VOLUME 31 NUMBER

AUGUST 1970

JOURNAL OF PHYSICS AND CHEMISTRY OF SOLIDS

AN INTERNATIONAL JOURNAL

Editor-in-Chief
HARVEY BROOKS
Cambridge, Mass.

Associate Editors

H. B. G. CASIMIR
Eindhoven

B. CHALMERS FRAZER
and
DAVID E. COX
Brookhaven

JACQUES FRIEDEL
Paris

I. M. LIFSHITZ
Khar'kov

INTERNATIONAL CONFERENCE ON ULTRASONIC ATTENUATION AND INTERNAL FRICTION

PERGAMON PRESS NEW YORK · OXFORD · LONDON · PARIS

THE JOURNAL OF PHYSICS AND CHEMISTRY OF SOLIDS

Editors

PROF. HARVEY BROOKS (*Editor-in-Chief*), 217 *Pierce Hall, Harvard University, Cambridge* 38, *Mass., U.S.A.*
PROF. DR. H. B. G. CASIMIR, *N.V. Philips' Gloeilampenfabrieken, Eindhoven, The Netherlands*
DR. B. CHALMERS FRAZER and DR. DAVID E. COX (*Assistant Editor*), *Brookhaven National Laboratory, Upton, Long Island, New York, U.S.A.*
PROF. JACQUES FRIEDEL, *Laboratoire de Physique des Solides, Bâtiment* 210, *Faculté des Sciences,* 91-*Orsay, France*
PROF. I. M. LIFSHITZ, *Chief, Theoretical Department, Institute of Physical Problems, Moscow V* 334, *Vorobevskoe Shosse 2, U.S.S.R.*

Editorial Advisory Board

U.S.A.

E. N. ADAMS, White Plains, N.Y.
D. ALPERT, Urbana, Ill.
L. APKER, Schenectady, N.Y.
J. BARDEEN, Urbana, Ill.
D. S. BILLINGTON, Oak Ridge, Tenn.
R. G. BRECKENRIDGE, Canoga Pk., Calif.
LEO BREWER, Berkeley, Calif.
E. BURSTEIN, Philadelphia, Penn.
J. A. BURTON, Murray Hill, N.J.
N. CABRERA, Charlottesville, Va.
G. C. DANIELSON, Ames, Iowa
G. J. DIENES, Long Island, N.Y.
J. C. FISHER, Schenectady, N.Y.
F. G. FUMI, Chicago, Ill.
H. K. HENISCH, University Park, Penn.
F. HERMAN, San Jose, Calif.
C. HERRING, Murray Hill, N.J.
A. R. VON HIPPEL, Cambridge, Mass.
J. H. HOLLOMON, Washington, D.C.
W. V. HOUSTON, Houston, Texas
H. B. HUNTINGTON, Troy, N.Y.
H. M. JAMES, Lafayette, Ind.
C. KITTEL, Berkeley, Calif.
W. KOHN, La Jolla, Calif.
J. A. KRUMHANSL, Ithaca, N.Y.
A. W. LAWSON, Riverside, Calif.
H. W. LEVERENZ, Princeton, N.J.
O. T. MARZKE, Pittsburgh, Penn.
B. T. MATTHIAS, La Jolla, Calif.
L. R. MAXWELL, Silver Spring, Md.
J. E. MAYER, La Jolla, Calif.
J. W. MITCHELL, Charlottesville, Va.
F. W. MONTROLL, Rochester, N.Y.
D. PINES, Urbana, Ill.
M. H. L. PRYCE, Los Angeles, Calif.
G. T. RADO, Washington, D.C.
H. REISS, Thousand Oaks, Calif.
J. R. REITZ, Dearborn, Mich.
A. ROSE, Princeton, N.J.
R. A. SMITH, Cambridge, Mass.
R. SMOLUCHOWSKI, Princeton, N.J.
F. H. SPEDDING, Ames, Iowa
D. TURNBULL, Cambridge, Mass.
J. H. VAN VLECK, Cambridge, Mass.
B. E. WARREN, Cambridge, Mass.
E. P. WIGNER, Princeton, N.J.
B. H. ZIMM, La Jolla, Calif.

Canada

R. E. BURGESS, Vancouver
W. B. PEARSON, Ottawa

United Kingdom

A. CHARLESBY, Shrivenham, Berks.
W. J. DUNNING, Bristol
F. C. FRANK, Bristol
H. JONES, London
A. B. PIPPARD, Cambridge
O. C. SIMPSON, Baldock, Herts
K. W. H. STEVENS, Nottingham
F. C. TOMPKINS, London

Czechoslovakia

J. TAUC, Praha

France

E. F. BERTAUT, Grenoble
J. BOK, Paris
B. DREYFUS, Grenoble
A. GUINIER, Orsay
A. HERPIN, Gif-sur-Yvette
B. JACROT, Grenoble
LOUIS NÉEL, Grenoble

Germany

ULRICH DEHLINGER, Stuttgart
R. HILSCH, Göttingen
G. LEIBFRIED, Aachen
E. MOLLWO, Erlangen
H. PICK, Stuttgart
W. WELKER, Erlangen

Israel

I. ESTERMANN, Haifa

Italy

F. G. FUMI, Palermo

Japan

TOSHINOSUKE MUTO, Tokyo

The Netherlands

A. MICHELS, Amsterdam
G. W. RATHENAU, Eindhoven

Sweden

J. O. LINDE, Stockholm
PER-OLOV LÖWDIN, Uppsala

Switzerland

G. BUSCH, Zurich
P. SCHERRER, Zurich

U.S.S.R.

G. S. ZHDANOV, Moscow

Publishing Offices

American Continent *Pergamon Press Inc., Maxwell House, Fairview Park, Elmsford, N.Y.* 10523
Rest of the World *Pergamon Press Ltd.*, 84-86 *Malahide Road, Coolock, Dublin* 5

Published monthly. Annual subscription for libraries, research establishments and all other multiple-reader institutions, £60 ($150.00), *private individuals whose departmental libraries subscribe, may obtain this Journal for their personal use at a reduced price of* £6 ($15.00) *per annum, including postage. All subscription enquiries are to be addressed to The Manager, Subscriptions Department, Pergamon Press, Headington Hill Hall, Oxford OX3 0BW, England. Back issues are available, write for Back Issues Price Lists.*

Copyright © 1970 Pergamon Press Ltd.

PERGAMON PRESS INC.
MAXWELL HOUSE, FAIRVIEW PARK, ELMSFORD, N.Y. 10523
HEADINGTON HILL HALL, OXFORD OX3 0BW

J. Phys. Chem. Solids Pergamon Press 1970. Vol. 31, pp. 895–904. Printed in Great Britain.

Accession number 82552
Date 30 11
SV02

CO-ORDINATION OF Yb^{3+} IN PHOSPHATE, SILICATE, AND GERMANATE GLASSES[†]

CHARLES C. ROBINSON and J. T. FOURNIER
Central Research Laboratory, American Optical Corp. Southbridge, Mass. 01550, U.S.A

(*Received* 10 *November* 1969)

Abstract – The optical absorption and emission spectra of Yb^{3+} in zinc–aluminophosphate, alkali–barium–silicate and alkali–barium–germanate glasses have been investigated at temperatures near 20°K. Analysis of the spectra within the framework of crystal field theory shows that in all three glasses the spectra are consistent with six co-ordinated Yb^{3+}. The observed splittings indicate crystal field components of symmetry lower than cubic, and the magnitude of the distortion fields are found to vary with glass type. A correlation of the absorption intensities with the magnitude of the distortion fields is also observed. Finally, a model rare earth site is proposed, and a mode of distortion which leads to trigonal fields at the rare earth site is discussed.

1. INTRODUCTION

IN A RECENT note the present authors submitted evidence for six-fold co-ordination of Yb^{3+} in phosphate, germanate, and silicate glasses derived from an application of crystal field theory to low temperature optical absorption and emission spectra[1]. To illustrate the results of our investigation, the spectra of Yb^{3+} in a lanthanum metaphosphate glass was discussed in detail, and the similarity of spectra in other glass hosts was noted. In the present work, an analysis of ytterbium spectra in a zinc–aluminophosphate glass, an alkali–barium–germanate glass, and an alkali–barium–silicate glass is presented.

The Yb^{3+} ion has ground configuration $4f^{13}$. This configuration gives rise to the multiplet ${}^2F_{7/2}$, ${}^2F_{5/2}$, with the $J = \frac{7}{2}$ level lying lowest. In the glass hosts studied, the J-levels are separated by about 10,500 cm^{-1}, and each J-manifold is split through interaction with the crystal field. It is found that in all three glass hosts the observed splittings are compatible with a distorted octahedral field. From a comparison of the splittings of the octahedral manifolds and of the observed absorption intensities, it is shown that the magnitude of the low symmetry components of the crystal field vary with glass type. Finally, model structures consistent with the observed spectra are discussed, and it is suggested that the environmental distortions lead to trigonal fields.

2. EXPERIMENTAL PROCEDURES

The glasses employed as hosts for the rare earth have multicomponent compositions typical of technical glasses. The nominal compositions determined from the batch mixtures are given in Table 1. Volatile materials in the starting mixtures which are expected to be lost through boil-off have been disregarded. Glasses containing approximately 1·5 wt % Yb_2O_3 were prepared for investigation of absorption spectra. Specimens containing approximately 8 wt % Yb_2O_3 and 2 wt % Nd_2O_3 were employed in the emission studies. The Yb^{3+} concentrations in the absorption samples have been determined first by carefully observing the batch weight before and after melting, and second by chemical analysis of the resulting glass. In the first method, it has been assumed that none of the rare earth is boiled away during the melting process. The results are summarized in Table 2. Also included are the

---

[†] Work supported in part by the U.S. Army Electronics Command, Fort Monmouth, New Jersey, under Contract No DAAB07-68-C-0313

Table 1. *Nominal compositions of* Yb^{3+} *doped glasses*

	Silicate glass Absorption sample	Emission sample		Germanate glass Absorption sample	Emission sample		Phosphate glass Absorption sample	Emission sample
	(Wt %)	(Wt %)		(Wt %)	(Wt %)		(Wt%)	(Wt %)
SiO_2	69·6	63·6	GeO_2	79·5	72·6	P_2O_5	71·5	65·4
Na_2O	7·5	6·8	Na_2O	4·9	4·5	Al_2O_3	9·9	9·0
K_2O	11·3	10·3	K_2O	7·4	6·8	ZnO	17·1	15·6
BaO	5·0	4·5	BaO	3·3	3·0	Yb_2O_3	1·5	8·0
Sb_2O_3	1·0	1·0	Sb_2O_3	0·7	0·6	Nd_2O_3		2·0
Al_2O_3	1·6	1·4	Al_2O_3	1·0	0·9			
ZnO	1·6	1·4	ZnO	1·0	0·9			
Li_2O	1·0	1·0	Li_2O	0·7	0·6			
Yb_2O_3	1·5	8·0	Yb_2O_3	1·5	8·0			
Nd_2O_3		2·0	Nd_2O_3		2·0			

Table 2. *Physical parameters of* Yb^{3+} *doped absorption samples*

Glass	Silicate	Germanate	Phosphate
Wt % Yb_2O_3 from analysis	1·38 ± 0·03	1·57 ± 0·07	1·6 ± 0·10
Density (g/cc)	2·536	3·952	2·726
Yb^{3+} ions/cc	(1·07 ± 0·02) 10^{20}	(1·89 ± 0·09) 10^{20}	(1·34 ± 0·08) 10^{20}
Index of refraction at 1000 nm	1·502	1·653	1·505

densities, the indices of refraction, and the Yb^{3+} concentrations in ions/cm^3 for the absorption specimens.

The neodymium added to the emission samples serves as a sensitizer for the Yb^{3+} emission. In all the glass hosts employed, Nd^{3+} has an emission line at about 1060 nm which interferes with the Yb^{3+} spectrum. However, the neodymium emission is strongly quenched by energy transfer to the ytterbium. This has been verified by examination of the characteristic Nd^{3+} emission in regions of the spectrum where the Yb^{3+} spectrum does not interfere. In all cases, the Nd^{3+} emission at 880 and 920 nm was barely discernible, and the weaker 1090 and 1350 nm lines were completely absent. It is assumed, therefore, that the neodymium makes a negligible contribution to the observed spectra.

A Cary Model 14 spectrophotometer and a Cary Model CD-151 liquid helium Dewar were utilized to measure the low temperature optical spectra. Samples were mounted in a copper cold finger which threads into the liquid helium container. The temperature of the cold finger was measured with a germanium thermistor. An estimate of the difference in temperature between the sample and the cold finger was obtained through the use of a copper constantan thermocouple embedded in the glass, with the reference junction clamped under the thermistor.

Absorption measurements were made on rectangular, polished glass flats of dimension 5 × 17 mm with thicknesses from 5 to 10 mm. A copper fixture was used to hold the samples in close contact with the cold finger. Silver impregnated vacuum grease and indium metal shims were employed to obtain good thermal contact. The emission samples had dimensions 17 × 5 × 5 mm and were clamped to the cold finger in such a manner to permit right angle illumination by a xenon arc lamp. A heat-screen filter, opaque to wavelengths longer than 800 nm, was inserted between the lamp and the sample.

3. ABSORPTION AND EMISSION SPECTRA OF Yb^{3+} IN GLASS HOSTS

The optical spectra of Yb^{3+} in the three glasses studied are shown in Fig. 1. In the case of the absorption spectra, we plot the absorbance α defined by the relation $I = I_0 \exp(-\alpha l)$, where I_0 and I are respectively the incident and transmitted intensities, and l is the sample thickness. The fluorescent intensities are plotted on an arbitrary scale; no attempt to measure the specific emission intensity has been made.

Principal absorption peaks are located at 917·0, 958·0 and 973·9 nm in the zinc–aluminophosphate glass. Emission bands with peaks near 981·0, 997·0, 1020·0 and 1054·0 nm are observed. The principal absorption and emission peaks in the alkali–barium–germanate glass are found at 973·0, 957·5 and 908·5 nm, and 981·5, 1002·0, 1024·0 and 1063·0 nm respectively. In the alkali–barium–silicate glass, principal absorption peaks appear at 910·0, 960·0 and 972·3 nm and emission peaks are found near 976·0, 1004·5, 1024·0 and 1065·5 nm.

In addition to the principal bands, secondary absorptions too weak to be evident in Fig. 1 are also observed. Peaks are found near 825, 870 and 934 nm in the phosphate glass, 830, 885 and 925 nm in the silicate glass, and 845 and 937 nm in the germanate glass. Base glass samples containing no rare earth are found to be free of the weak secondary absorptions. To determine whether these bands originate from other rare earth impurities introduced with the Yb_2O_3, the samples were examined for characteristic absorptions in other regions of the spectrum, but no bands were observed. Apparently, a small portion of the ytterbium ions are found in sites distinctly different from those occupied by the Yb^{3+} ions which give rise to the principal spectra.

Concentrating on the principal bands, it is seen from Fig. 1 that in all three cases the shortest wavelength emission band strongly overlaps the longest wavelength absorption. Because of the high Yb^{3+} concentrations in the specimens used for emission studies, the shortest wavelength emission band is distorted by self-absorption with a resulting shift in the observed peak position. Since previous investigation of the Yb^{3+} emission in a silicate glass shows negligible Stokes shifting[2], the long wavelength absorption peak has been employed to locate the lowest lying state of the excited multiplet.

Comparison of the Yb^{3+} spectra in the three types of glass shows a striking similarity in spectral features. The line shapes are similar in all three hosts, exhibiting the same asymmetries despite differences in widths and peak positions. Although the absolute intensities vary between glass types, the relative intensities of the lines are nearly equal in the three hosts. Furthermore, except for differences in linewidths, the zinc–alumino phosphate glass spectra are identical to the Yb^{3+} spectra observed in the lanthanum metaphosphate glass discussed in Ref. [1]. These results suggest that the Yb^{3+} ions reside in essentially similar sites in phosphate, silicate, and germanate glasses. An indication of the symmetry of this site is derived in the following section from a consideration of crystal field effects within the Yb^{3+} free ion multiplets.

4. CRYSTAL FIELD ANALYSIS OF Yb^{3+} SPECTRA

The single electron levels derived from the observed absorption and emission spectra are shown in Fig. 2. The degeneracies are completely resolved; each J-level exhibits the maximum number of Kramers doublets. While the complete splitting of the J-manifold degeneracy indicates low symmetry crystal field components at the rare earth site, the grouping of the Kramers doublets is compatible with six-fold coordination of the rare

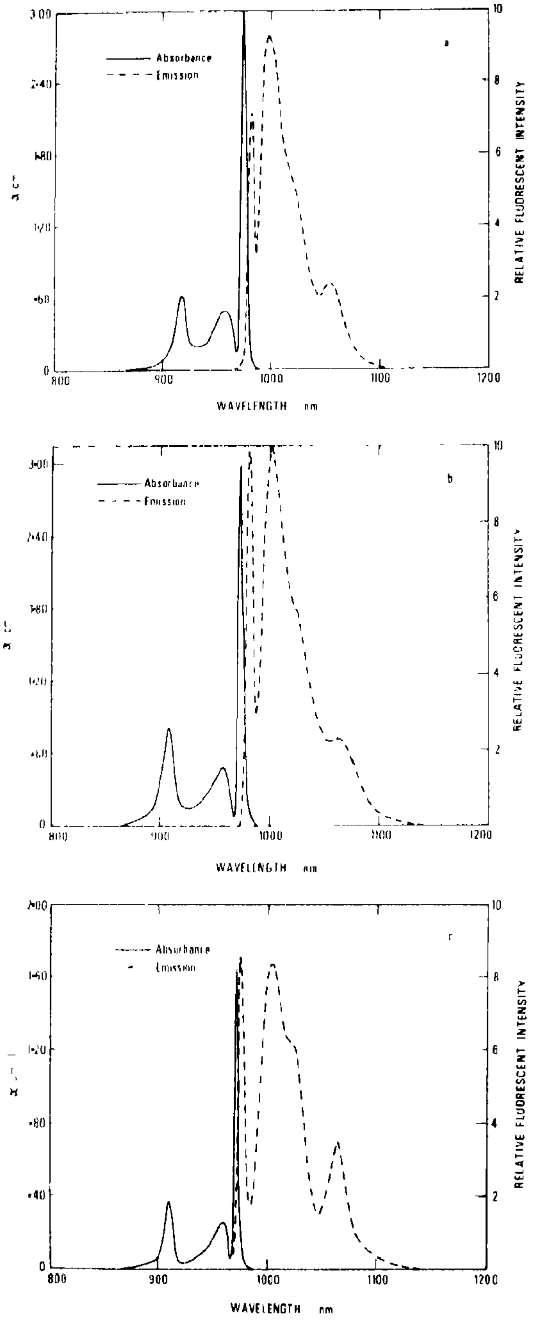

Fig. 1. Low temperature absorption and emission spectra of Yb^{3+} in the vicinity of 20°K. (a) zinc-aluminophosphate glass. (b) alkali-barium-germanate glass. (c) alkali-barium-silicate glass.

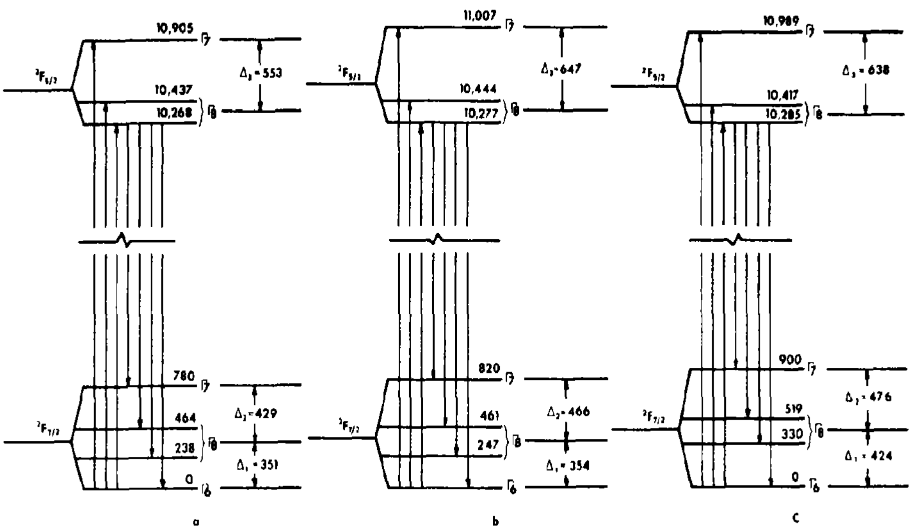

Fig. 2. Energy levels derived from the absorption and emission spectra. (a) Zinc–aluminophosphate glass (b) alkali–barium–germanate glass. (c) alkali–barium–silicate glass

earth at a site where the crystal field is predominantly cubic.

In a crystal field of cubic symmetry the six-fold degenerate $J = \frac{7}{2}$ manifold is split into a doublet and a quartet, and for octahedral (six-fold) coordination the quartet lies lowest[3]. Examination of the absorption spectra of the Yb^{3+} ion in the three glass hosts shows that in all cases the two lower doublets lie close together, as would be the case if these levels were split from the octahedral quartet by a perturbing field of lower symmetry. In Fig. 2, the observed Kramers doublets are grouped according to the octahedral states from which they are assumed to derive, and the resulting manifolds are labeled by the appropriate irreducible representations of the cubic group O_h. The $J = \frac{7}{2}$ manifold yields a quartet Γ_8 and two doublets Γ_6 and Γ_7. The consistency of the assignment shown in Fig. 2 is demonstrated by a quantitative consideration of the octahedral crystal field.

In the crystal field theory, the ion of interest is taken to reside in a potential V which can be expanded in spherical harmonics according to the relationship[4]

$$V = \sum_{l,m} B_{lm} r^l Y_l^m(\theta, \phi). \tag{1}$$

The effect of the potential V on the free ion energies and wavefunctions is determined by application of the interaction

$$\mathcal{H}_c = -e \sum_i V(\mathbf{r}_i). \tag{2}$$

where $-e$ is the charge on an electron, and $\mathbf{r}_i$ denotes coordinates of the ith electron. For rare-earth ions, matrix elements of $\mathcal{H}_c$ between $4f$ wavefunctions are required, and terms up to sixth order survive in the expansion of V. The form of the potential is further restricted by the symmetry of the environment. For a field of cubic symmetry O_h with z direction taken to lie along a three-fold axis C_3, the interaction $\mathcal{H}_c$ becomes

$$\begin{aligned}\mathcal{H}_c = {} & A_4{}^0 \sum_i (35 z_i{}^4 - 30 r_i{}^2 z_i{}^2 + 3 r_i{}^4) \\ & + A_4{}^3 \sum_i z_i (x_i{}^3 - 3 x_i y_i{}^2) \\ & + A_6{}^0 \sum_i (231 z_i{}^6 - 315 r_i{}^2 z_i{}^4 \\ & \quad + 105 r_i{}^4 z_i{}^2 - 5 r_i{}^6)\end{aligned}$$

$$+A_6^3 \sum (11 z_i^3 - 3 z_i r_i^2)(x_i^3 - 3x_i y_i^2)$$

$$+A_6^6 \sum (x_i^6 - 15 x_i^4 y_i^2 + 15 x_i^2 y_i^4 - y_i^6). \quad (3)$$

The A_l^m are simply related to the B_{lm} of equation (1), and depend explicitly on coordinates and charges of the surrounding ions in the lattice. In the case of an octahedral field due to six point ions of equal charge equidistant from the rare earth, direct evaluation shows the A_l^m are connected by the relationships

$$\frac{A_4^3}{A_4^0} = -10\sqrt{2}, \frac{A_6^3}{A_6^0} = \frac{35\sqrt{2}}{4}, \text{and} \frac{A_6^6}{A_6^0} = \frac{77}{8}.$$

Consequently, the octahedral field is uniquely specified by two independent parameters which can be chosen to be A_4^0 and A_6^0.

Since the ${}^2F_{7/2}$ and the ${}^2F_{5/2}$ manifolds are separated by about 10500 cm^{-1} while crystal field splittings of only a few hundred wavenumbers are observed, the energies of the crystal field levels can be determined by application of $\mathscr{H}_c$ within each J-manifold separately. The eigenfunctions in the presence of $\mathscr{H}_c$ are completely symmetry determined and appear in Table 3 expanded in a basis of free ion functions $|4f^{13}, {}^2F; J, M_J\rangle$. Evaluation of the energies of the crystal field levels is facilitated by application of the operator equivalent method[5]. The characteristic octahedral splittings are found to be

$$\Delta_1 = -1{\cdot}870 A_4^0 \langle r^4\rangle + 3{\cdot}776 A_6^0 \langle r^6\rangle, \quad (4.1)$$

$$\Delta_2 = -3{\cdot}117 A_4^0 \langle r^4\rangle - 4{\cdot}366 A_6^0 \langle r^6\rangle, \quad (4.2)$$

and

$$\Delta_3 = -3{\cdot}428 A_4^0 \langle r^4\rangle, \quad (4.3)$$

where $\langle r^4\rangle$ and $\langle r^6\rangle$ are expectation values

Table 3. Octahedral wavefunctions expanded in terms of basis functions $|4f^{13}, {}^2\mathrm{F}; \mathrm{J,M_J}\rangle$ *which diagonalize* $\mathbf{J}_z$ *with z axis along a* C_3 *axis of the octahedron*

$J = \frac{5}{2}$	Γ_7	$0{\cdot}6667\|\frac{5}{2}+\frac{5}{2}\rangle$	$-0{\cdot}7454\|\frac{5}{2}-\frac{1}{2}\rangle$	
		$0{\cdot}6667\|\frac{5}{2}-\frac{5}{2}\rangle$	$-0{\cdot}7454\|\frac{5}{2}+\frac{1}{2}\rangle$	
	Γ_8	$\|\frac{5}{2}+\frac{3}{2}\rangle$		
		$0{\cdot}7454\|\frac{5}{2}+\frac{5}{2}\rangle$	$+0{\cdot}6667\|\frac{5}{2}-\frac{1}{2}\rangle$	
		$-0{\cdot}7454\|\frac{5}{2}-\frac{5}{2}\rangle$	$+0{\cdot}6667\|\frac{5}{2}+\frac{1}{2}\rangle$	
		$\|\frac{5}{2}-\frac{3}{2}\rangle$		
$J = \frac{7}{2}$	Γ_7	$-0{\cdot}6236\|\frac{7}{2}+\frac{7}{2}\rangle$	$+0{\cdot}7454\|\frac{7}{2}+\frac{1}{2}\rangle$	$+0{\cdot}2357\|\frac{7}{2}-\frac{5}{2}\rangle$
		$0{\cdot}6236\|\frac{7}{2}-\frac{7}{2}\rangle$	$+0{\cdot}7454\|\frac{7}{2}-\frac{1}{2}\rangle$	$-0{\cdot}2357\|\frac{7}{2}+\frac{5}{2}\rangle$
	Γ_8	$\|\frac{7}{2}+\frac{3}{2}\rangle$		
		$-0{\cdot}5443\|\frac{7}{2}-\frac{5}{2}\rangle$	$-0{\cdot}4303\|\frac{7}{2}+\frac{1}{2}\rangle$	$-0{\cdot}7201\|\frac{7}{2}+\frac{7}{2}\rangle$
		$0{\cdot}5443\|\frac{7}{2}+\frac{5}{2}\rangle$	$-0{\cdot}4303\|\frac{7}{2}-\frac{1}{2}\rangle$	$+0{\cdot}7201\|\frac{7}{2}-\frac{7}{2}\rangle$
		$\|\frac{7}{2}-\frac{3}{2}\rangle$		
	Γ_6	$-0{\cdot}8050\|\frac{7}{2}+\frac{5}{2}\rangle$	$-0{\cdot}5093\|\frac{7}{2}-\frac{1}{2}\rangle$	$+0{\cdot}3044\|\frac{7}{2}-\frac{7}{2}\rangle$
		$0{\cdot}8050\|\frac{7}{2}-\frac{5}{2}\rangle$	$-0{\cdot}5093\|\frac{7}{2}+\frac{1}{2}\rangle$	$-0{\cdot}3044\|\frac{7}{2}+\frac{7}{2}\rangle$

of r^4 and r^6 for the $4f$ wavefunction of the rare earth in the glass. While these moments can be approximated employing free ion wavefunctions, we shall simply regard the products $A_4^0\langle r^4\rangle$ and $A_6^0\langle r^6\rangle$ as parameters to be deduced from the spectra.

The two splittings Δ_1 and Δ_2 in the $J = \frac{7}{2}$ manifold permit the evaluation of both $A_4^0\langle r^4\rangle$ and $A_6^0\langle r^6\rangle$. Since the octahedral splitting Δ_3 of the $J = \frac{5}{2}$ manifold involves $A_4^0\langle r^4\rangle$ exclusively, the optical data yields two independent values of the fourth order parameter. Comparison of the values provides a check of the consistency of our assignment of the Kramers doublet to parent octahedral manifolds. Parameter values determined from the observed splittings in the three glass types are listed in Table 4*. The two values of the fourth order parameter are found to be in good agreement.

From the preceding analysis, it is clear that the gross features of the Yb^{3+} spectra are consistent with a six-fold co-ordination of the rare earth in all three glass hosts. However, the observed splittings of the Γ_8 manifolds indicate departures from octahedral symmetry, and differences in the magnitudes of these splittings in the three glasses suggest that the low symmetry fields vary with glass type. A quantitative measure of this effect is the ratio of the splitting of the Γ_8 quartet of the $J = \frac{5}{2}$ level to the cubic splitting Δ_3. The ratios are found to be 0·207, 0·258 and 0·305 for the silicate, germanate and phosphate glasses respectively. This result indicates that low symmetry fields are the largest in the phosphate and smallest in the silicate with the germanate falling inbetween. Another indication of this effect is found in the observed intensities of the absorption spectra.

Table 4. Effective octahedral field parameters $A_4^0\langle r^4\rangle$ and $A_6^0\langle r^6\rangle$ for Yb^{3+} in alkali-barium-silicate, alkali-barium-germanate and zinc-aluminophosphate glasses

Glass type	$A_4^0\langle r^4\rangle$ $(J = \frac{5}{2})$	$A_4^0\langle r^4\rangle$ $(J = \frac{7}{2})$	$A_6^0\langle r^6\rangle$ $(J = \frac{7}{2})$
Silicate	$-186\ cm^{-1}$	$-176\ cm^{-1}$	$25\ cm^{-1}$
Germanate	$-189\ cm^{-1}$	$-162\ cm^{-1}$	$13\ cm^{-1}$
Phosphate	$-161\ cm^{-1}$	$-154\ cm^{-1}$	$17\ cm^{-1}$

The ${}^2F_{7/2} \leftrightarrow {}^2F_{5/2}$ transitions in the Yb^{3+} ion all occur between the states of the $4f^{13}$ configuration. In the free ion or in a centrosymmetric crystal field, such transitions are strictly parity forbidden. Magnetic dipole and electric quadruple transitions are allowed, but the intensities of rare earth lines are generally too great to be attributed to these radiative processes[6]. In solids, though, admixture into the $4f^n$ configuration of states from configurations of opposite parity (e.g. $4f^{n-1}5d$) by means of non-centrosymmetric components of crystal field permits so-called forced electric dipole transitions which are sufficiently strong to account for observed intensities. Although the intensities are related to the odd terms in the crystal potential in a rather complicated manner[7], an enhanced Yb^{3+} absorption in a particular glass can be taken as an indication of greater distortion in that host.

A convenient measure of the intensity of an optical band is the oscillator strength f which is related to the area under the absorption curve by the relationship[6]

$$f = \frac{mc}{n_0 \pi e^2} \int \alpha(\nu) \mathrm{d}\nu, \qquad (5)$$

---

*In Ref. [1], the crystal potential was expressed in a coordinate system with z axis along a four-fold (C_4) axis of the octahedron rather than along a three-fold (C_3) axis as has been done in the present work. The form of the crystal potential and resulting eigenfunctions differ in the two different schemes, and the magnitudes of the crystal field parameters differ In fact, the parameters are simply connected by relationships

$$\frac{A_4^0(C_4)}{A_4^0(C_3)} = -\frac{3}{2}, \text{ and } \frac{A_6^0(C_4)}{A_6^0(C_3)} = \frac{9}{16}.$$

The coordinate scheme with z axis along C_3 has been chosen because this symmetry axis survives in the rare-earth site model envisioned, while the C_4 axis is destroyed.

where n_0 is the volume density of absorbing centers. (Oscillator strengths calculated using this expression include *local* field effects implicitly). The oscillator strengths determined from the low temperature absorption spectra of Fig. 1 are shown in Table 5. For comparison, calculated values of the magnetic dipole contributions to the free ion oscillator strengths are also listed. (See Appendix for details). Since the experimental oscillator strengths exceed the magnetic dipole strengths by at least a factor of six, the observed differences in Yb^{3+} intensities in the three glasses are attributable to differences in electric dipole contributions. The oscillator strengths are seen to follow the same trend as the splittings of the Γ_8 manifolds, increasing in the order silicate–germanate–phosphate. It should be noted that the crystal field components which act to break the parity selection rule are not effective in splitting the J-manifolds since these terms are of the wrong parity to couple states within the $4f^n$ configuration. The observed trend in intensities thus provides an independent measure of site distortion.

Table 5. Experimental oscillator strengths f_{exp} determined from low temperature Yb^{3+} absorption spectra and the magnetic dipole oscillator strength f_{mag} calculated for the free Yb^{3+} ion

Glass	f_{exp}	f_{mag}
Silicate	$(1{\cdot}82 \pm 0{\cdot}08)10^{-6}$	$2{\cdot}59 \times 10^{-7}$
Germanate	$(2{\cdot}83 \pm 0{\cdot}13)10^{-6}$	$2{\cdot}86 \times 10^{-7}$
Phosphate	$(3{\cdot}66 \pm 0{\cdot}24)10^{-6}$	$2{\cdot}60 \times 10^{-7}$

5. DISCUSSION

The observed regularities in the Yb^{3+} spectra indicate that the rare earth is incorporated in the glass at sites of distinct symmetry. The peak positions are found to be consistent with a six-fold coordination of the rare earth, but the splitting of the Γ_8 quartets requires departures from octahedral symmetry. Furthermore, the crystal field components of symmetry lower than cubic are necessarily associated with non-random distortion of the environment since transitions to the states split from Γ_8 manifolds are resolved in both absorption and emission spectra.

A further indication of the structure of the glass in the vicinity of the rare earth is derived from consideration of the Yb^{3+} doped lanthanum metaphosphate glass discussed in Ref. [1]. This glass has composition $RE(PO_3)_3$, and, as previously noted, the Yb^{3+} spectra in this glass is nearly identical to the zinc–alumino–phosphate spectra. Taking the PO_4 tetrahedron as a basic structural unit[8, 9] leads to a network in which each rare earth is coordinated by three tetrahedra with each tetrahedron providing two nearest neighbor non-bridging oxygens to the rare earth. The two remaining oxygens associated with each tetrahedron are bridging oxygens shared by other PO_4 tetrahedra which are themselves adjacent to other rare earth ions. Each rare earth ion can be considered part of a locally well defined complex consisting of the three tetrahedra clustered about the rare earth. Variation in the P–O–P bond angle allows for randomness of the structure beyond the complex and permits one to consider only those contributions to the crystal field at the rare earth which arise from ions in the complex. A diagram of such a complex with the six non-bridging oxygens arranged to form a regular octahedron is shown in Fig. 3. Taken as a whole, the complex has D_3 symmetry with the C_3 axis of the octahedron being preserved as the prime symmetry axis. In this structure the ions of the complex beyond the six nearest neighbor oxygens contribute to trigonal components of the crystal field which act to split the octahedral degeneracies. Furthermore, consideration of ion sizes suggests that additional physical

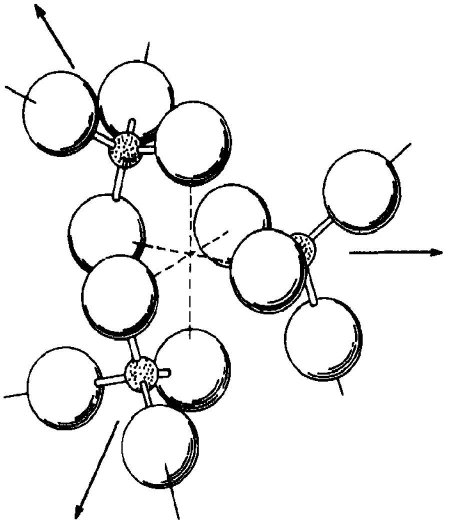

Fig. 3. 'Octahedral' complex constructed from undistorted glass-forming tetrahedra. Expansion of the central void by translation of each tetrahedron along the directions indicated by arrows leads to trigonal fields at the void

distortion of the structure which would augment the splitting can be expected.

The glass forming tetrahedron in lime-phosphate glass has P—O and O—O bond lengths of 1·57 Å and 2·56 Å respectively[10]. A structure such as that shown in Fig. 3 based on undistorted tetrahedra with these bond lengths can accommodate an ion with radius of only 0·53 Å at the central void, while the ionic radius of Yb^{3+} is about 1·0 Å. Of course, some differences in the dimensions of PO_4 tetrahedra in the lanthanum metaphosphate glass are expected, and the O—O distance between two non-bridging oxygens on a tetrahedron may be somewhat greater than 2·56 Å. Since covalent bonding effects strongly favor preservation of the PO_4 tetrahedron, though, changes in bond angle or bond length sufficient to permit octahedral coordination of the rare earth seem unlikely.

In attempting to visualize the actual cluster of tetrahedra about the rare earth, it is helpful to consider possible distortions of the octahedral structure which would permit inclusion of the Yb^{3+} ion at the central void. A possible mode of distortion which preserves the D_3 symmetry of the complex involves translation of the three undistorted tetrahedra by equal amounts along the three two-fold axes indicated by arrows in Fig. 3. To accommodate an ion of 1·0 Å radius, translation of each tetrahedron by 0·6 Å is required. In the expanded complex the nearest neighbor oxygens to the rare earth would be expected to provide the dominant contribution to the trigonal components of the crystal field which split the octahedral degeneracies. The non-bridging oxygens also give rise to non-centrosymmetric components of the crystal field in the distorted complex. Thus, in this model, the observed correlation between the splittings of the Γ_8 manifolds and the intensities of the optical bands which has been discussed in the preceding section is expected.

The striking similarity of the Yb^{3+} spectra in all the glasses studied suggests that the rare earth is incorporated at similar sites in phosphate, silicate and germanate glasses. In the case of the silicate and germanate glasses, the creation of six non-bridging nearest neighbor oxygens to the rare earth requires the inclusion of electron-donor modifier ions in the network. Assuming an energetic preference for local charge compensation, the modifier ions could well be included in the complex. In an idealized model, one might envision three alkali metal ions intercollated in the spaces between the tetrahedra on the two-fold axes directly opposite the silicon or germanium ions. While the abundance of alkali in the glasses investigated would certainly permit compensation of each rare earth by three metal ions, a more thorough investigation of the effects of alkali type and concentration on the rare earth spectra is required to establish the role of the modifier ions in rare earth glasses.

Acknowledgements—The authors acknowledge useful discussions with Professor R. H. Bartram and express their thanks to A. Cleri and L. Caplette for assistance in carrying out the optical measurements, to R. Graf for making the glass samples and to W. Reed for measuring the indices of refraction.

REFERENCES

1. ROBINSON C. C. and FOURNIER J. T., *Chem. Phys. Lett.* **3**, 517 (1969). In Fig. 1 of this reference the splitting Δ_1 should read $\Delta_1 = 558\ \text{cm}^{-1}$. The correct value of the splitting was employed in the calculation of the crystal field parameter $A_4{}^0\langle r^4\rangle$.
2. SNITZER E., *IEEE J. quant. Electron.* **QE-2**, 562 (1966).
3. LEASK R., LEASK M. J. M. and WOLF W. P., *J. Phys. Chem. Solids* **23**, 1381 (1962).
4. The ideas of the crystal field theory are well known and have been detailed in many reviews and texts. Presentations which are particularly relevant to the rare earths are found in JUDD B. R. *Operator Techniques in Atomic Spectroscopy*. McGraw-Hill, New York (1963), and WYBOURNE B. G., *Spectroscopic Properties of Rare Earths*. Interscience, New York (1965).
5. A useful collection of operator equivalents and matrix elements of these operators is found in LOW W. *Paramagnetic Resonance in Solids*. Supplement 2 to *Solid State Physics* (Edited by F. Seitz and D. Turnbull), Chap. 2. Academic Press, New York (1960). Several references to the original work of Stevens, Elliott, and Judd are found in this reference.
6. BROER L. J. F., GORTER C. J. and HOOGSCHAGEN J. *Physica* 11, 231 (1945).
7. JUDD B. R., *Phys. Rev.* **127**, 750 (1962).
8. VAN WAZER J. R., *Phosphorous and Its Compounds*, Vol. 1, p. 756. Interscience, New York (1958).
9. WESTMAN A. E. R., Constitution of phosphate glasses. *Modern Aspects of the Vitreous State* (Edited by J. D. Mackenzie), p. 63. Butterworths, London (1960).
10. BISCOE J., PINCUS A. G., SMITH C. S. and WARREN B. E., *J. Am. Ceram. Soc.* **24**, 116 (1941).

APPENDIX

To estimate the magnetic dipole contribution to the oscillator strength of the Yb^{3+} absorption band, the strength of the free ion $^2F_{7/2} \rightarrow {}^2F_{5/2}$ transition was calculated from the equation[6]

$$f_{\text{mag}} = \frac{8\pi^2 mn\nu}{3he^2} M_0{}^2,$$

$$M_0{}^2 = \frac{1}{(2J_i+1)} \frac{e^2}{4m^2c^2} \sum_{i,f} |\langle i|L+2S|f\rangle|^2.$$

Here, $|i\rangle$ and $|f\rangle$ are initial and final states between which the transitions occur, and the sums are over all states belonging to the two J-manifolds. Actually, all matrix elements needed for the Yb^{3+} calculation have been determined in Ref. [6], and the results reported there need simply be modified by insertion of the index of refraction n of the glass. Refractive indices for the three glasses considered are listed in Table 1 of the main text.

J. Phys. Chem. Solids Pergamon Press 1970. Vol. 31, pp. 905–912. Printed in Great Britain.

A NEW Mn^{2+} CENTRE IN CaF_2

G. G. P. VAN GORKOM
Philips Research Laboratories, N. V. Philips' Gloeilampenfabrieken, Eindhoven, The Netherlands

(*Received* 16 *June* 1969; *in revised form* 10 *November* 1969)

Abstract—An EPR, ENDOR and optical study of manganese in CaF_2 has been made. It was found that two different Mn^{2+} centres were present, both having cubic symmetry without axial components. One of these is well known in the literature and its EPR spectrum is characterized by a very small cubic field splitting and a well resolved fluor hyperfine structure.

The other centre shows no resolved superhyperfine structure and a larger cubic field splitting. The spin hamiltonian parameters of both centres have been determined accurately at three temperatures, 4·2, 77 and 295°K. This temperature dependence is discussed briefly. The ENDOR measurements have shown that the second Mn^{2+} centre is Mn^{2+} at a Ca^{2+} site with no fluorine first neighbours. Analysing the results of the EPR, ENDOR and optical measurements we have reached the conclusion that, most probably, centre II is Mn^{2+} at a Ca^{2+} site and surrounded by six or eight oxygen ions.

1. EPR RESULTS

AN EPR reinvestigation has been made of single crystals CaF_2:Mn. It turned out that in addition to the well known[1, 2, 3] Mn^{2+} centre (which is probably Mn^{2+} substitutionally for Ca^{2+}) another centre was present in a few crystals which as far as we know, has not been found before. In the following we shall first describe the well known centre (centre I) and then the new centre II.

(*a*) *Centre I*

The EPR spectrum of this centre can be described by the spin hamiltonian.

$$\mathcal{H} = g\beta\mathbf{H}\cdot\mathbf{S} + A\mathbf{S}\cdot\mathbf{I} - g_N\beta_N\mathbf{H}\cdot\mathbf{I} + \frac{1}{6}a\left[S_x^4 + S_y^4 + S_z^4 - \frac{1}{5}S(S+1) \times (3S^2+3S-1)\right] + \sum_j A_j^s\mathbf{S}\cdot\mathbf{I}_j \quad (1.1)$$

Here $S = 5/2$, $I = 5/2$, I_j is the fluorine nuclear spin of the jth neighbour, so $I_j = \frac{1}{2}$; g and g_N are the spectroscopic splitting factors of respectively the electrons and the manganese nucleus. A is the hyperfine coupling constant, A_j^s is the superhyperfine (s.h.f.) coupling constant which describes the interaction of the manganese $3d$ electrons with the surrounding fluorine nuclei.

The EPR transition frequencies for the transition $m_s \rightarrow m_s - 1$ are in first order given by

$$h\nu = g\beta H + Am_I + \frac{1}{6}a\frac{35}{20}\left[m_s^4 - (m_s-1)^4 - \frac{95}{14}\{m_s^2 - (m_s-1)^2\}\right] + \text{superhyperfine splitting term.} \quad (1.2)$$

The spectrum consists of 6 groups of lines situated around $g = 2{\cdot}002$ according to an isotropic hyperfine splitting of about 100 G. Each group contains a number of superhyperfine lines (linewidth: about 3 G), see Fig. 1. The s.h.f splitting constant K in the case of a Mn^{2+} ion with only *one* fluorine neighbour is given by

$$K = [(A_s + 2A_p)^2\cos^2\vartheta + (A_s - A_p)^2\sin^2\vartheta]^{1/2} \quad (1.3)$$

which can be rewritten as

$$K = [\{A_s + A_p(3\cos^2\vartheta - 1)\}^2 + 9A_p^2\sin^2\vartheta\cos^2\vartheta]^{1/2} \quad (1.4)$$

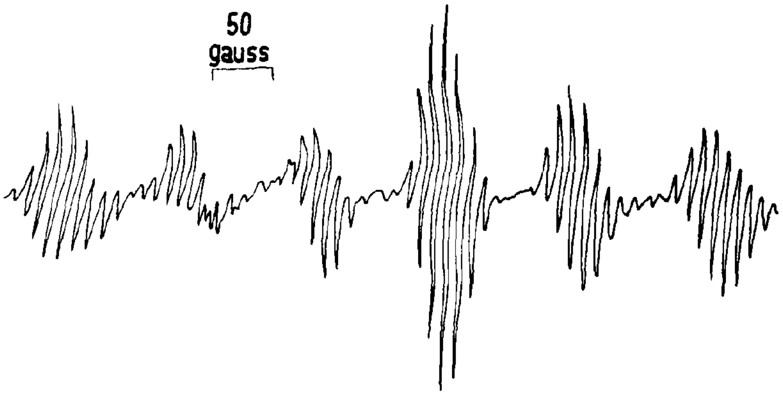

Fig. 1 EPR spectrum of centre I ($d\chi''/dH$ vs H) $T = 295°K$, $f = 9{\cdot}8$ GHz, H increases from left to right, $H \parallel [100]$

here A_s and A_p are respectively the isotropic and anisotropic parts of the superhyperfine interaction, ϑ is the angle between the magnetic field **H** and the line joining the manganese and fluorine ion.

It should be noted here that it is preferable to use formula (4) instead of the following formula used by Baker *et al.*[2]:

$$K = (A_s + 2A_p)\cos^2\vartheta + (A_s - A_p)\sin^2\vartheta$$
$$= A_s + A_p(3\cos^2\vartheta - 1) \qquad (1.5)$$

because of the fact that $g_N\beta_N\mathbf{H}\cdot\mathbf{I} <$ s.h.f. interaction energy.

Actually, the manganese ion has 8 fluorine neighbours, so for an arbitrary direction of **H** a very complicated superhyperfine pattern results.

For **H** in the 3 main directions [100], [110] and [111] however, the spectrum is quite simple and these 3 spectra are sufficient to determine $|A_s|$, $|A_p|$ and their relative signs. It turned out that $A_s/A_p > 0$.

Another complication arises since the fine structure term in (1.2) causes each s.h.f. line to split into 5 components. This splitting is not resolved in most cases but gives rise to a confusion of the s.h.f. line pattern. It turned out that the s.h.f. lines of the fourth group of the spectrum (corresponding to $M_I = \frac{1}{2}$ if we assume A to be negative) were least confused (see also Fig. 1). This can be explained by assuming a value for the fine structure splitting parameter a of about 0·5 G as in that case the second order hyperfine effect cancels the fine structure splitting of the $3/2 \to \frac{1}{2}$ and $-\frac{1}{2} \to -3/2$ transitions, so that the two lines coincide with the $\frac{1}{2} \to -\frac{1}{2}$ transition. This conclusion was confirmed by the results of a spectrum simulation of the whole spectrum with the aid of a computer: the experimental data are best fitted when $a = 0{\cdot}6$ G.

The measurements were performed at X band at 4·2, 77 and 295°K. The spin hamiltonian parameters which were derived from the measurements are given in Table 1 in which the results of [2] and [3] are given for comparison.

(*b*) *Centre II*

The EPR spectrum of the centre II differs considerably from the spectrum of centre I but it is certainly due to Mn^{2+}: the spectrum consists basically of 6 groups of lines according to an isotropic hyperfine splitting (with $I = 5/2$) of about 80 G; each group is resolved in 5 fine structure lines, so $S = 5/2$. Superhyperfine structure is either not resolved or not present, so A_s, $A_p < 0{\cdot}4$ G because the line width is again about 3 G. A typical result of the spectrum of centre II is shown in Fig. 2.

The local environment of the Mn^{2+} ion appeared to be exactly cubic as can be seen from

Table 1. *Spin Hamiltonian parameters of centre* I* = 90°K

	g			$\|A\|$ in 10^{-4} cm^{-1}			A_s in 10^{-4} cm^{-1}			A_p in 10^{-4} cm^{1}			a in 10^{-4} cm^{-1}		
	This work	[2]	[3]	This work	[2]	[3]	This work	[2]	[3]	This work	[2]	[3]	This work	[2]	[3]
295°K	2·002 ±0·001	—	2·0016 ±0·0005	95·2 ±0·1	—	95·3 ±1·0	8·6 ±0·1	—	8·8 ±0·5	2·7 ±0·2	—	—	0·6	—	—
77°K	2·002	1·998* +0·003	—	96·0	97·8* ±1·0	—	8·8	9·5* ±0·3	—	2·7	2·7* ±0·5	—	—	0·6*	—
4·2°K	2·002	—	—	96·2	—	—	8·9	—	—	2·7	—	—	—	—	—

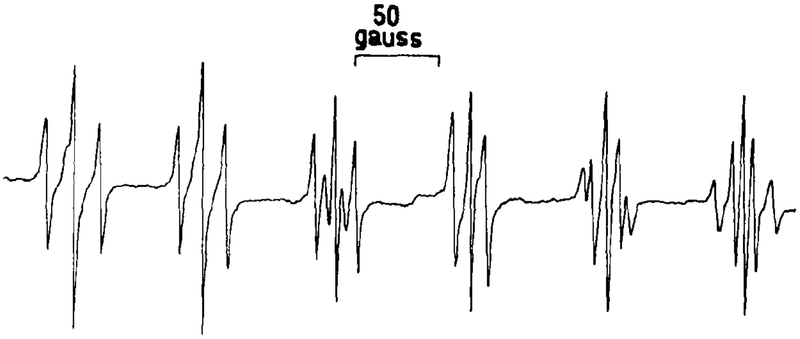

Fig. 2 EPR spectrum of centre II H in arbitrary direction. $T = 295°K$, $f = 9{\cdot}8$ GHz.

the fact that rotation of the applied steady magnetic field in a (111) plane does not affect the position of the fine structure lines at all. The width of the $\pm 5/2 \rightarrow \pm 3/2$ lines approximately equals the line width of the $\frac{1}{2} \rightarrow -\frac{1}{2}$ transition so that it can be concluded that no appreciable static strain was present in the investigated crystals.

The spin hamiltonians of centre II and centre I are identical and given by expression (1.1). The measurements were again performed at X band at 3 temperatures; the resulting values for the spin hamiltonian parameters are given in Table 2.

The value of a has been determined by looking at the angular dependence of the position of the fine structure lines; when **H** was rotated in a (110) plane the experimental results could be well explained by the theoretical cubic field angular dependence

$$P_{m_s-m_s-1} = \frac{1}{6}a\frac{35}{20}\Big[m_s^4 - (m_s-1)^4 - \frac{95}{14}\{m_s^2 - (m_s-1)^2\}\Big] \times [1 - \tfrac{5}{4}\sin^2\theta\,(1 + 3\cos^2\theta)] \qquad (1.6)$$

Where θ is the angle between H and the [100] axis.

The signs of A and a were determined from the relative intensities of the different fine structure lines at low temperatures. In order to achieve an accuracy of $0{\cdot}1\ 10^{-4}\,\mathrm{cm}^{-1}$ in the determination of A and a, it was necessary to take into account the second and third order terms in the hyperfine coupling; the precise values for a were determined with H along the [100] direction where the second order fine structure term is zero.

2. ENDOR MEASUREMENTS

As mentioned before, the EPR spectrum of centre II shows no resolved superhyperfine structure, the lines are inhomogeneously broadened due to the interaction of the Mn^{2+} ion with the surrounding fluorine nuclei, resulting in a linewidth of about 3 G. The number and relative positions of these nuclei can be detected with the use of ENDOR techniques; these experiments will now be described.

The ENDOR measurements were performed upon crystals containing centre II at 4·2°K using an X band EPR spectrometer. The ENDOR coil was placed at the centre of the cavity, which operates in the TE_{102} mode. The samples were mounted in the centre of the coil and in such a way that the steady magnetic field could be rotated in a (110) plane. With the use of a wideband power amplifier the output of a Hewlett-Packard type 8690 B sweep oscillator (with plug in unit 8698 B) was boosted to about 1 W. The ENDOR power was amplitude modulated (100 per cent modulation depth) at a frequency of about 200 c/s, the centre of the EPR absorption line being moderately saturated

Table 2. Spin Hamiltonian parameters of centre II

	g	A in $10^{-4}\,cm^{-1}$	a in $10^{-4}\,cm^{-1}$	A_s, A_p in $10^{-4}\,cm^{-1}$
295°K	$2{\cdot}002 \pm 0{\cdot}001$	$-74{\cdot}5 \pm 0{\cdot}1$	$+6{\cdot}2 \pm 0{\cdot}1$	$< 0{\cdot}4$
77°K	$2{\cdot}002 \pm 0{\cdot}001$	$-75{\cdot}5$	$6{\cdot}4$	$< 0{\cdot}4$
4·2°K	$2{\cdot}002 \pm 0{\cdot}001$	$-75{\cdot}5$	$6{\cdot}4$	$< 0{\cdot}4$

to obtain maximum signal to noise ratio (about 50 in best cases). The ENDOR linewidth was found to be about 40 kc/s. ENDOR transitions were observed in all five fine structure lines of each of the six hyperfine groups. This enables us to determine the signs of the superhyperfine parameter A_s and A_p unambiguously.

The crystal structure of CaF_2 is well known; each Ca^{2+} ion is surrounded by 8 fluorine ions at the corners of a cube at a distance of $\sqrt{3}$ (in units $\frac{1}{4}a_0 = 1{\cdot}361$ Å), the 24 second nearest neighbours are at distance $\sqrt{11}$, the 24 third and 32 fourth neighbours at $\sqrt{19}$ and $\sqrt{27}$ respectively. Only half the available body centres are occupied by Ca^{2+} ions; the empty body centres however have perfectly the same arrangement of fluorine neighbours, only the surrounding Ca^{2+} ions are in a different arrangement. Since we can observe only the interaction of the Mn^{2+} ion with the fluorine nuclei we cannot decide whether the Mn^{2+} ion is at a Ca^{2+} site (substitutionally replacing the Ca^{2+}) or at the alternative body centre. In the following derivation we will assume that Mn^{2+} is located at a Ca^{2+} site or alternative body centre. The spin Hamiltonian for the αth ($\alpha = 1, 2, \ldots 8$) first neighbour, interacting with the spin moment of the Mn^{2+} ion is:

$$\mathscr{H} = g_F \beta_N \mathbf{H}\cdot\mathbf{I}^\alpha + \mathbf{S}\cdot\mathbf{A}_F{}^\alpha\cdot\mathbf{I}^\alpha. \qquad (2.1)$$

It is assumed that the superhyperfine interaction is axially symmetric about the bond axis, so we write

$$\mathbf{S}\cdot A_F{}^\alpha\cdot\mathbf{I}^\alpha = A_\parallel{}^\alpha S_{z'} I^\alpha_{z'} + A_\perp{}^\alpha (S_{x'} I^\alpha_{x'} + S_{y'} I^\alpha_{y'})$$

where the z' axis is the bond axis (i.e. [111] direction). This is more conveniently written by

$$A_\perp{}^\alpha = A_s{}^\alpha - A_p{}^\alpha$$
$$A_\parallel{}^\alpha = A_s{}^\alpha + 2A_p{}^\alpha$$

to give the sum of an isotropic and anisotropic term with the same form as the dipole–dipole interaction term. The eigen values of the spin Hamiltonian (2.1) can then be shown to be

$$E_{m_F} = m_F\{[-g_F\beta_N H + A_s{}^\alpha m_s + (3\cos^2\theta^\alpha - 1)A_p{}^\alpha m_s]^2 + 9\sin^2\theta^\alpha \times \cos^2\theta^\alpha A_p{}^{\alpha 2} m_S{}^2\}^{1/2}.$$

The ENDOR frequencies are then, to second order given by:

$$\nu_E = \nu_0 - \{A_s{}^\alpha + (3\cos^2\theta^\alpha - 1)A_p{}^\alpha\} m_s + \frac{9}{2\nu_0}\sin^2\theta^\alpha\cos^2\theta^\alpha A_p{}^{\alpha 2} m_S{}^2 \qquad (2.2)$$

where ν_0 is the free fluorine nuclear frequency. A similar expression like (2.1) holds for more distant neighbours.

Let us first consider the ENDOR lines to be expected from the 8 nearest neighbours. Therefore it is necessary to express the term $3\cos^2\theta^\alpha - 1$ for each of the fluorines in the laboratory angle γ, which is the angle between **H** and the [001] direction but **H** always lying in a (110) plane. This can be readily done, the result is ($K \equiv 3\cos^2\theta - 1$):

$$K_1 = \sin^2\gamma + \sqrt{2}\sin 2\gamma$$
$$K_2 = \sin^2\gamma - \sqrt{2}\sin 2\gamma \qquad (2.3)$$
$$K_3 = \cos^2\gamma - 1.$$

So at an arbitrary angle γ three lines can be expected. A rotational diagram (H in (110) plane) has been recorded but no lines could be found which fit the expression (2.3). This means that if the Mn^{2+} ion is at a Ca^{2+} site or alternative body centre it has no fluorine first neighbours.

It can easily be shown that the 24 next nearest fluorine neighbours give 7 ENDOR lines with appropriate angular dependences; these are given by Hall and Schumacher[5]. These lines were found and certainly identified by their angular dependences which directly proves that Mn^{2+} is at a Ca^{2+} site or alternative body centre. However the lines were split up (the splitting varying with the direction of the magnetic field, maximum value: about 150 kc/s) which could be partly due to a misorientation of the crystal (the alignment could not be better than 1° in the present apparatus) but probably partly due to local imperfections (see also the discussion). The parameters A_s and A_p were determined but cannot be given very accurate because of the mentioned splitting of the lines; the results are given in Table 3.

Table 3. ENDOR results for centre II. *The experimental error is about* 20 kc/s; *however for the second shell the lines are split (see text) and the values quoted here are mean values*

Shell No.	A_s (Mc/s)	A_p (Mc/s)	Class dipole–dipole coupling (Mc/s)
2	−0·05	+0·99	+0·80
3	0	+0·38	+0·36
4	0	+0·21	+0·21

The remaining lines in the ENDOR spectrum could all be identified as belonging to third and fourth shell fluorine nuclei. The appropriate values of A_p are given in Table 3 too and are seen to be very close to the classical dipole–dipole coupling term; A_s is practically zero.

The conclusion that can be drawn from the ENDOR measurements is that the Mn^{2+} is at a Ca^{2+} site or alternative body centre, no fluorine nearest neighbours being present; second, third and fourth neighbours are present, but especially the second nearest neighbours are probably somewhat distorted from their lattice positions.

3. OPTICAL MEASUREMENTS

Some optical measurements have been carried out in addition to the EPR experiments. Both centres showed a very weak fluorescence when excited with electrons. The weakness of the fluorescence can be explained by the fact that the CaF_2 crystals contained 0·01 per cent Mn or less (see also later); moreover the optical transition which is responsible for the fluorescence ($^4T_{1g} \to {}^6A_{1g}$) is highly forbidden. This is reflected in the fact that the decay time of the fluorescing $^4T_{1g}$ level is quite large, see Table 4.

Table 4. Optical behaviour of both centres

	Decay time (msec)	Mean fluorescence wavelength in 10^{-10} m
centre I	60	4800
centre II	25	5500

Because of the weak signals, the fluorescence wavelength could not be measured accurately. The mean fluorescence wavelength of both centres is given in Table 4.

From these values and the energy diagram as given by Tanabe and Sugano[4] it can be estimated that the cubic field parameter $|10Dq|$ for centre II is roughly a factor of 2 larger than for centre I.

4. DISCUSSION

The CaF_2:Mn single crystals were grown from the melt (in Argon atmosphere) using the Czochralsky method. All crystals were grown under identical conditions, so at this moment we do not know under which precise conditions centre I or centre II is produced. Most crystals contained either centre I or centre II; only a few crystals contained both centres. Crystals in which centre I is present contain about 4×10^{-2} at% Mn; for centre II this figure is about 6×10^{-3} at% Mn, as has been determined by spectrochemical analysis and confirmed by the strength of the EPR signals. Some chemical experiments have been performed to try to convert centre I in centre II and vice versa. These will be discussed later.

Let us now consider the nature of centre I and centre II. We shall assume that centre I is Mn^{2+} substitutionally replacing Ca^{2+}, with no other impurities in the vicinity.

The results of the ENDOR measurements show that centre II is Mn^{2+} on a Ca^{2+} site or alternative body centre with fluorine first neighbours missing. Then other impurity ions must be present as first neighbours. These impurity ions must have zero nuclear spin because otherwise we should find superhyperfine structure in the EPR spectrum or in the ENDOR spectrum. We suppose these other impurity ions to be O^{2-}. The impurity complex is then most likely $(MnO_6)^{10-}$ or $(MnO_8)^{14-}$.

There are 2 important arguments for this assumption:

(1) The optical measurements have shown that centre II has a $|10Dq|$ value which is twice as large as for centre I, which can be expected (in the point-charge approximation) because the oxygen ions are, of course, double charged. Moreover, it is known that the oxides form more covalent bondings than fluorides; this gives more mixing of odd states into the $3d$ wave functions of the manganese increasing the transition probability for the ${}^4T_{1g}\rightarrow{}^6A_{1g}$ optical transition. The result is a shorter lifetime of the fluorescing state, as indeed has been found, see Table 4.

(2) Since we assume that the Mn^{2+} first neighbours are O^{2-} ions and the second Ca^{2+}, it seems worthwhile to compare the spin hamiltonian parameters of centre II with the parameters for the case CaO:Mn as given by Low and Rubins[6]:

$$|A| = (80{\cdot}7\pm0{\cdot}1)\times10^{-4}\,\text{cm}^{-1};\quad |a| = (6{\cdot}0\pm0{\cdot}3)\times10^{-4}\,\text{cm}^{-1}$$

and for centre II:

$$A = (-74{\cdot}5\pm0{\cdot}1)\times10^{-4}\,\text{cm}^{-1};\quad a = (+6{\cdot}2\pm0{\cdot}1)\times10^{-4}\,\text{cm}^{-1}.$$

The agreement is quite satisfactory, especially for the cubic field splitting parameter, giving an important support for the assumed nature of centre II.

Some of the available crystals were turpid, indicating a segregation of CaO. These crystals contained only centre II (but all the measurements in which the spin hamiltonian parameters have been determined, were performed upon clear crystals). This indicates that, at least in these crystals enough oxygen was present to form the assumed manganese-oxygen complex.

We expect the complex to be $(MnO_6)^{10-}$ rather than $(MnO_8)^{14-}$ because of the well known fact that Mn^{2+} is more stable in a sixfold coordination. A point to notice is that the needed charge compensation must be far away because otherwise the EPR spectrum could not be perfectly cubic. The precise orientation of the $(MnO_6)^{10-}$, or eventually $(MnO_8)^{14-}$ in the CaF_2 host lattice cannot be determined, neither by EPR nor by ENDOR techniques because the O^{16} nuclear (natural abundance: 99·9963 per cent) has zero magnetic moment, as was mentioned before.

Several other impurity complexes are known in the literature, for instance $(FeF_8)^{3-}$ in CdTe as described by Kravitz and Piper [7], but as far as we know, there are no impurity complexes in CaF_2 reported until now. By impurity complexes we do not mean the presence of nearby charge compensation, as for instance RE^{3+}-O^{2-} complexes in CaF_2, in which RE^{3+} is a triple charged rare earth ion and an O^{2-} ion present at a fluorine site to provide charge compensation. An excellent treatment of these charge compensation problems, especially RE^{3+}-H$^-$ is very recently given by Jones *et al.*[8].

Two chemical experiments have been performed, one to try to convert centre I in II and one to convert II in I. In the first experiment a CaF$_2$ crystal in which centre I is present was treated for 1 hr at 1000°C in oxygen atmosphere. After the treatment, different zones could be seen: the middle of the crystal was still clear, more outside there was a grey zone, the outer part of the crystal being brown. The clear part showed the EPR spectrum of centre I just as before the treatment; the grey and brown part showed neither the spectrum of centre I nor that of centre II, indicating that no Mn^{2+} was present any more. Indeed, the grey and brown colour is most probably produced by Mn^{3+} or Mn^{4+} surrounded by oxygen ions. So we conclude that oxygen had penetrated the crystal and oxidized the manganese to a higher degree of ionisation; furthermore it must be concluded that it seems to be impossible to produce centre II in this way.

The second experiment we tried was the following. A CaF$_2$ crystal containing centre II was heated for $\frac{1}{2}$ hr in fluor atmosphere at 800°C. It could be expected that at least a part of the oxygen ions would be replaced by fluor ions, producing centre I. However, the EPR spectrum was completely the same before and after the treatment.

It seems worthwhile to pay some attention to the measured temperature dependence of the spin hamiltonian parameters of both centres. Let us first consider the hyperfine splitting. As can be seen from the values given in Table 1 and Table 2, the hyperfine splitting factor A of both centres decreases with increasing temperature in, at least qualitative, accordance with the theory given by Simánek *et al.*[9, 10]. The temperature dependence of centre I has been studied by Huang *et al.*[11] in the temperature range 50–700°K; they find an excellent agreement with the theory of Simánek *et al.* but there is a small difference in the absolute value of A with the values given in this work.

The temperature dependence of the cubic field splitting parameter a of centre II (the a for centre I was too small to be measured accurately) shows the same tendency as in the former case, namely a decreases with increasing temperature. This tendency is the same as for the cases M_gO:Mn^{2+} and ZnS:Mn^{2+} reported by Walsh *et al.*[12]. They pointed out that the main cause of this effect is the thermal expansion of the lattice.

Finally the isotropic part of the superhyperfine splitting (for centre I) shows a small but significant decrease with increasing temperature. Thermal lattice expansion might give an important contribution to this effect because of decreasing direct overlap of the manganese and fluorine wave-functions, but there may be several other explanations.

Acknowledgements – The author wishes to thank Mr. J. W. de Jong for growing the single crystals, Mr. J. H Haanstra and Mr. J. A de Poorter for performing the optical measurements Dr J C. M Henning and Dr. J Dieleman for helpful advice.

REFERENCES

1 LOW W., *Phys. Rev.* **105**, 793 (1957)
2 BAKER J. M., BLEANEY B. and HAYES W., *Proc R Soc* **247**, 141 (1958).
3 VINOKUROV V. M and STEPONOV V. G., *Soviet Phys solid St* **6**, 303 (1964).
4. TANABE Y and SUGANO S., *J phys Soc. Japan* **9**, 753, 766 (1954)
5. HALL J. L. and SCHUMACHER R. T., *Phys. Rev* **127**, 1892 (1962).
6. LOW W and RUBINS R. S., *Phys. Lett.* **1**, 316 (1962).
7 KRAVITZ L. C. and PIPER W. W., *Phys. Rev.* **146**, 322 (1966).
8 JONES G. D., PELED S., ROSENWAKS S. and YATSW S., *Phys. Rev.* **183**, 353 (1969).
9 SIMÁNEK E. and ORBACH R., *Phys. Rev.* **145**, 191 (1966).
10. SIMÁNEK E. and HUANG Nai Li, *Phys. Rev. Lett* **17**, 699 (1966).
11. HUANG C. Y., REICHERT J. F. and GIGANTE J., *Phys. Lett.* **26A**, 219 (1968).
12. WALSH W. M Jr., JEANER J. and BLOEMBERGEN N., *Phys. Rev.* **139A**, 1338 (1965).

J. Phys. Chem. Solids Pergamon Press 1970. Vol. 31, pp. 913–926. Printed in Great Britain.

APPLICATION OF GROUP THEORY TO THE LATTICE DYNAMICS OF MAGNESIUM STANNIDE*

R. J. KEARNEY†
University of Idaho, Moscow, Idaho 83843, U.S.A.

and

T. G. WORLTON‡ and **R. E. SCHMUNK**
Idaho Nuclear Corporation, Idaho Falls, Idaho 83401, U.S.A.

(*Received* 24 *July* 1969; *in revised form* 23 *October* 1969)

Abstract – Group theoretical techniques have been applied to an analysis of the lattice dynamics of Mg_2Sn along directions of high symmetry and at certain points in the Brillouin zone. Matrix representations have been constructed for the symmetry elements in the group of the wave vector. These representations have been used to:

(1) determine the classification of the phonon modes for a given **q**,
(2) construct projection operators to determine the form of the eigenvectors for the atomic motions and from these construct unitary transformation matrices **U** which will be used to
(3) block diagonalize the dynamical matrix **D**.

The results obtained here are generally applicable to other fluorite structure crystals as well as Mg_2Sn.

1. INTRODUCTION

A GROUP theoretical analysis of the lattice vibrations in crystalline solids is extremely useful in a detailed study of experimental data. It is especially useful in fitting force constant models to experimentally measured dispersion curves. In the preceding paper[1], hereafter called KWS I, the experimental analysis of the lattice vibrations in Mg_2Sn is given. In this paper we shall classify the phonon modes according to their symmetry and block diagonalize the dynamical matrix along directions of high symmetry.

Two general methods for performing a group theoretical analysis of lattice vibrations in solids have recently been given[2, 3]. In this paper we will follow the methods outlined by Chen[2].

The basic problem is to solve the equations of motion of the lattice which in the harmonic approximation are:

$$M_\kappa \ddot{U}_\alpha\binom{l}{\kappa} = -\sum_{l',\kappa',\beta} \Phi_{\alpha\beta}(l\kappa, l'\kappa')\, U_\beta\binom{l'}{\kappa'} \qquad (1)$$

where $-\Phi_{\alpha\beta}(l\kappa, l'\kappa')$ is the force in the α direction on the κth atom in the lth cell due to a unit displacement of the κ'th atom in the l'th cell in a direction β; M_κ is the mass of the κth atom, and $U_\alpha\binom{l}{\kappa}$ is a displacement of the κth atom in the lth cell in the direction α. These equations can be simplified by the assumption

$$U_\alpha\binom{l}{\kappa} = \frac{U_\alpha(\kappa)}{\sqrt{M_\kappa}} \exp i\,[\mathbf{q}\cdot\{\mathbf{X}(l)+\mathbf{X}(\kappa)\} - \omega t] \qquad (2)$$

where $\mathbf{X}(l)$ denotes the position of the lth unit cell and $\mathbf{X}(\kappa)$ denotes the position of the κth atom in that cell.

This assumption leads directly to the equation:

$$\omega^2 U_\alpha(\kappa) = \sum_{\beta\,\kappa'} D_{\alpha\beta}^{\kappa\kappa'}(\mathbf{q})\, U_\beta(\kappa') \qquad (3)$$

where

$$D_{\alpha\beta}^{\kappa\kappa'}(\mathbf{q}) = \frac{1}{\sqrt{M_\kappa M_{\kappa'}}} \sum_{l'} \Phi_{\alpha\beta}(l\kappa, l'\kappa') \times \exp\{-i\mathbf{q}\cdot[\mathbf{X}(l)-\mathbf{X}(l')]\} \times \exp\{-i\mathbf{q}\cdot[\mathbf{X}(\kappa)-\mathbf{X}(\kappa')]\}. \qquad (4)$$

---

*Work done under the auspices of the United States Atomic Energy Commission.

†Supported in part by the United States Army Research Office, Durham.

‡Present address: Los Alamos Scientific Laboratory, Los Alamos, New Mexico 87544

The requirement for a solution to equation (3) is that

$$\det\left|\omega^2\delta_{\kappa\kappa'}\delta_{\alpha\beta} - D_{\alpha\beta}^{\kappa\kappa'}(\mathbf{q})\right| = 0. \qquad (5)$$

The ω's are the normal mode vibrational frequencies of the lattice. These, along with the complex polarization vectors U_α, are considered to be a solution to the problem. The expressions for the elements of the dynamical matrix $D_{\alpha\beta}^{\kappa\kappa'}(\mathbf{q})$ can be simplified considerably if symmetry coordinates for the lattice structure are used – that is, the **D** matrix can be brought into block diagonal form by a suitable similarity transformation.

The reducible matrix representations for the symmetry elements in the group of the wave vector are given by Chen's equation (2.21) as:

$$S_{\alpha\beta}^{\kappa\kappa'}(A,\mathbf{q}) = \delta_{A(\kappa),\kappa'}\, a_{\alpha\beta}\, e^{i\mathbf{q}\cdot\mathbf{R}_t}\, e^{-i\mathbf{G}\cdot(\mathbf{R}_\kappa - \mathbf{R}_t)} \qquad (6)$$

where **G** is determined from the requirement†

$$a^{-1}\mathbf{q} = \mathbf{q} + \mathbf{G}$$

and the $a_{\alpha\beta}$'s are elements of the 3×3 matrix representation of the rotational part of the symmetry elements. In equation (6) $\mathbf{R}_{\kappa'}$ is the position vector of atom κ' and $\mathbf{R}_t$ is a fractional translation which is zero for symmorphic groups.

The procedure begins with the construction of reducible matrix representations for the symmetry elements in the group of the wave vector. To initially simplify the dynamical matrix we will use the fact that the reducible matrix representation of all elements in the group of the wave vector commute with **D**, i.e. $\mathbf{D} = \mathbf{S}^{-1}\mathbf{D}\mathbf{S}$. This simplification is followed by the block diagonalization of **D** through $\mathbf{U}^{-1}\mathbf{D}\mathbf{U}$ where **U** is constructed from the orthogonal basis vectors which are discussed below.

To determine the number and multiplicity of different phonon modes at a given value of **q** the decomposition formula[4]

$$c_\alpha = \frac{1}{g}\sum_A \chi^{(\alpha)}(A)^*\chi(A) \qquad (7)$$

is employed. Here $\chi(A)$ and $\chi^{(\alpha)}(A)$ are the characters (traces) of the reducible representation matrices $S(A)$ and the αth irreducible representation (i.r.) of these elements. Each phonon mode will be labeled with the name of the corresponding i.r. The characters $\chi^{(\alpha)}(A)$ of the i.r. matrices are read directly from the character table for each element A of the αth i.r. In this formula g is the order of the group and c_α is the number of times the αth i.r. is contained in the reduction. In addition, the dimensionality of the αth i.r. gives the degeneracy of the phonon modes which transform according to the αth i.r. The projection operator technique is used to construct symmetry coordinates which form orthogonal basis vectors for the different i.r.'s. The eigenvectors or orthogonal basis vectors obtained from the projection operators can be normalized and used to construct the unitary transformation matrix **U** which will transform the dynamical matrix into block diagonal form.

2. Mg_2Sn PHONON SYMMETRY

The crystal structure of Mg_2Sn consists of three interpenetrating face-centered cubic lattices, one lattice of tin with origin (0, 0, 0) and two of magnesium with origins $(a/4) \times (1, 1, 1)$ and $(3a/4)(1, 1, 1)$. Each tin atom occupies a center of inversion symmetry and is surrounded by eight magnesium ions. The lattice constant has the value $a = 6{\cdot}758$ Å[5]. This fluorite structure along with its Brillouin zone is shown in Fig. 1. The notation used to label i.r.'s and symmetry points is due to Bouckaert, Smoluchowski and Wigner (BSW) [6]. The symmetry of the fluorite structure is described by the symmorphic space group O_h^5[7].

We shall use the following format for all our matrix representations:

---

† We found it necessary to use this relation rather than $a\mathbf{q} = \mathbf{q} + \mathbf{G}$ in order to obtain the correct symmetry reduction at the point W.

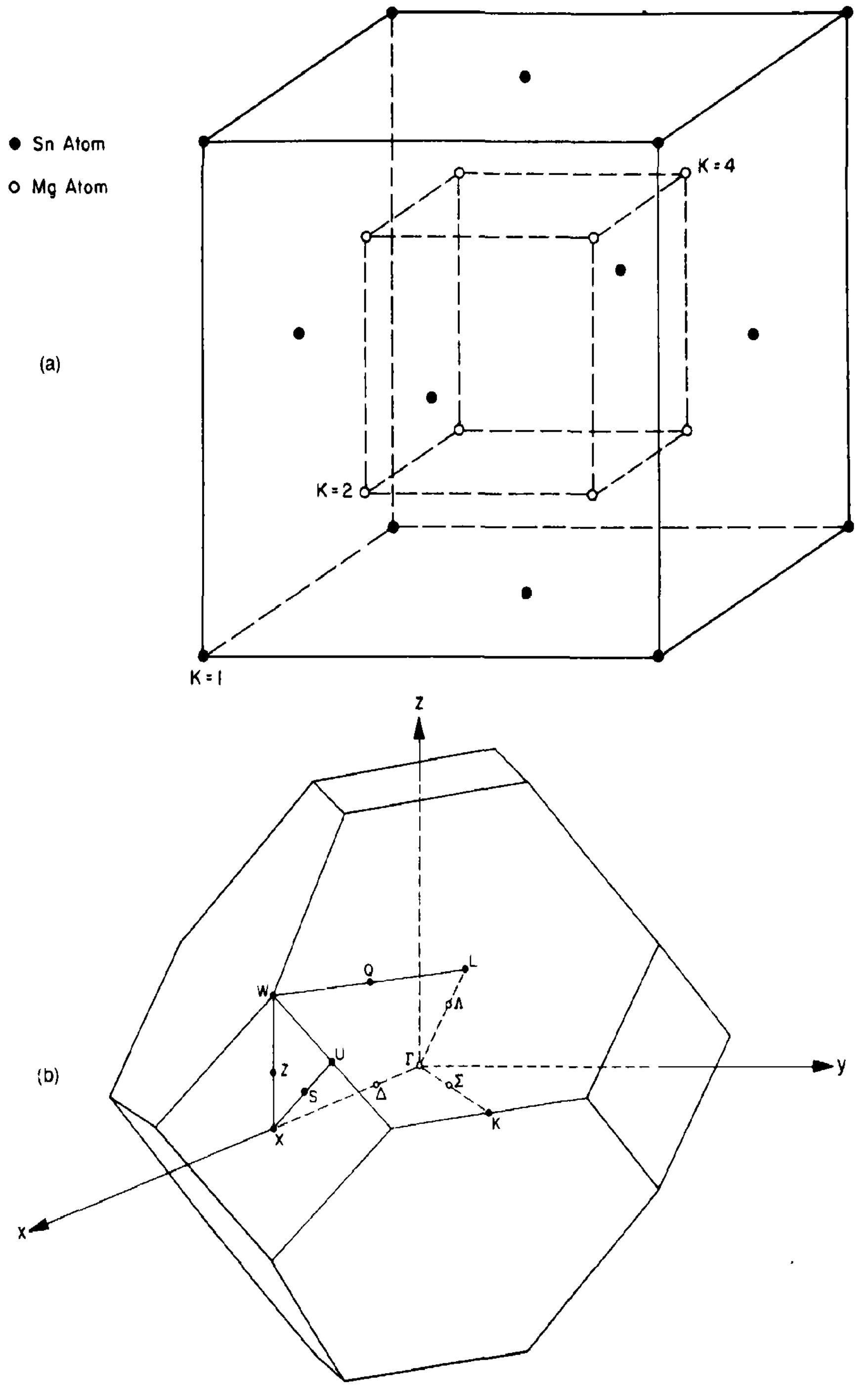

Fig. 1. (a) The crystal structure of magnesium stannide showing the conventional unit cell with side dimension a. The atoms are arranged on three interpenetrating face centered cubic lattices with their origins at (000) for the Sn atoms ($\kappa = 1$), and $(a/4)(111)$ and $(3a/4)(111)$ for the Mg atoms ($\kappa = 2, 4$). (b) Brillouin zone for Mg_2Sn with points and lines of high symmetry which have been included in the discussion of this paper labeled in the notation of Bouckaert, Smoluchowski and Wigner.

$$\begin{bmatrix} \binom{11}{\alpha\beta} & \binom{12}{\alpha\beta} & \binom{14}{\alpha\beta} \\ \binom{21}{\alpha\beta} & \binom{22}{\alpha\beta} & \binom{24}{\alpha\beta} \\ \binom{41}{\alpha\beta} & \binom{42}{\alpha\beta} & \binom{44}{\alpha\beta} \end{bmatrix}$$

where $\kappa = 1$ labels the Sn atom at $(0,0,0)$;
$\kappa = 2$ labels the Mg atom at $(a/4)(1,1,1)$;
$\kappa = 4$ labels the Mg atom at $(3a/4)(1,1,1)$; and $\alpha, \beta = x, y, z$.

Since the fluorite structure is symmorphic the exponential factors in equation (6) simplify to $\theta_{\kappa'} = \exp[-i\mathbf{G}\cdot\mathbf{R}_{\kappa'}]$. Noting that $\mathbf{R}_4 = -\mathbf{R}_2 + \mathbf{R}_l$ where $\mathbf{R}_l$ is a lattice translation vector we find that $\theta_4 = \theta_2^*$. The Sn atom is at the origin so $\theta_1 = 1$ for all symmetry operations. Table 1 lists the factor θ_2 for all symmetry lines and points of interest except the point Γ where we have the trivial result that $\theta_\kappa = 1$ for all symmetry operations. In Table 1 the rotational symmetry elements of O_h are labeled in the notation of Kovalev[8]. Other notations can be correlated to that of Kovalev by referring to Tables 3 and 4 of Warren[9].

Table 1 also indicates whether or not each symmetry operation interchanges the two Mg sublattices. If the Mg sublattices are interchanged the S matrix resulting from equation (6) has the form:

$$\mathbf{S}(A,\mathbf{q}) = \begin{bmatrix} \mathbf{A} & \mathbf{0} & \mathbf{0} \\ \mathbf{0} & \mathbf{0} & \theta_2^*\mathbf{A} \\ \mathbf{0} & \theta_2\mathbf{A} & \mathbf{0} \end{bmatrix}$$

where **A** refers to the 3×3 rotation matrix

Table 1. *The factor* $\theta_2 = \exp[-i\mathbf{G}\cdot\mathbf{R}_2]$ *which is used in equation* (6)

A†	INT‡	Δ	Σ	Λ	*Z*	*S*	*X*	*L*	*W*	*Q*
h_1		1	1	1	1	1	1	1	1	1
h_2							−1			
h_3					−1		−1		−1	
h_4		1					1			
h_5				1				1		
h_6				1				1		
h_{13}	*						−1	$-i$		
h_{14}	*	1					1			
h_{15}	*	1					1			
h_{16}	*		1				−1			
h_{17}	*							$-i$		
h_{18}	*					−1				
h_{19}	*							$-i$	$-i$	i
h_{21}	*								i	
h_{25}	*						−1	$-i$		
h_{26}	*	1			−1	−1	1		−1	
h_{27}	*	1					1			
h_{28}	*		1		1		−1		1	
h_{29}	*							$-i$		
h_{33}	*							$-i$		
h_{37}		1	1	1			1	1		
h_{38}							−1			
h_{39}							−1			
h_{40}		1					1			
h_{41}				1		1		1		
h_{45}				1				1		
h_{46}									i	
h_{48}									$-i$	

†To correlate these symbols with the notation used by other authors see reference [9]

‡In the column labeled INT * means that the two Mg sublattices are interchanged by that symmetry operation.

representing the symmetry operation A. For the cubic point groups these rotation matrices can be taken to be the $T_{1u}(\Gamma_{15})$ irreducible representation matrices. These are also listed in Tables 3 and 4 of Warren[9]. (Note that for h_{24} in Warren's Table 3, $(T_{1u})_{31}$ should be -1 instead of 1.) For the symmetry operations which do not interchange Mg sublattices the S matrices have the form:

$$\mathbf{S}(A,\mathbf{q})=\begin{bmatrix}\mathbf{A} & \mathbf{0} & \mathbf{0}\\ \mathbf{0} & \theta_2\mathbf{A} & \mathbf{0}\\ \mathbf{0} & \mathbf{0} & \theta_2^*\mathbf{A}\end{bmatrix}.$$

Before considering the different wave vector groups some general conditions can be given for the dynamical matrix. The reality of the eigenvalues ω^2 imposes the requirement that $\mathbf{D}$ be Hermitian: $D^{\kappa\kappa'}_{\alpha\beta}=D^{\kappa'\kappa*}_{\beta\alpha}$. If the point group of the crystal contains the inversion operation, which 0_h does, further simplifications† are $D^{11}_{\alpha\beta}=D^{11*}_{\alpha\beta}$, $D^{22}_{\alpha\beta}=D^{33*}_{\alpha\beta}$, and $D^{32*}_{\alpha\beta}=D^{23}_{\alpha\beta}$. By combining the last relation with the Hermitian property we obtain $D^{23}_{\alpha\beta}=D^{23}_{\beta\alpha}$. We shall call these requirements general conditions on $\mathbf{D}$. We now carry out the procedure in detail for wave vectors $\mathbf{q}$ along the lines $(2\pi/a)[\mathbf{00}\zeta]$, $(2\pi/a)[\zeta\zeta\mathbf{0}]$, $(2\pi/a)\times[\zeta\zeta\zeta]$, $(2\pi/a)[\mathbf{1}\zeta\mathbf{0}]$, and at the points $(2\pi/a)[\mathbf{1}\tfrac{1}{2}\mathbf{0}]$ and $(2\pi/a)[\tfrac{1}{2}\tfrac{1}{2}\tfrac{1}{2}]$.

1. Along the line Δ: $\mathbf{q}=(2\pi/a)[\mathbf{00}\zeta]$. The point group of the wave vector is C_{4v}.

We now impose the requirement that $\mathbf{S}^{-1}\mathbf{DS}=\mathbf{D}$ for all symmetry operations in the group of the wave vector. This plus the general requirements result in the following form for $\mathbf{D}$:

$$\begin{bmatrix}
d_{11} & 0 & 0 & d_{14} & d_{15} & 0 & d_{14} & -d_{15} & 0\\
0 & d_{11} & 0 & d_{15} & d_{14} & 0 & -d_{15} & d_{14} & 0\\
0 & 0 & d_{33} & 0 & 0 & d_{36} & 0 & 0 & d_{36}\\
d_{14} & -d_{15} & 0 & d_{44} & 0 & 0 & d_{47} & d_{48} & 0\\
-d_{15} & d_{14} & 0 & 0 & d_{44} & 0 & d_{48} & d_{47} & 0\\
0 & 0 & d_{36} & 0 & 0 & d_{66} & 0 & 0 & d_{69}\\
d_{14} & d_{15} & 0 & d_{47} & -d_{48} & 0 & d_{44} & 0 & 0\\
d_{15} & d_{14} & 0 & -d_{48} & d_{47} & 0 & 0 & d_{44} & 0\\
0 & 0 & d_{36} & 0 & 0 & d_{69} & 0 & 0 & d_{66}
\end{bmatrix}$$

The decomposition is found from equation (8) to be $2\Delta_1+\Delta_{2'}+3\Delta_5$. Thus when we transform to symmetry coordinates which reduce $\mathbf{D}$ to block diagonal form, the submatrices will be a 2×2 Δ_1, a 1×1 $\Delta_{2'}$, and two degenerate 3×3 Δ_5's. The projection operators are obtained from equation (2.26) of Chen's paper[2] which in our case is written:

$$\mathbf{P}^{(\alpha)}_{ij}(\mathbf{q})=\frac{1}{g}\sum_{A}\chi^{(\alpha)*}_{ij}(\mathbf{q},A)\mathbf{S}(\mathbf{q},A) \qquad (9)$$

where $\chi^{(\alpha)}_{ij}$ is the ij element of the αth i.r. The character tables and i.r.'s for all symmetry lines and points of the $0_h{}^5$ space groups are given by Slater[7]. These operators project from an arbitrary vector that part which transforms according to the corresponding i.r.

After application of each projection operator the resultant vectors can be decomposed into the proper number of basis vectors by inspection. The basis vectors should be normalized since we wish to use them to construct a unitary transformation matrix $\mathbf{U}$. Thus, $\mathbf{U}^{-1}=\mathbf{U}\dagger=\tilde{\mathbf{U}}^*$. For the Δ direction the unitary transformation matrix is:

$$\mathbf{U}=\begin{bmatrix}
0 & 0 & 0 & 1 & 0 & 0 & 0 & 0 & 0\\
0 & 0 & 0 & 0 & 0 & 0 & 1 & 0 & 0\\
1 & 0 & 0 & 0 & 0 & 0 & 0 & 0 & 0\\
0 & 0 & 0 & 0 & \frac{1}{\sqrt{2}} & 0 & 0 & \frac{1}{\sqrt{2}} & 0\\
0 & 0 & 0 & 0 & 0 & \frac{1}{\sqrt{2}} & 0 & 0 & \frac{1}{\sqrt{2}}\\
0 & \frac{1}{\sqrt{2}} & \frac{1}{\sqrt{2}} & 0 & 0 & 0 & 0 & 0 & 0\\
0 & 0 & 0 & 0 & \frac{1}{\sqrt{2}} & 0 & 0 & \frac{-1}{\sqrt{2}} & 0\\
0 & 0 & 0 & 0 & 0 & \frac{-1}{\sqrt{2}} & 0 & 0 & \frac{1}{\sqrt{2}}\\
0 & \frac{1}{\sqrt{2}} & \frac{-1}{\sqrt{2}} & 0 & 0 & 0 & 0 & 0 & 0
\end{bmatrix}$$
$$\underbrace{\qquad\qquad}_{\Delta_1}\;\underbrace{\qquad}_{\Delta_{2'}}\;\underbrace{\qquad\qquad\qquad}_{\Delta_5}\;\underbrace{\qquad\qquad\qquad}_{\Delta_5}$$

---

†Reference [3], equations (3.25) to (3.31).

The operation $\mathbf{U}^{-1}\mathbf{D}\mathbf{U}$ gives the result:

$$\mathbf{D}=\left[\begin{array}{ccccccccc}
d_{33} & \sqrt{2}d_{36} & 0 & 0 & 0 & 0 & 0 & 0 & 0\\
\sqrt{2}d_{36} & d_{66}+d_{69} & 0 & 0 & 0 & 0 & 0 & 0 & 0\\
0 & 0 & d_{66}-d_{69} & 0 & 0 & 0 & 0 & 0 & 0\\
0 & 0 & 0 & d_{11} & \sqrt{2}d_{14} & \sqrt{2}d_{15} & 0 & 0 & 0\\
0 & 0 & 0 & \sqrt{2}d_{14} & d_{44}+d_{47} & -d_{48} & 0 & 0 & 0\\
0 & 0 & 0 & -\sqrt{2}d_{15} & d_{48} & d_{44}-d_{47} & 0 & 0 & 0\\
0 & 0 & 0 & 0 & 0 & 0 & d_{11} & \sqrt{2}d_{14} & \sqrt{2}d_{15}\\
0 & 0 & 0 & 0 & 0 & 0 & \sqrt{2}d_{14} & d_{44}+d_{47} & -d_{48}\\
0 & 0 & 0 & 0 & 0 & 0 & -\sqrt{2}d_{15} & d_{48} & d_{44}-d_{47}\\
\multicolumn{2}{c}{\underbrace{\hspace{6em}}_{\Delta_1}} & \underbrace{\hspace{3em}}_{\Delta_{2'}} & \multicolumn{3}{c}{\underbrace{\hspace{12em}}_{\Delta_5}} & \multicolumn{3}{c}{\underbrace{\hspace{12em}}_{\Delta_5}}
\end{array}\right]$$

2. Along the line Σ: $\mathbf{q}=(2\pi/a)[\zeta\zeta 0]$. The point group of the wave vector is C_{2v}. Our procedure is identical to that used previously along Δ. Imposing the requirements $\mathbf{S}^{-1}\mathbf{D}\mathbf{S}=\mathbf{D}$, together with the general rules gives:

$$\begin{bmatrix}
d_{11} & d_{12} & 0 & d_{14} & d_{15} & d_{16} & d_{14} & d_{15} & -d_{16}\\
d_{12} & d_{11} & 0 & d_{15} & d_{14} & d_{16} & d_{15} & d_{14} & -d_{16}\\
0 & 0 & d_{33} & d_{34} & d_{34} & d_{36} & -d_{34} & -d_{34} & d_{36}\\
d_{14} & d_{15} & -d_{34} & d_{44} & d_{45} & d_{46} & d_{47} & d_{48} & d_{49}\\
d_{15} & d_{14} & -d_{34} & d_{45} & d_{44} & d_{46} & d_{48} & d_{47} & d_{49}\\
-d_{16} & -d_{16} & d_{36} & -d_{46} & -d_{46} & d_{66} & d_{49} & d_{49} & d_{69}\\
d_{14} & d_{15} & d_{34} & d_{47} & d_{48} & -d_{49} & d_{44} & d_{45} & -d_{46}\\
d_{15} & d_{14} & d_{34} & d_{48} & d_{47} & -d_{49} & d_{45} & d_{44} & -d_{46}\\
d_{16} & d_{16} & d_{36} & -d_{49} & -d_{49} & d_{69} & d_{46} & d_{46} & d_{66}
\end{bmatrix}.$$

The decomposition of the representation $\mathbf{S}_\Sigma$ is $3\Sigma_1+\Sigma_2+3\Sigma_3+2\Sigma_4$. The unitary transformation matrix is:

$$\mathbf{U}=\begin{array}{c}
\begin{array}{ccccccccc}
\multicolumn{3}{c}{\overbrace{\hspace{7em}}^{\Sigma_1}} & \overbrace{\hspace{1.5em}}^{\Sigma_2} & \multicolumn{3}{c}{\overbrace{\hspace{7em}}^{\Sigma_3}} & \multicolumn{2}{c}{\overbrace{\hspace{4em}}^{\Sigma_4}}
\end{array}\\
\left[\begin{array}{ccccccccc}
\frac{1}{\sqrt{2}} & 0 & 0 & 0 & 0 & 0 & 0 & \frac{1}{\sqrt{2}} & 0\\
\frac{1}{\sqrt{2}} & 0 & 0 & 0 & 0 & 0 & 0 & \frac{-1}{\sqrt{2}} & 0\\
0 & 0 & 0 & 0 & 1 & 0 & 0 & 0 & 0\\
0 & \frac{1}{2} & 0 & \frac{1}{2} & 0 & \frac{1}{2} & 0 & 0 & \frac{1}{2}\\
0 & \frac{1}{2} & 0 & \frac{-1}{2} & 0 & \frac{1}{2} & 0 & 0 & \frac{-1}{2}\\
0 & 0 & \frac{1}{\sqrt{2}} & 0 & 0 & 0 & \frac{1}{\sqrt{2}} & 0 & 0\\
0 & \frac{1}{2} & 0 & \frac{-1}{2} & 0 & \frac{-1}{2} & 0 & 0 & \frac{1}{2}\\
0 & \frac{1}{2} & 0 & \frac{1}{2} & 0 & \frac{-1}{2} & 0 & 0 & \frac{-1}{2}\\
0 & 0 & \frac{-1}{\sqrt{2}} & 0 & 0 & 0 & \frac{1}{\sqrt{2}} & 0 & 0
\end{array}\right]
\end{array}.$$

Then, $\mathbf{U}^{-1}\mathbf{D}\mathbf{U}$ gives the following block diagonal form for $\mathbf{D}$:

$$\begin{array}{ccccccccc}
d_{11}+d_{12} & \sqrt{2}(d_{14}+d_{15}) & 2d_{16} & 0 & 0 & 0 & 0 & 0 & 0 \\
\sqrt{2}(d_{14}+d_{15}) & \begin{array}{c} d_{44}+d_{45} \\ +d_{47}+d_{48} \end{array} & \sqrt{2}(d_{46}-d_{49}) & 0 & 0 & 0 & 0 & 0 & 0 \\
-2d_{16} & -\sqrt{2}(d_{46}-d_{49}) & d_{66}-d_{69} & 0 & 0 & 0 & 0 & 0 & 0 \\
0 & 0 & 0 & \begin{array}{c} d_{44}+d_{48} \\ -d_{45}-d_{47} \end{array} & 0 & 0 & 0 & 0 & 0 \\
0 & 0 & 0 & 0 & d_{33} & 2d_{34} & \sqrt{2}d_{36} & 0 & 0 \\
0 & 0 & 0 & 0 & -2d_{34} & \begin{array}{c} d_{44}+d_{45} \\ -d_{47}-d_{48} \end{array} & \sqrt{2}(d_{46}+d_{49}) & 0 & 0 \\
0 & 0 & 0 & 0 & \sqrt{2}d_{36} & -\sqrt{2}(d_{46}+d_{49}) & d_{66}+d_{69} & 0 & 0 \\
0 & 0 & 0 & 0 & 0 & 0 & 0 & d_{11}-d_{12} & \sqrt{2}(d_{14}-d_{15}) \\
0 & 0 & 0 & 0 & 0 & 0 & 0 & \sqrt{2}(d_{14}-d_{15}) & \begin{array}{c} d_{44}+d_{47} \\ -d_{45}-d_{48} \end{array} \\
\multicolumn{3}{c}{\underbrace{\hphantom{xxxxxxxxxxxxxxxxxxxxxxxxxxxxxxxxxxxx}}_{\Sigma_1}} & \underbrace{\hphantom{xxxxxxxx}}_{\Sigma_2} & \multicolumn{3}{c}{\underbrace{\hphantom{xxxxxxxxxxxxxxxxxxxxxxxxxxxxxxxxxx}}_{\Sigma_3}} & \multicolumn{2}{c}{\underbrace{\hphantom{xxxxxxxxxxxxxxxxxxxxxxxx}}_{\Sigma_4}}
\end{array}$$

3. Along the line Λ: $\mathbf{q} = (2\pi/a)[\zeta\zeta\zeta]$. The point group of the wave vector is C_{3v}. The decomposition of the **S** matrices is $3\Lambda_1 + 3\Lambda_3$. The relation $\mathbf{S}^{-1}\mathbf{D}\mathbf{S} = \mathbf{D}$ and the general requirements give:

$$\mathbf{D} = \begin{bmatrix} d_{11} & d_{12} & d_{12} & d_{14} & d_{15} & d_{15} & d_{14}^* & d_{15}^* & d_{15}^* \\ d_{12} & d_{11} & d_{12} & d_{15} & d_{14} & d_{15} & d_{15}^* & d_{14}^* & d_{15}^* \\ d_{12} & d_{12} & d_{11} & d_{15} & d_{15} & d_{14} & d_{15}^* & d_{15}^* & d_{14}^* \\ d_{14}^* & d_{15}^* & d_{15}^* & d_{44} & d_{45} & d_{45} & d_{47} & d_{48} & d_{48} \\ d_{15}^* & d_{14}^* & d_{15}^* & d_{15} & d_{44} & d_{45} & d_{48} & d_{47} & d_{48} \\ d_{15}^* & d_{15}^* & d_{14}^* & d_{45} & d_{45} & d_{44} & d_{48} & d_{48} & d_{47} \\ d_{14} & d_{15} & d_{15} & d_{47}^* & d_{48}^* & d_{48}^* & d_{44} & d_{45} & d_{45} \\ d_{15} & d_{14} & d_{15} & d_{48}^* & d_{47}^* & d_{48}^* & d_{45} & d_{44} & d_{45} \\ d_{15} & d_{15} & d_{14} & d_{48}^* & d_{48}^* & d_{47}^* & d_{45} & d_{45} & d_{44} \end{bmatrix}$$

The unitary transformation matrix is:

$$\mathbf{U} = \begin{array}{c} \left[\begin{array}{ccccccccc} \frac{1}{\sqrt{3}} & 0 & 0 & \frac{2}{\sqrt{6}} & 0 & 0 & 0 & 0 & 0 \\ \frac{1}{\sqrt{3}} & 0 & 0 & \frac{-1}{\sqrt{6}} & 0 & 0 & \frac{1}{\sqrt{2}} & 0 & 0 \\ \frac{1}{\sqrt{3}} & 0 & 0 & \frac{-1}{\sqrt{6}} & 0 & 0 & \frac{-1}{\sqrt{2}} & 0 & 0 \\ 0 & \frac{1}{\sqrt{3}} & 0 & 0 & \frac{2}{\sqrt{6}} & 0 & 0 & 0 & 0 \\ 0 & \frac{1}{\sqrt{3}} & 0 & 0 & \frac{-1}{\sqrt{6}} & 0 & 0 & \frac{1}{\sqrt{2}} & 0 \\ 0 & \frac{1}{\sqrt{3}} & 0 & 0 & \frac{-1}{\sqrt{6}} & 0 & 0 & \frac{-1}{\sqrt{2}} & 0 \\ 0 & 0 & \frac{1}{\sqrt{3}} & 0 & 0 & \frac{2}{\sqrt{6}} & 0 & 0 & 0 \\ 0 & 0 & \frac{1}{\sqrt{3}} & 0 & 0 & \frac{-1}{\sqrt{6}} & 0 & 0 & \frac{1}{\sqrt{2}} \\ 0 & 0 & \frac{1}{\sqrt{3}} & 0 & 0 & \frac{-1}{\sqrt{6}} & 0 & 0 & \frac{-1}{\sqrt{2}} \end{array}\right] \\ \underbrace{\hphantom{\frac{1}{\sqrt{3}}\;0\;\;0}}_{\Lambda_1}\quad\underbrace{\hphantom{\frac{1}{\sqrt{3}}\;0\;\;0}}_{\Lambda_3}\quad\underbrace{\hphantom{\frac{1}{\sqrt{3}}\;0\;\;0}}_{\Lambda_3} \end{array} .$$

The block diagonalized form of **D** is found to be:

$$
\mathbf{D}=\begin{array}{c}
\left[\begin{array}{ccccccccc}
d_{11}+2d_{12} & d_{14}+2d_{15} & d^*_{14}+2d^*_{15} & 0 & 0 & 0 & 0 & 0 & 0\\
d^*_{14}+2d^*_{15} & d_{44}+2d_{45} & d_{47}+2d_{48} & 0 & 0 & 0 & 0 & 0 & 0\\
d_{14}+2d_{15} & d^*_{47}+2d^*_{48} & d_{44}+2d_{45} & 0 & 0 & 0 & 0 & 0 & 0\\
0 & 0 & 0 & d_{11}-d_{12} & d_{14}-d_{15} & d^*_{14}-d^*_{15} & 0 & 0 & 0\\
0 & 0 & 0 & d^*_{14}-d^*_{15} & d_{44}-d_{45} & d_{47}-d_{48} & 0 & 0 & 0\\
0 & 0 & 0 & d_{14}-d_{15} & d^*_{47}-d^*_{48} & d_{44}-d_{45} & 0 & 0 & 0\\
0 & 0 & 0 & 0 & 0 & 0 & d_{11}-d_{12} & d_{14}-d_{15} & d^*_{14}-d^*_{15}\\
0 & 0 & 0 & 0 & 0 & 0 & d^*_{14}-d^*_{15} & d_{44}-d_{45} & d_{47}-d_{48}\\
0 & 0 & 0 & 0 & 0 & 0 & d_{14}-d_{15} & d^*_{47}-d^*_{48} & d_{44}-d_{45}
\end{array}\right]\\
\begin{array}{ccc}
\underbrace{\hspace{12em}}_{\Lambda_1} & \underbrace{\hspace{12em}}_{\Lambda_3} & \underbrace{\hspace{12em}}_{\Lambda_3}
\end{array}
\end{array}
$$

4. Along the line Z: $\mathbf{q}=(2\pi/a)[1\zeta 0]$. The point group of the wave vector is C_{2l}. The decomposition of the S matrices gives $3Z_1+2Z_2+2Z_3+2Z_4$.

The unitary **U** matrix found from the projection operators is:

$$
\mathbf{U}=\begin{array}{c}
\left[\begin{array}{ccccccccc}
0 & 0 & 0 & 0 & 0 & 1 & 0 & 0 & 0\\
1 & 0 & 0 & 0 & 0 & 0 & 0 & 0 & 0\\
0 & 0 & 0 & 0 & 0 & 0 & 0 & 1 & 0\\
0 & \frac{1}{\sqrt{2}} & 0 & \frac{1}{\sqrt{2}} & 0 & 0 & 0 & 0 & 0\\
0 & 0 & 0 & 0 & 0 & 0 & \frac{1}{\sqrt{2}} & 0 & \frac{1}{\sqrt{2}}\\
0 & 0 & \frac{1}{\sqrt{2}} & 0 & \frac{1}{\sqrt{2}} & 0 & 0 & 0 & 0\\
0 & \frac{1}{\sqrt{2}} & 0 & \frac{-1}{\sqrt{2}} & 0 & 0 & 0 & 0 & 0\\
0 & 0 & 0 & 0 & 0 & 0 & \frac{1}{\sqrt{2}} & 0 & \frac{-1}{\sqrt{2}}\\
0 & 0 & \frac{-1}{\sqrt{2}} & 0 & \frac{1}{\sqrt{2}} & 0 & 0 & 0 & 0
\end{array}\right]\\
\begin{array}{cccc}
\underbrace{\hspace{7em}}_{Z_1} & \underbrace{\hspace{5em}}_{Z_2} & \underbrace{\hspace{4em}}_{Z_3} & \underbrace{\hspace{4em}}_{Z_4}
\end{array}
\end{array}.
$$

The operators $\mathbf{S}^{-1}\mathbf{D}\mathbf{S}$ give:

$$
\mathbf{D}=\begin{bmatrix}
d_{11} & 0 & 0 & 0 & d_{15} & 0 & 0 & d_{15} & 0\\
0 & d_{22} & 0 & d_{24} & 0 & d_{26} & d_{24} & 0 & -d_{26}\\
0 & 0 & d_{33} & 0 & d_{35} & 0 & 0 & -d_{35} & 0\\
0 & d_{24} & 0 & d_{44} & 0 & d_{46} & d_{47} & 0 & d_{49}\\
d_{15} & 0 & -d_{35} & 0 & d_{55} & 0 & 0 & d_{58} & 0\\
0 & -d_{26} & 0 & -d_{46} & 0 & d_{66} & d_{49} & 0 & d_{69}\\
0 & d_{24} & 0 & d_{47} & 0 & -d_{49} & d_{44} & 0 & -d_{46}\\
d_{15} & 0 & d_{35} & 0 & d_{58} & 0 & 0 & d_{55} & 0\\
0 & d_{26} & 0 & -d_{49} & 0 & d_{69} & d_{46} & 0 & d_{66}
\end{bmatrix}.
$$

The block diagonalized dynamical matrix is:

$$\mathbf{D} = \left[\underbrace{\begin{matrix} d_{22} & \sqrt{2}d_{24} & \sqrt{2}d_{26} \\ \sqrt{2}d_{24} & d_{44}+d_{47} & (d_{46}-d_{19}) \\ -\sqrt{2}d_{26} & -(d_{46}-d_{49}) & d_{66}-d_{69} \\ 0 & 0 & 0 \\ 0 & 0 & 0 \\ 0 & 0 & 0 \\ 0 & 0 & 0 \\ 0 & 0 & 0 \\ 0 & 0 & 0 \end{matrix}}_{Z_1} \quad \underbrace{\begin{matrix} 0 & 0 \\ 0 & 0 \\ 0 & 0 \\ d_{44}-d_{47} & (d_{46}+d_{49}) \\ -(d_{46}+d_{49}) & d_{66}+d_{69} \\ 0 & 0 \\ 0 & 0 \\ 0 & 0 \\ 0 & 0 \end{matrix}}_{Z_2} \quad \underbrace{\begin{matrix} 0 & 0 \\ 0 & 0 \\ 0 & 0 \\ 0 & 0 \\ 0 & 0 \\ d_{11} & \sqrt{2}d_{15} \\ \sqrt{2}d_{15} & d_{55}+d_{58} \\ 0 & 0 \\ 0 & 0 \end{matrix}}_{Z_3} \quad \underbrace{\begin{matrix} 0 & 0 \\ 0 & 0 \\ 0 & 0 \\ 0 & 0 \\ 0 & 0 \\ 0 & 0 \\ 0 & 0 \\ d_{33} & \sqrt{2}d_{35} \\ -\sqrt{2}d_{35} & d_{55}-d_{58} \end{matrix}}_{Z_4} \right]$$

5. At the point W: $\mathbf{q} = (2\pi/a)[1\tfrac{1}{2}0]$. The point group of the wave vector is D_{2d}. The symmetry reduced dynamical matrix is:

$$\mathbf{D} = \begin{bmatrix} d_{11} & 0 & 0 & 0 & d_{15} & 0 & 0 & d_{15} & 0 \\ 0 & d_{22} & 0 & d_{24} & 0 & -id_{24} & d_{24} & 0 & id_{24} \\ 0 & 0 & d_{11} & 0 & -id_{15} & 0 & 0 & id_{15} & 0 \\ 0 & d_{24} & 0 & d_{44} & 0 & d_{46} & d_{47} & 0 & d_{49} \\ d_{15} & 0 & id_{15} & 0 & d_{55} & 0 & 0 & 0 & 0 \\ 0 & id_{24} & 0 & -d_{46} & 0 & d_{44} & d_{49} & 0 & -d_{47} \\ 0 & d_{24} & 0 & d_{17} & 0 & -d_{49} & d_{44} & 0 & -d_{46} \\ d_{15} & 0 & -id_{15} & 0 & 0 & 0 & 0 & d_{55} & 0 \\ 0 & -id_{24} & 0 & -d_{49} & 0 & -d_{47} & d_{46} & 0 & d_{44} \end{bmatrix}.$$

The unitary transformation matrix is:

$$\mathbf{U} = \begin{bmatrix} 0 & 0 & 0 & 0 & 0 & 1 & 0 & 0 & 0 \\ 0 & 0 & 0 & 0 & 1 & 0 & 0 & 0 & 0 \\ 0 & 0 & 0 & 0 & 0 & 0 & 0 & 1 & 0 \\ \frac{1}{2} & \frac{1}{2} & \frac{-1}{2} & \frac{1}{2} & 0 & 0 & 0 & 0 & 0 \\ 0 & 0 & 0 & 0 & 0 & 0 & \frac{1}{\sqrt{2}} & 0 & \frac{1}{\sqrt{2}} \\ \frac{-i}{2} & \frac{i}{2} & \frac{i}{2} & \frac{i}{2} & 0 & 0 & 0 & 0 & 0 \\ \frac{1}{2} & \frac{-1}{2} & \frac{1}{2} & \frac{1}{2} & 0 & 0 & 0 & 0 & 0 \\ 0 & 0 & 0 & 0 & 0 & 0 & \frac{1}{\sqrt{2}} & 0 & \frac{-1}{\sqrt{2}} \\ \frac{i}{2} & \frac{i}{2} & \frac{i}{2} & \frac{-i}{2} & 0 & 0 & 0 & 0 & 0 \\ \underbrace{\quad}_{W_1} & \underbrace{\quad}_{W_{1'}} & \underbrace{\quad}_{W_2} & \underbrace{\quad}_{W_{2'}} & & \multicolumn{2}{c}{\underbrace{\qquad\qquad}_{W_3}} & \multicolumn{2}{c}{\underbrace{\qquad\qquad}_{W_3}} \end{bmatrix}.$$

The operation $\mathbf{U}^{-1}\mathbf{DU}$ gives the following block diagonal form for the dynamical matrix:

$$\begin{bmatrix} \begin{matrix} d_{44}+d_{47} \\ -i(d_{46}-d_{49}) \end{matrix} & 0 & 0 & 0 & 0 & 0 & 0 & 0 & 0 \\ 0 & \begin{matrix} d_{44}-d_{47} \\ +i(d_{46}+d_{49}) \end{matrix} & 0 & 0 & 0 & 0 & 0 & 0 & 0 \\ 0 & 0 & \begin{matrix} d_{44}-d_{47} \\ -i(d_{46}+d_{49}) \end{matrix} & 0 & 0 & 0 & 0 & 0 & 0 \\ 0 & 0 & 0 & \begin{matrix} d_{44}+d_{47} \\ +i(d_{46}-d_{49}) \end{matrix} & 2d_{24} & 0 & 0 & 0 & 0 \\ 0 & 0 & 0 & 2d_{24} & d_{22} & 0 & 0 & 0 & 0 \\ 0 & 0 & 0 & 0 & 0 & d_{11} & \sqrt{2}d_{15} & 0 & 0 \\ 0 & 0 & 0 & 0 & 0 & \sqrt{2}d_{15} & d_{55} & 0 & 0 \\ 0 & 0 & 0 & 0 & 0 & 0 & 0 & d_{11} & -i\sqrt{2}d_{15} \\ 0 & 0 & 0 & 0 & 0 & 0 & 0 & i\sqrt{2}d_{15} & d_{55} \\ \underbrace{\qquad}_{W_1} & \underbrace{\qquad}_{W_{1'}} & \underbrace{\qquad}_{W_2} & \multicolumn{2}{c}{\underbrace{\qquad\qquad\qquad}_{W_{2'}}} & \multicolumn{2}{c}{\underbrace{\qquad\qquad}_{W_3}} & \multicolumn{2}{c}{\underbrace{\qquad\qquad}_{W_3}} \end{bmatrix}$$

6. The point L; $\mathbf{q} = (2\pi/a)[\frac{1}{2}\frac{1}{2}\frac{1}{2}]$. The point group of the wave vector is D_{3d}. The decomposition is $L_1 + L_3 + 2L_{2'} + 2L_{3'}$. The symmetry reduced dynamical matrix is:

$$\mathbf{D} = \begin{bmatrix} d_{11} & d_{12} & d_{12} & d_{14} & d_{15} & d_{15} & id_{14} & id_{15} & id_{15} \\ d_{12} & d_{11} & d_{12} & d_{15} & d_{14} & d_{15} & id_{15} & id_{14} & id_{15} \\ d_{12} & d_{12} & d_{11} & d_{15} & d_{15} & d_{14} & id_{15} & id_{15} & id_{14} \\ id_{14} & id_{15} & id_{15} & d_{44} & d_{45} & d_{45} & d_{47} & d_{48} & d_{48} \\ id_{15} & id_{14} & id_{15} & d_{45} & d_{44} & d_{45} & d_{48} & d_{47} & d_{48} \\ id_{15} & id_{15} & id_{14} & d_{45} & d_{45} & d_{44} & d_{48} & d_{48} & d_{47} \\ d_{14} & d_{15} & d_{15} & -d_{47} & -d_{48} & -d_{48} & d_{44} & d_{45} & d_{45} \\ d_{15} & d_{14} & d_{15} & -d_{48} & -d_{47} & -d_{48} & d_{45} & d_{44} & d_{45} \\ d_{15} & d_{15} & d_{14} & -d_{48} & -d_{48} & -d_{47} & d_{45} & d_{45} & d_{44} \end{bmatrix}.$$

The normalized eigenvectors form the unitary transformation matrix:

$$\mathbf{U} = \begin{array}{c} \begin{array}{ccccccccc} \underbrace{L_1} & \underbrace{L_3} & \underbrace{L_3} & \multicolumn{2}{c}{\underbrace{\qquad L_{2'} \qquad}} & \multicolumn{2}{c}{\underbrace{\qquad L_{3'} \qquad}} & \multicolumn{2}{c}{\underbrace{\qquad L_{3'} \qquad}} \end{array} \\ \begin{bmatrix} 0 & 0 & 0 & \frac{1}{\sqrt{3}} & 0 & \frac{2}{\sqrt{6}} & 0 & 0 & 0 \\ 0 & 0 & 0 & \frac{1}{\sqrt{3}} & 0 & \frac{-1}{\sqrt{6}} & 0 & \frac{1}{\sqrt{2}} & 0 \\ 0 & 0 & 0 & \frac{1}{\sqrt{3}} & 0 & \frac{-1}{\sqrt{6}} & 0 & \frac{-1}{\sqrt{2}} & 0 \\ \frac{1}{\sqrt{6}} & \frac{2}{\sqrt{12}} & 0 & 0 & \frac{1}{\sqrt{6}} & 0 & \frac{2}{\sqrt{12}} & 0 & 0 \\ \frac{1}{\sqrt{6}} & \frac{-1}{\sqrt{12}} & \frac{1}{2} & 0 & \frac{1}{\sqrt{6}} & 0 & \frac{-1}{\sqrt{12}} & 0 & \frac{1}{2} \\ \frac{1}{\sqrt{6}} & \frac{-1}{\sqrt{12}} & \frac{-1}{2} & 0 & \frac{1}{\sqrt{6}} & 0 & \frac{-1}{\sqrt{12}} & 0 & \frac{-1}{2} \\ \frac{-i}{\sqrt{6}} & \frac{-2i}{\sqrt{12}} & 0 & 0 & \frac{i}{\sqrt{6}} & 0 & \frac{2i}{\sqrt{12}} & 0 & 0 \\ \frac{-i}{\sqrt{6}} & \frac{i}{\sqrt{12}} & \frac{-i}{2} & 0 & \frac{i}{\sqrt{6}} & 0 & \frac{-i}{\sqrt{12}} & 0 & \frac{i}{2} \\ \frac{-i}{\sqrt{6}} & \frac{i}{\sqrt{12}} & \frac{i}{2} & 0 & \frac{i}{\sqrt{6}} & 0 & \frac{-i}{\sqrt{12}} & 0 & \frac{-i}{2} \end{bmatrix} \end{array}.$$

The block diagonalized dynamical matrix is:

$$\mathbf{D} = \begin{array}{ccccccccc} \overbrace{\qquad\qquad}^{L_1} & \overbrace{\qquad\qquad}^{L_3} & \overbrace{\qquad\qquad}^{L_3} & \multicolumn{2}{c}{\overbrace{\qquad\qquad\qquad\qquad}^{L_{2'}}} & \multicolumn{2}{c}{\overbrace{\qquad\qquad\qquad\qquad}^{L_{3'}}} & \multicolumn{2}{c}{\overbrace{\qquad\qquad\qquad\qquad}^{L_{3'}}} \\ \multicolumn{9}{c}{\left[\begin{array}{ccccccccc} \begin{matrix} d_{44}+2d_{45} \\ -i(d_{47}+2d_{48}) \end{matrix} & 0 & 0 & 0 & 0 & 0 & 0 & 0 & 0 \\ 0 & \begin{matrix} d_{44}-d_{45} \\ -i(d_{47}-d_{48}) \end{matrix} & 0 & 0 & 0 & 0 & 0 & 0 & 0 \\ 0 & 0 & \begin{matrix} d_{44}-d_{45} \\ -i(d_{47}-d_{48}) \end{matrix} & 0 & 0 & 0 & 0 & 0 & 0 \\ 0 & 0 & 0 & d_{11}+2d_{12} & \sqrt{2}(d_{14}+2d_{15}) & 0 & 0 & 0 & 0 \\ 0 & 0 & 0 & i\sqrt{2}(d_{14}+2d_{15}) & \begin{matrix} d_{44}+2d_{45} \\ +i(d_{47}-d_{48}) \end{matrix} & 0 & 0 & 0 & 0 \\ 0 & 0 & 0 & 0 & 0 & d_{11}-d_{12} & \sqrt{2}(d_{14}-d_{15}) & 0 & 0 \\ 0 & 0 & 0 & 0 & 0 & i\sqrt{2}(d_{14}-d_{15}) & \begin{matrix} d_{44}-d_{45} \\ +i(d_{47}-d_{48}) \end{matrix} & 0 & 0 \\ 0 & 0 & 0 & 0 & 0 & 0 & 0 & d_{11}-d_{12} & \sqrt{2}(d_{14}-d_{15}) \\ 0 & 0 & 0 & 0 & 0 & 0 & 0 & i\sqrt{2}(d_{14}-d_{15}) & \begin{matrix} d_{44}-d_{45} \\ +i(d_{47}-d_{48}) \end{matrix} \end{array}\right]} \end{array}$$

7. Further results of interest. At the symmetry point Γ ($\mathbf{q} = [\mathbf{000}]$) the decomposition is $2\Gamma_{15}+\Gamma_{25'}$. Each Γ representation is three fold degenerate. One of the Γ_{15}'s corresponds to the acoustic modes. The degeneracy of the other Γ_{15} is removed by the macroscopic **E** field which arises in non-polar crystals. Warren [9] gives a brief discussion along with pertinent references on this matter. See also the recent reference by Lucas[10].

At the point X ($\mathbf{q} = (2\pi/a)[\mathbf{001}]$) on the Brillouin zone boundary the decomposition is $X_1+X_{2'}+X_{4'}+X_5+2X_{5'}$. Along the line S ($\mathbf{q} = (2\pi/a)[\mathbf{1}\zeta\zeta]$) the decomposition is $3S_1+S_2+3S_3+S_4$. Along the line Q ($\mathbf{q} = (2\pi/a)$-$[\mathbf{1}-\zeta, \frac{1}{2}, \zeta]$) the decomposition is $4Q_1+5Q_2$. The point U ($\mathbf{q} = (2\pi/a)[\mathbf{1}\frac{1}{4}\frac{1}{4}]$) has the same symmetry as the line S and the point K ($\mathbf{q} = (2\pi/a)[\frac{3}{4}\frac{3}{4}\mathbf{0}]$) has the same symmetry as the line Σ. We list the pertinent compatability relations at Γ, X, L and W:

$$
\begin{aligned}
&\Gamma_{15} \rightarrow \Delta_1+\Delta_5, \Sigma_1+\Sigma_3+\Sigma_4, \Lambda_1+\Lambda_3\\
&\Gamma_{25'} \rightarrow \Delta_{2'}+\Delta_5, \Sigma_1+\Sigma_2+\Sigma_3, \Lambda_1+\Lambda_3\\
&X_1 \rightarrow \Delta_1, \Sigma_1, Z_1.\\
&X_{2'} \rightarrow \Delta_{2'}, \Sigma_3, Z_2\\
&X_{4'} \rightarrow \Delta_1, \Sigma_3, Z_3\\
&X_5 \rightarrow \Delta_5, \Sigma_2+\Sigma_4, Z_2+Z_3\\
&X_{5'} \rightarrow \Delta_5, \Sigma_1+\Sigma_4, Z_1+Z_4.\\
&\Lambda_3 \rightarrow L_3, L_{3'}\\
&\Lambda_1 \rightarrow L_1, L_{2'}\\
&W_1 \rightarrow Z_1, \quad W_{1'} \rightarrow Z_2, \quad W_2 \rightarrow Z_2, \quad W_{2'} \rightarrow Z_1,\\
&W_3 \rightarrow Z_3+Z_4.
\end{aligned}
$$

At the point X, S has the same compatability as along Σ.

The compatability relations and phonon mode symmetry classifications are in agreement with those given by Dolling *et al.*[11] and by Elliott and Thorpe[12]. Note that Dolling *et al.* use Koster[13] notation while Elliott and Thorpe use BSW as we have.

3. SUMMARY AND CONCLUSIONS

The lattice vibrational frequencies along the major symmetry directions of Mg_2Sn have been analyzed by group theoretical methods. The symmetry coordinates have been obtained for the major symmetry points and the dynamical matrix is displayed in block diagonal form. In some cases the symmetry coordinates uniquely determine the phonon polarization. These results are used in the previous paper both in the experimental data taking procedure and in the force constant model fitting. The phonon mode symmetry classifications should also be useful in interpretation of experimental transport phenomena data[14].

Acknowledgements – The authors would like to thank Dr. J. L. Warren of the Los Alamos Scientific Laboratory for reviewing the manuscript and Dr. R. M. Brugger for his continued support.

REFERENCES

1. KEARNEY R. J., WORLTON T. G. and SCHMUNK R. E., *J. Phys. Chem. Solids* **31**, 913 (1970).
2. CHEN S. H., *Phys. Rev.* **163**, 532 (1967)
3. MARADUDIN A. A. and VOSCO S. H., *Rev. mod. Phys.* **40**, 1 (1968).
4. TINKHAM M., *Group Theory and Quantum Mechanics* McGraw-Hill, New York (1964).
5. PEARSON W. B., *Lattice Spacings and Structures of Metals and Alloys*. Pergamon Press, Oxford (1958).
6. BOUCKAERT L. P., SMOLUCHOWSKI R. and WIGNER E., *Phys. Rev.* **50**, 58 (1936)
7. SLATER J. C., *Quantum Theory of Molecules and Solids*, V-2 McGraw-Hill, New York (1965)
8. KOVALEV O. V., *Irreducible Representations of the Space Groups* Gordon and Breach, New York (1965).
9. WARREN J. L., *Rev. mod. Phys.* **40**, 38 (1968).
10. LUCAS A. A., *Phys. Rev.* **162**, 801 (1967)
11. DOLLING G., COWLEY R. A. and WOODS A. D. B., *Can. J. Phys.* **43**, 1397 (1965)
12. ELLIOTT R. J. and THORPE M. F., *Proc. phys. Soc.* **91**, 903 (1967).
13. KOSTER G. F., Space Groups and Their Representations, In *Solid State Physics* (Edited by F. Seitz and D. Turnbull), Vol. 5 Academic Press, New York (1957)
14. FOLLAND N. O. and BASSANI F., *J. Phys. Chem. Solids* **29**, 281 (1968).

J. Phys. Chem. Solids Pergamon Press 1970. Vol. 31, pp. 927–938. Printed in Great Britain.

GALVANOMAGNETIC EFFECTS OF HOT ELECTRONS IN *n*-TYPE SILICON*†

H. HEINRICH

Institut für Angewandte Physik der Universität, A-1090 Vienna, and Ludwig-Boltzmann
Institut für Festkörperphysik, Vienna, Austria

and

M. KRIECHBAUM

Institut für Theoretische Physik der Universität, A-8010 Graz, Austria

(*Received* 13 *August* 1969; *in revised form* 13 *October* 1969)

Abstract – Measurements were performed of the transverse magneto-resistance of *n*-Si in different crystallographic directions at 77°K and at field strengths up to 5 kV/cm. For $j \parallel \langle 111 \rangle$ a normal behaviour was found whereas for $j \parallel \langle 100 \rangle$ a negative magnetoresistance and for $j \parallel \langle 110 \rangle$ a strong positive magnetoresistance was observed. Calculations have been performed based on a Maxwellian distribution and taking into account a repopulation of carriers between different valleys depending on the electric and magnetic fields. From the energy balance the electron temperatures were determined. Numerical calculations were done with different coupling strengths for different electron–phonon scattering mechanisms. Results are given for population number, mobility, Hall mobility, and magnetoconductivity for different sample orientations. Good agreement is obtained with experimental data.

1. INTRODUCTION

As is well known the conduction band of silicon consists of 6 equivalent minima oriented along the $\langle 100 \rangle$ axes in k-space. With a strong electric field applied parallel to the [100] direction, the valleys are separated into 2 cold and 4 hot ones. This difference in mean electron energy results in a transfer of electrons from the hot to the cold valleys. The application of a transverse magnetic field decreases the mobility in each valley and therefore causes a cooling of the electrons[1]. On the other hand the resulting Hall field causes a deviation of the electric field from the [100] direction so that the electrons of the valleys on the [100] axis will take up more energy from the field. One therefore can expect an equalization of the temperatures of both types of valleys and as a consequence an equalization of the particle numbers in the different types of minima. In this way a drastic change in magnetoresistance behaviour may be expected from this effect. When the current is parallel to the [110] direction and **B** is oriented along [001] three different types of valleys are present, while with **B** parallel to $[1\bar{1}0]$ only two types of energetically different valleys exist. Again one can expect that the magnetic field influences the electron numbers in the different valleys. Therefore it may be concluded that valuable information about the different scattering mechanisms present in *n*-type Si is obtainable from a study of hot electron magneto-resistance.

In this paper we report measurements of the transverse magnetoresistance of *n*-type Si at 77°K in electric fields up to 5 kV/cm and in magnetic fields between 1 and 6·5 kG. Within the range of 0·15–2 kV/cm a negative magnetoresistance is observed for samples oriented along the $\langle 100 \rangle$ crystallographic axis.

---

*Partly presented at the spring meeting of the DPG, Deutsche Physikalische Gesellschaft, in Munich, March 1969.

†Work supported by "Fonds zur Förderung der wissenschaftlichen Forschung".

In contrast, ⟨111⟩ samples always show a positive magnetoresistance within the investigated range of fields. For current parallel to [110] direction the magnetoresistance goes through a maximum when the electric field is increased and **B** is aligned parallel to [001]. A minimum is observed when **B** is parallel to [110].

Several authors treated the problem of hot electron magnetoresistance in semiconductors from a theoretical point of view[2–13]. In some of these papers ellipsoidal energy surfaces and different scattering mechanisms were taken into account. But in none of these papers the influence of the magnetic field on the repopulation of carriers is considered. Review articles on galvanomagnetic phenomena were written by Beer[14] and Bross[15]. Since it was expected that the magnetoresistance in *n*-type Si is a consequence of the particular band structure and a result of the different scattering mechanisms present in this material, one can hope to obtain a fair agreement between experiment and theory only when these facts are taken into account. In order to prove whether or not the above outlined model is applicable for the interpretation of the experimental results, we extend the transport theory of Herring and Vogt[16] to the case of hot electrons. We assume a Maxwellian distribution and take into account scattering by acoustic and intervalley phonons as well as impurity scattering. The magnetic field dependence of the conductivity tensor is solved exactly and the electron temperature in each valley is determined by the energy-balance equation.

The main features of the experimental results are explained by this model and quantitative agreement is obtained in most cases. The negative magnetoresistance is found to have the correct magnitude and to be in the observed range of electric field strengths. Discrepances at intermediate electric field strengths may be due to the fact that a Maxwellian distribution was used in the calculation. Calculated results are also given for the ratio of carrier populations in cold and hot valleys for different magnetic fields as well as electron temperatures as a function of the electric field intensity.

2. EXPERIMENTAL

Samples have been prepared from *n*-type Si with 5 Ω-cm room temperature resistivity. They were quadrangular in shape, having dimensions of about $10 \times 1 \times 1$ mm^3 with their long axis being parallel either to the ⟨100⟩, ⟨111⟩ or ⟨110⟩ crystallographic direction. Contacts were made by P-diffusion and Ni-plating of the end faces.

The schematic arrangement of the measuring equipment is shown in Fig. 1. A pulsed d.c. electric field of 8 nsec duration has been applied to the sample with a repetition rate of 50 Hz by discharging a coaxial line through a mercury wetted relay. The voltage drop across the sample and across a small current measuring resistance has been observed on a sampling oscilloscope and an *X-Y* recorder connected to it. The sample, mounted in the magnetic field, was held at liquid nitrogen temperature. A minimum change of the sample current due to the application of the magnetic field of about 10^{-3} could be observed by making use of the d.c.-offset of the sampling oscilloscope.

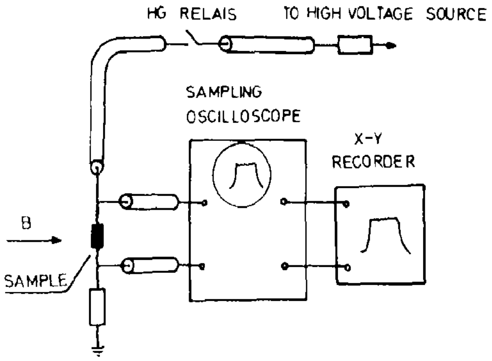

Fig. 1. Schematic arrangement of the measuring equipment.

3. EXPERIMENTAL RESULTS IN THE LIMIT OF ZERO MAGNETIC FIELD B

The value of the magnetoresistance has been measured at 77°K for samples being parallel either to the ⟨100⟩ or ⟨111⟩ or ⟨110⟩ crystallographic direction, up to 5 kV/cm for magnetic fields between 1 and 6·5 kG. When the magnetoresistance $\Delta R/RB^2$ for a fixed value of the electric field strength is plotted as a function of B, the experimental points are found to lie on a straight line, at least for small values of B. This is plotted in Fig. 2 for *a* ⟨100⟩ oriented sample, and three different electric field strengths. By extrapolating B toward zero we obtained a value of $(\Delta R/RB^2)_{B=0}$. This figure shows that the value of $\Delta R/RB^2$ decreases with increasing magnetic field strength in the near-ohmic range of 10 V/cm. For higher values of the electric field strength the magnetoresistance is negative and its behaviour is changed so that at 530 V/cm the absolute value of $\Delta R/RB^2$ increases with B.

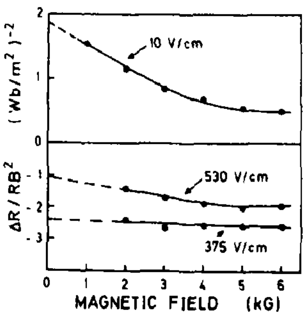

Fig. 2. Magnetoresistance vs. magnetic field strength for $\mathbf{j}\|[100]$ and $\mathbf{B}\|[011]$ for three characteristic electric field strengths. The dots indicate measured values. The scale is different for positive and negative values of the magnetoresistance.

Figure 3 shows the results of measurements for the magnetoresistance as a function of electric field strength for typical samples oriented along ⟨100⟩ and ⟨111⟩ crystallographic directions, respectively. For the ⟨111⟩ sample the magnetoresistance is positive within the investigated range of electric field strength. In contrast, the ⟨100⟩ sample exhibits a region of strong negative magnetoresistance. For the highest measured field strengths the magnetoresistance becomes positive again[17]. In Fig. 3 we have also plotted the ratio of electron concentrations in cold and hot valleys as obtained by Kästner *et al.*[18]. The region of negative magnetoresistance coincides roughly with the region in which electron transfer occurs. This indicates that repopulation of electrons plays a major role in interpreting this effect.

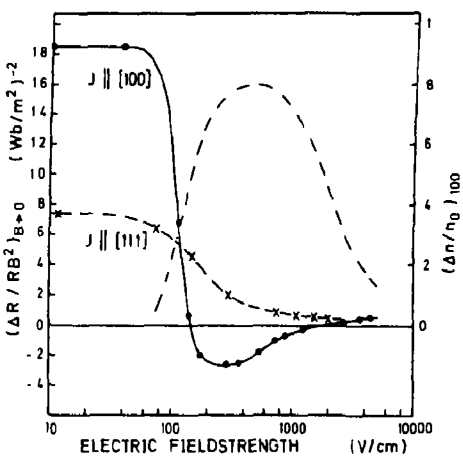

Fig. 3. Extrapolated transverse magnetoresistance (experimental) vs electric field strength for two different orientations of j. The dots and the crosses indicate measured values. *The dash-dotted curve is an average of* experimentally determined values of the population of the valleys on the [100] axis in k-space taken from Kästner *et al.*[18].

When the current is parallel to either [100] or [111] direction a simple calculation shows that a rotation of **B** in the transverse plane does not influence the magnetoresistance in the ohmic case. Within the experimental error this turned out to hold also under hot electron conditions. However, when the current is parallel to the [110] direction, the ohmic as well as the high field magnetoresistance depends strongly on the particular direction of **B** in the transverse plane. Results for this orientation are given in Fig. 4. For **B** parallel to [001] direction the magnetoresistance is stronger and exhibits a maximum as a function of applied electric field strength,

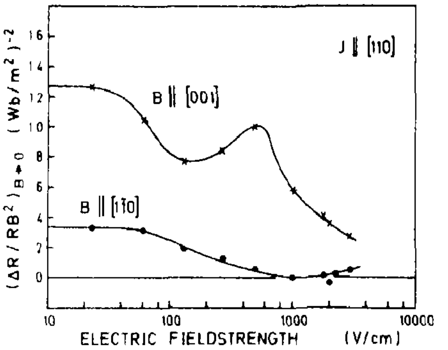

Fig 4 Extrapolated transverse magnetoresistance (experimental) vs. electric field strength for j‖[110] and two different orientations of **B**

while for the case of **B** parallel to [1$\bar{1}$0] a minimum is observed.

In Fig. 5 results of measurements of $\sigma(E)/\sigma_0$ are given which can be assumed to be equal to μ/μ_0. Also plotted are the ratios of $(\Delta R/RB^2)/(\Delta R/RB^2)_{E=0}$ for a sample oriented in ⟨111⟩ direction. It can be seen that the experimental points exhibit practically the same dependence on electric field strength as the ratio $(\mu/\mu_0)^2$. This indicates that the decrease of magnetoresistance with electric field strength is mainly due to the decrease in mobility for samples in ⟨111⟩ crystallographic direction where no carrier transfer is present.

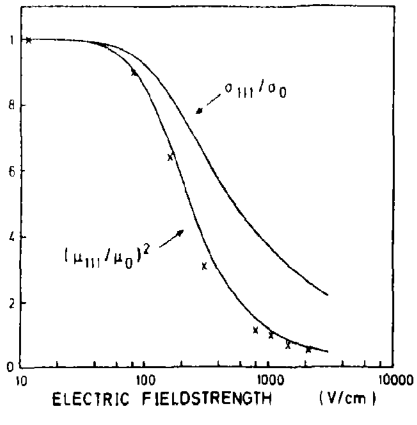

Fig. 5 Experimentally obtained values of the ratio of the conductivity to the ohmic conductivity for j‖[111]. The crosses indicate extrapolated experimental values of the transverse magnetoresistance normalized to unity for j‖[111]. Note the same behaviour with the square of the relative mobility (the mobility ratio was assumed to be equal to the conductivity ratio).

4. ANALYTICAL CONSIDERATIONS

When analyzing the dependence of the electric current on an externally applied electric field **E** and a magnetic field **B**, one has to solve a Boltzmann equation. Since it is impossible to solve this equation exactly with all scattering mechanisms included one has to make assumptions about the carrier distribution function depending on the number of carriers present. The samples used in the experiments had a donor concentration of about $1\times 10^{15}\,\mathrm{cm}^{-3}$. For this carrier concentration and 77°K lattice temperature the electron-electron scattering is sufficiently frequent compared to lattice scattering to maintain a Maxwellian distribution as a stationary state. This can be seen by making use of a criterion of Fröhlich and Paranjape [19] for the carrier concentration,

$$n = \frac{1}{4\pi}\frac{\epsilon^{3/2}m^{3/2}s^2\kappa^2}{k_0 T e^3\tau} \tag{1}$$

where ϵ is the mean electron energy, m is the effective electron mass, s the sound velocity, κ the dielectric constant, k_0 Boltzmann's constant, T lattice temperature, e electronic charge, and τ the relaxation time of electrons due to phonon scattering. Equation (1) is fulfilled up to about 800°K electron temperature. A more exact criterion by Dykman and Tomchuk [20] yields about the same results.

In the following it is therefore assumed that the symmetric part of the distribution function for electrons in each valley i is Maxwellian with a temperature $T_e^{(i)}$. Then for each valley the transport theory derived by Herring and Vogt [16] for ohmic case and many-valley semiconductors with ellipsoidal energy surfaces is applicable. In this theory the Boltzmann equation is solved to first order in **E** and exact in **B** by neglecting the influence of electron–electron scattering on the mobility. According to this theory the contribution to the total current $\mathrm{d}\mathbf{j}^{(i)}$, of electrons of the ith valley within an energy shell $\mathrm{d}\epsilon$ around ϵ is given by

$$\frac{\mathrm{d}j_{\alpha}^{(i)}}{\tau_{\alpha}} = \frac{2x\mathrm{e}^2E_{\alpha}^{(i)}\mathrm{d}n^{(i)}}{3m_{\alpha}} - \frac{\mathrm{e}\Sigma_{\beta\gamma}\epsilon_{\alpha\beta\gamma}B_{\gamma}^{(i)}\mathrm{d}j_{\beta}^{(i)}}{m_{\alpha}} \tag{2}$$

where

$$x = \frac{\epsilon}{k_0T_e^{(i)}} \tag{3}$$

with m_α the elements of the mass tensor, τ_α the elements of the relaxation time tensor. The subscript α runs from 1 to 3. $\epsilon_{\alpha\beta\gamma}$ is the third rank antisymmetric tensor, $\mathrm{d}n^{(i)}$ is the number of electrons in the energy shell $\mathrm{d}\epsilon$. Equation (2) defines a system of linear equations from which one can derive $\mathrm{d}\mathbf{j}^{(i)}$. By integrating over the energy one gets the current $\mathbf{j}^{(i)}$ from the ith valley proportional to $\mathbf{E}$ and one can define a mobility tensor $\boldsymbol{\mu}^{(i)}(\mathbf{B}, T_e^{(i)})$. The solution of the linear equations and the integration has to be done numerically. The electron temperature in each valley is derived by the method of energy balance,

$$\mathrm{e}\mathbf{E}\boldsymbol{\mu}^{(i)}(\mathbf{B},T_e^{(i)})\mathbf{E} = \left\langle\frac{\mathrm{d}\epsilon}{\mathrm{d}t}\right\rangle\Big|_{\text{lattice}} \tag{4}$$

where the brackets mean a Maxwellian average. The left hand side of equation (4) is the energy gain of an electron from the electric field and the right hand side is the energy loss due to scattering by lattice vibrations. The total conductivity tensor is then

$$\boldsymbol{\sigma}(\mathbf{B},T_e^{(1)},\ldots.\,T_e^{(g)}) = \mathrm{e}\sum_{i=1}^{g} n^{(i)}\mu^{(i)}(\mathbf{B},T_e^{(i)}) \tag{5}$$

where $g = 6$ is the number of equivalent valleys.

The relaxation times in n-Si with 77°K lattice temperature are mainly determined by acoustic, intervalley and ionized impurity scattering. The acoustic relaxation times are given by HV with the assumption of phonon equipartition and deformation potential scattering as (the numbers are slightly changed compared to HV, because we used different masses which were taken from Rauch *et al.*[21]):

$$\frac{1}{\tau_{\perp}} = A\left(1\cdot33\left(\frac{\Xi_d}{\Xi_u}\right)^2 + 1\cdot10\frac{\Xi_d}{\Xi_u} + 1\cdot19\right) \tag{6a}$$

$$\frac{1}{\tau_{\parallel}} = A\left(1\cdot38\left(\frac{\Xi_d}{\Xi_u}\right)^2 + 2\cdot30\frac{\Xi_d}{\Xi_u} + 1\cdot74\right) \tag{6b}$$

and

$$A = \frac{3m_tm_l^{1/2}k_0T\epsilon^{1/2}}{2^{3/2}\pi^4c_l\pi}\,\Xi_u^{\,2}.$$

c_l is an average elastic constant for longitudinal phonons. Ξ_d and Ξ_u are the deformation potential constants for dilatation and uniaxial shear. Equations (6) are derived taking into account the elastic anisotropy of the crystal.

The intervalley scattering was considered by Long[22] and Asche *et al.*[23–25]. These authors take into account separately the different phonon groups which take part in g-scattering (intervalley scattering between valleys with equal band edge direction in k-space) and f-scattering (different band edge direction). The intervalley relaxation time reads[22, 26].

$$\frac{1}{\tau_{iv}^{(s)}} = \frac{w_sT_{cs}}{T_0^{3/2}}\left[\left(\frac{\epsilon}{k_0}+T_{cs}\right)^{1/2}N_s + \left(\frac{\epsilon}{k_0}-T_{cs}\right)^{1/2}(N_s+1)\right] \tag{7}$$

where s runs over different possible intervalley transitions. N_s is the number of intervalley phonons present, T_{cs} their characteristic temperature, and $w_s/T_0^{3/2}$ is the coupling constant.

For ionized impurity scattering the relaxation times in a cubic crystal with ellipsoidal energy surfaces are given by [27]

$$[C\ln(4D^{-1})]\tau_{\parallel} = 5{\cdot}90 \qquad (8a)$$

and

$$[C\ln(4D^{-1})]\tau_{\perp} = 1{\cdot}57 \qquad (8b)$$

with

$$C = \frac{4ne^4 m_l^{1/2}}{\kappa^2 (2\epsilon)^{3/2} m_t}$$

and

$$D = \frac{\hbar^2}{2\epsilon m_t R^2}.$$

This derivation is based on the Born approximation for scattering by a screened Coulomb potential. The screening radius is calculated by an extension of the method of Dingle[28] to valleys with different temperatures and different occupation numbers. One gets for the screening radius

$$R = \frac{(\kappa k_0)^{1/2}}{e}\left(\sum_{i=1}^{9} \frac{n^{(i)}}{T_e^{(i)}}\right)^{-1/2}. \qquad (9)$$

The mean energy loss per electron to the lattice for acoustic phonon scattering is given by Conwell[29]

$$\left\langle\frac{d\epsilon}{dt}\right\rangle\Bigg|_{ac}^{(i)} = \frac{32\, m_t^2 m_l^{1/2} (k_0 T_e^{(i)})^{3/2}}{(2\pi)^{3/2} \rho \hbar^4}\left(1 - \frac{T}{T_e^{(i)}}\right)\Xi_0^2 \qquad (10)$$

with

$$\Xi_0^2 = \Xi_d^2\left\{\frac{2}{3} + \frac{1}{3}\frac{m_l}{m_t}\left(1 + \frac{\Xi_u}{\Xi_d}\right)^2\right\} \qquad (11)$$

and ρ being the density of the crystal. For intervalley phonon scattering the energy loss is [29]

$$\left\langle\frac{d\epsilon}{dt}\right\rangle\Bigg|_{iv}^{(i,s)} = \left(\frac{2}{\pi}\right)^{1/2} \frac{D_s^2 m_t m_l^{1/2}}{\pi\hbar^2 \rho} \times (k_0 T_e^{(i)})^{1/2} U(x_0^{(s)}, x_e^{(i,s)}) \qquad (12)$$

with

$$U(x_0, x_e) = \frac{\exp(x_0 - x_e) - 1}{\exp(x_0) - 1}\frac{x_e}{2} \times \exp\left(\frac{x_e}{2}\right) K_1\left(\frac{x_e}{2}\right) \qquad (13)$$

where

$$x_0^{(s)} = \frac{T_{cs}}{T}, \quad x_e^{(i,s)} = \frac{T_{cs}}{T_e^{(i)}},$$

and K_1 is a Bessel function of the second kind with imaginary argument.

The coupling constant D_s in equation (12) is related to the coupling constant in equation (7) by

$$D_s^2 = \frac{2^{1/2} k_0^{1/2} \pi \rho \hbar^2}{m_t m_l^{1/2}} \frac{w_s}{T_0^{3/2}} T_{cs}^2. \qquad (14)$$

Optical phonon scattering is not important in n-Si (Conwell[29], p. 103).

In order to calculate the particle numbers in the different valleys we start with an equilibrium condition

$$\sum_j{}'\left(\frac{\partial n}{\partial t}\right)_{j\to i} = \sum_j{}'\left(\frac{\partial n}{\partial t}\right)_{i\to j} \qquad (15)$$

where Σ_j' means the sum over all valleys except the valley i. $(\partial n/\partial t)_{i\to j}$ is the transfer rate of carriers from valley i to valley j. It is given by

$$\left(\frac{\partial n}{\partial t}\right)_{i\to j} = -\left\langle\frac{1}{\tau_{iv}^{(i\to j)}}\right\rangle n^{(i)} \qquad (16)$$

where the brackets again mean Maxwellian averages and $\tau_{iv}^{(i\to j)}$ is the intervalley relaxation time for scattering from valley i to valley j. One gets

$$\left(\frac{\partial n}{\partial t}\right)_{i\to j} = \sum_s \left(\frac{2}{\pi}\right)^{1/2} \frac{D_s^2 m_t m_l^{1/2} T_e^{(i)1/2}}{\pi\hbar^2 k_0^{1/2} \rho T_{cs}} \times V(x_0^{(s)}, x_e^{(i,s)}) n^{(i)} \qquad (17)$$

with

$$V(x_0, x_e) = \frac{\exp(x_0 - x_e) + 1}{\exp(x_0) - 1}\frac{x_e}{2}\exp\left(\frac{x_e}{2}\right) K_1\left(\frac{x_e}{2}\right). \qquad (18)$$

In equation (17) the sum runs over the different types of intervalley processes which lead to a scattering from valley i to valley j. With this one gets

$$n^{(i)} = n\left(a_i \sum_{j=1}^{g} \frac{1}{a_j}\right)^{-1} \tag{19}$$

with

$$a_i = \sum_{g} \frac{D_g^{\,2}}{T_{cg}} T_e^{(i)1/2} V(x_0^{(g)}, x_e^{(i,g)}). \tag{20}$$

Valley i and j have different band edge directions. Intervalley g-scattering does not enter here, because the two valleys on the same axis in k-space have the same magnetoresistance behaviour.

The coupling constants for the different scattering mechanisms are derived in the following way. From measurements of the ohmic magnetoresistance[30] one gets the ratio of the transverse to the parallel acoustic relaxation times $\tau_{ac,\perp}/\tau_{ac,\parallel}$ as 1·5. This together with equation (6) gives a quadratic equation for Ξ_d/Ξ_u. One solution is $\Xi_d = 0$. If one takes[31, 32] $\Xi_u = 8{\cdot}6\,\mathrm{eV}$ one gets $\Xi_0 = 10{\cdot}8\,\mathrm{eV}$ which is in good agreement with measurements of the energy loss[33]. In order to study the influence of different values of Ξ_d on the results, calculations have been performed with $\Xi_d = 0{\cdot}2\Xi_u$ which is also compatible with the results of Long and Myers[30]. However, with $\Xi_d = 0$ better general agreement with the present experiments is obtained.

The ratios of the coupling constants for the different intervalley scattering processes to an acoustic coupling constant are derived by Long[22] and Asche *et al.*[25] from the field dependence of the anisotropy of the conductivity and from the field dependence of the piezoresistivity. Several sets of values for these constants are given by these authors. We made runs on the computer for different sets of parameters. The values of the parameters are given in Table 1. for two different runs. The parameters of run 2 are the ones given by Asche *et al.*[25]. Note, however, that we compared the intervalley scattering to the transverse acoustic instead to an isotropic acoustic relaxation time. This may be done because the mobility without magnetic field is determined mainly by $\tau_\perp$.

Table 1. Data used in the numerical calculations. The elastic constants (c_1, c_{12}, c_{44}, c^*) are taken from Ref. [16]

$m_l/m_0 = 0{\cdot}90$	$\rho = 2{\cdot}33\,\mathrm{g/cm^3}$	$\kappa = 11{\cdot}8$
$m_t/m_0 = 0{\cdot}192$	$c_l = 1{\cdot}845 \times 10^{12}$ dyn/cm²	$n = 6 \times 10^{14}\,\mathrm{cm^{-3}}$
$c_{12} = 0{\cdot}801 \times 10^{12}$	$c_{44} = 0{\cdot}650 \times 10^{12}$	$c^* = -0{\cdot}426 \times 10^{12}$ dyn/cm²
$\Xi_d = 0$	$\Xi_u = 8{\cdot}6\,\mathrm{eV}$	$D_{0p} = 0$

Intervalley scattering parameters	Low energy g	Low energy f	High energy g	High energy f
Characteristic temperature T_{cg}(°K)	190	190	720	680
Intervalley phonon coupling strength D_g (erg/cm)	$2{\cdot}82 \times 10^{-4}$	0	$1{\cdot}07 \times 10^{-3}$ $3{\cdot}38 \times 10^{-3}$	1† 0 2†
w_g/w_a	0·3	0	0·3 3·0	1† 0·001* 2†

*This is the only process which contributes to scattering between valleys on different axes in k-space

†1 and 2 characterize the two different sets of parameters used in the calculations.

5. EXPERIMENTAL AND THEORETICAL RESULTS FOR B = 0

In Figs. 6–12 the calculated results are given, obtained with the constants listed in Table 1. It turned out that the coupling constants for intervalley phonons critically modifies the galvanomagnetic behaviour in the hot electron range. In Fig. 6 the ratio of mobility to ohmic mobility is given as a function of field strength for **j** parallel to [111] and [100] respectively. For comparison, also some experimental points are indicated for these two current directions. For the [100] direction the agreement is satisfactory for set 1 of the parameters. The discrepancy for [111] direction (set 1) at low field strengths stems probably from the fact that the doping of the samples is somewhat higher than assumed in the calculations. Therefore the contribution of the impurity scattering to the ohmic resistivity may not have been calculated correctly.

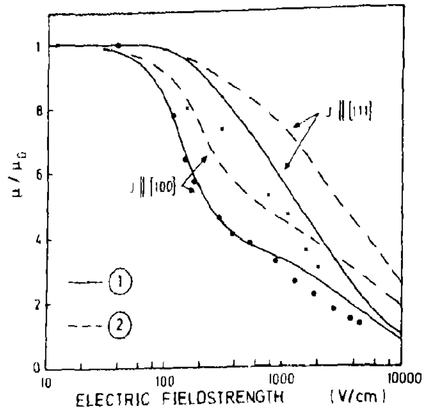

Fig. 6. Theoretically calculated mobility ratios vs electric field strength for two different orientations of j. The encircled numbers indicate results obtained for the two different sets of parameters. Experimental values are indicated by dots for j‖[100] and by crosses for j‖[111].

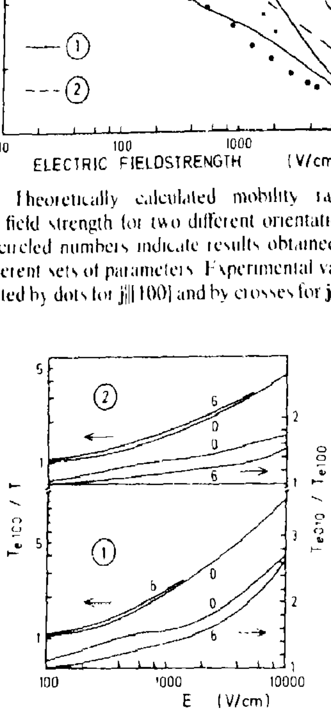

Fig. 7. Ratio of electron temperature to lattice temperature and ratio of electron temperatures of different valleys vs electric field strength for j‖[100] and B‖[011]. The numbers indicate the magnetic field strength in kG. 1 and 2 see Fig. 6.

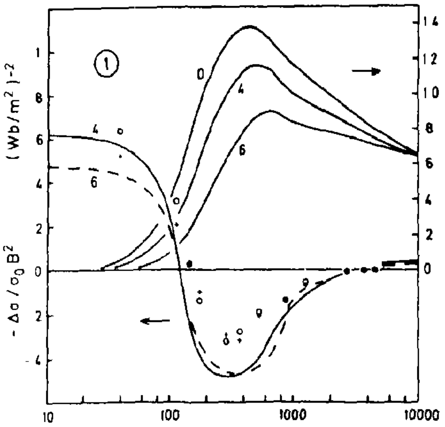

Fig. 8(a). Theoretically calculated transverse magnetoconductivity and relative population of valleys vs electric field strength for j‖[100] and B‖[011]. The numbers indicate the magnetic field strength in kG. The circles and the crosses indicate experimental values for 4 (circles) and 6 kG (crosses) respectively. The calculation was done with the set of constants No. 1.

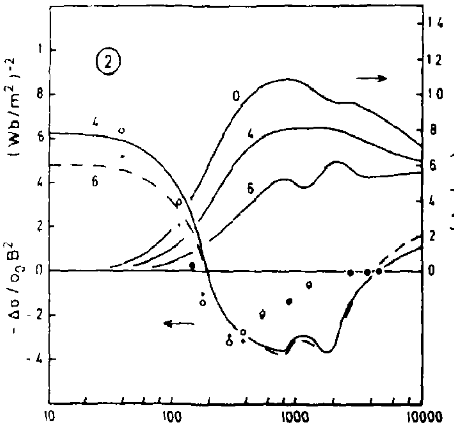

Fig. 8(b). Same as Fig. 8(a), but for the second set of parameters.

In Fig. 7 the electron temperatures are plotted vs. the electric field strength for j in the [100] direction and **B** parallel to [011]. Two different groups of valleys are present. It is obvious that the magnetic field causes a small increase of the temperature of the cooler valley and therefore a decrease of the ratio of the temperatures of the two groups of valleys. Figure 8(a) shows the result of the calculation of the transverse magnetoconductivity as well as the repopulation of carriers for the same directions of j and **B** as before. Experimental results of $\Delta\sigma/\sigma_0B^2$ for 4 and 6 kG (circles and crosses respectively) are indicated. The most significant result is that the above outlined model is able to give a negative magnetoresistance of approximately correct magnitude within the experimentally determined range of electric field strengths. It is also noted that the model qualitatively gives the correct dependence of magneto-

Accession number 82552
Date 3 ...

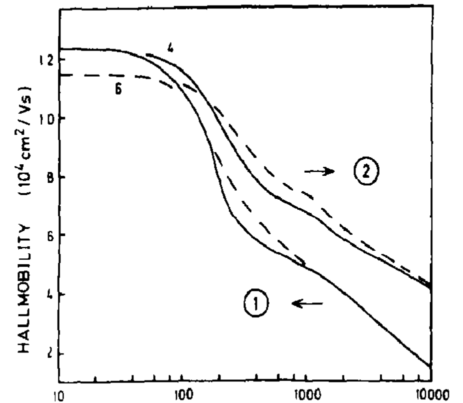

Fig. 9. Theoretically calculated Hall mobilities vs. electric field strength for j‖[100] and B‖[011]. The full and the dashed curves correspond to 4 and 6 kG respectively. 1 and 2 see Fig. 6.

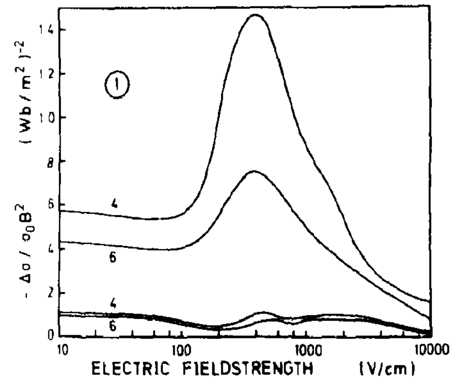

Fig. 10(a). Theoretically calculated transverse magnetoconductivity vs. electric field strength for j‖[011]. The upper two curves correspond to B‖[100], the lower two to B‖[011]. Numbers indicate field strength in kG. The calculation was done with the set of constants No. 1.

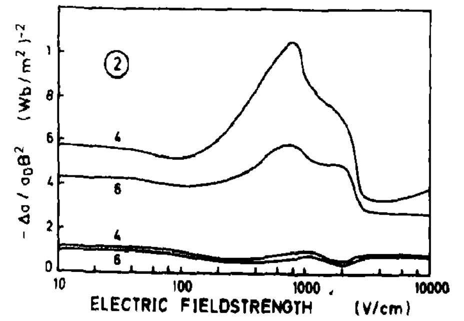

Fig. 10(b). Same as Fig. 10(a), but for the second set of parameters.

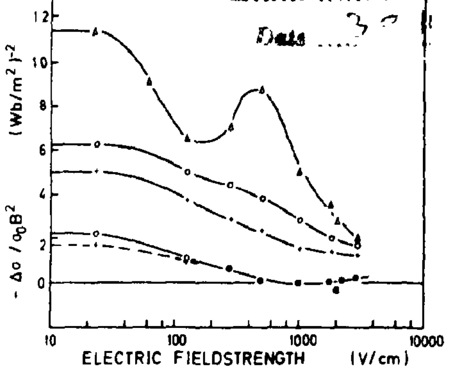

Fig. 10(c). Experimental values of transverse magnetoconductivity vs electric field strength for j‖[011]. The upper three curves correspond to B‖[100], the lower two to B‖[011]. ΔΔΔ 1 kG, 000 4 kG, +++ 6 kG.

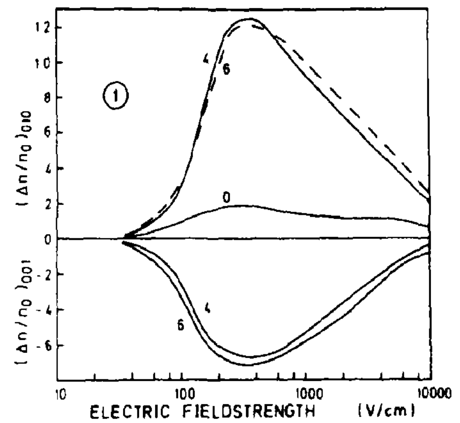

Fig. 11(a). Relative populations vs. electric field strength or j‖[011] and B‖[100] for two different valleys. The numbers indicate the magnetic field strength in kG. For $B = 0$ the population of the [001] valleys is the same as that for the [010] valleys. The calculation was done with the set of constants No. 1.

resistance on magnetic field. This is seen by comparison with the experimental points indicated in Fig. 8(a) and by comparison with Fig. 2. For low electric fields the magnetoresistance or the negative magnetoconductivity which are equal up to terms of first order in σ strongly decreases with increasing magnetic field. In the range of negative magnetoresistance both the experimental and theoretical values show only a weak dependence on magnetic field strength. Moreover,

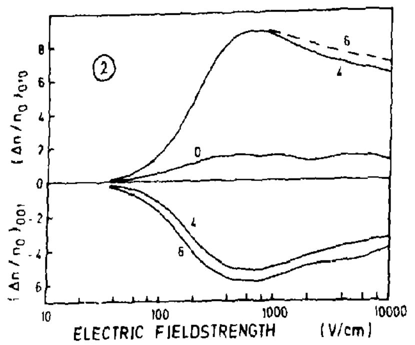

Fig. 11(b). Same as Fig. 11a, but for the second set of parameters.

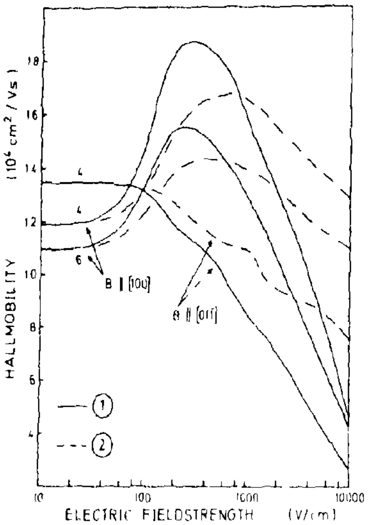

Fig. 12. Calculated Hall mobilities vs. electric field strength for **j**‖[011]. The numbers indicate the magnetic field strength in kG. For **B**‖[011] the 6 kG curve is very close to the 4 kG curve. 1 and 2 see Fig. 6.

for zero magnetoresistance for low and high electric field strength both the theoretical and experimental magnetoresistances are independent of *B*. Also included in Fig. 8(a) is the relative change in population of the valleys on the [100] axis in *k*-space. The maximum of the population roughly coincides with the maximum negative magnetoresistance. An applied magnetic field reduces the population of the valleys on the [100] axis and therefore acts towards an equalization of the particle numbers of the different valleys. Figure 8(b) gives the results for the second set of values of parameters, with the higher coupling strength *D* (see Table 1) for the high energy *g*-intervalley phonons. As is to be expected, the electrons lose much more energy in this process and therefore remain cooler, so that the maximum of the magnetoconductivity is shifted towards higher electric field strength. Figure 9 shows the calculated Hall mobilities vs. electric field strength for 4 and 6 kG magnetic field strength. In the ohmic case the Hall mobilities exhibit the normal behaviour, that is, the 6 kG curve is lower than the 4 kG curve. At about 200 V/cm this behaviour is changed and the Hall mobility for 6 kG is higher than for 4 kG.

For the case of **j** parallel to [011] and **B** pointing in the [01$\bar{1}$] direction one has again two different sets of valleys. However, for **B** aligned parallel to [100] the Hall field points in the [01$\bar{1}$] direction and there are therefore three different sets of valleys. The temperature of the valleys on the [100] axis is almost independent of **B** but the temperature of the valleys on the [010] axis is lowered and on the [001] axis is increased. In Figs. 10(a) and (b) the calculated magnetoconductivities for 4 and 6 kG are given for the two different orientations of **B**. The experimental values of the magnetoconductivity are given in Fig. 10(c). It can be seen that a magnetoconductivity maximum for **B** parallel to [100] is also exhibited by the calculated values although at higher values of the magnetic field intensity. In this case, however, the agreement between theory and experiment is only qualitative. Both the experimental and theoretical curves show a maximum of magnetoresistance at about 800 V/cm, but the theoretically calculated effect is much too high. The ohmic magnetoconductivity is again predicted correctly by the model. In Figs. 11(a) and (b) the corresponding populations of two different valleys are shown for **B** parallel to [100] only. For **B** parallel [01$\bar{1}$] the effect of the magnetic field on the population numbers is small. The magnetic field enhances the population of the valleys on the [010] axis in k-space and reduces the population of the other valleys as shown by Figs. 11. The great influence of the magnetic field on the relative population of the valleys is also expressed in the calculated Hall mobilities which are shown in Fig. 12. For **B** parallel [100] the Hall mobility is a maximum at electric field strengths near 300 V/cm.

6. DISCUSSIONS

We want to note that the proposed model is able to explain most of the experimentally observed features. Especially the peculiar and unexpected behaviour of magnetoresistance with current in [100] direction is analyzed. Obviously it is necessary to consider the dependence of the population of the valleys on the magnetic field. It remains to discuss the validity of some of the assumptions made in the calculations.

As can be seen from Fig. 7, the electron temperature raises to about 800°K in the cooler valleys and to about 2000°K in the hotter valleys. For **j** parallel to [011] the magnitudes are about the same. A Maxwellian distribution should therefore be established in the cooler valleys according to equation (1). In the hotter valleys the temperature raises well above the characteristic temperatures of all high energy phonons, and again a Maxwellian distribution is present according to Reik and Risken[34].

We have neglected the energy exchange between electrons of different valleys due to intervalley scattering processes in the energy balance-equation equation (4). Sample calculations reveal that it is much smaller than the energy exchange with the lattice.

The rate of energy loss to optical phonons and to the phonons involved in intervalley scattering is overestimated by a Maxwellian distribution. This result is true when the electron temperature is up to about twice as high as the characteristic temperature of these phonons, since the number of electrons in the high energy range is overestimated by the distribution. This probably causes a better agreement with experiment at least in the case **j** parallel to [100] for a lower coupling constant than that used by Asche *et al.*[25]. Also we note that in the case where an electron temperature is comparable to the characteristic temperature of an intervalley phonon both the Fröhlich–Paranjape criterion (equation (1)), and the assumption of a relaxation time for the intervalley scattering are not valid. But in this case the corresponding intervalley relaxation times are greater than the acoustic relaxation times so that this effect should not have much influence. Another important point is the influence of the magnetic field on the distribution function and especially on Paranjape's criterion equation (1). To our knowledge no estimate of this influence has been given so far. But as the magnetic field has a small influence only on the electron temperatures we assume that the effect on criterion equation (1) is also small.

At field strength up to 300 V/cm where all the effects mentioned above certainly are small it is clearly indicated that the experiments, especially the negative magnetoresistance, could only be explained by taking into account the effect of the magnetic field and the resulting Hall field on the electron temperatures and as a consequence on the population rates of the different valleys.

Acknowledgements—We want to express our deep gratitude to Professors Dr K. Baumann and Dr. K. Seeger for their continuous interest in this work and for many helpful discussions. Thanks are due also to the Mathematisches Institut der Technischen Hochschule. Vienna, and the Institut für Statistik der Universität, Vienna, for making available their computers. The possibility to use the experimental facilities of Professor B. Karlik is greatly appreciated

REFERENCES

1. Recently experimental results appeared which confirm this conclusion. (ASKENAZY S., PORTAL J. C., CLOT J., *Compt. rend.* **268B**, 1083 (1969)

2. SODHA M. S. and EASTMANN P. C., *Phys. Rev.* **110**, 1314 (1958)
3. CONWELL E. M., *Phys. Rev.* **123**, 454 (1961)
4. NAG B. R., DAS P. and PARIA H., *Proc. phys. Soc. Lond.* **81**, 736 (1963)
5. NAG B. R., DAS P. and PARIA H., *Proc. phys. Soc. Lond.* **82**, 728 (1963)
6. BUDD H. F., *Phys. Rev.* **131**, 1520 (1963)
7. BUDD H. F., *Phys. Rev.* **134**, A 1281 (1964)
8. DAS P. and NAG B. R., *Proc. phys. Soc. Lond.* **82**, 923 (1963)
9. MATZ D. and GARCIA-MOLINER F., *Phys. Status Solidi* **5**, 495 (1964), **7**, 205 (1964).
10. DAS P., *Proc. phys. Soc. Lond.* **86**, 387 (1965)
11. BUDD H. F., *Phys. Rev.* **140**, A 2170 (1965)
12. NAG B. R. and PARIA H., *Phys. Rev.* **150**, 632 (1966)
13. BUDD H. F., *Phys. Rev.* **175**, 241 (1968)
14. BEER A. C., *Solid-St. Phys. Suppl.* **4**, (1963)
15. BROSS H., *Festkorperprobleme* Friedr.-Vieweg, Braunschweig (1966)
16. HERRING C. and VOGT E., *Phys. Rev.* **101**, 944 (1956).
17. During preparation of this manuscript similar experimental results have been published by ASCHE M., BONDAR V. M. and SARBEJ O. G., *Phys. Status Solidi* **31**, K 143 (1969); for the case where a relatively strong magnetic field (9.6 kG) has been applied to a ⟨100⟩ oriented sample
18. KASTNER P., RÖTH E. P. and SEEGER K., *Z. Phys.* **187**, 359 (1965).
19. FRÖHLICH H. and PARANJAPE B. V., *Proc. phys. Soc. Lond.* **B69**, 21 (1956).
20. DYKMAN I. M. and TOMCHUK P. M., *Fizika tverd. Tela* **2**, 2228 (1960). English translation *Soviet Phys. solid-St.* **2**, 1988 (1960).
21. RAUCH C. J., STICKLER J. J., ZEIGER H. J. and HELLER G. S., *Phys. Rev. Lett.* **4**, 64 (1960).
22. LONG D., *Phys. Rev.* **120**, 2024 (1960).
23. ASCHE M. and SARBEJ O. G., *Phys. Status Solidi* **7**, 339 (1964).
24. ASCHE M., BOICHENKO B. L. and SARBEJ O. G. *Phys. Status Solidi* **9**, 323 (1965).
25. ASCHE M., BOICHENKO B. L., BONDAR V. M. and SARBEJ O. G., *Proc. 9th Int. Conf. Semicond., Moscow*, p. 793 (1968).
26. PAIGE E. G. S., *Prog. Semicond.* **8**, (1964).
27. EAGLES P. M. and EDWARDS D. M., *Phys. Rev.* **138**, A 1706 (1964)
28. DINGLE R. B., *Phil. Mag.* **46**, 831 (1955).
29. CONWELL E. M., *Solid-St. Phys. Suppl.* **9**, (1968).
30. LONG D. and MYERS J., *Phys. Rev.* **120**, 39 (1960).
31. BALSLEV I., *Phys. Rev.* **143**, 636 (1966).
32. BULTHUIS K., *Philips Res. Rep.* **23**, 25 (1968).
33. HESS K., private communication
34. REIK H. G. and RISKEN H., *Phys. Rev.* **124**, 777 (1961)

J. Phys. Chem. Solids Pergamon Press 1970. Vol. 31, pp. 939–946. Printed in Great Britain.

ANISOTROPY OF THE ULTRASONIC ATTENUATION IN MnF_2 NEAR THE NÉEL TEMPERATURE*

AKIRA IKUSHIMA†
Department of Physics and Materials Research Laboratory, University of Illinois, Urbana.
Ill. 61801, U.S.A.

(*Received* 23 *July* 1969; *in revised form* 6 *October* 1969)

Abstract – The anomalous ultrasonic attenuation α of longitudinal waves in MnF_2 was measured near the Néel point, T_N, as a function of temperature T and sound frequency f for different directions of the wave propagation **k**. The result for $T > T_N$ is expressed by the power-law formula, $\alpha \sim f^n|T-T_N|^{-\eta}$; $\eta = 0{\cdot}15 \pm 0{\cdot}01$, $n = 1{\cdot}8 \pm 0{\cdot}1$ for $\mathbf{k}\|[110]$; $\eta = 0{\cdot}14 \pm 0{\cdot}01$, $n = 1{\cdot}6 \pm 0{\cdot}1$ for $\mathbf{k}\|[100]$, and $\eta = 0{\cdot}16 \pm 0{\cdot}01$, $n = 1{\cdot}6 \pm 0{\cdot}1$ for $\mathbf{k}\|[001]$. However, the magnitude of the attenuation coefficient varied appreciably for different directions of the wave propagation, from which was deduced a relative value of the derivative of the antiferromagnetic exchange interaction between next-nearest neighbor spins, J_2, as $|(\partial J_2/\partial z)/(\partial J_2/\partial x)| = 2{\cdot}2$–$2{\cdot}6$ where x and z correspond to the [100] and [001] directions

1. INTRODUCTION

ULTRASONIC study has recently been recognized as a powerful way to investigate the dynamical aspects of the critical phenomenon associated with the second-order phase transition. Many experimental studies have been reported of anomalous increase of attenuation and decrease of the sound velocity near the magnetic transition point[1–8]. Various theoretical treatments have also been given for the behaviour of the sound attenuation due to the spin fluctuation near the transition point[9–17]. The thing of most importance in the problem should be to elucidate the physical meaning of the critical exponents, η and ζ, and of the parameter n which appear in the power-law formulae for the anomaly of the attenuation, α, and the velocity V as functions of the temperature T and the sound frequency f;

$$\alpha \sim f^n|T-T_N|^{-\eta}, \quad \Delta V/V_0 \sim |T-T_N|^{-\zeta}. \quad (1)$$

Kadanoff's[17] most recent theory for the attenuation, in which the decay rate of one sound wave into two, three or four other sound waves is treated with the scaling-law concept, predicted the values of the above quantities as $\eta = 1$, $n = 2{\cdot}0$ for the isotropic antiferromagnet, and $\eta = 4/3$, $n = 2{\cdot}0$ for the anisotropic antiferromagnet. These values agree well with the results in rare-earth metals [5, 6], but disagree with the observed values in a number of fluorides such as MnF_2[2, 3, 18], FeF_2[19] and $RbMnF_3$[4] and in CoO[7].

The other point of importance seems to be the dependence of the magnitude of the attenuation coefficient on the direction of the propagation vector of the sound. If we consider only longitudinal waves, the magnitude of the attenuation coefficient would be found from the spatial derivatives of the exchange interactions and from the number of the exchange interactions between spins which are affected by the sound waves. Thus, if we ignore possible difference of the critical exponent or the time factor of the spin fluctuation for different propagation direction of sound, we can obtain rather directly the relative value of the derivatives of the exchange interactions from the measured ratio of the orientation-dependent attenuation coefficients. The relative value of the derivatives should be very important in the study of the dynamics of the spin system.

This work was supported in part by the U.S. Atomic Energy Commission, Contract AT(11-1)-1198

[†] Present Address: The Institute for Solid State Physics, The University of Tokyo, Roppongi, Minato-ku, Tokyo 106 Japan.

The present author[18] has recently reported experimental results for the [100] longitudinal waves in MnF_2, where a detailed description was given for the experimental procedure used to obtain reliable data for the critical exponent, η, and for the behavior of the attentuation as a function of both of temperature and sound frequency. In this paper, the results of the attenuation experiment in MnF_2 for the other longitudinal waves will be presented. Finally, combining this with the previous results, a discussion will be given with a special emphasis on the process which would give a small η in MnF_2, $0{\cdot}14 \pm 0{\cdot}01$ for the [100] longitudinal waves for example, and the derivative of the exchange interaction. MnF_2 was studied because it is the most well understood antiferromagnet. Figure 1 shows the location of Mn ions and exchange interactions in MnF_2. Here J_2 is the strongest, antiferromagnetic interaction which predominantly determines the magnetic properties of this material.

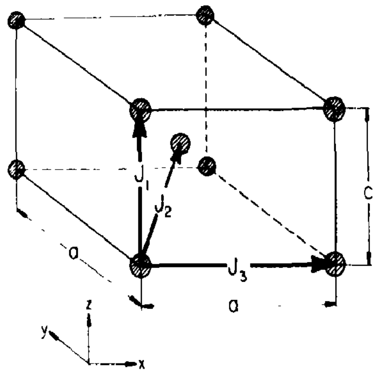

Fig. 1. Unit cell of MnF_2. J_1, J_2, J_3 are the exchange interactions between nearest neighbor spins, next-nearest neighbor spins, and 3rd nearest neighbor spins respectively. $a = 4{\cdot}87$ Å, $c = 3{\cdot}31$ Å[20].

2. EXPERIMENTAL PROCEDURE AND RESULTS

The present specimen was obtained from Semi Elements, Inc. The crystallographic orientations of surfaces to be used were determined by X-ray techniques to within 0·5° from the desired orientations. Then the same experimental procedure was employed as described in the previous paper[18].

Figure 2 shows the attenuation coefficient for three different longitudinal waves over a rather wide temperature range. The peak temperature was $(67{\cdot}31 \pm 0{\cdot}02)$°K, and did not shift for all directions of the sound propagation.

If we use here the usual power-law formula of the attenuation coefficient, value of the critical exponent, η, can be deduced from the most linear part of the plots shown in Figs.

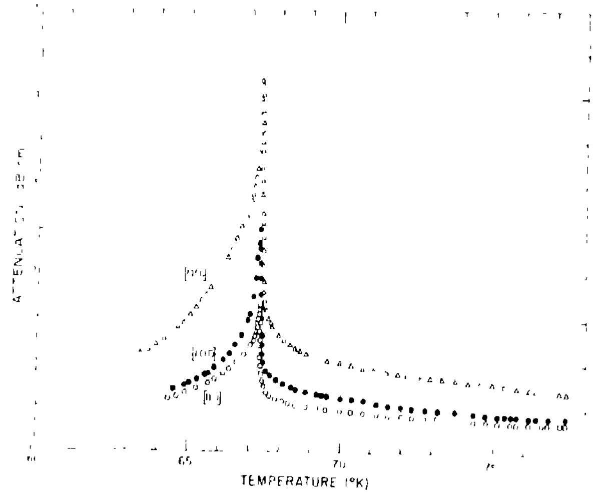

Fig. 2. Critical attenuation of 30 MHz longitudinal waves propagating along [110], [100] and [001] directions in MnF_2.

3–6. Table 1 summarizes the values of η for $T > T_N$ for three principal crystallographic directions. Figures 7 and 8 then show the frequency dependence of the attenuation for $T > T_N$, which give n equal to 1·8±0·1 for [110] and 1·6±0·1 for [001]. The value of n for [100] was 1·6±0·1 in the previous work[18].

A similar measurement was carried out for longitudinal waves propagating along an off-axis direction, which is also a direction for pure elastic modes. This direction is in the [110] plane, denoted as *[β] in equation (11)*, and is defined by an angle ϕ from the c-axis as given by equation (13). The value of η for this direction was found to be $0{\cdot}16_3$, which is again essentially the same as those for the other three directions.

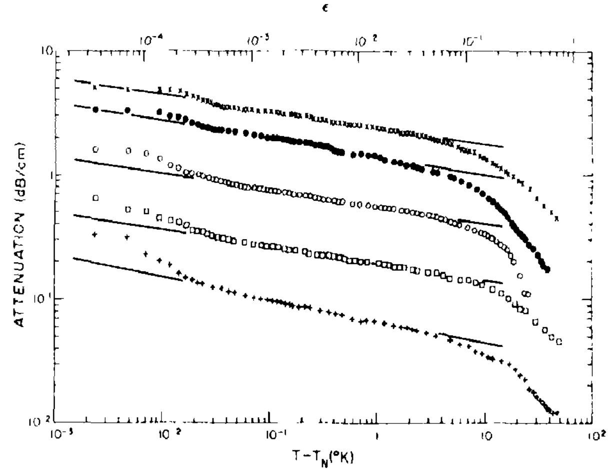

Fig. 3. Temperature dependence of the attenuation coefficient of the [110] longitudinal waves for $T > T_N$. + – 10 MHz, □ – 20 MHz, ○ – 30 MHz, ● – 50 MHz, x – 70 MHz.

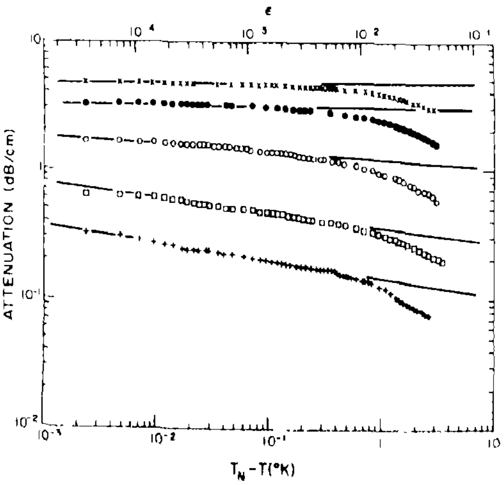

Fig. 4. Temperature dependence of the attenuation coefficient of the [110] longitudinal waves for $T < T_N$. + – 10 MHz, □ – 20 MHz, ○ – 30 MHz, ● – 50 MHz, x – 70 MHz.

Table 1

Frequency (MHz)	k‖[110]	k‖[100]	k‖[001]	k‖[β]
10	$0{\cdot}17_5$	$0{\cdot}13_8$	$0{\cdot}14_7$	
20	$0{\cdot}13_6$	.	$0{\cdot}17_1$	
30	$0{\cdot}13_6$	$0{\cdot}13_1$	$0{\cdot}17_1$	$0{\cdot}16_3$
50	$0{\cdot}14_4$	$0{\cdot}13_1$	$0{\cdot}14_4$	
70	$0{\cdot}13_3$	$0{\cdot}12_6$	$0{\cdot}14_1$	
90		$0{\cdot}15_0$		
110		$0{\cdot}15_2$		
Average	0·15±0·01	0·14±0·01	0·16±0·01	$0{\cdot}16_8$

Table 2 summarizes the values of the attenuation coefficient for 30 MHz at $\epsilon = 10^{-3}$, and the ratio of α_k to $\alpha_{[110]}$.

Neighbours and Moss[2] observed the same anisotropy in MnF$_2$, giving that the ratio of the attenuation in the [001] direction compared to [110] approximately from 2·5 to 3·6 depending on how we define the background level of the attenuation in Fig. 2 of Ref. [2]. Evans[3] also

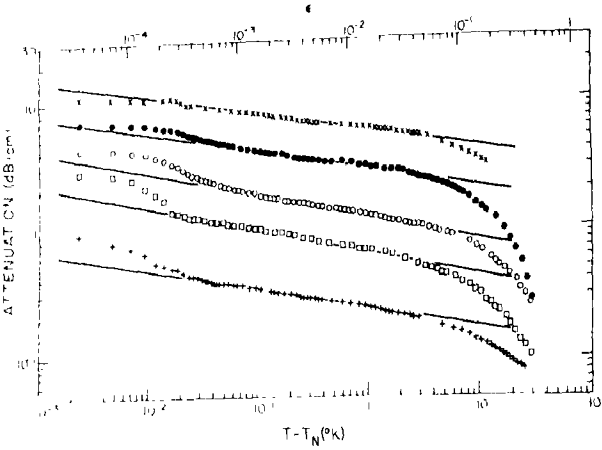

Fig. 5. Temperature dependence of the attenuation coefficient of the [001] longitudinal waves for $T > T_N$. + – 10 MHz, □ – 20 MHz, ○ – 30 MHz, ● – 50 MHz, x – 70 MHz

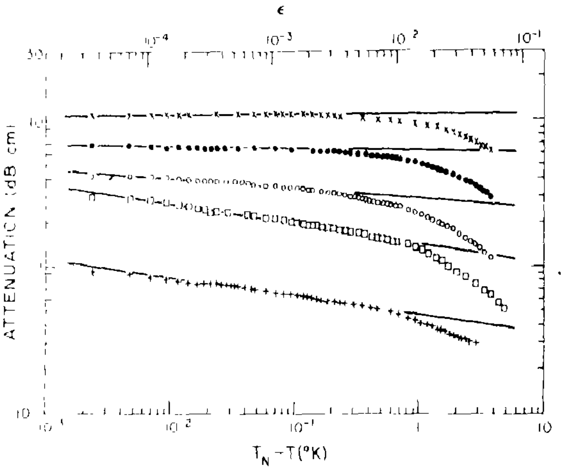

Fig. 6. Temperature dependence of the attenuation coefficient of the [001] longitudinal waves for $T < T_N$. + – 10 MHz, □ – 20 MHz, ○ – 30 MHz, ● – 50 MHz, x – 70 MHz

Table 2. Attenuation coefficient of 30 MHz longitudinal waves for T > T$_N$

k	α at $\epsilon = 10^{-3}$ (dB/cm)	$\alpha/\alpha_{[110]}$
[110]	$0{\cdot}7_8$	1
[100]	$1{\cdot}0_5$	1·3
[001]	$2{\cdot}0_0$	2·6
[β]	$1{\cdot}9_0$	2·6

measured the attenuation peak of the [100] longitudinal waves in MnF_2. However, he obtained a much larger peak, about 8 dB/cm at T_N for 30 MHz, which seems to the present author to be in some doubt.

3. DISCUSSION

(1) *Attenuation coefficient vs. temperature and frequency*

From the above experimental result, it

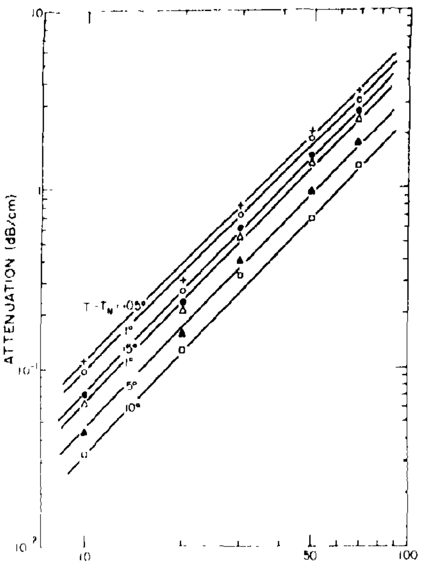

Fig. 7. Frequency dependence of the attenuation coeffi-of the [110] longitudinal waves for $T > T_N$. The temperature difference, $T-T_N$, is indicated in the figure.

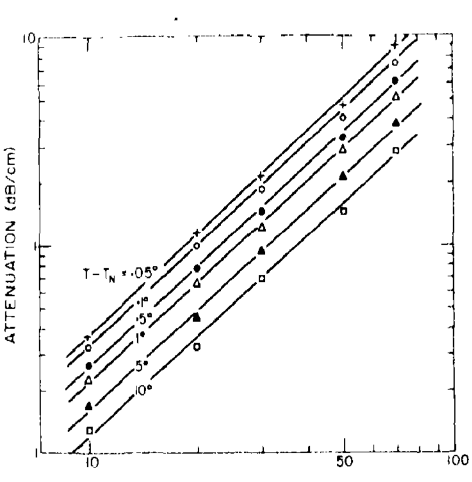

Fig. 8. Frequency dependence of the attenuation coefficient of the [001] longitudinal waves for $T > T_N$. The temperature difference, $T-T_N$, is indicated in the figure

appears that the magnitudes of η and n for $T > T_N$, an anomalous behavior of the attenuation in the vicinity of the Neel point ($T-T_N < 2\times 10^{-2}$°K for $T > T_N$) the frequency dependent η for $T < T_N$ and other features are definitely orientation-independent. A point to be mentioned here is the discrepancy between the present η and the values given by Neighbours and Moss[2] in MnF_2. They gave $\eta = 0{\cdot}42$ and $0{\cdot}38$ for the [001] and [110] longitudinal waves, respectively. The discrepancy might arise because Neighbours *et al.* did not measure the variation of the attenuation coefficient up to a temperature far enough from T_N to determine the background level. Although the most important temperature range for determining the value of η would be approximately $T_N \pm 2$°K, we may get a value even twice as large as the present one if we would take the magnitude of the attenuation coefficient at several degrees K above T_N as the background level.

(2) *Orientation dependence of the attenuation coefficient*

As was shown in Fig. 2, the magnitude of the attenuation coefficient depends rather strongly on the direction of the sound propagation. This result should in the first place be compared with the theoretical treatment of Tani and Mori[9]. Let us consider here two leading terms of the exchange interaction, J_1 and J_2, where J_1 is the ferromagnetic interaction between spin of the Mn ion at (0,0,0) and the one at (0,0,1), and J_2[*] is the antiferromagnetic interaction between spins at (0,0,0) and at $(\frac{1}{2},\frac{1}{2},\frac{1}{2})$ as shown in Fig. 1. In this approximation, the treatment by Tani and Mori predicts the following formulae:

$$\alpha_{[110]}T = [1+A(T/T_N)^2 \exp(-\lambda\epsilon^{1/2})/\epsilon^{1/2}]^2 \cdot \frac{8(\pi/6)^{1/2}(J'_{2r})^2[S(S+1)]^{3/2}(ak)^2\hbar}{[MVk_B(4J_2^2+J_1^2)]^{1/2}}. \quad (2)$$

$$\alpha_{[100]} = \begin{cases} \dfrac{2^{1/2}(4J_2^2+J_1^2)^{1/2}}{J_1}\cdot\alpha_{[110]} & \text{if } J_2 \simeq J_1 \quad (3) \\ \dfrac{8}{\pi}(Z\xi)^{1/2}\dfrac{|J_2|\cdot(4J_2^2+J_1^2)}{J_1^2}\cdot\alpha_{[110]} & \text{if } J_2 \gg J_1. \quad (4) \end{cases}$$

---

[*] The notations, J_1 and J_2, used throughout this paper correspond to J_2 and J_1 respectively in the theory of Tani and Mori.

$$\alpha_{[001]} = \begin{cases} 2^{-5/2}\left(\dfrac{c}{a}\right)^2 \dfrac{(2J'_{2z}+J'_{1z})^3(4J_2{}^2+J_1{}^2)^{1/2}}{(J'_{2x})^2|J'_{2z}J_1-2J'_{1z}J_2|}\cdot\alpha_{[110]} \quad \text{if } J_2 \simeq J_1 & (5) \\ \dfrac{1}{2\pi}(Z\xi)^{1/2}\left(\dfrac{c}{a}\right)^2 \dfrac{(2J'_{2z}+J'_{1z})^4|J_2|(4J_2{}^2+J_1{}^2)^{1/2}}{(J'_{2x})^2(J'_{2z}J_1-2J'_{1z}J_2)^2}\cdot\alpha_{[110]} \\ \qquad\qquad\qquad\qquad \text{if } J_2 \gg J_1. & (6) \end{cases}$$

Here, $J'_{1x} = \partial J_1/\partial x$, $J'_{1z} = \partial J_1/\partial z$ etc. at the equilibrium distance of the lattice: A and λ are constants having values of 0·48 and 2·8 respectively in MnF_2; $\epsilon = |T - T_N|/T_N$; S is the spin quantum number: a and c are the lattice parameters along the [100] and [001] axes respectively; k is the magnitude of the wave vector of the sound; M is the mass of the unit cell; V is the sound velocity; k_B is the Boltzmann constant; Z is the number of the nearest neighbor spins, and $\xi = 1-39[1+3/\{S+1)\}]/5Z^2$.

The magnitude of $\alpha_{[110]}$ and the value of the ratio, $\alpha_{[100]}/\alpha_{[001]}$, estimated from these formulae do not seem to be unreasonable in comparison with the measured values in MnF_2. However, the magnitudes of $\alpha_{[100]}$ and $\alpha_{[001]}$ are not compatible with the observed results. For example, the ratio, $\alpha_{[100]}/\alpha_{[110]}$, is calculated to be 15·6 or 420 depending on the case whether $J_1 \simeq J_2$ or $J_1 \ll J_2$ respectively, whereas the observed value of the ratio is only 1·3. In this estimate, the values $J_1 = 0{\cdot}32°K$ and $J_2 = -1{\cdot}76°K$ were used, as obtained from the neutron experiment on the spin waves [21].

The reason for the discrepancy between the theory and the observed result is considered as follows. Ultrasonic attenuation in the [100] and the [001] directions is physically different from that in the [110] direction in the sense that all the eight next-nearest neighbor interactions, J_2, around a certain spin contribute in the same way to the attenuation in the former cases, whereas only four of these eight interactions contribute in the latter case. If only the interaction, J_2, were important, the force acting on the spin system should be proportional to the spin Hamiltonian in the [100] and [001] cases, and the energy of the spin system should decay very slowly because of the kinematic slowing-down within the usual theoretical framework where the spin-lattice relaxation is ignored. This slowing-down is formally expressed as a very small value of g_k in equation (4.1) in the theory of Tani and Mori; this in turn makes the value of the attenuation very large as is shown in equation (4.3) of their theory, where g_k appears in the denominator. Generally speaking, the attenuation should be composed of α_F and α_R, where α_E is the part due to the energy-energy correlation function and α_R is the part arising from the correlation between the random forces. α_E should in principle be treated separately from α_R, and the decay time for α_E may be given by the spin-lattice relaxation time[22]. In the theory of Tani and Mori, this separation was not made, and therefore α_E was very much overestimated for $\alpha_{[100]}$ and $\alpha_{[001]}$. The importance of α_E would also be the reason of the small η in MnF_2[18].

Present results satisfy the relation that $\alpha_{[001]} > \alpha_{[100]} > \alpha_{[110]}$. The inequality is thought to be a reflection of the physical situation that the magnitude of the attenuation coefficient can be proportional to the square of the coupling strength between the spin system and the sound waves multiplied by the number of the exchange interactions affected by the sound waves. That is,

$$\alpha \sim |\sum_{l,m} i\mathbf{k}\cdot\mathbf{R}_{lm}\frac{\partial J_{lm}}{\partial \mathbf{R}_{lm}}\cdot\mathbf{k}|^2/V\ ,$$

where $\mathbf{k}$ is the wave vector of the sound, $\mathbf{R}_{lm} = \mathbf{R}_l - \mathbf{R}_m$ is the distance between spins l and m, and J_{lm} is the exchange interaction between these spins. For example, $\alpha_{[110]}$ would be smallest partly because the spin at $(\frac{1}{2},\frac{1}{2},\frac{1}{2})$ does not interact with spins at (1,0,0), (1,0,1), (0,1,0) and (0,1,1) for this longitudinal wave, thus reducing the number of J_2 affected by the sound waves. It would be worth noting here that the above quantity is equivalent to the static correlation function of the random force thoroughly investigated by Tani and Mori.

According to this simple interpretation, the attenuation coefficient for five directions in the tetragonal system for the pure longitudinal modes[22] can be written as

$$\alpha_{[110]} = Ka^2|J'_{2x}|^2/V_{[110]} \tag{7}$$

$$\alpha_{[100]} = Ka^2|J'_{2x}|^2/V_{[100]} \tag{8}$$

$$\alpha_{[001]} = Kc^2|J'_{2z}+\tfrac{1}{2}J'_{1z}|^2/V_{[001]} \tag{9}$$

$$\alpha_{[\pi]} = Ka^2|\sin^2\theta\cdot J'_{2x}+\frac{c}{a}\cos^2\theta\cdot J'_{2z} + \frac{c}{2a}\cos^2\theta\cdot J'_{1z}|^2/V_{[\pi]} \tag{10}$$

$$\alpha_{[\beta]} = Ka^2|\sin^2\phi\cdot J'_{2x}+\frac{c}{a}\cos^2\phi\cdot J'_{2z} + \frac{c}{2a}\cos^2\phi\cdot J'_{1z}|^2/V_{[\beta]} \tag{11}$$

where K is a common proportional factor, and $V_{[\cdot]}$ is the sound velocity for each direction. The direction denoted as $[\pi]$ is in (100) plane with an angle θ from c-axis given by

$$\cos\theta = A^{1/2}/(A+C)^{1/2}, \tag{12}$$

and the $[\beta]$-direction is in (110) plane with an angle ϕ from c-axis given by

$$\cos\phi = (2A-B)^{1/2}/(2A-B+C)^{1/2}, \tag{13}$$

where $A = c_{11}-2c_{44}-c_{13}$, $B = c_{11}-2c_{66}-c_{12}$ and $C = c_{33}-2c_{44}-c_{13}$, and c_{ij} are the elastic constants. From the values* of c_{ij} measured in the present specimens near T_N. These angles take values that $\theta = 50{\cdot}6°$ and $\phi = 45{\cdot}0°$.

First of all, equations (7) and (8) verify the experimental fact that $\alpha_{[100]}$ nearly equals to $\alpha_{[110]}$. The small difference may be due to higher order terms. Then, assuming that J'_{1z} might be small, we can deduce the value of the ratio, $|J'_{2z}/J'_{2x}|$, from these equations. The value is $2{\cdot}2 \pm 0{\cdot}2$ if we use the measured ratios of $\alpha_{[001]}/\alpha_{[110]}$ and $\alpha_{[001]}/\alpha_{[100]}$. Furthermore, this value is in good agreement with the value, 2·6, obtained from the ratio of $\alpha_{[\beta]}/\alpha_{[100]}$. Thus, the above procedure, although crude, seems to give a good estimate of the relative values of the attenuation coefficients for various directions of the longitudinal wave propagation. It has been reported that $J_{2x} = -8{\cdot}0\times10^{-8}$ erg cm^{-1}[16, 24]. Furthermore, the thermal expansion in MnF$_2$ measured by Gibbons[25] indicates that $J'_{2z} < 0$, which lets us conclude that $J_{2z} = -2\times10^{-7}$ erg cm^{-1}.

A theoretical estimate of these derivatives from the wave functions should be much desirable.

Acknowledgement – The present author would like to thank Dr. R. J. Maurer. Dr A V. Granto and other members of The University of Illinois for their hospitality, which made this work possible

REFERENCES

1. LUTHI B., PAPON P. and POLINA R. J., *Proc Conf. Magnetism* (1968).
2. NEIGHBOURS J R and MOSS R W, *Phys. Rev.* **173**, 542 (1968)
3 EVANS R. G., *Phys. Lett* **27A**, 451 (1968).
4 GOLDING B, *Phys. Rev. Lett* **20**, 5 (1968).
5. LUTHI B and POLLINA R. J, *Phys. Rev.* **167**, 488 (1968).
6. POLLINA R J. and LÜTHI B., *Phys. Rev.* **177**, 841 (1969).
7 IKUSHIMA A., *Phys Lett.* **29A**, 417 (1969).
8. LÜTHI B and POLLINA R J., *Phys. Rev Lett* **22**, 717 (1969).
9. TANI K. and MORI H., *Phys. Lett* **19**, 627 (1966)
10. OKAMOTO H., *Prog. theor. Phys* **37**, 1348 (1967).
11. BENNETT H. S. and PYTTE E., *Phys. Rev.* **155**, 553 (1967).
12. BENNETT H. S. and PYTTE E, *Phys. Rev.* **164**, 712 (1967).
13. KAWASAKI K., *Solid-St. Commun.* **6**, 57 (1968)
14. KAWASAKI K., *Phys Lett.* **26A**, 543 (1968).
15. KAWASAKI K., *Prog. theor. Phys.* **39**, 285 (1968).

---

*The measured results were, $c_{11} = 1{\cdot}41$, $c_{12} = 0{\cdot}51$, $c_{13} = 0{\cdot}22$, $c_{33} = 1{\cdot}72$, $c_{44} = 0{\cdot}30$, $c_{66} = 0{\cdot}76$ in unit of 10^{12} dyn/cm^2 at liquid nitrogen temperature. The error is less than 0·2 per cent. Details will be reported elsewhere

16 TANI K and MORI H. *Prog theor Phys.* **39**, 876 (1968)

17. KADANOFF L P, *J phys Soc. Japan* **26**, 122 (1969).

18. IKUSHIMA A, *J Phys Chem Solids* **31**, pp 939–946 (1970)

19. IKUSHIMA A, **31**, 939 (1970)
$\eta = 0{\cdot}75 \pm 10\%$ for $T > T_N$ and $0{\cdot}45 \pm 10\%$ for $T < T_N$.

20. BAUR W H, *Acta Crystallogr* **11**, 488 (1958).

21 OKAZAKI A, TURBERFIELD K C and STEVENSON R W H, *Phys Lett.* **8**, 9 (1964)

22 KAWASAKI K, *Phys Lett* **29A** 406 (1969).

23. BRUGGER K, *J appl Phys* **36** 759 (1965)

24 BENEDEK G B. and KUSHIDA T., *Phys Rev.* **118**, 46 (1960)

25. GIBBONS D F., *Phys. Rev.* **115**, 1194 (1959).

26 KAWASAKI K., and IKUSHIMA A., *Phys. Rev.*, in press.

Note added in proof The present author and his co-worker have recently obtained a direct proof that the small value of η in MnF_2 comes from a relaxation time other than that considered in the existing theories[26]. A discussion of $|J_{2z}/J_{1z}|$ is also given in that paper, and deduced the value of 2·7.

J. Phys. Chem. Solids Pergamon Press 1970. Vol. 31, pp. 947–962. Printed in Great Britain.

THE ELECTRICAL PROPERTIES AND DEFECT STRUCTURE OF PURE AND CHROMIUM-DOPED MnO

M. O'KEEFFE and M. VALIGI*
Chemistry Department, Arizona State University, Tempe, Ariz. 85281, U.S.A

(*Received* 25 *June* 1969; *in revised form* 2 *October* 1969)

Abstract – X-ray, chemical analysis and electrical studies have been made as a function of temperature and oxygen activity on pure and chromium-doped MnO. MnO always contains an excess of oxygen, the majority defect being the doubly ionized cation vacancy at lower concentrations of excess of oxygen. Chromium is incorporated substitutionally as Cr^{3+}. The heat and entropy of solution of 1 g atom oxygen at 1 atm into MnO are – 11 kcal and – 16·5 cal deg^{-1} respectively. It is concluded that MnO is either a 'hopping' type semiconductor with a band gap of 2·2 eV or that the band gap is even lower (about 1·85 eV) with 'band' conduction for electrons.

1. INTRODUCTION

THE REVIVAL of interest in the electrical properties of the simple transition metal oxides[1] has stimulated a re-examination of their chemical properties and, in particular, further investigation of the nature of the native defects responsible for many of their interesting properties. MnO is unique among these oxides in that it is observed[2, 3] that there is a minimum in the conductivity as a function of oxygen activity which has led to speculation about a possible *p-n* transition in this material. Several models have been proposed to account for this behavior, but experimental difficulties have precluded unambiguous determination of the defect structure. In this paper we show how the existence of a conductivity minimum can be exploited in crystals doped with Cr_2O_3 to obtain precise information about the non-stoichiometry. The observation of the conductivity minimum and its behavior on doping also provides a unique and very sensitive method of determining solubilities of dopants at *temperature*. Recognition of this fact has allowed us to explore in detail the mechanism of incorporation of an altervalent ion into MnO.

Relevant previous work includes Hall effect measurements[4–6] which have established that at high temperatures (*ca.* 1000°C) electron mobility is considerably greater than hole mobility, and chemical analysis[7] and gravimetric[3, 8, 9] measurements which indicate that in the range of conditions conveniently accessible, there is always an excess of oxygen over the stoichiometric composition MnO even at oxygen pressures below the conductivity minimum. At an oxygen pressure close to that of the conductivity minimum the Seebeck coefficient changes sign[8, 10, 11].

Hed and Tannhauser[8], in particular, discussed the electrical measurements and concluded that there is substantial evidence for the majority defect being the doubly ionized manganese vacancy*, V''_{Mn}, except possibly at higher oxygen contents. By way of contrast, other authors have proposed that at the lower oxygen pressures, there may be substantial concentrations of anion vacancies [11] or of cation interstitials[13]. However, as we discuss below, it appears likely that the conductivity minimum arises because of the high electron mobility and, in fact, the electron concentration, n, is always less than the hole concentration, p. This is supported by the observation[11] that the conductivity as a function of oxygen pressure makes a smooth transition from $\sigma \propto P_{O_2}^{1/6}$ to $\sigma \propto P_{O_2}^{-1/6}$.

---

*Present address: Istituto di Chimica Generale, Universitá di Roma, Italy.

*Here, and throughout, we use Kröger's notation[12].

2. THEORY

We consider here the defect equilibria expected in an oxide such as MnO in equilibrium with oxygen, and possibly containing an impurity ion as dopant. The argument is restricted to dilute solutions (not more than a few tenths of a percent) of defects so that their activities may be replaced to a good approximation by their concentrations and the methods of Kröger[12] may be applied to the various possible equilibria.

As mentioned above, and as also the results of this work will show, the predominant ionic defect close to stoichiometry in MnO is the doubly ionized cation vacancy, V''_{Mn}, produced according to the reaction

$$2MnO + \tfrac{1}{2}O_2 \rightarrow 2Mn^{\cdot}_{Mn} + V''_{Mn} + 3O_0. \quad (1)$$

At low concentration, the defects may be expected to behave ideally so that

$$[V''_{Mn}]p^2 = K_{ox}a \quad (2)$$

where K_{ox} is the equilibrium constant for reaction (1), p represents $[Mn^{\cdot}_{Mn}]$, the concentration of holes, and a is the activity of oxygen in the gas phase. We will, as is usual, adopt a standard state of gaseous oxygen at 1 atm so that $a = (P_{O_2}, \text{atm})^{1/2}$.*

It is also expected that other defects such as electrons Mn'_{Mn}, and manganese interstitials or oxygen vacancies are present in smaller quantities. If n is the electron concentration we have from the equilibrium

$$2Mn_{Mn} \rightarrow Mn'_{Mn} + Mn^{\cdot}_{Mn} \quad (3)$$

$$np = K_i \quad (4)$$

likewise, if $Y^{\cdot\cdot}$ represents $V^{\cdot\cdot}_O$ or $Mn_i^{\cdot\cdot}$

$$[Y^{\cdot\cdot}][V''_{Mn}] = K_s. \quad (5)$$

Now consider the incorporation of stable trivalent ions such as Cr^{3+} into MnO. We can write for the incorporation of Cr_2O_3 a reaction analogous to equation (1)

$$Cr_2O_3 \rightarrow 2Cr^{\cdot}_{Mn} + V''_{Mn} + 3O_0 \quad (6)$$

with an equilibrium constant analogous to equation (2)

$$[V''_{Mn}]x^2 = K_{Cr}a(Cr_2O_3) \quad (7)$$

where $x = [Cr^{\cdot}_{Mn}]$.

The condition expressing electrical neutrality in the crystal is in general

$$p + x + 2[Y^{\cdot\cdot}] = n + 2[V''_{Mn}]. \quad (8)$$

In the absence of ionic conductivity, the electronic conductivity is

$$\sigma = ne\mu_- + pe\mu_+. \quad (9)$$

In the subsequent discussion we will attach particular significance to the magnitude of various quantities at the conductivity minimum. Such quantities are denoted by subscript m. As p will always be an increasing function of a and n will always be a decreasing function of a it is clear that at σ_m

$$n_m e\mu_- = p_m e\mu_+ \quad (10)$$

so that from equation (4)

$$p_m = (bK_i)^{1/2} \quad (11)$$

where $b = \mu_-/\mu_+$ is assumed to depend on temperature only. At σ_m we obtain from the electrical neutrality condition (8) using equations (2), (4) and (11),

---

*Some authors replace a by $q = P(CO_2)/P(CO)$ which is a convenient variable experimentally. Clearly $a = qK$ where K is the equilibrium constant for the reaction $CO_2 \rightarrow CO + \tfrac{1}{2}O_2$.

$$a_m - \gamma/a_m = \beta x + \alpha \qquad (12)$$

where

$$\alpha = \frac{(bK_i)^{3/2}}{2K_{ox}}\left[\frac{b-1}{b}\right] \qquad (13)$$

$$\beta = bK_i/2K_{ox} \qquad (14)$$

$$\gamma = (bK_i)^2 K_s/K_{ox}^2. \qquad (15)$$

As a_m increases, a plot of a_m against x will approach a straight line of slope β and intercept at $x = 0$ of α. In fact, the experimental results to be described indicate rather clearly that $\gamma \ll a_m^2$ (for example a plot of a_m vs. x is accurately linear) showing that the concentrations of defects such as oxygen vacancies and manganese interstitials are quite negligible.

From the values of α and β thus obtained experimentally one has that

$$bK_i = (\alpha^2/\beta^2)[b/(1-b)]^2 \qquad (16)$$

and

$$K_{ox} = (\alpha^2/2\beta^3)[b/(1-b)]^2. \qquad (17)$$

The deviation from stoichiometry, δ in $MnO_{1+\delta}$, is given by

$$\delta = [V''_{Mn}] - [Y^{\cdot}] = (p + x - n)/2. \qquad (18)$$

In particular, for pure MnO at the conductivity minimum, from equations (4), (10), (11) and (16),

$$\delta_m = \alpha/2\beta. \qquad (19)$$

Equation (19) is particularly useful since δ_m can be determined independently by chemical or gravimetric analysis of appropriately heated samples, thus providing a check on the theory outlined above.

δ_m is in turn related to p_m by the expression

$$2\delta_m = p_m(b-1)/b. \qquad (20)$$

The value of b entering in these expressions can be calculated if μ_- is known, using the expression (*cf.* equations (9) and (10))

$$\sigma_m = 2p_m e\mu_+ \qquad (21)$$

whence

$$b \equiv \mu_-/\mu_+ = 1 + 4e\delta_m\mu_-/\sigma_m. \qquad (22)$$

Using the reported values of μ_- it will be shown that $b \gg 1$ (see for example, Table 2 below) so that the factor $b/(b-1)$ entering into many of the expressions above can be replaced by unity. This is equivalent to stating that $p_m \gg n_m$; this result will be used in what follows.

We turn now to a discussion of the factors controlling the solubility of chromium. When n and $[Y^{\cdot}]$ can be ignored, the condition for electrical neutrality, equation (8) becomes

$$p + x = 2[V''_{Mn}] \qquad (8a)$$

so that equation (2) can be written

$$(p+x)p^2 = 2K_{ox}a. \qquad (23)$$

When the manganous oxide is saturated with chromium (solubility x_0) $MnCr_2O_4$ will appear as a second phase. We choose this as our standard state so that in $MnCr_2O_4$, $a(Cr_2O_3) = 1$. Equation (7) becomes (using equation (8a))

$$(p + x_0)x_0^2 = 2K_{cr}. \qquad (24)$$

Eliminating p from equations (23) and (24) gives the explicit dependence of chromium solubility on oxygen activity

$$x_0 = \left[\frac{2K_{cr}}{(K_{ox}\,a/K_{cr})^{1/2} + 1}\right]^{1/3}. \qquad (25)$$

Two methods of determining x_0 have been employed in this work. The first method relies on the fact that a_m will vary linearly with x while chromium is still dissolving in MnO (equation (12)) whereas a_m will be constant when the concentration of added chromium exceeds x_0. The second method, suitable for higher temperatures when electrical measurements become difficult, relies on the fact that the lattice parameter of doped MnO varies smoothly with x until saturation is reached, beyond which point the lattice parameter does not change with increasing chromium concentration. Clearly, if x_0 is known at a given value of a, and K_{0x} determined from equation (17), K_0 can be obtained from equation (25).

A final point which we wish to take up in this section concerns possible deviations from ideality of the solution of defects. At concentrations corresponding to site fractions of less than 10^{-3}, the defects are typically ten interatomic distances or some 20 Å apart; under these circumstances one might reasonably expect the solution of defects to behave ideally. At higher concentrations one might expect to observe the effects of significant concentrations of associates (V''_{Mn} Mn_{Mn}), which may of course be written more simply as singly ionized vacancies V'_{Mn}. This association effect is noticed in the conductivity measurements[3,8] at higher oxygen pressures when the conductivity changes from dependence on a one-sixth to a one-quarter power of oxygen pressure. However, the results to be analyzed in this paper do not require considerations of this nature.

3. EXPERIMENTAL

All the results to be described were obtained with samples which were prepared from accurately weighed mixtures of Mn_3O_4 (United Mineral and Chemical Corp. Grade 1, total impurities less than 10 ppm) and from 0–5 at% Cr_2O_3 (Matheson, Coleman and Bell, Reagent Grade). The powders were mixed as an acetone slurry by prolonged grinding in a mortar. The dry powder was pressed at approximately 8 kbar into 1 cm dia. pellets which were then sintered for 5 hr at 1430°C in an atmosphere of tank hydrogen. After sintering the samples were rapidly cooled by removing them from the furnace while maintaining the hydrogen atmosphere. Metallographic examination showed that samples prepared in this way were dense and homogeneous with uniformly dispersed grains of spinel as a second phase in preparations containing higher chromium concentrations.

Specimens for electrical measurements were obtained by grinding the pellets to provide a rectangular bar, typically 1 × 2 × 8 mm, with two side arms. Platinum–platinum/10% rhodium thermocouples were bound to the ends with platinum wire which was then coated with platinum paste. Platinum leads were similarly affixed to the two side arms. Conductivity was measured at 400 Hz by the four-probe method. The thermoelectric power was determined by measuring the temperature at the two ends of the sample (typically 8–10° temperature difference) and the potential difference between the two platinum leads of the thermocouples.

Lattice parameter measurements were made using a Norelco back reflection camera with filtered Fe $K\alpha$ radiation at 25°C. There are three lines in this region: (420) at about 77°, (331) at 72° and (400) at 60·5°. Only for the (420) reflection were well-resolved α_1, α_2 doublets visible in every case. Several films were taken for each sample and each film was read several times. The lattice parameter a_0 calculated for each line was extrapolated to $\theta = 90°$ by plotting against $\phi \tan \phi$[14] where $\phi = 90° - \theta$. The precision of the measurement of a_0 was ±0·0004 Å.

Chemical analysis of the stoichiometric excess of oxygen in MnO_x was made by either the modified Bunsen–Rupp method[15] using apparatus similar to Deren *et al.*[16], or by the oxalate method of Fowler and Bright[17]. The two methods gave concordant results although the Bunsen–Rupp method gave higher precision and was preferred.

In the course of the work two methods of quenching samples were compared. The first, which we call 'slow quench' consisted of withdrawing the sample to a room temperature part of the furnace under controlled atmosphere. The second, 'rapid quench' consisted of dropping the sample from the hot zone of the furnace through 50 cm into a saturated aqueous solution of sodium chloride at 0°C.

Furnace gas atmospheres consisted of analyzed flowing stream of CO_2 and CO or of hydrogen containing 0·05% O_2 analyzed as water. Some experiments employed nitrogen containing a very small, unknown quantity of oxygen. An attempt was made to make some electrical measurements in manganese vapor at about 10^{-3} atm; however, the platinum thermocouples and contacts rapidly deteriorated at 1000°C precluding any reliable measurements under these conditions. Oxygen activities in the CO_2-CO mixtures relative to a standard state of pure oxygen gas at 1 atm were calculated according to the expression[18]

$$\log a = \log [P(CO_2)/P(CO)] + 4{\cdot}528 - 14575/T \qquad (26)$$

4. RESULTS

(a) *Lattice parameter measurements*

Measurements of lattice parameter were made on several series of $MnO-Cr_2O_3$ mixtures sintered at different temperatures and in different atmospheres. Results are shown in Fig. 1. As can be seen in the figure, the lattice parameter decreased linearly with increasing concentration until a saturated solution was obtained, at which point the lattice parameter is constant and $MnCr_2O_4$ appears as a second phase. The immediate important result is that the solubility of Cr_2O_3 in MnO can be seen to vary with temperature and with oxygen activity as might be expected. The observation of a decrease in lattice parameter provides strong support for the hypothesis that chromium is incorporated as $Cr^{\cdot}_{Mn}$ (rather than say, interstitially). In fact, using the method of Cimino[19], the decrease in lattice parameter is calculated to be 24×10^{-4} Å per atom percent $Cr^{\cdot}_{Mn}$ using the Goldschmidt radii for Cr^{3+} (0·65 Å) and for Mn^{2+} (0·91 Å). This should be compared with the observed value of 18×10^{-4} Å per atom percent observed for the series of experiments performed at 1430°C in H_2 (for which the concentration of $Mn^{\cdot}_{Mn}$ is expected to be negligibly small).

We also obtained precise lattice parameters for pure MnO prepared in different ways. These are reported in Table 1. Again, the

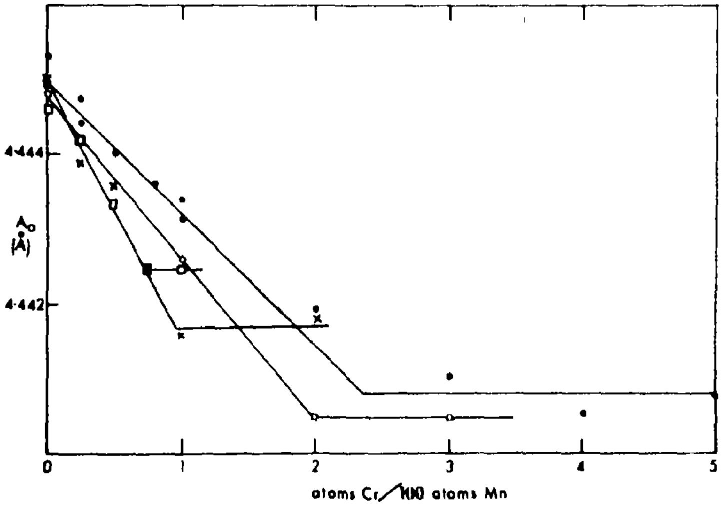

Fig. 1 Lattice parameter as a function of chromium concentration in $MnO-Cr_2O_3$ solid solutions ● 1430°C in H_2; ○ 1430°C in N_2, x 1300°C in $CO:CO_2 = 1:1$; □ 1200°C in $CO:CO_2 = 1.1$.

Table 1. *Lattice parameter* a_0, *at* 25°C *for* $MnO_{1+\delta}$

Preparation	δ	a_0(Å)
*1430°C H_2	$<1\times10^{-4}$	$4{\cdot}444_0$
†1430°C N_2	$5{\cdot}5\times10^{-4}$	$4{\cdot}444_8$
*1430°C $P(O_2) = 10^{-1}$ atm	6×10^{-2}	$4{\cdot}443_8$
†1300°C $P(CO_2)/P(CO) = 1$	$0{\cdot}7\times10^{-4}$	$4{\cdot}445_0$
*1200°C $P(CO_2)/P(CO) = 1$ rapid quench	$2{\cdot}2\times10^{-3}$	$4{\cdot}444_0$
†1200°C $P(CO_2)/P(CO) = 1$ slow quench	$0{\cdot}8\times10^{-4}$	$4{\cdot}444_6$

*Probably oxidized on cooling

†Probably reduced on cooling.

decrease of lattice parameter with increasing δ (in $MnO_{1+\delta}$) strongly supports the hypothesis that an oxygen excess is accompanied by V''_{Mn} and $Mn^{\cdot}_{Mn}$. It should be remarked however that the samples with an apparently large δ are inhomogeneous and have some surface oxidation so that no *quantitative* significance attaches to the variation of a_0 with δ.

(*b*) *Electrical measurements*

The main results of the electrical measurements are displayed graphically in Fig. 2 which shows how the conductivity of pure and doped MnO varies with oxygen-pressure in the region of the conductivity minimum and in Fig. 3, which shows typical plots of thermoelectric power as a function of oxygen pressure.

In Fig. 4 we have plotted the value of $\sigma_m(T)/\sigma_m$ (1000°C) for samples of pure and doped MnO vs. $1/T$. The points all fall on a line of slope $7{\cdot}00\times10^3$ deg corresponding to an 'activation energy' of 1·39 eV (in excellent agreement with the value of 1·37 eV given by Hed and Tannhauser[8] for the same quantity).

Figure 5 shows a_m plotted against the chromium concentration x, for doped samples at three temperatures. It may be seen that a_m is accurately linear in x implying that the term γ/a_m in equation (12) is negligible. From the intercept at $x = 0$ (α) and the slope (β) of these lines we can calculate the constants bK_i and K_{ox} using equations (16) and (17) (assuming $b \gg 1$). We can then calculate p_m (the hole concentration at the conductivity minimum) from equation (11) and the hole mobility μ_+ from equation (21). Finally, the value of x at which the breaks in the curves occur gives the solubility x_0 of chromium at a particular oxygen activity. This in turn allows one to calculate K_{cr} from equation (24) or (25). The results of these calculations are summarized in Table 2. Included in the table is the maximum solubility of chromium $x_{0,\max}$ this is simply (*cf.* equation (25)) $(2K_{cr})^{1/3}$ and represents the limiting solubility of chromium as the oxygen pressure

Table 2. *Derived constants for pure* MnO *at three temperatures**

	1000°C	1100°C	1200°C
K_{ox} (atm$^{-1/2}$)	$1{\cdot}48\times10^{-2}$	$1{\cdot}10\times10^{-2}$	$0{\cdot}84\times10^{-2}$
$2\delta_m = p_m$	$1{\cdot}28\times10^{-3}$	$2{\cdot}26\times10^{-3}$	$3{\cdot}70\times10^{-3}$
K_{cr}	$1{\cdot}0\times10^{-8}$	$3{\cdot}3\times10^{-8}$	$10{\cdot}3\times10^{-8}$
$x_{0,\max}$	$2{\cdot}7\times10^{-3}$	$4{\cdot}0\times10^{-3}$	$5{\cdot}9\times10^{-3}$
bK_i	$1{\cdot}62\times10^{-6}$	$5{\cdot}15\times10^{-6}$	$1{\cdot}38\times10^{-5}$
σ_m (ohm^{-1} cm^{-1})	0·125	0·36	0·66
μ_+ (cm^{2}v^{-1}s^{-1})	$6{\cdot}6\times10^{-3}$	$9{\cdot}3\times10^{-3}$	$1{\cdot}2\times10^{-2}$
b($\mu_- = 10$ cm^{2}v^{-1}s^{-1})	1500	1070	820

*The concentration unit is the (dimensionless) site fraction. To convert to cm^{-3}, concentrations should be multiplied by $4{\cdot}95\times10^{22}$ (at 1100°C).

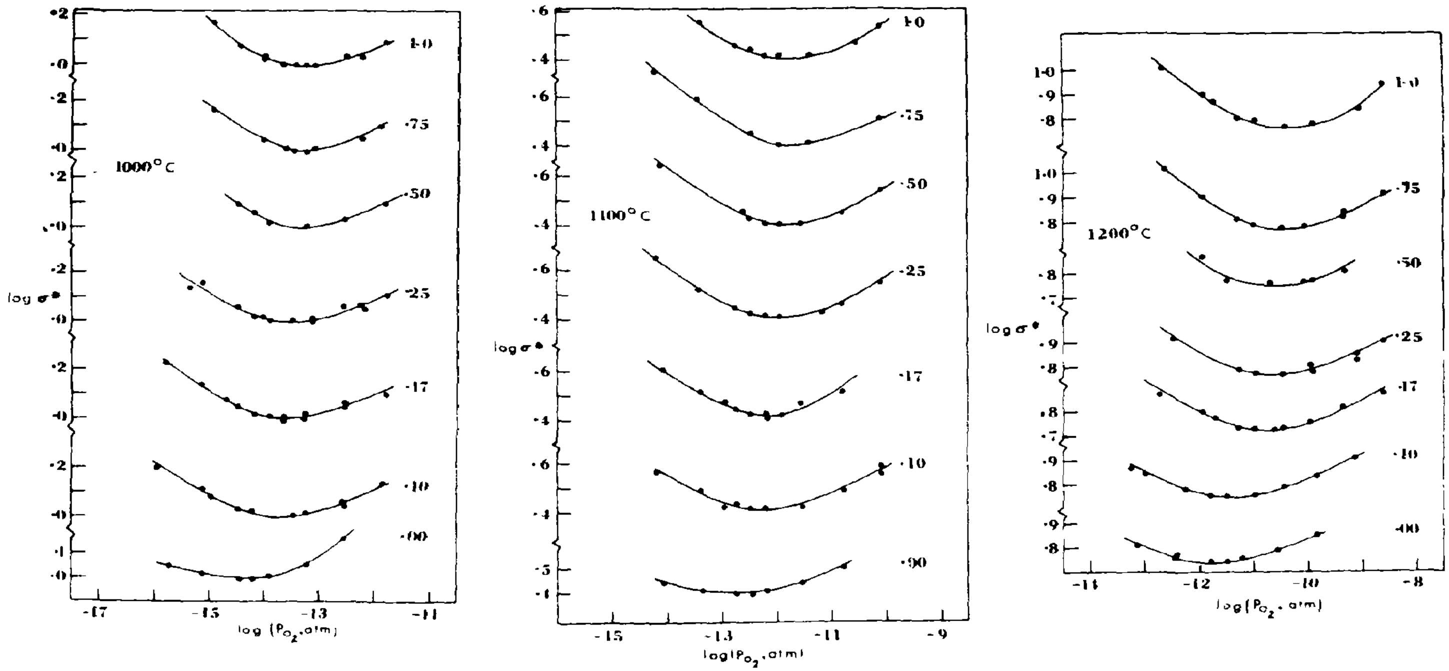

Fig. 2. Relative conductivity $\sigma^* = \sigma/\sigma_m$ (1000°C), at 1000°, 1100° and 1200°C as a function of oxygen pressure for pure and Cr doped MnO. The numbers on the curves are the atom percent Cr/Mn.

895
41
936

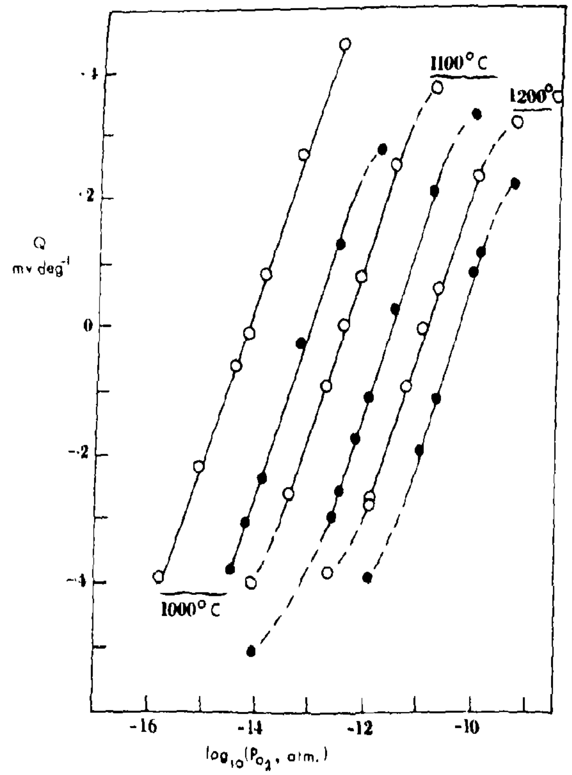

Fig. 3. Thermoelectric power Q as a function of oxygen pressure at three temperatures ○ for pure MnO; ● for MnO + 0·17% $CrO_{1.5}$

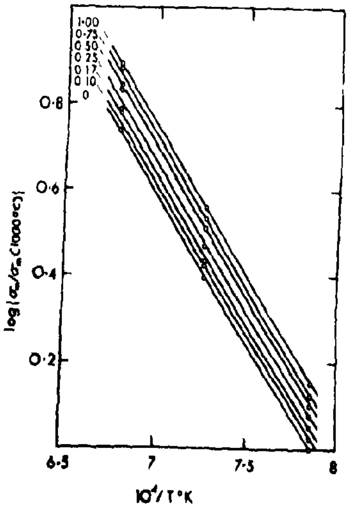

Fig. 4. $\sigma_m^* = \sigma_m/\sigma_m$ (1000°C) as a function of temperature for pure and Cr-doped MnO. The numbers on the curves are at.% Cr/Mn. Note the shift in zero for each curve.

goes to zero. Also included are the values of b and μ_+ calculated from the conductivity using equations (21) and (22).

Of some interest is the temperature dependence of some of these quantities. In Fig. 6 we show a plot of the logarithm of μ_+, K_{ox} and K_{cr} as a function of reciprocal temperature. From these plots we obtain, and discuss below, the activation energy for hole migration (0·51 eV, compare the value of 0·42 eV of Hed and Tannhauser[8]) and the heats of solution of oxygen and of chromium oxide in MnO.

(c) *Chemical analysis*

An important test of various methods of study of non-stoichiometric oxides lies in comparison of the concentrations of defects determined in various ways. In the case of

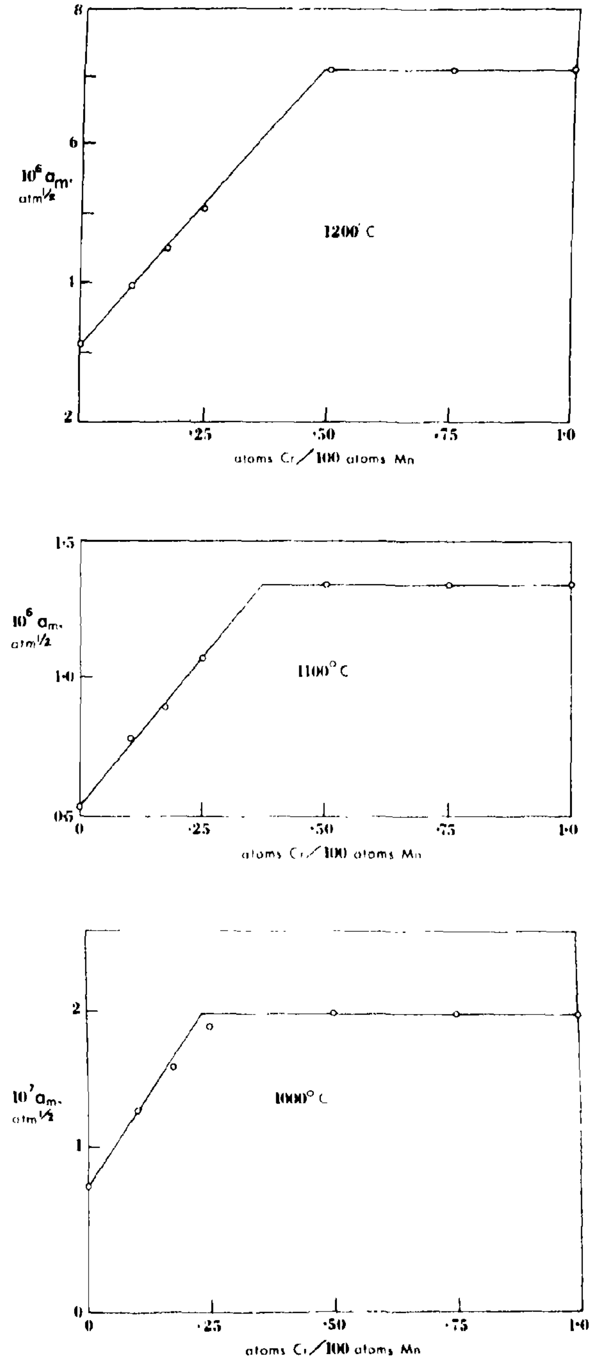

Fig. 5 The oxygen activity at minimum conductivity, a_m, as a function of chromium concentration in MnO-Cr_2O_3 solid solutions at three temperatures. The break in the curves occurs at the solubility point.

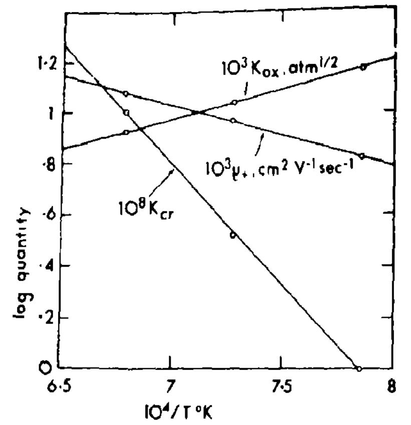

Fig. 6. Plot of hole mobility μ_+, and the constants relating to oxygen (K_{ox}) and chromium (K_{cr}) solubility as a function of temperature.

MnO a number of methods have been used to determine the extent of non-stoichiometry. The gravimetric method has been employed by Eror[3] and by Hed and Tannhauser[8, 9]. This method involves extrapolation to the ideal stoichiometry and is hindered by problems of evaporation of the sample. A second method is that used by Davies and Richardson [7] which involves chemical analysis of the quenched sample. This method is often criticized because of the difficulty in achieving a sufficiently rapid quench. Our results (in the table) comparing a 'slow quench' with a 'rapid quench' confirm this criticism as might be expected[20].

Another method, recently exploited by Fender and Riley[21] is to use the technique of coulometric titration of a known amount of oxygen into a crystal, combined with electrochemical determination of oxygen activity. This method is very accurate at the higher oxygen excess studied by Fender and Riley, but has the same difficulty of establishing a 'zero' as the gravimetric method.

Finally, one can derive the constants controlling the formation of defects from electrical studies of doped crystals. The results of the different kinds of measurement are compared in Table 3; it may be seen that there is little agreement between them. It should be remarked, however, that the electrical measurements have inherently much greater precision than other techniques for measuring defect concentrations.

5. DISCUSSION

(*a*) *Solubility of oxygen and chromium in MnO*

One of the most interesting features of this work is that it has proved possible to determine both the chromium solubility and the equilibrium constant for solution of oxygen solely from the variation of the oxygen pressure of the minimum conductivity with chromium concentration, i.e. from the data of Fig. 5. The essential information is contained in the values of K_{ox} and K_{cr} (Table 2 and Fig. 6). From these constants and their temperature dependence one can derive various thermodynamic quantities as follows.

Writing

$$K_{ox} = \exp(-\Delta G_1^\circ/RT),$$

it follows that

Table 3. Comparison of various techniques of determining the deviation from stoichiometry in MnO_{1+x}, *at* 1200°C *and* $P(CO_2)/P(CO) = 1$

Method	Authors	x	Comment
Slow quench	Davies, Richardson[7]	$<4 \times 10^{-4}$	(*a*)
Slow quench	(this work)	$1{\cdot}6 \times 10^{-4}$	
Rapid quench	(this work)	$4{\cdot}4 \times 10^{-3}$	
Gravimetric	Eror[3]	$6{\cdot}3 \times 10^{-4}$	(*b*)
Gravimetric	Hed, Tannhauser[9]	1×10^{-3}	
Electrical	(this work)	$1{\cdot}8 \times 10^{-3}$	

(*a*) Assuming with Davies and Richardson that x is a function of $P(O_2)$ only.
(*b*) Extrapolated from $P(O_2) = 7 \times 10^{-10}$ atm assuming $x \propto P(O_2)^{1/6}$.

$$-R\partial \ln K_{ox}/\partial(1/T) = \Delta H_1^\circ \qquad (27)$$

$$\partial(RT \ln K_{ox})/\partial T = \Delta S_1^\circ \qquad (28)$$

ere ΔH_1°, ΔS_1° refer to the solution of 1 g om of oxygen at 1 atm into $Mn_{1-x}O$ at the *ypothetical*) standard state $x = 1$. In the low ncentration region there are *non-interacting* ubly-ionized vacancies with $x \propto a^{1/3}$, so e configurational entropy is $-R \ln [x/(1-$ $]^3 = 3R \ln[(1-x)/x]$ and the partial molar antities (relative to oxygen at 1 atm) are

$$\Delta\bar{H}(1/2O_2) = \Delta H_1^\circ$$

$$\Delta\bar{S}(1/2O_2) = \Delta S_1^\circ + 3R \ln[(1-x)/x].$$

From the data of Fig. 6 and Table 2 we ive from equations (27) and (28) for the lution of oxygen at 1 atm in $Mn_{1-x}O$

$$H_1^\circ = \Delta\bar{H}(1/2O_2) = -11 \pm 2 \text{ kcal/g atom oxygen}$$

$$S_1^\circ = -16{\cdot}5 \pm 1{\cdot}5 \text{ cal deg}^{-1}\text{/g atom oxygen}$$

$$\bar{S}(1/2O_2) = 20{\cdot}6 \pm 1{\cdot}5 \text{ cal deg}^{-1}\text{/g atom oxygen at } x = 0{\cdot}002.$$

It is worth inquiring whether these values of ntropy and enthalpy of solution are reasonble. O'Keeffe and Moore[22] discussed the ntropy of solution of oxygen in some oxides cluding the closely related oxides NiO and oO, and recently Eror and Wagner[23] etermined the entropy of solution of oxygen CoO. From these results ($\Delta S^\circ \approx -10$ cal eg^{-1} in CoO and -14 cal deg^{-1} in NiO) it is lear that the value given above for MnO is easonable. Likewise, consideration[24] of a imple ionic model indicates that the enthalpy f solution should be intermediate between the ery exothermic value for FeO ($\Delta H^\circ \approx -65$ cal) and the very endothermic value for FeO $\Delta H^\circ \approx -65$ kcal) and the very endothermic value for NiO ($\Delta H^\circ \approx +60$ kcal) as is indeed the case.

It is interesting to compare the solution process from a slightly different point of view. If we change the standard state of oxygen to be the activity in equilibrium with MnO and Mn_3O_4 the thermodynamic quantities will refer to solution of Mn_3O_4 in MnO and can be calculated by summing

$$\begin{array}{rll}
(1) & 2MnO + 1/2O_2 \rightarrow 3O_0 + V''_{Mn} + 2Mn^{\bullet}_{Mn} & \Delta H_1^\circ \quad \Delta S_1^\circ \\
(3) & \underline{Mn_3O_4 \rightarrow 3MnO + 1/2O_2} & \underline{\Delta H_3^\circ \quad \Delta S_3^\circ} \\
(2) = (1) + (3) & Mn_3O_4 \rightarrow MnO + 3O_0 + V''_{Mn} + 2Mn^{\bullet}_{Mn} & \Delta H_2^\circ = \Delta H_1^\circ + \Delta H_3^\circ \text{ etc.}
\end{array}$$

Reaction (1) is the solution of oxygen already discussed, for reaction (3) at 1100°C, $\Delta H_3^\circ = 53{\cdot}5$ kcal and $\Delta S_3^\circ = 30{\cdot}2$ cal deg^{-1}, so that for the solution of Mn_3O_4 in MnO:

$$\Delta H_2^\circ = 43 \text{ kcal mole}^{-1}$$

$$\Delta S_2^\circ = 13{\cdot}7 \text{ cal deg}^{-1} \text{ mole}^{-1}.$$

Turning now to the solution of chromium in MnO, we chose as standard state the spinel $MnCr_2O_4$ so that the heat and entropy of solution of this spinel in MnO may be obtained from K_{cr}. We find in this way

$$\Delta H_{cr}^\circ = 48 \pm 5 \text{ kcal mole}^{-1}$$

$$\Delta S_{cr}^\circ = -2{\cdot}5 \pm 3 \text{ cal deg}^{-1} \text{ mole}^{-1}.$$

It is interesting, but not entirely unexpected, that the heats of solution of the two spinels $Mn[Mn_2^{3+}]O_4$ and $Mn[Cr_2]O_4$ are so similar. Equally interesting is speculation as to the origin of the greater entropy of solution of Mn_3O_4, however in view of the rather large uncertainty in these quantities a little unwise at this stage.

(*b*) *Defect equilibria*

Knowing the constants relating to defect formation as reported in Table 2 we can use the expressions developed earlier (notably equations (8a), (23), (25) and (4)) to calculate the concentration of defects in pure and doped MnO as a function of oxygen pressure. The result of such a calculation is shown in Fig. 7 for a temperature of 1100°C.

Noticeable in this diagram is the fact that in chromium doped MnO the logarithm of the various concentrations is not a linear function of the logarithm of oxygen pressure across most of the field of stability. It may also be seen that the limiting solubility of chromium is strongly dependent on oxygen pressure. Particularly noteworthy is the observation that the intrinsic point $p = n$ falls just outside the Mn–MnO boundary in striking vindication of the prediction by Kröger[25].

It should be possible now to calculate the electronic conductivity of Cr doped MnO as a function of oxygen pressure. Using the same data we have calculated the relative conductivity σ/σ_m in pure MnO, in MnO+2 at.% $CrO_{1.5}$ and in MnO saturated with Cr_2O_3. The curves are shown in Fig. 8. A striking difference in slope ∂ log σ/∂ log P_{O_2} between pure and Cr doped MnO at low oxygen pressures is predicted and apparently

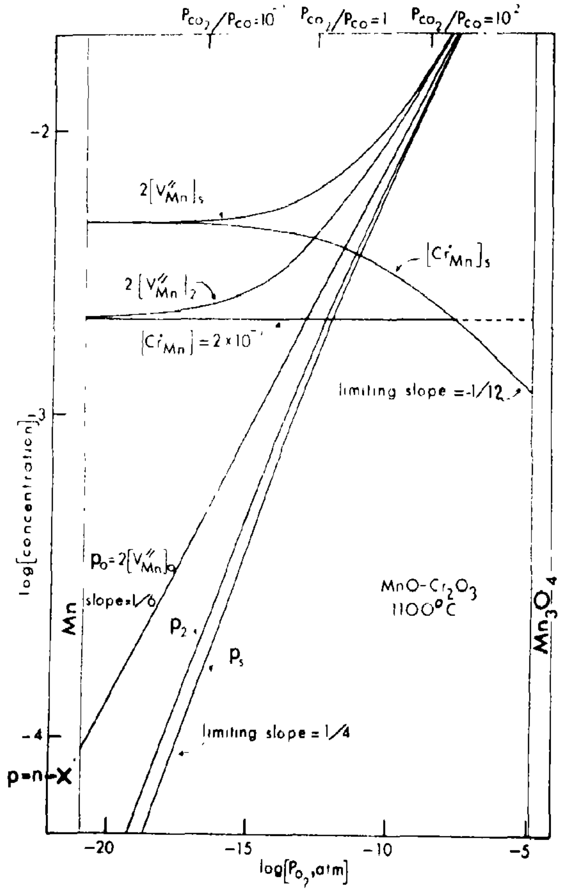

Fig. 7. Calculated concentrations of defects in pure and in Cr doped MnO. The curves refer to chromium concentration ([Cr_{Mn}]), hole concentration (p) and cation vacancy concentration ([V''_{Mn}]). The subscripts are s, saturated with chromium, 2, 0·2% chromium, O, pure MnO. Note the point $p = n$ at the lower left corner. The Mn/MnO and MnO/Mn_3O_4 boundaries are indicated.

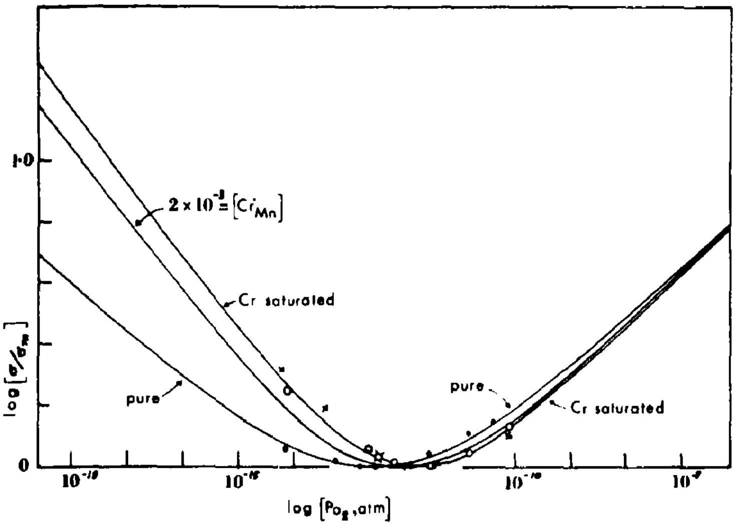

Fig. 8. The relative conductivity at 1100°C calculated for pure MnO, MnO doped with 0·2 at.% Cr_2O_3 and MnO saturated with Cr_2O_3. The experimental points are: ●, pure MnO; ○ and *x*, two samples of MnO saturated with Cr_2O_3 (some $MnCr_2O_4$ present).

rne out by the experimental results as own in the figure.

) *Electrical properties*

It proved essential in this work to have as ll as possible an understanding of the electri- il properties of MnO, in particular to under- and why MnO and NiO should have such teresting differences in behavior (NiO has) region of *n*-type thermoelectric power r example). To this end it is instructive to onsider an energy level diagram such as onstructed by McKinzie[10] following the ocedure of van Houten[26, 27]. These ithors and also Morin[28] have discussed e procedure for doing this at length so the tails are not repeated here. The essential ita used are the ionization energies for In[29]: $d^5 \rightarrow d^4$, 33·69 eV; $d^4s \rightarrow d^4$, 5·95 eV; $d^5s \rightarrow d^5$, 15·64 eV and $d^6 \rightarrow d^5$, ·87 eV; and for oxygen $O^{2-} \rightarrow O^-$, −8·9 eV. he Madelung potential at an ion site is 22·6 V. The crystal field stabilization iergies were taken to be: d^6, 0·3 eV; d^5s, , O; d^4, 1·5 eV. The most important quantity this kind of calculation is the polarization energy when an ion of different from normal charge is present in the lattice. In this instance, the critical quantity is the polarization energy when there is Mn^+ or Mn^{3+} in place of Mn^{2+}. To a fair approximation we can take the values calculated by van Houten for NiO, as most of the polarization will be the surrounding oxygen ions. However, because the polarizability of Mn^{2+} is larger than that of Ni^{2+}, this value will be an underestimate. van Houten's values are, for a rigid lattice 5·0 eV, and allowing ionic relaxation, 6·8 eV.*

From these data we obtain the energy level diagram shown in Fig. 9. In this diagram levels are identified as if they were occupied so that, for example, the level labelled Mn_{Mn} is a Mn^{2+} ion when occupied (and is a hole, Mn^{3+}, when empty). The highest filled band will correspond to the Mn_{Mn} level and the

---

*The value given for polarization energy by Dickens *et al.*[24] is clearly too large for MnO, although these authors agree with van Houten for NiO. The reason is that the polarizability of oxygen was taken to be larger in MnO: In fact, the refractive index[30] of MnO is actually smaller than that of NiO. The larger polarizability of Mn^{2+} results, however, in MnO having a much higher static dielectric constant than NiO[30].

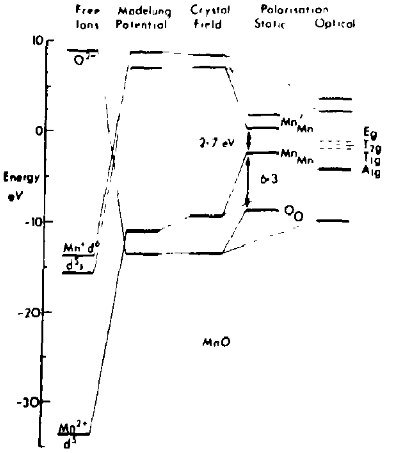

Fig. 9. Energy level diagram for MnO from McKinzie[10] based on a similar diagram of van Houten[26] for NiO.

lowest empty band will originate in the Mn'_{Mn} level so it can be seen that the *thermal* band gap for MnO should be somewhat less than 2·7 eV in contrast to the values of 5·4 eV found by the same method for NiO. The *optical* band gap will be larger, and is obtained by using the rigid-lattice value of the polarization energy. In this way a value of 5–6 eV is obtained.

The low band gap predicted for MnO suggests that a considerably higher electron concentration is expected in this oxide than in NiO. Also of interest is the observation[29] that for Mn^+ d^5s is 1·87 eV more stable than d^6 whereas for Ni^+ d^9 is 1·04 eV more stable than d^8s; the conduction band for MnO is therefore likely to have considerable s character and to be wider than the d-like conduction band in NiO. This explains the unusually high (for an ionic oxide) electron mobility in MnO.

Optical studies on MnO[31,32] do indeed indicate an optical band gap of about 4 eV and show also the energy levels characteristic of Mn^{2+} in an octahedral field so that the Mn^{2+} levels are fairly well localized.

The thermal band gap can be obtained from the experimental data in several ways. From equations (20) and (22), the minimum conductivity is

$$\sigma_m = 2e(K_i\mu_+\mu_-)^{1/2} \qquad (29)$$

and K_i is related to the thermal band gap energy ϵ_0 by

$$K_i = n_0 p_0 \exp(-\epsilon_0/kT) \qquad (30)$$

where n_0 and p_0 are respectively the conduction and valence band densities of states. From these two equations it follows that

$$-k\partial \ln \sigma_m/\partial(1/T) = \epsilon_0/2 - (k/2)\partial \ln \mu_+/\partial(1/T) - (k/2)\partial \ln \mu_-/\partial(1/T) \qquad (31)$$

From the data shown in Figs. 4 and 6, it has already been determined that $-k\partial \ln \sigma_m/\partial(1/T) = 1{\cdot}39$ eV and that $-k\partial \ln \mu_+/\partial(1/T) = 0{\cdot}52$ eV, so that from equation (31):

$$\epsilon_0 = 2{\cdot}26\,\text{eV} + k\partial \ln \mu_-/\partial(1/T). \qquad (32)$$

The high electron mobility suggests that μ_- is not a strong function of temperature so the first estimate of the band gap is $\epsilon_0 \doteq 2{\cdot}25$ eV.

A second method involves the data for the *isothermal* variation of the thermoelectric power, Q, with oxygen pressure. Becker and Frederikse[33] show that close to σ_m

$$\partial Q/\partial \ln P_{O_2} = (k\nu/2e)[\epsilon_0/kT) + A_+ + A_- - 2] \qquad (33)$$

here ν is $\partial \ln p/\partial \ln P_{O_2}$ equal in this case to 1/6 and A_+ and A_- are the kinetic energy terms that enter into the contributions from holes and electrons respectively to the thermoelectric power.

The data shown in Fig. 3 give for 1100°C, $\partial Q/\partial \ln P_{O_2} = 1{\cdot}18 \times 10^{-4}$ V deg^{-1} so that from equation (33)

$$\epsilon_0 = [2{\cdot}18 - 0{\cdot}118\,(A_+ + A_-)]\,\text{eV}. \qquad (34)$$

For the 'hopping' mechanism of conduction A_+, A_- are probably close to zero[1,27], so again $\epsilon_0 \approx 2{\cdot}2$ eV. An analysis along somewhat similar lines but utilizing other data over a wider range of concentrations was made by Crevecoeur and de Wit[34] using Jonker's[35] method of analysis of thermoelectric power gave a smaller band gap ($\leq 1{\cdot}84$ eV). As both Jonker's approach and equation (33) suppose that the mobility ratio b is constant, we prefer the larger value obtained here.

A final calculation of interest concerns the densities of states, n_0 and p_0. It was shown earlier that bK_i could be unambiguously determined from the variation with doping of the oxygen pressure at the conductivity minimum, equation (16). Referring to Table 2, the value of bK_i at 1100°C is (with concentration units of site fraction) $5{\cdot}15 \times 10^{-6}$. With $\epsilon_0 = 2{\cdot}2$ determined above

$$bK_i \exp{(\epsilon_0/kT)} = bn_0p_0 = 560 \text{ at } 1100°\text{C}. \tag{35}$$

Alternatively, if one were to accept the band gap of Crevecoeur and de Wit, $\epsilon_0 = 1{\cdot}84$ eV, the same calculation leads to

$$bn_0p_0 = 30. \tag{36}$$

As Jonker and van Houten[27] have discussed, there are usually two cases to consider: Conduction in a fairly wide band with density of states of the order of 10^{-3} (expressed as site fraction i.e. 10^{19}–10^{20} cm^{-3}) and in the 'hopping' regime the density of states becomes simply the concentration of ions, or unity in units of site fraction. A possible interpretation of the result expressed in equation (35) is therefore $b \sim 10^3$, $n_0 \sim p_0 \sim 1$. This would imply that the 'hopping' model applies to the transport of holes *and electrons* in MnO, despite the very high mobility of the latter. On the other hand equation (36) is consistent with 'band' conduction for electrons, for if we take $b \approx 10^3$, $p_0 \approx 1$ we obtain $n_0 \approx 3 \times 10^{-2}$ ($= 1{\cdot}4 \times 10^{21}$ cm^{-3}) and the usual expression for the density-of-states effective mass yields

$$(m^*/m) = h^2(n_0/2)^{2/3}/(2\pi mkT) \approx 3; \tag{37}$$

a perfectly acceptable value. The lower band gap would imply $A_- \approx 2$ in equation (34) and a rather large negative temperature dependence of μ_- (about T^{-3}, see equation (32)); also consistent with band conduction.

In view of current thinking about oxide semiconductors[1], the second possibility, with the lower band gap, seems the more likely, but to resolve the problem unambiguously a useful (but difficult) experiment would be to determine the temperature dependence of electron mobility.

6. CONCLUSION

Summary

This work has demonstrated that correctly interpreted studies of the electrical properties as a function of oxygen activity for doped crystals can be unusually productive. We have been able to derive in this way the equilibrium constants for incorporation of oxygen and chromium in MnO.

The electrical properties can be correlated with an energy level diagram based on the ionic model. The conduction levels are associated with Mn$^+$ and the valence levels with Mn^{2+} with an energy gap of 1·8–2·2 eV.

Acknowledgements—We have profited greatly from the earlier studies of and subsequent discussions with Dr. H L. McKinzie. This work was supported by the Air Force office of Aerospace Research, United States Air Force Office of Scientific Research, Office of Aerospace Research, United States Air Force, under AFOSR Grant No. AF-AFOSR-68-1371 M. V. gratefully acknowledges a research grant from C.N.R. Rome, Italy.

REFERENCES

1. ADLER D. In *Solid State Physics* (Edited by F. Seitz, D Turnbull and H Ehrenreich), Vol. 21, p. 1, Academic Press, New York (1968).
2. DUQUESNOY A. and MARION F., *C r hebd Séanc. Acad. Sci., Paris* **256**, 2862 (1963).
3. EROR N. G., Ph D. Thesis, Northwestern University (1965).
4. GVISHI M., TALLAN N. M. and TANNHAUSER D. S., *Solid State Commun.* **6**, 135 (1968).
5. deWIT H. J. and CREVECOEUR C., *Phys. Letts* **25A**, 393 (1967).
6. NAGELS P., DENAYER M., deWIT H. J. and CREVECOEUR C., *Solid State Commun.* **6**, 695 (1968).
7. DAVIES M. W. and RICHARDSON F. D., *Trans. Faraday Soc.* **55**, 604 (1959).

8. HED A. Z. and TANNHAUSER D. S., *J. chem. Phys.* **47**, 2090 (1967).
9. HED A. Z. and TANNHAUSER D. S., *J. electrochem. Soc.* **114**, 314 (1967).
10. McKINZIE H. L., Ph.D. Thesis, Arizona State University (1967).
11. LeBRUSQ H., OEHLIG J. and MARION F., *C. r. hebd. Séanc. Acad. Sci., Paris* **266**, 965 (1968).
12. KRÖGER F. A., *The Chemistry of Imperfect Crystals*. North Holland, Amsterdam (1964).
13. BOCQUET J.-P., KAWAHARA M. and LACOMBE P., *C. r. hebd. Séanc. Acad. Sci., Paris* **265**, 1318 (1967).
14. PARRISH W. and WILSON A. J. C., In *International Tables for X-ray Crystallography* (Edited by J. S. Kaspar and K. Lonsdale), Vol. 2, p. 216. Kynoch Press, Birmingham (1967).
15. SACHSE H. B., *Anal. Chem.* **32**, 529 (1960).
16. DEREN J., HABER J. and SLOCZYNSKI J., *Chem. Anal.* **6**, 659 (1961).
17. KOLTHOFF I. M. and BELCHER J. F., *Volumetric Analysis*, Vol. 3, p. 53. Interscience, New York (1957).
18. HAGEMARK K. and BROLL M., *J. inorg. nucl. Chem.* **28**, 2837 (1966).
19. CIMINO A., *J. phys. Chem.* **61**, 1676 (1957).
20. O'KEEFFE M., In *Chemistry of Extended Defects in Non-metallic Solids* (Edited by L. Eyring and M. O'Keeffe). North Holland, Amsterdam (1970).
21. FENDER B. E. F. and RILEY F. D., *ibid.*
22. O'KEEFFE M. and MOORE W. J., *J. chem. Phys.* **36**, 3009 (1962).
23. EROR N. G. and WAGNER J. B., *J. Phys. Chem. Solids* **29**, 1597 (1968).
24. DICKENS P. G., HECKINGBOTTOM R. and LINNETT J. W., *Trans. Faraday Soc.* **64**, 1489 (1968).
25. KRÖGER F. A., *J. Phys. Chem. Solids* **29**, 1889 (1968).
26. van HOUTEN S., *J. Phys. Chem. Solids* **17**, 7 (1960).
27. JONKER G. H. and van HOUTEN S., *Halbleiterprobleme* **6**, 118 (1961).
28. MORIN F. J., *Bell Syst. Tech. J.* **37**, 1047 (1958).
29. CHARKIN O. P. and DYATKINA M. E., *Zh. Struct. Khim.* **6**, 422 (1965); Engl. trans. *J. Structural Chem.* **6**, 397 (1965).
30. KINNEY T. B. and O'KEEFFE M., *Solid State Commun.* **7**, 977 (1969).
31. PRATT G. W. and COELHO R., *Phys. Rev.* **116**, 281 (1959).
32. NEWMAN R. and LOH E., *J. appl. Phys.* **32**, 470 (1961).
33. BECKER J. H. and FREDERIKSE H. P. R., *J. appl. Phys.* **33**, 447 (1962).
34. CREVECOEUR C. and deWIT H. J., *Solid State Commun.* **6**, 295 (1968).
35. JONKER G. H., *Philips Res. Rep.* **23**, 131 (1968).

J. Phys. Chem. Solids Pergamon Press 1970. Vol. 31, pp. 963–972. Printed in Great Britain.

RECOMBINATION AND TRAPPING IN *n*-TYPE COBALT-DOPED GERMANIUM

G. SUSILA

Department of Physics, Indian Institute of Science, Bangalore-12. India

(*Received* 29 *September* 1969)

Abstract – The role of cobalt centers in promoting the recombination and trapping processes in *n*-type germanium has been investigated. Data on lifetime measurements carried out by the steady-state photoconductivity and photo-magneto-electric methods in the temperature range 145 to 300°K on *n*-type germanium samples containing cobalt in the concentration range $1\cdot10^{13}$ to $5\cdot10^{14}/\text{cm}^3$ are presented The results are analysed on the basis of Sah–Shockley's multi-level formula to yield the capture cross-sections $S_p^{=}$ (hole capture cross-section at doubly negatively charged center) and S_n^{-} (electron capture cross-section at singly negatively charged center) and temperature dependence It is found that S_p^{-} is $(22\pm6)\,.\,10^{-16}\,\text{cm}^2$ and S_n^{-} is $\sim 0\cdot1\,.\,10^{-16}\,\text{cm}^2$ at 145°K. $S_p^{=}$ varies as T^{-n} ($n = 3\cdot5$ to $4\cdot5$) in the range 145–220°K; above 225°K the index '*n*' tends to a smaller value. S_n^{-} is practically temperature independent below 180°K and increases with increase of temperature above 180°K. The value of $S_p^{=}$ and its temperature variation lead one to the conclusion that during capture at attractive centers, the phonon cascade mechanism is responsible for the dissipation of the recombination energy.

1. INTRODUCTION

It is well-known from the work of Tyler, Newman and Woodbury[1] that cobalt in germanium gives rise to two deep levels in the forbidden gap, one at 0·30 eV from the conduction band and the other at 0·25 eV from the valence band and that these levels promote the electron-hole recombination processes. The 0·25 eV level represents the transition of cobalt centers from the neutral to singly negatively charged state and the 0·30 eV corresponds to the transition from singly negatively charged to doubly negatively charged state and the capture cross-sections that are involved in the recombination processes are S_n^0, S_p^-, S_n^- and $S_p^=$ where the subscript refers to the type of carrier captured and the superscript to the state of cobalt atom before capture. A value of $10\,.\,10^{-16}\,\text{cm}^2$ has been reported for S_n^0 by Glinchuk *et al.* [2]. Some stray values of S_n^- attributed to Glinchuk ($S_n^- = 0\cdot001\,.\,10^{-16}\,\text{cm}^2$ at 80°K and $< 10\cdot10^{-16}\,\text{cm}^2$ at 300°K) have been found quoted in the literature[3]. However, unlike its neighbours iron, manganese and nickel in the Periodic Table, no detailed investigations seem to have been carried out on the recombination cross-sections of cobalt centers in germanium and their temperature dependence. In this paper, the results of lifetime measurements on *n*-type cobalt-doped germanium samples are reported and some of the capture cross-sections of the cobalt centers have been estimated.

2. MATERIAL PREPARATION

Single crystals of *n*-type germanium were grown by Czochralski pulling technique. Cobalt doping was performed by adding to the melt germanium–cobalt pellets containing weighed amounts (10–60 mg) of cobalt (spectroscopically pure and procured from Johnson Mathey & Co., U.K.). The cobalt was free from nickel, iron etc. Even if these impurities were to be present in very small concentrations, it would have hardly mattered because the segregation coefficients of these impurities in germanium are also of the same order as that of cobalt. Also the presence of small quantities of shallow level impurities would have very little effect on the ultimate recombination processes in the temperature range under investigation. To get n-type crystals of different concentrations, antimony (Johnson Mathey Semiconductor grade I, spectroscopically pure) was used as the counterdopant. In all the cobalt-doped crystals, invariably lineage markings appeared at the latter portions of the crystals. Samples from the earlier regions exhibited dislocation densities of the order of a few hundreds to one thousand per cm^2, as estimated by counting the etch pits. Samples cut from the lower portions sometimes showed abnormal mobility behaviour and rather low effective cobalt concentration.

3. EXPERIMENTAL

Resistivity, Hall effect and lifetime measurements by the steady-state photoconductance (pc) and photo-magneto-electric (pme) methods were carried out on a large number of n-type cobalt-doped germanium samples in the temperature range 145-300°K using liquid oxygen as the refrigerent. For Hall effect measurements, a magnetic field of 3000 oersteds was used.

For lifetime measurements light from a tungsten filament lamp (36 W) powered by a constant current source and interrupted at 120 cps by a chopper disc was focussed on the specimen. An iris diaphragm to vary the injection level and a water filter of 3 cm thickness to ensure surface generation were interposed in the path of the beam. The photoconductivity signal obtained across the sample when a current was passed through it from a constant current source was amplified by a twin-T narrow band amplifier (band width 5 cps) and was fed to a phase-sensitive detector. The reference signal for the phase-sensitive detector was derived from a photocell on which was incident light from an auxiliary lamp and chopped by the same chopper, thus ensuring perfect synchronization of the signal and the reference. The detected d.c. output was measured by a galvanometer with a lamp and scale arrangement. The amplifier-phase-sensitive detector system were calibrated with signals of known magnitude. For pme effect, no current was sent through the crystal but the sample was subjected to a magnetic field in a direction perpendicular to that of light. The pme signal developed across the third perpendicular direction was measured in the same way as in the photoconductivity method. Using the pc and pme voltages the lifetimes τ_{pc} and τ_{pme} were calculated. The unknown intensity parameter occuring in the evaluation of τ_{pc} and τ_{pme} was estimated by the compensation method at room temperature, in which the pc signal was adjusted to cancel the pme signal. When there is no trapping which is usually the case at room temperature, $\tau_{pme} = \tau_{pc} = \tau_{comp}$. This assumption as can be seen later, was valid for most of the crystals. Since the value of intensity of the light estimated at room temperature was utilized for the calculation of lifetimes τ_{pc} and τ_{pme} at other temperatures, care was exercised to retain the crystal and other components in the optical system undisturbed throughout each set of measurements. The lifetime measurements were carried out under the conditions described by Karpova *et al.* [4].

In order to see whether linear recombination law is valid and to choose the proper intensity range in which the lifetime is practically independent of light intensity, τ_{pc} and τ_{pme} were measured for all the samples at different light intensities and the results for sample No. 48 are given in Fig. 1. Similar results were obtained for other samples also. It is seen from the figure that τ_{pc} and τ_{pme} are constant within a factor of 3 for a change of intensity by a factor 20 even at low temperatures. Major part of the changes are confined to the region of high-light intensity. All the measurements were carried out in the middle of the region to effect a compromise between the signal strength and low-injection level.

The front surface of the crystal was carefully etched to reduce surface recombination. Experiments were performed in vacuum and in different gas ambients (O$_2$, N$_2$, CO$_2$,

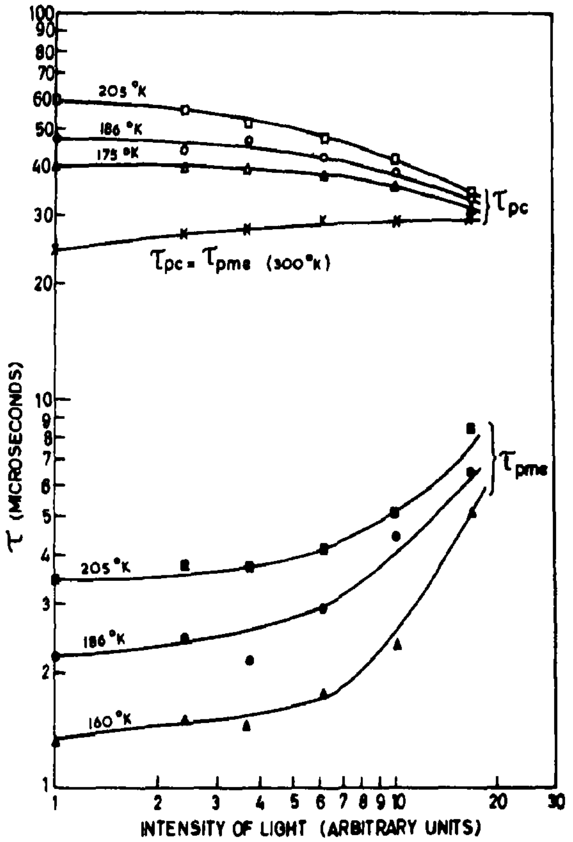

Fig. 1. Variation of τ_{pme} and τ_{pc} with light intensity for sample No. 48.

N_2O. Argon) to alter the surface recombination velocity. It was found that there was practically no change in the observed lifetime, thereby indicating that the surface recombination is small compared to bulk recombination.

4. RESULTS AND DISCUSSION

The variations of resistivity (ρ) and electron concentration (n_0) as a function of temperature for high-resistivity, cobalt-doped *n*-type samples show the characteristic slope of 0·30 eV in conformity with the results reported by Tyler and his coworkers for cobalt[1]. The lifetime values observed in cobalt-doped samples vary from 1 to 30 μ sec at 300°K depending on the cobalt concentration in contrast to at least 300 μ sec in the undoped material, thereby indicating that cobalt gives rise to efficient recombination centers. For the reliable estimation of capture cross-sections, low- and medium-resistivity samples were chosen and the results of τ_{pc} and τ_{pme} measurements as a function of temperature are given in Fig. 2 and the other pertaining data are presented in Table 1.

The cobalt concentration in each sample was estimated by one of the following methods as applicable: (1) from the difference in the two plateaus in the log n_0 vs. $1/T$ curve wherever two plateaus are clearly observed, (2) from the relative location of the sample in the grown crystal with respect to a sample in which two plateaus were obtained and (3) from the knowledge of the segregation

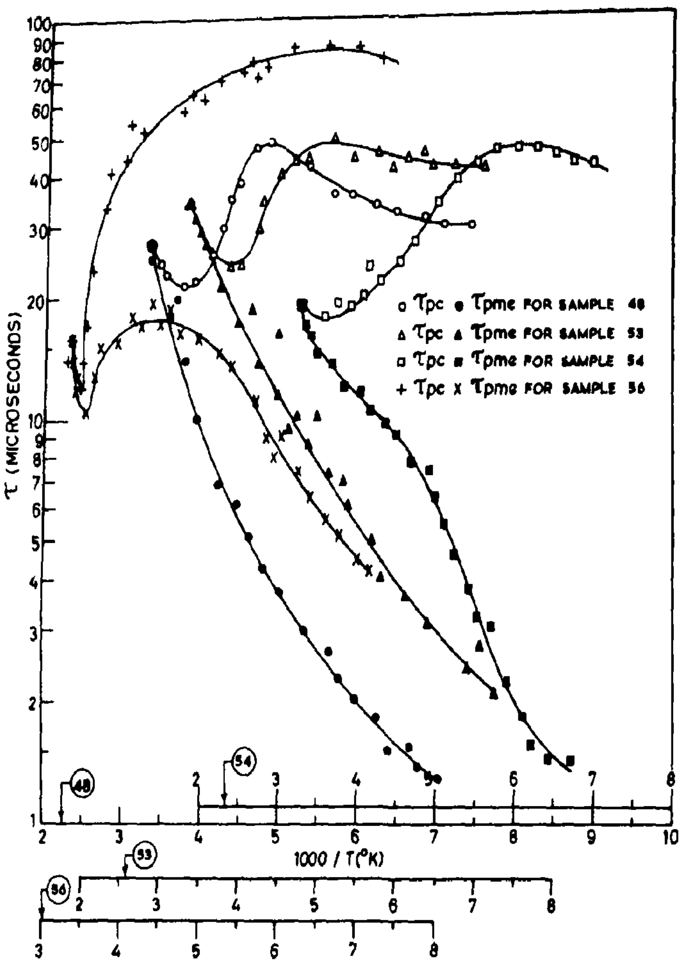

Fig. 2. Temperature variation of τ_{pmc} and τ_{pc} for n-type cobalt-doped germanium samples. Note (1) the shift in the horizontal scale for different samples; (2) the vertical scale should be divided by 10 for sample 54.

Table 1

Sample No.	Electron conc. n_0 at 300°K (No./cm³)	Cobalt conc. N_t (atoms/cm³)	Lifetime $\tau_{pmc} = \tau_{pc}$ at 300°K(μ sec)	S_p(T°K) ($\times 10^{-16}$ cm²)	S_n (T°K) ($\times 10^{-16}$ cm²)	Index 'n' in the power law AT^{-n}
48	$1{\cdot}44 . 10^{14}$	$2{\cdot}8 . 10^{13}$	28	28(145°K)	0·16(145°K)	3·8
53	$2{\cdot}43 . 10^{14}$	$- 1{\cdot}5 . 10^{13}$	34	28(145°K)	0·06(145°K)	3·5
54	$1{\cdot}37 . 10^{15}$	$4{\cdot}4 . 10^{14}$	1·9	15(155°K)	0·13(155°K)	4·15
56	$1{\cdot}15 . 10^{15}$	$- 1 . 10^{13}$ (Effective value calculated)	15·6		0·005(145°K)	4·5

coefficient of cobalt in germanium and the amount added to the melt.

Before analysing the results of the samples mentioned above, it is worthwhile to summarize the main features of τ_{pc} and τ_{pme} data.

(1) The τ_{pme} value decreases with increase of cobalt concentration throughout the temperature range investigated, thereby indicating that cobalt atoms are responsible for recombination.

(2) The τ_{pme} decreases with decrease of temperature.

(3) The log τ_{pc} vs. $1000/T$ curve shows the following features:

(a) immediately below room temperature (from 300°K to roughly 270°K), τ_{pc} decreases with decrease of temperature, following closely the τ_{pme} curve, (b) in the temperature range around 270–200°K, τ_{pc} increases rapidly to a value greater than the room temperature value and (c) at still lower temperatures (below 200°K), the curve shows a gradual decrease after reaching a maximum and in some crystals the decrease is followed by a plateau.

(4) The trapping ratio $K \equiv \tau_{pc}/\tau_{pme}$ at low temperatures increases with increase in cobalt concentration for a given carrier concentration.

The pronounced differences in the τ_{pme} and τ_{pc} values at low temperatures indicate that there is considerable amount of trapping as expected for *n*-type crystals with deep-level acceptor impurities. The fact that the trapping ratio depends on cobalt concentration shows that the cobalt centers themselves are responsible for trapping in addition to their role in recombination.

There are two aspects to the understanding of the main features of these curves. They are (1) the study of recombination proper without the complications of trapping. This is possible by the analysis of the τ_{pme} data which are not much influenced by trapping effects. (2) the study of trapping from the photoconductivity data.

The analysis of the τ_{pme} and τ_{pc} data and the identification of the relevant cross-sections therefrom are carried out on the basis of multilevel recombination statistics of Sah and Shockley[5] since cobalt introduces two acceptor levels. Under favourable conditions the formula can be reduced to the single-level form of Shockley and Read[6] as discussed below. (Actually it has been reported by Tyler[7] that cobalt gives rise to three levels of which the lower most donor level is near the valence band. However this is ignored because it becomes operative only at very low temperature and at high hole concentrations).

For the two-level case, Sah–Shockley's[5] expression for τ takes the form (for low-injection levels)

$$\frac{1}{\tau} = (n_0+p_0) \times\left[\frac{(f_0{}^0+f_1{}^0)}{\tau(n,0)\{p_0+p^*(\tfrac{1}{2})\}+\tau(p,1)\{n_0+n^*(\tfrac{1}{2})\}} + \frac{(f_1{}^0+f_2{}^0)}{\tau(n,1)\{p_0+p^*(\tfrac{3}{2})\}+\tau(p,2)\{n_0+n^*(\tfrac{3}{2})\}}\right]. \tag{1}$$

For meaning of symbols see Table 2.

For *n*-type samples where the Fermi-level lies above the intrinsic level, there will be no neutral cobalt sites. Hence $f_0{}^0$ can be equated to zero. Also, for low-resistivity crystals at low temperatures, the Fermi-level lies well above the second level, thereby ensuring that there are no singly negatively charged cobalt sites either (i.e. $f_1{}^0 = 0$ and $f_2{}^0 = 1$). Therefore the first term in the expression (1) can be deleted. $p_0 \ll n_0$ and $p^*(\tfrac{3}{2}) \ll n_0$. For example, even at room temperature for $n_0 = 10^{14}/\mathrm{cm}^3$, $p_0 \approx 5\,.\,10^{12}/\mathrm{cm}^3$, $p^*(\tfrac{3}{2}) \approx p(\tfrac{3}{2}) = 5{\cdot}8\,.\,10^{12}/\mathrm{cm}^3$ which will be even smaller when divided by γ, the degeneracy ratio. Hence for low-resistivity *n*-type samples, the expression for τ reduces to a very simple form at low temperatures.

$$\tau = \tau(p.2)\left[1+\frac{n^*(\tfrac{3}{2})}{n_0}\right] = \frac{1}{N_f S_p{}^{=} v}\left[1+\frac{n^*(\tfrac{3}{2})}{n_0}\right]. \tag{2}$$

Table 2. Meaning of the symbols

τ	lifetime; the subscript pc. pme, comp. refers to the value obtained by the respective methods
$E(\frac{3}{2})$	0·30 eV level from the conduction band
$E(\frac{1}{2})$	0·25 eV level from the valence band
$\gamma(\frac{1}{2})$ $\gamma(\frac{3}{2})$	the degeneracy ratios of the respective levels
n_0 and p_0	equilibrium concentrations of electrons and holes.
$n(\frac{1}{2})$	$N_c \exp -\left[\frac{E_c - E(\frac{1}{2})}{kT}\right]$
$p(\frac{1}{2})$	$N_v \exp\left[-\frac{E_v - E(\frac{1}{2})}{kT}\right]$
$n(\frac{3}{2})$	$N_c \exp -\left[\frac{E_c - E(\frac{3}{2})}{kT}\right]$
$p(\frac{3}{2})$	$N_v \exp\left[\frac{E_v - E(\frac{3}{2})}{kT}\right]$
$E^*(\frac{1}{2})$	$= E(\frac{1}{2}) + kT \log \gamma(\frac{1}{2})$
$E^*(\frac{3}{2})$	$= E(\frac{3}{2}) + kT \log \gamma(\frac{3}{2})$
$n^*(\frac{1}{2})$ $p^*(\frac{1}{2})$ $n^*(\frac{3}{2})$ $p^*(\frac{3}{2})$	are obtained by replacing $E(\frac{1}{2})$ and $E(\frac{3}{2})$ by $E^*(\frac{1}{2})$ and $E^*(\frac{3}{2})$ in the expressions for n and p
$n^*(\frac{1}{2})$	$= \gamma(\frac{1}{2}) n(\frac{1}{2})$; $p^*(\frac{1}{2}) = p(\frac{1}{2})/\gamma(\frac{1}{2})$
$n^*(\frac{3}{2})$	$= \gamma(\frac{3}{2}) n(\frac{3}{2})$; $p^*(\frac{3}{2}) = p(\frac{3}{2})/\gamma(\frac{3}{2})$
N_f	total concentration of cobalt centers
N_0, N_1 and N_2	concentration of neutral, singly negatively charged and doubly negatively charged cobalt centers
f_0^0	occupation probability for the neutral state (under equilibrium) = N_0/N_f
f_1^0	same for singly negatively charged state = N_1/N_f
f_2^0	same for doubly negatively charged state = N_2/N_f
S	capture cross-section (subscript refers to the type of carrier captured and superscript to the state of the center before capture) $\tau(n,0) = \frac{1}{N_f S_n^0 v}$, $\tau(n,1) = \frac{1}{N_f S_n^- v}$ $\tau(p,1) = \frac{1}{N_f S_p^- v}$; $\tau(p,2) = \frac{1}{N_f S_p^= v}$.
v	thermal velocity of the carriers

By identifying the measured τ_{pme} with τ in equation (2) and knowing $n^*(\frac{3}{2})$, n_0 and N_f, $S_p^=$ can be calculated. Further for the case of cobalt $n^*(\frac{3}{2})$ is of the order of $1{\cdot}6 \,.\, 10^{11}/\text{cm}^3$ at 200°K (within a factor of γ), which decreases very rapidly with decrease of temperature. Hence below 200°K, $\tau_{\text{pme}} \approx \tau(p,2)$ and any temperature variation of τ_{pme} *at low temperatures should be due to that of $S_p^=$ only.*

In the region of temperatures where there is a change in the charge state (from 2 to 1), f_1^0 cannot be ignored and it may be necessary to *examine the contribution of the other* capture cross-sections in the first term of equation (1).

The analysis of τ_{pc} data is not as simple as that of τ_{pme} in any temperature range. The difference between τ_{pc} and τ_{pme} particularly arises because of the large difference in the cross-sections for electrons and holes. It is the usual practice to deal with the ratio $\tau_{\text{pc}}/\tau_{\text{pme}} = K$ which can be expressed in terms of $\delta p_{\text{flaw}}/\delta p$ (the ratio of excess fixed charges due to trapping to the excess mobile charges) rather than with τ_{pc} alone. Since in the low- and medium-resistivity n-type materials only the upper level is operative and the expression for $\delta p_{\text{flaw}}/\delta p$ (see Ref. [8]) can be written as

$$\frac{\delta p_{\text{flaw}}}{\delta p} = N_f \times \frac{S_p^= f_2^0 - S_n^- f_1^0}{S_p^=[p_0 + p^*(\frac{3}{2})] + S_n^-[n_0 + n^*(\frac{3}{2}) + N_f(1 - f_2^0)]} \tag{3}$$

($f_1^0 + f_2^0 = 1$ since $f_0^0 = 0$).
p_0 and $p^*(\frac{3}{2}) \ll n_0$ and at low temperatures $f_2^0 \approx 1$. Hence

$$\frac{\delta p_{\text{flaw}}}{\delta p} = \frac{N_f}{n_0} \frac{S_p^=}{S_n^-}. \tag{4}$$

The trapping coefficient K is given by [8]

$$K = 1 + \frac{b}{b+1} \frac{N_f}{n_0} \frac{S_p^=}{S_n^-}. \tag{5}$$

Knowing $S_p^=$, N_f, n_0 and K, S_n^- and its temperature dependence can be evaluated.

At higher temperatures where $f_2^0 \neq 1$, the expression for K is

$$K = 1 + \frac{b}{b+1} \frac{N_f}{n_0} \frac{S_p^{=}}{S_n^{-}} (f_2^0)^2 \tag{6}$$

provided the relative magnitude of $S_p^{=}$ and S_n^{-} are favourable i.e., $(S_p^{=}/S_n^{-}) \gg 1$.

For the samples under investigation, n_0 varies from 10^{14} to $5 . 10^{15}/\text{cm}^3$. For a value of $\gamma \approx 10$ (the reasons for which are discussed below), $\tau_{\text{pme}} \approx \tau(p.2)$ at low temperatures and the values of $S_p^{=}$ for the different crystals lie in the range $(15$–$28) . 10^{-16}\,\text{cm}^2$ at 145°K. Since $n^*(\frac{3}{2})/n_0$ does not exceed 0·01 even at 200°K, the temperature variation of τ_{pme} in the region 145–200°K gives the temperature variation of $\tau(p,2)$ and hence that of $S_p^{=}$. Figure 3 gives the plots of $\log \tau_{\text{pme}}$ vs. $\log T$ for the different samples. It is found that the plots are linear at low temperatures, thereby showing that the temperature variation of $S_p^{=}$ obeys a power law AT^{-n} (n varying between 3·5 and 4·5 for the different samples).

If this power law were valid up to room temperature, then making use of the extrapolated values of $S_p^{=}$, it should be possible to fit up the experimental curve to the expression (2) by a proper choice of $n^*(\frac{3}{2})$ i.e. $\gamma(\frac{3}{2})$. For the operative cobalt level 0·30 eV, it was not possible to fit up the experimental curve for a single value of γ.

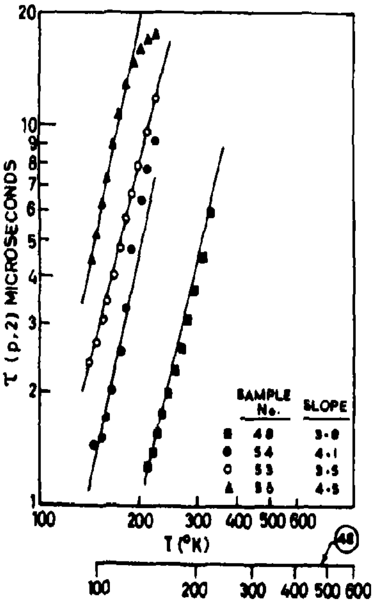

Fig. 3. $\text{Log}\,\tau(p,2) \approx \text{Log}\,\tau_{\text{pme}}$, (at low temperatures) vs $\log T$ for n-type cobalt-doped germanium samples. For sample 48 the horizintal scale is shifted. For sample 54 the vertical scale should be divided by 10.

This discrepancy may be due to (1) contribution from other terms in equation (1) if $f_1^0 \neq 0$ near room temperature and (2) change in the power law (i.e. a less steep variation of $S_p^{=}$ at higher temperatures). Rough estimates of the contribution of the first term to lifetime, τ, indicate that it will not completely account for the discrepancy mentioned above when $f_1^0 \neq 0$. This is further confirmed by the observation that in some crystals (for example N°: 53), in which the electron concentration is such that $f_1^0 = 0$ even at room temperature, the experimental τ_{pme} curve could not be fitted up to the expression using a single value of $\gamma(\frac{3}{2})$. Hence it is concluded that the temperature law for $S_p^{=}$ determined at low temperatures may not hold good right up to room temperature and the index n in the power law may tend to a smaller value around 200°K.

From the trapping ratio K, $S_p^{=}/S_n^{-}$ and hence S_n^{-} was determined at 145°K. The values of S_n^{-} determined for different crystals at about 145°K range from $(0{\cdot}05$ to $2) . 10^{-16}\,\text{cm}^2$. Using the expression (5) and assuming that S_n^{-} is temperature independent, the trapping coefficient K was calculated for the temperature range under investigation. The plot of K vs. $1/T$ for two samples are given in Fig. 4. The full line represents the calculated values of K and the dots represent the experimental points.

For most of the crystals the calculated and experimental values of K agree reasonably well at low temperatures, the calculated values being slightly higher than the experimental ones and this deviation increases with increase of temperature. The exact temperature dependence could not be found out due to uncertainty in the index n in the power law $S_p^{=} = AT^{-n}$ above 200°K. The calculation

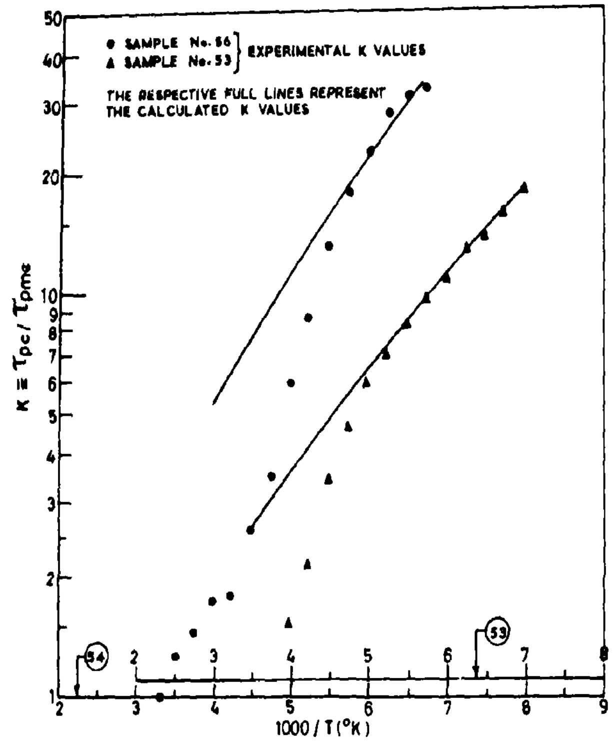

Fig. 4. Variation of K with temperature Note the shift in the temperature scale for sample 53.

of K in crystals whose log n_0 vs. $1/T$ plots exhibit two plateaus is rendered difficult due to uncertainty in $f_2{}^0$.

Some of the samples cut from the lower end of the grown crystals, which is rich in cobalt, exhibit the following anamolous behaviour. The pme and pc lifetimes are found to be larger than what would be expected for the cobalt concentration calculated from the knowledge of segregation coefficient. While the overall pattern of τ_{pc} and τ_{pme} curves at low temperatures and the initial dip in the τ_{pc} curve are similar to those found in other samples, the τ_{pme} curve shows a predominant hump around 225°K exhibiting values higher than that at room temperatures. Making use of the value of $S_p{}^=$ from other samples the effective cobalt concentration is determined and it is found to be an order of magnitude smaller than the expected value. However the trapping coefficient K at low temperature is considerably larger than what is expected for the small effective cobalt concentration. The value of $S_n{}^-$ estimated at 145°K is quite low ($0{\cdot}005 \,.\, 10^{-16}\,\mathrm{cm}^2$).

The large difference in the expected and the effective cobalt concentrations may be because of the deactivation of the levels due to the precipitation of cobalt atoms from the solid solution. The high trapping coefficient may be due to the inhomogeneities in the crystal due to large amount of precipitated cobalt. The hump is much too pronounced to be explained on the basis of changes in the power law for the temperature variation of $S_p{}^=$.

5. γ FOR THE LEVEL E (3/2)

One of the ubiquitous quantities involved in the analysis of lifetime data is the degeneracy ratio denoted by γ. The present knowledge of these ratios for impurity levels in the band gap of semiconductors is scanty. For cobalt levels in germanium, there seems to be no prior investigations on γ values and lack of this data has been a serious handicap in making quantitative calculations. An examination of the carrier concentration and recombination data gives us some idea about these ratios.

From the electron concentration data, the range of Fermi levels for the temperature range under investigation is determined for different samples. This range indicates that the effective energy level $E^*(\frac{3}{2})$ which is related to the true level $E(\frac{3}{2})$ by the relation

$$E^*(\tfrac{3}{2}) = E(\tfrac{3}{2}) + kT\log\gamma(\tfrac{3}{2}) \qquad (7)$$

should be situated above 0·30 eV level because the room temperature Fermi level lies above 0·30 eV even for those samples, which show two plateaus in the log n_0 vs. 1000/T curve. This implies that γ is greater than unity. By finding out the Fermi level at the temperature at which the electron concentration is n_0 (at low temperature) $+\frac{1}{2}N_f$ (i.e.) the upper cobalt level is half-populated), it is possible to calculate $\gamma(\frac{3}{2})$. The values of γ obtained for different samples on the basis of the above procedure ranges from 7 to 16. It should be pointed out that this method is not accurate because it is quite sensitive to the choice of the point at which the cobalt levels are supposed to be half-populated. Since the values range from 7 to 16, a round figure 10 has been utilized in order to make approximate estimates of the values of $n^*(\frac{3}{2})$ and $p^*(\frac{3}{2})$ for discussion purposes.

CAPTURE AT ATTRACTIVE CENTERS

The cross-section $S_p^=$ describes the capture process at an attractive center. The value of $S_p^=$ for cobalt in germanium has been found to be $(22\pm6) \,.\, 10^{-16}$ cm^2 at 145°K. The capture cross-section is not dependent on the electron concentration, thereby indicating that the Auger process is not taking place. By combining the temperature variation of $S_p^=$ with the low temperature value, the room temperature value of $S_p^=$ has been determined and it is found to be around $1 \,.\, 10^{-16}$ cm^2. It has been already mentioned that there must be a change in the magnitude of n to a lower value at higher temperatures. Therefore the extrapolated value of $1 \,.\, 10^{-16}$ cm^2 for room temperature can be considered as a lower estimate. The fairly large value of $S_p^=$ and its temperature dependence are characteristic of the cascade process of recombination proposed by Lax[9] where phonons take away the recombination energy. The observed value of about 4 for the index n at low temperature is in conformity with the Lax's theory which predicts a value 1 to 4 for attractive centers. The reasons for values of n higher than 4 observed in some specimens and for variation in 'n' among individual samples are not known. Such behaviour, however, is not peculiar to cobalt-doped germanium alone; values as high as 5 have been reported for manganese-doped germanium also[10]. The proposed less steep variations of $S_p^=$ at higher temperatures may be due to the contribution of optical phonons.

6. CAPTURE AT REPULSIVE CENTERS

The cross-section S_n^- obtained from trapping ratios is of the order of $0\cdot1 \,.\, 10^{-16}$ cm^2 at 145°K and it appears to be very weakly temperature dependent in the range 145–180°K. However above 180°K, it is not possible to account for the observed K values assuming that S_n^- is temperature independent. The value of S_n^- at room temperature from experimental K value (assuming $S_p^= \approx 1 \,.\, 10^{-16}$ cm^2, lower estimate) is $0\cdot3 \,.\, 10^{-16}$ cm^2. This will be even more if a lower index is used in the T^{-n} law of $S_p^=$. Allowing for this the value of S_n^- may be around $1 \,.\, 10^{-16}$ cm^2 at 300°K.

Further information on S_n^- may be obtained from a study of p-type cobalt-doped samples. Considering the fact that S_n^- is related to capture at repulsive centers, the magnitude of the cross-section is rather large. The same behaviour of S_n^- has been reported for other deep-level acceptor centers like iron, manganese, etc. in germanium[10, 11].

Acknowledgements – The author wishes to acknowledge her thanks to Professor R. S. Krishnan for his kind interest and encouragement and to Dr G. Suryan for his constant guidance and discussions. Author's thanks are also due to Mr M. Venkateswara Rao for growing the crystals.

REFERENCES

1. TYLER W. W., NEWMAN R. and WOODBURY H. H., *Phys. Rev.* **97**, 669 (1955).
2. GLINCHUK K. D., MISELYUK E. G. and FORTUNATOVA N. N., *Ukr. fiz. Zh.* **4**, 207 (1959).
3. SHEINKMAN M. K., *Fizika tverd. Tela* **7**, 28 (1965). *Soviet Phys. solid St.* **7**, 18 (1965).
4. KARPOVA I. V., ALEKSEEVA V. G. and KALASHNIKOV S. G., *Fizika tverd. Tela* **4**, 634 (1962); *Soviet Phys. solid St.* **4**, 461 (1962).
5. SAH C. T. and SHOCKLEY W., *Phys. Rev.* **109**, 1103 (1958).
6. SHOCKLEY W. and READ W. T., *Phys. Rev.* **87**, 835 (1952).
7. TYLER W. W., *J. Phys. Chem. Solids* **8**, 59 (1959); *Advances in Semiconductor Science* (Edited by H. Brooks), p. 59, Pergamon Press, Oxford (1959).
8. KALASHNIKOV S. G. and MOROZOV A. I., *Fizika tverd. Tela*, **2**, 2813 (1960); *Soviet Phys. solid St.* **2**, 2505 (1961).
9. LAX M., *Phys. Rev.* **119**, 1502 (1960).
10. LANDSBERG E. G. and KALASHNIKOV S. G., *Fizika tverd. Tela* **5**, 1067 (1963); *Soviet Phys. solid St.* **5**, 777 (1963).
11. KALASHNIKOV S. G., *Proc. Int. Conf. on Semiconductor Physics, Prague*, p. 241 (1960).

J. Phys. Chem. Solids Pergamon Press 1970. Vol. 31, pp. 973–982. Printed in Great Britain.

SUPERCONDUCTING PROPERTIES AND THE PHASE DIAGRAMS OF THE Pb-Bi AND Pb-In ALLOY SYSTEMS

J. E. EVETTS
Department of Metallurgy, University of Cambridge, England
and
J. M. A. WADE*
Cavendish Laboratory, University of Cambridge, England

(*Received* 14 *July* 1969; *in revised form* 24 *September* 1969)

Abstract—Magnetisation measurements have been made at 4·2°K on Pb–Bi and Pb–In alloys over a wide range of compositions. The resulting data for the variation with composition of the three critical fields and kappa is presented. For both alloy systems the superconducting measurements prove to be a powerful method for resolving uncertainties in the phase diagram

1. INTRODUCTION

We report here data on the primary superconducting properties of the Pb–Bi and Pb–In alloy systems. The measurements were made during the course of a more general research programme into flux movement in the Pb–In system[1], and flux pinning in the Pb–Bi system[2], and were necessitated by the paucity of data in the literature. We present our results in conjunction with the data given by other workers to provide fairly extensive information on critical fields and kappa values at 4·2°K over a wide range of alloy compositions. The experiments show also how superconducting measurements can be of use in resolving uncertainties in phase diagrams especially in the regime where room temperature diffusion is rapid.

2. EXPERIMENTAL METHODS

2.1 *Specimens*

The phase diagrams for Pb–Bi and Pb–In are given by Hansen and Anderko[3] and are shown in Fig. 1; all compositions will be quoted as atomic percentages. The alloys were made up from 5*N* purity starting materials and vacuum cast into glass tubes. The specimens, about 20 mm long and 1–2 mm dia., were annealed a few degrees below their melting points for periods of between 1–5 weeks. In the Pb–In alloys and the Pb–Bi epsilon phase there was little change after three days annealing, but in the Pb–Bi alpha phase there was a tendency for prismatic solidification to occur[4], which made it difficult to prepare very reversible alloys and would explain the anomalously high magnetic hysteresis observed by Livingston[5] for these alloys. Analyses were not in general carried out and except where indicated the compositions quoted are nominal, although the few Pb–Bi specimens that were analysed were all found to be within ½ per cent of their nominal compositions.

2.2 *Magnetisation measurements*

Complete hysteresis loops were plotted for the Pb–In specimens by a method of electronic integration. A Keithley 149 Millimicrovoltmeter was used to amplify the signal from roughly balanced pickup coils in the cryostat. The main pick-up coils consisted of two 8000 turn coils wound on a former 5 mm long with internal and external diameters of

---

*Present address: Institute of Physics, University of Oslo, Blindern, Oslo 3, Norway.

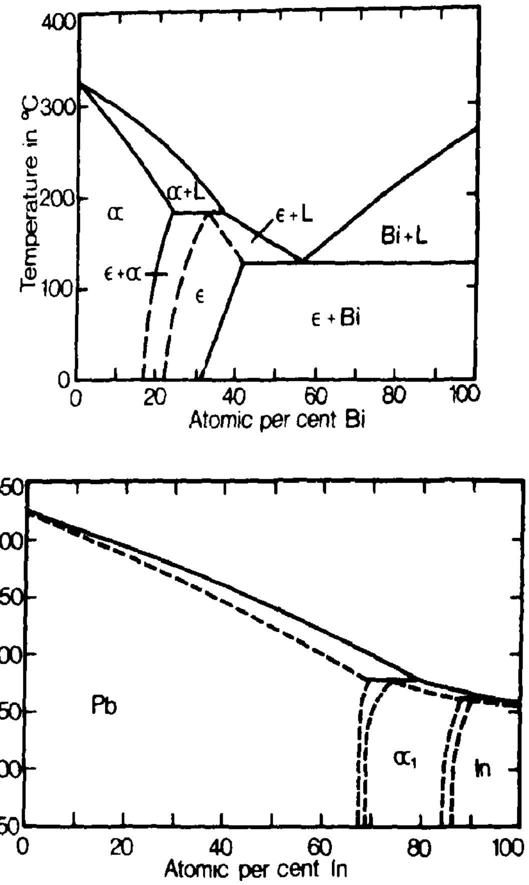

Fig. 1 Phase diagrams of (a) Pb–Bi and (b) Pb–In from Ref. [3].

3 and 13 mm. These coils were balanced to within 0·1 per cent and the specimen was placed in one of them. Before integrating an adjustable compensating signal was added to cancel any remaining contribution from the applied field. It came from a d.c. amplifier with a variable gain between zero and ±20, and was originally derived from a 200 turn 100 mm dia. coil attached to the magnet pole pieces outside the cryostat. The magnetic field was measured with a Hall probe, accurate to 1 per cent, so that hysteresis loops could be traced directly on an X-Y recorder with an estimated accuracy in $4\pi M$ of 2 G for a 2 mm specimen.

For the Pb–Bi alloys hysteresis loops were plotted point by point; the specimen was moved rapidly from one search coil to an oppositely wound coil in series with a Kipp A 53 ballistic galvanometer. Further details of the measurements, including the effect of jarring, are described in[2]. The accuracy was usually better than 1 per cent and for a 2 mm specimen, $4\pi M$ could be measured with an ultimate sensitivity of 0·3 G.

3. ANALYSIS OF RESULTS

3.1 *Normalisation*

Typical hysteresis loops are seen in Fig. 2; some hysteresis invariably remained, which has been shown[2] to arise almost entirely from pinning of flux lines at the surface interface. No treatment aimed at homogenizing the

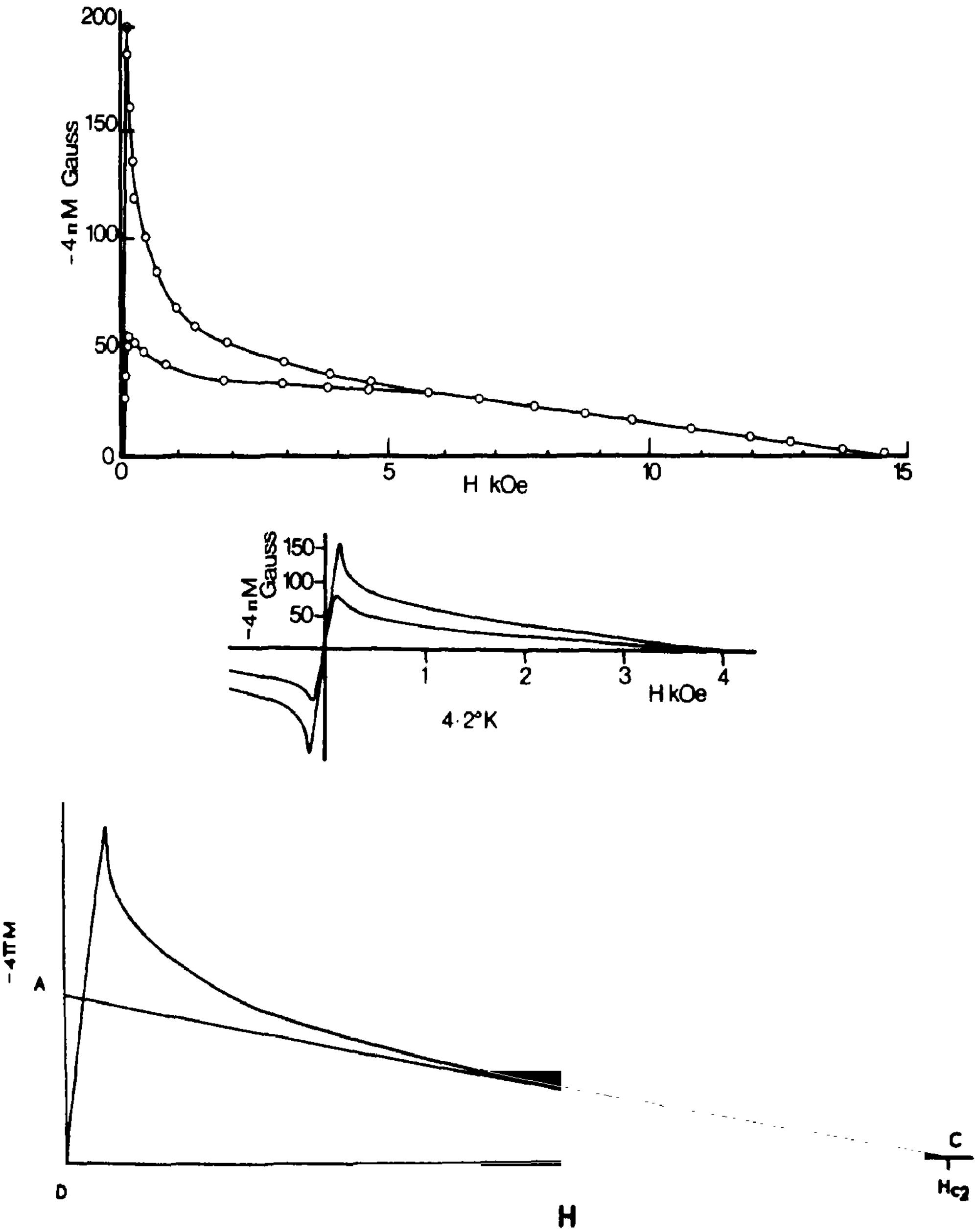

Fig. 2. Magnetisation curves (a) as measured for Pb-35% Bi, (b) as measured for Pb-30% In and (c) illustrating areas compared in deriving inequalities for κ_2/κ_1. ADC is the area under the straight line which coincides with the reversible curve at H_{c2}.

interior of the specimen will significantly improve the reversibility.

The ballistic magnetisation curves could be normalised directly to the diamagnetic slope since the readings started from zero field. Demagnetisation effects were small as long as the specimen was closely parallel to the applied field. For a 2 mm dia. specimen the slope deviates from unity by 2 per cent.

For the electronically integrated loops the initial slope could not normally be measured, so the curves were normalised to the slope of a line drawn from the origin to the point of first observable departure from linearity. This point, at H_{fp}, was taken as a first approximation to H_{c1}; a discussion of the procedure for extracting accurate estimates of H_{c1} from the curves is given below in Section 3.3. The true H_{c1} is invariably some tens of oersteds less than H_{fp}, but this is not important for the purpose of normalisation as the normalisation procedure is rather insensitive to the exact choice of H_{fp} provided that the zero field remanence is small.

3.2 *Evaluation of* H_{c2} κ_1 κ_2 *and* H_c

At high fields where the hysteresis is small the path of the reversible curve can be located accurately midway between the increasing and decreasing field curves. At lower fields it becomes increasingly difficult to deduce the path of the curve accurately in view of the uncertainty in H_{c1}: however the area under the curve and hence H_c can be found accurately as the area is insensitive (especially for large κ) to large variations in the detail of the curve near H_{c1}. For high kappa alloys ($\kappa > 10$) the reversible curves are very nearly linear down to less than half H_{c2}, so the slope at H_{c2} and the values of H_{c2} and H_c can all be determined accurately The maximum probable error (2 to 3 times the standard error) was estimated as 1·5 per cent for H_{c2}, 4 per cent for the slope at H_{c2} and 2 per cent for H_c. For smaller kappa values the error increases progressively. The maximum probable error estimates are indicated in the figures.

The results were interpreted as far as possible in terms of the temperature dependent Ginzburg–Landau theory[6, 7]. The values of H_{c2} and H_c were used to calculate κ_1, and κ_2 was obtained from the slope at H_{c2}. The different kappas have been defined by Maki [6]. The theory is not yet completely satisfactory, although it seems to be qualitatively correct[8, 9].

A powerful test of the theory is the value of the ratio κ_2/κ_1. By considering the inequality of the area under the reversible curve, $H_c^2/2$, and the area under the straight line which coincides with the reversible curve at high fields, $H_{c2}^2/(2{\cdot}36(2\kappa_2^2-1))$, definite inequalities restricting the range of variation of κ_2/κ_1 can be obtained (see diagram, Fig. 2(c)). These inequalities are a useful check on the full microscopic theoretical treatment and also give a clear physical picture of the consequence of a change in κ_2/κ_1.

It can be shown that κ_2 must always be greater than $0{\cdot}92\kappa_1$. Also when the fraction of total area of the reversible curve that lies above the straight line exceeds 0·15 one can show that $\kappa_2 > \kappa_1$. Experimentally we find this to be the case for alloys with roughly $\kappa < 7$. For $\kappa > 7$ one has $0{\cdot}92\kappa_1 < \kappa_2 < \kappa_1$.

The results indicate that for the Pb–In alloys κ_2 is significantly greater than κ_1 especially for small kappa. For the Pb–Bi alpha phase there is a transition across $\kappa_1 = \kappa_2$ at around Pb–20% Bi. For the epsilon phase κ_1 is significantly greater than κ_2 (taking a mean of all five compositions gives $\kappa_2 = (0{\cdot}95 \pm 0{\cdot}01)\kappa_1$); however the tendency for the ratio κ_2/κ_1 to decrease as kappa increases across the phase is hardly statistically significant.

The values obtained for kappa and the critical fields are given in Table 1 for Pb–Bi and in Table 2 for Pb–In. The variation with composition of kappa is shown in Fig. 3, and that of H_{c2} in Fig. 4. Some values obtained by previous workers[5, 10, 11] are also shown in the figures.

3.3 *Evaluation of* H_{c1}

It is difficult to obtain good values for the lower critical field. If there is any hysteresis it tends to be greatest near H_{c1} and the initial diamagnetic slope appears to extend beyond H_{c1}. The point of first observable departure

Table 1

At % Bi	T/T_c	H_{c2} (kOe)	H_c (Oe)	H_{c1} (H and A) (Oe)	H_{c1} (fitted) (Oe)	κ_1	κ_2	κ_3
40	0·50	17·7	909	141	156	13·7	13·1	15·7
37·5	0·50	16·5	874	137	151	13·4	12·8	15·4
34·9*	0·50	14·4	775	130	146	13·2	12·7	15·2
33·5*	0·50	13·4	738	118	134	12·9	12·6	14·9
31·1*	0·50	12·3	698	113	123	12·4	12·2	14·3
23	0·52	8·6	580	105	125	10·3	10·3	11·7
22·5	0·52	8·5	580	105	125	10·2	10·3	11·6
17·5	0·54	5·8	620	152	182	6·6	6·5	7·4
15	0·55	4·5	630	183	210	5·1	5·3	5·7
12	0·55	3·8	645	211	250	4·2	4·4	4·7
10	0·56	2·9	640	253	290	3·2	3·5	3·6
5	0·57	1·65	560	332	350	1·9	2·5	2·1
2·5	0·58	0·94	570	440	450	1·2	—	1·3

*Analysed by electron microprobe analysis.

Table 2

At% In	T/T_c	H_{FP} (Oe)	H_{c2} (kOe)	H_c (Oe)	H_{c1} (Oe)	κ_1	κ_2	κ_3
18	0·59	180	3·0	520	170	4·1	4·4	4·6
30	0·60	160	3·7	505	145	5·2	5·1	5·6
40	0·61	165	4·1	480	125	6·0	6·2	6·2
45	0·62	135	4·0	460	120	6·1	6·1	6·5
50	0·64	135	3·8	430	105	6·3	6·9	7·0
57	0·65	120	3·3	400	105	5·9	6·0	6·3
62	0·67	140	2·8	380	110	5·2	5·6	5·7
75	0·73	90	1·4	215	70	4·6	4·7	4·8
83	0·79	82	0·62	160	65	2·8	3·4	3·2
89	0·91	36	0·15	52	28	2·0	2·2	2·1

from linearity, H_{FP}, has often erroneously been taken as H_{c1}.

Two methods were used to obtain more accurate values for H_{c1}. The first method was to calculate κ_3 from Maki's[6] results using values of κ_1 obtained above, in conjunction with the critical temperature data of other workers[12]. The variation of H_{c1}/H_c with kappa has been computed by Harden and Arp[13] from the Abrikosov theory, and therefore a value for H_{c1} could readily be obtained. The process could be iterated if required, by re-drawing the supposed reversible curve to H_{c1} rather than H_{FP} and re-measuring the area to obtain better values for H_c and thus H_{c1}, but this was unnecessary in the present case on account of the fairly low hysteresis in the experimental curves.

The second method was to use directly the computed Abrikosov curves (for the high κ limit) giving the magnetisation near H_{c1} as a function of $(H-H_{c1})$, the form of the curve depending on H_c/κ_3. The experimental curve was fitted by the appropriate one of a set of theoretical curves using points in regions where hysteresis was low, i.e. well above H_{FP}.

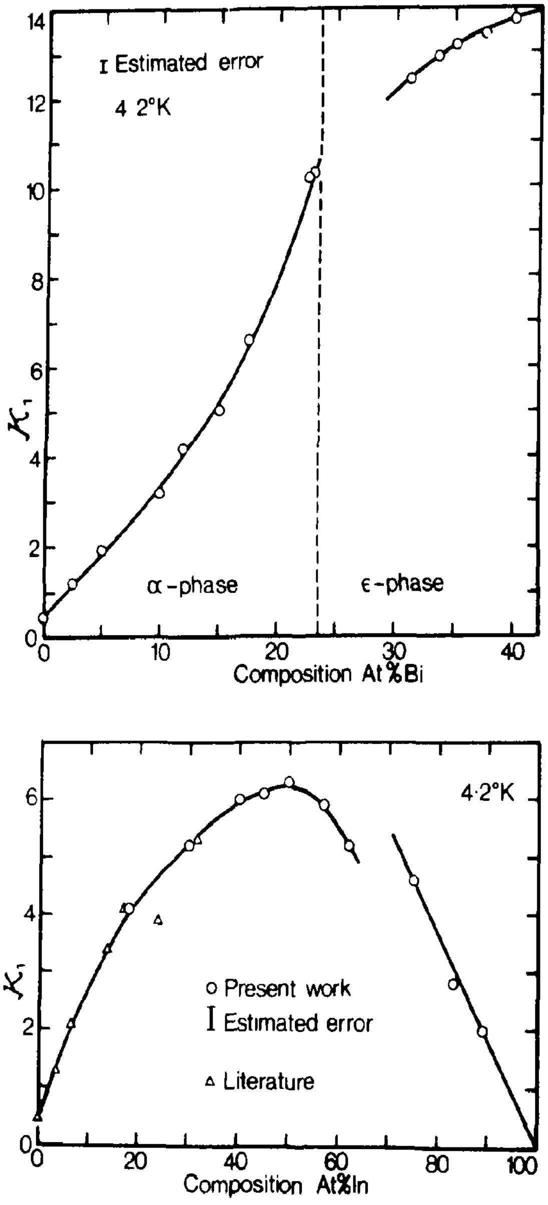

Fig 3 Measured values of κ_1 for (a) Pb–Bi and (b) Pb–In.

The precise low field shape of the Abrikosov curve then determined a value for H_{c1} and H_c/κ_3. Using Maki[6] this value of H_c could be checked against a new estimate of H_c redetermined from the area under the reversible curve and if necessary the process could be iterated In the case of the Pb–Bi system both methods for determining H_{c1} were used and the results compared. The first method gave results slightly below the second, the difference between the results increasing as kappa decreased. This difference may be related to

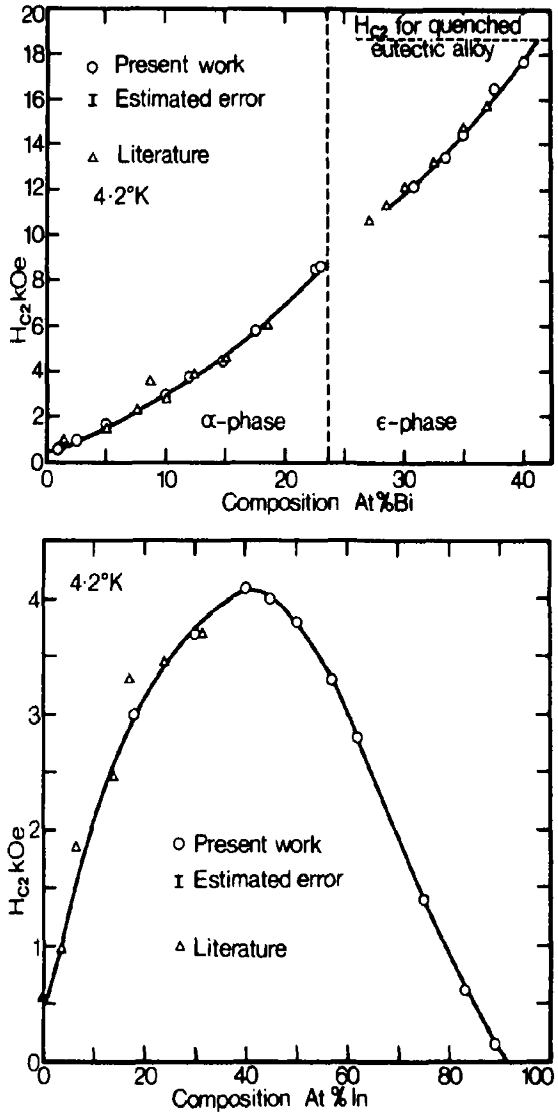

Fig. 4. Measured values of H_{c2} for (a) Pb-Bi and (b) Pb-In.

the inaccuracy of Abrikosov's expression for the magnetisation for small kappa values. In addition in the low kappa region the alloys can no longer be regarded as obeying the 'dirty limit' theory. Helfand and Werthamer[7] give data which shows that one should get significant deviation in these alloys when $\kappa < 2$, i.e. for compositions of less than 6% Bi.

In the case of the Pb-In system the first method was used to determine H_{c1}. Values obtained for both systems are shown in Fig. 5 together with the results of previous workers [5, 10].

4. THE ALLOY PHASE DIAGRAMS

For both systems the superconducting measurements indicate how uncertainties in the phase diagram may be investigated.

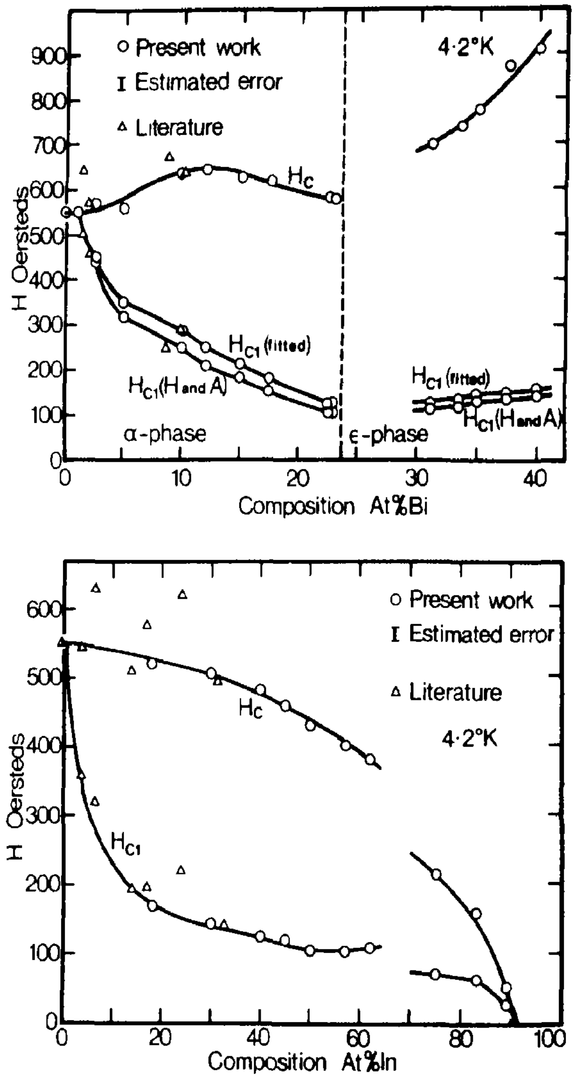

Fig. 5 Measured values of H_c and H_{c1} for (a) Pb-Bi and (b) Pb-In.

In the Pb-Bi system there is still considerable uncertainty as to the bismuth rich limit of the epsilon phase at the eutectic temperature. This uncertainty arises because epsilon phase alloys with more than 35% Bi are unstable at room temperature and precipitate bismuth. Room temperature diffusion is rapid and microstructures change significantly in the time taken to prepare a micrograph.

Superconducting measurements were made on a series of alloys with increasing bismuth content. They were annealed near the eutectic temperature and quenched rapidly into liquid nitrogen. Figure 4 shows the variation of H_{c2} with composition. The alloys remained nearly reversible up to over 40% Bi. For alloys over about 42% Bi the irreversibility started to increase, indicating the alloy was no longer single phase, while H_{c2} remained constant at 18·7 ± 0·3 kOe. This corresponded to a limiting composition for the epsilon phase of Pb-41% Bi, assuming a linear extrapolation to the phase edge.

The Pb–In phase diagram (Fig. 1) has two-phase regions in the neighbourhood of 68 and 87% In. The width of these regions is extremely uncertain. The analysis given below goes some way to resolving the uncertainty around 68% In and shows how a careful series of superconducting measurements could give valuable quantitative information.

In the two-phase region the hysteresis loop becomes more irreversible because of flux line pinning by the second phase particles[2]. Figure 6 shows the hysteresis loop for a 65% In alloy, the hysteresis revealing a marked field dependence. Similar loops were obtained for 70 and 83% In alloys, although the hysteretic features were less pronounced in the former case and only just discernible in the latter. There was absolutely no evidence of a second phase in alloys containing 62, 75 and 89% In.

The shape of the loop in Fig. 6 can be interpreted in terms of a simple model in which phase boundary pinning is proportional to $\Delta M/\sqrt{B}$. Here ΔM is the difference in equilibrium magnetisation of the phases and B is the flux density. The minimum in the hysteresis as a function of field arises because when two phases have similar H_c values but different kappa values their equilibrium magnetisation curves cross. At this point ΔM and therefore the pinning goes to zero, while similar reasoning suggests that the local maximum in the hysteresis at a somewhat higher field occurs at H_{c2} for the phase with the lower value of κ.

The compositions of the two phases present were thus estimated, by interpolating the results for H_{c2} across the two-phase region as in Fig. 4, to be about 64 and 70% In. A simple calculation of the pinning on the model described then yielded the points shown in Fig. 6, giving a markedly better fit with the $B^{-1/2}$ dependence than with B^{-1} or a pinning force independent of B. The scaling factor required to fit the experimental curve implied, using results in[2], that the precipitate particles (assumed spherical) had a diameter of roughly 10μm.

The particular specimen described was not quenched to low temperature and the simple two-phase structure assumed was almost certainly modified by diffusion to give the observed small discrepancies between the theoretical and experimental curves. The present results, however, cast considerable doubt on the accuracy in detail of the phase diagram as

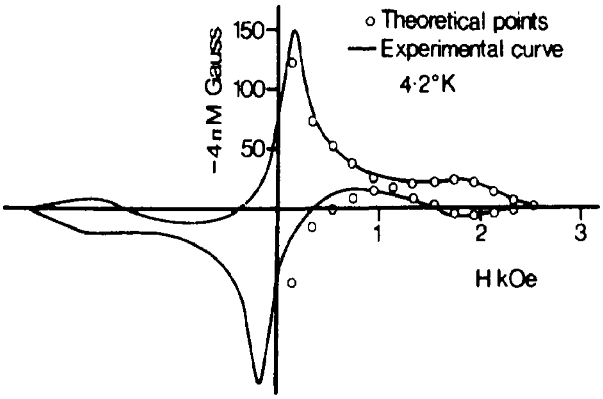

Fig. 6. Measured hysteresis loop for Pb-65% In alloy, with theoretical points calculated as described in the text

drawn in [3], and show that a systematic investigation would clearly define the phase boundaries in this situation where more conventional techniques cannot be applied.

Acknowledgement – Both authors express thanks to the Central Electricity Generating Board for financial support during the course of this work.

REFERENCES

1. WADE J. M. A., *Phil. Mag.* **20**, 1107.
2. CAMPBELL A. M., EVETTS J. E. and DEW-HUGHES D., *Phil. Mag.* **18**, 313 (1968).
3. HANSEN M. and ANDERKO K., *Constitution of Binary Alloys* McGraw-Hill, New York (1958).
4. TILLER W. A. and RUTTER J. W., *Can. J. Phys* **34**, 96 (1956).
5. LIVINGSTON J. D., *G.E. Res. Rept* No. 62-RL-3155 M (1962). *Phys. Rev.* **129**, 1943 (1963).
6. MAKI K., *Physics* **1**, 21 and 127 (1964). CAROLI C., CYROT M. and DE GENNES P. G., *Solid-St. Commun.* **4**, 17 (1966).
7. HELFAND E. and WERTHAMER N. R., *Phys. Rev. Lett.* **13**, 686 (1964).
8. FIETZ W. A. and WEBB W. W., *Phys. Rev.* **161**, 423 (1967).
9. ZOLLER P. and DILLINGER J. R., *Phys. Rev. Lett.* **20**, 1154 (1968).
10. DRUYVESTEYN W. F., VAN OOIJEN D. J. and BERBEN T. J., *Rev. mod. Phys.* **36**, 58 (1964). DRUYVESTEYN W. F., Thesis, Eindhoven (1965).
11. MALSEED C. and RACHINGER W. A., *Scripta Met.* **3**, 139 (1969).
12. MEISSNER W., FRANZ H. and WESTERHOFF H., *Ann. Phys.* **13**, 505 and 967 (1932). KING H. W., RUSSELL C. M. and HULBERT J. A., *Phys. Lett.* **20**, 600 (1966).
13. HARDEN J. L. and ARP V., *Cryogenics* **3**, 105 (1963)

J. Phys. Chem. Solids Pergamon Press 1970. Vol. 31, pp. 983–994. Printed in Great Britain.

CHARGE TRANSPORT THROUGH α-MONOCLINIC SELENIUM

J. M. CAYWOOD* and C. A. MEAD
California Institute of Technology, Pasadena, Calif. 91109, U.S.A.

(*Received* 24 *July* 1969; *in revised form* 23 *September* 1969)

Abstract – The existence of surface barriers on α-monoclinic selenium crystals has been demonstrated. Photometric measurements indicate electron barrier energies of 1·05 and 1·3 eV, respectively, for Ga and Au contacts. The mobilities of holes and electrons have been measured by a time-of-flight technique to be about 0·2 cm²/Vsec and 1·6 cm²/Vsec, respectively, at room temperature. The hole mobility was found to be limited by traps 0·23 ± 0·01 eV above the valence levels, while the electron mobility is an intrinsic mobility limited by scattering. It was found that in the region of low carrier density (i.e. no space charge effects) the collection efficiency was limited by diffusion of carriers into the metal contact.

1. INTRODUCTION

THE α-MONOCLINIC form of selenium was apparently first produced by Mitscherlich in 1855[1]. Later crystallographic studies were conducted by Muthmann[2] in 1890 and by Saunders[3] in 1900. The electrical and optical properties were first investigated by a group at Gottingen which, in 1926, reported limited measurements of index of refraction, dielectric constant, and photoconductivity[4, 5]. Although a detailed X-ray crystal structure determination was reported by Burbank[6] in 1950, no further work was done on the electrical or optical properties for over thirty years until Prosser measured the optical constants in the region of the long wavelength side of the absorption edge (0·876–0·592 μ) [7]. Capitalizing on Gudden and Pohl's discovery of mobile holes and electrons[5], Spear verified the mobility of carriers of both kinds and measured the mobility of electrons over a wide temperature range[8]. Recently the optical absorption constant has been measured to below 0·28 μ[9].

Since both holes and electrons are mobile, the absence of current flow with bias applied to the unilluminated sample clearly indicates that neither carrier can enter the crystal from the contacts. We have used the photoemission of electrons from different metal contacts into the selenium to demonstrate the existence of surface barriers and determine their energies.

In addition we report transient measurements similar to those of Spear[8], in which the transit time and collection efficiency of carriers excited by a short flash of light have been studied as a function of the sign and amplitude of the applied field, temperature of the sample, and intensity of the light pulse. From these results a simple and completely selfconsistent model for structures of this type has been constructed.

2. SURFACE BARRIERS

Sample preparation

The method of growing the crystals used in these studies was reported earlier[10]. Samples were prepared by lapping α-monoclinic, single crystals to platelets of the desired thickness and then etching the platelets in spectroscopic grade CS_2 in order to remove any surface damage resulting from the lapping. (The resulting platelets were 40–100 μ in thickness and had lateral dimensions of few mm.) The crystals were oriented prior to lapping so that the large surfaces which received the contacts lay in the (101) plane. Because the α-monoclinic form is thermodynamically unstable at room temperature (converting to the trigonal form in a period of a few years)[11], care was exercised throughout this procedure to avoid heating the crystals above room temperature (20–25°C) in order to avoid thermal damage to the crystal.

---

*Present address: Institute of Applied Physics, University of Basel, Basel, Switzerland.

Metallic contacts were made to the two sides of the platelets. Back contacts were made of gold or gallium while the front contact always consisted of a semitransparent gold dot deposited by vacuum evaporation. A shutter was used in all evaporations in order to minimize thermal damage due to exposure of the crystal to the hot filament. The gold back contacts were vacuum evaporated and then cemented to a copper substrate with silver paste. The gallium contacts were prepared by wetting the substrate with gallium and pushing the selenium platelet into the liquid gallium.

Experimental procedure

The energy of barrier contacts to an insulating material such as Se can best be determined by observing the photoemission of electrons from the metal into the conduction band of the material. As the photon energy is increased, essentially no current flows until the barrier energy is exceeded[12]. The current then increases as the square of the energy above the threshold. At still higher energies near the band gap, the onset of electron-hole pair creation in the semiconductor causes a further very rapid increase in current.

Light chopped at 45 Hz was focused from the exit slit of a Spex double monochromator onto the entire front surface of the sample by a 6:1 reducing mirror. Second and higher order light from the 0·5 μ blaze grating was eliminated by utilizing polished crystals of the series CdS_xS_{1-x} as filters. Bias was applied across the sample and the photocurrent detected by standard synchronous techniques. Reversing the polarity of the bias allowed the current from the front and back contacts to be investigated separately. Measurements were made on several samples with guard rings to assure that the current flow was predominantly through the crystal and not along its surface.

Results and discussion

The logarithm of the observed photocurrent is plotted as a function of photon energy in Fig. 1 for two polarities of applied bias. The sample on which these data were taken had both front and back contacts of gold, but the area of the back contact was larger by a factor of 10. The high energy portions of the two curves are quite similar, and are attributed to bulk free carrier creation. The energy at which the current begins to increase quite rapidly, 2·3 eV, is in good agreement with the earlier reported value for the optical absorption edge for α-monoclinic selenium[9]. The equality of the current for the two polarities is a strong indication that deep trapping is not important in these samples.

For photon energies less than about 1·8 eV, the current is increasing as would be expected from injection over a barrier, but the ratio of the currents for the two polarities is 40:1. Simple considerations of area of contacts accounts for a difference of ~ 10:1. The optical absorption length in gold for this wavelength is 130–150 Å[13] and the range in gold for hot electrons of the energies involved in this experiment is about 350 Å[14]. Since the thickness of the front contact is about 900 Å, electrons are essentially all generated at the front surface of the gold and then relax as they diffuse toward the selenium. Thus the front contact should be about 10 times less efficient at injecting electrons into the selenium as the back contact. However, about 70 per cent of the light which enters the selenium is absorbed before reaching the back contact leaving it more efficient by only a factor of 3. Thus the total photocurrent from the back contact should be approxi-

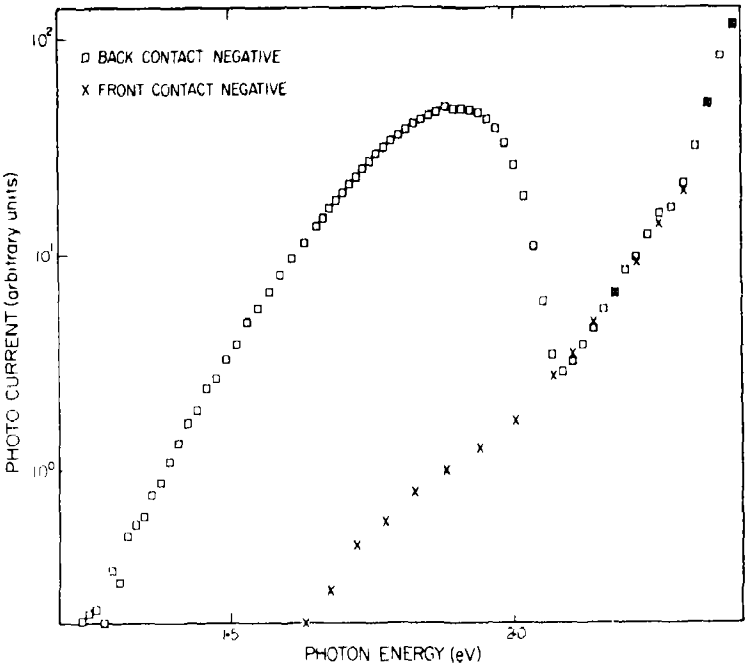

Fig. 1. Photocurrent vs photon energy for an α-Se sample with gold contacts. The back contact was larger than the front by approximately a factor of 10

mately 30 times as large as that from the front – as observed. The polarities of the bias involved in this experiment indicate that the carriers injected over the barriers are in fact electrons.

The sharp dip that occurs in the photocurrent from the back contact at photon energies between 1·9 and 2·1 eV is due to the sharp increase in the optical absorption constant of from $0{\cdot}166 \times 10^{+3}\,\mathrm{cm}^{-1}$ at 1·9 eV to $1{\cdot}805 \times 10^{3}\,\mathrm{cm}^{-1}$ at 2·1 eV [7]. Since this platelet was measured to be about 100 μ thick, the fraction of light entering the selenium crystal which reaches the back contact is about 0·3 at energies $<$ 1·8 eV, 0·2 at 1·9 eV, 0·0018 at 2·0 eV and $1{\cdot}4 \times 10^{-8}$ at 2·1 eV. Since it is clear that this absorption must account for a decrease in photocurrent, the electron which absorbs the photon must make a transition between two localized states (e.g. a bound exciton). As the photon energy increases, the energy which separates the absorbing localized states from the conducting states decreases and it becomes increasingly likely that the carrier will be thermally excited to a conducting state. At $h\nu \approx 2{\cdot}1$ eV, the current from this process becomes larger than the current coming over the barrier and continues as the dominant process until the photon energy is increased to the threshold for photogeneration of free carriers.

In Fig. 2 is plotted the square root of the normalized photocurrent for low photon energies plotted as a function of energy of incident photons for a sample with gold front contact and gallium back contact. This plot is linear over a large range of photon energy. The zero current intercept for the case in which the gold contact is biased negatively is about 1·3 eV, as it was for similar plots of cases in which both contacts were gold. However, in the case in which the gallium is biased negatively, the zero current intercept is 1·05 eV. This clear cut difference of threshold with differing contact materials

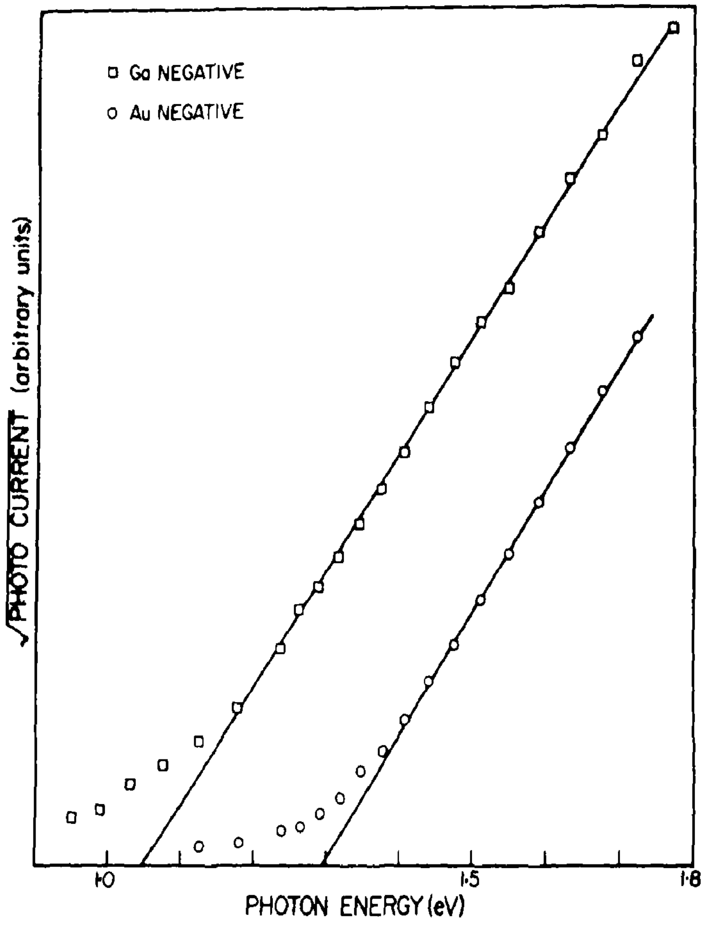

Fig. 2. Long wavelength photoresponse of α-Se sample with Au front contact and Ga back contact.

demonstrates that this photocurrent is indeed a contact phenomenon.

The sign of the bias indicates that the carriers being injected are electrons. The barriers to the injection of electrons from gallium and gold into Se are 1·05 eV and 1·3 eV, respectively. The electronegativity of gallium is 1·6 and that of gold is 2·4[15]. Thus, the ratio of the change of barrier height to the change of electronegativity is considerably less than one. Behavior of this type has been observed on other materials and is usually associated with surface states in the forbidden gap of the material.

3. MOBILITY MEASUREMENTS

Experimental procedure

All samples used in these experiments were typically 40 μ thick with both front and back contacts of gold. The front contact was approximately 10^{-3} cm^2 in area. The measurement consisted of generating carriers at the front surface with a flash of light and drawing the generated carriers across the crystal with an externally applied bias field. The light generated by an air pinch discharge lamp (Fischer Nanolite) with a half width of about 10 nanoseconds was focused onto the sample by a front surfaced mirror. A No. 5-60

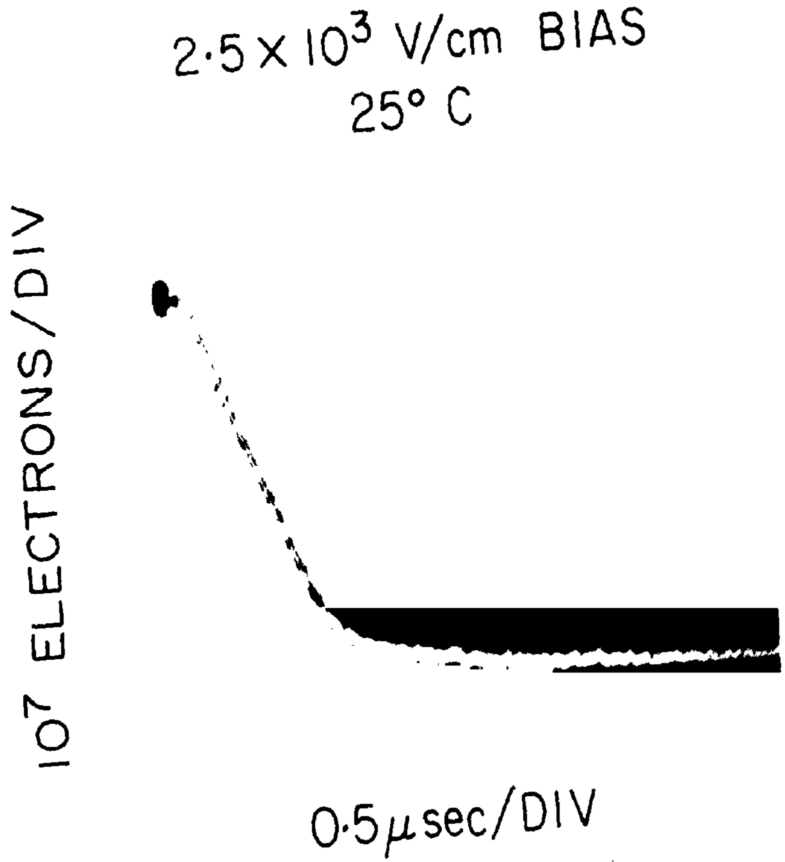

Fig 3 Typical oscilloscope trace of collected charge vs. time

Corning glass filter limited the light reaching the crystal to the wavelength range 0·33–0·52 μ. The absorption length in α-monoclinic selenium for light of these wavelengths ranges from 0·2 to 0·02 μ[9]. Intensity of light reaching the sample was controlled by neutral density filters of metal screen (in some cases mechanically supported by ultrasil fused silica) placed in the light beam.

The sample was contained in an electrostatically shielded box which was electrically integral with the amplifier. This shielding prevented electromagnetic pickup of the lamp discharge by the measuring circuit. Provision was made for varying the sample temperature which was monitored by a thermocouple.

Bias was applied to the front contact by a 0·002-in. dia. gold wire probe. The current pulse arising from optically generated carriers crossing the crystal was integrated by a passive RC integrator with a time constant of about 800 μsec (very much greater than any measured transit time), amplified by a Keithley model 105 pulse amplifier, and displayed on a high speed oscilloscope. The data was photographically recorded from the oscilloscope screen. In all measurement reported here, the generation length was very small, ~ 1/500 of the sample thickness, and the generation time (i.e. duration of the light flash) was much less than the time for the carriers to drift across the platelets. Under these conditions, the current arising from the charges going to the front contact contributed a negligible amount to the integrated current which is, therefore, a direct display of the induced change due to carriers of one sign drifting across the crystal. The sign of the carriers composing the charge sheet was determined by the polarity of the applied bias. In order to insure that the bias field was not distorted by trapped charge, the sample was shorted and illuminated with 10 light pulses before each measurement.

Results and discussion

A typical oscillograph trace is shown in Fig. 3. The maximum collected charge is $\approx 10^{-12}$C. The charge induced on the sample electrodes due to the applied bias is thus much larger than the charge in transit for applied fields greater than ≈ 750 V/cm. In the absence of deep trapping,* the risetime of the waveform shown corresponds directly to the transit time τ_t of carriers crossing the sample.

$$\frac{1}{\tau_t} = \frac{E\mu}{d}. \qquad (1)$$

The inverse transit time determined in this way is plotted as a function of applied electric field in Fig. 4. The plot results in a good linear relationship as expected from equation (1), where the slope of the straight line is μ/d. From plots of this type taken for the two bias polarities, mobilities of holes and electrons were determined as a function of sample temperature, and are shown in Fig. 5. The electron mobility, μ_e, shows a slight decrease with increasing temperature, suggesting that it is limited by lattice scattering. Typical values at room temperature ranged from 1·5 cm²/V-sec to 3·6 cm²/V-sec depending on the particular crystal.

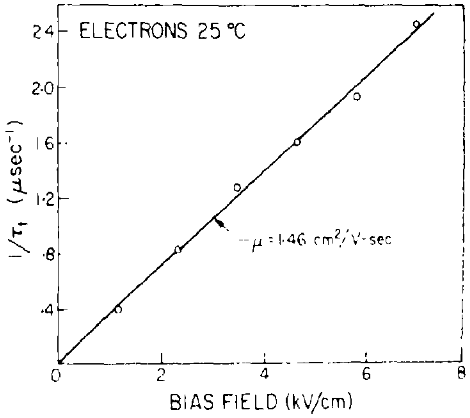

Fig. 4. Inverse transit time vs. bias field for electrons at 25°C.

---

*One indication that deep trapping is not important was noted in Section 2. A detailed discussion will be given in the next section.

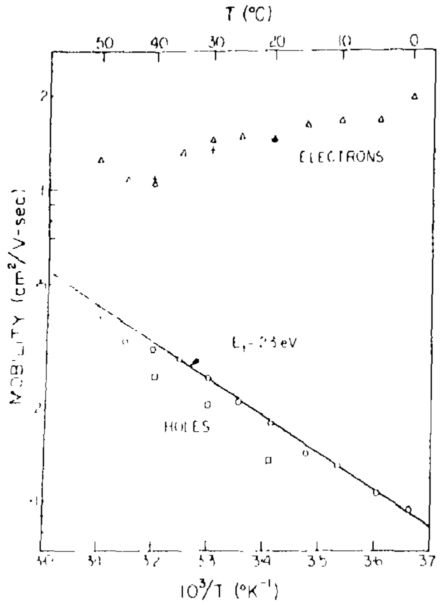

Fig. 5. Mobility of holes and electrons vs. inverse temperature. The circles ○ and triangles △ are data taken before heating the sample to the highest temperature used. Squares □ and pluses + were taken after heating.

The hole mobility, μ_h, exhibits an exponential increase with an activation energy of 0·23 eV, indicating that it is dominated by shallow trapping, in confirmation of the earlier work of Spear[8]. Tefft[16] has shown that behavior of this sort is consistent with a model in which the holes spend most of their time in traps so that the measured mobility is much less than the true lattice mobility, μ_{h0}, and is determined by the release time of the traps. The room temperature hole mobility of course, varied with the trap density, a typical value being 0·2 cm²/V-sec. We can use these values to estimate the trap density. The number of times the average hole is released from a trap, $\bar{n}$, is the product of the transit time and the emission probability

$$\bar{n} = \tau_t e_h = \tau_t v_{th}\sigma_h N_v e^{-E_t/kT} \qquad (2)$$

where e_h is the emission probability per unit time, v_{th} is the thermal velocity, σ_h is the cross section of the trap for holes, N_v the effective density of states in the valence band, and E_t is the trap activation energy[17]. During the time in which the hole is free, τ_f, it must drift a distance given by

$$\frac{d}{\bar{n}} = \tau_f \mu_{h0} E. \qquad (3)$$

But τ_f is just the mean time between trapping events, given by

$$\tau_f = \frac{1}{v_{th}\sigma_h N_t}. \qquad (4)$$

Combining equations (1–4) yields

$$N_t = \frac{\mu_{h0}}{\mu_h} N_v e^{-E_t/kT}. \qquad (5)$$

If we assume $N_v \sim 10^{19}/\mathrm{cm}^3$ and $\mu_{h0} \sim \mu_e$, we find $N_t \sim 10^{16}/\mathrm{cm}^3$, a value well within the bounds of credibility.

Further examination of Fig. 5 yields more information concerning the traps. The circles show the hole mobility as the sample temperature was being increased. These data fall on a straight line from which the 0·23 eV activation energy was derived. The squares are data taken after heating the sample to 50°C and fall on a lower line of the same slope. Thus we can conclude that the temperature cycle introduced more traps of the same activation energy as those initially present. We hypothesize that all these traps have a common origin; broken Se rings. The triangles and crosses show the electron mobility before and after heating the sample to 50°C. It is clear that the electron mobility was unaffected by the temperature cycle.

4. COLLECTION EFFICIENCY

When electron-hole pairs are created near a metal-semiconductor interface by a short burst of light, one can observe the resultant pulse of collected charge. For a uniform electric field, the behavior of this pulse can be divided into three cases. Figure 6(a) illustrates the case in which the collection efficiency, η, (the ratio of collected carriers to electron-hole pairs generated) is unity and all

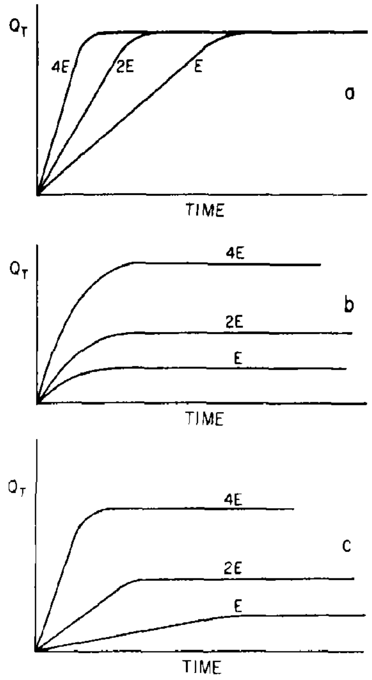

Fig. 6. Collected charge vs. time for three cases: (a) Collection efficiency unity and response time equal to transit time (inversely proportional to electric field), (b) Response time equal to bulk trapping time and collection efficiency proportional to electric field. (c) Both inverse response time and collection efficiency proportional to electric field.

of the carriers cross the sample without becoming deeply trapped. In this case the transit time, τ_t, is inversely proportional to the electric field, and the total collected charge is constant.

If the carriers are deeply trapped while crossing the sample, the risetime of the pulse is equal to the bulk trapping time, independent of electric field, but the collected charge is proportional to the electric field because increasing the field increases the distance the carrier travels before being trapped. This case, which is illustrated by Fig. 6(b), has been shown in the previous section to be inapplicable to our data.

The third case, in which both inverse transit time and collected charge are proportional to electric field, is illustrated by Fig. 6(c). This behavior is characteristic of the Se samples reported here. A plot of collected charge vs. Electric field at fixed light intensity is shown in Fig. 7.

A number of models have been proposed to explain data of this type. Tabak and Warter [18] have developed a model based on field aided thermal release from bound states. This model predicts an efficiency which increases exponentially with temperature.

$$\eta = \left[1 + \frac{1}{\tau_r \nu}\exp\left(\frac{\xi_t - e\left(\frac{eE}{\pi\epsilon}\right)^{1/2}}{kT}\right)\right] \qquad (5)$$

where τ_r is the lifetime for nonphotoconductive decay of the bound state, ν is the attempt-to-escape frequency, ξ_t is the binding energy of the state, e is the charge on an electron, and ϵ is the permittivity of the Se.

A number of authors[19] have discussed recombination in the region of generation. In wide band gap semiconductors, one would expect carriers of one polarity to become trapped. A carrier of the other sign would then recombine with the trapped carrier. Since the electric field drifts the more mobile species away from the less mobile, a higher field would decrease the time in which recombination can occur and raise the collection efficiency.

A model similar to that of recombination is

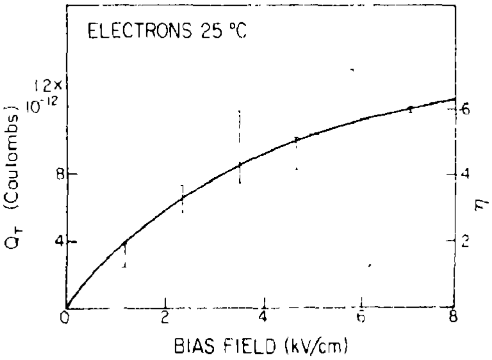

Fig. 7. Total collected charge for fixed light intensity as a function of applied electric field. Measured points for electrons at 25°C. The solid curve is the theoretical dependence (equation (8)) with vertical scale adjusted to fit at 7 kV

one in which both carriers are trapped in a narrow damaged layer near the surface. This model predicts a collection efficiency which is exponentially dependent upon the product of the mobility, μ, and the trapping time, τ_{tr}, in the damaged layer of carrier crossing the sample.

Although any or all of the above mechanisms may be operative, they are often unimportant compared with the effect of diffusion of carriers into the contact. The exceedingly short relaxation times of hot carriers in metals is responsible for the absence of carrier storage effects in Schottky barrier diodes. This relaxation time forces the density of both holes and electrons at the metal-semiconductor interface to be essentially zero. Under all conditions the carrier distribution created by the light must be spread by diffusion. The carrier sink provided by the metal contact keeps the gradient toward it steep and accentuates diffusion toward the contact while the bias field drifts the entire distribution away from the contact (for carriers of the sign which cross the crystal).

The fraction of generated carriers lost by this process can be evaluated quantitatively by solving the continuity equation for the carrier density, $n(x, t)$,

$$\frac{\partial n}{\partial t} = \mu\left(\frac{kT}{q}\frac{\partial^2 n}{\partial x^2} - E\frac{\partial n}{\partial x}\right) \tag{6}$$

under the boundary conditions $n(0, t) = n(d, t) = 0$ and the initial condition

$$n(x, 0) = \begin{cases} N_0 \exp(-\alpha x) & x > 0 \\ 0 & x < 0 \end{cases} \tag{7}$$

where the illuminated interface is at $x = 0$, the collecting contact is at $x = d$, α is the optical absorption constant for the incident light, and N_0 is the density of carriers generated at $x = 0^+$. This calculation, which is carried out in detail in the Appendix, yields

$$\eta = \frac{E/E_f}{1 + E/E_f} \tag{8}$$

where $E_f \equiv (\alpha kT/q)$ is an 'effective diffusion field'. This expression is plotted as the solid curve in Fig. 7.

The theory presented here makes a number of predictions beyond the field dependence given in equation (8). Since both the drift and diffusion terms in equation (6) are linear in mobility, it is evident that η must be independent of mobility and polarity of carrier. The form of equation (8) makes it clear that the efficiency predicted by this theory decreases as temperature and optical absorption constant increase. A further prediction is that the charge which diffuses into the contact does so in a time much shorter than the transit time so that the charge collection pulse should show a linear increase as shown in Fig. 6(c), not the rounded shape as in Fig. 6(b).

To establish the dominant mechanism which limits the collection efficiency, we first consider its temperature dependence. The collected charge, Q_r, as a function of temperature is shown in Fig. 8 for an applied field of approximately 10^3V/cm. The solid line is a least-squares fit to the data which *decreases* about 10 per cent for a temperature increase of 50°C in good agreement with the predictions of the diffusion model. If the binding energy of the state postulated in the field aided thermal release model were 0·1 eV, the collection efficiency would double between 0 and 50°C, a result which differs from the least squares fit by about three standard deviations. Despite an order of magnitude difference between the measured bulk mobilities of holes and electrons, the observed efficiencies for carriers of both signs were nearly identical, as shown in Fig. 9. If the efficiency were limited by trapping in a damaged surface layer, the products of the mobilities and the trapping times in the damaged layer, $\mu\tau_{tr}$, for carriers of the two polarities would have to be nearly equal.

The probability of an electron recombining in unit time,

$$P_r(t) = v_{th} N_t (1 - f)\sigma$$

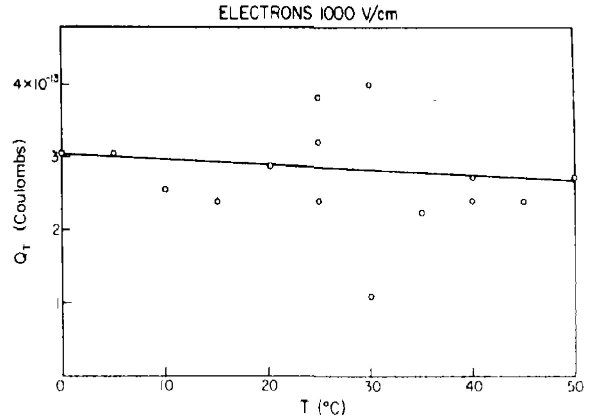

Fig. 8. Total collected charge at fixed light intensity as a function of temperature for a low applied field. The solid line is a linear least-square fit to the data.

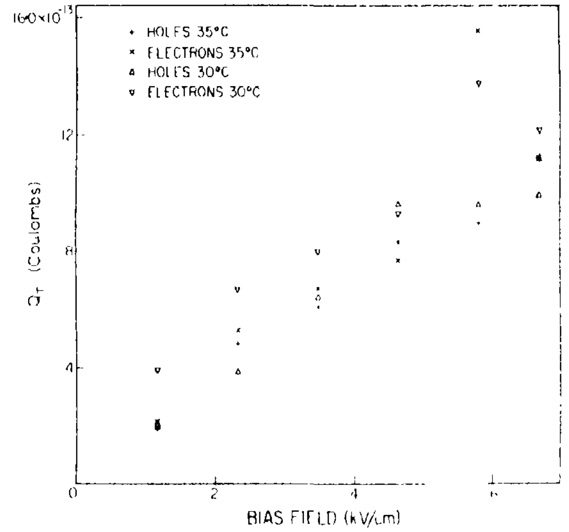

Fig. 9. Total collected charge at fixed light intensity as a function of electric field for both holes and electrons.

where v_{th} is the thermal velocity, σ is the capture cross section of the trap for electrons, N_t is the trap density, and f is the occupation factor which gives the fraction of the traps occupied by an electron[17].

$$N_t(1-f) = Q_0\alpha/A$$

where α is the absorption constant and A is the area of the contact. Since both the transmission of the filter and the spectral intensity of the source peak in the vicinity of 4200 Å, α will be taken to be $2\times10^5\ \text{cm}^{-1}$, the value at 4200 Å[20, 9]. Assuming that $v_{th} = 10^7$ cm/sec, that $\sigma = 10^{-15}\ \text{cm}^2$, the cross sectional area of an Se_8 molecule, and that $Q_0 \cong Q_{T\max}$, one finds that that recombination time is

$$\frac{1}{P_r} \cong 200\ \text{nsec}$$

while the time for an electron to cross the absorption region at a field of 1000 V/cm (a value at which half of the carriers must recombine if recombination is to be a tenable mechanism for the η variation) is about 1 nsec. Thus, the recombination rate is too small by about two orders of magnitude to explain the observed effect.

Although we have shown that in the case discussed here diffusion to the contact dominates that collection efficiency, other effects may be important in other cases. Nevertheless, diffusion to the interface must be present in all contact limited devices and places an upper limit on the attainable efficiency.

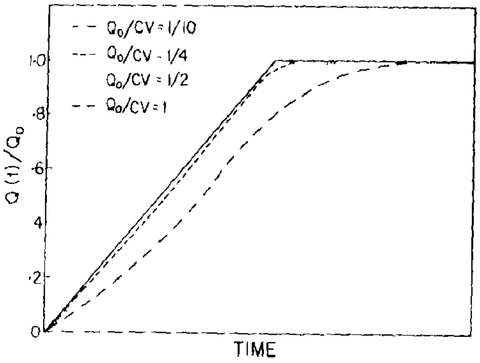

Fig. 10. Collected charge as a function of time based on the calculations of Weisz *et al.*[21] showing that the measured transit time is insensitive to space charge effects.

5. SPACE CHARGE EFFECTS

So far the discussion has been restricted to light intensities small enough that space charge plays no significant part. We now relax this restriction and examine what occurs as the light intensity increases. This problem has been treated theoretically in detail by Weisz *et al.*[21]. As long as the carriers which are generated at the front surface by a short pulse of light must either all begin to drift across the sample or recombine in a time short with respect to the transit time, no virtual cathode (i.e. a reservoir of charge which makes $E = 0$) can form. Simple integration of Poisson's equation then shows that the maximum amount of charge which can be drawn across the platelet is CV where C is the parallel plate capacitance of the sample and V the applied voltage. (It is shown in the Appendix that any virtual cathode must collapse in a time very much less than the transit time). In Fig. 10 is shown the result of a graphical integration of the curves presented by Weisz *et al.* for current as a function of time. In this figure, the integrated current, or charge, $Q(t)$, is normalized by dividing it by the total charge generated, Q_0, and plotted vs. time. Note that the effective transit time, as it has been obtained above from the experimental data, increases about 20 per cent as Q_0 increases from $1/10\,CV$ to CV, and that most of the increase in τ_t occurs as Q_0 increases from $1/2\,CV$ to CV.

In Fig. 11(a) the data for transit time as a function of light intensity is compared with the theoretical predictions of Weisz *et al.* as inferred from Fig. 10. The agreement is seen to be quite good, except for the highest light intensity.

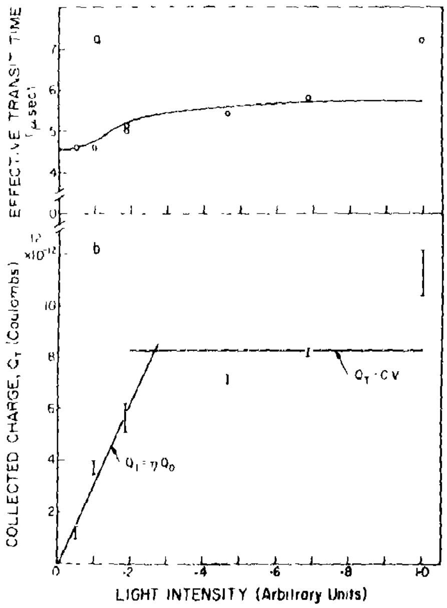

Fig. 11. Response time and total collected charge vs. light intensity. Measured points are for electrons at 23°C with a bias field of ≈ 6 kV/cm. Solid curves are theoretical dependence (see text).

One would expect that the collected charge, Q_T, would equal ηQ_0 for low light intensities, where Q_0 is the total charge generated by the light pulse. At higher light intensity the space charge would be increasingly effective in screening the bias field and the collection efficiency would decrease as the collected charge approaches the saturation value, CV. The data presented in Fig. 11(b) are again in good agreement with this sample picture, with the exception of the data taken at highest light intensity.

Extrapolation of Q_0 from low to higher light intensities suggests that a surface density of carriers of between $10^{16}/\text{cm}^3$ and $10^{17}/\text{cm}^3$ is created by the light flash. This would cause the surface sheet resistance of the selenium crystal to be in the vicinity of a few hundred ohms/□. Since the evaporated contact covered only about 1/10 of the surface, it is possible that the surface conductivity was modulated by the light flash to such an extent that the effective area of the contact increased enough that Q_T is equal to CV for the larger effective sample area. This model would explain the large increase in transit time for the case with $Q_T > CV$ because after the initial charge injection from the modulated surface the field lines would change rather drastically as the surface resistance rose. As would be expected, the collected charge vs. time curve displayed considerably more rounding for the high light intensity case than for those cases for which the light pulse was of lower intensity.

REFERENCES

1. MITSCHERLICH, *Berl. Akad. Monatber*, 409 (1855).
2. MUTHMANN E., *Z. Kristallogr.* **17**, 336 (1890).
3. SAUNDERS A. P., *J. phys. Chem.* **4**, 423 (1900).
4. KYROPOULOS S., *Z. Phys.* **40**, 618 (1927).
5. GUDDEN B. and POHL R., *Z. Phys.* **35**, 18 (1926).
6. BURBANK R. D., *Acta crystallogr.* **4**, 140 (1951).
7. PROSSER V., *Čs. Čas. Fys.* **10**, 35 (1960).
8. SPEAR W. E., *J. Phys. Chem. Solids* **21**, 110 (1961).
9. CAYWOOD J. M. and TAYNAI J. D., *J. Phys. Chem. Solids* **30**, 1573 (1969).
10. IIZIMA S. *et al.*, see orig. in *Proc. 1st Int. Symp. on Phys. of Se and Te.*
11. MARSH R. E., Private communication.
12. WILLIAMS R. and BUBE R. H., *J. appl. Phys.* **31**, 968 (1960).
13. *American Institute of Physics Handbook*, 2nd Edn., Section 6, p. 112. McGraw Hill, New York (1957).
14. SZE S. M. *et al.*, *Solid-St. Electron.* **7**, 509 (1964).
15. PAULING L., *The Nature of the Chemical Bond*, p. 93. Cornell University Press, Ithaca (1960).
16. TEFFT W. E., *J. appl. Phys.* **38**, 5265 (1965).
17. GROVE A. S., *Physics and Technology of Semiconductor Devices*, p. 131. Wiley, New York (1967).
18. TABAK M. D. and WARTER P. J., JR., *Phys. Rev.* **173**, 899 (1968)
19. Cf. BUILT H. C. and WEGNER H. E., *Rev. scient. Instrum.* **34**, 274 (1963); BROWN W. L., *IRE Trans.* **NS-8**, 2 (1961); MAYER J. W., *Nuclear Electronics*, p. 129. Organization for Economic Cooperation and Development, European Nuclear Energy Agency, Paris (1964).
20. FISCHER H. and RUPPEL W. B., *Appl. Optics* **3**, 769 (1964).
21. WEISZ S. Z. *et al*, *J. appl. Phys.* **39**, 2296 (1968).
22. *Bateman Manuscript Project, Integral Transforms*, Vol. 1, p. 74, (Eq. 2.4.26). McGraw-Hill, New York (1954).
23. BEAM W. R., *Electronics of Solids*, p. 272. McGraw-Hill, New York (1965).

APPENDIX

The problem to be solved is that of the behavior of an exponential initial distribution of carriers under the influence of drift and diffusion in the vicinity of a collecting contact. Formally one writes the continuity equation.

$$\frac{\partial n}{\partial t} = D\frac{\partial^2 n}{\partial x^2} - \mu E\frac{\partial n}{\partial x} \qquad \text{(A.1a)}$$

the initial condition

$$n(x,0) = \begin{cases} N_0 e^{-\alpha x} & x > 0 \\ 0 & x \leq 0 \end{cases} \qquad \text{(A.1b)}$$

and the boundary conditions

$$n(0,t) = n(d,t) = 0 \quad \forall t \qquad \text{(A.1c)}$$

where, D is the diffusion constant, n is the number of carriers, μ is the mobility, E is the electric field, α is the optical absorption constant, N_0 is the total number of carriers generated at the surface and d is the thickness of the crystal.

Separating variables, solving the equation, and applying the boundary conditions yields

$$n(x,t) = \sum_{m=1}^{\infty} A_m \exp\left[-\left(\frac{m\pi}{d}\right)^2 - \frac{F^2}{4D}t + \frac{Fx}{2D}\right]\sin\frac{m\pi x}{d} \qquad \text{(A.2)}$$

where $F \equiv \mu E$.

Using the initial condition to evaluate A_m, one obtains

$$n(x,t) = \frac{2N_0}{d}\exp\left(-\frac{F^2}{4D}t+\frac{Fx}{2D}\right)$$

$$\sum_{m=1}^{\infty}\frac{(m\pi/d)\exp\left[-\left(\frac{m\pi}{d}\right)^2Dt\right]\left\{1-(-1)^m\exp\left[-\left(\alpha+\frac{F}{2D}\right)d\right]\right\}\sin\frac{m\pi x}{d}}{\left(\alpha+\frac{F}{2D}\right)^2+\left(\frac{m\pi}{d}\right)^2}. \qquad \text{(A.3)}$$

Now if d is very large w.r.t. α, we can let $d \to \infty$ in such a way that $(l\pi/d) \to w$ and obtain

$$n(x,t) = \frac{N_0}{2}\exp\left(-\frac{F^2}{4D}t+\frac{Fx}{2D}\right)\int_0^{\infty}\frac{w\exp(-w^2Dt)\sin wx\,dw}{\left(\alpha+\frac{F}{2D}\right)^2+w^2} \qquad \text{(A.4)}$$

Evaluation of the integral produces[22]

$$n(x,t) = \left\{\frac{N_0}{2}\exp\left[-\frac{F^2}{4D}t+\frac{Fx}{2D}+\left(\alpha+\frac{F}{2D}\right)^2Dt\right]\right\}.$$

$$\left\{\exp\left[-\left(\alpha+\frac{F}{2D}\right)x\right]\mathrm{Erfc}\left[\sqrt{Dt}\left(\alpha+\frac{F}{2D}\right)-\frac{x}{2\sqrt{Dt}}\right]\right.$$

$$\left.-\exp\left[\left(\alpha+\frac{F}{2D}\right)x\right]\mathrm{Erfc}\left[\sqrt{Dt}\left(\alpha+\frac{F}{2D}\right)+\frac{x}{2\sqrt{Dt}}\right]\right\} \qquad \text{(A.5)}$$

However, equation (A.5) isn't very useful because what is really desired is the current flow out through the contact at $x = 0$. This current is given by

$$i(t)\Big|_{x=0} = Fn(0,t) - D\frac{\partial n(x,t)}{\partial x}\Big|_{x=0} \qquad \text{(A.6)}$$

The result of substituting equation (A.4) into equation (A.6) is

$$i(t)\Big|_{x=0} = \frac{2N_0D}{\pi}\exp\left[-\frac{F^2}{4D}t\right].$$

$$\int_0^{\infty}\frac{w^2\exp[-w^2Dt]}{(\alpha+(F/2D))^2+w^2}\,dw. \qquad \text{(A.7)}$$

The charge lost by time, t, as a result of the current of equation (A.7),

$$Q_L(t) = \int i(t')dt'$$

$$= \frac{-2N_0}{\pi}\left\{\int_0^{\infty}\frac{w^2dw}{[w^2+(\alpha+(F/2D))^2][w^2+(F/2D)^2]}\right.$$

$$\left.-\exp\left[-\frac{F^2}{4D}t\right]\int_0^{\infty}\frac{w^2\exp[-w^2Dt]\,dw}{[w^2+(\alpha+(F/2D))^2][w^2+(F/2D)^2]}\right\}. \qquad \text{(A.8)}$$

The time dependence is obviously segregated into the second term. Evaluation of the term before the integral places an upper bound on the relaxation time, $\tau_r = (4D/F^2)$. The ratio of the relaxation time to the transit time

$$\frac{\tau_r}{\tau_t} = \frac{4D}{Fd} = \frac{4kT/q}{V}$$

where V is the voltage across the sample, k is Boltzmann's constant and the Einstein relation has been used to evaluate D[23]. The smallest bias voltage ever employed in these measurements was 5 V so that

$$\frac{\tau_r}{\tau_t} \leq 0{\cdot}02$$

justifying an earlier assertion. Since the second term of equation (A.8) drops so rapidly with time (being always less than 1/100 of the first term after $0{\cdot}1\,\tau_t$), one can say *that essentially all of the charge which will be collected* at $x = 0$ is collected in the first small part of the transit time and approximate the lost charge, $Q_l(t)$, with a constant,

$$Q_l = \frac{2N_0}{\pi}\int_0^{\infty}\frac{w^2dw}{[w^2+(\alpha+(F/2D))^2][w^2+(F/2D)^2]} \qquad \text{(A.9)}$$

the first term of equation (A.8). By evaluating the residues of the poles of the integrand of equation (A.9), one finds

$$Q_L = \frac{N_0}{\alpha}\frac{1}{1+(E/E_F)} \qquad \text{(A.10)}$$

where $E_F = (\alpha kT/q)$ is an effective 'diffusion field'. Finally the charge transferred across the crystal is given by

$$Q_T = \frac{n_0}{\alpha}\frac{E/E_F}{1+(E/E_F)}. \qquad \text{(A.11)}$$

J Phys. Chem. Solids Pergamon Press 1970. Vol. 31, pp. 995–1010. Printed in Great Britain.

CALCULATION OF g-FACTORS OF Cu^{2+}-CENTERS IN II–VI-COMPOUNDS

UDO SCHERZ
3. Physikalisches Institut der Technischen Universität Berlin, Berlin, Germany

(*Received* 12 *September* 1969)

Abstract—The linear Zeeman effect of Cu^{2+}-centers with a d^9 configuration in tetrahedral and trigonally or tetragonally distorted tetrahedral crystal fields is investigated. The g-factors are calculated in terms of crystal field parameters and orbital reduction factors by using a tensor operator technique. The eigenfunctions of the energy levels of Cu^{2+} centers are presented first. In case of a tetrahedral crystal field the g-factors may be found without any approximation and the angular dependance of the g-factors is given. In case of trigonally or tetragonally distorted tetrahedral crystal fields the g-factors are calculated with magnetic field parallel or perpendicular to the axis of distortion. The formulas of the g-factors may also be used for Cu^{2+}-centers in octahedral and trigonally or tetragonally distorted octahedral crystal fields and for ions with a d^1 configuration

1. INTRODUCTION

In II–VI compounds g-factors of Cu^{2+} centers can be obtained by Zeeman effect and by EPR measurements. While EPR gives the splitting of the ground multiplet only, observation of the Zeeman effect makes it possible not only to find the g-factors of excited states but also the energy level diagram. The energy levels of Cu^{2+} centers and the corresponding g-factors can be calculated in terms of various unknown parameters so that the measurement of the g-factors gives further information about these parameters and helps to find the correct interpretation of the optical spectra. On the other hand EPR measurements are usually interpreted by using a spin Hamiltonian in which the g-factors and other hyperfine structure constants play the role of unknown parameters to be determined by experiment. In this paper we are primarily concerned with the Zeeman effect and the g-factors are calculated in terms of crystal field parameters whereas hyperfine structure and related topics are neglected.

Zeeman splittings of the energy levels of Cu^{2+} centers in II–VI-compounds had been observed by Dietz *et al.*[1] at $ZnO:Cu^{2+}$ crystals,* and by De Wit[2] and Wöhlecke[3] at cubic $ZnS:Cu^{2+}$ crystals. They also calculated the observed g-factors in terms of crystal field parameters and orbital reduction factors. The determination of the parameters of the spectra of cubic $ZnS:Cu^{2+}$ crystals, however, is not clear, and in the meantime new g-factors had been measured by Broser *et al.*[4] at $ZnO:Cu^{2+}$ crystals.

The aim of this paper is therefore to calculate all g-factors of Cu^{2+} energy levels from the standpoint of crystal field theory. In addition the angular dependence of the Zeeman splitting is investigated. The comparison of the calculated g-factors with experimental measurements and the determination of crystal field parameters and orbital reduction factors is given by Broser *et al.*[4].

Copper centers—and also centers of the other transition metal ions—in II–VI compounds are surrounded by four equal next neighbors which produce a crystal field of tetrahedral symmetry. The spectra of Cu^{2+} centers in cubic crystals (for instance cubic ZnS) may therefore be found by considering the influence of a crystal field, invariant under the transformations of the symmetry group T_d, on the spectrum of the free ion. In case of hexagonal crystals (for instance ZnO) the symmetry of the crystal field is C_{3v} which is a subgroup of T_d, and the trigonal axis is called the c-axis. For reasons of mathematical convenience these circumstances are best described by small trigonal distortions of tetrahedral crystal fields. In addition tetragonally distorted tetrahedral crystal fields (symmetry group D_{2d}) are considered here.

---

*They also found the same ground state g-factors by EPR measurements.

In a foregoing paper[5] the author calculated the energy spectra of Cu^{2+}-ions in tetrahedral or octahedral crystal fields with and without trigonal or tetragonal distortions. By using the most general effective Hamiltonian invariant under the transformations of the symmetry group considered, general energy matrices are derived and the corresponding eigenfunctions are given. The energy levels, which are the eigenvalues of the energy matrix, had been obtained approximately by making some assumptions about the relative order of magnitude of the parameters.

We can find the linear Zeeman splitting of the energy levels by calculating the matrices of a tensor operator in the eigenspace of the energy level considered. The g-factors are simply the differences of the eigenvalues of these matrices. The tensor operator used is a more general operator than $\mathbf{L}+2\mathbf{S}$ (orbital angular momentum and spin operator). So orbital reduction is taken into account and this produces new orbital reduction factors k, k' which appear in the formulas of the g-factors as new unknown parameters to be determined by experiment.

The eigenfunctions of the energy levels, necessary to calculate the g-factors, may be found from the energy matrices and eigenfunctions given in reference [5] for a d^1 configuration. The transition $d^1 \to d^9$ of Cu^{2+} can be done by replacing all parameters by their negative values[6]. All g-factors obtained in this paper, however, are identical for d^1 and d^9 configurations. This may be seen by a simple argument: the orbital reduction factors k, k' are dimensionless parameters and do not change their sign if transitions $d^1 \leftrightarrow d^9$ are considered. The dimension of all other parameters, occurring in the g-factors, is energy and they change their sign when the transition $d^1 \to d^9$ is carried out. Since the g-factor is a dimensionless function of the parameters, it must be invariant under the transitions $d^1 \leftrightarrow d^9$.

The transition from tetrahedral to octahedral crystal fields is just as simple. The energy matrices for this case may be found from those given in reference [5] by merely replacing Dq by its negative value. The same is true for the g-factors given in this paper.

2. g-FACTORS OF A d^9 CONFIGURATION IN A TETRAHEDRAL CRYSTAL FIELD

The first case studied is a d^9 configuration in a tetrahedral crystal field with energy levels[5]:

$$E(\Gamma_8(^2E)) = 6Dq + \frac{3\xi'^2}{20Dq}$$

$$E(\Gamma_8(^2T_2)) = -4Dq + \tfrac{1}{2}\xi - \frac{3\xi'^2}{20Dq}$$

$$E(\Gamma_7(^2T_2)) = -4Dq - \xi$$

where $\xi \ll 10Dq$, $\xi' \ll 10Dq$ has been assumed. The corresponding eigenfunctions may easily be found by an unitary transformation of the basis functions, given in Ref. [5], with which the energy matrices are defined. Making also the transition $d^1 \to d^9$ we find:

$$|\Gamma_8(^2E)1\rangle = a\cos\alpha + u_- \sin\alpha$$

$$|\Gamma_8(^2E)2\rangle = b\cos\alpha + v_- \sin\alpha$$

$$|\Gamma_8(^2E)3\rangle = a'\cos\alpha + u_+ \sin\alpha$$

$$|\Gamma_8(^2E)4\rangle = b'\cos\alpha + v_+ \sin\alpha$$

$$|\Gamma_7({}^2T_2)1\rangle = c$$

$$|\Gamma_8({}^2T_2)1\rangle = -a\sin\alpha + u_-\cos\alpha$$

$$|\Gamma_8({}^2T_2)2\rangle = -b\sin\alpha + v_-\cos\alpha$$

$$|\Gamma_8({}^2T_2)3\rangle = -a'\sin\alpha + u_+\cos\alpha$$

$$|\Gamma_8({}^2T_2)4\rangle = -b'\sin\alpha + v_+\cos\alpha$$

$$|\Gamma_7({}^2T_2)2\rangle = c' \qquad (1)$$

with

$$\sin 2\alpha = \frac{\sqrt{6}\xi'}{\sqrt{(10Dq-\frac{1}{2}\xi)^2+6\xi'^2}} = \frac{\sqrt{6}\epsilon}{\sqrt{1+6\epsilon^2}}$$

$$\epsilon = \frac{\xi'}{10Dq-\frac{1}{2}\xi} \ll 1$$

$$\cos 2\alpha = \frac{-10Dq+\frac{1}{2}\xi}{\sqrt{(10Dq-\frac{1}{2}\xi)^2+6\xi'^2}} = \frac{-1}{\sqrt{1+6\epsilon^2}} \qquad (2)$$

and a, b, c, a', b', c', u_-, ... are defined in Ref. [5]. The transition $d^1 \rightarrow d^9$ can be made by changing the signs of all parameters Dq, ξ, ξ', but cannot be made if the parameter ϵ is introduced. The formulas for the wave functions are different in both cases, the g-factors, however, remain unchanged.

To find the g-factors, for instance of the energy level $\Gamma_8({}^2E)$, with magnetic field in z-direction, we have to calculate the eigenvalues of the matrix

$$\langle\Gamma_8({}^2E)\nu|T_z+2S_z|\Gamma_8({}^2E)\mu\rangle \qquad (3)$$

with $T_z = T\gamma(T_1)$. This is due to the fact that the components of the orbital angular momentum operator L_x, L_y, L_z transform as α, β, γ basis functions of the irreducible representation T_1 if the symmetry transformations of the tetrahedral symmetry group T_d are applied. The matrix (3) may be found from (1) and the matrices

$$\langle E\gamma|T_z|E\gamma'\rangle = 0,$$

$$(\langle T_2\gamma|T_z|T_2\gamma'\rangle) = k\begin{pmatrix} 0 & i & 0 \\ -i & 0 & 0 \\ 0 & 0 & 0 \end{pmatrix},$$

$$(\langle T_2\gamma|T_z|E\gamma'\rangle) = k'\begin{pmatrix} 0 & 0 \\ 0 & 0 \\ 0 & 2i \end{pmatrix},$$

$$(\langle \tfrac{1}{2}M_s|2S_z|\tfrac{1}{2}M_s'\rangle) = \begin{pmatrix} 1 & 0 \\ 0 & -1 \end{pmatrix} \qquad (4)$$

which had been calculated by using the Wigner–Eckart theorem [6]

$$\langle\Gamma\gamma|V\gamma(\Gamma)|\Gamma'\gamma'\rangle = (d_r)^{-1/2}\langle\bar{\Gamma}\|V(\bar{\Gamma})\|\Gamma'\rangle\langle\Gamma\gamma|\Gamma'\gamma'\bar{\Gamma}\bar{\gamma}\rangle$$

and the double barred matrix elements given in [5]

$$\langle T_2\|T(T_1)\|T_2\rangle = i\sqrt{6}k,$$

$$\langle T_2\|T(T_1)\|E\rangle = -i2\sqrt{3}k',$$

where additional orbital reduction factors k, k' had been introduced, which are defined by

$$k = -i\langle t_2\xi|t_z(T_1)|t_2\eta\rangle$$

$$k' = -\frac{i}{2}\langle t_2\zeta|t_z(T_1)|ev\rangle.$$

The orbital reduction factors appear because of the more general character of the $T_\gamma(T_1)$ operator compared with L_z. Their difference from 1 expresses the fact that covalent bonding has been taken into account.

Performing the transformation of the basis functions given in Ref. [5] we get the following matrices of the tensor operator T_z+2S_z with the help of (4):

$$\begin{pmatrix} 1-k & 0 & 0 & & & \\ 0 & \frac{k-1}{3} & i\frac{\sqrt{2}}{3}(k+2) & & 0 & \\ 0 & i\frac{\sqrt{2}}{3}(k+2) & \frac{2k+1}{3} & & & \\ & & & k-1 & 0 & 0 \\ & 0 & & 0 & \frac{1-k}{3} & -i\frac{\sqrt{2}}{3}(k+2) \\ & & & 0 & i\frac{\sqrt{2}}{3}(k+2) & -\frac{2k+1}{3} \end{pmatrix} \begin{array}{c} a \\ b \\ c \\ a' \\ b' \\ c' \end{array} \begin{pmatrix} 0 & 0 & & \\ 0 & 2\sqrt{\frac{2}{3}}k' & & 0 \\ 0 & \frac{-2ik'}{\sqrt{3}} & & \\ & & 0 & 0 \\ & 0 & 0 & -2\sqrt{\frac{2}{3}}k' \\ & & 0 & \frac{-2ik'}{\sqrt{3}} \end{pmatrix}$$

$$\begin{pmatrix} u_- & v_- & u_+ & v_+ \\ 1 & & 0 & \\ & -1 & & \\ & & 1 & \\ & 0 & & 1 \end{pmatrix}. \tag{5}$$

By using these matrices (5) and the functions (1) the matrix elements (3) may easily be found:

$$\langle\Gamma_8(^2E)1|T_z+2S_z|\Gamma_8(^2E)1\rangle$$
$$= -\cos 2\alpha - k\cos^2\alpha$$
$$\langle\Gamma_8(^2E)2|T_z+2S_z|\Gamma_8(^2E)2\rangle$$
$$= \frac{k-1}{3}\cos^2\alpha + 2k'\sqrt{\frac{2}{3}}\sin 2\alpha - \sin^2\alpha$$
$$\langle\Gamma_8(^2E)3|T_z+2S_z|\Gamma_8(^2E)3\rangle$$
$$= -\langle\Gamma_8(^2E)1|T_z+2S_z|\Gamma_8(^2E)1\rangle$$
$$\langle\Gamma_8(^2E)4|T_z+2S_z|\Gamma_8(^2E)4\rangle$$
$$= -\langle\Gamma_8(^2E)2|T_z+2S_z|\Gamma_8(^2E)2\rangle$$

all non-diagonal elements being zero. In this paper all g-factors are calculated as the positive distances of the energy levels split by the magnetic field. We therefore have

$$g_{z1}(\Gamma_8(^2E)) = -2\cos 2\alpha + k(1+\cos 2\alpha),$$
$$g_{z2}(\Gamma_8(^2E)) = \frac{1-k}{3}(1+\cos 2\alpha) + 1$$
$$-\cos 2\alpha - \frac{8k'}{\sqrt{6}}\sin 2\alpha. \tag{6}$$

To simplify the formulas we expand in terms of powers of ϵ. From (2) we find up to ϵ^2:

$$\sin 2\alpha = \sqrt{6}\epsilon, \cos 2\alpha = -1+3\epsilon^2,$$
$$\sin^2\alpha = 1-\tfrac{3}{2}\epsilon^2, \cos^2\alpha = \tfrac{3}{2}\epsilon^2 \tag{7}$$

and therefore we finally get

$$g_{z1}(\Gamma_8(^2E)) = 2-3(2-k)\epsilon^2$$
$$g_{z2}(\Gamma_8(^2E)) = 2-8k'\epsilon-(2+k)\epsilon^2. \tag{8}$$

These g-factors had been given by De Wit[2] in linear approximation only. Similarly we calculate the g-factors of the $\Gamma_8(^2T_2)$ level. From (1) and (5) we find

$$\langle\Gamma_8(^2T_2)1|T_z+2S_z|\Gamma_8(^2T_2)1\rangle$$
$$= -\cos 2\alpha - k\sin^2\alpha$$
$$\langle\Gamma_8(^2T_2)2|T_z+2S_z|\Gamma_8(^2T_2)2\rangle$$
$$= \frac{k-1}{3}\sin^2\alpha - \cos^2\alpha - 2\sqrt{\frac{2}{3}}k'\sin 2\alpha$$
$$\langle\Gamma_8(^2T_2)3|T_z+2S_z|\Gamma_8(^2T_2)3\rangle$$
$$= -\langle\Gamma_8(^2T_2)1|T_z+2S_z|\Gamma_8(^2T_2)1\rangle$$
$$\langle\Gamma_8(^2T_2)4|T_z+2S_z|\Gamma_8(^2T_2)4\rangle$$
$$= -\langle\Gamma_8(^2T_2)2|T_z+2S_z|\Gamma_8(^2T_2)2\rangle$$

all non-diagonal matrix elements being zero. The g-factors are therefore

$$g_{z1}(\Gamma_8(^2T_2)) = -2\cos 2\alpha - k(1-\cos 2\alpha)$$

$$g_{z2}(\Gamma_8(^2T_2)) = \frac{1-k}{3}(1-\cos 2\alpha)+1 + \cos 2\alpha + \frac{8k'}{\sqrt{6}}\sin 2\alpha \qquad (9)$$

or with the approximations (7):

$$g_{z1}(\Gamma_8(^2T_2)) = 2(1-k) - 3(2-k)\epsilon^2,$$

$$g_{z2}(\Gamma_8(^2T_2)) = \tfrac{2}{3}(1-k) + 8k'\epsilon + (2+k)\epsilon^2. \qquad (10)$$

The g-factor of the two dimensional ground level $\Gamma_7(^2T_2)$ is found from the matrix elements

$$\langle\Gamma_7(^2T_2)1|T_z+2S_z|\Gamma_7(^2T_2)1\rangle = -\langle\Gamma_7(^2T_2)2|T_z+2S_z|\Gamma_7(^2T_2)2\rangle = \frac{2k+1}{3}$$

(non-diagonal elements are zero) where (1) and (5) have been used. From this we find without any approximation:

$$g_z(\Gamma_7(^2T_2)) = \tfrac{2}{3}(2k+1) \qquad (11)$$

which had already been given by De Wit[2].

If a Cu^{2+} ion with a d^9 configuration is placed in an octahedral crystal field we have simply to replace Dq by its negative value. In this case the g-factors (8) and (10) are given by changing the sign of the terms proportional to $k'\epsilon$ and interpreting ϵ as

$$\frac{\xi'}{10Dq+\frac{1}{2}\xi}.$$

The g-factor (11) remains unaltered.

3. ANGULAR DEPENDENCE OF THE g-FACTORS IN A TETRAHEDRAL CRYSTAL FIELD

The angular dependence of the Zeeman splitting of Γ_8-levels had already been discussed by Ayant *et al.*[7]. They gave, however, no g-factors in terms of crystal field parameters. To simplify the calculation we assume the magnetic field to have the direction

$$\mathbf{H} = H\left(\frac{\sin\theta}{\sqrt{2}}, \frac{\sin\theta}{\sqrt{2}}, \cos\theta\right)$$

where θ is an angle in the $(1\bar{1}0)$ plane. $\cos\theta = 1$, $1/\sqrt{3}$, 0 correspond to directions [001], [111] and [110] respectively. We define

$$u = \frac{\sin\theta}{\sqrt{2}},\ \mu = 2\operatorname{ctg}\theta,\ \frac{\mu^2}{2}+1 = \frac{1}{2u^2},$$

$$\frac{\mu^4}{4}+\mu^2+1 = \frac{1}{4u^4} \qquad (12)$$

and calculate $g(\theta)$ with the tensor operator

$$T = u\cdot[T_x+2S_x+T_y+2S_y+\mu(T_z+2S_z)] \qquad (13)$$

with $T_x = T_\alpha(T_1)$, $T_y = T_\beta(T_1)$. The matrix elements of the tensor operators may again be found by using the Wigner-Eckart theorem:

$$\langle E\gamma|T_x|E\gamma'\rangle = 0,$$

$$(\langle T_2\gamma|T_x|T_2\gamma'\rangle) = k\begin{pmatrix}0 & 0 & 0\\ 0 & 0 & i\\ 0 & -i & 0\end{pmatrix},$$

$$(\langle T_2\gamma|T_x|E\gamma'\rangle) = k'\begin{pmatrix}-i\sqrt{3} & -i\\ 0 & 0\\ 0 & 0\end{pmatrix}$$

$$\langle E\gamma|T_y|E\gamma'\rangle = 0,$$

$$(\langle T_2\gamma|T_y|T_2\gamma'\rangle) = k\begin{pmatrix}0 & 0 & -i\\ 0 & 0 & 0\\ i & 0 & 0\end{pmatrix},$$

$$(\langle T_2\gamma|T_y|E\gamma'\rangle) = k'\begin{pmatrix}0 & 0\\ i\sqrt{3} & -i\\ 0 & 0\end{pmatrix}$$

$$(\langle\tfrac{1}{2}M_s|2S_x|\tfrac{1}{2}M_s'\rangle) = \begin{pmatrix}0 & 1\\ 1 & 0\end{pmatrix},$$

$$(\langle\tfrac{1}{2}M_s|2S_y|\tfrac{1}{2}M_s'\rangle) = \begin{pmatrix}0 & -i\\ i & 0\end{pmatrix}.$$

Applying the unitary transformation given in Ref. [5] we find the matrices of $T_x + 2S_x$:

$$\begin{pmatrix} & 0 & & 0 & \frac{1-k}{\sqrt3} & \frac{i(2+k)}{\sqrt6} \\ & 0 & & \frac{1-k}{\sqrt3} & \frac{2}{3}(k-1) & \frac{i(2+k)}{3\sqrt2} \\ & & & \frac{i(2+k)}{\sqrt6} & \frac{i(2+k)}{3\sqrt2} & \frac{2k+1}{3} \\ 0 & \frac{1-k}{\sqrt3} & \frac{-i}{\sqrt6}(2+k) & & & \\ \frac{1-k}{\sqrt3} & \frac{2}{3}(k-1) & \frac{-i(2+k)}{3\sqrt2} & & 0 & \\ -\frac{i(2+k)}{\sqrt6} & -\frac{i(2+k)}{3\sqrt2} & \frac{2k+1}{3} & & & \end{pmatrix} \begin{array}{c} a \\ b \\ c \\ a' \\ b' \\ c' \end{array} \begin{pmatrix} & & -k'\sqrt{\frac32} & \frac{-k'}{\sqrt2} \\ & 0 & \frac{-k'}{\sqrt2} & \frac{-k'}{\sqrt6} \\ & & -ik' & \frac{-ik'}{\sqrt3} \\ -k'\sqrt{\frac32} & \frac{-k'}{\sqrt2} & & \\ \frac{-k'}{\sqrt2} & \frac{-k'}{\sqrt6} & 0 & \\ ik' & \frac{ik'}{\sqrt3} & & \end{pmatrix}$$

$$\begin{pmatrix} u_- & v_- & u_+ & v_+ \\ 0 & 0 & 1 & 0 \\ 0 & 0 & 0 & 1 \\ 1 & 0 & 0 & 0 \\ 0 & 1 & 0 & 0 \end{pmatrix}$$

and the matrices of $Ty + 2S_y$:

$$\begin{pmatrix} & 0 & & 0 & \frac{i(k-1)}{\sqrt3} & \frac{2+k}{\sqrt6} \\ & 0 & & \frac{i(k-1)}{\sqrt3} & i\frac{2}{3}(k-1) & \frac{-2-k}{3\sqrt2} \\ & & & \frac{2+k}{\sqrt6} & \frac{-2-k}{3\sqrt2} & \frac{i}{3}(1+2k) \\ 0 & \frac{i}{3}(1-k) & \frac{2+k}{\sqrt6} & & & \\ \frac{i(1-k)}{\sqrt3} & i\frac{2}{3}(1-k) & \frac{2-k}{3\sqrt2} & & 0 & \\ \frac{2+k}{\sqrt6} & \frac{-2-k}{3\sqrt2} & -\frac{i}{3}(1+2k) & & & \end{pmatrix} \begin{array}{c} a \\ b \\ c \\ a' \\ b' \\ c' \end{array} \begin{pmatrix} & & -ik'\sqrt{\frac32} & \frac{ik'}{\sqrt2} \\ & 0 & \frac{ik'}{\sqrt2} & \frac{-ik'}{\sqrt6} \\ & & -k' & \frac{k'}{\sqrt3} \\ ik'\sqrt{\frac32} & \frac{-ik'}{\sqrt2} & & \\ \frac{-ik'}{\sqrt2} & \frac{ik'}{\sqrt6} & 0 & \\ -k' & \frac{k'}{\sqrt3} & & \end{pmatrix}$$

$$\begin{pmatrix} u_- & v_- & u_+ & v_+ \\ 0 & 0 & i & 0 \\ 0 & 0 & 0 & i \\ -i & 0 & 0 & 0 \\ 0 & -i & 0 & 0 \end{pmatrix}$$

We first consider the ground level $\Gamma_7(^2T_2)$. The matrix elements of the tensor operator T are with respect to (1):

$$(\Gamma_7(^2T_2)1\left|\frac{1}{u}T\right|\Gamma_7(^2T_2)1\rangle = -\left\langle\Gamma_7(^2T_2)2\left|\frac{1}{u}T\right|\Gamma_7(^2T_2)2\right\rangle = \mu\frac{2k+1}{3}$$

$$\left\langle\Gamma_7(^2T_2)1\left|\frac{1}{u}T\right|\Gamma_7(^2T_2)2\right\rangle = (1+i)\frac{2k+1}{3}$$

and the g-factor is therefore independent of θ:

$$g(\Gamma_7(^2T_2)) = u\sqrt{\mu^2+2}\cdot\tfrac{2}{3}(2k+1)$$
$$=\tfrac{2}{3}(2k+1).$$

Proceeding now to the Γ_8 levels we find the following matrix of the operator T:

$$\langle T\rangle = u\cdot\begin{pmatrix} -\mu A & 0 & (1+i)C & (1-i)D \\ 0 & -\mu B & (1-i)D & (1+i)E \\ (1-i)C & (1+i)D & \mu A & 0 \\ (1+i)D & (1-i)E & 0 & \mu B \end{pmatrix} \qquad (14)$$

with the abbreviations:

for $\Gamma_8(^2E)$:

$$A = -\cos 2\alpha + k\cos^2\alpha$$
$$B = \frac{1-k}{3}\cos^2\alpha + \sin^2\alpha - \frac{4k'}{\sqrt{6}}\sin 2\alpha$$
$$C = \sin^2\alpha - \frac{3k'}{\sqrt{6}}\sin 2\alpha$$
$$D = \frac{1-k}{\sqrt{3}}\cos^2\alpha - \frac{k'}{\sqrt{2}}\sin 2\alpha$$
$$E = \frac{2}{3}(k-1)\cos^2\alpha + \sin^2\alpha + \frac{4k'}{\sqrt{6}}\sin 2\alpha$$

and for $\Gamma_8(^2T_2)$:

$$A = \cos 2\alpha + k\sin^2\alpha$$
$$B = \frac{1-k}{3}\sin^2\alpha + \cos^2\alpha + \frac{4k'}{\sqrt{6}}\sin 2\alpha$$
$$C = \cos^2\alpha + \frac{3k'}{\sqrt{6}}\sin 2\alpha$$
$$D = \frac{1-k}{\sqrt{3}}\sin^2\alpha + \frac{k'}{\sqrt{2}}\sin 2\alpha$$
$$E = \frac{2}{3}(k-1)\sin^2\alpha + \cos^2\alpha + \frac{k'}{\sqrt{6}}\sin 2\alpha.$$

The g-factors of the Γ_8 levels are the differences of the eigenvalues of the T-matrix (14) and we find:

$$g_1 = 2u\sqrt{X+\sqrt{Y}},\quad g_2 = 2u\sqrt{X-\sqrt{Y}} \qquad (15)$$

with

$$X = \frac{\mu^2}{2}(A^2+B^2) + C^2 + 2D^2 + E^2$$
$$Y = \frac{\mu^4}{4}(A^2-B^2)^2$$
$$+\mu^2[2D^2(A-B)^2 + (A^2-B^2)(C^2-E^2)]$$
$$+(C^2-E^2)^2 + 4D^2(C-E)^2.$$

The evaluation of the g-factors in terms of ϵ, k and k' can now be done by using the approximations (7). Neglecting terms proportional to ϵ^3 and higher we find in case of $\Gamma_8(^2E)$:

$$X = \frac{1}{u^2}[1 - 4k'\epsilon + (8k'^2 - 4 + k)\epsilon^2] \quad (16)$$
$$Y = \frac{1}{u^4}4k'^2\epsilon^2(4-3\Lambda(\theta))$$
$$\times\left(1-\left(\frac{1-k}{k'}+4k'\right)\epsilon\right)$$

and in case of $\Gamma_8(^2T_2)$:

$$X = \frac{1}{u^2}\left[\frac{5}{9}(1-k)^2 + \frac{4}{3}(1-k)k'\epsilon\right.$$
$$\left.+\left(8k'^2 - \frac{1}{3}(1-k)(8-5k)\right)\epsilon^2\right]$$
$$Y = \frac{1}{u^4}\frac{4}{3}(1-k)^2\left[\frac{4}{9}\left\{\frac{1}{3}(1-k)^2 - 2(1-k)k'\epsilon\right.\right.$$
$$\left.-((1-k)(5-2k)+9k'^2)\epsilon^2\right\}$$
$$\left.+\Lambda(\theta)\cdot\epsilon\{2(1-k)k' + (1-k+9k'^2)\epsilon\}\right]$$
$$(17)$$

with

$$\Lambda(\theta) = \sin^2 2\theta + \sin^4\theta. \qquad (18)$$

In the approximation used, u^2X is independent of θ, but $g_1(\Gamma_8(^2E))$ and $g_2(\Gamma_8(^2E))$ have an angular dependence which is of the same order of magnitude as the difference between them. If the magnetic field is in [111] direction, we have $\Lambda = \frac{1}{3}$ and we find from (15) and (16): $g_1(\Gamma_8(^2E)) = g_2(\Gamma_8(^2E))$, so that in this case the $\Gamma_8(^2E)$ quartet is split in two levels only. The difference of the two g-factors of the $\Gamma_8(^2E)$ level has a maximum for $\Lambda(\theta) = 0$ or $\theta = 0$, that is if the magnetic field is in [001] direction.

We consider now the $\Gamma_8(^2T_2)$ quartet. The angular dependence of the g-factors depends here on the numerical values of the parameters. The variation of the g-factors with θ might or might not be small compared with the difference between the two g-factors.

For both Γ_8 quartets we can say that if the two g-factors are equal, that means if they are split in two levels only, then this splitting is independent of θ. If the Zeeman splitting is independent of θ, then the $\Gamma_8(^2E)$ quartet is split in two levels only

4. *g*-FACTORS OF A d^9 CONFIGURATION IN A TRIGONALLY DISTORTED TETRAHEDRAL CRYSTAL FIELD

In a trigonally distorted tetrahedral crystal field a d^9 configuration has five doublets with energies[5]:

$$E(\Gamma_6(^2E)) = 6Dq+\frac{1}{2}D + \frac{1}{10Dq}\left(\frac{3}{2}\xi'^2 + 2K'\xi'\right)$$

$$E(\Gamma_4\Gamma_5(^2E)) = 6Dq-\frac{1}{2}D + \frac{1}{10Dq}\left(\frac{3}{2}\xi'^2 - 2K'\xi'\right)$$

$$E(\Gamma_4\Gamma_5(^2T_2)) = -4Dq+\frac{1}{2}\xi+K - \frac{1}{10Dq}\left(\frac{3}{2}\xi'^2 - 2K'\xi'\right)$$

$$E(\Gamma_6(^2T_2)) = -4Dq+\frac{1}{2}\xi-K - \frac{1}{10Dq}\left(\frac{3}{2}\xi'^2 + 2K'\xi'\right)$$

$$E(\Gamma_6(^2T_2)g) = -4Dq-\xi$$

where index g denotes the ground state and where

$$\xi_\perp = \xi_\parallel = \xi \ll 10Dq, \xi'_\perp = \xi'_\parallel = \xi' \ll 10Dq, \\ K \ll \xi, K' \ll \xi', \xi'_0 = 0$$

have been assumed. To find the corresponding eigenfunctions we have to perform the transition $d^1 \rightarrow d^9$ and to introduce the approximations into the wave functions given in Ref. [5]. The eigenfunctions of the $\Gamma_4\Gamma_5$ Kramers doublets may easily be found by an unitary transformation of the basis functions, given in Ref. [5], with which the energy matrices are defined. We find:

$$\begin{aligned}
|\Gamma_4\Gamma_5(^2E)1\rangle &= \cos\epsilon|u_+\tfrac{1}{2}\rangle - \sin\epsilon(\cos\beta|x_+\tfrac{1}{2}\rangle - \sin\beta|x_- -\tfrac{1}{2}\rangle) \\
|\Gamma_4\Gamma_5(^2E)2\rangle &= \cos\epsilon|u_- -\tfrac{1}{2}\rangle - \sin\epsilon(\sin\beta|x_+\tfrac{1}{2}\rangle + \cos\beta|x_- -\tfrac{1}{2}\rangle) \\
|\Gamma_4\Gamma_5(^2T_2)1\rangle &= -\sin\epsilon|u_+\tfrac{1}{2}\rangle - \cos\epsilon(\cos\beta|x_+\tfrac{1}{2}\rangle - \sin\beta|x_- -\tfrac{1}{2}\rangle) \\
|\Gamma_4\Gamma_5(^2T_2)2\rangle &= -\sin\epsilon|u_- -\tfrac{1}{2}\rangle - \cos\epsilon(\sin\beta|x_+\tfrac{1}{2}\rangle + \cos\beta|x_- -\tfrac{1}{2}\rangle)
\end{aligned} \tag{19}$$

with

$$\cos\beta = \frac{K'-\frac{1}{2}\xi'}{\sqrt{(K'-\frac{1}{2}\xi')^2+\frac{1}{2}\xi'^2}}.$$

$$\sin\beta = \frac{(1/\sqrt{2})\xi'}{\sqrt{(K'-\frac{1}{2}\xi')^2+\frac{1}{2}\xi'^2}}$$

$$\cos 2\epsilon = \frac{10Dq-\frac{1}{2}\xi-(D/2)-K}{\sqrt{(10Dq-\frac{1}{2}\xi-(D/2)-K)^2+2(2K'-\xi')^2+4\xi'^2}}$$

$$\sin 2\epsilon = \left[\frac{2(2K'-\xi')^2+4\xi'^2}{(10Dq-\frac{1}{2}\xi-(D/2)-K)^2+2(2K'-\xi')^2+4\xi'^2}\right]^{1/2}.$$

The calculation of the functions of the three Γ_6 doublets is a little more difficult, since we have to find the unitary matrix for the principal-axis transformation of the 3×3 energy matrix of the Γ_6 levels. To simplify the calculation we take advantage of the fact that the $\Gamma_6(^2E)$ level is far above the other two Γ_6 levels and that the non-diagonal elements are small compared with the diagonal elements of the energy. We first apply an unitary transformation which diagonalizes the matrix of the two $\Gamma_6(^2T_2)$ doublets:

$$\left(\begin{array}{cc} \begin{pmatrix} 6Dq+\frac{D}{2} & a & b \\ a & \lambda_1 & 0 \\ b & 0 & \lambda_2 \end{pmatrix}; & \begin{array}{l} \Gamma_6(^2E) \\ \Gamma_6(^2T_2) \\ \Gamma_6(^2T_2)g \end{array} \end{array}\right)$$

with $\lambda_1 = -4Dq+\frac{1}{2}\xi-K$

$$\lambda_2 = -4Dq-\xi$$

$$a = \xi'\cos\delta - \left(\sqrt{2}K'+\frac{1}{\sqrt{2}}\xi'\right)\sin\delta$$

$$b = -\xi'\sin\delta - \left(\sqrt{2}K'+\frac{1}{\sqrt{2}}\xi'\right)\cos\delta$$

and the transformed functions are:

$$\begin{pmatrix} |u_+ -\frac{1}{2}\rangle \\ \cos\delta|x_0\frac{1}{2}\rangle+\sin\delta|x_+ -\frac{1}{2}\rangle \\ -\sin\delta|x_0\frac{1}{2}\rangle+\cos\delta|x_+ -\frac{1}{2}\rangle \end{pmatrix}$$

and

$$\begin{pmatrix} |u_-\frac{1}{2}\rangle \\ \cos\delta|x_0-\frac{1}{2}\rangle+\sin\delta|x_-\frac{1}{2}\rangle \\ -\sin\delta|x_0-\frac{1}{2}\rangle+\cos\delta|x_-\frac{1}{2}\rangle \end{pmatrix}$$

with

$$\sin 2\delta = \frac{-\sqrt{2}\xi}{\sqrt{(\frac{1}{2}\xi-3K)^2+2\xi^2}}.$$

$$\cos 2\delta = \frac{\frac{1}{2}\xi-3K}{\sqrt{(\frac{1}{2}\xi-3K)^2+2\xi^2}}.$$

Before going further it must be pointed out that the method to calculate the energy levels and g-factors is an expansion of all quantities in terms of powers of the small numbers

$$\frac{\xi}{10Dq}, \frac{\xi'}{10Dq}, \frac{K}{\xi}, \frac{K'}{\xi}$$

As far as the g-factors are concerned we restrict ourselves to the linear approximation and neglect quadratic terms and higher. Following this concept we diagonalize the matrices

$$\begin{pmatrix} 6Dq+\frac{D}{2} & a \\ a & \lambda_1 \end{pmatrix} \text{ and } \begin{pmatrix} 6Dq+\frac{D}{2} & b \\ b & \lambda_2 \end{pmatrix}$$

separately and use the resulting functions as approximations of the exact eigenfunctions. A proof of this method to diagonalize a 3×3-matrix is given in the appendix. We further note that the matrix element b does not alter the eigenvalues and gives only quadratic terms to eigenfunctions and g-values. It may therefore be neglected.

We then find the following eigenfunctions:

$$|\Gamma_6(^2E)1\rangle = \cos\gamma|u_+ -\tfrac{1}{2}\rangle + \sin\gamma\left[\cos\delta|x_0\tfrac{1}{2}\rangle + \sin\delta|x_+ -\tfrac{1}{2}\rangle\right]$$

$$
\begin{aligned}
|\Gamma_6({}^2E)2\rangle &= \cos\gamma|u\ \tfrac{1}{2}\rangle \\
&\quad + \sin\gamma\,[\cos\delta\,|x_0 -\tfrac{1}{2}\rangle \\
&\quad + \sin\delta\,|x_-\tfrac{1}{2}\rangle\,] \\
|\Gamma_6({}^2T_2)1\rangle &= -\sin\gamma|u_+ -\tfrac{1}{2}\rangle \\
&\quad + \cos\gamma\,[\cos\delta\,|x_0\tfrac{1}{2}\rangle \\
&\quad + \sin\delta\,|x_+ -\tfrac{1}{2}\rangle\,] \\
|\Gamma_6({}^2T_2)2\rangle &= -\sin\gamma|u\ \tfrac{1}{2}\rangle \\
&\quad + \cos\gamma\,[\cos\delta\,|x_0 -\tfrac{1}{2}\rangle \\
&\quad + \sin\delta\,|x\ \tfrac{1}{2}\rangle\,] \\
|\Gamma_6({}^2T_2)g1\rangle &= -\sin\delta\,|x_0\tfrac{1}{2}\rangle + \cos\delta\,|x_+ -\tfrac{1}{2}\rangle \\
|\Gamma_6({}^2T_2)g2\rangle &= -\sin\delta\,|x_0 -\tfrac{1}{2}\rangle + \cos\delta\,|x\ \tfrac{1}{2}\rangle
\end{aligned} \tag{20}
$$

with

$$
\sin 2\gamma = -\frac{2a}{\sqrt{(10Dq - \frac{1}{2}\xi + (D/2) + K)^2 + 4a^2}}
$$

$$
\cos 2\gamma = -\frac{10Dq - \frac{1}{2}\xi + (D/2) + K}{\sqrt{10Dq - \frac{1}{2}\xi + (D/2) + K)^2 + 4a^2}}
$$

Expanding the trigonometric functions in power series up to linear terms only we get:

$$
\begin{aligned}
\cos\beta &= \frac{-1}{\sqrt{3}}\left(1 - \frac{4}{3}\frac{K'}{\xi'}\right), \\
\cos 2\epsilon &= 1 \\
\cos 2\delta &= \frac{1}{3} - \frac{16}{9}\frac{K}{\xi} \\
\cos 2\gamma &= 1 \\
\sin\beta &= \sqrt{\frac{2}{3}}\left(1 + \frac{2}{3}\frac{K'}{\xi'}\right) \\
\sin 2\epsilon &= \sqrt{6}\,\frac{\xi'}{10Dq} \\
\sin 2\delta &= -\frac{2\sqrt{2}}{3}\left(1 + \frac{2}{3}\frac{K}{\xi}\right) \\
\sin 2\gamma &= \frac{\xi'}{10Dq}\,(2\cos\delta - \sqrt{2}\sin\delta)\,.
\end{aligned} \tag{21}
$$

To find the g-factors with magnetic field parallel or perpendicular to the trigonal axis we have to calculate the matrices of the operators $T_z + 2S_z$ and $T_x + 2S_x$ respectively with the eigenfunctions of the energy levels. We remember that the trigonal axis is the z-axis and find:

$$
T_z = T_{a_0}(T_1),\ T_x = \frac{1}{\sqrt{2}}\,(T_{a_+}(T_1) - T_{a_-}(T_1))
$$

where the basis functions a_+, a_-, a_0 of irreducible representation T_1 are defined in Ref. [5]. The matrices of the T-operators with these functions may be found by using the Wigner–Eckart theorem. The Clebsch–Gordon coefficients have been given by Tanabe and Kamimura[6]. We find the following matrices:

$$
\langle E\gamma|T_z|E\gamma'\rangle = 0,
$$

$$
(\langle T_2\gamma|T_z|T_2\gamma'\rangle) = k\begin{pmatrix} -1 & 0 & 0 \\ 0 & 1 & 0 \\ 0 & 0 & 0 \end{pmatrix}
$$

$$
(\langle T_2\gamma|T_z|E\gamma'\rangle) = k'\sqrt{2}\begin{pmatrix} -1 & 0 \\ 0 & 1 \\ 0 & 0 \end{pmatrix}.
$$

$$
(\langle \tfrac{1}{2}M_s|2S_z|\tfrac{1}{2}M_s'\rangle) = \begin{pmatrix} 1 & 0 \\ 0 & -1 \end{pmatrix}
$$

and the orbital reduction factors are defined by

$$
k = -\langle t_2x_+|l_z(T_1)|t_2x_+\rangle,
$$

$$
k' = -\frac{1}{\sqrt{2}}\,\langle t_2x_+|l_z(T_1)|eu_+\rangle.
$$

It must be remembered that orbital reduction factors $k_\parallel$, $k_\perp$ and $k_\parallel'$, $k_\perp'$ can be defined in general. In this paper, however, we neglect the anisotropy of the spin orbit coupling parameters and orbital reduction factors. The matrices of the operator $T_z + 2S_z$ in the product spaces are:

$$\begin{pmatrix} 1-k & & & & & \\ & -1-k & & & & 0 \\ & & 1+k & & & \\ & & & -1+k & & \\ 0 & & & & 1 & \\ & & & & & -1 \end{pmatrix} \begin{array}{l} |x_+\tfrac{1}{2}\rangle \\ |x_+-\tfrac{1}{2}\rangle \\ |x_-\tfrac{1}{2}\rangle \\ |x_--\tfrac{1}{2}\rangle \\ |x_0\tfrac{1}{2}\rangle \\ |x_0-\tfrac{1}{2}\rangle \end{array} \begin{pmatrix} -k'\sqrt{2} & & & \\ & -k'\sqrt{2} & & 0 \\ & & k'\sqrt{2} & \\ & & & k'\sqrt{2} \\ & 0 & & \\ & & & \end{pmatrix}$$

$$\begin{array}{cccc} |u_+\tfrac{1}{2}\rangle & |n_+-\tfrac{1}{2}\rangle & |n_-\tfrac{1}{2}\rangle & |n_--\tfrac{1}{2}\rangle \end{array}$$

$$\begin{pmatrix} 1 & & & 0 \\ & -1 & & \\ & & 1 & \\ 0 & & & -1 \end{pmatrix}. \qquad (22)$$

The $g_{\|}$-factors, with magnetic field parallel to the trigonal axis, may now be found by using the eigenfunctions (19) and (20) with approximations (21) and the matrices of T_z+2S_z (22). We find:

$$g_{\|}(\Gamma_4\Gamma_5(^2E)) = 2-\frac{4k'\xi'}{10Dq}+\frac{8k'K'}{10Dq}$$

$$g_{\|}(\Gamma_4\Gamma_5(^2T_2)) = 2(1-k)+\frac{4k'\xi'}{10Dq}-\frac{8k'K'}{10Dq}$$

$$g_{\|}(\Gamma_6(^2E)) = 2-\frac{4k'\xi'}{10Dq} \qquad (23)$$

$$g_{\|}(\Gamma_6(^2T_2)) = \frac{2}{3}(1-k)-\frac{16}{9}(2+k)\frac{K}{\xi}-\frac{4k'\xi'}{10Dq}$$

$$g_{\|}(\Gamma_6(^2T_2)g) = \frac{2}{3}(2k+1)-\frac{16}{9}(2+k)\frac{K}{\xi}.$$

If the magnetic field is perpendicular to the trigonal axis, we use the following matrices:

$$\langle E\gamma|T_x|E\gamma'\rangle = 0,$$

$$(\langle T_2\gamma|T_x|T_2\gamma'\rangle) = \frac{k}{\sqrt{2}}\begin{pmatrix} 0 & 0 & 1 \\ 0 & 0 & 1 \\ 1 & 1 & 0 \end{pmatrix}$$

$$(\langle T_2\gamma|T_x|E\gamma'\rangle) = k'\begin{pmatrix} 0 & 1 \\ -1 & 0 \\ -1 & -1 \end{pmatrix},$$

$$(\langle \tfrac{1}{2}M_s|2S_x|\tfrac{1}{2}M'\rangle) = \begin{pmatrix} 0 & 1 \\ 1 & 0 \end{pmatrix}$$

The matrices of the operator T_x+2S_x in the product spaces are:

$$\begin{pmatrix} & 1 & & & \frac{k}{\sqrt{2}} & \\ 1 & & & & & \frac{k}{\sqrt{2}} \\ & & & 1 & \frac{k}{\sqrt{2}} & \\ & & 1 & & & \frac{k}{\sqrt{2}} \\ \frac{k}{\sqrt{2}} & & \frac{k}{\sqrt{2}} & & & 1 \\ & \frac{k}{\sqrt{2}} & & \frac{k}{\sqrt{2}} & 1 & \end{pmatrix} \begin{array}{l} |x_+\tfrac{1}{2}\rangle \\ |x_+-\tfrac{1}{2}\rangle \\ |x_-\tfrac{1}{2}\rangle \\ |x_--\tfrac{1}{2}\rangle \\ |x_0\tfrac{1}{2}\rangle \\ |x_0-\tfrac{1}{2}\rangle \end{array} \begin{pmatrix} & & k' & \\ & & & k' \\ -k' & & & \\ & -k' & & \\ -k' & & -k' & \\ & -k' & & -k' \end{pmatrix} \qquad (24)$$

$$\begin{array}{cccc} |n_+\tfrac{1}{2}\rangle & |n_+-\tfrac{1}{2}\rangle & |n_-\tfrac{1}{2}\rangle & |n_--\tfrac{1}{2}\rangle \end{array}$$

$$\begin{pmatrix} & 1 & & \\ 1 & & & \\ & & & 1 \\ & & 1 & \end{pmatrix}.$$

The $g_\perp$-factors, with magnetic field perpendicular to the trigonal axis, may now be found by using the eigenfunctions (19) and (20) with approximations (21) and the matrices of T_x+2S_x (24). We find.

$$g_\perp(\Gamma_4\Gamma_5(^2E)) = g_\perp(\Gamma_4\Gamma_5(^2T_2)) = 0$$

$$g_\perp(\Gamma_6(^2E)) = 4k'\xi'/10Dq$$

$$g_\perp(\Gamma_6(^2T_2)) = \frac{4}{3}(1-k)-\frac{8}{9}(2+k)\frac{K}{\xi}+\frac{4k'\xi'}{10Dq}$$

$$g_\perp(\Gamma_6(^2T_2)g) = \frac{2}{3}(2k+1)+\frac{8}{9}(2+k)\frac{K}{\xi}. \quad (25)$$

The g-factors of $\Gamma_6(^2T_2)g$ and $\Gamma_4\Gamma_5(^2E)$ have already been given by Dietz *et al.*[1], with some but not all quadratic terms included. The $g_\perp$-values of the two $\Gamma_4\Gamma_5$ Kramers-doublets are zero without any approximation. Therefore the measurement of these g-values may be used to check the whole treatment of the linear Zeeman effect by crystal field theory.

If more precise g-values are desired one has to evaluate the eigenfunctions of the Γ_6 energy levels in a higher approximation and then take quadratic terms into account. It must be remembered, however, that several other approximations had been introduced which might affect the g-values as well: the anisotropy of ξ, ξ', k, k' had been neglected and the parameter ξ_0' had been set equal to zero. But in principle the g-values might be calculated to any accuracy with the method used here.

We remark that the parameters which describe the trigonal crystal field D, K, K' may be positive or negative. They are defined in Ref. [5] so as to produce positive values for ZnO:Cu^{2+} (the definition in Ref. [1] is different by a factor -1 for K and K'). Therefore the g-factors depend on the order of the energy levels in the energy level diagram[5].

The angular dependence of the g-factors can be investigated with the additional operator

$$T_y+2S_y \text{ with } T_y = \frac{-i}{\sqrt{2}}(T_{a+}(T_1)+T_{a-}(T_1)).$$

If we introduce spherical polar coordinates with polar axis in direction of the trigonal axis we have

$$g^2(\theta) = g_\parallel^2\cos^2\theta + g_\perp{}^2\sin^2\theta$$

where θ is the angle between the direction of the magnetic field vector and the trigonal axis. This has already been given by Dietz *et al.*[1] and various other authors. Using the method of this paper Heinze[8] has proved this formula.

In case of a Cu^{2+} ion, with a d^9 configuration, in a trigonally distorted octahedral crystal field the same g-factors (23) and (25) result if Dq is replaced by its negative value. The formula of $g_\perp(\Gamma_6(^2E))$ of (25), however, remains unchanged, since we calculate g-factors here as positive numbers only.

5. g-FACTORS OF A d^9-CONFIGURATION IN A TETRAGONALLY DISTORTED TETRAHEDRAL CRYSTAL FIELD

In a tetragonally distorted tetrahedral crystal field, with symmetry group D_{2d}, a d^9 configuration has five doublets with energies: [5]

$$E(\Gamma_6(^2E)) = 6Dq+D+\frac{3\xi'^2}{20Dq}$$

$$E(\Gamma_7(^2E)) = 6Dq-D+\frac{3\xi'^2}{20Dq}$$

$$E(\Gamma_6(^2T_2)) = -4Dq+\frac{1}{2}\xi+F-\frac{3\xi'^2}{20Dq}$$

$$E(\Gamma_7(^2T_2)) = -4Dq+\frac{1}{2}\xi-F-\frac{3\xi'^2}{20Dq}$$

$$E(\Gamma_7(^2T_2)g) = -4Dq-\xi$$

where index g denotes the ground state and where

$$\xi_\perp = \xi_\parallel = \xi \ll 10Dq, \xi'_\perp = \xi'_\parallel = \xi' \ll 10Dq.$$

$$\xi_0' = 0, F \ll \xi, D \ll \xi$$

have been assumed. Using again the approximations given in the appendix and restricting to first power of the small quantities

$$\frac{\xi}{10Dq}, \frac{\xi'}{10Dq}, \frac{F}{\xi}, \frac{D}{\xi}$$

we find the following eigenfunctions of the energy levels

$$\begin{aligned}
|\Gamma_6(^2E)1\rangle &= \cos\gamma\left|u-\tfrac{1}{2}\right\rangle+\frac{i}{\sqrt{2}}\sin\gamma\left|\xi\,\tfrac{1}{2}\right\rangle \\
&\quad -\frac{1}{\sqrt{2}}\sin\gamma\left|\eta\,\tfrac{1}{2}\right\rangle \\
|\Gamma_6(^2E)2\rangle &= \cos\gamma\left|u\,\tfrac{1}{2}\right\rangle+\frac{i}{\sqrt{2}}\sin\gamma\left|\xi-\tfrac{1}{2}\right\rangle \\
&\quad +\frac{1}{\sqrt{2}}\sin\gamma\left|\eta-\tfrac{1}{2}\right\rangle \\
|\Gamma_7(^2E)1\rangle &= \cos\beta\left|v-\tfrac{1}{2}\right\rangle \\
&\quad +i\sin\beta\Big[\cos\alpha\left|\zeta-\tfrac{1}{2}\right\rangle \\
&\quad -\frac{1}{\sqrt{2}}\sin\alpha\left|\xi\,\tfrac{1}{2}\right\rangle+\frac{i}{\sqrt{2}}\sin\alpha\left|\eta\,\tfrac{1}{2}\right\rangle\Big] \\
|\Gamma_7(^2E)2\rangle &= \cos\beta\left|v\,\tfrac{1}{2}\right\rangle \\
&\quad +i\sin\beta\Big[-\cos\alpha\left|\zeta\tfrac{1}{2}\right\rangle \\
&\quad -\frac{1}{\sqrt{2}}\sin\alpha\left|\xi-\tfrac{1}{2}\right\rangle \\
&\quad -\frac{i}{\sqrt{2}}\sin\alpha\left|\eta-\tfrac{1}{2}\right\rangle\Big] \\
|\Gamma_6(^2T_2)1\rangle &= -\sin\gamma\left|u-\tfrac{1}{2}\right\rangle \\
&\quad +\frac{i}{\sqrt{2}}\cos\gamma\left|\xi\,\tfrac{1}{2}\right\rangle \\
&\quad -\frac{1}{\sqrt{2}}\cos\gamma\left|\eta\,\tfrac{1}{2}\right\rangle \qquad (26)
\end{aligned}$$

$$\begin{aligned}
|\Gamma_6(^2T_2)2\rangle &= -\sin\gamma\left|u\,\tfrac{1}{2}\right\rangle+\frac{i}{\sqrt{2}}\cos\gamma\left|\xi-\tfrac{1}{2}\right\rangle \\
&\quad +\frac{1}{\sqrt{2}}\cos\gamma\left|\eta-\tfrac{1}{2}\right\rangle \\
|\Gamma_7(^2T_2)1\rangle &= -i\sin\beta\left|v-\tfrac{1}{2}\right\rangle \\
&\quad -\cos\beta\Big[\cos\alpha\left|\zeta-\tfrac{1}{2}\right\rangle \\
&\quad -\frac{1}{\sqrt{2}}\sin\alpha\left|\xi\,\tfrac{1}{2}\right\rangle \\
&\quad +\frac{i}{\sqrt{2}}\sin\alpha\left|\eta\,\tfrac{1}{2}\right\rangle\Big] \\
|\Gamma_7(^2T_2)2\rangle &= -i\sin\beta\left|v\,\tfrac{1}{2}\right\rangle \\
&\quad -\cos\beta\Big[-\cos\alpha\left|\zeta\tfrac{1}{2}\right\rangle \\
&\quad -\frac{1}{\sqrt{2}}\sin\alpha\left|\xi-\tfrac{1}{2}\right\rangle \\
&\quad -\frac{i}{\sqrt{2}}\sin\alpha\left|\eta-\tfrac{1}{2}\right\rangle\Big] \\
|\Gamma_7(^2T_2)g1\rangle &= -i\sin\alpha\left|\zeta-\tfrac{1}{2}\right\rangle \\
&\quad -\frac{i}{\sqrt{2}}\cos\alpha\left|\xi\,\tfrac{1}{2}\right\rangle \\
&\quad -\frac{1}{\sqrt{2}}\cos\alpha\left|\eta\,\tfrac{1}{2}\right\rangle \\
|\Gamma_7(^2T_2)g2\rangle &= i\sin\alpha\left|\zeta\tfrac{1}{2}\right\rangle \\
&\quad -\frac{i}{\sqrt{2}}\cos\alpha\left|\xi-\tfrac{1}{2}\right\rangle \\
&\quad +\frac{1}{\sqrt{2}}\cos\alpha\left|\eta-\tfrac{1}{2}\right\rangle
\end{aligned}$$

with

$$\sin 2\alpha=\frac{\sqrt{2}\xi}{\sqrt{(\frac{1}{2}\xi-3F)^2+2\xi^2}}\simeq\frac{2\sqrt{2}}{3}\left(1+\frac{2}{3}\frac{F}{\xi}\right)$$

$$\cos 2\alpha=\frac{\frac{1}{2}\xi-3F}{\sqrt{(\frac{1}{2}\xi-3F)^2+2\xi^2}}\simeq\frac{1}{3}-\frac{16}{9}\frac{F}{\xi}$$

$$\sin 2\beta = \frac{-\xi'(2\cos\alpha + \sqrt{2}\sin\alpha)}{\sqrt{(10Dq - \frac{1}{2}\xi + F - D)^2 + \xi'^2(2\cos\alpha + \sqrt{2}\sin\alpha)^2}} \simeq \frac{-\sqrt{6}\xi'}{10Dq} \tag{27}$$

$$\cos 2\beta = \frac{10Dq - \frac{1}{2}\xi + F - D}{\sqrt{(10Dq - \frac{1}{2}\xi + F - D)^2 + \xi'^2(2\cos\alpha + \sqrt{2}\sin\alpha)^2}} \simeq 1$$

$$\sin 2\gamma = \frac{\sqrt{6}\xi'}{\sqrt{(10Dq - \frac{1}{2}\xi + D - F)^2 + 6\xi'^2}} \simeq \frac{\sqrt{6}\xi'}{10Dq}$$

$$\cos 2\gamma = \frac{10Dq - \frac{1}{2}\xi + D - F}{\sqrt{(10Dq - \frac{1}{2}\xi + D - F)^2 + 6\xi'^2}} \simeq 1.$$

The g-factors $g_{\parallel}$ and $g_{\perp}$ with magnetic field parallel and perpendicular to the tetragonal or z-axis respectively are calculated from the matrices of the tensor operators $T_z + 2S_z$ with $T_z = T_\gamma(T_1)$ and $T_x + 2S_x$ with $T_x = T_\alpha(T_1)$.

$$\langle E\gamma | T_z | E\gamma' \rangle = 0,$$

$$(\langle T_2\gamma | T_z | T_2\gamma' \rangle) = ik \begin{pmatrix} 0 & 1 & 0 \\ -1 & 0 & 0 \\ 0 & 0 & 0 \end{pmatrix}$$

$$(\langle T_2\gamma | T_z | E\gamma' \rangle) = 2ik' \begin{pmatrix} 0 & 0 \\ 0 & 0 \\ 0 & 1 \end{pmatrix}.$$

$$(\langle \tfrac{1}{2}M_s | 2S_z | \tfrac{1}{2}M_s' \rangle) = \begin{pmatrix} 1 & 0 \\ 0 & -1 \end{pmatrix}$$

$$\langle E\gamma | T_x | E\gamma' \rangle = 0,$$

$$(\langle T_2\gamma | T_x | T_2\gamma' \rangle) = ik \begin{pmatrix} 0 & 0 & 0 \\ 0 & 0 & 1 \\ 0 & -1 & 0 \end{pmatrix}$$

$$(\langle T_2\gamma | T_x | E\gamma' \rangle) = -ik' \begin{pmatrix} \sqrt{3} & 1 \\ 0 & 0 \\ 0 & 0 \end{pmatrix},$$

$$(\langle \tfrac{1}{2}M_s | 2S_x | \tfrac{1}{2}M_s' \rangle) = \begin{pmatrix} 0 & 1 \\ 1 & 0 \end{pmatrix}$$

and the orbital reduction factors are defined by

$$k = -i \langle t_2\xi | t_\gamma(T_1) | t_2\eta \rangle$$

$$k' = -\frac{i}{2} \langle t_2\zeta | t_\gamma(T_1) | ev \rangle.$$

As in the case of a trigonally distorted tetrahedral crystal field we have neglected the anisotropy of the orbital reduction factors. The matrices of the tensor operator $T_z = 2S_z$ therefore are:

$$\begin{pmatrix} 1 & & ik & & & \\ & -1 & & ik & & \\ -ik & & 1 & & & \\ & -ik & & -1 & & \\ & & & & 1 & \\ & & & & & -1 \end{pmatrix} \begin{array}{l} |\xi\tfrac{1}{2}\rangle \\ |\xi-\tfrac{1}{2}\rangle \\ |\eta\tfrac{1}{2}\rangle \\ |\eta-\tfrac{1}{2}\rangle \\ |\zeta\tfrac{1}{2}\rangle \\ |\zeta-\tfrac{1}{2}\rangle \end{array} \begin{pmatrix} & & & \\ & & & \\ & & & \\ & & & \\ & & 2ik' & \\ & & & 2ik' \end{pmatrix}$$

$$\begin{array}{cccc} |u\tfrac{1}{2}\rangle & |u-\tfrac{1}{2}\rangle & |v\tfrac{1}{2}\rangle & |v-\tfrac{1}{2}\rangle \end{array} \tag{28}$$

$$\begin{pmatrix} 1 & & & \\ & -1 & & \\ & & 1 & \\ & & & -1 \end{pmatrix}.$$

The matrices of the tensor operator T_x+2S_x are:

$$\begin{pmatrix} & 1 & & & & \\ 1 & & & & & \\ & & & 1 & ik & \\ & & 1 & & & ik \\ & & -ik & & & 1 \\ & & & -ik & 1 & \end{pmatrix}\begin{array}{l} |\xi\tfrac{1}{2}\rangle \\ |\xi-\tfrac{1}{2}\rangle \\ |\eta\tfrac{1}{2}\rangle \\ |\eta-\tfrac{1}{2}\rangle \\ |\zeta\tfrac{1}{2}\rangle \\ |\zeta-\tfrac{1}{2}\rangle \end{array}\begin{pmatrix} -ik'\sqrt{3} & & -ik' & \\ & -ik'\sqrt{3} & & -ik' \\ & & & \\ & & & \\ & & & \\ & & & \end{pmatrix}$$

$$\begin{array}{cccc} |u\tfrac{1}{2}\rangle & |u-\tfrac{1}{2}\rangle & |v\tfrac{1}{2}\rangle & |v-\tfrac{1}{2}\rangle \\ \end{array}$$

$$\begin{pmatrix} & 1 & & \\ 1 & & & \\ & & & 1 \\ & & 1 & \end{pmatrix}. \tag{29}$$

Inserting (27) into (26) and calculating the matrices of the tensor operator T_z+2S_z in the eigenspace of the energy levels we find with the help of (28):

$$\begin{aligned} g_{\parallel}(\Gamma_6(^2E)) &= 2 \\ g_{\parallel}(\Gamma_7(^2E)) &= 2+\frac{8k'\xi'}{10Dq} \\ g_{\parallel}(\Gamma_6(^2T_2)) &= 2(1-k) \\ g_{\parallel}(\Gamma_7(^2T_2)) &= \frac{2}{3}(1-k)-(2+k)\frac{16}{9}\frac{F}{\xi}-\frac{8k'\xi'}{10Dq} \\ g_{\parallel}(\Gamma_7(^2T_2)g) &= \frac{2}{3}(2k+1)-(2+k)\frac{16}{9}\frac{F}{\xi} \end{aligned} \tag{30}$$

and we remark that a g-value greater than two is expected for $\Gamma_7(^2E)$.

If the magnetic field is perpendicular to the tetragonal axis we find with the help of (29):

$$\begin{aligned} g_{\perp}(\Gamma_6(^2E)) &= 2-\frac{6k'\xi'}{10Dq} \\ g_{\perp}(\Gamma_7(^2E)) &= 2-\frac{2k'\xi'}{10Dq} \\ g_{\perp}(\Gamma_6(^2T_2)) &= \frac{6k'\xi'}{10Dq} \\ g_{\perp}(\Gamma_7(^2T_2)) &= \frac{4}{3}(1+k)-(2-k)\frac{8}{9}\frac{F}{\xi}-\frac{2k'\xi'}{10Dq} \\ g_{\perp}(\Gamma_7(^2T_2)g) &= \frac{2}{3}(1-2k)+(2-k)\frac{8}{9}\frac{F}{\xi}. \end{aligned} \tag{31}$$

The angular dependence of the g-factors may be found by also using the tensor operator T_y+2S_y with $T_y=T_\beta(T_1)$. Again the simple formula

$$g^2(\theta) = g_{\parallel}{}^2\cos^2\theta+g_{\perp}{}^2\sin^2\theta$$

results, where θ is the angle between the direction of the magnetic field and the tetragonal axis.

The tetragonal crystal field parameters D and F may be positive or negative and therefore the g-factors of the $\Gamma_7(^2T_2)$ doublets depend on whether the $\Gamma_7(^2T_2)$ or the $\Gamma_6(^2T_2)$ is the lower one.

In case of a Cu^{2+} ion, with a d^9 configuration, in a tetragonally distorted octahedral crystal field the same g-factors (30) and (31) result if Dq is replaced by its negative value. The formula of $g_{\perp}(\Gamma_6(^2T_2))$ of (31), however, remains unchanged, since we here calculate g-factors as positive numbers only.

Acknowledgement—The author thanks Professor I. Broser for his permanent interest in this work

REFERENCES

1. DIETZ R. E., KAMIMURA H., STURGE M. D. and YARIV A., *Phys. Rev.* **132**, 1559 (1963).
2. DE WIT M., *Phys. Rev.* **177**, 441 (1969)
3. WÖHLECKE M., *Diplomarbeit Technische Universitat Berlin* (1969).
4. BROSER I., SCHERZ U. and WÖHLECKE M., *J. Luminescence* **1**, 39 (1969).
5. SCHERZ U., *J. Phys. Chem. Solids* **30**, 2077 (1969).

6. TANABE Y. and KIMIMURA H., *J. phys. Soc. Japan* **13**, 394 (1958).
7. AYANT Y., BELORIZKY E. and ROSSET J., *J. Phys. Radium* **23**, 201 (1962).
8. HEINZE R.-I., *Diplomarbeit Technische Universität Berlin* (1969).

APPENDIX

In this section we give a proof of the method used to find approximately the eigenvalues and eigenfunctions of a real and symmetric matrix of the form

$$(\langle i|A|j\rangle) = \begin{pmatrix} a & \epsilon_1 & \epsilon_2 \\ \epsilon_1 & b & 0 \\ \epsilon_2 & 0 & c \end{pmatrix} \text{ with eigenfunctions} \begin{pmatrix} |1\rangle \\ |2\rangle \\ |3\rangle \end{pmatrix}.$$

If we have

$$\left|\frac{\epsilon_1}{a-b}\right| \ll 1, \left|\frac{\epsilon_2}{a-c}\right| \ll 1$$

we can develop eigenvalues λ_i and eigenfunctions $|\lambda_i\rangle$ of A in a power series of these small quantities and find up to the second order

$$\lambda_1 = a + \frac{\epsilon_1^2}{a-b} + \frac{\epsilon_2^2}{a-c}$$

$$|\lambda_1\rangle = \cos\alpha\cos\beta\,|1\rangle + \sin\alpha\,|2\rangle + \sin\beta\,|3\rangle$$

$$\lambda_2 = b - \frac{\epsilon_1^2}{a-b}$$

$$|\lambda_2\rangle = -\sin\alpha\,|1\rangle + \cos\alpha\,|2\rangle$$

$$\lambda_3 = c - \frac{\epsilon_2^2}{a-c}$$

$$|\lambda_3\rangle = -\sin\beta\,|1\rangle + \cos\beta\,|3\rangle$$

with

$$\sin 2\alpha = \frac{2\epsilon_1}{\sqrt{(a-b)^2+4\epsilon_1^2}},$$

$$\cos 2\alpha = \frac{a-b}{\sqrt{(a-b)^2+4\epsilon_1^2}}$$

$$\sin 2\beta = \frac{2\epsilon_2}{\sqrt{(a-c)^2+4\epsilon_2^2}},$$

$$\cos 2\beta = \frac{a-c}{\sqrt{(a-c)^2+4\epsilon_2^2}}$$

and we have simply diagonalised the two submatrices

$$\begin{pmatrix} a & \epsilon_1 \\ \epsilon_1 & b \end{pmatrix} \text{ and } \begin{pmatrix} a & \epsilon_2 \\ \epsilon_2 & c \end{pmatrix}$$

separately. To replace the trigonometric functions by power series we assume without loss of generality: $c < b < a$, $0 < \epsilon_1$, $0 < \epsilon_2$ and find up to the second order:

$$\sin\alpha = \frac{\epsilon_1}{a-b}, \quad \cos\alpha = 1 - \frac{1}{2}\frac{\epsilon_1^2}{(a-b)^2}$$

$$\sin\beta = \frac{\epsilon_2}{a-c}, \quad \cos\beta = 1 - \frac{1}{2}\frac{\epsilon_2^2}{(a-c)^2}$$

Introducing these approximations into the functions $|\lambda_i\rangle$ and calculating the matrix $\langle\lambda_i|A|\lambda_j\rangle$ we find up to the second order: λ_i for diagonal elements and zero for non-diagonal elements, except $\langle\lambda_2|A\lambda_3\rangle$ which is small of second order. Another unitary transformation, however, which transforms this matrix element to zero, would not change the eigenvalues up to the second order.

J. Phys. Chem. Solids Pergamon Press 1970. Vol. 31, pp. 1011-1018. Printed in Great Britain

ETUDE PAR RESONANCE ELECTRONIQUE DU TRITIUM ATOMIQUE FORME AU SEIN DE CRISTAUX DE FLUORURE DE LITHIUM IRRADIE AUX NEUTRONS

MARIA T. CAUSA*, DENIS RAOUX et CHRISTIANE TAUPIN
Laboratoire de Physique des Solides† Faculté des Sciences, 91-Orsay, France

(*Received* 25 *June* 1969)

Résumé – L'étude en RPE de monocristaux de LiF irradié aux neutrons a permis de mettre en évidence du tritium atomique en plusieurs sites cristallins dans la matrice. L'un d'eux a pu être identifié comme le site interstitiel $\frac{1}{4}, \frac{1}{4}, \frac{1}{4}$. L'interprétation quantitative du spectre RPE obtenu dans ce cas exige que les ions fluor proches voisins soient repoussés par l'insertion de l'interstitiel d'environ 20 pour cent de leur distance au centre de la maille.

Abstract – An EPR investigation of neutron irradiated LiF single crystals shows that atomic tritium may be found in several sites of the lattice. One of them has been identified: it is the $\frac{1}{4}, \frac{1}{4}, \frac{1}{4}$ interstitial site. Quantitative interpretation of this EPR spectrum needs the relaxation of the lattice. The nearest neighbour ions have to be pushed away from the interstitial site by 20 per cent of their distance

SI ON irradie aux neutrons thermiques un monocristal de LiF contenant 7% de Li^6, la réaction nucléaire Li^6 (n, α) H^3 produit au sein du cristal du tritium atomique (H^3). Si la dose d'irradiation est suffisamment élevée et si l'irradiation a été faite à basse température, on peut alors observer le spectre du tritium en résonance paramagnétique électronique (RPE).

Ce spectre a été décrit par Dweck *et al.*[1], ainsi que par Kazumata[2]; ces auteurs ont observé un doublet de deux raies simples sans structure. Nous avons observé des spectres analogues sur des échantillons irradiés à 77°K et réchauffés à la température ambiante. Par contre, les spectres que nous avons obtenus avec des cristaux conservés et étudiés à la température d'irradiation sont très différents de ceux qu'a observés Kazumata. Les raies sont larges et présentent une structure. Des conditions d'irradiation différentes (doses d'irradiation plus fortes, température réelle au cours de l'irradiation probablement plus basse) sont sans doute responsables de la présence de spectres nouveaux.

1. CONDITIONS EXPERIMENTALES ET DESCRIPTION DES SPECTRES A TRITIUM

Nous avons étudié des cristaux fournis par Harshaw, et irradiés au Centre d'Etudes Nucléaires de Grenoble à 77°K, après des recuits entre 77 et 600°K. La dose d'irradiation était de 10^{20} neutrons par cm^2. Nous avons ainsi observé des spectres correspondant à des concentrations atomiques de l'ordre de 10^{-5} en H^3, ce qui représente environ $\frac{1}{10}$ du nombre total de noyaux de Tritium libérés par la réaction nucléaire; la plupart des noyaux H^3 se trouvent donc sous forme non paramagnétique (ions ou molécules).

Le spectre RPE obtenu évolue beaucoup au cours de recuits. Il est simple pour des échantillons réchauffés au-dessus de la température ambiante: il comprend alors essentiellement un doublet de deux raies hyperfines sans structure (Fig. 1(a)) qui correspond au spectre déjà observé[1, 2]. Nous notons T° (Tritium atomique)* ce spectre. Par contre pour des échantillons non réchauffés au-dessus de 77°K, le spectre obtenu est très compliqué, divers centres sont simultanément présents, dont le centre V_k de Känzig[4]. Il existe cependant toujours un doublet dont l'écart hyperfin entre les deux raies et le facteur g sont voisins de ceux du spectre T° (Fig. 1(b)). Mais les deux raies sont larges et présentent une structure. Une de ces raies est représentée sur la Fig. 2(a); c'est la somme de cinq raies repérées par les lettres A, B, C, B, A; la raie C est très dissymétrique.

---

*Adresse permanente: Instituto de Fisica, Bariloche, Argentine.

†Laboratoire associé au C.N.R.S.

La Fig. 1(c) représente le spectre obtenu avec un échantillon réchauffé 1 h. à la température ambiante. La comparaison entre les spectres 1(b) et 1(c) montre que la raie C a cru énormément, les raies A et B beaucoup diminué en intensité sans se déplacer en position; en même temps la raie C est devenue plus étroite (de 20 à 10 G) et sa dissymétrie a beaucoup diminué. La raie C est donc due à la superposition de deux raies, qui ne sont pas centrées à la même valeur du champ magnétique: une d'elles s'élimine au cours des recuits, en même temps que les raies A et B. L'ensemble des raies A, B et de cette composante de la raie C correspond à un centre stable à basse température, que nous notons $T_i^{\circ *}$ et que nous étudions dans la 4° partie. L'autre composante de la raie C croit au cours des recuits et correspond au centre T° qu'on observe sur des échantillons

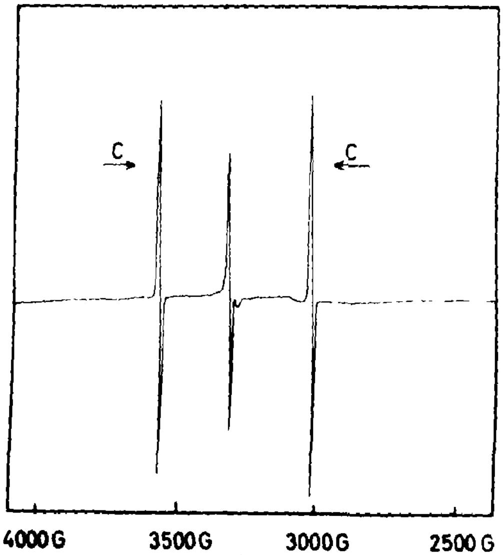

1(a).

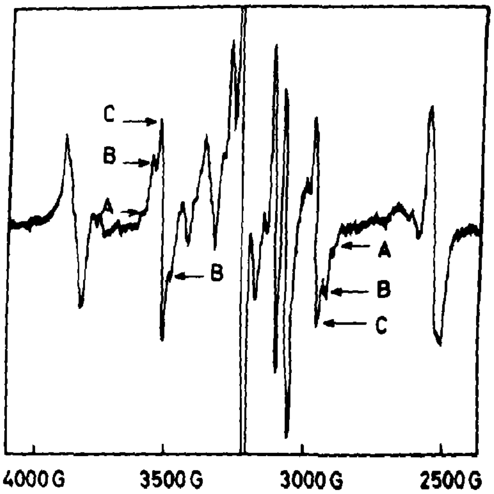

1(b).

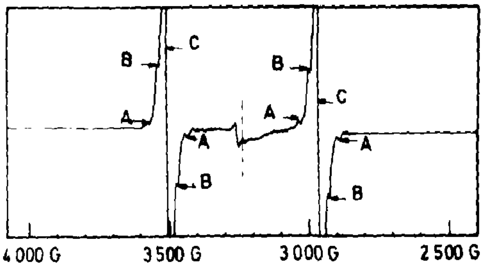

1(c).

Fig. 1. Spectre du LiF irradié aux neutrons. (a) échantillon réchauffé longtemps à l'ambiante (Spectre observé à température ambiante). (b) échantillon conservé à 77°K. (Spectre obtenu à 77°K) (c) échantillon réchauffé 1 h à l'ambiante. (Spectre obtenu à température ambiante) Les échelles ne sont pas les mêmes dans les trois cas.

---

*La notation que nous utilisons pour les centres à Tritium atomique est une extension de celle employée par Pick[3] pour les centres à Hydrogène atomique.

H_s° Hydrogène atomique en substitution dans le réseau. (centre U_3).

T° Tritium atomique (site mal identifié).

H_i° Hydrogène atomique en site interstitiel ½, ½, ½ (centre U_2).

T_i° Tritium atomique en site interstitiel ½, ½, ½.

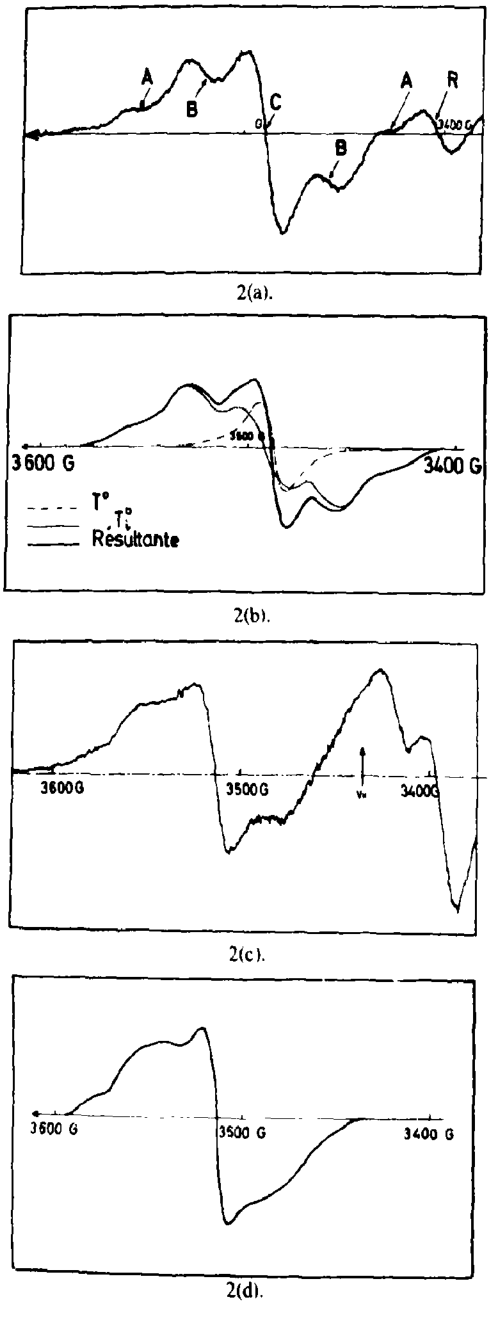

2(a).

2(b).

2(c).

2(d).

Fig 2 Raie du centre T_i° centrée à 3490 G. (a) Raie expérimentale pour H_0//[100] (la raie R n'appartient pas au centre T_i°). (b) Raie théorique pour H_0//[100] (c) Raie expérimentale pour H_0 dans le plan [100] et faisant un angle de 10° avec [011] (d) Raie théorique pour H_0 dans le plan [100] et faisant un angle de 10° avec [011].

réchauffés. Ce spectre est étudié dans la troisième partie.

Nous en concluons que l'atome H^3 peut occuper plusieurs sites du réseau, la probabilité de sa présence sur ces sites dépendant de la température de recuit. Cette évolution thermique est étudiée dans la deuxième partie.

2. EVOLUTION THERMIQUE DU NOMBRE DE CENTRES ENTRE 100 ET 600°K

Nous avons évalué les concentrations des centres T° et T_i°, après des recuits successifs de 10 min de 77 à 600°K. Les résultats sont représentés sur la Fig. 3. On constate que le centre T_i° s'élimine entre 220–270°K au profit du centre T°. Ces résultats sont analogues à ceux publiés par Hayes *et al.*[5] pour les centres H_i° et H_s° à hydrogène dans KCl, bien que les températures d'évolution que nous ayons observées soient plus élevées que celles observées par Hayes. Il y a là un effet de masse (H^3 au lieu de H^1), et aussi un effet dû au réseau de LiF; les températures de diffusion des divers centres colorés sont en effet plus élevées dans LiF que dans les autres halogénures alcalins.

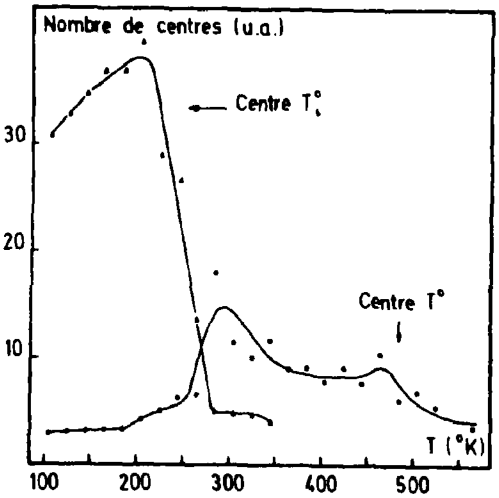

Fig. 3 Evolution thermique du nombre des centres T_i° et T°.

Au-dessus de la température ambiante, on observe une légère remontée du nombre de centres T° vers 470°K; Dweck[1] et Kazumata [2] ont signalé ce fait. Nous l'interprétons dans la troisième partie. Le centre T° s'élimine au-dessus de 500°K.

3. ETUDE DES CENTRES T° STABLES A TEMPERATURE AMBIANTE

L'hamiltonien d'un atome H^3 soumis à un champ magnétique extérieur $\mathbf{H}_0$ peut s'écrire:

$$\mathscr{H} = \mathscr{H}_0 + \mathscr{H}_1 + \mathscr{H}_2 \qquad (1)$$

$\mathscr{H}_0$ est la partie de l'énergie indépendante du spin de l'électron.

$$\mathscr{H}_1 = \beta \mathbf{H}_0 \bar{g}_e \mathbf{S} + \mathbf{I}_N \bar{A}_N \mathbf{S} \qquad (2)$$

est la partie de l'hamiltonien d'un atome libre H^3 dépendante du spin.

$$\mathscr{H}_2 = \sum_R \mathbf{I}_R \dot{A}_R \mathbf{S} \qquad (3)$$

est la partie dépendante du spin qui représente l'interaction avec le réseau. Comme $\mathscr{H}_1$ prédomine devant $\mathscr{H}_2$, le spectre de résonance est formé de deux raies ($I_N = \frac{1}{2}$ spin du noyau H^3) dont la distance donne a_N.

Nous avons mesure un facteur $g = 2{\cdot}004$ (calculé par la formule de Breit-Rabi) et un couplage hyperfin $a_N = 542{,}5$ G.

Nous avons en outre constaté que les deux composantes du doublet du spectre T° sont dissymétriques et de largeur variable avec la température de recuit; cette largeur décroit d'environ 20 G à 77°K à 1 G à 600°K. La dissymétrie diminue au cours de ces recuits et les raies deviennent gaussiennes à haute température. Nous en concluons que la raie est complexe et peut s'analyser en deux raies de largeurs différentes: une raie de 15–20 G et une autre de 1 G environ. Dweck *et al.* [1] avaient déjà signalé l'existence de raies larges sous les raies étroites pour des observations à 80°K. Au cours des recuits la raie large s'élimine au profit de la raie étroite. Rappelons ici un des résultats exposés dans la deuxième partie: le nombre de centres T° présente un faible maximum vers 470°K; la présence d'un tel maximum est difficile à expliquer si l'on n'admet pas qu'il existe plusieurs centres T°. En effet le nombre de centres T° a été calculé en utilisant la formule $N \alpha\, \Delta H_{pp}^2 \times h$, où h est la hauteur de raie et ΔH_{pp} la largeur pic à pic. Nous avons mesure ΔH_{pp} après chaque recuit: mais si une raie complexe est la superposition de deux raies de largeurs différentes, la raie large étant moins intense que la raie étroite, cette méthode sous estime le nombre total de centres, en négligeant la contribution provenant des ailes de la raie large. La remontée du nombre de centres observée à 470°K ne traduit donc pas une augmentation du nombre total de centres, mais l'élimination des centres donnant une raie large au profit de ceux qui donnent une raie étroite.

Tous ces faits nous conduisent à conclure que deux sites cristallins au moins sont occupés par les atomes de H^3 au-dessus de la température ambiante. Aucune structure n'ayant été observée sur ces raies, la méthode de RPE ne nous permet pas d'avancer plus avant dans l'identification de ces centres. Nous pouvons seulement remarquer que après des recuits à haute température, la raie très étroite indique que les atomes de H^3 se placent dans des sites cristallins très peu couplés au réseau.

4. ETUDE DU CENTRE T_i° STABLE A BASSE TEMPERATURE

(a) *Résultats expérimentaux*

Comme nous l'avons signalé, les raies du doublet obtenu avec un échantillon conservé à 77°K et étudié sans avoir été réchauffé sont complexes. Elles résultent de la superposition de la raie des centres T° (en partie responsable de la raie C) et de celles des centres T_i° dont le spectre comprend les raies A, B et en partie la raie C. La forme de la raie complexe obtenue dépend de l'orientation du champ magnétique par rapport au cristal. Le spectre représenté sur la Fig.

2(a) a été obtenu avec le champ magnétique directeur orienté suivant la direction[100] du cristal. C'est dans cette orientation que les raies A et B sont les mieux résolues.

(b) *Reconstitution théorique du spectre*

Tous les résultats expérimentaux ont pu être interprétés et une reconstitution précise du spectre a été possible en supposant que l'atome de H^3 occupe une position interstitielle $\frac{1}{4}, \frac{1}{4}, \frac{1}{4}$ dans le réseau (cf. Fig. 4).

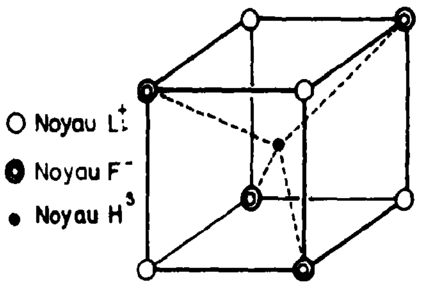

Fig 4. Situation du centre T_i° dans le réseau du LiF.

Si l'on suppose que l'interaction hyperfine avec chacun des 8 ions proches voisins est à symétrie axiale autour de la direction [111] qui le relie à l'atome H^3, et que le champ magnétique directeur est suffisamment fort pour quantifier réellement les spins de l'électron et des noyaux, l'équation d'interaction avec le réseau (3) s'écrit:

$$\mathscr{H}_2 = \sum_R \left(a_R + b_R\left(3\cos^2\theta_{ZR} - 1\right)\right)\mathbf{I}_R\mathbf{S} \qquad (4)$$

où R désigne les 8 ions proches voisins

θ_{ZR} l'angle entre le champ magnétique directeur et la direction[111] considérée.

a_R et b_R désignent les couplages hyperfins isotropes (terme de Fermi) et anisotropes (termes dipolaires).

Il n'y a donc pas de couplage dipolaire si cos $\theta_{ZR} = 1/\sqrt{3}$, c'est à dire si le champ magnétique H_0 est dirigé suivant une direction [100] du cristal. C'est donc pour cette orientation que le spectre doit être le mieux résolu. On retrouve ainsi un résultat expérimental cité dans le paragraphe 4a. Dans ce cas,

$$\mathscr{H}_2 = \sum_1^4 a_F\mathbf{I}_F\mathbf{S} + \sum_1^4 a_{L_i}\mathbf{I}_{L_i}\mathbf{S}. \qquad (5)$$

Nous avons étudié le centre T_i° dans des cristaux de LiF ordinaire (7% de Li^6) et de LiF dopé à 90% de Li^6. Malgré la différence de spin ($\frac{3}{2}$ pour Li^7, 1 pour Li^6) et le grand rapport des moments magnétiques de Li^7 et Li^6, les spectres obtenus sont très semblables: cela prouve que $a_F > a_{Li}$. La structure hyperfine observée est donc due aux ions F^- (raies A, B, C, B, A): l'interaction hyperfine avec les ions Li^+ n'est pas résolue et contribue seulement à la largeur et la forme des 5 raies élémentaires dont la somme reconstitue le spectre du centre T_i°.

Structure due aux ions F^-. Le spin total est $4 \times \frac{1}{2} = 2$. Il y a donc 5 raies d'intensité respectives 1, 4, 6, 4, 1, dont la distance est a_F.

Structure due aux ions Li^+. Chacune des 5 raies est en fait la somme de 13 raies: car le spin total des ions Li^+ est $4 \times \frac{3}{2} = 6$, d'intensité respectives 1, 4, 10, 20, 31, 40, 44, 40, 31, 20, 10, 4, 1 et dont l'équidistance est a_{Li}

La forme du spectre obtenu dépend donc des deux paramètres a_{Li}/a_F et Δ/a_F (Δ est la largeur pic à pic des raies élémentaires dues à l'interaction avec le lithium). Nous avons reconstitué les spectres expérimentaux à l'aide d'un ordinateur. Nous avons mesuré plusieurs grandeurs (hauteurs et pentes relatives) relevées sur les raies expérimentales A et B (relativement peu déformées par la présence du centre T°) et avons cherché les valeurs de a_{Li}/a_F et Δ/a_F qui donnent un bon accord avec ces mesures.

En mesurant l'écart entre les sommets A et B nous avons trouvé $a_F = 28$ G. Par reconstitution du spectre à la machine nous déduisons $a_{Li} = 5{,}5$ G et $\Delta = 11$ G. Cette méthode indirecte de mesure de a_{Li} et Δ est en fait très précise. Nous avons pu vérifier que a_{Li} était certainement supérieur à 5 G et inférieur à 6 G. Pour Δ la précision *est plus faible: Δ est certainement supérieur à 8 G (les raies du lithium sont alors résolues) et inférieur à 12 G.*

Nous avons ensuite reconstitué la partie centrale du spectre experimental (*raie C*) en ajoutant pour la raie T° une gaussienne de largeur pic à pic égale à 20 G et dont le centre est décalé de 5 G par rapport au centre de la raie T_i°, ce qui permet d'évaluer le couplage avec le noyau de Tritium pour le centre T_i°: 552 G environ.

La Fig. 2(b) représente la forme de raie ainsi obtenue que l'on peut comparer à la raie expérimentale (Fig. 2(a)).

Ce modèle a également permis de retrouver la variation des spectres expérimentaux avec l'orientation du champ H_0. En effet pour une orientation de H_0 différente de [100] les raies dues aux divers ions ne coincident plus et la structure devient moins nette; en particulier la raie centrale diminue considérablement. La reconstitution des spectres obtenus pour les orientations [110] et [111] a permis de trouver $b_F = 2{,}8$ G et $b_{Li} = 1{,}9$ G. (la précision de ces évaluations est moins bonne que pour les termes a_F et a_{Li}) La Fig. 2(c) représente le spectre expérimental pour H_0 situé dans un plan (001) et faisant un angle de 10° avec la direction [110]: la Fig. 2(d) reproduit le spectre théorique reconstruit pour cette même orientation.

Le modèle d'atome de H^3 dans un site interstitiel ½, ½, ½ nous permet donc d'interpréter avec un bon accord les spectres expérimentaux.

Ce centre T_i° est tout à fait analogue au centre H_i° observé dans de nombreux halogénures alcalins. Nous avons comparé nos résultats expérimentaux avec ceux publiés par divers auteurs pour les centres H_i° et cités par Lehnert et Spaeth [6].

Comme l'ont observé Lehnert et Spaeth [6], le rapport des densités de spin sur un anion et un cation proches voisins croit avec le rapport des rayons ioniques tandis que décroit la densité de spins sur le noyau du centre. Nos résultats sont compatibles avec cette observation. Nous voulons aussi signaler que, à la différence des centres H_i° précédemment étudiés la densité de spins de l'électron du centre T_i° sur son propre noyau de H^3 est plus forte que celle de l'électron de l'atome H^3 libre.

5. CALCULS THEORIQUES

Pour diverses raisons, notamment la faible différence des densités de spins sur le proton dans les centres H_i° et dans l'atome libre, le modèle utilisé généralement pour le calcul des centres H_i° admet que l'état fondamental de l'électron est essentiellement l'état fondamental $|1s\rangle$ de l'atome libre. Dans ce

Tableau 1. Résultats expérimentaux pour les centres H_i° et le centre T_i° dans LiF

	Site cristallin	KBr(7)	NaCl(7)	KCl(8)	RbCl(6)	T_i° LiF	Atome libre
Densité de spins (en u a)	Noyau	$301{,}5 \times 10^{-3}$	$304{,}8 \times 10^{-3}$	308.4×10^{-3}	310.8×10^{-3}	324×10^{-3}	$317{,}8 \times 10^{-3}$
	Anion	114×10^{-3}	106×10^{-3}	54.15×10^{-3}	39.5×10^{-3}	$18{,}65 \times 10^{-3}$	
	Cation	$\leq 70 \times 10^{-3}$	4×10^{-3}	4.714×10^{-3}	12.44×10^{-3}	8.87×10^{-3}	
Rapport des densités de spins	Anion/Cation	≥ 2	∼ 30	11.5	3.18	2.1	
Rapport des rayons ioniques	Anion/Cation	1,47	1,85	1.36	1,22	1,185*	
Paramètre du réseau		6,58	5,64	6,28	6,55	4,02	

*Rayons ioniques mesurés par rayons X dans LiF [9].

modèle la présence du réseau ne joue que par l'intermédiaire du principe de Pauli: la partie spatiale de la fonction d'onde de l'électron supplémentaire introduit dans le réseau doit être orthogonale à celles des électrons des ions proches voisins, ceci mélange à la fonction hydrogène une certaine proportion des fonctions d'onde des électrons des ions. L'anion ayant une taille supérieure à celle du cation, les recouvrements de ses orbitales avec l'orbitale de l'atome d'hydrogène sont supérieurs à ceux des orbitales cationiques et la proportion de fonctions d'onde des anions proches voisins mélangée à celle de l'hydrogène sera plus importante que celle des cations. La partie *s* des fonctions d'onde d'un ion produisant la densité de spin sur le site correspondant, on retrouve ainsi l'influence du rapport des rayons ioniques de l'anion et du cation[6]. Un modèle de ce type a été appliqué par de nombreux auteurs; tenant compte notamment des calculs de Spaeth[8], nous avons pour notre part orthogonalisé entre elles les fonctions d'onde des électrons des ions avant de les orthogonaliser avec la fonction d'onde de l'interstitiel hydrogène. Les calculs d'intégrales de recouvrement ont été faits en suivant la méthode exposée par Löwdin[10] et en utilisant les fonctions d'onde données par Morse *et al.*[11].

Nous avons obtenu les résultats portés dans la deuxième colonne du Tableau 2, la première colonne rappellant les résultats expérimentaux.

Tableau 2. T_1° dans LiF

Expérimental (G)	Calculé sans relaxation (G)	Calculé avec 20% de relaxation (G)
$a_N = 552$	$a_N = 654.4$	$a_N = 576.6$
$a_F = 28$	$a_F = 89.3$	$a_F = 28.2$
$a_{Li} = 5.5$	$a_{Li} = 17.9$	$a_{Li} = 4.9$

Nous avons obtenu par le calcul des valeurs qui sont toutes très supérieures aux résultats expérimentaux. Tous les auteurs cités qui ont utilisé des modèles de ce type pour calculer les centres H_i° ont obtenu des valeurs trop fortes pour a_N mais toujours trop faibles pour le couplage avec les ions halogènes. Il semble donc que le cas du LiF soit original: il faut admettre que les distances joignant le site interstitiel $\frac{1}{4}$, $\frac{1}{4}$, $\frac{1}{4}$ aux 8 ions proches voisins doivent être augmentées, l'atome H^3 interstitiel repoussant les voisins. Cette supposition est confirmée par des considérations géométriques. En effet si, en site interstitiel, l'atome H dispose d'un rayon de 0,9 Å pour se loger dans KCl, il ne dispose plus que de 0,65 Å dans le LiF, ce qui est très insuffisant pour un atome d'hydrogène de rayon voisin de 1 Å. Il est donc raisonnable de supposer qu'il repousse ses voisins les plus proches.

Nous avons donc supposé de la façon la plus simple, que les 4 ions F^- et les 4 ions Li^+ plus proches voisins étaient également repoussés dans les directions ⟨111⟩.

Pour un déplacement de 20 pour cent par rapport à la valeur normale de 3,48 Å nous avons obtenu les valeurs portées dans la troisième colonne du tableau II.

L'accord est alors bon avec les résultats expérimentaux.

La valeur un peu faible du couplage avec les ions Li^+ pourrait vouloir dire que les ions Li^+ sont un peu moins repoussés que les ions F^-, ce qui serait logique; mais il nous semble difficile d'apprécier réellement cette différence au seul vu des mesures RPE.

En ce qui concerne le couplage hyperfin avec le noyau central, l'accord est bien meilleur que pour les autres halogénures alcalins. En effet le LiF est le seul halogénure alcalin pour lequel la valeur expérimentale de ce couplage est supérieure à celle de l'atome libre; or l'orthagonalisation provoque toujours un accroissement de la densité de spin sur le noyau central.

6. CONCLUSIONS

Nous avons pu mettre en évidence plusieurs sites possibles pour un atome de H^3 dans un monocristal de LiF.

A basse température, le tritium occupe des sites interstitiels $\frac{1}{4}, \frac{1}{4}, \frac{1}{4}$ pour lesquels l'électron est relativement bien couplé au réseau. Il diffuse ensuite au cours des recuits vers des positions plus stables (centres T°) pour lesquelles le couplage avec le réseau est de moins en moins fort. Il semble qu'il existe au moins deux de ces positions, qui correspondent à des largeurs de raies bien différentes (20 G contre 1 G). Mais il ne nous a pas été possible d'identifier de façon précise ces sites, les raies obtenues alors ne présentant pas de structure nette.

Le spectre correspondant au site interstitiel par contre a pu être analysé et les caractéristiques des couplages hyperfins avec les ions du réseau ont pu être calculées par un modèle de fonction d'onde orthogonalisée aux ions du réseau à condition de supposer que les 8 ions proches voisins soient repoussés d'environ 20 pour cent de la distance normale, dans les directions ⟨111⟩. L'accord avec les valeurs expérimentales est alors très bon; meilleur que dans les calculs du même type publiés par divers auteurs pour d'autres halogénures alcalins. Le modèle très simple de fonction d'onde orthogonalisée semble donc mieux représenter la réalité dans les autres halogénures alcalins.

Remerciements – Nous exprimons notre gratitude à Madame le Professeur M. Lambert pour de nombreuses et fructueuses discussions.

L'un de nous (M.T.C.), bénéficiaire d'une bourse Joliot-Curie, remercie le Comité chargé de l'attribution de ces bourses.

REFERENCES

1. DWECK J. A., HOOPER H. O. et BRAY P. J., *Bull. Am. phys. Soc.* **7**, 51 (1962).
2. KAZUMATA Y., *Phys. Status Solidi* **25**, 563 (1968).
3. PICK H. Structure of trapped electron and trapped hole centers in Alkali Halides. *Optical Properties of Solids* (Edited by F. Abelès) North-Holland Amsterdam (1969).
4. CASTNER T. J., KÄNZIG W., *J. Phys. Chem. Solids* **3**, 178 (1957).
5. HAYES W., HODBY J. W., *Proc. R. Soc.* **A294**, 359 (1966).
6. LEHNERT G., SPAETH J. M., *Phys. Status Solidi* **31**, 703 (1969).
7. KERKHOFF F., MARTIENSSEN W. et SANDER W., *Z. Phys.* **173**, 184 (1963).
8. SPAETH J. M., *Z. Phys.* **192**, 107 (1966).
9. KRUG J., WITTE H. et WOFEL E., *Z. phys. Chem.* **4**, 36 (1955).
10. LÖWDIN P., *Adv. Phys.* **5**, 3 (1956).
11. MORSE P. M., YOUNG L. A. et HAURWITZ E. S., *Phys. Rev.* **48**, 948 (1935).

J. Phys. Chem. Solids Pergamon Press 1970. Vol. 31, pp. 1019-1026. Printed in Great Britain.

TIME DEPENDENT POLARISATION IN ALKALI HALIDES

K. C. KAO,* W. WHITHAM and J. H. CALDERWOOD
University of Salford, Salford, England

(*Received 6 March 1969, in revised form 20 June 1969*)

Abstract – Measurements were made on electric currents as a function of time immediately after the application of rectangular voltage pulses of various durations in NaCl, KCl, NaCl + Ca^{2+} and NaCl + Ba^{2+} at temperatures between 100 and 350°C. The rate of current decay immediately after the application of the field is identical with that immediately after the removal of the field and this phenomenon is independent of the mark/space ratio of the pulses. Analysis of the observed results indicates that this type of polarisation is intimately associated with the presence of dislocations and also interfacial polarisation determined by internal boundaries within the crystal. The observations do not support an interpretation based either on the space charges built up near blocking electrodes or on the orientation of divalent cation-vacancy complexes.

1. INTRODUCTION

DETERMINATIONS of the electrical conductivity of the alkali halides have been made from time to time since the end of the last century[1]. An aspect of these measurements which has served to complicate their interpretation is that on application of a steady unidirectional field the current is observed to decay from some higher initial value to a lower steady-state value over a period of time.

This current decay has given rise to debate amongst the investigators as to whether the initial or steady-state value of the current should be used in conductivity determinations. The choice between the two values has hinged upon the opinion of the investigator in regard to the underlying causal mechanism giving rise to the effect. Thus those investigators who favour the space-charge polarisation theory adopt the initial value of the current[2] whilst those who prefer the dielectric relaxation theory choose the steady-state current as the appropriate value[3].

Over the last decade a number of experiments have been reported which were aimed at establishing the cause of the effect. Unfortunately no definitive conclusions have been reached although some interesting and valuable observations were made. It would appear that the underlying causes are not simple; for instance, some mechanisms seem to predominate over others in different temperature regions. Thus, in the region −50°C to room temperature, a polarisation current has been observed which has been interpreted in terms of the relaxation of divalent impurity-vacancy complexes[4]. From room temperature up to about 400°C the polarisation seems to be intimately connected with the presence of line defects[3].

Above this temperature and up to the melting point the polarisation displays the characteristics of space-charge polarisation due to blocking electrode effects[5].

Some investigators[6] have also sought to distinguish between the effect of a blocking electrode and what is called 'interfacial polarisation' arising from thin insulating surface layers adjacent to the electrode. It is not entirely clear how the one effect can be distinguished from the other since on the face of it 'thin insulating surface layers' should give rise to space charge polarisation.

The purpose of this paper is to present further observations of the effect at moderate

---

[*] Now with the Electrical Engineering Department, University of Manitoba, Canada.

temperatures, including current observations in the time immediately following the application of the voltage, a region of time not previously investigated.

2. EXPERIMENTAL

Single crystals of sodium chloride and potasium chloride were grown by the Kyropoulos technique in dry nitrogen atmosphere, after preliminary evacuation to 10^{-3} torr. The laboratory crystal pulling apparatus utilised induction heating of the melt which was contained in a vitreous carbon crucible. In order to prepare doped specimens, divalent impurities were added to the melt in the form of barium chloride and calcium chloride. In all cases analar grade chemicals were used.

Some initial experiments were performed upon crystals obtained from Hilger and Watts Ltd., but the measurements on these did not differ significantly from the undoped home-grown specimens.

Specimens were cleaved from the ingot to a thickness of approximately 3 mm. Each specimen was then machined and polished as described in an earlier paper[7]. Gold, and in some cases, nickel electrodes were evaporated onto the specimen under a vacuum of 10^{-6} torr. No significant difference in the behaviour of the specimen could be attributed to the different electrode materials and so gold was used exclusively in the later stages of the experiment since some evidence of chemical attack of the nickel was apparent after subjecting the specimen to temperatures over 500°C. The deposited metal electrodes proved to be very prone to scratching on insertion and removal from the electrode system and a coating of colloidal graphite over the metal served to increase its durability.

The measuring circuit was as shown schematically in Fig. 1. Care had to be exercised in balancing the bridge, and ensuring that the initial part of the observed current decay was due to a real effect in the crystal, undistorted by any transient created by slight bridge unbalance. Oscilloscope probes having a capacitance compensation facility and trimming potentiometers were used to obtain the final balance. The variable air capacitor was used to balance out the steady state capacitance in order to suppress the very short term charging and discharging currents and to exhibit the longer term ones.

The electrode system, which held the specimen in position by means of nichrome spring-loaded electrical contacts, was constructed out of a machinable ceramic. A local heater

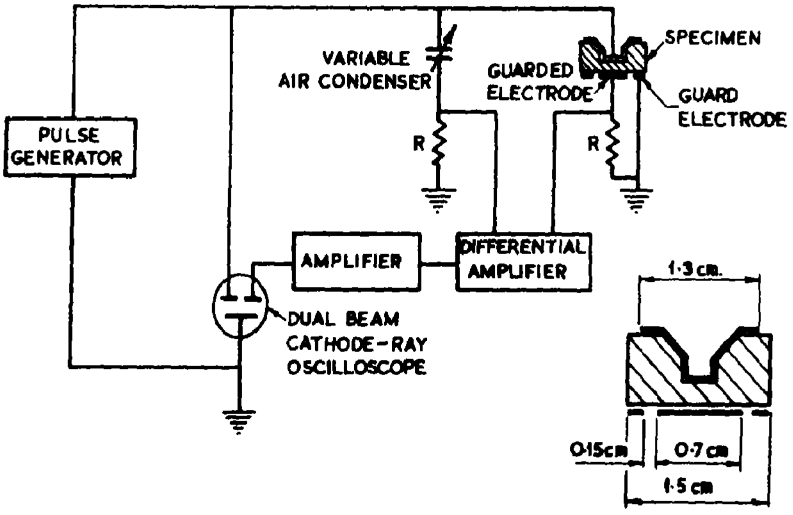

Fig. 1. Measuring circuit.

was wound on this structure, which made it possible to accurately control the temperature of the immediate crystal environment to ±0·5°C. Electrical leads and thermocouple wires were brought out of either side of the electrode system which fitted comfortably into a horizontal silica tube furnace for the experiments. The end of this silica tube could be sealed to vacuum tightness and the tube was filled with pure argon gas during the measurements. The divalent ion concentrations in the doped specimens were determined by a colourimetric titration technique using a micro-pipette and a sensitive indicator which was titrated against ethylenediamine-tetra-acetic acid.

The pulse generator provided a series of rectangular pulses of variable pulse duration, amplitude and frequency. Throughout the investigation the amplitude of the pulse used was 100 V with a rise time of 5 μsec, and the thickness of the specimen was in the region of 0·2–0·5 mm.

3. RESULTS

The time required for the current to decay from the initial value, i_0, to the final steady value, i_s, immediately after the application of a rectangular pulse is practically equal to that for the reverse current to decay to zero immediately after the removal of the field; in other words, the shaded area of $i-i_s$ is congruent with the shaded area under the reverse current curve as shown in Fig. 2. This observation was unaffected by the variation of the mark/space ratio of the pulses, and of the pulse duration provided that the duration of mark and space is long enough for the current to reach its steady value, and at temperatures between 100–350°C. There is no observable change in the current-time characteristics from pulse to pulse for a given temperature if the pulse-stressing time is not too long. It should be noted that prolonged pre-stressing with direct voltage did lower the steady value of the current at lower voltages and that at temperatures in the region of 400°C and above, the discharge curve exhibited a longer relaxation than the charge curve.

After a series of measurements from low to high temperatures, the steady conduction currents in a second series of similar measurements are lower than those in the first; and the higher the temperature to which the

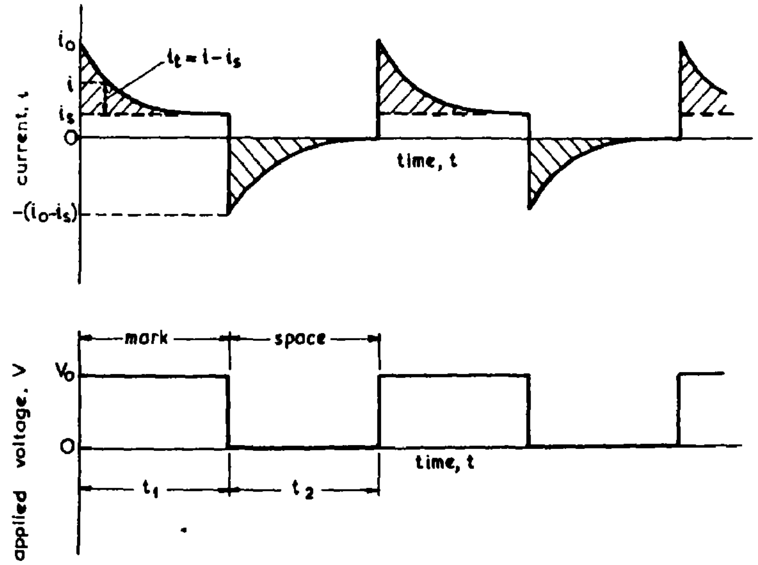

Fig. 2. Variation of current and voltage with time.

specimen is subjected, the more marked is the subsequent lowering of the steady conduction current at lower temperatures. A typical example of this phenomenon for NaCl is shown in Fig. 3.

In contrast with the steady state conduction current, the initial polarisation current, $i_0 - i_s$, does not show a decrease in value after a series of measurements from low to high temperatures, and sometimes, it even tends to increase. But the effect is erratic.

The total current can be resolved into a steady state conduction current, i_s, and a polarisation current, i_p, as shown in Fig. 2. The polarisation current does not obey any simple power law, but it may be appropriately expressed as the sum of two exponential terms

$$i_t = A\exp(-t/\tau_a) + B\exp(-t/\tau_b)$$

where τ_a and τ_b are time constants, and A and B are constants which depend on the material and vary from specimen to specimen of the same material.

The values of A and B are of the same order, and both increase with increasing temperature. Figure 4 shows the method used for analysing the polarisation current into two exponential terms for NaCl at 254°C.

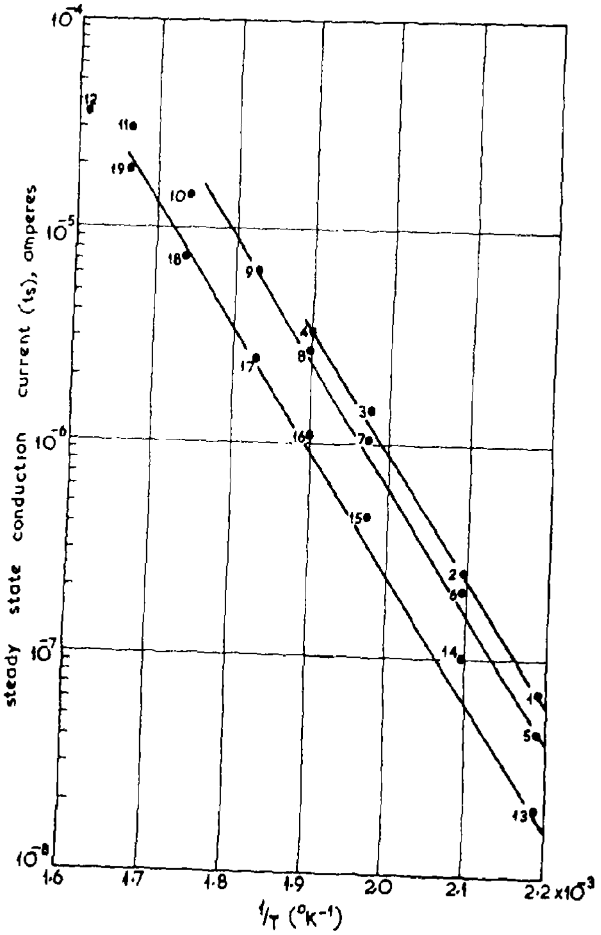

Fig. 3. Effect of conditioning

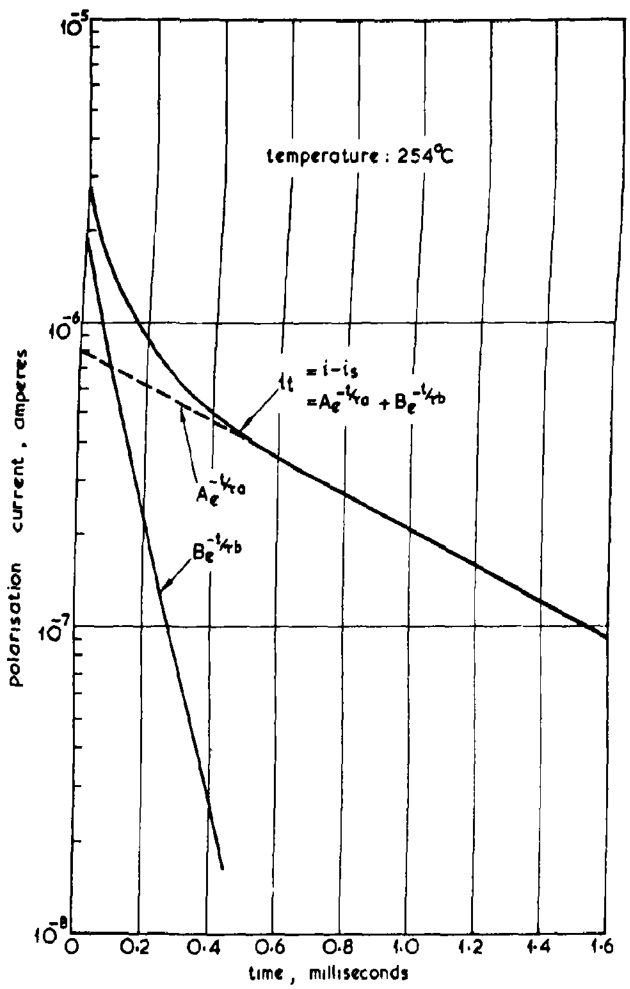

Fig. 4. Analysis of polarisation current in NaCl

The time constants obey the Arrhenius-type equation

$$\frac{1}{\tau} = G \exp(-\epsilon/kT)$$

where G is the frequency factor and ϵ is the activation energy of the reaction. Figures 5 and 6 show the variation of the two time constants with temperature, and from these curves the activation energies are calculated and given in Table 1. It can be seen that the two time constants give two different activation energies implying that there may be two mechanisms responsible for the polarisation.

Table 1. *Activation energies*

Crystal	Activation energy (eV)		
	ϵ_s	ϵ_a	ϵ_b
NaCl	1·13	1·09	0·76
KCl	0·99	1·04	0·80
NaCl + Ca^{2+}	1·00	0·97	0·72
NaCl + Ba^{2+}	0·99	1·00	0·79

It should be noted that as there are some divergencies from linear relationship between the plotted points, the straight lines drawn in Figs. 5 and 6 are clearly not unique.

It is known that over the temperature

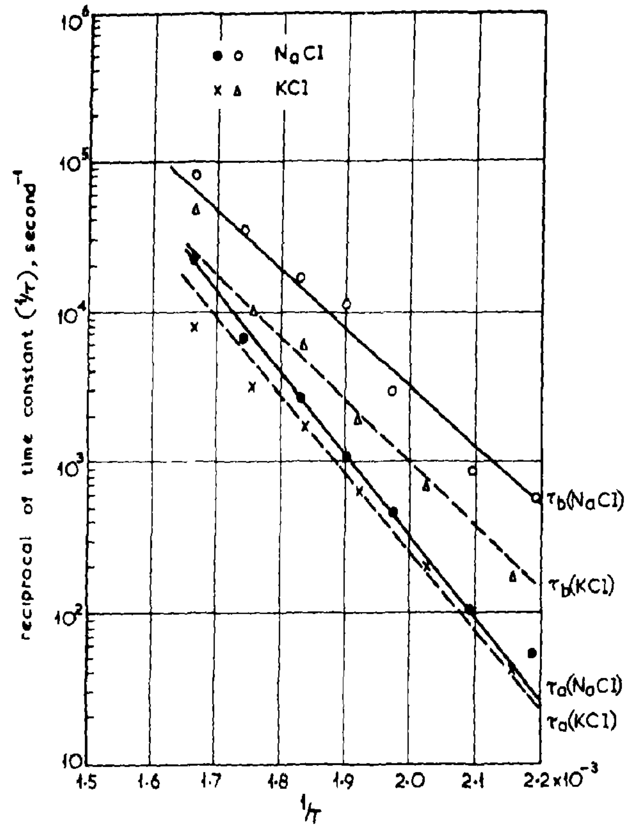

Fig. 5 Reciprocal of time constant vs. temperature for NaCl and KCl.

range under this investigation the steady-state conductivity increases with temperature as a result of increases in carrier mobility and the number of charge carriers which arise from complex dissociation. The steady-state conduction current is given by

$$i_s = \frac{\delta_0}{T}\exp(-\epsilon_s/kT)$$

where ϵ_s is the activation energy which is the sum of the activation energy for motion of a cation vacancy, ϵ_m, and part of the binding energy of a divalent ion-vacancy complex, ϵ_c. ϵ_m is of the order of 0·7–0·8 eV and ϵ_c is of the order of 0·2–0·5 eV. Values of ϵ_s given in Table 1 are in good agreement with the theoretical prediction. It is interesting to note that the values of ϵ_s are close to those of ϵ_a.

The introduction of divalent cations, such as Ca^{2+} and Ba^{2+}, into the crystal increased both the polarisation and the steady state conduction currents. This implies that the polarisation is associated with vacancies.

When the specimen was heated to about 400°C and then cooled rapidly to a lower temperature, say 200°C, the polarisation current was greatly increased. This implies that the polarisation is associated with dislocations produced by thermal quenching.

4. DISCUSSION

As the superposition principle[3] was obeyed below 400°C it is reasonable to rule out space-charge accumulation at the elec

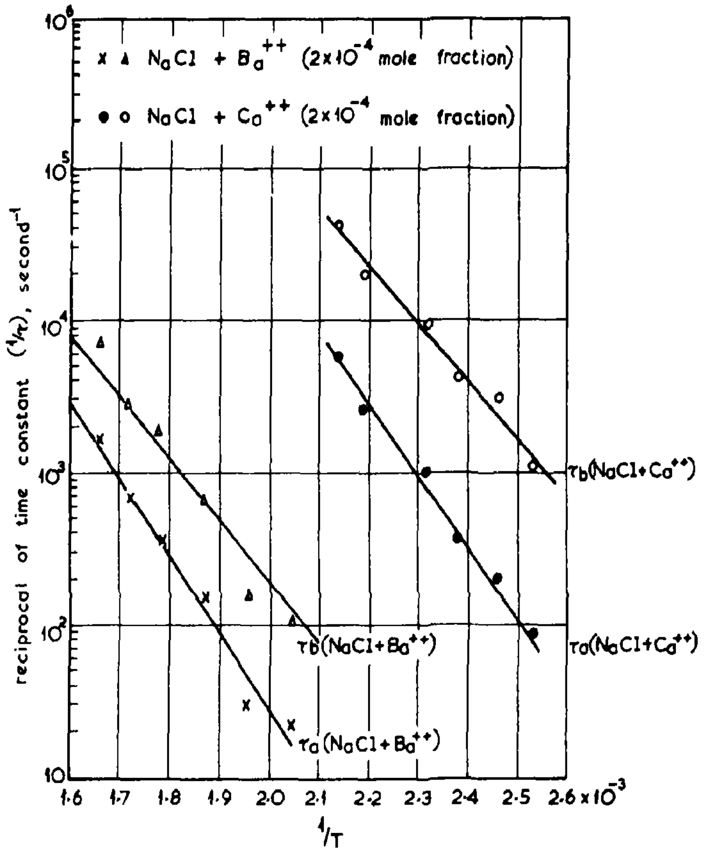

Fig. 6. Reciprocal of time constant vs. temperature for NaCl+Ca^{2+} and NaCl+Ba^{2+}.

trodes as an explanation for the observed polarisation since the non-linearity of the differential equations involved in space-charge polarisation theory[8] indicates a failure of this principle. However, there were indications that the higher temperature measurements were beginning to reveal such a failure and thus some evidence for space-charge polarisation above 400°C was established.

The two different activation energies for the time constants describing the polarisation current imply that there are two different polarisation mechanisms. In some specimens the analysis of the results indicated the presence of more than two exponential terms but accurate evaluation of these extra terms was prevented by the limited sensitivity of the instrumentation.

The shorter time constant reveals an activation energy close to the values for motion of charge carriers and for relaxation of impurity-vacancy complexes in NaCl[4]. In keeping with these results, the larger divalent impurity ion such as barium should exhibit a slower relaxation. However, the values of the time constants measured in the present work are some two orders of magnitude greater than what would be expected from impurity-vacancy relaxation at these temperatures, judging from the results of Dreyfus[4], Watkins[9], Haven[10]. Also, the polarisation effect measured here, increased with temperature whereas the impurity-vacancy relaxation should exhibit a decrease with temperature, due to thermal dissociation of the complexes. These facts preclude the interpretation of the shorter time constant in terms of impurity-vacancy relaxation and our observations are more in keeping with mechanisms associated with dislocations. It is likely that this shorter time constant is due to the migration of charged jogs on dislocation and to the displacement of the charged cloud of vacancies surrounding dislocations. The observation that thermal quenching and mechanical stressing increase the polarisation current associated with this term supports this contention.

The longer time-constant possesses an activation energy close to that of a steady-state conduction process. Thus an interfacial polarisation mechanism involving the migration of charge-carriers suggests itself. This could arise from large clusters of defects giving rise to regions of enhanced conductivity within the crystal, and producing a discontinuity of charge flow at their boundaries. However, it should be pointed out that this slower component too is intimately related to the presence of dislocations, since this component of polarisation also exhibits an increase on thermal quenching or mechanical stressing.

It is obvious from the above results and the associated work in this field that further experiments are required before the mechanisms under-lying this polarisation effect can be confidently established.

REFERENCES

1. LIDIARD A. B., *Handbuch der Physik* (Edited by S. Flugge, Vol 20, p 246. Springer Berlin (1957).
2. JOFFE A., *The Physics of Crystals* McGraw-Hill, New York (1928)
3. SUTTER P. H. and NOWICK A. S. *J. appl. Phys.* **34**, 734 (1963).
4. DREYFUS R. W., *Phys. Rev* **121**, 1675 (1961)
5. ALLNATT A. R. and JACOBS P. W. M., *J. Phys Chem Solids* **19**, 281 (1961)
6. WIMMER J. M. and TALLON N. M., *J. appl. Phys* **37** 3728 (1966).
7. HANSCOMB J. R., KAO K. C., CALDERWOOD J. H., O'DWYER J. J. and EMTAGE P. R., *Proc phys Soc* **88**, 425 (1966)
8. MACDONALD J. R., *Phys. Rev.* **92**, 4 (1963).
9. WATKINS G. D., *Phys. Rev* **113**, 91 (1959)
10. HAVEN Y., *J chem Phys* **21**, 171 (1953)

J. Phys. Chem. Solids Pergamon Press 1970. Vol. 31, pp. 1027–1040. Printed in Great Britain

COVALENCY AND HYPERFINE STRUCTURE CONSTANT *A* OF IRON GROUP IMPURITIES IN CRYSTALS

E. ŠIMÁNEK† and **K. A. MÜLLER**
IBM Zurich Research Laboratory, 8803 Rüschlikon, Switzerland

(*Received* 3 *February* 1969, *in revised form* 27 *May* 1969)

Abstract—The covalent reduction of the hyperfine splitting *A* of Mn^{2+} and other transition metal impurities in crystals is interpreted as resulting from the exchange polarization of the bonding orbitals containing 4*s*-admixture of the impurity. The calculated unpaired spin density responsible for the reduction of *A* is composed of two contributions. The first one results from the ligand → 4*s* transfer of the up-spin electron overcompensating the transfer of the down-spin electron. The second contribution is due to the difference between the 4*s*-radial wave function of up- and down-spin electrons. The latter effect is shown to be a dominating one on both the theoretical and experimental grounds. The theory is applied to discuss the relationship of *A* vs. covalency for 3*d* transition metal ions in various hosts. It is concluded that in covalent crystals the 4*s*-bonding of the impurity dominates over the 3*d*-bonding.

1. INTRODUCTION

HYPERFINE interaction of the isotope 55 of divalent manganese impurities in a solid was first reported by Schneider and England in ZnS[1]. Subsequently van Wieringen[2] investigated this interaction for Mn^{2+} substituted in a number of crystals. He showed that the hyperfine splitting *A* depended strongly on the host lattice. *A* was appreciably larger for ionic crystals than for covalently bonded ones[2].

In the free Mn^{2+} with configuration $3d^5$ the origin of the hyperfine splitting is the exchange polarization of the inner 1*s*, 2*s* and 3*s* orbitals as first computed by Heine[3] and Wood and Pratt[4] using the unrestricted Hartree-Fock method. In fact, due to the exchange interaction between electrons of parallel spin of the 3*d* and inner shell cores an attractive potential acts. Thus a net antiparallel polarization at the nucleus results, i.e. *A* in the isotropic term $\mathscr{H} = \mathbf{A \cdot SI}$ is negative. Extensive calculations of Watson and Freemann[5] show remarkable agreement with *A* as extrapolated from the data of the more ionic compounds. Remarkable because of the near cancellation of the very large parallel and antiparallel spin densities at the nucleus for a particular *s*-shell. In a free Mn^{2+} ion the hyperfine field $H_{hf} = -700$ kG which is due to the competition between the dominant and negatively polarized 2*s* and the positively polarized 3*s* shell[5, 6]. The relation between the hyperfine field H_{hf} at ^{55}Mn and the corresponding hyperfine splitting parameter *A* is

$$A[\mathrm{cm}^{-1}] = \frac{g_N \beta_N}{S} \cdot H_{hf} = 1 \cdot 4 \times 10^{-8} H_{hf} \quad [\mathrm{Gauss}] \qquad (1)$$

where g_N and β_N are the nuclear *g* factor of ^{55}Mn and nuclear magneton, respectively, and *S* is the total Mn^{2+} spin ($S = \frac{5}{2}$). Using (1) the calculated field $H_{hf} = -700$ kG corresponds to $A = -98 \times 10^{-4}\,\mathrm{cm}^{-1}$.

The relation between the parameter *A* and the bonding in crystals was put phenomenologically on a more quantitative basis by Matumura[7]. He plotted *A* vs. Pauling's covalency parameter derived from the elec-

---

† On leave from the Institute of Physics, Czechoslovak Academy of Sciences, Prague, Czechoslovakia.

tronegativity difference between the substitutional manganese and the ligands B, $x_{Mn}-x_B$ of the cluster $(Mn\,B_n)$ in a compound AB. Figure 1 shows such a graph where the more recent results of A have been included and the range of covalency has been extended to include homopolar structures. We computed the covalency in a particular cluster using the empirical relation of Hannay and Smyth[8],

$$c = 1-0{\cdot}16\,(x_{Mn}-x_B)-0{\cdot}035\,(x_{Mn}-x_B)^2. \tag{2}$$

We note that expression (2) was obtained by utilizing the electric dipole moments of hydrogenhalide diatomic molecules as a measure of the ionic character of the bond. The electronegativities x were taken from Gordy and Thomas[9]. Then following Pauling[10] the covalency of the cluster was calculated by dividing c by the number of ligands n.

First it is seen that A practically does not depend on the host cations. This is true for the SrF_2–CaF_2, the CaO–MgO series down to the MgTe–ZnTe one. Such a near independence on the host lattice was first noted by Müller[11] to occur for the hyperfine structure constant A of Mn^{4+} in various oxides, and ascribed to the dominance of nearest-neighbor interaction[11]. Subsequently, Geschwind[12] showed this to hold to a high degree of accuracy for Mn^{2+} as well as Fe^{3+} in the MgO–CaO series. This justifies our approach to consider only c/n and $x_{Mn}-x_B$ values of a cluster, and neglect the influence of the host cations which may act on A only via different $Mn^{2+}-B$ distances due to the changing sizes of the ions.

Taking the center of gravity of A for a particular series (MgO, CaO, SiO) the relation between A and the covalency parameter is certainly monotonic and except for stronger covalency linear within the relatively large

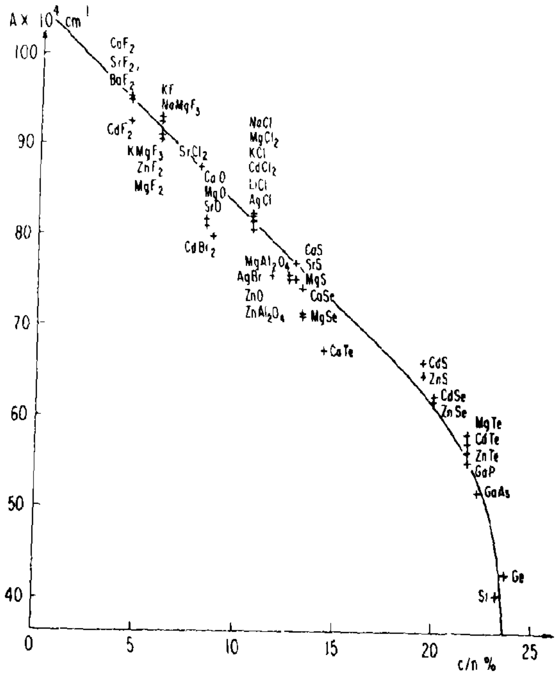

Fig. 1 The hyperfine interaction constant A of Mn^{2+} as a function of the covalency parameter c divided by the number of ligands. For a reference of A data see Table 1 in the Appendix.

uncertainty of *c/n* resulting from the not very accurate empirical electronegativity data. In Fig. 2 the *A* data of the isoelectronic Cr^{+} ion in various compounds are plotted against *c/n*. Although the amount of available data is more restricted one infers a linear relationship to hold for Cr^{+} into the region of strong covalency (Si, GaP). In contrast for Fe^{3+} the relation of *A* vs. *c/n* is not linear in the whole range (Fig. 3). Thus it appears that the divalent manganese is an intermediate case behaving like Cr^{+} in the more ionic region and like Fe^{3+} in the more covalent compounds.

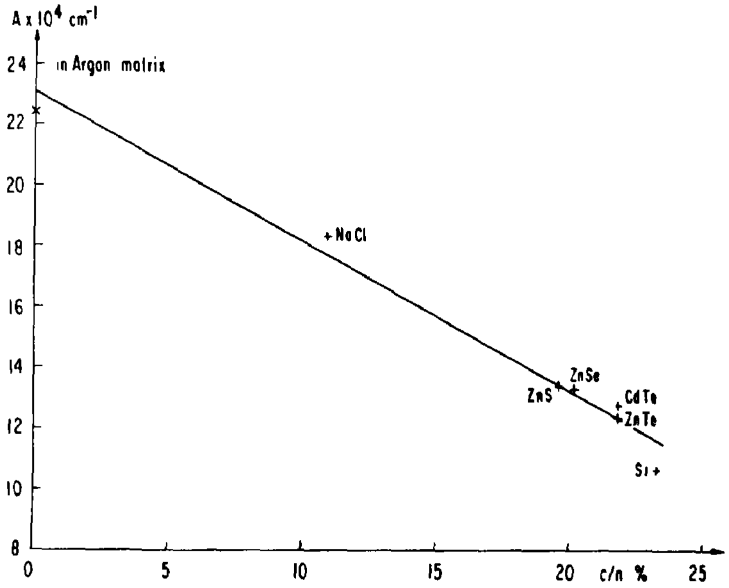

Fig. 2. The hyperfine interaction constant *A* of Cr^{+} as a function of the *c/n* ratio. A table of *A* values may be found in Ursu I., *Résonance Paramagnétique Electronique*, p. 400, Dunod, Paris (1968) (see also reference [17]).

A first qualitative discussion of the mechanism of covalent reduced *A* was presented by van Wieringen[2] and involved covalency hindered $3s \rightarrow 4s$ excitation *with a partially occupied 4s orbital*[2]. This was at a time when *A* was thought to be due to a Fermi contact interaction for the pure ion with an admixture of simple $3s \rightarrow 4s$ excitations, as also emphasized later by Abragam *et al.*[13]. Thus the first part of van Wieringen's model is not useful, but the second one of the contribution of the 4*s* orbital will be shown to be important. After the exchange polarization mechanism had been recognized as a source of the hyperfine field in the free ion, it was generally assumed[14] that the reduction of *A* was due to the decrease of the 3*d* electron spin density at the Mn^{2+} site due to covalency. The degree of exchange polarization is proportional to the 3*d* spin of the atom and therefore reflects 3*d* covalency.

Recently Estle and Holton[15] studied the superhyperfine interaction of the isoelectronic Fe^{3+}, Mn^{2+} and Cr^{+} ions in several II–VI compounds. They found to their surprise that the apparent percentage of delocalization of the antibonding 3*d* electrons in the $^{6}S_{5/2}$ state to the neighbor atoms was generally of the same amount of a few per cent as found in the ionic fluorides[15]. The present study was initiated by their work because from their data it appears that the 3*d* covalency cannot be the primary cause for the reduction of *A*. In view of the original suggestion by van Wieringen[2] and the calculations of the weak

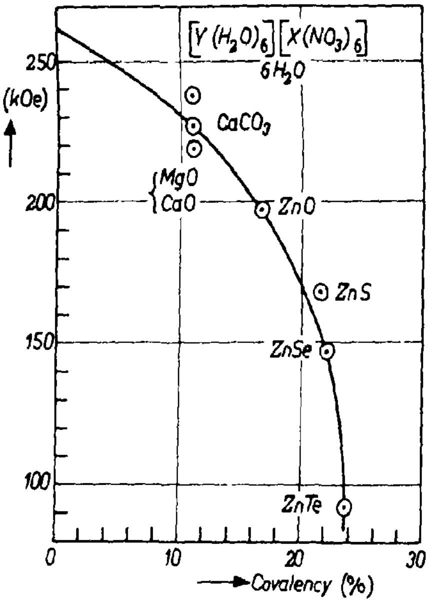

Fig. 3 Hyperfine field for Fe^{3+} vs c/n (after reference [19])

covalency by Hubbard *et al.*[16] where they found that the admixture of the 4*s* orbital is important, we decided to look at the exchange polarization of the 4*s* function participating in the bonding.

In a free atom the 4*s* orbital extends further out than the 3*d* one, thus the 3*d* exchange potential causes a large radial deformation of the parallel spin 4*s* orbital which induces a considerable positive 4*s* spin density at the nucleus. This exchange polarization is so large that it practically cancels the negative spin density due to the inner shells. For the Mn^0 atom with configuration $3d^54s^2$, Kasai [17] finds from EPR experiments $A = -26 \times 10^{-4}$ cm^{-1} only. Thus participation of the 4*s* function in filled bonding orbitals will reduce *A* to a substantial extent (to about a quarter of the free-ion value).

For instance, for substitutional manganese in silicon, $A = -40{\cdot}5 \times 10^{-4}$ cm^{-1}[18], i.e. less than half of the value found in ionic compounds. Of course in the covalent bonding of a manganese atom substituted into a crystal we have virtual transfer of electrons from the surrounding ligands to empty 3*d* (down-spin) as well as 4*s* and 4*p* (either spin) orbitals. Thus the covalency degree is strictly a mixture of the contributions from various shells. However, the results of Estle and Holton[15] and the remarkable 'linear' relationship between *A* and covalency for $3d^5$ Cr^+ and to a certain extent Mn^{2+}, suggests that the reduction of *A* is in this case proportional to a single covalency parameter, which, in view of what has been pointed out before, should be related *to the 4s covalent admixture of a cluster.*

While this study was in progress Henning [19] also pointed out the importance of a single covalency parameter and suggested that the reduction of *A* is produced by the exchange polarization of the bonding orbitals of a_{1g} symmetry. However he obtained a linear dependence with the covalency parameter λ_{a1} in the MOLCAO function which implies that *A* is proportional to the *square root of* the covalency in disagreement with the observed linear dependence in Cr^+ and Mn^{2+}.

In the next two sections the contribution investigated by Henning[19] as well as the radial 4*s*-exchange effect are obtained at once from a perturbation treatment of the exchange polarization of the bonding orbital. It is found that both contributions are proportional to the 4*s* transferred charge, i.e. proportional to $(\lambda_{a1})^2$! However, there is an important difference between the behavior of these terms with respect to the dependence on the bonding–antibonding energy separation. We find that the radial 4*s* effect is less dependent on this energy, and also seems to give a larger contribution than the polarization effect.

In Section 4(a) the derived expression for the covalent-induced hyperfine field is discussed in view of the experimentally observed linear relationship between *A* for Cr^+ and Mn^{2+} and its covalent bonding strength. Changes of the radial shape of 4*s*- and higher *s*-states due to coulomb screening are considered to explain the linear and partly linear behavior for Cr^+ and Mn^{2+}, respectively, and the nonlinear one for Fe^{3+}. In

Section 4(b) we estimate numerically the covalent-induced H_{hf} for Mn^{2+}: $KMgF_3$, and find that the contribution due to the radial 4s-effect is about 2·4 times stronger than that due to the bond-polarization effect considered by Henning[19].

Section 4(c) is devoted to a discussion of the systematics of hyperfine field in $3d^3$ series. We conclude the paper with Section 5, where physical reasons for the relatively strong 4s-covalency of transition metal ions in covalent crystals are discussed.

2. EXCHANGE POLARIZATION OF THE BONDING ORBITALS

In view of the conclusions we reached in the previous section, we shall assume that the dominant covalent contribution to A is due to the exchange polarization of the 4s-electrons admixed into the manganese configuration by covalent bonding. To describe this bonding we use a cluster model composed of a central manganese ion surrounded by nearest-neighbor ligands. This model is appropriate because of the small dependence of A on the cation in a compound, as already extensively discussed in the introduction.

We use the molecular orbital description, and take account only of the covalent mixing between the a_{1g} combination of ligand orbitals denoted as ϕ_L and the 4s-orbital of manganese. Thus we construct the a_{1g}-bonding orbital

$$\phi_B = N_B(\phi_L+\gamma_4\phi_{4s}) \tag{3}$$

where γ_4 is the $\phi_L \rightarrow \phi_{4s}$ transfer parameter.

In the 'restricted' Hartree–Fock approximation the orbital (3) is doubly occupied and the many-electron system we consider is described by a Slater determinant

$$\psi_0 = (3!)^{-1/2}\ \{\phi_d{}^+,\phi_B{}^+,\phi_B{}^-\ \} \tag{4}$$

where (+) and (−) denote the up- and down-spin, respectively. For simplicity, we consider only one unpaired d-electron ϕ_d of up-spin to be present. It is easy to extend the results to the real case of five d-electrons.

The presence of the unpaired $\phi_d{}^+$ electron yields an exchange potential and produces an unpairing of the 'closed' shell ($\phi_B{}^+$, $\phi_B{}^-$). This potential produces a distortion of a type: $\phi_B{}^+ \rightarrow \phi_B{}'^+$ so that the resulting Slater determinant takes the following 'unrestricted' form,

$$\psi = (3!)^{-1/2}\ \{\phi_d{}^+,\phi_B{}'^+,\phi_B{}^-\ \} \tag{5}$$

where $\phi_B{}'$ can be calculated using perturbation theory (see [20]),

$$\phi_B{}' = \phi_B + \sum_{n\geq 4} \frac{\langle\phi_d\phi_n|\phi_B\phi_d\rangle}{E_n - E_B}\phi_n \tag{6}$$

where ϕ_n are the unoccupied a_{1g} states of the complex which are solutions of the restricted Hartree–Fock approximation

$$\langle\phi_d\phi_n|\phi_B\phi_d\rangle = e^2\int d\tau\int d\tau' \frac{\phi_d^*(r')\phi_n^*(r')\phi_B(r)\phi_d(r)}{|\mathbf{r}-\mathbf{r}'|}. \tag{7}$$

In the framework of the configuration interaction, expression (6) corresponds to including promotion of a $\phi_B{}^+$ electron to the excited states $\phi_n{}^+$ via the exchange potential of $\phi_d{}^+$. At this point it seems useful to refer to the paper by Henning[19] who took into account only a single promotion $\phi_B \rightarrow \phi_4$, where ϕ_4 is the empty antibonding orbital,

$$\phi_4 = N_4\,[\phi_{4s} - (\gamma_4+S_4)\,\phi_l\,] \tag{8}$$

where

$$S_4 = \langle\phi_{4s}|\phi_l\,\rangle. \tag{9}$$

Physically, this type of promotion represents a certain type of exchange polarization of the bonding orbital ϕ_B with the following features. The attractive d-exchange potential produces a redistribution of the up-spin density between ϕ_L and ϕ_{4s}, but leaves the 4s-radial function unchanged. By admitting higher ($n > 4$) terms in the perturbation expansion (4) we allow the 4s electron of up-spin to be distorted radially. Since the 4s electron is mostly 'outside' of the 3d core, there is an inward attraction of the 4s density leading to a net positive unpaired s-density. We neglect the bonding of these excited s states ($\gamma_n = 0$) so that the 'antibonding' states ϕ_n for $n > 4$ are

$$\phi_n = N_n(\phi_{ns} - S_n\phi_l) \qquad (10)$$

where

$$S_n = \langle\phi_{ns}|\phi_l\rangle. \qquad (11)$$

Of course the ϕ_{ns} are less localized than ϕ_{4s} but the energy denominators are larger. Further the covalency of these states is an unknown parameter which is thus absorbed later into γ_4 and N_4.

The states ϕ_{ns} are the atomic s-states of the manganese ion. Since the radial deformation of the 4s-orbital mainly around the nucleus is important for hyperfine effects, the set of ϕ_{ns} states must also include the continuum of the manganese s-states. Thus the energies E_n lie rather high above the 4s state (more than 15 eV as shown later).

3. UNPAIRED s-DENSITY AT MANGANESE NUCLEUS

The modification of density of upward bonding electrons is from (6) to first order in exchange

$$(\phi_B')^2 - (\phi_B)^2 = 2\sum_{n\geq 4}\frac{\langle\phi_d\phi_n|\phi_B\phi_d\rangle}{E_n - E_B}\phi_B(r)\phi_n(r). \qquad (12)$$

By expressing ϕ_B and ϕ_n in terms of atomic orbitals, ϕ_{4s} and ϕ_{ns}, respectively, we obtain for the MO exchange integral in (12) an 'atomic' approximation

$$\langle\phi_d\phi_n|\phi_B\phi_d\rangle \simeq N_B N_n \gamma_4 \ \langle\phi_d\phi_{ns}|\phi_{4s}\phi_d\rangle. \qquad (13)$$

We note that in deriving (13) we have neglected all the integrals containing orbitals situated on different atomic sites.

The unpaired s-density at the ^{55}Mn nucleus ($r = 0$) can be calculated from (12) using (3) and (10). To see separately the two polarization effects, it is convenient to break expression (12) into two parts, as follows:

$$\begin{aligned}(\phi_B')^2 - (\phi_B)^2 &\cong N_B^2\gamma_4^2\bigg[2N_4^2\frac{\langle\phi_d\phi_{4s}|\phi_{4s}\phi_d\rangle}{E_4 - E_B}\phi_{4s}^2(0)\\ &\quad + 2N_4\sum_{n>4}\frac{\langle\phi_d\phi_{4s}|\phi_{ns}\phi_d\rangle}{E_n - E_B}\phi_{ns}(0)\phi_{4s}(0)\bigg].\end{aligned} \qquad (14)$$

In (14) we have used approximation (13) and assumed $N_n = 1$.

Now, we recognize that the first term ($n = 4$) on the right-hand side of (14) is essentially the contribution of the exchange polarized bond in the sense of Ref. [19]. The second term ($n > 4$) is the effect of radial 4s-polarization. The latter effect should be quantitatively related to the unpaired 4s-density in the $3d^5 4s^2$ configuration of Mn^0. In fact, a simple physical argument suggests that the radial 4s-hyperfine contribution should be given by the product of the hyperfine field of exchange polarized 4s-shells in Mn^0 and the probability of $3d^5 4s^2$ configuration. To check the validity of such an argument we apply the perturbation expansion to the 4s up-spin orbital in Mn^0, and obtain

$$\phi_{4s}' = \phi_{4s} + \sum_{n>4}\frac{\langle\phi_d\phi_{ns}|\phi_{4s}\phi_d\rangle}{E_n^a - E_4^a}\phi_{ns} \qquad (15)$$

where superscript (a) denotes the atomic energy level.

From this, the unpaired s-density at the ^{55}Mn nucleus is

$$(\phi_{4s}')^2 - (\phi_{4s})^2 \cong 2\sum_{n>4}\frac{\langle\phi_d\phi_{4s}|\phi_{ns}\phi_d\rangle}{E_n^a - E_4^a}\phi_{ns}(0)\phi_{4s}(0). \qquad (16)$$

By comparing (16) with the second term in (14) we see that the above simple argument does not hold exactly since there is a difference between the denominators of these two expressions.

As illustrated in Fig. 4, the difference is clearly due to the fact that in a covalent complex the electrons are "exchange" excited from the energy level E_B, whereas in the Mn^0 atom the 4*s*-electrons are excited from the E_{4s} level.

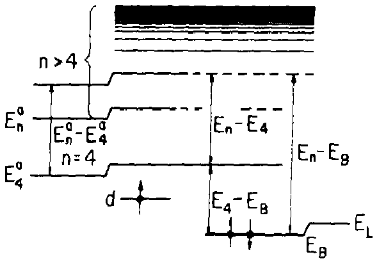

Fig. 4. The energy levels of a molecular complex (MnB_n). Also shown are the atomic energy levels of the *s* states of the manganese ion, denoted by E_n^0, and the ligand energy levels (E_l).

The difference $E_n - E_n^0$ (due to the antibonding effect) is quite small (1 eV or so) and hence the promotion energy in (12) can be written as follows,

$$\begin{aligned} E_n - E_B &= (E_n - E_4) + (E_4 - E_B) \\ &\cong (E_n^0 - E_4^0) + (E_4 - E_B). \qquad (17) \end{aligned}$$

Thus the presence of the term $(E_4 - E_B)$ produces a reduction of the radial exchange polarization as compared to what one expected using unpaired 4*s*-density in a free Mn^0 atom. In addition the second term of (14) is modified by Nn + 1 but this has been absorbed into N_4 and γ_4.

Some physical insight into this reduction process can be gained by applying the configuration interaction description to the 4*s*-covalency. The virtual charge transfer $\phi_l \rightarrow \phi_{4s}$ has certain dynamic features, which have been discussed previously[21]. It has been shown[21] that the charge transfer excited state has a lifetime given by $\hbar/\Delta E$, where ΔE is the promotion energy of the charge transfer. In our case this energy is $E_4^0 - E_L \approx E_4 - E_B$. In the configuration interaction method, the exchange polarization studied above can be incorporated by considering the higher-order perturbation term (second order in transfers, first order in intraatomic exchange). The reduction then can be interpreted as due to the finite lifetime of the electron transferred to the 4*s* state. The $\phi_{4s} \rightarrow \phi_{ns}$ excitations require a certain time, longer than $\hbar/(E_n^0 - E_4^0)$, and thus the polarization process may be dynamically reduced by the finite lifetime $\hbar/E_4 - E_B$.

Obviously, the degree of this reduction of spin density depends upon the distribution of energy levels in Fig. 4, and thus is a function of the bonding. We shall revert to this question in Section 4.

It is useful to rewrite expression (14) in terms of hyperfine field and take into account the presence of five unpaired 3*d*-electrons: This covalency-induced hyperfine field is then

$$\begin{aligned} \Delta H_{cov} &= \frac{8\pi}{3}\mu_B[(\phi_B')^2 - (\phi_B)^2] \\ &= \gamma_4{}^2 N_B{}^2 \left[\frac{2N_l{}^2 J}{E_4 - E_B} H_{4s} + N_4 H_{4s^2}^{\text{red}}\right] \qquad (18) \end{aligned}$$

where J is the energy difference between $3d^5\uparrow 4s\uparrow$ (^7S) and $3d^5\uparrow 4s\downarrow$ (^4S) states of Mn$^+$. H_{4s} is an average hyperfine field due to unpaired 4*s*-electrons in the above two configurations. We estimate this field from unrestricted Hartree–Fock calculations of Watson and Freeman[5] for Mn^0($3d^5 4s^2$). According to these calculations $H_{4s\uparrow} = 1750$ kG, $H_{4s\downarrow} = -1149$ kG and we take H_{4s} to be roughly an average of these two latter values so that $H_{4s} \approx 1500$ kG. $H_{4s^2}^{\text{red}}$ is the dynamically reduced hyperfine field of the exchange polarized $4s^2$ shell in Mn^0. In the "static limit" (when $E_n - E_4 \gg E_4 - E_B$), H_{4s^2} goes over to the free-atom value $H_{4s\uparrow} - H_{4s\downarrow} \cong 600$ kG[5].

4. DISCUSSION

(a) *General remarks*

Equation (18) suggests that there should be linear relationship between the covalent induced hyperfine field and the total charge transferred to the 4*s*-state of manganese. Indeed, according to (3) this charge turns out to be

$$Q_{4s} = 2N_B^2\gamma_s^2. \qquad (19)$$

Unfortunately, this factor is multiplied in (18) by the square bracket which is a function of various parameters ($E_4 - E_B$, N_4) dependent upon the degree of covalency. Thus, for instance, we expect the bonding–antibonding separation $E_4 - E_B$ to decrease appreciably on going from the ionic to covalent compounds. Consequently, both terms in the square bracket are expected to increase if other parameters such as ϕ_{4s}, ϕ_{ns} entering H_{4s^2}, $H_{4s^2}^{\text{red}}$ and J are kept constant. However, it should be stressed that (18) is based on the first order approximation (12) which is justified only if $\langle\phi_d\phi_B|\phi_n\phi_d\rangle \ll E_n - E_B$. In strongly covalent compounds $E_4 - E_B$ may be comparable to J and (18) is not applicable.

From (14) it is obvious that $H_{4s^2}^{\text{red}}$ would experience a weaker dependence on $E_4 - E_B$ than $1/(E_4 - E_B)$ (as encountered for the first term), because of the presence of excitations $E_n - E_4$ in the denominators of (14). To estimate this dependence quantitatively we would have to know the effective range of energies $E_n - E_4$. One possible way of estimating it would be to compare the numerically computed unrestricted Hartree–Fock wave function $\psi_{4s}'(r)$ with expansion (15) and find the coefficients of such an expansion.

A rough estimate of the lower limit of $E_n - E_4$ can be made by realizing that the most important excitations for exchange polarization are those involving the excited states of the continuum. Since the ionization energy of Mn^+ is 15 eV, we estimate $E_n - E_4 > 15$ eV.

Even if we take the average excitation energy $\langle E_n - E_4\rangle$ to be as large as 20 eV we still expect sizable changes of $H_{4s^2}^{\text{red}}$ due to changing $E_4 - E_B$. Thus, for instance, in the case of Mn^{2+}:$KMgF_3$ calculations of Hubbard *et al.*[16] indicate $E_4 - E_B \simeq 30$ eV. In very covalent cases we expect $E_4 - E_B$ to be comparable to the band-gap which is certainly less than 10 eV. Consequently, the average values of the denominators in (15) may change by about 100 per cent leading to changes of $H_{4s^2}^{\text{red}}$ of that order.

In view of these facts it is quite surprising that a linear relationship is observed between A of Mn^{2+} and Cr^+ and the degree of covalency. However, there may be additional effects compensating the one of $E_4 - E_B$.

First, the changes in bonding may be accompanied by changes of the radial wave functions ϕ_{1s} and ϕ_{ns}. Electrostatic screening by the 4*s* and 4*p* charge density causes a decrease of the hyperfine fields H_{4s} and $H_{4s^2}^{\text{red}}$ with increasing covalency. One can make a rough estimate of the 4*s* screening effect by comparing the hyperfine field of the 4*s* electron with up-spin in $Mn^0(3d^54s^2)$ and Mn^+ $(3d^54s)$. The calculations of Watson and Freeman[5] give $H_{4s\uparrow} = 1750$ kG for Mn^0. For the case of Mn^+ we use recent EPR results of Ikeya and Itoh[22] on Mn^+:KCl giving $A = 232\times10^{-4}\,\text{cm}^{-1}$. Assuming that the core polarization contribution to A is the same as in a free ion (-600 kG), we obtain $H_{4s\uparrow} \cong 2000$ kG. Thus about 15 per cent decrease of H_{4s} is expected on going from Mn^+ to Mn^0. The 4*p* screening in $3d^5$ $4s$ $4p$ vs. $3d^5$ $4s$ amounts to about 5 per cent change of H_{4s}[23]. The changes of $E_4 - E_B$ are difficult to assess but certain information can be drawn from the atomic energy levels (d^6) and $(3d^54s)$ which show an interesting systematic behavior along the sequence Cr, Mn^+, Fe^{2+} (see Fig. 5). These configurations correspond to the charge transfer from the ligand to the 3*d* and 4*s* atomic levels, respectively. It is possible that due to the low-lying $(3d^54s)$ configuration in Cr and Mn^+ the promotion energy $E_4 - E_B$ changes less

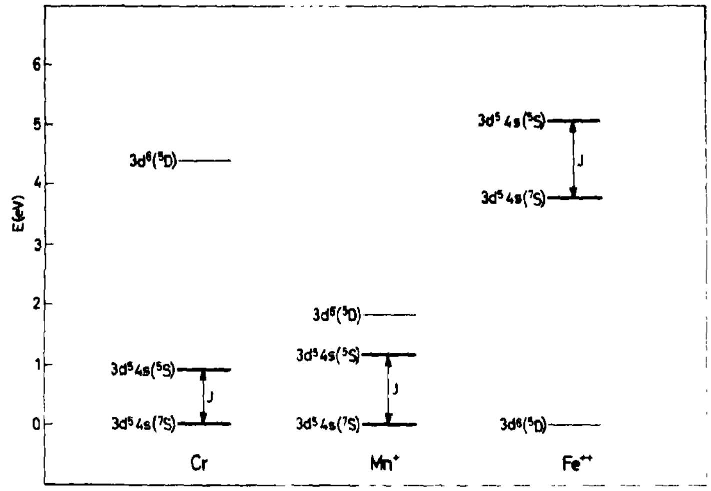

Fig. 5. The energy separations between configurations ($3d^6$) and ($3d^5 4s$) of the Cr^0, Mn^+ and Fe^{2+} ions[24]. The separation between $^7S(3d^5, 4s\uparrow)$ and $^5S(3d^5, 4s\downarrow)$ states defines the $3d-4s$ exchange integral J.

strongly with covalency. The large off-diagonal matrix elements then control the $E_1 - E_B$ separation to remain more or less constant in contrast to Fe^{3+}. This could explain the fact that the plots of A vs. covalency also develop a systematic increase in non-linearity on going from Cr^+ to Fe^{3+}.

The second possibility† may be that the amount of 4s-charge (19) is not a simple linear function of the covalency degree, which is defined by the electronegativity difference. Obviously, the latter difference must be related not only to the 4s, but also to the 3d and 4p covalencies. Although the 3d-covalency is found to be rather small, even in strongly covalent compounds (see [15]) the 4p effect is probably appreciable especially for tetrahedral bonds.

(*b*) *Numerical estimates*

Up to now we have only been concerned with some qualitative features of the above-derived covalent contribution to the hyperfine field. Now we should like to present more quantitative arguments showing the importance of the 4s-radial effect as compared with the contribution of the exchange polarized bond.

First let us consider a typical ionic case: Mn^{2+} in $KMgF_3$, for which we have a theoretical value of $(E_1 - E_B) \simeq 30$ eV (see Hubbard *et al.*[16]). For J we can use the free-ion value of 1 eV as given in the atomic energy level tables[24]. Using $H_{4s} \simeq 1500$ kG we arrive at an estimate

$$\frac{2J}{E_4 - E_B} H_{4s} \simeq 100\,\mathrm{kG}. \qquad (20)$$

To find a corresponding value of $H_{4s^2}^{\mathrm{red}}$ we write the second term in (14) as follows:

$$\sum_{n>4} \frac{\langle \phi_d \phi_{4s} | \phi_{ns} \phi_d \rangle}{E_n - E_B} \phi_{ns}(0)\, \phi_{4s}(0)$$

$$\cong \frac{1}{(E_n - E_4) + E_4 - E_B} \sum \langle \phi_d \phi_{4s} | \phi_{ns} \phi_d \rangle \phi_{ns}(0) \phi_{4s}(0). \qquad (21)$$

In the 'static' limit, $(E_4 - E_B) \to 0$ and the expression (21) then roughly corresponds to the hyperfine field of the exchange polarized $4s^2$ shell of Mn^0, which is about +600 kG (see Section 3). In keeping with the above discussion we use $\langle E_n - E_4 \rangle \simeq 20\,\mathrm{eV}$, $E_4 - E_B \simeq 30\,\mathrm{eV}$, and obtain from (19) the dynamically reduced hyperfine field

---

†See Note added in proof.

$$H^{\mathrm{red}}_{4s^2} = 600 \times \frac{\langle E_n - E_4 \rangle}{\langle E_n - E_4 \rangle + E_4 - E_B}\,\mathrm{kG} = 240\,\mathrm{kG}, \tag{22}$$

which is to be compared with the 100 kG contribution due to the bond polarization.

The importance of the radial polarization contribution in covalent compounds may be seen by inspecting the EPR measurements on Mn^{2+}, Fe^{3+} and Cr^{+} in II–VI compounds. Estle and Holton[15] find only several per cent of unpaired total spin summing over all the ions surrounding the transition metal impurity. Now it should be realized that the exchange polarization of the 4*s-bond* leads to a negative spin density at the ligands[25]. This is natural to expect, since predominantly the up-spin electron is transferred from ligands to the 4*s*-state of the transition metal ion. For example in the case of Mn^{2+}: ZnSe Estle and Holton[15] find A to be about 60 per cent of the free ion value, and if we wanted to explain all of it by the bond polarization, we should have to assume about 20 per cent of the up-spin to be transferred to the 4*s*-state. This would then produce 20 per cent of the total unpaired density on all the ligands. An accidental cancellation between the latter and a positive density due to 3*d*-covalency is improbable because it would have to occur for all the ions Fe^{3+}, Mn^{2+} and Cr^{+}; especially if one refers to the relative $3d^5 4s$ and $3d^6$ level positions shown in Fig. 5. We conclude that the exchange polarization of the 4*s-bond* must be much less than 20 per cent and hence cannot be the dominant cause of the strong reduction of A.

This indirectly proves that the 4*s-radial* effect must be dominant in strongly covalent compounds. It produces a sizable density at the Mn-nucleus without leaving appreciable spin densities at the ligands. Quantitative estimates of the bond polarization and 4*s*-radial effects in covalent compounds cannot be safely made because of the lack of knowledge of the parameters entering[18].

In addition, the theory presented in Sections 2 and 3 neglects the effects of the overlaps between ligands and inner *s*-shells of the metal ion. As shown earlier in connection with isomer shift of $^{57}\mathrm{Fe}$, these overlaps lead to an increase of the effective 4*s*-density[26]. This should produce an amplification of ΔH_{cov}, quite strong in ionic compounds, but difficult to estimate in the covalent compounds.

(*c*) 3d^3 *in octahedral surroundings*

The isoelectronic series of V^{2+}, Cr^{3+} and Mn^{4+} is a particularly interesting example where the insight gained here can be applied quantitatively. Geschwind[12] has pointed out that the hyperfine field H_{cp} practically does not vary from V^{2+} to Mn^{4+} in oxygen octahedral environment. This value amounts to $H_{cp} = -193 \pm 1{\cdot}5\,\mathrm{kG}$ per spin, if the small orbital contribution of the order of 3–5 kG is subtracted from the experimental value. This may be compared with the calculations of Freeman and Watson[27] for the free Mn^{4+} ion giving $H_{cp}(\mathrm{Mn}^{4+}) = -196\,\mathrm{kG}$.

We start with the interesting case of Mn^{4+}. Freeman and Watson[27] calculated the net spin density at the nucleus of manganese as a function of ionization (per spin). The 3*d* functions are more contracted for the larger ionization stages. This yields a more positive 3*s* exchange polarization and reduces the net negative spin density leading to a decrease of the magnitude of the net core polarization with ionization degree. Geschwind and coworkers[28] have taken the experimentally observed smaller values of A for Mn^{4+} as evidence for this trend. However, they overlooked an important point. In the oxides, a four-valent $3d^3$ ion shows appreciable 3*d* covalency coming mainly from the σ-bonding e_g orbitals (the antibonding ones not being occupied). This reduces the charge on the manganese ion, and consequently the above-mentioned contraction of the three occupied antibonding $3d$ functions is decreased. Thus the positive $3s$ exchange polarization is reduced compared to the free Mn^{4+} value.

A quantitative estimate of the net charge reduction of the Mn^{4+} ion can be made by using the computed covalency factor by Lacroix and Emch[29]. They found for $Mn^{4+}O_6$ $P_\sigma = 38$ per cent for e_g orbitals, and $P_\pi = 15$ per cent for t_{2g} orbitals including overlap (P_i being the probability of $3d$ occupation). The outflow of charge due to the three occupied t_{2g} antibonding orbitals is approximately compensated by the inflow of the corresponding charge of 3 bonding t_{2g} orbitals. The latter is, however, occupied by six electrons, and we obtain an inflow of $3(-0{\cdot}15\,e) = -0{\cdot}45e$. The reduction from four σ bonding e_g orbitals is $4(-0{\cdot}38e) = -1{\cdot}52e$.

Hence a charge reduction due to $3d$ covalency of about $-2e$ is present.† It should be noted, however, that this strong charge reduction comes mainly from *nonmagnetic bonding* orbitals and is thus accompanied by only a slight $3d$ spin reduction ($\simeq 15$) per cent). This means that the exchange polarization of a Mn^{4+} in an oxide environment should behave as a free Mn^{2+} ion with $H_{ep} \sim -285$ kG per spin instead of -200 kG (if $4s$ covalency and $3d$ spin reduction is neglected). We have thus to explain the considerable reduction observed (which is larger than that found for Mn^{2+} in oxygen environment).

We can do this quantitatively by assuming again that the exchange polarization of the bounding a_{1g} orbital is the cause of the reduction. Because it should be close to that of Mn^{2+} we can use the gauge curve of Fig. 1 with the hyperfine field per spin for Mn^{2+} in MgO neglecting a small $3d$-covalency of Mn^{2+}: MgO. From Fig. 1, $H_{ep} = -235$ kG; this value is further reduced owing to the loss of spin density of 15 per cent due to the π-bonding of the occupied antibonding t_{2g} orbitals, and yields 200 kG in good agreement with the measured values.

On the other side of the $3d^3$ series is V^{2+} which we now discuss. From the experimental hyperfine data of V^{2+} and Mn^{2+} in the most ionic compounds, the fluorines, it is found that the field per spin $H_{exp}(V^{2+})$ is 12 per cent smaller than $H_{exp}(Mn^{2+})$. This scales with the theoretical values for inner core polarization hyperfine fields in the neutral V^0 and Mn^0 atoms (V^{2+}h.f. core polarization calculation not being available). Assuming that actual free-ion values have the ratio of $H_{exp}(V^{2+})/H_{exp}(Mn^{2+})$ of fluorines, and using the extrapolated free H value for $H(Mn^{2+}) = 285$ kG (Fig. 1 and equation (1)), we obtain a value of $H(V^{2+}) = -250$ kG for the free V^{2+} ion. Since the experimental hyperfine field V^{2+} in MgO is near 200 kG, a reduction of about 20 per cent is found as compared to 17·5 per cent for Mn^{2+} in MgO. If we assume that the reduction is due to the *same* admixture of $4s$ vanadium and manganese wave functions in the bonding a_{1g} orbitals this is in line with our theory for the following reasons: the electronegativities are the same for both ions, and the positive exchange polarizations per spin of the $4s$ shell for neutral vanadium and manganese atoms coincide within 10 per cent[5]. Thus if we assume that the covalency deduced from the electronegativity differences is proportional to the $4s$ electron admixture in the a_{1g} orbital the result is obvious.

Similar considerations can be made for central hyperfine interaction parameters of transition metal ions for which less complete data are available.

5. CONCLUSIONS

The major conclusion to be drawn from the present study is the observation that the $4s$-bonding dominates over the $3d$ one. This is true at least in the very covalent crystals and for tetrahedral coordination, where sizable reductions of A are accompanied by small $3d$-covalency. This is quite an interesting fact from the point of view of the theory of covalency: especially because recent *a priori* calculations of covalency in highly ionic $KMnF_3$ indicate quite small (and smaller than for $3d$) $4s$-transfer[16]. It appears that the relative amount of $4s$-bonding increases on going to more covalent crystals, and the $4s$ orbitals contribute appreciably to the electronegativity of the transition ions. However, we have to point out that this observation should not be considered as a general rule for all transition metal ions. In the $4d$ and $5d$ series, the d-orbital covalency may play an important role for central hyperfine structure constants. Our results have been obtained using a quite simple model [30] and physical arguments rather than rigorous calculations of the complete system which is at present not accessible. Thus this does not exhaust all possible contributions.

---

†The $3d$ charge reduction is also reflected in the larger electronegativity of Mn^{4+} as compared to that of Mn^{2+}.

Acknowledgements – We should like to thank Dr. O. Schirmer for valuable comments on the manuscript and Professor R. Brout for a useful discussion

REFERENCES

1. SCHNEIDER E. E. and ENGLAND T. S., *Physica* **17**, 221 (1951).
2. VAN WIERINGEN J. S., *Disc. Faraday Soc.* **19**, 118 (1955).
3. HEINE V., *Phys. Rev.* **107**, 1002 (1957)
4. WOOD J. H. and PRATT G. W., Jr., *Phys. Rev.* **107**, 995 (1957).
5. WATSON R. E. and FREEMAN A. J., *Phys. Rev.* **123**, 2027 (1961).
6. WATSON R. E. and FREEMAN A. J., In *Hyperfine Interactions* (Edited by A. J. Freeman and R. B. Frankel. Academic Press, New York (1967)
7. MATUMURA O., *J. phys. Soc. Japan* **14**, 108 (1959).
8. HANNAY N. B. and SMYTH C. F., *J. Am. Chem. Soc.* **68**, 171 (1946).
9. GORDY W. and THOMAS W. J. O., *J. chem. Phys.* **24**, 439 (1956).
10. PAULING L., *The Nature of the Chemical Bond*, 3rd Edn. Cornell University Press, Ithaca (1960).
11. MÜLLER K. A., In *Paramagnetic Resonance* (Edited by W. Low), Vol. 1. Academic Press, New York (1963).
12. GESCHWIND S., In *Hyperfine Interactions* (Edited by A. J. Freeman and R. B. Frankel). Academic Press, New York (1967).
13. ABRAGAM A., HOROWITZ J. and PRYCE M. H. L., *Proc. R. Soc.* **230**, 169 (1955).
14. TITLE R. S., In *Physics and Chemistry of II–VI Compounds* (Edited by M. Aven and J. S. Prener) p. 265, North-Holland, Amsterdam (1967).
15. ESTLE T. L. and HOLTON W. C., *Phys. Rev.* **150**, 159 (1966).
16. HUBBARD J., RIMMER D. E. and HOPGOOD F. R. A., *Proc. Phys. Soc.* **88**, 13 (1966).
17. KASAI P. H., *Phys. Rev. Lett.* **21**, 67 (1968).
18. WOODBURY H. H. and LUGWIG G. W., *Phys. Rev. Lett.* **5**, 96 (1960).
19. HENNING J. C. M., *Physics Lett.* **24A**, 40 (1967).
20. ANDERSON P. W., *Solid St. Phys.* **14**, 99 (1963).
21. ŠIMÁNEK E. and TACHIKI M., *Phys. Lett.* **21**, 625 (1966).
22. IKEYA M. and ITOH N. *Solid State Comm.* **7**, 355 (1969).
23. STEUDEL H., Private communication.
24. MOORE C. E., *Atomic Energy Levels* National Bureau of Standard Circular No. 467, Vol. II. U. S. Government Printing Office, Washington (1952)
25. SCHIRMER O., *J. Phys. Chem. Solids* **29**, 1407 (1968).
26. ŠIMÁNEK E. and ŠROUBEK Z., *Phys. Rev.* **163**, 275 (1967)
27. FREEMAN A. J. and WATSON R. E., In *Magnetism IIA* (Edited by G. T. Rado and H. Suhl) Academic Press, New York (1965)
28. GESCHWIND S., KISLIUK P., KLEIN M. P., REMEIKA J. P. and WOOD D. L., *Phys. Rev.* **126**, 1684 (1962)
29. LACROIX R. and EMCH G., *Helv. phys. Acta* **35**, 592 (1962).
30. The approach with which the transition metal impurity-ligand atom *cluster* has been dealt is an open-shell MO–LCAO model rather than the Heitler–London picture. We note that Phillips has recently used an open-shell energy band model rather than the Heitler–London one to obtain from dielectric properties of AB type crystals the ionic character of the bonds of bulk crystals. See Phillips J. C. and van Vechten J. A., *Phys. Rev. Lett.* **22**, 705 (1969) and references quoted therein

Note added in proof. A new explanation of the non-linearity of A vs. c/n for Mn^{2+} and Fe^{3+} has been presented recently by us to result from the ionic covalent "phase" transition occurring for high c/n values. This explanation is supported by the sharp change of exciton absorption, metal–semiconductor interface behavior and the relative contribution of non-direct transitions plotted as a function of electronegativity differences of the constituents discussed by KURTIN S., McGill T. C. and MEAD C. A., *Phys. Rev. Lett.* **22**, 1433 (1969).

Appendix: Table 1

Compound	$-A$ $\times 10^4\,cm^{-1}$	T (°K)	Reference
CaF_2	95·3 ± 0·2	→ 0	SERWAY R. A., *Phys. Lett.* **26A**, 642 (1968)
SrF_2	95·2 ± 1	300	VINOKUROV V. M. and STEPANOV V. G., *Soviet Physics-solid State* **6**, 303 (1964)
BaF_2	94·9 ± 1	77	DRUMHELLER J. E., *J. chem. Phys.* **38**, 970 (1963)
CdF_2	92·5 ± 0·5	300	RANON U. and STAMIRES D. N., *Chem. Phys. Lett.* **2**, 286 (1968)
KF	92·9 ± 0·1	77	HALL T. P. P., HAYES W., STEVENSON R. W. H. and WILKENS J., *J. chem. Phys.* **38** 1977 (1963)
$NaMgF_3$	92·5 ± 1·5	300	OGAWA S., *J. phys. Soc. Japan* **15**, 1475 (1960)
$KMgF_3$	91·0 ± 0·5	300	HALL T. P. P., HAYES W., STEVENSON R. W. H. and WILKENS J., *J. chem. Phys.* **38**, 1977 (1963)
ZnF_2	90·7 ± 0·3	77	CLOGSTON A. M., GORDON J. P., JACCARINO V., PETER M. and WALKER L. R., *Phys. Rev.* **117**, 1222 (1960)
MgF_2	90·6	300	MATUMURA O., *J. phys. Soc. Japan* **14**, 108 (1959)
$SrCl_2$	87·4	20	DOBROWOLSKI W., JONES R. V. and JEFFRIES C. D., *Phys. Rev.* **104**, 1378 (1956)
CaO	81·6 ± 0·001	4·2	GESCHWIND S., In *Hyperfine Interactions* (Edited by A. J. Freeman and R. B. Frankel), p. 225 Academic Press, New York (1967)
MgO	81·5 ± 0·2	4·2	GESCHWIND S., In *Hyperfine Interactions* (Edited by A. J. Freeman and R. B. Frankel), p. 225 Academic Press, New York (1967)
SrO	80·9 ± 0·2	4·2	GESCHWIND S., In *Hyperfine Interactions* (Edited by A. J. Freeman and R. B. Frankel), p. 225 Academic Press New York (1967)
$CdBr_2$	79·8	300	KOGA H., HORAI K. and MATUMURA O., *J. phys. Soc. Japan* **15**, 1340 (1960)
NaCl	82·3 ± 0·3	300	WATKINS G. D., *Phys. Rev.* **113**, 79 (1959)
$MgCl_2$	82·0 ± 1·0	20–300	HALL T. P. P., HAYES W. and WILLIAMS F. I. B., *Proc. Phys. Soc.* **78**, 883 (1961)
KCL	81·8 ± 1·0	300	WATKINS G. D., *Phys. Rev.* **113**, 79 (1959)
$CdCl_2$	81·5 ± 0·2	20	HALL T. P. P., HAYES W. and WILLIAMS F. I. B. *Proc. Phys. Soc.* **78**, 883 (1961)
LiCl	81·4 ± 0·4	300	
	80·8 ± 0·5	300	WATKINS G. D., *Phys. Rev.* **113**, 79 (1959)
AgCl	80·0 ± 0·5	77	SCHNEIDER J. and SIRCAR S. R., *Z. Naturf.* **17a**, 155 (1962)
AgBr	75·6 ± 2	20–300	HAYES W., *Disc. Faraday Soc.* **26**, 58 (1959)
	75·7 ± 2	20–300	HENNIG K., *Phys. Status Solidi* **11**, 795 (1965)
$MgAl_2O_4$	75·4 ± 0·6	300	WALDNER F., *Helv. phys. Acta* **35**, 756 (1962)
ZnO	75·0 ± 0·05	20	HALL T. P. P., HAYES W. and WILLIAMS F. I. B., *Proc. Phys. Soc.* **78**, 883 (1961)
$ZnAl_2O_4$	74·9 ± 0·5	300	STAHL-BRADA R. and LOW W. *Phys. Rev.* **116**, 561 (1959)
CaS	76·8	77	AUZINS P., ORTON J. W. and WERTZ J. E., In *Paramagnetic Resonance I Jerusalem Conf.* (Edited by W. Low), p. 90 Academic Press, New York (1963)
SrS	76·8	77	AUZINS P., ORTON J. W. and WERTZ J. E., In *Paramagnetic Resonance I Jerusalem Conf.* (Edited by W. Low), p. 90. Academic Press, New York (1963)
MgS	74·8	77	AUZINS P., ORTON J. W. and WERTZ J. E., In *Paramagnetic Resonance I Jerusalem Conf.* (Edited by W. Low), p. 90. Academic Press New York (1963)
CaSe	74·05	77	AUZINS P., ORTON J. W. and WERTZ J. E. In *Paramagnetic Resonance I Jerusalem Conf.* (Edited by W. Low), p. 90. Academic Press New York (1963)
MgSe	71·2	300	MATUMURA O., *J. phys. Soc. Japan* **14**, 108 (1959)

Table 1 *(cont.)*

Compound	$-A$ $\times 10^4$ cm^{-1}	T (°K)	Reference
CaTe	67·2	300	MATUMURA O., *J. phys. Soc. Japan* **14**, 108 (1959)
CdS	66·0 ± 0·1	77	SCHNEIDER J., SIRCAR S. R. and RAUBER A., *Z. Naturf.* **18a**, 980 (1963)
ZnS	64·5 ± 0·1	77	SCHNEIDER J., SIRCAR S. R. and RÄUBER A., *Z. Naturf.* **18a**, 980 (1963)
CdSe	62·2 ± 0·1	77	SCHNEIDER J., SIRCAR S. R. and RÄUBER A., *Z. Naturf.* **18a**, 980 (1963)
	62·2	77	KUNII S., TOBITA S. and HIRAHARA E., *J. phys. Soc. Japan* **21**, 479 (1966)
ZnSe	61·7 ± 0·1	77	TITLE R. S., *Phys. Rev.* **131**, 2503 (1963)
MgTe	58·1	300	MATUMURA O., *J. phys. Soc. Japan* **14**, 108 (1959)
CdTe	57·5	4·2	TITLE R. S., *Phys. Rev.* **131**, 2503 (1963)
ZnTe	56·5	4·2	KIKUCHI C. and AZARBAYEJANI G. H., *J. phys. Soc. Japan* **17**, Suppl. B-1 453 (1962)
	56·2	10	WOODBURY H. H. and LUDWIG G. W., *Bull. Am. phys. Soc.* **6**, 118 (1961)
GaP	55	10	WOODBURY H. H. and LUDWIG G. W., *Bull. Am. phys. Soc.* **6**, 118 (1961)
GaAs	52·3	77	ALMELEH N. and GOLDSTEIN B., *Phys. Rev.* **128**, 1568 (1962)
	52·4 ± 0·5	77	BLEEKRODE R., DIELEMAN J. and VEGTER H. J., *Phys. Lett.* **2**, 355 (1962)
Ge	42·6 ± 0·3	1·5–77	WATKINS G. D., *Bull. Am. phys. Soc.* **2**, 345 (1957)
Si	40·5	4·2	WOODBURY H. H. and LUDWIG G. W., *Phys. Rev. Lett.* **5**, 96 (1960)

J. Phys. Chem. Solids Pergamon Press 1970. Vol. 31, pp 1041–1056. Printed in Great Britain.

TEMPERATURE DEPENDENCE OF THE SHORT WAVELENGTH TRANSMITTANCE LIMIT OF VACUUM ULTRAVIOLET WINDOW MATERIALS–II* THEORETICAL, INCLUDING INTERPRETATIONS FOR U.V. SPECTRA OF SiO_2, GeO_2, AND Al_2O_3

MICHAEL H. REILLY

Solid State Division, U.S. Naval Research Laboratory, Washington, DC 20390, U.S.A

(*Received* 15 *May* 1969)

Abstract–The short wavelength transmittance limits of LiF, MgF_2, CaF_2 and BaF_2 crystals have a temperature dependence which is consistent with a model of photoexcitation of localized excitons at momentarily thermally distorted regions of the lattice. The localized exciton is identified as a hole self-trapped in an F_2^- molecule + excited electron. The anomalous data for LaF_3 is hypothesized to be impurity controlled. In order to identify the relevant transitions in SiO_2 and Al_2O_3, a method is developed and employed for an LCAO-MO semiquantitative determination of valence bands, which seems generally advantageous for complex solids with important covalent bonding effects. The preceding model for fluorides is found to be plausible with extension to explain the Al_2O_3 data, while it is not so for the SiO_2 data, which is interpreted to be due to phonon assisted interband transitions. In general, the lowest transitions in the u.v. spectra of SiO_2, Al_2O_3, and, by inference, GeO_2, which is structurally isomorphic to SiO_2, are found to originate from oxygen lone pair orbital valence bands, and the u.v. spectra of amorphous and crystal specimens of these oxides are tentatively so interpreted, with the assistance of available experimental information

1. INTRODUCTION

THE PURPOSE of this paper is to theoretically interpret the experimental results obtained in the preceding paper [hereafter referred to as (I)]. In particular, we wish to explain the temperature dependence of the cut-off wavelength λ_{co}, which is defined in terms of the transmission T through approximately 1 mm thick slabs of the solid insulators under consideration as $T(\lambda_{co}) \approx 0{\cdot}1$–$0{\cdot}5$ per cent. A plot of λ_{co} vs. temperature is given in (I), Fig. 4, and is reproduced in Fig. 1 of this paper.

For these small transmission values, interference effects between front and back surfaces of the slab can be accurately ignored, and the expression for $T(\lambda)$ is

$$T(\lambda) = [1-R(\lambda)]^2 \exp[-4\pi k(\lambda)d/\lambda] \qquad (1)$$

where $R(\lambda)$ is the normal incidence reflectance at one vacuum-solid interface, d is the thickness of the slab, and $k(\lambda)$ is the extinction coefficient[1]. In the wavelength region under consideration, where $k \leqslant 10^{-4}$, $R(\lambda)$ is essentially constant, and the rapid variation of the exponential factor in equation (1) through the wavelength and temperature dependence of k gives the effect. This dependence is related microscopically to transitions from the ground to excited states of the solid as

$$k(\lambda,\beta) \propto \frac{\lambda^2}{n(\lambda)} \sum_{\alpha} \frac{\exp(-\beta E_{g\alpha})}{Z(\beta)} \sum_{j} |<g\alpha|M|j>|^2 \delta\left(\frac{2\pi\hbar c}{\lambda} - \epsilon_j + E_{g\alpha}\right).$$

where

$$Z(\beta) \equiv \Sigma_\alpha \exp(-\beta E_{g\alpha}), \qquad (2)$$

and we have introduced the temperature dependence through β, which is the inverse of

---

*Part I by Hunter W. R. and Malo S. A. *J. Phys. Chem. Solids* **30**, 2739 (1969).

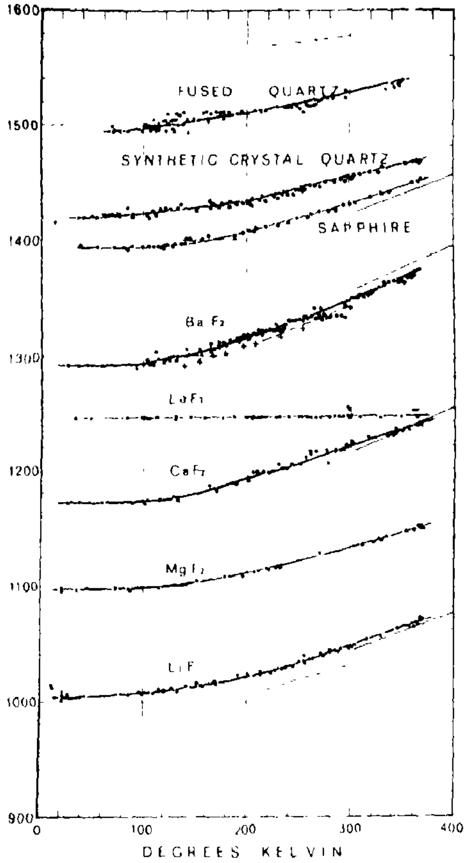

Fig. 1. Temperature dependence of λ_{co}.

the product of the temperature and Boltzmann's constant. Here M is the electric dipole operator for allowed transitions, $|g\alpha>$ represents the ground electronic and α'th vibrational state (the usual adiabatic approximation of the Born Oppenheimer Method[2] for the ground state is already implied here) with corresponding energy $E_{g\alpha}$, the $|j>$ represent excited states of the solid with corresponding energies ϵ_j, and $n(\lambda)$ is the index of refraction which is essentially constant in the wavelength and temperature region under consideration. A detailed interpretation of Fig. 1 is obtained from evaluation of equation (2), which involves the usual sum over final states and thermal average over initial states.

In principle, the evaluation of equation (2) might proceed by first finding the electronic states in a rigid lattice calculation, next including the mixing between them induced by the lattice vibrations (assuming their character is known) by means of perturbation theory, and finally calculating equation (2). The difficulties of actually carrying this out are enormous, of course, but suppose it were done. The temperature dependence of λ_{co} in Fig. 1 would be interpreted as the growth of phonon assisted transitions between rigid lattice electronic states with temperature. When the temperature increases to the point where the dominance of zero-point vibrations begins to subside, k begins to grow at a given wavelength, and the previously flat portion of λ_{co} begins to turn toward lower energy, which corresponds to the observed behavior in Fig. 1. In all the solids under consideration λ_{co} is on the order of 1 eV below the observed lowest exciton peak position. Hence, for example, one might have to consider processes involving excitation of a rigid lattice electronic transition with simultaneous absorption of a large number of phonons. Such phonon processes arise from a single phonon terms in high order perturbation theory or multiphonon terms in lower order perturbation theory. The value of specific models which pick out the most important effects and simplify the interpretation of Fig. 1 is thus evident.

In Section 2 a model is introduced to unify and explain the ionic solid fluoride data in Fig. 1, which in effect singles out the importance of certain short wavelength phonon lattice distortions. This model is found inadequate without extension to explain the oxide data, where covalent effects are important, and Section 3 discusses a method to handle their interpretation. Section 4 utilizes this method in an interpretation of the data for fused and crystal quartz (SiO_2). Section 5 similarly interprets the data for synthetic crystal sapphire (Al_2O_3). In the process of analyzing the oxide data certain new interpretations of the available optical data for these solids and GeO_2 arise, and these are discussed in Section 6. In Section 7 we draw some conclusions from this study.

2. INTERPRETATION FOR FLUORIDES

The first group of solids we consider are the metal fluorides, all of which behave similarly in Fig. 1 except for LaF_3, which will be discussed later. Because fluorine is highly electronegative these may all be assumed to be almost completely ionic, and by analogy with other alkali halides[3], the lowest absorption peak may be assigned to a direct exciton transition at Γ from the $2p$-like F^- valence band to the conduction band edge, mainly associated with the metal ion. In the Electron Transfer Model[4, 3], one considers it as the transfer of an electron from one of the F^- ions to a neighboring metal ion. Each of the λ_{c0} curves in Fig. 1 falls on the long wavelength side of the absorption peak by an amount substantially greater than the half-width of the peak. In LiF[5] λ_{c0} is about 0·8 eV lower than the peak position at room temperature. In CaF_2 and BaF_2[6] these amounts are 0·9 and 0·6 eV, respectively.

The model we use to describe the absorption in this energy region below the first exciton peak adopts the view[7] that the relevant transitions are from the ground state to localized exciton states at momentarily thermally distorted regions of the lattice. Specifically, it has been established through ESR studies[8] and intrinsic luminescence studies [3] on several halides[9], including LiF and CaF_2, that electronic excitation is accompanied by lattice relaxation which self-traps the hole such that the hole wave function is localized on an adjacent pair of F^- ions. The observed 'self-trapped exciton' then consists of a stable F_2^- molecule (or V_k center) + bound excited electron. We depict the self-trapping process for this exciton in Fig. 2 by plotting exciton energies vs. the separation R of a specified pair of adjacent F^- ions. This kind of diagram has previously been used to interpret the intrinsic luminescence of alkali halides[9]. As R decreases below its perfect lattice value R_{PL} in Fig. 2, where the ground state (GS) potential has its minimum, a perturbation potential arises which scatters exciton state solutions of the rigid lattice Hamiltonian. As R decreases below R_c a bound state of the perturbation potential or self-trapped exciton state STE1 breaks off from the continuum of scattered or 'free' translational states of the exciton. We have denoted these latter states by the FE shaded band in Fig. 2. The STE1 exciton state relaxes to an equilibrium at R_e. Wave functions for the translational motion of the FE states are spread throughout the solid while that for the STE1 state is localized in the vicinity of a given pair of fluorine ions. A second self-trapped exciton state STE2 is indicated in Fig. 2 to illustrate the possibility of higher energy bound states of the perturbation potential (e.g. see [9]). That a minimum finite distortion is required to self-trap the exciton is a consequence of the basically short range nature of the potential[10]. The square well potential

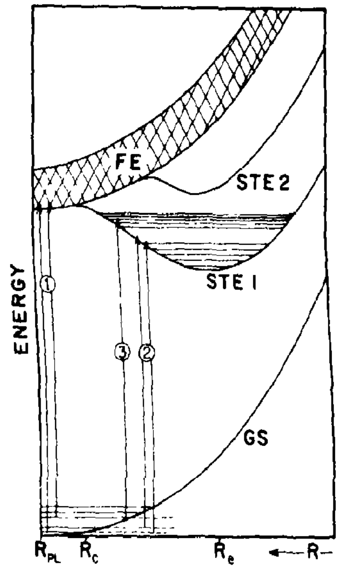

Fig. 2. Schematic potential curves for self-trapped exciton (STE) states, the lowest band of free exciton (FE) states, and the ground state (GS). The configuration coordinate R, increasing to the left in the abscissa axis, represents the separation between a pair of adjacent fluorine ions.

or 'particle in a box' problem is a useful analogy to consider in this regard. The value of R_c is approximately determined[11] when the increase in the F_2^- molecule binding energy associated with the change in R from R_{PL} to R_c just exceeds (but with opposite sign) the energy required to localize the exciton motion wave function on a pair of F^- ions (which is spread throughout the solid up to that point). The latter localization energy is a consequence of the uncertainty principle which indicates that localization in position implies delocalization in momentum with kinetic energy increase. Similar models have been discussed[7] and detailed[12] before in different contexts.

The above discussion indicates the type of distortion which can easily (i.e. without excessive increase in GS potential) produce the low energy transitions of interest here. In effect, the short wavelength phonons which change the separation between adjacent F^- ions are singled out as most important in the evaluation of k. We further assume for simplicity that the ground state distortions which produce the localized excitons at low energy are few and far enough between on the average that cooperative effects between different distorted regions can be ignored. We are now in a position to take over much of the theory for the optical properties of imperfections in the simplification of equation (2)[13]. We (1) treat each distorted region as an isolated impurity, (2) take Fig. 2 as the appropriate single configuration coordinate diagram, (3) make the Adiabatic Approximation for $|j>$ as well as $|g\alpha>$, so that

$$|g\alpha> \equiv \psi_g(\mathbf{r}, R)\,\chi_{g,\alpha}(R)$$

$$|j> \equiv \psi_{\mathrm{STE1}}(\mathbf{r}, R)\,\chi_{\mathrm{STE1}\,\gamma}(R),$$

where $\mathbf{r}$ represents the electronic coordinates, R is the configuration coordinate of Fig. 2, and γ refers to a vibrational state of the STE1 potential in Fig. 2, (4) employ the Condon Approximation, and (5) apply the classical approximation $E_{\mathrm{STE1},\gamma} \approx E_{\mathrm{STE1}}(R)$ for the highly excited vibrational states in the transitions of interest[12]. The final expression for $k(\lambda, \beta)$ in the wavelength region of Fig. 1 is

$$k(\lambda, \beta) \propto \frac{\lambda^2}{n} \sum_{\alpha} \frac{\exp(-\beta E_{g\alpha})}{Z(\beta)} \int \mathrm{d}R\, |\chi_{g\alpha}(R)|^2$$

$$\delta\left(\frac{2\pi\hbar c}{\lambda} - E_{\mathrm{STE1}}(R) + E_{g\alpha}\right)$$

$$= \lambda^2/n\, Z(\beta)^{-1}\, \Sigma_\alpha \exp(-\beta E_{g\alpha})$$

$$|E'_{\mathrm{STE1}}(R_\alpha)|^{-1}\, |\chi_{g\alpha}(R_\alpha)|^2, \quad (3a)$$

where R_α is defined by

$$|E'_{\mathrm{STE1}}(R_\alpha)|^{-1}\, |\chi_{g\alpha}(R_\alpha)|^2, \qquad (3b)$$

and $E'_{\mathrm{STE1}}(R_\alpha)$ is the derivative of E_{STE1} evaluated at R_α. It is seen that the α'th transition in equation (3) for a given wavelength can be represented by a vertical (arrowed) line at R_α as in Fig. 2, where three types of transitions are shown, labelled ①, ②, and ③. Type ① transitions contribute to the main absorption peak, but types ② and ③ transitions contribute at the lower energies under consideration.

There are two conflicting dependences in equation (3). The temperature dependence clearly favors small α transitions (e.g. the ② transitions in Fig. 2). This is especially so for low temperatures; e.g. $Z(\beta)^{-1} \exp(-\beta E_{g\alpha}) \to \delta_{\alpha,0}$ as $\beta \to \infty$. On the other hand, the factor $|\chi_{g\alpha}(R_\alpha)|^2$ is especially large for those large α transitions with R_α near the classical turning point, i.e. $E_{g\alpha} \approx E_g(R_\alpha)$. Hence, these large α transitions (e.g. the ③ transition in Fig. 2) are favored at high temperatures.

We would like to distinguish between two different cases for the critical distortion $R_{PL}-R_c$ in Fig. 2: in Case 1 it is small, and in Case 2 it is large. We are interested in a wavelength on the low energy side of the exciton peak position, so that, e.g. the ② (small α) and ③ (large α) transitions in Fig. 2 are under consideration. The R_α's associated with ② transitions are clearly farther into the tunneling region beyond the classical turning point for Case 2 than for Case 1, and we therefore expect that ③ transitions (near the classical turning point) are relatively more important in Case 2 than in Case 1 for a given temperature. This can be seen in more detail if we invoke the Harmonic Approximation[2] for the GS curve and note that $R_{\alpha+1} \approx R_\alpha$. Then

$$\left|\frac{\chi_{\nu,\alpha+1}(R_{\alpha+1})}{\chi_{\nu\alpha}(R_\alpha)}\right|^2 \approx \frac{1}{2(\alpha+1)}\left[\frac{H_{\alpha+1}(\gamma R_\alpha)}{H_\alpha(\gamma R_\alpha)}\right]^2$$

where H_n is the n'th order Hermite polynomial and γ is a parameter related to the curvature of the GS potential (e.g. see pp. 66–76 in [10]). For $\alpha = 0$, R_0 is well beyond the classical turning point in Fig. 2, and the dominance of the highest order terms of the H_0 and H_1 polynomials makes the above ratio larger in Case 2 than Case 1. This reasoning can be extended for $\alpha = 2$ compared to $\alpha = 1$, $\alpha = 3$ compared to $\alpha = 2$, etc., and as α increases R_α gradually approaches the classical turning point for some α_0 larger in Case 2 than in Case 1. From these considerations and equation (3), one would expect that as the temperature increases above absolute zero the $\alpha = 0$ transition loses predominance sooner, and successively higher α transitions become important more rapidly in Case 2 than in Case 1. Hence the curve of λ_{c0} vs. temperature (as in Fig. 1) should remain flat for a smaller temperature range, and then rise more rapidly with temperature in Case 2 than the corresponding curve in Case 1.

A quantitative specification of the configuration coordinate curve in Fig. 2 depends in a complicated way on the characteristics of each solid, and so it is somewhat risky to interpret the fluoride data of Fig. 1 in terms of Fig. 2. For the present discussion, however, we simply lean on the experimental evidence [3, 8, 9] that the V_k center and self-trapped exciton for a given halide have, for the most part, an identity largely independent of the host material. Then it seems plausible to assume that the most important variation in going from one fluoride to another is in R_{PL}–R_C. This critical distortion is expected to be large in solids where R_{PL} is large to start with, so that the increase in molecular binding of the F_2^- molecule, associated with the two-center overlap of F^- valence orbitals, can overcome the localization energy. From the observed crystal structure[14] it is found that the nearest F – F separation R_{PL} is, in increasing order: 2·57A for MgF_2, 2·73A for CaF_2, 2·84A for LiF, and 3·10A for BaF_2. One would predict that R_{PL}–R_C increases in the same order, and therefore that the steepness of the rise of the λ_{c0} curves beyond their flat portions in Fig. 1 should increase in this order. This is, indeed, the pattern exhibited in Fig. 1. Furthermore, the comparison between CaF_2 and BaF_2 is attractive since both have the same crystal structure. The temperature at which λ_{c0} begins its rise in Fig. 1 is less for BaF_2 than for CaF_2. Our model is thus consistent with Fig. 1. It also seems consistent with other optical data for the alkali halides, although this is a preliminary result.

The LaF_3 data in Fig. 1 is clearly anomalous with λ_{c0} showing no variation with temperature. The crystal structure shows a hexagonal unit cell with a basis of two La^{+3} ions, two F(1) ions and four $F(2)^-$ ions[14]. This unusual notation[14] is to label the two non-equivalent types of F^- ions, and our point ion calculations indicate that the highest valence band is principally associated with the $F(2)^-$ ions. We see no indication that V_k centers should not be associated with these ions, and so we hypothesize that the LaF_3 data is impurity controlled, as seems supported by other experimental evidence in (1). Further experiments on pure specimens would be helpful.

3. METHOD FOR TREATING COVALENT EFFECTS

If one were to assume that oxygen plays the same role in Al_2O_3 and SiO_2 as fluorine did in the preceding analysis, one would first note that the nearest O–O separation is 2·49A in Al_2O_3 and 2·60A in crystal quartz, and then predict that the Al_2O_3 curve should rise less steeply than the SiO_2 curves in Fig. 1. Quite the opposite behavior is observed. Indeed, the preceding model is not expected to apply directly to these solids, where covalent Al–O and Si–O bonding effects are important, and we shall develop interpretations for the associated transitions accordingly.

In solids like the fluorides, alkali halides, rare gas solids, and other ionic crystals, the valence states have a simple correspondence to states of an isolated atom or ion. For example, in solid xenon the highest valence bands are quantitatively well described by the tight-binding method, where the Bloch functions are almost entirely composed of Xe $5p$ atomic orbitals[15]. Occurring at lower energies is the $5s$-like valence band. In covalent solids one finds strong mixing between valence orbitals at the atomic level, and the tight-binding method is no longer applicable. In its place one utilizes sp, sd, and pd hybridization to pile up electronic charge between each adjacent pair of atoms forming a bond, and the equivalent set of basis orbitals thus formed, in conjunction with the approximation of weakly interacting hydrid orbitals (small overlap) in different bonds, can be and has been successfully used to order and interpret the valence levels of molecules in LCAO-MO theory[16]. Diatomic molecule concepts are thus brought to bear, and Walsh[17] has applied these simplifications to an interpretation of the energy levels and spectral transitions in polyatomic molecules. The extension to covalent solids is natural, and we shall employ it to interpret the electronic transitions of SiO_2 and Al_2O_3. After going through these applications of the method, where further explanation is found, the reader may want to see in somewhat greater detail how the method works for the relatively well understood tetravalent elements having the diamond structure in Appendix A.

4. INTERPRETATION FOR FUSED AND CRYSTAL QUARTZ (SiO_2)

Both the fused quartz and crystal α-quartz forms of SiO_2 consist of Si tetrahedrally bonded to four O atoms, each O atom being common to ('bridging') two such SiO_4 tetrahedra. Hence, each O is coordinated to two Si atoms and six O atoms, which are at respective distances of 1·61 A and 2·60–2·67 A in the α-quartz crystal[14], and the next neighbors beyond this are about 3·4 A distant. The Si–O–Si bond angle in the crystal is 144°, but it is found[18] in random network theory to vary over a range of about 40° with a mean value of about 150° in fused silica.

Orthogonal hybrid orbitals for each atom suggest themselves in connection with the well known maximum overlapping criterion for bond strength and the approximation of small overlap between hybrid orbitals in different bonds, which simplify this complex problem. Our choice of hybrid orbitals, formed from the $3s$ and $3p$ valence shells of Si and the $2s$ and $2p$ valence shells of O, is: (1) the four (sp^3) tetrahedral orbitals on each Si, each directed toward a neighboring O, and (2) four orthogonal hybrid orbitals on each O, two of which are directed toward the two near Si neighbors and the other two of which are directed away from this pair of atoms. It is then natural to isolate an Si–O–Si molecular unit,* which is depicted in Fig. 3, and relate it to the

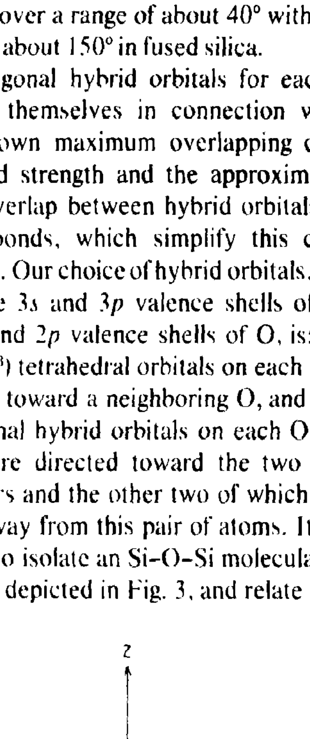

Fig. 3. Coordinate system and notation used to describe the Si–O–Si molecular unit. The subscripts (1) and (2) are used to distinguish the two Si atoms, and the bond angle is denoted by α. The X axis is perpendicular to the plane of the molecular unit.

---

*Essentially the same molecular unit was isolated by M. C. M. O'Brien [*Proc. R. Soc.* **A231**, 404 (1955)] in an analysis of color centers in quartz, which has features in common with the present analysis.

rest of the solid in a manner similar to that used by Walsh[17] for polyatomic molecules. Since Walsh treats triatomic molecules, we have chosen our coordinate system in Fig. 3 and the notation below to correspond to his, for comparison's sake. In this coordinate system, the orthonormal hybrid orbitals on the O atom are found in terms of the bond angle α to be: [19]

$$\begin{aligned} \phi_1 &\equiv 2^{-1/2}[(2-\csc^2\alpha/2)^{1/2}s-p_y \\ &\quad -(\cot\alpha/2)p_z] \\ \phi_2 &\equiv 2^{1/2}[(2-\csc^2\alpha/2)^{1/2}s+p_y \\ &\quad -(\cot\alpha/2)p_z] \\ \phi_3 &\equiv (\cot\alpha/2)s+(2-\csc^2\alpha/2)^{1/2}p_z \\ \phi_4 &\equiv p_x \qquad (90° \leq \alpha \leq 180°). \end{aligned} \tag{4}$$

Here ϕ_1 is directed toward the $Si_{(1)}$ atom and overlaps very strongly with one of its tetrahedral orbitals (and weakly with the others), denoted by $(sp^3)_1$. The same is true of ϕ_2 as related to $Si_{(2)}$ with $(sp^3)_2$ thus defined. ϕ_3 is a lone pair orbital in the plane of the molecule pointing away from the silicons in the +z direction. ϕ_4 is a lone pair orbital directed out of the plane of the molecule.

We obtain an LCAO-MO determination of the valence bands of solid SiO_2 by: (1) first considering the strong mixing of ϕ_1 with $(sp^3)_1$ and ϕ_2 with $(sp^3)_2$ in a localized bond approximation (cf. [16], pp. 72–75), (2) next considering the weaker mixing (because of smaller overlap integrals) of the two bond orbitals with each other and ϕ_3, and (3) finally including the still weaker mixing of these orbitals and ϕ_4 in the Si–O–Si molecular unit with the remaining hybrid orbitals, which are outside the molecular unit. In this manner, successively smaller perturbations are treated in steps, and the effect of the perturbation in one step is to split and/or shift somewhat the levels found in the preceding step. To treat step (3) in detail is, of course, a major undertaking, but its effect is to replace each discrete level at the end of step (2) by a quasi-continuous band of energies. This is similar, for example, to the replacement of the 5s and 5p levels of atomic xenon by the 5s-like and 5p-like energy bands in solid xenon[15]. The above steps are carried out in Fig. 4. From left to right: the one electron energies of the atoms are indicated approximately to scale as determined from the experimental ionization energies[16]; the hybrid atomic orbitals defined above are

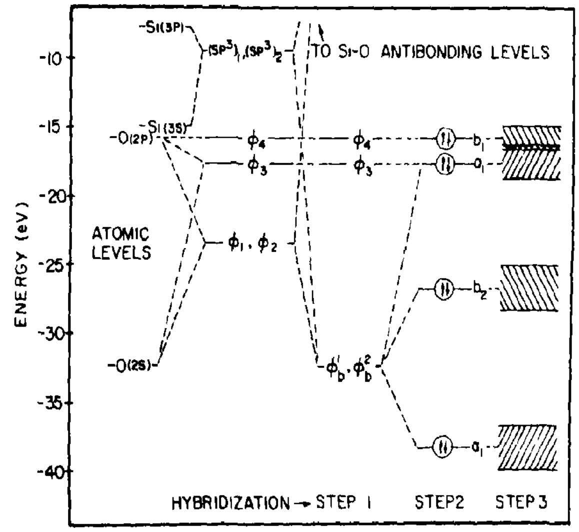

Fig. 4. Qualitative determination of the valence bands of crystal quartz (see text).

formed with corresponding energy changes, which are indicated approximately to scale in Fig. 4 for $\alpha = 144°$; the strong mixing of step (1) is depicted with the formation of Si–O bonding orbitals ϕ_b^1 and ϕ_b^2 in the approximation of localized bonds (the Si–O antibonding orbitals lie off scale); step (2) is performed with the level designations being the irreducible representation labels of the symmetry group C_{2v} of the molecular unit; and finally, the energy band formation of step (3) is indicated. One Si valence electron is associated with each of $(sp^3)_1$ and $(sp^3)_2$ and each O atom contributes 6 valence electrons. Consequently, these 8 valence electrons completely fill the valence levels as shown in Step 2 of Fig. 4; likewise, all the valence bands of this insulating solid are filled. Now and henceforth, the indicated energy scale locates the energies of the atomic hybrid orbitals and gives a qualitative handle on the energy separations between LCAO-MO valence bands (except that space limitation did not quite allow proper positioning of the lowest valence band with respect to the next higher one), but is otherwise not to be taken too seriously. For example, other effects left unaccounted for are partial ionic character of the bonding and interaction with extra-valency orbitals at higher energies, but these will very likely not affect the qualitative conclusions drawn from Fig. 4, as indicated by calculations on a great many molecules, such as H_2O[20], for example, which resembles our Si–O–Si molecular unit in many ways.

Among other conclusions which can be inferred from Fig. 4 (see Section 6), it is relevant here that the lower energy transitions originate from valence bands principally associated with lone pair orbitals on the oxygen atoms in fused and crystal quartz. In particular, we argue in Section 6 that the observed[21] lowest energy reflectance peak in SiO_2 corresponds to an exciton, the hole orbital part of which corresponds to the highest valence band band edge, i.e., the hole orbital is principally associated with the oxygen $2p$ orbital directed out of the plane of each Si–O–Si molecular unit. One might suspect that trapped hole formation with associated self-trapped exciton effects would play a role in producing the low energy transitions of interest beneath the first exciton reflectance peak, similarly as described for the fluorides. The condition for this would be that the lone pair $2p$ hole orbital on one oxygen should overlap quite strongly with the corresponding $2p$ orbital on a nearby oxygen, so as to enhance the covalent bonding associated with self-trapped hole formation. Inspection of the structure of α-quartz [14] reveals, however, that this bond would be very bent and thus very weak, as far as the six nearest neighboring oxygens are concerned. The corresponding bond with the oxygens about 3·4A away would also be very bent. One could think about mixing in states from the other oxygen lone pair orbital valence band at slightly lower energies; this would not unbend the bonds with the six nearby oxygens at 2·6A very much, but it definitely would unbend the bond with an oxygen 3·4 A away. This large distance and the energy separation between the different lone pair oxygen orbitals might, however, make trapped hole formation through this mixing improbable. Mixing in the Si–O bonding orbitals would unbend the nearby O–O bonds, but these orbitals are at such low energies as to make this mixing too small to be effective. Hence the possibility of self-trapped hole effects in the low energy absorption of interest here can not presently be ruled out, but it seems that the critical distortion $R_{PL}-R_C$ would be so large as to make this mechanism ineffective compared to any competing processes. Herein lies a major difference with the ionic solid fluorides. None of the F^- $2p$ orbitals separate from the others very much in energy by participating in bonds, and hence are available to promote self-trapped hole formation. Indeed, at the valence band edge, assumed to be at $\Gamma(k = 0)$, these p orbitals are degenerate in LiF, CaF_2, and BaF_2 for symmetry reasons.

There is experimental evidence that the lowest exciton peak in SiO_2 lies above the threshold for the continuum of interband transitions (see Section 6). Then it may be that the low energy transitions of interest are phonon assisted interband transitions, which can lead to the observed temperature dependence in Fig. 1, as discussed in Section 1. For these processes a wide energy range of the phonon spectrum can contribute, which may explain the lack of a rather well defined flat portion for the SiO_2 curves in Fig. 1, unlike the other curves. Of further interest in Fig. 1 is that λ_{c0} for fused quartz is almost 0·5 eV lower than λ_{c0} for crystal quartz, even though the lowest exciton peak positions[21] are apparently much closer together. This may indicate the effect of static lattice disorder in fused quartz which produces lower energy interband transitions associated with especially distorted local environments in the solid.

5. INTERPRETATION FOR CRYSTAL SAPPHIRE (Al_2O_3)

The preceding analysis for the valence bands of SiO_2 can also be carried out for the more complicated case of Al_2O_3. In this (corundum) structure[22] each Al is surrounded by six O's, three at a distance of 1·84A and the other three at a distance of 1·98A. Thus, each Al is considered to bond strongly with three O's and weakly with three O's. Each O is surrounded by four Al's, bonding strongly to two and weakly to the other two. The molecular unit which illustrates the central features of this structure, as well as the notation used below, is given in Fig. 5 (cf. Fig. 3–13 in Ref. [22]). For Al_2O_3, $t_1 = t_2 = t_3 \equiv s = 2{\cdot}74$A and $r = 4{\cdot}33$A. Each large circle in Fig. 5 represents two Al atoms, one on top of the other at the indicated height.

The cartesian coordinates of Al atoms in the corundum structure are

$$\pm[(0{\cdot}5\zeta_1 s, 0{\cdot}866\zeta_2 s, (1{\cdot}065+\zeta_3)r);$$
$$(0{\cdot}5\zeta_1 s, 0{\cdot}866\zeta_2 s, (0{\cdot}435+\zeta_3)r)],$$

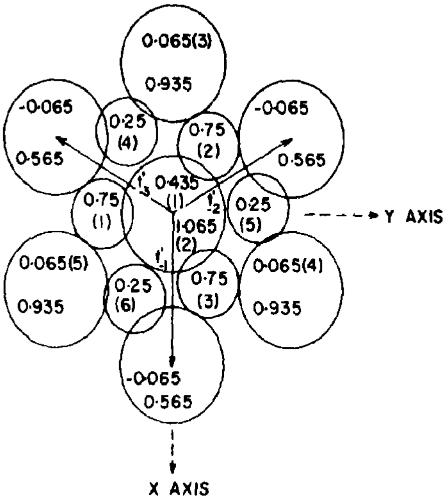

Fig. 5. Structure of the molecular unit used to describe crystal sapphire (Al_2O_3). Large spheres. Al: small spheres O. Heights of atoms are shown as multiples of r, the component of the trigonal system basis vectors t_1, t_2, t_3 along the z axis. The vectors t'_1, t'_2, t'_3 are the components of the vectors t_1, t_2, t_3 in the xy plane. Numbers in parentheses are used to identify atoms (see text)

and the cartesian coordinates of O atoms are

$$\pm\begin{bmatrix}(0{\cdot}5(-0{\cdot}909+\zeta_1)s, 0{\cdot}866(0{\cdot}303+\zeta_2)s, \\ (0{\cdot}75+\zeta_3)r); \\ (0{\cdot}5(0{\cdot}909+\zeta_1)s, 0{\cdot}866(0{\cdot}303+\zeta_2)s, \\ (0{\cdot}75+\zeta_3)r); \\ (0{\cdot}5\zeta_1 s, 0{\cdot}866(-0{\cdot}606+\zeta_2)s, (0{\cdot}75+\zeta_3)r)\end{bmatrix}$$

where ζ_1, ζ_2, and ζ_3 are any integers such that $\zeta_1+\zeta_2$ is an integral multiple of two and $\zeta_1+\zeta_3$ is an integral multiple of three.

With reference to the identifying numbers in parentheses in Fig. 5, one finds that Al(1) bonds strongly to O(4), O(5), and O(6), which in turn bond strongly to Al(3), Al(4), and Al(5), respectively; both Al(1) and Al(2) bond weakly to O(1), O(2), and O(3), each of which in turn bonds strongly to a pair of adjacent Al atoms at heights 0·935r and 0·565r; and O(4), O(5), and O(6) each bond weakly to an adjacent pair of Al atoms at heights 0·565r and −0·065r, superimposed in Fig. 5. Now if O(4), O(5), and O(6) sat at three corners of a regular tetrahedron with Al(1) at its center, the Al–O distance would be 1·76A instead of the observed 1·84A. This is close enough that the (sp^3) tetrahedral hybrid orbital basis set on each Al atom is appropriate (and convenient), formed from the $3s$ and $3p$ shells. The bonding (sp^3) orbitals on Al(1) are denoted by $(sp^3)_1{}^1$, $(sp^3)_1{}^2$, and $(sp^3)_1{}^3$, and the lone pair (sp^3) orbital on Al(1), which points in the z direction, is denoted by $(sp^3)_1{}^4$. The three bonding (sp^3) orbitals on Al(2) are directed toward an equilateral triangle of oxygen atoms at height $1·25r$ (not shown); the lone pair (sp^3) orbital on Al(2), which points in the $-z$ direction, is denoted by $(sp^3)_2{}^4$. The particular (sp^3) orbitals on Al(3), Al(4), and Al(5) which point toward O(4), O(5), and O(6) are denoted by $(sp^3)_3$, $(sp^3)_4$, and $(sp^3)_5$, respectively. On the other hand, if an oxygen atom sat in the middle of an equilateral triangle with the two strongly bonded Al atoms at two corners, the Al–O–Al bond angle and Al–O distance would be 120° and 1·85A, respectively, instead of the observed 119° and 1·84A. This is certainly close enough that the (sp^2, p) trigonal hybrid orbital basis set on each O atom is appropriate, formed from the $2s$ and $2p$ shells. The bonding (sp^2) orbitals on the i'th oxygen atom O(i) ($i = 4, 5, 6$) are denoted by $(sp^2)_i{}^1$ and $(sp^2)_i{}^2$. The lone pair (sp^2) orbitals on O(1), O(2), and O(3) are directed toward a point on the z axis midway between Al(1) and Al(2), and are denoted by $(sp^2)_1$, $(sp^2)_2$, and $(sp^2)_3$, respectively. Finally, the lone pair $2p$ orbitals on O(1), O(2), and O(3), directed out of the planes of the (sp^2) orbitals, are denoted by $(p)_1$, $(p)_2$, and $(p)_3$, respectively.

In the preceding paragraph, we have explicitly defined a number of hybrid orbitals, in order to describe the various bonding effects and thus deduce the valence bands of Al_2O_3, as was done for SiO_2. This is carried out in Fig. 6. In the 'hybirdization' step the eight Al(sp^3) orbitals defined above are referred to, i.e. $(sp^3)_1{}^1$, $(sp^3)_1{}^2$, $(sp^3)_1{}^3$, $(sp^3)_1{}^1$, $(sp^3)_2{}^4$, $(sp^3)_3$, $(sp^3)_4$, and $(sp^3)_5$. The above nine O(sp^2) orbitals are also indicated, i.e. $(sp^2)_4{}^1$, $(sp^2)_4{}^2$, $(sp^2)_5{}^1$, $(sp^2)_5{}^2$, $(sp^2)_6{}^1$, $(sp^2)_6{}^2$, $(sp^2)_1$, $(sp^2)_2$, and $(sp^2)_3$. Also indicated are the three O lone pair orbitals, $(p)_1$, $(p)_2$, and $(p)_3$. In step 1 we consider the strong bonding effects separately associated with each of three triatomic Al–O–Al molecules, i.e. Al(1)–O(4)–Al(3), Al(1)–O(5)–Al(4), and Al(1)–O(6)–Al(5). The hybrid orbitals involved in the

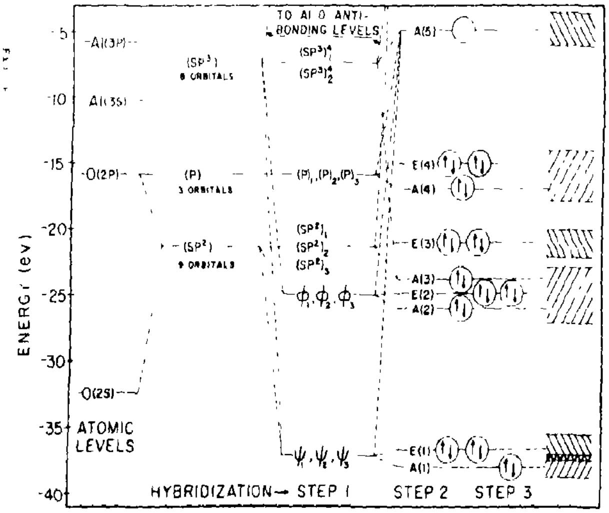

Fig. 6. Qualitative determination of the valence bands of crystal sapphire (see text).

mixing in the Al(1)–O(4)–Al(3) molecule are, for example, $(sp^3)_1^1$, $(sp^2)_4^1$, $(sp^2)_4^2$, and $(sp^3)_3$. Hence, ψ_1 and ϕ_1 correspond to a_1 and b_2 in Fig. 4 for this Al–O–Al molecule with ψ_2, ϕ_2, ψ_3, and ϕ_3 having the same relationship for the other two Al–O–Al molecules. The lone pair orbitals, $(sp^2)_1$, $(sp^2)_2$, and $(sp^2)_3$ correspond to ϕ_3 in Fig. 4, and the lone pair orbitals $(p)_1$, $(p)_2$ and $(p)_3$ correspond to ϕ_4 in Fig. 4. Actually Step 1 in Fig. 6 combines Steps 1 and 2 in Fig. 4. Step 2 in Fig. 6 primarily takes notice of the fact that $(sp^2)_1$, $(sp^2)_2$, and $(sp^2)_3$ rather strongly overlap $(sp^3)_1^1$ and $(sp^3)_2^4$ orbitals midway between Al(1) and Al(2) in Fig. 4, thus leading to the weak bonds in Al_2O_3. In addition, weaker mixing with the other orbitals in Step 1 is expected through their overlap in the region of the central aluminum atoms. The interactions in Step 2 are expected to be smaller than in Step 1 for two basic reasons: (1) the weak Al–O bonds are somewhat bent in character, and (2) the Al 3*s* and 3*p* atomic levels are much closer together than the O 2*s* and 2*p* atomic levels, which, for example, apparently precludes the kind of splitting in Step 2 as found between ψ_1 and ϕ_1 levels in Step 1. The functions for each level in Step 1 transform into each other under the operations of the symmetry group C_3, which has a one-dimensional irreducible representation *A* and a two-dimensional representation *E*. We therefore use these labels for the levels in Step 2. The discrete levels are replaced by bands of energies in Step 3 as before. Note that the mixing of the symmetric combination of the oxygen (sp^2) lone pair orbitals $[(sp^2)_1+(sp^2)_2+(sp^2)_3]$ with the symmetric combination of the aluminum (sp^3) lone pair orbitals $[(sp^3)_1^4+(sp^3)_2^4]$ is principally responsible for the weak Al–O bonding. The other combination $[(sp^3)_1^4-(sp^3)_2^4]$, corresponding to $A(5)$, is essentially Al–O non-bonding with a small Al–Al antibonding effect and with weak repulsion from lower *A* levels, which is the reason why the empty conduction band associated with $A(5)$ lies at relatively low energy. We shall discuss this a little further in the next Section.

As found for SiO_2 the highest filled valence band is associated with the oxygen (p) lone pair orbitals. It is seen from inspection of Fig. 5 that (p) orbitals on such adjacent pairs of oxygens as O(1) and O(6), which are 2·74A apart, overlap quite directly and might participate in trapped hole formation. The (sp^2) oxygen lone pair orbitals associated with the $E(3)$ valence bands should help this out slightly. Hence, we would not discount this possibility as the operative mechanism, similarly as for the fluorides. Suggestive in this regard is a well defined flat portion for the λ_{c0} curve in Fig. 1. Of further note, despite the fact that the lowest exciton peak position in crystal sapphire (corundum) is about 9·5 eV[23], while it is about 10·4 eV in crystal quartz [21], the room temperature λ_{c0} values in Fig. 1 are reversed, corresponding to about 8·7 eV in crystal sapphire and 8·5 eV in crystal quartz. This suggests something different about SiO_2, such as we have indicated.

6. TENTATIVE INTERPRETATIONS FOR SiO_2, GeO_2, AND Al_2O_3 SPECTRA

Present understanding of the u.v. spectra for SiO_2, GeO_2, and Al_2O_3 is very preliminary, and so it may be useful to discuss possible interpretations of the associated transitions, based on the results we have found in Fig. 4 and Fig. 6 and available experimental data. In addition to doing this, further experiments for sifting out one or another interpretation are suggested below.

First we consider the results of measurements for the optical constants of fused and crystal quartz[21]. Very similarly for both materials, four absorption peaks occur near 10·2, 11·7, 14·3, and 17·2 eV. In general, low-lying transitions originate from the higher valence bands. As part of the determination of these bands, it will be recalled that with the aid of hybridization concepts, the Si–O–Si molecular unit was isolated to describe the important bonding effects. The similarity of this molecular unit to H_2O was mentioned, where the (sp^3) orbital on each Si atom corresponds to the 1s orbital of H in LCAO-MO theory. The electronegativity (Pauling's) of H and Si are nearly equal, the maxima of the Si 3s and 3p radial functions are near the Bohr radius, and the 3s and 3p energies lie below and above one Rydberg, respectively. One might expect that the calculated valence levels of the H_2O molecule[20] would be near those for the Si–O–Si molecular unit, except that the H–O–H bond angle is 105° while the Si–O–Si bond angle in crystal quartz is 144°. Hence, one expects H–H bonding and anti-bonding effects to be stronger than the corresponding Si–Si effects, which is associated with a smaller separation between the lower a_1 and b_2 levels in Fig. 4[17]. Furthermore, one expects from equation (4) that the separation between the oxygen lone pair orbital levels in Fig. 4 will be no larger than for H_2O (where it is approximately 1·4 eV[20]), and that the oxygen 2s admixture in the Si–O bonds will be greater than in the H–O bonds. The separation between b_1 and b_2 levels in Fig. 4 is thus expected to be greater than the 7 eV calculated for H_2O[20], which gives us some confidence in our estimate that at least the three lower energy absorption peaks principally involve the oxygen lone pair hole orbitals. This differs from Ruffa's interpretation, which considered the lowest transitions to involve bond-breaking in a valence bond approximation[26]. Sak has previously noted the probable importance of oxygen non-bonding hole orbitals in the lowest transitions in a Private Communication [27].

At present there are no band calculations of quartz to assist the identification of excited electronic states, but the results of several optical experiments suggest certain characteristics of the excited state transitions with which we shall be concerned here. As emphasized by Phillip[21], the u.v. reflectance spectra of fused and crystal quartz[21, 27] are strikingly similar, despite the lack of long range order in the former, characterized by large variations in the Si–O–Si bond angle. This is particularly so for the two lowest peaks at 10·2 and 11·7 eV, and since we have associated them with oxygen lone pair hole orbitals, we would be inclined to guess that the Si influence in the associated excited electron states is secondary. For example, the excited electron state for the electron hole pair is probably not Si–O antibonding. One might guess that the 10·2 eV peak is a transition to an exciton state at Γ in the crystal, with the hole orbital corresponding to the oxygen 2p_x orbital in Fig. 3 and the electron orbital resembling the oxygen 3s orbital. This kind of transition would not be expected to change very much in passing to the glassy material. Two possibilities for the 11·7 eV peak are that it corresponds to the band to band transitions associated with the 10·2 eV exciton in the Wannier model, or that it corresponds to the oxygen 2p–3d exciton transition suggested by Pajasova[27]. Platzöder's data[28] is interesting in this regard; he finds that the 10·2 and 11·7 eV peaks strangely disappear into the background (instead of showing the typical broadening) as the temperature increases from about 0–300°C, while the 14·3 and 17·2 eV peaks remain unchanged in this temperature range. Although this 'disappearing' with temperature phenomenon seems not to have previously been studied theoretically, it may indicate a thermally enhanced instability of excitons degenerate with band to band (interband) transitions. Hence, we consider this as evidence that the 10·2 and 11·7 eV peaks are excitons degenerate with interband transitions. This suggests that the lowest conduction band edge of the crystal is away from Γ in the Brillouin Zone. It could be that the 11·7 eV peak is an exciton associated with the same conduction band as the 10·2 eV exciton, but with the other oxygen lone pair hole orbital valence band (a_1 in Fig. 4). It was found by Sigel[29] that, upon varying the alkali content of alkali silicate glasses, the 10·3 eV peak position was drastically effected, while the

11·7 eV peak position was not. This may be the result of the alkali (R) ions locating themselves on a line perpendicular to and symmetrically placed with respect to the plane of the original Si–O–Si molecular unit (R_2O replaces one of the Si atoms). The other oxygen lone pair orbital in the Si–O–Si plane may then not be affected too much, since the alkali ions would be approximately in its nodal plane. On the other hand, this particular piece of evidence may not be inconsistent with the above interband transition interpretation for the 11·7 eV peak. As another result of Sigel's work, the peak labelled A in Platzoder's Fig. 1 [28] may well be associated with a single non-bridging oxygen defect[29, 30].

Since GeO_2 has a structure isomorphic to crystal quartz[31], it seems appropriate to suggest a possible interpretation for its glassy and crystal u.v. spectra[27]. The principal characteristic of the reflectivity spectra of the glass are two broad peaks at 6·6 and 10·7 eV. The crystal spectrum shows a three-component structure in the 6·6 eV peak, but is otherwise very similar. The lowest energy component near 6 eV is apparently directly associated with the $Ge^{(2+)}$ impurity[32, 30], while no interpretation of the other two components has previously been suggested. These are a peak near 6·6 eV and something that resembles a shoulder near 8·3 eV. We propose that the 6·6 and 10·7 eV peaks in the crystal spectrum correspond to Γ exciton transitions associated with the same conduction band but with the two different oxygen lone pair orbital bands, similarly as for the above proposed interpretation of the 10·2 and 11·7 eV peaks in SiO_2. The fact that the oxygen lone pair orbital in the plane of the Ge–O–Ge molecule would have to be a few eV more removed from the out-of-plane oxygen lone pair orbital than was the case for SiO_2 is not inconsistent with equation (4) for ϕ_3 and the fact that the Ge–O–Ge bond angle[31] is only 130° (hence, more s admixture in the in-plane orbital). The shoulder-like component at 8·3 eV in the crystal GeO_2 reflectivity spectrum looks suspiciously like an M_2 Van Hove singularity in the interband density of states[33], and we take this as evidence that the 6·6 eV peak is an exciton degenerate with interband transitions, similarly as for SiO_2. The fact that this 8·3 eV structure almost disappears, merging into the tail of the broad 6·6 eV peak in the glass spectrum, could result from the disappearance of long range order in the glass. It may be, however, that the 8·3 eV structure has the same interpretation just given for the 10·7 eV peak.

Finally, we would like to comment on the u.v. spectrum of crystal and anodized films of Al_2O_3[23]. An exciton is found at 8·4 ± 0·3 eV in the amorphous film and 9·5 ± 0·1 eV in the crystal. The associated interband transition edge is found at 9·4 ± 0·4 eV in the film and 9·9 ± 0·1 eV in the crystal. Noteworthy is that the exciton peak and interband edge are much broader on the energy scale in the film than in the crystal, and the exciton peak position is 1 eV lower in the film than in the crystal. This is unlike the case for the materials previously discussed. For the moment, we can only hypothesize that, with respect to Fig. 6, the exciton and interband transitions in question are associated with the highest $E(4)$ valence band and the lowest $A(5)$ conduction band. The low-lying $A(5)$ conduction band, principally associated with the aluminum valency shells, had no counterpart in SiO_2 and GeO_2, and we might expect it to be quite drastically affected in passing from the crystal to the amorphous material.

The above interpretations of spectra are frankly heuristic; there are certainly other possibilities not covered here. It is hoped that the above may be a stimulus for further experimental and theoretical studies. One may expect to gain much information about the symmetry of orbitals involved in the lowest transitions (e.g. the oxygen lone pair $2p$ valency orbitals) by doing piezo-optical and polarized light experiments, once the difficulties of obtaining u.v. polarized light are overcome. One way of verifying the interpretation of excitons degenerate with interband transitions is through photoconductivity measurements [3]. Luminescence excitation spectra may also turn out to be helpful in this regard [3].

7. CONCLUSIONS

The temperature dependence of the short wavelength transmittance limit λ_{co} for the ionic fluoride window materials is found to be consistent with a model which describes the onset of absorption as due to the creation of localized excitons in momentarily thermally distorted regions of the crystal. These excitons are identified with the F_2^- molecule + excited electron system. The anomalous data for LaF_3, however, are tentatively interpreted to be controlled by the presence of impurities in the sample studied.

To explain the oxide data for λ_{co} vs. temperature, new interpretations for the fundamental excitations in this wavelength region were formed with the assistance of experimental data and according to the results of an LCAO-MO ordering and interpretation of valence bands. Covalent effects are found to be important, and, in particular, the relevant transitions are expected to originate from an oxygen lone pair orbital valence band for each of the oxides. While the preceding model for fluorides may well apply with extension to the synthetic crystal sapphire data, as we have discussed, this mechanism is not found to be as plausible for the fused and crystal quartz data. Instead, the evidence here seems to indicate that phonon assisted interband transitions give the temperature dependence of λ_{co}.

The method developed and employed here for the LCAO-MO determination of valence bands should be advantageous for a wide variety of complex solids where covalent bonding effects are important. Little more than observed or calculated one-electron energies and straightforward hybridization concepts are required to systemmatically isolate a molecular unit and semiquantitatively describe the gross covalent effects in the solid. Comparison of these molecular units with similar molecules on which calculations have been performed (e.g. Si–O–Si compared to H_2O) could probably be used for estimates to even better advantage than we have done once this idea has been further explored.

In the process of obtaining valence bands for SiO_2 and Al_2O_3 and surveying available optical spectra for these oxides and GeO_2, which has a structure isomorphic to SiO_2, tentative, new interpretations of these spectra arise, and are given in the preceding Section. The spectra for both the crystal and amorphous forms of these oxides are considered, and certain optical effects are identified with the destruction of long range order in going from the crystal to the amorphous material. It is hoped that these interpretations will serve as guidelines for further experimental studies, which stand to provide not only specific information about these solids but also general information about the physics of amorphous materials.

Acknowledgements—The author would like to thank Dr W. R. Hunter for providing his prepublication data and for other assistance. Special thanks are also due to Dr D. L. Griscom, who first pointed out to the author the existence of lone pair orbitals on the oxygen atoms in SiO_2 and stimulated the author's interest in hybridization concepts for their description, and to Dr. G. H. Sigel for several helpful discussions.

REFERENCES

1. For the case where interference effects are important, see, e.g. STERN F., In *Solid State Physics*, Vol. 15, pp. 324–7 (Edited by F. Seitz and D. Turnbull) Academic Press, New York (1963). See also TAUC J., In *The Optical Properties of Solids*, (Edited by J. Tauc), course 34, pp. 68–71, Academic Press, New York (1966).
2. BORN M. and OPPENHEIMER J. R., *Ann. Phys.* **84**, 457 (1927). See also BORN M. and HUANG K., *Dynamical Theory of Crystal Lattices* Oxford University Press, London (1954).
3. KNOX R. S. and TEEGARDEN K. J., In *Physics of Color Centers* (Edited by W. Beall Fowler). Academic Press, New York (1968).
4. *KNOX R. S., Theory of Excitons, Solid State Physics* Academic Press, New York *(1936).*
5. ROESSLER D. M. and WALKER W. C., *J. Phys. Chem. Solids* **28**, 1507 (1967).
6. MIYATA T. and TOMIKI T., *J. phys. Soc. Japan* **24**, 954 (1968).

7. TOYOZAWA Y., *Techn. Rept. of ISSP*, Series A, No. 119, (1964).
8. SEIDEL H. and WOLF H. C., In *Physics of Color Centers* (Edited by W. Beall Fowler). Academic Press, New York (1968).
9. KABLER M. N. and PATTERSON D. A., *Phys. Rev. Lett.* **19**, 652 (1967).
10. SCHIFF L. I., *Quantum Mechanics*, 3rd Edn, Chap. 2. McGraw-Hill, New York (1968).
11. FOWLER W. B., In *Physics of Color Centers* (Edited by W. Beall Fowler) p. 129. Academic Press, New York (1968).
12. TOYOZAWA Y., In *Polarons and Excitons* (Edited by C. G. Kuper and G. D. Whitfield). Plenum Press, New York (1962).
13. DEXTER D. L., In *Solid State Physics*, (Edited by F. Seitz and D. Turnbull) Vol. 6. Academic Press, New York (1958)
14. WYCKOFF R. W. G., *Crystal Structures*, 2nd Edn. Wiley, New York (1963–64).
15. REILLY M. H., *J. Phys. Chem. Solids* **28**, 2067 (1967)
16. BALLHAUSEN C. J. and GRAY H. B., *Molecular Orbital Theory* Benjamin, New York (1964)
17. WALSH A. D., *J. chem. Soc.*, pp. 2260–2289 (1953). Reprinted in [16]
18. BELL R. J. and DEAN P., *Nature, Lond.* **212**, 1354 (1966)
19. See e.g. the discussion of SLATER J. C., *Quantum Theory of Molecules and Solids*, Vol. 1, p. 203. McGraw-Hill, New York (1963)
20. ELLISON F. O. and SHULL H., *J. chem. Phys.* **21**, 1420 (1953); *ibid.* **23**, 2348 (1955).
21. PHILLIPS H. R., *Solid State Commun.* **4**, 73 (1966).
22. For a discussion of the corundum structure, see SLATER J. C., *Quantum Theory of Molecules and Solids*, Vol. 2, pp. 81–84. McGraw-Hill, New York (1965).
23. ARAKAWA E. T. and WILLIAMS M. W., *J. Phys. Chem. Solids* **29**, 735 (1968).
24. See e.g., TINKHAM M., *Group Theory and Quantum Mechanics* McGraw-Hill, New York (1964).
25. HERMAN F. *et al.*, In *Quantum Theory of Atoms, Molecules, and the Solid State* (Edited by P. O. Lowdin). Academic Press, New York (1966).
26. RUFFA A. R., *Phys. Status Solidi* **29**, 2 (1968).
27. PAJASOVA L., "Optical Properties of GeO_2 in the Ultraviolet Region", to be published in the Czechoslovak Journal of Physics.
28. PLATZÖDER K., *Phys. Status Solidi* **29**, K63 (1968).
29. SIGEL G. H., Ph.D. thesis, Georgetown University. 1968 (unpublished).
30. SIGEL G. H., Private communication
31. SMITH G. S. and ISAACS P. B., *Acta Crystallogr* **17**, 842 (1964)
32. GARINO-CANINA V., *C. r. hebd. Séanc. Acad. Sci.*, **242**, 1882 (1956); *ibid.* **247**, 593, 643 (1958).
33. TOYOZAWA Y., *et al.*, *J. phys. Soc. Japan* **22**, 1337, 1349 (1967)

APPENDIX A

In the tetravalent elements each atom is tetrahedrally coordinated to four neighboring atoms, and the smallest molecular unit which exhibits the bonding effects is the body-centered tetrahedron consisting of five atoms. The appropriate minimal set of hybrid orbitals includes (1) the four (sp^3) tetrahedral orbitals on the central atom which point toward the neighboring atoms, and (2) the tetrahedral orbital on each neighboring atom which points toward the central atom. We denote the tetrahedral orbital on the central atom which points toward the j'th neighbor by $(sp^3)^j$ $(j = 1, \cdots, 4)$, and we denote the tetrahedral orbital on the j'th neighbor which points toward the central atom by $(sp^3)_j$, thus making a total of eight hybrid orbitals. The stepwise procedure for obtaining valence and conduction bands associated with these valency shell orbitals is shown in Fig. 7. Here we first indicate the s and p atomic valency levels, as before, and next indicate the energy of the (sp^3) orbital, which is defined by its expectation value of atomic Hamiltonian: $E(sp^3) = 0{\cdot}25E(s) + 0{\cdot}75E(p)$. In Step 1 the four bonding orbitals $\phi_b(j)$ and four antibonding orbitals $\phi_a(j)$ $(j = 1, 2, 3, 4)$ are formed in a localized bond approximation. For the j'th bond, for example, these

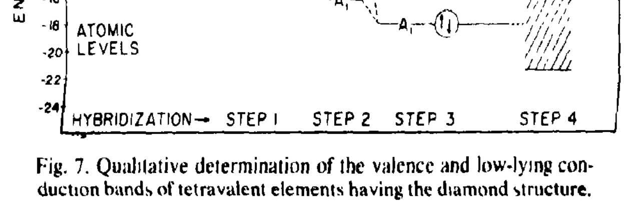

Fig. 7. Qualitative determination of the valence and low-lying conduction bands of tetravalent elements having the diamond structure.

are $(sp^3)_i \pm (sp^3)_j$, up to a normalizing factor, where the upper and lower sign possibilities are for $\phi_b(j)$ and $\phi_a(j)$, respectively. Each of these sets of four orbitals forms a reducible representation of the tetrahedral group T_d, the irreducible component representations of which are A_1 (1-dim.) and T_2(3-dim.)[24]. This explains the splittings and labels in Step 2. Since an s function transforms as A_1 and the three degenerate p functions transform at T_2, one may view each splitting in Step 2 as a decoupling of s and p functions on the central atom. Also included in this splitting is a bonding effect among nearest neighbors for A_1 and a small anti-bonding effect among these same atoms for T_2. In Step 3 we take account of the mutual repulsion between levels of the same symmetry, which has the effect of partially decoupling the central atom from its neighbors, thus taking account of other internal effects. In Step 4 each discrete level is replaced by a continuous band of energies, which has the effect of inserting similar coupling of the minimal set of hybrid orbitals we have used to the rest of the solid.

The above discussion and Fig. 7 correspond quite well to past interpretations of results of band structure calculations for tetravalent elements (see, e.g. [22], pp. 272–80). Actually, Fig. 7 corresponds most closely to the results for Ge[25]. As one goes from Ge to Si and C, the repulsion between A_1 levels in Step 3 of Fig. 7 becomes greater relative to the repulsion between T_2 levels, in making the correspondence to calculated results[25]. This is correlated with the relatively stronger overlap between s orbitals in Si and C. In C the calculated atomic $2s$ orbital even has its maximum beyond the $2p$ orbital maximum.

J. Phys. Chem. Solids Pergamon Press 1970. Vol. 31, pp. 1057–1067. Printed in Great Britain.

THE CRYSTAL STRUCTURE AND MAGNETIC SUSCEPTIBILITIES OF $MnNb_3S_6$, $FeNb_3S_6$, $CoNb_3S_6$ AND $NiNb_3S_6$

K. ANZENHOFER, J. M. VAN DEN BERG*, P. COSSEE and J. N. HELLE
Koninklijke/Shell-Laboratorium, Amsterdam, Holland

(*Received* 27 *June* 1969; *in revised form* 13 *November* 1969)

Abstract—The crystal structures of the ternary compounds MNb_3S_6 (M = Mn, Fe, Co, Ni) have been refined and their magnetic susceptibilities measured using single-crystal samples. With the values for the magnetic parameters a consistent theoretical picture of the electronic structure of MNb_3S_6 was derived.

1. INTRODUCTION

IN THE course of our investigation of the ternary transition metal sulfides M_xNbS_2 and M_xTaS_2 it was found that extra metal atoms M can be inserted into the octahedral holes between the prismatic layers of NbS_2 and TaS_2[1]. At $x = \frac{1}{3}$, the compounds MNb_3S_6 and MTa_3S_6 were found with an ordered distribution of the extra metal atoms. Their structure was determined using X-ray diffraction intensities collected from powder samples. Figure 1 shows this structure with all the relevant information included. There are in principle three different octahedral holes available in the space group $P6_322$ with the following position parameters.

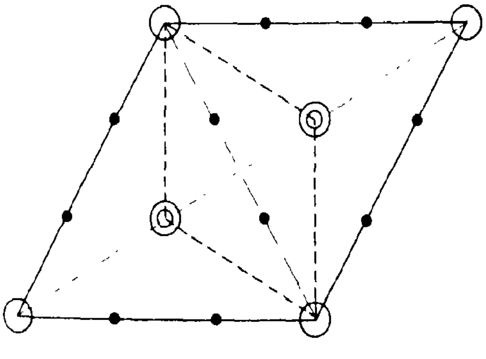

Fig. 1. Projection of the crystal structure of $Me_{1/3}NbS_2$ along the C axis. — — — = Original NbS_2 cell; ● = S; ○ = Nb; ◎ = Me

	x	y	z
(2b)	0	0	$\frac{1}{4}$
(2c)	$\frac{1}{3}$	$\frac{2}{3}$	$\frac{1}{4}$
(2d)	$\frac{2}{3}$	$\frac{1}{3}$	$\frac{1}{4}$

The structure analyses described in Ref. [1] showed position (2c) to be the most probable.

The magnetic susceptibilities of MNb_3S_6 obtained from the powder samples could reasonably be described with the Curie–Weiss formula

$$X_M - A_M = \frac{C_M}{T-\Theta}. \qquad (1)$$

Most compounds, however, contained oxide impurities. This was reflected in the term A_M which in some cases contained an excessively high positive contribution.

It became apparent that a detailed and unequivocal description of the structure and accurate magnetic parameters could be obtained only from measurements on pure samples. So, when we succeeded in preparing crystals of MNb_3S_6 by means of iodine vapour transport, both structural and magnetic investigations were repeated. The results obtained are presented in this paper and compared with those of the powder measurements.

---

*Present address: Bell Telephone Laboratories, Murray Hill, N.J. 07974, U.S.A.

With the much better values for the magnetic parameters a consistent theoretical picture can be given of the electronic structure of these compounds.

2. PREPARATION OF SINGLE CRYSTALS

Single crystals of MNb_3S_6 were grown by vapour transport reactions with iodine at 950–800°C. The ternary sulfides were obtained as a powder by heating the elements in the right proportions at 850°C for 80 hr. After 16 hr the reaction was interrupted for a homogenization by powdering. The powder finally obtained was used for growing the single crystals according to the following procedure. 2·5 g of the powder was degassed in a quartz ampulla of 50 cm^3 at 550°C in a vacuum of 10^{-5} torr for 1 hr. After 0·5 g of sublimed iodine had been added in a drying cabinet, the ampulla was sealed and heated in a three-zone oven according to Kershaw *et al.* [2]. The oven consisted of a quartz tube of 50 cm length and 3·5 cm dia. and three independently regulated Kanthal A heating elements. By keeping the ends of the oven at 950°C and the centre at 800°C, the compound was transported to the middle of the oven. The single crystals formed in this way were flakes of hexagonal shape with a maximum diameter of 5 mm and a thickness varying from about 0·05 to 0·4 mm.

3. COLLECTION AND CORRECTION OF X-RAY DIFFRACTION INTENSITIES

The intensity measurements were carried out on a Nonius automatic three-circle diffractometer with Zr-filtered Mo Kα radiation by θ–2θ scan. The crystals used for diffractometry were hexagonal prisms with dimensions d_1 and d_2 given in Table 1. The reflection pattern consists of two groups with systematically different intensities [1], viz.

(a) the very intense 'basic' reflections due to NbS_2. They do not contain extra-metal contributions and for their indices the relation h–$k = 3n$ holds;

(b) the less intense 'extra' reflections due to the extra metal only.

The crystals were rotated on the diffractometer about the $10\bar{1}0$ axis. Though only minor absorption corrections are to be expected under such conditions, the scan of an h00-reflection throughout the azimuth range of 2π yielded the typical picture shown in Fig. 2.

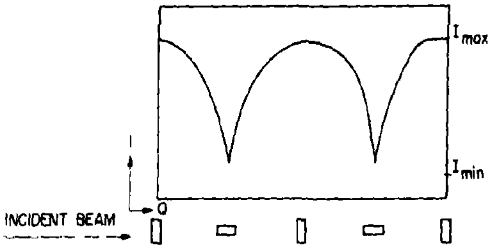

Fig 2. Crystal position.

This suggests that the MNb_3S_6 crystals are rather perfect, the reflection intensities being affected by primary extinction. In addition the split-up of intensities into $K\alpha_1$ and $K\alpha_2$ peaks at a θ of as low as 20° equally illustrates the perfectness of the crystals. To convert the measured intensities I_m into values I_{corr}, which are as reasonably as possible proportional to the squares of the corresponding structure factors, we first extrapolated the intensities to a value which would have been measured at $\varphi(I = I_{max})$. Then we applied a crude absorption correction factor for spherical specimens, using an effective absorption coefficient whose magnitude was estimated from the decrease of I_{max}/I_{min} with increasing θ.

As each of the two different groups of reflections needs its own correction scheme, the main problems were

(1) to give the right φ-correction (to obtain reasonable anisotropic temperature factors);

(2) to keep the two correction schemes for each compound on the same scale (to get reasonable occupation numbers for the extra metals).

All information relevant to data correction is presented in Table 1.

Table 1. Crystal data and constants essential for the correction scheme

Extra metal	Cell† constants		Crystal size (mm)		I_{max}/I_{min} extra reflections		I_{max}/I_{min} basic reflections		θ_{min}	N
					100	500	300	600		
	a	c	d_1	d_2	($\theta = 4{\cdot}1$)	($\theta = 20{\cdot}8$)	($\theta = 12{\cdot}3$)	($\theta = 25{\cdot}3$)		
Mn	5·782	12·629	0·25	0·45	1·6*	1·5*	1·5*	1·3*	14°	236
Fe	5·761	12·201	0·25	0·04	3·5	2·5	5·0	4·4	10°	204
Co	5·768	11·886	0·40	0·15	4·0	3·0	6·5	6·0	14°	278
Ni	5·758	11·897	0·30	0·15	3·5	3·0	5·5	4·8	10°	248

θ_{min} is the minimum value of θ, below which basic reflections are omitted from refinement.

N is the number of reflections involved in refinement.

*For this compound the position of the minimum intensity was not the same for all rotation axis reflections.

†The cell constants were taken from Ref. [1]; their accuracy is ± 0·001 Å.

4. STRUCTURE REFINEMENT

All refinement calculations were carried out with the ORFLS program by Busing and Levy [3]. The successive calculations for each structure were:

(a) Refinement of $z(\mathrm{Nb_I})$, $xyz(S)$, and the three occupation numbers of the extra metal positions. The scale factor and overall temperature factor were adjusted.

(b) From the R-factor obtained in this way a weighting scheme was derived according to Hughes [4]. The refinement was extended to the anisotropic temperature factors of all atoms being considered. As only position 2(c) appeared to be occupied by the extra metal, positions 2(a) and 2(b) were excluded from further refinement.

The atomic scattering factors were taken from the International Tables [5]; from f_{Nb} the real part of the anomalous dispersion was subtracted. The final disagreement factors R and R' are presented in Table 2. The final results of the refinement calculations are presented in Tables 3 and 4. Owing to the temperature factors being small the value of β_{33} is a very sensitive check on the validity of the adopted correction schemes, because from packing considerations we expect the following relations to hold between the average temperature vibration amplitudes:

$$\mathrm{Nb_I} \quad : U_{11}, U_{22} < U_{33}$$
$$\mathrm{Nb_{II}}\ \text{and}\ \mathrm{M} : U_{11}, U_{22} > U_{33}.$$

These relations appeared to hold for all four structures.

The most interesting interatomic distances are presented in Table 5. Their relation to the structural details appears from Fig. 3.

A rather strong trigonal distortion is present in the S octahedron about M, which can be characterized by the angle α [6]. The calculation of α is based on the hexagonal prisms obtained by duplicating the sulfur atoms via a mirror plane normal on (001) through M. The values for α can be compared with $\alpha = 84{\cdot}5°$ for an undistorted octahedron.

5. MAGNETIC SUSCEPTIBILITIES

The magnetic susceptibilities of the four compounds were measured on crushed single crystals with the Faraday balance in the temperature region 80–1000°K. An analysis of the extra metal content revealed that the concentration of extra metal, x, often differs from $\frac{1}{3}$. So, for the calculation of the magnetic parameters per extra metal atom the molecular weight had to be modified. For convenience, however, we refer to the compounds as $\mathrm{MNb_3S_6}$. In our discussion we assume that the magnetic moment μ does not depend

Table 2. Final disagreement factors R and R'

	$R = \frac{\Sigma \lVert F_o\rvert - \lvert F_c \rVert}{\Sigma \lvert F_o \rvert}\cdot 100$	$R' = \frac{\sqrt{\Sigma_w (F_o - F_c)^2}}{\sqrt{\Sigma_w (F_o^2 F_o)}}\cdot 100$
$MnNb_3S_6$	2·7	2·9
$FeNb_3S_6$	9·2	10·2
$CoNb_3S_6$	4·5	5·5
$NiNb_3S_6$	10·3	11·4

Table 3. Position and occupation parameters (λ) after refinement

	Atom	x	y	z	λ	$\sigma(x)$	$\sigma(y)$	$\sigma(z)$	$\sigma(\lambda)$
$Mn_{1/3}NbS_2$	Mn	$\frac{1}{3}$	$\frac{2}{3}$	$\frac{1}{4}$	0·163	—	—	—	0·003
	Nb_{II}	0	0	0	$\frac{1}{6}$	—	—	—	—
	Nb_I	$\frac{1}{3}$	$\frac{2}{3}$	−0·0006	$\frac{1}{3}$	—	—	0·00003	—
	S	0·33299	0·00394	0·37601	1	0·00019	0·00021	0·00007	—
$Fe_{1/3}NbS_2$	Fe	$\frac{1}{3}$	$\frac{2}{3}$	$\frac{1}{4}$	0·169	—	—	—	0·009
	Nb_{II}	0	0	0	$\frac{1}{6}$	—	—	—	—
	Nb_I	$\frac{1}{3}$	$\frac{2}{3}$	−0·0011	$\frac{1}{3}$	—	—	0·0002	—
	S	0·33261	0·00222	0·37213	1	0·0018	0·0016	0·0006	—
$Co_{1/3}NbS_2$	Co	$\frac{1}{3}$	$\frac{2}{3}$	$\frac{1}{4}$	0·159	—	—	—	0·006
	Nb_{II}	0	0	0	$\frac{1}{6}$	—	—	—	—
	Nb_I	$\frac{1}{3}$	$\frac{2}{3}$	−0·0013	$\frac{1}{3}$	—	—	0·0008	—
	S	0·33258	0·00075	0·36780	1	0·00046	0·00048	0·00018	—
$Ni_{1/3}NbS_2$	Ni	$\frac{1}{3}$	$\frac{2}{3}$	$\frac{1}{4}$	0·168	—	—	—	0·008
	Nb_{II}	0	0	0	$\frac{1}{6}$	—	—	—	—
	Nb_I	$\frac{1}{3}$	$\frac{2}{3}$	−0·0021	$\frac{1}{3}$	—	—	—	—
	S	0·33260	0·00098	0·36875	1	0·00089	0·00087	0·00034	—

appreciably on the concentration x for x slightly differing from $\frac{1}{3}$.

Throughout the temperature range considered, the compounds showed a temperature-dependent paramagnetic behaviour in accordance with the Curie–Weiss formula (equation (1)). The susceptibilities per gram-atom of M inserted are presented in Table 6. For the Ni system it remains doubtful whether the magnetic moment found in the range $x \approx 0{\cdot}15$ is also characteristic of $NiNb_3S_6$. In our discussion we will assume this to be so.

The magnetic parameters C_M, A_M, and Θ were obtained from a least-squares fit of the χ_M values observed between 80 and 1000°K to the Curie–Weiss formula. In Fig. 4 a $(\chi_M - A_M)^{-1}$ vs. T plot is presented, based on the A_M values as obtained from this least-squares refinement. The parameters are listed, together with their standard deviations, in Table 7. A comparison with the values obtained with powders (see Ref. [1]) shows that the latter were apparently not very reliable.

Especially for $CoNb_3S_6$ the difference between the single-crystal and powder parameters is striking. The value of A_M, very high in the powder, is approximately zero in the crystal; C_M is much larger in the single crystal. Essentially the same differences are observed with the other compounds, which suggests that in the powder samples impurities, probably oxides, were largely responsible for the excessively large positive contributions to

Table 4. Anisotropic temperature factor coefficients of the metal atoms The expression for the anisotropic temperature factor is here:
$[(\beta_{11}h^2+\beta_{22}k^2+\beta_{33}l^2+2\beta_{12}hk+2\beta_{13}hl+2\beta_{23}kl)]$

	Atom	β_{11}	β_{33}	$\sigma(\beta_{11})$	$\sigma(\beta_{33})$	U_{11}	U_{33}
$Mn_{1/3}NbS_2$	Mn	0·0113	0·0007	0·0006	0·00007	1·14	0·41
	Nb_{II}	0 0064	0·0015	0·0002	0·00007	0·65	0·85
	Nb_I	0·0062	0 0008	0·0001	0·00005	0·62	0·42
$Fe_{1/3}NbS_2$	Fe	0·021	0·021	0·003	0·0005	2·08	0·78
	Nb_{II}	0·0091	0·0022	0·0027	0·0006	0·90	1·24
	Nb_I	0·0091	0·0015	0·0015	0·0003	0·90	0 85
$Co_{1/3}NbS_2$	Co	0·0148	0·0008	0·0011	0·0001	1·47	0·46
	• Nb_{II}	0·00274	0·0008	0·0056	0·0001	0·27	0·46
	Nb_I	0·00262	0·00043	0·00041	0·00008	0·26	0·24
$Ni_{1/3}NbS_2$	Ni	0·0172	0·0022	0·0022	0·00043	1·71	1·24
	Nb_{II}	0·0083	0·0019	0·0019	0·0003	0·83	1·08
	Nb_I	0·0079	0·0011	0·0017	0·0002	0·79	0·62

For all metal atoms the relations hold: $\beta_{11}=\beta_{22}=\beta_{12}$, β_{33} independent, $\beta_{13}=\beta_{23}=0$. The U_{ii} were calculated with the relation $(x/4)i^{*2}U_{ii}=\beta_{ii}$ ($x_1=a$ etc.).

Table 5. Interatomic distances [Å] and trigonal distortion ($\alpha°$)

	2s-NbS_2'	$MnNb_3S_6$	$FeNb_3S_6$	$CoNb_3S_6$	$NiNb_3S_6$	2s-MoS_2'
M–S	(2·42)	2·519	2·445	2·385	2 389	(2·38)
M–Nb_I	(2·972)	3·168	3·066	2·987	2·999	(3 58)
Nb_I–S(1)	2·47	2·472	2·465	2·474	2·458	—
Nb_I–S(2)	2·47	2 508	2·497	2·499	2·496	—
S–S(3)	3·14	3·132	3·124	3·138	3·117	3·19
S–S(4)	3·31	3 338	3·324	3·329	3·321	3·16
S–S(5)	3·40	3·735	3·553	3·398	3·416	3·47
$\alpha°$(sec^6)	82·8	78·1	79·5	80·7	80·6	78·7

*See Ref. [6].

A_M. It is a well-known fact that in the preparation of this type of compound oxide formation is almost inevitable.

We feel that with our data from transported single crystals we have obtained reliable parameters. They give rise to some straightforward qualitative conclusions:

(a) The values for the magnetic moment ($\mu=\sqrt{8C_M}$ B.M.) suggest that 4, 4, 2, and 2 localized unpaired electrons are present in the Mn, Fe, Co and Ni compounds, respectively.

(b) Only Mn shows the expected diamagnetic behaviour of approximately $-0{\cdot}1\times10^{-3}$ e.m.u. per NbS_2 unit. The other compounds have positive contributions to A_M which are to be attributed to Pauli paramagnetism just as in pure NbS_2. The rather high positive values suggest that the electrons are delocalized in a narrow band.

(c) The Θ values suggest that the Mn com-

Table 6. Magnetic susceptibility measurements on MNb_3S_6

$Mn_{0.28}NbS_2$		$Co_{0.18}NbS_2$		$Fe_{0.34}NbS_2$		$Ni_{0.17}NbS_2$	
T (°K)	$\chi_M \times 10^3$	T (°K)	$\chi_M \times 10^3$	T (°K)	$\chi_M \times 10^3$	T (°K)	$\chi_M \times 10^3$
195·1	26·43	78·3	4·348	77 8	24·43	78·2	4·881
274·4	14 58	195·4	2·963	195 1	11·58	195·0	2·825
290·7	13·24	274·2	2·381	274·2	8·547	274·0	2·225
334·6	11 13	295·1	2·260	293·3	8·055	294·7	2·175
357 7	9·858	353 6	1·967	388·9	6·268	356·8	1·835
376·5	9 420	411 2	1·812	462·4	5·356	409·1	1·675
407 9	8·520	471·0	1·607	533·7	4·809	542·3	1·285
462·2	7 255	534·9	1·491	600·0	4·285	610·3	1 155
500·8	6 455	604·6	1·364	670·4	3·715	679 1	1·055
564·2	5·510	646·7	1·301	742·3	3·328	747·7	0·955
591·3	5·202	664·9	1·296	800·1	3·104	822·9	0·885
650·6	4 449	725·2	1·201	868·0	2·872	874·2	0·855
722·2	3 858	746·4	1 159	935 9	2 621	947·1	0·780
788·7	3 508	808·3	1 085	1067 9	2 261	1008 2	0·735
853 7	3·214	869·5	0·998	1122·3	2 088		
928·2	2·935	950·9	0·901				
995·8	2 734	1006·6	0·888				

Table 7. Magnetic parameters of MNb_3S_6 (crystalline) Standard deviations between brackets

M	$A_M\ 10^3$	Θ	C_M	$\mu(=\mu_B)$
Mn	0 330 (0·115)	93 (2)	2·73 (0·03)	4·68 (0·03)
Fe	−0·068 (0 085)	−30 (2)	2·64 (0·03)	4·60 (0·03)
Co	0·016 (0·023)	−157 (4)	1 02 (0·01)	2·86 (0·02)
Ni	−0 008 (0·024)	−90 (3)	0·82 (0·01)	2·56 (0·02)

pound will become ferromagnetic at low temperatures, whereas the others will be antiferromagnetic.

6. ELECTRIC CONDUCTIVITY

The compounds all remain metallic conductors, which is to be expected since the a_1-bands are only partly filled, just as in NbS_2 itself. Only the Mn compound with Mn^{3+} should contain a filled a_1-band and become a semi-conductor. However, the single crystals had not the ideal crystallographic formula $Mn_{0.33}NbS_2$, but only contained $Mn_{0.28}$ (from chemical analysis), which is a reason for the crystals maintaining their metallic character, also for the Mn compound. Unfortunately, the crystals were too small in one direction to permit a measurement of the anisotropy of the electric conductivity of the compound.

7. ELECTRONIC STRUCTURE

The trigonal symmetry of the crystal structure causes the *d*-orbitals of both M and Nb to split into *a* and *e*-representations. For the octahedral ions M the situation is quite simple. The fact that the octahedron is elongated along its trigonal axis makes it probable that one set of e_g-type orbitals is lower than a_g. In the trigonal prismatic surroundings of Nb the situation is more complicated. One possibility is that a_1 (d_{z^2}) is the lower and e_2 $(d_{x^2-y^2}, d_{xy})$ is in the middle (e_1 is always pushed up towards the highest posi-

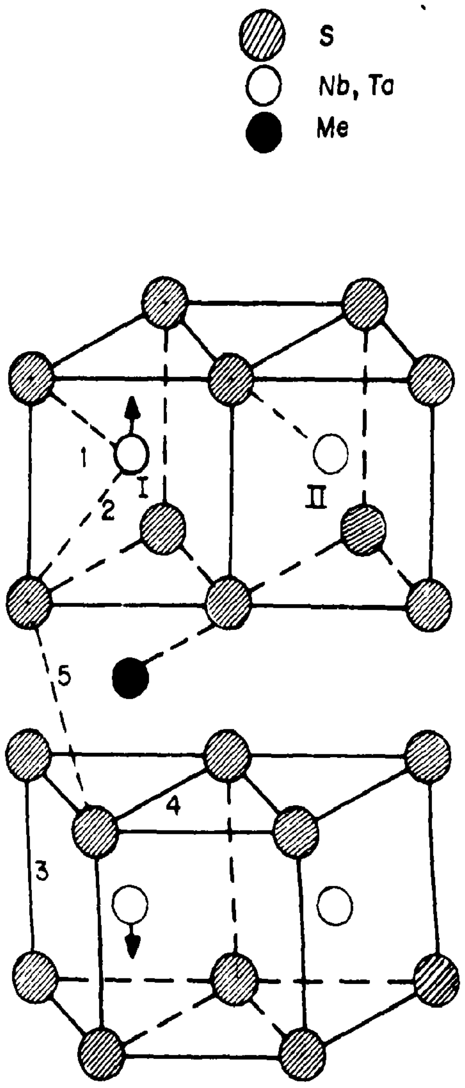

Fig 3 Numbering of interatomic distances relating to Table 6.

tion) or a_1 is in the middle and e_2 is most favourable.

Goodenough[7] postulates that e_2 is the lowest and he explains the electric and magnetic properties of compounds like WS_2 and NbS_2 by a mechanism in which the band, resulting from the interaction of the e_2 orbitals of neighbouring metals, is split up, by spin-orbit coupling, into two sub-bands.

In the following, we propose that a_1 should be lowest in our compounds as well as in NbS_2 and WS_2. The assumption that a_1 be the most favourable orbital easily explains why MoS_2 is a diamagnetic semi-conductor and why NbS_2 is a metallic conductor with a Pauli paramagnetism of $\approx 0{\cdot}1 \times 10^{-3}$ e.m.u./mole.

At this point of our discussion on the order of the *d*-levels about Nb, we should like to make the following observations.

In Goodenough's paper, Table 3 is presented for *trigonal bipyramidal* interstices (this table, incidentally, is not correct because in a trigonal bipyramid e_1 will be the lower set of orbitals; a_1 is in that case indeed very unfavourable). On page 474 it is mentioned that the cations in the layer structures of NbS_2 and WS_2 are in *trigonal bipyramidal* interstices and that Table 3 is applicable. However, Nb and W are in *trigonal prisms* and here it is not so obvious which is the more favourable, e_2 or a_1. We did not find any quantitative justification in Goodenough's article to support that e_2 is more favourable than a_1.

We have, however, carried out a qualitative estimate of the order of orbitals by two independent methods:

(a) A pure crystal field van Vleck type point charge calculation, using a formula derived by Koerts[8] and adapted to the geometry of the NbS_6 prism, shows that at least an improbably high effective nuclear charge of $Z > 7{\cdot}5$ is needed to bring e_2 below a_1. It is realized that a purely electrostatic approach is not quite realistic for these heavy-element sulfides. So, we do not regard these results as a proof, but rather as an indication that a prismatic geometry certainly does not exclude the a_1 orbital to be much more favourable than the e_2 set of orbitals.

(b) Semi-empirical Extended-Hückel calculations* for NbS_2, TaS_2, MoS_2 and WS_2 all result in a_1 being the most favourable orbital, followed by e_2. For NbS_2, in particular,

---

*Kindly performed by Dr. W. Th. A. M. van der Lugt of this laboratory.

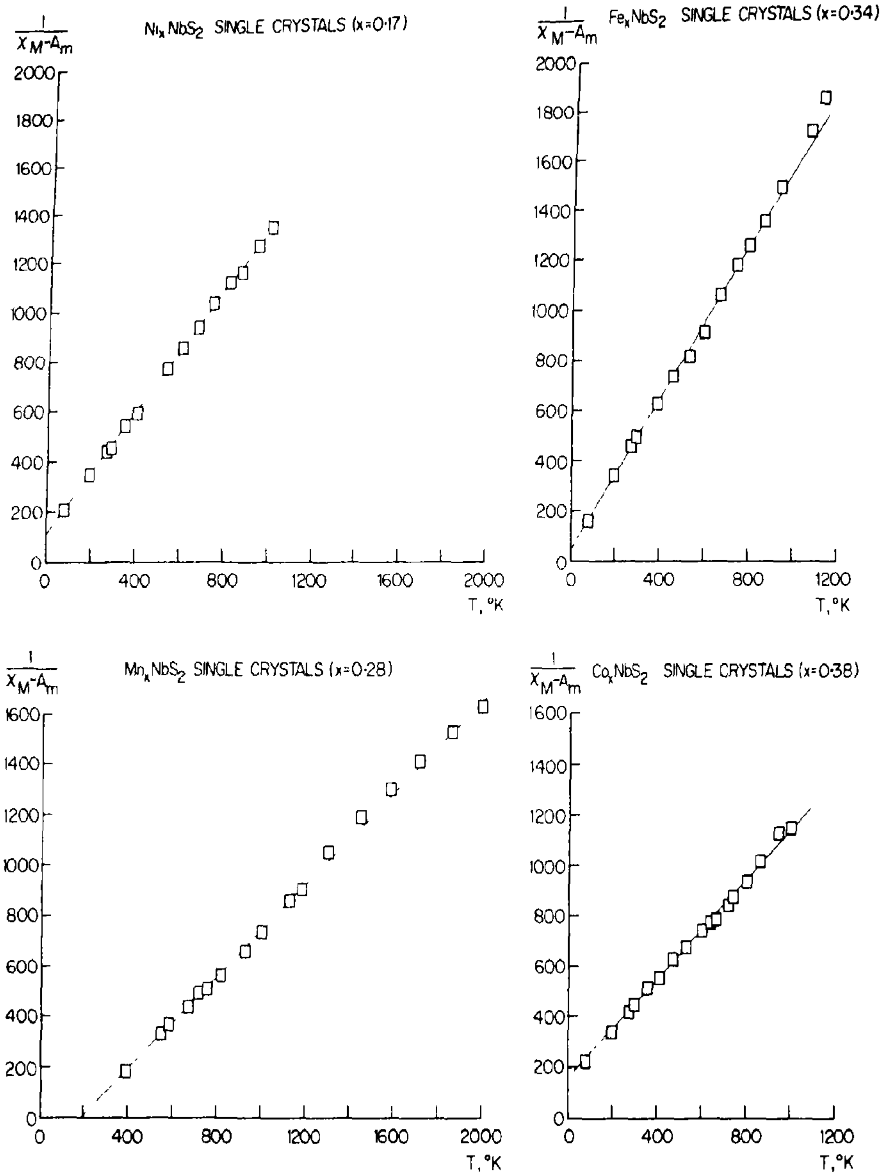

Fig. 4. $1/\chi_M - A_M$ vs T.

a_1 lies 3200 cm^{-1} below e_2, e_1 being 29,500 cm^{-1} above e_2.

We therefore prefer the interpretation that a_1 is lower than e_2, and thus arrive schematically at two systems of *d*-orbitals as shown in Fig. 5, as also suggested by Hulliger[9].

The relative positions on the energy scale of the M and Nb levels will depend on the metal M. The exact distribution of the electrons will be determined by the difference in 'ionization level', by possible interactions between M and the Nb layers and by the interelectronic repulsion.

In order to explain the magnetic data we

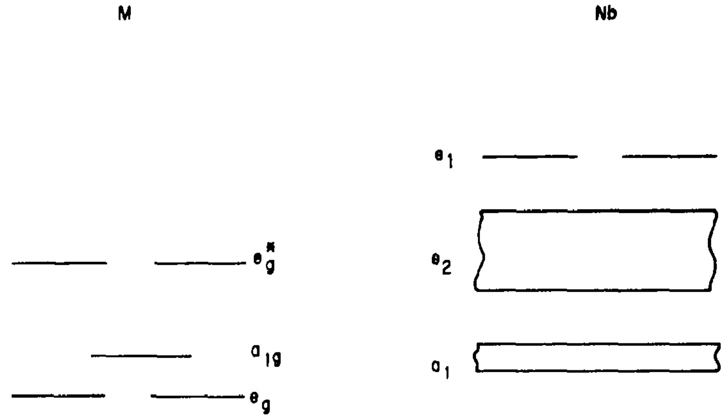

Fig. 5. Localized and delocalized d orbitals in MNb_3S_6.

arrive at the assignments of Table 8 for the electron distributions (the contributions to the a_1-band are formally given per 1 Nb atom, whereas physically we must consider 3 Nb atoms at one inserted M atom). Such an assignment not only explains the μ and A-values, but also the trend of the variation in Θ can be made plausible when the different possible magnetic interactions are taken into account (see below). This assignment brings the formal valencies of the ions at Mn^{3+}, Fe^{2+}, Co^{1+}, Ni^{2+}. The fact that only Mn becomes trivalent is in agreement with the known order of the ionization potentials. Going from Mn to Ni the energy of the levels of M will undoubtedly drop relative to those of Nb. One would rather have expected Mn^{3+}, Fe^{2+}, Co^{2+}, Ni^{2+} (which is actually found in the tantalum series (see Ref. [1]) or even Mn^{3+}, Fe^{2+}, Co^{2+}, Ni^{1+} if only ionization energies are taken into account. The only apparent inconsistency is then in the Co compound.

Table 8. Distribution of electrons localized and delocalized orbitals

Compound	M (localized)	Nb(delocalized)	Number of unpaired electrons	Pauli paramagnetism
$MnNb_3S_6$	$(e_g)^2(a_{1g})^1(e_g^*)^1$	$(a_1\text{-band})^2$	4	no
$FeNb_3S_6$	$(e_g)^3(a_{1g})^1(e_g^*)^2$	$(a_1\text{-band})^{5/3}$	4	yes
$CoNb_3S_6$	$(e_g)^4(a_{1g})^2(e_g^*)^2$	$(a_1\text{-band})^{4/3}$	2	yes
$NiNb_3S_6$	$(e_g)^4(a_{1g})^2(e_g^*)^2$	$(a_1\text{-band})^{5/3}$	2	yes

However, the doubly filled a_{1g}, e_g system and the half filled e_g^* system in both Co^{1+} and Ni^{2+} may have a special stability if the energy difference between a_{1g} and e_g^* is large enough.† It may also be that the a_{1g} level in the Co compound has come very close to the a_1 level of Nb, thus favouring its participation in the band. In that case too only the two e_g^* electrons contribute to the magnetic moment, but a formal valency for Co is then difficult to define. In fact the shortest distance between M and Nb occurs in the Co compound, which might support the latter assignment, if we bear in mind a critical distance R_c [10] between atoms, below which the electrons must be described as collective rather than localized.

---

†This suggestion was made, in a private discussion, by Professor C. Haas from Groningen University.

The above picture with the localized moments at the extra metal centres M is further confirmed by Mössbauer experiments, which indicate Fe^{2+} ions in octahedra†.

The presence of isolated moments of Mn^{3+} in a ferro-magnetically ordered state and of Fe^{2+} in an antiferromagnetic arrangement was confirmed by Van Laar *et al.*[11], who carried out neutron diffraction experiments at liquid helium temperatures.

8. MAGNETIC INTERACTIONS (Θ)

The values of Θ in Table 7 show that there is a magnetic interaction between the localized unpaired spins. We have *qualitatively* considered three types of interactions and have based ourselves on arguments put forward by Goodenough[10, 12].

(1) Superexchange interaction through intermediate S anions will take place mainly via the σ-bonding e_g^* orbitals, and we expect an antiferromagnetic interaction for all compounds, as no e_g^* orbital has more than one electron.

Table 9. Magnetic interactions among the extra metal atoms

M	Superexchange interaction	Interaction via Nb conduction electrons	Interaction via empty Nb orbitals	Suggested sum	Θ, °K exp.
Mn^{3+}	weakly antiferromagnetic	--	ferromagnetic	ferromagnetic	93
Fe^{2+}	antiferromagnetic	ferromagnetic	weakly ferromagnetic	—	−30
Co^{2+}	antiferromagnetic	--	—	antiferromagnetic	−157
Ni^{2+}	antiferromagnetic	—	—	antiferromagnetic	−90

(2) Interaction through conduction electrons may, according to Ruderman and Kittel[13], give rise to both ferromagnetic and antiferromagnetic coupling, dependent on atomic separation. Since in the Ni- and Co-compounds no localized electrons occur in the a_{1g} and e_g orbitals and in *ideal* $MnNb_3S_6$ no conduction electrons are available, only the Fe compound may show this type of interaction. We have assumed the distance in our compounds to be appropriate for a ferromagnetic coupling in order to explain the reduction of the expected strong antiferromagnetic superexchange in the iron compound to such a low value of −30°K.

(3) For direct interactions between the extra metal ions their mutual distances are obviously too large. However there may occur an interaction via empty orbitals of Nb. As the a_1-orbital of Nb is not empty, only e_g(M)–e_2(Nb)–e_g(M) is taken into account. In the Mn-compound two e_g orbitals are half filled and may give rise, via the empty e_2(Nb), to ferromagnetic coupling; in the Fe-compound only one e_g orbital is half filled and may also give rise to a ferromagnetic, though weaker, interaction via empty e_2(Nb).

The picture given here should be considered as purely qualitative, and for this reason the fifth column of Table 9 bears the heading 'suggested sum'. The simplified picture assumes all localized electrons to be localized on M and the *d* electrons of Nb delocalized through the Nb layers. The present model, however, so far explains consistently all the experimental data for the insertion compounds MNb_3S_6, MTa_3S_6 as well as the empty layer structures of NbS_2, TaS_2, MoS_2 and WS_2.

Acknowledgements—The authors wish to express their sincere thanks to Miss M. J. van Diepen, Miss M. Burink, Miss Y. van der Wel, and Mr. J. J. de Boer of this laboratory, who carried out the experiments and calculations involved in the work described.

REFERENCES

1. VAN DEN BERG J. M. and COSSEE P., *Inorg. chim. Acta* **2**, 143 (1968).

---

† J. van de Kraan and J. J. van Loef, private communication.

2. KERSHAW P., VLASSE M. and WOLD A., *Inorg. Chem.* **6**, 787 (1967).
3. BUSING W. R., MARTIN K. C. and LEVY H. A., *Oak Ridge National Lab. Res. Rep.* No. ORNL-TM-305 (1957)
4. HUGHES E., *J. Am. chem. Soc.* **63**, 737 (1941).
5. *International Tables for X-Ray Crystallography*, Vol. 3, p. 211 (1962).
6. BUNN C. W., *Chemical Crystallography*, p. 135 (1951).
7. GOODENOUGH J. B., *Phys. Rev* **171B**, 466 (1968).
8. KOERTS K., Thesis Leyden, p. 53 (1965).
9. HULLIGER F., *Structure and Bonding* **4**, 89 (1968).
10. GOODENOUGH J. B., *Colloque International sur des Dérivés Semimétalliques*. University of Paris (1965).
11. VAN LAAR B., RIETVELD H. M. and YDO D. J. W., Paper presented at *3rd Int. Conf. on Solid Compounds of Transition Elements, Oslo*, (1969).
12. GOODENOUGH J. B., *Magnetism and the Chemical Bond*, p. 165. Interscience, New York (1963).
13. RUDERMAN M. A. and KITTEL C., *Phys. Rev.* **96B**, 99 (1954).

J. Phys. Chem. Solids Pergamon Press 1970. Vol. 31, pp. 1069-1073. Printed in Great Britain.

THERMAL ANNEALING OF IRRADIATED LITHIUM HYDRIDE–I. MEASUREMENT OF STORED ENERGY*

H. W. NEWKIRK and H. R. LEIDER

Lawrence Radiation Laboratory, University of California Livermore, Calif. 94550, U.S A.

(*Received* 11 *August* 1969; *in revised form* 12 *November* 1969)

Abstract – The release of stored energy from irradiated LiH during thermal annealing was measured with a differential thermal analysis technique. For all samples irradiated with ^{60}Co γ-rays to doses between 1×10^9 and 5×10^{10} rad. at temperatures ranging from 40 to 270°C, the amount of stored energy was directly proportional to the amount of 'motionally narrowed' hydrogen seen in the material by pulsed nuclear magnetic resonance. The energy release is from the recombination reaction of free lithium and hydrogen that have been produced by irradiation; the energy for the reaction $Li_{(c)} + \frac{1}{2}H_{2(g)} \rightarrow LiH_{(c)}$ was ~20 kcal/mole. This is comparable to the standard heat of formation of LiH, $\Delta H_f^\circ = -21{\cdot}7$ kcal/mole.

1. INTRODUCTION

LITHIUM hydride is a particularly interesting material for radiation damage studies because the changes in some of its properties on irradiation are unusually large. Pretzel and his coworkers have provided a broad background of information on LiH and its irradiation behavior[1-6]. One of the more remarkable observations is that when LiH is irradiated, either externally as with γ-rays or internally as in tritium-containing material, very large increases in volume result if the irradiations are carried out above room temperature[6-9]. Accompanying the swelling is the formation of aggregates of metallic lithium and gaseous hydrogen within the lattice[6-9]. The state of these decomposition products has been characterized principally by nuclear magnetic resonance (NMR)[6-9]; it has been observed that as much as 10 per cent of the original hydrogen present in the lattice can be converted to a 'motionally-narrowed' gaseous form[7-9] by radiation. This gross decomposition is associated with volume changes of 25 per cent or more[6-9]. Recent electron microscopic studies have shown the presence of cubic, oriented bubbles in irradiated LiH [10], and NMR measurements of the angular dependence of the relaxation time of the hydrogen gas in irradiated single crystals clearly show that these are actually cubic hydrogen bubbles[11].

In light of the substantial decomposition of irradiated lithium hydride, it seemed important to measure the stored energy in such materials and to see whether the amount of H_2 and Li detected by NMR could be correlated with the total energy. If stored energy release is due to back-reaction of 'free' lithium and hydrogen, large amounts of energy would be seen, and this observation would confirm the interpretation of the NMR experiments[12].

Stored energy studies have been made on other irradiated ionic solids, particularly NaCl[13-15] and LiF[15]. Features of the energy release spectra were attributed to specific processes, such as aggregation of point defects and precipitation of colloidal metal particles. For LiF irradiated to more than 10^8 rad. with γ-rays, the stored-energy range values were very large, between 200–400 cal/g[15]. Energy of this magnitude must surely be due to back-reaction of lithium and fluorine produced by the irradiation. Similar values of stored energy have been observed in LiF irradiated with fast electrons[16].

---

*Work performed under the auspices of the U.S Atomic Energy Commission.

Radiation effects in LiF are in many respects similar to those seen in LiH. The formation of metallic lithium particles has been observed by X-ray techniques[17, 18] and by electron spin resonance (ESR)[19] and NMR[20]. Motionally-narrowed fluorine has been seen, as well[16, 19]. Also, bubbles of square shape have been seen directly with optical microscopes[21–27]; the presence of cavities was also inferred from X-ray scattering studies[23, 25, 28]. Microdifferential thermal analysis (DTA) has shown that the Li precipitates in LiF can have an anomalous f.c.c. crystallographic structure that can be converted by thermal annealing to the normal b.c.c. form[29]. A parallel investigation showed that in irradiated LiH only the normal b.c.c. lithium is formed[29, 30].

2. EXPERIMENTAL

The lithium hydride used in these experiments was synthesized at this Laboratory by direct combination of the elements, and crystals were grown in a manner similar to that described by Pretzel *et al.*[1]. The materials which were measured here are portions of those for which NMR measurements have been reported[8–10]. Lithium hydride was available which had been irradiated with ^{60}Co γ-rays to doses between 2×10^8 and 5×10^{10} rad. at Brookhaven National Laboratory. Irradiation temperatures ranged from 40 to 270°C. The LiH was always handled entirely under argon atmosphere in steel glove-boxes.

The differential thermal analyzer used in this investigation was obtained commercially[31, 32]. The calorimeter cell assembly is completely detachable and can be put into the argon glove-box for loading. The calorimeter construction follows the design principles of Boeresma[33] and can be operated up to 700°C. It consists of a silver heater block wound with resistance wire, a differential thermocouple with attached sample cups, reference thermocouple, and radiation shields. The entire system is contained within a small bell jar. A cup is permanently mounted on each junction of the differential thermocouple, one to contain the irradiated sample, and the other a reference material. The reference thermocouple is mounted within the heating block. It reads the calorimeter temperature and controls the rate of rise of temperature via an external programmer[31, 32].

Samples to be analyzed were ground in the glove-box and packed tightly into a platinum cup which fits snugly into the cups mounted on the differential thermocouple. The reference cup was filled with a similar amount of ground, unirradiated LiH. Sample size was typically ~25 mg. The calorimeter cell was assembled and sealed within the glove-box before removal. When the cell was mounted for measurement, it was continuously purged with dry helium (~10 cm³/sec) until the measurement was completed. An *X*-*Y* recorder displayed the system temperature as the abscissa and the differential temperature between reference and sample as the ordinate. The area above baseline was a measure of the energy released. The system was calibrated by determining the areas corresponding to the known heats of fusion of a large number of materials, namely, In, Sn, Cd, Pb, Zn, Al, $AgNO_3$, KNO_3, $NaNO_3$, $PbCl_2$ and AgCl. The calibration provided points for temperature and for energy per unit area between ~150 and 650°C. Temperature values are believed reliable to ±2°C and energy measurements to ±10 per cent. The calibration was done for a range of heating rates from 1·5 to 50°C/min. We always used the high heating rate, 50°C/min to make the measurements on irradiated LiH, because this minimized the time for possible reaction of accidental contaminants such as water and oxygen with the sample.

3. RESULTS AND DISCUSSION

In Fig. 1 several typical thermograms show DTA spectra from LiH irradiated at several temperatures. It was previously reported for LiH irradiated below 100°C that while a substantial amount of hydrogen was seen by pulsed NMR there was often no detectable metallic lithium[7, 8]. The curves in Fig. 1 show a similar result. For LiH irradiated above 100°C an endotherm is seen in the DTA spectrum corresponding to the melting of Li metal[18] but this endotherm is usually missing for material irradiated at low temperature. However, for those materials showing no Li, there is always a DTA peak in the vicinity of 225°C, and the lower the irradiation temperature the larger is this peak.

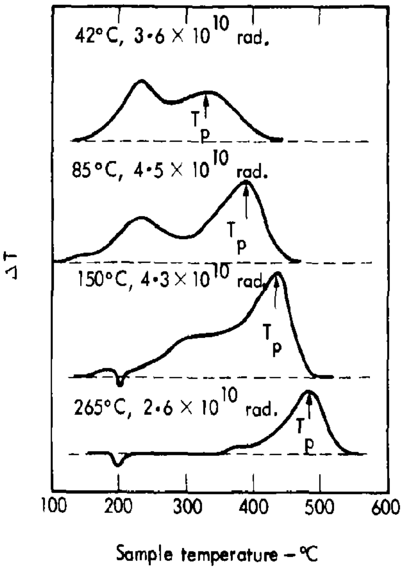

Fig. 1. Several typical DTA spectra for samples irradiated at different temperatures and radiation doses. The ordinate ΔT is differential temperature on an arbitrary scale. Note the presence of the melting curve for Li metal for materials irradiated at the higher temperatures. The temperature scale is uncorrected by calibration. The heating rate was 50°C/min in all cases.

We have found that annealing such irradiated LiH at 200–250°C results in the development of lithium metal aggregates that are detectable by both NMR and to DTA. Figure 2 compares samples from one irradiation batch. The upper curve shows the DTA spectrum of the LiH as irradiated, and the lower curve is the spectrum of a similar sample after heating to 225°C and cooling to room temperature. The development of a melting curve for Li is evident. Simultaneous with the appearance of Li precipitates is the disappearance (or diminution) of the 225°C peak. This feature of the DTA spectrum is probably due to recombination resulting when atomic lithium becomes mobile. Similar phenomena have been seen in NaCl[13, 14] and LiF[15].

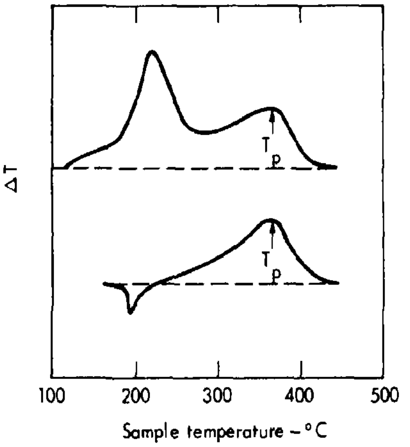

Fig. 2. DTA spectra of two samples from the same batch of LiH irradiated at 65°C with $5{\cdot}0 \times 10^{10}$ rad. Upper, DTA spectrum after the irradiation. Lower, DTA spectrum of irradiated material after it was annealed to 225°C to develop the Li metal aggregates. The temperature scale is uncorrected by calibration

The most prominent feature of the DTA curves is a high-temperature peak, labeled T_p in Fig. 1, which represents most of the stored-energy release. This peak occurs at higher temperatures for materials which have been irradiated at higher temperatures.

For a given irradiation temperature, this peak occurs at higher temperatures for materials which have received a higher irradiation dose. This variation of T_p with irradiation temperature and dose is similar to the trend of hydrogen bubble size[9, 10]. A mechanism for the stored-energy release is suggested by this observation and will be discussed in a subsequent paper[34].

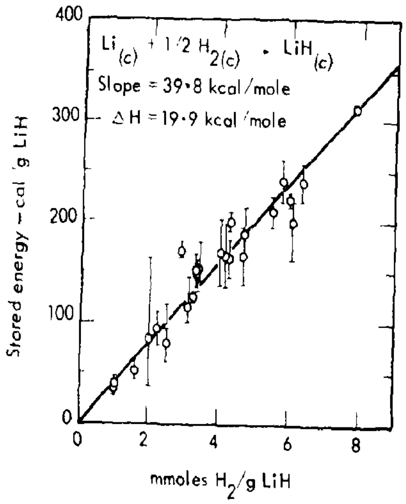

Fig 3. The relationship between stored energy and amount of motionally-narrowed hydrogen (as measured by NMR) for 24 samples. The line is a least-squares fit to the points. Each point is the average value for several measurements: the bars merely represent the experimental scatter. Moles of H_2 include a factor of $\frac{4}{3}$ to correct for the para-component. Materials shown were irradiated to doses between $1{\cdot}0 \times 10^9$ and $5{\cdot}1 \times 10^{10}$ rad at temperatures between 40 and 270°C.

One positive correlation has emerged from the measurement of stored energy. For all samples exposed to an irradiation dose of $\geq 10^9$ rad., a proportionality is found (Fig. 3) between the stored energy and the amount of 'motionally-narrowed' hydrogen measured by pulsed NMR[8, 9]. This motionally-narrowed hydrogen has been shown to be due to the presence of bubbles of gaseous H_2[7–10]; therefore, it is likely that the stored-energy release is due to the recombination of the hydrogen and lithium produced by irradiation. Figure 3 shows the relationship between the stored energy and the amount of H_2 present (corrected by a factor of $\frac{4}{3}$ due to the ortho-para equilibrium). The data shows that the energy of the reaction

$$Li_{(c)} + \tfrac{1}{2}H_{2(c)} \rightarrow LiH_{(c)}$$

is 19·9 kcal/mole. This value is comparable to the standard heat of formation of LiH, $\Delta H_f^\circ = -21{\cdot}7$ kcal/mole[35]. Although the reaction does not proceed under standard conditions, the comparison is consistent with the proposed explanation. The large variation seen for some samples is probably due to large-scale inhomogeneities in the distribution of lithium and hydrogen aggregates. The bars in Fig. 3 show the spread in the measurements. The average value of a sufficiently large number of measurements (up to 8 separate measurements) fits the general trend quite well. This satisfying relationship breaks down, however, for materials irradiated to $< 10^9$ rad.

Figure 4 shows stored energy plotted against motionally-narrowed hydrogen for several

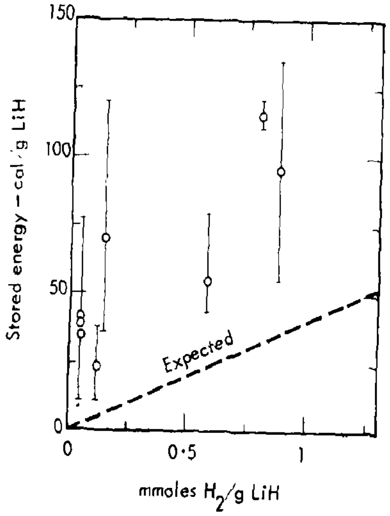

Fig 4. Stored energy vs. motionally-narrowed hydrogen for LiH irradiated to doses from $1{\cdot}5 \times 10^8$ and $5{\cdot}1 \times 10^8$ rad. at temperatures between 87 and 215°C. This plot shows 'excess' stored energy. The 'expected' line is the one fitted to the data in Fig. 4.

samples which have been irradiated to doses from 1·5 to 5 × 10^8 rad. It is clear that in these samples too much stored energy is found to be consistent with the above explanation. The thermograms are not remarkable except that some energy release is seen between 100 -200°C. If the stored energy release does indeed result from the back-reaction of free lithium and hydrogen, then in those samples plotted in Fig. 4, 'free' hydrogen must be present which is neither motionally-narrowed nor paramagnetic. If isolated H_2 molecules were trapped in the lattice, perhaps interstitially or in some configuration involving vacancies, they might not be able to rotate or librate and so might not be seen by pulsed NMR. It is not obvious that a hydrogen molecule trapped in a single vacancy or vacancy pair would be unable to rotate, but if this were true, there surely exist many such defects produced by radiation that might provide traps for molecules. This proposal requires that a large number of trapped isolated H_2 molecules be present, $\sim 10^{21}/\text{cm}^3$.

Acknowledgements—We wish to thank P. C. Souers and T. S. Blake for many helpful discussions. The support of C. M Griffith was invaluable in performing these experiments.

REFERENCES

1. PRETZEL F. E., RUPERT G. N., MADER C L., STORMS E. K., GRITTON G. V. and RUSHING C C., *J. Phys. Chem. Solids* **16**, 10 (1961).
2. PRETZEL F. E and RUSHING C. C , *J Phys. Chem. Solids* **17**, 232 (1961).
3. LEWIS W. B. and PRETZEL F. E., *J. Phys. Chem. Solids* **19**, 139 (1961).
4. PRETZEL F. E. and PETTY R L., *Phys. Rev.* **123**, 464 (1961).
5. PRETZEL F. E., GRITTON G. V., RUSHING C C., FRIAUF R. J., LEWIS W. B. and WALDSTEIN P., *J. Phys. Chem. Solids* **23**, 323 (1962).
6. PRETZEL F. E., LEWIS W. B., SZKLARZ E. G and VIER D. T., *J. appl. Phys. Suppl.* **33**, 510 (1962).
7. SOUERS P. C., JOLLY T. A. and CLINE C. F., *J. Phys. Chem. Solids* **28**, 1717 (1967).
8. SOUERS P. C., BLAKE T. S. PENPRAZE R. M. and CLINE C. F., *J. Phys. Chem. Solids* **30**, 2649 (1969).
9. SOUERS P. C., IMAI T., BLAKE T. S., PENPRAZE R. M. and LEIDER H. R., *Lawrence Radiation Lab. Rep.* No. UCRL-71835 (1969). *J. Phys. Chem. Solids* (In press).
10. IMAI T., *Phil. Mag.* (In press).
11. SOUERS P. C., BLAKE T. S. and PENPRAZE R. M., *Phil. Mag.* (In press).
12. Stored energy release has been observed when lithium hydride which had been irradiated at low temperature was allowed to warm to room temperature. L. H. Treiman, private communication of work in progress at the Los Alamos Scientific Laboratory.
13. KOBAYASHI K , *Phys. Rev.* **102**, 348 (1956).
14. BUNCH J. M., *Stored energy in irradiated sodium chloride*, Ph.D. Thesis, Univ. of Nebraska, Lincoln, Nebraska (1967).
15. ZAVADOVSKAYA E. K. and KUZ'MINA A V , *Soviet Phys. solid St.* **6**, 2677 (1965), (*Izv. Vysshikh Uchebuykh Zavedenii Fiz.* **1**, 175 (1965).
16. NEWKIRK H W , BLAKE T. S and SOUERS P. C., private communication of work in progress.
17. LAMBERT M., MAZIERES C. and GUINIER A., *J. Phys. Chem. Solids* **18**, 129 (1961)
18. MAZIERES C., *Annls Chim.*, Paris **6**, 613 (1961).
19. KIM Y W., KAPLAN R and BRAY P. J , *Phys Rev.* **117**, 740 (1960), KNUTSON C., HOOPER H and BRAY P. J , *J Phys. Chem. Solids* **27**, 147 (1966)
20. TAUPIN C., *Compt. rend.* **262**, 1617 (1966); *J. Phys. Chem. Solids* **28**, 41 (1967)
21. SENIO P , *Science* **126**, 208 (1957).
22. SENIO P. and TUCKER C W., Jr , *Knolls Atomic Power Lab. Rep.* No. KAPL-1727 (1957).
23. SMALLMAN R E. and WILLIS B. T M., *Phil. Mag.* **2**, 1018 (1957).
24. GILMAN J J. and JOHNSON W. G., *J appl Phys.* **29**, 877 (1958)
25. LAMBERT M. and GUINIER A , *Compt rend.* **244**, 2791 (1957)
26. WHAPHAM A. D. and MAKIN M J., *Phil Mag* **8**, 237 (1960)
27. MANNAMI M , AKISUE O and TANAKA K., Japan *J. appl. Phys.* **6**, 283 (1967)
28. LAMBERT M., LEFEBRE S. and GUINIER A., *Compt. rend.* **255**, 97 (1962).
29. LAMBERT M., BERGE P., MAZIERES C and GUINIER A., *Compt. rend.* **249**, 2054 (1959).
30. SMITH G., private communication.
31. The DuPont 900 DTA apparatus with plug-in calorimeter cell modulus. This apparatus is described in detail in reference [32].
32. CHIU J., *Analyt Chem.* **34**, 1841 (1962), SARASOHN I. M., In *Int. Conf on Thermal Analysis: First Conference, Aberdeen, Scotland, Sept 6–9, 1965* (Edited by J. P Redfern), p 53 MacMillan, New York (1965).
33. BOERESMA S. L., *J. Am. ceram. Soc.* **38**, 281 (1955).
34. LEIDER H. R. *J. Phys. Chem Solids*. (In press).
35. JANAF Thermochemical Data, compiled by the Dow Chemical Co , Midland, Michigan (September 30, 1967).

J. Phys. Chem. Solids Pergamon Press 1970. Vol. 31, pp. 1075–1083. Printed in Great Britain

A THEORY OF THE FIRST ORDER RAMAN SCATTERING OF LIGHT BY POLARITONS IN CRYSTALS OF THE ROCKSALT STRUCTURE

A. A. MARADUDIN* and **S. USHIODA**
Department of Physics, University of California, Irvine, Calif. 92664, U.S.A.

(*Received* 8 *September* 1969; *in revised form* 27 *October* 1969)

Abstract – In crystals of the rocksalt structure the electro-optic coefficient as well as the first derivative of the electronic polarizability with respect to an ionic displacement vanishes because every ion is at a center of inversion. Consequently, the zone center optical phonons are inactive in first order Raman scattering. However, these phonons are infrared active, and the transverse optical (TO) phonons form polaritons when the retardation of the Coulomb interaction is taken into account. Because of the axial vector character of the magnetic field, the first derivative of the electronic polarizability with respect to the macroscopic magnetic field associated with the polaritons does not vanish in rocksalt type crystals. Thus the polaritons in crystals of the rocksalt structure can give rise to first order Raman scattering. In this note we present a theory of the Raman scattering intensity by polaritons via the magneto-optic effect, and estimate the intensity of the light scattered by this mechanism.

THE USUAL explanation of why crystals of the rocksalt structure do not scatter light inelastically, by one phonon processes, is well known[1]. Every ion is at a center of inversion, and the first derivative of the electronic polarizability of the crystal with respect to an ionic displacement consequently vanishes identically. There is consequently no elasto-optic scattering by one phonon processes. For the same reason crystals of the rocksalt structure, unlike crystals of the zincblende structure, for example, have no first order Raman effect associated with the modulation of the electronic polarizability by a macroscopic electric field, either the longitudinal macroscopic field associated with the long wavelength longitudinal optical modes[2], or the transverse macroscopic field associated with the long wavelength transverse optical modes, when the retardation of the Coulomb interaction is taken into account[3]. Thus there is no electro-optic scattering by one phonon processes. Nevertheless, crystals of the rocksalt structure can display a first order Raman effect, through the modulation of the electronic polarizability by the macroscopic magnetic field to which the long wavelength transverse optical modes give rise when the retardation of the Coulomb interaction is taken into account. The elementary excitations in the crystal from which the scattering takes place are polaritons, which are the normal modes of the linearly coupled transverse phonon–photon system in the presence of a retarded Coulomb interaction[4]. In this paper we present a theory of this effect, magneto-optic scattering, and estimate the intensity of the light scattered by this mechanism.

Let us write the contribution to the electronic polarizability which is linear in the magnetic field and explicitly of zero order in the ionic displacements as

$$P_{\mu\nu} = \sum_{l\kappa\alpha} R^{(0)}_{\mu\nu\alpha}(l\kappa) H_\alpha(l\kappa) \tag{1}$$

where we assume that the macroscopic magnetic field has a spatial variation of the kind

$$H_\alpha(\mathbf{x}) = \bar{H}_\alpha e^{i\mathbf{k}\cdot\mathbf{x}} \tag{2}$$

and $H_\alpha(l\kappa) = H_\alpha(\mathbf{x} = \mathbf{x}(l\kappa))$, where $\mathbf{x}(l\kappa)$ is the position vector to the equilibrium position

---

*This research was supported in part by the Air Force Office of Scientific Research, Office of Aerospace Research, U.S.A.F., under AFOSR Grant No. 68-1448. Technical Report No. 69-23.

of the ion $(l\kappa)$. Writing $P_{\mu\nu}$ in this form is a formal device, which will yield in a direct way the condition that the wave vector of the scattered light equal the sum of the wave vectors of the incident light and the elementary excitation responsible for the scattering.

If we use the fact that $P_{\mu\nu}$ transforms as a second rank tensor under rotations of the crystal, and that an electric field is a polar vector while a magnetic field is an axial vector, it is straightforward to establish the transformation law for the coefficient $R^{(0)}_{\mu\nu\alpha}(l\kappa)$ under an operation of the space group of the crystal:

$$R^{(0)}_{\mu\nu\alpha}(LK) = |\mathbf{S}| \sum_{\mu'\nu'\alpha'} S_{\mu\mu'}S_{\nu\nu'}S_{\alpha\alpha'}R^{(0)}_{\mu'\nu'\alpha'}(l\kappa) \quad (3)$$

where $\mathbf{S}$ is a 3×3 real orthogonal matrix representative of the elements of the point group of the space group of the crystal, and (LK) is the lattice site into which the site $(l\kappa)$ is sent by the symmetry operation. It follows from this result that $R^{(0)}_{\mu\nu\alpha}(l\kappa)$ is independent of the cell index l, because of the translational symmetry of the crystal. Consequently we denote this coefficient by $R^{(0)}_{\mu\nu\alpha}(\kappa)$ in what follows.

The generalized principle of symmetry of the kinetic coefficients[5] has the consequence that $R^{(0)}_{\mu\nu\alpha}(\kappa)$ is antisymmetric in μ and ν,

$$R^{(0)}_{\mu\nu\alpha}(\kappa) = -R^{(0)}_{\nu\mu\alpha}(\kappa). \quad (4)$$

Used together with the condition that absorption is absent, this principle also requires that $R^{(0)}_{\mu\nu\alpha}(\kappa)$ be pure imaginary, and we express this condition by writing

$$R^{(0)}_{\mu\nu\alpha}(\kappa) = ir_{\mu\nu\alpha}(\kappa). \quad (5)$$

The point group of each lattice site in crystals of the rocksalt structure is 0_h. When we use the operations of this group in equation (3), and note equation (5), we find that the tensor $r_{\mu\nu\alpha}(\kappa)$ has only one independent, nonzero component for crystals of the rocksalt structure, and can be written in the form

$$r_{\mu\nu\alpha}(\kappa) = \epsilon_{\mu\nu\alpha}r(\kappa) \quad (6)$$

where $\epsilon_{\mu\nu\alpha}$ is the Levi-Civita symbol. This result is compatible with that expressed by equation (4), so that the latter does not yield any new restrictions on the form of $r_{\mu\nu\alpha}(\kappa)$, for crystals of the rocksalt structure.

If we expand the dielectric constant in powers of a uniform magnetic field,

$$\epsilon_{\mu\nu} = \epsilon^{(0)}_{\mu\nu} + i\sum_{\lambda} g_{\mu\nu\lambda}H_{\lambda} + \cdots \quad (7)$$

then the following relation holds between the coefficients $g_{\mu\nu\lambda}$ and the coefficients $r_{\mu\nu\lambda}(\kappa)$,

$$g_{\mu\nu\lambda} = \frac{4\pi}{\Omega_0}\sum_{\kappa} r_{\mu\nu\lambda}(\kappa) \quad (8)$$

where Ω_0 is the volume of a primitive unit cell.

We will see that it is only in the combination $g_{\mu\nu\lambda}$ that the coefficients $\{r_{\mu\nu\lambda}(\kappa)\}$ enter the expression for the scattered intensity. It is this result, coupled with the fact that the values of $g_{\mu\nu\lambda}$ can be obtained from experimental results on the Faraday effect in insulators or semiconductors, that ultimately enables us to estimate the intensity of scattering by polaritons through the magneto-optic effect.

In the context of the present problem the magnetic field entering into equation (1) is the transverse magnetic field established by the ionic vibrations when the retardation of the Coulomb interaction is taken into account. Our first task is to relate this field to the ionic displacement amplitudes.

It is known[6] that when the retardation of the Coulomb interaction is taken into account, a displacement field of the ions of the form

$$u_{\alpha}(l\kappa; t) = \frac{w_{\alpha}(\kappa)}{\sqrt{M_{\kappa}}}e^{i\mathbf{k}\cdot\mathbf{x}(l\kappa)-i\omega t} \quad (9)$$

where M_{κ} is the mass of the κ^{th} kind of ion, gives rise to a macroscopic electric field

$$\mathbf{E}(\mathbf{x}; t) = \bar{\mathbf{E}}\,e^{i\mathbf{k}\cdot\mathbf{x}-i\omega t} \quad (10)$$

which possesses both a longitudinal and a transverse part:

$$\mathbf{E}(\mathbf{x}; t) = \mathbf{E}^{\parallel}(\mathbf{x}; t) + \mathbf{E}^{\perp}(\mathbf{x}; t). \quad (11)$$

The longitudinal and transverse components are given by

$$\mathbf{E}^{\parallel}(\mathbf{x};t)=\bar{\mathbf{E}}^{\parallel}\,e^{i\mathbf{k}\cdot\mathbf{x}-i\omega t} \tag{12a}$$

$$\mathbf{E}^{\perp}(\mathbf{x};t)=\bar{\mathbf{E}}^{\perp}\,e^{i\mathbf{k}\cdot\mathbf{x}-i\omega t} \tag{12b}$$

where

$$\mathbf{k}\times\bar{\mathbf{E}}^{\parallel}=0,\quad \mathbf{k}\cdot\bar{\mathbf{E}}^{\perp}=0. \tag{12c}$$

The dielectric polarization due to the motion of the ions is given by

$$\mathbf{P}(\mathbf{x};t)=\bar{\mathbf{P}}\,e^{i\mathbf{k}\cdot\mathbf{x}-i\omega t}. \tag{13}$$

The amplitudes $\bar{\mathbf{E}}^{\parallel}$, $\bar{\mathbf{E}}^{\perp}$, and $\bar{\mathbf{P}}$ are related by

$$\bar{E}^{\parallel}_{\alpha}=-4\pi\sum_{\beta}\hat{k}_{\alpha}\hat{k}_{\beta}\bar{P}_{\beta} \tag{14}$$

$$\bar{E}^{\perp}_{\alpha}=\frac{4\pi}{n^2-1}\sum_{\beta}(\delta_{\alpha\beta}-\hat{k}_{\alpha}\hat{k}_{\beta})\bar{P}_{\beta} \tag{15}$$

where $\hat{\mathbf{k}}$ is a unit vector in the direction of $\mathbf{k}$, and

$$n=\frac{ck}{\omega} \tag{16}$$

is the refractive index of the optical wave under consideration.

The relation between $\bar{P}_{\alpha}$, the displacement amplitude $w_{\alpha}(\kappa)$, and the macroscopic field is[7]

$$\bar{P}_{\alpha}=\frac{1}{\Omega_0}\sum_{\kappa\beta}M_{\alpha\beta}(\kappa)\frac{w_{\beta}(\kappa)}{\sqrt{M_{\kappa}}}+\sum_{\beta}\chi^{(\infty)}_{\alpha\beta}\bar{E}_{\beta} \tag{17}$$

where Ω_0 is the volume of a primitive unit cell, $M_{\alpha\beta}(\kappa)$ is the transverse (or Born) effective charge tensor for the κ^{th} kind of ion, and $\chi^{(\infty)}_{\alpha\beta}$ is the electronic susceptibility.

If we substitute equations (14) and (15) into equation (17) and solve for $\bar{P}_{\alpha}$ as a function of $w_{\beta}(\kappa)$, we obtain

$$\bar{P}_{\alpha}=\frac{1}{\Omega_0}\sum_{\beta\gamma\kappa}S_{\alpha\beta}M_{\beta\gamma}(\kappa)\frac{w_{\gamma}(\kappa)}{\sqrt{M_{\kappa}}} \tag{18}$$

where $S_{\alpha\beta}$ is the 3×3 matrix inverse to

$$S^{-1}_{\alpha\beta}=\delta_{\alpha\beta}+4\pi\sum_{\gamma}\chi^{(\infty)}_{\alpha\gamma}\left[\hat{k}_{\gamma}\hat{k}_{\beta}-\frac{\delta_{\gamma\beta}-\hat{k}_{\gamma}\hat{k}_{\beta}}{n^2-1}\right]. \tag{19}$$

It follows, therefore, that the transverse electric field is given by

$$\bar{E}^{\perp}_{\alpha}=\frac{1}{\Omega_0}\frac{4\pi}{n^2-1}\sum_{\beta\gamma\delta\kappa}\times(\delta_{\alpha\beta}-\hat{k}_{\alpha}\hat{k}_{\beta})S_{\beta\gamma}M_{\gamma\delta}(\kappa)\frac{w_{\delta}(\kappa)}{\sqrt{M_{\kappa}}}. \tag{20}$$

If the macroscopic magnetic field is written in the form

$$\mathbf{H}(\mathbf{x};t)=\bar{\mathbf{H}}\,e^{i\mathbf{k}\cdot\mathbf{x}-i\omega t} \tag{21}$$

the amplitude $\bar{\mathbf{H}}$ is related to $\bar{\mathbf{E}}^{\perp}$ by the Maxwell equation

$$\bar{\mathbf{H}}=\frac{c}{\omega}\mathbf{k}\times\bar{\mathbf{E}}^{\perp} \tag{22}$$

and we obtain the general result

$$\bar{H}_{\alpha}=\frac{1}{\Omega_0}\frac{4\pi n}{n^2-1}\sum_{\beta\gamma\delta\lambda\mu\kappa}\epsilon_{\alpha\beta\gamma}\hat{k}_{\beta}(\delta_{\gamma\delta}-\hat{k}_{\gamma}\hat{k}_{\delta})S_{\delta\lambda}\times M_{\lambda\mu}(\kappa)\frac{w_{\mu}(\kappa)}{\sqrt{M_{\kappa}}}. \tag{23}$$

We now specialize this result to the case of crystals of the rocksalt structure. In this case the electronic susceptibility is isotropic, $\chi^{(\infty)}_{\alpha\beta}=\delta_{\alpha\beta}\chi^{(\infty)}$, and $S_{\alpha\beta}$ takes the simple form

$$S_{\alpha\beta}=\frac{\hat{k}_{\alpha}\hat{k}_{\beta}}{\epsilon_{\infty}}+(\delta_{\alpha\beta}-\hat{k}_{\alpha}\hat{k}_{\beta})\frac{n^2-1}{n^2-\epsilon_{\infty}} \tag{24}$$

where ϵ_{∞} is the optical frequency dielectric constant, $\epsilon_{\infty}=1+4\pi\chi^{(\infty)}$. The effective charge tensor is also isotropic,

$$M_{\alpha\beta}(\kappa)=\delta_{\alpha\beta}e(\kappa) \tag{25a}$$

with

$$e(+)=-e(-)=e^{*}. \tag{25b}$$

Substituting these results into equation (23) we obtain

$$\bar{H}_\alpha = \frac{1}{\Omega_0}\frac{4\pi n}{n^2-\epsilon_\infty}\sum_{\beta\kappa} T_{\alpha\beta}(\hat{\mathbf{k}})e(\kappa)\frac{w_\beta(\kappa)}{\sqrt{M_\kappa}} \tag{26}$$

where

$$T_{\alpha\beta}(\hat{\mathbf{k}}) = \sum_{\gamma\lambda}\epsilon_{\alpha\gamma\lambda}\hat{k}_\gamma(\delta_{\lambda\beta}-\hat{k}_\lambda\hat{k}_\beta). \tag{27}$$

In the long wavelength limit the equation satisfied by $w_\alpha(\kappa)$ is [7]

$$\omega^2 w_\alpha(\kappa) = \sum_{\kappa'\beta}\frac{f_{\alpha\beta}(\kappa\kappa')w_\beta(\kappa')}{(M_\kappa M_{\kappa'})^{1/2}} - \frac{1}{\sqrt{M_\kappa}}\sum_\beta M_{\beta\alpha}(\kappa)\bar{E}_\beta \tag{28}$$

where $f_{\alpha\beta}(\kappa\kappa')$ is related to the force constants associated with all the short range forces (including the Lorentz field) $\{\Phi_{\alpha\beta}(l\kappa;l'\kappa')\}$ by

$$f_{\alpha\beta}(\kappa\kappa') = \sum_{l'}\Phi_{\alpha\beta}(l\kappa;l'\kappa'). \tag{29}$$

If we substitute into equation (28) the expression for the macroscopic field given by equations (14), (15) and (18), it becomes

$$\omega^2 w_\alpha(\kappa) = \sum_{\kappa'\beta}\frac{f_{\alpha\beta}(\kappa\kappa')}{(M_\kappa M_{\kappa'})^{1/2}}w_\beta(\kappa') + \frac{4\pi}{\Omega_0}\sum_{\beta\gamma\delta\lambda\kappa'}\frac{M_{\beta\alpha}(\kappa)}{\sqrt{M_\kappa}} \times\left[\hat{k}_\beta\hat{k}_\gamma - \frac{\delta_{\beta\gamma}-\hat{k}_\beta\hat{k}_\gamma}{n^2-1}\right] \times S_{\gamma\delta}\frac{M_{\delta\lambda}(\kappa')}{\sqrt{M_{\kappa'}}}w_\lambda(\kappa'). \tag{30}$$

For the particular case of a crystal of the rocksalt structure the tensor $f_{\alpha\beta}(\kappa\kappa')$ takes the simple form

$$f_{\alpha\beta}(\kappa\kappa') = \delta_{\alpha\beta}f(\kappa\kappa') \tag{31a}$$

with

$$f(++) = -f(+-) = -f(-+) = f(--) = f = \mu\omega_T^2. \tag{31b}$$

In equation (31b) $\mu = M_+M_-/(M_+ + M_-)$ is the reduced mass of a primitive unit cell, and ω_T is the frequency of the transverse optical modes of infinite wavelength, in the absence of retardation. With the use of this result and those given by equations (24) and (25), we transform equation (30) into

$$\omega^2 w_\alpha(\kappa) = \sum_{\kappa'}\frac{f(\kappa\kappa')}{(M_\kappa M_{\kappa'})^{1/2}}w_\alpha(\kappa') + \frac{4\pi}{\Omega_0}\sum_{\kappa'\beta}\frac{e(\kappa)}{\sqrt{M_\kappa}} \times\left(\frac{\hat{k}_\alpha\hat{k}_\beta}{\epsilon_\infty} - \frac{\delta_{\alpha\beta}-\hat{k}_\alpha\hat{k}_\beta}{n^2-\epsilon_\infty}\right) \times\frac{e(\kappa')}{\sqrt{M_{\kappa'}}}w_\beta(\kappa'). \tag{32}$$

We divide the solutions of this equation into two types: (a) those for which

$$\frac{w_\alpha(+)}{\sqrt{M_+}} = \frac{w_\alpha(-)}{\sqrt{M_-}} = \frac{\eta_\alpha}{\sqrt{M_c}} \tag{33}$$

where $M_c = M_+ + M_-$ is the mass of a unit cell; and (b) those for which

$$\sqrt{M_+}w_\alpha(+) = -\sqrt{M_-}w_\alpha(-) = \sqrt{\mu}\xi_\alpha. \tag{34}$$

With these definitions $\boldsymbol{\eta}$ and $\boldsymbol{\xi}$ are unit vectors.

The equations determining η_α and ξ_α are obtained by substituting equations (33) and (34) into equation (32):

$$\omega^2\eta_\alpha = 0 \tag{35a}$$

$$\omega^2\xi_\alpha = \omega_T^2\xi_\alpha + \frac{4\pi(e^*)^2}{\mu\Omega_0}\sum_\beta \times\left(\frac{\hat{k}_\alpha\hat{k}_\beta}{\epsilon_\infty} - \frac{\delta_{\alpha\beta}-\hat{k}_\alpha\hat{k}_\beta}{n^2-\epsilon_\infty}\right)\xi_\beta. \tag{35b}$$

The solutions of equation (35a) are

$$\omega = 0 \tag{36a}$$

$$\boldsymbol{\eta} = \boldsymbol{\eta}(j), \quad j = 1,2,3, \tag{36b}$$

where $\{\boldsymbol{\eta}(j)\}$ $(j = 1, 2, 3)$ are any three mutually perpendicular unit vectors. A convenient realization of these vectors is

$$\eta_\alpha(j) = \delta_{\alpha j}. \tag{36c}$$

If we assume that $\boldsymbol{\xi}$ is parallel to $\mathbf{k}$, we find that the equation it satisfies is

$$\omega^2\xi_\alpha = \omega_T^2\xi_\alpha + \frac{4\pi(e^*)^2}{\mu\Omega_0\epsilon_\infty}\xi_\alpha, \tag{37}$$

which yields the frequency

$$\omega^2 = \omega_T^2 + \frac{4\pi(e^*)^2}{\mu\Omega_0\epsilon_\infty} \equiv \omega_T^2 + \omega_p^2 = \omega_L^2 \tag{38}$$

where ω_L is the frequency of the longitudinal optical modes of infinite wavelength. If we assume that $\boldsymbol{\xi}$ is perpendicular to $\mathbf{k}$, the equation it satisfies is

$$\omega^2\xi_\alpha = \omega_T^2\xi_\alpha - \frac{4\pi(e^*)^2}{\mu\Omega_0}\frac{1}{\dfrac{c^2k^2}{\omega^2} - \epsilon_\infty}\xi_\alpha. \tag{39}$$

The frequencies obtained from this equation are found to be

$$\omega_\pm^2(\mathbf{k}) = \tfrac{1}{2}\left\{\omega_L^2 + \frac{c^2k^2}{\epsilon_\infty} \pm \left[\left(\omega_L^2 + \frac{c^2k^2}{\epsilon_\infty}\right)^2 - 4\frac{c^2k^2\omega_T^2}{\epsilon_\infty}\right]^{1/2}\right\}. \tag{40}$$

These solutions are just the dispersion relations for the two branches of the polariton spectrum for crystals of the rocksalt structure (see Fig. 1). Thus, we can classify the solutions of equation (35b) as

$$\boldsymbol{\xi}(4) \perp \boldsymbol{\xi}(5) \perp \boldsymbol{\xi}(6), \quad \omega_4^2 = \omega_5^2 = \omega_\pm^2. \tag{41a}$$

$$\boldsymbol{\xi}(6) = \hat{\mathbf{k}}, \quad \omega_6^2 = \omega_L^2. \tag{41b}$$

Here $\boldsymbol{\xi}(4)$ and $\boldsymbol{\xi}(5)$ are any two unit vectors which are perpendicular to each other, and which are both perpendicular to $\boldsymbol{\xi}(6)$. Explicit expressions for $\boldsymbol{\xi}(4)$ and $\boldsymbol{\xi}(5)$ will not be needed in what follows.

Thus, for crystals of the rocksalt we can label the eigenvectors of equation (32) by an index $j(= 1,2,\ldots 6)$, and we have explicitly that

$$w_\alpha(+|j) = \left(\frac{M_+}{M_c}\right)^{1/2}\delta_{\alpha j}, \quad j = 1,2,3 \tag{42a}$$

$$w_\alpha(-|j) = \left(\frac{M_-}{M_c}\right)^{1/2}\delta_{\alpha j}, \quad j = 1,2,3 \tag{42b}$$

$$w_\alpha(+|j) = \left(\frac{\mu}{M_+}\right)^{1/2}\xi_\alpha(j), \quad j = 4,5,6 \tag{42c}$$

$$w_\alpha(-|j) = -\left(\frac{\mu}{M_-}\right)^{1/2}\xi_\alpha(j), \quad j = 4,5,6. \tag{42d}$$

We now expand $u_\alpha(l\kappa)$ in terms of normal coordinates

$$u_\alpha(l\kappa) = \frac{1}{(NM_\kappa)^{1/2}}\sum_{\mathbf{k}j} w_\alpha(k|\mathbf{k}j)\,e^{i\mathbf{k}\cdot\mathbf{x}(l\kappa)}Q(\mathbf{k}j) \tag{43}$$

where the $\{w_\alpha(\kappa|\mathbf{k}j)\}$ are the continuations to finite wave vectors of the eigenvectors $\{w_\alpha(\kappa|j)\}$. In the long wavelength limit, which is the only case of interest here, the equation of motion satisfied by $Q(\mathbf{k}j)$ on the assumption that it has a time dependence of the form of $\exp(-i\omega t)$, is found to be

$$-\ddot{Q}(\mathbf{k}j) = \omega_j^2Q(\mathbf{k}j) + \frac{4\pi(e^*)^2}{\mu\Omega_0}V(\mathbf{k}\omega;j)Q(\mathbf{k}j) \tag{44}$$

$$\omega_j^2 = 0, \quad j = 1,2,3 \tag{45a}$$

$$= \omega_T^2, \; j = 4,5,6 \tag{45b}$$

$$V(\mathbf{k}\omega;j) = 0, \quad j = 1,2,3 \tag{46a}$$

$$= -\frac{1}{\dfrac{c^2k^2}{\omega^2} - \epsilon_\infty}, \quad j = 4,5 \tag{46b}$$

$$= \frac{1}{\epsilon_\infty}, \quad j = 6. \tag{46c}$$

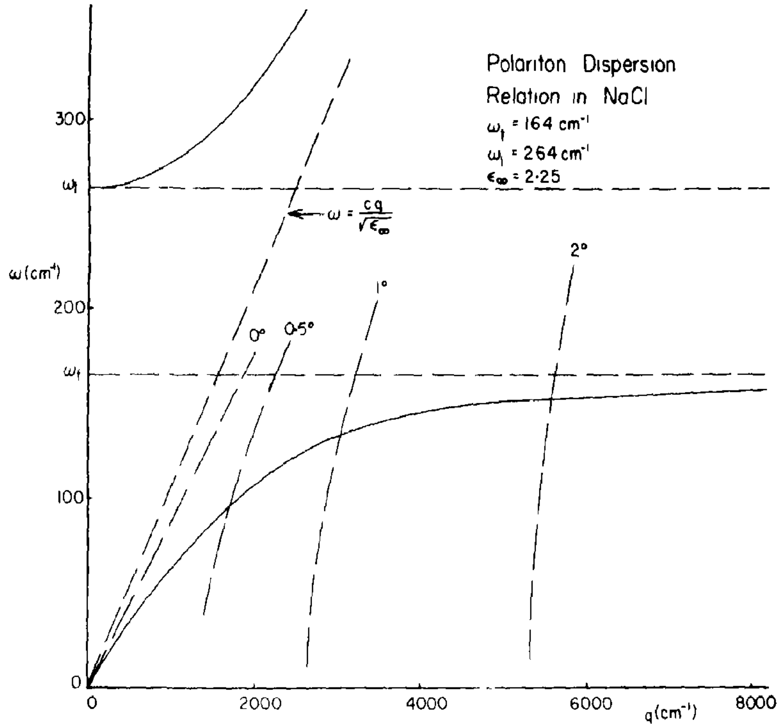

Fig. 1. The polariton dispersion relation for the rocksalt crystal. The dashed curves denote allowed values of frequency and wave vector transfer at 0°, 0·5°, 1° and 2° scattering angles for the exciting light at 6328 Å

With these results in hand, we can now turn to a calculation of the intensity of light scattered by polaritons through the magneto-optic effect.

The rate of Raman scattering per unit solid angle into the frequency range $(\omega_s, \omega_s + d\omega_s)$ is given by[8]

$$I(\omega_s)\,d\omega_s = \frac{\omega_0^4}{2\pi c^3} \sum_{\alpha\beta\gamma\lambda} n_\alpha n_\beta i_{\alpha\gamma\beta\lambda}(\omega) E_\gamma^- E_\lambda^+\,d\omega_s \tag{47}$$

where ω_0 is the frequency of the incident light, $\omega = \omega_s - \omega_0$ is the shift in the frequency of the light on scattering, **n** is a unit vector which defines the polarization of one linearly polarized component of the scattered light, and $\mathbf{E}^+$ and $\mathbf{E}^-(=(\mathbf{E}^+)^*)$ are the amplitudes of the positive and negative frequency components of the incident field. The tensor $i_{\alpha\gamma\beta\lambda}(\omega)$ is given by

$$i_{\alpha\gamma\beta\lambda}(\omega) = \frac{1}{2\pi} \int_{-\infty}^{\infty} dt\, e^{i\omega t} \langle p_{\beta\lambda}^{\dagger}(t) p_{\alpha\gamma}^{-}(0) \rangle, \tag{48}$$

where, in the present problem,

$$p_{\alpha\gamma}^{-} = (p_{\alpha\gamma}^{+})^{+} = \sum_{l\kappa\mu} R_{\alpha\gamma\mu}^{(0)}(\kappa) H_\mu(l\kappa)\, e^{iq\cdot x(l\kappa)} \tag{49}$$

and $\mathbf{q} = \mathbf{k}_s - \mathbf{k}_0$ is the difference between the wave vectors of the scattered and incident light. The operator $p_{\beta\lambda}^{+}(t)$ is the Heisenberg operator

$$p_{\beta\lambda}^{+}(t) = e^{i(t/\hbar)H} p_{\beta\lambda}^{+}(0)\, e^{-i(t/\hbar)H} \tag{50}$$

where H is the Hamiltonian of the system of vibrating ions and the associated electromagnetic field. The angular brackets in equation (48) denote an average over the canonical ensemble defined by the Hamiltonian H.

If a displacement field (9) gives rise to a macroscopic magnetic field (21), with an amplitude given by equation (23), then by superposition the displacement field given by equation (43) gives rise to a macroscopic field

$$H(\mathbf{x};t)=\sum_{\mathbf{k}}\bar{H}_\alpha(\mathbf{k})\,\mathrm{e}^{i\mathbf{k}\cdot\mathbf{x}-i\omega t}\tag{51}$$

where

$$\begin{aligned}\bar{H}_\alpha(\mathbf{k})&=\frac{4\pi}{\Omega_0}\frac{n}{n^2-1}\sum_{\beta\gamma\delta\lambda\mu\kappa'}\\&\quad\times\sum_j\epsilon_{\alpha\beta\gamma}\hat{k}_\beta(\delta_{\gamma\delta}-\hat{k}_\gamma\hat{k}_\delta)S_{\delta\lambda}\\&\quad\times M_{\lambda\mu}(\kappa')\frac{w_\mu(\kappa'|\mathbf{k}j)}{(NM_{\kappa'})^{1/2}}Q(\mathbf{k}j)\end{aligned}\tag{52}$$

which for crystals of the rocksalt structure simplifies to

$$\begin{aligned}\bar{H}_\alpha(\mathbf{k})&=\frac{4\pi}{\Omega_0}\frac{n}{n^2-\epsilon_\infty}\sum_j\\&\quad\times\left\{\sum_{\kappa'\beta}T_{\alpha\beta}(\hat{\mathbf{k}})e(\kappa')\frac{w_\beta(\kappa'|\mathbf{k}j)}{(NM_{\kappa'})^{1/2}}\right\}Q(\mathbf{k}j).\end{aligned}\tag{53}$$

When we substitute equations (51) and (53) into equation (49), we obtain for $p^-_{\alpha\gamma}$ the result that

$$\begin{aligned}p^-_{\alpha\gamma}&=i\sum_{l\kappa\mu}r_{\alpha\gamma\mu}(k)\frac{4\pi}{\Omega_0}\\&\quad\times\sum_{\mathbf{k}j}\frac{n}{n^2-\epsilon_\infty}\sum_{\rho\kappa'}T_{\mu\rho}(\hat{\mathbf{k}})e(\kappa')\\&\quad\times\frac{w_\rho(\kappa'|\mathbf{k}j)}{(NM_{\kappa'})^{1/2}}\mathrm{e}^{i(\mathbf{k}-\mathbf{q})\cdot\mathbf{x}(l\kappa)}Q(\mathbf{k}j)\\&=iN^{1/2}\frac{n}{n^2-\epsilon_\infty}\sum_\mu g_{\alpha\gamma\mu}\sum_j\\&\quad\times\left\{\sum_{\rho\kappa}T_{\mu\rho}(\hat{\mathbf{q}})e(\kappa).\frac{w_\rho(\kappa|\mathbf{q}j)}{M_\kappa{}^{1/2}}\right\}Q(\mathbf{q}j)\end{aligned}\tag{54}$$

where n is now (cq/ω), and we have used equation (8) to simplify this result. Inasmuch as $w_\rho(\kappa|\mathbf{q}j)/M_\kappa{}^{1/2}$ is independent of κ for $j=1,2,3$, then in view of equation (25b) only the optical modes contribute to $p^-_{\alpha\gamma}$, which we rewrite as

$$\begin{aligned}p^-_{\alpha\gamma}&=iN^{1/2}\frac{e^*}{\mu^{1/2}}\frac{n}{n^2-\epsilon_\infty}\\&\quad\times\sum_j^{\text{opt.}}\sum_{\mu\rho}g_{\alpha\gamma\mu}T_{\mu\rho}(\hat{\mathbf{q}})\xi_\rho(j)Q(\mathbf{q}j).\end{aligned}\tag{55}$$

Therefore, the elements of the tensor $i_{\alpha\gamma\beta\lambda}(\omega)$ are given by

$$\begin{aligned}i_{\alpha\gamma\beta\lambda}(\omega)&=N\frac{(e^*)^2}{\mu}\frac{n^2}{(n^2-\epsilon_\infty)^2}\\&\quad\times\sum_{jj'}^{\text{opt.}}\sum_{\mu\rho}\sum_{\nu\sigma}g_{\beta\lambda\nu}g_{\alpha\gamma\mu}\\&\quad\times T_{\nu\sigma}(\hat{\mathbf{q}})T_{\mu\rho}(\hat{\mathbf{q}})\xi_\sigma(j)\xi_\rho(j')\\&\quad\times\frac{1}{2\pi}\int_{-\infty}^{\infty}\mathrm{d}t\,\mathrm{e}^{-i\omega t}\\&\quad\times\langle Q^*(\mathbf{q}j;t)Q(\mathbf{q}j';0)\rangle.\end{aligned}\tag{56}$$

To evaluate the Fourier transform of the correlation function, we introduce the (retarded) double time Green's function [9]

$$\begin{aligned}G(\mathbf{q}j;\mathbf{q}j';t)&=\langle\langle Q^*(\mathbf{q}j;t);Q(\mathbf{q}j';0)\rangle\rangle\\&=-i\theta(t)\langle[Q^*(\mathbf{q}j;t),Q(\mathbf{q}j';0)]\rangle\end{aligned}\tag{57}$$

where $\theta(t)$ is the Heaviside unit step function. If we introduce the Fourier transform of this function by

$$G(\mathbf{q}j;\mathbf{q}j';t)=\int_{-\infty}^{\infty}\mathrm{d}E\hat{G}(\mathbf{q}j;\mathbf{q}j';E)\,\mathrm{e}^{-iEt}\tag{58}$$

then it is the case that

$$\frac{1}{2\pi}\int_{-\infty}^{\infty}\mathrm{d}t\,\mathrm{e}^{-i\omega t}\langle Q^*(\mathbf{q}j;t)Q(\mathbf{q}j';0)\rangle$$

$$= \frac{i}{e^{\beta\hbar\omega}-1}$$

$$\times [\hat{G}(\mathbf{q}j;\mathbf{q}j';\omega+i0)-\hat{G}(\mathbf{q}j;\mathbf{q}j';\omega-i0)]. \tag{59}$$

The Green's function $G(\mathbf{q}j;\mathbf{q}j';t)$ obeys the equation of motion

$$-\hbar^2\frac{d^2}{dt^2}G(\mathbf{q}j;\mathbf{q}j';t)$$

$$= i\hbar^2\delta(t)\langle[\dot{Q}^*(\mathbf{q}j),Q(\mathbf{q}j')]\rangle$$

$$-\hbar^2\langle\langle\ddot{Q}^*(\mathbf{q}j;t);Q(\mathbf{q}j';0)\rangle\rangle. \tag{60}$$

The commutator of $Q^*(\mathbf{q}j)$ and $Q(\mathbf{q}j')$ is

$$[\dot{Q}^*(\mathbf{q}j),Q(\mathbf{q}j')] = -i\hbar\delta_{jj'}. \tag{61}$$

Consequently, taking the Fourier transform of equation (60) and making use of equations (61) and (44–46), we obtain

$$\hat{G}(\mathbf{q}j;\mathbf{q}j';E) = \delta_{jj'}\frac{\hbar}{2\pi}$$

$$\times\frac{1}{E^2-\omega_j^2-\dfrac{4\pi(e^*)^2}{\mu\Omega_0}V(\mathbf{q}E;j)}. \tag{62}$$

Combining the results given by equations (56), (59) and (62), we obtain the result that

$$i_{\alpha\gamma\beta\lambda}(\omega) = N\hbar\frac{sgn\omega}{e^{\beta\hbar\omega}-1}\frac{(e^*)^2}{\mu}\frac{n^2}{(n^2-\epsilon_\infty)^2}$$

$$\times\sum_{\mu\rho}\sum_{\nu\sigma}g_{\alpha\gamma\mu}\,g_{\beta\lambda\nu}T_{\mu\rho}(\hat{\mathbf{q}})T_{\nu\sigma}(\hat{\mathbf{q}})$$

$$\times\{\hat{q}_\rho\hat{q}_\sigma\delta(\omega^2-\omega_l^2)+(\delta_{\rho\sigma}-\hat{q}_\rho\hat{q}_\sigma)\mathscr{S}(\omega)$$

$$\times[\delta(\omega^2-\omega_+^2(\mathbf{q}))+\delta(\omega^2-\omega_-^2(\mathbf{q}))]\} \tag{63}$$

where

$$\mathscr{S}(\omega) = \frac{\omega^2\omega_p^2}{(\omega^2-\omega_T^2)^2}\left[1+\frac{\omega^2\omega_p^2}{(\omega^2-\omega_T^2)^2}\right]^{-1} \tag{64}$$

is the phonon strength function which has been used in previous discussions of polariton theory[2]. This function may be introduced upon noting the identity

$$\frac{\omega_\pm^2(\mathbf{q})-(c^2q^2/\epsilon_\infty)}{\omega_+^2(\mathbf{q})-\omega_-^2(\mathbf{q})}\delta(\omega^2-\omega_\pm^2(\mathbf{q}))$$

$$= \pm\mathscr{S}(\omega)\delta(\omega^2-\omega_\pm^2(\mathbf{q})) \tag{65}$$

which follows from equations (39) and (40).

If we use the result, which follows from equations (6) and (8), that for crystals of the rocksalt structure

$$g_{\alpha\gamma\mu} = \epsilon_{\alpha\gamma\mu}g \tag{66}$$

and the explicit expression for $T_{\alpha\beta}(\hat{\mathbf{q}})$ given by equation (27), we obtain finally as the only non-zero element of $i_{\alpha\gamma\beta\lambda}(\omega)$ (in the case that $\mathbf{q} = (q,0,0)$)

$$i_{xyxy}(\omega) = N\hbar\frac{sgn\omega}{e^{\beta\hbar\omega}-1}\mathscr{S}(\omega)\frac{(e^*)^2}{\mu}$$

$$\times\frac{n^2}{(n^2-\epsilon_\infty)^2}g^2$$

$$\times[\delta(\omega^2-\omega_+^2(\mathbf{q}))+\delta(\omega^2-\omega_-^2(\mathbf{q}))]$$

$$= i_{zxzx}(\omega). \tag{67}$$

Now let us estimate the intensity of scattering via the present mechanism and consider the feasibility of observing this effect experimentally. The value of g in the limit of ω going to zero (for a static magnetic field) can be estimated from the data on Faraday rotation of a crystal at the wavelength of the exciting light λ_0. The Faraday rotation angle per unit length of a crystal is given by[10]

$$\theta = \frac{\pi}{\lambda_0}(n_+-n_-) \tag{68}$$

where n_+ and n_- are the indices of refraction for light of positive and negative helicity propagating in the direction of the magnetic field. n_+ and n_- can be derived from the expression for the dielectric constant $\epsilon_{\mu\nu\lambda}(H)$, equation (7), in the presence of a magnetic field. When the magnetic field is along the z-axis, i.e. $\mathbf{H} = (0,0,H_z)$, in a crystal of the rocksalt structure, we have

$$n_\pm = [\epsilon^{(0)} \pm gH_z]^{1/2}. \tag{69}$$

Combining equation (68) and equation (69), we obtain the relation between g and θ in the limit of $gH_z/\epsilon^{(0)} \ll 1$

$$g = \frac{\lambda_0 \sqrt{\epsilon^{(0)}}\theta}{\pi H_z}. \tag{70}$$

The value of g calculated for n-type PbS at $\lambda_0 = 10\mu$ from the Faraday rotation data of Palik *et al.*[11] is approximately $1{\cdot}0 \times 10^{-7}\,\mathrm{G}^{-1}$.

A rough idea of the relative strength of the magneto-optic scattering can be obtained by comparing the magnitude of $i_{xyxy}(\omega)$ in equation (67) with the electro-optic scattering contribution $i^{(EO)}_{xyxy}(\omega)$ in a crystal lacking a center of inversion. The electro-optic contribution to Raman scattering by polaritons in a zincblende type crystal can be shown to be

$$i^{(EO)}_{xyxy}(\omega) = N\hbar \frac{sgn\omega}{e^{\beta\hbar\omega} - 1}$$

$$\times \mathcal{T}(\omega) \frac{(e^*)^2}{\mu} \frac{1}{(n^2 - \epsilon_\infty)^2} Q^2$$

$$\times [\delta(\omega^2 - \omega_+{}^2(\mathbf{q})) + \delta(\omega^2 - \omega_-{}^2(\mathbf{q}))] \tag{71}$$

where Q is the single non-zero electro-optic tensor element[12]. Thus the ratio between the magneto-optic and the electro-optic contributions to Raman scattering by polaritons is roughly of the order of

$$\frac{i^{(MO)}_{xyxy}(\omega)}{i^{(EO)}_{xyxy}(\omega)} \approx \frac{n^2 g^2}{Q^2}. \tag{72}$$

The value of Q in zincblende type II–VI compounds such as ZnS and ZnSe is typically of the order of 5×10^{-6} esu[13]. For n-type PbS at $\lambda_0 = 10\mu$ the ratio in equation (72) becomes

$$\frac{i^{(MO)}_{xyxy}(\omega)}{i^{(EO)}_{xyxy}(\omega)} \approx 10^{-1}.$$

Since the electro-optic contribution to Raman scattering by polaritons is experimentally observable[14], the first order Raman scattering by polaritons via the magneto-optic effect in lead salts of the rocksalt structure should also be experimentally observable.

Finally, we point out that although we have emphasized crystals possessing the rocksalt structure in the present discussion, the general results presented here predict and describe the first order Raman effect from polaritons associated with i.r. active modes in arbitrary, centrosymmetric crystals.

REFERENCES

1. BORN M. and HUANG K., *Dynamical Theory of Crystal Lattices*, p. 371. Oxford University Press, New York (1954).
2. POULET H., *Ann Phys.* **10**, 908 (1955); LOUDON R., *Adv. Phys.* **13**, 423 (1964).
3. BURSTEIN E., USHIODA S. and PINCZUK A., *Solid State Comm* **6**, 407 (1968)
4. Reference [1], section 8
5. LANDAU L. D. and LIFSHITZ E. M., *Electrodynamics of Continuous Media*, Section 82. Addison-Wesley, Reading, Mass. (1960).
6. Reference [1], section 44.
7. Reference [1], section 33.
8. Reference [1], sections 19 and 49.
9. ZUBAREV D. N., *Usp Fiz. Nauk* **71**, 71 (1960); [English translation: *Soviet Physics – Uspekhi* **3**, 320 (1960).
10. NYE J. F., *Physical Properties of Crystals*, p. 262 Clarendon, Oxford (1957).
11. PALIK E. D. and MITCHELL D. L., *Phys. Rev.* **135**, A763 (1964).
12. The third rank tensor $Q_{\mu\nu\lambda}$ is defined by a relation similar to equation (7) in which iH_λ is replaced by E_λ. $Q_{\mu\nu\lambda}$ is related to the nonlinear susceptibility by an approximate relation $Q_{\mu\nu\lambda} = 4\pi(\partial\chi_{\mu\nu}/\partial E_\lambda) \cong 4\pi d^{2\omega}_{\mu\nu\lambda}$, where $\chi_{\mu\nu}$ is the electronic susceptibility of the crystal.
13. ROBINSON F. N. H., *Bell Syst. Tech J* 913. May–June 1967).
14. USHIODA S., PINCZUK A., TAYLOR W. and BURSTEIN E., *Proc. 1967 Int. Conf. II-VI Semiconducting Compounds* Benjamin, New York (1967).

J. Phys. Chem. Solids Pergamon Press 1970. Vol. 31, pp. 1085–1097. Printed in Great Britain.

LATTICE DYNAMICS OF MAGNESIUM STANNIDE AT ROOM TEMPERATURE*

R. J. KEARNEY
University of Idaho, Moscow, Idaho 83843, U.S.A.

and

T. G. WORLTON† and R. E. SCHMUNK
Idaho Nuclear Corporation, Idaho Falls, Idaho 83401, U.S.A.

(*Received* 24 *July* 1969; *in revised form* 23 *October* 1969)

Abstract – Neutron inelastic scattering has been used to determine the frequency–wave vector phonon dispersion relation of Mg_2Sn at room temperature along the [00ζ], [ζζ0] and [ζζζ] symmetry directions. The frequency of the i.r. active optical mode was found to be $5{\cdot}56\times10^{12}\,\mathrm{sec}^{-1}$ in excellent agreement with i.r. absorption measurements. Slopes of the acoustic modes were in good agreement with elastic constant data. Both rigid ion and shell models have been least squares fit to the experimentally measured frequencies. A satisfactory fit to the experimental data was obtained with 9 and 10 parameter shell models, but no satisfactory fit was found for the 7 parameter rigid ion model. The best fitting model was used to calculate the vibration frequencies along the [1ζ0] direction in addition to the directions for which measurements were made.

1. INTRODUCTION

Mg_2Sn is a fluorite structure semiconducting compound whose electrical properties have been studied extensively[1–6]. However, knowledge of both the electronic and lattice properties are prerequisite to a thorough understanding of the physical properties of a crystal. A preliminary calculation of the lattice vibrations of Mg_2Sn for the principal symmetry directions was made by Davis *et al.*[7] using experimentally determined elastic constants and i.r. measurements. These data, however, are not sufficient to obtain a good description of the lattice vibration frequencies except possibly in the long wavelength limit. Inelastic neutron scattering provides a method of measuring the normal modes of vibration throughout the Brillouin zone. The frequency and wave vector (ω and $\mathbf{q}$) of phonons which take part in the coherent single inelastic scattering of thermal neutrons from a solid are given by the following equations of conservation of energy and momentum:

$$\Delta E = |E - E_0| = \hbar\omega(\mathbf{q}),$$
$$\mathbf{Q} \equiv \mathbf{k}_0 - \mathbf{k} = 2\pi\boldsymbol{\tau} \pm \mathbf{q}, \qquad (1)$$

where E_0, $\mathbf{k}_0$ and E, $\mathbf{k}$ are respectively the neutron energy and wave vector before and after scattering, and $\boldsymbol{\tau}$ is a reciprocal lattice vector. By making a series of neutron scattering measurements with a single crystal sample it is possible to obtain extensive information about the phonon dispersion relation, i.e. the relationship between ω and $\mathbf{q}$ for the normal modes of vibration of a crystal.

In this paper we report on an experimental study of the lattice dynamics of Mg_2Sn by inelastic thermal neutron scattering which was made using a three axis spectrometer at the Materials Testing Reactor. Experimental measurements were made for $\mathbf{q}$ along [00ζ], [ζζ0] and [ζζζ] symmetry directions. The symmetry properties of the fluorite structure which are derived in a companion paper[8]

---

*Work done under the auspices of the U.S. Atomic Energy Commission.

†*Present address*: Los Alamos Scientific Laboratory, Los Alamos, New Mexico 87544, U.S.A.

(hereafter referred to as KWS II) were used to classify the branches of the dispersion relation. The experimental data have been compared with rigid ion and shell models whose parameters were evaluated by a least squares fitting routine to give the best agreement between the individual models and the data. The rigid ion model fit the experimental data very poorly whereas both nine and ten parameter versions of the shell model fit the data very well. No attempt was made to calculate any thermodynamic properties from the models since the low Debye temperature[9] indicates that there would be appreciable anharmonic contributions to these properties[10]. The cost of computer time needed for accurate frequency distribution calculations was also an important consideration.

Single crystal inelastic scattering experiments have been performed elsewhere on CaF_2 [11], and UO_2[12], both of which have the fluorite structure. Some of the results of the UO_2 experiment will be discussed and related to the present experiment.

2. LATTICE DYNAMICS

The crystal structure of Mg_2Sn consists of three interpenetrating face-centered cubic lattices: one lattice of tin ions with origin (0, 0, 0) and two of magnesium ions with origins at $(a/4)(1, 1, 1)$ and $(3a/4)(1, 1, 1)$. Each tin ion occupies a center of inversion symmetry and is surrounded by eight magnesium ions. A drawing of the unit cell with atoms labeled as in the present paper is given in KWS II and also by Whitten *et al.*[13]. The lattice constant has the value $a = 6{\cdot}758$ Å[14].

In the harmonic approximation the vibrational frequencies $\omega(\mathbf{q})$ of the lattice are the solutions of the secular equation:

$$\alpha, \beta = x, y, z$$

$$\det|\omega^2(\mathbf{q})\delta_{\alpha\beta}\delta_{\kappa\kappa'} - D^{\kappa\kappa'}_{\alpha\beta}(\mathbf{q})| = 0, \qquad (2)$$

$$\kappa\kappa' = 1, 2, 4$$

Terms in this equation are defined in the Appendix. The dynamical matrix **D** is of the order 9×9, and hence, there are nine eigenvalues ω, or nine branches of the dispersion relation for an arbitrary direction of **q**. Three branches are acoustic and six branches are optic. For wave vectors **q** in directions of high symmetry **D** can be reduced to lower order matrices which simplifies the work in solving the above equation, and the number of distinct branches of the dispersion relation may be reduced because of degeneracies. In addition, along directions of high symmetry the eigenvectors for the normal modes of vibration are often constrained by symmetry whereas along some arbitrary direction they usually are not, a point which is used to advantage in planning and completing the experimental measurements. In KWS II the reduction of the dynamical matrix and the classification of the phonon branches according to symmetry are discussed.

Briefly, in the $[00\zeta]$ direction there are three transverse branches, each doubly degenerate, and three longitudinal branches. The same statement applies for the $[\zeta\zeta\zeta]$ direction where again all branches have pure polarizations. For waves propagating along $[\zeta\zeta 0]$ there are three transverse branches which are polarized along $[\zeta\bar{\zeta}0]$. The other six branches for this direction of propagation do not have symmetry determined polarizations.

3. EXPERIMENTAL METHOD AND RESULTS

Experimental measurements reported here were made using a three-axis spectrometer installed at the Materials Testing Reactor (MTR). The spectrometer, which has been described elsewhere[15] consisted of two units: (1) a monochromator facility for producing a monoenergetic beam of neutrons; and (2) a sample platform and energy analyzer unit which were mounted on a large diameter rotary table. All measurements were made in the 'constant Q' mode with the incident neutron energy held constant. During the initial phase of the experiment the spectrometer was installed at the HB-3 beam hole of the MTR, utilizing two spherical aluminum crystals with the (111) planes of the two crystals aligned in the 'parallel' configuration to produce a monochromatic beam with a wavelength of 1·349 Å. A third aluminum crystal, again using the (111) planes, was utilized as an analyzer crystal.

Because of the low beam intensity at the sample position ($< 1\times 10^6$ neutrons/cm^2/sec) and the poor statistics on many of the phonon scans[16] the measurements were repeated with the spectrometer installed at the HT-1 south beam hole of the MTR. In the second series of measurements a beryllium crystal, (002) planes, was used as monochromator giving a flux of 5×10^6 neutrons/cm^2/sec at the sample position with a neutron wavelength of 1·227 Å. Horizontal collimation of 0·3° FWHM was used between monochromator and sample positions and 0·5° FWHM between sample and analyzer positions. The use of a copper crystal as an analyzer gave a further increase in counting rate which overall amounted to a factor of 15 due to changes in both monochromator and analyzer crystals. The efficiency of data collection was improved considerably during the second series of measurements through the interfacing of the spectrometer to a PDP-9 computer[17]. The necessary constants were read into the computer for each phonon scan along with a sequence of numbers which dictated the order in which the measurements were to be performed. All spectrometer angle settings were calculated by the PDP-9 including angle corrections to get from the final angles of one scan to the initial angles of the next scan. Automatic operation by the computer included the recording and resetting of data and monitor scalers and the incrementing of the spectrometer angles through digital pulses supplied from the computer to Slo-Syn stepping motors.

The Mg_2Sn single crystal was grown by a modified Bridgman technique. Its shape is that of a cone with a base diameter of 1·95 cm and a length of 5·95 cm. Resistivity and Hall coefficient measurements on similar samples show a residual carrier concentration of $\approx 10^{16}$ cm^{-3}. Although specific experiments to determine the mosaic spread of the sample were not performed, it is estimated to be approximately 5 min of arc.

All measurements were restricted to scattering in the $(1\bar{1}0)$ plane, and data were obtained for waves propagating in the symmetry directions $[00\zeta]$, $[\zeta\zeta0]$ and $[\zeta\zeta\zeta]$. For both $[00\zeta]$ and $[\zeta\zeta\zeta]$ directions where the number of branches is reduced to six by degeneracy data were obtained on all branches. However, along $[\zeta\zeta0]$ data were obtained for only six of the nine branches because the polarization for the other three branches was normal to the scattering plane. Structure factor and focusing considerations were used as a guide in determining the reciprocal lattice position for maximum intensity of the various phonon modes. The results of Elliott and Thorpe[18] were also helpful in the choice of lattice point. Figure 1 shows the $(1\bar{1}0)$ reciprocal lattice plane with the structure zone and Brillouin zones outlined. Alphabetically labeled points have been included in the figure to indicate the region in k-space in which a given branch was investigated, letters A–F for the Λ direction, G–L for the Σ direction and M–S for the Δ direction with the branches for each direction labeled in order of increasing frequency. In Fig. 2 data peaks are displayed for each of the six Λ branches for constant Q scans taken at $\zeta = 0{\cdot}3$. The time required for the constant Q scans varied typically from a few minutes for the low frequency acoustic modes to about 4 hr for the optic modes.

The measured normal mode frequencies for Mg_2Sn are listed in Table 1 and the data are displayed in Fig. 3. Errors on the data are generally in the range 1–2 per cent. The group theory notation used is that of Bouckaert *et al.* [19]. For the symmetry directions $[00\zeta]$ and $[\zeta\zeta\zeta]$ the diamonds indicate modes having transverse polarization and the circles indicate longitudinal modes while along $[\zeta\zeta0]$ the polarizations are not necessarily pure for the observed branches. Initial slopes of the acoustic branches are in very good agreement with the

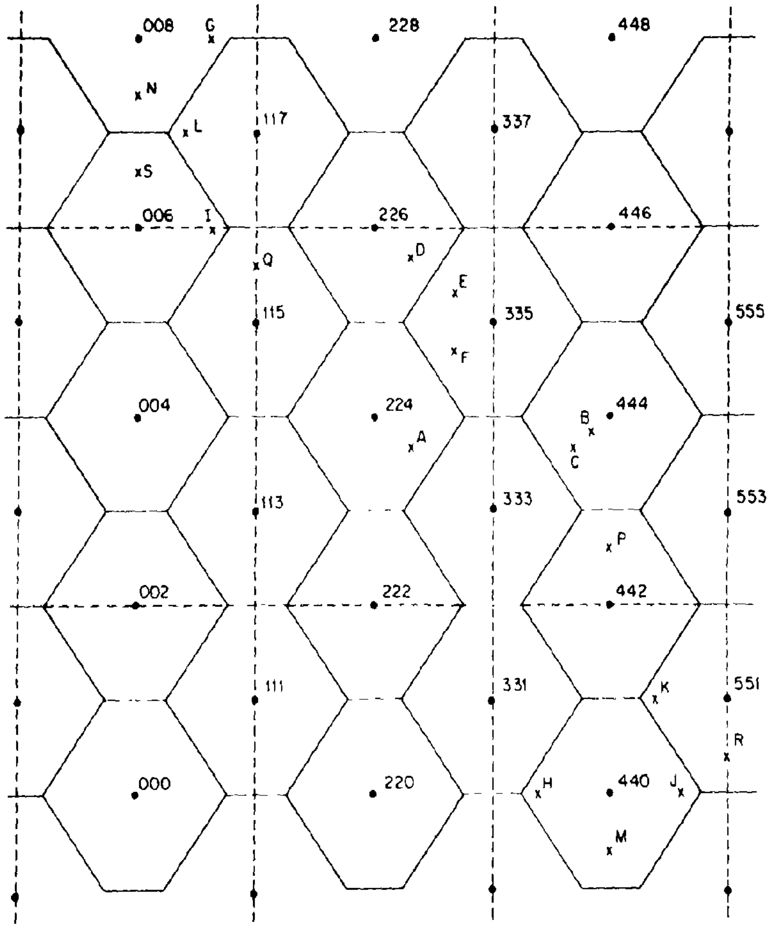

Fig. 1. Reciprocal space plot for Mg_2Sn showing the Brillouin zone outline (solid lines) in the scattering plane of the experiment along with an outline of the periodic range of the dynamic structure factor (dashed lines). Alphabetically labeled points indicate the region in which the various branches were measured, points A–F for the $[\zeta\zeta\zeta]$ direction, G–L for the $[\zeta\zeta 0]$ direction, and M–S for the $[00\zeta]$ direction with the label in order of increasing frequency for each direction.

elastic constant data of Davis *et al.*[7] and the observed $TO(\Gamma)$ mode for which $\nu = 5{\cdot}56 \times 10^{12}\,\mathrm{sec}^{-1}$) is in very good agreement with the i.r. absorption data ($\nu = 5{\cdot}57 \times 10^{12}\,\mathrm{sec}^{-1}$) of Kahan *et al.*[20]. We were unable to observe the $LO(\Gamma)$ mode corresponding to the end point of the Δ_1 optical branch, so the open point shown in the data figure was determined from the Lyddane–Sachs–Teller relation[21] using the frequency of the $TO(\Gamma)$ mode cited above and the dielectric constant data of Kahan *et al.* The dispersion relation data for Mg_2Sn are quite similar to the dispersion relation for UO_2[12] except for the fact that acoustical and optical modes are clearly separated along the three symmetry directions in Mg_2Sn while they are not for UO_2.

Lipson and Kahan[3] have deduced from a fitting procedure based on optical absorption measurements that the electron transition to the conduction band in Mg_2Sn is indirect and requires a phonon energy of 0·008 eV. Piezoresistance measurements[5, 6] show the conduction band to have a minimum along the

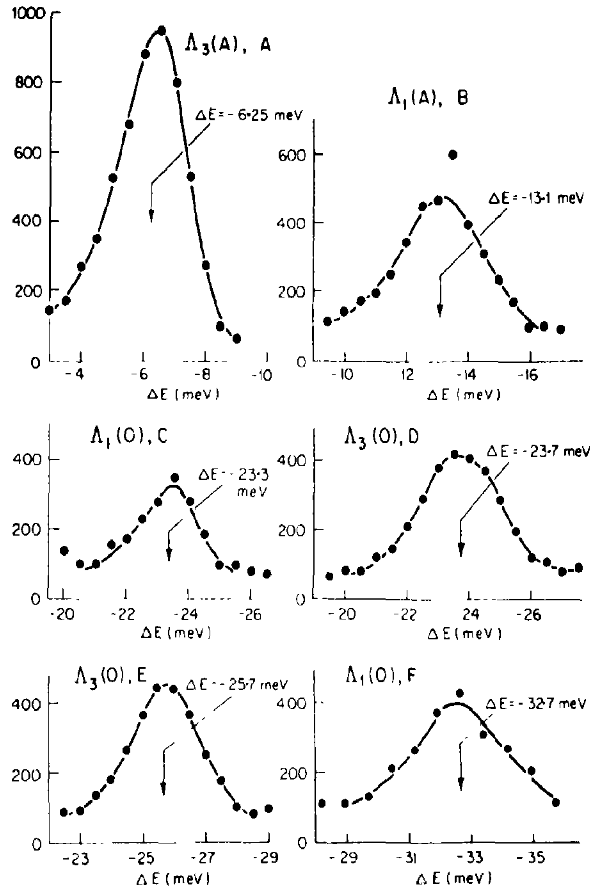

Fig. 2. Data peaks obtained for each of the six Λ branches at $\zeta = 0{\cdot}3$ with the spectrometer operated in the 'constant Q' mode. The letter identification assigned to each peak is used to identify the location in k-space where the measurement was made as indicated in Fig. 1.

[00ζ] direction while the valence band maximum is at the zone center. Hence the phonon which assists in the electron transition lies along [00ζ]. Neutron inelastic scattering in the present experiment shows that the energy value 0·008 eV occurs at approximately $\zeta = 0{\cdot}55$ on the Δ_5 acoustic branch which puts the conduction band minimum inside the Brillouin zone. However, since Mg_2Sn is a symmorphic group (unlike silicon it has neither glide planes nor screw axes) we suspect that the minimum is actually on the zone boundary. This is in agreement with recent band calculations performed by Au-Yang and Cohen[22]. Presumably the optical absorption data must be compared with a phonon energy of 0·0091 ± 0·0001 eV, assuming that only this mode contributes.

4. MODELS

Three different models based on the Born–von Karman theory of lattice dynamics have been employed to calculate the lattice vibration frequencies of Mg_2Sn. The simplest model is the rigid ion model which treates each ion as a charged particle. Dynamical matrix elements for a rigid ion model of the fluorite lattice were first derived by Srinivasan[23] and

Table 1. Observed phonon frequencies for Mg_2Sn *in units of* 10^{12} *sec*$^{-1}$

Direction	$\zeta = aq/2\pi$	$\Delta_5(A)$	$\Delta_1(A)$	$\Delta'_2(0)$	$\Delta_5(0)$	$\Delta_5(0)$	$\Delta_1(0)$
[00ζ]	0·2	0·89	1·40	6·42	5·55	6·58	6·92
	0·4	1·60	2·45	6·14	5·30	6·56	7·33
	0·6	1·96	3·22	5·32	4·95	6·66	8·11
	0·8	2·21	3·55	4·75	4·72	6·73	8·78
	1·0	2·21	3·68	4·47	4·58	6·79	9·07
		$\Sigma_1(A)$	$\Sigma_1(A)$	$\Sigma_4(0)$	$\Sigma_3(0)$	$\Sigma_1(0)$	$\Sigma_1(0)$
[ζζ0]	0·2	1·85	1·25	5·38	6·52	6·29	
	0·4	3·02	2·13	5·08	6·11	5·86	7·42
	0·5	3·26					
	0·6	3·22	2·71	4·67	5·74	6·26	7·5
	0·8	2·96	3·31	4·50	5·09	6·67	8·12
	0·9	2·32	3·59	4·47			
	1·0	2·21	3·68	4·45	4·58	6·79	9·07
		$\Lambda_3(A)$	$\Lambda_1(A)$	$\Lambda_3(0)$	$\Lambda_3(0)$	$\Lambda_1(0)$	$\Lambda_1(0)$
[ζζζ]	0·1	0·72	1·18	5·57	6·55	6·24	
	0·2	1·28	2·42	5·63	6·38	5·74	7·62
	0·3	1·51	3·17	5·74	6·21	5·65	7·82
	0·4	1·57	3·45	5·86	6·11	5·79	7·63
	0·5	1·60	3·43	5·97	6·00	5·91	7·60

$\nu_{TO}(\Gamma_{15}) = 5{\cdot}56$.
$\nu_{TO\,TO}(\Gamma'_{25}) = 6{\cdot}67$.

Ganesan and Srinivasan[24]. They considered Ca–F (I–II and I–IV) and F–F (II–II, II–IV and IV–IV) short range interactions plus the long range Coulomb interaction, which gave a total of five independent parameters in the model. The model of Ganesan and Srinivasan was later extended to include third neighbors (I–I interaction) and applied to Mg_2Si and Mg_2Ge by Whitten *et al.*[13] and Chung *et al.*[25].

A qualitative description of the data can be obtained using the rigid ion model, but this model fails rather badly in describing the high frequency longitudinal optic modes of ionic crystals. By taking into account the polarizability of the ions a much better description of the dispersion relations can be obtained. This can be done by means of a shell model which considers each ion to be made up of a core and a shell which are coupled together, but are able to move separately giving a net polarization to the ion. The vibrational frequencies are obtained as solutions to the secular equation (2) where the dynamical matrix $D_{\alpha\beta}^{\kappa\kappa'}(\mathbf{q})$ is given in the shell model [26, 27] as:

$$\mathbf{D} = (\mathbf{R} + \mathbf{ZCZ}) - (\mathbf{T} + \mathbf{ZCY})(\mathbf{S} + \mathbf{YCY})^{-1} \times (\mathbf{T}^{\dagger} + \mathbf{YCZ}). \quad (3)$$

Here **R**, **T**, and **S** are 9×9 matrices representing the core–core, core–shell and shell–shell interactions, respectively, **Y** and **Z** are 9×9 diagonal matrices representing the shell and ion charges and **C** is a 9×9 matrix representing the long range Coulomb interaction. The adiabatic approximation which sets the shell mass equal to zero has been introduced in order to obtain equation (3) from the equations of motion. To further reduce the number of parameters it is assumed, as usual, that the overlap forces act only between the shells of neighboring ions. In this approximation, **T** = **R** and **S** = **R** + **K**, and because the force constant matrices must be real-symmetric or Hermitian, $\mathbf{T}^{\dagger} = \mathbf{T}$. **K** is a diagonal matrix such that $K_{\alpha\alpha}(\kappa)$ is the core–shell coupling constant for the κth atom. The dy-

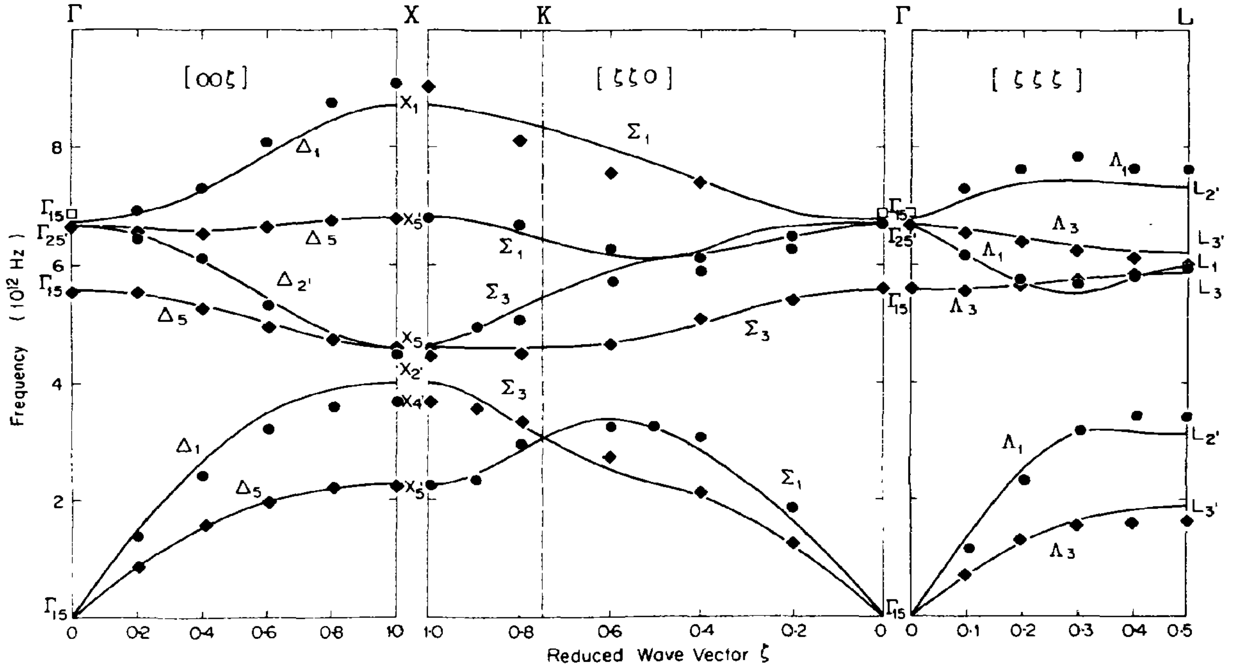

Fig. 3. Phonon dispersion relation of Mg_2Sn for the three symmetry directions [00ζ], [ζζ0] and [ζζζ]. Diamonds and round points indicate branches having transverse and longitudinal polarizations respectively for the Δ and Λ branches whereas the Σ branches of this experiment do not have symmetry determined polarizations The curves in the figure are the result of a ten parameter shell model which was least squares fit to the data.

namical matrix for fluorite type crystals is a 9×9 Hermitian matrix since there are three atoms in the primitive unit cell, not all related by inversion symmetry.

The most complete work to date on a fluorite type crystal was done by Dolling *et al.*[12] who measured the dispersion curves of UO_2 using neutron inelastic scattering and fitted their data with several models including the third neighbor shell model. Short range terms used in the present paper are the same as those used by Dolling *et al.* with the corrections noted in the Appendix. Formulas are also given in the Appendix for relating the parameters of Davis[7] to those of Dolling. The elements of the short range matrix given by Axe[28] are the same as those given by Dolling if the U–U interaction is neglected and the force constants defined in terms of $e^2/2V$, instead of e^2/V. (Here $V = a^3/4$ is the volume of the primitive unit cell.)

Davis *et al.* used acoustic, i.r. and Raman data to evaluate the parameters of both shell and rigid ion models for Mg_2Sn. Because of the limited amount of experimental information which Davis *et al.* had available it was necessary for them to restrict the number of parameters in their models. In their shell model only the Sn ion was assumed polarizable and one other parameter was assumed equal to zero. Their models gave a fairly good fit to the acoustic modes but gave a poor fit to the optic modes.

Whitten *et al.*[13] calculated the Coulomb coupling terms which can be used for the Sn–Mg^{II} and Sn–Mg^{IV} coupling while Kellerman's [29] NaCl results can be used for the Sn–Sn and Mg^{II}–Mg^{II} plus Mg^{IV}–Mg^{IV} interactions. Rather than use these published values which were only accurate to 1 or 2 decimal places, a computer program was written which was used to make calculations accurate to five decimal places[30]. These values were then read into the computer as a table at the beginning of the program used for the least squares fitting.

In the present experiment classification of the branches in Fig. 3 was made after comparing with the calculated frequencies found for the various submatrices in KWS II, using preliminary values of the force constants. By using the block diagonalized dynamical matrix it was possible to identify each branch uniquely and thus be certain that each of the calculated eigenvalues was paired with the proper experimental frequency for the least squares fitting of the models to the experimental data. Starting with the parameters given by Davis *et al.* the parameters of the rigid ion (model I) and shell models (models II and III) were obtained by least squares fitting to the dispersion curves in the $[00\zeta]$, $[\zeta\zeta 0]$ and $[\zeta\zeta\zeta]$ directions. Parameters of the models are presented in Table 2 and results of the calculations with these models are displayed in Fig. 3 (model III) and in Fig. 4 (models I and II). A good fit to the experimental data was obtained with the ten parameter model (III) and with the nine parameter shell model (II) which considered only the Sn ion polarizable.

In model III the shell charge on the Mg ion was fixed at $-8{\cdot}0\,e$ because it tended to physically unrealistic values when allowed to vary. (Values ranging up to 500 e in magnitude were obtained in the fitting.) Even in model III which considered both ions polarizable, the polarizability of the Mg ion was negligible. Calculation of the polarizability of the Sn ion 10·24 and 10·40 for models II and III (units of Å^3) respectively. Tessman *et al.*[31] report a value of 3·4 Å^3 for the electronic polarizability of the Sn^{4+} ion.

Elastic constants were not included in the least squares fitting but were calculated for each of the models after fitting to the neutron data. The equations used are given in the Appendix. They were obtained by extending the recently published equations of Srinivasan [32] to third neighbors using the equations given by Chung *et al.*[25]. As can be seen in Table 3, model I gives a poor fit to the elastic constant data as well as to the neutron data. Of course, it would have been possible to obtain a rigid ion model which gave excellent

Table 2. Values obtained for lattice dynamics model parameters by least squares fit of the models to the dispersion relation data of Table 1

	Sn–Mg		Mg_{II}–Mg_{IV}		Sn–Sn		
Model	A_1*	B_1*	A_2*	B_2*	A_3*	B_3*	
I	5·73	2·37	2·17	0·12	3·42	−2·07	
II	21·34	−3·00	0 24	0 29	0·10	0·97	
III	19·71	−2·45	0·60	0·21	1 71	0·25	
	Z_1†	Z_2†	Y_1†	Y_2†	K_1	K_2	χ^2
I	−1·03	0·52	0	0	—	—	2·70
II	−2·07	1·04	−4·90	0	132	—	1·96
III	−1·94	0·97	−5·18	−8·0	153	10^7	1·66

The parameter χ^2 indicates the quality of fit in the least squares computation.
*Short range parameters in units of e^2/V.
†Charge parameters in units of e

Table 3. Elastic constants, polarizability, and equilibrium check (E.C.) calculated from the parameters of Table 2

Model	C_{11}	C_{12}	C_{14}	α_{Sn}(Å^3)	E.C
I	0·691	0·361	0·159	0	−1·131
II	0·856	0·235	0·355	10·24	1 317
III	0·918	0·419	0·333	10·40	0·085
Exp.*	0·824	0·208	0·366	3·4	—

Elastic constants are in units of 10^{12} dyn/cm^2.
†Experimental data from reference [7].

values of the elastic constants if the neutron data were ignored, but all rigid ion models considered gave a very unsatisfactory description of the dispersion curves. Model II gives very good values of the elastic constants and model III gives quite good values for C_{11} and C_{14}, but C_{12} is high by a factor of 2. From this standpoint model II would appear to be preferable although model III gives a slightly better fit to the neutron scattering data.

Another check of the credibility of the models can be obtained from the equilibrium condition which can be derived from the cohesive energy of the unit cell:

$$\Phi = \tfrac{1}{2}\alpha_M Z_1 Z_2 e^2/r + 8\phi_1(r') + 6\phi_2(r) + 6\phi_3(r'') \tag{4}$$

where the Madelung constant $\alpha_M = 5{\cdot}818$ is in terms of the Mg–Mg separation, $r = 3{\cdot}379$ Å, $r' = \sqrt{3}/(2r)$, and $r'' = \sqrt{2}r$. At the equilibrium separation the cohesive energy should be a minimum resulting in the relation

$$B_1 + B_2 + 2B_3 - \tfrac{1}{6}\alpha_M Z_1 Z_2 = 0 \tag{5}$$

where B_1, B_2 and B_3 are short range force constants defined by Dolling *et al.*[12] in units of e^2/V.

The condition that $(\partial\Phi/\partial r)_{r=r_0}$ be equal to zero was not used as a constraint in the fitting, but it is interesting that the best fitting model comes the closest to satisfying this condition. Models I, II and III give values of −1·13, 1·32 and 0·085, respectively for the left hand side of equation (5). From considerations of the equilibrium conditions, elastic constants and from the fitting of the neutron data it appears that models II and III give realistic physical pictures of the forces binding the Mg_2Sn crystal.

While developing the computer programs for the fluorite structure force constants given by Dolling *et al.*[12] were used to calculate the vibration frequencies and elastic constants of UO_2. It was found that the calculated elastic constants were twice the values reported by Dolling *et al.* and that the calculated frequencies of vibration were high by a factor of $\sqrt{2}$. After dividing the force constants by 2 and the charges by $\sqrt{2}$ the calculations came into

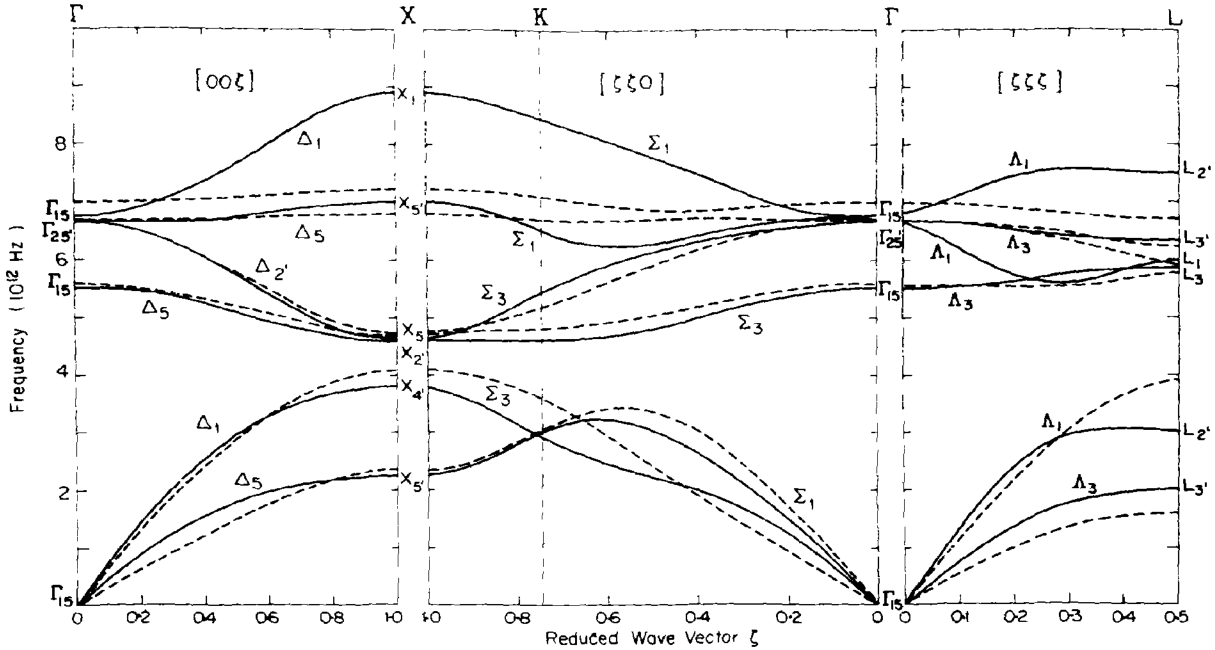

Fig. 4. Calculated phonon dispersion relation for Mg_2Sn based on a *nine* parameter shell model (solid curves) and a seven parameter rigid-ion model (dashed lines) where each model was least squares fit to the *neutron* scattering data.

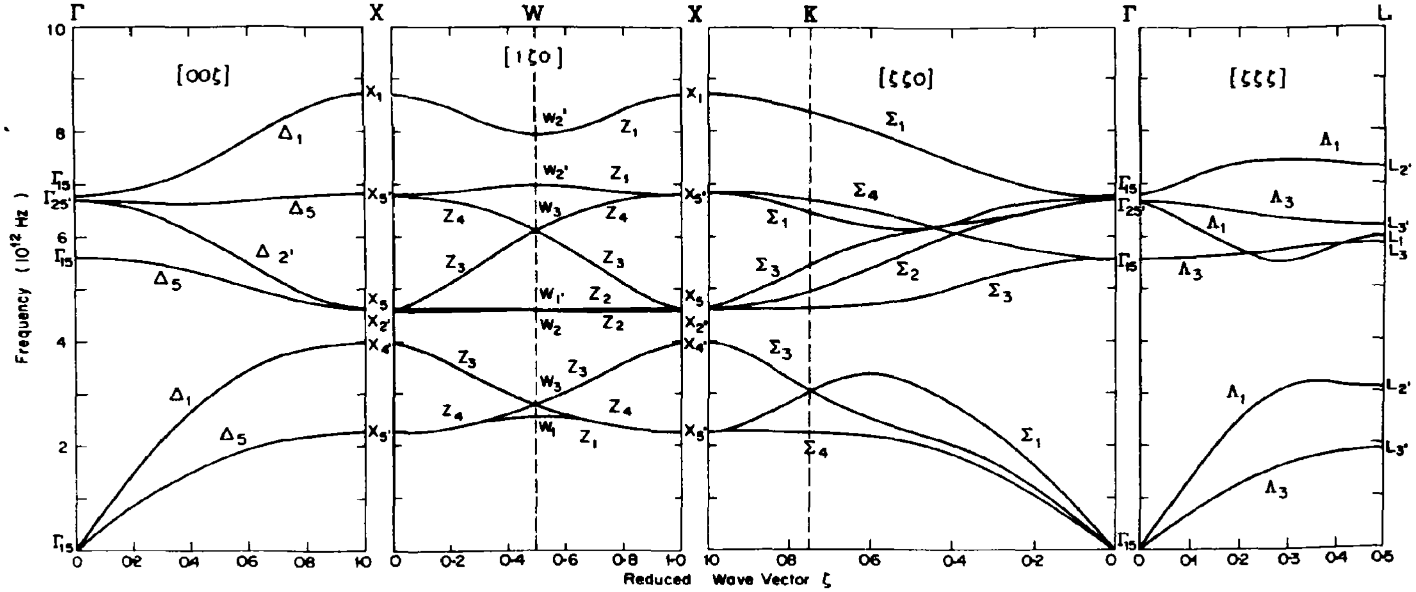

Fig. 5. Calculated phonon dispersion relation for Mg_2Sn based on the ten parameter shell model which was least squares fit to the neutron scattering data. Shown are the predictions of this model for the directions investigated in this experiment (Δ, Σ, and Λ) and for the Z direction as well. Included for the Σ direction are branches which were not investigated experimentally (Σ_2 and Σ_4).

agreement with those quoted by Dolling *et al.* It would appear that these authors actually used units of $(e^2/2V)$ rather than (e^2/V) in their calculation. A check of the equilibrium condition was made for UO_2 using these corrected values in equation (5). The values obtained for the four models were −0·43, 0·48, 1·1 and 0·58 for models I, II, III and IV, respectively. On this basis their model IV would appear to be superior to model III although the latter gives a slightly better fit to the neutron scattering data.

In addition to the frequency calculations made for the branches of the dispersion relation of Mg_2Sn which were measured experimentally, frequencies were calculated for the Σ_2 and Σ_4 branches and for all the branches along [1ζ0]. The results of these calculations for model III are shown in Fig. 5. Symmetry points in the Brillouin zone and the branches of the dispersion relation are labeled according to BSW notation[19]. Along the [1ζ0] there are nine distinct branches which degenerate to seven at the point W. For Mg_2Sn the two Z_2 branches are very close together and become accidentally degenerate at W.

5. SUMMARY

The phonon dispersion relation has been measured in the present experiment along the symmetry directions [00ζ], [ζζ0] and [ζζζ] for Mg_2Sn by slow neutron scattering. These results are quite similar to those reported for UO_2 except that a distinct separation of acoustical and optical branches occurs for Mg_2Sn while it does not for UO_2. Rigid ion as well as nine and ten parameter versions of the shell model have been least squares fit to the data with the ten parameter shell model giving the best overall agreement with the data.

Acknowledgements—The authors would like to thank a number of people who assisted with the experiment: Mr. R. E. Brown and Mr. D. E. Jackson for their assistance with the electronics, Mr. W R. Beck for the construction of collimators and other equipment used in the initial phase of the experiment, Mr. J. K. Boyter for programming assistance, Dr. W. R. Myers for programming the spectrometer control program for the PDP-9 and Dr. R. M. Brugger for his support. One of us (R.J.K.) would like to thank the Associated Western Universities for support during part of his stay at the MTR and Idaho Nuclear Corporation for their support of a personnel exchange over a period of one semester.

REFERENCES

1. BLUNT R. F., FREDERIKSE H. P. and HOSLER W R., *Phys. Rev.* **100**, 663 (1955)
2. LICHTER B. D., *J. Electrochem. Soc.* **109**, 819 (1962).
3. LIPSON H G. and KAHAN A., *Phys. Rev.* **133**, A800 (1964).
4. UMEDA J., *J Phys. Soc Japan* **19**, 2052 (1964).
5. KAISER K. B. and KEARNEY R. J., *Phys. Rev.* **162**, 716 (1967).
6. CROSSMAN L D. and DANIELSON G. C., *Phys. Rev* **171**, 867 (1968).
7. DAVIS L. C., WHITTEN W. B., and DANIELSON G. C., *J Phys. Chem Solids* **28**, 439 (1967).
8. KEARNEY R J., WORLTON T. G. and SCHMUNK R E., *J. Phys. Chem. Solids* **31**, (1970).
9. JELINEK F J., SHICKELL W. D and GERSTEIN B. C., *J. Phys. Chem. Solids* **28**, 267 (1967).
10. RAUBENHEIMER L. J. and GILAT G., *Phys. Rev.* **157**, 586 (1967).
11. CRIBIER D., FARNOUX B. and JACROT B., *IAEA*, Vol. II, p. 225. Vienna (1963).
12. DOLLING G., COWLEY R. A. and WOODS A D. B., *Can J Phys.* **43**, 1397 (1965).
13. WHITTEN W B., CHUNG P. L. and DANIELSON G. C., *J Phys. Chem Solids* **26**, 49 (1965).
14. PEARSON W. B., *Lattice Spacings and Structures of Metals and Alloys*. Pergamon Press, New York (1958).
15. OSTHELLER G. L., SCHMUNK R E., and KEARNEY R. J., Idaho Nuclear Corporation Report, IN-1129, May 1968
16. KEARNEY R. J., WORLTON T. G and SCHMUNK R. E., *Bull Am. Phys. Soc.* **13**, 87 (1968).
17. MYERS W. R., Idaho Nuclear Corporation Report, IN-1287, July 1969.
18. ELLIOTT R. J. and THORPE M. F., *Proc. Phys. Soc.* **91**, 903 (1967).
19. BOUCKAERT L. P., SMOLUCHOWSKI R. and WIGNER E., *Phys. Rev.* **50**, 58 (1936).
20. KAHAN A., LIPSON H. G., and LOEWENSTEIN E. V., *Proc 7th Int. Conf. Physics of Semiconductors*, Paris, p. 1067 (1964).
21. LYDDANE R. H., SACHS R. G. and TELLER E., *Phys. Rev.* **59**, 673 (1941).
22. AU-YANG M Y and COHEN M. L., *Phys. Rev.* **178**, 1358 (1969).
23. SRINIVASAN R., *Proc. Phys. Soc. (London)* **72**, 566 (1958).
24. GANESAN S. and SRINIVASAN R., *Can. J. Phys.* **40**, 74 (1962).
25. CHUNG P L., WHITTEN W. B. and DANIELSON G. C., *J. Phys. Chem. Solids* **26**, 1753 (1965).
26. WOODS A D. B., COCHRAN W. and BROCKHOUSE B. N., *Phys. Rev* **119**, 980 (1960).

27. COWLEY R. A., *Proc. R. Soc.* (*London*) **A268**, 121 (1962).
28. AXE J. D., *Phys. Rev.* **139**, A1215 (1965).
29. KELLERMAN E. W., *Phil. Trans. R. Soc.* (*London*) **238**, 513 (1940).
30. BOYTER J. K. and WORLTON T. G., Idaho Nuclear Corporation Report, IN-1226, October 1968.
31. TESSMAN J. R., KAHN A. H. and SHOCKLEY W., *Phys. Rev.* **92**, 890 (1953).
32. SRINIVASAN R., *Phys. Rev.* **165**, 1054 (1968).

APPENDIX

The elements of the short range matrix **R** are as found in Dolling *et al.* [12] with the following two corrections:

$$R^{11}_{\alpha\alpha} = (8/3)(A_1 + 2B_1) + 2(A_3 + B_1)(2 - \cos\xi_\alpha(\cos\xi_\beta + \cos\xi_\gamma)) + 4B_3(1 - \cos\xi_\beta\cos\xi_\gamma)$$

$$R^{22}_{\alpha\alpha} = (4/3)(A_1 + 2B_1) + 2A_2 + 4B_2.$$

These elements can be related to those given by Davis *et al.* [7] by the relations:

$\alpha_1 = (A_1 + 2B_1)/3$

$\beta_1 = (A_1 - B_1)/3$

$\alpha_2 = B_3$

$\beta_2 = (A_3 + B_3)/2$

$\gamma_2 = (A_3 - B_3)/2$

$\alpha_3 = A_2$

$\beta_3 = B_2.$

It should be noted that for both the short range matrix and the Coulomb matrix $D^{\kappa\kappa'}_{\alpha\beta} = D^{\kappa\kappa'}_{\beta\alpha}$, $D^{12}_{\alpha\beta} = D^{14*}_{\alpha\beta}$, and $D^{22}_{\alpha\beta} = D^{44}_{\alpha\beta}$. Used in connection with the Hermetian property these relations reduce the number of independent elements of both **R** and **C** from 81 to 24. The 24 independent elements of **C** were read into the computer for each value of the wave vector and the other elements defined in terms of the elements read in. In the symmetry directions considered some of the 24 elements were identical because of the equivalence of different components of the wave vector.

The equations for the elastic constants were obtained by adding the third neighbor terms given by Chung *et al.* [25] to the equations given by Srinivasan [32]. Note that Srinivasan has taken $a_0 = a/2$, and defined force constants in units of $e^2/2V = e^2/4a_0^3$.

$$C_{11} = (2/a)[1/3(A_1 + 2B_1) + A_2 + A_3 + B_3 + 3{\cdot}0512\,Z_2^2](e^2/V)$$

$$C_{12} = (2/a)[A_1/3 - 4B_1/3 - B_2 + A_3/2 - 5B_3/2 - 5{\cdot}4044\,Z_2^2](e^2/V)$$

$$C_{44} = (2/a)\left\{(A_1 + 2B_1)/3 + B_2 + A_3/2 + 3B_3/2 - 1{\cdot}5256\,Z_2^2 - \frac{[5{\cdot}0288\,Z_2^2 - \frac{1}{3}(A_1 - B_1)]^2}{[\frac{1}{3}(A_1 + 2B_1) + A_2 + 2B_2]} - \frac{(5{\cdot}0288\,Z_2)^2}{2K_2}\right\}(e^2/V)$$

J. Phys. Chem Solids Pergamon Press 1970. Vol. 31, pp. 1099-1111. Printed in Great Britain.

EXPANSIONS OF THE FREE ENERGY NEAR A PHASE TRANSITION

DANIEL J. AMIT*
Department of Physics, Brandeis University Waltham, Mass. 02154, U.S.A

(*Received* 30 *June* 1969; *in revised form* 21 *October* 1969)

Abstract—A phenomenological theory describing the uniform and non-uniform properties of a system near a critical point is proposed. This theory allows for quite general exponents satisfying certain relations e.g scaling relations. The form of the expansion in powers of the order-parameter is different from previous attempts to generalize the Landau-Ginzburg theory. This change in the form of the expansion allows for the allocation of a well defined region in the order-parameter temperature plane in which the theory is expected to be a good approximation. The expectation is reinforced by a recent experiment of Ho and Litster. The proposed expansion includes in a natural way a possible logarithmic divergence in the specific heat without affecting other properties with logarithm terms. The determination of the parameters in the theory is discussed both for cases in which the order-parameter is experimentally accessible and for cases, like the superfluid, in which it is not accessible.

1. INTRODUCTION

THE POSSIBILITY of finding an expansion of the free energy of a system in the neighbourhood of a non-classical phase transition has recently received a fair amount of attention [1, 2]. The desire to obtain an expansion of this type stems from the great usefulness of the Landau[3] and Landau-Ginzburg[4] theories which described all phase transitions qualitatively and some, like superconductivity, quantitatively. The Landau-Ginzburg theory would predict the same critical exponents for all phase transitions i.e. the classical exponents[5]. This, as is well known, is not borne out by experiments[6]. Two other difficulties appear in the 'straight' Landau-Ginzburg theory: (*a*) The relative fluctuations in the order parameter diverge as one approaches the critical point[7] so that there is a region around the critical point, sometimes quite small, from which the theory is excluded; (*b*) While the exponents satisfy all the 'scaling relations'[8] but one, namely $d\nu' = 2-\alpha'$, this violation is serious as it involves the violation of the rigorous inequality $d\nu' > 2-\alpha'$, proved by Josephson[9]. d is the number of dimensions, ν' and α' are the critical exponents of the correlation length and the specific heat below the transition temperature. Thus the Landau-Ginzburg theory is not an acceptable theory of the critical region.

The attempts to generalize the phenomenological theory invariably[1, 2] interpreted the Landau-Ginzburg theory as an expansion in powers of ψ/ϵ^{β} where ψ is the order parameter, ϵ—the dimensionless temperature difference from the critical point and β—the critical exponent of the equilibrium order-parameter. Thus, for example, the local part of the free energy in the Landau-Ginzburg case could be viewed as

$$A_1\epsilon\psi^2+A_2\psi^4 = \epsilon^2[A_1(\psi^2/\epsilon)+A_2(\psi^2/\epsilon)^2]. \quad (1)$$

The generalization was made by letting the exponents of ϵ in the coefficients of the various powers of ψ (which were taken to be integral) assume non-integral values but keeping a small number of terms. Since in the (ψ,ϵ) plane only the origin is a singular point this form of expansion must imply that one cannot approach $\epsilon = 0$ with finite order parameter

---

*Permanent address: Department of Theoretical Physics, Hebrew University, Jerusalem.

[10]. Such an expansion could be meaningful in regions of the (ψ, ϵ) plane denoted by A1 and A2 in Fig. 1. There is nothing special about region A1, above the transition, and such an expansion in that region was proposed by Griffiths[11] where for the sake of generality an infinite number of terms is kept. But in the above mentioned theories[1, 2] it was assumed that such an expansion can also be carried out below the transition i.e. the region A2 of Fig. 1. Furthermore, it was believed (or hoped) that the region A2 would extend some finite amount beyond the coexistence curve (marked by x_0 in Fig. 1), so that the equilibrium value of ψ, $\bar{\psi}(\epsilon)$, could be determined in this region, thus giving one relation between the coefficients. In fact, the only reasonable procedure for finding $\bar{\psi}(\epsilon)$ was by minimizing the free energy as a function of $x = \psi / |\epsilon|^{\beta}$ from the right. That is from values of $x > x_0$ where

$$\bar{\psi}(\epsilon) = x_0(-\epsilon)\beta. \qquad (2)$$

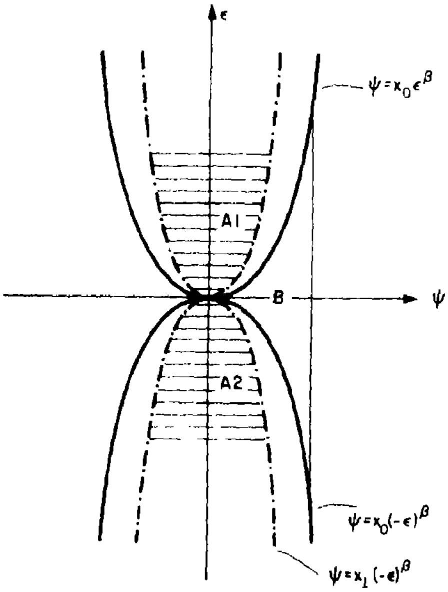

Fig. 1. The ψ–ϵ plane. The curve $\psi = x_0(-\epsilon)^{\beta}$ is the coexistence curve. A1 and A2 are the regions of expansion in refs. (1, 2) with $x_1 > x_0$. Region B is the region where the expansions of Section 7 are used

Clearly, even if such a series existed *it would not be able to give us any information about the behaviour of the various thermodynamic quantities along the critical isotherm* (the ψ axis in Fig. 1[12]). Moreover, the transition from $\epsilon > 0$ to $\epsilon < 0$, which is important for the proximity effect[13], is very artificial.

In this work it will be argued that it is more pleasing to have an expansion in the region B of Fig. 1 with a small number of terms. This is for $(\psi / |\epsilon|^{\beta})$ large or $|\epsilon\psi^{-1/\beta}|$ small. This region includes both positive and negative ϵ values. The proposed expansion is analytic in ϵ and thus, like in the original Landau theory [3], the change in sign of the term linear in ϵ brings about the instability and broken symmetry. All the coefficients retain their values on crossing the critical isotherm. As far as the values of ψ off the positive real axis are concerned we assume that there is a complete symmetry in the critical region and that ψ can be replaced by $|\psi|$. This presented a difficulty in expansions which had non-integer powers of ϵ since one could not reasonably assume a symmetry between ϵ and $(-\epsilon)$. In fact, such theories postulate two different functions in the disjoint regions A_1 and A_2 with no way of connecting them within the expansion. To support the belief that region B can be extended to the coexistence curve we will call to our aid the recent illuminating experiment of Ho and Litster[14] on the equation of state of a ferromagnet.

The main advantages of the proposed expansion are:

(a) It has a well defined region in the $\psi\epsilon$-plane in which it is a good description of the free energy. Thus, for example, the coexistence curve and the critical isotherm are within the range of one and the same expansion. This is to be contrasted with the former expansions which were to hold in an ambiguous vicinity of the coexistence curve.

(b) In the case of a logarithmic divergence of the specific heat this behaviour is naturally encompassed in the expansion. No other properties are logarithmically infected.

We will also carry along a term describing the price, in free energy, of spatial inhomogeneities of the order parameter. This will be done in a way which allows for non Ornstein–Zernike behaviour of the correlation function for large wave numbers[15].

It will be shown that if a description of the proposed type with a local order-parameter averaged over a volume of the scale of the correlation length should exist for *a priori* reasons then Josephson's inequality[9] follows. On the other hand, if the exponents are fixed phenomenologically then Josephson's inequality insures us against fluctuations in the order parameter becoming greater than the local value itself, as we approach T_c. This is in contrast to the difficulty present in the Landau–Ginzburg theory.

In order to be able to use the proposed expansion in the analysis of inhomogeneous situations, restricted geometries, etc., one has, first of all, to determine phenomenologically the coefficients. The experimental information needed in this case will be discussed.

In Section 2 the free energy functional is postulated. The requirements on the homogeneous function due to the broken symmetry are discussed. The bulk properties of the system are discussed in Section 3. This is mostly a recapitulation of such arguments as those of Widom[16] and Griffiths[11] which show that the scaling relations between the exponents of the bulk properties have been built in. Section 4 is devoted to the critical behaviour of the correlation function. The connection between the long wave-length behaviour of the correlation function is made following Josephson[15, 2a]. The remaining exponent relations which are implied by the postulated free energy are exhibited. In Section 5 we spell out our conception about the meaning of spatial variations described by the free energy functional. The expansions, for $\alpha > 0$ and $\alpha = 0$, of the local part of the free energy in region B of Fig. 1 are stated in Section 7. The relevant non-vanishing coefficients are discussed. Finally, in Section 8 we discuss in detail the experimental information necessary for determining the exponents and coefficients which appear in the expanded free energy. This is done for three most common cases, namely, when there is a field conjugate to the order parameter experimentally accessible and either $\alpha > 0$ or $\alpha = 0$ and the third case is no conjugate field and $\alpha = 0$ (the case of superfluids). It is interesting to point out that for the determination of the exponents in the free energy one does not need, in the practical cases, to use the relation $d\nu = 2-\alpha$. Even for the superfluid where one measures the superfluid density it is shown that if the superfluid density exponent is 2/3 then so is ν in any number of dimensions.

2. THE FREE ENERGY AND EQUILIBRIUM ORDER PARAMETER

We postulate a free energy which is a functional of a spatially varying order-parameter $\psi(r)$. For simplicity we take it to be a real scalar. The generalization to complex or vector order-parameter does not cause any problem. It will be written as:

$$\mathscr{F}(X,\epsilon,\{\psi\}) = F_0(X,\epsilon) + \int \mathrm{d}^3r\,[A_0|\nabla\psi|^2 + \psi^{\delta+1}\phi(\epsilon\psi^{-1/\beta})] \tag{3}$$

where F_0 is an analytic function of ϵ and X denotes a set of thermodynamic variables which are needed to specify the state and $\epsilon = (T-T_c)/T_c$. A_0 may depend on ϵ and we define:

$$A_0 = a_0|\epsilon|^{-\sigma}. \tag{4}$$

The need for this type of behavior is discussed in Section 4.* The field h conjugate to ψ is obtained from the free energy as a functional derivative with respect to $\psi(r)$. We have:

---

*The behavior of A_0, equation (4), could not describe the contribution of spatial inhomogeneities near the critical isotherm. It may possibly be generalized to read $A_0 = b_0|\psi|^{-\sigma/\beta}$. This may affect the spatial behavior of ψ in restricted geometries but will not change any of the conclusions reached hereafter. The restriction of this term to the neighborhood of the $\epsilon = 0$ line is discussed in Section 7 I am grateful to the referee for pointing out this ambiguity.

$$h(r) = \Omega^{-1}\frac{\delta\mathscr{F}(X,\epsilon,\{\psi\})}{\delta\psi(r)} \tag{5}$$

which is the equation of state.

δ and β are left arbitrary. Clearly, the Landau–Ginzburg free energy is a special case of (3) when $\delta = 3$ and $\beta = 1/2$ and we keep only the two lowest order terms, the zeroth and first, in the expansion of ϕ in powers of its argument.

It is further assumed that (3) includes the effects of fluctuations since the order parameter is averaged over volumes of size ξ^d where ξ is the correlation length and d is the number of dimensions [17].

At equilibrium the order parameter is uniform and its value is to be found by minimizing $\psi^{\delta+1}\phi(x)$ with respect to ψ. The equation is:

$$h(\psi,\epsilon) = \beta^{-1}\psi^{\delta}[\beta(\delta+1)\phi(x) - x\phi'(x)] = 0 \tag{6}$$

where $\phi' = \mathrm{d}\phi(x)/\mathrm{d}x$ and

$$x = \epsilon\psi^{-1/\beta}. \tag{7}$$

We restrict ourselves, for the moment, to $\psi > 0$. The shape of the coexistence curve is given by:

$$\bar{\psi}(\epsilon) = x_0(-\epsilon)^{\beta} \tag{8}$$

where $-x_0 < 0$ satisfies equation (7) together with:

$$\frac{\partial^2}{\partial\psi^2}[\psi^{\delta+1}\phi(x)]_{\bar{\psi}} > 0. \tag{9}$$

Using $\bar{\psi}$, equation (8), the inequality reads:

$$\bar{\psi}^{\delta-1}[\delta(\delta+1)\phi(-x_0) - \beta^{-1}(2\delta+1-\beta^{-1}) \times (-x_0)\phi'(-x_0) + \beta^{-2}(-x_0)^2\phi''(-x)] > 0. \tag{10}$$

That the inequality (10) be satisfied is a special case of the requirement of convexity of the free energy since the left hand side of (10) is the susceptibility at that point in the (ψ,ϵ) plane [19]. The requirement has to be imposed on ϕ everywhere in the plane.

For $\epsilon > 0$ or $x > 0$ equation (6) should have no zeros, except $\psi = 0$.

3. SPECIFIC HEAT AND SUSCEPTIBILITY AT EQUILIBRIUM

In the previous section we formulated the ansatz for the free energy and identified β by equation (8). Requiring that the critical behaviour of the equilibrium bulk properties be described by our ansatz we now proceed to identify δ and to exhibit the scaling relations implied by the ansatz for these properties. We treat the cases $\alpha > 0$ and $\alpha = 0$ in turn.

(a) $\alpha > 0$

If we are above the transition $\epsilon > 0$ and as $\psi \to 0$ we have $x \to \infty$. How does ϕ behave? We know that along the ϵ-axis where $\psi = 0$, the specific heat, at constant X and $h = 0$, diverges as $\epsilon^{-\alpha}$ which implies a term behaving like $\epsilon^{2-\alpha}$ in $\mathscr{F}$. Thus, as $\psi \to 0$ and ϵ is small we must have for the asymptotic behaviour of ϕ:

$$\phi(x)_{x\to\infty} \sim \varphi_0 x^{2-\alpha} + \varphi_1 x^{\mu} \tag{11}$$

and in order that the leading term in $C_{h=0}$ be $\epsilon^{-\alpha}$ the ψ's in $\psi^{\delta+1}\phi(x)$ must cancel. Hence the following relation must exist

$$\beta(\delta+1) = 2-\alpha. \tag{12}$$

In order to turn (12) into a scaling relation we only have to identify δ. This is done with the aid of equation (6). If we set $x = 0$ in (6) we obtain h as a function of ψ along the critical isotherm, ψ-axis. If we take the limit of $x \to 0$ then as long as $\phi(0)$ is bounded $x\phi'(x)$ vanishes at $x = 0$. Thus we must have $\phi(0) > 0$ for ψ to be finite for finite field along the critical isotherm. δ acquires its conventional meaning, namely

$$\psi \sim h^{1/\delta} \text{ for } \epsilon = 0. \tag{13}$$

The derivation of (12) does nothing more than to show that we built this scaling relation into our theory.

Next we calculate the specific heat for $\epsilon < 0$. Again at X fixed and $h = 0$. That is, along the coexistence curve. Along this curve ψ is given by (8) and the contribution to the free energy is:

$$\psi^{\delta+1}\phi(-x_0) = x_0{}^{\delta+1}\phi(-x_0)(-\epsilon)^{\beta(\delta+1)}$$
$$= x_0{}^{\delta+1}\phi(-x_0)(-\epsilon)^{2-\alpha}. \qquad (14)$$

But, by definition for $|\epsilon| \to 0$ the singular part of the free energy is

$$\mathscr{F}_{\text{sing.}} \sim (-\epsilon)^{2-\alpha'} \text{ for } \epsilon < 0. \qquad (15)$$

We find

$$\alpha = \alpha'. \qquad (16)$$

This result is subject only to the assumption that the same function ϕ describes the critical part of the free energy at both small and large x[20].

The specific heat has a symmetric exponent about $\epsilon = 0$ but not necessarily the same coefficient.

(b) $\alpha = 0$

In this case the singular term in the specific heat, along the $\psi = 0$ line for $\epsilon > 0$, is $\ln \epsilon$. This corresponds to an $\epsilon^2 \ln \epsilon$ term in $\mathscr{F}$, ϕ must therefore behave like:

$$\phi(x)_{x\to\infty} \sim \varphi_0 x^2 \ln x \qquad (17)$$

combined with (3) we find that

$$\beta(\delta+1) = 2 \qquad (18)$$

as it should according to (12), if the logarithmic divergence is to correspond to the limit $\alpha \to 0$. But (17) is not satisfactory since as $\psi \to 0$ at small but finite ϵ it will diverge. Hence in the $\alpha = 0$ case we must have an additional term in (3). The local part of the integrand will read:

$$\psi^{\delta+1}\phi(x) - \varphi_0\epsilon^2 \ln(\psi^{-1/\beta}). \qquad (19)$$

This does not result in a homogeneous free energy but the equation of state is still homogeneous[11]. Clearly, by adding and subtracting $\varphi_0\epsilon^2 \ln \epsilon$, in equation (19), we could have maintained the homogeneity of the ψ-dependent term but $F_0(X, \epsilon)$ would not have been analytic in ϵ. This latter was the approach taken in ref. [2*a*]. Since in Section 2 we use equation (6) for determining the equilibrium order parameters the results are unaffected. The singular term along the $\psi = 0$-line will be: $\varphi_0\epsilon^2 \ln \epsilon$. While along the coexistence curve it will be:

$$\epsilon^2 [\phi(-x_0) - \varphi_0 \ln(x_0{}^{-1/\beta})] + \varphi_0\epsilon^2 \ln \epsilon.$$

Thus, as is well known, in the $\alpha = 0$ case the specific heat diverges logarithmically on both sides of $\epsilon = 0$ with the same coefficient. On top of this there may be superposed a finite discontinuity.

The lowest order term in $\phi(x)$, when $x \to \infty$, equation (11), cancels out of the expression for h, equation (6), upon using equation (12). Thus in order to calculate the susceptibility χ we have to look for the next order term near the critical isochore. There has to be a term which will leave a ψ in equation (7) so that we get a finite susceptibility along the positive ϵ-axis. On inserting (11) in (6) we will have $\mu = \beta(\delta - 1) = 2 - \alpha - 2\beta$. Similarly, along the coexistence curve we find from (6) that $\chi^{-1} \propto \psi^{\delta-1}$. In both cases we find, respectively, that

$$\chi = \begin{cases} (2\varphi_1)^{-1}\epsilon^{-\gamma} & \epsilon > 0 \\ [\delta(\delta+1)\phi(-x_0) \\ \quad + \delta\beta^{-1}x_0\phi'(-x_0)]^{-1}(-\epsilon)^{-\gamma'} & \epsilon < 0 \end{cases} \qquad (20)$$

where

$$\gamma = \gamma' = 2 - \alpha - 2\beta. \qquad (21)$$

4. CORRELATION FUNCTIONS AND THEIR EXPONENTS

The correlation function of fluctuations in the order parameter is defined as:

$$g(r-r') = \langle \delta\psi(r)\delta\psi(r')\rangle \qquad (22)$$

where

$$\delta\psi(r) = \psi(r) - \bar{\psi} = \Omega^{-1/2}\sum_k \delta\psi(k)e^{ik\cdot r}. \qquad (23)$$

Its Fourier transform is:

$$G(k) = \int d^3 r e^{-ik\cdot r} g(r) = \langle \delta\psi(k)\delta\psi(-k)\rangle. \qquad (24)$$

It can be easily shown that if we take

$$\delta\psi(r) = \Omega^{-1/2}\psi_k \cos(k\,.\,r) \qquad (25)$$

insert it in equation (3) for the free energy then

$$G(k) = \tfrac{1}{2}(\partial^2\mathscr{F}/\partial\psi_k{}^2)_0{}^{-1} = \frac{k_B T}{2A_0 k^2 + \theta_0''} \qquad (26)$$

k_B is Boltzmans constant and the 0 subscript indicates that the derivative has to be taken at equilibrium where all $\psi_k = 0$ and $\psi = \bar{\psi}$. θ_0'' is given by:

$$\theta_0'' = \frac{\partial^2}{\partial\psi^2}[\psi^{\delta+1}\phi(x)]_0 = \chi^{-1}(\epsilon) \qquad (27)$$

with χ as the initial isothermal susceptibility:

$$\chi = ((\partial/\partial)(\psi/h))_T. \qquad (28)$$

From (26) and (27) we have for the $k \to 0$ limit of $G(k)$

$$\lim_{k \to 0} G(k) = k_B T\chi(\epsilon). \qquad (29)$$

Clearly, our original free energy can at best describe spatial variations of very long wavelength. These can indeed be expected to have a correlation function of the generalized Ornstein–Zernike type[31]. This type of behavior seems to be of a general nature above T_c[21]. Below T_c the two dimensional Ising model provides a counter example[21]. We shall not consider such cases here and hope that they can be accounted for by starting the non-local part of the free energy in momentum space with a power different than two. This type of approach was applied to HeII by Guyon and Maki[23]. One can compensate, of course, by having different σ's above and below T_c. Through this behavior of the correlation function we define the correlation length. Namely:

$$G(k)_{k \sim \xi^{-1}} \frac{\Gamma(T)}{k^2+\xi^{-2}}. \qquad (29a)$$

That is: ξ^{-1} is defined as the position of the pole of $G(k)$ along the imaginary k axis. Hence in our case we have

$$\xi^{-2} = \chi^{-1}/2A_0 \sim |\epsilon|^{\gamma+\sigma};$$

$$\Gamma(T) = \tfrac{1}{2}k_B T A_0{}^{-1} \sim |\epsilon|^{\sigma}$$

or if

$$\xi \sim |\epsilon|^{-\nu} \qquad (30)$$

then

$$2\nu = \gamma + \sigma. \qquad (31)$$

We do not distinguish between ν and ν' since, from the fact that $\gamma = \gamma'$ and the postulate that σ is symmetric, it follows that they are equal. For large k, $G(k)$ may behave non-classically but since the wave-length is short the behaviour cannot be critical in temperature. By definition we have

$$G(k)_{k\ \infty} \sim k^{-2+\eta}. \qquad (32)$$

We assume with Josephson[15] that at some k proportional to ξ^{-1} the two limiting behaviors merge. Equating (26) and (32) at $ka\xi^{-1}$ we find:

$$\chi \sim \xi^{2-\eta} \qquad (33)$$

or

$$\gamma = \nu(2-\eta). \qquad (34)$$

Combined with (31) this gives us the value of σ we have to use in order to make the matching possible, i.e.

$$\sigma = \eta\nu. \qquad (35)$$

5. FLUCTUATIONS AND THE REMAINING SCALING RELATION

As long as one is content with bulk thermodynamic properties of the system any set of exponents α, α', β, γ, γ', δ that satisfy relations (12), (16) and (21) is acceptable. This includes for example the original Landau theory with $\alpha = \alpha' = 0$, $\beta = \frac{1}{2}$, $\gamma = \gamma' = 1$ and $\delta = 3$. Fluctuations in the order parameter below T_c will be small compared to the average order parameter. This is trivial since the fluctuations increase with the first power of the volume when the susceptibility is assumed finite, while the square of the equilibrium order parameter varies as the volume to the second power[24].

Once we start considering local fluctuations and correlations the exponents ν, ν' and η come in and new restrictions appear. Thus one finds, for example, that the Landau $\delta = 3$ is incompatible with an Ornstein–Zernike behaviour of the correlation function[9*b*]. That is, the Landau–Ginzburg theory cannot be carried up to the critical point. A more primitive argument for an excluded region around T_c inherent in the Landau–Ginzburg theory was given by Ginzburg[7]. Finally, Josephson[9] showed that using rigorous thermodynamic arguments and plausible assumptions on the correlation functions results in the inequalities:

$$d\nu > 2-\alpha, d\nu' > 2-\alpha'. \qquad (36)$$

These, of course, are not satisfied by the Landau-Ginzburg theory and exclude it as a theory of a temperature interval which includes the critical point.

The extension of the generalized Ornstein–Zernike correlation function to $k = (\mu\xi)^{-1}$ and of the power behavior of the correlation function up to this value of k implies the assumption that at distances smaller than $(\mu\xi)$ the local values of the order parameter are very strongly correlated while outside this length they are almost uncorrelated. Thus, if we want to give the theory a meaning as regards spatial variations of the order-parameter we have to average the order parameter over volumes of linear dimensions $(\mu\xi)$. The theory which describes the variations inside such a volume is, of course, much more complicated. On the other hand, it also does not make sense to take the averaging volume to have a linear dimension which diverges faster than ξ as we approach T_c. The very small correlations between different regions inside the volume will render a uniform average value ascribed to the whole volume very artificial. The differential equation (5) describing spatial variations will give variations on a scale much smaller than the scale over which we coarse-grained the order parameter.

We are mainly interested in the spatial variations of the order-parameter while we are near the coexistence line. Otherwise, we have to build into the theory a dependence of the correlation length on magnetic field. This limitation is made clear by noticing that the correlation length will not be infinite along the critical isotherm, since we assumed that the susceptibility there is finite.

Once we restrict ourselves to these cells of linear dimension $(\mu\xi)$ the question of fluctuations becomes important. The question of whether the fluctuations in the average order parameter in such a region still leave us with a well defined quantity. This quantity is proportional to the equilibrium value of the order-parameter per unit volume times the volume of the cell. Denote the volume of the cell V_ξ, then:

$$V_\xi = (\mu\xi)^d \qquad (37)$$

where d is the number of dimensions. The total order-parameter in the cell will be ψ_ξ where

$$\psi_\xi = \int_{V_\xi} dr\psi(r). \qquad (38)$$

The fluctuation in the square of the order-parameter is given by Nyquist's theorem as

$$\langle(\psi_\xi - \bar{\psi}_\xi)^2\rangle \approx k_B T V_\xi \chi \qquad (39)$$

where χ is the bulk susceptibility. The average value of ψ_ξ is $V_\xi\bar{\psi}(\epsilon)$. We therefore have for the ratio of the fluctuations to the square of the order-parameter:

$$\frac{\langle(\psi_\xi-\bar{\psi}_\xi)^2\rangle}{(\bar{\psi}_\xi)^2}\approx k_BT_cV_\xi^{-1}\chi(x_0)^{-2}$$
$$\times(-\epsilon)^{-2\beta}\propto\mu^{-d}\epsilon^{d\nu'-(2-\alpha)}. \tag{40}$$

This result can be viewed in two ways:

Firstly, if we assume that a theory of the type described in the preceeding sections has to exist throughout the critical region then we must have:

$$d\nu'>2-\alpha$$

which is Josephson's inequality.

Secondly, if we take β, δ, ν from experiment, and this is after all a phenomenological theory, then Josephson's theorem[9] implies that the fluctuations will not blow up. If the strict inequality holds in (36) then there is always a temperature region close enough to T_c in which the description of spatial variations in the system, where the order-parameter is averaged over a volume of dimensions proportional to ξ, is self consistent. When the equality holds, as is for example the case for He at the lambda transition (see Section 7 below), the relative fluctuations are temperature independent[1b]. But ξ still has a numerical coefficient, which can be varied to make (40) very small, in our formulation it is a_0 in equation (4). This, however, has to be checked against experiment in nonuniform situations to find whether the coeffcient a_0 is of the correct order of magnitude. For example, if one uses for HeII the type of theory proposed in Ref.[1] where the exponent η to be set to be zero and $a_0=\hbar^2/2m$ one finds that the magnitude of the derived correlation length describes the situation in films fairly well and the relative fluctuations are temperature independent but small[1b].

6. EXPANSIONS

All we have done so far is essentially to recapitulate the considerations leading from the homogeneous free energy to scaling relations: we found the representation (3) more convenient to use than that of Ref. [2a] because the $\psi\rightarrow-\psi$ symmetry can be easily expressed. Furthermore, as was stated in the introduction, if an expansion with a small number of terms is to give a good description in a region near the critical point which includes the coexistence curve it is going to be in region B of Fig. 1. That is, when $|x|=|\epsilon|\cdot|\psi|^{-1/\beta}$ is small. This approach, we believe, is supported by at least one experiment, i.e. that of Ho and Litster[14]. On the other hand, the old approach[1] though borne out above the transition, $\epsilon>0$[14], has no support below the transition. Thus we expand $\phi(x)$ in powers of x and keep as small a number of terms as is necessary to obtain a non-vanishing specific heat along the critical isotherm. Of course, one may have to add more terms in order to describe higher temperature derivatives of the free energy. These, however, are rarely measured and will not be discussed here. The higher order terms should not contribute appreciably to the critical behaviour of the quantities under consideration.

We now proceed to discuss the different terms which should appear in the expansion. In doing this the case of a logarithmic divergence of the specific heat is treated separately.

(a) $\alpha>0$:

$\phi(x)$ is an analytic function of x in region B and thus we write:

$$\psi^{\delta+1}\phi(x)=\psi^{\delta+1}(f_0+f_1x+f_2x^2).$$

That $f_0\neq0$ follows from the fact that we have to have finite susceptibility along the critical isotherm. This point was discussed in Section 3.

Next we argue that $f_1\neq0$[12]. In the homogeneous system this is the 'critical' term that will contribute to an order-parameter dependent part to the entropy along the critical isotherm. Let $\mathcal{S}$ be the entropy per unit volume, then:

$$\frac{\partial \mathscr{S}}{\partial \psi} = -\Omega^{-1} \frac{\partial^2 \mathscr{F}}{\partial \psi \partial \epsilon}\bigg|_{\epsilon=0} = -\frac{1-\alpha}{\beta} \psi^{(1-\alpha)/\beta - 1} \tag{41}$$

where use has been made of equation (12). Thus if we define a critical exponent κ [22]

$$\left(\frac{\partial \mathscr{S}}{\partial \psi}\right)_{\epsilon=0} \sim -\psi^{\kappa} \tag{42}$$

then:

$$\kappa = (1-\alpha)/\beta - 1. \tag{43}$$

But by a Maxwell relation we have:

$$\left(\frac{\partial \mathscr{S}}{\partial \psi}\right)_T = \left(\frac{\partial h}{\partial T}\right)_\psi \tag{44}$$

which is a measurable quantity.

Finally the quadratic term is the one giving the behaviour of the specific heat along the critical isotherm. We find that:

$$f_2 \psi^{\delta+1} x^2 = f_2 \epsilon^2 \psi^{\delta+1-2/\beta} = f_2 \epsilon^2 \psi^{-\alpha/\beta} \tag{45}$$

The specific heat at fixed order-parameter along the ψ-axis in Fig. 1 is:

$$C_\psi(\psi) \underset{\psi \to 0}{\sim} -2T_c f_2 \psi^{-\alpha/\beta}. \tag{46}$$

If another critical exponent is introduced via:

$$C_\psi(\psi) \sim \psi^{-\theta} \tag{47}$$

then

$$\theta = \alpha/\beta. \tag{48}$$

From (43) and (48) we find [12]

$$\theta + \kappa = \beta^{-1} - 1. \tag{49}$$

This relation is equivalent to the relation equation (11) of Ref. [22] if one takes account of the facts that on the critical isotherm fixed ψ is fixed h and $\psi \sim h^{1/\delta}$. It is a direct consequence of homogeneity in addition to the assumption that all the pertinent quantities equations (42) and (47) derive their leading terms from the critical part of the free energy.

Thus we propose in region B to use:

$$\begin{aligned} \mathscr{F}(X, \epsilon, \{\psi\}) &= F_0(X, \epsilon) + \int d^3r [A_0 |\nabla\psi|^2 \\ &\quad + f_0 \psi^{\delta+1} + f_1 \epsilon \psi^{\delta+1-1/\beta} \\ &\quad + f_2 \epsilon^2 \psi^{\delta+1-2/\beta}] \qquad (50) \\ &= F_0(X, \epsilon) + \int d^3r [A_0 |\nabla\psi|^2 \\ &\quad + f\ \psi^{(2-\alpha)/\beta} + f_1 \epsilon \psi^{(1-\alpha)\beta} \\ &\quad + f_2 \epsilon^2 \psi^{-\alpha/\beta}]. \end{aligned}$$

(b) $\alpha = 0$:

As we discussed in Section 3 the local part of $\mathscr{F}$ is, equation [19],

$$F_{\text{local}} = \psi^{\delta+1} \phi(x) - \varphi_0 \epsilon^2 \ln \psi^{-1/\beta}.$$

Once again, in $\phi(x)$ terms to order ϵ^2 or x^2 are kept. Inserting [40] into the expression for F_{local} we have

$$\begin{aligned} F_{\text{local}}(\psi) &= f_0 \psi^{\delta+1} + f_1 \epsilon \psi^{\delta+1-1/\beta} \\ &\quad + f_2 \epsilon^2 \psi^{\delta+1-2/\beta} - \varphi_0 \epsilon^2 \ln \psi^{-1/\beta}. \end{aligned}$$

But this time $\beta(\delta+1) = 2$ hence:

$$F_{\text{local}}(\psi) = f_0 \psi^{2/\beta} + f_1 \epsilon \psi^{1/\beta} + f_2 \epsilon^2 - \varphi_0 \epsilon^2 \ln \psi^{-1/\beta}. \tag{51}$$

And the full free energy functional in the $\alpha = 0$ case is:

$$\begin{aligned} F(X, \epsilon, \{\psi\} &= F_0(X, \epsilon) + \\ &\quad + \int d^3r [A_0 |\nabla\psi|^2 + f_0 \psi^{2/\beta} \\ &\quad + f_1 \epsilon \psi^{1/\beta} + \varphi_0 \epsilon^2\, ln \psi^{1/\beta}]. \qquad (52) \end{aligned}$$

The term $f_2 \epsilon^2$ has been absorbed into F_0.

To end this section we remark that there is complete symmetry between ψ and $-\psi$ in the neighborhood of the critical point. Hence in (50) and (52) we can replace ψ by its absolute value and relax the restriction $\psi > 0$.

7. PHENOMENOLOGICAL DETERMINATION OF COEFFICIENTS

At first glance it may seem that it would be more difficult to determine the coefficients in the new type of expansion than in the expansions of Ref. [1a], since there are more of them. However, the different nature of the expansion and its associated, well defined, region of application make this task rather easier. When one used expansions with ψ/ϵ^{β} small one had to assume that the region in which the expansion is a good approximation (region A in Fig. 1) stretches beyond the coexistence curve. How far beyond this curve is unclear. Thus in determining the coefficients of the local part of the free energy one is restricted to the measurements along the coexistence curve. In the present theory the region in which the expansions are expected to be accurate is region B in Fig. 1 in which one has two variables ϵ, h at one's disposal. One could proceed with the complete survey of the region as was done by Ho and Litster[14] but any point in this region gives a relation between the three coefficients, once β and δ are known.

Of course, it is much more advantageous to obtain a closed form of the equation of state in the whole critical region. It is a much bolder proposition than presented here. However, so far only a parametric representation of the equation of state was constructed[25]. This type of representation is in terms of h and ϵ rather than ψ and ϵ and thus, it seems to us, is less convenient for representing nonuniform situations. Those are usually considered in the neighborhood of the coexistence curve and there such expansions as were proposed in the previous section are adequate. For such problems as the proximity effect between the ordered and the disordered phases our expansion will not suffice. In that case we will need to know the expansion in the neighborhood of the $\psi = 0$ line, for $\epsilon > 0$.

There are four coefficients to be determined in the proposed expansions. These are:

$\alpha > 0; a_0, f_0, f_1, f_2$ in equation (50)
$\alpha = 0; a_0, f_0, f_1, \varphi_0$ in equation (52).

Each one of the above two cases splits into two subcases according to whether the field conjugate to the order-parameter is experimentally accessible or not. In what follows we shall leave out the case $\alpha > 0$ and field not accessible and discuss the other three cases.

(a) $\alpha > 0$

This is a quite simple case as is demonstrated by the detailed investigation of Ho and Litster[14]. One determines β and δ by measuring the equilibrium order-parameter along the coexistence curve and along the critical isotherm, respectively. The second measurement gives f_0, directly. If ψ behaves along the critical isotherm as

$$\psi = uh^{1/\delta} \tag{53}$$

then we have:

$$f_0 = u^{-\delta}/(\delta + 1). \tag{54}$$

The first measurement gives β and a relation between f_0, f_1, f_2. If along the coexistence curve

$$\bar{\psi} = x_0(-\epsilon)^{\beta}$$

then x_0 is the positive root of the equation:

$$(2-\alpha)f_0 - (1-\alpha)f_1 x_0^{-1/\beta} - \alpha f_2 x_0^{-2/\beta} = 0. \tag{55}$$

When $\epsilon > 0$ the second term changes sign and the equation should not have any roots. A third relation between the three coefficients can be obtained for example by measuring the specific heat along the coexistence curve. In fact one point is sufficient since if

$$C_{h=0}(\epsilon)(-\epsilon)^{2-\beta(\delta+1)} = v \tag{56}$$

then

$$v = -T_c(2-\alpha)(1-\alpha)(f_0 - f_1 x_0^{-1/\beta} + f_2 x_0^{-2/\beta}) x_0^{(2-\alpha)/\beta}. \tag{57}$$

We mention the coexistence curve and critical isotherm only since these are the two lines, in region B (of Fig. 1), on which one of the two variables ϵ or h is fixed which enter the critical point. A check of consistency may then be performed by measuring any point in region B i.e.

$$h = h(\psi, \epsilon).$$

In particular the specific heat along the critical isotherm is completely determined by f_2.

Finally, one has to determine A_0. In order to do this one can use a scattering experiment at low k in order to obtain the correlation length. Clearly, the closer we get to T_c the longer the wavelength we have to use since $k\xi < 1$ must be satisfied. From the measured ξ we obtain ν' and using equation (34) we have also η. If it is found that

$$\xi(\epsilon) = \xi_0(-\epsilon)^{-\nu'} \tag{58}$$

along the coexistence curve, then for a_0 of (4) we have

$$a_0 = \tfrac{1}{2}\chi_0^{-1}\xi_0^2 \tag{59}$$

where χ_0 is the coefficient in the susceptibility along the coexistence curve given by:

$$\begin{aligned}\chi_0^{-1} = \beta^{-2}x_0^{\delta-1}[&(2-\alpha-\beta)(2-\alpha)f_0\\ &-(1-\alpha-\beta)(1-\alpha)f_1x_0^{-1/\beta}\\ &+(\alpha+\beta)\alpha f_2x_0^{-2/\beta}].\end{aligned} \tag{60}$$

(b) $\alpha = 0$, *h accessible:*

This case is even simpler than the preceding one. In order to determine f_0, f_1 and φ_0 one does not have to use measurements along the critical isotherm at all. It is enough to measure the specific heat along the $h = 0$ curve above and below the critical temperature and the shape of the coexistence curve. From the logarithmic divergence of $C_{h=0}$ and β we have $\delta = 2/\beta - 1$.

If the coefficient of the logarithm in the specific heat is C_0 then

$$\varphi_0 = -C_0/2T_c. \tag{61}$$

The shape of the coexistence curve is

$$\bar{\psi} = x_0(-\epsilon)^{\beta} \tag{62}$$

where x_0 satisfies

$$2f_0 - f_1x_0^{-1/\beta} + \varphi_0x_0^{-2/\beta} = 0 \tag{63}$$

which is a relation between f_0 and f_1 since φ_0 is known. The third relation is determined from the discontinuity in $C_{h=0}$ across the critical point. If this discontinuity is denoted by ΔC then:

$$\begin{aligned}\Delta C &= \lim\,[C(-\epsilon) - C(\epsilon)]\\ &= -2T_c[f_0x_0^{2/\beta} - f_1x_0^{1/\beta}\\ &\qquad + \varphi_0 \ln(x_0^{1/\beta}) + \tfrac{3}{2}\varphi_0].\end{aligned} \tag{64}$$

Once again, measurements along the critical isotherm can be used to check the validity of the free energy ansatz. A_0 is determined as equation (59) but now

$$\begin{aligned}\chi_0^{-1} = \beta^{-1}x_0^{\delta-1}[&2(2-\beta)f_0 - (1-\beta)f_1x_0^{-1/\beta}\\ &-\beta\varphi_0x_0^{-2/\beta}].\end{aligned} \tag{65}$$

(c). $\alpha = 0$, *h inaccessible:*

There are three popular systems with this property. Namely, superfluids, superconductors and antiferromagnets. The first two are clearly analogous, the third one can also be shown to be analogous to the former two[26]. We will discuss this case in the language of the superfluid.

In the case of the superfluid A_0 plays a much more crucial role than in the systems discussed before. The reason is that the measurable quantity is the superfluid density ρ_s rather than the order-parameter which is the quasi-average of the field operator[15]. The order-parameter is complex but the symmetry between ψ and $-\psi$ mentioned at the end of Section 6 can be extended to all phases of the order-parameter and in the free energy the absolute value of ψ appears. A_0

relates ρ_s to the square of the order-parameter via[15]:

$$\rho_s = 2A_0(m\hbar)^2|\psi|^2 \qquad (66)$$

where ρ_s is the mass density of the superfluid. The traditional way of treating the problem [27, 1] was to postulate

$$A_0 = \hbar^2/2m \qquad (67)$$

thus having

$$\rho_s = m|\psi|^2. \qquad (68)$$

This identifies $|\psi|^2$ with the superfluid number density. It also implies $\eta = 0$. The other two coefficients in an expansion of this type are determined from $\rho_s(\epsilon)$ and the discontinuity of the specific heat. Clearly, the arbitrary determination of A_0 hides the fact that there really is one undetermined coefficient and one undetermined exponent i.e. β or η. This situation persists in the present theory despite the fact that there are four coefficients as opposed to three in the Ginzburg-Pitaevskii theory[27].

Assume for the moment that β is known. Then, of course, we will have all the exponents. Defining ζ – the superfluid density exponent, by

$$\rho_s = \rho_0(-\epsilon)^{\zeta} \qquad (69)$$

and if we include in our exponent relations also $d\nu = 2-\alpha$ then [30, 28]

$$\zeta = \nu \qquad (70)$$

in three dimensions or $\zeta = (d-2)\nu$ in d dimensions. But this scaling relation is not implied by our ansatz. The measured value of ζ for the superfluid is 2/3. We will proceed to show now that in this case we will have

$$\nu = \tfrac{2}{3} \qquad (71)$$

independently of the number of dimensions and of the above mentioned exponent relation.

Proof: From (66) we have:

$$\zeta = 2\beta - \eta\nu \qquad (72)$$

together with (21) and (34) we find

$$\zeta = 2(1-\nu). \qquad (73)$$

Hence $\zeta = 2/3 = >, \nu = 2/3$, Q.E.D.

The value $\zeta = 2/3$ occurs for the superfluid and the antiferromagnet[26]. It does not correspond to the superconductor but we believe that the superconductor has not been brought into the critical region.

A corollary of the above proposition is that in three dimensions $\alpha = 0$ and $\zeta = 2/3$ implies the equality in Josephson's inequality equation (36). If $\alpha = 0$ and $\zeta = 2/3$ in any higher number of dimensions then

$$d\nu > 2.$$

Finally, it follows that $\alpha = 0$ and $\zeta = 2/3$ is impossible in two dimensions.

From equation (73) we have ν if ζ is measured i.e.

$$\nu = 1 - \tfrac{1}{2}\zeta. \qquad (74)$$

Now if, as we assumed above, β is known then we can find from our exponent relations γ, δ and η. We still have to determine a_0, f_0, f_1 and φ_0. ρ_0 of equation (69) can be measured [28, 29] thus we have one relation

$$\rho_0 = 2a_0(m/\hbar)^2 x_0^2 \qquad (75)$$

where x_0 is the root of equation (63), φ_0 can be determined, again, from the logarithmic term in the specific heat and equation (61). A third relation between f_0, f_1 and φ_0 is provided by equation (64). This is all we can derive from bulk properties of the superfluid. So we are left with one undetermined coefficient, and one undetermined exponent.

If the Ginzburg-Pitaevskii[27] postulate is used then we have $\beta = 1/3$ and $a_0 = n^2/2m$ and everything is fixed. One can, of course, use this hypothesis and proceed to calculate various effects in films etc. But if, for example, agreement is not very good and the results turn out to be sensitive to the value of β then there may be a possibility of using the film data to determine β.

Acknowledgements – I am very grateful to Drs. H. Wagner and A. Leggett for many stimulating discussions over a long period, to Professor H. Callen, who was patient enough to listen to most of what was written above and finally even to read the first draft of the manuscript and make very helpful comment, and to D. Stauffer for making many useful comments on the first manuscript.

REFERENCES

1. (a) MAMALADZE YU. G., *Eksperim Zh. i Teor Fiz.* **52**, 739 (1966), Soviet Phys.–J.E.T.P. **25**, 479 (1967).
   (b) AMIT D. J., *Phys. Letters* **26A**, 466 and 488 (1968).
2. (a) AMIT D. J. and LUBAN M., *Phys. Letters* **27A**, 487 (1968)
   (b) WONG V. K., *Phys. Letters* **27A**, 358 (1968).
   (c) STENSCHKE H., *Z. Physik* **216**, 456 (1968)
   (d) STAUFFER D., *Z. Physik* **221**, 122 (1969) where many more references can be found.
3. LANDAU L. D., *Fiz. J. Sovjet* **11**, 545 (1937); English translation in Collected Papers of LANDAU L. D., ed. HAAR TER D. (Pergamon Press, London, 1965).
4. GINZBURG V. L. and LANDAU L. D., *Eksperim Zh. i. Tero. Fiz.* **20**, 1064 (1950).
5. FISHER M. E., *Rep. Prog. Phys.* **30**, 615 (1967).
6. HELLER P., *Rep. Prog. Phys.* **30**, 731 (1967).
7. GINZBURG V. L., *Fiz. Tverd. Tela.* **2**, 2031 (1960), *Sov. Phys. solid State* **2**, 1824 (1960).
8. See e.g. Ref. (5) and earlier references there cited
9. (a) JOSEPHSON B. D., *Proc. Phys. Soc.* **92**, 276 (1967)
   (b) GUNTON J. D. and BUCKINGHAM M. J., *Phys. Rev. Letters* **20**, 143 (1968).
10. This point was made explicit in Ref. (2a).
11. GRIFFITHS R. B., *Phys. Rev* **158**, 176 (1967).
12. AMIT D. J. and WAGNER H., (unpublished) see also refs (2d) and (22).
13. BURKHARDT T. W. and STAUFFER D., (Report, Max Planck Institute, unpublished, June 1968).
14. HO J. T. and LITSTER J. D., *Phys. Rev. Letters* **22**, 603 (1969).
15. JOSEPHSON B. D., *Phys. Letters* **21**, 608 (1966).
16. WIDOM B., *J. Chem. Phys.* **43**, 3898 (1965).
17. PATASHINSKII A. Z. and POKROVSKII V. L., *Zh. Eksperim. i. Teor. Fiz.*, **50**. 439 (1966); *Soviet Phys.–J.E.T.P.* **23**, 292 (1966).
18. STENSCHKE H. and FALK G., *Z. Physik* **210**, 111 (1968).
19. See e.g. Ref. (11). In particular the discussion leading to Eq. (18) of Ref. (11).
20. That this is not self evident see Ref. (9a), appendix 1
21. KADANOFF L. P., *Nuovo Cim.* **44B**, 276 (1966); MIGDAL A. A., *Zh. Eksperim. i Teor. Fiz* **55**, 1964 (1968).
22. Similar exponents have been defined in COOPERSMITH M. H., *Phys. Rev.* **167**, 478 (1968).
23. GUYON E. and MAKI K., *J. Physique* **30**, 63 (1969)
24. LEVANYUK A. P., *Zh. Eksperim. i. Teor. Fiz* **36**, 810 (1959); *Soviet Phys.–J.E.T.P.* **9**, 571 (1959).
25. SCHOFIELD P., *Phys. Rev. Letters* **22**, 606 (1969)
26. HALPERIN B. I. and HOHENBERG P. C., *Phys. Rev* **177**, 952 (1968)
27. GINZBURG V. L. and PITAEVSKII L. P., *Soviet Phys.–J.E.T.P.* **7**, 858 (1958)
28. TYSON J. A., *Phys. Rev.* **166**, 166 (1968).
29. CLOW J. R. and REPPY J. D., *Phys. Rev. Letters* **16**, 887 (1966).
30. KADANOFF L. P., GOTZE W., HECHT R., LEWIS E. A., PALCIAUSCAS V. V., RAYL M., SWIFT J., ASPNES D. and KANE J., *Rev. mod. Phys.* **39**, 395 (1967).
31. By generalized Ornstein-Zernike correlation function we mean a behaviour of the form Eq. (29) with Γ possibly critically ϵ-dependent

J. Phys. Chem. Solids Pergamon Press 1970. Vol. 31, pp. 1113–1119. Printed in Great Britain.

THERMODYNAMICS OF POINT DEFECTS WITH EXPLICIT CONCENTRATION DEPENDENT INTERACTIONS

R. D. FOUCHAUX
Department of Physics, Lehigh University, Bethlehem, Pa. 18015, U.S.A.

(*Received* 25 *July* 1969; *in revised form* 15 *October* 1969)

Abstract—Thermodynamic quantities related to point defects in thermal equilibrium are discussed under the assumption that these quantities are explicit functions of the defect concentration, n, as well as pressure P, and temperature, T. It is shown that if the partial Gibbs free energy per defect resulting from the interaction among defects becomes comparable with kT, there will be a large enhancement of the temperature coefficient of defect concentration, $\delta n/\delta T$, as well as the thermal expansion coefficient, the specific heat and the isothermal compressibility.

Some experimental results on the silver and alkali halides are discussed as examples We suggest that the volume increment per defect in ionic crystals may be strongly temperature dependent.

1. INTRODUCTION

PROPERTIES of point defects in thermal equilibrium have been interpreted in terms of various partial thermodynamic quantities such as free energy, enthalpy, volume, and entropy per defect[1]. These quantities, when properly defined, are crucial parameters in the correlation of experiments involving a wide variety of defect properties. In ionic crystals ionic conductivity and diffusion, as well as defect enhanced thermal expansion, specific heat and compressibility are basic defect-related properties.

In the silver halides, there is a particularly interesting situation in that there is one dominant defect species, the Frenkel defect, which is present in comparatively large concentrations at elevated temperatures[2, 3, 4]. These defects are charged, and therefore must interact over long range through the coulomb interaction. Although this fact has been recognized for some time, it is comparatively recently that detailed work has been done using the coulomb interaction[1, 5, 6, 7]. Abbink and Martin's ionic conductivity studies and Weber and Friauf's[8] recent diffusion mechanism studies stress the role of interactions between defects in their interpretations. They conclude that explicit inclusion of defect-defect long range interactions is mandatory for the interpretation of their experimental results.

Although the specific interaction model to be used is questionable on theoretical as well as experimental grounds, the Debye–Hückel (DH) theory of strong electrolytes[9] seems most useful at this time.

The DH model can be cast in a form in which the Gibbs free energy per defect, g, is an explicit function of defect concentration, n, as well as pressure, P, and temperature, T. We will treat this in more detail below. First, we give some general thermodynamic arguments.

2. THEORY

We write the Gibbs free energy of a crystal of N molecules (or formula elements) containing n defects of a single species (as Frenkel defects) as

$$G(P,T,n) = G_0(P,T) + G_D(P,T,n) - TS_c(n) \quad (1)$$

where G_0 is the partial free energy of a hypothetical defect free crystal, G_D the partial free energy of the defects and S_c is the entropy of mixing. For Frenkel defects, with $N_i =$ the number of interstitial sites,

$$S_c = +k \log \frac{N_i!N!}{(n!)^2(N_i-n)!(N-n)!}. \qquad (2)$$

We define the chemical potential for Frenkel defects

$$\mu = \left(\frac{\partial G}{\partial n}\right)_{P,T}.$$

For thermal equilibrium at a particular P, T, the condition of equilibrium is that

$$\mu = 0 = \frac{\partial G_D}{\partial n} - T\frac{\partial S_c}{\partial n}. \qquad (3)$$

Using (2) and the usual Sterling approximation, we obtain

$$\mu(P,T,n) = \frac{\partial G_D(P,T,n)}{\partial n} + kT\left(\log \frac{n^2}{(N-n)(N_i-n)}\right). \qquad (4)$$

We also have the equilibrium volume,

$$V(P,T,n) = \frac{\partial G}{\partial P} = V_0(P,T) + V_D(P,T,n), \qquad (5)$$

the entropy

$$S(P,T,n) = -\frac{\partial G}{\partial T} = S_0(P,T) + S_D(P,T,n) + S_c(n), \qquad (6)$$

and the enthalpy

$$H(P,T,n) = G + TS = H_0(P,T) + H_D(P,T,n) \qquad (7)$$

where the meaning of each term is obvious.

The partial quantities referring to the defects are usually expressed in a manner which is a first approximation to the more general forms above. We list these for comparison

$$G_D(P,T,n) = ng(P,T) \qquad (8)$$

with equation (4) yields, if $n \ll N$,

$$\mu = g - T\frac{\partial S_c}{\partial n} = g + 2kT \log \frac{n}{\sqrt{N_i N}} = 0 \qquad (9)$$

or

$$\frac{n}{\sqrt{N_i N}} = e^{\frac{-g}{2kT}} \qquad (9a)$$

when solved explicitly for n.

Equations (5), (6) and (7) yield respectively,

$$V_D = nv(P,T), \qquad (10)$$

$$S_D = ns(P,T), \qquad (11)$$

and

$$H_D = nh(P,T). \qquad (12)$$

With these definitions,

$$g = h - Ts, \qquad (13)$$

$$\frac{\partial g}{\partial P} = v, \qquad (14)$$

$$-\frac{\partial g}{\partial T} = s, \qquad (15)$$

and so on.

With the linear concentration dependence of the free energy, it is possible to solve equation (9) explicitly for the concentration $n(P, T)$ and thus to eliminate n from the free energy function. Under these conditions, the interpretation of experiments in terms of the partial thermodynamic functions g, v, s, h, etc. is unambiguous. However, where we cannot solve equation (4) explicitly for n, we must be more careful. In this case, we formally treat $G(P, T, n)$ as a function of three independent variables P, T, n and apply, where appropriate, the equilibrium condition,

$$\mu(P,T,n)=0, \qquad (3)$$

as a subsidiary condition.

For example, the experimental thermal expansion coefficient is measured at constant pressure and at equilibrium defect concentration. It is defined as

$$\beta=\frac{1}{V}\left(\frac{\delta V}{\delta T}\right)_P=+\left\{\frac{\partial V}{\partial T}-\left(\frac{\partial V}{\partial n}\right)\left(\frac{\partial \mu}{\partial T}\right)\Big/\frac{\partial \mu}{\partial n}\right\}\Big/V \qquad (16)$$

The isothermal compressibility is

$$\kappa=-\frac{1}{V}\left(\frac{\delta V}{\delta P}\right)_T=-\left\{\frac{\partial V}{\partial P}-\left(\frac{\partial V}{\partial n}\right)\left(\frac{\partial \mu}{\partial P}\right)\Big/\frac{\partial \mu}{\partial n}\right\}\Big/V, \qquad (17)$$

and the specific heat is

$$C_P=\left(\frac{\delta H}{\delta T}\right)_P=\frac{\partial H}{\partial T}-\left(\frac{\partial H}{\partial n}\right)\left(\frac{\partial \mu}{\partial T}\right)\Big/\frac{\partial \mu}{\partial n}. \qquad (18)$$

When this is done correctly, some of the difficulties in the correlation of experiments in the silver halides and other ionic crystals may disappear.

3. THE CONCENTRATION EQUATION

Several workers have, by a method of Koch and Wagner[2], measured the equilibrium concentrations of Frenkel defects in silver chloride[2, 4, 6, 10]. Although there is some variation in the interpretation, there is fairly general agreement in the basic data when differences in purity of 'pure' materials are taken into account. We will use the results of Abbink and Martin here as standard, with some remarks on other work when appropriate. Values of $n/N=x$ are plotted in the form $\log x$ vs. $1/kT$. We obtain from equation (4), with $n \ll N, N_i$:

$$\frac{\delta \log x}{\delta T}=\frac{1}{x}\frac{\delta x}{\delta T}=-\frac{1}{x}\frac{\partial \mu/\partial T}{\partial \mu/\partial x}$$
$$=\frac{\partial H_D/\partial x}{2kT^2\left(1+\dfrac{x}{2kT}\dfrac{\partial^2 G_D}{\partial x^2}\right)}$$

or

$$\frac{\delta \log x}{\delta(1/kT)}=-\frac{\partial H_D/\partial x}{2\left(1+\dfrac{x}{2kT}\dfrac{\partial^2 G_D}{\partial x^2}\right)}. \qquad (19)$$

If $G_D(P,T,x)=Nxg(P,T)$, this gives

$$\frac{\delta \log x}{\delta(1/kT)}=-\frac{h}{2},$$

however, where defect-defect interaction is included,

$$\frac{\partial^2 G}{\partial x^2}\neq 0,$$
$$\frac{\partial H_D}{\partial x}\neq h$$

and the result is modified

We will use the Debye-Hückel Theory as a model to illustrate the changes. In Debye-Hückel Theory, as applied by Abbink and Martin, the concentration formula is written

$$2kT\left(\log\sqrt{\frac{N}{N_i}}x+\log\gamma\right)+g'(P,T)=0 \qquad (20)$$

where

$$-\log\gamma=\frac{e^2b}{2DkT(1+bR)} \qquad (21)$$

and

$$b^2=\frac{8\pi e^2x}{VDkT} \qquad (22)$$

is the Debye-Hückel screening parameter. R is a parameter related to the closest possible interstitial-vacancy spacing.

Thus by comparison with equation (4), we identify

$$\frac{\partial G_D}{\partial x}=g'-\frac{e^2b}{D(1+Rb)}$$
$$=g'(P,T)-g''(P,T,x) \qquad (23)$$

To write the Debye-Hückel term g'' as a **partial Gibbs** free energy, we should express it **as a function of P, T, x**.

energy of the defects and S_c is the entropy of mixing. For Frenkel defects, with N_i = the number of interstitial sites,

$$S_c = +k \log \frac{N_i! N!}{(n!)^2 (N_i - n)! (N - n)!}. \qquad (2)$$

We define the chemical potential for Frenkel defects

$$\mu = \left(\frac{\partial G}{\partial n}\right)_{PT}.$$

For thermal equilibrium at a particular P, T, the condition of equilibrium is that

$$\mu = 0 = \frac{\partial G_D}{\partial n} - T\frac{\partial S_c}{\partial n}. \qquad (3)$$

Using (2) and the usual Sterling approximation, we obtain

$$\mu(P, T, n) = \frac{\partial G_D(P, T, n)}{\partial n} + kT\left(\log \frac{n^2}{(N-n)(N_i - n)}\right). \qquad (4)$$

We also have the equilibrium volume,

$$V(P, T, n) = \frac{\partial G}{\partial P} = V_0(P, T) + V_D(P, T, n), \qquad (5)$$

the entropy

$$S(P, T, n) = -\frac{\partial G}{\partial T} = S_0(P, T) + S_D(P, T, n) + S_c(n), \qquad (6)$$

and the enthalpy

$$H(P, T, n) = G + TS = H_0(P, T) + H_D(P, T, n) \qquad (7)$$

where the meaning of each term is obvious.

The partial quantities referring to the defects are usually expressed in a manner which is a first approximation to the more general forms above. We list these for comparison

$$G_D(P, T, n) = ng(P, T) \qquad (8)$$

with equation (4) yields, if $n \ll N$,

$$\mu = g - T\frac{\partial S_c}{\partial n} = g + 2kT \log \frac{n}{\sqrt{N_i N}} = 0 \qquad (9)$$

or

$$\frac{n}{\sqrt{N_i N}} = e^{\frac{-g}{2kT}} \qquad (9a)$$

when solved explicitly for n.

Equations (5), (6) and (7) yield respectively,

$$V_D = nv(P, T), \qquad (10)$$

$$S_D = ns(P, T), \qquad (11)$$

and

$$H_D = nh(P, T). \qquad (12)$$

With these definitions,

$$g = h - Ts, \qquad (13)$$

$$\frac{\partial g}{\partial P} = v, \qquad (14)$$

$$-\frac{\partial g}{\partial T} = s, \qquad (15)$$

and so on.

With the linear concentration dependence of the free energy, it is possible to solve equation (9) explicitly for the concentration $n(P, T)$ and thus to eliminate n from the free energy function. Under these conditions, the interpretation of experiments in terms of the partial thermodynamic functions g, v, s, h, etc. is unambiguous. However, where we cannot solve equation (4) explicitly for n, we must be more careful. In this case, we formally treat $G(P, T, n)$ as a function of three independent variables P, T, n and apply, where appropriate, the equilibrium condition,

$$\mu(P, T, n) = 0, \tag{3}$$

as a subsidiary condition.

For example, the experimental thermal expansion coefficient is measured at constant pressure and at equilibrium defect concentration. It is defined as

$$\beta = \frac{1}{V}\left(\frac{\delta V}{\delta T}\right)_P = +\left\{\frac{\partial V}{\partial T} - \left(\frac{\partial V}{\partial n}\right)\left(\frac{\partial \mu}{\partial T}\right)\Big/\frac{\partial \mu}{\partial n}\right\}\Big/V \tag{16}$$

The isothermal compressibility is

$$\kappa = -\frac{1}{V}\left(\frac{\delta V}{\delta P}\right)_T = -\left\{\frac{\partial V}{\partial P} - \left(\frac{\partial V}{\partial n}\right)\left(\frac{\partial \mu}{\partial P}\right)\Big/\frac{\partial \mu}{\partial n}\right\}\Big/V, \tag{17}$$

and the specific heat is

$$C_P = \left(\frac{\delta H}{\delta T}\right)_P = \frac{\partial H}{\partial T} - \left(\frac{\partial H}{\partial n}\right)\left(\frac{\partial \mu}{\partial T}\right)\Big/\frac{\partial \mu}{\partial n}. \tag{18}$$

When this is done correctly, some of the difficulties in the correlation of experiments in the silver halides and other ionic crystals may disappear.

3. THE CONCENTRATION EQUATION

Several workers have, by a method of Koch and Wagner[2], measured the equilibrium concentrations of Frenkel defects in silver chloride[2, 4, 6, 10]. Although there is some variation in the interpretation, there is fairly general agreement in the basic data when differences in purity of 'pure' materials are taken into account. We will use the results of Abbink and Martin here as standard, with some remarks on other work when appropriate. Values of $n/N = x$ are plotted in the form $\log x$ vs. $1/kT$. We obtain from equation (4), with $n \ll N, N_i$:

$$\frac{\delta \log x}{\delta T} = \frac{1}{x}\frac{\delta x}{\delta T} = -\frac{1}{x}\frac{\partial\mu/\partial T}{\partial\mu/\partial x}$$
$$= \frac{\partial H_D/\partial x}{2kT^2\left(1 + \dfrac{x}{2kT}\dfrac{\partial^2 G_D}{\partial x^2}\right)}$$

or

$$\frac{\delta \log x}{\delta(1/kT)} = -\frac{\partial H_D/\partial x}{2\left(1 + \dfrac{x}{2kT}\dfrac{\partial^2 G_D}{\partial x^2}\right)}. \tag{19}$$

If $G_D(P, T, x) = Nxg(P, T)$, this gives

$$\frac{\delta \log x}{\delta(1/kT)} = -\frac{h}{2},$$

however, where defect-defect interaction is included,

$$\frac{\partial^2 G}{\partial x^2} \neq 0,$$

$$\frac{\partial H_D}{\partial x} \neq h$$

and the result is modified.

We will use the Debye-Hückel Theory as a model to illustrate the changes. In Debye-Hückel Theory, as applied by Abbink and Martin, the concentration formula is written

$$2kT\left(\log\sqrt{\frac{N}{N_i}}x + \log\gamma\right) + g'(P, T) = 0 \tag{20}$$

where

$$-\log\gamma = \frac{e^2 b}{2DkT(1 + bR)} \tag{21}$$

and

$$b^2 = \frac{8\pi e^2 x}{VDkT} \tag{22}$$

is the Debye-Hückel screening parameter. R is a parameter related to the closest possible interstitial-vacancy spacing.

Thus by comparison with equation (4), we identify

$$\frac{\partial G_D}{\partial x} = g' - \frac{e^2 b}{D(1 + Rb)}$$
$$= g'(P, T) - g''(P, T, x) \tag{23}$$

To write the Debye-Hückel term g'' as a partial Gibbs free energy, we should express it as a function of P, T, x.

Equation (22) shows that we have not done this, since V appears explicitly rather than P The dielectric constant D is also an explicit function of pressure, temperature and perhaps defect concentration[7] In fact, the temperature dependence of D may be crucial here, for its increase of a factor of about 1·5 in the termperature range from 400 to 680°K may dominate the behavior of g''.

In the following, for purposes of illustration, we will ignore the term Rb with respect to unity for the reasons that the minimum defect spacing is uncertain, and if the defect concentration is small enough, $Rb \ll 1$ for any reasonable value of R. We also treat D as constant.

We can evaluate equation (19) as follows:

$$\frac{\partial S_D}{\partial x} = \frac{-\partial^2 G_D}{\partial T \partial x} = -\frac{\partial g'}{\partial T} + \frac{e^2}{D}\frac{\partial b}{\partial T} = +s' - \frac{e^2 b}{2DT}, \tag{24}$$

$$\begin{aligned}\frac{\partial H_D}{\partial x} &= \frac{\partial}{\partial x}(G_D + TS_D)\\ &= g' + Ts' - \frac{3e^2b}{D} = h' - \frac{3e^2b}{D},\end{aligned} \tag{25}$$

$$x\frac{\partial^2 G_D}{\partial x^2} = -\frac{xe^2}{D}\left(\frac{\partial b}{\partial x}\right) = -\frac{e^2 b}{2D}. \tag{26}$$

Thus,

$$\frac{\delta \log x}{\delta(1/kT)} = -\frac{h' - \frac{3}{2}(e^2b/D)}{2\left(1 - \frac{e^2b}{4kTD}\right)}. \tag{27}$$

In silver chloride, $h' \approx 1{\cdot}4$ eV. For $x = 10^{-4}$ ($T \approx 300$°C or 573°K) Abbink gives $|\log \gamma| = 0{\cdot}27$, which means $\frac{3}{2}(e^2b/D) \approx 0{\cdot}04$ eV $\ll h'$, therefore

$$\frac{\delta \log x}{\delta(1/kT)} \approx -\frac{h'}{2\left(1 - \frac{|\log \gamma|}{2}\right)}$$

or roughly 13 per cent larger in magnitude than $h'/2$, the expected result with no defect-defect interaction. Abbink and Martin obtained a value of $h' = 1{\cdot}44$ eV by an analysis consistent with this approach. The notable result here is that the defect-defect interaction energy must merely be comparable with kT and not h' to cause appreciable changes in the slope of the concentration curve.

It is tempting to speculate that since the temperature coefficient of defect formation, $\delta x/\delta T$, becomes infinite when $e^2b/4kTD = 1$, that some drastic change such as melting must occur in the crystal if the defect concentration becomes large enough We could estimate an upper bound to the concentration of defects at the melting point by setting $e^2 b_{max}/D = 4KT_{(melt)}$. The resulting b_{max} corresponds to a concentration $x_{max} = 8 \times 10^{-3}$. However, $b_{max}^{-1} \approx 4$ Å under these conditions and the quantitative accuracy of DH theory where the shielding radius is of the order of a lattice parameter is highly suspect at best. The increase of the dielectric constant mentioned above may be very significant here

Perhaps a better comparison is to compare various estimates of the largest value of g'' by Sevenich and Kliewer[7] with $kT_{(melt)} = 0{\cdot}0627$ eV. Their estimates range between 0·04 and 0·16 eV, the higher limit occurring when the variation of dielectric constant is ignored. However, the value of $x(\partial^2 G_D/\partial x^2)$ is smaller than g'' and in fact goes to zero in some of these estimates The value of dielectric constant was based on an extrapolation from 680°K to the melting point of 728°K

4. SPECIFIC HEAT MEASUREMENTS

With the DH model, equation (18) becomes

$$\begin{aligned}C_P &= (C_P)_0 + \frac{\partial H_D}{\partial T} + \frac{Nx\left(h' - \frac{3e^2b}{2D}\right)}{2kT^2\left(1 - \frac{e^2b}{4DkT}\right)}\\ &= (C_P)_0 + \Delta C_P\end{aligned} \tag{28}$$

The term $(C_P)_0$ is the hypothetical perfect crystal specific heat. $\partial H_D/\partial T$ is a (presumably small) contribution due to the explicit temperature change of the enthalpy of defects already in the crystal at temperature T as the crystal is heated from T to $T + dT$ and the third term is a contribution due to the formation of new defects.

In 1950, Kobayashi[11] interpreted his specific heat measurements as indicating that Schottky defects must contribute an appreciable enthalpy to the crystal near the melting point. We see that this is not necessary, since the factor $(1 - e^2b/4DkT)$ in the denominator of the third term can account for the curvature of his $\log(T^2 \Delta C_P)$ vs. T^{-1} plot. Although Kobayashi gives a value of 1·53 eV for the enthalpy of formation of Frenkel defects, his data are consistent with $h' = 1{\cdot}44$ eV. Since extrapolation or calculation of 'perfect crystal' specific heat is questionable, it is probably not fruitful to attempt to correlate concentration magnitudes with partial enthalpy due to defects.

5. ENTROPY OF FORMATION

Although there is considerable disagreement in the literature as to the value of the entropy of formation for Frenkel defects in silver chloride[4, 6, 10] it is agreed that it is probably more than a factor of 3 higher than the entropy of formation of vacancies in nobel metals[12], for example.

The value given by Abbink and Martin should be the same as our $s' = (h' - g')/T$ and equals $8{\cdot}1 \times 10^{-4}$ eV/°K. Equation (24) gives

$$s' = \frac{\partial S_D}{\partial x} + \frac{e^2 b}{2DT} \cong \frac{\partial S_D}{\partial x} - k \log \gamma \qquad (29)$$

using equation (21).

Again, with Abbink's value of $\gamma = 0{\cdot}76$ for $x = 10^{-4}$, we obtain $-k \log \gamma = 0{\cdot}23 \times 10^{-4}$ eV/°K, apparently only a small fraction of the total entropy per defect.

It appears that the defect-defect interaction does not account for the large entropy of formation of defects in ionic crystals as compared with metals as suggested by Fouchaux and Simmons[5].

6. VOLUME CONTRIBUTED BY DEFECTS

Fouchaux and Simmons pointed out that when the partial volume of the crystal associated with defects, V_D, obtained through certain extrapolation procedures is compared with nv, using n estimated from Ebert and Teltow and v from Abey and Tomizuka[13] at defect concentrations approximately appropriate to the melting point of 728°K, the value of V_D exceeds nv_F by a factor of 1·8–3·5. However, the value of v used was determined at 527°K. At that temperature, V_D is rather small, but there is good agreement with nv if we use Abbink and Martin's value of $x = 2 \times 10^{-5}$ at that temperature.

We will investigate two possibilities for the apparent discrepancy: (1) that v increases at large concentrations because of defect-defect interaction, and (2) that v increases at high temperature through an unspecified explicit temperature effect.

For the defect-defect interaction we had, using the DH model,

$$V_D = \frac{\partial G_D}{\partial P} = n\left\{v' - \frac{\partial}{\partial P}\left(\frac{e^2 b}{D}\right)\right\}. \qquad (30)$$

If we ignore the possible pressure dependence of D, the second term in the bracket becomes

$$\frac{\partial}{\partial P}\left(\frac{e^2 b}{D}\right) = \frac{e^2 b}{2D}\kappa \qquad (31)$$

where κ is the compressibility. This term is of necessity positive so the volume per defect would be decreased if such a term were significant. We estimate, however, that the term is very small compared to v'.

To address ourselves to the possibility of explicit temperature dependence of v, it is more convenient to consider the thermal expansion coefficient β than the volume per defect directly.

From equation (16) we obtain

$$V\beta = \frac{\partial V_0}{\partial T} + \frac{\partial V_D}{\partial T} - \frac{\partial V_D}{\partial n}\frac{\partial \mu}{\partial T}\Big/\frac{\partial \mu}{\partial n}$$

where the term to be investigated first is $\partial V_D/\partial T$. In the DH model

$$\frac{\partial V_D}{\partial T} = n\left\{\frac{\partial v'}{\partial T} - \frac{\partial}{\partial T}\left(\frac{e^2 b \kappa}{2D}\right)\right\}.$$

Since the second term requires explicit information on $\kappa(T)$ and $D(T)$ as well as $b(T)$, we cannot be very quantitative, but an order of magnitude estimate suggests a completely negligible contribution. The first term, however, may not be negligible. We turn to an indirect argument here. Zieten[14] has measured the thermal expansion of silver chloride as a function of added divalent impurity ion (Cd) concentration, c. In the structure sensitive temperature range $T \leq 200°\mathrm{C}$, he found a fairly large concentration dependence for the thermal expansion coefficient. We need only assume that the volume $V(T, c)$ is a differentiable function of the form $V(T, c) = V_0(T) + cv_c(T)$, where v_c is the volume per defect of the impurity plus cation vacancy, to obtain

$$\frac{\partial v_c}{\partial T} = \beta v_c + V\frac{\partial \beta}{\partial c}.$$

The term βv_c is small $(\sim 10^{-4}\,\Omega/°\mathrm{K})$ where Ω is the formula volume. At 200°C, we obtain $\partial\beta/\partial c \approx 10^{-2}/°\mathrm{K}$ giving $\partial v_c/\partial T \approx 10^{-2}\Omega/°\mathrm{K}$. If we assume that the Frenkel defect behaves similarly to the substitutional impurity plus cation vacancy, which seems reasonable, then a term $(\partial v_c/\partial T)\Delta T$ could contribute enough extra volume to triple the volume per defect in the temperature range of 200°K from 527°, where v for Frenkel defects was measured, to the melting point.

The third term, $(-\partial V'_d/\partial n)(\partial\mu/\partial T)/(\partial\mu/\partial n)$ gives the familiar defect contribution to the thermal expansion modified by defect-defect interaction terms. In the DH model, the result is

$$-\frac{\partial V_D}{\partial n}\frac{\partial \mu}{\partial T}\bigg/\frac{\partial \mu}{\partial n} = Nx\,\frac{(h' - 3e^2b/2D)v'}{2kT^2(1 - e^2b/4DkT)}.$$

Again, we see the possibility of a large increase as $e^2b/4DkT \rightarrow 1$. Even without this effect, the combined terms

$$Nx\left(\frac{\partial v'}{\partial T} + \frac{h'v'}{2kT^2}\right)$$

could provide the observed discrepancy in the measured and extrapolated thermal expansion coefficients up to quite close to the melting point.

Finally, we mention the work of Kurnick [15] on silver bromide in which he suggested a large v at high temperatures compared to the value observed at lower temperatures. Although the method used was criticized as insensitive to high temperatures and is based on uncertain values of mobilities, the result is reasonable. Its interpretation does not, however, require appreciable Schottky defect concentrations.

6. COMPRESSIBILITY

The experimental value to be expected from compressibility measurements at temperatures where large defect concentrations exist depends strongly on the experimental conditions. If the conditions are such that the equilibrium defect concentration is maintained, equation (17) will hold. The appearance of $\partial\mu/\partial n$ in the denominator of the last term would again cause a very large compressibility if the defect-defect interaction energy per defect becomes comparable to kT. On the other hand, it is not clear that such conditions would hold for methods utilizing the speed of sound, etc. No high temperature compressibility measurements seem to be available.

Simmons and Baluffi[12] have pointed out that in equilibrium measurements of point defect concentrations by the method of comparing thermal expansion measured by macroscopic methods with X-ray measurements, the sample must be completely unconstrained. This requirement may be even more stringent in the case of ionic crystals because of the possibility of very large compressibility increases near the melting point. In fact a large increase in volume increment per defect together with an increase in compressibility would combine their effect in such a way as to cause erroneously low concentration measurements near the melting temperature (see below).

7. SUMMARY AND DISCUSSION

We have indicated how a general equilibrium approach to defect properties in crystals may lead to a better understanding of the correlation between basic experiments.

Silver chloride was used as an example in which many apparent discrepancies among experiments have been shown not to be in conflict. Some comments on alkali halides may be appropriate. Ionic conductivity studies [16, 17] have typically shown the upward curvature of $\log \sigma T$ vs. $1/T$ curves which we attribute to defect-defect interactions, while measurements by Von Guerard, Peisl, and Waidelich [18] of equilibrium concentration of Schottky defects in potassium chloride do not appear to show this effect, and these authors draw a straight line through their $\log x$ vs. $1/T$ curve.

I believe this result is inconclusive. When the limits of experimental error given by Von Guerard *et al.*, are considered a curvature of the amount seen in the ionic conductivity studies is not excluded. In fact, if results below 600°C, where the errors are greatest, were ignored, a small upward curvature might fit the data better. Furthermore the sample could have been under some small constraint which under the conditions mentioned above might not be negligible. Such a condition could hide an upward curvature toward the high temperature end.

Because the dielectric constant in the alkali halides is smaller than that in silver halides, the interaction effects would be expected to be larger in alkali halides than silver salts at comparible defect concentrations. The Debye–Hückel theory has been less successfully applied to alkali halides than silver halides at this time. This may be because the Schottky defect is less amenable to the type of statistical treatment implicit in the *DH* theory, since there are fewer sites for an anion vacancy near a cation vacancy than there are interstitial sites.

As in silver halides, the volume expansion of alkali halides appears to be larger than would be expected if there is a fixed volume increment per defect [19].

Acknowledgements – The author thanks Professor R. O. Simmons for comments on an earlier manuscript of this paper. He also thanks Dr M. H. Reilly for a conversation concerning problems in the alkali halides

REFERENCES

1. LIDIARD A. B., *Handb. Phys.* **20**, 246 (1956) gives a comprehensive review with earlier references.
2. KOCH E. and WAGNER C., *Z. phys. Chem.* **B38**, 295 (1937).
3. TELTOW J., *Ann. Phys.* **5**, 63, 71 (1949).
4. EBERT I. and TELTOW J., *Ann. Phys.* **15**, 268 (1955).
5. FOUCHAUX R. D. and SIMMONS R. O., *Phys. Rev.* **136A**, 1664 (1964)
6. ABBINK H. C. and MARTIN D. S. JR., *J. Phys. Chem. Solids* **27**, 205 (1966)
7. SEVENICH R. A. and KLIEWER K. L., *J. chem. Phys.* **48**, 3045 (1968)
8. WEBER M. D. and FRIAUF R. J., *J. Phys. Chem. Solids* **30**, 407 (1969).
9. DEBYE P. and HUCKEL E., *Phys. Z.* **24**, 185 (1923)
10. MÜLLER P., *Phys. Status Solidi* **9**, K193 (1965); **12**, 775 (1965).
11. KOBAYASHI K., *Sci. Rep. Res. Inst., Tohoku Univ. Series* I **34**, 112 (1950).
12. SIMMONS R. O. and BALUFFI R. W., *Phys. Rev.* **129**, 1533 (1963).
13. ABEY A. E. and TOMIZUKA C. T., *J. Phys. Chem. Solids* **27**, 1149 (1966).
14. ZIETEN W., *Z. Phys.* **146**, 451 (1956).
15. KURNICK S. W., *J. chem. Phys.* **20**, 218 (1952).
16. DAWSON D. K. and BARR L. W., *Phys. Rev. Lett.* **19**, 844 (1967).
17. FULLER R. G., REILLY M. H., MARQUARDT C. L. and WELLS J. C. JR., *Phys. Rev. Lett.* **20**, 662 (1968).
18. VON GUERARD B., PEISL H. and WAIDELICH W., *Phys. Status Solidi* **29**, K59 (1968).
19. MERRIAM M. F., SMOLUCHOWSKI R. and WEIGAND D. A., *Phys. Rev.* **125**, 65 (1962)

J. Phys. Chem. Solids Pergamon Press 1970. Vol. 31, pp. 1121–1135. Printed in Great Britain.

ETUDE DE LA SURFACE DE SOLIDES PAR RMN DE LIQUIDES ADSORBE–I. ORIGINE DU DEPLACEMENT ET DE LA LARGEUR DES RAIES DANS LE CAS DES CARBONES

S. GRADSZTAJN[*], **J. CONARD et H. BENOIT**[*]
Institut d'Electronique Fondamentale, Laboratoire Associé au CNRS, Faculté des Sciences 91, Orsay, France

(*Received* 5 *June* 1969; *in revised form* 14 *October* 1969)

Résumé – Cette étude en RMN haute résolution donne des informations sur la microtexture de la surface solide et la nature des liens qui l'unit à l'adsorbat. Dans les carbones l'anisotropie diamagnétique des parties cristallisées est à l'origine du déplacement des raies de résonance Un modèle en feuillets pour l'organisation locale du solide au voisinage des pores permet de calculer ce déplacement, et les valeurs obtenues sont en bon accord avec l'expérience Une interaction scalaire avec les électrons célibataires ou une modification de la constante d'écran due à une liaison chimique demeurent négligeables dans les cas de liquides non polaires présentés ici. L'observation de la largeur des raies RMN du proton et du fluor montre l'existence de deux causes de largeurs superposées, une largeur d'origine dipolaire et une distribution du champ local diamagnétique L'analyse de ces deux causes de largeur permet d'évaluer des temps de corrélation pour certains mouvements des molécules adsorbées.

Abstract – High Resolution NMR study of liquids adsorbed on solids gives information on the solid texture and the bond between solid and adsorbed molecules For Carbons, diamagnetic anisotropy of crystalized parts is responsible for the observed line shift A foil stack pattern for the local organization around the pores, allows us to calculate this shift and gives a good agreement with the experimental values. Scalar interaction with unpaired electrons or change in screening constant by a chemical bond are negligible effects in the case of non polar adsorbed molecules studied here. From proton or fluor line width studies, it is possible to deduce the existence of two causes of line width: A width of dipolar origine and a distribution of the local magnetic field Correlations times for some type of motions may be evaluated

1. INTRODUCTION

L'ÉTUDE par RMN des liquides adsorbés à la surface d'un solide montre un déplacement et un élargissement des raies par rapport à celles du liquide libre.

Les déplacements des raies ont été généralement attribués à trois causes:

(1) L'interaction de contact entre les électrons non appariés du solide et les spins nucléaires du liquide adsorbé[1–3].

(2) La déformation du nuage électronique de la molécule adsorbée[4] (effet d'écran).

(3) Un champ local aux sites où sont adsorbées les molécules de liquide et dont l'origine est la susceptibilité diamagnétique anisotrope du solide[5, 6].

Dans le cas des carbones ces trois causes de déplacement peuvent être envisagées. La première semblait à priori la plus probable étant donné le rapprochement que l'on peut faire entre les déplacements particulièrement grands observés et la grande concentration en centres paramagnétiques des carbones. On sait d'autre part, par les expériences de polarisation dynamique[7–10] et par les mesures de temps de relaxation[11, 12] que des interactions entre les électrons des carbones et les noyaux des liquides adsorbés existent.

Nous montrons par ce travail que les grands déplacements observés doivent être attribués en fait à l'existence d'un champ local anisotrope d'origine diamagnétique. Nous avons étudié également le rôle de ce champ local dans l'élargissement des raies.

---

[*] Faculté des Sciences de Paris.

2. CHOIX DES SOLIDES ET DES LIQUIDES ET METHODE EXPERIMENTALE

2.1 *Les solides*

La nature et les propriétés des carbones utilisés sont résumées dans le Tableau 1.*

Les carbones NC et Carbolac ont été choisis pour leur grande surface spécifique, ce qui permet d'obtenir des signaux mesurables pour de très faibles recouvrements de la surface par le liquide (inférieurs à une couche monomoléculaire BET).

Les cokes de saccharose ont été choisis pour leur propriétés magnétiques bien connues en RPE et en RMN[10, 11, 13].

Les noirs de carbones; Spheron et Graphon, ont été choisis pour la forme sphèrique de leurs grains, leur texture et leur état de graphitation étudiés par ailleurs[17].

Tous les carbones contiennent beaucoup d'électrons célibataires (Tableau 1) souvent tres délocalisés[14–16].

Les noirs de carbones sont naturellement sous forme de poudres fines (100–200 Å); les autres carbones ont été broyés ($\phi < 80\mu$). Ils présentent des pores dont la forme est généralement mal connue et dont les plus petits ont des dimensions de 7 Å environ. Ils contiennent d'autre part des cristallites[17] dont les dimensions et le nombre croissent avec la température de traitement (HTT) du carbone. Les poudres de carbones sont donc isotropes à l'échelle macroscopique mais fortement anisotrope à l'échelle des micropores et des cristallites (Tableau 1).

2.2 *Les liquides*

Les liquides étudiés sont:

(1) Le benzène et l'eau, qui, adsorbés sur des carbones, ont déjà été étudiés par polarisation dynamique[8–10].

(2) Les fluoro benzènes (C_6HF_5 et C_6H_5F) pour lesquels on peut étudier simultanément la résonance magnétique du fluor et du proton.

(3) Des liquides non polaires à deux composantes chimiques bien séparées (Toluène, Xylène) pour lesquels ont peut étudier séparément le comportement des deux composantes (protons des groupes CH_3 d'une part et protons du cycle aromatique d'autre part).

2.3 *Préparation des échantillons et méthode expérimentale*

Les carbones sont dégazés à 250°C et 10^{-4} torr pendant 48 hr. Le tube contenant les carbones est ensuite mis en communication avec celui contenant le liquide préalablement dégazé. Les quantités de liquides adsorbés sont déterminées par pesées.

Les mesures de RMN sont faites sur un spectromètre Varian à haute résolution, muni d'une stabilisation en champ à 60 MHz sur la raie du proton de l'eau (référence externe).

Les mesures de déplacement des raies de liquide adsorbé par rapport à celles du liquide libre ont été faites par la méthode de substitution. La précision de ces mesures est determinee essentiellement par le pointé du sommet des raies larges de liquide adsorbé.

3. RESULTATS EXPERIMENTAUX CONCERNANT LES DEPLACEMENTS DES RAIES

3.1 *Effet du champ directeur* H_0

Dans tous les cas examiné (Tableau 2) les déplacements ont lieu vers les champs croissants à fréquence fixe (Fig. 1) et sont rigoureusement proportionnels au champ directeur H_0 (d'autres mesures ont été faites à 15, 1 MHz, 56, 4 MHz et dans certains cas à 100 MHz).

3.2 *Effet de la nature de l'adsorbat et de l'adsorbant*

Les déplacements sont caractéristiques du carbone et pratiquement indépendants du liquide adsorbé et du noyau résonnant (Tableau 2).

Dans le cas des liquides non polaires à deux composantes chimiques, un déplacement

---

*Nous remercions M. le Professeur J. B Donnet (ESCM) et M. P. Chiche (CERCHAR) pour les nombreux échantillons de carbones qu'ils nous ont fournis et pour les discussions fructueuses que nous avons eu avec eux.

Tableau 1. *Propriétés des carbones utilisés*

Nature	Nom	Surface BET en (m²/g)	Dimension des grains	*d*: Densité de la poudre	*D'* Densité vraie des grains	Dimension des cristallites Diamètre*	épaisseur	RPE		RMN des protons du carbone
Carbone actif de noix de coco activé à la vapeur d'eau à 900°C (Taux d'usure 65%)	NC	1 330	< 80 μ	0.4	2.15	20 à 60 Å	~10 Å	raie large 100G raie étroite 0,5G $N_s > 10^{18}$ spins/g		Pas de signal
Noirs de carbone	Carbolac	1 000	100 Å	0.05	1.8			$\Delta H = 2$G	$N_s = 10^{21}$	
	Spheron 6	120	250 Å	à	à	18 à 20 Å	3 à 4 plans			
	Graphon	80	200 Å	0.1	1.9		10.5–14 Å	$\Delta H = 3,8$G	$N_s = 10^{20}$	Pas de signal
Cokes de saccharose GFEC	S 400	300	< 80 μ	0.3	1.4			$\Delta H = 4$G	$N_s = 2\ 10^{19}$	$\Delta H = 4,1$G
traités à 400° et 650°	S 650	~ 300	< 80 μ	0.3	~ 1.4			$\Delta H = 1$G	$N_s = 10^{20}$	$\Delta H = 4,4$G

*Réf [17]. Les carbones.

ΔH: largeurs des raies RMN ou RPE (G)

N_s: concentration en centres paramagnétiques (spins/g).

Tableau 2. Valeurs expérimentales du déplacement et de la largeur des raies à 60 MHz pour H *et 56, 4 MHz pour* F *(θ est le recouvrement de la surface en nombre de couches monomoléculaires BET)*

Carbone	Liquide adsorbe et noyau résonnant		Déplacement (Hz)		Largeur (Hz)	
			$\theta \sim 2$	$\theta < 1$	$\theta \sim 2$	$\theta < 1$
NC (1.330 m^2/g)	Eau	*H*	470 ± 15	520	300 ± 20	550
	Toluène	*H*	440		330	
	Benzene	*H*	440	500	340	500
	C_6H_5F	*H*	435		290	
		F	430		290	
	C_6HF_5	*H*	425		480	
		F	445		600	
Carbolac (1000 m^2/g)	Eau	*H*	220 ± 15	370	80 ± 20	140
	Toluene	*H*	260		100	
	Benzène	*H*	240	380	70	130
Spheron 6 (120 m^2/g)	Benzène	*H*	50 ± 20	80	120	130
	2 raies	*H*	400	500	210	300
Graphon (80 m^2/g)	Benzene	*H*	800 ± 30		600 ± 40	
S-400 (300 m^2/g)	Eau	*H*	160 ± 30		830 ± 40	
	Benzène	*H*	120		~1000	
S 650	Eau	*H*	200 ± 30		~1000	
	Benzene	*H*	210		~1000	

différent pour les deux composantes a été observé mais la différence est très faible (toujours inférieure à 30 Hz) par rapport au déplacement global des deux raies et généralement à la limite de l'erreur expérimentale.

3.3 *Effet du recouvrement de la surface*

Le déplacement diminue (Fig. 2) lorsque le recouvrement θ de la surface augmente (θ = nbre de couches monomoléculaires évaluées d'après la surface BET).

Cette propriété n'a pas été observée pour les cokes de saccharose S 400 et S 650 pour lesquels les raies très larges ne permettent pas d'obtenir une bonne précision aux faibles recouvrements.

Dans le cas du carbone actif NC on voit apparaître une deuxième raie élargie mais non déplacée pour $\theta \sim 5$ (Fig. 4). Cette raie s'élimine facilement par dégazage à température ambiante. La raie déplacée par contre ne s'élimine qu'au moyen d'un dégazage prolongé à 200 ou 300°C. Dans le cas du noir de carbone Spheron 6 on observe également 2 raies (Tableau 2) mais dont les intensités diminuent simultanément pendant le dégazage.

3.4 *Effet de la température*

Quel que soit le carbone, nous n'avons pu mettre en évidence aucune variation du déplacement avec la température entre −80 et +35°C. Ces expériences ont été faites pour différents liquides adsorbés (eau, benzène, toluène) et pour différents recouvrements ($\theta < 1$ et $\theta > 1$.)

3.5 *Effet de la densité de la poudre et de la forme de l'échantillon*

Les poudres de carbones utilisées ont des densités apparentes faibles (Tableau 1). Une compression de la poudre ayant pour effet de multiplier la susceptibilité volumique de la poudre par un facteur 3 modifie le déplacement de moins de 10 pour cent. Nous avons vérifié également que la forme de l'échantillon (tube à bulbe sphèrique au lieu d'un tube cylindrique) avait un effet du même ordre de grandeur dans le cas des noirs de carbones et du carbone NC.

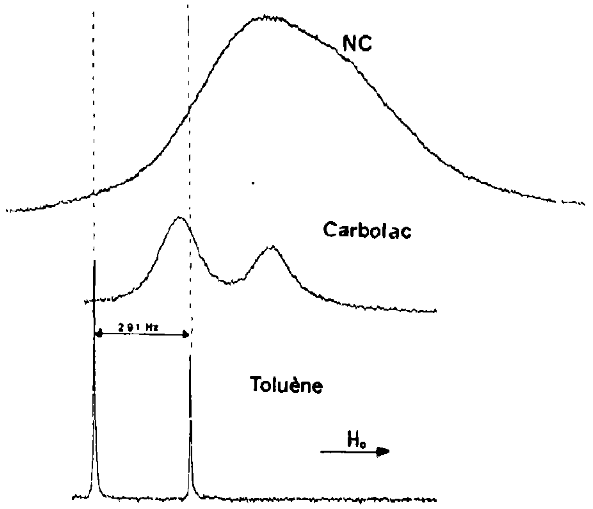

Fig. 1. Déplacement et élargissement des raies de liquide adsorbé sur différents carbones. De bas en haut: – Toluène pur; Toluène adsorbé sur le noir de carbone Carbolac; Toluène adsorbé sur le carbone actif NC.

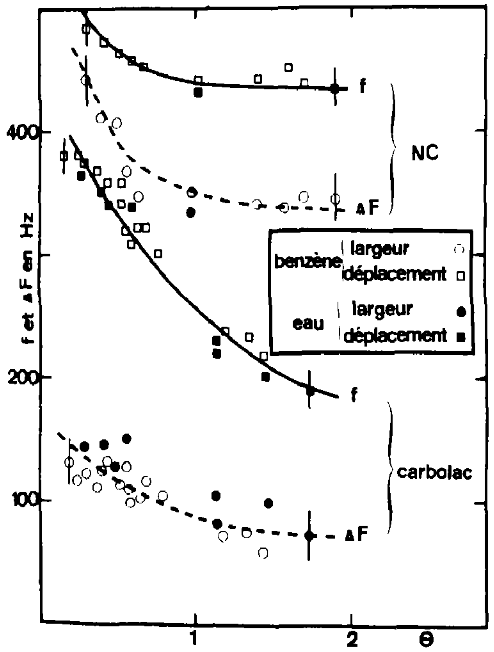

Fig. 2. Variation de la largeur ΔF et du déplacement f des raies en fonction du recouvrement θ de la surface. Les liquides adsorbés sont l'eau et le benzene. Les carbones sont le noir de carbone Carbolac et le carbone actif NC. Le recouvrement θ est exprimé en nombre de couches monomoléculaires statistiques évalué d'après la surface BET du carbone.

4. ORIGINE DU DEPLACEMENT DES RAIES

Nous discutons maintenant l'importance relative des différentes causes de déplacement.

4.1 *Interaction de contact entre les électrons non appariés et les spins nucléaires*

Cette interaction donne lieu à un déplacement mesuré en Hertz:

$$f = A\frac{\gamma_e}{\gamma_N}\frac{h\nu_0}{4kT}$$

A constante d'interaction hyperfine exprimée en Hz,

γ_N, γ_e rapports gyromagnétiques du noyau et de l'électron,

T temperature

ν_0 fréquence de mesure.

Lorsqu'on diminue la température de 100° on devrait observer une augmentation relative du déplacement $\Delta f/f \sim \frac{1}{3}$. Le fait que nous n'ayons observé aucune variation du déplacement avec la température (cf. 3.4) montre que la totalité du déplacement ne peut pas s'expliquer par cet effet.

L'interaction de contact, si elle existe, est donc masquée par d'autres causes de déplacement. Sa contribution au déplacement est certainement inférieure à 10 pour cent dans le cas des carbones NC, Spheron 6 et Graphon, à 15 pour cent dans le cas du Carbolac et à 30 pour cent dans le cas des cokes de saccharose S 400 et S 650.

4.2 *Déformation du nuage électronique des molécules adsorbées*

Une telle interaction donne des déplacements 'chimiques' variables avec la nature de la molécule adsorbée[4]. Dans le cas des molécules à 2 composantes on devrait observer une variation importante de l'écart des deux composantes du spectre entre l'état libre et l'état adsorbé. De plus dans le cas des fluorobenzènes (C_6HF_5 et C_6H_5F) on obtiendrait un déplacement beaucoup plus grand pour le fluor que pour le proton du fait de la grande différence des écrans électroniques de ces deux atomes. Au contraire, les résultats expérimentaux montrent (Tableau 2) que les différences des déplacements obtenus pour les différents liquides adsorbés sur un même carbone et les différents noyaux résonnants sont toujours inférieurs à 50 Hz.

Alors que dans le cas du gel de silice[4] cette interaction semble être la cause essentielle du déplacement, dans le cas des carbones cette cause ne peut contribuer que pour 10–15 pour cent au déplacement observé.

4.3 *Effet de la susceptibilité diamagnétique à l'échelle de l'échantillon.*

Le champ H vu par le noyau résonnant peut s'écrire: $\mathbf{H} = \mathbf{H}_0 + \mathbf{h}_1 + \mathbf{h}_2 + \mathbf{h}_3$ où $\mathbf{H}_0$ est le champ appliqué, $\mathbf{h}_1$ le champ démagnétisant dû à la forme de l'échantillon, $\mathbf{h}_2$ le champ de Lorentz[18], et $\mathbf{h}_3$ le champ dû à la matière à l'intérieur de la sphère de Lorentz.

Si nous choisissons une sphère de Lorentz qui ne contienne qu'un grain de la poudre (hypothèse raisonnable étant donné la faible densité d des poudres (cf. Tableau 1), le champ $\mathbf{h}_1 + \mathbf{h}_2$ est celui dû à l'ensemble des autres grains et dépend de la forme de l'échantillon et de la densité d la poudre. Si χ_{vp} est la susceptibilité volumique de la poudre: $\chi_{vp} = d\chi_m$ où d est la densité de la poudre et χ_m sa susceptibilité massique (cf. Tableau 1), on a $\mathbf{h}_1 + \mathbf{h}_2 = -(2\pi/3)\chi_{vp}\mathbf{H}_0$ pour un échantillon cylindrique et $h_1 + h_2 = 0$ pour un échantillon sphèrique.

Le déplacement des raies correspondant dans le cas d'un liquide adsorbé est proportionnel à $\Delta h = -(2\pi/3)(\chi_{vp} - \chi'_v)H_0$ dans le cas d'un échantillon cylindrique (χ'_v étant la susceptibilité volumique du liquide). Ce déplacement est nul si l'échantillon est sphèrique.

Le calcul du déplacement dû à ce champ $\mathbf{h}_1 + \mathbf{h}_2$ donne des valeurs faibles (10–35 Hz) par rapport à celles que nous observons (Tableau 2). De plus, les valeurs de χ_{vp} et χ'_v étant voisines, ce déplacement peut avoir lieu dans le sens du champ croissant ou décroissant suivant le signe de $(\chi_{vp} - \chi'_v)$. Enfin le fait que la compression de la poudre et la forme de l'échantillon n'affectent que faiblement (cf. 3.5.) le déplacement montre bien que la partie macroscopique: $\mathbf{h}_1 + \mathbf{h}_2$ du champ dû à la matière diamagnétique contribue pour moins de 10 pour cent au déplacement observé.

4.4 *Effet de la susceptibilité diamagnétique à l'échelle d'un grain*

A l'intérieur d'un grain, les pores où est adsorbé le liquide sont entourés de matière diamagnétique plus ou moins anisotrope et plus ou moins dense suivant le carbone considéré. Le champ h_3 crée par cette matière de susceptibilité volumique moyenne $\chi_v = \chi_m \cdot D$ où D est la densité vraie du grain (voir Tableau 1 et 3) dépend de la forme des grains [21], de la forme des pores, de leur orientation par rapport au champ magnétique $\mathbf{H}_0$ et de la disposition des cristallites autour des pores. Ce champ h_3 est proportionnel au champ magnétique H_0 et indépendant de la température et de la nature du liquide adsorbé. Il ne varie pas avec la forme extérieure de l'échantillon ni avec la densité de la poudre. On peut remarquer de plus (Tableau 3) que les

Tableau 3. Déplacement des raies calculés d'après le modèle b *et susceptibilités magnétiques apparentes de ce modèle pour les différents carbones*

Carbone	$\bar{\chi}_m$ (cgs par g)	$\bar{\chi}_l$ (cgs par cm³)	Déplacement max calculé (Hz)		Valeurs expérimentales du déplacement (Hz)	Valeurs des susceptibilités apparentes correspondant aux déplacements expérimentaux dans un modèle de pores plans		
			Pores cylindriques	Pores plans		$\chi_\perp$ (cgs par cm³)	$\chi_\parallel$ (cgs par cm³)	$\chi_\perp/\chi_\parallel$
S 400	$-0{,}45\ 10^{-6}$	$-0{,}62\ 10^{-6}$	78	310	160	$-1{,}3\ 10^{-6}$	$-0{,}3\ 10^{-6}$	4,3
S 650	$-0{,}6\ 10^{-6}$	$-0{,}84\ 10^{-6}$	102	410	200	$-1{,}6\ 10^{-6}$	$-0{,}4\ 10^{-6}$	4
Carbolac	$-0{,}8\ 10^{-6}$	$-1{,}48\ 10^{-6}$	186	745	370	$-2{,}9\ 10^{-6}$	$-0{,}7\ 10^{-6}$	4,1
NC	$-0{,}7\ 10^{-6}$	$-1{,}5\ 10^{-6}$	188	755	500	$-3{,}5\ 10^{-6}$	$-0{,}5\ 10^{-6}$	7
Spheron 6	$-0{,}85\ 10^{-6}$	$-1{,}57\ 10^{-6}$	197	790	500	$-3{,}6\ 10^{-6}$	$-0{,}6\ 10^{-6}$	6
Graphon	$-2\ 10^{-6}$	$-3{,}7\ 10^{-6}$	462	1 850	900	$-7{,}3\ 10^{-6}$	$-1{,}9\ 10^{-6}$	3,8

$\bar{\chi}_m$ est la susceptibilité massique moyenne· ces mesures nous ont été communiquées par M Zanchetta, Centre de Recherches de Magnétochimie—Talence.

$\bar{\chi}_l$ est la susceptibilité volumique moyenne· $\chi_l = \frac{1}{3}\chi_\perp + \frac{2}{3}\chi_\parallel = D\chi_m$ (cf. Tableau 1).

Les déplacements max. ont été calculés pour une anisotropie maximale: $\chi_\parallel = 0$ et $\chi_\perp = 3\chi_l$.

déplacements observés varient comme la susceptibilité χ_l des carbones.

La forme et la disposition des pores et des cristallites à l'intérieur d'un grain de carbone étant mal connue nous calculerons le champ h_3 dans le cas de modèles simples.

Ces modèles doivent rendre compte de l'ordre de grandeur observé pour le déplacement, du fait que le déplacement a toujours lieu vers les champs croissants et que (sauf pour les cokes de saccharose) il varie avec le recouvrement.

4.5 *Calcul du champ local* h_3

(a) *Grains de matière isotrope.* Nous admettons que pour un carbone donné les pores ont tous la même forme (ellipsoïdes, cylindres allongés, ou fissures planes) et qu'ils sont répartis et orientés au hasard dans un grain. On peut montrer alors (cf. annexe et Tableau 4) que le champ local h_3 à l'intérieur d'un pore créé par la matière isotrope du grain présente une distribution variable avec la forme du pore (Fig. 3) mais que la valeur moyenne de h_3 (sur toutes les orientations des pores) est nulle, quelle que soit leur forme.

Dans le cas de grains de matière isotrope on peut donc selon la forme des grains[21] et des pores observer une dispersion des déplacements dus au champ local h_l qui conduit éventuellement à un élargissement ou a une dissymétrie des raies de résonance, le centre de gravité de celle ci n'étant pas déplacé.

(b) *Grains de matière anisotrope.* Nous admettrons que chaque pore est entouré de matière anisotrope dont la direction de facile aimantation est perpendiculaire à la plus grande dimension du pore, l'ensemble des pores et des régions anisotropes qui les entourent étant toujours orienté au hasard dans le grain.

Ce modèle décrit une situation où les pores seraient entourés de cristallites ou de couches aromatiques organisées à l'échelle de quelques cycles, les plans aromatiques étant préférentiellement parallèles à un plan contenant la ou les plus grandes dimensions du pore.

Soient $\chi_\perp$ et $\chi_\parallel$ les susceptibilités volumiques apparentes perpendiculaire et parallèle à la direction préférentielle des plans aromatiques dans la région qui entoure le pore.

Dans ce cas $\mathbf{h}_3 = \mathbf{h}'_3 + \mathbf{h}''_3$ où $\mathbf{h}'_3$ est le champ démagnétisant dû à la forme du pore dans une matière anisotrope ($\chi_\perp \neq \chi_\parallel$) et $\mathbf{h}''_3$ le champ démagnétistant dû à forme du grain constitué de matière isotrope en moyenne ($\bar{\chi} = \frac{2}{3}\chi_\parallel + \frac{1}{3}\chi_\perp$).

Les valeurs moyennes du champ h_3 ont été calculées de cette façon (cf. Annexe) pour des pores sphèriques, cylindriques (ellipsoïde

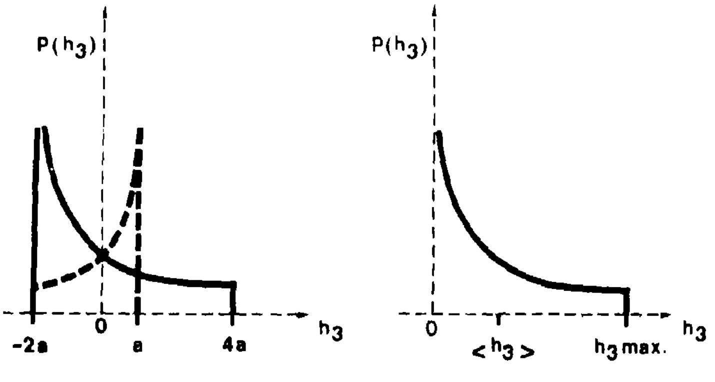

Fig. 3. Distribution du champ local h_3. *A gauche:* Cas de grains sphèriques de matière isotrope avec des pores plans — ou cylindriques --- $a = (2\pi/3)\chi_l H_0$ et $(h_l) = 0$. *A droite:* Distribution du champ local au voisinage d'un cristallite.

Tableau 4. Calcul du champ local pour différentes formes de pores

Forme du pore	Champ démagnétisant dans le pore: h''_3 Matière anisotrope	 Matière isotrope	$\langle h_3\rangle = \langle h'_3\rangle + \langle h''_3\rangle$ Matière anisotrope	 Matière isotrope
Sphère	$h''_3 = \frac{4\pi}{3}H_0(\chi_{\parallel}\cos^2\alpha + \chi_{\perp}\cos^2\beta$ $+\chi_{\perp}\cos^2\gamma)$	$h''_3 = \frac{4\pi}{3}H_0\chi$		$h_3 = 0$
$N_x = N_y = N_z = \frac{1}{3}$	$\langle h''_3\rangle = \frac{4\pi}{3}H_0\bar{\chi}$	$\langle h''_3\rangle = \frac{4\pi}{3}H_0\bar{\chi}$	$\langle h_3\rangle = 0$	$\langle h_3\rangle = 0$
Cylindre	$h''_3 = 2\pi H_0(\chi_{\parallel}\cos^2\beta + \chi_{\perp}\cos^2\gamma)$	$h''_3 = 2\pi H_0\bar{\chi}(\cos^2\beta + \cos^2\gamma)$		$h_3 = 2\pi H_0\bar{\chi}\left(\frac{1}{3} - \cos^2\alpha\right)$
$N_x = 0$ $N_y = N_z = 1/2$	$\langle h''_3\rangle = \frac{2\pi}{3}H_0(\chi_{\perp} + \chi)$	$\langle h''_3\rangle = \frac{4\pi}{3}H_0\bar{\chi}$	$\langle h_3\rangle = \frac{2\pi}{9}H_0(\chi_{\perp} - \chi)$	$\langle h_3\rangle = 0$
Plans	$h''_3 = 4\pi H_0\chi_{\perp}\cos^2\gamma$	$h''_3 = 4\pi H_0\overline{\chi\cos^2\gamma}$		$h_3 = 4\pi\bar{\chi}H_0\left(\cos^2\gamma - \frac{1}{3}\right)$
$N_x = N_y = 0,$ $N_z = 1$	$\langle h''_3\rangle = \frac{4\pi}{3}H_0\chi_{\perp}$	$\langle h''_3\rangle = \frac{4\pi}{3}H_0\bar{\chi}$	$\langle h_3\rangle = \frac{4\pi}{3}H_0(\chi_{\perp} - \bar{\chi})$	$\langle h_3\rangle = 0$

ayant un axe infini) ou plans (ellipsoïde ayant deux axes infinis) et conduisent aux déplacements représentés dans le Tableau 3.

On constate que les valeurs expérimentales sont dans tous les cas plus grandes que les valeurs maximales calculées pour des pores cylindriques et plus petites que les valeurs maximales calculées pour des pores plans. (Ces valeurs maximales correspondent à une anisotropie maximale: $\chi_{\parallel} = 0$ et $\chi_{\perp} = 3\bar{\chi}$.

Les valeurs expérimentales sont donc en accord avec un modèle de pores plans, l'anisotropie de la matière diamagnétique qui entoure les pores étant variables d'un carbone à l'autre. Les valeurs des susceptibilités apparentes et de l'anisotropie: $\chi_{\perp}/\chi_{\parallel}$ que l'on peut déduire de ce modèle (Tableau 3) sont toujours éloignées de celles du graphite monocristallin:

$$\chi_{\perp} = 48{,}6\ \text{cgs/cm}^3$$
$$\chi_{\parallel} = 1{,}1\ \text{cgs/cm}^3$$
$$\chi_{\perp}/\chi_{\parallel} = 44.$$

Dans le cas du Graphon la grande valeur obtenue pour $\chi_{\parallel}$ ($\chi_{\parallel} = 1{,}9$) est en bon accord avec l'existence de petits cristallites ayant une orientation préférentielle suivant le plan du pore mais non pas rigoureusement parallèles à celui-ci.

Le remplissage de la porosité par le liquide modifie la susceptibilité moyenne du grain et a pour effet de diminuer le déplacement.

(c) *Liquide adsorbé sur les cristallites.* Dans le cas de certains carbones les dimensions des cristallites sont connues par rayons X (Tableau 1) ont peut alors calculer le champ local h_3 en admettant que les molécules de liquide sont adsorbés sur les cristallites qui constituent les parois des pores. Ces molécules subissent alors un champ local: $\mathbf{h}_3 = \mathbf{h}_3' + \mathbf{h}_3'' + \mathbf{h}_3'''$ où $\mathbf{h}_3'$ et $\mathbf{h}_3''$ sont les champs démagnétisants dûs à la forme du pore et à la forme du grain dans une matière isotrope en moyenne et $\mathbf{h}_3'''$ est le champ au voisinage d'un cristallite. Nous avons vu (Section (a) et Annexe) que le champ $\mathbf{h}_3' + \mathbf{h}_3''$ dans ce cas présente une distribution mais que sa valeur moyenne $\langle \mathbf{h}_3' + \mathbf{h}_3'' \rangle$ est nulle quelle que soit la forme des pores. On aura donc ici $\langle h_3 \rangle = \langle h_3''' \rangle$. Le déplacement est déterminé par le champ au voisinage d'un cristallite.

Pour rendre compte du déplacement vers les champs magnétiques croissants, il faut alors admettre que les molécules sont adsorbées sur les faces des cristallites, parallèles aux plans aromatiques, qui tapissent le pore. Un tel pore peut être plan ou prismatique.

Nous avons calculé h_3''' dans le cas d'un cristallite formé de plusieurs (1, 2 ou 3) plans de 30 cycles aromatiques (ce qui correspond aux cristallites observés dans le cas des carbones NC et spheron 6) en remplaçant chaque cycle par un dipôle ponctuel. Nous admettons que la première couche de molécules adsorbées se trouve à 3,5 Å du cristallite (distance égale à la distance entre les plans du cristallite). Le champ h_3''' subi par une molécule de liquide située au milieu de la face plane d'un tel cristallite varie avec l'orientation de celui-ci par rapport à $\mathbf{H}_0$. Les déplacements de raies correspondants ont les valeurs suivantes à 60 MHz:

1 seul plan aromatique $f_{\max} = 1476$ Hz
2 plans aromatiques $f_{\max} = 1579$ Hz
3 plans aromatiques $f_{\max} = 1614$ Hz

1 $f_{\min} = 0$ $\langle f \rangle = 492$ Hz
2 $f_{\min} = 0$ $\langle f \rangle = 529$ Hz
3 $f_{\min} = 0$ $\langle f \rangle = 538$ Hz.

Les valeurs $f_{\max}$ et $f_{\min}$ correspondent respectivement aux plans aromatiques perpendiculaires et parallèles à $\mathbf{H}_0$, les valeurs $\langle f \rangle$ sont les déplacements moyens pour toutes les orientations du cristallite.

Ces valeurs moyennes sont obtenues par le déplacement des molécules soit d'un pore à l'autre (pores plans) soit d'un cristallite à l'autre (pores prismatiques).

Le déplacement moyen calculé de cette façon est en bon accord avec l'ordre de grandeur de ceux que nous observons dans le cas des carbones NC et Spheron. (cf. Tableau 2).

Le champ h_3''' diminue rapidement lorsque la distance à la surface augmente ce qui explique la variation du déplacement avec le recouvrement.

4.6 *Discussion*

L'existence d'un champ local dû à la matière diamagnétique à l'intérieur d'un grain de carbone est, parmi les hypothèses envisagées pour expliquer le déplacement des raies de résonance des liquides adsorbés, la seule qui soit en accord avec l'ensemble des résultats expérimentaux. Les différents modèles utilisés pour calculer ce champ local, montrent:

(1) Que ce champ local ne donne lieu à un déplacement des raies que si les pores où est adsorbé le liquide sont entourés de matière anisotrope (modèle a).

(2) Qu'une forme de pores plans rend compte de l'ordre de grandeur du déplacement observé dans tous les carbones étudiés et que l'on peut en déduire une valeur de l'anisotropie locale à l'échelle des micropores (modèle b).

(3) Que dans le cas des carbones traités à haute température et qui contiennent de nombreux cristallites révélés par rayons X, les molécules sont pour la majeure partie adsorbées sur les faces planes (plans aromatiques) de ces cristallites (modèle c). Ceci est en accord avec l'existence de pores plans ou prismatiques ayant ces cristallites pour paroi.

(4) Le champ local h_3 possède toujours une distribution autour de sa valeur moyenne qui peut avoir des répercussions sur la forme et la largeur des raies.

Le modèle en feuillets proposé par Emmet [25] et généralement admis pour les carbones [17] est donc en bon accord avec l'ensemble de nos résultats expérimentaux. Toutefois dans le cas des carbones traités à haute température et contenant des cristallites de graphite un modèle de pores prismatiques convient également.

Nous précisons donc ici nos résultats présentés antérieurement[5] et nous arrivons dans le cas des carbones a une conclusion sur l'origine du déplacement analogue à celle à laquelle est arrivé Geschke[6] à partir de résultats expérimentaux de nature différente.

4.7 *Cas particuliers*

La présence de deux raies de résonance dans le cas des carbones NC et du noir de Carbone Spheron 6 (cf. 3.3) s'explique par l'existence de deux sites d'absorption pour lesquels le champ local h_3 est différent.

La raie déplacée correspond aux molécules adsorbés à la paroi des pores sur la matière anisotrope (modèle c), qui sont difficiles à extraire par dégazage.

La raie non déplacée correspond à des molécules se trouvant au centre des macropores, (loin des parois) ou à l'extérieur des grains.

5. RESULTATS EXPERIMENTAUX CONCERNANT LA LARGEUR DES RAIES

L'étude de la largeur et de la forme des raies en fonction du champ H_0, de la température et du recouvrement de la surface montre que l'on peut classer les carbones en deux catégories:

(1) Ceux pour lesquels la largeur de raie des liquides adsorbés est de type homogène et reste constante lorsque H_0 varie.

(2) Ceux pour lesquels les largeurs de raies sont de type inhomogène et varient avec H_0.

5.1 *Raies de type homogène*

Pour les fréquences de mesure 15,1, 56,4 et 60 MHz le noir de carbone Carbolac donne les résultats les plus caractéristiques de ce type de raies à savoir:

(a) la largeur des raies reste constante lorsque H_0 varie (15,1, 56,4 et 60 MHz).

(b) la largeur de raie augmente lorsque la température diminue.

(c) la largeur de raie augmente lorsque le recouvrement diminue (Fig. 3) sa forme reste toujours symétrique et approximativement Lorentzienne.

(d) la largeur de raie est sensiblement la même pour les différentes molécules adsorbées étudiées (Tableau 2).

(e) la saturation des raies est caractéristique des raies homogènes [19].

A 100 MHz on observe pour ce carbone des raies élargies par rapport à celles observées pour des fréquences de mesures inférieures ou égales à 60 MHz et qui présentent les propriétés des raies inhomogènes (cf. paragraphe suivant 5.2).

5.2 *Raies de type inhomogène*

Le carbone actif NC donne pour les liquides examinés (sauf C_6HF_5) les résultats les plus caractéristiques de ce type de raies à savoir:

(a) la largeur de raie, comme le déplacement, croit avec H_0.

(b) la largeur de raie, comme le déplacement ne varie pas avec la température entre −80° et +35°.

(c) la largeur décroit lorsque le recouvrement θ de la surface augmente (Fig. 2).

Pour θ 1 on observe une raie dissymétrique (Fig. 5) et la dissymétrie de cette raie augmente avec H_0.

Pour θ 3 on observe une raie symétrique.

La deuxième raie qui apparaît pour $\theta \sim 5$ est symétrique également (Fig. 4).

(d) la largeur des raies est sensiblement la même pour tous les liquides examinés sauf pour C_6HF_5 (Tableau 2).

(e) les expériences d'écho de spin faites sur le même carbone (NC + benzène) ont montré [11] que le temps de relaxation T_2 obtenu par cette méthode est plus grand que celui mesuré à partir des largeurs de raies ce qui confirme le caractère inhomogène des raies.

Les raies observées pour le proton et le fluor de C_6HF_5 adsorbé sur le carbone NC sont beaucoup plus larges (Tableau 2) que celles des autres liquides et présentent les propriétés des raies homogènes (cf. 5.1).

6. ORIGINE DE LA LARGEUR DES RAIES

Les interactions dipolaires inter et intramoléculaires sont à l'origine d'un champ local dont la valeur moyenne est nulle mais dont la distribution a une largeur de 15 à 30 kHz avant rétrécissement par le mouvement.

Le champ local h_3 d'origine diamagnétique (cf. 4.4) présente également une distribution due d'une part à la forme et à l'orientation aléatoire des pores à l'intérieur d'un grain (Fig. 3), et d'autre part à la forme et à l'orientation aléatoire des grains lorsqu'ils ne sont pas sphèriques [21].

La largeur homogène dipolaire (15–30 kHz) est rétrécie par tous les mouvements (translation et rotation) des molécules adsorbées, que nous caractérisons par un temps de corrélation global τ_c.

La largeur inhomogène due à la forme et à l'orientation des pores (0,5–3 kHz à 60 MHz) peut être rétrécie par les mouvements de déplacement des molécules d'un pore à l'autre

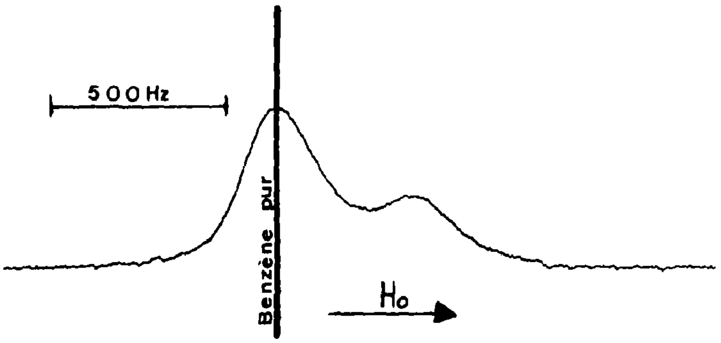

Fig. 4 Benzène adsorbé sur le carbone NC dans le cas d'un grand recouvrement ($\theta \sim 10$).

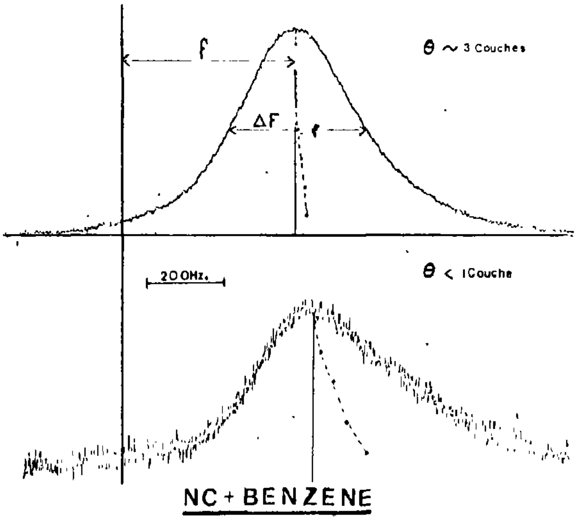

Fig. 5. Benzène adsorbé sur le carbone actif NC, on remarque la dissymétrie de la raie obtenue pour un faible recouvrement.

ou d'un cristallite à l'autre, dans le même grain, s'ils sont assez rapides. En effet ces mouvements, de temps de corrélation τ_D, modifient la valeur de champ h_3 vu par une molécule donnée. Ce type de mouvements est un cas particulier de l'ensemble des mouvements des molécules adsorbées décrit précédemment (de temps de corrélation τ_c).

La largeur inhomogène due à la forme (non sphèrique) des grains et à leur orientation (120–300 Hz à 60 MHz) n'est pas rétrécie par les mouvements des molécules dont la probabilité de changer de grain est très faible en raison de la grande porosité d'un grain et des faibles recouvrements considérés.

On obtient un ordre de grandeur du temps de correlation τ_c par la formulae.

$\Delta\omega \simeq \tau_c \overline{\Delta\omega_0^2}$ (20 ch. X) où $\Delta\omega$ est la largeur de raie rétrécie par le mouvement et $\overline{\Delta\omega_0^2}$ le second moment de la raie avant rétrécissement, la condition pour qu'il y ait. un rétrécissement étant $\tau_c < 1/\Delta\omega$.

6.1 *Cas des raies de type homogène: Noir de carbone Carbolac*

Dans ce cas la cause de largeur prédominante est vraisemblablement la largeur dipolaire. Celle-ci est en effet indépendante de H_0, elle croit lorsque le mouvement des molécules est ralenti, ce qui est en bon accord avec les variation de la largeur observées en fonction de la température et du recouvrement.

Pour le noir de carbone Carbolac (dont les grains sont sphèriques) la cause de largeur inhomogène est encore négligeable à 60 MHz et on a: $\tau_D < 10^{-4}$ sec et $\tau_c \sim 8\,10^{-7}$ sec (τ_c a été calculé dans le cas du benzène adsorbé en monocouche et à température ambiante).

Lorsque le champ directeur H_0 augmente, la largeur d'origine dipolaire reste constante alors que la largeur de type inhomogène, rétrécie par le mouvement, augmente proportionnellement à H_0^2 et peut devenir apparente. C'est ce qu'on observe à 100 MHz et on peut en déduire: $\tau_D \sim 5\,10^{-5}$ sec.

On remarque que le temps de corrélation τ_D lié aux mouvements de déplacement des molécules qui modifient h_3 est 100 fois plus grand que celui lié à la mobilité globale des molécules adsorbées.

6.2 *Cas des raies de type inhomogène: Carbone actif NC*

Dans ce cas, la largeur inhomogène due à la distribution du champ local h_3 est prédominante, ce qui explique la variation de la largeur de raie avec H_0, son indépendance de la température et le fait que les raies du proton et du fluor aient la même largeur dans le cas du C_6H_5F (cf. 6.3).

Dans le cas du carbone NC les grains ne sont pas sphèriques, on a donc toujours une cause de largeur inhomogène non rétrécie par le mouvement des molécules adsorbées et qui à 60 MHz, peut être évaluée à 270 Hz: $\Delta H \simeq 3\bar{\chi}_1 H_0$[21].

Cette cause de largeur peut expliquer la dissymétrie de la raie[21–22] observée pour les faibles recouvrements à 60 MHz (Fig. 5) et qui disparait pour un champ directeur 4 fois plus faible (15,1 MHz).

6.3 *Cas des raies du proton et du fluor du pentafluorobenzène*

Les raies beaucoup plus larges observées dans le cas de C_6HF_5 adsorbé sur le carbone NC (Tableau 2) s'expliquent de la façon suivante: la molécule C_6HF_5, beaucoup plus lourde que les autres molécules étudiées, a des mouvements plus lents à température égale, le rétrécissement par le mouvement est alors moins efficace et la largeur dipolaire devient prédominante.

De plus, le fait que la largeur de la raie du fluor soit plus grande que la largeur de la raie du proton confirme la contribution importante de la largeur dipolaire. On sait en effet (20 Chap. VIII) que le second moment de la raie a une expression différente selon que l'interaction dipolaire a lieu entre spins identiques ou spins différents. Dans le cas de C_6HF_5 on obtient en tenant compte du rétrécissement des raies par le mouvement un rapport des largeurs: $(\Delta\omega_H/\Delta\omega_F) = 0{,}56$. La valeur expérimentale de ce rapport: $0{,}80 \pm 0{,}05$ (Tableau 2) trop grande s'explique par la contribution résiduelle de la largeur inhomogène due au champ local.

Il est alors possible de calculer la partie dipolaire de la largeur et d'en déduire pour une monocouche à température ambiante $\tau_c \sim 10^{-6}$ sec.

6.4 *Discussion*

Les deux causes de largeurs de raies mises en évidence dans les paragraphes précédents sont toujours présentes simultanément dans le cas des carbones, mais selon la grandeur du champ H_0 et du temps de corrélation τ_D qui régit le déplacement des molécules adsorbées l'une des causes peut devenir prépondérante ou négligeable par rapport à l'autre.

Les ordres de grandeurs que l'on déduit de ces considérations pour le temps de corrélations caractérisant les mouvements des molécules adsorbées en monocouche montrent que pour les deux carbones la mobilité des molécules dans la phase adsorbée est comparable.

7. CONCLUSION

Le diamagnétisme anisotrope à l'échelle microscopique des carbones est à l'origine d'un champ local important qui explique les grands déplacements de raies des liquides adsorbés et leur largeur de type inhomogène dans certains cas.

Les déplacements importants dus à ce champ local masquent ceux dus à la déformation du nuage électronique des molécules adsorbées et à la différence de susceptibilité macroscopique de la poudre de carbone et du liquide adsorbé. Ces deux effets ne peuvent intervenir que pour environ 15 pour cent dans le déplacement observé des raies. Malgré la concentration importante en centres paramagnétiques des carbones, nous n'avons pu mettre en évidence dans aucun des cas examinés dans cet article, une contribution au déplacement de l'interaction scalaire entre les électrons du carbone et les spins nucléaires du liquide adsorbé.

Nous montrons que l'étude du déplacement, de la largeur et de la forme des raies de RMN haute résolution peut apporter des renseignements nouveaux sur la texture, et l'anisotropie magnétique du solide à l'échelle microscopique, et sur la mobilité des molécules adsorbées[23, 24].

REFERENCES

1. GRAHAM D et PHILLIPS W. D, *Solid Gas Interface*, p. 22 Butterworth, London (1957).
2. CONARD J, *C. r. Acad Sci. Paris* **259**, 1107 (1964).
3. GESCHKE D. et PFEIFER H, XIVe Colloque Ampère. Ljubljana (1966).
4. GESCHKE D., *Z. Naturf.* **23a**, 689 (1968).
5. GRADSZTAJN S., *C r. Acad. Sci. Paris* **266**, 817 (1968)
6. GESCHKE D., *Z. phys. Chim.* **239**, 138 (1968)
7. MOTCHANE J L. et UEBERSFELD J, *C. r. Acad. Sci. Paris* **246**, 2121 (1958).
8. KREBS J. J., *J. chem Phys.* **34**, 326 (1961).
9. GRIVET J P., *C. r. Acad Sci. Paris* **259**, 776 (1964).
10. LEGRAND A. P., Thèse, Paris, Fac. des Sciences No. AO 2510 (1968).
11. ESTRADE H, Thèse, Paris, Fac. des Sciences No. AO 2509 (1968)
12. THOMPSON J. K, KREBS J. J. et RESING H. A, *J chem. Phys.* **43**, 3853 (1965).
13. CONARD J et GRADSZTAJN S., *J Phys* **28**, 551 (1967).
14. CONARD J, Thèse, Orsay, Fac. des Sciences, No. A 112 (1965).
15. UEBERSFELD J., et ERB E. J., *J. phys. Radium* **16**, 340 (1955)
16. INGRAM D. J E., *Free Radical as studied by electron spin Resonance* Butterworth, London (1958).
17. PACAULT A, *Les Carbones* Masson, Paris (1965).
18. KITTEL C, *Introduction à la Physique de l'État Solide*, Chaps 7 et 9. Dunod, Paris (1958)
19. PORTIS, *Phys. Rev.* **91**, 1071 (1953)
20. ABRAGAM A., *Les Principes du Magnétisme Nucléaire*. Presses Universitaires de France (1961).
21. DRAIN L. E, *Proc. phys. Soc* **80**, 1380 (1962).
22. SOBEL A, *J. Phys. Chem. Solids* **28**, 185 (1967).
23. GRADSZTAJN S. et CONARD J., *C. r. Acad. Sci. Paris* **262**, 1213 (1966).
24. RIOU A., GRADSZTAJN S, CONARD J., DONNET J. B., COUDERC P et PAPIRER E, *C. r. Acad. Sci. Paris* **268**, 297 (1969).
25. EMMET P H, *Chem. Rev.* **43**, 69 (1948)

ANNEXE

Le champ démagnétisant à l'intérieur d'une cavité de forme ellipsoïdale dû à la matière diamagnétique qui l'entoure peut s'écrire:

$$\mathbf{h}'_3 = 4\pi\mathbf{H}_0(\chi_\parallel N_x \cos^2\alpha + \chi_\parallel N_y \cos^2\beta + \chi_\perp N_z \cos^2\gamma)$$

où α, β et γ sont les angles directeurs de H_0 dans le axes $Oxyz$ de l'ellipsoïde, N_x, N_y, N_z sont les facteurs démagnétisants suivant les axes Ox, Oy et Oz.
$(N_x + N_y + N_z = 1)$. $\chi_\parallel$ et $\chi_\perp$ sont les susceptibilites volumiques parallèle et perpendiculaire au plan XOY (ici le plan aromatique) On prend l'axe Oz de l'ellipsoïde suivant la direction de facile aimantation.

La valeur moyenne $\langle h'_3\rangle$ du champ h_3 pour toutes les orientations de H_0 est

$$\langle h'_3\rangle = \frac{4\pi}{3}H_0[\chi_\parallel N_x + \chi_\parallel N_y + \chi_\perp N_z]$$

Le champ demagnetisant dans un grain sphèrique est

$$\mathbf{h}''_3 = -\frac{4\pi}{3}[\chi_\parallel \cos^2\alpha + \chi_\parallel \cos^2\beta + \chi_\perp \cos^2\gamma]\mathbf{H}_0$$

$(N_x = N_y = N_z = \frac{1}{3})$ et sa valeur moyenne pour toutes les orientations de H_0 est $\langle h''_3\rangle = -(4\pi/3)\bar{\chi}H_0$ où $\bar{\chi} = \frac{2}{3}\chi_\parallel + \chi_\perp$ est la susceptibilité volumique moyenne.

Le champ local $\mathbf{h}_l$ pour différentes formes de pores dans un grain sphèrique $\mathbf{h}_l = \mathbf{h}'_3 + \mathbf{h}''_3$ est donné dans le Tableau 3

J. Phys. Chem. Solids Pergamon Press 1970. Vol. 31, pp. 1137–1141. Printed in Great Britain.

DIPOLE SUMS FOR HEXAGONAL, TETRAGONAL AND ORTHORHOMBIC LATTICES WITH A BASIS

P. BRÜESCH and M. LIETZ
Brown Boveri Research Center, Baden, Switzerland

(*Received* 6 *October* 1969)

Abstract – Mackenzie's method for calculating dipole sums is generalized to orthorhombic, tetragonal and hexagonal lattices with a basis. Specific examples, such as the hcp structure, are treated numerically.

1. INTRODUCTION

IN PROBLEMS of lattice dynamics and spin wave theory one often encounters sums of point dipoles which converge very slowly in an oscillatory manner. Based on the Ewald–Born lattice sum formulas[1, 2], Mueller[3] has given expressions for the Lorentz factors of simple hexagonal and tetragonal lattices as a function of the axial ratio of the unit cell, c/a. The application of this method is made complicated by the fact that an arbitrary parameter must be chosen so that all the series occurring in the expressions for the Lorentz factors converge rapidly. Furthermore the actual calculation of the sums in more complicated lattices is tedious because the vectors of both, the direct and the reciprocal lattices occur.

In their recent study of the dipolar effects on spin waves in thin films, Benson and Mills[4] encountered certain dipole sums for the simple cubic lattice which they converted to rapidly converging series by applying a method due originally to Mackenzie[5] and described by van der Hoff and Benson[6]. The same method has also been used in the studies of normal modes of a semi-infinite ionic crystal by Tong and Maradudin[7]. The evaluation of the sums by this method is simpler than by using Mueller's expressions, mainly because no arbitrary parameters and no reciprocal lattice vectors occur. Furthermore Mueller's expressions are valid only for zero wave vector ϕ (all dipoles parallel and in phase), whereas Mackenzie's method is not restricted to $\phi = 0$.

The purpose of this note is to generalize Mackenzie's method to hexagonal, tetragonal and orthorhombic lattices with a basis.

In Section 2 we give the general expressions for the dipole sums. Section 3 contains the application to the examples of the simple orthorhombic, tetragonal and hexagonal lattices. In addition we consider the frequently observed hexagonal closed packed structure which has not previously been treated in the literature.

We also have formulated this method for the general lattice with a basis. Then the expressions become rather lengthy. We do not give them here because in most applications only the simpler expressions will be needed.

2. GENERAL FORMULAS

In the method applied by Benson and Mills[4] the sums are carried out over infinite planes. The generalization for hexagonal lattices is done most easily if the two dimensional hexagonal lattice with lattice constant a is decomposed into two orthorhombic sublattices with lattice constants a and $b = \sqrt{3}a$. Arbitrary a and b, of course, correspond to the general orthorhombic lattice, whereas for $a = b$ we are concerned with the tetragonal lattice. Using Benson's and Mills' notation, the sums we are concerned with have the form

$$D_{ij}(\phi_x, \phi_y, L_z) = \sum_{L_x, L_y}{}' e^{i\phi_x L_x} e^{i\phi_y L_y} \times \left[\frac{\delta_{ij}}{(L_x^2 + L_y^2 + L_z^2)^{3/2}} - \frac{3L_i L_j}{(L_x^2 + L_y^2 + L_z^2)^{5/2}}\right]. \quad (1)$$

The prime on the summation indicates that when $L_z = 0$ the term with $L_x = L_y = 0$ is to be excluded.

For an orthorhombic lattice the lattice vector $\mathbf{L} = (L_x, L_y, L_z)$ has components

$$L_x = \rho_x + l_x a, \; L_y = \rho_y + l_y b, \; L_z = \rho_z.$$

Here $\boldsymbol{\rho} = (\rho_x, \rho_y, \rho_z)$ is the vector from the origin (at which the field is evaluated) to a nearby point of a two dimensional orthorhombic lattice in the plane ρ_z = constant, over which the summation is carried out (see Fig. 1). l_x and l_y are integers ranging from $-\infty$ to $+\infty$.

We consider first the plane $\rho_z \neq 0$. The generalization of the method described by Benson and Mills is straightforward and only the results will be given. For the orthorhombic lattice we find

$$D_{xx}(\phi_x, \phi_y, \rho_z) = \frac{4\pi}{a^3 b} \sum_{n, m = -\infty}^{+\infty} e^{2\pi i\left(n\frac{\rho_x}{a} + m\frac{\rho_y}{b}\right)} \times \frac{(\pi n + \frac{1}{2}\phi_x a)^2}{\gamma_{nm}} \cdot e^{-2|\rho_z|\gamma_{nm}}$$

$$D_{yy}(\phi_x, \phi_y, \rho_z) = \frac{4\pi}{ab^3} \sum_{n, m = -\infty}^{+\infty} e^{-2\pi i\left(n\frac{\rho_x}{a} + m\frac{\rho_y}{b}\right)} \times \frac{(\pi m + \frac{1}{2}\phi_y b)^2}{\gamma_{nm}} \cdot e^{-2|\rho_z|\gamma_{nm}} \quad (2)$$

$$D_{zz}(\phi_x, \phi_y, \rho_z) = \frac{4\pi}{ab} \sum_{n, m = -\infty}^{+\infty} e^{-2\pi i\left(n\frac{\rho_x}{a} + m\frac{\rho_y}{b}\right)} \times \gamma_{nm} e^{-2|\rho_z|\gamma_{nm}},$$

where

$$\gamma_{nm} = \left[\frac{1}{a^2}(\pi n + \tfrac{1}{2}\phi_x a)^2 + \frac{1}{b^2}(\pi m + \tfrac{1}{2}\phi_y b)^2\right]^{1/2}. \quad (3)$$

Let us now consider the case $\rho_z = 0$. Following Benson and Mills we define

$$S_y(\phi_x, \phi_y) = \sum_{L_x, L_y}{}' \frac{L_y^2}{(L_x^2 + L_y^2)^{5/2}} \cdot e^{i\phi_x L_x} e^{i\phi_y L_y},$$

$$S_x(\phi_x, \phi_y) = \sum_{L_x, L_y}{}' \frac{L_x^2}{(L_x^2 + L_y^2)^{5/2}} \cdot e^{i\phi_x L_x} e^{i\phi_y L_y}. \quad (4)$$

The summation excludes the term with both L_x and $L_y = 0$. In terms of these quantities we have

$$D_{xx}(\phi_x, \phi_y, 0) = -2S_x(\phi_x, \phi_y) + S_y(\phi_x, \phi_y)$$

$$D_{yy}(\phi_x, \phi_y, 0) = S_x(\phi_x, \phi_y) - 2S_y(\phi_x, \phi_y) \quad (5)$$

$$D_{zz}(\phi_x, \phi_y, 0) = S_x(\phi_x, \phi_y) + S_y(\phi_x, \phi_y).$$

Again, the derivation can be generalized easily. The expressions for the orthorhombic lattice are as follows

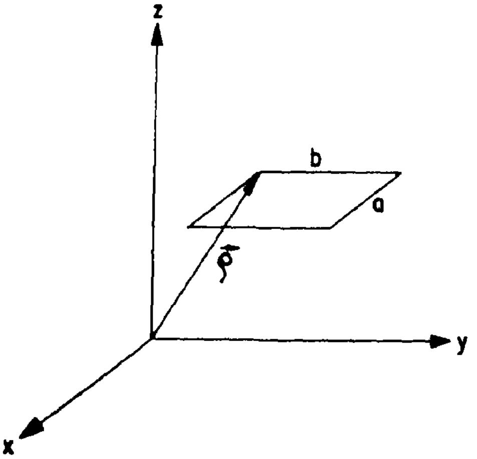

Fig. 1. Description of geometry used in the lattice sums. The a, b, and c axis of the orthorhombic lattice are assumed to be parallel to the x, y, and z axis, respectively.

$$S_x(\phi_x, \phi_y) = \frac{8}{3b^3} \sum_{l_x=-\infty}^{+\infty} \sum_{n=-\infty}^{+\infty} e^{i\phi_x a\left(l_x+\frac{\rho_x}{a}\right)} e^{-2\pi i n\frac{\rho_y}{b}}$$
$$\times (\pi n+\tfrac{1}{2}\phi_y b)^2 \cdot K_2\left\{2\frac{a}{b}\cdot\left|l_x+\right.\right.$$
$$\left.\left.+\frac{\rho_x}{a}\right|\cdot\left|\pi n+\tfrac{1}{2}\phi_y b\right|\right\}, \qquad (6)$$

$$S_y(\phi_x, \phi_y) = \frac{8}{3a^3} \sum_{l_y=-\infty}^{+\infty} \sum_{n=-\infty}^{+\infty} e^{i\phi_y b\left(l_y+\frac{\rho_y}{b}\right)} e^{-2\pi i n\frac{\rho_y}{b}}$$
$$\times (\pi n+\tfrac{1}{2}\phi_x a)^2 \cdot K_2\left\{2\frac{b}{a}\cdot\left|l_y\right.\right.$$
$$\left.\left.+\frac{\rho_y}{b}\right|\cdot\left|\pi n+\tfrac{1}{2}\phi_x a\right|\right\}.$$

$K_2\{x\}$, the modified Bessel function of order two[8], converges rapidly for large values of x. If $\rho_x = 0$ in $S_x(\phi_x, \phi_y)$ the term with $l_x = 0$ in the sum is excluded, and correspondingly for $S_y(\phi_x, \phi_y)$.

To obtain the contribution of the whole lattice, the summation over the layers can be carried out explicitly. Let the equidistant sequence of all sublattice layers with the same basis (ρ_x, ρ_y) be described by $\rho_z(s) = r_0 + \rho_{z0}\cdot s$, $(s = 0, \pm 1, \pm 2 \ldots)$. The notation is explained in Fig. 2. Then

$$D_{xx}(\phi_x, \phi_y) = \sum_s D_{xx}\{\phi_x, \phi_y, \rho_z(s)\}$$
$$= D_{xx}(\phi_x, \phi_y, r_0) + \frac{8\pi}{a^3 b} \sum_{n,m}^{+\infty} e^{2\pi i\left(n\frac{\rho_x}{a}+m\frac{\rho_y}{b}\right)}$$
$$\times \frac{(\pi n+\frac{1}{2}\phi_x a)^2}{\gamma_{nm}} \cosh(2r_0\gamma_{nm})$$
$$\times \frac{e^{-2\rho_{z0}\gamma_{nm}}}{1-e^{-2\rho_{z0}\gamma_{nm}}}, \qquad (7)$$

For the evaluation of $D_{xx}(\phi_x, \phi_y, r_0)$ formula (2) applies if $r_0 \neq 0$, and (6) if $r_0 = 0$. D_{yy} and D_{zz} can be expressed correspondingly

3. EXAMPLES

In the following we consider only the case $\phi_x = \phi_y = 0$ and write $D_{xx}(0, 0, \rho_z) = D_{xx}(\rho_z)$ etc. To illustrate the method and to compare with Mueller's results we first consider the simple orthorhombic, tetragonal and hexagonal lattices. Finally the results for the hexagonal closed packed structure are given.

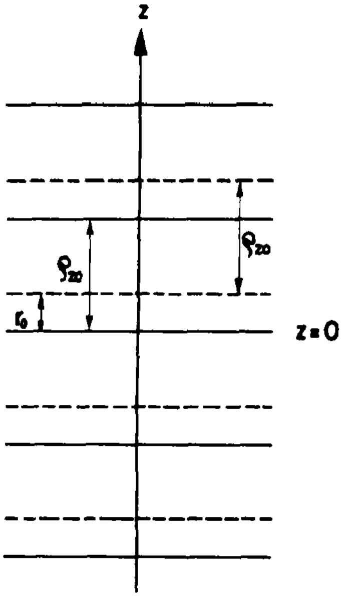

Fig. 2. ρ_{z0} is the distance between equivalent layers. r_0 is either zero or the distance between the plane $z = 0$ and the nearest nonequivalent plane

(a) *Simple orthorhombic lattice*

Let a, b and c be the lattice constants of the orthorhombic lattice. The total dipole sums are given by (7), where $\rho_{z0} = c$ and $r_0 = 0$.

Putting $\rho_x = \rho_y = 0$ in (6) we obtain

$$S_x = \frac{4\pi^2}{9a^2 b} + \frac{32\pi^2}{3b^3} \sum_{l=1}^{\infty} \sum_{n=1}^{\infty} n^2 K_2\left(2\pi\frac{a}{b}nl\right)$$
$$S_y = \frac{4\pi^2}{9ab^2} + \frac{32\pi^2}{3a^3} \sum_{l=1}^{\infty} \sum_{n=1}^{\infty} n^2 K_2\left(2\pi\frac{b}{a}nl\right). \qquad (8)$$

Substitution of (8) into (5) yields $D_{xx}(0)$, $D_{yy}(0)$ and $D_{zz}(0) = -D_{xx}(0) - D_{yy}(0)$.

The simple tetragonal lattice, where $a = b \neq c$ has already been studied by Mueller[3] who expressed his results in terms of the Lorentz factors L_x, L_y, L_z as a function of the axial ratio of the unit cell, c/a. In order to compare with Mueller we express L_x, L_y, L_z in terms of D_{xx}, D_{yy}, D_{zz}. From the expression of the local field, $F_x = E_x + (4\pi/v)L_x p_x = E_x - D_{xx}p_x$ (p_x = dipole moment, v = volume of the unit cell) and from $L_x + L_y + L_z = 1$ we obtain

$$L_x = L_y = -\frac{v}{4\pi}D_{xx}, L_z = 1-2L_x. \quad (9)$$

If $c/a > 2$ we have $D_{xx}(c) \ll D_{xx}(0)$ and therefore $D_{xx} \approx D_{xx}(0)$. Evaluation of the sums yields

$$L_x = L_y \approx -\frac{v}{4\pi}D_{xx}(0) = 0{\cdot}359 \cdot c/a$$

in agreement with Mueller. For $c/a = 1$ we obtain $L_x = L_y = L_z = \frac{1}{3}$, the well known Lorentz factor for the cubic structure.

For $c/a = \frac{1}{2}$ the contributions with $\rho_z \neq 0$ become important. Evaluation of the sums gives $L_x(0) = 0{\cdot}180$, the other layers contribute $-0{\cdot}445$, so that $L_x \approx -0{\cdot}265$ in accordance with Mueller (see Fig. 1 in Ref.[3]).

(b) *Simple hexagonal lattice*

Each two dimensional hexagonal lattice is decomposed into two orthorhombic sublattices (1) and (2) with $\rho_x^{(1)} = \rho_y^{(1)} = 0$ and $\rho_x^{(2)} = a/2$, $\rho_y^{(2)} = b/2 = (\sqrt{3}/2)a$. If $D_{xx}^{(1)}(\rho_z)$ and $D_{xx}^{(2)}(\rho_z)$ denote the contributions from sublattices (1) and (2) respectively we have

$$D_{xx}(\rho_z) = D_{xx}^{(1)}(\rho_z) + D_{xx}^{(2)}(\rho_z) \quad (10)$$

Using (6), (5) and (10) and $D_{xx}(0) = D_{yy}(0)$ we obtain

$$D_{xx}(0) = -\frac{16\pi^2}{27a^3}[1+18(S_1+S_2)] \quad (11)$$

where

$$S_1 = \sum_{l=1}^{\infty}\sum_{n=1}^{\infty} n^2K_2[2\sqrt{3}\pi nl]$$
$$S_2 = \sum_{l=0}^{\infty}\sum_{n=1}^{\infty} (-1)^n n^2K_2[2\sqrt{3}\pi n(l+\tfrac{1}{2})]. \quad (12)$$

From (7) we obtain for the total sum

$$D_{xx} = D_{yy} = D_{xx}(0) + \frac{16\pi^2}{a^3\sqrt{3}} \times \sum_{\substack{n,m=-\infty \\ n+m=\text{even}}}^{+\infty} n^2\left(n^2+\frac{m^2}{3}\right)^{-1/2} \cdot \frac{e^{-2\pi\left(n^2+\frac{m^2}{3}\right)^{1/2}\frac{c}{a}}}{1-e^{-2\pi\left(n^2+\frac{m^2}{3}\right)^{1/2}\frac{c}{a}}} \quad (13)$$

$$D_{zz} = -2D_{xx}.$$

For $c/a > 1, 5$ we have again $D_{xx} \approx D_{xx}(0)$, and evaluation of the sums (12) gives

$$L_x = L_y \approx -\frac{v_{\text{hex}}}{4\pi}D_{xx}(0) = 0{\cdot}380 \cdot c/a.$$

Mueller finds $L_x = 0{\cdot}370 \cdot c/a$, probably due to inaccurate calculation.

(c) *Hexagonal closed packed structure*

There are two inequivalent sites α and β in the unit cell, one at the origin $x_\alpha = y_\alpha = z_\alpha = 0$ (at which the field is evaluated) and the other at $x_\beta = a/2$, $y_\beta = a/2\sqrt{3}$, $z_\beta = c/2$. The field produced by the dipoles α is given by $D_{\alpha x} = D_{xx}(0) + 2D_{xx}(c) + \ldots$, whereas the field of the dipoles β is given by $D_{\beta x} = 2D_{xx}(c/2) + 2D_{xx}(3c/2) + \ldots$. Since for the ideal hcp structure $c/a = \sqrt{(8/3)} = 1{\cdot}633$ we have again $D_{xx}(c) \ll D_{xx}(0)$. The corresponding Lorentz factors are therefore given by

$$L_{\alpha x} \approx -\frac{v_{\text{hex}}}{4\pi}D_{xx}(0) = 0{\cdot}380\, c/a$$

(see simple hexagonal lattice with $c/a > 1{\cdot}5$) and

$$L_{\beta x} = -\frac{v_{\text{hex}}}{4\pi} \cdot D_{\beta x}. \quad (14)$$

If $D_{\beta x}^{(1)}$ and $D_{\beta x}^{(2)}$ are the contributions of the two orthorhombic sublattices (1) and (2) of the β layers, with components $\rho_x^{(1)} = a/2$, $\rho_y^{(1)} = a/2\sqrt{3}$ and $\rho_x^{(2)} = 0$, $\rho_y^{(2)} = -a/\sqrt{3}$, we obtain from (7) and using the symmetry properties of the lattice

$$D_{\beta x} = \frac{16\pi^2}{\sqrt{3}a^3}\sum_{\substack{n,m=-\infty \\ n+m\ \text{even}}}^{+\infty} e^{\frac{2\pi}{3}im} n^2\left(n^2+\frac{m^2}{3}\right)^{-1/2} \times \frac{e^{-2\pi\left(n^2+\frac{m^2}{3}\right)^{1/2}\frac{c}{2a}}}{1-e^{-2\pi\left(n^2+\frac{m^2}{3}\right)^{1/2}\frac{c}{a}}} \quad (15)$$

The results for $L_{\alpha x}$, $L_{\beta x}$ and $L_x = L_{\alpha x} + L_{\beta x}$ are given in Table 1 for $1{\cdot}5 \leq c/a \leq 2{\cdot}0$.

Table 1. Lorentz factors L_x of the hcp structure as a function of the axial ratio of the unit cell, c/a, with contributions $L_{\alpha x}$, $L_{\beta x}$ of the two inequivalent sites α and β

c/a	$L_{\alpha x}$	$L_{\beta x}$	L_x
1·5	0·570	0·134	0·704
1·6	0·608	0·100	0·708
1·633	0·621	0·091	0·712
1·7	0·646	0·075	0·721
1·8	0·684	0·056	0·740
1·9	0·722	0·041	0·763
2·0	0·760	0·030	0·790

Acknowledgement—The authors wish to record their gratitude to Dr S. Straessler who brought the method of Mackenzie to their attention They also wish to thank Professor D. L. Mills for making available the work of Tong and Maradudin prior to its publication

REFERENCES

1. EWALD P. P., *Ann. Phys.* **49**, 117 (1916).
2. BORN M. and GOEPPERT-MAYER M., *Handb. Phys.* **24**, 770 (1927).
3. MUELLER H., *Phys. Rev.* **47**, 947 (1935). *Phys. Rev.* **50**, 547 (1936)
4. BENSON H. and MILLS D. L., *Phys. Rev.* **178**, 839 (1969).
5. MACKENZIE J. K., Ph D Thesis, University of Bristol (1949) (unpublished)
6. VAN DER HOFF B. M. E. and BENSON G. C., *Can. J. Phys.* **31**, 1087 (1953)
7. TONG S. Y. and MARADUDIN A. A., Normal modes of a semi-infinite ionic crystal (preprint (1969))
8. *Handbook of Mathematical Functions* (Edited by Milton Abramowitz and Irene A. Stegun), p 374. Dover, New York (1965).

J. Phys. Chem. Solids Pergamon Press 1970. Vol. 31, pp. 1143-1149. Printed in Great Britain.

MANY-BODY PERTURBATION THEORY FOR NON-ORTHOGONAL BASIS STATES

D. J. NEWMAN

Department of Physics, Queen Mary College, Mile End Road, London E.1., England

(*Received* 5 *September* 1969)

Abstract – A simple extension of Brueckner–Goldstone time independent perturbation theory is made to allow the use of non-orthogonal basis states. This has advantages for composite electronic systems in that the 'natural' one electron states (i.e. those which produce the most rapid convergence of the perturbation series) are frequently non-orthogonal. The formalism is applied to the case of a pair of overlapping systems and is further specialized to give expressions relevant to the crystal field problem. A possible application to electron correlation in large atoms is also discussed.

1. INTRODUCTION

PREVIOUS publications[1, 2, 3] have introduced several methods of dealing with non-orthogonal basis states. In particular it has been shown how to formulate energy expressions to arbitrary order in the overlap integrals[3]. The main defect of the previous work is that the expressions obtained became very complicated beyond second order in perturbation theory and are not simply related to the conventional theories of perturbation expansions to arbitrary order. These difficulties arose partly because an explicit zero'th order Hamiltonian was not identified and partly because an attempt was made to avoid one electron matrix elements involving unoccupied (and unexcited) states appearing in the results.

The reason for using non-orthogonal basis states in perturbation theory is that it is sometimes possible to determine a closer approximation to the exact eigenstates in this way than is given by any known orthogonal set. A systematic orthogonalization procedure can, of course, be used, but this does not help us to determine the new zero'th order Hamiltonian $\hat{H}_0$. Besides this, a 'natural' excited state begins to look quite unnatural when it has been orthogonalized with respect to many other *unoccupied* excited states. A characteristic example of this situation is a system composed of many atoms or ions. Here the natural basis states are in many cases the states determined by the Hartree–Fock potentials associated with the individual atoms.

In this paper we first generalize the Brueckner–Goldstone form of time independent perturbation theory to non-orthogonal basis states, i.e. in terms of a non-Hermitian $\hat{H}_0$. An explicit expression for $\hat{H}_0$ is then obtained and the formalism is specialized to the case of two overlapping systems, each of which has internally orthogonal unperturbed states. These results are then used to obtain expressions for the crystal field up to third order in perturbation theory and to identify the infinite sums which shift the denominators.

The notation used for the creation and annihilation operators of non-orthogonal states is identical to that described in Ref. [3]. We also find it convenient to use generalizations of some of the results obtained by Kelly[4, 5, 6] for atomic systems.

2. PERTURBATION THEORY WITH NON-ORTHOGONAL BASIS STATES

We first generalize the usual Brueckner–Goldstone perturbation formalism to the case in which the total manybody (Hermitian) Hamiltonian $\hat{H}$ is split into non-Hermitian components. Let

$$\hat{H} = \hat{H}_0 + \hat{H}' \quad \text{where} \quad \hat{H}_0 \neq \hat{H}_0^{\dagger}.$$

It is necessary to distinguish the right and left many-particle eigenfunctions of $\hat{H}_0$:

$$\hat{H}_0|\xi_n\rangle = E_n|\xi_n\rangle \quad \text{and} \quad \langle\xi^r|\hat{H}_0 = \langle\xi^r|E_r, \tag{2.1}$$

where $\langle\xi^r|\xi_n\rangle = \delta_n{}^r$. We now adapt the argument of Brueckner[7] in the form given by March *et al.*[8] to nonorthogonal basis states.

Suppose that the true ground state is represented by $|\psi\rangle$ so that

$$\hat{H}|\psi\rangle = E|\psi\rangle \quad \text{and} \quad \langle\psi| = (|\psi\rangle)^\dagger = \langle\xi^r|\psi_r,$$

where the summation convention has been employed. For convenience we choose the normalisation $\langle\psi|\xi_0\rangle = \psi_0 = 1$. The eigenvalue equations then give

$$\langle\psi|\hat{H}_0|\xi_0\rangle = E_0$$

$$\langle\psi|\hat{H}|\xi_0\rangle = \langle\psi|\hat{H}_0|\xi_0\rangle + \langle\psi|\hat{H}'|\xi_0\rangle = E,$$

and we define

$$\Delta E = E - E_0 = \langle\psi|\hat{H}'|\xi_0\rangle.$$

In order to develop the perturbation series we introduce projection operators

$$\hat{P} = |\xi_0\rangle\langle\xi^0| \quad \text{and} \quad \hat{Q} = 1 - \hat{P} = \sum_{r\neq 0}|\xi_r\rangle\langle\xi^r|,$$

so that $\langle\psi| = \langle\xi^0| + \langle\psi|\hat{Q}$. Substituting this expression into the identity

$$\langle\psi|(E_0 - \hat{H}_0) = \langle\psi|(E_0 - E + \hat{H}')$$
$$= \langle\psi|(\hat{H}' - \Delta E)$$

then gives

$$\langle\psi| = \langle\xi^0| + \langle\psi|(\hat{H}' - \Delta E)\frac{\hat{Q}}{E_0 - \hat{H}_0}. \tag{2.2}$$

It should be noted that, with this choice of $\hat{Q}$, $\hat{Q}\hat{H}_0 = \hat{H}_0\hat{Q}$, so that the order of numerator and denominator in equation (2.2) does not need to be specified. Iterating this equation for $\langle\psi|$ gives

$$\langle\psi| = \langle\xi^0|\sum_{n=0}^{\infty}\left\{(\hat{H}' - \Delta E)\frac{\hat{Q}}{E_0 - \hat{H}_0}\right\}^n$$

and

$$\Delta E = \langle\xi^0|\sum_{n=0}^{\infty}\left\{(\hat{H}' - \Delta E)\frac{\hat{Q}}{E_0 - \hat{H}_0}\right\}^n\hat{H}'|\xi_0\rangle.$$

A further iteration can then be carried out for the energy expansion $E = \sum_\lambda E^{(\lambda)}$ to get linked cluster expressions (denoted by subscript L) which are formally the same as those obtained by Brueckner

$$E^{(0)} = \langle\xi^0|\hat{H}_0|\xi_0\rangle_L = E_0,$$

$$E^{(1)} = \langle\xi^0|\hat{H}'|\xi_0\rangle_L = \langle\hat{H}'\rangle_{0L},$$

$$E^{(2)} = \left\langle\hat{H}'\frac{\hat{Q}}{E_0 - \hat{H}_0}\hat{H}'\right\rangle_{0L},$$

$$E^{(3)} = \left\langle\hat{H}'\frac{\hat{Q}}{E_0 - \hat{H}_0}\hat{H}'\frac{\hat{Q}}{E_0 - \hat{H}_0}\hat{H}'\right\rangle_{0L}, \text{etc.} \tag{2.3}$$

In most problems the perturbative Hamiltonian represents the sum of a single particle potential and a two particle interaction potential. We therefore write

$$\hat{H}' = a^{i+}a^j\langle i|V|j\rangle + \tfrac{1}{2}a^{i+}a^{j+}a^k a^l\langle ij|g|lk\rangle,$$

where the significance of the covariant and contravariant suffices is as defined in Ref. [3]. The evaluation of products of annihilation and creation operators between $|\xi_0\rangle$ and $\langle\xi^0|$ gives results which are a trivial generalization of those for orthogonal states, e.g.

$$\langle\xi^0|a^{i+}a^j|\xi_0\rangle = \langle a^{i+}a^j\rangle_0 = S^{i\underline{j}},$$

$$\langle a^{i+}a^{j+}a^k a^l\rangle_0 = S^{i\underline{l}}S^{j\underline{k}} - S^{i\underline{k}}S^{j\underline{l}},$$

$$\langle a^{i+}a^{j+}a^k a^l a_t{}^+ a^s\rangle = (S^{i\underline{s}}S^{j\underline{k}} - S^{i\underline{k}}S^{j\underline{s}})\delta_{\underline{t}}{}^l$$
$$+ (S^{i\underline{l}}S^{j\underline{s}} - S^{i\underline{s}}S^{j\underline{l}})\delta_{\underline{t}}{}^k$$

$$\text{if} \quad t \neq s. \tag{2.4}$$

In these expressions an underlined suffix indicates that only occupied states in $|\xi_0\rangle$ give a non-zero result; tilde underlining indicates that only states *not* in $|\xi_0\rangle$ give a non-zero result.

Substituting these and similar expressions into equation (2.3) we obtain the following results for the energy contributions in terms of matrix elements formed from one electron states:

$$
\begin{aligned}
E^{(1)} &= \langle \xi^0 | \hat{H}' | \xi_0 \rangle = S^{ij} \langle i | V | \underline{j} \rangle \\
&\quad + \tfrac{1}{2} (S^{il} S^{j\underline{k}} - S^{i\underline{k}} S^{jl}) \langle ij | g | \underline{lk} \rangle, \\
E^{(2)} &= \left\langle \xi^0 \middle| \hat{H}' \frac{\hat{Q}}{E_0 - H_0} \hat{H}' \middle| \xi_0 \right\rangle \\
&= [S^{i\underline{s}} \langle i | V | \underline{t} \rangle + (S^{i\underline{s}} S^{j\underline{k}} - S^{i\underline{k}} S^{j\underline{s}}) \\
&\quad \times \langle ij | g | \underline{tk} \rangle] [S^{k\underline{t}} \langle k | V | s \rangle \\
&\quad + (S^{l\underline{t}} S^{m\underline{r}} - S^{l\underline{r}} S^{m\underline{t}}) \\
&\quad \times \langle lm | g | \underline{sr} \rangle] / (\epsilon_s - \epsilon_t) \qquad (2.5)
\end{aligned}
$$

(the summation convention is not applied to denominator suffices). In the second equation we have included only one electron excitations $(\underline{s} \to \utilde{t})$, the tilde underlining being used to indicate that only excited single particle states are summed over; ϵ_i are the one electron eigenvalues of H_0.

The basically simple form of the above equations may be made more explicit by the introduction of matrix elements with raised suffices. We write

$$V^i{}_j = S^{ik} \langle k | V | j \rangle,$$

$$G^{ij}{}_{kl} = S^{ir} S^{jm} \langle rm | g | kl \rangle, \; G^{ij}{}_{\underline{kl}} = G^{ij}{}_{kl} - G^{ij}{}_{lk},$$

and $U^i{}_j = V^i{}_j + G^{i\underline{k}}{}_{j\underline{k}}$.
Then, for example,

$$E^{(2)} = U^s{}_{\underline{t}} U^t{}_{\underline{s}} / (\epsilon_s - \epsilon_t). \qquad (2.6)$$

This formulation makes it trivial to generate expressions for the higher order terms of the perturbation series. Each term is related to a Goldstone diagram in the usual way with the following extra rules:

(a) All state summations involve one covariant and one contravariant suffix in the numerator.

(b) On each symbol the right hand side covariant suffices are summed over a restricted range (i.e. over only occupied *or* only unoccupied states according to whether the ingoing line represents a hole or a particle).

It is worth noting that, because of the restriction of some summations to occupied states, the perturbation series is quite different to the one that would have been obtained by initially orthogonalizing all states. Some examples of diagrams and their interpretation are given in Fig. 1.

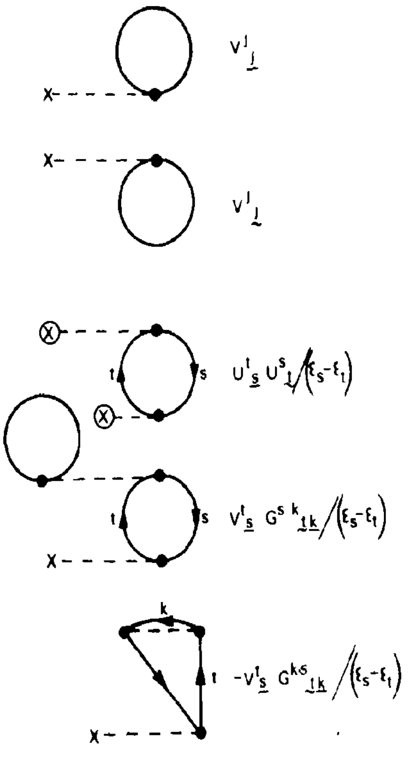
X
$V^j{}_{\underline{j}}$
X
$V^j{}_{\underline{j}}$
⊗
t
s
$U^t{}_{\underline{s}} U^s{}_{\utilde{t}} / (\epsilon_s - \epsilon_t)$
⊗
t
s
$V^t{}_{\underline{s}} G^{sk}{}_{\utilde{t}\underline{k}} / (\epsilon_s - \epsilon_t)$
X
k
t
$-V^t{}_{\underline{s}} G^{ks}{}_{\utilde{t}\underline{k}} / (\epsilon_s - \epsilon_t)$
X

Fig 1 Examples of the interpretation of Goldstone energy diagrams. Note that the line entering a node always corresponds to the covariant suffix with restricted range.

Diagrams giving single particle excitation contributions to $E^{(3)}$ are shown in Fig. 2. The corresponding expressions are

$$E^{(3)} = -U^r_sU^s_tU^t_r/(\epsilon_s-\epsilon_t)(\epsilon_t-\epsilon_r)$$
$$+U^r_sU^s_tU^t_r/(\epsilon_r-\epsilon_t)(\epsilon_t-\epsilon_s)$$
$$+U^t_qG^{sq}_{tp}U^p_s/(\epsilon_s-\epsilon_p)(\epsilon_t-\epsilon_q). \quad (2.7)$$

For convergence of the perturbation series it is usually necessary to identify all those terms of $E^{(3)}$ with $t = s$, $p = q$, as the first terms of an infinite series which shifts the denominators [5]. Then we replace $\epsilon_s-\epsilon_t$ by

$D_{st} = \epsilon_s - \epsilon_t + U^s_s - U^t_t - G^{st}_{st}$(no summations) in equation (2.6).

Now suppose that systems A and B are brought together so as to be both overlapping and interacting. The joint overlap matrix of the one-particle states $S_{ij} = \langle i|j\rangle$ is taken as the metric tensor of our formalism. We note that $S_{\alpha\beta} = \delta_{\alpha\beta}$, $S_{\mu\nu} = \delta_{\mu\nu}$, $S_{\alpha\mu} \neq 0$ and[3]

$$[a_\alpha^+, a_\mu]_+ = [a_\alpha, a_\mu^+]_+ = S_{\alpha\mu}.$$

The orthogonality of states within systems A and B implies that

$$S^{\mu\nu}S_{\nu\alpha} = -S^{\mu\alpha}, \quad S^{\alpha\beta}S_{\beta\nu} = -S^{\alpha\nu}. \quad (3.2)$$

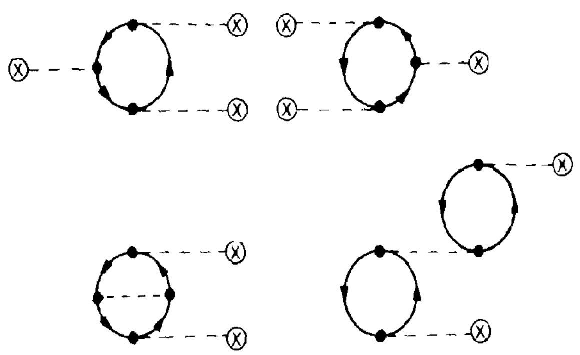

Fig. 2. Contributions to $E^{(3)}$ arising from single particle excitations. See equation (2.7)

3. OVERLAPPING SYSTEMS

Consider two non-interacting systems of electrons A, B with independently diagonalized Hamiltonians:

$$\hat{H}_A = \sum_\alpha \epsilon_\alpha{}^A a_\alpha{}^+ a_\alpha \quad H_B = \sum_\mu \epsilon_\mu{}^B a_\mu{}^+ a_\mu. \quad (3.1)$$

In general we shall use suffices $\alpha, \beta, \gamma \ldots$ for A and $\mu, \nu, \tau \ldots$ for B. Suffices ranging over the one-particle states of both systems will be written $i = \alpha, \mu$; $j = \beta, \nu$; $k = \gamma, \tau$. It is convenient for the present discussion to avoid the problems associated with defining complete sets of states by arbitrarily truncating the ranges of the suffices: $\alpha = 1 \ldots N_A$; $\mu = N_A + 1, \ldots, N$. The number of electrons in system A, denoted n_A, is presumed to satisfy $n_A \leq N_A$. Similarly $n_B \leq N - N_A = N_B$.

The natural 'reference state' based on the ground states of the constituent systems in isolation is produced by creating electrons in the lowest energy levels of both systems:

$$|\Psi_0\rangle = \prod_\mu^{n_B} a_\mu{}^+ \prod_\alpha^{n_A} a_\alpha{}^+|0\rangle = \prod_\alpha^{n_A} a_\alpha{}^+ \prod_\mu^{n_B} a_\mu{}^+|0\rangle.$$

A simple modification of $\hat{H}_A$ and $\hat{H}_B$ gives operators which are separately eigen-operators of $|\Psi_0\rangle$ and similarly defined excited states; we write

$$\hat{H}(A) = \epsilon_\alpha{}^A a_\alpha{}^+ a^\alpha, \quad \hat{H}(B) = \epsilon_\mu{}^B a_\mu{}^+ a^\mu, \quad (3.3)$$

where an obvious summation convention has been employed. These operators take the same energy eigenvalues in the overlapping (but non-interacting) system as $\hat{H}_A$ and $\hat{H}_B$ have in the isolated systems.

These properties, combined with the fact that $\hat{H}(A)$ and $\hat{H}(B)$ commute, lead up to define a non-Hermitian unperturbed Hamiltonian

$$\hat{H}_0 = \hat{H}(A) + \hat{H}(B) = \epsilon_i a_i^{+} a^i.$$

It should be emphasised that this expression for $\hat{H}_0$ is, in fact, quite general and is implied by equation (2.1). The perturbation, corresponding to the interaction of the two systems, is then given by $\hat{H}' = \hat{H} - \hat{H}_0$ where the full Hamiltonian may be written in explicitly invariant form[3] as

$$\hat{H} = a^{i+}a^j\langle i|T + V^c|j\rangle + \tfrac{1}{2}a^{i+}a^{k+}a^l a^j\langle ik|g|jl\rangle.$$

In this expression T represents the kinetic energy terms, and V^c the total potential energy of the combined system. An external potential can be introduced if required; it involves no new considerations.

Our first problem is to eliminate from $\hat{H}'$ those matrix elements of T which do not appear in $\hat{H}_0$. We write

$$\hat{T} = a^{i+}a^j\langle i|T|j\rangle,$$

where, according to equations (3.1), we have

$$(T + V^A)|\alpha\rangle = \epsilon_\alpha{}^A|\alpha\rangle$$

and

$$(T + V^B)|\mu\rangle = \epsilon_\mu{}^B|\mu\rangle.$$

In these equations V^A and V^B are often the self-consistent Hartree–Fock potentials associated with systems A and B respectively. It follows that

$$\hat{T} = \hat{H}_0 - a^{i+}a^\beta\langle i|V^A|\beta\rangle - a^{i+}a^\nu\langle i|V^B|\nu\rangle \quad (3.4)$$

and

$$\begin{aligned}\langle\alpha|T|\mu\rangle &= \epsilon_\alpha{}^A\langle\alpha|\mu\rangle - \langle\alpha|V^A|\mu\rangle \\ &= \epsilon_\mu{}^B\langle\alpha|\mu\rangle - \langle\alpha|V^B|\mu\rangle. \quad (3.5)\end{aligned}$$

The perturbative part of the Hamiltonian is thus

$$\hat{H}' = \hat{H} - H_0 = a^{i+}a^j\langle i|V|j\rangle + \tfrac{1}{2}a^{i+}a^{k+}a^l a^j\langle ik|g|jl\rangle,$$

where the potential V is defined by

$$\begin{aligned}\langle i|V|\beta\rangle &= \langle i|V^c - V^A|\beta\rangle, \\ \langle i|V|\nu\rangle &= \langle i|V^c - V^B|\nu\rangle.\end{aligned} \quad (3.6)$$

This makes the non-Hermitian character of $\hat{H}'$ explicit. In many problems it is convenient to eliminate either V^A or V^B from the cross matrix elements between systems A and B by means of equation (3.5). In particular we may choose to completely reformulate the perturbation series with an Hermitian potential defined according to either of the following relations:

$\bar{V} = V$ in all matrix elements other than

$$\langle\alpha|V|\nu\rangle = \langle\alpha|\bar{V}|\nu\rangle + (\epsilon_\alpha - \epsilon_\nu)\langle\alpha|\nu\rangle, \quad (3.7)$$

$\bar{\bar{V}} = V$ in all matrix elements other than

$$\langle\mu|V|\beta\rangle = \langle\mu|\bar{\bar{V}}|\beta\rangle - (\epsilon_\beta - \epsilon_\mu)\langle\beta|\mu\rangle. \quad (3.8)$$

Note that neither $\bar{V}$ nor $\bar{\bar{V}}$ are scalar potentials because of the distinction between $\langle\alpha|V|\beta\rangle$ and $\langle\mu|V|\nu\rangle$.

4. FORMULATION OF CRYSTAL FIELD THEORY

In order to demonstrate the power of the results obtained in Sections 2 and 3 we apply them to the problem of formulating expressions for the electron energies in a one-particle crystal field. Approximate solutions to this problem to second order are well known and have been used in numerical calculations [9, 10].

System B is taken to be the outer shells of a closed shell ion combined with a central point potential. System A is a single electron in an open shell of another ion which overlaps B. The set of states considered is taken to include only the occupied states of B and the degenerate open shell states of A. Hence the only excitations will be of electrons from B to A.

We shall further suppose that each energy level in the open shell system transforms as a distinct irreducible representation of the symmetry group C_{ω} of the combined system. This avoids the introduction of a generalised perturbation theory for degenerate systems [6]. It also allows us to obtain the following results for the components of S^{ij} in terms of the pivotal quantities defined in our previous work[3]:

$$\left.\begin{aligned} S^{\alpha\beta} &= \delta_{\alpha\beta}({}^{(B)}S_{\alpha\alpha})^{-1},\\ S^{\alpha\nu} &= {}^{(B)}\delta_{\alpha}{}^{\nu}S^{\alpha\alpha}. \end{aligned}\right\} \qquad (4.1)$$

In these equations the prefix 'B' indicates that all pivots in system B have been accounted for. Combining these results with the relation (3.2) we also get

$$S^{\alpha\nu} = -S_{\alpha\nu}S^{\alpha\alpha}. \qquad (4.2)$$

In crystal field theory we are interested in the energy dependence of the total system on the state occupied by the single electron in system A. We may therefore omit all energy terms independent of this state (henceforth denoted α). If the denominators $D_{\mu\beta}$ are then taken to be functions of the B states (μ) alone, several subtractions of constant terms may be performed (e.g. see Ref. [10]) to give the following energy contributions up to third order:

$$E_\alpha{}^{(1)} = U^\alpha{}_\alpha$$

$$E_\alpha{}^{(2)} = U^\alpha{}_\mu U^\mu{}_\alpha / D_\mu$$

$$\begin{aligned} E_\alpha{}^{(3)} = {} & U^\alpha{}_\mu U^\mu{}_\nu U^\nu{}_\alpha / D_\mu D_\nu \\ & - U^\alpha{}_\mu G^{\mu\alpha}{}_{\nu\alpha} U^\nu{}_\alpha / D_\mu D_\nu \end{aligned}$$

$$(\mu \neq \nu \text{ in summations})$$

where $U_i{}^j$ is the quantity defined in Section 2 and the denominator may be written

$$D_\mu = \epsilon_\beta - \epsilon_\mu + U^\beta{}_\beta - U^\mu{}_\mu - G^{\beta\mu}{}_{\beta\mu}$$

$$(\text{no summations}).$$

To first order this is identical with the denominator used in our numerical calculations[10].

In order to compare these results with the expressions used for previous numerical calculations let us write the V terms in $E_\alpha{}^{(1)}$ explicitly as

$$V_\alpha{}^\alpha = S^{\alpha\alpha}(\langle\alpha|V|\alpha\rangle - S_{\alpha\mu}\langle\mu|V|\alpha\rangle).$$

We notice that here only one cross matrix element $\langle\mu|V|\alpha\rangle$ occurs compared with two in equation (4.5) of Ref. [9]. This difference arises because of the implicit use of V (defined in equation (3.8)) rather than V in the previous work. Substitution of equation (3.8) into the expression given above for $E_\alpha{}^{(2)}$ leads to a partial cancellation of the denominator so that the cross matrix element missing from $E_\alpha{}^{(1)}$ appears. The numerical importance of these terms has been demonstrated (Ref. [10], Table 4) and this shows that the present formalism (with V) gives a more slowly convergent perturbation series than the transformed series in terms of $\bar{V}$. It must be emphasized, however, that both series are expressed in terms of the same basis states (defined by H_0): the transformation merely redistributes the non-Hermitian part of V among the different terms of the perturbation series. The need to consider transformations of this type does not arise in conventional perturbation theory.

5. DISCUSSION

We have developed a perturbation expansion for nonorthogonal basis states and have shown that it provides a more systematic way of obtaining results in crystal field theory than any presently available technique. The chief merit of the present approach is that all expressions may be fully represented by the familiar Goldstone diagrams, only two extra rules of interpretation being required.

The formalism has many applications outside crystal field theory; in fact it is relevant to most problems involving electrons in molecules and crystals where the natural basis states are obviously nonorthogonal. Even in the theory of electron correlation in single atoms it is found necessary, because of convergence difficulties, to use excited electronic states which are nonorthogonal to the occupied (Hartree–Fock) ground states[5]. This is an interesting case because the numerical calculations made by Kelly[4, 5] show explicitly that nonorthogonal basis states lead to quicker convergence. For small atoms the overlap integrals involved are very small and may be neglected, so the improved convergence is seen to depend only on the choice of physically reasonable excited states. In the case of larger atoms there will be a greater degree of nonorthogonality so that the formalism developed in this paper will be required.

The theory given in Section 3 can be adapted to the atomic problem by letting system A represent the states derived from the Hartree–Fock solution and system B the states derived from a modified potential V^B. $V^A - V^B$ is taken to be the potential due to a single outer shell electron.

Acknowledgements—The author is grateful to Dr J. S. Marsh and Professor K. W. H Stevens for helpful discussions

REFERENCES

1. BISHTON S S and NEWMAN D. J., *J. Phys. Chem. Solids* **29**, 1245 (1968).
2. NEWMAN D. J, *Chem Phys. Lett.* **1**, 684 (1968).
3. NEWMAN D J, *J Phys Chem. Solids* **30**, 1709 (1969).
4. KELLY H P., *Phys Rev.* **131**, 684 (1963)
5. KELLY H. P, *Phys. Rev* **136**, B896 (1964)
6. KELLY H P, *Phys Rev* **144**, 39 (1966).
7. BRUECKNER K. A, *Phys. Rev.* **100**, 36 (1955)
8. MARCH N H., YOUNG W H and SAMPANTHAR S, *The Many-Body Problem in Quantum Mechanics* Cambridge University Press (1967).
9. ELLIS M M. and NEWMAN D J., *J chem Phys.* **47**, 1986 (1967)
10. ELLIS M M. and NEWMAN D J, *J. chem. Phys* **49**, 4037 (1968).

J. Phys. Chem. Solids Pergamon Press 1970. Vol. 31, pp. 1151-1161. Printed in Great Britain

HIGH-FREQUENCY BEHAVIOR OF HOT ELECTRONS IN ONE-VALLEY POLAR SEMICONDUCTORS*

E. BONEK, H. W. PÖTZL† and K. RICHTER
Institut für Hochfrequenztechnik, Technische Hochschule Wien, Austria

(*Received* 12 *August* 1969)

Abstract – A semiphenomenological theory is developed for the high-frequency conductivity of polar semiconductors in the hot electron region. A mean energy relaxation time is calculated from the energy loss to polar optical phonons. A mean momentum relaxation time is obtained from the experimental d.c. current vs. field characteristic thus accounting for any elastic scattering processes present. By this theory, the small-signal conductivity is calculated in dependence on frequency, heating d.c. field, polarization of the a.c. field, and sample properties. The results are compared with new experimental data of *n*-InSb at 35 GHz. Good agreement is found, and it is shown that the elastic scattering processes have to be included. For *n*-type GaAs this theory is successfully applied in the low-field region where the electron transfer between the valleys is negligible. Three independent methods for the determination of the mean momentum relaxation time are used to demonstrate the applicability of this concept.

1. INTRODUCTION

An anisotropic small-signal a.c. conductivity is found in semiconductors when a strong d.c. electric field is simultaneously applied to cause deviations of the average electron energy from thermal equilibrium with the lattice[1, 2]. As this anisotropy is not due to the complicated band structure of elemental semiconductors, materials with isotropic effective mass and mobility of the carriers exhibit the same effect [3-6]. Sufficiently high frequencies of the probing a.c. field cause pronounced relaxation effects and the anisotropic small-signal conductivity (ASC) does not depend only upon the bias field but also upon the frequency. This frequency dependence may be used to study the scattering processes in the hot-electron region. Because of the great interest which has been paid to technically important polar semiconductors exhibiting microwave emission, e.g. GaAs and InSb, reliable results for the ASC are desirable to estimate important parameters of these materials. The (limited) application of the one-valley model even for GaAs is justified at fields sufficiently beneath threshold because electron transfer to the upper valley can be neglected in this region.

A simple successful approach to the small-signal microwave conductivity based upon the assumption of a monoenergetic electron distribution has been originated by Gibson *et al.*[7] some years ago. This method has been refined by application of transport theory. In principle, two ways are practicable: (a) the assumption of a test distribution containing parameters which are usually determined by momentum and energy balance and (b) the direct determination of the distribution function from the Boltzmann equation.

For polar semiconductors the first method has been applied to the problem of calculating the ASC by Das *et al.*[8], assuming a drifted Maxwell-Boltzmann distribution with time-dependent drift momentum and electron temperature. A similar approach of Kopetz and Pötzl[9] included the effect of impurity scattering. A calculation of the small-signal conductivity based upon an exact solution of the Boltzmann equation was tried by Conwell [10]. However, the simplifications necessary to

---

*This work was supported by the Ludwig-Boltzmann-Gesellschaft, Wien.

†Lehrkanzel für Physikalische Elektronik, Technische Hochschule Wien, Austria.

obtain an analytical solution restrict this work to the high energy electrons and do not yield a proper account for the whole distribution. Therefore, macroscopic quantities as the conductivity cannot be derived from these results. A Monte-Carlo-method calculation of the small-signal conductivity parallel to the heating field has been carried out by Rees[11]. The disadvantage of this most rigorous method, however, is a loss of physical insight and the need of huge amounts of computer time and storage place. Huber[12] has extended works by Dykman *et al.*[13] to the small-signal high-frequency case, considering electron–electron, impurity, and polar optical scattering. The integral equation for the symmetric part of the distribution is solved, for not too low carrier concentrations[14] by a Maxwell–Boltzmann distribution. The rather complicated method employed in this work does not lead to any substantial improvement in agreement between theory and experiment as compared to[9].

Summarizing all the existing work on the small-signal conductivity seems to indicate the following:

(1) The inclusion of all relevant scattering mechanisms for polar semiconductors in a calculation of the ASC seems rather cumbersome and difficult, and has not been carried out so far.

(2) Rather poor agreement between experiment and theory for both polar and non-polar materials was found so far because of conclusion (1).

(3) Better agreement of ASC data with calculated results can be obtained if the small-signal calculations are based rather on experimentally than theoretically derived velocity-field characteristics.

(4) The Maxwell–Boltzmann distribution for the carriers, shifted in momentum space and assuming an effective carrier temperature, offers great convenience for theoretical treatment without concealing any important effect. Although not correctly describing the microscopic aspect of the problem, it is well suited for the description of macroscopic quantities like d.c. and a.c. current density and conductivity. The reason is that momentum and energy balance equations are the essential tools to obtain a macroscopically correct description of the hot electron phenomena.

Therefore, a new semiphenomenological theory is suggested by this paper which is very well suited to describe the high-frequency behavior of polar semiconductors. Concerning the scattering processes, only one assumption is made: the energy exchange between the carriers and the lattice takes place via polar optical phonons only. This is reasonable because neither ionized impurity scattering nor electron–electron collisions contribute to the energy balance. Any assumption concerning the mechanisms influencing the momentum balance is avoided by the use of the experimentally obtained d.c. characteristic. This theory is developed in Section 2. In Section 3 new detailed experimental data are presented and compared with the theory of Section 2 and some other theoretical approaches. A new microwave method for the determination of the momentum relaxation time in the presence of hot electrons is described in Section 4.

2. THEORY

In the light of the above discussion it seems reasonable to use a drifted Maxwell–Boltzmann distribution. The drifted Maxwellian $f(\mathbf{p})$ of electrons in momentum space

$$f(\mathbf{p}) = \frac{n}{\sqrt{2\pi k_B T_e(t) m^{*3}}} \exp\left\{-\frac{[\mathbf{p}-\mathbf{p}_E(t)]^2}{2m^* k_B T_e(t)}\right\} \tag{1}$$

is characterized by two parameters, namely the drift momentum $\mathbf{p}_E$ and the electron temperature T_e (we retain only the first order term in $\mathbf{p}_E$). Dealing with the a.c. conductivity both have to be assumed as depending on time. The electron density n and the isotropic effective mass m^* are assumed to be constant.

Inserting $f(\mathbf{p})$ into the Boltzmann equation

$$B(f)=\frac{\partial f}{\partial t}-e\mathbf{E}\cdot\nabla_p f+\left(\frac{\partial f}{\partial t}\right)_c=0, \quad (2)$$

in which E denotes the electric field and $(\partial f/\partial t)_c$ the collision operator, one obtains the equations of momentum and energy balance by carrying out the integrals

$$\int \mathbf{p}B(f)\,\mathrm{d}^3p=0 \int \frac{p^2}{2m^*}B(f)\,\mathrm{d}^3p=0$$

over the whole momentum space. These equations can be written as

$$\frac{\partial \mathbf{p}_E}{\partial t}=-e\mathbf{E}-\frac{\mathbf{p}_E}{\tau_m(T_e)}, \quad (3)$$

$$\frac{\partial T_e}{\partial t}=-\frac{2e}{3k_Bm^*}\mathbf{E}\cdot\mathbf{p}_E-\frac{T_e-T_L}{\tau_\epsilon(T_e)}, \quad (4)$$

in which T_L denotes the lattice temperature. These balance equations can be regarded as a Drude theory generalized to hold for the hot electron case. The influence of collisions is expressed by characteristic time constants τ_m, τ_ϵ which only depend on the electron temperature. They will be denoted as *mean* relaxation times not to be confused with the usual relaxation times which depend on $p^2/2m^*$ and hence on the position in momentum space. The mean relaxation times are related to the whole electron ensemble rather than to individual electrons.

The mean relaxation times can be calculated explicitly for the different types of relaxation processes as acoustical, optical, piezoelectrical, polar optical and ionized impurity scattering. For polar optical scattering (p.o.) one obtains[10]

$$\left(\frac{1}{\tau_m}\right)_{\text{p.o.}}=\frac{2}{3}\frac{eF_R}{\sqrt{2\pi m^*k_B\theta}}\frac{x_e^{3/2}e^{x_e/2}}{e^{x_0}-1}$$

$$\left[(e^{x-x_e}+1)\,K_1\left(\frac{x_e}{2}\right)+(e^{x_0-x_e}-1)\,K_0\left(\frac{x_e}{2}\right)\right] \quad (5)$$

$$\left(\frac{1}{\tau_\epsilon}\right)_{\text{p.o}}=\frac{4}{3}\frac{eF_R}{\sqrt{2\pi m^*k_B\theta}}\frac{x_0x_e^{3/2}e^{x_e/2}}{e^{x_0}-1}$$

$$\frac{e^{x_0-x_e}-1}{x_0-x_e}K_0\left(\frac{x_e}{2}\right). \quad (6)$$

In these equations F_R denotes the coupling field of p.o., θ means the Debye temperature of the p.o. phonons and

$$x_0=\theta/T_L,\ x_e=\theta/T_e. \quad (7)$$

The theory by Das *et al.*[8] is equivalent to the balance equations (3) and (4) with the mean p.o. relaxation times (5), (6) inserted. However, the authors failed to obtain even qualitative agreement with experiment. Kopetz and Pötzl[9] have shown that semi-quantitative agreement can be obtained by a more realistic choice of the coupling field F_R (520 V/cm instead of 330 V/cm) and by accounting for ionized impurity scattering. Mukhopadhyay and Nag[15] recently stated that ionized impurity scattering is not essential for this improvement. However, it is seen from [9] that it does essentially improve the d.c. current-field characteristic. Furthermore, the results presented in Section 3 indicate the importance of impurity scattering for the ASC. Thus the conclusion by Mukhopadhyay and Nag does not seem to be valid, and impurities will be included simply by using the experimentally obtained d.c. characteristic. This allows to check the 'extended Drude theory' without introducing possible errors by neglect of additional scattering mechanisms.

Thus the following procedure is carried out: The d.c. electron temperature and the mean energy relaxation time will be calculated from p.o. scattering only. Therefore, the electron temperature T_e for any point of the steady current density (j_0) vs. field-strength (E_0) characteristic is given by (4), which yields

$$\frac{T_e-T_L}{\tau_\epsilon(T_e)}=\frac{2}{3k_Bn}j_0E_0. \quad (8)$$

If τ_ϵ is inserted from (6) the following equation for the temperature parameter x_e is obtained

$$\sqrt{\frac{2\pi m^*}{k_B\theta}\,\frac{j_0E_0}{2eF_Bn}} = x_e{}^{1/2}\,e^{x_e/2}\,K_0\left(\frac{x_e}{2}\right)\frac{e^{x_0-x_e}-1}{e^{x_0}-1}. \tag{9}$$

A coefficient n_2 which characterizes the temperature dependence of τ_ϵ is calculated from

$$n_2 = \frac{x_e}{\tau_\epsilon}\frac{d\tau_\epsilon}{dx_e} = \frac{x_e\,e^{x_0-x_e}}{e^{x_0-x_e}-1} - \frac{1}{2}(x_e+3) - \frac{x_e}{x_0-x_e} - \frac{\frac{x_e}{2}\cdot K_0'\left(\frac{x_e}{2}\right)}{K_0\left(\frac{x_e}{2}\right)}. \tag{10}$$

The differential conductivity is dj_0/dE_0, the mean momentum relaxation time is given by

$$\tau_m = \frac{m^*}{e^2n}\frac{j_0}{E_0} \tag{11}$$

according to (3) and a parameter S characterizing the deviations from Ohm's law is defined by

$$S = \frac{1-\frac{E_0}{j_0}\cdot\frac{dj_0}{dE_0}}{1+\frac{E_0}{j_0}\cdot\frac{dj_0}{dE_0}}. \tag{12}$$

These quantities are sufficient to derive the ASC by a small-signal analysis. As shown in the Appendix, the following results are obtained

$$\sigma_{r\perp} = \frac{\sigma_{\text{int}}}{1+(\omega\tau_m)^2};\ \sigma_{i\perp} = \frac{\sigma_{\text{int}}}{1+(\omega\tau_m)^2}(-\omega\tau_m) \tag{13}$$

$$\sigma_{r\parallel} = \sigma_{\text{int}}\cdot\frac{1-S^2+\omega^2\tau_\epsilon'(\tau_\epsilon'+S\tau_m)}{(1+S)^2+\omega^2[\tau_\epsilon'^2-2S\tau_\epsilon'\tau_m+\tau_m{}^2(1+\omega^2\tau_\epsilon'^2)]} \tag{14}$$

$$\sigma_{i\parallel} = \omega\cdot\sigma_{\text{int}}\cdot\frac{2S\tau_\epsilon'-\tau_m(1-S+\omega^2\tau_\epsilon'^2)}{(1+S)^2+\omega^2[\tau_\epsilon'^2-2S\tau_\epsilon'\tau_m+\tau_m{}^2(1+\omega^2\tau_\epsilon'^2)]}. \tag{15}$$

The subscripts $\perp$ and $\parallel$ mean crossed and parallel a.c. and d.c. electric fields, respectively, and

$$\sigma_{\text{int}} = \frac{j_0}{E_0},\ \tau_\epsilon' = \frac{\tau_\epsilon}{1+n_2(T_e-T_0)/T_e}. \tag{16}$$

3. RESULTS AND DISCUSSION

n-*InSb*

New data on high-mobility *n*-InSb were taken at 77°K and 35 GHz to be compared with the theoretical approach as outlined in Section 2. The zero d.c. field parameters of the sample used (III) are given in Table 1 along with the respective quantities for another sample (II) which was experimentally investigated earlier[6]. The experimental set-up and procedure to obtain values of the ASC was the same as already reported[6, 16].

Figures 1 and 2 show the electron temperature T_e and the relaxation times versus electric field. Both T_e and τ_ϵ have been calculated according to Section 2.

The experimental d.c. characteristics yield τ_m as plotted by solid lines ($m^* = 0{\cdot}0152\ m_0$). The data points for τ_m were derived from ASC measurements parallel and perpendicular to the d.c. field by methods to be discussed in Section 4. The curves for T_e, τ_m and τ_ϵ were employed in our calculations of the ASC.

Figures 3 and 4 show the real and imaginary part of the ASC in comparison with our theory and with the theoretical result by Mukhopadhyay and Nag[15] who neglect impurity scattering. At low d.c. field our theory is clearly better suited to describe the experimental results for σ_r which proves that

Table 1. Sample characteristics at 77°K and zero d.c. field

Sample	Mobility	Carrier density	$\omega\tau_m$ at 35 GHz
II	470,000 cm²/Vsec	$1{\cdot}3 \times 10^{14}$ cm^{-3}	0·85
III	650,000 cm²/Vsec	1×10^{14} cm^{-3}	1·18

impurity scattering is essential in this region. This should become even more pronounced for lower-mobility samples.

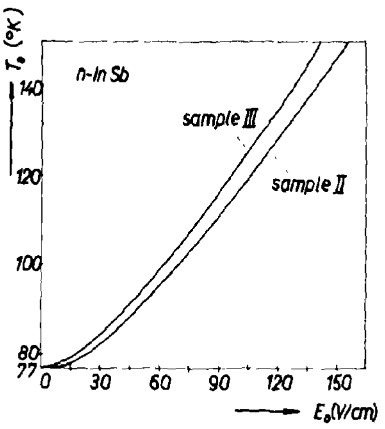

Fig. 1. Electron temperature calculated from polar optical scattering.

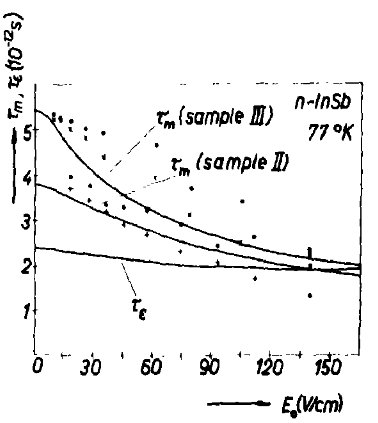

Fig. 2 Mean relaxation times. Solid curves are for theoretical values (τ_ϵ) and d.c.-measured values (τ_m) Data points were derived from microwave measurement perpendicular (sample II: +++, sample III: ×××) and parallel (sample II: ○○○, sample III: ●●●) to the heating d.c. field.

To give insight into the frequency behavior of the ASC, Figs. 5, 6 and 8 show our theoretical results (σ_r and σ_i, respectively) for sample II at a set of different frequencies. For comparison the experimental results are

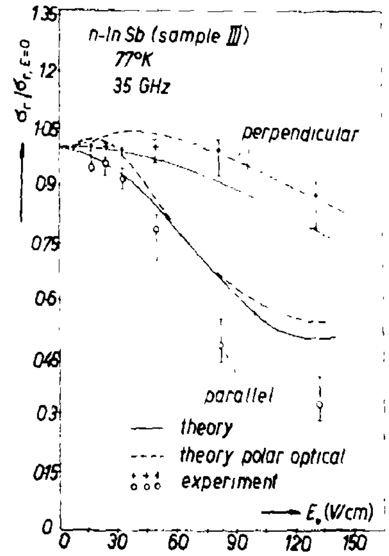

Fig. 3 Real part of the ASC of a high-mobility sample (sample III)

included at 35 GHz which have already been reported[6]. The essential features of the frequency dependence of the ASC apparent from Figs. 5 and 6 can be summarized as follows:

(a) At low frequencies ($\omega\tau_m \ll 1$) the small slope conductivity $\sigma_{\rm diff}$ is obtained for the parallel case and the higher d.c. conductivity for the perpendicular case, leading to a pronounced anisotropy. Both are decreasing with increasing electric field. The anisotropy is given by $\sigma_{r\parallel} = \sigma_{r\perp}(1-S)/(1+S)$.

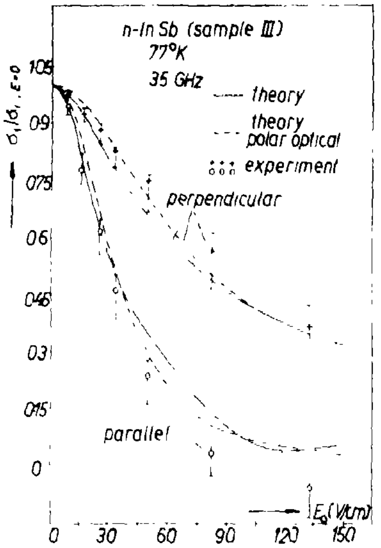

Fig. 4. Imaginary part of the ASC of a high-mobility sample (sample III).

(b) At frequencies at which relaxation effects become effective (e.g. 35 GHz) the decrease with electric field becomes less pronounced while the anisotropy is only slightly reduced.

(c) At even higher frequencies $\sigma_{r\parallel}$ increases in the lower field region and the anisotropy is reversed there. It still decreases in the higher field region. At 70 GHz there is hardly any anisotropy and the conductivities remain fairly constant.

(d) At high enough frequencies both conductivities increase with electric field and the anisotropy is again pronounced but reversed everywhere. Thus, e.g. in the frequency range of the cyanide laser (891 GHz), the absorption for parallel d.c. and a.c. fields must be much stronger than for transverse polarization of the laser radiation. This anisotropy at high frequencies is a consequence of momentum and energy exchange taking place at about the same rate by p.o. scattering. In this high frequency limit we obtain

$$\sigma_{r\parallel} = \sigma_{r\perp}\left(1 + S\frac{\tau_m}{\tau_\epsilon}\right).$$

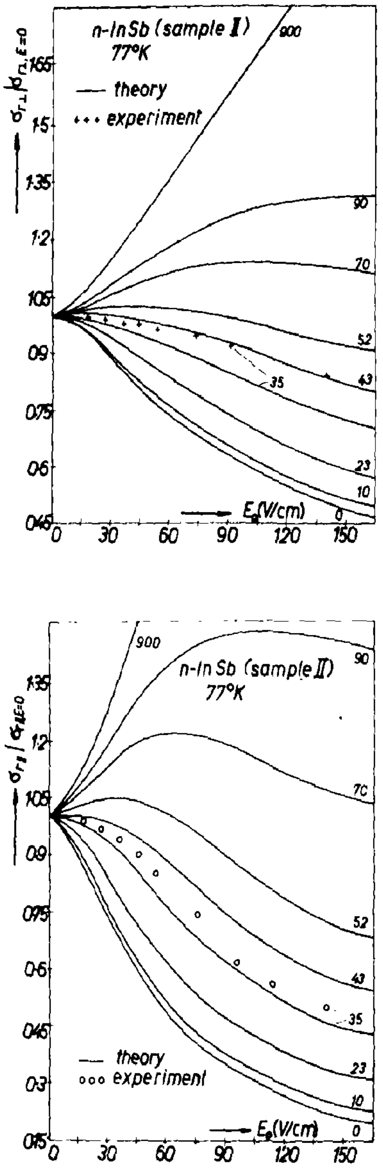

Fig. 5. Real part of the microwave conductivity perpendicular (a) and parallel (b) to the d.c. field, calculated for sample II. Parameter of the curves is the frequency in GHz.

Of course, the theory is only applicable up to frequencies $\omega < kT_L/\hbar$, $\hbar$ being Planck's constant divided by 2π.

It should be noted that an increase of τ_m and τ_ϵ is equivalent to an increase of frequency. At

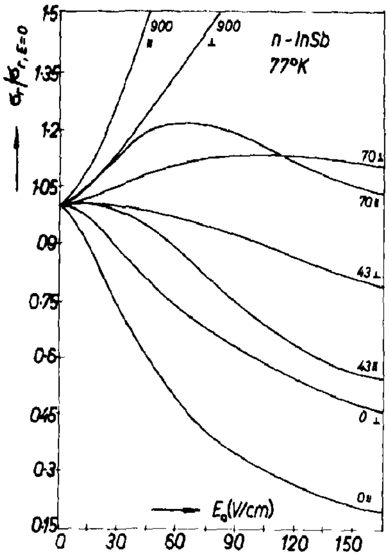

Fig. 6. Anisotropy of the real part of the ASC in dependence upon frequency and electric field

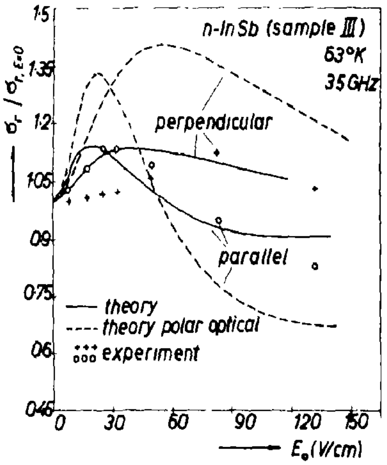

Fig. 7. Preliminary data of the real part of the ASC at 63°K in comparison with theory.

lower temperatures therefore, one has to expect a behavior similar to that at increased frequency. Preliminary data for the real part of the ASC at 63°K and 35 GHz are presented in Fig. 7. The theoretical curves included are calculated as well by our theory as by that of Ref. [15]. The experimentally observed rise in zero field momentum relaxation time at 63°K ($\omega\tau_m \approx 1{\cdot}4$) over the 77°K value was some 30 per cent, while the p.o. mobility alone increases almost by a factor 2. This great difference is caused by the increasing influence of impurity scattering at lower temperatures. Consequently, the curves according to [15] neglecting impurity scattering lie far off the experimental values. Therefore, it must be assumed that the agreement between our experiments and the theory by

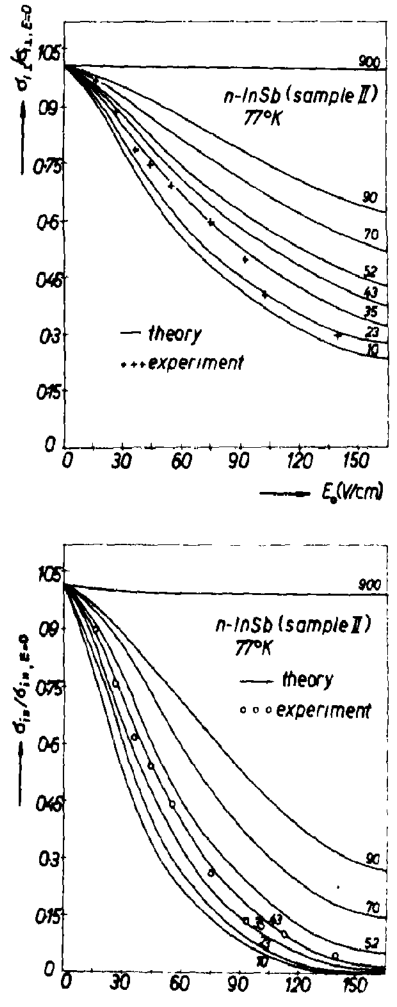

Fig. 8. Imaginary part of the microwave conductivity perpendicular (a) and parallel (b) to the d.c field, calculated for sample II. Parameter of the curves is the frequency in GHz.

Mukhopadhyay and Nag claimed in [15] is accidental. The increase of $\sigma_{r\parallel}$ in the lower field region, shown by the curve of Mukhopadhyay and Nag presented in Fig. 3, is also a consequence of the omission of impurity scattering and the corresponding overestimation of τ_m. (In Fig. 1 of Ref. [15] this increase is not indicated because of an inaccuracy of this figure.)

The theoretical curves for σ_i at different frequencies (Fig. 8) show that it is much less sensitive to variations in $\omega\tau_m$. At high frequencies the decrease with electric field becomes less pronounced and the change of sign of $\sigma_{i\parallel}$ ceases to take place. Finally both $\sigma_{i\parallel}$ and $\sigma_{i\perp}$ approach the isotropic constant value $-\epsilon\omega_p^2/\omega$, where ω_p denotes the plasma frequency of the carriers. Clearly, there is no influence of scattering in this limit

n-GaAs

Quite some interest has been paid recently to the small-signal microwave conductivity of GaAs, mainly because it presents a tool to estimate the upper frequency limit of Gunn effect devices[11, 17]. Measurements of the small-signal microwave conductivity parallel to the d.c. field have been performed by Vlaardingerbroek *et al.*[18] at 140 GHz up to fields of 2·5 kV/cm. In this region no electron transfer from the [000] valley to the [100] valleys takes place. Therefore the one-valley approach for the microwave conductivity below threshold seems reasonable and rewarding. Our calculations done for a zero field mobility of 7500 cm^2/Vsec are shown together with results of Ref. [18] in Fig. 9 along with calculations by Rees[11]. Our theoretical curve neatly flows into the experimental curve, which starts not before a field strength of 1·5 kV/cm, probably because of experimental uncertainties at lower fields. Quantitatively, the results of Ref. [11] are somewhat off in the 1·5 kV/cm region. The conductivity plateau which occurs both in experiment and in Rees' calculations would occur in our theory in a field region above threshold field. This is due to the underestimation of hot carriers in a Maxwell–Boltzmann distribution. To shift the plateau to about 2·5 kV/cm a zero field mobility of 17000 cm^2/Vsec would have to be assumed which, of course, is unrealistically high. Similarly, the conductivity plateau already occurs at about 1·5 kV/cm in Ref. [11] instead of 2 kV/cm in experiment, because Rees used much higher zero field mobilities (9500 cm^2/Vsec) than did Vlaardingerbroek *et al.* (< 8200 cm^2/Vsec). Thus the plateau seems to be originated by heating effects in the [000] valley and not by electron transfer to the [100] valleys.

4. MEAN MOMENTUM RELAXATION TIME

A decisive quantity in the calculation of the ASC is the mean momentum relaxation time as was shown in the two previous sections. This relaxation time is an appropriate quantity to describe both d.c. and a.c. phenomena. The dependence of τ_m on the electric d.c. field was deduced from three different sets of measurements to check on this assertion.

The first – manifest – method is to obtain τ_m from the velocity-field characteristic of the semiconductor. For the two *n*-type InSb samples II and III, τ_m is calculated from (11) and plotted in Fig. 2 (solid lines). This method obviously requests the knowledge of the density and effective mass of the carriers.

A second method circumvents this restriction by determining τ_m from ASC data in case of perpendicular a.c. and d.c. fields. This method first reported in [5] yields close agreement with the d.c.-measured τ_m as shown in Fig. 2 (II: +++, III: ×××). The mean momentum relaxation time is calculated by the ratio of the imaginary and real parts of the conductivity:

$$\tau_{m\perp} = -\frac{1}{\omega}\cdot\frac{\sigma_{i\perp}}{\sigma_{r\perp}}. \tag{17}$$

However, for reasons of experimental simplicity the arrangement with parallel a.c. and d.c. fields[7, 8, 19, 20] seems to be more customary than with perpendicular fields. The

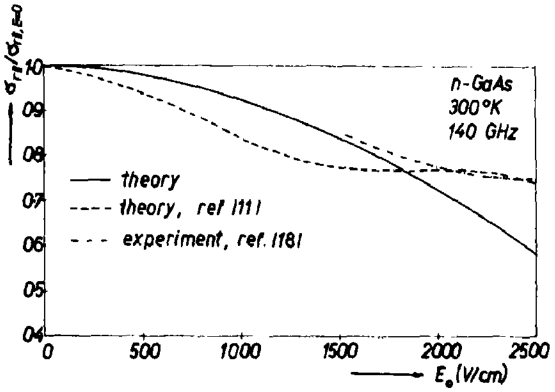

Fig. 9. Small-signal microwave conductivity of *n*-GaAs in direction of heating d.c. field near frequency limit of Gunn-effect devices.

parallel field configuration is mainly applied to high resistivity semiconductors. To extend the microwave measurement of τ_m to the parallel case and, last not least, to examine the consistency of the ASC data, a new method has been developed. In the following this method is described by which the mean momentum relaxation time is derived from the ASC data parallel to the heating d.c. field.

Starting from the equations for the parallel small-signal conductivity (14) and (15), one obtains two linear equations in τ_ϵ' and τ_m, respectively,

$$1-S=-\omega\tau_\epsilon'(\omega\tau_m\cdot R+I)+R(1+S)-I\cdot\omega\tau_m \quad (18)$$

$$\omega\tau_\epsilon'(1-R+I\cdot\omega\tau_m)=R\cdot\omega\tau_m+(1+S)I, \quad (19)$$

where S is defined by (12), and R and I by

$$R+jI=\frac{\sigma_{r\parallel}+j\sigma_{i\parallel}}{\sigma_{\mathrm{int}}} \qquad (j=\sqrt{-1}). \quad (20)$$

Elimination of τ_ϵ' yields the pertinent equation for $\tau_{m\parallel}$

$$\tau_{m\parallel}=\frac{1}{\omega}\cdot\frac{-I(2-S)+\sqrt{D}}{2(R^2+I^2)} \quad (21)$$

$$D=I^2(4-4S+S^2)-4(R^2+I^2)\times[(R^2+I^2)(1+S)+1-S-2R]. \quad (22)$$

Note that all quantities controlling $\tau_{m\parallel}$ are accessible to measurement.

This 'parallel' relaxation time is plotted in Fig. 2 as data points (II: ○○○, III: ●●●). Because of the specific structure of (21), quantities of approximately the same order of magnitude are substracted from each other which evidently enhances the effect of experimental uncertainties. Nevertheless, there exists fair agreement with the relaxation time values obtained by the first two methods. Further, it is an advantage of the new method that the quantity D from (22) is sensitive to experimental errors. Thus it could be found out that values of the parallel a.c. conductivity for a sample with high resistivity[5] were much too low for d.c. fields above 50 V/cm. Mathematically, this results in a negative value of D, which would lead to physically senseless complex relaxation times. Thus the method reveals experimental errors. The sample serves as a cover of a circular hole in a reflection-type TE_{102} cavity, cut along lines of current flow to suppress unwanted radiation [21, 6]. At zero d.c. field the thickness of the sample was about three times the penetration depth of the electromagnetic wave in the semiconductor. The resonator is well closed.

However, the penetration depth increases with increasing field until energy radiates through the sample and the resonator is not closed any more. This loss of energy appears as an erroneously low real and imaginary part of the conductivity. By this error an additional anisotropy has been pretended leading to the incorrect conclusion that the anisotropy is more pronounced for higher mobility samples[6]. The use of thicker and/or lower-resistivity samples (II, III) excluded this error in later measurements.

5. CONCLUSIONS

The new theory developed is very well suited to describe the high-frequency behavior of polar semiconductors. The inclusion of elastic scattering processes results in substantial improvement in the agreement with experiment, especially at low temperatures and low d.c. fields. The anisotropy of the small-signal conductivity reverses its sign in the high frequency limit, but does not disappear as a consequence of the high-rate energy exchange by polar optical scattering. In contrary, the contribution of the free carriers to the dielectric constant becomes isotropic and field-independent in this limit. Although a one-valley approximation is made, the theory is applicable to n-GaAs at fields below threshold for Gunn-oscillations where a Monte-Carlo-calculation fails to produce quantitative agreement with experimental results.

The new method of determining τ_m from a.c. conductivity measurements parallel to the d.c. field proves the consistency of the mean momentum relaxation time concept. It also allows to check the reliability of the results of microwave measurements.

REFERENCES

1. GUNN M. W., *Proc. IEEE* **52**, 851 (1964)
2. GERSHENZON E. M., GURVICH Yu. A. and LITVAK-GORSKAYA L. B., *Soviet Phys. solid-St* **7**, 1111 (1965).
3. PÖTZL H. W. and RICHTER K., *Proc. IEEE* **55**, 1497 (1967)
4. PÖTZL H. W. and RICHTER K., *Arch. elekt. Übertr.* **21**, 649 (1967).
5. RICHTER K. and BONEK E., *J. appl. Phys.* **39**, 4035 (1968).
6. RICHTER K. and BONEK E., *Phys. Status Solidi* **31** 579 (1969).
7. GIBSON A. F., GRANVILLE J. W. and PAIGE E. G. S., *J. Phys. Chem. Solids* **19**, 198 (1961).
8. DAS P., RIFKIN R. H. and POOLE J. J., *Electron. Lett* **3**, 515 (1967).
9. KOPETZ H. and PÖTZL H. W., *Electron. Lett* **4**, 79 (1968).
10. CONWELL E. M., *High Field Transport in Semiconductors*, p. 272 ff. Academic Press, New York (1967)
11. REES H. D., *Solid-St. Commun.* **7**, 267 (1969).
12. HUBER F. X., Ph.D. Thesis, Lehrkanzel f. Physikal. Elektronik, Technische Hochschule Wien (1968)
13. DYKMAN I. M. and TOMCHUK P. M., *Soviet Phys. solid-St.* **4**, 798 (1962): This article contains reference to earlier work DYKMAN I. M. and TOMCHUK P. M., *Soviet Phys. solid-St* **4**, 2600 (1962); GRIGORJEV N. N., DYKMAN I. M. and TOMCHUK P. M., *Soviet Phys. solid-St* **7**, 2719 (1966).
14. FROHLICH H. and PARANJAPE B. V., *Proc. phys. Soc.* **B-69**, 21 (1956).
15. MUKHOPADHYAY D. and NAG B. R., *Electron. Lett.* **5** 20 (1969)
16. RICHTER K., *IEEE Trans.* **MTT-17**, 339 (1969)
17. GRASL L. M. and ZIMMERL O. F., *Arch. elekt. Ubertr* **23** 165 (1969)
18. VLAARDINGERBROEK M. T., BOERS P. M. and ACKET G. A., *Philips Res. Repts.* **24**, 379 (1969)
19. ARTHUR J. B., GIBSON A. F. and GRANVILLE J. W., *J. Electron.* **2**, 145 (1956).
20. CONWELL E. M., FOWLER V. J. and ZUCKER J., Contract No. DA 36-039-SC-89174, US Army Signal Res. Dev. Lab., Fort Monmouth, N.J., 1963
21. SEIFERT F., *Arch. elekt. Ubertr.* **19**, 492 (1965)

APPENDIX

The starting point for the calculation of the ASC is the balance equations of momentum (3) and energy (4), which are repeated here for completeness' sake

$$\frac{\partial \mathbf{p}'_E}{\partial t} = -e\mathbf{E}' - \frac{\mathbf{p}'_E}{\tau_m(T'_e)} \tag{A1}$$

$$\frac{dT'_e}{dt} = -\frac{2e}{3k_B m^*}\mathbf{E}' \cdot \mathbf{p}'_E - \frac{T'_e - T_l}{\tau_e(T'_e)} \tag{A2}$$

Inserting time-varying quantities for drift momentum $\mathbf{p}'_E$, electric field $\mathbf{E}'$, and electron temperature T'_e in the form

$$\begin{aligned} \mathbf{p}'_E &= \mathbf{p}_E + \mathbf{p}_{E1} \cdot e^{j\omega t} \\ \mathbf{E}' &= \mathbf{E}_0 + \mathbf{E}_1 \cdot e^{j\omega t} \\ T'_e &= T_e + T_{e1} \cdot e^{j\omega t} \end{aligned} \tag{A3}$$

where

$$\begin{aligned} p_{E1} &\ll p_E \\ E_1 &\ll E_0 \\ T_{e1} &\ll T_e \end{aligned}$$

one obtains two linear equations for $\mathbf{p}_{E1}$, $\mathbf{E}_1$, and T_{e1}, when products of small-signal perturbation are neglected,

$$(1+j\omega\tau_m)\mathbf{p}_{E1}+\frac{n_1}{T_e}\mathbf{p}_E T_{e1}=-e\tau_m\mathbf{E}_1 \qquad (A4)$$

and

$$e\tau_\epsilon\mathbf{E}_0\cdot\mathbf{p}_{E1}+\left(1+j\omega\tau_\epsilon+n_2\frac{T_e-T_l}{T_e}\right)m^*\frac{3}{2}k_B T_{e1}$$
$$=-e\tau_\epsilon\mathbf{p}_E\cdot\mathbf{E}_1. \qquad (A5)$$

n_2 is defined by (10), n_1 similarly by

$$n_1=\frac{x_e}{\tau_m}\frac{d\tau_m}{dx_e} \qquad (A6)$$

Two different pairs of scalar equations are found from (A4) and (A5) for the two cases of parallel and perpendicular a.c. and d.c. fields, from which T_{e1} may be eliminated and the complex small-signal conductivity defined as

$$\sigma=\sigma_r+j\sigma_i=-\frac{enp_{E1}}{m^*E_1}. \qquad (A7)$$

Introducing the integral conductivity

$$\sigma_{\text{int}}=\frac{-enp_0}{m^*E_0}=\frac{e^2\tau_m n}{m^*} \qquad (A8)$$

and splitting in real and imaginary parts yields the result

$$\sigma_{r\perp}=\frac{\sigma_{\text{int}}}{1+(\omega\tau_m)^2},\ \sigma_{i\perp}=\frac{-\omega\tau_m\sigma_{\text{int}}}{1+(\omega\tau_m)^2} \qquad (A9)$$

$$\sigma_{r\parallel}=\sigma_{\text{int}}\frac{[1+(n_2-n_1)(T_e-T_l)/T_e][1+(n_2+n_1)(T_e-T_l)/T_e]+\omega^2\tau_\epsilon[\tau_\epsilon+\tau_m n_1(T_e-T_l)/T_e]}{[1+(n_2+n_1)(T_e-T_l)/T_e]^2+\omega^2\{\tau_\epsilon^2-2n_1\tau_\epsilon\tau_m(T_e-T_L)/T_e+\tau_m^2[1+n_2(T_e-T_l)/T_e]^2+\omega^2\tau_\epsilon^2\tau_m^2\}} \qquad (A10)$$

$$\sigma_{i\parallel}=\sigma_{\text{int}}\omega\frac{2n_1\tau_\epsilon(T_e-T_l)/T_e-\tau_m[1+n_2(T_e-T_l)/T_e][1+(n_2-n_1)(T_e-T_l)/T_e]-\omega^2\tau_m\tau_\epsilon^2}{[1+(n_2+n_1)(T_e-T_l)/T_e]^2+\omega^2\{\tau_\epsilon^2-2n_1\tau_\epsilon\tau_m(T_e-T_l)/T_e+\tau_m^2[1+n_2(T_e-T_L)/T_e]^2+\omega^2\tau_\epsilon^2\tau_m^2\}}. \qquad (A11)$$

A simplification for the parallel conductivity can be made by considering the low-frequency limit $\omega\to 0$, where $\sigma_{r\parallel}$ (A10) becomes the differential conductivity dj_0/dE_0. Then,

$$S=\frac{1-\dfrac{1}{\sigma_{\text{int}}}\dfrac{dj_0}{dE_0}}{1+\dfrac{1}{\sigma_{\text{int}}}\dfrac{dj_0}{dE_0}}=\frac{n_1(T_e-T_l)/T_e}{1+n_2(T_e-T_l)/T_e} \qquad (A12)$$

$$\sigma_{r\parallel}=\sigma_{\text{int}}\frac{1-S^2+\omega^2\tau_\epsilon'(\tau_\epsilon'+S\tau_m)}{(1+S)^2+\omega^2[\tau_\epsilon'^2-2S\tau_\epsilon'\tau_m+\tau_m^2(1+\omega^2\tau_\epsilon'^2)]}, \qquad (A13)$$

$$\sigma_{i\parallel}=\omega\sigma_{\text{int}}\frac{2S\tau_\epsilon'-\tau_m(1-S+\omega^2\tau_\epsilon'^2)}{(1+S)^2+\omega^2[\tau_\epsilon'^2-2S\tau_\epsilon'\tau_m+\tau_m^2(1+\omega^2\tau_\epsilon'^2)]} \qquad (A14)$$

by introducing a modified energy relaxation time

$$\tau_\epsilon'=\frac{\tau_\epsilon}{1+n_2(T_e-T_l)/T_e}. \qquad (A15)$$

J. Phys. Chem. Solids Pergamon Press 1970. Vol. 31, pp. 1163–1169. Printed in Great Britain.

TIME DEPENDENT PHONON DISTRIBUTION IN HOT ELECTRON EXPERIMENTS

K. BAUMANN, M. KRIECHBAUM
Institut für theoretische Physik der Universität Graz, Austria

and

H. KAHLERT
Institut für Angewandte Physik der Universität Wien and Ludwig Boltzmann-Institut für Festkörperphysik, Wien, Austria

(*Received* 8 *August* 1969)

Abstract—In hot electron experiments at low temperature it is essential to take into account two properties of the phonon distribution. (1) It is not an equilibrium distribution, and (2) it is not stationary. The latter property may be demonstrated by measuring its influence on the electron mobility It is shown that the current should increase if impurity scattering is dominant, and decrease if acoustic phonon scattering is dominant Both of these effects have been confirmed experimentally.

1. INTRODUCTION

IF A STRONG electric field is applied to a semiconductor a stationary state is established within a time of the order of the collision time of the carriers. This state is characterized by a balance between the rate at which the electrons gain energy from the field, and the rate at which they transmit energy to the lattice. However, a corresponding balance condition is not fulfilled by the lattice, and hence the stationarity of this state is only an approximative one. For this reason in hot electron experiments a strong electric field is applied to the semiconductor for a few microseconds only. The energy transmitted to the lattice during this time is small because the number of carriers is extremely small as compared with the number of lattice atoms. However, even a small energy gain of the lattice has important consequences if the total energy content of the lattice is also very small. It turns out that at liquid helium temperatures the change of the lattice energy during one microsecond is of the same order of magnitude as the thermal energy of the lattice. Furthermore, the relaxation time describing the establishment of thermal equilibrium in the lattice is large compared with one microsecond. Hence the energy gain of the lattice cannot be described by an increased lattice temperature. Rather, a deviation of the photon distribution from equilibrium is produced.

A theory of the time-dependent phonon distribution in semiconductors with a conduction band of standard type was given by Paranjape and Paranjape[1]. Baumann, Kocevar and Kriechbaum[2] worked out the phonon distribution in n–Ge at 4°K 1 μsec after application of a strong voltage pulse. The changing state of the lattice acts back on the conduction electrons, and the electron mobility will change with time. In the present paper we report on an experimental and theoretical study of the resulting time dependence of the electron current.

2. THEORY

An analysis of the change of current with time leads to formidable numerical integrations if the many-valley structure of the conduction band of germanium is taken into account. Hence we shall base our calculations on the standard band model. Apart from this simplification, the same assumptions will be made as in [2].

Thus, all donors (5×10^{15} cm^{-3}) are assumed to be ionized. Electrons in the conduction band have a Maxwellian velocity distribution. Electron scattering by long-wave acoustic lattice vibrations and by ionized impurities is taken into account. In the evaluation of the latter the Born approximation is used; according to Blatt's estimates[3] this should cause practically no error for an electron temperature of 50°K or more. The most severe deficiency of our analysis is the negligence of the many-valley structure, and of electron electron scattering.

In [2] the question of the phonon relaxation mechanisms was discussed in detail. The conclusion was that practically no phonons are lost during an observation time of the order of 1 μs and a sample dimension of the order of 1 mm. The phonon scattering mechanisms (all of which we shall ignore) have the effect of making the phonon distribution isotropic and of populating equally the various possible polarizations. We can ignore the randomization in direction since in our standard band treatment the phonon distribution never deviates from isotropy. Our reason for ignoring the collisions which transform phonons of one polarization into another is the following: In a standard band crystal only longitudinal phonons are coupled to the electrons. Therefore transformation of two thirds of the emitted longitudinal phonons into transverse ones by surface scattering will be an important effect. It will influence strongly the time-dependence of the electric current. But obviously this is a specific property of the standard band model. A much weaker effect is to be expected in n-germanium. We are thus justified to use the following phonon Boltzmann equation:

$$\frac{\partial N_{\mathbf{q}}}{\partial t} = \frac{{\Xi_q}^2}{4\pi^2\hbar\rho s}\int \delta(E(\mathbf{k}+\mathbf{q}) - E(\mathbf{k}) - \hbar\omega(q))$$

$$\times\{(N_{\mathbf{q}}+1)f(\mathbf{k}+\mathbf{q}) - N_{\mathbf{q}}f(\mathbf{k})\}\,\mathrm{d}^3k. \qquad (1)$$

Here, Ξ is a deformation potential constant which should be chosen as [4]

$$\Xi = \Xi_d + \tfrac{1}{3}\Xi_u. \qquad (2)$$

This choice guarantees an optimal agreement between the properties of our model and of true n-germanium; Ξ_d and Ξ_u are the deformation potential constants for volume dilatation and uniaxial shear. The mass density of the crystal is ρ, and s is the longitudinal sound velocity. It has been shown in [2] that the conditions are such as to justify the approximation of the electron distribution by an undisplaced Maxwellian distribution:

$$f(\mathbf{k}) = \frac{n}{N_c(T_e)}\exp\left\{-\frac{E(\mathbf{k})}{KT_e}\right\} \qquad (3)$$

where n is the carrier concentration, T_e the electron temperature, K Boltzmann's constant, and

$$N_c(T_e) = 2(2\pi mKT_e/h^2)^{3/2} \qquad (4)$$

the effective density of states in the conduction band. Combining (1) and (3) and performing the integration (using $E(\mathbf{k}) = \hbar^2k^2/2m$) leads to

$$\frac{\partial N_{\mathbf{q}}}{\partial t} = \frac{\Xi^2m^2KT_en}{2\pi\rho sh^4N_c(T_e)}\left\{(N_{\mathbf{q}}+1)\exp\left(-\frac{\hbar\omega}{KT_e}\right)\right.$$

$$\left. - N_{\mathbf{q}}\right\}\exp\left\{-\frac{\hbar^2}{2mKT_e}\left(\frac{q}{2}-\frac{m\omega}{\hbar q}\right)^2\right\} \qquad (5)$$

or

$$\frac{\partial N_{\mathbf{q}}}{\partial t} = Q - PN_{\mathbf{q}} \qquad (6)$$

$$P = \{\exp(\hbar\omega/KT_e) - 1\}Q, \qquad (7)$$

$$Q = \frac{\Xi^2n}{2h\rho s}\,\frac{(2\pi)^{3/2}m^{1/2}}{(KT_e)^{1/2}}$$

$$\times\exp\left\{-\frac{\hbar^2}{2mKT_e}\left(\frac{q}{2}+\frac{m\omega}{\hbar q}\right)^2\right\}. \qquad (8)$$

Next we consider the energy balance. The average rate of change of the energy of an electron is

$$\left\langle\frac{dE}{dt}\right\rangle = e\mu F^2 - \frac{1}{8\pi^3 n}\int \hbar s q \frac{\partial N_q}{\partial t} 4\pi q^2 \mathrm{d}q. \qquad (9)$$

The brackets indicate an average over the electron distribution. The strength of the applied electric field is denoted by F; μ is the electron mobility. The second term on the right-hand side represents the energy transferred to the lattice. Since the deviation from stationarity of the electrons is small we put the left-hand side equal to zero and get

$$e\mu F^2 = \frac{\hbar s}{2\pi^2 n}\int_0^\infty q^3\{Q - PN_q\}\,dq. \qquad (10)$$

The electron mobility is calculated from

$$\mu = \frac{e\langle E\tau(E)\rangle}{m\langle E\rangle} \qquad (11)$$

In order to minimize the error introduced by neglecting the electron mass anisotropy, different electron masses should be used in $E(k)$ and in μ. In equation (11), the conductivity mass is to be used if F$\|$[100].

The electron relaxation time $\tau(E)$ is given by

$$\tau = \{(\tau_L)^{-1} + (\tau_I)^{-1}\}^{-1}, \qquad (12)$$

τ_L is the contribution from acoustic lattice vibrations, and τ_I from ionized impurity scattering. The lattice term is determined from the equation

$$\frac{1}{\tau_L(E)} = \int (1-\cos\vartheta)\Lambda(E\cos\vartheta)2\pi\sin\vartheta\,\mathrm{d}\vartheta, \qquad (13)$$

where ϑ denotes the electron scattering angle, and $\Lambda 2\pi\sin\vartheta \mathrm{d}\vartheta \mathrm{d}t$ the probability for scattering by an angle between ϑ and $\vartheta + \mathrm{d}\vartheta$ during the time interval $\mathrm{d}t$. The wave number q of the phonon belonging to scattering by an angle ϑ is given by

$$\hbar q = (2mE)^{1/2}(2 - 2\cos\vartheta)^{1/2}, \qquad (14)$$

if the inelasticity of the scattering is neglected. Furthermore,

$$\Lambda(E, \cos\vartheta) = \frac{\Xi^2 m^2}{2\rho\pi^2\hbar^4 s}E(2 - 2\cos\vartheta)^{1/2} \times (N_q + \tfrac{1}{2}). \qquad (15)$$

The relaxation time for Rutherford scattering has been given by Dingle[5]. He finds

$$\frac{1}{\tau_I(E)} = \frac{\pi n e^4}{(2m)^{1/2}\epsilon^2} \times\left\{\ln(1+\xi) - \frac{\xi}{1+\xi}\right\}E^{-3/2}, \qquad (16)$$

where ϵ is the dielectric constant, and

$$\xi = 8mR^2E/\hbar^2 \qquad (17)$$

$$R^2 = \frac{\epsilon K T_e}{e^2 n}.$$

Equations (6), (10) and (11) permit a determination of T_e, μ and N_q for arbitrary times. We have performed a numerical evaluation of these three functions. The results for N are shown in Fig. 1. The curves might be com-

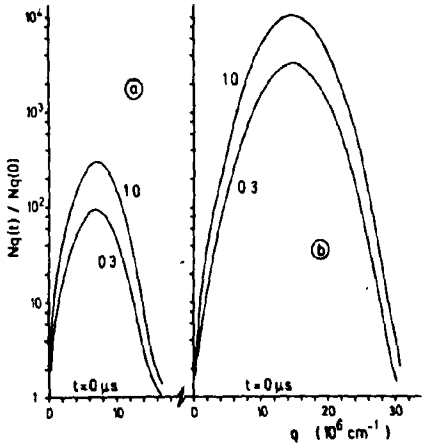

Fig. 1. Phonon numbers N_q at $t = 0{\cdot}3\,\mu$sec and $t = 1{\cdot}0\,\mu$sec. The electron temperature at $t = 0\,\mu$sec is taken as 70°K (a) and 150°K (b).

pared with Fig. 4 of [2]. There is a discrepancy in the predicted maximum values of N_q. However, Fig 2 of [2] shows that the longitudinal branch is strongly suppressed in the [001] direction which has been chosen for presentation in Fig. 4 of [2]. Thus the results of a many-valley and of a standard band calculation do not differ so much on the average.

The change of conductivity with time is by far not as large as one would expect from the large increase in phonon number. This is connected with the fact that Rutherford scattering is dominant at $T_e = 70$°K whereas it is not at 150°K. As a consequence, the change of σ with time is positive at the smaller electron temperature but negative at the bigger one. The relative change of the conductivity at $t = 0·3\,\mu$sec and at $t = 1\,\mu$sec is given in Table 2.

Table 1. Constants used in the calculation. Ξ_d and Ξ_u are taken from Ito et al.[6].

ρ 5·35 g/cm^3	m_l 1·46 × 10^{-27} g	Ξ_d −10·5 eV
s 5·4 × 10^5 cm/s	m_t 7·47 × 10^{-29} g	Ξ_u 18·7 eV
ϵ 16	T 4·2°K	n 5 × 10^{15} cm^{-3}

Table 2. Calculated temperatures and relative change of conductivity

t (μsec)	$T_e(t)$ (°K)		$(\sigma_t - \sigma_0)/\sigma_0$ (%)	
	a	*b*	*a*	*b*
0	70	150		
0·3	83	149	+12·6	−11·0
1·0	96	154	+20·6	23·5

3. EXPERIMENTAL PROCEDURES

For the measurement of low temperature breakdown at 4·2°K two sets of samples from two different crystals of n-type germanium were used. The first set was taken from a single crystal with a net donor concentration of $5·0 \times 10^{14}\,\text{cm}^{-3}$ and a Hall mobility of 3400 cm^2/Vsec at 300°K. Parallelepipeds were cut with their long axis parallel to the [100] direction. The transverse dimensions of these samples were varied between 5·2 × 7·0 mm^2 and 0·5 × 2·3 mm^2. To this type of samples contacts were made by alloying tin containing 1 per cent antimony. The large current contacts completely covered the end faces of the samples. The potential contacts were in the form of small tin spheres with a contact area of about 0·05–0·01 mm^2. These potential contacts were placed asymmetrically at the side faces of the samples as shown in Fig. 2. It turned out during the measurements that an anomalous potential drop at the cathode may occur at this type of current contact, which possibly influences the conductivity in the bulk material by emission of phonons travelling into the volume between the potential probes. By placing one potential probe approximately 1 cm away from the cathode one assures that no phonons have the possibility of reaching the area between the potential probes within the first microsecond of a current pulse, since the longitudinal sound velocity in Ge has a value of $5·4 \times 10^5$ cm/sec.

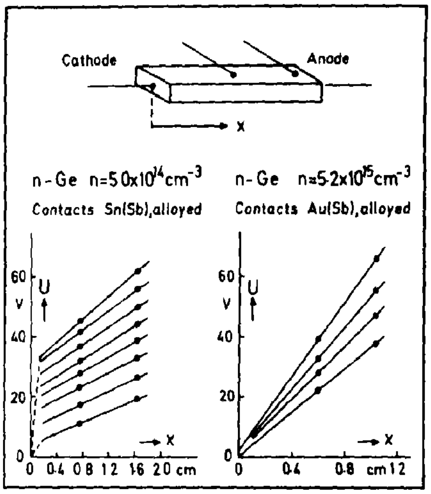

Fig. 2. Sample geometry and potential distribution

The other set of samples was taken from a single crystal with a net donor concentration of $5·2 \times 10^{15}\,\text{cm}^{-3}$ and a Hall mobility of 2910 cm^2/Vsec at 300°K. Oriented samples were cut with their long axis parallel to the [100] and [111] direction. The transverse dimensions of these samples varied between 0·32 × 0·18 mm^2 and 0·28 × 0·09 mm^2. To the endfaces of the samples current contacts were made by alloying, in hydrogenic atmosphere, gold containing a few per cent antimony. 70 μm thick platinum wires were soldered to the sidefaces of the samples as potential probes. For this type of contacts it was proved that up to a field strength of about 70 V/cm no marked cathode drop was built up as is shown by Fig. 2. Nevertheless the potential probe next to the cathode was placed far enough away from the cathode, that even at the occurance of a phonon emission from the cathode there would be no influence on the mobility of carriers in the region between the potential probes within the first microsec after application of the voltage.

Voltage pulses of 1–3 μsec duration and a repetition rate between 1 and 20 Hz were applied to the samples by discharging a 50 Ω coaxial cable of suitable length over a mercury wetted relay. The field strength was calculated from the voltage drop between the potential probes measured with a differential amplifier. The current density was taken from the voltage drop across a series resistor small compared with the sample resistance. Both signals were displayed simultaneously at the screen of a dualtrace oscilloscope and photographed, or they were picked up by a sampling oscilloscope and plotted by a x-y-recorder vs. time.

4. EXPERIMENTAL RESULTS

In Fig. 3 the observed dependence of conductivity σ on the electric field strength E is shown for the two materials under investigation. Values of σ were calculated from the voltage and current traces 100 nsec after the beginning of the pulse. Note that for the lower curve (a) taken with the material of $n = 5{\cdot}0 \times 10^{14}$ cm^{-3} carriers the experimental points from samples with the smallest cross dimension ranging from 5 to 0·5 mm are all on the same curve within the experimental error[7]. After the $\sigma - E$ characteristics were measured with CP4 polished samples the surfaces were sandblasted and characteristics measured again. Not the least influence of the surface quality on the $\sigma - E$ characteristic was observed. The maximum of conductivity with these samples occurs at a field strength of about 16 V/cm. For the samples with $n = 5{\cdot}2 \times 10^{15}$ cm^{-3} the breakdown field strength is higher and the maximum of the conductivity occurs at about 100 V/cm, again followed by a region of decreasing conductivity with increasing field strength. The voltage and current pulses across a sample with $n = 5{\cdot}0 \times 10^{14}$ cm^{-3} are shown in Fig. 4. While the voltage across the potential probes (upper trace) remains essentially constant during the 2 μsec pulse, one observes a marked decrease in

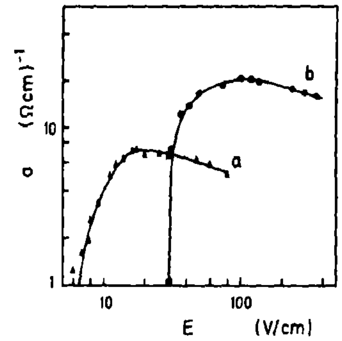

Fig. 3. Electrical conductivity of n-type germanium with $n = 5{\cdot}0 \times 10^{14}$ cm^{-3} (curve a taken from Ref. [7] and $n = 5{\cdot}2 \times 10^{15}$ cm^{-3} (curve b) vs electrical field strength at 4·2°K

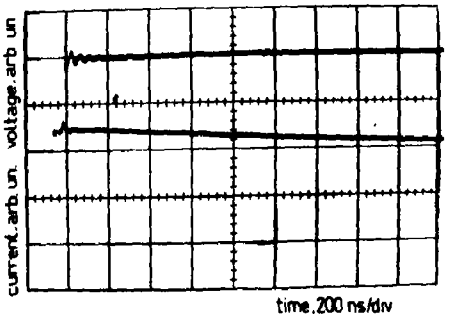

Fig. 4. Voltage and current vs time at a field strength of 35·2 V/cm ($n = 5{\cdot}0 \times 10^{14}$ cm^{-3}, [100])

current (lower trace). The distance between the cathode and the cathode near potential probe was 12 mm in this case. Thus any phonons created at the cathode during the 2 μsec pulse should not have influenced the mobility between the potential probes. In Table 3 the relative decreases of current and therefore of conductivity are summarized for some values of field strength well above saturation of low temperature breakdown[8].

Table 3. Relative change in conductivity for various materials and field strength investigated

Carrier concentration, Crystallogr direction	Field strength (V/cm)	$(\sigma_t - \sigma_0)/\sigma_0$ (t = 1 μsec) (%)
n 5·0 × 10^{14} cm^{-3} 100	26·4	6·5
	35·2	-6·1
	54·5	9·2
n 5·2 × 10^{15} cm^{-3} 100	31·5	+2·9
	38·3	-5·1
	52·9	6·2
n 5·2 × 10^{15} cm^{-3} 111	50	+0
	100	-8·3
	152	8·7

A typical result obtained with a sample cut in [111] direction from a crystal with $n = 5{\cdot}2 \times 10^{15}$ cm^{-3} is shown in Fig. 5. Again the upper trace shows the voltage across the potential probes, which decreases slowly. This decrease is caused by the properties of the 3 μsec discharge cable used in this experiment. The lower trace representing the current pulse decreases faster. By dividing the height of the voltage pulse through the height of the current pulse at a given time one gets a number which is proportional to the resistivity of the sample. As the voltage pulse is not completely constant one has to take into account during the calculation of the true time dependence of the conductivity that σ depends on E as shown in Fig. 3. In consequence the time dependence of current, which one would measure with a perfectly constant voltage pulse should be larger as measured in our case, if the field strength applied to the sample exceeds the value corresponding to the maximum value of conductivity. Current pulses at three different values of field strength with a sample cut in [100] direction from the same crystal are shown in Fig. 6. The voltage pulses not shown in this diagram were essentially flat. At the lowest field strength the current increases with time. At a higher value of E it is fairly constant with time and at the highest field strength shown in Fig. 6 the current decreases.

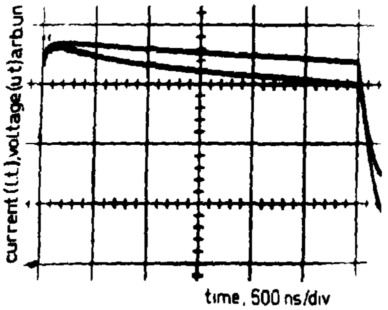

Fig. 5. Voltage and current vs. time at a field intensity of 100 V/cm ($n = 5{\cdot}2 \times 10^{15}$ cm^{-3}, [111]).

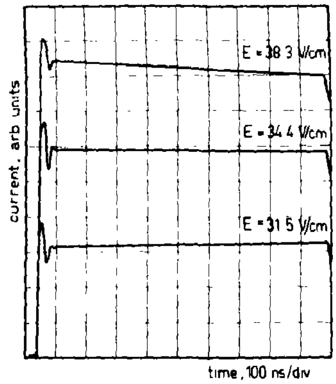

Fig. 6. Current vs time at three different field intensities ($n = 5{\cdot}2 \times 10^{15}$ cm^{-3}, [100]).

The relative changes of conductivity within the first microsecond at several values of E with samples cut parallel to the [100] and the [111] directions are also summarized in Table 3.

5. DISCUSSION

A comparison of the theoretical and experimental time dependence of conductivity shows that qualitative agreement between experiment and theory is obtained. However the calculations are based on the standard band model neglecting the many valley structure of the conduction band of germanium and also only an electron temperature (Table 2) rather than the observed field intensity (Table 3) is calculated. Nevertheless the experimental verification of the theoretical time dependence of mobility and the nonexistence of any dimensional effect seems to confirm the conclusions about the phonon-relaxation mechanism pointed out in our previous paper [2].

Conwell[9] assumed that the phonons emitted by the hot electrons are eliminated as soon as they reach the surface of the sample. On the basis of this assumption, which is in contradiction to the well known thermal boundary resistance between solids and liquid helium[10], a marked dependence of electric conductivity on sample dimensions was to be expected. Since we did not observe any dimensional effects we conclude that the phonons are nearly totally reflected at the germanium–helium interface. This conclusion is also satisfactory from the point of view of elasticity theory.

The observation of dimensional dependence of conductivity in agreement with Conwell's theory was reported by Zylbersztejn and Conwell[11]. We suspect that these effects will disappear if proper care is taken to eliminate effects of a cathode fall etc. from the experiment. A true dimensional effect as postulated by Conwell must necessarily be zero at the beginning of the voltage pulse and reach its maximum value at a time of the order of L/s ($\approx 1\ \mu$sec for $L = 5$ mm). Zylbersztejn, however, observed dimension-dependent but time-independent currents[12]. Zylbersztejn argued that Conwell's view of phonon boundary scattering is also supported by another experiment performed by him [13]. It would be interesting to repeat this experiment in order to find out if the results are compatible with diffuse boundary scattering of the phonons.

Acknowledgements – We have profited from discussions with Professor Seeger. Our thanks are also due to the Fonds zur Forderung der wissenschaftlichen Forschung. Vienna, and to the Ludwig Boltzmann Gesellschaft. Vienna, for financial support. The numerical calculations have been performed at the Rechenzentrum, Graz, and at the Mathematisches Institut der Technischen Hochschule, Vienna.

REFERENCES

1. PARANJAPE V. V. and PARANJAPE B. V., *Phys. Rev.* **166**, 757 (1968).
2. BAUMANN K., KOCEVAR P. and KRIECHBAUM M., *J. Phys. Chem. Solids* **31**, 95 (1970).
3. BLATT F. J., *J. Phys. Chem. Solids* **1**, 262 (1957).
4. BARDEEN J. and SHOCKLEY W., *Phys. Rev.* **80**, 72 (1950).
5. DINGLE R. B., *Phil. Mag.* **46**, 831 (1955).
6. ITO R., KAWAMURA H. and FUKAI M., *Phys. Lett.* **13**, 26 (1964).
7. BAUMANN K., KOCEVAR P., KRIECHBAUM M., KAHLERT H. and SEEGER K., *Proc. 9th Int. Conf. Semicond. Physics, Moscow*, p. 757 (1968).
8. ZAVARITSKAYA E. I., from Skobel'tsyn Electrical and optical properties of semiconductors **37**, 33 (1968).
9. CONWELL E., *Phys. Rev.* **135**, A814 (1964).
10. JOHNSON A. B. and LITTLE C. D., *Phys. Rev.* **130**, 596 (1963).
11. ZYLBERSZTEJN and CONWELL E., *Phys. Rev. Lett.* **11**, 417 (1963).
12. ZYLBERSZTEJN A., private communication.
13. ZYLBERSZTEJN A., *Phys. Rev. Lett.* **19**, 838 (1967).

J. Phys. Chem. Solids Pergamon Press 1970. Vol. 31, pp. 1171–1183. Printed in Great Britain.

ETUDE PAR RAYONS X ET NEUTRONS DE LA SERIE ISOMORPHE ATiTO$_5$ (A = Cr, Mn, Fe, T = TERRES RARES)

G. BUISSON
Centre d'etudes Nucleaires, Cedex 85, 38-Grenoble-Gare, France

(*Received* 15 *July* 1969)

Résumé–Les composés ATiTO$_5$ sont isomorphes à Mn$_2$HoO$_5$ pour les terres rares de la première série dont le rayon ionique r(T) est compris entre r(Pr) et r(Gd). Dans les préparations cette structure est en compétition avec celles du type pyrochlore et pérovskite de formule respective Ti$_2$T$_2$O$_7$ et ATO$_3$. Un des buts de cette étude fut de déterminer dans ATiTO$_5$ la distribution des ions A^{3+} et Ti^{4+} sur les deux sites possibles, dont l'un possède un environnement octaédrique en oxygène et l'autre un environnement de cinq oxygènes disposés au sommet d'une pyramide à base carrée Une étude par diffraction de neutron sur CrTiNdO$_5$ et FeTiNdO$_5$ a montré que 95% du Cr^{3+} et 57% du Fe^{3+} vont respectivement sur le site octaédrique. Ce comportement s'explique facilement par des considérations de champ cristallin. Dans CrTiNdO$_5$, à 13°K Cr^{3+} et Nd^{3+} s'ordonnent magnétiquement en même temps pour donner naissance à une structure non colinéaire où les moments de Nd sont dans le plan *XY* (+Gx-Ay) ainsi que les moments de 5% d'atome de Cr^{3+} sur le site pyramide à base carrée (+Ay) mais les 95% des moments des atomes de Cr^{3+} sur le site octaédrique sont suivant *z* (+Az), couplés dans une même représentation. Le groupe de Shubnikov est Pbam'. Dans FeTiNdO$_5$, Nd n'est pas ordonné et les moments magnétiques de Fe sont dans le plan *XY* avec une configuration non colinéaire CxFy sur les deux sites. Le groupe de Shubnikov est $P_{2_1}b'$ am'. La direction des moments de Nd^{3+} dans CrTiNdO$_5$ et de Fe^{3+} dans FeTiNdO$_5$ fait un angle voisin de 12° avec l'axe des *Y*. On ne peut expliquer la direction des moments dans CrTiNdO$_5$ que par couplage anisotrope antisymétrique. Nous n'avons pas observé d'ordre magnétique pour MnTiNdO$_5$ à 1·5°K

Abstract–The compounds ATiTO$_5$ are isomorphous with HoMn$_2$O$_5$ when the rare earth ionic radius is intermediate between that of Gd and Pr. Pyrochlore (T$_2$Ti$_2$O$_7$) and perowskite (ATO$_3$) structures are found simultaneously. A purpose of this study was to investigate the distribution of A^{3+} and Ti^{4+} in ATiTO$_5$ over the two different available sites having an octahedral and square pyramid oxygen environment. A neutron diffraction study of Nd compounds has shown that A^{3+} occupation of the octahedral site was 95% and 57% when A^{3+} is Cr^{3+} and Fe^{3+} respectively. This is easily interpreted using crystal field theory. In CrTiNdO$_5$ both Cr and Nd spins become ordered below 13°K Nd^{3+} spins lie in the *XY* plane (+Gx-Ay). Cr^{3+} ions in octahedral sites (95%) have spins along the *z* axis (+Az) while the remaining Cr^{3+} ions square pyramid sites (5%) have spins in the *XY* plane (+Ay). Shubnikov group is Pbam' In FeTiNdO$_5$, Nd^{3+} spins are not ordered at 1·5°K Fe^{3+} spins lie in *XY* plane with a CxFy configuration for both sites. Shubnikov group is $P_{2_1}b'$ am'. For these two compounds the spin direction in the *XY* plane makes an angle of approximately 12° with the *Y* axis In CrTiNdO$_5$ the spin direction can be explained only by assuming anisotropic exchange. No magnetic ordering was observed for MnTiNdO$_5$.

UN NOUVEAU composé de formule TMn$_2$O$_5$ avec T = terre rare, a été décrit pour la première fois en 1964[1, 2]. Ce composé était caractérisé par la coéxistence de Mn^{3+} et de Mn^{4+} en proportion stoéchiométrique dans la structure.

L'étude cristalline révélait que ces atomes de Mn étaient disposés sur deux sites distincts, dont l'environnement était octaédrique pour l'un, et de 5 oxygènes disposés au sommet d'une pyramide à base carrée pour l'autre (Fig. 1).

La structure magnétique du composé isomorphe BiMn$_2$O$_5$[3] démontrait la complexité des interactions magnétiques et permettait de préciser la place des Mn^{3+} et Mn^{4+} sur les deux sites correspondants.

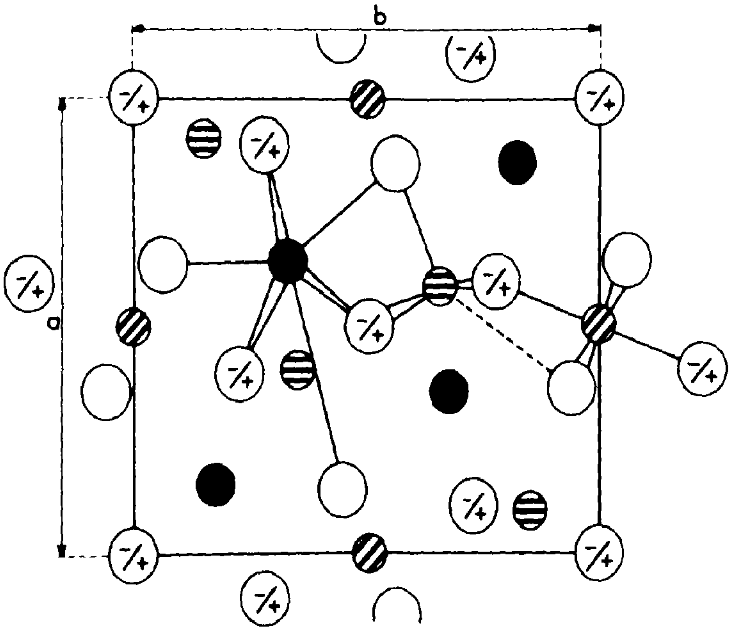

Fig. 1. Projection de la structure de $HoMn_2O_5$ dans le plan *b*.

Nous nous proposons dans ce mémoire* de faire l'étude par rayons X et par Neutrons des propriétés chimiques et physiques des composés $ATiTO_5$ isomorphes à Mn_2TO_5 (A^{3+} = Cr, Mn, Fe) (T = terres rares)

1. DOMAINE DE STABILITE

Le mélange des oxydes de A^{3+} (Cr_2O_3, Fe_2O_3, Fe_2O_3 ou Mn_2O_3) avec TiO_2 et T_2O_3 en proportion stoéchiométrique est finement broyé et porté au four pendant 48 hr à température fixe.

La poudre est analysée par rayons X. La Fig. 2 résume les résultats des produits obtenus en fonction des différentes terres rares et de la température. Nous obtenons les composés isomorphes de formule $ATiTO_5$ avec les terres rares dont le rayon ionique est compris entre celui de Pr et de Gd inclus, dans des domaines de températures variables suivant le cation A^{3+} mais en moyenne entre 1000° et 1300°C. Ces composés isomorphes à Mn_2TO_5 sont en compétition avec deux autres structures, pyrochlore et pérovskite de formules respectives $T_2Ti_2O_7$ et TAO_3.

On peut remarquer sur la Fig. 2 que pour les terres rares de petits rayons ioniques, c'est la structure pyrochlore qui est la plus stable, la limite de formation dépendant à la fois de la température et du cation A^{3+}. Pour les terres rares de grands rayons ioniques c'est la structure pérovskite qui est la plus stable.

Il est difficile d'obtenir des produits purs et il éxiste toujours un mélange entre ces trois structures et les produits de départ. C'est entre 1200° et 1300° que nous avons préparé les composés les plus purs en recuisant et rebroyant le mélange des oxydes pendant plusieurs jours. Les composés $ATiTO_5$ étant formés, ils se décomposent au point de fusion en donnant lieu soit à la pérovskite soit au pyrochlore.

Nous avons cherché à obtenir les composés isomorphes avec d'autres cations A^{3+}. Nos résultats n'ont pas été concluants avec A^{3+}

---

*Thèse n° 3405.

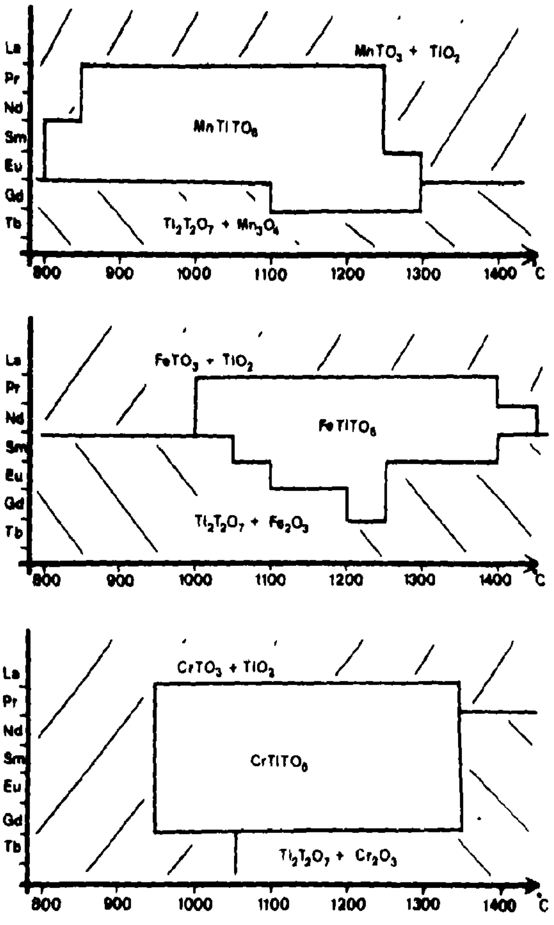

Fig. 2. Diagrammes de phase A$_2$O$_3$-TiO$_2$-T$_2$O$_3$ en fonction de la température.

= Ga, Al, Ti, Co, Rh. Nous avons d'autre part essayé de remplacer le Ti^{4+} par Ge^{4+} et Zr^{4+} sans obtenir les produits isomorphes cherchés.

2. DONNEES CRISTALLOGRAPHIQUES PAR Rx

Nous avons indéxé les clichés de poudre de rayon X sur chambre de 360 mm avec la longueur d'onde du chrome. La maille est orthorombique. Les groupes d'espaces possibles sont Pbam ou Pba2 ce qui confirme l'isormophie avec TMn$_2$O$_5$.

Le Tableau 1 donne la valeur des paramètres pour les différentes terres rares et pour les différents cations A^{3+}. Le Tableau 2 résume l'indexation d'un cliché de poudre pour la longueur d'onde du Cr.

3. ETUDE PAR DIFFRACTION NEUTRONIQUE

L'étude de la structure aux Rx aurait certainement permis de situer avec précision la place de la terre rare ainsi que celle des cations de transition 3*d*. mais les facteurs de diffusion des cations A^{3+} et Ti^{4+} étant voisins, il ne nous aurait pas été possible de différencier sur les sites correspondants.

Par contre, avec les neutrons, la longueur de Fermi b(Ti) étant négative, et celle *b*(Fe) et *b*(Cr) positive nous pouvons prévoir qu'il sera facile de déterminer la position res-

Tableau 1. *Paramètres des mailles orthorhombiques de* $ATiTO_5$

	Cr			Fe			Mn		
	b	*b*	*c*	*a*	*b*	*c*	*a*	*b*	*c*
Pr	7,58	8,68	5,81	7,57	8,72	5,855	7,59	8,72	5,83
Nd	7,56	8,67	5,80	7,54	8,71	5,85	7,55	8,69	5,82
Sm	7,50	8,62	5,79	7,50	8,69	5,83	7,49	8,65	5,81
Eu	7,475	8,60	5,785	7,47	8,67	5,825	7,46	8,60	5,805
Gd	7,45	8,59	5,785	7,43	8,65	5,82	7,43	8,56	5,795

pective de ces cations. Quant aux ions d'oxygène il est bien connu que $b(0)$ est suffisamment grand pour permettre leur positionnement. A basse température, nous avons d'autre part la contribution dû à l'ordre des atomes magnétiques; par leurs moments magnétiques nous pourrons ainsi confirmer les paramètres des sites dans lesquels ils se placent et déterminer la structure magnétique du composé.

1. $CrTiNdO_5$

La Fig. 3 représente les diagrammes de neutrons à la longueur d'onde $\lambda = 1,106$ A enregistrés à la température ambiante et à 4,2°K.

Affinement de la structure cristalline. Il est difficile d'affiner avec précision la structure en considérant le faible nombre de raies nucléaires non multiples par rapport au grand nombre de paramètres qui-interviennent. D'autre part nous ne connaisson pas le pourcentage de Cr ou de Ti sur les 2 sites $4h$ et $4f$ (voir le Tableau 3 pour les différents sites ou ils peuvent se trouver); nous devons donc introduire une variable supplémentaire qui fixe la distribution de ces cations.

Pour affiner la structure nous avons employé un programme spécialement écrit pour les raies multiples par BASSI du CEN/G. Nous l'avons utilisé en introduisant succéssivement différents pourcentages de Cr sur le site $4h$ ou son complément sur le site $4f$. Par itérations nous n'avons observé une convergence des valeurs que pour des pourcentages compris entre 0 et 6% de Cr^{3+} sur le site $4h$. Le résidu cristallographique le plus bas correspond à 0% de Cr^{3+} sur le site $4h$ et 100 pour cent sur le site $4f$. Cependant le calcul montre certaines incompatibilités des distances interatomiques en particulier sur les sites $4f$ et $4h$. Les distances interatomiques les plus vraisemblables, correspondent à un affinement avec 5% de Cr^{3+} et 95% de Ti^{4+} sur le site $4h$ et 95% de Cr^{3+} et 5% de Ti^{4+} sur le site $4f$.

Le Tableau 3 donne le résultat de cet affinement.

Structure magnétique. Par mesure magnétique nous observons à 13°K un point de transition qui correspond à un ordre magnétique coopératif du Cr et de la terre rare. La transition correspondant à l'ordre du Cr seul n'est pas appréciable. Pour observer l'ordre du Cr seul nous avons dû opérer en diffraction neutronique à plus haute température, dans un vase à température variable. Le diagramme obtenu à 30°K est sensiblement identique à celui correspondant à la température ambiante, aux impuretés près, qui sont Cr_2O_3 et $NdCrO_3$ ordonnés magnétiquement à ces températures et représentés sur la Fig. 3

Nous en déduisons qu'à 30°K le Cr^{3+} n'est pas ordonné. Le diagramme à 4,2°K qui correspond à l'ordre du Cr et de la terre rare, permet d'observer des intensités magnétiques qui s'indexent dans la maille cristalline, donc $\mathbf{k} = 000$.

Théorie macroscopique de Bertaut. Les cations en position $4g$ sont numérotés de

Tableau 2. Indexation d'un cliché de poudre de $FeTiSmO_5$ (λCR)

HKL	$Sin^2\,\theta obs$ ($\times 10^{-4}$)	$Sin^2\,\theta calc$ ($\times 10^{-4}$)	HKL	$Sin^2\,\theta obs.$ ($\times 10^{-4}$)	$Sin^2\,\theta calc$ ($\times 10^{-4}$)
001	391	386	251	5670	5663
110		407	510	6014	6005
111	802	793	152	6133	6121
120	940	928	323	6273	6268
021	1092	1081	350	6462	6443
210	1117	1107	143		6487
201	1325	1319	440	6512	6512
121		1314	520		6526
211	1502	1493	160		6488
002	1552	1544	061	6661	6641
220	1638	1628	432	6848	6840
130	1806	1797	351		6829
112	1960	1951	441	6918	6898
221	2029	2014	521		6912
131	2197	2183	333	7141	7137
310	2251	2272	403	7219	7206
022		2239	062	7810	7799
230	2485	2497			
202		2477	423	7907	7901
311	2664	2659	134	7974	7973
212		2650	442	8065	8056
140	3030	3013	360	8359	8354
222	3188	3172	343		8353
321		3180	451	8451	8462
132	3347	3341	314		8449
141	3414	3399	540	8625	8611
003	3480	3474	170	8756	8746
330	3672	3663	433		8770
400	3740	3732	532	8943	8939
113	3884	3881	611		8957
331	4050	4049	541	9001	8997
232		4041	144	9189	9189
401	4128	4118	270	9454	9446
042	4334	4324	063	9732	9729
123	4412	4402	271	9836	9832
150	4582	4577	334		9839
332	5214	5207	404	9903	9908
402	5284	5276	362		9898
412	5462	5450			

1 à 4 ainsi que ceux en position *4h*; ceux en position *4f* de 5 à 8

$$\begin{array}{llll}
X\,Y\,0 & -1- & X\,Y\,0{,}5 & 0{,}5\;0\,Z-5 \\
\bar{X}\,\bar{Y}\,0 & -2- & \bar{X}\,\bar{Y}\,0{,}5 & 0{,}5\;0\,\bar{Z}-6 \\
0{,}5-X,\,0{,}5+Y,\,0 & -3- & 0{,}5-X,\,0{,}5+Y,\,0{,}5 & 0\;0{,}5\,Z-7 \\
0{,}5+X,\,0{,}5-Y,\,0 & -4- & 0{,}5+X,\,0{,}5-Y,\,0{,}5 & 0\;0{,}5\,\bar{Z}-8
\end{array}$$

L'énergie est invariante dans le groupe

cristallographique (et magnétique). du cristal. Les modes magnétiques compatibles avec la symétrie du cristal sont vecteurs de base

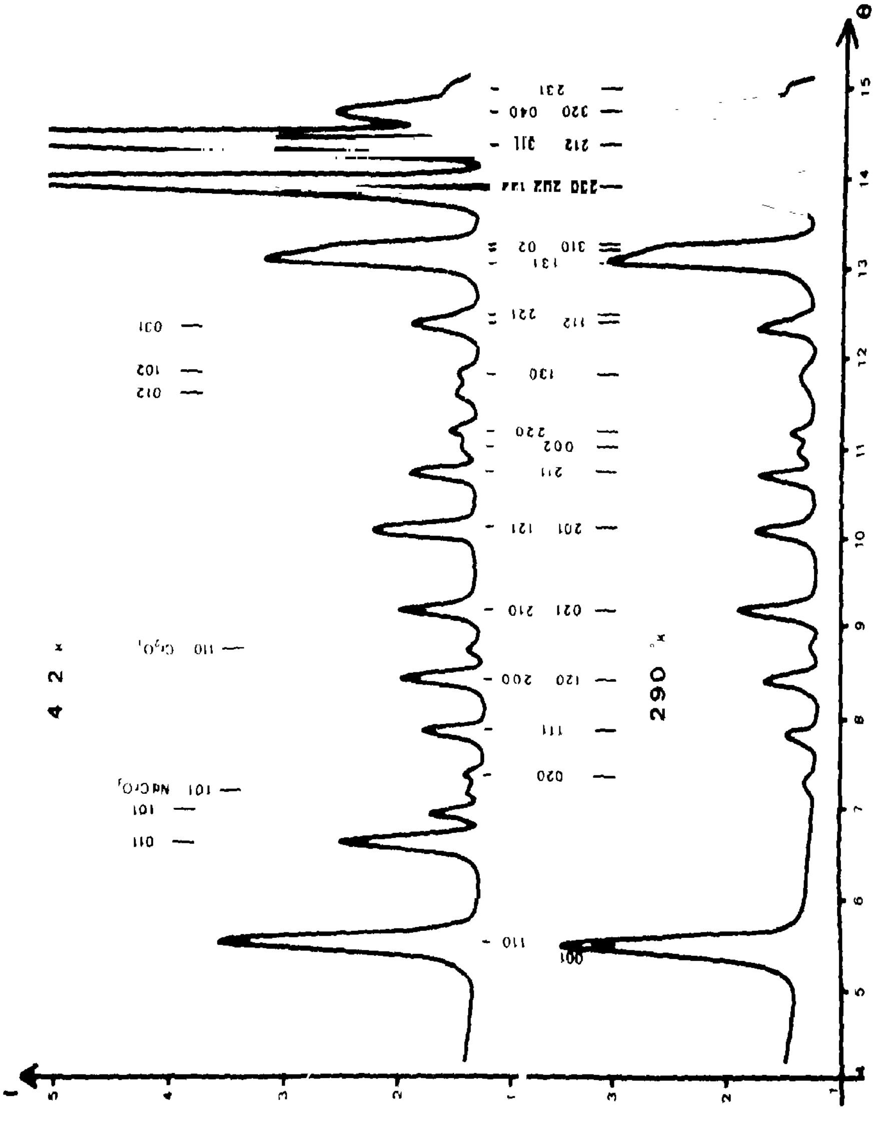

Fig 3. Diagrammes de diffraction neutronique de $CrTiNdO_5$ ($\lambda = 1.106$ Å).

Tableau 3. Paramètres cristallins de $CrTiNdO_5$

	X	*Y*	*Z*	Pbam
Nd	0,142	0,172	0,0	4*g*
5% Cr 95% Ti	0,124	−0,134	0,5	4*h*
95% Cr 5% Ti	0,0	0,5	0,252	4*f*
0	0,111	−0,285	0,260	8*i*
0	0,186	0,433	0,0	4*g*
0	0,156	0,444	0,5	4*h*
0	0,0	0,0	0,300	4*e*

des représentations du groupe. Une méthode pour trouver les vecteurs de base est celle de l'opérateur de projection, connaissant les représentations irréductibles du groupe. Lorsque **k** = 0, il suffit d'utiliser les représentations du groupe ponctuel m m m. Le Tableau 4 donne la transformation des spins sur l'action des opérateurs de symétrie. Le Tableau 5 donne les modes compatibles suivant les 8 représentations correspondant à P 222 × $\bar{1}$. Les lettre F G C A correspondent aux arrangements bien connus des spins.

Tableau 4. Transformations des spins par les opérateurs de symétrie.

e	2_1x	2_1y	$2z$	$\bar{1}$	$\bar{1}2_1x$	$\bar{1}2_1y$	$\bar{1}2z$
S_1x	$+S_4x$	$-S_3x$	$-S_2x$	$+S_2x$	$+S_3x$	$-S_4x$	$-S_1x$
S_1y	$-S_1y$	$+S_3y$	$-S_2y$	$+S_2y$	$-S_3y$	$+S_4y$	$-S_1y$
S_1z	$-S_4z$	$-S_3z$	$+S_2z$	$+S_2z$	$-S_3z$	$-S_4z$	$+S_1z$
S_5x	$+S_8x$	$-S_8x$	$-S_5x$	$+S_8x$	$+S_7x$	$-S_7y$	$-S_6x$
S_5y	$-S_8y$	$+S_8y$	$-S_5y$	$+S_6y$	$-S_7y$	$+S_7y$	$-S_8y$
S_5z	$-S_8z$	$-S_8z$	$+S_5z$	$+S_8z$	$-S_7z$	$-S_7z$	$+S_8z$

Tableau 5. Représentations irréductibles du groupe Pbam pour **k** = 000 *et* **k** = 00½

	Site 4g et 4*h*	Site 4*f*	*k* = 000 Groupes de Shubnikov
Γ_1	Cz	Cz	Pbam
Γ_2	Cx Fy	Cx Fy	Pb'am'
Γ_3	Fx Cy	Fx Cy	Pba'm'
Γ_4	Fz	Fz	Pb'a'm
Γ_5	Ax Gy	Gz	Pb'a'm'
Γ_6	Gz	Ax Gy	Pb'am
Γ_7	Az	Gx Ay	Pba'm
Γ_8	Gx Ay	Az	Pbam'

$$F = S_1 + S_2 + S_3 + S_4 \qquad C = S_1 + S_2 - S_3 - S_4$$
$$G = S_1 - S_2 + S_3 - S_4 \qquad A = S_1 - S_2 - S_3 + S_4$$

Il en est de même pour S_5, S_6, S_7, S_8

Configurations magnétiques observées. Lorsque l'énergie est d'ordre deux dans les spins les modes couplés doivent appartenir à une même représentation irreductible.

La seule structure compatible avec les intensités observées correspond à la représentation Γ_8. En effet nous expliquons les intensités magnétiques observées, en admettant l'existence des modes +Gx et −Fy sur les sites 4*g* (Nd^{3+}) et Ay sur le site 4*h* (5% Cr^{3+}) et +Az sur le site 4*f* (95% de Cr). Les moments magnétiques font un angle de 12° avec l'axe des *y* pour le site 4*g*; ils sont suivant *y* pour le site 4*h* et suivant *z* sur le site 4*f*.

La Fig. 4 représente la direction des moments magnétiques sur les différents sites.

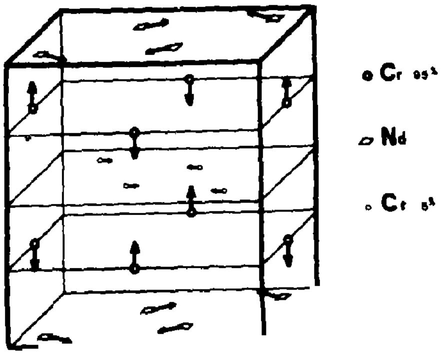

Fig. 4. Structure magnétique de $CrTiNdO_5$

Le Tableau 6 donne la correspondance entre Iobs. et I théorique pour les différentes réflexions.

Nous avons pris les valeurs du facteur de forme *f* de Nd de[4] et pour Cr^{3+} de[5]. Nous devons remarquer que la décroissance des facteurs *f* des références citées ci-dessus n'est pas assez prononcée puisque les intensités théoriques restent systématiquement plus élevées aux grands angles que celles observées.

La précision sur le site à 5% de Cr^{3+} est insuffisante pour pouvoir préciser l'angle des spins avec l'axe des *y*.

2. *FeTiNdO*$_5$

La Fig. 5 représente les diagrammes obtenus par diffraction neutronique ($\lambda = 1,106$ Å) à la température ambiante et à 1,5°K.

Affinement de la structure cristalline. Le problème est identique à celui du produit $CrTiNdO_5$. Nous n'avons que peu de raies de diffraction, un grand nombre de paramètres à affiner, et le pourcentage de Fe^{3+} sur le site 4*h* et 4*f* n'est pas connu. Par affinements successifs, en faisant varier le pourcentage de Fe sur le site 4*h*, nous avons observé une convergence des valeurs pour des pourcentages de Fe compris entre 48 et 40 pour cent.

Les distances interatomiques les plus vraisem-blables correspondent à 43% de Fe^{3+} ou 57% de Ti^{4+} sur le site 4*h*, et 57% de Fe^{3+} ou 43% de Ti^{4+} sur le site 4*f*.

Le Tableau 7 résume le résultat de cet affinement.

Tableau 7. Paramètres cristallins de $FeTiNdO_5$

	X	*Y*	*Z*	Pbam
Nd	0,136	0,184	0,0	4*g*
43% Fe^{3+} 57% Ti^{4+}	0,088	−0,156	0,5	4*h*
57% Fe^{3+} 43% Ti^{4+}	0,0	0,5	0,238	4*f*
O	0,107	−0,296	0,247	8*i*
O	0,206	0,429	0,0	4*g*
O	0,179	0,404	0,5	4*h*
O	0,0	0,0	0,285	4*e*

Tableau 6. Intensités magnétiques observées et calculées pour $CrTiNdO_5$

HKl	I cal.	I obs
001 110	31	28
020	4	0
011	353	355
101	97	99
111	78,6	75
120 200	125,5	130
021 210	13	25
121 201	320	292
211	118	99
002	0	0
220	46,4	37
012	179,6	146
130 102	23	15
221 031 112	220,4	180

R = 10,5%; μNd = 2,89 μB ± 0,15. μCr = 2,95 μB ± 0,15.

Structure magnétique. Le diagramme à 1,5°K s'indexe en doublant la maille cristalline suivant C. Le vecteur de propagation est donc $\vec{k} = (00\tfrac{1}{2})$.

Théorie Macroscopique de Bertaut. Les cations sont numérotés de 1 à 4 dans la position 4*h* et de 5 à 8 dans la position 4*f* comme pour $CrTiNdO_5$.

On emploie la même méthode que précédemment, c'est à dire celle de l'opérateur de projection, mais il faut trouver les représentations irréductibles correspondant au vecteur $k = 00\tfrac{1}{2}$. On emploie alors la méthode d'Olbrychski, qui étudie les relations entre éléments générateurs

$$\begin{aligned} 2_{1x} &= (2_x|\tfrac{1}{2}\tfrac{1}{2}0) & (2_{1x})^2 &= (\epsilon|100) \\ 2_{1y} &= (2_y|\tfrac{1}{2}\tfrac{1}{2}0) & (2_{1y})^2 &= (\epsilon|010) \\ \bar{1} &= (\bar{1}|000) & (\bar{1})^2 &= (\epsilon|000) \end{aligned}$$

$$\begin{aligned} 2_{1x}2_{1y} &= (\epsilon|1\bar{1}0)2_{1y}2_{1x} \\ 2_{1x}\bar{1} &= (\epsilon|110)\bar{1}\ 2_{1x} \\ 2_{1y}\bar{1} &= (\epsilon|110)\bar{1}\ 2_{1y} \end{aligned}$$

ce qui donne les relations suivantes entre

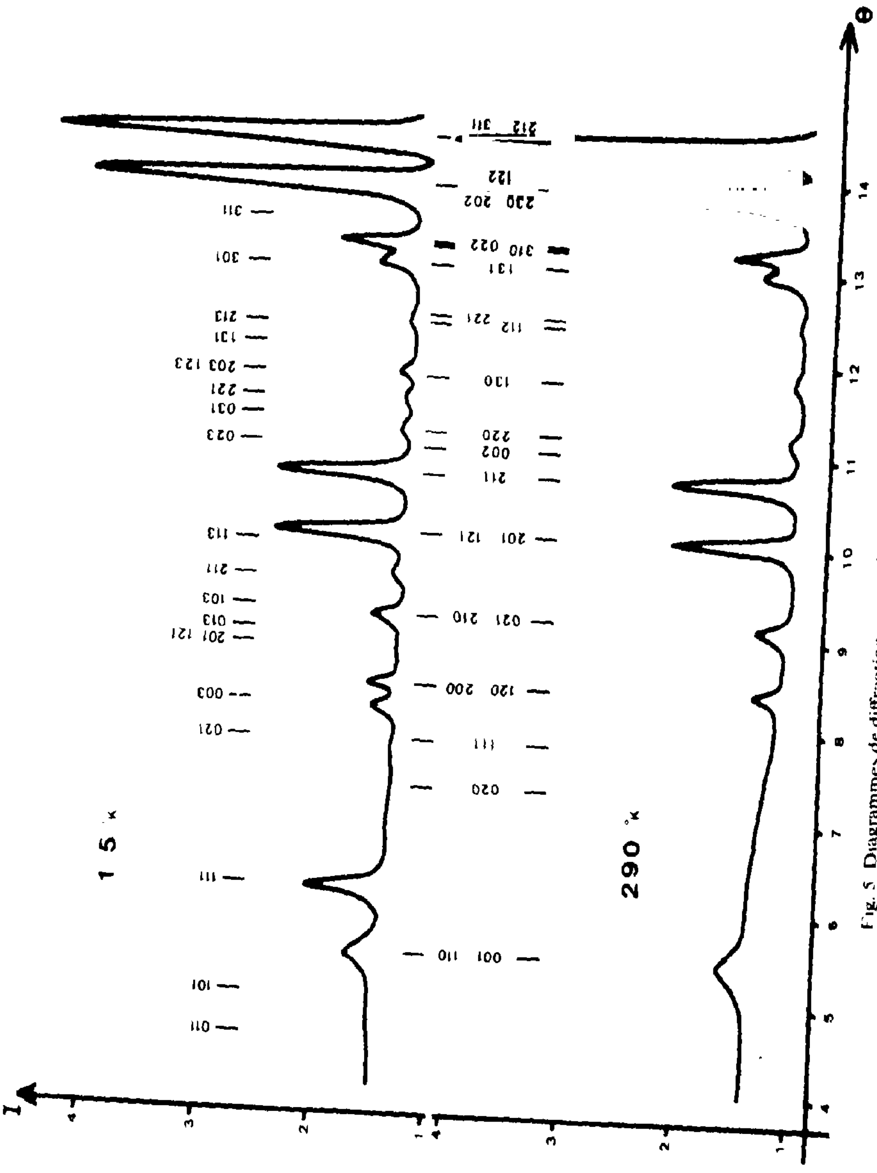

Fig. 5 Diagrammes de diffraction neutronique de $FeTiNdO_5$ ($\lambda = 1.106$ Å).

matrices représentatives pour $h = 00\,0{,}5$

$$(D(2_{1x}))^2 = +1 \quad (D(2_{1y}))^2 = +1$$

$$(D(\bar{1}))^2 = +1$$

$$D(2_{1x})\,D(2_{1y}) = D(2_{1y})\,D(2_{1x})$$

$$D(2_{1x})\,D(\bar{1}) = D(\bar{1})\,D(2_{1x})$$

$$D(2_{1y})\,D(\bar{1}) = D(\bar{1})\,D(2_{1y})$$

Ces matrices commutent, donc les représentations irreductibles sont de dimension 1 et comme il y a 8 éléments dans le groupe ponctuel, il y aura 8 représentations irréductibles. Ceci était prévisible, car il n'y a pas d'élément générateur de translation suivant z. Par la méthode de l'opérateur de projection on obtient ainsi les mêmes modes compatibles que dans le cas de CrTiNdO$_5$ (Tableau 5).

Configurations magnétiques observées. La seule structure compatible avec les intensités observées correspond à la représentation Γ2 (Tableau 5) Le groupe de Shubnikov est P_{2c} b'am'. Nous expliquons les intensités magnétiques observées, en admettant l'existence des modes $-Cx+Fy$ sur le site $4h$ (43% de Fe), et $+Cx-Fy$ sur le site $4f$ (57% Fe). La faiblesse des intensités observées ne nous permet pas de trancher entre ces modes et $-Cx+Fy$ sur $4h$ et $-Cx+Fy$ sur $4f$. Les moments magnétiques sur les 2 sites font un angle de 15° avec l'axe des y.

La Fig. 6 représente la direction des moments sur les différents sites. Le Tableau 8 donne la correspondance entre I obs. et I calculées.

Nous avons pris les valeurs de f pour le fer, de [6].

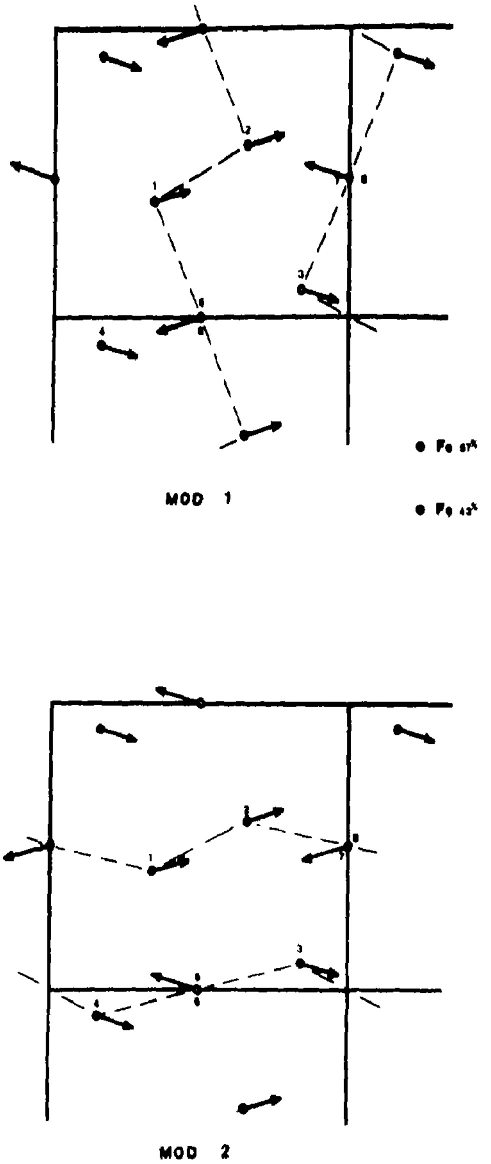

Fig. 6 Projection de la structure magnétique de FeTiNdO$_5$ (la maille double suivant c).

3. *MnTiNdO$_5$*

Pour ce composé l'étude est différente, en effet les b(Mn) et b(Ti) sont négatifs et de valeurs identiques. Il sera donc impossible de les distinguer par affinement sur les intensités nucléaires.

Il reste uniquement la détermination de la structure magnétique. Or le diagramme de Diffraction Neutronique à 1,5°K est identique à celui obtenu à température ambiante. Les Mn^{3+} ne sont pas encore ordonnés magnétiquement.

Tableau 8. *Intensités magnétiques, observées et calculées pour* $FeTiNdO_5$

Hkh	I cal_1	I obs	I cal_2
001	0	0	0
011	0,3	5	5,4
101	2,3		0
111	87	87	87
021	5,6	0	5,6
003	55,6	55,1	55,6
201	5,2	15	5,2
121	7,7		1,7
013	4,6	0	0
103	0	0	5
211	18,5	24	30,6
113	12.1	15	12.1
023	4.9	0	4,9
031	5	0	0
221	18,9	23	18,9
203	41,9	44	41,9
123	6,9		8,3
131	0	0	0
213	24	26	16,5
301	0		0
311	24,9	30	24,9

S(eff) = 0,935 (théorique); R_1 = 15%, R_2 = 18%.

4. DISCUSSIONS

Environment des atomes de transition 3d

La structure possèdant deux sites différents, l'un octaédrique l'autre "pyramide à base carrée" est assez exceptionnelle pour que l'on se demande quels sites vont choisir les différents cations.

Basolo et Pearson (7) donnent les valeurs théoriques des niveaux d'énergie des orbitales *d* dans des champs cristallins de différentes symétries en particulier pour un octaèdre, une pyramide à base carrée et un tétraèdre (Tableau 9).

Ces calculs ont été faits par la méthode du champ cristallin, en assimilant les ligands à des charges ponctuelles et pour des symétries idéales que nous n'observons que très rarement dans les composés.

D'après ce tableau on peut calculer l'énergie de stabilisation due à l'action du champ cristallin sur les électrons 3*d*. Cette énergie dépend de la symétrie et du nombre des électrons 3*d*, donc variera pour les différents cations (Tableau 10).

Ti^{4+} ne possède aucun électron 3*d* et l'énergie de stabilisation sera donc nulle pour n'importe quelle symétrie. Seules interviennent alors les hybridations d'orbitales *s*, *p*, *d*, la covalence et la taille des rayons ioniques. Donc. théoriquement, Ti^{4+} peut aller sur n'importe quel des deux sites. L'expérience montre qu'il va dans un octaèdre (structure pérovskite) mais aussi sur des sites bipyramides à base triangulaire (8) comme l'énergie de stabilisation est sensiblement la même pour une bipyramide et une pyramide à base carrée nous pouvons donc penser une dans les composés $ATiTO_5$, la position du Ti^{4+} sur les 2 sites est indifférente, et il pourra donc aussi bien se trouver dans la site octaédrique que dans le site pyramide à base carrée. C'est ce que nous observons dans nos différents composés.

Si nous considérons maintenant Cr^{3+}, nous pouvons observer de la même façon qu'il est peu probable de le trouver dans un

Tableau 9. *Niveaux d'énergie des orbitales* d *dans des champs cristallins de différentes symétries (d'après Basolo et Pearson)*

	dx^2-y^2	dy^2	dxy	dxz	dyz
Pyramide à base carrée	9,14 *dq*	0,86 *dq*	−0,86 *dq*	−4,57 *dq*	−4,57 *dq*
Octaèdre	6 *dq*	6 *dq*	−4 *dq*	−4 *dq*	−4 *dq*
Tétraèdre	−2, 67 *dq*	−2,67 *dq*	1,78 *dq*	1.78 *dq*	1,78 *dq*

Tableau 10. *Energie de stabilisation du champ cristallin pour différents cations*

	Cr^{3+}	Mn^{3+}	Fe^{3+}	Ti^{4+}
Octaèdre	− 12 *dq*	− 6 *dq*	0	0
Tétraèdre	− 3,56 *dq*	− 1,78 *dq*	0	0
Pyramide à base carrée	− 10 *dq*	− 9,14 *dq*	0	0

tétraèdre, puisqu'il perd 8,44Dq par rapport à l'octaèdre, de même dans notre cas, Cr^{3+} aura tendance à rester sur le site octaédrique plutôt que sur le site "pyramide à base carrée", puisqu'il perd alors 2Dq d'énergie. C'est ce que nous observons, mais alors que l'on ne connait pas de Cr^{3+} sur un site tétraèdrique, nous en observons 5 pour cent sur le site "pyramide à base carrée", ce qui peut s'expliquer par la faible différence de stabilisation.

En ce qui concerne Fe^{3+}, les énergies de stabilisation sont identiques pour tous les sites, et nous pouvons en tirer les mêmes conclusions que pour Ti^{4+}. C'est ce que nous observons puisqu'il y a pratiquement équipartition du Fe^{3+} sur les 2 sites. Il faut cependant remarquer une légère préférence du Fe^{3+} pour le site octaédrique (57%), qui ne peut pas s'expliquer par une différence de rayon ionique, ceux du Fe^{3+} et Ti^{4+} étant sensiblement identiques ou bien Fe^{3+} préferait donc l'environnement octaèdrique, ou bien Ti^{4+} le site "pyramide à base carrée".

Quant à Mn^{3+}, théoriquement il préferera nettement le site pyramide à base carrée (gain de 3,14 Dq par rapport à l'octaèdre). Nous n'avons pu le vérifier sur les composés avec Ti, mais nous avons observé que sur le composé isomorphe $BiMn_2O_5$, les ions Mn^{3+} vont sur ce site. D'autre part le fait que le composé $MnTiNdO_5$ ne soit pas ordonné à 1,5°K peut être dû à l'isolement des Mn^{3+} dans la structure, puisqu'ils ne sont situés que sur le site 4*h* (pyramide à base carrée): la liaison magnétique entre les plans des Mn distants de $c = 5,81$ devient alors très faible, le site 4*f* étant occupé par Ti^{4+} diamagnétique.

Interactions magnétiques

La première remarque concerne l'angle que font les spins avec l'axe des *y*: 12° pour le spin de Nd dans $CrNdTiO_5$ et 15° pour celui de Fe dans $FeNdTiO_5$. Si l'on ajoute que nous avions trouvé un angle de 13° entre la direction des spins avec l'axe des *X* dans $BiMn_2O_5$, on se rend compte que la direction d'anisotropie diffère de 90°. Elle correspond à la symétrie des sites: en effet dans $BiMn_2O_5$ les moments magnétiques sont dirigés à peu près dans la direction de l'axe de la pyramide à base carrée, pour le composé avec le fer ils sont parallèles au plan de base de la pyramide, et pour Nd dans $NdCrTiO_5$ où l'environnement est constitué de 8 oxygènes voisins de la terre rare, la direction des moments magnétiques reste parallèle au plan de symétrie de la terre rare et à la base carée de la pyramide.

La deuxième remarque se rapporte aux interactions Cr-Nd Deux Cr en $z = 0,25$ et $-0,25$ sont couplés entre eux par de fortes interactions négatives à 90°. Ces deux atomes de Cr sont de part et d'autre d'un plan d'atome de Nd ($z = 0$) et les interactions par pont d'oxygène sont identiques, ils devraient donc se coupler de la même façon par rapport à Nd dans le cas d'interactions isotropes; or leurs moments étant opposés nous devons en conclure que les interactions Cr-Nd doivent être anisotropes et antisymétriques.

La troisième remarque est relative aux interactions Fe-Fe entre les atomes des sites 4*h* et 4*f*. Les deux atomes de fer du site 4*f* (57% de Fe) qui sont situés symétriquement par rapport au Fe du site 4*h* ($z = 0,5$), dont les interactions d'échange s'effectuent par le même oxygène avec un angle voisin de 120°, ont leurs moments magnétiques de même sens et opposés à ceux de ce deuxième site. L'échange est donc isotrope et s'effectue suivant les lignes parallèles de la Fig. 6.

La quatrième remarque est, que deux

atomes de Fe^{3+} du site $4h$, situé en XY et $\bar{X}\bar{Y}$ sont couplés ferromagnétiquement comme dans Fe_2CaO_4 et $UFeO_4$ (9) et (10) à l'opposé de ceux de Cr^{3+} et de Mn^{3+} dans $CrTiNdO_5$ et Mn_2BiO_5.

Il faut remarquer que cette interaction se fait par pont d'oxygène légèrement supérieur à 90° ($Fe_{(7)}O_{(7)}Fe_{(7)} = 1000° 18'$) et pour des distances entre atomes de fer de 3,04 Å. On retrouve cette distance 3,06 Å entre deux atomes de fer sur le site $4f$ couplés parallèlement, alors qu'elle est de 2,78 Å entre les 2 atomes couples antiparallèlement ($Fe_{(3)}O_{(5)}Fe_{(3)} = 78°22'$) oú cette courte distance suggère un échange direct comme dans (9) et (10).

Remerciements—Nous remercions Monsieur le Professeur Bertaut pour l'attention qu'il a apporteé à ce travail, nous remercions mademoisselle Martin pour son aide pour la préparation chimique des drivers composés

REFERENCES

1. QUEZEL-AMBRUNAZ S., BERTAUT E. F. et BUISSON G., *C.r. hebd. Seanc Acad. Sci., Paris* **258**, 3025 (1964)
2. BERTAUT E. F., BUISSON G., DURIF A., MARESCHAL J., MONTMORY M. C. QUEZEL-AMBRUNAZ S., *Bull Soc. Chim. France* 1132 (1965).
3. BERTAUT E. F., BUISSON G., QUEZEL-AMBRUNAZ S. et QUEZEL G., *Solid State Commun.* **5**, 25, (1967).
4. KOEHLER W. C. et WOLLAN E. O., *Phys. Rev.* **92**, 1380 (1953).
5. TAKEI W. J., COX D. E et SHIRANE G., *Phys. Rev.* **129**, 2008, (1963).
6. BROCKHOUSE *et al*. *Phys. Rev.* **98**, 1721, (1955).
7. BASOLO F. et PEARSON R. G., *Mechanism of Inorganic Reaction*, p. 55. Wiley, New York (1958).
8. GUILLEN M. et BERTAUT F F., *Cr hebd. Seanc Acad. Sci., Paris* 262, 962 (1966).
9. BERTAUT E. F., CHAPPERT J., APOSTOLOV A. et SEMENOV V., *Bull. Sté Franc. Min. et Crist.*, **89**, 206, (1966).
10. BACMANN M., BERTAUT E. F. et BLAISE A., *Cr. hebd, Seanc Acad. Sci., Paris* **266**, 45 (1968).

J. Phys. Chem. Solids Pergamon Press 1970. Vol. 31, pp. 1185–1188. Printed in Great Britain.

TECHNICAL NOTES

Recombination luminescence in NaCl*

(Received 6 October 1969; in revised form 25 November 1969)

A LOW-temperature luminescence arising from the recombination of an electron with a V_k center (self-trapped hole) has been identified previously in various alkali halides [1–3]. Experimental proof that a particular emission band arises from the decay of a (V_k+e^-) state can be achieved by orienting the V_k centers along one of the ⟨110⟩ directions, and then observing a linear polarization in the emitted light when electrons are released in the crystal and recombine with V_k centers. Previous work on NaCl[1] revealed two prominent emission bands at low temperature, with peaks at 3·36 and 5·38 eV. These bands were attributed to (V_k+e^-) recombination luminescence, although a positive identification by the polarization properties was not given. In this work we have investigated further these emission bands in NaCl. We conclude that the high-energy band is definitely due to (V_k+e^-) recombination and is σ polarized; the low-energy band is only weakly polarized (if at all) but does arise from (V_k+e^-) recombination.

V_k centers were produced in crystals of NaCl(Tl), NaCl(Ag) and NaCl(Pb) by X-irradiation at either liquid nitrogen temperature (LNT) or liquid helium temperature (LHeT). V_k centers were identified in NaCl (Tl) and NaCl(Pb) by observation of the electron spin resonance spectrum at LNT, using a Varian V4502-06 X-band spectrometer. ESR measurements were made with the magnetic field parallel to both ⟨100⟩ and ⟨110⟩ directions. The ESR spectrum in NaCl(Pb) showed strong absorption due to V_k centers, and the observed spectrum was in agreement with earlier work of Castner and Känzig[4]. The Pb concentration in this crystal was nominally 10^{-1} mole per cent; the crystal was annealed at 400°C for a few minutes and then quenched to room temperature before X-irradiation. X-irradiation of two different crystals of NaCl(Tl), with Tl concentrations of about 10^{-2} and 10^{-1} mole percent respectively, resulted in only a small concentration of V_k centers relative to the crystal of NaCl(Pb). The V_k concentration in NaCl(Pb) was a factor of 10 larger than in the 10^{-1} mole per cent NaCl(Tl), and a factor of 40 larger than in the 10^{-2} mole per cent NaCl(Tl). ESR experiments were not performed in NaCl(Ag).

V_k centers were identified in NaCl(Ag) and NaCl(Pb) by measurement of the anisotropic absorption spectrum[5] of the u.v. band with a Cary model 14R spectrophotometer and a Glan–Thompson polarizer. At LNT we find this anisotropic absorption band to have a peak energy of 3·28 eV and a full width at half maximum of 1·10 eV. This peak energy is in reasonably good agreement with previous measurements quoted by Gucker[6], but disagrees with the value reported by Schmidt [7]. X-irradiation of the two different crystals of NaCl(Tl) at either LNT or LHeT produces an absorption band (or bands) whose peak occurs at 3·5 eV, but which does not become measurably dichroic after exposure to linearly polarized light. As indicated above, ESR experiments showed that a relatively small concentration of V_k centers is produced in these crystals. We attribute the u.v. absorption band in irradiated NaCl(Tl) to absorption by both Tl^0, and Tl^{2+} centers, by

---

* Work supported by the U.S. Atomic Energy Commission under Contract No. AT(30-1)-3842.

analogy with the known absorption bands of these centers in KCl[8]. Optical experiments on the ($V_k + e^-$) recombination process were not performed in NaCl(Tl) for the above reasons.

In an experiment to determine the thermal stability of V_k centers, an irradiated crystal of NaCl(Ag) (nominal 0·1 mole per cent Ag) was warmed at a rate of 3°K/min above LNT. The maximum rate of change of the V_k absorption band occurred at a temperature of about 151°K. In other experiments a prominent thermoluminescence glow peak was observed in NaCl(Tl) and NaCl(Ag) at 151 and 147°K respectively. As these three experiments were not performed at exactly the same warming rate, we believe that the above temperatures correspond to the same phenomenon, viz. the diffusion of V_k centers and their annihilation at electron-excess sites.

The two emission bands of interest in this work reach their maximum intensity in the range below 40°K. The temperature dependence of the intensity of the 3·36 and 5·38-eV bands is shown in Fig. 1. These data were obtained during X-ray excitation of nominally pure NaCl. The ordinate represents the relative number of quanta in the two bands; the low-energy band is approximately 10 times more intense than the high-energy band. The intensity of both bands continues to fall above 80°K.

As a consequence of the temperature dependence of Fig. 1, experiments on the identification of these bands were performed at LHeT; the actual temperature of the crystal was typically ≃ 7°K. Identification of the 5·38-eV band as a ($V_k + e^-$) emission band was achieved by polarization experiments, as described previously[2, 3], in NaCl(Ag) and NaCl(Pb). A distinct σ-polarization was observed in both crystals, and the results of an experiment in NaCl(Pb) are shown in Fig. 2. In this experiment, a crystal of NaCl (Pb) was X-rayed at LNT, producing V_k-centers and F-centers, and then cooled to LHeT. Illumination in the F-band stimulated luminescence emission with the characteristic peaks at 3·36 and 5·38 eV. The V_k centers were then oriented along the [0$\bar{1}$1] direction of the crystal by well known methods[5]. To investigate a possible polarization of the 5·38-eV luminescence as a consequence of this orientation, a Polacoat PL-40 analyzer [9] was inserted between the crystal and monochromator-detector system. The crystal was then illuminated with F light along the [010] direction, and the luminescence emitted in the [100] direction passed through the

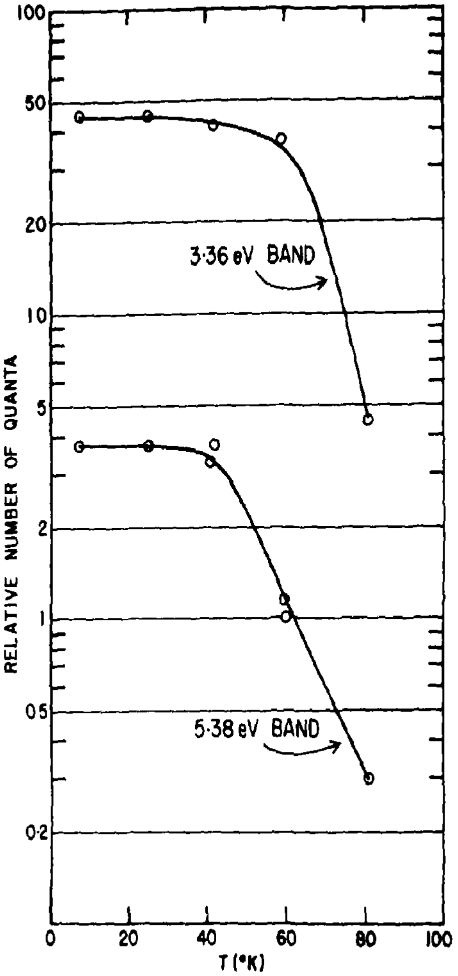

Fig. 1. Temperature dependence of intensity of (V_k + e^-) emission bands in NaCl. Data were obtained during X-ray irradiation of nominally pure NaCl. The ordinate represents the relative number of quanta in the two bands.

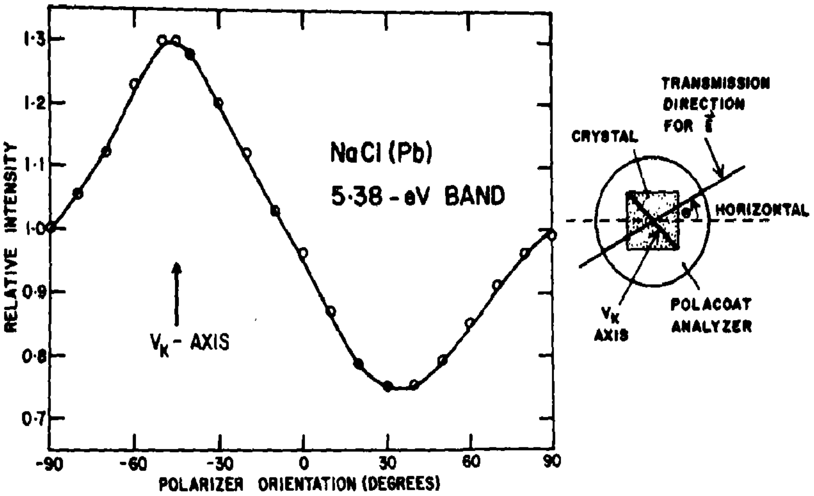

Fig. 2. Relative intensity of light (5·38-eV band) transmitted through a Polacoat PL-40 analyzer, as a function of angle of rotation of the analyzer. The angle θ is measured from the horizontal to the easy axis of the analyzer. The [011] direction of the crystal is at 45° and the $[0\bar{1}1]$ direction is along $-45°$. V_k centers were previously oriented into the $[0\bar{1}1]$ direction. The experiment was performed in NaCl(Pb) at a temperature ≃ 7°K. Emission was excited by optical excitation in the F-band.

analyzer to the monochromator-detector. The geometrical arrangement is shown in Fig. 2, where the [100] direction is perpendicular to the paper. In Fig. 2 we plot the intensity of the 5·38-eV band as the analyzer is rotated relative to the crystal, and a peak is observed when the easy axis of the analyzer (transmission direction for E) is parallel to the axis of oriented V_k centers. The polarizer orientation relative to the crystallographic axes of the crystal, as given in Fig. 2, was determined by a visual alignment of the analyzer with the vertical axis of the cryostat, hence with the [001] direction of the crystal. Angular measurements are therefore subject to a systematic error of several degrees. The significant result of Fig. 2 is the fact that a polarization in the luminescence is clearly established by orientation of the V_k centers, and that the electric vector of the emitted radiation is along the V_k axis. The 5·38-eV band is therefore σ polarized.

It was not possible to identify positively the low-energy emission band (3·36 eV) in the same way, as this band overlaps almost perfectly the dichroic V_k absorption band at 3·28 eV; therefore, an unpolarized emission would appear to be Π polarized due to self-absorption in the crystal. In an experiment on NaCl(Ag), we observed a Π-polarized emission in the 3·36-eV band with a polarization amounting to $-6 \pm 1·5$ per cent. (Polarization is here defined as $(I_\parallel - I_\perp)/(I_\parallel + I_\perp)$, where $I_\parallel$ and $I_\perp$ represent the light intensities observed with the polarizer transmission axis parallel and perpendicular to the axis of aligned V_k centers.) The contribution of dichroic self-absorption to this polarization is estimated from other data as $-3 \pm 1·5$ per cent. The observed polarization in emission is thus small, and within the limits of error it may be zero. We cannot, therefore, make a definitive statement regarding the polarization of the low-energy band.

Additional evidence concerning the origin of the low-energy emission band was obtained in another experiment. A crystal of NaCl(Ag) that was X-rayed at LNT was cooled to LHeT; optical excitation of electrons (from Ag^0) produced both the 3·36 and 5·38-eV emission bands, and in addition a narrower emission band at 5·15 eV. We attribute the latter band to radiative decay of Ag^+ excited states (formed by $Ag^{2+} + e^-$). An Ag^+ luminescence at 4·96 eV at room temperature has been identified previously[10, 11]. The crystal was then warmed to 166°K, resulting in the annihilation of V_k-centers; upon cooling again to LHeT, optical excitation of electrons produced neither the 3·36 nor the 5·38-eV emission band. The narrow Ag^+ emission at 5·15 eV was still prominent, however, indicating that electrons were in fact still released by optical excitation. We conclude that both the 3·36 and 5·38-eV emission bands arise from the same center, and that they result from the radiative decay of $(V_k + e^-)$ states.

The results of this work therefore support previous tentative assignments of the origin of these two bands[1, 12]. Although a definite polarization was not measured for the low-energy band in this work, it seems reasonable to interpret it as a transition from a triplet state by virtue of its relatively long lifetime[12].

Acknowledgements – We wish to thank Janet Seiner for her participation in the experiments, and R. D. Ewing for use of the ESR spectrometer

Department of Physics R. B. MURRAY
University of Delaware, H. B. DIETRICH
Newark, Delaware 19711, *U.S.A.* F. J. KELLER

REFERENCES

1. KABLER M. N., *Phys. Rev.* **136**, A1296 (1964)
2. MURRAY R. B. and KELLER F. J., *Phys. Rev.* **137**, A942 (1965)
3. MURRAY R. B. and KELLER F. J., *Phys. Rev.* **153**, 993 (1967).
4. CASTNER T. G. and KANZIG W., *J. Phys. Chem. Solids* **3**, 178 (1957)
5. DELBECQ C. J., HAYES W. and YUSTER P. H., *Phys. Rev.* **121**, 1043 (1961)
6. GUCKER E. F., *Helv. Phys. Acta* **41**, 493 (1968).
7. SCHMIDT H. J., *Z. Phys.* **166**, 447 (1962).
8. DELBECQ C. J., GHOSH A. K. and YUSTER P. H., *Phys. Rev.* **151**, 599 (1966)
9. This analyzer transmits about 50 per cent of the light in the 5.38-eV region. Available from Polacoat Inc., Blue Ash, Ohio
10. ETZEL H. W. and SCHULMAN J. H., *J. Chem. Phys.* **22**, 1549 (1954)
11. ONAKA R. and YANO S., *J. phys. Soc. Japan* **20**, 1740 (1965)
12. KABLER M. N. and PATTERSON D. A., *Phys. Rev. Lett.* **19**, 652 (1967).

---

*Permanent address: Clemson University, Clemson, South Carolina. 29631, U.S.A.

J. Phys. Chem. Solids Vol. 31, pp. 1188–1190.

Mode Grüneisen parameters for single crystal Al_2O_3

(*Received 18 April* 1969, *in revised form 28 October* 1969)

SINGLE crystal Al_2O_3, (sapphire of corundum), crystallizes in the trigonal lattice, point group 3m[1]. Its thermodynamic properties have been extensively investigated over the last years[2–11]. As the pressure derivatives of its elastic moduli have recently become available[12], it is of interest to compute the mode Grüneisen parameters[13–14] for the above material, and correlate their values with its other known thermodynamic data.

A scheme for calculating the scalar mode Grüneisen parameters $\gamma(p, \mathbf{q})$, from the pressure derivatives of the elastic moduli for cubic, tetragonal, hexagonal and orthorhombic crystals has recently been described[15]. Here, $\gamma(p, \mathbf{q})$ is defined as:

$$\gamma(p, \mathbf{q}) = -[\partial \ln \omega(p, \mathbf{q})/\partial \ln V]_T \qquad (1)$$

where $\omega(p, \mathbf{q})$ is the angular frequency of a normal vibrational mode with wave vector $\mathbf{q}$ and polarization index p $(p = 1, 2, 3)$, V the volume and T and temperature. The calculation is done in the framework of the anisotropic continuum model, neglecting dispersion and the contribution of the optical modes. The above computation may be easily extended to trigonal crystals, the relation between $\gamma(p, \mathbf{q})$ and the pressure derivatives of the elastic moduli being given by

$$\begin{aligned}\gamma(p, \mathbf{q}) = -\tfrac{1}{2} &+ (N_1{}^2K_1{}^T + N_2{}^2K_2{}^T \\ &+ N_3{}^2K_3{}^T)/K_V{}^T \\ &+ [\partial \ln c(p, \mathbf{q})/\partial P]_T/(2K_V{}^T). \qquad (2)\end{aligned}$$

Here, $c(p, \mathbf{q})$ is the effective elastic modulus for the propagation mode $p, \mathbf{q}$, (ie. ρv^2, where ρ is the density, v the sound velocity). N_1, N_2 and N_3 the direction cosines of q, K_1^T, K_2^T and K_3^T the linear isothermal compressibilities parallel to the X, Y and Z axis respectively, K_V^T the volume isothermal compressibility and P the hydrostatic pressure.

A computer program to evaluate $\gamma(p, \mathbf{q})$ has been written. The program calculates $c(p, \mathbf{q})$ and $\partial c(p, \mathbf{q})/\partial P$ over a grid of 125 points in the range bounded by the spherical triangle defined by the range of colatitudes θ 0–180°, and azimuths ϕ 0–120°. At each point the three corresponding values of $c(p, \mathbf{q})$ and $\partial c/\partial P$ are evaluated, and hence, the three quantities $\gamma(p, \mathbf{q})$ are determined. The results of the calculation for some directions of high symmetry are shown in Figs. 1 and 2, where 1 refers to the longitudinal mode, 2 and 3 to the fast and slow shear modes respectively. As can be seen from the slight dependence of the values of $\gamma(p, \mathbf{q})$ on the azimuth angle in Fig. 1, and from their near symmetry with respect to the [010] axis in Fig. 2, single crystal Al_2O_3 behaves nearly as if its structure is hexagonal. This is really not surprising, as the stiffness modulus c_{14} is relatively small, and the rhombohedral angle is very close to the value for the hcp structure (55°20′ vs. 53°47″).

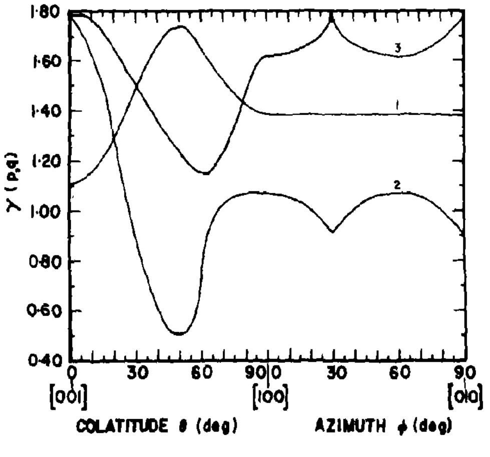

Fig. 1. Values of the mode Grüneisen parameters in the XZ and XY planes.

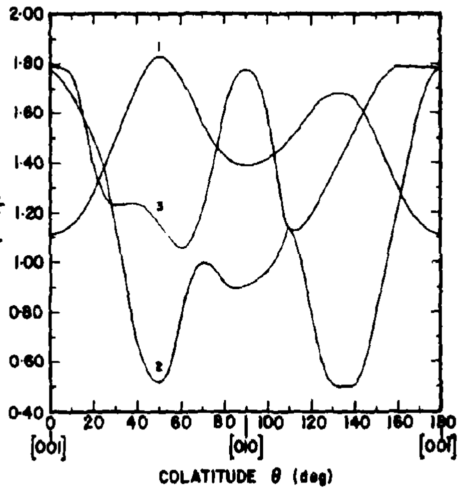

Fig. 2. Values of the mode Gruneisen parameters in the YZ plane.

From the values of $\gamma(p, \mathbf{q})$, the low and high temperature limit of their thermal average, γ_L and γ_H may be computed[16]. The latter values, together with the corresponding quantities derived from thermal expansion data[8, 9], are shown in Table 1. It is interesting to note the good agreement between the thermal expansion and elastic values for

Table 1. Values of γ_L and γ_H as derived from elastic and thermal expansion data

	γ_l	γ_H
Elastic	1·24	1·28
Thermal expansion	1·30 (100°K)*	1·32 (1470°K)*

*Ref.[9].

both γ_L and γ_H. The usual case for ionic crystals[15-17] is that the thermal expansion and elastic values of γ_L agree, while there is a discrepancy between the two values for γ_H. The reason for this is that the assumptions on which the calculation of the elastic γ_L and γ_H is based are well fulfilled at low temperatures, while at high temperatures, there is a considerable contribution due to the excitation of optical phonons. The fact that for Al_2O_3 there is a good agreement between the thermal expansion and elastic values of γ_H might indicate that even at a temperature of 1470°K optical phonons do not contribute appreciably to the thermal expansion.

Aerospace Research Laboratories, Wright-Patterson Air Force Base, Ohio 45433, U.S.A.
D. GERLICH*†

REFERENCES

1. PALACHE C., BERMAN H. and FRONDEL C., in *Dana's System of Mineralogy* Wiley, New York (1944).
2. WACHTMAN J. B Jr., TEFFT W. F. LAM D. J. and STINCHFIELD R. P., *J. Res. natn Bur. Stand.* **64A**, 213 (1960)
3. MAYER W. G. and HIEDEMAN E. A., *Acta crystallogr.* **14**, 323 (1961).
4. ALEXANDROV K. S. and RYZHOVA T. V., *Soviet Phys. Crystallogr.* **6**, 228 (1961)
5. BERSTEIN B. T., *J. appl. Phys.* **34**, 169 (1963).
6. TEFFT W. E., *J. Res. natn. Bur. Stand.* **70A**, 277 (1966).
7. RAMAMURTHY I., *J. Phys. Chem. Solids* **28**, 363 (1967)
8. WACHTMAN J. B. Jr., SCUDERI T. G. and CLEEK G. W., *J. Am. ceram. Soc.* **45**, 319 (1962).
9. SCHAUER A., *Can. J. Phys.* **43**, 523 (1965).
10. FURUKAWA G. T., DOUGLAS T. B., McCOSKEY R. E. and GINNINGS D. C., *J. Res. natn. Bur. Stand.* **57**, 67 (1956).
11. FUGATE R. Q. and SWENSON C. A., *J. appl. Phys.* **40**, 3034 (1969).
12. GIESKE J. H. and BARSCH G. R., *Phys. Status Solidi* **29**, 121 (1968).
13. BRUGGER K., *Phys. Rev.* **137**, A1826 (1965).
14. BRUGGER K. and FRITZ T. C., *Phys. Rev.* **157**, 524 (1967).
15. GERLICH D., *J. Phys. Chem. Solids* **30**, 1638 (1969).
16. SCHUELE D. E. and SMITH C. S., *J. Phys. Chem. Solids* **25**, 801 (1964).
17. GERLICH D., *Phys. Rev.* **168**, 947 (1968).

---

*Holder of a National Research Council Senior Resident Research Associateship supported by the Aerospace Research Laboratories, USAF.

†On sabbatical leave from Department of Physics and Astronomy, Tel Aviv University, Ramat Aviv, Israel.

J. Phys. Chem. Solids Vol. 31, pp. 1190–1192.

Electron mobility in nonstoichiometric cerium dioxide at high temperatures*

(*Received* 6 *October* 1969)

NONSTOICHIOMETRIC cerium dioxide, $Ce_{1+y}O_2$, may be classified as a metal excess, *n*-type semiconductor on the basis of experimental observations[1-4]. This metal excess may arise from the presence of a defect structure involving either anion vacancies or cation interstitials. Recent investigations[5, 6] have favored a defect model consisting of electrons localized at cerium ions at normal lattice sites and cerium interstitials in one or more states of ionization.

The electrical conductivity study[6] is consistent with the assumption that the electrons are localized. Hence the electronic conduction mechanism may be regarded as a 'hopping type' process. An experimental activation energy for motion 0·18 eV was calculated from this data in the temperature and oxygen pressure region where quadruply ionized cerium interstitials predominate.

The electron mobility in nonstoichiometric cerium dioxide, $Ce_{1+y}O_2$, may also be calculated by combining electrical conductivity and thermogravimetric data for the temperature and oxygen region where the defect predominates in one state of ionization. The objective of this note is to report the results of such calculations to establish (1) the magnitude of the electron mobility at elevated temperatures and (2) the temperature dependence of the

---

*This work was supported by the U.S. Atomic Energy Commission. This is AEC Report COO-1441-8.

mobility in order to test the previously proposed 'hopping type' conduction model[6].

The concentration of charge carriers, n, was obtained from the thermodynamic data[7] at 100°C intervals between 800–1200°C in the oxygen pressure region where quadruply ionized cerium interstitials are assumed to predominate[6]. The electronic mobility, μ, was then calculated from the relation

$$\sigma = ne\mu$$

by using the values of σ and n corresponding to the same temperature and oxygen partial pressure. The results of these calculations for two sintered conductivity specimens[6] of 70 and 85 per cent theoretical density respectively and one arc cast large grain polycrystalline specimen[7] of approximately 100 per cent theoretical density are shown in Table 1. Where possible the mobility was calculated for at least two different values of P_{O_2} at each temperature. In general the agreement between these values of μ at each temperature is consistent with the assumption that a single state of ionization for the defect predominates. The temperature dependence of the mobility is illustrated in Fig. 1 where the log of the average value of μ is plotted as a function of the reciprocal temperature. It can be seen that the order of magnitude of the mobility is 10^{-2} cm²/v-sec and the mobility increases exponentially with increasing temperature. The activation energies shown in Fig. 1 were calculated from the slopes of the least squares lines using the data in Table 1. It should be noted that although the absolute value of μ varies slightly with the density of the sintered conductivity specimens, the activation energies appear to be independent of the density within experimental error in the range of densities investigated. In addition, the absolute values of μ for both the 85 per cent dense specimen and the arc melted specimen are extremely close, indicating the μ values are probably close to that of the single crystal and the grain boundaries are not contributing appreciably to the scattering.

The above calculation of the mobility

Table 1. Electron mobility in $Ce_{1+y}O_2$ for various temperatures and oxygen partial pressures

Temp (°C)	P_{O_2} (atm)	Electron mobility (cm²/V-sec) 70%*	 85%*	 Arc cast†
800	$1{\cdot}00 \times 10^{-15}$	$5{\cdot}63 \times 10^{-3}$	$7{\cdot}54 \times 10^{-3}$	
	$1{\cdot}00 \times 10^{-16}$	$5{\cdot}90 \times 10^{-3}$	$7{\cdot}55 \times 10^{-3}$	
	$5{\cdot}54 \times 10^{-16}$			$7{\cdot}28 \times 10^{-3}$
900	$1{\cdot}00 \times 10^{-12}$	$6{\cdot}16 \times 10^{-3}$	$8{\cdot}52 \times 10^{-3}$	
	$1{\cdot}00 \times 10^{-13}$	$6{\cdot}06 \times 10^{-3}$	$8{\cdot}28 \times 10^{-3}$	
	$1{\cdot}00 \times 10^{-14}$	$6{\cdot}09 \times 10^{-3}$	$8{\cdot}04 \times 10^{-3}$	
	$1{\cdot}24 \times 10^{-13}$			$8{\cdot}11 \times 10^{-3}$
1000	$1{\cdot}00 \times 10^{-10}$	$6{\cdot}32 \times 10^{-3}$	$8{\cdot}85 \times 10^{-3}$	
	$1{\cdot}00 \times 10^{-11}$	$6{\cdot}41 \times 10^{-3}$	$9{\cdot}03 \times 10^{-3}$	
	$1{\cdot}16 \times 10^{-11}$			$9{\cdot}19 \times 10^{-3}$
1100	$1{\cdot}00 \times 10^{-9}$	$8{\cdot}71 \times 10^{-3}$	$1{\cdot}11 \times 10^{-2}$	
	$1{\cdot}00 \times 10^{-10}$	$7{\cdot}90 \times 10^{-3}$	$1{\cdot}04 \times 10^{-2}$	
	$5{\cdot}60 \times 10^{-10}$			$1{\cdot}07 \times 10^{-2}$
1200	$1{\cdot}00 \times 10^{-7}$	$8{\cdot}68 \times 10^{-3}$	$1{\cdot}09 \times 10^{-2}$	
	$1{\cdot}00 \times 10^{-8}$	$8{\cdot}03 \times 10^{-3}$	$1{\cdot}04 \times 10^{-2}$	
	$1{\cdot}37 \times 10^{-8}$			$1{\cdot}18 \times 10^{-2}$
	$1{\cdot}21 \times 10^{-7}$			$1{\cdot}01 \times 10^{-2}$
	$1{\cdot}58 \times 10^{-8}$			$1{\cdot}16 \times 10^{-2}$

*Percent theoretical density (sintered specimen).
†Arc cast ceria.

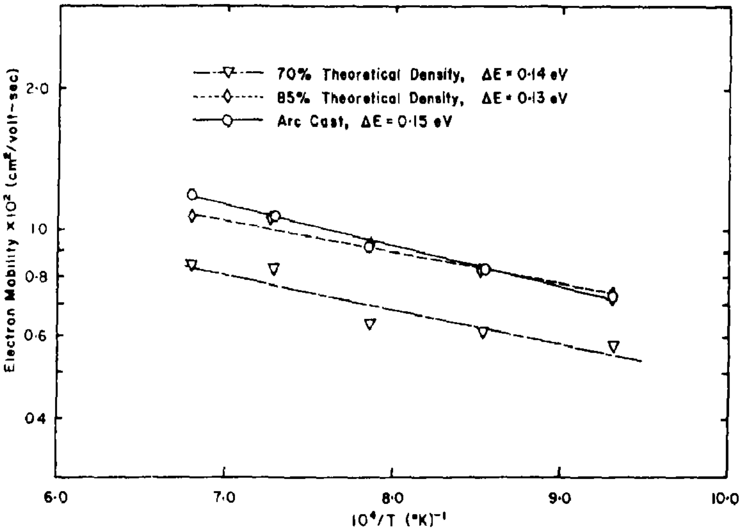

Fig. 1

requires knowledge of the defect structure. The actual results of this calculation, however, vary little with the precise nature of the defect since the number of carriers is approximately the same for different defect structures. Hence if the defect structure used in this calculation is not entirely correct, the magnitude of the mobility will not be drastically affected[8]. Also the temperature dependence of the mobility is entirely independent of the assumed defect structure provided the assumption of a single state of ionization predominating is valid. Hence the experimental activation energy can be obtained directly from the data alone.

In addition, it is reasonable to suspect that a compositional dependence of the mobility may exist as the departures from stoichiometry become large. This would be due to the reduction in normal sites available for 'hopping'[6]. To check this supposition and to verify the observed temperature dependence of the mobility, high temperature Hall mobility measurements are currently in progress in this laboratory.

Acknowledgements—The authors wish to thank Dr. Walter Class of the Materials Research Corporation for providing the arc cast ceria and Mr. Frank Brugner for his help with the electrical conductivity measurements on the arc cast ceria specimen

R. N. BLUMENTHAL
R. J. PANLENER

Metallurgy and Materials Science,
College of Engineering,
Marquette University,
Milwaukee,
Wisc. 53233, U.S.A.

REFERENCES

1. BRAUER G., GINGERICH K. A. and HOLTZSCHMIDT U., *J. inorg. nucl. Chem.* **16**, 77 (1960)
2. BEVAN D. J. M. and KORDIS J., *J. inorg. nucl. Chem.* **26**, 1509 (1964)
3. GREENER E. H., WIMMER J. M. and HIRTHE W. M., *Rare Earth Research II*, (Edited by Karl S. Vorres), p. 534. Gordon and Breach, New York (1964)
4. BLUMENTHAL R. N. and LAUBACH J. E., *Anisotropy in Single Crystal Refractory Compounds*, Vol. 2, p. 137. Plenum Press, New York (1968).
5. KOFSTAD P. and HED A. Z., *J. Am. ceram. Soc.* **50**, 681 (1967).
6. BLUMENTHAL R. N., LEE P. W. and PANLENER R. J. to be published in *J. electrochem. Soc.*
7. BLUMENTHAL R. N., *Atomic Energy Rep No.* COO-1441-10
8. BLUMENTHAL R. N., KIRK J. C., Jr. and HIRTHE W. M., *J. Phys. Chem. Solids*, **28**, 1077 (1967)

J. Phys. Chem. Solids Vol. 31, pp. 1193-1195.

Low temperature neutron diffraction studies on Li(*D*, *T*)*

(*Received* 6 *October* 1969)

A CONSIDERABLE amount of evidence[1, 2] has been collected indicating that lithium tritide undergoes changes in lattice parameter, a_0, as a result of the tritium decay, provided the sample temperature is maintained below −7°C. This material does not, however, suffer these lattice changes when stored at higher temperatures. This material undergoes bulk expansion as a result of radiation damage, but only at the reduced temperature does this bulk expansion correspond to the lattice expansion. At the higher temperatures the radiation damage produces bulk expansion by other mechanisms, primarily the formation of gas bubbles. Pretzel[1–2] has suggested that this low temperature lattice expansion is the result of the ^{3}He decay product occupying an interstitial position in the cubic lattice with the corresponding formation of an *F*-center. This lattice distortion is such that the average volume increase per (*F*-center-^{3}He) interstitial pair is 12–14 Å^3 (2, 3). This lattice expansion has been measured by a low temperature X-ray diffraction technique and a value of 13·7 Å^3 per ^{3}He was determined[2].

This study was undertaken to verify Pretzel's data and to observe the changes in lattice parameter once this expanded salt is warmed to 23°C. This study was possible with neutron diffraction, whereas, due to the extensive radiation damage, the X-ray lines became so diffuse on warming the sample that the annealing studies were not possible.

A sample of ^{7}LiD$_{0\cdot6}$T$_{0\cdot4}$ was loaded into a sealed sample holder designed to fit the cryostat used for low temperature neutron diffraction studies. The front and back faces of this sample holder were $\frac{1}{8}$ in. thick copper plates, which served as an internal reference standard. The neutron source was the Omega West Reactor at LASL, the diffractometer using monochromatic neutrons with $\lambda = 1\cdot1420$ Å.

Initially, an ambient temperature (23°C) pattern was run from 25·0 to 81·0° 2θ. This scan covered the (111), (200), (220), (311), (222), (400) and (331) peaks of Li(*D*, *T*). The copper from the sample holder gave the (111), (200), (220), (311), (222) and (400) peaks in this region of 2θ. Analysis of these data indicated that sufficient data could be obtained by simply scanning the (111) and (311) peaks on Li(*D*, *T*) and the (200) and (220) peaks for copper. The sample was cooled to liquid nitrogen temperature and periodically these four peaks were scanned. After 187 days of continuous storage at low temperature the sample was quickly warmed to room temperature and the annealing of the expanded lattice was monitored by scanning the (111) peak of the Li(*D*, *T*). Occasionally the complete spectrum would be run and these runs confirm that the value for lattice parameter, a_0, obtained from the (111) peak was in excellent agreement with that obtained by fitting all seven Li(*D*, *T*) peaks. There was some fluctuation in ambient temperature during this annealing stage, but the temperature was continuously monitored and the data were corrected for thermal expansion to 23°C. Here a value of 36×10^{-6}°C^{-1} was used for the coefficient of thermal expansion, α[4].

Table 1 gives the initial and final values of a_0 for this material at 23°C and at liquid nitrogen temperatures. Also listed are the corresponding values for the reference copper.

The agreement for the total change observed at 23°C and at liquid nitrogen temperature is quite good, as are the initial and final values for copper. Figure 1 is a plot of a_0 vs. time for the period of low temperature storage. The lattice parameter increased a total of 0·0110 Å over this period for a total growth of 0·272 per cent. This gives a growth rate of 0·0014 per cent per day, compared to a value of 0·0038

---

*Work done under the auspices of the U.S. Atomic Energy Commission.

Table 1. *Experimentally determined* a_0's (Å)

Material	Temp (°C)	Initial (Å)	After 187 days (Å)	Change (Å)
$\text{LiD}_{0\cdot6}\text{T}_{0\cdot4}$	23	4·0666 ± 0·0004	4·0770 ± 0·0004	0·0104 ± 0·0006
$\text{LiD}_{0\cdot6}\text{T}_{0\cdot4}$	−190	4·0465 ± 0·0005	4·0575 ± 0·0005	0·0110 ± 0·0008
Cu	23	3·6147 ± 0·0003	3·6147 ± 0·0004	
Cu	−190	3·6031 ± 0·0003	3·6035 ± 0·0006	

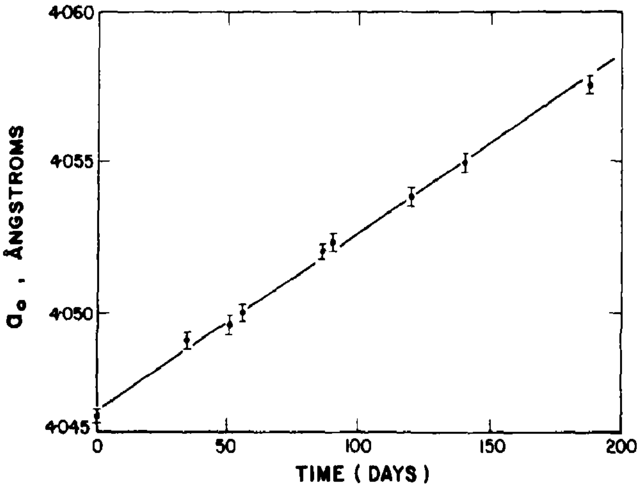

Fig. 1. Observed lattice expansion for $^{7}\text{LiD}_{0\cdot6}\text{T}_{0\cdot4}$ stored at liquid nitrogen temperature.

per cent per day reported by Pretzel and Anderson[2] for $\text{LiH}_{0\cdot12}\text{T}_{0\cdot88}$. This is, in fact, very good agreement when the dose rate correction is included (0·0038 × 0·4/0·88 = 0·0017 per cent per day). The period of 187 days is such that there were $6{\cdot}6 \times 10^{20}\beta$ decays per cm^3 of sample and likewise $6{\cdot}6 \times 10^{20}$ ^{3}He's formed per cm^3. If indeed the total 0·272 per cent linear expansion is due to the formation of interstitial ^{3}He's this would correspond to a lattice distortion of 12·4 Å^3 per ^{3}He. This volume increase is in very good agreement with that reported earlier[1, 2].

On warming to 23°C there was a definite relaxing of the expanded lattice. The salt did not anneal back to the initial room temperature value of 4·0666 Å, but some 80 per cent of the total lattice expansion was eventually recovered. It was felt that this annealing might well be a first order phenomenon, dependent only on the concentration of interstitial ^{3}He. The lattice parameter at 23°C was therefore fit to the following equation:

$$a_0 = Ae^{-Bt} + C$$

where

a_0 = lattice constant
A = intercept
B = slope α $1/t_{1/2}$
C = baseline = final value of a_0.

Figure 2 is a plot of the least squares fit of the data to the calculated line. This fit gave the following values for the parameters:

A = 0·0082 ± 0·0001 Å,
B = 0·0164 ± 0·0008 hr^{-1}; $t_{1/2}$ = 42·3 ± 2·0 hr,
C = 4·0688 ± 0·0001 Å.

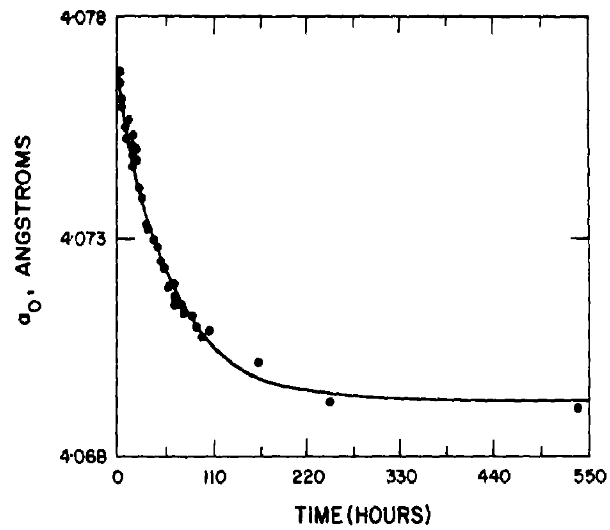

Fig 2. Room temperature annealing curve for expanded $^7LiD_{0.6}T_{0.4}$ lattice. The solid line is the least squares fit to the equation: $a_0 = Ae^{-Bt}+C$

The value of $A+C$ then gives the 23°C lattice parameter after 187 days storage at liquid nitrogen temperature. It is encouraging that the total expansion determined from these parameters of 0·0104 Å is in such good agreement with the 0·0110 Å expansion measured at the low temperature. The final 23°C value of 4·0688 Å corresponds to a net total expansion of 0·0022 Å, or 0·05 linear per cent Earlier X-ray diffraction studies did not indicate any net lattice expansion of Li(D, T) stored at ambient temperatures. The 0·05 per cent expansion detected here is probably due to the limited solubility of ^{3}He in the Li(D, T) lattice at 23°C.

It is felt that the low temperature lattice expansion of Li(D, T) is due to the formation of interstitial ^{3}He. When the sample is then warmed to room temperature the ^{3}He is able to diffuse out of this site, allowing the distorted lattice to relax back toward its initial a_0. There is however, some net expansion due probably to the limited solubility of ^{3}He in Li(D, T).

Acknowledgements—The authors are indebted to Dr. Dwayne T. Vier for his support and many helpful discussions. The help of Mr. W. L. Drumhiller in sample preparation and D Foshee and R Briesmeister in taking data was greatly appreciated.

Los Alamos Scientific Laboratory, J. L ANDERSON
University of California, A. L. BOWMAN
Los Alamos, G P. ARNOLD
New Mexico 87544, U.S.A.

REFERENCES

1. PRETZEL F. E., LEWIS W. B., SZKLARZ E. G. and VIER D T., *J. appl. Phys.* **33S**, 510 (1962).
2. PRETZEL F E. and ANDERSON J. L., *Los Alamos Scientific Lab. Rep* No LA-3501-MS (1966).
3. PRETZEL F. E., VIER D T., SZKLARZ E. G. and LEWIS W B., *Los Alamos Scientific Lab Rep.* No LA-2463 (1961)
4. ANDERSON J. L., NASISE J., PHILLIPSON K and PRETZEL F. E., *J Phys. Chem. Solids* **31**, pp 613-618 (1970).

J. Phys. Chem. Solids Vol. 31, pp 1195-1197

Magnetic susceptibility and Mössbauer spectrum of $NH_4Fe^{3+}Fe^{II}(CN)_6^*$

(*Received* 15 *July* 1969)

1. INTRODUCTION

It is difficult to prepare stoichiometric Prussian Blues and their analogs which contain a full complement of the associated alkali ions. In the process of preparation and purification some alkali is invariably washed out and replaced by the transition metal or other heavy metal ion present in the reaction mixture.

In the course of an investigation of the magnetic properties of complex cyanides of transition metals we have prepared the compound $NH_4Fe^{3+}Fe^{II}(CN)_6$, measured its magnetic susceptibility as a function of temperature, and determined its Mössbauer spectrum

2. PREPARATION AND ANALYSIS

$NH_4Fe^{3+}[Fe^{II}(CN)_6]$ (prep. I) (superscripts in Arabic numerals denote high-spin oxidation states; Roman numerals, low-spin states) was prepared by the slow addition of a hot solution (70°C) of $NH_4Fe(SO_4)_2 \cdot 12H_2O$ to a hot solution (70°C) of $(NH_4)_4Fe(CN)_6$. The precipitate was allowed to stand overnight, and was then centrifuged and washed three times with water. It was then dried in a vacuum desiccator at room temperature.

Analysis, calculated for $NH_4FeFe(CN)_6$: NH_3, 5·96%; Fe, 39·08%. Found: NH_3, 5·81%, Fe, 39·02%. Ratio, mols Fe/mols NH_3 = 2·05.

$NH_4Fe[Fe(CN)_6]$ (prep. II) was also prepared by the addition of $(NH_4)_2Fe(SO_4)_2 \cdot 6H_2O$ in a solution containing a fifty-fold excess of NH_4Cl to a solution of $K_4Fe(CN)_6$, also in a solution containing a fifty-fold excess of NH_4Cl.

3. MAGNETIC SUSCEPTIBILITY MEASUREMENTS

Magnetic susceptibilities were measured on a Gouy balance over the temperature range 75°–373°C. The calculated molar susceptibilities, averaged for three samples and corrected for diamagnetism ($\chi_{dia.} \times 10^6 = -140$ cm^3 mol.$^{-1}$), are given in Table 1.

Table 1. Magnetic susceptibilities

T (°K)	75	195	295	373
$\chi \times 10^6$ (cm^3 mol^{-1})	5925	2260	1470	1165

The susceptibility follows Curie's law, $\chi = 4{\cdot}36/T$. These results are shown in Fig. 1.

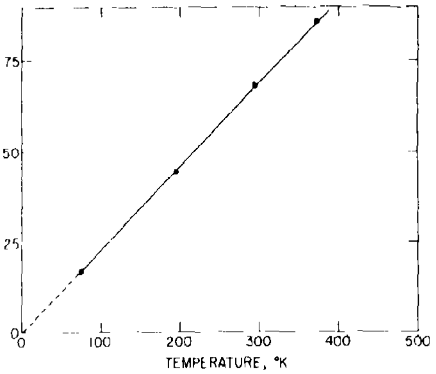

Fig. 1. Inverse molar susceptibility of $NH_4Fe[Fe(CN)_6]$ vs temperature.

4. MÖSSBAUER SPECTRA

The room temperature Mössbauer absorption spectra were obtained using a source of ^{57}Co diffused into a copper matrix. This source gave a single line with nearly natural line width. The spectra of $K_4Fe(CN)_6$ and $NH_4Fe^{3+}[Fe^{II}(CN)_6]$ prepared from (a) $NH_4Fe(SO_4)_2 \cdot 12H_2O$ and $K_4Fe(CN)_6$ and (b) $(NH_4)_2Fe(SO_4)_2 \cdot 6H_2O$ and $K_3Fe(CN)_6$ are shown in Fig. 2.

5. X-RAY DIFFRACTION

An X-ray powder diffraction pattern of $NH_4FeFe(CN)_6$ (prep. I) was obtained, and the reflections indexed on the basis of a cubic unit cell 10·181 ± 0·006 Å on edge. Only reflections with *h,k,l* all even or all odd were observed.

6. DISCUSSION

The presence of reflections in the X-ray diffraction pattern of the type, *h,k,l* odd, shows that the NH_4^+ ions are ordered in the 1/4 1/4 1/4; 1/4 3/4 3/4; ∩ positions, and calculations of the intensities of the 111 and 311 reflections confirmed this, the CN^- ions making very little contribution, as shown earlier by van Bever[1].

The magnetic moment calculated from the susceptibility data is $\mu = 5{\cdot}91\beta$, in good agree-

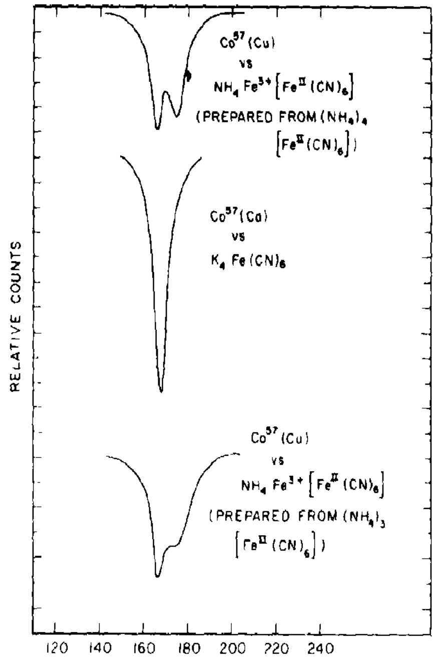

Fig 2

ment with the value $5{\cdot}916\beta$ expected for the Fe^{3+} ion in the $^6A_{1g}$ state. Unfortunately this result, by itself, does not unambiguously rule out the alternative structure, $NH_4Fe^{2+}[Fe^{III}(CN)_6]$, which has the same number of unpaired electrons. However, it is unlikely that Curie's law would be followed in the alternative case, as inferred from the work of Bozorth *et al.*[2], or that the moments would be independent of temperature.

The Mössbauer spectra of $NH_4Fe^{3+}[Fe^{II}(CN)_6]$ (preps. I and II), shown in Fig. 2, consist of two absorption maxima which can be assigned unequivocally to 'low-spin' Fe^{2+} and 'high-spin' Fe^{3+}, which verifies the valence distribution indicated. The absence of any observable quadrupole splitting is in agreement with the X-ray and analytical results which show an ordered stoichiometric structure.

The Mössbauer spectra we observed are generally cleaner than those reported by Duncan and Wigley[3] for $KFe^{3+}[Fe^{II}(CN)_6]$ whose compounds may have contained some iron, as well as alkali, in interstitial positions.

In agreement with previous results[3], both preparations of $NH_4Fe^{3+}[Fe^{II}(CN)_6]$ give essentially identical spectra, indicating that the same final compound is formed regardless of the oxidation states of the starting materials. The somewhat poorer resolution and increased line width of the Fe^{3+} ion observed in prep. II samples might be due to either a slight departure from ideal stoichiometry or the presence of some interstitial water in this preparation which could cause an increase in the spin relaxation time of this ion. Since prep. I samples gave cleaner spectra, the X-ray and magnetic measurements reported were made on this material.

Chemistry Department,
Brookhaven National Laboratory,
Upton,
N.Y. 11973, U.S.A.

N. ERICKSON
N. ELLIOTT

REFERENCES

1. VAN BEVER A. K., *Rec. trav. Chim.* **57**, 1259 (1938).
2. BOZORTH R. M., WILLIAMS H. J. and WALSH DOROTHY E., *Phys. Rev.* **103**, 572 (1956).
3. DUNCAN J. F. and WIGLEY P. W., *J. chem. Soc.* 1120 (1963).

for sample (e) which has a carrier concentration of about 3×10^{15} cm^{-3} at room temperature.

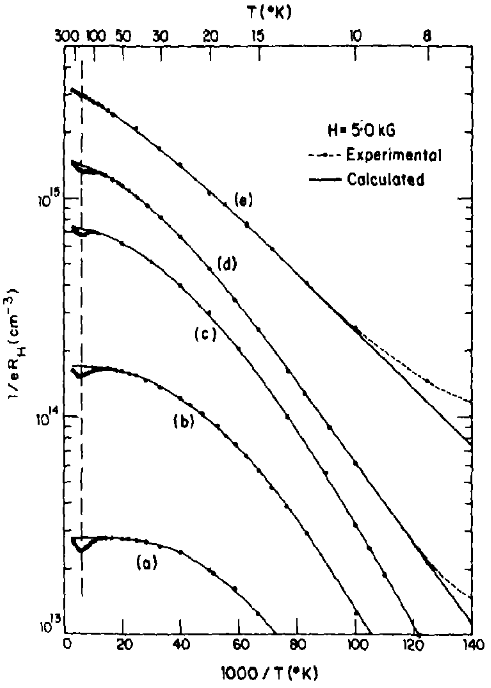

Fig. 1. Temperature variation of $1/eR_H$ measured at 5 kG for a series of samples with carrier concentrations from about $2{\cdot}5 \times 10^{13}$ to $3{\cdot}0 \times 10^{15}$ cm^{-3}. At low temperatures the carrier concentration decreases due to shallow donor deionization. At high temperatures the temperature variation of the Hall factor for polar mode scattering is observed which decreases with increasing impurity density.

Table 1. *Properties of* GaAs *samples as determined from analysis of Hall effect measurements*

Sample	N_D (cm^{-3})	N_A (cm^{-3})	E_D (meV)
a	$4{\cdot}8 \times 10^{13}$	$2{\cdot}1 \times 10^{13}$	5·52
b	$2{\cdot}0 \times 10^{14}$	$4{\cdot}1 \times 10^{13}$	5·09
c	$1{\cdot}1 \times 10^{15}$	$3{\cdot}3 \times 10^{14}$	3·88
d	$2{\cdot}1 \times 10^{15}$	$6{\cdot}0 \times 10^{14}$	3·29
e	$4{\cdot}7 \times 10^{15}$	$1{\cdot}6 \times 10^{15}$	1·89

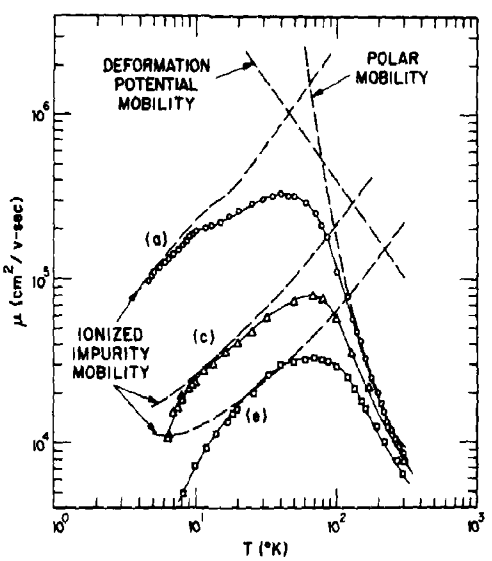

Fig. 2. Temperature variation of Hall mobility at 5 kG for three samples. In the temperature range from 300 to 77°K the mobility of sample (a) is dominated by polar mode scattering. Samples (c) and (e) show increased effects of ionized impurity scattering

For the purest sample (indicated by (a) in Figs. 1 and 2) the effect is observable in the temperature range from about 77 to 300°K, and for this sample the mobility in this temperature range is limited almost entirely by polar mode scattering, as indicated in Fig. 2. The polar mobility shown in this figure was calculated using the equation of Petritz and Scanlon[11]. Also shown in Fig. 2 are the deformation potential mobility determined from the theory of Bardeen and Shockley[12], and the ionized impurity mobilities determined from the Brooks–Herring[13] equation using values of N_D, N_A, and n obtained from analyses of Hall effect measurements for the various samples over the temperature range 4·2–300°K.

It is apparent that the mobility for samples (c) and (e) is affected by a larger contribution of ionized impurity scattering, and this could mask the temperature variation of the scattering factor due to polar mode scattering. Because of this, sample (a), which has a total ionized impurity density of only 7×10^{13} cm^{-3}, was used for subsequent measurements.

4. TEMPERATURE AND MAGNETIC FIELD DEPENDENCE

The experimental variation of the Hall constant for magnetic fields of 0·5, 5·0, 50·0 and 90·0 kG is shown in Fig. 3. The slight decrease in R_H observed at high temperatures for $H = 50·0$ and 90·0 kG may represent an increase in carrier concentration due to ionization of a deeper donor level. The experimental variation of the scattering factor with temperature determined from $r_H = R_H/R_{90kG}$, for $H = 0·5$, 5·0 and 50 kG is shown in Fig. 4, along with the theoretical variation calculated by Lewis and Sondheimer[2] and Devlin[5]. The scattering factor is plotted as a function of $z = \theta/T$ where a longitudinal optical phonon temperature of $\theta = 423$°K [14] was used. The Hall factors measured at 0·5 and 5·0 kG are in qualitative agreement with both calculations, although the shape of the curves agrees more closely with Devlin's results. As mentioned previously, in the limit of high magnetic fields the scattering factor should be independent of temperature and approximately equal to 1, and this is the case for the results at 50 kG.

It would be interesting to experimentally determine the minimum in the temperature variation indicated by the theory at high temperatures. Unfortunately, in GaAs there is a large variation in Hall constant in this high temperature range due to two-band conduction involving the higher lying ⟨100⟩ conduction band minima[15] which obscures the relatively smaller temperature variation due to polar mode scattering.

Since a universal relaxation time cannot be defined for temperatures less than θ, the usual criterion for the breakdown of low field Hall effect theory, $\mu B \rightarrow 1$, does not apply, and the Hall coefficient factor is not simply a function of μB alone, but is also a function of temperature. However, the variation with magnetic field of the Hall factor for polar mode scattering has also been calculated[2, 5], and the results of Devlin's calculations for three different temperatures as well as the experimental variation of r_H for comparable temperatures are shown in Fig. 5. There is considerable scatter in the data, but the theoretical and experimental curves are in remarkably good agreement at the higher values of μB.

The variation of the Hall factor with degeneracy has also been calculated by Lewis and Sondheimer, and they predict a continuous decrease of r_H with increasing degeneracy at a fixed temperature. In GaAs,

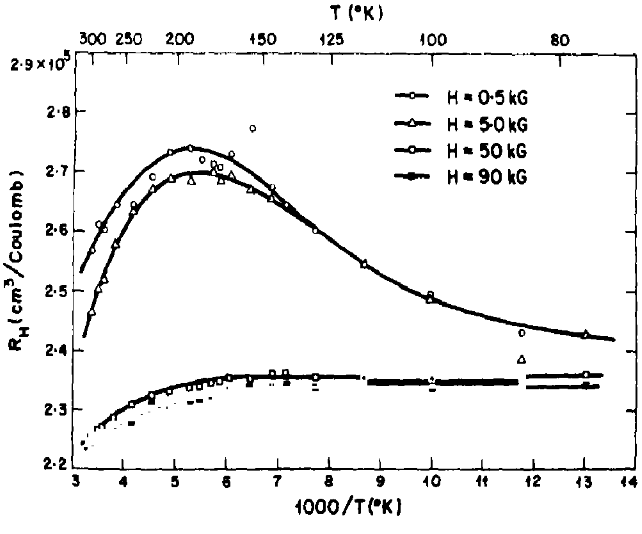

Fig. 3. Temperature variation of the Hall coefficient, R_H, for magnetic fields of $H = 0·5$, 5, 50 and 90 kG.

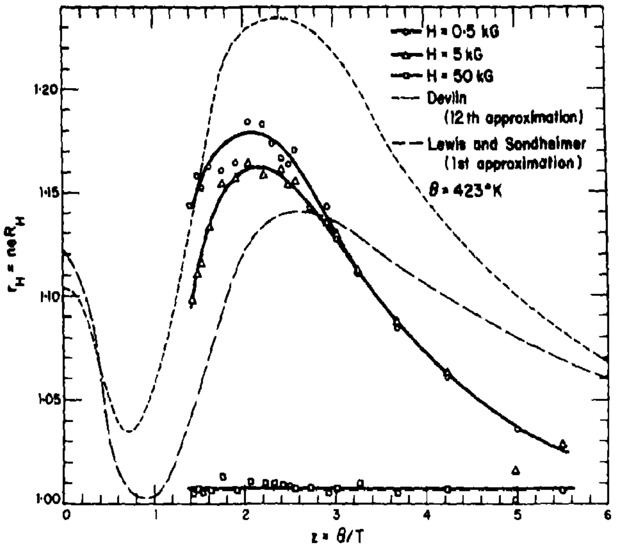

Fig. 4 Temperature dependence of the Hall factor for polar mode scattering for both theory and experiment. The dependence is qualitatively the same The effect disappears at 50 kG.

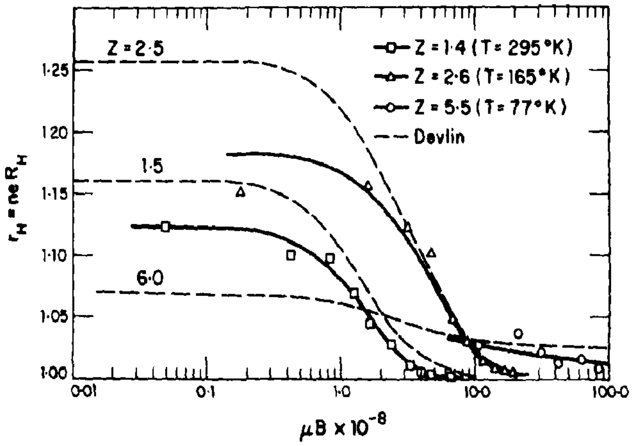

Fig. 5. Magnetic field dependence of the Hall factor for polar mode scattering for both theory and experiment. Since a universal relaxation time cannot be defined for polar mode scattering, the scattering factor does not approach 1 for the same value of μB at different temperatures.

however, the effects of ionized impurity scattering also increase for increasing degeneracy, as previously indicated, so it is not possible to examine the variation of r_H with degeneracy alone. The disappearance of the dip in Fig. 1 with increasing carrier concentration from sample (*a*) to sample (*e*) is probably due mainly to the increasing contribution of ionized impurity scattering, since at the temperature of the dip the Fermi energy is still 3 *kT* below the bottom of the conduction band for sample (*e*). The results of Lewis and Sondheimer predict essentially no change in the scattering factor at this degeneracy level.

5. CONCLUSIONS

The experimental variation of the Hall factor for polar mode scattering with temperature and magnetic field is in as good agreement with the theory as can be expected. Although Devlin[5] estimates the accuracy of his calculation for the temperature variation of the Hall factor to be better than 10 per cent, the experimental variation of the Hall factor would be expected to be affected by band structure, sample and magnetic field inhomogeneity, screening, and other scattering mechanisms which are not taken into account in the theory.

Practically, the effect of the Hall factor for polar mode scattering on the calculated carrier concentration and mobility is small and is evident only in high purity GaAs. At a magnetic field of 5 kG, which is commonly used for the characterization of GaAs, the error introduced by assuming $r_H = 1$ is at most about − 15 per cent at room temperature, and at 77°K the error is at most about −3 per cent. However, the error would result in a calculated carrier concentration at 77°K which was higher than the calculated carrier concentration at room temperature. This anomaly in calculated carrier concentration has been observed[16] in other similar epitaxial GaAs samples. Another interesting and potentially important effect of the temperature variation of r_H can be observed in Fig. 3. Although the high field data clearly show a decrease in R_H at high temperatures, possibly caused by the presence of a deeper donor level, this effect is completely masked in the low field data by the temperature variation of the scattering factor. Consequently, the presence of a small concentration of deeper donors might not be revealed in low magnetic field Hall coefficient data, especially if taken only at a few isolated temperatures such as 300 and 77°K.

Acknowledgements—We would like to thank R. C. Hancock for performing the Hall measurements, L. Krohn for preparing the GaAs samples, and the M.I.T. Francis Bitter National Magnet Laboratory for providing the facilities for the high field measurements.

REFERENCES

1. HOWARTH D. J. and SONDHEIMER E. H., *Proc. R. Soc.* **A219**, 53 (1953)
2. LEWIS B. F. and SONDHEIMER E. H., *Proc. R. Soc.* **A227**, 241 (1954).
3. EHRENREICH H., *J. Phys. Chem. Solids* **9**, 129 (1959)
4. DELVES R. T., *Proc. phys. Soc.* **73**, 572 (1959).
5. DEVLIN S. S., *Physics and Chemistry of II–VI Compounds* (Edited by M. Aven and J. S. Prener), p. **551** North-Holland, Amsterdam (1967); DEVLIN S. S., Thesis, Case Institute of Technology (1964)
6. SEEGER A., *Can. J. Phys.* **34**, 1278 (1956).
7. MARPLE D. T. F., *Phys. Rev.* **129**, 2466 (1963).
8. SEGALL B., LORENZ M. R. and HALSTED R. E., *Phys. Rev.* **129**, 2471 (1963).
9. KNIGHT J. R., EFFER D. and EVANS P. R., *Solid-St. Electron* **8**, 178 (1965).
10. VAN DER PAUW L. J., *Philips Res. Rep.* **13**, 1 (1958)
11. PETRITZ R. L. and SCANLON W. W., *Phys. Rev.* **97**, 1620 (1955); EHRENREICH H., *J. Phys. Chem. Solids* **8**, 130 (1959)
12. BARDEEN J. and SHOCKLEY W., *Phys. Rev.* **80**, 72 (1950).
13. BROOKS H., *Adv. Electronics electron Phys.* **7**, 158 (1955)
14. FRAY S. J., JOHNSON F. A., QUARRINGTON J. E. and WILLIAMS N., *Proc. phys. Soc.* **77**, 215 (1961).
15. AUKERMAN L. W. and WILLARDSON R. K., *J. appl. Phys.* **31**, 939 (1960)
16. SOLOMON R., *Proc. Int. Symp. GaAs, Dallas*, p. 17. Institute of Physics and The Physical Society, London, (1969).

J. Phys. Chem. Solids Pergamon Press 1970. Vol. 31, pp. 1205–1220. Printed in Great Britain.

CONDUCTIBILITE, NOMBRES DE TRANSPORT ET AUTODIFFUSION DES IONS DANS DIFFERENTS MONOCRISTAUX DE CHLORURE DE SODIUM

F. BENIERE, M. BENIERE et M. CHEMLA
Laboratoire d'Electrochimie, Faculté des Sciences de Paris, 10, rue Cuvier, 75, Paris 5e France

(*Received* 15 *July* 1969; *in revised form* 27 *November* 1969)

Résumé – Les mesures de la conductivité, des nombres de transport et des coefficients d'autodiffusion de Na^+ et Cl^- ont été effectuées avec une reproductibilité de 1 pour cent dans des monocristaux de NaCl purs et dopés par des ions Sr^{2+}. Les contributions des lacunes cationiques, des lacunes anioniques et des paires de lacunes ont pu être séparées, ce qui a permis d'obtenir, à partir de l'ensemble des grandeurs expérimentales, les véritables valeurs des enthalpies et entropies de formation et de migration des défauts. La relation de Nernst–Einstein a pu alors être étudiée en toute rigueur; cette relation se vérifie avec une précision de 2 pour cent, alors que la théorie des corrélations prévoyait un facteur multiplicatif égal à 0,78. Il semble donc que dans le système étudié, le modèle du réseau rigide, dont la conséquence est l'existence d'effets de corrélations, mérite d'être reconsidéré.

Abstract – The measurements of conductivity, transport numbers and self diffusion coefficients of Na^+ and Cl^- have been made with an accuracy of 1 per cent in single crystals of pure and Sr^{2+}-doped NaCl. The contributions of cation-vacancies, anion-vacancies and vacancy-pairs have been separated; this has allowed to reach, from the whole of the experimental data, the true values of the enthalpies and entropies of defects formation and migration. The Nernst–Einstein relation has then been strictly studied; this relation is verified with an accuracy of 2 per cent, whereas the correlation theory had forecast a multiplicative factor equal to 0,78. It seems therefore that in the studied system, the rigid lattice model, the consequence of which is the existence of correlation effects, is worth being reconsidered.

1. INTRODUCTION

De nombreux travaux ont eu pour objet l'étude des défauts dans les cristaux ioniques, dans le but d'établir la nature des défauts et les paramètres fixant leurs concentrations et leurs mobilités. Les méthodes expérimentales les plus employées et les plus directes sont la mesure de la conductibilité et de l'autodiffusion des ions. Il semble bien admis que les défauts prédominants dans le cristal de chlorure de sodium sont du type de Schottky, c'est à dire des lacunes cationiques et anioniques, dont une partie peut s'associer pour former des paires de lacunes. La mesure de la conductivité reflète la somme des migrations des deux espèces d'ions dans les lacunes libres; d'autre part, la mesure des coefficients d'autodiffusion par l'utilisation de traceurs radioactifs permet de suivre individuellement chacun des ions, mais donne la somme des mécanismes de diffusion par les lacunes libres et par les paires de lacunes. On se rend ainsi compte que dans chaque cas, il y a compétition entre au moins deux mécanismes.

Ainsi, dans le cas du chlorure de sodium, étudié par des mesures de conductivité[1–9], d'autodiffusion du cation[10–12] et de l'anion [12–16] et de nombres de transport[17], les contributions dues aux lacunes libres et aux paires de lacunes n'avaient pu être chiffrées séparément. Ainsi, Dreyfus et Nowick[4] ont calculé les paramètres de formation et de migration des défauts uniquement à partir des mesures de conductivité en négligeant la mobilité de l'anion: on se rend compte du caractère approximatif de cette hypothèse en remarquant que les coefficients de diffusion de Cl^- et Na^+ sont dans le rapport 1 à 4 environ à 700°C.

Dans le présent travail, après avoir mis au point des méthodes de mesures de grande précision, nous nous sommes proposés de rechercher les valeurs les plus sûres relatives aux processus de transport afin de tester les théories actuellement proposées.

Nos résultats expérimentaux portent sur les grandeurs suivantes:

(a) mesures de la conductibilité électrique et des nombres de transport.

(b) coefficients d'autodiffusion* des anions et des cations dans des cristaux de haute pureté: ces mesures permettent de déterminer la somme des processus de diffusion par lacunes libres et par paires de lacunes.

(c) coefficients d'autodiffusion dans des cristaux dopés par des ions Sr^{2+}; grâce à la mise au point d'une technique de dopage par diffusion, nous avons pu préparer des monocristaux de concentrations en ions Sr^{2+} bien connues. Il devient alors possible de faire varier les concentrations de défauts, ce qui permet de calculer séparément la contribution des paires.

L'ensemble des résultats expérimentaux ainsi obtenus permet d'examiner la validité de la relation de Nernst–Einstein afin de rechercher l'intervention du facteur de corrélation.

2. THEORIES ACTUELLES DE LA FORMATION ET DE LA MIGRATION DES DEFAUTS

(1) *Concentration des défauts*

Les conceptions actuelles[19] supposent, qu'en raison de l'agitation thermique, une certaine fraction des sites du réseau de chlorure de sodium se trouvent vacants. Si n^+ et n^- sont les concentrations des lacunes cationiques et anioniques, ces grandeurs obéissent au produit de solubilité:

$$n^+ \cdot n^- = \exp\left(-\frac{Gd}{kT}\right) = \exp\left(\frac{Sd}{k}\right)\exp\left(-\frac{Hd}{kT}\right) \quad (1)$$

Sd: variation d'entropie pour former un couple de défauts,

Hd: variation d'enthalpie pour former un couple de défauts,

T: température absolue,

k: constante de Boltzmann.

En plus de ces lacunes 'thermodynamiques' existent des lacunes dues à la présence d'impuretés résiduelles ou volontairement introduites. On considère que les impuretés monovalentes (K^+...) se substituent à des ions du réseau sans modifier sensiblement les propriétés du cristal. Par contre, les impuretés ioniques de valence supérieure à 1 doivent introduire des lacunes afin de respecter la neutralité électrique. Si on suppose que les impuretés cationiques bivalentes (Ca^{2+}, Sr^{2+}...) sont prépondérantes et en concentration égale à C, la relation d'électroneutralité s'écrit:

$$n^+ = C + n^-. \quad (2)$$

En outre, les défauts ponctuels de charges opposées sont susceptibles de s'associer en partie pour former des groupements qui ne participent pas à la conductibilité.

Un cation bivalent peut s'associer à une lacune cationique, par attraction électrostatique, pour former un 'complexe' et l'on doit considérer l'équilibre:

$$\text{cation bivalent} + \text{lacune cationique} \rightleftharpoons \text{complexe}.$$

Dans le domaine des fortes concentrations de lacunes dues aux impuretés, l'application de la loi d'action de masse donne selon Lidiard [19]:

$$\frac{p}{(1-p)^2} = 12\,C\exp\left(-\frac{G_c}{kT}\right) \quad (3)$$

où p est le degré d'association et G_c l'énergie libre d'association, de valeur négative puisque la réaction d'association est exoénergétique.

D'autre part, deux lacunes de signes contraires présentent également une attraction électrostatique[20] ce qui conduit à un nouvel équilibre qui, combiné à l'équation (1), donne la concentration n_p des paires:

---

*Seuls les résultats des mesures antérieurement décrites [11] et [16] ont été rappelés.

$$n_p = 6\exp\left(\frac{-G_d - G_p{}^a}{kT}\right) \qquad (4)$$

où $G_p{}^a$ est l'énergie libre d'association de deux lacunes pour former une paire.

Les valeurs des coefficients d'autodiffusion et de la conductivité sont proportionnelles à la concentration des défauts. A haute température les défauts thermodynamiques prédominent et les énergies d'activation comprendront l'énergie de migration et l'énergie de formation du défaut (domaine intrinsèque). Par contre, lorsque la concentration des lacunes dues aux impuretés l'emporte, l'énergie d'activation ne comprendra plus l'énergie de migration de défaut (domaine extrinsèque dans lequel il faudra de plus éventuellement faire la part des complexes).

(2) *Diffusion*

On démontre[21] que le coefficient d'autodiffusion d'un ion dans la structure cubique à faces centrées (12 ions plus proches voisins d'un ion de même espèce) est égal à:

$$D = \frac{\nu a^2}{3} \times 12\,n$$

où

$$\left(-\frac{G_m}{kT}\right) = \nu_0 \exp\left(\frac{S_m}{k}\right)\exp\left(-\frac{H_m}{kT}\right) \qquad (5)$$

ν_0: fréquence propre, supposée généralement égale à la fréquence de Debye.

S_m et H_m: variations d'entropie et d'enthalpie lors de la migration d'un ion d'un site à l'autre.

a: distance anion-cation

n: fraction de défauts.

Les coefficients de diffusion représentent la somme des contributions des lacunes libres et des paires de lacunes.

La contribution due aux paires de lacunes est, en raison de la relation (4), indépendante de la concentration en cations bivalents C et identique pour les mouvements du cation et de l'anion:

Soit D_p le coefficient de diffusion par les paires:

$$D_p = D\,\mathrm{op}\exp\left(-\frac{H_p}{kT}\right).$$

Finalement, tant que l'on peut négliger la fraction de complexes, les coefficients de diffusion de Na^+ et Cl^- son égaux à D^+ et D^- tels que:

$$D^+ = 4a^2\nu^+ \cdot \frac{+C + (C^2 + 4\exp - (Gd/kT))^{1/2}}{2} + \mathrm{Dop}\exp\left(-\frac{Hp}{kT}\right) \qquad (6)$$

$$D^- = 4a^2\nu^- \cdot \frac{-C + (C^2 + 4\exp - (Gd/kT))^{1/2}}{2} + \mathrm{Dop}\exp\left(-\frac{Hp}{kT}\right). \qquad (6\,\text{bis})$$

Nous verrons plus bas qu'il est possible de définir, en ce qui concerne les mouvements du sodium, un domaine extrinsèque dans un intervalle de températures et de concentrations pour lequel on peut négliger la part des lacunes thermodynamiques et des complexes. Le coefficient de diffusion de Na^+ est alors égal à:

$$D_2{}^+ = 4a^2\nu_0 C\exp\left(\frac{Sm^+}{k}\right)\exp\left(-\frac{Hm^+}{kT}\right). \qquad (7)$$

Les coefficients de diffusion de Na^+ et Cl^- dans le cristal pur dans le domaine intrinsèque sont respectivement égaux à:

$$D_1{}^+ = 4a^2\nu_0\exp\left(\frac{Sd/2 + Sm^+}{k}\right) \times \exp\left(-\frac{Hd/2 + Hm^+}{kT}\right) + \mathrm{Dop}\exp\left(-\frac{Hp}{kT}\right) \qquad (8)$$

$$D_1{}^{-}=4a^2\nu_0\exp\left(\frac{Sd/2+Sm^{-}}{k}\right)\times\exp\left(-\frac{Hd/2+Hm^{-}}{kT}\right)+\mathrm{Dop}\exp\left(-\frac{Hp}{kT}\right). \tag{9}$$

(3) *Conductibilité*

Dans un système idéal, dépourvu d'effets de corrélation et de paires neutres, la conductibilité et les coefficients de diffusion devraient être reliés par la relation de Nernst–Einstein:

$$\sigma=\frac{Ne^2}{kT}(D_1{}^{+}+D_1\ )$$

où N est le nombre d'ions par unité de volume et e la charge de l'électron.

Dans l'étude expérimentale, en l'absence d'effets de corrélation, des valeurs de $(D_1{}^{+}+D_1\ )/\sigma$ supérieures à la valeur théorique traduiront la présence des paires de lacunes.

Lorsque l'expression de Dp peut être calculée, les expressions de $(D_1{}^{+}-D_p)$ et $(D_1{}^{-}-D_p)$ peuvent à leur tour être calculées, ce qui permet d'éliminer l'influence des paires dans la relation de Nernst–Einstein qui doit ainsi s'écrire:

$$\sigma=\frac{Ne^2}{kT}(D_1{}^{+}+D_1{}^{-}-2Dp).$$

Dans le domaine intrinsèque, la conductibilité est la somme des conductibilités partielles:

$$\sigma=\sigma^{+}+\sigma=\frac{Ne^2}{kT}4a^2\nu_0\exp\left(-\frac{Hd-TSd}{2kT}\right)\times\left(\exp\frac{Sm^{+}}{k}\exp-\frac{Hm^{+}}{kT}+\exp\frac{Sm^{-}}{k}\exp-\frac{Hm^{-}}{kT}\right). \tag{10}$$

Dans le domaine extrinsèque où la concentration de lacunes est pratiquement égale à celle du dopant, la conductibilité s'écrira:

$$\sigma_2=\frac{Ne^2}{kT}4a^2\nu_0C\exp\left(\frac{Sm^{+}}{k}\right)\exp\left(-\frac{Hm^{+}}{kT}\right). \tag{11}$$

(4) *Nombres de transport*

Il est possible de séparer les contributions anionique et cationique à la conductivité par la mesure des nombres de transport, ce qui permet en principe de calculer σ^{+} et σ^{-}.

Cependant la précision des mesures étant insuffisante (de l'ordre de 3 pour cent), nous nous contenterons de vérifier que les nombres de transport sont compatibles avec les mesures de coefficients de diffusion, selon les relations:

$$\frac{t^{+}}{t^{-}}=\frac{\sigma^{+}}{\sigma^{-}}=\frac{D_1{}^{+}-Dp}{D_1{}^{-}-Dp}. \tag{12}$$

(5) *Facteur de corrélation*

La preuve du mécanisme lacunaire proposé dans le cas du chlorure de sodium pourrait être fournie par la mise en évidence du facteur de corrélation; Bardeen et Herring[22] ont montré que si on considère la succession des sauts d'un ion radioactif, on constate qu'après le premier saut de l'ion qui l'amène dans la lacune, le second saut n'est pas parfaitement aléatoire, c'est à dire que les probabilités de sauter vers les 12 plus proches voisins ne sont pas identiques mais qu'au contraire la probabilité du saut le ramenant dans sa position initiale est plus grande. Les calculs développés par LeClaire et Lidiard[23] ainsi que par Compaan et Haven[24] ont montré que dans cette hypothèse le coefficient de diffusion D^* mesuré à l'aide d'un isotope serait inférieur au coefficient d'autodiffusion vrai d'un facteur $f=0{,}7815$ dans le cas de NaCl.

Si, à partir de la mesure de la conductibilité, on calcule la valeur du coefficient de diffusion:

$$D_{\mathrm{calc}}=\frac{kT}{Ne^2}\sigma$$

la théorie des corrélations doit conduire à la relation:

$$\frac{D^*_{\text{mes.}}}{D_{\text{calc.}}} = f.$$

On se rend compte que l'étude expérimentale du rapport $(D_1^+ + D_1^- - 2Dp)/\sigma$ sera un test sensible de la théorie des corrélations, car la présence du facteur f donnerait des valeurs environ 20 pour cent inférieures à la valeur théorique de Nernst–Einstein.

3. METHODES EXPERIMENTALES

Toutes les mesures ont été effectuées sur des monocristaux fabriqués par 'Harshaw' et 'Quartz et Silice' ainsi que sur des monocristaux Harshaw dopés par des ions Sr^{2+}. Afin de conserver les propriétés structurales du monocristal, les cristaux sont dopés par diffusion. Ce résultat est obtenu en déposant sur les faces de trois plaquettes de cristal empilées la même quantité d'une solution méthylique de $SrCl_2$, à laquelle on a ajouté dans un rapport bien déterminé, du chlorure de ^{90}Sr qui joue le rôle de radioindicateur. L'ensemble, maintenu dans une feuille de platine, est introduit dans une ampoule de quartz de haute pureté, scellée sous atmosphère de gaz chlorhydrique. Les cristaux sont alors recuits à 760°C jusqu'à homogénéisation complète par diffusion de la concentration des ions Sr^{2+}. L'utilisation du ^{90}Sr permet de vérifier en tout point l'homogénéité du dopant et de calculer sa concentration.

Les monocristaux sont clivés à la dimension voulue et les faces sont dans tous les cas aplanies au microtome jusqu'à l'obtention de parallélépipèdes à surfaces planes, ce qui est obtenu par des coupes finales de 1 μ d'épaisseur.

La constance de la température, à quelques centièmes de degré près, est assurée par des régulations électroniques à action proportionnelle. La température est repérée par des thermocouples nickel chrome–nickel allié étalonnés, construits symétriquement, dont la soudure chaude est placée au voisinage immédiat des échantillons et la soudure froide plongée dans un bain eau distillée + glace. Dans ces conditions, l'erreur globale sur la température est de ±0,1°. D'autre part, la tension aux bornes des thermocouples est enregistrée en fonction du temps pendant toute la durée des expériences. Signalons enfin que toutes les expériences qui suivent ont été effectuées dans des tubes de quartz identiques dans les mêmes conditions de mesure de la température, ce qui rend leur comparaison particulièrement valable.

(1) *Diffusion*

Les ions radioactifs sont déposés à l'interface de deux cristaux par sublimation de $^{22}NaCl$ ou $Na^{36}Cl$ (^{22}Na et ^{36}Cl sont émetteurs β de périodes respectivement égales à 2,6 et 5×10^5 ans). Après diffusion et clivage des bords, les échantillons, dont la surface est alors égale à environ 1 cm², sont fixés sur le banc du microtome et réglés parallèlement au plan du rasoir au moyen d'une lunette autocollimatrice. Les découpes, de 2 μ d'épaisseur, tombent directement dans des coupelles ensuite pesées au 1/100 mg et dont la radioactivité est mesurée au compteur β. Notons que ce microtome de précision, spécialement conçu pour les substances dures, permet une grande régularité des découpes; cette régularité rendrait superflue la pesée, si elle n'était nécessaire à la détermination de l'épaisseur de la première coupe et à la connaissance de l'activité spécifique en ^{90}Sr, donc de la concentration des ions Sr^{2+} dans le cas des cristaux dopés. Les coefficients de diffusion sont déduits de l'équation:

$$A(x) = \frac{Q}{2\sqrt{\pi D t}} \exp\left(-\frac{x^2}{4Dt}\right).$$

(2) *Conductibilité*

La difficulté dans les mesures de conductivité réside dans le choix des électrodes qui doivent assurer un bon contact et ne pas contenir d'éléments susceptibles de diffuser dans le cristal. Nous avons résolu ce problème en réalisant des dépôts de platine sur les faces du cristal, par évaporation sous vide. Le dépôt doit être effectué lentement afin de ne pas trop élever localement la température du cristal. La couche de platine ainsi déposée adhère bien au cristal et assure un bon contact électrique sur toute la surface, et cela jusqu'au voisinage du point de fusion de NaCl. Nous pensons que ceci constitue une amélioration très nette par rapport aux électrodes obtenues par dépôt de graphite, qui perdent leur adhérence à haute température et peuvent contenir des impuretés dopant le cristal.

En effet, nous avons constaté par l'usage de suspensions de graphite colloïdal que les mesures de conductibilité n'étaient pas reproductibles, en ce sens que l'on observait une augmentation constante de la conductibilité en fonction du temps principalement dans le domaine extrinsèque, ce qui est caractéristique de la présence d'impuretés. Ce phénomène n'a pas été retrouvé avec des dépôts de platine et les valeurs de σ demeuraient les mêmes à 1 pour cent près au cours d'un cycle d'élévation et d'abaissement de la température.

La conductivité est mesurée de 10 en 10°C chaque fois que la température est stabilisée, à l'aide d'un pont d'impédance, alimenté par un générateur de fréquence, l'équilibre étant repéré par un amplificateur de zéro.

Quatre types de cristaux de puretés différentes ont été étudiés (Fig. 1.). Pour chaque espèce, nous avons effectué trois séries de mesures de conductivité sur des échantillons différents, afin d'étudier la reproductibilité des mesures. Ainsi, afin d'étudier l'influence éventuelle des dimensions géométriques des échantillons, nous avons fait varier l'épaisseur entre 1,65 et 4,49 mm et la surface entre 0,416 et 1,725 cm^2, ce qui a montré que la mesure de la conductivité est indépendante des dimensions du cristal. En ce qui concerne la reproductibilité des mesures, il faut distinguer celles qui sont indépendantes de la nature du cristal (à haute température, domaine intrinsèque) et celles qui dépendent de la pureté (à basse température, domaine extrinsèque). Dans le premier cas, à température donnée, l'écart moyen est de 1 pour cent tandis que dans le second cas, l'écart moyen est égal à 2 pour cent, prouvant ainsi la qualité de la méthode de fabrication des cristaux dopés.

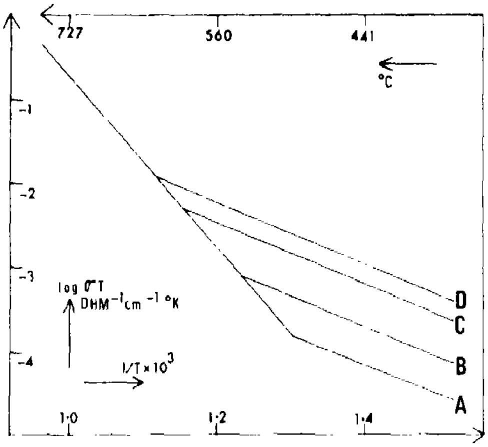

Fig. 1. Conductivité des cristaux. *A*: Harshaw; *B*: Quartz et Silice; *C*. dopés à 12×10^{-6} ions Sr^{2+}; *D*: dopés à 27×10^{-6} ions Sr^{2+}.

(3) *Nombres de transport*

Un ensemble de trois monocristaux identiques est maintenu dans un dispositif de serrage en platine iridié. L'utilisation de monocristaux à faces aplanies au microtome permet, d'une part d'obtenir de bonnes surfaces de contact, et d'autre part de les séparer facilement après l'expérience. Nous avons rejeté le principe des couches protectrices de $BaCl_2$ introduites par Tubandt[17], qui par diffusion de Ba^{2+} dopent les cristaux de NaCl, ce qui revient à fausser par excès le nombre de transport de Na^+. Par contre, dans notre méthode, le cristal anodique donne par sa perte de poids le nombre de transport t^+; d'autre part, le sodium formé à la cathode s'échappe de l'interface cristal-électrode et donne un dépôt d'oxyde sur les bords du cristal facilement détachable. La perte de poids du cristal cathodique, proportionnelle à t^-, permet un contrôle supplémentaire. Contrairement aux expériences de diffusion et conductivité, le système est placé dans un tube de quartz ouvert à l'air, ce qui permet au chlore de se dégager et au sodium de s'oxyder. L'intensité de courant adoptée est de l'ordre de 0,2 mA, et la durée de 20 h, ce qui correspond à une masse de chlorure de sodium électrolysée de l'ordre de 8 mg; la quantité de courant est mesurée à l'aide d'un voltamètre à argent.

La réalisation de telles expériences est particulièrement délicate en raison de la faible conductibilité des cristaux qui ne peuvent pas subir une électrolyse prolongée sans se détériorer partiellement. La reproductibilité des mesures nous indique une précision d'environ 3 pour cent, mais il nous parait nécessaire de rappeler que les valeurs expérimentales de nombres de transport ne sont utilisées que pour confirmer les mécanismes déduits des expériences de diffusion et conductibilité.

4. ENTHALPIES ET ENTROPIES DE FORMATION ET DE MIGRATION DES DEFAUTS

L'autodiffusion des ions et la conductibilité ionique sont, dans tous les cas, la résultante de plusieurs mécanismes dus à plusieurs espèces de défauts; il faut en effet distinguer les lacunes thermodynamiques, les lacunes induites par les impuretés, les paires de lacunes et les associations impureté-lacune.

Nous avons pu cependant, par l'application des précédentes méthodes à des monocristaux de chlorure de sodium de puretés variables, séparer chacun des termes avec la meilleure précision possible.

(1) *Enthalpie de migration des cations*

Le plus souvent, les paramètres thermodynamiques ont été calculés uniquement à partir de mesures de conductivité. A titre d'exemple, nous avons représenté la conductivité sous la forme de la quantité log σT en fonction de $1/T$, mesurée dans des cristaux contenant 12×10^{-6} ions Sr^{2+} (Fig. 2). On observe les régions suivantes

$\theta > 650°C$: section presque rectiligne qui représente la somme des conductivités des deux ions dans le domaine intrinsèque.

$510 < \theta < 650°C$: zone coudée due à la superposition de la migration dans les lacunes thermodynamiques et dans les lacunes induites par les impuretés.

$415 < \theta < 510°C$: section rectiligne, correspondant au domaine extrinsèque, habituellement attribuée à une concentration fixe de lacunes dues aux impuretés.

$\theta < 415°C$: la courbe s'incurve de nouveau dans le sens d'une augmentation de l'énergie d'activation, ce qui indique qu'une partie des lacunes est susceptible de s'associer aux cations bivalents pour donner des complexes.

Une valeur d'énergie d'activation déduite de la première section n'est pas directement exploitable; en effet:

(a) *Aux lacunes thermodynamiques* il faut ajouter les lacunes dues aux impuretés en concentration relative d'autant plus importante que la température est plus basse. Ceci a souvent conduit, en supposant que cette énergie d'activation était la somme $(Hd/2 + Hm^+)$, à attribuer une valeur trop faible à cette somme. Par contre, l'utilisation de cristaux très purs pour lesquels le coude se produit à la température de 492°C, permet d'obtenir un large domaine des hautes températures où la concentration des lacunes dues aux impuretés est négligeable;

(b) *Même dans ce dernier cas* il faut tenir compte non seulement de la conductivité cationique mais aussi de la contribution des anions, calculée plus loin à partir des mesures des coefficients de diffusion et des nombres de transport.

Par contre, l'enthalpie de migration de Na^+ (Hm^+) peut se déduire directement de la mesure de la pente de la courbe entre 415 et 510°C. En effet dans ce domaine de température et pour cette concentration en impuretés bivalentes, la participation des anions à la conductibilité est négligeable puisque le coefficient de diffusion de Cl^- est environ cent fois plus faible que celui de Na^+ et qu'en outre sa valeur est attribuée aux paires neutres. D'autre part la contribution des associations Sr^{2+}-lacune, qui correspond à une migration

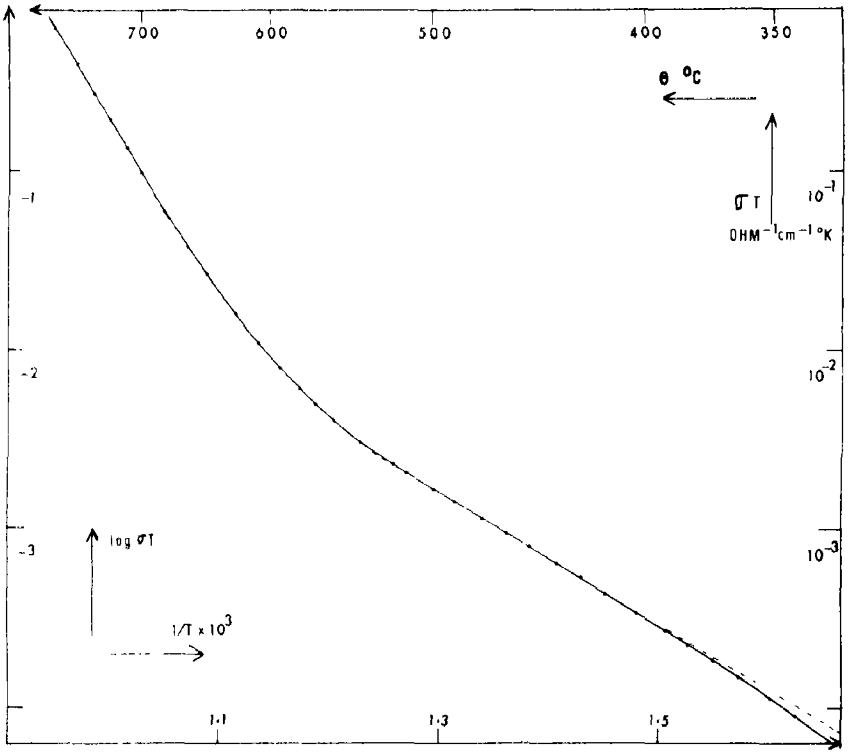

Fig. 2. Conductivité des cristaux C (contenant 12×10^{-6} ions Sr^{2+}).

des ions Sr^{2+}, est égale au nombre de transport de ces ions. Cette valeur est négligeable puisque le degré d'association p des ions Sr^{2+} avec les lacunes est négligeable dans ce domaine de température pour cette teneur en dopant.

On peut donc admettre que la conductibilité dans le domaine extrinsèque est due essentiellement à la migration des cations par lacunes libres.

Nous avons effectué les mesures de la conductibilité dans les cristaux de puretés différentes. Le meilleur ajustement des points expérimentaux à la fonction théorique (11):

$$\sigma = \frac{\sigma_0}{T}\exp - \frac{H}{kT}$$

a été calculé selon la méthode des moindres carrés.

Les résultats obtenus dans le domaine extrinsèque sont groupés dans le Tableau 1 dans lequel sont indiqués: la nature du cristal, l'intervalle de température dans lequel a été effectué l'ajustement, les grandeurs σ_0 et H, ainsi que la température de raccordement avec l'extrapolation de la section pseudo-linéaire obtenue à haute température.

Le mécanisme proposé est en outre confirmé par la mesure des coefficients de diffusion de Na^+ dans les cristaux du type D qui peuvent être représentés par l'équation (7):

$$D_2{}^+ = 3{,}53 \times 10^{-6} \exp - \frac{0{,}72}{kT} \text{cm}^2/\text{sec}.$$

Finalement nous pouvons attribuer à l'enthalpie de migration de Na^+ la valeur de 0,72 eV.

(2) *Enthalpie de formation d'un couple de lacunes*

Il est alors possible de calculer l'enthalpie de formation des défauts de Schottky Hd si

Tableau 1. Paramètres de la conductivité extrinsèque

Cristaux	Nature	Intervalle de température (°C)	σ_0 ($\Omega^{-1}\,cm^{-1}\,°K$)	H (eV)	Température de coude (°K)
A	Harshaw purs	386–419	5,30	0,70	765,5
B	Quartz et Silice	397–478	22,1	0,72	811
C	Harshaw dopés $12 \times 10^{-6}\,Sr^{2+}$	415–509	84,1	0,72	868
D	Harshaw dopés $27 \times 10^{-6}\,Sr^{2+}$	406–535	169	0,73	895

l'on connait la somme $(Hd/2)+Hm^+$. Pour cela nous nous portons vers les coefficients d'autodiffusion de Na^+ mesurés aux hautes températures que l'on peut représenter globalement par l'équation (8):

$$D = 33{,}16 \exp - \frac{1{,}975}{kT}\ \mathrm{cm^2/sec}.$$

Pour atteindre le terme de migration par lacunes libres, il faut en outre retrancher la faible contribution (de l'ordre de 4 pour cent) des paires dont le calcul est indiqué au paragraphe 4: nous arrivons ainsi pour la diffusion du cation par les lacunes cationiques à l'équation:

$$D = 29{,}51 \exp\left(-\frac{1{,}97}{kT}\right)$$

soit

$$\frac{Hd}{2} + Hm^+ = 1{,}97.$$

D'où

$$Hd = 2{,}50\ \mathrm{Ev}.$$

Afin de connaître la concentration des lacunes thermodynamiques donnée par l'équation (1) nous devons déterminer Sd.

(3) *Entropie de formation d'un couple de lacunes*

La valeur de Sd, variation d'entropie de formation d'un couple de défauts, peut être calculée par comparaison des équations (7) et (8).

Soit par l'intersection des deux courbes $\log D^+$ correspondant respectivement aux coefficients de diffusion du cation dans les domaines intrinsèque et extrinsèque obtenus dans des cristaux de concentration en cations bivalents égale à C; Le point d'intersection se produisant à la température T_0 donne la relation:

$$\exp\left(\frac{Sd}{2k}\right) \exp\left(-\frac{Hd}{2kT_0}\right) = C \qquad (13)$$

d'où l'on tire:

$$\exp\left(\frac{Sd}{2k}\right) = 258.$$

Soit par la comparaison des termes de fréquence:

$$\frac{D_{0\mathrm{int}}}{D_{0\mathrm{ext}}} = \frac{\exp\,(Sd/2k)}{C}$$

ce qui donne:

$$\exp\left(\frac{Sd}{2k}\right) = 254$$

en bon accord avec la précédente détermination:

on en tire:

$$\frac{Sd}{2k} = 5{,}55.$$

Soit:

$$Sd = 0{,}96 \times 10^{-3}\,\mathrm{eV}\,d^{0-1}$$

L'équation (1) donne alors la concentration de lacunes à toute température:

$$(n^+ \cdot n^-)^{1/2} = 258 \exp - \frac{2{,}50}{2kT}$$

ainsi au point de fusion (800°C):

$$n^+ = n^- = 3{,}50 \times 10^{-4}.$$

L'équation (13) permet d'évaluer la concentration en cations du type Sr^{2+} d'un cristal 'pur', tant que cette concentration reste suffisamment faible pour ne pas avoir à tenir compte de l'équilibre (3); la température T_0 est donnée dans ce cas par l'intersection des courbes log $(D_1{}^+)$ et log (D_2 calc). Par exemple, dans les cristaux Harshaw et Quartz et Silice, C est respectivement égal à $1{,}55 \times 10^{-6}$ et $4{,}7 \times 10^{-6}$ (à condition d'exprimer les concentrations en équivalent de strontium).

(4) *Enthalpie de migration des anions*

L'interprétation des mesures des coefficients de diffusion du chlore est plus délicate car le rôle des paires de lacunes est alors loin d'être négligeable. En effet dans notre travail antérieur sur l'autodiffusion de Cl^- dans des cristaux dopés[16] nous avons observé que le coefficient de diffusion du chlore commence par décroitre en raison de la présence d'impuretés cationiques bivalentes. Ce résultat était interprété qualitativement par une diminution de la concentration des lacunes anioniques due à la relation du produit de solubilité (1). Cependant, nous avions noté qu'à plus basse température, D devenait presque indépendant de la concentration en dopant, ce qui mettait en évidence la présence de paires de lacunes.

Fuller[25] a séparé les contributions des lacunes anioniques et des paires de lacunes dans le cas du chlorure de potassium en utilisant des cristaux également dopés par des ions Sr^{2+}. Nous avons préféré une méthode d'itération à sa méthode autocohérente. En effet, la connaissance de la concentration des lacunes permet d'adapter les mesures des coefficients de diffusion de Cl^- à l'équation (6 bis) avec deux paramètres de moins. La méthode est la suivante:

Les mesures précédentes relatives au cation nous ont permis de calculer une première valeur de Gd. D'autre part la concentration C du dopant est connue. Ces valeurs peuvent alors être reportées dans l'équation (6 bis) dans laquelle subsisteront alors deux inconnues: la fréquence de saut de l'anion ν^- ainsi que le coefficient de diffusion des paires. Afin de pouvoir résoudre ce système nous tirons parti du fait que si l'on dispose des coefficients de diffusion de l'anion D et D' à une même température pour deux cristaux de concentration C et C' en impuretés bivalentes, la différence $D-D'$ est indépendante de la participation des paires. (En effet c'est une conséquence du produit de solubilité (1) que la proportion des paires demeure constante quelle que soit la teneur en dopant).

On peut ainsi en tirer l'expression de la fréquence de saut des anions dans les lacunes libres ν^- et ensuite obtenir le coefficient de diffusion des paires. Ce dernier est ensuite retranché du coefficient de diffusion de ^{22}Na du domaine intrinsèque ce qui permet d'améliorer la valeur de Gd qui est reportée dans le même programme et ainsi de suite.

Nous avons utilisé les mesures précédemment publiées[16]; rappelons que dans le cristal Harshaw les coefficients de diffusion de Cl^- sont représentés par l'équation:

$$D = 60{,}7 \exp\left(-\frac{2{,}14}{kT}\right) \text{cm}^2/\text{sec}.$$

La diffusion de l'anion par les lacunes libres dans le cristal est donnée par l'équation:

$$D = 4a^2\nu_0 \exp\left(\frac{Sd/2 + Sm^-}{k}\right) \times \exp - \left(\frac{Hd/2 + Hm^-}{kT}\right) = 36{,}2 \exp\left(-\frac{2{,}11}{kT}\right) \text{cm}^2/\text{sec}.$$

On en déduit la valeur de Hm^- égale à 0,86 eV.

La diffusion par les paires de lacunes est représentée par l'expression:

$$Dp = 5200 \exp\left(-\frac{2{,}63}{kT}\right) \text{cm}^2/\text{sec}.$$

dont l'enthalpie d'activation est la somme:

$$Hd + H_p{}^a + H_m{}^p = 2{,}63 \text{ eV}$$

où $H_p{}^a$ est l'enthalpie d'association lacune cationique + lacune anionique, et $H_m{}^p$ est l'enthalpie de migration d'une paire de lacunes.

Les valeurs des enthalpies sont groupées dans le tableau récapitulatif ci-dessous:

Enthalpies de formation et de migration des lacunes (en eV)

Hd	*Hm⁺*	*Hm⁻*
2,50	0,72	0,86

(5) *Entropies de migration des cations et des anions*

Outre l'entropie de formation de lacune il reste à déterminer les entropies de migration. Ces dernières grandeurs ne sont pas directement accessibles; seuls les termes préexponentiels sont calculables:

$$4a^2\nu_0 \exp\frac{Sm^+}{k} = 0{,}114$$

$$4a^2\nu_0 \exp\frac{Sm^-}{k} = 0{,}140.$$

Cependant si l'on adopte arbitrairement pour ν_0 la fréquence de Debye: $\nu_0 = 4{,}55 \times 10^{12}$ sec^{-1}, on obtient les valeurs suivantes:

$$\frac{Sm^+}{k} = 2{,}07 \quad \text{et} \quad \frac{Sm^-}{k} = 2{,}27$$

Soit:

$$Sm^+ = 1{,}78 \times 10^{-4} \text{ eV d}^{0^{-1}}$$

et

$$Sm^- = 1{,}96 \times 10^{-4} \text{ eV d}^{0^{-1}}.$$

Les valeurs des entropies sont indiquées dans le tableau suivant, à titre de comparaison:

Entropies de formation et de migration des lacunes

$Sd/2k$	Sm^+/k	Sm^-/k
5,55	2,07	2,27

(6) *Mise en évidence des conductibilités individuelles*

Nous avons vu que la conductibilité intrinsèque est la somme de la conductibilité cationique et de la conductibilité anionique; afin de le vérifier, nous avons effectué les mesures des nombres de transport, qui sont données dans le tableau 2 comparativement aux rapports: $r = (D_1{}^+ - D_p)/(D_1{}^+ + D_1{}^- - 2Dp)$ calculés aux températures correspondantes. L'accord est dans les limites de l'indétermination expérimentale du nombre de transport égale à 3 pour cent; ces mesures montrent une fois encore que la mobilité de l'anion ne doit pas être négligée devant la mobilité du cation dans le domaine intrinsèque.

Tableau 2. Nombres de transport

θ (0°C)	580	600	650
t^+	0.81	0.83	0.84
r	0.845	0.839	0.825

Remarquons que ces valeurs sont très différentes des anciennes mesures de Tubandt (1931) qui à 600°C trouvait $t^+ = 0.95$[17], probablement pour les raisons signalées dans le chapitre des méthodes expérimentales. Ce point semble confirmé par la différence des valeurs des nombres de transport obtenus dans KCl, d'une part par cet auteur et, d'autre part plus récemment (1957) par Kerkhoff[18]. Par exemple à 600°C, le premier auteur attribue à t^+ la valeur de 0,88, alors que le second donne la valeur de 0,70.

Enfin, nous avons comparé la conductibilité intrinsèque à la diffusion due aux lacunes libres, afin de vérifier l'équation (10). Dans ce but nous avons représenté les mesures de σ par la fonction approchée:

$$\sigma = \frac{\sigma_0}{T} \exp - \frac{H}{kT}$$

dans l'intervalle des températures comprises entre 600 et 720°C. Le meilleur ajustement des paramètres σ_0 et H à partir des valeurs expérimentales a été calculé par la méthode des moindres carrés; finalement on obtient:

$$\sigma T = 0{,}2006 \times 10^{10} \exp - \frac{1{,}998}{kT}\, \Omega^{-1}\,\mathrm{cm}^{-1}\,{}^{\circ}\mathrm{K}.$$

En effet, la conductibilité est égale, en toute rigueur, à la somme de deux exponentielles, ce qui explique la légère courbure généralement observée dans le domaine intrinsèque; cependant on peut en première approximation, représenter cette somme par une seule exponentielle.

La même programme a été utilisé afin de représenter la somme des coefficients de diffusion du cation et de l'anion après soustraction de la contribution des paires, dans le même intervalle de température, ce qui revient à poser l'identité:

$$D_0^{+} \exp\left(-\frac{H^{+}}{kT}\right) + D_0^{-} \exp\left(-\frac{H^{-}}{kT}\right) \equiv$$

$$D_0 \exp - \frac{H}{kT} = D.$$

On obtient ainsi:

$$D = 49{,}0 \exp - \frac{1{,}995}{kT}\, \mathrm{cm}^2/\mathrm{sec}.$$

L'argument et le terme préexponentiel des fonctions calculées: D et $\sigma T \times k/Ne^2$ sont comparées ci-dessous.

$D_0 = 49{,}0$	$H = 1{,}995$
$\frac{\sigma_0 k}{2} = 48{,}4$ Ne^2	$H = 1{,}998$

Cet excellent accord entre les valeurs de la conductivité et des coefficients de diffusion démontre, d'une part la qualité des méthodes expérimentales, et, d'autre part la validité des équations (8), (9) et (10). L'étude rigoureuse de la relation de Nernst-Einstein devient ainsi possible.

5. RELATION DE NERNST-EINSTEIN

Au premier abord il semble que c'est dans le domaine intrinsèque que la relation de Nernst-Einstein est le plus directement applicable, car dans ce domaine, nous avons vu que les concentrations des lacunes anioniques et des paires de lacunes sont négligeables devant la concentration des lacunes cationiques; aussi on peut s'attendre à ce que dans ce domaine la conductibilité et la diffusion de Na^+ s'exercent par le même mécanisme, à savoir la migration des lacunes cationiques.

Cependant on se trouve devant un double écueil; si les cations bivalents sont introduits en trop forte concentration, une fraction de ceux-ci donne des complexes qui ne participent pas à la conductibilité mais qui peuvent contribuer à la diffusion, ce qui conduit à un rapport $D^*/D_{\mathrm{calc}} > 1$; si au contraire cette concentration est trop faible (domaine extrinsèque des cristaux purs), on constate alors que la relation de Nernst-Einstein n'est plus applicable (Figs. 3 et 4). Ce point semple ne pouvoir s'interpréter que par la méconnaissance de la nature des impuretés résiduelles présentes. Cependant nous avons constaté expérimentalement qu'entre ces deux situations extrêmes la relation de Nernst-Einstein se trouvait vérifiée dans le domaine

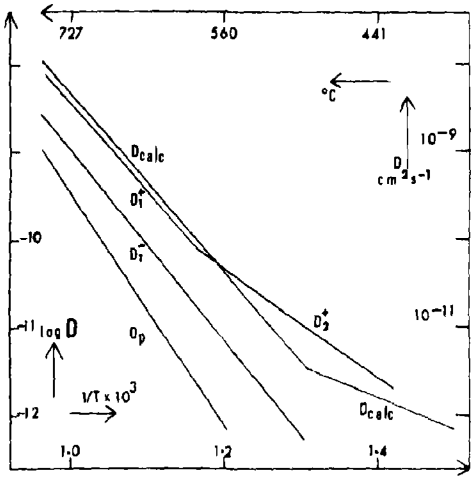

Fig. 3. Comparaison des coefficients de diffusion mesurés et calculés dans les cristaux *A*.

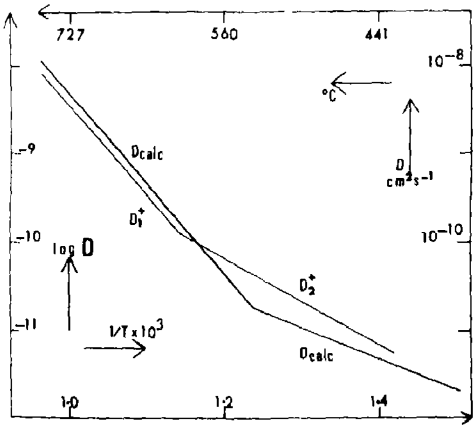

Fig. 4. Comparaison des coefficients de diffusion mesurés et calculés dans les cristaux *B*.

extrinsèque avec une précision de l'ordre de 4 pour cent lorsque la concentration en Sr^{2+} est égale à 27×10^{-6} (Fig. 5).

En résumé, les résultats obtenus dans le domaine extrinsèque ne permettent pas un test rigoureux de la relation de Nernst-Einstein.

Par contre, dans le domaine intrinsèque, dans lequel interviennent à la fois, les lacunes libres, cationiques et anioniques, et les paires de lacunes dans la comparaison des valeurs de D^* et $D_{\text{calc.}}$, nous avons vu que chaque terme a pu être déterminé de façon précise.

Nous avons comparé, d'une part les valeurs de *D* calculées à partir des mesures de conductivité, qui, selon l'équation (10) représentent la somme des migrations par les lacunes libres, cationiques et anioniques, à d'autre part, la somme des coefficients de diffusion de l'anion et du cation dus aux lacunes libres (donnée par les mesures de *D* Na^+ et DCl^- après déduction de la contribution des paires (Dp)).

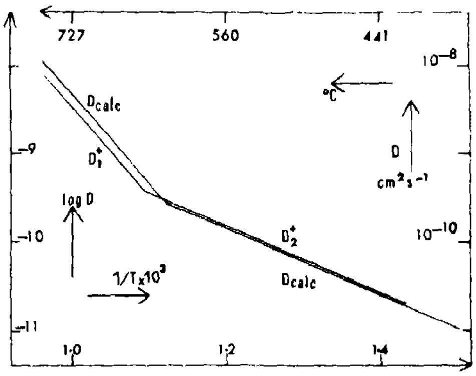

Fig. 5. Comparaison des coefficients de diffusion mesurés et calculés dans les cristaux *D*

Le Tableau 3 représente quelques unes de ces mesures; afin d'éviter les erreurs d'arrondi, les calculs (sur ordinateur) ont été effectués avec un nombre supérieur de décimales.

La valeur moyenne obtenue pour le rapport D^*/D_{calc} calculée sur plus de cent mesures effectuées entre 600 et 720°C dans douze échantillons différents est la suivante:

$$\frac{D^*}{D_{\text{calc}}} = 1{,}04 \pm 0{,}02;$$

Enfin, il faut tenir compte des effets isotopiques puisque les coefficients de diffusion ont été déterminés par les isotopes ^{22}Na et ^{36}Cl alors que le chlorure de sodium est constitué d'une part, de ^{23}Na et d'autre part, de $^{35}Cl + {}^{37}Cl$ dans le rapport 3 à 1.

Tableau 3. Verification de la relation d'Einstein

θ (°C)	$D_1^+ - D_p$	$D_1^- - D_p$	$D_1^+ + D_1^- - 2D_p$	D_{calc} (Nernst–Einstein)	$\frac{D_1^+ + D_1^- - 2D_p}{D_{calc}}$
721,5	$3{,}10 \times 10^{-9}$	$7{,}43 \times 10^{-10}$	$3{,}84 \times 10^{-9}$	$3{,}73 \times 10^{-9}$	1,03
699,3	$1{,}83 \times 10^{-9}$	$4{,}23 \times 10^{-10}$	$2{,}26 \times 10^{-9}$	$2{,}18 \times 10^{-9}$	1,035
676,3	$1{,}04 \times 10^{-9}$	$2{,}30 \times 10^{-10}$	$1{,}27 \times 10^{-9}$	$1{,}21 \times 10^{-9}$	1,05
652,0	$5{,}52 \times 10^{-10}$	$1{,}17 \times 10^{-10}$	$6{,}69 \times 10^{-10}$	$6{,}36 \times 10^{-10}$	1,05
629,9	$3{,}01 \times 10^{-10}$	$6{,}12 \times 10^{-11}$	$3{,}62 \times 10^{-10}$	$3{,}44 \times 10^{-10}$	1,05
606,5	$1{,}54 \times 10^{-10}$	$2{,}98 \times 10^{-11}$	$1{,}83 \times 10^{-10}$	$1{,}76 \times 10^{-10}$	1,04

Pour le calcul de l'effet isotopique nous prenons la simple loi en $1/\sqrt{M}$, mise en évidence expérimentalement par *M*. Chemla[13] par l'étude de la diffusion du couple d'isotopes ^{22}Na–^{24}Na dans NaCl, sans faire intervenir le facteur de corrélation dont nos expériences ne confirment pas l'existence; on obtient ainsi:

$$^{23}D = \sqrt{\frac{22}{23}}\,{}^{22}D$$

soit:

$$D^+ = 0{,}978\,{}^{22}D$$

et:

$$\begin{aligned} D &= \tfrac{3}{4}\,{}^{35}D + \tfrac{1}{4}\,{}^{37}D \\ &= \frac{3}{4}\sqrt{\frac{36}{35}}\,{}^{36}D + \frac{1}{4}\sqrt{\frac{36}{37}}\,{}^{36}D. \end{aligned}$$

Soit:

$$D = 1{,}007\,{}^{36}D$$

et finalement, compte tenu des effets isotopiques, le rapport moyen D^*/D_{calc} prend la valeur:

$$\frac{D^*}{D_{calc}} = 1{,}02 \pm 0{,}02.$$

6. CONCLUSION

Il ressort de ce travail que l'étude de la validité de la relation de Nernst–Einstein et de l'intervention des effets de corrélation dans les halogénures alcalins nécessite un examen approfondi de tous les mécanismes qui participent aux processus de transport. En particulier, notre attention doit être portée sur les mécanismes élémentaires qui, par leur nature, peuvent apporter des écarts, c'est à dire essentiellement la diffusion par paires de lacunes et par associations cations bivalents-lacune cationique.

C'est grâce à des mesures rendues très précises par une technique élaborée que nous avons pu présenter une synthèse de l'ensemble des résultats expérimentaux portant sur les processus de transport: autodiffusion des anions et des cations, conductibilité électrique et nombres de transport. Ces mesures, associées à notre méthode de production de cristaux dopés de concentrations bien connues, nous ont permis de présenter un ensemble cohérent des valeurs thermodynamiques rendant compte de toutes les grandeurs expérimentales obtenues.

Pour résumer le chemin suivi dans ce développement thermodynamique, nous nous contenterons de rappeler les étapes qui ont conduit à la détermination de chacune de ces valeurs.

(1) Les mesures de conductibilité et de coefficients d'autodiffusion dans le domaine extrinsèque de cristaux dopés ont permis de calculer l'enthalpie de migration Hm^+.

(2) Cette valeur portée dans les mesures des coefficients d'autodiffusion du cation dans le domaine intrinsèque a permis d'atteindre une première valeur approchée de l'enthalpie de formation d'un couple de lacunes.

(3) Par comparaison des coefficients d'autodiffusion du cation dans des cristaux dopés, nous avons pu calculer l'entropie de formation d'un couple de lacunes.

(4) L'étude de la diffusion de l'anion dans des cristaux dopés a mis en évidence l'intervention d'un produit de solubilité qui provoque une diminution du nombre de lacunes anioniques libres lorsque la concentration des lacunes cationiques augmente. En outre, la variation du coefficient de diffusion de l'anion avec la concentration en dopant montre la nécessité de faire intervenir un processus par paires de lacunes et permet le calcul du coefficient de diffusion par paires.

(5) Il devient ainsi possible, compte tenu de tous ces processus élémentaires, d'aboutir à un examen approfondi de la validité de la relation de Nernst-Einstein dans les cristaux ioniques.

Les calculs ainsi développés, légèrement corrigés de l'effet isotopique dû à l'emploi de ^{22}Na et ^{36}Cl aboutissent à un ensemble de valeurs telles que:

$$1{,}00 \leqslant D^*/D_{\text{calc.}} \leqslant 1{,}04.$$

Ce résultat, afin de trouver sa pleine signification, nécessite une discussion approfondie de la précision avec laquelle il est obtenu. Cette discussion doit porter sur les mesures de D^*, D_{calc} et T. Nous avons vu dans le chapitre des méthodes expérimentales comment nous avons tenté d'obtenir la plus grande précision possible sur T de façon à déterminer au mieux les valeurs de D et σ en valeur absolue; D'autre part, l'expression qui nous intéresse est le rapport D^*/D_{calc} ; rappelons qu'afin d'éliminer l'influence de la température, les mesures de D et σ ont été effectuées au moyen de cellules et de méthodes de mesure de la température identiques.

La précision sur les mesures des coefficients de diffusion a été antérieurement discutée[26]. Grâce en particulier au haut degré de perfectionnement de la technique de découpage, l'erreur sur D^* est égale à ± 1 pour cent.

En ce qui concerne la conductibilité électrique, l'appareillage donne une précision supérieure à 1/1000 sur les valeurs des résistances. Cependant les mesures effectuées d'un échantillon à l'autre montrent des fluctuations de ± 1 pour cent. La raison de cet écart provient de l'erreur sur la détermination des dimensions du cristal, erreur égale à 0,02 mm. Les échantillons étant des parallélépipèdes de dimensions moyennes: 10 × 10 × 2 mm, il en résulte une erreur de 1 pour cent dans la détermination de $\sigma = (l/R)(1/S)$. La valeur de cet écart est par ailleurs concrétisée par la différence entre les masses des échantillons obtenues, d'une part, par pesée et, d'autre part, par application de la relation $m = \rho \times l \times S$, différence de l'ordre de 1 pour cent.

En conclusion, le rapport $D^*/D_{\text{calc.}}$ est déterminé avec une précision de ±2 pour cent, bien en accord avec l'ensemble des mesures, et prend ainsi la valeur: 1,02 ± 0,02.

Or, la théorie des corrélations prévoyait pour ce rapport la valeur de 0,7815.

Par conséquent, on peut affirmer que dans le cas du chlorure de sodium, la relation de Nernst-Einstein est bien vérifiée, sans introduire le facteur de corrélation.

La théorie des corrélations telle qu'elle a été établie par Le Claire et Lidiard[23] est mathématiquement irréprochable; puisque nos résultats expérimentaux aboutissent à la vérification de la relation de Nernst-Einstein sans l'intervention du facteur de corrélation, nous devons réexaminer le modèle sur lequel est fondée cette théorie.

La théorie du mécanisme de diffusion par lacunes représente les mouvements dans le réseau par une succession de 'photographies' sur lesquelles les ions, et par conséquent les lacunes sont situées après chaque saut aux noeuds du réseau. Ce modèle rigide, où les ions et les lacunes sont discernables, conduit à la corrélation des sauts successifs d'un ion marqué.

Afin de rechercher un modèle où n'apparaissent pas d'effets de corrélation, il faut admettre, soit un mécanisme interstitiel que les calculs theoriques d'énergie d'activation ont repoussé, soit un mécanisme lacunaire moins rigide dans le temps et dans l'espace; on pourrait ainsi envisager les deux hypothèses suivantes:

(1) Il est raisonnable de penser qu'à courte distance les ions vibrent en phase, ce qui rend probables les successions de quelques sauts colinéaires dont l'effet est d'éloigner la lacune qui vient de permettre le saut de l'ion marqué, rendant ainsi plus aléatoire son deuxième saut.

(2) L'image représentant la lacune comme un volume vide parfaitement centré sur un noeud du réseau est en contradiction avec la relaxation des ions. Nachtrieb *et al.*[27] supposent même que, dans les métaux, le petit volume englobant la lacune et les atomes voisins est aussi désordonné que dans l'etat liquide. Nos résultats semblent indiquer que dans le cas du chlorure de sodium, il n'est pas possible de fixer la position des ions au voisinage de la lacune. Si on suppose ainsi la lacune délocalisée dans une petite région du réseau, le nombre de sauts possibles dans le réseau du chlorure de sodium pourrait être très supérieur à 12, ce qui conduirait à une décorrélation des sauts.

REFERENCES

1. LEHFELDT W. *Z. Phys.* **85**, 717 (1933).
2. FIZEL H. et MAURER R. *J. chem. Phys.* **18**, 1003 (1950).
3. JAIN S. et DAHAKE S. *Phys. Lett.* **3**, 308 (1963).
4. DREYFUS R. et NOWICK A. *J. appl. Phys.* **33**, 473 (1962).
5. BIZOUARD M. PANTALONI J. et LAM PHAM, *C.r. Acad. Sci. Paris* **264**, 1461 (1967).
6. ROTHMAN S. BARR L., ROWE A. et SELWOOD P., *Phil. Mag.* **14**, 50 (1966).
7. KIRK D. et PRATT P., *Proc. Br. Ceram. Soc.* **9**, 215 (1967).
8. BROWN N. et HOODLESS I., *J. Phys. Chem. Solids* **28**, 2297 (1967).
9. ALNATT A. et PANTELIS P., *Solid St. Commun.* **58**, 116 (1969).
10. MAPOTHER D. CROOKS N. et MAURER R., *J. chem. Phys.* **18**, 1231 (1950).
11. BENIERE F. et CHEMLA M., *C.r. Acad. Sci. Paris* **266**, 660 (1968).
12. LAURENT J. et BENARD J., *J. Phys. Chem. Solids* **3**, 7 (1957).
13. CHEMLA M., *Ann. Phys.* **1**, 959 (1956).
14. LAURANCE N. *Phys. Rev.* **120**, 57 (1960).
15. BARR L., MORRISON J. et SCHROEDER P., *J. appl. Phys.* **36**, 624 (1965).
16. BENIERE F., BENIERE M. et CHEMLA M., *C.r. Acad. Sci. Paris* **267**, 633 (1968).
17. TUBANDT C., REINHOLD H. et LIEBOLD G., *Z. anorg. Chem.* **197**, 225 (1931).
18. KERKHOFF *Z. Phys.* **130**, 449 (1957).
19. LIDIARD A. B., *Handbuch der Physik*, Vol. 21 Springer. Berlin (1957).
20. THARMALINGAM K. et LIDIARD A. B., *Phil. Mag.* **6**, 1157 (1961).
21. ADDA Y. et PHILIBERT J., *La Diffusion dans Les Solides*, *Paris* (1966).
22. BARDEEN J. et HERRING C., *Imperfections in Nearly Perfect Crystals* Wiley, New York (1952).
23. LE CLAIRE A. et LIDIARD A. B., *Phil. Mag.* **1**, 518 (1956).
24. COMPAAN K. et HAVEN Y., *Trans. Faraday Soc.* **52**, 786 (1956).
25. FULLER R., *Phys. Rev.* **142**, 524 (1966).
26. BENIERE F., BENIERE M. et CHEMLA M., *J. chim. Phys.* **66**, 898 (1969).
27. NACHTRIEB N. et HANDLER G., *Acta Metall.* **2**, 797 (1954).

J. Phys. Chem. Solids Pergamon Press 1970. Vol. 31, pp. 1221–1224. Printed in Great Britain.

THERMAL ANNEALING OF IRRADIATED LITHIUM HYDRIDE–II

A PROPOSED MECHANISM*

H. R. LEIDER

Lawrence Radiation Laboratory, University of California, Livermore, Calif. 94550, U.S.A

(*Received* 11 *August* 1969; *in revised form* 12 *November* 1969)

Abstract – Radiation causes considerable internal decomposition of lithium hydride, ultimately resulting in gross swelling and formation of bubbles of hydrogen and particles of metallic lithium. When irradiated LiH is heated, stored energy is evolved as the free lithium and hydrogen back-react to form LiH. A mechanism is proposed that describes the back-reaction as proceeding by H_2 molecules 'redissolving' in the lattice, and then migrating to Li particles, where recombination occurs. An expression is developed that relates the size and the concentration of the hydrogen bubbles to the temperature characterizing the release of the stored energy. The data are shown to be consistent with this model

IRRADIATION results in substantial decomposition of LiH into Li metal aggregates and H_2 bubbles[1-4]. Measurements of stored energy yield values which are consistent with the assumption that thermal annealing causes a back-reaction between the 'free' Li and H_2 to form LiH. Assuming the reaction to be

$$Li_{(c)} + \frac{1}{2}H_{2(c)} \rightarrow LiH_{(c)},$$

the energy found is ~ 20 kcal/mole[5], which is close the standard heat of formation of LiH[6].

A model for the recombination process can be developed that combines the results of several independent experiments to explain the stored energy release; namely, pulsed NMR measurement of 'free' Li and H_2[1], swelling due to irradiation[1], electron microscope observation of bubble sizes[4] and the stored energy measurements themselves[5].

Several possible mechanisms for the back-reaction can be readily visualized. For instance, diffusion of bubbles[7] may result in collisions between H_2 bubbles and Li 'bubbles', causing back-reaction. In such a process either the H_2 bubbles or the Li aggregates might be mobile. Likewise, the back-reaction could be due to the 're-solution' of either H_2 or Li, or both, in the lattice, followed by their migration as atoms or molecules to recombination sites. Combinations of bubble motion and molecular diffusion can also be considered. However, one experimental finding indicates a particular choice of model. When examined by electron microscopy, thermally annealed crystals (those in which the back-reaction is complete) are seen to retain individual cubic voids, just as are found in irradiated material examined before annealing[8]. What is more, their edges and corners are still sharp and well-defined, without marked coalescence. This observation is inconsistent with a process involving bubble collisions or with the back-reaction occurring at the site of H_2 bubbles, as would be expected if Li were to migrate. Thus the possibility that the hydrogen leaves the bubbles and then diffuses to Li sites where back-reaction occurs seems more likely.

Consider the following assumptions:

(1) Stored energy measured by differential thermal analysis (DTA) represents the energy

---

*Work performed under the auspices of the U.S. Atomic Energy Commission.

released from the back-reaction of 'free' hydrogen and lithium produced by irradiation[5]. For simplicity we will regard the stored energy as being entirely released at the temperature of the principal peak of the DTA spectrum, T_p. This is appropriate if the energy release at T_p is actually proportional to the total stored energy.

(2) The hydrogen which is observed as a 'motionally-narrowed' species by pulsed NMR exists as bubbles of gas[3,4]; the lithium occurs as small, metallic aggregates [1-3].

(3) The observed macroscopic swelling of irradiated LiH is due entirely to hydrogen bubbles; the lithium aggregates form only when free volume is available[1].

If the over-all back-reaction mechanism can be described as a permeation process, then the rate depends on the product of the rate[9] at which H_2 molecules 'dissolve' in the lattice and the rate at which they subsequently migrate to lithium sites.

The rate of solution will depend on the frequency of collision of H_2 molecules with the bubble walls, the total surface area associated with the bubbles, and an exponential term containing the heat of solution; the rate of migration will depend on the diffusion coefficient and the distance the H_2 molecules must migrate. Since the Li aggregates have not been directly observed, it is assumed that their distribution is the same as that of the hydrogen bubbles, so that the distance between hydrogen and lithium aggregates is approximated by the cube-root of the bubble concentration. Then the rate is

$$\phi = \left[K_1 \frac{[H_2]}{\Delta V} r^2 \rho T_p{}^{1/2} \exp\left(-\frac{\Delta H_s}{RT_p}\right)\right] \times \left[K_2 (\rho^{1/3})^2 \exp\left(-\frac{\Delta H_m}{RT_p}\right)\right] \qquad (1)$$

and

$$\phi = \frac{K[H_2]r^{-1}}{(1+\Delta V)} \rho^{2/3} T_p{}^{1/2} \exp\left(-\frac{\Delta H_s + \Delta H_m}{RT_p}\right) \qquad (2)$$

where ΔV = fractional volume increase on irradiation,

r = average bubble edge length,

ρ = bubble concentration; $\rho = \Delta V / r^3(1+\Delta V)$ from Assumption 3 above,

$[H_2]$ = concentration of 'motionally-narrowed' hydrogen,

T_p = temperature of the principal DTA peak,

ΔH_s = heat of solution,

ΔH_m = activation energy for migration.

The first term in brackets in equation (1) is the rate of solution; in the second bracket is the expression for the rate of migration [i.e. $(D/x^2) \propto (1/t)$].

The rate of energy released at T_p is:

$$\frac{dE}{dt} \propto \phi = k\Delta T,$$

where ΔT = temperature rise at T_p.

From Assumption (1),

$$\frac{\Delta T(1+\Delta V)}{[H_2]} = \text{a constant.} \qquad (3)$$

This quantity is constant to within a factor of ~ 2 for all the measurements. It is plausible to attribute at least part of the deviation from constancy to experimental causes. Differences in heat transfer properties from sample to sample because of imperfect packing of powdered samples can affect ΔT considerably.

$$\frac{\Delta T(1+\Delta V)}{[H_2]} = C = \frac{\phi(1+\Delta V)}{[H_2]} \qquad (4)$$

and

$$C = kr^{-1}\rho^{2/3}T_p{}^{1/2} \exp\left(-\frac{\Delta H}{RT_p}\right) \qquad (5)$$

where

$$\Delta H = \Delta H_m + \Delta H_s,$$

so that

$$\frac{r\rho^{-2/3}}{T_p{}^{1/2}} = A \times \exp\left(-\frac{\Delta H}{RT_p}\right) = Q. \qquad (6)$$

Figure 1 shows that this functional dependence is followed reasonably well. Table 1 lists the measured quantities used to calculate Q for Fig. 1. If the activation energy for migration of H_2 molecules in LiH is similar to that for ^3He, namely $\Delta H_m \approx 30$ kcal/mole[10], then the heat of solution for H_2 in LiH would be $\Delta H_s \approx 50$ kcal/mole; however, at the moment this is mere conjecture.

In the above discussion the hydrogen is always considered to be molecular. This is justified by the fact that in irradiated LiH, the only paramagnetism observed is that associated with Li metal aggregates or F-centers[2, 11]. This is so even during irradiation at 80°K. If atomic hydrogen did exist, even transitorily, it might be expected that these atoms could have been seen by a technique as sensitive as electron spin resonance. Moreover, the V-type optical

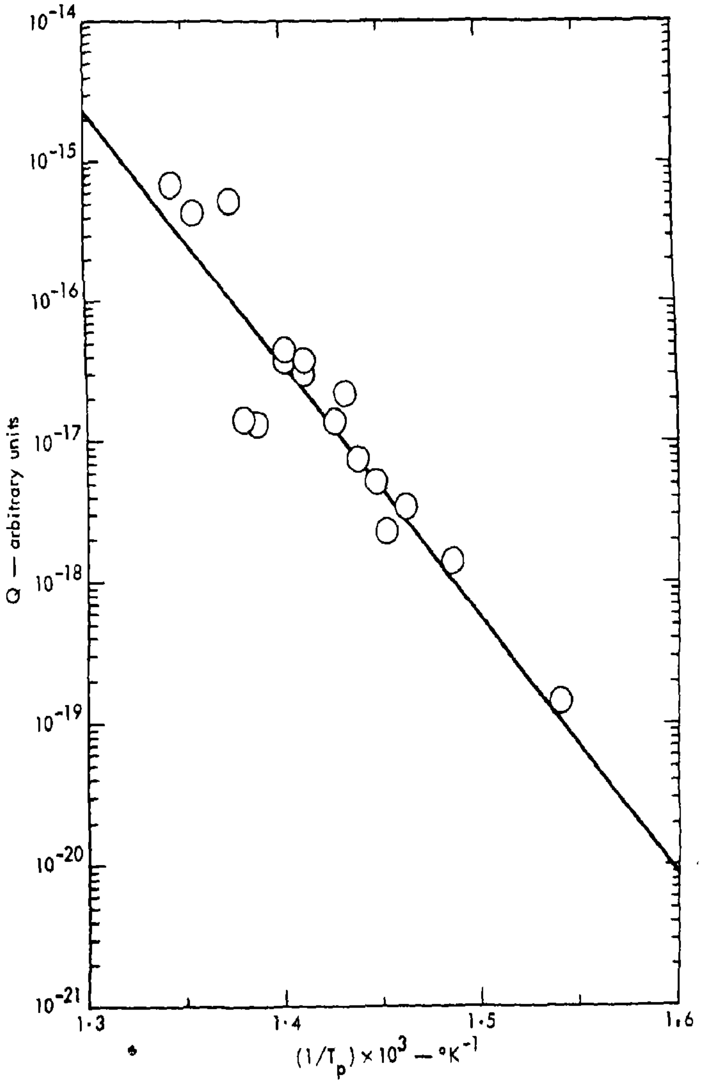

Fig. 1. A plot of log Q vs. $1/T_p$. The line is a least-squares fit to the points; the slope corresponds to $\Delta H = 83{\cdot}4$ kcal/mole. The terms are defined in the text.

Table 1. The data used to calculate the quantities plotted in Fig. 1. The terms are defined in the text

T_p (Ref.[5]) (°K)	ΔV (Refs.[1, 8]) (cm³/cm³)	[H_2] (Refs.[1, 8]) $[H]_2$ (10^{21} molecules/cm³)	r (Ref.[8]) (Å)	ρ (bubbles/cm³)	Dose (Refs.[1, 8]) (10^9 rad.)
649·8	0·046	1·29	80	$8{\cdot}5\times10^{16}$	1·2
673·2	0·097	2·15	205	$1{\cdot}0\times10^{16}$	7·0
684·0	0·064	1·46	250	$3{\cdot}3\times10^{15}$	1·3
688·8	0·114	2·06	245	$6{\cdot}9\times10^{15}$	7·0
693·7	0·230	2·63	405	$3{\cdot}2\times10^{15}$	43·0
695·7	0·161	1·72	400	$2{\cdot}2\times10^{15}$	14·3
698·6	0·018	0·40	340	$4{\cdot}5\times10^{14}$	0·5
701·5	0·065	1·41	395	$1{\cdot}0\times10^{15}$	1·3
708·3	0·249	2·20	725	$5{\cdot}2\times10^{14}$	22·1
708·3	0·116	1·96	640	$3{\cdot}9\times10^{14}$	3·2
713·2	0·072	1·46	570	$3{\cdot}6\times10^{14}$	1·3
713·2	0·129	1·95	690	$3{\cdot}5\times10^{14}$	3·5
721·0	0·154	1·77	485	$1{\cdot}1\times10^{15}$	7·0
724·9	0·160	1·76	500	$1{\cdot}1\times10^{15}$	7·0
727·7	0·104	0·96	1485	$2{\cdot}8\times10^{13}$	3·6
737·6	0·112	0·88	1430	$3{\cdot}4\times10^{13}$	3·6
743·4	0·062	1·02	1450	$1{\cdot}9\times10^{13}$	25·8

absorption bands seen in irradiated LiH have been interpreted as being from molecular hydrogen trapped in the lattice[12]. These *V*-centers were found to be relatively stable to thermal or optical bleaching. Analogous sorts of diatomic molecules are also produced in alkali halides by irradiation[13].

One other observation supports the idea that hydrogen molecules are trapped in the LiH lattice. For several samples irradiated to relatively low doses ($<5\times10^8$ rad.), the measured stored energy was much larger than was expected from the amount of motionally-narrowed hydrogen seen by pulsed NMR[5]. This observation can be explained by a requirement that 'free' hydrogen be present which is neither paramagnetic nor able to move. A plausible interpretation is that a considerable quantity of isolated H_2 molecules is somehow trapped in the lattice in these samples.

Acknowledgements—Thanks are due to P. C. Souers, R. H. Condit, H. W. Newkirk and J. S. Kane for many valuable discussions and for a critical reading of the manuscript.

REFERENCES

1. SOUERS P. C., JOLLY T. A. and CLINE C. F., *J. Phys. Chem. Solids* **38**, 1717 (1967); SOUERS P. C., BLAKE T. S., PENPRAZE R. M. and CLINE C. F., *J. Phys. Chem. Solids* **30**, 2669 (1969).
2. PRETZEL F. E., LEWIS W. B., SZKLARZ E. G. and VIER D. T., *J. appl. Phys. Suppl.* **33**, 510 (1962); PRETZEL F. E., VIER D. T., SZKLARZ E. G. and LEWIS W. B., *Los Alamos Scient. Lab. Rep.* No LA-2463 (1961).
3. SOUERS P. C., BLAKE T. S. and PENPRAZE R. M., *Phil. Mag.* (In press)
4. IMAI T., *Phil Mag.* (In press).
5. NEWKIRK H. W. and LEIDER H. R., *J. Phys. Chem. Solids* **31**, 1069 (1970).
6. JANAF Thermochemical Data, compiled by the Dow Chemical Co., Midland, Michigan (September 30, 1967).
7. For example, KELLY R., *Phys. Status Solidi* **21**, 457 (1961), and the references cited therein.
8. SOUERS P. C. and IMAI T., private communication of work in progress.
9. For example, see JOST W., *Diffusion*, Chap. 7. Academic Press, New York (1960).
10. HOLT J. B., ALMASSY M. and CRAWFORD R., *Bull. Am. ceram. Soc.* **48**, 394 (1969)
11. LEWIS W. B. and PRETZEL F. E., *J. Phys. Chem. Solids* **19**, 139 (1961)
12. PRETZEL F. E. and RUSHING C. C., *J. Phys. Chem. Solids* **17**, 232 (1961).
13. SCHULMAN J. H. and COMPTON W. D., *Color Centers in Solids*. MacMillan, New York (1962).

J. Phys. Chem. Solids Pergamon Press 1970. Vol. 31, pp. 1225–1234. Printed in Great Britain.

ANTIFERROMAGNETISM OF A γ IRON-NICKEL-CHROMIUM ALLOY (NON-MAGNETIC STAINLESS STEEL)

YOSHIKAZU ISHIKAWA, YASUO ENDOH and TEIJI TAKIMOTO
The institute for Solid State Physics, University of Tokyo, Tokyo, Japan

(*Received* 15 *July* 1969; *in revised form* 3 *November* 1969)

Abstract – Long range antiferromagnetic order has been detected in a single crystal of f.c.c. $Fe_{0.70}Ni_{0.15}Cr_{0.15}$ by neutron diffraction techniques. The antiferromagnetic structure resembles that of γ manganese in that the average magnetic moments in alternate (001) planes are parallel or antiparallel to [001]. The fluctuation of the magnetic moments exhibits short range correlation in the (001) plane. The moment per atom is $0{\cdot}40 \pm 0{\cdot}03\ \mu_B$ and the Néel temperature was estimated to be $21° \pm 1°$K. The induced magnetization $M(H)$ is not a linear function of the applied field H, but it obeys a simple relation $M^2 = -A + B{\cdot}H/M$. The result suggests that a ferromagnetic interaction exists between the induced magnetization.

1. INTRODUCTION

THERE has been a long debate on the magnetic ground state of iron with the f.c.c. structure (γFe). Based on magnetic susceptibility measurement of a stainless steel alloy ($Fe_{0.73}Ni_{0.09}Cr_{0.18}$), Kondorsky and Sedov first suggested γ iron to be antiferromagnetic with a Néel temperature of about 40°K[1]. The antiferromagnetic spin structure of γFe was determined by Abrahams *et al.* by a neutron diffraction study of γ iron precipitated in a single crystal of copper[2]. The deduced spin structure resembled that of γ manganese[3], but with the spin vector inclined at about 19° from the normal to the ferromagnetic sheet. The moment per atom was $0{\cdot}7\ \mu_B$ and the Néel temperature 8°K. These results, however, have been questioned[4] since the precipitated phase of iron in copper is not pure γFe but contains some copper. F.c.c. Fe–Mn alloys that are antiferromagnetic have also been investigated in order to understand the antiferromagnetism of γFe[5–7]. Neutron diffraction studies have demonstrated that the antiferromagnetic structure consists of four different sublattice, each containing one spin aligned in one of the four different [111] directions[6, 7]. Recent studies of this alloy system, however, have revealed that the interaction between the manganese atom spins plays a more important role than that between those of iron atoms in determining the spin structure [7, 8]. Thus the magnetic properties of γ iron cannot be estimated by simple extrapolation of these or related γ Fe–Mn alloys.

The iron rich f.c.c. Fe–Ni–Cr alloy which has almost the same composition as the so called 'non-magnetic' stainless steel is another γ iron alloy stable at low temperatures. The antiferromagnetism of this alloy was suggested by Mössbauer effect studies[9], but the long range antiferromagnetic order had not been detected by neutron diffraction [10, 11].

We have studied systematically the magnetic properties of the Fe–Ni–Cr alloys and found that the ferromagnetism of the alloys depends mainly on the concentration of nickel and that the alloy containing less than 20 at. per cent nickel is not ferromagnetic at 4·2°K [12]. The antiferromagnetism of the Fe–Ni–Cr alloy was therefore examined by using a single crystal of $Fe_{0.70}Ni_{0.15}Cr_{0.15}$. The magnetization was also measured to provide further information concerning the anomalous magnetic properties of non magnetic stainless steels[11]. The results are discussed within the framework of both the itinerant electron and the localized spin models.

2. NEUTRON DIFFRACTION STUDY

The single crystal of $Fe_{0\cdot70}Ni_{0\cdot15}Cr_{0\cdot15}$ was grown by the Bridgman method. The crystal was cut into a cylindrical form with its long axis along the [110] crystallographic direction and was mounted in a low temperature cryostat on a neutron diffraction spectrometer of the Institute for Solid State Physics at the JRR-3 reactor. The crystal dimensions were 24 mm in length and 4 mm in dia. The magnetic reflections 001, 110 and 112 were measured with monochromatic neutrons of $\lambda = 1\cdot24$ Å in a temperature range between 2°K and 300°K. The contamination of the $\lambda/2$ component in the incident beam was minimized by using monochromatic neutrons from the 311 reflection of a distorted germanium monochromator. The intensity ratio of $\lambda/2$ component was estimated to be $1\cdot4\times10^{-4}$. The effect of secondary extinction was evaluated by measuring various nuclear reflections at room temperature and the wave length dependence of the intensity of a nuclear reflection. In spite of the large crystal size, the effect was found to be negligible except for the strongest 002 line. For example the integrated intensity of the 110 reflection at 300°K is just that expected from the $\lambda/2$ contamination.

The magnetic reflections 001, 110 and 112 were found at 4·2°K as shown in Fig. 1, and indicate the existence of long range antiferromagnetic order. It is noted that the line width of the 001 reflection is almost twice as broad as that of the 220 nuclear reflection. This reflection is clearly broader than any possible Bragg reflection or the resolution function at the 001 position, the line width of which was estimated from the high angle lines to be approximately 1·9°. The structure amplitude $F^2(hkl)(=I_{hkl}\sin 2\theta)$ obtained from the integrated intensities I_{hkl} of the magnetic reflections as well as the nuclear reflections determined at 4·2°K are normalized with respect to the 220 reflection and are summarized in Table 1. The values in the table are corrected for contamination of the $\lambda/2$ component. The error for the 110 reflection is mainly statistical, estimated from the results

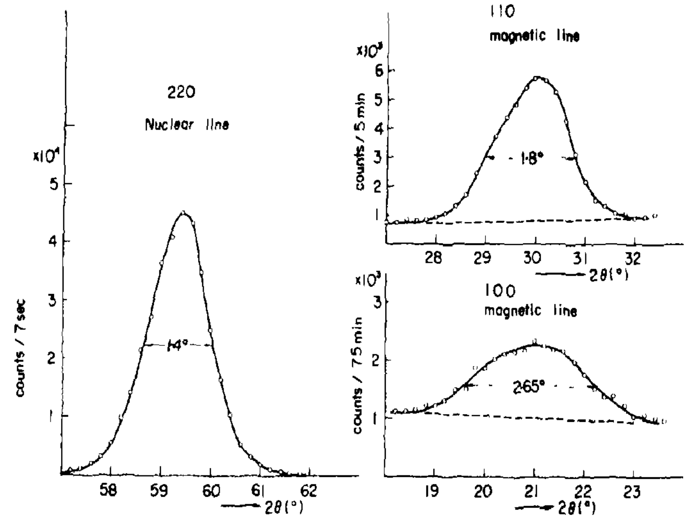

Fig. 1. Nuclear and magnetic reflections measured with $\theta-2\theta$ scans at 4·2°K from a single crystal of $Fe_{0\cdot70}Cr_{0\cdot15}Ni_{0\cdot15}$.

of two experiments, while for the other magnetic reflections, the error was due mainly to the subtraction of the background.

Table 1. Structure amplitudes at 4·2°K *normalized relative to* 220

hkl	$I_{hkl}\sin 2\theta/I_{220}\sin 2\theta_{220}$
002	0·950
220	1·000
001	$2{\cdot}1\pm0{\cdot}2\times10^{-4}$
001 (3° off)	$1{\cdot}7\pm0{\cdot}2\times10^{-4}$
001 (elastic)*	$0{\cdot}4\pm0{\cdot}4\times10^{-4}$
110	$24{\cdot}1\pm0{\cdot}06\times10^{-4}$
112	$1{\cdot}8\pm0{\cdot}1\times10^{-4}$

*001 (elastic) is the estimated value of the coherent elastic scattering in the 001 reflection.

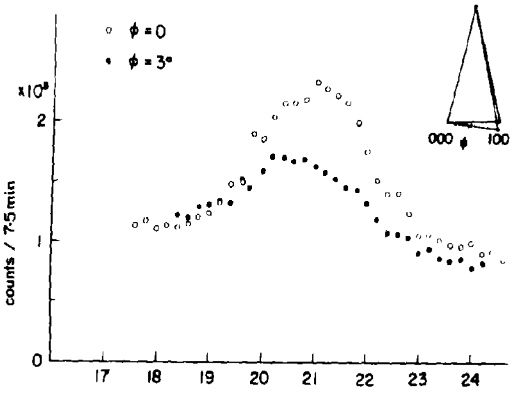

Fig. 2. Bragg (○) and off-Bragg (○) 001 reflections at 4·2°K. The off-Bragg reflection was measured with $\theta-2\theta$ scans after rotating the crystal 3 deg from the Bragg position around the [110] axis.

The angular spread of the 001 reflection suggests that there is some contribution other than coherent elastic scattering, such as coherent inelastic scattering by spin waves or quasielastic scattering due to short range correlation. To determine whether this was so, the crystal was rotated by three degrees from the Bragg angle about the [110] axis. In this condition, coherent elastic scattering would be excluded from the peak observed with θ–2θ scans. The results are shown in Fig. 2, where off-Bragg-angle-reflections are denoted by closed circles. The integrated intensity of this reflection is listed as 001 (3° off) in Table 1. The difference between this reflection and the total 001 reflection is found to be almost the same order of magnitude as the $\lambda/2$ component of the 002 reflection. Therefore the coherent elastic scattering, if it exists, contributes at most one third of the total 001 reflection.

The temperature dependence of the magnetic reflections, 110 and 001 were measured from 2 to 100°K and the results are shown in Fig. 3. The peak intensity of the 110 reflection decreases monotonically with increasing temperature. The Néel temperature is estimated from the figure to be 21 ± 1°K. The rate of decrease of the integrated intensities with increasing temperature becomes slower than that of the peak value as the Néel temperature is approached, as shown in Fig. 4, where the sublattice magnetization estimated from both the peak value and integrated intensity of the 110 reflection is plotted against temperature on a normalized scale. In contrast with the 110 reflection, the temperature variation of the peak intensity of the 001 reflection is quite anomalous. It decreases slightly as the temperature increases from 2 to 20°K, but then increases sharply, followed by a gradual decrease to 100°K. This tendency is almost the same as for the integrated intensities which were examined at 2, 4·2 and 77°K. This temperature variation is characteristic of critical scattering. Therefore the main part of the 001 reflection is concluded to be due to short range correlation. Such quasi-elastic scattering seems to exist also at the 110 position above the Néel temperature, as can be seen from Figs. 3 and 4.

3. ANTIFERROMAGNETIC STRUCTURE

The presence of the 001, 110 and 112 magnetic reflections suggests that the spin structure of this alloy is given in general by Fig. 5. This is the antiferromagnetic structure proposed for γFe precipitated in copper. If we assume that the moment is inclined from the [001] axis by θ in the plane which makes

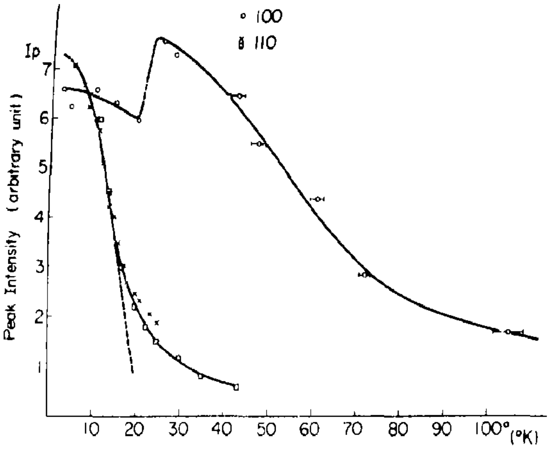

Fig. 3 Temperature variation of the peak intensities of 110 and 001 reflections. The peak intensities are not corrected for λ/2 contamination.

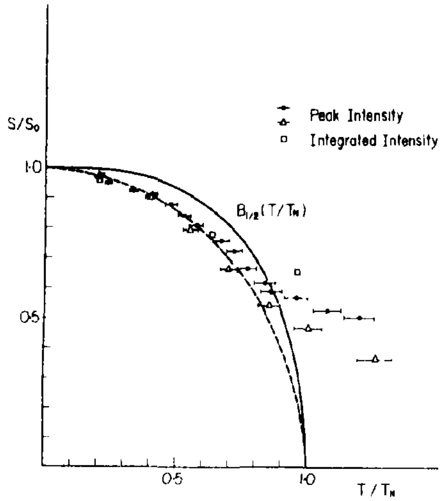

Fig. 4 Temperature variation of the sublattice moment, estimated from both peak and integrated intensities of the 110 reflection.

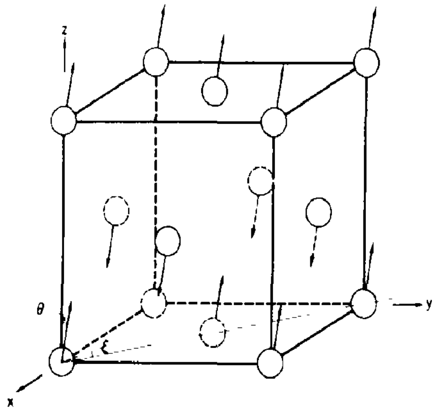

Fig. 5. General spin structure of γFe

an angle of ξ from the (110) plane, the magnetic structure amplitudes $|F(hkl)|^2$ of the three magnetic reflections are given by

$$|F(001)|^2 = A\frac{16}{3}\sin^2\theta$$

$$|F(110)|^2 = A\frac{16}{3}(\cos^2\theta + \sin^2\theta\cos^2\xi)$$

$$|F(112)|^2 = A\frac{16}{3}[1-\frac{1}{3}(\sin\theta\sin\xi - \sqrt{2}\cos\theta)^2]^2$$

where A is $(e^2\gamma/mc^2)^2S^2f^2$ and the antiferromagnetic domains are assumed to be distributed equally in three principal crystallographic directions. The assumption seems to be reasonable for our crystal, because no anisotropy was detected by magnetic susceptibility measurements for this single crystal. By adopting the magnetic form factor of iron determined for γFe-Mn alloys[7], the average magnetic moment $2S$ and the angle of inclination θ are evaluated from the 110 and 112 reflections to be $0{\cdot}40 \pm 0{\cdot}03\ \mu_B$ and 0 degrees respectively. The angle θ estimated from the 001 reflection is $4 \pm 4°$. The angle ξ could not be determined for the spin system with such a small value of θ. The observed intensities are, therefore, consistent with the conclusion that the magnetic moment aligns almost parallel or antiparallel to the [001] axis.

4. MAGNETIZATION MEASUREMENTS

The magnetization for a single crystal of $Fe_{0.70}Ni_{0.15}Cr_{0.15}$ was measured by means of a vibrating sample magnetometer in a temperature range between 2 and 300°K. The crystal used in the experiment was cut from the same ingot from which the neutron diffraction crystal was obtained. The hysteresis loop along the [100] axis measured at 4·2°K in magnetic fields up to 20 kOe is shown in Fig. 6. No anisotropy of magnetization was detected.

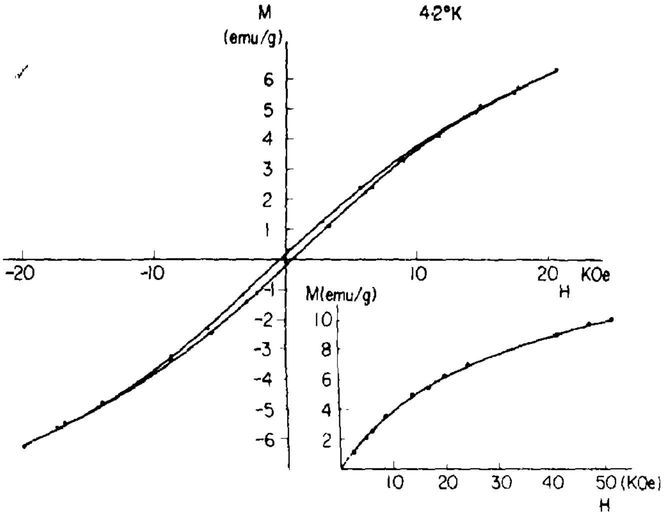

Fig. 6. Hysteresis loop of a single crystal of $Fe_{0.70}Cr_{0.15}Ni_{0.15}$ measured at 4·2°K in the [001] axis by means of a vibration sample magnetometer The magnetization curve in the lower part was measured with an extraction type magnetometer.

In contrast with the ordinary antiferromagnetic substance, the crystal has a remanence at 4·2°K and the magnetization shows a slight tendency to saturate. The remanence decreases rapidly with increasing temperature from 2 to 4·2°K and disappears above 7°K. It decays with time at 4·2°K. This can be attributed to the ferromagnetic small clusters existing parasitically in the crystal, the origin of which may be due to the inhomogeneity of the specimen. The specimen was cooled to 4·2°K in a magnetic field through the Néel temperature, but no shift of the hysteresis was observed at 4·2°K. In order to determine the bulk magnetic properties, the magnetization measurements were extended up to magnetic fields of 50 kOe with an automatic extraction type magnetometer incorporated in a superconducting magnet apparatus. The result of this experiment is illustrated in the inset to Fig. 6. It was found that the magnetization M obeys a simple relation

$$M^2 = -A + BH/M \qquad (1)$$

over a whole range of the field studied as shown in Fig. 7, where A and B are constants. In Fig. 8 are plotted the temperature variations of the magnetization in two magnetic fields of 20 and 3 kOe. A hump was found around the Néel temperature in the magnetiza-

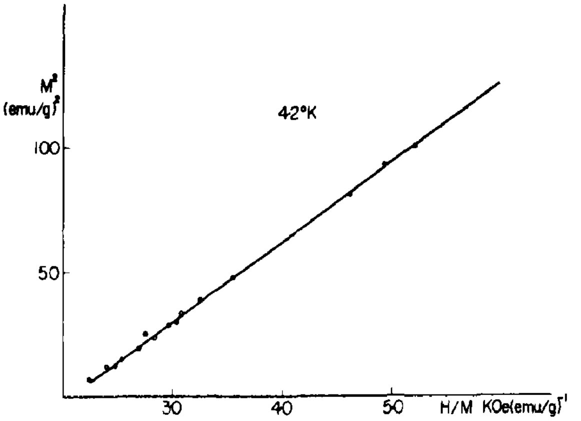

Fig. 7. M^2vs.H/M plot of magnetization at 4·2°K.

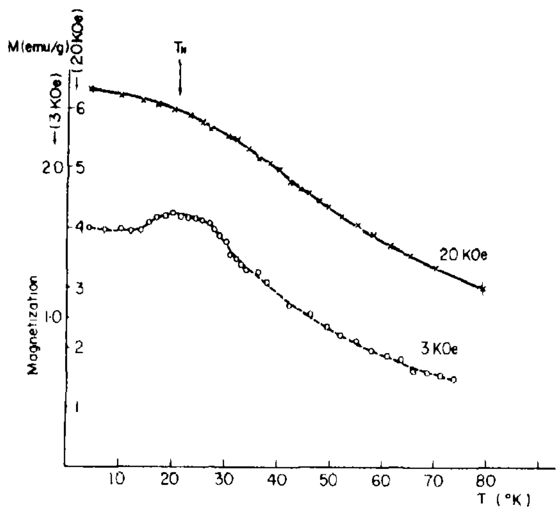

Fig. 8. Temperature variation of magnetization at 3 kOe and 20 kOe

tion at 3 kOe, but the magnetization at high fields decreases almost monotonically with temperature without exhibiting any distinct peak at the Néel temperature.

5. DISCUSSION

(1) *Magnetic structure*

The antiferromagnetic structure of non magnetic stainless steel more closely resembles that of γ iron precipitated in copper than that of γ iron-manganese alloys in the sense that the observed 001 reflection is not extremely small compared with the 110 magnetic reflection. Careful investigation of the 001 reflection, however, suggests that the main part of the reflection is not due to coherent elastic Bragg scattering.

The cross section $d^2\sigma/d\Omega dE$ for neutrons scattered magnetically from a wave vector $\mathbf{k}_0$ to a wave vector $\mathbf{k}$ and from an energy E_0 to an energy E' is in general proportional to the response function $S(\mathbf{Q}\omega)$. $\mathbf{Q}$ and ω are defined by

$$\mathbf{Q} = \mathbf{k}_0 - \mathbf{k}$$

and

$$\hbar\omega = E_0 - E.$$

$S(\mathbf{Q}\omega)$ is the Fourier transform over space and time of the spin pair correlation function, and is given for the cubic system by

$$S(\mathbf{Q}\omega) = (2\pi)^{-1}\Sigma_\alpha (1-\hat{Q}_\alpha^2)\,\Sigma_R \int_{-\infty}^{\infty} \exp(i\mathbf{QR} - i\omega t)\,dt\,\langle S_0^\alpha(0)S_R^\alpha(t)\rangle, \tag{2}$$

where α denotes the cartesian coordinates x, y and z, and $\mathbf{Q}_\alpha$ the α-direction cosine of $\mathbf{Q}$.

Equation (2) shows that only the spin pair correlation on the plane perpendicular to the scattering vector $\mathbf{Q}$ contributes to the magnetic scattering. Since no appreciable Bragg scattering was observed at the 001 position, the most probable magnetic structure is that the average magnetic moments are aligned parallel to the [001] axis (which we take as the z axis), but the moments have a component on the (001) plane (x or y component) which correlate with neighboring spins in short range order. This correlation represented by $\langle S_0^x(0)S_R^x(t)\rangle$ or $\langle S_0^y(0)S_R^y(t)\rangle$, produces the quasielastic scattering at the 001 position. The correlation is found to persist up to 90°K. Spin waves propagating in a direction perpendicular to the spin axis (the z axis) also contribute to the 001 reflection below the Néel temperature. In our experiment we did not make an energy analysis, therefore, it is not clear whether the 001 reflection contains any coherent inelastic scattering by spin waves.

It is noted that if the total intensity of the 001 reflection is assumed to be due to coherent elastic scattering, the angle of inclination θ estimated from this reflection is 14·3°. This value is very close to the value of $\theta = 18{\cdot}7°$ determined for iron precipitated in copper [2]. It is doubtful, therefore, if the 001 reflection of γ iron precipitated in copper is really due to coherent elastic scattering. The spin structure proposed for γFe is hard to understand from the theoretical point of view. The presence of such a diffuse 001 reflection seems to be characteristic of the antiferromagnetism of γ phase alloys. A broad 001 reflection was detected by neutron diffraction in γMn–Pd alloy [13], γMn–Cu alloys [3] and γFe–Mn alloys [14].

The sublattice magnetization decreases with increasing temperature more rapidly than the Brillouin curve with $S = \frac{1}{2}$ as shown in Fig. 4. The tendency is the same as that for the temperature dependence of the iron atom moment in γFe–Mn alloys [7] and may be considered characteristic of the iron atom moment in the f.c.c. structure. Abrahams *et al.* used the Brillouin function $B_{1/2}$ to estimate the Néel temperature of γ iron from the observations made at 4·6, 4·2 and 1·4°K. It is possible that they underestimated the Néel temperature.

(2) *Magnetic properties*

The magnetic properties of antiferromagnetic γFe–Ni–Cr alloys are different from those of typical antiferromagnetic alloys such as Cr–Mn or Fe–Mn alloys. The magnetization curve shows a tendency to saturate in a high magnetic field and is found to follow equation (1). This relation has been reported to hold either for a ferromagnetic substance near the Curie temperature [15] or for the case where the induced moment M is small compared with the saturation magnetization. The latter situation is realized in weak band ferromagnetism [16] such as $ZrZn_2$ [17]. The fact that the extrapolation of M^2 gives a negative value (Fig. 7) indicates that the substance as a whole is not ferromagnetic. It also excludes the possibility that the observed magnetization is due to ferromagnetic impurities in the sample.

It is important to investigate under what conditions this relation holds for an antiferromagnetic substance. The free energy $F(H,T)$ of the antiferromagnetic system in a magnetic field H and temperature T can be expanded in a power series of the relative induced magnetization $\delta M/M_0$ (cf. Appendix)

$$F(H,T) = F(0,0) + \frac{1}{2}A(T)\left(\frac{\delta M}{M_0}\right)^2$$

$$+\frac{1}{4}B(T)\left(\frac{\delta M}{M_0}\right)^4-H\delta M-\frac{1}{2}a(\delta M)^2$$

$$=F(0,0)+\frac{1}{2}\left(\frac{1}{\chi_0}-a\right)(\delta M)^2$$

$$+\frac{1}{4}B(T)\left(\frac{\delta M}{M_0}\right)^4-H\delta M \qquad (3)$$

where a is a magnetic interaction coefficient between neighboring induced magnetic moments and χ_0 the magnetic susceptibility of the non-interacting system respectively. M_0 is the saturation magnetization of the system. $B(T)$ is usually of the same order of magnitude as $A(T)$ as shown in the appendix. When $\delta M/M_0$ is small, expansion terms higher than $(\delta M/M_0)^6$ can be neglected and we obtain a relation

$$(\delta M)^3=\left[\frac{M_0^4}{B(T)}\right]\cdot H-\left[\frac{(A-aM_0^2)M_0^2}{B(T)}\right]\cdot\delta M, \qquad (4)$$

using the equilibrium condition $\partial F/\partial\delta M=0$. Therefore the linear relation between $(\delta M)^2$ and $H/\delta M$ generally holds, when $\delta M/M_0 \ll 1$. For this relation to be appreciable, the intercept of the δM^2vs. $H/\delta M$ line on the ordinate, which is given by $-[(A-aM_0^2)/B]\cdot M_0^2$, must be of the same order of magnitude as δM^2. This requires that $(A-aM_0^2)/B \ll 1$, because $\delta M/M_0 \ll 1$. Since A is of the same order of magnitude as B, it is essential that a is positive and is close to $1/\chi_0$. We therefore conclude that there exists a positive interaction between the induced magnetization in the antiferromagnetic Fe–Ni–Cr alloy.

Two models can be proposed to interpret the magnetic properties of this alloy. One is an itinerant antiferromagnetic model and the other is a localized spin model in which two types of magnetic moments exist. The magnetization process was calculated for both models and the results are shown in Appendix I and II. In the itinerant electron model, χ_0 is the Pauli paramagnetic susceptibility and is proportional to the density of states at the Fermi surface $D(\epsilon_F)$. a is the intra-atomic interaction coefficient between the itinerant electron spins. Therefore a is always positive and $(1/\chi_0-a)$ can be small and positive depending on the density of states at the Fermi energy. When $(1/\chi_0-a)>0$, the ferromagnetism does not appear even if a is positive. The antiferromagnetism occurs when the splitting of the band due to antiferromagnetic order reduces the whole energy of the system [18]. As the ferromagnetism appears with a slight increase of the electron to atom ratio in the alloy, it is reasonable to suppose that $(1/\chi_0-a)$ for this alloy is small. The magnetic properties of the Fe–Ni–Cr alloy are compatible with a band antiferromagnetism in which the Stoner condition for the appearance of ferromagnetism is just broken.

Another model consists of localized moments m_1 loosely coupled with the antiferromagnetic lattice having moments m_0. The localized moments have a positive interaction between themselves, but they align antiferromagnetically in zero field. The magnetization process of this system was calculated for a simple case in the Appendix. It is found that the relation (4) also holds in this case. $(1/\chi_0-a)$ which is equal to $(m_0J_{01}-2m_1J_{11})/nm_1$ (for notations see Appendix) is positive and is also expected to be small for this alloy. Actually this model corresponds to the case where the moments in the iron rich regions form an antiferromagnetic lattice due to the negative iron–iron interaction, while the ferromagnetically interacting moments in the nickel rich regions, which are weakly coupled with the antiferromagnetic regions, behave just as the localized spins in a magnetic field. The nickel rich regions must not be ferromagnetic clusters that can be saturated in magnetic fields of 50 kOe. If the ferromagnetic regions have appreciable coupling with the antiferromagnetic lattice, then field cooling through the Néel temperature may induce unidirectional anisotropy [19]. This is not the case for this alloy.

The temperature dependence of the magnetization in both low and high fields can be interpreted in terms of either model. We cannot determine from the magnetic properties which model is appropriate for this alloy.

It is finally noted that the magnetic moment induced in a field of 50 kOe is about 0·1 μ_B per $Fe_{0\cdot7}Ni_{0\cdot15}Cr_{0\cdot15}$. Considering that the saturation magnetic moment is much higher than this value ($\delta M/M_0 \ll 1$), we cannot attribute the induced moment to the nickel atom alone. Therefore it is considered that the antiferromagnetic structure is modified by the external field of 50 kOe in any model. It should be very interesting to make neutron diffraction and Mössbauer effect studies of this alloy in high fields, and both of these investigations are in preparation.

Acknowledgement—The authors would like to thank Professor S. Chikazumi for reading the manuscript and discussion, Mr. T. Maruyama for assistance with the magnetization measurements, and Dr. O. S. Rodbell for suggestions concerning the presentation of the manuscript.

REFERENCES

1 KONDORSKY E. I. and SEDOV V. L., *J. appl. Phys.* **31S**, 331 (1960)
2 ABRAHAMS S. C., GUTTMAN L. and KASPER J. S., *Phys. Rev.* **127**, 2052 (1962).
3 MENEGHETTI D. and SIDHU S. S., *Phys. Rev* **105**, 130 (1957)
4 ARROTT A., *Magnetism* 11B (Edited by Rado and Suhl), p. 397. Academic Press, New York (1966).
5 KOUVEL J. S. and KASPER J. S., *J. Phys. Chem. Solids* **24**, 529 (1963).
6 UMEBAYASHI H. and ISHIKAWA Y., *J. phys. Soc Japan* **21**, 1281 (1966)
7 ISHIKAWA Y. and ENDOH Y., *J. phys. Soc. Japan* **23**, 205 (1967).
8 ENDOH Y. and ISHIKAWA Y., In preparation.
9 GONSER U., MEECHAN C. J., MUIR A. H. and WIEDERSICH H., *J. appl. Phys.* **34**, 2327 (1963)
10 NATHANS R. and PICKART S. J., *J. Phys. Chem. Solids* **27**, 183 (1964).
11 MARDION B., DE VRIES G., TOURNIER R and VOYER R. *C.r. Acad. Sci.* **259**, 4552 (1964).
12. ISHIKAWA Y. and TAKIMOTO T., *J. phys. Soc. Japan*, To be published.
13 HICKS T. J., PEPPER A. R. and SMITH J. H., *Proc. phys. Soc.* **1**, 1683 (1968).
14 ARROTT A., private communication and ISHIKAWA Y. and ENDOH Y. To be published.
15. ARROTT A., *Phys. Rev* **108**, 1394 (1957).
16 WOHLFARTH E. P., *J. appl. Phys.* **39**, 1061 (1968).
17. OGAWA S. and SAKAMOTO N., *J. phys. Soc Japan* **22**, 1214 (1968).
18. YAMASHITA J., ASANO S. and WAKOH S., *J. appl. Phys.* **39**, 1274 (1968)
19. KOUVEL J. S., *J. Phys. Chem. Solids* **24**, 795 (1963).
20 SHIMIZU M., *Proc. phys. Soc.* **86**, 147 (1965).

APPENDIX I

In itinerant antiferromagnetism, the expansion of the free energy in a power series of the induced moment can be done in the same way as in the case of paramagnetism, which has been reported by several authors[16], [20]. According to their results, $A(0)$ and $B(0)$ are given by

$$A(0) = \frac{M_0^2}{\chi_0} = \frac{n^2N}{2D(\epsilon_F)},$$

$$B(0) = \gamma A(0) = \frac{1}{8}A(0)\left[\frac{n}{D(\epsilon_F)}\right]^2\left(\nu_1^2 - \frac{1}{3}\nu_2\right),$$

$$\nu_m = \frac{D^{(m)}(\epsilon_F)}{D(\epsilon_F)},$$

where $D(\epsilon_F)$ is the density of states at the antiferromagnetic Fermi energy and $D^{(m)}(\epsilon_F)$ the mth derivative. All other notations are the same as those in the Ref [16] For a parabolic band, B/A is calculated to be 2/27.

APPENDIX II

For the case of a localized spin system, we consider a simple model in which the localized moments m_1 are weakly coupled with the antiferromagnetic lattice composed of the moments m_0 as indicated in Fig. 9 A magnetic field is applied in a direction perpendicular to the

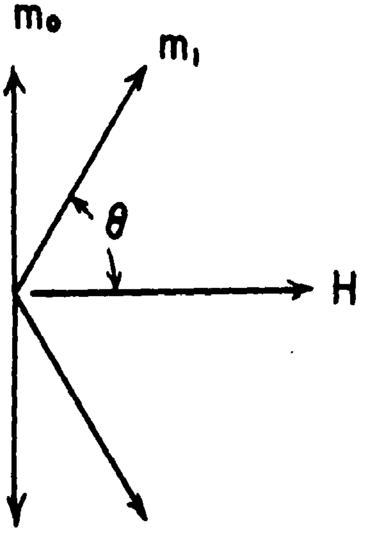

Fig 9. Simple localized spin model proposed to explain the case where relation (4) holds for the antiferromagnetic system.

antiferromagnetic axis and the antiferromagnetic structure is assumed to be undisturbed by the field. The magnetic energy of the system is written by

$$
\begin{aligned}
E &= -nm_1 H\cos\theta - nJ_{01}m_0m_1\sin\theta - \frac{n}{2}J_{11}m_1^2\cos 2\theta \\
&= -n\delta m_1 H - nJ_{01}m_0\sqrt{m_1^2-(\delta m_1)^2} - nJ_{11}(\delta m_1)^2 \\
&\quad + \frac{n}{2}J_{11}m_1^2,
\end{aligned}
\tag{6}
$$

where J_{01} and J_{11} are the interaction coefficients between m_1 and m_0 and between two moments m_1 respectively, and n is the number of the localized moment.

When induced magnetization $\delta M(=n\delta m_1)$ is sufficiently small compared with the saturation magnetization M_0 $(=nm_1)$, the energy E can be expanded as a series of $\delta M/M_0$ and the relation

$$
H = (J_{01}m_0 - 2J_{11}m_1)\left(\frac{\delta M}{M_0}\right) + \frac{1}{2}J_{01}m_0\left(\frac{\delta M}{M_0}\right)^3 \tag{7}
$$

is obtained, using the equilibrium condition $\partial E/\partial\delta M = 0$. This is the same relation as equation (4). B/A is 1/2 in this case.

This argument can be extended to the general case where many different localized spins exist and the antiferromagnetic spins m_0 also contribute to the induced magnetization δM. The result is that equation (4) holds to the extent that $(\delta m_1/m_1)^5$ can be neglected for any kind of localized moment.

J. Phys. Chem. Solids Pergamon Press 1970. Vol. 31, pp. 1235-1246. Printed in Great Britain.

THE THERMOELECTRIC PROPERTIES OF QUATERNARY CHALCOGENIDES

J. J. CURRY* and S. R. POLLACK
School of Metallurgy and Materials Science, University of Pennsylvania, Philadelphia, Pa., U.S.A.

(*Received* 14 *October* 1969)

Abstract—Four compounds of the general composition 12_236_4 have been studied to ascertain their thermoelectric properties. Measurements were performed on pressed and sintered samples. The compounds were identified by their Debye-Scherrer pattern and metallographic examination confirmed the presence of a single phase. Determinations were made of the thermoelectric power, the electrical conductivity, Hall coefficient, optical reflectivity and microhardness. The results of this investigation indicate that the bandgap in these semiconductors is less than 0·5 eV. The electronic properties are discussed in terms of alloy and ionized impurity scattering

1. INTRODUCTION

IN RECENT years there has been considerable interest in the crystal chemistry of ternary and quaternary compounds[1-3]. It is only of late that papers describing the properties of such compounds have appeared[4]. These papers have been restricted mainly to ternary compounds and literature on quaternary compounds is virtually nonexistant. This investigation is concerned with the thermoelectric properties of four quaternary chalcogenides belonging to the class 12_236_4. Crystal chemical considerations of these compounds have been elucidated by Parthé[5]. Four compounds were chosen on the basis of range of lattice parameter and thermoelectric hot probe measurements.

The purpose of the investigation is twofold:

(1) to elucidate the properties of these materials in order to understand the nature of their conductivity;

(2) to determine their potential usefulness as thermoelectric energy converters.

Chosen for study were $AgCd_2InTe_4$, $CuCd_2InTe_4$, $CuZn_2InTe_4$ and $CuCd_2InSe_4$. Measurements were made to determine the thermoelectric power, electrical conductivity, Hall coefficient, optical reflectivity and microhardness. In this manner these compounds could be characterized and possible correlations with structure could be sought. On the basis of these measurements, determinations of the Fermi energy, carrier concentration, effective mass and scattering mode were made for the telluride compounds. Bipolar conduction accounts for the properties of the selenide compound. Due to the extremely low conductivities exhibited by all of these compounds, they would not make suitable thermoelectric energy converters.

2. EXPERIMENTAL PROCEDURES

(a) *Preparation*

Stoichiometric amounts of the constituent elements were weighed and placed in a vycor capsule. The purity of the constituents is shown in Table 1. The capsule was then evacuated to a pressure of approximately 10^{-5} torr and sealed off. Following this evacuation the sample contained within the vycor capsule was placed in a muffle furnace initially at room temperature and the controller set for a temperature above the melting point of the compound. This was usually in the 850-950°C range. The capsule was held at this elevated temperature for 4 hr during which time the capsule was periodically agitated to enhance

---

*[*] *Present address*: Bell Telephone Laboratories, Allentown, Pa. 18103, U.S.A.

Table 1. Elements used in compound preparation and their major impurities

Element	Purity	Supplier and stock number
Silver (sponge)	99·999% Ca 8 ppm Cu 2 ppm	ESPI K-4700
Cadmium (powder)	99·999% Bi 3 ppm Mg 3 ppm Pb 2 ppm	ESPI K-977 M
Copper (wire)	99·999% Sb 1 ppm As 1 ppm	ESPI K 1432 F
Indium (powder)	99·9995% Cu 1 ppm Pb 1 ppm Tl 1 ppm	ESPI K-2813 K
Selenium (powder)	99·999% Te 1 ppm	ESPI K-4662 B
Tellurium (lump)	99·9999% S trace	COMINCO HPM-5860
Zinc (powder)	99·9999% Cd trace	ESPI K-5601 K

mixing of the elements. At the end of this period, the capsule was quenched to 0°C in an ice-water bath. The solid ingot was removed from the tube and crushed into a fine powder. The powder was pressed to form cylindrical samples from which the various experimental shapes could be cut. These cylindrical pellets were then placed in a vycor tube and sealed off in the manner mentioned above. They were then annealed at a temperature below the melting point (usually 750°C) for 24 hr. Following the 24 hr period, the samples were allowed to furnace cool. This technique resulted in single phase, polycrystalline samples having the proper crystallographic parameters and reproducible electrical properties.

Lattice parameters were obtained by the Debye–Scherrer technique. The values of the lattice parameters obtained in this investigation were in complete agreement with those found by Parthé *et al.*[6]. It was not possible to observe superstructure lines in the powder patterns. This is due to the fact that the atomic scattering factors of all of the elements are quite close. It is therefore not known whether the structure is a cubic zincblende structure, $F\bar{4}3\,m$, or the stannite structure, $I\bar{4}2\,m$. The indexing of the pattern agrees with both structures. In the cubic structure there is a single formula unit ($1_2 2_2 3 6_4$) in a cubic unit cell of size a. In the stannite structure there are two formula units in a cell with a c dimension of $2a$. The value of the lattice parameter a, found in all of the single phase compounds is given below:

$AgCd_2InTe_4$	6·438 Å
$CuCd_2InTe_4$	6·336 Å
$CuZn_2InTe_4$	6·153 Å
$CuCd_2InSe_4$	5·934 Å.

Metallographic investigation of the sinter-annealed powder specimens indicated that all of the compounds formed in the above fashion were single phase and had an extremely small grain size (less than 1 μ). Various attempts were made to grow single crystal specimens, but these all resulted in two-phase materials having powder patterns which could not be indexed. Only the rapid quenching from the liquid provided single phase compounds with the proper lattice parameter. Apparently there is a segregation of components in the liquid under slow cooling. This precluded single crystal growth by either the solution growth or directional cooling means.

The pellets of the compounds that were formed from the pressed and sintered powder were cut into the various shapes necessitated by individual experiments with the use of a Brown and Sharpe diamond slicing wheel. In this manner it was possible to achieve the maximum sample flexibility with the minimum of sample waste.

(b) *Electrical measurements*

Measurement of the thermoelectric power of the compounds was performed with the aid of cylindrical samples 7 mm in dia. and approximately 5 mm high. The cylinder was pressed between two copper blocks. Three compression springs applied a sufficient pressure to allow a low resistance (both thermal and electrical) contact to be made to the sample. On the faces of the copper blocks immediately adjacent to the sample were copper constantan thermocouples having a junction approximately 0·001 in. in thickness. The couples were mounted in shallow slots in the faces and held in place with a light application of Metaplast silver conductive epoxy. Both blocks were equipped with small heaters and one of the blocks was mounted on a cold finger inside of a dewar system. The dewar system shown in Fig. 1 was so designed that it was possible to make a simple change of test fixture on top of the cold finger in order to measure the electrical conductivity and Hall coefficient. By filling the bottom dewar with liquid nitrogen it was possible to vary the temperature of the sample from 77 to 350°K. In addition to sample considerations, which will be discussed later, it was found that the setup was most stable in the range 100–300°K. The voltages developed by the couples were fed into twin differential amplifiers of high sensitivity and precision. The thermal e.m.f. was measured by a Keithley milli-microvoltmeter. This is shown in Fig. 2. The system was calibrated against a 99·999 per cent silver specimen, and corrections were made for the thermoelectric power of copper as given by Blatt *et al.*[7]. The values so obtained were then compared to the data of Blatt *et al.*[7] for the absolute thermoelectric power of silver. The agreement of the data was excellent. Using this arrangement it was possible to measure the thermoelectric power to within 2·0 per cent with a reproducibility of 1·0 per cent.

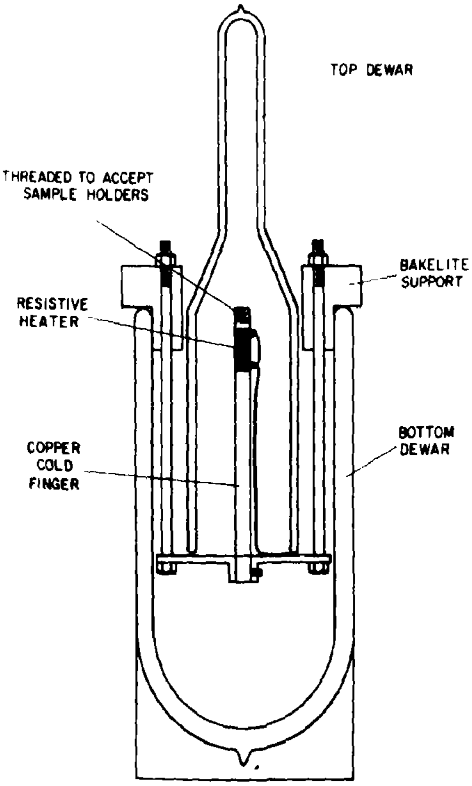

Fig. 1. Variable temperature system used in this investigation.

For the measurement of the electrical conductivity and Hall coefficient, thin rectangular slabs were cut from the larger cylinders. The slabs so cut were generally 12 mm long, 2–3 mm wide and 0·1–0·5 mm thick. Samples of this type having a length–width ratio of 4 or greater produce a negligible shorting effect[8] for the Hall measurements. In addition the thin slabs provided reasonable current densities at low current. Four terminal measurement was made of the electrical conductivity. Two copper leads for the purpose of introducing current were affixed to ends of the slab with Metaplast or Aquadag, both of which provided sturdy ohmic contact. The probe leads were 0·002 in. chromel wires that were either spot welded or, in the case of the high resistivity compounds, tacked with a small bead of Aquadag. The leads were so arranged that by proper selection one could either measure Hall voltage (in the presence of a magnetic field) or the electrical conductivity. Measurement of the Hall coefficient was made at fields of 10 and 20 kG. The Hall voltages

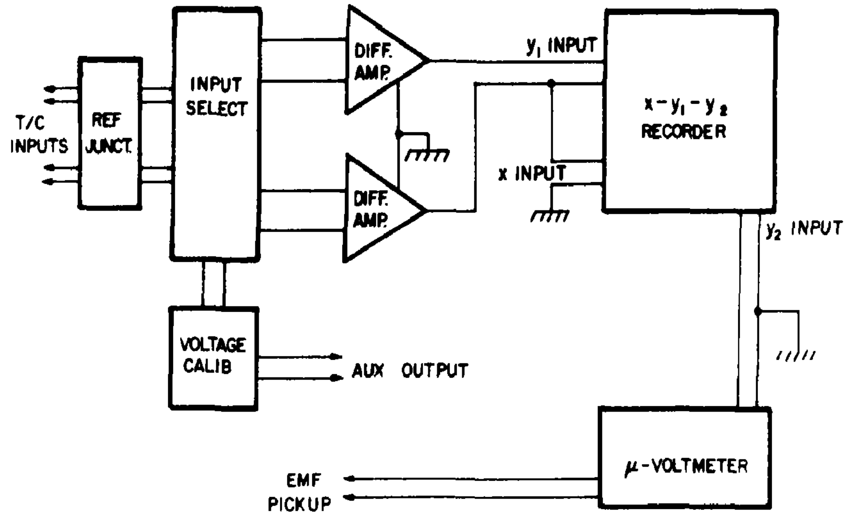

Fig. 2. Block diagram showing the necessary instrumentation for the measurement of the thermoelectric power

obtained were always linear in field and no traces of magnetoresistivity were noted. Measurements were always made for both directions of current flow and magnetic field to eliminate thermoelectric and thermomagnetic effects. By mounting the slab on an anodized aluminum holder with rubber cement, thermal stability was achieved. The anodized holder was placed on the cold finger and a thermocouple affixed to the sample with Metaplast. The electrical conductivity could be measured to within 1·5 per cent and the Hall coefficient to within 1·75 per cent. Reproducibility for both was better than 1·0 per cent.

(c) *Optical measurements*

Measurement of the optical reflectivity was made using the Cary Model 14 spectrophotometer equipped with a specular reflectance attachment. Samples were mounted in bakelite metallographic mounts and polished using diamond paste lapping and various water-alumina polishes finishing with a 0·05 μ wet alumina polish. Measurement of the relative reflectivity was made in the 2000–25,000 Å range. Using the technique of Fochs[9], it is possible to measure the fundamental absorption edge and hence the optical bandgap of the semiconductor. This technique precluded the necessity of thin transmission samples.

(d) *Microhardness*

Knoop microhardness measurements were made on as-quenched annealed samples in order to determine the microhardness without introducing variations due to powder pressing problems. The compressed and sintered samples had a density of between 80 and 90 per cent. Although the as-quenched and annealed samples showed large voids, there were large enough solid regions to do microhardness measurements. These measurements were performed to see if the microhardness conformed to Kurnakov's law as shown by Zalar[10] in his ternary studies. Also following the trend of Goodman[11] and Mooser and Pearson[12] possible correlations could be sought between the energy gap obtained from optical measurements and the microhardness (essentially a measure of bond strength).

3. RESULTS AND DISCUSSION

The tellurides

All of the tellurides showed high thermoelectric powers. Figure 3 shows the thermoelectric power, Hall coefficient, electrical conductivity and Hall mobility (defined as the product of the electrical conductivity and Hall coefficient) for $CuCd_2InTe_4$. The data presented is that obtained from a representative sample. As mentioned earlier, the range of measurement is restricted to 100-300°K. Not only is the variable temperature system most stable in this region, it is also the temperature regime which allows reproducibility of measurement. It has been found that at temperatures much higher than 350°K, there is a noticeable change in electronic properties on recycling the sample. This change is accompanied by a measureable weight loss. It was therefore necessary to restrict measurements to the 100-300°K range in order to provide necessary reproducibility and stability. Returning to Fig. 3, it can be seen the Hall coefficient remains essentially constant as a function of temperature indicative of a nearly constant carrier concentration. Both the thermoelectric power and Hall coefficient indicate *p*-type conduction. Also the Hall mobility is quite low and has an approximate $T^{0.5}$ dependence.

Figure 4 shows the same properties for $CuZn_2InTe_4$. The properties show a similar

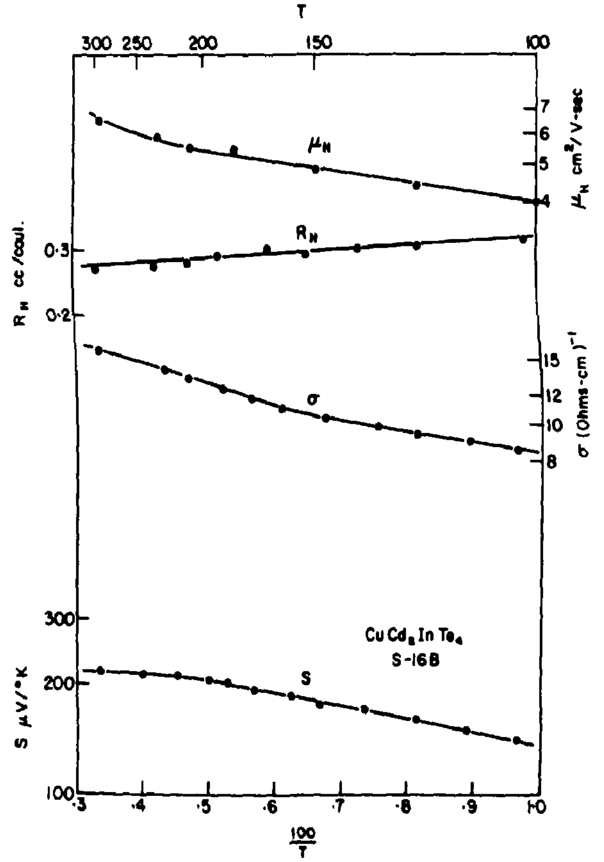

Fig. 3. The thermoelectric power (*S*), the electrical conductivity (σ), Hall coefficient (R_H) and Hall mobility (μ_H) of $CuCd_2InTe_4$ as a function of temperature.

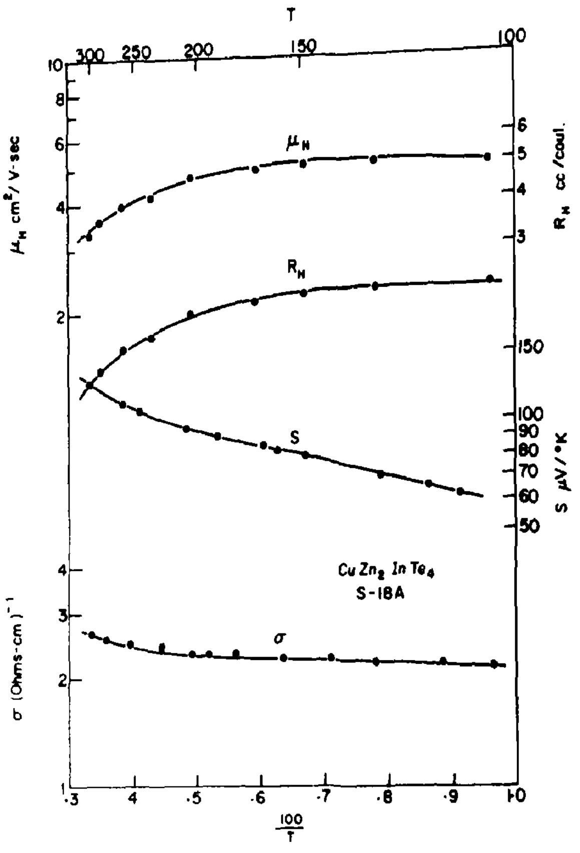

Fig. 4. The thermoelectric power (S), the electrical conductivity (σ), Hall coefficient (R_H) and Hall mobility (μ_H) of CuZn$_2$InTe$_4$ as a function of temperature.

variation with temperature with the notable exception of the Hall mobility which varies as $T^{-0.59}$. The Hall mobility is of the same magnitude as found in CuCd$_2$InTe$_4$.

Figure 5 shows the same properties of AgCd$_2$InTe$_4$. This compound bears a resemblance to CuZn$_2$InTe$_4$. The electrical conductivity shows an extremely small temperature dependence over the range of measurement and the Hall mobility gives a good fit to a $T^{-0.72}$ dependence. Several points are evident from this data. The tellurides all show large thermoelectric powers being on the order of 200 μV/°K at room temperature. The electrical conductivities are quite low. This is due to the mobility of the holes which is on the order of several cm^2/V-sec. A knowledge of the thermoelectric power and temperature variation of the mobility and Hall coefficient provide the necessary information to interpret the data. The thermoelectric power is given by

$$S = \frac{k}{e}(A - E_f/kT) \quad \text{Non-degenerate or lightly degenerate case} \qquad (1)$$

where E_f is the Fermi energy, k is Boltzmann's constant and A is a constant at a given temperature and is dependent on the scattering mechanism. A can be evaluated from a knowledge of the temperature dependence of the

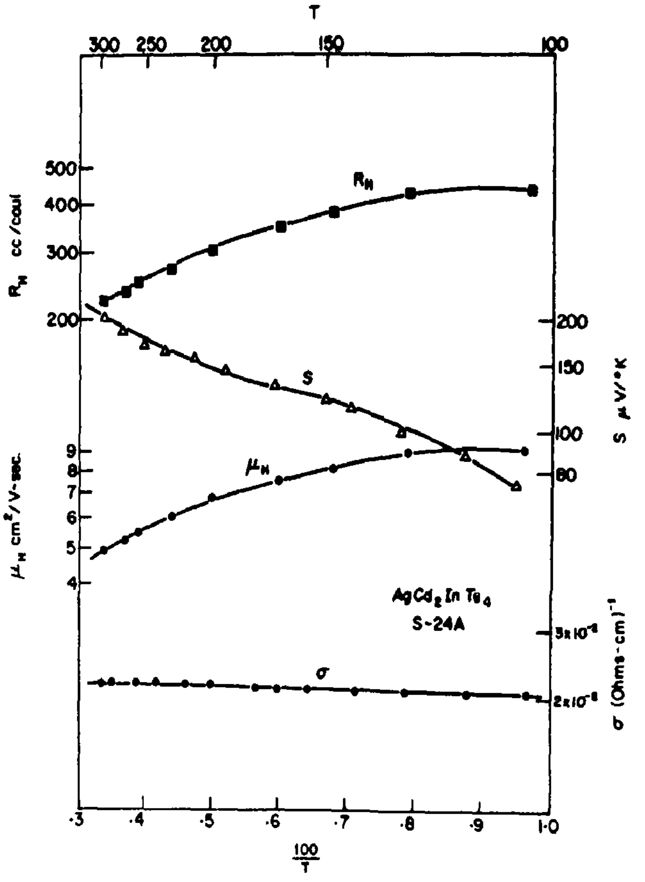

Fig. 5. The thermoelectric power (S), the electrical conductivity (σ), Hall coefficient (R_H) and Hall mobility (μ_H) of $AgCd_2InTe_4$ as a function of temperature.

mobility[13]. When A is known, it is thus possible to evaluate the Fermi energy at a given temperature. If the Hall coefficient is taken to be

$$R_H = \frac{1}{pe} \tag{2}$$

then it is possible to arrive at the carrier concentration. The carrier concentration is also given by

$$p = \frac{4}{\sqrt{\pi}}\left(\frac{2\pi m^* kT}{h^2}\right)^{3/2} F_{1/2}(E_f/kT) \tag{3}$$

where $F_{1/2}(E_f/kT)$ is the Fermi integral of ½ order. This function has been tabulated. Since p and E_f are known, equation (3) allows the calculation of the effective mass, although the effective mass so obtained is usually at variance with effective masses obtained from optical or reasonance phenomena[4, 14]. In other compounds, it will be used here in the absence of a better value.

The results of this type of analysis are shown in Table 2 where a cross-section of the pertinent properties are shown for the tellurides at 300°K. Consider the data on $AgCd_2InTe_4$ and $CuZn_2InTe_4$. The samples all show a slight degeneracy. For effective masses that are this low, it is not possible that ionized impurity scattering or lattice scattering could

Table 2. Data obtained on the tellurides at 300°K

	$AgCd_2InTe_4$		$CuCd_2InTe_4$		$CuZn_2InTe_4$	
	S24A	S24B	S13B	S16B	S18A	S20A
Thermoelectric power (uV/°K)	207	197	198	215	153	130
Electrical conductivity $(\Omega\text{-cm})^{-1}$	0·0218	0·0276	18·37	15·71	2·604	2·850
Hall mobility (cm²/V-sec)	4·95	4·52	4·95	4·16	3·31	1·89
Hall coefficient (cc/coul)	227·0	164·0	0·236	0·265	1·270	0·630
E_f/kT	0·38	0·56	0·72	0·50	0·85	1·40
Carrier concentration (cm^{-3})	$5{\cdot}32\times10^{16}$	7·37	$5{\cdot}12\times10^{19}$	4·56	$0{\cdot}951\times10^{19}$	1·91
m^*/m_0	0·016	0·019	1·34	1·38	0·41	0·52
Temperature dependence of hall mobility	$T^{-0.72}$	$T^{-0.65}$	$T^{0.52}$	$T^{0.49}$	$T^{-0.87}$	$T^{-0.59}$

be the responsible scattering mechanisms. The temperature dependence is clearly different.

A possible mechanism for the scattering could be alloy scattering. This was first described by Weisberg[15] and qualitatively by Brooks[16]. This scattering is caused by a random distribution of inhomogeneities in the compound. These inhomogeneities may be in the form of impurity clusters, disordered regions or regions of compositional fluctuation. Regions of this type develop a space charge around them in order to establish charge neutrality in the bulk. As given by Weisberg, the mobility is

$$\mu = \frac{e}{(2m^*kT)^{1/2}} \cdot \frac{1}{N_s S} \qquad (4)$$

where S is the effective area of the scatterer and N_s is the concentration of the space charge regions. The creation of space charge regions of this type has been found to decrease the mobility of certain samples of GaAs by almost two orders of magnitude[17]. Although the actual regions of compositional fluctuation are small, it has been found that the space charge surrounding this region can be of a size that is several orders of magnitude larger[18]. As can be seen from equation (4) the temperature dependence is $T^{-0.5}$. It is believed that the departures from this $T^{-0.5}$ dependence are due to an energy dependence of the scattering which Weisberg's model does not assume. Also there may be a slight temperature dependence due to the size of the space charge region. This scattering mode will lead to mobilities of several cm²/V-sec even when the effective mass is 0·01 m_0 using equation (4) and the values of m^* and μ. Calculations show slightly overlapping space charge regions producing the effect of a sample containing many micro p–n junctions. The results of this calculation show that alloy scattering could result in the low mobilities and experimental temperature dependence of the mobility found in $CuZn_2InTe_4$ and $AgCd_2InTe_4$. Returning to $CuCd_2InTe_4$, it can be seen that the effective mass is high. It is believed that the scattering here is a mixture of ionized impurity scattering and alloy scattering. With an effective mass of approximately 1·4 m_0 it is possible that the ionized impurity scattering could make an appreciable contribution to the total mobility. If the mobility due to ionized impurity scattering was on the order of 15–20 cm²/V-sec, then the combined effect of the two processes could result in a mobility dependence of $T^{0.5}$. It is not known, however, why the effective mass should be so much larger in $CuCd_2InTe_4$ than in the other two tellurides. This remains to be answered.

The selenide

Figure 6 shows a plot of the electrical conductivity and thermoelectric power for copper cadmium indium selenide. It can be seen that these properties differ sharply from the properties of the tellurides. The thermoelectric power is quite low being on the order of 15 μV/°K at room temperature. The electrical conductivity is also much smaller than those found in the tellurides. This low conductivity made a precise Hall measurement impossible due to voltage fluctuations at the pickup probes. The maximum value for the Hall coefficient could be set at 3·29 cm³/Cb. The low Hall coefficient and thermoelectric power lead one to suspect ambipolar conduction. The thermoelectric power due to contributions from both electrons and holes is given by:

$$S = \frac{|S_h|\sigma_h - |S_e|\sigma_e}{\sigma_h + \sigma_e} \tag{5}$$

The electrical conductivity and Hall coefficient are given by:

$$\sigma = \sigma_h + \sigma_e \tag{6}$$

$$R_H = \frac{1}{e}\frac{p\mu_h^2 - n\mu_e^2}{(p\mu_h + n\mu_e)^2}. \tag{7}$$

It can be seen from these equations that the thermoelectric power and Hall coefficient are given by a difference of terms so that even if

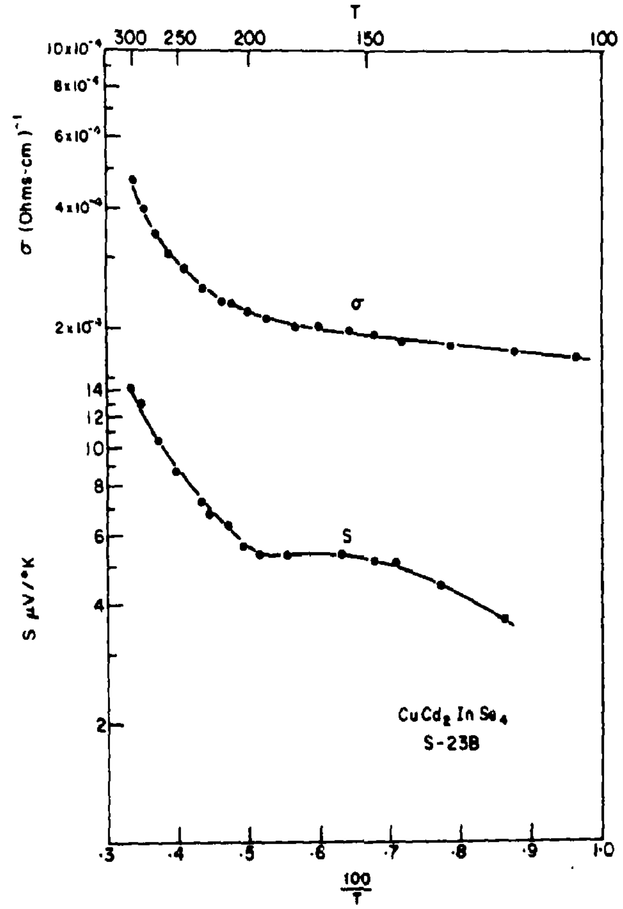

Fig. 6. The thermoelectric power (S) and electrical conductivity (σ) of $CuCd_2InSe_4$ as a function of temperature

the individual terms are large, if they are approximately equal their difference will be small. These are the three equations for which experimental data was taken. There are, however four unknowns: the carrier concentrations and mobilities for both the electrons and the holes. A parametric solution was tried, with the ratio of electron mobility to hole mobility serving as a convenient parameter. It was further assumed that the scattering mechanism for the holes is the same as for the electrons and both the electrons and holes have an effective mass equal to the free electron mass. These conditions were assumed in the absence of any data to the contrary. Calculations were performed which indicated that under these conditions and for a unit ratio of carrier mobilities that the carrier mobility is $1\cdot6\times10^{1}$ cm²/V-sec with a hole concentration of $4\cdot69\times10^{16}$ and an electron concentration of $4\cdot26\times10^{16}$ at room temperature. The value of the energy gap under these conditions could also be calculated and was found to be 0·32 eV. The calculation shows that the two band scheme gives a reasonable explanation of the empirical data.

Optical reflection measurements over the range of 25,000 Å to 2000 Å were performed in accordance with the procedures of Fochs [9]. The experimental data show that there are no sharp reflection maxima in the far visible and i.r. ranges. This is shown in Fig. 7. The maxima, occuring at higher energies, are most likely due to interband transitions similar to those found by Greenaway and Cardona[19] in InSb. A measurement on single crystal specimens would have provided an insight into the band structure of the compounds, however, the position of the maximum in a polycrystalline material provides little information other than indicating the presence of a transition. From the optical reflection measurements taken over the aforementioned range, it can be stated that the energy gap of these compounds must be less than 0·5 eV. The energy gap value cal-

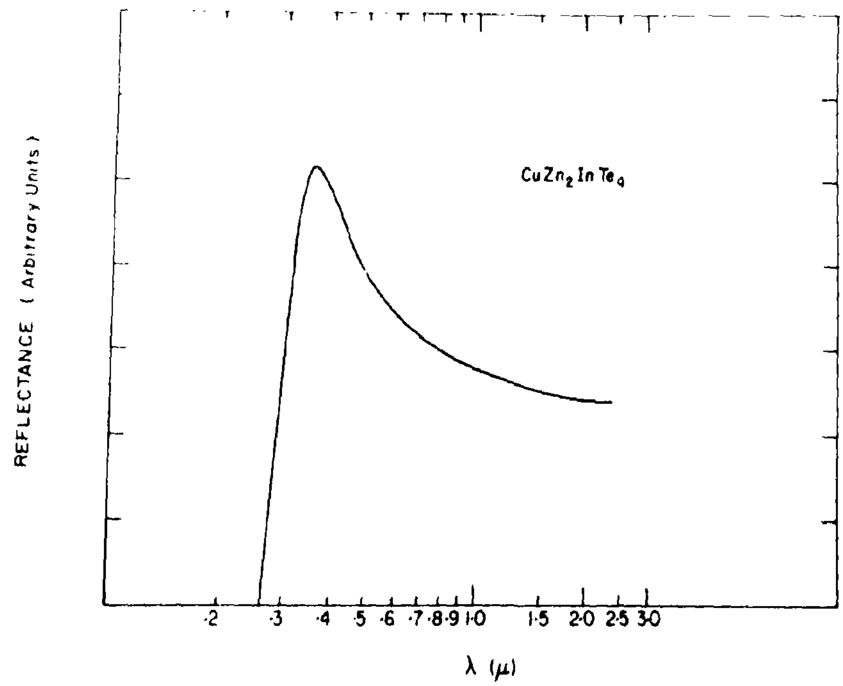

Fig 7 Optical reflectance vs. wavelength for $CuZn_2InTe_4$

culated for $CuCd_2InSe_4$ is in qualitative agreement with this observation.

The results of the microhardness investigation are shown in Fig. 8. The Knoop microhardness under a load of 300 g is shown plotted against the reciprocal of the lattice parameter. This plot is similar to the one presented by Zalar[10]. It appears that Kurnakov's law is followed by these compounds. The selenide is 'softer' than the tellurides, however Zalar's data indicates the ternary selenides were softer than the ternary tellurides. The plot is presented here to represent an empirical relation found in these compounds which has been found by others in binary and ternary compounds. Since the grain size was small (1 μ), it might be argued that the conductivity is limited by high resistance paths at the grain boundaries. In order to test this hypothesis, the electrical conductivity was measured under ac conditions in the range 10 hz–200 khz. If the grains were interconnected by high resistance paths, one could consider the analog of inter-grain coupling by capacitors of high leakage resistance. At low frequencies the impedance of the sample should be limited by capacitively shunted conductances, representing the grain boundaries. However as the frequency is increased this impedance will become less and less due to a decrease in the capacitive reactance. Therefore the ac conductivity as a function of frequency should show an increasing conductivity with increasing frequency. Measurements of several samples of each of the four compounds showed that over the aforementioned range, the conductivity remained constant within instrumental resolution of 2 per cent. The conductivity does not seem to be limited by the grain boundaries.

4. CONCLUSIONS

The use of powder metallurgical techniques resulted in the formation of single phase quaternary chalcogenides having reproducible electrical properties. Measurements of the thermoelectric power, electrical conductivity and Hall coefficient were made to characterize the properties of the material. Measurements were also made to ascertain the bandgap of the semiconductors using optical reflection techniques.

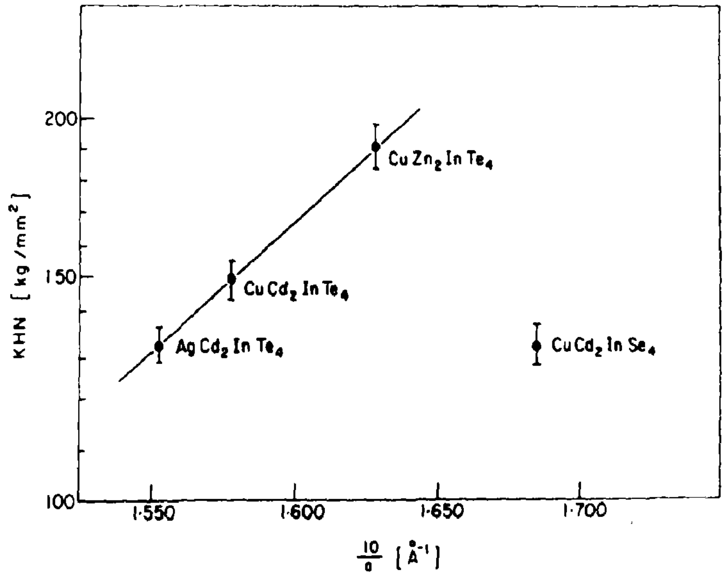

Fig. 8. Knoop microhardness vs. the reciprocal of the lattice parameter for the compounds studied in this investigation

As a result of this investigation it was determined that the tellurides and the selenide studied would not make suitable thermoelectric materials. Although the tellurides had high thermoelectric powers, the electrical conductivity was too low to attain a high figure of merit. In the selenide, the thermoelectric power was quite small, on the order of 15 μV/deg. and also had a low electrical conductivity.

The results for the tellurides were analyzed to obtain the carrier concentrations, Fermi energies and effective masses. In $AgCd_2InTe_4$ and $CuZn_2InTe_4$, the predominant scattering mode was determined from the temperature dependence of the Hall mobility and the magnitude of this mobility. In $CuCd_2InTe_4$, there is a large contribution from ionized impurity scattering in addition to the alloy scattering. This was determined from the temperature dependence of the Hall mobility and consideration of the high effective mass of the holes in this compound.

The results for the selenide were analyzed by the consideration of a two band scheme in which both electrons and holes take part in the conduction. In addition this work was extended to a determination of the energy gap in terms of the ratio of electron to hole mobilities for given electrical properties. Since it was not possible to measure the Hall coefficient exactly in this compound, there was no information generated on the scattering mechanism. However, in consideration of the low mobilities found in the selenide, it is improbable that the effective mass of the carriers is high enough to result in an ionized impurity scattering mobility that is this low. Alloy scattering effects are likely present in the selenide also. Unless alloy scattering is circumvented in the compounds by the development of better preparational techniques, all of the compounds studied would not make suitable thermoelectric materials. $AgCd_2InTe_4$ may possibly be a promising material if the effects of alloy scattering can be eliminated. The effective mass in this compound is low enough to provide high mobilities in either the ionized impurity mode or the lattice mode of scattering.

Acknowledgements – I would like to thank E. Parthé for some helpful suggestions. This work was sponsored by the Institute for Direct Energy Conversion of the University of Pennsylvania under a grant from the National Aeronautics and Space Administration.

REFERENCES

1. PARTHE E., *Crystal Chemistry of Tetrahedral Structures*. Gordon and Breach, New York (1964).
2. GORYUNOVA N. A., *Chemistry of Diamond-Like Semiconductors* Chapman and Hall, London (1965).
3. KOSHKIN V. M., KOMNIK Y. F. and ORLOVA S. D., Some characteristics of the chemical bond in multicomponent semiconducting compounds. *Chemical Bond in Semiconductors* (Edited by N. N. Sirota). Consultants Bureau, New York (1967).
4. BORSCHEVSKII A. S., GORYUNOUA N. A., KESAMANLY F. P. and NASLEDOU D. N., *Phys. Status Solidi* **21**, 9 (1967)
5. PARTHE E., 'Wurtzite and Zincblende Type Structures. *Intermetallic Compounds* (Edited by J. H. Westbrook) Wiley, New York (1967).
6. PARTHE E., YVON K. and DEITCH R. H., *Acta crystallogr* **B25**, 1164 (1969).
7. BLATT F. J., GARBER M., KROPSCHOT R. H. and SCOTT B., *Aust. J. Phys.* **13**, 233 (1960).
8. VOLGER J., *Phys. Rev* **79**, 1023 (1950)
9. FOCHS P. D., *Proc. phys. Soc. Lond.* **B69**, 42, 154, 162 (1956)
10. ZALAR S. M., *Experimental Studies of Chalcopyritic Compound $CuInTe_2$*. Raytheon Res Report T-445, Waltham, Mass (1963).
11. GOODMAN C. H. L., *J. Electron.* **1**, 115 (1955)
12. MOOSER E. and PEARSON W. S., *J. Electron.* **2**, 629 (1956)
13. IOFFE A. F., *Physics of Semiconductors*. Academic Press, New York (1960).
14. SMITH R. A., *Semiconductors*. Cambridge University Press, Cambridge (1959).
15. WEISBERG L. R., *J. appl. Phys.* **33**, 1817 (1962).
16. BROOKS H., *Adv. Electronics electron Phys.* **7**, 144 (1955)
17. BUBE R. H., MacDONALD H. E. and BLANC J., *J. Phys. Chem. Solids* **22**, 173 (1961).
18. GOSSICK B. R., *J. appl. Phys* **30**, 1214 (1959).
19. GREENAWAY D. L. and CARDONA M., *Proc. Int. Conf. on the Physics of Semiconductors*, p. 666. Institute of Physics and Physical Society of London, London (1962).

ETUDE DU SYSTEME TANTALE-HYDROGENE: DIAGRAMME D'EQUILIBRE ET STRUCTURE ELECTRONIQUE

F. DUCASTELLE, R. CAUDRON et P. COSTA
O.N.E.R.A.-29, Avenue de la Division Leclerc, 92 Chatillon, France

(*Received* 19 *March* 1969; *in revised form* 14 *October* 1969)

Résumé – L'étude de la chaleur spécifique électronique et de la susceptibilité magnétique des alliages du système Ta–H confirme la validité du modèle de bandes rigides *d* déjà avancé pour divers hydrures de métaux de transition; on peut en effet établir un parallélisme assez étroit entre le comportement de ces composés et celui des alliages iso-électroniques Ta–W. Au cours de cette étude nous avons été conduits à préciser par des expériences de résistivité et de diffraction X, un certain nombre de points obscurs du diagramme binaire Ta–H. Nous avons en particulier donné la limite du domaine de solubilité primaire de l'hydrogène dans le tantale, confirmé la structure orthorhombique des composés voisins de la composition $TaH_{0.5}$ et précisé leur domaine d'existence.

Abstract – The study of the electronic specific heat and of the magnetic susceptibility of Ta–H compounds has been carried out in order to check the validity of the rigid *d* band model, which has already been put forward for several transition metals hydrides. The behaviour of these compounds has been shown to be quite similar to the behaviour of the isoelectronic alloys Ta–W. During this work, we had to bring some precisions on some obscure points of the binary diagram Ta–H through resistivity and X-ray diffraction experiments. In particular we determined the solubility limits of the Ta-rich solid solution and of the orthorhombic compound near $TaH_{0.5}$.

INTRODUCTION

ON SAIT que, comme beaucoup de métaux de transition, le tantale peut absorber de grandes quantités d'hydrogène[1, 2].

Dans la plupart des cas, la nature de la liaison métal-hydrogène n'est pas clairement élucidée[3, 4]. Un modèle fréquemment proposé est celui des bandes rigides, l'hydrogène s'ionisant pour donner son électron à la bande *d* du métal[5–8]. Ce modèle paraît assez valable pour PdH[9–11] et semble convenir aux hydrures des métaux de la colonne V, sur la base de mesures de susceptibilité magnétique (NbH, TaH[3], VH[12], ou de déplacement de Knight (VH[13], NbH[14]). Il rend compte également de la variation de la chaleur de dissolution de l'hydrogène dans les métaux de transition en fonction de la concentration électronique *e*/*a*[8]; cette grandeur se présente en effet comme une fonction décroissante du remplissage électronique de la bande *d*, modulée par des pics (V, Nb; alliages Mo–Rh; Pd, Ni) associés à l'existence de fortes densités d'états dans cette bande, qui favorisent la constitution d'un écran à la charge du proton.

Nous avons voulu confirmer les résultats précédents sur les métaux de la colonne V à partir de mesures de chaleur spécifique électronique. Parmi les trois systèmes (V–H), (Nb–H), (Ta–H), le troisième se singularise par une très forte solubilité primaire à l'ambiante de l'hydrogène dans le tantale; c'est la raison pour laquelle nous l'avons choisi pour nos expériences.

Les mesures de chaleur spécifique nous ont malheureusement montré que cette solubilité ne se conservait pas à plus basse température. Elles nous ont toutefois permis,

(1) de préciser le diagramme de phases Ta–H pour lequel la littérature comportait des renseignements contradictoires. Il nous a été pour cela nécessaire de reprendre les expériences de susceptibilité magnétique de Stalinski, et de faire des mesures de résistivité.

(2) d'étudier la variation de la densité d'états au niveau de Fermi pour des composés plus riches en hydrogène TaH_x ($x = 0,47, 0,58$).

1. PREPARATION DES ECHANTILLONS

Les échantillons ont été préparés par absorption directe d'hydrogène suivant la méthode décrite par Sieverts et de nombreux auteurs[1-4]. L'hydrogène provient de la décomposition de l'hydrure de titane TiH_2. L'absorption d'hydrogène se fait après dégazage sous vide [10^{-5} torr] par refroidissement lent [50°C/hr] depuis 400°C jusqu'à la température ambiante. On procède ensuite à un recuit d'homogénéisation de 48 hr à 300°C. Pour faciliter cette homogénéisation, on utilise des tiges de tantale d'environ 1 mm² de section.

Le tantale de départ est du tantale Johnson-Matthey en barreaux de 4,5 mm de dia. contenant: Al: 20 ppm; Si: 10 ppm; Fe: 8 ppm; Nb: 200 ppm. Ces barreaux sont laminés au diamètre désiré, puis nettoyés, polis mécaniquement et recuits. Nous avons également utilisé du tantale en poudre Johnson-Matthey pour les mesures de susceptibilité magnétique [impuretés métalliques sauf Nb < 150 ppm; Nb: 100 ppm].

La concentration en hydrogène de nos échantillons a été déterminé par pesées, par analyse volumétrique [fusion sous hélium] et par mesure des paramètres cristallins. Nous avons également dosé l'oxygène et l'azote; la teneur en oxygène ne dépasse jamais 100 ppm, celle en azote 50 ppm. Les paramètres ont été mesurés sur des clichés de diffraction de rayons X [méthode des poudres], à température ambiante.

Le système TaH comporte, à l'ambiante, deux phases, α et β; pour les faibles concentrations en hydrogène, la phase α, qui conserve le réseau cubique centré du métal, et dont le paramètre croît linéairement avec le nombre d'atomes d'hydrogène par atomes de métal; la phase β de haute teneur en hydrogène en dérive par une distorsion orthorhombique qui peut s'analyser comme le produit d'une dilatation suivant l'axe [001] ($c_0 \neq a_0$) et d'une faible distorsion angulaire dans le plan (001), mesurée par ϵ [voir Fig. 1 et Tableau 1(b)].

Les mesures de paramètres à l'ambiante nous ont conduits aux résultats figurant dans les Tableaux 1(a) et 1(b).

Pour la phase α, on peut écrire: $a_0 = 3,306 + 0,15x$ (Å) avec $x = H/Ta$ en atomes.

La largeur de raie correspond à une incertitude sur le paramètre de $\pm 2 \cdot 10^{-3}$ Å. Ce nombre nous donne l'ordre de grandeur du défaut d'homogénéité des échantillons, qui

Tableau 1(a). *Paramètres cristallins* (*phase* α)

Phase α	a_0 (Å)
Ta	3,306
$TaH_{0,06}$	3,315
$TaH_{0,10}$	3,322
$TaH_{0,15}$	3,328
$TaH_{0,20}$	3,338

Tableau 1(b). *Paramètres cristallins* (*phase* β)

Phase β	Réseau cubique deformé				Réseau orthorhombique		
	a_0	c_0	c_0/a_0	ϵ	a	b	c
*$TaH_{0,32}$	3,368	3,395	1,008	0,3°	4,76	4,76	3,395
*$TaH_{0,41}$	3,368	3,395	1,008	0,3°	4,76	4,76	3,395
$TaH_{0,58}$	3,376	3,415	1,111	0,5°	4,77	4,79	3,415
$TaH_{0,61}$	3,382	3,425	1,012	0,5°	4,78	4,80	3,425

*échantillons biphasés, la concentration indiquée correspond à la composition nominale de l'échantillon.

ϵ est la distorsion angulaire.

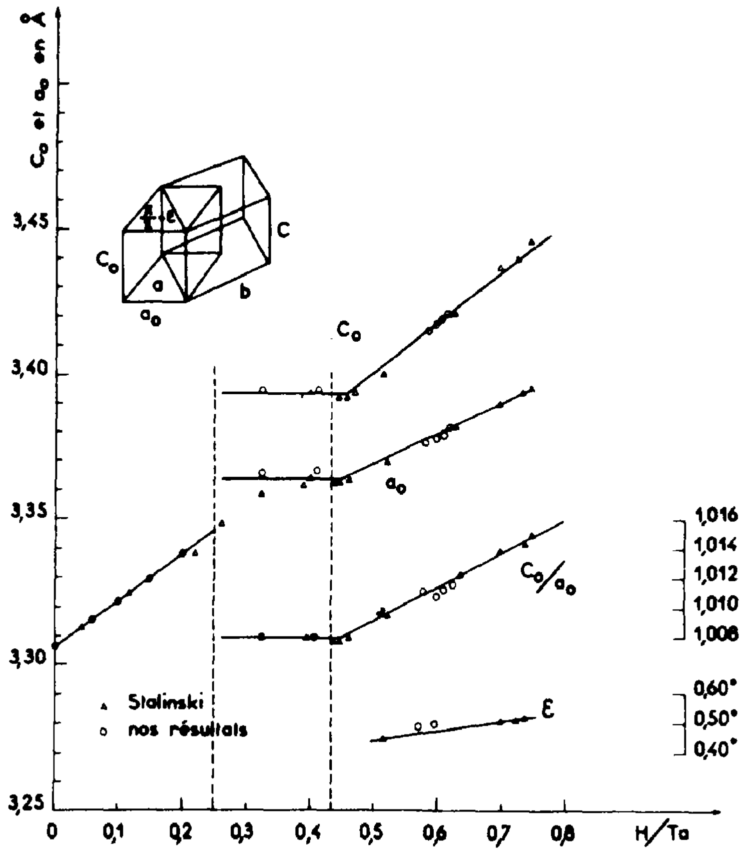

Fig. 1. Système TaH: paramètres cristallins à la température ambiante.

correspond à un écart moyen $|\overline{\Delta x}|$ de l'ordre de 0,02.

2. DETAILS EXPERIMENTAUX

(1) *Chaleur spécifique*

Les mesures de chaleur spécifique ont été faites dans un calorimètre adiabatique déjà décrit par ailleurs[15, 16].

Les échantillons sont refroidis par un gaz d'échange (^{3}He). Les mesures ont été faites entre 1,5 et 9°K, et comportent chacune soixante points environ.

Les échantillons, d'un poids d'environ 65 g étaient placés dans un container en cuivre de 7 g.

(2) *Susceptibilité magnétique*

Pour les mesures de susceptibilité magnétique, on utilise la méthode de Curie–Faraday; les forces sont mesurées à l'aide d'une balance électronique Sartorius dont la sensibilité est de 1 μg; l'électro-aimant est équipé de pièces polaires donnant une force constante; les points intermédiaires entre la température ambiante et 77°K s'obtiennent par effet Joule dans un bobinage entourant l'échantillon. La puissance de chauffage est asservie à la mesure de température.

(3) *Résistivité*

On a employé la méthode potentiométrique classique. Les lectures de tension se font sur un pont Tinsley qui permet d'apprecier 0,03 μV environ.

Le contact des fils sur l'échantillon est assuré par un dépôt de laque à l'argent. Ces fils, deux en cuivre, deux en or-cobalt, permettent de mesurer les tensions et les températures aux extrémités de l'échantillon, séparées d'environ six centimètres.

Deux bobinages enroulés autour de blocs de cuivre situés à chaque extrémité permettent d'annuler par effet Joule le gradient de température, et d'élever la température de l'ensemble.

3. RESULTATS

(1) Chaleur spécifique

On a porté sur des graphiques (Figs. 2 et 3) C_p/T en fonction de T^2. Les discontinuités à basse température correspondent à la transition supraconductrice.

On sait qu'à basse température, la chaleur spécifique dans l'état normal peut s'écrire $C_p = \gamma T + \alpha T^3$, γ caractérisant la contribution des électrons de conduction, et α celle des phonons.

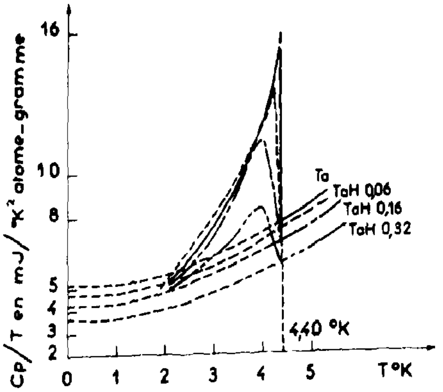

Fig. 3. Chaleurs spécifiques des composés Ta–H pour l'état supraconducteur.

γ est obtenu en extrapolant les courbes à $T^2 = 0$, α en prenant leurs pentes; les courbes sont bien linéaires, ce qui justifie cette extrapolation.;

Les précisions relatives sur α et γ sont $\Delta\alpha/\alpha \simeq 0{,}04$, $\Delta\gamma/\gamma \simeq 0{,}04$.

Le coefficient γ est directement relié à la densité d'états $n(E_F)$ au niveau de Fermi

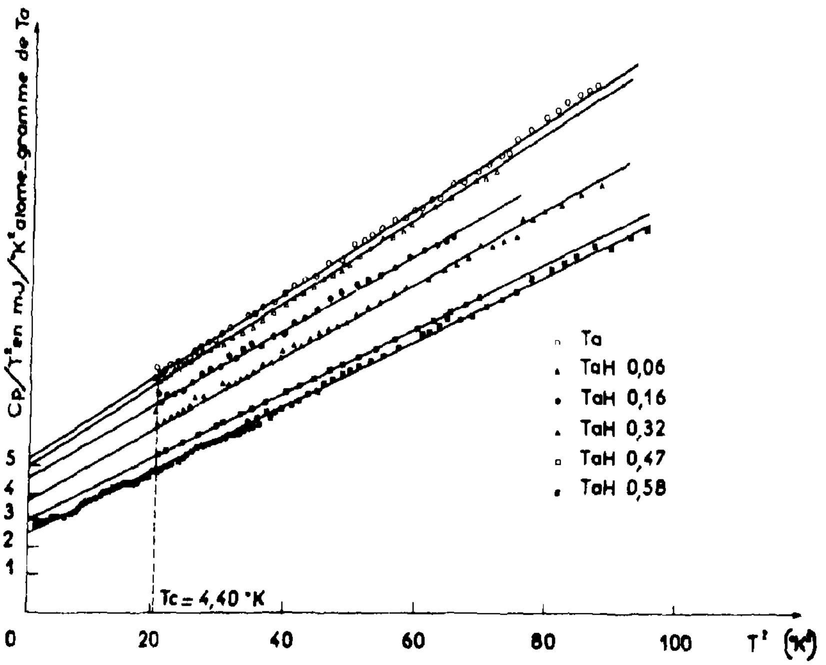

Fig. 2. Chaleurs spécifiques des composés Ta–H pour l'état normal.

[$n(E_F)$ pour l'ensemble des états de spin]. Quant à α, on peut le relier à la température de Debye Θ_D:

$$\alpha = \frac{12\pi^4}{5} \cdot Nk_B \cdot \frac{1}{\Theta_D{}^3}$$

Nous avons reporté les valeurs de γ, $n(E_F)$, α et Θ_D dans le Tableau 2.

Les valeurs indiquées pour TaH_x, $x = 0{,}06$; 0,16; 0,32, sont des valeurs globales. Ces échantillons étant biphasés à basse température (cf. Section 4(a)), on vérifie la linéarité des propriétés entre $x = 0$ et $x = 0{,}32$, aux erreurs de mesure près (sur x et sur les chaleurs spécifiques).

$$\frac{0{,}004}{0{,}06} \simeq \frac{0{,}012}{0{,}16} \simeq \frac{0{,}027}{0{,}32} = 0{,}75 \pm 0{,}1$$

$$\frac{0{,}35}{0{,}06} \simeq \frac{0{,}78}{0{,}16} \simeq \frac{1{,}67}{0{,}32} = 5{,}5 \pm 0{,}5.$$

Les valeurs obtenues pour le tantale pur sont en accord avec celles données par White *et al.*[17] ($\gamma = 5{,}68$ mJ/°K^2; $\Theta_D = 245$°K). Nous n'avons pas, comme ce dernier, observé de courbure appréciable de la courbe $C_p/T = f(T^2)$; cela explique que notre valeur de γ soit plus faible.

La température critique T_c, bien définie dans le cas du tantale ($T_c = 4{,}40$°K) l'est moins bien pour les hydrures (Fig. 3).

(2) *Résistivité*

Nous avons mesuré la résistivité de six échantillons: Ta, $TaH_{0,16}$, $TaH_{0,32}$, $TaH_{0,41}$, $TaH_{0,47}$ et $TaH_{0,58}$, de 4,2°K à l'ambiante pour Ta, de 4,2°K ou 77°K à 350°K pour les hydrures.

La courbe relative au tantale pur présente les caractéristiques connues: apparition de la supraconductivité à 4,40°K, et légère concavité négative.

Les courbes relatives à $TaH_{0,16}$ et $TaH_{0,32}$, fort semblables aux basses températures, présentent des anomalies étalées entre 250 et 310°K (Fig. 4).

Enfin les courbes relatives à $TaH_{0,41}$, $TaH_{0,47}$ et $TaH_{0,58}$ présentent deux anomalies dont l'une, correspondant à la température la plus élevée, est fort aigüe (Fig. 5).

Par ailleurs, la résistivité résiduelle de $TaH_{0,58}$ est forte, (Tableau 3).

Tableau 3

H/Ta	résistivité résiduelle en $\mu\Omega$ cm
0	0,27
0,16	0,42
0,58	3,9

Les mesures de résistance sont obtenues à une précision d'environ 1 ‰, mais l'évaluation du facteur de forme conduit à des erreurs sur la résistivité de l'ordre de 5 pour cent.

(3) *Susceptibilité magnétique*

Nous avons voulu reprendre les expériences

Tableau 2

Echantillon	γ_1 (mJ/°K^2) par atome g de Ta	$n(E_F)$ en états par atome g de Ta	α (mJ/°K^4) par atome g de Ta	Θ_D (°K)
Ta	5,28	1,12	0.138	241
*$TaH_{0,06}$	4,93		0,134	
*$TaH_{0,16}$	4,50		0.126	
*$TaH_{0,32}$	3,61		0,111	
$TaH_{0,47}$	2,86	0,61	0.089	280
$TaH_{0,58}$	2,42	0,51	0.096	273

*Echantillons biphasés à basse température.

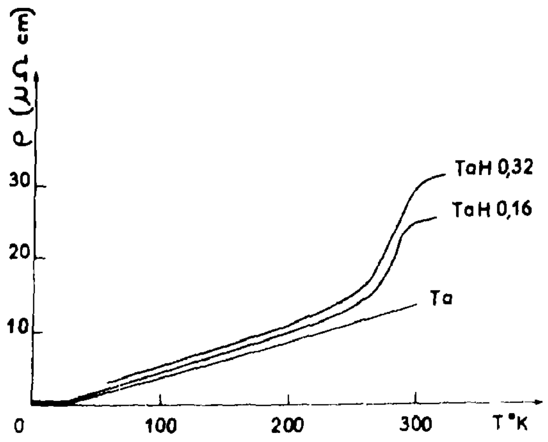

Fig. 4 Résistivités des composés Ta–H pour H/Ta < 0.40.

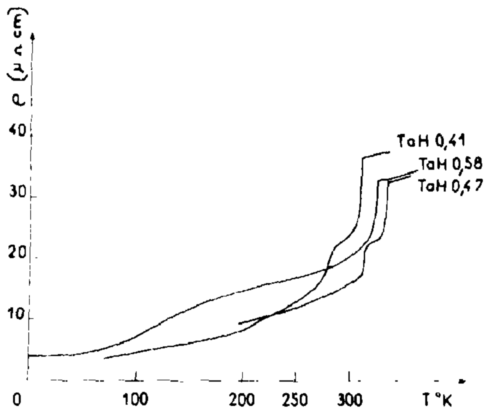

Fig 5 Résistivités des composés Ta–H pour H/Ta > 0,40

de susceptibilité de Stalinski qui ne présentent aucune des anomalies observées en résistivité. Nos résultats les ont pleinement confirmées:

La susceptibilité décroît quand H/Ta croît, et ceci d'autant plus qu'on s'approche de la concentration limite H/Ta = 0,75.

La susceptibilité dépend très peu de la température ($0 \leq \Delta\chi/\chi \leq 0{,}02$ entre 77° et 320°K), le sens de variation étant inversé vers les hautes teneurs. Nos résultats sont résumés dans le Tableau 4; la précision relative des mesures est estimée à 1 pour cent.

Tableau 4

χ (10^{-6} u e m/at. Ta)		H/Ta (atomes)
77°K	295°K	
147	145	0.16
147	144	0,20
	115	0,55
114	113	0,58
109	109	0.61

4. INTERPRETATION DES RESULTATS

(a) *Diagramme d'équilibre* Ta–H

A notre connaissance, aucune étude systématique de ce diagramme n'a été faite, en particulier pour les températures inférieures à 300°K. Un certain nombre de divergences apparaissaient en outre sur les mesures à l'ambiante.

(1) *Domaine de solubilité primaire de l'hydrogène dans le tantale cubique centré.* Stalinski[3] annonçait une solubilité primaire de l'hydrogène jusqu'à $TaH_{0,37}$. Wallace[18], donnait par contre un diagramme tout à fait contradictoire reposant sur des expériences de rayons X et de résistivité non publiées, mais qui semblaient concorder avec d'anciennes mesures de chaleur spécifique de Kelley entre 50 et 300°K[19].

Nos résultats confirment en gros les hypothèses de Wallace. Nous avons pu préciser la limite de solubilité primaire (Fig. 6) en nous appuyant sur nos mesures de résistivité ($TaH_{0,16}$ et $TaH_{0,32}$) et sur les mesures de Kelley.

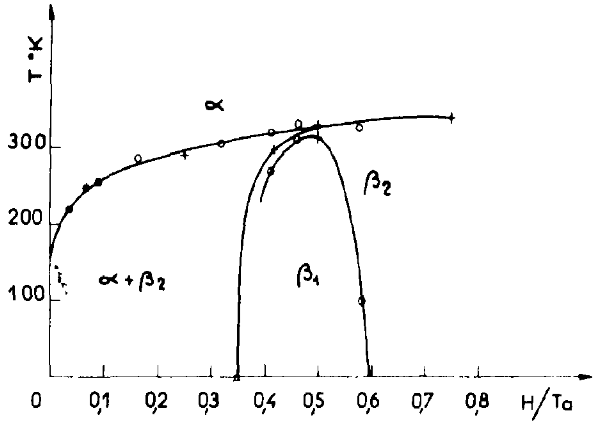

Fig. 6. Diagramme d'équilibre TaH. Points déduits des mesures de Kelley: ●, de Wallace: ×. Points déduits de nos mesures de résistivité: ○, chaleur spécifique: △, paramètres cristallins: +.

Dans les deux cas, on constate des anomalies étalées entre 150 et 300°K, la limite supérieure dépendant de la concentration en hydrogène. Ces anomalies correspondent certainement à l'apparition de la phase β de symétrie orthorhombique décrite en I.

D'autres faits expérimentaux confirment cette interprétation: Nos mesures de chaleur spécifique électronique montrent, d'une part que la température d'apparition de la supraconductivité est indépendante de H/Ta pour H/Ta = 0,06; 0,16; 0,32, d'aute part que le pic de chaleur spécifique correspondant s'étale et diminue d'amplitude. Pour un échantillon supraconducteur monophasé, C_p/T doit tendre vers zéro quand la température tand vers zéro.

Cette condition n'est pas remplie; elle ne serait d'ailleurs pas compatible avec la condition d'égalité des aires combrises entre la courbe C_p/T (T) relative à l'état supraconducteur, et la courbe extrapolée relative à l'état normal. [Cette égalité traduit l'égalité des entropies à $T = T_c$ (température critique) pour l'état supraconducteur et l'état normal]. Il faut donc décomposer C_p en deux contributions, celle qui correspond au tantale presque pur, et celle qui correspond à la phase β (non supraconductrice) (Fig. 2). En faisant ce découpage, on trouve comme limite de solubilité, de l'hydrogène dans la phase β H/Ta = 0,35 à 4,2°K.

La résistivité résiduelle de $TaH_{0,16}$ est trop voisine de celle de Ta pur pour correspondre à un composé monophasé. Elle correspond bien par contre à ce qu'on attend pour un mélange de tantale à faible résistivité résiduelle et de phase β à forte résistivité résiduelle (on additionne les conductivités).

La limite de solubilité à la température ambiante (~ 290°K) est difficile à préciser; ceci d'autant plus que les clichés de diffraction de rayons X sont difficiles à interpréter: les raies des deux phases sont très voisines; leur séparation est souvent du même ordre que leur épaisseur. Ainsi, un long recuit en ampoule scellée de l'échantillon $TaH_{0,32}$ nous a permis de séparer les raies de la phase β qui n'étaient pas visibles après le premier traitement. Ceci nous conduit à placer la limite de solubilité à $H/Ta \approx 0,25$ au lieu de 0,37 [3].

(2) *Domaine d'existence et nature de la phase.* Wallace a montré pour Ta_2H l'existence de deux phases β_1 et β_2 pour lesquelles le réseau métallique a la même symétrie. Les transitions $\alpha - \beta_2$ et $\beta_2 - \beta_1$, ont été observées en chaleur spécifique, en résistivité et en analyse thermique différentielle. La diffraction de neutrons a en outre révélé l'existence d'un ordre des hydrogènes dans β_1. Mais, à la différence des autres auteurs [3, 20, 21], Wallace attribue la structure quadratique aux phases β.

Nos expériences prouvent que le réseau est bein orthorhombique en raison de la séparation desraies 042 et 402. Elles confirment pour les échantillons $TaH_{0,41}$, $TaH_{0,47}$, $TaH_{0,58}$, l'existence d'une double transition, aux températures indiquées dans le Tableau 5 (cf. Fig. 5).

Tableau 5

	Température de transition	
H/Ta	(°K)	
	$\beta_1 - \beta_2$	$\beta_2 - \alpha$
0,41	275	322
0,47	315	334
0,58	100	328

Nous pouvons compléter le diagramme en ce qui concerne la limite α, $(\alpha + \beta_2)$. Les limites β_2, $(\beta_1 + \beta_2)$ et $(\beta_1 + \beta_2)$, β_1 sont plus difficiles à définir. On peut supposer que β_1 correspond à une phase ordonnée centrée sur la concentration $H/Ta = 0,5$. Nos échantillons $TaH_{0,47}$ et $TaH_{0,58}$ seraient donc monophasés à basse température.

(3) *Notons encore* que Saba et Wallace ont trouvé un double pic de chaleur spécifique pour la transition α, β_2 [22], mais aucune explication concluante n'a pu être donnée, d'autant plus que les courbes de résistivité ne présentent qu'une seule anomalie.

Nous pouvons donc à présent esquisser un diagramme d'équilibre compatible avec tous les résultats connus (Fig. 6), en nous servant des idées de Wallace et en les corrigeant sur quelques points.

Il demeure un doute quant à l'ordre des transitions β_1, β_2, et β_2, α pour $H/Ta \geqslant 0,5$, les domaines biphasés n'ayant jamais été mis en évidence, soient qu'ils n'existent pas, soient qu'ils soient extrêmement réduits. La nature de l'ordre dans β_1 reste également à élucider.

De façon générale, le diagramme proposé doit être considéré comme indicatif. Des études plus approfondies (diffraction de neutrons en particulier) sont nécessaires pour préciser l'étendue des domaines β_1 et β_2.

(b) *Structure de bandes*

(1) *Les propriétés électroniques des alliages de substitution* des métaux de transition voisins d'une même ligne dans le tableau périodique s'interprètent bien avec le modèle des bandes rigides [9, 23], la bande *d* se remplissant quand on augmente la concentration électronique. Nous avons tenté d'appliquer ce modèle aux composés (Ta–H) et comparé dans cet esprit les différentes courbes expérimentales dont nous disposions: chaleurs spécifiques électroniques et susceptibilités magnétiques des composés Ta–H; chaleurs spécifiques et susceptibilités magnétiques des alliages Ta–W [24, 25], (Figs. 7 et 8).

Pour les composés Ta–H, seules sont intéressantes évidemment les mesures portant sur des échantillons monophasés. Remarquons cependant que la susceptibilité est pratique-

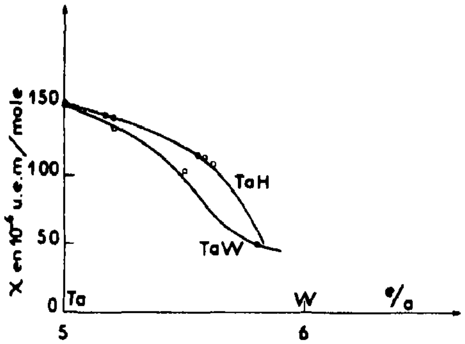

Fig. 7. Susceptibilité magnétique de TaH et TAW. TAH. courbe en trait plein: mesures de Stalinski. O: nos résultats. TAW, □: mesures de Taniguchi[26].

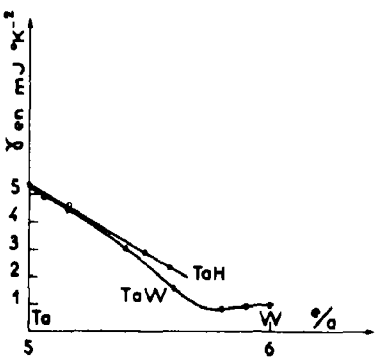

Fig. 8. Chaleur spécifique électronique de TaH et TaW: ● TaW[27]; O TaH: nos résultats.

ment indépendante de la température, même pour des échantillons qui ont présenté des anomalies de résistivité ou de chaleur spécifique; on en déduit que la variation de la densité d'états au niveau de Fermi pour $0 \leq H/Ta \leq 0{,}36$ coincide avec la variation linéaire qu'on attend pour un mélange biphasé et qui est effectivement observée sur les valeurs de (cf. Section 2).

La comparaison des résultats évoqués plus haut conduit aux résultats suivants:

(a) *Les valeurs de* γ présentent des lois de variation comparable pour Ta–H et Ta–W; $n(E_F)$ décroît sensiblement quand e/a croît.

(b) *L'écart entre les valeurs de* $n(E_F)$ déduites de la susceptibilité (en l'identifiant à un terme de Pauli) et de la chaleur spécifique sont analogues pour les deux types d'alliages. On est donc, pour l'essentiel conduit à un schéma proche du modèle de bandes rigides, en accord avec les résultats obtenus pour le déplacement du Knight de V et Nb dans les hydrures correspondants[13, 14].

(c) *Les courbes homologues* (susceptibilité, ou coefficient γ) indiquent toutefois une décroissance moins prononcée dans le cas de Ta–H. Ce résultat signifie vraisemblablement que la charge d'écran autour du proton n'est pas uniquement constituée par des électrons dans des états de bande d; mais d'autres hypothèses peuvent aussi être avancées: rétrécissement de la bande d dû à l'augmentation de la distance entre atomes métalliques; déformation de la bande au voisinage du niveau de Fermi associé à la distorsion de la maille cubique. Ce phénomène semble fréquent pour les hydrures de transition les plus concentrés[26].

(2) *Température de Debye*. Pour les métaux et alliages de transition, l'énergie de cohésion et les grandeurs élastiques qui lui sont reliées, dont en particulier la température de Debye, présentent un maximum en milieu de série qui s'interprète bien dans l'approximation des liaisons fortes[23]. Pour la troisième série de transition, ce maximum correspond au tungstène.

Qualitativement, on comprend donc que la température de Debye croisse quand H/Ta croît, c'est-à-dire quand on se rapproche de la situation du tungstène en remplissant la bande d. Là encore cependant cet effet est plus faible que pour les alliages de transition:

$$\Theta_D(\mathrm{TaH}_{0,58}) = 273°\mathrm{K};\ \Theta_D(\mathrm{Ta}_{0,4}\mathrm{W}_{0,6}) = 317°\mathrm{K}.$$

(3) *Supraconductivité*. On a vu que les anomalies de chaleur spécifique dues à l'apparition de la supraconductivité pour $H/Ta < 0{,}5$ s'interprètaient par l'existence d'un mélange de tantale et de phase non supraconductrice. De fait $\mathrm{TaH}_{0,58}$ n'est pas supraconducteur au dessus de 2°K. On sait d'ailleurs que dans les séries de transition, la température critique est maximum pour $e/a = 5$, et que

la supraconductivité disparaît rapidement au-delà, cet effet étant lié à la décroissance de $n(E_F)$.

Par exemple, les alliages Ta–W ne sont plus supraconducteurs à partir de $Ta_{0,75}W_{0,25}$ [27].

Dans notre hypothèse d'un remplissage de la bande *d*, la disparition de la supraconductivité pour Ta_2H a donc certainement même origine. La situation est analogue dans le cas des composés Nb–H [28].

Remerciements – Les auteurs tiennent à remercier M. le Professeur R. Castaing, Directeur Général de l'Onera pour le soutien qu'il a bien voulu accorder à ce travail, et à M. le Professeur Friedel pour les conseils qu'il leur a donnés.

REFERENCES

1. SIEVERTS A and COSTA **A.**, **Z.** *anorg. Chem.* **187**, 155 (1930)
2. HÄGG G., *Z. phys. Chem.* **11**, 433 **(1931)**.
3. STALINSKI B., *Zesz. nauk. Politech.* **wrocl. 4, 25** (1957).
4. LIBOWITZ G. G., *The Solid State Chemistry of Binary Metal Hydrides* Benjamin, New-York (1965).
5. JONES D. W., PESSALL N. and McQUILLAN A. D., *Phil. Mag.* **6**, 455 (1961)
6. JONES D. W. and McQUILLAN A. D., *J. Phys. Chem. Solids* **23**, 1441 (1962)
7. JONES D. W., *J. less-common Metals* **6**, 100 (1964).
8. JONES D. W., *Phil. Mag.* **9**, 100, 709 (1964).
9. MOTT N. F. and JONES H., *The Theory of the Properties of Metals and Alloys.* Oxford University Press (1936).
10. TSUCHIDA T., *J. phys. Soc. Japan* **18**, 7 (1963).
11. MACKLIET C. A. and SCHINDLER A. I., *Phys. Rev.* **146**, 2, 463 (1963).
12. ZAMIR D., *Phys. Rev.* **140**, 271 (1965).
13. BETSUYAKU H., TAKAGI Y. and BETSUYAKU Y., *J. phys. Soc. Japan* **16**, 1089 (1964).
14. ZAMIR D. and COTTS R. M., *Phys. Rev.* **124**, 666 (1964).
15. CONTE R., Thèse Orsay (1964).
16. CAUDRON R. and COSTA P., *2nd. Conf. des Composés Solides d'éléments de Transition, Groningue* (1967).
17. WHITE D., CHOU C. and JOHNSTON H. L., *Phys. Rev.* **109**, 3, 797 (1958).
18. WAITE T. R., WALLACE W. E. and CRAIG R. S., *J. chem. Phys.* **24**, 634 (1956).
19. KELLEY K. K., *J. chem. Phys.* **8**, 316 (1940).
20. BRAUER G. and HERMANN R., *Z. anorg. allg. Chem.* **274**, 11 (1953).
21. PEDERSEN B., KROGDAHL T. and STOKKELAND O. E., *J. chem. Phys.* **42**, 72 (1965).
22. WALLACE W. E.; SABA W. G., WALLACE W. E., SANDMO H. and CRAIG R. S., *J. chem. Phys.* **35**, 2148 et 2156 (1961).
23. FRIEDEL J., *Theory of Magnetism in Transition Metals*, p. 283 Academic Press, N.Y. (1967).
24. BUCHER E., HEINIGER F. and MULLER J., L.T.P. Vol. 9, p. 1059, Plenum Press, N.Y. (1965).
25. TANIGUCHI S., TEBBLE R. S. and WILLIAMS D. E. G., *Proc. R. Soc.* **265**, 1325, 502 (1962).
26. DUCASTELLE F. and COSTA P., à paraître.
27. HULM J. K. and BLAUGHER R. D., *Phys. Rev.* **123**, 5 (1961).
28. RAUCH G. C., ROSE R. M. and WULFF J., *J. less-common Metals* **8**, 99 (1965).

J. Phys. Chem. Solids Pergamon Press 1970. Vol. 31, pp. 1257–1262. Printed in Great Britain.

ANOMALIES IN THE DIELECTRIC CONSTANT OF THE $Pr_{1-x}Nd_xAlO_3$ SYSTEM

W. A. NORDLAND and L. G. VAN UITERT
Bell Telephone Laboratories, Incorporated, Murray Hill, N.J. 07974, U.S.A

(*Received* 10 *October* 1969)

Abstract—The low frequency (1 kHz) values of the dielectric constant of the $Pr_{1-x}Nd_xAlO_3$ system have been measured between 300 and 5°K. In pure $PrAlO_3$ anomalies have been observed which involve, (1) a first order phase transformation at 205°K; (2) a second order phase transformation at 151°K; (3) a change from a twinned to an untwinned structure around 80°K; and (4) a magnetically induced re-orientation of the crystallographic axes below 80°K. Pure $NdAlO_3$ on the other hand showed no anomalies over this temperature range. For the mixed crystals $Pr_{1-x}Nd_xAlO_3$, the 205°K transformation, was found to shift to lower temperatures in a linear fashion with increasing amounts of Nd^{3+} ions. The 151°K transformation behaved similarly but appeared to become first order when the concentration of Nd^{3+} approached 50 per cent

1. INTRODUCTION

A GENERAL interest in the rare-earth orthoaluminates, particularly those which contain the lighter rare-earth metals such as Pr and Nd, has precipitated a series of studies of these systems. Two low temperature phase transformations in $PrAlO_3$ have been reported elsewhere[1] as well as a magnetic field induced re-orientation of the crystallographic axes[2]. Crystallographic studies[3], specific heat measurements[4] and spectroscopic studies[5] have also been made. In conjunction with these we report the results of an investigation of the unclamped dielectric constant of pure $PrAlO_3$, pure $NdAlO_3$ and $Pr_{1-x}Nd_xAlO_3$ for $x - 0{\cdot}05$, 0·1, 0·25, 0·5 and 0·75. These materials have been reported to be slightly distorted perovskites[6] and have $F\bar{3}2/c \equiv D_{3d}^6$ symmetry at room temperature[3]. A rhombohedral unit cell derives from a slight distortion from true cubic structure. In these experiments the measuring electric field, E, was always directed parallel to an edge of the pseudo-cube which is the natural growth form[6]. The principal values of the electric susceptibility tensor could not be determined since E was not in general parallel to the appropriate crystallographic directions. In addition, presence of a twinned structure precluded the determination of the principal values of the dielectric tensor in the low temperature phases. Two anomalies were observed in pure $PrAlO_3$ in which the measured dielectric constant, ϵ, changes by about 3 per cent and which correspond to structural phase transformations. A step change at 205°K (see Fig. 1(a)) which has a temperature hysteresis of 3° indicates a first order transformation. A slope change without a temperature hysteresis at 151°K is consistent with a second order transformation. The symmetry has been identified to be monoclinic $I112/m \equiv C_{2h}^3$ between 205 and 151°K and triclinic $I1 \equiv C_i^1$ below 151°K[3]. No anomalies were observed in pure $NdAlO_3$; however, the effect of increasing amounts of Nd^{3+} ions in the $PrAlO_3$ lattice was observed to cause these transformations to take place at correspondingly lower temperatures as might be expected. These results together with other investigations may aid in the understanding of ion–ion interactions in the rare earth aluminates.

Several tests were performed to determine whether non-centrosymmetric structures were present in any of the low temperature phases of pure $PrAlO_3$. Hysteresis loop tests for ferroelectricity gave negative results. Pyroelectric tests for spontaneous electric polarization using the method of Chynoweth[7] and the second harmonic generation test for absence of a center of symmetry gave mainly negative results[8]. These latter two tests did, however, give inconclusive evidence of an asymmetric structure in some highly twinned samples. The observation of these effects in such cases can be explained by the fact that with the centrosymmetric structures proposed, the boundary regions between adjacent twins cannot be centrosymmetric. Also, a very slight shift of the array of Pr atoms can result in an asymmetric structure which would not be in conflict with the structure calculations[9].

2. EXPERIMENTAL

The variations in ϵ which correspond to these anomalies were a small fraction of the measured dielectric constant ($\epsilon \approx 25$), therefore, an automatically balancing, high sensitivity, capacitance bridge system was used to resolve them. The system used for these measurements* was operated at a signal frequency of 1 kHz and has a resolution of 0·02 pF. Continuous readout of changing capacitance coupled with high sensitivity permitted slow temperature scanning and recording of extremely small variations in ϵ. The curves in Fig. 1 were derived from X-Y recorder traces in which a d.c. voltage proportional to the sample capacitance was plotted vs. temperature.

The samples were mounted on a brass block together with two GaAs temperature sensors and an Advance wire heating coil. This apparatus was mounted in a helium dewar which was initially cooled to near 80°K by liquid N_2 placed in the outer dewar chamber. Further cooling to 5°K was accomplished by transferring liquid helium vapor to the inner dewar chamber via a standard helium transfer

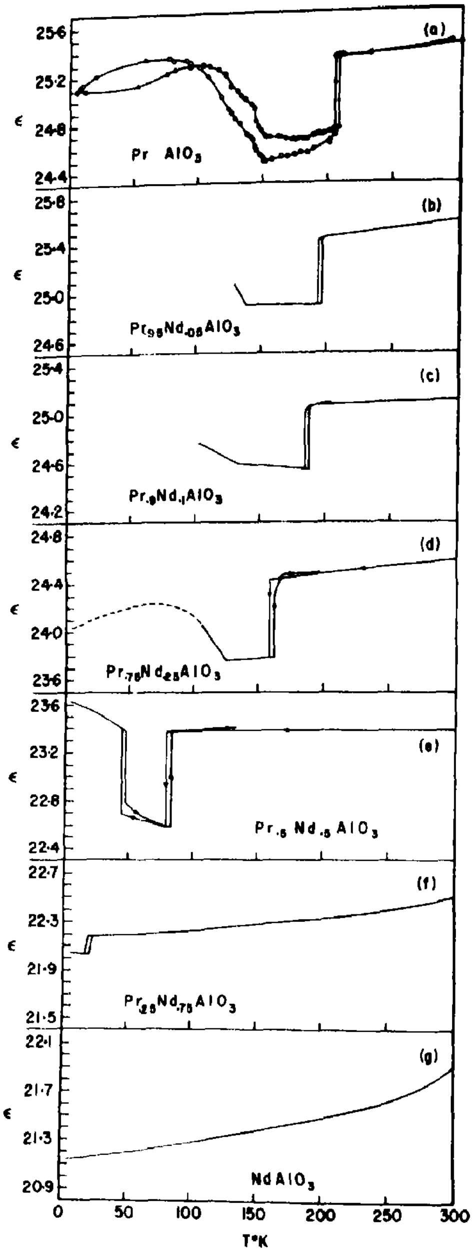

Fig. 1. The dielectric constant is plotted vs. T for the various values of x which were tested in the Pr$_{1-x}$Nd$_x$AlO$_3$ system. In each figure the temperature was cycled in both directions over the range shown. The step anomaly at 205°K had a 3°K hysteresis. The slope change at 151°K in (a) through (d) had no hysteresis but the step change at 47°K in (e) had ~ 1° hysteresis. The overall hysteresis below 205°K in (a) is thought to be due to the presence of different twin structures during the return part of the temperature cycle.

---

*A General Radio Type 1680 Automatic Capacitance Bridge which consists of a self balancing bridge, a digitizing unit and an analog converter.

tube. One of the GaAs sensors was calibrated to an accuracy of about ±0·1°K. Its output was read on a digital voltmeter with a resolution of ±0·1°K. The other sensor was used to provide feedback to a temperature control system which supplied controlled power to the heater wound on the sample holder. The overall system performance provided a temperature control of ±0·25°K down to about 40°K and about ±0·5°K down to 5°K.

The samples were platelets cut from flux grown crystals which normally grow in the form of parallelopipeds. In each case, samples were cut along directions which were parallel to the growth edges. Sample sizes were typically 12–25 mm^2 with thicknesses ranging from 0·08 to 0·4 mm. The absolute values of capacitance were in the 10–20 pF range. Generally the samples were single crystals in the trigonal phase and twinned in the low temperature phases. Aluminum electrodes ~1000 Å thick were evaporated on opposite faces of the platelets. Aluminum foil strips were connected to these electrodes with a conductive epoxy cement. When mounted the samples were suspended freely by their connecting foil strips. This method of attachment was found to be necessary in order to reduce mechanical strain due to differences in thermal expansion coefficients between the sample and the sample holder.

3. OBSERVATIONS

The dielectric constant, ϵ, of pure $NdAlO_3$, shown in Fig. 1(g), was without anomalies and varied only about 2 per cent between 300 and 5°K.

Pure $PrAlO_3$ (Fig. 1(a)) on the other hand undergoes a first order transformation to monoclinic symmetry at 205°K, and exhibits a step change in ϵ of about 2½ per cent to a lower value. A 3° temperature hysteresis is also associated with this anomaly. The temperature at which this transformation occurred was found to vary over several degrees for different samples. This variation is believed to be due to the presence of extrinsic strain. Evidence of this was the ability to change the transformation temperature by stressing the sample near the critical temperature. A slope change at 151°K is accounted for by the transformation to the triclinic structure. The slope change and the absence of hysteresis observed at this temperature are consistent with the identification of this transformation as being of second order. The 151°K transformation was unaffected by external stress in contrast to the 205°K transformation. Several samples were fabricated with semitransparent Al electrodes about 200 Å thick. This permitted simultaneous visual observation of the twin structure along with the capacitance measurement. A series of twin patterns which changed rapidly with temperature were observed visually in going from 151 to 80°K. Over this temperature range ϵ was observed to increase about 2 per cent. Near 80°K most samples assumed a relatively stable finely twinned structure, in some cases, however, large untwinned regions suddenly appeared. A step change in ϵ to a lower value (not shown in Fig. 1(a) because of its variability) was associated with this sudden change. Several 'as grown' samples which had not had mechanical treatment such as cutting, grinding, and polishing, were observed to become single domain in the triclinic phase near 80°K. Thus, it appears that this twin structure may in some cases be attributed to extrinsic strain.

The overall hysteresis below the 205° transformation shown in Fig. 1(a) only occurred if the sample was taken below ~120°K in any given cycle. If T was reversed above 120°K, the increasing T curve was coincident with the decreasing T curve, as was the case in 1(b), 1(c) and 1(d). Since the samples tended to be highly twinned in the triclinic phase with new sets of orientations occurring during successive cycles, the hysteresis can arise from a structural anisotropy due to the small distortion of the lattice from cubic symmetry. It has been proposed that the magnitude of such an anisotropy could be expected to be of the order of 1–2 per cent[10], as was observed.

Figures 1(b)–1(f) show the effects of increasing amounts of Nd^{3+} ions in the $PrAlO_3$ lattice. It is important to note that the lower temperature transformation in the $x = 0{\cdot}5$ curve (1(e)) exhibits a step anomaly with a temperature hysteresis, ≈1°, suggesting a first order transformation instead of the second order transformation observed for this anomaly with $x > 0{\cdot}5$. The $x = 0{\cdot}75$ curve (1(f)) exhibits a 0·8 per cent step anomaly at ~20°K which appeared to have some hysteresis also. The temperature at which this anomaly occurred varied over several degrees in the sample tested making it difficult to be precise as to its nature. A twinned structure appeared at this temperature and continued to be in evidence down to 5°K. Comparison of the curves in Fig. 1 also reveals a gradual decrease in the absolute value of ϵ with increasing Nd concentration.

Figure 2 shows the various anomalies observed in the $Pr_{1-x}Nd_xAlO_3$ system plotted as a function of temperature. The coordinates of the single anomaly observed with $x = 0{\cdot}75$ are on the upper curve which represents the first order transformations and, therefore, also suggests that it is a first order type. This upper curve can be seen to be quite linear whereas the lower temperature anomaly appears to vary differently. It should be noted that since the error in temperature can be considered as negligible on the scale given in Fig. 2, and since the value of x is the same for both curves, one must explain the deviation from a simple curve of the lower T anomaly points, especially since the upper T anomaly points fit a linear curve. It should also be noted that several samples of pure $PrAlO_3$ were measured and the upper T anomaly was reproducible within 5° and the lower T anomaly within 2°.

Reorientation of the crystallographic axes has been found to occur in $PrAlO_3$ in the triclinic phase when a magnetic field of about 15 *kg* is applied perpendicular to the pseudotetragonal or c axis. This effect has been described in some detail elsewhere[2]. Using this effect we have observed a change in ϵ of 1–2 per cent when the c axis was switched from being parallel to E to being parallel to the magnetic field, H, where E and H were mutually perpendicular. This change, therefore, represents the dielectric anisotropy for E parallel and perpendicular to c. A dimensional change associated with this effect usually destroys the electrodes after one or two 'switches' making quantitative measurements of the effect difficult. We have not studied the effect of a magnetic field on the mixed $Pr_{1-x}Nd_xAlO_3$ system except for the $x = 0{\cdot}75$ case where below the 20°K anomaly, an effect of magnetic field on the dielectric constant was observed. The effect of magnetic field up to 20 kg on both phase transformation temperatures in pure $PrAlO_3$ was studied, however, and no effect was observed within experimental error.

4. SUMMARY

We have measured the unclamped dielectric constant of $PrAlO_3$ crystals and observed the anomalies due to two phase transformations and the structural re-orientation of the crystallographic axes in the triclinic phase by a magnetic field. A dielectric anisotropy of ~1·5 per cent has also been observed by the use of this latter effect which is probably an average value due to the presence of a twinned structure. Interesting effects took place on the phase transformations as Nd^{3+} ions were substituted for Pr^{3+} ions. Both transformations shifted to lower temperatures as the amount of Nd_{3+} increased. The second order transformation appeared to change character when the concentration approached 50 per cent. Investigations of these effects may aid in the understanding of ion–ion interactions in the rare-earth ortho-aluminates as well as the crystal field theory appropriate to these materials.

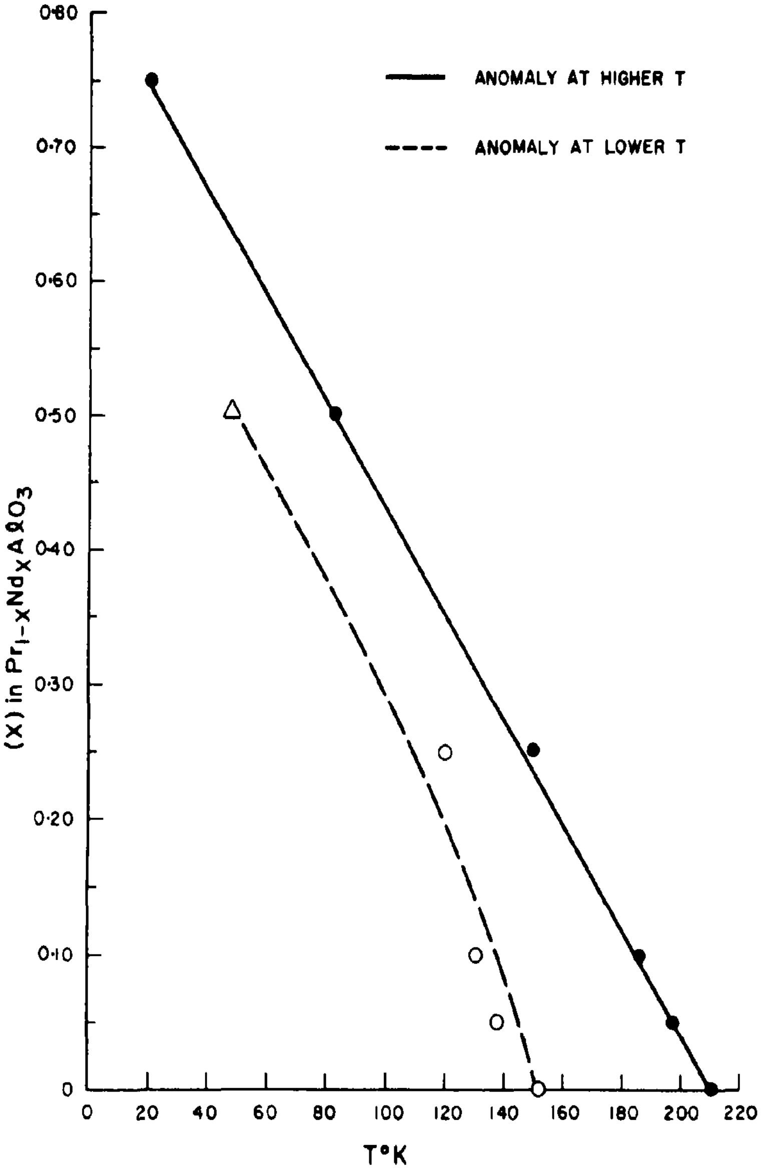

Fig. 2. The anomalies observed in the $Pr_{1-x}Nd_xAlO_3$ system are shown on a plot of x vs. T. The solid linear curve represents the first order transformation which occurred at higher T. The dashed nonlinear curve represents the second order transformation (circle points) which appears to have become a first order type (triangular point) for $x \rightarrow 0{\cdot}5$.

Acknowledgements—The authors wish to express indebtedness to Drs. E. Cohen and L. A. Riseberg for suggesting and discussing these experiments, and we give special recognition to W. H. Grodkiewicz for growing the large, high quality crystals without which these experiments would not have been possible.

REFERENCES

1. COHEN E., RISEBERG L. A. NORDLAND W. A., BURBANK R. D., SHERWOOD R. C. and VAN UITERT L. G., *Phys. Rev.* **186**. 476 (1969)
2. RISEBERG L. A., COHEN E., NORDLAND W.

A. and VAN UITERT L. G., *Phys. Lett.* **30A**, 4 (1969).
3. BURBANK R. D., *Acta crystallogr Suppl.* **A25**, S227 (May 1, 1969). Also *J appl. Cryst* (In press).
4. RYDER E. J (To be published).
5. COHEN E., RISEBERG I. A., NORDLAND W. A. (To be published).
6. GELLER S. and BALA V. B., *Acta crystallogr.* **9**, 1019 (1956). *Crystallographic Studies of Perovskite-like Compounds – II. Rare Earth Aluminates.*
7. CHYNOWETH A. G., *J. appl. Phys.* **27**, 78 (1956).
8. KURTZ S. K. private communication.
9. BURBANK R. D., private communication.
10. COHEN E., private communication.

J. Phys. Chem. Solids Pergamon Press 1970. Vol. 31, pp. 1263–1272. Printed in Great Britain.

EFFETS DE TAILLE DANS LES SOLUTIONS SOLIDES DE L'ALUMINIUM AVEC LES METAUX DE TRANSITION DE LA PREMIERE SERIE

JEAN BLETRY

Laboratoire de Physique des Solides*, Faculté des Sciences, 91, Orsay, France

(*Received* 7 *October*, 1968; *in revised form* 22 *September* 1969)

Résumé – On a préparé par trempe ultra rapide de l'état liquide une série de solutions solides des métaux de transition (Ti, V, Cr, Mn, Fe, Co, Ni) dans l'aluminium jusqu'à une concentration de 2–5 pour cent *at*.

La variation du paramètre de réseau de ces solutions solides avec le type d'impureté est en accord qualitatif mais non quantitatif avec celle calculée par Blandin et Deplante.

Les causes possibles des écarts observés sont discutées.

Abstract – A series of solid solutions of transition metals (Ti, V, Cr, Mn, Fe, Co, Ni) in Aluminium has been prepared by splat cooling method, up to concentration of 2–5 per cent *at*.

The variation of the lattice parameter of these solid solutions with the different impurities is in qualitative but not quantitative agreement with the calculation by Blandin and Deplante. The possible cause of the observed discrepancy are discussed.

1. INTRODUCTION

LA NOTION d'état lié virtuel *d*[1] permet d'analyser la structure électronique des impuretés de transition en substitution dans le réseau d'un métal normal. Grâce à ce modèle, il est possible d'expliquer la variation de certaines propriétés physiques de ces solutions solides en fonction du nombre atomique du métal de transition dissous. Ainsi Déplanté[2] a pu calculer, au prix de très nombreuses approximations, la variation du paramètre de la maille qui résulte de la dissolution d'une impureté de transition dans une matrice d'aluminium. Malheureusement la quasi-insolubilité de ces métaux (et plus particulièrement du fer, du cobalt et du nickel) dans l'aluminium interdisait jusqu'alors une vérification expérimentale sûre de ces prévisions théoriques.

Pour surmonter cette difficulté, nous avons utilisé la technique des trempes ultrarapides de Duwez[3] car elle permet de préparer des solutions solides métastables Al–T très fortement sursaturées en T. Nous avons donc pu étudier les variations du paramètre cristallin de ces alliages en fonction de la concentration en métal de transition et cela dans de bonnes conditions puisque les variations à mesurer étaient notables. Nos résultats, pour les sept métaux de la série Ti, V, Cr, Mn, Fe, Co, Ni, n'ont pas été conformes aux prévisions: nous avons essayé d'interpréter ce désaccord en discutant les diverses approximations employées par Déplanté.

2. METHODES EXPERIMENTALES

(1) *Préparation des solutions solides* Al–T

Les alliages Al–T ont été préparés au four à induction dans des creusets en glucine, réfractaire très résistant à l'aluminium à haute température. La concentration en impuretés parasites ne dépassait pas 1 pour cent de la concentration en métal de transition. Des bâtonnets de 20 mg environ ont ensuite été prélevés sur ces alliages pour être trempés. A cette fin, nous avons employé les appareils de trempe ultrarapide construits par Dixmier[4]. Leur principe consiste à écraser une goutte d'alliage liquide entre deux parois froides. Les lamelles ainsi obtenues ont une épaisseur de 4 à 10 μ et une surface de quelques mm^2.

---

*Laboratoire associé au C.N.R.S.

(2) *Mesures de paramètre*

Les alliages d'aluminium préparés par trempe ultrarapide sont microcristallisés. La taille moyenne des grains, estimée à l'aide des largeurs de raies, est voisine de 1000 Å. Pour obtenir les diagrammes de diffraction de ces poudres, nous avons choisi l'enregistrement photographique avec une chambre Seeman–Bohlin travaillant par réflexion et associée à un monochromateur. Cette méthode présente deux avantages:

(a) La grande étendue du domaine d'angle couvert permet de déceler l'apparition de raies supplémentaires provenant d'un début de précipitation du métal de transition en une phase intermédiaire.

(b) La chambre est très dispersive, condition indispensable pour des mesures précises de paramètre.

Pour déterminer les faibles variations Δa du paramètre a de ces solutions solides en fonction de la concentration atomique C en élément de transition dissous (de l'ordre de quelques pour cent), nous avons utilisé une méthode différentielle: Après avoir évaporé sur nos échantillons une mince couche d'aluminium, nous avons mesuré la distance des raies données par la solution solide considérée et par l'aluminium pur. Toutefois la raie de l'alliage trempé est tellement élargie qu'elle se superpose à celle de l'aluminium (Fig. 1). Afin de séparer la raie fine de l'étalon de la raie large de la solution solide, nous avons comparé de la façon suivante les densitogrammes du diagramme de la solution solide seule: $I_{1S}(\theta)$ et du mélange aluminium + solution solide: $I_2(\theta)$: On retranche tout d'abord de $I_2(\theta)$, $RI_{1S}(\theta) = I_{2S}(\theta)$, le coefficient R étant ajusté pour que la différence soit nulle en dehors de la raie de l'aluminium. Cette différence donne alors le profil vrai $I_{2\mathrm{Al}}(\theta)$ de la raie de l'aluminium d'où la distance angulaire des deux raies $I_{2\mathrm{Al}}(\theta)$ et $I_{2S}(\theta)$. Finalement, compte tenu de la précision des pointés, l'erreur absolue sur le paramètre ne dépasse pas: $\Delta a \simeq 0{,}0007$ Å.

Il serait illusoire d'espérer mieux vu la largeur des raies des solutions solides. Ce serait d'ailleurs inutile car la principale incertitude affectant nos mesures est l'incertitude sur la concentration.

(3) *Mesures de concentration*

Le but de l'expérience étant la mesure de $\Delta a/Ca$, celle-ci n'a de sens que si l'erreur sur C est aussi réduite que possible. Or la teneur en métal de transition des lamelles obtenues par trempe ultrarapide peut différer de façon considérable de la valeur nominale de la concentration de l'alliage mère. Il est donc nécessaire de mesurer la concentration des échantillons mêmes qui servent aux déterminations de paramètre.

Le choix de la méthode de mesure a été dicté par la masse de métal de transition à doser qui, pour un échantillon de 5 μ d'épaisseur et de 5 mm^2 de surface et une concentration de quelques pour cent, est d'environ 10^{-6} g. On ne peut espérer doser avec précision une si faible masse à l'aide d'une méthode chimique. Nous avons donc utilisé la microsonde électronique.

Pratiquement on déduit du rapport k_T des intensités X de longueur d'onde λ_T émergeant de la solution solide Al-T et du témoin de transition T pur, la concentration massique C_T en T dans l'échantillon. Pour cela nous avons établi une courbe d'étalonnage en suivant la méthode préconisée par Philibert [5]. Les différentes corrections nécessaires pour obtenir C_T à partir de k_T sont affectées d'une incertitude théorique. En effet, ces corrections sont calculées en se fondant sur de nombreuses approximations et sur le choix d'un modèle de trajectoires électroniques. Elles sont donc sujettes à caution. Toutefois l'écart relatif entre k_T et C_T ne dépasse pas 20 pour cent et il est légitime d'espérer que l'erreur relative commise en calculant ces corrections est inférieure à 5 pour cent. Par

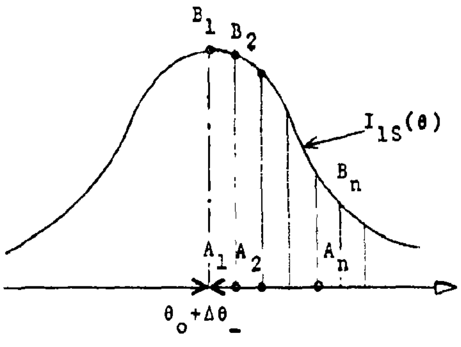

DENSITOGRAMME N° 1

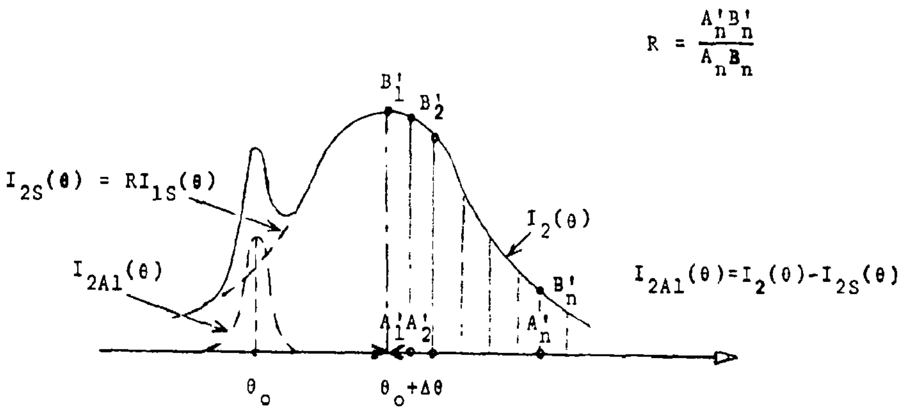
$R = \frac{A'_nB'_n}{A_nB_n}$
B'_1
B'_2
$I_{2S}(\theta) = RI_{1S}(\theta)$
$I_{2Al}(\theta)$
$I_2(\theta)$
B'_n
$I_{2Al}(\theta)=I_2(\theta)-I_{2S}(\theta)$
A'_1
A'_2
A'_n
θ_o
$\theta_o+\Delta\theta$

DENSITOGRAMME N° 2

Fig. 1. Mesure de la distance de deux raies voisines dont l'une est fine et l'autre large

ailleurs, la mesure de k_T est entachée d'erreurs expérimentales qui entraînent une incertitude supplémentaire sur C_T estimée à moins de 5 pour cent[6]. Au total, l'erreur relative sur la concentration C_T n'excède pas 10 pour cent.

3. RESULTATS EXPERIMENTAUX

(1) *Variations du paramètre a des solutions solides* Al–T *avec la concentration atomique* C *en impureté de transition* T

L'effet se caractérise par la quantité $p = (da/adC)_{C=0}$ donnant la variation relative du paramètre de l'aluminium par pour cent d'impureté dissous et pour une dilution infinie. Nos résultats sont consignés dans le Tableau 1.

L'amplitude des variations de p est six fois plus faible en moyenne que celle qui a été prévue par Déplanté[2].

Une première explication de cet écart serait la mise en solution incomplète de l'impureté dans le réseau de l'aluminium. La concentration réelle de la solution solide serait alors inférieure à la concentration globale mesurée à la sonde.

Mais dans cette éventualité les atomes d'impureté qui ne sont pas en solution doivent être soit à l'état de métal libre, soit liés à l'aluminium sous forme d'un composé plus riche en atomes dissous.

Dans le cas des échantillons les mieux trempés (les plus minces) qui, seuls ont été utilisés pour nos mesures de paramètre, nous avons pu vérifier que l'on pouvait écarter ces deux possibilités.

α *Présence de grains de métal de transition à l'état libre.* Ces alliages trempés ont fait l'objet très récemment[13] de mesures de susceptibilités magnétiques.

L'appareil utilisé, d'une très grande sensibilité permet de déceler quelques ppm d'impureté ferromagnétique dans l'échantillon. Nous avons ainsi constaté que les alliages à base de Fe, Co, Ni, n'étaient pas ferromagnétiques: il n'y a donc pas de petits cristaux de ces métaux à l'état pur dans les échantillons.

On parvient à la même conclusion dans le cas des alliages contenant des métaux de transition paramagnétiques. Leur susceptibilité ne suit pas une loi en $1/T$ comme celle de ces métaux à l'etat pur.

β *Présence de précipités* $Al_\alpha T_\beta$. La formation de précipités, au cours de la solidification, prévue par le diagramme d'équilibre thermique peut être suivie sur une série d'échantillons ayant subi des trempes de rapidité croissante.

Les diagrammes de $R-X$ des lamelles les plus épaisses ($> 50\mu$) font apparaître une deuxième phase solide reconnaissable aux raies caractéristiques du composé intermédiaire cependant que les raies de l'aluminium ne sont pas déplacées.

Pour une vitesse de trempe supérieure les raies de l'aluminium sont dédoublées: une composante du doublet correspond à de l'aluminium pur, l'autre à la solution solide. La position de cette raie déplacée est fixe mais son intensité variable suivant l'état de recuit de l'alliage; en même temps, les raies de la seconde phase diminuent en intensité.

Lorsque la vitesse de trempe est suffisante [$e < 10\mu$] la raie de l'aluminium pur a totalement disparu au profit d'une augmentation d'intensité de la raie déplacée. Enfin les raies du composé intermédiaire sont totalement absentes.

Le fait qu'on n'observe pas de déplacement intermédiaire pour les raies de l'aluminium prouve que la précipitation de $Al_\alpha T_\beta$ est discontinue. Lorsque celle-ci est amorcée dans un grain elle se développe très rapidement.

Par conséquent si le diagramme de RX ne présente qu'un seul système de raies déplacées pour l'aluminium, nous devons admettre qu'aucune ségrégation n'a eu lieu.

L'impureté est nécéssairement dans le réseau de l'aluminium.

(2) *Particularités des différentes solutions solides* Al-T

(a) *Solutions solides* Al-Ti. Il faut noter que dans ce cas la valeur de p est moins certaine que les valeurs obtenues pour les autres métaux de la série de transition. En effet, nous n'avons fait qu'une seule mesure et il n'est pas sûr que dans l'alliage considéré tout le titane soit dissous. La valeur réelle de $|da/adC|$ peut donc être supérieure à la valeur

Tableau 1

Impureté de transition	Ti	V	Cr	Mn	Fe	Co	Ni	Cu
Numero atomique Z	22	23	24	25	26	27	28	29
$\frac{da}{adC}$ expérimental	−0,032	−0,143	−0,170	−0,137	−0,136	−0,105	−0,044	−0,120
$\frac{da}{adC}$ calculé	−0,704	−0,796	−0,722	−0,511	−0,241	−0,019	+0,074	0,000

ci-dessus. Cependant le signe de l'effet est sûr et son ordre de grandeur probablement correct.

(b) *Solutions solides* Al–V. Dans le cas du vanadium la sursaturation obtenue par trempe ultrarapide est anormalement faible. En effet, bien que la solubilité naturelle du vanadium dans l'aluminium vers 650°C atteigne 0,20 pour cent, sa solubilité après trempe n'excède pas 2 pour cent. Au contraire, la solubilité du fer, du cobalt et du nickel passe dans les mêmes conditions de quelques 0,01 à 5 pour cent (cf. Tableau 2).

Ce phénomène peut sans doute s'interpréter en se référant à notre étude de la vitesse de trempe[6]. Nous avons montré que l'efficacité de la trempe dépendait essentiellement de la durée de la solidification de la goutte d'alliage liquide et que cette solidification se déroulait au voisinage de la température de fusion. Le Tableau 2 montre que la solidification de l'alliage Al 95%–V 5% se produit vers 1100°. Cette température bien plus élevée que pour les autres éléments de la série explique que la diffusion du vanadium dans l'aluminium soit plus rapide, ce qui permet une organisation des atomes en un mélange de deux phases: la solution solide et la phase $Al_{11}V$. La solution solide a un paramètre constant indépendant de la concentration en vanadium et la phase précipitée se manifeste par l'apparition des 4 raies les plus intenses de son diagramme de poudre ($d = 2{,}450$, 2,208, 2,182, 2,089 Å). Naturellement ces raies sont très élargies et très peu intenses.

(c) *Solutions solides* Al–Cr *et* Al–Mn. Après une trempe ultrarapide les limites de solubilité du chrome et du manganèse dans l'aluminium sont les plus grandes de toute la série de transition et dépassent certainement 6 pour cent.

Les variations du paramètre de l'aluminium en fonction de la concentration en manganèse et en chrome prolongent parfaitement les résultats obtenus par Falkenhagen et Hofmann [7] puis Varich et Burov [8].

(d) *Solutions solides* Al–Fe. La préparation de ces solutions solides a rencontré quelques difficultés. En effet l'alliage n'est homogène que si la trempe est très rapide, c'est-à-dire quand la lamelle est très mince ($e < 5\,\mu$[6]). Dans le cas contraire, nous avons constaté que le paramètre de l'alliage est égal à celui de l'aluminium. Et pourtant l'analyse à la microsonde montre que le fer est réparti de façon uniforme (à l'échelle du $1\,\mu^2$) dans l'alliage. Si ce fer n'est pas en solution solide, il doit être concentré dans une très fine phase précipitée. D'après le diagramme d'équilibre ce serait la phase $Al_{13}Fe_4$[9]. Néanmoins nous n'avons pas trouvé sur le diagramme de diffraction de l'alliage les raies caractéristiques de cette phase, probablement parce qu'elles sont très peu intenses en raison de la basse symétrie de $Al_{13}Fe_4$ (monoclinique). Donc, même quand on constate une variation de paramètre, on ne peut être sûr que tout le fer donné par l'analyse soit en solution solide.

(e) *Solutions solides* Al–Co *et* Al–Ni. Pour le cobalt et le nickel, le déplacement des limites de solubilité produit par trempe ultrarapide est considérable. Les meilleures

Tableau 2

Impureté de transition	Ti	V	Cr	Mn	Fe	Co	Ni	
Solubilité naturelle	≈ 0	0,2	≈ 0	≈ 0	≈ 0	≈ 0	≈ 0	Les solubilités sont en % atomiques
Solubilité après une trempe classique	0,1?	0,6	1,5	1,8	≈ 0	≈ 0	≈ 0	
Solubilité après une trempe ultrarapide	2?	2	> 6	> 6	5	5	5	
Température de solidification de l'alliage Al 95%–T 5% (°C)		1100	920	790	900	900	730	

trempes permettent d'en dissoudre jusqu'à 5 pour cent atomique alors que la solubilité naturelle de ces éléments est de quelques ppm. C'est pourquoi aucune valeur de $a(C)$ n'avait été obtenue auparavant.

(3) *Etude des largeurs de raies des diagrammes des poudres* Al–T

La trempe ultrarapide des alliages Al–T donne des solutions solides dont les raies sont très larges. Nous avons cherché la cause de cet élargissement. Deux modèles se présentent à l'esprit:

(a) *L'élargissement est dû à un pur effet de taille des cristallites.* Les grains de la solution solide seraient parfaitement cristallisés mais leur petite taille élargirait les domaines de diffraction de Bragg. Par la formule de Scherrer on peut alors tirer de la largeur d'une raie à mi-intensité un ordre de grandeur de la dimension moyenne L des grains:

$$\Delta_{1/2}(2\theta) = \frac{0{,}9\lambda}{L\cos\theta_{hkl}}$$

$\left\{\begin{array}{l}\theta_{hkl}\text{: angle de Bragg de la raie considérée,}\\ \lambda\text{: Longueur d'onde utilisée.}\end{array}\right.$

(b) *L'élargissement est dû a un pur effet de distorsion.* Dans ce cas les grains de la solution solide sont gros mais mal cristallisés. L'élargissement des domaines de diffraction est dû aux distorsions du réseau dont le paramètre varie d'un point à un autre d'un grain. Si l'on admet que ces distorsions peuvent être représentées par une statistique de répartition des paramètres de largeur Δa, la largeur à mi-hauteur est donnée par:

$$\Delta_{1/2}(2\theta) = 2\frac{\Delta a}{a}tg\theta_{hkl}.$$

L'expérience montre[6] que cette seconde hypothèse est préférable. Une question se pose alors: Quelle est l'origine de cette répartition statistique des paramètres? Là encore on peut envisager deux modèles:

(a) *Les divers grains de solution solide sont bien cristallisés mais n'ont pas la même concentration.* Dans ce cas l'alliage n'est pas homogène à l'échelle microscopique. La statistique de répartition des paramètres reproduit alors la statistique du nombre des grains ayant une concentration donnée. Les analyses effectuées à la microsonde rendent cette hypothèse peu vraisemblable. En effet, la largeur statistique maximum des inhomogénéités de concentration ΔC est déterminée par ces mesures. De ΔC on déduit les fluctuations de paramètre Δa et une largeur de raie théorique $\Delta_{1/2}(2\theta)$. Dans tous les cas cette largeur calculée est environ dix fois plus petite que la largeur effectivement mesurée.

(b) *Nous sommes donc conduits à admettre que les différents grains de solution solide ont sensiblement la même composition (ce qui est logique puisque la trempe se fait à partir de l'état liquide homogène) mais que le fait essentiel est la distorsion du réseau.* Quelle est l'origine de ces distorsions? Tout d'abord la trempe ultrarapide introduit de nombreux défauts même dans un métal pur. D'autre part, la substitution d'atomes de transition aux atomes d'aluminium perturbe le réseau de façon considérable puisqu'il est impossible de réaliser cette substitution à l'état d'équilibre. Ainsi pour des vitesses de trempe voisines (c'est-à-dire des épaisseurs d'échantillon égales), la largeur des raies croît d'une façon à peu près linéaire avec la concentration en impuretés dissoutes. Toutefois nous n'avons pas cherché à étudier quantitativement les distorsions du réseau et ne pouvons préciser davantage ce point.

4. INTERPRETATION THEORIQUE

Au facteur 6 près, et si l'on normalise la courbe théorique à la valeur expérimentale trouvée pour les solutions solides Al–Cu, la forme de la courbe expérimentale reproduit assez bien celle de la courbe calculée (Fig. 2).

Pour essayer d'interpréter ce désaccord, il convient d'examiner les diverses approximations qui ont été faites dans le calcul théorique.

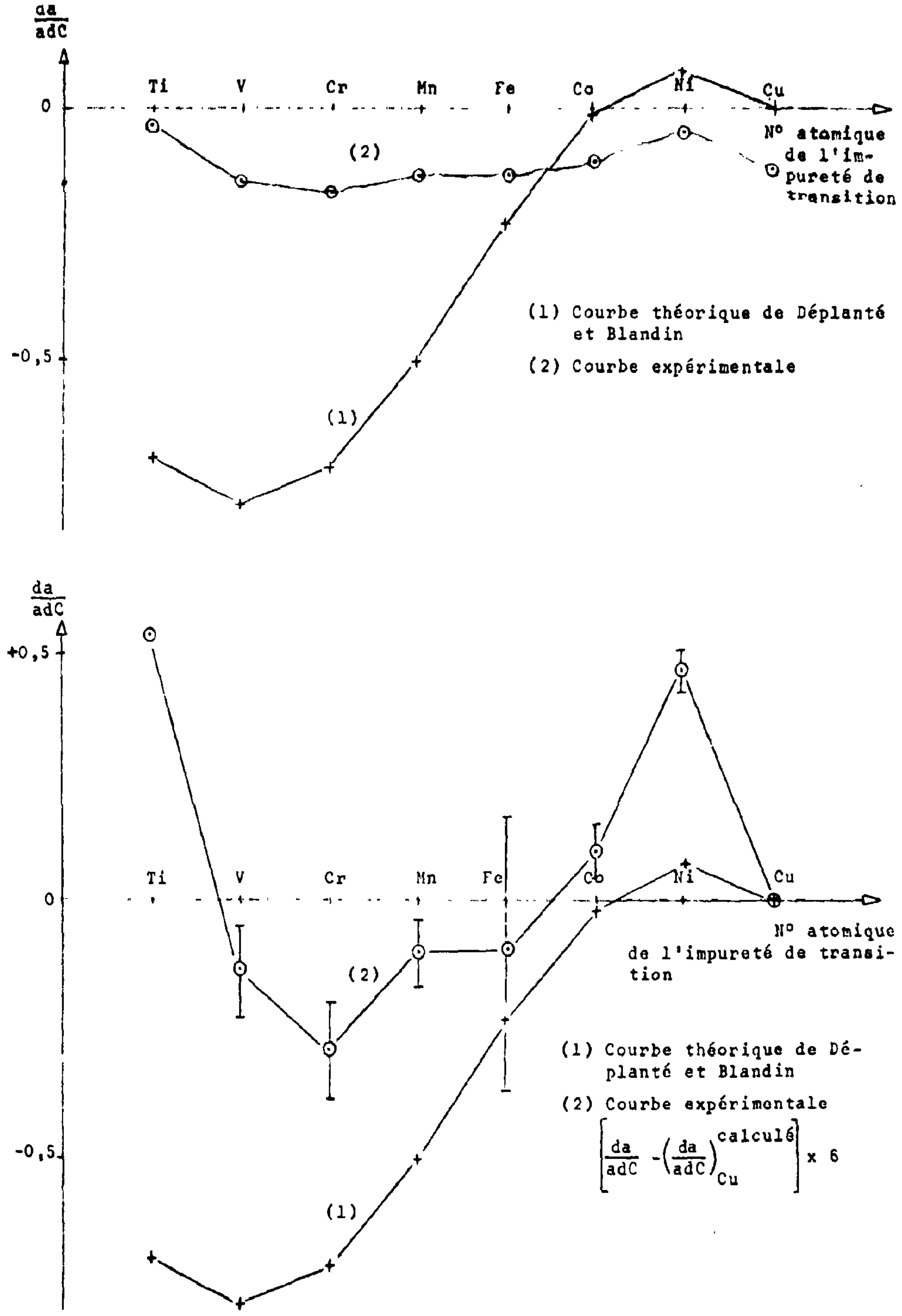

Fig. 2. Comparaison des valeurs expérimentales et théoriques de *da/adC*.

A cette fin nous rappellerons les étapes successives du calcul de Déplanté.

L'introduction d'un atome de transition en substitution dans le réseau de l'aluminium perturbe fortement la structure électronique de la matrice. Les électrons se réarrangent autour de cette charge ionique supplémentaire de manière à lui faire écran et des oscillations de densité électronique apparaissent autour de l'impureté. On suppose tout d'abord que les électrons de conduction de l'aluminium pur peuvent être traités comme des électrons libres de répartition spatiale uniforme et que la perturbation possède la symétrie sphérique. On analyse alors les fonctions d'onde des électrons de conduction en harmoniques sphériques et l'on montre qu'il apparaît autour de l'impureté un champ électrique dont la forme asymptotique à grande distance est:

$$E(r)_{r\to\infty} = \frac{e\alpha}{2\pi k_F}\frac{\sin(2k_Fr+\phi)}{r^3}$$

avec

$$\alpha\sin\phi = \sum_{\sigma l}(-1)^l(2l+1)\sin^2\delta_{l\sigma}(E_F)$$

$$\alpha\cos\phi = \sum_{\sigma l}(-1)^l(2l+1)\sin\delta_{l\sigma}(E_F)\times\cos\delta_{l\sigma}(E_F)$$

où $\delta_{l\sigma}$ est le déphasage introduit par la perturbation dans la $l^{\text{ème}}$ composante sphérique d'un électron de conduction de spin σ au niveau de Fermi E_F (correspondant au vecteur d'onde k_F).

Un ion de la matrice d'aluminium voisin de l'impureté est donc soumis à une force $F(r) = zeE(r)$ si ze est sa charge. L'action de l'ensemble de ces forces produit la contraction ou la dilatation du réseau. Les premières approximations du calcul consistent:

(a) *A suppposer que la forme asymptotique du champ électrique perturbateur est valable à la distance* R_0 *des premiers voisins.*

(b) *A négliger totalement l'action de ce champ sur les autres voisins.*

On suppose alors que la solution solide est idéale (c'est-à dire que les différents atomes d'impuretés sont répartis au hasard sur les noeuds du réseau de l'aluminium) puis à l'aide d'une approximation élastique on montre que la variation relative du paramètre cristallin a par unité de concentration s'écrit:

$$\frac{da}{adC} = \frac{1}{18\pi}\frac{nze^2\chi}{\Omega k_F}\frac{\alpha\sin(2k_FR_0+\phi)}{R_0^2}$$

n: nombre de premiers voisins = 12 pour un réseau cubique à faces centrées

χ: compressibilité de la matrice.

Ω: volume atomique de la matrice.

Le problème se ramène donc au calcul des déphasages $\delta_{l\sigma}(E_F)$ dont dépendent α et ϕ. On utilise pour cela la règle de somme de Friedel[10] qui relie la charge ionique supplémentaire à écranter Ze aux déphasages $\delta_{l\sigma}(E_F)$:

$$Z = \frac{1}{\pi}\sum_{l\sigma}(2l+1)\delta_{l\sigma}(E_F).$$

Comme l'atome d'aluminium a trois électrons de conduction et l'atome de transition N électrons $3d$ et $4s$ en dehors des couches pleines, il est naturel de prendre[11]:

$$Z = N-3.$$

Cela revient à ignorer la contribution à l'effet de taille due aux couches internes ou encore à négliger la différence de période entre l'aluminium et les métaux de transition.

Par ailleurs les impuretés de transition donnent naissance au phénomène de niveau lié virtuel décrit par Friedel[1]. L'énergie E_d des états $3d$ de l'élément de transition tombe dans le quasicontinuum de la bande de conduction de l'aluminium. Il se produit alors un effet de résonance entre la composante d des états de conduction de l'aluminium et les états $3d$. Les niveaux $3d$ sont élargis en énergie et il apparaît un excès de probabilité de présence localisé au voisinage de l'impureté et lié à l'amplitude anormalement grande de la composante d des électrons de conduction. En termes de déphasage cela se traduit par une rapide variation de δ_2 qui passe de 0 à π au voisinage de E_d sur une largeur en énergie croissant avec $E_d - E_0$ (E_0 énergie du bas de la bande de conduction de l'aluminium). Lorsqu'on parcourt la série de transition, les états E_d de la couche d traversent le niveau de Fermi de l'aluminium ($E_d \simeq E_F$), le niveau lié virtuel se remplit progressivement et les variations de $\delta_{2\sigma}(E_F)$ sont importantes. Au contraire les déphasages δ_0 et δ_1 restent à peu près constants. D'autre part, la largeur du niveau lié virtuel est grande car l'énergie de Fermi de l'aluminium est élevée ($E_d - E_0 = E_F - E_0 = 12$ eV) et il n'y a pas de decouplage des deux directions de spin[11]. $\delta_{2\sigma}$ est indépendant de σ et

$$Z = \frac{2}{\pi}(\delta_0 + 3\delta_1 + 5\delta_2)$$

si l'on néglige les déphasages d'ordre $l > 2$.

Pour tenir compte de la contribution à l'écran des composantes $s(l = 0)$ et $p(l = 1)$ en même temps que de l'effet de différence de période entre l'aluminium et les métaux de transition, il est naturel de rapporter les effets de taille à celui du cuivre dans l'aluminium. En effet, puisque δ_0 et δ_1 varient lentement avec Z il est logique de supposer que les composantes s et p produisent le même écran pour toutes les impuretés de la première série de transition et pour le cuivre de structure électronique $3d^{10}4s^1$[11]. Or le cuivre dissous dans l'aluminium possède une couche d pleine qui peut être traitée comme une couche interne. On considère alors que la charge ionique supplémentaire introduite par le cuivre dans l'aluminium: $+e - 3e = -2e$ est écrantée par les composantes sphériques s et p des électrons de conduction.

Il reste à expliquer la différence entre les valeurs mesurées et calculées de l'amplitude des variations de p avec le numéro atomique Z de l'impureté de transition dissoute. Déplanté a montré[12] que l'assimilation de la "compressibilité de l'impureté" à celle de la matrice peut entraîner une erreur relative sur p comprise entre 0,8 et 1,5 et ne saurait donc expliquer le facteur 6 observé.

L'approximation la plus discutable vient de la façon dont est traitée la réaction de la matrice au déplacement des ions voisins de l'impureté. Cette réaction est calculée dans un modèle d'élasticité linéaire; ceci suppose que les déplacements ne sont pas trop importants. Or, les déplacements prédits impliquent des variations locales de volume de l'ordre de 20 pour cent (pour Ti, V, Cr, Mn). La limite de l'élasticité linéaire étant généralement atteinte pour des variations relatives de volume de l'ordre de 0,1, on est donc largement sorti de ce cadre. Par ailleurs, les effets non linéaires sont probablement plus importants pour des contractions comme c'est le cas pour les impuretés de transition dans l'Aluminium. Dans un modèle plus approprié, toute la partie gauche de la courbe théorique devrait donc se trouver largement remontée en ordonnées.

5. CONCLUSION

La mesure des variations du paramètre de l'aluminium avec la concentration en impureté de transition pour sept élements de la série (Ti, V, Cr, Mn, Fe, Co, Ni) a été entreprise pour les comparer à des valeurs calculées.

Malgré une différence d'amplitude entre les valeurs observées et calculées le modèle des états liés virtuels d décrit d'une façon satisfaisante l'allure des variations de p tout au long de la première série de transition. En particulier on verifie bien que dans l'aluminium les 2 niveaux liés virtuels de spin opposé ont la même énergie moyenne car en présence d'un découplage l'allure des phénomènes serait très différente.

REFERENCES

1. FRIEDEL J., *Can. J. Phys.* **34**, 1190 (1956).
2. DÉPLANTÉ J. L. et BLANDIN A., *J. Phys. Chem. Solids* **26**, 381 (1965).
3. DUWEZ P. et WILLENS R H., *Trans. metall. Soc. A.I.M.E.* **227**, 362 (1963).

4. DIXMIER J. et GUINIER A., *Mém. scient. Revue Métall.* **1**, 53 (1967)

5. PHILIBERT J., *L'analyse Quantitative en Microanalyse par Sonde Électronique* Publication de l'IRSID (1965).

6. BLÉTRY J., Thèse 3° Cycle (1968)

7. FALKENHAGEN G. et HOFMANN W., *Z Metallk.* **43**, 69 (1952).

8. BUROV L. M. et VARICH N. I., *Physics Metals Metallogr.* **16**, 33 (1963).

9. BLACK P. J., *Acta. crystallogr.* **8**, 175 (1955).

10. FRIEDEL J., *Nuovo cim.* **7**, 287 (1958).

11. BLANDIN A. et FRIEDEL J., *J. Phys. Radium* **20**, 160 (1959).

12. DÉPLANTÉ J. L., Thèse 3° Cycle (1963).

13. SADOC J. F., Thèse 3° Cycle (1969).

J. Phys. Chem. Solids Pergamon Press 1970. Vol. 31, pp. 1273–1280. Printed in Great Britain.

THE ROLE OF *K* SHELL IONIZATION IN THE FORMATION OF *F* CENTERS IN ALKALI HALIDES AT 78°K–I. KBr*

BALTASAR A. CRUZ-VIDAL† **and HENRY J. GOMBERG**

Physics Department, University of Puerto Rico at Mayagüez, and Puerto Rico Nuclear Center,
Mayagüez, Puerto Rico 00708, U.S.A.

(*Received* 2 *September* 1969)

Abstract—Within the uncertainty of the experiment, the rate of *F* center formation per unit energy retained in Harshaw KBr irradiated at 78°K at equal energy flux is the same (0·78 ± 0·02 *F* center/keV) whether the incident-photon energy is 13·4 keV or 14·1 keV. (The *K* edge of bromine is at 13·5 kev) Since a large background of multiply ionized atoms is expected whether the incident-photon energy is 13·4 keV or 14·1 keV, the above result is not sufficient evidence to conclude that a Varley mechanism of *F* center formation is not operative. Each of the monochromatic beams was the X-ray fluorescent output either of powdered RbCl filtered with a thin layer of NaBr or of powdered $Sr(NO_3)_2$ filtered with RbCl. The half-width of each monochromatic beam was 330 eV. An air ionization chamber used to measure the flux was calibrated with a calorimeter

1. INTRODUCTION

SEVERAL models have been suggested for the mechanism of formation of Frenkel defects in defectless regions of alkali halides[1–5]. The model suggested by Varley[1] requires multiple ionization of a halogen prior to displacement from its normal lattice position. Researchers interested in understanding the mechanism of displacement of a halogen ion from its normal lattice position have measured the efficiency of *F* center formation[6–8]. Also, several studies of the formation of *F* centers in alkali halides during exposure to ultraviolet light have been made[9–11]. Furthermore, since an initial ionization in an inner shell of a halogen ion leads by means of an Auger cascade to a multiple ionization[12], selective ionization of an inner shell can be used to test a multiple-ionization mechanism of formation of *F* centers[13]. Thus, J. Sharma and R. Smoluchowski[14] tested the efficiency of formation of *F* centers in KCl and in KBr at room temperature and at liquid-nitrogen temperature as a function of incident photon energy in an energy range which included the halogen *K*-absorption edge. At room temperature they found no change in the efficiency of *F* center formation as the incident-photon energy became larger than the halogen *K*-absorption energy. However, at liquid-nitrogen temperature they found that in KBr and in KCl the efficiency of formation of *F* centers increased by a factor of 1·1 and 2·5, respectively, when the incident-photon energy became larger than the halogen *K*-absorption energy.

In the present paper the measurement of the relative efficiency of formation of *F* centers in KBr at 78°K during exposure to monochromatic X-ray photons of energy either above (14·1 keV) or below (13·4 keV) the halogen *K*-absorption energy (13·5 keV) is reported. Two succeeding papers—but on RbBr and on KCl—disclose results similar to those reported here for KBr.

2. EXPERIMENTAL METHOD AND CONTROL

The X-ray beam from a Machlett AEG-50S tungsten-target X-ray tube operated at 45 kvp

---

[*] This work is based on a thesis submitted by B. A. Cruz-Vidal to the Physics Department, Harvard University in partial fulfillment of the requirements for a Ph D.

[†] Oak Ridge Graduate Fellow, 1964–67, under appointment from The Oak Ridge Institute of Nuclear Studies.

in a General Electric XRD-5 machine was incident at a 45° angle on an aluminum planchet called a radiator. The radiator was filled with a compound of an element whose K_α fluorescence is either above or below the bromine K-absorption energy. All other elements in the compound were of low atomic weight. The fluorescence emitted perpendicular to the incident beam by the radiator was filtered by a thin film of a compound containing low atomic weight elements and an element whose K-absorption edge lies between the K_α and the K_β energies of the element of interest in the radiator. The filtered fluorescence of the radiator, consisting almost exclusively of K_α fluorescence, was incident on the sample. The half-width of the filtered monochromatic output was approximately 330 eV.

A radiator made of firmly pressed RbBr powder was used with a filter of NaBr for irradiation with photons of energy below the bromine K-absorption energy (13·5 keV). The K_α-emission energy of Rb is 13·4 keV. For irradiations with photons of energy above the bromine K-absorption energy, a $Sr(NO_3)_2$ powder radiator was used with a RbCl filter. The K_α-emission energy of Sr is 14·1 keV.

The filtering compound was finely ground and then suspended in a fresh solution of equal parts of Carter's 465 household cement and acetone. The resulting suspension was poured onto a 0·001 in. thick mylar film stretched on a plexiglass frame. A uniform film resulted when the mixture was dried slowly under low humidity conditions. The filters were tested using ordinary crystal diffraction. The criterion for a good filter was that it looked uniform and reduced the intensity of the K_β fluorescence to less than 2 per cent of the total fluorescent output. See Figs. 1 and 2.

An air ionization chamber was used to measure the relative value of the monochromatic flux of the two radiator-filter combinations. A system manufactured by the Victoreen Instrument Company was used. It consists of a cylindrical condenser, model 651, and an electrometer, model 570 condenser R-meter. The readings in the R-meter are in 'r-units,' a measure of absorbed energy in the air space of the ionization chamber. This reading is converted to an incident-energy-flux measurement as follows: Let μ/ρ be the mass-energy transfer coefficient of air for a given incident-photon energy; ρ, the density of air; d, the depth of the absorption chamber along the direction of incidence of the radiation; I_0, the number of photons incident on the chamber; and I_a, the number of photons absorbed in the chamber; then, to a first approximation I_0 is given by

$$I_0 = \frac{I_a}{\mu d}.$$

The flux incident on the chamber, F_0, is proportional to I_0/At, where A is the face area of the chamber and t is the exposure time. Thus,

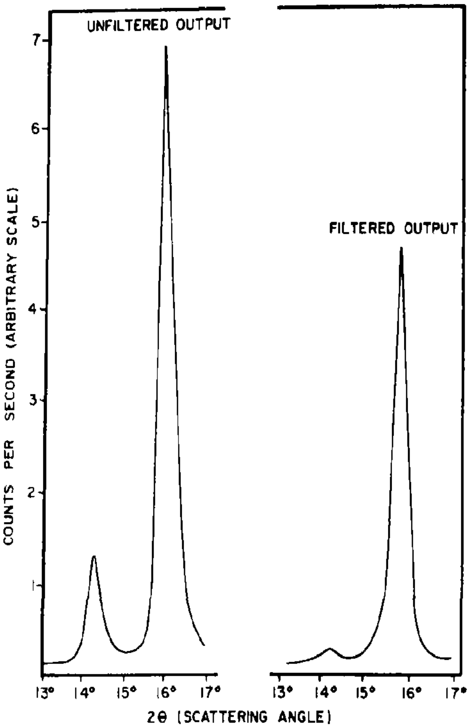

Fig. 1. Spectrum analyses of the fluorescent emission of the RbCl radiator—before and after NaBr filtration. A quartz diffraction crystal was used.

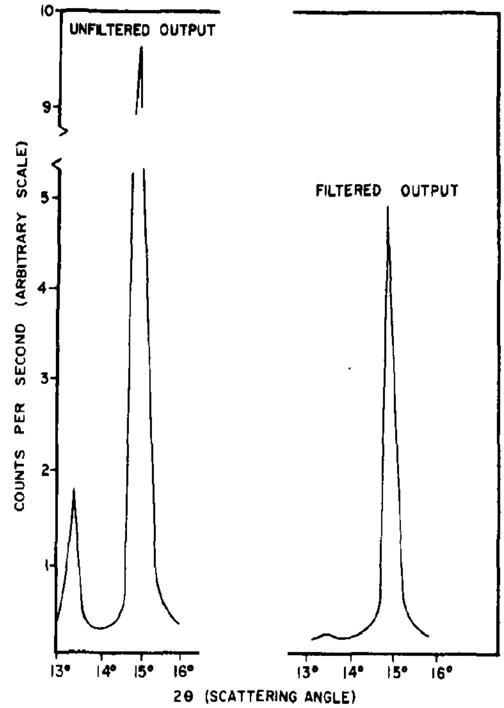

Fig. 2. Spectrum analyses of the fluorescent emission of the $Sr(NO_3)_2$ radiator–before and after RbCl filtration. A quartz diffraction crystal was used.

the incident flux, F_0, in units of energy per unit area per unit time is given by:

$$F_0 = C\frac{I_a}{(\mu/\rho)t},$$

where t is the exposure time, and C is the factor required to change the reading of the R-meter (which is proportional to I_a) from '*r*-units' to units of absorbed energy per unit mass.

A calorimetric calibration of the dosimeter was made. The result (shown in Table 1), based on limited data, is: $C = (11{\cdot}7 \pm 0{\cdot}2)$ ergs/'*r*-unit'-g. The calorimeter, which operates at liquid-nitrogen temperature, had been designed and built at the University of Michigan[15]. The incident X-ray flux is admitted to the calorimeter vessel through an aluminized mylar window (0·001 in. thick) and a cold beryllium window (0·002 in. thick), and then is totally absorbed by a cold but electrically and thermally insulated gold target. The gold target consists of two layers of gold foil and a coiled heater wire of known resistance located between the foil layers. Two thermistors, thermally connected to the back of the target, form two resistances of a Wheatstone bridge. When radiation is absorbed by the calorimeter, heat from the target brings about a change in the resistance of the thermistors. This causes an imbalance in the Wheatstone

Table 1. The energy equivalent of one 'r-unit' measured by the Victoreen 651 Ionization Chamber and 570 Electrometer. The corrections indicated in the third column were included in the second column. Also, the values in the second column were corrected for the absorption of a 0·002 in. beryllium window in the path of the beams. No correction for loss due to Compton scattering has been included

Photon energy (keV)	Energy equivalent of one '*r*-unit' (ergs/'*r*-unit'-g)	Fraction of incident flux lost by *L* fluorescence by the calorimeter's gold target	Average energy equivalent of one '*r*-unit' (ergs/'*r*-unit'-g)
13·4	12·3	0·019	11·7±0·2
14·1	11·3	0·03	
14·9	12·1	0·034	
15·7	11·2	0·028	

bridge. The imbalance is recorded in a fast moving strip-chart recorded; the slope of the signal on the chart changes with a change in the energy absorbed by the target. The dissipation of a known amount of energy in the resistance coil of the gold target permits the response of the recorder to be calibrated in energy units. Table 1 shows the values obtained for the energy equivalent of one 'r-unit' for several of the photon energies used.

For all the experiments reported here, the incident-energy flux was:

$$F_0 = (3{\cdot}85 \pm 0{\cdot}08) \times 10^{16}\ \mathrm{eV/cm^2\text{-}hr}.$$

Since this value is affected by the choice of values of the mass-energy transfer coefficient used, those values are given here: 2·20 $\mathrm{cm^2/g}$ at 13·4 keV, and 1·93 $\mathrm{cm^2/g}$ at 14·1 keV. The given uncertainty in F_0 reflects only the uncertainty (±2 per cent) in the relative dosimetry: i.e., the uncertainty in the knowledge that the flux, F_0, was the same in all the runs. The actual uncertainty in F_0 is larger (2·7 per cent) for it must include the uncertainty (1·6 per cent) in the energy calibration of the response of the dosimeter. Since the experiment is intended to compare the efficiency of F center formation during exposure to 13·4 keV incident photons with the efficiency of F center formation during exposure to 14·1 keV incident photons, only the relative value of the fluxes must be known.

A dewar manufactured by Superior Air Products was used in this work. At the bottom of the dewar there are two windows optically aligned with two parallel holes drilled through a copper rod which was kept at liquid-nitrogen temperature. The sample was mounted with vacuum grease in front of one of the holes in the rod. The other hole was left unobstructed to serve as a reference for the optical measurements. The irradiation window consisted of a tightly stretched mylar film 0·001 in. thick. The opposite window was quartz. With the dewar filled with liquid nitrogen, the temperature on the face of the crystal was 78°K.

Throughout an experimental run a sample was exposed only to one incident photon energy, and each run was done with a different sample. The current of the X-ray tube, always operated at 45 kvp, was adjusted to achieve the same incident energy flux on the sample regardless of incident-photon energy used (i.e., regardless of the radiator-filter combination used). The runs were interrupted at regular time intervals to make the optical measurements. Since the spectrophotometer was a manual Beckman DU, the measurements were usually limited to the peak of the F band; but a few points away from the band were included to verify the proper operation of the instrument. Unfortunately, the peak of the α band was beyond the range of accurate measurement of the spectrophotometer.

Smakula's equation[16, 17] gives the rate of F center formation per unit face area per unit time:

$$\frac{\mathrm{d}(Nd)}{\mathrm{d}t} = K\frac{\mathrm{d}A}{\mathrm{d}t},^{*}$$

where K is a constant, characteristic of the particular crystal and its temperature; N is the number of F centers per unit volume; d is the depth of coloration; and $A = \log_{10}(I_0/I_T)$ is the absorbance at the peak of the F band and is measured directly by the spectrophotometer. (I_0 and I_t are respectively the incident and the transmitted intensity at the peak of the F band.) For KBr at 78°K the value of K is $5{\cdot}6 \times 10^{15}\ \mathrm{cm^{-2}}$.

The number of F centers formed per unit incident energy, ($\mathrm{d}F/\mathrm{d}E_i$), is

$$\frac{1}{F_0}\frac{\mathrm{d}(Nd)}{\mathrm{d}t}.$$

The rate of F center formation per unit energy *retained* in the sample, ($\mathrm{d}F/\mathrm{d}E_a$), is given by the following equation:

---

[*] The derivative of the half-width of the absorption band was assumed to be zero.

$$\frac{\mathrm{d}F}{\mathrm{d}E_a} = K\frac{1}{1-fF_0}\frac{1}{}\frac{\mathrm{d}A}{\mathrm{d}t}, \tag{1}$$

where f is the fraction of the incident flux which is lost by fluorescence through the front face of the sample.

In the discussion that follows, the fraction (f) of energy lost by fluorescence from a diatomic slab during its exposure to a photon energy larger than the K-absorption energy of an element in the slab is computed following the derivation by W. J. Veigele and N. J. Roper[18]. The probability of fluorescence occurring after an initial K shell ionization caused by scattering of an incident photon has been neglected. Assuming that the slab is infinitely thick, Equation 10 in the paper by W. J. Veigele and N. J. Roper[18] can be integrated to yield

$$f = \frac{F_{\text{front}}}{F_0} = \frac{\tau_0}{\mu_0}\frac{\bar{\omega}_K}{2}\frac{(r_K-1)}{r_K}\frac{h\nu_f}{h\nu_0}$$

$$\left[1-\frac{\mu_f}{\mu_0}\ln\left(1+\frac{\mu_0}{\mu_f}\right)\right] \tag{2}$$

where F_{front} is the fluorescent flux lost through the front of the slab, $h\nu_f$ is the energy of the fluorescent photon, $h\nu_0$ is the incident-photon energy, τ_0/ρ is the probability (in g-cm^2) per unit path length for photoelectric interaction in the slab at the incident-photon energy, μ_0/ρ and μ_f/ρ are the mass-energy transfer coefficients in the slab at the incident-photon energy and at the fluorescent photon energy, respectively, (ρ is the density of the slab), r_K is the K jump ratio, and $\bar{\omega}_K$ is the K shell fluorescent yield. Since the contribution of Compton scattering to the mass-energy transfer coefficient of medium-weight atoms at about 10 keV is only 1 g/cm^2, τ_0 is assumed equal to μ_0. For an infinitely thick KBr crystal exposed to incident photons of 13·4 keV, f is zero. For a crystal exposed to incident photons of 14·1 keV, f is equal to 0·117.* A calculation of the fluorescence transmitted through the slab shows that for the samples that were used the transmission is negligible. Also, the fluorescence through the front face of the sample is not changed appreciably by the approximation that the samples were infinitely thick.

All samples used were cleaved from the same single crystal of KBr obtained from The Harshaw Chemical Company. They were 0·5–0·8 mm thick, sufficiently thick to absorb all the radiation incident on the sample.

3. EXPERIMENTAL RESULTS

1. *The rate of* F *center formation per unit energy retained in* KBr *at 78°K*

Figure 3 shows the growth curves of coloration at the peak of the F band for KBr crystals which were each exposed at 78°K to monochromatic X-ray photons of either 13·4 keV or 14·1 keV. For each sample the absorbance is plotted against time of exposure to X-rays. The lines on the figure are the least-square-straight lines which best fit the experimental points in the region of the growth curve that seems to be linear. The slope of the least-square-straight line fitted to each set of experimental points is given in Table 2.

The rate of growth of absorbance per hour of exposure to X-rays, ($\mathrm{d}A/\mathrm{d}t$), is larger in the runs in which 13·4 keV photons were used than in the runs in which 14·1 keV photons were used. Therefore, the rate of F center formation per unit *incident* energy, ($\mathrm{d}F/\mathrm{d}E_i$), is larger in the runs in which 13·4 keV photons were used than in the runs in which 14·1 keV photons were used. However, as a result of the fluorescent loss correction, the rate of F center formation per unit energy *retained* in KBr at 78°K is the same, within the uncertainty of the result, whether 13·4 keV, or 14·1 keV is the incident-photon energy:

$$\frac{[\mathrm{d}F/\mathrm{d}E_a]_{14\cdot1\,\text{keV}}}{[\mathrm{d}F/\mathrm{d}E_a]_{13\cdot4\,\text{keV}}} = 1{\cdot}03 \pm 0{\cdot}05.$$

(See Table 2.) The value of the uncertainty was arrived at by combining the following

---

*For the purpose of this calculation it was assumed that 80 per cent of the fluorescent output was K_α radiation and the remainder was K_β.

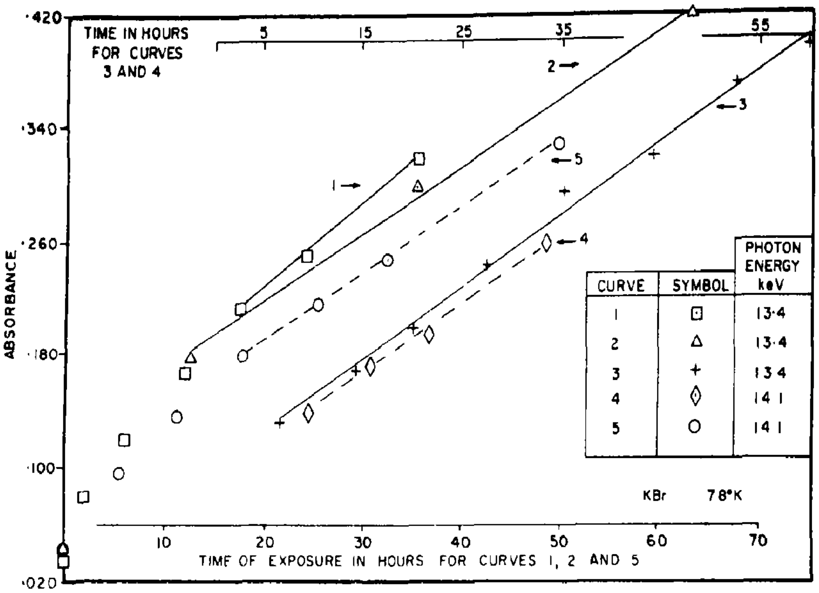

Fig. 3. Absorbance at the peak of the F band of KBr irradiated at 78°K and plotted as a function of exposure time. For each run the incident photon energy is given in the inset. All runs were made at the same energy flux. For each run the straight line is the least-square fit to the experimental points through which the line is drawn.

Table 2. Slopes, (dA/dt), of the experimental curves of Fig. 3 and their uncertainties and the values of the efficiency, (dF/dE$_a$), of formation of F center per unit retained energy in KBr *at 78°K. For all experimental runs the incident flux was* (3·85 ± 0·08) × 10^{16} eV/cm^2-hr

Curve number	Incident photon energy (keV)	$\frac{dA}{dt}$ × 10^{-3} hr^{-1}	Average of the slopes × 10^{3} hr^{1}	$\frac{dF}{dE_a}$ (keV^{-1})
1		6·0 ± 0·8%		
2	13·4	4·9 ± 2·2%	5 3 ± 4·3%	0·77 ± 0·04
3		5 1 ± 1 1%		
4		4·8 ± 2·1%		
	14·1		4·8 ± 1·1%	0 79 ± 0·02
5		4·7 ± 0·6%		

uncertainties: the probable error (4·3 per cent) of the average of the three values of the slopes of the growth curves of coloration for runs using 13·4 keV photons, the probable error (1·1 per cent) of the average value of the slope of the growth curves using 14·1 keV photons, and the uncertainty (2 per cent) in the measurements of the incident flux by the dosimeter.

4. FURTHER DISCUSSION OF EXPERIMENTAL ERRORS

Since the uncertainty in the time measurements is negligible, the per cent uncertainty in $(\mathrm{d}A(t)/\mathrm{d}t)$ is the same as the per cent uncertainty in the change of absorbance ΔA. Therefore, if one assumes that the difference $A(t_n)-A(t_1)$ is used in the computation of the slope, then the probable error of the slope is given by the equation:

probable error of

$$\frac{\mathrm{d}A(t)}{\mathrm{d}t}=0\cdot67\frac{\sqrt{2}S}{A(t_n)-A(t_1)}\times 100\%. \quad (3)$$

In this equation, S is the standard error of the estimate of a value for the absorbance $A(t)$ at time t given by the least-square-straight line fitted to the n measured values $A_1, A_2, \ldots, A_n$ at times $t_1, t_2, \ldots, t_n$, respectively. The value of S is given by the equation:

$$S^2=\frac{1}{n}\sum_{i=1}^{n}(A_i-A(t_i))^2.$$

For each of the curves in Fig. 3 the probable error of the slope was calculated and is shown in Table 2.

Any variation of the relative value of the incident-energy fluxes at the two photon energies was caused only by uncertainties in the dosimetry readings and in the values used for the mass-energy transfer coefficient of air. Under low humidity conditions the dosimetry readings gave results whose uncertainty was not larger than ±2 per cent. This fact refers only to the uncertainty in the knowledge that the energy fluxes were the same in the runs in which 13·4 keV photons were used as in the runs in which 14·1 keV photons were used. The uncertainty in the values of the mass-energy transfer coefficient is primarily a systematic error and has been neglected.

Any statement given in units of energy, such as the energy of formation of one *F* center, contains uncertainties which originate from the calorimetric calibration of the dosimeter and from the use of Smakula's equation, as well as those which originate from the optical measurements and from the readings of the dosimeter.

The uncertainty of the calorimetric calibration of the dosimeter is 1·6 per cent. This uncertainty is the probable error of the average of the calorimetric calibrations of the dosimeter for incident-photon energies of 13·4 keV, 14·1 keV, 14·9 keV, and 15·7 keV. This uncertainty agrees with the inherent accuracy of the calorimeter.

5. DISCUSSION

The efficiency of formation of *F* centers per unit energy absorbed in a KBr crystal while exposed at 78°K at equal energy flux to monochromatic X-ray photons of 13·4 keV or 14·1 keV shows no dependence on the incident photon energy. This result does not support J. Sharma's[14] observation that in KBr at liquid–nitrogen temperature the efficiency of formation of *F* centers per unit incident energy at photon energies just above the halogen *K* edge was 1·1 times the efficiency of formation at energies just below the *K* edge.

The work of T. A. Carlson, W. E. Hunt, and M. O. Krause[19] indicates that a large number of multiply ionized ions are produced when a bromine ion is ionized either in the *K* shell or in the *L* shell. Because a negative bromine ion and an atom of krypton, which was studied by Carlson and coworkers, are isoelectronic, an inner-shell ionization should lead to a similar degree of ionization in either atom. Therefore, in either atom, either a *K*-shell or an *L*-shell ionization should result in an average loss of five to seven electrons. Thus, the bromine *K* edge should be insensitive to selective ionization in the *K* shell even if a multiple ionization of the halogen in an alkali halide crystal were a sufficient condition for the formation of vacancies.

The details of the mechanism of *F* center formation in alkali halides by ionizing radiation remain to be unraveled. Certainly, the mechanism proposed by D. Pooley[4] and by

H. N. Hersh[5] is successful in explaining luminescent and variable temperature phenomena, as well as ultraviolet radiation damage in alkali halides. On the other hand, the insensitivity of K-shell ionization that is reported in the present paper does not eliminate the possibility that a multiple ionization of the halogen can lead to F center formation by a Varley-type mechanism. This possibility exists because no significant change is expected in the probability distribution of ions as the energy of the incident photons crosses the K edge of bromine.

Acknowledgements—Several discussions with Dean Harvey Brooks, with Professor R. Smoluchowski, and with Professor F. Vazquez Martinez are gratefully acknowledged. Thanks are due to Mr J. E. Aguiar and Dr P. Paraskevoudakis for making the calorimetric measurements used to calibrate the dosimeter, and to Mrs. M. Kay for programming the necessary calculations.

REFERENCES

1. VARLEY J. H. O., *Nature, Lond.* **174**, 886 (1954); *J. nucl. Energy* **1**, 130 (1954); *J. Phys. Chem. Solids* **23**, 985 (1962).
2. SMOLUCHOWSKI R. and WIEGAND D. A., *Discuss. Faraday Soc.* **31**, 151 (1961).
3. KLICK C. C., *Phys. Rev.* **120**, 760 (1960).
4. POOLEY D., *Solid State Commun.* **3**, 241 (1965); *Proc. phys. Soc.* **87**, 245 (1966); *Proc. phys. Soc.* **87**, 257 (1966).
5. HERSH H. N., *Phys. Rev.* **148**, 928 (1966).
6. RABIN H. and KLICK C. C., *Phys. Rev.* **117**, 1005 (1960).
7. HALL T. P. P., POOLEY D. and WEDEPOHL P. T., *Proc. phys. Soc.* **83**, 635 (1964).
8. COMINS J. D. and WEDEPOHL P. T., *Solid State Commun.* **4**, 537 (1966).
9. HALL T. P. P., POOLEY D., RUNCINAM W. A. and WEDEPOHL P. T., *Proc. phys. Soc.* **84**, 719 (1964); POOLEY D. and RUNCINAM W. A., *Solid State Commun.* **4**, 351 (1966).
10. GOLDSTEIN F. T., *Solid State Commun.* **4**, 621 (1966).
11. LUSHCHIK CH. B., VITOL I. K. and ELANGO M. A., *Fiz. Tverd. Tela* **10**, 2753 (1968) (English transl.); *Soviet Phys. solid St.* **10**, 2166 (1969).
12. BURHOP F. H. S., *The Auger Effect and Other Radiationless Transitions.* Cambridge University Press (1952).
13. DURUP J. and PLATZMAN R. L., *Discuss. Faraday Soc.* **31**, 156 (1961).
14. SHARMA J. and SMOLUCHOWSKI R., *Phys. Rev.* **137**, A259 (1965).
15. PARASKEVOUDAKIS P., GOMBERG H. J. and AGUIAR J. E., To be published in *Proc. of the 1st European Cong. on Radiation Protection*, Menton, France. October (1968).
16. SCHULMAN J. H. and COMPTON W. D., *Color Centers in Solids.* MacMillan, New York (1962).
17. MARKHAM J. J., *F Centers in Alkali Halides.* Academic Press, New York (1966).
18. VEIGELE W. J. and ROPER N. J., *J. appl. Phys.* **37**, 4309 (1966).
19. CARLSON T. A., HUNT W. E. and KRAUSE M. O., *Phys. Rev.* **151**, 41 (1966).

J. Phys. Chem. Solids Pergamon Press 1970. Vol. 31, pp. 1281–1285. Printed in Great Britain.

THE ROLE OF *K* SHELL IONIZATION IN THE FORMATION OF *F* CENTERS IN ALKALI HALIDES AT 78°K–II. RbBr*

BALTASAR A. CRUZ-VIDAL, FERNANDO DÍAZ-HERNÁNDEZ†, and HENRY J. GOMBERG
Physics Department, University of Puerto Rico at Mayagüez, and Puerto Rico Nuclear Center,
Mayagüez, Puerto Rico 00708, U.S.A.

(*Received* 2 *September* 1969)

Abstract – Within the uncertainty of the experiment, the rate of *F* center formation per unit energy retained in freshly cleaved RbBr (grown from purified material under a bromine–argon atmosphere by Professor R. O. Pohl, Cornell University) irradiated at 78°K at approximately equal energy flux is the same (0·342 ± 0·005 keV^{-1}) whether the incident-photon energy is 13·4, 14·1, 14·9, or 15·7 keV. (The *K* edge of bromine is at 13·5 keV and the *K* edge of rubidium is at 15·2 keV.) Each of the monochromatic beams was the X-ray fluorescent output of RbCl filtered with a thin layer of NaBr, of $Sr(NO_3)_2$ filtered with RbCl, of $Y_2(CO_3)_3 \cdot 3H_2O$ filtered with $Sr(NO_3)_8$, or of Zr filtered with $Sr(NO_3)_2$. The half-width of each monochromatic beam was 330 eV.

1. INTRODUCTION

THE EXPERIMENTAL method is described in detail in the preceding paper in this volume (hereafter referred to as Paper I)[1]. The work discussed in Paper I shows that in Harshaw KBr irradiated at 78°K the efficiency of *F* center formation per unit energy *retained* in the crystal is the same, within the uncertainty of the result, whether 13·4 keV or 14·1 keV is the incident-photon energy, where the *K*-absorption edge of bromine is at 13·5 keV. The present paper presents the result of an identical experiment, but the sample is RbBr. The experiment provides a verification of the result given in Paper I and yields some evidence on the accuracy of the fluorescent correction required to calculate the fraction of the incident energy that is retained in the crystal. This evidence is obtained from the present study because additional incident-photon energies of 14·9 and 15·7 keV have been used, energies which are on either side of the rubidium *K*-absorption edge (15·2 keV).

2. EXPERIMENTAL METHOD

The method of generation of monochromatic X-rays was described in Paper I[1]. In addition to the radiators of RbBr powder filtered with NaBr and of $Sr(NO_3)_2$ powder filtered with RbCl, radiators of $Y_2(CO_3)_3 \cdot 3H_2O$ powder and of Zr metal each filtered by the same $Sr(NO_3)_2$ filter were used. Thus, the energies used in the experiment were 13·4 keV, 14·1 keV, 14·9 keV, and 15·7 keV, obtained from the K_α fluorescence of Rb, Sr, Y, and Zr, respectively. These monochromatic beams had at most a contamination of 2 per cent from K_β fluorescence and had a half-width of about 330 eV.

The dosimeter was the Victoreen model 651 air ionization chamber and model 570 condenser R-meter, described previously [1]. The conversion from absorbed dose to incident flux is a function of the values used for the mass-energy transfer coefficient, μ/ρ, of air: 2·20 cm²/g at 13·4 keV, 1·93 cm²/g at 14·1 keV, 1·63 cm²/g at 14·9 keV, and 1·40 cm²/g at 15·7 keV. These values are consistent with the values given by A. H. Compton and S. K. Allison[2], G. W. Grodstein[3], R. T. Berger[4], and A. J. Bearden[5] (except for a possible small systematic shift of the same sign and the same relative size for all of the values that were used).

---

*This work is based on a thesis submitted by F. Díaz-Hernández to the Department of Physics of the University of Puerto Rico in partial fulfillment of the requirements for an M.S.

†Now a graduate student in the Division of Engineering and Applied Physics, Harvard University, Cambridge, Mass. 02138, U.S.A.

Several samples of RbBr were irradiated at 78°K with monochromatic X-ray photons whose energy was either above, between, or below the K-absorption edges of bromine and rubidium. Each sample was exposed to only one photon energy throughout a run, and each run was done with a different sample. The current in the X-ray tube was varied between runs to achieve approximately the same incident-energy flux on the face of each sample. At regular time intervals, usually from eight to twelve hours, the irradiation was stopped, and the absorbance at the peak of the F band was measured. After a period of exposure to approximately 100 hr, a growth curve of the F band was obtained. A straight line was fitted to the experimental points in the region which seemed to be linear.

All the samples used were freshly cleaved from the same single RbBr crystal grown from purified material in a bromine–argon atmosphere by Professor R. O. Pohl's group at the Laboratory of Atomic and Solid State Physics at Cornell University.

Equation (1) of Paper I[1] gives the rate of F center formation per unit energy *retained* in the sample. In this equation the value of the constant K for RbBr at 78°K is $5{\cdot}6 \times 10^{15}$ cm^{-2}.

Equation (2) of Paper I[1] gives the fraction, f, of the incident flux lost through the front face of a RbBr crystal as a result of bromine K-shell ionization when the incident-photon energy is 14·1 keV or 14·9 keV. However, when the incident photon energy is 15·7 keV (larger than the rubidium K-absorption energy), f is the sum of the contributions of the K fluorescence of bromine and the K fluorescence of rubidium. In equation (2) of Paper I the factor $(r_K - 1)/r_K$ gives the probability that photoionization will occur in the K shell. When the incident-photon energy is above two nearby K-absorption edges, and subscripts are assigned to the absorption edges, subscript 1 is assigned to the edge of higher energy and subscript 2 to the edge of lower energy, then the probability of photoionization in the K_1 shell is $(r_{K_1} - 1)/r_{K_1}$ and in the K_2 shell is $[(r_{K_2} - 1)r_{K_2}][1 - (r_{K_1} - 1)/r_{K_1}]$.[*] The separate contributions of K_α and K_β fluorescence have been included in the calculation of f. Eighty per cent of the fluorescent flux is due to K_α fluorescence and twenty per cent is due to K_β fluorescence. For each incident-photon energy Table 1 gives the fraction, f, of the incident flux that is lost by fluorescence through the front face of a RbBr crystal.

Table 1. *Fraction,* f, *of the incident energy flux lost by fluorescence through the front face of a* RbBr *crystal*

Incident photon energy (keV)	f
13·4	0
14·1	0·092
14·9	0·083
15·7	0·127

3. EXPERIMENTAL RESULTS

(a) *The rate of* F *center formation per unit energy retained in* RbBr *at 78°K*

Figures 1 and 2 show the growth curves of the F band obtained when the crystal was exposed to X-ray photons of either 13·4 keV, 14·1 keV, 14·9 keV, or 15·7 keV. For each experimental run the straight line is the

---

[*] The proof of this result is analogous to the discussion on L edges that starts on p. 530 of Compton and Allison [2]

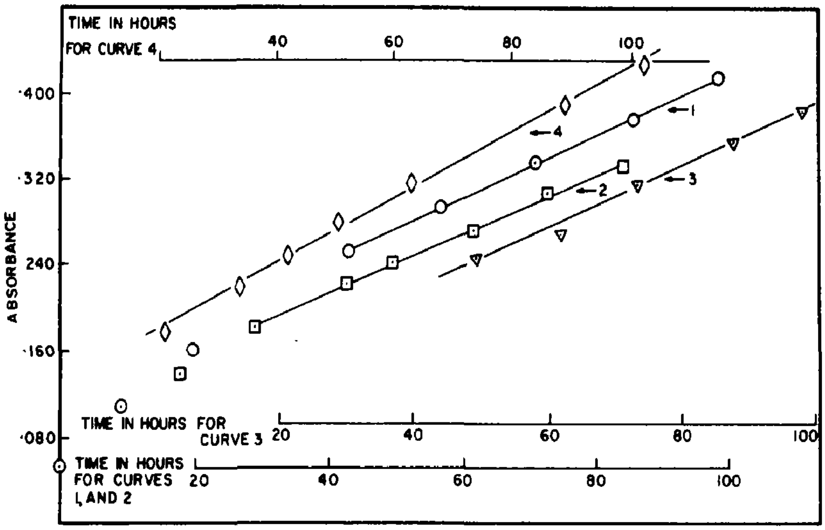

Fig. 1. Absorbance at the peak of the *F* band of RbBr irradiated at 78°K and plotted as a function of exposure time For each run the incident-photon energy was 13·4 keV. The curves presented in Figs. 1 and 2 were made at approximately the same energy flux, which is given in Table 2. For each run the straight line is the least-square fit to the experimental points through which the line is drawn.

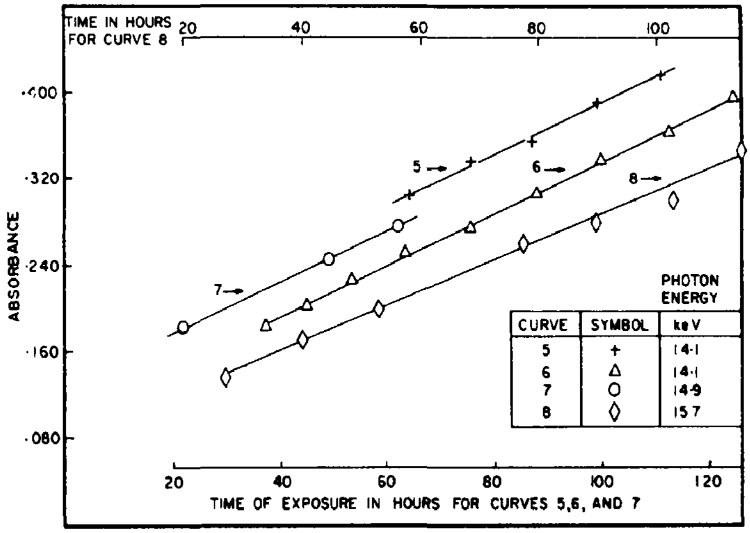

Fig 2. Absorbance at the peak of the *F* band of RbBr irradiated at 78°K and plotted as a function of exposure time. For each run the incident-photon energy is given in the inset. All runs presented in Figs. 1 and 2 were made at approximately the same energy flux, which is given in Table 2. For each run the straight line is the least-square fit to the experimental points through which the line is drawn.

least-square fit to the experimental points in the region of the growth curve which seems to be linear. The slope of each of the lines (the rate of growth of absorbance, A, per unit time of exposure, $\mathrm{d}A/\mathrm{d}t$) is given in Table 2. For each incident-photon energy Table 2 gives the average of the slopes of the curves in Figs. 1 and 2.

The evidence presented in Table 3 shows that, within the uncertainty of the experiment, the efficiency of F center formation per unit energy *retained* in RbBr at 78°K is the same whether the incident-photon energy is 13·4 keV, 14·1 keV, 14·9 keV, or 15·7 keV.

(b) *The experimental uncertainty*

Two sources of uncertainty affect the result that the efficiency of formation of F centers per unit energy *retained* in RbBr at 78°K is the same whether the incident-photon energy is 13·4 keV, 14·1 keV, 14·9 keV, or 15·7 keV. These sources of uncertainty are: the inaccuracy in the readings of the absorbance at the peak of the F absorption band and the inaccuracy in the *relative* values of the radiation fluxes used in the experimental runs. Other errors affecting the result stated above are systematic and were discussed in Paper I[1].

Table 3. *The efficiency of formation of* F *centers in* RbBr *at 78°K during exposure to monochromatic X rays. The indicated uncertainties include uncertainties in the optical measurements and in the dosimetry and do not include the uncertainty (1·6 per cent) in the energy calibration of the dosimetry*

Incident photon energy (keV)	Efficiency of formation of F centers per: incident energy $\frac{\mathrm{d}F}{\mathrm{d}E_i}$ (keV^{-1})	retained energy, $\frac{\mathrm{d}F}{\mathrm{d}E_a}$ (keV^{-1})
13·4	0·351 ± 2·3%	0·351 ± 0·008
14·1	0·309 ± 2·3%	0·340 ± 0·008
14·9	0·313 ± 2·2%	0·341 ± 0·008
15·7	0·291 ± 3·5%	0·334 ± 0·012

The inaccuracy in the *relative* values (not the absolute values) of the fluxes is estimated to be two per cent.

Equation (3) of Paper I[1] gives the per cent uncertainty of the slope for each of the curves in Figs. 1 and 2. The computed values for the per cent uncertainty of each of the slopes of those curves are given in Table 2 along with each value of the slope. As seen from Table 2 the computed uncertainty of a

Table 2. *Slopes of the experimental curves. The incident flux is based on the results of measurements with the Victoreen Air Ionization Chamber Model 651. The 'r-unit' refers to one unit in the scale of the Victoreen Model 570 Electrometer*

Curve number	Incident-photon energy (keV)	Slope of least square straight line (× 10^4 hr^{-1})	Average of slopes (× 10^4 hr^{-1})	Percentage probable error of the average	Incident flux $\left(\frac{\text{'r-unit'-g}}{\text{cm}^2\text{-sec}}\right)$
1	13·4	29·3 ± 0·8%	29·1	1·2%	1·81 ± 0·04
2	13·4	27·8 ± 0·6%			
3	13·4	28·2 ± 0·5%			
4	13·4	31·0 ± 1·6%			
5	14·1	23·7 ± 1·8%	23·8	1·1%	1·68 ± 0·03
6	14·1	23·9 ± 1·1%			
7	14·9	23·7 ± 0·8%	23·7	0·8%	1·65 ± 0·03
8	15·7	23·3 ± 2·8%	23·3	2·8%	1·74 ± 0·04

slope was usually one to two per cent and its range was from one-half to three per cent. These values are reasonable in view of the estimated accuracy (three per cent) of a single reading of the absorbance and in view of the fact that each growth curve usually consisted of five to eight experimental points. In those cases where more than one growth curve was obtained for the same incident-photon energy, the probable error of the average value of the slope has been computed. These results are presented in Table 2.

4. DISCUSSION

(a) *The role of halogen* K*-shell ionization in the formation of* F *centers in alkali halide crystals*

The efficiency of formation of *F* centers per unit energy retained in RbBr at 78°K is the same, within the uncertainty of the experiment, whether the incident photon energy is 13·4 keV or 14·1 keV. In Paper I [1] a similar result in KBr is reported. In both cases the rate of growth of coloration due to the presence of *F* centers is not sensitive to the incident-photon energy. However, since an *L*-shell ionization in a bromine ion is expected to result in extensive multiple ionization[6], the results of the present paper and of Paper I are not conclusive evidence that a multiple ionization of the halogen will not lead to vacancy formation in an alkali halide crystal.

The equality of the efficiency of *F* center formation when the incident-photon energy is above or below the rubidium *K* edge (15·2 keV) indicates that the fluorescent correction [7] used in this work is basically correct. Furthermore, this result does not support the observation by N. Itoh, J. Sharma, and R. Smoluchowski[8] that in RbBr the efficiency of *F* center formation increased as the incident-photon energy increased through both the Br edge and the Rb edge.

REFERENCES

1. CRUZ-VIDAL B. A. and GOMBERG H. J., *J. Phys. Chem. Solids* **31**, 1273 (1970).
2. COMPTON A. H. and ALLISON S. K., *X Rays in Theory and Experiment*. Van Nostrand New York (1943).
3. GRODSTEIN G. W., *X-Ray Attenuation Coefficients from 10 keV to 100 MeV* National Bureau of Standards, Circular 583 (1957).
4. BERGER R. T., *Rad. Res.* **15**, 1 (1961).
5. BEARDEN A. J., *J. appl. Phys.* **37**, 1681 (1966).
6. CARLSON T. A., HUNT W. E. and KRAUSE M. O., *Phys. Rev.* **151**, 41 (1966).
7. VEIGELE W. J. and ROPER N. J., *J. appl. Phys.* **37**, 4309 (1966).
8. ITOH N., SHARMA J. and SMOLUCHOWSKI R., *1965 Int. Symp. on Color Centers in Alkali Halides*, Urbana, Illinois, Abstract No. 95

J. Phys. Chem. Solids Pergamon Press 1970. Vol. 31, pp. 1287–1290. Printed in Great Britain.

THE ROLE OF *K*-SHELL IONIZATION IN THE FORMATION OF *F* CENTERS IN ALKALI HALIDES AT 78°K–III. KCl*

BALTASAR A. CRUZ-VIDAL, LAUREANO NIÑO-ROJAS† and HENRY J. GOMBERG

Physics Department, University of Puerto Rico at Mayagüez and Puerto Rico Nuclear Center,
Mayagüez, Puerto Rico 00708, U.S.A.

(*Received* 2 *September* 1969)

Abstract—Within the uncertainty of the experiment, the rate of *F* center formation per unit energy retained in Harshaw KCl irradiated at 78°K at equal energy flux is the same whether the incident-photon energy is below (2·62 and 2·81 keV), between (3·31 and 3·59 keV), or above (3·69 and 4·01 keV) the chlorine (2·82 keV) and potassium (3·61 keV) *K* edges. Since an initial photoionization in the L_{II} or L_{III} subshell of a chlorine ion is expected to result in an average loss of 2·3 electrons, while an initial photoionization in the *K* shell is expected to result in an average loss of 4·2 electrons, the result reported here indicates that the multiple ionization of the halogen (Varley mechanism) is not the dominant mechanism of Frenkel defect formation in KCl at 78°K. Each of the beams used was the X-ray fluorescent output of LiCl, or of $K_2C_2O_4 \cdot H_2O$, or of CaO.

1. INTRODUCTION

Two PREVIOUS papers, hereafter referred to as Paper I[1] and Paper II[2], have shown that the efficiency of *F* center formation in KBr and RbBr at 78°K and irradiated at equal intensity is the same whether the incident-photon energy is below (13·4 keV) or above (14·1 keV for the KBr experiment; 14·1, 14·9, or 15·7 keV for the RbBr experiment) the bromine *K* edge (13·5 keV).

The present paper reports a similar result using KCl exposed at 78°K at equal energy intensity to incident-photon energies either below (2·62 and 2·81 keV), between (3·31 and 3·59 keV), or above (3·69 and 4·01 keV) the *K*-absorption edges of chlorine (2·82 keV) and of potassium (3·61 keV).

J. Sharma and R. Smoluchowski[3] found that the efficiency of formation of *F* centers in KCl at liquid-nitrogen temperature increased by a factor of 2·5 as the incident-photon energy became larger than the *K*-absorption energy of chlorine. T. A. Carlson and coworkers[4] observed that for argon atoms ionized in the *K* shell the average loss of electrons is 4·2, and the probability of a loss of three or less electrons is small. They also observed that for argon atoms ionized in the L_I subshell the average loss of electrons is 3·3, while if ionized in the L_{II} or L_{III} subshell the average loss of electrons is 2·3. Since an argon atom is isoelectronic to a chlorine ion, a similar average degree of ionization can reasonably be expected to result in a chlorine ion after the corresponding inner-shell ionization. Using a computer model of the events that would follow the multiple ionization of chlorine in a KCl lattice, L. T. Chadderton and coworkers[5] predicted that the loss of three or four electrons by a chlorine ion in a KCl lattice would lead to the formation of stable Frenkel defects. On the other hand, the same calculation predicted that the loss of one or two electrons by a chlorine ion in a KCl lattice would not lead to the formation of stable Frenkel defects. Thus, based on Carlson's experimental result[4] and Chadderton's calculation[5], if the multiple ionization of the halogen in an alkali halide were to be the initial step in the formation of Frenkel defects, the efficiency of F center formation in KCl should be higher when the incident photons can ionize the K shell of chlorine than when the incident photons can not ionize the K shell.

---

*This work is based on a thesis submitted by L. Niño-Rojas to the Department of Physics of the University of Puerto Rico in partial fulfillment of the requirements for an M.S.

†Present address: Universidad Pedagógica y Tecnológica de Colombia, Tunja, Boyacá, Colombia.

2. EXPERIMENTAL METHOD

The experimental method is described in detail in Paper I.[1]

A general Electric EA50 tungsten-target tube operated at 45 kvp was used to excite the fluorescence of either LiCl powder, $K_2C_2O_4 \cdot H_2O$ powder, or CaO powder which had been pressed tightly into an aluminum planchet (radiator). Thus, beams were obtained consisting primarily of the K_α fluorescence (80 per cent of the fluorescent output) and K_β fluorescence of the heavier element in the radiator. For each radiator both the K_α and K_β emission is either below, between, or above the K-absorption edge of chlorine (2·82 keV) and potassium (3·61 keV). Thus, the beams used were: of 2·62 and 2·81 keV, from the K_α and K_β emission of chlorine; of 3·31 and 3·59 keV, from the K_α and K_β emission of potassium; and of 3·69 and 4·01 keV, from the K_α and K_β emission of calcium.

The radiator was always mounted directly under the beam of the X-ray tube as described in Paper I.[1] However, in this experiment the radiator was in vacuum and no filter was used. The beam from the X-ray tube passed through a thin (0·008 in) beryllium window before striking the radiator at an angle of 45 degrees. The vessel of the radiator was connected by means of a vacuum-tight quick coupling to the experimental dewar described previously.[1] The moderate vacuum surrounding the radiator was separated from the higher vacuum in the dewar by a thin (0·00050 in.) mylar window.

The thermoluminescence from several ribbon LiF thermoluminescent dosimeters (Harshaw Chemical Company, TLD-700), $\frac{1}{8}$ in. × $\frac{1}{8}$ in × 0·035 in, was used to measure the relative value of the energy-flux output at the position of the sample for each radiator at a given current of the X-ray tube operated at 45 kvp. The thermoluminescence of the dosimeter was measured with a ConRad model 5100 instrument. The reading of this instrument is in arbitrary units: counts*. The thickness of the dosimeter is sufficient for total absorption of the incident beams. The curves of the dosimeter's response plotted against the current of the X-ray tube always operated at 45 kvp were linear and extrapolated to zero dose for zero current. The response of each LiF ribbon piece varied by at most 2 per cent from the average value of the six pieces that were used. A correction was introduced for this systematic variation. During exposure the LiF pieces were covered by a 0·0005 in. thick mylar film. Likewise, the window for the KCl irradiation consisted of tightly stretched 0·0005 in. thick mylar. For all the experimental runs the incident flux was 720 counts/cm²/sec.

Several KCl samples, freshly cleaved from a large single crystal obtained from the Harshaw Chemical Company, were irradiated at 78°K with the fluorescent beams described above. Throughout a run a sample was exposed to only one of the fluorescent beams, and each run was made with a different sample. The current in the X-ray tube was varied between runs to achieve the same incident-energy flux on the sample regardless of incident-photon energy. At regular time intervals, usually 24–48 hr, the irradiation was momentarily interrupted to measure the absorbance at the peak of the F band. Also, the absorbance far from the peak of the F band was regularly measured to verify the proper operation of the spectrophotometer (Beckman DU). Thus, growth curves of the absorbance at the peak of the F band as a function of irradiation time were obtained.

For KCl at 78°K the value of the constant

---

*A calibration is supplied with the dosimeters for Cobalt 60 γ rays when the thermoluminescence is measured with a Harshaw model 2000 Thermoluminescent Analyzer: 0·501 nc/R ± 3 per cent. The response of the dosimeters read in a ConRad 5100 instrument will be calorimetrically calibrated in the future.

K in the form of Smakula's equation given in equation (1) of Paper I[1] is $6{\cdot}22 \times 10^{15}$ cm^{-2}.

The KCl samples that were used were sufficiently thick (about 1 mm) to absorb all the incident flux. However, depending on the incident-photon energy, a fraction, f, of the incident flux is reradiated as K_α and K_β fluorescence of potassium and chlorine. The calculation of the fluorescent-loss fraction, f, yields* the following values: $f = 1{\cdot}52 \times 10^{-2}$ for irradiation with calcium fluorescence, $f = 1{\cdot}07 \times 10^{-2}$ for irradiation with potassium fluorescence, and $f = 0$ for irradiation with chlorine fluorescence. The details of this calculation have been described in Papers I and II.[1, 2]

3. EXPERIMENTAL RESULTS

1. *The rate of* F *center formation per unit energy retained in* KCl *at 78°K*

Figure 1 shows the growth curves of the F band obtained when the crystal was exposed to X-ray photons of either 2·62 and 2·81 keV, 3·31 and 3·59 keV, or 3·69 and 4·01 keV. For each experimental run the straight line is the least-square fit to the experimental points in the region of the curve which seems to be linear. The slope of each of the lines is given in Table 1.

The evidence presented in Table 1 shows that, within the accuracy of the experiment, the efficiency of F center formation per unit energy *retained* in KCl at 78°K irradiated at equal energy flux does not vary appreciably whether the incident-photon energy is below, between, or above the chlorine and potassium K-absorption edges.

4. EXPERIMENTAL ERRORS

The uncertainty in the slopes shown in Table 1 is calculated using equation (3) of Paper I; however, for curves 2 and 3 of Fig. 1, the standard deviation, S, used in equation (3) is

$$S^2 = \sum_{i=1}^{n} \frac{1}{n}(s_i)^2,$$

where s_i is the standard deviation of the value A_i of the absorbance at time t_i and n is the number of experimental points in the curve.

The uncertainty in the time measurements is negligible.

The probable error of the dosimeter's response (as a measure of the relative value of the fluxes) is estimated to be 2 per cent.

Table 1. *The energy of formation of* F *centers in* KCl *at 78°K per unit retained energy,* dF/dE_a. *The approximated energy distribution of the incident* X*-ray beam is shown in the first column. The unit* (*counts*)$^{-1}$ *refers to the reading of the Harshaw LiF TLD-700 ribbon dosimeter in a ConRad 5100 Readout Instrument*

Incident-photon energy distribution	$\frac{dA}{dt}$ ($\times 10^{1}$ hr^{-1})	$\frac{dF}{dE_i}$ ($\times 10^{-5}$ counts^{-1})	$\frac{dF}{dE_a}$ ($\times 10^{-5}$ counts^{-1})
80%: 2·62 keV 20%, 2·81 keV	4·20 ± 0·06	10·1 ± 0 3	10·1 ± 0·3
80%· 3·31 keV 20%: 3·59 keV	3·8 ± 0·3	9·1 ± 0·8	9·2 ± 0·8
80%, 3·69 keV 20%: 4·01 keV	4·3 ± 0·3	10·3 ± 0·8	10·5 ± 0·8

5. DISCUSSION

Within the accuracy of the experiment, the rate of formation of F centers in KCl at 78°K and irradiated at equal energy flux by incident photons of 2·62 and 2·81 keV, of 3·31 and 3·59 keV, and of 3·69 and 4·01 keV shows no appreciable dependence on the incident-photon energy.

Since the work of T. A. Carlson and coworkers[4] shows that an initial K-shell ionization in a chlorine ion should result in the average loss of four electrons, while an initial L-shell

---

*The incident flux is assumed to be 80 per cent K_α and 20 per cent K_β radiation. Likewise the fluorescence emitted by the crystal is assumed to be 80 per cent K_α and 20 per cent K_β radiation.

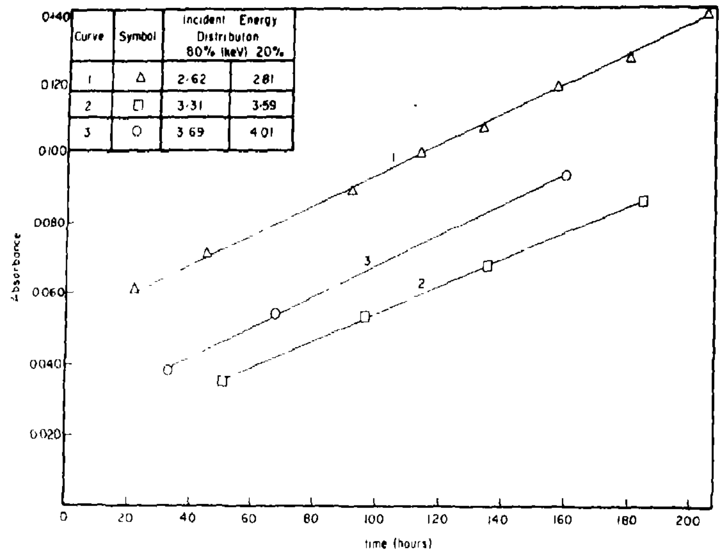

Fig. 1. Absorbance at the peak of the *F* band of KCl at 78°K and plotted as a function of exposure time. For each run the incident-phon energy distribution is approximately given in the inset. All runs were made at the same incident-energy flux. For each run the straight line is the least-square fit to the experimental points through which the line is drawn.

ionization should result in the average loss of two or three electrons, the result stated in the above paragraph indicates that a multiple-ionization mechanism such as described by L. T. Chadderton and coworkers[5] is not the dominant mechanism of Frenkel defect formation in alkali halides at liquid-nitrogen temperature. Also, the result reported above fails to confirm the observation of J. Sharma [3] that the efficiency of formation of *F* centers in KCl at liquid-nitrogen temperature increased by 250 per cent as the incident-photon energy became larger than the energy of the *K*-absorption edge of chlorine. The result reported above is based on irradiations with photon energies somewhat far from the *K*-absorption energy, while Sharma's result is based on irradiations with a beam whose energy changed smoothly along the face of a KCl sample in an energy range which included the chlorine *K*-absorption edge. There is some evidence that higher-shell photoionization cross sections change irregularly with incident-photon energy in the soft X-ray energy range.[6] However, such changes may not occur in the innermost shell, or if they do they are not likely to be sufficiently large to account for Sharma's[3] result.

REFERENCES

1. CRUZ-VIDAL B. A. and GOMBERG H. J., *J. Phys. Chem. Solids* **31**, 1273–1280 (1970).
2. CRUZ-VIDAL B. A., GOMBERG H. J. and DIAZ-HERNANDEZ F., *J. Phys. Chem. Solids* **31**, 1281–1285 (1970).
3. SHARMA J. and SMOLUCHOWSKI R., *Phys. Rev.* **137**, A259 (1965).
4. CARLSON T. A., HUNT W. E. and KRAUSE M. O., *Phys. Rev.* **151**, 41 (1966).
5. CHADDERTON L. T., MORGAN D. V. and TORRENS I. McC., *Phys. Lett.* **20**, 329 (1966).
6. KRAUSE M. O., *Phys. Rev.* **177**, 151 (1969); MANSON S. T. and COOPER J. W., *Phys. Rev.* **165**, 126 (1968) and *Phys. Rev.* **177**, 157 (1969); COMBET FARNOUX F. and HENO Y., *Compt. Rend.* **264** B, 138 (1967); COMBET FARNOUX F., *ibid.* **264** B, 1728 (1967).

J. Phys. Chem. Solids Pergamon Press 1970. Vol. 31, pp. 1291–1294. Printed in Great Britain.

DISTRIBUTION OF HYDROXIDE IONS IN DOPED ALKALI HALIDE CRYSTALS

THOMAS G. STOEBE

Division of Metallurgical Engineering, University of Washington, Seattle, Wash. 98105, U.S.A.

(*Received* 25 *August* 1969)

Abstract—The available information concerning the distribution of hydroxide ions in alkali halide crystals is reviewed. The various possible reactions among the hydroxide ions and divalent cation impurities and their accompanying charge compensating cation vacancies are given and discussed in terms of the available ionic conductivity and optical absorption data. The possible hydroxide ion complexes are discussed in terms of ESR results. Complexes containing hydroxide ions, each on their own anion site, with cation impurities and vacancies on adjacent sites are indicated as being the most probable to occur. Different geometries of such a complex are discussed in terms of the available experimental data.

1. INTRODUCTION

THE PRESENCE of hydroxide ions in alkali halide crystals has been shown to influence greatly their electrical[1–3] and optical[1, 3, 4] properties. In these crystals, the hydroxide ions may exist as separate substitutional ions, in complexes, or in precipitate phases in the lattice. The actual distribution of these hydroxide ions have been investigated using electron spin resonance (ESR)[5–8] and optical absorption techniques[1, 3, 8, 9]. However, no consistent picture of the overall dispersion of the hydroxide ions in doped alkali halide crystals has emerged.

Any study of the distribution of a particular imperfection in an ionic lattice must consider the overall defect state of the crystal. The necessary information may be obtained from studies of electrical conductivity[10], thermal depolarization of impurity-vacancy dipoles (often called ionic thermo-currents or I.T.C.) [11], and related investigations[12]. In addition to the vacancies present due to thermal equilibrium, an alkali halide crystal MX containing n divalent cation impurity ions F^{2+} will also contain n extrinsic cation vacancies to maintain charge neutrality[12]. At high temperatures these extrinsic vacancies will be free in the lattice, while at lower temperatures, divalent cation-vacancy dipoles will be formed; at still lower temperatures the dipoles aggregate into clusters and finally (near room temperature) into a superlattice precipitate containing divalent cations, vacancies, and host ions[13]. In heavily doped crystals a precipitate of the form FX_2 is also observed[14].

In crystals containing hydroxide ions, ionic conductivity measurements show a large decrease in conduction compared with crystals free of hydroxide ions[1, 3]. This indicates that the extrinsic vacancies are tied up through interactions involving the hydroxide ions in the crystal. The extrinsic vacancies are still important in crystals containing moderate amounts of dopants, however, since a conductivity knee corresponding to extrinsic vacancies is observed in this case[3]. Furthermore, thermal depolarization results have shown the presence of divalent cation-vacancy dipoles in crystals containing OH ions[7].

In KCl:Ca:OH, Fritz *et al.*[1] have shown that Ca^{2+} and OH^- ions react in a ratio 1:2 to form a product which they interpret as $Ca(OH)_2$. These authors suggest a reaction between a Ca^{2+} ion, its associated cation vacancy, and two OH^- ions on anion sites to form a $Ca(OH)_2$ molecule which could occupy the space provided by all four original sites.

In NaF:Mn:OH, Laj *et al.*[7, 8] have suggested a model with two OH^- ions on one anion site neighboring the divalent cation; the ESR results of this work are inconsistent with the four-site model of Fritz *et al.*[1].

In LiF:Mg:OH, a large number of infrared absorption bands are observed[3] in the region between 2·68 and 2·85 μ. The 2·68 μ peak has been shown to be due to OH^- ions free in the lattice, while the remainder correspond to various forms of $Mg^{2+}-OH^-$ complexes. The major absorption peak, at 2·80 μ, is presumably due to the most stable form of the complex. These complexes cannot be due to the aggregation of simple complexes into larger ones, since the ESR lines do not broaden[15]. Rather, it is supposed that several forms of divalent impurity–OH^- ion complexes exist giving rise to the observed absorption peaks. It is the purpose of this paper to evaluate the merit of various possible models for the structure of these complexes.

2. DEFECT EQUILIBRIA

The equilibrium among vacancies and impurities must consider the overall charge neutrality of the crystal. A number of possible reactions which may take place in such a system are given below. Here a modified Kroger nomenclature is used[12], with +, –, and 0 indicating the effective charge of each species with respect to its own sublattice. The reactions are written for a general alkali halide *MX* containing impurities *F* and vacancies *V*; the subscripts represent the type of site occupied by the species and the net charge of each species is given with respect to the neutral *MX* lattice.

Since ionic conductivity measurements at low temperatures in OH-doped crystals show the large depression discussed above, those reactions showing free vacancies (i.e. numbers (2), (4) and (6)) must be discarded. In addition, free OH ions should be observable using infrared absorption measurements if reactions 2 and 3 are to be important[9, 3].

The infrared absorption results permit one to determine whether the OH ions in the lattice are free (broad 2·68 μ absorption) or in complex form (2·72–2·84 μ absorption peaks)[3, 9]. The usual absorption spectrum in OH-doped crystals show the broad 2·68 μ absorption only after the sharp peak spectrum is developed[3]. Thus, free OH ions are only present in the lattice after the OH complexes are fully developed. This observation rules out reaction (3) as an important step in the complexing behavior of the OH ions.

The products of reactions (6) and (7) include the anion vacancy which must be formed in the reaction

$$(OH)_X^0 + (OH)_X^0 \rightarrow [2(OH)]_X^- + V_X^+$$

where the reactant represents two OH^- ions each on an anion site, and the product includes two OH^- ions on one anion site. The four-site $Ca(OH)_2$ model of Fritz *et al.* [1] can be represented by reaction 7 with the vacancy pair bound to the complex. The

Reaction		Comments
(1)	$F_M^+ + V_M^- + 2(OH)_X^0 \rightleftarrows (F_M V_M)^0 + 2(OH)_X^0$	Reactants all free, products, dipoles, unreacted OH
(2)	$\rightleftarrows (F_M(OH)_X)^+ + (OH)_X^0 + V_M^-$	Free vacancies, free OH.
(3)	$\rightleftarrows (F_M(OH)_X V_M)^0 + (OH)_X^0$	Free OH.
(4)	$\rightleftarrows (F_M(OH)_X(OH)_X)^+ + V_M^-$	Free vacancies
(5)	$\rightleftarrows (F_M(OH)_X(OH)_X V_M)^0$	2(OH) ions on two *X* sites.
(6)	$\rightleftarrows (F_M[2(OH)]_X)^0 + V_M + V_X^+$	2(OH) ions on one *X* site; Free vacancies.
(7)	$\rightleftarrows (F_M[2(OH)]_X)^0 + (V_M V_X)^0$	Vacancy pairs, perhaps bound to complex.

$Mn(OH)_2$ model proposed by Laj *et al.*[7, 8] corresponds to the complex in reaction 7 without the bound vacancy pair.

The feasibility of reactions (6) and (7) may be open to question due to the considerable energy required to place two OH^- ions on one anion site. Size factor considerations alone indicate that even in KCl, where the OH^- ion diameter[16] (2·72 Å) is smaller than the Cl^- diameter[17] (3·26 Å), the substitution of two OH^- ions for one Cl^- ion would be difficult; the difficulty would be lessened by the arrangement of the two OH^- ions along the more spacious ⟨110⟩ or ⟨111⟩ directions in the NaCl lattice. The difficulty of such a substitution will be considerably greater, however, in the corresponding fluorides (F^- average dia. 2·36 Å)[17].

Electrostatic considerations indicate considerable difficulty in placing two negative ions on one anion site, and the probability of such a process occurring should be closely related to that for placing two host anions on one site, which is not observed in these alkali halides[12].

The overall energy involved in reactions (6) and (7) includes the energy to form a vacancy near the complex and the repulsive electrostatic and elastic (size factor) energies, less the binding energy of the resultant complex. It is probable that in different alkali halides these energy terms will vary. Thus, the existence of $Ca(OH)_2$ on the four-site model of Fritz *et al.*[1] (i.e. with the bound vacancy pair) may be energetically favorable in KCl, but it is probably energetically unfavorable in fluorides, since it is not observed in the ESR results. Similarly, the formation of $Mn(OH)_2$ molecules in fluorides on two adjacent sites seems energetically unfavorable.

3. DISCUSSION

The defect equilibria which seem energetically favorable and which are compatible with the observed experimental results are reactions (1) and (5). The product and reactant species in reaction (1) have all been observed in conductivity[1, 3] thermal depolarization [7, 8] and optical absorption[1, 3, 7, 9] studies. The product complex of reaction (5) may take on a variety of forms in the lattice, as illustrated in two dimensions in Fig. 1. The vacancy in this complex is expected to be attracted to the OH^- ion (or ions) in fluorides, because this would reduce the strain energy of the (too large) OH^- ion; in chlorides and bromides the vacancy would probably be repulsed by the (too small) OH^- ion but the vacancy would still be electrostatically attracted by the

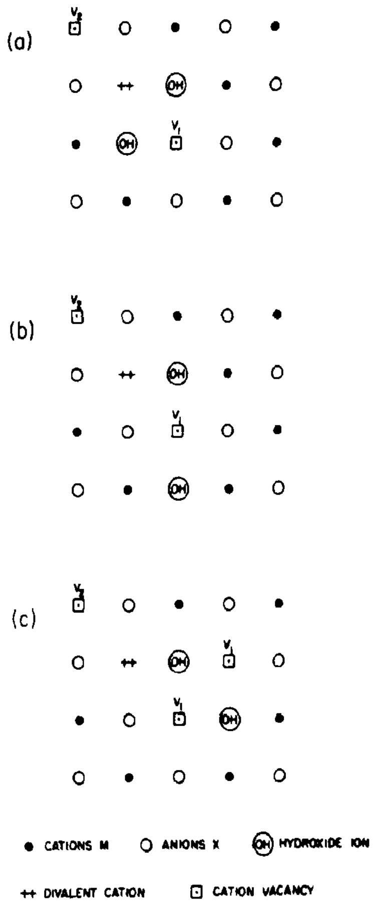

Fig. 1. Possible geometries for impurity–vacancy–hydroxide complexes resulting from reaction (5) (see text). Several possible vacancy positions are indicated by V_1 and V_2 depending on whether the vacancy and the OH^- ion attract or repel.

divalent cation impurity. In the geometrical configurations shown in Fig. 1, V_1 represents the case of a cation vacancy attracted both to F_M^+ and OH^-, and V_2 represents the case of a cation vacancy attracted by F_M^+ but repulsed by OH^-.

The ESR results[6–8] in fluorides show one spectrum with orthorhombic symmetry and a second, somewhat less stable spectrum with axial symmetry. The complex in Fig. 1(a) satisfies the axial symmetry with the axis perpendicular to the plane of the paper, and has been suggested previously[7, 8]. The orthorhombic spectrum corresponds to one missing fluorine in the nearest neighbor shell to the divalent impurity. This is satisfied by complexes in Figs. 1(b) and 1(c).

Each of the different complex geometries shown in Fig. 1 may be expected to give a slightly different infrared absorption frequency. In the process of approaching equilibrium, many different geometries are present, of which only a few are shown in Fig. 1. In the present interpretation, one step in the approach to equilibrium corresponds to the complex in Fig. 1(a) which gives rise to the axially symmetrical ESR spectrum. Complete equilibrium is reached with the complex corresponding to the orthorhombic ESR spectrum, which corresponds to the complexes in Figs. 1(b) or 1(c), and should correspond to the dominant 2·80 μ absorption peak.

Except in heavily doped crystals, one would not expect actual precipitation of a separate phase of $F(OH)_2$ where vacancies would be annihilated at an incoherent interface. This would cause a broadening of the ESR lines due to interactions between paramagnetic ions, which has not been observed.

The complexes illustrated in Fig. 1 seem, therefore, to be reasonable choices for the stable complexes present at room temperature in alkali halide crystals containing hydroxide ions and divalent cations. While other choices cannot be ruled out on the basis of the available data, the other possibilities discussed above seem less likely to occur. The variety of sharp i.r. absorption peaks observed in such crystals, and the dependence of their relative intensities on heat treatment [3], indicates that many different complex geometries do occur during the approach to equilibrium. While these less stable complexes may be related to any of the reactions given above, reaction 5 and the geometries given in Fig. 1 seem to represent the most stable complexes, at least in alkali fluoride systems.

Acknowledgements—The author wishes to thank Dr. C. Laj for supplying his results prior to publication and Dr. H. I. Dawson for valuable discussions. This work was supported by P.H.S. Research Grant No. EC 00125 from the Environmental Control Administration.

REFERENCES

1. FRITZ B., LUTY F. and ANGER J., *Z. Phys.* **174**, 240 (1963).
2. DREYFUS R. W., *Appl. Phys. Lett.* **3**, 175 (1963)
3. STOEBE T. G., *J. Phys. Chem. Solids* **28**, 1375 (1967).
4. NAKAJIMA T., *J. appl. Phys.* **39**, 4811 (1968).
5. CHANG T. I., TANTTILA W. H. and WELLS J. S., *J. chem. Phys.* **39**, 2453 (1963).
6. BOTTCHER R., WINDSCH W. and LUDKE W., *Phys. Status Solidi* **20**, 121 (1967)
7. LAJ C., Thesis, Orsay (1969).
8. BIANCHINI A., MARTINELLI M., SANTUCCI S., BERGE P. and LAJ C., *Phys. Lett.* **29A**, 522 (1969)
9. MEISTRICH M. L., *J. Phys. Chem. Solids* **29**, 1119 (1968)
10. See, for example, in LiF: STOEBE T. G. and PRATT P. L., *Proc. Br. ceramic. Soc.* **9**, 181 (1966); in NaCl: KIRK D. L. and PRATT P. L., *Proc. Br. ceramic Soc.* **9**, 215 (1966); in KCl: FULLER R. G., MARQUARDT C. L., REILLY M. H. and WELLS J. C., *Phys. Rev.* **176**, 1036 (1968).
11. See, for example, BUCCI C., *Phys. Rev.* **164**, 1200 (1967); LAJ C. and BERGE P., *J. Phys.* **28**, 821 (1967).
12. For a general discussion, see KROGER F. A., *Chemistry of Imperfect Crystals*. Wiley, New York (1964).
13. SUZUKI K., *J. phys. Soc. Japan* **16** 67(1961).
14. BARSIS E., LILLEY E. and TAYLOR A., *Proc. Br. ceramic Soc.* **9**, 203 (1967).
15. LAJ C., private communication.
16. PAUS H. and LUTY F., *Phys. Status Solidi* **12**, 341 (1965).
17. TOSI M. P. and FUMI F. G., *J. Phys. Chem. Solids* **25**, 45 (1964)

J. Phys. Chem. Solids Pergamon Press 1970. Vol. 31, pp. 1295–1306. Printed in Great Britain.

MOMENTS DEVELOPMENTS AND THEIR APPLICATION TO THE ELECTRONIC CHARGE DISTRIBUTION OF *d* BANDS

F. DUCASTELLE and F. CYROT-LACKMANN[*]
Laboratoire de Physique des Solides,[†] Faculté des Sciences, 91-Orsay, France

(*Received* 4 *August* 1969)

Abstract – A systematic study of the *d* electronic charge distribution of transition metals is presented. The calculations are done in a tight binding scheme using an extension of the expansion of the density of states of the *d* band in its moments. The results are in agreement with experiments, showing a contrasting behaviour for the various crystalline structures; the top of the band having a marked T_{2g} character in the *f.c.c.* structure, and in a *b.c.c.* one, the antibonding states having a slight predominant E_g character.

INTRODUCTION

THE ELECTRONIC properties of transition metals are usually described by first principles band structure calculations. One makes use of various techniques which directly solve a given one electron crystal wave equation[1]; for example, the simple tight binding scheme, the augmented plane wave method (*APW*), the Green's function method (*KKR*). More recently, interpolation schemes have been used which short circuit many of these calculational complexities[2]. They have numerically verified that the band structure of transition metals can be described to a good approximation by the overlapping and hybridization of an *s* band with a tight binding *d* band.

These methods are very cumbersome to describe effects related to disorder. This is an important failure. Such effects exist for example in liquid transition metals, in alloys or in disordered crystalline transition metals, (pure crystals with extended defects, surfaces, . . .).

With this in mind, one of us has developed a technique using an expansion in moments of the density of states in the tight binding scheme, which has been applied with some success to disordered systems[3, 4]. Some attempts have also been made using a small number of moments to compute the melting heat, the cohesive energy and the surface tension of transition metals[3, 4]. This is justified by a complete study of an *s* band which supports the idea that the knowledge of only a few moments is sufficient to give a good estimate of these properties.

Our aim, in this paper is to analyze in detail the moments of the density of states for a *d* band, and to show how these moments may be used to investigate the effect of the crystalline field on the electronic charge distribution of transition metals. There are numerous other possible applications of this method, such as the study of cohesive energy, binding energies, elastic constants, stacking fault energy, magnetic properties of crystals.

1. EXPANSION IN MOMENTS

In the following work, we shall use a simple tight binding scheme, neglecting spin orbit-coupling and mixing with the *s* band[‡]. The one electron Hamiltonian is then simply written in terms of a sum of spherical atomic potentials located on the various lattice sites $\mathbf{R}_i$:

---

[*] Also at Laboratory of Atomic and Solid State Physics, Cornell University, Ithaca, N.Y. 14850, U.S.A.

[†] Associé au C.N.R.S.

[‡] The spin orbit coupling term may in fact have some effect particularly for the heavy metals of the second and third series[5, 6], and *sd* mixing on the noble metals.

$$H = T + \sum_i V(\mathbf{r} - \mathbf{R}_i) \tag{1}$$

In the tight binding scheme, the band is described as a linear combination of the atomic d orbitals located at all the lattice sites, $\phi_\lambda(\mathbf{r} - \mathbf{R}_i)$, labelled according to their magnetic quantum number, $\lambda = 1, \dots, 5$. The ϕ_λ are set up as usual to form basis functions for the irreducible representations of the cubic point group Γ_i, and are varying as xy, yz, zx, $x^2 - y^2$ and $3z^2 - r^2$, multiplied by appropriate function of r. They satisfy

$$\{T + V(\mathbf{r} - \mathbf{R}_i)\}\phi_\lambda(\mathbf{r} - \mathbf{R}_i) = E_0\phi_\lambda(\mathbf{r} - \mathbf{R}_i)$$

where E_0 is the energy of the d level of the free atom.

We will assume that the atomic orbitals located on various sites are orthogonal to each other, and we will keep only the two center overlap integrals. Using E_0 as the zero energy point, we define the 5×5 matrices $H(\mathbf{R})$, $\beta(\mathbf{R})$, α and $\alpha(\mathbf{R})$, which have the following elements:

$$\begin{aligned} H_{\lambda\lambda'}(\mathbf{R}) &= H_{\lambda\lambda'}(\mathbf{R}_i - \mathbf{R}_j) \\ &= \int \phi_\lambda^*(\mathbf{r} - \mathbf{R}_i) H \phi_{\lambda'}(\mathbf{r} - \mathbf{R}_j)\,\mathbf{dr} \end{aligned}$$

with:

$$\begin{aligned} \text{if } \mathbf{R} \neq 0 \quad H_{\lambda\lambda'}(\mathbf{R}) &= \beta_{\lambda\lambda'}(\mathbf{R}) \\ &= \int \phi_\lambda^*(\mathbf{r}) V(\mathbf{r} - \mathbf{R}) \phi_{\lambda'}(\mathbf{r} - \mathbf{R})\,\mathbf{dr} \end{aligned}$$

$$\begin{aligned} \text{if } \mathbf{R} \neq 0 = \alpha_{\lambda\lambda'} &= \sum_i \alpha_{\lambda\lambda'}(\mathbf{R}_i) \\ &= \int \phi_\lambda^*(\mathbf{r}) \Big\{\sum V(\mathbf{r} - \mathbf{R}_i)\Big\} \phi_{\lambda'}(\mathbf{r})\,\mathbf{dr} \end{aligned} \tag{2}$$

The matrix β is symmetric, and hence as shown by Slater and Koster[7] its elements can be written as linear combinations of three two-center overlap integrals $dd\sigma$, $dd\pi$ and $dd\delta$ corresponding to the values $|m| =$ 0, 1, and 2 of the projection of the orbital momentum on the z axis. In the same way, the elements of $\alpha(\mathbf{R})$ can be written as functions of $dd\sigma'$, $dd\pi'$ and $dd\delta'$.

The electronic wave functions may be chosen to transform under the symmetry operations of the point group G_p of the lattice, as its irreducible representations Γ_i. But, in general, it is impossible to reduce the matrix $\beta(\mathbf{R})$ following the representations Γ_i. Therefore, one can decompose the trace of the matrix β following partial traces on sub spaces associated with Γ_i, and write:

$$Tr\,\beta(\mathbf{R}) = \sum_i Tr_{\Gamma_i}\beta(\mathbf{R}) \tag{3}$$

$Tr\,\alpha(\mathbf{R})$ may be similarly decomposed, but since $\alpha = \sum_{\mathbf{R}_i \neq 0} \alpha(\mathbf{R}_i)$ is invariant with respect to Gp:

$$\langle \Gamma_i | \alpha | \Gamma_j \rangle = \alpha(\Gamma_i)\delta_{ij} \tag{4}$$

(1) *Moments of the density of states*

The successive moments m_p of the density of states per atom are defined by:

$$m_p = \int E^p n(E)\,\mathrm{d}E = \frac{1}{N} Tr H^p. \tag{5}$$

Using an expansion over the set of tight binding atomic orbitals, this may be written in terms of the matrix $H(\mathbf{R})$:

$$m_p = Tr \sum_{\mathbf{R}_1 \dots \mathbf{R}_p} H(\mathbf{R}_1) H(\mathbf{R}_2) \dots H(\mathbf{R}_p). \tag{6}$$

with

$$\sum \mathbf{R}_p = 0$$

Defining the partial densities of states $n_\Gamma(E)$, we shall write:

$$\begin{aligned} m_p(\Gamma_i) &= \int E^p n_{\Gamma_i}(E)\,\mathrm{d}E \\ &= Tr_{\Gamma_i} \sum_{\mathbf{R}_1 \dots \mathbf{R}_p} H(\mathbf{R}_1) \dots H(\mathbf{R}_p) \end{aligned}$$

with

$$\sum \mathbf{R}_p = 0 \tag{7}$$

with

$$n(E) = \sum_i n_{\Gamma_i}(E) \tag{8}$$

$$m_p = \sum_i m_p(\Gamma_i).$$

In the case of a non degenerate band, and for either a perfect lattice or a disordered one, the moments can be computed using a walk counting technique on the lattice[4]. These moments can also be expressed as integrals involving Newton sums of the roots of the secular equation (8).

Here, we want to work out some analytical expression for the first moments as a function of the two-center overlap integrals, and we shall use an extension of the walk counting technique to the case of a degenerate band. It is, in fact, rather straight forward to give the following rules for the computation of the moment m_p, of order p; one has to: (a) enumerate the closed circuits going successively through $q \leq p$ neighbouring atoms; (b) associate the matrix $\beta(\mathbf{R})$ with each of the q paths parallels to $\mathbf{R}$, and the matrix α with each of the $p-q$ nodes; (c) evaluate the trace of the product of matrices associated with this circuit; (d) sum the contributions of all possible closed circuits.

Due to the peculiar properties of the matrices $\beta(\mathbf{R})$ and of the trace, the contribution of a circuit is independent of the direction in which the path is described, of the position of the origin in the circuit, and of its orientation in the lattice.

It is then possible with this procedure to compute analytically the first moments as a function of the two-center overlap integrals, and using a computer the moments of high order.

(2) *Computation of the first moments*

(a) *Overlap integrals.* Using atomic orbitals deduced from the Slater rules[9], the two-center overlap integrals will only depend on two parameters for a whole transition series, i.e. the effective charge and the interatomic distance. A priori, due to the symmetry properties, one has:

$$dd\pi > 0;\ dd\sigma, dd\delta < 0$$
$$|dd\delta| \ll dd\pi < |dd\sigma|.$$

More precisely, assuming some shape for the atomic potentials, one can compute these integrals, but in actual fact only a few of the transition metals have yet been investigated. A systematic study of the variation of these integrals is currently in progress and the results will be presented elsewhere[10].

It must be pointed out, however, that ambiguities in the choice of the atomic potentials may limit the accuracy with which these integrals can be computed. The atomic potentials should in principle be computed in a self consistent way. In fact, the potential is usually chosen to be that of the positive ions, instead of the potential of the neutral atoms as is required by the Hartree scheme. This choice has the advantage that one uses the same energy E_0, potentials $V(\mathbf{r})$ and atomic orbitals in the solid as in the gas; also, it takes into account in some way the intra-atomic correlations through a Wigner–Seitz modification of the Hartree scheme. It is then reasonable to assume that these correlation effects are similar both in the solid and the free atom[6].

The numerical values one gets for the overlap integrals are thus estimates, especially for the crystal field type α integrals. Indeed, they involve the long range part of the potential which is screened out to some extent by d and s electrons and their computed values are certainly too large.

One may use the results given by an interpolation scheme, as first suggested by Slater and Koster[7], and recently extended by various authors[2] to get some other numerical values for these overlap integrals with an accuracy of 5–10 per cent. In principle, one can also get the α type overlap integrals. However since these integrals depend on the distance between the s and d bands which

Table 1. *Two centers overlap integrals for* FCC *metals (eV)*

$dd\sigma$	$dd\pi$	$dd\delta$	$\frac{dd\sigma}{dd\pi}$	Metal	Reference
−0·34	0·185	−0·03	1·85	Ni	11
−0·53	0·31	−0·11	1·70	Ni	12
−0·53	0·24	−0·03	2·20	Ni	13
−0·29	0·21	−0·04	1·38	Ni	14
−0·38	0·21	−0·03	1·81	Ni	15
−0·25	0·11	−0·01	2·27	Ni	15
−0·35	0·175	−0·02	2·00	Cu	16
−0·34	0·18	−0·03	1·89	Cu	15
−0·65	0·27	−0·01	2·40	Fe	17

varies strongly with the approximation made; it is then difficult to get some precise answer. But in any case, these crystal field integrals can be reasonably taken as being a small fraction of the β ones.

We have listed in Tables 1 and 2 some of the numerical values of the two-center type β overlap integrals which have been computed for the *FCC* and *BCC* crystalline structures.

One may notice that if the absolute values of these overlap integrals are rather different, the ratios $(dd\sigma)/dd\pi$ and $dd\sigma(1)/dd\sigma(2)$ are on the contrary quite similar and independent of the structure. Here $dd\sigma(1)$ and $dd\sigma(2)$ denote respectively overlap integrals between first and second nearest neighbours. Thus, in the following, as a simplification in the computation of the moments, we will assume that

$$dd\delta = 0;\ \frac{dd\sigma}{dd\pi} = -2 \text{ and}$$

$$\frac{dd\sigma(2)}{dd\sigma(1)} = 0{\cdot}5 \text{ for a } BCC \text{ Lattice}$$

$$= 0 \quad \text{for an } FCC \text{ Lattice}$$

and we will take $|dd\sigma| = \beta$ as a parameter.

(b) *Analytical expression*. The zero order moment gives the number of d electrons for a filled band, i.e. $m_0 = 5$.

The first order moment gives the average shift of the band, and

$$m_1 = Tr\alpha = \sum_i p_i\alpha(\Gamma_i) = 5\bar{\alpha}$$

where p_i is the dimension of the subspace Γ_i.

In fact, in the following, we will use the central moments of the density of states normalised to the unity

$$\mu_n = \frac{\int (E-\bar{\alpha})^n(E)\,\mathrm{d}E}{\int n(E)\,\mathrm{d}E}. \tag{9}$$

One may notice that if the matrice α is a scalar, its effect is only a simple shift of the band $\bar{\alpha}$.

But, in general, the matrix α is not a scalar, and the $\alpha(\Gamma_i)$ defined by (4) are different. This leads also to a distortion of the band besides its shift. As a first approximation, we will neglect this effect in our computation because the crystal field integrals being much smaller than the β ones.

In some cases, the differences between the shifts of the sub-bands may be of some importance, and we will estimate their effects using a pertubation expansion (cf. Appendix and Section 2(c).

The second order moment is thus related to the width of the band and is written as:

$$\mu_2 = \frac{1}{5}\sum_i Z_i[dd\sigma^2(i) + 2dd\pi^2(i) + 2dd\delta^2(i)] \tag{10}$$

Table 2. *Two centers overlap integrals for* BCC *metals (eV)*

$dd\sigma(1)$	$dd\pi(1)$	$dd\delta(1)$	$\frac{\lvert dd\sigma(1)\rvert}{dd\pi(1)}$	$dd\sigma(2)$	$dd\pi(2)$	$\frac{\lvert dd\sigma(2)\rvert}{dd\pi(2)}$	$\frac{dd\sigma(1)}{dd\sigma(2)}$	Metal	Reference
−1 13	0·62	−0·10	1·8	−0·52	0·24	2·15	2·2	Cr	18
−1·05	0·45	−0·05	2·3	−0·405	0·13	3·0	2·6	Fe	19
−0·74	0·49	−0·09	1·5	−0·45	0·21	2·1	1·65	Fe	20
−0·66	0·43	−0·07	1·5	−0·405	0·33	1·2	1·65	Fe	21
−0·73	0·51	−0·06	1 4	−0·41	0·19	2·15	1·8	Fe	17

where Z_i is the number of neighbours of the i^{th} shell.

We will keep only the integral between the first nearest neighbours in compact structures, and between the first and second neighbours in a *BBC* structure (cf. Tables 1 and 2).

The computation of the other moments will depend on the crystalline structure and hence will become increasingly difficult. We shall give here only the result for the third order moment for various crystalline structures.

The location of the first nearest neighbours of any atom is the same for all compact crystalline structures. Therefore, in keeping only overlap integrals between nearest neighbours, the third order moment μ_3 is the same for all the compact structures, such as *FCC* and *CPH*. More precisely, one can write for μ_3:

$$\begin{aligned}5\mu_3 = {} & 9(dd\pi + dd\delta)^2(3dd\sigma + dd\delta) \\ & - \tfrac{3}{32}(dd\sigma + 4dd\pi + 3dd\delta^3) \\ & - \tfrac{27}{4}(dd\sigma - dd\delta)^2(dd\delta - dd\pi) \\ & + (dd\delta - dd\pi)^3 \\ & + \tfrac{9}{2}dd\pi(dd\sigma + 3dd\delta) \\ & \times (dd\sigma + 4dd\pi + 3dd\delta).\end{aligned}$$

For a non degenerate band, all the compact structures have the same moments, and therefore the same density of states. Now, due to the degeneracy of the *d* band, this is not true. The computation of μ_4, already rather tedious will lead to results different for an *FCC* lattice and a *CPH* one. These differences in μ_4 or in moments of higher order, will then dominate the behaviour of the relative stability of the *FCC* and *CPH* phases, and thereby the value of the stacking fault energy [22].

The first moments $\mu_p(\Gamma_i)$ of the partial density of states $n_{\Gamma_i}(E)$, which is defined by (8), can also be easily computed.

Thus, the effect of a cubic field is to split the atomic five fold degenerate *d* levels into threefold and two fold degenerate levels: the former having T_{2g} symmetry with atomic orbitals *xy*, *yz*, *zx* ($\Gamma_{25'}$ representation) and the latter having E_g symmetry with atomic orbitals $x^2 - y^2$ and $3z^2 - r^2$ (Γ_{12} representation).

For an *FCC* lattice, we have:

$$\mu_2(T_{2g}) = 3dd\sigma^2 + 4dd\pi^2 + 5dd\delta^2$$

$$\mu_2(E_g) = \tfrac{3}{2}(dd\sigma^2 + 4dd\pi^2 + 3dd\delta^2)$$

and

$$\begin{aligned}\mu_3(T_{2g}) = {} & 3(3dd\sigma + dd\delta)(dd\pi + dd\delta)^2 \\ & - 2(dd\pi - dd\delta)^3 \\ & + \tfrac{3}{2}(dd\pi - dd\delta)(dd\sigma - dd\delta)^2\end{aligned}$$

$$\begin{aligned}\mu_3(E_g) = {} & \tfrac{9}{8}(dd\pi - dd\delta)(dd\sigma - dd\delta)^2 \\ & - \tfrac{3}{64}(dd\sigma + 4dd\pi + 3dd\delta)^3 \\ & + \tfrac{9}{4}dd\pi(dd\sigma + 3dd\delta) \\ & \times (dd\sigma + 4dd\pi + 3dd\delta).\end{aligned}$$

The effect of a hexagonal crystalline field is to split the *d* levels into one non degenerate level of A_{1g} symmetry and two twofold degenerate levels of symmetry E_{1g} and E_{2g}. These levels correspond respectively to an absolute value of the projection of the orbital momentum of $m = 0$, $|m| = 1$ and $|m| = 2$, i.e. to the ϕ_5, ϕ_2 and ϕ_3, ϕ_1 and ϕ_4 atomic orbitals.

The moments $\mu_2(\Gamma_i)$ and $\mu_3(\Gamma_i)$ can be written as a function of the moments of the *FCC* lattice:

$$\mu_j^{CPH}(A_{1g}) = \mu_j^{FCC}(T_{2g})$$

$$\mu_j^{CPH}(E_{1g}) = \frac{2\mu_j^{FCC}(E_g) + \mu_j^{FCC}(T_{2g})}{3}$$

$$\text{for } j = 2, 3 \qquad (11)$$

$$\mu_j^{CPH}(E_{2g}) = \frac{\mu_j^{FCC}(E_g) + 2\mu_j^{FCC}(T_{2g})}{3}.$$

In a *BCC* lattice, we will also take into account the overlap integrals between second nearest neighbours as they are fairly close to the first ones.

The second order moment is given by (10) and the partial moments $\mu_2(T_{2g})$ and $\mu_2(E_g)$ write easily as:

$$\mu_2(T_{2g}) = \tfrac{8}{9}[3dd\sigma^2(1)+2dd\pi^2(1)+4dd\delta^2(1)] + 2[2dd\pi^2(2)+dd\delta^2(2)]$$

$$\mu_2(E_g) = \tfrac{8}{3}[2dd\sigma^2(1)+dd\delta^2(1)] + 3[dd\sigma^2(2)+dd\delta^2(2)].$$

We get for the third order moment μ_3:

$$\tfrac{5}{72}\mu_3 = A^2[2dd\pi(2)+dd\delta(2)] + \frac{2C^2}{27}[dd\sigma(2)-4dd\pi(2)-3dd\delta(2)] - 2B^2[dd\sigma(2)+D^2[dd\sigma(2)+dd\delta(2)]]$$

with

$$A = \frac{3dd\sigma(1)+2dd\pi(1)+4dd\delta(1)}{9}$$

$$B = \frac{3dd\sigma(1)-dd\pi(1)-2dd\delta(1)}{9}$$

$$C = dd\pi(1)-dd\delta(1)$$

$$D = \frac{2dd\pi(1)+dd\delta(1)}{3}$$

and

$$\frac{\mu_3(T_{2g})}{24} = A^2[2dd\pi(2)+dd\delta(2)] - 2B^2 dd\delta(2) - \tfrac{4}{27}C^2[2dd\pi(2)-dd\delta(2)]$$

$$\frac{\mu_3(E_g)}{72} = \frac{C^2}{27}[dd\sigma(2)-3dd\delta(2)] + \frac{D^2}{2}[dd\sigma(2)+dd\delta(2)].$$

(c) *Numerical values*. Using the results of (a) and (b), we have listed in Tables 3, 4 and 5, the numerical values of the first moments μ_2, μ_3, and μ_4 and of the ratios $\mu_3/\mu_2^{3/2}$ and μ^4/μ_2^2 for the *FCC*, *CPH* and *BCC* crystalline structures. We have also presented the results for a non degenerate band.

In particular, one may notice that the moments are different for an *FCC* lattice and a *CPH* one, their difference being quite small (of the order of a few percents), and almost independent of the c/a ratio[22].

Table 3. *First moments for* FCC *structure* (*β units*)

	T_{2g}	E_g	Total band	Non degenerate band
μ_2	4·0	3·0	3·6	12
μ_3	1·75	−0·61	−1·30	−48
μ_4	31·9	14·1	24·8	+540
$\frac{\mu_3}{\mu_2^{3/2}}$	−0·22	−0·12	−0·19	−1·15
$\frac{\mu_4}{\mu_2^2}$	2·0	1·6	1·9	+3·75

Table 4. *First moments for* CPH *structure* (*β units*)

	A_{1g}	E_{1g}	E_{2g}	Total band	Non degenerate band
μ_2	4·0	3·3	3·7	3·6	12
μ_3	−1·75	−1·0	−1·37	−1·30	−48
μ_4	30·9	19·4	25·2	24·0	540
$\frac{\mu_3}{\mu_2^{3/2}}$	−0·22	−0·13	−0·17	−0·19	−1·15
$\frac{\mu_4}{\mu_2^2}$	1·9	1·75	1·9	1·85	3·75

Table 5. First moments for BCC *structure (β units)*

	T_{2g}	E_g	Total band	Non degenerate band
μ_2	3·3	2·1	2·8	9·5
μ_3	0·15	−2·24	−0·81	−36
μ_4	18	10	14·8	366
$\frac{\mu_3}{\mu_2^{3/2}}$	0·02	−0·76	−0·17	−1·25
$\frac{\mu_4}{\mu_2^2}$	1·64	2·28	1·83	4·05

2. DENSITY OF STATES AND ELECTRONIC ASPHERICITY

(1) *Density of states*

In a cubic structure, the location of the limits of the *d* band is fairly well known, and therefore one can get the width W as a function of the two center overlap integrals.

Thus in an FCC lattice, the bottom of the *d* band is located in X_3, and its top in X_5 [11, 12] and:

$$X_5 = -(3dd\sigma + dd\delta) + \alpha(T_{2g})$$
$$X_3 = 3(dd\sigma - dd\delta) - 4dd\pi + \alpha(T_{2g})$$

and

$$W_{FCC} = 2(-3dd\sigma + 2dd\pi + 2dd\delta) \sim 8\beta.$$

In a BCC lattice, the location of the extremities of the *d* band may depend on the method of computation. Usually, it corresponds either to the point H of the Brillouin zone, or to the point N [18, 19, 21]. Since this leads to the same order of magnitude for the width, we will compute it assuming that the bottom of the band and its top are respectively located in H_{12} and $H_{25'}$;

$$H_{25'} = -\tfrac{8}{9}[3dd\sigma(1) + 2dd\pi(1) + 4dd\delta(1)] + 2[2dd\pi(2) + dd\delta(2)] + \alpha(T_{2g})$$
$$H_{12} = -\tfrac{8}{3}[2dd\pi(1) + dd\delta(1)] + 3[dd\sigma(2) + dd\delta(2)] + \alpha(E_g)$$

and

$$W_{BCC} = \tfrac{8}{9}[-3dd\sigma(1) + 4dd\pi(1) - dd\delta(1)] - 3dd\sigma(2) + 4dd\pi(2) - dd\delta(2) + \alpha(T_{2g}) - \alpha(E_g)$$
$$W_{BCC} \sim 7\beta + \alpha(T_{2g}) - \alpha(E_g) \leqslant 7\beta.$$

In any case, one can verify that $W \sim 4\sqrt{\mu_2}$; for a non degenerate band, this would be $W \sim 3,5\sqrt{\mu_2}$.

From the numerical values of the first moments listed in Tables 3–5, one can get some more information about the shape of the total density of states $n(E)$ and of the partial ones. Indeed μ_2, $\mu_3/\mu_2^{3/2}$, μ_4/μ_2^2 respectively reflect some characteristic features of the width of the band, its asymmetry and the importance of its wings.

Thus, one can notice that since $\mu_3/\mu_2^{3/2}$ is smaller for a *d* band than for a non degenerate one, the *d* band is somewhat more symmetric. This is due to the fact that now the overlap integrals are not all negative, as was the case for an *s* band. A similar effect occurs in μ_4/μ_2^2 which is also smaller for a *d* band than for an *s* band; therefore the *d* band will be less spread out.

The same kind of conclusions can be drawn for the partial density of states. Thus, one expects in an FCC lattice the sub-band T_{2g} to be broader than the E_g one; in a CPH lattice, the three sub-bands to be of similar shape; and in a BCC lattice, the sub-band E_g to be much more asymmetric than the T_{2g} one.

These qualitative features of the *d* band as seen by inspection to the first few moments, are in agreement with the more precise description given by a full band structure computation[19, 21, 27].

(2) *Electronic* d *asphericity*

It is clear from the previous discussion that the electronic charge distribution surrounding an atom will not in general be spherical in a transition metal*. This effect can be investigated experimentally either by diffraction of X rays or of polarized neutrons. The X rays experiments lead to a knowledge of the total electronic charge distribution, whereas the neutron experiments using ferromagnetic materials, give informations about the charge distribution of impaired electrons. It should be noticed that the impaired electrons, which are responsible for the magnetization, have their energies lying between the two spin up and spin down Fermi levels E and E. Since the departure from spherical symmetry is usually quite large for the impaired electrons charge distributions, the experiments can give some more precise answers.

The electronic charge distribution can be written:

$$Z(E) = \int^{E} n(E')\,\mathrm{d}E' \qquad (12)$$

and

$$Z_{\Gamma_i}(E) = \int^{E} n_{\Gamma_i}(E')\,\mathrm{d}E'$$

We will compute $Z(E)$ and $Z_{\Gamma_i}(E)$ using for the density of states a curve fitted to its first moments.†

Here we will take a gaussian multiplied by a polynomial[23] and with the first moments, this can be written:

$$n_{\Gamma i}(X_i) = \frac{p_i}{\sqrt{2\pi\mu_2(\Gamma_i)}}\,\mathrm{e}^{-X_i^2/2}$$

$$\times\left[1+\frac{A_i-3}{24}(3-6X_i^2+X_i^4)\right.$$

$$\left.+\frac{B_i}{2}X_i\left(-1+\frac{X_i^2}{3}\right)\right] \qquad (13)$$

with

$$X_i = \frac{E-\alpha(\Gamma_i)}{\sqrt{\mu_2(\Gamma_i)}};\; A = \frac{\mu_4(\Gamma_i)}{\mu_2^2(\Gamma_i)};$$

$$B_i = \frac{\mu_3(\Gamma_i)}{\mu_2^{3/2}(\Gamma_i)}$$

and

$$n(E) = \sum_i n_{\Gamma_i}(E).$$

It must be pointed out that in all the following numerical computations, the dominating term in $Z(E)$ comes from the first term on the right hand side of (13); the moments μ_3 and μ_4 then have quite a negligible effect.

(a) FCC *structure*. In the first figure we have plotted the results of a computation of $Z(E)$ and of $Z_{\Gamma_i}(E)$ for the two symmetries T_{2g} and E_g. $Z(E)$ can also be written as

$$Z(E) = Z_{T_{2g}}(E) + Z_{E_g}(E).$$

In these computations, we have neglected the possible shift of the band. But, if, as we expect, the two sub-bands have the same shift, the curves $Z_{T_{2g}}(E)$ and $Z_{E_g}(E)$ will have the same relative position.

The only transition metals having an *FCC* structure can be found at the ends of the series. Here, we will describe the ferromagnetic materials, e.g. Ni, Co, and some dilute alloys. In the following, we will assume that the two spin up and spin down densities of states $n\uparrow(E)$ and $n\downarrow(E)$ can be obtained by a simple rigid exchange splitting of the total density of states.

Experimental results on Nickel can be interpreted as corresponding to a strong T_{2g} character of the unpaired electrons. More precisely, Mook[24] gave a population of T_{2g} orbital of 81 per cent, while some older results [25] have been interpreted[26] as corresponding to a T_{2g} population of 75 per cent. A distribution of spherical symmetry would correspond to a population of T_{2g} orbitals of 60 per cent and E_g orbitals of 40 per cent.

---

*In principle, one would have to take into account this departure from spherical symmetry and use non spherical atomic potentials and wave functions. This would lead to an additional small crystal field splitting.

†We have neglected the overlap between the *d* orbitals. This can lead to a quite negligible additional asphericity.

Any value over 60 per cent for the T_{2g} orbitals indicates that the spin density tends to point along the body diagonals (111) of the cube, and any value less than 60 per cent along the cube axes (100).

Assuming 0.55 holes in the spin down band $n\downarrow(E)$, we find that the population of T_{2g}, given by

$$t_m = \frac{Z_{T_{2g}}}{Z_{T_{2g}} + Z_{E_g}} \text{ is 70 per cent.}$$

Our result is then a little too small. This is probably due to the fact that a small number of moments are unable to describe the well-known prominent peak at the top of the band of Ni. This peak might be mainly responsible for the T_{2g} character, as suggested by Hodges and Ehrenreich[27].

Using the results of a Green's function band structure computation, Wakoh and Yamashita[28] give a rate of 74 per cent T_{2g} for the magnetic electrons. They also give a value of 59 per cent for the proportion t_e of T_{2g} symmetry corresponding to the total electronic charge density. The total electronic charge distribution is then nearly completely spherical, as one could have guessed from Fig. 1. More precisely, we find a proportion t_e of 60 per cent, i.e. a spherical distribution.

The magnetic form factor of a dilute ferromagnetic alloy **Pd** Fe with 1·3 per cent of Fe has been measured by Philips[29]. He has emphasized the aspherical shape of the unpaired electronic distribution, which can be assumed to have a proportion t_m of 80 per cent of T_{2g} symmetry.

The 4*d* electrons play in **Pd** a role, somewhat similar to the 3*d* electrons in Ni. Neglecting the distortion of the band due to the addition of a small amount of Fe, one would expect in our model a similar behaviour to that of Ni, with a strong T_{2g} character for the unpaired electrons.* One also might expect a strong T_{2g} character for the unpaired electrons in some other possible *FCC* ferromagnetic alloys, such as **Pd** Ni.

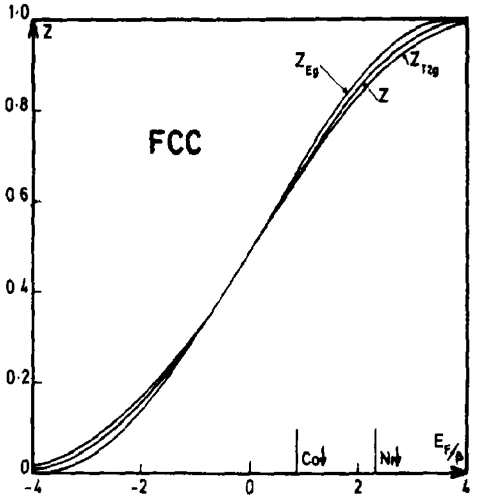

Fig. 1. *FCC* structure: number of electrons $Z(E_g)$, $Z(T_{2g})$ and Z for the sub-bands and the total band, the density of states being normalized to unity.

Weiss[30] has interpreted the data of Menziger and Paoletti[31] on the *FCC* phase of Cobalt by assuming a proportion of the unpaired electrons in the T_{2g} orbitals of 44 ± 4 per cent. Thus, there would be an excess of E_g orbitals which is contrary to the situation in the case of Ni.

Here, assuming 1·7 holes in the spin down band $n\downarrow(E)$, we find a relative occupation of 61 per cent for the T_{2g} orbitals. It could be seen that the T_{2g} orbitals in our computation are slightly in excess, but as one can easily see from Fig. 1, a very small relative displacement would reverse this effect. Thus, if we take into account a small difference between the shifts of the sub-bands, we find now a slight over occupation for the E_g orbitals.

In an *FCC* structure, the electronic states have then a predominant T_{2g} character at the top of the band. But at lower energies, this reverses and the E_g character predominates.

(b) CPH *structure*. We have seen (cf.

---

*We have neglected the spin orbit coupling which would reduce the T_{2g} and E_g symmetries.

Section 2.1) that the density of states will probably have a similar shape in an *FCC* structure and in a *CPH* one. The partial densities of states $n_\Gamma(E)$ can be related to each other using (11) and (13). Thus from the results for the *FCC* structure, one can guess that the A_{1g} will be predominant at the top of the band.

For the *CPH* phase of Co, our model leads to a very small departure from the spherical symmetry for the unpaired electrons, as we find the following occupation for the orbitals:

$$A_{1g}\text{: } 20{\cdot}3\% \quad E_{1g}\text{: } 39{\cdot}5\% \quad E_{2g}\text{: } 40{\cdot}2\%.$$

This agrees with the experimental results of Moon[32] who obtained a nearly spherical charge distribution with a deviation of the order of 0·2 per cent excess of E_{1g} orbital. This result has also been obtained theoretically by Hodges and Ehrenreich[27] using an interpolated band picture.

(c) *BCC structure*. The Figs. 2(a) and 2(b) represent the curves $Z(E)$ and $Z_\Gamma(E)$ for the respective cases $\bar{\alpha} = 0$; and $\alpha = -\beta/2$, $\alpha(T_{2g}) - \alpha(E_g) = -\beta/2$. In that last case, we have taken two different shifts for the two sub-bands T_{2g} and E_g (cf. Appendix). The Fig. 2 suggests that there will be some noticeable deviation from a spherical distribution, although the *BCC* transition metals have their Fermi levels near to the middle of the band.

For example, we have listed in the Table 6 the results of various experiments and computations done on Fe. t_m and t_c denote the relative proportion of T_{2g} symmetry for the unpaired spin density and for the total charge density, respectively. In our computation, we assumed 4·6d electrons with spin up, and 2·4d electrons with spin down, in accordance with the magnetization data and with a $3d^7$ configuration.

We have also listed in the Table 7, the relative proportion t_c of T_{2g} symmetry for two different occupations of the d band, which correspond respectively to the cases of V, Nb, Ta ($Z = 3{\cdot}4$) and Cr, Mo, W ($Z = 4{\cdot}6$). These metals have a band which is not completely half filled and therefore the electrons have a predominant T_{2g} symmetry. The situation would be reversed for metals with more than half their band filled. Unfortunately, there are very few experimental results on these metals. De Marco and Weiss[35] have interpreted their experimental results on *V* in

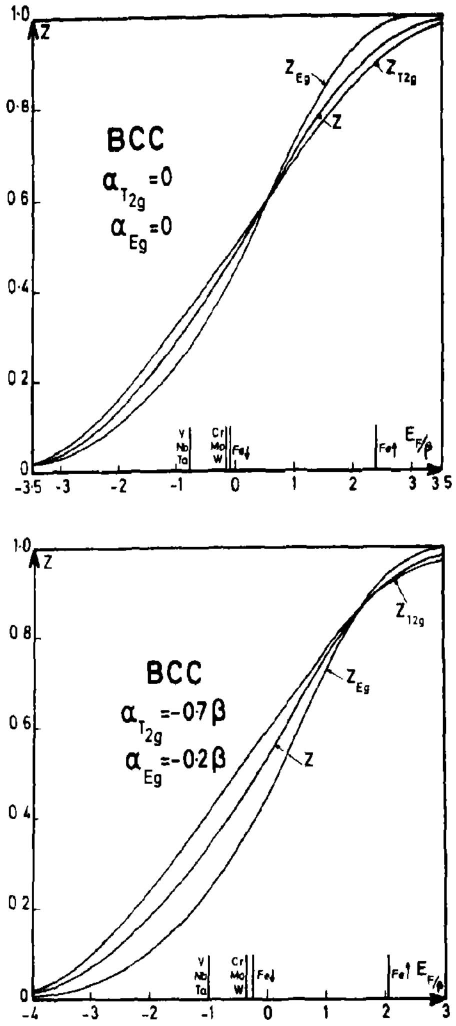

Fig 2 *BCC* structure· number of electrons $Z(E_g)$, $Z(T_{2g})$ and Z for the sub-bands and the total band, the density of states being normalized to unity. (2a) with $\bar{\alpha} = 0$; (2b) with $\bar{\alpha} = -\beta/2$; $\alpha(T_{2g}) - \alpha(E_g) = -\beta/2$.

Table 6. t_m *and* t_e *values for iron* (%)

t_m	t_e	Method	Reference
50	—	Polarized neutrons	25, 26
47	70	Polarized neutrons and X rays	34
46	62	Band structure computation	28
48	62	Band structure computation	33
47	57	Band structure computation	34
49	59	Band structure computation	19
53	60	This work	
50	62	This work	

Table 7. t_e *values for* BCC *metals* (%)

Z	$t_e(\bar{\alpha}-0)$	$t_e\left[\bar{\alpha}=-\frac{\beta}{2}, \alpha(T_{2g})-\alpha(E_g)=-\frac{\beta}{2}\right]$
3·4	68·0	72·5
4·6	63·5	69·0

assuming a relative rate t_e of 81 per cent, which seems rather too large.

Cr is a special case as it is antiferromagnetic. The unpaired electrons will then correspond to electron states in the band structure which are in the neighbourhood of the gap. Therefore they represent only a small fraction of the electronic states, lying near the Fermi level. Looking then at the results of a band structure computation done by Asano and Yamashita [36], we can expect that the electrons perturbed by the formation of new boundaries zones will be of predominant T_{2g} symmetry. This may explain the experimental results of Moon and Koehler[37] who gave an occupation t_m of 79 per cent.

3. CONCLUSION

In a tight binding scheme, we have described the *d* band of transition metals using an expansion of the density of states in its moments. The moments can be expressed as a function of the two center overlap integrals. Therefore they depend only on simple parameters, such as the filling of the *d* band, and the crystalline structure.

From the numerical results of the first moments, we have been able to obtain some qualitative features of the total density of states and of the partial densities of states of the sub-bands due to the crystal field splitting.

We have done a systematic study of the electronic *d* asphericity of the transition metals, using results obtained from the first moments. Indeed, if a precise knowledge of the density of states requires a large number of moments, a semiquantitative description of the electronic charge distribution can be obtained very easily using the first moments. The results are in reasonable agreement with the experiments. In particular we find that: for an *FCC* structure, the peak at the top of the band has a strong T_{2g} character; for *CPH* metals, the distribution of electrons is nearly spherical; for a *BCC* structure, the antibonding part of the density of states has a slightly predominant E_g character while the bonding part has a slightly predominant T_{2g} character.

Acknowledgements—We would like to thank Pr J. Friedel for stimulating discussions. One of us (F.C.) would like also to thank Drs G. Chester and N. Ashcroft for their hospitality at Cornell University, where a part of this work has been done.

REFERENCES

1. See for example CALLAWAY J., *Energy band theory*. Academic Press, New York (1964).
2. MUELLER F. M., *Phys. Rev* **153**, 659 (1967). HODGES L., EHRENREICH H. and LANG N. D., *Phys. Rev* **152**, 505 (1966). PHILLIPS J. C., *Adv. Phys.* **17**, 179 (1968). HUBBARD J., *Proc. R. Soc.* **92**, 921 (1967). EHRENREICH H. and HODGES L., *Method in Computational Physics*, Vol. 8, p. 149. Academic Press, New York (1968).
3. CYROT-LACKMANN F., *Adv. Phys.* **16**, 393 (1967); Thèse de Doctorat d'Etat, Orsay (1968).

of little consequence for the properties under study of the glasses investigated were not altered by this cooling procedure.

The NMR spectra of the samples were recorded using a Varian model V-4200B wide line NMR spectrometer operating at a modulation frequency of 400 c/s. The magnet employed was a 9 in. Varian Associated electromagnet with Fieldial control. All spectra were taken at room temperature with a scan rate of 2 G/min. The following discussion is concerned primarily with the ^{51}V NMR results since they yield the most useful information concerning the glass structure.

3. NMR RESULTS AND ANALYSIS

The derivative curve shown in Fig. 1 is typical of the NMR spectra of the ^{51}V nucleus for mole percentages of V_2O_5 from 60–80 per cent. (All references to percentages of the glass in this paper refer to mole per cent of V_2O_5 content in the glass.) This curve represents the derivative of a very large asymmetric absorption curve caused by a large amount of broadening due to either quadrupole or magnetic interactions or both. Similar curves were obtained at resonant frequencies from 8 to 16 MHz. Below 8 MHz the aluminum NMR line from the Varian probe is superimposed on the vanadium line making quantitative information very difficult to obtain.

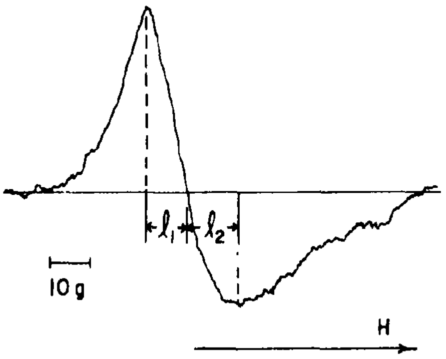

Fig. 1. First derivative of the ^{51}V resonance of 80 mole % V_2O_5 phosphate glass at 12 MHz.

The phosphorous isotope ^{31}P is 100 per cent abundant and has a nuclear spin of $I = \frac{1}{2}$, consequently having no quadrupole moment. Figure 2 shows a typical phosphorous spectrum of 70 mole per cent glass at 16 MHz.

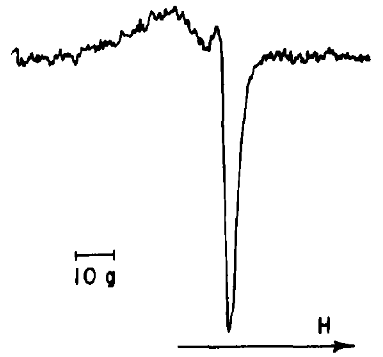

Fig. 2. First derivative of the ^{31}P resonance of 70 mole % V_2O_5 phosphate glass at 16 MHz.

The low field side of the spectrum is broadened out. This broadening of the phosphorous line can be accounted for if there exists a distribution of local magnetic fields. The small peak on the low field side of the spectra in Fig. 2 is presumably due to those phosphorous nuclei which are not appreciably affected by the magnetic interaction taking place in the glass. It would be expected that only those phosphorous nuclei which are near neighbors to a vanadium atom would contribute to the line broadening.

The shape of the ^{51}V NMR line observed for an amorphous or polycrystalline sample depends upon the magnitude and symmetry properties and distribution of the electric field gradient at the vanadium site. If the electric field gradient is small, satellite transitions (e.g. $m = \pm\frac{3}{2} \leftrightarrow \pm\frac{1}{2}$, $m = \pm\frac{5}{2} \leftrightarrow \pm\frac{3}{2}$ and $m = \pm\frac{7}{2} \leftrightarrow \frac{5}{2}$) distinct from the central transition ($m = \frac{1}{2} \leftrightarrow -\frac{1}{2}$) would be expected. For large electric field gradients the central transition becomes asymmetric and will show structure [6, 9] if the broadening is small enough. In the case of glassey materials, the satellite lines are usually broadened to such a degree that they are not observable [12, 13]. In the present study measurement of the intensity of the ^{51}V lines compared to the intensity of the V_2O_5 NMR spectrum indicates that only the central $+\frac{1}{2} \leftrightarrow -\frac{1}{2}$ transitions are contained in the observed resonance. In addition, no distinct satellite lines were observed in the glasses.

The spectra obtained were analyzed employing the relationship previously developed[10, 11] and given in equation (1) for the measure of the asymmetry of the line $\Delta l = l_2 - l_1$ (see Fig. 1) of the central transition due to quadrupole and anisotropic magnetic shift interactions in a polycrystalline sample.

$$\Delta l = (\nu_Q^2/30\nu)[I(I+1)-\tfrac{3}{4}] + 12(\nu K_{\parallel})^3/35\sigma^2 \tag{1}$$

where $\nu_Q = 3e^2qQ/2I(2I-1)h$. $K_{\parallel}$ is the third component of the diagonal anisotropic magnetic shift tensor, σ is the peak-to-peak width of the first derivative of the resonance line and eq is the largest component in the principal axis system of the electric field gradient tensor at the nucleus. For simplicity, axial symmetry has been assumed for both the field gradient and magnetic shift tensor.

The procedure employed is to plot Δl against frequency and by curve fitting to extract the values of the quadrupole coupling constant $C_Q = e^2qQ/h$, and anisotropic magnetic shift $K_{\parallel}$. It would appear from equation (1) that the data would fit a curve of the form $\Delta l = a/\nu + b\nu^3$. However, the experimental data as illustrated in Fig. 3 fit a relationship of the form $\Delta l = a/\nu + b\nu$. This can be explained by a broadening of the resonance line due to a distribution of values of coupling constant C_Q, asymmetry parameter η and $K_{\parallel}$ centered about some average C_Q and $K_{\parallel}$. Such broadening has been believed to alter the resonance line shape in borate glasses [13]. It is extremely difficult to include variations of C_Q, $K_{\parallel}$ and η in a theoretical discussion of line shapes so that the usual procedure is to approximate the effects of such variations on an analysis where single values of coupling constant and shift are assumed. The line broadening can be expressed by

$$\sigma^2 = \sigma_d^2 + \sigma_Q^2 + \sigma_m^2 \tag{2}$$

where σ_d is the dipolar contribution, σ_Q the quadrupolar contribution including variations in the asymmetry parameter, η and σ_m the

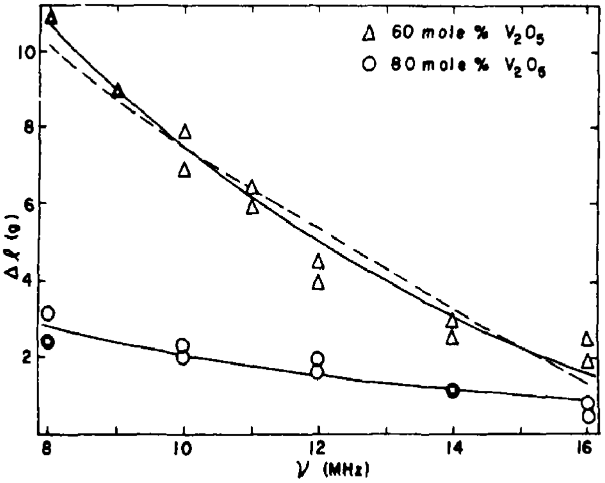

Fig. 3. The line asymmetry parameter Δl for the ^{51}V resonance as a function of frequency ν for 60 and 80 mole % V_2O_5 phosphate glass The dashed curve is a least squares fit of $\Delta l = a/\nu + b\nu^3$. The solid lines are least square fits of $\Delta l = a/\nu + b\nu$.

magnetic shift contribution to the line width. The quantity σ_Q will vary inversely as the resonant frequency, σ_m will be proportional to the frequency and σ_d is assumed to be constant over the range of frequencies employed in these investigations. For large values of σ_m, that is, at high frequencies, σ_m will dominate and $\sigma \approx \sigma_m + \sigma_d^2/2\sigma_m$ for small values of σ_d compared to σ_m. A rough estimate[9] for σ_d due to ^{51}V nuclei in VO$_2$ is 5 g. At 16 MHz the line width of 80 per cent vanadium phosphate glass is 24 g.

Since $\sigma_m = R\nu$ where R is a constant, the contribution from the magnetic interaction to the line asymmetry Δl becomes $12K_{\parallel}^3\nu/35R^2$ which results in an expression $\Delta l = a/\nu + b\nu$ in agreement with the experimental data. A check of the line width data shows agreement with this expression for frequencies above 12 MHz. At lower frequencies the line width will be dominated by σ_Q and σ_d. However, at frequencies below about 12 MHz the quadrupole broadening is so dominant that Δl will assume a $1/\nu$ dependence.

Figures 3 and 4 show experimental values of Δl for different percentages of vanadium phosphate glass plotted against frequency. More than one sample of each composition was examined and in many cases two data points lie on top of one another. This is indicated by placing a circle within the other data point. The method of least squares has been used to fit the curve $\Delta l = a/\nu + b\nu$ to the data. Table 1 lists the values of a, b and C_Q with their standard deviations determined by this analysis. Figures 5 and 6 show respec-

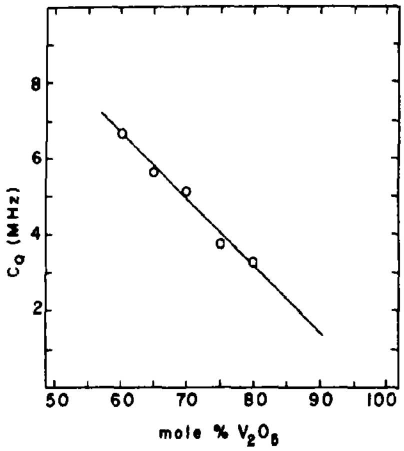

Fig. 5. Quadrupole coupling constant C_Q for ^{51}V as a function of V$_2$O$_5$ content in vanadium phosphate glass

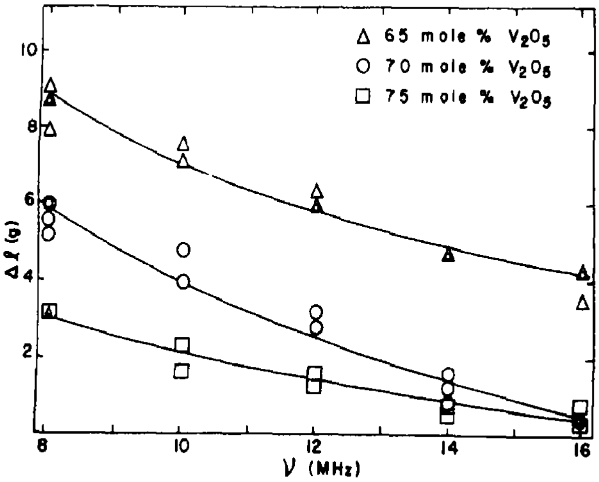

Fig. 4. The line asymmetry parameter Δl for the ^{51}V resonance as a function of frequency ν for 65, 70 and 75 mole % V$_2$O$_5$ phosphate glass. The solid lines are least square fits of $\Delta l = a/\nu + b\nu$.

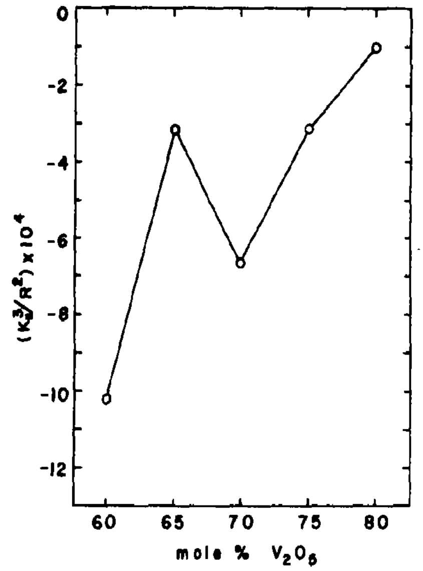

Fig 6. Anisotropic shift of ^{51}V resonance as a function of V_2O_5 content in vanadium phosphate glass.

tively the quadrupole coupling constant C_Q and $K_{\parallel}^3/R^2$ plotted against glass composition.

Figure 7 shows a plot of the isotropic magnetic shift K. These values are also included in Table 1. The values of K were measured relative to that of the aluminum line from the Varian probe at 16 Mc/sec, but were converted to that of an unshifted vanadium line using the Knight shift of aluminum of 0·162 per cent. Hence this procedure of indirect measurement will not affect the relative accuracy of these values of K.

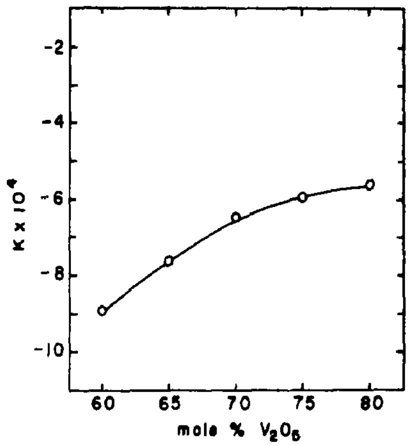

Fig. 7 Isotropic shift of ^{51}V resonance as a function of V_2O_5 content in vanadium phosphate glass.

4. QUADRUPOLE COUPLING CONSTANT

It is apparent from Fig. 5 that for glass between 60 and 80 per cent V_2O_5 the quadrupole coupling constant decreases linearly within experimental accuracy. This dependence can be employed to estimate the valence state of the V ions in the glass. The results of

Table 1. *NMR Parameters for* V *ions in* V_2O_5–P_2O_5 *glasses*

V_2O_5 (%)	a (g(MHz))	b (g/(MHz))	C_Q (MHz)	$(K_{\parallel}^3/R^2)\times 10^4$	$K\times 10^4$
60	104·66	−0·3142	6·77	−10·27	−8·94
65	71·00	−0·0137	5 59	−3·195	−7·70
70	59·70	−0·2046	5·15	−6·709	−6·47
75	30·51	−0·0966	3·66	−3·150	−5·95
80	25·13	−0·0478	3·32	−1·564	−5·59

Standard deviations

VO (%)	δa (g(MHz))	δb (g/(MHz))	δC_Q (MHz)	$\delta(K_{\parallel}^3/R^2)\times 10^4$
60	1·03	0·0080	0·033	0·262
65	0·86	0·0067	0·034	0·219
70	0·87	0·0066	0·037	0·217
75	1·22	0·0090	0·073	0·262
80	1·05	0·0083	0·069	0·242

both Munakata[1] and Rao[3] using chemical and X-ray analysis indicate that the lowest valency state of vanadium in vanadium phosphate glasses prepared in air is V^{4+}. Since the vanadium in V_2O_5 is mostly in the V^{5+} state, vanadium must exist as both V^{4+} and V^{5+} ions in vanadium phosphate glasses. Various authors[4, 14, 15] using EPR have found that the V^{4+} ion exists as the vanadyl ion VO^{2+} in borosilicate, sodium borate and vanadium phosphate glasses. The VO^{2+} ions are six co-ordinated with one of the bonds being covalent, stronger and shorter than the others which are more ionic in character. This gives the V^{4+} ion an approximate axial symmetry along the covalent bond.

The quadrupole coupling constant has been measured[16] in polycrystalline VO_2 where vanadium exists in the V^{4+} state. It has been found that $\nu_Q = 0{\cdot}5$ MHz which is equivalent to a coupling constant $C_Q = 14\nu_Q = 7$ MHz for V^{4+} in VO_2. Garnastansky and Stager[17] have measured C_Q in single crystals of V_2O_5 where vanadium is in the V^{5+} state, and have determined the value of $C_Q = 805$ KHz. Previous authors[18, 19] using polycrystalline samples of V_2O_5 have reported a coupling constant for the V^{5+} ion of 752 and 780 kHz. The coupling constant determined from the single crystal will be taken as the more reliable.

If a straight line is fitted to the data of Fig. 5 by the method of least squares, then

$$C_Q = 17{\cdot}26 - 17{\cdot}66P \qquad (3)$$

where C_Q is in MHz and P is the mole per cent of V_2O_5 in the glass divided by 100. The V^{51} NMR spectrum in the glass is the resultant of the various spectra of V^{4+} and V^{5+} ions present in the glass. The quadrupole coupling constant C_Q obtained then must be the average C_Q. The fact that the NMR spectra of the V^{4+} and V^{5+} ions are not individually observable is probably due to the large line width caused by diverse distortions of the co-ordination symmetry which manifests itself as σ_Q and σ_m mentioned earlier. These distortions are inherent in the amorphous nature of glass [12, 13].

If C_Q is an average, then it follows that

$$C_Q = (n_4C_4 + n_5C_5)/n_v, \qquad (4)$$

$$n_v = n_4 + n_5 \qquad (5)$$

where n_4 and n_5 are the density of V^{4+} and V^{5+} ions respectively, C_4 and C_5 are the quadrupole coupling constants for V^{4+} and V^{5+}, and n_v is the density of vanadium atoms present in the sample. Equation (4) appears to be a reasonable first approximation to a rather complex problem which requires the addition of electric field gradient tensors whose components are not known. Substituting for C_Q from equation (3) and the values of $C_4 = 7$ MHz and $C_5 = 0{\cdot}805$ MHz, equations (4) and (5) can be reduced to

$$n_4 = (2{\cdot}66 - 2{\cdot}84P)n_v \qquad (6)$$

$$n_5 = (-1{\cdot}66 + 2{\cdot}84P)n_v \qquad (7)$$

for the concentration of V^{4+} and V^{5+} ions. It has been assumed that the coupling constants for vanadium in VO_2 and V_2O_5 are good representative values for the coupling constants for the V^{4+} and V^{5+} ions in the glass. From equations (6) and (7) it is apparent that n_4 and n_5 are zero at $P = 0{\cdot}936$ and $P = 0{\cdot}585$ respectively. Only between the ranges of about 60–90% V_2O_5 can the empirical relations expressed by equations (6) and (7) be expected to be true, that is only where the coupling constant C_Q depends linearly on vanadium concentration (P) and only if a glass can be formed at the percentage.

5. MAGNETIC SHIFT

The negative values for K and $K_p{}^3/R^2$ in Table 1 would indicate that core polarization of the vanadium atom is taking place. This core polarization is most likely caused by an electrostatic coupling of a $3d$ electron to the inner shell electrons such as the $3s$ electrons.

The V^{4+} ion of VO^{2+} in $VO(H_2O)_5{}^{2+}$ has an unpaired electron placed in a practically nonbonding $3d_{xy}$ vanadium orbital[20]. Hochstrasser[4] believes from EPR measurements this to be somewhat the case for V^{4+} ions in borosilicate glass. Calculations[15] by Hecht and Johnson using EPR confirm this view for V^{4+} in sodium borate glass. From the shifts reported[17] for V^{5+} in V_2O_5 single crystals where there are no unpaired $3d$ electrons the isotropic shift is a negative $K = -0{\cdot}567 \times 10^{-4}$.

The increasing or less negative values for K and $K_{\parallel}^{3}/R^{2}$ with increasing vanadium content then indicate that the concentration of V^{4+} ions is decreasing while that of the V^{5+} ions is increasing. This is of course what was found from the quadrupole coupling constant calculations and merely supports this view. This conclusion is also supported by Nagiev[4] who found that the number of V^{4+} ions increased as the concentration of P_2O_5 increased in vanadium phosphate glasses. Measurements of the magnetic susceptibility[3] showed that it decreased as the percentage of V_2O_5 increased. This evidence further supports our data since the unpaired d electron of the V^{4+} ion is responsible for the magnetic susceptibility.

The low value of $K_{\parallel}^{3}/R^{2}$ for 65 per cent is apparently real since three different glasses of this concentration gave a comparative value. There appears to be no obvious explanation for this low value at 65 per cent.

6. RESISTIVITY

Semiconducting glasses are those amorphous materials which have a volume resistivity less than $10^{9}\,\Omega$-cm at 25°C and have a negative temperature coefficient of resistivity. Vanadium phosphate glasses with or without other metal oxides are electronic semiconductors. Their resistivity is time independent[21] as opposed to ionic conductors. Through the work of Munakata[1] and Rao[3] it is known that the resistivity is strongly dependent on the concentration of V^{4+} and V^{5+} ions in the glass as well as the total vanadium content. Both authors have shown that the electrical conductivity is decreased with an increasing concentration of the lower valence states of vanadium, namely V^{4+}. Denton *et al.*[21] were the first to suggest that these glasses are *n* type semiconductors. The fact that there is no *p* type conduction has been confirmed several times[1, 3, 22, 23].

It has been proposed that the mechanism [24] for conduction in the V_2O_5–P_2O_5 glasses is the transfer of an electron from an ion of lower valence to one of higher valence. Rao [3] has suggested that the basic unit of conduction is that of the VO_6 groups with the vanadium ion in different valence states. These VO_6 groups are linked as chains or sheets, depending on the concentration of vanadium, to provide a path for conduction of the electrons. Rao[3] has measured the activation energy ΔE at 54, 81·5 and 90·5% V_2O_5 content. (Rao's percentages are based on the system V_2O_5–P_4O_{10} so that his percentages must be transformed into the system V_2O_5–P_2O_5 by the equation $P = T/(2-T)$ where P and T are the percentages divided by 100 expressed in the systems using P_2O_5 and P_4O_{10} respectively.) These three values plotted against V_2O_5 content lie on a straight line given by the empirical equation $\Delta E = 0{\cdot}6 - 0{\cdot}4\,P$. It has been determined[3] that the temperature dependence of the resistivity is given approximately by $\rho = \rho_0 \exp(\Delta E/kT)$.

Figure 8 is a graph of $ln\rho$ plotted against the per cent of V_2O_5 at 25°C for vanadium phosphate glasses melted in air for the two cases where ρ_0 is proportional to the ratio n_4/n_5 and proportional to $1/n_5$. The black circles are data points taken from the papers of Rao[3]. (These data have been converted from $\log_{10}$ to natural log base and from the system P_4O_{10} to the system P_2O_5 using the previously given equation.) The rational for choosing ρ_0 proportional to n_4/n_5 and $1/n_5$ is that various authors[1, 3, 4] have suggested that the resistivity is highly dependent on one or another of these quantities.

As can be seen from Fig. 8, there is no rea-

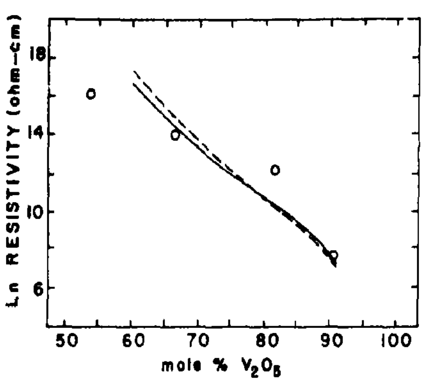

Fig. 8. Ln resistivity plotted against V_2O_5 content. The circles are the data points of Rao[3]. The solid line is $\rho \propto 1/n_5$. The dashed line is $\rho \propto n_4/n_5$.

son to choose either one or the other parameter as being dominant and responsible for electronic conduction in vanadium phosphate glass. Moreover one can say that there must exist some other complex mechanism such as mobility of the conduction electrons which plays a more sensitive role in determining the resistivities of these glasses. Any mechanism will certainly depend on the general concentration of V^{5+} ions since the general trend of the curves in Fig. 8 is in the right direction towards decreasing resistivity with an increasing concentration of V^{5+} ions present in the glass.

7. CONCLUSION

Empirical relations have been found for the concentration of V^{4+} and V^{5+} ions as a function of the mole percent of V_2O_5 between 60 and 90 per cent. At percentages less than 50 per cent, a picture develops of mostly V^{4+} ions, with very few V^{5+} ions, interspersed among the PO_4 chains and groups causing a shortage of conduction electrons which gives the glass its very high resistivity. At around 50 per cent there are enough vanadium atoms among the PO_4 groups that additional vanadium atoms coming into the structure have a very good probability of connecting onto an oxygen already bound to another vanadium instead of a phosphorous, and of starting to form VO_6 groups[3] mainly of V^{5+} character. Electrons are probably made available in this process of VO_6 group formation and the conduction carrier concentration increases. There seems to be no reason at present to attribute this increased conductivity directly either to the density of V^{5+} ions or to the ratio of V^{5+}/V^{4+} ions present but that the general increase of V^{5+} ions for increasing concentrations of V_2O_5 present must affect some other mechanism such as mobility which is mainly responsible for the widely varying values of resistivity which have been reported in the literature. Certainly more experimental work needs to be done on determining unknown quantities such as those mentioned above before any model for conduction can be selected in the vanadium phosphate glass system.

REFERENCES

1. MUNAKATA M., *Solid-St. Electron.* **1**, 159 (1960).
2. LANDSBERGER F. R., BAUGHER J. F., OJA T and BRAY P. J., *Bull. Am. phys. Soc.* **12**, 720 (1967)
3. RAO B. V. J., *J. Am. ceram. Soc.* **49**, 605 (1966) and **48**, 311 (1965)
4. NAGIEV V. M., *Soviet Phys. solid St.* **7**, 2204 (1966).
5. MACKENZIE J. D., *Modern Aspects of the Vitreous State* Vol 3 Butterworths, London (1964).
6. COHEN M. H. and REIF F., *Solid St. Phys.* **5**, 321 (1957)
7. JONES W. H., Jr., GRAHAM T. P. and BARNES R. G., *Phys. Rev.* **132**, 1898 (1963).
8. CASABELLA P. A., *J. chem. Phys.* **40**, 149 (1964).
9. NARITA K., UMEDA J. and KUSUMOTO H., *J. chem. Phys.* **44**, 2710 (1966).
10. FRANCE P. W. and HOOPER H. O. To be published
11. FRANCE P. W., Ph.D. Thesis, Wayne State University (1967)
12. BRAY P. J., LEVENTHAL M. and HOOPER H. O., *Physics Chem. Glasses* **4**, 47 (1963).
13. SILVER A. H. and BRAY P. J., *J. chem. Phys.* **29**, 984 (1958).
14. HOCHSTRASSER G., *Physics Chem. Glasses* **7**, 178 (1966).
15. HECHT H. G. and JOHNSTON T. S., *J. chem. Phys.* **46**, 23 (1967)
16. UMEDA J., KUSUMOTO H., NARITA K. and YAMADA E., *J. chem. Phys.* **42**, 1458 (1965).
17. GORNOSTANSKY S. P. and STAGER C. V., *J. chem. Phys.* **46**, 4959 (1967).
18. RAGLE J. L., *J. chem. Phys.* **35**, 753 (1961).
19. NAGASAWA H., TAKESHITA S. K. and TOMONO Y., *J. phys. Soc. Japan* **19**, 764 (1964).
20. BORCHERTS R. H. and KIKUCHI C. H., *J. chem. Phys.* **40**, 2270 (1964).

21. DENTON E. P., RAWSON H. and STANWORTH J. E., *Nature, Lond.* **173**, 10 (1954).
22. HAMBLEN D. P., WEIDEL R. A., and BLAIR G. E., *J. Am. ceram. Soc.* **46**, 499 (1963).
23. BAYNTON P. L., RAWSON H., and STANWORTH J. E., *J. electrochem. Soc.* **104**, 237 (1957).
24. IOFFE V. A., PATRINA I. B. and POVEROVSHAYA I. S., *Soviet Phys. solid St.* **2**, 609 (1960).

J. Phys. Chem. Solids Pergamon Press 1970. Vol. 31, pp. 1317–1323. Printed in Great Britain.

A NOTE ON THE DETERMINATION OF THE DENSITY OF PHONON EIGENSTATES FROM THE INELASTIC INCOHERENT NEUTRON SCATTERING*

D. T. KEATING
Brookhaven National Laboratory, Upton, N.Y. 11973, U.S.A.

(*Received* 2 *October* 1969; *in revised form* 24 *November* 1969)

Abstract – A method for determining the density of phonon eigenstates of a harmonic crystal from the inelastic incoherent neutron scattering is described. The neutron scattering contains, in addition to the one phonon process, multiphonon processes. This scattering, including multiphonon processes, can always be expressed as a Fourier integral transform of a function of the phonon eigenstates, and if the scattering is measured while keeping the magnitude of the scattering vector constant, the phonon eigenstates can be obtained by appropriate Fourier inversions. The method is illustrated using the phonon eigenstates recently determined for vanadium at 300°K from the measurement of the thermal diffuse X-ray scattering. Assuming that the only effect of temperature is the change in the occupation number of the eigenstates, the influence of temperature on the scattering, and the frequency distribution in the one phonon approximation is discussed. The integrated multiphonon processes are 16·6, 63·5 and 165 per cent of the one phonon process at 300, 1000 and 2000°K.

1. DEVELOPMENT OF METHOD

A METHOD for the direct determination of the density of phonon eigenstates of a harmonic crystal from the measured neutron inelastic incoherent scattering is described. The treatment is valid when the restoring forces are linear in the displacements and the crystal eigenstates are those of harmonic oscillators. The method is described for cubic bravais lattice types of one atomic species. The extension of the method to more complex crystals has not been considered. The method takes advantage of the obvious fact that the Fourier integral time transformation of the multiphonon formulation is the series expansion of the exponential function, whose argument involves the Fourier integral transform of the phonon eigenstates. Thus the scattering, including multiphonon processes, can always be expressed as a Fourier integral transform of a function of the phonon eigenstates, and provided the scattering is measured keeping the magnitude of the scattering vector constant, the phonon eigenstates can be obtained by appropriate Fourier inversions.

As the starting point we write the inelastic incoherent scattering in the multiphonon symmetric formulation following Sjölander [2] and Turchin [3] as

$$\begin{aligned}(b^{-2}d\sigma_{\text{inc}}/d\Omega d\omega-\delta(\omega)) &= (1+\omega/\omega_0)^{1/2}\exp\left[-\frac{m\omega(\chi)}{M\omega(0)}-\omega/\omega(T)\right]\\ &\quad\times\sum_{n=1}^{\infty}(m\omega(\chi)/M)^n G_n(\omega)/n!,\qquad(1)\end{aligned}$$

where b is the incoherent scattering amplitude; $d\sigma_{\text{inc}}/d\Omega d\omega$ is the second order double differential incoherent cross section; ω is the difference between the scattered circular frequency ω' and incident frequency ω_0 of the neutron; m and M are the neutron and atomic masses; and $\chi^2=|\kappa_0|^2+|\kappa|^2-2|\kappa|\,|\kappa_0|\cos 2\theta$, κ_0 and κ being the wavevectors of the incident and scattered neutron, and 2θ being the angle of scattering. The circular frequency associated with the scattering vector, χ, is $\omega(\chi)=\hbar\chi^2/(2m)$, where $\hbar$ is Planck's constant divided by 2π. The circular frequency associated with the absolute temperature T, is $\omega(T)=2kT/\hbar$, where k is Boltzmann's constant. The circular frequency $\omega(0)$ is defined by

---

*Work performed under the auspices of the U.S. Atomic Energy Commission.

$$1/\omega(0)=\int_0^{\omega_m}\frac{f(\omega)}{\omega}\coth(\omega/\omega(T))\,\mathrm{d}\omega, \qquad (2)$$

$f(\omega)\mathrm{d}\omega$ is the number of eigenstates between ω and $\omega+\mathrm{d}\omega$ divided by the total number of eigenstates. The maximum vibrational frequency of the crystal is ω_m. The usual Debye Waller factor is then $m\omega(\chi)/(M\omega(0))$. The quantity $G_n(\omega)$ is defined by

$$G_n(\omega)=\int_{-\infty}^{+\infty}G_1(\omega-\omega'')G_{n-1}(\omega'')\,\mathrm{d}\omega'', \qquad (3)$$

and

$$G_1(\omega)=\frac{f(|\omega|)}{2\omega\sinh(\omega/\omega(T))}. \qquad (4)$$

These G's differ from Sjölander's[2] only by his factor $\gamma(0)$ or $1/\omega(0)$. The delta function $\delta(\omega)$ in equation (1) eliminates the elastic peak in the scattering.

The function $G_1(\omega)$ is an even function and we define its Fourier integral cosine transforms as

$$1/\omega(t)=2\int_0\frac{f(\omega)\cos\omega t}{2\omega\sinh(\omega/\omega(T))}\,\mathrm{d}\omega. \qquad (5)$$

The Fourier transform of the n multiple Faltung−integral[4] for $G_n(\omega)$ is then $\omega^{-n}(t)$. The transform of the nth term in the sum of equation (1) is then $(m\omega(\chi)/(M\omega(t)))^n/n!$. Recognizing these terms as the terms in the expansion of $\exp(m\omega(\chi)/(M\omega(t)))$, and using the fact that formally the transform of a sum is the sum of the transforms of each term, we write for equation (1)

$$(b^{-2}\mathrm{d}\sigma_{\mathrm{inc}}/\mathrm{d}\Omega\mathrm{d}\omega-\delta(\omega))$$

$$=\pi^{-1}(1+\omega/\omega_0)^{1/2}\exp\left[-\frac{m\omega(\chi)}{M\omega(0)}-\omega/\omega(T)\right]$$

$$\times\int_0^\infty\left[\exp\frac{m\omega(\chi)}{M\omega(t)}-1\right]\cos\omega t\,\mathrm{d}t. \qquad (6)$$

Equation (6) expresses the double differential cross section for a particular frequency change and scattering angle as a Fourier integral cosine transform. Given $f(\omega)$ the scattering can be evaluated readily using equations (5) and (6).

The integrand in equation (6) can be solved for by inversion of the frequency dependent factors if $\omega(\chi)$ is invarient with frequency within the range for which the double differential cross-section is non vanishing. $\omega(\chi)$ can be kept constant if the scattering angle is varied with ω according to equation (7).

$$\cos 2\theta=[(\omega-\omega(\chi))/(2\omega_0)+1]/(1+\omega/\omega_0)^{1/2}. \qquad (7)$$

The angle for elastic scattering is given by $\cos 2\theta_{\mathrm{elastic}}=1-\omega(\chi)/(2\omega_0)$. Equation (7) is plotted in Fig. 1 for various choices of $\omega(\chi)/\omega_0$ between $2-\sqrt{3}$ and 4·0. The choices correspond to elastic scattering angles of 30, 60, 90, 120 and 180 deg. For example with $\omega(\chi)/(\omega_0=4\cdot0$ the change in circular frequency upon scattering can range from zero to eight times the incident frequency. By proper choice of $\omega(\chi)$ and ω_0 a range in ω can be selected within which the scattering essentially vanishes, and for each value of ω in the range there is an appropriate detector angle determined by equation (7).

Denoting the Fourier integral cosine transform of the frequency dependent factor in equation (6) as

$$T(t)=\exp\frac{m\omega(\chi)}{M\omega(0)}\int_0^\infty(b^{-2}\mathrm{d}\sigma_{\mathrm{inc}}/\mathrm{d}\Omega\mathrm{d}\omega-\delta(\omega))$$

$$\times(1+\omega/\omega_0)^{-1/2}\exp(\omega/\omega(T))\cos\omega t\,\mathrm{d}\omega, \qquad (8)$$

the distributions of eigenstates is found by Fourier inversion, or

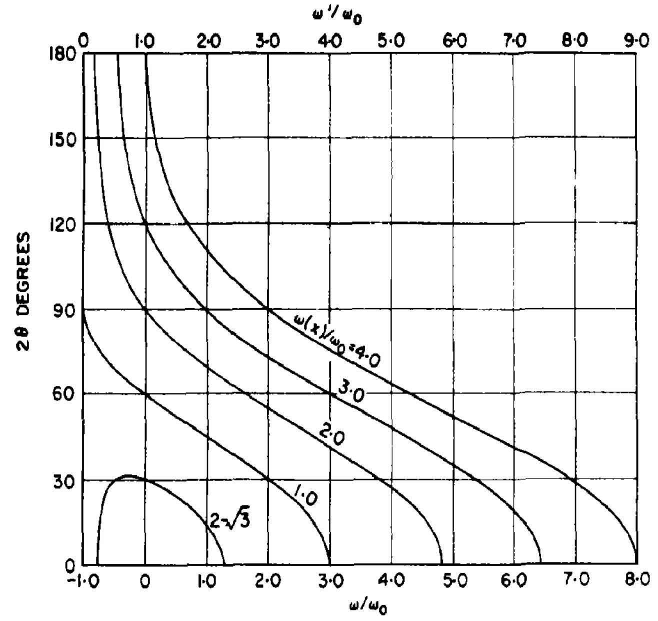

Fig. 1. Loci of detector angles, 2θ, vs. ω'/ω_0 (top) and ω/ω_0 (bottom) which maintain $\omega(\chi)$ constant. The choices of $\omega(\chi)/\omega_0$ give elastic scattering at 30, 60, 90, 120 and 180 deg.

$$f(\omega)=\frac{M\omega}{\pi m\omega(\chi)}\sinh\left(\omega/\omega(T)\right)\times\int_0^\infty \ln(T(t)+1)\cos\omega t\,\mathrm{d}t. \qquad (9)$$

Equation (9) allows the direct determination of the phonon eigenstates from the scattering.

Consider that the scattering has been measured with $\omega(\chi)$ fixed according to equation (7). If one were to assume that the linear term in the expansion of the exponential in equation (6) is adequate, (one phonon approximation) the frequency distribution, $f_M(\omega)$, derived from the scattering is

$$f_M(\omega)=\frac{M\omega}{m\omega(\chi)}\sinh\left(\omega/\omega(T)\right)(1+\omega/\omega_0)^{-1/2}\times\exp\left(\frac{m\omega(\chi)}{M\omega(0)}+\omega/\omega(T)\right)\times\left(b^{-2}\mathrm{d}\sigma_{\mathrm{inc}}/\mathrm{d}\Omega\mathrm{d}\omega-\delta(\omega)\right). \qquad (10)$$

The frequency $f_M(\omega)$ contains all the higher order phonon processes, and $f_M(\omega)-f(\omega)$ integrated over ω gives a numerical estimate of the multiphonon contribution in the one phonon approximation, equation (10).

2. DISCUSSION

To illustrate the method consider the density of phonon eigenstates of vanadium pictured in Fig. 2. Colella and Batterman[1] computed this distribution from seven neighbor atomic force constants derived from thermal diffuse scattering of X-rays at 300°K. The frequency is in units of 10^{12} rad. sec^{-1}, and the distribution is in reciprocal units. The distribution has a well defined maximum frequency of $47{\cdot}8\times10^{12}$ rad. sec^{-1}. Assuming that the only influence of temperature is the change in the mean occupation number of the phonon states, equation (6) was used to calculate the scattering from vanadium at 300, 1000 and 2000°K in Fig. 3. The values $\omega_0=25{\cdot}0$ and $\omega(\chi)=75{\cdot}0$ in units of 10^{12} rad. sec^{-1} were chosen corres-

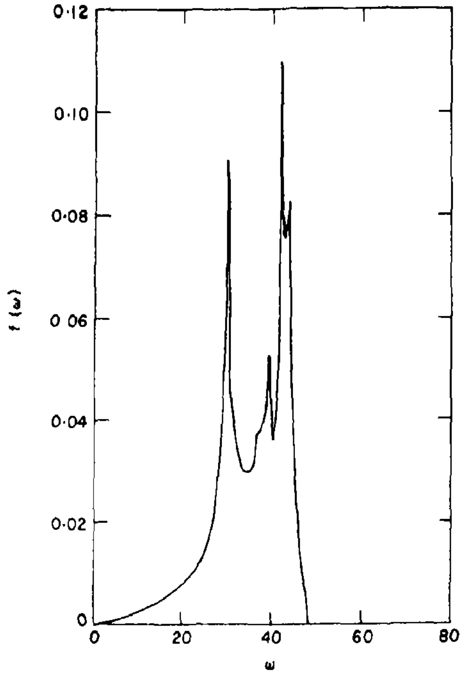

Fig. 2. The distribution, $f(\omega)$, of phonon eigenstates in vanadium. The abscissa is in units of 10^{12} rad. sec^{-1}, and the ordinate in reciprocal units.

ponding to the locus $\omega(\chi)/\omega_0 = 3{\cdot}0$ in Fig. 1. These choices correspond to an incident neutron energy of 0·0165 eV or a wavelength of 2·24 Å and a scattering vector of 4·86 Å^{-1}. In Fig. 3 the ordinate is in units of $(10^{12}$ sterad. rad. sec$^{-1})^{-1}$, and the changes in scale should be noted. The high frequency tails extending beyond the maximum crystal frequency are due to the higher order phonon processes. These tails increase in magnitude and extent as the temperature is raised. When equations (8) and (9) are used the frequency distribution, $f(\omega)$, in Fig. 2 is recovered. If one were to treat these scattering data in the one phonon approximation, equation (10), then the phonon distribution, $f_M(\omega)$, of Fig. 4 is found. The correct frequency distribution is readily observable, but the contributions of the higher phonon processes are appreciable and contain structure. The multiphonon contributions in $f_M(\omega)$ are 16·6, 63·5 and 165 per cent of the correct distribution at 300, 1000 and 2000°K respectively.

While the method offers attractive features, present technology presents serious obstacles to the direct recovery of $f(\omega)$ by application of equations (8) and (9). The incoherent scattering in Fig. 3 is extremely small, resulting in serious problems of statistical accuracy and resolution. Recently Page[5] collected scattering data at some 23 scattering angles using time of flight techniques, but was forced to combine data for groups of detector angles to improve his statistics. Page was careful to make allowance for multiphonon contributions, but was still left with a high energy tail, which could not be properly accounted for by any single one of the four possible sources he considered. He concluded, 'that no single process can account for all of the tail; if the tail is an experimental effect it must be an unusual aggregate of several small factors'. Frequency distributions calculated from dispersion relations (obtained either with X-rays or neutrons) assume that the eigenstates of the crystal are those of harmonic oscillators and do not predict a high energy tail. It would be interesting to design an experiment to take full advantage of this exact method of correcting for multiphonon effects. Failure of such an experiment to remove the high energy tail might lead to a more serious scrutiny of the applicability of the harmonic approximation. Such an experiment is difficult, since the neutron energies used in this example require chopper speeds near the mechanical limit of present choppers. Electronically chopped beams employing magnetic monochromators may increase the useful range of time of flight techniques[6]. It should be noted that the wavelengths implied by this example are quite suitable for using crystal monochromators such as pyrolytic graphite[7] combined with velocity selectors to eliminate harmonics passed by the monochromators. In any case, equation (6) is useful in calculating the exact scattering including all multiphonon processes.

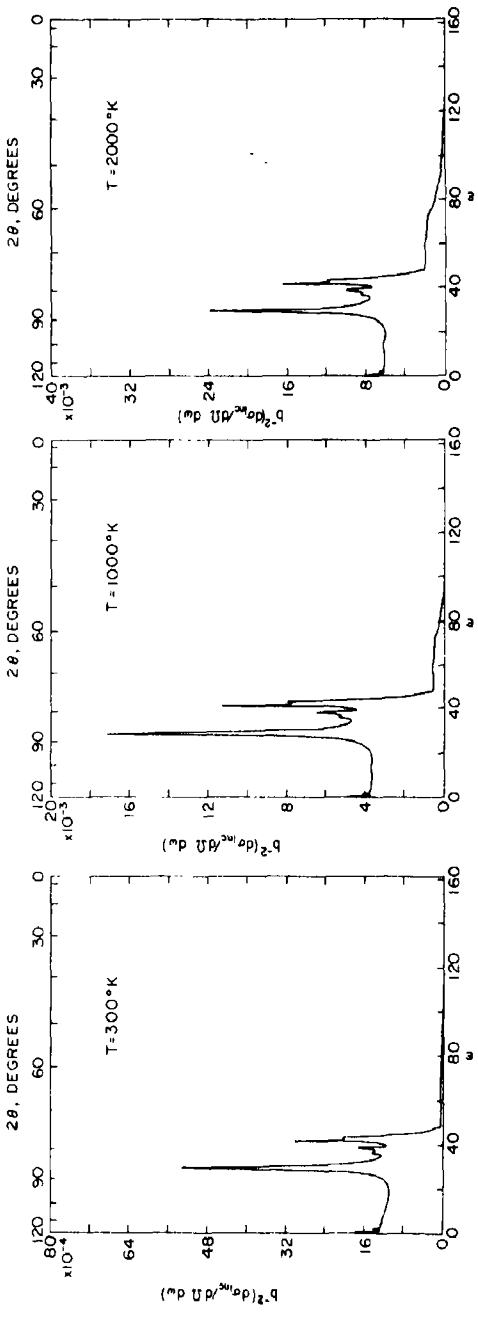

Fig. 3. The scattering predicted by equation (6) for vanadium at 300, 1000 and 2000°K. The abscissa is in units of 10^{12} rad. sec^{-1}, and the ordinate in units of $(10^{12}$ steradians radians sec$^{-1})^{-1}$.

J. Phys. Chem. Solids Pergamon Press 1970. Vol. 31, pp. 1325–1343. Printed in Great Britain.

ELECTRONIC STRUCTURE OF β'-NiAl

Y. YAMAGUCHI*, T. AOKI and J. O. BRITTAIN
Department of Materials Science, Northwestern University, Evanston, Ill 62201, U.S A.

(*Received* 25 *July* 1969, *in revised form* 14 *November* 1969)

Abstract – The electrical resistivity, Hall effect, and magnetoresistance of β'-phase NiAl ($45 \sim 60$ at% Ni, CsCl-type structure) have been measured on about ten specimens of different compositions. A resistance minimum and negative magnetoresistance were found in these materials. These are the first extensive observations of such phenomena in the not-dilute, and not-semiconducting intermetallic compounds. A qualitative discussion for the influence of the defect structure on the electrical resistivity, resistance minimum, negative magnetoresistance, and the optical properties is developed.

1. INTRODUCTION

THE INTERMETALLIC compound NiAl has a β'-phase ($45 \sim 60$ at% Ni) B2 structure (isotypic with CsCl) and is a $\frac{3}{2}$ electron compound. Bradley and Taylor[1] pointed out the peculiar behavior of the lattice parameter and the density vs. the composition from which the defect structure was deduced; that is, vacancies at Ni sites in the composition range of $45 \sim 49$ at% Ni and substitutional Ni atoms at Al sites in the Ni rich region. Cooper's work [2] indicates that the defect state in the compositional range of ~ 49 to 50 at% Ni is substitutional Al atoms at Ni sites. The striking color change associated with the variation of composition was also pointed out by Bradley and Taylor[1]. Therefore the normal reflectance of β'-NiAl was measured by Sanbongi *et al.*[3] and more extensive optical studies were done by Rechtien *et al.*[4] N.M.R. studies were reported by Miyatani *et al.*[5], Seitchik and Walmsley[6] and West[7]. The Knight shift of Al in β'-NiAl is positive and small ($\simeq 0{\cdot}055 \sim 0{\cdot}058$ per cent), and independent of composition. No change of the Knight shift between room temperature and liquid N_2 temperature was observed. It was concluded from NMR studies that *s*-character at Al nucleus site in β'-NiAl is much smaller than that of Al atom in pure Al. The electronic specific heat[6,8] and the magnetic susceptibility[7,9,10] were studied on several alloys of different compositions in a limited temperature region. β'-NiAl is considered nonmagnetic ($\chi = 1{\cdot}4 \times 10^{-7}$ *c.g.s/g*) at room temperature and remains non-ferromagnetic at 6·5°K[10]

In contrast with the development of modern techniques utilizing quantum effects for high purity specimens, the electronic structure and properties of alloys[11], especially those which contain transitional elements, have not been the object of intensive study. However, there is a merit in investigating the properties of alloys in which the electron density is easily varied via chemical composition. Due to defects in these alloys the physical purity is far from the quantum condition $\omega_c\tau > 1$ (ω_c = cyclotron frequency, τ = relaxation time). In the case of stoichiometric β'-NiAl, $\omega_c\tau$ is estimated to be $2{\cdot}8 \times 10^{-7} H$ (*H* is in Oersted) at 4·2°K.

In the present paper the ordinary transport phenomena, electrical resistivity, Hall effect, and magnetoresistance will be described in detail. The electronic structure of β'-NiAl will be discussed based on the transport phenomena, optical properties and the band calculation by Adachi *et al.*[12].

---

*Present address: Department of Applied Physics, University of Tokyo, Tokyo, Japan.

2. EXPERIMENTAL

The alloys used in this study were made by melting in a NRC unit under a partial pressure of He using recrystallized alumina crucibles and a cold copper mold. Later, an arc melting furnace was used to prepare alloys. Some efforts were made to produce single crystals via the Bridgman technique[4]. The difference between nominal compositions and chemically analyzed compositions when the NRC melting apparatus was employed can be found in Ref. [4]. The Al was 99·995 wt.% and the decarburized Ni was better than 99·96 wt.%. Fe was the only transitional impurity found ($\leq$ 0·009 wt.%) in the alloys.

Prior to machining specimens the ingots were well annealed at 1200°C for about 20 hr under a reduced argon pressure. Some specimens were annealed again at 500°C for 3 ~ 10 hr in quartz ampules under vacuum after machining.

The specimens for electrical resistivity measurements and for Hall effect and magnetoresistance measurements were cut from ingots and planed by a servomet spark machine and finished by mechanical polishing. The former's dimensions are $\sim 1 \times 1{\cdot}5 \times 12$ mm^3 and the latter's $\sim 0{\cdot}16 \times 1{\cdot}3 \times 10$ mm^3.

The electrical leads were spot-welded using the thin platinum wire. Some specimens of low Ni compositions were so brittle that soldering was employed to attach leads. In that case the ends were electroless plated prior to the soldering. Since the Hall voltage was estimated to be $\sim 10^{-7}$ V, the measurements were made via the three probes method [13].

Electrical resistivity was measured by a Leeds and Northrup *K*-3 potentiometer. A calibrated germanium thermometer and a Cu-constantan thermocouple were used for temperature measurements. The Hall and magnetoresistance measurements utilized a Keithley-147 nanovolt null detector, a Keithley-260 nanovolt source and an *X*-*Y* recorder. The data were plotted point by point on an *X*-*Y* recorder at each magnetic field up to 32 kOe. The primary current direction was inverted for the electrical resistivity measurements. For the Hall and magnetoresistance measurements, both the primary current and the magnetic field were inverted to avoid some spurious effects.

3. RESULTS

(a) *Electrical resistivity*

Figure 1 shows the compositional dependence of the electrical resistivity at 297, 77 and 4·2°K. The open and crossed data points represent results on specimens annealed at 1200°C prior to machining. The solid data points represent results on specimens that were given a second anneal of 3 hr at 500°C in vacuo after mechanical polishing.

It has been generally accepted[2, 14] that the formation of vacancies in Ni-poor region results from the high stability of 3 conduction electrons per unit cell configuration which is preserved by maintaining just one Al atom in each unit cell. The conduction electron density as a function of the compositional is calculated based on the Hume–Rothery model, where lattice parameters by Cooper[2] and Bradley and Taylor[1] and the number of Al atoms in a unit cell are used. The result is shown in Fig. 2. As there is some question about the concentration of Al substitutional atoms in the low Ni region, two branches are drawn in the figure. Although the number of conduction electrons per unit cell is constant in the low Ni region, the conduction electron density (cm^{-3}) is not constant, due to the change of lattice parameters.

In order to examine the relaxation time effect explicitly the residual resistance ration ($\equiv R_{297°K}/R_{4{\cdot}2°K} = R.R.R.$) is plotted in Fig. 3, where open and solid circles indicate the same as before. The values of *R.R.R.* of this material are so small that modern techniques to attack the electronic structure by studying os-

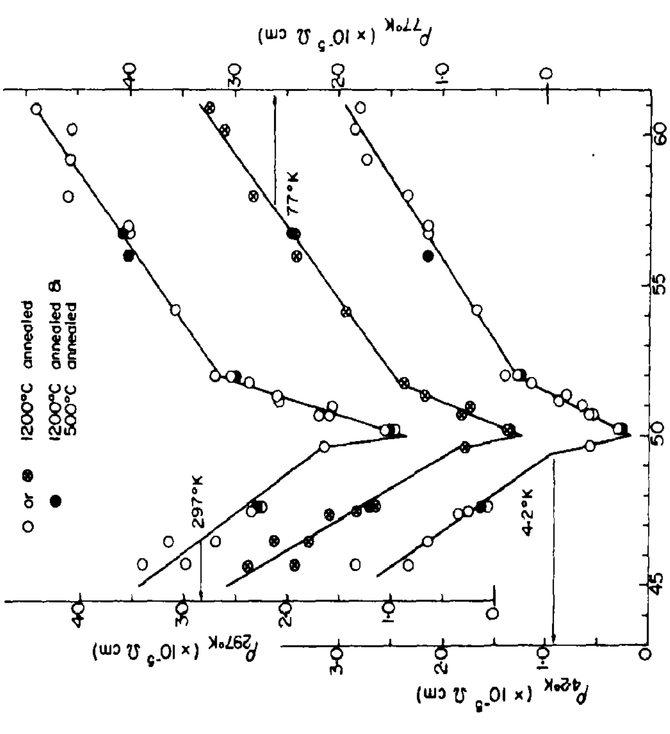

Fig. 1. The electrical resistivity as a function of the composition at 297, 77 and 4·2°K.

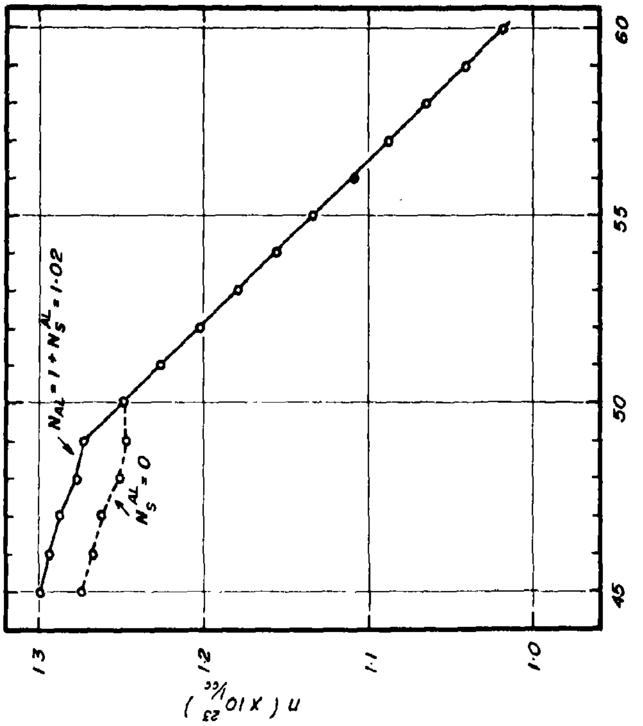

Fig. 2. Calculated conduction electron density as a function of the composition based on the Hume-Rothery model.

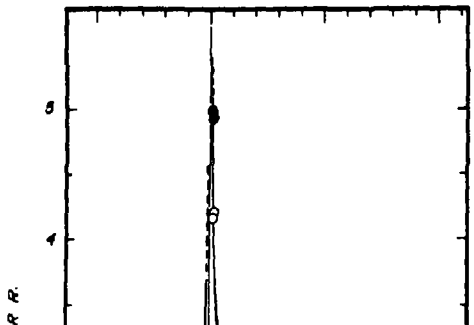

Fig 3 The residual resistance ratio (= R R.R) as a function of the composition The meaning of open and solid circles is the same as Fig. 1. The solid line is obtained from the solid lines in Fig. 1

cillatory behaviors seems impossible. Only $50{\cdot}1_6$ at% Ni specimen is a single crystal and its *R.R.R.* increased from 4·2 to 5 through the annealing process in the final shape. The low *R.R.R.* is thought to be a result of lattice defects in β'-NiAl and the inability to produce a stoichiometric β'-NiAl compound. The temperature dependent part of the electrical resistivity,

$$\rho(\mathrm{T}) = \rho_{297^\circ\mathrm{K}} - \rho_{4\cdot 2^\circ\mathrm{K}} \qquad (1)$$

is plotted as a function of composition in Fig. 4. It should be noted $\rho(\mathrm{T})$ is fairly constant in two regions of 45 ~ 49 at% Ni and 52 ~ 60 at% Ni. The correspondence of Fig. 1 and Fig. 4 suggests the formation of clusters of vacancies in β'-NiAl alloys with less than ~ 49 at% Ni and clusters of substitutional atoms in alloys with greater than ~ 52 at% Ni. The hypothesis of the point defect clustering is also supported by evidence from x-ray diffraction studies of ordering in β'-NiAl[15], and also by NMR studies in β'-NiAl and β'-CoAl[7].

Measurements of the temperature dependence of the electrical resistivity revealed a compositionally dependent resistance minimum phenomenon, Fig. 5. While resistance minimum has been reported in dilute alloys and semiconducting compounds, this appears to be the first detailed investigation of the phenomenon in a non-semiconducting intermetallic compound.

(b) *Hall effect*

Nine specimens of different compositions in β'-phase were utilized in measuring the Hall coefficients ($R_H = V_H/H$) at room temperature and 4·2°K. The transverse Hall voltage, V_H, is defined* in this paper as follows:

$$\mathbf{V}_H = \tfrac{1}{4}[\mathbf{V}(\mathbf{H},\mathbf{I}) - \mathbf{V}(-\mathbf{H},\mathbf{I}) + (-\mathbf{H},-\mathbf{I}) - \mathbf{V}(\mathbf{H},-\mathbf{I})] \qquad (2)$$

and combines four readings of the primary current **I**. Since variations in the primary current from 0·2 to 1·5 *A* produced no change in the observed Hall coefficient, the magnitude of the primary current was varied in this range in order to produce about 1 μV in V_H at 30kOe. The gain of the Keithley-147 nanovolt null detector and the *X-Y* recorder were adjusted for 1 μV to correspond to 50 mm. The experimental error is estimated $\approx \pm 6 \times 10^{-9}$ V in measuring V_H.

Figure 6 shows the Hall coefficients, R_H, as a function of magnetic field at 297 and 4·2°K.

---

*This is a conventional method to obtain the Hall coefficient But the Ettingshausen effect cannot be separated from the Hall effect. See, for example, LINDBERG O., *Proc. IRE* **40**, 1414 (1952).

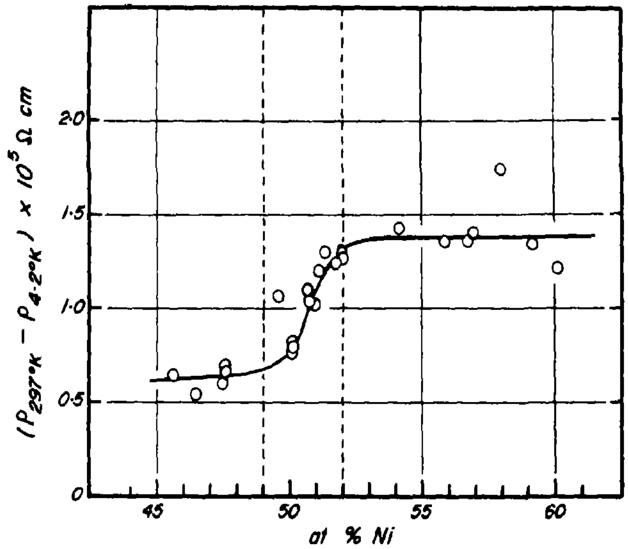

Fig. 4. The temperature dependent part of the electrical resistivity as obtained $\rho(T) = \rho_{297°K} - \rho_{4.2°K}$.

First, it is noteworthy that $R_{//}$ is positive in the composition range less than 58 at% Ni at both 297 and 4·2°K. Secondly, the absolute magnitude of $R_{//}$ is larger at 297°K than at 4·2°K. Ignoring the magnetic field dependence, the mean values of $R_{//}$ are plotted as a function of composition in Fig. 7, where the vertical line through the data points indicates the variation of $R_{//}$ for the various magnetic fields.

(c) *Magnetoresistance*

The transverse magnetoresistance, $(\Delta\rho/\rho_0)_{tr} \equiv [(\rho(H)-\rho(0))/\rho(0)]_{tr}$, of eight specimens was measured between 4·2 and 1·8°K in magnetic fields from ~ 5 to 32 kOe. Two kinds of behavior were observed: in the first, a reversal of sign from positive to negative occurred between 3 ~ 2°K, while the second always had a negative magnetoresistance in this temperature range. The absolute magnitude is relatively small, of the order of $10^{-4} \sim 10^{-3}$ at 30 kOe. The typical temperature dependences are shown in Figs. 8 and 9, where the latter is plotted on a log–log scale. Figure 8 shows that $(\Delta\rho/\rho_0)_{tr}$ saturated at lower temperatures and higher magnetic fields. Similar behavior was observed in another specimen ($50{\cdot}1_6$ at% Ni) which also shows the sign reversal. The quadratic dependence of the magnetoresistance on the magnetic field, which is expected at low fields from the well known transport theory and Yoshida theory[16] in the case of negative sign, does not seem to hold in β'-NiAl (Fig. 9), although there may be some experimental inaccuracy, especially at lower fields where the magnitude of the magnetoresistance is very small. These experimental results suggest that the transport properties of β'-NiAl are similar to those of dilute magnetic alloys [16], e.g. Cu–Mn, and degenerate semiconductors[17]. If the negative magnetoresistance described above originated from something like localized magnetic moments through the s–d exchange interaction, we might reasonably expect the same order of the longitudinal magnetoresistance. Therefore the longitudinal magnetoresistance was measured on three specimens, $47{\cdot}6_3$, $50{\cdot}7_5$, and $51{\cdot}9_8$ at% Ni. The magnitude and temperature dependence of the longitudinal and transverse

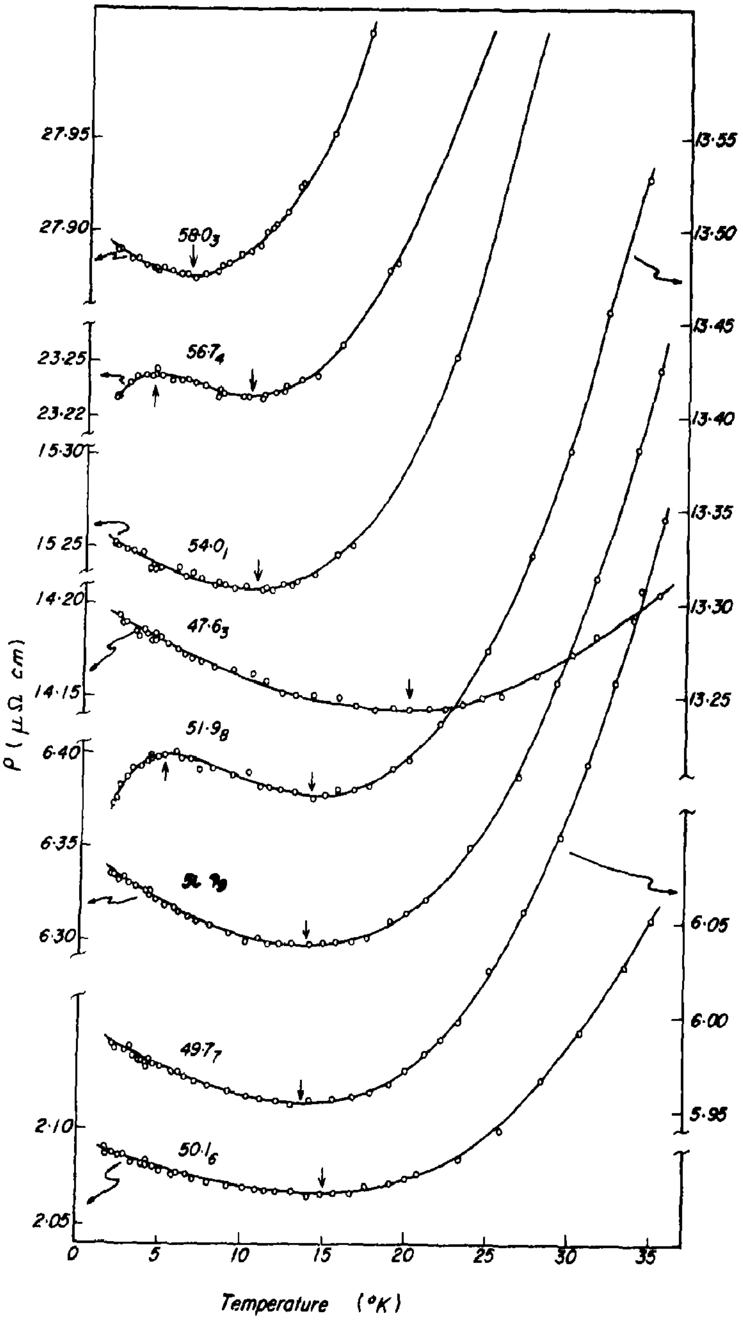

Fig. 5. Temperature variation of the electrical resistivities for eight specimens. It should be noteworthy that they show resistance minimum phenomena.

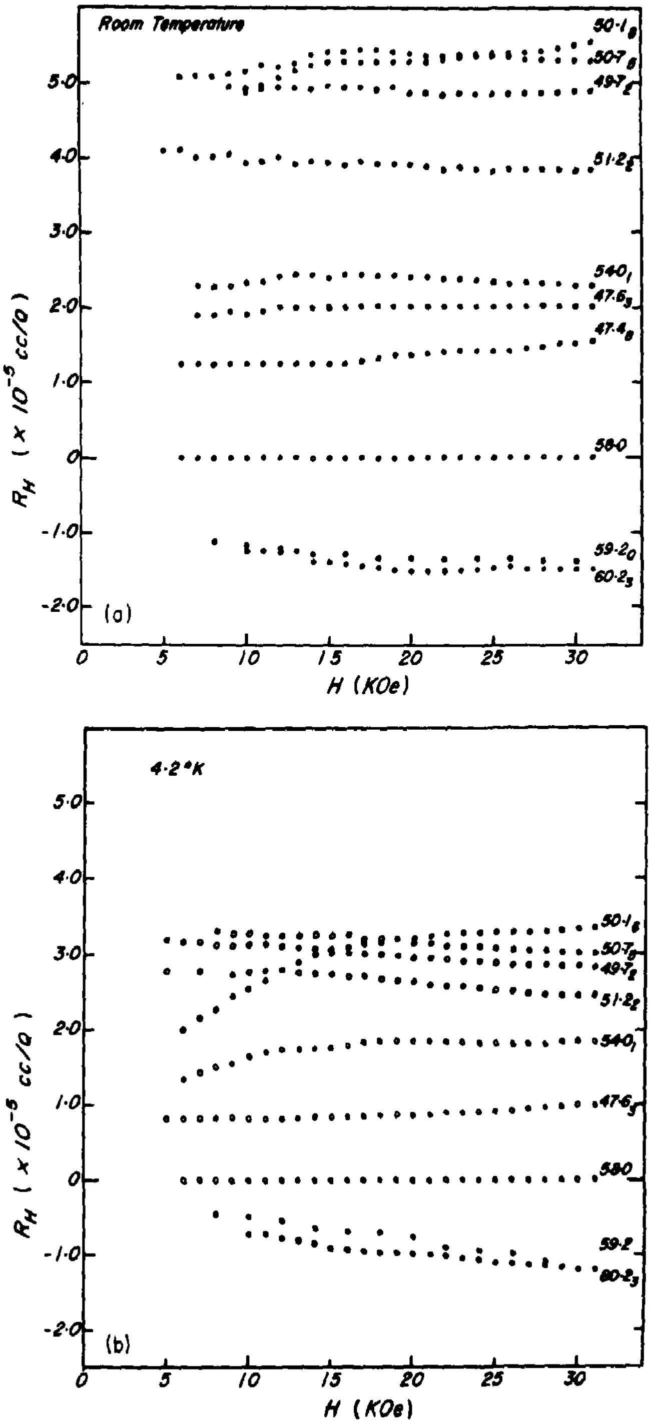

Fig. 6. Hall coefficients of β'-NiAl as a function of the magnetic field at 297°K (a) and 4·2°K (b).

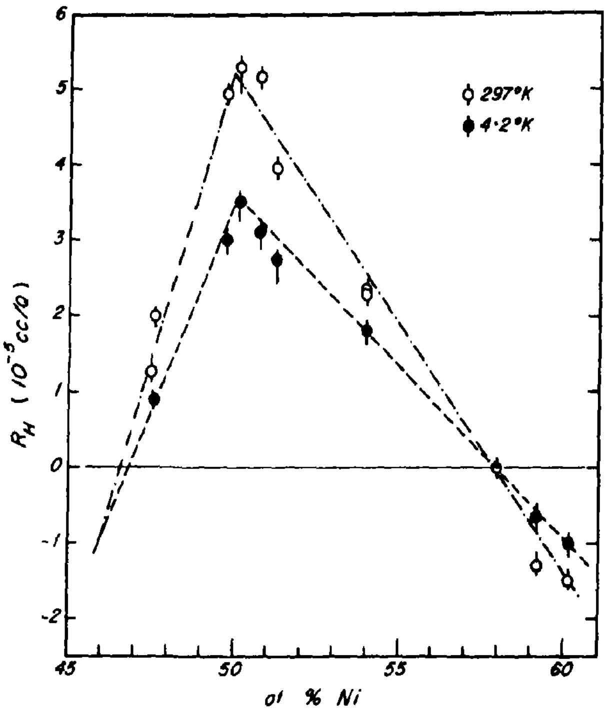

Fig. 7. Hall coefficient as a function of composition.

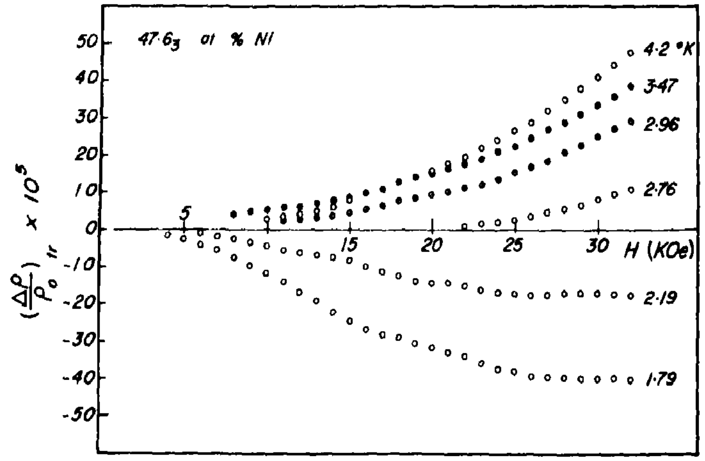

Fig. 8. Transverse magnetoresistance of $47{\cdot}6_3$ at% Ni.

magnetoresistance were similar for these three alloys. (Compare Figs. 9 and 10 for the 50·75 at% Ni alloy). Table 1 is a summary of the magnetoresistance measurements of all specimens.

4. DISCUSSION

(a) *Electrical resistivity*

The positive Hall coefficient and its composition dependence suggest a two-carrier model in β'-NiAl. The electrical resistivity, ρ,

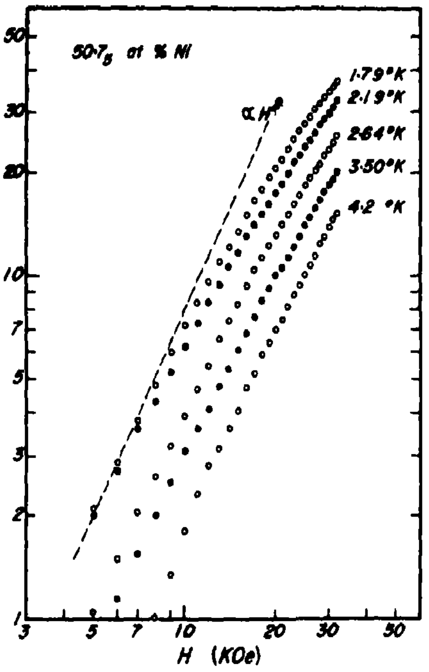

Fig. 9 Transverse magnetoresistance of 50·7$_5$ at% Ni (log–log plot).

is therefore expressed as

$$\rho = \frac{1}{\sigma} = \frac{1}{\sigma_e + \sigma_h} \tag{3}$$

$$= \left(\frac{n_e e^2 \tau_e}{m_e^*} + \frac{n_h e^2 \tau_h}{m_h^*}\right)^{-1} \tag{4}$$

where suffixes e and h mean electrons and holes respectively. The contribution of the holes to the resistivity will depend on the topology of the Fermi surface. Since the defect concentration in β′-NiAl is high, the electrical resistivity should be determined mostly by the defects. If we replot the electrical resistivity as a function of concentration of substitutional atoms or of vacancies, we can obtain the resistivity increment per unit substitutional atom or vacancy (in the unit of at%). Assuming that the resistivity data can be expressed in terms of a linear function with respect to the defect concentration, we have drawn the four straight lines shown in Fig. 1 and calculated the resistivity change due to the reported

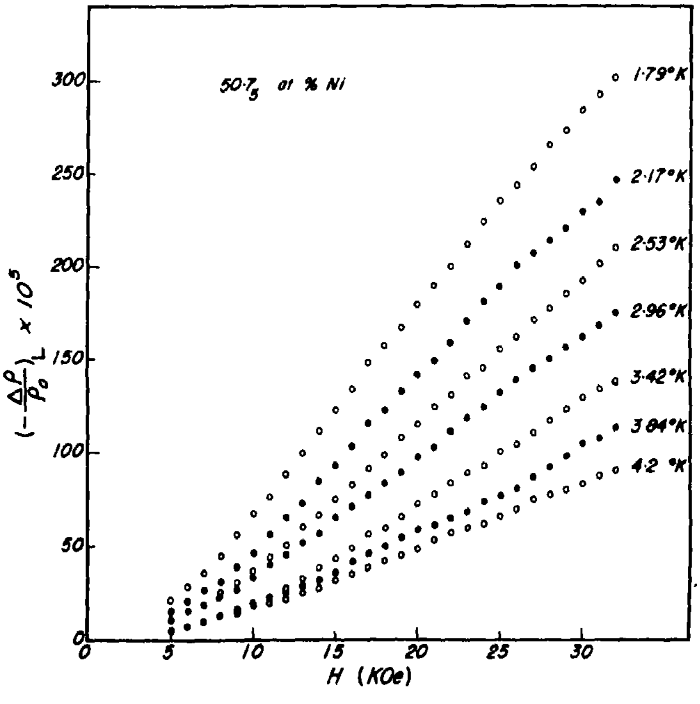

Fig. 10. Longitudinal magnetoresistance of 50·7$_5$ at% Ni.

defect state. The results to a good approximation are:

$$\frac{d\rho}{dN_S^{Ni}} = 9\cdot 0\,\mu\Omega\cdot\text{cm/at\%}\ (297^\circ\text{K})$$

$$50 \sim 52\ \text{at\% Ni}$$

$$= 5\cdot 6\,\mu\Omega\cdot\text{cm/at\%}\ (4\cdot 2^\circ\text{K})$$

$$= 2\cdot 0\,\mu\Omega\cdot\text{cm/at\%}\ (297^\circ\text{K})$$

$$52 \sim 60\ \text{at\% Ni}$$

$$= 1\cdot 9\,\mu\Omega\cdot\text{cm/at\%}\ (4\cdot 2^\circ\text{K})$$

and

$$\frac{d\rho}{dN_S^{Al}} \cong 70\,\mu\Omega\cdot\text{cm/at\%}\ (297^\circ\text{K})$$

$$49\cdot 5 \sim 50\ \text{at\% Ni}$$

$$\cong 40\,\mu\Omega\cdot\text{cm/at\%}\ (4\cdot 2^\circ\text{K})$$

$$\frac{d\rho}{dN_v} = 1\cdot 6\,\mu\Omega\cdot\text{cm/at\%}\ (297^\circ\text{K})$$

$$45 \sim 49\cdot 5\ \text{at\% Ni}$$

$$= 2\cdot 0\,\mu\Omega\cdot\text{cm/at\%}\ (4\cdot 2^\circ\text{K}).$$

The resistivity contribution due to isolated point imperfections, aggregates of point defects, and the lattice strain associated with the defects have been investigated by many individuals. Although the problem has not been solved satisfactorily either experimentally or theoretically, it is generally accepted that the scattering effects due to point defects are additive in the low concentrations. In the case of β'-NiAl we consider isolated vacancies or antistructure defects will contribute to the resistivity in an additive fashion in the range of 49·5 ~ 52 at% Ni. But as the defect concentration increases complexes or clusters will form and the conduction carriers will be scattered by the complexes as well as the isolated point defects. Two knees at 49·5 and 52 at% Ni in Fig. 1 are explained by this idea and supported by X-ray diffraction[15] and NMR studies[7]. The theories[18,19] developed to explain the increase in resistivity in a metal or dilute alloy due to an arbitrary distribution of point imperfections and to the lattice strain around them lead to a resistivity change/at% defect that is more than an order of magnitude too small for the observed resistivity changes in β'-NiAl for small deviations in stoichiometry. It should be noted that the resistivity change in β'-NiAl for large deviations in stoichiometry was much smaller and of the same magnitude as that observed in dilute alloys. This suggests a drastic decrease of the scattering of the carriers due to the clustering of point defects.

Let us now turn our attention to the resistance minima observed in Fig. 6. In the case of dilute magnetic alloys Kondo[20] proposed a theory which explained resistance minimum phenomena fairly well. By Kondo's theory the electrical resistivity is expressed as:

$$\rho = aT^5 + c\rho_0 - c\rho_1 \log T \qquad (5)$$

where the first and second terms are the lattice contribution and the residual resistivity, respectively, and the third term is due to the s–d exchange interaction. Here c is the concentration of magnetic impurity atoms. From equation (5), the temperature T_m at which the minimum occurs, and the depth of the minimum are given by

$$T_{\min} = \left(\frac{\rho_1}{5a}\right)^{1/5} c^{1/5} \qquad (6)$$

and

$$\rho_{T=0} - \rho_{\min} = \rho_1 c\left\{\log\left(\frac{T_{\min}}{T_0}\right) - \frac{1}{5}\right\}. \qquad (7)$$

In β'-NiAl we have to examine whether any localized magnetic moment exists. Höhl[9] suggested from the magnetic susceptibility measurement (82 ~ 870°K, for 49·9 at% Ni) that a small fraction (< 1 per cent) of Ni atoms had unfilled d-shells at lower temperatures. As the temperature goes up, the number of d-holes increases and the decrease of the susceptibility which obeys the Curie law is cancelled out so that the measured susceptibility is not particularly temperature-sensitive. On the other hand, West[7], Seitchik and Walmsley[6], and Miyatani *et al.*[5] concluded that the 3 d-band of β'-NiAl is completely filled. If we consider the substitutional Ni atoms in the non-stoichiometric alloys having a magnetic moment other than that in the ordered NiAl matrix, we would have higher $T_{\min}$ at higher Ni compositions. This is inconsistent with the experimental results as seen in Fig. 5, Fig. 11(a) and Table 1. The assumption that vacancies would create some magnetic moments in β'-NiAl is also denied by the same reason. Therefore, the only possibility of the existence of localized magnetic moments is due to some unknown magnetic impurities. Figures 11(a) and (b) shows the composition dependence of $T_{\min}$ and $\{\rho(2°\mathrm{K}) - \rho(T_{\min})\}/\rho(2°\mathrm{K}) \times 100\ (\%)$. $T_{\min}$ decreases as Ni concentration increases and the latter looks like the shape of *R.R.R.* (Fig. 3). The resistivity data was also replotted against $\log T$ in order to determine whether the temperature dependence of the resistivity of β'-NiAl was logarithmic at low temperatures. It was found that the resistivity was not simply proportional to $\log T$ but exhibited a tendency to saturate at very low temperatures. A similar observation has been observed in β'-CoAl [23,24] and in β'-CoGa, and NiGa[24]. Therefore the behavior depicted seems to reflect the intrinsic electronic structure rather than some foreign impurities.

Only two specimens, $51{\cdot}9_8$ and $56{\cdot}7_4$ at% Ni show the resistance maximum also. A clear explanation is not easy at this stage.

The explanation of the above observation may lie in localized spin fluctuations[21] which predicts a weak resistance minimum and a low temperature logarithmic dependence. If it is found that there is a critical concentration near the stoichiometric composition at which the impurity states approach the magnetic limit in our system, the localized spin fluctuation model may be accepted. However, at this time there is no data concerning such magnetic states.

(b) *Hall effect*

Some of the specimens have magnetic-field-dependent Hall coefficients. By the standard transport theory the Hall coefficient for a two-band model is expressed as[22]

$$R_H = \frac{-n_e e\mu_e^2 + n_h e\mu_h^2 + (-n_e e + n_h e)\mu_e^2\mu_h^2H^2}{(-n_e e\mu_e + n_h e\mu_h)^2 + (-n_e e + n_h e)^2\mu_e^2\mu_h^2H^2} \qquad (8)$$

where μ is the mobility of the electrons or

Table 1. Characteristics of the specimens. The blank means no measurements were done about the quantity concerned

Sample No.	Composition (at% Ni)	$T_{\min}$ (°K)	$T_{\max}$ (°K)	$\left(\frac{\Delta\rho}{\rho_0}\right)_{tr}$ 4·2°K	$\left(\frac{\Delta\rho}{\rho_0}\right)_{tr}$ 1·8°K	$\left(\frac{\Delta\rho}{\rho_0}\right)_1$	T_0(°K)
4	$47{\cdot}6_3$	20	No	+	−	−	
5	$49{\cdot}7_2$	13·5	No	−	−		~ 1
18	$50{\cdot}1_8$	15	No	+	−		
7	$50{\cdot}7_5$			−	−	−	1·1 ~ 1·6
3	$50{\cdot}9_9$	14	No				
14	$51{\cdot}9_8$	14	5	−	−	−	
17	$54{\cdot}0_1$	10·5	No	−	−		1·1 ~ 1·9
10	$56{\cdot}7_4$	10	4				
11	$58{\cdot}0_3$	6·5	No	−	−		1·7
13	$60{\cdot}2_3$			−	−		1 ~ 1·5

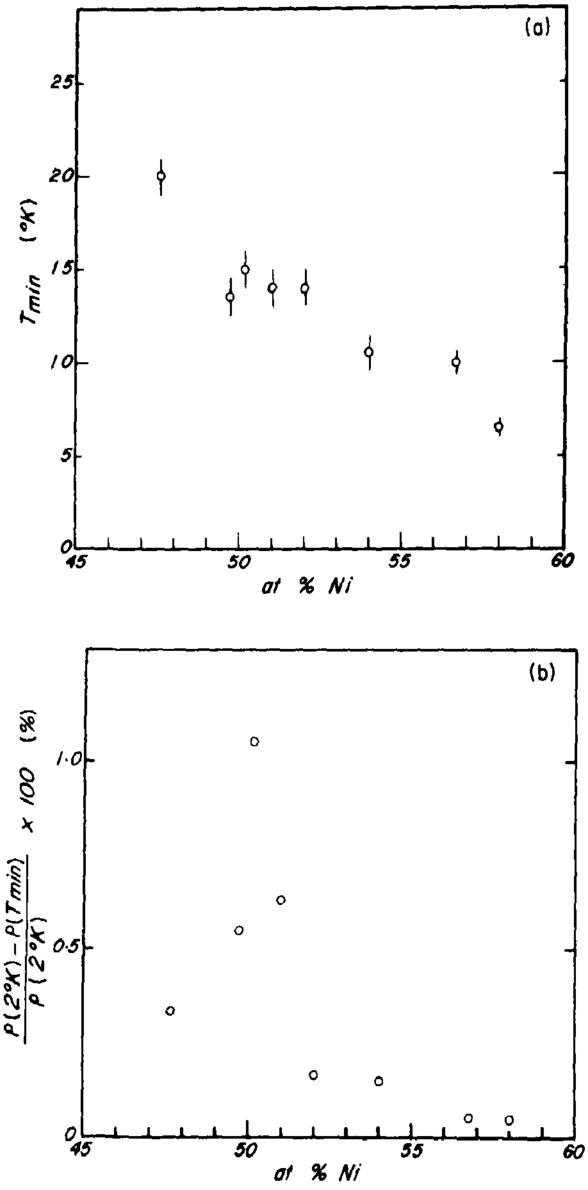

Fig. 11. The composition dependence of T_{min} (a), and $\{\rho(2°K) - \rho(T_{min})\}/\rho(2°K) \times 100$ (%) (b).

holes. In the weak field limit the well known formula

$$R_H = -e\frac{n_e\mu_e^2 - n_h\mu_h^2}{(\sigma_e+\sigma_h)^2} \qquad (9)$$

is obtained. For β'-NiAl 30 kOe is considered to be a weak magnetic field according to the estimation of $\omega_c\tau (= 1/c\mu H)$. Therefore, we should expect a constant R_h in the magnetic field range investigated because β'-NiAl is non-magnetic. At 4·2°K the $50{\cdot}1_6$ at% Ni (single crystal specimen) had a smaller R_H

in the lower fields. This field dependence differs from the usual two carrier effect, for example, in p-Ge[25]. It is also different from the behavior of ferromagnetic materials[26]. From a log–log plot, we know the Hall voltage varies as $H^{1\cdot 5}$ up to 15 kOe and as H above it (Fig. 12). Such a field dependence of the Hall voltage is hard to explain because there is little possibility that the structure of the Fermi surface would be affected by some quantum mechanical effects.

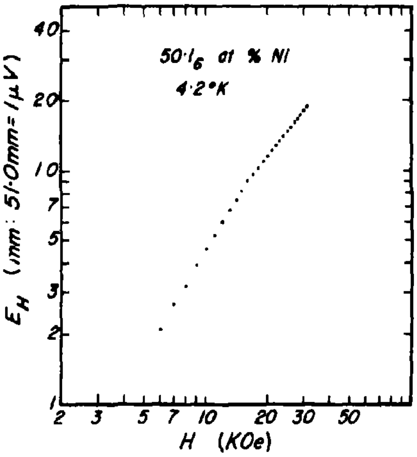

Fig. 12 Hall voltage for 50·1$_6$ at% Ni specimen as a function of the magnetic field at 4·2°K.

We only notice here the average value of R_H as a function of composition. The composition dependence of R_H in β'-NiAl has characteristics similar to those of β-CuZn[27], where compensation occurs and $|R_H|$ ($R_H = -0{\cdot}6\times10^{-5}$ cc/Q) becomes smaller than that of Cu ($R_H = -5{\cdot}2\times10^{-5}$ cc/Q) due to hole pockets at the corners of the first and second zones. From Fig. 7 and equation (9) it is concluded

$$\frac{n_e}{n_h} < \left(\frac{\mu_h}{\mu_e}\right)^2 \qquad (10)$$

in the range of 46 ~ 58 at% Ni. It is reasonably supposed that the number of electrons is larger than that of holes. Therefore the hole mobility is larger than the electron mobility in order to satisfy equation (10). However, it is impossible to separate the behavior of the electrons and holes without having four independent equations of n_e, n_h, μ_e, and μ_h.

Let us consider the Fermi surface by the single OPW method. Figure 13 shows the Brillouin zone and symmetry points for β'-NiAl. At stoichiometry the lattice constant[2] $a = 2{\cdot}885\times10^{-8}$ cm and the Fermi vector k_F is

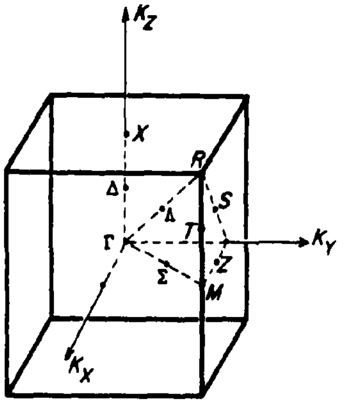

Fig. 13 Simple cubic Brillouin zone for β'-NiAl and symmetry points.

$$k_F = \left(\frac{3}{8\pi}n_0\right)^{1/3} = \left(\frac{3}{8\pi}\cdot\frac{3}{a^3}\right)^{1/3} = 0{\cdot}7101\,\frac{1}{a}$$
$$= 2{\cdot}462\times10^{7}\,\text{cm}^{-1} \qquad (11)$$

where the assumption that the conduction electron density n_0 is determined by three electrons per one Al atom, is made. On the other hand the diagonal length of the first Brillouin zone, $\overline{\Gamma M}$, is

$$\overline{\Gamma M} = \frac{1}{a}\sqrt{\tfrac{1}{2}} = 0{\cdot}0701\,\frac{1}{a} = 2{\cdot}451\times10^{7}\,\text{cm}^{-1}. \qquad (12)$$

This situation is illustrated in Fig. 14. The Fermi surface is associated not only with the first zone but also with the second, third and fourth zone. However, if we would take many

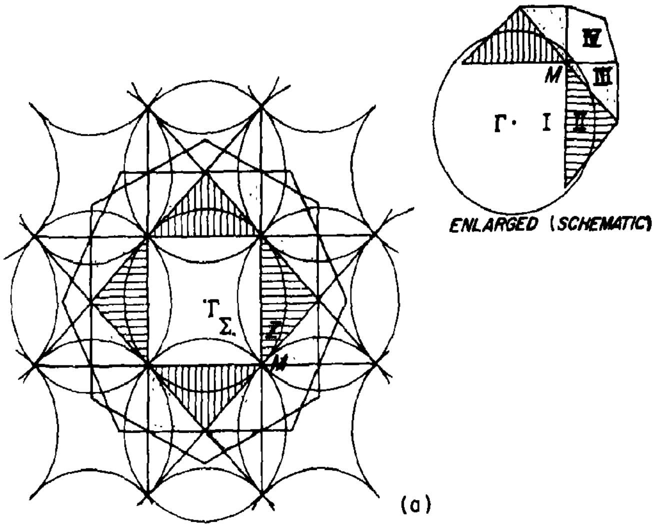

(a)

ΓMZ PLANE

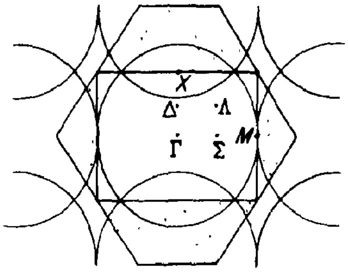

(b)

XΓMR PLANE

Fig. 14. Fermi surface by the single OPW and Brillouin zones for (a) ΓMR plane and (b) XΓMR plane.

OPW's, the third and fourth zone would not be related with the Fermi surface.

In the single OPW approximation, $k_F = \overline{\Gamma M}$ will be satisfied if 2·962 electrons per Al atom are supplied. As the Ni content increases, the Fermi surface shrinks and k_F becomes $2{\cdot}300 \times 10^7$ cm^{-1} compared with $\overline{\Gamma M} = 2{\cdot}467 \times 10^7$ cm^{-1} at 60 at% Ni. In the alloys of the higher Ni concentration a hole surface resulted from the corners at point M in the first zone and this will contribute to the conduction process. The experimental results, on the other hand, suggest that the hole contribution becomes less at higher Ni concentrations. This apparent inconsistency is rationalized by assuming the appropriate curvature of the band (= large effective mass) near point M.

In the alloys of the lower Ni concentration, the Fermi surface expands; for example, $k_F = 2{\cdot}494 \times 10^7$ cm^{-1}, $\overline{\Gamma M} = 2{\cdot}467 \times 10^7$ cm^{-1}, and $\overline{\Gamma R} = 3{\cdot}022 \times 10^7$ cm^{-1} at 45 at% Ni. The hole surface will be near point R only in the first zone and becomes smaller in the second zone. On the other hand the electron contribution increases. Therefore, we should expect R_H to be dominated by electrons in this composition range.

Adachi, Katayama, and Hirone[12] have

calculated the energy band structure of CsCl type NiAl, CoAl and FeAl alloys by the Wigner–Seitz method. They assumed Cu^+ Hartree potential and Al^{3+} Hartree potential for Ni and Al respectively. The defect structures of NiAl and CoAl were neglected. The curves of E vs. **k** are shown in Fig. 15. The hole surface at point R is consistent with the aforementioned crude approximation by the single OPW. The energy band model of β′-NiAl suggests the existence of two kinds of holes with different effective mass. At higher Ni concentrations point M also becomes a hole surface as indicated in Fig. 15, calculations by Adachi *et al.*, also suggest that the major electron surface is along $X\Delta$ direction. It may be concluded that the energy band structure model lends support to electron approximation, thus Jones' interpretation[28] of the Hume-Rothery rule is reasonable.

(c) *Magnetoresistance*

The experimental results of the magnetoresistance strongly suggest the existence of the s–d exchange type interaction in β′-NiAl. According to Yoshida's theory the negative magnetoresistance is proportional to the average magnetization due to localized spins.

$$-\frac{\Delta\rho}{\rho_0} = S(T)H^2 \propto M^2 \propto (\chi H)^2. \quad (13)$$

If we plot $\lim_{H\to 0} S^{-1/2}$ vs. temperature, we obtain information about the coupling of localized spins. Figure 16 shows such an analysis of 50·57 at% Ni specimens. If a linear relation is assumed, different paramagnetic Curie–Weiss temperatures, T_0, are obtained for the different magnetic fields. The lower field gives the paramagnetic Curie–Weiss temperature because there is less effect of the normal positive magnetoresistance. In Table 1 values of T_0 for various compositions are listed. There is only a small variation in T_0 with composition if the experimental errors are also considered.

A recent review by Daybel and Steyert[29] has discussed the effects due to small numbers of transition element impurities. Since in intermetallic compounds as β′-NiAl it is impossible to subtract the phonon contribution from the measured resistivity, the analysis becomes extremely difficult. The question of whether localized moments do or do not exist has not been resolved with a high certainty. The results of NMR and magnetic susceptibility measurements[6–10] suggest a probable absence of localized moments. However, since there are no thermoelectric power measurements at low temperatures, this question is not firmly resolved.

The specimen preparation technique may somewhat affect the transport properties, especially the magnetoresistance effect. The 51·98 at% Ni specimen showed a small temperature dependence of the magnetoresistance and also had a much larger T_0 value than specimens of other compositions. This specimen has been found to be consisted of only two or three grains, i.e. quasi single crystal.

In a previous paper[30] deviations from the stoichiometry seemed to cause an anomalous behavior in the electrical resistivity and the magnetoresistance. The magnitude of the negative magnetoresistance was expected to increase as the composition deviates from stoichiometry. However, the experimental results showed the opposite. If we assume that vacancies and/or substitutional atoms of Ni have localized magnetic moments, one again would expect the magnitude of the negative magnetoresistance to increase with departure from stoichiometry, contrary to the experimental observations. Therefore, the negative magnetoresistance in β′-NiAl is not due to its peculiar defect structure.

As shown in Fig. 9~10 the field dependence of the negative magnetoresistance deviates from H^2 law at high magnetic fields, that is, the normal (positive) component begins to dominate at these high fields. We expect that the sign reversal may occur at the magnetic fields of the order of 10^5 Oe at 1·8°K.

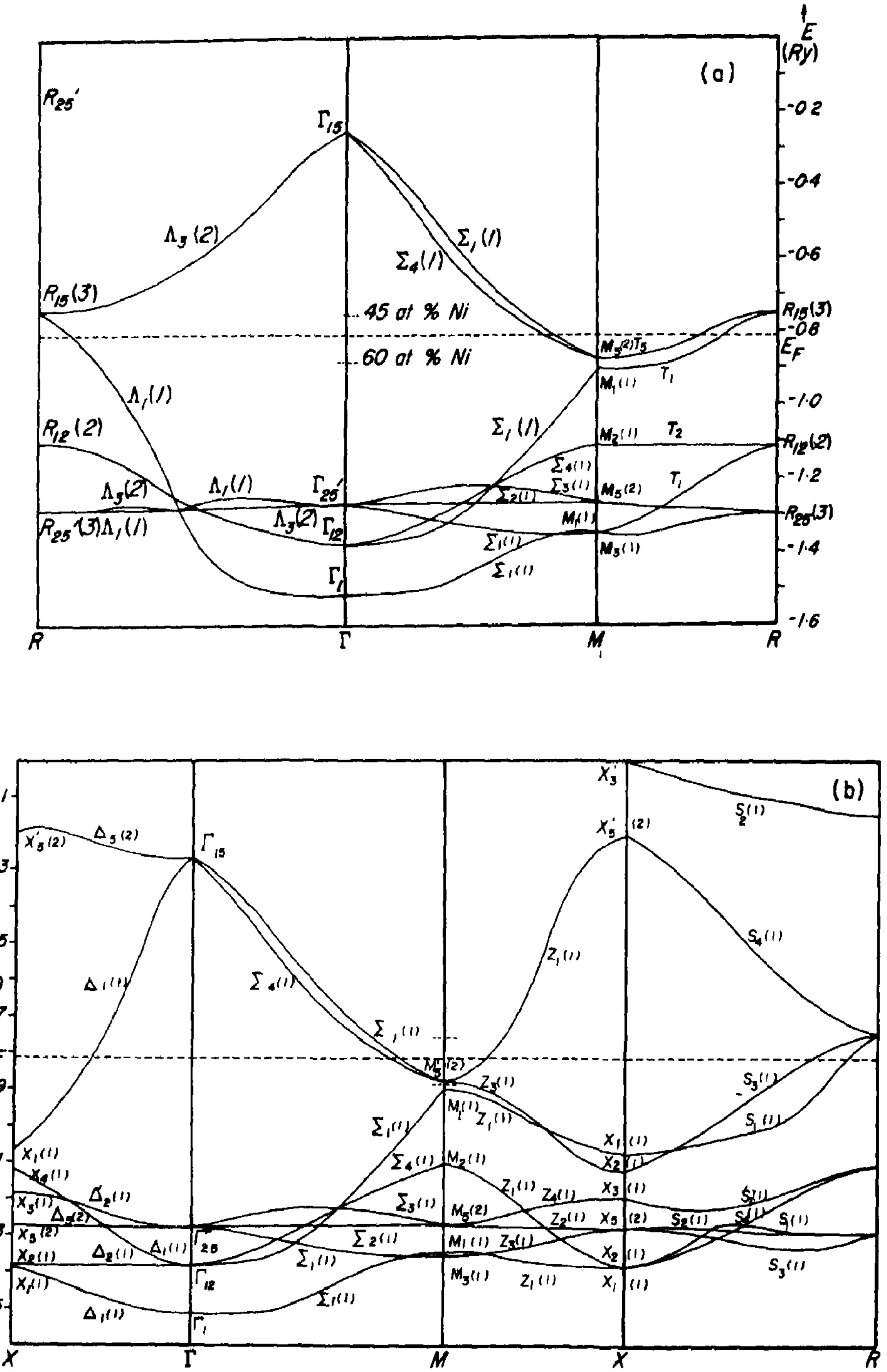

Fig. 15. Energy band for β'-NiAl by K. Adachi, T. Katayama and T. Hirone (unpublished). The Fermi energy, E_f, is for the stoichiometry. The defect structure was neglected for the calculation (the Wigner-Seitz method).

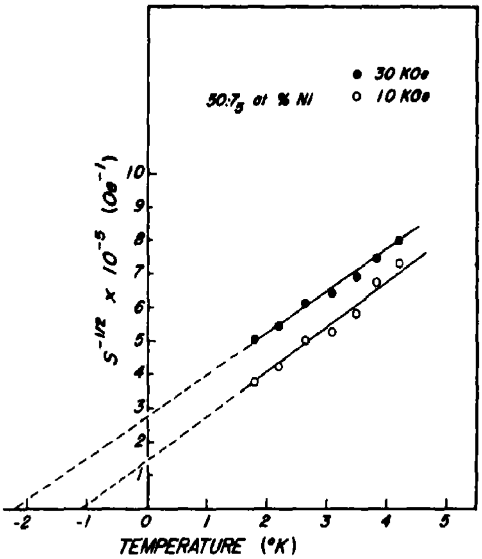

Fig. 16. $S^{1/2}$ vs. temperature for 50·7$_5$ at% Ni specimens.

The resistance minimum and the negative magnetoresistance have also been found by the present authors in the course of extensive studies on the similar β'-phase intermetallic compounds such as CoAl, CoGa and NiGa [31]. It is very suggestive that all of these are considered to be Hume-Rothery $\frac{3}{2}$ electron compounds and contain 3*d*-transitional elements.

Kondo[30] suggested that if there was a very small Fermi surface in β'-NiAl we might expect $-\Delta\rho/\rho_0 \propto (\mu_B H)^2$, where μ_B is Bohr magneton. The optical measurements[4] and the energy band calculation by Adachi *et al.* [12] are rather negative for this speculation.

(d) *Optical properties*

Optical constants *n* and *k* were measured in this laboratory between 0·7 and 6 eV of the photon energy on β'-NiAl[32] and CoAl, CoGa, and NiGa[33]. β'-NiAl showed three or four peaks in the dielectric constants, ϵ_1 and ϵ_2, in the energy range studied. On the other hand, three other compounds had only one or two peaks. Rechtien *et al.*[4] have examined the optical transitions based on a rigid band and the single OPW model. In this section we will discuss the interband transitions taking into consideration the band calculation by Adachi *et al.*

One may expect three different interband transitions in metals: (1) the transition which is independent of the Fermi surface, that is, the transition from lower lying bands to higher lying bands, (2) the transition from the Fermi surface to higher lying bands, and (3) the transition from lower lying bands to the Fermi surface.

Experimentally Rechtien *et al.* have found four peaks (or shoulders), at 1·5 ~ 2·0 (γ), 2·5 (α), 4·0 (β), and 5·1 (δ) eV, in ϵ_2 curves. Only one of these transitions, 4·0 eV (β), is independent of composition and appeared in all four compounds. This is the case (1) which is likely to occur at the *R* point, $R_{12}(2) \rightarrow R_{15}(3)$, where the interband density of states is expected to be large because these are symmetry interband points[34]. The calculated energy difference of these levels is 4·9 eV. The second type of interband transition will occur at three positions, $F.S. \rightarrow R_3(2)$ point (0·14 ~ 2·04 eV)*, $F.S. \rightarrow S_4(1)$ (0·14 ~ 4·2 eV)*, and $\Sigma_4(1) \rightarrow \Sigma_1(1)$ (0 ~ 0·5 eV)*. The transitions in the nearly parallel band that are realized in the last transition strongly affects the intraband transitions and compounds the difficulty of determining the free electron contributions[4]. Case (3) is associated with many levels at different positions in the Brillouin zone. Three interband transitions among them are considered to be relatively dominant due to nearly parallel band effects (general interband points). Along the symmetry line *RS* we expect two such transitions of $S_1(1) \rightarrow F.S.$ (0·34 ~ 1·64 eV)* and $S_1(1)$, $S_4(1) \rightarrow F.S.$ (4·6 ~ 4·9 eV)*. Another is that of $T_2 \rightarrow F.S.$ (≃ 3·1 eV) in high Ni composition. One also expects interband transitions along $X\Delta$, MZ, $R\Lambda$, and $M\Sigma$ symmetry lines; these transitions cover almost all of the energy ranges studied, though the transition-strength is determined by the specific interband density of states.

---

*The energy ranges are due to the compositional range in the β'-NiAl phase (i.e. 45 to 60 at% Ni).

Granting the rigid band model and taking into account the shift of peaks, the α peak is supposed to correspond to the transition of $F.S. \rightarrow \Lambda_3(2)$ and $F.S. \rightarrow S_4(1)$. The energy difference, however, is not exactly equal to the observed one. The peak shift of these transitions with composition are consistent with the shift of the Fermi surface. The β peak, which is independent of composition, should correspond to the transition of $R_{12}(2) \rightarrow R_{15}(3)$. The γ peak, which is prominent at high Ni composition, will be associated with the transition of $S_1(1) \rightarrow F.S.$ As for the δ peak, the experimental difficulty of determining this peak precisely makes it precarious to assign transitions at this time. The numerical discrepancies between experimental and calculated values as seen above are consistent with the many assumptions made to solve the Schrödinger equation from the viewpoint of the one-electron spectra.

Figure 17 is the calculated normal reflectance of several typical colored specimens from the optical constants n and k. The blue color in low Ni compositions probably comes from the α peak. The yellowish color in high Ni compositions will be due to the γ peak. This interpretation suggests that the drastic color change with the variation of the composition originates from the interband transitions associated with the Fermi surface.

Finally, the plasma frequency will be shifted largely from the simple calculated value due to the mixing of the interband transitions even below 1 eV. Therefore, the infrared measurement is highly desirable to detect the pure free electron behavior in β'-NiAl.

5. CONCLUDING REMARKS

No direct measurements on the shape and the size of the Fermi surface of β'-NiAl have been made. All the measurements described in this paper are indirect approaches to the electronic structure of β'-NiAl. The band calculation in such an intermetallic compound

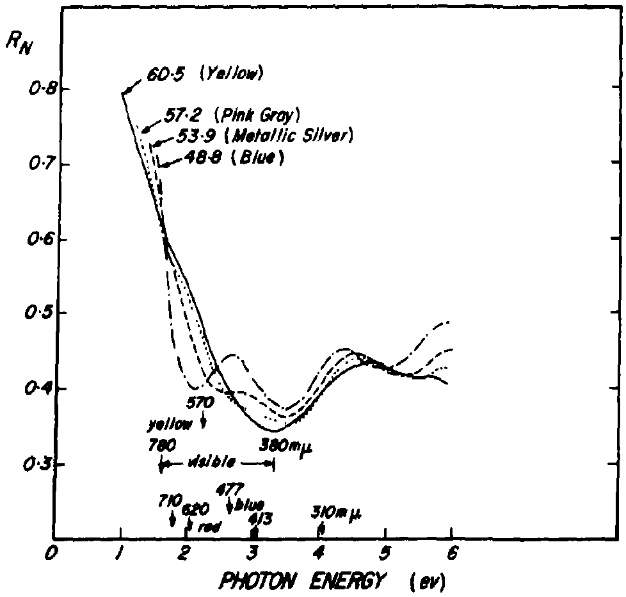

Fig. 17. Normal reflectance of several typical colored specimens of β'-NiAl.

has the eternal problem of deciding the true potential in the compound. The Hume-Rotherby rule should be applied carefully to this material because the transport properties are not simple. The anomalous transport properties have not been fully explained. The existence of the s–d exchange interaction mechanism would be ascertained by measuring the thermoelectric power at low temperatures. The basic question of whether the recently discussed s–d mechanism for dilute-alloys is applicable or not, is beyond our scope at the present stage.

Acknowledgements – The authors express their thanks to Drs. T. Hughes, J. J. Rechtien, and D. A. Kiewit in thier laboratory for the assistance of the preparation of the crystals and optical measurements. Magnetic facility of the Materials Research Center ARPA were used for measurements. Thanks are due to Professors K. Adachi, T. Kakayama, and T. Hirone for showing their unpublished work on the band calculation of β'-NiAl. Professor K. Adachi, Dr. J. Kondo and Dr. Y. Sawada are also acknowledged for suggesting various points. Professor T. Sugawara and his coworkers have kindly given the authors the chance to check the existence of the resistance minimum. One of the authors (Y. Y.) wishes to thank Professor S. Tanuma for his encouragement and suggestions.

REFERENCES

1. BRADLEY A. J. and TAYLOR A., *Proc. R. Soc.* **A159**, 56 (1937).
2. COOPER M. J., *Phil Mag.* **8**, 811 (1963).
3. SANBONGI T., HAGIWARA R. and YAMADAYA T., *J. phys. Soc. Japan* **21**, 923 (1966).
4 RECHTIEN J. J., KANNEWURF C. R. and BRITTAIN J. O., *J. appl. Phys.* **38**, 3045 (1967).
5. MIYATANI K., EHARA S., SATO T. and TOMONO Y., *J phys. Soc. Japan* **18**, 1345 (1963).
6. SEITCHIK J. A. and WALMSLEY R. H., *Phys. Rev.* **131**, 1473 (1963).
7. WEST G. H., *Phil. Mag.* **9**, 979 (1964); *ibid.* **15**, 855 (1967).
8. WALLACE W. E. and CRAIG R., *Phase Stability in Metals and Alloys*, p. 255, *loc. cit.*
9. HÖHL M., *Z. Metallk.* **51**, 85 (1960).
10. BRODSKY M. B. and BRITTAIN J. O., *J. Appl. Phys.* **40**, 3615 (1969).
11. In this paper the word 'alloys' mean 'intermetallic compounds' too.
12. ADACHI K., KATAYAMA T. and HIRONE T., unpublished.
13. LOGAN J. K. and MARCUS J. A., *Phys. Rev.* **88**, 1234 (1952).
14. RAYNOR G., *Progress in Metal Physics* (Edited by B. Chalmers), Vol. 1, p. 15. Interscience, New York (1949).
15 HUGHES T. J., LAUTENSCHLAGER E. P., COHEN J. B. and BRITTAIN J. O., to be published.
16. There are a number of articles of anomalous transport phenomena in dilute magnetic alloys. Many of them will be found in *Progress in Low Temperature Physics* (Edited by C. J. Gorter). Vol. 4, Chap. 4. North–Holland, Amsterdam (1964).
17. For example, KATAYAMA Y. and TANAKA S., *Phys. Rev.* **153**, 873 (1967).
18. ALFRED L. C., *Phys. Rev.* **152**, 693 (1966).
19. DAMASK A. C. and DIENES G. J., *Point Defects in Metals*, p. 173. Gorden and Beach, New York (1963).
20. KONDO J., *Prog. theor. Phys.* **32**, 37 (1964).
21. KIM D. J., *Phys. Rev.* **146**, 455 (1966).
22. ALLGAIER R. S., *J. appl. Phys.* **38**, 5095 (1967).
23. CASKEY G. R. and SELLMYER D. J., *J. appl. Phys* **40**, 1476 (1969).
24. AOKI T., Ph.D. Thesis, Northwestern University (1969).
25. WILLARDSON R. K., HARMAN T. C. and BEER A. C., *Phys. Rev.* **96**, 1512 (1954); BEER A. C., *Solid State Physics* (Edited by F. Seitz and D. Turnbull). Vol. 4 Academic Press, New York (1963).
26 PUGH E. M. and ROSTOKER N., *Rev. mod. Phys.* **25**, 151 (1953). PUGH E. M., *Phys Rev.* **97**, 647 (1955)
27. JOHNSON K. H. and AMAR R., *Phys. Rev.* **139**, 760 (1965). FRANK V., *Danske Videnskab Selskag. Math-Fys. Medal.* **30**, 1 (1955) ARLINGHAUS F. J., *Phys. Rev.* **157**, 491 (1967).
28 MOTT N. F. and JONES H., *The Theory of the* Oxford (1936). JONES H., *Proc R. Soc* **49**, 250 (1937).
29. DAYBELL M. D. and STEYERT W. A., *Rev. mod. Phys.* **40**, 380 (1968).
30 YAMAGUCHI Y. and BRITTAIN J. O., *Phys. Rev Lett.* **21**, 1447 (1968).
31. YAMAGUCHI Y., AOKI T. and BRITTAIN J. O. (To be published).
32. RECHTIEN J. J., Ph.D. Thesis, Northwestern University (1966); and also Ref [4].
33. KIEWIT D. A. and BRITTAIN J. O., *J. appl. Phys.* **41**, (1970).
34. PHILLIPS J. C. *Solid State Physics* (Edited by F. Seitz and D. Turnbull), Vol. 18, p. 67. Academic Press, New York (1966).

J. Phys. Chem. Solids Pergamon Press 1970, Vol. 31, pp. 1345–1351. Printed in Great Britain.

EFFECT OF PRESSURE AND TEMPERATURE ON THE LATTICE PARAMETERS OF RHENIUM

LIN-GUN LIU, TARO TAKAHASHI and WILLIAM A. BASSETT

Department of Geological Sciences and Space Science Center University of Rochester,
Rochester, N Y. 14627, U.S.A

(*Received* 3 *September* 1969, *in revised form* 5 *November* 1969)

Abstract–The effect of pressure on the lattice parameters, hence the molar volume, of the hexagonal close-packed phase of rhenium (Re) was determined at room temperature up to 350 kbar by means of X-ray diffraction employing a diamond–anvil high-pressure cell. The initial bulk modulus of rhenium calculated from the volume data is 3·50 ± 0·15 Mbar. The crystallographic axis ratio, c/a, is virtually independent of pressure. No phase transformation was observed within the pressure range studied. The mean coefficients of linear thermal expansion were determined to be $(7{\cdot}03 \pm 0{\cdot}10) \times 10^{-6}{}^\circ C^{-1}$ for the a-axis and $(4{\cdot}96 \pm 0{\cdot}07) \times 10^{-6}{}^\circ C^{-1}$ for the c-axis in a temperature range of 12–428°C at a pressure of 1 bar by means of the X-ray diffraction method.

1. INTRODUCTION

RHENIUM (Re) is a Group 7 element which crystallizes in a hexagonal close-packed (hcp) structure up to its melting temperature, 3180°C. Bridgman[1] investigated the effect of pressure on the volume of elemental rhenium at room temperature and discovered that rhenium is least compressible of all the metals investigated. Kaufman[2] made a systematic thermodynamic study of binary alloys of various transition elements including rhenium. Assuming ideal solutions in the alloy systems of Mo–Re, Nb–Re, and Ta–Re, he estimated the difference in the Gibbs free energies for the hcp and bcc phases in rhenium to be –520 cal/mole at 300°K and the difference in the volumes of these two phases to be in a range of 0·02–0·48 cm³/mole. Kaufman (personal communication) speculated that the hcp rhenium might undergo a phase transformation to the b.c.c. phase under high pressures somewhere between 45 and 1100 kbar at room temperature. We, thus, undertook a study of rhenium up to 350 kbar at room temperature in order to search for the phase transformation as well as to redetermine the value of bulk modulus by means of the X-ray diffraction method utilizing a diamond–anvil high-pressure cell. Furthermore, the coefficient of thermal expansion for rhenium was determined by means of an X-ray diffractometer.

2. EXPERIMENTAL METHOD

A high-pressure X-ray diffraction camera designed by Bassett *et al.*[3] was used in the present study. The high pressure cell of this camera consists of two ⅛ carat gem quality diamond anvils driven by a piston screw assembly. When a polycrystalline sample is compressed between the anvil faces, a maximum pressure is produced at the center of the sample area. A finely collimated X-ray beam (approximately 50 μ in dia.) of filtered molybdenum K_α radiation passes through one of the anvils and impinges on the central part of the sample area where the maximum pressure and minimum pressure gradient exist thus producing a high resolution diffraction pattern. Diffracted rays pass out through the other anvil to a curved film having a radius of 50 mm and allowing a maximum dispersion of 45° in 2θ.

The sample consists of a mixture of powdered (submicron size) rhenium metal (99 per cent pure or better) and sodium chloride, which serves as an internal pressure standard. The resulting X-ray diffraction patterns thus consist of the diffraction lines for rhenium and for sodium chloride. The diffraction lines, (100), (002), (101), (102), (110), (103), (112) and (201) for rhenium, and the lines (200), (220) and (222) for sodium chloride were measured and used for the computation of the lattice parameters. The lattice parameters thus calculated are estimated to have an accuracy of ±0·15 per cent, and the volumes ±0·45 per cent.

The pressures to which the samples were subjected were calculated from the lattice dimension or molar volume of NaCl. To obtain a reliable pressure-volume relationship for NaCl at room temperature, the vibrational formulation of the Hildebrand equation was used as shown in detail by Weaver et al.[4]. The pressure–volume relationship thus calculated is in agreement with the experimental data of Bridgman[5] up to 100 kbar within 0·8 per cent in pressure for a given volume. On the basis of the uncertainties in various parameters used for the computation, the precision for the pressure–volume relationship in NaCl has been estimated to be ±2·5 per cent. The accuracy of the pressure values reported in this paper has been estimated to be also ±2·5 per cent.

An X-ray diffractometer (GE XRD-5) equipped with a heating stage similar to the design of Skinner *et al.*[6] was used to study the thermal expansion of rhenium. A sample consisting of a mixture of powdered rhenium and platinum, the latter of which serves as an internal standard, was heated through a temperature range of 12–428°C under 1 bar pressure of helium atmosphere. The 2θ angles for the (100), (002) and (101) diffraction peaks for rhenium and for the (111) diffraction peak for platinum produced by CuK$_\alpha$ radiation were measured to within 0·005°. The temperature was measured to ±1°C with a chromel–alumel thermocouple, which was embedded in the powdered sample to eliminate the effect of direct radiation from the heating elements. The measurements were made at room temperature, 12°C, 69°, 254°, 428°, 137° and room temperature in that order. The lattice parameters measured for heating and cooling cycles of the sample were found to be identical. This is consistent with the observation made by Conway and Losekamp[7]. No evidence of phase change or reaction was observed at a temperature of 428°C for 2 hr.

3. EFFECT OF PRESSURE

The experimental results are listed in Table 1, and also plotted in Figs. 1 and 2. The isothermal bulk modulus at zero pressure, $K_0 = -V(\partial P/\partial V)_T$, can be calculated by means of the least-squares fit of the pressure-volume data to the Birch–Murnaghan equation:

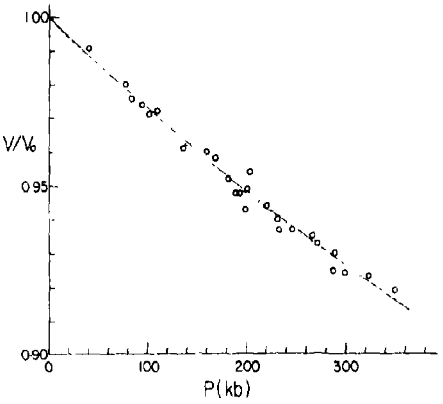

Fig. 1. The effect of pressure on the volume of rhenium up to 350 kbar at room temperature. The solid curve indicates the least squares fit of the data to the two parameter Birch–Murnaghan equation, and the dashed curve indicates the least squares fit of the data to the Birch–Murnaghan equation with $\xi = 0$.

$$P = (\tfrac{3}{2})K_0[(V_0/V)^{7/3} - (V_0/V)^{5/3}] \times \{1 - \xi[(V_0/V)^{2/3} - 1]\},$$

where V is the volume at pressure P, V_0 the volume at zero pressure, and $\xi = (\tfrac{3}{4})(4 - K_0')$, where K_0' is the pressure derivative of K, $(\partial K/\partial P)_T$, evaluated at $P = 0$. The values of K_0 and ξ for rhenium thus computed are

Table 1. Experimental data for the effect of pressure on the lattice parameters and the molar volume of rhenium at 23° ± 2°C

	NaCl			Rhenium				
Run No.	a (Å)	V/V_0	P (kbar)	c (Å)	a (Å)	c/a	V (cm³/mole)	V/V_0
1DS	5·640	1·000	0	4·456	2·761	1·614	8·86	1·000
15UP 9	5·411	0·883	40	4·435	2·755	1·610	8·78	0·991
3LD 130	5·276	0·819	78	4·428	2·742	1·615	8·68	0·980
9UP 35	5·258	0·810	84	4·425	2·739	1·616	8·65	0·976
15UP 5	5·227	0·796	95	4·411	2·739	1·610	8·63	0·974
15UP 6	5·210	0·788	102	4·410	2·734	1·613	8·60	0·971
15UP 7	5·187	0·778	110	4·418	2·734	1·616	8·61	0·972
9UP 26	5·127	0·751	137	4·390	2·727	1·610	8·51	0·961
9UP 28	5·081	0·731	161	4·394	2·724	1·613	8·50	0·960
9UP 36	5·060	0·722	170	4·390	2·723	1·613	8·49	0·958
9UP 30	5·039	0·713	183	4·385	2·716	1·615	8·43	0·952
9UP 29	5·027	0·708	190	4·378	2·713	1·614	8·40	0·948
9UP 31	5·020	0·705	194	4·378	2·713	1·614	8·40	0·948
3LD 118	5·010	0·701	200	4·371	2·707	1·614	8·35	0·943
3LD 129	5·006	0·699	202	4·375	2·714	1·612	8·41	0·949
3LD 108	5·003	0·698	204	4·385	2·719	1·613	8·45	0·954
3LD 128	4·976	0·687	222	4·372	2·709	1·614	8·37	0·944
3LD 112	4·960	0·680	232	4·360	2·706	1·611	8·32	0·940
3LD 119	4·957	0·679	235	4·355	2·704	1·611	8·30	0·937
3LD 113	4·940	0·672	247	4·363	2·701	1·615	8·30	0·937
3LD 114	4·911	0·660	268	4·360	2·699	1·615	8·29	0·935
3LD 115	4·906	0·658	272	4·352	2·699	1·613	8·27	0·933
3LD 110	4·886	0·650	288	4·334	2·693	1·609	8·19	0·925
3LD 116	4·883	0·649	290	4·348	2·695	1·613	8·24	0·930
3LD 121	4·873	0·645	300	4·340	2·689	1·614	8·18	0·924
3LD 124*	4·845	0·634	324	4·332	2·691	1·610	8·18	0·923
3LD 125*	4·820	0·624	350	4·331	2·684	1·614	8·14	0·919

*High-pressure B2 phase of NaCl[14] exist.

$K_0 = 3{\cdot}50 \pm 0{\cdot}15$ Mbar and $\xi = 0{\cdot}8 \pm 1{\cdot}0$. The uncertainty values represent those at a 50 per cent confidence level. On the other hand, if the ξ parameter is assumed to be zero, ($K_0' = 4$) of the least-squares fit of the data to the Birch–Murnaghan equation yields a value of $K_0 = 3{\cdot}36 \pm 0{\cdot}15$ Mbar. In Fig. 1, the results of these calculational schemes are compared, and are barely distinguishable.

In Fig. 2, the linear compressions along the a- and c-crystallographic axes are shown. The least-squares fit of the data to a linear equation yields a relationship:

$$\Delta a/a_0 = (0{\cdot}97 \pm 0{\cdot}10)\Delta c/c_0,$$

where a_0 and c_0 are the lattice dimensions at

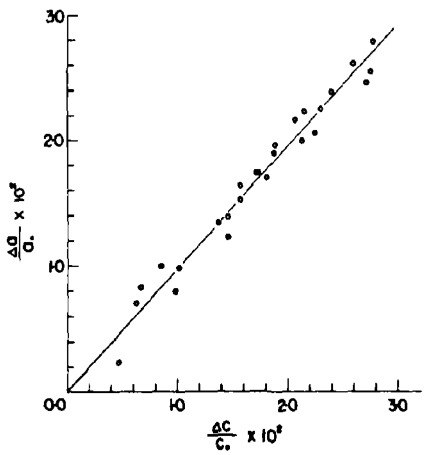

Fig. 2. The plot of the linear compressions along the a-axis and the c-axis. The straight line indicates the least squares fit: $\Delta a/a_0 = (0{\cdot}97 \pm 0{\cdot}10)\Delta c/c_0$.

zero pressure and room temperature, and Δa and Δc are the change in the a and c axes. The uncertainty represents one standard deviation. This indicates that the axial ratio, c/a, is virtually independent of pressure.

Bridgman[1] determined the effect of pressure on the volume of rhenium at room temperature up to 30 kbar, and obtained a bulk modulus of 3·71 Mbar. The precision of his volume measurements is presumably ±3 per cent in $\Delta V/V_0$ or ±0·1 Mbar for K_0 value. If our experimental data for a range of 0–110 kbar were fitted to a linear equation as done by Bridgman[1] for his data, we obtain a K_0 value of 3·69 Mbar, which compares well with Bridgman's value. Therefore, the difference between Bridgman's value and our value, which was calculated by means of the Birch–Murnaghan equation, can be attributed to the difference in the data processing methods.

The adiabatic bulk modulus for a single crystal of rhenium was determined to be 3·635 Mbar at 25°C by Shepard and Smith[8] by means of the ultrasonic technique. The adiabatic bulk modulus, K_S, can be related to the isothermal bulk modulus, K_T by the equations:

$$K_S = (1 + \gamma\alpha_v T)K_T \text{ and } \gamma = (\alpha_v V K_S)/C_p.$$

where γ is the thermodynamic Grüneisen parameter, α_v the volume thermal expansivity, T the temperature, V the molar volume, and C_p the specific heat at constant pressure. On the basis of the values of the isothermal bulk modulus, the volume thermal expansivity, and the molar volume determined by the present work, the thermodynamic Grüneisen parameter, γ, can be calculated to be 2·38 ± 0·03 for rhenium, where the value of C_p, 6·14 cal/mole deg, given by Stull and Sinke[9] was used. Hence, the adiabatic bulk modulus by Shepard and Smith[8] is equivalent to the isothermal bulk modulus of 3·587 Mbar. Therefore, the result of this work, 3·50 ± 0·15 Mbar, is in agreement with the ultrasonic value within the experimental uncertainties. If this ultrasonic value is accepted for the K_0 value, then the corresponding value for K_0' can be calculated to be $2{\cdot}2 \pm 0{\cdot}5$ by means of the least-squares fit of the data to the Birch–Murnaghan equation.

4. EFFECT OF TEMPERATURE

The effect of temperature on the lattice parameters for rhenium and platinum are listed in Table 2 and also plotted in Fig. 3. The mean coefficients of linear thermal expansion were calculated by means of the least-squares fit of the experimental data to the equation:

$$L/L_{25} = 1 + \alpha(T - 25)$$

where L is the linear dimension of unit cell at temperature T°C, L_{25} the linear dimension at 25°C, and α the mean coefficient of linear thermal expansion. The values thus calculated are:

$$\alpha_a = (7{\cdot}03 \pm 0{\cdot}10) \times 10^{-6}\,{}^{\circ}\mathrm{C}^{-1}, \text{ along the } a\text{-axis}$$

$$\alpha_c = (4{\cdot}96 \pm 0{\cdot}07) \times 10^{-6}\,{}^{\circ}\mathrm{C}^{-1},$$

along the c-axis for rhenium and

$$\alpha_a = (9{\cdot}17 \pm 0{\cdot}13) \times 10^{-6}\,{}^{\circ}\mathrm{C}^{-1} \text{ for platinum.}$$

On the basis of these values, the mean coefficient of the volume thermal expansion

Table 2. The experimental data for the lattice parameters of rhenium and platinum at various temperatures

T	Re		Pt
(°C)	a/a_{25}	c/c_{25}	a/a_{25}
12·5	0·99993[†]	0·99998	0·99992
25	1·00000	1·00000	1·00000
69·5	1·00036	1·00025	1·00041
137·0	1·00091	1·00054	1·00112
254·0	1·00181	1·00114	1·00214
428·0	1·00268	1·00200	1·00365

[†] The uncertainty is estimated to be ±0·00010.

Table 3. Comparison of the thermal expansion data for rhenium

	α_v 10^{-6}°C^{-1}	α_a 10^{-6}°C^{-1}	α_c 10^{-6}°C^{-1}	Methods	Range of measurements (°C)	Temperature range for the α values
Sims *et al.*[13]	19·8	—	—	Bulk		
Conway and Losekamp[7]	17·7	—	—	Bulk	25–2500	25°C
Agte *et al.*[11]	21·8 ± 1·1	4·7 ± 0·4	12·5 ± 0·9	X-ray	25–1917	Mean over the range of measurements
Pawar and Deshpande[12]	20·6	7·9	4·8	X-ray	25–354	Mean over the range of measurements
This work	19·0 ± 0·2	7·03 ± 0·10	4·96 ± 0·07	X-ray	12–428	Mean over the range of measurements

*Conway and Losekamp express their results in terms of average linear thermal expansion by $\alpha_l = 5{\cdot}89 \times 10^{-6} + 17{\cdot}1 \times 10^{-10}\,(t-25)$, where t is in °C

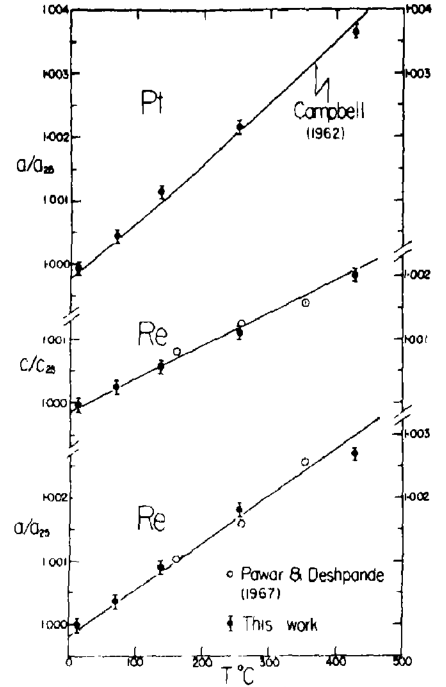

Fig. 3. The lattice parameters of rhenium and platinum as a function of temperature between 12 and 428°C. The data points obtained by Pawar and Deshpande[12] are indicated by open circles, and our data with solid circles.

for rhenium can be calculated:

$$\alpha_v = (19{\cdot}0 \pm 0{\cdot}2) \times 10^{-6}\,{}^{\circ}\mathrm{C}^{-1}.$$

The results for platinum which was used as an internal standard are in good agreement with the data obtained by Campbell[10] as shown in Fig. 3. The thermal coefficient values for rhenium by various investigators are tabulated in Table 3 along with the results of this work. It is seen that the volume thermal expansion data for these five studies are nearly in agreement, whereas the linear thermal expansion data of Agte *et al.*[11] differ substantially from the values of Pawar and Deshpande[12] and of ours. A close agreement between the values of Pawar and Deshpande and ours indicates that the result of Agte *et al.*[11] are probably in error.

5. THE *c/a* AXIS RATIO

The *c/a* axis ratio in rhenium is virtually independent of volume, when it is compressed by 10 per cent of the original volume. The mean *c/a* ratio for 27 measurements up to 350 kbar is 1·613 with a standard deviation of ±0·002 in the *c/a* ratio or 0·1 per cent. On the other hand, the *c/a* ratio varies with temperature; it decreases by 0·1 per cent for a volume expansion of 1 per cent (at 500°C). More quantitatively the effect of pressure and temperature can be expressed as:

$$-0{\cdot}013 < (\partial \ln (c/a)/\partial \ln V)_T < 0{\cdot}013$$
$$(\partial \ln (c/a)/\partial \ln V)_p = -0{\cdot}109 \pm 0{\cdot}007.$$

Thus, the effect of temperature on the *c/a* axis ratio is at least one order of magnitude greater than the effect of pressure.

The thermal expansivity is a manifestation of the anharmonicity in lattice vibrations, whereas the compressibility or bulk modulus is primarily a manifestation of harmonic properties in solids. Thus, it appears that the variation in *c/a* ratio depends mainly on a difference in anharmonicity in different directions in the rhenium structure.

Acknowledgements—We are grateful to Dr. Larry Kaufman, Man Labs Inc., Cambridge, Mass. U.S.A., for suggesting a study of rhenium under high pressure, and for providing a sample of rhenium. We also thank J. Scott Weaver for his assistance in the thermal expansion measurements and for his critical comments on the manuscript. This work was partially supported by a National Science Foundation Grant, GA-1430.

REFERENCES

1. BRIDGMAN P. W., *Proc. Am. Acad. Arts Sci.* **84**, 111 (1955).
2. KAUFMAN L., *Phase Stability in Metals and Alloys* (Edited by P. S. Rudman, J. Stringer and R. I. Jaffer), p. 125. McGraw Hill, New York (1967).
3. BASSETT W. A., TAKAHASHI T. and STOOK P. W., *Rev. scient. Instrum* **38**, 37 (1967).
4. WEAVER J. S., TAKAHASHI T. and BASSETT W. A., *Symposium on the Accurate Characterisation of High Pressures* (Edited by E. Lloyd). National Bureau of Standard, Washington, D.C. (In press).
5. BRIDGMAN P. W., *Proc. Am. Acad. Arts Sci.* **76**, 1 (1945).
6. SKINNER B. J., STEWART D. B. and MORGENSTERN J. C., *Am. Miner.* **47**, 962 (1962).
7. CONWAY J. B. and LOSEKAMP A. C., *Trans. AIME* **236**, 702 (1966).

8. SHEPARD M. L. and SMITH J. F., *J. appl. Phys.* **36**, 1447 (1965).
9. STULL D. R. and SINKE G. C., *Thermodynamic Properties of the Elements*, p. 233. American Chemical Society, Washington, D.C. (1956).
10. CAMPBELL, U.S. Bur. Mines, Inform. Circ. 8102 (1962).
11. AGTE C., ALTERTHUM H., BECKER K., HEYNE G. and MOERS K., *Z. anorg. Chem.* **196**, 129 (1931).
12. PAWAR R. R. and DESHPANDE V. T., *Curr. Sci.* **36**, 120 (1967).
13. SIMS C. T., GRAIGHEAD C. M., and JAFFEE R. I., *Trans AIME* **203**, 168, (1955).
14. BASSETT W. A., TAKAHASHI T., MAO H. K. and WEAVER J. S., *J appl. Phys.* **39**, 319 (1968).

J. Phys. Chem. Solids Pergamon Press 1970. Vol. 31, pp. 1353–1359. Printed in Great Britain.

INFRARED QUENCHING OF THE LUMINESCENCE AND PHOTO-HALL EFFECT OF ZnS:Cu AND CdS:Cu CRYSTALS*

CHARLEY B. BURGETT† and CHUN C. LIN
Department of Physics, University of Wisconsin, Madison, Wisc 53706, U S.A

(*Received* 20 *October* 1969)

Abstract—The infrared quenching of the green luminescence of ZnS:Cu and the 1·0-μ luminescence of CdS:Cu has been studied. A quenching band at 2·4μ was found for ZnS:Cu in addition to the two well-known bands at 0·8μ and 1·2μ. The new quenching band is identified as hole transition from the *e* state of Cu^{2+} to the valence band. The transient stimulation effect produced by the quenching radiation can be explained as the transfer of electrons from slow centers to fast centers using the unassociated pair model. For CdS:Cu three quenching bands centered around 0·8–0·9, 1·4, and 2·5μ have been observed, and they can be ascribed to hole transitions among the two crystal-field states of Cu^{2+} and the valence band. Quenching of photo-Hall effect by radiation of 0·8–0·9 and 1·2–1·3μ has been observed for both ZnS:Cu and CdS:Cu. The reduction of Hall mobility may be interpreted as the result of two-carrier conduction. For CdS:Cu quenching of photoconductivity was also found at 2·5μ.

1. INTRODUCTION

THE LUMINESCENCE of ZnS crystals has been a subject of interest for over fifty years. Although various models have been proposed to explain the mechanism of the luminescence, only in recent years have serious attempts been made to describe the electronic processes in terms of the atomic constituents of the crystals. The green luminescence has long been thought of as transitions to the Cu^{2+} impurity centers from electrons in the conduction band or from electron traps in shallow donor levels[1, 2]. Shionoya and his co-workers[3, 4, 5] have recently proposed the unassociated donor–acceptor pair emission mechanism for the green luminescence, i.e. transition from a co-activator donor level to the copper acceptor level. According to crystal field theory, the ground state $(3d)^9$ of a free Cu^{2+} ion is split into two levels in a tetrahedral crystal lattice and the spacing between these two levels is about 5800 cm^{-1} in the case of ZnO:Cu[6]. Indeed the recent work of Broser, Maier, and Schulz[7] has established that the i.r. luminescence near 1·5μ and absorption at 1·3μ are due to the transitions between the two crystal-field levels of the Cu^{2+} ion. Although the hole in Cu^{2+} is normally located in the upper level which is responsible for the green luminescence, the presence of a lower level of the Cu^{2+} center suggests the possibility of optical quenching effects other than the 0·8μ band[1, 8, 9] and the strong correlation between the green and the i.r. luminescence. In this paper we shall report some studies of quenching of the green luminescence of ZnS and CdS crystals with special reference to the energy levels of the Cu center. I.R. quenching of the photo-Hall effect has also been examined in conjunction with the luminescence experiments. The results of this work have shown that the stimulation of the green and i.r. luminescence can be explained by Shionoya's unassociated model and that the three different i.r. quenching modes of the green luminescence and of the photo-Hall effect and photoconductivity can all be attributed to the energy levels of the Cu center.

---

*Supported by the U.S. Office of Naval Research.

†Present address: Texas Instruments Incorporated, Dallas, Texas 75222, U.S.A.

2. EXPERIMENT

The crystal samples were grown by the vapor-phase method with Cl as coactivator. For the luminescence experiments, an electron gun operated at 10 kV and 0·1–50μA and modulated at 200 cps was used as the primary source of excitation. A photomultiplier was used to detect the visible luminescence. The a.c. component (200 cps) of the photomultiplier output was amplified and phase-detected. For studying the transient stimulation, the d.c. output of the photomultiplier was monitored and measured by a Keithley electrometer. In the case of i.r. emission, a PbS detector was used. A 75W tungsten–halogen lamp with quartz bulb supplied the secondary radiation for quenching and stimulation. Selection of the quenching radiation and of the luminescence bands was accomplished by means of thin-film dielectric interference filters. In order to produce a constant flux of quenching (or exciting) radiation as a function of frequency, the intensity of the monochromatic beam was normalized by the use of neutral density filters.

For mobility measurements, the Hall voltage was generated and modulated at a frequency of 2 cps by a rotating permanent magnet of 5000 G. For ZnS crystals the contact leads were made by melted indium baked at about 500°C in H_2[10], whereas pressed or melted indium contacts were satisfactory for CdS. Because of the high sample resistance, the Hall voltage was monitored by an electrometer with $10^{14}\Omega$ input resistance, acting as a unity-gain impedance-matching device. It transformed the Hall voltage to a low impedance signal which was then fed to the amplifier and phase detection system. Two light beams, one for photo-excitation and one for quenching, were directed onto the crystal by means of a quartz light pipe.

3. LUMINESCENCE OF ZnS:Cu CRYSTALS

The visible part of the luminescence of the ZnS crystals used in this work is predominantly 'green' in the wavelength range of 0·45–0·55μ. With electron-beam excitation alone, luminescence in the i.r. region of 1·45–1·75μ was also observed. The intensity of the i.r. luminescence is greatly enhanced by doping the crystals with additional amounts of copper, followed by annealing.

(a) *Quenching and stimulation of the green luminescence*

It is well known that the green luminescence of ZnS may be quenched by radiation of 0·8μ and of 1·2μ, and that the quenching efficiency of the 1·2-μ band decreases as the temperature is reduced from 300 to 77°K[1, 8]. Our crystals show the same kind of quenching behavior. In each of the quenching bands the application of i.r. radiation produced a transient stimulation of the luminescence followed by steady-state quenching. The similarity between the quenching and stimulation behaviors has been previously noted[8, 9]. While it has been well confirmed that the quenching of the green luminescence is due to transition of holes from the Cu^{2+} center to the valence band or to an excited state slightly above it, the origin of the stimulation effect is not as clear, although it has been commonly ascribed to release of electrons from traps[1, 9]. Using the unassociated pair model proposed by Era, Shionoya and Washizawa[4], we can ascribe the quenching and stimulation to the same mechanism. According to these authors, the green luminescence arises from donor–acceptor (unassociated) pair emission. Pairs with large separation have small transition probabilities and act as slow centers whereas close pairs have a larger transition probability and are faster. When quenching radiation is applied, holes are excited from Cu^{2+} ions to the valence band and may be captured by a fast center. This, in effect, transfers holes from the slow centers to the fast ones, giving rise to a momentary increase of the luminescence. The long-term quenching then sets in as a result of a drop in the Cu^{2+} concentration because the holes excited to the valence band may also be captured by non-radiative centers. Thus both optical stimulation and quenching result from the same process of hole transfer from the acceptor to the valence band and should have the same spectral response. The former occurs when the freed holes are captured by the fast centers, whereas transfer of holes to the non-radiative centers results in quenching. In fact, if the crystals are relatively free of non-radiative centers, the transient stimulation would still occur, but very little long-term quenching would be observed.

(b) *Excitation of the i.r. luminescence*

The i.r. emission and absorption at 1·2–1·6μ have been identified by Broser, Maier and Schulz[7] as due to transitions between the two levels resulting from the crystal-field splitting of the ground state of the Cu^{2+} ion in a tetrahedral field. In Fig. 1 are shown the two crystal-field energy levels (e and t_2) of a d-electron in tetrahedral symmetry. It has been pointed out by several workers that the i.r. emission can be excited by radiation of 0·8μ and of 1·3μ[8, 9, 11]. Both peaks were found in our samples. The two peaks in the excitation spectrum were ascribed to transition of holes from Cu^{2+} centers to the valence band and to an excited state of the Cu^{2+} centers. Since the low-frequency peak of the excitation spectrum occurs at the same frequency as the i.r. absorption studied by Broser *et al.*, we may identify the hole excited state as the lower crystal-field level of Cu^{2+}.

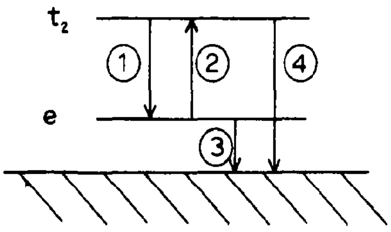

Fig. 1. The two crystal-field energy levels, t_2 and e, of a d-electron in the ZnS lattice relative to the valence band. The arrows indicate hole transitions.

Our samples show an original level of i.r. emission under electron beam bombardment only. When the exciting radiation is turned on, the intensity of the i.r. emission first rises sharply and then falls back slowly to a steady-state level somewhat higher than the original value. The sharp rise of the intensity is due to an increase in the number of holes in the e level of Cu^{2+} as produced by exciting radiation. The excitation process, however, also increases the rate of depletion of the Cu^{2+} ions through transfer of holes to non-radiative centers, thus causing a slow decrease of the i.r. emission.

(c) *Quenching of green luminescence by radiation at* 2–3μ

According to the two-level scheme of the Cu^{2+} center as shown in Fig. 1, i.r. radiation corresponding to hole transition 3 will remove the holes in the e level, and, if there is a sufficient degree of thermal excitation of holes from t_2 to e, may reduce the hole population in the t_2 level and thereby cause quenching of the green luminescence. To test this point, we have examined the quenching spectrum between 2 and 3 μ and found a small quenching peak around 2·4μ at room temperature and no quenching at 77°K. The results are listed in Table 1. This quenching peak

Table 1. *Percentage quenching of the 'green' luminescence of* ZnS:Cu *and* CdS:Cu *and of photoconductivity of* CdS:Cu *by i.r. radiation of* 2·1–2·9μ

Wavelength (μ)	ZnS Lum.	CdS Lum.	CdS Photocond.
2·1	0	0	0
2·2	3	0	1
2·3	9	6	4
2·4	12	8	5
2·5	11	12	7
2·7	5	4	7
2·9	0	0	0

corresponds well to the energy difference between transition 4 (0·8μ) and transition 1 (1·2–1·3μ) in Fig. 1. Initial stimulation was also observed in association with this quenching.

Because both the 2·4-μ and 1·2-μ quenching of the green luminescence require thermal excitation, it should be possible to use a two-step optical excitation without the aid of thermal activation. We have therefore conducted a double quenching experiment with simultaneous irradiation of 2–3μ and 1·2-μ wavelength. At 77°K, the use of 1·2-μ irradiation produced a small quenching and no quenching was observed with 2–3μ alone. Upon application of both 1·2-μ and 2–3μ radiation, the quenching efficiency was increased by about one-half of the previous values. The results of this experiment support the assignment of the 2·4-μ radiation as causing hole ejection to the valence band from the lower Cu^{2+} level.

The quenching of the green luminescence by the 1·2-μ and by the 2·4-μ radiation requires a thermal activation energy of 0·5 eV and 0·9 eV respectively. We can take the temperature at which the thermoluminescence becomes maximum (called T^*), as an indication of the temperature region where thermal activation is efficient. Using the approximate formula which resulted from the theory of Randall and Wilkins[12], we obtain $T^* \simeq$ 200°K for an activation energy of 0·5 eV and $T^* \simeq 360$°K for 0·9 eV activation. This is in qualitative agreement with the observation that the 1·2-μ quenching band decreases in efficiency at 77°K whereas the quenching by 2·4-μ radiation disappears at 77°K.

4. LUMINESCENCE OF CdS:Cu CRYSTALS

Similar studies of the luminescence behavior have been made on CdS:Cu crystals. The luminescence which corresponds to the green emission of ZnS:Cu occurs at 1·0μ, but will be designated as the 'green' band to facilitate comparison with the ZnS crystals. We have measured the quenching of this 'green' band by i.r. radiation of various frequencies. The experimental data in Fig. 2 show two bands centered around 0·8–0·9μ and 1·4μ. As in the case of ZnS : Cu, the low-frequency quenching peak decreases in efficiency at liquid N_2 temperature.

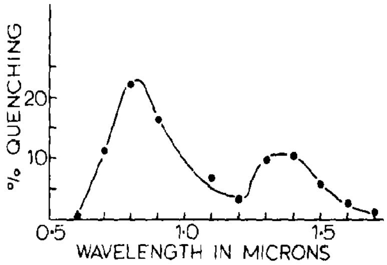

Fig. 2. Percentage quenching of the 1·0-μ luminescence of CdS : Cu by i.r. radiation of 0·7–1·7μ. No measurements were made with quenching radiation of 1·0μ because of the difficulty of isolating the quenching radiation from the detector.

The emission spectrum of CdS:Cu at 1·7μ (corresponding to the 1·6-μ band of ZnS:Cu) has been studied quite extensively[8, 13]. It can be excited by 0·8–0·9-μ and 1·4–1·5-μ radiation. Our samples exhibit the same excitation behaviors as those reported in the literature. We see that the two excitation peaks of 1·7-μ emission again coincide with the two quenching peaks of the 'green' luminescence. Broser, Maier, and Schulz[7] have assigned the 1·7-μ emission and the 1·5-μ absorption of CdS:Cu to the transition between the two crystal-field levels of the $(3d)^9$ state of Cu^{2+}. Thus we have a completely analogous situation to the case of ZnS:Cu and the same energy level diagram of Fig. 1 applies to CdS : Cu as well.

This analogy is further evidenced by the observation of quenching of the 'green' luminescence by i.r. radiation at 2·3–2·8μ. Percentage quenching at various wavelengths may be found in Table 1.

5. PHOTO-HALL EFFECT AND PHOTOCONDUCTIVITY

Since the optical quenching of luminescence of both ZnS:Cu and CdS:Cu is associated with ejection of holes to the valence band, one may expect to observe a change in the Hall mobility under i.r. radiation as a result of the hole conduction. When both electrons and holes are making appreciable contributions to electric conduction, the conductivity and Hall mobility μ_H are related to the concentrations n and p and mobilities μ_n and μ_p of the electrons and holes as

$$\begin{aligned}\sigma &= pe\mu_p + ne\mu_n,\\ \mu_H &= (p\mu_p^2 - n\mu_n^2)/(p\mu_p + n\mu_n).\end{aligned} \tag{1}$$

Consider a photoconductor under band-gap (primary) photoexcitation. As the i.r. (secondary) radiation is introduced, the electron carrier density decreases markedly[14]. Although the holes begin to contribute to σ, the net result is a quenching of photoconductivity, which has been studied extensively[14]. The situation of the Hall effect is rather different, since in the case of one-carrier (electron) conduction, the Hall voltage should be independent of the carrier density or the conductivity provided that μ_n remains constant. Bube, McDonald, and Blanc[15] have found that for CdS the Hall mobility varies only by a factor of two over the range of $n = 10^{10}$ to $10^{15}\,\text{cm}^{-3}$. However, one may expect a much more drastic decrease in the Hall mobility if there are sufficient numbers of hole carriers to cancel the mobility due to electron conduction. Indeed, a substantial reduction of the photo-Hall mobility was observed previously for CdS but no spectral dependence of the quenching was reported[15].

We have measured the Hall mobilities of our samples and their variation under i.r. irradiation. At first only band-gap radiation was used, and the Hall mobility of the CdS crystals remained essentially constant (98 cm^2/V-sec) over the range of electron density of $10^9\,\text{cm}^{-3}$ to $3 \times 10^{11}\,\text{cm}^{-3}$. With the secondary i.r. radiation, the change of the Hall mobility with respect to the frequency of the quenching radiation is shown in Fig. 3. For comparison, the electric conductivity data are also included in this graph. One notes that between 0·9 to 1·0μ, the Hall mobility is reduced by over 95 per cent whereas the decrease of conductivity is only 80 per cent. As a further test, we removed the quenching radiation and lowered the intensity of the primary excitation until σ was again reduced to 20 per cent of its initial value. Under this condition, we found no change of the Hall mobility from the original value of 98 cm^2/V-sec. Thus the quenching of the Hall mobility is too large to be explained by the change of electron mobility due to charge scattering effects and is therefore attributed to the introduction of two-carrier conductivity. The two maxima of quenching of photo-Hall effect in Fig. 3 appear at about the same frequencies as those associated with the quenching of the 1·0μ luminescence. Similar experiments on the quenching of the Hall mobility have been performed for the ZnS crystals. The results are given in Fig. 4. The electric measurements are generally more difficult to make in the case of ZnS because of the long response time of the Hall voltage. Again we see two peaks near 0·9μ and 1·3μ similar to the ones found in the luminescence experiments. Our observation of the quenching of photo-Hall effect therefore gives additional evidence for the generation of holes in the valence band by the 0·8–0·9μ and 1·2–1·3μ i.r. radiation.

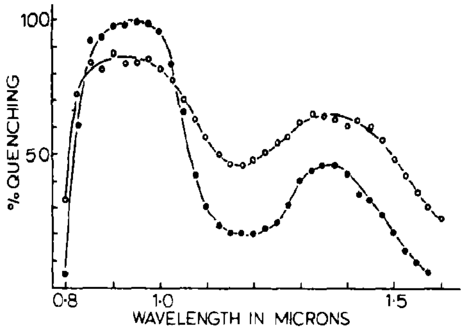

Fig. 3. Percentage quenching of the Hall mobility (dots) and photoconductivity (circles) of CdS:Cu by i.r. radiation of 0·8–1·6μ.

In the region around 2·6μ, optical quenching of photoconductivity of CdS:Cu was

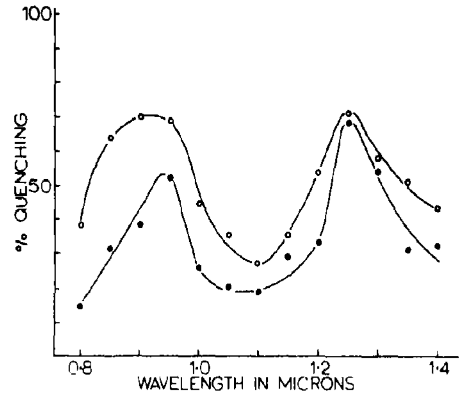

Fig. 4. Percentage quenching of the Hall mobility (dots) and photoconductivity (circles) of ZnS:Cu by i.r. radiation of 0·8–1·4μ.

observed and the data are summarized in Table 1. When a broad-band filter for the entire range of 2–3μ was used to select the secondary radiation, the photoconductivity can be quenched by 25 per cent. Attempts were made to detect the quenching of Hall mobility, but only a very small reduction (about 5 per cent) of the Hall voltage was found even under broad-band i.r. irradiation of 2–3μ. In the case of ZnS:Cu, the crystals produced too much noise to obtain reliable measurements of small quenching effects. Becuase of the 0·9 eV thermal activation energy required, the transition 3 as indicated in Fig. 1 is an inefficient process for transferring holes from the Cu^{2+} center to the valence band. The 2·4μ radiation may shift the Fermi level sufficiently to reduce the electron carrier density and the conductivity, but may not produce significant hole density to alter the Hall mobility.

Because of the marked difference in the decay rate for luminescence and conductivity, it has been previously concluded that the luminescence activator and the sensitizing centers for photoconductivity are not identical. However, there is some disagreement on their identification in the literature. Era, Shionoya, Washizawa, and Ohmatsu[5] suggested that a copper impurity atom in very close proximity to an activator may act as the sensitizer, whereas Kang, Phipps, and Bube[2] identified the sensitizing centers to the cation vacancies. The observation of optical quenching at 0·8μ tends to place the sensitizer level about 1·2–1·3 eV above the valance band, the same location as the luminescence activator. Since the 1·3-μ absorption of ZnS:Cu is associated with the crystal-field splitting of the $(3d)^9$ state of Cu^{2+}, it is reasonable to assign the 1·3-μ quenching of the photo-Hall effect to excitation of holes from t_2 to e in Fig. 1. This is in line with the closely associated copper pairs as sensitizer as suggested by Era *et al.*[5]. It is also compatible with cation-vacancy model since ejection of holes from the copper atoms may cause a transfer of holes from the cation vacancy.

6. SUMMARY

The two crystal-field energy levels of a *d*-electron of Cu^{2+} in the ZnS crystal lattice relative to the valence band are shown in Fig. 1. A new quenching band at 2·3–2·8μ has been observed for the green luminescence of ZnS:Cu. This may be ascribed to the transition of holes from the lower crystal-field level to the valence band. All three quenching bands of the green luminescence (0·8, 1·2, 2·4μ) are accompanied by an initial stimulation. It is suggested that the stimulation effect may be explained as the result of transfer of holes from the slow to the fast luminescence centers using the unassociated pair model.

Three quenching bands at 0·8–0·9, 1·4, and 2·5μ have been observed for the 1·0-μ luminescence of CdS:Cu. These can be explained in terms of the crystal-field energy levels of Cu^{2+} in the CdS lattice similar to the case of ZnS.

Quenching of photo-Hall effect by 0·8–0·9-μ and 1·3–1·4-μ radiation has been observed for both ZnS:Cu and CdS:Cu. The reduction of the Hall mobility may be interpreted as due to the introduction of hole conduction produced by the i.r. radiation. A small quenching of the photoconductivity by 2·5μ radiation was seen for CdS:Cu, but we were unable to detect quenching of photo-Hall effect at this wavelength.

Acknowledgement – We wish to thank Dr. H. Samelson for the crystals.

REFERENCES

1. CURIE D., *Luminescence in Crystals*. Wiley, New York (1963).
2. KANG C. S., PHIPPS P. B. P. and BUBE R. H., *Phys. Rev.* **156**, 998 (1967).
3. SHIONOYA S., ERA K. and WASHIZAWA Y., *J. phys. Soc. Japan* **21**, 1624 (1966).
4. ERA K., SHIONOYA S. and WASHIZAWA Y., *J Phys. Chem Solids* **29**, 1827 (1968).
5. ERA K., SHIONOYA S., WASHIZAWA Y. and OHMATSU H., *J. Phys. Chem. Solids* **29**, 1843 (1968).
6. WEAKLIEM H. A., *J. chem. Phys.* **36**, 2117 (1962).
7. BROSER I., MAIER H. and SCHULZ H. J., *Phys. Rev.* **140**, A2135 (1965).
8. BROWNE P. F., *J. Electron.* **2**, 1 (1956–67).
9. MEIJER G., *J. Phys. Chem. Solids* **7**, 153 (1958).
10. BLOUNT G. H., FISHER M. W., MORRISON R. G. and BUBE R. H., *J. electrochem. Soc.* **113**, 690 (1966).
11. APPLE E. F and PRENER J. S., *J Phys. Chem. Solids* **13**, 81 (1960).
12. See p. 163 of Ref.[1]; RANDALL J. T. and WILKINS M. H. F., *Proc R. Soc.* **A184**, 366 (1945).
13. BRYANT F. J. and COX A. F. J., *Proc. phys. Soc.* **87**, 551 (1966).
14. BUBE R. H., *Phys. Rev.* **99**, 1105 (1955).
15. BUBE R. H., MACDONALD H. E. and BLANC J., *J. Phys. Chem. Solids* **22**, 173 (1961).

J. Phys. Chem. Solids Pergamon Press 1970. Vol. 31, pp. 1361–1373. Printed in Great Britain.

COLORATION OF LiF BY 3·0 MeV ^{3}He, ^{40}Ar, ^{84}Kr, AND 2·0 MeV ^{129}Xe IONS

K. L. VANDER LUGT*, J. COMAS and E. A. WOLICKI
Naval Research Laboratory, Wash. D.C. 20390, U.S.A.

(*Received* 6 *October* 1969)

Abstract – Coloration studies of alkali halide crystals have been extended by investigating the color centers produced in LiF by 3·0 MeV ^{3}He, ^{40}Ar, ^{84}Kr, and 2·0 MeV ^{129}Xe ions. From the *F*-center growth curves it has been determined that 666 eV and 1150 eV are expended per *F*-center created by the ^{3}He and ^{40}Ar ions respectively; the curves are linear up to approx $2{\cdot}3 \times 10^{18}$ F/cc and $2{\cdot}4 \times 10^{18}$ F/cc, respectively. The optical absorption spectra of the damage produced by the ions have been quantitatively resolved and compared to the damage produced by gamma rays by means of a least squares Gaussian curve fitting computer program. For the ^{40}Ar-, ^{84}Kr- and ^{129}Xe-irradiations the data are best fitted by the formation of 3 bands near 3·22, 2·97 and 2·22 eV and the ^{3}He data by a small band near 2·90 eV. Damage profile curves, obtained by etching, yield penetration depths which agree qualitatively with calculated values and show that the damage is fairly uniform.

1. INTRODUCTION

EVEN though extensive studies on the defects (color centers) produced in alkali halide crystals upon exposure to X-rays, gamma rays, u.v. rays, electrons, protons and neutrons have been made, little information on the defects produced by energetic massive ions has been reported. The following considerations provide a strong incentive for extending alkali halide coloration studies to include irradiation by energetic massive ions. (1) Since the penetration depth is expected to be small (1–10μ), defect concentrations up to 10^{20} per cm^{3} could be measured optically. It would thus be possible to investigate those portions of defect growth curves which are otherwise often too opaque for optical measurements. Also, from the slope of the growth curve the number of defects produced per incident ion, and thus the number of electron volts expended per defect created, could be calculated. (2) Since the known color centers are produced by ionization mechanisms and no color centers due solely to direct displacements have been verified, the creation of new color centers due to direct displacement damage could be systematically investigated by employing ions whose mass varied over a considerable range. (3) A profile study of the induced damage as a function of depth could be correlated with theoretical stopping power calculations to yield information on the relative defect producing capability of ionization and direct displacement mechanisms. Such a study would be especially valuable if defects due solely to direct displacements were found. (4) A search for color centers due to the implanted ion themselves could be conducted. In particular, a recent theoretical paper has suggested the possibility of a new color center formed by an inert gas atom trapped in the potential well of an *F*-center[1].

In view of the above considerations, ion beams of ^{3}He, ^{40}Ar, ^{84}Kr, and ^{129}Xe have been employed to irradiate single crystals of LiF at room temperature. The results obtained are the subject of the present paper.

2. EXPERIMENTAL PROCEDURE

(A) *Crystals*

Lithium fluoride was employed in this investigation since preliminary coloration studies indicated that with LiF the damage

---

*NRC Postdoctoral Research Associate
Present address: Augustana College, Sioux Falls, S.D

was stable at room temperature and was also unaffected by room light. Although color centers in LiF have not been as extensively studied as those in KCl or KBr, for example, the dominant color centers in LiF irradiated at room temperature have been identified[2]. In addition, it has been reported that in LiF, unlike in other alkali halides, the radiation damage is independent of the irradiation flux [3]. This property would greatly facilitate any attempt to correlate theoretical stopping power calculations with experimental profile studies.

To facilitate cleaving, the crystals* were first hardened by exposure to ^{60}Co (10^6R) gamma rays. Samples approximately $6\times6\times\frac{1}{2}$ mm^3 were then cleaved and subsequently annealed for several hours at 450°C to remove the damage induced by the gamma-ray irradiation.

(B) *Ion accelerator*

The NRL 5 MV Van de Graaff accelerator was used to produce beams of 3·0-MeV ^{3}He, ^{40}Ar, ^{84}Kr, and 2·0-MeV ^{129}Xe ions. The ion beams were magnetically analyzed before striking the target and the beam current on target was measured and integrated in a Faraday cup arrangement which had a negatively biased guard ring located at its entrance to suppress secondary electrons.

Since charge exchange processes may be expected to increase with increasing atomic number of the incident ion and increasing pressure in the beam transport tubing, pressure in the beam tube was maintained at 10^{-5} torr or lower during irradiations. In addition, tests were made for the presence of a neutral beam component which would produce damage in the target but not be measured as an electrical current. In these tests a deflecting voltage was applied to the beam so as to prevent the singly ionized beam component from reaching the target, and three permanent magnets were placed along the beam transport tube between the deflecting plates and the target in order to deflect any beam particles which had become ionized after passing through the deflecting plates. The combined electrostatic and magnetic deflections reduced the beam measured at the target by a factor of ⩾ 50. A LiF crystal was then irradiated for ten minutes under conditions such that a beam current much larger than that used in the actual irradiations was present before the deflecting plates. The coloration produced in this way was extrapolated to the small beams and small total charge collected during the actual irradiations from which the dose curves were obtained. The neutral beam component obtained from these measurements introduced a correction of about 3 per cent to the dose delivered to the target.

In order to provide uniform irradiation over the target the beam spot was scanned electrostatically over an area somewhat larger than the sample size. Slits were then used to limit the beam to a well defined rectangular area which was larger than the crystal samples which were irradiated. The area bombarded was measured and used together with the integrated beam charge in calculating the total number of ions per cm^2 incident on the sample.

Effects due to heating of the crystals by the incident beam were evaluated in a series of preliminary irradiations. Final irradiations consisted of repeated short runs with beam intensities of 6×10^{-9} A or less into target areas of approximately 1 cm^2. Under these pulsed, low intensity, bombarding conditions no heating effects in LiF were observed. It is estimated that the surface temperature does not rise above 85°C for the most intense beam used. Even though effects due to electrostatic charging of the samples were expected to be small at the very low bombarding currents used, the following precaution was taken. The area irradiated by the beam was made purposely larger than the LiF sample so that a portion of the beam would strike the solid brass plate on which they were mounted. The secondary electrons produced at the brass plate around the periphery of the target served to keep the surface effectively neutralized. The coloration produced was measured at room temperature with a Cary 14 optical spectrophotometer several hours after irradiation.

---

*The samples were cleaved from a single block of LiF purchased from the Harshaw Chemical Co., Cleveland, Ohio, U.S.A.

3. RESULTS AND DISCUSSION

(A) F-*Center growth curves*

Typical growth curves of *F*-centers produced in alkali halide crystals subjected to ionizing radiation at room temperature indicate that coloration proceeds in three stages [4, 5]: (1) an early stage in which the coloration increases rapidly and terminates after a relatively low dose, (2) a second stage in which the coloration rises slowly, and (3) a final stage where saturation is approached. Early interpretations were that in the first, or intrinsic stage, anion vacancies initially present in the crystal simply captured an electron liberated by the radiation. Recent studies[5], however, have suggested that this stage is more complex and that both isolated and clustered anion vacancies are actually being created. The latter subsequently trap electrons to become *F*-centers. Finally, for large doses the probability for formation of an *F*-center becomes equal to that for dissociation and saturation is reached.

In the present study coloration depths are on the order of a few microns so that defect concentrations in the range of 10^{17}/cc to 10^{21}/cc can be measured. Thus the regions of the growth curves which can be observed are the second and third stages. *F*-center growth curves (plotted as *F*-centers/cm^2 vs. incident ions/cm^2) for both ^{3}He and ^{40}Ar-ion bombardment are illustrated in Fig. 1. In order to convert the optical density measurements of the *F*-band (247 nm) into *F*-centers/cm^2, Smakula's equation[6, 7] was employed using an oscillator strength of unity and a half-width for the *F*-band of 0·70 eV. The data are presented as a log–log plot since it covers several orders of magnitude in both parameters.

In order to observe the transition from the second stage to the third stage more closely, the lower portions of the growth curves are redrawn as a linear plot in Fig. 2. It is seen that the ^{3}He growth curve is linear up to approximately 2×10^{15} *F*-centers/cm^2 and that the ^{40}Ar curve is linear up to approximately 5×10^{14} *F*-centers/cm^2.

It is interesting to note that Farge *et al.*[8] have reported that a log–log plot of the *F*-center growth curve from X-ray irradiated LiF should have a slope of $\frac{1}{2}$. Their model involves the recombination of interstitials and *F*-centers after the initial or primary creation of Frenkel pairs by ionizing radiation. The presence of dislocation loops play an important role in their mechanism. In our case, however, the primary defects are not caused entirely by ionization mechanisms and it is likely that the number and type of dislocations produced by the massive ion bombardment are very different from those produced by X-rays.

Damage profile curves have been obtained using the chemical polishing solution described by Gilman and Johnston[9]. The samples were held with teflon coated tweezers in a 1·5 per cent solution of ammonium hydroxide in distilled water and rinsed with acetone. The etching periods varied from 60 sec for the ^{3}He samples to 6 sec for the ^{129}Xe samples. Damage profile curves were obtained by plotting the number of *F*-centers remaining vs. etching time. Etching rate measurements were obtained using a Bendix electronic indicator with an accuracy $\pm 0{\cdot}2 \times 10^{-6}$ in. The etching rate in the damaged region was found to be approximately the same for the He-, Ar-, and Kr- and Xe-irradiated LiF targets. An etching rate of about 0·8 μ/min was obtained while etching the samples in the solution at room temperature.

The etching measurements showed that the coloration was fairly uniform along the penetration depth for all the bombarding particle

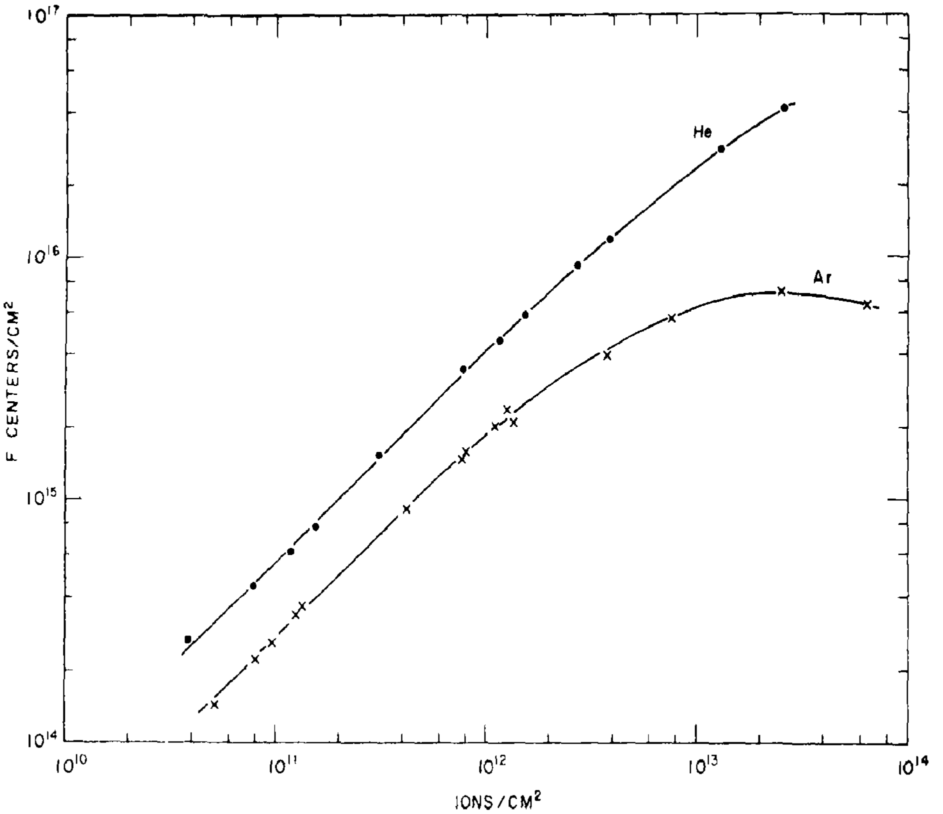

Fig. 1 Log-log plot of the F-center growth curves in LiF produced by 3 MeV ^{3}He and ^{40}Ar ion bombardment

species. For ^{3}He and ^{40}Ar in particular, such uniform coloration does not correspond to the calculated variations in stopping power vs. penetration depth.

The total stopping power, $(dE/dX)_{\text{electronic}}$ plus $(dE/dX)_{\text{nuclear}}$, of 3·0 MeV ^{3}He, ^{40}Ar, ^{84}Kr and 2·0 MeV ^{129}Xe ions vs. energy is shown in Fig. 3. For ^{3}He, dE/dX attains a maximum value near the end of its range, i.e. when the incident energy has been reduced to only 0·35 MeV. At 0·35 MeV the dE/dX is $\sim 0{\cdot}45 \times 10^{10}$ eV/cm; at 3·0 MeV, when it is just entering the surface, dE/dX is $0{\cdot}189 \times 10^{10}$ eV/cm, so the ^{3}He energy loss has come down by a factor of 2·4. For ^{40}Ar the dE/dX is lowest at the end of its range, where it is $\sim 1{\cdot}05 \times 10^{10}$ eV/cm, and highest as the ^{40}Ar just enters the surface, where it is $\sim 2{\cdot}4 \times 10^{10}$ eV/cm. The $(dE/dX)_{\text{total}}$ for ^{40}Ar has changed by a factor of about 2·4 but in the opposite direction from ^{3}He. For ^{84}Kr and ^{129}Xe the ratios of the nuclear and electronic contributions are different, while the $(dE/dX)_{\text{electronic}}$ is very nearly the same for both. The increase in the $(dE/dX)_{\text{total}}$ for Xe is due entirely to its large nuclear component. The total energy loss for both ^{84}Kr and ^{129}Xe is nearly constant throughout the particles penetration into LiF, changing by only 15–20 per cent.

The etching measurements were consistent with the calculated ratios of the penetration depths. A range of 8·61 μ for 3·0 MeV ^{3}He in LiF was obtained using stopping powers for ^{3}He in Li and F calculated by Williamson *et al.*[10]. For ^{40}Ar, ^{84}Kr and ^{129}Xe nuclear and electronic stopping powers in Li and F were

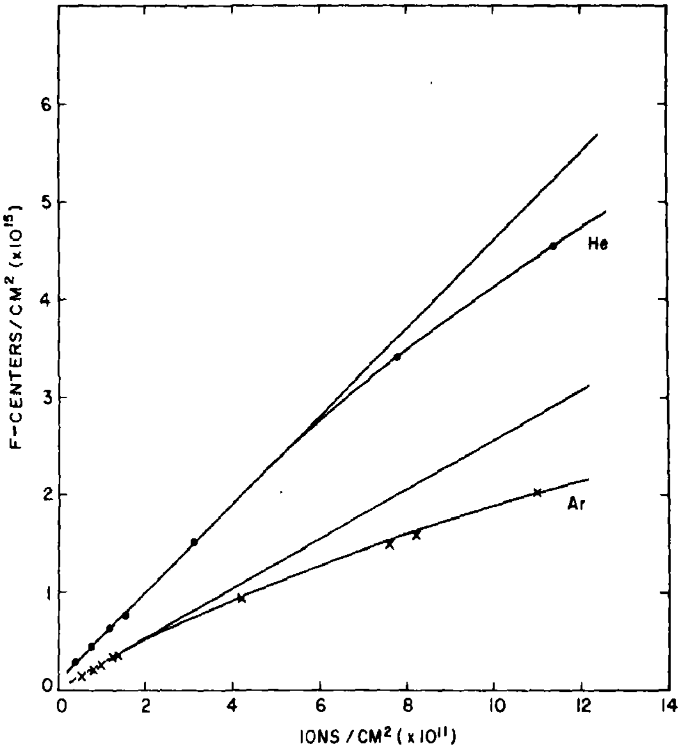

Fig. 2. Linear plot of the low dose portion of the F-center growth curves in LiF produced by 3 MeV ^{3}He and ^{40}Ar ion bombardment.

calculated using the theory of Lindhard *et al.* [11]. For heavy ion nuclear collisions the large angle scatterings are important in the energy loss process. Therefore the ranges obtained for ^{40}Ar, ^{84}Kr and ^{129}Xe were corrected to projected ranges so as to correspond to penetration depths of the ions into the LiF crystal. Projected ranges obtained for 3·0 MeV ^{40}Ar, ^{84}Kr and 2·0 MeV ^{129}Xe ions, respectively, were 2·05, 1·50 and 0·71 μ.

Since the coloration was found to be nearly uniform, the calculated values of the penetration depths can be used to convert F-centers/cm^2 to F-centers/cc. It is estimated that the F-center concentrations at which the growth curves (Fig. 2) become nonlinear are $2{\cdot}3 \times 10^{18}$ F-centers/cc and $2{\cdot}24 \times 10^{18}$ F-centers/cc for the ^{3}He- and ^{40}Ar-ion bombardment respectively. One interpretation of this close agreement is that the concentration at which an F-center growth curve becomes nonlinear does not depend upon the type of radiation or its rate of energy loss. An alternative possibility, however, is that the transition of the F-center growth curve from the second stage to stage three may be governed by the rate of the back reaction involved with the type of irradiation employed. For example, many X-rays may pass through a given region and F-centers already formed may be partially destroyed by a subsequent ray. In such cases energy is dissipated in unproductive events and the growth curves would become nonlinear at lower concentrations.

In the present case, however, even for an integrated particle flux of 4×10^{11}/cm^2, the average distance between tracks may be taken to be about 160 Å. This implies that the ion tracks do not overlap to a great extent, thus reducing at least one source of back reaction.

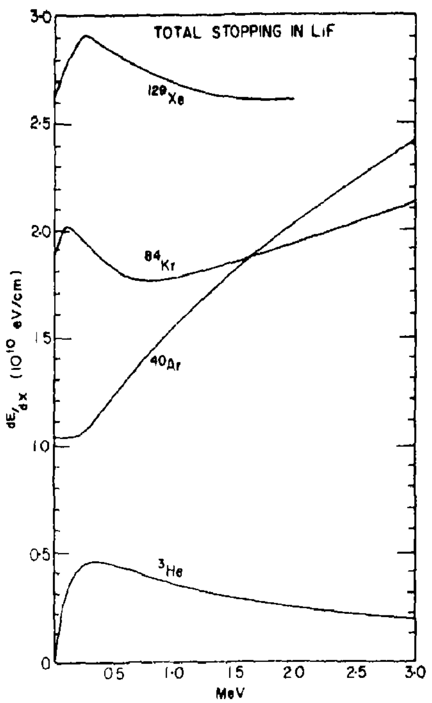

Fig. 3. Total stopping power, $(dE/dX)_{\text{electronic}}$ plus $(dE/dX)_{\text{nuclear}}$, of ^{3}He, ^{40}Ar, ^{84}Kr and ^{129}Xe in LiF.

This assumed lack of overlap is consistent with recent electron microscope observations on Ni-ion irradiated Si by Mazey *et al.*[12]. They observed damaged regions of approximately 50 Å in dia. when a 'thinned' Si crystal was subjected to a dose of 1×10^{13} 80 KeV Ne ions per cm^2. From Fig. 2 it is seen that the ^{3}He and ^{40}Ar curves become nonlinear at doses of approximately 4×10^{11} ions/cm^2 and 2×10^{11} ions/cm^2 respectively. Since the diameter of the damage track of a ^{3}He ion is expected to be smaller than that for an ^{40}Ar ion, it would be expected that the ^{3}He growth curve be linear to a higher dose than the ^{40}Ar curve.

From the linear portion of the growth curves an accurate determination of the number of *F*-centers produced per incident ion can be obtained. It is found that 4500 *F*-centers are created per ^{3}He ion and that 2600 *F*-centers are created per ^{40}Ar ion. Since each ion has an incident energy of 3·0 MeV, average energies of 666 eV and 1150 eV are expended per *F*-center produced by ^{3}He and ^{40}Ar ions respectively. These efficiencies can be compared to values ranging from 850 eV/*F*-center to 3800 eV/*F*-center for irradiation of LiF at liquid-helium temperature by 2·0 MeV electrons and various energy X-rays [13]. The relative magnitudes of the efficiencies for ^{3}He and ^{40}Ar in the present study are consistent with the X-ray and electron liquid-helium study in that, for irradiations with high track ionization densities, the efficiency decreases as the ionization density increases. Further comparisons are difficult due to the difference in sample temperatures.

A final observation from the growth curves in Fig. 2 is obtained by extrapolation of the linear portions. The intersections with the abscissa are $8{\cdot}5 \times 10^{13}$ *F*-centers/cm^2 and $1{\cdot}7 \times 10^{13}$ *F*-centers/cm^2 for ^{3}He and ^{40}Ar respectively. The ratio of these values is 5·0 while the ratio of the estimated penetration depths is 4·8. This agreement indicates that the concentration at which the first stage saturates is directly proportional to the penetration depth, and that with massive ion bombardment the initial concentration of negative ion vacancy sources (both direct and indirect) for LiF crystals prehardened and annealed is approximately $9{\cdot}5 \times 10^{16}$ *F*-centers/cc.

(B) *Search for color centers created by direct displacements*

In addition to the *F*-band (247 nm) the absorption spectra of both ^{3}He and ^{40}Ar bombarded crystals exhibited other bands in both the visible and u.v. regions. The spectrum of a ^{3}He irradiated crystal appeared quite similar to that obtained by room temperature irradiation by gamma rays, i.e. composed of *F* and *F*-aggregate bands. However, it was immediately evident that the spectra produced by ^{40}Ar contained an additional band, or bands, in the *M* band (445 nm) region.

In an effort to catalog the new color center bands, both spectra were quantitatively resolved with a computer into individual Gaussian bands and compared to a similarly resolved spectra obtained from a sample which had received gamma-ray irradiation. A general computer program designed to perform a least squares analysis for nonlinear functions[14] was employed to decompose an optical absorption spectrum into its component Gaussian bands. The program input consisted of: (1) the data points, taken at intervals of 1 nm, from the continuous spectrum furnished by the Cary spectrophotometer, (2) initial guesses as to the Gaussians present, i.e. the number present, their height in optical density (o.d.), the positions of the band maximums in nm (λ_m), and the band-widths at half maximum in eV (ΔW), and (3) which, if any, of the three parameters per Gaussian were to be held fixed. The computer varied those parameters not fixed in such a way as to obtain the best fit to the data, and then plotted on the same graph the data points, the individual Gaussian bands, and the total absorbance resulting from the addition of these Gaussians. Since room temperature gamma-ray irradiation of LiF produces no known color centers attributed solely to direct displacement damage, the following procedure was employed in order to compare the three resolved spectra.

The spectrum of a gamma-ray (10^7R) irradiated crystal was analysed by estimating the parameters of the six dominant F- and F-aggregate color center bands known to exist in gamma-ray irradiated LiF, i.e. the F, M, R_1, R_2, R_N[15] and F_3^+[16] bands. A rather broad band under the high energy side of the F-band was also included. There were thus 21 parameters and all were allowed to vary. The resulting fit to the data is shown in Fig. 4. In this figure, and in those which follow, the data are represented by open circles, the resolved individual Gaussians by the broken lines, and the fit by the solid line. The final values of the parameters for the gamma-ray produced spectrum are given in Column 1 of Table 1. These seven bands then became the standards by which the ^{3}He and ^{40}Ar produced spectra were compared.

In order to analyze the spectra produced by the ions, the positions and band-widths of the standard bands were held fixed and only their heights were allowed to vary. Furthermore, since the R_1, R_2, and R_N bands arise from the same defect, their heights were always held in the fixed ratio (1·0:0·68:0·21) found in the gamma-ray produced spectrum analysis. If this procedure of varying the five remaining parameters failed to produce a satisfactory fit, additional Gaussians were added to the program input and allowed to vary until a good fit was obtained. The analysis thus employed the minimum number of new Gaussians necessary to obtain a good fit. Each additional Gaussian needed corresponds to a color center band contained in the spectra of the ion bombarded crystals but not in that of the gamma-ray irradiated crystal.

The final results for a ^{3}He-(1·3 × 10^{13} ions/cm^2) produced spectrum are illustrated in Fig. 5 and tabulated in Column 2 of Table 1. In this case only one additional band at 2·9 eV was needed. It is represented in Fig. 5 by the dash-dot curve. It is important to note that this is a relatively weak band and could possibly be the result of several bands, such as those found in the ^{40}Ar case discussed below. Similarily, the fit for a ^{40}Ar-(3·8 × 10^{12} ions/cm^2) produced spectrum is shown in Fig. 6 and tabulated in Column 3 of Table 1. In this case three additional bands at 3·21 eV, 2·97 eV, and 2·22 eV were needed. An enlarged view of both the known bands and the three new bands is shown in Fig. 7. Again, in these figures the new bands are represented by dash-dot curves.

Support for the assignment of the three new bands in the ^{40}Ar-produced spectrum was sought by extending the study to include other massive ions. Thus, samples were bombarded with 3·0 MeV ^{84}Kr and 2·0 MeV ^{129}Xe ions. The spectra produced by these ions were then analyzed with the procedure outlined above. As with the ^{40}Ar-produced spectrum, both the

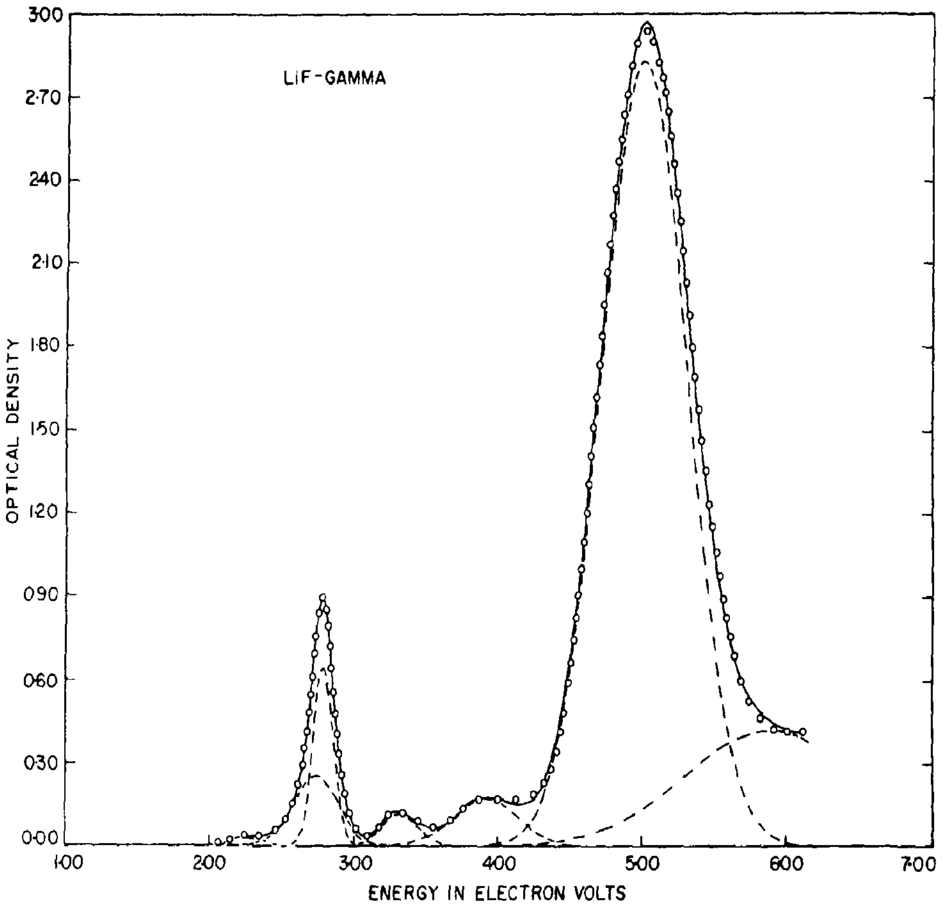

Fig. 4. Resolved spectrum of a gamma-ray irradiated (10^7R) sample of LiF. The open circles represent the data, the broken curves are the resolved Gaussian bands corresponding to the known color centers, and the solid curve is the subsequent fit to the data.

^{84}Kr- and ^{129}Xe-produced spectra require three additional Gaussian bands in order to obtain a good fit. Moreover, with one exception, viz., the half-width of the band at 3·17 eV in the ^{84}Kr spectrum, the positions and half-widths of the three bands agreed quite well. Since the accuracy of the optical density measurements is about 0·005, the values given in Table 1 for the smaller bands are less reliable than the larger ones.

No special effort was given to obtaining a close fit for any of these spectra in the region of the *F*-band (4–6 eV) for the following reasons: (1) *F*-bands are known not to be exactly Gaussian, (2) there are several bands expected to lie in the *F*-band region (for example M_F, R_F, *L*, *K*, and *Z* bands) but not all of their positions and band widths are known, (3) the origin of the band at 5·77 eV is not known to the authors and may be an approximation to some combination of those mentioned above, (4) the shape of the error curve (the difference between the data and the fit) in the *F*-band region is nearly the same for all five spectra and resembles the second derivative of the *F*-band. This regularity of error indicates that no large underlying band exists in only some of the spectra and in view

Table 1. Tabulations of Gaussian parameters yielding the best computer fit to the data for LiF colored with gamma rays and inert gas ions. Band heights are in optical density (o.d.), *bandwidths in eV* (ΔW), *and positions of band maximums in nm* (λm).

Gamma ray	He	Ar	Kr	Xe	Parameter	Designation of center
0·208	0·167	0·0437	0·062	0·012	o.d.	X
1·38	fixed	fixed	fixed	fixed	ΔW	
210·6(5·88 eV)	fixed	fixed	fixed	fixed	λm	
1·41	1·66	0·180	0·321	0·168	o.d.	F
0·70	fixed	fixed	fixed	fixed	ΔW	
247·5(5·00 eV)	fixed	fixed	fixed	fixed	λm	
0·087	0·016	0·0066	0·017	0·0040	o.d.	R_1
0·516	fixed	fixed	fixed	fixed	ΔW	
316·6(3·92 eV)	fixed	fixed	fixed	fixed	λm	
0·060	0·011	0·0045	0·012	0·003	o.d.	R_2
0·292	fixed	fixed	fixed	fixed	ΔW	
374·6(3·31 eV)	fixed	fixed	fixed	fixed	λm	
0·017	0·003	0·0013	0·003	0·0008	o.d.	R_n
0·248	fixed	fixed	fixed	fixed	ΔW	
552·5(2·24 eV)	fixed	fixed	fixed	fixed	λm	
0·126	0·100	0·0267	0·035	0·022	o.d.	F_3^+
0·376	fixed	fixed	fixed	fixed	ΔW	
453·9(2·72 eV)	fixed	fixed	fixed	fixed	λm	
0·323	0·287	0·0374	0·0659	0·035	o.d	M
0·163	fixed	fixed	fixed	fixed	ΔW	
445·1(2·78 eV)	fixed	fixed	fixed	fixed	λm	
		0·0142	0·014	0·0085	o.d.	3·22 eV
		0·707	1·15	0·748	ΔW	
		385·5(3·22 eV)	391·6(3·17 eV)	388·5(3·19 eV)	λm	
	0·050	0·0286	0·027	0·012	o.d.	2·97 eV
	0·440	0·376	0·325	0·282	ΔW	
	427·9(2·90 eV)	417·4(2·97 eV)	415·2(2·99 eV)	414·4(2·99 eV)	λm	
		0·0066	0·006	0·007	o d.	2·22 eV
		0·350	0·378	0·434	ΔW	
		558·7(2·22 eV)	564·9(2·19 eV)	563·7(2·20 eV)	λm	

of reasons (1) through (3), discovery of a new small band in the F-band region would be very difficult.

In the M-band region (2–4 eV) the fit obtained in all five spectra was good. The conclusion of this analysis is that in addition to creating the color centers produced by electromagnetic irradiation, massive ion bombardment creates additional damage. If this damage consists of specific color centers which can be represented by Gaussian absorption bands, the values listed in Table 1 for these new bands can be assumed to be approximately correct. Of course, if the bands are not Gaussian then the entire analysis fails. Colloidal bands are usually non-Gaussian and in LiF the wavelengths of bands attributed to colloids are either near 290 nm or on the low energy side of the M band. The mechanism producing these new color centers may well be that of direct displacement collisions, but further work will be needed to verify this and to propose specific defect models.

F-center growth curves for ^{84}Kr- and ^{129}Xe-ion bombardment were also obtained, but the very small absorption coefficients involved made any quantitative analysis unreliable. These heavier ions did follow the expected trend, however, in that estimates of the efficiencies for F-center production decreased as the mass of the bombarding species increased.

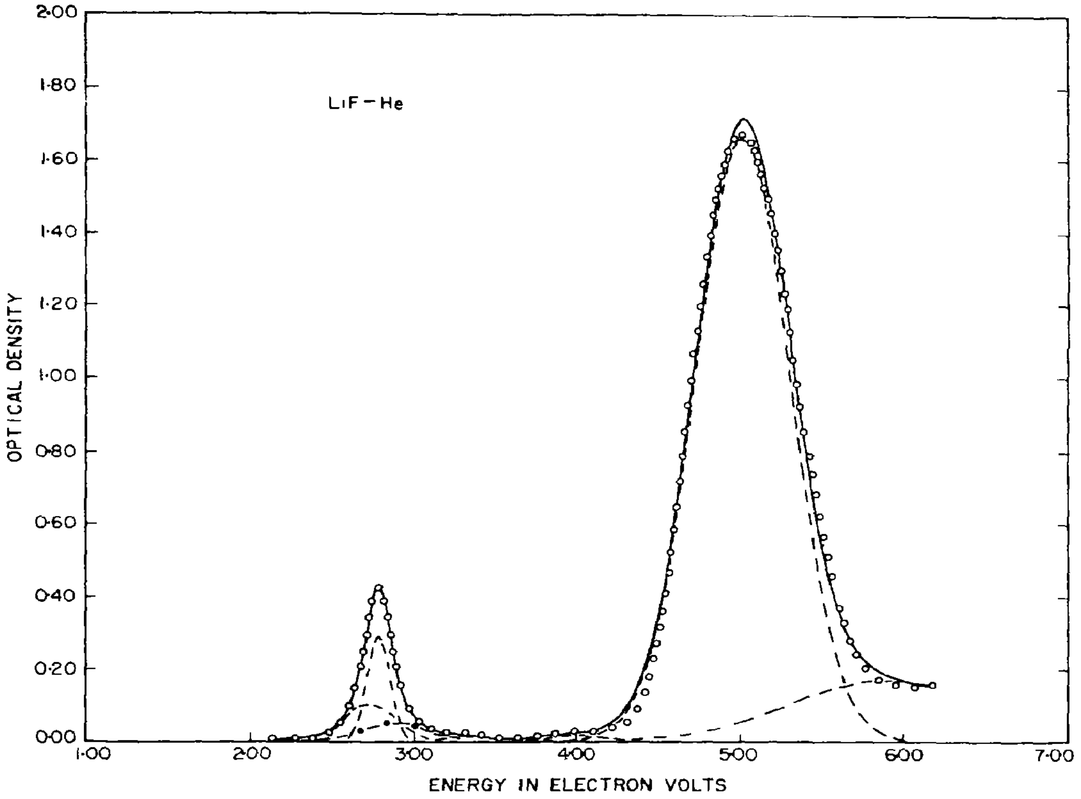

Fig. 5. Resolved spectrum of a LiF sample bombarded with 3 MeV ^{3}He ions ($1 \cdot 3 \times 10^{13}$ ions/cm^2). The new band (see text) is represented by the dash-dot curve.

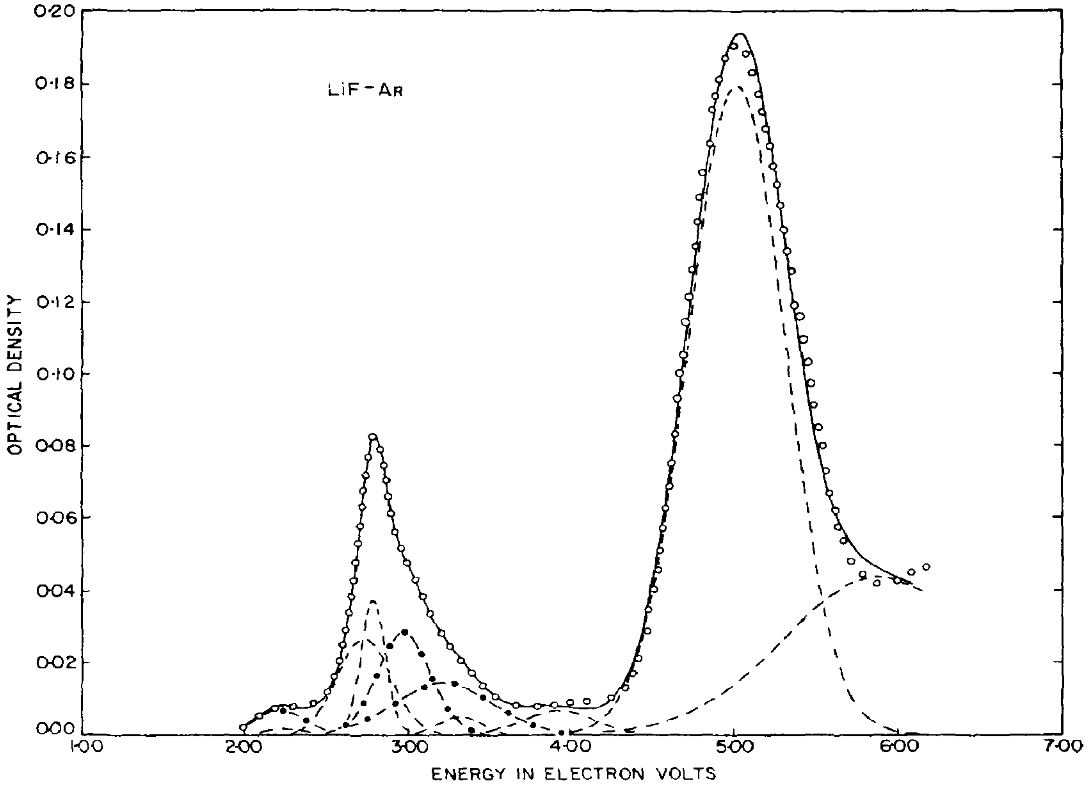

Fig. 6 Resolved spectrum of a LiF sample bombarded with 3 MeV ^{40}Ar ions ($3 \cdot 8 \times 10^{12}$ ions/cm^2). The three new bands (see text) are represented by the dash-dot curves.

Finally, in view of the results presented, it appears that the observation of a new color center due to the imbedded inert gas atoms themselves would be difficult in LiF bombarded at room temperature. Ritz[17] has examined alkali halides bombarded with 5 MeV rare-gas ions at 6°K and did not detect any rare-gas centers. The minimum number of color centers optically detectable is approximately 10^{14} per cm^2 so that an ion dose larger than this would certainly be required. The growth curves in Fig. 1 were terminated at 3×10^{13} ions/cm^2, yet even at this dose well developed absorption bands are already present throughout the visible and near u.v. regions of the spectra. These bands would strongly mask any very weak additional band even if it were stable at room temperature.

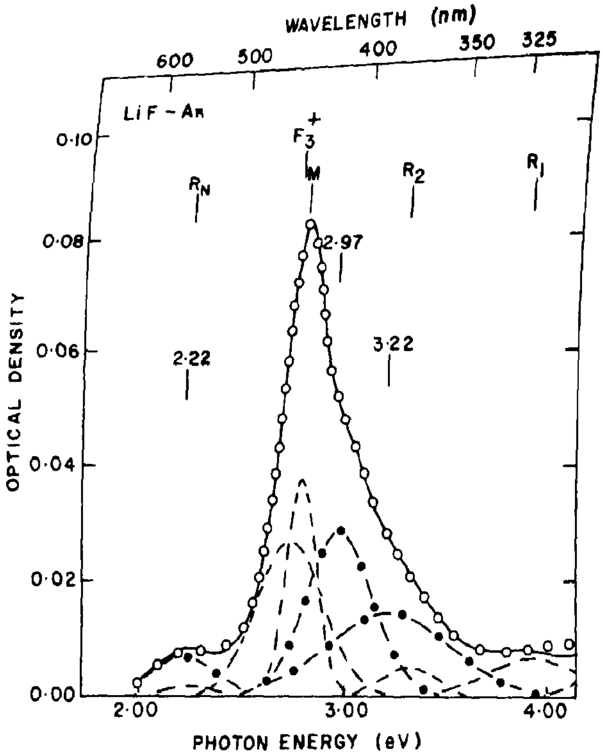

Fig. 7. Enlargement of the M-band region of Fig. 6 indicating the positions of the three new bands near 2·22, 2·97 and 3·22 eV.

4. CONCLUSIONS

(1) Optical studies of radiation damage in alkali halide crystals can successfully be extended to include irradiation by uniform beams of energetic massive ions.

(2) In addition to those known color centers created in LiF by irradiation with electromagnetic rays or light particles, bombardment by energetic massive ions produces additional defects.

(3) Damage profile curves of LiF showed that the coloration produced was fairly uniform along the penetration depth for all the bombarding particle species.

(4) The new defects created by ^3He ions exhibit a small band (or bands) near 2·90 eV while those created by ^{40}Ar, ^{84}Kr and ^{129}Xe ions exhibit in each case bands near 3·22, 2·97, and 2·22 eV.

(5) The second stage of the *F*-center growth curves produced by ^3He and ^{40}Ar ions are linear up to approximately $2{\cdot}3\times10^{18}$ *F*-centers/cc and $2{\cdot}24\times10^{18}$ *F*-centers/cc respectively. Saturation of the ^{40}Ar produced *F*-center concentration occurs at about $3{\cdot}4\times10^{19}$ *F*-centers/cc.

(6) From the slope of the linear portion of the growth curves it is determined that 4500 *F*-centers are created per incident 3 MeV ^3He ion and that 2600 *F*-centers are created per incident 3 MeV ^{40}Ar ion. These values correspond to efficiencies of 666 and 1150 eV per *F*-center respectively.

Acknowledgements—We are indebted to Dr. B. J. Faraday for his interest and many fruitful discussions. We wish to thank Mr. J. J. Halpin for his assistance with the computer analysis and Drs. M. N. Kabler and V. Ritz for their helpful comments. The critical comments by Dr. W. Dale Compton of the University of Illinois are gratefully acknowledged.

REFERENCES

1. SMITH D. Y., *Phys. Rev.* **166**, 848 (1968).
2. COMPTON W. D. and RABIN H., *Solid St. Phys.* (Edited by F. Seitz and D. Turnbull), Vol. 16. Academic Press, New York (1964).
3. WHAPHAM A. D. and MAKIN M. J., *Phil. Mag* **5**, 237 (1960).
4. MARKHAM J., *F-Centers in Alkali Halides*. Academic Press, New York (1966).
5. CRAWFORD J. H., JR., *Adv. Phys.* **17**, 93 (1968).
6. SMAKULA A., *Z. Phys.* **59**, 603 (1930)
7. DEXTER D. L., *Phys. Rev.* **101**, 48 (1956).
8. FARGE Y., DURAND P. and LAMBERT M., *Int. Symp. on Color Centers, Rome* (1968) Abstract 58.
9. GILMAN J. J. and JOHNSTON W. G., *Dislocations and Mechanical Properties of Crystals*, p. 116. Wiley, New York (1957).
10. WILLIAMS C. F., BORUOT J. P. and PICARD J., Centre d'Etudes Nucleaires De Saclay Rapport (Erratum) CEA-R3042 (1966).
11. LINDHARD J., SCHARFF M. and SCHIOTT H. E., *Mat.fys. Meddn.* **33**, No. 14 (1963)
12. MAZEY P. J., NELSON R. S., and BARNES R. S., *Phil. Mag.* **17**, 1145 (1968).
13. RITZ V. H., *Phys. Rev.* **113**, A1452 (1964).
14. DANIELS W. E., General least squares with statistics. *Univ. of Maryland Tech. Rep.* No. 579 (1966).
15. VANDER LUGT K. L. and KIM Y. W., *Phys. Lett.* **22**, 50 (1966).
16. NAHUM J. and WIEGAND D. A., *Phys. Rev.* **154**, 817 (1967).
17. RITZ V. H., *Bull. Am. phys. Soc.* **14**, 376 (1969).

J. Phys. Chem. Solids Pergamon Press 1970. Vol. 31, pp. 1375–1379. Printed in Great Britain.

MAGNETIC FIELD EFFECTS ON PHOTO-ENHANCED CURRENTS IN ORGANIC CRYSTALS*

N. E. GEACINTOV, M. POPE and S. FOX†
Radiation and Solid State Physics Laboratory and Chemistry Department, New York University, N.Y. 10003, U.S.A.

(*Received* 31 *July* 1969; *in revised form* 29 *September* 1969)

Abstract – An anisotropy in the effect of a magnetic field on the photo-enhanced bulk conductivity in anthracene and tetracene single crystals was found. In anthracene this effect may be explained in terms of a triplet exciton-trapped hole interaction. In tetracene it is mainly a consequence of singlet exciton fission into triplet excitons.

1. INTRODUCTION

THE MAGNETIC field dependence of the photoconductivity of anthracene and tetracene was first described by Frankevich *et al.*[1–4]. They ascribed their results to the effect of the magnetic field on charge-transfer (Wannier type) excitons which in some cases could be produced by triplet excitons.

In this paper we present evidence that the effect of a magnetic field on photo-induced bulk conductivity may be understood in terms of singlet exciton fission (in tetracene) and triplet exciton interaction with other paramagnetic species (such as trapped holes) in anthracene and tetracene.

We used single crystals of anthracene and tetracene, illuminated through a semitransparent evaporated gold electrode. The back electrode was a small droplet of mercury. The incident light was perpendicular to the *ab* plane of the crystal and was in the first singlet absorption region for both anthracene and tetracene. This light will not induce an electron photocurrent under the present experimental conditions[5, 6].

A gold electrode is able to inject holes into tetracene and anthracene in total darkness [7, 8]. When the electrode is at a positive potential, a space charge limited current can be produced. The effect of light on the observed current in this case where a gold electrode is used would be chiefly due to the reduction in the filled trap density; this would in turn produce an increase in the measured current. The current that flows in the presence of light under these circumstances has been referred to as a photo-enhanced current[9].

The changes in steady-state photocurrents were measured as a function of the orientation of the magnetic field vector $\vec{H}$ with respect to the *b* axis in the *ab* plane of the crystals.

2. RESULTS

In tetracene the fractional change in the current $\Delta i/i$ when $\vec{H} = 3{\cdot}4$ kG is strongly anisotropic, exhibiting sharp resonances as shown in Fig. 1; furthermore, the magnitude as well as the sign of $\Delta i/i$ is a function of wavelength of illumination. When light is weakly absorbed (wavelength $\lambda = 565$ nm, absorption coefficient $k \leq 3000\,\text{cm}^{-1}$) $\Delta i/i$ is negative (Fig. 1). When strongly absorbed light is used ($400\text{ nm} < \lambda < 520$ nm, $k = 10^4 - 10^5\,\text{cm}^{-1}$), $\Delta i/i$ is positive.

In anthracene the effect of the magnetic field on the photoconductivity was measured in the first singlet absorption band ($\lambda = 360$–400 nm, $k \sim 10^5\,\text{cm}^{-1}$); $\Delta i/i$ is negative and exhibits pronounced anisotropy (Fig. 2). It was also

---

*This work was supported by the National Science Foundation and the U.S. Atomic Energy Commission.

†This is part of a dissertation (S.F.) in partial fulfillment of requirements for the Ph.D. degree at New York University.

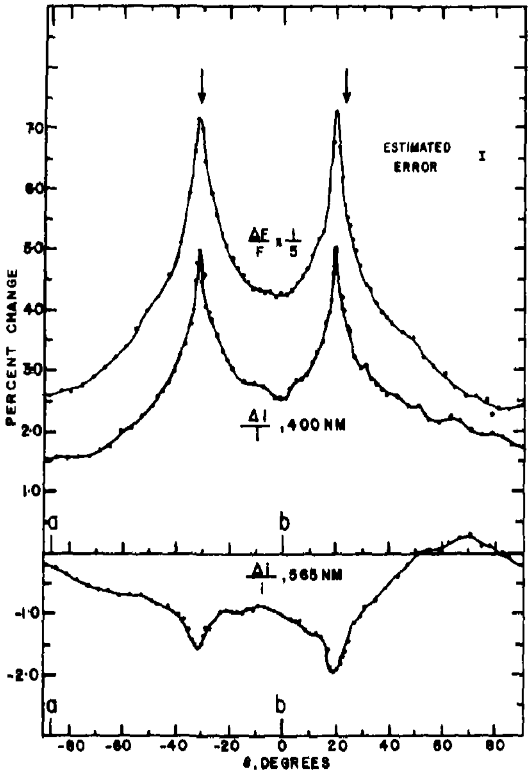

Fig. 1. Tetracene crystal (175 μm thick). Effect of magnetic field $H = 3400$ G on fluorescence F and hole photocurrent i. H rotated in ab crystal plane. Photocurrents measured with 250 V across crystal, current with $H = 0$ was $8{\cdot}5\times 10^{-9}$ A/cm^2 at 400 nm and $1{\cdot}4\times 10^{-7}$ A/cm^2 at 565 nm. At 565 nm light is weakly ($k \leq 3\times 10^{1}$ cm^{-1}) absorbed. The b axis is at 0. The resonances calculated from equation 1 (with $D/E = -0{\cdot}077$)[10] are shown by heavy arrows. $T = 298$°K. ϕ = typical estimated error

noted that $\Delta i/i$ decreased with increasing voltage.

There was no noticeable effect of $\vec{H}$ on the dark currents which were at least 100 times smaller than the photo-enhanced currents.

3. DISCUSSION

In tetracene, singlet exciton fission into two triplet excitons is a very efficient process at room temperature[10, 11]. This process can be inhibited by the application of an external magnetic field and the singlet exciton density may be increased thereby by as much as 40 per cent. It can also be calculated (using data and equations given in [12]) that there is a concomitant *decrease* in the triplet exciton density of about 1–2 per cent. The generation of singlets via triplet–triplet exciton fusion and the resulting delayed fluorescence are decreased in both anthracene[13] and tetracene [14] in the presence of a magnetic field. All these magnetic field effects are anisotropic with respect to the orientation of $\vec{H}$. For every 180° of rotation in the ab or ac plane, two resonances are observed. Maxima in the prompt fluorescence of tetracene and minima in the delayed fluorescence of tetracene and anthracene are observed at these special orientations.

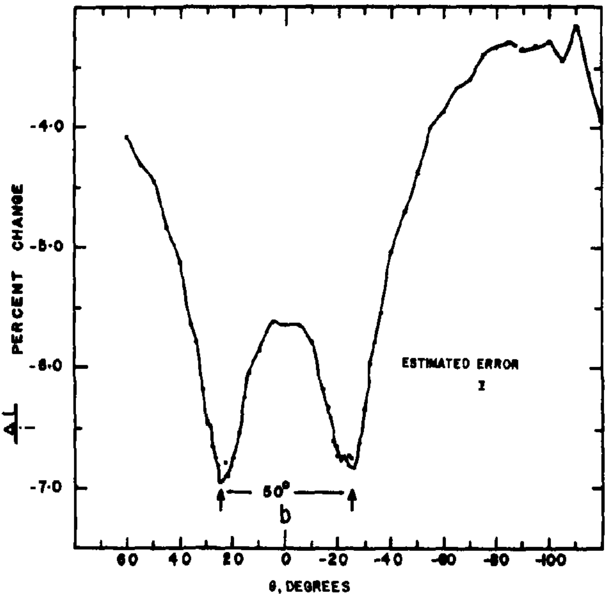

Fig. 2. Anthracene crystal (100 μm thick) Effect of magnetic field $H = 3400$ G on hole photocurrent i. $\vec{H}$ rotated in ab crystal plane Photocurrents measured with 24 V across crystal; current with $H = 0$ was $1{\cdot}3 \times 10^{-9}$ A/cm² at 366 nm. The b axis is at 0 and the resonances were calculated from equation 1 (with $D/E = -0{\cdot}0974$)[17] are indicated by heavy arrows $T = 298$°K. ϕ = typical estimated error.

The field directions at which these effects occur correspond to orientations at which a particular type of level-crossing resonance occurs[13, 15]. The resonances occur at orientations of $\vec{H}(\vec{H} > 2000\,\mathrm{G})$ for which $W_{0,0} = W_{+1,-1}$, where the latter quantities refer to the energies of the $|0, 0>$ and $|+1, -1>$ triplet exciton pair states (each triplet exciton is characterized by the appropriate spin quantum number $M_s = 0, \pm 1$). Also, at these orientations $W_0(\vec{H}) = 0$, where W_0 is the energy of the $|0>$ triplet exciton.

Knowing the orientation of the crystal zero field splitting tensor, or the orientation of the molecular axes in the lattice, $W_0(H)$ can be calculated. If D and E are the zero-field splitting parameters, and $L_{1,2}$, $M_{1,2}$, $N_{1,2}$ are the orientations of the long, short and normal axes of molecules 1 and 2, respectively, in the anthracene or tetracene unit cell, the resonances occur at orientations of $\vec{H}$ for which[10]

$$W_0 = \frac{D}{2}\left[\frac{2}{3} - (\cos^2(\vec{N}_1, \vec{H}) + \cos^2(\vec{N}_2, \vec{H}))\right]$$

$$-\frac{E}{2}\Big[(\cos^2(\vec{L}_1, \vec{H}) + \cos^2(\vec{L}_2, \vec{H}))$$

$$-(\cos^2(\vec{M}_1, \vec{H}) + \cos^2(\vec{M}_2, \vec{H}))\Big] = 0.$$

The calculated resonance points for tetracene are shown in Fig. 1 by arrows. They are in reasonable agreement with the observed fluorescence resonance peaks*. The discrepancy in the left hand peak (~ 1·5°) and the right hand peak (~ 3·5°) in Fig. 1 is more than can be accounted for in terms of experimental error (± 1°). The shape of $\Delta i/i$ at 400 nm reproduces the fluorescence curve except that $\Delta i/i$ is smaller in magnitude by a factor of about seven.

---

*Since reference[10] was published, the apparatus was considerably improved, which permitted a more accurate location of the two peaks in Fig. 1. We are grateful to Dr. P. Avakian for communicating to us the location of the crystallographic a and b axes with reference to the $\Delta F/F$ peaks. With these improvements and corrections the agreement between theory and experiment is not quite as good as implied in Fig. 2 of reference[10] as is evident in Fig. 1 of this paper.

The conclusion to be drawn in the case of tetracene provided with gold electrodes is that at 400 nm the magnetic effects on the hole current are mainly a consequence of the increase in the concentration of singlet excitons produced by the decrease in the fission of singlet excitons into two triplets; the singlet excitons in turn detrap the holes already injected by the electrode. This is demonstrated by the *positive* sign of $\Delta i/i$ and the anisotropy as shown in Fig. 1.

Using light of $\lambda = 565$ nm (Fig. 1), it was found that i was decreased by $\vec{H}$. This decrease implies that the hole density in traps was increased by $\vec{H}$, or that hole detrapping was reduced. Since it is the triplet exciton concentration that is reduced by $\vec{H}$, and not the singlet exciton concentration, the magnetic effects of 565 nm are due mainly to the interactions of triplet excitons. (The interaction rate between a triplet exciton and a trapped hole is also reduced in a magnetic field – see below.)

In anthracene, there is no exciton fission, and at the light intensities used in this experiment, there is no triplet–triplet exciton fusion process of any significance; yet there is a significant effect of $\vec{H}$ on $\Delta i/i$ that depends on the orientation of the magnetic field (Fig. 2). We interpret this effect in terms of an interaction between a triplet exciton (produced by intersystem crossover from a singlet state) and another paramagnetic species, namely a free or a trapped hole, in which process the triplet exciton is annihilated. As before, the holes are injected by the gold electrode and produce a space charge that limits the current. In the presence of an external magnetic field, we assume that the efficiency of triplet exciton annihilation by the holes is reduced. This produces a larger space charge than when $\vec{H} = 0$, and the photoenhanced current drops, as is observed. Furthermore, if the applied voltage is increased the reservoir of injected holes is depleted and the density of holes near the positive electrode decreases. Hence, the effect of the external magnetic field should diminish as the voltage across the crystal is increased, as is observed.

The effect of a magnetic field on triplet exciton annihilation by paramagnetic centers (free radicals) and the theory of the interaction were discussed by Ern and Merrifield[16]. A trapped hole (or electron) has a spin of $\pm\frac{1}{2}$ and thus may act like a paramagnetic center. The resonances occur at orientations for which $W_{0,\pm 1/2} = W_{+1,\mp 1/2}$[16]. Since the field orientation dependence of W is due to the zero field splitting parameters of the triplet excitons only, the resonance orientations can also be calculated by equation (1). The same result is obtained from equation (4) of Ref. [16] which, however, is written in terms of the *crystal* zero-field splitting tensor.

The anisotropy and *negative* sign of the effect of $\vec{H}$ on $\Delta i/i$ in Fig. 2 thus supports the contention made above that the magnetic effect is due to a decreased interaction between triplet excitons and holes. The resonances for triplet–triplet and triplet–electron interactions are the same and these processes cannot be distinguished by the magnetic field anisotropy alone.

In conclusion, it is apparent that the use of magnetic field in photoconductivity studies is invaluable in assessing the role played by triplet excitons, particularly in their interaction with carriers. Further detailed studies may also provide information about the diffusion length of the triplet exciton and the spatial distribution of traps.

Acknowledgements – We would like to express our gratitude to Professor M Furst for helpful discussions and to Mr C Penn for his technical assistance.

REFERENCES

1. FRANKEVICH E. L. and BALABANOV E. I.; *Fiz. Tverd. Tela* **8**, 855 (1966). *Soviet Phys. solid St.* **8**, 682 (1966).
2. FRANKEVICH E. L., BALABANOV E I. and VSELYUBSKAYA. G V.; *Fiz. tverd. Tela* **8**,

1970 (1966). *Soviet Phys. solid St.* **8**, 1567 (1966).
3. FRANKEVICH E. L. and SOKOLIK I. A.; *Zh. Eksp. Teor. Fiz.* **52**, 1189 (1967); *Soviet Phys. JETP* **25**, 790 (1967).
4. RUSIN B. A. and FRANKEVICH E. L., *Phys. Status Solidi* **33**, 885 (1969).
5. POPE M. and KALLMANN H., In *Symposium on Electrical Conductivity in Organic Solids* (Edited by H. Kallmann and M. Silver). p. 83. Interscience, New York (1961).
6. MULDER J.; *Philips Res. Rept.* **1968**, Suppl. No. 4.
7. MEHL W.; *Solid State Commun.* **6**, 549 (1968).
8. BAESSLER H., HERRMANN G., RIEHL N. and VAUBEL G., *J. Phys. Chem. Solids* **30**, 1579 (1969).
9. MANY A., LEVINSON J. and TEUCHER I.; *Molec. Crystallogr.* **5**, 273 (1968).
10. GEACINTOV N., POPE M. and VOGEL F.; *Phys. Rev. Lett.* **22**, 593 (1969).
11. MERRIFIELD R. E., AVAKIAN P. and GROFF R. P.; *Chem. Phys. Lett.* **3**, 155 (1969).
12. POPE M., GEACINTOV N. and VOGEL F., Molecular Crystals, *Mol. Cryst. Liq. Cryst.* **6**, 83 (1969).
13. JOHNSON R. C., MERRIFIELD R. E., AVAKIAN P. and FLIPPEN R. B., *Phys. Rev. Lett.* **19**, 285 (1967)
14. GROFF R. P., AVAKIAN P. and MERRIFIELD R. E., *J. Luminescence* **1**, In press.
15. MERRIFIELD R. E., *J. chem. Phys.* **48**, 4318 (1968).
16. ERN V. and MERRIFIELD R. E., *Phys. Rev. Lett.* **21**, 609 (1968)
17. VAN DER WAALS J. H. and TER MATEN G., *Mol. Phys.* **8**, 301 (1964).

J. Phys. Chem. Solids Pergamon Press 1970. Vol. 31, pp. 1381–1387. Printed in Great Britain

THE ANNEALING OF THE EPR-SIGNAL PRODUCED IN SILICON BY PLASTIC DEFORMATION

F. D. WÖHLER and H. ALEXANDER*
Institut für Metallphysik der Universität Gottingen, Germany
and
W. SANDER†
I. Physikalisches Institut der Universitat Gottingen, Germany

(*Received* 29 *September* 1969)

Abstract – In silicon an EPR signal is produced by plastic deformation. The annealing behavior of this signal has been investigated, and the dislocation density and structure has been studied by the etch pit technique and by electron microscopy. The EPR-signal anneals in one stage with an activation energy of (1·36 ± 0·1) eV, and the dislocation structure is fundamentally altered. This change, which is probably caused by diffusion of divacancies, is considered responsible for the observed decrease of the EPR-signal.

1. INTRODUCTION

IN 1965 ALEXANDER *et al.*[1] found an EPR-signal in silicon, which had been produced by plastic deformation and whose magnitude was proportional to the dislocation density. The signal was almost isotropic with a g-value of $2{\cdot}0043 \pm 0{\cdot}0009$ and a linewidth of 11 Oe. The authors supposed, that the signal occurs, if there are unpaired electrons in the cores of dislocations.

The above experiments were made with single-crystals, which had been deformed at constant load at relatively low temperatures. In order to decide whether there was a small anisotropy of the signal, it was of prime importance to investigate crystals with a high dislocation density and a dislocation structure which was as anisotropic as possible. The latter can be produced by predominant slip on one slip system. Dynamic deformation (with constant cross-head speed) at higher temperatures seemed to be promising in this respect. Such experiments were performed between 800 and 1125°C. An unexpected result was obtained: crystals, which were deformed at different temperatures T_v, until they had the same dislocation density N‡, showed that the intensity I of the resonance signal increased inversely to the temperature. Figure 1 illustrates the relative intensity

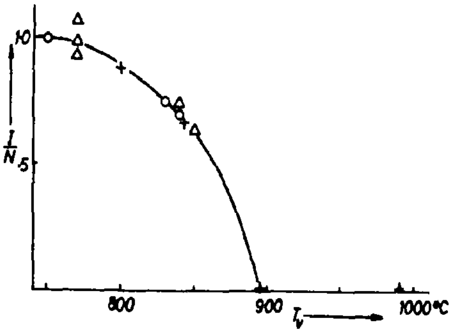

Fig. 1. The ratio of signal intensity I and dislocation density N (arbitrary units) vs. deformation temperature T_v. ○ from [1]; △ statically deformed crystals; + dynamically deformed crystals.

---

*Present address: Abteilung für Metallphysik im II Physikalischen Institut der Universität zu Köln, (5) Köln 41, Universitätsstr. 14 Germany.

†Present address: 2 Physikalisches Institut der Technischen Hochschule, 51 Aachen 1, Templergraben 55, Germany.

‡The etch pit density revealed by using Sirtl's etch [2] is taken as N.

I/N of the signal as a function of T_v. The EPR data obtained from statically deformed crystals in former experiments fit into the same $I/N - T_v$ curve as those of the dynamically deformed crystals. The scattering of the values about the $I(N)$-curve in Ref. [1] (Fig. 2) turns out to be a result of the different deformation temperatures used in the experiments reported. No signal was found at $T_v >$ 895°C. In the light of these results, one has to assume that the signal-producing centers anneal during the deformation and the following time of cooling. The degree of annealing depends on T_v. To achieve a high relative signal intensity the temperature of deformation must be as low as possible. Although the deformation rate increases at higher temperatures the decrease in time during which the crystal is at high temperatures is overcompensated by the effect of accelerated annealing. The lower limit of the deformation temperature is about 750°C (because of the brittle-ductile transition).

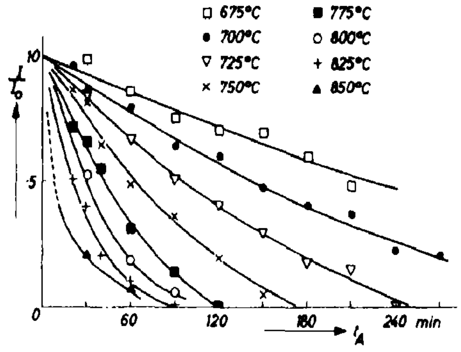

Fig. 2 Isothermal annealing curves. I/I_0. relative signal intensity; t_A: annealing time.

A precise investigation of the annealing process was considered important to identify the centers which produced the EPR signal. This is the purpose of this paper. Uniformally deformed samples were tempered in vacuum isothermally or isochronally. The intensity of the EPR-signal was measured after each stage of annealing and the result analysed according to Meechan and Brinkman[3].

2. EXPERIMENTAL

A single crystal* grown by floating zone was sawn into samples of square cross-section $3 \times 3 \times 17\,mm^3$ (doping: $5 . 10^{13}$ atoms of B/cm^3, resistivity: $400\Omega\,cm$ at 20°C). The density of grown-in dislocations was about $10^4\,cm^{-2}$. The specimen axes were parallel to ⟨123⟩, one pair of sides being (111). After mechanical and chemical polishing the samples were deformed by static compression at 770°C in an apparatus described elsewhere [4]. Forming gas (8% H_2, 92% N_2 purest) served as an inert protecting atmosphere. The creep curve passed into the range of hardening (11 per cent shear strain) at a resolved shear stress on the primary glide system of 1·6 kg/mm², where the corresponding dislocation density was $N = (5 \pm 1) . 10^8\,cm^{-2}$. The time of cooling after the deformation was shortened to some minutes by opening the furnace. During this time the crystal was kept under load. The intensities of the signal I_0 after deformation differed from crystal to crystal by no more than 8 per cent. A quartz glass tube evacuated to 10^{-6} torr was used for annealing. A pre-heated cylindrical furnace could be pushed over the tube, the temperature being measured by a thermocouple situated close to the sample. The increase of temperature was observed until the annealing temperature was attained (after 5 min), so that the amount of annealing during this period could be taken into account. This correction was noticeable only for temperatures above 800°C.

The EPR was measured with a Varian spectrometer V-4500 at a frequency of 9·3 GHz. The sample was situated on a quartz support together with a standard sample (Si with $2{\cdot}10^{14}$ atoms of P/cm^3) in the coolant (liquid hydrogen at 20·4°K). The magnetic field was modulated with 100 kHz, and the differentiated absorption curve was recorded. In general the intensity I of the signal, i.e. the ordinate of the maximum of the absorption curve, must be determined by integrating the differentiated curve with respect to H. If the shape of the absorption line does not alter (as in our case), I is proportional to the difference in slope at the inflection points of the absorption curve, i.e. proportional to the difference between the ordinates of the maxima of the differentiated curve. It was shown by repeated grinding: the signal decreases with the mass and is therefore not produced preferentially by surface layers. Thus, I can be suitably related to the unit of mass of the sample.

---

*We are indebted to the AEG Research Institute for giving us the crystal.

3. RESULTS

(a) *The activation energy of the annealing process*

12 samples were tempered isothermally at 8 temperatures between 675 and 850°C (Fig. 2). The variation of the intensity I after tempering, divided by its initial value I_0, during the time of tempering could be well reproduced. The limit of detection of this signal was 10 per cent of the initial intensity. 4 samples were tempered isochronally (Fig. 3). The isochrone showed only one stage of annealing. The analysis of these curves was performed according to Meechan and Brinkman[3]. This method is independent of whether the centers that produce the signal migrate through the lattice until they become inactive at a sink, or lattice defects migrate to the centers and 'poison' them. If the migration through the lattice can be activated by a single energy E, the general formula

$$\frac{dn}{dt} = f(n)\,e^{-E/kT} \qquad (1)$$

is valid (n: density of active centers). The function $f(n)$ must be monotonic. The relation between the density of centers and the intensity of signal $I = I(n)$ must be single valued and monotonic. Then

$$\frac{dI}{dt} = \frac{dI}{dn} f(n)\,e^{-E/kT} = F(n)\,e^{-E/kT}. \qquad (2)$$

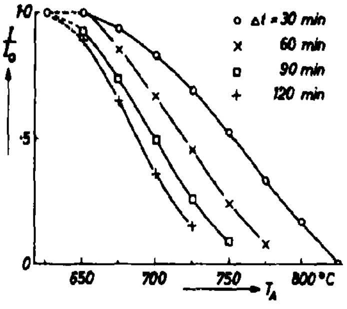

Fig. 3. Isochronal annealing curves: I/I_0, relative signal intensity; T_A: annealing temperature.

The activation energy E of migration can be determined either by a family of isotherms or by a combination of one isotherm and of one isochrone. If equations (1) and (2) are justified, then:

$$\int_{I_0}^{I} \frac{dI}{F(n(I))} = e^{-E/kT}\,t \qquad (3)$$

and for intersections through the family of isotherms with I/I_0 as a parameter

$$e^{-E/kT}\,t = \theta \qquad (4)$$

is valid (θ: a constant depending on I/I_0). Figure 4 shows the resultant logarithmic straight lines with the slope $E = (1{\cdot}37 \pm 0{\cdot}1)$ eV. A plot of I/I_0 vs. θ combines all the isotherms to one "reduced isotherm":

$$\frac{I}{I_0} = 1 - C(1 - e^{-K_0\theta}) \qquad (5)$$

with $C = 1{\cdot}3$ and $K_0 = 10^{-3}\,\mathrm{sec}^{-1}$ (Fig. 5).

From combining pairs of one isotherm and one isochrone one obtains $E = (1{\cdot}35 \pm 0{\cdot}1)$ eV. So it can be concluded that the migration through the lattice, on which is based the annealing of the signal, can be described by an Arrhenius formula with a distinct activation energy of $(1{\cdot}36 \pm 0{\cdot}1)$ eV.

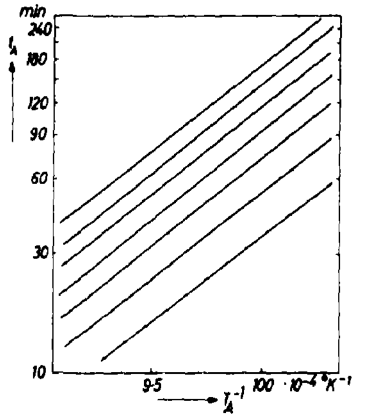

Fig. 4. The annealing time t_A as a function of the annealing temperature T_A (from Fig. 2). Parameter of the curves: I/I_0

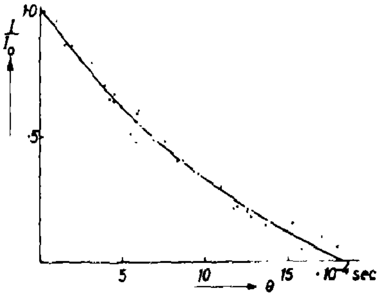

Fig. 5. The reduced isotherm (see text)

(b) *Density and structure of dislocations*

The dislocation density N was determined with an electron microscope before and after tempering by shadowed replicas of an etched (111) side face. It remained constant within the accuracy of the method (20 per cent). However, whereas before tempering the etch pits were homogeneously spread over the surface (without taking into account the arrangement in slip lines), after tempering they formed a cell-like structure: areas of 10–20 μm dia. with few etch pits were surrounded by walls of about 1 μm thickness containing 10 times as many pits.

A sample tempered and afterwards deformed for a second time showed fresh slip lines which were superimposed on these cells.

The dislocation structure in the interior of the crystals was investigated by transmission electron microscopy (TEM) using slices cut parallel to the primary glide plane $(1\bar{1}1)$. Two samples used for determining the activation energy were investigated. Figure 6(a) shows the dislocations after standard deformation. The arrow (parallel to [011]) marks the direction of the primary system burgers vector. One can also see a kind of cell structure. Dense arrangements of dislocations form nearly straight tangles parallel to both the [110] and [101] directions. The dislocations are predominantly of edge type, but they show numerous bent segments. The tangles, 0·5–1 μm thick, form the boundaries of the cells which are 3–5 μm in dia. and contain few dislocations. A completely different structure (compare Fig. 6(b)) is to be seen after tempering for 40 min at 825°C ($I/I_0 = 0{\cdot}2$). The above two ⟨110⟩ directions in the primary glide plane are shown again. However, in this case straight 60°-dislocations of about 100 μm length were parallel to these directions. These dislocations form groups separated from each other by about 10 μm. Sometimes they form dense bundles which cannot be resolved. An accurate determination of the dislocation density was not possible neither in Fig. 6(a) nor in Fig. 6(b). It is certain, however, that by annealing N is not diminished in the same degree as the intensity of the signal.

4. DISCUSSION

Without doubt the EPR-signal in question is produced by plastic deformation.* (See folio 1387.) The thermal treatment which is connected with the deformation does not participate in the production (as the reference sample shows), but it even causes a partial reduction of the signal intensity. One sample, which was redeformed after an annealing process showed the same signal which was nearly as strong after the second deformation as after the first one. Thus the signal produced is independent of the thermal and plastic history of the sample.

Of all the lattice defects which are caused

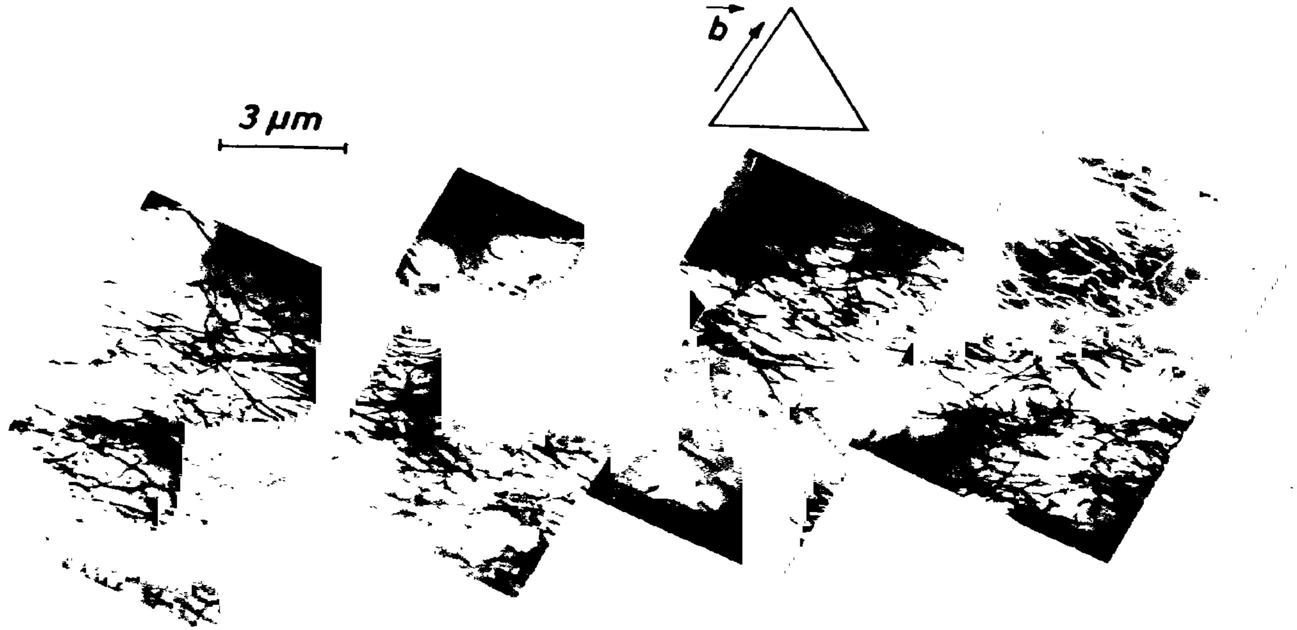

Fig. 6(a). The dislocations in the primary glide plane of a crystal deformed at 770°C to a shear strain $a = 0{\cdot}11$, cooled under load. The triangle shows the three {1 10] directions, the arrow the glide direction for the main glide system.

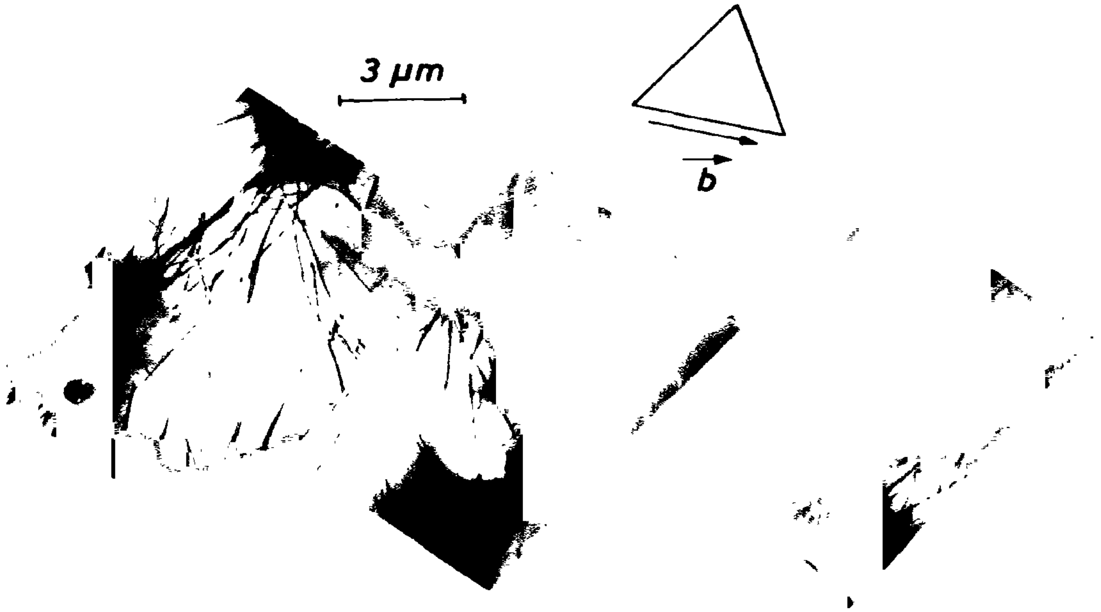

Fig. 6(b). The dislocations in the primary glide plane of a crystal deformed as the crystal of Fig. 6(a) and then annealed for 2 × 20 min at 825°C ($I/I_0 = 0{\cdot}2$).

by plastic deformation (dislocations, vacancies, interstitial atoms, diffused-in foreign atoms, and combinations of these defects), we consider dislocations responsible for the signal for the following reasons:

(1) Crystals deformed at the same temperature show an intensity of the EPR signal proportional to the dislocation density[1].

(2) The EPR-spectra of the most simple lattice defects are known[5] and are different from ours.

(3) In the range of doping investigated so far, (B up to $1{\cdot}6\,.\,10^{16}\,\mathrm{cm}^{-3}$, P: $2\,.\,10^{14}\,\mathrm{cm}^{-3}$) the resonance signal occurs independently of the doping material and the crystal growth technique (i.e. floating zone or crucible). These facts suggest an intrinsic lattice defect.

For the reduction during annealing in the EPR caused by the dislocations or by certain sections of them the following processes must be considered:

(a) The tempering may reduce the density of dislocations; (b) lattice defects (e.g. foreign atoms) may diffuse to the active centers on the dislocations and inactivate them; (c) it is possible that only certain types of dislocations, i.e. dislocations of certain orientations with respect to the burgers vector, cause a signal. A variation in the spectrum of the dislocation types during the annealing process may then make the signal disappear; (d) jogs and kinks in the dislocations could be the centers which cause the signal. Their density may also decrease by annealing without a variation of the dislocation density.

cf. (a) Both the counting of etch pits as well as the TEM exposures taken up until now show that the dislocation density does not decrease to the same degree as the signal intensity. This process cannot explain the recovery.

cf. (b) Our investigations have not suggested up till now, that a defect, which diffuses from the lattice to the dislocations and segregates there, inactivates the resonance centers. After the standard deformation the crystal contains about $2 \cdot 10^{14}\,\mathrm{cm}^{-3}$ active resonance centers[1]. It is possible that during annealing the crystal absorbs foreign atoms of a concentration which is comparable with this value. If these atoms were responsible for the disappearance of the signal, it is improbable that in this now homogeneously impure crystal as many active centers should be present after the second deformation as after the first.

As a test of the model (b) one may derive from the kinetics of the annealing of the signal (5) the kinetics of the hypothetical precipitation to the dislocations. If one assumes, that the number of precipitated defects is proportional to the number of inactivated centers, from (5) follows the fraction w of defects precipitated to dislocations

$$w \sim 1 - e^{-K_0\theta} = 1 - e^{-K(T)t} \qquad (6)$$

This relationship indeed fits Ham's theory of precipitation of lattice defects to dislocations[6, 7], where $K(T) = \lambda_0{}^2 D$ ($\lambda_0{}^2 = 2\pi N$; D = diffusion coefficient of the defect). If one puts from our results: $D = D_0 \exp(-1{\cdot}36\ \mathrm{eV/kT})$ and $N = 5\,.\,10^8\,\mathrm{cm}^{-2}$, the preexponential factor D_0 is $3\,.\,10^{-7}\,\mathrm{cm}^2/\mathrm{sec}$. This value is about $2\,.\,10^3$ times smaller than the normally accepted value (calculated from the Debye frequency and entropy of migration $S_w \sim k$).

cf. (c) and (d) The observed change of dislocation structure on the primary slip plane after tempering for 40 min is surprisingly strong if one considers the relatively low annealing temperature of 825°C. It causes a marked mechanical recovery of the crystal [8]. Predominantly straight dislocations with burgers vectors at 60° angles to their lengths are produced by tempering (Fig. 6(b)). Most probably the density of the 'singularities' in the dislocation lines (jogs, kinks) decreases as well: The dislocations lose jogs by absorbing the divacancies produced during the deformation, whereas the relatively low number of curved dislocations as compared to long straight ones in the micrographs shows the decrease of the kink density. In this context the results of Khiznichenko *et al.*[9] should be mentioned. These authors found a maximum of internal friction at 110°K and 250 Hz in silicon and they assume that this is due to the movement of kinks along dislocations. The height of the internal friction maximum decreases by 50 per cent during a thermal treatment equivalent to ours. This also indicates that a strong decrease of the kink density is caused by our annealing. Whether or not the parallel decrease of the density of jogs and kinks with the intensity of the EPR-signal is coincidental (process (d)), cannot be decided until a detailed theory of the dislocations jogs or kinks as EPR centers has been developed.

Process (c) could also be responsible for the disappearance of the EPR-signal as shown by our electron micrographs. It seems plausible that a dislocation with a burgers vector at 60° angle to its length would show a barely detectable EPR signal because of broadening by the spin-spin interaction between closely neighbouring unpaired electrons (separation of dangling bonds 4 Å). The unpaired electrons are more distant from each other along dislocations having an angle smaller than 60° between their burgers vector and length so that a narrower signal can be expected.

If we assume that the variation of the dislocation structure according to one of the processes (c) or (d) causes the signal to disappear, then the meaning of the measured activation energy of 1·36 eV has to be considered. The following formula describes the motion of dislocations in their glide plane, which has taken place as is evident from Figs. 6(a) and 6(b):

$$v = B_0 \tau_{\mathrm{eff}}\, e^{\;Q/kT} \tag{7}$$

(v: dislocation velocity, τ_{eff}: effective shear stress at the dislocation, $B_0 = 4\,.\,10^7\ \mathrm{mm}^3/\mathrm{kg\ sec}$, $Q = 2{\cdot}2\ \mathrm{eV}$)[10]. Considerable internal stresses which can give rise to dislocation motion even in the unloaded crystal are caused by the dislocation density attained (10^8 to $5\,.\,10^8\ \mathrm{cm}^{-2}$). Using our previous assumption we are forced to conclude, from the activation energy of 1·36 eV, that for the motion of dislocations in the unloaded crystal a second process must take place apart from that of thermally activated motion in the glide plane described in equation (7). In the range of temperature and dislocation density considered here this second process must be the slower one determining the velocity despite its smaller activation energy*. Here the motion of divacancies V_2, which are produced in the diamond lattice during deformation, to the dislocations must be considered. The absorption of V_2 takes place at the jogs and causes more or less localized climb. This on the one hand diminishes the jog density, as demanded by (d), on the other hand it can exhaust obstacles for the conservative motion of dislocations and thereby can be a starting mechanism for the annealing process described in (c). Using different methods[11, 12], values between 1·2 and 1·3 eV are determined for the migration energy of the divacancies. According to these results divacancies already anneal in about 15 min below 300°C, and may not endure the post-deformation cooling period as a free defect.†

Cheng *et al.*[12] found a dependence of the annealing of the divacancies on the oxygen content in their samples and concluded that the divacancies disappeared by forming complexes with O-atoms. These complexes can dissociate at higher temperatures and set free divacancies. The composite process of dissociation of the complexes and migration of the freed divacancies to the dislocations has a higher activation energy (1·36 eV?) than the migration of a divacancy to the next O-atom (1·2 eV).

---

*An investigation describing the development of the dislocation structure during annealing is under way [8].

†This is consistent with the negative result of our attempt to find the EPR signal of the positively charged divacancies after deformation. To guarantee the necessary state of charge of the divacancies, Si heavier doped with B ($1{\cdot}6 \cdot 10^{18}\ \mathrm{cm}^{-3}$) was used for this experiment.

The EPR centers investigated by us had a half life time of 140 min at 700°C. From this results an average diffusion length given by

$$\sqrt{\overline{s^2}} = \sqrt{2D \, . \, t} = 7 \cdot 5 \, . \, 10^4 \, a \qquad (8)$$

(a = distance of a single jump) with the usual pre-exponential factor. This is about 100 times longer than the average distance of dislocations in our samples. This means the same as the above mentioned comparison of $K(T)$ with D_0 from Ham's theory: the time constant of our process is rather large regarding the activation energy and the dislocation distances.

5. CONCLUSION

The EPR signal produced by plastic deformation in silicon anneals in one stage with an activation energy of ($1 \cdot 36 \pm 0 \cdot 1$) eV in material weakly doped with B grown by the floating zone method. In the course of annealing which reduces the signal intensity below the limit of detection (10 per cent of the initial value) the dislocation structure on the primary glide plane is fundamentally altered. This change is considered responsible for the disappearance of the EPR-signal. Probably the diffusion of the divacancies produced by deformation to the dislocations is decisive for the motion of the dislocations.

Acknowledgements – The authors wish to thank Professor Dr. P. Haasen and Professor Dr. R. Hilsch for the possibility of working in their institutes and for valuable discussions. They also thank Dr. K. P. Chik for correspondence about migration entropy and Dr. M. Desvaux for comments on the text. The Deutsche Forschungsgemeinschaft and the Fraunhofergesellschaft supplied the apparatus.

REFERENCES

1. ALEXANDER H., LABUSCH R. and SANDER W., *Solid-St. Commun.* **3**, 357 (1965).
2. SIRTL E. and ADLER A., *Z. Metallk.* **52**, 529 (1961).
3. MEECHAN C. J. and BRINKMAN J. A., *Phys. Rev.* **103**, 1193 (1956).
4. BERNER K. and ALEXANDER H., *Acta metall.* **15**, 933 (1967).
5. CORBETT J. W., *Solid State Physics Suppl.* **7**. (Edited by F. Seitz and D. Turnbull). Academic Press. New York (1966).
6. HAM F. S., *J. Phys. Chem. Solids* **6**, 335 (1958).
7. HAM F. S., *J. appl. Phys.* **30**, 915 (1959).
8. WOHLER F. D., unpublished results.
9. KHIZNICHENKO L. P., KROHMER P. F., KAIPNAZAROV D. K., OTENIAZOV E., YUSUPOVA D. and ZOTOVA L. G., *Phys. Status Solidi* **21**, 805 (1967).
   KROHMER P. F. and KHIZNICHENKO L. P., *Phys. Status Solidi* **21**, 811 (1967).
10. ALEXANDER H. and HAASEN P., *Solid State Physics* (Edited by F. Seitz and D. Turnbull), Vol. **22**, p. 27. Academic Press, New York (1968).
11. WATKINS G. D. and CORBETT J. W., *Phys. Rev.* **138**, A543 (1965).
12. CHENG L. J., CORELLI J. C., CORBETT J. W. and WATKINS G. D., *Phys. Rev.* **152**, A761 (1966).

**Note added in proof.* Recently V. A. Gražulis and Yu. A. Osipàn reported on a EPR-signal in deformed Si which they attribute to the dislocations, as we did[1] (Materials of the Conf. on Defects of Structure in Semiconductors, Nowosibirsk 1969 p. 374. Private communication by D. R. Labusch)

J. Phys. Chem. Solids Pergamon Press 1970. Vol. 31, pp. 1389–1397. Printed in Great Britain.

ON THE MIGRATION OF V_K-CENTERS IN ALKALI HALIDES

K. S. SONG*
Institut de Physique, Faculté des Sciences, Strasbourg, France

(*Received* 22 *July* 1969; *in revised form* 29 *September* 1969)

Abstract—The small polaron migration theory is applied to the problem of reorientation and diffusion of V_K-centers in alkali halides. The Huang–Rhys S factor is calculated for 60°, 90° and 180° jumps of V_K-centers in function of the displacement of the two halogen ions of the V_K-center Activation energy, jump frequency and the tunnel effect are evaluated for KI and KCl, there is a satisfactory agreement with experimental data.

1. INTRODUCTION

SINCE the first work of Castner and Känzig[1] which established the existence of the self-trapped hole, the so-called V_K-center, in alkali halide crystals X-rayed at low temperature, many properties of this new hole center have been studied optically and by ESR technique.

Among these the migration study of V_K-centers carried out by Murray and Keller [2–4] on several alkali halides is of considerable interest. V_K-centers are oriented along a particular direction in the crystal by bleaching with linearly polarized light in the V_K absorption band. Then by studying the anisotropy of optical absorption and of ESR, Murray and Keller[2] established that the V_K-centers reorient preferentially through 60° jumps to one of its 8 adjacent sites, a jump of 90° being negligible. A subsequent study[3] indicated that 180° jump was also negligible in the temperature range studied.

In this range of temperature, around 90°K for KI and around 150°K for KCl, the jump motion is characterized by an activation energy which is typically a few tenth of eV[2–4].

On the other hand an approximate temperature independent afterglow is observed at much lower temperature range. This afterglow was found anisotropic and Delbecq *et al.*[5] attributed this to a 'tunneling' of the hole along the V_K axis.

In this paper we propose an interpretation of these data based on the small polaron theory. The possibility of applying the polaron theory was previously hinted by Murray and Keller[3].

The small polaron migration was studied by Yamashita and Kurosawa[6, 7] for the problem of electrical conductivity of NiO, while Holstein[8] studied this question extensively with a linear molecular chain. Applying the polaron theory to V_K-centers may seem questionable at first sight. As shown in a previous paper[9] we have shown that for the stabilization of a trapped hole between two halogen ions, the molecular binding between the two ions is more decisive than the polarization of the lattice by the hole. Beside optical phonons, which is represented by the polarization of the lattice around the hole, acoustical phonons should contribute to the stabilization through molecular binding. In this sense the V_K-center may be looked on as a polaron with important acoustical phonon contribution.

In Section 2(a) we will present briefly the theory of Yamashita and Kurasawa adapted for V_K-center. Calculation of Huang–Rhys S factor for 60°, 90° and 180° jumps will be given in Section 2(b). We will show that the jump probability decreases sharply in this order. In Section 2(c) we will study the temperature dependence of the jump probability for the entire temperature range and define such quantities as the activation energy, the jump frequency and the relative intensity of the tunnel effect at very low temperature. In Sections 3(a) and 3(b) we will evaluate these quantities for KI and KCl and compare these results with the experimental data. In spite of the very approximate nature of the parameters used there is a qualitative agreement between them. We finally will discuss in Section 4 some of the basic assumptions of the theory of Y-K.

---

*Present address: Dept. of Physics, Faculty of pure and applied science, University of Ottawa, Canada.

2. THEORY

(a) *Small polaron migration theory*

We present here very briefly the essential results of the theory of small polaron migration due to Y-K[6].

The Hamiltonian of the system consisting of a hole and the lattice can be written in the following way:

$$H = H_0 + H_{\text{int}}$$
$$H_0 = H_{el} + H_l$$

where

$$H_{el} = \frac{p^2}{2m} + U(r-0) + U(r-0') \quad (1)$$

and H_l is the perfect lattice Hamiltonian in which the potential energy is written in terms of the lattice point displacements $\Delta\mathbf{R}_i$ in the harmonic approximation.

$U(r-0)$ is the potential of the halogen ion located at 0 which the hole of the V_K-center sees.

The interaction Hamiltonian consists of two parts:

$$H_{\text{int}} = H_1 + H_2 \quad (2)$$

$$H_1 = \sum_{R_j \neq 0,0'}' U(r-R_j)$$

$$H_2 = \delta_{nn'} U' \sum_{R_j} \mathbf{R}_j \,.\, \Delta\mathbf{R}_j / |R_j| + \hat{\delta}_{nn'} V' \mathbf{R}_{nn'} \,.\, (\Delta\mathbf{R}_{n'} - \Delta R_n)/|R_{nn'}| \quad (3)$$

where

$\delta_{nn'}$ is the usual Kronecker's delta

and

$\hat{\delta}_{nn'} = 1$ if n and n' are nearest neighbours
0 otherwise

U' and V' are respectively the first derivatives with respect to the distance between the ions of the self-energy and the transfer energy of the hole.

H_1 is the remaining terms in the crystal potential after the deduction of $U(r-0)$ and $U(r-0')$.

Instead of employing the continuum model as did Y-K[6] we expressed the electron-lattice interaction term H_2 explicitly in terms of a few ionic displacements directly concerned[9, 10]

We have previously used this model to study the relative stability of one-center trapped and two-center trapped electron[9]. We found that for the V_K-center stability, against the one-center trapped configuration, $V' \gtrsim U'$ is necessary for most of the cases studied.

The essential point in the theory of migration of Y-K is to assume that H_2 is more important than H_1 and treat H_2 in zeroth-order while H_1 is considered as a small perturbation. This may be qualitatively the case for V_K-centers in alkali halides, because V_K-centers may be considered localized on ionic sites, though this is not a stationary state of the system. The rôle of H_1 is then to provoke transitions between the eigenstates of $H_0 + H_2$ centered on different sites.

In our previous work[9] we have solved the Schrödinger equation approximately, in which the hole wave function was of following form:

$$\Psi(r) = \frac{1}{\sqrt{2}}[\phi(r-0) + \phi(r-0')]. \quad (4)$$

The Schrödinger equation was then solved by variational method with $\Delta\mathbf{R}_i$ as variational parameters. We thus obtained the lattice relaxation around the hole directly.

The transition probability of the whole system, the hole and the relaxed lattice around it, to jump from one site to another is given by equation (45) of Y-K[6].

$$W = \frac{2\pi}{\hbar}|J|^2 \exp\{-S(2n+1)\}\frac{1}{\hbar\omega} \times I_0\{2S\sqrt{n(n+1)}\} \tag{5}$$

where ω is a suitable mean frequency of all phonons contributing to the jump,

$$n = 1/[\exp(\hbar\omega/kT) - 1]$$

is the phonon distribution function,

$$J = \int \Psi(r-R_m)H_1\Psi(r-R_{m+1})d\tau \tag{6}$$

is the transfer energy between two adjacent V_K wave functions.

$$S = \sum_{q,\mu=1\cdot 2} \frac{\omega_q}{2\hbar}[\delta Q_q{}^\mu(R_m - \delta Q_q{}^\mu(R_{m+1})]^2 \tag{7}$$

is the well-known Huang-Rhys factor*, $dQ_q{}^\mu$ being the displacement of the real normal coordinates[11] due to the local relaxation of lattice. Their relation to ΔR_j will be given in the next section.

I_0 is the modified Bessel function of order zero. This part of the above expression comes directly from the original formula of Huang and Rhys[12] by putting the number of net absorbed (or emitted) phonons $p = 0$, because during the jump of a V_K-center from R_m to R_{m+1} the net population of phonons is not altered.

(b) *Calculation of S factor*

We will evaluate S factor for three cases for which the angles between the initial and the final V_K axis are respectively 60°, 90° and 180°.

First we calculate the displacement δQ_q of the normal coordinate for only a small number of lattice points relaxation, namely that of the two halogen ions forming the V_K-center: Δ (Fig. 1). Relaxations of more ions should be included to obtain a better estimation of the S factor, however this entails a considerably lengthy calculation. Though these lattice relaxations can be calculated theoretically[9, 10, 13] the calculated values are not very reliable and they are not available in general. We know at best approximate values of the equilibrium distance of free $X_2{}^-$ from Person's work[14], from which we can deduce approximate values of Δ. We thus limited the lattice points displacements to that of the two halogen ions.

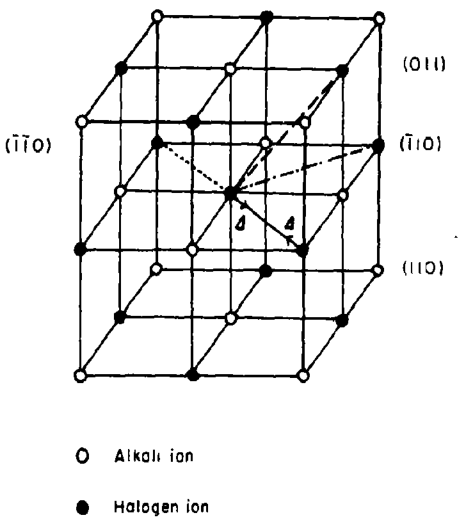

Fig. 1. Displacement of ions around a V_K-center We have taken into account only Δ of the two halogen ions 60° jump: (110) → (011), 90° jump: (110) → (1̄10); 180° jump. (110) → (110)

We believe that phonons other than the longitudinal optical ones contribute to the stabilization of the V_K-center. However, in order to simplify our calculation we will consider only the longitudinal optical phonons whose frequency will be considered constant and set equal to ω.

---

*The formula [28] of Y-K[6] giving the definition of the S factor is in error. π in the denominator should be dropped. This is also the case with the formula [12.5] of Appel[15].

In the original definition [4-21] of Huang and Rhys [12], $\hbar$ should be brought from numerator to denominator.

δQ is related to the lattice point displacement ΔR_j through the following definition[12]:

$$\delta Q_q = \frac{1}{\sqrt{2}}(\delta Q_q{}^1 + i\delta Q_q{}^2)$$
$$= \sqrt{\frac{\bar{M}}{N}} \sum_{R_j} \frac{\mathbf{q}}{|q|} \cdot \Delta \mathbf{X}_j\, e^{-iq.R_j} \qquad (8)$$

where

$\bar{M} = [(M_+M_-)/(M_+ + M_-)]$	the reduced mass
$\Delta \mathbf{X}_j = \Delta \mathbf{R}_j{}^- - \Delta \mathbf{R}_j{}^+$	the displacement of the halogen ion relative to the alkali ion.

N is the total number of unit cells in the crystal. δQ_q as defined above can be expressed immediately in terms of Δ. The exact summation over **q** in the first Brillouin zone is lengthy to perform, so we have replaced the Brillouin zone by a sphere of equal volume with radius q_0:

$$\frac{4\Pi}{3} q_0{}^3 = v_{BZ} = \frac{4}{a^3}(2\pi)^3$$

hence

$$q_0 = \frac{2}{a}(3\pi^2)^{1/3}.$$

This, then permit a straightforward integration in $|q|$ and we obtain the following results:

$$60^\circ. \quad S = 0{,}8881\, \bar{M}\omega_0\Delta^2$$
$$90^\circ: \quad S = 1{,}4858\, \bar{M}\omega_0\Delta^2 \qquad (9)$$
$$180^\circ: \quad S = 2{,}6982\, \bar{M}\omega_0\Delta^2$$

where $\bar{M}$ is expressed in atomic weight
ω_0 in unit of 10^{13}
Δ in unit of Ångstrom.

As we see the critical parameter in the S factor is the lattice displacement Δ. We will evaluate S factors from these expressions in Section 3(a). We can conclude without further numerical calculation that 60° jump is more favorable than other processes.

2(c) *Variation of the transition probability with temperature*

The variation of the transition probability with temperature is discussed in the review article of Appel[15] on polaron.

We are not going into the detail of this problem, but derive a few quantities which we need for the analysis of the experimental data in the next section. As we will shortly see, a typical value of S is found to be situated between $50 \sim 100$ for V_K-centers in alkali halides (compared to about $20 \sim 30$ for F-centers).

Table 1 gives the value of the temperature dependent factor of the transition probability for $S = 100$. Figure 2 shows the variation of $\log W$ with temperature (in $\hbar\omega/kT$). It is well-known that two distinct regions of temperature can be defined[8, 15]. In the high temperature region, $\hbar\omega/kT < 1$, one can

Table 1. Variation of the transition probability W *with temperature;* $W_0(T) = \exp.\{-S(2n+1)\}I_0\{2S\sqrt{n(n+1)}\}$ for $S = 100$

$\hbar\omega/kT$	W_0	$\log W_0$
∞	$3{\cdot}7\times10^{-44}$	-100
10	$1{\cdot}0\times10^{-43}$	$-99{\cdot}002$
8	$2{\cdot}9\times10^{-43}$	$-97{\cdot}935$
6	$6{\cdot}2\times10^{-41}$	$-92{\cdot}573$
5	$4{\cdot}4\times10^{-38}$	$-87{\cdot}131$
4	$8{\cdot}7\times10^{-36}$	$-80{\cdot}733$
3	$1{\cdot}5\times10^{-29}$	$-66{\cdot}360$
2	$3{\cdot}6\times10^{-22}$	$-49{\cdot}363$
1·4	$8{\cdot}7\times10^{-17}$	$-36{\cdot}981$
1·2	$7{\cdot}0\times10^{-15}$	$-32{\cdot}589$
1·0	$6{\cdot}6\times10^{-13}$	$-28{\cdot}041$
0·8	$6{\cdot}9\times10^{-11}$	$-23{\cdot}396$
0·2	$9{\cdot}0\times10^{-5}$	$-9{\cdot}317$
0·1	$7{\cdot}6\times10^{-4}$	$-7{\cdot}187$
0·02	$2{\cdot}4\times10^{-3}$	$-6{\cdot}022$
0·01	$2{\cdot}1\times10^{-3}$	$-6{\cdot}176$

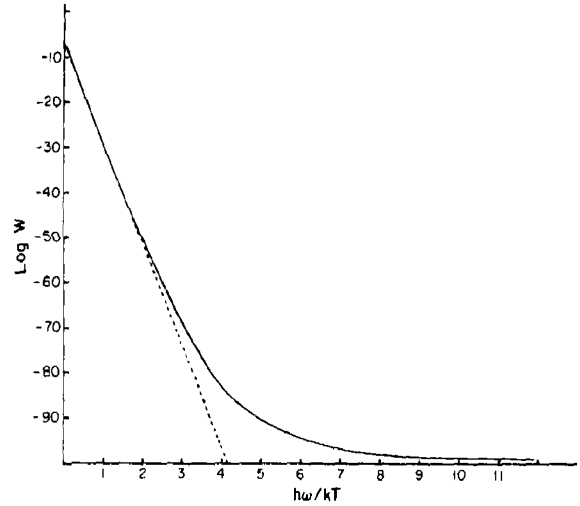

Fig. 2. Variation of the transition probability W with temperature. Log W is charted against $\hbar\omega/kT$. Dashed straight line shows that an activation energy can be defined at high temperature region, $\hbar\omega/kT < 1$. For low temperature, $\hbar\omega/kT > 8$, log W is almost independent of temperature $S = 100$.

define an 'activation energy' and a jump frequency, while for $\infty > \hbar\omega/kT > 8$, $\log W$ is practically temperature independent.

Using the asymptotic development of the modified Bessel function[16] the transition probability can be put in the following form in the limit of high temperature, $\hbar\omega/kT \to 0$:

$$W = \nu\, e^{-E_a/kT} \tag{10}$$

where

$$\nu = \frac{2\pi}{\hbar}\frac{|J|^2}{\hbar\omega}\sqrt{\frac{\hbar\omega/kT}{4\pi S}} \tag{11}$$

$$E_a = \frac{S}{4}\hbar\omega$$

E_a can be regarded as an activation energy if we assume that ν is constant over a limited interval of temperature, which is reasonable for the analysis of experimental data. ν is then the jump frequency. However as we will see in the next section, the measurements are taken in the temperature region where $\hbar\omega/kT$ is typically $\simeq 2$. In this region the deviation of the exact formula[5] from the asymptotic form is considerable and we must take the derivative of $\log W(1/kT)$ as the activation energy. The jump frequency also should be calculated locally. As is shown in Fig. 2, W attains the maximum at $\hbar\omega/kT = 2/S$ before going to zero at $\hbar\omega/kT = 0$. The maximum point is situated at $\hbar\omega/kT = 0.02$ for $S = 100$. The experimentally interesting region is thus very far from this point.

The next quantity we will define is the temperature at which the asymptotic expression of $W(T)$[10] gives the value for very low temperature. This temperature may be considered characteristic of the 'tunnel effect' of V_K-centers, as the migration is approximately temperature independent in this region of temperature, $\hbar\omega/kT > 8$.

The definition of Tc is evident from Fig. 2, and we put

$$\sqrt{\frac{\hbar\omega/kT_c}{4\pi S}}\, e^{-S\hbar\omega/4kTc} = e^{-S}$$

which gives

$$kTc = \frac{S\hbar\omega}{4(S + \frac{1}{2}\log(\hbar\omega/kTc) - \frac{1}{2}\log S - \frac{1}{2}\log(4\pi))}$$

$$\simeq \frac{\hbar\omega}{4} \text{ for large values of } S \tag{12}$$

Tc is thus approximately independent of the value of S, for large values of S.

3. COMPARISON WITH EXPERIMENTS

(a) *Preferential jump of* V_K*-centers*

In a series of experiments on V_K-centers in KCl[2] and KI[3] Murray and Keller have established that the migration of V_K-centers in the temperature range studied ($\Delta T \simeq 20°$), slightly below the respective decay temperature ($\simeq 110°K$ for KI and $\simeq 200°K$ for KCl) was by a succession of 60° jumps, with one of the two halogen ions remaining in the new V_K-center. 90° jumps were eliminated quite easily through optical anisotropy study. Possibility of V_K-centers migrating along the axis (180° jumps) was examined[3] by studying the isothermal decrease of the principal V_K absorption band and of the afterglow which is due to the recombination of migrating V_K-center with impurity trapped electron. Assuming that the jump frequency is not greatly different for a 60° jump and a 180° jump, which is a sound hypothesis as we will see in Section 4, they have concluded that at the temperature range studied 180° jump is either negligibly small or has approximately equal activation energy. In this section we will discuss these results and evaluate the activation energy E_a and the jump frequency ν. We will study KCl and KI for which precise data are available.

The most important parameter we need is the amount of the displacement of the two halogen ions. The values proposed by Person [14] give some indication. As we neglect other relaxations, which renders a quantitative calculation impossible, we will contend with the values proposed by Person for free X_2^-.

From the expression (9) we obtain the following results:

KI

$$\omega = 2{\cdot}7\times 10^{13}/\text{sec}[18]$$
$$\Delta = 0{\cdot}925\ \text{Å}[14]$$
$$S(60°) = 61$$

KCl

$$\omega = 4{\cdot}02\times 10^{13}[18]$$
$$\Delta = 0{\cdot}925\ \text{Å}[14]$$
$$S(60°) = 57.$$

We have not given the corresponding values for 90° and 180° jumps, as they are immediately evaluated from (9). They are roughly 2 times and 3 times that of 60° respectively. The temperature range in which the measurements were undertaken is respectively $85 \sim 105°K$ for KI[3] and $150 \sim 170°K$ for KCl[2]. This is equivalent, in unit of $\hbar\omega/kT$, respectively to $2{\cdot}42 \sim 1{\cdot}96$ and $2{\cdot}05 \sim 1{\cdot}81$. We are in the region where the activation energy can be defined though it is slightly dependent on temperature.

Following the remarks we have given in the previous section, we have evaluated locally, at $\hbar\omega/kT = 2$, the activation energy for 60° jumps. We also give in the parenthesis the values for the high temperature limit.

KI
$E_a = 0{\cdot}21$ eV ($0{\cdot}27$ eV), $E_a^{\text{exp}} = 0{\cdot}27$ eV [3]
KCl
$E_a = 0{\cdot}29$ eV ($0{\cdot}37$ eV), $E_a^{\text{exp}} = 0{\cdot}54$ eV [2].

The calculated values are in good qualitative agreement with experimental data in spite of simplifications we have adopted. From these values we can conclude that the S factor has values several times larger than in the case of F-centers in alkali halides. Yamashita and Kurosawa[6] have obtained $S = 10$ for a one-center trapped hole in NaCl using their continuum model.

The activation energies for 90° and 180° jumps are respectively 0·42 eV and 0·77 eV for KI according to our calculation. This means that in the temperature range studied, 90° and 180° jumps are quite negligible compared to that with 60° reorientation. However, because of the simplification we brought in this evaluation, in particular the neglect of lattice point relaxations other than those of the two halogen ions, we can not make quantitative comparison between these processes. The relaxation of the two halogen ions being the most important, we think that the influence of other ions would not be such that the qualitative conclusion we draw should be modified.

We now evaluate the jump frequency ν according to our definition given in the previous section. Instead of the expression [11] which is valid only in the limit of high temperature, we draw a straight line tangent to $\log W(1/kT)$ and from the ordinate at the origin we obtain the jump frequency. To evaluate this quantity we need J, the transfer energy. This quantity is difficult to estimate without a reliable potential. Instead we put $J = 0{,}1$ eV, which is derived from the experimental values of band-width of KCl[17]. In this way the following value is obtained:

$$\nu = 2 \times 10^{12}\,\text{sec}^{-1}$$

with

$$J = 0{,}1\,\text{eV}, \hbar\omega/kT = 2$$
$$\omega = 4 \times 10^{13}\,\text{sec}^{-1}$$

this value can be compared favourably with $\nu = 5 \times 10^{12}$ sec^{-1}[2]. However, because of the uncertainty in the value of J we have employed, this result is only indicative as to the order of magnitude.

(b) *Anisotropic tunneling effect at low temperature*

Persistent afterglow was observed at low temperature by Delbecq *et al.*[5] and Murray and Keller[3] in KCl[Ag] and KI[Tl] respectively. This luminescence is approximately temperature independent from 5°K up to about 75°K for KI and 140°K for KCl. This luminescence was found to be due to the recombination of V_K-centers and impurity-trapped electrons. Preoriented V_K-centers give rise to polarized luminescence which Delbecq *et al.*[5] have attributed to the tunneling effect of holes along the V_K axis.

In this section we study this phenomenon and examine whether the axial migration of hole may predominate the 60° jump at these temperatures.

As Fig. 2 shows, a constant activation energy can be defined only for region where $\hbar\omega/kT < 1$. For lower temperature the exact curve departs considerably from the straight line. For a small interval of temperature, however, one can attribute this departure to a 'tunneling effect' as did Murray and Keller [3]. In the case of our example with $S = 100$, we find the following:

$$E_a = 23\hbar\omega \;(\text{at } \hbar\omega/kT = 1)$$
$$W = W_0(\mathrm{e}^{-23\hbar\omega/kT} + \delta) \text{ at } \hbar\omega/kT = 1{\cdot}4$$

where

$$\delta = \mathrm{e}^{-33{\cdot}8} = 10^{-14{\cdot}3}.$$

With $\hbar\omega = 0{\cdot}018$ eV we find that this 'tunneling effect' contribution is equivalent to the hopping contribution at $T = 140$°K. This value is of the same order of magnitude as that found by Murray and Keller[3] for KI at $T \simeq 90$°.

We, however, draw attention to the fact that this is not to be taken for a real tunneling effect, but to be attributed to the deviation from a simple thermal activation type law.

One can talk about tunneling effect, however, at much lower temperature; $\hbar\omega/kT > 8$ (Fig. 2).

In this region $\log W$ curve is practically flat and we may talk about a temperature independent tunnel effect, characterized by the temperature $kT_c \simeq \hbar\omega/4$. This temperature is approximately 52°K for KI. For intermediate region of temperature only the exact expression[5] can describe the situation satisfactorily.

The anisotropy observed by Delbecq *et al.* [5] on KCl poses the question whether or not at very low temperature, $T < 20$°K, the predominant process (by tunneling effect) is 180° jump or 60° and 90° jumps. We find that $J(60°) > J(180°)$ and $S(60°) > S(180°)$ is necessary to ensure the inversion of importance of 60° and 180° jumps going to the lower temperature. The first condition is not in-acceptable, but the second one seems less probable according to our calculation of Section 2(b). We supposed that the 180° jumps predominate at low temperature. This, however, is not necessary to have anisotropy different from zero.

Anisotropy is defined as

$$A = \frac{I_{\parallel} - I_{\perp}}{I_{\parallel} + I_{\perp}}$$

where $I_{\parallel}$ and $I_{\perp}$ are intensities of luminescence parallel or perpendicular to the V_K axis.

If the migration of V_K-centers is due entirely to 60° (and 90°) jumps, then the optically oriented V_K-centers will lose completely their polarization after a few jumps, and we should have $I_{\parallel} = I_{\perp}$; $A = 0$. If, on the other hand, 180° jumps are not negligible, without necessarily being the dominant process, $I_{\parallel}$ and $I_{\perp}$ would not be equal and the anisotropy would be different from zero.

A precise measurement of the degree of anisotropy of the afterglow at very low temperature, $T < 20°$K, may provide us some indication as to the question of whether or not $S(60°)$ is greater than $S(180°)$.

4. DISCUSSION

We have studied the migration of V_K-centers in alkali halides by applying the small polaron hopping theory of Yamashita and Kurosawa. The essential assumptions lying under this theory are:

(1). the polaron binding energy, expressed by $S\hbar\omega$, is greater than the valence bandwidth,

(2). the transfer energy J is small, so that it may be considered as perturbation.

The first condition is apparently satisfied, because S is typically $\simeq 60$ and the bandwidth is less than 1 eV[17]. The second condition is linked to the question whether the hopping motion is adiabatic or not. The theory of Y–K and Holstein is a non-adiabatic theory: the hole moves so slowly from one site to another that the lattice has time to relax around it. The generally accepted criteria is that $J < \hbar\omega$[15].

This condition is apparently not satisfied in our case, though we have not evaluated J between two adjacent V_K wave functions. The largest term in the transfer energy of 60° *jump is roughly given by*

$$\frac{1}{4}\left[\left\langle\phi_x\left(\frac{\Delta}{\sqrt{2}},\frac{\Delta}{\sqrt{2}},0\right)\middle|H_1\middle|\phi_z\left(0,\frac{\Delta}{\sqrt{2}},\frac{\Delta}{\sqrt{2}}\right)\right\rangle + \left\langle\phi_y\left(\frac{\Delta}{\sqrt{2}},\frac{\Delta}{\sqrt{2}},0\right)\middle|H_1\middle|\phi_y\left(0,\frac{\Delta}{\sqrt{2}},\frac{\Delta}{\sqrt{2}}\right)\right\rangle\right].$$

We have assumed $J \simeq 0{,}1$ eV in Section 3(a) and this value is several times greater than that of $\hbar\omega$ we employed.

We believe that we are in an intermediate region where neither of the two approximations is quite justified. For the adiabatic case only qualitative study exists[7, 15]. Before proceeding to a more rigorous study in this direction, a reliable evaluation of J is desired with a suitable crystal potential.

In spite of certain assumptions which need further examinations, we have presented here an interpretation of the experimental data on V_K-center migration which is satisfactory on the whole. A few experimental measurements could be suggested to allow further understanding of the problem:

(1) A precise measurement of the activation energy and the jump frequency over a more extended interval of temperature may permit to judge whether our interpretation is right. In the adiabatic case the jump frequency is a certain mean frequency of the lattice vibration[7, 1] which can be varied by replacing the halogen atoms by its isotopes.

(2) Anisotropy measurements of the afterglow at very low temperature $T < 20°$K, may be of interest to determine the relative importance of the axial migration of V_K-centers, compared to that with 60° jumps. The model we propose show that the intensity of the afterglow at very low temperature is equiv-

alent to that of hopping motion with $kT_c \simeq \hbar\omega/4$.

(3) We have calculated recently the self-trapping of hole in solid argon[10]. We found that the V_K-like trapping is stable energetically.* In this case, however, the activation energy for migration should be at least an order of magnitude smaller than in a typical alkali halides, because of the low phonon frequencies. The activation energy is proportional to the square of the phonon frequency. This indicates that the V_K-centers, even if they are formed in rare gas solids, should be observable only at very low temperature.

REFERENCES

1. CASTNER T. G. and KÄNZIG W., *J. Phys. Chem. Solids* **3**, 178 (1957)
2. KELLER F. J. and MURRAY R. B., *Phys. Rev. Lett.* **15**, 198 (1965). KELLER F. J., MURRAY R. B., ABRAHAM M. M. and WEEKS R. A., *Phys. Rev.* **154**, 812 (1967)
3. KELLER F. J. and MURRAY R. B., *Phys. Rev.* **150**, 670 (1966).
4. MURRAY R. B. and KELLER F. J., *Phys. Rev.* **137**, A942 (1965).
5. DELBECQ C. J., GHOSH A. K. and YUSTER P. H., *Proc. Int. Symp. on Color Centers in Alkali Halides, Urbana* (1965).
6. YAMASHITA J. and KUROSAWA T., *J. Phys. Chem. Solids* **5**, 34 (1958).
7. YAMASHITA J. and KUROSAWA T., *J. phys. Soc. Japan* **15**, 802 (1960).
8. HOLSTEIN T., *Ann. Phys.* **8**, 325, 343 (1959).
9. SONG K. S., *J. phys. Soc. Japan* **26**, 1131 (1969).
10. SONG K. S., *Calculation on Self-Trapping of Hole in Solid Argon.* (to be published).
11. BORN M. and HUANG K., *Dynamical Theory of Lattices*. Oxford University Press, Oxford.
12. HUANG K. and RHYS A., *Proc. R. Soc.* **A204**, 406 (1950).
13. DAS T. P., JETTE A. N. and KNOX R. S., *Phys. Rev.* **134**, A1079 (1964).
14. PERSON W. B., *J. chem. Phys.* **38**, 109 (1963).
15. APPEL J., *Solid St. Phys.* **21**, 193. Academic Press, New York (1968).
16. *Handbook of Mathematical Functions* (Edited by Abromowitz and I. A. Stegun), p. 377. National Bureau of Standards U.S.A. (1964).
17. PANATT L. G. and JOSSEM E. L., *Phys. Rev.* **97**, 916 (1955).
18. BEALL FOWLER W., *Physics of Color Centers*, p. 629. Academic Press, New York (1968).
19. DRUGER S. D. and KNOX R. S. *J. Chem. Phys.* **30**, 3143 (1969)

---

*Since the submission of the present paper we learned of the work of Druger and Knox[19] giving the same conclusion.

J. Phys. Chem. Solids Pergamon Press 1970. Vol. 31, pp. 1399–1403. Printed in Great Britain.

ETUDE DES EFFETS SUPERFICIELS DANS LES TRANSFORMATIONS DES ACIDES STANNIQUES PAR L'EFFET MÖSSBAUER ET PAR DIFFRACTION DES RAYONS X

P. B. FABRITCHNYI, A. M. BABECHKIN et A. N. NESMEIANOV
Chaire de chimie nucléaire, Faculté de chimie, Université de Moscou, U.S.S.R.

(*Received* 16 *December* 1968; *in revised form* 27 *May* 1969)

Résumé – A partir des résultats expérimentaux les carrés des amplitudes moyennes des vibrations des noyaux d'étain $\langle x^2\rangle$ sont calculés en fonction de la température du recuit précédent pour les échantillons des acides α- et β-stanniques. On a montré que le grossissement des microcristaux de SnO_2 est accompagné de diminution des valeurs de $\langle x^2\rangle$. Pour les particules de SnO_2 dont le diamètre radiographique a atteint à ≈ 25 Å, le grossissement suivant ne provoque pas le changement des valeurs de $\langle x^2\rangle$.

Abstract – Surface effects associated with thermal annealing of α- and β-stannic acids were studied by means of Mossbauer effect and X-ray diffraction. Mean square displacements of tin nuclei $\langle x^2\rangle$ are found from experimental data as a function of annealing temperature. It is shown that increase in SnO_2 crystal size is accompanied by the decrease in $\langle x^2\rangle$. For SnO_2 particles whose average diameter is more than ≈ 25 Å as determined by diffuse X-ray scattering, further increase in the crystal size does not cause any change in the $\langle x^2\rangle$.

1. INTRODUCTION

LA POSSIBILITÉ d'observer les effets de surface dans les spectres Mössbauer est due au fait que les atomes superficiels ont le spectre de vibration différent de celui des atomes en masse[1, 2, 3]. En outre, l'environnement des atomes dans les couches superficielles, en principe, n'est pas le même que celui des atomes à l'intérieur du cristal, ce que doit se manifester par la différence des champs internes.

L'étude des effets de surface dans les solides à l'aide de la spectroscopie Mössbauer est exempte de quelques difficultés qui empêchent d'utiliser cette méthode pour la recherche des défauts internes du cristal. Ainsi on peut examiner les proprietés de surface dans les conditions quand tous les atomes superficiels se trouvent dans les positions équivalentes et éviter ainsi l'effet de 'superposition' dû au environnement variant des atomes Mössbauer ce qui est dans le cas lorsqu'on examine les proprietés des composés superficiels contenants les atomes résonnants (l'adsorbant luimême ne les contient pas).

L'application de l'effet Mössbauer peut être utile dans presque tous les domaines de la chimie d'état solide où les effets de surface jouent un rôle important. En particulier, l'effet Mössbauer doit permettre d'étudier les processus qui sont accompagnés par le changement de la surface specifique des particules dans les systèmes dispersifs des solides dans les cas, lorsque la susceptibilité des autres méthodes n'est pas suffisante.

Un système convenable pour l'étude des processus pareils presentent les acides stanniques qui se composent des agglomérés des microcristaux de SnO_2 et des molécules d'eau absorbée[4, 5]. Il est connu que les propriétes physiques et chimiques des acides stanniques fraîchement préparés se différencient notablement de celles des acides vieillis; on distingue, respectivement, les formes α et β. La forme α est peu stable et se transforme en celle β qui est le stade intermédiaire, lui-même mal défini, de l'évolution d'acide α-stannique à SnO_2 anhydre. Les acides stanniques ont fait l'objet de nombreux travaux (voir l'aperçu[6]), cependant le problème du mécanisme de leurs transformations n'est pas encore complètement résolu.

Dans la littérature on ne peut citer que quelques travaux[7, 8] contenants l'étude de ces acides par l'effet Mössbauer. Ces premiers travaux ont montré que la dépendance thermique de l'intensité de la raie résonnante dans les acides stanniques fraîchement préparés se différencie notablement de celle pour SnO_2. Sous tous les autres rapports les spectres Mössbauer des acides stanniques sont tout à fait anologues à ceux de SnO_2.

2. PREPARATION ET METHODE EXPERIMENTALE

Les acides α- et β-stanniques ont été préparés par réactions généralement employées:

$$SnCl_4 + NH_4OH \longrightarrow SnO_2{\cdot}mH_2O \quad (\alpha\text{-forme})$$

$$Sn + HNO_3 \longrightarrow SnO_2{\cdot}nH_2O \quad (\beta\text{-forme}).$$

Les précipités ainsi obtenus ont été lavés et puis sechés à la température ambiante. Ensuite les échantillons des acides stanniques étaient soumis au chauffage pendant trois heures à la température entre 40 et 1000°C.

Les spectres Mössbauer ont été enregistrés sur un spectromètre à accélération constante. La source utilisée était $^{119m}SnO_2$. L'épaisseur des absorbeurs était constante et égale à $0{\cdot}75$ mg/cm^2 ^{119}Sn. Dans tous les cas le déplacement isomérique et la largeur de la raie résonnante étaient identiques (avec une précision $\pm 0{\cdot}05$ mm/sec) aux paramètres correspondants d'absorbeur de SnO_2 préparé à partir de SnO:

$$SnO + \tfrac{1}{2}O_2 \longrightarrow SnO_2.$$

Cet absorbeur-étalon avait le déplacement isomérique $\delta = -2{\cdot}60$ mm/sec par rapport à une source β-^{119m}Sn et la largeur expérimental à mi-hauteur $\Gamma_{exp} = 1{\cdot}45$ mm/sec avec la source $^{119m}SnO_2$ utilisée dans ce travail. Ajoutons enfin que la valeur du carré de l'amplitude moyenne des vibrations des noyaux d'étain en direction de $\gamma\,\langle x^2\rangle = 0{\cdot}9\,.\,10^{-18}$ cm^2 trouvée pour cet absorbeur était la limite inférieure de celles trouvées pour les échantillons des acides stanniques.

Les diffractogrammes des échantillons examinés ont été obtenues avec la radiation CuK_α. Le diamètre radiographique des cristallites de SnO_2 dans les acides stanniques a été determiné à partir de l'élargissement des raies X. Nous avons tenu compte de l'élargissement instrumental en utilisant un étalon interne de CdO.

3. ANALYSE DES RESULTATS ET DISCUSSION

La particularité des acides stanniques est une grande dépendance de la probabilité d'absorbtion résonnante du degré du vieillissement.

En utilisant l'expression générale pour la probabilité f' des processus sans agitation thermique:

$$f' = \exp\left(-\frac{4\pi^2\langle x^2\rangle}{\lambda^2}\right) \qquad (1)$$

où λ est la longueur d'onde du rayonnement γ; nous avons calculé des valeurs de $\langle x^2\rangle$ pour les échantillons des acides stanniques après le recuit thermique. Les valeurs de f' qui sont nécessaires pour ce calcul ont été déterminées selon la méthode de surface décrite par Shirley, Kaplan et Axel[9], en utilisant la valeur du coefficient de la conversion interne α égale à $6{\cdot}3$ et celle de la largeur du niveau exité du noyau ^{119}Sn, égale à $2{\cdot}4\,.\,10^{-8}$ eV.

La Fig. 1 représente les variations de $\langle x^2\rangle$ en fonction de la température du recuit précédent pour les expériences avec les deux formes des acides examinés. On voit que dans la region des températures basses, les valeurs de $\langle x^2\rangle$ pour la forme β sont inférieurs à celles

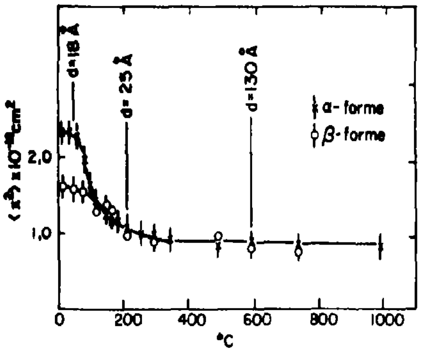

Fig. 1. Variation des valeurs du carré de l'amplitude moyenne des vibrations des noyaux d'etain $\langle x^2 \rangle$ en fonction de la température du recuit précédent pour les échantillons des acides α- et β-stanniques $\bar{d}$ = diamètre radiographique des cristallites de SnO_2. Absorbeurs des acides stanniques étaient au cours des expériences Mossbauer à la température de l'azote liquide.

d'acide α-stannique. La différence entre $\langle x^2 \rangle$ pour ces deux formes diminue avec élévation de la température du recuit. Cette allure des courbes $\langle x^2 \rangle = F(T_{\text{recuit}})$ correspondant à la transition, bien connue dans la chimie, de forme α à celle β, manifeste le fait que les acides stanniques sont les systèmes dispersifs où les microparticules de SnO_2 se différencient par leur grosseur.

L'influence du degré de dispersion sur $\langle x^2 \rangle$ dans les microcristaux peut se manifester sous deux aspects opposés. D'un coté, dans le microcristal il est impossible d'avoir une existence des vibrations thermiques avec les longueurs d'ondes beaucoup plus grandes que sa propre dimension. L'apparition dans le spectre de vibration des atomes internes du microcristal un tel 'cutoff' des frequances basses provoquerait une croissance lente de $\langle x^2 \rangle$ avec dimension. On a observé cet effet[10] dans le cas des microcristaux de Au pour les particules avec les diamètres moyens égales à 60 et à 200 Å.

D'autre part, la diminution des dimensions doit s'accompagner de l'augmentation de $\langle x^2 \rangle$ due au fait que les atomes dans les couches superficielles ont les amplitudes des vibrations plus grandes que celles des atomes internes. On a signalé cet effet dans le travail [11] où on a montré que les particules d'étain avec $d \approx 250$ Å possèdent $\langle x^2 \rangle$ plus grand que celui pour les particules avec $d \approx 600$ Å.

Les travaux déjà cités montrent que dans l'étude des transformations des acides stanniques à l'aide de la spectroscopie Mössbauer il est intéressant d'évaluer la grosseur des microparticules de SnO_2 dans les stades différents. Nous avons pour cela utilisé la diffraction des rayons X. Le diamètre moyen $\bar{d}$ des cristallites de SnO_2 dans les échantillons des acides stanniques a été déterminé à partir de l'élargissement des raies X.

La comparaison des diamètres radiographiques ainsi obtenus avec les valeurs de $\langle x^2 \rangle$ fournies par l'effet Mössbauer est compliquée, malheureusement, par le fait que les valeurs de $\bar{d}$ ne sont que les moyennes de la fonction de répartition de dimension; les conditions de préparation des acides stanniques suggèrent que cette fonction ne doit pas être étroite.

Nous n'avons pas décelé la différence entre les diamètres radiographiques de SnO_2 dans les acides α- et β-stanniques qui étaient soumis au même traitement thermique, par conséquent, les valeurs de $\bar{d}$ présentées sur la Fig. 1 ont rapport à tout les deux formes des acides examinés.

On peut voir sur la Fig. 1 qu'en général, la valeur de $\langle x^2 \rangle$ trouvée pour les acides stanniques qui se caractérisent par le diamètre radiographique de SnO_2 plus grand, est inférieure à celle pour les échantillons avec $\bar{d} \approx 18$ Å.

Ce fait met en évidence l'influence décisive dans le cas de microcristaux de SnO_2 d'effet de surface dû à l'affaiblissement des interactions entre les atomes internes dans les couches superficielles. Au contraire, l'effet de modification du spectre des vibrations des atomes internes dans les microparticules n'est pas important dans ce cas. Cette conclusion confirme celle du travail précédent[12] où la faible dépendance thermique de la fraction f' d'absorption 'sans recul' dans le réseau cristallin de SnO_2 était expliquée par le rôle prédominant pour les atomes d'étain des vibrations optiques qui se caractérisent par longueur d'onde courte.

La Fig. 1 montre que la diminution forte des valeurs de $\langle x^2 \rangle$ se passe lorsque l'augmentation des diamètres radiographiques des microparticules de SnO_2 est relativement faible.

Nous attribuons ce fait à la contribution différente des particules superpetites ($\bar{d} < 10$ Å) aux valeurs fournies par la diffraction des rayons X et par l'effet Mössbauer. Dans les expérience aux rayons X ces particules ne sont que les domaines amorphes qui ne peuvent pas provoquer les phénomènes notables de diffraction. Par contre, dans le cas d'effet Mössbauer, les particules superpetites font la contribution la plus importante à la valeur de $\langle x^2 \rangle$. Le traitement thermique à des temperatures basses des échantillons des acides stanniques ne fait possible que les processus qui se caractérisent par l'énergie d'activation la plus faible; c'est pourquoi un tel recuit provoque en majeur partie la disparition des particules les plus petites. Ceci permet d'expliquer les résultats obtenus. Ces observations permettent aussi de conclure que les processus du grossissement des microcristaux de SnO_2 dans les transformations des acides stanniques sont essentiellement ceux de la recristallisation. En outre, la différence entre les proprietés de deux formes des acides stanniques parait être due à celle de la fraction des particules superpetites dans la fonction de la répartition de dimension.

Il nous a paru intéressant d'examiner le rôle des molécules d'eau absorbée dans les transformations qui se passent dans les acides stanniques. D'un coté, l'absence dans les spectres Mössbauer du déplacement isomérique par rapport à la source de SnO_2 montre que le carré de la fonction d'onde près de noyau d'étain reste le même:

$$|\Psi(0)|^2_{\alpha\text{-forme}} = |\Psi(0)|^2_{\beta\text{-forme}} = |\Psi(0)|^2_{SnO_2}$$

c'est-à-dire, la présence des molécules d'eau absorbée ne change pas notablement la configuration éléctronique autour des noyaux d'étain même les plus proches. L'absence dans tous les cas des changements de la forme et de la largeur de la raie résonnante montrent aussi que l'environnement au moins le plus proche des atomes d'étain dans les transformations des acides stanniques ne change pas. Cependant, on peut supposer la corrélation entre la teneur en eau absorbée et le changement de $\langle x^2 \rangle$ parce que tous les deux sont dus aux effets superficiels.

La Fig. 2 représente la variation de $\langle x^2 \rangle$ pour les deux formes des acides stanniques en fonction de la perte d'eau ρ. On peut voir de la Fig. 2 que la perte des premières quantités d'eau ne correspond pas au changement notable des valeurs de $\langle x^2 \rangle$. Comme on pouvait le prévoir, l'acide α-stannique contient beaucoup plus d'eau plus facile à éliminer que la forme β.

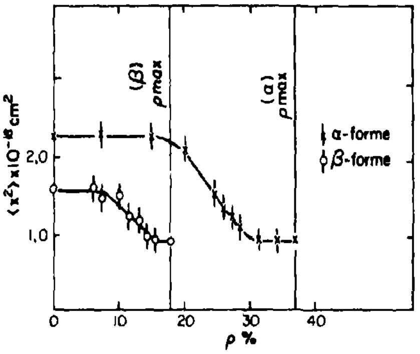

Fig. 2 Variation de $\langle x^2 \rangle$ en fonction de la perte d'eau après le recuit thermique pour les deux formes des acides stanniques.

$$\left(\rho = \frac{\text{la perte de poids après le recuit}}{\text{le poids initial d'échantillon}} \cdot 100\%\right).$$

Ensuite, la perte d'eau absorbée accompagne les processus de recristallisation de SnO_2. Enfin, on peut constater que la perte des dernières quantités d'eau ne correspond pas au changement notable des valeurs de $\langle x^2 \rangle$ ce qui est dû probablement à la limite supérieur de la susceptibilité de la méthode utilisée.

4. CONCLUSIONS

On a montré l'influence décisive de l'effet de surface sur la valeur de $\langle x^2 \rangle$ pour les microparticules de SnO_2 dont le diamètre radiographique est inférieur à ≈ 25 Å.

La comparaison des résultats fournis par l'effet Mössbauer et par la diffraction des rayons X nous permet de conclure que les processus du grossissement des particules de SnO_2 sont essentiellement ceux de la recristallisation.

Enfin, les résultats de cette étude montrent que l'effet Mössbauer permet d'examiner les processus qui s'accompangent par le changement des dimensions des particules dans les systèmes très dispersifs des solides lorsque la susceptibilité des autres méthodes n'est pas suffisante.

Remerciements – Nous tenons très particulièrement à remercier ici Dr. Pokrovskii B.I. qui a bien voulu analyser nos échantillons par la diffraction des rayons X. Nous remercions également le Professeur Kovba L.M. pour les discussions que nous avons eues ensemble.

BIBLIOGRAPHIE

1. MARADUDIN A. A., *Rev. mod. Phys.* **36**, 428 (1964).
2. RICH M., *Phys. Lett.* **4**, 153 (1963).
3. VAIL J., *Can. J. Phys.* **45**, 2661 (1967).
4. WEISER H. B. et MILLIGAN W. O., *J. phys. Chem.* **36**, 3010 (1932).
5. DONALDSON J. D. et FULLER M. J., *J. inorg. nucl. Chem* **30**, 1083 (1968).
6. PASCAL P., Nouveau Traité de Chimie Minérale, Vol. 8, p. 285. Masson & Cie, Paris (1963)
7. BONTSHEV I., SKORTCHEV, ORMANDGIEV S., EMERSLEBEN O., CRISTOV D., KAMENOV P. et DANAILOV G., *Ann. Univ Sofia, fac. de phys.* **58**, 71 (1963/64).
8. DUBININ V. M., KORDUK S L., LISITCHENKO V. L. et SMOILOVSKII O N *Ukr. fiz. Zh.* **10**, 1368 (1965).
9. SHIRLEY D A., KAPLAN M et AXEL P., *Phys Rev.* **123**, 816 (1961)
10. MARSHALL S W et WILENZICK R M, *Phys. Rev. Lett.* **16**, 219 (1966).
11. SUZDALEV I. P., HEN M, GOLDANSKII V. I. et MAKAROV E F., *Zh. eksp. teor fiz.* **51**, 118 (1966).
12. KAGAN U., *Zh. eksp. teor fiz.* **41**, 659 (1961).

J. Phys. Chem. Solids Pergamon Press 1970. Vol. 31, pp. 1405–1408. Printed in Great Britain.

TECHNICAL NOTES

Thermal properties of nickel hexammine salts at the phase transition

(*Received* 23 *September* 1969; *in revised form* 22 *December* 1969)

NICKEL hexammine chloride $Ni(NH_3)_6Cl_2$ is cubic at room temperature and has the space group Fm3m[1]. It has a phase transition at $T_c \approx 77°K$ that can be seen as a sudden broadening of the Ni^{2+} ESR line[2]. This indicates a distortion of the cubic crystal field seen by the Ni^{2+} ions with spin $S = 1$. The transition shows about 5° thermal hysteresis and an isotope shift. The dielectric constant increases from $\epsilon = 6{\cdot}0$ above T_c to $\epsilon = 8{\cdot}5$ below T_c[3]. Proton NMR[4] and low temperature specific heat measurements [5, 6] show that the ammonia groups in this crystal rotate around their 3-fold symmetry axes by tunnelling with frequencies of the order of 10^{10} Hz even at liquid helium temperatures. Since the symmetry of the NH_3 group does not fit that of the lattice, there are several equivalent orientations of the ammonia, and we believe the phase change is primarily an order–disorder transition in the NH_3 orientation. We have measured the specific heat around T_c to find the entropy of transition which might give information about the change of order. We also report that the heat conductivity of this salt and the isomorphous crystal $Ni(NH_3)_6Br_2$ is very low above T_c, of the same order as in completely disordered solids like glass, but at the transition it increases by a factor 3. Heat conductivities usually do not change very much at phase transitions, only in KH_2PO_4-type crystals are changes of the same magnitude reported [7]. For comparison we have measured the conductivity of NH_4Cl which has an order–disorder transition at $T_c = 243°K$.

Single crystals of $Ni(NH_3)_6Cl_2$ were grown in a thermostatically controlled bath at about 30°C from a solution of $NiCl_2.6H_2O$ p.a. in distilled water with NH_3 added to saturation. For specific heat work it was advantageous to grow them around a small heating spiral of 0·03 mm constantan wire to insure good heat contact. Growth on a wire also gave octahedra with plane parallel faces for conductivity work. $Ni(NH_3)_6Br_2$ was grown in a similar way, while NH_4Cl grew best with urea added to the solution.

The specific heat of two crystals weighing 15·8 mg and 14·9 mg was measured by monitoring the temperature as a function of time during heating and cooling. The samples were suspended in vacuum with 0·05 mm copper/constantan thermocouples glued on. The reference temperature was the wall of the container immersed in liquid nitrogen boiling under constant pressure. The heat leak corrected and averaged results of several runs are shown in Fig. 1. The heat capacity λ peaks correspond to an entropy of transition $\Delta S = \int (\Delta C_p/T)\,dT = (4{\cdot}0 \pm 0{\cdot}4)k_B$ per molecule where k_B is Boltzmann's constant. The exact shape of the specific heat

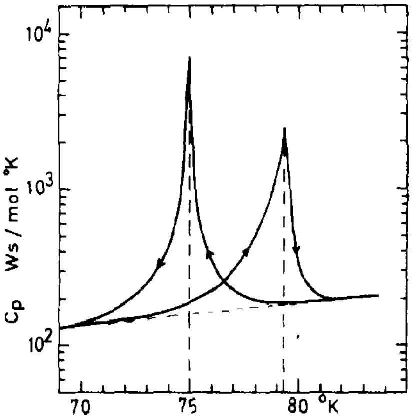

Fig. 1. Averaged specific heat of $Ni(NH_3)_6Cl_2$.

anomaly as a function of $(T_c - T)$ close to T_c is very difficult to determine, and it is probably strongly influenced by impurities and the causes of thermal hysteresis.

The averaged heat conductivity across crystals of octahedral shape and side edge about 3 mm is shown in Fig. 2. The crystals were glued between a copper block and a thin piece of copper foil with a heater attached to the foil. One thermocouple junction was between the crystal and the foil and the other on the block. The block temperature was measured with copper and germanium resistance thermometers. Because of the large heat of transition, dynamic effects will give an apparent peak in conductivity near T_c unless the temperature is varied very slowly. This may be the cause of the peak observed at the λ-point in CH_4[8]. Most of the conductivity change at the transition takes place within a 1°K interval. The uncertainties in the data are caused mainly by the contact resistance, and the possible error is about 10 per cent at T_c and above, increasing to perhaps 30 per cent at the lowest temperatures and the highest conductivities.

The conductivity of NH_4Cl is considerably higher than that of the hexammines, and it changes much less at the transition. This salt has also been studied by Simson[9] and recently by Bausch and Waidelich[14] (note added in proof).

In cubic $Ni(NH_3)_6Cl_2$ above T_c each ammonia is surrounded in the plane of the triangular H_3 groups by a square of the 4 nearest Cl^- ions[1]. The protons polarize to some extent the closest Cl^- ions, and we believe that the NH_3-Cl^- interactions are mainly responsible for the barriers to NH_3 rotation. The direct NH_3-NH_3 interaction is probably small. In a perfect 4-fold symmetric potential set up by the Cl^- neighbours a 30° rotation of the NH_3 group will bring it back to an equivalent position. But a 30° rotation probably also results in some readjustment of the neighbours and a slight tilting of the NH_3 symmetry axis. Distortion of the Cl^- lattice around one ammonia will be felt by the neighboring NH_3 groups, and below T_c the structure is locked in a permanent distortion with greater NH_3 order.

The measured entropy change at the transition is very close to $k_B \ln 2$ per NH_3 group $(6 \ln 2 = 4{\cdot}16)$. If this is a change in configurational entropy alone upon going to a more ordered state, there must be just half the number of allowed NH_3 orientations below T_c and there the 4-fold symmetry of the Cl^- square must be reduced to 2-fold. A rhombic distortion as suggested in Fig. 3(a) is very

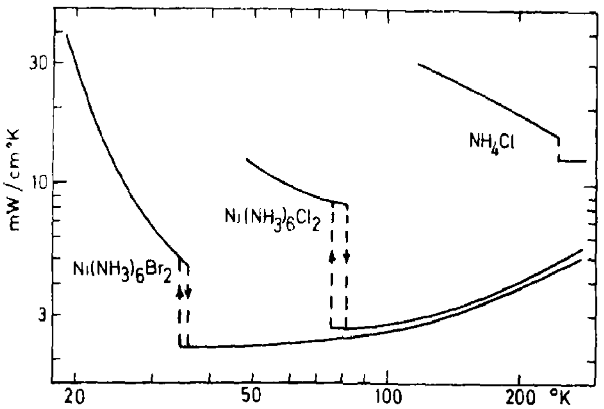

Fig. 2. Averaged thermal conductivities of $Ni(NH_3)_6Cl_2$, $Ni(NH_3)_6Br_2$ and NH_4Cl.

likely to occur and it would have this ordering effect if NH_3 orientations A and B in Fig. 3(b) are split in energy by more than k_BT_c. However, the distortion of the lattice will probably contribute to ΔS and no firm conclusions on the transition can be reached from the specific heat data. Our transition entropy value for $Ni(NH_3)_6Cl_2$ is in good agreement with data on the similar salt $Ni(NH_3)_6(NO_3)_2$ which has $\Delta S = (3{\cdot}85 \pm 0{\cdot}25)k_B$ per molecule at $T_c = 243°K$[10], but where ordering of NO_3 groups may be involved. The transition in the nitrate is easily undercooled, while we have observed no undercooling in the chloride. For $Ni(NH_3)_6I_2$ a much smaller value $\Delta S = k_B \ln 3$ at $T_c = 19{\cdot}5°K$ has been reported[5].

The heat conductivity of the hexammines is surprisingly low above T_c. The approximate formula for heat conductivity $K = Cvl/3$ gives a phonon mean free path as short as $l \approx 3Å$ if we assume a mean phonon velocity $v \approx 2000$ m/sec. Although a large part of the measured specific heat C is associated with optical phonons of small group velocity and with localized rotations of the NH_3 groups so that the acoustic phonon mean free path is longer than the estimate above, the small conductivity indicates strong phonon scattering. The resistance in KH_2PO_4 has been explained by a coupling between acoustic phonons and the ferroelectric mode[11]. The model for the hexammine suggested in Fig. 3 has the required scattering mechanism above T_c. Any lattice wave that instantaneously deforms the Cl^- square will make the NH_3 orientations A and B slightly nonequivalent, and rotation transitions between these states will scatter the phonons. The scattering is most efficient for phonons having the same frequency as the AB jump rate which probably is of the order 10^{11}–10^{12} Hz. In the permanently distorted lattice below T_c no such coupling between acoustic phonons and NH_3 rotations is possible, and here the conductivity of the hexammines show the normal behavior of crystalline solids.

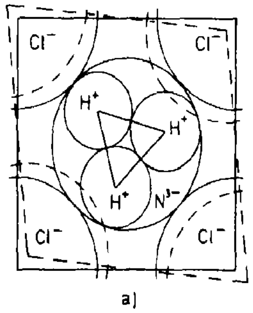

Fig. 3 (a). Position of NH_3 group in square of 4Cl ions in $Ni(NH_3)_6Cl_2$. Suggested deformation is shown with dashed lines

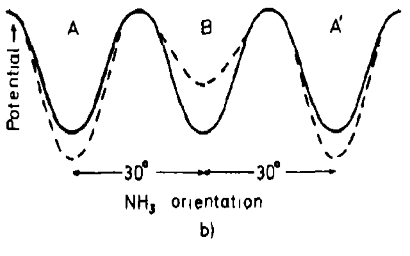

Fig. 3 (b). Barriers to NH_3 rotation with changes upon suggested deformation shown dashed.

Disorder for only the light hydrogen atoms is not enough to insure very short phonon mean free paths as can be seen from the measurements on NH_4Cl. Here the conductivity change at the order–disorder transition is only about 20 per cent and the added resistivity above T_c is less than $\frac{1}{10}$ of that for $Ni(NH_3)_6Cl_2$. NH_4Cl is cubic and the structure is disordered with respect to the two possible orientations of the NH_4 groups above T_c[12]. But the symmetry is such that the energies of the two NH_4 states are influenced in the same way by an uniaxial compression, and we expect no coupling between acoustic phonons and NH_4 rotations. The ultrasonic attenuation in NH_4Cl is approximately the same above and below T_c[13], while we predict strong attenuation of short ultrasonic waves in the hexammines above T_c.

In the suggested model for the hexammines the orientations A and A' are not equivalent in an electric field if the axis of the NH_3 dipole is somewhat tilted in the equilibrium position. To explain the greater dielectric constant below T_c[3] we must assume greater tilting in the distorted lattice.

Acknowledgements – We are grateful to Norges Almenvitenskapelige Forskningsråd and to NTH's Fond for support of this work

Physics Department, A. ELGSAETER
Norwegian Institute of Technology, I. SVARE
Trondheim,
Norway

REFERENCES

1. WYCKOFF R. W. G., *Crystal Structures*, 2 Edn., Vol. 3, p. 783 Interscience, New York (1965)
2. AIELLO G., PALMA M. U. and PERSICO F., *Phys. Lett.* **11**, 117 (1964).
3. AIELLO G., and PALMA-VITTORELLI M. B., *Phys. Rev. Lett.* **21**, 137 (1968)
4. KIM P. H., *J. phys. Soc. Japan* **15**, 445 (1960).
5. Van KEMPEN H., DUFFY Jr. W. T., MIEDEMA A. R. and HUISKAMP W. J., *Physica* **30**, 1131 (1964).
6. Van KEMPEN H., GAROFANO T., MIEDEMA A. R. and HUISKAMP W. J., *Physica* **31**, 1096 (1965)
7. SUEMUNE Y., *J. phys. Soc. Japan* **22**, 735 (1967)
8. GERRITSEN A. N. and van der STAR P., *Physica* **9**, 503 (1942)
9. SIMSON C., *Naturwissenschaften* **38**, 559 (1951).
10. LONG E. A. and TOETTCHER F. C., *J. Am. chem. Soc.* **64**, 629 (1942).
11. INOUE M., *J. phys. Soc. Japan* **26**, 420 (1969)
12. LEVY H. A. and PETERSON S. W., *Phys. Rev.* **86**, 766 (1952).
13. GARLAND C. W. and JONES I. S., *J. chem. Phys.* **42**, 4194 (1965)
14. BAUSCH W. and WAIDELICH W., *Phys. Lett.* **30A**, 190 (1969)

J. Phys. Chem. Solids Vol. 31, pp. 1408–1412

Electron paramagnetic resonance study of Mn^{2+} in $(NH_4)_2Mg_2(SO_4)_3$ and $(NH_4)_2Zn_2(SO_4)_3$ crystals

(*Received* 27 *August* 1969; *in revised form* 9 *December* 1969)

ELECTRON paramagnetic resonance studies of Mn^{2+} have been reported earlier in several crystals[1–3]. Information was obtained about the position of the paramagnetic ion, spin-Hamiltonian parameters and lattice defects. EPR studies of different paramagnetic ions in Langbeinites, whose general composition is $(M^{1+})_2(M^{2+})_2(SO_4)_3$ where M^{1+} = K, Rb, Tl or NH_4 and M^{2+} = Ca, Cd, Co, Ni, Mg or Zn, have been taken up to define the environment of the paramagnetic ion in these crystals and also to obtain the information about the associated lattice defects and the crystal field parameters. Langbeinites will particularly form interesting series since both monovalent and divalent sites are available for the substitution of the paramagnetic ion. The results obtained from the EPR studies of Mn^{2+} in $(NH_4)_2Cd_2(SO_4)_3$[4], $(NH_4)_2Co_2(SO_4)_3$ and $(NH_4)_2Ni_2(SO_4)_3$[5] have been reported earlier. The present paper deals with the results obtained from the EPR studies of Mn^{2+} in $(NH_4)_2Mg_2(SO_4)_3$ and $(NH_4)_2Zn_2(SO_4)_3$ single crystals.

The detailed X-ray data regarding the atomic positions in $(NH_4)_2Mg_2(SO_4)_3$ and $(NH_4)_2Zn_2(SO_4)_3$ does not seem to be available in the literature. The detailed data regarding the crystal structure of $K_2Mg_2(SO_4)_3$ which is isomorphic to $(NH_4)_2Mg_2(SO_4)_3$ and $(NH_4)_2Zn_2(SO_4)_3$ is reported earlier[6]. The lattice parameters of many isomorphic salts of Langbeinites excluding that of $(NH_4)_2Zn_2(SO_4)_3$ is available in the literature[7]. Langbeinite series crystalizes in space group $P2_13$ with cubic symmetry and there are four molecules per unit cell. The edge length of the tetramolecular unit of $(NH_4)_2Mg_2(SO_4)_3$ is 9·979 Å. Since $(NH_4)_2Mg_2(SO_4)_3$ and $(NH_4)_2Zn_2(SO_4)_3$ are isomorphic to $K_2Mg_2(SO_4)_3$ the structural data available regarding $K_2Mg_2(SO_4)_3$ can be treated as applicable to $(NH_4)_2Mg_2(SO_4)_3$ and $(NH_4)_2Zn_2(SO_4)_3$ but for the slight changes in lattice parameters and inter-atomic distances. The structure is a grouping of sulphate tetrahedra and metal atoms. There are two crystallographically non-equivalent divalent metal atoms (Mg^{2+} or Zn^{2+}) and two nonequivalent monovalent metal atoms the difference between the environment of the two nonequivalent monovalent metal atoms.

In order to grow single crystals of Mn^{2+} doped $(NH_4)_2Mg_2(SO_4)_3$, magnesium sulph- divalent metal atoms is much less compared to $((NH_4)^+)$. Each divalent atom is surrounded by six oxygen atoms which forms slightly distorted octahedron. The distances between oxygen atoms and divalent metal atoms (Mg^{2+} or Zn^{2+}) in two octahedra are different which in turn gives rise to the non-equivalency between the two divalent metal ions. The monovalent atom $((NH_4)^+)$ coordination cannot be sharply defined, there are four oxygens around one type of monovalent atom and three oxygens around second type of monovalent atom. The difference between the environment of two non equivalent ate ($MgSO_4 \cdot 7H_2O$) and ammonium sulphate $((NH_4)_2SO_4)$ are mixed in stochiometric proportion. Little quantity (approximately 0·5 per cent by weight) of manganese sulphate ($MnSO_4 \cdot 4\text{–}5H_2O$) has been added to the mixture of magnesium sulphate and ammonium sulphate and the saturated solution is prepared. The crystals are grown by the slow evaporation of the saturated solution at room temperature. Similar procedure is adopted to grow the single crystals of Mn^{2+} doped $(NH_4)_2Zn_2(SO_4)_3$ by using zinc sulphate ($ZnSO_4 \cdot 7H_2O$) instead of magnesium sulphate. The crystals are found to grow with large {110} faces. A varian V-4502 EPR *X*. band spectrometer with 100 kc/sec modulation has been used to study the EPR. The microwave cavity was a TE_{011} mode cylindrical cavity with the axis parallel to the rotation axis of the magnet and perpendicular to the direction of the magnetic field. As a reference for magnetic field strength the resonance line of DPPH is used. The magnetic field is measured using a varian NMR gaussmeter while the frequency of the proton signal is measured by a Beckman counter. IBM 1620 computer has been used for doing the calculations.

The EPR spectrum of Mn^{2+} in orthorhombic field is expected to show five fine structure transitions, each of which will show six hyperfine components. When one of the principal axes (x, y and z) of a Mn^{2+} ion parallels the magnetic field, the energy level separations of the spin system correspond to an extreme value. The orientation of these axes can be found by searching for the magnetic field direction, where the fine structure lines of the EPR spectra lie at an extremum in energy. The measurements in both the crystals are done by rotating the magnetic field in a $(\bar{1}10)$ plane of the crystal. The fine structure lines are found to have two extrema in $(\bar{1}10)$ plane and the two extrema are separated by 90° in each case. The z axis was assigned to the direction with large separation between the $M = -\frac{3}{2} \rightarrow -\frac{5}{2}$ and $M = \frac{5}{2} \rightarrow \frac{3}{2}$ transitions. The direction of the second extrema was called x axis. The z axis in $(NH_4)_2Mg_2(SO_4)_3$ makes an angle of 35° with [110] axis in $(\bar{1}10)$ plane and this happened to be the [111] axis also. The z axis in $(NH_4)_2Zn_2(SO_4)_3$ makes an angle of 38° with [110] axis in $(\bar{1}10)$ plane and this happened to be [111] axis also. In a cubic crystal the [111] axis is expected to make 35° angle with [110] axis in $(\bar{1}10)$ plane. The observation of z axis at 38° from [110] axis in $(NH_4)_2Zn_2(SO_4)_3$ instead of at 35° might be due to the slight misorientation of the crystal. The x axis makes an angle of 90° with [111] axis or z axis in $(\bar{1}10)$ plane. The y axis in both the crystals is perpendicular to zx plane and it coincides with $[\bar{1}10]$ axis. In the neighbourhood of static magnetic field parallel to the z and x axis in both the crystals the measurements were made by rotating the crystals about it's $[\bar{1}10]$ axis which was held perpendicular to the direction of the magnetic field to make sure about the extrema observed. The resonance lines in the y direction in both the crystals are grouped close together and so no accurate magnetic field measurements of their positions could be made. Magnetic field measurements are done along the z and x directions in both the crystals. It may be noted here that in addition to the thirty resonance lines due to Mn^{2+} magnetic complex in one environment, there are some very weak lines. Probably these lines are due to Mn^{2+} in some other environment. The study of this weak spectra could not be done because of the relative intensity of this weak spectra under discussion in both the crystals.

The EPR measurements on $(NH_4)_2Mg_2(SO_4)_3$ and $(NH_4)_2Zn_2(SO_4)_3$ are analyzed using the spin Hamiltonian appropriate for Mn^{2+} in a rhombic crystalline electric field[8]

$$\begin{aligned}\mathcal{H} = {} & \beta(g_x H_x S_x + g_y H_y S_y + g_z H_z S_z) \\ & + D(S_z^2 - (\tfrac{1}{3})S(S+1)) + E(S_x^2 - S_y^2) \\ & + \frac{a}{6}(S_x^4 + S_y^4 + S_z^4 - (\tfrac{1}{5})S(S+1) \\ & \times (3S^2 + 3S - 1)) \\ & + A_x S_x I_x + A_y S_y I_y + A_z S_z I_z \qquad (1)\end{aligned}$$

where the terms have their usual meaning. a, D and E are cubic, axial and rhombic crystal field parameters, respectively, and A is the hyperfine constant. The expressions used to obtain the energy differences of the energy levels of spin Hamiltonian given in equation (1) are found in Table 1. The spin Hamiltonian parameters obtained using the expressions given in Table 1 are given in Table 2. The spin Hamiltonian parameters obtained for Mn^{2+} in $(NH_4)_2Cd_2(SO_4)_3$ crystal [4] and $(NH_4)_2Co_2(SO_4)_3$ crystal[5] are also given in Table 2 for comparison sake. It may be noted here that the spin Hamiltonian used for Mn^{2+} in $(NH_4)_2Cd_2(SO_4)_3$ crystal[4] corresponds to Mn^{2+} in tetragonal crystalline electric field. For the case of Mn^{2+} doped $(NH_4)_2Co_2(SO_4)_3$ crystal[5] the spin Hamiltonian described in equation (1) and the expressions given in Table 1 are used.

Experimentally, only the relative signs are determined. The second order shifts permit the determination of relative signs of the various measured parameters. For negative D/A, the separations of sextets decrease on the low field side while for positive D/A the separations of sextets decrease on the high field side for the magnetic field parallel to z axis. In the case of Mn^{2+} negative A is commonly accepted. In the present experiments the separations of sextets decreases towards the high field side and hence D/A is positive which in turn results D to be negative.

The EPR results can be best explained by assuming that Mn^{2+} substitute for Mg^{2+} in the case of $(NH_4)_2Mg_2(SO_4)_3$ and for Zn^{2+} in the case of $(NH_4)_2Zn_2(SO_4)_3$. Such replacement would not be unexpected, given the similarity of ionic radii (0·66 Å for Mg^{2+}, 0·74 Å for Zn^{2+} and 0·80 Å for Mn^{2+}) and the identity of charge. When Mn^{2+} substitute for Mg^{2+} or Zn^{2+} positions one expects two different spectra because of the availability of two nonequivalent sites. However, the

Table 1. Fine structure and hyperfine structure splittings

(a) Fine structure

Energy differences for $H \| Z$.

$H_1\ (M = \frac{5}{2} \rightarrow \frac{3}{2}) = H_0 + 4D + 9E^2/(H_1 - D) - 5E^2/(H_1 - 3D) + 2a$

$H_2\ (M = \frac{3}{2} \rightarrow \frac{1}{2}) = H_0 + 2D + 9E^2/(H_2 + D) - 9E^2/(H_2 - D) - 5E^4/(H_2 - 3D) - (\frac{5}{2})a$

$H_3\ (M = \frac{1}{2} \rightarrow -\frac{1}{2}) = H_0 - 9E^2/(H_3 - D) + 5E^2/(H_3 + 3D) + 5E^2/(H_3 - 3D) - 9E^2/(H_3 + D)$

$H_4\ (M = -\frac{1}{2} \rightarrow -\frac{3}{2}) = H_0 - 2D - 9E^2/(H_4 + D) + 9E^2/(H_4 - D) - 5E^2(H_4 + 3D) + (\frac{5}{2})a$

$H_5\ (M = -\frac{3}{2} \rightarrow -\frac{5}{2}) = H_0 - 4D + 9E^2/(H_5 + D) - 5E^2/(H_5 + 3D) - 2a$

For $H \| X$ or $H \| Y$, substitute for D and E, respectively,

$-(\frac{1}{2})(D - 3E)$ and $-(\frac{1}{2})(E + D)$

or

$-(\frac{1}{2})(D + 3E)$ and $-(\frac{1}{2})(E - D)$

(b) Hyperfine structure

$H\ (m \leftrightarrow m) = -Am - (A^2/2H_0)(I(I+1) - m^2 + (2M - 1)m) - m^2 + (2M - 1)m)$

Table 2. Spin-Hamiltonian parameters of Mn^{2+} *in* $(NH_4)_2Mg_2(SO_4)_3$ *and* $(NH_4)_2Zn_2(SO_4)_3$ *single crystals*

	g_z	g_x	$D \times 10^{-4}\,\mathrm{cm}^{-1}$	$E \times 10^{-4}\,\mathrm{cm}^{-1}$	$a \times 10^{-4}\,\mathrm{cm}^{-1}$	$A_z \times 10^{-4}\,\mathrm{cm}_{-1}$	$A_x \times 10^{-4}\,\mathrm{cm}^{-1}$
$(NH_4)_2Mg_2(SO_4)_3$	2·008	2·004	−236·0	60·95	2·81	−89·1	−87·0
	±0·001	±0·001	± 0·2	± 2·0		± 1·0	± 1·0
$(NH_4)_2Zn_2(SO_4)_3$	2·008	2·010	−236·9	69·4	5·62	−89·9	−86·6
	±0·001	±0·001	± 0·2	± 2·0		± 1·0	± 1·0
$(NH_4)_2Co_2(SO_4)_3$[5]	2·0036	2·0036	−231·0	68·7	2·0	−88·4	−86·8
	±0·0008	±0·0008	± 0·2	± 2·0		± 1·0	± 1·0
$(NH_4)_2Cd_2(SO_4)_3$[4]	2·000	—	−157·3	—	5·4	−94·3	—
	±0·002		± 1·3		±1·0	± 1·8	

presence of only one Mn^{2+} magnetic complex in both the crystals suggests that the Mn^{2+} ions are substituting for only one type of Mg^{2+} or Zn^{2+} sites. Substitution for $(NH_4)^+$ appears improbable because of the difference in charge.

In conclusion, the results obtained in the present study can be compared with the results obtained for Mn^{2+} doped $(NH_4)_2Cd_2(SO_4)_3$ and $(NH_4)_2Co_2(SO_4)_3$ crystals [4, 5]. The resolution of the spectral lines was very good in the present experiments and Mn^{2+} doped $(NH_4)_2Co_2(SO_4)_3$ while it was pretty poor in the case of Mn^{2+} doped $(NH_4)_2Cd_2(SO_4)_3$. This has been noted by the author himself. The comparison of the spin-Hamiltonian parameters obtained in the present study and those in Mn^{2+} doped $(NH_4)_2Co_2(SO_4)_3$ and $(NH_4)_2Cd_2(SO_4)_3$ crystals [5, 4] suggests that the crystalline field experienced by Mn^{2+} substituting for Mg^{2+}, Zn^{2+} and Co^{2+} in single crystals of $(NH_4)_2Mg_2(SO_4)_3$, $(NH_4)_2Zn_2(SO_4)_3$ and $(NH_4)_2Co_2(SO_4)_3$ respectively, is nearly same, and more than that experienced by Mn^{2+} ions substituting for Cd^{2+} in single crystals of $(NH_4)_2Cd_2(SO_4)_3$. The reason for this might be due to the difference in the lattice parameter of these salts. Another point of interest is the value of A. It has been pointed by Van Wieringen [9] that the magnitude of A decreases with increasing covalency of the magnetic complex. From the electronegativity of Mn^{2+} and negative ions and the numbers of the surrounding negative ions, the amount of the ionic character or covalency can be calculated after Pauling [10]. Matumura [11] has shown that the relationship between the magnitude of A and the ionicity is a linear one if the degree of covalency is calculated according to Pauling's rule [10]. From Matumura's curve we obtain that for $A = 94.3 \times 10^{-4}\,cm^{-1}$, $88{\cdot}4 \times 10^{-4}\,cm^{-1}$, $89{\cdot}9 \times 10^{-4}\,cm^{-1}$ and $89{\cdot}1 \times 10^{-4}\,cm^{-1}$, as is the case respectively for Mn^{2+} in $(NH_4)_2Cd_2(SO_4)_3$, $(NH_4)_2Co_2(SO_4)_3$, $(NH_4)_2Zn_2(SO_4)_3$ and $(NH_4)_2Mg_2(SO_4)_3$, there is about 96·0 per cent, 93·5 per cent, 94·5 per cent and 94·25 per cent ionicity respectively. This suggests that these crystals are more of ionic character.

Acknowledgements – Thanks are due to Professors Putcha Venkateswarlu and J. Mahanty for their continuous interest in the progress of the work.

Department of Physics, B. V. R. CHOWDARI*
Indian Institute of Technology,
Kanpur,
India

REFERENCES

1. BOWERS K. D. and OWEN J., *Rep. Prog. Phys.* **18**, 304 (1955)
2. LOW W., *Paramagnetic Resonance in Solids*, Academic Press, New York (1960).
3. ALTSHULER S. A. and KOZREV B. M., *Electron Paramagnetic Resonance*, Academic Press, New York (1964).
4. TATSUZAKI I., *J. phys. Soc. Japan*, **17**, 582 (1962).
5. CHOWDARI B. V. R., *J. Phys. Chem. Solids* **30**, 2747 (1969)
6. ZEMANN V. A and ZEMANN J., *Acta crystallogr* **10**, 409 (1957).
7. WYCKOFF R. W. G., *Crystal Structures*, Interscience New York **3**, 217 (1965)
8. LOW W., *Paramagnetic Resonance in Solids*, p. 46. science New York **3**, 217 (1965)
9. VAN WIERINGEN J. S., *Disc. Faraday Soc.* **19**, 118 (1955).
10. PAULING L., *The Nature of Chemical Bond*, Cornell University Press, New York (1940).
11. MATUMURA O., *J. phys. Soc. Japan* **14**, 108 (1959)

---

[*] Research Fellow of National Institute of Sciences of India

Present address Department of Nuclear Engineering, Nagoya University, Nagoya, Japan.

J. Phys. Chem. Solids Vol. 31, pp. 1412–1416.

Exo-electron emission from activated $CaSO_4$ phosphors

(*Received* 25 *September; in revised form* 3 *December* 1969)

IT IS NOW commonly accepted that the emission of electrons from the surface of solids (exoelectron emission: *EEE*) is conditioned by the concentration and distribution of active traps in the surface layer of the material. Unfortunately, there is not too much known about the nature of these traps. The correspondence in glow *EEE* and thermoluminescence (*TL*) curves which has been shown for a number of substances, would indicate that in some cases these traps must be of the same origin for both phenomena[1, 2]. Kramer[3] pointed out on the base of band theory of *TL* and *EEE*, that the traps for luminescence and for *EEE* are often identical. However for the *EEE* activator centers are not necessary. Lepper[4] showed also that activator levels contributed by the manganese impurity in the $CaSO_4$ phosphors are necessary for *TL* but not for *EEE* effect. In the experimental material published so far in general on the *EEE* there is no information on the role of the concentration of the activator centers on the *EEE* intensity.

In the present paper the authors give results of studies on the effect of activators concentration on the *EEE* intensity for $CaSO_4$ phosphors doped by manganese and lead. In contrast to our previous work[5] amorphous powder samples of $CaSO_4$ phosphor were used because of better sensitivity to ionizing radiation than the crystalline one. It was also found impossible to prepare monocrystalline samples doped with higher concentration of given activators than ~0·1 per cent.

The powder amorphous samples of $CaSO_4$ phosphors doped by manganese and lead were prepared by Watanabe's method[6] and by precipitation. The basic amount of $Ca(NO_3)_2 . 4H_2O$ with various parts of $Pb(NO_3)_2$ or $MnCl_2 . 4H_2O$ were dissolved in 50 ml of water and precipitated by a dilute (50 per cent) sulphuric acid. The coagulation was washed by water on the Büchner slit-sieve funnel and after drying was heated at 900°C for 20 min in a normal atmosphere.

The Watanabe's method of preparing of $CaSO_4$ doped phosphors was the following: $CaSO_4 . 2H_2O$ with various amount of $PbSO_4$ or $MnSO_4 . 4H_2O$ were mixed with concentrated sulphuric acid into a sherry. The mixture was left at room temperature for 48 hr and occasionally stirred. The water was driven off at 80–90°C and the sulphuric acid at 250–300°C and heated the same way as precipitated one.

The concentration of lead in $CaSO_4$ phosphors was estimated after dissolving in a nitric acid by polarography. The estimation of manganese in $CaSO_4$ phosphors was carried on by colorimetric measurement of anions MnO_4^- on the spectrophotometer at the wavelength of 520 nm after previous oxidation of Mn(II) by periodate in the presence of phosphoric and sulphuric acid[7]. The concentrations of manganese and lead were established with the maximum errors of about ±3 per cent.

The activated phosphors were fixed on copper disks (15 × 15 × 1 mm) by silicone varnish. The samples were irradiated with X-rays from Machlett tube (40 kV, 30 mA) at room temperature and 50 mm focus distance. The *EEE* and *TL* intensities were measured on a laboratory apparatus described recently elsewhere[5].

The shape of glow *EEE* and *TL* curves for doped $CaSO_4$ phosphors with various quantity of lead or manganese was practically the same and were independent on the nature of activator or its concentration, however, the intensities of *EEE* and *TL* were different. The curves showed one maximum only. The activation energy of traps (trap-depth) $\Delta\epsilon$ was calculated from glow curves for considering if the nature of the traps are identical. The values $\Delta\epsilon$ were calculated using Booth's equation[8] and from the graphical dependence of $\Delta\epsilon$ on various glow temperatures given recently by Hofmann and Gobrecht[9]. From their graphical dependence is possible to write down a simple formula $\Delta\epsilon = 540/T_m$, where T_m is a glow temperature, which is valid for the range of glow temperatures of the $CaSO_4$ doped phosphors. The estimation values are given in Table 1 for $CaSO_4(Pb)$ and $CaSO_4(Mn)$ phosphors prepared by both methods. (The average values of $\Delta\epsilon$ given in Table 1 were obtained from measurements of

Table 1. Trap-depths for $CaSO_4$ *phosphors calculated from the glow* EEE *and* TL *curves*

Sample	Trap-depth From *TL* glow curves Booth method (eV)	 $\Delta\varepsilon = 540/T_m$ (eV)	 From *EEE* glow curves Booth method (eV)	 $\Delta\varepsilon = 540/T_m$ (eV)
$CaSO_4(Pb)_P$*	0·61	0·62	0·64	0·65
$CaSO_4(Pb)_W$*	0·61	0·62	0·63	0,65
$CaSO_4(Mn)_P$	0·69	0·67	0·68	0·67
$CaSO_4(Mn)_W$	0·69	0·67	0·66	0·65

*The letters *P* and *W* in all tables indicate the way of sample preparation. *P* means precipitation method and *W* Watanabe's one.

all phosphors with various concentration of activators. The deviations from the average values were not higher than ±10 per cent.)

The samples of $CaSO_4$(Pb) and $CaSO_4$(Mn phosphors were irradiated by the same dose and the glow *EEE* and *TL* curves were recorded. The dependence of areas under glow *EEE* and *TL* curves (intensity of *EEE* and *TL*) against concentration of activators are plotted in Figs. 1 and 2. The survey of optimum concentration of activators is given in Table 2. The phosphors with the optimum concentration were irradiated by identical doses and the relative sensitivities of phosphors were established and are summarized in Table 3. The relative sensitivity for a 'pure' $CaSO_4$ phosphor, prepared by the same way as activated ones, is also given in Table 3. (*TL* glow curve for the 'pure' $CaSO_4$ was not observed even if a high dose was applied to the phosphor).

Table 2. The optimum concentration of activators in $CaSO_4$ *phosphors (in wt. %)*

Sample	Optimum concentration for *EEE* (%)	 for *TL* (%)
$CaSO_4(Pb)_P$	0·75	1·60
$CaSO_4(Pb)_W$	1·40	5·50
$CaSO_4(Mn)_P$	0·05	0·24
$CaSO_4(Mn)_W$	0·14	0·75

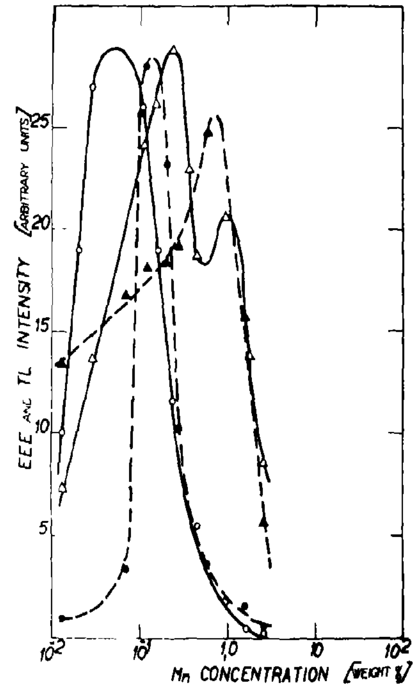

Fig. 1. The dependence of *EEE* and *TL* intensities on the Mn concentrations. (Full curves in Fig. 1 and Fig. 2 belong to the samples prepared by Watanabe's method and dashed to the samples prepared by precipitation. Triangles mark the *TL* intensities and circles the *EEE* intensities).

Comparing the values of trap-depth for *EEE* and *TL* traps (see Table 1) one can notice only a small difference between them. The traps are supported from that point of view to be identical for both phenomena.

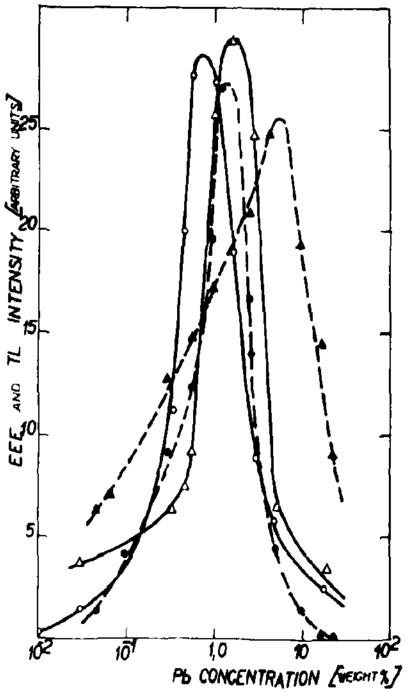

Fig. 2. The dependence of *EEE* and *TL* intensities on the *Pb* concentrations.

Table 3. The relative sensitivities of CaSO$_4$ *phosphors with optimum concentration of activators*

Sample	Relative sensitivity of *EEE*	*TL*
CaSO$_4$ 'pure'$_P$	0·01	—
CaSO$_4$ 'pure'$_W$	0·05	—
CaSO$_4$(Pb)$_P$	1·5	0·81
CaSO$_4$(Pb)$_W$	3·3	6·8
CaSO$_4$(Mn)$_P$	63·7	34·6
CaSO$_4$(Mn)$_W$	67·4	39·4

The number of traps in an unactivated sample of CaSO$_4$ is dependent only on the way of its preparation. If the sample is prepared according to Watanabe's method, i.e. in a high excess of anions SO$_4^{2-}$ the number of created traps is higher than that prepared by the precipitation method, as one can see from *EEE* measurement (see Table 3).

The *EEE* and *TL* intensities increase with increasing concentration of activator undoubtedly in consequence of the increasing of traps and activator centers (see Figs. 1 and 2 initial part of curves). If a definite concentration of activator in the phosphor is reached (so called optimum concentration) the *EEE* and *TL* gain the maximum values and during the next increasing of the concentration of activator are decreased. The values of optimum concentrations of activators for *EEE* and *TL* are rather different and depend on the way of sample preparation and on the nature of activator. As it was expected this value for the Watanabe's method of preparation is higher than for precipitation one. The difference between various values of optimum concentrations for manganese and lead can be explained by oxidation of Mn(II) during preparation period. It was established experimentally by us that only ~ 40 per cent of manganese is imbeded in the form of Mn(II); the rest undergoes oxidation on Mn(IV) and was not estimated by used analytical method.

It is urgent to emphasize that activators are only necessary for *TL* but for *EEE* seem to be unnecessary (see Table 3). However, the influence of activator is indirect i.e. it increases concentration of traps which electron can be trapped in and released from and increases the number of emitted electrons. More experiments will have to be carried on for a better understanding of the *EEE* mechanism doped CaSO$_4$ phosphors and for making a general conclusion. The experiments in this field are in a progress.

REFERENCES

1. NASSENSTEIN H., *Z. Naturf.* **10**, 144 (1955).
2. BOHUN A. and DOLEJŠÍ J., *Czech. J. Phys.* **9**, 578 (1959).
3. KRAMER J., *Proc. 2nd Int. Conf. on Luminescence Dosimetry, Gatlinburg*, p. 180 (1968).
4. LEPPER J., *Z. Naturf.* **10**, 47 (1955).
5. SPURNÝ Z., NOVOTNÝ J., and HOLOHLAVSKÁ H., *Proc. 2nd Int. Conf. on Luminescence Dosimetry, Gatlinburg*, p. 220 (1968).
6. WATANABE K., *Phys. Rev.* **83**, 785 (1951).

7. CHARLOT G., *Colorometric Determination of Elements*, p. 291. Elsevier, Amsterdam (1964).
8. BOOTH A. H., *Can. J. Chem.* **32**, 214 (1954).
9. GOBRECHT H. and HOFMANN D., *J. Phys Chem. Solids* **27**, 509 (1966)

J. NOVOTNEÝ
Z. SPURNÝ
M. BÍNOVÁ

Faculty of Technical and Nuclear Physics,
Prague 1,
Brehová 7,
Czechoslovakia

J Phys Chem Solids Vol. 31, pp 1416–1417

Ultrasonic measurement of the electrocaloric effect in KH_2PO_4

(*Received* 29 *September* 1969;
in revised form 24 *October* 1969)

IF AN ELECTRIC field is applied along the c axis of a KH_2PO_4 crystal, the temperature of which T is slightly above its ferroelectric transition point T_c, and after a while it is switched off, a transient increase in the attenuation of Mhz longitudinal ultrasonic waves, propagating parallel to the c axis, may result. This observation can readily be explained by invoking the electrocaloric effect, i.e. the change in the temperature of the sample induced by an adiabatic change in its polarization. When the field is switched on, the temperature of the sample increases. This increase, however, does not affect the ultrasonic attenuation since the latter is independent of temperature for $T \gtrsim T_c$[1]. While the field is on, the sample loses heat and cools down, its temperature approaching that of the heat bath T_B. If the field is sufficiently large and if it has been applied long enough, its adiabatic removal will temporarily cool the sample to or below its transition temperature. When this happens, the ultrasonic attenuation increases; it has been observed that rapid cooling of the sample across its transition point leads to increased attenuation. This explains our observation.

The onset of this effect corresponds to the case in which the removal of the field cools the sample right to its transition temperature. If the field is switched off much faster than the thermal relaxation rate of the sample, this point can be determined rather accurately as it involves a sudden decrease in the amplitudes of the whole train of ultrasonic echoes. One can make use of this fact to carry out measurements of the electrocaloric effect. An electric field is applied to the sample for a period of time sufficient to re-establish thermal equilibrium with the heat bath. Subsequently, the field is switched off and the effect on the attenuation observed. The field is varied, and this procedure is repeated at constant T_B until the onset of the increase in attenuation is determined. In this way, the value of the field the adiabatic removal of which induces a temperature change equal to $T_B - T_c$ can be measured for different values of T_B.

The circles in Fig. 1 represent experimental data thus obtained with 10 MHz ultrasonic waves. The solid line is a theoretical curve calculated from the thermodynamic relation [2] $\Delta T \cong T_B - T_c = -\beta T(2c\rho)^{-1}P^2$, in the linear dielectric constant approximation $E =$

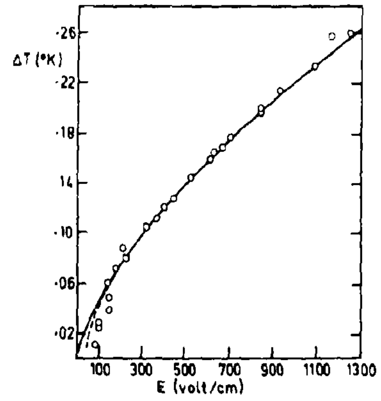

Fig. 1 Experimental results (circles) and theoretical calculations showing the change in temperature ΔT induced by the adiabatic removal of an electric field E. The solid curve corresponds to the linear dielectric constant approximation. The broken line indicates corrections due to the rapid increase of the heat capacity in the vicinity of the ferroelectric transition temperature.

$\beta(T-T_c)P$. Since in our case $T-T_c=\Delta T$, the relation between the temperature change ΔT and the electric field E becomes

$$\Delta T = -(T/2c\beta\rho)^{1/3}E^{2/3}. \qquad (1)$$

The constant $\beta = 3{\cdot}8\ 10^{-3}$ c.g.s. was taken from Reese[3]; the heat capacity c erg/gr was derived from the molar heat capacity at zero field $C_0 = 100$ J/mole[4]; $\rho = 2{\cdot}34$ g/cm^3 and $T = 121$°K. It can be seen that the agreement between theory and experiment is good except at low values of the field. There are, however, two factors which have so far been neglected, and which can lead to improved agreement in this region. First, the heat capacity increases steeply in the vicinity of T_c[5]. The broken line in Fig. 1 shows the corrections obtained by taking this fact into account. Second, the Curie temperature is somewhat lower than T_c[1, 3], i.e. $T_0 = T_c-\delta$. Accordingly, the equivalent of equation (1) is

$$\Delta T(\Delta T+\delta)^2 = -\frac{TE^2}{2\rho c\beta}.$$

This correction should improve agreement for $\Delta T < \delta$. The magnitude of δ calculated from data presented by Reese[3] is too small to have any practical significance. The real value is probably larger[1, 3], but it is not known with sufficient accuracy. To obtain good agreement in Fig. 1 a value of $\delta \simeq 0{\cdot}01$°K is needed. However, the experimental errors in this region of the figure are quite large and no such conclusion is justified. The data presented here compare well with those obtained by Reese[5], except at high values of the electric field; the deviations due to nonlinearities in the dielectric constant observed by Reese are absent in Fig. 1. Direct measurements of the electrocaloric effect were carried out also by Baumgartner[6]. His data, however, were taken at much larger fields than here and at an unspecified temperature. Therefore, no meaningful comparison with his results can be made.

The method described here has the advantage that it allows a rapid and direct measurement of the change in the temperature of the sample. However, the electric field and the temperature of the sample can not be varied independently.

Department of Physics,
The Hebrew University,
Jerusalem,
Israel

M. SHIMSHONI
E. HARNIK

REFERENCES

1. HARNIK E. and SHIMSHONI M., *Phys. Lett.* **29A**, 620 (1969)
2. MERZ W. J., *Phys. Rev.* **91**, 513 (1953)
3. REESE W., *Solid State Commun.* **7**, 969 (1969).
4. REESE W. and MAY L. F., *Phys. Rev.* **162**, 510 (1967).
5. REESE W., *Phys. Rev.* **181**, 905 (1969).
6. BAUMGARTNER H., *Helv. phys. Acta* **23**, 651 (1950).

J. Phys. Chem. Solids Vol 31, pp 1417-1419.

Dielectric properties of single-domain melt-grown BaTiO$_3$

(*Received* 22 *October* 1969)

THE LOW and high frequency c-axis dielectric constants of clear melt-grown BaTiO$_3$ crystals have been remeasured. Unusually large crystals ($8\times8\times2$ mm^3) grown from solution by top seeding a TiO$_2$-rich melt[1] have made it possible to measure the high frequency clamped dielectric constant ϵ_c' at much lower frequencies (75 MHz) with greater precision than possible in previous experiments. Earlier measurements[2] were made on crystals which contained 180° domain walls (anti-parallel domains). The results reported here were obtained using a poled sample completely free of anti-parallel domains.

The values obtained for the room temperature (23°C) unclamped (stress-free) and clamped (strain-free) dielectric constants in single domain BaTiO$_3$ are ϵ_c (1 kHz) = 135 and ϵ_c' (75 MHz) = 60, respectively. These values compare with our previously published values

[2] of ϵ_c (100 kHz) = 150 and ϵ_c' (250 MHz) = 80. The new values of ϵ_c and ϵ_c' were found to be independent of the presence of 180° domains. It is noteworthy that our value of ϵ_c' is substantially higher than the value $\epsilon_c' \approx 40$ measured optically from polariton dispersion data[3]. The origin of this discrepancy is not known.

In Fig. 1 we show the temperature dependence of the unclamped dielectric constants measured at 1 kHz on a single-domain crystal. These results differ somewhat from those reported previously[2, 4]. From these data we find a ferroelectric-paraelectric transition temperature $T_c = 135°C$, a Curie constant $C = 1{\cdot}8 \times 10^5 °C$, and Curie–Weiss temperature $T_0 = 112°C$. It is of interest to note that the peak dielectric constant is given closely by $C/(T_c - T_0)$.

The temperature dependence of the spontaneous polarization P_s was also remeasured. By measuring P_s at two different temperatures and using the specific heat corrected pyroelectric data given earlier[2] we determined the temperature dependence of P_s. Except for an *increase* in P_s of 0·01 C/m^2 at all temperatures the previously published curve of P_s vs. T is correct. Thus, at 23°C, $P_s = 0{\cdot}26\ C/m^2$.

Crystals of $BaTiO_3$ slow cooled through the transition temperature in the presence of a poling field of several kV/cm usually contain anti-parallel domains (see Ref. [2] for poling

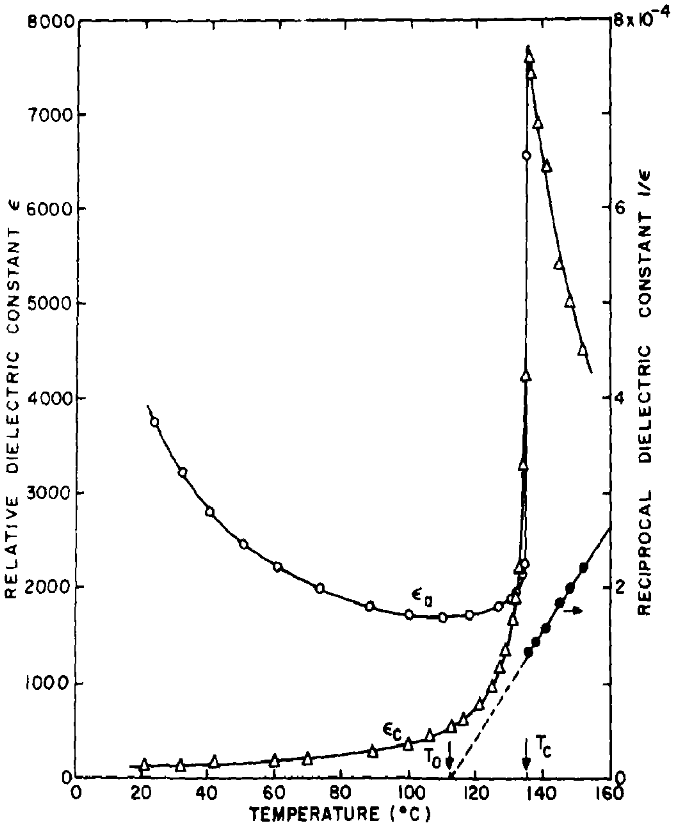

Fig. 1. Temperature dependence of the low frequency (1 kHz) dielectric constants in single-domain $BaTiO_3$ in the cubic and tetragonal phases. The reciprocal dielectric constant is also plotted as a function of temperature in the cubic phase.

details). These 180° domains can be observed by placing the crystal between crossed polarizers under a polarizing microscope. By rotating the crystal with the *c*-axis in the plane of the polarizers so as to obtain good contrast, regions made up of short dense lines can be identified under low magnification (25–50 ×). Under higher magnification the lines appear to be dagger-shaped. These regions are associated with 180° domains and usually form near crystal imperfections and the crystal edges where the polarization terminates. The 180° domains can be removed as follows:

(1) Crystals that have been poled to remove the 90° domains should be carefully polished and all chips or cracks must be removed.

(2) Silver paste electrodes are then applied to the two surfaces perpendicular to the *c*-axis.

(3) With the sample placed under a polarizing microscope, spring contact connections are made.

(4) The direction of the pyroelectric signal is determined with a microvoltmeter by slightly heating the sample (for example, with the illumination from the microscope lamp). This step determines the direction of the net polarization.

(5) A static field of 3–5 kV/cm is then applied to the sample along the direction of P_s and the sample is poled for several hours or until the domains disappear. For a sample that has cracks or extensive surface damage, the final poling step may take several days or longer, since these faults act as 'barriers' and impede the motion of the anti-parallel domains.

Acknowledgements – We wish to thank A. Linz of MIT for providing the $BaTiO_3$ crystals used in this study.

Bell Telephone Laboratories, Inc., I. CAMLIBEL
Murray Hill, M. DIDOMENICO, JR.
New Jersey, S. H. WEMPLE
N.J. 07974, *U.S.A.*

REFERENCES

1. LINZ A., BELRUSS V. and NAIMAN C. S., *J. electrochem. Soc.* **112**, 60C (1965).
2. WEMPLE S. H., DIDOMENICO M. JR. and CAMLIBEL I., *J. Phys. Chem. Solids* **29**, 1797 (1968).
3. PINCZUK A., BURSTEIN E., USHIODA S., *Solid State Commun.* **7**, 139 (1969)
4. JOHNSON C. J., *Appl. Phys. Lett.* **7**, 221 (1965).

J. Phys. Chem. Solids Vol. 31, pp. 1419–1422

Electron paramagnetic resonance of Mn^{2+} in zinc acetate dihydrate

(*Received* 16 *April* 1969; *in revised form* 20 *June* 1969)

THE PARAMAGNETIC resonance of undiluted manganese acetate tetrahydrate was studied by Abe and Morigaki[1]. There are some EPR studies reported, on diluted manganese acetate by Kumugai *et al.*[2], Hayashi *et al.* [3] and Ingram[4]. Kumugai *et al.* and Hayashi *et al.* studied the EPR of $Mn(CH_3COO)_2 \cdot 3H_2O$ diluted with zinc ions, while Ingram reported the EPR of $(Mn\text{-}Zn)(CH_3COO)_2 \cdot 4H_2O$. In this paper, we report the resonance absorption of divalent manganese in zinc acetate dihydrate.

The crystal structure of zinc acetate dihydrate was reported by van Niekerk, Shoening and Talbot[5]. The unit is monoclinic with cell dimensions $a_0 = 14{\cdot}50$ Å, $b_0 = 5{\cdot}32$ Å, $c_0 = 11{\cdot}02$ Å and $\beta = 100°0'$. The four formula units in the tetramolecular unit cell are derived by the operation of the space group of symmetry $C2/c$. The projection of the unit cell along its b_0 axis is given in Fig. 1[6]. For $C2/c$ space group symmetry, the equivalent atoms are in the following positions:

$$\pm(0, u, \tfrac{1}{4}; \tfrac{1}{2}, u+\tfrac{1}{2}, \tfrac{1}{4})$$

and

$$\pm(x, y, z; x, \bar{y}, z+\tfrac{1}{2}; x+\tfrac{1}{2}, y+\tfrac{1}{2}, z; x+\tfrac{1}{2}, \tfrac{1}{2}-y, z+\tfrac{1}{2}).$$

The zinc atom lies on the two fold axis, parallel to *b*-axis. The six nearest neighbours of zinc atom, forming a greatly distorted octahedron, are two oxygen atoms (O_1 and

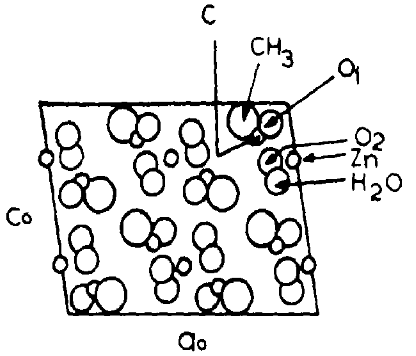

Fig. 1 The monoclinic structure of zinc acetate dihydrate, projected along its b_0-axis (left hand axes).

$O_1{}^0$) at a distance of 2·17 Å, two more oxygen atoms of the two acetate groups (O_2 and $O_2{}^0$) at 2·18 Å and two water molecules (H_2O and H_2O^0) at 2·14 Å. The atoms or molecules with a superscript 'O' are obtained from the corresponding non-subscripted ones by a two fold rotation parallel to *b*-axis, through the zinc atom. The nearest neighbours subtend angles at Zn^{2+} as given below:

$$O_1\text{-}Zn\text{-}O_1{}^0 = 158°,\ O_2\text{-}Zn\text{-}O_2{}^0 = 85°,$$
$$H_2O\text{-}Zn\text{-}H_2O^0 = 94°.$$

The Mn^{2+} ion is doped substitutionally, in the lattice of $Zn(CH_3COO)_2.2H_2O$ at Zn^{2+}, by adding a small quantity of $Mn(CH_3COO)_2.4H_2O$ (about 2 per cent by weight) to $Zn(CH_3COO)_2.2H_2O$. The single crystals of Mn^{2+} doped $Zn(CH_3COO)_2.2H_2O$ were grown by slow evaporation, at constant temperature of the saturated solution in distilled water, of $Mn(CH_3COO)_2.4H_2O$ and $Zn(CH_3COO)_2.2H_2O$. The crystals grew in the form of thin plates parallel to bc plane.

The experiments have been carried out at room temperature using the Varan *V*-4502 EPR spectrometer, operating at *X*-band microwave frequency. The magnetic field was modulated with 100 kc/sec frequency and was calibrated by the standard field marker DPPH. The intensity of the magnetic field at the DPPH resonance field was measured by the proton resonance frequency using Gertsch Model FM-3, VHF-frequency meter.

The divalent manganese ion has an outer shell configuration of $(3d)^5$ electrons and hence the ground state $^6S_{5/2}$. In a field of orthorhombic or lower symmetry, the ground state splits into three Kramer's doublets and this gives rise to the fine structure of EPR of Mn^{2+}. The manganese nucleus Mn^{55} (100 per cent abundant) has a nuclear spin $I = 5/2$ which gives rise to hyperfine structure due to the interaction between the nucleus and the electrons. The number of allowed transitions obeying the selection rule ($\Delta M = \pm 1, \Delta m = 0$) is 30.

A single group of 30 allowed transitions have been observed along all the directions. Considering Zn^{2+} to be the origin as regards the orientation of the other atoms or molecules relative to Zn^{2+}, two of the four molecules of $Zn(CH_3COO)_2.2H_2O$ are identical, while the other two are derived from the above pair by a reflection in the crystallographic a.c. plane. As far as the magnetic resonance properties are concerned, all the four sites of Zn^{2+} are identical and hence the observation of single group of 30 line absorption spectrum. Similar observation has been made for the tetramolecular calcium tungstate ($CaWO_4$) and pyroxene diopside ($CaMg_2Si_2O_6$). The EPR of Mn^{2+} ion in $CaWO_4$ was studied by Hempstead and Bowers[7] and that in $CaMg_2Si_2O_6$ by Vinokurov *et al.*[8], and in both the cases a single group of 30 lines has been observed indicating that all the paramagnetic complexes are magnetically equivalent. The principal *y*-axis coincided with the two-fold symmetry axis (crystallographic *b*-axis).

The observed spectra have been analyzed using the spin-Hamiltonian

$$\mathcal{H} = \beta(g_z H_z S_z + g_x H_x S_x + g_y H_y S_y) + D\left(S_z{}^2 - \frac{S(S+1)}{3}\right) + E(S_x{}^2 - S_y{}^2)$$

$$+A_zS_zI_z+A_xS_xI_x+A_yS_yI_y.$$

The spin-Hamiltonian constants are given in Table 1.

Table 1. Spin Hamiltonian constants of Mn^{2+} *in zinc acetate dihydrate at room temperature.* A_x, A_y, *and* A_z *are taken as negative and accordingly the signs of other constants have been assigned*

$g_z = 2·0013 \pm 0·001$
$g_x = 2·0014 \pm 0·001$
$g_y = 2·0024 \pm 0·001$
$D = 248 \pm 0·5$ G.
$E = -25·5 \pm 1·5$ G.
$A_z = -89·6 \pm 0·5$ G.
$A_x = -89·9 \pm 0\ 5$ G.
$A_y = -89·3 \pm 0·5$ G.

The linewidths are of the order 7G, while the sharpest line has a width of about 3G. This smallness of the linewidth is due to the fact that four of the six ligands surrounding Mn^{2+} are oxygens, which because of their zero nuclear spin, do not contribute to the dipolar interaction between the spins of the ligand nucleus and the paramagnetic ion.

The linewidths of $M = +\frac{1}{2} \rightarrow -\frac{1}{2}$ transition are small as compared to the linewidths of fine structure transitions involving higher quantum numbers. This variation of linewidth with the fine structure transition has been observed to be minimum along the crystallographic *b*-axis. This phenomenon has been observed in some cases previously[7, 9] and is explained as due to static fluctuation of local crystalline field.

The intensity of the allowed transitions goes off very rapidly as the direction of the magnetic field is changed from either the principal *z*-axis or the principal *xy* plane. In Mn^{2+}:$SrCl_2$[10], same phenomenon has been observed and has been explained theoretically by Bir[11].

Besides the ($\Delta M = \pm 1, \Delta m = 0$) transitions, nuclear forbidden ($\Delta M = \pm 1$, $\Delta m = \pm 1$) transitions have been observed. The assignment $\Delta m = \pm 1$ has been made by studying intensity variation of the forbidden transition with the direction of the magnetic field off the principal axis[12].

The nuclear forbidden transitions have been observed in many systems[12–17], of cubic, axial and orthorhombic symmetries. The occurrence of nuclear forbidden transitions has been explained in terms of second order mixing of the hyperfine constant A, with the fine structure constant 'a'[18], 'D'[12, 13] or 'D' and 'E'[16] for the cases of cubic, axial or orthorhombic symmetries.

The strong angular dependence of the allowed and forbidden transitions, as has been observed in the present case and in Mn^{2+}:$SrCl_2$[10] is explained by Bir[11] as due to the strong angular dependence of the overlap integral of the nuclear spin functions.

For the orthorhombic symmetry, assuming g to be isotropic the separation of the forbidden doublets ($\Delta m = \pm 1$) in $M = \frac{1}{2} \rightarrow -\frac{1}{2}$ transition is given as [16]

$$\Delta H = \frac{17B^2}{2H_0} + \frac{2\gamma\beta_N}{g\beta}H - \Big[Q'(3\cos^2\theta - 1) + 3Q''\sin^2\theta\cos 2\phi - \frac{4B^2D}{H_0^2}(3\cos^2\theta - 1)\Big] \times (2m+1) - \frac{25}{2}\frac{A^3}{H_0^2}(2m+1)$$

where Q' and Q'' are quadrupole interaction terms of the Mn^{55} nucleus with the electric field gradient. We have obtained from separations of forbidden doublets at $\theta = 10°$ and $15°$ from *z*-axis in *zx* plane, $Q' = 0·402$ G and $Q'' = 4·7$G.

Acknowledgements—One of the authors (R.J.) wishes to thank the Council of Scientific and Industrial Research, India for the award of Junior Research Fellowship and Mr. K. V. S. Rao for helpful discussions.

Department of Physics,
Indian Institute of Technology,
Kanpur, India

R. JANAKIRAMAN
G. C. UPRETI

REFERENCES

1. ABE H. and MORIGAKI H., In *Paramagnetic Resonance* (Edited by W. Low), Vol. 2, p. 567. Academic Press, New York (1963).
2. KUMUGAI H., ONO K., HAYASHI I. and KAMBE K., *Phys. Rev.* **87**, 374 (1952).
3. HAYASHI I. and ONO K., *J. phys. Soc. Japan* **8**, 270 (1953).
4. INGRAM D. J. E., *Proc. phys. Soc. Lond.* **A66**, 412 (1953).
5. VAN NIEKERK J. N., SHOENING F. R. L. and TALBOT J. H., *Act crystallogr.* **6**, 720 (1953).
6. WYCKOFF R. W. G., In *Crystal Structures* (Edited by R. W. G. Wyckoff), Vol. 5, p. 329, Wiley, New York (1966).
7. HEMPSTEAD C. F. and BOWERS K. D., *Phys. Rev* **118**, 131 (1960).
8. VINOKUROV V. M., ZARIPOV M. M. and STEPANOV V. G., *Soviet Phys. solid St.* **6**, 870 (1964).
9. VANIER J., *Can. J. Phys.* **42**, 494 (1964).
10. KORNFELD M. I. and SACHOVA L. S., *Soviet Phys. solid St.* **5**, 1625 (1964).
11. BIR G. L., *Soviet Phys. solid St.* **5**, 1628 (1964).
12. BLEANEY B. and RUBINS R. S., *Proc. phys. Soc. Lond.* **77**, 103 (1961).
13. BLEANEY B. and RUBINS R. S., *Proc. phys. Soc. Lond.* **78**, 778 (1961).
14. WOLGA G. J. and TSENG R., *Phys. Rev.* **133A**, 1563 (1964).
15. FRIEDMAN E. and LOW W., *Phys. Rev.* **120**, 408 (1960).
16. SHRIVASTAVA K. N. and VENKATESWARLU P., *Proc. Ind. Acad. Sci.* **63**, 311 (1966).
17. LUDWIG G. W. and WOODBURG H. H., *Bull. Am. phys. Soc.* **5**, 158 (1960).
18. DRUMHELLER J. E. and RUBINS R. S., *Phys. Rev.* **133A**, 1099 (1964).

J. Phys. Chem. Solids Pergamon Press 1970. Vol. 31, pp. 1423-1434. Printed in Great Britain.

MÖSSBAUER EFFECT STUDIES OF SOME DIMERIC IRON COMPOUNDS

A. N. BUCKLEY, I. R. HERBERT, B. D. RUMBOLD and G. V. H. WILSON
Department of Physics, Monash University, Clayton, Victoria 3168, Australia

and

K. S. MURRAY
Chemistry Department, Monash University, Clayton, Victoria 3168, Australia

(*Received* 15 *January* 1970)

Abstract—A detailed experimental study of the temperature dependence of the asymmetry in the Mössbauer spectra of the dimeric iron compounds (Fe salen Cl)$_2$ and (Fe salen)$_2$O is reported. It is proposed that the integral asymmetry of the quadrupole doublet from (Fe salen Cl)$_2$ is due to anisotropy in the recoilfree fraction. A theoretical study of relaxation effects describes approximately the temperature dependence of the peak height asymmetry, the main defect of the theoretical treatment being probably the neglect of crystal field splittings. Observations of the spectra at 4·2°K in applied fields of up to 90 kOe verify that the ground state for both compounds has zero spin and also lead to information concerning the polarity and asymmetry of the electric field gradients.

1. INTRODUCTION

We have recently reported[1] observations of the Mössbauer spectra of the dimeric iron compound (Fe salen Cl)$_2$ where salen = N,N'-Ethylenebis-(salicylaldiminato) anion. The spectra consist of a quadrupole doublet which is symmetric at 4·2°K and asymmetric at 78 and 298°K. A qualitative explanation was given in terms of the effects of intermolecular spin–spin relaxation. We describe here a more detailed study of the temperature dependence of the spectra obtained in zero applied magnetic field, observations of the spectra from (Fe salen Cl)$_2$ and (Fe salen)$_2$O in applied fields of up to 90 kOe and the results of a theoretical study of the effects of spin relaxation on the zero field spectra.

The dimeric iron(III) Schiff-base complexes (Fe salen Cl)$_2$ and (Fe salen)$_2$O were first prepared by Pfeiffer and Tsumaki[2] and their magnetic susceptibilities determined over a limited temperature range by Klemm and Raddatz[3]. X-ray structure studies[4] of (Fe salen Cl)$_2$ showed that the two iron ions are octahedrally coordinated and stereochemically equivalent. The dimer is formed by the sharing of two ligand oxygen atoms by both iron atoms, the resulting intramolecular Fe–Fe distance being 3·291 Å. From measurements of the susceptibility, Gerloch *et al.*[5] showed that the effective magnetic moment per iron ion decreases from 5·36 μ_B at 300°K to 3·75 μ_B at 82°K and that this temperature dependence could be well explained by assuming antiferromagnetic exchange between the two iron ions such that $\mathscr{H} = -2JS_1 . S_2$ with an exchange integral $J = -7{\cdot}5 \pm 0{\cdot}6\,\mathrm{cm}^{-1}$ and a g-value of 2·02. From the susceptibility at high temperatures ($T \gg |J|/k$) the iron spin state was unambiguously shown to be $S = \frac{5}{2}$. Reiff *et al.*[6] extended the susceptibility studies down to 22°K and arrived at virtually the same values of g and J.

The crystal structure of (Fe salen)$_2$O has not yet been reported. However crystal structure studies of (Fe salen)$_2$O . py_2[7, 8] indicate that the dimer involves two (Fe salen) moieties bridged by an oxygen atom, the oxo-bridge being bent to an angle of 139°.

The iron ions are penta-coordinated as the pyridine molecules are not bonded to them. The structure of (Fe salen)$_2$O is probably very similar. The temperature dependence of the susceptibility is well explained[9] by antiferromagnetic exchange between the two iron ions with $S = \frac{5}{2}$, $g = 2{\cdot}00$ and a large exchange integral J of order $-95\ \text{cm}^{-1}$. However because the susceptibility has not been measured to temperatures $\gg |J|/k$ this spin assignment is not unambiguous and a value $S = \frac{3}{2}$ is also possible.

2. EXPERIMENTAL

The complexes were prepared as described by Lewis and co-workers[5, 9] and microanalysed. Room temperature magnetic susceptibilities were measured as a further check on purity.

The Mossbauer spectra were obtained with source and absorber at the same temperature by means of a constant acceleration electromagnetic drive and 400 channel pulse-height analyser operating in time mode. The zero field spectra were obtained using a 10 mCi source of ^{57}Co in Pd. For the high field spectra a 10 mCi source of ^{57}Co in Cu together with an Oxford Instrument Company 100 kOe superconducting solenoid was used. The absorbers were microcrystalline and thin, typically of the order of 6 mg of natural iron/cm^2, in order to avoid any broadening of the resonance lines. Room temperature spectra were taken with the absorber at 90 and at 45° to the detection axis to test for any preferred orientation in the samples. The spectral parameters (isomer shift, quadrupole splitting, peak height and area ratios) were obtained using an iterative curve fitting procedure[10].

3. MÖSSBAUER SPECTRA IN ZERO APPLIED MAGNETIC FIELD

Mössbauer spectra of (Fe salen Cl)$_2$ were obtained at a number of temperatures between 4–300°K. Both the isomer shift of $+0{\cdot}62$ mm/sec with respect to sodium nitroprusside and the quadrupole splitting of $1{\cdot}38$ mm/sec were essentially temperature independent in this range. For an Fe^{3+} ion this is a normal isomer shift; the quadrupole splitting is large as expected for the strongly anisotropic environment of each iron site. The spectra obtained at 4·2, 78 and 298°K have been published previously[1]. At 4·2°K the quadrupole doublet is effectively symmetric; at higher temperatures the peak heights and intensities of the two lines are different. No difference in the asymmetry at 298°K was observed with the absorber at 45° to the incident γ-rays, indicating the absence of any preferred orientation. In Fig. 1 the ratios of the height and area of the peak at positive velocity to the height and area respectively of the peak at negative velocity are plotted against temperature.

We propose that the integral asymmetry of the quadrupole doublet is due to the Karyagin effect[11], i.e. the anisotropy in the recoil-free fraction. A dimeric molecule such as (Fe salen Cl)$_2$ might be expected to exhibit a fairly strong Karyagin effect at higher temperatures. However to test whether an asymmetry of order 9 per cent at the relatively low temperature of 150°K is feasible we now make an estimate of the effect of this upon the f-value. For atomic vibrations having tetragonal symmetry, the f-value for a polycrystalline material may be expressed[11, 12] as

$$f' = e^{-\kappa^2\langle x^2\rangle}\int_0^1 e^{-\epsilon\cos^2\theta}\, d\cos\theta \qquad (1)$$

where $\epsilon = \kappa^2(\langle z^2\rangle - \langle x^2\rangle)$.

The area ratio, $R = I_{3/2}/I_{1/2}$ of the two peaks is then given by

$$R = \frac{\int_0^1 (1+\cos^2\theta)\, e^{-\epsilon\cos^2\theta}\, d\cos\theta}{\int_0^1 (5/3-\cos^2\theta)\, e^{-\cos^2\theta}\, d\cos\theta} \qquad (2)$$

where the electric field gradient (EFG) is assumed to have the same symmetry as the atomic vibrations. The area ratio plotted in Fig. 1 equals R if the EFG is positive or $1/R$ if it is negative. As discussed below, it is almost certain that the EFG is negative but we consider both possibilities here. Flinn *et al.*[13] have evaluated the integrals in (2) numerically and plotted R as a function of ϵ. From our value of the area ratio we can therefore determine ϵ and at 150°K we obtain from expression (1):

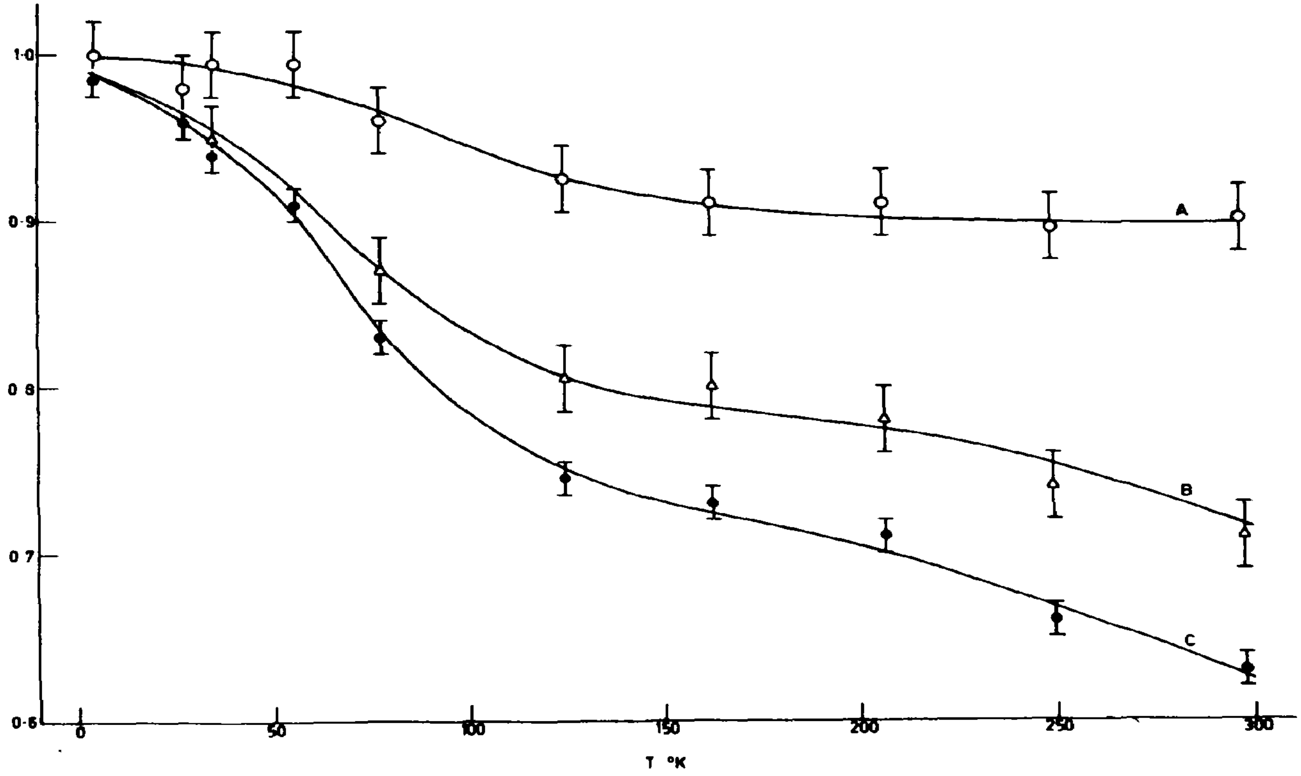

Fig. 1. Temperature dependence of the area (A), peak height (C) and corrected peak height (B) ratios of the quadrupole doublet components of (Fe salen Cl)$_2$.

$$f' = 0{\cdot}66\,e^{-\kappa^2\langle z^2\rangle} \text{ if the EFG is negative } (R > 1, \epsilon < 0, \langle z^2\rangle < \langle x^2\rangle)$$

$$\text{and} \qquad (3)$$

$$f' = 0{\cdot}80\,e^{-\kappa^2\langle x^2\rangle} \text{ if the EFG is positive } (R < 1, \epsilon > 0, \langle x^2\rangle < \langle z^2\rangle)$$

where in both cases we have chosen the exponential factor involving the axis (x or z) along which the least vibration takes place.

At 150°K we have measured the f-value of (Fe salen Cl)$_2$ and obtained $f' = 0{\cdot}57 \pm 0{\cdot}05$. This value can satisfy either of equations (3), i.e. the coefficients 0·66 and 0·80 are not too small. However, assuming a negative EFG, if the integral asymmetry at 150°K was as large as 15 per cent, the f-value calculated from (1) would be too small. Hence the magnitude of the observed integral asymmetry is not too large to lead to any inconsistency in the recoilfree fraction. The form of the temperature dependence of the integral asymmetry is similar to that observed by Stöckler and Sano[14] for polymeric $(CH_3)_3SnF$.

Curve B in Fig. 1 represents the temperature dependence of the peak height ratio corrected for the integral asymmetry, i.e. this is the peak height ratio which would be observed in the absence of the Karyagin effect. We believe that this asymmetry in the peak heights is due to relaxation effects. An antiferromagnetic coupling between two $S = \frac{5}{2}$ ions described by $\mathscr{H} = -2J\,\mathrm{S}_1 . \mathrm{S}_2$ leads to a series of multiplets with resultant spin $S' = 0, 1, \ldots, 5$. The ground state is $S' = 0$. Assuming that the crystal field splitting of the multiplets is small in comparison with J, the energy is given by $E(S') = -JS'(S'+1)$, taking the ground state energy as zero. Hence the multiplet energies are spread over $30|J|$. At 4·2°K the observed quadrupole doublet is symmetric. For a single magnetic ion such a spectrum could only be observed if the ionic relaxation was much faster than the precessional frequency of the nuclei in the hyperfine magnetic fields. However for a dimeric molecule with antiferromagnetic exchange such a spectrum is expected regardless of relaxation if the temperature is low enough for only the $S' = 0$ state to be significantly populated, since $\langle S_1^z\rangle$ and $\langle S_2^z\rangle$ must then vanish.

At higher temperatures multiplets with $S' \neq 0$ will also be populated. The first excited multiplet ($S' = 1$) is centred at about $2|J| \approx 15\,cm^{-1}$. The states, other than those for which $M' = 0$, in these higher multiplets will have non-vanishing magnetic hyperfine matrix elements. The observed peak height asymmetry is typical of the effect of fluctuating hyperfine fields with an electronic correlation time which is comparable with the nuclear precession time for the $I_z = \pm\frac{1}{2} \rightarrow I_z = \pm\frac{3}{2}$ transitions but still sufficiently fast for nuclei undergoing transitions to the $\pm\frac{1}{2}$ excited states to experience effectively the zero time averaged magnetic field[15]. This is strictly true only when the hyperfine fields are parallel to the principal axis of the EFG; when they are perpendicular, it was shown by Blume and Tjon[16] that it is the line to the $I_z = \pm\frac{1}{2}$ excited states which broadens first. The dominant spin relaxation process here will be that of mutual spin flips involving the $|S', M'\rangle$ states of different molecules. For spin flips induced by dipolar coupling between the molecules, the only process which conserves energy is when the M' value of one molecule increases and that of the other decreases by one. Since the crystal field splitting of different multiplets will be different, conservation of energy also requires that such spin flips can only be between pairs of molecules which have the same S' values. As the temperature is raised and the populations of the higher multiplets increase it is expected that the peak height asymmetry would increase, since states with higher S' values will have larger hyperfine fields, and also the relaxation should become slower because, as more states become populated, the probability of a particular molecule having a neighbour in a state suitable for flipping will decrease. However this trend will be reduced somewhat because the dipolar interaction between molecules in higher S' multiplets will be stronger thus tending to reduce the relaxation time. Hence qualitatively the increased peak height asymmetry at higher temperatures is accounted for by assuming that exchange energy dominates the spin Hamiltonian leading to an increase in magnetic hyperfine interaction and slower ionic relaxation as the temperature increases. A quantitative study of this is described below.

The Mössbauer spectrum of (Fe salen)$_2$O obtained at 298°K was similar to that reported by Bancroft *et al.*[17]. The peak height ratio was found to be $0{\cdot}97 \pm 0{\cdot}01$ and an area ratio of $1{\cdot}00 \pm 0{\cdot}01$ was obtained. The absence of any Karyagin effect here is not surprising when the probable structure of this dimeric molecule is considered. The anisotropic vibration parameters estimated[8] for the iron atoms from X-ray studies of (Fe salen)$_2$O.py_2 suggest that the thermal motion is nearly a vibrational sphere. However, of course, the vibrational frequencies relevant to Mössbauer and X-ray diffraction are different. At 78°K the spectrum was symmetrical. As discussed previously[18] this asymmetry of 3 per cent at room temperature is reasonable since for this complex $|J|/k \simeq 137$°K. Also the actual relaxation rate will depend upon the chemical structure and particularly upon the dimer-dimer distances.

4. MÖSSBAUER SPECTRA IN APPLIED MAGNETIC FIELDS

Spectra obtained with (Fe salen)$_2$O and (Fe salen Cl)$_2$ in various applied fields of up to 90 kOe at 4·2°K are shown in Figs. 2 and 3. These are very similar to theoretical spectra calculated by Collins and Travis[19] for the case of no hyperfine magnetic field with a detection axis parallel to the applied field and a randomly oriented EFG. Comparison between the observed and theoretical splittings leads to values for the field acting at the nuclei as given in Table 1. The field at the nuclei is always a little less than the applied field. We believe that this discrepancy is significant and must represent some kind of shielding phenomenon such as a small induced negative hyperfine field. However the striking feature of the observed spectra is the lack of any substantial hyperfine field. In the absence of strong exchange, one expects to observe a hyperfine field of order −300 to −550 kOe at the nuclei of Fe^{3+} ions with such a large ratio of the applied field, H_a, to temperature as used here[20]. The observation that there is no such field under these conditions in a compound which at higher temperatures exhibits a large paramagnetic susceptibility together with relaxation broadened Mössbauer spectra is definitive evidence for a spin zero ground state with an exchange integral much larger in magnitude than $g\mu_B H_a$. Hence our spectra support very well the earlier interpretations of the temperature dependent susceptibility in terms of antiferromagnetic coupling within the dimeric molecules.

Table 1. Comparison of applied magnetic fields and the fields acting at the nuclei as deduced from the Mössbauer spectra

Applied field (kOe)	Observed field at the iron nuclei (kOe)	
	(Fe salen)$_2$O	(Fe salen Cl)$_2$
30	24 ± 3	21 ± 3
50	44 ± 5	39 ± 5
90	88 ± 6	85 ± 6

The computed spectra of Collins and Travis[19] show that when the EFG asymmetry parameter $\eta = (V_{xx} - V_{yy})/V_{zz}$ is zero, an applied field causes the $\pm\frac{1}{2} \rightarrow \pm\frac{3}{2}$ line to split into a poorly defined doublet. The $\pm\frac{1}{2} \rightarrow \pm\frac{1}{2}$ line splits into a triplet with well resolved outer lines and a weak inner line. For $\eta \neq 0$ a weak inner line appears between the two $\pm\frac{3}{2}$ lines and for $\eta = 1$ the spectrum is symmetrical, both the $\pm\frac{1}{2}$ and $\pm\frac{3}{2}$ lines splitting into identical triplets. An examination of the (Fe salen)$_2$O spectra shows unambiguously that the line at negative velocity is from the $\pm\frac{1}{2} \rightarrow \pm\frac{1}{2}$ transitions so that the EFG is

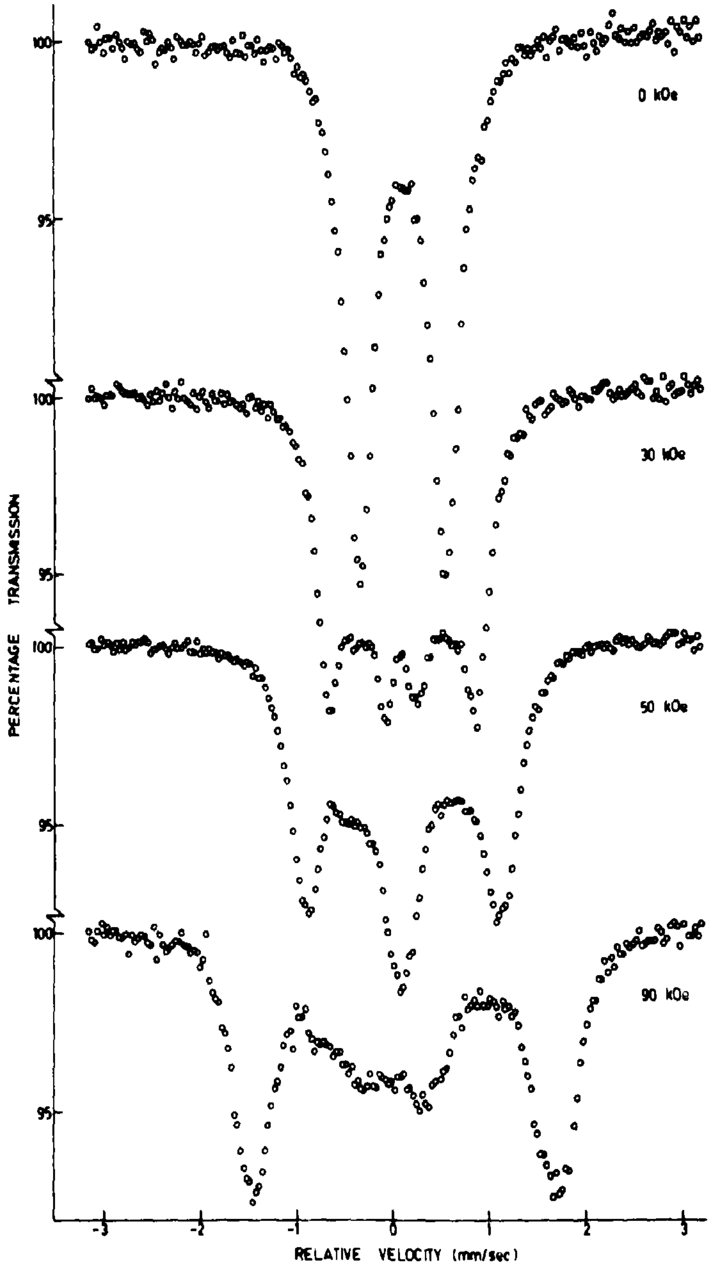

Fig. 2. Mössbauer spectra of (Fe salen)$_2$O at 4·2°K in various applied magnetic fields.

positive. The lack of any strong asymmetry in the spectra shows that η is of the order of 0·8. Comparison with the room temperature zero field spectrum then shows that it is the $\pm\frac{3}{2}$ line which broadens so that it can also be concluded that the hyperfine field is parallel to the principal axis of the EFG.

The spectra of (Fe salen Cl)$_2$ in applied

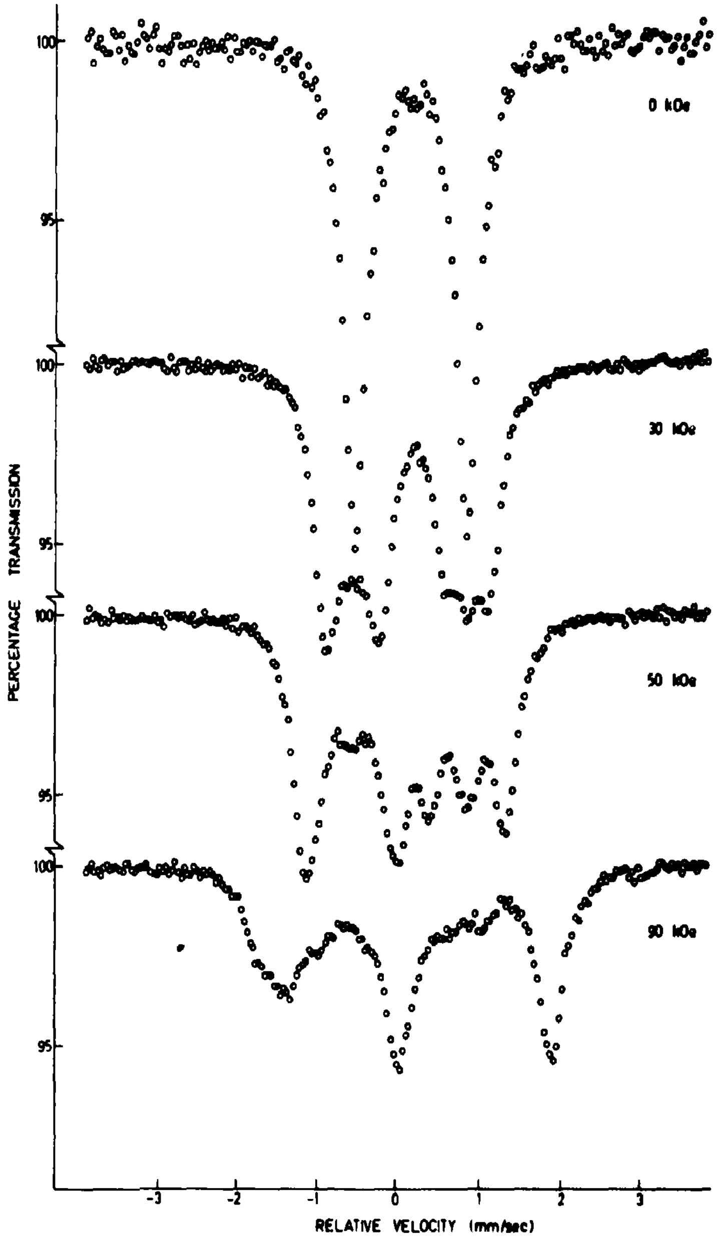

Fig. 3. Mössbauer spectra of (Fe salen Cl)$_2$ at 4·2°K in various applied magnetic fields.

fields indicate that η is small but certainly non-zero. The lines at negative velocity are consistently broader than those at positive velocity, especially in 90 kOe. Also the inner line of the triplet at positive velocity is considerably more intense than that at negative velocity. Hence there can be little doubt that for this complex the EFG is negative. A comparison with higher temperature zero field spectra then shows that the hyperfine field must be perpendicular to the principal axis of the EFG. However there is a small element of doubt here since the central peak of the $\pm\frac{1}{2}$ triplet is considerably more intense than in the spectra calculated by Collins and Travis. Since no integral asymmetry is observed in the zero field spectra of either complex at 4·2°K, no distortion of the applied field spectra due to the Karyagin effect is expected.

5. THEORY OF THE RELAXATION EFFECTS

As described above, it is expected that the dominant ionic relaxation process will be mutual spin flips between ions with the same value of S' and with M' values differing by one. Hence at any given temperature the zero field spectrum will be a superposition of independent relaxation spectra from each of the six multiplets. We have made calculations of such spectra using the stochastic model of Anderson[21] as modified for Mössbauer calculations[15, 22].

For each multiplet we assume the Hamiltonian

$$\mathscr{H}(t) = \mathscr{H}_0 + Q\{3I_z^2 - I^2 + \tfrac{1}{2}\eta(I_+^2 + I_-^2)\} + g\mu h(S')I_z f(t) \qquad (4)$$

where $\mathscr{H}_0$ is the unperturbed Hamiltonian, μ the nuclear magnetic moment and $f(t)$ is the function of time which describes the fluctuation of the electron spin component S_z. Hence for the S' multiplet $f(t)$ can take on the values $-S', -S'+1, \ldots, S'$. The quantity $h(S')$ is the hyperfine magnetic field for a molecule with total spin S' when in the state $M' = S'$. By the Wigner–Eckart theorem within the multiplet S' the hyperfine field for the state $|S'M'\rangle$ will be proportional to M'. Also for a symmetric dimer $\langle S_1^z\rangle = \langle S_2^z\rangle = \frac{1}{2}M'$ so provided that we may neglect the contribution to the hyperfine field at the nucleus from the spin of the other atom in the molecule, the hyperfine fields for all $|S'M'\rangle$ states are proportional to M'. Hence in (4) we may write

$$h(S') = \tfrac{1}{2}HS'/S = HS'/5 \qquad (5)$$

where H is the normal hyperfine field for an Fe^{3+} ion. Taking $H = 550$ kOe[20] equation (5) means that the Hamiltonian (4) for each multiplet is completely defined.

To calculate the spectra we assume that the nuclei do not change their states during the time averaging of the electron spin, i.e. that the nuclear relaxation is much slower than the electronic relaxation. We also assume that the electronic relaxation is a Markov process and that for a given molecule the transition probability between the states $|S'M_1'\rangle$ and $|S'M_2'\rangle$ is of the form[23]

$$W(M_1' \rightarrow M_2') = C|\langle M_2'|S_\pm'|M_1'\rangle|^4 n(M_2'). \qquad (6)$$

Here the fourth power enters because the golden rule for a single transition $M_1' \rightarrow M_2'$ involves the square of the matrix element and the assumption of a spin flip involves a corresponding transition $M_2' \rightarrow M_1'$ for a neighbouring molecule. $n(M_2')$ is the fractional population of the M_2' level. Assuming that crystal field splittings are small, then all levels in a given multiplet have the same population given by

$$n(S') = e^{JS'(S'+1)/kT} \Big/ \sum_{S''=0}^{5} e^{JS''(S''+1)/kT}. \qquad (7)$$

We define an effective relaxation time parameter τ as the reciprocal of the constant C and τ is now the only adjustable parameter in the theory which gives the spectra from all multiplets.

For the case of axial symmetry and an EFG which is parallel to the hyperfine fields, $\eta = 0$ and the Hamiltonian (4) is then diagonal in I_z. As above, for a number of temperatures, the spectrum was calculated as a superposition of spectra from each multiplet. For the S' multiplet the contribution of each Zeeman line to the spectrum is obtained by inversion at each velocity point of a transition rate $2(2S'+1)\times 2(2S'+1)$ real matrix A. The resulting line shape is a normal six line Zeeman pattern folded together according to the time average of the stochastic factor. In the calculations the experimental line-width of 0·3 mm/sec was assumed. For very slow relaxation, say $\tau > 10^{-6}$ sec, the final total spectrum was a superposition of the symmetric doublet from the $S'=0$ state and undistorted six line spectra from the other multiplets. For fast relaxation, say $\tau < 10^{-12}$ sec, almost symmetric quadrupole doublets resulted at all temperatures. For an intermediate range the spectrum, at temperatures

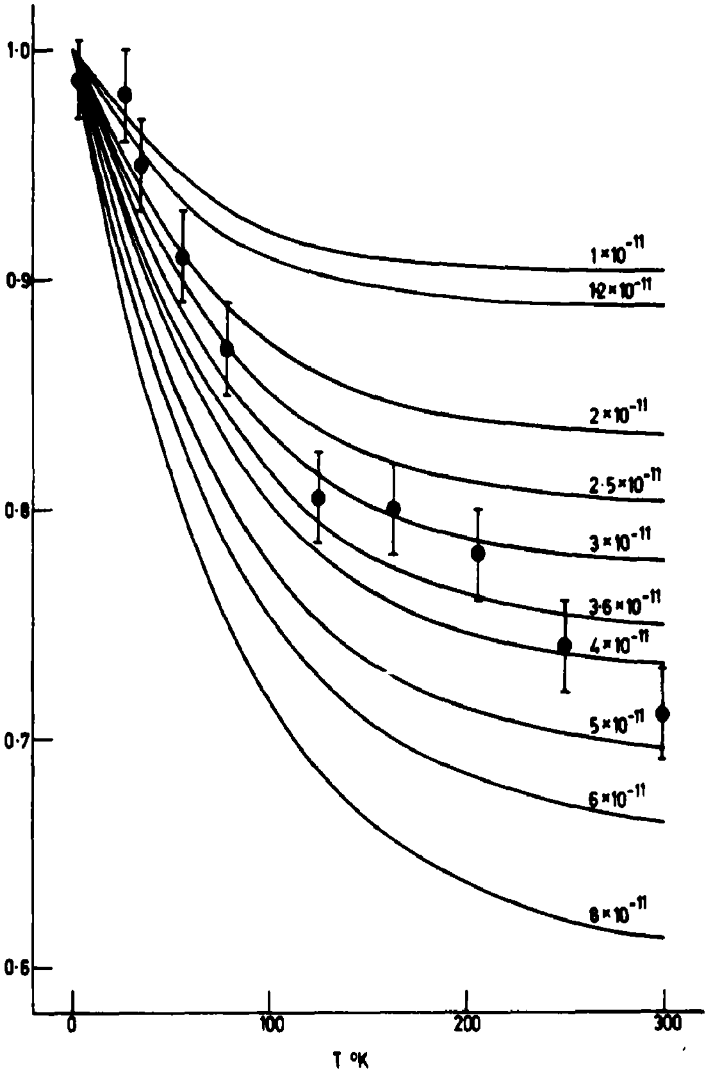

Fig. 4. Temperature dependence of the calculated peak height ratio, with the EFG parallel to the hyperfine fields, for $(\text{Fe salen Cl})_2$ for various values of the relaxation parameter τ (given in sec). The experimental peak height ratio corrected for the integral asymmetry is also plotted.

high enough for $S' \neq 0$ states to be populated, was an asymmetric quadrupole doublet with a temperature dependent peak height asymmetry which is plotted in Fig. 4 for various values of τ. Over this range of τ the area ratio was always unity showing that relaxation effects could not account for the observed integral asymmetry.

Spectra were also calculated for the case of axial symmetry but with the hyperfine fields perpendicular to the principal axis of the EFG according to the Hamiltonian

$$\mathscr{H} = \mathscr{H}_0 + Q'(3I_x^2 - I^2) + g\mu h(S')I_z f(t). \tag{8}$$

To perform the calculations the equivalent

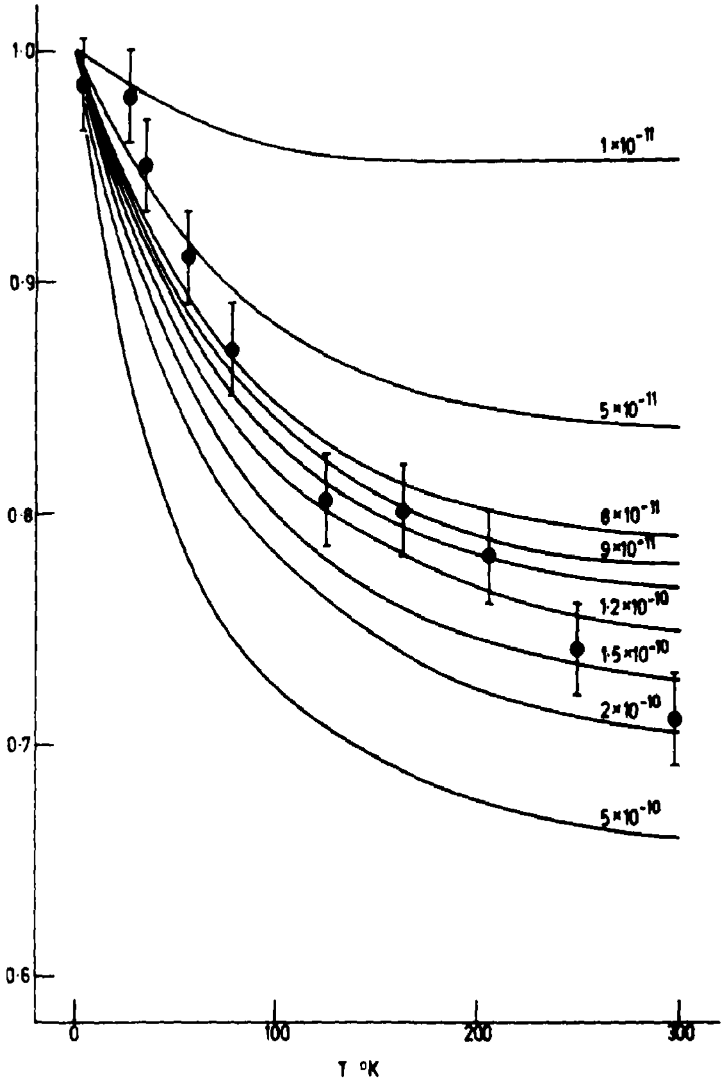

Fig. 5. Temperature dependence of the calculated peak height ratio, with the EFG perpendicular to the hyperfine fields, for (Fe salen Cl)$_2$ for various values of the relaxation parameter τ (given in sec). The experimental peak height ratio corrected for the integral asymmetry is also plotted.

Hamiltonian (4) was used[16] with $Q = -\frac{1}{2}Q'$ and $\eta = -3$. The problem is now somewhat more complex since the Hamiltonian is no longer diagonal in I_z and the fluctuating field can induce transitions between the quadrupolar eigenstates. This is allowed for by modifying the matrix A with a matrix B involving the previously forbidden $\Delta m_I = \pm 2$ transitions as derived by Blume and Tjon[16]. The results obtained were similar to those for a parallel EFG except that now it is the $\pm\frac{1}{2}$ line instead of the $\pm\frac{3}{2}$ line which exhibits the strongest relaxation broadening. The peak height ratio is plotted against temperature for various values of τ in Fig. 5.

The observed peak height ratios for (Fe salen Cl)$_2$ are also plotted in Figs. 4 and 5. It is seen that the theory leads to an approximate description of the observed results. However the only adjustable parameter τ exhibits some temperature dependence varying from about $2{\cdot}5 \times 10^{-11}$ sec to 4×10^{-11} sec for a parallel EFG and from about 8×10^{-11} sec to $1{\cdot}5 \times 10^{-10}$ sec for a perpendicular EFG. This defect in the theory may well be due to our neglect of crystal field splitting. A significant splitting of the $S' = 1$ multiplet could appreciably affect the spectra obtained at low temperatures.

Spectra were also calculated for a perpendicular EFG without pure axial symmetry, i.e. with a non-zero asymmetry parameter $\eta' = (V_{yy} - V_{zz})/V_{xx}$. Taking the value $\eta' = 0{\cdot}3$ only changed the value of τ for the best fit of the data from 1×10^{-10} sec to $1{\cdot}4 \times 10^{-10}$ sec.

The results of these calculations may be applied to any compound with antiferromagnetically coupled $S = \frac{5}{2}$ ion pairs since the ratios plotted in Figs. 4 and 5 are functions of T/J.

6. CONCLUSIONS

After allowing for an integral asymmetry due to anisotropy in the recoil free fraction, the zero field spectra of (Fe salen Cl)$_2$ are described approximately by a model in which crystal field splittings are assumed to be small in comparison with the intramolecular exchange and the dominant electronic relaxation process is that of mutual dipole induced spin flips. The 3 per cent peak height asymmetry obtained with (Fe salen)$_2$O at 298°K is also consistent with a similar relaxation effect since the exchange integral is much larger for this compound. Spectra obtained from both compounds at 4·2°K in large applied fields do not exhibit any appreciable hyperfine field verifying that the ground state involves zero total spin. For (Fe salen)$_2$O the EFG is positive with a large departure from axial symmetry. The principal axis of the EFG is parallel to the hyperfine magnetic fields. For (Fe salen Cl)$_2$ the symmetry is more nearly axial. The EFG is probably negative and perpendicular to the hyperfine magnetic fields.

Acknowledgements—We would like to thank Dr. P. Hannaford for valuable discussions. This project was supported by grants from the Australian Research Grants Committee and the Australian Institute for Nuclear Science and Engineering. It was carried out during the tenure of an I.C.I.A.N.Z. Research Fellowship by A. N Buckley, A Monash Graduate Scholarship by I R Herbert and a Commonwealth Postgraduate Award by B. D. Rumbold.

REFERENCES

1. BUCKLEY A. N., WILSON G. V. H. and MURRAY K. S., *Solid St. Commun.* **7**, 471 (1969).
2. PFEIFFER P., BREITH E., LÜBBE E. and TSUMAKI T., *Annl Chem.* **503**, 84 (1933).
3. KLEMM W. and RADDATZ K. H., *Z anorg. allg Chem.* **250**, 207 (1942).
4. GERLOCH M. and MABBS F. E., *J. chem. Soc.* 1900 (1967).
5. GERLOCH M., LEWIS J., MABBS F. E. and RICHARDS A., *J. chem. Soc.* 112 (1968).
6. REIFF W. M., LONG G. J. and BAKER W. A., JR., *J. Am. chem. Soc.* **90**, 6347 (1968).
7. GERLOCH M., McKENZIE E. D. and TOWL A. D. C., *Nature, Lond.* **220**, 906 (1968).
8. GERLOCH M., McKENZIE E. D. and TOWL A. D. C., *J. chem. Soc.* 2850 (1969).
9. LEWIS J., MABBS F. E. and RICHARDS A., *J. chem. Soc.* 1014 (1967).
10. PRICE D. C., to be published.
11. KARYAGIN S. V., *Dokl. Akad. Nauk SSSR* **148**, 1102 (1963). [English translation; *Soviet Phys. Dokl.* **148**, 110 (1963)].

12. GOL'DANSKII V. I., MAKAROV E. F., SUZDALEV I. P. and VINOGRADOV I. A., *Phys. Rev. Lett.* **20**, 137 (1968).
13. FLINN P. A., RUBY S. L. and KEHL W. L., *Science* **143**, 1434 (1964).
14. STÖCKLER H. A. and SANO H., *Phys. Rev.* **165**, 406 (1968).
15. BLUME M., *Phys. Rev. Lett.* **14**, 96 (1965).
16. BLUME M. and TJON J. A., *Phys. Rev.* **165**, 446 (1968).
17. BANCROFT G. M., MADDOCK A. G and RANDL R. P., *J. chem. Soc.* 2936 (1968).
18. BUCKLEY A. N., WILSON G. V. H. and MURRAY K. S., *Chem. Commun* 718 (1969).
19. COLLINS R. L and TRAVIS J C., *Mossbauer Effect Methodology* **3**, 123 (1967).
20. WICKMAN H. H. and WERTHEIM G. K., *Phys. Rev.* **148**, 211 (1966).
21. ANDERSON P. W., *J. phys. Soc. Japan* **9**, 316 (1954).
22. BOYLE A. J. F. and GABRIEL J. R., *Phys. Lett.* **19**, 451 (1965).
23. BLUME M., *Phys. Rev. Lett.* **18**, 305 (1967).

Note added in proof. (a) In this paper, statements concerning the sign of the EFG in fact refer to the sign of V_{zz}, which is opposite to that of $\nabla . E$. (b) It has been brought to our notice by S. V. Karyagin that the effect upon quadrupole doublets due to anisotropy in the recoil-free fraction should be referred to as the 'Gol'danskii–Karyagin effect'.

J. Phys. Chem. Solids Pergamon Press 1970. Vol. 31, pp. 1435–1441. Printed in Great Britain.

THE MÖSSBAUER ISOMER SHIFT IN ^{119}Sn – I. PSEUDOPOTENTIAL APPROACH

J. E. INGLESFIELD
Cavendish Laboratory, Cambridge, England

(*Received* 7 *November* 1969; *in revised form* 29 *December* 1969)

Abstract – The orthogonalization procedure for obtaining the electronic wave-function at the nucleus in Sn from the pseudo-wave-function is compared with a matching calculation, and the agreement is good. An expression is obtained for the total charge density at the nucleus in terms of the pseudopotential

1. INTRODUCTION

THE ISOMER shift of Mössbauer nuclei, in which the resonance frequency of the γ-ray depends on the charge density of the atomic electrons at the nucleus, provides an interesting tool to study the effect of crystal structure on the electronic structure of a crystal. In this paper we show how the pseudopotential formalism may be used to calculate the total electron charge density at the nucleus of an atom in a crystal, and we apply our results to the case of Sn. In a subsequent paper we calculate the isomer shift in α-^{119}Sn, β-^{119}Sn and ^{119}SnMg$_2$ and consider the change in shift under pressure, and the agreement with experiment is good. Our method may also be easily modified to calculate the structure-dependence of the Knight shift, which depends on the charge density at the nucleus produced by electrons at the Fermi level rather than the total charge density at the nucleus.

The advantage of the pseudopotential method of treating metallic crystals is that the energies and wave-functions of the conduction electrons *outside* the atomic cores may be calculated by a perturbation expression, the structure-dependence of the wave-function appearing in first and higher order terms. It is usually sufficient for simple metals to calculate wave-functions to first order and of course the success of the method is related to the nearly-free-electron like behaviour of the conduction electrons outside the atomic cores. To obtain the actual rapidly varying wave-function ψ_k inside the core from the smooth pseudo-wave-function ϕ_k is easy for orthogonalized plane wave pseudopotentials, when ψ_k inside the core is obtained simply by making ϕ_k orthogonal to the core states by a Schmidt procedure. This method has been discussed in connection with Knight shift calculations by Holland[1], and in Section 2 of this paper we shall discuss this 'orthogonalization procedure' in connection with finding the total electron density at the nucleus in ^{119}Sn.

We know that *in practice* there is no difference between the OPW form and other forms of the pseudopotential[2], including the model potential of Heine and Abarenkov[3, 4]. This suggests that the orthogonalization procedure will give a good approximation to ψ_k inside the core from a ϕ_k derived from any pseudopotential. However it is possible to find ψ_k exactly knowing ϕ_k by a matching calculation, because ψ_k is just the solution of the Schrödinger equation inside the core which matches on to ϕ_k at the core radius. In Section 3 we shall show how the matching procedure to determine $\psi_k(0)$ at the nucleus can be reduced to a form comparable with the orthogonalization procedure, and in fact we shall see that the two methods agree surprisingly well for Sn. One of the conclusions from Sections 2 and 3 is that if ϕ_k is made up of one or two plane waves having the same $|\mathbf{k}|$, for example at a Brillouin zone boundary or well inside a zone, $\psi_{\mathbf{k}}(0)$ is approximately proportional to $\phi_{\mathbf{k}}(0)$ the constant of proportionality being relatively independent of $\mathbf{k}$.

In Section 4 we shall use the results of Sections 2 and 3 to express the total conduction electron density at the nucleus in a given crystal structure as a sum over the reciprocal lattice vectors $\mathbf{g}$ to first order in the total pseudopotential $V(\mathbf{g})$. This result is very convenient for calculating the effect of structural and volume changes on the isomer shift. In summing the effects of $V(\mathbf{g})$ on $|\psi_{\mathbf{k}}(0)|^2$ through the Fermi sphere there is cancellation from the states on either side of the Brillouin zone boundary, and as in a calculation of the band-structure energy[5] the change in electron density at the nucleus comes from the states well away from the zone boundary. In the complete first-order perturbation calculation we shall see that the total conduction electron density at the nucleus is *not* simply proportional to the pseudo-electron density there.

2. THE ORTHOGONALIZATION PROCEDURE FOR THE ISOMER SHIFT

The frequency of the γ-ray emitted by a given Mössbauer nucleus changes from crystal structure to crystal structure, the shift in frequency being given by:

$$\delta \propto (\langle r^2\rangle_e - \langle r^2\rangle_g)(\rho(0)_1 - \rho(0)_2), \quad (1)$$

where $\langle r^2\rangle_e$ is the mean square nuclear radius in the excited state, $\langle r^2\rangle_g$ the radius in the ground state, and $(\rho(0)_1 - \rho(0)_2)$ the difference between the electronic (s-wave) density at the nucleus in the two crystal structures. We shall assume that the core states in the Mössbauer atom undergo little change as we vary the crystal structure, so:

$$\rho(0)_1 - \rho(0)_2 = \rho_v(0)_1 - \rho_v(0)_2, \quad (2)$$

where $\rho_v(0)$ is the valence or conduction electron density at the nucleus. Clearly,

$$\rho_v(0) = \sum_{\mathbf{k}} \left|\psi_{\mathbf{k}}(0)\right|^2, \quad (3)$$

the sum being over all occupied states $\psi_{\mathbf{k}}$.

Now in the pseudopotential method we find, usually by perturbation theory, the pseudo-wave-function $\phi(\mathbf{r})$ which is the same as $\psi(\mathbf{r})$ outside the ion cores and has the same energy. We know that the real wave-function must be orthogonal to the core functions and we expect that with any pseudopotential the orthogonalization procedure will be a fairly satisfactory method for obtaining $\psi_{\mathbf{k}}$ from $\phi_{\mathbf{k}}$, especially if the core is small and there are lots of core states:

$$\psi_{\mathbf{k}}(\mathbf{r})_{op} = \phi_{\mathbf{k}}(\mathbf{r}) - \sum_{\mathbf{r}_l,\alpha} \psi_\alpha(\mathbf{r}-\mathbf{r}_l) \int \psi_\alpha^*(\mathbf{r}'-\mathbf{r}_l) \phi_{\mathbf{k}}(\mathbf{r}')\, d^3\mathbf{r}'. \quad (4)$$

The summation is over all atomic sites $\mathbf{r}_l$ and over all core states ψ_α. Equation (4) gives us a wave-function $\psi_{\mathbf{k}}(\mathbf{r})_{op}$ which is certainly orthogonal to the core states and is the same as the real wave-function outside the core.

Equation (4) gives us a particularly simple form for $\psi_{\mathbf{k}}(0)$ when we expand $\phi_{\mathbf{k}}(\mathbf{r})$ as a sum of plane waves over the reciprocal lattice vectors $\mathbf{g}$:

$$\phi_{\mathbf{k}}(\mathbf{r}) = \sum_{\mathbf{g}} a_{\mathbf{k}+\mathbf{g}} \exp\{i(\mathbf{k}+\mathbf{g}) \cdot \mathbf{r}\}. \quad (5)$$

Let us consider the wave-function at the nucleus at the origin. Then the core wave-functions from neighbouring atoms do not overlap, and so (4) becomes:

$$\begin{aligned}\psi_{\mathbf{k}}(0)_{op} &= \sum_{\mathbf{g}} a_{\mathbf{k}+\mathbf{g}} - \sum_{\alpha} \psi_\alpha(0) \sum_{\mathbf{g}} a_{\mathbf{k}+\mathbf{g}} \int \psi_\alpha^*(\mathbf{r}) \exp\{i(\mathbf{k}+\mathbf{g}) \cdot \mathbf{r}\}\, d^3\mathbf{r} \\ &= \sum_{\mathbf{g}} a_{\mathbf{k}+\mathbf{g}} f(|\mathbf{k}+\mathbf{g}|) \quad (6)\end{aligned}$$

where

$$f(k) = 1 - \sum_{\alpha} \psi_\alpha(0) \int \psi_\alpha^*(\mathbf{r}) \exp(i\mathbf{k} \cdot \mathbf{r})\, d^3\mathbf{r}.$$

We note that the sum in (6) over core states reduces to a sum over the s-states alone. The advantage of (6) is that we now have a function $f(k)$ which is simply a *property of the Mössbauer atom*, and the effects of potential in the crystal due to structure, different neighbouring atoms and so on are all contained in the coefficients $a_{\mathbf{k}+\mathbf{g}}$.

Figure 1 shows $f(k)$ for Sn calculated using the Herman and Skillman[6] values for the

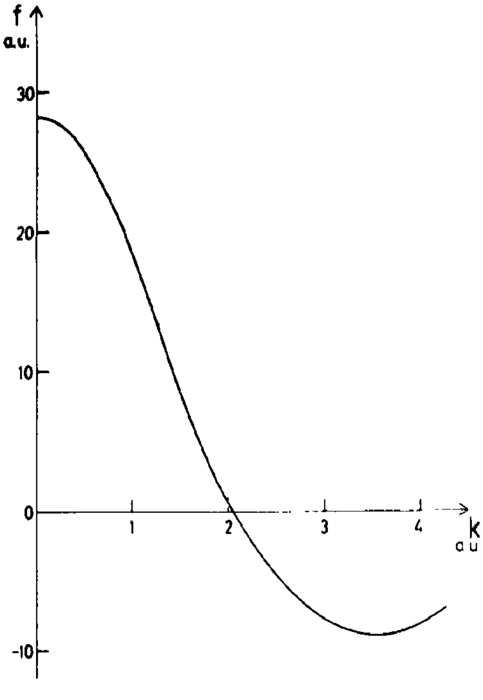

Fig 1. $f(k)$ for Sn; orthogonalization procedure.

core wave-functions. We note that $f(k)$ does not vary much over the range of **k**-vectors 0 to k_F (in β-Sn $k_F = 0{\cdot}87$ a.u.)*.

Now *to zeroth order*,

$$\phi_{\mathbf{k}}(\mathbf{r}) = n \exp(i\mathbf{k}\,.\,\mathbf{r})$$

where n is a normalising constant, so from (6) $\rho_v(0)$ is simply proportional to the free-electron density at the origin. Also if

$$\phi_{\mathbf{k}}(\mathbf{r}) = \frac{n}{\sqrt{2}}\{\exp(i\mathbf{k}\,.\,\mathbf{r}) \pm \exp(-i\mathbf{k}\,.\,\mathbf{r})\},$$

as near a Brillouin zone boundary, $\psi_{\mathbf{k}}(0)$ is proportional simply to $\phi_{\mathbf{k}}(0)$, the constant of proportionality $f(k)$ being roughly independent of k.

3. MATCHING PROCEDURE

To obtain the actual wave-function inside the ion core in a matching (APW-type) calculation we must integrate the Schrödinger equation outwards with the core potential $V(r)$ at the energy E of the pseudo-wave-function, so that the resulting function has the same amplitude at the radius of the core R_c as the pseudo-wave-function. The slopes will automatically match at R_c, if the correct energy E on an absolute scale is used in the integration outwards, because the real wave-function is the same as the pseudo-wave-function at R_c. If the radius R_c is fairly small the potential due to all other atoms does not vary much over the core, and so inside R_c the potential is the same as the free atom potential $V_a(r)$ apart from a constant term:

$$V(r) = V_a(r) + V_0, \quad r < R_c. \tag{7}$$

As we are interested essentially in a Hartree calculation it is the free *atom* potential which enters (7) and not the potential of the atom minus the valency electrons – the conduction electron density inside the core will be very close to the valence electron density in the free atom. Outside the ion core where nearly all the changes in conduction electron density occur, the dielectric screening function which enters the pseudopotential matrix elements ensures that our calculation is of a Hartree SCF type.

In this exact matching calculation we can write down immediately that:

$$\psi_{\mathbf{k}}(0) = \frac{\psi_{E,s}(0)}{\psi_{E,s}(R_c)} x\sigma_{\mathbf{k}}(R_c) \tag{8}$$

where $\psi_{E,s}(r)$ is the s-wave solution obtained by integrating the Schrödinger equation inside the core with energy E, and $\sigma_{\mathbf{k}}(R_c)$ is the s-wave part of $\phi_{\mathbf{k}}$ at R_c:

---

*We use atomic units in which $e = \hbar = m = 1$.

$$\sigma_{\mathbf{k}}(R_c) = \sum_{\mathbf{g}} a_{\mathbf{k}+\mathbf{g}} \frac{\sin(|\mathbf{k}+\mathbf{g}|R_c)}{|\mathbf{k}+\mathbf{g}|R_c}. \quad (9)$$

Equation (8) is exact for *any* pseudopotential but we can see that it has a rather different form from (6). We can however simplify (8) because we are going to determine it by perturbation theory only to first order. To first order in the pseudopotential $E(\mathbf{k})$ is given by the free-electron energy $E_0+\hbar^2k^2/2m$ so our final expression for (8) is:

$$\psi_{\mathbf{k}}(0) = F(k) \sum_{\mathbf{g}} a_{\mathbf{k}+\mathbf{g}} \frac{\sin(|\mathbf{k}+\mathbf{g}|R_c)}{|\mathbf{k}+\mathbf{g}|R_c} \quad (10)$$

where $F(k) = \psi_{E,s}(0)/\psi_{E,s}(R_c)$ evaluated at *the free-electron energy*. The structure-dependence now enters (10) only through the Fourier coefficients $a_{\mathbf{k}+\mathbf{g}}$, and this is the expression we shall subsequently use in Section 4.

A problem arises in calculating $F(k)$ because of the unknown constants V_0 in (7) and the energy E_0 of the bottom of the conduction band. Fortunately we can eliminate these constants by determining the energy of the bottom of the band relative to the free atom by a Wigner–Seitz procedure. Let us write the Schrödinger equation to be integrated outwards from $r=0$ as:

$$\{-\hbar^2/2m\,\nabla^2 + V_a(r)\}\psi_{E,s}(r) =$$

$$(\hbar^2k^2/2m + E_0 - V_0)\psi_{E,s}(r), \quad r < R_c. \quad (11)$$

This equation is the free atom Schrödinger equation with energy $(\hbar^2k^2/2m+E_0-V_0)$, which at the bottom of the band becomes simply (E_0-V_0). But we know that at the bottom of the band the pseudo-wave-function is more or less constant outside the core, so (E_0-V_0) is that energy at which $\psi_{E,s}(r)$ has zero radial derivative at R_c. With this result we have calculated $F(k)$ for Sn using the Herman–Skillman atomic potential for $V_a(r)$ and a core radius R_c of 2·13 a.u. (cf. the Animalu and Heine[4] core radius of 2 a.u.), and this is shown in Fig. 2. We see that it is a slowly varying function of k over the range 0 to k_F which further vindicates our approximation of evaulating it at the free-electron energy.

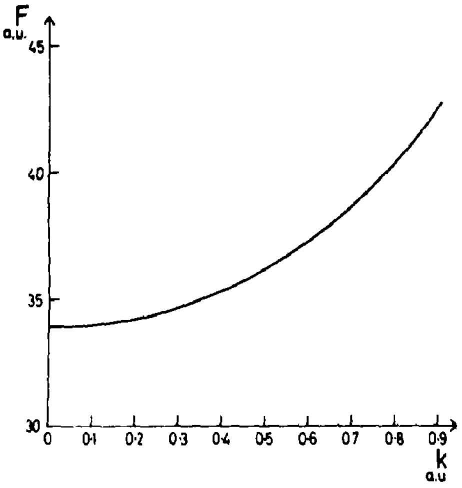

Fig. 2. $F(k)$ for Sn: matching procedure, $R_c = 2{\cdot}13$ a.u.

We can now compare directly the orthogonalization and matching procedures for a one or two plane wave pseudo-wave-function. Although we shall use (10) in our full perturbation treatment in § 4 where many Fourier components $V(\mathbf{g})$ of the potential are mixed in, we expect that a good approximation for $\psi_{\mathbf{k}}(0)$ is:

$$\psi_{\mathbf{k}}(0) \approx \sum_{\mathbf{g}} a_{\mathbf{k}+\mathbf{g}}\, b(|\mathbf{k}+\mathbf{g}|) \quad (12)$$

where

$$b(k) = F(k)\frac{\sin(kR_c)}{kR_c}.$$

This will be a fair approximation because the only coefficients $a_{\mathbf{k}+\mathbf{g}}$ which are large, are those for which

$$|\mathbf{k}+\mathbf{g}| \approx k,$$

and also because $F(k)$ varies slowly. We now have an expression (12) which has just the same form as (6) with the function $b(k)$ replacing $f(k)$. Figure 3 shows $b(k)$ and we can see that it has a very similar form to $f(k)$, but about 20 per cent larger. This result shows that the orthogonalization procedure must work fairly well for determining $\psi_{\mathbf{k}}(0)$ from *any* pseudopotential, confirming our assertions of Section 1.

4. PERTURBATION THEORY AND $\rho v(0)$

Having obtained expressions (6) and (10) for $\psi_{\mathbf{k}}(0)$ in terms of the Fourier coefficients $a_{\mathbf{k}+\mathbf{g}}$ we shall now calculate the total conduction electron density at the origin, using first order perturbation theory[7] to evaluate $a_{\mathbf{k}+\mathbf{g}}$. That is,

$$a_{\mathbf{k}+\mathbf{g}}=\frac{a_{\mathbf{k}}V(\mathbf{g})}{E(\mathbf{k})-E(\mathbf{k}+\mathbf{g})}. \qquad (13)$$

To first order in the pseudopotential we obtain from (10):

$$|\psi_{\mathbf{k}}(0)|^2=b(k)^2|a_{\mathbf{k}}|^2+F(k)^2$$

$$\sum_{\mathbf{g}}{}' \left\{\frac{\sin(kR_c)\sin(|\mathbf{k}+\mathbf{g}|R_c)}{(kR_c)(|\mathbf{k}+\mathbf{g}|R_c)}\right.$$

$$\left.(a_{\mathbf{k}}a^*_{\mathbf{k}+\mathbf{g}}+\text{c.c.})\right\}\cdot \qquad (14)$$

We note that the pseudopotential matrix elements $V(\mathbf{g})$ which enter (13) and (14) must be evaluated from an origin at the Sn nucleus under consideration.

The normalization condition on $|a_{\mathbf{k}}|^2$ is rather tricky because we want the *real* wave-function and not the pseudo-wave-function to be normalized to unity over the crystal volume, and we only know the real wave-function in terms of a matching calculation or the orthogonalization procedure. We know that the real one-electron density $|\psi_{\mathbf{k}}(\mathbf{r})|^2$ looks like the pseudo-density $|\phi_{\mathbf{k}}(\mathbf{r})|^2$[7] apart from an 'orthogonalization hole' on each atom, and this affects the normalization.

The standard pseudopotential result for the normalization of the pseudo-wave-function is that

$$|a_{\mathbf{k}}|^2=1/N(\Omega-\Omega_{oh}) \qquad (15)$$

where N is the number of atoms, Ω is the volume per atom and Ω_{oh} is the volume of the orthogonality hole. The exact size of Ω_{oh} is not important being much smaller than Ω but we have used a value of 28 a.u., which we have derived in the following way. If Ω_c is the volume of the atomic core outside which the actual wave-function is the same as the pseudo-wave-function, the total one-electron charge outside the cores is:

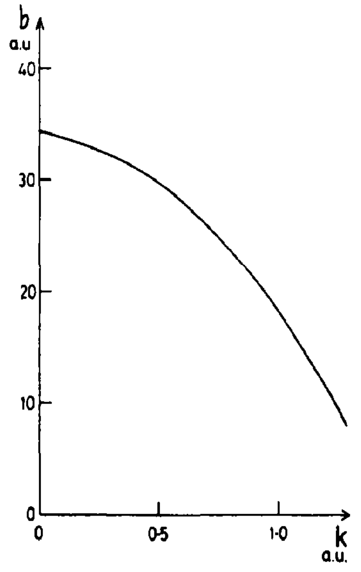

Fig. 3. $b(k)$ for Sn; matching procedure.

$$\text{charge (outside)} \approx N(\Omega-\Omega_c)|a_{\mathbf{k}}|^2. \quad (16)$$

Now inside the cores the wave-function looks like the combination of atomic $s-$, $p-$ .... wave-functions which matches on to $\phi_{\mathbf{k}}$ at R_c and we have found by integrating the charge density inside a core-radius of 2·28 a.u. that:

$$\text{charge (inside)} \approx N\times 22\,|a_{\mathbf{k}}|^2. \quad (17)$$

$$\text{So the total charge} = N(\Omega - \Omega_c + 22)|a_{\mathbf{k}}|^2 = N(\Omega - 28)|a_{\mathbf{k}}|^2,$$

which must equal unity by normalization.

We can now sum (14) over all the states inside the Fermi sphere to obtain an expression for the conduction electron density at the nucleus:

$$\rho_c(0) = \frac{Z}{\Omega - \Omega_{oh}}\left[\overline{b^2} + \sum_{\mathbf{g}}{}' \mathscr{R}\{V(\mathbf{g})\} J(k_F, g)\right] \tag{18}$$

where

$$J(k_F, g) = (3/\pi k_F^3) \int_{k<k_F} \mathrm{d}^3\mathbf{k} \, \frac{F(k)^2 \sin(kR_c) \sin(|\mathbf{k}+\mathbf{g}|R_c)}{(k^2 - |\mathbf{k}+\mathbf{g}|^2)(kR_c)(|\mathbf{k}+\mathbf{g}|R_c)}.$$

In this expression Z is the number of conduction electrons per atom, $\overline{b^2}$ is the average of $b(k)^2$ through the Fermi sphere, and the sum is over all non-zero reciprocal lattice vectors **g**. We see that the real part of the matrix element of the total pseudopotential in the crystal is multiplied by a function $J(k_F, g)$, which we have determined for Sn (Fig. 4). J is very dependent on the Fermi wavevector k_F, and becomes very small for g beyond $2k_F$. The corresponding expression for the pseudo-electron density at the nucleus is:

$$\rho_{ps}(0) = \frac{Z}{\Omega - \Omega_{oh}}\left[1 + \sum_{\mathbf{g}}{}' \mathscr{R}\{V(\mathbf{g})\} \chi(k_F, g)\right] \tag{19}$$

where

$$\chi(k_F, g) = (3/\pi k_F^3) \int_{k<k_F} \mathrm{d}^3\mathbf{k} \, \frac{1}{(k^2 - |\mathbf{k}+\mathbf{g}|^2)}.$$

J is *not* proportional to χ, which is the standard perturbation function[8], so there is no direct relation between the full first order electron density and the pseudo-electron density.

The first term in (18) can immediately be identified as the free-electron contribution to $\rho_p(0)$, the second term containing all the effects of the crystal potential $V(\mathbf{g})$. Although the states on either side of the Brillouin zone boundary are the most strongly affected by $V(\mathbf{g})$ they cancel each other out in the integral for J and effectively only contribute the free-electron term to $\rho_p(0)$. The largest contribution to J comes from states away from the Brillouin zone boundary, which is just the same situation as the contribution by $V(\mathbf{g})$ to the total energy of the Fermi sphere[5].

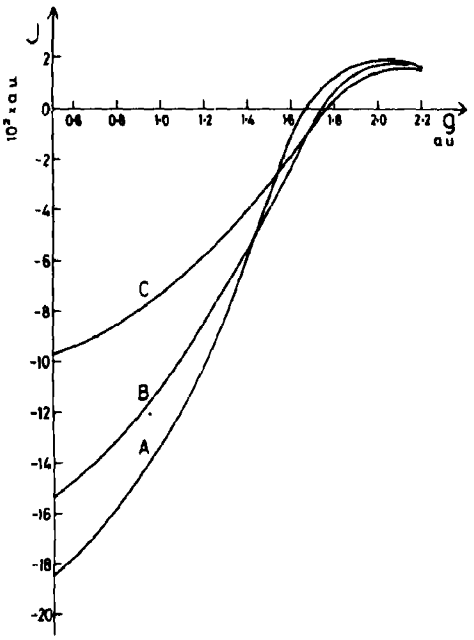

Fig. 4. $J(k_F, g)$ for Sn, A: $k_F = 0\cdot767$ a.u., B. $k_F = 0\cdot799$ a.u., C: $k_F = 0\cdot867$ a.u.

Acknowledgements – I should like to thank Dr. V. Heine and Dr. J. B. Pendry for their help. Financial support was provided by AERE (Harwell).

REFERENCES

1. HOLLAND B. W., *Phys. Status. Solidi* **28**, 121 (1968).
2. COHEN M. L. and HEINE V., *Solid State Physics* (Edited by F. Seitz, D. Turnbull, and H. Ehrenreich). To be published.
3. HEINE V. and ABARENKOV I., *Phil. Mag.* **9**, 451 (1964)
4. ANIMALU A. O. E. and HEINE V., *Phil. Mag.* **12**, 1249 (1965)
5. WILLIAMS A. R. and WEAIRE D., *J. phys. C: Solid State Phys.* **3**, 386 (1970).

6. HERMAN F. and SKILLMAN S., *Atomic Structure Calculations*. Prentice-Hall, N.J. (1963).
7. HARRISON W. A., *Pseudopotentials in the Theory of Metals*. Benjamin, New York (1966).
8. HEINE V., *The Physics of Metals* (Edited by J. M. Ziman), Vol. 1. Cambridge University Press, Cambridge (1969).

J. Phys. Chem. Solids Pergamon Press 1970. Vol. 31, pp. 1443-1448. Printed in Great Britain.

THE MÖSSBAUER ISOMER SHIFT IN ^{119}Sn–II. EFFECTS OF CRYSTAL STRUCTURE

J. E. INGLESFIELD
Cavendish Laboratory, Cambridge, England

(*Received* 7 *November* 1969)

Abstract—The different electron densities at the ^{119}Sn nucleus in α-Sn, β-Sn and $SnMg_2$ which give rise to isomer shifts are studied in terms of a pseudopotential expression. The effects of volume changes are examined, and in $SnMg_2$ the observed increase in electron density at the nucleus under pressure may be connected with an observed increase in electrical conductivity.

1. INTRODUCTION

IN A PREVIOUS paper[1] we showed that the contribution of the conduction electrons to the total electron density at the nucleus of a tin atom, which determines the isomer shift of Mössbauer γ-rays emitted by ^{119}Sn, can be expressed as a simple formula using the pseudopotential method to describe the effects of crystal structure on the conduction electron wave-functions. The first term in our formula is a free-electron contribution and the second term, a sum over reciprocal lattice vectors, depends on crystal structure. In this present paper we shall use the results of[1] to study the change in isomer shift of ^{119}Sn under pressure, and as we go from crystal structure to crystal structure.

In Sections 2 and 3 of this paper we shall determine the isomer shifts of β-Sn and $SnMg_2$ relative to α-Sn, and the agreement with experiment is qualitatively correct[2]. As we go from structure to structure the change in the average free-electron density and the different band-structure both cause the electron density at the nucleus to change, but as we shall see in Sections 2 and 3 the observed isomer shifts arise because the change in average electron density predominates.

Möller and Mössbauer[2] found from isomer shift measurements that when β-Sn is compressed the electron density at the nucleus decreases, and we shall show in Section 4 that this effect can *partly* be explained by the results of[1]. As β-Sn is compressed the free-electron density increases but the band-structure term decreases, though not enough to explain the results of[2]. This suggests that changes in the core states under compression may play some role in explaining the decrease in electron density at the nucleus.

The change under pressure of the isomer shift in $SnMg_2$ is particularly interesting because there is a sudden increase in electron density at the nucleus at 20–30 kbar. This in fact coincides with a breakdown in the semiconducting properties of $SnMg_2$, and Möller first suggested that the two are related. We show in Section 5 how the effects of a semiconductor band-gap on the electron density can be calculated and our results for $SnMg_2$ demonstrate that Möller's explanation is correct: the states directly underneath the band-gap are p-like with respect to the ^{119}Sn nuclei, so when the semiconducting properties break down the electron density at the nucleus increases.

2. THE ISOMER SHIFT IN DIFFERENT STRUCTURES

The isomer shift δ in the frequency of the γ-rays emitted by ^{119}Sn in two different environments 1 and 2 is related to the changes in electron density at the nucleus $\rho(0)$ by the following expression[1, 2]:

$$\delta = A(\rho(0)_1 - \rho(0)_2) \qquad (1)$$

where it is known from experiment that the constant of proportionality A, a property of the Mössbauer nucleus alone, is positive. In our work we assume that only the conduction (or valency) electron density $\rho_v(0)$ alters, i.e:

$$\delta = A(\rho_v(0)_1 - \rho_v(0)_2), \tag{2}$$

and we calculate $\rho_v(0)$ from the expression derived in[1]:

$$\rho_v(0) = \frac{Z}{\Omega - \Omega_{oh}}\left[\overline{b^2} + \sum_{g}{}' \mathscr{R}\{V(\mathbf{g})\} J(k_F, g)\right] \tag{3}$$

Z is the valency, Ω is the volume per atom and Ω_{oh} is the effective volume of the atomic core which is more or less excluded for the conduction electrons. $\overline{b^2}$ is the average 'penetration' of the conduction electrons and is a property solely of the Mössbauer atom. All the dependence of $\rho_v(0)$ on the crystal potential enters in the second term which is a sum over the reciprocal lattice vectors $\mathbf{g}$ (except $g = 0$), the corresponding pseudopotential matrix elements being $V(\mathbf{g})$. We have calculated the function $J(k_F, g)$ for Sn, and it is strongly dependent on the Fermi wave-vector k_F[1].

The interesting point about (3) is that the factor $Z/\Omega - \Omega_{oh}$ is simply the mean conduction electron density in the crystal, taking into account the excluded volume Ω_{oh}. The product $Z\overline{b^2}/\Omega - \Omega_{oh}$ is just the free-electron contribution to $\rho_v(0)$.

The experimental results which we now wish to interpret are the values of δ, relative to α-Sn at 0 kbar, shown in Table 1. Another result which we shall later consider, derived by Lees and Flinn[3], is that the isomer shift in an ideal Sn^{2+} ion relative to $SnMg_2$ is 2·86 mm/sec. In this context the 'ideal' Sn^{2+} ion is one with no $5p$ electrons and in which the s-electrons are in free $5s$ orbitals with no covalency effects, and this value of δ has been obtained by extrapolation from the isomer shift in various stannous salts.

Table 1. *Isomer shifts relative to* α-Sn *at zero pressure*

Compound	Atomic volume (a.u.)	Isomer shift (mm/sec)
β-Sn	181·5	+0·56
α-Sn	232·1	0
$SnMg_2$	175	−0·15

We can now explain the results of Table 1 simply in terms of changes in mean electron density. Let us ignore the first-order band-structure contribution to $\rho_v(0)$ and write to zeroth order:

$$\rho_v(0) = \frac{Z\overline{b^2}}{\Omega - \Omega_{oh}}. \tag{4}$$

The mean volumes per atom Ω are given in Table 1 and we have estimated Ω_{oh} to be 28 a.u.,* and so from (4):

$$\rho_v(0)_{\beta\text{-Sn}} = 1{\cdot}33\,\rho_v(0)_{\alpha\text{-Sn}}.$$

In $SnMg_2$,

$$Z = 2\tfrac{2}{3}$$

and so:

$$\rho_v(0)_{SnMg_2} = 0{\cdot}93\,\rho_v(0)_{\alpha\text{-Sn}}.$$

These results agree qualitatively with the observed isomer shifts but as we shall see in Section 3 putting in the band-structure tends to make the ratios of $\rho_v(0)$ nearer unity. From these zeroth order results the isomer shifts relative to α-Sn are in the ratio:

$$\frac{\delta_{\beta\text{-Sn}}}{\delta_{SnMg_2}} = -\frac{0{\cdot}33}{0{\cdot}07} = -4{\cdot}7$$

which compares quite favourably with the experimental result of −3·7.

3. BAND-STRUCTURE AND THE ISOMER SHIFT

To determine $\rho_v(0)$ and hence the constant A in (1) we must determine the band-structure contribution, the sum over the reciprocal lattice vectors in (3). This contribution is fairly large in α-Sn and SnMg$_2$. We can see from the variation of J with k_F (Fig. 4 of Ref.[1]) that if $V(\mathbf{g})$ for low g is predominantly negative, as in these structures, the band-structure contribution increases with decreasing k_F, and this tends to cancel out the volume changes of the zeroth order term.

---

*We use atomic units throughout in which $e = \hbar = m = 1$.

As usual[5] $V(\mathbf{g})$ can be factorised into a product of a structure factor $S(\mathbf{g})$ and an atomic pseudopotential matrix element, and for α-Sn and β-Sn we obtain:

$$V(\mathbf{g}) = S(\mathbf{g})v_{\mathrm{Sn}}(g) \qquad (5)$$

where $S(\mathbf{g}) = (1/N)\Sigma_{\mathbf{r}_j}\exp(i\mathbf{g}\,.\,\mathbf{r}_j)$.

N is the total number of atoms and v_{Sn} is the pseudopotential of the Sn atom, for which we use Animalu and Heine's[6] tabulated form-factor. $S(\mathbf{g})$ is a sum over atomic sites $\mathbf{r}_j$ *measured from an* Sn *atom at the origin.* In SnMg$_2$ we have similarly:

$$V(\mathbf{g}) = (v_{\mathrm{Mg}}S_{\mathrm{Mg}} + v_{\mathrm{Sn}}S_{\mathrm{Sn}})\,. \qquad (6)$$

The effect of the band-structure term is to increase $\rho_v(0)$ in all three cases (Table 2). Figure 1 shows v_{Sn} and the positions of the contributing reciprocal lattice vectors $\mathbf{g}$ in α- and β-Sn. For all these vectors the real part of $S(\mathbf{g})$ is positive and so for the smaller values of g $\mathcal{R}\{V(\mathbf{g})\}$ is strongly negative. But from the form of J the smaller g's make the largest contribution to $\rho_v(0)$, and so the band-structure terms increase the electron density at the nucleus. We see from Table 2 that the effect of the band-structure terms is to increase $\rho_v(0)$ for α-Sn and SnMg$_2$ much more than for β-Sn, but because the zeroth order term predominates the qualitative results of Section 2 still hold.

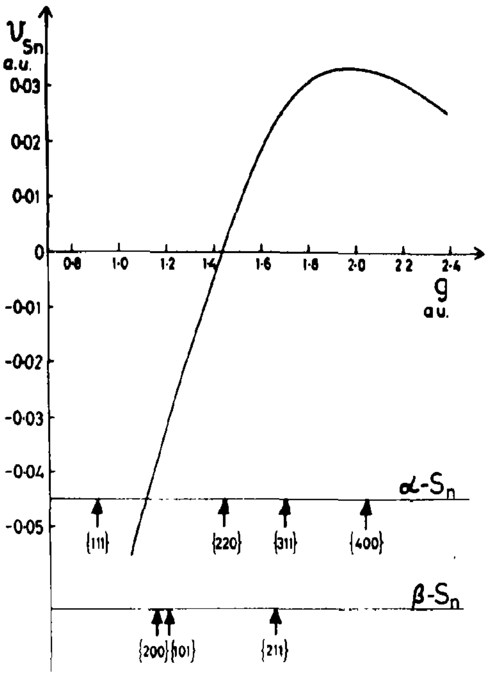

Fig. 1. $v(g)$ for Sn, Ω = 182 a.u., with positions of reciprocal lattice vectors in α-Sn and β-Sn

Table 2. *Electron densities at the* ^{119}Sn *nucleus*

Material	Free-electron contribution (electrons per a.u. of volume)	$\rho_v(0)$
β-Sn	19·5	23·1
α-Sn	14·6	21·3
SnMg$_2$	13·4	21·1

Because of the unknown constant A in (1) we cannot make a direct comparison between our calculated $\rho_v(0)$'s and the δ's shown in Table 1 but following Möller we can conveniently express our results in terms of the isomer shift in Sn^{2+} relative to SnMg$_2$. To a good approximation $\rho_v(0)$ for 'ideal' Sn^{2+} is just the same as the density at the origin of the $5s^2$ electrons in a free Sn atom, and from Herman–Skillman[4] we obtain:

$$\rho_v(0)_{\mathrm{Sn}^{2+}} = 35{\cdot}2 \text{ electrons/a.u. volume.} \qquad (7)$$

Then from (7), Table 2 and the result of Lees and Flinn it follows that a value of

$$(\rho_v(0)_1 - \rho_v(0)_2) = 14{\cdot}1 \text{ electrons/a.u. volume}$$

corresponds to an isomer shift of 2·86 mm/sec. Hence,

$$A = \frac{2 \cdot 86}{14 \cdot 1} = 0 \cdot 203 . \tag{8}$$

With this value of A we can compare Tables 1 and 2 obtaining the following theoretical values for the isomer shifts of β-Sn and $SnMg_2$ relative to α-Sn at 0 kbar:

$$\delta_{\beta\text{-Sn}} = +0 \cdot 37 \text{ mm/sec}$$
$$\delta_{SnMg_2} = -0 \cdot 04 \text{ mm/sec}$$

The value for the shift of β-Sn is in good agreement with the observed shift, +0·56 mm/sec. The shift for $SnMg_2$ is too small but when we take into account the effects of the semiconductor band-gap in this substance (Section 5) again excellent agreement is obtained.

4. CHANGES IN THE ISOMER SHIFT OF β-Sn UNDER PRESSURE

When β-Sn is compressed by 100 kbar so that the volume is reduced to 0·87 of the volume at zero pressure it is found that the isomer shift is *reduced* by 0·15 mm/sec. This means that a reduction in atomic volume is causing the electron density at the nucleus to decrease. We saw in Section 2 that we could understand the changes in δ with structure largely in terms of the mean electron density, but clearly this change under pressure cannot be understood simply in these terms. As the volume is reduced the mean electron density increases but the contribution from the band-structure term decreases markedly, but not by quite enough to explain the observed result.

There are two reasons for the *decrease* in the band-structure contribution as the volume is reduced. As Ω decreases k_F increases and $|J|$ decreases. We saw in Section 3 that this causes a decrease in $\rho_v(0)$. Also as Ω decreases the reciprocal lattice vectors move outwards and from Fig. 1 the potential $V(\mathbf{g})$ for the smallest and most important g's becomes less attractive, again causing a decrease in $\rho_v(0)$. As k_F increases the screening of $V(\mathbf{g})$ by the conduction electrons increases, via the dielectric constant $\epsilon(g)$[5], but this reduces $\rho_v(0)$ by a *negligible* amount compared with the other effects.

Differentiating (3) we obtain:

$$\frac{d\rho_v(0)}{d\Omega} = -\frac{\rho_v(0)}{\Omega - \Omega_{oh}} + \frac{Z}{\Omega - \Omega_{oh}} \left[{\sum_{\mathbf{g}}}' \mathscr{R}\{V(\mathbf{g})\} \times \frac{dJ}{d\Omega} + \mathscr{R}\left\{\frac{dV}{d\Omega}\right\} J \right] \tag{9}$$

where

$$\frac{dV}{d\Omega} = -\frac{V}{\Omega} - \frac{g}{3\Omega}\frac{\partial V}{\partial g}$$

because V is the matrix element taken between plane waves normalized to unity over the crystal volume. In differentiating $\rho_v(0)$ we ignore the weak dependence of $\overline{b^2}$ on k_F. We can see that the first term in (9) corresponds to the increase in mean electron density as the volume decreases, and the second term is produced by the band-structure effects. We expect that the second term will be particularly large in β-Sn because the smallest values of g coincide with the steep part of the pseudopotential, i.e. $\partial V/\partial g$ large and positive.

The calculated value of $d\rho/d\Omega$ for β-Sn is

$$\frac{d\rho_v(0)}{d\Omega} = -0 \cdot 151 + 0 \cdot 107$$
$$= -0 \cdot 044 \text{ electrons/(a.u. volume)}^2.$$

This is not in agreement with the experimental result which is that $d\rho/d\Omega$ is positive, but we can see that the change in band-structure contribution does to a large extent cancel out the effect of change in the mean density. The discrepancy with experiment means that either higher order terms in $\rho_v(0)$ must be considered, or that there are changes in the core states. Nevertheless we have shown that a large part of the effect of pressure on the isomer shift of β-Sn can be understood in our terms.

5. SEMICONDUCTOR EFFECTS IN $SnMg_2$

When $SnMg_2$ is compressed a rapid parabolic change in the isomer shift sets in at 20–

30 kbar corresponding to an increase in electron density at the nucleus, the change in δ at a pressure of 30 kbar being + 0·1 mm/sec. The volume changes only by about 6 per cent and so the mechanism for the increase in charge density seems unlikely to be the changes in $\rho_v(0)$ discussed in Section 4 which would certainly be linear over this change of volume. However over just this range 20–30 kbar the electrical resistance of $SnMg_2$, a semiconductor at zero pressure, suddenly falls and the two phenomena seem likely to be connected [2]. The fact that at the lower pressures $SnMg_2$ is a semiconductor means that expression (3) for $\rho_v(0)$ is not complete and there is an extra contribution to the charge density at the nucleus. The dramatic change in δ then arises from the disappearance of semiconducting properties and the corresponding extra term.

The derivation of $\rho_v(0)$ in [1] ignored completely the distortions of the Fermi sphere of electrons by the Brillouin zone, and we know [5] that this is a valid approximation in metals. It implies however that the states which we might expect to contribute most to $\rho_v(0)$, namely those on either side of the Brillouin zone boundaries where the perturbation due to $V(\mathbf{g})$ is strongest, contribute in total only a free-electron term, and *all the band-structure contribution to* $\rho_v(0)$ *comes from states away from the boundaries*. Suppose we have a metal with a Brillouin zone boundary for which $V(\mathbf{g})$ is real and positive. Then the pseudo-wave-functions for the states directly underneath the zone boundary look like $\sqrt{2}\sin(kr)$ and each state contributes nothing to $\rho_v(0)$. On the other hand the states above the boundary look like $\sqrt{2}\cos(kr)$ and these contribute $2b(k)^2$([1],(12)), $b(k)$ being the 'penetration' of a wave $\exp(i\mathbf{k}\,.\,\mathbf{r})$. So the total contribution of a pair of states on either side of the boundary is $2b(k)^2$ which is just the same as their free-electron contribution without the band gap. The band-structure part of $\rho_v(0)$ contains no contribution from the states on either side of the zone boundaries. This 'metallic' situation is correctly treated in the evaluation of the function $J(k_F, g)$ which is a principal-value integral ([1], (18)).

However in a semiconductor there is a band-gap at the Jones' zone boundary [7] which completely surrounds the Fermi region of electrons and so *there is no cancellation of the band-structure contribution to* $\rho_v(0)$ *from the states directly under the zone boundary*. It is this band-structure contribution which is the extra effect we have ignored in semiconducting $SnMg_2$, but we can determine its approximate size by a Penn [8] model of a semiconductor in which there is an isotropic spherically symmetric band-gap at the Fermi surface (Fig. 2).

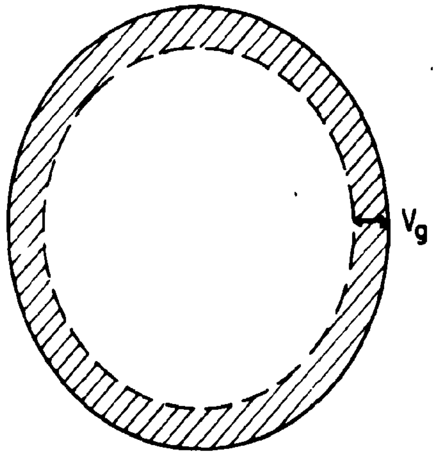

Fig. 2. Isotropic band-gap model of semiconducting $SnMg_2$. The shaded states give no contribution to $\rho_v(0)$.

In $SnMg_2$, which has the fluorite structure, the Jones' zone is made up from {220} planes and the corresponding band gap $2|V(220)|$ is 0·018 a.u. from Animalu and Heine's form factors [6]. Because $V(220)$ is real and positive the pseudo-wave-functions directly underneath the zone are sine-like with respect to an Sn atom at the origin. To determine $\rho_v(0)$ it is reasonable to assume that for all states *away* from the zone boundary expression (3) is valid using J determined from ([1], (18)). On the other hand the effect of the states directly underneath the zone boundary is given correctly in terms of Fig. 2. To a good approximation the number of these sine-like states is[9]:

$$n = |V(220)| \times \text{Density of states at } k_F$$

$$= \frac{3ZN|V(220)|}{2E_F} \qquad (10)$$

where E_F is the Fermi energy. These n states in fact contribute nothing to $\rho_v(0)$ whereas in (3) they have been *effectively* treated as giving the free electron contribution to $\rho_v(0)$ of $b(k_F)^2/N(\Omega - \Omega_{oh})$ ([1], (12), (15)). So in semiconducting SnMg$_2$:

$$\rho_v(0) = \rho_v(0)_{\text{Metallic}} + \Delta\rho \qquad (11)$$

where $\rho_v(0)_{\text{Metallic}}$ is given by (3) and:

$$\Delta\rho = -\frac{3ZN|V(220)|}{2E_F} \times \frac{b(k_F)^2}{N(\Omega - \Omega_{oh})}$$

$$- 1{\cdot}5 \times \frac{b(k_F)^2 Z}{\Omega - \Omega_{oh}} \times \frac{|V(200)|}{E_F}. \qquad (12)$$

$\Delta\rho$ turns out to be

$$-0{\cdot}48 \text{ electrons/a.u. volume.} \qquad (13)$$

Our interpretation of the change in δ (following [2]) is that as the pressure is increased $\rho_v(0)_{\text{Metallic}}$ remains essentially unaltered, but the band-structure changes just sufficiently for electrons to overflow out of the Jones' zone and the extra, semiconductor, contribution $\Delta\rho$ to vanish. This would imply an increase in the isomer shift of

$$+0{\cdot}48 \times 0{\cdot}203 = +0{\cdot}096 \text{ mm/sec.}$$

and this is exactly the change observed in going to 30 kbar. Combining (13) with the calculation of $\rho_v(0)_{\text{Metallic}}$ from Table 2 we obtain the isomer shift of SnMg$_2$ relative to α-Sn at 0 kbar to be

$$\delta_{\text{SnMg}_2} = -0{\cdot}14 \text{ mm/sec.},$$

in agreement with Table 1.

Acknowledgements—I should like to thank Dr. V. Heine for his help and encouragement. The work has been supported by a grant from AERE (Harwell).

REFERENCES

1. INGLESFIELD J. E., *J. Phys. Chem. Solids* **31**, 1435 (1970).
2. MOLLER H. S., *Z. Phys.* **212**, 107 (1968).
3. LEES J. and FLINN P. A., *Phys. Lett.* **19**, 186 (1965)
4. HERMAN F. and SKILLMAN S., *Atomic Structure Calculations* Prentice-Hall, N.J. (1963).
5. HARRISON W. A., *Pseudopotentials in the Theory of Metals* Benjamin, New York (1966)
6. ANIMALU A. O. E. and HEINE V., *Phil. Mag.* **12**, 1249 (1965)
7. MOTT N. F. and JONES H., *The Theory of the Properties of Metals and Alloys*. Oxford University Press, Oxford (1936).
8. PENN D., *Phys. Rev.* **128**, 2093 (1962)
9. HEINE V. and JONES R. O., *J. Phys. C.* **2**, 719 (1968) (Ref [2])

J. Phys. Chem. Solids Pergamon Press 1970. Vol. 31, pp. 1449-1454. Printed in Great Britain.

THE SYSTEM $Nb_3Sn_{1-x}Sb_x$ AND THE DENSITY OF STATES MODEL FOR Nb_3Sn*

L. J. VIELAND
RCA Laboratories, Princeton, N.J. 08540, U.S.A.

(*Received* 30 *September* 1969; *in revised form* 1 *December* 1969)

Abstract – The temperature of the cubic-tetragonal transformation in Nb_3Sn, and the magnitude of the tetragonal distortion, are found by X-ray measurements to be independent of Sb doping over the range studied, $0 < x < 0{\cdot}15$. However, the addition of a small amount of Sb results in a c/a ratio greater than unity, while for pure Nb_3Sn, $a > c$. These results are discussed in terms of the density of states model of the lattice transformation in β-tungsten superconductors.

1. INTRODUCTION

LABBÉ and Friedel have shown[1] that much of the anomalous behavior of the high T_c, β-tungsten superconductors can be understood in terms of a band model comprising two main features; a strongly energy dependent density of states within a few hundred degrees of the Fermi level at 0°K, and a threefold degeneracy of the relevant d-band which is removed by a low temperature distortion from cubic to tetragonal symmetry. Cohen *et al.*[2] proposed a particularly simple density of states representation (square band) which leads to striking agreement between theory and experiment for most of the properties of these unusual metals[2, 3]. However, the model is phenomenological, and although some experimental observations remain unexplained [3], its limitations are not clearly defined. The necessary fine structure in the density of states is not derivable from band structure calculations, which are made on a relatively coarse energy scale. Similarly, direct observation of this structure by a technique such as soft X-ray emission appears to be out of the question. One simple line of attack which remains open is the classic method of effecting small changes in electron concentration by means of doping, and correlating these changes with suitable physical properties. The major premise of the method is the validity of the rigid band approximation.

A convenient system to look at is the Nb_3-Sn-Nb_3Sb pseudo-binary, about which some useful information is already at hand[4-6]. The replacement of Sn by neighboring Sb in the periodic table should introduce minimum perturbations other than the desired change in electron concentration.

2. THEORY

The parameters of the square band density of states model (ignoring the small overlapping s-band contribution) are N_0, U_2 and T_0, where N_0 is the d-band density of states in the cubic state, U_2 is the deformation potential relating the shift in the band edge with uniaxial strain along the ⟨100⟩ direction, and T_0, which is the distance from the Fermi level at 0°K to the near band edge, is the quantity adjustable by alloying. The number of electrons (holes) in the nearly empty (full) band for $Nb_3Sn_{1-x}Sb_x$ alloys is

$$N_0kT_0' = N_0kT_0 \pm x\Delta v/4$$

where Δv, the difference in valence between Sb and Sn, is probably, but not necessarily

---

*The research reported in this paper was jointly sponsored by NASA, George C. Marshall Space Flight Center, Alabama, under Contract No NAS-8-21384 and RCA Laboratories, Princeton, New Jersey.

[7], + 1. Since N_0kT_0 is about 0·04 states/atom for Nb_3Sn[3], and since the d-band carriers are thought to be holes, the model suggests a maximum solubility of $x \approx 0{\cdot}16$.

T_0 is a characteristic temperature which enters exponentially into the temperature dependence of many physical properties of Nb_3Sn. A particularly useful one for our purpose is the martensitic (cubic → tetragonal) transformation temperature T_m. According to the model, T_m is [nearly] the temperature at which the negative contributions of the d-band carriers to the free energy difference between the cubic and tetragonal states just balances the contribution from all other sources to the binding energy. This is given by[2],

$$\tfrac{4}{3}N_0U_2{}^2(1-e^{-T_0/T_m}) = A_{11}-A_{12},$$

where $A_{11}-A_{12}$ is the lattice contribution to the elastic constant for the shear strain carrying the lattice from cubic to tetragonal.

Since for Nb_3Sn $T_0/T_m \sim 1{\cdot}6$[3], we have

$$\delta T_m = \pm\frac{x}{4N_0k(1{\cdot}6)} \approx 300x\,°\mathrm{K},$$

so that changes in T_m accompanying small additions of Sb should be readily detected.

3. EXPERIMENTAL

Samples were prepared by cold pressing—325 mesh powders at 30 t.s.i. into ¼ in. thick by ½ in. dia. pellets, and sintering in a nearly static helium atmosphere for 16 hr. A series having $x = 0$, 0·05, 0·10, 0·15 was made at 1250°C, and one sample with $x = 0{\cdot}20$ was prepared at 1100°C. The latter showed some unreacted Nb and Sn (Sb) by anodization and microscopic examination[8] in addition to the usual (~ 2 per cent) NbO and other unidentified phases, while X-ray powder patterns showed only β-W phases. Lattice constants were determined with CuK_α radiation on a $36/\pi$ cm camera by the extrapolation method of Cohen, with a precision of ±0·0002 Å. The low temperature X-ray work was carried out in a liquid helium cryostat fitted with Be windows, using ordinary diffractometer and detector techniques. Powdered samples were sprinkled on to a lightly greased flat copper stage suspended from the He bath by a stainless steel tube. Temperatures were measured with a Au–2·1% Co vs. Cu thermocouple with the cold junction attached to the He bath, allowing the temperature to be read to ±0·1°K with a portable potentiometer. A Pt resistance thermometer was used to calibrate the thermocouple. Superconducting transition temperatures were determined inductively.

4. RESULTS

Both T_c and a_0 are found to decrease linearly with Sb concentration, the data being in good agreement with that of earlier work. In Fig. 1, the circles represent transition midpoints, the bars transition extremities. The sample designated by the triangle ($x = 0{\cdot}2$) showed two β-W phases, with $a_0 = 5{\cdot}277$ for the minor phase, estimated to be 10–20 per cent of the sample volume from X-ray intensities. A second phase was also seen in the T_c measurement, with a broad transition between 7·5 and 10°K accounting for 20 per cent of the total inductance change. Extrapolating the lattice constant data gives $x = 0{\cdot}56$ for the minor phase. A materials balance then gives 18 per cent for the proportion of this phase. The high T_c phase showed a transition much like that of the other doped samples but with a small tail (5 per cent) extending up to 17·4°K. Annealing for 66 hr at 980°C resulted in no change in either T_c or the diffraction pattern for this specimen. A miscibility gap extending from $0{\cdot}3 < x < 0{\cdot}7$ at 1200° has been reported[5], so that this unusual behavior appears to be strongly temperature dependent.

Transformation temperatures are shown at the top of Fig. 1. The squares represent the temperature at which an observable shift in position of the intensity maximum was noted,

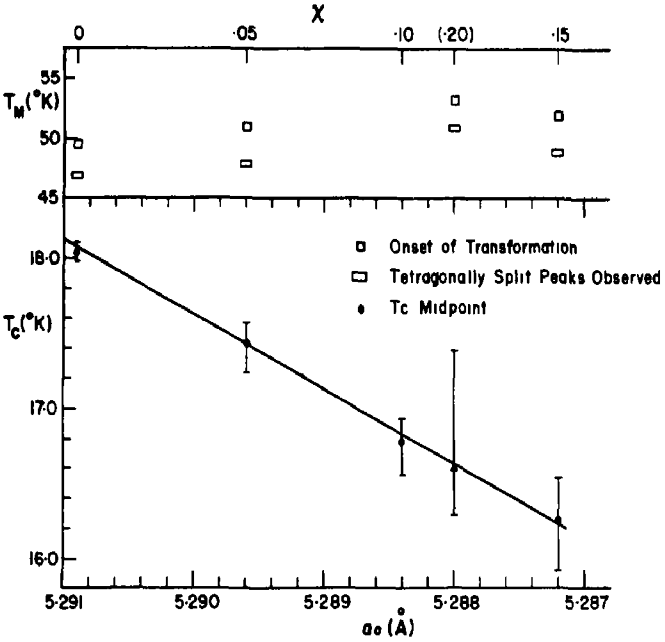

Fig. 1. T_c and T_m for $Nb_3Sn_{1-x}Sb_x$. Compositions of samples of various lattice constants are shown at the top. The sample designated by Δ had a second β-W phase, not shown, richer in Sb (see text).

while the rectangles indicate the temperature at which the transformation is evident in an unambiguous way (appreciable line splitting). Within the framework of the theory discussed above, T_m is found to be invariant.

The course of the transformation is shown in Fig. 2 for the two samples of extremal lattice constant, $x = 0$ and $x = 0{\cdot}15$. The {400} peak proved to be the simplest to study, by virtue of its reasonable intensity, absence of degeneracy in $\Sigma(h^2+k^2+l^2)$, and sufficient resolution of the tetragonal splitting. As seen in the figure, there is a decrease in resolution of the $K_{\alpha_1} - K_{\alpha_2}$ lines above T_m, and a reduction of intensity of the main (K_{α_1}) peak. Presumably this is due to an increase in thermal diffuse scattering and/or fluctuations accompanying the vanishing of the elastic constant C_{11}-C_{12} at T_m. For both samples, the onset of the transformation is marked by a shift of the peak maximum to higher angle. The d spacing in the tetragonal state is given by

$$d = d_{\text{cubic}}\left\{1+\left(\frac{\epsilon}{2}\right)\frac{h^2+k^2-2l^2}{h^2+k^2+l^2}\right\}.$$

where $\epsilon = \frac{2}{3}(a/c-1)$. For the {400} set we have $d_2 = d_c(1+\epsilon/2)$ and $d_1 = d_c(1-\epsilon)$, where the subscripts 1, 2 indicate the relative intensities. For positive ϵ the shift near T_m should be to lower angle. At low temperatures, where $\epsilon > 2\times10^{-3}$, four peaks should be observed (two for each wavelength radiation), with the main peak double the intensity of any other peak and the splitting $\delta\theta(d_2) = \frac{1}{2}\delta\theta(d_1)$. For $x = 0$ we find $\epsilon = +(3{\cdot}5\pm0{\cdot}5)\times 10^{-3}$, although the intensity distribution, which was found to be weakly dependent on sample mounting, is not strictly consistent with a simple tetragonal splitting. Other workers have reported tetragonalities between $2{\cdot}4\times10^{-3}$ and $4{\cdot}1\times10^{-3}$[9]. The shift

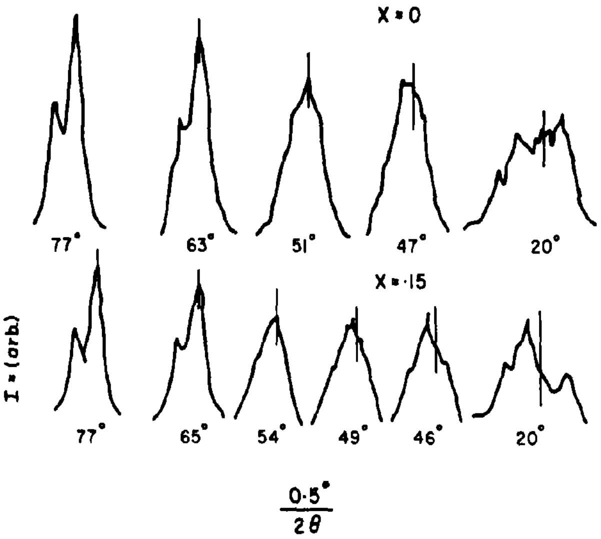

Fig. 2. {400} X-ray intensities as a function of temperature for the two extremal compositions. The vertical lines mark the position of the K_{α_1} peak maximum in the cubic state.

to higher angles near T_m could be the result of a decrease in volume of the unit cell, but analysis of the shift in centroid for several peaks reveals no consistent pattern. The transformation is volumeless, within experimental error.

For the $x = 0{\cdot}15$ sample we find the remarkable result that the splitting is of the same magnitude, but of opposite sign, with $\epsilon = -(3{\cdot}2 \pm 0{\cdot}5) \times 10^{-3}$. In this case the peak intensities are entirely consistent with the splitting.

Figure 3 shows the {400} and {440} diffraction patterns for the single phase samples at 20°K. The {440} peaks arise from planes having $d_2 = d_c(1-\epsilon/4)$ and $d_1 = d_c(1+\epsilon/2)$, the increased dispersion at higher angle leading to a $\delta\theta$ virtually the same as for the {400} reflections. The $x = 0{\cdot}05$ sample appears to have both ϵ^+ and ϵ^- components, while for $x = 0{\cdot}10$, although the intensities are not well behaved, the splitting appears to be similar to the $x = 0{\cdot}15$ sample. Again for the latter, the {440} reflection allows us to assert that for this sample there is essentially no material remaining which is either cubic, or transformed but of opposite sign.

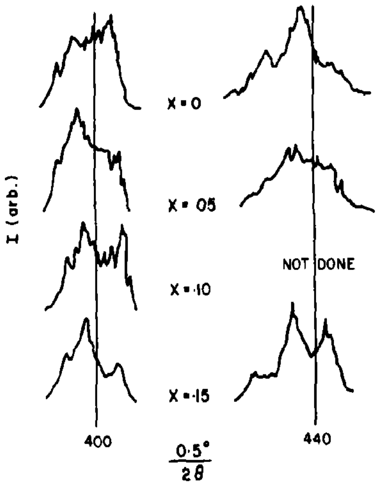

Fig. 3. {400} and {440} reflections at 20°K. Vertical lines mark the position of the K_{α_1} peak maximum in the cubic state.

5. DISCUSSION

It is clear that the relationship between T_0 and x predicted on the basis of the rigid band model is not borne out by the data. The invariance of T_m suggests that in order to approach the data from the point of view of the density of states model, the band parameters should be taken as unaffected by the addition of Sb. The question of why the band filling (T_0) is not variable can be set aside, and the interesting implications of the change of sign of the tetragonality examined in terms of a fixed band.

The sign and magnitude of the spontaneous strain below T_m are given by the usual condition of minimum free energy. Near T_m, it is useful to write the free energy difference between the cubic and tetragonal states as a power series in the strain (cf. Ref.[1]); $\delta F \approx A\epsilon^2+B\epsilon^2+C\epsilon^4+\cdots$, where each coefficient is the sum of both the electronic terms, calculable exactly in terms of the parameters of the model, and lattice terms representing all other contributions. Setting $\delta F=0$ at T_m, and requiring that $\partial\delta F/\partial\epsilon|_T=0$, the spontaneous strain is seen to be $\epsilon(T_m)\approx -B/2C$; that is, ϵ depends solely on the higher order elastic constants. Now, one of the outstanding successes of the square band representation for Nb_3Sn is the correct prediction of the strain near T_m, based on the electronic terms alone, and using parameters determined from cubic state data. We may, therefore, ignore the lattice contributions, and assert that in the absence of a changing electronic contribution, the model does not readily admit a change in the sign of ϵ. The presumably small perturbation found necessary to alter the sense of the transformation implies the smallness of terms of odd order in ϵ in a proper free energy expansion near T_m[10]. This supports the conclusion drawn from specific heat measurements that the transformation is second order, or near second order ($B(T_m)\approx 0$), and that the expansion must contain terms other than those given by the band model if it is to properly account for the details of the behavior near T_m[11].

The strain at low temperatures is equally problematic. A general result of the band theory of the transformation is that the predicted strain at 0°K is a factor of two smaller when $c > a$, regardless of the form assumed for the density of states as a function of energy Instead, we find the magnitude of the strain to be independent of sign.

Finally, we have the interesting result that T_c varies smoothly with x, which can be interpreted as indicating that the density of states is little affected by the change in sign of ϵ^*. This is borne out by magnetic susceptibility measurements, which show no difference in the decrease in susceptibility which accompanies the transformation for pure Nb_3Sn and for $Nb_3Sn_{0.85}Sb_{0.15}$[12]. T_c is known, however, to be a strong function of uniaxial stress applied in the ⟨100⟩ direction [13], this effect being several orders of magnitude larger than for ordinary superconductors, and in semi-quantitative agreement with the band model. If the density of states interpretation of this result is correct, then it is necessary to suppose that the band structure in the tetragonal state depends on the magnitude of the strain, but not the sign, suggesting that the band splitting below T_m is symmetric about the cubic band edge.

6. CONCLUSIONS

Significant modifications of the band model of the lattice transformation in β-W superconductors will have to be made in order to account for the data presented here. The question of the level at which the theory requires amendment is not resolved, but the difficulties encountered are certainly not dependent on the particular form chosen to represent the density of states. A possible modification of the theory clearly suggested by the data lies in the direction of postulating a band splitting independent of the sign of ϵ.

---

[*] At 0°K the model gives for the ratio of the density of states at the Fermi level for ϵ^+ splitting ($a > c$, Fermi level in one sub-band), to that for ϵ^- splitting, $N_0^+/N_0^- \approx (\frac{1}{2})^{1/n+1}$ where $N(E)\alpha E^n$, and $n=-\frac{1}{2}, 0, \frac{1}{2}$ are the exponents for the labbé–Friedel band, square band, and free electron band respectively

However, the failure of Sb doping to alter the band filling represents an unexpected rigidity in the model, and raises some doubts about its fundamental validity. Before credible alteration of the theory can be made, it would appear desirable to investigate other dopants and band structure sensitive properties in an attempt to find evidence for the model of the sort originally sought in this study.

Acknowledgements – The generous assistance of R. Paff in helping with the X-ray measurements is gratefully acknowledged, as are the efforts of R. Miller, who made the T_c measurements. The author is indebted to Drs R. W. Cohen and G. D. Cody for helpful criticism of the manuscript.

REFERENCES

1. LABBÉ J. and FRIEDEL J., *J. Phys. Radium* **27**, 153, 303 (1966).
2. COHEN R. W., CODY G. D. and HALLORAN J. J., *Phys. Rev. Lett.* **19**, 840 (1967).
3. CODY G. D., COHEN R. W. and VIELAND L. J. *Proc. 11th Int. Conf. on Low Temperature Physics*, p. 1009 (1968).
4. REED T. B., GATOS H. C., LaFLEUR W. J. and RODDY J. T., *Metallurgy of Advanced Electronic Materials* (Edited by G. E. Brock), p. 71. Interscience, New York (1963).
5. BACHNER F. J., GOODENOUGH J. B. and GATOS H. C., *J. Phys. Chem. Solids* **28**, 889 (1967).
6. HAGNER R. and SAUER E., *Naturwissenschaften* **49**, 444 (1962).
7. PAULING L., *Trans. ASM* **48A**, 220 (1956).
8. PICKLESIMER W. L., *Oak Ridge National Lab. Rep.* No. 2296 (1957).
9. MAILFERT R., BATTERMAN R. W., and HANAK J. J., *Phys. Lett.* **24A**, 315 (1967); KING H. W., COCKS F. H. and POLLACK J. T. A., *ibid* **26A**, 77 (1967); MEDVEDEV S. A., KISELEVA R. V. and MIKHAILOV V. V., *Fiz. tverd. Tela* **10**, 746 (1968); transl. *Soviet Phys. solid St.* **10**, 584 (1968).
10. LANDAU L. D. and LIFSHITZ E. M., *Statistical Physics*, Chap. 14. Pergamon Press, Oxford (1958).
11. VIELAND L. J. and WICKLUND A. W., *Solid St. Commun.* **7**, 37 (1969).
12. RAYL M. and CODY G. D., private communication
13. McEVOY J. P., *Int. Conf. on the Science of Superconductors* Stanford University Press (1969).

J. Phys. Chem. Solids Pergamon Press 1970. Vol. 31, pp. 1455–1460. Printed in Great Britain.

ELECTROLUMINESCENCE DUE TO INTERNAL FIELD EMISSION IN KI

C. PARACCHINI and G. SCHIANCHI
Istituto di Fisica dell 'Università, Parma, Italy, Gruppo Nazionale di Struttura della Materia of C.N.R.

(*Received* 14 *November* 1969)

Abstract – The luminescence obtained by the radiative recombination of electrons and holes injected from metal colloids in KI single crystals under a.c. excitation has been studied as a function of the applied voltage and of the frequency; voltage and brightness waves have been compared.

The results are discussed on the basis of Fischer's model. The experimental brightness voltage relation $B = \xi V^4$ is justified with a double emission mechanism.

UP TO a few years ago, electroluminescence phenomena have been mainly studied in semiconductors and low gap dielectrics[1]. In spite of the great amount of work done, an ultimate comprehension of the subject is still lacking, and several models have been proposed to explain the experimental results so far obtained. Moreover, the case of insulators luminescence under a.c. excitation turns out to be of particularly difficult understanding. For this last case Fischer[2, 3], studying ZnS, presented a critical review of the up to date situation, proposing two possible mechanisms: (a) *double field emission*, (b) *inverted impact ionisation*.

Both these models are based on internal field emission, and require the existence of conducting lines embedded in the crystal. In the first case carriers of opposite sign are injected from the tips of the conducting lines facing the electrodes. At the field reversal electrons recombine radiatively with the trapped holes injected during the previous half-cycle. Carriers are field emitted according to the Fowler–Nordheim law.

In the second case the electric field pulls electrons out of the traps surrounding the positive end of the conducting lines. Free electrons are then accelerated, creating carrier pairs by impact ionisation. The holes are then trapped, and the excess electrons flow into the conducting line, being field emitted at the negative end. Here they recombine with holes trapped during the previous half-cycle. The number of carrier pairs increases as $\exp(-\text{const}/\sqrt{V})$, and the brightness-voltage relation applying to this case is that of Alfrey–Taylor:

$$B = B_0 \exp(-a/\sqrt{V}).$$

A great uncertainty generally exists about which of the two models has to be preferred, though the first one, due to the lower field required, appears to be in some cases more probable. In fact some experimental results, as the brightness-voltage curve or the light output versus time, which ought to be closely connected with the excitation mechanism, can often be interpreted with both models.

More recently, the direct conversion of electrical energy into light by the recombination of opposite carriers has been studied in wide gap insulators too, like silver and alkali halides, with the main purpose of understanding the involved mechanisms. Meczynska and Oczkowski[4] verified Fischer's and Maeda's models in AgBr and AgCl; Unger and Teegarden[5] were the first to observe a persistent electroluminescent effect in an alkali halide salt, injecting electrons from silver or indium contacts. In a preliminary work[6], we observed an electroluminescence effect in KI single crystals containing potassium colloids, and showed that light emission was due to the electron-hole recombination via V_k centers.

The purpose of this work is to improve the previous experimental results – particularly the unusual brightness-voltage relation – and to justify them in terms of carrier internal field emission.

EXPERIMENTAL

KI single crystals, grown in N_2 atmosphere by Kyropoulos method in our own laboratory, and then reduced to cubes of approximately 1 cm side, were electrolytically colored by the standard method (coloring temperature 600°C, applied field 400 V/cm). The samples were then cleaved in slices 0·5–4 mm thick, and heated at ~100°C for some hours in order to obtain an intense colloidal band. This band was found to present its maximum at ~850 mμ, in good agreement with available data[7]. We noticed that the presence of OH considerably favours the coagulation of F centers.

The specimens so prepared have been placed, to avoid electrical discharges, in a carefully evacuated container (~10^{-6} mm Hg), between two copper electrodes, one of which was in direct thermal contact with the liquid nitrogen reservoir, in order to make all the measurements at ~78°K. To avoid the effect of thermal contractions during the experiment, the crystal slices were sandwiched between the electrodes with the aid of soft stainless steel springs.

The applied voltage was generally a sinusoidal one with the frequency ranging from 50 to 200 Hz. The emitted light was observed perpendicularly to the electric field with a trialkali photomultiplier (EMI 9558 QA), and the photocurrent measured with a Keitley 414 micromicroammeter, or displayed on a Tektronix 535 A oscilloscope. The electric field was provided by a Wavetek 116 function generator, and amplified by a power amplifier followed by a step up transformer. The brightness-voltage curves were 'obtained plotting' on a $x-y$ recorder the integrated photocurrent vs. the r.m.s. applied voltage.

Preliminary measurements have been performed on white (not colored) specimens, no light emission being obtained even by direct contact between the sample and the copper electrodes, up to fields of ~60 kV/cm at 200 Hz. Such a result supports the idea that no appreciable carrier injection is present at the contacts between the crystal and the electrodes. Moreover, the colloid rich specimens show light emission with an electric field greater than 10 kV/cm even with mylar or teflon blocking contacts, confirming that in this case electroluminescence arises from internal carrier generation.

EXPERIMENTAL RESULTS

The results we present here deal mainly with the dependence of light emission on the electrical excitation. In fact we assume that the nature of the optical recombination is already proved[6].

In Fig. 1 the light output is plotted as a function of the external voltage amplitude, the frequency of the applied field being 200 Hz. The experimenatl points are very well fitted by the formula:

$$B = \xi V^4,$$

where B is the brightness and ξ a proportionality factor (curve A). From Fig. 2, showing the brightness-voltage curves for two other frequency values, it is possible to see that the slope of the curves does not depend on the excitation frequency, at least in the examined range. A dependence of brightness on the external voltage of the type $B = \xi V^\alpha$, with α ranging between 2–8, was observed by other authors on several materials[3, 8], but over voltage and brightness short ranges only. In these cases experimenatl results are better fitted by Alfrey–Taylor formula,

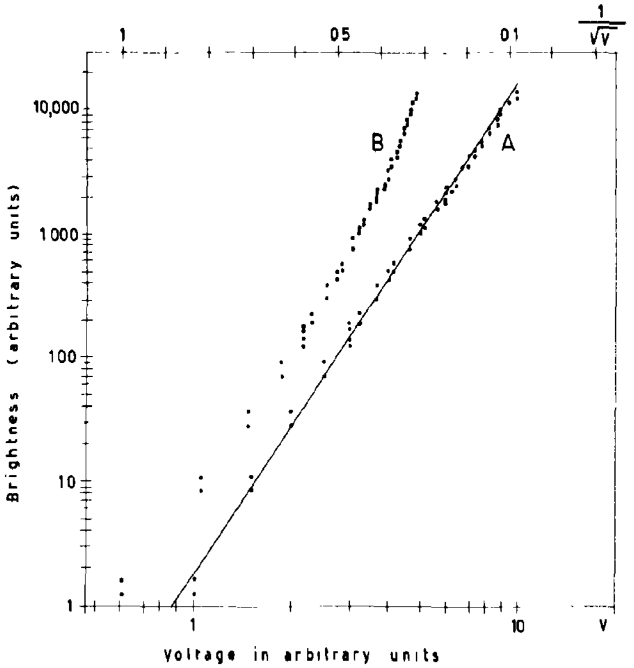

Fig. 1. Brightness vs. voltage. Sinusoidally varying field: 200 Hz; max. applied voltage: $8 \cdot 10^4$ V/cm peak to peak. Curve *A*: the experimental points are plotted on a log-log scale. Curve *B*: the same points of curve *A* plotted in a semilog-scale as a function of $1/\sqrt{V}$.

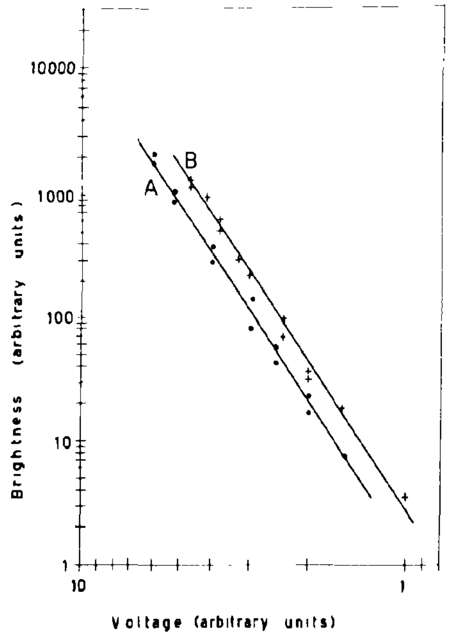

Fig. 2. Brightness vs. voltage. Sinusoidally varying field; curve *A*: 50 Hz. Curve *B*: 500 Hz.

which has been extensively verified over large ranges in the most cases of electroluminescent cells. The rather unusual result in our case is that the power dependence of the light output from the applied voltage approximates the experimental behaviour much better than an exponential law of the Alfrey-Taylor type (Fig. 1, curve *B*).

The dependence of the brightness on the applied field frequency, as shown in Fig. 3, has been found to be a linear one in the range from 50 to 2000 Hz for two different voltage amplitudes (10 and 30 kV/cm). No light emission was obtained under a d.c. field.

Figure 4 is a direct photograph of brightness and voltage waves at 200 Hz. Light waves present no evidence for 'primary' and 'secondary' peaks, and the light peaks are in phase with the voltage ones.

DISCUSSION

Our experimental results are consistent with the double emission model suggested by Fischer[2, 3] as alternative hypothesis to the inverted impact ionisation. When the field is applied to the sample, electrons and holes are alternatively field emitted from the opposite sides of the colloids. Free holes cause a lattice deformation, remaining self trapped (V_K centers); electrons, in the following half cycle, are emitted into the positive space charge sheath of previously trapped holes. Electrons and self trapped holes recombine radiatively if the temperature is sufficiently low (less than 80°K in KI). The field emission current density is governed by the Fowler-Nordheim law:

$$j = AE^2 e^{-a/E}$$

where E is the local field, A and a are proportionality factors, this law applying for both carriers.

As potassium has a low electron work function ($\phi \sim 2$eV), electrons are more probably emitted with respect to holes at the beginning of every half cycle, and their

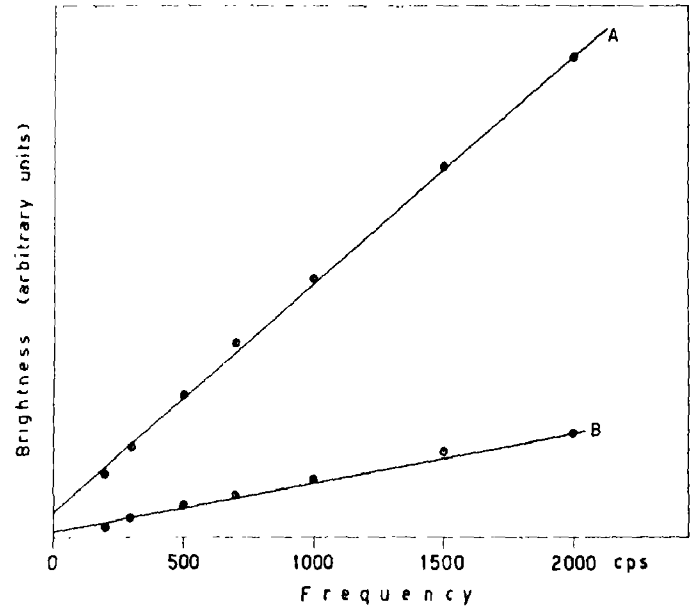

Fig. 3 Brightness vs frequency. Sinusoidally varying field, curve *A*: 30 kV/cm. Curve *B*: 10 kV/cm.

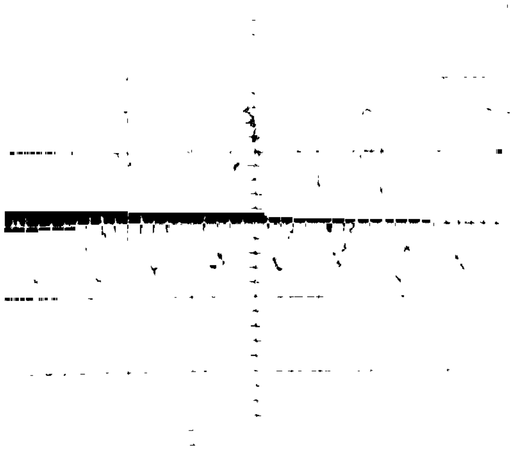

Fig. 4. Brightness and voltage waves at 200 Hz.

emission lowers the Fermi level, so favouring the subsequent injection of holes from colloids. In this, case, assuming the neutrality of potassium colloids, the number of injected holes during half a cycle will be equal to the number of injected electrons, that is:

$$n_+ = n_- = \int_{\text{halfcycle}} AE^2\, e^{-a/E}\, dt,$$

where the local field E must be a periodical function of the same frequency of the applied voltage. If the external voltage varies sinusoidally, we can take $E(t) = E_0 \cos\omega t$, E_0 being the amplitude of the local field, and the exponential factor in the preceding formula becomes $\exp[-a/(E_0 \cos t)]$.

Assuming now E_0 to be one or two orders of magnitude higher than a, $\exp(-a/E_0)$ is practically a constant, and n_+ and n_- reduce to be both proportional to E_0^2. The brightness B is proportional both to the number n_- of electrons injected during half a cycle and to the number n_+^* of holes self trapped in the same time. Supposing that all injected holes are self-trapped, $n_+^* = n_+$ and

$$B \propto n_+ n_- \propto E_0^4$$

in agreement with our experimental results.

This model is quantitatively consistent with available experimental values: the proportionality factor a has been evaluated to be $a = 6{\cdot}8.10^7\ \phi^{3/2}.f(y)$, where $f(y)$ is a dimensionless elliptic function of the variable $y = 3{\cdot}79.10^{-4}\ (E^{1/2}/(\phi-\epsilon))$, where the kinetic energy ϵ of the field emitted carriers has been considered negligible with respect to ϕ[9]. In our case a can be assumed to be of the order of 10^6 V/cm. Supposing E_0 ranging between 10^7 and 10^8 V/cm, the factor $\exp(-a/E_0)$ will be between 0·9–0·99. Such great values for E_0 are not surprising, for it is well known that the local field can far exceed the breakdown limit[10]. This argument is not restricted to the case of sinusoidally varying applied voltage; but it is valid for any periodic function with E_0 as recurrent maximum value.

The linear rise of brightness with increasing frequency shown in Fig. 2 has been observed in the same range by other authors[8]. It is usually simply explained assuming that the integrated light output over a single cycle does not depend on the period over a rather wide frequency range. On this basis, the number of carriers emitted during a single semicycle is governed by the applied field amplitude only[11].

The dependence of brightness on time over a single excitation cycle is in agreement with Fischer's model: in fact the light emission is contemporary to the field emission of electrons from the metal colloids.

The phase shift between light and voltage waves can give information about the intensity of the field due to self trapped holes. In fact they create a space charge getting its maximum value during the last period of every half-cycle, and remaining unreduced until electrons begin to flow toward it. The field created by this space charge is a periodic one, and its maxima anticipate by nearly $\pi/2$ those of the external field. When the latter is zero, space charge has its maxima, and, if its field would be strong enough, it could succeed in pulling electrons out of colloids, thereby giving rise to brightness waves anticipated with respect to external field. The fact that we did not observe any phase shift in the examined frequency range, suggests that in this case space charge can be neglected, and does not influence the phenomenon.

CONCLUSIONS

Metallic colloids embedded in an alkali halide single crystal under the effect of applied field inject electrons and holes according to the Fowler–Nordheim law. These carriers are emitted only during a short time following the application of the field. Later the polarization of the crystal or/and the space charges created by the injected carriers inhibit any further field emission from the colloids.

Applying an alternating field, electrons and holes are successively field emitted from the opposite sides of the colloids, and the former recombine with V_K centers created by the latter. The observed electroluminescence gives information about the mechanism of carrier emission and recombination, in agreement with the double emission model.

Acknowledgements—The authors are grateful to Professor R. Fieschi and Mr. P. A. Benedetti for helpful discussions.

REFERENCES

1. THORNTON P. R., *The Physics of Electroluminescence Devices*, Spon, London (1967).
2. FISCHER A. G., *J. electrochem. Soc.* **110**, 793 (1963).
3. FISCHER A. G., SHRADER R. E. and LARACH S., *Review Article in Photoelectronic Material and Devices* (Edited by S. Larach). Van Nostrand, New York (1965).
4. MECZYNSKA H. and OCZKOWSKI H. L., *Acta phys. pol.* **34**, 147 (1968).
5. UNGER S. and TEEGARDEN K., *Phys. Rev. Lett.* **19**, 1229 (1967).
6. PARACCHINI C. and SCHIANCHI G., *Phys. Status Solidi* **36**, K1 (1969).
7. SCOTT A. B., SMITH W. A. and THOMPSON M. A., *J. Phys. Chem.* **57**, 757 (1953)
   SAROJINI K. A., *Br. J. appl. Phys.* **18**, 679 (1967).
8. P. CHUKOVA YU., *Proc. P. N. Lebedev phys. Inst.* **37**, 127 (1968).
9. DYKE W. P. and DOLAN W. W., *Adv. Electronics Electron Phys* **8**, 91 (1956).
10. von HIPPEL A., GROSS E. P., JELATIS J. G. and GELLER M., *Phys. Rev.* **91**, 568 (1953).
11. PIPER W. W. and WILLIAMS F. E., *Solid State Physics*, Vol. 6, p. 145, Academic Press, New York

J. Phys. Chem. Solids Pergamon Press 1970. Vol. 31, pp. 1461–1466. Printed in Great Britain.

NMR AND ELECTRON MICROSCOPY STUDIES ON IRRADIATED LITHIUM HYDRIDE*

P. C. SOUERS, T. IMAI, T. S. BLAKE, R. M. PENPRAZE and H. R. LEIDER
Lawrence Radiation Laboratory, University of California, Livermore, Calif. 94550, U.S.A.

(*Received* 28 *July* 1969; *in revised form* 12 *November* 1969)

Abstract—Gamma-irradiated lithium hydride has been studied with pulsed NMR and electron microscopy. Cubic voids were seen in the micrographs, and were shown to be hydrogen gas bubbles. Formation of these bubbles caused LiH to swell as much as 25 volume per cent on irradiation. The average bubble size seems to be mainly a function of the irradiation temperature; the average size ranges from 80–1500 Å for irradiation temperatures between 120 and 265°C. Hydrogen gas in the bubbles gives rise to a motionally-narrowed NMR signal. The longitudinal relaxation time T_1 appears to be a function only of the gas density, as is expected for gases. The transverse relaxation time T_{2m} is strongly affected by wall interactions and, therefore, decreases markedly with decreasing bubble size.

1. INTRODUCTION

LITHIUM hydride is unusual in that it shows very large volume expansion when irradiated. Pretzel[1, 2] found volume increases up to 35 per cent for lithium hydride irradiated with low-energy electrons. We have previously irradiated LiH with ^{60}Co γ-rays and have observed expansions as large as 25 per cent volume per cent[3]. Maximum swelling occurs for irradiations at temperatures of 150–200°C; no swelling occurs at temperatures above 300°C. The motionally-narrowed lithium and hydrogen signals that are produced by radiation[3] were studied using pulsed nuclear magnetic resonance (NMR). The amplitude of the NMR signals increases with increasing swelling. The resonance from the[7] Li shows a Knight shift characteristic of the metallic form[2, 4, 5] and thus indicates precipitation of the lithium due to the irradiation. The magnitude of the hydrogen signal shows a temperature variation which is explained by assuming that the hydrogen exists as diatomic molecules and undergoes an ortho-para transition. The density of the hydrogen gas was calculated in two ways: (1) by comparison of the longitudinal relaxation time T_1 to reported measurements of T_1 vs. gas density[6], and (2) by assuming that all the observed swelling is due to the formation of gas bubbles which contain the amount of H_2 measured by NMR. Densities arrived at in these two ways are in close agreement for most samples, supporting the assumption that the increase in volume is due to formation of gas bubbles. Electron microscopic examination of irradiated LiH has shown the presence of 'cubic' porosity[7]. The walls of the cubic voids are nearly always parallel to the (100) planes of the lattice. A pronounced anisotropy of the measured transverse relaxation time T_{2m} as a function of LiH crystal orientation in the magnetic field is evidence that the cubic bubbles contain the H_2 gas[8].

NMR measurements of motionally narrowed lithium and hydrogen show a maximum atomic ratio, ^{7}Li/H, of about $\frac{3}{4}$ rather than unity, as is expected from stoichiometry. However, since decomposition of 1 cm^3 of LiH can yield 1·27 cm^3 of Li metal, only 0·79 (1/1·27) of the precipitated metal can fit within the original volume. This fraction is comparable to that experimentally observed, and strongly indicates that Li precipitates only in the amount that can occupy available volume due to radiation decomposition of the lattice. The H_2 gas bubbles apparently create extra volume in their formation.

---

*This work was performed under the auspices of the U.S. Atomic Energy Commission.

X-ray studies have shown that the lattice parameter of LiH increases by less than 0·2 per cent on irradiation[9, 10] so that the process which produces the large volume changes is one which does not cause equivalent lattice distortion. This is additional confirmation that bubble formation causes the swelling.

The radiation-induced decomposition of LiH has also been studied by differential thermal analysis measurements of stored energy[11]. The magnitude of the stored energy is consistent with that expected from the back-reaction of the amounts of Li and H_2 seen by NMR. Similar effects have been seen in neutron-irradiated LiF, which expands more than 20 per cent when irradiated at 80°C[12]. Stored energy measurements on irradiated LiF are also consistent with back-reaction of decomposition products[13]. Broad-line NMR measurements have shown up to 2 per cent of the LiF fluorine is converted to a motionally-narrowed form, presumably gaseous, in similarly irradiated material[14]. 'Square' bubbles have also been observed with the optical microscope in irradiated LiF which has been thermally annealed[15-17].

2. EXPERIMENTAL

The LiH was synthesized from the elements [2, 3]. Single LiH crystals were irradiated from 0·5 to 47 gigarads (Grad.) with ^{60}Co γ-rays over the temperature range 40-450°C. The swellings, NMR spin counts of H_2 and ^{7}Li, and approximate relaxation times have been reported[3] for all but one series at 7 Grad., which also gave results consistent with the previously reported data. All data are incorporated in the results of this paper.

Electron microscopic examination of the irradiated LiH was done by direct carbon replication[7]. The LiH was cleaved in a dry argon atmosphere, and carbon was deposited normal to the cleavage faces. A Pt/20 per cent Pd alloy was shadow-cast on the carbon at a shallow angle to provide contrast.

Most of the replicas were examined at about 30,000×. A few pictures were also made with other microscopes at 80,000×. About 250-1000 bubbles for each sample were carefully measured for size under a magnifying glass. Care was taken to photograph representative sections of each sample. Many of the high dose samples showed a fuzziness on the replicas that often obscured smaller bubbles. This problem also appeared in low-dose, low temperature samples where bubbles ~100 Å in size were often not seen. This undesirable effect may be due to surface contamination of the LiH during irradiation and storage despite all efforts to keep a clean argon atmosphere. We note in this paper only those bubble sizes where background fuzziness did not appear to affect the definition of the smaller bubbles.

The NMR was done with the same 15 MHz, phase-coherent pulsed spectrometer used previously[3]. Ion decays were blocked out of the pre-amplifier; therefore the ^{7}Li and H_2 signals mentioned in this paper refer to the motionally-narrowed species formed on irradiation.

T_1 was measured by the usual 180-90° sequence; T_{2m} was obtained from the 90-180°-spin echo sequence[18]. All the relaxation times were measured at room temperature; that is, between 20-25°C. This temperature spread is probably partly responsible for the scatter in the data. The T_{2m}'s were taken both on samples consisting of many crystal chips and also on oriented single crystals. Relaxation times for H_2 were accurate to ±5 per cent.

3. RELAXATION TIME AND BUBBLE SIZE

Hydrogen gas at high pressures has been studied by pulsed NMR up to 150 atm[6, 19], and T_1 was found to be a function of the density only; T_1 and T_2 were found to be almost equal in these experiments[20]. Equal relaxation times are expected for gases in which the molecular collision frequency is much greater than the NMR frequency and where relaxation occurs only by a dipolar mechanism[21]. Methane, which relaxes by internal mechanisms, as does H_2, has been studied as a function of container size[22]. T_1 was found to be constant; however, T_{2m} decreased as the container size decreased because of interaction between the molecules and the walls. These results suggest that T_{2m} for the motionally-narrowed H_2 in LiH is related to the bubble size. The lowest pressure seen in irradiated LiH is about 800 atm[3]. This is much higher than those in all the reported experiments, so that a considerable extrapolation is needed to apply the same considerations to this work.

In these experiments T_1 remains unchanged between room temperature and 77°K for all samples where $T_1 \leq 200$ msec. Therefore, we have assumed that in these cases (pressure ≤ 4000 atm at 25°C) T_1 is a function of gas density alone. It is also assumed that T_2, the transverse relaxation time for macroscopic gas, equals T_1 in these cases. Thus, the measured transverse relaxation time T_{2m} may be expressed by

$$\frac{1}{T_{2m}} = \frac{1}{T_1} + \frac{1}{T_{2w}}. \qquad (1)$$

Here, T_{2w} is the time characteristic of a.c. relaxation processes between gas molecules and bubble walls. The quantity T_{2w} may be used as a measure of bubble size once it has been calibrated.

T_{2m} for H_2 is measured by the 90–180°-spin echo sequence[18]. The diffusion constant of the H_2 gas is very high, $D \approx 10^{-3}$ cm²/sec, as predicted from gas kinetic theory. Despite this, the well-known NMR diffusion effects [18] do not appear because the nuclei cannot diffuse very far before hitting the bubble walls. The nuclei are thereby forced to remain in the same magnetic fields throughout the spin echo sequence. This restricted diffusion yields an apparent diffusion constant D' such that [22]

$$D' = \frac{(a_H)^4}{10D(T_{2m})^2}. \qquad (2)$$

In a bubble with edge length $a_H \approx 1000$ Å, $D' \approx 10^{-15}$ cm²/sec. This is far to small a value to cause any observable effects. Thus, the 90–180°-spin echo T_{2m} is equivalent to the T_{2m} of the Carr–Purcell sequence, the usual procedure for eliminating diffusion effects[18].

Since T_{2m} is a strong function of orientation in crystals[8], the single crystal measurements must be related to those on randomly oriented crystal chips such as are usually measured in our experiments. T_{2w}, derived from equation (1), is the quantity dependent on angle. In a single crystal tilted at 45°, let the angle α be the angle of rotation about an axis running vertically, along a (110) direction of the crystal. We have previously found that[8]

$$\frac{T_{2w}(\alpha)}{T_{2w}(0)} = \frac{2}{|(1 - 3\cos^2\alpha)|}. \qquad (3)$$

This expression is derived by assuming interaction of nuclear magnetic dipoles in the H_2 gas with cubic walls oriented parallel with the (100) directions of the crystal. A mean angle of interaction between the d.c. magnetic field direction and bubble walls was assumed. The ratio $T_{2w}(\alpha)/T_{2w}(0)$ is normalized to 1·00 at $\alpha = 0°$.

$T_{2w}(\alpha)$ may be randomized by using an approximate average using only three orientations of the cube; namely (100), (110), and (111), which occur at $\alpha = 0°$ and 180°, 90° and 54°44′ and 125°16′ respectively. For these orientations there are, respectively, 6 cube sides, $T_{2w}(\alpha)/T_{2w}(0)$ ratio = 1·00; 12 cube edges, ratio = 0·50; and 8 cube corners, ratio = 0·00. We now average over these three orientations:

$$\frac{1}{T_{2w}} = \frac{1}{T_{2w}(0)}\left[\sum_{k=1}^{3} F_k\left(\frac{1 - 3\cos^2\alpha_k}{2}\right)^2\right]^{1/2} \qquad (4)$$

Here F_k is the fraction of each orientation. A 'random' value, $T_{2w} = 1{\cdot}7\,T_{2w}(0)$, is obtained in this way.

4. RESULTS

The size of the bubbles in irradiated LiH as a function of irradiation temperature is shown in Fig. 1. The H_2 bubble sizes are the average edge lengths of the cubic bubbles seen by the electron microscope. It is difficult to estimate an error in the bubble size, since the width of the size distribution at half height is about ±50 per cent of the average value itself. However, errors from not including the smaller unseen bubbles in the average were estimated by also measuring the fractional area, $\Delta A/A_0$, occupied by the bubbles in the photographs. This was converted to the dilatation $\Delta V/V_0$, using:

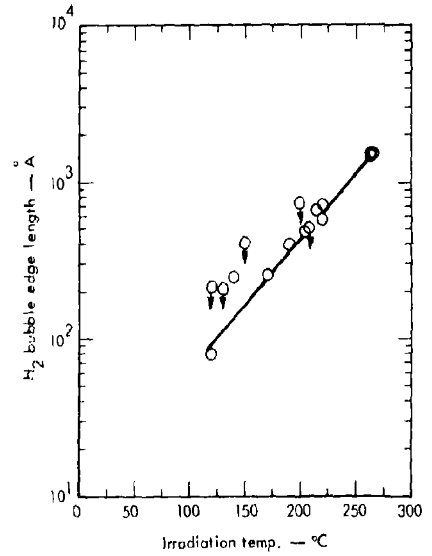

Fig. 1. Average edge length of H_2 bubbles as a function of LiH irradiation temperature

$$\frac{\Delta V}{V_0} = \left[1 + \frac{\Delta A}{A_0}\right]^{3/2} - 1. \tag{5}$$

This $\Delta V/V_0$ was compared with the swelling volume measured by flotation. Seven samples showed computed swellings 50–150 per cent of the measured values. Those samples where the micrograph $\Delta V/V_0$ was less than 20 per cent of the floatation value probably had the smaller bubbles obscured. These points are shown as an upper limit in size in Fig. 1.

The H_2 relaxation times, T_1 and T_{2w}, are plotted against the H_2 bubble edge size in Fig. 2. The error in determining T_{2w} is shown by the bars. The error becomes larger with increasing bubble size because as T_1 and T_{2m} approach one another, the difference of the reciprocals becomes less certain. For the 1500 Å, T_1 and T_{2m} (now = T_2) are identical within the resolution of the spectrometer, and T_{2w} cannot be determined. The open circles are randomly oriented LiH samples; the closed circles are for single crystals, which have been 'randomized' as described above. T_1 of course, shows no orientation dependence.

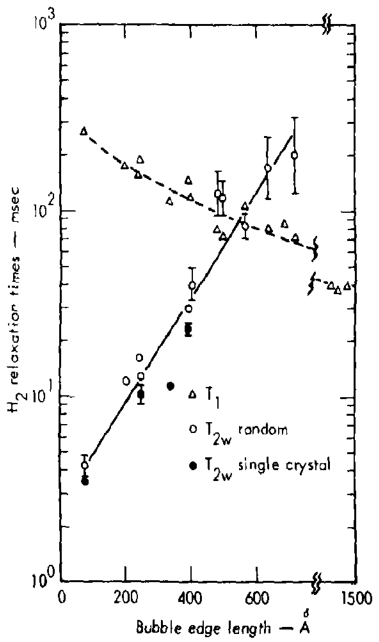

Fig. 2. H_2 relaxation times, T_1 and T_{2w}, as a function of H_2 bubble edge length

5. DISCUSSION

The H_2 bubble edge sizes (Fig. 1) are mostly a function of irradiation temperature, since maximum values seem to have been reached even at low doses. If the bubble size curve is extrapolated to lower temperatures, we get about 20 Å at room temperatures. This is perhaps a lower limit on what might be called a bubble, and it is at this temperature that large swellings first occur on irradiation[1, 2]. At lower temperatures, there is presumably not enough thermal energy available for diffusion processes to form bubbles, and large swelling does not occur[1, 2].

The simplest relationship between T_{2w} and the H_2 bubble size one might expect is that T_{2w} is inversely proportional to the molecular collision frequency with the walls, i.e. the product of the gas density and the square of the mean distance across the bubble. The data do not agree with this simple kinetic description, however, and the $T_{2w}-a_H$ curve is presented as an empirical relationship.

It is seen in Fig. 2 that T_1 decreases smoothly with increasing bubble size. This suggests that the gas pressure in the bubbles may be in equilibrium with the surface energy of the walls, since T_1 is proportional to the gas density. The expression for equilibrium between pressure and surface energy of a cubic in a solid is[23]

$$P=\frac{4\gamma}{a_H} \tag{6}$$

where P is the pressure, a_H is the bubble edge size, and γ is the surface tension. Applying it to samples where $a_H \gtrsim 200$ Å, we calculate values of γ in the range of 1990–4080 ergs/cm^2. These very large numbers may be compared with a calculated γ for (100) surfaces of LiF of 473·5 ergs/cm^2[24, 25]. Apparently, equilibrium with surface tension is not achieved in the H_2 bubbles in these samples. Possibly the large pressure in the bubbles is supported, at least in part by the strength of the lattice. Hardness and yield stress of alkali halides are substantially increased by irradiation[26]. Similar effects in LiH might also be expected[2], and would enhance the capacity to maintain high stresses. In four samples where a_H was estimated to be ≈ 20 Å (from T_{2w}), $\gamma \approx 250$ ergs/cm^2. This is not an unreasonable value, and perhaps in these cases, equilibrium with surface energy does occur. These materials were all irradiated at low dose and showed only small expansions, the order of 1 volume per cent.

It is perhaps worth noting that for these samples which may be in equilibrium, thermal annealing at 400°C removed all the expansion caused by irradiation. In those samples where high values for γ were deduced, annealing merely caused back-reaction of Li and H_2, but did not remove the swelling; cubic bubbles were still found in annealed material of this sort.

Unfortunately, the Li aggregates have not yet been identified with the electron microscopy. However, recent X-ray studies[27] have shown the presence of large, oriented crystallites of Li in irradiated LiH. The metal is in the normal b.c.c. form, and particle sizes are $\gtrsim 1000$ Å in the several samples examined thus far. The lower size limit is inferred from the sharpness of the diffraction spots from the Li particles.

Acknowledgements—We wish to thank H W Newkirk, G S. Smith, C F. Cline and J Mitchell for helpful discussions. We wish also to thank D. Cassidy of the Brookhaven National Laboratory for his help in the irradiations

REFERENCES

1. PRETZEL F. E., LEWIS W. B., SZKLARZ E. G. and VIER D. T., *J. appl. Phys Suppl.* **33**, 510 (1962)
2. PRETZEL F. E., VIER D. T., SZKLARZ E. G. and LEWIS W. B., *Los Alamos Lab. Rep.* No. LA-2463 (1961).
3. SOUERS P. C., JOLLY T. A. and CLINE C. F., *J. Phys. Chem. Solids* **23**, 1717 (1967); SOUERS P. C., BLAKE T. S., PENPRAZE R. M., and CLINE C. F., *J Phys. Chem Solids* **30**, 2649 (1969)
4. GUTOWSKY H S. and McGARVEY B. R., *J. chem. Phys* **20**, 1472 (1952), DOYLE W. T., INGHAM E. T. E. and SMITH M. J. A., *Phys Rev. Lett.* **3**, 338 (1959).
5. KNIGHT W. D., *Solid State Physics* (Edited by F. Seitz and D. Turnbull), Vol 2, p. 93. Academic Press, New York (1956).
6. LIPSICAS M. and HARTLAND A., *Phys. Rev* **131**, 1187 (1963)
7. IMAI T., *Phil. Mag.* **21**, 281 (1970).
8. SOUERS P. C., BLAKE T. S. and PENPRAZE R. M., *Phil. Mag.* **21**, 287 (1970).
9. PRETZEL F E. and PETTY R. L., *Phys Rev.* **123**, 464 (1961).

arsenic is far from being so. Indeed arsenic tends towards a layer-like crystal structure. Any particular atom is sited on one of the (111) planes and has three nearest neighbours on the adjacent parallel plane; three next nearest neighbours lie on another (111) plane on the other side of the given atom but much further away. The nearest neighbour (A_1) and next nearest neighbour (A_2) distances are 2·51 Å and 3·15 Å respectively. Thus planes normal to the trigonal [111] direction occur in pairs in which the atoms are comparatively close together, while these double layers are more widely spaced. Three different arrangements of the atoms on the planar networks are extant. A projection on to the *xy plane* (Fig. 2(a)) shows the relationship between these networks, labelled A, B, C, which follow sequentially along the z-axis and are separated by the short and long interplanar spacings in turn. The crystal structure is described by the sequence, shown in Fig. 2(b), 123123123 of three types of double layer network.

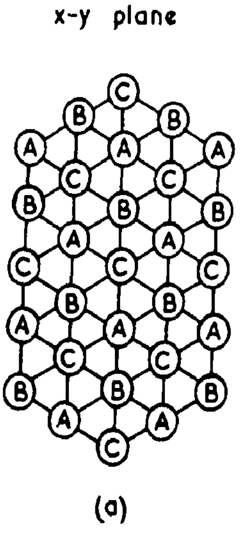

Fig. 2(a). The arrangement of the three types of atomic networks A, B and C for arsenic shown projected onto the xy plane.

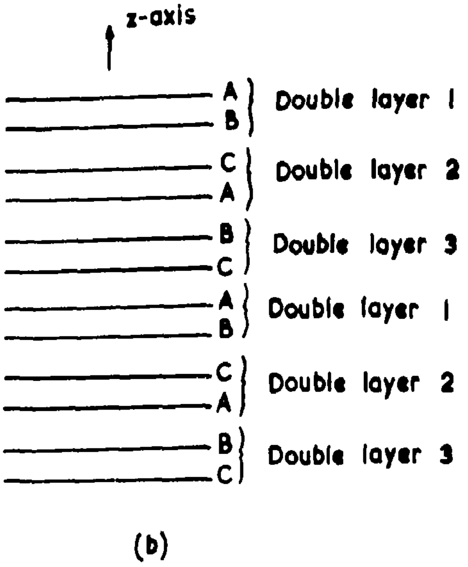

Fig. 2(b). The sequential nature of the planes normal to the z-axis in arsenic. Single planes are separated alternatively by u_0(= 2·2531 Å) and w_0(= 1·2529 Å) and are arranged in sequence *ABCABC*. The double layer planes follow the order 123123123.

Binding between successive double layers is weak – as evidenced by the ease of cleavage to expose (111) planes – while on the other hand within the double layers atoms are bound tightly. The crystal chemistry of the group *VB* semimetals has been discussed in some detail in relation to the band structure[1]. Plausibly the deeper lying, outer shell s^2 electrons participate less in the interatomic binding than do the three p electrons; a valency of three commonly occurs for these elements. For arsenic in particular, bonding within the double layer planes would arise essentially from overlap of the p^3 orbitals, resulting in three bonds almost at right angles. The interbond angle in the layer planes is actually 97°12′, some sp hybridisation probably occurs. On this basis the gross features of the band structure become understandable[1]: two bands, essentially s-bonding and s-antibonding, are completely occupied, while three nearly full, predominantly p-bonding bands overlap slightly with nearly empty, p-antibonding bands to give the characteristic semimetallic behaviour. Antimony and bismuth do not exhibit such pronounced layer structure and cannot have bonds localized within the double layers to the same extent as in arsenic.

The present concern is to report and interpret the elastic constants of arsenic. Comparison between the data and that for bismuth [3] and antimony[4] point to a marked difference between the interatomic binding in arsenic on the one hand and in bismuth and antimony on the other. Mechanical and thermal properties characteristic of layer-like structures would be anticipated for arsenic and the elastic constants attest to this. In particular the linear compressibility is much greater across the cleavage planes than along them, where in fact it is negative. Direct evidence is put forward that the atomic planes are loosely connected along the trigonal direction; this is suggestive of the model for arsenic, much quoted in textbooks, that the double layer planes are held together largely by van der Waals forces. This model is tested here. No previous quantitative assessments are available. Such a model cannot be used for rigorous computations: the high z-axis electrical conductivity[5] and the known Fermi surface point to some degree of orbital overlap between the double layer planes. However it is particularly suited to calculation because to a first approximation interlayer cohesion only need be considered. The exact nature of the interatomic binding within each double layer is not of paramount importance, provided that it is tight and the double layers can be taken as being rigid. The lattice sums of the potential energy are computed assuming a Lennard-Jones 6-n potential along the trigonal direction. Hence the energy of cohesion between the double layer planes is calculated. To assess the validity of the model, calculated linear thermal expansion and compressibility are compared with experimental data.

2. EXPERIMENTAL DETAILS AND RESULTS

The elastic constants were obtained from ultrasound velocity measurements on single crystals grown by the vapour phase method [6] from 99·9995 per cent purity arsenic. Crystal perfection was good; back reflection Laue X-ray photographs showed the pinpoint spots which evidence unstrained material. Dislocation etch pit density was of the order of 10^4cm^{-2} on the (111) cleaved surfaces. Further indications of the state of perfection of these crystals can be gleaned from carrier mobilities and densities obtained from the low field magnetoresistivity tensor[5]. For the A7 structure, the tensor component signs can depend upon the definition of a right-handed $(+x, +y, +z)$ axial set in the particular crystal under investigation[3, 7]. In the present instance, this is so for unambiguous determination of the sign of C_{14}. The co-ordinate system used here is illustrated in Fig. 1. The trigonal (z) axis, formed by the intersection of three mirror planes mutually orientated at ±120°, lies along the long body diagonal of the primitive rhombohedral unit cell defined from the lattice translation vectors $\mathbf{a}_1$, $\mathbf{a}_2$, $\mathbf{a}_3$. The bisectrix (y) axis, for which there are three options, is defined by projecting an $\mathbf{a}_i$ on to the trigonal plane; the positive y direction is taken outwards from the origin 0 of the $\mathbf{a}_i$. A positive binary (x) axis completes the right-handed set. The axis can be identified from Laue back-reflection photographs by reference to the relationship between the A7 crystal structure and a distorted cubic structure: the [100] directions show pseudo-fourfold symmetry and the body diagonal directions (except [111]) show pseudo-threefold symmetry. The quadrant in the mirror plane formed by the $+y$ and $+z$ axes contains a pseudo-threefold axis and that formed by the $-y$ and $+z$ axes a pseudo-fourfold axis. One practical approach to assignment of such a right-handed system in a particular crystal is to inspect etch pits on the (111) cleaved surfaces. We have found the unique orientation of these etch pits in arsenic crystals. This has proved useful for crystal orientation for the elastic constant measurements among others. For the sake of completion the etch pit orientation on antimony crystals grown from the melt[8] has been looked at.

Crystals were cleaved to expose the (111) planes and etched. Pits on antimony, produced by Dash I[9], are almost triangular, while those for arsenic, produced by an etch composed of two parts hydrofluoric acid, 1 part nitric acid and 1 part glacial acetic acid[6], have somewhat rounded sides. Straight slip lines, mutually oriented at 120°, are observed on the (111) plane for both antimony and arsenic along the $[10\bar{1}]$ directions, that is parallel to the three binary axes. Etch pits on a given plane all have the same orientation and each side of any pit, or rather in arsenic the tangent to the side centre, is parallel to the slip lines. The task remaining is to determine how the etch pits are orientated with respect to the $+x$ and $+y$ axes, when the $+z$ axis is defined as the outward normal from the cleaved surface. Etch pits in arsenic and antimony show the same orientation: a vector drawn from the centre normal to a pit side points along $+y$ axis. A cleavage plane can be exposed on opposite sides of a crystal; there are thus two possible definitions of the $+z$ axis as outward normals to these faces. For consistency of the orientation rule, the etch pits must point in opposite directions on these two faces. This has been confirmed.

Brown *et al.*[7] suggest for bismuth that a unique assignment of $+x$, $+y$ and $+z$ axes can be made using a twinning plane. If the (111) plane is intersected by a twinning plane such that a $-z$ axis intercepts the twinning plane below the (111) surface, then the $+y$ axis points from the binary line, defined as the intersection of the two planes, to an origin where the z-axis cuts the surface (see Fig. 2 of their paper). This rule is correct, if, as described in the literature[10], the twinning planes are (110) in Miller indices referred to the large face centred rhombohedron or (211) referred to the primitive rhombohedral cell. We have examined, by use of Laue back-reflection X-ray photographs, the crystallography of a large (2 cm × 1 cm × 1 cm) twinned crystal of arsenic. The twin plane, which is somewhat broadened, has been shown to be the (110). The (111) planes on either side of the twin plane have been exposed by cleaving and the etch pit orientation examined. The results, illustrated in Fig. 3, verify experimentally that the rule proposed[7] holds for arsenic. Further, the relationship between this (110) plane and the right-handed $+x$, $+y$, $+z$ set has been proved geometrically.

Crystals, aligned to within ±1° of the prerequisite directions, were planed to have faces flat and parallel to within 0·0002 cm and about 1 cm apart. Ultrasonic wave transit times were measured by the single-ended pulse-echo technique at a carrier frequency of 10 MHz. Further details of the technique and experimental apparatus may be found elsewhere [3, 11, 12]. Resonant, gold plated, quartz transducers, X-cut for longitudinal and Y-cut for transverse, were used to excite the ultrasound. The transducers were bonded to the crystal surfaces most satisfactorily with tensol cement. Room temperature ultrasonic wave velocities, determined as the statistical mean from the results of many experiments on several different crystals, are presented in Table 1. There are six Voigt elastic stiffness constants for $R\bar{3}m$ crystals; these are best represented by the matrix[3]

$$C_{ij} = \begin{vmatrix} C_{11} & C_{12} & C_{13} & C_{14} & 0 & 0 \\ C_{12} & C_{11} & C_{13} & -C_{14} & 0 & 0 \\ C_{13} & C_{13} & C_{33} & 0 & 0 & 0 \\ C_{14} & -C_{14} & 0 & C_{44} & 0 & 0 \\ 0 & 0 & 0 & 0 & C_{44} & C_{14} \\ 0 & 0 & 0 & 0 & C_{14} & C_{66} \end{vmatrix}. \qquad (9)$$

Ultrasonic wave velocities are related[3] to the elastic stiffness constants C_{ij} by the set of equations (1–8) in Table 1. Eight velocities have been measured experimentally to allow two redundant checks for the six stiffness constants. To obtain the C_{ij}, a computer programme has been devised, producing a least-mean-squares fit to all eight velocities. The method is described in detail elsewhere[5].

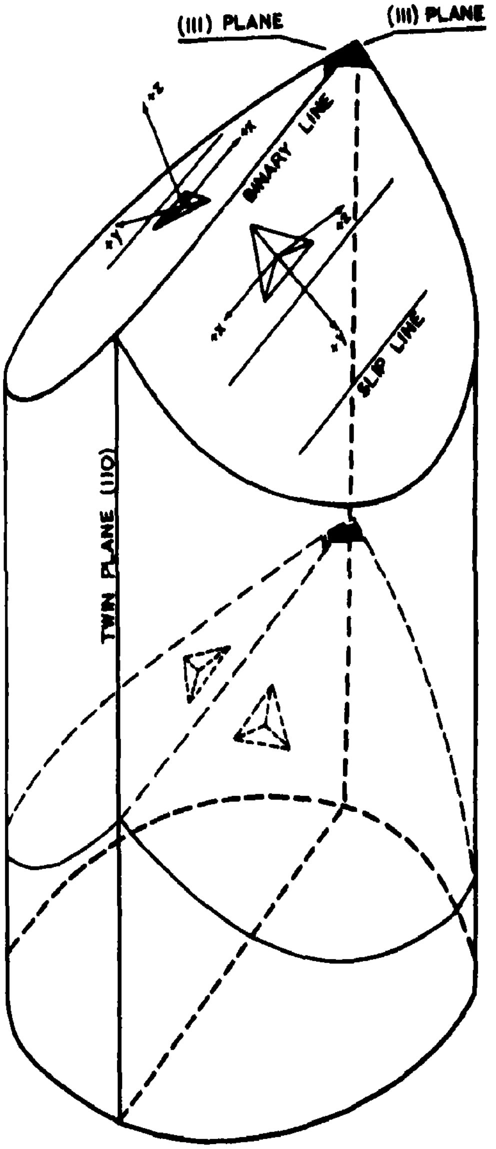

Fig. 3. Schematic of the orientation found for a twinned arsenic crystal. Etch pit orientation on the (111) cleaved surfaces and one of the three sets of slip lines (each parallel to a possible binary x direction) are illustrated. The intersection of the (111) planes on either side lies parallel to a binary direction; the twin plane, which is the (110), contains a binary direction. The relationship between etch pits and the Cartesian $(+x, +y, +z)$ coordinate system on either side of the twin plane is shown.

Each of the velocities is calculated, by inserting an arbitrary set of parameters into the equations (1–8), then divided by the corresponding experimental value and then compared to unity to compute a parameter *SUMSQ* which is minimized.

$$SUMSQ = \sum_{i=1}^{8} \left|\frac{\text{calculated } \rho v_i^2}{\text{measured } \rho v_i^2} - 1{\cdot}0\right|^2. \qquad (10)$$

The density of arsenic is taken as 5·766 g cm^{-3}. Calculated values for the C_{ij} for arsenic, together with those of bismuth and antimony are presented in Table 2(a). In addition, Table 2(b) includes the elastic compliances S_{ij}, where S_{ijkl} is the reciprocal tensor of C_{ijkl} (the usual matrix notation giving constants C_{ij} and S_{ij} is used, replacing 11 by 1, 22 by 2, 33 by 3, 23 by 4, 13 by 5, and 12 by 6). The transformation is affected by

$$S_{ij} = (-1)^{i+j}\Delta_{ij}^c/\Delta^c \qquad (11)$$

where Δ^c is the determinant of the C_{ij} terms and Δ_{ij}^c is the minor of the element C_{ij}.

For lattice stability, the crystal strain energy $\frac{1}{2}C_{ij}\epsilon_i\epsilon_j$ must be positive. To ensure this, the principal minor determinants of successive orders of the matrix C_{ij} (equation (9)) must all be greater than zero[13]. For R$\bar{3}m$ crystals, the principal minors are

$$C_{66},\ C_{44}C_{66}-C_{14}^2,\ C_{33}C_{44}(C_{44}C_{66}-C_{14}^2),$$

$$(C_{44}C_{66}-C_{14}^2)[(C_{11}C_{33}-C_{13}^2)C_{44}-C_{14}^2C_{33}],$$

$$(C_{44}C_{66}-C_{14}^2)[C_{44}(C_{11}-C_{12})(-2C_{13}^2+C_{33}$$

$$\times\{C_{11}+C_{12}\})+2C_{14}^2(2C_{13}^2-C_{12}C_{33})].$$

For all three elements, these requirements are satisfied, serving as an additional check on the experimental data.

The Debye temperature has been calculated from the elastic constant data using the harmonic series expansion method[14]. Accurate assessment requires low temperature elastic constants, but the value obtained ($\theta_D = 250$°K) from the room temperature data compares favourably with that (282°K) derived from

Table 1. Elastic stiffness constant equations and room temperature experimental velocities in arsenic crystals

Equation No	Elastic stiffness constant equations	Propagation direction	Polarisation direction	Experimental velocity (×10⁻⁵ cm/sec)
1	$\rho v_1^2 = C_{11}$	100	100	4·79
2	$\rho v_2^2 = \frac{1}{2}[(C_{66}+C_{44})+\{(C_{44}-C_{66})^2+4C_{14}^2\}^{1/2}]$	100	001	2·99
3	$\rho v_3^2 = \frac{1}{2}[(C_{66}+C_{44})-\{(C_{44}-C_{66})^2+4C_{14}^2\}^{1/2}]$	100	010	1·89
4	$\rho v_4^2 = C_{33}$	001	001	3·20
5	$\rho v_5^2 = C_{44}$	001	100 or 010	2·05
6	$2\rho v_6^2 = \frac{1}{2}(C_{11}+C_{33})+C_{44}-C_{14}$ $+\{(\frac{1}{2}C_{11}-\frac{1}{2}C_{33}-C_{14})^2+(C_{13}+C_{44}-C_{14})^2\}^{1/2}$	0, 1/√2, 1/√2	0, 1/√2, 1/√2	4·32
7	$2\rho v_7^2 = \frac{1}{2}(C_{11}+C_{33})+C_{44}-C_{14}$ $-\{(\frac{1}{2}C_{11}-\frac{1}{2}C_{33}-C_{14})^2+(C_{13}+C_{44}-C_{14})^2\}^{1/2}$	0, 1/√2, 1/√2	0, −1/√2, 1/√2	1·38
8	$\rho v_8^2 = \frac{1}{2}(C_{66}+C_{44})+C_{14}$	0, 1/√2, 1/√2	100	2·43

Table 2(a). Elastic stiffness constants in units of 10^{10} cm^{-2} dyn *at room temperature*

	C_{11}	C_{12}	C_{13}	C_{14}	C_{33}	C_{44}	C_{66}	*SUMSQ*	Source
As	123·6	19·7	62·3	−4·16	59·1	22·6	51·9	0·010	This work
Sb	99·4	30·9	26·4	21·6	44·5	39·5	34·2	0·019	[4]
Bi	63·22	24·42	24·4	7·20	38·11	11·30	19·40	0·000	[3]

Table 2(b). Elastic compliance constants in units of 10^{-13} cm^2 dyn^{-1} *at room temperature*

	S_{11}	S_{12}	S_{13}	S_{14}	S_{33}	S_{44}	S_{66}	Source
As	46·6	36·8	−88·0	1·8	202·4	44·9	19·6	This work
Sb	16·2	6·1	−5·9	12·2	29·5	38·6	44·6	[4]
Bi	25·74	8·01	−11·35	21·50	40·77	115·9	67·51	[3]

specific heat measurements[15]. The energy change most easily computed from theoretical models is that associated with the compressibility, the measure of dilatation without shear under hydrostatic pressure. The volume compressibility in terms of the compliance constants is

$$\beta_v = S_{11}+S_{22}+S_{33}+2(S_{12}+S_{23}+S_{31}). \quad (12)$$

The linear compressibility, defined as the relative decrease in length of a line when the crystal is subjected to unit hydrostatic pressure, has two components for rhombohedral materials, these are

$$\beta_l = S_{11}+S_{12}+S_{13} \quad (13)$$

$$\beta_z = (S_{11}+S_{12}+S_{13}) - (S_{11}+S_{12}-S_{13}-S_{33}) \quad (14)$$

for length changes perpendicular and parallel to the trigonal axis respectively. Calculated compressibilities for arsenic, antimony and bismuth are collected in Table 3. Arsenic is the least compressible, so far as bulk dilatation is concerned. But along the trigonal axis, it is the most compressible: of the three elements, arsenic is the most weakly bound along this direction. Most striking and significant is the difference in sign of the two linear compressibilities β_t and β_z for arsenic. When the crystal is subjected to a hydrostatic pressure, it enlarges on the xy plane. A similar effect is shown by graphite[16] and by tellurium[17], crystals also having highly anisotropic structures. In arsenic, in particular, this property is understandable on the basis of weak interlayer binding. The resultant large compressibility produces a big change in the spacing between the double layers and the enhanced repulsive forces direct atoms outwards in the xy plane.

Table 3. *Linear and volume compressibilities in units of* 10^{-13} cm^2/dyn

	β_t	β_z	β_v	Source
As	−4·6	26·4	17·2	This work
Sb	4·1	17·5	25·8	[4]
Bi	6·38	18·07	30·83	[3]

3. LATTICE SUMMATIONS IN THE VAN DER WAALS MODEL FOR ARSENIC

Lattice properties can be computed from appropriate summations of the potential energy interactions of the atoms in the crystal. The layer-like structure of arsenic, the ready cleavage and the great anisotropy of the linear compressibilities β_t and β_z suggest that certain properties will be dominated by the interlayer cohesion. Certainly this is so[18] for the related semimetal graphite, which also has a layer structure. The purpose now is to calculate the lattice summations of the potential energy along the trigonal direction only in a model of rigid double layer planes interacting with each other by van der Waals forces. To probe this model for arsenic the results will be used to calculate z-axis compressibility and thermal expansion and the energy of cohesion. Then the theoretical assessments will be compared with experiment. The potential energy Φ between two interacting arsenic atoms located on unpaired trigonal planes is written as the sum of a van der Waals attractive term and a repulsive overlap term.

$$\Phi = A\left(\frac{b}{r^n} - \frac{1}{r^6}\right), n > 6. \tag{15}$$

Here r is the atomic separation and A and b are positive constants. Physically the London dispersion effect arises from interaction between momentarily induced atomic dipoles: to obtain the van der Waals attractive potential between the atoms, the atomic polarizability α is required[19–22]. Taking the first atomic ionization potential of arsenic as 10·05 eV, we estimate $4{\cdot}9\times 10^{-24}$ cm^3 for α. Buckingham [23] using self consistent field, wave functions and including electron exchange, has given general relationships between the van der Waals constant A and the polarizability α. For two identical atoms with N electrons in the outer shell, his expressions take the form

$$A = \frac{3}{4}\frac{\alpha^{1/2}e^2}{\sqrt{(\alpha/N)}} \tag{16}$$

which gives A as 230×10^{-60} ergs cm^6 for arsenic. Once A is known, a quantitative expression for the lattice potential energy ψ can be obtained from appropriate summations of Φ. The approach follows that used for graphite[18], although the detailed summation procedures for the A7 structure are more complex.

The potential energy function $\psi(Z_p)$ for interaction between an atom at the origin O with all the atoms on the p^{th} plane at a distance Z_p along the normal to the (111) planes is

$$\psi(Z_p) = A\sum_m \left[b(Z_p{}^2 + d_m{}^2)^{-n/2} - (Z_p{}^2 + d_m{}^2)^{-6/2}\right]. \tag{17}$$

Figure 4 shows the definition of d_m; it is at this point that the three different types of atomic arrangement (Fig. 2(a)) are taken into account. The values of d_m for one type of plane are different from those of the other two. All three types of planes have an identical number σ of atoms per unit area. To simplify, it is convenient to replace direct sums

$$s^n(Z_p) = \sum_m (Z_p{}^2 + d_m{}^2)^{-n/2} \qquad (18)$$

by integrals of the form

$$S^n(Z_p) = 2\pi\sigma \int_0^\infty (Z_p{}^2 + \gamma^2)^{\;n/2}\gamma \,.\, \mathrm{d}\gamma$$

$$= \frac{2\pi\sigma}{n-2} \cdot Z_p{}^{2-n}. \qquad (19)$$

Extensive machine computations have shown that the difference between $s^n(Z_p)$ and $S^n(Z_p)$ is negligible and this replacement is permissable. We can now write

$$\psi(Z_p) = A\,[bS^n(Z_p) - S^6(Z_p)\,]. \qquad (20)$$

Next the potential energy per unit area for interaction between two semi-infinite arsenic crystals can be obtained by summing $\psi(Z_p)$ over all values of Z_p and multiplying by the number of atoms per cm² on each plane

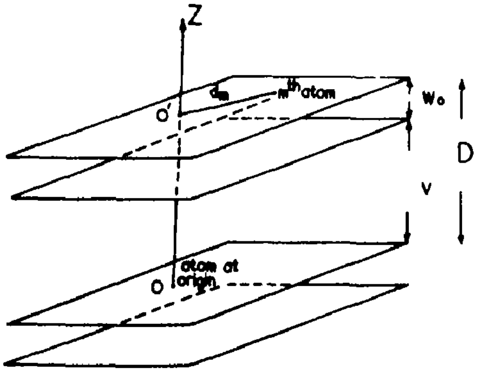

Fig. 4. A schematic diagram of the double layer planes d_m is the distance of the mth atom on the pth plane from O', the point at which the normal from the origin O intersects that pth plane sited Z_p and O.

$$\sum_p \psi(Z_p) = \sigma A\left[b \sum_p S^n(Z_p) - \sum_p S^6(Z_p)\right]. \quad (21)$$

To describe the full range of Z_p it is convenient to use three series expressions e_p, f_p and g_p, where

$$e_p = D\left(\frac{v}{D} + p\right),\; f_p = D\left(1 + \frac{w'_0}{D} + p\right),$$

$$g_p = D(1+p), \quad p = 0, 1, 2\ldots$$

v and w'_0 are respectively the distances between and within the double layers (see Fig. 4) and D is equal to $v + w'_0$. Hence

$$\sum_{p=0}^{\infty} S^n(e_p) = \frac{2\pi\sigma D^{2-n}}{n-2} \sum_{p=0}^{\infty} \left(\frac{v}{D} + p\right)^{2-n}. \quad (22)$$

This summation may be written in terms of the polygamma function $\phi^{(k)}$

$$\sum_{p=0}^{\infty} S^n(e_p) = (-1)^n \frac{2\pi\sigma D^{2-n}}{(n-2)!} \frac{(n-3)}{\phi(u/D)} \quad (23)$$

where

$$\overset{(k)}{\phi}(r) = (-1)^{k+1}k! \sum_{m=0}^{\infty} (r+m)^{-(k+1)}.$$

When the same substitution is made for the other terms, the potential energy function is obtained as

$$\psi(v) = 2\pi\sigma^2 A\Bigg[\frac{(-1)^n bD^{2-n}}{(n-2)!}$$
$$\times\left(\overset{(n-3)}{\phi}(v/D) + \overset{(n-3)}{\phi}(1 + w'_0/D) + 2\overset{(n-3)}{\phi}(1)\right)$$
$$-\frac{D^{-4}}{4!}\Bigg(\overset{(3)}{\phi}(v/D) + \overset{(3)}{\phi}(1 + w'_0/D)$$
$$+ 2\overset{(3)}{\phi}(1)\Bigg)\Bigg]. \qquad (24)$$

The constant b is determined from the equilibrium condition $(\mathrm{d}\psi/\mathrm{d}v)_{v=v_0} = 0$. Expressions for the derivatives of $\psi(v)$ with respect to v are obtained by noting that

$$\frac{d\phi^{(n)}}{dv\phi}(v/D) = \frac{w'_0}{D^2}\overset{(n+1)}{\phi}(v/D) \qquad (25)$$

and

$$\frac{d\phi^{(n)}}{dv\phi}(1+w_0/D) = -\frac{w_0}{D^2}\overset{(n+1)}{\phi}(1+w_0/D). \qquad (26)$$

These derivatives are required for calculation of the compressibility and thermal expansion. Numerical values of the polygamma functions were obtained for the first thousand terms by use of a computer. The potential energy functions $\psi(v)$ are plotted for three values ($n = 8, 10, 12$) of the repulsive exponent in Fig. 5.

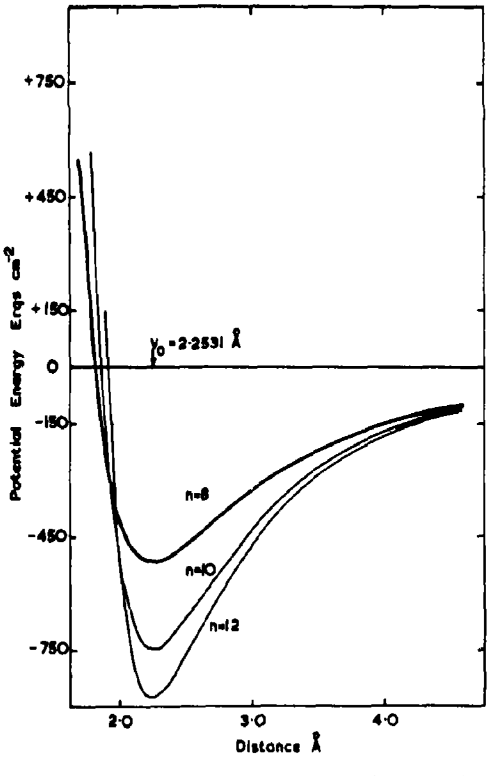

Fig. 5. The potential energy function $\psi(v)$ for interaction between two semi-infinite arsenic crystals. The results for the repulsive exponent $n = 8, 10, 12$ are shown, with the curve for $n = 8$ drawn in the thicker line.

4. DISCUSSION

Now that the experimental data for compressibility is available, it becomes possible to see how well the van der Waals model accounts for the measured lattice properties. A reasonable approximation is to replace the total volume change under hydrostatic compression with that due to the interplanar contraction, when the total energy change is equal to that in the lattice potential energy $\psi(v)$ alone. Then the z-axis linear compressibility may be expressed by

$$\frac{1}{\beta_z} = v\left(\frac{d^2\psi(v)}{dv^2}\right)_{v=v_0}. \qquad (27)$$

Calculated values of β_z, taking the repulsive exponent n as 8, 10 and 12 in equation (24), are compared in Table 4 with the experimental result. Best agreement obtains when n is 8.

An independent assessment of the model can be obtained by recourse to thermal expansion data. The thermal expansion is a symmetric tensor of second rank with two independent components for rhombohedral crystals, one (δ_{33}) describing expansion along the z-axis and the other (δ_{11}) in the xy plane. In layer-type crystals anisotropy is enhanced and the thermal expansion coefficient δ_{33} of arsenic is much the greater, again relating to the weak interlayer binding. The linear expansion coefficient δ_{33} can be estimated from the potential energy function $\psi(v)$ following Zhdanov [24] whence

$$\delta_{33} = \frac{Gk}{(v+w'_0)B} \qquad (28)$$

where k is Boltzmann's constant and B and G are respectively the harmonic and anharmonic restoring force constants for a linear chain of coupled oscillators in a potential $\psi(v)$ and are given by

$$B = (v+w'_0)/\beta_z,$$
$$G = -\frac{1}{2}\left(\frac{d\beta_z}{dv}\right)_{v=v_0}. \qquad (29)$$

The values of δ_{33} calculated in this way are

Table 4. Measured and calculated values of linear compressibility, thermal expansion and interlayer cohesive energy for three values of repulsive exponent

Repulsive exponent (n)	Linear compressibility ($\beta_z \times 10^{14}$ cm^2 dyn^{-1}) Measured[*]	Linear compressibility ($\beta_z \times 10^{14}$ cm^2 dyn^{-1}) Calculated[*]	Linear thermal expansion $\delta_{33} \times 10^5$ deg^{-1} Measured[†]	Linear thermal expansion $\delta_{33} \times 10^5$ deg^{-1} Calculated[†]	Interlayer cohesive energy (erg cm^{-2})
8	26·4	21·74	5·0	5·87	515
10		10·92		3·90	746
12		7·39		1·27	875

[*] This work

[†] Ref [25].

given in Table 4. Agreement with the experimental value[25] is good, again when the repulsive exponent is 8. In this case the interlayer cohesive energy is 515 ergs cm^{-2} (0·391 eV/atom) a ratio of 1 : 7·7 of the total cohesive energy (3·0 eV/atom). For graphite where the van der Waals model is certainly a better approximation than it is for arsenic, the same ratio is 1:39. So the magnitude of the calculated interlayer cohesive energy is reasonable. No experimental estimates exist for this parameter or the closely related heat of wetting.

The results in Table 4 demonstrate that the simple model of arsenic as a double layer structure held by van der Waals forces can give the correct order of magnitude for the linear compressibility and the thermal expansion along the z-axis. Indeed when the repulsive exponent is taken as 8, agreement is good. Plausibly there is a high proportion of this type of bonding along the z-axis. The model has the virtue of simplicity and allows a clear insight into the nature of lattice and mechanical properties of arsenic.

REFERENCES

1. COHEN M. H., FALICOV L. M. and GOLIN S., *I.B.M.J. Res. Dev.* **8**, 215 (1964).
2. FALICOV L. M. and GOLIN S., *Phys. Rev.* **137**, A871 (1965).
3. ECKSTEIN Y., LAWSON A. W. and RENEKER D. H., *J. appl. Phys.* **31**, 1534 (1960).
4. EPSTEIN S. and DeBRETTEVILLE A. P., *Phys. Rev.* **138**, A771 (1965).
5. JEAVONS A. P. and SAUNDERS G. A., *Proc. R. Soc.* **A310**, 415 (1969).
6. JEAVONS A. P. and SAUNDERS G. A., *Br. J. appl. Phys.* **1**, 869 (1968).
7. BROWN R. D., HARTMAN R. L. and KOENIG S. H., *Phys. Rev.* **172**, 598 (1968).
8. OKTU O. and SAUNDERS G. A., *Proc. phys. Soc.* **91**, 156 (1967).
9. WERNICK J. H., HOBSTETTER J. N., LOVELL L. C. and DORSI D., *J. appl. Phys.* **29**, 1013 (1958).
10. HALL E. O., *Twinning and Diffusionless Transformations in Metals* p. 57. Butterworths, London (1954).
11. ALPER T. and SAUNDERS G. A., *J. Phys. Chem. Solids* **28**, 1637 (1967).
12. PACE N. G., SAUNDERS G. A., SUMENGEN Z. and THORP J. S., *J. mat. Sci.* **4**, 1106 (1969).
13. BORN M. and HUANG K., *Dynamical Theory of Crystal Lattices*, Chap. 3. Clarendon Press, Oxford (1963).
14. BELLIS D. D., BHATIA A. B. and HORTON G. K., *Phys. Rev.* **104**, 43 (1956).
15. TAYLOR W. A., McCOLLUM D. C., PASSENHEIM B. C. and WHITE H. W., *Phys. Rev.* **161**, 652 (1967).
16. RILEY D. P., *Proc. phys. Soc.* **57**, 486 (1945).
17. BRIDGMAN P. W., *Proc. Am. Acad. Arts Sci.* **60**, 305 (1925).
18. GIRIFALCO L. A. and LAD R. A., *J. chem. Phys.* **25**, 693 (1956).
19. SLATER J. C. and KIRKWOOD J. G., *Phys. Rev.* **37**, 682 (1931).
20. LONDON F., *Trans. Faraday Soc.* **33**, 8 (1937).
21. MARGENAU H., *Rev. mod. Phys.* **11**, 1 (1939).
22. MOTT N. F. and SNEDDON I. N., *Wave Mechanics and its Applications*, Chap. 7. Clarendon Press, Oxford (1948).
23. BUCKINGHAM R. A., *Proc. R. Soc.* **A160**, 94 (1937).
24. ZHDANOV G. S., *Crystal Physics*, Chap. 14. Oliver & Boyd, London (1965).
25. KLEMM W., SPITZER H., NIERMANN H., *Angew. Chem.* **72**, 985 (1960).

J. Phys. Chem Solids Pergamon Press 1970. Vol. 31, pp. 1477–1484. Printed in Great Britain.

RELAXATION TIME OF ELECTRON-PHONON SYSTEMS*

G. D. MAHAN†

Institute of Theoretical Science and Department of Physics, University of Oregon, Eugene, Oregon 97403, U.S.A.

(*Received 7 April 1969, in revised form 21 October 1969*)

Abstract – A new definition is proposed for the electronic relaxation time of electron–phonon systems. This is the relaxation time measured in electrical resistivity, or in the Drude contribution to the optical dielectric function. The proposed expression reduced to Baym's result at zero frequency and to the Ron and Tzoar result at high frequency. The present result has the advantage that it is valid over the entire range of frequencies of interest

1. INTRODUCTION

THE FREQUENCY dependent relaxation time $\tau(\omega)$ of an electronic system can not be defined in a rigorous way. For example, the different measurements of a relaxation time usually measure a different average over the physical properties of a system[1, 2]. A further difficulty is that the relaxation time $\tau(\omega)$ can not be defined in terms of some explicit correlation function as can, for example, the conductivity be defined in terms of a Kubo formula. A d.c. relaxation time can be defined in terms of the d.c. conductivity $\sigma = ne^2\tau/m$, but there is no unique way to extend this definition to finite frequencies. One possible way to define a $\tau(\omega)$ is by deriving a transport equation for the electrons, and then interpreting the scattering integral as a relaxation time[1]. Another possible way is to assume that the Drude formula

$$\epsilon_1(\omega) = 1 - \frac{\omega_p^2}{\omega(\omega + i/\tau(\omega))} \qquad (1.1)$$

is valid in simple metals for frequencies below the interband thresholds. This assumption permits a derivation of τ from the definition of the dielectric function, which can be rigorously defined in terms of a correlation function [3, 4].

In this article, we shall propose a definition of the relaxation time $\tau(\omega)$ for a free electron gas based upon the Drude formula. Thus we are concerned with the relaxation time associated with electrical conductivity, which is different than that associated with the shear viscosity or the thermal conductivity. Furthermore, this relaxation time is not that of an individual electron, but represents some average over all of the electrons participating in the electrical conduction.

This investigation was stimulated by the experimental results of Bennett and Bennett on the optical properties of Ag, Au and Al[5]. The Bennetts found that the Drude formula was valid at optical frequencies below the interband threshold. In this frequency range the $\tau(\omega)$ was found to be nearly independent of frequency, and furthermore the value of τ was equal to the d.c. relaxation time obtained by measuring the electrical resistance. Thus they found experimentally that the frequency dependent relaxation time $\tau(\omega)$ is nearly independent of frequency in the range ($0 \leq \omega \leq 2{\cdot}0\,\text{eV}$). It is important to note that Bennetts' samples were very pure so that phonon scattering is the important contribution to τ, and the experiments were performed at room temperatures.

---

*Research supported by National Science Foundation, Grant 669-G P-7647.

†Alfred P. Sloan Research Fellow

A partial explanation of this phenomena has already been provided by the work of Ron[3], Tzoar[4] and Hopfield[6]. They calculate an electronic relaxation time τ from the electron-phonon interaction which shows a remarkable independence of ω in the range $0 \leq \omega \leq \omega_p$ where ω_p is the plasma frequency. This basically accounts for Bennetts' data except for one feature. In the limit of zero frequency, the Ron, Tzoar and Hopfield equation does not reduce to the correct temperature dependent d.c. relaxation time. Our model for the d.c. result is the form proposed by Baym[1]. The formula we derive is similar to Baym's at d.c. and to Ron and Tzoar at high frequency.

It has the feature that at high temperatures (greater than the Debye energies), the d.c. and high frequency relaxation times are the same, thereby explaining the experimental result.

Our basic assumption in the calculation is that it is adequate to evaluate $1/\tau(\omega)$ to first order in the square of the electron–phonon matrix element $M_{q\lambda}$. So we assume the existense of a series.

$$1/\tau(\omega) = \sum_{q\lambda} |M_{q\lambda}|^2 F_{q\lambda}(\omega) + O(M^4) \qquad (1.2)$$

in which it is sufficient to keep just the first term. However, the first term can still be quite complicated. For example, the term $F_{q\lambda}(\omega)$ should include the effects of electron–electron interaction, interband transition (i.e. crystal structure), and multiple scattering. Our calculation is done for a free electron gas. So our expression (2.11) does not include band structure effects, but does include electron–electron scattering and multiple scatterings consistent with the approximation of only including terms to $|M_{q\lambda}|^2$. So we are mainly concerned with the simple metals (e.g. Al) where $M_{q\lambda}$ is "small", and it is usually adequate to calculate quantities to order $|M_{q\lambda}|^2$. Our aim is to get right the other factors, which are due to electron–electron interaction etc. Most previous calculations have been content to evaluate terms to order $|M_{q\lambda}|^2$. The only exception of which we are aware is Baym's result for $\omega = 0$, yet even those applying Baym's results simplify to terms of order $|M_{q\lambda}|^2$.

Our method of obtaining $\tau(\omega)$ begins from the definition of the $k = 0$ transverse dielectric function $\epsilon_\perp(\omega)$ in terms of a correlation function. By manipulating this correlation function, we are able to express it as a power series in $|M_{q\lambda}|^2$.

$$\epsilon_\perp(\omega) = \epsilon_\perp^{(0)} + \sum_{q\lambda} |M_{q\lambda}|^2 \epsilon_\perp^{(2)}(\mathbf{q}, \lambda, \omega) + O(M^4). \qquad (1.3)$$

The first term in (1.3) contains terms independent of $|M_{q\lambda}|^2$. Now from the Drude equation (1.1), we can expand

$$\epsilon_\perp(\omega) = 1 - \frac{\omega_p^2}{\omega^2}(1 - i/\tau\omega - 1/(\tau\omega)^2 + \cdots). \qquad (1.4)$$

Because a term $(1/\tau)^n$ is proportional to $|M_{q\lambda}|^{2n}$, or even higher powers of $M_{q\lambda}$, it follows that the term $\omega_p^2/\tau\omega^3$ is the only one proportional to $|M_{q\lambda}|^2$. So this term can be identified with the second term in (1.3), which establishes a proportionality between $\epsilon_\perp^{(2)}$ in (1.3) and F in (1.2). Thus we are able to derive (1.2) from (1.3). Note that this identification does not depend upon the convergence of the expansion in (1.4). It is valid for $\omega\tau \ll 1$, and even for $\omega \to 0$. The result for $\tau(0)$ is equivalent to the answer obtained from d.c. transport theory. For example it has the $(1 - \cos\theta)$ factor in the integration over wave vectors.

Our formula for the relaxation time has the form

$$1/\tau(\omega) = \frac{m}{ne^2\omega} Re \int_{t'}^{\infty} \mathrm{d}t\, e^{i\omega(t-t')} \times \left\langle \left[\frac{\partial}{\partial t} j_\nu(t), \frac{\partial}{\partial t'} j_\nu(t') \right] \right\rangle.$$

The idea of defining the relaxation time as a correlation function of time-derivative quantities is not new. Mori and Kawasaki [7] proposed that the relaxation time for spins be defined by the correlation function $[\dot{S}(t), \dot{S}(t')]$. This idea was expanded by Sandy and Jones[8], who used a dielectric relaxation time defined in terms of $[\dot{P}(t), \dot{P}(t')]$.

2. RELAXATION TIME

The density and current correlation functions can be defined in the Matsubara notation as[9, 10]

$$\pi(i\omega) = -\int_0^\beta \mathrm{d}\tau\, \mathrm{e}^{i\omega\tau}\langle T_\tau j_\nu(\tau) j_\nu(0)\rangle \tag{2.1}$$

$$\chi(q, i\omega) = -\int_0^\beta \mathrm{d}\tau\, \mathrm{e}^{i\omega\tau}\langle T_\tau \rho(q,\tau)\rho(-q,0)\rangle. \tag{2.2}$$

The current correlation function (2.1) is given for the case of zero wave vector. This reflects our interest in the optical dielectric problem (1.1), which is also defined at vanishing wave vector. After evaluating these correlation functions, the related retarded functions (π_R, X_r) are obtained by letting $i\omega \to \omega + i\delta$. The transverse $\epsilon_\perp(\omega)$ and longitudinal $\epsilon(q,\omega)$ dielectric functions are defined in terms of the retarded functions [9, 10]

$$\epsilon_\perp(\omega) = 1 - \frac{\omega_p^2}{\omega^2} - \frac{4\pi}{\omega^2}\pi_R(\omega) \tag{2.3}$$

$$1/\epsilon(q,\omega) = 1 + \frac{4\pi e^2}{q^2}\chi_R(q,\omega). \tag{2.4}$$

If we assume that the Drude equation (1.1) is valid, then comparing it with (2.3) gives

$$\pi_R(\omega) = -\frac{ne^2}{m}\frac{1}{1 - i\omega\tau}. \tag{2.5}$$

Our derivation begins by integrating by parts on the τ integral in equation (2.1). The first integration yields

$$\pi(i\omega) = \frac{1}{i\omega}\langle [j_\nu(0), j_\nu(0)]\rangle$$
$$+ \frac{1}{i\omega}\int_0^\beta \mathrm{d}\tau\, \mathrm{e}^{i\omega\tau}\left\langle T_\tau\left(\frac{\partial}{\partial\tau} j_\nu(\tau)\right) j_\nu(0)\right\rangle.$$

The first term is a way of writing the result

$$\langle [j_\nu(0), j_\nu(0)]\rangle = \langle j_\nu(\beta) j_\nu(0)$$
$$- j_\nu(0) j_\nu(0)\rangle$$

and this term vanishes. In the second term the bracket may be rewritten as

$$\left\langle T_\tau \left(\frac{\partial}{\partial\tau'} j_\nu(\tau')\right)_{\tau'=0} j_\nu(-\tau)\right\rangle.$$

Integrating by parts again gives

$$\pi(i\omega) = \frac{1}{(i\omega)^2}\left\langle\left[j_\nu(0), \left(\frac{\partial}{\partial\tau} j_\nu(\tau)\right)_{\tau=0}\right]\right\rangle$$
$$+ \frac{1}{(i\omega)^2}\int_0^\beta \mathrm{d}\tau\, \mathrm{e}^{i\omega\tau}$$
$$\times \left\langle T_\tau\left(\frac{\partial}{\partial\tau} j_\nu(\tau)\right)\left(\frac{\partial}{\partial\tau'} j_\nu(\tau')\right)_{\tau'=0}\right\rangle. \tag{2.6}$$

We will show that the first term vanishes for a free electron gas. In a free electron gas the positive charge is spread uniformly over the system. There are no energy bands nor interband contributions to j_ν or ρ. The Hamiltonian for the electron–phonon system is

$$\mathscr{H} = \mathscr{H}_0 + \mathscr{H}_{\text{el-ph}} + \mathscr{H}_{\text{el-el}}$$

$$\mathscr{H}_0 = \sum_{\mathbf{p}} \xi_{\mathbf{p}} C_{\mathbf{p}}{}^{+} C_{\mathbf{p}} + \sum_{\mathbf{q}\lambda} \omega_{\mathbf{q}\lambda} a^{+}_{\mathbf{q}\lambda} a_{\mathbf{q}\lambda}$$

$$\mathscr{H}_{\text{el-ph}} = \sum_{\mathbf{q}\lambda} M_{\mathbf{q}\lambda} A_{\mathbf{q}\lambda}\rho(\mathbf{q})$$

$$\mathscr{H}_{\text{el-el}} = \frac{V}{2V}\sum_{qpk}\frac{4\pi \mathbf{e}^2}{q^2} C^{+}_{\mathbf{k}+\mathbf{q}} C^{+}_{\mathbf{p}-\mathbf{q}} C_{\mathbf{p}} C_{\mathbf{k}}$$

where λ is the phonon polarization, and

$$A_{q\lambda} = (a_{q\lambda} + a^{\dagger}_{q\lambda})$$

$$\rho(q) = \sum_{p} C^{\dagger}_{p+q} C_{p}$$

$$j_{\nu} = \frac{e}{m} \sum_{p} p_{\nu} C_{p}^{\dagger} C_{p}.$$

Evaluate

$$\begin{aligned} \frac{\partial}{\partial \tau} j_{\nu}(\tau) &= [\mathcal{H}, j_{\nu}(\tau)] \\ &= [\mathcal{H}_{\mathrm{el-ph}}(\tau), j_{\nu}(\tau)] \\ &= -\frac{e}{m} \sum_{q\lambda} M_{q\lambda} A_{q\lambda}(\tau) q_{\nu} \rho(q, \tau). \end{aligned}$$

In this case the first term in (2.6) does vanish, and the remaining term may be written as

$$\begin{aligned} \pi(i\omega) &= \frac{e^2}{m^2 (i\omega)^2} \sum_{qq'\lambda\lambda'} M_{q\lambda} M_{q'\lambda'} q_{\nu} q'_{\nu} \cdot \\ &\cdot \int_0^{\beta} d\tau\, e^{i\omega\tau} \langle T_{\tau} A_{q\lambda}(\tau) A_{q'\lambda'}(0) \\ &\times \rho(q, \tau) \rho(q', 0) \rangle. \end{aligned} \tag{2.7}$$

This formula is exact for a free electron gas. It provides the point of departure for the remaining discussion.

In most electron gas problems the electron–phonon interaction is considered to be "weak" in that it is usually adequate to calculate quantities to order $|M_{q\lambda}|^2$. If we adopt this approximation in (2.7), then we can evaluate the bracket $[T_{\tau} A(\tau) \ldots]$ while neglecting any further effects of the electron–phonon interaction. In this case the bracket exactly equals

$$\delta_{\lambda\lambda'} \delta_{q, q'} \mathcal{D}(q, \lambda, \tau) \chi(q, \tau)$$

where $\mathcal{D}$ is the phonon Greens function and $\chi(q, \tau)$ is the correlation function defined in (2.2). In this approximation χ contains no electron–phonon contributions, but it is exact in so far as electron–electron interactions. We take $\mathcal{D}(q, \lambda, \tau)$ as the exact phonon Green's functions, although this is slightly inconsistent since this implies that $\mathcal{D}$ contains electron–phonon contributions to its self energy. Denote with a prime the $\pi(i\omega)$ evaluated by this approximation

$$\begin{aligned} \pi'(i\omega) &= \frac{e^2}{m^2 (i\omega)^2} \sum_{q\lambda} |M_{q\lambda}|^2 q_{\nu}^2 \\ &\times \frac{1}{\beta} \sum_{i\omega} \mathcal{D}(q, \lambda, i\omega_1) \chi(q, i\omega + i\omega_1). \end{aligned}$$

After evaluating the sum over $i\omega_1$ we get for the retarded function

$$\begin{aligned} \pi'_R(i\omega) &= \frac{1}{4\pi m^2 \omega^2} \sum_{q\lambda} |M_{q\lambda}|^2 q_{\nu}^2 q^2 \\ &\times \int_{-\infty}^{\infty} \frac{d\omega'}{2\pi} n(\omega') \cdot \\ &\cdot \left\{ 2 D_R^{*}(q, \lambda; \omega' - \omega) \, Im \frac{1}{\epsilon(q, \omega')} \right. \\ &\left. - A_{\lambda}(q, \omega) \left(\frac{1}{\epsilon(q, \omega + \omega')} - 1 \right) \right\} \end{aligned} \tag{2.8}$$

where $A_{\lambda}(q, \omega)$ is the phonon spectral function which is derived from the retarded Green's function

$$A_{\lambda}(\mathbf{q}, \omega) = -2 Im D_R(\mathbf{q}, \lambda, \omega)$$

and $n(\omega') = (e^{\beta\omega'} - 1)^{-1}$. In deriving (2.8) we have used (2.4) to relate $\chi_R(\mathbf{q}, \omega)$ to the inverse of the dielectric function.

We wish to relate (2.8) to a relaxation time $\tau(\omega)$. In calculating $1/\tau(\omega)$, we are usually content to calculate those terms for which

$$1/\tau \sim |M_{q\lambda}|^2.$$

Now expand (2.5)

$$\pi_R(\omega) = -\frac{ine^2}{m\tau\omega}(|1 - i/\tau\omega + \cdots). \tag{2.9}$$

This series suggests that terms in $\pi_R(\omega)$ which are proportional to $|M_{\lambda q}|^2$ contribute to the leading term in (2.9). Whereas terms $|M_{\lambda q}|^4$ in $\pi_R(\omega)$ could arise from either of the first two terms ($1/\tau$ or $1/\tau^2$) in (2.9 . We deduce, by comparing (2.8) and (2.9) that $1/\tau(\omega)$ is given to order $|M_{\lambda q}|^2$ by $\pi_R'(\omega)$

$$1/\tau(\omega) = -\frac{m\omega}{ne^2} Im\,\pi_R'(\omega). \qquad (2.10)$$

We emphasize that our equating of the first term in (2.9) to $\pi_R'(\omega)$ is based on a matrix element argument. This identification is valid even when the second term is larger than the first, which occurs at $\tau\omega < 1$. By taking the imaginary part of (2.8), and rearranging it slightly, we get

$$1/\tau(\omega) = (4\pi ne^2 m\omega)^{-1} \sum_{q\lambda} |M_{q\lambda}|^2 q_\nu^2 q^2 \times \int_{-\infty}^{\infty} \frac{d\omega'}{2\pi} A_\lambda(\mathbf{q},\omega')\, Im \frac{1}{\epsilon(q,\omega+\omega')} \times [n(\omega') - n(\omega+\omega')]. \qquad (2.11)$$

This expression is our final, most general, formula for $\tau(\omega)$. It has been derived assuming that the Drude formula (1.1) is valid. It is not an exact expression since we have made the common and apparently well founded (for simple metals) assumption that it is adequate to take only terms proportional to $|M\ |^2$. Within these limitations and assumptions the resulting expression (2.11) appears to contain all electron–electron interactions exactly.

Another way to demonstrate the plausibility of (2.11) is to relate this definition of $\tau(\omega)$ to those derived previously. We will now show that (2.11) does reduce to prior results in the proper limits. The chief virtue of the present result is that it appears valid for all values of temperatures ($1/\beta$) and frequency. Previous results appear to be valid over limited areas of the frequency-temperature range.

Baym[1] derived a result for the d.c. relaxation time. In (2.11) we take the limit of zero frequency by

$$\lim_{\omega\to 0} \frac{1}{\omega} [n(\omega') - n(\omega+\omega')] = -\frac{\partial}{\partial\omega'} n(\omega') = -\beta n(\omega') n(-\omega').$$

So our result is[11]

$$1/\tau(0) = \frac{-\hbar\beta}{4\pi ne^2 m} \sum_{q\lambda} |M_{q\lambda}|^2 q^2 q_\nu^2 \times \int_{-\infty}^{\infty} \frac{d\omega'}{2\pi} A_\lambda(q,\omega') n(\omega') n(-\omega')\, Im \times \frac{1}{\epsilon(q,\omega')}. \qquad (2.12)$$

This can be made to resemble Baym's result equation (8) by the following alterations. First, the matrix element is taken to be

$$M_{q\lambda} = \frac{v_0(q)}{V_0} \left(\frac{\hbar V_0}{2MV\omega_{q\lambda}}\right)^{1/2} (\hat{\epsilon}_{q\lambda} \cdot \mathbf{q})$$

where $v_0(q)$ is the unscreended electron-ion interaction. V_0 is the unit cell volume and M is the ion mass. Then Baym defined $S'(q,\omega)$ which is

$$S'(q,\omega) = -\frac{n(-\omega)}{2M} \sum_\lambda A_\lambda(q,\omega) \times (\epsilon_{q\lambda} \cdot \mathbf{q})^2 / \omega_{q\lambda}.$$

Secondly, in

$$Im \frac{1}{\epsilon(q,\omega')} = -\frac{\epsilon_2(q,\omega')}{|\epsilon(q,\omega')|^2}$$

Baym's result corresponds to taking the Random Phase Approximation for ϵ_2 in the limit of small ω'

$$\epsilon_2(q,\omega') = \frac{2e^2 m^2 \omega'}{\hbar^3 q^3} \theta(2p_F - q).$$

We finally get Baym's result[11]

$$1/\tau(0)=\frac{m}{12\pi^3 Z\hbar}\int_0^{2p_F}q^3\mathrm{d}q\int_{-\infty}^{\infty}\frac{\mathrm{d}\omega'}{2\pi}\times\left|\frac{v_0(q)}{\epsilon(q,\omega')}\right|^2 S'(q,\omega')\beta\omega' n(\omega'). \tag{2.13}$$

So we obtain Baym's result from our (2.12) by taking ϵ_2 in the *RPA*. This suggests that our result (2.12) is a slight improvement over Baym's in that it is valid for any form of $\epsilon(q,\omega)$. Numerical calculations by Dynes and Carbotte[12] indicate that Baym's result does give a good quantitative account of the temperature dependence of the resistivity of simple metals.

Ron[3] has also derived a frequency dependent relaxation time for electron-phonon systems. His approach is similar to that used here, in that he derives a result for the frequency dependent conductivity and relates it to $\tau(\omega)$ through the Drude expression. In spite of these similarities in approach, the present result is different than Ron's. In particular, the two results differ dramatically at zero frequency where Ron's result is qualitatively different than (2.12) or (2.13). This comparison is unfair because Ron explicitly specifies that his $\tau(\omega)$ is valid at high frequency ($\omega\tau \gg 1$) and not at low frequency.

A comparison of the two results at high frequency show that they are very similar in this regime. In order to compare with Ron's result, we need to assume in (2.11) that the phonons are well defined eigenstates[13]

$$A_\lambda(\mathbf{q},\omega)=2\pi[\delta(\omega'-\omega_{q\lambda})-\delta(\omega'+\omega_{q\lambda})]. \tag{2.14}$$

In evaluating (2.11) in the high frequency limit, we can neglect the term $n(\omega\pm\omega_{q\lambda})$. We get for $\omega \gg (1/\beta,\omega_{q\lambda})$

$$1/\tau(\omega)=(4\pi ne^2\omega)m)^{-1}\sum_{q\lambda}|M_{q\lambda}|^2 q_\nu^2 q^2\times\cosh(\beta\omega_{q\lambda}/2)Im\frac{1}{\epsilon(q,\omega)}. \tag{2.15}$$

In deriving this result we have neglected the phonon frequency $\omega_{q\lambda}$ in $\epsilon(q,\omega\pm\omega_{q\lambda})$. Making the same approximation on Ron's result yields the same result as (2.15). Thus Ron's result is the same as (2.11) at high frequency but not at low frequencies.

Another feature of (2.11) is that at high temperatures ($\beta\omega_{q\lambda} \ll 1$), $\tau(\omega)$ is remarkably independent of frequency. At high temperatures, the high frequency result (2.15) becomes

$$1/\tau(\omega)=(4\pi ne^2 m\omega)^{-1}\sum_{q\lambda}|M_{q\lambda}|^2 q_\nu^2 q^2\left(\frac{2}{\beta\omega_{q\lambda}}\right)\times Im\frac{1}{\epsilon(q,\omega)}.$$

The d.c. relaxation term from (2.12) obtained by using (2.14) is

$$1/\tau(0)=(4\pi e^2 nm)^{-1}\sum_{q\lambda}|M_{q\lambda}|^2 q_\nu^2 q^2\left(\frac{2}{\beta\omega_{q\lambda}^2}\right)\times Im\frac{1}{\epsilon(q,\omega_{q\lambda})}.$$

These two results are numerically similar for frequencies less than the plasma frequency ($\omega \lesssim \omega_p$) because the factor

$$\frac{1}{\omega}Im\frac{1}{\epsilon(q,\omega)}$$

is remarkably insensitive to ω in this range. This is shown explicitly by the numerical calculations of Ron and Tzoar[4]. This insensitivity to ω appears to explain Bennetts' optical data taken at room temperature. For optical experiments at helium temperatures, one expects that the $\tau(\omega)$ in the Drude term is to still be a relative insensitive function of ω (given by (2.15)), but this τ will be different than measured at d.c. (given by (2.12)). Of course, interband terms will change $\tau(\omega)$ dramatically, so this insensitivity to frequencies only is valid below the threshold for interband transitions.

3. DISCUSSION

Hopfield[6] and Ferrell[14] have suggested an equation for calculating the phonon and interband contributions to the transverse dielectric function. Their result is similar to that used by Ron and Tzoar[3, 4] and corresponds to using

$$\epsilon_2(\omega) = \frac{\omega_p^2}{\omega^3\tau(\omega)} \tag{3.1}$$

where the high frequency $\tau(\omega)$ is defined in (2.15). The present derivation of this result, by the integration by parts method in Section 2 provides an alternate derivation to that suggested by Hopfield and Ferrell. If we had started from the electron–ion interaction or from the electron–impurity interaction, instead of from the electron–phonon interaction, we could derive a formula analogous to (2.15) for these interactions by the same technique.

Foo and Hopfield[15] point out that the Hopfield–Ferrell formula has a broader interpretation than originally suggested. For example, suppose that one used (3.1) and (2.15) to calculate $\epsilon_2(\omega)$ to order $|M_{q\lambda}|^2$ in the electron–phonon interaction. In this case the proper interpretation to put on the longitudinal dielectric function $\epsilon(q, \omega)$ in (2.15) is that it contains the effects of all interactions except the electron–phonon. So it includes the effects of interband transitions as well as electron–electron interactions. It follows that the best way to calculate the strength of phonon-assisted interband transitions is to use (2.15) with the interband terms included in $\epsilon(q, \omega)$. This is formally equivalent to, but perhaps computationally easier than, the usual method of treating phonon-assisted transitions as a higher-order vertex correction[16].

In an earlier article[17] we reported the calculation of some vertex corrections to the interband transitions in sodium. These results are now regarded as gross overestimates because, as shown by several groups[18, 19], the proper inclusion of renormalization reduces the effect considerably. There is another reason why the strength of these plasmon-assisted interband transitions is considerably reduced. After the electron virtually emits the plasmon, the electron goes into a virtual intermediate state. This intermediate state is characterized by a short relaxation time because electrons in this state can emit real plasmons. This high damping in the intermediate state should reduce the probability of these plasmon-assisted transitions. The same considerations imply that the plasmoron peak should be less than present theoretical predictions[20–22] and may explain why the effect is not observed experimentally[23].

The present discussion of the Hopfield–Ferrell formula suggests that there is a better way of calculating such vertex corrections. They must all be equivalent to corrections to the dielectric function $\epsilon(q, \omega)$. This follows immediately from the assertion that $\epsilon(q, \omega)$ contains the effects of all electron–electron interactions. Thus the best way to evaluate these vertex corrections is to calculate a better dielectric function. This is the approach followed by Young[24]. However, his estimates of the corrections to $\epsilon_2(q, \omega)$ appear to be too large because he did not account for the high damping in the intermediate electron states which was mentioned above.

REFERENCES

1. BAYM G., *Phys. Rev.* **135**, A1691 (1964).
2. RICE M. J. and SHAM L. J., *Phys. Lett.* **28A**, 7 (1969); erratum **29A**, 488 (1969)
3. RON A., *Phys. Rev.* **131**, 2041 (1963)
4. RON A. and TZOAR N., *Phys. Rev.* **131**, 1943 (1963)
5. BENNETT H. E. and BENNETT J. M., *Optical Properties and Electronic Structure of Metals and Alloys* (Edited by F. Abeles) Wiley, New York (1966).
6. HOPFIELD J. J., *Phys. Rev.* **139**, A419 (1965)
7. MORI H. and KAWASAKI K., *Prog. theor. Phys. Kyoto* **27**, 529 (1962)
8. SANDY F. and JONES R. V., *Phys. Rev.* **168**, 481 (1968).
9. PINES D. and NOZIERES P., *Quantum Liquids*, Vol. 1. Benjamin, New York (1966).

10. ABRIKOSOV A. A., GORKOV L. P. and DZYALOSHINSKI I. E., *Methods of Quantum Field Theory in Statistical Physics*. Prentice Hall, Engelwood, Cliffs, N J (1963)
11. This relaxation time does contain the $(1-\cos\theta)$ factor obtained for transport phenomena.
12. DYNES R. C. and CARBOTTE J. P., *Phys. Rev.* **175**, 913 (1968)
13. This spectral function should have a renormalization factor but that has already been included by using the correct $\omega_{\mathbf{q}\lambda}$ in the definition of $M_{\mathbf{q}\lambda}$
14. FERRELL R. A., *Optical Properties and Electronic Structure of Metals and Alloys* (Edited by F. Abeles) Wiley, New York (1966)
15. FOO E-Ni and HOPFIELD J. J., *Phys. Rev.* **173**, 635 (1968)
16. NETTEL S. J., *Phys. Rev.* **150**, 421 (1966).
17. MAHAN G. D., *Phys. Lett.* **24A**, 708 (1967)
18. BEEFERMAN L. and EHRENREICH H., (private communication).
19. WATAKE M. and YASUHARA H., *Phys. Lett.* **28A**, 329 (1968). (to be published).
20. HEDIN L., LUNDQVIST B. I. and LUNDQVIST S., *Solid St. Commun.* **5**, 237 (1967)
21. LUNDQVIST B. I., *Phys. condensed Matter* **6**, 193, 206 (1967); **7**, 117 (1968).
22. LONGE P. and GLICK A., (to be published); *Phys. Rev. Lett.* **15**, 589 (1965).
23. CUTHILL J. R., DOBBYN R. C., McALISTER A. J. and WILLIAMS M. L., *Phys. Rev.* **174**, 515 (1968).
24. YOUNG C. Y., *Phys. Rev.* **183**, 627 (1969).

J. Phys. Chem. Solids Pergamon Press 1970. Vol. 31, pp. 1485–1490. Printed in Great Britain.

COHESIVE ENERGIES OF NH_4Cl AND NH_4Br

C. S. N. MURTHY and Y. V. G. S. MURTI
Department of Physics, Indian Institute of Technology, Madras, Madras-36, India

(*Received* 29 *September* 1969)

Abstract—The Born Model is used to calculate the room temperature cohesive energies of NH_4Cl and NH_4Br. The computed values are respectively 155·0 and 148·2 kcal/mole. Comparison with experimental cohesive energies determined from a thermo-chemical cycle shows the predominance of ionic binding and suggests a probable contribution of 4·4 and 4·0 kcal/mole due to hydrogen bonding in NH_4Cl and NH_4Br respectively.

1. INTRODUCTION

THE BORN Model[1] has been successfully used to account for the cohesion of most of the alkali halides with the NaCl structure. Some of them show a dimorphic transition to CsCl structure under high pressures, their relative stabilities[1, 2] being the subject of several inconclusive investigations in the past. Notable differences exist in the properties (colour centres, ionic mobilities and defect formation, elastic anisotropy) of the solids crystallising in the two lattices. These may be presumably of a structural origin and there is clearly a need for a better understanding of the cohesion in the salts of the CsCl type. Towards this end, we have computed the cohesive energies under standard thermodynamic conditions (negligible pressure and room temperature) of seven crystals of the CsCl type: CsCl, CsBr, CsI, TlCl, TlBr, NB_4Cl, NH_4Br and the results on the ammonium halides are reported here.

The ammonium halides present an interesting system for study in view of their polymorphism and the possible internal rotation of the ammonium ion[3]. NH_4Cl and NH_4Br at room temperature have a simple cubic space lattice of the CsCl type, with the tetrahedral ammonium ions oriented at random with respect to the two equivalent positions in the unit cell (the hydrogen atoms pointing towards one tetrahedral set of surrounding anions in some cells and towards the other set in other cells). It was inferred by Waddington[4] from his infra-red studies that the ammonium ions in the lattices of NH_4Cl and NH_4Br are locked in by hydrogen bonding.

Bleick[5], assuming a point charge model, computed the cohesive energies of ammonium halides using the Born–Mayer potentia[1] wherein second neighbour repulsions are considered explicitly. He deduced a value of 8·95 eV for the proton affinity of ammonia (P_{NH_3}) from his lattice energy calculations in agreement with the theoretical value (9·0 eV) of Mulliken[6]. Ladd and Lee[7], in their thermodynamical studies of ammonium halides, calculated the lattice energies with a single exponential repulsive potential and using the Van der Waals coefficients of rubidium halides. The thermodynamic correction was neglected in their calculations and thus their values for the cohesive energy may be considered to be low in absolute magnitude by a few kcal/mole. Vetchinkin *et al.*[8], considering the charge distribution of the ammonium ion in NH_4Cl, made an approximate estimate of 10 kcal/mole for the contribution of hydrogen bonding.

To decide upon the nature of binding in the ammonium halides, it is advisable to compare the theoretical and experimental cohesive energies but the lack of a measured value for

P_{NH_3} prevented the earlier workers from following this procedure. A number of values based on the molecular orbital calculations have been reported in the literature[9 10]. However, in order to assess the magnitude of the hydrogen bonding in these salts, we approach the problem by calculating the cohesive energy from a thermochemical cycle using the value deduced by Russel *et al.*[11] from their *H*-ion scattering measurements. This is compared with the cohesive energy computed on the Born model. Moreover, as the single crystal elastic constants data of NH_4Cl and NH_4Br[12, 13] are available, it seemed appropriate to recalculate the lattice energies for these salts under standard thermodynamic conditions using the equation of state pertaining to the crystal data employed. Thus the thermo-dynamic correction is taken care of and the calculations are expected to improve as found by the present authors in the case of TlCl and TlBr. The calculations are carried out with the single exponential and double exponential Born-Mayer repulsive potential and the results indicated a predominantly ionic character of binding for NH_4Cl and NH_4Br.

2. DETERMINATION OF REPULSIVE PARAMETERS

The lattice energy W_L of an ionic crystal is composed of an attractive and a repulsive part. The Born Model assumes that the attractive part $-W_A(r)$ is given by the Madelung energy and by the dipole–dipole and dipole–quadrupole Van der Waals interaction energies and postulates a plausible form for the dependence of the repulsive part $W_R(r)$ on the interionic distance. The parameters entering a particular form of $W_R(r)$ are determined from crystal data in standard thermodynamic conditions by means of the equation of state and its volume derivative at constant temperature in the vibrational Hildebrand form[1]. The equations which are strictly correct for a quasi harmonic solid of CsCl type at zero pressures and at classical temperatures can be written as

$$\frac{dW_L}{dr} = \frac{8r^2T\beta}{\sqrt{3}K_T} \tag{1}$$

$$\frac{d^2W_L}{dr^2} = \frac{8\sqrt{3}r}{K_T}\left\{1 + T\left[\frac{1}{K_T}\left(\frac{\partial K_T}{\partial T}\right)_p + \frac{\beta}{K_T^2}\left(\frac{\partial K_T}{\partial P}\right)_T + \tfrac{2}{3}\beta T\right]\right\} = \frac{8\sqrt{3}r}{K_T}F(T,P) \tag{2}$$

where β is the volume thermal expansion coefficient, K_T is the isothermal compressibility of the solid. If one uses the single exponential form $B\exp(-r/\rho)$ for $W_R(r)$, equations (1) and (2) lead to

$$W_L(r) = \left[-\frac{\alpha_r e^2}{r}(1-\rho/r) - \frac{8r^2T\beta\rho}{\sqrt{3}K_T} - \frac{C_r}{r^6}\left(1-\frac{6\rho}{r}\right) - \frac{D_r}{r^8}\left(1-\frac{8\rho}{r}\right)\right] \tag{3}$$

$$r/\rho = \sigma/\tau. \tag{4}$$

Where:

$$\tau = \frac{\alpha_r e^2}{r} + \frac{6C_r}{r^6} + \frac{8D_r}{r^8} - \frac{8r^3T\beta}{\sqrt{3}K_T}$$

and

$$\sigma = \frac{8\sqrt{3}}{K_T}r^3F(T,P) + \frac{2\alpha_r e^2}{r} + \frac{42C_r}{r^6} + \frac{72D_r}{r^8}$$

where α_r, C_r and D_r are the Madelung constant and the Van der Waals coefficients referred to the nearest neighbour distance. The values of the coefficients C_r and D_r are taken from Bleick[5]. The repulsive parameter ρ is determined from equation (4). If one considers explicitly the second neighbour repulsions by adopting the double exponential repulsive potential so that

$$W_L(r) = -\frac{\alpha_r e^2}{r} - \frac{C_r}{r^6} - \frac{D_r}{r^8} + 8C_{+-}b$$

$$\times \exp[(r_+ + r_- - r)/\rho] + 3b\left[\exp\left(\frac{2r_+}{\rho}\right)\right.$$

$$\left.\times C_{++} + C_{--}\exp\left(\frac{2r_-}{\rho}\right)\right]\exp\left(\frac{-1\cdot 155r}{\rho}\right). \quad (5)$$

The quantities c_{+-}, c_{--}, c_{++} are the Pauling coefficients.

Equations (1) and (2) can be rewritten as

$$r = r_+ + r_- + \rho \ln\left\{8C_{+-}\frac{br}{\tau\rho}\left[1 + \frac{6\times 1\cdot 155}{16}\right.\right.$$

$$\times\left\{\frac{C_{++}}{C_{+-}}\exp\left(\frac{r_+ - r_-}{\rho}\right) + \frac{C_{--}}{C_{+-}}\exp\left(\frac{r_- - r_+}{\rho}\right)\right\}$$

$$\left.\left.\times\exp\left(\frac{-0\cdot 155\,r}{\rho}\right)\right]\right\} \quad (6)$$

$$\frac{\left(\frac{r}{\rho}\frac{\tau}{\sigma} - 1\right)}{\left(\frac{1\cdot 155\,r}{\rho}\frac{\tau}{\sigma} - 1\right)} = \frac{-6\times 1\cdot 155}{16}$$

$$\times\left[\frac{C_{++}}{C_{+-}}\exp\left(\frac{r_+ - r_-}{\rho}\right) + \frac{C_{--}}{C_{+-}}\exp\left(\frac{r_- - r_+}{\rho}\right)\right]$$

$$\times\exp\left(\frac{-0\cdot 155\,r}{\rho}\right). \quad (7)$$

The repulsive parameters b, ρ are evaluated from equations (6) and (7) using $r_+ = 1{\cdot}43$ Å, $r_{\mathrm{Cl}^-} = 1{\cdot}81$ Å and $r_{\mathrm{Br}^-} = 1{\cdot}96$ Å and the calculations were carried out on an IBM 1620 computer. The experimental crystal data used is listed in Table 1.

Table 1. *Crystal data for* CsCl *type* NH_4Cl *and* NH_4Br *at room temperature and at atmospheric pressure*

Experimental parameter		NH_4Cl	NH_4Br
$10^8\, r$	cm	3·348	3·505
$10^{12}\, K_T$	cm²/dyn	5·580	6·440
$10^{12}\dfrac{1}{K_T}\left(\dfrac{\partial K_T}{\partial P}\right)_T$	cm²/dyn	−43·160	−68·890
$10^4\ \dfrac{1}{K_T}\left(\dfrac{\partial K_T}{\partial_T}\right)$	°K⁻¹	4·730	9·410
$10^4\, \beta$	°K⁻¹	1·659*	1·792*
$10^{12}\, \tau$	ergs	16·906	16·055
$10^{12}\, \sigma$	ergs	144·068	136·821

*Ref [15].

Data analysis

The past authors made use of Bridgman's [14] Volume compression data for determining the isothermal compressibility and its temperature and pressure coefficients. His data were taken on pressed polycrystalline samples which one might expect to be more compressible than single crystals. Moreover, since the compressibilities derived from velocity of sound measurements would give information more representative of zero pressure than those derived by extrapolation of compressions at high pressures, we used the elastic constants data. From the adiabatic compressibility (K_S) the isothermal compressibility (K_T) at various temperature is deduced from the well known thermodynamic relation

$$K_T = K_S + \frac{TM\beta^2}{C_P d}$$

where C_P is the specific heat per mole at constant pressure, M is the molecular weight and d is the density. The temperature variation of β[15] and C_P[16] are taken into account. The isothermal compressibility at various pressures is calculated considering the pressure dependence of β and d using the procedure adopted by Morse and Lawson [17]. The temperature and pressure coefficients of K_T at zero pressure are obtained from the slopes of $K_T - T$ and $K_T - P$ curves respectively.

To the lattice energy given by equations (3) and (5) the internal vibrational energy, which is usually estimated on a Debye Model, is added to give the cohesive energy at room temperature. In view of the anomalous thermal behaviour of NH_4Cl and NH_4Br the internal energy estimated from the specific heat data is used[5]. The values of the cohesive energies in standard thermodynamic conditions are cited in Table 2 together with their deviations indicated in parenthesis from the experimental values.

3. EXPERIMENTAL COHESIVE ENERGIES

The thermo-chemical process giving the reactions and the corresponding enthalpy changes, is the same as that adopted by Bleick[5], except that it is used to obtain the enthalpy of formation of the crystal at room temperature rather than at the absolute zero, from the dispersed ions at the absolute zero. The cohesive energies (W_c kcal./mole) given in column 2 of Table 2 are calculated at room temperature and at atmospheric pressure using the recent thermo-chemical data, wherever available.

*Reactions

			NH_4Cl	NH_4Br
$NH_4X(C, 298°K)$	$\xrightarrow{W_c}$	$NH_4^+(g, 0°K) + X^-(g, 0°K)$	W_c	W_c
$NH_4^+(g, 0°K)$	$\xrightarrow{P_{NH_3}}$	$NH_3(g, 0°K) + H^+(g, 0°K)$	216·7	216·7
$H^+(g, 0°K)$	$\xrightarrow{I(H)}$	$H^0(g, 0°K)$	−313·5	−313·5
$X^-(g, 0°K)$	$\xrightarrow{I(X)}$	$X^0(g, 0°K)$	85·8†± 1·0	80·5†±0·4
$NH_3(g, 0°K)$	$\xrightarrow{\Delta h_1}$	$NH_3(g, 298°K)$	2·4‡	2·4
$H^0(g, 0°K) + X^0(g, 0°K)$	$\xrightarrow{\Delta h_2}$	$H^0(g, 298°K) + X^0(g, 298°K)$	3·0‡	3·0
$H^0(g, 298°K)$	$\xrightarrow{\frac{1}{2}D(H_2)}$	$\frac{1}{2}H_2(S, 298°K)$	−51·5‖	−51·5
$X^0(g, 298°K)$	$\xrightarrow{-\frac{1}{2}D(X)}$	$\frac{1}{2}X_2(S, 298°K)$	−28·9†	−26·8†
$NH_3(g, 298°K)$	$\xrightarrow{\Delta H(NH_3)}$	$\frac{1}{2}N_2(S, 298°K)$‡ $\frac{3}{2}H_2(S, 298°K)$	10·9§	10·9
$\frac{1}{2}N_2(S, 298°K) + \frac{3}{2}H_2(S, 298°K) + \frac{1}{2}H_2(S, 298°K)$‡ $\frac{1}{2}X_2(S, 298°K)$	$\xrightarrow{\Delta H(NH_4X)}$	$NH_4X(C, 298°K)$	−75·7§	−64·7§

* The letters C, S and g denote crystal, standard state and gas respectively.

†Ref. [1].

‡The enthalpy changes Δh_1 and Δh_2 are estimated from the equipartition law neglecting vibrations for ammonia.

§Ref. [16].

‖Ref. [18].

4. DISCUSSION

The uncertainties of the various data with the exception of the electron affinities and the proton affinity amount to a fraction of a kilocalorie per mole. The accuracy in the value of W_c depends largely on the uncertainty of the value used for the proton affinity of ammonia. The result that the experimental W_c is less than that of the theoretical value reflects the uncertainty in the magnitude of P_{NH_3} used which is clearly an overestimate by at least 0·2 eV. Even though this uncertainty was not quoted by the authors[11] it is clear from the discussion in their paper, the value of 9·4 eV may be too large by about 0·2 to 0·4 eV. If we take 9·0 eV for P_{NH_3} the experimental energies will exceed the computed values by 4·4 and 4·0 kcal./mole for NH_4Cl and NH_4Br respectively. These probably represent upper limits for the Hydrogen bonding contribution. If one considers the hydrogen bonding energy of about 10 kcal./mole estimated by Vetchinkin [8], the proton affinity gets reduced to 8·72 eV. However, very recently Haney and Franklin[19] determined the heat of formation of NH_4^+ ions from electron impact measurements and deduced the P_{NH_3} to be 8·98 eV.

Table 2. Room temperature cohesive energies (kcal./mole)

Crystal	Experimental value	Computed value Single exponential form	 Double exponential form
NH_4Cl	−150·2	−155·1(−4·9)	−155·0(−4·8)
NH_4Br	−143·0	−148·3(−5·3)	−148·2(−5·2)

This suggests that Vetchinkin's value for the hydrogen bonding energy in NH_4Cl is overestimated.

Before concluding we determine how well the Born Model is applicable for these by adopting two criteria. One method is to verify the Szigeti (20, 21) equations. Szigeti developed two equations relating the experimental parameters of a Born model which can be written as

$$9MVW^2(\epsilon_S - n^2) = 4\pi(n^2+2)^2(Ze)^2 \qquad (9)$$

$$Mr^2W^2K_T(\epsilon_S+2) = 3V(n^2+2) \qquad (10)$$

where Ze is the charge on an ion, V is the molecular volume W is the infrared absorption frequency, M is the reduced mass of the ions, r is the nearest neighbour distance. The value of e calculated from equation (9) is called e^*, the effective charge. Its ratio to the electronic charge, e is less than one, and the difference between e^*/e and 1 is a measure of the overlap distortion of the ions and the non-centrality of the forces[22]. Similarly, the calculated K_T^* is not usually equal to the experimental value K_T and the ratio of K_T^*/K_T may be either greater or less than 1, with the difference due to non-centrality of forces or next-nearest neighbour interactions [23]. The value of e^*/e and K_T^*/K_T along with experimental values at room temperature used in calculating them are presented in Table 3.

We see that the large deviation of K_T^*/K_T from unity needs further discussion. The second derivation of Szigeti is based on the Born Model of ionic crystals for the stability of a static lattice, unlike that of his relation for e^*. It is strictly applicable only at very low temperatures. Thus the deviations of K_T^*/K_T from 1 cannot be taken to indicate the failure of Born Model as the room temperature values of the experimental parameters are used. The second and sensitive test of the nature of binding and hence the applicability of Born Model is the validity of Cauchy's relation. The ratio of C_{12}/C_{44} at room temperature is found to be 0·986 and 1·083 for NH_4Cl and NH_4Br respectively. This shows that these salts are largely ionic because with homopolar binding we should not expect the relation $C_{12} = C_{44}$ to be satisfied[25].

Table 3. Experimental values used for evaluating Szigetti equations

Parameter	NH_4Cl	NH_4Br	Ref.
ϵ_S	6·96	7·3	[16]
n^2	2·698	2·927	[24]
$10^{-13}W$(sec^{-1})	3·66	3·178	[16]
$10^{+23}M$(g)	1·909	2·33	
$10^{12}K_T$(cm^2/dyn)	5·58	6·44	
e^*/e	0·94	0·93	
K_T^*/K_T	0·57	0·59	

In the light of the above considerations, it appears fairly certain that the cohesion in these salts is predominantly ionic and the hydrogen bonding contribution is less than 5 kcal./mole. in NH_4Cl and NH_4Br.

Acknowledgements—The authors would like to thank Professor C. Ramasastry for his interest and encouragement.

REFERENCES

1. TOSI M. P., *In Solid State Physics* (Edited by F. Seitz and D. Turnbull), Vol. 16, p. 42–74. Academic Press, New York (1964).

2. SEITZ F., *The Modern Theory of Solids*. p. 89. McGraw-Hill, New York (1940).

3. HAMILTON W. C. and IBERS J. A., *Hydrogen Bonding in Solids*, p. 222. BENJAMIN, New York (1968).

4. WADDINGTON T. C., *J. chem. Soc*. 4340 (1958).

5. BLEICK W. E. *J chem Phys.* **2**, 160 (1934).

6. MULLIKEN R. S., *J. chem. Phys.* **1**, 492 (1933).

7. LADD M. F. C. and LEE W H., *J inorg nucl Chem*. **13**, 218 (1960).

8. VETCHINKIN S. I., PSENICHNOV E. A. and SOKOLOV N. D., *Zh. Fiz. Khim*. **33**, 1269 (1959).

9 MOCCIA R., *J chem. Phys*. **40**, 2176 (1964).

10. RAJAGOPAL P., *Z Naturf*. **20a**, 1557 (1965).

11 RUSSEL A. S., FONTANA C M and SIMONS J H., *J chem. Phys* **9**, 381 (1941)

12 GARLAND C. W. and RENARD R., *J. chem. Phys* **44**, 1130 (1966).

13 GARLAND C. W and YARNELL C F *J chem Phys* **44**, 1112 (1966).

14. BRIDGMAN P. W., *Phys Rev*. **38**, 182 (1931)

15. SHARMA S. S., *Proc. Indian Acad. Sci.* **A31**, 339 (1950).

16. See *International Critical Tables of Numerical Data*. McGraw-Hill, New York (1933).

17. MORSE G. E. and LAWSON A. W., *J. Phys. Chem. Solids* **28**, 939 (1967).

18. SLATER J. C., *Introduction to Chemical Physics*, p. 132. McGraw-Hill, New York (1939).

19. HANEY M. A. and FRANKLIN J. L., *J. chem. Phys*. **50**, 2028 (1969).

20. SZIGETI B., *Trans. Faraday. Soc*. **45**, 155 (1949).

21. SZIGETI B., *Proc. R. Soc*. **A204**, 51 (1950).

22. HANLON J. E. and LAWSON A. W., *Phys. Rev.* **133**, 472 (1959).

23 JONES G. A., MARTIN D. H., MAWER P. A. and PERRY C. H., *Proc. R. Soc*. **261**, 10 (1961).

24. TESSMAN J. R., KHAN A. H. and SHOCKLEY W., *Phys. Rev*. **93**, 890 (1953).

25. MOTT N F. and GURNEY R. W., *Electronic Processes in Ionic Crystals*, p. 10. Oxford University Press, (1957).

J. Phys. Chem. Solids Pergamon Press 1970. Vol. 31, pp. 1491–1510. Printed in Great Britain.

SOLUTION TO THE ANDERSON EXCHANGE NARROWING MODEL FOR $I > \frac{1}{2}$*

HORACIO A. FARACH, EDWIN F. STROTHER and CHARLES P. POOLE, Jr.
University of South Carolina, Columbia, S.C. 29208, U.S.A.

(*Received* 15 *September* 1969)

Abstract – The Anderson exchange and motional narrowing model of a resonance spectrum was solved for two distinct cases having nuclear spin values of $I = \frac{1}{2}, 1, \frac{3}{2}, 2$, and $\frac{5}{2}$. In the absence of exchange interactions the spectrum consists of $n = 2I + 1$ resolved lines of equal intensity and separated by the frequency $2\omega_0$. Case (a) corresponds to equal transition probability to all other lines of the spectrum, while allowed transitions for case (b) occur only between adjacent lines. For both cases the initial effect of increasing the magnitude of the exchange interaction ω_e is the broadening and drawing together of the spectral lines. At higher exchange frequencies the spectrum is dominated by a single exchange narrowed component while the other $n - 1$ lines are broadened beyond detection. For case (a) exchange narrowing occurs when $\omega_e > 2(n-1)\omega_0$ and for case (b) it occurs when $\omega_e > 2(n-1)^2\omega_0$. In the limit of strong exchange all of the hyperfine components collapse to the spectral center of gravity for case (b), as contrasted with case (a) in which only the inner ($M_I = 0$ or $\pm\frac{1}{2}$) components actually collapse to the center

Values of the ratio ω_e/ω_0 at each hyperfine component's point of collapse to the center were determined. The variations of the line positions, widths and relative intensities were calculated as a function of the exchange frequency Asymptotic formulae were derived for the limits of large and small exchange.

1. INTRODUCTION

A NUMBER of years ago, P. W. Anderson[1] formulated a mathematical model for exchange and motional narrowing which he referred to as the 'Random frequency-modulation model'. In this classical paper he derived determinantal expressions for an arbitrary spin, and deduced perturbation formulae for the extremes of very small and very large exchange. His solutions provide the width and position of each line in the spectrum. In addition, he solved the spin $\frac{1}{2}$ problem exactly. The results of this paper have been found useful in interpreting the experimental data of many workers, and it is widely considered as the fundamental paper on exchange narrowing.

Since its publication, not much additional work has been carried out to solve Anderson's equations. Sack[2] deduced integral solutions for the line widths of the various lines, but his expressions are too complex for convenient use. Some workers have tended to extrapolate the results of Anderson's exact solution for spin $\frac{1}{2}$, and to draw conclusions therefrom concerning the higher spin cases. The general belief concerning the validity of this extrapolation has hindered progress toward a fuller understanding of exchange narrowing. Indeed, the general solutions to Anderson's equations which we present below exhibit some rather novel and unexpected features which should be experimentally observable.

The treatment presented here extends the Anderson approach to higher spin states, without any modification in the theory. Other authors have treated this problem from a more sophisticated or more general viewpoint, and the relationship of our approach to theirs will be clarified below. Much of this recent work in the field of relaxation and hyperfine structure[3–6] has been motivated by a desire to interpret relaxation effects in Mössbauer spectra, whereas the present formulation is more applicable to the electron spin resonance of transition metal ions, and to exchange effects in NMR for nuclei with $I > \frac{1}{2}$.

2. THE ANDERSON MODEL

Anderson's classic paper contains the

---

*Supported in part by Air Force Office of Scientific Research Grant No. 1139-68.

theoretical background for his theory, so we will be content to present his final equations. The basic parameters which enter into the theory are the hyperfine coupling constant A_0 and the exchange frequency ω_e. In the absence of exchange the observed hyperfine spectrum arising from a nuclear spin I is assumed to consist of $2I+1$ equally spaced hyperfine lines, and each line is assumed to have the same amplitude and zero width.

Anderson considers two simple cases of his model which he characterizes as 'typical of two possible extremes'. In case (a) we consider transitions as being equally coupled to all other lines of the spectrum while in case (b) the transitions occur only to the nearest lines. For spin I one must solve a $(2I+1)$ by $(2I+1)$ symmetrical square matrix. For case (a) the off-diagonal matrix elements are all $\omega_e/2I$ while for case (b) the off-diagonal matrix elements are $\omega_e/2$ adjacent to the diagonal ones, and zero otherwise. The diagonal matrix elements of case (a) with the eigenvalue λ are

$$[-(\omega_e-\lambda)-iM_IA_0] \tag{1}$$

where M_I runs consecutively over integral or half-integral values. Case (b) has the same diagonal matrix elements except for the two end or corner positions where $M_I=\pm I$, for which $-\omega_e$ is replaced by $-\omega_e/2$. As a result, if all of the matrix elements in a row or column are summed only the value $-\lambda-iM_IA_0$ will be obtained. For the case $I=\frac{1}{2}$ both matrices are identical, and this is the case that was solved exactly by Anderson. It might be mentioned in passing that Anderson employs the symbol $m/2$ for M_I and $2\omega_0$ for A_0, and as a result some of his summations are in steps of two. For $I=\frac{5}{2}$ the eigenvalue matrix for Anderson's case (a) is

$$\begin{vmatrix} \omega_e+\frac{5i}{2}A_0-\lambda & \frac{\omega_e}{5} & \frac{\omega_e}{5} & \frac{\omega_e}{5} & \frac{\omega_e}{5} & \frac{\omega_e}{5} \\ \frac{\omega_e}{5} & -\omega_e+\frac{3i}{2}A_0-\lambda & \frac{\omega_e}{5} & \frac{\omega_e}{5} & \frac{\omega_e}{5} & \frac{\omega_e}{5} \\ \frac{\omega_e}{5} & \frac{\omega_e}{5} & -\omega_e+\frac{i}{2}A_0-\lambda & \frac{\omega_e}{5} & \frac{\omega_e}{5} & \frac{\omega_e}{5} \\ \frac{\omega_e}{5} & \frac{\omega_e}{5} & \frac{\omega_e}{5} & -\omega_e-\frac{i}{2}A_0-\lambda & \frac{\omega_e}{5} & \frac{\omega_e}{5} \\ \frac{\omega_e}{5} & \frac{\omega_e}{5} & \frac{\omega_e}{5} & \frac{\omega_e}{5} & -\omega_e-\frac{3i}{2}A_0-\lambda & \frac{\omega_e}{5} \\ \frac{\omega_e}{5} & \frac{\omega_e}{5} & \frac{\omega_e}{5} & \frac{\omega_e}{5} & \frac{\omega_e}{5} & -\omega_e-\frac{5i}{2}A_0-\lambda \end{vmatrix} \tag{2}$$

while that for Anderson's case (b) is

$$\begin{vmatrix} -\frac{\omega_e}{2}+\frac{5}{2}iA_0-\lambda & \frac{\omega_e}{2} & 0 & 0 & 0 & 0 \\ \frac{\omega_e}{2} & -\omega_e+\frac{3}{2}iA_0-\lambda & \frac{\omega_e}{2} & 0 & 0 & 0 \\ 0 & \frac{\omega_e}{2} & -\omega_e+\frac{i}{2}A_0-\lambda & \frac{\omega_e}{2} & 0 & 0 \\ 0 & 0 & \frac{\omega_e}{2} & -\omega_e-\frac{i}{2}A_0-\lambda & \frac{\omega_e}{2} & 0 \\ 0 & 0 & 0 & \frac{\omega_e}{2} & -\omega_e-\frac{3i}{2}A_0-\lambda & \frac{\omega_e}{2} \\ 0 & 0 & 0 & 0 & \frac{\omega_e}{2} & -\frac{\omega_e}{2}-\frac{5i}{2}A_0-\lambda \end{vmatrix}. \tag{3}$$

The corresponding matrices for other values of I are easily written down.

3. THE POLYNOMIAL EQUATIONS

To solve the exchange narrowing problem one may either diagonalize the matrix directly, or equate the determinant of the matrix to zero and find the roots λ of the resulting $(2I+1)$-th order polynomial equation. Each procedure was carried out on a computer, and answers obtained by these two methods were compared to check the accuracy of the calculations. Additional checks were obtained by the use of the perturbation formulae to be presented below.

The first step in solving the matrix equations consists in casting them in a symmetrical, dimensionless form. The appropriate changes of variable for case (a) with $I = \frac{5}{2}$ are

$$S = \frac{5}{\omega_e}\left(-\omega_e - \lambda + \frac{5i}{2}A_0\right) - 1 \qquad (4)$$

$$T = \frac{5}{\omega_e}\left(-\omega_e - \lambda + \frac{3i}{2}A_0\right) - 1 \qquad (5)$$

$$U = \frac{5}{\omega_e}\left(-\omega_e - \lambda + \frac{i}{2}A_0\right) - 1 \qquad (6)$$

$$W = 5\frac{\lambda}{\omega_e} + 6 \qquad (7)$$

$$X = \frac{5A_0}{2\omega_e} \qquad (8)$$

where of course $U^* = \frac{5}{\omega_e}\left(-\omega_e - \lambda - \frac{i}{2}A_0\right) - 1$, etc.

This gives the corresponding matrix

$$\begin{matrix} S+1 & 1 & 1 & 1 & 1 & 1 \\ 1 & T+1 & 1 & 1 & 1 & 1 \\ 1 & 1 & U+1 & 1 & 1 & 1 \\ 1 & 1 & 1 & U^*+1 & 1 & 1 \\ 1 & 1 & 1 & 1 & T^*+1 & 1 \\ 1 & 1 & 1 & 1 & 1 & S^*+1 \end{matrix} \qquad (9)$$

and its equivalent polynomial equations

$$\begin{aligned} &SS^*TT^*UU^* + (S+S^*)(TT^*UU^*) \\ &\quad + (T+T^*)(SS^*UU^*) + (U+U^*) \\ &\quad \times (SS^*TT^*) = 0 \end{aligned} \qquad (10)$$

and

$$\begin{aligned} &W^6 - 6W^5 + 35W^3X^2(W-4) \\ &\quad + 259WX^4(W-2) + 225X^6 = 0 \end{aligned} \qquad (11)$$

The analogous expressions for case (b), $I = \frac{5}{2}$ are

$$S = \frac{1}{\omega_e}(-\omega_e - 2\lambda + 5iA_0) \qquad (12)$$

$$T = \frac{1}{\omega_e}(-2\omega_e - 2\lambda + 3iA_0) \qquad (13)$$

$$U = \frac{1}{\omega_e}(-2\omega_e - 2\lambda + iA_0) \qquad (14)$$

$$W = 2\left(1 + \frac{\lambda}{\omega_e}\right) \qquad (15)$$

$$X = \frac{A_0}{\omega_e} \qquad (16)$$

$$\begin{matrix} S & 1 & 0 & 0 & 0 & 0 \\ 1 & T & 1 & 0 & 0 & 0 \\ 0 & 1 & U & 1 & 0 & 0 \\ 0 & 0 & 1 & U^* & 1 & 0 \\ 0 & 0 & 0 & 1 & T^* & 1 \\ 0 & 0 & 0 & 0 & 1 & S^* \end{matrix} \qquad (17)$$

$$\begin{aligned} &SS^*TT^*UU^* - UU^*(ST + T^*S^* - 1) \\ &\quad - SS^*(TU + T^*U^* - 1) - SS^*TT^* \\ &\quad + [ST + S^*T^*] + [SU^* + S^*U] - 1 = 0 \end{aligned} \qquad (18)$$

$$\begin{aligned} &W^6 - 2W^5 + (35X^2 - 4)W^4 + 4(2 - 5X^2)W^3 \\ &+ (259X^4 - 40X^2 + 3)W^2 + 2(-9X^4 + 4X^2 - 3)W \\ &+ (225X^6 - 36X^4 + 3X^2) = 0. \end{aligned} \qquad (19)$$

The corresponding expressions for other

values of nuclear spin I are easily written down by analogy with these cases.

The basic polynomial equations for the nuclear spins $\frac{1}{2} \leq I \leq \frac{5}{2}$ are listed in Tables 1–4 for Anderson cases (a) and (b). The equations in Tables 1 and 3 follow a certain sequential order in the two series $I = \frac{1}{2}, \frac{3}{2}, \frac{5}{2}, \ldots$ and $I = 1, 2, 3, \ldots$ The equations in Tables 2 and 4 also exhibit certain analogous symmetries, but to a lesser extent than those in Tables 1 and 3. Symmetries in the $S, T, U, \ldots$ equations allow one to write down those for higher values of the nuclear spin I.

The parameters X, W, S, T, and U in the

Table 1. The equations obtained by multiplying out the determinant for Anderson case (a). The parameters X *and* W *are listed in Table 2*

I	S	T	U	Equation
$\frac{1}{2}$	$-W+iX$	—	—	$SS^*+(S+S^*)=0$
1	$-W+2iX$	$-W$	—	$(W-1)SS^*+W(S+S^*)=0$
$\frac{3}{2}$	$W+3iX$	$W+iX$		$(SS^*TT^*)+(S+S^*)(TT^*)+(T+T^*)(SS^*)=0$
2	$-W+4iX$	$W+2iX$	$-W$	$(W-1)(SS^*)(TT^*)+W(S+S^*)(TT^*)+W(T+T^*)(SS^*)=0$
$\frac{5}{2}$	$-W+5iX$	$-W+3iX$	$-W+iX$	$SS^*TT^*UU^*+(S+S^*)(TT^*)(UU^*)+(T+T^*)(SS^*UU^*)$ $+(U+U^*)(SS^*TT^*)=0$

Table 2. The W*-polynomial equation for Anderson case (a) with the dimensionless parameters* W *and* X *defined. These equations are derived from the corresponding ones presented in Table 1, where $A_0 = 2\omega_0$*

I	X	W	Equation
I	IA_0/ω_r	$2I\left(\frac{\lambda}{\omega_r}+1\right)+1$	$\sum_{n=0}^{2I+1} C_n(X)W^n = \sum_{m\ \text{even}} B_m(W)X^m = 0$
$\frac{1}{2}$	$\frac{A_0}{2\omega_r}$	$\frac{\lambda}{\omega_r}+2$	$(W^2-2W)+X^2=0$
1	$\frac{A_0}{\omega_r}$	$2\frac{\lambda}{\omega_r}+3$	$(W^3-3W^2)+4(W-1)X^2=0$
$\frac{3}{2}$	$\frac{3A_0}{2\omega_r}$	$3\frac{\lambda}{\omega_r}+4$	$(W^4-4W^3)+10(W^2-2W)X^2+9X^4=0$
2	$\frac{2A_0}{\omega_r}$	$4\frac{\lambda}{\omega_r}+5$	$(W^5-5W^4)+20(W^3-3W^2)X^2+64(W-1)X^4=0$
$\frac{5}{2}$	$\frac{5A_0}{2\omega_r}$	$5\frac{\lambda}{\omega_r}+6$	$(W^6-6W^5)+35(W^4-4W^3)X^2+259(W^2-2W)X^4+225X^6=0$

Table 3. The equations obtained by multiplying out the determinant for Anderson case (b). The parameters X *and* W *are defined in Table 4*

I	S	T	U	Equation
$\frac{1}{2}$	$1-W+iX$	—	—	$SS^*-1=0$
1	$1-W+2iX$	$-W$	—	$WSS^*+(S+S^*)=0$
$\frac{3}{2}$	$1-W+3iX$	$-W+iX$	—	$SS^*TT^*-(ST+S^*T^*)-SS^*+1=0$
2	$1-W+4iX$	$-W+2iX$	$-W$	$WSS^*TT^*-W(ST+S^*T^*)+SS^*(T+T^*)$ $-(S+S^*)+W=0$
$\frac{5}{2}$	$1-W+5iX$	$-W+3iX$	$-W+iX$	$SS^*TT^*UU^*-SS^*(TU+T^*U^*-1)$ $-UU^*(ST+S^*T^*-1)-SS^*TT^*+[ST+S^*T^*]$ $+(SU^*+S^*U^*)-1=0$

Table 4. The W*-polynomial equation for Anderson case (b). The dimensionless parameters* X *and* W *are the same for each nuclear spin* I. *These equations were derived from the corresponding ones in Table* 3, *where* $A_0 = 2\omega_0$

I	X	W	Equation
I	A_0/ω_e	$2\left(1+\frac{\lambda}{\omega_e}\right)$	$\sum_{n=0}^{2I+1} C_{n(x)}W^n = \sum_{m\ \mathrm{even}} B_{m(W)}X^m = 0$
$\frac{1}{2}$	A_0/ω_e	$2\left(1+\frac{\lambda}{\omega_e}\right)$	$W^2-2W+X^2=0$
1	A_0/ω_e	$2\left(1+\frac{\lambda}{\omega_e}\right)$	$W^3-2W^2+W(4X^2-1)+2=0$
$\frac{3}{2}$	A_0/ω_e	$2\left(1+\frac{\lambda}{\omega_e}\right)$	$W^4-2W^3+2W^2(5X^2-1)+2W(-X^2+2)+9X^4-2X^2=0$
2	A_0/ω_e	$2\left(1+\frac{\lambda}{\omega_e}\right)$	$W^5-2W^4+W^3(20X^2-3)+2W^2(-4X^2+3)+W(64X^4-12X^2+1)-2=0$
$\frac{5}{2}$	A_0/ω_e	$2\left(1+\frac{\lambda}{\omega_e}\right)$	$W^6-2W^5+W^4(35X^2-4)+4W^3(-5X^2+2)+W^2(259X^4-40X^2+3)$ $+2W(-9X^4+4X^2-3)+(225X^6-36X^4+3X^2)=0$

equations of Tables 1–4 are dimensionless since they are normalized relative to the exchange frequency ω_e. One should note that the W-equation for each case may be considered as a polynomial in W with the form

$$\sum_{n=0}^{2I+1} C_n(X)\,W^n = 0 \tag{20}$$

where the coefficients C_n are functions of X. These coefficients exhibit certain regularities such as

$$\left.\begin{aligned} C_{2I+1} &= 1 \\ C_{2I} &= -(2I+1) \end{aligned}\right\}\text{Case (a)}$$
$$\left.\begin{aligned} C_{2I+1} &= 1 \\ C_{2I} &= -2 \end{aligned}\right\}\text{Case (b)} \tag{21}$$

and all C_n are non-zero for $0 \leq n \leq 2I+1$. The W-equation may also be considered as a polynomial in X

$$\sum B_m(W)X^m = 0 \tag{22}$$

with the coefficients B_m considered as functions of W. Only even powers of X occur, and all such powers appear from the constant (X^0) to the highest terms (X^{2I+1} for half integral spin and X^{2I} for integral spin I).

When the W-equation is written as a polynomial in λ it becomes very complicated, so such expressions will not be written down here. It is more convenient to let the computer make this variable change.

4. SOLUTIONS OF THE EXCHANGE MODEL

The eigenvalues λ of the matrices (roots of the polynomial equations) are in general complex

$$\lambda = -\Delta\omega + iP. \tag{23a}$$

The real part $\Delta\omega$ is the linewidth, and the imaginary part P is the position of the hyperfine component. The roots may be labeled with the parameters μ where

$$\lambda_\mu = -\Delta\omega_\mu + iP_\mu \tag{23b}$$

$\Delta\omega_\mu > 0$ and P_μ is positive for $\mu > 0$, negative for $\mu < 0$ and vanishes for $\mu = 0$. The line positions P_μ are symmetrical about the center point of the spectrum

$$\begin{aligned} P_\mu &= -P_{-\mu} \\ P_0 &= 0. \end{aligned} \tag{24}$$

The linewidth $\Delta\omega = \frac{1}{2}\Delta\omega_{1/2}$ may be looked upon as half of the full absorption linewidth at half amplitude. Since we assume infinitely narrow or 'δ-function' lineshapes $\Delta\omega_\mu$ is zero for all hyperfine components when $A_0/\omega_e \gg 1$ and the observed exchange-narrowed singlet again becomes infinitely narrow in the very strong exchange limit $A_0/\omega_e \ll 1$. These asymptotic limits will be discussed below where the ranges of validity will be more accurately defined. Figures 1–6 present the variation of the widths and positions of the hyperfine components for several nuclear spin states using Anderson's cases (a) and (b), while Tables 5–7 give asymptotic and transition point values. The solid lines in these figures are the computer calculated results while the dotted lines show the limiting behavior. For ease of comparison the plots for half integral spins are on the left and the integral spins are on the right. In these figures one should note that the abscissa scale is $\omega_e/(n-1)\omega_0$ for case (a) and $\omega_e/(n-1)^2\omega_0$ for case (b), where the notation $\omega_0 = A_0/2$ is used. As shown on Figs. 1 and 4, the final hyperfine line of each spectrum collapses into the center in the range from $\frac{1}{2}$ to 2 on the abscissa scale, so these scales are convenient to use. What this means physically is that exchange narrowing predominates when $\omega_e > 2(n-1)\omega_0$ for Anderson case (a) and when $\omega_e > 2(n-1)^2\omega_0$ for Anderson case (b). The usually accepted criterion omits the factor $(n-1)$ or $(n-1)^2$, so the exchange frequency ω_e deduced from a comparison of the Anderson theory with experimental data will be rather large for high values of the nuclear spin. This must be borne in mind when comparing the Anderson theory with other theoretical formulations of exchange narrowing.

Before proceeding it will be helpful to say a few words about the ordinate scales. Since the overall hyperfine pattern covers a range of $4I\omega_0$, it is appropriate to normalize the position to $P/(n-1)\omega_0$, as was done on Figs. 1 and 4. The linewidth of all hyperfine components except the exchange narrowed singlet in the center $(P=0)$ is approximately equal to the exchange frequency ω_e in the two limits $\omega_e \gg \omega_0$ and $\omega_e \ll \omega_0$. As a result it is appropriate to normalize the ordinate linewidth scale of Figs. 2 and 3 of case (a) to $\Delta\omega/(n-1)\omega_0$ and the scale on Fig. 5 of case (b) to $\Delta\omega/(n-1)^2\omega_0$. Figure 6 of case (b) shows the details of the exchange narrowed singlet which has a width $1/(n-1)$ as great as the broadest component, so the ordinate $\Delta\omega/(n-1)\omega_0$ is appropriate. The abscissae and ordinates of the other figures are less likely to

Table 5. Asymptotic values of the normalized line positions $P/\omega_0 = 2P/A_0$ *for weak and strong exchange. Cf. equations* (28), (30) *and* (37)

			Case (a)		Case (b)	
n	I	M_I	$\omega_e \ll (n-1)\omega_0$	$\omega_e \gg (n-1)\omega_0$	$\omega_e \ll (n-1)\omega_0$	$\omega_e \gg (n-1)^2\omega_0$
2	$\frac{1}{2}$	$\pm\frac{1}{2}$	± 1	0	± 1	0
3	1	0	0	0	0	0
		± 1	± 2	$\pm\frac{2}{\sqrt{3}}$	± 2	0
4	$\frac{3}{2}$	$\pm\frac{1}{2}$	± 1	0	± 1	0
		$\pm\frac{3}{2}$	± 3	$\pm\sqrt{5}$	± 3	0
5	2	0	0	0	0	0
		± 1	± 2	$\pm[6-2\sqrt{29/5}]^{1/2}$	± 2	0
		± 2	± 4	$\pm[6+2\sqrt{29/5}]^{1/2}$	± 4	0
6	$\frac{5}{2}$	$\pm\frac{1}{2}$	± 1	0	± 1	0
		$\pm\frac{3}{2}$	± 3	$\pm[\frac{1}{3}(35-4\sqrt{7})]^{1/2}$	± 3	0
		$\pm\frac{5}{2}$	± 5	$\pm[\frac{1}{3}(35+4\sqrt{7})]^{1/2}$	± 5	0

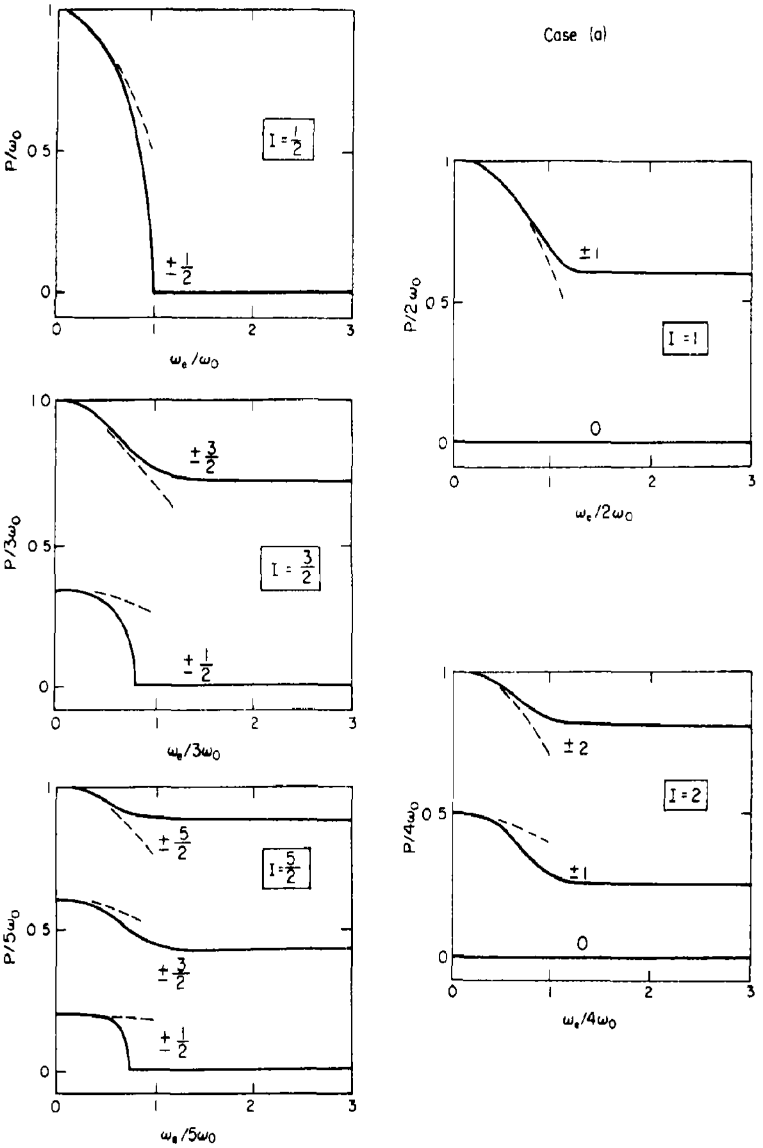

Fig. 1 The dependence of the magnitude of the position P (solid curves) of various component lines on the exchange frequency ω_e for case (a). The ordinate $|P|$ where $P_{M_I} = -P_{-M_I}$. Both the ordinate and abscissa are normalized relative to $(2I\omega_0) = (IA_0)$. The asymptotic behavior (dashed curve) for $\omega_e \ll 2I\omega_0$ is also shown. Table 7 gives the exchange frequencies at which the $\pm\frac{1}{2}$ lines collapse to zero.

lead to confusion, so they will not be explicated until later.

Bearing in mind the precautions noted in the previous paragraph, we will proceed to a discussion of the calculated results presented in Figs. 1–6 by the solid line curves. Cases (a) and (b) are identical for $I = \frac{1}{2}$.

(a) *Anderson case (a)*

The remarkable thing about the hyperfine

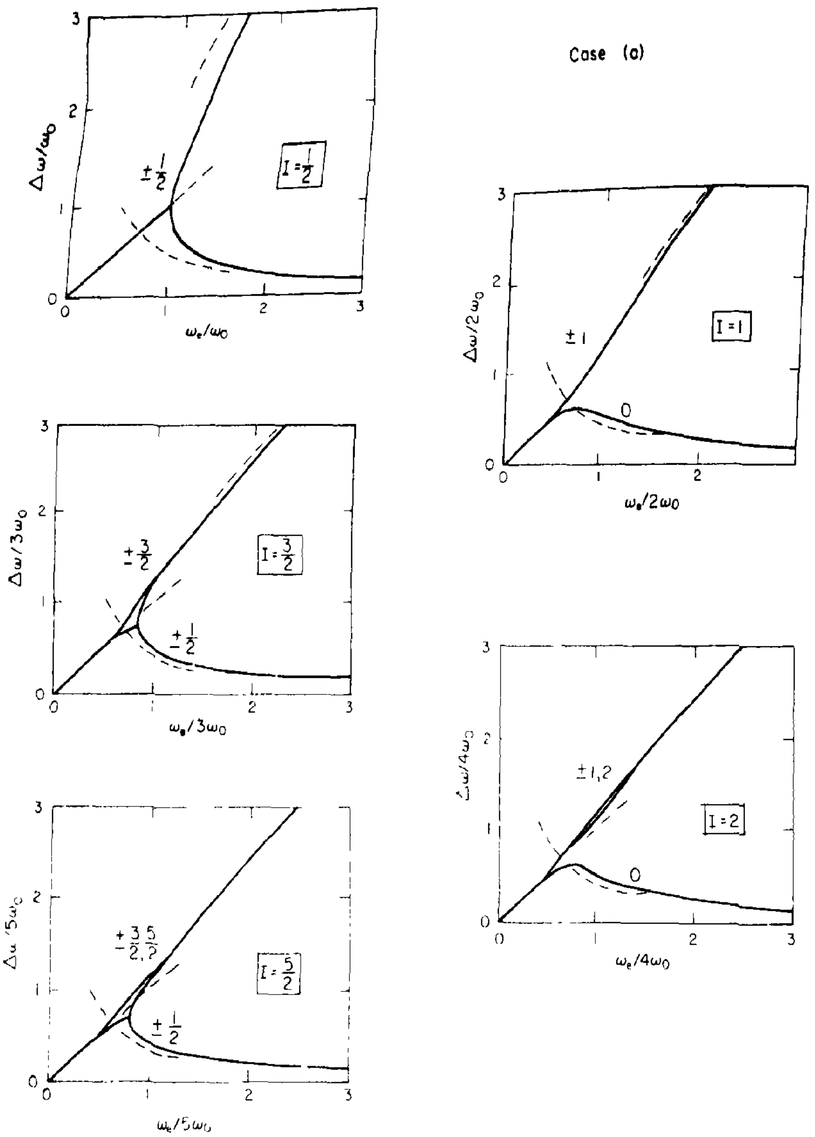

Fig. 2. The dependence of the linewidth $\Delta\omega$ (solid curves) on the exchange frequency ω_e for case (a). Both the ordinate and abscissa are normalized relative to $2I\omega_0$. The asymptotic behavior (dashed curves) at large and small ω_e is shown.

pattern of case (a) is how only one component is exchange narrowed. For integral spin ($I = 1, 2$) the central $M_I = 0$ line is infinitely narrow at zero exchange, increases to a peak width of $\Delta\omega \sim 0{\cdot}6(n-1)\omega_0$ near $\omega_e \sim 0{\cdot}7(n-1)\omega_0$, as shown on Figs. 2 and 3, and then gradually narrows to another delta function linewidth as $\omega_e \to \infty$. For half integral spin the $M_I = \pm\frac{1}{2}$ lines collapse rather abruptly into the center at or somewhat below exchange rates of $\omega_e \sim (n-1)\omega_0$, with the transition shifting to slightly lower values of ω_e with increasing nuclear spin I, as shown on the left hand side of Fig. 1. The values of

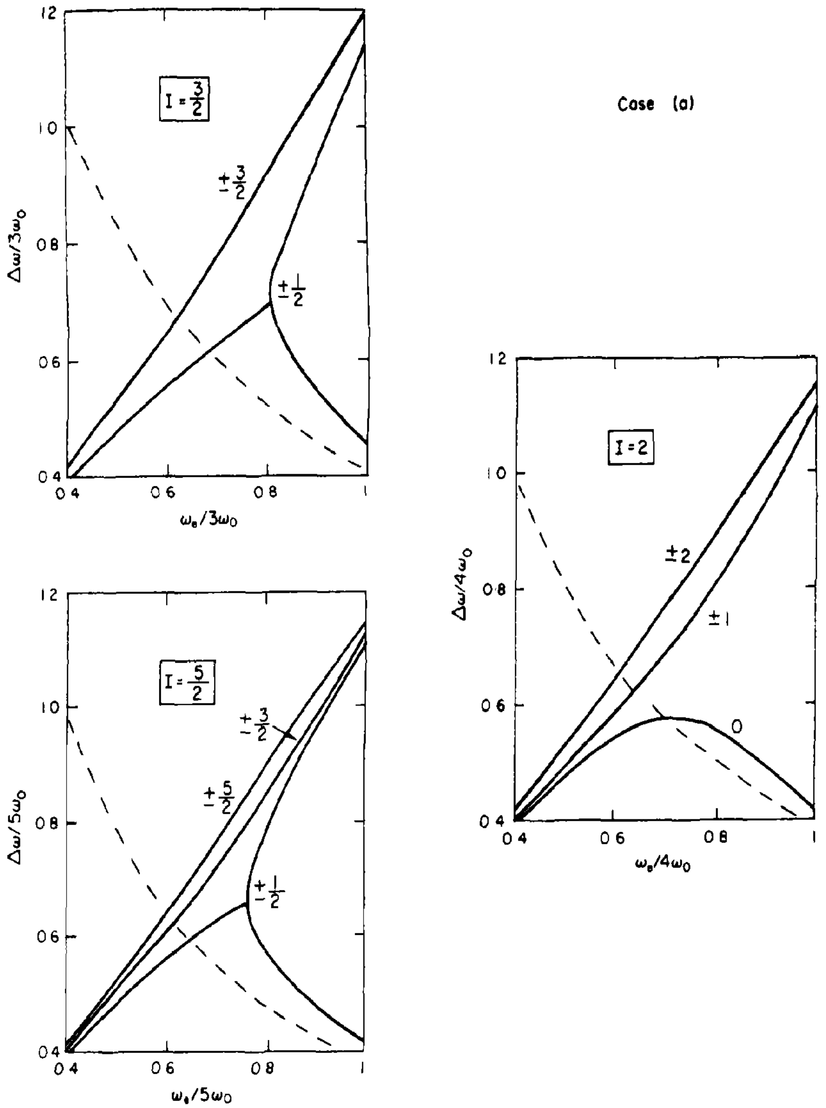

Fig. 3. Detailed plots of the linewidth behavior from Fig. 2 near the onset of exchange narrowing.

ω_e/ω_0 at the transition are listed in Table 7. The linewidths for the exchange narrowed component near $\omega_e \sim (n-1)\omega_0$ for both the integral and half integral case are quite similar, as shown in Fig. 2 and the detailed plots of Fig. 3. The main difference is that the $M_I = 0$ linewidth goes through a maximum value and then narrows, whereas the width of the $M_I = \pm\frac{1}{2}$ line stops rather abruptly at its peak value and splits into two components which form a very smooth curve as it passes vertically past this transformation point. The lower component proceeds to exchange narrow at $\omega_e \gg (n-1)\omega_0$, while the upper one broadens to infinity. In the strongly exchange narrowed region only the narrow line is observable experimentally.

A remarkable result characteristic of this

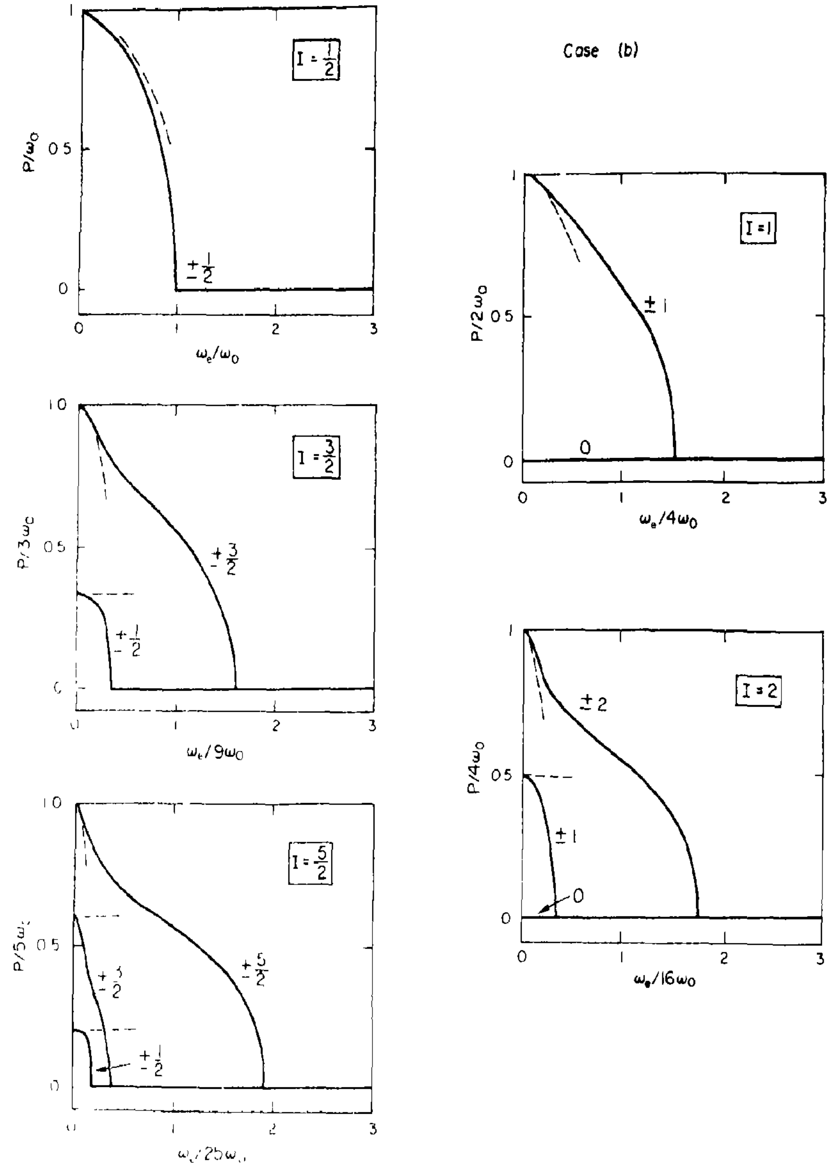

Fig. 4 The dependence of the magnitude of the position P on the exchange frequency ω_e for case (b) using the notation of Fig. 1. For each graph the position P is normalized relative to $2I\omega_0$, while the abscissa is normalized to $(2I)^2\omega_0$. Table 7 gives the exchange frequencies at which the various components collapse to zero.

model is the manner in which $(n-1)$ components of an n component hyperfine pattern broaden to infinity beyond the transition near $\omega_e(n-1)\omega_0$. Indeed the linewidth for $\omega_e \gg (n-1)\omega_0$ is proportional to ω_e with a proportionality constant close to unity, as shown in Table 6. The lines with $I > \frac{1}{2}$ assume positions intermediate between the center of the pattern and their positions $2\omega_0 M_I$ in the absence of exchange narrowing, as shown on

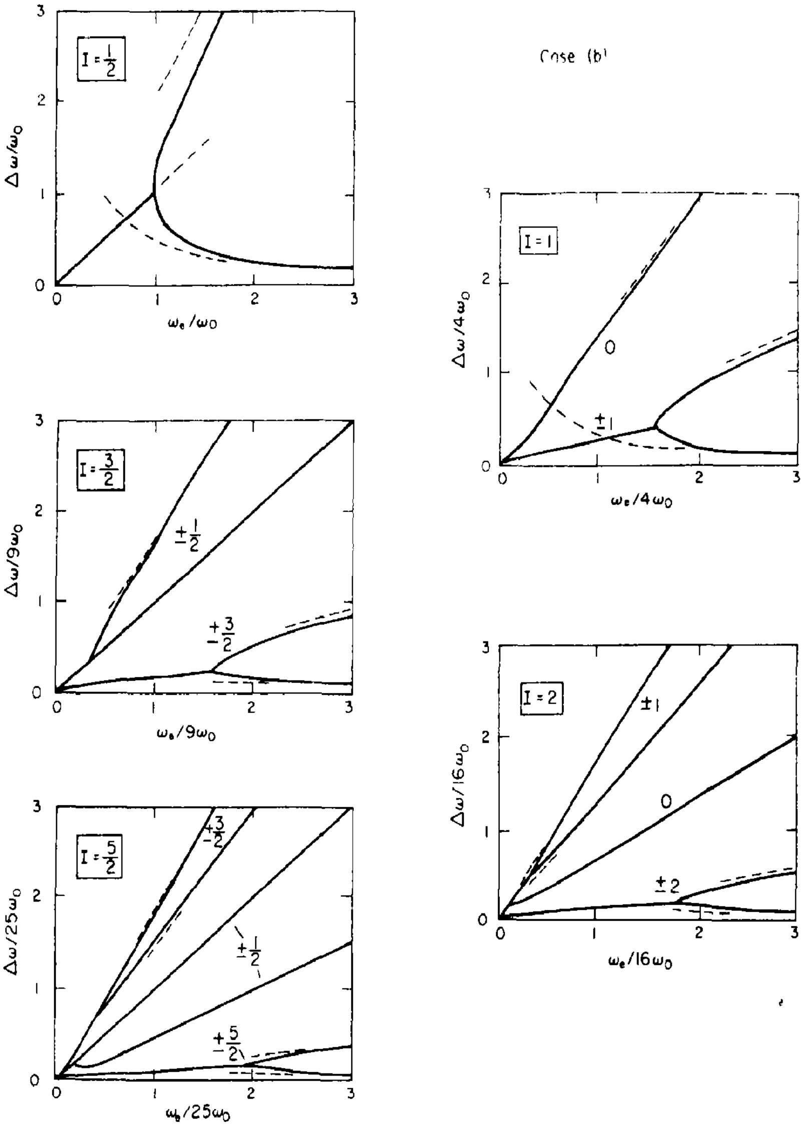

Fig. 5. The dependence of the linewidth $\Delta\omega$ (solid curves) on the exchange frequency ω_e for case (b) using the notation of Fig. 2. Both ordinates and abscissae are normalized relative to $(2I)^2\omega_0$.

Fig. 1 and Table 5. Specific asymptotic relations in this region will be derived in the next section. While the $(n-1)$ outer lines are broadening the remaining line in the center exchange narrows with the width

$$\Delta\omega = \frac{\omega_0^2}{\omega_e}\frac{(n-1)^2(n+1)}{3n} \tag{25}$$

as shown by Anderson[1]. As a result all but one hyperfine line broadens beyond detection, and only the exchange narrowed central line is observed.

(b) *Anderson case (b)*

Appreciable exchange narrowing for Anderson case (b) sets in for $\omega_e > (n-1)^2\omega_0$,

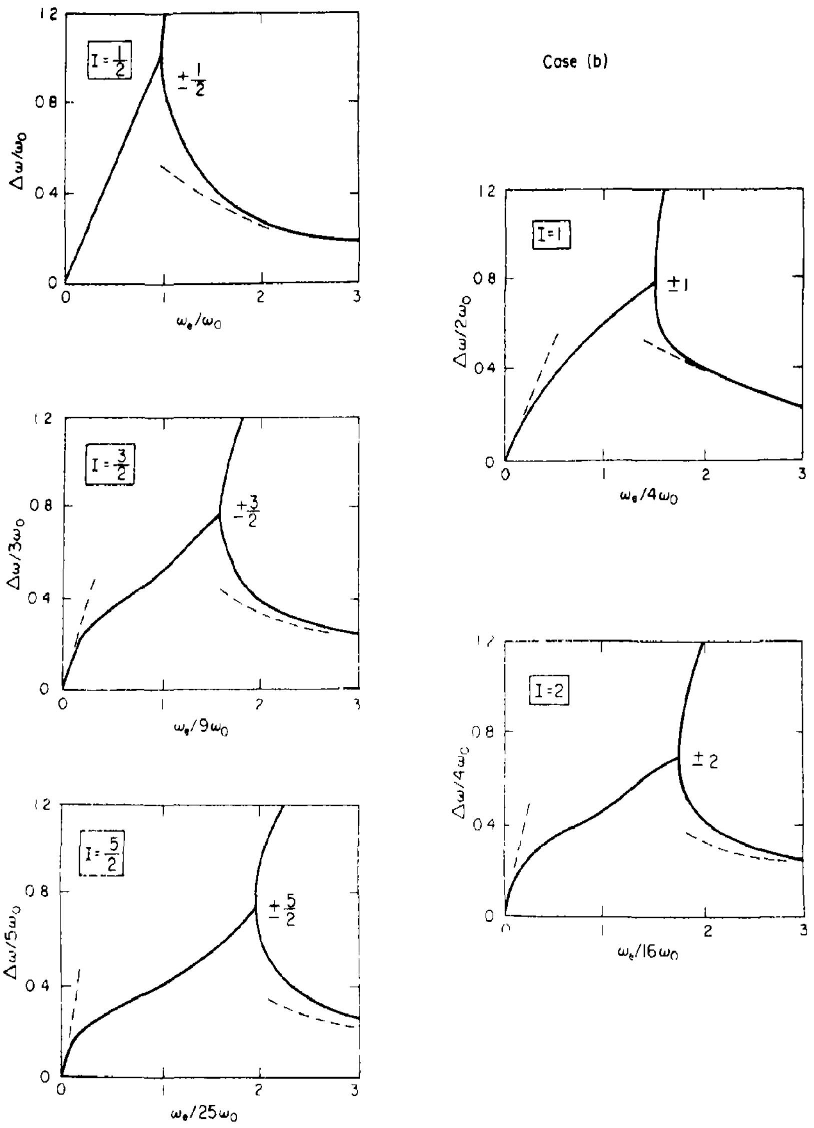

Fig. 6 Detailed plots of the linewidth behavior from Fig. 5 near the onset of exchange narrowing. The abscissa is normalized to $(2I)^2\omega_0$ as in Fig. 5, but the ordinate is normalized relative to $2I\omega_0$ which differs from Fig. 5

which means that higher values of the exchange frequency ω_e are needed than in case (a). As a result the abscissa scales of Figs. 4-6 are normalized by the factor $(n-1)^2\omega_0$. For spin $I > 1$ where more than one hyperfine line collapses to the center the outermost one $M_I = \pm I$ does so beyond the point $\omega_e/(n-1)^2\omega_0 = 1$, while the remaining lines at $|M_I| < I$ fall into the center below this value, as Fig. 4 indicates. The lines $M_I = \pm I$ collapse last, $M_I = \pm(I-1)$ next, then $M_I = \pm(I-2)$, etc. Each of these transitions

Table 6. Asymptotic values of the normalized linewidth $\Delta\omega/\omega_e$ *of the various hyperfine components for weak and strong exchange. Cf. equations* (28), (33), (24), (29), (30), (25) *and* (26)

			Case (a)		Case (b)	
n	I	M_I	$\omega_e \ll (n-1)\omega_0$	$\omega_e \gg (n-1)\omega_0$	$\omega_e \ll (n-1)\omega_0$	$\omega_e \gg (n-1)^2\omega_0$
2	$\frac{1}{2}$	$\pm\frac{1}{2}$	1	$\left\{\begin{matrix} \frac{1}{2}\left(\frac{\omega_0}{\omega_e}\right)^2 \\ 2 \end{matrix}\right\}$	1	$\left\{\begin{matrix} 2 \\ \frac{1}{2}\left(\frac{\omega_0}{\omega_e}\right)^2 \end{matrix}\right.$
3	1	0	1	$\frac{16}{9}\left(\frac{\omega_0}{\omega}\right)^2$	1	$\frac{3}{2}$
		± 1	1	$\frac{3}{2}$	$\frac{1}{2}$	$\left\{\begin{matrix} \frac{1}{2} \\ \frac{16}{3}\left(\frac{\omega_0}{\omega_e}\right)^2 \end{matrix}\right.$
4	$\frac{3}{2}$	$\pm\frac{1}{2}$	1	$\left\{\begin{matrix} \frac{15}{4}\left(\frac{\omega_0}{\omega_e}\right)^2 \\ \frac{7}{4} \end{matrix}\right\}$	1	$\left\{\begin{matrix} (1+\sqrt{2}) \\ 1 \end{matrix}\right.$
		$\pm\frac{3}{2}$	1	1	$\frac{1}{2}$	$\left\{\begin{matrix} (1-\sqrt{2}) \\ \frac{51}{3}\left(\frac{\omega_0}{\omega_e}\right)^2 \end{matrix}\right.$
5	2	0	1	$\frac{32}{5}\left(\frac{\omega_0}{\omega_e}\right)^2$	1	$(1+\frac{1}{4}\sqrt{6+2\sqrt{5}})$
		± 1	1	$\frac{5}{4}$	1	$\left\{\begin{matrix} (1+\frac{1}{4}\sqrt{6-2\sqrt{5}}) \\ (1-\frac{1}{4}\sqrt{6-2\sqrt{5}}) \end{matrix}\right.$
		± 2	1	$\frac{5}{4}$	$\frac{1}{2}$	$\left\{\begin{matrix} (1-\frac{1}{4}\sqrt{6+2\sqrt{5}}) \\ \frac{208}{5}\left(\frac{\omega_0}{\omega_e}\right)^2 \end{matrix}\right.$
6	$\frac{5}{2}$	$\pm\frac{1}{2}$	1	$\left\{\begin{matrix} \frac{175}{18}\left(\frac{\omega_0}{\omega_e}\right)^2 \\ \frac{6}{5} \end{matrix}\right\}$	1	$\left\{\begin{matrix} (1+\frac{1}{2}\sqrt{3}) \\ \frac{3}{2} \end{matrix}\right.$
		$\pm\frac{3}{2}$	1	$\frac{9}{5}$	1	$\left\{\begin{matrix} 1 \\ \frac{1}{2} \end{matrix}\right.$
		$\pm\frac{5}{2}$	1	$\frac{9}{5}$	$\frac{1}{2}$	$\left\{\begin{matrix} (1-\frac{1}{2}\sqrt{3}) \\ \frac{259}{3}\left(\frac{\omega_0}{\omega_e}\right)^2 \end{matrix}\right.$

begins gradually, and then the position rapidly decreases to zero in the neighborhood of the transition point.

As each line with $|M_I| < I$ reaches the origin it splits into two components with different linewidths, as shown in Fig. 5. With increasing ω_e each line broadens with a width $\Delta\omega$ close to ω_e. Table 6 gives the constant $K \sim 1$ in the expression

$$\Delta\omega = K\omega_e \tag{26}$$

for each component in the exchange narrowing region. It follows that for large ω_e these lines broaden beyond detection. When the $M_I = \pm I$ lines collapse into the origin they split into a component which broadens beyond detection in accordance with equation (25), and another which exchange narrows in accordance with ($n > 2$)

$$\Delta\omega = \frac{(n^4-1)}{15}\left[\frac{\omega_0^2}{\omega_e}\right]. \tag{27}$$

As Fig. 6 indicates, the linewidths slightly above the $M_I = \pm I$ collapse point change

Table 7. Values of the ratio ω_e/ω_0 at the points where the various hyperfine components collapse into the center line

			ω_e/ω_0 at disappearance	
n	I	M_I	Case (a)	Case (b)
2	$\frac{1}{2}$	$\pm\frac{1}{2}$	1·000	1·000
3	1	0	0	0
		± 1	—	6·183
4	$\frac{3}{2}$	$\pm\frac{1}{2}$	2·472	3·081
		$\pm\frac{3}{2}$	—	14·43
5	2	0	0	0
		± 1	—	5·598
		± 2	—	28·01
6	$\frac{5}{2}$	$\pm\frac{1}{2}$	3·825	4·486
		$\pm\frac{3}{2}$	—	9·429
		$\pm\frac{5}{2}$	—	48·22

very rapidly with variations in ω_e. Thus for $\omega_e \gg (n-1)^2\omega_0$ one outer ($M_I = \pm I$) component in the spectrum is exchange narrowed and the other $(n-1)$ component are broadened beyond detection.

5. PERTURBATION SOLUTIONS

In his classic paper[11] Anderson presented some perturbation formulae for the cases of very high and very low exchange. For case (a) and $\omega_0 = A_0/2 \gg \omega_e/(n-1)$ all of the lines shift, and the position and width are

$$P_M = MA_0 - \frac{1}{A_0}\left[\frac{\omega_e}{2}\right]^2\left[\frac{M}{|M|}\right]_{j=(I+1-|M|)} \sum (1/j) \quad (28)$$

$$\Delta\omega_M = \omega_e \quad (29)$$

while for case (b) and $A_0/2 \gg (n-1)^2\omega_e$ all of the lines except the end ones are unshifted

$$\left.\begin{aligned} P_I &= IA_0 - \frac{\omega_e^2}{4A_0} \\ \Delta\omega_I &= \frac{\omega_e}{2} \end{aligned}\right\} \quad |M| = I$$

$$\left.\begin{aligned} P_M &= MA_0 \\ \Delta\omega_M &= \omega_e \end{aligned}\right\} \quad |M| < I. \quad (30)$$

In Figs. 1–6 these formulae are plotted as dotted lines and compared with the exact solutions for Anderson cases (a) and (b). One should note that the perturbation behavior is not indicative of the true shift of the lines near $A_0 \sim 2(n-1)\omega_e$. In fact for case (a) the outside lines for which $|M| > \frac{1}{2}$ never even collapse to an exchange narrowed singlet, while in case (b) every line collapses to the center. The opposite impression is given by the perturbation expressions.

In the limit of strong exchange, to a first approximation we may rewrite the W'' equation of Tables 2 and 4 with $x = 0$ and $\lambda = -\Delta\omega$. For case (a) the equations have the form

$$W^{n-1}(W-n) = 0 \quad (31)$$

where from column 3 of Table 2

$$W = n-(n-1)\frac{\Delta\omega}{\omega_e}. \quad (32)$$

Therefore, substituting equation (32) into equation (31) the asymptotic linewidth of the $(n-1)$ broadened hyperfine components are all found to have the following value.

$$\Delta\omega = \left(\frac{n}{n-1}\right)\omega_e. \quad (33)$$

The width of the exchange narrowed component was derived by Anderson[1], and is given by equation (25).

To obtain the position for case (a) in the strong exchange region, one may write for the five broadened lines when $I = \frac{5}{2}$

$$W = 5\left(\frac{-\Delta\omega + iP}{\omega_e}\right) + 6 \tag{34}$$

$$= 5\frac{iP}{\omega_e} \tag{35}$$

using the previously derived value of $\Delta\omega$ in equation (33). Since ω_e is so large it follows that $|P| \ll \omega_e$. The asymptotic form of the W-equation of Table 2 is

$$3\left(\frac{P}{\omega_0}\right)^4 - 70\left(\frac{P}{\omega_0}\right)^2 + 259 = 0 \tag{36}$$

where we neglect W and x relative to unity. This has the four solutions

$$\frac{P}{\omega_0} = \pm\left[\frac{1}{3}(35 \pm 4\sqrt{7}\right]^{1/2} \tag{37}$$

as listed in Table 5. The remaining two lines have the position $P = 0$ corresponding to the root $W = n$ of equation (31). In this case the width comes from the next order equation using

$$W = -\frac{5\Delta\omega}{\omega_e} + 6 \tag{38}$$

in the asymptotic expression where $\Delta\omega \ll \omega_e$, and higher powers of x are neglected. This gives

$$W^3[W^2(W-6) + 35(W-4)x^2] = 0 \tag{39}$$

Using $x = 5\omega_0/\omega_e$ from Table 2, we obtain

$$-36\left(\frac{5\Delta\omega}{\omega_e}\right) + 70\left(\frac{5\omega_0}{\omega_e}\right)^2 = 0 \tag{40}$$

which gives the asymptotic linewidth corresponding to equation (24) for the exchange narrowed line.

A similar approach may be used in treating the strong exchange limit of case (b) by writing the W-equation of Table 4 with x set equal to zero. For $I = \frac{5}{2}$ this provides the polynomial

$$W(W^5 - 2W^4 - 4W^3 + 8W^2 + 3W - 6) = 0 \tag{41}$$

where from column 2 of Table 4

$$W = 2 + \frac{2\lambda}{\omega_e} \tag{42}$$

with the obvious solution $W = 0$, and the other known solution $W = 2$ for the exchange narrowed line, where λ vanishes to a first approximation. Therefore, the equation may be simplified by dividing by $(W-2)$ to give the simple quadratic expression

$$W(W-2)(W^4 - 4W^2 + 3) = 0 \tag{43}$$

which is easily solved for W^2. The roots are listed in Table 6. The exchange narrowed line is treated by writing the next approximation

$$W = W_0 - \frac{2\Delta\omega}{\omega_e} \tag{44}$$

where $W_0 = 2$ and $\Delta\omega \ll \omega_e$, substituting it into the total W-equation and cancelling the terms in W_0 which correspond to equation (19). Retaining only terms in $\Delta\omega/\omega_e$ and $x^2 = (2\omega_0/\omega_e)^2$ gives

$$\begin{aligned}&\left(\frac{2\Delta\omega}{\omega_e}\right)[6W_0^5 - 10W_0^4 - 16W_0^3 + 24W_0^2\\ &+ 6W_0 - 6] - \left(\frac{2\omega_0}{\omega_e}\right)^2[35W_0^4 - 20W_0^3\\ &- 40W_0^2 + 8W_0 + 3] = 0.\end{aligned} \tag{45}$$

Inserting $W_0 = 2$ and evaluating gives

$$\Delta\omega = \frac{259}{3}\frac{\omega_0^2}{\omega_e} \tag{46}$$

as shown in Table 6. This agrees with the general expression (26).

The asymptotic behavior for both cases at large exchange frequencies is plotted on Figs. 1–6 using dashed curves. In a couple of places such as the $\pm\frac{1}{2}$ lines of the $I = \frac{3}{2}$ case on Fig. 5 arrows were drawn on the solid curves to indicate that the perturbation solution is too close to the exact one to be indicated separately.

One should note that the perturbation formulae have various ranges of validity. The low exchange limit position and linewidth formulae are valid for

$$\omega_e \ll (n-1)\omega_0 \quad \text{Case (a)} \qquad (47)$$

$$\omega_e \ll (n-1)\omega_0 \quad \text{Case (b)} \qquad (48)$$

while the high exchange rate position and linewidth expressions are applicable when

$$\omega_e \gg (n-1)\omega_0 \quad \text{Case (a)} \qquad (49)$$

$$\omega_e \gg (n-1)^2\omega_0 \quad \text{Case (b).} \qquad (50)$$

All of the inequalities of case (a) contain the factor $(n-1)$, while in case (b) the same factor $(n-1)$ occurs at low exchange and its square $(n-1)^2$ appears at high exchange. These inequalities may be deduced from an examination of Figs. 1–6.

The $(n-1)$ lines which are broadened beyond detection at high exchange rates follow the overall behavior shown on Fig. 7. At intermediate exchange frequencies between the inequalities of equations (47–50), the linewidth of both cases (a) and (b) gradually passes from its low exchange asymptote to its high-exchange asymptote in the manner shown in Fig. 7. Sometimes the high exchange asymptote is approached from above and sometimes from below. Some lines exhibit a discontinuity at the point of collapse of the position to the center, but despite this the overall behavior is of the type shown on Fig. 7. This makes the asymptotic solutions particularly useful in deducing the overall behavior of a hyperfine multiplet over large variations in exchange.

The asymptotic behavior of the $I = \frac{3}{2}$ case was treated in some detail to illustrate the method for obtaining asymptotic solutions of the equations. This approach may be employed to obtain the overall behavior of the hyperfine patterns for $I > \frac{3}{2}$ without solving the whole problem. However, great care should be exercised in applying these perturbation methods to higher spin cases.

6. DISCUSSION

The exchange narrowing problem for n equally spaced, equally strong lines corresponding to the nuclear spins $I = \frac{1}{2}, 1, \frac{3}{2}, 2$ and $\frac{5}{2}$ was solved for two particular cases. Case (a) corresponds to equal transition probability to all other lines of the spectrum, so it exhibits a transition matrix with all off-diagonal elements equal to $\omega_e/(n-1)$. Case (b) corresponds to allowed transitions only between adjacent lines, so the immediate off-diagonal elements are $\omega_e/2$ and all others are 0. For each case the transition probability from each line is ω_e. It is easy to write down transition matrices for intermediate cases and solve them by the methods discussed here. To obtain an overall picture of exchange narrowing we have solved exactly the problem for high nuclear spins in these two cases. Anderson[1] solved the $I = \frac{1}{2}$ case and gave perturbation formulae for the higher nuclear spins.

Extrapolations from the perturbation formulae for $I > \frac{1}{2}$ by analogy with the $I = \frac{1}{2}$ exact solution are not always valid. For example, in case (a) the lines for $|M_I| > \frac{1}{2}$ never coalesce. For $I = 2$, the low exchange perturbation formulae of case (a) for the $M_I = \pm 1$ lines, show a movement toward the spectral center of gravity, while the corresponding formula of case (b) exhibits no such change. Nevertheless, as Figs. 1 and 4 indicate, it is the case (b) lines that eventually merge at the center, the case (a) ones merely shift inward from $P = \pm 2{\cdot}00\omega_0$ and then

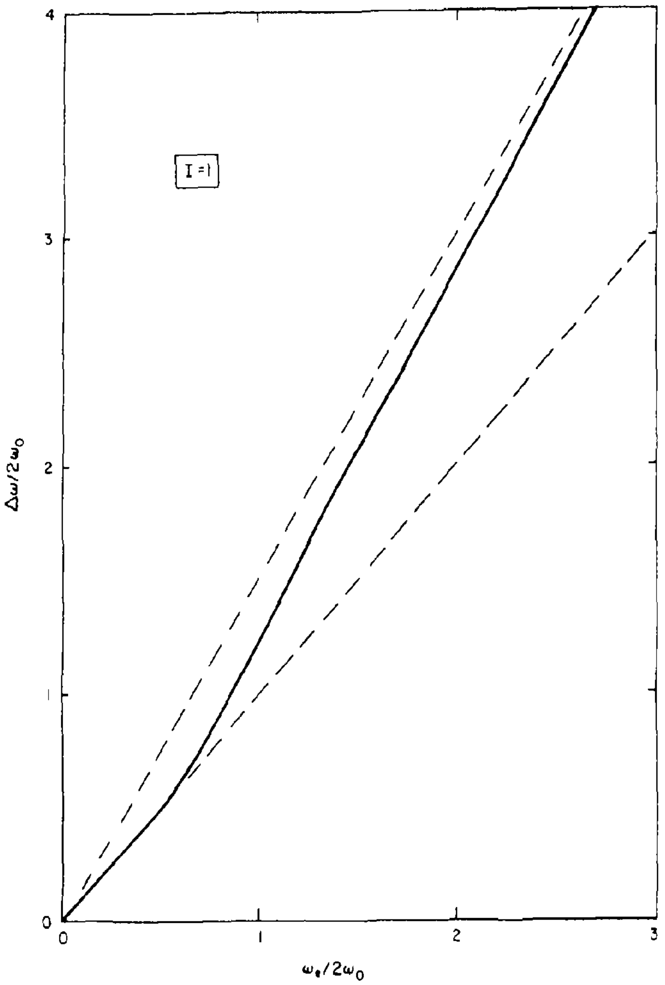

Fig. 7 Illustration of the manner in which the linewidth of a broadened hyperfine component transforms from its linear behavior at small ω_e to its modified linear behavior at high ω_e. For the case shown $I = 1$, $M_I = \pm 1$, the slope is 1 near the origin, and it is $\frac{3}{2}$ at large exchange

gradually approach $P = \pm 1{\cdot}09\omega_0$ while they broaden beyond detection. Indeed for $I = 2$, low exchange, and case (b) the $M_I = \pm 1$ lines which exhibit no shift in first order collapse to the origin faster than the $M_I = \pm 2$ lines with the pronounced first order shift.

In case (b) exchange narrowing does not occur until the last or $M_I = \pm I$ hyperfine pair has emerged at the center. Beyond that point the asymptotic narrowing region is approached quite rapidly. In case (a) the onset of narrowing for half integral spin also takes place quite soon after the coalescence if the $M_I = \pm\frac{1}{2}$ lines, and the integral spin patterns behave similarly on the $\omega_e/(n-1)\omega_0$ scale.

The Anderson theory assumes a hyperfine pattern of delta function line shapes which are subject to an exchange interaction. As this interaction increases in magnitude it gradually broadens the lines, causes them to merge into a single wide resonance line of width $\Delta\omega \sim \frac{2}{3}(n-1)\omega_0$, and then broadens most of the component lines beyond detection while exchange narrowing the dominant component back to an infinity narrow line. This process is observable experimentally, and its details can be checked with the theory.

The line broadening of the component lines for the hyperfine patterns with $I > \frac{1}{2}$ is so pronounced below the onset of exchange narrowing that the pattern collapses into a singlet before that point is reached. The values of ω_e/ω_0 at which resolution is lost are now being studied. They may be estimated from the value of ω_e/ω_0 at which $P-\Delta\omega$ of the outside $M_I = I$ line equals the value $P+\Delta\omega$ of the adjacent line $M_I = I-1$

$$P_I - P_{I-1} = \Delta\omega_I + \Delta\omega_{I-1} \qquad (51)$$

since $\Delta\omega$ is the halfwidth of the line. Beyond

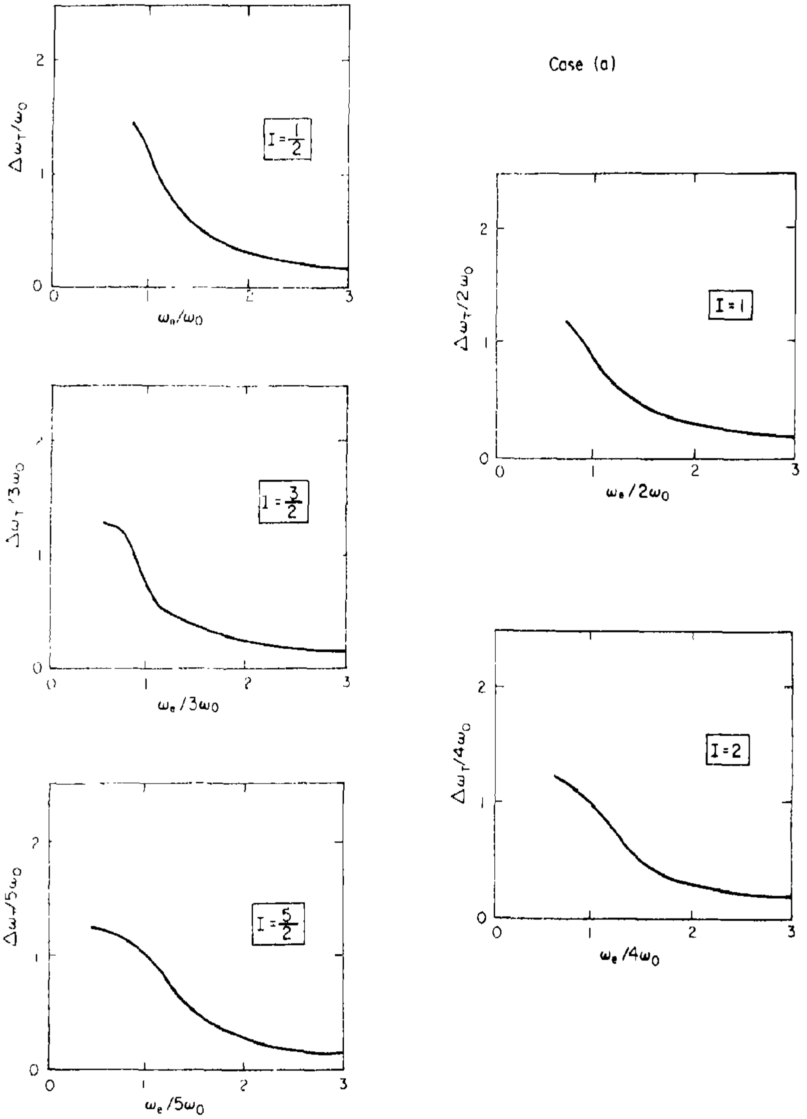

Fig. 8. Dependence of the overall total linewidth $\Delta\omega_T/2I\omega_0$ on the exchange rate $\omega_e/2I\omega_0$ after the collapse of the component lines to a singlet for case (a).

the point of merger and up to the neighborhood where exchange narrowing sets in, the resonance line may be assumed to have the overall halfwidth $\Delta\omega_T$ of the outermost component line

$$\Delta\omega_T = P_l + \Delta\omega_l. \qquad (52)$$

With the onset of exchange narrowing the central exchange narrowing component may be considered as dominant when all other component lines are more than five times as broad, to give in this region

$$\Delta\omega_l = K\frac{{\omega_0}^2}{\omega_{e2}} \qquad (53)$$

where the constant K is listed in columns 5

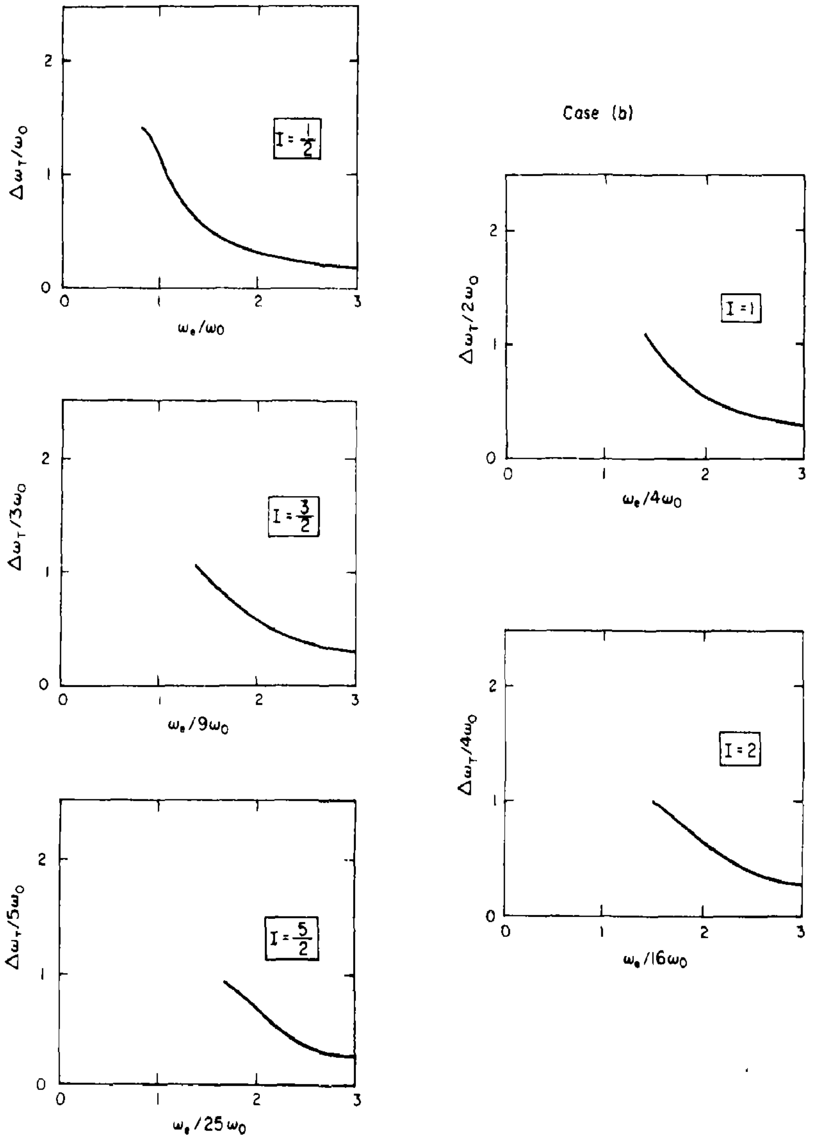

Fig. 9. Dependence of the overall total linewidth $\Delta\omega_T/2I\omega_0$ on the exchange rate $\omega_e/(2I)^2\omega_0$ after the collapse of the component lines to a singlet for case (b).

and 7 of Table 6. Thus, data from several of the figures and tables may be employed to obtain the approximate linewidth behavior of the observed singlet from the point where the hyperfine structure collapses to the region of exchange narrowing.

A more satisfactory procedure to obtain this behavior consists in assuming that each component line has a position given by Fig. 1 (or 4), a width given by Fig. 2 (or 5) and a constant integrated area. Computer spectra were synthesized from Lorentzian line-shapes and the data of these figures. The overall halfwidths of the resulting singlets are plotted in Figs. 8 and 9 for cases (a) and (b). The curves in these figures start at the point of coalescence of the hyperfine structure, and begin to approach the asymptotic linewidth of equation (53) at the highest plotted values of the abscissa. Structure is resolved at the low values of the abscissa before the beginning of each curve.

Figures 8 and 9 are approximations which can be compared with experimental data. If the exchange frequency ω_e is not known, it would be difficult to deduce which case is present from experimental data. The details of the line shape before the coalescence of the hyperfine pattern are quite sensitive to the particular case (a) or (b). The authors are extending this study to a more exact calculation of these spectra and figures using the approach of Stack[2]. It is planned to give various lineshape criteria for explicating partially exchange-narrowed spectra. Others[16, 17] have also recently studied line shapes in the presence of rapid exchange.

REFERENCES

1. ANDERSON P. W., *J. phys. Soc. Japan* **9**, 316 (1954).
2. SACK R. A., *Molec. Phys.* **1**, 163 (1958).
3. MATTHIAS E. and SHIRLEY D. A., Eds., *Hyperfine Structure and Nuclear Radiations*, Chap. 11. North-Holland, Amsterdam (1968)
4. BLUME M. and TJON J. A., *Phys. Rev.* **165**, 446, 456 (1968)
5. BLUME M., *Phys. Rev.* **174**, 351 (1968).
6. GABRIEL H., BOSSE J. and RANDER K., *Phys Status Solidi* **27**, 301 (1968).
7. DEKKER A. J., *Hyperfine Interactions* (Edited by A. J. Freeman and R. B. Frankel), p. 679. Academic Press, New York (1967).
8. KUBO R., *J. phys. Soc. Japan* **9**, 935 (1954)
9. VAN DER WOUDE F. and DEKKER A. J., *Phys. Status Solidi* **13**, 181 (1966)
10. JESSON J. P., WEIHER J. F. and TROFIMENKO S., *J. chem. Phys.* **48**, 2058 (1968).
11. WERTHEIM G. K., GUGGENHEIM H. J. and BUCHANAN D. F., *Phys. Rev.* **169**, 465 (1968)
12. POPLE J. A., SCHNEIDER W. G. and BERNSTEIN H. J., *High Resolution Nuclear Magnetic Resonance*, p. 223. McGraw-Hill, New York (1959).
13. GUTOWSKY H. S. and HOLM C. H., *J. chem. Phys.* **25**, 1228 (1956)
14. ABRAGAM A., *The Principles of Nuclear Magnetism*, p. 450. Oxford University Press (1961).
15. STROTHER E. F., FARACH H. A. and POOLE C. P., Jr., *Bull. Am. phys. Soc.* **14**, 435 (1969).
16. GORDON R. G. and McGINNIS R. P., *J. chem. Phys.* **49**, 2455 (1968).
17. JOHNSON C. S., Jr and HOLZ J. B., *J. chem. Phys.* **50**, 4420 (1969)

J. Phys. Chem. Solids Pergamon Press 1970. Vol. 31, pp. 1511–1524. Printed in Great Britain.

MAGNETISM AND BONDING IN A $D8_8$ STRUCTURE; MÖSSBAUER AND MAGNETIC INVESTIGATION OF THE SYSTEM Mn_5Si_3–Fe_5Si_3

K. S. V. L. NARASIMHAN*, W. M. REIFF†, H. STEINFINK* and R. L. COLLINS‡
The University of Texas at Austin, Austin, Texas 78712, U.S.A.

(*Received* 9 *June* 1969)

Abstract – The Mössbauer spectra and magnetic measurements of the phases $Mn_{5-x}Fe_xSi_3$, $1 \leq x \leq 5$, and Mn_5Si_3 were obtained from 4·2°K to above room temperature. The compounds crystallize with the hexagonal $D8_8$ structure (Mn_5Si_3 type), space group $P6_3/mcm$. The first iron atom substitutes into the 4(d) site. The second iron occupies mainly the 6(g) site while the third iron occupies both the 6(g) and 4(d) sites of the space group. The fourth iron substitutes in such a manner that 4(d) sites are completely occupied by iron and only one Mn is left in 6(g). The phases Mn_4FeSi_3 and $Mn_3Fe_2Si_3$ show antiferromagnetic behavior similar to Mn_5Si_3; $MnFe_4Si_3$ is ferromagnetic and displays a magnetization curve similar to Fe_5Si_3. The data indicate that iron in the 4(d) site can be described on the basis of a low spin $3d^5$ configuration with covalent bonding between it and the surrounding six silicon atoms. Covalency is assigned on the basis of the internal field value $H_n \approx 130$ kG. The 6(g) iron displays about 50 per cent covalent and 50 per cent metallic character. A magnetic structure for $MnFe_4Si_3$ and Fe_5Si_3 is proposed in which canting of the sublattice magnetizations is considered

1. INTRODUCTION

THE MAGNETIC structures of Fe_5Si_3 and Mn_5Si_3 have been investigated by neutron diffraction techniques, Mössbauer spectroscopy, and by susceptibility measurements [1–6]. Both compounds crystallize with the $D8_8$ structure and Fe_5Si_3 is ferromagnetic while Mn_5Si_3 is antiferromagnetic. The $D8_8$ type structure has the space group symmetry $P6_3/mcm$ (193) and contains two formula weights of composition M_5Si_3 (M = metal atom) in the unit cell. The metal ions are situated in two independent crystallographic sites designated 6(g) and 4(d) and the formula can be written as $(M_3)(M_2)Si_3$ to indicate the respective site occupants. The crystal structure of Mn_5Si_3 was first determined by Amark *et al.*[7] and more recently by Aronsson[8] and by Lander and Brown[9]. The environment of the metal ion in the 4(d) site consists of six silicon atoms at the corners of a distorted octahedron. In Mn_5Si_3 the six distances from Mn in 4(d) to silicon vary from 2·413 to 2·419 Å. The distances between adjacent 4(d) atoms, stacked parallel to the c axis in the form of a linear chain is 2·406 Å, while the distances between chains exceeds 5 Å. The Mn in the 6(g) sites form triangles around the c axis at $z = \frac{1}{4}$ and $z = \frac{3}{4}$, and the two triangles are rotated by 60° with respect to each other.

Mössbauer data obtained on carbon stabilized samples of Fe_5Si_3[1] were found to exhibit a hyperfine split pattern consisting of a set of sharp lines with an internal field $H_n = 137$ kG, superposed on a more diffuse six line pattern for which the estimated internal field ranged from 180 to 240 kG. The field $H_n = 137$ kG was assigned to iron in 4(d) sites and it was estimated that such iron has a $\Delta E = 0{\cdot}35$ mm/sec. The principle component of the electric field gradient tensor was assumed axially symmetric and of positive sign. The iron exhibiting larger internal fields was presumed to correspond to the

---

*Materials Science Laboratories, Department of Chemical Engineering.
†Department of Chemistry.
‡Department of Physics.

$6(g)$ sites of the $D8_8$ structure. The same values of H_n for the two sites were also found by Shinjo and Nakamura[3]. The present spectra are better resolved than those in Ref. [3] and no spectra were presented in Ref. [1].

Several spin schemes have been proposed for Fe_5Si_3[1-3, 10] which, however, are not in accord with each other. The postulate advanced to explain the spin of atoms in the $4(d)$ position of the $D8_8$ structure assumes that they are purely metallic, even though they are closely surrounded by a slightly distorted octahedral arrangement of silicon atoms and as a result considerable covalent bonding should exist. In order to investigate the spin arrangements in the $4(d)$ and $6(g)$ sites in greater detail we undertook a study of the phases $Mn_{5-x}Fe_xSi_3$, $0 \leq x \leq 5$. We investigated the Mössbauer spectra of the series $Mn_{5-x}Fe_xSi_3$, $1 \leq x \leq 5$, over a large range of temperature and in the case of Fe_5Si_3 in the presence of an external magnetic field. The spectra and magnetic measurements have been determined systematically for all the members of the series in order to obtain a reasonable picture of the change in electronic and magnetic structure as a function of composition. Through the Mössbauer measurements, it has also been possible to follow the mode of substitution of iron for manganese in $4(d)$ and $6(g)$ lattice sites. This is not possible via X-ray methods as the scattering power of iron and manganese are not sufficiently different. The mode of substitution is significantly related to the change in magnetic behavior from the antiferromagnetic Mn_5Si_3 to the strongly ferromagnetic Fe_5Si_3.

2. EXPERIMENTAL

Iron and manganese of 99·99 per cent nominal purity and silicon of 99·99 per cent purity were used to prepare the phases. Quantities of the powdered elements which yielded the desired stoichiometry were sealed into an evacuated vycor tube and heated for 36 hr at 800°C. The reacted material was then placed into an alumina crucible and melted in an induction furnance in an argon atmosphere and the molten product cooled over a two hour period. The phase Fe_5Si_3 was prepared by arc melting the stoichiometric mixture on a water cooled hearth followed by sealing the arc melted button into a vycor tube and annealing it at 900°C for 36 hr and then quenching it by dropping it into water.

X-ray diffraction patterns using a diffractometer were obtained for all preparations and the diagrams showed lines which were due only to the $D8_8$ structure with shifts in the 'd' spacings as expected for the solid solutions. Precise lattice parameters were obtained from X-ray powder paterns of specimens exposed in a 114·6 mm dia. Straumanis type camera, using unfiltered FeK radiation. A least squares refinement of measured 2θ values yielded the lattice constants shown in Table 1.

Magnetic susceptibility measurements were carried out using the Faraday method and the procedure and precision of measurements have been previously described[11]. The magnetization measurements were done with a vibrating sample magnetometer of the Foner type[12]. This instrument has a reproducibility better than 1 per cent and can detect changes in magnetic moment of 5×10^{-5} e.m.u. The instrument was calibrated with spectrosopically pure nickel.

Mössbauer spectra were obtained using a constant acceleration drive operated in the time mode. Data were accumulated in a 400 channel analyzer. The source used was 75 mC of Co^{57} diffused into copper foil and used at room temperature. Calibrations were obtained using 0·00127 cm, 99·99 per cent iron foil. Samples consisted of finely ground powders suspended in a spray adhesive between filter paper discs. Samples ranged in thickness from 200 to 400 mg/in². The spectra were fitted by least squares analysis assuming Lorentzian line shapes and using a modified National Bureau of Standards computer program[13]. The reproducibility for

Table 1. *Magnetic and crystal parameters of* $Mn_{5-x}Fe_xSi_3$ *Phases. Numbers in parentheses refer to standard deviations*

Phase	Curie temp. T_c or Néel temp. T_n (°K)	Weiss temp. θ_p (°K)	μ_{eff}[a] (Paramagnetic) Per metal atom in Bohr magnetons	μ_{eff}[a] (Ferromagnetic) Per metal atom in Bohr magnetons	Lattice constants A	
					a_0	c_0
Mn_5Si_3	62	−9·1	4·05		6·901 (0·006)	4·812 (0·002)
Mn_4FeSi_3	99	10.4	4·35		6·873 (0·014)	4·782 (0·002)
$Mn_3Fe_2Si_3$	162	12·4	3·34		6·864 (0·019)	4·780 (0·004)
$Mn_2Fe_3Si_3$	160	256·6	3·44		6·862 (0·005)	4·779 (0·001)
$MnFe_4Si_3$	325	346·0	3·52	1·11	6·770 (0·014)	4·728 (0·005)
Fe_5Si_3	376			0·89	6·757 (0·021)	4·717 (0·002)

[a] Relative error in μ_{eff} (paramagnetic) and μ_{eff} (ferromagnetic) is 1·6 and 0·5 per cent respectively.

values of the isomer shifts, δ, and quadrupole splitting, ΔE, obtained from mathematical fitting of the data was ±0·01 mm/sec. For magnetically split spectra, error in determination of internal fields is estimated as ±5 kG.

The spectrum of Fe_5Si_3 in an externally applied field was obtained using a superconducting magnet such that the applied field, H_0, is parallel to the direction of gamma-ray propagation. Refrigerants used to obtain low temperature spectra were dry ice-isopropanol slushes, liquid nitrogen and liquid helium. Mineral oil was used as a heat transfer medium for temperatures above room temperature.

3. MÖSSBAUER MEASUREMENTS

(a) Mn_4FeSi_3

The phase Mn_4FeSi_3 shows the least complicated spectral behavior of the series $Mn_{5-x}Fe_xSi_3$. At room temperature, Fig. 1(a), a symmetric quadrupole doublet with relatively narrow lines, Table 2, is observed. The small ΔE for this system, Table 3 indicates a small but definite distortion of electronic symmetry. As the temperature is decreased magnetic splitting occurs, Fig. 1(b) and 1(c), and a single six line pattern results at 4·2°K. Although the peak heights of the spectrum at 4·2°K differ from the expected 3:2:1:1:2:3 ratios, the areas of the six peaks do indicate an essentially random distribution of internal field directions in this sample. For a magnetically ordered, polycrystalline sample, the relative areas of the six absorptions are related to the angle θ between the γ-ray propagation direction and internal field directions by the equation [14]:

$$\langle\cos^2\theta\rangle = \frac{A_1+A_3+A_4+A_6-(A_2+A_5)}{\sum_{i=1}^{6} A_i}$$

where the A_i are the respective absorption areas. In the present case $\langle\cos^2\theta\rangle = 0{\cdot}27$, while for a perfectly random orientation of internal field directions $\langle\cos^2\theta\rangle = \frac{1}{3}$. The observation of a single six line pattern at 4·2°K and a 'clean' room temperature quadrupole doublet leads to the conclusion that essentially all of the first iron to be substituted into Mn_5Si_3 goes preferentially into a single crystallographic site.

The low value of the internal field corresponding to spectrum 1(c) suggests that the bonding to this iron is strongly covalent.

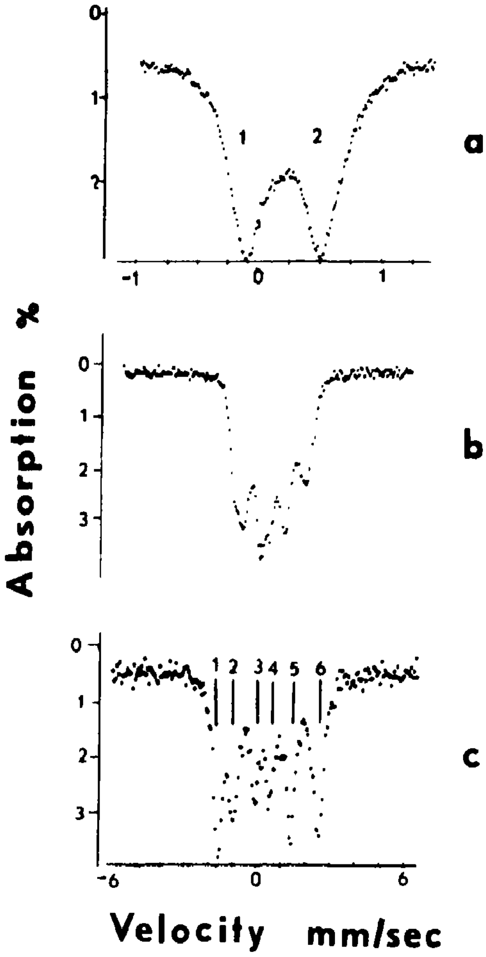

Fig. 1 Mossbauer spectrum of Mn_4FeSi_3 at (a) 300°K, (b) 78°K, (c) 4·2°K

For example, it has been well demonstrated for high spin Fe^{+3}, that H_n decreases with increasing covalency and that H_n is, in fact, a more sensitive measure of covalency than the isomer shift[15, 16]. This has been found with both tetrahedral and octahedral stereochemistries for a variety of ligands. Comparison with the values of H_n found by Johnson *et al.*[1], and Shinjo and Nakamura [3], and in this work, Table 4, for Fe_5Si_3 indicates that the iron of Mn_4FeSi_3 is in a 4(*d*) site, i.e. within a slightly distorted octahedral array of silicon.

The spectrum of Mn_4FeSi_3 at 4·2°K is indicative of combined quadrupole and magnetic hyperfine interactions[17]. In Fig. 1(c) the center of the inner four peaks is shifted to lower velocity such that the difference in splitting between lines 1 and 2 and lines 5 and 6 is 0·4 of the room temperature quadrupole splitting. The foregoing difference is a measure of the quadrupole splitting [14, 17] for a magnetically split spectrum assuming an axially symmetric electric field gradient. In general, the value of ΔE for the case of combined magnetic and quadrupole interactions is dependent on the angle θ, between the internal field H_n, and the principle component V_{zz}, of the electric field gradient tensor[14, 17]. In the present case, assuming ΔE is temperature independent, a ratio of $\Delta E(4{\cdot}2°K)/\Delta E(300°K) = 0{\cdot}4$ leads to a calculated angle $\theta = 63°$. Landet *et al.*[4],

Table 2. Line widths (Γ)[a]

Compound	Temp.(°K)	Γ_1	Γ_2	Γ_3	Γ_4	Γ_5	Γ_6
Mn_4FeSi_3	300	0·39	0·44				
	195	0·36	0·42				
	78	0·39	0·57	0·41	0·60	0·50	0·49
	4·2	0·39	0·56	0·41	0·57	0·49	0·51
$Mn_3Fe_2Si_3$	400	0·30	0·36	0·36	0·38		
	78	0·29	0·75	0·57	0·32	0·81	0·70
	3·0	0·51	0·71	0·74	0·47	0·69	0·65
$Mn_2Fe_3Si_3$	300	0·30	0·32	0·27	0·35		
	195	0·28	0·29	0·25	0·34		
$MnFe_4Si_3$	470	0·32	0·33	0·29	0·36		
	420	0·32	0·34	0·29	0·35		

[a] All line widths in mm/sec relative to iron foil for which ⟨Γ⟩ observed ≈ 0·27 mm/sec.

Table 3. *Mössbauer data*^(a)^

Compound	Temp. (°K)	Isomer shift (δ) 4(*d*)(1, 3)*	Isomer shift (δ) 6(*g*)(2, 4)*	Quadrupole splitting (Δ*E*) 4(*d*)(1, 3)*	Quadrupole splitting (Δ*E*) 6(*g*)(2, 4)*
Mn_4FeSi_3	300	0·21		0·60	
	195	0·28		0·59	
	4·2	0·25		0·24	
$Mn_3Fe_2Si_3$	400	0·14	0·38	0·56	0·55
	300	0·21	0·40	0·48	0·56
	195	0·29	0·44	0·51	0·58
$Mn_2Fe_3Si_3$	300	0·19	0·43	0·54	0·55
	195	0·24	0·45	0·47	0·48
$MnFe_4Si_3$	470	0·11	0·33	0·50	0·63
	420	0·14	0·37	0·50	0·64
	300	0·23	0·36	0·51	0·61

(a) All data in mm/sec relative to natural iron foil.

*Identification of sites, enumerated on spectra.

Table 4. *Internal fields*^(a)^

Compound	Temp. (°K)	4(*d*)	6(*g*)
Mn_4FeSi_3	78	97	
	4·2	128	
$Mn_3Fe_2Si_3$	78	101	
	4·2	111	
	3·0	123	
$Mn_2Fe_3Si_3$	78	123	187
	4·2	137	228
$MnFe_4Si_3$	195	116	177
	78	132	209
	4·2	139	226
Fe_5Si_3	300	91	168
	78	123	228
	4·2	132	243

(a) All fields in kilo-Gauss relative to iron foil for which the internal field at 300°K is taken as 330 ± 3 kG [22].

determined a value of 90° for this angle from a neutron diffraction study of the isomorphous Mn_5Si_3 phase. In light of the assumptions made, $\theta = 63°$ is a reasonable value for Mn_4FeSi_3. This value of θ, with a shift of the center of the inner four lines of Mn_4FeSi_3 toward negative velocity, indicates V_{zz} is negative at a 4(*d*) site. Johnson, *et al.*[1] assigned a positive value to V_{zz} for 4(*d*) sites in Fe_5Si_3 and this may have resulted from assuming $\theta \approx 0°$ for 4(*d*) iron of Fe_5Si_3. However this angle is difficult to determine with any certainty from the complex spectrum of Fe_5Si_3. Using a point charge model and interatomic angles and distances based on the parameters of the isomorphous Mn_5Si_3 [8], a negative V_{zz} is calculated for 4(*d*) sites. This can only be taken as qualitative theoretical support for the results of this investigation since covalency and π bonding effects are undoubtedly very large as indicated by the small value of H_n.

(b) $Mn_3Fe_2Si_3$

Figures 2(a–d) show the Mössbauer behavior of $Mn_3Fe_2Si_3$ over a wide range of temperature. From the higher temperature spectra, it is evident that more than one crystallographic type of iron is present in the system. On the basis of isomer shift and quadrupole splitting at several temperatures, Table 3, absorptions 1 and 3 of Figs. 2(a) and 2(b) are assigned to a quadrupole doublet resulting from 4(*d*) type iron as in Mn_4FeSi_3. Peak 2 and the shoulder at positive velocity labeled 4 are assigned to another quadrupole doublet having a splitting of similar magnitude to the preceding 4(*d*) iron but a more positive isomer shift in all cases. In the following discussion this new doublet is attributed to iron in 6(*g*) lattice sites. The spectrum of $Mn_3Fe_2Si_3$ remains constant down to 78°K at which temperature magnetic

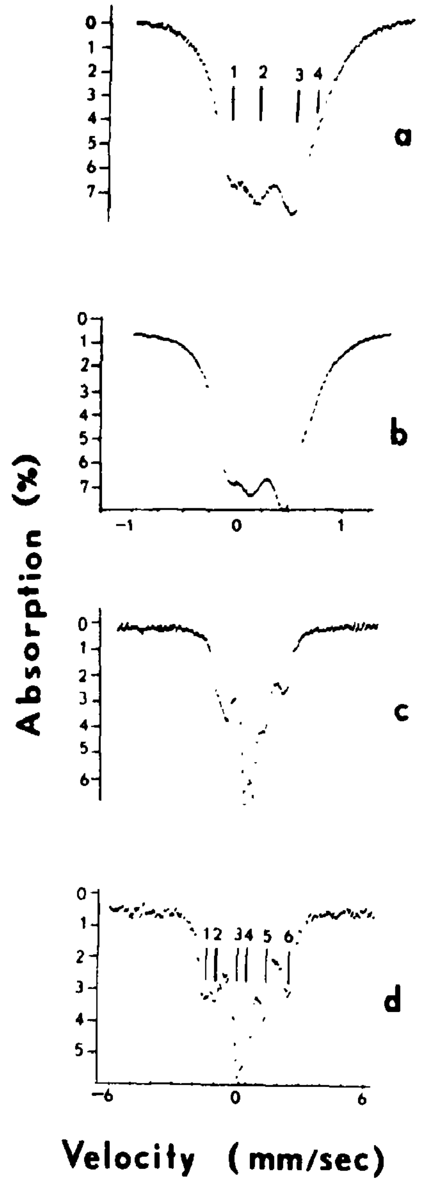

Fig. 2. Mossbauer spectrum of Mn$_3$Fe$_2$Si$_3$ at (a) 400°K, (b) 300°K, (c) 78°K, (d) 3·0°K.

splitting is noticeable. The general shape of this spectrum is reminiscent of that of Mn$_4$FeSi$_3$ at 78°K except for the two very intense peaks labeled 3 and 4. The spectrum at 4·2°K is essentially the same as that shown in Fig. 2(d) for 3·0°K, i.e. only one type of iron appears to be significantly split by magnetic hyperfine interaction and the magnitude of H_n, Table 4, indicates this to be 4(*d*) iron.

The neutron diffraction study of Lander, *et al.* indicates that two of the 6(*g*) sites of Mn$_5$Si$_3$ are not magnetically ordered[4] although crystallographically all 6(*g*) sites are equivalent. Hence, a possible explanation for the absence of noticeable splitting of the inner lines 3 and 4 of Mn$_3$Fe$_2$Si$_3$ is that a large fraction of the second iron preferentially occupies the magnetically random 6(*g*) sites. Such preferential occupation is difficult to explain along the usual lines of different crystal field stabilization energies of the sites involved. The exact electronic configurations for 4(*d*) and 6(*g*) sites are not known and the 6(*g*) coordination environment is rather complex. On the other hand, the entropy of the system is expected to increase with filling of 6(*g*) as well as 4(*d*) sites. This suggests that 6(*g*) sites are only slightly higher in energy than 4(*d*) in Mn$_4$FeSi$_3$ and Mn$_3$Fe$_2$Si$_3$ phases.

We next consider the relative occupation factors for different sites. The unknown *f* factors (recoil free fractions)[17] and their temperature dependence prevent an exact analysis. However, the analysis at high and low temperature would be expected to differ significantly if the *f* values differ appreciably. A least squares fit to the spectrum of Mn$_3$Fe$_2$Si$_3$ at 400°K indicates peak 2 and shoulder 4 to correspond to 38 per cent of the total area or therefore 0.76 iron atoms in 6(*g*) sites. From a similar fit to the spectrum of Mn$_3$Fe$_2$Si$_3$ at 3·0°K the intense absorptions 3 and 4 correspond to 42 per cent of the total absorption area. This includes the inner peaks of magnetically split 4(*d*) iron. If saturation effects are neglected, then the 6(*g*) iron accounts for 31 per cent of the total absorption area, i.e. 0·62 6(*g*) iron atoms. However, saturation is not negligible since peaks 3 and 4 of Mn$_4$FeSi$_3$ correspond to 25 per cent of the total area for spectrum 1(*c*). Using this factor to account for 4(*d*) intensity in peaks 3 and 4 of Fig. 2(d), 6(*g*) absorption corresponds to 25 per cent of the total absorption area, i.e. 0·50 6(*g*) iron atoms. This is a reasonable lower bound on the amount of 6(*g*) iron present. Possibly, all of the 6(*g*) absorption area of $Mn_3Fe_2Si_3$ at 3·0°K is not confined to the more intense central peaks as evidenced by the broadness (Table 2) of the peaks of spectrum 2(*d*) in Fig. 2. However, the approximate agreement of the percentage of total area corresponding to 6(*g*) iron for 400°K and 3°K indicates that a significant fraction (between $\frac{1}{2}$–$\frac{3}{4}$) of the second iron goes into 6(*g*) sites on formation of $Mn_3Fe_2Si_3$.

(c) $Mn_2Fe_3Si_3$

The Mössbauer spectrum at 300°K, Fig. 3(a), shows the same general pattern of four lines as in $Mn_3Fe_2Si_3$ although the increased 6(*g*) content leads to a better resolved spectrum. As for $Mn_3Fe_2Si_3$, lines 1 and 3 correspond to quadrupole split 4(*d*) iron while 2 and 4 represent similarly split 6(*g*) iron atoms. A least squares computer fit indicates that the spectra at 300°K and 195°K can be reconstructed from separate peaks as shown in Fig. 3(b) for the spectrum at 300°K where the area ratio $(A_1+A_3)/(A_2+A_4)$ is 1 . 1. This implies that occupation of 4(*d*) and 6(*g*) sites is nearly equal for $Mn_2Fe_3Si_3$.

On decreasing the temperature, the system clearly shows two separate hyperfine patterns where the more diffuse pattern corresponding to a larger internal field is assigned to iron in 6(*g*) sites. It is reasonable to conclude that magnetically split 6(*g*) sites of $Mn_2Fe_3Si_3$ are now being occupied.

(d) $MnFe_4Si_3$

A similar situation occurs in this phase except that the initial broadening effects of magnetic hyperfine splitting are evident even at room temperature. Comparison shows that the spectrum, Fig. 4(b), is very similar to that of $Mn_2Fe_3Si_3$ at 300°K except that peaks 1 and 2 of the latter compound have coalesced into one broad intense peak in $MnFe_4Si_3$ at room temperature. Increasing the temperature to 420°K results in rapid fluctuation of internal magnetic fields causing line 4 in the spectrum of $MnFe_4Si_3$ to narrow while the sloping baseline at positive velocity disappears. Similar behavior occurs for the

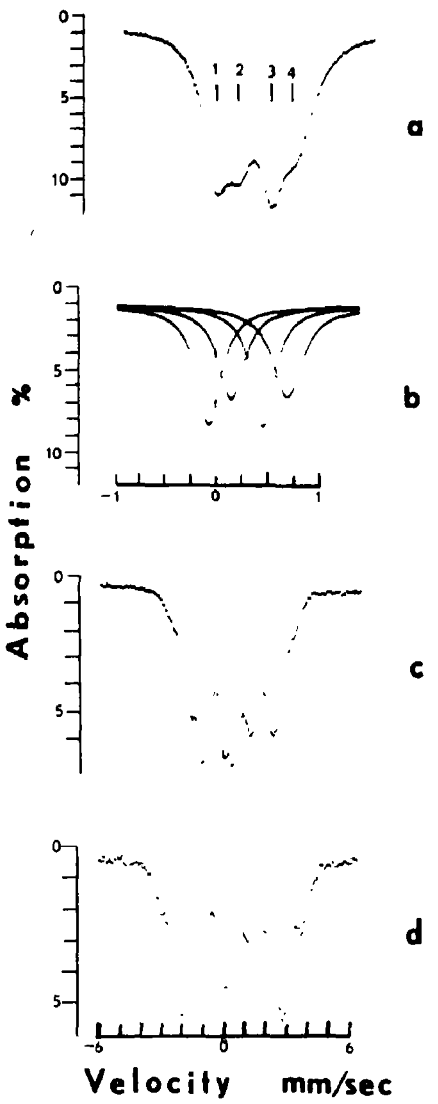

Fig. 3. Mössbauer spectrum of $Mn_2Fe_3Si_3$ at (a) 300°K, (b) computer reconstructed spectrum at 300°K in terms of 4(*d*) and 6(*g*) absorptions, (c) 78°K, (d) 4·2°K.

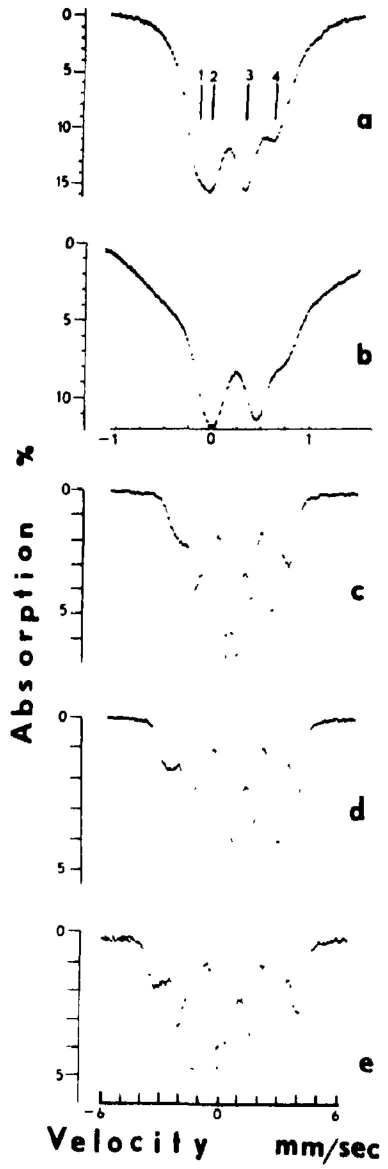

Fig. 4. Mossbauer spectrum of $MnFe_4Si_3$ at (a) 470°K, (b) 300°K, (c) 195°K, (d) 78°K, (e) 4·2°K

broad absorption at negative velocity, and at 470°K, Fig. 4(a), a shoulder corresponding to peak 1 of 4(*d*) iron is evident. The best fit to the latter spectrum shows $(A_1+A_3)/(A_2+A_4)=$ 0·95, or nearly equal occupation of 4(*d*) and 6(*g*) sites as in $Mn_2Fe_3Si_3$.

It is well known that for quadrupole split iron showing magnetic hyperfine splitting the $|\frac{3}{2}, \pm\frac{3}{2}\rangle \rightarrow |\frac{1}{2}, \pm\frac{1}{2}\rangle$ transitions narrow more slowly than $|\frac{3}{2}, \pm\frac{1}{2}\rangle \rightarrow |\frac{1}{2}, \pm\frac{1}{2}\rangle$ transitions on going from a 6 line pattern to a quadrupole doublet[18]. The kets are the magnetic sublevels of the excited and ground nuclear energy states of ^{57}Fe. With increasing temperature, the magnetic splitting can disappear and leave only a quadrupole doublet. Hence the behavior of $MnFe_4Si_3$ with increasing temperature is taken as tentatively indicating $V_{zz} < 0$ for 4(*d*) iron and $V_{zz} > 0$ for 6(*g*) iron.

With decreasing temperature the phase $MnFe_4Si_3$ behaves in much the same way as $Mn_2Fe_3Si_3$ except that magnetic interaction is now stronger and essentially complete hyperfine splitting occurs at higher temperatures. A comparison of the internal fields at different temperatures, Table 4, shows this trend of increasing ferromagnetic interaction with increasing number of iron atoms.

(e) Fe_5Si_3

The Mössbauer spectrum of Fe_5Si_3 at 300°K has the same general appearance as that shown in Fig. 5(a) at 4·2°K. The internal fields corresponding to 4(*d*) and 6(*g*) iron of $Mn_2Fe_3Si_3$ and $MnFe_4Si_3$ are calculated on the basis of two overlapping six line patterns as shown for Fe_5Si_3 at 4·2°K, where the lower pattern in Fig. 5(a) is that for 4(*d*) iron and the middle pattern for 6(*g*). It is evident that there is more uncertainty in the estimation of H_n for 6(*g*) iron than 4(*d*). This is in part attributable to the fact that the 6(*g*) sites are not all magnetically equivalent. For example, in Fe_5Si_3, fields corresponding to 6(*g*) iron range from about 190 to 240 kG. Johnson *et al.*[1] made a similar observation for carbon stabilized Fe_5Si_3. Secondly, absorptions (dashed lines) attributable to Fe_3Si impurity are also present. This complicating feature was also found in the spectrum of Fe_5Si_3 by Shinjo and Nakamura[3], who determined internal fields of 195 ± 10 and 305 ± 10 kG

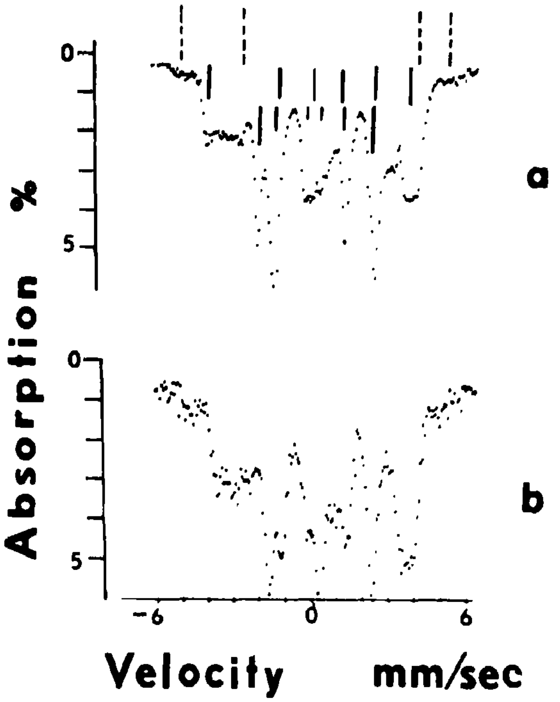

Fig. 5. Mössbauer spectrum of Fe_5Si_3 at (a) 4·2°K, $H_{\text{applied}} = 0$, (b) 4·2°K, $H_{\text{applied}} = 26$ kG.

for the two types of iron in Fe_3Si and which agree with those found here. Hence, in Table 4 only the maximum value of H_n for 6(g) iron at each temperature is reported.

In an effort to understand better the nature of magnetic ordering in Fe_5Si_3, spectra were taken in external magnetic fields. A small field of the order of 1000 G had no effect on the spectrum at 4·2°K. A large field, 26 kG, caused a small decrease in the internal fields of both kinds of iron and although the signal to noise ratio is now lower, H_n for 4(d) iron is estimated as 122 ± 10 kG while the maximum value for 6(g) is 227 ± 10 kG. The decrease in the respective internal fields is somewhat smaller than that expected if the system were a perfect ferromagnet with internal fields parallel. The system is magnetically saturated at this applied field and temperature, Fig. 7, and on this basis it is possible to make a crude calculation of the angle between the internal fields from their observed decrease in an external field, assuming the resultant of the internal fields is collinear with the applied field. In the present case, this amounts to maximum angle of about 112°. Therefore it is assumed that the spins of the corresponding magnetic sublattices are canted at a maximum by approximately this angle. This result must be taken as approximate since the decreases in H_n are small and difficult to estimate accurately from the spectrum. Furthermore, it is seen that the intensities of the spectral absorptions change in a complicated way which is not readily correlated with the observed decreases in internal fields.

4. MAGNETIC MEASUREMENTS

The inverse magnetic susceptibilities of these compounds above their transition temperatures are shown as function of temperature in Fig. 6. Mn_5Si_3 exhibits typical antiferromagnetic behavior as expected and the Neel temperature, 62°K, agrees with previously reported values[4, 19]. The variation in the susceptibility as iron is introduced into the structure reflects the decreasing antiferromagnetic influence and the concomitant increase of ferromagnetic spin arrangements as the iron concentration increases. The transition temperatures also increase as the Fe_5Si_3 end member is approached. The high temperature data for Fe_5Si_3 is not shown because this phase is unstable[20]. Table 1 summarizes the data from the magnetic measurements. In Fig. 7 are shown the magnetization curves for these materials. For $Mn_{5-x}Fe_xSi_3$, $x = 1, 2$, the curves reflect the antiferromagnetic behavior and for $x = 4, 5$ ferromagnetism is clearly evident. However, for $x = 3$ an intermediate state of magnetization can be inferred.

5. MAGNETIC STRUCTURE

The behavior of the susceptibility of the solid solution phases can be understood on the basis of the spin structures for the end members, Mn_5Si_3 and Fe_5Si_3. The Mössbauer data show that the substitution of the first iron atom for manganese occurs in the 4(*d*) position. The susceptibility and magnetization curves for $(Mn_3)(MnFe)Si_3$ indicate that the spin structure of this compound is only very slightly affected by the introduction of the iron atom and the effect is mainly manifested by an increase of the Néel and Weiss temperatures. The Mössbauer data for the phase $Mn_3Fe_2Si_3$ show that the second iron atom occupies mainly the 6(*g*) position in the structure and an approximate formula indicating the probable distribution is $(Mn_{2\cdot35}Fe_{0\cdot65})(Mn_{0\cdot65}Fe_{1\cdot35})Si_3$. The magnetization for this phase, Fig. 7, is nearly unchanged from that of Mn_4FeSi_3 and the implication

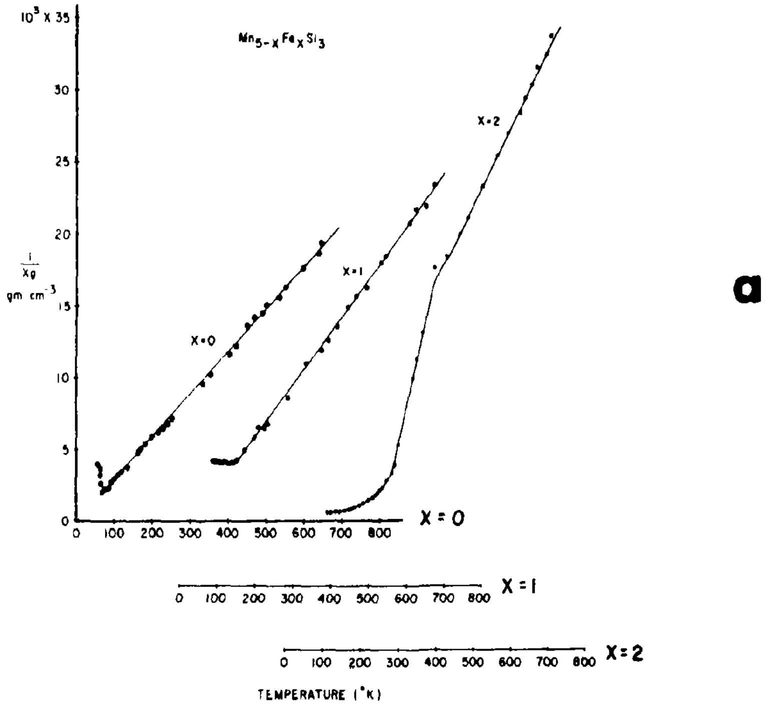

Fig. 6. (a) $1/\chi$ vs. T as a function of increasing iron concentration in the Mn_5Si_3–Fe_5Si_3 system.

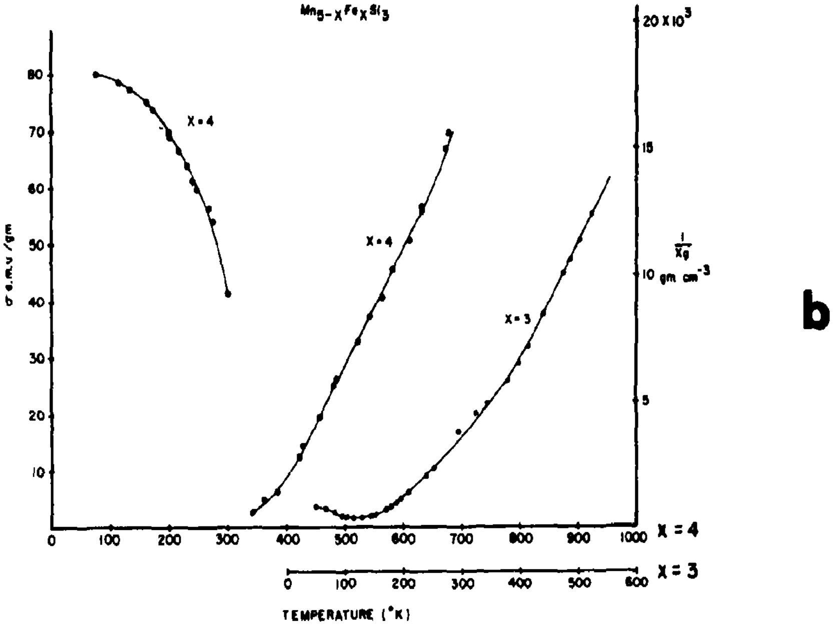

Fig. 6(b). $1/\chi$ vs. T for $Mn_2Fe_3Si_3$ and $MnFe_4Si_3$. The magnetization vs. T for the latter compound is also shown.

must be drawn that the spin structure of this phase remains essentially unaltered except for a further increase in the Néel and Weiss temperatures. However, the susceptibility curve, Fig. 6(a), shows evidence of ferromagnetic interaction from the change in slope at about 350°K. This could be due to a predominant ferromagnetic interaction of the iron atoms in the 4(*d*) sublattice. The overall antiferromagnetic behavior becomes dominant at about 200°K.

Mössbauer data obtained for $Mn_2Fe_3Si_3$ can be interpreted on the basis that most of the third iron atom occupies a 6(*g*) position but with a definite increase of iron present in 4(*d*) sites. Thus a probable formulation is $(Mn_{1.5}Fe_{1.5})(Mn_{0.5}Fe_{1.5})Si_3$. The magnetic behavior exhibited by this phase indicates that its spin structure must be quite different from the previous compositions. The Mössbauer spectra are consistent with magnetically ordered 6(*g*) sites. The susceptibility and magnetization curves for this material definitely show the presence of ferromagnetic interactions with a sharp increase in the Weiss constant. The abrupt change in the transition temperature also supports this view of the spin structure. We attempted to obtain the ferromagnetic component of the magnetization, σ_0, from an extrapolation of the high field part of the σ vs. H curve on the assumption that the magnetization can be expressed as $\sigma = \sigma_0 + \chi H$ where χ is the antiferromagnetic susceptibility. The curve does not show a large degree of horizontal character at the fields available to us so that an extrapolation is expected to yield a low value of σ_0. A value of 0·09 μ_B per metal atom is obtained from the extrapolation of the high field portion of the curve. A moment of 0·26 μ_B per metal atom is calculated on the basis of the following assumptions: (a) Iron contributes 1 μ_B per atom [1] and manganese contributes 0·4 μ_B per atom [4] in the 4(*d*) site and the iron and manganese spins are oppositely aligned. The resultant moment for the 4(*d*) sublattice is 1·3 μ_B. (b)

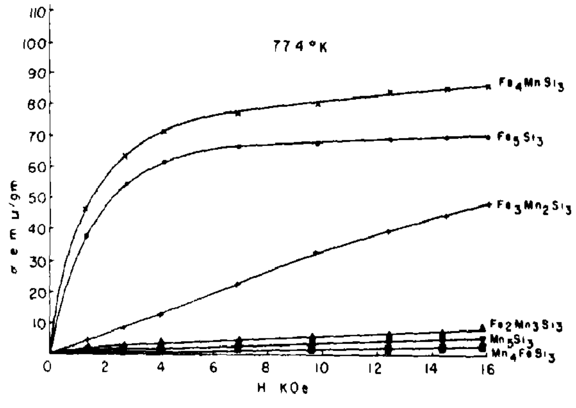

Fig. 7. Magnetization vs. magnetic field intensity for the system $Mn_{5-x}Fe_xSi_3$, $0 \leq x \leq 5$.

The magnetic structure of the 6(*g*) sublattice retains the antiferromagnetic arrangement as in Mn_5Si_3[4]. Thus the total moment for $(Mn_{1.5}Fe_{1.5})(Mn_{0.5}Fe_{1.5})Si_3$ is 1·3 μ_B or 0·26 μ_B per metal atom. Since the material is not sufficiently saturated only a qualitative support for this spin scheme is to be expected.

As indicated by the Mössbauer data, the introduction of the fourth iron atom to form the phase $(MnFe_2)(Fe_2)Si_3$ places two iron atoms into the 6(*g*) and two into the 4(*d*) positions and clearly ferromagnetic coupling among the atoms exist now in both sublattices. The behavior of the susceptibility and magnetization curves, Figs. 6, 7, is typical for a ferromagnetic compound. The magnetization curve for Fe_5Si_3 is included for the sake of completeness. Powdered samples of $MnFe_4Si_3$ and Fe_5Si_3 were oriented in a magnetic field of about 14 kG and their X-ray diffraction patterns showed a strong enhancement of the 00*l* and a nearly complete disappearance of *hkl* lines indicating that the easy axis of magnetization is the *c* axis.

The difference in the permanent moments observed for Fe_5Si_3 and $MnFe_4Si_3$, Table 1, is significant. It can be explained on the basis that the ferromagnetic moment of one sublattice is canted with respect to the other and that the cant angle is a function of the composition. It was previously pointed out that the Mössbauer data are consistent with a maximum cant angle of about 112° for Fe_5Si_3. The value 1·11 μ_B/metal atom for the observed moment in $(MnFe_2)(Fe_2)Si_3$ can be accounted for on the basis that the atoms in the sublattices have parallel spin alignments, the sublattices are coupled parallel, and manganese occupies the magnetically random 6(*g*) positions. Using the values of 1 μ_B for 4(*d*) iron and 1·55 μ_B for 6(*g*)[1] iron the calculated moment is 1·02 μ_B/metal atom. It must be realized that such good agreement may be fortuitous but both the Mössbauer and magnetic data lend credence to this magnetic structure. The same magnetic structure for Fe_5Si_3, i.e. random magnetic sites in 6(*g*), would again give rise to an expected moment of 1·02 μ_B as compared to the observed value of 0·9 μ_B. However, a cant angle of 120° between the sublattices will produce a resultant moment of 0·9 μ_B. The required cant angle is close to the maximum value deduced from the Mössbauer spectrum of Fe_5Si_3 in an external field. Evidence for random spin in some of the 6(*g*) sites comes from the range of internal fields observed for 6(*g*) iron in Fe_5Si_3 in the present investigation and also that of Johnson *et al.*[1]. Lander *et al.*[4] remarked that it is difficult to understand why the 6(*g*) sites are divided into two magnetically non equivalent groups one of which is random in Mn_5Si_3. This difficulty still exists in the case of $MnFe_4Si_3$ and Fe_5Si_3. Perhaps the 'randomness' of the spin structure is due to a third sublattice for which the periodicity extends over many crystallographic unit cells. This could also account for the considerable range of hyperfine field values which are observed.

6. BONDING IN $D8_8$ STRUCTURE

The bonding between an atom in the 4(*d*) site and surrounding silicon atoms is expected to be primarily covalent and the measured hyperfine field value confirms this expectation. Thus, it is reasonable to postulate that the low spin configuration is assumed by the metal atoms[21]. If Fe is considered to have contributed three of its electrons to the conduction band then the resultant low spin $3d^5$ configuration would contain one unpaired electron and give rise to a moment of 1 μ_B in agreement with the reported value for that position by Johnson, *et al.*[1]. It should be noted that the observed isomer shift, Table 3, for 4(*d*) iron is consistent with a low spin $3d^5$ configuration[23]. The discussion of the electronic configuration for the occupant of the 6(*g*) site is considerably more complicated because of the very complex near neighbor environment. The metal atom is bonded to five Si forming a trigonal bipyramid. The metal atom itself is outside this polyhedron. The covalent bonding to Si can be considered to impart a low spin, d^5, configuration, i.e. 1 μ_B contribution to the observed moment. In addition there are ten other metal atoms nearby, six 6(*g*) atoms at distances varying from 2·82*A* to 2·87*A* and four 4(*d*) atoms at 2·95*A*. If one considers metallic type bonding to exist among these and assumes that the resultant contribution to the magnetic moment will be as in α iron, namely 2·2 μ_B, then an approximate 50–50 mixture of metallic and covalent bonding could account for the observed moment of 1·55 μ_B for an atom in the 6(*g*) site.

The explanations offered by Kanematsu [10] and by Lecocq, *et al.*[2] for the magnetic moment observed in Fe_5Si_3 rests on the assumption that the iron atom in the 4(*d*) site is purely metallic and that covalent bonding exists between iron in 6(*g*) and silicon. Kanematsu's theory assigns 2 μ_B to the 4(*d*) site and 1 μ_B to the 6(*g*) site iron atom and he calculates a resultant moment per atom of 1·4 μ_B. We believe that the assignment of the moments in the sublattices and the assumption of parallel coupling is not supported by our results. Similarly Lecocq *et al.* assign a moment of 2·2 μ_B to the 4(*d*) Fe as in α iron and a moment of 0·606 μ_B to 6(*g*) Fe by analogy with nickel and obtain a calculated moment of 1·243 μ_B/Fe atom for Fe_5Si_3, still in rather poor agreement with the measured value.

Acknowledgements—Research of the Materials Science group is sponsored by the Air Force Office of Scientific Research, Office of Aerospace Research, United States Air Force and the National Science Foundation. One of us, W.M.R., is pleased to thank the Chemistry Department of the University of Texas for the N.S.F.-U.S.D.P. Faculty Associate Award extended to him during the course of this research. The support of the Robert A. Welch Foundation is also gratefully acknowledged by R.L.C.

REFERENCES

1. JOHNSON C. E., FORSYTH J. B., LANDER G. H. and BROWN P. J., *J. appl. Phys.* **39**, 465 (1968).
2. LECOCQ Y., LECOCQ P. and MICHEL A., *C.r. Acad. Sci. Paris* **258**, 5655 (1964)
3. SHINJO T. and NAKAMURA Y., *J. phys. Soc. Japan* **18**, 797 (1963).
4. LANDER G. H., BROWN, P. J. and FORSYTH J. B., *Proc. phys. Soc.* **91**, 332 (1967).
5. CON K. V., *C.r. Acad. Sci. Paris* **260**, 111 (1965)
6. ÜBELOCKER E and LECOCQ P., *C.r. Acad. Sci. Paris* **262**, 793 (1966).
7. AMARK K., BOREN B. and WESTGREN A., *Metallwirt.* **15**, 835 (1936).
8. ARONSSON B., *Acta chem. scand.* **14**, 1414 (1960).
9. LANDER G. H. and BROWN P. J., *Phil. Mag.* **16**, 141 (1967).
10. KANEMATSU K., *J. phys. Soc. Japan* **17**, 85 (1962).

11. NARASIMHAN K. S. V. L., STEINFINK H. and GANAPATHY E. V., *J. appl. Phys.* **40**, 51 (1969).
12. FONER S., *Rev. scient. Instrum.* **30**, 548 (1959).
13. RHODES E., O'NEAL W. and SPIJKERMAN J. J., *NBS Tech Note* **404**, 108 (1966).
14. GRANT R. W., *The Mossbauer Effect and Its Application in Chemistry* (Edited by C. Seidel and R. Herber). *Advances in Chemistry Series*, No. **68**, American Chemical Society, Washington, D. C. (1967).
15. EDWARDS P. R. and JOHNSON C. E., *J. chem. Phys.* **49**, 211 (1968).
16. RICKARDS R., JOHNSON C. E. and HILL H. A. O., *J. chem. Phys.* **48**, 5231 (1968).
17. WERTHEIM G. H., *Mossbauer Effect: Principles and Application.* Academic Press, New York (1964).
18. BLUME, M., *Phys. Rev. Lett.* **14**, 96 (1965).
19. LETUN S. M., GEL'D P. V. and SEREBRENNIKOV N. N., *Russ. J. of inorg. Chem.* (Engl. transl.) **10**, 683 (1965).
20. HANSEN M., *Constitution of Binary Alloys*, p. 173, McGraw-Hill, New York (1958).
21. ORGEL L. E., *An Introduction to Transition-Metal Chemistry: Ligand Field Theory.* Wiley, New York (1962).
22. PRESTON R. S., HANNA S. S. and HEBERLE J., *Phys. Rev* **128**, 2207 (1962).
23. REIFF W. M., BAKER W. A., Jr. and ERICKSON N. E., *J. Am. chem. Soc.* **90**, 4794 (1968).

J. Phys. Chem. Solids Pergamon Press 1970. Vol. 31, pp. 1525–1529. Printed in Great Britain.

ELASTIC DISTORTIONS AND INTERACTIONS OF POINT DEFECTS IN KBr*

K. BACHMANN†
Department of Physics and Materials Research Laboratory,
University of Illinois, Urbana, Ill. 61801, U S.A

and

H. PEISL‡
Department of Physics and Coordinated Science Laboratory,
University of Illinois, Urbana, Ill. 61801, U.S.A.

(*Received* 29 *September* 1969; *in revised form* 19 *December* 1969)

Abstract – Using elasticity theory one can describe the lattice distortion due to the *H* center in KBr by the following stress tensor

$$P = \begin{pmatrix} 7\cdot9 & -0\cdot7 & 0 \\ -0\cdot7 & 7\cdot9 & 0 \\ 0 & 0 & -4\cdot4 \end{pmatrix} \times 10^{-12}\,\text{erg}.$$

The distortion field around an *H* center is evaluated. The elastic interaction between two *H* centers and between an *H* center and its anticenter, the *F* center, is discussed.

1. INTRODUCTION

THE DISTORTION of a crystal lattice due to a point defect can be described in terms of elastic multipoles[1–4]. Actual experimental determination of the parameters necessary to fully describe a defect in this way has been limited to a few favorable cases of impurities[4–9] or simple isotropic defects [10].

Low temperature X-irradiation of alkali halides produces various types of defects in these materials[11]. The defects are of the Frenkel type[12]. Among others the well-known *F* center is produced, together with the *H* center as an anticenter. What follows deals with the *H* center in KBr. The atomic structure of the *H* center has been studied extensively by optical and resonance techniques[13]. The *H* center can be described as a Br_2^- molecule sitting on an anion site in the KBr lattice (see Fig. 1) with its axis parallel to a [110] direction. Thus it is a crowdion type of interstitial defect. One expects the distortion field around such a defect to be anisotropic. Recently two independent experiments have been reported [14–16] which, combined, allow the description of the *H* center as an elastic multipole.

Using the experimental data we evaluate the value of the tensor which describes the distortion due to this defect and extrapolate these results to calculate the elastic displacements of the neighboring lattice atoms. We also estimate the elastic interaction between two *H* centers and between an *H* center and an *F* center.

2. ELASTICITY THEORY

Following Kröner[2], we describe the *H* center by a double force tensor **P**. The defect is replaced by a set of body forces acting on the medium. As a consequence, the introduction of a random distribution of such

---

*This research was supported in part by the U S. Atomic Energy Commission under Contract AT (11-1)-1198 and by the Joint Services Electronics Program under Army Contract DAAB-07-67-C-0199.

†Present address: Forschungszentrum Brown, Boveri and Cie, 5401 Baden, Switzerland.

‡Permanent address: I. Physikalisches Institut der Techn. Hochschule, 61 Darmstadt, Germany.

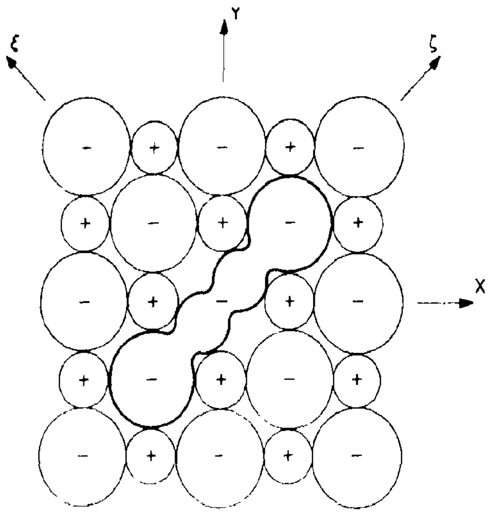

Fig. 1. Model of the *H* center in KBr

defects will change the dimensions of a crystal. A concentration c of defects in a finite crystal gives a relative change of the volume [1]

$$\Delta V/V = c(\text{trace}\,\mathbf{P})/(3C_s\,.\,a^3/8),\ \text{where} \qquad (1)$$

C_s is the bulk modulus and a is the lattice constant $= 6{\cdot}59$ Å. For a cubic crystal the bulk modulus is:

$$C_s = (C_{11}+2C_{12})/3. \qquad (2)$$

Equation (1) permits the determination of the trace of the tensor **P** if one measures the volume change produced by a known concentration of the defects. Balzer *et al.*[14, 15] have measured the macroscopic volume change and the change in lattice parameter of KBr crystals in which a known concentration of defects have been introduced and subsequently annealed. The concentration of the defects has been determined from optical absorption measurements. They obtained a volume change per *H* center $(\Delta V/V)/c_H = 0{\cdot}6 \pm 0{\cdot}2$[15]. Using the low temperature elastic constants of KBr[5]

$$C_{11} = 0{\cdot}428 \times 10^{12}\ \text{dyn/cm}^2$$
$$C_{12} = 0{\cdot}055 \times 10^{12}\ \text{dyn/cm}^2$$
$$C_{44} = 0{\cdot}0505 \times 10^{12}\ \text{dyn/cm}^2$$
$$C_s = 0{\cdot}179 \times 10^{12}\ \text{dyn/cm}^2$$

we obtain

$$\text{trace}\,\mathbf{P} = 11{\cdot}4 \times 10^{-12}\ \text{erg}. \qquad (3)$$

Elastic multipoles can be influenced by an external elastic field. The interaction energy E_{int} with a stress field $\boldsymbol{\epsilon}$ is

$$E_{\text{int}} = -\mathbf{P}\,.\,\boldsymbol{\epsilon}. \qquad (4)$$

The energy levels of the defect in the perfect crystal have orientational degeneracy. By applying a uniaxial stress one can partially remove this degeneracy. At appropriate temperatures the defects reorient, thereby making the crystal dichroic. Bachmann *et al.*[15] measured the anisotropy of the tensor **P**. They define a tensor **P**′ = **P**-(trace **P**/3) and obtain for **P**′

$$\mathbf{P}' = \begin{pmatrix} +4{\cdot}8 & & \\ & -8{\cdot}2 & \\ & & +3{\cdot}4 \end{pmatrix} \times 10^{-12}\ \text{erg}. \qquad (5)$$

Combining equations (3) and (5), we get the actual tensor **P**

$$\mathbf{P} = \begin{pmatrix} 8{\cdot}6 & & \\ & -4{\cdot}4 & \\ & & 7{\cdot}2 \end{pmatrix} \times 10^{-12}\ \text{erg}. \qquad (6)$$

The principal axes of the tensor **P** are the principal axes ξ, η, ζ of the center, as shown in Fig. 1. A proper transformation of axes gives **P** in the usual crystal coordinates x, y, z

$$\mathbf{P} = \begin{pmatrix} 7{\cdot}9 & -0{\cdot}7 & 0 \\ -0{\cdot}7 & 7{\cdot}9 & 0 \\ 0 & 0 & -4{\cdot}4 \end{pmatrix} \times 10^{-12}\ \text{erg}. \qquad (7)$$

3. ELASTIC DISTORTION FIELD

Knowing the tensor **P**, we are able to calculate the elastic distortions around the defect. Shuey and Beyeler[4] have done this in a general way. They expand the elastic field created by a defect in terms of spherical harmonics. As it seems to be impossible to give an exact solution for a cubic medium they use only as many harmonics as they used in their exact solution for an isotropic medium. The distortion field for the unit double force tensor is represented by three terms. The invariant cubic field is

$$\mathbf{u}_1 = -\frac{1}{\sqrt{4\pi}}\frac{5}{3C_{11}+2C_{12}+4C_{44}}\frac{Y^1_{00}}{r^2} \qquad (8)$$

(Symmetry Γ_1),
a doublet:

$$\mathbf{u}_3 = \sum_M \frac{1}{10K_3}\frac{1}{r^2}\left[\frac{47C_{11}+16C_{12}+74C_{44}}{\sqrt{3\pi}}\mathbf{Y}^1_{2M} - \frac{9(3C_{11}+4C_{12}+C_{44})}{\sqrt{2\pi}}\mathbf{Y}^3_{2M}\right] \qquad (9)$$

(Symmetry Γ_3) $M = 0, 2c$,
and a triplet:

$$\mathbf{u}_5 = \sum_M \frac{1}{10K_5 r^2}\left[\frac{137C_{11}+52C_{12}+230C_{44}}{3\sqrt{3\pi}}\mathbf{Y}^1_{2M} - \frac{3(8C_{11}+13C_{12}+5C_{44})}{\sqrt{2\pi}}\mathbf{Y}^3_{2M}\right] \qquad (10)$$

(Symmetry Γ_5) $M = 1c, 1s, 2s$.

In equations (8–10) C_{11}, C_{12}, C_{44} are the cubic elastic constants given before, K_3 and K_5 are abbreviations for the following combinations of the C's.

$$K_3 = \tfrac{1}{25}\left[(47C_{11}+16C_{12}+74C_{44})\right.$$
$$\left.(3C_{11}-C_{12}+C_{44}) - \tfrac{18}{7}(3C_{11}+4C_{12}+C_{44})^2\right]$$

$$K_5 = \tfrac{1}{75}\left[(137C_{11}+52C_{12}+230_{44})\right.$$
$$\left.(C_{11}+C_{12}+5C_{44}) - \tfrac{6}{7}(8C_{11}+13C_{12}+5C_{44})^2\right].$$

$\mathbf{Y}^1_{00}$, $\mathbf{Y}^1_{2M}$ and $\mathbf{Y}^3_{2M}$ are the vector harmonics as defined by

$$\mathbf{Y}^1_{00} = -\frac{x\mathbf{i}+y\mathbf{j}+z\mathbf{k}}{\sqrt{4\pi r}}, \mathbf{Y}^1_{20} = \frac{2z\mathbf{k}-x\mathbf{i}-y\mathbf{j}}{2\sqrt{2\pi r}},$$

$$\mathbf{Y}^3_{20} = \frac{-1}{4r^3}\sqrt{\frac{3}{\pi}}[z(2z^2-3x^2-3y^2)\,\mathbf{k} +$$
$$+ (4z^2-x^2-y^2)(x\mathbf{i}+y\mathbf{j})],$$

$$\mathbf{Y}^1_{22S} = \sqrt{\frac{3}{2\pi}}\frac{x\mathbf{j}+y\mathbf{i}}{2r},$$

$$\mathbf{Y}^3_{22S} = \frac{-1}{2r^3\sqrt{\pi}}[y(4x^2-y^2-z^2)\mathbf{i}$$
$$+ x(4y^2-x^2-z^2)\mathbf{j} + 5\,xyz\,\mathbf{k}]$$

x, y, z are the coordinates and r the distance from the origin of the lattice site.

To obtain the actual distortion fields one has to multiply the unit components given in equations (8–10) by the components of the tensor **P**. The total distortion of a lattice point is the sum of the three distortions. To do so we have to write the tensor **P** in the same spherical notation used for the vector harmonics.

$$P_s = \tfrac{1}{3}(P_{xx}+P_{yy}+P_{zz})$$
$$= 3{\cdot}8 \times 10^{-12}\,\text{erg}.$$
$$P_0 = 1/\sqrt{6}(2P_{zz}-P_{xx}-P_{yy})$$
$$= -10{\cdot}0 \times 10^{-12}\,\text{erg}$$
$$P_{2s} = \sqrt{2}P_{xy} = -0{\cdot}99 \times 10^{-12}\,\text{erg}.$$

The displacements of several lattice points are given in Table 1 and Fig. 2. The largest expansion of the lattice occurs in $[1\bar{1}0]$ direction perpendicular to the molecular axis of the H center. The lattice is also expanded parallel to the molecular axis whereas it is contracted in the third direction [001].

This calculation of lattice distortion is formally exact only at large distances from the defect due to the use of elasticity theory and

Table 1. Displacements of the neighbors of an H *center in* KBr. *The internuclear axis of the* H *center is parallel to* [*110*]. *Unit distance is the nearest neighbor spacing* a/2 = 3·295 Å

Lattice site	Displacement
(1, 0, 0)	(+0·108, −0·0072, 0)
(0, 0, 1)	(0, 0, −0·137)
(1, 1, 0)	(+0·028, +0·028, 0)
$(1, \bar{1}, 0)$	(+0·048, −0·048, 0)
(1, 0, 1)	(+0·045, 0·0025, −0·029)
(1, 1, 1)	(+0·0048, +0·0048, −0·0050)
$(1, \bar{1}, 1)$	(+0·013, −0·013, +0·0002)

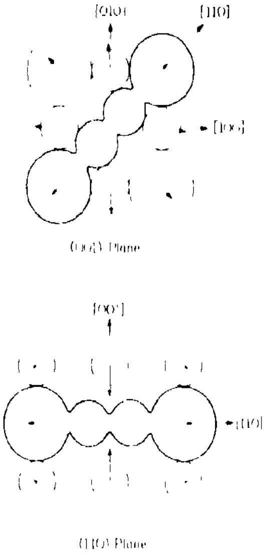

Fig. 2. Elastic displacement of ions in a [001] and a $[1\bar{1}0]$ plane surrounding an *H* center in KBr (Displacement magnification 4*x*)

to the neglect of higher harmonics in the field expansion. However it is expected to give an order of magnitude estimate even for the nearest neighbors. Only an atomistic calculation of the defect neighborhood could give eventually more accurate results in this region. (Dienes *et al.*[16] have made such a calculation for the *H* center in KCl. If one takes into account the different host lattices their results agree quite well with ours.)

4. ELASTIC INTERACTION

Two defects with at least one of them having a nonisotropic tensor **P** interact elastically. Shuey and Beyeler[4] have calculated the elastic interaction energies. Using their results we are able to calculate the elastic interaction of an *H* center with another *H* center or of an *H* center with an *F* center. We find that the energetically most favorable configurations of two *H* centers are those where the connection line between the two *H* centers is along [110] and where the internuclear axes of the defects are either both parallel to [101] or where one is parallel to [101] and the other parallel to $[10\bar{1}]$. The elastic interaction energies are $-0{\cdot}25/n^3$ eV and $-0{\cdot}24/n^3$ eV respectively. ($n = 1, 2, 3, \ldots$ depending whether the centers are first, second or higher order neighbors along the considered connection line). The least favorable configurations have two *H* centers with a connection line along [110] and with both their internuclear axes parallel to $[1\bar{1}0]$. In this case the interaction energy is $+0{\cdot}38/n^3$ eV.

Using the **P** tensor for the *F* center given by von Guerard *et al.*[10], we calculate the interaction energy for an *H* center–*F* center pair. We find that the most favorable configuration is the one where the connection line between the defects is along [001] and where the molecular axis of the *H* center is parallel to [110]. The elastic interaction energy of this configuration is $-0{\cdot}043/n^3$ eV. A very unfavorable configuration with an interaction energy of $+0{\cdot}076/n^3$ eV is the following: connection line between the centers along [110] and internuclear axis of the *H* center parallel to $[1\bar{1}0]$.

We would like to emphasize that the calculation of Shuey and Beyeler deals only with the elastic interaction energy of point defects. For extended defects the electrical interaction energy has to be taken into account. Although the defects are electrically neutral with respect to the lattice, an electric interaction arises from the extended charge clouds of the defects. In fact, for a pair of

H centers a simple calculation shows that the electrical interaction energy is of the same order of magnitude as the elastic interaction energy. The simplest approximation one can make is that the *H* center can be described by two point charges each having charge of $e/2$, separated along the internuclear axis. For a charge separation of $b = 0{\cdot}38\,a$ the electrical interaction energies for the two most favorable positions are $-0{\cdot}06/n^3$ eV and $-0{\cdot}44/n^3$ eV respectively. None of the other configurations becomes more favorable by adding the electrical term. Furthermore the influence of the electrical polarisation field created by the displacement of the surrounding ions as well as the polarization of the ions themselves has to be taken into account.

REFERENCES

1. ESHELBY J. D., *Solid State Phys.* Vol. 3, p 79. Academic Press, New York. (1956)
2. KRÖNER E., *Ergebn. angew. Math.* **5**, (1958).
3. NOWICK A. S and HELLER W. R, *Adv. Phys.* **12**, 251 (1963)
4. SHUEY R. T. and BEYELER H. U., *Z. Angew. Math. Phys. (ZAMP)*, **19**, 278 (1968).
5. KÄNZIG W., *J. Phys. Chem. Solids* **23**, 479 (1962)
6. VON WALDKIRCH Th., ZELLER H. R. and KÄNZIG W., *Helv. Phys. Acta* **40**, 823 (1967)
7. HÄRTEL H. and LUTY F., *Phys. Status Solidi* **12**, 347 (1965).
8. PAUS H. and LUTY F., *Phys. Status Solidi* **12**, 341 (1965)
9. BYER N. E. and SACK H. S, *J. Phys. Chem. Solids* **29**, 677 (1968).
10. VON GUERARD B., PEISL H. and WAIDELICH W., *Z. Phys.* **220**, 473, (1969).
11. See e.g. SCHULMAN J H., and COMPTON W. D., *Color Centers in Solids*, Pergamon Press, Oxford (1963)–CRAWFORD J. H Jr., *Adv. Phys.* **17**, 93 (1968).
12. BALZER R., PEISL H. and WAIDELICH W., *Phys. Lett.* **27A**, 31 (1968);–*Phys. Status Solidi* **27**, K165 (1968); **28**, 207 (1968)
13. DUERIG W H. and MARKHAM J. J., *Phys Rev.* **88**, 1043 (1952) COMPTON W. D. and KLICK C C., *Phys. Rev.* **110**, 349 (1958) KANZIG, W and WOODRUFF T. O, *J. Phys. Chem. Solids* **9**, 70 (1958).
14. BALZER R., PEISL H. and WAIDELICH W., *Phys. Status Solidi* **31**, K29 (1969).
15. BACHMANN K. and KANZIG W., *Phys. kondens. Mater.* **7**, 284 (1968).
16. DIENES G. J., HATCHER P. D, and SMOLUCHOWSKI R., *Phys. Rev* **157**, 692 (1967).

J. Phys. Chem. Solids Pergamon Press 1970. Vol. 31, pp. 1531–1537. Printed in Great Britain.

CHALEUR SPECIFIQUE, SUPRACONDUCTIVITE ET ORDRE CRISTALLIN D'ALLIAGES DE STRUCTURE A 15 A BASE DE VANADIUM

P. SPITZLI, R. FLÜKIGER, F. HEINIGER, A. JUNOD,
J. MULLER et J. L. STAUDENMANN
Institut de Physique de la Matière Condensée, Université de Genève, 1211 Genève, Switzerland

(*Received* 7 *November* 1969; *in revised form* 17 *December* 1969)

Résumé– La chaleur spécifique à basse température et la température de transition supraconductrice ont été mesurées dans des alliages de structure A 15 de vanadium avec d'autres éléments de transition tels que Os, Ir, Pt, Au, Rh, Pd, Co et Ni. Nous avons observé une corrélation remarquable entre la chaleur spécifique électronique et le taux d'occupation des chaînes de la structure A 15 par les atomes de vanadium.

Abstract–The low temperature specific heat and the superconducting transition temperature have been measured in binary alloys of vanadium with Os, Ir, Pt, Au, Rh, Pd, Co and Ni exhibiting the A 15 type structure. The results show a remarkable correlation between the electronic specific heat and the rate of occupation of the chain-sites in this structure by atoms of vanadium.

1. INTRODUCTION

DANS DES travaux précédents[1, 2] sur des composés du type A 15 à base de niobium, nous avons trouvé que la température de transition supraconductrice, T_c, et la chaleur spécifique électronique, γ, dépendent fortement des conditions de préparation des échantillons et de leur degré d'ordre. Ces résultats et ceux trouvés par van Reuth *et al.*[3] dans les composés V_3Au, également du type A 15, font penser que l'influence de l'ordre cristallin sur T_c se manifeste principalement par l'intermédiaire de la forme de la bande du vanadium et par la densité d'états électroniques au niveau de Fermi. Dans ce travail, nous avons étudié plus en détail la corrélation entre la température critique T_c, la densité d'états électroniques et le degré d'ordre cristallin dans une série d'alliages $V_{1-\beta}X_\beta$ de structure A 15, où X signifie un élément de transition tel que Os, Ir, Pt, Au, Rh, Pd, Co et Ni.

2. RESULTATS EXPERIMENTAUX

Pour le présent travail tous les échantillons ont été préparés au four à arc sous atmosphère d'argon, les pertes en poids restant toujours inférieures à 1 pour cent. Les mesures s'effectuaient, soit directement au lingot de fusion tel qu'il était obtenu après un refroidissement rapide à partir du point de fusion, soit après un recuit entre 600 et 1050°C (Tableau 1). Tous les échantillons ont été analysés par diffraction de rayons X à l'aide d'une caméra Guinier-de Wolff, et à l'exception de l'échantillon $V_{0\cdot78}Ni_{0\cdot22}$ ils se présentaient tous de phase A 15 pure.

La chaleur spécifique a été mesurée entre 1·5 et 4·2°K pour les alliages dont le T_c était inférieur à 1·5°K. Pour les autres alliages, elle a été étendue à des températures plus élevées de façon à pouvoir séparer sans ambiguité les contributions des électrons et du réseau et déterminer le coefficient de la chaleur spécifique électronique γ et la température de Debye θ_0. Les résultats de nos mesures, ensemble avec les conditions de préparation, sont rassemblés dans le Table 1.

La température de transition supraconductrice, la température de Debye θ_0 et la chaleur spécifique électronique sont représentées dans la Fig. 1. A première vue,

Table 1

Système $A_{1-\beta}B_\beta$	Concentration atomes B β[% at]	Traitement thermique	Constante réticulaire a[Å]	Température de transition T_c[°K]	Chaleur spécifique électronique γ[mJ/at-g°K^2]	Température de Debye θ_0[°K]
V–Co	25·0	400 h à 800°C	4·688 ± 0·003	< 0·015$^{5)}$	2·78 ± 0·01	560 ± 15
V–Ni	22·0[*]	310 h. à 820°C	4·708 ± 0·001	0·35$^{6)}$	4·5 ± 0·2	
V–Rh	25·0	75 h à 1053°C	4·785$^{4)}$	< 0·015$^{5)}$	2·51 ± 0·05	485 ± 10
V–Pd	25·0	75 h à 1050°C	4·825$^{4)}$	0·08$^{6)}$	5·00 ± 0·05	400 ± 15
V–Os	50·0	Lingot de fusion	4·808 ± 0·003	5·15	4·76 ± 0·02	385 ± 5
V–Ir	25·0	75 h à 1050°C	4·788$^{4)}$	< 0·015$^{5)}$	1·97 ± 0·05	460 ± 10
"	31·0	Lingot de fusion	4·792 ± 0·002	0·91	3·67 ± 0·02	414 ± 7
"	37·0	Lingot de fusion	4·789 ± 0·003	1·71	4·34 ± 0·01	395 ± 5
V–Pt	28·0	Lingot de fusion	4·825 ± 0·004	1·50	6·32 ± 0·03	471 ± 10
"	25·0	75 h. à 1050°C	4·817$^{4)}$	3·20	7·19 ± 0·10	511 ± 20
"	22·2	Lingot de fusion	4·817 ± 0·002	0·98	5·15 ± 0·02	400 ± 15
V–Au	25·0	Lingot de fusion	4·882 ± 0·003	< 0·90	9·03 ± 0·05	379 ± 15
"	25·0	120 h. à 1000°C et 120 h. à 850°C		1·60	11·10 ± 0·05	398 ± 20
"	25·0	200 h à 600°C et refroidissement lent		2·20	12·11 ± 0·05	387 ± 20

[*] L'échantillon $V_{0·78}Ni_{0·22}$ ne comprenait qu'environ 80% de phase A 15, d'où la grande incertitude sur les paramètres de la chaleur spécifique

il semble être difficile de trouver une corrélation entre ces grandeurs si on compare des systèmes d'alliages différents. Par contre en comparant les alliages $V_{1-\beta}X_\beta$ pour un élément X donné, le comportement de la température de transition supraconductrice reflète les variations de la chaleur spécifique électronique, que ces variations soient dues à la concentration β(V – Pt, V – Ir) ou au traitement thermique (V_3Au). Notons aussi que la chaleur spécifique électronique des alliages A 15 à base de vanadium est du même ordre que celle des alliages à base de niobium, tandis que les températures de transition T_c de ces derniers sont en général plus élevées. Pour faciliter cette comparaison, nous avons calculé sur la base de la théorie de McMillan[7] relative aux supraconducteurs à couplage fort le paramètre de couplage électrons–phonons λ en admettant pour le paramètre d'interaction de Coulomb effective μ^* des valeurs 0·18 (points dans la Fig. 2) et de 0·13 et 0·20 (limites inférieures et supérieures des barres de la Fig. 2). Ce choix peut paraître arbitraire, mais il semble raisonnable d'utiliser, dans le cas de bandes de caractère 3 *d*, une valeur pour μ^* plus élevée que la moyenne de 0·13 postulée pour l'ensemble des alliages des métaux de transition. Cependant, il est difficile d'indiquer une valeur maximale pratiquement admissible pour des métaux paramagnétiques ayant une faible largeur de bande. Au voisinage de 6 électrons par atome, les valeurs obtenues pour le λ des alliages V–X sont comparables à celles des alliages Nb–X. Pour 6·2–6·5 électrons par atome, le paramètre λ des alliages à base de vanadium reste appréciablement au-dessous de celui des alliages à base de niobium. Ceci est très prononcé cans le cas du V_3Pd. L'alliage $V_{0·50}Os_{0·50}$ par contre prend une position intermédiaire; nous pensons que la substitution sur les chaînes de la structure A 15 d'atomes d'Os aux atomes de V change partiellement le caractère 3 *d* des fonctions d'ondes qui semble être plutôt défavorable à la supraconductibilité.

Notons que la théorie de McMillan offre une description intéressante surtout pour les alliages des métaux de transition à structure cubique centrée. Entre autre, les valeurs empiriques de la densité d'états non renormalisée de ces alliages sont en bon accord avec les résultats calculés par la

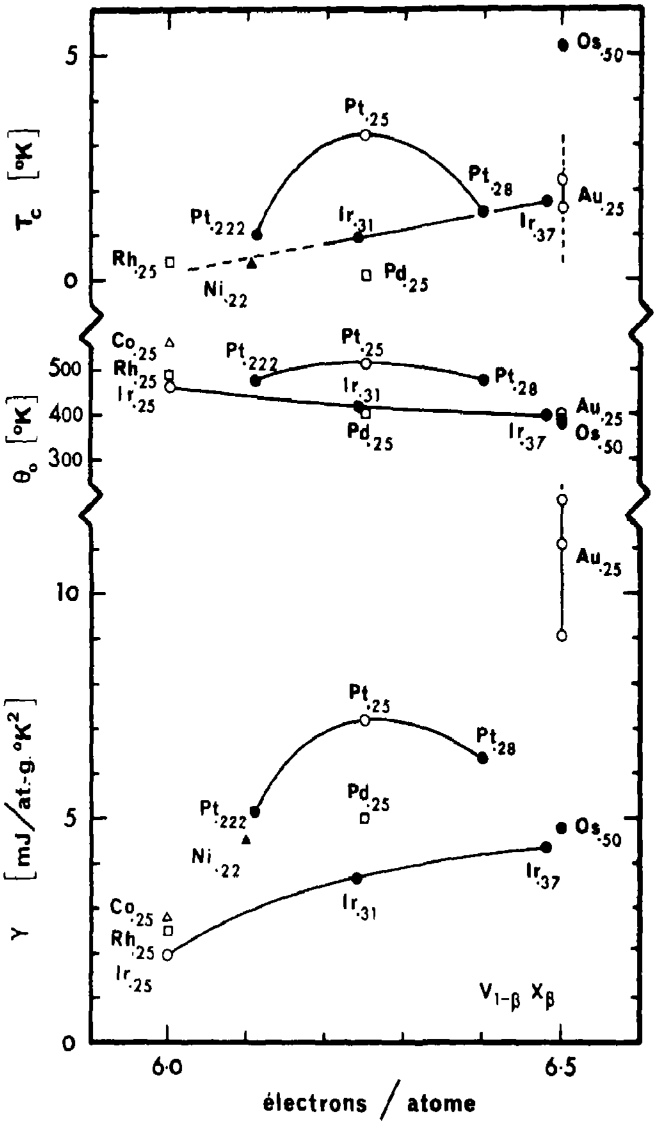

Fig. 1 Température de transition, T_c, température de Debye, θ_0, et coefficient de la chaleur spécifique électronique, γ, d'alliages A 15 de composition $V_{1-\beta}X_\beta$.

méthode APW (voir Fig. 10 de la Réf. [7]. Par contre, le modèle linéaire proposé par Labbé et Friedel[8, 9], quoique mathématiquement simple, est plus particulièrement adapté à la structure A 15. Dans le contexte de la présente étude, ce modèle a le mérite de prévoir explicitement une forte dépendance de T_c de la densité d'états. Toutefois, ce problème ne pourra être discuté de manière plus détaillée que lorsque seront disponibles les résultats concernant les séries d'alliages A 15 basées sur d'autres élements de transition que le vanadium.

3. ORDRE CRISTALLIN ET DENSITE D'ETATS

Comparant les chaleurs spécifiques électroniques, γ, des composés V_3X à celles des composés correspondants Nb_3X,

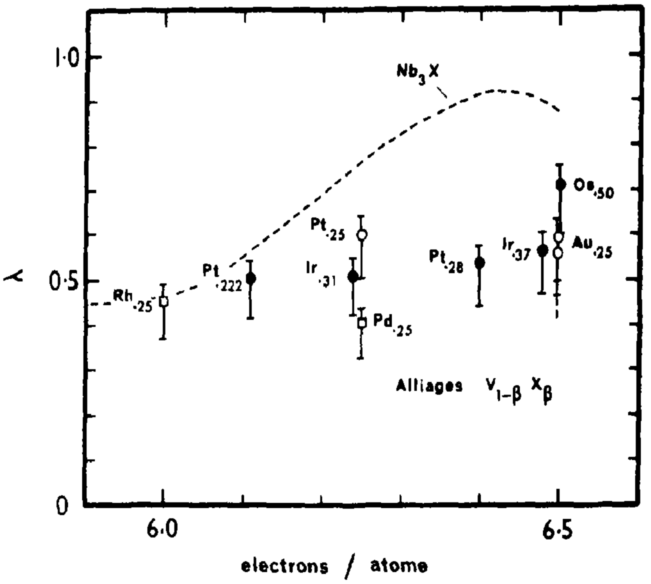

Fig. 2 Paramètre du couplage électrons–phonons, λ

on constate une augmentation semblable de γ en fonction du nombre d'électrons par atome entre 6·0 et 6·5. Pour les alliages stoechiométriques et ordonnés, γ augmente dans ce domaine d'un facteur 5 ou plus. Pour des alliages $A_{1-\beta}B_\beta$ avec $\beta > 0{\cdot}25$, ou pour des alliages avec un ordre cristallin imparfait on trouve par contre des valeurs de γ plus basses. Ce fait nous a amenés à comparer les chaleurs spécifiques électroniques avec un paramètre d'ordre r_a, décrivant l'ordre cristallin sur les chaînes de la structure A 15. En fait la structure A 15 consiste en un réseau cubique comprenant deux types de sites différents. Les sites b forment un réseau cubique centré et les sites a composent des chaînes dans les 3 directions ⟨100⟩ du réseau. Dans un alliage de formule $A_{1-\beta}B_\beta$, le paramètre r_a définissant la fraction des sites a occupés par des atomes A (par du vanadium ou du niobium dans notre cas) peut être déterminé à l'aide des paramètres d'ordre de Bragg-Williams[4]:

$$S_A = \frac{r_a - (1-\beta)}{\beta} \quad \text{et} \quad S_B = \frac{r_b - \beta}{1-\beta}$$

Dans un alliage A 15 on a par maille élémentaire 6 sites a, 2 sites b et, d'après Waterstrat et van Reuth[10], pratiquement pas de lacune; il en résulte que les taux d'occupation r_a et r_b sont liés à la concentration β. On trouve cette relation en écrivant que le nombre d'atomes B aux sites b plus le nombre d'atomes B aux sites a est égal au nombre total d'atomes B dans la maille élémentaire:

$$2r_b + 6(1-r_a) = 8\beta.$$

On peut ainsi exprimer le paramètre r_a en fonction des paramètres d'ordre S_A ou S_B:

$$r_a = 1-\beta(1-S_A) =$$
$$\tfrac{4}{3}(1-\beta) - \tfrac{1}{3}(1-\beta)(1-S_B).$$

Pour les alliages stoechiométriques, $\beta = 0{\cdot}25$, $S_A = S_B = S$ d'où $r_a = \frac{1}{4}(S+3)$, et il est possible d'estimer avec une bonne précision les valeurs de S simplement en comparant les conditions de préparation et dans certains cas les températures critiques de la supraconductivité de nos échantillons avec celles des alliages dont le degré d'ordre a été déterminé par diffractométrie[3, 4, 10, 11]. Pour les alliages non-stoechiométriques le paramètre r_a ne peut dépasser une valeur maximale $r_a(\max)$ déterminée par la concentration:

$$r_a(\max) = 1 \text{ si } \beta < 0{\cdot}25,$$

$$r_a(\max) = \tfrac{4}{3}(1-\beta) \text{ si } \beta > 0{\cdot}25.$$

Ainsi, lorsque $\beta < 0{\cdot}25$, le terme $-\beta(1-S_A)$ intervenant dans l'expression de r_a est une correction due à une déviation du degré d'orde maximum, déviation qui, chez van Reuth et Waterstrat[4], est décrite par le paramètre $S = S_A$. De même, lorsque $\beta > 0{\cdot}25$ le terme $-\frac{4}{3}(1-\beta)(1-S_B)$ est la correction décrite par le paramètre d'ordre $S = S_B$. Dans ce dernier cas, le taux d'occupation des chaînes, r_a, est principalement déterminé par la concentration β, et l'influence du paramètre S n'est pas importante, du moins pour nos échantillons. Les paramètres S, permettant de calculer les corrections, ont été estimés par comparaison des conditions de préparation de nos échantillons avec celles de Waterstrat et van Reuth[10]. Dans la Fig. 3, nos résultats pour la chaleur spécifique électronique γ sont reportés en fonction du nombre d'électrons par atome, avec en indice les valeurs du paramètre S. Dans cette même figure, nous avons essayé de tracer le graphe de la chaleur spécifique électronique en fonction du nombre d'électrons par atome, ceci pour les alliages de vanadium et d'un élément $5\,d$ pour les cas où les sites a sont occupés uniquement par des atomes de vanadium. Ayant ainsi défini un $\gamma_0(5d)$, 'idéal' nous avons porté dans la Fig. 4 le rapport γ/γ_0 en fonction du paramètre r_a.

La Fig. 4 met en évidence une corrélation étroite entre la densité d'états électroniques

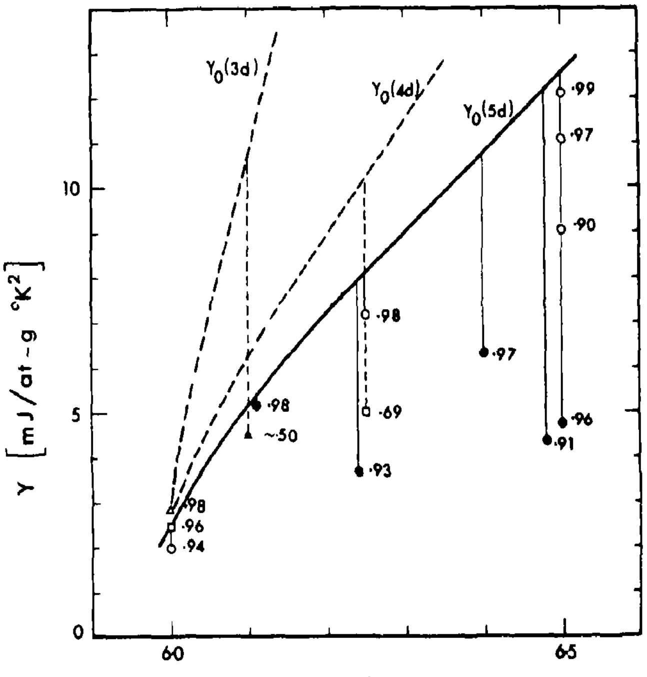

Fig. 3. Coefficient de la chaleur spécifique électronique, γ, et paramètre d'ordre. ○ V-5d, □ V-4d, △ V-3d, symboles pleins: alliages nonstoechiométriques.

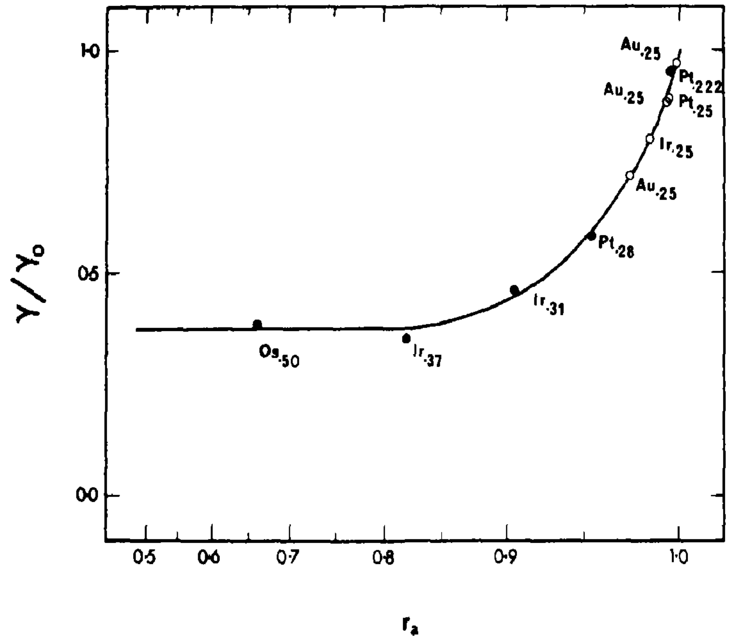

Fig. 4. Corrélation entre la densité d'états réduite et le taux d'occupation des chaînes par des atomes de vanadium.

et le degré d'ordre des alliages A 15 de vanadium avec un élément 5 *d*. Il est remarquable que cette corrélation ne dépende pas du nombre d'électrons par atome, ni du fait que le désordre peut provenir soit d'un traitement thermique adéquat, soit d'une déviation de la concentration stoechiométrique. Il faut également noter l'importance de ce désordre cristallin pour la densité d'états électroniques: pour $r_a = 0{\cdot}93$, donc en ayant remplacé un atome de vanadium sur 14 par un élément d'une valence différente, on trouve que la densité d'états totale est réduite de 50 pour cent. Selon Labbé[9, 12], une telle situation peut être décrite d'une manière satisfaisante en considérant des chaînes linéaires perturbées par des atomes différents et en admettant que le niveau de Fermi soit voisin d'une pointe de la densité d'états d'une sous-bande *d*.

Pour les alliages avec un élément 4 *d* il faut noter que le V_3Pd est très désordonné, $S = 0{\cdot}69$; il en résulte que si la corrélation $\gamma/\gamma_0 = f(r_a)$, trouvée pour les alliages de vanadium avec un élément de la série 5 *d*, est aussi valable pour les alliages avec des éléments 4 *d*, la densité d'états électroniques du V_3Pd ordonné devrait être le double de la valeur mesurée. Sur la base de ce raisonnement on obtient pour la densité d'états idéale relative aux alliages de vanadium avec un élément 4 *d* la courbe $\gamma_0(4\,d)$ de la Fig. 3. D'une manière analogue nous avons représenté la densité d'états hypothétique relative aux alliages avec un élément 3 *d*.

Initialement les résultats pour les alliages non-stoechiométriques nous ont amenés à comparer les valeurs γ avec un paramètre d'ordre relatif aux chaînes de la structure A 15 plutôt qu'avec le paramètre d'ordre du type Bragg-Williams. En effet le degré d'ordre relatif aux sites b semble avoir assez peu d'influence sur la densité d'états. Ceci est confirmé par des mesures plus anciennes, effectuées dans le système d'alliages $(Nb_{1-\alpha}V_\alpha)_3Au$[13]. En négligeant d'abord l'occupation de sites a par des atomes d'Au, le paramètre r_a, défini comme ci-dessus, vaut

$r_a = \alpha$ pour $\alpha \geq 0{\cdot}5$, et si on définit r_a par rapport au Nb, $r_a = 1-\alpha$ pour $\alpha \leq 0{\cdot}5$. Dans ce système, la chaleur spécifique γ baisse jusqu'à 50 pour cent en substituant du Nb au V ou du V au Nb dans les alliages V_3Au et Nb_3Au respectivement. L'effet serait encore plus marqué si ces alliages binaires étaient parfaitement ordonnés. En se basant sur un γ_0 interpolé linéairement entre Nb_3Au et V_3Au ordonnés on observe une et V_3Au ordonnés on observe une dépression maximale de γ dans le système ternaire qui est comparable à celle donnée par la Fig. 4. La variation de γ/γ_0 en fonction de r_a par contre semble être plus faible au voisinage de $r_a = 1$. Il est possible, lors de la substitution d'un faible pourcentage d'atomes dans les chaînes, que la perturbation soit moins grande si les atomes échangés ont la même valence.

4. CONCLUSIONS

Nous avons trouvé dans ce travail que la densité d'états électroniques d'alliages du type A 15 à base de vanadium ou de niobium dépend fortement du taux d'occupation des chaînes de cette structure par la même espèce d'atomes, ceci pour un nombre d'électrons par atome compris entre 6·2 et 6·5. Dans ce domaine, la forte augmentation de la densité d'états des alliages parfaitement ordonnés, lorsque le nombre d'électrons croît, indique que le niveau de Fermi s'approche d'une pointe de la densité d'états; par suite, dans chaque cas, l'abaissement de la densité d'états s'explique par une modification de la bande *d* due à un désordre sur les chaînes. Pour conclure on peut dire que si l'ordre cristallin a une aussi grande influence sur la structure de bande, inversement la structure électronique doit être un facteur important, limitant l'ordre et les domaines d'homogénéité des phases A 15.

Remerciements—Nous remercions MM. E. C. van Reuth et R. M. Waterstrat de la communication d'une partie de leurs résultats avant la publication ainsi que M. J. Labbé de nous avoir informé de ses résultats récents. Le présent travail a été soutenu par le Fonds National Suisse et la Commission fédérale pour l'encouragement de la recherche scientifique.

REFERENCES

1. FLUKIGER R., SPITZLI P., HEINIGER F. et MULLER J., *Phys. Lett.* **29A**, 407 (1969)
2. SPITZLI P., FLUKIGER R., HEINIGER F. et MULLER J., *Phys. Lett.* **30A**, 170 (1969)
3. VAN REUTH E. C., SCHOEP G. K., KLAASSEN T. O. et POULIS N. J., *Physica* **37**, 476 (1967).
4. VAN REUTH E. C. et WATERSTRAT R. M., *Acta crystallogr.* **B24**, 186 (1968)
5. BLAUGHER R. D., HEIN R. A., COX J. E. et WATERSTRAT R. M., *J. Low Temp. Phys.* **1**, 539 (1969).
6. HEIN R. A., COX J. E., BLAUGHER R. D. et
7. McMILLAN W. L., *Phys. Rev.* **167**, 331 (1968).
8. LABBÉ J. et FRIEDEL J., *J. Phys.* **27**, 153 (1966).
   WATERSTRAT R. M., *Solid State. Commun.* **7**, 381 (1969).
   LABBÉ J., BARISIC S. et FRIEDEL J., *Phys. Rev. Lett.* **19**, 1039 (1967).
9. LABBÉ J., Thèse, Paris (1968)
10. WATERSTRAT R. M. et VAN REUTH E. C., *Third Bolton Landing Conference, Lake George, N.Y.* (1969)
11. VAN REUTH E. C., WATERSTRAT R. M., BLAUGHER R. D., HEIN R. A. et COX J. E., *Proc.* LT 10, Vol IIb, p. 137 (1967).
12. LABBE J., communication privée
13. HEINIGER F., BUCHER F. et MULLER J., *Phys. kondens. Mater.* **5**, 243 (1966)

J. Phys. Chem. Solids Pergamon Press 1970. Vol. 31, pp. 1539–1545. Printed in Great Britain.

ELECTRICAL CONDUCTIVITY IN NH_4Cl AND ND_4Cl SINGLE CRYSTALS

R. G. FULLER* and **F. W. PATTEN**
U.S. Naval Research Laboratory, Wash. D.C. 20390, U.S.A.

(*Received* 24 *October* 1969; *in revised form* 15 *December* 1969)

Abstract – Electrical conductivity measurements are reported for normal and deuterated ammonium chloride single crystals in the temperature regions which characterize the pure and the impurity-dominated materials. We conclude from the data that conductivity in ammonium chloride is due to the formation of either cation or anion vacancies and a subsequent process controlled by a proton transfer Our results are found to be consistent with a model proposed by Herrington and Staveley.

1. INTRODUCTION

It was noted, during studies on radiation-induced point defects in ammonium halide single crystals[1, 2], that hydrogen migrates fairly rapidly through these crystals at room temperature. This effect may be seen directly in the electron paramagnetic resonance spectra of ND_3Cl color centers[2] in deuterated single crystals. If these crystals are exposed to the atmosphere for short periods of time, proton hyperfine interactions from hydrogen which has exchanged with deuterium atoms in the ammonium group become pronounced in the spectra. These measurements may, in fact, be used to determine the rate of hydrogen diffusion in ammonium halide crystals. The mechanism of such a rapid diffusion is still in doubt, however. A likely explanation is that this mechanism is the same as that proposed to explain electrical conductivity in the ammonium halides, which is also dependent on motion of hydrogen atoms. Diffusion and conductivity are then related by the Nernst-Einstein equation.

Electrical conductivity measurements on the ammonium halides were obtained first by Herrington and Staveley[3]. They found that ammonium chloride, in particular, is a significantly better intrinsic conductor than any of the alkali halides. Since conductivity in this material is due entirely to ionic motion, as it is in the alkali halides, they were lead to consider processes peculiar to the ammonium halides which might lead to lower activation energies for ion migration. When single crystals were doped with either divalent cation or divalent anion substitutional impurities the conductivity was enhanced by about the same factor, implying that anions and cations make comparable contributions to the conductivity. By contrast, cation motion predominates in the alkali halides. Several other properties of NH_4Cl single crystals seemed of special relevance: (1) the heat capacity is larger than can be explained by lattice and molecular harmonic motions, (2) the thermal expansion coefficient is anomalously high and (3) the vapor pressure is high, measurable even at room temperature. These suggest that at room temperature and below there is a significant amount of dissociation within the crystal matrix, of the form $NH_4^+ + Cl^- \rightarrow NH_3 + HCl$. Herrington and Staveley finally proposed a three-stage mechanism for ionic conduction (Fig. 1) based on this ease of dissociation: (1) NH_3 and HCl are formed by a proton transfer, adjacent to either a positive or negative ion vacancy; (2) either NH_3 or HCl moves into the vacancy; (3) a reverse proton transfer occurs forming NH_4^+ and Cl^- again, one of which has exchanged its position

---

*Present address: Physics Department, University of Nebraska, Lincoln, Nebr. 68508, U.S.A.

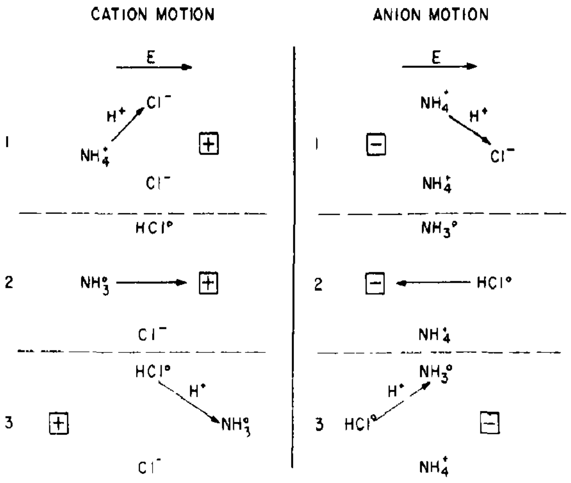

Fig. 1. Mechanism for ionic conduction in NH_4Cl (Shown in 110 plane.)

with the vacancy. A succession of these exchanges, under the influence of the applied electric field, results in a net transfer of charge.

A test of this hypothesis could be achieved by measuring the conductivities of both normal and deuterated ammonium chloride over some temperature interval. If a proton exchange is the controlling process in the above mechanism, in the sense that it has the highest activation energy (excluding the activation energy for vacancy production), then the attack frequency of the moving particle and hence the preexponential factor in the conductivity equation will be affected greatly upon deuteration of the crystal. The results of such measurements, reported in the following sections, show unambiguously that electrical conductivity in NH_4Cl is dependent on motion of hydrogen ions, in agreement with the mechanism proposed by Herrington and Staveley.

2. THEORY

Electrical conductivity may be expressed as the sum of the individual contributions of the different charge carriers in the material:

$$\sigma = \sum_i N_i z_i e \mu_i \qquad (1)$$

where σ is the conductivity and where N_i, $z_i e$ and μ_i are the number, charge and mobility of the ith type of carrier, respectively. If, as in the alkali halides, the charge carriers are anions and cations, their contributions to the conductivity are determined by the concentrations of vacant lattice sites as well as the ion mobilities[4]. The equation for the conductivity can be written as

$$\sigma = \sigma_a + \sigma_c = N_a e \mu_a + N_c e \mu_c, \qquad (2)$$

where N_a and N_c are the numbers of anion and cation vacancies per unit volume and where μ_a and μ_c are the anion and cation mobilities. The equations for the vacancy concentrations and ion mobilities are well known[5], and in our notation are:

$$N_a N_c = N_0^2 = N^2 \exp(-g/kT), \qquad (3)$$

$$\mu_a = \frac{4a^2 e \nu_a}{kT} \exp(-\Delta g_a/kT), \qquad (4)$$

$$\mu_c = \frac{4a^2 e \nu_c}{kT} \exp(-\Delta g_c/kT), \qquad (5)$$

where N is the number of ions, either anions or cations, per unit volume, g is the Gibbs energy of Schottky defect formation, a is the anion–cation distance, ν_a and ν_c are the anion and cation jump attempt frequencies, and Δg_a and Δg_c are the Gibbs energies of anion and cation migration. The Gibbs energy can be expressed as the enthalpy minus the product of absolute temperature and entropy, $g = h - Ts$.

In an Arrhenius plot of log (σT) vs. $1/T$ one would interpret curvature as an indication that both anions and cations make contributions to the conductivity. This is the case for alkali halides[6, 7]. On the other hand, barring the unlikely coincidence of equal activation energies, a linear Arrhenius plot would indicate that one charge carrier predominates and that the conductivity can be expressed as a single exponential,

$$\sigma T = \frac{4Na^2e^2\nu}{k}\exp\left[\frac{-g/2-\Delta g}{kT}\right]$$
$$= A_0 \exp\left(-[h/2+\Delta h]/kT\right). \quad (6)$$

This appears to be the situation for NH_4Cl. According to classical rate theory, the jump attempt frequency is proportional to the inverse square root of the mass of the vibrating ion[5]. In the case of NH_4Cl and ND_4Cl this means that if the mechanism for conduction is the motion of the anions, the conductivity of NH_4Cl and ND_4Cl would be the same; if the mechanism is cation motion, the ratio of NH_4Cl conductivity to ND_4Cl conductivity would be $\sqrt{11/9}$; if the mechanism for conduction is dominated by motion of a hydrogen ion, then the above ratio takes on the value $\sqrt{2}$.

In vacancy controlled mechanisms it is possible to separate the formation and migration energies from one another by putting a known amount of divalent cation impurity into the crystal. The cation vacancy concentration is then enhanced and the anion vacancy concentration is depressed. Then the equations for vacancy concentration are

$$N_c = N_a + N_i \quad (7)$$

where N_i is the number of impurity ions per unit volume, while equation (3) still holds for the product of the vacancy concentrations[5]. Consequently, the activation enthalpy for conduction changes from $h/2+\Delta h_c$ to Δh_c, and the conductivity can be expressed as

$$\sigma T = \frac{4a^2e\nu_c}{k}N_i \exp\left(-\Delta g_c/kT\right)$$
$$= C_0 \exp\left(-\Delta h_c/kT\right). \quad (8)$$

3. EXPERIMENTAL PROCEDURE

NH_4Cl single crystals have the CsCl crystal structure in the temperature region from 184·3 to −30·5°C, which encompasses the interval of experimental investigation. Crystals, very nearly cubic in habit, were grown from saturated aqueous solution with urea added to suppress dendritic growth. Starting materials were either Fisher or Mallinckrodt analytic reagent grade materials. Some crystals were grown by slow evaporation of the solution in a temperature controlled chamber. Larger (up to 1 cm^3), and more perfect, crystals were grown by starting with a saturated solution at about 40°C in a closed vessel which was immersed in a water bath regulated to within 0·01°C/day. The temperature was then lowered by about 0·2°C/day over a period of weeks. The resulting crystals were colorless, perfect cubes. It was not possible to detect the presence of any urea impurity by using NMR and i.r. absorption techniques.

Deuterated single crystals were prepared by dissolving analytic grade NH_4Cl and urea in 99·85 mole-% D_2O and evaporating to dryness four times before growing crystals in a temperature-regulated solution; it is expected that 99·0 per cent deuteration was achieved for the freshly grown crystals. While handling the crystals in preparation for the conductivity measurements, they were exposed to the atmosphere with some consequent exchange of hydrogen for deuterium. An NMR analysis of some of these samples showed that the level of deuteration was 90 ± 5 per cent during measurements of the conductivity.

The samples were cut to about 1 × 7 × 7 mm size, polished, and painted with dag electrodes before being installed between the platinum contacts of the conductivity sample holder. The samples were kept in a dry argon atmosphere during the measurements of the conductivity. The conductivity measurements were made using standard a.c. bridge techniques.

4. RESULTS

A plot of log (σT) vs. $1000/T$ for NH_4Cl, $NH_4Cl:SrCl_2$ and ND_4Cl is shown for the temperature interval 180–60°C in Fig. 2. The concentration of Sr in the doped material was found to be about 55 ppm, using the flame emission spectroscopy analysis technique. There is good linearity observed for both the NH_4Cl and ND_4Cl curves over two decades of values on the ordinate within the high temperature, intrinsic region from 180 to 130°C. This implies that there is only one value for the activation enthalpy within the exponential of the conductivity equation, equation (6), and hence there is only one mechanism for conduction within this temperature interval. This contrasts with the situation for the alkali halides, whose conductivity plots show definite curvature in the high temperature regime. It should be remarked that when measurements were

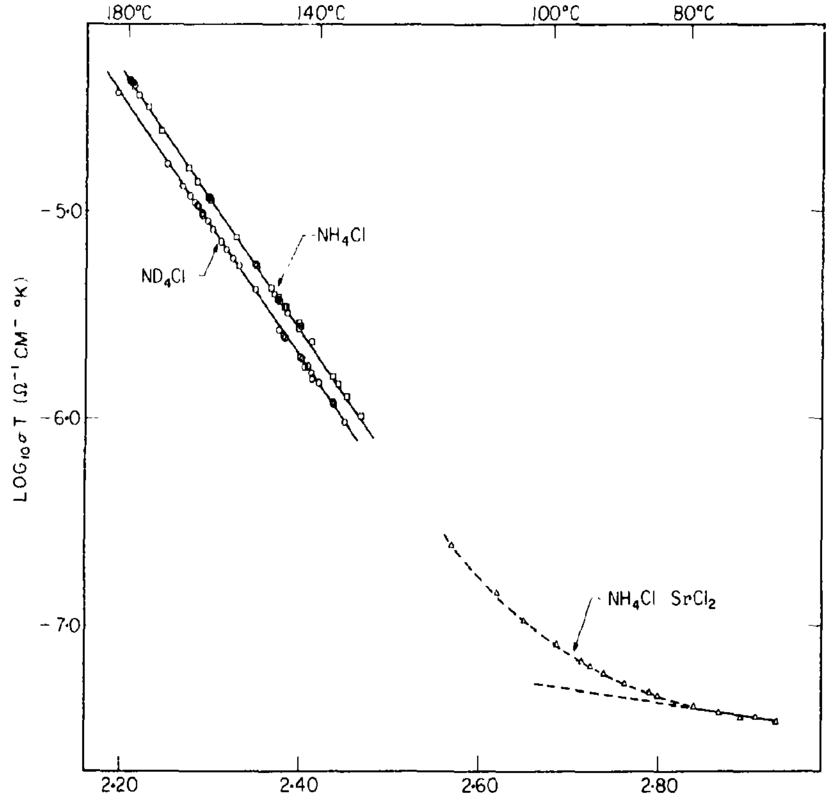

Fig. 2. The conductivity-absolute temperature product as a function of reciprocal temperature for NH_4Cl, ND_4Cl and $NH_4Cl:SrCl_2$ single crystals. The solid lines are a result of a least squares computer fit of a first degree polynomial to the data (only the five data points in the low temperature extreme of $NH_4Cl:SrCl_2$ were fitted).

attempted at temperatures higher than about 180°C, the increased vapor pressure of NH_4Cl caused a boiloff of material to occur, degrading the sample and preventing further measurements.

The low temperature, impurity dominated or extrinsic conductivity region, is represented by the temperature interval from 130 to 60°C in the figure. Within this region, the doped material, $NH_4Cl:SrCl_2$, has conductivity values higher than those for the extrapolated linear plot of data in the intrinsic region. This shows that cation vacancies, induced by charge compensation of the substitutional Sr^{2+} ions, are an essential part of the conductivity mechanism at these temperatures. In the linear portion of this region at the low temperature extreme, the conductivity equation again may be simplified to a single exponential, of the form of equation (8). There is now a single contribution to the activation enthalpy, that of the migration enthalpy of the charge carrier. This value is given in Table 1, along with the activation enthalpy for the intrinsic region.

The linear fit to the ND_4Cl data in the figure has the same slope as the NH_4Cl data in the intrinsic region, leading to the same value for the activation enthalpy within this temperature interval. In all of the above cases, a linear relation was computer-fitted to the data points using a least-squares routine.

Table 1

Material	Conductivity* (Ω^{-1} cm^{-1})	Activation enthalpy (eV)
NH_4Cl	$8{\cdot}14\times10^{-9}$	1·26
ND_4Cl	$6{\cdot}07\times10^{-9}$	1·26
$NH_4Cl:SrCl_2$	—	0·15

*At 420°K.

5. DISCUSSION

The differences in conductivity for NH_4Cl and ND_4Cl single crystals in the intrinsic region cannot be ascribed to differences in impurity concentrations since the same starting materials were used for both crystals, except that the deuterated crystals were grown from a D_2O solution. Also, the excellent fit of a single exponential to both sets of data implies that the conductivity measurement is dominated by the motion of a single charged particle across a potential barrier which is identical in both crystals. We conclude that the conductivity mechanism either is a single charge transfer process, or it is a sequence of charge transfers in which one jump (the controlling process) is associated with a significantly higher activation enthalpy than the others.

In either case, the parallel displacement of the two conductivity curves in the intrinsic region is due to a different preexponential constant in equation (6), and therefore there must be a difference in the jump attempt frequency, ν, of the charge carrier for the normal and deuterated material. Since this quantity is inversely proportional to the square root of the mass of the charge carrier, the ratio of conductivities for any particular temperature in the intrinsic region is

$$(\sigma T)_H/(\sigma T)_D = \nu_H/\nu_D = (m_D/m_H)^{1/2}. \quad (9)$$

where the subscripts H and D refer to the NH_4Cl and ND_4Cl cases, respectively. From the data of Fig. 2 we find that $(\sigma T)_H/(\sigma T)_D = 1{\cdot}34$, evaluated within the linear region. Of the limited number of charge carriers which could exist in this material, only the bare proton/deuteron has a sufficiently high value for the mass ratio to fit the data: $(m_D/m_H)^{1/2} = 1{\cdot}414$. The discrepancy between these two numbers is easily explained by the fact that the ND_4Cl crystals were not completely deuterated. Letting x represent the fraction of the total charge carriers in ND_4Cl crystals which result from hydrogen substitution, then

$$(\sigma T)_H/(\sigma T)_D = \sqrt{2}/[1+(\sqrt{2}-1)x]. \quad (10)$$

When equation (10) is evaluated for the value of the conductivity ratio given above, it is found that $x = 0{\cdot}14$. Thus the experimental result can be accounted for by assuming only 86 per cent deuteration of the ND_4Cl crystals, which is in excellent agreement with the result of the NMR analysis given in Section 3.

It appears very likely, from this evidence, that the charge carrier controlling the process of charge transport in NH_4Cl is a proton. The results of divalent cation impurity substitution indicate that vacancies, of either polarity, are also required within the mechanism. These ingredients are both contained within the Herrington–Staveley model, pictorially represented in Fig. 1. Processes 1 and 3 in the dual picture are a forward and reverse proton switch. Process 2, the intermediate charge-transfer process, results in a displacement of the cation/anion vacancy by one lattice spacing along a ⟨100⟩ direction. Each step is aided by the applied electric field and contributes a portion of the total motion of the charge. Our results are consistent with this model. Furthermore, if the initial proton transfer is the controlling process of the mechanism, process 2 must have a much lower activation enthalpy.

The measured activation enthalpy (Δh_c) for conduction in strontium doped ammonium chloride in the impurity-dominated region is, from Table 1, 0·15 eV. This value represents, from equation (8), the migration enthalpy of the charge carrier, equal to that of the controlling process, step 1 of Fig. 1. The measured activation enthalpy ($h/2+\Delta h_c$) of 1·26 eV in the intrinsic region of the conductivity curve leads to a value of 2·22 eV for the enthalpy (h) of formation of vacancy-pairs (Schottky defects) in pure NH_4Cl. These may be compared with the values for CsCl[8] of 0·6 and 0·3 eV for the enthalpies of cation and anion vacancy mobility, respectively, and 1·8 eV for the enthalpy of Schottky defect formation.

The above values for NH_4Cl differ from those reported by Herrington and Staveley, which are $\Delta h_c = 0{\cdot}75$ eV and $h/2+\Delta h_c = 1{\cdot}15$ eV, so that $h = 0{\cdot}80$ eV. Our disagreement principally is with the measurement of activation enthalpy in the extrinsic region of the conductivity curve. On examining their data, we observed an intermediate temperature region in their conductivity curves for doped samples in which the measurements seem to correspond very well to those of our extrinsic region. Their measurement of an activation enthalpy at even lower temperatures, which they attribute to the motion of the charge carrier of the high temperature mechanism, may, in fact, be associated with some form of charged aggregate.

Thus the energy of Schottky defect formation in NH_4Cl is in substantial agreement with the value quoted for isomorphous CsCl. The low value found for the activation enthalpy for migration of the charge carrier, compared to ionic mobilities in CsCl or alkali halides, is what one might intuitively expect for a mechanism dominated by a proton exchange. The identical process has recently been examined theoretically by Clementi[9], in his study of the transitional states in the $NH_3 + HCl \rightarrow NH_4Cl$ reaction. From his potential diagrams[10], we estimate a barrier height of about 0·5 eV for the gas phase reaction, using an interatomic distance appropriate to the solid. However, the problem is modified greatly by the presence of the Madelung potential in the solid. It would be desirable to calculate the effect of this contribution on Clementi's potential energy diagram for the free space reaction, though this appears to be a very difficult problem.

6. CONCLUSION

Conductivity in ammonium chloride seems to be dependent on formation of Schottky defects as in the alkali halides. However, the conductivity mechanism is not the simple ion motion found in alkali halides, but is a process which is apparently dominated by a proton transfer. Such a mechanism has been suggested by Herrington and Staveley and our results, based on measurements of normal and deuterated ammonium chloride single crystals, are in agreement with this model. Our conductivity data are somewhat different from those reported previously. In particular, the activation enthalpy for conduction in the extrinsic region is considerably smaller than was indicated. It is asserted that this value is essentially the activation enthalpy of the proton transfer.

Acknowledgements – The authors wish to express their gratitude to M. N Kahler and M. H. Reilly for their advice, and to R Black for performing the analyses for strontium impurity in our samples.

REFERENCES

1. PATTEN F W. and MARRONE M J., *Phys. Rev.* **142**, 513 (1966).
2. PATTEN F. W., *Phys. Rev.* **175**, 1216 (1968).
3. HERRINGTON T. M. and STAVELEY L. A K., *J. Phys. Chem. Solids* **25**, 921 (1964).
4. FULLER R G, MARQUARDT C. L., REILLY M. H. and WELLS J. C., Jr, *Phys. Rev* **176**, 1036 (1968)
5. LIDIARD A. B, in *Handbuch der Physik* (Edited by S. Flugge), Vol. 20, Part 2, pp. 246–349. Springer, Berlin (1957)
6. FULLER R. G and REILLY M. H, *Phys. Rev Lett.* **19**, 113 (1967)
7. SUPTITZ P. and TELTOW J, *Phys Status Solidi* **23**, 9 (1967).
8. HARVEY P J. and HOODLESS I M, *Phil Mag* **16**, 543 (1967)
9. CLEMENTI F., *J. chem. Phys* **46**, 3851 (1967), **47**, 2323 (1967); **47**, 3837 (1967)
10. *Ibid*, **47**, 3839 (Fig. 1) (1967).

J. Phys. Chem. Solids Pergamon Press 1970. Vol. 31, pp. 1547–1551. Printed in Great Britain.

TRIVALENT AND TETRAVALENT CHROMIUM IN THE SELENO-SPINEL SERIES $CuCr_{0\cdot3}Rh_{1\cdot7-x}Sn_xSe_4$

R. P. VAN STAPELE and F. K. LOTGERING

Philips Research Laboratories, N.V. Philips' Gloeilampenfabrieken, Eindhoven, Netherlands

(*Received* 24 *October* 1969; *in revised form* 1 *December* 1969)

Abstract–The Curie constant per gramatom chromium varies from 1·03 for $x = 0$ to 1·86 for $x = 1$ in the mixed crystal series $CuCr_{0\cdot3}Rh_{1\cdot7-x}Sn_xSe_4$. This is interpreted as a transition from tetravalent to trivalent chromium. The ferromagnetic ordering occurring for $x = 0$ is found to be destroyed rapidly by Sn substitution.

1. INTRODUCTION

IN AN earlier paper[1] the authors have shown that the saturation magnetizations and Curie constants of the ferromagnetic seleno-spinels $CuCr_yRh_{2-y}Se_4$ are in agreement with the chromium occurring mainly in the tetravalent state for $y < 1$. In this series of mixed crystals the valency of chromium has been studied on materials with a varying Cr content. The present paper reports a change of the Curie constant per gramatom chromium from 1·03 to 1·86 in the series $CuCr_{0\cdot3}Rh_{1\cdot7-x}Sn_xSe_4$ having a constant Cr content (cf. the spin-only values 1·00 for Cr^{4+} and 1·87 for Cr^{3+}). We consider this as a further confirmation that Cr^{4+} can be present in certain Cu-containing sulpho–and seleno-spinels contrary to Goodenough's[2] statement that Cr^{4+} is not stable in these substances.

2. EXPERIMENTAL PROCEDURE AND RESULTS

Hahn and Strick[3] have reported the existence of the seleno-spinels $CuCrMeSe_4$ with Me = Ti or Sn. Attempts to prepare $CuCrMeSe_4$ and $CuRhMeSe_4$ at 800°C failed for Me = Ti but yield a pure spinel phase in the cases of Me = Sn. Samples of $CuCr_{0\cdot3}Rh_{1\cdot7-x}Sn_xSe_4$ with $x = 0\cdot1$, 0·2, 0·3, 0·4, 0·7 and 1·0 were prepared at 500°C from the elements in the usual way in evacuated silica ampoules. In addition the materials were ground and fired at 800°C three times. The X-ray diagrams showed a pure spinel phase except for the samples with $x = 0\cdot4$ and 0·7, in which cases two very weak non-identified reflections were present. The susceptibilities at room temperature measured after the third and fourth firing were equal within a few percent except for $x = 0\cdot4$ and 0·7, in which cases the difference was ~9 per cent.

Figure 1 gives some $\chi_m^{-1}-T$ curves for $CuCr_{0\cdot3}Rh_{1\cdot7-x}Sn_xSe_4$. The susceptibilities were corrected for temperature-independent paramagnetism or diamagnetism using the susceptibilities at room temperature measured on samples of $CuRh_{2-x}Sn_xSe_4$[4] (Fig. 2). The only magnetic ions in $CuCr_{0\cdot3}Rh_{1\cdot7-x}Sn_xSe_4$ are the Cr ions, which occur in a rather small concentration so that the determination of C_m is not very accurate. From the marked change in slope of the $\chi_m^{-1}-T$ curves in Fig. 1 it is seen, however, that a change of the Curie constant per gramatom Cr is observed for beyond the experimental error.

Figure 3 gives some of the magnetization curves measured on $CuCr_{0\cdot3}Rh_{1\cdot7-x}Sn_xSe_4$. The replacement of Rh in $CuCr_{0\cdot3}Rh_{1\cdot7}Se_4$ by Sn seems to destroy the ferromagnetic ordering. This is seen from a drop of the moment at 4·2°K below 0·6 μ_B/molecule and

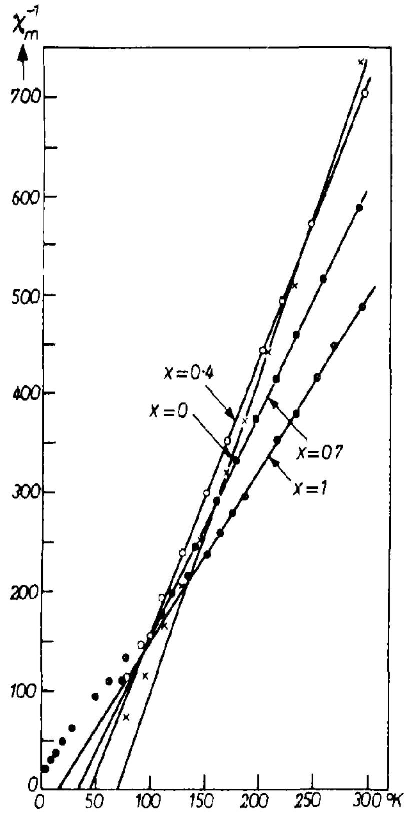

Fig. 1. $CuCr_{0.3}Rh_{1.7-x}Sn_xSe_4$ with $x = 0$, 0·4, 0·7 and 1·0. Reciprocal molar susceptibility as a function of temperature. Susceptibility corrected using Fig. 2 (see text).

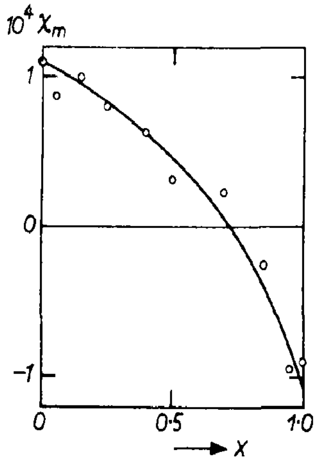

Fig. 2. $CuRh_{2-x}Sn_xSe_4$[4]. Molar susceptibility at room temperature as a function of composition.

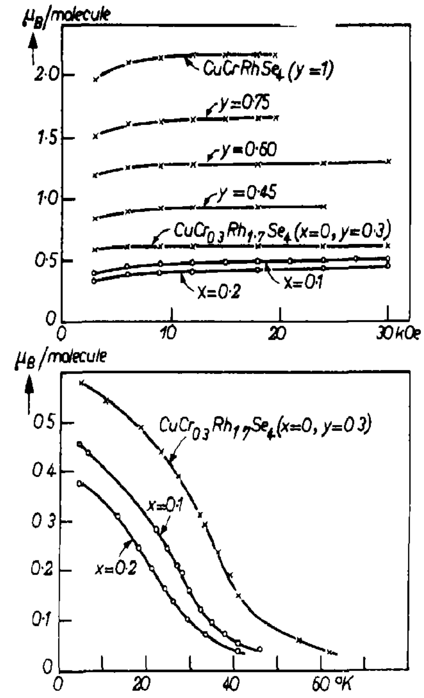

Fig. 3. $CuCr_{0.3}Rh_{1.7-x}Sn_xSe_4$ (circles) and $CuCr_yRh_{2-y}Se_4$ (crosses). Magnetization at 4·2°K as a function of field strength (top) and as a function of temperature for $H = 6$ kOe (bottom).

an increasing slope of the magnetization curves for increasing Sn content (Fig. 3). For $x = 0{\cdot}3$ the magnetic behaviour can hardly be called ferromagnetic as we measured at 4·2°K a steady increase of the magnetization with the field and a very narrow hysteresis loop (Coercive force ~50 oe; remanence ~0·1 G cm^3 g^{-1} i.e. ~0·01 μ_B/molecule).

We replaced 0·4 Rh in $CuCrRhSe_4$ by Sn and found a similar effect. Whereas T_c = 270°K and the saturation, being 2·18 μ_B/molecule, is easily attained (Fig. 3) for $CuCrRhSe_4$ we found that the Sn substitution decreased T_c to 140°K and had the effect of preventing complete saturation at 4·2°K for $H = 30$ kOe. The magnetization at 4·2°K and $H = 30$ kOe was increased to 2·7 μ_B/molecule, showing a transition from Cr^{4+} into Cr^{3+} as a result of the Sn substitution.

Figure 4 gives several quantities of

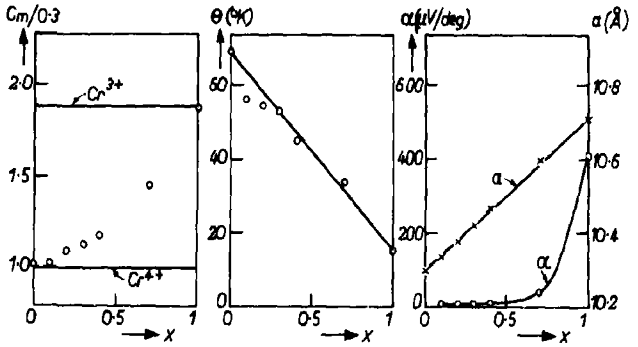

Fig. 4. CuCr$_{0\cdot3}$Rh$_{1\cdot7-x}$Sn$_x$Se$_4$. Curie constant per gramatom chromium $C_m/0{\cdot}3$, paramagnetic Curie temperature θ, Seebeck coefficient α and cell edge a as a function of composition. Paramagnetic data corrected for temperature-independent susceptibility (see text).

CuCr$_{0\cdot3}$Rh$_{2-x}$Sn$_x$Se$_4$ as a function of the Sn content. From the Seebeck coefficients it is seen that the material is p-type metallic conducting for $x \neq 1$ and semiconducting for $x = 1$. This was confirmed by some resistivity measurements. For $x = 1$ we found $\rho = 30$ ohm cm at room temperature and an activation energy of 0·13 eV for temperatures between 290 and 100°K. For $x = 0{\cdot}1$ and $0{\cdot}7$ we measured $\rho \sim 10^{-3}$ ohm cm at room temperature and at 78°K.

Since the paramagnetic Curie temperature of CuCr$_{0\cdot3}$Rh$_{1\cdot7-x}$Sn$_x$Se$_4$ for small x (Fig. 4) was found to be considerably lower than the value $\theta = 120$°K reported earlier[1] for $x = 0$, we reinvestigated CuCr$_y$Rh$_{2-y}$Se$_4$ with $y = 0{\cdot}30$, 0·45 and 0·60. The old samples were prepared by two heat treatments (at 700 and 750°C) starting from the components* CuCr$_2$Se$_4$ and CuRh$_2$Se$_4$. We prepared these materials using the same procedure but with one additional firing at 750°C, and the materials were ground longer after each firing. The susceptibilities χ_m (295°K) measured on the new samples after the second and third firing are mutually in reasonable agreement but differ considerably from χ_m(295°K) measured on the old samples (e.g. $\chi_m^{-1} = 735$ and 750 for the new samples, and $\chi_m^{-1} = 610$ for the old sample with $y = 0{\cdot}30$).

Figure 5 gives θ, C_m and μ_f of CuCr$_y$Rh$_{2-y}$Se$_4$ measured on the new samples after the second firing in the case of $y = 0{\cdot}30$, 0·45 and 0·60. The susceptibilities were corrected for temperature-independent paramagnetism using the value $1{\cdot}1 \,.\, 10^{-4}$ of CuRh$_2$Se$_4$ (see Fig. 2. For increasing Cr content this correction becomes less reliable but also less important). Whereas θ differs considerably from the values given in Ref. [1] (e.g. $\theta = 66$ or 120°K* for $y = 0{\cdot}30$), the values of C_m and μ_f are in good agreement (e.g. $C_m = 0{\cdot}33$* or 0·29*; $\mu_f = 0{\cdot}64$ or 0·57 μ_B/molecule for $y = 0{\cdot}30$). Since θ changes rapidly with the composition y (Fig. 5), we think that the poor reproducibility of θ and χ_m(295°K) arises from relatively small deviations from complete mixing of the small amount of CuCr$_2$Se$_4$ with the excess of CuRh$_2$Se$_4$, and the present values are more reliable than those given in Ref. [1]. For several samples of both series of mixed crystals it was verified at 78 and

---

*In Ref. [1] it is mentioned incorrectly that the CuCr$_y$Rh$_{2-y}$Se$_4$ samples had been prepared from the elements. In fact the preparation started from mixtures of CuCr$_2$Se$_4$ and CuRh$_2$Se$_4$.

*Without correction for temperature-independent paramagnetism

J. Phys. Chem. Solids Pergamon Press 1970. Vol. 31, pp. 1553-1563. Printed in Great Britain

THERMOELECTRIC POWER OF IONIC CRYSTALS-V. THERMOELECTRIC POWER OF POTASSIUM BROMIDE AND SODIUM BROMIDE USING BROMINE GAS ELECTRODES

HIDEOKI HOSHINO and MITSUO SHIMOJI
Department of Chemistry, Faculty of Science, Hokkaido University, Sapporo, Japan

(*Received* 27 *October* 1969)

Abstract—The thermoelectric powers of single crystals of KBr and NaBr, undoped and doped with $BaBr_2$, were measured as a function of temperature between 400–540°C using bromine gas electrodes. Slight discolouration of the crystals, observed after the thermoelectric power measurements, suggests that stoichiometric excess of bromine presumably yield cation vacancies and holes The transport numbers of the holes can be neglected under the experimental condition of interest, as inferred from Mollwo's work The experimental results of the thermoelectric power are interpreted in terms of theoretical expressions for homogeneous and heterogeneous thermoelectric power. The values of heats of transport of both cation- and anion vacancies are in agreement with those of heats of activation for migration of respective ions, as predicted from the non-equilibrium theory based upon the Fokker-Planck equation (papers I and III of this series) It is quantitatively shown that the heterogeneous thermoelectric powers of the KBr and NaBr crystals being in contact with the inert metal electrodes may depend on the electrode materials and on the purity of the crystals.

1. INTRODUCTION

ON THE thermoelectric power measurements of the alkali halide crystals, the alkali metal electrodes can not be used because of their active nature. Therefore, the inert metal electrodes, such as Pt[1-7], Rh[5], Ag[9] and graphite[2, 6-8] have been employed for the systems: NaCl[1-3], KCl[2, 4, 5], NaBr [6], KBr[7], KI[8] and LiF[9]. In this case the expressions for the heterogeneous thermoelectric power have very complex forms [5, 10-12], resulting from some reactions associated with the contact between the metal electrodes and the salts, since they have no common ion. Although there have been done some devices[3-8] to obtain the values of the heats of transport of lattice defects, the discussions have been unsatisfactory[6-8]; the unknown parameters have been introduced to interpret the reactions related to the behavior of the excess electrons at the surface of the crystal.

In this paper the thermoelectric power of KBr and NaBr crystals was measured using the bromine gas electrodes in place of the inert metal electrodes. The thermoelectric power measurements of the solid electrolytes due to the halogen gas electrodes have first been made by Reinhold[13] on the systems, Ag-, Cu- and Pb halides and recently on the AgI system by Wagener[14]. There has been no attempt to measure the thermoelectric power of alkali halide crystals using halogen gas electrodes until now except the cases of molten alkali halides[15, 16].

It should be noted that, when some alkali halide crystals, e.g. KBr and KI, have been annealed in their halogen gas atmosphere at high temperatures, the formation of the V-centres[17-23] and an enhancement of the electrical conductivity[17, 23, 24] have often been observed. Such a conductivity change may be caused by cation vacancies and holes both resulted from dissolution of the halogen molecules. According to Mollwo[17], under the present experimental conditions (70mm Hg bromine gas atmosphere and 400–540°C), the concentrations of dissolved bromine atoms in KBr crystals were much less than those of the Schottky defect pairs produced thermally. In these cases the analysis of the thermoelectric power may be done practically taking cation and anion vacancies into consideration.

The purposes of the present paper are, (1) to measure the thermoelectric power of KBr and NaBr crystals using the bromine gas electrodes, (2) to determine the values of heats of transport of the respective lattice defects, (3) to compare these values with the predictions based on the nonequilibrium statistical mechanics (I and III of this series) and (4) to estimate the heterogeneous thermoelectric powers of KBr and NaBr in the cases of Pt- and graphite electrodes. The heterogeneous thermoelectric power due to the halogen electrodes can be estimated from the experimental data of the heat capacity[25, 26]. Then the values of homogeneous part can be separated theoretically from those of the total thermoelectric power. Thus, the quantities in the theoretical expressions derived from the irreversible thermodynamics[10, 11, 27–30] can be discussed by making use of the conductivity results.

2. EXPERIMENTAL PROCEDURES

Single crystals of KBr and NaBr, pure and doped with $BaBr_2$, were prepared by the Kyropoulos technique[31]. Cleaved specimens were used. The concentrations of barium impurities were determined by the colourimetric method[32]. As used previously [13] graphite was employed as an electrode meterial. This substance is known[33–35] to react with bromine and to form the stable intercalation complexes such as C_8Br and $C_{16}Br$. The graphite electrodes were cut out as thin as possible from the graphite rod with impurity of metals less than 35 ppm and polished using emery papers. Then they were baked in vacuum at 600°C for 24 hr. The thermoelectric power measurements were carried out under the condition that there were no temperature gradients within the graphite electrodes. The pressure of bromine gas was maintained at 70 mm Hg throughout the measurements by circulating over the liquid bromine cooled always at 0°C using ice-water coolant[36].

The cell used is shown in Fig. 1. The sample chamber was made from the Pyrex glass. The crystal was held between the graphite electrodes and mildly pressed by an alumina tube. Two calibrated alumel-chromel thermocouples, which were kept in alumina tubes, were placed in contact with each electrode in order to measure respective temperatures as accurately as possible. At the start of each run the chamber was evacuated including the bromine trap which was held at liquid nitrogen temperature during this procedure. At 540°C the chamber was filled with the 70 mm Hg bromine gas. After annealing the crystal which

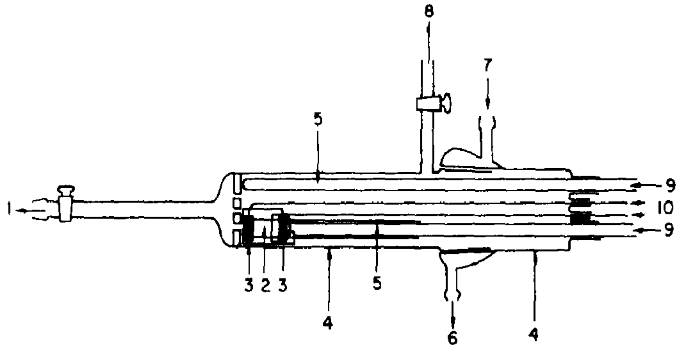

Fig. 1. Electrode assembly employed. 1. To vacuum pump; 2. Crystal; 3. Graphite electrodes; 4. Pyrex glass; 5. Alumina tubes; 6. Water outlet; 7. Water inlet; 8. To bromine trap; 9. a.c thermocouples, 10. Pt wires.

was immersed in this bromine gas atmosphere at 400°C for 12 hr, the thermoelectric power measurements were begun. Other experimental arrangements and techniques were the same as before[6, 7].

After the thermoelectric power measurements had been made each crystal was quenched in the bromine gas. The crystals were coloured slightly yellow. The optical absorption measurements of the crystals were made in the region of wavelengths from 200 to 600 mμ at room temperature.

3. RESULTS

The thermoelectric power of a crystal at one temperature was determined from the slope obtained by plotting thermoelectric potentials against temperature differences. As a typical example the result of a crystal of KBr doped with $5{\cdot}55\times10^{-4}$ $BaBr_2$ obtained at 500°C is shown in Fig. 2. In Figs. 3–6 the results of thermoelectric power, θ, of the crystals are shown as a function of temperature, together with the results of electrical conductivities of the same crystals obtained under the bromine atmosphere by employing a d.c. method, the

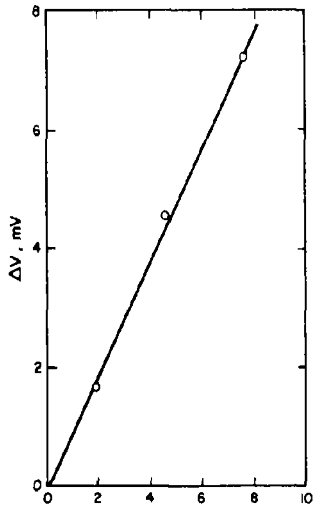

Fig. 2. Potential differences across a KBr+$5{\cdot}55\times10^{-4}$ $BaBr_2$ at 500°C plotted against the temperature differences recorded by the thermocouples.

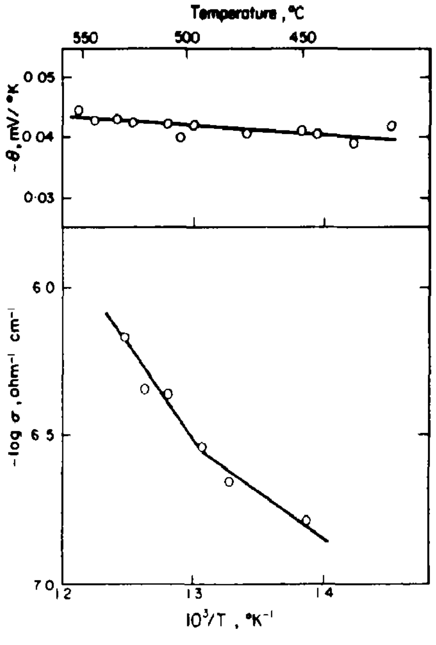

Fig. 3. Thermoelectric power and electrical conductivity of KBr crystals both measured in bromine gas atmosphere as a function of temperature.

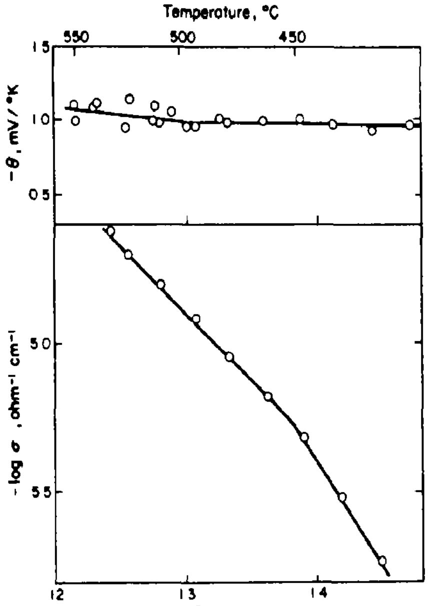

Fig. 4. Thermoelectric power and electrical conductivity of KBr+$5{\cdot}55\times10^{-4}$ $BaBr_2$ crystals both measured in bromine gas atmosphere as a function of temperature.

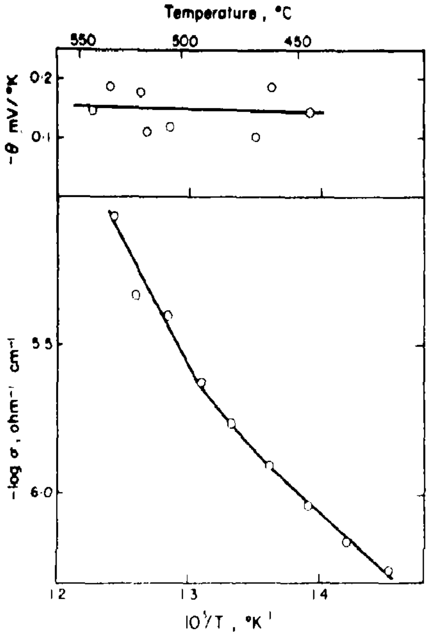

Fig. 5. Thermoelectric power and electrical conductivity of NaBr crystals both measured in bromine gas atmosphere as a function of temperature

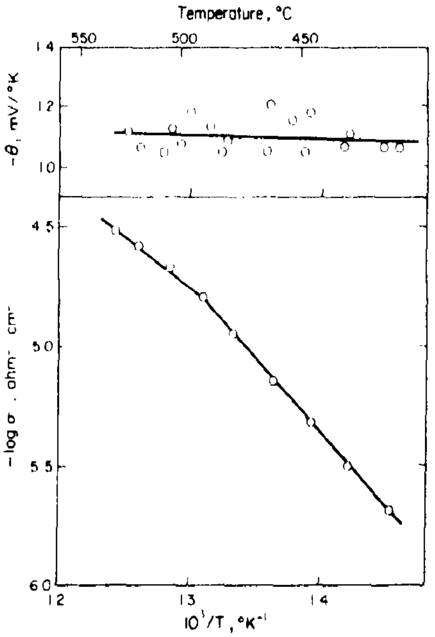

Fig. 6. Thermoelectric power and electrical conductivity of NaBr + 2.5×10^{-4} BaBr$_2$ crystals both measured in bromine gas atmosphere as a function of temperature

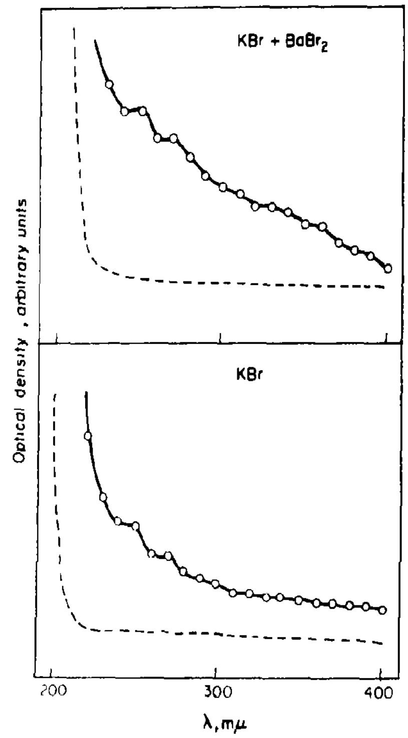

Fig. 7. Optical density (in arbitrary units) of KBr and KBr + 5.55×10^{-4} BaBr$_2$ employed in thermoelectric power measurements in bromine gas (○) together with that of untreated samples (---) as a function of wavelength

details of which will be reported later. The experimental errors of these thermoelectric power measurements were about 5 per cent for all the crystals.

From these figures it is seen that (1) the values of thermoelectric powers are always negative and more negative with increasing temperature, (2) the thermoelectric powers of crystals containing barium ions are always more negative than those of pure crystals and (3) the values of electrical conductivities depend significantly on temperature, while the thermoelectric powers are insensitive to it. The last behavior is similar to that found in the measurements of the crystals of KBr and NaBr in which Pt- and graphite electrodes were used[6, 7].

In Figs. 7 and 8 the results of optical absorption measurements at room tempera-

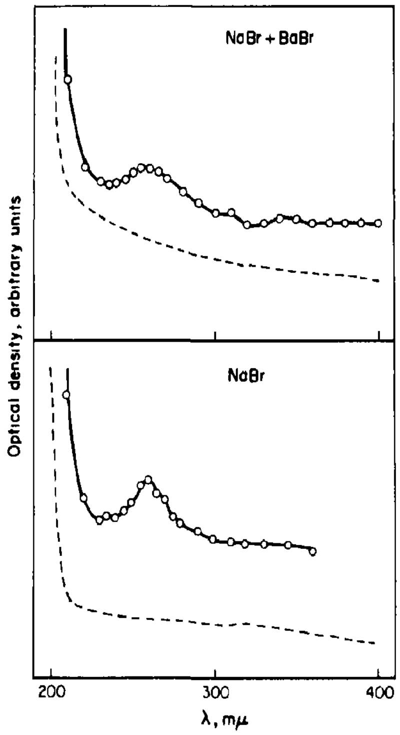

Fig. 8. Optical density (in arbitrary units) of NaBr and NaBr + 2·5 × 10^{-4} $BaBr_2$ employed in thermoelectric power measurements in bromine gas (○) together with that of untreated samples (---) as a function of wavelength.

ture are shown. The characteristic absorption maxima of the crystals, employed for the thermoelectric power measurements, are found in the ultraviolet regions and can be attributed to the excess bromine introduced into the host crystals[17, 18].

4. ANALYSIS OF RESULTS

1. *The contribution of holes*

The results of the ultraviolet absorption (Figs. 7 and 8) display that the excess bromine is dissolved in the KBr and NaBr (pure and doped with $BaBr_2$) crystals and its concentrations in the pure crystals are nearly the same as those in the $BaBr_2$ doped crystals. In the thermoelectric power measurements the bromine gas can be considered to be in equilibrium with the crystal as in the case of Mollwo's experiment[17]. Under these conditions the contribution of holes has to be taken into consideration. If the transport number of holes were approximately estimated from the ratio of the hole conductivity to the total conductivity, then this value may be about 0·05 at 500°C for pure KBr; the hole conductivity obtained by Mollwo[17] was about $2 \times 10^{-8} \Omega^{-1}\text{cm}^{-1}$ and the total conductivity about $4 \times 10^{-7} \Omega^{-1}\text{cm}^{-1}$. Then, the contribution of holes to the total current may be negligible within experimental errors. In the KBr crystal doped with $BaBr_2$ the total conductivity is much larger than that in pure KBr, so the contribution due to the holes may also be negligible. The same considerations may be expected in the cases of pure- and $BaBr_2$ doped NaBr crystals. Thus, we arrive at the conclusion that the effects of lattice defects on the electrical properties of the crystals immersed in the 70 mm Hg bromine gas atmosphere may be similar to those in an inert gas atmosphere[6, 7].

2. *Theoretical relations*

In the present thermoelectric power measurements the arrangement devised by Reinhold[13] was used:

$$M''|M', X_2|_T MX \text{ (or } MX + M_I X_2)|_{T+\Delta T} X_2, \quad M'|M''. \tag{1}$$

When ionic crystal, MX (or $MX + M_I X_2$), being in contact with electrodes, M', is placed in a temperature difference, ΔT, at a temperature, T, under a halogen atmosphere, X_2, a thermoelectric potential, $\Delta\phi$, appears between leads, M'', attached to the electrodes. In the present case M' corresponds to graphite and M'' to Pt.

The thermoelectric power, θ, of the system at zero current is given by

$$\theta = \Delta\phi/\Delta T, \tag{2}$$

$$= \theta_{\text{hom},MX} + \theta_{\text{het},MX} + Q_{M''}, \tag{3}$$

where $\theta_{\text{hom}\,MX}$ is the homogeneous thermoelectric power of the crystal MX arising from the thermal diffusion of lattice defects in the bulk, $\theta_{\mathrm{het}.MX}$ is the heterogeneous thermoelectric power caused by the difference in contact potentials between electrodes and crystals and $Q_{M'}$ is the absolute thermoelectric power of metal leads. The values of $Q_{M'}$ for Pt have been obtained by Cusack and Kendall [37].

The expression for the heterogeneous thermoelectric power, $\theta_{\mathrm{het}.MX}$, has been given, in principle, by Haga[26]. The halogen atom in MX near the contact surface with graphite electrode is in equilibrium with that in the gaseous phase at the same temperature, so that

$$\mu_{MX}^{X} = \mu_{X_2}^{X_2}/2, \qquad (4)$$

where μ_{MX}^{X} and $\mu_{X_2}^{X_2}$ are the chemical potential of a halogen atom in MX and that of a halogen molecule in the gaseous phase, respectively. Further a reaction takes place at the contact between MX and graphite:

$$X \rightleftharpoons X^{-} - e^{-}, \qquad (5)$$

where e^{-} denotes the electron. Considering the electrochemical equilibrium for this reaction (5), we obtain the expression for the heterogeneous thermoelectric power arising from the cell as follows:

$$\theta_{\mathrm{het}.MX} = (S_{MX} - S_{X_2})/2e, \qquad (6)$$

where $-e$ is the electronic charge, S_{MX} is the entropy of a perfect crystal MX and S_{X_2} is the entropy of a halogen molecule in the gaseous phase, which is expressed as

$$S_{X_2} = S_{X_2}\,(p_{X_2} = 1\ \mathrm{atm.}) - R \ln p_{X_2}\,(\mathrm{atm.}). \qquad (7)$$

Here, R is the gas constant and p_{X_2} is the pressure of halogen gas. A half of S_{MX} may be assumed to be equal to the entropy of a halogen ion in a crystal MX as proposed by Wagner[25]. Pitzer's modification[38], which may be better in the liquid state, has not been employed in this work. The values of S_{MX} and S_{X_2} were calculated from the experimental values of heat capacities[39, 40].

The expression for the homogeneous thermoelectric power of the crystal MX, $\theta_{\mathrm{hom}.MX}$, has been given previously[11] by means of irreversible thermodynamics [27–30]. The expression for a pure MX crystal containing the Schottky disorder, $\theta_{\mathrm{hom}.MX}(1)$, is given by

$$Te\,\theta_{\mathrm{hom}.MX}(1) = [t_{(+)}(Q_{(+)}^{*} + h_{(+)}^{v}) - t_{(-)}(Q_{(-)}^{*} + h_{(-)}^{v})], \qquad (8)$$

where

$$h_{(+)}^{v} = h_{(-)}^{v} = h_s^{0}/2 + Zx_{(+)}^{0}\omega_{(+)(-)} - \beta e^{2}(3 + 2\beta b)(1 + \mathrm{d}\ln\epsilon/\mathrm{d}\ln T)/4\epsilon(1 + \beta b)^{2}. \qquad (9)$$

In equation (8) $t_{(i)}$ and $Q_{(i)}^{*}$ are the transport number and the heat of transport of respective lattice defects. In equation (9) h_s^{0} is the heat of formation of a Schottky defect pair. The second and third terms on the right hand side of equation (9) represent the interaction between a cation vacancy and an anion vacancy in their nearest neighbour distance and the Coulomb interactions between these defects, respectively, as shown in paper I [11]. These two terms were found to be much smaller than the first term in the temperature ranges under consideration. The expression for a crystal MX containing divalent impurity ions, $\theta_{\mathrm{hom}.MX}(\xi)$, becomes

$$Te\,\theta_{\mathrm{hom}.MX}(\xi) = Q_{(+)}^{*} + p\chi/(1 + p), \qquad (10)$$

where $\xi^{2} \gg 1$. In equation (10) p is the degree of association and χ is the heat of association between a cation vacancy and a divalent impurity ion. ξ is the ratio of the concentration of unassociated cation vacancies in an impure crystal to the concentration of cation vacancies in a pure crystal at the same temperature.

3. *Homogeneous thermoelectric power*

According to equation (3) the values of

$\theta_{\text{hom}.MX}$ of each crystal can be determined by subtracting the values of $Q_{M''}$ and $\theta_{\text{het}.MX}$ from the measured thermoelectric power. In Figs. 9 and 10 $\theta_{\text{hom}.MX}$ for pure and impure KBr and NaBr crystals obtained in this way is shown as a function of temperature. In all the cases $\theta_{\text{hom}.MX}$ decreases with increase of temperature.

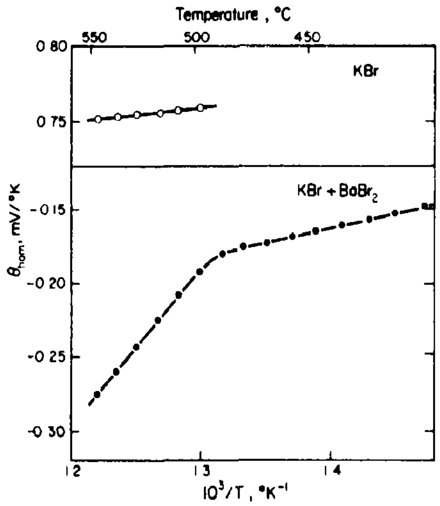

Fig. 9. Homogeneous thermoelectric power of pure KBr crystals (○) and KBr crystals containing BaBr$_2$ (●) obtained from the measurements in bromine gas as a function of temperature

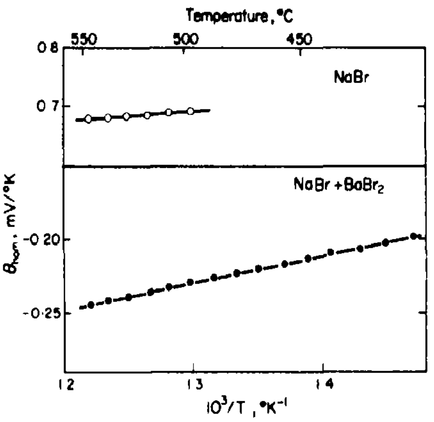

Fig 10. Homogeneous thermoelectric power of pure NaBr crystals (○) and NaBr crystals containing BaBr$_2$ (●) obtained from the measurements in bromine gas as a function of temperature.

4. *Heat of transport*

The values of the heats of transport of cation vacancies $Q^*_{(+)}$, can be obtained from equation (10) by knowing the values of p and χ, both of which have already been determined for KBr crystals containing BaBr$_2$[7] and NaBr crystals doped with BaBr$_2$[6]. In Table 1 the values of $Q^*_{(+)}$, which are determined by considering changes in p, in 'association' and 'dissociation' regions[41], are shown together with the values of χ, and of the heat of activation for motion of cations, h_+^J. Owing to the uncertainties involved in p the values of $Q^*_{(+)}$ are dispersed. However, the absolute values of $Q^*_{(+)}$ are not different from the values of h_+^J.

The values of the heat of transport of anion vacancies, $Q^*_{(-)}$, can be determined by equation (8) using the values of the transport number of cation vacancies, $t_{(+)}$,[42, 43] and the heat of formation of a Schottky defect pair, $h^F_{(+)}$,[6, 7]. In Table 2 the values of $Q^*_{(-)}$ are given together with those of $t_{(+)}$, $h^F_{(+)}$ and the heat of activation for motion of anions, h_-^J. It is seen that $Q^*_{(-)}$ is nearly independent of temperature. In the KBr crystals the absolute values of $Q^*_{(-)}$ are in good agreement with the values of h_-^J. However, in NaBr both

Table 1. *Heats of transport of a cation vacancy for* KBr *and* NaBr *crystals*

Material	$-Q^*_{(+)}$ (eV) Association ($p = 1$)	 Dissociation ($p = p(T) < 1$)	χ (eV)	h_+^J (eV)
KBr	0·5±0·2	0·3±0·3	0·81	0·83
NaBr	0·5±0·1	0·4±0·1	0·62	0·80

Table 2. Heats of transport of an anion vacancy for KBr *and* NaBr *crystals*

Material	*Temperature* (°C)	$t_{(+)}$	$-Q^*_{(-)}$ (eV)	$h^J_{(+)}$ (eV)	h^J_- (eV)
KBr	497	0·73[(a)]	1·1	1·20	1·04[(c)]
	527	0·71[(a)]	1·2		
	547	0·69[(a)]	1·2		
NaBr	497	0·95[(b)]	3·1	0·86	1·17[(b)]
	527	0·94[(b)]	3·1		
	547	0·93[(b)]	3·0		

[(a)] ROLFE J., *Can. J. Phys.* **42**, 2195 (1964).
[(b)] SCHAMP H. W. and KATZ E., *Phys. Rev.* **94**, 828 (1954).
[(c)] MAYCOCK J. N., *J. appl. Phys.* **35**, 1512 (1964).

values are not in so good agreement. This may partly be due to the uncertainties involved in the transport number of anion vacancies.

5. DISCUSSION

1. *Relation between* Q^* *and* h^J

In order to interpret the heat of transport appearing in the phenomenological equations we have developed a general treatment on the microscopic flow processes with thermal, concentration and electric potential gradients [11, 7] on the basis of the Fokker-Planck equation [44, 45]. This leads to the relation between heat of transport and heat of activation for migration,

$$|Q_l^*| = h_r^J. \qquad (11)$$

where l is for lattice defects and r for corresponding ions. This is the same result as obtained for thermal diffusion by Allnatt and Rice [46] and by Schottky [47]. As pointed out in the previous section (see Tables 1 and 2), the absolute values of $Q^*_{(+)}$ and of $Q^*_{(-)}$ are, within experimental errors, in good agreement with those of h_+^J and h_-^J, respectively. These results seem to satisfy the theoretical prediction, i.e. equation (11).

2. *Theoretical evaluation of thermoelectric power*

As described in Section 4, the total thermoelectric power can be calculated using equations (3) and (6–10). In Figs. 11 and 12 these theoretical values are compared with the

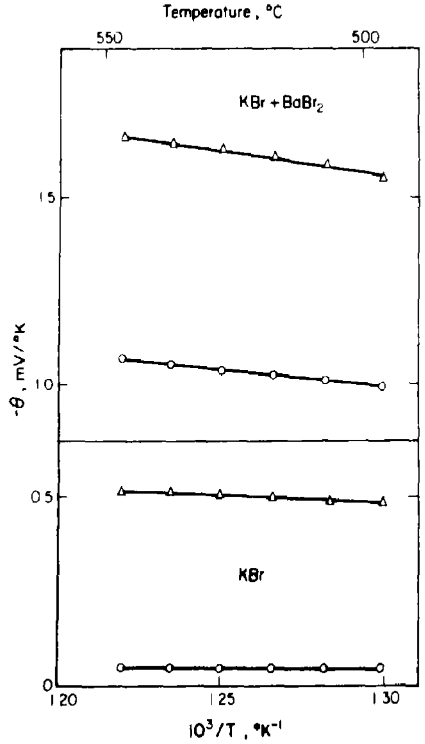

Fig. 11. Total thermoelectric power of pure and impure KBr crystals using bromine gas electrodes as a function of temperature. Open circles represent the values obtained from the experiments and triangles those calculated from the theory

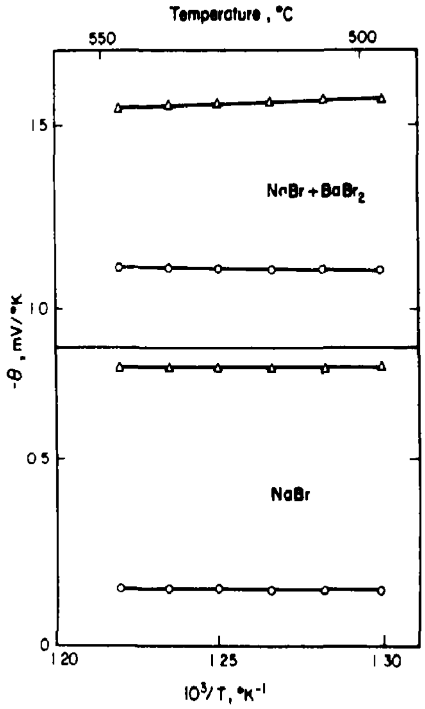

Fig. 12. Total thermoelectric power of pure and impure NaBr crystals using bromine gas electrodes as a function of temperature. Open circles represent the values obtained from the experiments and triangles those calculated from the theory.

values obtained experimentally. It is seen from these figures that the sign and temperature-dependence of theoretical thermoelectric power are in agreement with those of the experimental one. Since $Q_{M''}$ and theoretical $\theta_{\mathrm{het}.MX}$ are of little temperature-dependence, the slopes may chiefly be due to the effect of $\theta_{\mathrm{hom}.MX}$. But the experimental values are less negative in order of magnitude by about 0·4–0·6 mV/°K than the calculated ones. The present calculation of $\theta_{\mathrm{het}.MX}$ has been made on the basis of the Wagner's expression[25], i.e. equation (6). But even if the Pitzer's expression[40] were used the differences were found to remain between 0·3–0·5 mV/°K. Then, these theoretical computations may be regarded as a measure of the sign and the temperature-dependence of the thermoelectric power. The difference may mainly be attributed to the estimation of $\theta_{\mathrm{het}.MX}$, especially the entropy of a halogen ion in a crystal. Another origin of the difference may be considered to exist in the experimental errors involved in the conductivity parameters, such as transport numbers and degrees of association etc.

3. *Problems related to the results with non-halogen electrodes*

From our previous thermoelectric power measurements done using inert Pt and graphite electrodes[6, 7] the absolute values of $Q^*_{(+)}$ have been determined to be 1·0 and 0·75 eV for KBr and NaBr systems, respectively, which roughly agreed with the values determined by using bromine gas electrodes; 0·5±0·2 eV for KBr and 0·5±0·1 eV for NaBr systems. However, definite values for $Q^*_{(-)}$ were not obtained[6, 7] because of the unknown parameters involved in the heterogeneous thermoelectric power, θ_{het} arising from the contact between the crystal and the Pt or graphite electrodes. Therefore, the thermoelectric power measurement due to bromine gas electrodes has an advantage in that the heat of transport of an anion vacancy may be evaluated.

In our previous studies[11, 7] it has been proposed that in alkali halide crystals being in contact with inert metal electrodes the electrons from metal electrodes may enter the region near the crystal surface and that can be trapped by some anion vacancies. From this the expression for θ_{het} has been given by equation (4.5) in paper I[11]. Assuming the formation of *F*-centres (corresponding to *excess metallic elements*) at the surface of the crystal, we find the relation

$$e\theta_{\mathrm{het.}}(\xi) = -S_F - \partial[kT\ln\{n_F{}^s(\xi) \\ /n_{(-)}(\xi)\}]/\partial T, \quad (12)$$

which is equivalent to equation (4.8) in paper I. Here, S_F is the partial entropy of the *F*-centre formation, $n_F{}^s$ is the concentration of the *F*-centres at the surface of the crystal and

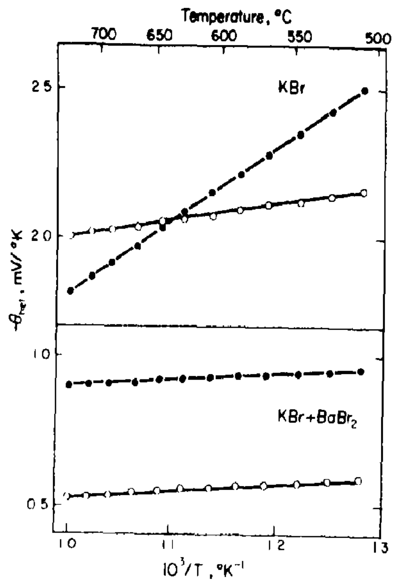

Fig. 13. Heterogeneous thermoelectric power of pure and impure KBr crystals using Pt (○) or graphite (●) electrodes as a function of temperature.

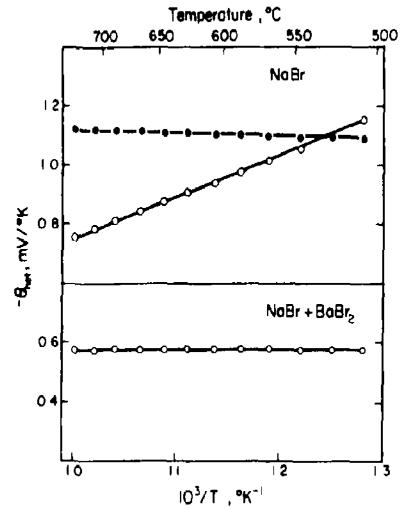

Fig. 14. Heterogeneous thermoelectric power of pure and impure NaBr crystals using Pt (○) or graphite (●) electrodes as a function of temperature.

$n_{(-)}$ is the concentration of an anion vacancy in the bulk of the crystal. When $\xi = 1$ the expression for pure crystals, θ_{het} (1), is obtained. No reliable computation is now available for the respective parameters (except for $n_{(-)}$) appearing in equation (12), but the values of

Table 3. Experimental results of thermoelectric power of KBr *and* NaBr *crystals measured using* Pt *and graphite electrodes*

Material	Electrode	Thermoelectric power (mV/°K)
KBr	graphite	$\theta = 1{\cdot}92 \times 10^3/T + 0{\cdot}22$ (580–680°C)
	Pt	$\theta = -4{\cdot}61 \times 10/T - 1{\cdot}84$ (516–693°C)
KBr + BaBr$_2$	graphite	$\theta = -1{\cdot}03 \times 10^3/T - 0{\cdot}72$ (485–670°C)
	Pt	$\theta = -1{\cdot}07 \times 10^3/T - 0{\cdot}30$ (550–640°C)
NaBr	graphite	$\theta = -7{\cdot}12 \times 10/T - 1{\cdot}064$ (446–670°C)
	Pt	$\theta = -1{\cdot}59 \times 10^3/T + 0{\cdot}82$ (624–729°C)
NaBr + BaBr$_2$	Pt	$\theta = -7{\cdot}52 \times 10^2/T + 0{\cdot}505$ (602–719°C)

$\theta_{\text{het.}}$ can be determined using the values of the total θ observed[6, 7] (Table 3), the absolute thermoelectric power of Pt lead wires[39] and the theoretical $\theta_{\text{hom.}}$ of the crystals. The results are shown in Figs. 13 and 14 as a function of temperature. These figures show that the heterogeneous thermoelectric powers for the crystals containing divalent cation impurities are nearly constant and those for pure crystals show some dependence on temperature and on electrode materials. The temperature-dependence observed for the pure crystals may partly be due to the uncertinties involved in the transport numbers which appear in the calculated homogeneous thermoelectric power.

REFERENCES

1 CHRISTRY R W., HSUEH Y. W. and MUELLER R. C., *J chem. Phys.* **38**, 1647 (1963).
2. NIKITINSKAYA T. I. and MURIN A N., *Zh. Tekh Fiz.* **25**, 1198 (1955).
3. ALLNATT A. R. and CHADWICK A. W., *J. chem. Phys.* **47**, 2372 (1967)
4. ALLNATT A R. and JACOBS P. W. M., *Proc R. Soc.* **A267**, 31 (1962).
5. JACOBS P. W. M. and MAYCOCK J. N., *Trans. Am. Inst. metall. Engrs* **236**, 165 (1966).
6. HOSHINO H. and SHIMOJI M., *J Phys. Chem. Solids* **28**, 1169 (1967)
7 HOSHINO H and SHIMOJI M, *J Phys Chem. Solids* **29**, 1431 (1968).
8. ITAMI T., HOSHINO H and SHIMOJI M., *J Phys. Chem. Solids* **30**, 1603 (1969)
9. CURIEN H. and MIHAILOVIC Z., *C R Acad. Sci. Paris* **248**, 2982 (1959)
10. ALLNATT A. R. and JACOBS P W. M, *Proc. R. Soc.* **260**, 350 (1961).
11. SHIMOJI M. and HOSHINO H., *J Phys. Chem. Solids* **28**, 1155 (1967).
12. ALLNATT A R. and JACOBS P. W. M, *Can. J Phys.* **46**, 1635 (1968).
13. REINHOLD H., *Z anorg. allg. Chem.* **171**, 181 (1928).
14. WAGENER K., *Z. phys. Chem.* **21**, 74 (1959).
15. FISCHER W., *Z. Naturf.* **21a**, 281 (1966).
16. DETIG R. H. and ARCHER D H., *J. chem. Phys.* **38**, 661 (1963).
17. MOLLWOE., *Annln. Phys.* **29**, 394 (1937).
18. NAKAI Y, *J. phys. Soc. Japan* **13**, 1424 (1958).
19. SCHULMAN J. H. and COMPTON W. D., *Color Centers in Solids*. Pergamon Press, Oxford (1963).
20. SEITZ F., *Rev. mod. Phys.* **18**, 384 (1946); *ibid* **26**, 7 (1954).
21 MARKHAM J. J., *F-centres in Alkali Halides, Solid State Physics*, Suppl. 8. Academic Press, New York (1966).
22. HERSH H. N., *Phys. Rev* **105**, 1410 (1957).
23. FORBES H. L. and LYNCH D W, *J. Phys. Chem Solids* **25**, 621 (1964).
24. BARR L. W. and DAWSON D. K., *Proc. Br. ceram. Soc.* **5**, 77 (1965).
25. WAGNER C., *Annln Phys.* **3**, 629 (1929).
26. HAGA E., *J. phys. Soc. Japan* **14**, 992 (1959).
27. DE GROOT S. R., *Thermodynamics of Irreversible Processes*. North-Holland, Amsterdam (1951)
28. DE GROOT S. R. and MAZUR P., *Nonequilibrium Thermodynamics*. North-Holland, Amsterdam (1962)
29. PRIGOGINE I., *Étude Thermodynamique des Phénomènes Irreversible*. Maison Desoer, Liege (1947)
30. DENBIGH K. G., *The Thermodynamics of the Steady State* Mathuen, London (1958).
31. KYROPOULOS S., *Z. anorg. allg. Chem* **154**, 308 (1926).
32 SANDELL E. B., *Colorimetric Determination of Traces of Metals*. Interscience, New York (1959).
33. UBBELOHDE A. R. and LEWIS F. A., *Graphite and Its Crystal Compounds*. Oxford University Press, London (1960)
34. MANDELCORN L., *Non-Stoichiometric Compounds* Academic Press, New York (1964).
35. DUDORF W., *Z anorg. allg Chem.* **245**, 383 (1941)
36. SCHEFFER F. E. C. and VOOGD M., *Recl Trav. chim. Pays-Bas Belg.* **45**, 216, 221, 223 (1926)
37. CUSACK N. and KENDALL P., *Proc. phys. Soc.* **72**, 898 (1958).
38 PITZER K. S., *J. phys. Chem* **65**, 147 (1961).
39. KELLEY K. K, *Bull. U.S. Bur Mines* NO. 476, (1949), Critical evaluation of high-temperature heat capacities of inorganic compounds.
40. KUBACHEWSKI O. and EVANS E. L. L., *Metallurgical Thermochemistry*. Pergamon Press, Oxford. (1958).
41 DREFUS R. W and NOWICK A S., *J. appl. Phys* **33**, 473 (1962).
42. ROLFE J., *Can. J Phys* **42**, 2195 (1964).
43. SCHAMP H. W. and KATZ E., *Phys. Rev.* **94**, 828 (1954).
44 KITTEL C, *Elementary Statistical Physics*. Wiley, New York (1958).
45. CHANDRASEKHAR S, *Rev mod. Phys.* **15**, 1 (1943).
46 ALLNATT A. R and RICE S. A, *J. chem. Phys* **33**, 573 (1960).
47. SCHOTTKY G., *Phys. Status Solidi* **8**, 357 (1965).

J. Phys. Chem. Solids Pergamon Press 1970. Vol. 31, pp. 1565–1571. Printed in Great Britain.

MÖSSBAUER EFFECT IN B8 ALLOYS OF NICKEL WITH ^{121}Sb AND ^{119}Sn*

H. Z. DOKUZOGUZ†, **L. H. BOWEN** and **H. H. STADELMAIER**
Departments of Chemistry and Engineering Research, North Carolina State University, Raleigh, N.C. 27607, U.S.A.

(*Received* 23 *October* 1969)

Abstract – Nickel forms intermetallic compounds of the B8 (NiAs–Ni_2In) structure with antimony (NiSb), tin (Ni_3Sn_2), and germanium (Ni_3Ge_2) A continuous solid solution of the same structure type exists between NiSb and Ni_3Sn_2 and, as discovered in the present study, between NiSb and Ni_3Ge_2 Both ^{119}Sn and ^{121}Sb Mossbauer effect measurements have been made on a series of compositions of the Ni–Sn–Sb ternary system, and the ^{121}Sb spectra have been taken for a series from the Ni–Ge–Sb ternary system. The isomer shifts for both ^{119}Sn and ^{121}Sb show systematic variations within the first series, consistent with partial transfer of valence electrons from the non-transition metals to nickel The isomer shifts for ^{121}Sb in the Ge system are identical within experimental error with corresponding samples from the Sn system. Additional alloys have been studied to clarify the electron transfer occurring in these systems

THE STUDY of the ^{119}Sn Mössbauer effect in alloys of tin with transition metals, for example, palladium[1], [2] and platinum[3], has led to interesting and significant conclusions concerning the local electron density at the tin site. Isomer shifts for ^{119}Sn in the above binary metallic systems vary in approximately linear fashion with transition metal concentration, as the *s* electron density shifts away from tin to the transition metal nucleus, although some fine structure was observed in the Pd–Sn system[2] and correlated with other structural information.

Recent studies of the Mössbauer effect in ^{121}Sb[4], [5] have shown that the isomer shift for this nuclide has a much larger variation (about 20 mm/sec range) than that for ^{119}Sn and consequently greater sensitivity to small variations in electron density. It was, therefore, of interest to apply this technique to an alloy system containing antimony and a transition metal. Because of the interest in our laboratory in the B8 structure type and because of the available structural information on the continuous solid solution of the B8 type between NiSb and Ni_3Sn_2[6], we have concentrated on this system in the present work. Besides having a well-defined structure, this ternary solid solution provides the opportunity to observe easily the Mössbauer effect in two of the three components. In the course of this study, certain features of the Mössbauer spectra caused us to look for an alternate system of the same structure. Indeed, a B8 type continuous solid solution was also found between NiSb and Ni_3Ge_2, and studied as well.

The $B8_1$ structure, exemplified by NiSb, has the hexagonal unit cell shown in Fig. 1. The Sb is surrounded by six Ni atoms at the apices of a right-trigonal prism, while the coordination about Ni is six Sb atoms in a distorted octahedral array, with two additional Ni neighbors along the *c* axis. In the $B8_2$ structure, as for example Ni_2In, there are two Ni sites, Ni_I being the same as in $B8_1$, and Ni_{II} being the two additional positions which are unfilled in the $B8_1$ unit cell (Fig. 1). In

---

*This work was supported by the National Science Foundation grant GP-8087. Based in part on the Ph.D. thesis in the Department of Chemistry, North Carolina State University, 1969, of H. Z. Dokuzoguz.

†American Cyanamid Company, Piney River, Va. 22964, U.S.A.

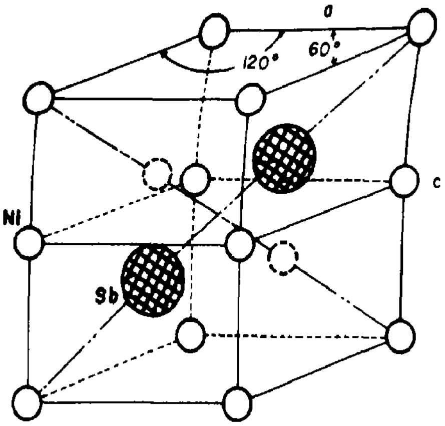

Fig. 1. Unit cell of the B8$_1$ structure. The atomic arrangement for NiSb is shown. Vacant positions occupied by Ni$_{II}$ in the B8$_2$ structure are also indicated as broken circles.

Ni_2In the Ni$_{II}$ site has five close In neighbors at the apices of a trigonal-bipyramid. The compounds Ni_3Sn_2 and Ni_3Ge_2 lie midway between B8$_1$ and B8$_2$, and have half the Ni$_{II}$ sites filled.

A separate X-ray diffraction study comparing calculated and observed structure factors verified the following assumptions concerning the atomic arrangement in the ternary alloys.* In both NiSb–Ni_3Sn_2 and NiSb–Ni_3Ge_2, the tin or germanium atoms are substituted into Sb positions. The excess nickel fills the Ni$_{II}$ position partially. Even in the germanium alloys the structure factors are not sensitive to ordering between germanium and antimony, so it is uncertain whether the atom replacing antimony is ordered. The tin ternary alloys are slightly distorted into a lower orthorhombic symmetry not reported by Gladyshevskii and Cherkashin[6]. The ratio a to b of the orthorhombic lattice constants is very close to $1/\sqrt{3}$. The germanium alloys remain truly hexagonal throughout the composition range.

Structural information on the systems of interest here is summarized in Table 1. We have also included our values for the lattice constants of the Ni–Ge–Sb ternary system, previously unreported. In addition to the B8 alloys, we also studied the compounds $Ni_{1.5}Sb$ and SnSb to provide additional information on the electron distribution in the Ni–Sn–Sb system.

Table 1. Lattice parameters for alloys of the B8 type

Alloy	*c*	*a*	*c/a*	Reference
NiSb	5·137 Å	3·936 Å	1·305	(b)
Ni_3Sn_2	5·182 Å	4 110 Å	1·261	(b)
I (Sn)[a]	5·149 Å	3·975 Å	1·295	(b)
II (Sn)	5 151 Å	4·040 Å	1·275	(b)
III (Sn)	5·167 Å	4·080 Å	1·266	(b)
Ni_3Ge_2	5·034 Å	3·964 Å	1·270	(c)
I (Ge)[a]	5·131 Å	3·906 Å	1·314	(d)
II (Ge)	5 118 Å	3·883 Å	1·318	(d)
III (Ge)	5·029 A	3·861 Å	1·302	(d)

[a] The alloy designated I (Sn) has the composition $Ni_{0.529}Sn_{0.118}Sb_{0.353}$, II (Sn) is $Ni_{0.556}Sn_{0.222}Sb_{0.222}$, and III (Sn) is $Ni_{0.583}Sn_{0.333}Sb_{0.084}$. The alloys I (Ge), II (Ge), and III (Ge) have corresponding atomic compositions with Ge replacing Sn

[b] PEARSON W. B., *A Handbook of Lattice Spacings and Structures of Metals and Alloys*, Vol. 2, p. 1139 Pergamon Press, Oxford, (1967).

[c] *Ibid*, p 979.

[d] This work

EXPERIMENTAL

Preparation and characterization of compounds

The materials were prepared using 99·80% pure Ni, 99·99% Sn, 99·999% Ge, and 99·98% Sb. Each compound was obtained by melting the components in a sealed quartz glass capsule evacuated to 10^{-4} mm Hg, followed by slow cooling in air. After checking for weight loss, the sample was sectioned, and one part polished by standard techniques to be examined with a metallographic microscope for phase purity. If pure, the other part of the sample was crushed and passed through a −325 mesh screen to obtain a powder less than 43 μ in dia. for X-ray and Mössbauer measurements. The SnSb sample was heat treated for 48 hr at 300°C. The $Ni_{1.5}Sb$ was melted at 1500°C, followed by a 24 hr anneal at 1000°C and quenching in water. The resulting material was very hard and ductile and could not be powdered as the other materials, but only be crushed into small chunks. No X-ray pattern was taken of this material, but microscopic examination showed only a single phase. The X-ray diffraction patterns were obtained with a 114·6 mm dia. powder camera, using filtered Cu radiation. In those cases where lattice parameters have been reported, the interplanar spacings observed were in agreement within 0·005 Å. For the Ni–Ge–Sb ternary series, the indexed X-ray patterns were used to calculate the values of the unit cell parameters reported in Table 1.

---

*R. A. Jones and H. H. Stadelmaier, unpublished research.

Mössbauer spectra

An SnO_2 source containing approximately 100 μc each of ^{119m}Sn and ^{121}Sn was used. The same source therefore could be used for both ^{119}Sn and ^{121}Sb Mössbauer spectroscopy by isolating either the 24 keV ^{119m}Sn gamma or the 8 keV escape peak from the ^{121}Sb 37 keV gamma. A xenonmethane proportional counter, an Austin Science Associates constant acceleration drive, and Nuclear Data 512 channel analyzer were used. The velocity scale was calibrated with a Pd (^{57}Co) source and 1 mil iron foil (New England Nuclear Corp.). All spectra except for the standards were taken at liquid nitrogen temperature for both source and absorber (77–84°K).

The $Ni_{15}Sb$ had to be measured in the form of small irregular chunks. All other materials were mixed in powder form with powdered dextrose, and sealed in Lucite such as to give a uniform thickness of about 10 mg/cm^2 Sb or Sn, depending upon which spectrum was being observed.

Analysis of data

Enough counts were collected in each case except $Ni_{15}Sb$ to give a signal/noise ratio of 25–30. The mirror images of the spectrum were folded and fitted to one or more Lorentzian curves, using the Triangle Universities Computing Center IBM 360/75. In the case of ^{119}Sn spectra, the two Lorentz peaks of the quadrupole doublet were constrained to have equal intensities and widths. This constrained fit was equally good as that when the two peaks were not constrained and gave consistently more realistic widths. In no case was there evidence for the eight-line quadrupole splitting of ^{121}Sb.

In addition to the computer-generated errors, other errors have been estimated for reporting the data in Tables 2 and 3. These

Table 2. ^{119}Sn *Mössbauer parameters. All isomer shifts* (IS) *are relative to the* $^{119}SnO_2$ *source. For conversion to an* α-Sn *scale, subtract* 2·25 *mm/sec. The observed splitting between the symmetric doublet is given as the quadrupole splitting* (QS). *The full width at half maximum* (Γ) *of an individual peak is reported*

Absorber	*IS* (mm/sec)	*QS* (mm/sec)	Γ (mm/sec)
Ni_3Sn_2	2·15 ± 0·04	1·20 ± 0·08	1·26 ± 0·06
III (Sn)	2·21 ± 0·04	1·24 ± 0·08	1·41 ± 0·06
II (Sn)	2·25 ± 0·04	1·25 ± 0·08	1·32 ± 0·06
I (Sn)	2·31 ± 0·04	1·13 ± 0·08	1·42 ± 0·06
β-Sn	2·90 ± 0·04	0·52 ± 0·08	0·92 ± 0·06
SnSb	3·09 ± 0·05	0·49 ± 0·10	1·15 ± 0·07

Table 3. ^{121}Sb *Mössbauer parameters. All isomer shifts* (IS) *are relative to the* $^{121}SbO_2$ *source. The full width at half maximum* (Γ) *and observed percent effect* (ε) *are also reported. For conversion to an* InSb *scale,* 8·15 *mm/sec should be added to the given* IS *values*

Absorber	*IS* (mm/sec)	Γ (mm/sec)	ε (%)
Sb	−11·21 ± 0·07	2·85 ± 0·07	6·07 ± 0·06
SnSb	−10·10 ± 0·07	3·02 ± 0·08	5·08 ± 0·06
NiSb	−8·42 ± 0·06	3·49 ± 0·08	5·57 ± 0·06
I (Sn)	−8·02 ± 0·06	3·19 ± 0·08	5·05 ± 0·06
I (Ge)	−8·02 ± 0·05	3·20 ± 0·06	10·83 ± 0·08
II (Sn)	−7·85 ± 0·06	3·94 ± 0·08	4·34 ± 0·04
II (Ge)	−7·87 ± 0·05	3·30 ± 0·07	11·06 ± 0·09
III (Sn)	−7·52 ± 0·06	3·27 ± 0·08	4·61 ± 0·05
III (Ge)	−7·61 ± 0·06	2·96 ± 0·07	10·73 ± 0·10
$Ni_{15}Sb$	−5·92 ± 0·13	5·0 ± 0·40	1·01 ± 0·04

include errors in the velocity calibration, errors in folding the spectra, and errors in zero velocity determination.

RESULTS

A summary of the Mössbauer parameters determined is given in Tables 2 and 3. It should be pointed out that when the quadrupole splitting for ^{119}Sn is $QS \equiv e^2qQ/2 = 1{\cdot}25$ mm/sec (largest observed here), and assuming the field gradient q is the same for both Sn and Sb in a given type of compound, the separation in the eight-line quadrupole spectrum of ^{121}Sb would be on the order of $e^2qQ/4$, where $Q = -0{\cdot}07$ barn for ^{119}Sn[7] and $-0{\cdot}26$ barn for ^{121}Sb[4]. This gives about 2·3 mm/sec as the ^{121}Sb splitting, or the same magnitude as the theoretical width of 2·1 mm/sec[7]. Thus, it would be surprising to find observable quadrupole splittings for ^{121}Sb in these alloys. The observed line widths for ^{121}Sb are generally larger than theoretical, but not overly so considering the finite absorber thickness and imperfect nature of the source, as well as the unresolved quadrupole splittings.

The quadrupole splittings (QS) observed for ^{119}Sn (Table 2) fall into two categories. In the case of β-Sn and SnSb, the splitting is small and of the same magnitude as the splitting in the source. However, in the four compounds with nickel, the splitting is definitely present in the absorber. Considering the B8 structure, with its trigonal prismatic site for Sn and with a varying number of occupied Ni_{II} sites, it is expected to find QS. The lack of any appreciable variation in QS among the four B8 compounds indicates the symmetry of the electron distribution about Sn is not appreciably affected by filling in Ni_{II} sites.

The absorption intensities observed for ^{121}Sb were large and easily analyzed (Fig. 2). One surprising result for the Ni–Sn–Sb system was the appearance of a second peak at about 2 mm/sec, which increased in intensity as the relative amount of Sn increased (Fig. 3). The widths of the peak at 2 mm/sec

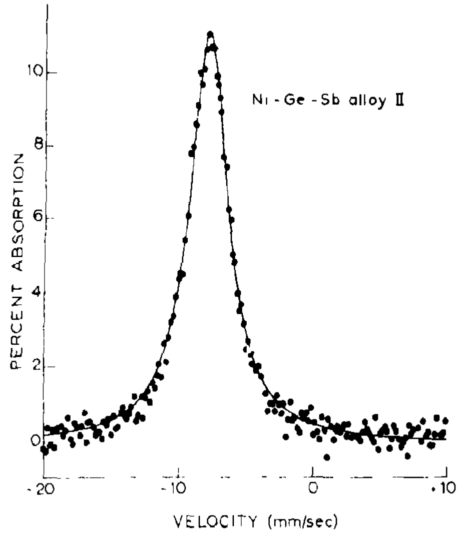

Fig. 2 ^{121}Mossbauer spectrum for alloy II (Ge).

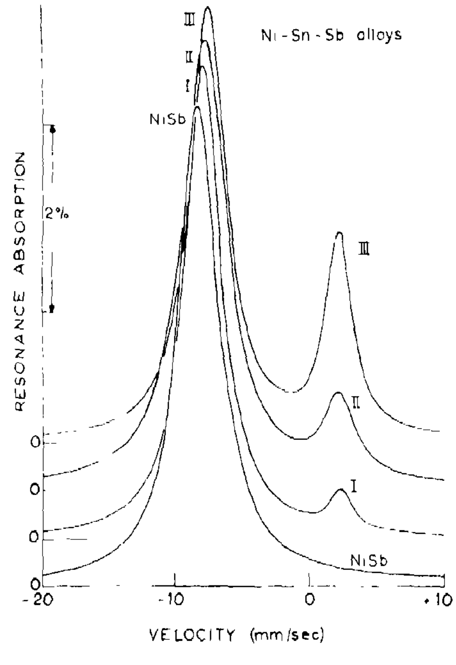

Fig. 3 ^{121}Sb Mossbauer spectra for the alloys in the Ni–Sn–Sb ternary system. The data points have been omitted for clarity, but have a similar scatter to those shown in Fig. 2. The appearance of a second peak at + 2 mm/sec is due to ^{119}Sn absorption, not ^{121}Sb (see discussion in Results section) were generally smaller than those of the one at -8 mm/sec. A small second peak at 3 mm/sec was also observed for SnSb. This second peak was the object of much speculation. However, its cause was resolved after several months. The obvious possibility of oxide coating or other phase impurities was ruled out by careful microscopic and X-ray analysis. Upon retaking the spectrum of alloy III(Sn), which had the largest second peak, that peak was reduced in intensity. It was then realized that the peak appeared only when Sn was present in the absorber, and that the reduction in intensity was consistent with the 250 day half-life of ^{119m}Sn. Indeed, a peak at 2 mm/sec was also then observed for Ni_3Sn_2, which could not exhibit ^{121}Sb absorption. Thus, the second peak is due in all cases to ^{119}Sn resonant absorption. Because the single channel analyzer is set for the escape peak from ^{121}Sb at 8 keV, part of the background in the channel is due to ^{119m}Sn 24 keV gammas that have been degraded in energy by Compton scattering in the absorber, or have deposited only part of their energy in the detector. Since resonance in the absorber is possible before these events, the appearance of a ^{119}Sn absorption peak is understandable in a relatively new source with both activities present.

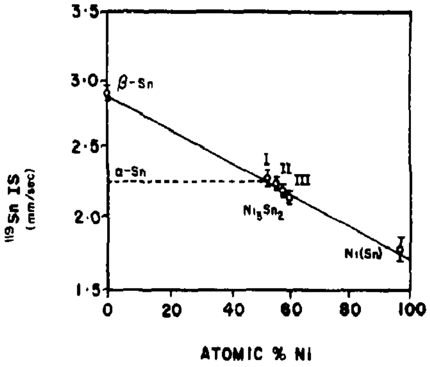

Fig. 4. Isomer shift vs atomic percent nickel for ^{119}Sn. The point for the dilute solution of Sn in Ni was taken from Cordey-Hayes M., *Chemical Applications of Mossbauer Spectroscopy* (Edited by V I Goldanskii and R. H. Herber), p. 326, Academic Press, New York (1968).

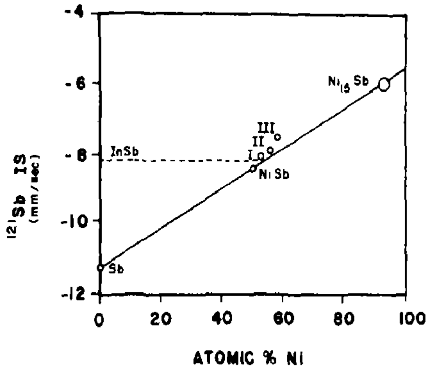

Fig. 5. Isomer shift vs. atomic percent nickel for ^{121}Sb.

Plots have been made in Figs. 4 and 5 of isomer shift vs. atomic percent nickel. To a first approximation both the ^{119}Sn and ^{121}Sb plots are linear. The ^{121}Sb isomer shifts for the corresponding Ni-Ge-Sb and Ni-Sn-Sb ternaries are the same within the experimental error. The opposite signs of the slopes for ^{119}Sn and ^{121}Sb are expected, as the nuclear radius difference between excited and ground state has the opposite sign in the two nuclides [4]. Other similarities may be noted. The ^{119}Sn isomer shift for α-Sn (2·25 mm/sec) [8] and the ^{121}Sb isomer shift for InSb ($-8{\cdot}15 \pm 0{\cdot}06$ mm/sec) each lie at about 50% Ni on the plots in Figs. 4 and 5. If one assumes an electron configuration of $5s^1p_3$ for each of these[4], the ternary alloys also have a $5s$ electron density of about one at both Sn and Sb nuclei. The graphical calibration of Ruby *et al.*[4] can be used to determine the total $5s$ electron transfer from Sn or Sb to Ni if certain assumptions are made. The isomer shift from the configuration $5s^0p^3$ to $5s^2p^3$ is approximately -22 mm/sec for ^{121}Sb and $+3{\cdot}8$ mm/sec for ^{119}Sn from the graphs[4]. The slopes of isomer shift vs. atomic percent Ni are $-1{\cdot}25$ mm/sec for ^{119}Sn and 5·91 for ^{121}Sb (Figs. 4 and 5). Assuming a constant $5p^3$ shielding, the $5s$ electron transfer which occurs between 0 and 100 atomic percent Ni is therefore about 0·7 for Sn and 0·5 for Sb.

Ignoring p shielding, the corresponding numbers would be 0·5 for Sn and 0·4 for Sb. In both cases, the slopes are in the direction of decreasing $5s$ electron density with increasing Ni content.

Upon closer examination, the ^{121}Sb isomer shifts for the ternary compounds I, II, and III seem to lie slightly off the line through the binary Ni–Sb points (Fig. 5), in the direction of higher $5s$ electron transfer away from Sb. The indication is that Sb in the B8 ternary alloys loses $5s$ electrons somewhat more easily than in the binary compounds. With the lower precision available for isomer shift determination in the ^{119}Sn spectra, a corresponding effect for Sn cannot be observed.

The behavior of the Sn and Sb in these alloys is similar to that of Sn in Pd-Sn[1], [2] and Pt-Sn[3]. In the latter cases, it was concluded that some of the $5s$ electrons are transferred from Sn into the unfilled d-bands of the transition metals.

It is reasonable to assume that the $3d$-band of the Ni atom also is filled in the Ni–Sb and Ni–Sn systems by transferring $5s$-electrons from Sn and Sb. According to Crangle and Martin[9] the magnetic amount of Ni decreases linearly with increasing atomic percent Sb and Sn in dilute binary solid solutions. From their plots, it can be inferred that the magnetic moment vanishes around 8 atomic percent Sb and 9% Sn in these systems. They interpret their results first by assuming that in pure Ni the number of unoccupied $3d$-states per atom is about 0·55. Then, they calculate the number of electrons transferred to the unoccupied $3d$-band of Ni from the Sn and Sb atoms to be 3·29 and 4·27, respectively. The remaining 0·7 valence electrons are assumed either to be transferred into nonmagnetic conduction levels in the alloy, or remain bound to the Sn and Sb atoms.

Pearson[10] points out that in compounds having B8 type structure the electrical properties vary with their c/a ratios. On the basis of existing electrical and magnetic properties, he concludes that when c/a is much less than 1·50 (this ratio is 1·63 for a perfect B8 structure in which the Ni atoms are in precisely octahedral holes) metallic conduction occurs. In all of the B8 type compounds and alloys studied here this ratio is well below 1·50 (see Table 1). Therefore, one expects them to be metallic due to the formation of a $3d$-band as a result of interaction between $3d$ shells of Ni. Based on the observed Ni–Ni distances, Dudkin[11] also concludes that NiSb is metallic. From the isomer shift values and the magnetic data it can be concluded that some of the $5s$ electrons are transferred from Sn and Sb partially to fill the $3d$-band of Ni, and partially to go into nonmagnetic conduction bands of the alloys.

Considering the above information on electron transfer from Sn and Sb to Ni, it was of interest to determine the isomer shifts for both components of the binary SnSb, to see what effect removing the transition metal d-bands would have on the electron transfer. Of course, SnSb does not have the B8 structure, so that an exact comparison cannot be made. The X-ray pattern for this alloy agreed with that of Hägg and Hybinette [12], that of a rhombohedrally distorted cubic structure. Since the atomic scattering factors of Sn and Sb are similar, it is impossible to know whether the two are ordered in a distorted NaCl array or arranged randomly on the lattice points. The small quadrupole splitting observed for Sn in this alloy (Table 2) suggests a symmetric local environment. The isomer shifts for Sn and Sb fit well with the proposed electron transfer scheme for the B8 structures. The ^{119}Sn spectrum for this alloy has been reported previously[13] and our isomer shift (IS) value of $3{\cdot}09 \pm 0{\cdot}05$ mm/sec is in excellent agreement with the earlier determination, after correcting for the difference in source used. The IS for ^{121}Sb of $-10{\cdot}10 \pm 0{\cdot}07$ mm/sec has not been previously reported. Comparing these values with those of the pure elements (Tables 2 and 3), it is seen that both the SnSb IS values are more positive than those of the metals. Considering the difference in sign of the nuclear radius change, one can say the 5 *s* electron density at the Sn site is greater in SnSb than in β-Sn, whereas the density at the Sb site is slightly less than in Sb. The IS value for ^{121}Sb in SnSb reported here is essentially the same as that reported for a dilute solution of Sb in β-Sn[14]. In both cases the Sb presumably has near neighbors of Sn. The small electron transfer indicated by the IS values occurs from Sb to Sn.

Thus, it appears that the transition metal is necessary for any large amount of electron transfer to occur. It can be expected that in the dilute solution range, before the Ni *d*-bands are filled, both IS values for ^{119}Sn and ^{121}Sb will be constant, as observed for the Pd–Sn system[2]. The fact that the *s* electron transfer calculated for Sb to Ni is somewhat less than that for Sn over the entire range of compositions is perhaps to be expected on the basis that Sb has more valence electrons, and a transfer mechanism would logically involve a smaller *s* character on a percentage basis if the additional valence electron were primarily *p*, and if Sb and Sn are behaving similarly toward Ni. The detailed structure in a metallic system is apparently a minor factor in electron localization. However, the transition metal *d*-bands seem to be filled at the expense of any non-transition metal present. It also appears that both *s* and *p* electrons are transferred from the non-transition metal.

Acknowledgement—The assistance of Miss M. L. Fiedler in preparation and characterization of the samples is gratefully acknowledged.

REFERENCES

1. IBRAIMOV N. S. and KUZ'MIN R. N., *Zh. éksp. teor. Fiz.* **48**, 103 (1965); *Soviet Phys. JETP* **21**, 70 (1965).
2. CORDEY-HAYES M. and HARRIS I. R., *Phys. Lett.* **24A**, 80 (1967).
3. KANEKAR C. R., RAO K. R. P. M. and RAO V. U. S., *Phys. Lett.* **19**, 95 (1965).
4. RUBY S. L., KALVIUS G. M., BEARD G. B. and SNYDER R. E., *Phys. Rev.* **159**, 239 (1967).
5. BOWEN L. H., STEVENS J. G. and LONG G. G., *J. chem. Phys.* **51**, 2010 (1969)
6. GLADYSHEVSKII E. I. and CHERKASHIN E. E., referenced in PEARSON W. B., *A Handbook of Lattice Spacings and Structures of Metals and Alloys*, Vol 2, p. 1139 Pergamon Press, Oxford (1967).
7. MUIR A. H., JR., ANDO K. J. and COOGAN H. M., *Mossbauer Effect Data Index*. Interscience, New York (1967)
8. LEES J. K. and FLINN P. A., *J. chem. Phys.* **48**, 882 (1968).
9. CRANGLE J. and MARTIN M. J. C., *Phil. Mag.* **4**, 1006 (1959).
10. PEARSON W. B., *Can. J. Phys.* **35**, 886 (1957)
11. DUDKIN L. D., *Dokl. Akad. Nauk SSSR* **127**, 1203 (1959); *Soviet Phys. Dokl.* **4**, 903 (1960).
12. HAGG G. and HYBINETTE A. G., *Phil. Mag.* **20**, 913 (1935).
13. BRYUKHANOV V. A., DELYAGIN N. N., KUZ'MIN R. N. and SHPINEL V. S., *Zh. éksp. teor. Fiz.* **46**, 1996 (1964), *Soviet Phys. JETP* **19**, 1344 (1964).
14. RUBY S. L., *Mossbauer Effect Methodology* (Edited by I. J. Gruverman), Vol. 3, p. 203. Plenum Press, New York (1967)

J. Phys. Chem. Solids Pergamon Press 1970. Vol. 31, pp. 1573–1585. Printed in Great Britain.

THEORY OF IMPURITY STATES IN SYSTEMS WITH LONG RANGE INTERACTIONS–SPIN WAVES IN Tb–Ho ALLOYS

J. A. BLACKMAN*
Department of Theoretical Physics, Oxford University, England and Department of Physics, Atomic Energy Establishment Riso, Roskilde, Denmark

(*Received* 18 *March* 1969; *in revised form* 20 *October* 1969)

Abstract – The theoretical treatment of impurity problems is generally restricted to cases involving interactions of short range. We present here a discussion of the long range case and show how certain of the impurity terms may be treated exactly. One term remains intractable, however, but it is shown that, under some circumstances, this may to a good approximation be neglected. In particular the spin wave spectrum of the rare earth alloy Tb–Ho is considered, a system in which the angular momenta are coupled by the long range Rudermann-Kittel interaction, and in which resonant magnon modes have been observed experimentally. A discussion is also given of the likely behaviour of spin waves in other Tb-rare earth alloys.

1. INTRODUCTION

THEORETICAL studies of the effect of impurities on the spectrum of elementary excitations in solids have in most cases been limited to cases in which the perturbation due to the impurities is of short range. The simplest cases are (1) the lattice vibration problem in which the impurity mass is different from the host mass – e.g. Montroll and Potts[1], Mahanty *et al.*[2], and (2) the electronic problem in which an impurity introduces a perturbing potential localized to the defect site itself – e.g. Koster and Slater[3]. The slightly more complicated case is treated in the paper of Wolfram and Callaway[4]. They considered the spin-wave spectrum of a simple cubic ferromagnet with nearest neighbour exchange coupling. Associated with impurities are changes in spin and coupling constants. Their problem reduced to one of matrix algebra involving 7×7 matrices. Because of the point symmetry of the defect site the problem was further simplified by a little elementary group theory.

As the range of the defect potential increases, so also does the dimensionality of the matrices involved, and the problem rapidly becomes too difficult to handle by the Wolfram and Callaway method. This is in fact the case in the Tb–Ho alloys studied by Bjerrum Møller *et al.*[5], where the exchange coupling is due to the Rudermann-Kittel interaction. They studied the spin wave spectrum of this alloy and observed what appears to be a resonant state within the magnon band.

In this paper we discuss the extended perturbation single impurity problem using a Hamiltonian appropriate to the Tb–Ho system. It is shown that immediately tractable single site perturbation terms occur (mainly due to the anisotropy), and also troublesome long range terms appear due to the exchange. An account is given of the source of these long range terms and a method described whereby some of them can be manipulated into a tractable form. A final unmanageable term remains, however, which prevents an exact solution of the problem. It is suggested that under appropriate conditions this may be justifiably neglected.

The only other papers dealing with long-range interactions in impurity problems are those of Elliott and Taylor[6] (Debye model of phonons), Hermanson[7] (excitons), and Page and Strauch[8] (U-centres). Page and Strauch have developed a method of dealing with the vibrations of charged impurities with long-range Coulomb interactions in crystals, which is in many ways analogous to ours. In fact they find that they can only treat a part of the long-range interaction which occurs in ionic crystals[9], and we can only treat a similar part in the general case (see Section 4).

---

*Present address: Dept. of Physics and Astronomy, University of Maryland, College Park, Md. 20740, U.S.A.

2. SPIN-WAVES IN PURE TERBIUM

Below 216°K terbium orders ferromagnetically with all moments aligned in the basal plane of the hexagonal close packed lattice, and at 30° to the direction joining nearest neighbours. The simplest Hamiltonian that will provide a description of the system is of the form

$$H=-\tfrac{1}{2}\sum_{\substack{i,j\\ \alpha,\beta}} J_{ij}^{\alpha\beta}\mathbf{S}_i^{\alpha}\cdot\mathbf{S}_j^{\beta}+\sum_{i,\alpha}\,[B(S_{iz}^{\alpha})^2$$
$$-\tfrac{1}{2}G\{(S_{ix}^{\alpha}+iS_{iy}^{\alpha})^6+(S_{ix}^{\alpha}-iS_{iy}^{\alpha})^6\}] \quad (2.1)$$

α, β are labels of the atoms in unit cells i, j: **S** is the total angular momentum operator; $J_{ij}^{\alpha\beta}$ is the indirect exchange parameter describing the coupling between spins on sites $\mathbf{R}_i^{\alpha}$ and $\mathbf{R}_j^{\beta}$. It is defined with $J_{ii}^{\alpha\alpha}=0$, so that we can take the unrestricted sum. The remaining terms arise from the crystal field anisotropy. The z-direction is along the hexagonal c-axis. With B and G positive the tendency is for alignment along the x-direction. The crystal field terms in S_z^4 and S_z^6 are neglected for the moment. Their effect is discussed later, however (see Section 5(2)). Within the spin wave approximation the usual transformation to boson operators is made:

$$\begin{aligned} S_{ix}^{\alpha} &= S-a_{i\alpha}^{+}a_{i\alpha} & \qquad S_{i+}^{\alpha} &= (2S)^{1/2}a_{i\alpha} \\ S_{\pm} &= S_y\pm iS_z & \qquad S_{i-}^{\alpha} &= (2S)^{1/2}a_{i\alpha}^{+} \end{aligned} \quad (2.2)$$

The Hamiltonian (2.1) is written in bilinear form:

$$H=\text{const.}-S\sum_{\substack{i,j\\ \alpha,\beta}} J_{ij}^{\alpha\beta}(a_{i\alpha}^{+}a_{j\beta}-a_{i\alpha}^{+}a_{i\alpha})$$
$$+\sum_{i,\alpha}\left[-\frac{BS}{2}(a_{i\alpha}^{+}-a_{i\alpha})^2+GS^5\left\{6a_{i\alpha}^{+}a_{i\alpha}\right.\right.$$
$$\left.\left.+\frac{15}{2}(a_{i\alpha}^{+}+a_{i\alpha})^2\right\}\right]. \quad (2.3)$$

Using the canonical transformations of Niira [10] and Oguchi[11], the Hamiltonian (2.3) can be diagonalized—see, for example, Lindgård *et al.*[12]. An expression for magnon energy eigenvalues, λ_{ik}, is obtained:

$$\lambda_{ik}=S[\omega_{ik}^2+2(B+21GS^4)\omega_{ik}$$
$$+72GS^4(B+3GS^4)]^{1/2} \quad (2.4)$$

where

$$\omega_{ik}=J_0+J_0'-J_k\mp|J_k'| \quad (2.5)$$

i denotes the spin-wave branch. In (2.5) the upper sign refers to the acoustic and the lower sign to the optical magnon modes. The Fourier transforms of the exchange parameters are defined by:

$$\begin{matrix}(\alpha=\beta):J_k\\ (\alpha\neq\beta):J_k'\end{matrix}={J_k}^{\alpha\beta}$$
$$=\sum_{(i-j)}J_{ij}^{\alpha\beta}\,e^{i\mathbf{k}}\,.\,(\mathbf{R}_i^{\alpha}-\mathbf{R}_j^{\beta}).$$

3. PERFECT CRYSTAL GREEN'S FUNCTIONS

It is convenient to set up the problem in a Green's function formalism. We employ the double-time, temperature-dependent, retarded Green's function as discussed in the review paper by Zubarev[13]. For example, the Green's function for the operators $A(t)$ and $B(t')$, which are in the Heisenberg representation, is defined by

$$\langle\langle A(t);B(t')\rangle\rangle=-i\theta(t-t')\langle[A(t),B(t')]\rangle, \quad (3.1)$$

$\langle\ldots\rangle$ indicates an average over a grand canonical ensemble, and $\theta(t)$ is the step function. Since we are dealing with boson operators we use the commutator of the operators. The properties of the Green's functions can be determined by the equations of motion:

$$i\hbar\frac{\mathrm{d}}{\mathrm{d}t}\langle\langle A(t);B(t')\rangle\rangle=\hbar\delta(t-t')\langle[A(t),B(t)]\rangle+\langle\langle[A(t),H(t)];B(t')\rangle\rangle. \tag{3.2}$$

It is convenient to work with the frequency transform throughout, defined by

$$\langle\langle A;B\rangle\rangle_\omega=\int_{-\infty}^{\infty}e^{i\omega t}\langle\langle A(t);B(0)\rangle\rangle\,\mathrm{d}t. \tag{3.3}$$

In (3.3) ω is understood to have a small positive imaginary part. We will use units in which $\hbar=1$.

The following four types of magnon operator Green's functions are defined:

$$\begin{aligned} g&=\langle\langle a;a^+\rangle\rangle_\omega; & h&=\langle\langle a^+;a^+\rangle\rangle_\omega\\ \tilde g&=\langle\langle a^+;a\rangle\rangle_\omega; & \tilde h&=\langle\langle a;a\rangle\rangle_\omega. \end{aligned} \tag{3.4}$$

By use of expressions (2.3), (3.2) and (3.3) it is straightforward to set up the equations of motion of the Green's functions of (3.4). They are conveniently grouped together in one matrix equation of the form

$$\begin{pmatrix}\omega I-P & Q\\ Q & \omega I+P\end{pmatrix}^{\alpha\delta}_{lj}\begin{pmatrix}g & \tilde h\\ -h & -\tilde g\end{pmatrix}^{\delta\beta}_{jl'}=\begin{pmatrix}I & O\\ O & I\end{pmatrix}^{\alpha\beta}_{ll'} \tag{3.5}$$

where

$$\begin{aligned} P^{\alpha\delta}_{lj}&=-S[J^{\alpha\delta}_{lj}-(J_0+J'_0)I^{\alpha\delta}_{lj}]+\Phi SI^{\alpha\delta}_{lj}\\ Q^{\alpha\delta}_{lj}&=-\Psi SI^{\alpha\delta}_{lj}\\ I^{\alpha\delta}_{lj}&=\delta_{lj}\delta_{\alpha\delta}\\ \Phi&=B+21GS^4\\ \Psi&=B-15GS^4. \end{aligned} \tag{3.6}$$

It is then a simple matter to invert (3.5) to obtain the perfect crystal Green's functions explicitly:

$$\begin{pmatrix}g & \tilde h\\ -h & -\tilde g\end{pmatrix}^{\alpha\beta}_{lj}=\frac{1}{2}\sum_k\left[\frac{\begin{pmatrix}\omega+S(\omega_{1k}+\Phi) & S\Psi\\ -S\Psi & \omega-S(\omega_{1k}+\Phi)\end{pmatrix}}{\omega^2-\lambda^2_{1k}}\pm\frac{\begin{pmatrix}\omega+S(\omega_{2k}+\Phi) & S\Psi\\ -S\Psi & \omega-S(\omega_{2k}+\Phi)\end{pmatrix}}{\omega^2-\lambda^2_{2k}}\right]\times e^{ik\cdot(R_l-R_j)}. \tag{3.7}$$

In (3.7) the upper sign refers to $\alpha=\beta$, and the lower sign to $\alpha\neq\beta$.

4. IMPURE CRYSTAL GREEN'S FUNCTIONS

Let us consider now a single impurity introduced in a unit cell $l=0$, and on sublattice θ. Suppose the presence of the defect causes the following changes in the parameters of the problem:

$$S\to S';\;B\to B';\;G\to G';\;J^{\theta\alpha}_{0l}\to\mathcal{J}^{\theta\alpha}_{0l}.$$

To simplify matters it will be assumed that the change in J is by a numerical factor only:

$$\text{i.e. }\mathcal{J}^{\theta\alpha}_{0l}=\mu J^{\theta\alpha}_{0l}.$$

The most obvious value of μ for this problem is the ratio $(\lambda'-1)/(\lambda-1)$, where λ and λ' are the Lande factors of host and impurity ions respectively. The appearance of the factor $(\lambda-1)^2$ in the indirect coupling between two ions of total angular momentum **S** (see de Gennes[14]) is replaced by $(\lambda-1)(\lambda'-1)$ when one of the ions has total angular momentum **S**$'$. To the Hamiltonian (2.3) is thus added the perturbation:

$$\begin{aligned} H_{\text{defect}}={}&-\sqrt{S}(\mu\sqrt{S'}-\sqrt{S})\\ &\times\sum_{l,\alpha}J^{\theta\alpha}_{0l}(a^+_{0\theta}a_{l\alpha}+a^+_{l\alpha}a_{0\theta})\\ &+\sum_{l,\alpha}J^{\theta\alpha}_{0l}[(\mu S'-S)a^+_{a\alpha}a_{a\alpha}+S(\mu-1)a^+_{0\theta}a_{0\theta}]\\ &+\sum_{l,\alpha}[-\tfrac{1}{2}(B'S'-BS)(a^+_{0\theta}-a_{0\theta})^2+(G'S'^5\\ &-GS^5)\{6a^+_{0\theta}a_{0\theta}+\tfrac{15}{2}(a^+_{0\theta}+a_{0\theta})^2\}]. \end{aligned} \tag{4.1}$$

The Green's functions in the presence of impurities are denoted by capital letters. Note, we have used the symbol G to denote both a

Green's function and an anisotropy constant. This is to accord with conventional usage. No confusion should arise, however, as the meaning will always be clear from the context. The perturbation (4.1) produces additional terms in the equations of motion and (3.5) is modified to the form

$$\begin{pmatrix} \omega I-P & Q \\ Q & \omega I+P \end{pmatrix}_{lj}^{\alpha\delta}\begin{pmatrix} G & \tilde{H} \\ -H & -\tilde{G} \end{pmatrix}_{jl'}^{\delta\beta}$$

$$= \begin{pmatrix} I & O \\ O & I \end{pmatrix}_{ll'}^{\alpha\beta} - a\begin{pmatrix} I & O \\ O & I \end{pmatrix}_{l0}^{\alpha\theta}\begin{pmatrix} J & O \\ O & -J \end{pmatrix}_{0j}^{\theta\gamma}$$

$$\times\begin{pmatrix} G & \tilde{H} \\ -H & -\tilde{G} \end{pmatrix}_{jl'}^{\gamma\beta} - a\begin{pmatrix} J & O \\ O & -J \end{pmatrix}_{l0}^{\alpha\theta}\begin{pmatrix} G & \tilde{H} \\ -H & -\tilde{G} \end{pmatrix}_{0l'}^{\theta\beta}$$

$$+ b\begin{pmatrix} J & O \\ O & -J \end{pmatrix}_{l0}^{\alpha\theta}\begin{pmatrix} G & \tilde{H} \\ -H & -\tilde{G} \end{pmatrix}_{ll'}^{\alpha\beta}$$

$$+\begin{pmatrix} \Delta_2 I & \Delta_1 I \\ -\Delta_1 I & -\Delta_2 I \end{pmatrix}_{l0}^{\alpha\theta}\begin{pmatrix} G & \tilde{H} \\ -H & -G \end{pmatrix}_{0l'}^{\theta\beta} \qquad (4.2)$$

where

$$a = \sqrt{S}(\mu\sqrt{S'} - \sqrt{S});\; b = \mu S' - S$$
$$\Delta_1 = -(B'S' - BS) + 15(G'S'^5 - GS^5)$$
$$\Delta_2 = (B'S' - BS) + 21(G'S'^5 - GS^5)$$
$$+ S(\mu - 1)(J_0 + J_0'). \qquad (4.3)$$

The second term on the right-hand side of (4.2) may be simplified by summing over j and γ and introducing modified Green's functions defined by

$$(JG)_{ll'}^{\alpha\beta} = J_{lj}^{\alpha\gamma}G_{jl'}^{\gamma\beta}. \qquad (4.4)$$

A corresponding set is also defined:

$$(GJ)_{ll'}^{\alpha\beta} = G_{lj}^{\alpha\gamma}J_{jl'}^{\gamma\beta}. \qquad (4.5)$$

Thus we may write (4.2) in Dyson form as

$$\begin{pmatrix} G & \tilde{H} \\ -H & -\tilde{G} \end{pmatrix}_{ll'}^{\alpha\beta} = \begin{pmatrix} g & \tilde{h} \\ -h & -\tilde{g} \end{pmatrix}_{ll'}^{\alpha\beta} + \begin{pmatrix} g & \tilde{h} \\ -h & -\tilde{g} \end{pmatrix}_{l0}^{\alpha\theta}$$

$$\times\begin{pmatrix} \Delta_2 & \Delta_1 \\ -\Delta_1 & -\Delta_2 \end{pmatrix}\begin{pmatrix} G & \tilde{H} \\ -H & -\tilde{G} \end{pmatrix}_{0l'}^{\theta\beta}$$

$$+\begin{pmatrix} g & \tilde{h} \\ -h & -\tilde{g} \end{pmatrix}_{l0}^{\alpha\theta}\begin{pmatrix} -a & O \\ O & a \end{pmatrix}$$

$$\times\begin{pmatrix} JG & J\tilde{H} \\ -JH & -J\tilde{G} \end{pmatrix}_{0l'}^{\theta\beta}$$

$$+\begin{pmatrix} gJ & h\tilde{J} \\ -hJ & -g\tilde{J} \end{pmatrix}_{l0}^{\alpha\theta}\begin{pmatrix} -a & O \\ O & a \end{pmatrix}$$

$$\times\begin{pmatrix} G & \tilde{H} \\ -H & -\tilde{G} \end{pmatrix}_{0l'}^{\theta\beta} + \begin{pmatrix} g & \tilde{h} \\ -h & -\tilde{g} \end{pmatrix}_{ll}^{\alpha\delta}$$

$$\times\begin{pmatrix} bJ & O \\ O & -bJ \end{pmatrix}_{l0}^{\delta\theta}\begin{pmatrix} G & \tilde{H} \\ -H & -\tilde{G} \end{pmatrix}_{ll'}^{\delta\beta}$$

$$(4.6)$$

Denoting the 2×2 pure and impure crystal matrices by γ and Γ respectively we may write (4.6) in the simpler form

$$\Gamma_{ll'}^{\alpha\beta} = \gamma_{ll'}^{\alpha\beta} + \gamma_{l0}^{\alpha\theta}V_1\Gamma_{0l'}^{\theta\beta} + \gamma_{l0}^{\alpha\theta}V_2(J\Gamma)_{0l'}^{\theta\beta}$$
$$+ (\gamma J)_{l0}^{\alpha\theta}V_2\Gamma_{0l'}^{\theta\beta} + \gamma_{ll}^{\alpha\delta}U_{l0}^{\delta\theta}\Gamma_{il'}^{\delta\beta} \qquad (4.7)$$

where

$$V_1 = \begin{pmatrix} \Delta_2 & \Delta_1 \\ -\Delta_1 & -\Delta_2 \end{pmatrix};\; V_2 = \begin{pmatrix} -a & O \\ O & a \end{pmatrix};$$

$$U = \begin{pmatrix} bJ & O \\ O & -bJ \end{pmatrix}. \qquad (4.8)$$

Equation (4.7) approaches still nearer to a familiar form if we obtain the equation of motion for the Green's function matrices $(J\Gamma)$ and (ΓJ), and also another one $(J\Gamma J)$. These are combined in a single 4×4 matrix expression:

$$\begin{pmatrix} \Gamma & \Gamma J \\ J\Gamma & J\Gamma J \end{pmatrix}_{ll'}^{\alpha\beta} = \begin{pmatrix} \gamma & \gamma J \\ J\gamma & J\gamma J \end{pmatrix}_{ll'}^{\alpha\beta} + \begin{pmatrix} \gamma & \gamma J \\ J\gamma & J\gamma J \end{pmatrix}_{l0}^{\alpha\theta}$$

$$\times\begin{pmatrix} V_1 & V_2 \\ V_2 & O \end{pmatrix}\begin{pmatrix} \Gamma & \Gamma J \\ J\Gamma & J\Gamma J \end{pmatrix}_{0l'}^{\theta\beta}$$

$$+\begin{pmatrix} \gamma & \gamma J \\ J\gamma & J\gamma J \end{pmatrix}_{ll}^{\alpha\delta}\begin{pmatrix} U & O \\ O & U \end{pmatrix}_{l0}^{\delta\theta}$$

$$\times\begin{pmatrix} \Gamma & \Gamma J \\ J\Gamma & J\Gamma J \end{pmatrix}_{il'}^{\theta\beta} \qquad (4.9)$$

The 'V' part of (4.9) looks very much like the expression obtained in the 'isotopic' impurity problem, and it can be handled in a similar way.

It is useful to make a comparison with the work of Wolfram and Callaway[4]. The defect matrix (equation (27) in their paper) has dimensions $z+1\times z+1$, where z is 6 in the simple cubic case. Its only non-zero elements are down the diagonal and along the first row and down the first column. The corresponding quantity in our case has the same format but the dimensionality is very large because of the long-range of the interactions.

In the above manipulation we have managed to include all the nondiagonal terms and the $(00, \theta\theta)$ diagonal element in the 'V' part of (4.9). The remaining diagonal terms form the 'U' part. It is fairly clear that this treatment will enable us to deal with all the 'V' terms exactly, but the 'U' terms are still intractable. The origin of the various impurity terms can be understood from the perturbation expression (4.1). The terms within the third summation are the single ion anisotropy contribution. This part of course is straightforward to handle as it is just a point defect problem. The spin-flip part of the exchange (JS^+S^-) gives rise to the first summation in (4.1). It is this part that is responsible for all offdiagonal elements of the impurity matrix. These, as has been stated, can be dealt with exactly, and are contained in the 'V' part of (4.9). The remaining terms in (4.1) come from that part of the exchange term of the form JS^xS^x (where x is the axis of quantization. In terms of boson operators it is made up of two parts, one containing only the operators for the impurity site, and the other in terms of operators for the host lattice sites. Performing the summation over i and α, the impurity ion part looks like a single ion term and can be treated on the same basis as the anisotropy terms. This accounts for the μ-dependent part in Δ_2 (equation (4.3)). The remaining term, which occurs as

$$\sum_{i,\alpha} J_{0i}^{\theta\alpha}(\mu S' - S)a_{i\alpha}^{+}a_{i\alpha}$$

in the defect Hamiltonian (4.1), gives the 'U' term in (4.9).

It is of interest to see if, under any circumstances, we can approximate by dropping the 'U' term completely, and taking the 'V' term only as the perturbation. We have examined the effect of doing this on the short range coupling case of Wolfram and Callaway[4]. Using their notation, the exact condition for an s-like resonant or localized mode is (their equation (42)

$$\epsilon = \frac{-1+(1-\sigma)\mathscr{G}_{12}(E-3)}{3\mathscr{G}_{11}+\mathscr{G}_{12}\{(\sigma-1)(E-3)+(E-6)\}} \tag{4.10}$$

where $\epsilon = (J'-J)/J$, and $\sigma = S'/S$. J is the exchange constant between host atoms, and J' that between the impurity and the host atoms. If we drop the diagonal 'U' term and look for the approximate resonance condition a quadratic equation in ϵ is obtained whose roots are

$$\epsilon = \frac{3(\mathscr{G}_{11}-2\sigma\mathscr{G}_{12})\pm\sqrt{[9\mathscr{G}_{11}^2+12\sigma(E-3)\mathscr{G}_{11}\mathscr{G}_{12}]}}{6\sigma\mathscr{G}_{12}}. \tag{4.11}$$

In their dimensionless units the bottom of the band is at energy $E = 3$ and the top at $E = -3$; $\mathscr{G}_{11}$ and $\mathscr{G}_{12}$ refer to the real parts of the Green's functions defined in their paper. To obtain a true resonance one also requires that its width is positive. A determining condition for this in the exact case is for the derivative of the resonant ϵ with respect to energy, $d\epsilon/d(-E)$, to be positive. With modes whose width is negative, one gets a dip rather than a peak in the density of states. These 'anti-resonance' states do not concern us here, however. We have compared the values of ϵ obtained from the exact expression (4.10) and the appropriate root of the approximation (4.11) for a number of different σ, viz. 3/7, 1, 2. The conclusion reached in this analysis are very interesting and can be summarized as follows:

(a) For $\sigma = 1$ and 2, resonant states exist only in the lower part of the band (between energies 3 and ~ 1). The agreement between the two expressions is to within 1·5 per cent over the whole energy range, but for the most part it is better than 0·2 per cent. This is not shown in diagrammatic form as the two curves are virtually indistinguishable.

(b) For $\sigma = 3/7$, resonant states exist in the lower part of the band (between $E = 3$ and $\sim 0{\cdot}1$; see Fig. 1), and in the upper part (between $E = \sim -1{\cdot}1$ and -3; see Fig. 2). Between 3 and 1 the errors are small and similar in magnitude to those of (a) above; e.g. the worst agreement is near $E = 2{\cdot}8$ with $\epsilon_{\text{exact}} = -0{\cdot}921$ and $\epsilon_{\text{approx}} = -0{\cdot}933$. Nearer the centre of the band the deviation becomes much greater (Fig. 1). This can be understood as it is in this region that the width of the resonance becomes suddenly much larger. When the resonance is narrow and the impurity modes are well localized, we expect the 'V' part of the perturbation to be more important than the 'U' part since it is the former that is more sensitive to resonance behaviour on the defect site itself. In fact, in the region of broad resonance, the approximate theory gives resonances of negative width (i.e. antiresonances). Therefore, at least in the case examined, a resonance given by our theory will be a very good approximation to the true resonance of the exact theory. Resonances may occur, however, over a wider energy range than is predicted by the approximate theory, in the way described here. The 'U' part cannot be neglected, therefore, for a broader resonance. In the upper part of the band (Fig. 2) the agreement is again good, the worst being at $E = -3$ with $\epsilon_{\text{exact}} = 0{\cdot}654$ and $\epsilon_{\text{approx}} = 0{\cdot}631$.

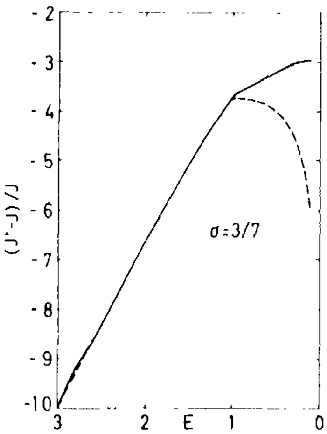

Fig. 1. Exact (full line) and approximate (broken line) positions of resonant modes in lower half of band

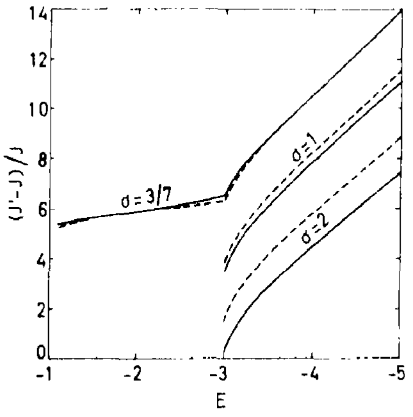

Fig. 2. Exact (full line) and approximate (broken line) positions of resonant modes in upper half of the band, and localized modes above the band

(c) In all cases the positions of bound states below the band as calculated by the two methods are in good agreement (better than 2 per cent), though it should be noted that these are not true bound states as they only occur for antiferromagnetic coupling between the impurity and the host lattice. Their occurrence merely serves to indicate that we have chosen the wrong ground state.

(d) The agreement for bound states above the band (Fig. 2) is very dependent on σ. It is reasonable for $\sigma < 1$, but becomes worse as σ increases.

The implication of the above comparison, then, is that, for narrow resonances within the band, our method gives a good approximation to the position of the resonant mode. A warning comment is required at this point, however. In the above analysis, we have been looking for the value of ϵ required to give a resonance at a particular energy. Had we been determining the resonant energy for a particular ϵ, however, we would have encountered certain difficulties. Reference to the in-band curves for $\sigma = 3/7$ in Fig. 2 shows that a small change in ϵ gives a large change in the position of the resonant energy. It is clearly seen that, for curves of this sort with small slope, large errors may occur through an approximate determination of the resonant energy positions, even though the exact and approximate curves lie very close together. In applying this method, therefore, one should check to see if small variations of any of the parameters associated with the impurity produce large changes in the position of the resonant energy.

5. NUMERICAL CALCULATIONS

1. *Parameters for terbium*

For interest we have performed the calculation, neglecting the 'U' term, for the Tb–Ho case. The resonant magnon mode position will be determined by the usual determinantal relation

$$Re\,[\det\,(I-\gamma_{00}^{00}\mathrm{V})] = 0 \qquad (5.1)$$

where, in this expression, γ and V represent the 4×4 matrices appearing in (4.9).

The basic four Green's functions g, $\bar{g}$, h, $\bar{h}$ can be calculated from a knowledge of the density of magnon states in pure terbium, and the remaining modified Green's functions are then easily determined (see Appendix).

As the only complete data so far available is that for 90°K, we have used this in the calculations, together with the effective values of the anisotropy constants at this temperature. The density of states for pure terbium has been calculated by Gylden Houmann[15], and a numerical integration using his data enabled us to evaluate the Green's functions we require. The other parameters of terbium that we need are J_0, J_0', B, G. We have taken the values of Goodings[16], as they are mutually consistent within a spin wave theory such as the one we are using. His figures are:

$$B = 0{\cdot}4\,\mathrm{meV} \quad G = 7{\cdot}5\times 10^{-7}\,\mathrm{meV}$$
$$J_0 = 0{\cdot}758\,\mathrm{meV} \quad J_0' = 0{\cdot}577\,\mathrm{meV}.$$

Values of J_{ij} out to varying numbers of neighbours have been given by several authors and their magnitudes and signs very markedly. However, the sums agree remarkably closely. Gylden Houmann[15] gives a value of J_0 of 0·788 meV, and Lindgård[17] gives values of J_0 and J_0' of 0·828 meV and 0·588 meV respectively. Lindgård's[17] estimate of B agrees closely with that of Goodings, being 0·39 meV. Gylden Houmann[15], however, prefers a value of B of 0·28 meV and a value of G roughly double that of Goodings. More recent measurements[18], however tend to confirm a value of B of about 0·4 meV. Appropriate values of B' and G' of holmium are much more difficult to assess. They are discussed, together with general remarks on the heavy rare earths, in the following subsection.

(2) *Impurity parameters*

In the above analysis we have implied that one can neglect the higher order anisotropy terms in a spin wave calculation. This is generally not true, and in this sub-section we shall illustrate the importance of the terms in S_z^4 and S_z^6 by way of a rough point charge calculation. The full crystal field anisotropy is written, via the operator equivalent technique (Stevens[19]), as

$$\begin{aligned} H_{an} = {} & \alpha A_2{}^0\langle r^2\rangle\,[3S_z{}^2 - S(S+1)] \\ & +\beta A_4{}^0\langle r^4\rangle\,[35S_z{}^4 - 30S(S+1)S_z{}^2 \\ & +25S_z{}^2 - 6S(S+1) + 3S^2(S+1)^2] \\ & +\gamma A_6{}^0\langle r^6\rangle\,[231S_z{}^6 - 315S(S+1)S_z{}^4 \\ & +735S_z{}^4 + 105S^2(S+1)^2S_z{}^2 \\ & -525S(S+1)S_z{}^2 + 294S_z{}^2 - 5S^3(S+1)^3 \\ & +40S^2(S+1)^2 - 60S(S+1)] \\ & -\gamma A_6{}^6\langle r^6\rangle\tfrac{1}{2}[(S_x+iS_y)^6 + (S_x-iS_y)^6] \end{aligned} \qquad (5.2)$$

where $A_n{}^m$ are constants determined by the distribution of charges surrounding the rare earth ion, and $\langle r^n\rangle$ are the mean values of r^n

over the $4f$ electron distribution. α, β, γ are numerical factors that have been evaluated [19]. Note that the opposite sign appears in the A_6^6 term to that usually used as we have taken the x-axis to coincide with that of magnetic alignment in terbium. Equation (5.2) may be put in the form

$$H_{an} = \text{const.} + BS_z^2 + DS_z^4 + FS_z^6 - \tfrac{1}{2}G[(S_x + iS_y)^6 + (S_x - iS_y)^6] \quad (5.3)$$

which is more useful for spin wave calculations. The constants B, D, F, G may be calculated by assuming point charges on the nearest neighbour sites, the effect of charges on the more distant sites being screened out by the conduction electrons. These are evaluated and displayed in Table 1. The calculation is based on the figures of Kasuya[20], although we have assumed tripositive ions on the nearest neighbour sites. The column headed (B_2^0) indicates the contribution to B from the A_2^0 term in (5.2), and similarly for the other symbols in parentheses.

An interesting point about this calculation is the occurrence of a negative B for holmium and a positive B for erbium. The signs of B in these two cases would give a tendency for magnetic ordering different from that observed experimentally, at least at low temperatures. This indicates that the higher order terms (in D and F) will be important, and one should therefore consider their effect in a spin wave calculation.

The treatment of Niira[10] does, in fact, include contributions from the D and F terms. He first replaced the angular momentum operators by spin wave operators and then rearranged the latter in the normal order (creation operators always written to the left of destruction operators). The commuting of the spin wave operators to obtain normal ordering results in terms bilinear in these operators for all the anisotropy terms. Using this procedure it is possible to obtain an effective B, defined by

$$B_{\text{eff}}^N = B + 3SD + (45/4)S^2F \quad (5.4)$$

All the expressions used in this paper are valid within the Niira approximation if B is replaced by B_{eff}^N as defined by (5.4). The values of B_{eff}^N from the point charge calculation are shown in Table 2.

A slight refinement of Niira's analysis appears in the paper of Brooks, Goodings and Ralph[21]. They give effective values of B and G defined by

$$\begin{aligned} B_{\text{eff}}^{BGR}S = {} & 3\alpha A_2^0\langle r^2\rangle(S-\tfrac{1}{2}) - 30\beta A_4^0\langle r^4\rangle \\ & \times(S-\tfrac{1}{2})(S-1)(S-\tfrac{3}{2}) \\ & + 105A_6^0\langle r^6\rangle(S-\tfrac{1}{2})(S-1)(S-\tfrac{3}{2}) \\ & \times(S-2)(S-\tfrac{5}{2}) \end{aligned} \quad (5.5\text{a})$$

$$\begin{aligned} G_{\text{eff}}^{BGR}S^5 = {} & \gamma A_6^6\langle r^6\rangle(S-\tfrac{1}{2})(S-1)(S-\tfrac{3}{2}) \\ & \times(S-2)(S-\tfrac{5}{2}). \end{aligned} \quad (5.5\text{b})$$

Again all equations in this paper are still applicable if we replace B and G by their effective values defined by (5.5). Table 3 shows the point charge calculation of these effective parameters. The contribution to B_{eff}^{BGR} from each of the three terms in (5.5a) is shown in the columns headed (b_n^0).

These tables clearly indicate the relative importance of the various anisotropy terms in the spin wave theory. Because of the dominance of the lowest order term it is not too critical which expression one uses for the effective parameters in the case of terbium, dysprosium or thulium. However, holmium and erbium require a much more careful treatment.

In our case of Tb–Ho alloys the effective values for Tb at 90°K are fairly well established and have already been listed in Section 5(1). However, appropriate values of B' and G' for holmium are very difficult to assess. This is partly for reasons made clear by the tables (viz. no one dominant anisotropy term), and partly because the holmium is embedded in a lattice of different atoms, although the similarity between the rare earths might lead one to believe that the values would not be too different from those for pure hol-

Table 1

	S	λ	(B_2^0)	(B_4^0)	(B_6^0)	B	(D_4^0)	(D_6^0)	D	F	G
Units			(meV)	(meV)	(meV)	(meV)	(10^{-2} meV)	(10^{-2} meV)	(10^{-2} meV)	(10^{-4} meV)	(10^{-5} meV)
Tb	6	$\frac{3}{2}$	0·3474	0·0890	−0·0360	0·4004	−0·2522	0·2752	0·0230	−0·509	0·390
Dy	7·5	$\frac{4}{3}$	0·2377	−0·0575	0·0737	0·2539	0·1067	−0·3625	−0·2558	0·433	−0·328
Ho	8	$\frac{5}{4}$	0 0849	−0·0336	−0·1097	−0·0584	0·0552	0·4750	0·5302	−0·500	0·378
Er	7·5	$\frac{6}{5}$	−0·0937	0·0372	0·1225	0 0660	−0·0691	−0·6021	−0·6712	0·719	−0 543
Tm	6	$\frac{7}{6}$	−0·3637	0·0961	−0·1273	−0·3949	−0·2406	0·9725	0·7319	−1·798	1·358

Table 2

meV	B	$3SD$	$(45/4)S^2F$	B^{X}_{eff}
Tb	0·4004	0·0041	−0·0205	0·3840
Dy	0·2539	−0·0576	0·0274	0·2237
Ho	−0·0584	0 1272	−0·0360	0·0328
Er	0·0660	−0·1510	0·0455	−0·0395
Tm	−0·3949	0·1318	−0·0728	−0·3359

mium. We require, however, effective values at 90°K, and since transitions in the magnetic ordering occur at temperatures below this it is likely that extrapolations from pure holmium would be extremely inaccurate.

Because of this uncertainty in B' and G' we have plotted (Fig. 3) the variation of the resonant energy with these two parameters. Resonances do occur at energies higher than those shown in the figure, but soon become less clearly defined and eventually disappear altogether. The diagram covers the region of interest, however. As 'best' values of B' and G' we have used the figures of Table 3, and scaled them so that the corresponding quantities for terbium agree with those measured experimentally. The resonance thus determined occurs at 4·25 meV with a width of 0·88 meV. This agrees well with the experimental figures of Bjerrum Møller *et al.*[5], viz. a resonance at about 4 meV with width 1 meV. The uncertainty in the parameters for holmium will probably put an accuracy of about ±0·5 meV on our estimate of the resonance position.

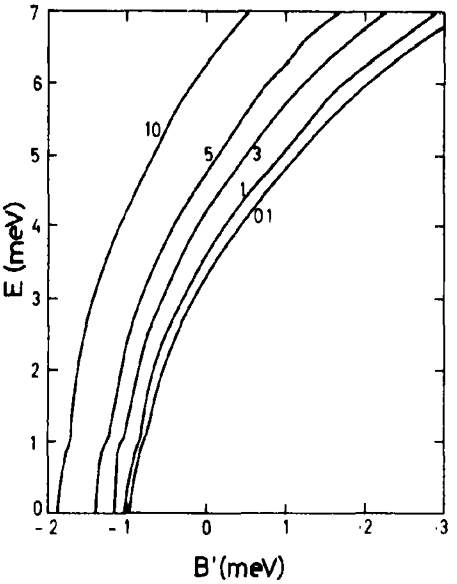

Fig. 3. Curves showing variation of resonant energy, E, with B' and G', for the λ' and S' of holmium. The figures on the curves represent the ratio G'/G.

6. OTHER Tb-RARE EARTH ALLOYS

The good agreement, over a wide range of resonant energies, between the exact and approximate theories in our discussion of the Wolfram and Callaway case, and the close agreement between theoretical and experimental results for the Tb–Ho alloy would lead one to hope that fairly accurate predictions could be made about the spin wave behaviour in other Tb-rare earth alloys. With thulium or erbium as the defect atoms, however, the region of interest appears to be one in which the approximate theory is rather

Table 3

meV	$\langle b_2^0\rangle$	$\langle b_4^0\rangle$	$\langle b_6^0\rangle$	B^{BGR}_{eff}	$G^{BGR}_{\text{eff}}\times 10^6$
Tb	0 3184	0·0445	−0·0066	0·3563	0·872
Dy	0·2219	−0·0333	0·0197	0·2083	−1·038
Ho	0·0796	- 0·0202	−0·0320	0·0274	1·301
Er	−0·0875	0·0216	0·0327	−0·0332	−1·718
Tm	−0·3333	0·0425	−0·0236	−0·3144	3·025

unsatisfactory. The theory is better suited to the case of dysprosium, but here resonance behaviour may be difficult to observe.

We consider first Dy as impurity atoms in the Tb lattice. Scaling the anisotropy constants of Table 3 in the way described for Ho gives resonance behaviour at 7·2 meV and at 8·5 meV. It is quite possible, however, that these resonances would not be observed experimentally. In this energy region (and above) the density of states of Tb shows a markedly peaked behaviour. A resonant mode (which is characterised by an increase in the density of states) occurring in this region is very likely to be masked by the peaky nature of the density of states in the host lattice. In fact, our calculations on the Tb–Ho alloy indicated a second resonant mode at a higher energy (10·3 meV), but this can be expected to be masked for similar reasons, a fact which is confirmed by the failure to observe such a mode experimentally. From the point of view of numerical calculations, the determinant (5.1) changes sign from positive to negative passing through zero at 4·24 meV in the Tb–Ho case. However, in the higher energy regions discussed above, for both Tb–Ho and for Tb–Dy, this determinant shows a rapid oscillatory behaviour as a function of energy and a much more marked sensitivity to the values of the anisotropy constants of the impurity. This is due to the rapidly varying magnitude of the Green's functions reflecting the peaky nature of the density of states. Thus, for Tb–Dy alloys, there is the possibility of resonant magnon modes in the energy region mentioned, but it is likely that they will be unobservable because of the peakiness of the host density of states.

Thulium and erbium, as impurities, offer the possibility of interesting phenomena, because of the negative sign of B in both cases which would tend to cant the spins out of the basal plane toward the c-axis. If this effect is sufficiently strong we would expect that it would be manifested by a bound state below the zero of energy indicating a wrongly chosen ground state. The situation is not as simple as in the Wolfram and Callaway case as the analogous situation there simply meant that the ground state was one with the impurity spin antiferromagnetically aligned to those of the host lattice. In our case a wrongly chosen ground state type of bound state will be much more complicated as we have to consider the resultant of two competing effects: the tendency of a negative B to align the spin along the c-axis, and the opposing exchange tending to keep the impurity spin aligned with those of the Tb lattice in the basal plane. At present we are simply trying to determine whether a new ground state is a likely possibility.

Let us consider Tb–Tm. The curves for this alloy are similar in form to those of Tb–Ho (Fig. 3), but shifted somewhat to the right. We are interested in the value of B_{Tm} for which the curves go to zero energy. A smaller B_{Tm} should then indicate a wrongly chosen ground state. Calculations show, however, that a bound state will occur for a B_{Tm} that is positive. This is, of course, unreasonable physically, and so one must conclude that our approximation breaks down for the very low energy region in much the same way as it did for bound states above the band in the Wolfram and Callaway case. The reason appears to be that bound states of this sort will be rather diffuse, and any tendency for the impurity spin to cant appreciably out of the basal plane will cause the neighbouring spins to do likewise to minimise the energy. Thus the 'U' term that we have neglected will become important.

The behaviour of the approximate theory in two limits is of some interest, however. We performed a calculation to determine the condition for a bound state with G' and S' unchanged from the values in Tb, but (a) a change in B only, and (b) a change in λ only. In case (a) it required a B' of $-0{\cdot}8$ meV to produce a bound state. This is, of course, an exact solution since it is simply a single ion term that is changing. In (b) it required a λ'

of 0·99 ($\mu = -0{\cdot}01$) to produce a bound state. This is clearly in good agreement with physical expectations, since the change from ferromagnetic to antiferromagnetic alignment is expected at $\mu = 0$. Between these two limits the behaviour is not what one would expect physically through, and so the very low energy region is obviously one in which the approximation breaks down. Since the curves are similar to those of Tb–Ho (Fig. 3), it appears that the omission of the 'U' term causes too rapid a fall off to zero energy, and so the gradient in this region is expected to be actually less steep.

Since the exchange factor μ for Tm is $\frac{1}{3}$, one would expect that a B' of much smaller magnitude than −0·8 would be sufficient to involve us in a new ground state problem, and it is very probable that a value of the order indicated by Table 3 would be enough. Some experimental studies of the magnetic ordering in Tb–Tm alloys would be very interesting.

Of course, even a small negative B' does, in a sense, involve us in a new ground state problem as there will be some tendency for tilting out of the basal plane, but it does not necessarily imply a major instability (bound state). In erbium, B' is small and negative, but it does also have the further complication of a negative G', which will encourage a tilting within the basal plane but at an angle to the host spins. The exchange coupling is reduced below that of Tb–Ho but not as much as Tb–Tm. Certainly, if there is a resonance, it will lie very low in the band, and even if an instability of the type likely for Tb–Tm does not occur, a bound state within the energy gap is quite a likely possibility. Experiments on the spin wave spectrum of Tb–Er alloys might well prove an interesting study, and because of the expected temperature dependence of the effective B', observations over a range of temperatures could give some sort of indication of the effect of varying B'.

Acknowledgements – I should like to express my appreciation to Dr. R. J. Elliott for his advice and interest throughout this work, and to Professor A. R. Mackintosh and Dr. P. A. Lindgård for useful discussions on the anisotropy of the rare earths.

REFERENCES

1. MONTROLL E. W. and POTTS R. B., *Phys. Rev.* **100**, 525 (1955).
2. MAHANTY J., MARADUDIN A. A. and WEISS G. H., *Prog. theor. Phys.* **20**, 369 (1955).
3. KOSTER G. F. and SLATER J. C., *Phys. Rev.* **96**, 1208 (1954).
4. WOLFRAM T. and CALLAWAY J., *Phys. Rev.* **130**, 2207 (1963)
5. BJERRUM MØLLER H., GYLDEN HOUMANN J. C. and MACKINTOSH A. R., *J. appl. Phys.* **39**, 807 (1968).
6. ELLIOTT R. J. and TAYLOR D. W., *Proc. R. Soc.* **296**, 161 (1967)
7. HERMANSON J., *Phys. Rev.* **150**, 660 (1966)
8. PAGE, J. B. Jr. and STRAUCH D., *Phys. Status Solidi* **24**, 469 (1967).
9. PAGE J. B. Jr., private communication
10. NIIRA K., *Phys. Rev.* **117**, 129 (1960)
11. OGUCHI T., *Phys. Rev.* **111**, 1063 (1958).
12. LINDGARD P. A., KOWALSKA A. and LAUT P., *J. Phys. Chem. Solids* **28**, 1357 (1967)
13. ZUBAREV D. N., *Usp. Fiz. Nauk.* **71** 71 (1960), English translation. *Soviet Phys. Usp.* **3**, 320 (1960)
14. de GENNES P. G., *Compt. Rend.* **247**, 1836 (1958)
15. GYLDEN HOUMANN J. C., Thesis submitted to the Technical University of Denmark (1968)
16. GOODINGS D. A., *J. phys. C (Proc. phys. Soc.)* **1**, 125 (1968).
17. LINDGARD P. A., *Neutron Inelastic Scattering*, Vol. 2 p. 93. IAEA, Vienna (1968).
18. MACKINTOSH A. R., private communication
19. STEVENS K. W. H., *Proc. phys. Soc.* **A65**, 209 (1952)
20. KASUYA T., *Magnetism IIB* (Edited by G. T. Rado and H. Suhl), p. 215. Academic Press, New York (1966)
21. BROOKS M. S. S., GOODINGS D. A. and RALPH H. I., *J. phys. C. Proc. phys. Soc.* **1**, 132 (1968).

APPENDIX

Useful relationships between the Green's functions may be found. We give one example of how the relationships may be derived and summarize the results. From (3.7) we may write, in an obvious notation

$$g_{ij}^{\alpha\beta} = \tfrac{1}{2} \sum_{k} (X_{1k} \pm X_{2k})\, e^{i\mathbf{k}\cdot(\mathbf{R}_i^{\alpha}-\mathbf{R}_j^{\beta})}. \quad (A.1)$$

Hence

$$(Jg)_{ij}^{\alpha\beta} = \tfrac{1}{2} \sum_{k} \left[(J_k + J_k')X_{1k} \pm (J_k - J_k')X_{2k} \right] e^{i\mathbf{k}\cdot(\mathbf{R}_i^{\alpha}-\mathbf{R}_j^{\beta})}. \quad (A.2)$$

But from (2.5)

$$\omega_{lk} = \epsilon_0 - \epsilon_{lk}$$

where

$$\epsilon_0 = J_0 + J_0'; \; \epsilon_{ik} = J_k \pm J_k' \tag{A.3}$$

and so

$$(Jg)_{ij}^{\alpha\beta} = \tfrac{1}{2} \sum_k e^{i\mathbf{k}\cdot(\mathbf{R}_i^{\alpha} - \mathbf{R}_j^{\beta})}[\epsilon_{1k}X_{1k} \pm \epsilon_{2k}X_{2k}]. \tag{A.4}$$

But from (3.7),

$$\epsilon_{ik}X_{ik} = \frac{\epsilon_{ik}(\omega + S\omega_{ik} + S\Phi)}{\omega^2 - \lambda^2}. \tag{A.5}$$

This expression simplifies to give

$$\epsilon_{ik}X_{ik'} = \frac{1}{S} + \frac{(\epsilon_0 S - \Phi S - \omega)}{S} X_{ik} - \frac{S^2\Psi^2}{\omega^2 - \lambda_{ik}^2}. \tag{A 6}$$

Hence (A.4) may be written in the form

$$(Jg)_{ij}^{\alpha\beta} = \frac{1}{S}\delta_{ij}\delta_{\alpha\beta} + \frac{(\epsilon_0 S + \Phi S - \omega)}{S} g_{ij}^{\alpha\beta} - \Psi h_{ij}^{\alpha\beta}. \tag{A 7}$$

Similar procedures with the other quantities eventually give us a set of relations which can conveniently be summarized in the following form

$$\begin{pmatrix} Jg & J\tilde{h} \\ -Jh & -J\tilde{g} \end{pmatrix}_{ij}^{\alpha\beta} = \begin{pmatrix} gJ & \tilde{h}J \\ -hJ & -\tilde{g}J \end{pmatrix}_{ij}^{\alpha\beta} = \begin{pmatrix} 1/S & O \\ O & -1/S \end{pmatrix} \delta_{ij}\delta_{\alpha\beta}$$

$$+ \begin{pmatrix} \dfrac{\epsilon_0 S + \Phi S - \omega}{S} & \Psi \\ \Psi & \dfrac{\epsilon_0 S + \Phi S + \omega}{S} \end{pmatrix} \begin{pmatrix} g & \tilde{h} \\ -h & -\tilde{g} \end{pmatrix}_{ij}^{\alpha\beta} \tag{A.8}$$

$$\begin{pmatrix} JgJ & J\tilde{h}J \\ -JhJ & -J\tilde{g}J \end{pmatrix}_{ij}^{\alpha\beta} = \begin{pmatrix} 1/S & O \\ O & -1/S \end{pmatrix} J_{ij}^{\alpha\beta}$$

$$+ \begin{pmatrix} \dfrac{\epsilon_0 S + \Phi S - \omega}{S} & \Psi \\ \Psi & \dfrac{\epsilon_0 S + \Phi S + \omega}{S} \end{pmatrix}$$

$$\times \begin{pmatrix} Jg & J\tilde{h} \\ -Jh & -J\tilde{g} \end{pmatrix}_{ij}^{\alpha\beta}. \tag{A.9}$$

J. Phys. Chem. Solids Pergamon Press 1970. Vol. 31, pp. 1587-1593. Printed in Great Britain.

FORCE-CONSTANT MODELS OF LATTICE VIBRATIONS IN RARE-EARTH HALIDES

G. E. STEDMAN and D. J. NEWMAN
Department of Physics, Queen Mary College, Mile End Road, London E.1., England

(*Received* 13 *October* 1969)

Abstract—Various harmonic force models are used to fit experimental $k = 0$ lattice vibration frequencies in $LaCl_3$, $CeCl_3$, $PrCl_3$ and $LaBr_3$. It is shown that a very approximate model using only two parameters gives a reasonable fit to six or more frequencies. This is not greatly improved by the use of more sophisticated models. The $k = 0$ eigenvector for a particular choice of force constants is also given.

1. INTRODUCTION

THE AIM OF this work is to use simple harmonic force models to fit the experimental lattice vibration frequencies in several rare-earth halides. This has intrinsic interest in that it provides a test of the usefulness of such a model for ionic crystals of low symmetry. However, the main justification for our analysis is that it lays the foundation for a comprehensive study of the interaction between phonons and localized electrons in this material which will be the subject of later publications. The rare-earth halides were chosen with this application in mind; they make very suitable host crystals for the study of rare-earth electronic spectra[1]. Added advantages are the considerable amount of Raman, infrared and vibronic data that has recently become available[2-8] and the previous analysis of $LaCl_3$ lattice vibrations given by Murphy, Caspers and Buchanan[6] (referred to in the following as MCB).

We shall use the same general procedure as MCB, to which the reader is referred for a description of the crystalline structure of the hexagonal rare-earth chlorides and bromides as well as the symmetry coordinates for the $k = 0$ modes. Some changes of sign were found necessary in their table of symmetry coordinates, so a corrected and simplified version of this is repeated as Table 1 of this paper*. It is of interest to use a more general set of parameters than the five force constants defined by MCB. We make $a_4 \neq a_5$ and introduce an extra force constant (a_6) to represent the coupling between pairs of nearest neighbour rare-earth ions in a unit cell. A similar force constant will be appropriate for nearest neighbour rare-earth ions along the c-axis, but this has no observable effect on the $k = 0$ modes. A more radical improvement is made by the use of a 'tensioned' spring model which has additional parameters (d_i) to describe the fractional displacement of ions from the minimum of the quadratic approximation to the potential at the equilibrium position. A total of 12 parameters are then defined in the model, but various constaints are used in the fitting procedures to reduce this to a manageable number.

2. EXPERIMENTAL DATA

There are three sources of experimental data on lattice vibration frequencies. That obtained by Raman spectroscopy is by far the most useful as, in this case, it is relatively easy to find all the observable transitions and to determine their group theoretical assignments. A considerable amount of vibronic

---

*We are grateful to Mr. S. Latner for an independent check of these corrections.

Table 1. *Symmetry coordinate transformation table. All elements have been multiplied by* $\sqrt{6}$. *The same transformation relations hold between either the first or second labels of each pair. Coordinates and degrees of freedom are labelled as in MCB. The coordinates of ions labelled* i + 4 *are given by* $\mathbf{r}_{i+4} = \mathbf{r}_i$ *for* u *representations and* $\mathbf{r}_{i+4} = -\mathbf{r}_i$ *for* g *representations*

Symmetry co-ordinates	C_{6h} reprs	x_1	y_1	x_2	y_2	x_3	y_3	x_4	y_4	z_1	z_2	z_3	z_4
1, 3	A_g, B_u				1	$-\frac{1}{2}\sqrt{3}$	$-\frac{1}{2}$	$\frac{1}{2}\sqrt{3}$	$-\frac{1}{2}$				
2, 4	A_g, B_u			1		$\frac{1}{2}$	$\frac{1}{2}\sqrt{3}$	$-\frac{1}{2}$	$-\frac{1}{2}\sqrt{3}$				
5, 11	E_{2g}, E_{1u}		$\sqrt{3}$										
6, 12	E_{2g}, E_{1u}	$-\sqrt{3}$											
7, 13	E_{2g}, E_{1u}				1		1		1				
8, 14	E_{2g}, E_{1u}			1		1		1					
9, 15	E_{2g}, E_{1u}				1	$\frac{1}{2}\sqrt{3}$	$-\frac{1}{2}$	$-\frac{1}{2}\sqrt{3}$	$-\frac{1}{2}$				
10, 16	E_{1g}, E_{1u}			1		$\frac{1}{2}$	$\frac{1}{2}\sqrt{3}$	$\frac{1}{2}$	$-\frac{1}{2}\sqrt{3}$				
17, 19	A_u, B_g									$\sqrt{3}$			
18, 20	A_u, B_g										1	1	1
21, 23	E_{1g}, E_{2u}										$\sqrt{2}$	$-\frac{1}{2}\sqrt{2}$	$-\frac{1}{2}\sqrt{2}$
22, 24	E_{1g}, E_{2u}											$\frac{1}{2}\sqrt{6}$	$-\frac{1}{2}\sqrt{6}$

data also exists, but not all observed transitions correspond to $k = 0$ excitations and the assignments that can be made are seldom unique. Reflection and absorption experiments have also been made giving values of the infra-red active LO and TO modes.

The difference between the LO and TO frequencies of a mode with a given group theoretical assignment implies a singularity in the dispersion curves at $k = 0$. This is brought about by the long range interactions between electric dipole moments, which are non-zero only in the case of infra-red active modes. No theory exists for a crystal as complex as the anhydrous chlorides which relates the observed LO and TO frequencies with the single frequency (ω_0) predicted by the the harmonic force model. We therefore use, as a working hypothesis, the result obtained by Balkanski[9] for the blende and Wurtzite crystals (which neglects the effects of ionic polarization):

$$\omega_0^2 = \frac{1}{3}(\omega_{L0}^2 + 2\omega_{T0}^2).$$

This formula has been used to estimate values of ω_0 for $PrCl_3$ using the results of Berreman *et al.*[3]. Values of ω_0 for $LaCl_3$ have also been estimated using measured TO frequencies[4–6] and the $PrCl_3$ LO frequencies.

There has been some disagreement in the literature regarding the assignments to be given to the Raman frequencies, but there is good reason to believe that this problem has now been settled. All six Raman frequencies are known for $CeCl_3$[8], $PrCl_3$[5] and $LaBr_3$ [2]; five are known for $LaCl_3$[2, 5] and $NdCl_3$ [5]. The missing $LaCl_3$ E_{2g} mode is probably degenerate with the A_g mode at 175 cm^{-1}. This data is used as the main raw material for the fits to the harmonic oscillator model discussed in the next section (Tables 2–5).

The use of vibronic data is made difficult by the fact that there is very little agreement between the results given by Richman, Satten and Wong[7] and those given by Cohen and Moos[4]. In the latter work definite identifications are only given for those lines already observed by other means, and none of the remaining lines has a possible identification which is at all related to the frequencies predicted by our fits to the Raman data. A useful feature of the work of Richman, Satten and Wong[7] is their attempt to coordinate the corresponding lines of the $LaBr_3$ and $LaCl_3$ spectra. This should be most reliable at the top and bottom of their frequency table. On this basis we accept their values of the B_u frequencies which accord well with our fits in both cases. We also suggest that the low frequency B_g mode should be at 98·1 cm^{-1} in $LaCl_3$ (80·8 cm^{-1} in $LaBr_3$) which Richman et al.[7] identify as a two (B_g) phonon process. This gives a reasonable correspondence with both the $LaCl_3$ and $LaBr_3$ fits.

Table 2. *Force constant analysis of* $LaCl_3$ *data. All frequencies are given in* cm^{-1}. *Force constants* (a_i) *are given in* gcm^{-2}

		Experiment (Wt.)*		2-Parameter fit	4-Parameter fit	5-Parameter fit	Alternative 5-Parameter fit
A_g	(1)	175	(1)	175	182	178	175
	(2)	210	(1)	211	213	211	216
E_{2g}	(1)	106	(1)	82	88	95	85
	(2)	175	(0·7)	172	175	174	170
	(3)	217	(1)	232	231	230	227
E_{1g}		186	(1)	188	191	189	186
A_u		184	(0·5)	189	173	185	190
E_{1u}	(1)	176	(0·5)	149	147	150	147
	(2)	232	(0·5)	216	210	213	227
B_g	(1)	98	(0·3)	89	94	97	83
	(2)			240	237	237	230
B_u	(1)			125	137	133	125
	(2)	248	(0·3)	244	245	241	237
E_{2u}				188	191	189	174
a_1				11·0	10·0	10·8	11·1
a_2				3·6	2·9	2·9	4·1
a_3				11·0	10·0	10·8	11·6
a_4				3·6	2·9	2·9	2·3
a_5				3·6	2·9	2·9	3·8
a_6				(0)	(0)	2·9	(0)
$d_1 = d_3$				(0)	−0·145	−0·072	(0)
$d_2 = d_4 = d_5$				(0)	0·292	0·153	(0)
γ					1·7	1·6	

*We minimise $\Sigma[(\text{Expt}-\text{Theor}) \times \text{Wt.}]^2$.

3. THE FITTING PROCEDURE

The force constant matrix is set up as described in MCB and then block diagonalized by the transformation to symmetry coordinates given in Table 1. It must be emphasised, however, that these symmetry coordinates do *not* give a complete block diagonalization in the sense that each row of each irreducible representation is associated with a separate block. The reason for this is that the two dimensional representations of the unit cell group C_{6h} are not fully reduced, so that the well known theorem on block diagonalization does not fully apply. In fact, any rotation about the c-axis commutes with the two dimensional representations of the generators (C_6 and i) of C_{6h}. Hence, the real symmetry coordinates of two dimensional representations produced by the projection operator method are indeterminate to this extent. This gives rise to extra elements in both the E_{1u} and E_{2g} blocks of the force matrix.

Some restrictions on the twelve parameters defined in Section 1 are required and various possibilities suggested by the X-ray data[10] have been tried. The variation of distance between differently orientated ionic pairs in

Table 3. Force constant analysis of $CeCl_3$ *data. All frequencies are given in* cm^{-1}. *Force constants are given in* $g\,cm^{-2}$

	Experiment	2-Parameter fit	5-Parameter fit
A_g (1)	183	177	181
(2)	216	214	213
E_{2g} (1)	106	83	95
(2)	180	173	178
(3)	218	235	230
E_{1g}	193	189	193
A_u		189	185
E_{1u} (1)		149	152
(2)		219	218
B_g (1)		90	94
(2)		242	243
B_u (1)		125	133
(2)		248	251
E_{2u}		189	193
$a_1 = a_3$		11·0	9·9
$a_2 = a_4 = a_5$		3·7	2·9
a_6		(0)	0·2
$d_1 = d_3$		(0)	−0·040
$d_2 = d_4 = d_5$		(0)	0·030
γ			4·6

the crystal is quite small: e.g. the standard deviations are 1·0 per cent for Cl^- *and 0·6 per cent for* $Nd^{3+}-Cl^-$ *in* $NdCl_3$. *It is therefore not unreasonable to take* $a_6 = 0$, $a_1 = a_3$ *and* $a_2 = a_4 = a_5$ *which, with all* $d_i = 0$, *reduces the total number of parameters to two. (In almost* all cases we have assumed $a_4 = a_5$ which corresponds to the rare-earth ion having a D_{3h} site symmetry. It also makes the E_{1g} and E_{2u} modes degenerate.)

The relative displacements from equilibrium d_i are subject to similar considerations and, in the results quoted in this paper, we have invariably taken $d_1 = d_3$, $d_2 = d_4 = d_5$ and $d_6 = 0$, although this is almost certainly less accurate than the corresponding restrictions on the a_i.

4. RESULTS

Tables 2–5 display the results of force constant analyses carried out for $LaCl_3$, $CeCl_3$, $PrCl_3$ and $LaBr_3$. In all cases other than $LaCl_3$ the fits are made to Raman data alone, but all

Table 4. Force constant analysis of $PrCl_3$ *data. All frequencies are given in* cm^{-1}. *Force constants are given in* $g\,cm^{-2}$

	Experiment	2-Parameter fit	3-Parameter fit	4-Parameter fit	5-Parameter fit
A_g (1)	183	179	176	185	183
(2)	214	215	212	217	215
E_{2g} (1)	106	84	105	90	98
(2)	179	174	176	178	179
(3)	217	237	234	236	232
E_{1g}	198	189	187	193	193
A_u	(192)	187	186	178	183
E_{1u} (1)	(176)	150	148	150	153
(2)	(222)	219	216	216	216
B_g (1)		90	102	95	99
(2)		242	240	240	236
B_u (1)		126	124	138	143
(2)		251	247	250	244
E_{2u}		189	187	192	193
$a_1 = a_3$		10·8	10·7	10·4	10·6
$a_2 = a_4 = a_5$		3·9	3·7	3·1	2·5
a_6		(0)	2·7	(0)	0·5
$d_1 = d_3$		(0)	(0)	−0·117	−0·111
$d_2 = d_4 = d_5$		(0)	(0)	0·227	0·240
γ				1·7	2·0

Table 5. Force constant analysis of $LaBr_3$ *data. All frequencies are given in* cm^{-1}. *Force constants are given in* gcm^{-2}

	Experiment	2-Parameter fit	3-Parameter fit	4-Parameter fit
A_g (1)	116	116	114	122
(2)	138	139	137	143
E_{2g} (1)	83	72	84	79
(2)	139	122	127	124
(3)	146	158	158	159
E_{1g}	122	120	118	124
A_u		139	137	133
E_{1u} (1)		107	106	110
(2)		150	148	147
B_g (1)	(81)	80	88	86
(2)		165	165	164
B_u (1)		80	79	88
(2)	(167)	163	160	166
E_{2u}		119	117	123
$a_1 = a_3$		8·9	8·6	7·8
$a_2 = a_4 = a_5$		4·0	3·9	4·1
a_6		(0)	2·2	(0)
$d_1 = d_3$		(1)	(1)	−0·030
$d_2 = d_4 = d_5$		(1)	(1)	0·016
γ				3·6

derived frequencies are tabulated and in some cases may be compared to (bracketed) experimental data which is not used in the fits. Only five Raman frequencies have been positively identified for $LaCl_3$ so it is useful to use the plentiful data from other sources. Relative weights assigned to the data are given in Table 2.

The most characteristic result is the high accuracy obtained using fits in which only two force constants are varied (one for the metal–ligand and one for the ligand–ligand interaction). The use of a larger number of parameters usually results in only a marginal improvement in the mean square error so that deviations obtained relative to the two parameter fit are probably not very significant. It is found, for example, that the metal–metal force constant a_6 assumes a value which is too large to be physically reasonable unless the parameters d_i are also allowed to vary. In 5-parameter fits of the latter type there is a considerable reduction in the ligand–ligand force constant but little change in the metal–metal constant relative to the two parameter fits; agreement with the lowest E_{2g} frequency is noticeably improved. The alternative 5-parameter fit to $LaCl_3$ data with $d_i = 0$ also gives a reasonable overall fit although in this case agreement with the lowest E_{2g} frequency remains bad. The relative magnitudes of the a_i obtained in this fit bear no particular relationship to the distances between similar pairs of ions and are therefore probably not significant.

The force constants obtained for the three systems $LaCl_3$, $CeCl_3$ and $PrCl_3$ are remarkably consistent, especially in view of the extended set of data used in the $LaCl_3$ analysis Results not quoted here show explicitly that the $LaCl_3$ force constants are insensitive to the number of input data used. The relative magnitude of the metal–metal and metal–halide force constants obtained in our analyses differs considerably from that of MCB. In the $LaBr_3$ the metal–halide force constant is shown to be rather smaller than in the chlorides, but the halide–halide force constant is very similar.

The fractional displacements d_i are constrained to have the correct signs appropriate to each type of bond (i.e. $d_1, d_3 < 0, d_2, d_4, d_5 > 0$). This also makes them of the correct sign to account for the stability of the lattice. An explicit consideration of the forces acting on the halide ion in the plane perpendicular to the c-axis leads to two independent stability equations which are very nearly consistent under the constraints $d_1 = d_3, a_1 = a_3$, $d_2 = d_4 = d_5$ and $a_1 = a_4 = a_5$. These equations give the equilibrium condition

$$\gamma = -d_1a_1/d_2a_2 \sim 1.$$

Calculated values of γ (given in Tables 2–5) are in the range 1·6–4·6. We therefore conclude that the lattice equilibrium cannot be consistently reproduced by our final parameters, the d_i values fluctuate too much during the fitting for the final γ to be very meaningful (although we note that γ is nearer to 1 for larger values of d_i).

A similar attempt was also made to compare results with the equilibrium conditions for stresses in the lattice[11]. In this case, however, it was found impossible to derive consistent equations for the short range force parameters[12]; long range effects are certainly more important in this case.

In Table 6 we give the complete eigenvector for $k = 0$ phonons in the rare-earth chlorides for a particular choice of force constant. This is found to be quite insensitive to the small variation of force constants obtained in the different fits.

In a future publication we shall employ the force constants derived in this paper to determine the elastic constants of the lattice and hence sound velocities and ion–lattice coupling constants.

Table 6. Eigenvector for $\mathrm{k} = 0$ *phonons in the rare-earth chlorides* ($\mathrm{a}_1 = \mathrm{a}_3 = 11{\cdot}0$, $\mathrm{a}_2 = \mathrm{a}_4 = \mathrm{a}_5 = 3{\cdot}6$) *The symmetry coordinate vector* S_i *is defined in Table* 1. $\mathrm{W}_i = \mathrm{S}_i$ *for* $\mathrm{i} = 21$ *to* 24

$$\begin{bmatrix} W_1 \\ W_2 \end{bmatrix} = \begin{bmatrix} -0{\cdot}13 & 0{\cdot}99 \\ 0{\cdot}99 & 0{\cdot}13 \end{bmatrix} \begin{bmatrix} S_1 \\ S_2 \end{bmatrix}$$

$$\begin{bmatrix} W_3 \\ W_4 \end{bmatrix} = \begin{bmatrix} 0{\cdot}49 & 0{\cdot}87 \\ 0{\cdot}87 & 0{\cdot}49 \end{bmatrix} \begin{bmatrix} S_3 \\ S_4 \end{bmatrix}$$

$$\begin{bmatrix} W_5 \\ W_6 \\ W_7 \\ W_8 \\ W_9 \\ W_{10} \end{bmatrix} = \begin{bmatrix} 0{\cdot}87 & 0{\cdot}08 & 0{\cdot}10 & -0{\cdot}13 & 0{\cdot}41 & 0{\cdot}19 \\ 0{\cdot}08 & 0{\cdot}87 & -0{\cdot}13 & 0{\cdot}10 & 0{\cdot}19 & -0{\cdot}41 \\ 0{\cdot}24 & 0{\cdot}33 & 0{\cdot}73 & 0{\cdot}15 & 0{\cdot}07 & 0{\cdot}52 \\ 0{\cdot}33 & -0{\cdot}24 & 0{\cdot}15 & -0{\cdot}73 & 0{\cdot}52 & -0{\cdot}07 \\ 0{\cdot}19 & -0{\cdot}16 & -0{\cdot}13 & 0{\cdot}63 & 0{\cdot}71 & -0{\cdot}07 \\ 0{\cdot}16 & 0{\cdot}19 & 0{\cdot}63 & -0{\cdot}13 & 0{\cdot}07 & 0{\cdot}72 \end{bmatrix} \begin{bmatrix} S_5 \\ S_6 \\ S_7 \\ S_8 \\ S_9 \\ S_{10} \end{bmatrix}$$

$$\begin{bmatrix} W_{11} \\ W_{12} \\ W_{13} \\ W_{14} \\ W_{15} \\ W_{16} \end{bmatrix} = \begin{bmatrix} 0{\cdot}75 & 0 & 0{\cdot}66 & 0 & 0 & 0 \\ 0 & 0{\cdot}75 & 0 & 0{\cdot}66 & 0 & 0 \\ 0{\cdot}51 & -0{\cdot}08 & 0{\cdot}59 & -0{\cdot}09 & -0{\cdot}17 & 0{\cdot}58 \\ 0{\cdot}08 & 0{\cdot}51 & 0{\cdot}09 & 0{\cdot}59 & -0{\cdot}58 & -0{\cdot}17 \\ 0{\cdot}11 & 0{\cdot}38 & 0{\cdot}13 & 0{\cdot}44 & 0{\cdot}78 & 0{\cdot}12 \\ 0{\cdot}38 & 0{\cdot}11 & -0{\cdot}44 & 0{\cdot}13 & -0{\cdot}12 & -0{\cdot}78 \end{bmatrix} \begin{bmatrix} S_{11} \\ S_{12} \\ S_{13} \\ S_{14} \\ S_{15} \\ S_{16} \end{bmatrix}$$

$$\begin{bmatrix} W_{17} \\ W_{18} \end{bmatrix} = \begin{bmatrix} 0{\cdot}75 & 0{\cdot}65 \\ 0{\cdot}65 & 0{\cdot}75 \end{bmatrix} \begin{bmatrix} S_{17} \\ S_{18} \end{bmatrix}$$

$$\begin{bmatrix} W_{19} \\ W_{20} \end{bmatrix} = \begin{bmatrix} -0{\cdot}92 & 0{\cdot}39 \\ 0{\cdot}39 & 0{\cdot}92 \end{bmatrix} \begin{bmatrix} S_{19} \\ S_{20} \end{bmatrix}$$

Acknowledgements – G. E. S. is grateful to the Science Research Council for a Research Assistantship.

REFERENCES

1. DIEKE G. H., *Spectra and Energy Levels of Rare-Earth Ions in Crystals* Interscience, New York (1968).
2. ASAWA C. K., SATTEN R. A. and STAFSUDD O. T., *Phys. Rev.* **168**, 957 (1968).
3. BERREMAN D. W., UNTERWALD F. C. and VARSANYI F., *Bull. Am. phys. Soc.* **12**, 372 (1967).
4. COHEN E. and MOOS H. W., *Phys. Rev.* **161**, 258 and 268 (1967).
5. HOUGEN J. T. and SINGH S., *Proc. R. Soc. Lond.* **A277**, 193 (1964).
6. MURPHY J., CASPERS H. H. and BUCHANAN R. A., *J. chem. Phys.* **40**, 743 (1964).
7. RICHMAN I., SATTEN R. A. and WONG E., *J. chem. Phys.* **39**, 1833 (1963)
8. KIEL A., DAMEN T., PORTO S. P. S., SINGH S. and VARSANYI F., *Phys. Rev.* **178**, 1518 (1969).
9. BALKANSKI M., *Elementary Excitations in Solids* (Edited by G. Nardelli), NATO Advanced Study Institute, Cortina. Plenum Press, New York (1969).
10. MOROSIN B., *J. chem. Phys.* **49**, 3009 (1968).
11. BORN M. and HUANG K., *Dynamical Theory of Crystal Lattices*. Clarendon Press, Oxford (1964)
12. STEDMAN G. E., Thesis, London (1968)

c

r

l

J. Phys. Chem. Solids Pergamon Press 1970. Vol. 31, pp. 1595–1611. Printed in Great Britain.

ANHARMONIC WIDTHS AND SHIFTS IN SIMPLE METALS. APPLICATION TO ALUMINIUM

ROLF SANDSTRÖM
Department of Theoretical Physics, Royal Institute of Technology, S-100 44 Stockholm 70, Sweden

and

THURE HÖGBERG
AB Atomenergi, Studsvik, Fack, S-611 01 Nyköping 1, Sweden

(*Received 7 April 1969; in revised form 23 July 1969*)

Abstract—The theory of the anharmonic effects in a coupled electron–phonon system is presented and applied to free-electron metals. The phonon self-energy is evaluated by means of a diagram expansion and the choice of diagrams which must be retained is carefully investigated. It is shown that the anharmonic terms can be described by the same effective potential that is used to obtain the harmonic frequencies. Further, it is found that for free-electron metals it is quite satisfactory to include only terms of the lowest order in the ion–electron potential. Calculations have been made for the phonon widths at 80° and 300°K in aluminium. The quasiharmonic, third order and fourth order shifts are taken into account. Results are presented for two local ion-electron potentials. One is given by Johnson and Westin and the other by Schneider and Stoll, both are obtained by fitting the potential to the harmonic frequencies. The calculated values are compared with the experimental results of Stedman *et al.* The widths are found to be in agreement with the experimental values in most cases. For the Johnson–Westin potential this is also true for the shifts.

1. INTRODUCTION

CALCULATIONS of phonon widths have been presented in several papers[1–4].

The theory for anharmonic widths and shifts in dielectric solids is presented e.g. by Maradudin and Fein[1] who have also carried out calculations for a nearest neighbour central-potential model for Pb. Cowley *et al.*[2, 3] have calculated widths and several other anharmonic properties for the alkali halides KBr and NaI, using a shell model. Bohlin and Högberg[4] have used a Leonard-Jones potential to obtain widths for rare gas solids and for Al. In one communication[5] the Bohlin–Högberg results are compared with some of the present calculations. As far as the authors are aware, the only fairly complete set of measurements of widths and shifts has been made by Stedman *et al.*[6] for Al.

In principle, a Born–von Karman model can yield phonon frequencies which are as accurate as is desired for a metal, however, it is believed (see e.g. [7, 8]) that the actual forces are of a quite different long-range nature. A number of authors have used pseudo-potentials to obtain phonon frequencies with both non-local and local potentials. The non-local potential is usually obtained from the atomic wave-functions (e.g. [9, 10]). The local pseudo-potential has a few parameters which are in most cases fitted to the dispersion curves (e.g. [9, 11, 12]). Some of these fitted potentials describe the phonon frequencies with good accuracy.

The theory of the metallic electron–phonon system is not greatly altered by the use of a non-local rather than a local ion–electron potential. It has therefore been decided to use a local potential, since the formalism is then somewhat simplified. In the theoretical section of this paper, the many body theory is used to show that the anharmonic terms can be described by the same effective ion–ion potential as is used in the harmonic approximation. This turns out to be a result of some generality. It is also shown that for free electron metals the ion–electron potential can be estimated satisfactorily by taking into account only the lowest order terms. This is also confirmed by comparison with calculations of higher order contributions to the harmonic frequencies, made by R. Johnson[12]. (Since his results have not been published, one example is presented here.)

This result has been used to calculate the line widths at 80° and 300°K and the shifts between 80° and 300°K for Al, and to compare them with the experimental values. The local potentials used are taken from Johnson and Westin[12] and Schneider and Stoll[11]. The formalism and results are presented in section 3. For the evaluation of widths and shifts the summations have been made over approx. 4000 points in the first Brillouin zone and 25 shells in the reciprocal lattice. For both the harmonic frequencies and the anharmonic terms, the Coulombic part is obtained by the use of Ewald summation. Some numerical details are presented in section 4. Finally the results are discussed in section 5.

2.a *The model*

The following usual assumptions are made:

(1) The metal comprises a Bravais lattice of rigid ions with Z conduction electrons for each ion.

(2) The so-called 'small core' approximation applies, that is the overlap between the ions is so small that it can be approximated by a local potential. The remainder of the direct ion–ion interaction consists only of the Coulomb interaction between point charges.

(3) The ion–electron potential $v(q)$ is local. The assumption of a *local* potential simplifies the formalism, but the extent of the numerical calculations would not have been changed drastically if methods similar to those of Vosko *et al.*[10] had been used. Vosko *et al.* found that the non-local potential could be satisfactorily approximated by a local potential for small values of

$$q\left(q \leq 2\cdot\frac{2\pi}{a}\right).$$

(4) $|v(q)|/E_F \ll 1$ for $q > k_F$ where k_F is the fermi momentum, so that $v(q)/E_F$ can be used as an expansion parameter.

(5) The anharmonic expansion is valid. This means that the system must not be too close to a phase transition.

The following Hamilton operator is obtained:

$$H = -\sum \frac{\hbar^2}{2M}\nabla_N{}^2 - \sum \frac{\hbar^2}{2m}\nabla_n{}^2 + \underbrace{\tfrac{1}{2}{\sum}' \Phi(\mathbf{R}_{N_1}-\mathbf{R}_{N_2})}_{\text{ion–ion part}} + \underbrace{\tfrac{1}{2}{\sum}' \frac{e^2}{|\mathbf{r}_{n_1}-\mathbf{r}_{n_2}|}}_{\text{electron–electron part}} + \underbrace{\sum_{n,N} v(\mathbf{r}_n-\mathbf{R}_N)}_{\text{ion-electron part}} \qquad (2.1)$$

$\mathbf{R}_N(\mathbf{r}_N)$ is the position of the N'th ion (electron). $M(m)$ is the mass of an ion (electron). The following notations are introduced (the inclusion of a constant part U_0 leads the different contributions to correspond to a stable lattice):

$$\Phi = \tfrac{1}{2}\sum_{N_1,N_2}{}' \frac{e^2Z^2}{|\mathbf{R}_{N_1}-\mathbf{R}_{N_2}|} - \frac{U_0}{2}$$

$$V_e = \tfrac{1}{2}\sum_{n_1,n_2}{}' \frac{e^2}{|\mathbf{r}_{n_1}-\mathbf{r}_{n_2}|} - \frac{U_0}{2}$$

$$V = \sum_{n,N} v(\mathbf{r}_n - \mathbf{R}_N) + U_0. \qquad (2.2)$$

An effective ion–ion potential Φ^E is also introduced; this is used to determine the harmonic frequencies and

$$F = \Phi^E - \Phi. \qquad (2.3)$$

The different potentials are expanded as usual around the equilibrium positions $\mathbf{X}_N = \mathbf{R}_N - \mathbf{u}_N$. $u_{\alpha_1 N_1}$ is written as $u(1)$.

$$\Phi+V=\Phi^{E}+V-F=\Phi_0{}^{E}+\sum_1 \Phi^{E}(1)u(1)+\dots$$
$$+V_0+\sum_1 V(1)u(1)+\tfrac{1}{2}\sum V(1,1)u^2(1)+\dots$$
$$-F_0-\sum F(1)u(1)-\tfrac{1}{2}\sum F(1,2)u(1)u(2)-\dots \quad (2.4)$$

with the conventional notation $F(1,2)=\frac{\partial^2 F}{\partial u(1)\partial u(2)}$ etc. taken at the equilibrium positions. Thus

$$H_{\text{harm}}=\tfrac{1}{2}\sum_{1,2}\Phi^{E}(1,2)u(1)u(2). \quad (2.5)$$

Expressed in phonon variables and electron operators this gives

$$H_{\text{harm}}=\sum_{\lambda}\hbar\omega(\lambda)(n(\lambda)+\tfrac{1}{2}) \quad (2.6)$$
$$H=H_0+H_{\text{anh}}$$

where

$$H_0=\sum_{\mathbf{k}}\hbar\epsilon_0(k)c_{\mathbf{k}}{}^{+}c_{\mathbf{k}}+H_{\text{harm}} \quad (2.7\text{a})$$

and

$$H_{\text{anh}}=\underline{\sum \Phi^{E}(\lambda_1)A_{\lambda_1}}+\tfrac{1}{6}\sum\Phi(\lambda_1,\lambda_2,\lambda_3)$$
$$\times A_{\lambda_1}A_{\lambda_2}A_{\lambda_3}$$
$$+\frac{1}{24}\sum_{\lambda_1\lambda_2\lambda_3\lambda_4}\Phi(\lambda_1,\lambda_2,\lambda_3,\lambda_4)A_{\lambda_1}A_{\lambda_2}A_{\lambda_3}A_{\lambda_4}$$
$$+\dots+\sum_{\mathbf{k},\mathbf{g}}{}' V(-\mathbf{k},\mathbf{k}+\mathbf{g})c^{+}_{\mathbf{k}+\mathbf{g}}c_{\mathbf{k}}$$
$$+\sum_{\mathbf{k}\mathbf{q}\lambda_1}V(-\mathbf{k},\mathbf{k}+\mathbf{q},\lambda_1)c^{+}_{\mathbf{k}+\mathbf{q}}c_{\mathbf{k}}A_{\lambda_1}+\dots$$
$$+\tfrac{1}{2}\frac{1}{\Omega}\sum_{\mathbf{k}_1\mathbf{k}_2\mathbf{q}}c^{+}_{\mathbf{k}_1}c^{+}_{\mathbf{k}_2}V_q{}^{c}c_{\mathbf{k}_2+\mathbf{q}}c_{\mathbf{k}_1-\mathbf{q}}$$
$$\underline{-\sum_{\lambda_1}F(\lambda_1)A_{\lambda_1}}-\tfrac{1}{2}\sum F(\lambda_1,\lambda_2)A_{\lambda_1}A_{\lambda_2}. \quad (2.7\text{b})$$

Details of the notation are explained in Appendix A. Since both Φ^{E} and F represent potentials in a Bravais lattice (which always has inversion symmetry) and we have made an expansion around the equilibrium positions the underlined terms vanish. Note that F is expanded only to second order.

2.b *Diagram expansion*

If the anharmonic shifts $\Delta(\lambda,\omega)$ and half-widths $\Gamma(\lambda,\omega)$ are small as compared with the harmonic frequency $\omega(\lambda)$ then (see [1])

$$\lim_{\delta\to+0}-\Sigma(\lambda,\omega+i\delta)=\Delta(\lambda,\omega)\mp i\Gamma(\lambda,\omega) \quad (2.8\text{a})$$

where $\Sigma(\lambda,+i\omega_l)$ is the diagonal part of the phonon self-energy defined from

$$G(\lambda,i\omega_l)=\frac{2\omega(\lambda)}{\omega_l{}^2+\omega^2(\lambda)-2\omega(\lambda)\Sigma(\lambda,i\omega_l)}. \quad (2.8\text{b})$$

To obtain Σ a diagram expansion is made, and H_0 as defined in equation (2.7a) is taken as a zero approximation. The harmonic and the Hartree approximations are included in H_0. The phonon and electron propagators are defined in Appendix A. Some of the lowest order diagrams are shown in Fig. 1. The different propagators and vertices are explained in the diagram dictionary in Appendix B. Zero momentum transfer diagrams of type A and B disappear (they are cancelled exactly by the contributions from U_0). Further, in Fig. 2(a) the notation for the screened polarization is introduced, where $\epsilon_0(q,\omega)$ is the ordinary Hartree dielectric function. The equation in Fig. 2(b) is obtained in the same way. The value at the screening ring indicates which dielectric function should be used.

The number of *screened* electron–electron interaction lines in a diagram is referred to as the electron–electron order. In order to clarify

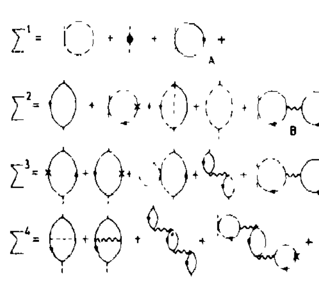

Fig. 1. Phonon self-energy parts of different orders. The diagrams marked A and B vanish (see text).

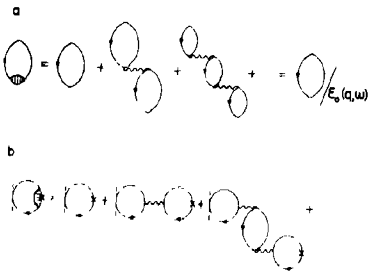

Fig. 2(a, b) Notation for screening.

the discussion, two further numbers are associated with each diagram: the *anharmonic degree* and the *electron–lattice number*. The anharmonic degree of a diagram is obtained by cutting off all the phonon lines. The separate diagram parts are then denoted phonon vertices. The anharmonic degree of a vertex is given as the number of phonon lines which emerge minus two (see [1]). The electron-lattice number of a phonon vertex is given as the number of factors $v(q)$ minus two. This is a convenient measure of the size of a diagram, since for each increasing electron–lattice order the diagram is roughly multiplied by a factor $|v(q)|/E_F$ for $q \sim k_F$ (see Abrikosov *et al.* [13]).

The contributions from all vertices are summed and give the total anharmonic degree and electron–lattice number. The question then arises as to what kind of higher electron–electron order diagrams should be retained in the polarization part. This point has been dealt with in great detail in the literature (see [10] for references). It has been found that these diagrams are not negligible, but since the actual evaluation of such diagrams would be extremely lengthy some approximation recipes have been developed. In the present calculations one of the standard methods has been chosen (see next section).

The introduction of the potential F enables us to obtain not only the anharmonic terms but also the harmonic frequencies. We can choose F (which up to now has not been determined) to cancel an arbitrary number of the diagrams of zero anharmonic degree. All these diagrams will then be included in the harmonic approximation. Since we want F as a non-retarded potential we only pick out ω independent diagrams. The conventional choice for harmonic frequencies in free electron metals is obtained if we take the diagrams in Fig. 3(a). To see this we evaluate the different diagrams in Fig. 3(a) using the diagram dictionary in Appendix B. We also use the formula following equation (2.11) which is straightforward to deduce. We thus get for the different parts in Fig. 3(a)

$$\sum \frac{N^2}{\Omega^2}\left(\frac{\hbar}{2MN}\right)(-i)^2 v^2(\mathbf{q}+\mathbf{g})\frac{|(\mathbf{q}+\mathbf{g}).\mathbf{e}(\mathbf{q}j)|^2}{\omega(\mathbf{q}j)}$$

$$\cdot\Omega\frac{1}{\hbar}\frac{(\mathbf{q}+\mathbf{g})^2}{4\pi e^2}\frac{(\epsilon_0(\mathbf{q}+\mathbf{g},0)-1)}{\epsilon_0(\mathbf{q}+\mathbf{g},0)};$$

$$\sum_{\mathbf{g}}{}'\left(\frac{N}{\Omega}\right)^2\left(\frac{\hbar}{2MN}\right)(-i)^2 v^2(\mathbf{g})\frac{|\mathbf{g}\mathbf{e}(\mathbf{q}j)|^2}{\omega(\mathbf{q}j)}$$

$$\cdot\Omega\frac{1}{\hbar}\frac{g^2}{4\pi e^2}\frac{(\epsilon_0(\mathbf{g},0)-1)}{\epsilon_0(\mathbf{g},0)};$$

$$\sum_{\alpha_1\alpha_2}-\frac{N^2}{\Omega}\frac{1}{2MN}$$

$$\cdot\left\{\sum_{\mathbf{g}}(\mathbf{q}+\mathbf{g})_{\alpha_1}(\mathbf{q}+\mathbf{g})_{\alpha_2}F(\mathbf{g}+\mathbf{q})-\sum_{\mathbf{g}}{}'\mathbf{g}_{\alpha_1}\mathbf{g}_{\alpha_2}F(\mathbf{g})\right\}$$

$$\cdot\frac{e_{\alpha_1}(\mathbf{q}j)e_{\alpha_2}(\mathbf{q}j)}{\omega(\mathbf{q}j)}.$$

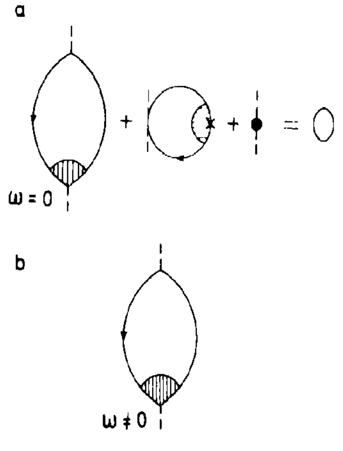

Fig. 3. (a) Diagrams which must be included in the harmonic approximation. (b) Self-energy contribution from the polarization part.

The equation in Fig. 3(a) thus gives

$$F(q)=-\frac{q^2}{4\pi e^2}v^2(q)\frac{\epsilon_0(q,0)-1}{\epsilon_0(q,0)}. \quad (2.9a)$$

The harmonic frequencies are determined from the potential $\Phi^E(q)$ and

$$\Phi^E(q)=\Phi(q)+F(q)=\Phi(q)-\frac{q^2}{4\pi e^2}\cdot v^2(q)\frac{\epsilon_0(q,0)-1}{\epsilon_0(q,0)} \quad (2.9b)$$

which is the expected result. It is essential to include the contribution from the imaginary part of the diagram in Fig. 3(b). This contribution is evaluated and discussed for the case of Al by Björkman *et al.*[14] and Johnson[15]. Johnson has also estimated the imaginary part of the diagrams in Fig. 8 and found that, as expected, they are negligible.

The anharmonic expansion for $T < T_{\text{Debye}}$ is believed to be rapidly convergent, as confirmed by the present and by earlier calculations; this justifies the step of taking into account only the lowest order diagrams for anharmonicity. The numerical evaluation of higher order diagrams would be extremely lengthy. Since there are no diagrams of degree 1, all diagrams of degree 2 are retained. Some diagrams of anharmonic degree 2 are then drawn in Fig. 4(a) and (b), with the electron-lattice numbers 0 and 1 respectively.

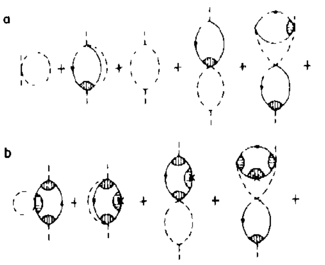

Fig. 4. Some diagrams of lowest anharmonic order. (a) Diagrams with electron-lattice number 0. (b) Diagrams with electron-lattice number 1.

It can be seen that even for the lowest anharmonic and electron-lattice orders there are quite a few diagrams. In order to simplify the notation, the three-phonon vertex is introduced in Fig. 5(a) and the four-phonon vertex in Fig. 5(b). The figures in the vertex, triangle and square refer to the electron-lattice number. To a close approximation, ω can be put equal to zero for the polarization in the vertex part. All the diagrams of anharmonic degree 2 are written as in Fig. 6. These are now of the same form as the corresponding terms for a dielectric solid, and it will be shown here that these vertices can be deduced from the same effective ion-ion potential as that used in the harmonic case. To illustrate this, the different terms in the three-phonon vertex are evaluated as an example. For the notation see Appendix A and B.

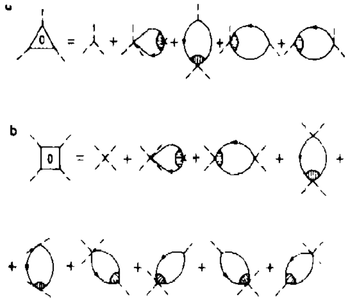

Fig. 5. Three and four phonon vertices with electron-lattice number 0

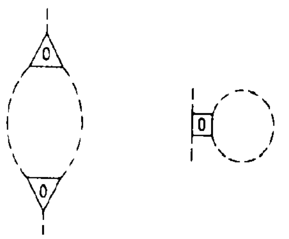

Fig. 6. All diagrams to lowest anharmonic and electron-lattice order.

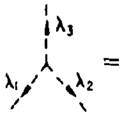

$$= V(\lambda_1,\lambda_2,\lambda_3) = \left(\frac{\hbar}{2MN}\right)^{3/2} \sum_{1,2,3} \frac{\Phi(1,2,3)e^{i(\mathbf{q}_1\cdot\mathbf{R}_1+\mathbf{q}_2\cdot\mathbf{R}_2+\mathbf{q}_3\cdot\mathbf{R}_3)}}{[\omega(\lambda_1)\omega(\lambda_2)\omega(\lambda_3)]^{1/2}} \cdot e_{\alpha_1}(\lambda_1)e_{\alpha_2}(\lambda_2)e_{\alpha_3}(\lambda_3)$$

$$= \left(\frac{\hbar}{2MN}\right)^{3/2} \frac{N^2}{\Omega} \sum_q (-i)^3 \frac{\mathbf{q}\cdot\mathbf{e}(\lambda_1)\mathbf{q}\cdot\mathbf{e}(\lambda_2)\mathbf{q}\cdot\mathbf{e}(\lambda_3)}{[\omega(\lambda_1)\omega(\lambda_2)\omega(\lambda_3)]^{1/2}} \Phi(q)\left(-\frac{1}{\hbar}\right)$$

$$\{\Delta(\mathbf{q}_1-\mathbf{q})+\Delta(\mathbf{q}_2-\mathbf{q})+\Delta(\mathbf{q}_3-\mathbf{q})\}\,\Delta(\mathbf{q}_1+\mathbf{q}_2+\mathbf{q}_3) \quad (2.10)$$

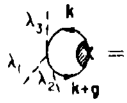

= 0 because the **g** and the − **g** parts cancel

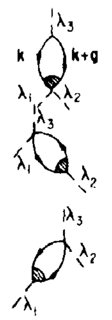

$$= \frac{N^2}{\Omega}\left(\frac{\hbar}{2MN}\right)^{3/2} \sum_q (-i)^3(-1)|v_q|^2$$

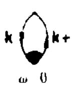

$$\frac{\mathbf{q}\cdot\mathbf{e}(\lambda_1)\mathbf{q}\cdot\mathbf{e}(\lambda_2)\mathbf{q}\cdot\mathbf{e}(\lambda_3)}{[\omega(\lambda_1)\omega(\lambda_2)\omega(\lambda_3)]^{1/2}}$$

$$\begin{Bmatrix} \Delta(+\mathbf{q}+\mathbf{q}_1+\mathbf{q}_2)\Delta(\mathbf{q}-\mathbf{q}_3) \\ -\Delta(+\mathbf{q}+\mathbf{q}_2)\Delta(-\mathbf{q}+\mathbf{q}_1+\mathbf{q}_3) \\ -\Delta(+\mathbf{q}+\mathbf{q}_1)\Delta(-\mathbf{q}+\mathbf{q}_2+\mathbf{q}_3) \end{Bmatrix} \quad (2.11)$$

since

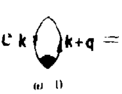

$= \frac{1}{\hbar}\frac{q^2\Omega}{4\pi e^2}\left(\frac{\epsilon_0(q,0)-1}{\epsilon_0(q,0)}\right)$ the effective vertex potential is

$$\Phi(q) - \frac{q^2v^2(q)}{4\pi e^2}\frac{\epsilon_0(q,0)-1}{\epsilon_0(q,0)}$$

and this is the same as the harmonic potential. The same could easily be shown for the four-phonon vertex.

We thus obtain the total contributions to the three- and four-phonon vertex in Fig. 5 as

$$\Phi^{T}(\lambda_1,\lambda_2,\lambda_3) = \left(\frac{\hbar}{2MN}\right)^{3/2}\frac{N^2}{\Omega}\sum_q (-i)^3 \frac{\mathbf{q}\cdot\mathbf{e}(\lambda_1)\mathbf{q}\cdot\mathbf{e}(\lambda_2)\mathbf{q}\cdot\mathbf{e}(\lambda_3)}{[\omega(\lambda_1)\omega(\lambda_2)\omega(\lambda_3)]^{1/2}}$$

$$\cdot\left[\Phi(q) - \frac{q^2}{4\pi e^2}v^2(q)\frac{\epsilon_0(q,0)-1}{\epsilon_0(q,0)}\right]\{\Delta(\mathbf{q}_1-\mathbf{q})+\Delta(\mathbf{q}_2-\mathbf{q})+\Delta(\mathbf{q}_3-\mathbf{q})\}$$

$$.\,\Delta(\mathbf{q}_1+\mathbf{q}_2+\mathbf{q}_3) \quad (2.12)$$

$$\Phi^{F}(\lambda_1,\lambda_2,\lambda_3,\lambda_4) = \left(\frac{\hbar}{2MN}\right)^{4/2}\frac{N^2}{\Omega}\sum_q i^4 \frac{\mathbf{q}\cdot\mathbf{e}(\lambda_1)\mathbf{q}\cdot\mathbf{e}(\lambda_2)\mathbf{q}\cdot\mathbf{e}(\lambda_3)\mathbf{q}\cdot\mathbf{e}(\lambda_4)}{[\omega(\lambda_1)\omega(\lambda_2)\omega(\lambda_3)\omega(\lambda_4)]^{1/2}}$$

$$\left[\Phi(q) - \frac{q^2}{4\pi e^2}v^2(q)\frac{\epsilon_0(q,0)-1}{\epsilon_0(q,0)}\right]\{\Delta(\mathbf{q}) - \Delta(\mathbf{q}+\mathbf{q}_4) - \Delta(\mathbf{q}+\mathbf{q}_3) - \Delta(\mathbf{q}+\mathbf{q}_2)$$

$$-\Delta(\mathbf{q}+\mathbf{q}_1)+\Delta(\mathbf{q}+\mathbf{q}_3+\mathbf{q}_1)+\Delta(\mathbf{q}+\mathbf{q}_3+\mathbf{q}_2)+\Delta(\mathbf{q}+\mathbf{q}_2+\mathbf{q}_4)\}\,\Delta(\mathbf{q}_1+\mathbf{q}_2+\mathbf{q}_3+\mathbf{q}_4). \quad (2.13)$$

The lowest order anharmonic contributions (Fig. 6) take the form

$$\sum^{3}(\lambda, i\omega_l) = \frac{1}{\hbar^2}\tfrac{1}{2}\sum_{\lambda_1\lambda_2}|\Phi^E(-\lambda,\lambda_1,\lambda_2)|^2\frac{1}{\beta}\sum_{i\omega_l=i\omega_{l_1}+i\omega_{l_2}} D_0(\lambda_1, i\omega_{l_1})\,D_0(\lambda_2, i\omega_{l_2}) \qquad (2.14)$$

$$\sum^{4}(\lambda, i\omega_l) = -\frac{1}{\hbar}\tfrac{1}{2}\sum_{l_1}\Phi^E(\lambda,\lambda_1,-\lambda,-\lambda_1)\frac{1}{\beta}\sum_{i\omega_{l_1}} D_0(\lambda_1, i\omega_{l_1}). \qquad (2.15)$$

These results are now formally identical to the results for a dielectric solid if the effective potential Φ^E is changed to an atom–atom potential (see [1]).

Terms with electron-lattice number 1 are next considered. The diagrams in Fig. 7 must now be included in the polarization part, giving

$$\epsilon_1(q,\omega) = \epsilon_0(q,\omega) + \frac{4\pi e^2\hbar}{q^2\Omega}. \text{ [Diagrams in Fig. 7]}$$

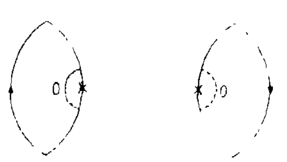

Fig. 7. The unscreened polarization parts with electron-lattice number 1

The corresponding diagrams in the harmonic approximation are given in Fig. 8(a). It is equally possible to use the diagrams in Fig. 8(b) to the same order of expansion, which seems more systematic. The anharmonic vertices are presented in Figs. 9 and 10. These vertices (as well as those of higher electron-lattice order) can also be deduced from a (many-body) potential. Thus for the diagrams in Figs. 9 and 10 a three-body potential is needed.

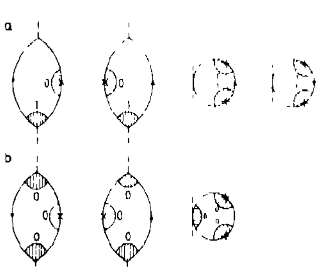

Fig. 8 Diagrams with electron-lattice number 1 which contribute in the harmonic approximation.

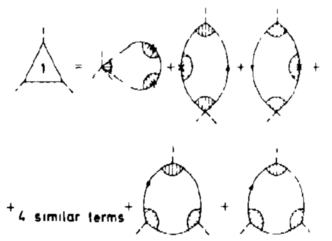

Fig. 9 The three phonon vertex with electron-lattice number 1.

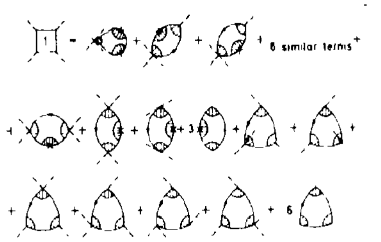

Fig. 10 The four phonon vertex with electron-lattice number 1

Now follows a comparison of the size of the first order diagrams with that of the zero order diagrams. Al is taken as an example since calculations have been performed of its higher order terms. All potentials we used for Al satisfy the expression

$$|v(q)| \lesssim 0{\cdot}1\, E_F \text{ for } q > k_F$$

which means that terms will be roughly a magnitude smaller for each increasing electron–lattice order. Johnson [12] has calculated the harmonic frequencies for Al, and he has included diagrams of the type shown in Fig. 8.

The results for one potential with and without the first order terms are plotted in Fig. 11, where it can be seen that the difference is roughly 15 per cent of the experimental value. The harmonic frequencies were fitted when the first order terms were included. Such a calculation is very time consuming and cannot be carried out particularly accurately. Johnson has also included second order diagrams and has found that their contribution is of the order of a few per cent. These results are also plotted in Fig. 11. It thus appears that the simple rule for estimating the size of vertices is quite reasonable. Since there are two vertices in the third order anharmonic terms, the first order diagrams are roughly 30 per cent of the zero order diagrams. For the fourth order anharmonic terms the corresponding figure is 15 per cent.

To sum up, it has been seen that for $T < T_{\text{Debye}}$ the important contributions to the self-energy consist of two parts. These are the lowest order anharmonic terms and the imaginary part of the polarization (Fig. 3(b)). The anharmonic terms are obtained using the same potential as in the harmonic case. It is found that if the ion–electron potential is obtained by fitting the harmonic frequencies it is essential to use the same electron–lattice order in the harmonic and in the various anharmonic vertices. This result will probably be easy to apply in a generalised form for other physical situations where coupling between quasi-particles is involved. It also appears probably that a complete inclusion of first order terms will affect the anharmonic terms by ≤ 5 per cent, which is far below the present-day level of instrumental resolution. These conclusions all apply to anharmonic calculations where the combination of ion–electron potential and dielectric function applies in the same way as for the harmonic case. The changes in the fitted ion–electron potential and in the dielectric function which are observed when first order terms are included may not cancel. They might even operate in the same direction if they are used to calculate other properties. In such cases the inclusion of first (and eventually higher) order terms is essential even in free electron metals such as Al which have an expansion parameter $|v(q)/E_f| \gtrsim 0{\cdot}05$ for $q \approx k_F$.

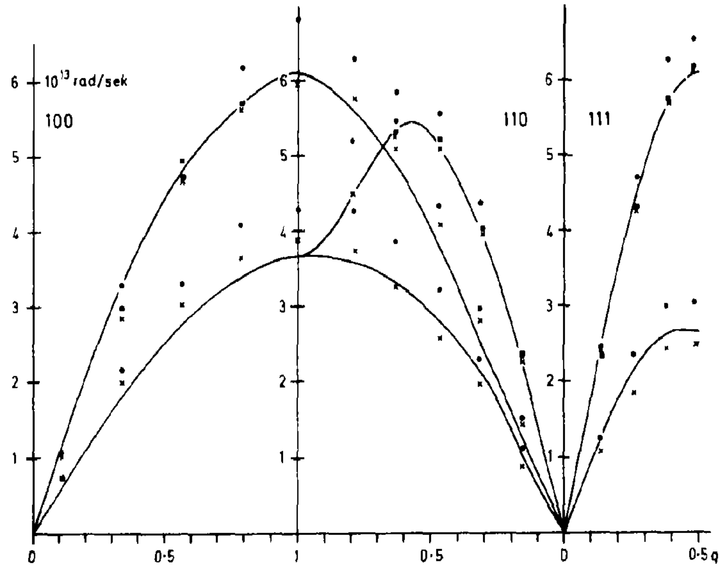

Fig. 11 Higher electron–lattice order contributions to the harmonic frequencies (from [12]) Dots, only the zero order terms; crosses, including first order terms; squares, including second order terms.

3. FORMALISM FOR THE CALCULATIONS

In these calculations, widths $\Gamma(\lambda,\omega)$ and shifts $\Delta(\lambda,\omega)$ have been evaluated to the lowest anharmonic and electron-lattice order. Using equations (2.8, 2.14 and 2.15) carrying out the sum over l_1 we obtain (see also [1])

$$\Gamma(\lambda,\omega)=\frac{\pi\hbar}{16N\omega(\lambda)}\sum_{\lambda_1\lambda_2}\Delta(\mathbf{q}+\mathbf{q}_1+\mathbf{q}_2)$$

$$\cdot\frac{1}{\omega(\lambda_1)\omega(\lambda_2)}$$

$$\cdot\left|\Phi^E(\lambda,\lambda_1,\lambda_2)\right|^2\{[n(\lambda_1)+n(\lambda_2)+1]$$

$$[\delta(\omega-\omega(\lambda_1)-\omega(\lambda_2))$$

$$-\delta(\omega+\omega(\lambda_1)+\omega(\lambda_2))]$$

$$+[n(\lambda_1)-n(\lambda_2)]$$

$$.[\delta(\omega+\omega(\lambda_1)-\omega(\lambda_2))$$

$$-\delta(\omega-\omega(\lambda_1)+\omega(\lambda_2))]\}$$

$$\Delta^4(\lambda,\omega)=\frac{\hbar}{8N\omega(\lambda)}\sum_{\lambda_1}\frac{\Phi^E(-\lambda,\lambda,-\lambda_1,\lambda_1)}{\omega(\lambda_1)}$$

$$.(2n(\lambda_1)+1)$$

$$\Delta^3(\lambda,\omega)=\frac{\hbar}{16N\omega(\hbar)}\sum_{\lambda_1\lambda_2}\Delta(\mathbf{k}+\mathbf{k}_1+\mathbf{k}_2)$$

$$.\frac{\left|\Phi^E(\lambda,\lambda_1,\lambda_2)\right|^2}{\omega(\lambda_1)\omega(\lambda_2)}$$

$$\cdot\left\{\frac{(n(\lambda_1)+n(\lambda_2)+1)}{(\omega-\omega(\lambda_1)-\omega(\lambda_2))_p}\right.$$

$$-\frac{(n(\lambda_1)+n(\lambda_2)+1)}{(\omega+\omega(\lambda_1)+\omega(\lambda_2))_p}$$

$$+\frac{n(\lambda_1)-n(\lambda_2)}{(\omega+\omega(\lambda_1)-\omega(\lambda_2))_p}$$

$$\left.-\frac{n(\lambda_1)-n(\lambda_2)}{(\omega-\omega(\lambda_1)+\omega(\lambda_2))_p}\right\} \qquad (3.1)$$

$$\Phi^E(\lambda,\lambda_1,\lambda_2)=\frac{i}{N\,.\,M^{3/2}}$$

$$.\sum_{\alpha\beta\gamma}e_\alpha(\lambda)e_\beta(\lambda_1)e_\gamma(\lambda_2)$$

$$\cdot\phi_{\alpha\beta\gamma}(\mathbf{q},\mathbf{q}_1,\mathbf{q}_2)$$

where

$$\phi_{\alpha\beta\gamma}(\mathbf{q},\mathbf{q}_1,\mathbf{q}_2)=\phi_{\alpha\beta\gamma}(\mathbf{q})+\phi_{\alpha\beta\gamma}(\mathbf{q}_1)+\phi_{\alpha\beta\gamma}(\mathbf{q}_2)$$

and

$$\phi_{\alpha\beta\gamma}(\mathbf{q})=\phi^C_{\alpha\beta\gamma}(\mathbf{q})+\phi^E_{\alpha\beta\gamma}(\mathbf{q})$$

$$\Phi^E(\lambda,-\lambda,\lambda_1,-\lambda_1)=$$

$$\frac{8}{M^2}\sum_{\alpha\beta\gamma\delta}e_\alpha(\lambda)e_\beta(\lambda)e_\gamma(\lambda_1)e_\delta(\lambda_1)\,.\,\phi_{\alpha\beta\gamma\delta}(\mathbf{q},\mathbf{q}_1)$$

$$\phi_{\alpha\beta\gamma\delta}(q,q_1)=\tfrac{1}{8}\{2[\phi_{\alpha\beta\gamma\delta}(0)-\phi_{\alpha\beta\gamma\delta}(\mathbf{q})$$

$$-\phi_{\alpha\beta\gamma\delta}(\mathbf{q}_1)]+\phi_{\alpha\beta\gamma\delta}(\mathbf{q}+\mathbf{q}_1)+\phi_{\alpha\beta\gamma\delta}(\mathbf{q}-\mathbf{q}_1)\}$$

$$\phi_{\alpha\beta\gamma\delta}(\mathbf{q})=\phi^C_{\alpha\beta\gamma\delta}(\mathbf{q})+\phi^E_{\alpha\beta\gamma\delta}(\mathbf{q}) \qquad (3.2)$$

ϕ^C and ϕ^E refer to the two different terms in the ion–ion potential*

$$V(q)=\frac{4\pi(Ze)^2}{q^2}-\frac{q^2}{4\pi e^2}|v(q)|^2\frac{\epsilon(q,0)-1}{\epsilon(q,0)} \qquad (3.3)$$

where $v(q)$ is the ion–electron potential and $\epsilon(q,0)$ the dielectric function. With the use of Ewald summation it is possible to deduce the form of $\phi^C_{\alpha\beta\gamma}(\mathbf{q})$, and $\phi^C_{\alpha\beta\gamma\delta}(\mathbf{q})$.

$$\phi^C_{\alpha\beta\gamma}(q)=\frac{4\pi}{v_c}\sum_{\mathbf{g}}\frac{(\mathbf{q}+\mathbf{g})_\alpha(\mathbf{q}+\mathbf{g})_\beta(\mathbf{q}+\mathbf{g})_\gamma}{(\mathbf{q}+\mathbf{g})^2}$$

$$\cdot e^{-\frac{1}{4\eta^2}(\mathbf{q}+\mathbf{g})^2}$$

$$+\sum_{\mathbf{R}}{}'\sin(\mathbf{q}\,.\,\mathbf{R})\left\{R_\alpha R_\beta R_\gamma\frac{\phi_{\text{III}}(R)}{R^3}\right.$$

$$\left.+(R_\gamma\delta_{\alpha\beta}+R_\beta\delta_{\alpha\gamma}+R_\alpha\delta_{\beta\gamma})\frac{\phi_{\text{II}}(R)}{R^2}\right\};$$

$$\phi^C_{\alpha\beta\gamma\delta}(\mathbf{q})=\frac{4\pi}{v_c}$$

$$\cdot\sum_{\mathbf{g}}\frac{(\mathbf{q}+\mathbf{g})_\alpha(\mathbf{q}+\mathbf{g})_\beta(\mathbf{q}+\mathbf{g})_\gamma(\mathbf{q}+\mathbf{g})_\delta}{(\mathbf{q}+\mathbf{g})^2}$$

$$\cdot e^{\frac{(\mathbf{q}+\mathbf{g})^2}{4\eta^2}}$$

---

*The exchange overlap is found to be negligible in Al (see [10]). We have thus chosen

$$\Phi(q)=4\pi\frac{(Ze)^2}{q^2}-$$

$$+\sum_{\mathbf{R}}{}' \cos(\mathbf{q}\cdot\mathbf{R})\left\{\frac{R_\alpha R_\beta R_\gamma R_\delta}{R^4}\,\phi_{\mathrm{IV}}(R)\right.$$
$$+(R_\alpha R_\beta \delta_{\gamma\delta}+R_\alpha R_\gamma \delta_{\beta\delta}+R_\alpha R_\delta \delta_{\beta\gamma}$$
$$+R_\beta R_\delta \delta_{\alpha\gamma}+R_\gamma R_\delta \delta_{\alpha\beta}+R_\beta R_\gamma \delta_{\alpha\delta})$$
$$\cdot\frac{\phi_{\mathrm{III}}(R)}{R^3}+(\delta_{\alpha\beta}\delta_{\gamma\delta}+\delta_{\beta\gamma}\delta_{\alpha\delta}+\delta_{\alpha\gamma}\delta_{\beta\delta})$$
$$\left.\cdot\frac{\phi_{\mathrm{II}}(R)}{R^3}\right\}-\frac{8}{5}\frac{1}{\sqrt{\pi}}$$
$$\cdot\,\eta^5(\delta_{\alpha\beta}\delta_{\gamma\delta}+\delta_{\beta\gamma}\delta_{\alpha\delta}+\delta_{\alpha\gamma}\delta_{\beta\delta}) \qquad (3.4)$$

$$\phi_{\mathrm{II}}(R)=\frac{3}{R^3}\operatorname{erfc}(\eta R)+\frac{6}{R^2}\frac{\eta}{\sqrt{\pi}}e^{-\eta^2R^2}$$
$$+\frac{4\eta^3}{\sqrt{\pi}}e^{-\eta^2R^2}$$

$$\phi_{\mathrm{III}}(R)=-\left\{\frac{15}{R^4}\operatorname{erfc}(\eta R)+\frac{30}{R^3}\frac{\eta}{\sqrt{\pi}}e^{-\eta^2R^2}\right.$$
$$\left.+\frac{20}{R}\frac{\eta^3}{\sqrt{\pi}}e^{-\eta^2R^2}+8\cdot R\frac{\eta^5}{\sqrt{\pi}}e^{-\eta^2R^2}\right\}$$

$$\phi_{\mathrm{IV}}(R)=\frac{105}{R^5}\operatorname{erfc}(\eta R)+\left\{\frac{210}{R^4}+\frac{140}{R^2}\eta^2\right.$$
$$\left.+56\eta^4+16R^2\eta^6\right\}\cdot\frac{\eta}{\sqrt{\pi}}e^{-\eta^2R^2}$$

R and **g** are the lattice vectors in direct and reciprocal space respectively. η is an arbitrary parameter which is chosen to make both the direct and the reciprocal sums converge rapidly. v_c is the volume of the lattice cell, which equals $a^3/4$ for the f.c.c. case where a is the lattice parameter. For free electron metals several formulae for $\epsilon(q,0)$ have been published. Here a form suggested by Hubbard has been used

$$\epsilon(q,0)=1+\frac{\epsilon_0(q,0)-1}{1-\frac{1}{2}\dfrac{q^2}{q^2+k_F^2+k_{TF}^2}(\epsilon_0(q,0)-1)} \qquad (3.5)$$

where $\epsilon_0(q,0)$ is the Lindhard dielectric function and k_F and k_{TF} are the Fermi radius and the Thomas–Fermi screening radius respectively.

Several authors have published calculations of the dispersion curves for Al with a local ion–electron potential. The local potential has a few parameters which are fitted to the dispersion curves. Some of these fitted potentials describe the phonon frequencies quite accurately. Here two potentials have been used principally. One is that given by Johnson and Westin[12], and the other that due to Schneider and Stoll[11]. The Johnson–Westin potential is obtained through a series expansions of $v(r)$ in direct space

$$v(r)=e^2\frac{Z(r)}{r}=-e^2\left\{\frac{Z}{r}+\frac{1}{r}\sum_{i=0}^{m}A_ir^ie^{-\alpha r}\right\};\ Z=3. \qquad (3.6)$$

After Fourier transformation it takes the form

$$v(q)=-4\pi Ze^2\left\{\frac{1}{q^2}+\frac{B_0}{q^2+\alpha^2}+\frac{B_1}{(q^2+\alpha^2)^2}+\cdots\right\} \qquad (3.7)$$

where

$$B_0=\frac{A_0}{3},\ B_1=\frac{\alpha}{3}(A_1\alpha-A_2)$$
$$B_2=\frac{8}{3}A_2\alpha^2\quad\text{etc.}\ \ldots$$

The series expansion is terminated by setting $B_i=0$ for $i>3$. When $r\to 0$, the requirement $Z(r)=11$ (the two S-electrons are included in the nuclear charge) sets the value of A_0 to 8 and that of B_0 to $\frac{8}{3}$. The value of α^{-1} must be about the size of the ion and it is found to be non-critical. α is fixed and B_1, B_2, B_3 are fitted to the dispersion curves in the symmetry directions. The Schneider–Stoll potential is of a similar type and is given as

$$v(q)=-\frac{4\pi Ze^2}{q^2}+\frac{1}{n}\sum_n\gamma_nH_n(qr_n) \qquad (3.8)$$

where

$$H_1=\frac{1}{[1+(qr_1)^2]^2};\quad H_2=\frac{qr_2}{[1+(qr_2)^2]^3}.$$

The parameter values are given in [5] and [11]. In their report Johnson and Westin have given several sets of parameters which are quite different but nevertheless describe the phonon frequencies well. These different parameter sets have been used in the present calculations in an attempt to avoid fortuitous results.

The $(1/q^2)$ term in $v(q)$ causes numerical problems because it decreases too slowly to zero for large q-values. On the other hand it is not possible to eliminate this term without making drastic assumptions. It is true, of course, that the concept of a local potential is somewhat doubtful for large q-values. Some kind of cut-off might be justified for the harmonic frequencies, but it is made only with difficulty for the anharmonic terms. Indeed a major contribution from $q \approx 5\cdot(2\pi/a)$ has been found. Hence it is felt that the error is smaller if a cut-off is not used when fitting the harmonic frequencies and calculating the anharmonic terms. The results from one of the Johnson–Westin potentials and from the Schneider-Stoll potential will be presented below.

The harmonic dispersion curves for both of these potentials have been published earlier (see [5] and [11]).

In Figs. 12 and 13 the phonon widths are given together with the experimental values for 80° and 300°K. The difference between the phonon frequencies for 300° and 80°K, including the quasi-harmonic shift and third and fourth-order shifts is plotted in Fig. 14. The results for the Johnson–Westin potential are also given in Table 1.

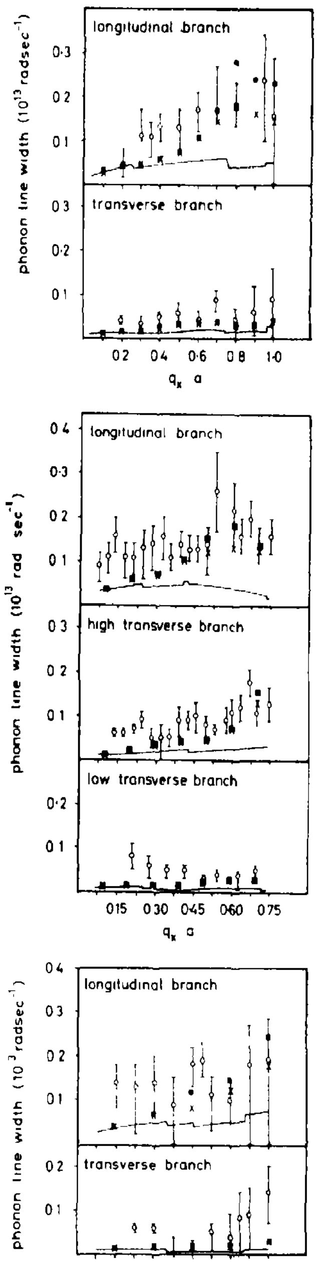

Fig. 12. Widths for Al ($T = 80$°K). Open circles, experimental values, squares, calculated with the Johnson–Westin potential, crosses, calculated with the Schneider-Stoll potential; lines electron-phonon contribution to the widths. (a) 100 direction, (b) 110 direction, (c) 111 direction.

4. NUMERICAL DETAILS

The integrands of $\Gamma(\lambda,\omega)$ and $\Delta(\lambda,\omega)$ contain $\omega(\lambda)$, $\phi_{\alpha\beta\gamma}(\mathbf{q})$, $\phi_{\alpha\beta\gamma\delta}(\mathbf{q})$ etc. all of which require time consuming computation owing to the sums in the reciprocal lattice. It has been found necessary to carry out the sums for the first 25 shells. A table has therefore been constructed for $\omega(\lambda)$, $e(\lambda)$, $\phi_{\alpha\beta\gamma}(\mathbf{q})$, $\phi_{\alpha\beta\gamma\delta}(\mathbf{q})$ at equidistant points 1/48 of the BZ. If $\Gamma(\lambda,\omega)$

Table 1. *Widths* (2Γ) *and shifts* (Δ) *for the Johnson–Westin potential at* 300° *and* 80°*K*

q_x	Mode	$\omega(\lambda)$	Γ	$-\Delta$	$-\Delta_{qh}$	$-\Delta_3$	Δ_4
100 direction							
0·1	L		4	12	17	42	54
		0·890	0			19	26
	T		5	20	9	42	33
		0·564	1			14	16
0·2	L		14	25	33	83	102
		1·787	2			37	48
	T		19	47	18	83	66
		1·108	2			20	32
0·3	L		28	32	48	97	126
		2·747	5			48	61
	T		48	51	26	118	99
		1·624	5			41	47
0·4	L		30	27	61	111	164
		3·537	7			61	80
	T		90	37	34	120	129
		2·097	10			49	61
0·5	L		41	45	71	161	205
		4·201	14			81	99
	T		77	15	42	111	158
		2·516	9			55	75
0·6	L		79	57	79	205	244
		4·753	28			100	117
	T		78	12	48	123	184
		2·873	10			62	87
0·7	L		154	86	87	268	275
		5·210	57			126	132
	T		70	11	54	133	205
		3·170	10			67	96
0·8	L		307	46	94	196	281
		5·651	119			99	135
	T		54	13	59	134	211
		3·435	9			69	100
0·9	L		246	6	98	128	287
		5·901	98			72	139
	T		42	11	62	137	222
		3·566	7			70	104
1·0	L		226	4	99	131	293
		5·968	90			74	141
	T		52	2	61	135	235
		3·560	9			69	110
110 direction							
0·1	L		12	22	25	73	88
		1·373	1			30	42
	T_1		10	29	13	61	47
		0·800	1			21	23
	T_2		7	24	9	39	20
		0·543	1			13	9
0·2	L		63	20	48	114	165
		2·660	9			55	78
	T_1		43	50	26	114	93
		1·597	4			41	44
	T_2		17	45	19	70	34
		1·132	2			25	15
0·3	L		55	28	68	127	208
		3·836	14			69	100
	T_1		74	33	38	124	136
		2·394	9			58	65
	T_2		32	57	28	84	28
		1·832	4			31	14
0·4	L		83	30	79	167	249
		4·632	28			86	119
	T_1		54	10	51	124	175
		3·187	9			73	83
	T_2		50	64	35	92	45
		2·347	6			40	22
0·5	L		137	54	86	204	244
		5·213	52			100	118
	T_1		45	44	64	179	203
		3·966	11			93	97
	T_2		49	56	41	101	72
		2·779	7			49	35
0·6	L		180	79	85	221	231
		5·361	69			108	112
	T_1		76	82	75	247	233
		4·628	25			119	112
	T_2		50	54	47	119	104
		3·137	7			58	50
0·7	L		155	110	84	299	258
		5·183	57			139	124
	T_1		166	124	80	291	219
		5·096	62			134	106
	T_2		53	48	52	134	139
		3·408	9			66	67
111 direction							
0·1	L		26	30	31	97	112
		1·731	3			39	53
	T		11	29	13	56	38
		0·769	1			19	17
0·2	L		44	−18	59	94	205
		3·359	9			64	98
	T		29	50	25	93	66
		1·500	3			33	31
0·3	L		97	30	84	157	248
		4·856	35			83	120
	T		41	40	34	104	71
		2·170	5			41	34
0·4	L		126	35	97	167	276
		5·824	50			87	134
	T		48	56	38	114	93
		2·472	6			47	44
0·5	L		210	72	99	243	297
		6·090	86			117	144
	T		58	45	39	116	114
		2·487	8			50	54

$\omega(\lambda)$ is in units of 10^{13} rad/sec; the widths and shifts are in units of 10^{10} rad/sec. For each mode the upper figures are at 300°K, the lower at 80°K. Δ_{qh} is the difference in harmonic frequency between $a = 4{\cdot}050$ ($T = 300$°K) and $a = 4{\cdot}033$ ($T = 80$°K). Δ is the total difference between the phonon frequencies at 300 and 80°K.

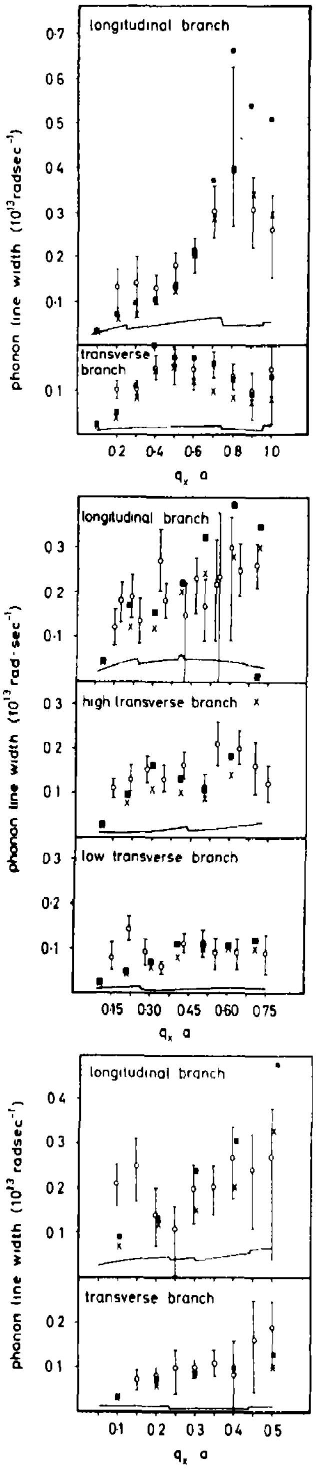

Fig. 13. The same as Fig. 12 for $T = 300°K$.

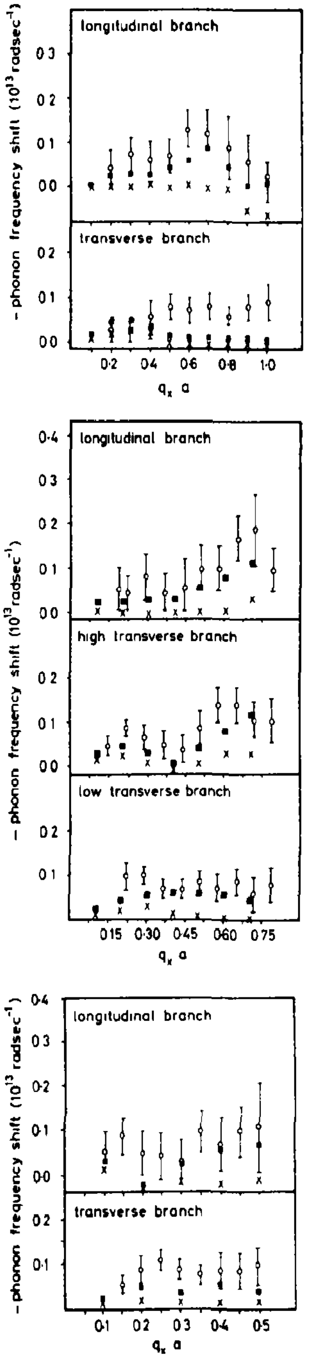

Fig. 14. Minus the shifts between 300° and 80°K for Al Open circles, experimental values; squares, calculated with the Johnson–Westin potential; crosses, calculated with the Schneider–Stoll potential. (a) 100 direction; (b) 110 direction; (c) 111 direction.

etc. are only evaluated for the points in the table, no interpolation is needed. In fact it is necessary to pass beyond the first *BZ*. The sums for $\phi_{\alpha\beta\gamma}(\mathbf{q})$ and $\phi_{\alpha\beta\gamma\delta}(\mathbf{q})$ do not converge, but this is not as serious as might be thought. The quantities which are needed are

$$\phi_{\alpha\beta\gamma}(\mathbf{q},\mathbf{q}_1,\mathbf{q}_2)\ \text{for}\ \mathbf{q}+\mathbf{q}_1+\mathbf{q}_2=0$$

and $\phi_{\alpha\beta\gamma\delta}(\mathbf{q},\mathbf{q}_1)$; these do converge provided that the same number of shells are included in the sums for $\phi_{\alpha\beta\gamma}(\mathbf{q})$:s etc. (Due to the non-convergence the condition $\mathbf{q}+\mathbf{q}_1+\mathbf{q}_2=\mathbf{g}$ is changed to $\mathbf{q}+\mathbf{q}_1+\mathbf{q}_2=0$.) As a consequence $\phi_{\alpha\beta\gamma}(\mathbf{q})\neq\phi_{\alpha\beta\gamma}(\mathbf{q}+\mathbf{g})$ but instead

$$\phi_{\alpha\beta\gamma}(\mathbf{q}+g)-\phi_{\alpha\beta\gamma}(\mathbf{g})=\phi_{\alpha\beta\gamma}(\mathbf{q})-\phi_{\alpha\beta\gamma}(0)\simeq\phi_{\alpha\beta\gamma}(\mathbf{q}).\quad(4.1)$$

Values for $\mathbf{q}$ outside the first *BZ* are thus easily obtained. For $\phi_{\alpha\beta\gamma\delta}(\mathbf{q})$ the corresponding expression is

$$\phi_{\alpha\beta\gamma\delta}(\mathbf{q}_1+\mathbf{g})-2\phi_{\alpha\beta\gamma\delta}\left(\frac{\mathbf{q}_1+\mathbf{q}_2}{2}+\mathbf{g}\right)$$
$$+\phi_{\alpha\beta\gamma\delta}(\mathbf{q}_2+\mathbf{g})$$
$$\simeq\phi_{\alpha\beta\gamma\delta}(\mathbf{q}_1)-2\phi_{\alpha\beta\gamma\delta}(\mathbf{q}_1+\mathbf{q}_2)+\phi_{\alpha\beta\gamma\delta}(\mathbf{q}_2).\quad(4.2)$$

With the aid of this formula it is possible to make the table smaller. The limits of the table used for the f.c.c. case are $1\geqslant q_x\geqslant q_y\geqslant q_z\geqslant 0$ in units of $(2\pi/a)$.

Because of the long computing times and the necessarily large core space it would be rather difficult to use a mesh finer than 0·1 in $\mathbf{q}$ space; this corresponds to about 4000 points in the first *BZ*. Steps of both 0·1 and 0·2 have been used in order to estimate the error in the integration. A typical result is seen in Fig. 15. If the integrand varied smoothly the error would on average be a factor smaller than the difference between the results. Since this is not the case it is only possible to estimate the error to the same order of magnitude as the difference.

The δ-functions and the principal values are approximated in the usual way as

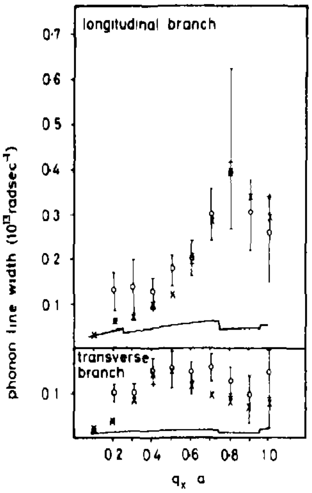

Fig. 15. Comparison between two different integration meshes (0·1 crosses and 0·2 daggers). The studied case is the same as in Fig. 13(a).

$$\delta(x)=\frac{1}{\pi}\frac{\epsilon}{x^2+\epsilon^2},\quad P\left(\frac{1}{x}\right)=\frac{\epsilon}{x^2+\epsilon^2}.$$

The choice of ϵ must be made with great care (see Bohlin and Högberg[4]). Too large an ϵ-value flattens out the structure in the $\Gamma(\lambda)$ and $\Delta(\lambda)$ curves. Too small a value, on the other hand, makes the integrand very uneven and the result becomes uncertain. A value of $\epsilon=0{\cdot}1\cdot10^{13}$ rad/sec has been used for the 0·1 mesh and $\epsilon=0{\cdot}2\cdot10^{13}$ rad/sec for the 0·2 mesh. This should be compared with the maximum phonon frequency in Al which is about $6\cdot10^{13}$ rad/sec.

For the Coulomb part it has been found quite sufficient to sum over 3 shells in direct space and eight shells in reciprocal space. For the 'electronic' part of the potential the question of how many shells is included is more critical. Johnson and Westin[12] have made a very careful examination of the number of shells needed if their potential is to yield accurate (better than 1‰) phonon frequencies. They found that they needed appr. twenty-five shells when they approximated the sum for large $\mathbf{g}$ values with an integral.

The assymptotic behaviour is the same for $\phi_{\alpha\beta\gamma}(\mathbf{q}, \mathbf{q}_1, \mathbf{q}_2)$ and $\phi_{\alpha\beta\gamma\delta}(\mathbf{q}, \mathbf{q}_1)$ as for the corresponding harmonic term. In practice, however, the $\phi_{\alpha\beta\gamma}(\mathbf{q}, \mathbf{q}_1, \mathbf{q}_2)$:*s* etc. converge more slowly, but since there is no need for the same accuracy twenty-five shells are sufficient.

5. DISCUSSION OF THE RESULTS

The results presented in Figs. 12, 13 and 14 for the widths and shifts in Al will now be discussed. It can be seen that for the widths there is good agreement with the experimental values in most cases. This is also true for the shifts for the Johnson–Westin potential; however, the agreement is less satisfactory for the Schneider–Stoll potential. A comparison of the widths for the two different potentials provides a method of estimating the extent to which the results are affected by a change of potential. The other Johnson–Westin potentials do not give quite so good agreement with the experimental values. The general trend for the potentials used is that a better fit of the harmonic frequencies yields widths that agree better with the experimental values. This is of course support for this type of fitted potential. As a result of the cancellations between the contributions from the two different parts of the potential (at least for small values of q) and other uncertainties discussed in section 5, the error in the numerical evaluation is probably around 20 per cent for the widths. The fact that the agreement between experiment and theory is less good for $T = 80°$K might in part depend on the difficulty obtaining experimental values at such a low temperature. The widths here are quite small and it is difficult to separate out the influence of the instrumental resolution.

The calculated shifts are the sum of six terms which almost completely cancel each other, and which themselves contain numerical uncertainties. The different contributions to the shift, i.e. the quasi-harmonic shift and the third and fourth order shifts, are of the same order of magnitude; this means that they must all be calculated accurately. Accordingly, the shifts are highly sensitive to small changes in the potential which explains the different results for the two potentials.

It is concluded that the use of local potentials fitted to the harmonic frequencies is justified for the calculation of anharmonic terms. In an earlier section it was found highly unlikely that higher order terms would affect the result appreciably.

Subsequent to the completion of this work, a preprint has been received from Buyers and Cowley[17] presenting measurements and calculations of widths and shifts for K. They used the potential $V^T(q)$ in [16] which corresponds to $\Phi^E(q)$ in this paper. $V^T(q)$ is a potential which is of short range character both in direct and in reciprocal space and is obtained through fitting to the harmonic frequencies. The use of a short range potential was found somewhat questionable in section 3 but it simplifies the calculations considerably. Buyers and Cowley obtained acceptable agreement between the calculated and the experimental shifts but not quite such good agreement for the widths. We are indebted to the authors for sending us this report.*

Acknowledgements – The authors wish to thank Dr. R. Johnson and Dr. L. Bohlin for many helpful discussions. One of us (R. S.) is indebted to the Swedish Nature Science Research Council for financial support. A major debt of gratitude is, however, owed to I. Ebbsjo who made all the data programs.

REFERENCES

1. MARADUDIN A. A. and FEIN A. E., *Phys. Rev.* **128**, 2589 (1962).
2. COWLEY R. A., *Adv. Phys.* **12**, 421 (1963).
3. COWLEY E. R. and COWLEY R. A., *Proc. R. Soc.* **A287**, 259, **A292**, 209 (1965).
4. BOHLIN L. and HOGBERG T., *J. Phys. Chem. Solids* **29**, 1805 (1968).
5. HOGBERG T. and SANDSTROM R., *Phys. Status Solidi* **33**, 169 (1969).

---

*The authors' attention was recently drawn to a review [18] on anharmonic crystals which contains some of the results of [17].

6. STEDMAN R. and NILSSON G., *Phys. Rev.* **145** 492 (1966).
7 SHAM L. J. and ZIMAN J. M., *Solid St. Phys.* **15**, (1963).
8. ZIMAN J. M., *Adv. Phys.* **13**, 89 (1964)
9. HARRISON W. A., New York, *Pseudo-potentials in the Theory of Metals*, Benjamin – (1966).
10. VOSKO S. H., TAYLOR R. and KEECH G. H., *Can. J. Phys.* **43**, 1187 (1965).
11. SCHNEIDER T. and STOLL E., *Phys. Kond. Materie* **5**, 331 (1966).
12 JOHNSON R. and WESTIN A., On phonons in simple metals – II. Calculated dispersion curves in Aluminium AB Atomenergi, Studsvik, Sweden (Unpublished).
13 ABRIKOSOV *et al.*, *Quantum Field Theoretical Methods in Statistical Physics* Pergamon Press, Oxford (1965).
14 BJORKMAN G., LUNDQVIST B. I. P. and SJÖLANDER A., *Phys. Rev.* **159**, 551 (1967)
15 JOHNSON R., Electronic contributions to the phonon damping in metals AB Atomenergi, Studsvik, Sweden, Report AE-328 (1968).
16 COWLEY R. A., WOODS A. D. B. and DOLLING G., *Phys. Rev.* **150**, 487 (1966).
17. BUYERS W. J. L. and COWLEY R. A., Crystal dynamics of potassium – II. The anharmonic effects (Preprint)
18 COWLEY R. A., *Rep. Progr. Phys.*, **31**, 1123 (1968)

APPENDIX A

Notations and definitions of the propagators

The free phonon propagator

$$D^0(\lambda, u) = \langle T(A_\lambda(u) A_\lambda^+(0))\rangle \qquad (A\ 1)$$

$\lambda = \mathbf{q}j$ (wavenumber vector and polarization index)
$A_\lambda = a_\lambda + a^+_\lambda$, a_λ boson operator

$$[a_{\lambda_1}, a^+_{\lambda_2}] = \delta_{\lambda_1\lambda_2}$$

T time-ordering operator,

$$A_\lambda(u) = e^{\frac{H_0 u}{\hbar}} A_\lambda e^{-\frac{H_0 u}{\hbar}}$$

$\omega(\lambda)$ harmonic frequencies; $\beta = \frac{\hbar}{kT}$ where T is the temperature.

$$D^0(\lambda, i\omega_l) = D_l^0(\lambda) \underset{\text{def}}{=} \int_0^\beta D^0(\lambda, u) e^{+i\omega_l u}\, du$$

$$= \frac{2\omega(\lambda)}{\omega_l^2 + \omega^2(\lambda)}, \omega_l = \frac{\pi}{\beta} 2l \quad \text{for bosons.} \qquad (A\ 2)$$

The free electron propagator

$$G^0(k, u) = \langle T(c_{\mathbf{k}}(u) c_{\mathbf{k}}^+(0))\rangle \qquad (A.3)$$

$c_{\mathbf{k}}$ fermion operator

$$[c_{\mathbf{k}_1}, c^+_{\mathbf{k}_2}]_+ = \delta_{\mathbf{k}_1\mathbf{k}_2}$$

$$\epsilon_0(k) = \frac{\hbar k^2}{2m}; \quad \mu = \frac{\hbar k^2 F}{2m}; \quad \text{(fermi frequency)}$$

$$G_l^0(k) = G^0(k, i\omega_l) = \int_0^\beta G^0(k, u) e^{i\omega_l u}\, du =$$

$$\frac{1}{[i\omega_l - (\epsilon_k - \mu)]} \qquad (A.4)$$

$$\omega_l = \frac{\pi}{\beta}(2l + 1) \text{ for fermions}$$

$\mathbf{g}$ reciprocal lattice vectors

Σ' *means that the zero momentum transfer should be* omitted. The full phonon propagator is written

$$D(qjj', u) = \langle T(\tilde{A}_\lambda(u)\tilde{A}_{\lambda'}^+(0))\rangle = \langle T(A_\lambda(u) A_{\lambda'}^+(0) S(\beta))\rangle_c \qquad (A\ 5)$$

(only connected diagrams in the last term)

$\tilde{A}_\lambda(u) = e^{Hu} A_\lambda e^{-Hu}$ (Heisenberg respresentation).

$$S(\beta) = T \exp - \int_0^\beta \frac{H_{\text{anh}}(u)}{\hbar}\, du$$

$${}^1S(\beta) = T\left(-\int_0^\beta \frac{H_{\text{anh}}(u)}{\hbar}\, du\right)$$

$${}^2S(\beta) = T\left(+\tfrac{1}{2}\int_0^\beta \frac{H_{\text{anh}}(u_1)}{\hbar}\frac{H_{\text{anh}}(u_2)}{\hbar}\, du_1\, du_2\right)$$

give the first and the second order diagrams etc.
Turning directly to the frequency dependent propagators

$$D(\lambda, u) = \frac{1}{\beta}\sum_l D(\lambda, i\omega_l) e^{-i\omega_l u}$$

$$D(\lambda, i\omega_l) = \int_0^\beta D(u) e^{i\omega_l u}\, du. \qquad (A\ 6)$$

APPENDIX B
(DIAGRAM DICTIONARY)

The diagrams are similar to those for temperature dependency used in [1] and [15].

(1)

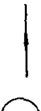

$$\mathbf{k}, \omega_l \equiv \frac{1}{[+i\omega_l - (\epsilon_k - \mu)]}$$

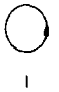

$$\mathbf{k}, \omega_l \equiv \tau \to +0 \frac{1}{\beta}\sum_{k,\omega_l} \frac{e^{i\omega_l\tau}}{[i\omega_l - (\epsilon_k - \mu)]}$$

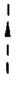

$$\lambda, \omega_l \equiv \frac{2\omega(\lambda)}{[\omega_l^2 + \omega^2(\lambda)]}.$$

(2) Vertices

(a) *Phonon–phonon part*

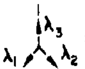

$$\equiv V(\lambda_1, \lambda_2, \lambda_3) = \left(\frac{\hbar}{2MN}\right)^{3/2} \sum_{1,2,3} \cdot \frac{\Phi(1,2,3)e_{\alpha_1}(\lambda_1)e_{\alpha_2}(\lambda_2)e_{\alpha_3}(\lambda_3)}{[\omega(\lambda_1)\omega(\lambda_2)\omega(\lambda_3)]^{1/2}}, e^{i[\mathbf{q}_1\mathbf{R}_1+\mathbf{q}_2\mathbf{R}_2+\mathbf{q}_3\mathbf{R}_3]}.$$

$1 = \mathbf{R}_1\alpha_1$, $\mathbf{e}(\lambda)$ phonon eigenvector

$$\Phi\begin{pmatrix}\mathbf{q}_1\mathbf{q}_2\mathbf{q}_3\\ \alpha_1\alpha_2\alpha_3\end{pmatrix} = +\frac{N^2}{\Omega}\sum_q (-i)^3 q_{\alpha_1}q_{\alpha_2}q_{\alpha_3}\Phi(q) \cdot \{\Delta(\mathbf{q}_1-\mathbf{q})+\Delta(\mathbf{q}_2-\mathbf{q})+\Delta(\mathbf{q}_3-\mathbf{q})\} \cdot \Delta(\mathbf{q}_1+\mathbf{q}_2+\mathbf{q}_3)$$

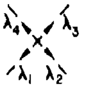

$$\equiv V(\lambda_1\lambda_2\lambda_3\lambda_4) = \left(\frac{\hbar}{2MN}\right)^{4/2} \sum_{1,2,3,4} \cdot \frac{\Phi(1,2,3,4)e_{\alpha_1}(\lambda_1)e_{\alpha_2}(\lambda_2)e_{\alpha_3}(\lambda_3)e_{\alpha_4}(\lambda_4)}{[\omega(\lambda_1)\omega(\lambda_2)\omega(\lambda_3)\omega(\lambda_4)]^{1/2}} \cdot e^{i[\mathbf{q}_1\mathbf{R}_1+\mathbf{q}_2\mathbf{R}_2+\mathbf{q}_3\mathbf{R}_3+\mathbf{q}_4\mathbf{R}_4]}$$

$$\Phi\begin{pmatrix}q_1q_2q_3q_4\\ \alpha_1\alpha_2\alpha_3\alpha_4\end{pmatrix} = \frac{N^2}{\Omega}\sum_q i^4 q_{\alpha_1}q_{\alpha_2}q_{\alpha_3}q_{\alpha_4}\Phi(\mathbf{q})\{\Delta(\mathbf{q})-\Delta(\mathbf{q}+\mathbf{q}_1) - \Delta(\mathbf{q}+\mathbf{q}_3)-\Delta(\mathbf{q}+\mathbf{q}_2)-\Delta(\mathbf{q}+\mathbf{q}_1) + \Delta(\mathbf{q}+\mathbf{q}_3+\mathbf{q}_4)+\Delta(\mathbf{q}+\mathbf{q}_1+\mathbf{q}_2) + \Delta(\mathbf{q}+\mathbf{q}_2+\mathbf{q}_4)\}\,\Delta(\mathbf{q}_1+\mathbf{q}_2+\mathbf{q}_3+\mathbf{q}_4)$$

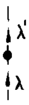

$$= F(\lambda,\lambda') = \sum_{\mathbf{g},\alpha_1\alpha_2} -\frac{N^2}{\Omega}\frac{1}{2MN}\{(\mathbf{g}+\mathbf{q})_{\alpha_1}(\mathbf{g}+\mathbf{q})_{\alpha_2} \cdot F(\mathbf{g}+\mathbf{q}) - g_{\alpha_1}g_{\alpha_2}F(g)\}\frac{e_{\alpha_1}(\lambda)e_{\alpha_2}(\lambda')}{[\omega(\lambda)\omega(\lambda')]^{1/2}}$$

$F(q)$ represents the ion–electron–ion interaction (see equation (2 3)).

(b) *Electron–electron part*

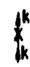

$$\equiv V(-\mathbf{k}_1,\mathbf{k}_2) = v(\mathbf{k}_2-\mathbf{k}_1)\ \frac{N}{\Omega}\ [\mathbf{k}_2 \neq k_1]$$

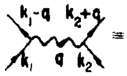

$$\equiv \frac{v_c(q)}{\Omega} = \frac{4\pi e^2}{q^2}\ \frac{1}{\Omega}.$$

(c) *Electron–phonon part*

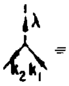

$$= V(-\mathbf{k}_1,\mathbf{k}_2,\lambda) = \frac{N}{\Omega}\left(\frac{\hbar}{2MN}\right)^{1/2}(-i)v(\mathbf{k}_2-\mathbf{k}_1)\ \frac{(\mathbf{k}_2-\mathbf{k}_1)\cdot\mathbf{e}(\lambda)}{[\omega(\lambda)]^{1/2}}$$

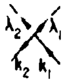

$$\equiv V(-\mathbf{k}_1,\mathbf{k}_2,\lambda_1,\lambda_2) = \frac{N}{\Omega}\left(\frac{\hbar}{2MN}\right)^{2/2}(-i)^2 v(\mathbf{k}_2-\mathbf{k}_1)\ \frac{(\mathbf{k}_2-\mathbf{k}_1)\cdot\mathbf{e}(\lambda_1)(\mathbf{k}_2-\mathbf{k}_1)\cdot\mathbf{e}(\lambda_2)}{[\omega(\lambda_1)\omega(\lambda_2)]^{1/2}}.$$

(3) In every vertex energy and momentum are conserved (up to a reciprocal lattice vector)

N.B. in a 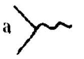 vertex there is complete momentum conservation

(4) A factor $\left(-\frac{1}{\hbar}\right)^n(-1)^F\frac{1}{p}(2S+1)^F\cdot\left(\frac{1}{2}\right)^L$

- n the order of the diagram
- F the number of fermion loops
- L the number of fermi loops which give a new diagram when the direction of the propagator is changed.
- p the permutation degree (see [1])

Example.

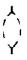 $p = 2!$ 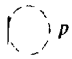 $p = 2!$ 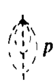 $p = 3!2!$.

(5)

Intermediate $\mathbf{k}, \omega_l \Longleftrightarrow$

$$\sum_{\mathbf{k}}\cdot\frac{1}{\beta}\sum_{\omega_l}$$

J. Phys. Chem. Solids Pergamon Press 1970. Vol. 31, pp. 1613-1619. Printed in Great Britain.

AN ELECTRON MICROSCOPIC INVESTIGATION OF THE DECOMPOSITION OF V_2O_5

R. J. D. TILLEY* and B. G. HYDE

School of Chemistry, University of Western Australia, Nedlands, Western Australia 6009

(*Received* 21 *March* 1969; *in revised form* 21 *May* 1969)

Abstract – The decomposition of vanadium pentoxide at temperatures up to 400°C in vacuum has been investigated using transmission electron microscopy. A number of new phases has been found, two of which may be ordered super-lattices of anion vacancies in vanadium pentoxide. No evidence of crystallographic shear was observed.

1. INTRODUCTION

At the commencement of this study, only one intermediate phase was known in the composition range VO_2-V_2O_5, the V_6O_{13} phase characterised by Aebi[1]. Its structure can be derived geometrically from that of V_2O_5 by crystallographic shear[2, 3, 4]. Some electron microscope observations were said to support a dislocation mechanism for the production of shear planes in V_2O_5[5, 6] and to show the early stages of the conversion of V_2O_5 to V_6O_{13} by this mechanism. Recent Leed studies have been similarly interpreted [7].

An interest in the mechanism of formation of such phases led us to study this system using transmission electron microscopy and diffraction. Our experiments were designed to throw light on the early stages of reduction of V_2O_5 and, because of this, low temperatures were selected. Transmission electron microscopy is a suitable technique for these studies, as it is able to reveal lattice defects on a small scale.

In the interim period V_3O_7, an oxide intermediate in composition between V_2O_5 and V_6O_{13}, has been reported by several workers [8, 9]. Its structure is unknown. Another recent investigation of the vanadium-oxygen system has revealed three additional phases[10] also of unknown structure and close in composition to V_6O_{13}. A series of low temperature studies of the reduction of both ammonium vanadate, NH_4VO_3, and V_2O_5 in hydrogen[11] have revealed several new phases in the region of V_6O_{13}-VO_2 and although the authors have deduced compositions of some of these phases[12] structures are unknown.

2. EXPERIMENTAL

Single crystals of V_2O_5 up to $0{\cdot}5\times0{\cdot}5\times5{\cdot}0$ mm were grown by cooling a melt of 99% V_2O_5 in a platinum boat, in air, at approximately 5°/hr. Cleavage parallel to (001)† is easy, and samples suitable for transmission electron microscopy were obtained using adhesive tape or by lightly crushing in an agate mortar. These cleavage fragments were mounted on carbon films. Some crystals were thinned chemically, using a 10 volume solution of H_2O_2, to provide large plates which did not have to be supported on carbon films. All crystals studied were of (001) habit.

In initial experiments V_2O_5 was reduced by heating the crystals in the microscope by focussing the electron beam after removing the condenser aperture. To obtain more controlled reduction, V_2O_5 platelets were heated in sealed, evacuated, pyrex glass tubes for 1–5 days at temperatures ranging from 100 to 450°C. The reduced crystals were then mounted on carbon films, and studied with a Hitachi HU-11B electron microscope fitted with a tilting stage. Dark field micrographs were taken using the displaced aperture technique.

---

*Present address: Department of Materials Science, University of Bradford, England.

†We use the notation of R. G. Wyckoff[13], and the lattice parameters of Bachmann *et al* [14], i.e $a_0 = 11{\cdot}510$ Å, $b_0 = 3{\cdot}563$ Å, $c = 4{\cdot}369$ Å, space group Pmmn.

X-ray powder patterns were obtained with a Guinier-type focussing camera.

3. ELECTRON MICROSCOPE OBSERVATIONS

3.1 *Beam-heated crystals*

Beam-heating is ill-defined, and the effects varied from crystal to crystal. However, they yielded an outline of the stages in the decomposition of V_2O_5 crystals at approximately 10^{-4} Torr. which was consistent with the results obtained from crystals heated under more controlled conditions of temperature and pressure. The reaction was rapid; leading to small crystallites of product, and making contrast interpretation difficult. Extinction contours first took on a ragged appearance, which coarsened into a domain texture, the domain size depending on crystal thickness and beam intensity (Figs. 1 and 2). Continued heating caused the domain pattern to be replaced by an ill-defined mottled contrast (Fig. 3). Figures 1 and 2 show the formation of a superstructure (Figs. 1c, 2c,) followed by another phase (Figs. 1d, 2d,) termed VO_x, which existed in two twin-related forms corresponding to the two domain orientations observed. This was confirmed by dark field observations. In the VO_x diffraction patterns, the angle between the reciprocal lattice rows that are almost parallel to the V_2O_5 **a*** direction (α in Fig. 4) varies with the proportion of VO_x present. When it is the minor component it is constrained by the V_2O_5: as its proportion increases, the constraint diminishes and decreases to zero. Thus, between the diffraction pattern of Fig. 2d (showing constrained VO_x) and that of Fig. 3 (in which all the V_2O_5

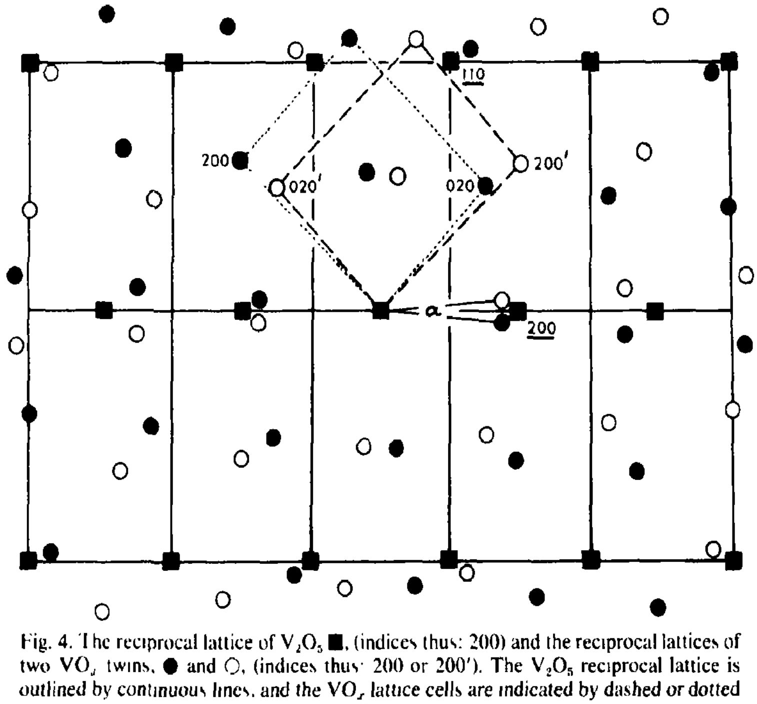

Fig. 4. The reciprocal lattice of V_2O_5 ■, (indices thus: 200) and the reciprocal lattices of two VO_x twins, ● and ○, (indices thus: 200 or 200'). The V_2O_5 reciprocal lattice is outlined by continuous lines, and the VO_x lattice cells are indicated by dashed or dotted lines.

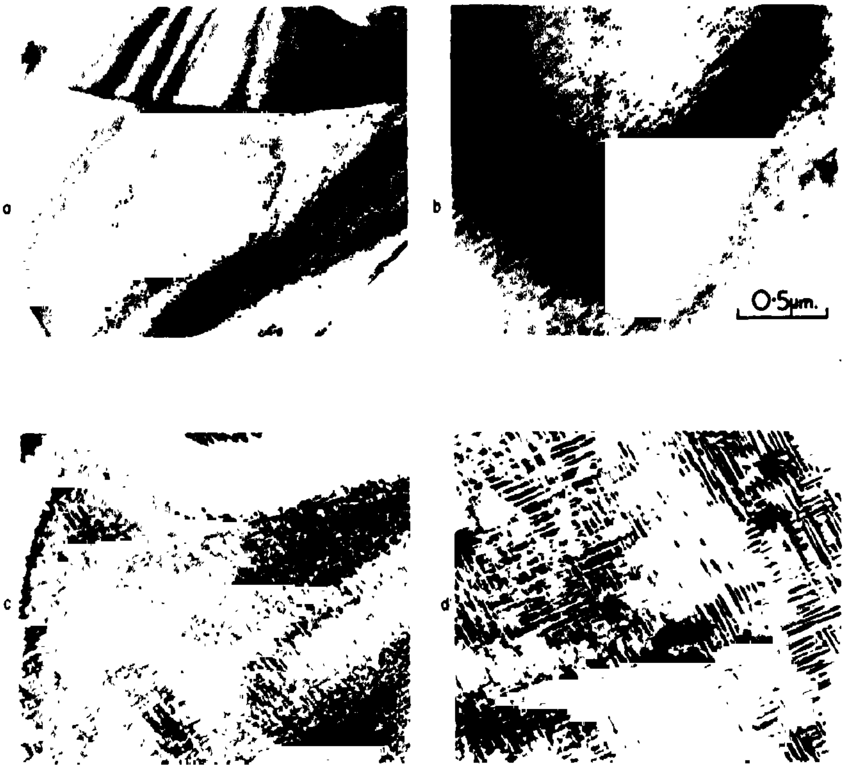

Fig. 1(a–d). Successive stages in the decomposition of V_2O_5 by beam heating, showing the development of a domain texture. All are at the same magnification.

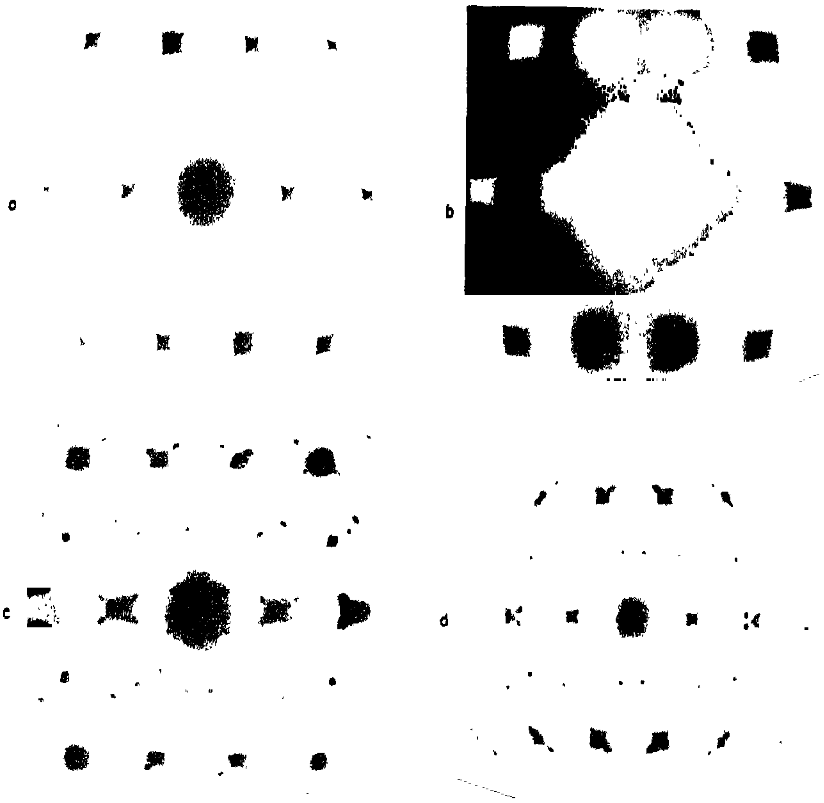

Fig 2(a–d). A series of diffraction patterns corresponding to the sequence of changes shown in Fig. 1.

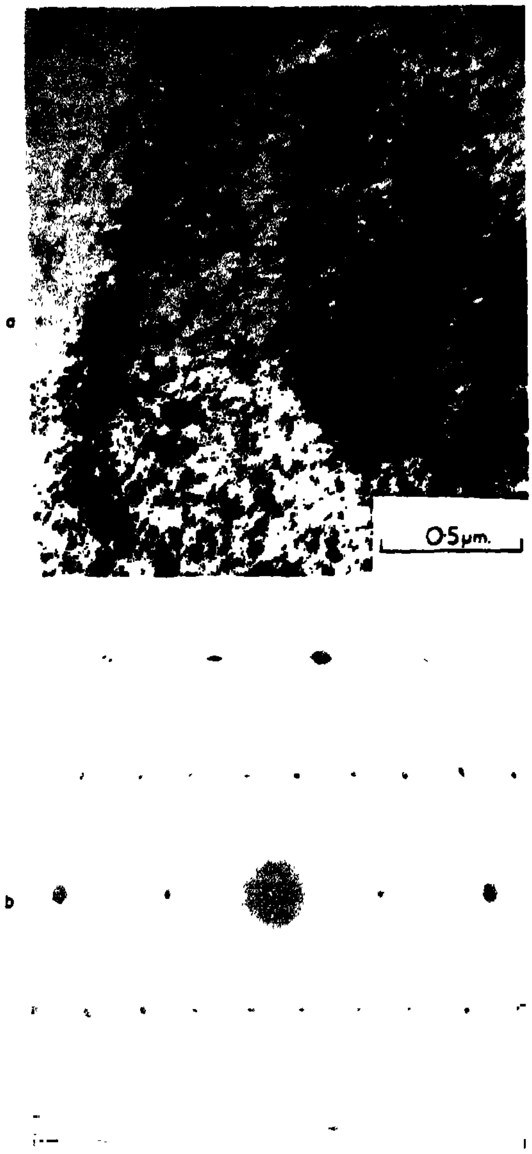

Fig. 3(a, b). The final stage in the decomposition of V_2O_5 by beam heating. Two twin forms of the final product are present causing the mottled contrast in (a).

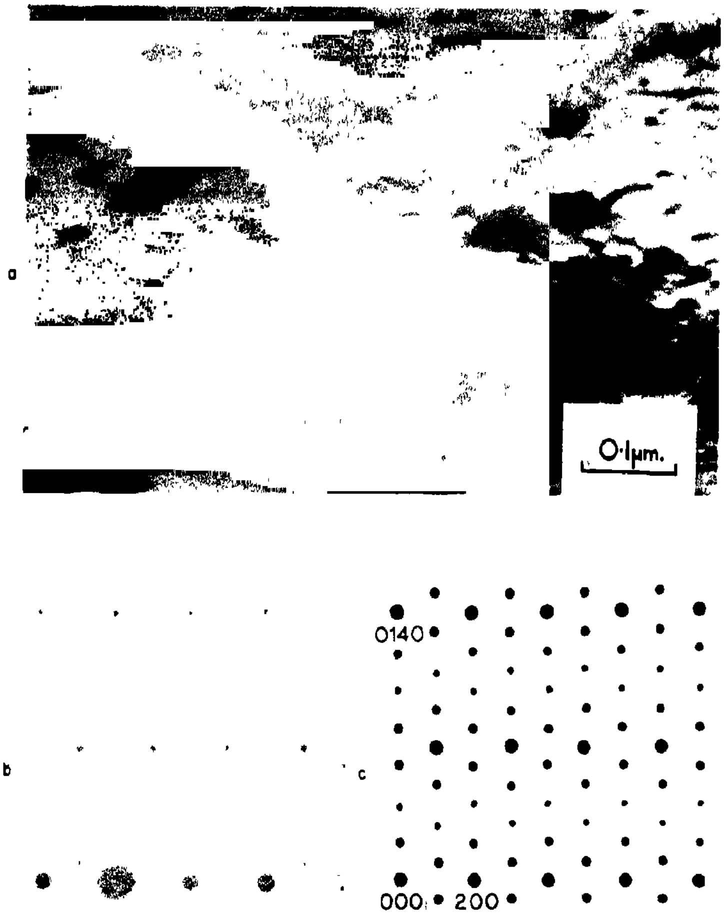

Fig. 5. (a) and (b) are a micrograph and diffraction pattern of a crystal of the 'seven-fold superlattice' type. Note streaking parallel to **a*** and extension of superlattice spots parallel to **b***. (c) is a diagram of the diffraction pattern. The indices refer to the superlattice cell. The largest spots represent V_2O_5 reflections; the 200 spot marked is also the V_2O_5 200 spot, and the 0 14 0 spot is the V_2O_5 020 spot.

has decomposed) a continuous decrease in α is observed. More intense heating caused evaporation and melting, and the study was limited to the above sequence.

To confirm the thermal origin of these effects, some crystals were examined on a heating stage in a JEM 6A electron microscope. These decomposed in exactly the same way; as did larger crystals not supported on carbon.

3.2 *Annealed crystals*

Crystals annealed at 100°C for 5 days showed a superstructure not observed in the beam-heating studies. Image contrast was invariably weak (Fig. 5a) and the presence of the new structure was indicated by the diffraction pattern (Figs. 5b and c). Both micrographs and diffraction patterns resemble those reported by Gillis and Remaut[6]. Superlattice reflections were not intense enough to give useful dark field images, and the weak contrast could not be related to the superlattice diffraction patterns in this way. Tilting allowed other reciprocal lattice sections to be intersected, and the complete reciprocal lattice to be constructed. The layer $z = 1$ is at a height of $\frac{1}{2}\mathbf{c}^*_{V_2O_5}$ above the zero layer. A unit cell can be chosen with $\mathbf{a}^*$ and $\mathbf{b}^*$ parallel to the equivalent V_2O_5 reciprocal axes (Fig. 5c). The accuracy of tilting does not allow the direction of $\mathbf{c}^*$ to be determined with precision, but does reveal that it is almost normal to the zero layer. Hence the dimensions of the approximately orthorhombic unit cell are

$$a_0 = a_0'(11{\cdot}5\ \text{Å}),\ b_0 = 7b_0'(24{\cdot}9\ \text{Å}),$$
$$c_0 = 2c_0'(8{\cdot}7\ \text{Å})$$

where the primes indicate V_2O_5 parameters. This is termed the seven-fold superlattice. Beam heating of these crystals caused decomposition identical with that observed in previously unreacted V_2O_5 crystals.

Some crystals also gave diffraction patterns showing the superlattice formed by beam-heating. The pattern was never complete, and frequently co-existed with the seven-fold superlattice spots. Its reciprocal lattice spacing parallel to $\mathbf{c}^*_{V_2O_5}$ was not found. In the reciprocal lattice layer observed, assuming that in the ideal case all rows of superlattice spots extend infinitely, a cell was deduced with $\mathbf{a}^* \equiv \mathbf{a}^*_{V_2O_5}$ and $\mathbf{b}^*$ along $\mathbf{g}_{510}$, with $|\mathbf{b}^*| = \frac{1}{24}|\mathbf{g}_{510}|$, that is, $a_0 = 11{\cdot}51$ Å and $b_0 = 46{\cdot}5$ Å. This will be referred to as the 24-fold superlattice. It is found that the V_2O_5 and VO_x reflections coincide with some of the reflections from this superlattice. Two twin orientations are also present (Fig. 6).

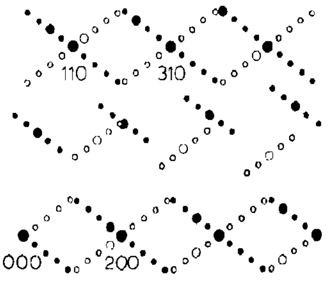

Fig. 6. Diagram of the diffraction pattern of the '24-fold superlattice', (compare with Fig. 2(c)). The spots which are also part of the VO_x reciprocal lattice are drawn larger than the superlattice spots. The indices refer to the V_2O_5 cell.

Crystals prepared by heating above 150°C were diphasic, containing VO_x and V_2O_5. The VO_x formed corners of the original platelets, or triangular domains extending in from the crystal edges (Fig. 7). The traces of the domain boundaries lay between $\langle 130\rangle_{V_2O_5}$ and $\langle 150\rangle_{V_2O_5}$, often varying between these limits along a single domain (c.f. Fig. 7). The boundaries were approximately normal to (001) and were therefore close to $\{410\}_{V_2O_5}$. The presence of VO_x twins was confirmed by selected area diffraction; one having its boundary close to $(410)_{V_2O_5}$ and the other close to $(\bar{4}10)_{V_2O_5}$. Tilting revealed fringes at these boundaries. The crystal is considerably distorted during its conversion from V_2O_5 to VO_x. The resulting stress often caused it to rupture, particularly when the twin forms came into contact (Figs. 7 and 8). In addition it may produce mechanical twinning of the V_2O_5 matrix[15].

V_2O_5 heated at 200–250°C often showed VO_x regions in the central part of the crystal, as well as at the edges. Also thin plate-like precipitates were observed (Fig. 9). At these precipitates, contrast was strongly dependent upon both the operating reflection **g** and the deviation of the reflecting planes from the Bragg position, s. Using the criteria of Ashby and Brown[16], the strain field was found to be similar to that produced by vacancy loops, that is, in the dark field the bright image side faced +**g**.

Heating above 250°C transformed thinner platelets into a mosaic of VO_x twins. As before, tilting of these crystals allowed the reciprocal lattice of the VO_x to be determined. The new $z = 1$ layer was not a simple fraction of $\mathbf{c}^*_{V_2O_5}$ above the zero layer in this case, but $\mathbf{c}^*_{VO_x}$ is perpendicular to it as far as can be judged from the available diffraction patterns. Thus the cell is approximately orthorhombic with parameters

$$a_0 = 8{\cdot}1\ \text{Å},\ b_0 = 10{\cdot}4\ \text{Å},\ c_0 = 16{\cdot}1\ \text{Å}$$

The relationship between a_0 and b_0 and the V_2O_5 cell is shown in Fig. 4. The c axis is parallel to $\mathbf{c}_{V_2O_5}$.

3.3 *Interpretation*

We presume that the superstructure phases and VO_x are formed by oxygen loss from V_2O_5, but our experiments have not yielded structures or compositions. The two superlattices appear to precede the formation of VO_x. The seven-fold superlattice is apparently identical with that observed but not commented on by Gillis and Remaut[6], and the contrast observed within these crystals resembles sets of weak, parallel, but not straight fringes (Fig. 5a). Otherwise the crystals appear homogeneous, and it is unlikely that the features represent precipitates of the superstructure, as the contrast is weak and not typical of that due to strain. Other contrast effects associated with precipitates, such as interfacial Moiré patterns[17] have never been observed. These features only occur in the seven-fold superlattice structure, and not in V_2O_5 itself. They are not elements of shear planes as the contrast is not typical of α-boundaries[18]. Also shear planes would be expected to extend or become more numerous upon further heating of the crystals[19] and this does not happen upon beam heating. Likewise, crystals annealed for longer times do not produce these features in greater profusion, as would be expected for precipitates or shear planes. At present no satisfactory model has been found to account for this contrast, but it may arise at boundaries between regions containing different arrays of ordered vacancies. The observation that the beam decomposition of these crystals is similar to that of V_2O_5 indicates that the degree of reduction is small and that this superstructure is perhaps nearer in composition to V_2O_5 than is the 24-fold superstructure. Therefore, although no composition data are available, it seems possible that this material differs from V_2O_5 only in containing ordered arrays of anion vacancies. Structure factors have been computed for V_2O_5 with various ordered arrangements of oxygen vacancies. It was found that either of the arrangements shown in Fig. 10 gives the correct extinctions to reproduce the observed superlattice diffraction pattern. However, agreement between calculated and observed intensities is not good, and a more complex grouping of vacancies may be necessary.

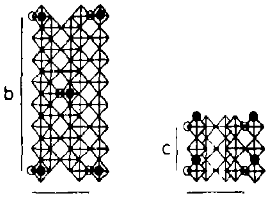

Fig. 10 Arrangements of oxygen vacancies (● or ○) in an idealised V_2O_5 matrix, which give rise to 'seven-fold superlattice' diffraction patterns.

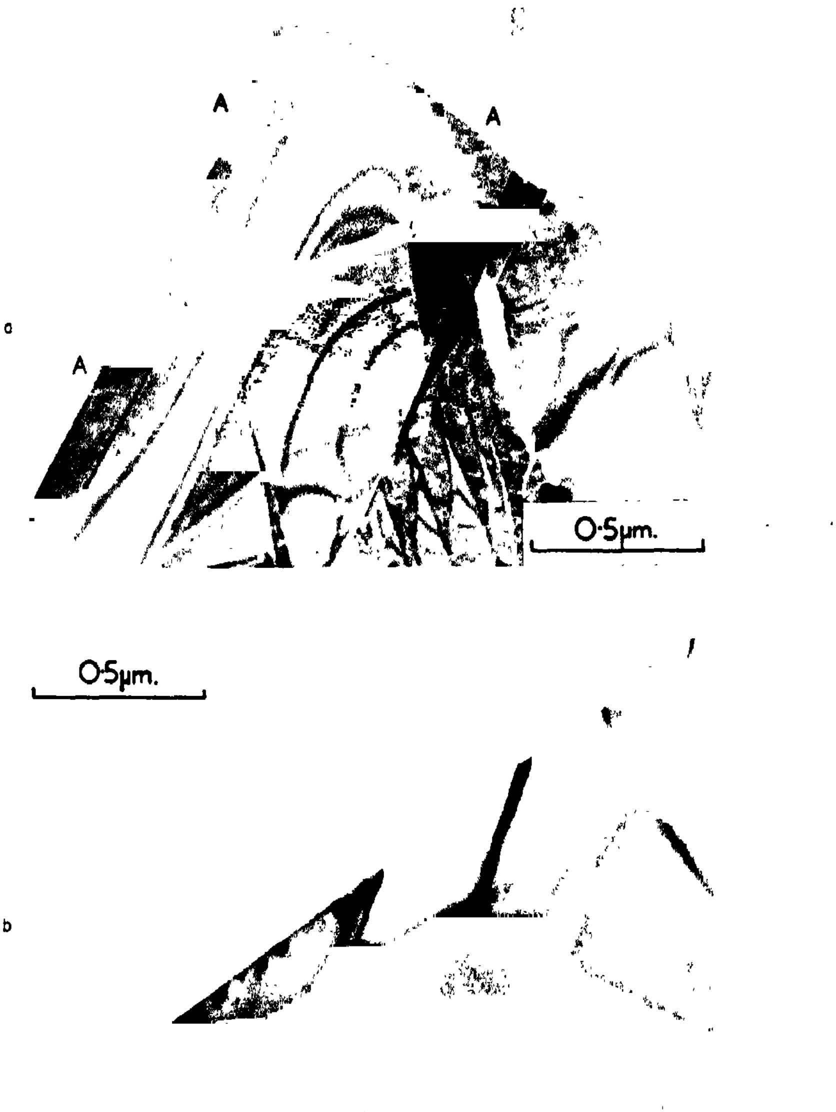

Fig. 7. (a) A crystal extensively converted to domains of VO_x which are labelled A.
(b) Small triangular domains of VO_x coherent with the V_2O_3 matrix

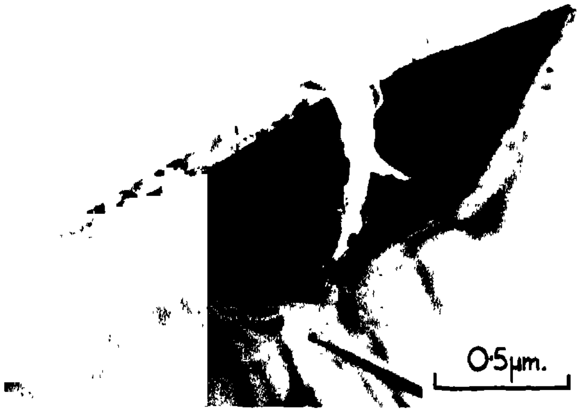

Fig. 8. Rupture of the crystal between domains of the twin forms of VO_x.

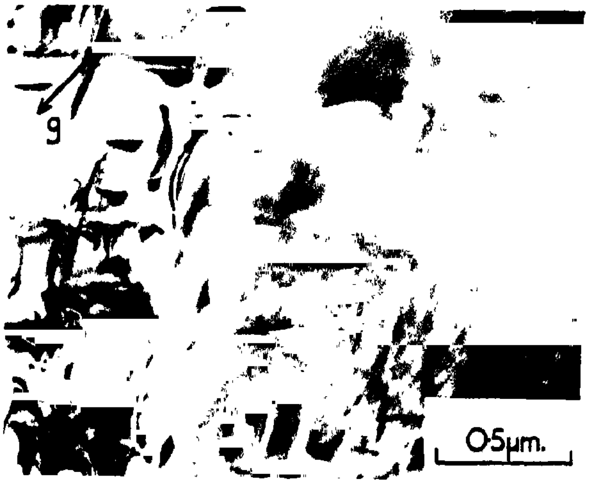

Fig 9. Precipitates in the V_2O_5 matrix. The operating reflection is $\overline{3}10$.

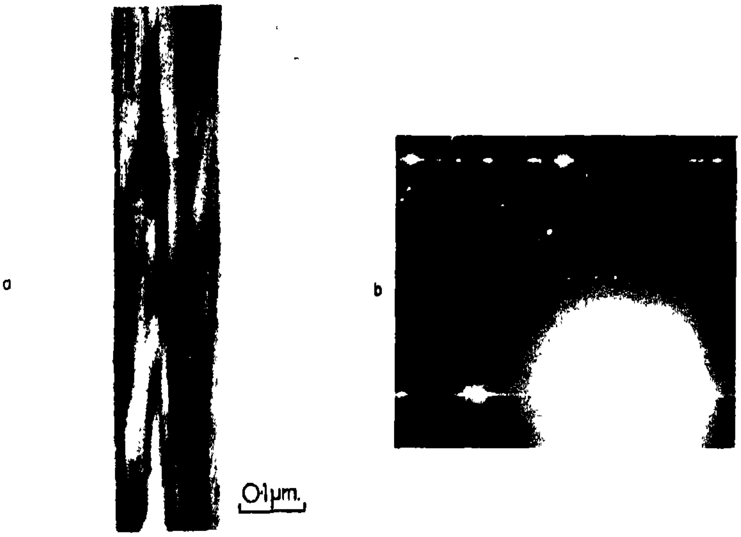

Fig. 11 (a) Crystals of needle shaped habit formed by vapour growth above 350°C on V_2O_5 crystals *in vacuo*, and (b), diffraction pattern of crystal in (a)

Until more accurate electron diffraction intensities can be obtained using *n*-beam theory, no further information can be obtained on this point.

The 24-fold superlattice is similar to that observed in Leed studies of V_2O_5[7]. We have insufficient data to define it in detail, but it appears to be closely related to the lattices of VO_x and V_2O_5 (Fig. 6). The precipitate features observed (see Fig. 9) may be plates of this superlattice form, which transform to VO_x as the degree of reduction increases. Diffraction patterns could not be used to confirm this because they showed only faint streaks (through V_2O_5 spots, normal to the precipitates). Similarly it was impossible to show that they were VO_x. The fact that diffraction contrast suggested a lattice collapse has not been fully exploited in this respect as the strain field around a thin precipitate of VO_x is impossible to calculate from the incomplete information available. The lattice contraction of the VO_x matrix parallel to $\mathbf{b}_{V_2O_5}$ and the lattice expansion parallel to $\mathbf{a}_{V_2O_5}$ are of the order of 10 per cent. The effect of this in the elastically anisotropic V_2O_5 crystal is difficult to approximate, and the rotation of lattice planes also adds an indeterminate strain. On the other hand, if the 24-fold superlattice is a simple superlattice of oxygen vacancies, little strain energy would be expected. Until the structures of these phases are known it is not possible to be categorical about the interpretation of strain contrast.

During beam heating, the fully ordered superlattices are rarely observed. It is reasonable to assume that this is because vacancy ordering is too slow or temperatures are too high. Short range ordering would lead to the extensive streaking observed on most diffraction patterns (c.f. Fig. 2). Figure 4 shows that the VO_x 040 reflection is coincident with 310 or $\bar{3}10$ of V_2O_5 according to which twin is considered. Hence, in the conversion to VO_x, the planes corresponding to $\{310\}_{V_2O_5}$ retain the same spacing and orientation. However, the appearance of the VO_x 020 reflection indicates that their constitution has changed in some way. The strain at the interface between VO_x and V_2O_5 is due to rotation of planes other than the {310} set and to changes in their interplanar spacings. The effect is not large enough to cause rupture of the lattice between V_2O_5 and VO_x, but is sufficient to cause splitting between twins of VO_x (Fig. 8). The change of shape of V_2O_5 crystals partly transformed to VO_x is in accord with a simple displacive transformation[20]. Such a deformation may be reproduced fairly precisely using a shear parallel to $(310)_{V_2O_5}$, but this does not result in a composition change. Until the structure of VO_x is known, no mechanism for its formation can be proposed without making gross assumptions.

4. X-RAY AND OPTICAL MICROSCOPE INVESTIGATIONS

Samples which, in the electron microscope appeared to be completely converted to VO_x, gave X-ray powder patterns corresponding to V_2O_5 with only a few weak extra lines. X-ray powder patterns of samples annealed below 250°C for several days, showed no new lines, although when examined in the electron microscope many of these showed large quantities of VO_x. In the optical microscope VO_x (blue-green) is readily distinguished from V_2O_5 (yellow). In this way we confirmed that only the thinnest V_2O_5 crystals had transformed to VO_x. Grinding V_2O_5 single crystals to a powder before heating in vacuum did not assist the production of VO_x. This is because the grinding action tends to produce roughly cubic crystallites, whereas rapid reaction appears to involve crystals thin in a direction parallel to $\mathbf{c}_{V_2O_5}$. The greatest extent of reaction was observed with thin plates, which had been prepared by cleaving with adhesive tape. The VO_x formation is less sensitive to V_2O_5 crystal dimensions in directions parallel to **a** or **b**.

Heating in sealed tubes at above 350°C for prolonged periods (up to 60 days), and heating in a dynamic vacuum of 10^{-6} Torr. were both unsuccessful in producing pure VO_x. X-ray powder patterns taken of samples heated in the range of 350°-400°C usually showed several weak lines not belonging to V_2O_5, and not fitting VO_x *d*-values calculated from the electron microscope data. All such lines were weak, and the accuracy of measurement is low. The most reliable measurements are included in Table 1. The only agreement with the literature is with the phases reported by Sata and Ito[12]. Examination of these samples in the electron microscope showed that most thin crystals, which, by virtue of their morphology were taken as originally being V_2O_5 platelets, had considerably altered. Their appearance suggested that much material had evaporated and their diffraction patterns were indexed as V_6O_{13}. Thus reduction to the phases of Sata and Ito[12] is possible. These samples also showed groups of needles at the crystal edges which appear to have grown by vapour transport. They were examined in the electron microscope (Figs. 11a and b). It was difficult to orient them to give simple diffraction patterns and the considerable streaking present hindered accurate measurement. However, the diffraction patterns are consistent with the available data for V_3O_7[8, 9, 21], but not with that for V_6O_{13}. The streaking on the diffraction pattern indicates disordered planar defects in the crystal, and these are revealed in the micrograph (Fig. 11b). These could be disordered shear planes, but as the reaction is most likely to involve growth from the vapour phase they do not throw light on the formation of VO_x.

Table 1. Values of $\sin^2\theta$ and interplanar spacings, d, *of non V_2O_5 lines occurring on X-ray photographs of V_2O_5 annealed at 350–400°C in vacuum*

$\sin^2\theta$ CuKα_1	d Å
0·0140	6·50
0·0340	4·17
0·0435	3·68
0·0475	3·53
0·0530	3·34
0·0567	2·23

Samples annealed for 40 or more days at 400°C were reduced to a mixture of V_6O_{13} and a phase tentatively indexed as V_3O_7. These results, and the blue-green colour of VO_x, lend credence to the suggestion that the phases found with the electron microscope are produced by oxygen loss from V_2O_5. This suggests that to produce pure VO_x it will be necessary to heat V_2O_5 at less than 250°C for long times. Techniques to encourage reaction at low temperatures, especially hydrothermal preparation, may be essential for preparation of reasonable quantities of these phases.

5. CONCLUSIONS

Following the report by Gillis and Remaut [6], we sought evidence for the occurrence of crystallographic shear in V_2O_5, but found nothing to suggest that VO_x is derived from V_2O_5 by such a mechanism, or that V_2O_5 transforms directly to V_6O_{13}.

It was discovered that the reaction is complex and that a number of phases exist which have not been reported previously. The effect of crystal size was also found to be of great importance, and the rate of reaction is closely related to the thickness of the crystal parallel to $c_{V_2O_5}$. Reactions observed to take place in thin crystals in a few seconds were extremely slow in normal powders and are virtually completely inhibited in thick crystals.

This preliminary report contains only a phenomenological description of the changes observed. Further work, particularly structural studies are needed before this region of the vanadium–oxygen phase diagram is understood.

Acknowledgements—We are indebted to the Australian Research Grants Committee and Professor J. Quirk, and to Dr. L. N. D. Lucas for making available electron microscopy facilities; also to Dr. D. J. M. Bevan for use of a Guinier camera. One of us (R.J.D.T.) was Australian Titan Products Research Fellow in Inorganic Chemistry in the University of Western Australia. We are pleased to acknowledge financial support received from AFOSR (SRC)-OAR, U.S.A.F. Grant No. AF-AFOSR-853-67, and also from the Research Grants Committee of this University.

We are especially grateful to Dr. L. A. Bursill for advice and discussion, and also for Fig. 1d.

6. REFERENCES

1. AEBI F., *Helv. chim. Acta* **31**, 8 (1948)
2. WADSLEY, A. D., *Rev. pure. appl. Chem.* **5**, 165 (1955).
3. WADSLEY A. D., *Acta. crystallogr.* **10**, 261 (1957) S., *Phys. Status Solidi* **11**, 689 (1965).
4. ANDERSON J. S. and HYDE B. G., *J. Phys. Chem. Solids* **28**, 1393 (1967).
5. GILLIS E., *C. R. hebd. Séanc. Acad. Sci., Paris* **258**, 4765 (1964).
6. GILLIS E. and REMAUT G., *C. R. hebd. Séanc. Acad. Sci., Paris* **262B**, 1215 (1966).
7. FIERMANS L. and VENNIK J., *Surf. Sci.* **9**, 187 (1968).
8. THOMAS D., TUDO J. and TRIDOT G., *C. R. hebd. Séanc. Acad. Sci., Paris* **265C**, 183 (1967).
9. KOSUGE K., *J. Phys. Chem. Solids* **28**, 1613 (1967).
10. THEOBALD F., CABALA R. and BERNARD J., *C. R. hebd. Séanc. Acad. Sci., Paris* **266C**, 1534 (1968).
11. SATA T., KOMADA E. and ITO Y., *Kogyo Kagaku Zasshi* **71**, 643 (1968).
12. SATA T. and ITO Y., *Kogyo Kagaku Zasshi* **71**, 647 (1968).
13. WYCKOFF R. G., *Crystal Structures*, Vol II, 2nd Edn Interscience, New York (1964).
14. BACHMANN H. G., AHMED F. R. and BARNES W. H., *Z. Krist.* **115**, 110 (1961).
15. TILLEY R. J. D. and HYDE B. G., To be published.
16. ASHBY M. F. and BROWN L. M., *Phil. Mag.* **8**, 1083, 1649 (1963).
17. HIRSCH P. B., HOWIE A., NICHOLSON R. B., PASHLEY D. W., and WHELAN M. J. *Electron Microscopy of Thin Crystals*. Butterworths, London, (1965)
18. GEVERS R., van LANDUYT J. and AMELINCKX S., *Phys. Status Solidi* **11**, 689 (1965).
19. BURSILL L. A., *Proc. R. Soc.* **A311**, 267 (1969).
20. BUERGER M. J., In *Phase Transformations in Solids* (Edited by R. Smoluchowski), p. 183. Wiley, New York (1951).
21. ANDERSSON S. and WADSLEY A. D., Private communication.

J. Phys. Chem. Solids Pergamon Press 1970. Vol. 31, pp. 1621-1639. Printed in Great Britain

SOME CONSIDERATIONS REGARDING THE APPLICATION OF A LINEAR CHAIN MODEL TO SOME COMPOUNDS OF THE β-W STRUCTURE

M. WEGER†

Laboratoire de Physique des Solides,‡ Faculté des Sciences, 91-Orsay, France

(Received 16 May 1969)

Abstract – In A_3B compounds possessing the A15 (β-W) lattice, such as V_3Si, "A" atoms are arranged in families of interpenetrating linear chains. As a consequence, the electronic band structure may display one-dimensional properties. A model lattice is considered by the tight-binding approximation, and it is shown that sections of the constant energy surfaces are approximately planes, and the wave functions are concentrated on chains perpendicular to these planes, even for quite strong interchain coupling. The symmetries of $3d$ states localized on atoms of a single chain are investigated, for the cubic and strained states of the lattice. It is shown that for some bands, the interchain coupling vanishes for $k = 0$; for these bands, it is conceivable that the density of states displays a sharp maximum there. It is also shown that due to the special symmetry of the lattice, a uniform uniaxial strain can open up a gap at the center of several of the bands of the linear chains, and this effect may also lead to a lattice instability.

1. INTRODUCTION

EVEN before the advent of the BCS theory, Frohlich[1] suggested that a one dimensional chain of metallic atoms, possesses an instability against distortion analogous to a second-order Jahn–Teller effect, and that this instability may be associated with superconductivity. This instability is due to interaction of electrons with phonons of wavevector $q = 2k_F$, where k_F is the Fermi momentum, and it results in a static deformation possessing this wavevector. Later, the suggestion was made[2], that in some alloys, possessing the A15 (β-W) crystal structure, notably V_3Si and Nb_3Sn, vanadium (or niobium) atoms are arranged in linear chains, such that the distance between atoms in the same chain is considerably less than between atoms belonging to different chains; and if the band structure of d-electrons can be described by the tight binding model, this property should give rise to an approximately one-dimensional band structure, which has inherent instabilities which may account for some of the peculiar properties of these alloys. Friedel and Labbé [3] suggested, that when $k_F \simeq 0$, the singularity in the density of states of a one-dimensional system at $k = 0$, enhances this instability, and, moreover, the large density of states is responsible for high superconducting transition temperatures, and thus the high value of T_c and the lattice instability are related. Barisic and De Gennes[4] suggested, that a one-dimensional structure should give rise to a large anisotropy in the upper critical field, H_{c2}. It is the purpose of this note to discuss some of the properties of the linear chains in crystals possessing the A15 symmetry.

In section 2, a simple model of a lattice consisting of two families of linear chains is treated in the tight-binding approximation. It is shown how this model displays 'one dimensional' properties, namely, sections of the constant-energy surfaces are planar, and the wavefunctions belonging to these states, are predominantly situated on chains perpendicular to these surfaces. It is shown that these 'one dimensional' properties persist even when the interchain coupling is not weak compared with the intrachain coupling; moreover, when the interchain coupling becomes weak, the 'one dimensionality' becomes very large. In section 3, the symmetry properties of individual chains of the A15 lattice are treated by analysing the representations of the group $P4_2/mmc$ which is a subgroup of $Pm3n$, the space group of the A15 lattice, containing only these operations which leave one chain invariant. The band structure is described for a d-band localized on one chain, and the effects of other bands, and interchain coupling, are discussed qualitatively. The effect of strain on the band structure is treated by considering the representations of subgroups containing the symmetry operations of the distorted lattice. It turns out, that a salient feature of the chains of the A15 structure, is that they possess a symmetry slightly lower than that of an isolated chain, because of their environment. First, they lack total rotational invariance; second, and more important, a translation by $a/2$ (the distance between neighbouring atoms) is a symmetry operation for an isolated linear chain, but not for the A15 lattice; instead, a screw-axis involving a translation by $a/2$ along the chain, followed by a rotation of 90° around the chain, transforms the chain into itself. As a result, the zone boundary is at $k_x = \pi/a$, while for a linear chain it would be at $k_x = \pi/(a/2)$; but, because of the screw axis, an extra degeneracy is present at the zone-boundary, preventing the existance of a gap for non-degenerate bands. Doubly degenerate bands may, however, be split at $k_x = \pi/a$, which they would not in a linear chain; and a distortion to a tetragonal state, produces a gap at the zone boundary even for non-degenerate levels.

---

†On leave from the Department of Physics, the Hebrew University, Jerusalem, Israel.

‡Laboratoire associé au C.N.R.S.

In section 4, an attempt is made to account for some of the singular properties of V_3Si, Nb_3Sn, etc. in light of preceding work, and the results of sections 2 and 3.

2. A SIMPLE LINEAR CHAIN MODEL

Consider the following two-dimensional model; (Fig. 2): There are two families of

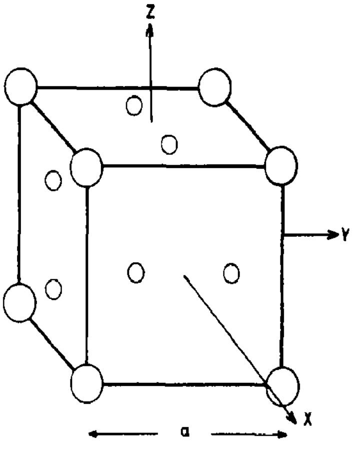

Fig. 1. The structure of the A15 lattice

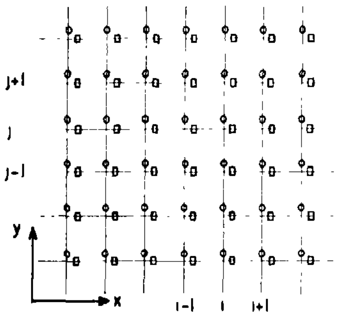

Fig. 2(a)

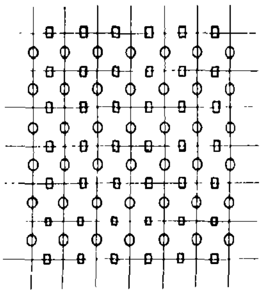

Fig. 2(b)

Fig. 2. (a) A two dimensional network of two families of linear chains, used as a model to demonstrate 'one-dimensionality'. (b) A centered two-dimensional lattice. Here the interchain coupling vanishes at the zone boundary, for bands with s or d_{xy} type symmetry.

lines, in the x and y directions; each atom belongs to one, and only one of the families. In the tight binding approximation, assume that the interaction integral between nearest neighbours on the same line is J_1, between neighbours belonging to different lines of the same family is zero, and between nearest neighbours belonging to different families, it is J_2. Then the system can be described by the Hamiltonian

$$= J_1 \sum_{ij} (a^*_{i,j+1} a_{i,j} + \text{c.c.}) + J_1 \sum_{ij} (b^*_{i+1,j} b_{i,j} + \text{c.c.}) + J_2 \sum_{ij} (a^*_{i,j} b_{i,j} + \text{c.c.})$$

$a^*_{ij} b^*_{ij}$ are creation operators for electrons on atoms in cell ij belonging respectively to the two families of chains. The wavefunctions and energies are given by

$$\psi = \alpha \sum_{ij} a^*_{i,j} \exp[i(k_x di + k_y dj)] + \beta \sum_{ij} b^*_{i,j} \exp[i(k_x di + k_y dj)]$$

$$E = J_1(\alpha^2 \cos k_x d + \beta^2 \cos k_y d) + J_2 \alpha\beta$$

where, for band A,

$$2\alpha^2 = 1 + \{1 + |J_2/2J_1(\cos k_y d - \cos k_x d)|^2\}^{-1/2}$$

$$\beta^2 = 1 - \alpha^2; \quad \text{and for band B,} \quad \alpha^B = -\beta^A; \quad \beta^B = \alpha^A$$

The surfaces of constant energy are shown in Fig. 3(a), for the case $J_1 = J_2$. Because of the relationship

$$E^B(k_x d, k_y d) = -E^A(\pi - k_y d, \pi - k_x d),$$

the surfaces of bands A and B are identical, if points Γ and M are interchanged, and E replaced by $-E$. The Fermi surface for occupation of $\frac{1}{2}$ electron per atom per spin, is shown in Fig. 3(b).

It is seen, that the constant energy surfaces are approximately squares, perpendicular to the x and y axes. When $J_2 < J_1$, this effect is even more marked. Moreover, at a section of the constant energy surface perpendicular to the x-axis, the wavefunctions are predominantly localised on chains in the x direction, and vice versa. Quantitatively, one may define a degree of 'one dimensionality' as the radius of curvature of the constant energy surfaces, divided by k; or, as the ratio α^2/β^2 of the components of the wavefunction on the two families of chains. This quantity is plotted as function of k_x (for $k_y = 0$) for several values of J_2/J_1, in Fig. 4. Alternative measures of 'one dimensionality' are, the inverse distance between the corresponding plane sections of the Fermi surfaces of the two bands, and the number of atoms along a chain, an electron follows on the average before passing to a different chain (approximately $v_F/a|E^A - E^B|\beta^2$). These quantities are also essentially equal to the quantity α^2/β^2, plotted in Fig. 4.

It is seen, that already for $J_2 = 2J_1$, a considerable degree of one-dimensionality is present for values of k_x which are not too small. However, for $k_x \approx 0$, the energy surfaces are circles, even for J_1 considerably larger than J_2. For comparison, the band structure for a single family of chains, with next nearest neighbour interaction J_2, is plotted in Fig. 3(c), for $J_2 = J_1/2$. For this model, to get the same 'one dimensionality' (say, defined as the inverse distance between the plane sections of the $E = 0$ energy surface), as for the preceding two family model with $J_2 = J_1$, requires here $J_2 = J_1/4$. Moreover, for large values of J_1/J_2, the one-dimensionality here increases linearly with this quantity, while for the two-family model, it increases quadratically. Qualitatively, this may be explained as follows. For motion of electrons along the chain, the forward scattering amplitudes add; however, for scattering to chains of a different family, successive scatterings correspond to different final states, and thus transition probabilities, rather than amplitudes, add, and the scattering is much weaker. This argument holds only when the product of the transition probability and the time the electron stays on an atom, is small; thus, when

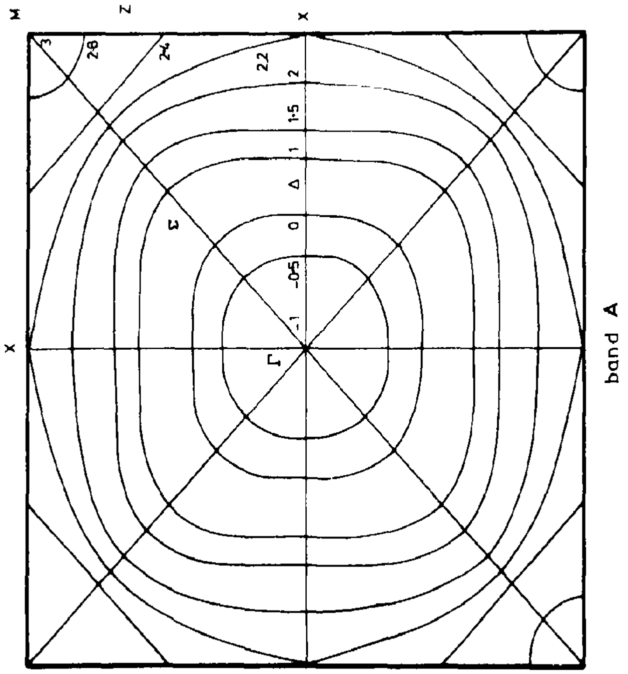

Fig. 3(a) Part 1

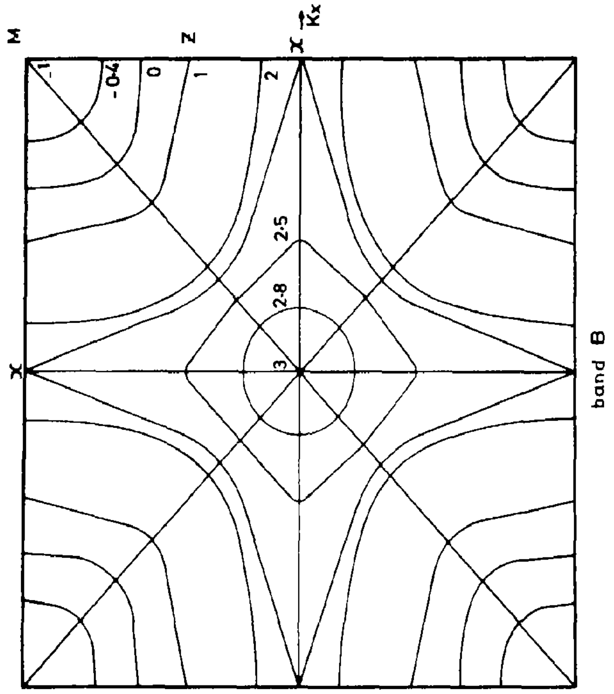

Fig. 3(a) Part 2

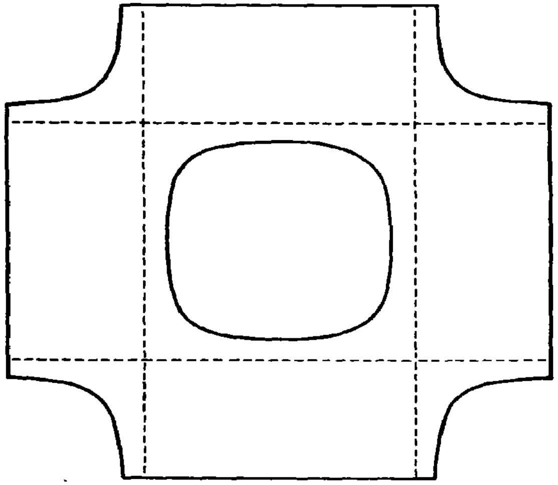

Fig 3(b)

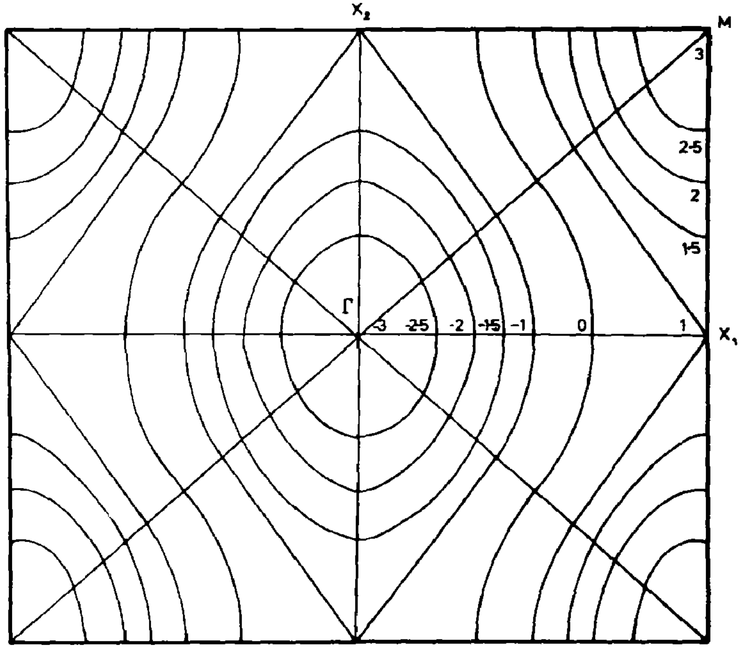

Fig. 3(c)

Fig 3 (a) Constant energy surfaces for the lattice of Fig 2a, when the interchain coupling equals the nearest neighbour intrachain coupling, for the two bands, *A* and *B*. (b) the Fermi surface corresponding to band structure (a), for an occupation of one electron per atom There are two sections, belonging to the two bands The dashed lines indicate the Fermi surface for an ideal one-dimensional model[2] (c) Constant energy surfaces for a two-dimensional rectangular lattice with one family of chains, when the interaction in the *x*-direction is twice as strong as in the *y*-direction. The structure is anisotropic, but less 'one-dimensional' than that of (a), as described in text

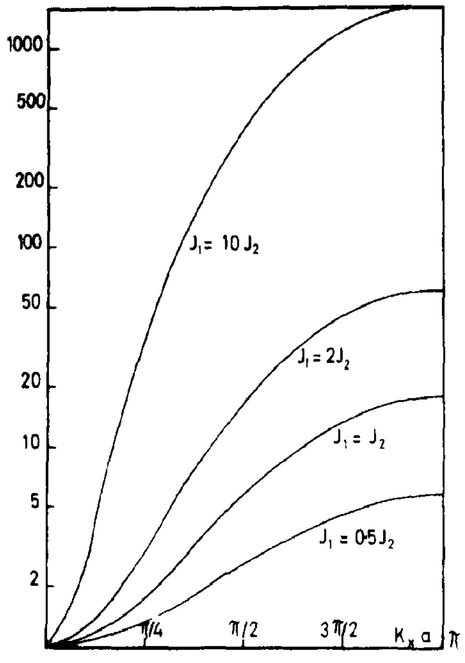

Fig. 4. The 'one-dimensionality', as defined in text, as function of the momentum along the Δ axis, for several values of interchain coupling J_2, for the lattice of Fig. 2a. For band A, electrons with momenta in the x-direction are preferentially localised on chains in the y-direction, and for band B, on chains in the y-direction. Along the M–Z–X axis ($k_y a = \pi$), the same graph applies, when $k_x a$ is replaced by $\pi - k_x a$. It is seen that there is appreciable 'one-dimensionality' even for relatively strong interchain coupling, except for small momenta, and for momenta along the line $k_x = k_y$

the electron stands still ($k = 0$), it does not apply.

Another salient feature of this model, is the Van-Hove singularity (saddle point) at point X. This saddle point gives rise to a singularity in the density of states:

$$n(E) = \begin{cases} 2(1/J_1{}^2 + 4/J_2{}^2)^{1/2} ln\,[4x_0{}^2\beta^2|J_1|/(E_x - E)] & E < E_x \\ 2(1/J_1{}^2 + 4/J_2{}^2)^{1/2} ln\,[4x_0{}^2\alpha^2|J_1|/(E - E_x)] & E > E_x \end{cases}$$

where x_0 is a number of order unity. As pointed out by Labbé and Friedel[3], a singularity in the density of states may give rise to a lattice instability, manifesting itself in a martensitic transformation, and/or a softening of the elastic constants, as observed experimentally for V_3Si^5, Nb_3Sn^6, and V_3Ge^7. The contribution to the elastic constants is given approximately by[7]

$$\delta(C_{11} - C_{12}) = -\tfrac{1}{4} n(E_F)(\partial E^A/\partial e_{xx} - \partial E^B/\partial e_{xx})^2$$

Thus, a large value of $n(E_F)$ helps to create a softening, however, it is also necessary that the volume-conserving strain $e_{yy} = -e_{xx}$ remove the degeneracy between $E^A(\pi, 0)$ and $E^B(0, \pi)$; when $J_2 \gg J_1$, this degeneracy is not effectively removed by the applied strain. Thus, a lattice softening, or instability, may also be accentuated by strong 'one dimensionality'. For the one-family model discussed here, with $J_1 = J_2$, there are also degenerate Van-Hove singularities at $\mathbf{k} = \frac{\pi}{d}(1, 0)$ and $\frac{\pi}{d}(0, 1)$; but $\partial E^A/\partial e_{xx} = \partial E^B/\partial e_{xx} = 0$; while when $J_1 \neq J_2$, the two Van-Hove singularities are not degenerate; thus, no appreciable softening may be expected there.

The A15 structure, projected on a plane, is a centered lattice, rather than a primitive one; thus, it might be tempting to consider a two-dimensional centered lattice of linear chains (Fig. 2(b)). In this case, the energy is given by:

$$E = J_1(\alpha^2 \cos k_x d + \beta^2 \cos k_y d) + J_2 \alpha\beta \cos\frac{k_x d}{2} \cos\frac{k_y d}{2}$$

and thus the constant energy surface of the band is exactly a square at the zone boundary (i.e. the zone boundary is a constant energy surface), the wavefunctions there are completely localized on their respective family of chains, and the density of states has an $E^{-1/2}$ singularity. However, when states of opposite parity are admitted (i.e. a p-band in addition to the d_{x^2} band considered so far) the term in J_2 no longer vanishes identically. If there is considerable admixture of such states, the very strong singularity may be smeared out. Thus, it is important to bear in mind, that for certain bands, and at certain high symmetry points (or lines, or planes), the interchain interaction integral vanishes, thus enhancing 'one dimensional' properties.

Thus, it appears that a linear chain structure may indeed result in a 'one dimensional' band structure, displaying some of the properties observed in β-W compounds, though, probably not near $k = 0$. The A15 structure has some additional complications, and requires a somewhat more detailed discussion.

3. THE BAND STRUCTURE OF AN ISOLATED LINEAR CHAIN OF THE A15 LATTICE IN THE TIGHT-BINDING APPROXIMATION

Consider linear chains, of, say, vanadium atoms, in the x-direction, surrounded, say, by silicon atoms (Fig. 5). The distance between neighbouring vanadium atoms is $a/2$, where a is the size of the cubic unit cell. The symmetry operations under which the chain is invariant are given in Table 1. The symmetry operations of the group $Pm3n$, of the complete A15 symmetry, are obtained by adding the rotations around the threefold axes in the (111) directions. These operations interchange the chains. The group $Pm3n$ is discussed by Gorzkowski [8]. Consider Bloch functions with $k_y = k_z = 0$. (In the linear chain model, the energy is independent of k_y, k_z.) Then, for $k_x = 0$, $k_x = 2\pi/a$ (point Γ), and $k_x = \pi/a$ (point X), the Bloch waves form an irreducible representation of the symmetry group. The classes are defined in Table 2, and the character table for the irreducible representations is given in Table 3. The representations with positive characters under T^2 correspond to point Γ, while those with a negative character correspond to point X. At intermediate values of k_x, (point Δ), the symmetry operations, and characters of irreducible representations, are given in Table 4. Figure 6, shows the correlation diagram between the various representations.

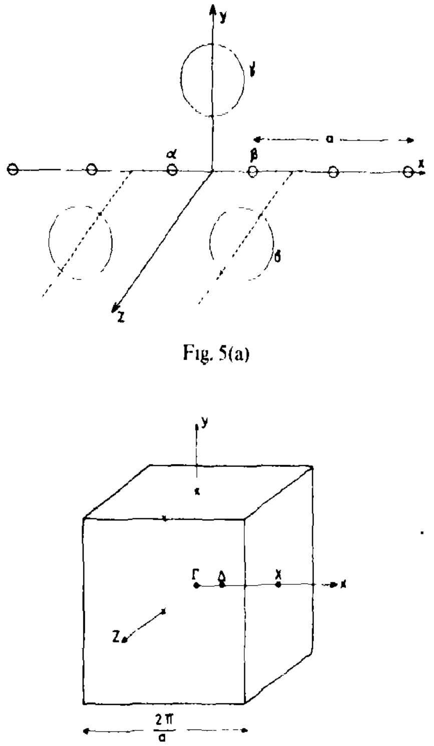

Fig. 5(a)

Fig. 5(b)

Fig. 5. (a) A linear chain of the A15 lattice, with some of its environment, illustrating its symmetry. (b) The first Brillouin zone of the A15 lattice, illustrating the points investigated in this work. The points marked 'x' are also considered briefly (Table 6).

Table 1. Symmetry operations for the linear chains in the x*-direction*

Operation	Point x, y, z transforms into
E	x, y, z
C_2	$x, -y, -z$
C_2'	$-x, -y, z$
C_2''	$-x, y, -z$
m_x	$-x, y, z$
m_y	$x, -y, z$
m_z	$x, y, -z$
I	$-x, -y, -z$
T	$x+a/2, z, y$
T^2	$x+a, y, z$

In order to get a crude idea of the band structure, let us make the following simplifying assumptions: the energy is given by $E_m(k) = E_m^0 - E_m \cos k_x a/2$, as in the tight binding model, E_m is proportional to the overlap between neighbouring atoms†. The potential has the symmetry of a linear chain; different *d*-states are not permitted to mix. A crude sketch of the band structure in the zeroth order under these assumptions is shown in thin lines in Fig. 7.

A slightly better model is obtained, if components of the crystalline potential with the proper symmetry are introduced, and if different *d*-states are permitted to mix. The

Table 2. The classes for points Γ, X. *The group is isomorphic to the group at points* Γ, X, *of the diamond lattice*

	Operations
$\mathscr{C}_1$	E
$\mathscr{C}_2$	Tm_x, TI, T^3m_x, T^3I
$\mathscr{C}_3$	C_4
$\mathscr{C}_4$	C_2, T^2C_2''
$\mathscr{C}_5$	$TC_2', TC_2'', T^3C_2', T^3C_2''$
$\mathscr{C}_6$	m_x, T^2m_x
$\mathscr{C}_7$	T, TC_2, T^3, T^3C_2
$\mathscr{C}_8$	I, T^2I
$\mathscr{C}_9$	m_y, m_z
$\mathscr{C}_{10}$	$Tm_y, Tm_z, T^3m_y, T^3m_z$
$\mathscr{C}_{11}$	T^2m_y, T^2m_z
$\mathscr{C}_{12}$	C_2'', T^2C_2'
$\mathscr{C}_{13}$	T^2C_2
$\mathscr{C}_{14}$	T^2

Table 3. Character table for the irreducible representations at points Γ *and* X

Representation		Class														Functions belonging to the representation	
		$\mathscr{C}_1$	$\mathscr{C}_{14}$	$\mathscr{C}_3$	$\mathscr{C}_{13}$	$\mathscr{C}_6$	$\mathscr{C}_8$	$\mathscr{C}_9$	$\mathscr{C}_{11}$	$\mathscr{C}_4$	$\mathscr{C}_{12}$	$\mathscr{C}_7$	$\mathscr{C}_2$	$\mathscr{C}_{10}$	$\mathscr{C}_5$		
Γ bonding	Γ_1	1	1	1	1	1	1	1	1	1	1	1	1	1	1	$x_\alpha^2 + x_\beta^2$	
	Γ_2	1	1	1	1	1	1	1	1	1	1	−1	−1	−1	1	$(y^2-z^2)_\alpha + (y^2-z^2)_\beta$	
	Γ_3	1	1	1	1	1	1	−1	−1	−1	−1	1	1	−1	−1	$yz_\alpha + yz_\beta$	
	Γ_4	1	1	1	1	1	1	−1	−1	−1	−1	−1	−1	1	1	$xyz_\alpha - xyz_\beta$	
	Γ_5	2	2	−2	2	2	−2	0	0	0	0	0	0	0	0	$xy_\alpha - xy_\beta$ $xz_\alpha - xz_\beta$	
Γ antibonding	Γ_1'	1	1	1	1	−1	−1	1	1	−1	−1	−1	1	1	1	$x_\alpha^2 - x_\beta^2$	
	Γ_2'	1	1	1	1	−1	1	1	1	−1	−1	1	−1	1	−1	$(y^2-z^2)_\alpha - (y^2-z^2)_\beta$	
	Γ_3'	1	1	1	1	1	−1	−1	−1	1	1	−1	1	1	−1	$yz_\alpha - yz_\beta$	
	Γ_4'	1	1	1	1	1	−1	−1	−1	1	1	1	−1	−1	1	$xyz_\alpha + xyz_\beta$	
	Γ_5'	2	2	2	−2	−2	2	0	0	0	0	0	0	0	0	$xy_\alpha + xy_\beta$ $xz_\alpha + xz_\beta$	
X	X_1	2	2	2	−2	0	0	2	−2	0	0	0	0	0	0	x_α^2 x_β^2	$(y^2-z^2)_\alpha$ $(y^2-z^2)_\beta$
	X_2	2	−2	2	−2	0	0	−2	2	0	0	0	0	0	0	yz_α yz_β	xyz_α xyz_β
	X_3	2	−2	−2	2	0	0	0	0	2	−2	0	0	0	0	$xy_\alpha + xy_\beta$ $xz_\alpha - xz_\beta$	
	X_4	2	−2	−2	2	0	0	0	0	−2	2	0	0	0	0	$xy_\alpha - xy_\beta$ $xy_\alpha + xz_\beta$	

---

†E_m^0 is chosen arbitrarily, but crudely to correspond with the band structure calculated by Mattheiss[9] using the APW method

Table 4. Character table for point Δ (the group here is infinite)

Representation	Operation E	C_2	m_y, m_z	T	Functions transforming under this representation	
Δ_1	1	1	1	$e^{ika/2}$	$x_\alpha^2 e^{-ika/4} + x_\beta^2 e^{ika/4}$	$(y^2-z^2)_\alpha e^{-ika/4} - (y^2-z^2)_\beta e^{ika/4}$
Δ_1'	1	1	1	$-e^{ika/2}$	$x_\alpha^2 e^{-ika/4} - x_\beta^2 e^{ika/4}$	$(y^2-z^2)_\alpha e^{-ika/4} + (y^2-z^2)_\beta e^{ika/4}$
Δ_2	1	1	-1	$e^{ika/2}$	$yz_\alpha e^{-ika/4} + yz_\beta e^{ika/4}$	$xyz_\alpha e^{-ika/4} + xyz_\beta e^{ika/4}$
Δ_2'	1	1	-1	$-e^{ika/2}$	$yz_\alpha e^{-ika/4} - yz_\beta e^{ika/4}$	$xyz_\alpha e^{-ika/4} - xyz_\beta e^{ika/4}$
Δ_5	2	-2	0	0	$xy_\alpha e^{-ika/4} - xy_\beta e^{ika/4}$ $xz_\alpha e^{-ika/4} - xz_\beta e^{ika/4}$	$xy_\alpha e^{-ika/4} + xy_\beta e^{ika/4}$ $xz_\alpha e^{-ika/4} + xz_\beta e^{ika/4}$

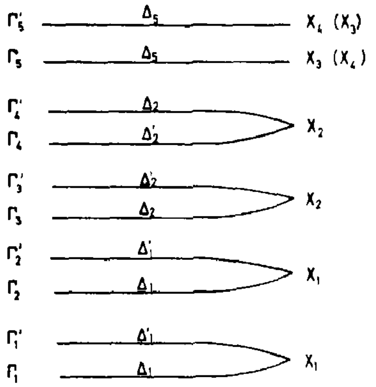

Fig. 6. The correlation of states along the Δ axis. The representations X_3 and X_4 are quite similar, and whether a state belongs to one or the other depends on the coordinate system chosen.

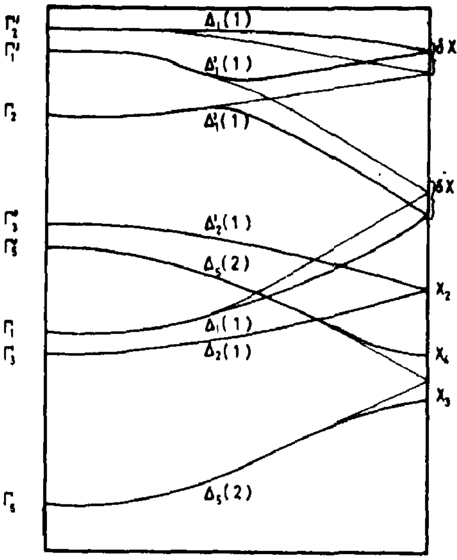

Fig. 7. The band structure for an individual linear chain, in the tight binding approximation. The fine lines, indicate the zeroth-order approximation; the heavy lines indicate the effect of coupling between different d-bands of the same chain. Some of the relevant parameters for this structure are given in Table 5.

effects of these corrections are shown by heavy lines in Fig. 7. Table 5 gives some parameters relevant to this figure.

Corrections to this approximation

It is possible to consider qualitatively the effects of the vanadium s-band, and the silicon s- and p-bands. If states of these bands possess the same symmetry as the d-states, and if they are not too far removed in energy, they will mix with the d-states, and as a result the wavefunction will be more extended in space, and the energy will depend on k_y and k_z. As a result, the bands may be broader and less 'one dimensional'. In Table 6, non-d-states, possessing the same symmetry as d-states at point Γ, are listed. It is seen, that all d-bands can mix with silicon s- and p-states, except the antibonding d_{yz}, which, therefore, could be particularly narrow.

One may also consider the interaction between various chains, parallel or perpendicular.

In order to estimate this effect, the wavefunctions have been calculated at the point of maximum overlap between the corresponding neighbours (Table 7). The interaction integrals,

Table 5. Corrections to the zeroth order band structure due to intrachain coupling

Let the energy levels in the zeroth order be given by:

$$E_m(k_x) = E_m^0 - E_m \cos k_x a/2$$

and let V be the component of the crystaline potential possessing the symmetry of $f(y^2-z^2)\cos 2\pi x/a$, where f is an odd function. Then, mixing of the d-states by this potential, causes the following corrections to the effective mass at point Γ, and to the energy levels at point X:

$$\frac{\hbar^2}{a^2}\left(\frac{1}{m^*_{xx}}\right)_{\Gamma_1} = E_{\Gamma_1} - \frac{(d_{x^2}|V|d_{y^2-z^2})^2}{(E_{\Gamma_2}+E_{\Gamma_1})+(E^0_{\Gamma_2}-E^0_{\Gamma_1})}$$

$$\frac{\hbar^2}{a^2}\left(\frac{1}{m^*_{xx}}\right)_{\Gamma_2} = E_{\Gamma_2} - \frac{(d_{x^2}|V|d_{y^2-z^2})^2}{(E_{\Gamma_2}+E_{\Gamma_1})-(E^0_{\Gamma_2}-E^0_{\Gamma_1})}$$

$$\frac{\hbar^2}{a^2}\left(\frac{1}{m^*_{yy}}\right)_{\Gamma_1} = E_{\Gamma_1} \quad \frac{\hbar^2}{a^2}\left(\frac{1}{m^*_{xx}}\right)_{\Gamma'_5} = -E_{\Gamma'_5}$$

$$\frac{\hbar^2}{a^2}\left(\frac{1}{m^*_{xx}}\right)_{\Gamma'_2} = -E_{\Gamma'_1} + \frac{(d_{x^2}|V|d_{y^2-z^2})^2}{(E_{\Gamma'_2}+E_{\Gamma'_1})+(E^0_{\Gamma'_2}-E^0_{\Gamma'_1})}$$

$$\frac{\hbar^2}{a^2}\left(\frac{1}{m^*_{xx}}\right)_{\Gamma'_1} = -E_{\Gamma'_1} + \frac{(d_{x^2}|V|d_{y^2-z^2})}{(E_{\Gamma'_2}+E_{\Gamma'_1})-(E^0_{\Gamma'_2}-E^0_{\Gamma'_1})}$$

$$\frac{\hbar^2}{a^2}\left(\frac{1}{m^*_{xx}}\right)_{\Gamma_5} = E_{\Gamma_5} - \frac{(d_{xy}|V|d_{xy})^2}{2E_{\Gamma_5}}$$

$$\frac{\hbar^2}{a^2}\left(\frac{1}{m^*_{xx}}\right)_{\Gamma'_5} = -E_{\Gamma'_5} + \frac{(d_{xy}|V|d_{xy})^2}{2E_{\Gamma'_5}}$$

$$\delta E_{X_1} = \frac{(d_{x^2}|V|d_{y^2-z^2})^2}{[(E^0_{\Gamma_2}-E^0_{\Gamma_1})^2+(d_{x^2}|V|d_{y^2-z^2})^2]^{1/2}}$$

$$E_{X_1} - E_{X_4} = 2(d_{xy}|V|d_{xy})$$

depend also on the volume of large overlap, and the potentials, but it is believed, that the relative value of $|\psi|^2$ gives at least a crude idea of the relative magnitude of the interaction integrals. It is seen, that for the d_{x^2} band, the nearest neighbour interaction is predominant; for the d_{yz} and $d_{y^2-z^2}$ bands, the next-nearest neighbour interaction is predominant, hence these bands cannot be expected to display a 'one dimensional' character. The situation of the d_{xy}, d_{xz} bands is intermediate. The nearest neighbour and next-nearest neighbour interactions appear to be of the same order. Bearing in mind the considerations of section 2, it appears that these bands may display some 'one dimensional' character. Estimates of the interaction integrals derived from Mattheiss' calculation[9] are also shown. It is seen, that agreement with the simple, semi-qualitative considerations, is surprisingly good at point Γ. However, if one tries to extend this agreement and compare the present structure with the structure calculated by Mattheiss along the Δ-axis, no agreement whatsoever is obtained.

In addition to the value of the overlap, symmetry considerations are also an important factor affecting interactions between different families of chains.

Interaction between perpendicular chains can be expected to be strong if states of the same symmetry have the same (or nearly the same) energy. This occurs at point Γ for some of the states, but not all, for example, a state Γ_1, on chains in the y- and z-directions, also has a Γ_1 symmetry when referred to the x-direction (considering the symmetry operations which are common to these families of chains), but Γ'_1 states do not possess this property.

In other words, the states Γ_1 of chains in the x-, y- and z-directions, belong to a reducible representation of the complete group, *Pm3n*, and the irreducible representations of the complete group, necessarily contain states belonging to different chains, while the states Γ'_1 belong to a triply degenerate, irreducible representation of *Pm3n*, and thus are eigenstates at point Γ even if mixing between different chains is allowed.

Table 8 shows the construction of wavefunctions of the whole lattice, from those of the individual chains, at point Γ. Thus, states Γ_1, Γ_2, Γ_5, Γ'_3, Γ'_4, Γ'_5 on chains in the x-direction, mix with corresponding states on chains in the y- and z-directions; while states Γ_3, Γ_4, Γ'_1, Γ'_2 do not, and therefore may be expected to be more 'one dimensional'.

Another factor to be considered, is the width and anisotropy of the bands. Bands which are relatively wide, and anisotropic, *Table* 6. *Symmetry of non*-d-*functions at the point* $k_x = 0$; k_y, $k_z = 0, \pi/a$

The symbols are defined in Fig. 5. The group at points $\mathbf{k} = (\pi/a)(0, 1, 0)$ and $\mathbf{k} = (\pi/a)(0, 0, 1)$ is *mmm* and it does not contain the operation *T*; hence Γ_1 and Γ_2 are indistinguishable, etc., and Γ_5, Γ_5' decompose. Vanadium *p*-functions do not mix with vanadium *d*-functions of the same chain, because of opposite parity. However, when interaction between chains is considered, they must be taken into account.

Representation \ k	(000)	(011)	(010)	(001)	Typical *d*-functions possessing this symmetry
Γ_1	$s^\gamma + s^\delta$ $s^\alpha + s^\beta$	$p_y{}^\delta + p_z{}^\gamma$ $s^\alpha + s^\beta$	s^γ $p_y{}^\delta$ $s^\alpha + s^\beta$	s^δ $p_z{}^\gamma$ $s^\alpha + s^\beta$	d_{x^2}
Γ_2	$s^\gamma - s^\delta$	$p_y{}^\delta - p_z{}^\gamma$			$d_{y^2-z^2}$
Γ_3		$p_z{}^\delta + p_y{}^\gamma$			d_{yz}
			$p_z{}^\delta$	$p_y{}^\gamma$	
Γ_4		$p_z{}^\delta - p_y{}^\gamma$			
Γ_5	$p_z{}^\gamma$ $p_y{}^\gamma$	s^γ	s^δ $p_y{}^\gamma$	s^γ $p_z{}^\delta$	d_{xy}
	$p_y{}^\delta$ $p_z{}^\delta$	s^δ	$p_z{}^\gamma$	$p_y{}^\delta$	d_{xz}
Γ_1'	$p_x{}^\gamma - p_x{}^\delta$ $s^\alpha - s^\beta$	$s^\alpha - s^\beta$	$p_x{}^\gamma$ $s^\alpha - s^\beta$	$p_x{}^\delta$ $s^\alpha - s^\beta$	d_{x^2}
Γ_2'	$p_x{}^\gamma + p_x{}^\delta$				$d_{y^2-z^2}$
Γ_3'					d_{yz}
Γ_4'					
Γ_5'		$p_x{}^\gamma$ $p_x{}^\delta$	$p_x{}^\delta$	$p_x{}^\gamma$	d_{xy} d_{xz}

Table 7a. *Estimate of* ψ^2 *at the point of maximum overlap. The radial dependence of the wavefunction is taken as* $f(r) = \exp(-qr)$, *where* $q = 0{\cdot}27\ \text{Å}^{-1}$

There are two nearest neighbours on the same chain, eight near neighbours on orthogonal chains for states d_{x^2}, $d_{y^2-z^2}$, d_{yz}, and four for states d_{xz}, d_{xz}. There are four neighbours on parallel chains for states d_{x^2}, $d_{y^2-z^2}$, d_{yz} and two for states d_{xy}, d_{xz}. The estimate of ψ^2 for neighbours on parallel chains is very unreliable, because of the large distance, and presence of intervening atoms.

State	Same chain	Orthogonal chain	Parallel chain
$d_{x^2}(\Gamma_1, \Gamma_1')$	0·7	0·03	0·05
$d_{y^2-z^2}(\Gamma_2, \Gamma_2')$	0·1	0·1	0·15
$d_{yz}(\Gamma_3, \Gamma_3')$	0·1	0·2	0·1
$d_{xy}, d_{xz}(\Gamma_5, \Gamma_5')$	0·5	0·2	0·1

may mix at point Γ, but for $k_x \neq 0$, states possessing the same symmetry but belonging to different families of chains, may possess very different energies, and hence not mix very much, thus, though all states Γ_1, Γ_2, Γ_3', Γ_4' mix at $k_x = 0$, Γ_1 may mix less than the rest for $k_x \neq 0$, because the corresponding band is broader and more anisotropic.

Effects of distortion

Let us consider briefly the effects of strain in the (100), (111), and (110) directions on the symmetry properties. The strain has two effects: it destroys the equivalence between the three families of chains, present in the cubic state; and it changes the properties of the individual chains. A strain in the (100) direction reduces the symmetry of the crystal

Table 7b. Energy levels from Mattheiss'[9] calculation for V_3Si

The present assignment is somewhat arbitrary, since only some wavefunctions are given there. E''' is determined from the difference between the centers of gravity of the bonding and antibonding states; the interchain coupling is estimated from the splitting of the bonding (or antibonding) states.

It is seen, that for the d_{x^2}, d_{xy} and d_{zx} states, a 'one-dimensional' model may be a reasonable approximation, but not for states $d_{y^2-z^2}$, d_{yz}, as may be expected from intuitive considerations

State	Energy (Ry)	Present assignment		E''' (Ry)	Interchain coupling (Ry)
Γ_1	0		Γ_1		
Γ_{12}	0·1	d_{x^2}	Γ_1	0·17	0·03
Γ_{25}	0·4		Γ'_1		
Γ_2	0·35		Γ_2		
Γ_{12}	0·26	$d_{y^2-z^2}$	Γ_2	0·06	0·03
Γ_{15}	0·42		Γ'_2		
Γ'_{25}	0		Γ_3		
Γ'_1	0	d_{yz}	Γ'_3	0·09	0·09
Γ'_{12}	0·28		Γ'_3		
Γ_{15}	−0·2		Γ_5		
Γ_{25}	0·08	d_{xy}	Γ_5	0·22	0·02
Γ'_{15}	0·31	d_{zx}	Γ'_5		
Γ'_{25}	0·3		Γ'_5		

from cubic to tetragonal. Thus, it maintains the symmetry of one family of chains (those in the x-direction), but destroys the screw-axis symmetry elements of the chains in the y- and z-directions. The group that is left is mmm, which has 8 one dimensional representations. The correlation with the original group is shown in Table 9. It is seen that the degeneracy at point X is lifted. This effect is similar to the one postulated by Frohlich[1], however, the difference is, that Frohlich postulated the lifting of this degeneracy by a phonon with wavenumber $q = \pi/(a/2)$, while here a phonon with wavenumber $q = 0$ can cause this effect. Such a phonon has a much lower energy. When the degeneracy is lifted, a singularity in the density of states is produced, which is similar to the singularity at $k = 0$, and may give rise to similar effects. (A second order

Table 8. Formation of states of the whole A15 lattice, from states of individual chains

'G' means Gorzkowski's notation[8]; 'BSW' means Bouchaert, Smoluchowski, and Wigner's notation. 'Γ_1^x' means a Γ_1 state, on chains in the x-direction (i.e. d_{x^2}) It is seen, that eigenstates of the lattice, may be eigenstates of individual chains, for states Γ'_1, Γ'_2, Γ_3, Γ_4.

Individual chain states	Linear combinations of individual chain states forming eigenstates of the lattice	G	BSW
$3\Gamma_1$	$\Gamma_1^x + \Gamma_1^y + \Gamma_1^z$	1^+	Γ_1
	$\Gamma_1^x - \frac{1}{2}(\Gamma_1^y + \Gamma_1^z)$ $\Gamma_1^y - \Gamma_1^z$	3^+	Γ_{12}
$3\Gamma'_1$	$\Gamma_1'^x$ $\Gamma_1'^y$ $\Gamma_1'^z$	5	Γ_{25}
$3\Gamma_2$	$\Gamma_2^x + \Gamma_2^y + \Gamma_2^z$	2^+	Γ_2
	$\Gamma_2^x - \frac{1}{2}(\Gamma_2^y + \Gamma_2^z)$ $\Gamma_2^y - \Gamma_2^z$	3^+	Γ_{12}
$3\Gamma'_2$	$\Gamma_2'^x$ $\Gamma_2'^y$ $\Gamma_2'^z$	4	Γ_{15}
$3\Gamma_3$	Γ_3^x Γ_3^y Γ_3^z	5^+	Γ'_{25}
$3\Gamma'_3$	$\Gamma_3'^x + \Gamma_3'^y + \Gamma_3'^z$	1	Γ'_1
	$\Gamma_3'^x - \frac{1}{2}(\Gamma_3'^y + \Gamma_3'^z)$ $\Gamma_3'^y - \Gamma_3'^z$	3	Γ'_{12}
$3\Gamma_4$	Γ_4^x Γ_4^y Γ_4^z	4^+	Γ'_{15}
$3\Gamma'_4$	$\Gamma_4'^x + \Gamma_4'^y + \Gamma_4'^z$	2^-	Γ'_2
	$\Gamma_4'^x - \frac{1}{2}(\Gamma_4'^y + \Gamma_4'^z)$ $\Gamma_4'^y - \Gamma_4'^z$	3	Γ'_{12}
$3\Gamma_5$	$\Gamma^x_{5_{xy}} + \Gamma^z_{5_{yz}}$ $\Gamma^y_{5_{yz}} + \Gamma^x_{5_{zx}}$ $\Gamma^z_{5_{zx}} + \Gamma^y_{5_{xy}}$	5	Γ_{25}
	$\Gamma^x_{5_{xy}} - \Gamma^z_{5_{yz}}$ $\Gamma^y_{5_{yz}} - \Gamma^x_{5_{zx}}$ $\Gamma^z_{5_{zx}} - \Gamma^y_{5_{xy}}$	4^-	Γ_{15}

Table 8 (*contd.*)

Individual chain states	Linear combinations of individual chain states forming eigenstates of the lattice	G	BSW
$3\Gamma_5'$	$\Gamma_{5_{xy}}'^{x}+\Gamma_{5_{xy}}'^{y}$ $\Gamma_{5_{yz}}'^{y}+\Gamma_{5_{yz}}'^{z}$ $\Gamma_{5_{zx}}'^{z}+\Gamma_{5_{zx}}'^{x}$	4^+	Γ_{15}'
	$\Gamma_{5_{xy}}'^{x}-\Gamma_{5_{xy}}'^{y}$ $\Gamma_{5_{yz}}'^{y}-\Gamma_{5_{yz}}'^{z}$ $\Gamma_{5_{zx}}'^{z}-\Gamma_{5_{zx}}'^{x}$	5^+	Γ_{25}'

Jahn–Teller distortion; a large electronic density of states; a contribution to the elastic constants; a contribution to the electron–phonon coupling responsible for superconductivity; etc.) Also, the doubly degenerate Δ_5 state is split. The effects of strain in the (100) direction have been discussed in great detail by Barisic and Labbé[3].

A strain in the (011) direction, maintains two families of chains, y and z, equivalent, while family x is different. The symmetry group for the family in the x-direction, is given in Table 10; that of the families in the y- and z-directions, is m. For symmetry m, all degeneracy is lifted. For the chains in the x-direction, the double degeneracy at point X is maintained; (there is no longer a screw-axis operation, but a glide-plane still exists). The degeneracy of states Δ_5 is lifted except at point X.

A strain in the (111) direction, maintains all families equivalent; the symmetry group is given in Table 11. The degeneracy of Δ_5 is lifted, but the degeneracy at point X remains. The lifting of the Δ_5 degeneracy could give rise to a softening of the elastic constant C_{44}, an effect observed in V_3Ge[7].

4. APPLICATION OF THE LINEAR CHAIN MODEL TO SOME V_3X, Nb_3X COMPOUNDS

In a number of papers, Friedel, Labbé and Barisic[3] considered a linear chain model for

Table 9. *Correlation between the representations of the group of the undisturbed chain, and those of the group* mmm, *describing chains under strain perpendicular to their length. The designation of the representations of* mmm *is that of Jones*[10]

$P4_2/mmc$ (mmm)	$P4_2/mmc$ (mmm)
$\Gamma_1-\Gamma_1^+$	$X_1 <^{X_1^+}_{X_3}$
$\Gamma_2-\Gamma_1^+$ $\Gamma_3-\Gamma_1^+$	$X_2 <^{X_3^+}_{X_1}$
$\Gamma_4-\Gamma_3^+$	$X_3 <^{X_2^-}_{X_2^+}$
$\Gamma_5 <^{\Gamma_2^+}_{\Gamma_4^+}$	$X_4 <^{X_1^+}_{X_4^-}$
$\Gamma_1'-\Gamma_3^-$	$\Delta_1-\Delta_1^+$
$\Gamma_2'-\Gamma_1$ $\Gamma_3'-\Gamma_1$ $\Gamma_4'-\Gamma_1$	$\Delta_1-\Delta_1^+$ $\Delta_2-\Delta_1^+$
$\Gamma_5' <^{\Gamma_2^-}_{\Gamma_4^-}$	$\Delta_2'-\Delta_1$
	$\Delta_5 <^{\Delta_2}_{\Delta_4}$

Correlation diagram for representations of *mmm*.

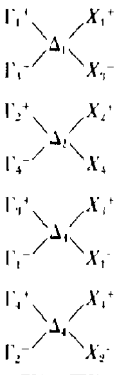

β-W compounds. Some of the assumptions of this model, are:

(1) That all interaction integrals, except the

Table 10. *Irreducible representations of the group corresponding to strain in the* (011) *direction* (Pcc/m)

Class Representation	E	T^2	C_2	T^2C_2	m_x T^2m_x	I T^2I	T T^3	TC_2 T^3C_2	TI T^3I	Tm_x T^3m_x	Typical functions belonging to the representation
Γ_{13}	1	1	1	1	1	1	1	1	1	1	Γ_1, Γ_3
Γ_{24}	1	1	1	1	1	1	−1	−1	−1	−1	Γ_2, Γ_4
Γ'_{13}	1	1	1	1	−1	−1	−1	−1	1	1	Γ'_1, Γ'_3
Γ'_{24}	1	1	1	1	−1	−1	1	1	−1	−1	Γ'_2, Γ'_4
Γ_{51}	1	1	−1	−1	1	−1	−1	1	1	−1	$(xy+xz)_\alpha-(xy+xz)_\beta$
Γ_{52}	1	1	−1	−1	1	−1	1	−1	−1	1	$(xy-xz)_\alpha-(xy-xz)_\beta$
Γ'_{51}	1	1	−1	−1	−1	1	1	−1	1	−1	$(xy+xz)_\alpha+(xy+xz)_\beta$
Γ'_{52}	1	1	−1	−1	−1	1	−1	1	−1	1	$(xy-xz)_\alpha+(xy-xz)_\beta$
X_{12}	2	−2	2	−2	0	0	0	0	0	0	X_1, X_2
X_{34}	2	2	−2	2	0	0	0	0	0	0	X_3, X_4

Table 11. *Irreducible representations of the group corresponding to strain in the* (111) *direction* (P2/c)

Class Representation	E	T^4	I T^2I	T^4	T^4I	Typical functions belonging to the irreducible representation
Γ_{135}	1	1	1	1	1	$\Gamma_1, \Gamma_3, (xy+xz)_\alpha+(xy+xz)_\beta$
Γ_{245}	1	1	1	−1	−1	$\Gamma_2, \Gamma_4, (xy-xz)_\alpha+(xy-xz)_\beta$
Γ'_{135}	1	1	−1	−1	1	$\Gamma'_1, \Gamma'_3, (xy+xz)_\alpha-(xy+xz)_\beta$
Γ'_{245}	1	1	−1	1	−1	$\Gamma'_2, \Gamma'_4, (xy-xz)_\alpha-(xy-xz)_\beta$
X	2	−2	0	0	0	X_1, X_2, X_3, X_4

nearest neighbour interaction J_1, vanish for all d-bands.

(2) That there are no crystalline field contributions to the energy.

Thus, the one dimensional structure gives rise to a $E^{-1/2}$ singularity in the density of states at point Γ

$$(\mathbf{k}=0,\ \mathbf{k}=\frac{2\pi}{a}(1,0,0),\ \text{etc.}).$$

It is assumed that the Fermi level is situated near this singularity, and as a result, the density of states is high and strongly energy dependent, there is a lattice softening, etc. Moreover, it is assumed that the d-band in question, is the d_{yz}, $d_{y^2-z^2}$ band (the two being degenerate in this model). For these bands, the overlap between nearest neighbours is small, hence, with assumption (1), this band turns out to be extremely narrow. Thus, the Labbé–Friedel model accounts for the following experimental observations:

(a) The high electronic density of states, at the Fermi level, as determined from the electronic specific heat, the susceptibility, etc. [11], and which gives rise to the high superconducting transition temperatures; the strong energy dependence of the density of states near the Fermi level, as manifested by the temperature dependence of the susceptibility, the Knight shift, the nuclear relaxation times [11], etc.

(b) The lattice softening[6], in particular the softening of the elastic constants $C_{11}-C_{12}$, which is not accompanied by a softening of C_{44}, or of the bulk modulus $C_{11}+2C_{12}$, and the martensitic transformation to the tetragonal state[5].

(c) The repopulation of *d*-states, as observed by the change of the Knight shift in the tetragonal state[12].

The difficulty encountered by the Labbé-Friedel model is, that it requires a very low next-nearest neighbour interaction integral. Specifically, this integral, J_2, must be small compared with the Fermi energy of approximately 5 meV, for the density of states to display the $E^{-1/2}$ behaviour there. Since the bandwidth is assumed to be approximately 1 eV, this requires that the next-nearest neighbour interaction be at least two orders of magnitude smaller than the nearest neighbour interaction, and this for the d_{yz}, $d_{y^2-z^2}$ bands. However, as shown in Table 7, it appears that for these bands, the next-nearest neighbour interaction is larger than the nearest neighbour interaction since the wavefunctions point away from the nearest neighbours. For the other bands, whose width is closer to 5 eV, the next nearest neighbour interaction must be about three orders smaller than the nearest neighbour interaction, for the density of states to display an $E^{-1/2}$ dependence at $E_F = 5$ meV; while it appears that the ratio J_1/J_2 is probably more in the range 3–10 (when account is taken of the number of neighbours, too). The argument in favour of this model is, that it accounts for the experimental observations of the average quantities (like specific heat, elastic constants, etc.), while experimental data on the band structure is not yet available to prove or disprove the model. However, this argument should be regarded with caution. It is characteristic of one dimensional systems in general, that they display singularities which are not present in three dimensional systems. Consider the following examples.

(a) There is an anomaly in the electron-phonon interaction, for phonons with wavevector $q = 2k_F$. For three dimensional systems, this anomaly[13] manifests itself in a small kink in the phonon ω vs. q curves, and has hardly any effect on the bulk properties, like electronic specific heat, elastic constants, etc. In one dimensional systems, this same interaction gives rise to the Frohlich instability [1], which manifests itself in major alterations of the bulk properties; namely, a change in the crystal structure, a gap opening up in the band, etc. Generally, a Frohlich singularity manifests itself in a periodic distortion, with wavevector $q = 2k_F$, rather than a uniform strain, as is the case in V_3Si, etc. However, for the special symmetry of the A15 lattice, a uniform distortion may have equivalent effects, as discussed in section 3.

(b) Interactions between electrons, whether direct or indirect, are enhanced in one dimensional systems[2, 14]. In a 'pure' one-dimensional system, this enhancement may be reduced by a larger effective screening[14]; however, in a metal, it is likely that screening is due predominantly to electrons of other bands, and is thus 'normal', while the interaction between electrons on a chain displays a singularity, enhancing the effective density of states.

(c) In a three dimensional system, the density of states function displays a 'weak' singularity (derivative going to infinity like $E^{-1/2}$) at band edges; in a one dimensional system, the singularity is strong, the density of states itself rising to infinity like $E^{-1/2}$ (the Labbé-Friedel model[3]).

(d) In the model of section 2, the Van-Hove singularities at point X, don't contribute significantly to softness of the lattice in an 'ordinary' system, while for a 'one-dimensional' (linear chain) model, they result in a lattice instability.

Any of the four examples cited here, yields an infinity in the effective density of states, elastic constants, etc, and thus can account for anomalies as large as we please. But for this very reason, the observation of large anomalies cannot be regarded as a proof for one of the models, rather than another. Moreover, two-dimensional systems also display anomalies, though weaker than for one-dimensional systems (such as a finite discontinuity in the density of states function), and anomalies like those may also be sufficient to account for the anomalous properties of Nb_3Sn[15].

A difference between possibilities (a, b) on the one hand, and (c, d) on the other, is that for (c, d) it is the bare density of states which is enhanced, while for (a, b) it is an effective, dressed density of states which displays a singularity, and therefore magnetic properties (like the susceptibility and Knight shift) should be enhanced differently (less, for interaction via phonons) from non-magnetic properties (like electronic specific heat, nuclear relaxation times, etc.)[16]. Experimentally, for V_3Si, the electronic specific heat yields a density of states of approximately 6 states per atom per eV, and the temperature dependent component of the susceptibility also yields this value. On this basis, essentially, Clogston and Jaccarino originally proposed the narrow band model for these alloys[11]. On the other hand, for Nb_3Al, as pointed out by Willens *et al.*[17], the 'magnetic' density of states is very small compared with the 'non-magnetic' one. Thus, it appears that the Labbé–Friedel model may account for the singularities of V_3Si, and likewise V_3Ga, and perhaps Nb_3Sn, but perhaps not for the singularities of all compounds with this crystal structure.

The Labbé–Friedel model is so simple, and it proved so successful, that it probably must be quite near the truth. However, the preceding considerations indicate that a more thorough consideration of the wavefunctions, and effective interactions integrals, is required to establish this model firmly.

The band structure of several A_3B compounds was calculated by Mattheiss[9], employing the APW method. The difficulty with band calculations of this kind, is that it is hard to get a resolution of 10 meV in energy, which is approximately the width of the peak in the density of states function required to account for the anomalies. Moreover, with the APW method, it is hard to evaluate the effects of lattice distortion, while the lattice distortion (martensitic transformation, softness of elastic constants,) is one of, if not the main, feature characterising the anomaly. Another criticism of the application of the APW method to this system was pointed out by Friedel. The distance between vanadium's nearest neighbours in V_3Si is 2·36 Å, while in vanadium metal it is 2·63 Å. Because of the closer distance, the approximation of d-functions as non-overlapping spheres, inherent in the APW method, is not so good, and it is possible that the strongly overlapping d-functions form something closer to a chemical bond, which may perhaps be better described by something like the tight binding approximation. This argument may apply to the d_{x^2} and d_{xy}, d_{xz} functions, which form σ and π bonds, but probably not to the d_{yz}, $d_{y^2-z^2}$ functions, which overlap only very little. Also, from Mattheiss' calculation it is not clear in what sense A_3B compounds are different from other metals and why just they display the strange anomalies. However, a calculation of this type, if it provides detailed information about the wavefunctions, in addition to energy levels (i.e. the fraction of d-character, the fraction of d-functions localised on a given family of chains, etc.) can probably serve as a key for understanding the properties of the band structure even with 10 meV resolution, if, for example, tight binding is regarded as an interpolation scheme and the parameters adjusted to the gross structure calculated by the APW method. An interesting feature of Mattheiss' calculation, is that the derivatives dE/dk vanish at point X, in the direction of the Δ line. It is not obvious, from elementary symmetry considerations, why all these derivatives must vanish. (See Fig. 7 here, for example.) If this vanishing is correct, it may throw light on some additional property of the A_3B lattice, and incidentally, contribute to a large increase in the density of states at point X. Thus, it appears that the peculiar properties of the A15 lattice, have not yet been fully accounted for.

The considerations of the preceding sections, suggest a number of possibilities to account for the anomalies in the density of states. For the bonding d_{yz}, and antibonding $d_{y^2-z^2}$, d_{x^2} bands, the effective next-nearest neighbour interaction integral vanishes at point Γ. The antibonding d_{x^2} band is probably so high above the Fermi level, (about 5 eV according to the estimates of Table 7), that it most likely cannot account for the observed anomalies. As for the d_{yz} and $d_{y^2-z^2}$ bands, the nearest neighbour interaction is probably weak, due to lack of overlap, thus these bands may be expected to provide sharp peaks in the density of states function, near $k = 0$, and the wavefunctions may be localised on the appropriate family of chains. In Table 12, the matrix for the d_{yz} band, in the tight binding approximation, is given. Since probably $J_2 > J_1$, the one-dimensionality of these bands is limited to the close vicinity of the $k_x = 0$ surface. If the interaction between parallel chains, J_3, is neglected, the surfaces of constant energy, for $k_x \neq 0$, are not planes, but their distance from the $k_x = 0$ plane is twice as large for $k_y = k_z = 0$ than for $k_y = \pi/a$, $k_z = 0$. However, near $k_x = 0$, this band structure provides an $E^{-1/2}$ singularity in the density of states.

The factor that could most likely smear out this $k = 0$ singularity, is admixture of d_{xy}, d_{xz} and vanadium $4p$ states, belonging to different chains. Assuming that the width of the d_{xy}, d_{xz} band is of order 1 eV, and that of the $4p$ band of order 10 eV, then roughly, 5% admixture of the first, and 0·5% admixture of the second, are sufficient to wash out the peak. The admixture of $4p$ states into the bonding $d_{y^2-z^2}$, Γ_2 state, was estimated by Mattheiss[9] to be about 0·4%: estimates for the other states are not available, but most likely do not differ by orders magnitude. However, the APW method introduces also plane wave states, whose physical nature here is not very clear, but which could in principle smear out the singularity. It is also instructive to note that the dublet of the $d_{y^2-z^2}$ antibonding band, Γ_{15}, at 0·5 Ry, of Mattheiss' calculation is extremely flat along the Δ axis. The dublet of the bonding d_{yz} band, Γ'_{25}, however, is not very flat. Thus, it appears that the existence of sharp peaks near point Γ for the bands for which this is allowed by symmetry, cannot as yet be ruled out, or, for that matter, be regarded as firmly established.

Another possibility is, that the anomaly is due to states near point X. For the center of the appropriate band ($E \approx 0$) at point X (see Fig. 8), the energy varies on the zone face, essentially like $(J_2^2/J_1)\,(k_y^2+k_z^2)a^2/2$; if we assume $J_1 \approx 1$ eV, $J_2 \approx 0{\cdot}2$ eV, then over about half of the zone face, the energy is within 0·01 eV from the energy at point X. The energy level diagrams given by Mattheiss, indeed indicate that some bands are very flat on the zone face, near point X. If the energy

Table 12. The Hamiltonian matrix of the d_{yz} *states on the three families of chains in the tight binding approximation*

J_1 is the nearest neighbour interaction, J_2 the next-nearest neighbour interaction, and J_3 the interaction with the nearest neighbour on a parallel chain $\Gamma_3{}^x$ means a Γ_3 state on a chain in the x-direction, etc. The matrix elements not written down are obtained from the given ones by a cyclic permutation of x, y, z.

$$\langle\Gamma_3{}^x|\mathscr{H}|\Gamma_3{}^x\rangle = J_1(1+\cos ak_x) - 2J_3(\cos ak_y + \cos ak_z)$$

$$\langle\Gamma_3'{}^x|\mathscr{H}|\Gamma_3'{}^x\rangle = -J_1(1+\cos ak_x) - 2J_3(\cos ak_y + \cos ak_z)$$

$$\langle\Gamma_3{}^x|\mathscr{H}|\Gamma_3'{}^x\rangle = iJ_1 \sin ak_x$$

$$\langle\Gamma_3{}^x|\mathscr{H}|\Gamma_3{}^y\rangle = \langle\Gamma_3'{}^x|\mathscr{H}|\Gamma_3{}^y\rangle = \langle\Gamma_3{}^x|\mathscr{H}|\Gamma_3{}^z\rangle = \langle\Gamma_3{}^x|\mathscr{H}|\Gamma_3'{}^z\rangle = 0$$

$$\langle\Gamma_3{}^x|\mathscr{H}|\Gamma_3'{}^y\rangle = -4J_2\cos(ak_z/2)\sin(ak_x/2)$$

$$\langle\Gamma_3'{}^x|\mathscr{H}|\Gamma_3'{}^y\rangle = 4J_2\cos(ak_z/2)\cos(ak_x/2)$$

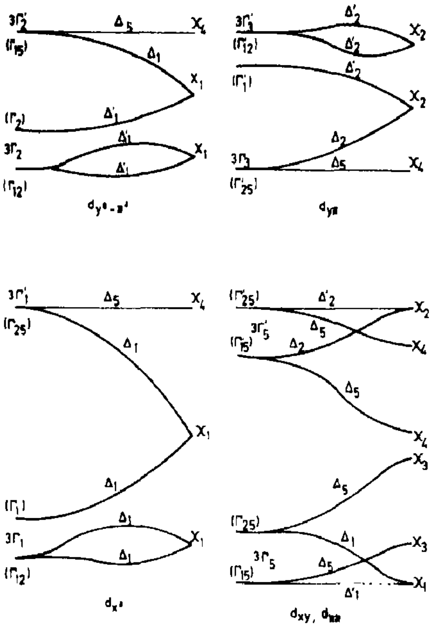

Fig. 8. Effect of interchain coupling, for the individual components of the d-band. The strongly energy dependent band, corresponds to states predominantly of chains in the direction of k. For bands Γ_1', Γ_2', Γ_3, the degenerate triplet at $k = 0$ indicates that states localised on individual chains are eigenstates. The diagram is qualitative only.

dependence on k_x along the Δ axis, at point X, is quadratic, $E = J_1 k_x^2 a^2/2$, then about 5–10 per cent of the states for a non-degenerate band, and 10–20 per cent for a doubly-degenerate band, like $d_{xy}d_{xz}$, in the zone are within 0·01 eV of E_X. This is probably an overestimate, since for the states of the d_{xy}, d_{xz} bands, the energy dependence is indeed quadratic, but probably with a factor larger than J_1; while for the d_{x^2} band, the dependence is probably linear. Nevertheless, it is seen, that one can account for approximately 7 per cent of the states in the zone, per chain, per spin, being within 0·01 eV, as indicated by the experiments[11]. Moreover, when the density of states is high in the first place, interaction with phonons, etc., results in further enhancement[16].

The softness accompanying the high density of states, can also be accounted for. For the singularities near point Γ, the Labbé–Friedel model applies. Near point X, a uniaxial strain has two effects: (a) it opens up a gap, due to elimination of the glide-plane symmetry element; and (b) it results in repopulations among states corresponding to the three points X (along the (100), (010), and (001) directions). Both of these effects result in softness of order[7] $\delta(C_{11}-C_{12}) \approx -n(E_F)\,(\partial J_1/\partial e_{xx} - \partial J_1/\partial e_{yy})^2$, where e_{ij} is the strain tensor. This amount is sufficient to account for the experimental softening in V_3Si, Nb_3Sn, etc[5, 6].

Thus, the peculiar properties of V_3Si, Nb_3Sn, etc. may be the result of the Fermi surface lying near point X, $\mathbf{k} = \frac{\pi}{a}(100)$, and, (1) The density of states there being high, as a result of the energy varying with k_y and k_z only like $(J_2^2/J_1)(k_x^2 + k_y^2)a^2$, roughly; (2) the electron–phonon interaction (Kohn anomaly[13]) being enhanced by the flatness of the Fermi surface, resulting in many electronic states interacting with the same phonon; (3) the phonons interacting predominantly with the electrons, being $\omega \approx 0$ phonons; (4) the density of states being further enhanced by feedback effects, through electron phonon interaction [16], etc. For the first three properties, one dimensionality, as defined in section 2, is a necessary and sufficient condition, except for (3), where the existence of a symmetry element like a glide plane may also be necessary. (The original Frohlich model[1] does not display this property).

However, this account for the peculiar properties of the A15 lattice, must at present be regarded as tentative, since there is as yet no direct evidence as to what electronic states are responsible for them.

5. CONCLUSION

The electronic band structure of alloys like V_3Si appears to be complicated, and probably not yet properly understood. Therefore, it is hard to make definite conclusions, and it is only possible to point towards factors which might possibly give rise to anomalies similar to the ones observed experimentally. It appears that the following factors may be of relevance: (a) The linear chain structure causes the distance of the next-nearest neighbour to be some 22 per cent larger than the nearest neighbour separation. As a result, the next-nearest neighbour interaction may be somewhat weaker than the nearest neighbour interaction: however, it is unlikely that the difference amounts to several orders of magnitude. (b) Because of the topology of the linear chain structure, a next-nearest neighbour interaction which is only somewhat weaker than the nearest neighbour interaction, may cause sections of the constant energy surfaces to be planar and the wavefunctions to be localised predominantly on one family of chains. (c) Because of the symmetry of the lattice, the next-nearest neighbour interaction may vanish for some values of the crystal momenta, for some bands, and this may give rise to sharp peaks in the density of states there. (d) Because of the special symmetry of the environment of the linear chains of the A15 lattice, doubly degenerate bands split at the center of the Brillouin zone characterising an individual chain; this splitting may give rise to singularities (sharp peaks) in the density of states there. Non-degenerate bands do not split in a perfect crystal, but do in a distorted crystal, and this splitting too may give rise to a lattice instability.

It thus appears that the linear chain model may account for the anomalies observed in various A_3B compounds, but it is not yet clear which band is responsible for the anomalies, and in what way; also, it is not yet clear whether other models may not account for the anomalies as well. Thus, further information about the nature of the electronic wavefunctions is necessary in order to draw more clear-cut conclusions.

Acknowledgements—The author wishes to acknowledge stimulating discussions with J. Labbé and S. Barisic, and in particular, this work was initiated by many suggestions and valuable criticism by Professor Friedel. The assistance of Mlle. Schnitzer and Mlle. Lavignolle in a difficult typing job is also deeply appreciated.

6. REFERENCES

1. FROHLICH H., *Proc. R. Soc.* **A223**, 296 (1954).
2. WEGER M., *Rev. mod. Phys.* **36**, 175 (1964).
3. LABBÉ J. and FRIEDEL J., *J. Physique.* **27**, 153, 303 (1966); *Phys. Rev.* **158**, 647 (1967); BARISIC S. and LABBÉ J., *J. Phys Chem. Solids* **28**, 2477 (1967) *Phys. Rev. Lett.* **19**, 1039 (1968).
4. BARISIC S. and DE GENNES P. G., *Solid State Commun.* **6**, 281 (1968).
5. BATTERMAN B. W. and BARRETT C. S., *Phys. Rev.* **145**, 296 (1966); TESTARDI L. R., SODEN R. R., GREINER E. S. and CHIRBA V. G., *Phys. Rev.* **154**, 385, 399 (1967); WEGER M., SILBERNAGEL B. G. and GREINER E. S., *Phys. Rev Lett.* **13**, 521 (1964).
6. KELLER K. R. and HANAK J. J., *Phys Rev* **154**, 628 (1967).
7. ROSEN M., KLIMKER H. and WEGER M., *Phys. Rev.* **184**, 466 (1969).
8. GORZKOWSKI W., *Phys. Status Solidi* **3**, 910 (1963).
9. MATTHEISS L. F., *Phys. Rev.* **138**, A112 (1965).
10. JONES H., *The Theory of Brillouin Zones and Electronic Structure in Crystals* North-Holland, Amsterdam (1960).
11. CLOGSTON A. M. and JACCARINO V., *Phys. Rev.* **121**, 1357 (1961); MORIN F. J. and MAITA J. P., *Phys. Rev.* **129**, 1115 (1963); CLOGSTON A. M., GOSSARD A. C., JACCARINO V. and YAFET Y., *Rev. mod. Phys.* **36**, 170 (1964); *Phys. Rev. Lett.* **9**, 262 (1962), SILBERNAGEL B. G., WEGER M., CLARK W. G. and WERNICK J. H., *Phys. Rev* **153**, 535 (1967).
12. GOSSARD A. C., *Phys. Rev.* **149**, 246 (1966).
13. WOLL E. J. and KOHN W., *Phys. Rev* **126**, 1693 (1962); LABBÉ J., Faculté des Sciences, Orsay. (unpublished)
14. LITTLE W. A., *Phys. Rev.* **134**, A1416 (1964).
15. COHEN R. W., CODY F. D and HALLORAN J. J., *Phys. Rev. Lett.* **19**, 840 (1967).
16. CLOGSTON A. M., *Phys. Rev.* **136**, A8 (1964).
17. WILLENS R. H., GEBALLE T. H., GOSSARD A. C., MAITA J. P., MENTH A., HULL G. W. and SODEN R. R., *Solid State Comm.* **7**, 837 (1969).

J. Phys. Chem. Solids Pergamon Press 1970. Vol. 31, pp. 1641-1642. Printed in Great Britain.

TECHNICAL NOTES

Ionicity of some polar crystals

(*Received* 1 *December* 1969)

SOME physical and chemical properties of crystals are influenced by the bonding nature of the lattice, which is represented by the ratio of covalency to ionicity in the case of polar crystals. Hitherto, this ratio in the bonding *A*–*B* has been given by the electronegativity difference between atom *A* and *B*. However, the electronegativity has been defined mainly in connection with molecular bond, so that more appropriate criteria based on the properties of solid lattice should be necessary in order to express the bonding nature of the solid lattice.

It was noted previously that $(LO/TO)^2$ is a liner function of q^{*2} for III–V compounds [1] and for II–VI compounds[2], where q^* is the effective charge defined by Szigeti [3] and (LO) and (TO) are the phonon frequencies of longitudinal optical and transverse optical blanch at the Brillouin zone edge, respectively. Marshall and Mitra [4] noted also that plotting $(\omega_{LO}-\omega_{TO})/\omega_{TO}$ against q^* for these compound gives straight lines with different slopes, where ω_{LO} and ω_{TO} are the frequencies of longitudinal optical and transverse at the zone center ($k = 0$).

As the Lyddane–Sachs–Teller relation, $(\omega_{TO}/\omega_{LO})^2 = \epsilon_\infty/\epsilon_0$ shows, the quantity $(\omega_{TO}/\omega_{LO})^2$ indicates some degree of the ionicity of the polar crystal. The effective

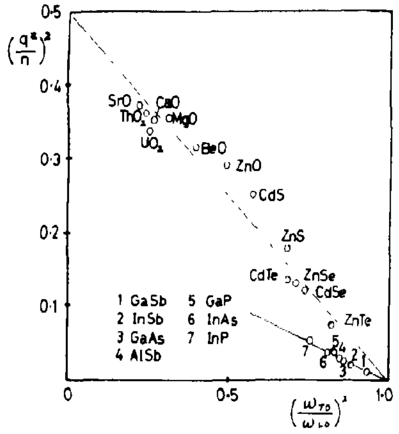

Fig. 1. Correlation of the effective charge of polar crystals with the ratio of the optical frequencies.

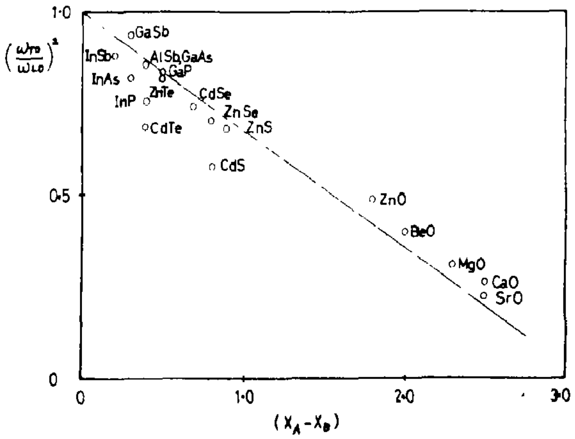

Fig. 2. Plotting the ratio of optical frequencies against electronegativity difference.

charge per one formal valency, (q^*/n) is considered to show this degree also, n being formal valence number of the bond. We can find that plotting $(q^*/n)^2$ against $(\omega_{TO}/\omega_{LO})^2$ gives straight lines for III–V compounds, for II–VI compound and for some oxides as shown in Fig. 1.

In this figure we can find that chalcogenides fall on one line and that AB_2 type compounds fall on this line by using effective charge per one formal valency. No such correlation exists for alkali-halides, for which the effective charge is explained successfully by shell model[5]. It is interesting that this relation holds good for oxides in spite of the large ionicity of oxides which is comparable with that of alkali-halides. Plotting $(\omega_{TO}/\omega_{LO})^2$ against usual electronegativity difference $(X_A - X_B)$ defined by Pauling[6] is shown in Fig. 2. Except for a few compounds a linear relation is held between them. In conclusion it may be said that the quantities $(q^*/n)^2$ and $(\omega_{TO}/\omega_{LO})^2$ can indicate the ionicity of polar crystals except some compounds such as alkali-halides. The values of q^*, ω_{TO} and ω_{LO} are adopted from Refs. [4] and [7–14].

JUN TATENO

Japan Atomic Energy Research Institute,
Tokai-mura, Naka-gun, Ibaraki-ken,
Japan

REFERENCES

1. KEYES R. W., *J. chem. Phys.* **37**, 72 (1962).
2. MARSHALL R. and MITRA S. S., *Phys. Rev.* **134**, A1019 (1964).
3. SZIGETI B., *Trans. Faraday Soc.* **45**, 155 (1949).
4. MITRA S. S. and MARSHALL R., *J. chem. Phys.* **41**, 3158 (1964)
5. HANLON J. E. and LAWSON A. W., *Phys. Rev.* **113**, 472 (1959)
6. PAULING L., *The Nature of the Chemical Bond.* 3rd Edn., Cornell Universities Press (1960).
7. KLEINMAN D. A. and SPITZER W. G., *Phys. Rev.* **113**, 127 (1960).
8. HASS M. and HENVIS B. W., *J. Phys. Chem. Solids* **23**, 1099 (1962).
9. HALSTED R. E., LORENZ M. R. and SEGALL B., *J. Phys. Chem. Solids* **22**, 109 (1961).
10. AXE J. D. and PETTIT G. D., *Phys. Rev.* **151**, 676 (1966).
11. JACOBSON J. L. and NIXON E. R., *J. Phys. Chem. Solids* **29**, 967 (1968).
12. LOH E., *Phys. Rev.* **166**, 673 (1968).
13. DEUTSCH T., *Proc. Int. Conf. Phys. Semicond.* England, 505 (1962).
14. COLLINS R. J. and KLEINMAN D. A., *J. Phys. Chem. Solids* **11**, 190 (1959).

J. Phys. Chem. Solids Vol. 31, pp. 1642–1644.

On the anomalous *F*-colouring behaviour of irradiated alkali halides

(*Received* 1 *December* 1969)

IN TWO recent papers to this journal[1, 2], Mehendru, Mitra and Sootha have reported the occurrence of rather strong anomalies in the *F*-colouring curve of KCl (Mn) irradiated with X-rays. They indicate that the same behaviour is not observed in pure KCl. In this letter we would like to call the attention to similar effects, which have been observed in the past by several authors and, recently, investigated in our laboratory and, in part, reported to the current literature.

In 1953, Platt and Markham[3] found that the rate and shape of the *F*-curve of X-rayed NaCl, depended on the dose of the partial irradiations and the time elapsed between them. By changing these two magnitudes the authors were able to produce clear anomalies in the shape of the curve. Strong changes were also obtained by Nowick[4, 5] in thermally and mechanically treated NaCl, and have been also observed in the curves reported by a number of authors[6]. This anomalous behaviour has been usually attributed to the thermal bleaching of the *F*-band and the possible influence of some other colour centers.

Over the last three years, we have carried out a very detailed investigation on the anomalous colouring of NaCl[7–9], and it has been well established that it appears whenever the irradiation is resumed after a certain interruption time. The magnitude of this effect depends, aside of the interruption time, on the type and intensity of radiation. The anomalous colouring zones, which have been termed 'transient regions of colouring', are not observable when the dose given to the crystal after the interruption is sufficiently high. On the contrary, if the dose is short enough, a clear decrease in the *F*- center concentration is produced. Then, when the crystal is irradiated with short partial doses separated by interruptions, the colouring is accomplished through succesive transient regions and a anomalous *F*-curve can be obtained[7].

Primarily, the change in the shape of the *F*-growth curve after an interruption, is a consequence of two basic phenomena: a thermally activated retrapping in the lattice of anion vacancies which have been liberated

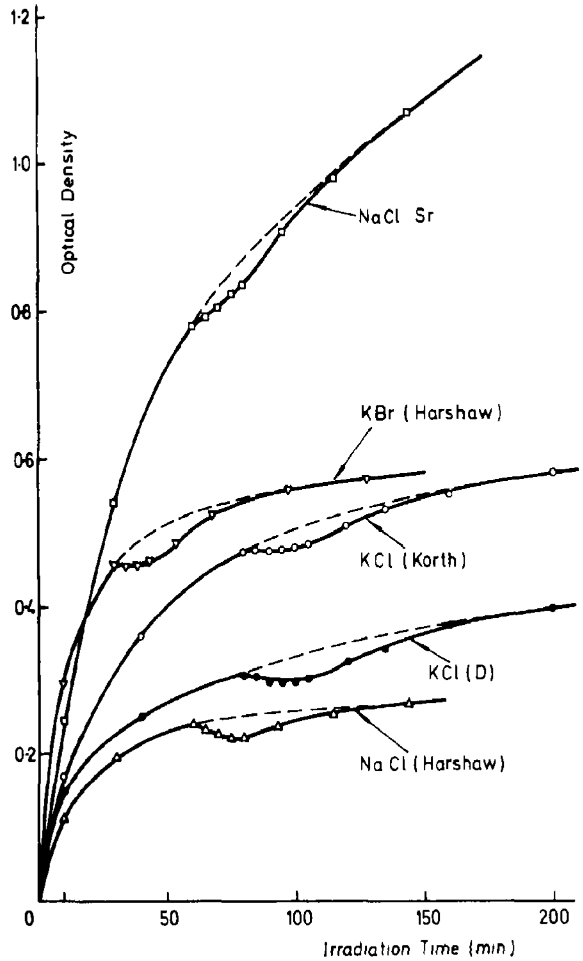

Fig. 1 Anomalous behaviour in the *F*-curves of X-rayed (120 kV, 13 mA, 2 mmAl filter) NaCl, KCl and KBr samples (see, text) Sample thicknesses are as follow: NaCl (Sr), $d = 1{\cdot}2$ mm; KBr (Harshaw), $d = 3{\cdot}0$ mm; KCl (Korth), $d = 1{\cdot}2$ mm, KCl (D), $d = 1{\cdot}3$ mm; NaCl (Harshaw), $d = 1{\cdot}0$ mm. The KCl (D) has been kindly supplied by Mr. E. Dominguez.

by radiation and F-center bleaching induced by ionizing radiation[8]. The role of the F-center thermal bleaching has been shown to be very small and cannot explain the observed effect at all[8, 9].

Essentially, the same behaviour as in pure NaCl has been observed in Ca^{+2} and Sr^{+2} doped NaCl.

Lately, we have tried to determine whether the transient colouring effects exist in other alkali halides and, therefore, some anomalous behaviour can be expected. So far our experiments have indicated the existence of transiente zones in X and γ rayed KCl and KBr. In fact, short irradiations interrupted by different times, have been very succesfully used, as irradiation procedure, to colour KCl in a very striking way[10]. On the other hand, in LiF (Harshaw) we have been unable to detect anomalous colouring with the same procedure and type of radiation.

Figure 1 illustrates the rather strong changes produced in the F-curve of a number of X-irradiated (120 kV, 13 mA, 2 mmAl filter) NaCl, KCl and KBr samples, by a reduction of the partial irradiation dose. In the case of the NaCl samples, the time elapsed between these short irradiations was longer than the normal measuring time (~ 10 min) to make the effect more apparent. In fact, similar anomalous curves can be obtained by just increasing the interruption times without altering the partial irradiations doses.

Although the indian workers do not give full details on how their anomalous curves are obtained, the effect appears to be the same one detected in our laboratory which might be magnified in their KCl (Mn) samples.

It might be worthwhile to point out that anomalous effects in the M-center growth curve have been also reported by Dahnke and Thommen[11] for X-rayed KCl and, more recently, by Sanchez and Agulló-López[12] for γ-irradiated NaCl. In the latter case, the effects are closely related to the transient colouring regions observed in the F-curve, whereas the anomalies reported by Dahnke and Thommen are attributed to some M-centers which are thermally unstable.

Acknowledgement—The authors gratefully acknowledge the continuos encouragement of Dr. Vigón.

División de Física,
Junta de Energía Nuclear,
Madrid, Spain

C. SÁNCHEZ
F. JAQUE
F AGULLÓ-LÓPEZ

REFERENCES

1. MEHENDRU P. C. and MITRA V., *J. Phys. Chem. Solids* **30**, 1021 (1969).
2. MEHENDRU P. C. and SOOTHA G. D., *J. Phys. Chem. Solids* **30**, 1012 (1969)
3. PLATT R. T., Jr. and MARKHAM J. J., *Phys. Rev.* **92**, 40 (1953)
4. NOWICK A. S., *Phys. Rev.* **111**, 16 (1958).
5. AMELINCKX S., *Proc. Int. School of Physics 'Enrico Fermi'*, p. 465 XVIII Course (1960).
6. See for example: BRON W. E., *Phys. Rev.* **119**, 1853 (1960)
7. AGULLO-LOPEZ F., *Solid State Commun.* **4**, 275 (1966)
8. SANCHEZ C. and AGULLO-LOPEZ F., *Phys. Status. Solidi* **29**, 217 (1968).
9. SANCHEZ C. and AGULLO-LOPEZ F., *Solid State Commun.* **5**, 495 (1967).
10. JAQUE F., SANCHEZ C. and AGULLO-LOPEZ F., *Solid State Commun.* **7**, 553 (1969).
11. DAHNKE H. G. and THOMMEN K., *Z. Phys* **184**, 367 (1965).
12. SANCHEZ C. and AGULLO-LOPEZ F., *Crystal Lattice Defects* **1**, 109 (1969)

J. Phys. Chem. Solids Vol. 31, pp. 1644–1647.

Wachtman's equation and the temperature dependence of bulk modulus in nonoxide solids

(*Received* 15 *October* 1969; *in revised form December* 1 1969)

A RECENT short communication[1] showed the possibility of the validity of Wachtman's equation for explaining the temperature dependence of bulk modulus in nonoxide solids. Wachtman *et al.*, in 1961, suggested [2] an equation for the temperature dependence of Young's modulus in oxide compounds. Anderson carried out[3] an interpretation of the parameters involved in the equation while considering a corresponding equation for the temperature dependence of the bulk modulus:

$$B_s = B_0 - bT\exp(-T_0/T)$$

where $b = 3R\gamma\delta/V_0$.

Here V_0 is the specific volume per 'average atom', B_0 is the bulk modulus at 0°K, R the gas constant, γ the Grüneisen parameter and δ the Anderson–Grüneisen parameter. Anderson further wrote the equation as

$$B_s = B_0 - (\gamma\delta/V_0)\int C_v \mathrm{d}T. \qquad (1)$$

The integral $\int C_v dT$ being the thermal energy, E, in the Mie-Grüneisen equation of state, the equation (1) can be modified, and can now be written as

$$B_s = B_0 - \frac{\gamma\delta T}{V_0}\frac{E(\Theta/T)}{T} \qquad (2)$$

where Θ is the characteristic temperature of the solid. This equation was shown to hold good for explaining the temperature dependence of bulk modulus in MgO[3].

In this article we present some results to confirm the conclusion[1] reached earlier. Calculations of bulk modulus at various temperatures using equation (2) have been carried out in nonoxide solids TlBr, CaF_2, BaF_2, NaCl, Al and Li. There, probably, is a value in such correlating equations for prediction of equation of state data in ambients inaccessible to direct experiment, for example in the core of planets.

The temperature dependence of elastic constants and γ in TlBr have been recently reported by Morse and Lawson[4]. Using these values of bulk modulii and γ, the temperature variation of Anderson–Grüneisen parameter, δ, is evaluated from equation (2) and is shown in Fig. 1 alongwith the variation of γ as given by Morse and Lawson. The values of $E(\Theta/T)/T$ have been taken from the tables given in a convenient form[5] for various values of (Θ/T). Both γ and δ were previously thought to be virtually independent of temperature. The average value, δ_{av}, comes out to be 5·23. Assuming the Dugdale–MacDonald relationship[6], Chang has recently shown[7] $\delta = 2\gamma$. The values of δ_{av} and the values of γ are now used to calculate the bulk modulii at different temperatures (Fig. 2). A good agreement with the experimental values was found when the room temperature value of γ and $\delta(= 2\gamma)$ were used.

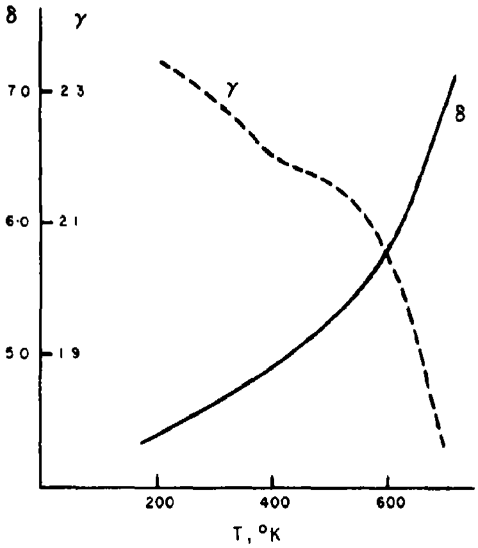

Fig. 1. The temperature variation of δ and γ in TlBr

The temperature dependence of bulk modulus in Al in the temperature range 293–925°K have been recently reported [8]. The value of Grüneisen parameter, γ, calculated as 2·17 agrees very well with the high temperature value of 2·27 determined from third order elastic constants. With an arbitrary value of B_0, and $\delta = 2\gamma$, the bulk modulii at different temperatures are shown in Fig. 2 along with the experimental values.

The temperature and pressure variation of the elastic constants of CaF_2 and BaF_2 have been given by Wong and Schuele[9] alongwith the temperature variation of γ. Calculations of the temperature dependence of bulk modulus in CaF_2 using these values of γ and $\delta = 2\gamma$ have been represented in

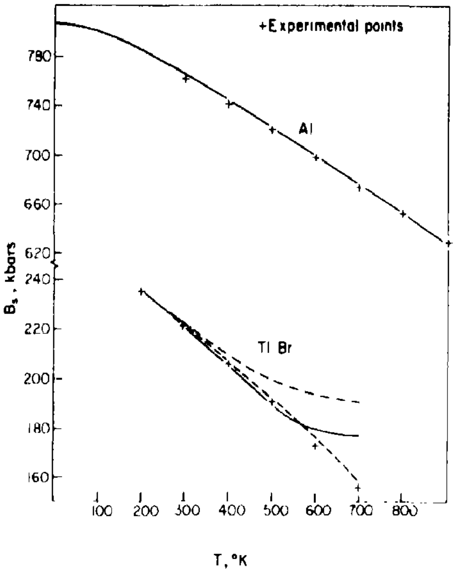

Fig. 2. The temperature dependence of bulk modulus in TlBr and Al TlBr ——— Using $\delta = 5{\cdot}23$; -.-.-.-.- $\delta = 2\gamma$(γ temperature dependent). ·········· Using room temperature value of γ and $\delta (= 2\gamma)$ Al. ——— Using $\delta = 2\gamma$.

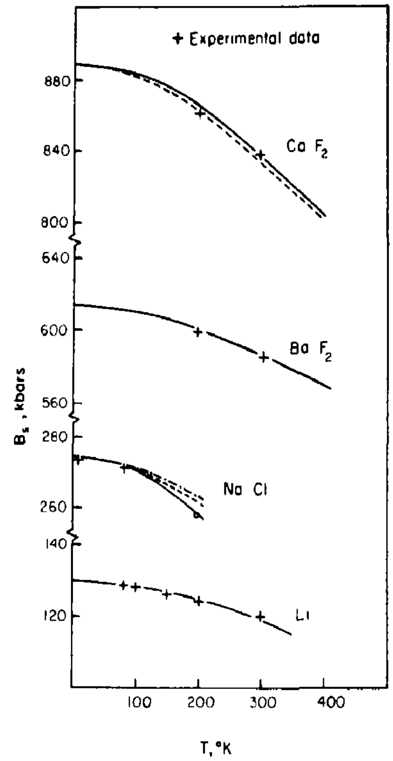

Fig. 3 Temperature dependence of B_s in BaF_2, CaF_2, NaCl and Li CaF_2: ——— Using $\delta = 2\gamma$, γ temperature dependent; ------ Using $\delta = (dB_T/dP) - 1$; BaF_2. ——— Using $\delta = (dB_T/dP) - 1$; NaCl: ○ Experimental value, Ref. [14], ——— Using $\gamma = 1{\cdot}43$ and $\delta = 5{\cdot}64$; ------ Using $\delta = 3{\cdot}57$; -·-·-·- Using $\delta = 4{\cdot}04$; Li ——— Estimated value using $(\gamma\delta)$.

Fig. 3. From thermodynamical considerations Chang showed[7] that the pressure dependence of the bulk modulus at constant temperature is related to δ by $\delta = (dB_T/dP) - 1$. Using this value of δ and the room temperature value of γ, B_s at various temperatures were calculated and are included in Fig. 3. The value of B_0 used is for the best fit of the theory and experiment. Similar calculations were performed for BaF_2 and the results are given in Fig. 3. The calculated values correspond to $\delta = (dB_T/dP) - 1$. The estimated values of B_s for $\delta = 2\gamma$ come out to be only slightly higher than the experimental ones.

The elastic constants of NaCl at 4·2 and 77·3°K have been reported by Fugate and Schuele[10]. The value of γ is taken from Born and Huang[11] and the different values of δ from Mathur and Singh[12]. The value of B_0 is selected for the best fit between theory and experiment, and the temperature dependence of B_s is included in Fig. 3.

The variation of bulk modulus with temperature in the range 78–298°K for Li are now available[13]. However, value of neither γ nor δ is known. The value of $(\gamma\delta)$, therefore, is calculated as follows:

Assuming that γ and δ are not much temperature dependent, the bulk modulus at any two temperatures can be written as,

$$B_{T_1} = B_0 - \frac{(\gamma\delta)}{V_0} T_1 \left[\frac{E(\Theta/T)}{T}\right]_{T=T_1}$$

$$B_{T_2} = B_0 - \frac{(\gamma\delta)}{V_0} T_2 \left[\frac{E(\Theta/T)}{T}\right]_{T=T_2}.$$

Therefore,

$$B_{T_1} - B_{T_2} = \frac{(\gamma\delta)}{V_0}\left\{T_2\left[\frac{E(\Theta/T)}{T}\right]_{T=T_2} - T_1\left[\frac{E(\Theta/T)}{T}\right]_{T=T_1}\right\}.$$

The value of $(\gamma\delta)$ can now be evaluated from the experimental values of B_s at any two temperatures, and, in turn, is used to calculate the bulk modulii at various temperatures with a proper arbitrary parameter B_0. A comparison of the estimated and experimental values are given in Fig. 3.

In all the cases examined, a good agreement is found between the calculated and experimental values; and, therefore, Wachtman's equation, as modified by Anderson, can very well be used for estimating the bulk modulii even at temperatures at which the experiments have not been carried out. Generally, it is observed that the estimation is quite near to the experimental points when the room temperature value of γ and $\delta = 2\gamma$ are used. We thus confirm our earlier conclusion[1] that the Wachtman's equation can safely be used for calculating the temperature dependence of bulk modulus in oxide and nonoxide solids.

Acknowledgements—The author is grateful to Professor G. S Verma and Dr M. M Joshi for their interest in the work. Financial assistance from the Department of Atomic Energy, India is thankfully acknowledged

S. RAJAGOPALAN

Ultrasonic and Solid State Research Laboratory,
Physics Department,
Allahabad University,
Allahabad,
India

REFERENCES

1. RAJAGOPALAN S., *Solid State Commun.* **7**, 1649 (1969).
2. WACHTMAN J. B., TEFFT W. E., LAM D. G. Jr. and APSTEIN C. S., *Phys. Rev.* **122**, 1754 (1961).
3. ANDERSON O. L., *Phys. Rev.* **144**, 553 (1966).
4. MORSE G. E. and LAWSON A. W., *J. Phys. Chem. Solids* **28**, 939 (1967).
5. *American Institute of Physics Handbook*, Chap. 7, Table 4, McGraw-Hill, New York (1957).
6. DUGDALE J. S. and McDONALD D. K. C., *Phys. Rev.* **89**, 832 (1953).
7. CHANG Y. A., *J. Phys. Chem. Solids* **28**, 697 (1967)
8. GERLICH D. and FISHER E. S., *J. Phys. Chem. Solids* **30**, 1197 (1969)
9. WONG C. and SCHUELE D. E., *J. Phys. Chem. Solids* **29**, 1309 (1968).
10. FUGATE R. Q. and SCHUELE D. E., *J. Phys. Chem. Solids* **27**, 493 (1966).
11. BORN M. and HUANG K., *Dynamical Theory of Crystal Lattices*. Clarendon Press, Oxford (1954).
12. MATHUR V. K. and SINGH S. P., *J. Phys. Chem. Solids* **29**, 959 (1968).
13. SLOTWINSKI T. and TRIVISONNO J., *J. Phys. Chem. Solids* **30**, 1276 (1969).
14. BARTELS R. A. and SCHUELE D. E., *J. Phys. Chem. Solids* **26**, 537 (1965).

J. Phys. Chem. Solids Vol. 31, pp. 1647–1649.

Magnon–phonon interaction in the itinerant electron model of ferromagnetism

(*Received* 11 *September* 1969;
in revised form 14 *November* 1969)

We want to present here a derivation of the bilinear magnon–phonon coupling using as a starting point the electron–phonon coupling and the itinerant electron model of ferromagnetism. The consequences of this coupling are well known and have been discussed by Kittel[1] from a phenomenological point of view.

The model Hamiltonian for a metallic ferromagnet in the presence of a magnetic field H is[2]

$$H_{\mathrm{el}} = \sum_{\mathbf{k}\sigma} \epsilon_{\mathbf{k}\sigma} C^{+}_{\mathbf{k}\sigma} C_{\mathbf{k}\sigma} + \frac{U}{N} \sum_{\mathbf{k}\mathbf{k}'\mathbf{q}} C^{+}_{\mathbf{k}+\mathbf{q}\uparrow} C_{\mathbf{k}\uparrow} C^{+}_{\mathbf{k}'-\mathbf{q}\downarrow} C_{\mathbf{k}'\downarrow} \tag{1}$$

with

$$\epsilon_{\mathbf{k}\sigma} = \epsilon_{\mathbf{k}} - \sigma\mu H \tag{2}$$

where $\epsilon_{\mathbf{k}}$ is the energy of the Bloch state $|\mathbf{k}\sigma\rangle$ and μ is the Bohr magneton. $C^{+}_{\mathbf{k}\sigma}$ is the creation operator of an electron in the state $|\mathbf{k}\sigma\rangle$. U is the Coulomb integral, $\sigma = (\uparrow, \downarrow)$.

Following Rajagopal and Joshi[3] we take the electron–phonon interaction in the form

$$H_{\text{el-ph}} = \frac{1}{\sqrt{N}} \sum_{\mathbf{kq}\lambda} \sum_{\sigma\sigma'} g^{\lambda}_{\sigma\sigma'}(\mathbf{q}) C^{+}_{\mathbf{k+q}\sigma} C_{\mathbf{k}\sigma'} b_{\mathbf{q}\lambda} + h.c. \quad (3)$$

The parameter $g^{\lambda}_{\sigma\sigma'}(\mathbf{q})$ measures the strength of the coupling. $b_{\mathbf{q}\lambda}$ is the destruction operator for a phonon of momentum **q** and polarization λ. From this interaction Hamiltonian we consider only those terms which give direct magnon–phonon coupling, i.e. we shall keep as interaction Hamiltonian

$$H_{\text{mag-ph}} = \frac{1}{\sqrt{N}} \sum_{\mathbf{kq}\lambda} g^{\lambda}_{\downarrow\uparrow}(\mathbf{q}) B^{+}_{\mathbf{kq}} b_{\mathbf{q}} + h.c. \quad (4)$$

where

$$B^{+}_{\mathbf{kq}} = C^{+}_{\mathbf{k+q}\downarrow} C_{\mathbf{k}\uparrow}.$$

Furthermore, since we shall be interested only in the qualitative aspects of the interaction we shall drop in what follows the polarization index λ. For an isotropic model, angular momentum conservation implies that only circularly polarized phonons would be coupled to the magnons. The total Hamiltonian of the system is then:

$$H = H_{\text{el}} + H_{\text{ph}} + H_{\text{mag-ph}} \quad (5)$$

where

$$H_{\text{ph}} = \sum_{\mathbf{q}} \omega^{\text{PH}}_{\mathbf{q}} b^{+}_{\mathbf{q}} b_{\mathbf{q}}$$

is the free phonon Hamiltonian.

Following the equation of motion method [4] we try now to find simultaneous eigenfrequencies within the random-phase approximation (RPA) corresponding to the excitation created by $b^{+}_{\mathbf{q}}$ (phonons) and

$$B^{+}_{\mathbf{q}} = \sum \alpha_{\mathbf{k}} B^{+}_{\mathbf{kq}} \text{ (magnons)}$$

$\alpha_{\mathbf{k}}$ can be determined later, in solving for the eigenfrequencies. After a simple calculation we find:

$$\begin{aligned} i\dot{B}^{+}_{\mathbf{kq}} = [H, B^{+}_{\mathbf{kq}}] = (\epsilon_{\mathbf{k+q}\downarrow} - \epsilon_{\mathbf{k}\uparrow}) B^{+}_{\mathbf{kq}} & \\ - \frac{U}{N} \sum_{\mathbf{k'q'}} C^{+}_{\mathbf{k+q}\downarrow} C_{\mathbf{k-q'}\uparrow} C^{+}_{\mathbf{k'-q'}\downarrow} C_{\mathbf{k'}\downarrow} & \\ - \frac{U}{N} \sum_{\mathbf{k'q'}} C_{\mathbf{k}\uparrow} C^{+}_{\mathbf{k'+q'}\uparrow} C_{\mathbf{k'}\uparrow} C^{+}_{\mathbf{k+q-q'}\downarrow} & \\ + \frac{1}{\sqrt{N}} \sum_{\mathbf{q'}} g^{*}(\mathbf{q'}) (C^{+}_{\mathbf{k+q-q'}\uparrow} C_{\mathbf{k}\uparrow} & \\ - C^{+}_{\mathbf{k+q}\downarrow} C_{\mathbf{k'+q'}\downarrow}) b^{+}_{\mathbf{q'}} & \quad (6) \end{aligned}$$

and

$$i\dot{b}^{+}_{\mathbf{q}} = [H, b^{+}_{\mathbf{q}}] = \omega^{\text{PH}}_{\mathbf{q}} b^{+}_{\mathbf{q}} + \frac{g(\mathbf{q})}{\sqrt{N}} \sum_{\mathbf{k}} B^{+}_{\mathbf{kq}} \quad (7)$$

within the RPA equation (6) becomes:

$$\begin{aligned} i\dot{B}^{+}_{\mathbf{kq}} = (E_{\mathbf{k+q}\downarrow} - E_{\mathbf{k}\uparrow}) B^{+}_{\mathbf{kq}} & \\ + \frac{U}{N} (n_{\mathbf{k+q}\downarrow} - n_{\mathbf{k}\uparrow}) \sum_{\mathbf{k'}} B^{+}_{\mathbf{k'q}} & \\ + \frac{g^{*}(\mathbf{q})}{\sqrt{N}} (n_{\mathbf{k}\uparrow} - n_{\mathbf{k+q}\downarrow}) b^{+}_{\mathbf{q}} & \quad (8) \end{aligned}$$

where

$$E_{\mathbf{k}\sigma} = \epsilon_{\mathbf{k}\sigma} + \frac{U}{N} n_{\sigma}$$

with

$$n_{\sigma} = \sum_{\mathbf{k}} n_{\mathbf{k}\sigma} = \sum_{\mathbf{k}} \langle C^{+}_{\mathbf{k}\sigma} C_{\mathbf{k}\sigma} \rangle.$$

Fourier transforming equations (7) and (8) and eliminating $b^{+}_{\mathbf{q}}$ we obtain

$$\begin{aligned} \Omega B^{+}_{\mathbf{kq}} = (E_{\mathbf{k+q}\downarrow} - E_{\mathbf{k}\uparrow}) B^{+}_{\mathbf{kq}} + \frac{1}{N} (n_{\mathbf{k+q}\downarrow} - n_{\mathbf{k}\uparrow}) & \\ \left[U - \frac{|g(\mathbf{q})|^{2}}{\Omega - \omega^{\text{PH}}_{\mathbf{q}}} \right] \sum_{\mathbf{k'}} B^{+}_{\mathbf{k'q}} & \quad (9) \end{aligned}$$

for the Fourier amplitudes $B^{+}_{\mathbf{kq}}(\Omega)$.

Multiplying equation (9) by α , and summing over **k** we are led to a set of homogeneous equations involving the $B^{+}_{\mathbf{kq}}$. The independence of the $B^{+}_{\mathbf{kq}}$ implies a new set of equations for the $\alpha_{\mathbf{k}}$ from which we obtain the following eigenvalue equations[4]

$$\frac{1}{N}\sum_{\mathbf{k}}\frac{1}{\Omega-E_{\mathbf{k+q}\downarrow}-E_{\mathbf{k}\uparrow}}(n_{\mathbf{k+q}\downarrow}-n_{\mathbf{k}\uparrow})\left[U-\frac{|g(\mathbf{q})|^2}{\Omega-\omega_{\mathbf{q}}^{PH}}\right]=1. \quad (10)$$

Assuming a spherical Fermi surface for evaluating the sum in equation (10) we obtain to second order in **q**

$$\left[U-\frac{|g(\mathbf{q})|^2}{\Omega-\omega_{\mathbf{q}}^{PH}}\right]\left\{\frac{n\downarrow}{\Delta}\left[1-\frac{\epsilon_{\mathbf{q}}}{\Delta}\left(1-\frac{4}{5}\frac{\epsilon_{F\downarrow}}{\Delta}\right)\right]-\frac{n\uparrow}{\Delta}\left[1+\frac{\epsilon_{\mathbf{q}}}{\Delta}\left(1+\frac{4}{5}\frac{\epsilon_{F\uparrow}}{\Delta}\right)\right]\right\}=1 \quad (11)$$

where $\Delta=\Omega-Um-2\mu H$, $m=\sum_{\mathbf{k}}(n_{\mathbf{k}\uparrow}-n_{\mathbf{k}\downarrow})$ is the net moment, and $\epsilon_{F\sigma}$ is the Fermi energy for the up and down bands respectively. Taking now $\mu H \ll Um$ and using the magnon frequency

$$\omega_{\mathbf{q}}^{M}=2\mu H+\epsilon_{\mathbf{q}}\left[\frac{n}{m}-\frac{4}{5}\frac{1}{Um^2}(\epsilon_{F\uparrow}n_{\uparrow}-\epsilon_{F\downarrow}n_{\downarrow})\right]$$

the roots of equation (11) can be written as:

$$\Omega=\frac{\omega_{\mathbf{q}}^{PH}+\omega_{\mathbf{q}}^{M}}{2}\pm\left[\left(\frac{\omega_{\mathbf{q}}^{PH}-\omega_{\mathbf{q}}^{M}}{2}\right)^2+|g(\mathbf{q})|^2m\right]^{1/2}. \quad (12)$$

We see from (12) that the gap at resonance

$$\Delta\Omega=|g(\mathbf{q})|m^{1/2}$$

is directly related to the electron–phonon coupling.

BLAS ALASCIO
ARTURO LÓPEZ

Centro Atomico Bariloche,
Comision Nacional de Energía Atómica,
Instituto de Fisica,
"Dr José A Balseiro",
Universidad Nacional de Cuyo,
San Carlos de Bariloche,
Rio Negro – Argentine

REFERENCES

1. KITTEL C., *Phys. Rev.* **110**, 836 (1958).
2. HERRING C., *Exchange Interactions among Itinerant Electrons* (Edited by W. G. Rado and H Suhl), Vol. 4. Academic Press, New York (1966).
3. RAJAGOPAL A. K. and JOSHI S K., *Phys. Lett* **24A**, 95 (1967).
4. See for instance: BLANDIN A., *Theory of Condensed Matter*. IAEA, Vienna (1966).

J. Phys. Chem. Solids Vol. 31, pp. 1649–1650

Field emission in high magnetic fields

(*Received* 17 *September* 1969)

THE BEHAVIOR of a field emission current in a magnetic field has been of interest for some time[1, 2]. Blatt[3] was the first to theoretically investigate such behavior for a gas of free electrons at the absolute zero of temperature. His results showed that the current should exhibit oscillations which are periodic in H^{-1}. Independently, and very shortly after Blatt's calculation, Gogadze, Itskovich, and Kulik[4] considered the more general case of an arbitrary Fermi surface and non-zero temperature, with the restriction that the electron orbits around the extremal areas are closed and non-self-intersecting. Both papers consider the case for which the Fermi energy is independent of magnetic field, and for which the Fermi energy oscillates with magnetic field. Gogadze *et al.*[4] estimated that observable oscillations in both cases are a possibility only when the current originates from small pockets of electrons with low effective masses. This was essentially the same conclusion reached by Blatt. Numerical estimates of the amplitude of the oscillations from both calculations indicate effects on the order of 2 or 3 per cent at 1 tesla for an electron pocket with an effective mass of $\sim 10^{-2} m_0$. At 3 teslas the amplitudes should be nearly 10 per cent of the emission current in zero magnetic field.

In addition to the oscillatory terms, Blatt[3] predicted a monotonic dependence of emission current on magnetic field. For the case of small pockets and low effective mass a quadratic decrease in current with magnetic field is expected. (Gogadze, *et al.*[2] did not discuss this part of the current.)

As suggested by Blatt, bismuth should be a suitable substance to use to search for the effects described above. The carriers are located in small pockets and have low effective masses. Several attempts have been made in this laboratory to observe this effect, not only in bismuth, but in zinc, tantalum, and tungsten as well. In no instance has any influence of magnetic field on the emission current been found. Current levels have ranged from 10^{-11} to 10^{-8} A, and magnetic field strengths up to 10 teslas have been used. It is particularly noteworthy that not even the monotonic decrease in current has been detected. In bismuth, for example, where the monotonic term should be quadratic, the current should have decreased by about 4 per cent at 1 tesla (at which point the oscillations should be on the order of 2 per cent) and by nearly 40 per cent at 3 teslas. (At 3 teslas the oscillations should be about 10 per cent of the zero field current level.)

The emission currents that were obtained were sufficiently stable over long enough periods of time that effects as small as ±1 per cent should have been readily detected. Cathodes of bismuth and zinc were prepared from pre-oriented single crystals, and cathodes of tantalum and tungsten were prepared from high purity polycrystalline wire. The emission chamber could be evacuated to a pressure between 10^{-5} and 10^{-6} torr by a conventional oil diffusion pump and cold trap assembly, and then submerged in liquid helium to be cryopumped to pressures estimated to be at least less than 10^{-11} torr. Field desorption techniques were employed to clean the emitting surfaces in high vacuum. Most of the experimental runs were made at temperatures near 1·2°K, which were obtained by pumping on the helium bath covering the vacuum chamber. The chamber itself was optically baffled from its pumping line to prevent backstreaming from the warmer parts of the system.

The theoretical investigations mentioned above consider only the case of a longitudinal magnetic field, i.e. emission current parallel to the magnetic field direction. A calculation of the behavior of the current when the magnetic field is perpendicular to the direction of current flow in the case of field emission has apparently not yet been made. Both orientations were tried in the course of these experiments, and the same null results were obtained in every case. Cathodes cut and etched from single crystals of bismuth and zinc were always mounted such that the trigonal axis of Bi and *c* axis of Zn were parallel to the magnetic field for both the longitudinal and transverse field orientations.

At the present time no definite explanation can be given for the failure of these experiments to substantiate the theory. It is felt that the experimental conditions sufficiently met the requirements of the calculations as presented in [3] and [4]. A closer look at the theories is perhaps justified. In particular, the fact that the emitting surface is not an infinite plane but is finite and three-dimensional ought to be investigated. The three-dimensional nature of the cathode implies that electrons with less then the maximum velocity parallel to the magnetic field will still have the same tunneling probability as those for which the velocity parallel to H is a maximum, provided they approach the metal surface perpendicularly. This in turn would cause the total current to be composed of electrons from many Landau levels, and could conceivably wash out any possible magnetic field effects.

Lewis Research Center,
Cleveland,
Ohio 44135,
U.S.A.

D. J. FLOOD

REFERENCES

1. HARDIN W. R., BLAIR J. C. and EINSPRUCH N. G., *Cryogenics* **5**, 138 (1965).
2. VAN OOSTROM A. G. J., *Phillips Res. Rep. Suppl.* No. 1 (1966).
3. BLATT F. J., *Phys. Rev.* **131**, 166 (1963).
4. GOGADZE G. A., ITSKOVICH F. I. and KULIK I. O., *Soviet phys. JETP* **19**, 622 (1969).

J. Phys. Chem. Solids Vol. 31, pp. 1651–1653.

The density of α-monoclinic selenium

(*Received* 14 *October* 1969)

THE α-MONOCLINIC modification of selenium is composed of puckered rings of 8 atoms each, 4 rings to the unit cell. The crystallographic parameters have been measured quite accurately[1]:

$$a = 9{\cdot}05 \pm 0{\cdot}01 \text{ A}$$
$$b = 9{\cdot}07 \pm 0{\cdot}01 \text{ A}$$
$$c = 11{\cdot}61 \pm 0{\cdot}01 \text{ A}$$
$$\beta = 90°46' \pm 5'$$

where a, b, c are the lengths of the three axes of the unit cell and β is the angle between the non-orthogonal axes. The volume of the unit cell is:

$$\begin{aligned} v &= a \times b \times c \times \sin(90°46') \\ &= 9{\cdot}529 \pm 0{\cdot}029 \times 10^{-22}\,\text{cm}^3. \end{aligned} \quad (1)$$

The weight of the atoms in the unit cell is $32 \times 78{\cdot}96$ a.m.u. (the atomic weight of selenium), which is $4{\cdot}1938 \pm 0{\cdot}0005 \times 10^{-21}$ g/unit cell. The density is simply given by this weight divided by the volume of the unit cell (equation (1)):

$$\rho = w/v = 4{\cdot}401 \pm 0{\cdot}016\ \text{g/cm}^3. \quad (2)$$

The crystals used were grown from a solution[2] of selenium dissolved in CS_2. Densities were determined for amorphous and α-monoclinic selenium. Each density was determined by 4 weighings on an analytic chain balance, whose error was ±0·2 mg.

The method used was that of displacement weighing. The weighing flask was suspended empty in air and weighed (w'_1). Next, the flask was immersed in a liquid and weighed (w'_2). Third, the flask was dried, filled with selenium, suspended in air and weighed (w'_3). Finally, the filled flask was immersed in the liquid (see Fig. 1) and weighed (w'_4).

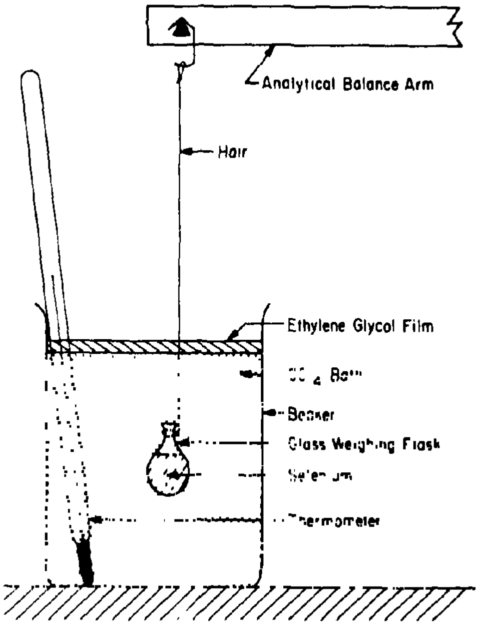

Fig. 1. Apparatus for density measurement.

$$\begin{aligned} w'_1 &= w'_g - \rho_a v_g \\ w'_2 &= w'_g - \rho_L(T_1) v_g \\ w'_3 &= w'_g + w'_{Se} - \rho_a(v_g + v_{Se}) \\ w'_4 &= w'_g + w'_{Se} - \rho_L(T_2)(v_g + v_{Se}) \end{aligned} \quad (3)$$

w'_g and w'_{Se} are the weights of the glass weighing flask and the selenium respectively. Similarly, v_g and v_{Se} are the respective volumes. $\rho_L(T_1)$ and $\rho_L(T_2)$ are the densities of the liquid at the temperatures T_1 and T_2 respectively. Since the temperature was not maintained constant, it was recorded at each weighing. ρ_a is the density of air.

Defining:

$$\rho_{Se} = w'_{Se}/v_{Se} \quad (4)$$

and solving (3), we have:

$$\rho_{Se} = \frac{(w'_3 - w'_1)}{(w'_3 - w'_4)/(\rho_L(T_2) - \rho_a) - (w'_1 - w'_2)/(\rho_l(T_1) - \rho_a)} + \rho_a \quad (5)$$

The error in ignoring ρ_a is less than 10^{-3}; yielding:

$$\rho_{Se} = \frac{(w_3 - w_1)}{(w_3 - w_4)/\rho_L(T_2) - (w_1 - w_2)/\rho_L(T_1)}. \quad (6)$$

The small glass weighing flasks were blown from 2 mm i.d. pyrex glass tubing. For small quantities of material, strong flasks were made weighing less than 0·3 g which held over 1 g of material. They were suspended from the balance by a human hair, which was thin enough to displace very little liquid, and weighed about 1 mg. Carbon tetrachloride (CCl_4) was chosen as the liquid for several reasons. First, selenium is insoluble[3] in it. Second, its viscosity is low and it wets glass and selenium, virtually eliminating trapped air bubbles. Third, CCl_4 is relatively dense, making $(w_3 - w_4)$ significant in equation (6). Fourth, it is readily available in high purity. Fifth, its density as a function of temperature is accurately known. Its disadvantage is its high rate of evaporation at room temperature, creating thermal gradients in the bath. To combat this, the CCl_4 surface was covered by a thin layer of ethylene glycol, which has a very low vapor pressure. It is less dense than CCl_4 and the two liquids are immiscible. Thus, the ethylene glycol will prevent evaporative cooling, stabilizing the temperature of the bath (see Fig. 1).

Table 1. Calculated and experimental densities of amorphous and α-monoclinic selenium

Crystal modification	Density (g/cm^3) Experimental	Calculated	Literature[5]
amorphous	4 265 ± 0·014	—	4·26
α-monoclinic	4 389 ± 0·015	4·401 ± 0 016	4·50

The density of the CCl_4 as a function of temperature was taken from Ref. [4]. A linear fit was made:

$$\rho_L(T) = 1{\cdot}5940 - 0{\cdot}00192 \times (T - 20{\cdot}0) \qquad 15 \leq T \leq 25 \quad (7)$$

where T is the liquid temperature in degrees Centigrade and ρ_L is the density of the CCl_4.

Errors in measurement were as follows. The four weights were correct to within 0·2 mg, out of about 300, 100, 1100 and 600 mg for w_1, w_2, w_3 and w_4 respectively. The temperature was known to within 0·1°C. The error due to thermal expansion of the glass flasks was less than 10^{-4} for maximum temperature fluctuations observed. Thus, the estimated overall experimental error was approximately 0·3 per cent.

Density measurements were made on amorphous and α-monoclinic selenium. The results are given in Table 1. The results show that the method gives the accepted experimental value for the density of amorphous selenium, and the new experimental density for α-monoclinic selenium agrees well within experimental error with the density calculated from X-ray data.

The published density values[6–11] range from 4·44 to 4·51 g/cm^3. These are unreasonably high, compared with the calculated value of 4·40 g/cm^3. The α-monoclinic form of selenium is metastable, however, and converts irreversibly to the higher density trigonal form ($\rho \simeq 4{\cdot}8$ g/cm^3). The conversion will take place at room temperature over a period of a few years[12]. Heating will accelerate the process[13]. It seems likely that the previous density measurements were made on partially converted material.

Acknowledgements – The authors gratefully acknowledge the work of Mr. Sigeru Iizima, who grew the α-monoclinic selenium crystals and who did some preliminary density measurements This work was financed through the National Aeronautics and Space Administration, and the Jet Propulsion Laboratory.

California Institute of Technology, Pasadena,
Calif. 91109, *U.S.A.*

J. D. TAYNAI
M. -A. NICOLET

REFERENCES

1. BURBANK R. D., *Acta crystallogr.* **4**, 140 (1951).
2. IIZIMA S. and NICOLET M-A , *JPL Space Programs Summary*. Vol 3. p. 70 (1967).
3. MOODY J W. and HIMES R. C., *Mat Res. Bull.* **2**, 703 (1967).
4. TIMMERMANS J., *Physico-Chemical Constants of Pure Organic Compounds*, Vol 1. p 221; Vol. 2. pp. 184, 434. Elsevier, New York (1950) and (1965)
5. *Handbook of Chemistry and Physics* 49th Edn. Chemical Rubber Co , Cleveland, Ohio (1968).
6. MITSCHERLICH M., *Ann chem Phys.* **46**. 301 (1856).
7. RAMMELSBERG K , *Pogg.* (Wied) *Ann. Phys.* **152**, 151 (1874).
8. PETERSEN F *Z. phys. Chem.* **8**. 612 (1891).
9. SAUNDERS A P *J phys. Chem.* **4**, 423 (1900).
10. COSTE M., *Compt Rend* **149**, 674 (1909)
11. SNEED M., *et al*, *Comprehensive Inorganic Chemistry*. Vol. 8. p. 16. Van Nostrand, New York (1961)
12. MARSH R E., Senior Research Fellow, California Institute of Technology. Pasadena. California. private communication.
13. MUTHMANN W , *Z. Kristallogr.* **17**. 336 (1890)

J. Phys. Chem. Solids Pergamon Press 1970. Vol. 31, pp. 1657–1667. Printed in Great Britain.

ELECTROMAGNETIC GENERATION OF ULTRASONIC WAVES IN METALS

E. ROLAND DOBBS
Department of Physics, University of Lancaster, Lancaster, England

(*Received* 25 *October* 1969)

Abstract—The discovery, early development and theory of the electromagnetic generation of pure shear and quasicompressional ultrasonic waves in metals is reviewed. It is shown that the four equations of Quinn lead to a satisfactory explanation of the periodic ionic displacements excited electromagnetically in metals in the presence of a static magnetic field over a wide range of temperature, frequency and magnetic field. Recent measurements of resonant effects found in directly generated shear waves in bismuth at helium temperatures are described The giant quantum oscillations in the generated signal have much larger amplitudes than those previously observed in the ultrasonic attenuation, but similar periods. A low field resonance occurs in the generated signal at 10–50 MHz and 30–70 G, where the magnetic field has a negligible effect on the attenuation Applications of the method to the generation of millimetre wave ultrasonics, to the non-destructive testing of metals and to the study of the solid state are briefly considered.

1. INTRODUCTION

THE GENERATION of ultrasonic waves directly from electromagnetic currents, without using a piezoelectric or magnetosrictive transducer, was discovered accidentally in Denmark by Saermark and Larsen[1] early in 1967. They were propagating helicons in an aluminum crystal at helium temperatures by placing a small coil on each side of an aluminum disk (the size of a dime), exciting one coil at 1–2 MHz and observing the signal received in the second coil as the magnetic field produced by a superconducting solenoid around the system was increased from 10–40 kG. To their surprise, sets of acoustic standing waves were generated corresponding to the diameter and thickness of the disk. As these were size-controlled, they were sharp resonances and the acoustic resonator had a Q larger than 10^4, so that a highly stable frequency source was necessary for the observations. The resonances were superimposed on helicon waves and were shown to be helicon-acoustic modes.

The conditions for the production of these shear waves seemed very restrictive: helium temperatures, static magnetic field vector $\mathbf{B}_0$ parallel to the ultrasonic wave vector $\mathbf{q}$ and magnetic field large enough to make $\omega_c\tau \gg 1$, where $\omega_c = e\mathbf{B}_0/mc$ is the cyclotron frequency of the electrons of mass m, charge $-e$ and relaxation time τ. Thus acoustic shear waves would only be generated under conditions for the propagation of helicon waves.

In the spring of 1967 Houck, Bohm, Maxfield and Wilkins[2] at Cornell University made a 'transducer' from the new effect by bonding a metal disk of aluminum to one end of a delay rod of quartz and detecting the shear waves with an AC-cut quartz at the other end. They showed that the 'transducer' would work in a non-resonant mode through r.f. generation at the surface of the aluminum disk over a wide range of magnetic fields. Further, they proved that the interaction producing the shear waves operated at magnetic fields well away from the 'cross-over' point where the phase velocities of the helicon modes and the shear vibrations coincide.

Then I am glad to say Professor Bohm spent the Summer with us at Lancaster and with him, Betjemann, Meredith and I[3] showed that the restrictive conditions for the production of ultrasonic waves electromagnetically did not apply at all. The method worked with 'low' magnetic fields when $\omega_c\tau < 1$, it worked when the static field $\mathbf{B}_0$ was normal to $\mathbf{q}$ and it even worked at room temperature in a copper rod from the machine shop! What was perhaps more surprising was that it worked *just as well* at 10 MHz in an aluminum rod at room temperature as it did in an aluminum single crystal at helium temperatures. Evidently it was a classical effect and we concluded that the Lorentz force on the electronic current in the skin depth was responsible for the generation.

Before describing our experiments I must mention the interesting result of Abeles[4], who showed that at 9·3 GHz electromagnetic generation and detection of shear waves was possible in the *absence of a static magnetic field* in a very clean, thin film of indium, evaporated on to an optically polished surface of a crystal rod of pure germanium, and placed in a microwave cavity at helium temperatures. The minimum conditions for electromagnetic generation of ultrasonic waves in metals are evidently *either* helium temperatures and no magnetic field *or* a steady magnetic field (of a few kilogauss in practice) at any temperature.

2. EXPERIMENTAL

The experimental arrangement we have used for making measurements on the electromagnetic generation of shear waves is shown in outline in Fig. 1. A conventional pulsed ultrasonic system operating at 10 or 15 MHz drives a small, flattened coil placed close to the plane face of a cylindrical metal sample, so than an r.f. magnetic field is generated at the surface of the metal. When a static, solenoidal field $\mathbf{B}_0$ of a few kilogauss was applied to the sample from an external magnet, a shear wave was excited at the metal surface within the electromagnetic skin depth. The sample geometry ensures that at megahertz frequencies, where the acoustic wavelength is much less than the diameter of the rod, a plane wave propagates normal to the flat face along the cylindrical axis Oz. The delayed output from a suitable quartz transducer bonded to the other flat face was then amplified and displayed. The sensitivity of this coil-resonant transducer system was such that in a field of 10 kG the signal to noise ratio was about 50:1 for room temperature measurements in a tin crystal. This was substantially greater than using a coil–coil system and so was preferred for the early experiments.

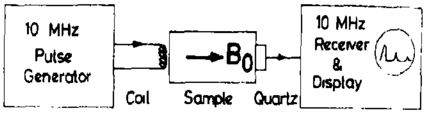

Fig. 1. Experimental arrangement for observing the direct generation of ultrasonic shear waves at the surface of a cylindrical metal rod in a solenoidal field $\mathbf{B}_0$.

The polarization of the generated sound wave was found to depend on the relative orientation of the propagation direction $\mathbf{q}$ and the static field $\mathbf{B}_0$. In Fig. 2(a) with the helicon geometry the ionic motion was ξ_x and so a shear wave was propagated and detected by a suitably oriented AC-cut quartz. No compressional wave was detected when the AC-cut quartz was replaced by an X-cut. However, when the system was placed in an electromagnet with $\mathbf{B}_0$ normal to $\mathbf{q}$ and parallel to the applied r.f. field $\mathbf{B}$, as shown in Fig. 2(b), a compressional wave was detected with the X-cut quartz. With this geometry, shear waves were also generated when the AC-cut quartz was oriented to detect ξ_y.

To verify that the shear waves have a preferred polarization direction in the helicon geometry, we studied the signal amplitude as the coil was rotated—this was easy at room temperature—about Oz. Using a long tin sample, maximum amplitude was recorded when the coil was parallel to Ox and zero amplitude when it was perpendicular to Ox, as expected. The effect on the amplitude A_c of the compressional signal of rotating $\mathbf{B}$ in the plane of the surface of the sample, with $\mathbf{B}_0$ fixed along Ox, is shown in Fig. 3.

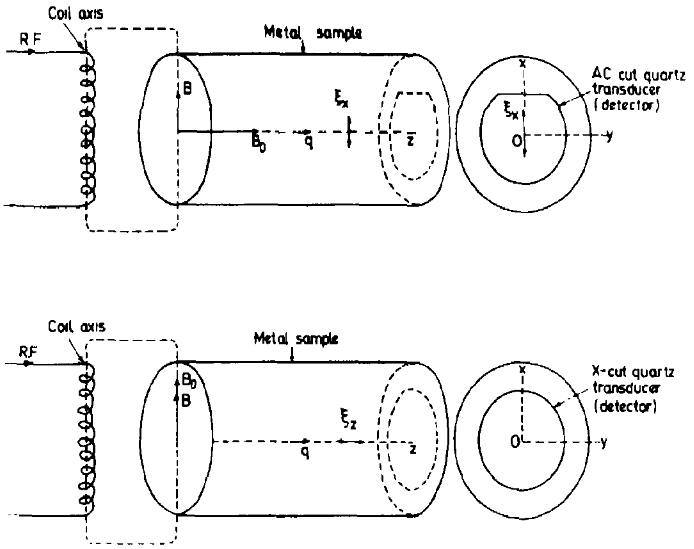
Coil axis
RF
Metal sample
B
ξx
B0
q
z
x
O
y
AC cut quartz transducer (detector)
Coil axis
RF
Metal sample
B0
B
ξz
q
z
x
O
y
X-cut quartz transducer (detector)

Fig. 2. Sample, coil and magnetic field orientations for generating and detecting ultrasonic waves. (Upper) Shear waves. (Lower) quasi-compressional waves.

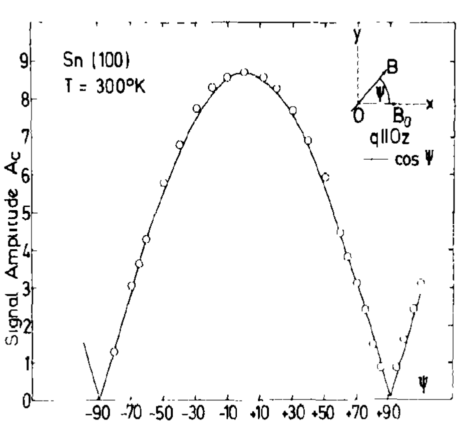

Fig. 3. Cosine variation of signal amplitude A, as $\mathbf{B}$ is rotated about Oz with $\mathbf{B}_0$ fixed. Maximum signal for $\mathbf{B}$ parallel to $\mathbf{B}_0$.

When **B** is parallel to Ox, ξ_z and ξ_y are coupled to each other via the Lorentz force on the ions

$$\frac{Ze}{c}\frac{\partial \boldsymbol{\xi}}{\partial t}\times \mathbf{B}_0$$

where Ze is the ionic charge and $\boldsymbol{\xi}$ the ionic displacement vector, producing both compressional and shear waves, as shown by Meredith, Watts-Tobin and Dobbs[5]. When **B** is parallel to Oy, ξ_z and ξ_y are coupled via the Lorentz force, but as *neither* is coupled to **B**, no sound waves are generated with this geometry. For intermediate orientations, the signal amplitude A_c is seen to fit closely the expected cosine variation.

Houck *et al.*[2] showed that the amplitude of the generated shear wave was proportional to $\mathbf{B}_0$ up to 50 kG at helium temperatures. We extended their measurements to 110 kG and to 77K (Fig. 4) in niobium. The generation appeared to be saturating at high fields at 77 K, but the magnetic attenuation was not negligible at these high fields. By observing successive echos, a correction was made for the absorption in the sample, and the generated signal was then found to be linear in $\mathbf{B}_0$. The increase in signal strength is striking: at 100 kG the signal-noise ratio was about 500! The absorption in the magnetic field was measured directly (Fig. 5) and found to be proportional to $\mathbf{B}_0^2$, in agreement with that calculated by Alpher and Rubin[6].

Thomas, Turner and Bohm[7] have observed the electromagnetic generation of shear waves in the presence of a magnetic field up to 500 MHz and it is reasonable to

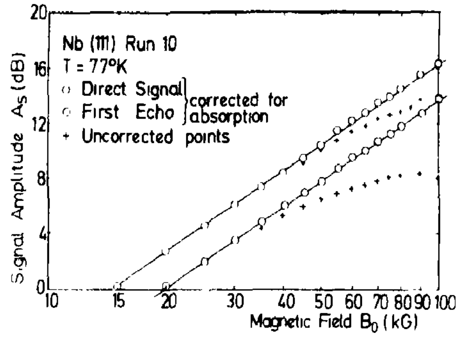

Fig. 4. Signal amplitude A_S in Nb (111) at 77 K, including correction for absorption.

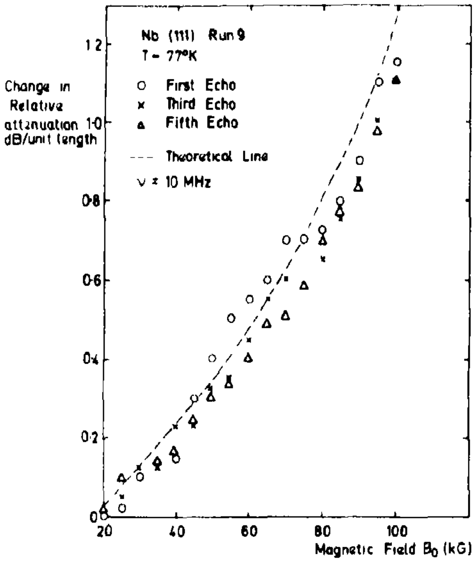

Fig. 5. Change in relative attenuation of shear waves in Nb (111) at 77 K as a function of magnetic field B_0

expect that compressional waves could similarly be generated by ultra high frequencies. Thomas *et al.* also used two identical pairs of Helmholtz coils, arranged to have their axes mutually orthogonal and lying in the plane of the surface, to produce both left-hand and right-hand, circularly polarized, 10 MHz waves at 4·2 and 77 K in an aluminum rod. Such circular modes cannot easily be generated with quartz transducers, although Einspruch[8] has proposed a generator based on a quarter-wave plate.

Meredith *et al.*[5] found that the generated signal (but not, of course, the attenuation) was inversely proportional to the bulk density d of the sample. After correcting for different transducer efficiencies, the efficiency of generation in aluminum was shown to be *three times* greater than in tin, as would be expected from the relative density of the two metals. Gaerttner, Wallace and Maxfield [9] have confirmed this density dependence (the factor is actually ds_t, where s_t is the velocity of sound) for metals with densities as low as 1·74 (Mg) and as high as 19·3 (W). They have also shown that the efficiency of generation at room temperature falls off at frequencies above 10 MHz, when the acoustic wavelength λ is no longer large compared with the skin depth δ, that is, when $\beta^2 \rightarrow 1$, where $\beta = 2\pi^2(\delta/\lambda)^2$.

3. THEORETICAL

At the same time as we[3] published our preliminary results, Quinn[10] published, as he put it, the 'four equations which describe completely the physics of the problem in the general case'. The problem is to find wave solutions of the ionic displacements ξ given by

$$\xi = \xi_0 \exp i(\omega t - \mathbf{q}\,.\,\mathbf{r}).$$

Following Mattis and Dresselhaus[11] the metal sample is considered to occupy the half-space $z > 0$, and to conserve electrons we suppose that its mirror image occupies the half-space $z < 0$. This is equivalent to assuming that the conduction electrons are reflected specularly at the surface, which is simple, and satisfactory when the electronic mean free path is much less than the acoustic wavelength. It can then be shown[5, 11] that the total electric current $\mathbf{J}$ is the sum of the ionic current $n_0e\xi$, the electronic current $\mathbf{j}_e$ and the fictitious surface current $\mathbf{j}_0$, so that

$$\mathbf{J} = in_0e\omega\xi + \mathbf{j}_e + \mathbf{j}_0 \qquad (1)$$

where there are n_0 conduction electrons per unit volume.

Maxwell's equations[10, 12] may be written in the form

$$\mathbf{J}(\mathbf{q},\omega) = \Gamma . \mathbf{E}(\mathbf{q},\omega) \quad (2)$$

where the electric conductivity tensor Γ is given by

$$\Gamma = \frac{ic^2q^2}{4\pi\omega}\left(1-\frac{\omega^2}{c^2q^2}\right)1-\frac{ic^2}{4\pi\omega}\mathbf{qq}.$$

For either of the geometries in Fig. 2 this reduces[5] to a simple function of $\beta\sigma_0$, where β is the skin depth parameter already defined and σ_0 is the static conductivity, equal to $n_0e^2\tau/m$ in the relaxation-time approximation.

The electronic transport equation of Cohen, Harrison and Harrison[13] may be written in the form[10]

$$\mathbf{j}_e(\mathbf{q},\omega) = \boldsymbol{\sigma}(\mathbf{q},\omega) . [\mathbf{E}(\mathbf{q},\omega)-(im\omega/e\tau)\boldsymbol{\xi}(\mathbf{q})] + n_0e\mathbf{D} . \mathbf{q}(\mathbf{q} . \boldsymbol{\xi}) \quad (3)$$

where $\mathbf{q} = (0,0,q)$ in the simple cases, $\boldsymbol{\sigma}(\mathbf{q},\omega)$ is the electronic magneto-conductivity tensor, $\mathbf{D} = (2\epsilon_F/3e^2n_0)(1+i\omega\tau)^{-1}$, $\boldsymbol{\sigma}$ is the diffusion tensor, and ϵ_F is the Fermi energy. As Quinn[10] has pointed out the electronic current is composed of three terms: the conduction current, the collison drag current and the diffusion current. In the helicon geometry the diffusion current vanishes and equation (3) becomes simply

$$j_{e\pm}(q) = \sigma_{\pm}(q,\omega)[E_{\pm}(q)-(im\omega/e\tau)\xi_{\pm}(q)]$$

where the transverse components are given by $E_{\pm} = E_z \pm iE_y$, etc.

The fourth and final equation given by Quinn is the equation of motion of the ions

$$M\frac{\partial^2\boldsymbol{\xi}}{\partial t^2} = C_l \operatorname{grad}\operatorname{div}\boldsymbol{\xi} - C_t \operatorname{curl}\operatorname{curl}\boldsymbol{\xi} + Ze\mathbf{E} + \frac{Ze\partial\boldsymbol{\xi}}{c\partial t}\times\mathbf{B}_0 - \frac{Ze}{\sigma_0}\mathbf{j}_e - \frac{Zn_0e^2}{\sigma_0}\frac{\partial\boldsymbol{\xi}}{\partial t} \quad (4)$$

where C_l and C_t are elastic moduli for compressional and shear waves associated with the short range forces between ions and the last two terms are the collision drag force.

The wave solution $\boldsymbol{\xi}(q)$ in the bulk metal required is found for each geometry by eliminating $\mathbf{J}$, $\mathbf{E}$ and $\mathbf{j}_e$ between the four equations. The simplest solution, for the helicon geometry, was given by Quinn

$$\xi_{\pm}(q) = -\frac{Ze\omega}{M\sigma_0}\frac{(1-\sigma_0R_{\pm})}{f(q,\omega)}j_{0\pm}(q), R^{\pm} = \frac{1}{\sigma_{\pm}} \quad (5)$$

where

$$f(q,\omega) = (\omega^2-s_t^2q^2\pm\Omega_c\omega)(\omega-i\sigma R_{\pm}\beta\omega) + (iZm\omega^2/M\tau)(1-i\beta)(1-\sigma_0R_{\pm}) \quad (6)$$

is familiar from helicon–phonon interaction studies. Thus Quinn showed that these four equations led to the generation of ultrasonic waves through the helicon–phonon interaction in the skin depth of the metal.

At Lancaster we[5] applied the Quinn equations to our results on aluminum and found, at low frequencies where $ql \ll 1$(l = electronic mean free path) and $\omega\tau \ll 1$, the ionic displacement amplitudes associated with both the phononlike and the plasmonlike excitations of the uncoupled system, that is, well away from the helicon–phonon cross-over. We were able to show that the same equations gave the correct attenuation at high and low temperatures, as well as the correct generation over a wide range of $\omega_c\tau$. In particular for shear waves generated as in Fig. 2(a) at high temperatures

$$\xi_1(z,t) = \frac{iB_0\mathbf{B}(z=0+)e^{i\omega[t-(z/s_t)]}e^{-q''z}}{4\pi ds_t\omega[1-(ic^2\omega/4\pi s_t^2\sigma_0)]} \quad (7)$$

where

$$q'' = \frac{c^4\Omega_c^2\omega^2}{8\pi s_t^5\Omega_p^2\sigma_0[1+(c^2\omega/4\pi s_t^2\sigma_0)^2]}, \quad (8)$$

Ω_c is the ionic cyclotron frequency $= ZeB_0/Mc$ for ions of mass M and charge Ze and Ω_P is the ionic plasma frequency given by

$\Omega_P^2 = 4\pi n_0 Ze^2/M$. The amplitude of the generated signal is seen in (7) to be proportional to B_0 and inversely proportional to ds_t, as found experimentally. The attenuation is shown in (8) to increase as B_0^2 and this expression was used to obtain the theoretical line in Fig. 5, where it agrees with the data on niobium at 77 K.

At helium temperatures the conductivity σ_0 is high and the magnetic attenuation is negligible (when $ql < 1$), so that the generated signal is approximately

$$\xi_1(z,t) = \frac{iB_0\mathbf{B}(z=0+)e^{i\omega(t-z/s_t)}}{4\pi d s_t \omega}.$$

Experimentally this has been verified in tin and niobium[5] crystals in fields up to 110 kG and in gold and aluminum[7] crystals up to 150 kG.

An analysis of the generation in the absence of a magnetic field observed by Abeles[4] has been given by Southgate[14]. He shows that in the case of a very clean, thin film the *diffuse* reflection of the electrons at its surfaces can produce the generation observed in the high frequency, anomalous limit. But it falls off as d/l (d = thickness), so that thick samples are not satisfactory. In fact at very high frequencies (above 40 GHz) a multilayer film, of alternate layers of long and short mean free path, is calculated to be the most efficient. A recent paper by Alig[15] confirms Southgate's result that all the generation takes place within the skin depth and shows, for shear waves, that in the presence of a magnetic field B_0 the power generated is proportional to B_0^2.

4. BISMUTH

As well as classical effects, it is of interest to study quantum effects in metals through measurements of directly generated acoustic waves. In the helicon geometry, giant quantum oscillations[16] are known to be observed in a few metals having reasonable values of their fundamental period

$$\Delta\left(\frac{1}{B_0}\right) = \frac{e\hbar}{m_c \epsilon_F c}, \tag{9}$$

where m_c is the cyclotron mass associated with the electron orbits about B_0. For bismuth with B_0 along the binary axis the fundamental is about $\frac{1}{15}$ kG^{-1} so that the giant oscillations in the acoustic attenuation are readily observed[17–20]. Thomas, Hsu and I[21] have recently seen for the first time similar giant quantum oscillations in directly generated shear waves in bismuth at helium temperatures and at 10 MHz, using a superconducting solenoid.

In the presence of a magnetic field B_0 the energy states of the conduction electrons are given by

$$\epsilon = (n+\tfrac{1}{2})\hbar\omega_c + \hbar^2 k_z^2/2m^* \pm \tfrac{1}{2}\gamma\hbar\omega_c \tag{10}$$

where n is an integer numbering the Landau level, k_z is the component of electron wave vector in the direction of B_0, m^* is the effective mass, $\gamma = \frac{1}{2}g^* m_c/m$ and g^* is the effective g-factor for the Zeeman splitting of the spin states. Under certain assumptions, Cohen and Blount[22] have shown that $|\gamma| = 1$. Toxen and Tansal[17] have shown that the giant oscillations are a consequence of the stringent selection rules that must be satisfied when an acoustic phonon is adsorbed by a conduction electron. In particular the only electrons that can absorb a phonon without changing Landau levels ($\Delta n = 0$), while conserving energy and momentum, are those electrons drifting in phase with the phonon. The electrons that are available to make such transitions are, of course, limited to those near the Fermi level ϵ_F, which at a finite temperature is broadened by about kT.

In Fig. 6 we show the energy levels given by (10), neglecting the parabolic term in k_z, which is very small compared with ϵ_F for those electrons that interact. When the magnetic field is large ($\hbar\omega_c \gg kT$) the Landau levels are sharp and widely spaced. The ultrasonic attenuation only exhibits the

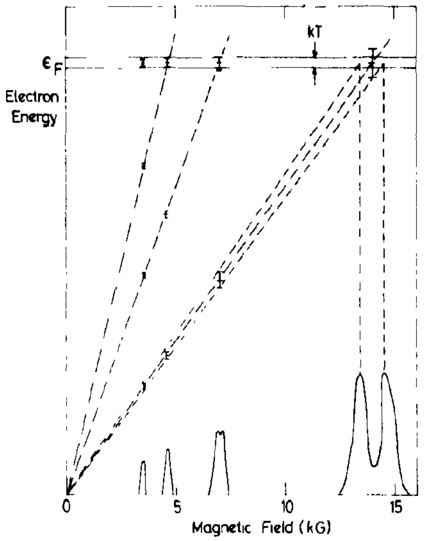

Fig. 6. The energy of the electrons increases continuously with magnetic field, but the ultrasonic attenuation only exhibits giant quantum oscillations when a Landau level coincides with the Fermi level ϵ_F. At high fields and at helium temperatures the spin-splitting of the Landau levels in bismuth is greater than their thermal broadening and a double oscillation is observed

oscillations (shown along the abscissa) when B_0 is such that a Landau level is intersecting the Fermi level. For a wide range of field (e.g. 8–12 kG) the attenuation is independent of B_0, since there are no conduction electrons available to absorb the sound! At sufficiently high fields, the oscillations show the spin-splitting of the Landau levels and the γ values can be measured[18].

We have observed (Fig. 7) the giant quantum oscillations in both the attenuation (upper trace), plotted as change in pulse-height of the signal, and in the generated signals (lower trace). It is interesting to note that the peaks do not occur at exactly the same fields in each case, but the measured periods (Fig. 8) for both fast and slow shear oscillations are seen to have the same period as those from the attenuation minima. However, the generated signals were *an order of magnitude* larger than the attenuation changes, as can be seen in Fig. 9 for the giant oscillation corresponding to the highest field Landau level. Here the generated signal is corrected for the small absorption (maximum of 4 dB) in the transit of the sample to the receiver (Fig. 1). For this sample at 10 MHz and 1·3 K, $ql \sim 10$, $\omega_c\tau > 10$ and $\beta \sim 0{\cdot}3$. Although we could see the giant oscillations in the attenuation quite easily at 50 MHz, we were unable to observe the generated signals at higher frequencies, perhaps because the etched surface of our sample was not sufficiently clean and flat.

In looking at the generation at lower magnetic fields using a copper solenoid, we found a

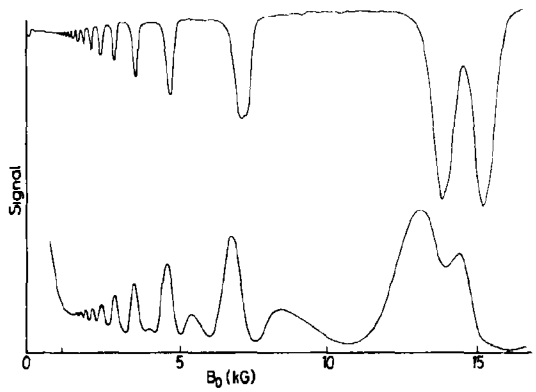

Fig. 7. The upper trace shows the giant quantum oscillations in the absorption of sound in a bismuth crystal and the lower trace the corresponding oscillation in the electromagnetically generated signals. (Arbitrary amplitudes, not to same vertical scale for each trace).

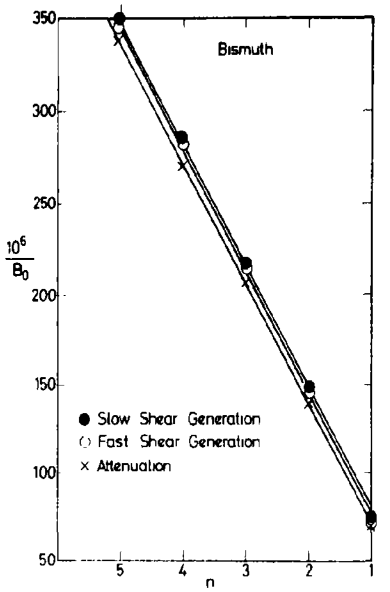

Fig. 8. Periodicity in the reciprocal of the magnetic field for three sets of giant quantum oscillations in bismuth. Pulse-height minima in the attenuation readings and maxima in the generated signals have the same period, $7.0 \times 10^{-5}\,G^{-1}$.

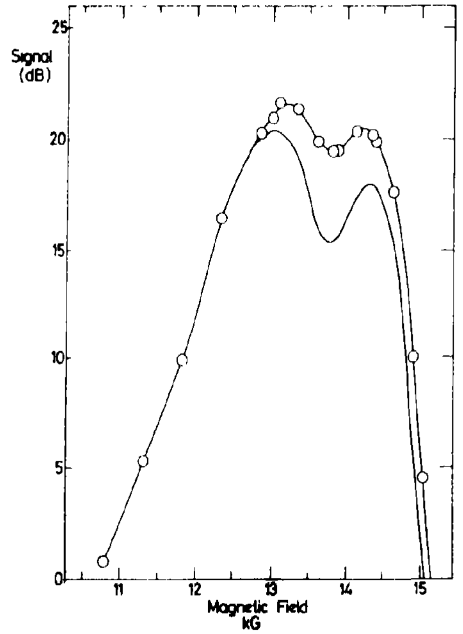

Fig. 9. Giant quantum oscillation of the directly generated, 10 MHz acoustic shear waves in bismuth at 1·3 K – signal observed at detector, ○–○ signal corrected for field-dependent attenuation in the sample

surprising result, which we have not yet fully understood. At a particular low field – less than 100 G – there is a resonance giving an enormous signal. In Fig. 10(a) at 30 G the slow shear resonance is at its peak (marked), in (b) at 10 G it has nearly disappeared. The fast shear resonance is at a higher field, so that the fast shear signals are seen below their

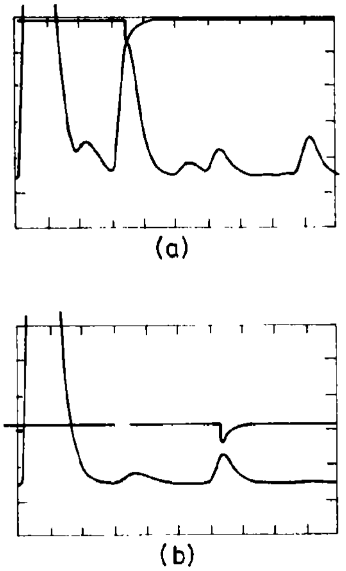

Fig. 10. Ultrasonic signals seen in bismuth at helium temperatures with low magnetic fields, using the experimental arrangement of Fig. 1. (a) At 30 G the large slow shear resonance marked at T produces its own reflection at $3T$. Also present are the fast shear signal at t and its two reflections at $3t$ and $5t$, off resonance, and a piezoelectric signal at $2T$ from the quartz transducer. (b) At 10 G the slow shear signal is off resonance, the fast shear signals have disappeared, but the piezoelectric signal (marked) is unchanged, since there is a negligible change in the attenuation with magnetic field.

resonant amplitude in (a) and have disappeared in (b). The signal that does not change with B_0 marked in (b), is generated by electromagnetic coupling to the quartz detector (seen also as a saturating pulse at $t = 0$) and is unchanged in amplitude because the magnetic *attenuation* is negligible, although the *generation* is strongly field dependent.

The resonances for slow shear generation at 4·2 K (Fig. 11) and for slow and fast shear generation at 1·5 K (Fig. 12) are seen to begin

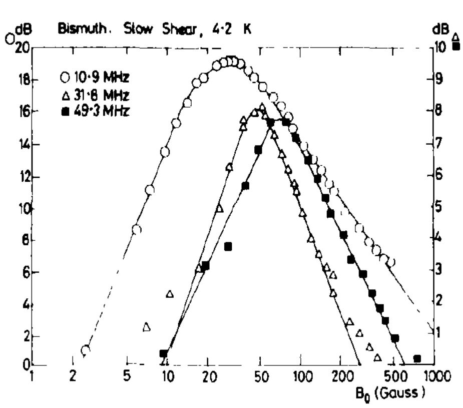

Fig. 11. Amplitudes of the directly generated slow shear signals in bismuth at 4·2 K ○, 10·9 MHz; $B_{max} = 30$ G, △, 31·8 MHz; $B_{max} = 47$ G; ■, 49·3 MHz; $B_{max} = 71$ G

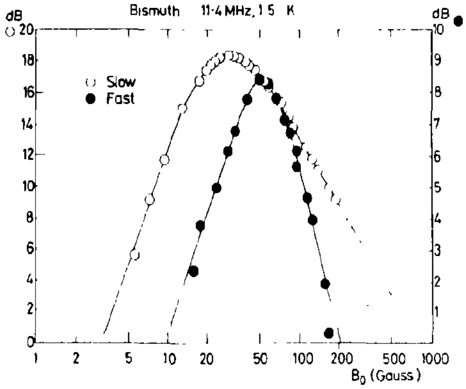

Fig. 12. Amplitudes of the directly generated shear signals in bismuth at 11·4 MHz and 1·5 K. ○, Slow shear; $B_{max} = 30$ G; ●, Fast shear; $B_{max} = 51$ G.

at very low fields and to disappear at a few hundred gauss, before the first of the quantum oscillations (Fig. 7) begins to appear. A comparison of Figs. 9, 11 and 12 shows that the low field resonance had a similar amplitude to the largest quantum oscillation at 10 MHz. The resonance peakB_{max} moves to higher fields (Fig. 11) as the frequency ω is increased with $B_{max} \sim \omega^{1/2}$ and also as the velocity is increased (Fig. 12) with $B_{max} \sim s_t$. It disappears on warming to 77 K. It is clear that the resonance is associated with electronic currents within the skin depth of the crystal, but its appearance cannot be explained by the simple theory[5] of plane shear waves in an isotropic metal. A different solution of the Quinn equations is probably required.

It is evident from these preliminary results that the study of the electromagnetic generation of acoustic phonons in metals and semimetals at helium temperatures provides an important new method of investigation of the electronic properties of solids, which should show any variation in these properties between the bulk metal and its surface.

5. APPLICATIONS

Besides its wide application in solid state physics, the technique of electromagnetic generation can be applied to the non-destructive testing of metals and to the generation of microsound at millimetre wave frequencies. At frequencies of 1–10 MHz transducers of quartz or barium titanate are commonly used and these have to be bonded to the sample under test with a suitable liquid, grease or epoxy resin. For measurements at very high or very low temperatures bonding can be a problem, while the 'ringing in' of transducers can easily damage very pure crystals, so that the 'bondless' transducer of Fig. 1 is attractive. Here the r.f. coil is quite small and need not touch the sample, although it must be quite close to the sample. The acoustic signal strength generated by the coil in the presence of the magnetic field $\mathbf{B}_0$ depends also on the strength of r.f. field $\mathbf{B}$ (equation (37)). For convenience a small flat coil has been used in many experiments and the r.f. field $\mathbf{B}$ is then only the fringing field. The effect of moving such a coil away from the surface of the sample is shown in Fig. 13, where the fringing field is seen to fall off exponentially with distance and so give on this logarithmic plot an 'apparent attenuation' of 180 dB cm^{-1}. Clearly the coil should be within 0·2 mm or 0·008 in. of the aluminum surface if less than 3 dB of generated signal is to be lost.

A more efficient coil system has recently been devised by Legg and Meredith[23] for non-destructive testing. It consists of

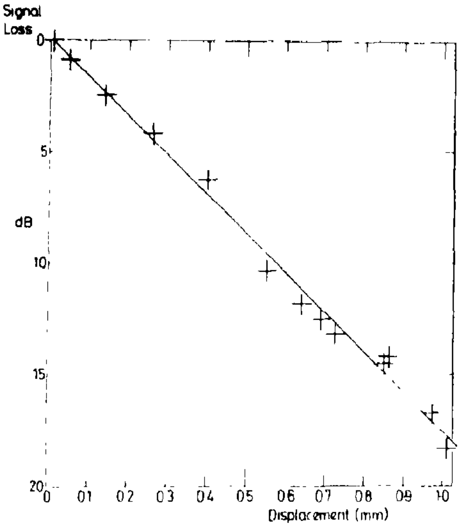

Fig. 13. The loss in amplitude of the directly generated shear signal in an aluminum crystal at 100 K as the generating coil was displaced up to 1 mm from the aluminum surface. The 'apparent attenuation' of 18 dB mm^{-1} is due to the exponential decrease of the induced r.f. field **B**.

two concentric, plane coils wound as a flat spiral, (Fig. 14), the outer acting as the transmitting and the inner as the receiving coil. A permanent magnet *NS* producing about 4 kG surrounds the coils and provides a field $\mathbf{B}_0$ parallel to part of the radial r.f. field **B**, thus generating quasicompressional waves in accordance with Fig. 2(b). Wallace, Houck, Bowers, Maxfield and Gaerttner [24] have demonstrated the drastic change of echo pattern that occurs when directly generated shear waves are scattered by a 1 mm hole oriented along **q**. Legg and Meredith have shown that they can detect an artificial flaw in a standard test block (Fig. 14) with directly generated compressional waves. The resultant echo pattern (Fig. 15) shows both the reduced amplitude (high apparent attenuation) of the signals from the back of the block and small signals from the flat end of the 'flaw'. However, the sensitivity of detection (at 5 kG) is substantially less than with conventional techniques and the detection of flaws near the surface, which is easy in the usual water bath technique, can only be done by generation from each end of the sample. It is therefore probable that electromagnetic generation techniques will be limited to special cases such as high speed, automatic testing of strip or sheet and measurements at extreme temperatures, where bonding is a problem.

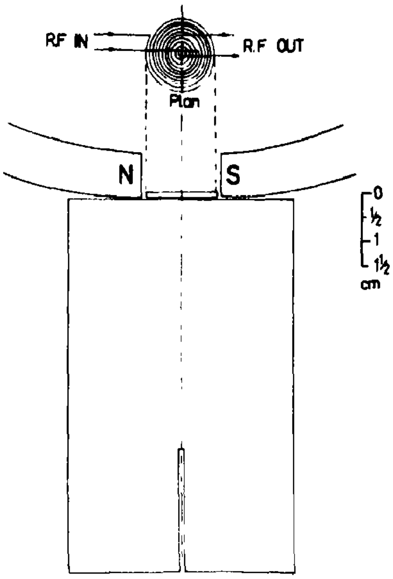

Fig. 14. The experimental arrangement for detecting an artificial flaw in a metal test block. A permanent magnet NS encloses the concentric pair of spirally wound 'pancake' coils, which generate and detect the compressional waves without touching the test block

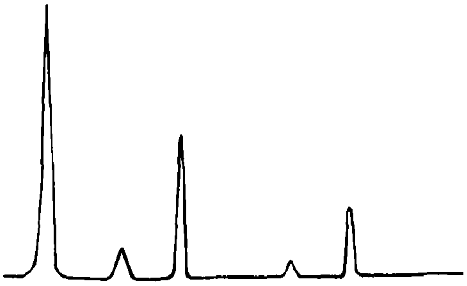

Fig. 15. Small reflections from the artificial flaw and large reflections from the end faces of the test block, using the arrangement of Fig. 14.

Abeles[4] has pioneered the generation of microwave acoustics in the absence of a static field in very clean, thin films. Southgate[14] has shown that for frequencies above 40 GHz this technique, or a modification of it using multilayer transducers, may be the most efficient way of producing sound from millimetre wavelength electromagnetic waves. Perhaps this technique will be used to generate phonons at thermal frequencies.

In conclusion I would like to emphasize that most of the effects that have been studied in the past by measuring small changes in ultrasonic attenuation could well be dramatically enhanced in the electromagnetically generated signals, as we have found in the giant quantum oscillations in bismuth. Although a static magnetic field is required at room temperature, several authors[4, 25, 26] have shown that this is not necessary at helium temperatures in pure metals. There are thus many interesting possibilities for further studies on solids.

Acknowledgements – It gives me much pleasure to thank Professor C. Elbaum for inviting me to present this paper at Brown University, Rhode Island. It was written while the author was a summer visitor at the Department of Physics, Wayne State University, and it is a pleasure to thank Dr. R. L. Thomas and D. Hsu for their collaboration on the measurements in bismuth, Dr G. Turner and Dr. N. Tepley for helpful discussions and Vice-President H. V. Bohm for the invitation to Detroit. My thanks are also due to Dr. D. J. Meredith and K. O. Legg for kindly supplying me with details of their recent experiments at Lancaster prior to publication.

REFERENCES

1. SAERMARK K. and LARSEN P. K., *Phys. Lett.* **24A**, 374 and 668 (1967).
2. HOUCK J. R., BOHM H. V., MAXFIELD B. W. and WILKINS J. W., *Phys. Rev. Lett.* **19**, 224 (1967).
3. BETJEMANN A. G., BOHM H. V., MEREDITH D. J. and DOBBS E. R., *Phys. Lett.* **25A**, 753 (1967)
4. ABELES B., *Phys. Rev. Lett.* **19**, 1181, (1967)
5. MEREDITH D. J., WATTS-TOBIN R. J. and DOBBS E. R., *J. acoust. Soc. Am.* **45**, 1393 (1969)
6. ALPHER R. A. and RUBIN R. J., *J. acoust. Soc. Am.* **26**, 452 (1954).
7. THOMAS R. L., TURNER G. and BOHM H. V., *Phys. Rev. Lett.* **20**, 207 (1968)
8. EINSPRUCH, N., *J. acoust. Soc. Am.* **36**, 971 (1964).
9. GAERTTNER M. R., WALLACE W. D. and MAXFIELD B. W., *Phys. Rev.* **184**, 702 (1969)
10. QUINN J. J., *Phys. Lett.* **25A**, 522 (1967).
11. MATTIS D. C. and DRESSELHAUS G., *Phys. Rev.* **111**, 403 (1958).
12. RODRIGUEZ S., *Phys. Rev.* **130**, 1778 (1963).
13. COHEN M. H., HARRISON M. J. and HARRISON W. A. *Phys. Rev.* **117**, 937 (1960)
14. SOUTHGATE P. D., *J. appl. Phys.* **40**, 22 (1969).
15. ALIG C. R., *Phys. Rev.* **178**, 1050 (1969).
16. GUREVICH V. L., SKOBOV V. G. and FIRSOV Yu. A., *Zh. eksp. teor. Fiz.* **40**, 786 (1961).
17. TOXEN A. M. and TANSAL S., *Phys. Rev.* **137A**, 211 (1965)
18. MASE S., FUJIMORI Y. and MORI H., *J. phys. Soc. Japan* **21**, 1744 (1966)
19. KOROLYUK A. P., *Zh. eksp. teor. Fiz.* **51**, 697 (1966); English transl. *Soviet Phys. JETP* **24**, 461 (1967)
20. GUIRA M., MARCON R., PAPA T. and WANDERLINGH F., *Phys. Rev.* **179**, 645 (1969)
21. DOBBS E. R., THOMAS R. L. and HSU D. *Phys. Lett.* **30A**, 338 (1969)
22. COHEN M. H. and BLOUNT E. I., *Phil. Mag.* **5**, 115 (1960)
23. LEGG K. O. and MEREDITH D. J., (To be published.)
24. WALLACE W. D., HOUCK J. R., BOWERS R., MAXFIELD B. W. and GAERTTNER M. R. *Rev. scient. Instrum.* **39**, 1863 (1968)
25. WALLACE W. D., GAERTTNER M. R. and MAXFIELD B. W., *Bull. Am. phys. Soc.* **14**, 64 (1969).
26. THOMAS R. L., TURNER G. and HSU D., *Phys. Lett.* **30A**, 316 (1969).

J. Phys. Chem. Solids Pergamon Press 1970. Vol. 31, pp. 1669–1672. Printed in Great Britain

APPLICATION OF TRANSLATIONALLY INVARIANT WAVEFUNCTIONS IN A MAGNETIC FIELD TO FREQUENCY AND WAVELENGTH DEPENDENT TRANSPORT PHENOMENA*

H. L. GRUBIN† and T. KJELDAAS, JR.
Polytechnic Institute of Brooklyn, Brooklyn, N.Y. 11201, U.S.A.

(*Received* 5 *September* 1969)

Abstract—Density matrix techniques are used to analyze magneto transport effects in solids. The representation used consists of wave functions that are simultaneous eigenfunctions of the magnetic Bloch Hamiltonian and the magnetic translation operators. This procedure yields results for both ordinary magnetic field dependent transport phenomena in general band structures and those due to magnetic breakdown. The conductivity tensor governing ultrasonic Doppler-shifted cyclotron resonance is analyzed, i.e. the wave vector **q** is parallel to the magnetic field **B**, the latter being parallel to the z-axis. Using a simplified periodic potential model in which $V(x, y, z) = V(x, y) + V(z)$, the contributions to $\sigma(\mathbf{q}, \omega, \mathbf{B})$ are separated into a part expressing magnetic breakdown effects and a part that is largely semiclassical in composition. Of significance here is the explicit dependence of some of the terms on magnetic quasi-particle parameters such as the magnetic field dependent effective mass $M_{J,c}$.

The magnetic quasi-particle contribution to $\sigma(\mathbf{q}, \omega, \mathbf{B})$ is analyzed in a regime where the electron mean free path Λ satisfies the condition $q\Lambda \gg 1$. It is found that increments appear in the conductivity that are periodic in $1/B$. These increments lead to spikes in the attenuation of ultrasound and helicons outside the absorption edge.

WE REPORT on a theoretical investigation of wave-propagation in solids in a uniform magnetic field **B**. The theory is formulated independently of the usual semiclassical approximations so as to include the effect of periodic potential broadening of the cylotron energy levels[1]. In the past[2, 3] we have included studies of various relevant transport coefficients. In the present report we limit ourselves to a description of the results for shear wave propagation parallel to the magnetic field, thus describing one of the magneto-acoustic effects as well as helicon propagation. A main result is the appearance of peaks in the attenuation coefficient outside the absorption edge[4]. The width of the peaks is related to the broadening of the energy levels induced by the periodic potential.

Density matrix techniques, patterned after the work of Tosima, Quinn and Lampert[5], are used to discuss magneto-transport effects by Bloch electrons. The formulation is sufficiently general to yield results for both ordinary magnetic field dependent transport coefficients in general band structures and those due to magnetic breakdown. Although we include the crystalline potential, the results are formally similar to the free electron calculation of Ref. [5].

The representation for our purposes are translationally invariant wave functions $\Omega^{\sigma}_{n\kappa}(\mathbf{r})$ that are simultaneously eigenfunctions of the Bloch Hamiltonian

$$\mathcal{H}_0 = \frac{1}{2m}\left(\mathbf{P} - \frac{e\mathbf{A}_0}{c}\right)^2 + V(\mathbf{r}) \tag{1}$$

and the commuting subset of operators.

$$\tau(\mathbf{R}) = \exp i\left(\mathbf{P} + \frac{e\mathbf{A}_0}{c}\right).\mathbf{R}/\hbar \tag{2}$$

---

*Work supported by U.S. Air Force Office of Scientific Research.

†*Present address.* United Aircraft Research Laboratories, East Hartford, Conn. 06118, U.S.A.

for a particle of charge e, mass m. $\mathbf{A}_0 = \frac{1}{2}\mathbf{B}\times\mathbf{r}$ and $V(\mathbf{r}) = V(\mathbf{r}+\mathbf{R})$. $\mathbf{R}$ is a crystal lattice vector. The functions $\Omega^{\sigma}_{n\kappa}$ are closely related to those discussed earlier[6] but are in a convenient form for the present study. A summary of their properties is contained in an Appendix.

We consider a collection of N_e independent electrons in the periodicity domain V subject to the Hamiltonian

$$\mathscr{H} = \mathscr{H}_0 + \mathscr{H}_1 + \mathscr{H}_2 \tag{3}$$

where

$$\mathscr{H}_1 = \frac{-\mathrm{e}}{2mc}\left[\left(\mathbf{P}-\frac{\mathrm{e}\mathbf{A}_0}{c}\right).\mathbf{A}_1(\mathbf{r},t)+\mathbf{A}_1(\mathbf{r},t)\right.$$
$$\left.\times\left(\mathbf{P}-\frac{\mathrm{e}\mathbf{A}_0}{c}\right)\right]+\mathrm{e}\varphi_1(\mathbf{r},t). \tag{4}$$

$\mathbf{A}_1(\mathbf{r},t)$ and $\phi_1(\mathbf{r},t)$ are the vector and scalar potentials of the space and time dependent perturbation. H_2 denotes the electron interaction with thermal phonons, impurity scattering centers, etc.

We treat the electron response using a density matrix formalism and take H_2 as having the effect of relaxing the density matrix to its thermal equilibrium value. We assume a constant relaxation time τ. Using a simplified periodic potential model with $V(x,y,z) = V(x,y) + V(z)$ we calculate the Fourier transform of the transverse current density per electron. We consider the orientation where the wave vector q is parallel to the magnetic field $\mathbf{B}$, the latter parallel to the z-axis.

In the limit of zero q, and for a spatially uniform field E_x, the transverse conductivity coefficients are separated into a part due to the effects of broadened bands and a part largely semiclassical in composition. For the broadened band contributions $\sigma'_{yx} = 0$ and

$$\sigma'_{xx} = \frac{\mathrm{e}^2}{mV}\frac{\tau}{1-i\omega\tau}\frac{m}{\hbar^2}\sum_{nj\kappa\sigma}\rho^{\circ}_{nj\kappa}$$
$$\times\frac{\partial^2\epsilon_n}{\partial\kappa_x{}^2} \equiv \frac{\mathrm{e}^2\tau}{M_{xx}V}\cdot\frac{1}{1-i\omega\tau} \tag{5}$$

is the conductivity coefficient of a particle of mass M_{xx} in an r.f. electric field. M_{xx} is zero in the zero periodic potential limit. For a finite potential M_{xx} exhibits structure as a function of magnetic field when a broadened level crosses the Fermi surface[2]. In equation (5) the band index n is associated with motion in the x-y plane, the index j with motion along the z-axis. (See notational discussion in the Appendix).

For finite q, the situation important to magneto-acoustics, the transverse current density is separated into two parts: one with and one without frequency dependent coefficients. The frequency independent part is identified as a magnetization current[7]. The frequency dependent part is

$$\mathbf{j}(q,\omega) = \frac{-\mathrm{e}^2}{mV}\overleftrightarrow{I}(q,\omega).\mathbf{E}(q,\omega)/i\omega \tag{6}$$

with

$$\dot{I}(q,\omega) = -m\hbar\omega\sum_{\nu,\nu'}\frac{\rho^{\circ}_{\nu'}-\rho^{\circ}_{\nu}}{\mathrm{e}_{\nu'}-\mathrm{e}_{\nu}}$$
$$\frac{\langle\nu'|\mathbf{V}(-q)|\nu\rangle\langle\nu|\mathbf{V}(q)|\nu'\rangle}{\mathrm{e}_{\nu'}-\mathrm{e}_{\nu}+\hbar\omega+i\hbar/\tau}. \tag{7}$$

$I(q,\omega)$ is a dyadic,

$$\mathbf{V}(\pm q) = \frac{1}{2m}\times\left\{\left(\mathbf{P}-\frac{\mathrm{e}\mathbf{A}_0}{c}\right)\mathrm{e}^{\pm iqz}\right.$$
$$\left.+\mathrm{e}^{\pm iqz}\left(\mathbf{P}-\frac{\mathrm{e}\mathbf{A}_0}{c}\right)\right\}.$$

ν denotes the magnetic quantum numbers and ρ°_{ν} is the Fermi-Dirac distribution function for particles with energy ϵ_{ν}.

$\mathbf{j}(q,\omega)$ is examined for the case when the electrons are free along the z-axis. The important band index is now associated with motion in the x-y plane, perpendicular to $\mathbf{B}$. Separating $\overleftrightarrow{I}(q,\omega)$ into a part that is diagonal in the band indices n, and an off diagonal part and evaluating for a potential possessing four-fold symmetry in the x-y plane we obtain

$$j^{\pm}(q,\omega)=\frac{e^2\tau}{mV}G^{\pm}E^{\pm}+\sigma^{D}_{xx}E^{+} \tag{8}$$

where $E^{\pm}=E_x\pm iE_y$, $j^{\pm}=j_x\pm ij_y$. G^{+} contains off diagonal contributions of the components I_{xx} and I_{xy} and is basically a semiclassical quantity. In the limit of zero periodic potential $G^{\pm}$ reduces to equation (9) of Ref. [4]. For terms diagonal in the magnetic band index

$$\sigma^{D}_{xx}=\frac{e^2\tau}{V}\cdot\frac{1}{\hbar^2}\sum_{n\kappa_x\kappa_y k\sigma}\rho^{\circ}_{n\kappa_x\kappa_y k}\times\frac{\partial^2\epsilon_n}{\partial\kappa_x{}^2}\Big/1+i\tau\left(\frac{\hbar qk_z}{m}-\omega\right) \tag{9}$$

where k_z varies from minus to plus infinity.

σ^{D}_{xx} is readily evaluated by changing the sum over $\kappa_x\kappa_y k_z$ into an integration and letting $\kappa_x Na=\vartheta$, $\kappa_y Na=\varphi$, $k_z=k_f\zeta$ (k_f is the wave vector at the Fermi surface). We have

$$\sigma^{D}_{xx}=-\sigma_0\frac{3}{2(6\pi^2)^{2/3}}\sum_l{}'\frac{V_l}{\hbar^2 b/m}\int'\times\frac{d\vartheta\,d\varphi\,d\zeta\cos\vartheta}{1+i(q\Lambda\zeta-\omega\tau)} \tag{10}$$

where the sum and integration are over occupied states (denoted by primes). The symbols $\Lambda=\hbar k_f\tau/m$, $\sigma_0=e^2\tau/mV$, and $b=|e\mathbf{B}|\hbar C$.

To arrive at equation (10) the quantities in equation (9) were approximated using perturbation theory. The periodic potential is treated as a perturbation of the Landau levels, denoted by the symbol l. V_l is the expectation value of the first Fourier expansion term of the periodic potential between symmetrized free electron states. Thus equation (10) is a sum over broadened Landau states.

We examine the real part of σ^{D}_{xx} for the situation $q\Lambda\gg 1$ where the denominator has a strong minimum at $\zeta_0=\omega\tau/q\Lambda$. For the real part of σ^{D}_{xx}, the reciprocal denominator is treated as a Dirac delta-like function of constant area $\pi/q\Lambda$ centered at ζ_0. Then

$$Re\,\sigma^{D}_{xx}=-\frac{\sigma_0}{2}\cdot\frac{3}{(6\pi^2)^{2/3}}\frac{\pi}{q\Lambda}\sum_l{}'\frac{V_l}{\hbar^{-2}b/m}\times\int'_{\zeta=\zeta_0}d\vartheta\,d\varphi\cos\vartheta. \tag{11}$$

For metals $\zeta_0\ll 1$. Thus the important value of k_z is $k_z\approx 0$. At $k_z\approx 0$ the broadened Landau levels are generally completely occupied, with the possible exception of the highest level. This level contributes only if there are values of κ_x and κ_y for which the electron energy $\epsilon_l(\kappa_x,\kappa_y,k_z)=\mu^0$, μ^0 being the electron energy at the Fermi surface. For this case

$$\left|Re\,\sigma^{D}_{xx}\right|=\frac{3\pi}{4q\Lambda}\sigma_0\left(\frac{128}{9\pi}\right)^{1/3}\frac{V_{l_f}}{\hbar^2 b/m}\beta_{l_f} \tag{12}$$

where l_f is the value of the Landau level at the Fermi surface. The quantity β_{l_f} is a number between zero and one and is dependent on the position of the Fermi surface.

The amplitude of equation (12) consists of a product of two factors. The factor $3\pi\sigma_0/4q\Lambda$ is the amplitude of the semiclassical expression evaluated in the limit of large $q\Lambda$. The other factor is approximately equal to the ratio of the broadening, as given by perturbation theory, to the Landau level spacing. Thus the entire effect can be described as follows. When the Fermi level falls inside the broadened band ($k_z\approx 0$) the electrons give an additional conductivity that ordinary electrons would have in the absence of a magnetic field, provided they have a reciprocal mass reduced by the ratio of the band width to the Landau level spacing. (In the case of the quantity M_{xx} discussed in connection with the $q=0$ conductivity, similar considerations apply. However, it is necessary in that case to consider a range of values of k_z, slightly complicating the issue.) Since the effect only occurs for such values of the magnetic field that the Fermi level falls inside the broadened level it is clear that increments in the conductivity that are periodic in $1/B$ occur. These peaks will reflect themselves in periodic changes in the soundwave attenuation. The height of the peak directly measures the width of the broadened band, thus providing an opportunity for an experimental determination of this quantity.

REFERENCES

1. HARPER P. G., *Proc. phys. Soc.* **A68**, 879 (1955).
2. GRUBIN H. L. and KJELDAAS T., Jr., *Bull. Am. phys. Soc. Ser. II* **12**, 398 (1967), and *Phys. Rev.* (to be published).
3. GRUBIN H. L., *Dissertation*, Polytechnic Institute of Brooklyn (1967) (Unpublished). Copies available from University Microfilms, Ann Arbor, Michigan.
4. KJELDAAS T., Jr., *Phys. Rev.* **113**, 1473 (1959).
5. TOSIMA S., QUINN J. J., LAMPERT M. A., *Phys. Rev.* **137**, A883 (1965).
6. BROWN E., *Phys. Rev.* **133**, A1038 (1964); ZAK J., *Phys. Rev.* **134**, A1607 (1964).
7. SLATER J. C. and FRANK N. H., *Electromagnetism*, Chap. 6. McGraw-Hill, New York (1947).

APPENDIX A

The functions $\Omega^q_{n\boldsymbol{\kappa}}(\mathbf{r})$ satisfy magnetic periodic boundary conditions [6] $\tau(N_i\mathbf{a}_i)\Omega^q_{n\boldsymbol{\kappa}}(\mathbf{r})$ where $N_i\mathbf{a}_i$ is a macroscopic length, $\mathbf{a}_i$ is a primitive lattice vector and N_i is an integer ($i = 1, 2, 3$). This condition restricts $\mathbf{B}$ to values given by

$$\mathbf{b} \equiv \frac{e\mathbf{B}}{\hbar c} = \frac{2\pi q}{N}\frac{\mathbf{a}_3}{\Delta} \tag{A.1}$$

where q and N are integer and $\Delta = (\mathbf{a}_1 \times \mathbf{a}_2)\,.\,\mathbf{a}_3$. With this restriction $\Omega^q_{n\boldsymbol{\kappa}}(\mathbf{r})$ is chosen to be an eigenfunction of $\mathscr{H}_0$ and the commuting subset

$$\{\tau(n_1\mathbf{d}_1), \tau(n_2N\mathbf{a}_2), \tau(n_3\mathbf{a}_3)\} \tag{A.2}$$

where $n_i (i = 1, 2, 3)$ is an integer. The eigenvalues of this operator are

$$\left\{\exp i\left(\boldsymbol{\kappa}+\sigma\frac{q}{N}\mathbf{K}_1\right)\cdot n_1\mathbf{a}_1, \exp i\boldsymbol{\kappa}\cdot n_2N\mathbf{a}_2, \exp i\boldsymbol{\kappa}\cdot n_3\mathbf{a}_3\right\} \tag{A.3}$$

where σ varies from 0 to $N-1$, $\boldsymbol{\kappa} = \kappa_x\hat{x}_0 + \kappa_y\hat{y}_0 + \kappa_z\hat{z}_0$ (orthorhombic systems are considered) with

$$\kappa_x = 2\pi\nu_1/N_1a_1, \nu_1 = 0, \pm 1, \ldots, \pm\tfrac{1}{2}N_1/N - 1, -\tfrac{1}{2}N_1/N,$$
$$\kappa_y = 2\pi\nu_2/N_2a_2, \nu_2 = 0, \pm 1, \ldots, \pm\tfrac{1}{2}N_2/N - 1, -\tfrac{1}{2}N_2/N,$$
$$\kappa_z = 2\pi\nu_3/N_3a_3, \nu_3 = 0, \pm 1, \ldots, \pm\tfrac{1}{2}N_3/2 - 1, -\tfrac{1}{2}N_3,$$

and $\mathbf{K}_i = 2\pi(\mathbf{a}_j \times \mathbf{a}_k)\Delta^{-1}$ $i, j, k, = 1, 2, 3$ et cyclic.

The eigenvalues of $\mathscr{H}_0$ are $\epsilon_n(\boldsymbol{\kappa})$ where n is a band index. $\epsilon_n(\boldsymbol{\kappa})$ is independent of σ and each level is at least N fold degenerate. $\epsilon_n(\boldsymbol{\kappa})$ has the property [2, 7]

$$\epsilon_n(\boldsymbol{\kappa}) = \epsilon_n(\boldsymbol{\kappa}+\mathrm{K}) \tag{A.4}$$

with $\mathrm{K} = n_1\mathbf{K}_1/N + n_2\mathbf{K}_2/N + n_3\mathbf{K}_3$. K is a vector of a *magnetic reciprocal lattice*.

For the situation when the periodic potential is written as $V(x, y, z) = V(x, y) + V(z)$, and $\mathbf{B}$ is along the z-axis the wave function is separable into $\psi_{z\,jk_z}\,\Omega^{q(x,y)}_{n\kappa_x\kappa_y}$ with energy $\epsilon_j(\kappa_z) + \epsilon_n(\kappa_x, \kappa_y)$. Here ψ_{jk_z} is a one dimensional Bloch wave function and $\Omega^q_{n\kappa_x\kappa_y}$ is a two dimensional magnetic wave function. When the electrons are free along the z-axis, the wave function reads $e^{ik_z z}\,\Omega^{q(x,y)}_{n\kappa_x\kappa_y}$ with appropriate normalization. Here k_z varies from minus infinity to plus infinity and the energy is $\hbar^2k_z^2/2m + \epsilon_n(\kappa_x, \kappa_y)$.

J Phys. Chem Solids Pergamon Press 1970. Vol. 31, pp. 1673-1676. Printed in Great Britain

NONLINEAR ATTENUATION OF MICROSOUND IN SEMICONDUCTING CdS

J. ZUCKER and S. ZEMON

Bayside Research Center of General Telephone & Electronics Laboratories Incorporated,
Bayside, N.Y. 11360, U S.A.

(*Received 5 September 1969*)

Abstract—The room temperature attenuation of acoustic waves in semiconducting CdS was measured in zero electric field from 0·2 to 5 GHz using Bragg scattering techniques. The waves were in narrow intense packets of acoustic power which had been amplified from thermal noise by electrons with supersonic drift velocities. Evidence is given for phonon-phonon interactions among the various modes in the packet.

1. INTRODUCTION

It is well known that propagating acoustic packets containing shear waves over a broad region spanning UHF and microwave frequencies can be generated in a piezolelectric semiconductor such as CdS by application of a field high enough to cause the electrons to flow with greater than sonic velocity[1]. These waves constitute a convenient source of acoustic shear-wave energy for attenuation measurements, obtained without the use of transducers or costly high-power microwave or UHF generators. We have made attenuation measurements at room temperature on such waves in semiconducting CdS in zero applied field in the frequency range from 0·2 to 5 GHz, using Bragg scattering of a He-Ne laser beam as a probe for the acoustic intensity. Our results are substantially different from that expected for single frequency waves in the same frequency band. This we believe to be due to phonon-phonon interactions among the various modes in the packet.

2. EXPERIMENTAL TECHNIQUE

A standard laser beam Bragg scattering probe which has been described elsewhere[1] was used for detecting the acoustic waves. The important parameters of this probe are: light wavelength, 6328 Å, power $\leqslant 40$ mW, acoustic frequency resolution ± 50 MHz, spatial resolution, $\sim 200\,\mu$, equivalent noise input to photomultiplier $\sim 2\times 10^{-15}$ W/cycle and directional resolution $\pm 0{\cdot}5$ deg. The data reported here were taken on two similar semiconducting CdS samples with carrier concentration of about $2\times 10^{15}\,\text{cm}^{-3}$, room temperature mobility about $300\,\text{cm}^2/\text{V}$ sec and dimensions of the order of $1\times 1\times 4\,\text{mm}^3$. Their long (current) directions were perpendicular to the crystallographic c axis. The acoustic waves investigated are the piezoelectrically active modes for this orientation, i.e. the shear modes propagating in the basal plane polarized parallel to the c axis. Low resistance contacts to the samples were prepared with an indium amalgam applied to chromic acid etched ends and heated at 400°C for 30 min in a forming gas atmosphere.

Short, intense voltage pulses were applied to the sample which served to amplify a broad spectrum of acoustic waves in narrow packets from the thermal acoustic noise background [1]. The characteristic of these packets have been extensively treated elsewhere[1-5]. The pulse duration was less than one-half the transit time for acoustic shear waves from cathode to anode to allow a sufficiently long field-free drift region in which the attenuation measurements could be made.

3. EXPERIMENTAL RESULTS

Attenuation was measured for several strain levels by varying either the amplitude or the length of the excitation pulse. Starting spectra for two of these levels of strain in the vicinity of f_{mi}, the frequency of maximum intensity, are shown in Fig. 1. The high-strain curve is peaked at 0·6 GHz while the low-strain curve is peaked at 1·2 GHz. For both curves, the frequency separation of the half-intensity points roughly equals f_{mi} which is much lower than the frequency of maximum net gain ($f_{mn} \sim 3$ GHz) predicted by linear theory[6, 7]. The downshift in f_{mi} with increasing intensity has previously been observed[1–3], and has been attributed to parametric amplification of subharmonics at the expense of the higher frequency modes contained in the acoustic packet[5, 8]. The intensity was peaked in the current direction, falling to half its intensity at roughly ±5° from the current direction. The strain in a frequency interval of 100 MHz around the peak and in a cone angle of 1° about the current direction was estimated to be 4×10^{-5} for the high-strain case and 7×10^{-6} for the low-strain case from the light scattering efficiency[9], $I(f)/I_0$. The photomultiplier signal half-width of 0·1 μsec gave an upper bound of 180 μ for the acoustic packet half-width.

The attenuation was studied both during the persistent acoustoelectric current I_{ae} that flows after the applied voltage V has fallen to zero, and after I_{ae} had essentially decayed to zero. In the first region, the decay is not exponential for modes below f_{mi} which still grow for some time after V has fallen to zero.

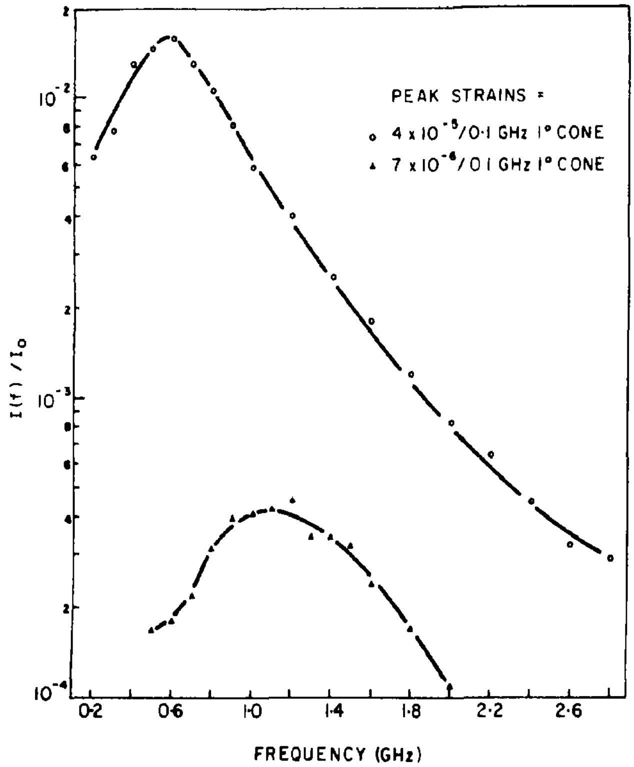

Fig. 1. Spectra of acoustic packets for peak strains of 4×10^{-5} (circles) and 7×10^{-6} (crosses).

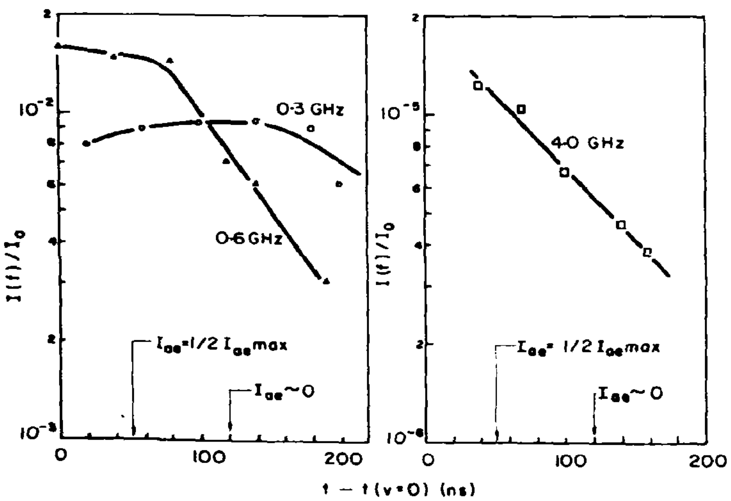

Fig. 2. Acoustic intensity as represented by ratio of light scattered by modes about frequency f to incident light, $I(f)/I_0$ vs time-of-flight after applied voltage has fallen to zero for 0·3 GHz (circles), 0·6 GHz (crosses) and 4·0 GHz (boxes). These frequencies are below, at and above f_m. The times for which I_{ae} has fallen to 0·5 its maximum value and by more than an order of magnitude are marked on the time axis.

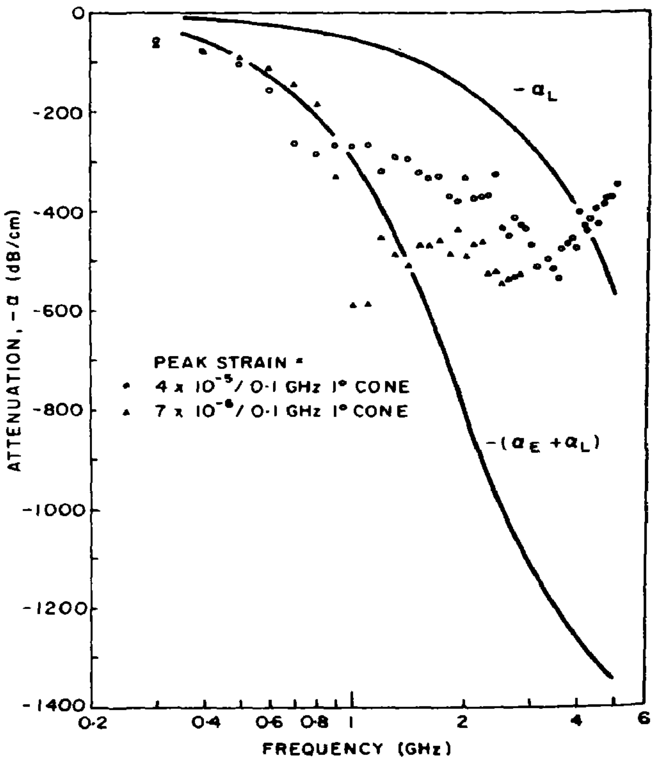

Fig 3. Attenuation vs. frequency for the high strain (circles) and low strain (crosses) spectra of Fig. 1. For comparison, curves for α_l and $\alpha_E - \alpha_l$ are included (solid lines).

The behavior during this time for the high-strain case is plotted in Fig. 2 for modes below, at and higher than f_{mi}.

After the current has fallen to zero, the attenuation curves at all frequencies could be approximated by exponentials. The attenuation in dB/cm as a function of frequency is shown in Fig. 3 for both the high-strain (circles) and low-strain (crosses). For comparison, the lattice loss, α_L[7], and the sum of α_L and the electronic attenuation α_E[6], calculated for a frequency of maximum α_E of 3·5 GHz are plotted in the same figure. The data are in fair agreement with $\alpha_E+\alpha_L$ only for the lowest frequencies. In the vicinity of f_{mi}, the absolute magnitude of the observed attenuation $|\alpha|$ is greater than $|\alpha_E+\alpha_L|$, while for frequencies much greater than f_{mi}, $|\alpha|<|\alpha_E+\alpha_L|$.

4. DISCUSSION

The important features of the attenuation data can be explained qualitatively by assuming that phonon–phonon interactions due to acoustoelectric nonlinearities[10] are operative among the modes of the intense acoustic packet. This model predicts that acoustic energy is transferred from the most intense modes into the weaker modes. Thus, the growth of the low frequency modes in zero field can be ascribed to parametric amplification[5, 8], the slow decay of the high-frequency modes to harmonic generation[11, 12] and mixing, and the attenuation maximum in the frequency range of the most intense modes to the depletion of these modes by the aforementioned processes.

Acknowledgements—We are indebted to A. Ganguly and E. M. Conwell for useful discussions, and L. Johrden and L. Vivenzio for technical assistance.

REFERENCES

1. ZUCKER J. and ZEMON S., *Appl. phys. Lett.* **9**, 398 (1966), Erratum: *Appl. Phys. Lett.* **10**, 212 (1967)
2. ZUCKER J., ZEMON S., and WASKO J. H., *II–VI Semiconducting Compounds 1967 Int. Conf.* (edited by D. Thomas), pp. 919–927. Benjamin, New York (1967).
3. ZUCKER J., ZEMON S. A. and WASKO J. H., *Proc. of the 9th Int. Conf. on the Phys. of Semiconductors, Moscow*, p. 904. Nauka, Leningrad (1968).
4. ZUCKER J., ZEMON S., CONWELL E. M. and GANGULY A. K., *Proc. of the Int. Conf. on Light Scattering Spectra of Solids* (Edited by George B. Wright), p. 615. Springer-Verlag, Berlin (1968).
5. ZEMON S. and ZUCKER J., *IBM J. Res. Develop.* **13**, 494 (1969)
6. WHITE D. L., *J. appl. Phys.* **33**, 2547 (1962).
7. BATEMAN T. B. and McFEE J. H., *J. appl. Phys.* **39**, 4471 (1968).
8. ZEMON S., ZUCKER J., WASKO J. H., CONWELL E. M. and GANGULY A. K., *Appl. phys. Lett.* **12**, 378 (1968)
9. HOPE L. L., *Phys. Rev.* **166**, 883 (1968)
10. HUTSON A. R., *Phys. Rev. Lett.* **9**, 296 (1962)
11. KROGER H., *Appl. phys. Lett.* **4**, 190 (1964).
12. TELL B., *Phys. Rev.* **136A**, A772 (1964)

J. Phys. Chem. Solids Pergamon Press 1970 Vol. 31, pp. 1677–1679. Printed in Great Britain.

CHANGE IN VELOCITY OF HIGH FREQUENCY TRANSVERSE SOUND AT THE SUPERCONDUCTING TRANSITION TEMPERATURE*

J. L. STEVENS and A. HOUGHTON
Physics Department, Brown University, Providence, R.I. 02912, U.S.A.

(*Received* 5 *September* 1969)

Abstract—The change in velocity of transverse sound at the transition temperature consists of two parts (1) a static part (usually estimated to be 1–10 ppm arising from the difference in the elastic constants between the superconducting and normal states, and (2) a purely dynamical effect due to Meissner Screening of the transverse electromagnetic fields at the transition temperature. It is shown that under suitable conditions, as first suggested by Ozaki and Mikoshiba, the second mechanism can give rise to much larger changes in the velocity of high frequency sound. In fact for Al at a sound wave frequency of 10^{6} c/s and $ql = 10$ (here q is the wave number of the sound wave and l is the electron mean free path) the relative change in velocity can be as much as 1 part per thousand. The results of a detailed microscopic calculation of the relative change in velocity $(v_s - v_n)/v_n$ are presented for weak coupling type I superconductors.

1. INTRODUCTION

It is well known that due to a difference in the elastic constants between the superconducting and normal states, there is a static change in the velocity of transverse sound of the order of one to ten parts per million. However, there is under suitable circumstances a much larger change due to the interaction of the electron system with the sound wave. This effect, which is a result of the sudden change in the screening of transverse electromagnetic fields at the transition temperature, was first pointed out by Ozaki and Mikoshiba[1]. These authors, who used a two fluid model to estimate the size of the effect, found that the relative change in velocity $(v_s - v_n)/v_n$ was strongly mean free path dependent and could be as large as 7×10^{-4} at $T/T_c = 0{\cdot}99$ and $ql = 10$, here q is the wave vector of the sound wave and l is the electron mean free path. As it is now possible using conventional techniques to determine changes of velocity to one part in 10^{7}, it should be possible to measure this change extremely accurately. For this reason a calculation, using microscopic theory, of the change in velocity of high frequency transverse sound as a function of temperature and mean free path was undertaken. It is shown that the change in velocity at high ql is even larger than that predicted by Ozaki and Mikoshiba.

2. VELOCITY OF TRANSVERSE SOUND

The model we have used to describe an isotropic, type I superconductor is essentially the same as the BCS[2] model. The model consists of an electron gas weakly coupled to a lattice of positive ions. Embedded in this superconductor are randomly placed nonmagnetic impurities. The effect of these impurities is described by a collision time $1/\Gamma$.

The velocity of a transverse sound wave can be obtained from the equation of motion of the ionic system[3]

$$\ddot{\xi} = -c_s^2\nabla\times(\nabla\times\xi) + F/\rho_i \qquad (1)$$

where $\xi \propto \exp i(\mathbf{q}\cdot\mathbf{r} - \omega t)$ is the ionic displacement, c_s is the velocity of sound in the normal state assumed to be a constant, and ρ_i is the

---

*Supported in part by the Advanced Research Project Agency, the U.S. Army Office of Research, Durham, North Carolina, and the National Science Foundation.

ionic mass density. The forces on the ions, appearing on the right hand side of equation (1) are a short range force characterised by an elastic constant and the dissipative force density F due to the electronic system. If the frequency of the sound wave is less than 10^9 sec^{-1} the dissipative force density can be written

$$F = q^2\xi\left[\frac{mv_F^2N}{5} + \langle[\tau_{yz}, \tau_{yz}]\rangle(q,z) - \frac{(\langle[\tau_{yz}, j_y]\rangle(q,z))^2}{\frac{N}{M} + \langle[j_y, j_y]\rangle(q,z)}\right] = q^2\xi(L+iK). \tag{2}$$

Here v_F is the Fermi velocity, m and N are the electron mass and number density and j_y, τ_{yz} are the electronic particle current and stress tensor respectively. The brackets, $\langle\ \rangle$, denote both a statistical average and an average over the random placements of the impurities. The second term in equation (2) is the collision drag force exerted by the electrons on the ions and the third term is due to the self-consistent electromagnetic field.

Using equations (1) and (2) we may write the dispersion relation for transverse sound waves as

$$\omega^2 = c_s^2q^2 - q^2(L+iK)/\rho_i. \tag{3}$$

Writing $\omega = \omega_1 - i\omega_2$, the attenuation and the

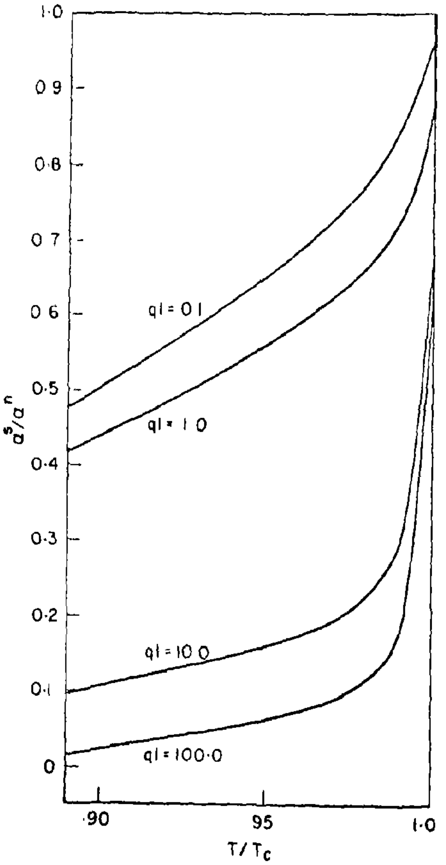

Fig. 1. The relative attenuation of transverse sound as a function of reduced temperature and ql.

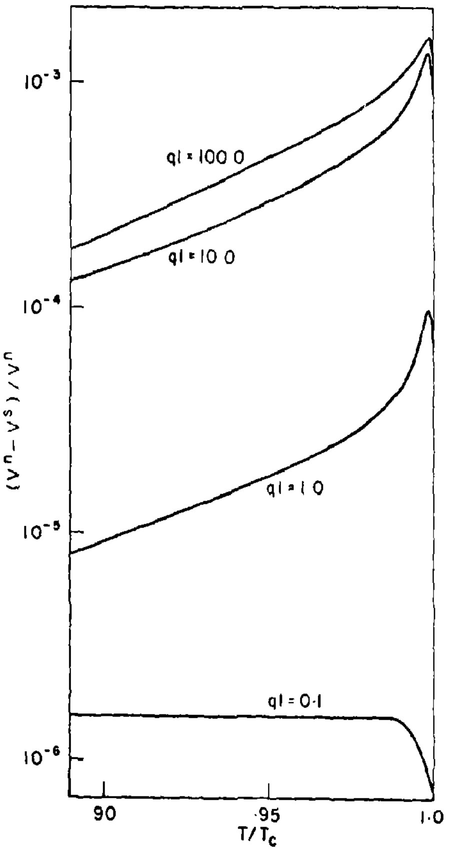

Fig. 2. The relative change in velocity of transverse sound as a function of reduced temperature and ql.

phase velocity of sound are given by

$$\omega_2 \cong qK/2\rho_l c_s \tag{4}$$

$$v_s \cong c_s[1-\tfrac{1}{2}(L/\rho_l c_s^2-(K/2\rho_l c_s^2)^2)]. \tag{5}$$

The correlation functions of equation (2) were expressed in terms of the Gorkov one-particle thermal Green's functions and computed by the usual methods[5].

3. RESULTS

The relative change in attenuation and velocity of sound are shown in figures one and two respectively. We have chosen parameters corresponding to Aluminum and the sound wave frequency has been taken to be 10^6 c/s. In Fig. 1 we have plotted the relative attenuation of transverse sound as a function of reduced temperature for several values of ql. This figure shows the drastic decrease in the attenuation near the critical temperature due to the sudden onset of the Meissner effect followed by a more gradual decrease at lower temperatures. This change in the form of the attenuation characteristic was first verified experimentally by Claiborne and Morse[6]. In Fig. 2 we have plotted the corresponding change in velocity of sound as a function of reduced temperature. It is seen from the figure that the change in velocity of sound is much greater than the static change for large values of ql.

REFERENCES

1. OZAKI H. and MIKOSHIBA N., *Phys. Lett.* **23**, 52 (1966)
2. BARDEEN J., COOPER L. N. and SCHRIEFFER J. R., *Phys. Rev.* **108**, 1175 (1957)
3. RODRIGUEZ S., *Phys. Rev.* **130**, 1778 (1963).
4. See for example TSUNETO T., RUTGERS *The State University, 1964* (Unpublished). MAKI K., *Phys. Rev.* **148**, 370 (1966).
5. KADANOFF L. P. and FALKO I. I., *Phys. Rev.* **136**, A1170 (1964).
6. CLAIBORNE L. T. and MORSE R. W., *Phys. Rev.* **136**, A893 (1964)

J. Phys. Chem. Solids Pergamon Press 1970 Vol. 31, pp. 1681-1685. Printed in Great Britain.

LONGITUDINAL ULTRASONIC ATTENUATION IN TYPE II SUPERCONDUCTORS: CLEAN LIMIT*

HILDA A. CERDEIRA†, W. N. COTTINGHAM‡ and A. HOUGHTON
Department of Physics, Brown University, Providence, R.I. 02912, U.S.A.

(*Received* 5 *September* 1969)

Abstract—The attenuation of longitudinal sound in clean type II superconductors, near H_{c_2}, has been calculated using a non-perturbative method. It is shown that at low frequencies the attenuation rate depends strongly on the direction of propagation of the wave, and on impurity concentration

1. INTRODUCTION

IN THIS paper we present a procedure for calculating the transport coefficients of clean type II superconductors near H_{c_2} which does not depend on an expansion in powers of the order parameter. The theory is used to study the attenuation of longitudinal sound in pure Niobium in magnetic fields close to the upper critical field. It is shown that the attenuation coefficient of longitudinal sound depends strongly on the direction of propagation, and is markedly dependent on impurity concentration even when $ql \gg 1$ and $\xi_0 \ll l$, here q is the wave vector of the sound wave, l is the electron mean free path and ξ_0 is the pure superconductor coherence distance.

2. THE ATTENUATION COEFFICIENT

In the low frequency limit $\omega_s < \pi T_{c_0}$, provided $ql \gg 1$, the attenuation coefficient of longitudinal sound is given by

$$\alpha_L = Re\frac{q^2}{i\omega_s\rho_{\text{ion}}v_s}\left(\frac{P_F{}^2}{3m}\right)^2\langle[n,n]\rangle(\mathbf{q},\omega_s). \qquad (1)$$

In equation (1) q and ω_s are the wave vector and frequency of the sound wave, p_F is the Fermi momentum and $\langle[n,n]\rangle(q,\omega_s)$ is the volume average of the density–density correlation function. The correlation function is obtained by analytic continuation of the thermal product $\langle[n,n]\rangle(q,\omega_0)$ from the set of discrete points $\omega_0 = 2m\pi T$ to $z = \omega_s - i\delta$. If we assume that, in the vicinity of H_{c_2}, the nearly uniform and constant magnetic field inside the superconductor can be replaced by its space average, the magnetic induction **B**, and treat the magnetic field dependence semiclassically, the thermal product can be written

$$\langle[n,n]\rangle(\mathbf{q},\omega_0) = 2T\sum_{\omega}\int d^3r\int d^3r'$$
$$\times e^{-i\mathbf{q}(\mathbf{r}-\mathbf{r}')}[G_{\omega+}(\mathbf{r},\mathbf{r}')G_{\omega}(\mathbf{r}',\mathbf{r})$$
$$-\int d^3r_1\int d^3r_2 G^0{}_{\omega_+}(\mathbf{r}-\mathbf{r}_1)G_{\omega_+}(\mathbf{r}',\mathbf{r}_1)$$
$$\times V(\mathbf{r}_1,\mathbf{r}_2)G_{\omega}(\mathbf{r}_2,\mathbf{r}')G^0{}_{-\omega}(\mathbf{r}_2-\mathbf{r})] \quad (2)$$

here $\omega = (2n+1)\pi T$ and $\omega_+ = \omega+\omega_0$.
The Green's function $G_\omega(\mathbf{r},\mathbf{r}')$ appearing in equation (2) satisfies the equation

$$G_\omega(\mathbf{r},\mathbf{r}') = G_\omega{}^0(\mathbf{r}-\mathbf{r}') - \int d^3r_1\int d^3r_2$$
$$\times G_\omega{}^0(\mathbf{r}-\mathbf{r}_1)V(\mathbf{r}_1,\mathbf{r}_2)G^0_{-\omega}(\mathbf{r}_1-\mathbf{r}_2)G_\omega(\mathbf{r}_2,\mathbf{r}'), \qquad (3)$$

$G^0(\mathbf{r}-\mathbf{r}')$ is the normal metal Green's function in the absence of a magnetic field and the function V is defined by:

$$V(\mathbf{r}_1,\mathbf{r}_2) = \Delta(\mathbf{r}_1)\Delta^*(\mathbf{r}_2)\,e^{-ieB(x_1+x_2)(y_1-y_2)} \qquad (4)$$

---

[*] Supported in part by the Advanced Projects Agency, the U.S. Army Office of Research, Durham, North Carolina, and the National Science Foundation

[†] Brown University Predoctoral Fellow

[‡] Permanent Address: Physics Department, University of Bristol, England.

the magnetic field having been chosen to be in the z direction.

It has been shown[1] that iterative solutions to equation (3) lead in certain cases to unphysical results even in the limit $B \to H_{c_2}$; recently, however, Brandt *et al.*[2] have solved equation (3) approximately by a method which avoids the iteration procedure. These authors note that when $(H_{c_2} - B) \ll H_{c_2}$ the order parameter $\Delta(\mathbf{r})$ is given by the Abrikosov solution of the Ginzburg–Landau equations

$$\Delta(\mathbf{r}) = \sum_n C_n \, e^{in\alpha y} \, e^{-eB(x-\alpha n/2eB)^2} \qquad (5)$$

and therefore $G(\mathbf{r}, \mathbf{r}')$ when considered as a function of sum and difference coordinates, has the periodicity of the flux line lattice with respect to the sum coordinate. Fourier analyzing equation (3) and noting that the dominant contribution to G is obtained if V is replaced by $\langle V \rangle$, an average over its sum coordinate they obtain in the infinite mean free path limit

$$G_\omega(\mathbf{p}, \mathbf{k}) = \delta_{k,0}\left[i\omega - \xi_p + \frac{i\sqrt{\pi}\Delta^2}{k_c V_f \sin\theta} W\left(\frac{i\omega + \xi_p}{K_c v_F \sin\theta}\right)\right]^{-1} \qquad (6)$$

where the wave vector $k_c = (2eB)^{1/2}$ is inversely proportional to the spacing between flux lines,

$$\Delta^2 = |\overline{\Delta}|^2,$$

$$\xi_p = p^2/2m - \mu,$$

θ is the angle between **p** and **B** and

$$W(z) = \frac{i}{\pi}\int_{-\infty}^{\infty} dt \, \frac{e^{-t^2}}{z-t}. \qquad (7)$$

If we restrict our calculations to the clean limit $k_c l \gg 1$, scattering effects due to impurities are included in the theory by simply replacing ω by $\tilde{\omega} = \omega(1 + i/2\tau|\omega|)$. Corrections to the order parameter and the electromagnetic vertices are negligible to order $1/k_c l$ and $1/ql$ respectively. We should point out that as $k_c \to 0$ when $T \to T_c$ this theory is not valid too close to the transition temperature. Making this replacement and performing the analytic continuation of equation (2) we obtain

$$\alpha_L = \frac{-q}{v_s \rho_{\text{ion}}}\left(\frac{p_F{}^2}{3m}\right)^2 Im \int \frac{d\omega}{2\pi i}[f(\omega + \omega_s) - f(\omega)]$$
$$\times [\langle [n, n] \rangle (\mathbf{q}; \omega + \omega_s + i/2\tau, \omega + i/2\tau)$$
$$- \langle [n; n] \rangle (\mathbf{q}; \omega + \omega_s + i/2\tau, \omega - i/2\tau)] \quad (8)$$

where

$$\langle [n, n] \rangle (\mathbf{q}; \omega + \omega_s + i/2\tau, \omega - i/2\tau)$$
$$= 2\int \frac{d^3p}{(2\pi)^3} G_{\omega+\omega_s+i/2\tau}(\mathbf{p} + \mathbf{q}, 0) G_{\omega - i/2\tau}(\mathbf{p}, 0)$$
$$\times \left[1 - \int \frac{d^3p'}{(2\pi)^3} G^0{}_{(\omega+\omega_s+i/2\tau)}(\mathbf{p} + \mathbf{q} + \mathbf{p}')\right.$$
$$\left.\times G^0{}_{-(\omega - i/2\tau)}(\mathbf{p} + \mathbf{p}') v(\mathbf{p}', 0)\right] \qquad (9)$$

$$V(\mathbf{p}', 0) = (\Delta/k_c)^2 2(2\pi)^2 \delta(p_z') \, e^{-(p_x'^2 + p_y'^2)/k_c{}^2} \qquad (10)$$

is the Fourier transform of $\langle V \rangle$ and $f(\omega)$ is the Fermi function.

In order to make further analytic progress we assume that $qv_F \gg \Delta^2/k_c V_F$. It is then possible to integrate over the magnitude of **p** and the polar angle, with the result that

$$\alpha_L = \frac{m^2}{v_s{}^2 \rho_{\text{ion}}}\left(\frac{p_F{}^2}{3m}\right)^2 \int \frac{d\phi}{2\pi}\int \frac{d\omega}{2\pi}$$
$$\times [f(\omega) - f(\omega + \omega_s)] I(\omega, \theta) \quad (11)$$

where

$$I(\omega, \theta) = (2Re\, K(z_0) - 1)(2Re\, K(z_0{}^+) - 1)$$
$$- 2(\Delta/k_c v_F \sin\theta)^2$$
$$\times Re\left[K(z_0) K(z_0{}^+) \times \frac{i\sqrt{\pi} w(z_0{}^+) - i\sqrt{\pi} w(z_0)}{z_0{}^+ - z_0}\right.$$
$$\left. + K(z_0{}^+) K^*(z_0) \frac{i\sqrt{\pi} w(z_0{}^+) - i\sqrt{\pi} w(z_0^*)}{z_0{}^+ - z_0^*}\right] (12)$$

z_0 is the solution of the equation

$$z_0 = \frac{2(\omega+i/2\tau)}{k_e v_F \sin\theta} + i\sqrt{\pi}(\Delta/k_e V_F \sin\theta)^2 W(z_0)$$

$$z_0^+ = z_0(\omega+\omega_s)$$

$$K(z_0) = [1 - i\sqrt{\pi}(\Delta/k_e v_F \sin\theta)^2 W(z_0)]^{-1}$$

$$\sin\theta = (1-\sin^2\phi\sin^2\alpha)^{1/2}$$

and α is the angle between **q** and **B**. Note that $[2Re\,K(z_0)-1] = N(\omega,\theta)$ is the angular dependent density of states found by Brandt *et al.*[2]. In deriving equation (12) we have made use of the fact that when $ql \gg 1$ the only electrons contributing to the absorption are those moving essentially perpendicular to the direction of propagation of the wave.

From the form of equation (12) it can be immediately seen that under the conditions specified above the attenuation will be strongly anisotropic. In particular we note that if $\sin\theta = 0$, the density of states is singular and the function

$$I(\omega,\theta=0) = \tfrac{1}{2}[1+(\omega^2-\Delta^2)/|\omega^2-\Delta^2|] \quad (13)$$

the BCS coherence factor. In general the form of equation (12) is such that for an arbitrary geometry the attenuation coefficient can only be obtained by numerical computation. It is possible, however, to make further progress in the simple case of parallel propagation (**q**||**B**). If we assume $\omega_s\tau \ll 1$, the usual experimental situation, then keeping terms to first order in ω_s we find

$$\alpha_L^s = -\frac{m^2}{v_s^2\rho_{\text{ion}}}\left(\frac{p_F^2}{3m}\right)^2 \omega_s \int \frac{d\omega}{2\pi}\frac{\partial f(\omega)}{\partial\omega}$$
$$\times\left[[2Re\,K(z_0)-1]^2 - 2(\Delta/k_e v_F)^2\right.$$
$$\times Re\left[K^2(z_0)\,i\sqrt{\pi}W'(z_0) + |K(z_0)|^2\right.$$
$$\left.\left.\times\frac{i\sqrt{\pi}W(z_0)-i\sqrt{\pi}W(z_0^*)}{z_0-z_0^*}\right]\right]. \quad (14)$$

In the region of validity of the theory $(H_{c_2}-B) \leqq H_{c_2}$ the parameter $(\Delta/k_e v_F) \cong (\Delta/\Delta_{BCS}) \ll 1$ and therefore $K(z_0)$ can be expanded in powers of $(\Delta/k_e v_F)^2$. Further if we use the property of the $W(z)$ function

$$i\sqrt{\pi}W(z^+) = [i\sqrt{\pi}W(z)]^* \quad (15)$$

we find

$$\alpha_L^s = -\frac{m^2}{v_s^2\rho_{\text{ion}}}\left(\frac{p_F^2}{3m}\right)^2 \omega_s \int \frac{d\omega}{2\pi}\frac{\partial f(\omega)}{\partial\omega}$$
$$\times\left[1-2(\Delta/k_e v_F)^2\right.$$
$$\times\left[\frac{k_e l\,Im\,(i\sqrt{\pi}W(z_0))}{1+(\Delta/k_e v_F)^2 k_e l\,Im\,(i\sqrt{\pi}W(z_0))}\right.$$
$$\left.\left.-Re\,i\sqrt{\pi}W'(z_0)\right]\right]. \quad (16)$$

2. RESULTS

The attenuation coefficient for longitudinal sound propagating parallel to the magnetic field in Nb at 4·2°K has been obtained from equation (16), by numerical computation, for three values of $k_e l$. The results of this calculation are shown in Fig. 1, where $\alpha_r^2 = (\alpha_s-\alpha_n)^2/(\alpha_n)^2$ is plotted vs. B/H_{c_2}. The physical parameters used in determining these curves were: Δ^2, which was taken from Eilenberger's paper[3], H_{c_2} (4·2°K) = 2680 G[4], V_F = 3·0 × 10^7 cm/sec and the density of states[5] $N(0)$ = 5·6 × 10^{34} erg/cm^3. We would like to point out the following features of Fig. 1: (1) α_r^2 varies markedly with mean free path even when $k_e l \gg 1$ and follows the trend found experimentally by Forgan and Gough[6], this is in contrast to the theoretical predictions of Maki[7], also shown in this figure, which are mean free path independent under these conditions; (2) α_r^2 is, apart from a small region close to H_{c_2}, a linear function of $(H_{c_2}-B)$ down to fields $B/H_{c_2} = 0·98$ at which point it starts to deviate from straight line behavior this is also consistent with Ref. [6]. It is not possible at this time to make an absolute comparison of theory with experiment as the only theoretical results we have are at a temperature of 4·2°K, whereas the available experimental

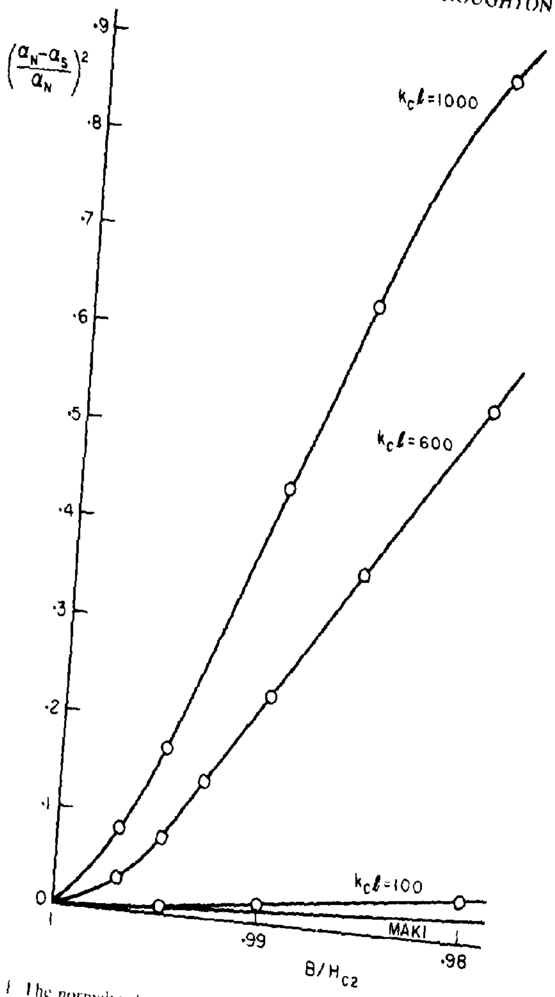

Fig. 1. The normalized attenuation in the mixed state at 4·2°K as a function of B/H_{c2}.

data[6, 8] is for temperatures of 2·02°K and 1·3°K. We do not expect, however, the absolute magnitude of the attenuation to change much in this temperature range. it would therefore appear that the theoretical values of α_l^2 agree qualitatively with the experiment results of Forgan and Gough whose purest sample gives $\alpha_l^2 \simeq 0·4$ at $B/H_{c2} \simeq 0·98$. A detailed discussion of these points together with calculations of the attenuation as a function of direction of propagation for different temperatures will be given elsewhere.

Acknowledgement – The authors would like to thank Drs M. Cyrot and W. B. Hibler III for several helpful discussions of points contained in this paper. They also thank Dr. Hibler for sending them his calculation of the order parameter.

REFERENCES

1. See for example CYROT M. and MAKI K., *Phys. Rev.* **156**, 433 (1967); MAKI K., *Phys. Rev.* **156**, 437 (1967).

2. BRANDT U., PESCH W. and TEWORDT L., *Z. Phys.* **201**, 209 (1967).
3. EILENBERGER G., *Phys. Rev.* **153**, 1584 (1967).
4. McCONVILLE T. and SERIN B., *Phys. Rev.* **140**, A1169 (1965).
5. LEUPOLD H. A. and BOORSE H. A., *Phys. Rev.* **134**, A1322 (1964).
6. FORGAN E. M. and GOUGH C. E., *Phys. Lett.* **26A**, 602 (1968).
7. MAKI K., *Phys. Rev.* **156**, 437 (1967).
8. KAGIWADA R., LEVY M., RUDNICK I., KAGIWADA H. and MAKI K., *Phys. Rev. Lett.* **18**, 74 (1967).

J. Phys. Chem. Solids Pergamon Press 1970. Vol. 31, pp. 1687–1691. Printed in Great Britain

ULTRASONIC ATTENUATION IN A TYPE II SUPERCONDUCTING ALLOY

B. R. TITTMANN
Science Center, North American Rockwell Corporation, Thousand Oaks, Calif 91360, U.S.A

(*Received* 5 *September* 1969, *in revised form* 1 *November* 1969)

Abstract – Ultrasonic attenuation measurements have now been obtained on a magnetically reversible type-II superconductor with both a high Ginzburg–Landau parameter ($\kappa_G > 1$) and with BCS coherence length > electronic mean free path. For applied fields close to H_{c_2}, the data appear to agree with dirty-limit ($\xi_0/l \gg 1$) theory which predicts a linear dependence of α on H. At fields farther from H_{c_2}, $\alpha(H)$ deviates from linearity and appears to fit empirically to a parabolic function of H. At very low fields, $H \gtrsim H_{c_1}$ the H- and T-dependence is in apparent agreement with another theory. Physical insight into the behavior in this region could be obtained with a model in which vortices are replaced by cylinders of completely normal material imbedded in a superconducting matrix

1. INTRODUCTION

MUCH THEORETICAL and experimental work has been carried out on the ultrasonic attenuation in clean type II superconductors characterized by having an electronic mean free path greater than the BCS coherence length, $l > \xi_0$, and having a small Ginzburg–Landau parameter, $\kappa_G \approx 1$. Although there have been theoretical[1–5] studies of the dirty regime characterized by $l < \xi_0$ and $\kappa_G > 1$ only few experimental investigations[6, 7] have been reported and discussed in the light of recent theory[1–5]. One[6] of these is confined to high-field superconducting alloys, and does not study electron–phonon interaction which is basic to the present investigation. The other experiment[7], performed on the alloy Mo-25 per cent *Re* ($\kappa_G \cong 4$), yielded a linear dependence of the electronic attenuation on magnetic field near the upper critical field H_{c_2} in qualitative agreement with the dirty limit theory[1–5].

However, the measured slope was in disagreement with the predicted value and did not show the temperature dependence expected from the theory[1–5] For $H \ll H_{c_2}$ no mention was made of the degree of magnetic reversibility and no interpretation was given for the ultrasonic data.

The present experiments were undertaken to see if a more quantitative comparison with the theory[1–5] was feasible and in particular to explore the region in which $H \ll H_{c_2}$ where few data for the electronic attenuation in the dirty regime are available. For this purpose a well characterized magnetically reversible crystal with reasonable T_c and H_{c_2} values and moderately high κ_G and ξ_0/l values was necessary. These requirements could be fulfilled with the solid solution alloy V-5·6 at% Ta and single, oriented crystals of this composition were grown by H. Nadler of this laboratory. Previous caloric[8] and magnetization[9] studies and the present resistivity and ultrasonic data combine to render the alloy a well-characterized metal with $\kappa_G \approx 5$ and $\xi_0/l \approx 5$. The ultrasonic measurements[10] display a substantial electron–phonon interaction, a high degree of magnetic reversibility, theoretically[11–13] predicted upper critical fields H_{c_2} and a behavior consistent with previous studies[8, 9] so that a quantitative comparison with theory is possible. The lack of hysteresis (except near the field of first flux penetration H_{fp}) means that the attenuation data in the range $H_{fp} < H \ll H_{c_2}$ is physically significant and, therefore, its magnitude and temperature dependence should be amenable to detailed analysis and quantitative interpretation.

2. EXPERIMENTAL TECHNIQUE

The apparatus and measurement techniques used in this experiment are essentially the same as those already described elsewhere

[14], except that the experimental arrangement allowed measurement on specimens with relatively low demagnetizing coefficient. Sample shape is well known to influence the initial flux penetration field H_{fp} and the slope [15, 16] of the magnetization curve near H_{c_2} in type-II superconductors, the latter especially when the condition[16] $(2\kappa_G^2 - 1)\beta \gg 1$ is not satisfied. Although in the present experiment $\kappa_G \approx 5$ so that the above condition is satisfied, it was possible to reduce the effective demagnetization factor[17] to $n_{ef} \approx 0{\cdot}015$ by placing the cylindrical sample (length $L = 3{\cdot}8$ cm, dia. $D = 1{\cdot}3$ cm) in between tapered cylindrical conductors machined from polycrystalline rods of nominally V-5·6 at% Ta composition.

The attenuation was measured by the pulse method at a frequency of 0·54 GHz for *longitudinal waves along the* ⟨110⟩ *direction and parallel to the applied magnetic field.* The magnetic fields of initial flux penetration H_{fp} and the upper critical fields H_{c_2} are clearly defined by the attenuation data both for increasing and decreasing fields. The only hysteresis was found near $H = 0$ where some flux trapping can be expected.

3. RESULTS

For dirty limit $\xi_0/l \gg 1$ superconductors no simple theoretical expression is available describing the attenuation over the whole extent of its magnetic field dependence but theoretical predictions have been made for two limits: the region[2] for fields close to the flux penetration field H_{fp} and the region[1, 3–5] for fields close to H_{c_2} corresponding respectively, to the limits of isolated, weakly interacting vortex lines, or $D/S < 1$, and to the case of many strongly interacting vortex lines forming a very dense lattice, or $D/S \approx 1$ (where D is the effective core diameter and S is the spacing between vortex lines).

(1) *Ultrasonic attenuation for* H < H$_{c_2}$

A theoretical expression for the electronic attenuation of longitudinal soundwaves $\alpha(H,T)/\alpha_n$ as a function of applied magnetic field H near H_{c_2} is given[1, 3–5] for the limit $\xi_0/l \gg 1$ by

$$\alpha(H,T)/\alpha_n = 1 - \frac{e\rho_n c}{8\pi^2 k_B T_c}\,\frac{H_{c_2} - H}{[2\kappa_2^2(t) - 1]\beta}\,C_2(t) \tag{1}$$

where $C_2(t)$ is a universal function[1] of the reduced temperature $t \equiv T/T_c$, e is the electronic charge, k_B is Boltzmann's constant, c is the speed of light, $\beta = 1{\cdot}16$, and ρ_n is the normal state electronic resistivity. Equation (1) predicts a linear dependence of the attenuation on the applied field near H_{c_2}. Figure 1, which shows the measured attenuation as a function of the field for three different temperatures, exhibits indeed such a linear dependence near H_{c_2}. In order to verify equation (1), the magnetization parameter κ_2 was calculated from the data and compared with values obtained in previous[8, 9] studies. In terms of the slope at H_{c_2} of the field dependent attanuation curve the parameter κ_2 may be written as

$$\kappa_2^2 = \frac{1}{2} + \frac{ec\rho_n C_2(t)}{16\pi^2 k_B T_c \beta\, \partial\alpha(t)/\partial H}. \tag{2}$$

From the measured values of the resistivity ρ_n, the transition temperature T_c, the numerical values[1] of $C_2(t)$, the observed slopes and equation (2) the parameter κ_2 was calculated. Figure 2 displays the ultrasonic values of κ_2 in rough agreement with previous values obtained directly from caloric[8] and magnetization[9] data. For $T \approx T_c$ the accuracy of $(\partial\alpha/\partial H)$ at $H = H_{c_2}$ is limited because of the limited region for which the curve is linear. The extrapolation to $T = T_c$ of the values of $\kappa_2(T)$ yields $\kappa_2(T = T_c) = \kappa_G \approx 4{\cdot}7$. A comparison with theory[11–13] of the temperature dependence of κ_2 shows no disagreement for $\xi_0/l \approx 5$ without p-wave scattering. The theory [1, 3–5] does not predict the field $H < H_{c_2}$ down to which the linear solution holds, nor how the length of the linear segment changes with temperature. However, an estimate has been made[18] that the linear dependence

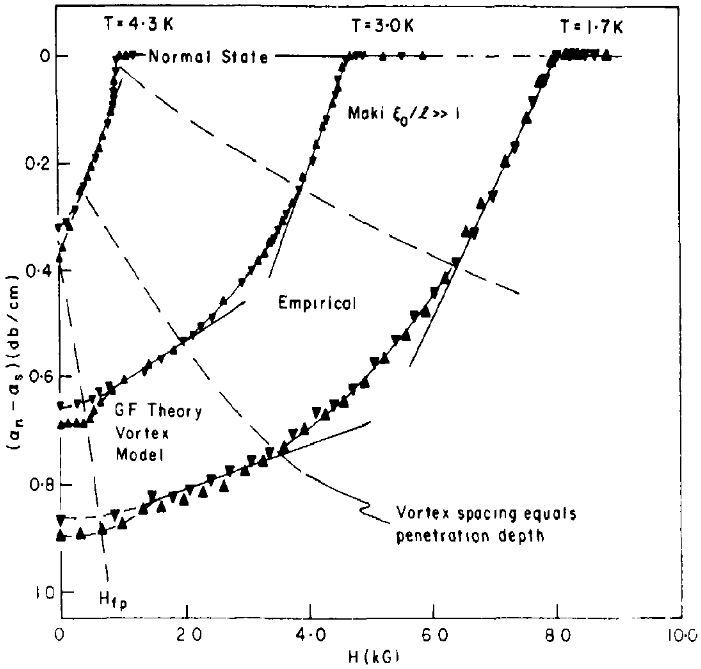

Fig. 1 Ultrasonic attenuation α_s relative to the attenuation α_n in the normal state as a function of magnetic field H for three representative temperatures at a frequency $f \approx 0{\cdot}54$ GHz in a sample of V-5 6 at% Ta (with transition temperature $T_c = 4{\cdot}7$°K, and normal state resistivity $\rho_n = 4\ 1 \times 10^{-6}$ Ωcm).

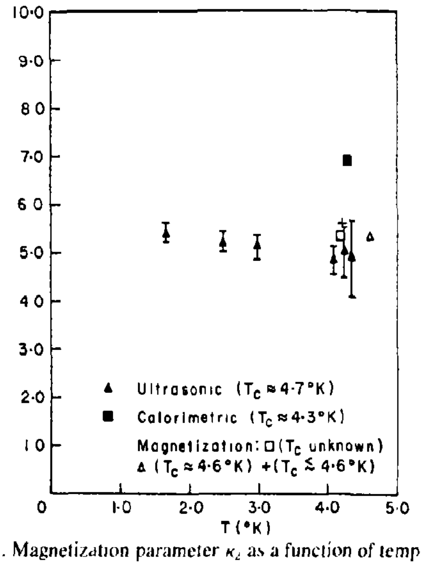

Fig. 2. Magnetization parameter κ_2 as a function of temperature. The values obtained with the help of equation (1) from ultrasonic data on a single crystal oriented along the (110) direction are compared with values obtained directly from previous caloric[8] and magnetization[9] data on polycrystalline samples of nominally V-5 at% Ta composition.

should hold in the regime $(H_{c_2} - H)/H_{c_2} \ll [(\xi_0/l)(1 - T/T_c)]^2$. The observed temperature dependence is in reasonable agreement with this criterion for the $\xi_0/l \approx 5$ purity value of the V-5·6 at% Ta specimen.

(2) *Ultrasonic attenuation for* H $\gtrsim$ H_{fp}

For weak magnetic fields such that $Be\lambda^2 \ll 1$ the electronic attenuation $\alpha(H, T)/\alpha_n$ as a function of the applied magnetic field B is given[2] by

$$\frac{\alpha(H,T)}{\alpha_n} = \left(\frac{\alpha_s}{\alpha_n}\right)_{\text{BCS}} + k(T)\frac{B}{H_{c_2}}$$

$$k(T) = A\,\kappa_G^{2/3}\frac{\Delta_0}{2k_BT}\cosh^2\frac{\Delta_0}{2k_BT} \qquad (2)$$

where Δ_0 is the temperature dependent superconducting energy gap as given by the BCS theory[19], λ is the penetration depth and A is a proportionality constant. Equation (2) predicts a linear dependence of the attenuation on the applied field[20] H near H_{fp} in agreement with the data on Fig. 1. From the ultrasonic data for H_{c2}, κ_G, and T_c plus the tabulated values[21] for the energy gap it was possible to calculate the slopes of the attenuation as a function of temperature. As shown in Fig. 3, the theoretical slopes when fitted to the data near $T = T_c$ $(A \simeq 0{\cdot}31)$ are in reasonable agreement with those obtained from the ultrasonic data except in the region $T \to 0$°K.

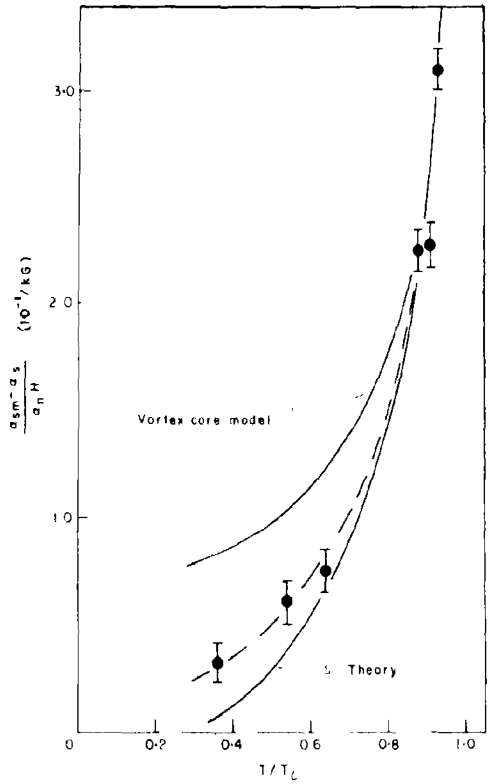

Fig. 3 Electronic attenuation per unit field $[\alpha(H,T) - \alpha(H = O,T)]/H = (\alpha_{sm} - \alpha_s)/\alpha_n H$ as a function of temperature in the low magnetic field region $H_{fp} < H < H_{c2}$. The ultrasonic data is compared with theory[2] and the results of a simple vortex core model.

In an effort to gain physical insight into the behavior of the attenuation in this region a model was constructed in which vortices were replaced by cylinders for which the energy gap parameter is nearly zero. The matrix surrounding the cylinders acts with a BCS zero field energy gap. If the normal core and matrix have nearly the same moduli, the total attenuation is given by

$$\alpha(H,T) = (\alpha_s + \alpha_B)[1 - V(H,T)] + (\alpha_n + \alpha_B)\, V(H,T) \tag{3}$$

where $\alpha_s = \alpha(H = O, T)$, $\alpha_n = \alpha(H = H_{c2}, T)$, α_B is the non-electronic background attenuation, and $V(T)$ is the total volume of normal material assumed to be made up of N cores each of diameter D and unit length. With the substitution of $\alpha_s/\alpha_n = 2/(\exp \Delta_0/k_B T + 1)$ from the BCS theory[19] and taking $N = H/\phi_0$, the slopes are given by

$$\frac{\alpha(H,T) - \alpha_s}{\alpha_n H} = \frac{\pi}{4}\frac{D^2}{\phi_0}\tanh\frac{\Delta_0}{2k_B T} \tag{4}$$

where $\phi_0 = 2{\cdot}1 \times 10^{-7}$ G cm^2 (the flux quantum). The predicted[22] Ginzburg-Landau coherence distance for the dirty limit $\xi_0/l \gg 1$ is

$$\xi_G^2 = 0{\cdot}723\,(\xi_0 l)/(1 - T/T_c).$$

A reasonable fit of the calculated slopes to the experimental values in the temperature regime near $T = T_c$ could be obtained when $D \approx 2\xi_G$. Although the agreement near $T = 0$°K is poor, it is interesting to find approximate agreement with experiment in the magnitude and temperature dependence of the attenuation for such a simple model.

One might expect the above considerations to break down when the vortices are made to approach (by increasing the field H) one another to within the critical distance given [22] by the penetration depth λ. This is born out by the data such as shown in Fig. 1 where the limits of linear dependence of attenuation on field approximately coincide with field values H_{crit} such that the critical spacing $S_c \approx (H_{\mathrm{crit}}/\phi_0)^{-1/2} \approx \lambda$.

(3) *Ultrasonic attenuation for* $H_{fp} < H < H_{c2}$

As seen in Fig. 1 the data exhibits a substantial transition region lying between the two limits $H \approx H_{fp}$ and $H \approx H_{c2}$. Apparently no

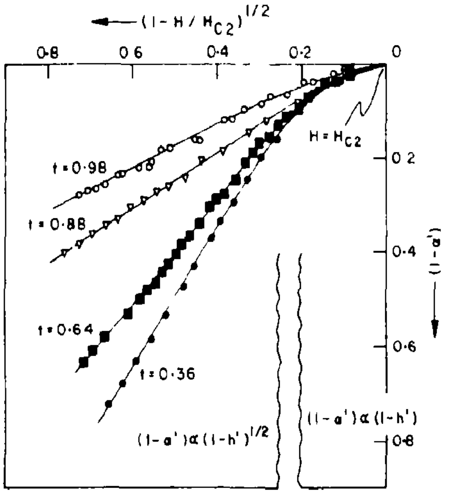

Fig. 4 Electronic attenuation $(1-\alpha')$ as a function of field $(1-H/H_{c2})^{1/2}$ for several temperatures where $\alpha' = \alpha(H, T)/\alpha(H = H_{c2}, T)$ Note that far away from H_{c2} the data agree well with $(1-\alpha') \propto (1-h')^{1/2}$ where $h' = H/H_{c2}$.

theoretical treatment covers this region. Figure 4 shows the field dependent attenuation below H_{c2} down to about $H/H_{c2} = 0{\cdot}3$ plotted against $(1-H/H_{c2})^{1/2}$. The resulting linear plots suggest that $(1-\alpha') \propto (1-h')^{1/2}$ where $\alpha' = \alpha(H, T)/\alpha(H = H_{c2}, T)$ and $h' = H/H_{c2}$ is a possible empirical fit.

4. CONCLUSION

For magnetic field values sufficiently close to the upper critical field H_{c2}, the field and temperature dependence of the attenuation is not in disagreement with the dirty-limit theory. The only hysteresis observed in the ultrasonic measurements is near $H = 0$ where some flux trapping can be expected. This magnetic reversibility makes it possible to interpret the data in the range $H \ll H_{c2}$. The field and temperature dependence appears to be in agreement with the theory. Physical insight into the behavior in this regime could be obtained by a model which replaces vortices by cylinders in which the energy gap parameter is nearly zero. An empirical fit to the data was possible in the region of intermediate field values yielding a parabolic field dependence of the attenuation. Although most of the field dependence of the attenuation thus appears to be described by three different functions, it is interesting to note that the data behaves as if it might just as well be described by a single smoothly varying function if such were available.

REFERENCES

1. MAKI K., *Superconductivity* (Edited by R. D. Parks). Vol 2, p. 1035. Marcel Dekker, New York, (1969). (The factor $\frac{1}{4}\pi^2$ in equation (224) is in error and should read $\frac{1}{8}\pi^2$; this has been confirmed by K. Maki, private communication.)
2. GALAIKO V. P. and FALKO I. I., *J. exp. theor. Phys.* **52**, 976 (1967); English transl: *Soviet Phys JETP* **25**, 646 (1967)
3. MAKI K. and FULDE P., *Solid St. Commun.* **5**, 21 (1967).
4. McLEAN F. B. and HOUGHTON A., *Phys. Rev.* **157**, 350 (1967).
5. MAKI K., *Phys. Rev.* **148**, 370 (1968)
6. SHAPIRA Y. and NEURINGER L. J., *Phys. Rev.* **154**, 375 (1967), also NEURINGER L. J. and SHAPIRA Y., *Phys. Rev. Lett.* **17**, 81 (1966).
7. GOTTLIEB M., JONES C. K. and GARBUNY M., *Phys. Lett.* **25A**, 107 (1967)
8. HAKE R. R. and BRAMMER W. G., *Phys. Rev.* **133**, A719 (1964).
9. CAPE J. A., unpublished data for polycrystalline V-5 at% Ta, also BARNES L. J. and HAKE R. R., unpublished.
10. TITTMANN B. R. and BOMMEL H. E., *Phys. Lett.* **28A**, 396 (1968).
11. HELFAND E. and WERTHAMER N. R., *Phys. Rev. Lett.* **13**, 686 (1968), *Phys. Rev.* **147**, 288 (1966)
12. WERTHAMER N. R., HELFAND E. and HOHENBERG P. C., *Phys. Rev.* **147**, 295 (1966).
13. EILENBERGER G., *Phys. Rev.* **153**, 584 (1967)
14. TITTMANN B. R. and BÖMMEL H. E., *Rev. scient. Instrum.* **39**, 614 (1968); *Rev. scient. Instrum.* **38**, 1491 (1967).
15. KULIK I. O., JETP PIS'MA v Redaktsiyu **3**, 395 (1966); English Transl *JETP lett.* **3**, 259 (1966).
16. CAPE J. A. and ZIMMERMAN J. M., *Phys. Rev.* **153**, 416 (1967).
17. STONER E. C., *Phil. Mag.* **36**, 803 (1945).
18. MAKI K., Private communication.
19. BARDEEN J., COOPER L. and SCHRIEFFER J., *Phys. Rev.* **108**, 1175 (1957).
20. Since $\kappa_{t} \approx 5$ for this material, $|4\pi M| \ll H$ in the range $0{\cdot}2 < H/H_{c2} < 1{\cdot}0$ (e.g. at $H = 0{\cdot}5 H_{c2}$, $|4\pi M| = (H - H_{c2})/(2\kappa_2^2 - 1)\beta \approx 0{\cdot}009 H_{c2} \ll H$) so that $B \approx H$
21. MÜHLSCHLEGEL B., *Z. Phys.* **155**, 313 (1959).
22. See, eg De Gennes P. G., *Superconductivity of Metals and Alloys* (Translated by P. A. Pincus). Benjamin, New York (1966).

J. Phys. Chem. Solids Pergamon Press 1970. Vol. 31, pp. 1693–1700. Printed in Great Britain.

HYPERSONIC ATTENUATION IN NIOBIUM IN THE MIXED STATE*

JAMES N. LANGE
Department of Physics, Oklahoma State University, Stillwater, Okla. 74074, U.S.A.

(*Received* 5 *September* 1969; *in revised form* 11 *November* 1969)

Abstract—The hypersonic attenuation of longitudinal and transverse modes in niobium is observed throughout the mixed state. The field dependence of the attenuation is shown not to be directly dependent on the normal state volume in the mixed state. The transverse and longitudinal attenuation have similar field dependences with the longitudinal mode coupling more strongly than the transverse mode to the vortices. The frequency and conductivity dependence of the phonon attenuation in the Meissner state exhibits features which are not strictly similar to the behavior of the attenuation in insulators, and might be associated with the coupling of the pair states to the lattice.

1. INTRODUCTION

THE MIXED state in Type II superconductors exists in a magnetic field interval bounded by two critical fields. The lower critical field (H_{c_1}) is the local value of the field at which flux begins to penetrate the material. Below the lower critical field, the Meissner state exists in which no flux penetrates the interior of the superconductor. Above the upper field (H_{c_2}) the material is in the normal state. In the mixed state ($H_{c_1} < H < H_{c_2}$), the interior of the material is penetrated by quantized lines of flux or vortices. The interaction of these vortices with each other and the lattice almost entirely determines the electrical transport properties of this state. A convenient means of investigating the response of the vortices to electromagnetic excitation is through observation of the acoustic parameters of the superconductor in the mixed state. The acoustic wave distorts the lattice and generates a local electromagnetic field in the bulk of the material which interacts with the flux filaments and superconducting regions. Propagation of the wave is modified by the reaction of the vortices to the lattice field and can be characterized in two limits. When the external field is close to H_{c_2}, the density of vortices is high and considerable interaction occurs between the filaments. Calculations of the acoustic attenuation near H_{c_2} in the pure[1] and dirty[2] limits have been in substantial agreement with the observations[3, 4]. At magnetic fields just above H_{c_1} the vortex density is low and each filament is more nearly isolated. This low field region of the mixed state, is of particular interest in this investigation.

A model of an isolated vortex consisting of an essentially normal core of radius ξ (coherence length) about which supercurrents circulate, was suggested by Caroli, deGennes, and Matricon[5] and is used in the following to relate the acoustic properties to the vortex state. Motion of the vortex as a whole leads to a viscous force similar to the Magnus force acting on superfluid vortices[6]. As pointed out by Barden and Stephen[7], the viscous force acts through the relaxation of the normal electrons of the vortex core, to the lattice reference frame. This is the major source of resistance in the mixed state as proposed by Kim *et al.*[8], who suggested the relative motion between the supercurrents and vortices results in current, in effect, being driven through the normal core of the vortex. Periodic distortion of the lattice reference

---

*This work supported by the National Science Foundation.

frame by the acoustic wave, results in a viscous force between the normal core and the lattice, as well as interactions of the vortex with supercurrents generated to shield the lattice electromagnetic field.

The conductivity and frequency dependence of transverse and longitudinal waves are determined to provide information on the response of the vortex to the local exciting field. The magnetic field dependence of the stiffness in the mixed state is used to determine the fraction of the material in the normal state. The hypersonic attenuation computed from the normal component is always less than that observed, indicating the interaction of the acoustic phonon with the vortex cannot be simply described by a two fluid approximation. The coupling of the acoustic phonon to the vortex appears to depend on phase coherence of the two particle transition probabilities similar to that encountered in describing the temperature dependence of the acoustic attenuation.

As the temperature decreases in the superconducting state, the normal electronic component of the acoustic attenuation rapidly approaches zero. The remaining attenuation is dependent on the strength of the normal process phonon interactions. Since the acoustic phonon does not have enough energy to excite the pair state across the energy gap, the attenuation reflects processes similar to those observed in insulators. The analogy between the low temperature attenuation in the Meissner state and that in insulators is not complete because of the unique phonon coupling mechanism resulting from the lattice distortions associated with the pair which has no obvious analog in insulators.

2. EXPERIMENTAL ARRANGEMENT

The hypersonic wave is generated by a quartz transducer placed in a high electric field point of a tunable microwave cavity. The wave is coupled to the specimen through a thin silicone oil (200-centistoke) band. The same quartz crystal is used as a receiver. The measurement accuracy (−3 per cent) is the same in the low field region as in the normal state because of the use of a logarithmic detection technique. The single crystals are etched before each measurement to remove surface damage with a resulting reproducibility of the field dependence of the attenuation of better than 10 per cent. The wave vector is along the [110] direction of specimen I and along the [100] direction in specimen II. The displacement of the transverse modes in both specimens, is oriented so the velocity is dependent on the C_{44} elastic modulus. The residual resistance is determined by extrapolating the high field resistivity, measured by a four probe technique, to zero field (Table 1). This is necessary because of the significant magnetoresistance of niobium. The critical magnetic fields are determined by simultaneous measurement of the magnetization and field dependence of the elasticity[9].

3. MIXED STATE

At fields above H_{c_2} (normal state) the attenuation is observed to be a linear function of the conductivity and a quadratic function

Table 1. *Characteristics of the single crystal niobium specimens containing approximately* 100 ppm *tantalum**

Specimen	Critical field at 4·2°K (kOe) H_{c_1}	H_{c_2}	Residual resistance ($\mu\Omega$ · cm) 4·2°K $H = 0$	Resistance ratio $\rho_{300}/\rho_{4\cdot 2}$
I	1·32	2·95	0·233	67
II	1·34	3·49	0·669	30

*Impurity reported by the Materials Research Corporation.

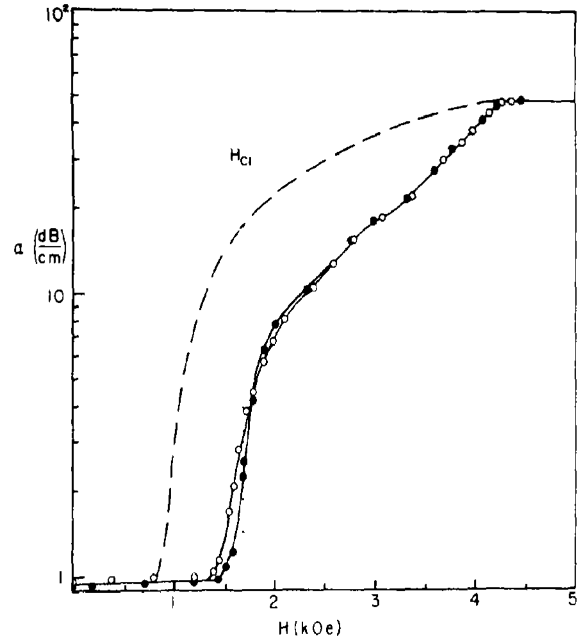

Fig. 1. The magnetic field dependence of the longitudinal mode attenuation at a temperature of 1·6°K and a frequency of 1 GHz for specimen 1. The open circles correspond to measurements with the field perpendicular to the propagation direction, while the closed circles are for the field parallel to the propagation direction. The dotted line represents the first critical field (H_{c_1}) as determined from elasticity and magnetization measurements. The dashed curve is obtained from equation (1) and the field dependence of the elastic stiffness in the mixed state.

of the frequency. This behavior is characteristic for an electron mean free path (l) less than the acoustic wavelength[10]. The field dependence of the attenuation in the mixed state (Fig. 1) for magnetic fields less than, but close to H_{c_2} is consistent with the predictions of the field dependence in the dirty limit ($\xi < l$). Estimates based on the residual resistivity indicate the coherence length is limited by the electron mean free path[11].

The hypersonic attenuation at lower fields ($H \sim H_{c_1}$) in the mixed state, might be thought to be related to the same mechanism that leads to a resistance to transport current flow in the mixed state. The flow resistance is due to the equivalent currents which flow through the normal core of the vortex as a result of the relative motion of the superconducting regions and the vortex. The flow resistivity (ρ_f) in the mixed state is observed to be a linear function of magnetic field[12] with $\rho_f/\rho_N = H/H_{c_2}$. This emperical relation is independent of the composition of the superconductor and suggests the flow resistivity follows a law of corresponding states. This relationship can be written in terms of the field dependent normal volume in the mixed state by using the model of the vortex suggested earlier. Then $\rho_f/\rho_N \propto N(H)\xi$[2] where $N(H)$ is the number of vortices per unit area and ξ is the coherence length. It would seem reasonable to postulate a similar dissipative mechanism for the acoustic wave where the driving currents result from the shielding of the periodically distorted lattice fields by supercurrents. The attenuation would then be proportional to the normal volume and given by $\alpha(H) = \alpha_N V_N(H)/V_0$ where α_N is the normal state attenuation, $V_N(H)$ is the field dependent normal state volume, and V_0 is the total volume. The field dependence of the normal volume in the mixed state is determined from the field dependence of the elastic stiffness. Observations of the stiffness in the mixed state for both type I and type II superconductors indicate the field dependence of the stiffness is directly related to the fraction of normal volume analagous to the magnetization in this field region. Using the normal volume computed from the stiffness measurements on the same specimen, the dashed curve in Fig. 1 is computed. In order to make a direct comparison between the calculated and observed attenuation, without concern for demagnetization effects, only regions above H_{c_1} are considered. In this field range, the calculated and observed values are seen to be quite different. Attenuation results from interaction of the normal core with supercurrents generated to shield the lattice fields and the difference in velocity between the lattice ions and the vortex core. If this relative motion is the same in the superconducting state as in the normal state, the attenuation would be directly proportional to the normal volume. This is contrary to the observation that the measured attenuation is always less than the calculated value in the mixed state and indicates the motion of the normal core in the mixed state more closely follows the motion of the lattice than would occur if the vortex were surrounded by normal electrons. The superconducting region surrounding the vortex apparently inhibits the motion of the core less than do the normal electrons with a reduction in viscosity of the core with respect to the lattice frame. In addition, since the superconducting exterior region is moving with the lattice to shield the local fields, there is also a reduction of the current driven through the normal core by the relative motion of

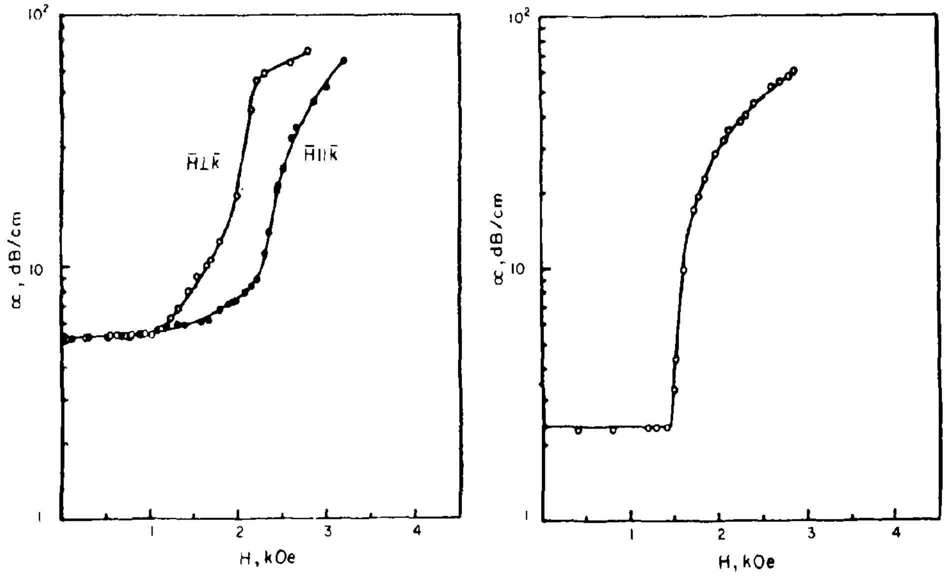

Fig. 2. The transverse mode attenuation at 1·6°K and 1 GHz for specimen II, on the left, and specimen I, on the right, as a function of applied magnetic field. The acoustic displacement is oriented so that the C_{44} elastic constant determines the velocity of propagation in both specimens.

the vortex with respect to the exterior supercurrents.

The longitudinal attenuation in the mixed state is observed to be related to the conductivity in both its field dependence and magnitude. In the low conductivity material (specimen II), an anisotropy in the attenuation is observed with a larger attenuation for propagation perpendicular to the direction of the field than parallel to it in fields near H_{c_1}. The attenuation in the Meissner state is similar for both specimens and well above the measurement limitations of the experimental apparatus.

The field dependence of the attenuation of transverse waves exhibits features similar to the longitudinal mode, although measurements are not performed over the entire mixed state due to the high attenuation near H_{c_2} (Fig. 2). The difference in field dependence of the attenuation is apparent for the specimens of different conductivity. An anistropy in the attenuation of the transverse mode as well as the longitudinal mode is present for the lower conductivity specimen. The origin of this anisotropic behavior is not clear and may be related to the structure of the lower conductivity specimen although not in any obvious way. A comparison of the relative coupling of the longitudinal and transverse modes to the vortex can be obtained through subtracting the Meissner attenuation from the observed value in the mixed state. If the attenuation is primarily due to the normal core electrons, the ratio of the transverse to longitudinal attenuation should agree with the calculation of Pippard which gives a ratio of $\infty_T/\infty_L = 5{\cdot}56$. The observed ratio at a field of 2·5 kOe is only 3·75, showing less transverse attenuation than the free electron model would predict if the waves coupled similarly to the vortex. This indicates a reduced coupling of the transverse mode or possibly a different effective dissipation for the transverse mode.

At lower frequencies (0·58 GHz), a larger segment of the mixed state transverse attenuation could be observed before the attenuation increased beyond the capabilities of the apparatus. A comparison of the lower frequency attenuation in the mixed state for the longitudinal and transverse modes (Fig. 3) shows a similarity in field dependence. At a field of approximately 3·5 kOe an inflection point in the attenuation is apparent for both modes. Above this inflection point the longitudinal attenuation behaves as predicted in high field limit for dirty superconductors.

A quadratic frequency dependence is observed for the low temperature normal state ($H > H_{c_2}$) longitudinal attenuation. At fields close to H_{c_2} in the mixed state, there is also a quadratic frequency dependence for both the longitudinal and transverse modes, consistent with an absorption process involving normal electrons in the $ql < 1$ limit. At lower fields in the mixed state ($H \sim H_{c_1}$), the frequency dependence is more complicated and is, on the average, a linear function of frequency (Fig. 4). In this region of the mixed state the vortex density is low and the vortices may be able to respond more dynamically to the acoustically induced field, thus leading to a different frequency response than in the high density region.

4. MEISSNER STATE

In the Meissner state, no vortices are present and the acoustic attenuation originates from two sources. One component is due to the unpaired electrons at finite temperatures [13] while the other results from phonon interactions. At 1·6°K, the unpaired electron component is negligible and the attenuation is a result of phonon interactions. The nature of the coupling between the acoustic phonons and thermal phonon distribution contains a unique feature which has no analogy among phonon interactions in insulators. This coupling mechanism results from the distortion of the lattice necessary to form the boss-like superconducting pair. The longitudinal and transverse modes exhibit a complicated frequency dependence in the temperature range where phonon interactions dominate

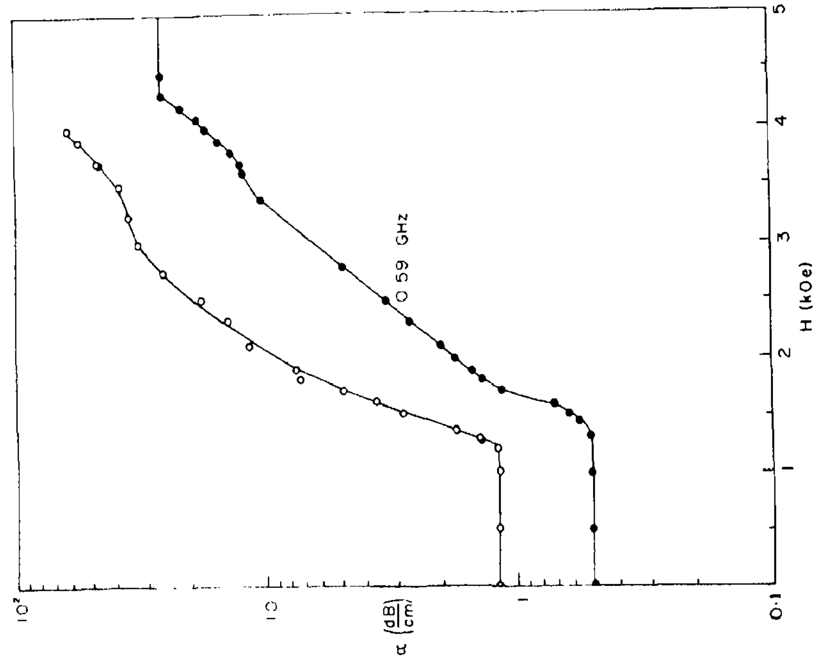

Fig. 3. The longitudinal (closed circles) and transverse (open circles) attenuation at a temperature of 1·6°K and a frequency of 0·58 GHz as a function of applied magnetic field.

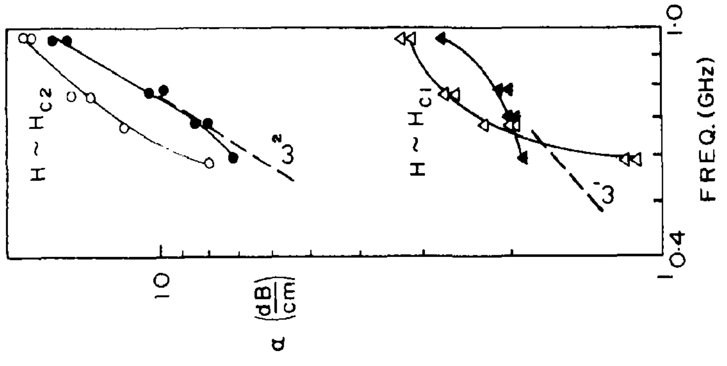

Fig. 4. The frequency dependence of the longitudinal attenuation for specimen I (open symbols) and specimen II (filled symbols) at various field values.

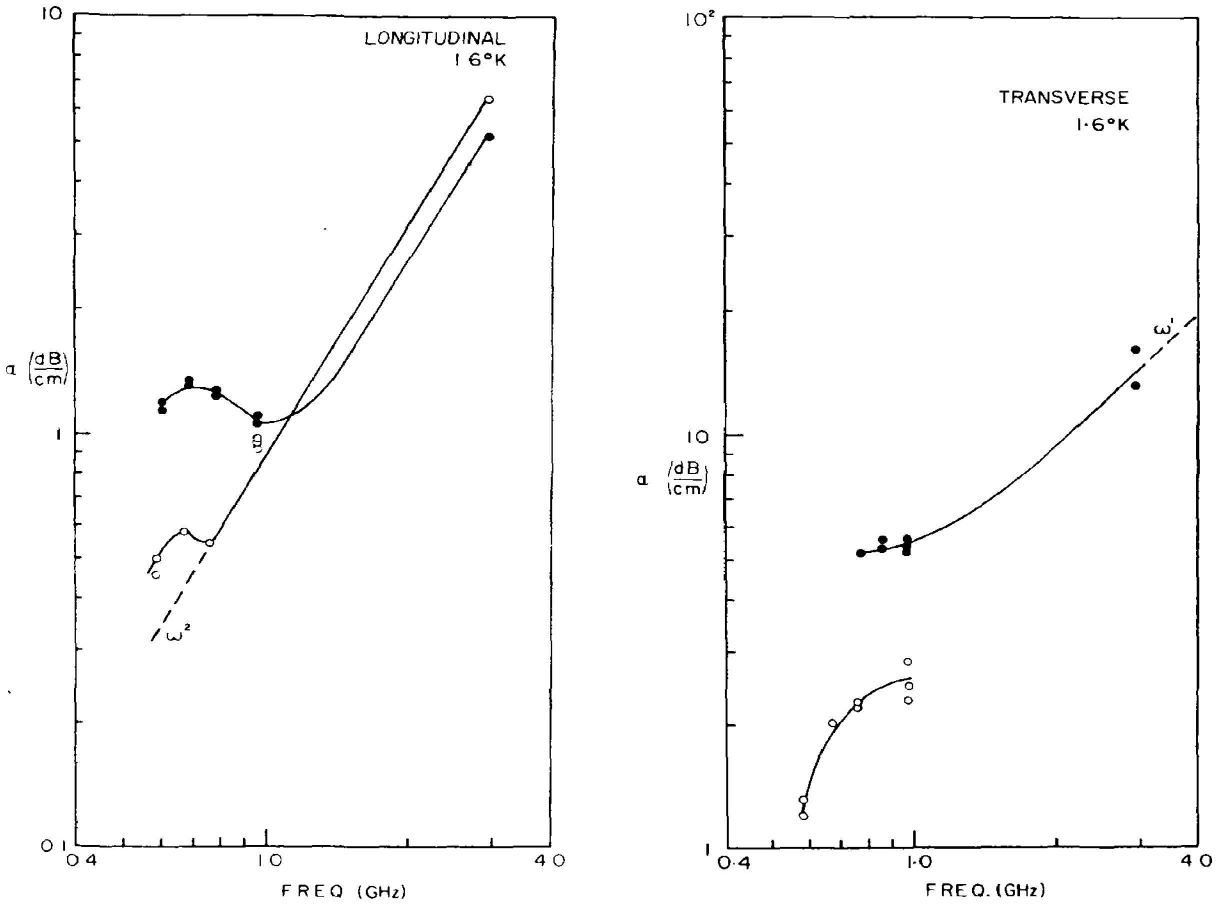

Fig 5 The frequency dependence of the longitudinal and transverse mode attenuation at 1·6°K in the Meissner state. The attenuation is primarily due to phonon interactions in both specimen I (open symbols) and specimen II (filled symbols)

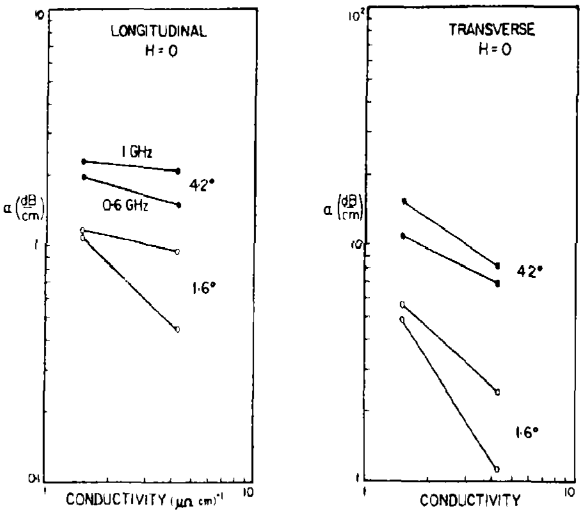

Fig. 6. The residual conductivity dependence of the longitudinal and transverse mode attenuation in the Meissner state, at various temperatures and frequencies. The normal state conductivity is assumed to be inversely related to the impurity and imperfection distribution.

(Fig. 5). The larger average frequency dependence of the longitudinal mode is consistent with the frequency dependence in some insulators. The longitudinal mode, after the attenuation due to the unpaired electrons is subtracted, exhibits a decrease in attenuation with increasing temperature for the high purity material. This behavior is not typical of insulators unless some relaxation absorption occurs at lower temperatures.

Both modes exhibit a larger attenuation for the specimen with the higher impurity and imperfection concentration (Fig. 6), with the transverse mode having the largest slope. The ratio of the residual resistances indicates an impurity and imperfection concentration about three times greater in one specimen compared to the other. Insulators, such as rutile[14], do not exhibit such a strong impurity dependence as observed in niobium for the same ratio of imperfections and in the same temperature range. The sensitivity of the attenuation to impurities and the unusual temperature dependence of the phonon component, are features of the phonon interactions which might be associated with the coupling of phonons to the bose-like superconducting quasiparticles.

REFERENCES

1. MAKI K., *Phys. Rev.* **156**, 437 (1957)
2. McLEAN F. B. and HOUGHTON A., *Phys. Rev.* **157**, 350 (1967).
3. KAGIWADA R., LEVY M., RUDNICK I., KAGIWADA H. and MAKI K., *Phys. Rev. Lett.* **18**, 74 (1967)
4. GOTTLIEB M., JONES C. K. and GARBUNY M., *Phys. Lett.* **25A**, 107 (1967)
5. CAROLI C., deGENNES P. and MATRICON J., *Phys. Lett.* **9**, 307 (1964)
6. deGENNES P. G. and MATRICON J., *Rev. mod. Phys.* **36**, 45 (1965)
7. BARDEEN J. and STEPHEN M. J., *Phys. Rev.* **140**, A1197 (1965).
8. KIM Y. B., HEMPSTEAD C. F. and STRAND A. R., *Phys. Rev.* **139**, A1163 (1964).
9. GOODRICH G. and LANGE J., *Phys. Rev.* **188**, 728 (1969)
10. PIPPARD A. B., *Phil. Mag.* **46**, 1104 (1955)
11. FINNEMORE D. K., STROMBERG T. F. and SWENSON C. A., *Phys. Rev.* **149**, 231 (1966)
12. REED W. A., FAWCETT E. and KIM Y. B., *Phys. Rev. Lett.* **14**, 790 (1965).
13. BARDEEN J., COOPER L. N. and SCHRIEFFER J. R., *Phys. Rev.* **108**, 1175 (1957).
14. LANGE J., *Phys. Rev.* **176**, 1030 (1968).

J. Phys Chem. Solids Pergamon Press 1970 Vol. 31, pp. 1701–1707. Printed in Great Britain

DIRECT GENERATION OF SOUND IN METALS AND ACOUSTIC NUCLEAR SPIN RESONANCE*

J. J. QUINN
Physics Department, Brown University, Providence, R I. 02912, U.S A

(*Received* 5 *September* 1969)

Abstract – The basic equations describing the direct electromagnetic generation of sound in a metal are studied. The boundary conditions are taken to be those applicable for specular reflection of the conduction electrons at the surface The resonances of the surface impedance associated with setting up a standing acoustic wave in a metallic plate are evaluated, and the contribution of direct acoustic generation and subsequent acoustic NMR to the nuclear magnetic resonance signal is investigated

1. INTRODUCTION

DURING the past few years there has been a considerable amount of effort devoted to the study of direct electromagnetic excitation of acoustic waves in metals. Most experiments [1–9] have been carried out at frequencies in the mega-Hertz range in the presence of a d.c. magnetic field oriented either perpendicular or parallel to the surface of the metal. For this situation the rate of acoustic generation is found to be proportional to the d.c. magnetic field strength over a considerable range of magnetic fields. Abeles[10] has investigated direct generation of acoustic waves in indium films at microwave frequencies in the absence of an applied magnetic field. The analysis of Abeles' results seems to depend critically on the diffuse reflection of the conduction electrons at the boundary of the metal[10, 11], while the lower frequency results do not. It is considerably simpler mathematically (but probably quite unrealistic) to apply boundary conditions appropriate for specular reflection at the metallic surface. Therefore, in this note we limit our consideration to the low frequency acoustic generation for which specular reflection boundary conditions can be assumed. We investigate the acoustic standing wave resonances of a thin metallic plate placed in an r.f. coil. For frequencies of the order of 10 MHz, resonances of high quality ($Q \simeq 10^3$–10^4) can readily be obtained at modest magnetic field strengths. For this situation a simple local theory of conductivity can be applied provided the d.c. magnetic field is larger than a few thousand Gauss. We also evaluate the contribution to the nuclear magnetic resonance signal due to the acoustic generation and subsequent acoustic NMR[13]. Under ideal conditions enhancement of the NMR signal by a factor of 10^2 seems possible. The method may prove useful in studying NMR in bulk single crystals of a number of metals.

2. GENERAL THEORY

We consider the model of a metal used by Rodriguez[14] to study the magnetic field dependence of the velocity of sound. The metal is thought to consist of a lattice positive ions of charge ze and mass M, and a gas of free electrons of charge $-e$ and mass m. The short range forces between the ions are accounted for by two 'unrenormalized' elastic constants, c_l associated with compressional distortions, and c_t' associated with shear distortions. In addition we introduce a phenomenological phonon relaxation time τ_p associated with the non-electronic damping of sound.

---

*Supported in part by the Advanced Research Projects Agency and by the National Science Foundation.

The equation of motion for the ionic displacement $\boldsymbol{\xi}$ is

$$M(\ddot{\boldsymbol{\xi}}+\dot{\boldsymbol{\xi}}/\tau_p)=c_l\boldsymbol{\nabla}(\boldsymbol{\nabla}\times\boldsymbol{\xi})-c_l\boldsymbol{\nabla}(\boldsymbol{\nabla}\times\boldsymbol{\xi})+ze\,\mathbf{E}$$
$$+\frac{ze}{c}\dot{\boldsymbol{\xi}}\times\mathbf{B}_0+\mathbf{F}. \tag{1}$$

The first two terms on the right hand side are short range forces between the ions. The next two are the electrostatic force, and the Lorentz force on the ions due to the d.c. magnetic field $\mathbf{B}_0$. The last term $\mathbf{F}$, the collision drag force, is given by $(zm/\tau)(\langle\mathbf{v}\rangle-\dot{\boldsymbol{\xi}})$, where $\langle\mathbf{v}\rangle$ is the average electronic velocity at position $\mathbf{r}$, and $\dot{\boldsymbol{\xi}}$ the local ionic velocity. $\mathbf{F}$ is simply the change in momentum per unit time of an ion due to collisions with conduction electrons. The collision drag force can also be expressed as $(-ze/\sigma_0)(\mathbf{j}_e+\mathbf{j}_I)$, where $\sigma_0=n_0e^2\tau/m$ is the d.c. conductivity and $\mathbf{j}_e$ and $\mathbf{j}_I$ are the electronic and ionic current densities respectively. The electric field and electron current density appear in two other equations. The first of these is the wave equation

$$\frac{\partial^2\mathbf{E}}{\partial z^2}+\frac{\omega^2}{c^2}\mathbf{E}=\frac{4\pi i\omega}{c^2}\mathbf{j}. \tag{2}$$

Here we have assumed that the metal surface is a plane of constant z, so that the electric field $\mathbf{E}$ varies in the z-direction only, and that $\mathbf{E}$ itself is in the $x-y$ plane. The wave equation (2) results from the two Maxwell equations $\boldsymbol{\nabla}\times\mathbf{E}=-c^{-1}\dot{\mathbf{B}}$, and $\boldsymbol{\nabla}\times\mathbf{B}=c^{-1}\dot{\mathbf{E}}+4\pi c^{-1}\mathbf{j}$, when we assume dependence of the form $\exp(i\omega t)$. Because of the existence of the metal surface at $z=0$, the electric field $\mathbf{E}(z)$ need not be a differentiable function of z at $z=0$. We define Fourier transforms of $\mathbf{E}(z)$ and $\mathbf{j}(z)$ by the perscription

$$\mathbf{E}(q)=\int_{-\infty}^{\infty}\mathrm{d}z\,\mathrm{e}^{iqz}\mathbf{E}(z). \tag{3}$$

The Fourier transform of the first term on the left hand side of equation (2) is given by

$$\int_{-\infty}^{\infty}\mathrm{d}z\,\mathrm{e}^{iqz}\frac{\partial^2\mathbf{E}(z)}{\partial z^2}=\Delta\mathbf{E}_0'-iq\,\Delta\mathbf{E}_0-q^2\mathbf{E}(q). \tag{4}$$

Here the constants $\Delta\mathbf{E}_0'$ and $\Delta\mathbf{E}_0$ are defined by the equations

$$\Delta\mathbf{E}_0'=\left(\frac{\partial\mathbf{E}(z)}{\partial z}\right)_{z=0-}-\left(\frac{\partial\mathbf{E}(z)}{\partial z}\right)_{z=0+},$$

and (5)

$$\Delta\mathbf{E}_0=\mathbf{E}(0-)-\mathbf{E}(0+).$$

The result in equation (4) is obtained by integrating by parts realizing that $\mathbf{E}(z)$ need not be continuous at $z=0$.

For the case of a perfectly rigid lattice, the Fourier transform of the total current $\mathbf{j}(z)$ appearing in equation (2) is entirely electronic.

$$\mathbf{j}(q)=\mathbf{j}_e(q)=\boldsymbol{\sigma}(q)\cdot\mathbf{E}(q), \tag{6}$$

where $\boldsymbol{\sigma}(q)$ is the wave number and frequency dependent conductivity of the electron gas. Using equations (5) and (6) one can solve equation (2) for the Fourier transform of $\mathbf{E}(z)$

$$E(q)=\frac{\Delta E_0'-iq\,\Delta E_0}{q^2-(\omega^2/c^2)+(4\pi i\omega/c^2)\,\sigma(q)}. \tag{7}$$

Knowing $E(q)$, we can easily evaluate $E(z)=\int(\mathrm{d}q/2\pi)E(q)\,\mathrm{e}^{-iqz}$ and the surface impedance $Z=(4\pi/c)[E(z)/H(z)]_{z=0}$. For the case of diffuse reflection, one wishes to replace the semi-infinite metal by an infinite one in which $E(z)=0$ for $z<0$. This means that, on the average, an electron arriving at the metal surface is replaced by an electron traveling from the opposite direction (from $z<0$) and passing through the $z=0$ plane as if no surface were present. In diffuse reflection at the surface the electron loses its memory that the electric field $E(z)$ has acted upon it as it approached from $z>0$. This is mimicked by requiring that its replacement coming from $z<0$ pass through a field free region. The integration over q from $-\infty$ to $+\infty$ can usually be performed by deforming the contour into the upper or lower half of the complex q-plane depending upon where e^{iqz} converges. The boundary conditions for diffuse reflection are obtained by requiring that $\Delta E_0' = -E'(0+)$ and $\Delta E_0 = -E(0+)$ be so chosen that the integration of $E(q)\,e^{-iqz}$ gives zero for $z < 0$.

For specular reflection, the electron retains a memory of the electric field which has acted on it as it approached the surface. This means that when we replace the semi-infinite metal by infinite one, both sides of the surface $z = 0$ must be mirror images of one another. Therefore $\mathbf{\Delta E}_0 = 0$ and $\mathbf{\Delta E}_0' = -2\mathbf{E}'(0+)$. For this case, the constant $\mathbf{\Delta E}_0'$ can equally well be thought of in terms of 'fictitious' surface current sheet with

$$\mathbf{\Delta E}_0' = \frac{4\pi i\omega}{c^2}\,\mathbf{j}_0(q), \tag{8}$$

or

$$\mathbf{j}_0(z) = \boldsymbol{\alpha}\delta(z) = \frac{c^2\mathbf{\Delta E}_0'}{4\pi i\omega}\,\delta(z). \tag{9}$$

The strength α of the current sheet can be shown to be proportional to the strength of the a.c. magnetic field at the surface i.e. $\boldsymbol{\alpha} = (c/2\pi)\mathbf{H}(0)$. In using this formulation of the boundary condition, we think of the total current density as the sum of $\mathbf{j}_e$, the electronic current density, $\mathbf{j}_i$, the ionic current density and $\mathbf{j}_0$, the fictitious surface current density. This total current appears on the right hand side of the Fourier transform of the wave equation (2). Since we have taken account of the discontinuity in $\mathbf{E}(z)$ at $z = 0$, the Fourier transform of equation (2) becomes

$$\mathbf{j}(q) = \Gamma\mathbf{E}(q), \tag{10}$$

where $\Gamma = ic^2q^2/4\pi\omega(1 - \omega^2/c^2q^2)$ for the case which we have considered in equation (2), viz. **E** normal to the direction of propagation. In general, we can allow **E** to be oriented arbitrarily with respect to **q**, and equation (10) becomes a tensor equation where the tensor $\mathbf{\Gamma} = ic^2q^2/4\pi\omega(1 - \omega^2/c^2q^2)\ \mathbf{1} - ic^2/4\pi\omega\ \mathbf{qq}$.

The final equation involving **j** and **E** is the constitutive equation for the electronic current density,

$$\mathbf{j}_e(q) = \boldsymbol{\sigma}(q)\cdot[\mathbf{E}(q) - (mi\omega/e\tau)\,\boldsymbol{\xi}(q)] + [2E_F/3e(1 + i\omega\tau)]\,\boldsymbol{\sigma}(q)\cdot\mathbf{q}(\mathbf{q}\cdot\boldsymbol{\xi}(q)). \tag{11}$$

The total current $\mathbf{j}(q)$ is the sum of the electronic current density given by equation (11) and the ionic current density $\mathbf{j}_i(q) = n_0 ei\omega\,\boldsymbol{\xi}(q)$.

For the general case in which the d.c. magnetic field is oriented at an angle θ with the normal to the metal surface, we choose $\mathbf{B}_0$ to define the z-direction and choose **q** to lie in the $y-z$ plane. Then we can solve equations (10) and (11) for the electric field **E** in terms of $\mathbf{j}_0$ and $\boldsymbol{\xi}$.

$$\begin{aligned}\mathbf{E}(q) = &-(\mathbf{1} - \mathbf{R}\cdot\mathbf{\Gamma})^{-1}\\ &\times\left[\frac{n_0 ei\omega}{\sigma_0}(\mathbf{1} - \sigma_0\mathbf{R}) + \frac{2E_F}{3e(1 + i\omega\tau)}\mathbf{qq}\right]\\ &\times\xi(q) - (\mathbf{1} - \mathbf{R}\cdot\mathbf{\Gamma})^{-1}\cdot\mathbf{R}\cdot\mathbf{j}_0(q).\end{aligned} \tag{12}$$

By substituting this expression for **E** in equation (1) and writing $\mathbf{j}_i + \mathbf{j}_l$ as $\mathbf{\Gamma}\cdot\mathbf{E} - \mathbf{j}_0$, we obtain the following tensor equation for the ionic displacement $\boldsymbol{\xi}$

$$\begin{aligned}&\Bigg\{\left(\omega^2 - \frac{i\omega}{\tau_p} - s_t^2q^2\right)\mathbf{1} - (s_l^2 - s_t^2)\,\mathbf{qq} + i\omega\Omega_c\mathbf{T}\\ &\quad - \frac{ze}{M}(\mathbf{1} - R_0\mathbf{\Gamma})\cdot(\mathbf{1} - \mathbf{R}\cdot\mathbf{\Gamma})^{-1}\\ &\quad\times\left[\frac{n_0 ei\omega}{\sigma_0}(\mathbf{1} - \sigma_0\mathbf{R}) + \frac{2E_F}{3e(1 + i\omega\tau)}\mathbf{qq}\right]\Bigg\}\cdot\boldsymbol{\xi}(q)\\ &\qquad = \frac{ze}{M}[(\mathbf{1} - R_0\mathbf{\Gamma})\cdot(\mathbf{1} - \mathbf{R}\cdot\mathbf{\Gamma})^{-1}\\ &\qquad\quad\times\mathbf{R} - R_0\,\mathbf{1}]\cdot\mathbf{j}_0(q).\end{aligned} \tag{13}$$

Here $\Omega_c = ze\mathbf{B}_0/mc$ is the cyclotron frequency of the ions; $R_0^{-1} = \sigma_0 = n_0e^2\tau/m$ is the d.c. conductivity, and $\mathbf{R} = \boldsymbol{\sigma}^{-1}$ is the resistivity tensor. The quantities s_l and s_t are unrenormalized sound velocities; E_F is the Fermi energy; **1** denotes the unit matrix, and **T** stands for the matrix whose only non-vanishing elements are $T_{xy} = -T_{yx} = 1$. This equation is valid for an arbitrary orientation of the d.c. magnetic field, for arbitrary values of the parameters ql, $\omega_c\tau$ and qv_F/ω_c, and includes both semi-classical and quantum effects if the quantum mechanical conductivity and resistivity tensors are used[15]. The general expressions are rather complicated, and normally one restricts one's attention to the simpler cases of $\mathbf{B}_0$ normal to the surface (helicon geometry[16]) and $\mathbf{B}_0$ parallel to the surface (Gantmaker geometry[17]). The first of the two cases involves slightly less arithmetic, so we shall investigate it in detail, and leave the slightly more complicated case as an exercise for the interested reader[18].

3. HELICON-GEOMETRY

For the helicon geometry, it is convenient to introduce circularly polarized coordinates defined by

$$\xi_\pm = \xi_x \pm i\xi_y. \qquad (14)$$

For this case it is not difficult to demonstrate that the solution of equation (13) can be written [12]

$$\xi_\pm(q) = -\frac{ze\omega}{M\sigma_0}\frac{(1-\sigma_0 R_\pm)}{f_\pm(q,\omega)}j_{0\pm}(q). \qquad (15)$$

where $R_\pm^{-1} = \sigma_\pm = \sigma_{xx} \pm i\sigma_{xy}$, and

$$\begin{aligned} f_\pm(q,\omega) = {} & \left(\omega^2 - \frac{i\omega}{\tau_p} - s_t^2 q^2 + \Omega_c\omega\right) \\ & \times (\omega - i\beta\omega\sigma_0 R_\pm) \\ & + \frac{zmi\omega^2}{M\tau}(1-i\beta)(1-\sigma_0 R_\pm). \end{aligned} \qquad (16)$$

The simplified form of equation (12) appropriate for the helicon geometry is

$$E_\pm(q) = \frac{i\omega m}{e\tau}\frac{(\sigma_\pm - \sigma_0)}{\sigma_\pm - i\beta\sigma_0}\xi_\pm(q) - \frac{j_{0\pm}(q)}{\sigma_\pm - i\beta\sigma_0}. \qquad (17)$$

By substituting the solution of equation (15) into equation (17) we obtain an expression for $E_\pm(q)$ in terms of $j_{0\pm}(q)$. Knowing $E_\pm(q)$, we need only calculate $\int E_\pm(q)e^{-iqz}dq/2\pi$ to obtain $E_\pm(z)$. A quantity of considerable interest to an experimenter is the surface impedance. It is given by

$$\begin{aligned} Z = {} & \frac{8\omega i}{c^2}\int_0^\infty dq\left(q^2 - \frac{\omega^2}{c^2} + \frac{4\pi i\omega}{c^2}\sigma_\pm\right)^{-1} \\ & \times\left[1 + \frac{zmi\omega^2}{M\tau}\frac{(1-\sigma R_\pm)^2}{\sigma_0 R_\pm f_\pm(q,\omega)}\right]. \end{aligned} \qquad (18)$$

The first term is the normal surface impedance in the absence of acoustic generation. The second term is the change in Z due to acoustic generation.

The function $f_\pm(q,\omega)$ is a cubic function of ω whose roots are the two acoustic waves (propagating in opposite directions) and the helicon wave[16]. Each of the roots has both a real and an imaginary part, giving the dispersion and attenuation of the wave. Obviously the change in surface impedance due to acoustic generation depends in a critical way on the nature of these roots.

4. RESONANCES OF A THIN PLATE

Consider a metal plate of thickness d place within an r.f. coil. The boundary conditions appropriate to specular reflection at each surface are obtained by choosing the surface current density to be given by

$$\mathbf{j}_0(z) = \boldsymbol{\alpha}\sum_{n=-\infty}^{\infty}(-)^n\delta(z-nd). \qquad (19)$$

The constant $\boldsymbol{\alpha}$ is again equal to $(c/2\pi)\mathbf{H}(0)$, where $\mathbf{H}(0)$ is the a.c. magnetic field strength at the surface. The Fourier transform of $\mathbf{j}_0(z)$ is given by

$$\mathbf{j}_0(q) = d^{-1}\boldsymbol{\alpha}\sum_{l=-\infty}^{\infty}\delta_{q,(2l+1)\pi/d}. \qquad (20)$$

where $\delta_{q,q'}$ is zero unless $q = q'$, in which case it has the value of unity. All the equations of the previous section up to equation (18) will hold for the present case if equation

(20) is used for $\mathbf{j}_0(q)$ instead of equation (8). This causes a change in the expression for the surface impedance, since only the particular discrete set of values of $q = (2l+1)\pi/d$, where l is an integer, contribute to the integral. For the change in Z due to acoustic generation we obtain

$$\Delta Z = \frac{2zmi\omega^2}{dM\tau} \sum_{q_n} (1 - i\beta\sigma_0 R_\pm)^{-1} \frac{(1-\sigma_0 R_\pm)^2}{f_\pm(q_n, \omega)}. \tag{21}$$

All functions of q appearing in equation (21) are to be evaluated at $q_n = (2n+1)\pi/\mathrm{d}$ when n is an integer. If the helicon frequency and the acoustic wave frequency are sufficiently different (i.e. $\omega_H = c^2q^2\omega_c/\omega_p{}^2 \ll s_tq$), and if the local theory of conduction is applicable, we may approximate $f_\pm(q, \omega)$ as follows

$$f_\pm(q,\omega) \simeq (\omega - s_tq - \Delta_+)(\omega + s_tq - \Delta_-)$$
$$[\omega \mp \omega_H(1 \pm i/\omega_c\tau)], \tag{22}$$

where

$$\Delta_\pm(q) \approx \pm\frac{i}{2\tau_p} \pm \frac{\Omega_c\omega_H}{2s_tq}\left[1 \pm i\frac{\omega_H}{s_tq}\frac{1}{\omega_c\tau}\right]. \tag{23}$$

Obviously ΔZ displays resonances at $\omega = sq_n + Re\Delta_+(q_n)$. The maximum amplitude of ΔZ at resonance is determined by the value of the imaginary part of $\Delta_+(q_n)$. For the value of ΔZ at resonance we obtain

$$(\Delta Z)_{\mathrm{res}} = \frac{8\pi}{d}\frac{\Omega_c\omega_c}{\omega_p{}^2}\left[\frac{1}{2\tau_p} + \frac{\Omega_c\omega_H{}^2}{2s_t{}^2q^2}\frac{1}{\omega_c\tau}\right]^{-1}. \tag{24}$$

For pure metals at low temperatures $\frac{1}{2}\tau_p{}^{-1}$ is usually much larger than the second term. In this situation the non-electronic damping of sound dominates the attenuation and determines the quality of the resonance[19]. For frequencies of the order $\omega \simeq 10^7\,\mathrm{sec}^{-1}$, Q's of 10^3 to 10^4 are not unusual leading to $\tau_p \approx 10^{-4}$ to 10^{-3} sec.

5. ACOUSTIC NUCLEAR MAGNETIC RESONANCE

In a standard NMR experiment in a metal, the applied r.f. field does not penetrate beyond the skin depth. However, we have just seen that the r.f. field can generate acoustic waves, and that these acoustic waves penetrate into the bulk. The acoustic waves can interact with the nuclear spins and cause NMR in the bulk of the sample. In this section we consider the change in the NMR signal due to generation of acoustic waves. The acoustic wave-nuclear spin coupling is taken to be that suggested by Quinn and Ying[13], although coupling via other mechanisms can be treated in a similar way. The experimental arrangement considered in this section has the advantage of utilizing a standard NMR spectrometer; no transduces are necessary because the acoustic waves are generated directly by the r.f. field. The only added requirement is that the sample have flat parallel faces.

The nuclear spin magnetization is given by

$$M_\pm = \chi_\pm B_\pm, \tag{25}$$

where the nuclear susceptibility $\chi_\pm$ is given by

$$\chi_\pm = \frac{\pm i\gamma M_0 T_2}{1 + i\omega T_2 \pm i\gamma B_0 T_2}. \tag{26}$$

Here γ is the nuclear gyromagnetic ratio, and M_0 the nuclear saturation magnetization in the direction parallel to the d.c. field $\mathbf{B}_0$. T_2 is the transverse nuclear relaxation time. The expression for $\chi_\pm$ was determined by solving the Bloch equation for the nuclear magnetization. If one includes the nuclear spin magnetization, the Maxwell equation for $\nabla \times \mathbf{B}$ becomes

$$\nabla \times \mathbf{B} = \frac{1}{c}\frac{\partial \mathbf{E}}{\partial t} + \frac{4\pi}{c}\mathbf{j} + 4\pi\,\nabla \times \mathbf{M}. \tag{27}$$

If we assume all the a.c. quantities vary as $\exp(i\omega t - iqz)$, then equation (27) together with the Maxwell equation for $\nabla \times \mathbf{E}$ can be combined to obtain the result (for circulary polarized waves)

$$j_\pm(q) = i\beta\sigma_0\nu_\pm E_\pm(q), \tag{28}$$

where $\nu_\pm = 1-4\pi\chi_\pm$. In obtaining this result we have made use of equation (25) to express $M_\pm$ in terms of $B_\pm$, and written $B_\pm = \pm i\ (cq/\omega)E_\pm$, which is from the Maxwell equation for $\nabla\times\mathbf{E}$.

If we use equation (28) instead of equation (8) and go through the same procedure as outlined in the previous sections we obtain an equation identical to equation (15), but now $f_\pm(q,\omega)$ is given by

$$f_\pm(q,\omega) = (\omega^2-(i\omega/\tau_p)-s_t^2q^2\pm\Omega_c\omega)$$
$$\times(\omega-i\beta\omega\sigma_0R_\pm\nu_\pm)$$
$$+\frac{zmi\omega^2}{M\tau}(1-i\beta\nu_\pm)(1-\sigma_0R_\pm) \quad (29)$$

instead of equation (16). The change in surface impedance due to acoustic generation is

$$\Delta Z = \frac{2zmi\omega^2}{dM\tau\sigma_0}\sum_{qn}\frac{(1-\sigma_0R_\pm)^2}{(1-i\beta\sigma_0R_\pm\nu_\pm)f_\pm(q,\omega)}. \quad (30)$$

For $\omega = sq$ and $sq \gg \omega_H$, $f_\pm(q,\omega)$ is approximately $2s^2q^2(\omega-sq-\Delta)$, where

$$\Delta = \Delta_1+i\Delta_2 = \frac{i}{2\tau_p}+\frac{\Omega_c\omega_H}{2s_tq}\left[1+i\nu_{2\pm}+i\frac{\omega_H}{s_tq\omega_c\tau}\right]. \quad (31)$$

If the non-electronic damping dominates, as it certainly does at low temperatures, the expression for ΔZ at a standing wave resonance is

$$(\Delta Z)_{\text{res}} \approx \frac{16\pi}{d}\frac{\Omega_c\omega_c}{\omega_p^2}\tau_p$$
$$\times\left\{1-\frac{\Omega_c\omega_c}{\omega_p^2}\frac{c^2}{s_t^2}\omega\tau_p\left(\nu_{2+}+\frac{c^2\omega}{s_t^2\omega_p^2\tau}\right)\right\}. \quad (32)$$

The appearance of ν_{2+}, the imaginary part of $-4\pi\chi_+$, leads to an acoustic contribution to the nuclear magnetic resonance signal. It is of interest to compare the contribution to NMR coming from equation (32) with Z_0, that due to the usual NMR signal from the skin depth. We find for this enhancement factor

$$\left(\frac{(\Delta Z)_{\text{res}}}{Z_0}\right)_{\text{NMR}} \approx 2^{5/2}\frac{\delta_0}{d}\frac{\omega\tau}{(1+\omega_c^2\tau^2)^{1/2}}\left(\frac{c\omega_c}{s_t\omega_p}\Omega_c\tau_p\right)^2.$$

Here δ_0 is the classical skin depth. For a thin plate ($d \simeq 0{\cdot}1$ cm) of ^{39}K in a field of 30 k, we estimate the enhancement factor to be of the order of 70.

6. SUMMARY

We have written down the basic equations describing direct electromagnetic generation of sound in a metal in the presence of a uniform magnetic field. The general equation valid for an arbitrary orientation of the d.c. magnetic field is studied in detail for the simple helicon geometry ($\mathbf{B}_0$ normal to the surface). We also investigate the acoustic standing wave resonances in the surface impedance of a metallic plate, and evaluate the contribution to the NMR signal due to acoustic generation and subsequent acoustic NMR. Under ideal conditions, the enhancement factor of the NMR signal due to acoustic generation can be of the order of 10^2.

Acknowledgement – The author would like to thank G. M. Seidel and R. Gordon for a number of helpful discussions.

REFERENCES

1. LARSEN P. K. and SAERMARK K., *Phys. Lett.* **24A**, 374 and 668 (1967); **26A**, 296 (1968).
2. HOUCK J. R., BOHM H. V., MAXFIELD B. W. and WILKINS J. W., *Phys. Rev. Lett.* **19**, 224 (1967).
3. BEIJEMANN A. G., BOHM H. V., MEREDITH D. J. and DOBBS E. R., *Phys. Lett.* **25A**, 753 (1967).
4. THOMAS R. L., TURNER G. and BOHM H. V., *Phys. Rev. Lett* **20**, 207 (1968).
5. GANTMAKER V. F. and DOLGOPOLOV V. T., *Zh. ETF Pis. Red.* **5**, 17 (1967), English translation: *Soviet Phys. JETP Lett.* **5**, 12 (1967).
6. GARDUKOV Yu. P. and PEROV A. P., *Zh. ETF Pis Red* **8**, 666 (1968); English translation *Soviet Phys JETP Lett.* **8**, 412 (1968)
7. MEREDITH D. J., WATTS-TOBIN R. J. and DOBBS E. R., *J. acoust. Soc. Am.* **45**, 1393 (1969).
8. GAERTTNER M. R., WALLACE W. D. and MAXFIELD B. W., *Phys. Rev.* **184**, 702 (1969).
9. TURNER R., LYALL K. R. and COCHRAN J. F., *Can. J. Phys.* **47**, 2293 (1969).

10. ABELES B., *Phys. Rev. Lett.* **19**, 1181 (1967).
11. SOUTHGATE P. D., *J. appl. Phys.* **40**, 22 (1969).
12. QUINN J. J., *Phys. Lett.* **25A**, 522 (1967)
13. QUINN J. J. and YING S. C., *Phys. Lett.* **23**, 61 (1966).
14. RODRIGUEZ S., *Phys. Rev.* **130**, 1778 (1963).
15. QUINN J. J. and RODRIGUEZ S., *Phys. Rev.* **128**, 2487 (1962).
16. QUINN J. J. and RODRIGUEZ S., *Phys. Rev.* **133**, A1589 (1964).
17. GANTMAKHER V. F., *Zh. eksp. teor. Fiz.* **43**, 345 (1962); English translation. *Soviet Phys. JETP* **16**, 247 (1963).
18. It will be helpful to note that for both of the simple geometries the left hand side of equation (12) is given in a useful and compact form in Ref. [14]. In this paper the normal modes of the infinite material were the subject of interest and $\mathbf{j}_0$ was therefore taken to be zero.
19. KRAVCHENKO V. Ya., *Zh. eksp. teor. Fiz.* **54**, 1494 (1968; English translation: *Soviet Phys. JETP* **27**, 801 (1968).

J. Phys. Chem Solids Pergamon Press 1970. Vol. 31, pp. 1709–1717. Printed in Great Britain

PERFORMANCE AND APPLICATIONS OF MICROWAVE PHOTON–PHONON DOUBLE-QUANTUM DETECTION IN MgO

ALAN J. BUDREAU and PAUL H. CARR
Air Force Cambridge Research Laboratories, Office of Aerospace Research, L. G. Hanscom Field, Bedford, Mass 01730, U S A.

(*Received* 5 *September* 1969)

Abstract – Microwave phonons at 3·1, 4·7, and 9·3 GHz were generated with CdS thin-film transducers, propagated through Fe^{2+}-doped MgO at 1·5 K, and detected with a photon–phonon double-quantum detector. In comparing double-quantum detection with the conventional piezoelectric method, it was found that the energy detecting properties of the former yielded exponential decays even when the latter did not. The field, frequency, and angular dependencies of the double-quantum detector were measured and interpreted. A shift from the double-quantum absorption to a slowly decaying saturation signal of opposite sign was observed as the phonon frequency approached that of the photons. The better precision made possible by the exponential echo pattern of the double-quantum detector was used to obtain accurate values for phonon attenuation. The frequency dependence of attenuation in MgO at 1·5 °K was measured for the first time. This dependence could be fitted to a term proportional to frequency (of about 0·3 dB/cm-GHz) which indicated the presence of scattering from dislocations, and a frequency-independent term (of about 0·4 dB/cm) attributed to boundary scattering. Double-quantum detection was also used to detect the scattered phonons observed between the echoes, and to demonstrate that they represented elastically scattered phonons. Longitudinal to-transverse mode conversion in one sample correlated with the presence of small-angle grain boundaries, as indicated by X-ray diffraction and laser ultramicroscope observations

1. INTRODUCTION

THE DOUBLE-QUANTUM detection of 9·45 GHz phonons in Fe^{2+}-doped MgO with 9·21 GHz photons was first observed by Schiren [1]. In an earlier paper, we studied the frequency dependence of the photon–phonon detector and discovered a new Raman-type transition[2]. The purpose of the present paper is two-fold. The first is to report on the characteristics of the double-quantum detector, and in particular, to contrast the second-order photon–phonon transition with the first-order spin–phonon and spin–photon transitions observed by Lewis and Stoneham [3]. The second is to describe the use of the double-quantum detection as a method for measuring the frequency dependence of the attenuation[4] (to the best of our knowledge, this is the first such measurement at 1·5 °K), for observing the spectral distribution of scattered phonons, and for studying longitudinal-to-transverse mode conversion.

The double-quantum detector has the advantage of detecting phonon power directly, while the microwave signal observed by the conventional piezoelectric method is proportional to the integral of the acoustic wavefront across the transducer surface, i.e. is phase-sensitive. Thus, nonparallelism of the sample endfaces or misalignment of the crystalline axes produces the ragged decay[5] observed in Fig. 1 (bottom). On the other hand, the echoes detected at the same time by the double-quantum method decay exponentially (Fig. 1, top). This has allowed us to measure the absolute attenuation of the phonons as a function of frequency, and thereby to determine the nature of the scattering mechanism. Andrews and Strandberg[6] attempted to measure the absolute

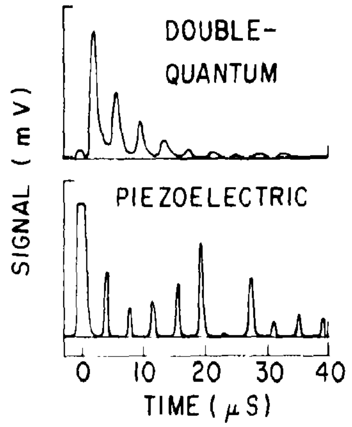

Fig. 1 Comparison of double-quantum and piezoelectric echoes for sample I at 4·7 GHz. Note that the two detectors are on opposite ends of the rod, producing the time difference between the two sets of peaks.

attenuation of 9 GHz phonons with a superconducting bolometer on one end of an X-cut quartz sample, but the loss of most of the acoustic energy in the bolometer precluded measurement of the intrinsic loss in the quartz.

The piezoelectric method can detect only the coherent phonons whose surfaces of constant phase are parallel to the end faces of the sample. Double-quantum detection is sensitive not only to these phonons in the primary beam but also to those scattered from it. The scattered phonons produce the ramp between the echoes observed by double-quantum detection in Fig. 1 (top). The presence of scattered phonons was also observed with a superconducting bolometer by Andrews and Strandberg. They were not, however, able to observe the spectral distribution of these scattered phonons, as bolometers are broad-band detectors. The double-quantum detector, on the other hand, has a narrow bandwidth and a center frequency which can be tuned by varying a static magnetic field. We have taken advantage of this characteristic to measure the spectral distribution of the scattered phonons.

Double-quantum detection is also a convenient means of measuring the polarization of the phonons. Either the longitudinal or the transverse mode may be observed by the choice of the angle between the rod axis and the magnetic field. This property proved useful in revealing a case of anomalous mode conversion in one of our samples.

2. EXPERIMENTAL METHOD

MgO rods were supplied by the Norton Company. CdS transducers, typically resonant at 3 GHz, were deposited on the end faces. Phonons were generated with a CdS transducer and detected by both the conventional piezoelectric method and the double-quantum detector as shown in Fig. 2. A magnetron was used to produce 0·5 μsec electromagnetic pulses which were then fed to a coaxial resonant cavity. This cavity was tuned with a movable ceramic disk to resonate in overtone modes at about 3·1, 4·7, or 9·3 GHz. Longitudinal microwave phonons were generated with a CdS transducer deposited on the end of the (100)-oriented 3 mm-dia. rod shown in Fig. 2. When the reflected phonon pulse returned to the

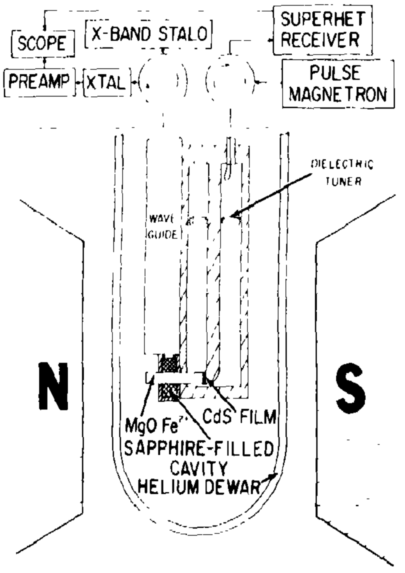

Fig. 2 Experimental apparatus for double-quantum and piezoelectric detection. The electromagnet could be rotated about the vertical axis.

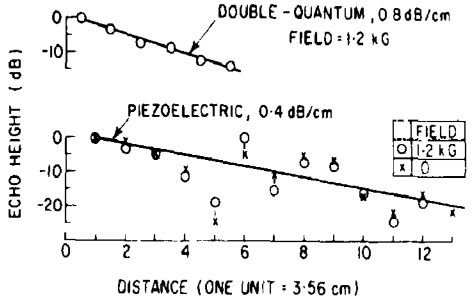

Fig. 3. Comparison of the decay patterns of sample I at 3·1 GHz by double-quantum (top) and piezoelectric phonon pulse echoes. The double quantum decay was observed at 1·2 kG, and the piezoelectric echoes were observed both at this and at zero field.

transducer, it was detected with a superheterodyne receiver. The electromechanical conversion efficiency (of the order of 10^{-5}), attenuation, and acoustic power were measured from these echoes[5, 7]. The double-quantum detection took place when the phonon pulse was inside a separate sapphire-filled TE_{012} rectangular cavity, resonant at 8·7 GHz. The cavity was positioned with the microwave magnetic field perpendicular to the static magnetic field. The photon–phonon double-quantum transition was manifest by an increase in the absorption in the rectangular cavity of photon power from an X-band frequency-stabilized CW source, as detected by a 1N23 diode which was d.c. biased for optimum sensitivity.

The stabilized CW source was fine-tuned to the detector cavity by minimizing the noise output of the video amplifier. The minimum was presumably due to nulling the FM noise in the source. The CW power level was adjusted to produce the maximal signal-to-noise ratio for the (pulse) double-quantum signal. This optimum was about 2 mW. At power levels substantially above this, the decrease in signal-to-noise ratio was due to saturation of the detector diode, and not to saturation of the spin system. This was checked by placing calibrated attenuators between the CW source and the cavity and between the cavity and the diode. In each experimental run the amplitude of the double-quantum output was calibrated by measuring the height of the first double-quantum signal as a function of the power to the reentrant cavity. The exponential decay of the double-quantum echoes was measured in this way (see Fig. 3).

The cavity configuration shown in Fig. 2 could be modified to generate transverse waves by applying the electric field in the plane of the CdS film. This was done by shortening the cavity centerpost and placing the rod end between it and the lower cavity wall. The rod as shown in Fig. 2 had the ends outside of the sapphire-filled cavity. This configuration allowed double-quantum detection of the phonon pulse before reflection from the end face and thus eliminated this possible source of mode conversion. In another modification, we mounted the rod with its end flush with the inside wall of the cavity. The latter configuration had the advantage of additively combining the outgoing and reflected pulses to enhance the strength of the detected signal.

The entire experimental assembly was installed in a cryogenic dewar system filled with liquid helium. A temperature of approximately 1·5 °K was obtained by pumping on the liquid helium.

3. DISCUSSION OF RESULTS

(a) Double-quantum detection

The double-quantum transition is characterized by the simultaneous absorption of a photon and a phonon. The double-quantum signal appeared as a series of exponentially-decaying echoes, peaking at the magnetic field at which the sum of the photon and the phonon energies equaled the transition from $M = -1$ to $M = +1$ (Fig. 1 and Ref. [2]. We checked the absolute sign of the observed signals by first determining that the rectangular cavity was undercoupled. The pulses produced by the double-quantum transition were of opposite sign than the CW absorption dip of the cavity resonance. It could then be readily shown that these double-quantum peaks were absorptions, as expected. As pointed out by Shiren, the double-quantum method is suitable for detecting fast pulses, as the intrinsic rise and fall times are both of the order of T_2, the spin–spin relaxation time. Our experimental rise and fall times were limited by the 2 MHz bandwidth of the video amplifier.

A boxcar integrator on the scope output and a rotating coil magnetometer were connected to an *X-Y* plotter to obtain plots of output vs. magnetic field. The observation that the number of transitions observed in such plots was a function of frequency, and the presence of new transitions, has been reported[2]. In addition, we found an appreciable change in the character of the signal as the phonon frequency approached that of the photons. For all experiments where the difference between the phonon and photon frequencies was significantly greater than the homogeneous linewidth of about 10 MHz, the narrow asymmetrical peak, sharper on the high-field side, as in the center trace of Fig. 4 (9·01 DQ), was observed. When the two frequencies approached to within 20 MHz, on the other hand, the magnetic field scans became much broader and more symmetrical (Fig. 4, 8·60 DQ, 8·64 DQ). At the same time, there appeared a signal of opposite sign which decayed with a time constant of about 25 μsec (Fig. 5). The amplitude of this latter signal increased, and that of the double-quantum decreased, as the frequencies became closer, so that when they were within a few MHz, the double-quantum signal could no longer be seen. This observation seems to correspond with that of Lewis and Stoneham [3], who, using approximately equal frequencies, reported slowly decaying signals representing decreased absorption, which they attributed to spin saturation. Further, their line-widths were similar to those we obtained when the gate was placed on the slowly decaying signal (Fig. 4, 8·64 Saturation). They offered no explanation for their failure to obtain double-quantum signals. Although they obtained traces[3, 8] which were qualitatively similar to our Fig. 5, Lewis and Stoneham performed experiments in varying field and frequency which indicated a different origin for their signals.

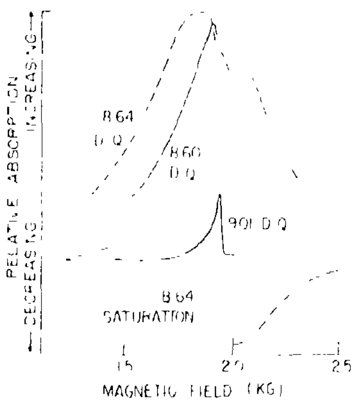

Fig. 4. Detector output as a function of magnetic field for photon frequency of 8·62 GHz. Phonon frequencies in GHz, are as indicated. Upper three traces: gate, 1 μsec, placed on first double-quantum peak. Lower dashed trace: identical conditions to upper dashed trace except that gate was increased to 12 μsec and shifted to begin 10 μsec after the first double-quantum peak. Thus the lower dashed trace measured the variation of the baseline.

The remainder of this paper deals with the more general case, in which the phonon and photon frequencies differed by at least 100 MHz. Under these conditions, the negative saturation signals of Fig. 5 were absent.

(b) *Applications of double-quantum detection*

(1) *Frequency-dependence of the attenuation.* The experimental attenuation measurements made in the manner illustrated in Fig. 3 are summarized in Table 1. The large spread in the attenuation made by piezoelectric detection is due to the uncertainty in fitting the observed echoes to an exponential. This method of estimating the attenuation does, however, come within a factor 2 of being equal to the absolute attenuation measured by the double-quantum method.

The experimental uncertainty for the double-quantum attenuation data was within 10 per cent for a given run. The greater

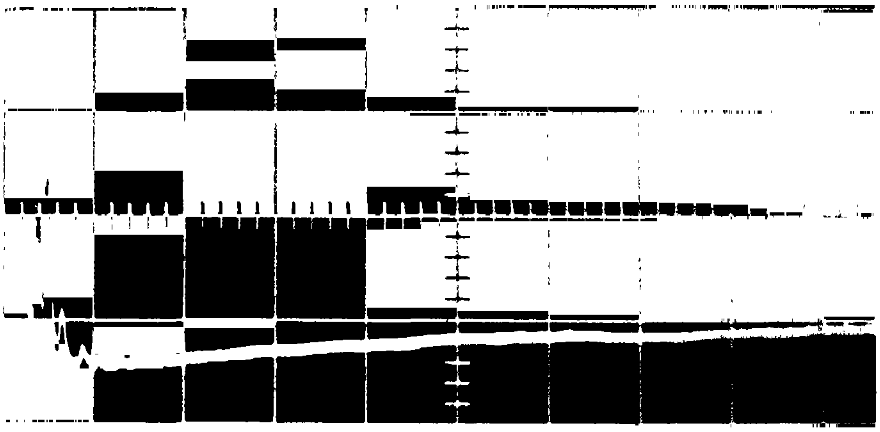

Fig. 5 Oscilloscope trace showing the narrow double-quantum absorption pulses superposed on the exponential decay of opposite sign due to spin-saturation. The photon frequency was 8·62 GHz and phonon frequency 8·63 GHz. Time scale: 1 large division equals 10 μsec

Table 1. *Frequency-dependence of the attenuation in* (100) MgO: Fe^{2+}

Sample	Frequency (GHz)	Attenuation (dB/cm) Piezoelectric	Attenuation (dB/cm) Double-quantum	Ramp* (dB)
1	3·1	0·4 ± 0·2	0·8	
	4·7	2·3 ± 2·0	1·5 ± 0·5	−10·0 ± 1·7
	9·0	3·0 ± 1·0	2·3 ± 0·3	−8·3 ± 1·3
2	3·1	2·6 ± 1·0	1·4	
	4·7	2·3 ± 1·4	2·2 ± 0·3	−10·8
	9·0	4·4 ± 2·0	3·2 ± 0·5	−3·2 ± 2·4
3	4·7	2·5 ± 1·0	2·1	
	9·0	1·5 ± 1·0	2·4	
4	4·7	2·7 ± 1·0	1·4	
	9·0	2·7 ± 1·0	2·8	−3·4

*Measured in dB below the echo peaks

uncertainty in the table was observed from one run to the next. Between runs the rod was warmed up to room temperature and removed from the experimental cavities. Where there was no tabulated uncertainty for the double-quantum attenuation, only one set of data was available. The change in attenuation from run to run followed no set pattern. On some successive runs it increased, whereas on others it decreased. Dislocation motion due to the thermal gradients in cycling the sample from 300 °K to 1·5 °K and changes in the mounting stresses are the most likely causes.

The frequency-dependence of the attenuation gives an indication of the scattering mechanism. Scattering from external boundaries of the sample and from grain boundaries would be expected to be frequency independent while scattering from strain-field dislocations would be proportional to the frequency [9, 10]. The attenuation measured by the double-quantum method is plotted as a function of the frequency in Fig. 6. Although there is considerable experimental scatter, the attenuation is approximately proportional to the frequency, with a slope of 0·27 dB/cm-GHz. The zero intercept of 0·4 dB/cm is the frequency independent component, attributed to scattering from boundaries at 1·5 °K. Using the estimate of 10^8 scattering centers/cm^2 obtained from laser microscope data (see below) we calculated the expected slope based on the expressions given for screw dislocations by Klemens[9], and for edge dislocations by Carruthers[11] and by Klemens[9]. These three expressions yielded slopes of $5·7 \times 10^{-4}$ dB/cm-GHz, $1·6 \times 10^{-2}$ dB/cm-GHz, and 5×10^{-4} dB/cm-GHz respectively. These are all to be regarded as order of magnitude estimates. Klemens[9] pointed out that the formalism he gave could underestimate the scattering by as much as an order of magnitude. Moss[12] observed that there was a tendency of the theories to underestimate the scattering, and Carruthers' expression yielded a closer fit. It is interesting

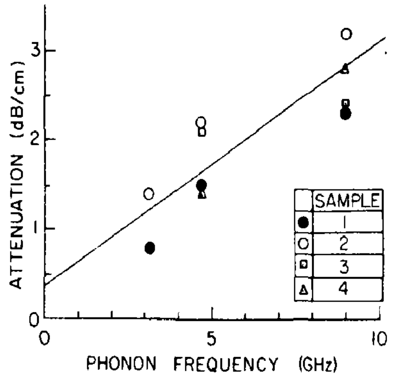

Fig. 6. Attenuation of longitudinal phonons in MgO at 1·5 °K measured as a function of frequency by the double quantum method for four different samples.

to note that, if we use the constants which Holland obtained from an emperical fit to his thermal conductivity data and scale up the number of dislocations to correspond to our sample, we obtain a predicted attenuation of 0·8 dB/cm-GHz. This is in reasonable agreement with our data.

The linear frequency dependence was too small for the attenuation to be due to the absorption of phonons by $\Delta M = \pm 1$ spin-phonon transitions between energy levels whose spacing corresponded to the phonon frequency[13, 14]. This was also confirmed by comparing the attenuation of 9·3 GHz phonons measured by piezoelectric detection at the 1·9 kG field required (the photons were at 8·7 GHz) for double-quantum detection with that measured at zero field (where the spin-phonon interaction was negligible). Individual echoes increased or decreased in amplitude, but there was no observable change in the overall attenuation. The attenuation changes at 3·1 GHz (lower set of data, Fig. 3) and 4·7 GHz were also negligible. The failure of the spin-phonon interaction to cause appreciable attenuation was most likely due to the fact that the $\Delta M = \pm 1$ transition was saturated by the first pulse (as indicated by the presence of the slowly decaying saturation signal in Fig. 5).

(2) *Scattered phonons.* The double-quantum method detects not only the phonons in the incident beam (i.e. the echoes in Fig. 1), but also those scattered from the main beam (the ramp between the echoes). The ramp in Fig. 1 was observable only after the first longitudinal echo. This was consistent with the fact that the phonons scattered from the main beam travel a longer path in arriving at the rectangular detection cavity. As we noted earlier, when the difference between the photon and phonon frequencies was greater than 100 MHz, the ramp was due to scattered phonons and not to the saturation of the spin system. This was confirmed in Fig. 7, where the ramp height and the peak heights of the echoes were plotted for the same rod on different runs. On the first run the echoes decayed with an attenuation of 2·9 dB/cm and the ramp decayed with the same attenuation but was 5·3 dB below the level of the decaying echo peaks. On the second run the echo attenuation increased to 3·8 dB/cm and the ramp decay was only 0·8 dB below that of the echoes.

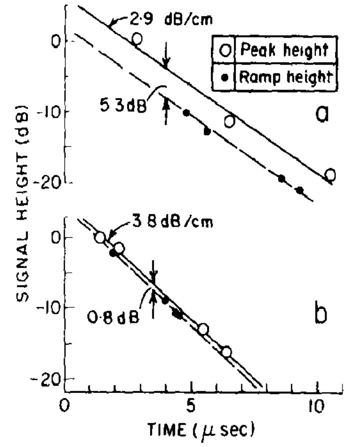

Fig. 7. Attenuation and ramp height of sample 2 at 1·5 °K compared for two different runs. Both runs were at *X*-band with separation of phonon and photon frequencies greater than 0·1 GHz. The ramp height increased with the attenuation showing that it consisted of scattered phonons.

The possible causes for the change in attenuation on different runs were discussed in the previous section. Inasmuch as the number of spins in the sample remained the same, we would not expect phonon scattering from the spins to have been the dominant scattering mechanism. The ramps of different samples (Table 1) were also found to correlate with the attenuation. This result was consistent with the view that the ramp was composed of phonons scattered from the primary beam.

Double-quantum detection also allowed us to determine the polarization of the scattered phonons and their energy spectrum. Polarization was examined by varying the angle between the rod-axis and the magnetic field (see Fig. 8). The ramp height was independent of this angle, indicating that the polarization of the phonons was random, and therefore

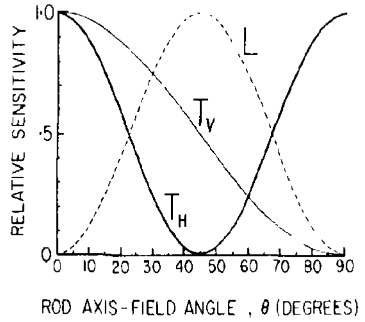

Fig. 8. Angular dependence of double-quantum detection for each of the three modes which propagate along the (100) axis. L is longitudinally polarized. T_V is transversely polarized, with motion normal to the plane of rotation of the magnetic field, and T_H is transversely polarized, in the plane of rotation

that the scattering process was isotropic. The spectral distribution of the scattered phonons was studied by comparing the line-shape (field dependence as in Fig. 4) of the scattered phonons of the ramp with that of the unscattered phonon echoes. Initial experiments seemed to indicate the presence of inelastically scattered phonons downshifted in frequency[15]. However, a careful repetition of the measurements failed to confirm the preliminary results. Thus, within experimental uncertainty, no difference could be found between the spectral distribution of the scattered and unscattered phonons, and all observed scattering was elastic.

(3) *Longitudinal-to-transverse mode conversion.* The angular dependence of the double-quantum sensitivity is different for longitudinal and transverse waves[14], as is illustrated in Fig. 8. Detection of longitudinal waves propagating along the (100) axis is most efficient when the rod axis makes a 45° angle to the magnetic field, and that of transverse waves is most efficient at 0°. This angular dependence was used to study the anomalously large transverse component present in sample 2. Figure 9 compares the double-quantum signals at 0° and 45° with the piezoelectric output (lower part). The upper trace in the top part of the figure shows the longitudinal echoes (velocity $8{\cdot}9 \times 10^5$ cm/sec) observed when the magnetic field was oriented at an angle of 45° with respect to the rod axis. The end of the rod was protruding outside the end of the rectangular cavity as in Fig. 2. Thus, the first two echoes were closely spaced with a high ramp amplitude between them. The next lower trace of Fig. 9 shows the transverse echoes observed with the field at 0°. The observed velocity was $6{\cdot}6 \times 10^5$ cm/sec, the same velocity obtained in piezoelectric experiments by changing the center-post configuration of the cavity to produce a transverse electric field. The transverse phonons were not observed in the piezoelectrically detected echoes shown in the bottom part of the figure.

We believe that the longitudinal-to-transverse mode conversion occurred at small angle sub-grain boundaries in the end of the crystal on which the CdS transducer was deposited. Since such a process would yield incoherent transverse phonons, they would not be detected piezoelectrically.

X-ray diffraction and laser ultramicroscope examinations were performed on both sample 1 and sample 2. While both departed from perfect crystalline structure, only sample 2 showed small angle grain boundaries. At the end on which the CdS transducer was deposited, the sample was actually divided into three crystals with slightly different angular orientations. This is evidenced by the splitting of each spot in the X-ray diffraction pattern from this end of the sample as shown in Fig. 10(a), where the splitting of each spot in the pattern (actually each spot has three components indicating the presence of structures of three slightly different angular orientations, but only two show in this reproduction) reveals the presence of more than one angular orientation. For comparison, the diffraction pattern observed at the opposite end of the sample, Fig. 10(b), is that expected from single crystal MgO.

Samples 1 and 2 were compared by examination with the laser ultramicroscope, which is a sensitive indicator of light scattering centers[17]. Both samples had a moderately high concentration of scattering centers of the order of 10^8 per cm^2 with apparently random distribution. The identification of the scattering centers as dislocations has not been compared with the more traditional methods of studying dislocations, but their concentration, distribution, and pattern of occurrence are so similar that there is little doubt as to their nature. The samples differed in that sample 2 had many bands or ribbons with very high concentrations of scattering centers, as shown in a typical photograph (Fig. 11(a)). The majority of such bands were found at the end with the CdS transducer. Small angle grain boundaries normally have a higher concentration of dislocations than the bulk of a specimen, and it is probable that the bands we see in the photographs are composed of the dislocations associated with the grain boundaries rather than the boundaries themselves. Figure 11b is a typical scattering pattern for sample 1. A second distinction between the two specimens was that the bands in sample 2 tended to traverse the rod diametrically while in sample 1 they generally looped in from the cylindrical surface, more or less parallel to the rod axis, and then loop out again, leaving the center of the rod free of grain boundaries, as shown schematically in Fig. 12. In comparing the frequency dependence of samples 1 and 2 in Fig. 6, one can see that the frequency dependent component is approximately the same but that the frequency-independent component for sample 2 is larger than from sample 1. This is consistent with the fact that the scattering from the more numerous grain boundaries in sample 2 is frequency independent[9].

4. CONCLUSIONS

Double-quantum detection has proved to be a useful tool in studying the attenuation of gigahertz phonons. Its energy-detecting property allowed more accurate and consistent measurements than piezoelectric detection. In addition, its ability to be magnetically tuned and to selectively measure the intensity of different modes of propagation gave it unique power as a diagnostic tool. Attenuation in MgO samples at 1·5°K was shown to be chiefly due to scattering from dislocations and boundaries. Anomalous longitudinal-to-transverse mode conversion in one sample was clearly evident in the double-quantum data yet completely hidden in the piezoelectric output. The anomalous acoustic behavior was shown to correlate with imperfections in crystal structure as revealed by ultramicroscope and X-ray diffraction measurements.

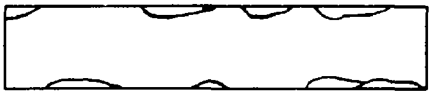

SAMPLE #1 1·5 dB/cm

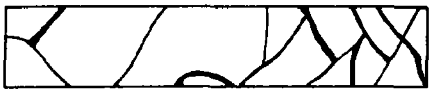

SAMPLE #2 2·2 dB/cm

Fig 12. Schematic drawings comparing the patterns of optical scattering centers observed in samples 1 and 2. This is based on a series of photographs including those of Fig 10 The CdS transducer was deposited on the right hand end of sample No. 2 X-ray diffraction from this end (Fig 10(a)) also showed the existance of small angle grain boundaries. The longitudinal to transverse mode conversion observed Fig. 9, for sample 2 is attributed to scattering at these grain boundaries

Acknowledgements – We wish to thank C A Pitha of the Solid State Sciences Laboratory, Air Force Cambridge Research Laboratories, for the laser ultramicroscope examinations, and H Posen and J A. Bruce, also of the Solid State Sciences Laboratory, for the X-ray diffraction measurements. We are indebted to J. Silva of the Microwave Physics Laboratory for technical assistance. We also wish to thank J. De Klerk of Westinghouse Research Laboratories, Pittsburgh, for fabricating cadmium sulfide transducers and for helpful discussions.

REFERENCES

1 SHIREN N. S., *Phys. Rev. Lett* **6**, 168 (1961).
2 CARR P H. and BUDREAU A. J., *Phys. Rev. Lett.* **21**, 976 (1968).

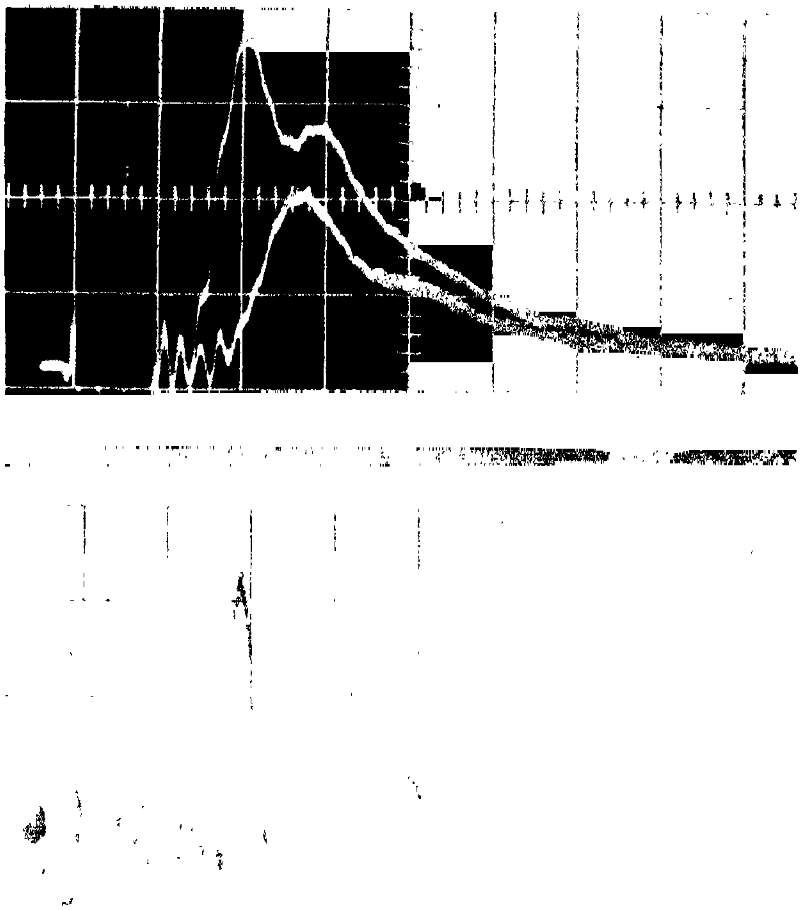

Fig. 9. Double-quantum and piezoelectric signals, sample 2 at 9·3 GHz. Uppermost trace obtained at rod-axis magnetic field angle of 45° for maximum sensitivity to longitudinally polarized phonons. Second trace down at 0° for maximum sensitivity to transversely polarized phonons. Bottom trace, made piezoelectrically, shows no evidence of either transverse phonons or (scattered) ramp between echoes.

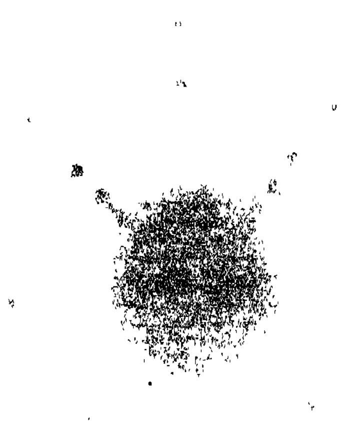

Fig. 10(a). X ray diffraction patterns of the regions near the two ends of sample 2. (a) taken near the CdS transducer, reveals by the splitting of each spot that small angle grain boundaries are present. (b) of the opposite end, yields the pattern expected from the (100) face of a single crystal MgO.

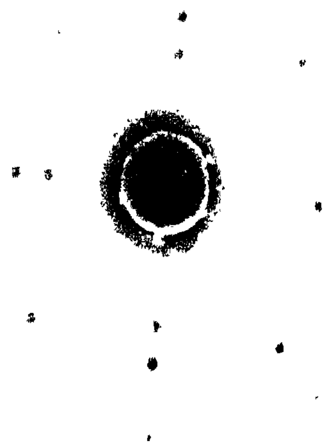

Fig. 10(b).

Fig 11(a). Typical LASER ultramicroscope photographs of sample 2 (a), and sample 1 (b) The area in each case is approximately 0·8 × 1·0 mm with a depth of field of about 10 μ. The long axis of each photograph coincides with the rod axis.

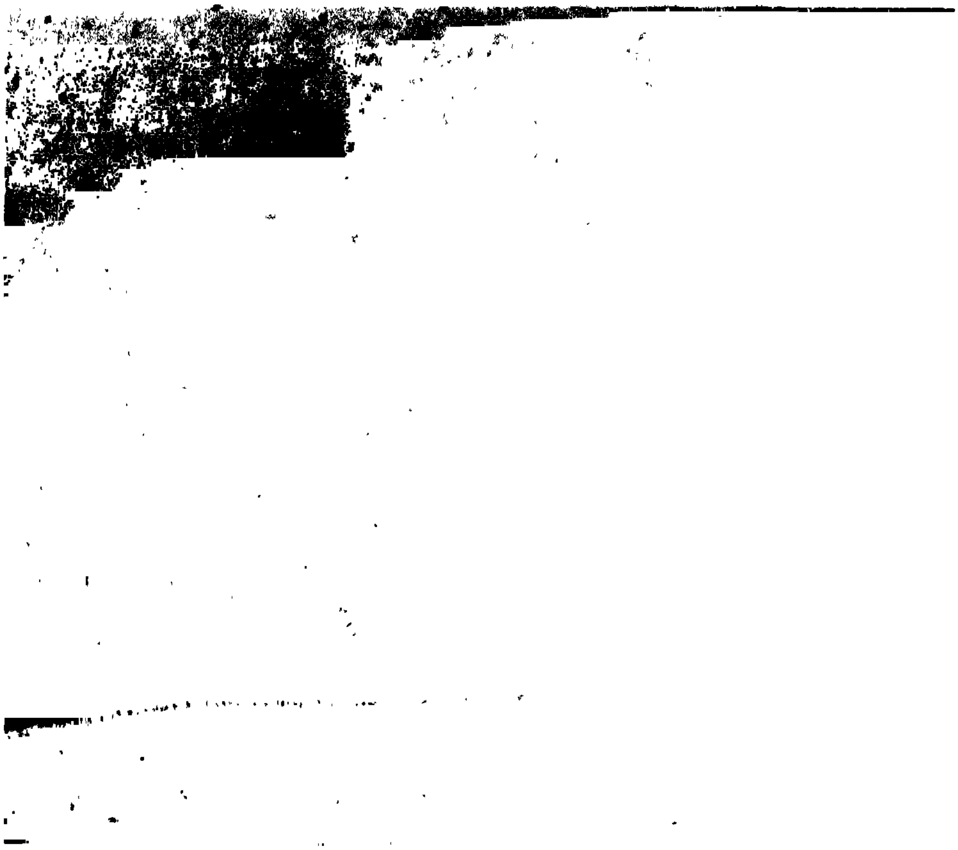

Fig. 11(b).

3. LEWIS M. F. and STONEHAM A. M., *Phys. Rev.* **164**, 271 (1967).
4. BUDREAU A. J., CARR P. H. and PITHA C. A., *Conf. on Ultrasonic Attenuation and Internal Friction in Crystalline Solids*, Providence, R. I. (1969).
5. CARR P. H. and STRANDBERG M. W. P., *J. Phys. Chem. Solids* **23**, 923 (1962).
6. ANDREWS J. M. and STRANDBERG M. W. P. *J. appl. Phys.* **38**, 2660 (1967).
7. CARR P. H., *J. acoust. Soc. Am.* **41**, 75 (1967).
8. LEWIS M. F., *Phys. Lett.* **17**, 183 (1965).
9. KLEMENS P. G., *Solid St. Phys.* **7**, 4 (1958).
10. HOLLAND M. G., *IEEE Trans.* **SU-15**, 18 (1968).
11. CARRUTHERS P., *Rev. mod. Phys.* **33**, 92 (1961).
12. MOSS M., *J. appl. Phys.* **37**, 4168 (1966).
13. DOBROV W. I., *Phys. Rev.* **134**, A734 (1964).
14. McMAHON D. H., *Phys. Rev.* **134**, A128 (1964).
15. CARR P. H. and BUDREAU A. J., *IEEE Trans.* **SU-16**, 36 (1969).
16. SHIREN N. S., *IBM Res. Paper* No. RC-1691 (1966).
17. POWELL R. C., *Air Force Cambridge Res. Lab. Rep.* No. 67 0648 (1967).

J. Phys. Chem. Solids Pergamon Press 1970. Vol. 31, pp. 1719–1727. Printed in Great Britain.

THE PROPAGATION AND ATTENUATION OF ACOUSTIC WAVES IN FERROMAGNETIC METALS*

B. A. HUBERMAN, R. ITO and E. BURSTEIN

Physics Department and Laboratory for Research on the Structure of Matter University of Pennsylvania, Philadelphia, Penn. 19104, U.S A.

and

Y. SAWADA

Physics Department, Osaka University, Toyonaka, Japan

(*Received* 8 *October* 1969)

Abstract – The physics underlying the propagation and attenuation of acoustic waves in ferromagnetic metals is discussed The propagating modes are considered as coupled acoustic phonon–magnon–photon modes and their dispersion relation is derived for both ferromagnetic insulators and metals by treating the modes as electromagnetic waves The damping of the coupled modes is discussed in terms of the individual damping mechanisms for the acoustic phonons, magnons and photons and their relative content as a function of frequency Data on the attenuation of high frequency (220 MHz) sound waves at low temperatures in ferromagnetic Ni is presented and discussed

1. INTRODUCTION

WE PRESENT in this paper a discussion of the physics underlying the propagation and attenuation of acoustic (A) waves in ferromagnetic metals in a magnetic field under conditions where the field within the crystal is uniform.

The acoustic waves in ferromagnetic crystals are actually coupled acoustic phonon–magnon–photon modes which arise from the magneto-elastic interaction of acoustic phonons (acoustic waves) with magnons (spin waves)[1, 2] and the magnetic-dipole interaction of photons (electromagnetic (EM) waves) with magnons[3]. (A direct coupling of acoustic phonons with photons may occur via a piezoelectric interaction in ferromagnetic crystal which are also piezo-electric, but we will for present purposes omit this coupling in our discussions). In the case of insulators, the dispersion relation for the coupled modes can be obtained by solving the coupled equations of motion for the acoustic phonons, magnons and photons. In the case of metals, one must also include the equation of motio for the single particle excitations of th plasma, and the resulting dispersion relatio for the coupled modes is found to depen on the magnitudes of ω_c, Ω_k and τ_e, whe ω_c is the cyclotron frequency of the electron Ω_k is the wave vector (k) dependent frequenc of the coupled modes and τ_e is the electro relaxation time. Since the coupled mode involve photons, they can also be regarde as EM waves in a medium of dielectric con stant $\epsilon(\omega, k)$ and magnetic permeabilit $\mu(\omega, k)$, i.e. the dispersion relation of th coupled modes is identical to the dispersio relation for the EM waves.

In discussing the attenuation of the couple acoustic phonon–magnon–photon modes, it i useful to do so in terms of the acousti phonon–magnon and photon strengths of th modes. This type of approach which has bee taken in the case of light scattering b coupled plasmon-LO phonon modes[4] an coupled photon-TO phonon modes (polari tons)[5] has the advantage of providing a intuitive basis for discussing the attenuatio of the coupled modes.

The attenuation of the coupled modes i due, in part, to the 'damping' processe

---

*Research supported in part by the U.S. Office of Naval Research and by the Advanced Research Projects Agency.

When one includes the damping of the modes, there will be an upper limit to the value of $\epsilon_\perp(\omega,k)\mu_\perp(\omega,k)$ and, therefore, an upper limit to the value of the k vector of the modes in the Ω_{k_1} branch. Beyond that maximum k value, which is determined by the magnitude of the magnon damping, the phonons and photons are no longer coupled to the magnons. In most crystals, the exchange term, Ak^2 is appreciable only at k values greater than 10^7[2], which is well beyond the maximum k value for the coupled modes in most ferromagnetic insulators. It can therefore be neglected in discussing the propagation of the coupled phonon–magnon–photon modes. (The effect of very large (magnon) damping is to completely smear out the region of anomalous dispersion so that the modes will be effectively uncoupled at all values of the wave vector. This happens for example when the width of the uncoupled magnon resonance is large compared to the splitting Δ of the coupled phonon–magnon modes at large k values.)

It is useful to express the acoustic phonon, magnon and photon character of the Ω_k modes in terms of their acoustic phonon-strength $\mathscr{S}_A(\Omega_k)$, magnon-strength $\mathscr{S}_M(\Omega_k)$, and photon-strength $\mathscr{S}_H(\Omega_k)$ which are defined by

$$\langle \mathbf{u}(\Omega_k)^2\rangle = \mathscr{S}_A(\Omega_k)\langle \mathbf{u}^\circ(\Omega_k)^2\rangle \tag{7}$$

$$\langle \mathbf{M}(\Omega_k)^2\rangle = \mathscr{S}_M(\Omega_k)\langle \mathbf{M}^\circ(\omega_m(k))^2\rangle \tag{8}$$

$$\langle \mathbf{H}(\Omega_k)^2\rangle = \mathscr{S}_H(\Omega_k)\langle \mathbf{H}^\circ(\Omega_k)^2\rangle \tag{9}$$

where $\mathbf{u}^\circ(\Omega_k)$ is the elastic displacement amplitude of the uncoupled phonons at Ω_k; $\mathbf{M}^\circ(\omega_m(k))$ is the magnetization amplitude of the uncoupled magnons at $(\omega_m(k))$; and $\mathbf{H}^\circ(\Omega_k)$ is the magnetic field of the uncoupled photons at Ω_k.

The phonon–magnon and photon-strengths of the modes are functions of frequency and wave-vector. In general, for a given k and a given coupling constant, the closer a coupled mode is to an uncoupled in frequency, the greater the admixture of that mode. In the Ω_{k_1} branch, the modes are acoustic phonon in character at $k=0$, i.e. $\mathbf{u}\pm(\Omega_k)\approx u^\circ\pm(\Omega_k)$ and $\mathscr{S}_A(\Omega_k)\approx 1$. As k increases the magnon content increases while the phonon content decreases. At large k values the Ω_{k_1} modes are magnon in character, i.e. $\mathbf{M}(\Omega_k)\approx \mathbf{M}^\circ(\omega_m(k))$ and $\mathscr{S}_M(\Omega_k)\approx 1$. For the Ω_{k_2} branch, the $k=0$ modes are an admixture of photons and magnons. As k increases the photon strength decreases and the Ω_{k_2} modes become largely magnon in character. With further increasing k the magnon strength decreases while the phonon strength increases. At large k values the modes are predominantly phononlike, i.e. $\mathscr{S}_A(\Omega_k)\approx 1$. For the Ω_{k_3} branch, the $k=0$ modes are an admixture of photons and magnons, and as k increases the magnon strength goes to zero and the photon strength goes to unity. One notes that modes with appreciable photon strength have little phonon strength and those modes with appreciable phonon strength have small photon strength.

In general, when acoustic waves are transmitted into the crystal, only those modes that have appreciable phonon strength will be 'excited', namely, the Ω_{k_1} modes at $\Omega_{k_1}<\omega_m-\Delta$ and the Ω_{k_2} modes at frequencies $\Omega_{k_2}>\omega_m$. There will be effectively no excitation of the modes which have little phonon strength, namely, the Ω_{k_3} modes and the $\Omega_{k_2}\lesssim\omega_m$ modes. On the other hand, when *EM* waves are transmitted into the crystal only those modes which have non-negligible photon strength will be appreciably excited, namely, the Ω_{k_2} mode at $\Omega_{k_2}\lesssim\omega_m$ and all the Ω_{k_3} modes.

For purposes of discussing the attenuation of the modes with appreciable phonon content one can, to a good approximation treat the Ω_{k_1} modes having $\Omega_k<\omega_m-\Delta$ and the Ω_{k_2} modes having $\Omega_k>\omega_m$ as coupled phonon–magnon modes. We take the frequencies as real and consider the wave vector k as complex, i.e. $\mathbf{k}=\mathbf{k}_1+i\mathbf{k}_2$. Therefore the attenuation per unit length of path of the propagating modes, (in the form of either plane waves or quasi-monochromatic pulses), which correspond to the spatial damping of the Poynting vector, is given by $\mathscr{A} = 2k_2$. The attenuation per unit time is in turn given by $\Gamma = vk_2$ where v is the velocity of energy transport (in regions away from anomalous dispersion v is equal to the group velocity).

In crystals where the attenuation of the coupled phonon–magnon modes is dominated by magnon damping one obtains the following expression for the attenuation per unit length in terms of the phonon and magnon-strengths of the modes.

$$\mathscr{A} = \frac{2\Delta\tau_m \mathscr{S}_M \Omega_k}{\Omega_k v_p \Delta\tau_m^2 \mathscr{S}_A + 2\mathscr{S}_M v_p}. \tag{10}$$

Where τ_m is the magnon relaxation time and $v_p = \Omega_k/k$ is the phase velocity. We note that $\mathscr{A}$ exhibits a peak when $\mathscr{S}_M(\Omega_k)$ is unity and v_p is small, namely, at $\Omega_k = \omega_m - \Delta$,

$$\mathscr{A}_{\max} \approx \frac{\Delta\tau_m \Omega_k}{v_p}. \tag{11}$$

At frequencies away from resonance, such that $\Omega_k \gg \omega_m$ and $\Omega_k \ll \omega_m - \Delta$, $\mathscr{S}_A(\Omega_k) \approx 1$ and the expression for $\mathscr{A}$ becomes

$$\mathscr{A} \approx \frac{2\mathscr{S}_M(\Omega_k)}{\tau_m}. \tag{12}$$

As mentioned earlier, the coupled modes with appreciably photon strength have negligible phonon strength and occur in different parts of the dispersion curves than the coupled modes with appreciable phonon strength and negligible photon strength. Accordingly experiments carried out with incident *EM* waves and those carried out with incident *A* waves involve different branches of the dispersion curves. In the case of *EM* wave experiments one observes a 'ferromagnetic' resonance at $\omega = \Omega_{k_1} = \omega_{0H}$ $\gamma_G B_0 = \gamma_G(H_0 + 4\pi M_s)$, whereas in the case of *A* wave experiments one observes a 'ferroacoustic' resonance at $\omega = \Omega_{k_1} = \gamma_G H - \Delta$. In 'ferromagnetic' resonance, the damping of magnons generally takes place via non-linear processes[7], whereas in 'ferroacoustic' resonance, the damping of magnons is believed to involve spin-lattice relaxation processes[2–6].

3. FERROMAGNETIC METALS

In addition to the interactions which play a role in the ferromagnetic insulator, one has, in the case of metals, the interaction of acoustic phonons, magnons and photons with the single particle elementary excitations of the electron plasma.

The strong interaction of photons with the electron plasma appreciably modifies the form of the dispersion curves for the electromagnetic modes and, thereby, the form of the dispersion curve of the coupled phonon–magnon–photon modes. One of the major effects of the modification of the dispersion curve of the uncoupled photons is to change the value of the wave vector at which the uncoupled phonons, magnons and photons cross one another. The absorption of *EM* radiation by the electron excitations contributes an additional strong damping mechanism that will lead to attenuation of the propagating coupled modes whenever they have a non-negligible photon strength. Since the interaction of phonons and magnons with the electron excitations are relatively weak, the forms of the dispersion curves for the uncoupled phonons and magnons are essentially unaffected. The coupling of phonon and magnon with the electron plasma excitations does however provide additional damping mechanisms for the coupled phonon–magnon–photon modes.

The dispersion relation for the coupled phonon–magnon–photon modes in a ferromagnetic metal are obtained by solving the coupled equations of motion for phonons, photons, magnons and the electron excitations taking into account the electron–photon interaction and the magnetoelastic interaction between phonons and magnons, but neglecting the much weaker electron–phonon and electron–magnon interactions. We will use the alternative approach of obtaining the dispersion relation directly from the *EM* wave equation (equation (5)). For this purpose we will use a model in which the interaction of the photons with the electron excitations is contained in $\epsilon_{\pm}(\omega, k)$ and the phonon–magnon and photon magnon interactions are contained in $\mu_{\pm}(\omega, k)$ (we will neglect the contributions of the electrons to $\mu(\omega, k)$). Since the coupling of the phonons and magnons with the electron plasma is neglected, $\mu_{\pm}(\omega, k)$ has the same form as in the case of the ferromagnetic insulator (equation (6)). The dielectric constant $\epsilon_{\pm}(\omega, k)$ will correspond to that of the electron plasma in a magnetic field. (The nature of the modes resulting from the interactions of helicon and magnons alone has been treated in detail by Stern and Callen[8] and Glick and Callen[9]).

When one neglects spatial dispersion (i.e. non-local) effects, the dielectric constant of the electron plasma (assumed to be uncompensated) is, on the basis of a simple electron gas model, given by[10]

$$\epsilon(\omega, k) = \epsilon_0 \pm \frac{\omega_p^2}{\omega(\omega \pm \omega_c) + i\tau_e^{-1}} = \epsilon_1(\omega) + i\epsilon_2(\omega) \tag{13}$$

where the + and − signs correspond to the circularly polarized *EM* modes which are cyclotron resonance active and inactive respectively; ω_p is the plasma frequency; $\omega_c = eB_0/m^*c = \gamma B_0$ is the cyclotron frequency of the electrons; and τ_e is the electron relaxation time. In general γ_e and γ_G have the same sign, so that the circularly polarized photon modes which are cyclotron resonance active will also be the ones that couple with the magnons. We also note that γ_e and γ_G have essentially the same magnitude and, therefore, ω_c will be approximately equal to $\omega_{0B} = \gamma_G B_0$. Since the frequency region of interest for acoustic attenuation is in the vicinity of $\omega_{0H} = \gamma_G H_0$, the cyclotron frequency will be much larger than the frequency of the incident acoustic waves. (In the case of uncompensated plasmas, $\epsilon_{\pm}(\omega, k)$ will have contributions from both electrons and holes.) Non-local effects can be taken into account by introducing the Doppler-shifted frequency $\omega' = \omega + \mathbf{k}\,.\,\mathbf{v}$ and summing over the velocity distribution of the electrons at the Fermi surface in the Landau sub-bands. These non-local effects manifest themselves in the phenomenon of Doppler shifted cyclotron resonance[10].

On introducing the expressions for $\epsilon_{\pm}(\omega, k)$ and $\mu_{\pm}(\omega, k)$ into the *EM* wave equation, one obtains the following dispersion relation for the coupled acoustic phonon–magnon–photon modes.

$$k^2c^2 = \omega^3\left\{\left[\epsilon_0 \pm \frac{\omega_p^2}{\omega(\omega \pm \omega_c) + i\tau_e^{-1}}\right]\right.$$
$$\left.\times\left[1 \pm \frac{4\pi\omega_s}{\omega_m + \Delta v_1^2k^2 \pm \omega}\right]\right\}. \tag{14}$$

It should be noted that the expression given by Akhiezer *et al.*[1] corresponds to the case when $\omega\tau_e \ll 1$ and $\omega_c\tau_e \ll 1$, and $\epsilon(\omega, k) = i4\pi\sigma_0/\omega$.

The form of the photon dispersion curves is determined by the magnitudes of $\omega\tau_e$ and $\omega_c\tau_e$. In most experimental situations where $\omega < 10^{10}$ cps, one generally finds that in the ferromagnetic metals the condition $\omega\tau_e \ll 1$ holds. On the other hand, depending on the magnitude of B_0 and the perfection of the crystal, both situations $\omega_c\tau_e \ll 1$ and $\omega_c\tau_e \gg 1$ can be encountered. When $\omega\tau_e \ll 1$ and $\omega_c\tau_e \ll 1$ as in the case of low resistivity ratio samples, $\epsilon_2(\omega, k)$ is much larger than $\epsilon_1(\omega, k)$. Therefore in the absence of any coupling with phonons and magnons, the dispersion relation for the *EM* modes will have the form

$$c^2k_1^2 \approx 2\pi\sigma_0\omega. \tag{15}$$

In this situation the frequency of the modes has a quadratic dependence on wave vector. Under these conditions, $k_1 \approx k_2$ so that propagating *EM* modes are heavily damped. The phase velocity of the modes is given by $v_p = (2c^2/\epsilon_2)^{1/2} = (c^2\omega/2\pi\sigma_0)^{1/2}$ and at given ω is considerably smaller than in the case of insulators. Accordingly, the point at which the uncoupled photon and magnon modes cross occurs at larger k values than in the insulator case, and comes closer to the point at which the uncoupled phonon and magnon modes cross. Furthermore, unlike the insulator case, there will be a crossing of the uncoupled phonons and photon modes at k values below that for the crossing of the photon and magnon modes.

For $\omega_c\tau_e > 1$ and $\omega_c/\omega > 1$, as may be encountered in high resistivity ratio samples, $\epsilon_1(\omega, k)$ is larger than $\epsilon_2(\omega, k)$ and $k_1 > k_2$. In the case of the cyclotron resonance active modes the photon modes correspond to weakly damped helicon waves (or to Alfvén waves in compensated plasmas). The dispersion relation for the propagating waves will have the form

$$c^2k^2 \approx \frac{\omega\omega_{p^2}}{\omega_c}. \tag{16}$$

When one takes into account the Doppler shift in cyclotron frequency, the helicon waves at a given magnetic field are strongly attenuated at frequencies above $\omega = \omega_c - v_F$ where v_F is the Fermi velocity of the electrons[11].

As can be seen from equation (6), the frequency of the helicon modes has a quadratic dependence on wave vector, the phase velocity is equal to $c(\omega_c\omega/\omega_p{}^2)^{1/2}$ which at a given frequency is considerably smaller than in the $\omega_c\tau_e \ll 1$ case. Also the k values at which the helicon and magnon modes cross are even larger than in the case $\omega_c\tau_e \ll 1$. In fact this crossover point will occur at higher k values than that for the phonon–magnon curves, and the crossing point between phonons and helicons will occur at even larger k values than that for the helicon–magnon modes. It should also be noted that the helicon–magnon coupling is much larger than the phonon–magnon coupling (i.e. $4\pi\omega_s \gg \Delta$).

A calculation of the detailed form of the dispersion curves of the coupled photon–phonon–magnon modes is much more difficult than in the case of insulators, particularly when the crossings of the photon–magnon curves occurs at wave vector values comparable or larger than those for phonons and magnons and has not as yet been carried out for the various conditions on $\omega_c\tau_e$. (When the photon and magnon curves cross at k values much smaller than the crossing point for photons and magnons, as in the case of very low conductivity, the situation is similar to that of the insulator case, and can be calculated fairly readily).

As in the case of insulators, there are three branches in the dispersion curves. At k approaching zero the modes correspond to coupled helicon-magnon modes whose frequency varies quadratically with wave vector (they have been observed by Grimes in nickel[12]); to modes with negligible magnon and photon content which correspond to acoustic phonon modes; and to modes at $\Omega_k = \omega_{0B} = \gamma_G B$ with negligible phonon content which correspond to coupled magnon–photon modes. At large values of k, the modes of the lowest branch have a frequency $\Omega_k = \omega_m - \Delta$ and are magnon in character; the modes of the next higher branch are acoustic phonon in character and the modes of the highest branch are photon in character; At intermediate k values, the modes will have mixed photon, magnon and phonon character. In those regions of ω and k where all three uncoupled modes come close to one another, the phonon, magnon and photon strengths of the coupled modes will be comparable to one another and it should be possible to excite the coupled modes either with incident acoustic waves or *EM* waves.

The attenuation of the coupled modes will be determined by the photon, magnon and phonon strengths and by the specific mechanisms which are responsible for the damping of the uncoupled modes.

The attenuation of the coupled modes via photon–electron excitations, the so-called eddy current damping, has been treated by Kittel[2] and Akhiezer[1], who consider it to be the dominant damping mechanism for coupled modes with an appreciable photon content. Other mechanisms, such as nonlinear interactions, have been discussed by Haas and Callen[7]. Since, as shown by Abraham[13] the damping of magnons via magnon–electron scattering is relatively small at low temperatures, the damping of the coupled modes with appreciable magnon content and negligible photon content is determined by other mechanisms, such as spin-lattice interactions.

4. EXPERIMENTS IN NICKEL

There have been relatively few investigations of acoustic wave propagation in ferromagnetic metals. Early investigators were primarily concerned with attenuation by domain-walls[15, 16] Luthi[14] have investigated acoustic birefringence in Ni in an external magnetic field for transverse waves propagating at right angles to the magnetic field and has obtained an estimate for the magneto-elastic coupling constant. However, they used a dispersion relation which neglected the coupling to photons and therefore neglected the role played by the electron excitations.

We have carried out low temperature (liquid Helium temperature) measurements of acoustic wave attenuation in Ni single crystal in an external magnetic field using a standard pulse echo technique. Transverse ultrasonic pulses, 2 μsec duration, at a frequency of 200–300 MHz were generated by *AC* cut quartz transducers attached to the Ni crystals with a low temperature (NONAC) cement. The Ni was cut and polished in an almost spherical, ellipsoidal shape with the unique axis parallel to[111] the easy magnetization axis, and with small flat faces parallel to the (111) planes. The resistivity ratio of the samples was 25 and, on the basis of magnetization measurements the samples were found to saturate at 1·9 kG. The use of frequencies above 100 MHz allowed us to obtain data on the attenuation of the coupled modes in the vicinity of the uncoupled acoustic phonon–magnon crossing point at magnetic fields well above saturation and thereby to avoid complications from domain wall damping.

Our data on the magnetic field dependence of the attenuation of transverse and longitudinal waves at 220 MHz ($\omega = 1{\cdot}2 \times 10^9$) for H_0 and **k** parallel to [111] are shown in Fig. 2. The structure which appears below 2 kG is due to domain wall effects. The attenuation of the transverse waves exhibits a peak at 2·3 kG. An estimate of the magnon frequency at this magnetic field [$\omega_{0H} = \gamma_G(H_0 - LM_s)$] which is extremely senitive to the value of the demagnetization factor (L), indicates that it is comparable to the frequency of the acoustic waves. The attenuation of the longitudinal waves is considerably smaller than the transverse waves and exhibits no appreciable dependence on magnetic field above 2 kG.

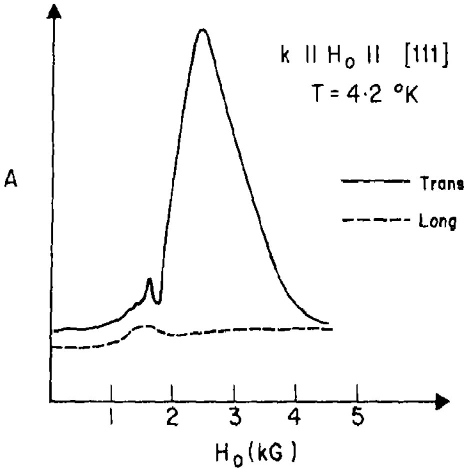

Fig. 2. The attenuation ($\mathscr{A}$) of *A* waves (220 MHz) in nickel at liquid helium temperatures. The full lines denote transverse sound waves while the dashed lines denote longitudinal sound waves.

On the basis of the measured resistivity ratio of 25, $\omega_c\tau_c$ is estimated to be of the order of 10^{-3}. Therefore, the appropriate dispersion relation to use corresponds to that given in equation (15) for the case where $\epsilon_2(\omega, k) \gg \epsilon_1(\omega, k)$. Furthermore, the acoustic phonon, magnon and photon curves are estimated to cross in the same region of frequency and wave vector. In this situation the nature of the coupled modes excited by incident acoustic waves is very sensitive to the parameters which determine $\epsilon(\omega, k)$ and $\mu(\omega, k)$. In the absence of detailed information about these parameters we have not attempted to calculate detailed dispersion curves at the present time.

We plan to carry out studies of the propagation of acoustic wave in high resistivity ratio crystals in order to observe the coupling of phonons and magnons with helicons. Since the coupled modes which are excited by incident acoustic waves in our experiments are an admixture of photons as well as phonons, it may be possible also to excite the coupled modes with incident EM waves. We plan also to investigate this possibility.

Acknowledgements—We wish to acknowledge valuable discussions with D. L. Mills and the assistance of P. J. Flanders in obtaining the magnetization curves for the nickel samples

REFERENCES

1. AKHIEZER A. I., BARIAKHTAR V. G. and PELETMINSKII S. V., *Soviet Phys JETP* **8** 157 (1959).
2. KITTEL C., *Phys Rev* **110**, 836 (1958) and SCHLOMANN E., *J. appl. Phys* **31**, 1647 (1960)
3. KITTEL C., *Quantum Theory of Solids* Wiley, New York (1967).
4. VARGA B., *Phys. Rev* **137A**, 1896 (1965) and BURSTEIN E., PINCZUK A. and IWASA S., *Phys Rev.* **157**, 611 (1967).
5. USHIODA S., PINCZUK A., TAYLOR W. and BURSTEIN E., *Proc Conf. on II–VI Semiconductor Compounds* (Edited by D. G. Thomas), p 1185. Benjamin, New York (1967).
6. LUTHI B., *Helv phys. Acta* **37**, 185 (1964).
7. HAAS C. W. and CALLEN H., *Magnetism* (Edited by Rado and Suhl), Vol 1, p 50. Academic Press, New York (1963).
8. STERN E. A. and CALLEN E., *Phys Rev* **131**, 512 (1963).
9. GLICK A. J. and CALLEN E., *Phys Rev* **169**, 530 (1968).
10. BUCHSBAUM S. J., *Plasma Effects in Solids*. Dunod, Paris (1964).
11. KJELDAS T., Jr., *Phys Rev* **113**, 147 (1959)
12. GRIMES C. C., *Plasma Effects in Solids* Dunod. Paris (1964).
13. ABRAHAM E., *Phys. Rev* **98**, 387 (1955).
14. LUTHI B., *Appl. Phys. Lett.* **8**, 107 (1966).
15. BOZORTH R. M., MASON W. P. and McSKIMIN H. J., *Bell Syst tech J* p 970, October (1951)
16. WEST F. G., *J appl. Phys* **29**, 480 (1958)

J. Phys. Chem. Solids Pergamon Press 1970. Vol. 31, pp. 1729–1733. Printed in Great Britain.

ULTRASONIC DONOR-SPIN RESONANCE IN GERMANIUM

T. ISHIGURO and N. MIKOSHIBA
Electrotechnical Laboratory, Mukodai, Tanashi, Tokyo, Japan

(*Received* 5 *September* 1969)

Abstract – Experimental results of ultrasonic spin resonance in As-doped Ge are presented The concentration of As atoms are between $1{\cdot}7 \times 10^{16}$ and $1{\cdot}4 \times 10^{17}$ cm^{-3} The anisotropic behavior, the intensity and the line width of resonant absorption are compared with either the theory of shallow impurity states, or the experimental results of ESR

1. INTRODUCTION

HASEGAWA[1] and Roth[2] investigated theoretically the spin-lattice relaxation of shallow donor states in germanium through a direct phonon process. The mechanism of the relaxation is due to a modulation of the g factor by lattice vibrations. In the ESR experiments under uniaxial stress, Wilson[3] found the anisotropy of the g value with respect to the magnetic field direction. It is expected, therefore, that an ultrasonic wave is absorbed resonantly by the donor spins via the direct phonon process[4] and the absorption measurement gives direct information of the spin-lattice relaxation mechanism. The observation of such an ultrasonic spin resonance (USR) in As-doped germanium has been reported by the present authors[5] and by Lockwood *et al.*[6].

In this paper the results of further experiments are described in detail and are compared with the theoretical results and with the experimental data on ESR[3]. The difference between experiment and theory of the absorption intensity pointed out in the previous paper[5] is discussed in more detail based on the concentration dependence of the resonant absorption without saturation effect. The concentration and temperature dependences of the linewidth ΔH (the magnetic field splitting of the absorption of half-maxima) are also discussed based on the simple model.

The theoretical expression of the absorption coefficient α[4] for isolated donors is given by

$$\alpha = (\pi N_d \hbar^3 \omega^4 / 2 g \mu_B \rho v_s^3 k T)$$
$$(g' \Xi_u / 3 g \Delta E)^2 F g(H), \qquad (1)$$

where ω is the angular frequency of the ultrasonic wave, ρ is the density, v_s is the sound velocity, T is the temperature, $g' = (g_l - g_t)/3$, $g = (g_l + 2g_t)/3$, g_l and g_t being the longitudinal and transverse component of the g tensor in a single valley of the conduction band, μ_B is the Bohr magneton Ξ_u is the deformation potential constant related to the shearing strain, ΔE is the valley-orbit splitting of the ground state, F is the anisotropy factor, and $g(H)$ is the shape function of the resonant absorption, $\int_0^\infty g(H)\mathrm{d}H = 1$. The anisotropy factor for the longitudinal wave propagating in the [110] direction is shown in Fig. 1.

2. EXPERIMENTAL PROCEDURE

The longitudinal ultrasonic wave of 9·26 ~ 9·38 GHz, which propagates in the [110] direction, is generated by the piezoelectric effect either in X-cut quartz bonded to a Ge sample or in ZnS thin film evaporated on the sample. Reflection of the pulsed acoustic power through the sample is gated, integrated and presented on a recorder as a function of magnetic fields. The experiments were performed in the liquid helium temperature range. Though the magnetic field was rotated in the (110) plane in the previous report[5], it is

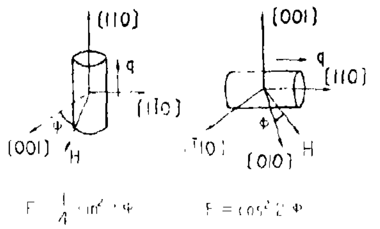

Fig. 1. Experimental configuration and corresponding anisotropy factor F.

now rotated in the (001) plane because of the larger absorption coefficient.

The samples were single crystals which were X-ray-oriented along symmetry axis, cut and polished. The concentrations of donors N_d and acceptors N_a were estimated from the Hall coefficient at 300°K, the Hall mobility at 77°K, and the ionized impurity scattering formula[7]. In Table 1 are tabulated the values of N_d, the compensation ratio $K = N_a/N_d$, and the sample lengths. The sample length was selected so that the fluctuation of N_d is less than 10 per cent throughout the sample.

3. EXPERIMENTAL RESULTS AND DISCUSSIONS

(a) *Saturation and large background absorption*

For the sample with highest concentration (GB7) in Table 1, any trial to observe an echo of ultrasonic waves of 9·3 GHz was in vain, because of very large non-resonant absorption in the sample. On the other hand, for the sample with concentration lower than $1{\cdot}7 \times 10^{16}\,\text{cm}^{-3}$ (GB1), it was not successful to observe the resonant absorption because of the saturation effect.

Table 1. Samples employed in the experiment. N_d donor concentration, K. compensation ratio, L: sample length

Sample	N_d ($10^{16}\,\text{cm}^{-3}$)	K (%)	l (mm)
GB1	1·7	25	13·9
GB2	7·2	5·5	10·7
GC4	8·5	8·2	12·4
GC6	14	9·2	8·4
GB7	25	4·1	13·1

It should be remarked here about the non-resonant background absorption. For the samples whose concentrations are less than $10^{17}\,\text{cm}^{-3}$, the relaxation absorption between the singlet and triplet of As donors[8] is less than 1 dB/cm[9]. On the other hand, in the samples whose concentrations are higher than $2 \times 10^{17}\,\text{cm}^{-3}$, some donor electrons can move freely throughout the sample and the Hall effect is measurable at liquid helium temperature[10], and hence an additive large absorption due to 'conduction' electrons appears[11].

In Fig. 2 is shown the acoustic power (P) dependence of the maximum attenuation coefficient (α_m) for GB2 at 1·5°K. The solid line in the figure represents the relation $\alpha/(1+aP)$ with the appropriate value of the saturation parameter a. In Fig. 2 is also shown the power dependence of ΔH, which increases with P in the highly saturated condition. In all cases it was impossible to measure α in the limit of $P \to 0$ in good S/N. Therefore, all of the data, except for the anisotropy, were obtained by extrapolating 6 data or more for the different acoustic power to the limit of $P \to 0$. As pointed out in Ref. [4], P should be less than about $10^{-5}\,\text{W/cm}^2$ in order to avoid the saturation. Since the power used was supposed to be $10^{-1} \sim 10^{-5}\,\text{W/cm}^2$, it is

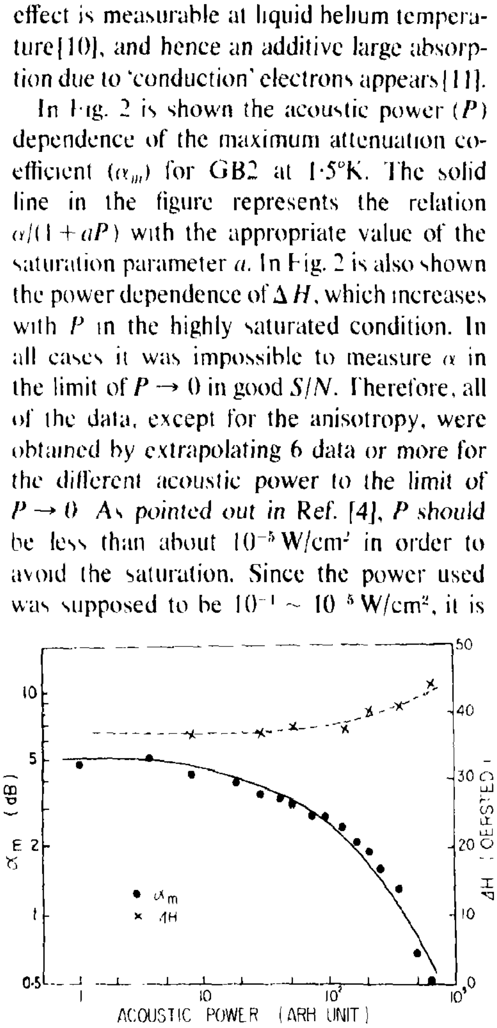

Fig. 2. Acoustic power dependence of the maximum amplitude of resonant absorption and the linewidth for the sample GB2 at 1·49°K and 9·268 GHz.

natural that we could not completely avoid the saturation[12].

(b) g *Value*

The g value obtained in our experiment was close to 1·570[3] and the deviations from this value were less than 0·3 per cent. The noticeable systematic deviation from this value was not observed. It was reported[3] that the change of the g value under the stress of the order of 10^3 g/mm^2 is several percents. Since the uniaxial stress by the microwave ultrasonic wave in our experiment is of the order of $10^{-1} \sim 10$ g/mm^2, the g shift due to the stress is negligible.

(c) *Line shapes*

In the samples used in this experiment, the hyperfine structure due to As nucleus is averaged out and the line shapes were close to the Gaussian type for GB1 and close to the Lorentzian type for GC6. The line shapes of GB2 and GC4 are rather close to the Lorentzian. Because of the different types of line shapes we take in what follows the absorption intensity $I = \int \alpha dH$ due to USR as the experimental data. This enables us to compare the experimental data with the theory without the influence of the line shapes.

(d) *Anisotropy*

Figure 3 shows the anisotropy of I with respect to the magnetic field direction under the experimental configuration shown in Fig. 1(b). The data were taken under the good S/N condition where we could not avoid the saturation effect. The anisotropy is well described by the formula of F in Fig. 1(b). On the other hand, ΔH shows the minimum in the [010] direction. In the configuration of Fig. 1(a), the decrease in ΔH with ψ is also observed[5]. Hence, the anisotropic behavior in USR is qualitatively consistent with that of ESR[3]. In the later section we discuss ΔH at $\phi = 0$, where the broadning due to dislocations is absent[3].

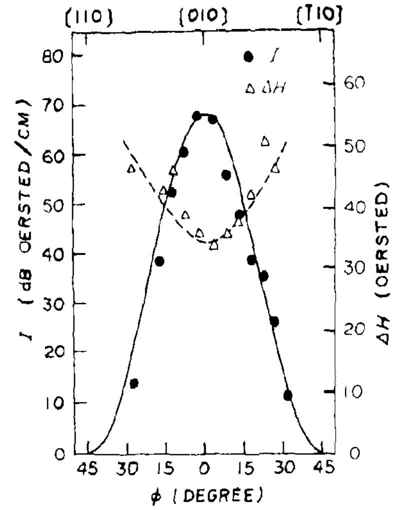

Fig. 3. Anisotropy of I and ΔH in the experimental configuration shown in Fig. 1(b) for the sample GC4 at 1·5°K and 9·340 GHz.

(e) *Concentration and temperature dependences*

The concentration dependences of I and ΔH are shown in Fig. 4 and the temperature dependences of I and ΔH are shown in Fig. 5 and Fig. 6, respectively. For the samples with lower concentrations I is proportional to $1/T$ (the Curie law), while for GC6 I deviates from the $1/T$ law. Such a deviation from the Curie law in the higher concentrations has been observed in the magnetic susceptibility[13] and in the intensity of ESR in Si[14] and attributed to the exchange interaction between donor electrons[15]. The evidence for exchange interaction is also seen from the results shown in Fig. 4, in which the experimental values of I deviates from the calculated value without exchange interaction. This calculated curve was obtained by equation (1) for isolated donors with the following numerical parameters: $g = 1{\cdot}57$, $g' = -0{\cdot}35$, $\Xi_u = 19$ eV, $\Delta E = 4{\cdot}15 \times 10^{-3}$ eV, $\rho = 5{\cdot}35$ g/cm^3, $v_s = 5{\cdot}44 \times 10^5$ cm/sec, and $\omega = 5{\cdot}84 \times 10^{10}$ sec^{-1}. In Fig. 4 is also shown a theoretical concentration dependence of I after Sonder and Schweinler[15], who treated the exchange

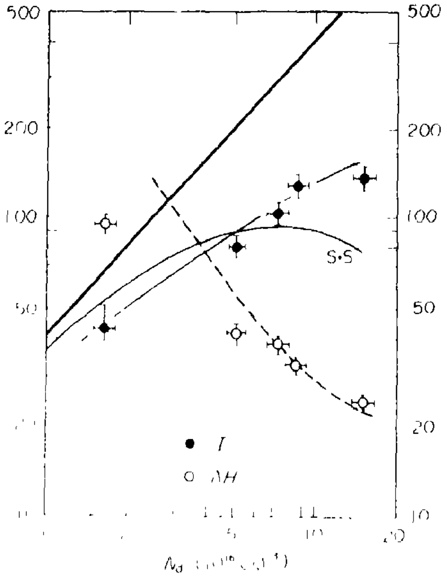

Fig. 4 Concentration dependence of the absorption intensity I and the linewidth ΔH at $\phi = 0°$ at $T = 1·5°K$. The thick solid line is the calculated absorption intensity for isolated donors and the thin solid line (S–S) is the corrected one after Sonder–Schweinler[15]

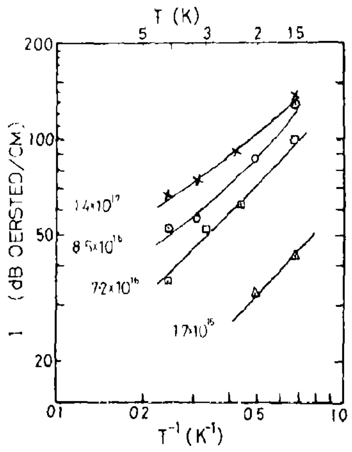

Fig. 5 Temperature dependence of I at $\phi = 0°$. All of the data are normalized to 9·3 GHz on the basis of ω^4 dependence as shown in equation (1).

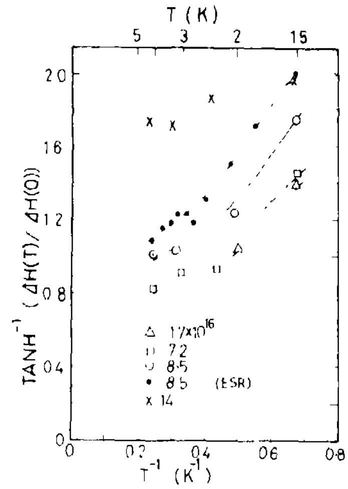

Fig. 6 Temperature dependence of ΔH for USR and ESR at $\phi = 0°$. As the value of $\Delta H(0)$ (ΔH at $T \to 0$) the following values are used: 108 oersted for (GB1), 42·5 oersted (GB2), 36 oersted (GC4) and 24 oersted (GC6) and 16·5 oersted (peak to peak linewidth of ESR measurement)

interaction between donor electrons on the basis of the hydrogen molecule model and the random distribution of donors. The absorption intensity is reduced from the Curie law by a factor $(3·7\,kT/m^*A)^{\alpha}(1+\alpha)^{-1}$ where α is N_d/Bm^{*3}, $A = 3·79 \times 10^{-2}$ eV, $B = 1·91 \times 10^{18}$ cm^{-3}, $m^* = 0·24$ for As atoms. This model for donor interactions explains the decrease of I qualitatively.

As mentioned in item (c), the hyperfine structure is averaged out and the line shape changes gradually from Gaussian to Lorentzian as the donor concentration increases. This feature indicates that the line shapes are motionally narrowed by hopping motion of donor electrons. In the case of motional narrowing, the concentration and temperature dependences are expressed by [3, 14]

$$\Delta H \propto \exp\,(2R_0/a_0)\,\tanh\,(|\Delta|/2kT), \quad (2)$$

where $R_0 = 0·62\ (N_d)^{-1/3}$, a_0 is an effective Bohr radius, and Δ is the activation energy for hopping. The dotted curve in Fig. 4 shows the concentration dependence of ΔH with $a_0 = 100$ Å, which value was obtained by Wilson[3] in the ESR experiment. This curve fits to the experimental data in the higher concentration, but deviates from the data in

GB1 where the motional narrowing is not complete.

Although the data of ESR[3, 14] have been analyzed by using equation (2), the temperature dependence of ΔH in USR cannot be described by equation (2) as shown in Fig. 6. In order to make clear the validity of equation (2) we performed an ESR experiment for the sample which has the concentration and dimension close to GC4. The peak to peak linewidth ΔH_p obtained by the modulation method shows the temperature dependence similar to that of USR (Fig. 6). This fact indicates that the effect of acoustic waves (USR) on the hopping motion is not different from that of electromagnetic waves (ESR).

(f) *Effective magnetoelastic coupling constant*

For Ge of cubic symmetry, magnetoelastic coupling matrix has two independent components G_{11}, and G_{44}[16], where $G_{11} = 0$ since a longitudinal stress applied along the ⟨100⟩ directions does not change the valley population and hence does not modulate the g tensor. Comparing the absorption coefficient given by equation (1) with that of the phenomenological expression[6, 16] the value of G_{44} for the isolated donors is given by the relation: $G_{44}^2 = (g'\Xi_u/3\Delta E)^2\pi/2$. This leads to $|G_{44}| = 670$ per unit strain. On the other hand the experimental data give the following values: $|G_{44}| = 530$ (GB1), 390 (GB2), 380 (GC4), 330 (GC6). The decrease of G_{44} value with increasing concentration may be due to the increase of the exchange coupling between donor atoms.

Note added in proof. The measurements of USR for the sample of $N_d = 5{\cdot}2 \times 10^{16}\,\text{cm}^{-3}$ and $K = 5{\cdot}0$ per cent were performed after the submission of this paper. The data are included in Fig. 4.

Acknowledgements – The authors would like to express their thanks to Professor W. Sasaki, Professor K. Shogenji and Dr. C. Yamanouchi for supplying the Ge single crystals. They are also indebted to Dr. S. Maekawa for his helpful discussion and for reading the manuscript and to H. Unoki and H. Ue for offering the facilities of ESR measurement. Finally they extend their thanks to members of Physics Division for their support in the course of this work.

REFERENCES

1. HASEGAWA H., *Phys. Rev.* **118**, 1523 (1960).
2. ROTH L. M., *Phys. Rev.* **118**, 1534 (1960).
3. WILSON D. K., *Phys. Rev.* **134**, A265 (1964).
4. MIKOSHIBA N., SUZUKI K., and ISHIGURO T., *J. phys. Soc. Japan* **24**, 337 (1968).
5. ISHIGURO T., MIKOSHIBA N., and SUZUKI K., *Phys. Rev. Lett.* **21**, 1340 (1968). The theoretical value of *I* quoted in this reference should be reduced by a factor of 2
6. LOCKWOOD H. F., ETZOLD K. F. and JOSEPHSON B. JR., *Phys. Rev. Lett.* **21**, 1471 (1968)
7. BROOKS H., In *Advances in Electronics and Electron Physics* **7**, 87 (1955).
8. POMERANTZ M., *Proc. IEEE* **53**, 1438 (1965)
9. SUZUKI K. and MIKOSHIBA N., *Phys. Lett.* **23**. 44 (1966); *ibid.* (errata) **23**, 560 (1966); KWOK P. C., *Phys. Rev.* **149**, 666 (1966)
10. YAMANOUCHI C., *J. phys. Soc. Japan* **20**, 1029 (1965).
11. ISHIGURO T. and MIKOSHIBA N., Unpublished
12. The description in Ref. [4] that the pulse-echo technique could avoid the saturation effect is not correct
13. DAMON D. H. and GERRITSEN A. N., *Phys. Rev.* **127**, 405 (1962).
14. MAEKAWA S. and KINOSHITA N., *J. phys. Soc. Japan* **20**, 1447 (1965).
15. SONDER E. and SCHWEINLER H. C., *Phys. Rev.* **117**, 1216 (1960).
16. DOBROV W. I., *Phys. Rev.* **134**, A734 (1964)

J. Phys. Chem. Solids Pergamon Press 1970 Vol. 31, pp. 1735–1740 Printed in Great Britain.

ELASTIC AND MAGNETOELASTIC EFFECTS IN RARE EARTH METALS*

T. J. MORAN and B. LUTHI
Physics Department, Rutgers, The State University, New Brunswick, N.J 08903, U S A

(*Received* 5 *September* 1969)

Abstract – The elastic and magnetoelastic properties of Gd, Tb, Dy and Ho are described as a function of temperature and magnetic field in the paramagnetic and ferromagnetic phases. It was found that the longitudinal sound velocity along the *c*-axis exhibits an H^2 field dependence in the paramagnetic state. In the ferromagnetic region it was found that Gd, Dy and Tb exhibited several competing magnetoelastic effects for shear sound waves propagating along the *c*-axis. A qualitative explanation of these effects is presented.

1. INTRODUCTION

PREVIOUS work in cubic ferromagnets such as the garnets[1] and magnetite[2] has led to a good understanding of magnetoelastic effects in these materials. In this paper we have extended the same type of measurements to the Rare Earth metals Gd, Tb, Dy and Ho. These metals, which are quite similar elastically, all have a hexagonal magnetic structure. This, coupled with the giant magnetostriction exhibited by them, makes them an interesting subject for investigation.

In this paper we begin with a section on the elastic properties in zero field and the effect of magnetic ordering on them. Then we describe magnetoelastic effects in the paramagnetic state and finally the magnetoelastic properties of Gd, Tb and Dy in the ferromagnetic state.

The measurements were made using the ultrasonic techniques described in Ref.[2]. The sound velocities for *c*-axis propagation and transition temperatures of the samples used are given in Table 1.

2. RESULTS AND DISCUSSION

(a) *Elastic properties*

Figure 1 shows the temperature dependence of the longitudinal sound velocity and attenuation along the *c*-axis in Gd. It can be seen from the figure that near the Curie temperature both the sound velocity and attenuation show large anomalies due to critical scattering effects [3, 4]. Around 220°K another anomaly of the same order of magnitude can be seen[5, 6]. In this temperature range the easy axis undergoes a sharp, continuous change from the *c*-axis to close to the basal plane[7, 8]. Below 220°K there is a slow change in the easy axis direction until it reaches a cone angle of approx. 40° with respect to the *c*-axis at 60°K. A saturating magnetic field will remove the anomalies in velocity[5] and attenuation indicating that they are caused by domain wall scattering. Similar effects were observed in magnetite near its easy axis change[2].

Tb, Dy and Ho show anomalies similar to the Curie point anomaly in Gd at their Neél points. The temperature dependences of the longitudinal sound velocities and attenuations have been given elsewhere (see Fig. 9 in Ref.[4]). Dy undergoes a first order transition to the ferromagnetic state at 85°K. Due to bond problems we were unable to measure the sound velocity changes through this transition. However, at higher temperatures in the antiferromagnetic state where we could measure, the sample could be driven ferromagnetic with

---

*Supported by the National Science Foundation.

Table 1. Sound velocities for c-axis propagation and transition temperatures

Sample	v_{long}	v_{shear}	T_N	T_c
GdII	2·9 . 10^5 cm/sec	1·6 . 10^5 cm/sec		290·1°K
Tb	2·9 . 10^5 cm/sec	1·66 . 10^5 cm/sec	227·6°K	222°K
DyB	2·95 10^5 cm/sec	1·7 . 10^5 cm/sec	177·0°K	85°K°K
Ho	2·95 . 10^5 cm/sec	1·7 . 10^5 cm/sec	132·1°K	

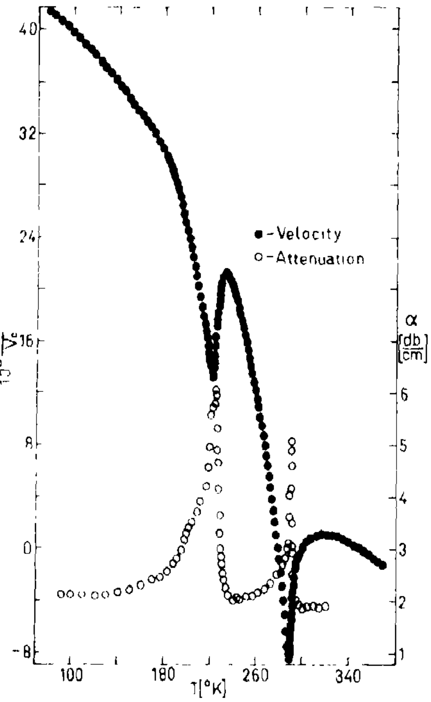

Fig. 1. Temperature dependence of the longitudinal ultrasonic attenuation and changes in the longitudinal sound velocity from the 300°K reference velocity in Gd. Sound propagation along the c-axis, ν = 50 MHz.

a sufficiently large field. Figure 2 shows the longitudinal sound velocity along the *c*-axis as a function of magnetic field at 167°K. The field is applied along the easy *a*-axis. It can be seen from the figure that between 12 kOe–15 kOe there is a very sharp jump in the velocity of about 2·7 per cent which indicates the onset of ferromagnetism. The figure has not been corrected for the magnetostrictive expansion which amounts to approximately 5 per cent of the total change shown [9].

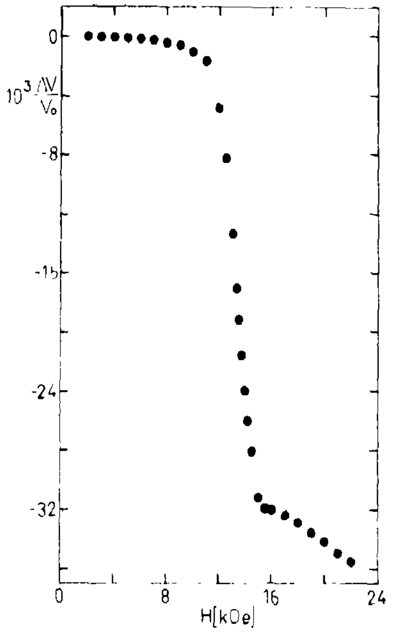

Fig. 2. Magnetic field dependence of the change in sound velocity from the zero field reference velocity in Dy when the sample is driven ferromagnetic. Sound propagation along the *c*-axis, *H* applied along the *a*-axis, *T* = 167°K.

(b) *Magnetoelastic effects in the paramagnetic region*

Figure 3 shows the magnetic field dependence of the longitudinal sound velocity along the *c*-axis in Dy for fields applied along the *a*-axis at various temperatures in the paramagnetic region. Figure 4 shows similar data for Ho. From both figures it can be seen that for reduced temperatures $(T - T_N)/T_N$ greater than 0·1 above the Neél points of Dy and Ho the velocities exhibit an H^2 field dependence. The data in these figures have not been corrected for magnetostrictive expansion which is

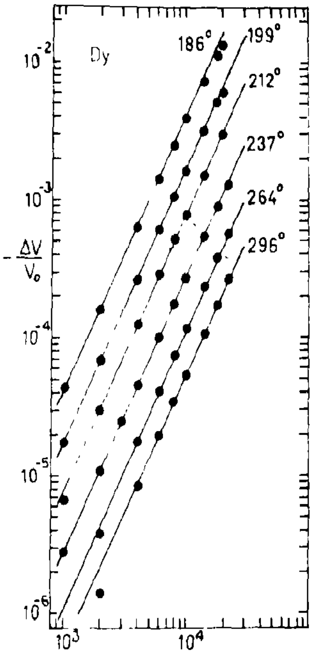

Fig. 3. Magnetic field dependence of the changes in longitudinal sound velocity from the zero field reference velocity in the paramagnetic state of Dy. Sound propagation along the c-axis, H applied along the a-axis.

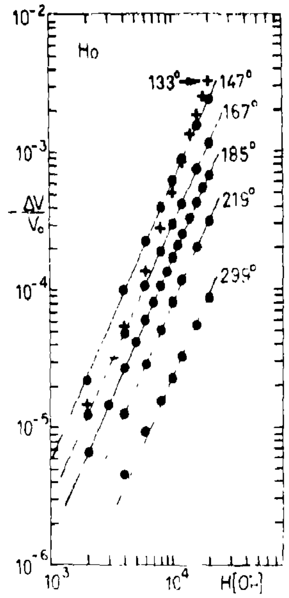

Fig. 4. Magnetic field dependence of the changes in longitudinal sound velocity from the zero field reference velocity in the paramagnetic state of Ho. Sound propagation along the c-axis, transverse H

estimated from published data[9, 10] to amount to about 5 per cent of the greatest change shown. This expansion also has an H^2 field dependence for temperatures outside the critical region[11].

For both materials the effect increases as the transition temperature is approached. Close to the transitions other effects such as suppression of critical scattering (see Fig. 11 in Ref. [4]) begin to appear. Critical suppression causes an increase in the sound velocity with field. In Fig. 3 the deviation at $T = 186°K$ is thought to be due to this effect. In Fig. 4 at $T = 133°K$ it can be seen that less of an effect is present at low fields, but there is an overall velocity decrease with field at a greater than H^2 rate. Both Tb and Gd show an H^2 dependence for $(T-T_n)/T_n > 0{\cdot}1$. Close to the transition they behave similar to Dy[4].

This behavior can be explained by means of the following spin-phonon Hamiltonian (written in an abreviated way):

$$H = \tfrac{1}{2}c\epsilon^2 + \sum_{ij} \partial J/\partial\epsilon\,\epsilon\,\mathbf{S}_i\,.\,\mathbf{S}_j + \sum_{ij} \partial^2 J/\partial\epsilon^2\,\epsilon^2\mathbf{S}_i\,.\,\mathbf{S}_j \tag{1}$$

where the first term denotes the elastic energy (c = elastic constant), the second the volume magnetostrictive part and the last a higher order term in the expansion of the exchange constant J in terms of the strain, ϵ. Similar single ion magnetostrictive terms can be included in (1).

The second term in (1) is the important spin-phonon coupling term responsible for the critical effects shown in zero field attenuation and sound velocity[4]. The last term in (1) did not have to be considered for these critical effects.

In the presence of a magnetic field this last term (or an equivalent single ion term) gives a contribution to the sound velocity proportional to χH^2 (χ = spin susceptibility). Hence it can be seen from Figs. 3 and 4 that $\partial^2 J/\partial\epsilon^2 <$

0 for Dy and Ho. Such is also the case for Gd and Tb which exhibit similar behavior far from the transition.

Close to T_n one observes critical suppression effects arising from the second term in equation (1). These are discussed in Ref. [4].

(c) *Magnetoelastic effects in the ferromagnetic state*

Figure 5 shows the field dependence of the shear sound velocity with propagation direction along the c-axis and polarization direction both parallel and perpendicular to the magnetization for Gd at 79°K and Tb at 140°K. Figure 6 shows a similar plot for Dy at 79°K and in addition a plot of the difference in the velocity changes for the two geometries after saturation. Tb exhibited the same type of behavior shown in Fig. 5 for all temperatures in the range of 220–140°K.

It can be seen in Fig. 5 that the large change in velocity from zero field to saturation (which might arise from domain effects) is isotropic in Gd. The difference in saturation fields is related to demagnetizing effects caused by the rectangular cross section of the sample used. For Tb it can be seen that the changes up to saturation are highly anisotropic with the absolute value of the change for the perpendicular mode geometry being almost three times that of the parallel mode. As can be seen from Fig. 6, Dy exhibits the same type of anisotropy, but in this material the parallel mode velocity increases with field. However, the absolute

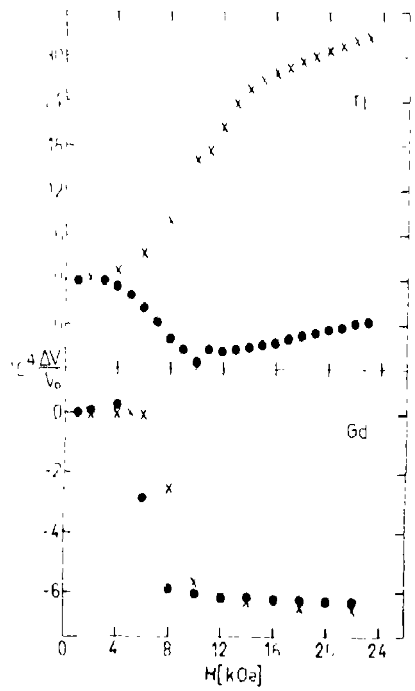

Fig. 5. Magnetic field dependence of the changes in shear sound velocity from the zero field reference velocity for Tb at 140°K (upper section) and Gd at 79°K (lower section). Sound propagation along c-axis. X, polarization perpendicular to H and parallel b-axis. ●, polarization parallel to H and b-axis.

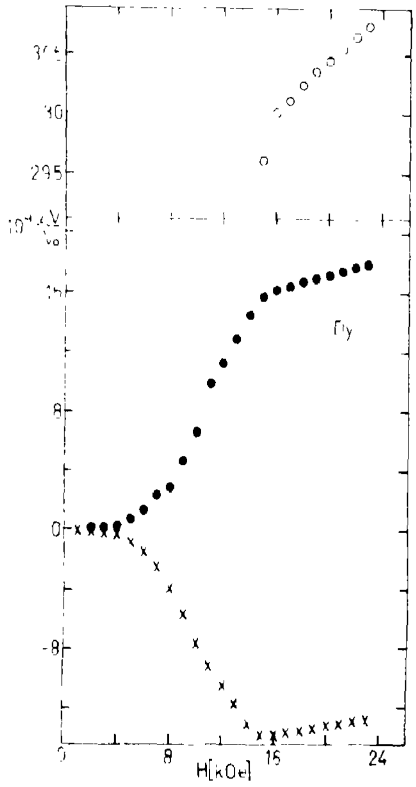

Fig. 6. (Lower section) magnetic field dependence of the changes in shear sound velocity from the zero field reference velocity for Dy at 79°K. Sound propagation along the c-axis. X, polarization perpendicular to H and a-axis. ●, polarization parallel to H and a-axis. (Upper section) Difference in the velocity changes of the two orientations shown in the lower section after saturation. $\Delta V/V_0(R\|H) - \Delta V/V_0(R \perp H)$.

value of the change is almost the same for the two modes.

After saturation at 10 kOe in Gd the mode parallel to the magnetization shows less of a decrease with field than does the perpendicular mode. In Tb, after saturation at 12 kOe, the perpendicular modes shows more of an increase with field and in Dy above 14 kOe the parallel mode shows more of an increase. The difference in the two modes for Dy is seen to be linear above saturation from the upper section of Fig. 6.

A linear theory of magnetoelastic interactions[1, 2] predicts that only the mode with magnetization and polarization parallel should show a field dependence after saturation. It was found in cubic materials[1, 2] that this *field dependence arose from a linear coupling* of spin waves and phonons. For hexagonal materials we obtain a dispersion relation for the coupled mode given by:

$$(\omega^2 - v^2k^2)(\omega^2 - \omega_m{}^2) = \sigma\gamma H, v^2k^2 \qquad (2)$$

where for $\mathbf{M}_0$ parallel to the a axis the spin wave frequency ω_m, is given by[12]:

$$(\text{Tb, Dy})\,\omega_m{}^2 = \gamma^2(H - NM_0 \pm 36K_6{}^6/M_0)$$
$$(H - NM_0 + 4\pi M_0 + 2K_2/M_0 \pm 6K_6{}^6/M_0)$$
$$(\text{Gd})\,\omega_m{}^2 = \gamma^2[H - NM_0][H - NM_0 + 4\pi M_0$$
$$-(2/M_0)(K_2 + 2K_4)] \qquad (3)$$

where $\sigma = \gamma(B^\epsilon)^2/\rho\mathbf{M}_0v^2$ is a measure of the strength of the interaction; k, the phonon wave vector; γ, the gyromagnetic ratio; v, the sound velocity; $\mathbf{M}_0$, the saturation magnetization; N, the demagnetizing factor; K_2, K_4 and $K_6{}^6$ are anisotropy constants; B^ϵ, the magnetoelastic coupling constant[11]; and ρ is the density.

From equation (2) the group velocity change with field (identical to the phase velocity change in this case) can be obtained easily (for $\omega_m \gg \omega$)[2]:

$$\Delta v/v_0 = -\gamma H\sigma/2\omega_m{}^2. \qquad (4)$$

For values of the anisotropy field large compared to the applied field ($2K_2/M_0 = 3\,.\,10^5$ G for Dy) this equation predicts a linear increase in velocity with field. If one assumes that the cause of the field dependence of the uncoupled mode is isotropic, the difference in the two modes would be the velocity change predicted by equation (3). It can be seen that the difference plotted in Fig. 6 for Dy is linear as predicted by theory. The coupling constant, B^ϵ, which is obtained from the difference in the two modes is $2{\cdot}7\,.\,10^8$ erg/cm^3 for Dy, in fair agreement with the value obtained from magnetostriction data[10] which is approximately twice that obtained above.

For Gd the difference in the two modes is very small, but it appears to have the field *dependence predicted by (3). However, the* coupling constant, $B^\epsilon = 9\,.\,10^7$ erg/cm^3 is almost three times the value obtained from magnetostriction data[13].

For Tb the difference in the two modes decreases instead of increasing and the absolute value of the change up to saturation is extremely anisotropic. In this case we have no reliable way to separate the different effects and compare them with theory.

It is thought that the field dependence of the coupled mode may arise from terms in the Hamiltonian similar to the last term in equation (1), or nonlinear terms not covered in this analysis.

In conclusion it appears that the rare earth metals exhibit very interesting effects arising from volume magnetostrictive type interactions as well as linear spin wave-phonon coupling. These effects are not well understood in detail yet.

REFERENCES

1. LUTHI B., *Appl. Phys. Lett.* **6** 234 (1965). *J. appl. Phys.* **37**, 990 (1966).
2. MORAN T. J. and LUTHI B., *Phys. Rev.* **187**, 710 (1969).
3. LUTHI B. and POLLINA R. J., *Phys. Rev.* **167**, 488 (1968).
4. LUTHI B., MORAN T. J. and POLLINA R. J., This Conference.
5. LONG M. Jr., WAZZAN A. R. and STERN R., *Phys. Rev.* **178**, 775 (1969).

6. Our sample GdI exhibited this anomaly at a temperature of 260°K, due to a different anisotropy resulting from impurities.
7. CORNER W. D., ROE W. C. and TAYLOR K. N. R., *Proc. phys. Soc. Japan* **17**, 1310 (1962).
8. GRAHAM C. D. Jr., *J. phys. Soc. Japan* **17**, 1310 (1962).
9. RHYNE J. J., Ph.D. Thesis, Iowa State Univ. (1965).
10. CLARK A. E., DeSAVAGE B. F. and BOZORTH R., *Phys. Rev.* **138**, A216 (1965).
11. CALLEN E. and CALLEN H., *Phys. Rev.* **139**, A455 (1965).
12. COOPER B. R., *Solid State Physics*, Vol. 21. Academic Press, New York (1968).
13. ALSTAD J. and LEGVOLD S., *J. appl. Phys.* **35**, 1752 (1964).

J. Phys. Chem. Solids Pergamon Press 1970. Vol. 31, pp. 1741–1758 Printed in Great Britain

SOUND PROPAGATION NEAR MAGNETIC PHASE TRANSITIONS*

B. LÜTHI, T. J. MORAN and R. J. POLLINA

Department of Physics, Rutgers, The State University, New Brunswick, N.J 08903, U.S.A.

(*Received 5 September* 1969)

Abstract—Experimental results on critical velocity and critical attenuation changes are presented and discussed Whereas the critical velocity changes show a uniform behavior for all substances studied, namely a frequency independent and a weak temperature dependent effect, the critical attenuation changes show a wide variety of behavior for different materials. A given substance can be characterized by the following physical parameters: spin structure (ferro- or antiferromagnet), magnetic anisotropy and range of spin interaction. In this way the rare earth metals Gd, Tb, Dy and Ho can be nicely accounted for by present theories. In insulators the coupling of the sound to the energy density of the spin system seems to be very important as shown in EuO, and also in $RbMnF_3$ and MnF_2 These latter antiferromagnets are not fully understood yet however. In addition other results (CoO, FeF_2) are discussed and results for Cr presented

1. INTRODUCTION

In the past, research in the field of phase transitions has been concentrated mainly on equilibrium phenomena. Systematic investigations of transport properties are scarce. Consequently equilibrium phenomena have been reviewed extensively recently[1–3]. Preliminary reviews of nonequilibrium phenomena can be found in Refs.[4, 5 and 6]. There exists a great variety of experimental techniques for the study of transport properties. In the case of magnetic phase transitions there are for example the tools of inelastic neutron scattering, electrical resistivity measurements, thermal conductivity and diffusivity experiments, ultrasonic propagation studies and NMR and EPR linewidth investigations.

The purpose of this paper is to review the field of ultrasonic propagation and thermal conductivity near magnetic phase transitions and to add some new results of critical attenuation and of critical changes of sound velocity. We concentrate our study on magnetic crystals exhibiting second order phase transitions, although some cases will be mentioned where the magnetic transition is more complicated.

It is now a well established fact[1–3] that equilibrium properties exhibit qualitatively and also quantitatively the same behavior near critical points for different phase transitions This fact is precisely brought out in the so-called scaling law theory (see Refs.[1] and [2]) which states that the various thermodynamic derivatives should depend only on one parameter, the so-called correlation length ξ, which measures the spatial extent of a fluctuation and which diverges on approaching the critical point T_c.

On the other hand, transport properties are not expected to show such a universality. In fact, as will be also shown in this article, a precise knowledge of the interaction Hamiltonian is required This is actually to be expected, since transport coefficients depend on transition rates which in turn depend sensitively on the matrix elements of the interaction. In the case of sound propagation near a magnetic phase transition the interaction Hamiltonian is the spin-phonon Hamiltonian.

Before we proceed we would like to list the main results of our study.

(1) The critical changes in sound velocity at magnetic phase transitions are frequency independent and have a rather weak temperature

---

*Supported by the National Science Foundation.

dependence (logarithmic: $(\Delta V/V) \propto -\omega^0 \ln \epsilon$ or a power law: $(\Delta V/V) \propto -\omega^0 \epsilon^{-\zeta}$ with the critical exponent $\zeta < 0{\cdot}2$), ϵ being the reduced temperature $\epsilon = (T - T_c)/T_c$ in agreement with theoretical predictions.

(2) The critical changes in sound wave attenuation closely follow a quadratic frequency dependence while the temperature dependence varies widely for different substances. The variation of the critical exponent η ($\alpha \propto \omega^2 \epsilon^{-\eta}$ where η should not be confused with the generalised Ornstein–Zernike η) can be characterized by the following parameters: Spin structure (ferro or antiferromagnets), degree of magnetic anisotropy of the spin interaction and range of the exchange interaction. For example the critical attenuation of the heavy rare earth metals Gd, Tb, Dy and Ho with rather long range exchange interactions can be very well explained by present theories, while insulators such as $RbMnF_3$ and MnF_2 are still not satisfactorily accounted for.

(3) In the case of thermal conductivity there exist very few relevant experiments, but they seem to be explicable along the same line as the ultrasonic attenuation.

In the next section we give a short presentation of the theories developed for these effects. After a brief survey of the experimental techniques we discuss the experimental results for the ultrasonic attenuation. After this we present and discuss the critical changes in sound velocity. These data will be for the most part new results. Finally we comment on thermal conductivity experiments and related topics.

2. THEORY

There have been a number of theories developed for the case of ultrasonic attenuation at magnetic phase transitions[7–13]. We shall review them by first discussing the spin-phonon coupling mechanism and by giving an expression for the critical attenuation coefficient. Then we discuss the theories by emphasizing the approximations made and their range of validity. Finally we mention the theory for the critical velocity change.

(a) *Coupling mechanism*

The spin-phonon interaction responsible for the critical effects arises in most cases via the strain modulation of the exchange interaction (volume magnetostrictive coupling). We shall discuss cases where the coupling arises through other processes such as single ion effects. With volume magnetostrictive coupling the interaction Hamiltonian reads [7, 14]:

$$H_{s-ph} = \sum_{i,\delta} \left(\frac{\hbar}{2M\omega_q}\right)^{1/2} \frac{1}{\delta}\frac{\partial J}{\partial \boldsymbol{\delta}} (q \,.\, \boldsymbol{\delta})(\boldsymbol{\delta} \,.\, \mathbf{e}_q) (b_q e^{iq\,\mathbf{R}_i} - b_q^\dagger e^{-iq\mathbf{R}_i}) \mathbf{S}_i \,.\, \mathbf{S}_{i+\delta}. \quad (1)$$

Here $\boldsymbol{\delta}$ is the vector connecting sites $\mathbf{R}_i$ and $\mathbf{R}_{i+\delta}$, $\partial J/\partial \boldsymbol{\delta}$ is the first Taylor expansion coefficient of the exchange interaction $J(\boldsymbol{\delta})$, b_q and $b_q^\dagger$ are the phonon operators, ω_q the soundwave frequency, M the mass of the crystal, $\mathbf{e}_q$ the polarization vector of the sound wave and S_i the spin on site i. It will be shown below that the critical sound attenuation experiments can be explained with this type of interaction. In particular we show that higher order terms in the phonon operators (scattering processes) need not be taken into account.

(b) *Expression for the critical attenuation coefficient*

By calculating the number of phonons with wavevector q absorbed minus those (induced) emitted one finds for the attenuation coefficient

$$\alpha\,[14]: \quad \alpha = \sum b(\delta,\delta',q) \int_0^\infty dt\, e^{i\omega t} e^{iq\,(\mathbf{R}_i - \mathbf{R}_j)} \langle \mathbf{S}_i \,.\, \mathbf{S}_{i+\delta} \mathbf{S}_j(t) \,.\, \mathbf{S}_{j+\delta'}(t) \rangle_{eq}$$

with

$$b(\delta,\delta',q) = \left(\frac{1}{\delta}\frac{\partial J}{\partial \delta}\right)^2 (\boldsymbol{\delta} \,.\, \mathbf{e}_q)(\boldsymbol{\delta}' \,.\, \mathbf{e}_q)(\boldsymbol{\delta} \,.\, \mathbf{q})(\boldsymbol{\delta}' \,.\, \mathbf{q}) (1 - e^{(\hbar\omega_q/KT)})(2eM\hbar\omega)^{-1}. \quad (2)$$

Equation (2) shows that α is proportional to the space time Fourier Laplace transform of a four-spin correlation function. This result, the starting point of all further calculations, can also be derived with arguments from irreversible thermodynamics[7, 15]. As in the case of Brownian motion, the sound attenuation coefficient can be expressed as an integrated time dependent correlation function of random forces originating from the spin phonon interaction (1). With the random stress $F_q = \partial H_{s-ph}/\partial \epsilon_q$ (ϵ = strain) equation (2) is readily obtained.

(c) *Conventional theories*

For the evaluation of the four-spin correlation function the aforementioned theories can be divided into 2 groups, the so-called conventional theories[7–10] and the improved theories due to Kawasaki[11] and Laramore–Kadanoff[13]. We outline below the main steps and assumptions of the conventional theories, which are rather transparent, and we indicate the improvements[11, 13] on these theories afterwards. We follow closely the arguments given by Kawasaki[10].

The conventional theories make three approximations:

(1) Factorization of the four-spin correlation function: for the paramagnetic region one is then left with products of two two-spin correlation functions:

$$\alpha_q = \sum_{\delta\delta' k} B(\delta,\delta',q,k) Re \int_0^\infty e^{i\omega t} dt \, \langle \mathbf{S}_k \mathbf{S}_{-k}(t) \rangle \langle \mathbf{S}_{k+q} \mathbf{S}_{k-q}(t) \rangle \tag{3}$$

where the two-spin correlation functions are Fourier transformed and B is the corresponding Fourier transform of b in equation (2). One expects this factorization to break down close to T_c [8].

(2) Use of the hydrodynamic form for the two spin correlation function: Although one has a k-sum in equation (3) one assumes the hydrodynamic form $\langle S_k S_{-k}(t) \rangle = \langle S_k S_{-k} \rangle e^{-t/\tau_k}$ which is valid only for $k\xi \ll 1$ with ξ = correlation length and where τ_k is the characteristic decay time of the spin fluctuations. For an isotropic ferromagnet it has the form [16] $1/\tau_k = Dk^2$ with D = spin diffusion coefficient. With $\langle S_k S_{-k} \rangle \propto \xi^2$ equation (3) becomes, neglecting the sound wave vector q compared to k,

$$\alpha \propto \int d^3k \frac{\xi^4 1/\tau_k}{\omega^2 + 1/\tau_k^2}.$$

(3) Approximation: $\omega \ll 1/\tau_c$. With this approximation the attenuation becomes finally

$$\alpha \propto \frac{\omega^2 \chi^{1/2}}{1/\tau_c} \tag{4}$$

where χ is the spin susceptibility, $\tau_c = \tau_{k\sim\xi^{-1}}$, and where we have indicated the ω^2 dependence of α stemming from the linear q dependence of H_{s-ph} (equation (1)). Any experimental evidence giving support to a ω^2 dependence of α will indicate that the H_{s-ph} (equation (1)) is sufficient and that one has not to go to higher order terms in the phonon variables (see Section 4).

Equation (4) indicates that the 'critical slowing down' of the spin fluctuations[16], $1/\tau_c$, enhances the singularity in the attenuation, α. This is a consequence of the third approximation which says that compared to the transit time of a sound wave the spin fluctuation decay time is still much shorter despite the critical slowing down.

Using the various expressions for τ_c[17, 18] one gets from equation (4) the temperature dependence or critical exponent, η, ($\alpha \propto \omega^2 \epsilon^{-\eta}$, ϵ = reduced temperature) for the conventional theories shown in Table 1. Tani and Mori[7] evaluate the correlation function differently. We list their values separately.

(d) *Theories of Kawasaki and Laramore–Kadanoff*

The conventional theories tend to overestimate the effect of correlations. This can be shown, for example, by calculating the specific

Table 1. Theoretical exponent η for critical ultrasonic attenuation in ferro (F)-and antiferro (AF)-magnets

	Isotropic		Anisotropic	
	F	AF	F	AF
Tani and Mori[7]	1	1		
Conventional theories[8–10]	$\frac{7}{3}$	$\frac{5}{3}$	$\frac{3}{2}$	$\frac{1}{2}$
Kawasaki[11], Laramore-Kadanoff[13]	$\frac{5}{4}$	1	$\frac{4}{3}$	$\frac{4}{3}$
energy density coupling	0	0		

heat using the above approximations; the result is[8] $C \propto \chi^{1/2}$. In fact, as pointed out by Bennett[19], if one replaces correspondingly in equation (4) $\chi^{1/2}$ by C one gets

$$\alpha \propto \frac{\omega^2 C}{1/\tau_c} \tag{5}$$

which is essentially the result of the improved theories[11–13]. These theories, while retaining the third approximation and the hydrodynamic form of the spin fluctuations, manage to circumvent the first two approximations. Kawasaki[11] uses scaling law arguments to determine the four-spin time-independent correlation function, Laramore and Kadanoff [13] use the mode-mode coupling theory of Kadanoff and Swift[20] to estimate the correlation function. The result of these calculations (equation (5)) for the various cases can be found in Table 1.

It is important to stress that the third approximation mentioned above is common to all these theories. Because τ_c diverges as one approaches T_c, this condition will be violated as one gets close enough to T_c. We shall dwell on this particular point later on in Sections 4(b) and (d).

(c) *Coupling to energy fluctuations*

An important variant of these theories outlined above occurs if the H_{s-ph} (1) is proportional to the exchange Hamiltonian, H_{ex}; e.g. if in the corresponding expressions

$$H_{s-ph} = \sum_i A e^{i\mathbf{q}\cdot\mathbf{R}_i} z_i' b_i \mathbf{S}_0 \cdot \mathbf{S}_{R_i},$$

$$H_{ex} = \sum_i z_i J_i \mathbf{S}_0 \cdot \mathbf{S}_{R_i} \tag{6}$$

each individual term of H_{s-ph} is proportional to the corresponding term in H_{ex}. Here A is the amplitude of the sound wave, z_i is the number of neighbors ($\mathbf{R}_i$) for a given site 0. z_i' is in general, however, different from z_i, e.g. in general the sound wave couples only to part of the spin energy density. Two examples shall illustrate this ($\hat{\mathbf{q}}$ = soundwave propagation direction): (1) EuO ($z_1 = 12, z_2 = 6$); $\hat{\mathbf{q}} = (1,0,0)$: $z_1 = 8$, $z_2 = 2$; $\hat{\mathbf{q}} = (1,1,0)$: $z_1' = 2+8$ (different coupling strength), $z_2' = 4$; $\hat{\mathbf{q}} = (1,1,1)$: $z_1' = 6$, $z_2' = 6$. (2) RbMnF$_3$ ($z_1 = 6$, $z_2 = 12$); $\hat{\mathbf{q}} = (1,0,0)$: $z_1' = 2$, $z_2' = 8$, $\hat{\mathbf{q}} = (1,1,0)$: $z_1' = 4$, $z_2' = 2+8$ (different coupling strength), $\hat{\mathbf{q}} = (1,1,1)$: $z_1' = 6$, $z_2' = 6$.

So only in the case of propagation along the (1, 1, 1) direction for RbMnF$_3$ and with the neglect of next nearest neighbor coupling, is the spin-phonon coupling truly a coupling to the energy density of the spin system.

If this holds, then the attenuation is proportional to an energy-energy correlation function instead of a four-spin correlation function:

$$\alpha_q \propto \omega^2 \int_0^\infty dt\, e^{i\omega t} \langle E_q E_{-q}(t) \rangle . \tag{7}$$

Now $\langle E_q E_{-q}(t) \rangle = \langle E_q E_{-q} \rangle e^{-\Lambda q^2 t}$ with $\Lambda = \kappa/C$ = energy diffusion constant, κ = spin thermal conductivity. In this case $q\xi \ll 1$ as well as $\omega \gg \Lambda q^2$ (kinematical slowing down) is well obeyed so that

$$\alpha_q \propto \omega^2 \frac{\kappa}{V^2}. \tag{8}$$

Hence the critical attenuation is directly proportional to κ. This fact was noted by various people[7, 13, 21, 22].

A factorization approximation type of calculation[23] and scaling law arguments[24] show κ to be nondivergent for an isotropic ferromagnet. For an isotropic antiferromagnet the situation is less clear. Two different applications of scaling laws showed in one case κ to be nondivergent[24] and in the other case[25] divergent as $\epsilon^{-1/3}$. A factorization type of calculation[26] again shows κ to be nondivergent. The corresponding values for the critical attenuation exponent are listed in Table 1.

(f) *Critical changes in sound velocity*

There exist, so far, three calculations[27-29] of the change in sound velocity as one approaches T_c and they give the result

$$\frac{\Delta V}{V} \propto -\omega^0 C. \tag{9}$$

This result is valid independent of whether the material is ferro or antiferromagnetic, isotropic or anisotropic. The reason for this is the fact that the spin fluctuation relaxation time, τ_c, does not enter equation (9). One also notes that $\Delta V/V$ is frequency independent.

Equation (9) can be obtained, in principle, by using second order perturbation theory to calculate the frequency shift of sound waves due to the spin phonon interaction, H_{s-ph} (1). Here we demonstrate how this result follows from a simple thermodynamic model[30, 31]: Consider the free energy to be composed of an elastic part and a magnetic part; $F = (B\epsilon^2/2) + Tf(T/T_c)$ where B is the bulk modulus, ϵ the strain and where the magnetic part shall have the simple functional dependence shown. With $T_c = T_c(V)$, the total isothermal bulk modulus is $B_T = V(\partial^2 F/\partial V^2)_T = B - (1/T_c)(\mathrm{d}T_c/dV)^2 C_v$ where $C_v = -T(\partial^2 F/\partial T^2)_V$ and where we have neglected terms involving $\partial^2 T_c/\partial V^2$. The isothermal sound velocity is $v = v_0 - (v_0^2/2BT_c)(\mathrm{d}T_c/\mathrm{d}V)^2 C_v$ (with v_0 = sound velocity far away from T_c) which is of the form of equation (9). In this model the adiabatic and isothermal sound velocities give the same behavior close to T_c, because[32] $v_{ad} = v_T - (T\beta^2/2Cp)v_T{}^3\rho$ where β = differential thermal expansion.

In summary, the theories discussed above are capable of producing a variety of critical attenuation exponents, dependent on whether the material is ferro- or antiferromagnetic, isotropic or anisotropic and whether or not the sound wave couples to the energy density of the spin system (see Table 1). The velocity changes on the other hand are predicted to have no such variety.

3. EXPERIMENTAL TECHNIQUES

We shall discuss two types of experiments: ultrasonic attenuation and velocity measurements. In both cases we employed a pulse-echo technique.

For the attenuation measurements we measured successive echo heights using a calibrated attenuator. This has advantages over amplitude measurements of a single echo in that it is relatively insensitive to electronic nonlinearity, instability and changes in the acoustic impedance of the bond material. To get the critical attenuation one has to subtract a background attenuation arising from other sources (anharmonic terms, imperfections, spurious geometric effects). This one can do by measuring the attenuation change far above the critical temperature and then extrapolating the background attenuation into the critical region. For the heavy rare earth metals with their similar elastic properties, one can test this extrapolation procedure by comparing the background attenuation of these samples in the same temperature range. One usually gets a good estimate for the background attenuation by measuring to $\epsilon \sim 0{\cdot}1$ above T_c. In MnF$_2$ we were forced to measure to much higher temperatures. A bad choice for the background attenuation may seriously affect the critical exponent η.

For the velocity measurements we used a phase comparison method[33] capable of detecting transit time changes to 1 part in 10^7.

Bond instabilities can seriously affect these measurements as was noticed in $RbMnF_3$. The choice of the background velocity change is more ambiguous than in the attenuation case. One usually takes a linear extrapolation of the high temperature slope[21, 29, 34]. However, since it turns out that the critical velocity changes usually have a much weaker dependence on temperature, the background choice is not so critical. A correction for the nonlinear thermal expansion is usually necessary to obtain the velocity changes from the transit time data.

For the thermometry, we used thermocouples or germanium resistors. The temperature resolution with thermocouples was about 20 mdeg and with germanium resistors about 1 mdeg. Great care was usually taken to ensure thermal equilibrium conditions and small thermal gradients (measured with differential thermocouples).

4. EXPERIMENTAL RESULTS AND DISCUSSION

We start with a discussion of the spin-phonon coupling mechanism, then present the critical sound attenuation and then discuss the critical changes in sound velocity. Finally we review the thermal conductivity experiments.

(a) *Coupling mechanism*

In previous publications[35, 36] we have shown that the coupling mechanism responsible for critical attenuation is of volume magnetostrictive nature. This we did by demonstrating that shear waves only experience critical behavior for propagation in off-symmetry directions. In such directions a shear wave always has longitudinal components. This result is compatible with the form of the spin phonon interaction Hamiltonian of equation (1). Physically it means that the change in length of the vector connecting the two spin sites is of first order in the strain for a longitudinal wave, but of second order in the strain for a shear wave propagating along a symmetry axis. One can estimate the coupling strengths for the volume magnetostrictive coupling from the pressure dependence of the Curie temperature, or from forced magnetostriction experiments, or from the anomalous thermal expansion effect; and for the linear magnetostrictive coupling, from linear magnetostriction experiments.

There are some cases where shear waves propagating along symmetry directions experience critical behavior, because the linear magnetostrictive (single ion) coupling constants are rather large: Dy[36, 18] and CoO [37]. Cr[18], as an itinerant antiferromagnet, is a special case. They will be discussed below. Coupling constants for the various materials, normalized to reduce magnetization, are shown in Table 2.

(b) *Critical attenuation*

We classify the investigated materials into 4 categories: (1) rare earth metals (2) ideal Heisenberg ferro- and antiferromagnets (3) other insulators (4) itinerant magnets.

(1) *Rare earth metals*. The heavy rare earth metals are known[38] to have localized magnetic moments composed of the 4*f* electrons and to have a long range exchange interaction via conduction electrons. This long range interaction, together with considerable single ion magnetocrystalline anisotropies, is responsible for the complicated spin structures found in these materials in the ordered state.

In previous publications[35, 36] we have shown extensive measurements of these materials. Here we would like to add two important results: (a) We have measured another Dy-sample (Dy *B*) of different origin than the Dy *A* (Table 2) and have found the same critical exponent as for Dy *A*. The roll off region due to impurities[36] in Dy *B* was slightly different from the one in Dy *A*, but did not affect the power law region. (b) From magnetoelastic studies[39] in our Gd 1 sample [35] we noticed a strange anisotropy behavior of this crystal. Subsequent measurements on a new crystal Gd 2 gave a critical exponent of

Table 2. Various physical properties of the crystals

	Material origin of our crystals	T_N, T_c	Anisotropy parameter a	Coupling constant (normalized to reduced magnetization) B_l (10^6 erg/cc)	B_{shear} (10^6 erg/cc)	Sound velocities along (001) at 300°K v_l (10^5 cm/sec)	v_s (10^5 cm/sec)
Gd I	IBM	290·4					
Gd II	α-crystals	290·1	$5\cdot10^{-4}$	9000	20	2·9	1·6
Tb	Metals Research	227·6	−0·4	7500	1280	2·9	1·6
Dy A	IBM	177·3					
			−0·3	6000	1440	2·95	1·7
Dy B	Metals Research	177·0					
Ho	IBM	132·1		2200	460	2·95	1·7
EuO	IBM	69·4	$4\cdot10^{-3}$	2700	40	4·6	2·7
$RbMnF_3$	IBM	83	$5\cdot10^{-6}$		0·2		
MnF_2	Optovac Inc	67·3	$3\cdot10^{-2}$	1300		6·25	2·8
FeF_2			0·6				
CoO		289·3		3000	2000 40000 (long)		
Ni		630					
Cr	Metals Research	311				6·6	3·8

$\eta = 1\cdot6$ compared to $\eta = 1\cdot2$ for Gd 1 (see Fig. 1).

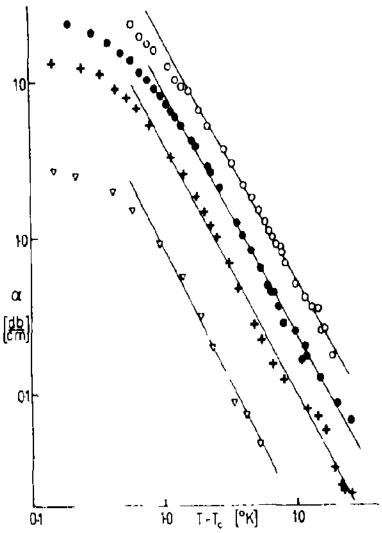

Fig. 1 Temperature dependence of critical longitudinal ultrasonic attenuation in Gd 2 along c-axis ∇, 10 MHz ($\eta = 1\cdot70$); +, 30 MHz ($\eta = 1\cdot62$), ●, 50 MHz ($\eta = 1\cdot63$), o, 70 MHz ($\eta = 1\cdot57$)

The long range nature of the exchange interaction[38] makes these rare earth metals good candidates for a description by the Kawasaki, Laramore–Kadanoff theories[11–13] discussed in Section 2(d). From Table 3 we see that for these materials η lies between 1·0 and 1·6; the same range as the theories predict. One can go even further in comparing theory and experiment by classifying these materials according to the anisotropy parameter, a[40] (Table 2). $a = 5\,.\,10^{-4}$ for Gd makes Gd an isotropic substance in the ϵ-range considered. Therefore, $\eta = 1\cdot6$ for Gd 2 fits nicely with theoretical predictions. The case of Dy, Tb and Ho requires special attention for the following reason: The strong uniaxial anisotropy in these crystals (Table 2) forces the spins to lie in the hexagonal plane. With no hexagonal anisotropy present, the spin dynamics in this case is equivalent to the isotropic Heisenberg antiferromagnet[41]. However, Tb and Dy have significant hexagonal anisotropies. For Tb at $T = 0$ the spin-wave energy gap $\Delta = ((36K_6^6/M)(2K_2/M))^{1/2} \simeq 10^5$ G, which is very large. Therefore, one can classify Tb and Dy as anisotropic materials. The exponent η of 1·24 and 1·37 for these

Table 3. Comparison of experimental and theoretical critical exponents

Material	ϵ-range	$\eta_{\exp}$	References	η_{theor}
Gd II	$10^{-3}-10^{-1}$	$1{\cdot}63 \pm 0{\cdot}1$	this work	$\frac{5}{3}$
Tb	$7\cdot10^{-3}-7\cdot10^{-2}$	$1{\cdot}24 \pm 0{\cdot}1$	[36]	$\frac{4}{3}$
Dy A		$1{\cdot}37 \pm 0{\cdot}1$	[36]	
	$3\cdot10^{-3}-10^{-1}$	$1{\cdot}26 \pm 0{\cdot}1$	this work	$\frac{4}{3}$
Dy B		0·8 (shear)	[36, 18]	
Ho	$3\cdot10^{-3}-10^{-1}$	$1{\cdot}0 \pm 0{\cdot}1$	[36]	$1, \frac{4}{3}$
EuO		0	[21, 44]	0
RbMnF$_3$	$4\cdot10^{-3}-4\cdot10^{-2}$	$0{\cdot}28 \pm 0{\cdot}05$	this work	?
		0·32	[46]	
MnF$_2$	$10^{-3}-3\cdot10^{-2}$	$0{\cdot}13-0{\cdot}16$ $\pm 0{\cdot}02$	[53], this work	$1, \frac{4}{3}$
FeF$_2$		$0{\cdot}75 \pm 0{\cdot}08$	[54]	$\frac{1}{2}$
Ni	$3\cdot10^{-3}-3\cdot10^{-2}$	1·4	[58]	1·4
Cr	$3\cdot10^{-3}-3\cdot10^{-2}$	$4{\cdot}24 \pm 0{\cdot}6$ $1{\cdot}77 \pm 0{\cdot}2$ (shear)	this work	

two materials then lies very close to the theoretically predicted one of $\frac{4}{3}$. The case of Ho is not clear at present due to lack of sufficient experimental information. We tentatively classify it as a borderline case between isotropic and anisotropic[36, 18]. The exponent $\eta = 1{\cdot}0$ for Ho compares favorably with theoretical predictions for an isotropic antiferromagnet.

Additional evidence that these rare earth metals can be well described by theory, has been given by Laramore and Kadanoff[13] who calculated the absolute magnitude of the critical attenuation using known coupling constants. Their agreement with experiment [36] is surprisingly good, indicating that for the rare earth metals not only the temperature and frequency dependence, but also the magnitude of the effect is well understood.

The observed roll off in critical attenuation close to T_N in these materials[36] is believed to be an impurity effect and not a breakdown of conditions such as $\omega\tau_c \ll 1$ (Section 2 (c), (d)) or $k\xi \ll 1$, which would show a marked frequency dependence contrary to observations (see Section 4(d)).

Critical shear wave attenuation: In Dy we also observed shear wave critical attenuation along the c-axis[36]. In this case the spin phonon coupling is of linear magnetostrictive (single-ion type) character. The particular form of the interaction Hamiltonian and a conventional type of theory for this case was discussed elsewhere[18]. The result of this study was that one can simultaneously explain semiquantitatively both the different critical exponent (Table 3) and the smaller effect compared to the corresponding longitudinal attenuation.

(2) *Ideal Heisenberg ferro- and antiferromagnets*. EuO[42] and RbMnF$_3$[43] are good examples of ideal Heisenberg ferro- and antiferromagnets. The range of the exchange interaction is predominantly only nearest neighbor and the anisotropy factor a is small (Table 2).

EuO. In EuO no evidence for critical attenuation was found[21, 44] both for longitudinal and shear waves along (100) and (110) crystallographic directions for the frequency range 10–200 Mc/sec. Instead, what one finds is a sharp increase in attenuation below T_c. This attenuation can be removed with the application of a moderate magnetic field[44], indicating that this increase is due to sound wave-domain wall interactions. From coupling constant considerations (Table 2), a noticeable critical attenuation effect should be observable for the measured frequency range [21].

The absence of any noticeable critical attenuation was explained with the coupling of the soundwave to the energy density of the spin system[21], as explained in Section 2(e). As noticed there, $z_l' \neq z_l$ for any symmetry direction in EuO. Therefore, the sound wave spin energy density coupling is not complete, although this may result only in a reduction factor for equivalent sites and nearest neighbor coupling only. The additional experimental evidence to support this conjecture, namely the proportionality between the magnetic specific heat C and the differential thermal expansion β, has been checked only for $|T-T_c| > 5°\text{K}$, a region where the Pippard relations[45] still seem to hold. Due to the approximate nature of this sound wave energy density coupling in EuO, we expect the occurrence of critical attenuation at higher frequencies; a search for it was started in our laboratory.

$RbMnF_3$. Contrary to EuO, antiferromagnetic $RbMnF_3$ has been shown to exhibit a clear critical attenuation effect[46, 47] with a critical exponent $\eta \sim 0{\cdot}3$. In Fig. 2 we show results from our study of a (111) oriented single crystal[48] for the frequency range 70–230 MHz. Included in the figure for comparison is Golding's result for 150 MHz. From the results, one can clearly see two power law regions with corresponding critical exponents; $\eta = 0{\cdot}28$ for $\epsilon < 4 \,.\, 10^{-2}$ and $\eta = 0{\cdot}7$ for $\epsilon > 4 \,.\, 10^{-2}$. It should be emphasized that the high temperature power law exponent has a somewhat larger error due to the sensitive background attenuation correction. In both regions α follows closely a ω^2-law. Such a two power law region has been observed in other substances as well: MnF_2 and CoO to be discussed below, but not in the rare earth metals.

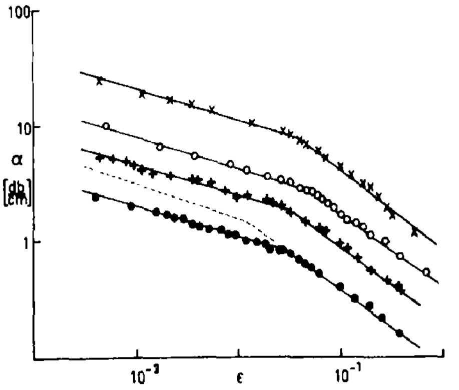

Fig. 2. Temperature dependence of critical longitudinal ultrasonic attenuation in $RbMnF_3$ along a (111)-direction. ●, 70 MHz ($\eta = 0{\cdot}28$); +, 110 MHz ($\eta = 0{\cdot}27$); 0, 150 MHz ($\eta = 0{\cdot}28$); ×, 230 MHz ($\eta = 0{\cdot}28$). ---- Golding's 150 MHz result for (100)-direction

There have been several suggestions to explain both the critical exponent $\eta = 0{\cdot}3$ and the break in power law for $\epsilon \sim 4 \,.\, 10^{-2}$.

We have already discussed in Section 2e the diverging views[24–26] with regard to the effect of a sound wave-energy density coupling in an isotropic antiferromagnet. It should be pointed out again that for sound propagation along a (111) direction in $RbMnF_3$ the sound wave-energy density coupling is complete if only the nearest neighbor interaction is important. Further theoretical work is needed to clear up whether $\eta = 0$ or $\frac{1}{3}$ in this case.

Other attempts to explain the experimental results have included spin-lattice[49] or spin energy-lattice relaxation[22] terms. The idea is that whereas the critical spin relaxation time is temperature dependent $\tau_c^{-1} = \omega_x \epsilon$, the spin lattice relaxation time τ_L is only weakly or not dependent on ϵ. Therefore, each relaxation process dominates in a different ϵ-region. In this way one could account in principle for the two power law regions as well as for the two critical exponents. For the Mn^{2+}-ion typically $\tau_l \sim 10^{-8}$ sec, so with $\tau_c^{-1} \sim 10^{12}\,\epsilon$ the crossover region $\epsilon_0 \sim 10^{-4}$ is too small. In addition, it is not clear how quantitatively the two values $\eta = 0{\cdot}3$ and $0{\cdot}7$ would follow, although precisely such values are stated in Ref. [49].

Another relaxation mechanism, coupling of the spin motion to the F^{19} nuclear spin system, again did not give the correct order of magnitude for the break in the power law region and had to be discarded[13].

In summary it seems that further work is needed to completely explain these interesting phenomena (see also Section 4 d).

From Fig. 2 we deduce for $\epsilon < 4 \,.\, 10^{-2} (\alpha_{111}/\alpha_{100}) \simeq 2{\cdot}6$.

(c) *Other insulators*. Here we discuss the results on MnF$_2$, FeF$_2$ CoO. Since these substances have quite different anisotropy factors and coupling constants, we discuss them separately.

MnF$_2$. The first evidence[50] of critical attenuation was found in MnF$_2$. Subsequently it was investigated at different places[18, 51, 52, 53]. Below we show some of our results. Figure 3 gives the total attenuation vs. temperature for various frequencies along the c-axis. In Fig. 4 we show the critical attenuation deduced from Fig. 3 in a power law plot. We noticed that in order to estimate the background attenuation correctly we had to measure more than 40°K above the Néel point.

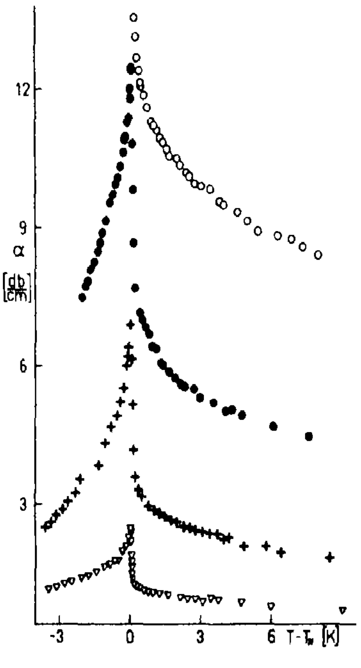

Fig. 3. Attenuation of sound in MnF$_2$ along (001)-direction. ∇, 15 MHz, +, 30 MHz; ●, 50 MHz; 0, 70 MHz.

This may explain the lower critical exponent deduced from this experiment[18, 53] compared to some reported[51, 52] higher ones. What can be seen clearly from Fig. 4 is a break in the power law, similar to the one found in RbMnF$_3$, but now for $\epsilon \simeq 0{\cdot}1$. Similar behavior can be seen in the results of Ref. [53]. The frequency dependence of the critical attenuation turns out to be $\omega^{1{\cdot}8}$, still close enough to ω^2 to warrant a quadratic frequency dependence. Ikushima[53] shows similar results, except his frequency dependence is $\omega^{1{\cdot}6}$.

From Table 3 one sees that the most reliable values for the critical exponents close to T_c are $\eta = 0{\cdot}13$–$0{\cdot}16$ for different propagation directions. These values are much smaller than any theoretical predictions. For $\epsilon > 0{\cdot}1$, $\eta \simeq 1$. The anisotropy parameter, $a = 3 \,.\, 10^{-2}$ (Table 2) for this material, suggests that it is a border line case between isotropic and anisotropic for the ϵ-range considered. Although one cannot explain at present the critical exponent η, it seems that the anisotropy of both the critical attenuation and critical velocity changes are fairly well understood [29, 53] by assuming different coupling constants for different propagation directions.

FeF$_2$. This material has the same crystal and magnetic structure as MnF$_2$, but the magnetocrystalline anisotropy is much larger than in MnF$_2$ (Fe^{2+} has a large single ion in anisotropy, Table 2). This makes it an attractive substance to test the theory for anisotropic materials. Ikushima's[54] result of $\eta = 0{\cdot}75$ for longitudinal waves, although quite a bit larger than say MnF$_2$, is not in agreement with the theoretical predictions $\eta = \frac{1}{4}$. The large single ion anisotropy of this substance suggests that single ion magnetoelastic coupling may perhaps be non-negligible compared to the volume magnetostrictive coupling. For longitudinal attenuation along the c-axis, these 2 mechanisms should give, however, the same type of singularity theoretically.

CoO. In CoO Ikushima[37] found a slightly

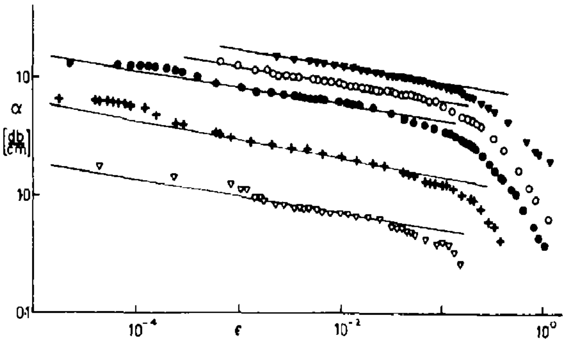

Fig. 4. Temperature dependence of critical longitudinal ultrasonic attenuation in MnF$_2$(001). ▽, 15 MHz ($\eta = 0{\cdot}140$); +, 30 MHz ($\eta = 0{\cdot}151$); ●, 50 MHz ($\eta = 0{\cdot}136$); ○, 70 MHz ($\eta = 0{\cdot}142$); ▼, 90 MHz ($\eta = 0{\cdot}136$).

stronger critical effect for shear waves than for longitudinal ones. The frequency dependence was approximately linear. The results indicate, again, two power law regions.

CoO exhibits a cubic tetragonal crystallographic transformation at the para-antiferromagnetic phase transition. In addition, the spin structure in the ordered state is a multi spin axis antiferromagnet[55]. According to Kanamori[55] (Table 2) the linear magnetoelastic coupling constants are of the same order or even larger than the volume magnetostrictive one. One consequence is that shear waves must exhibit a critical attenuation effect as observed. It is clear that CoO with these peculiar properties is not a good candidate for description by the idealized models.

The same remark applies to the case of EuSe, which also exhibits strange magnetoelastic properties at the phase transition[56]. EuSe is believed to have a first order phase transition to a complicated spin structure at $T_N = 4{\cdot}6$°K[57].

(4) *Itinerant ferro- and antiferromagnets.* We discuss briefly critical attenuation results for Ni and Cr.

In Nickel, critical effects on sound propagation have been observed[58]. In the temperature region where the condition $\omega\tau_c < 1$ is fulfilled (see Section 2(d)), the power law exponent was $\eta = 1{\cdot}4$ in rather good agreement with the Kawasaki and Laramore–Kadanoff theories. It should be emphasized that in Ni the range of the exchange interaction is longer than in any of the insulators. In addition, in Ni, due to its high T_c and high purity, it was possible to measure close enough to T_c so that the condition $\omega\tau < 1$ broke down. The measurements showed a frequency dependent transition to this region where the attenuation and velocity extremas showed a marked frequency dependence[58].

In Cr we studied a single crystal of moderate purity (electrical resistance ratio of 300). Figures 5 and 6 show power law plots of ultrasonic critical attenuation for longitudinal and shear waves with propagation direction along a (110) axis. They yield quite unusually large effects with $\eta_l = 4{\cdot}24$ and $\eta_{sh} = 1{\cdot}77$. From the results in these two figures it follows that equally good fits would probably have been possible for temperature-dependences other than a power law dependence. It should be emphasized that we found a quadratic frequency dependence for both longitudinal and shear critical attenuation and not a linear one as reported in the literature[59].

Theoretically, critical sound attenuation for itinerant magnets has just started to be calculated[60]. In view of the special nature of the magnetic behavior of Cr, especially its phase transition of the first order[61, 62], no attempt

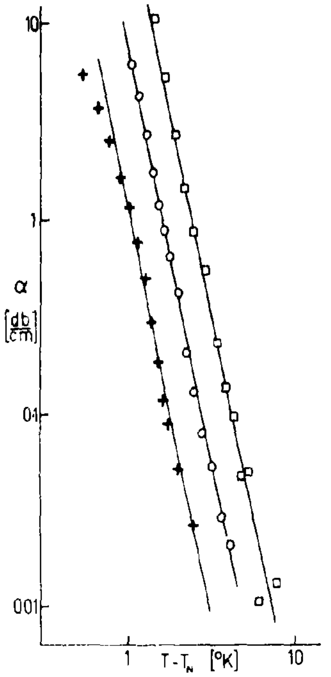

Fig. 5. Temperature dependence of critical longitudinal ultrasonic attenuation in Cr (110). +, 30 MHz ($\eta = 4{\cdot}24$), ○, 70 MHz ($\eta = 4{\cdot}20$), □, 150 MHz ($\eta = 4{\cdot}28$).

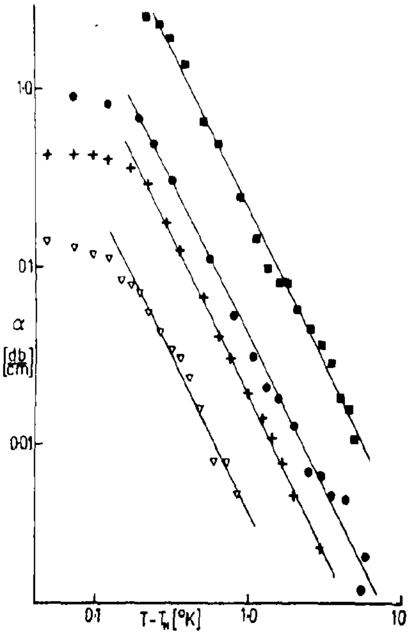

Fig. 6. Temperature dependence of shear ultrasound in Cr (110). ▽, 14 MHz ($\eta = 1{\cdot}76$); +, 30 MHz ($\eta = 1{\cdot}77$), ●, 50 MHz ($\eta = 1{\cdot}76$; □, 130 MHz ($\eta = 1{\cdot}77$).

is made here to analyze and interpret our data.

(5) *Attenuation below the critical point.* Very little information is available on the critical attenuation in the ordered region. The formation of domains seriously interferes with the critical attenuation and presents another attenuation mechanism for sound waves via domain wall interactions. In certain cases, such as for the *c*-direction propagation in MnF_2, this effect should be rather small. Our measured critical exponent for the attenuation in this case is $\eta = 0{\cdot}05$ compared to $\eta_{+} = 0{\cdot}15$ above T_N. It is usually found that $\eta < \eta_{+}$. No theory has been developed for this case yet.

In summary, we can conclude that critical sound attenuation is well understood for the rare earth metals. The insulators are much less well understood, mainly because their short range spin interaction permits other forms of spin phonon coupling such as phonon-spin energy density. In addition it seems that other relaxation mechanisms have to be taken into consideration than just the critical relaxation of spin and energy fluctuations.

(c) *Critical changes in sound velocity*

Although there have been several indications of critical velocity changes near T_c [21, 46, 63, 64], a quantitative test of equation (9), such as frequency and temperature dependence has been carried out only recently [29, 34]. Here we would like to discuss these results and present more experimental results for $RbMnF_3$ and the rare earth metals Gd, Tb, Dy and Ho.

(1) *$RbMnF_3$.* In $RbMnF_3$ we encountered experimental problems due to bond breaks as discussed in Section 3 [48]. The scatter of the experimental results in Fig. 7 is due to this cause. Nevertheless, within the error limit, the critical velocity change is frequency independent as shown previously for Dy [34]. The minimum in the velocity change occurred, within the temperature resolution of 10 mdeg, at the same temperature as the attenuation maximum. Figure 8 shows a semilog plot

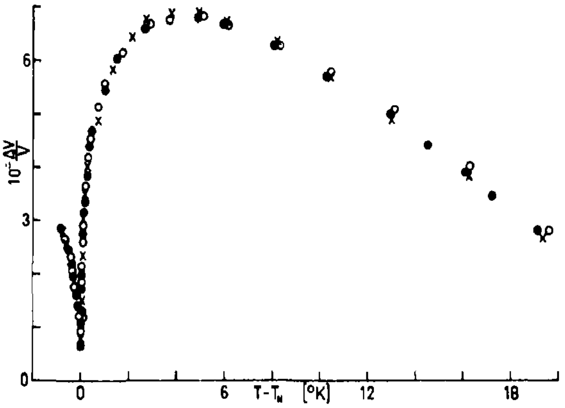

Fig. 7 Critical velocity change in $RbMnF_3$ (111) ×, 30 MHz, ●, 50 MHz, ○, 70 MHz.

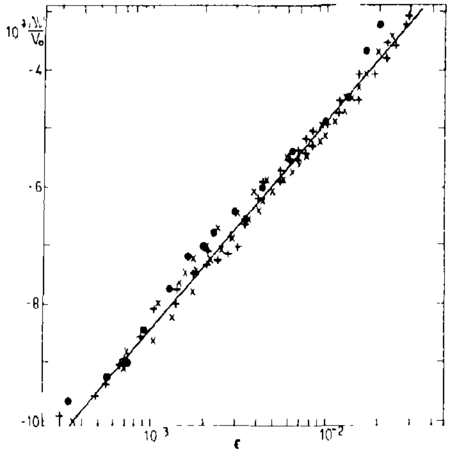

Fig. 8 Temperature dependence of critical velocity changes in $RbMnF_3$ (111) (linear background subtracted) ●, 30 MHz, ×, 50 MHz, +, 70 MHz.

taken from the data of Fig. 7 with a linear background correction, as in the case of EuO [21]. The semilog plot of Fig. 8 is obeyed for 2 decades in the reduced temperature, indicating a rather nice agreement with the theoretical prediction of equation (9). From our results and the ones of Ref. [64], we get an anisotropy

$$\left(\frac{\Delta V}{V_0}\right)_{111} \Big/ \left(\frac{\Delta V}{V_0}\right)_{100} = 1{\cdot}2 \pm 0{\cdot}3.$$

(2) *MnF_2*. In MnF_2 there exist measurements of critical velocity changes for different crystallographic directions, performed on the same crystal[29]. The results again show a frequency independent temperature variation. The critical exponent for the velocity changes is 0·12, small enough to compare favorably with theoretical predictions (equation (9)). In addition, the anisotropy observed in the velocity change could be explained in the same manner as that observed for the attenuation [53].

The case of EuO we discuss in Section 4(e).

(3) *Rare earth metals*. For the rare earth metals Gd, Tb, Dy and Ho we found the velocity minimum consistently at a smaller temperature than the attenuation maximum as shown, for example, in Fig. 9 for Ho. The insert in Fig. 9 shows that at T_N (attenuation peak) the velocity curve changes slope, indicating that the attenuation maximum must be regarded as the critical point, a procedure we followed in the evaluation of our results. The differences between T_N and the velocity minima are 1°K for Gd II, 0·17°K for Dy B and 0·9°K for Ho. A similar behavior was observed before in MnTe[63]. Figure 10 shows a semilog plot for the rare earth metals. The backgrounds were estimated again as linear extrapolations from the higher temperature slopes as in Fig. 9. Thermal expansion corrections were also applied and amounted to

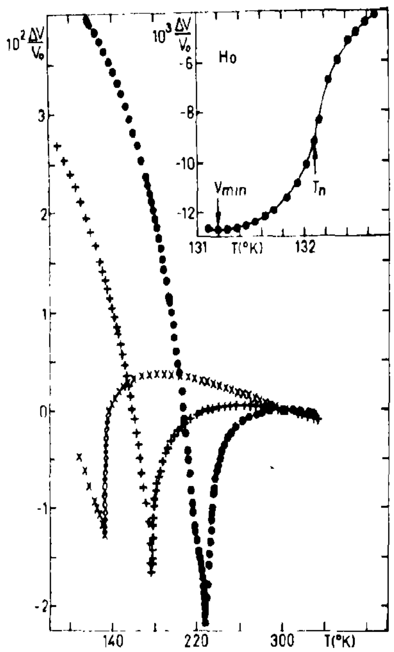

Fig. 9. Changes in sound velocity for rare earth metals (corrected for thermal expansion) ×, Ho; +, Dy; ●, Tb. The inset is an expanded plot of the velocity change near T_N in Ho.

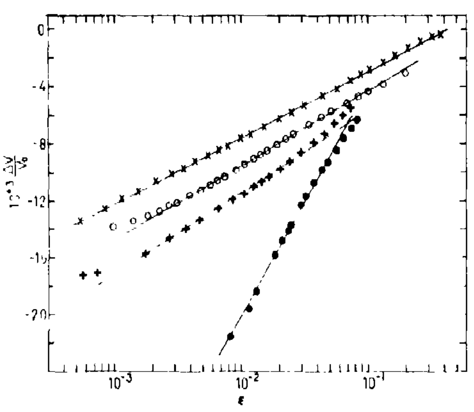

Fig. 10. Temperature dependence of critical velocity changes (linear background subtracted) ×, Ho, ○, Gd; +, Dy; ●, Tb (Arbitrary origin for the velocity scale)

a change of 5 per cent. Figure 10 shows that a logarithmic temperature dependence is well obeyed in these substances, with ϵ ranges similar to the ones for the attenuation[36].

(d) *Relaxation time for spin fluctuations*

It was pointed out[28, 29] that the ratio of the critical velocity changes to the critical attenuation gives the relaxation rate or the sum of relaxation rates if more than one relaxation mechanism is present. Equations (5) and (9) give

$$\frac{1}{\tau} \simeq -\frac{\omega^2}{V_0'} \frac{\Delta V/V_0'}{\alpha} \tag{10}$$

Equation (10) was tested with reasonable success for Dy[34].

First we use this relation to verify that the third approximation $\omega\tau_r \ll 1$, common to all the ultrasonic attenuation theories involving sound-spin fluctuation coupling (see Section 2(c) and (d)), is well obeyed for the rare earth metals. We choose for each metal the temperature where the impurity induced roll off in attenuation begins and the power law region ends, because this is the temperature region most likely to affect this condition. Defining ν' as $2\pi\nu'\tau = 1$, we get for Gd II: $\epsilon = 3 \,.\, 10^{-3}$, $\nu' = 300$ MHz; Tb: $\epsilon = 8 \,.\, 10^{-3}$, $\nu' = 1100$ MHz; Dy: $\epsilon = 2{\cdot}5 \,.\, 10^{-3}$, $\nu' = 2100$ MHz; Ho: $\epsilon = 3 \,.\, 10^{-4}$, $\nu' = 600$ MHz. So the result is that the condition is still fulfilled to a good degree for the frequency range measured and that the interpretation of the rolling off region as an impurity effect, valid.

Secondly, relation (10) can be used to analyze the less well understood cases such as $RbMnF_3$ and MnF_2: In $RbMnF_3$, from Fig. 2 and Fig. 8 we get for the smallest $\epsilon = 4 \,.\, 10^{-4}$ a $\nu' = 400$ MHz. To test a possible violation of the condition $\omega\tau \ll 1$, for example, a check on the frequency dependence of the critical attenuation is worthwhile. As shown in Fig. 2 there are no indications of such a violation up to 230 MHz, for which $\omega\tau \sim 0{\cdot}6$. Note that no such condition would occur if the coupling of the sound would be to the energy density of the spin system (see Section 2(e)).

Even more stringent is the condition for MnF_2[29] where for $\epsilon = 10^{-3}$, $\nu' = 60$ MHz. Again, however, an approximate ω^2-law for the attenuation is still observed.

The first clear experimental evidence of sound propagation in a region where $\omega\tau < 1$ no longer holds was given for Nickel[58], as discussed in Section 4(b4).

The conclusion of this Section is that while the rare earth metals are well described by the Kawasaki and Laramore–Kadanoff theories, this is not the case for the insulating antiferromagnets, $RbMnF_3$ and MnF_2. The persistence of an ω^2 law in the attenuation, despite the violation of $\omega\tau \ll 1$, suggests strongly that the coupling mechanism involves, at least in part, coupling to the spin energy density[22, 29, 53].

(e) *Sound velocities in an applied magnetic field*

Preliminary data on the effect of a magnetic field on the changes in velocity near the magnetic phase transition are given in Fig. 11. Here is plotted the relative change for a 10 kOe field $v(H,T)-v(O,T)/v(O,T)$ vs. $T-T_N$. Similar results for higher fields were obtained. Surprisingly enough, these changes are for the most part still negative changes and only close to $T_c(\epsilon \leq 0{\cdot}1)$ does one notice a positive trend indicating a suppression of critical fluctuations. In order to understand these results one has to take recourse to a more general interaction Hamiltonian than equation (1) which we write in a less detailed way:

$$H_{\text{int}} = \sum_{ij} \frac{\partial J}{\partial \epsilon} \epsilon \mathbf{S}_i \,.\, \mathbf{S}_j + \frac{1}{2} \sum_{ij} \frac{\partial^2 J}{\partial \epsilon^2} \epsilon^2 \mathbf{S}_i \,.\, \mathbf{S}_j \qquad (11)$$

where we write simply the strain ϵ for the phonon variables. The first term in (11) was responsible for the effects of critical attenuation and critical velocity changes in zero field. The second term was not included for the critical attenuation because it would lead to a ω^1 attenuation dependence not observed in the experiment (see Section 4(b)) and it was not included for the critical velocity changes because it would not exhibit any divergence [27, 29]. In the presence of a magnetic field, however, this second term gives a contribution proportional to H^2, a dependence observed by the results shown in Fig. 11 for $\epsilon > 0{\cdot}1$ [39]. The first term gives a contribution proportional to H^4, a dependence only observed for Holmium for $\epsilon \simeq 0{\cdot}05$[39]. Depending on the magnitude of $\partial^2 J/\partial \epsilon^2$, the critical suppression for $\epsilon < 0{\cdot}1$ is more or less pronounced. The biggest effect can be seen for Gd and only an indication of it for EuO (Fig. 12). The critical suppression of the sound velocity change, seen for $\epsilon < 0{\cdot}1$, means a suppression

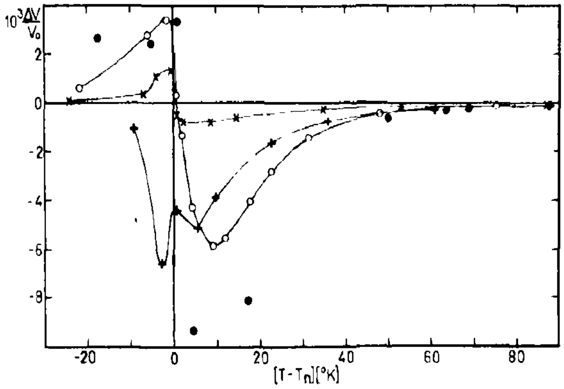

Fig. 11 Difference in the longitudinal sound velocity at 10 kOe from that at 0 field. $[v(10\,\text{kOe}, T) - v(O, T)]/V(O, T)$ as a function of temperature. ○, Gd; ●, Tb; +, Dy, ×, Ho The velocities are not corrected for magnetostrictive length changes which amount to *ca* 5 per cent of the change at each temperature

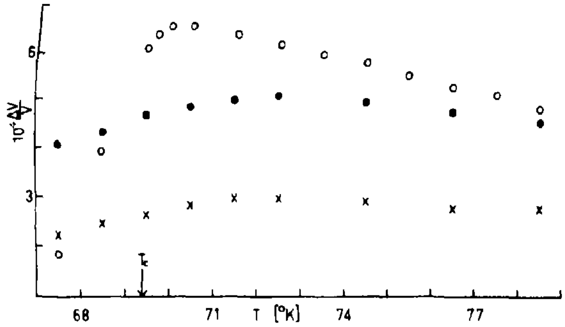

Fig. 12. Critical change in sound velocity in EuO with constant applied magnetic field ○, $H = 0$ kOe, ●, $H = 6$ kOe; ×, $H = 18$ kOe. The data has been corrected for field dependent thermal expansion (see text).

of the specific heat C in a magnetic field according to equation (9). It is well known that measurements of specific heat near T_c only give a suppression of C close to T_c, but an increase farther out[31, 65, 66]. This additional effect is superimposed on the effect described above of $\partial^2 J/\partial\epsilon^2$. It is particularly important for EuO.

In Fig. 12 we show velocity changes for $H = 0·6$ and 18 kOe for EuO. The $H = 0$ curve is the same as in Ref. (21). Field dependent thermal expansion corrections[66] were applied. From this figure one can notice again an H^2-dependence for $T - T_c > 5$°K and a weaker dependence closer to T_c. That we do not see a more clear cut suppression of critical fluctuations in this case has again to do with the particular dependence of $C(H)$ (see the analogous $\beta(H)$-dependence for the differential thermal expansion for the same fields in Ref.[66]). Finally, Fig. 13 shows velocity changes as a function of magnetic field near T_c. The pronounced dip at 1 kOe in the ordered region is a rather interesting domain wall effect. Its suppression at $T = 69·4$ gives a more accurate determination of T_c than the onset of attenuation did[21, 44].

So this magnetic field dependence of the velocity changes in the paramagnetic region exhibits a number of interesting effects which one can describe qualitatively. Analogous measurements for the critical attenuation are in progress in our laboratory.

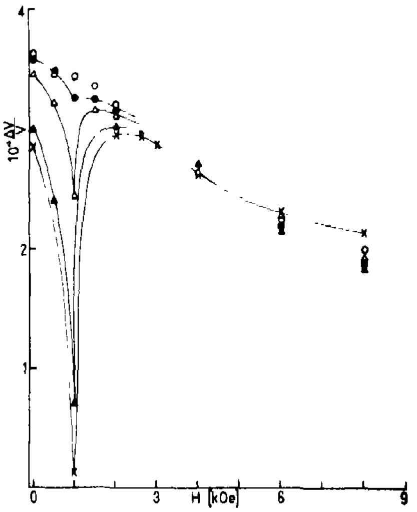

Fig. 13. Determination of T_c in EuO from isotherms of velocity changes as a function of magnetic field. ○, 69·6°K ●, 69·4°K, △, 69·3°K; ▲, 69·1°K, ×, 68·9°K $T_c = 69·4 \pm 0·1$°K

(f) *Thermal conductivity experiments*

Thermal conductivity experiments and ultrasonic attenuation experiments are closely related. In fact, in the expression for the thermal conductivity[14], $\kappa = \frac{1}{3}\sum_q C v^2 \tau_q$, part of the relaxation rate $1/\tau_q$ is directly related to the critical sound wave attenuation, $1/\tau_q^c = \alpha_q v$ (v = sound velocity). Thus taking all the other possible scattering mechanisms into account, a simple q-integration gives $\kappa(T)$. This simple relationship is true as long as $T_c \ll \theta_D$ = Debye temperature; e.g. as long as $\omega = vq$ is a good approximation for the thermal phonon.

Theoretically, in the case of thermal conductivity, only the phonon-spin energy density coupling (Section 2(e)) was considered and since the lowest order process does not give a singularity, higher order processes had to be taken into account[14, 67]. But, of course, the more general phonon-spin coupling (Section 2) gives an effect in lowest order as in the ultrasonic attenuation and has to be considered as well.

A number of experiments have been performed which gave an effect, namely, a dip in thermal conductivity in the vicinity of the magnetic phase transition. We mention here some cases where the condition $T_c \ll \theta_D$ is met to a high degree: $K_3Fe(CN)_6$[68] (T_N = 0·13°K) and $CuK_2Cl_4 . 2H_2O$[69] (T_c = 0·88°K). In the latter substance a critical scattering rate of $1/\tau \propto \omega^2\epsilon^{-1/2}$ accounted for the critical dip in thermal conductivity quantitatively. It is interesting to note that it is rather close to the expression used to explain critical scattering of sound in rare earth metals. A sufficiently large applied field removed the critical dip.

There are a number of other magnetic substances which exhibit a similar kind of phenomenon; however, the condition $T_c \ll \theta$ is no longer met very well and we will not discuss them here.

5. CONCLUSION

In this paper we have shown that, whereas the critical changes in sound velocity show a uniform behavior, namely a frequency independent weak temperature dependence in agreement with theory, the critical changes in sound attenuation show quite different behavior for different materials.

One class of materials, the rare earth metals with their long range spin interaction, nicely follow theoretical predictions. The same seems to be true for Nickel. EuO was explained with a coupling of the sound wave to the energy density of the spin system. $RbMnF_3$, MnF_2 and FeF_2 are not yet understood. A competition between energy density coupling and the usual spin coupling or spin phonon relaxation mechanism may explain the small critical exponents for the attenuation.

A given sample can thus be characterized by the following parameters: (1) spin structure (ferro- or antiferromagnetic); (2) magnetic anisotropy; (3) range of exchange interaction (possibility of phonon spin energy density coupling).

Acknowledgement – We have benefitted from discussions with numerous people. Dr. M. Shafer provided us with many single crystals used in this research.

REFERENCES

1. KADANOFF L. P. *et al., Rev. mod. Phys.* **39**, 395 (1967).
2. FISHER M. E., *Rep. Prog. Phys.* **30**, 615 (1967).
3. HELLER P., *Rep. Prog. Phys.* **30**, 731 (1967).
4. *Critical Phenomena*, NBS Misc. Publ. 273 (1966).
5. KADANOFF L. P., Comments on *Solid St. Phys.* **1**, 5 (1968).
6. CRAIG P. P. and GOLDBURG W. I., *J. appl. Phys.* **40**, 964 (1969).
7. TANI K. and MORI H., *Prog. theor. Phys.* **39**, 876 (1968), *Phys. Lett.* **19**, 627 (1966).
8. BENNETT H. S. and PYTTE E., *Phys. Rev.* **155**, 553 (1967); *ibid* **164**, 712 (1967).
9. OKAMOTO H., *Prog. theor. Phys.* **37**, 1348 (1967).
10. KAWASAKI K., *Solid St. Commun.* **6**, 57 (1968).
11. KAWASAKI K., *Phys. Lett.* **26A**, 543 (1968).
12. KADANOFF L. P., *J. phys. Soc. Japan Suppl.* **26**, 122 (1969) *Phys. Rev.* **187**, 619 (1969).
13. LARAMORE G. E. and KADANOFF L. P.
14. STERN H., *J. Phys. Chem. Solids* **26**, 153 (1965).
15. REIF F., *Fundamentals of Statistical Mechanics*, Chap. 15. McGraw-Hill, New York (1965).
16. deGENNES P. G., *Magnetism*. (Edited by Rado and Suhl), Vol. 3, Academic Press, New York (1963).
17. HALPERIN B. I. and HOHENBERG P. C., *Phys. Rev.* **177**, 952 (1969).
18. LÜTHI B., PAPON P., and POLLINA R. J., *J. appl. Phys.* **40**, 1029 (1969).
19. BENNETT H. S., *Phys. Rev.* **181**, 978 (1969).
20. KADANOFF L. P. and SWIFT J. *Phys. Rev.* **166**, 89 (1968).

21. LÜTHI B. and POLLINA R. J., *Phys. Rev. Lett.* **22**, 717 (1969).
22. KAWASAKI K., *Phys. Lett.* **29A**, 406 (1969).
23. HUBER D. L., *Solid St. Commun.* **6**, 685 (1968).
24. KAWASAKI K., *Prog. theor. Phys.* **40**, 706 (1968).
25. WAGNER H., (Unpublished)
26. HUBER D. L., private communication.
27. KASHCHEEV V. N., *Phys. Lett.* **25A**, 71 (1967)
28. BENNETT H. S., *Phys. Rev.* **185**, 801 (1969)
29. KAWASAKI K. and IKUSHIMA A. preprint.
30. POKROVSKII V. L., *Soviet Phys.-solid St.* **10**, 2852 (1969).
31. ARGYLE B. E., MYIATA N. and SCHULTZ T. D., *Phys. Rev.* **160**, 413 (1967).
32. LANDAU L. D. and LIFSHITZ E. M., *Theory of Elasticity*, Sect. 6 **6** Pergamon Press, Oxford (1959).
33. MORAN T. J. and LÜTHI B., *Phys. Rev.* **187**, 710 (1969)
34. MORAN T. J. and LÜTHI B., *Phys. Lett.* **29A**, 665 (1969).
35. LÜTHI B. and POLLINA R. J., *Phys. Rev.* **167**, 488 (1968)
36. POLLINA R. J. and LÜTHI B., *Phys. Rev.* **177**, 841 (1969)
37. IKUSHIMA A., *Phys. Lett.* **29A**, 417 (1969).
38. ELLIOTT R. J., *Magnetism* (Edited by Rado and Suhl), Vol. 2. Academic Press, New York (1965) MOLLER H. B., HOUSMANN J. C. G. and MACKINTOSH A. R., *J. appl. Phys.* **39**, 807 (1968).
39. MORAN T. J. and LÜTHI B., this conference. Gd 1 showed an easy axis change at 260°K, contrary to Gd 2, which showed it at 220°K, the commonly accepted temperature. This indicates that Gd 1 has a larger magnetic anisotropy. An impurity analysis for Gd 1 and 2 can be found in R. J. Pollina thesis, Rutgers University 1969.
40. As in Ref. [18] we introduce the anisotropy parameter $[a = J_{\parallel}(q = 0) - J_{\perp}(q = 0)]/[J_{\parallel}(q = 0) + J_{\perp}(q = 0)]$ where the anisotropic Hamiltonian reads $H = \sum_{ij} (J_{\perp}(i\delta) S_i^x S_\delta^x + J_{\parallel}(i\delta) S_i^z S_\delta^z$. For $\epsilon \approx a$ one does notice the effect of anisotropy
41. KAWASAKI K., private communication
42. McGUIRE T. R., ARGYLE B. E., SHAFER M. W. and SMART J. S., *J. appl. Phys.* **34**, 1345 (1962)
43. HEANEY D. F., FREISER M. J. and STEVENSON R. W. H., *Phys. Rev. Lett.* **9**, 212 (1962)
44. SHAPIRA Y. and REED T. B., *J. appl. Phys.* **40**, 1197 (1969)
45. See for example PIPPARD A. B., *Classical Thermodynamics*, p. 142. Cambridge University Press, Cambridge.
46. GOLDING B., *Phys. Rev. Lett.* **20**, 5 (1968).
47. LÜTHI B. and POLLINA R. J., *Bull. Am. phys. Soc.* **14**, 418 (1969).
48. The $RbMnF_3$ crystal used in our study had on its length of 8 mm a 2 mm long crystallite with a misorientation of 5° off the (1 1 1)-direction. The resulting bond breaks did not affect the critical attenuation but did affect the critical changes in sound velocity.
49. OKAMOTO H. and MORI H., *Phys. Lett.* **27A**, 151 (1968).
50. NEIGHBOURS J. R. OLIVER R. W. and STILLWELL C. H., *Phys. Rev. Lett.* **11**, 125 (1963).
51. NEIGHBOURS J. R. and MOSS R. W., *Phys. Rev.* **173**, 542 (1968)
52. EVANS R. G., *Phys. Lett.* **27A**, 451 (1968).
53. IKUSHIMA A., *Phys. Lett.* **29A**, 364 (1969) and submitted to *J. Phys. Chem. Solids.*
54. IKUSHIMA A., private communication.
55. The most recent paper on CoO with important references contained in it is BERTAUT E. F., *J. Phys. Chem. Solids* **30**, 763 (1969). see also KANAMORI K., *Prog. theor. Phys.* **17**, 197 (1957)
56. GOLDING B. and BUEHLER E., *Solid St. Commun.* **7**, 747 (1969).
57. KUZINA Ch., *Bull. Arbeitsgemeinschaft Magnetismus* (1969).
58. GOLDING B. and BARMATZ M., *Phys. Rev. Lett.* **23**, 223 (1969).
59. O'BRIEN E. J. and FRANKLIN J., *J. appl. Phys.* **37**, 2809 (1966)
60. PAULSON R. H. and SCHRIEFFER J. R., *Phys. Lett.* **27A**, 289 (1968).
61. ALS-NIELSEN J. and DIETRICH O. W., *Phys. Rev. Lett.* **22**, 290 (1969).
62. LEE E. W. and ASGAR M. A., *Phys. Rev. Lett.* **22**, 1436 (1969).
63. WALTHER K., *Solid St. Commun.* **5**, 399 (1967).
64. MELCHER R. L., BOLEF D. I. and STEVENSON R. W. H., *Solid St. Commun.* **5**, 735 (1967).
65. CONNELLY D. L., LOOMIS J. S. and MAPOTHER D. E., unpublished report
66. ARGYLE B. E. and MIYATA N., *Phys. Rev.* **171**, 555 (1968)
67. KAWASAKI K., *Prog. theor. Phys.* **29**, 801 (1963).
68. van KEMPEN H., Thesis, University of Leiden (1965).
69. DIXON G. S. and WALTON D., *Phys. Rev.* **185**, 735 (1969)

J. Phys. Chem. Solids Pergamon Press 1970. Vol. 31, pp. 1759–1764. Printed in Great Britain

ULTRASONIC ATTENUATION NEAR THE LAMBDA TRANSITION IN NH_4Cl AT HIGH PRESSURES*

C. W. GARLAND and D. D. SNYDER
Department of Chemistry and Center for Materials Science and Engineering,
Massachusetts Institute of Technology, Cambridge, Mass. 02139, U.S.A.

(*Received* 5 *September* 1969)

Abstract– The attenuation coefficient α of longitudinal ultrasonic waves propagating in the [100] direction of NH_4Cl has been measured as a function of both temperature and pressure in the vicinity of the lambda line. For seven different temperatures between 241–270°K measurements were carried out at 10, 20 and 30 MHz as the pressure was varied from 1 to 3500 bar. Lines of constant attenuation lie parallel to the lambda line in the ordered phase; however, such lines of constant attenuation in the disordered phase converge toward the lambda line as the pressure is increased. In both phases, isobaric values of α vary like $|T-T_\lambda(p)|^{-1}$ near the lambda line, where $T_\lambda(p)$ is the transition temperature at pressure p.

1. INTRODUCTION

THE LAMBDA transition in ammonium chloride is well established as an order-disorder transition involving the relative orientations of the NH_4^+ ions in a CsCl-type cubic structure [1]. In the ordered phase all the NH_4^+ ions are oriented 'parallel' to each other, while in the disordered phase they are randomly distributed with respect to two equivalent orientations. Thus the ordering in NH_4Cl is directly analogous to spin ordering in a simple-cubic ferromagnet.

Both the ultrasonic velocity and attenuation are 'anomalous' near this transition, although the only quantitative high-pressure work has been concerned with velocity measurements. Garland and Renard[2] used the pulse-superposition method to determine both longitudinal and shear velocities at 20 MHz over a wide range of temperature and pressure. Shear waves exhibited a distinct step-like velocity anomaly but gave no indication of unusual attenuation. These shear data thus provide an accurate indication of the pressure dependence of the transition temperature. In contrast, longitudinal waves showed a very sharp velocity minimum and were strongly attenuated near the lambda transition All the velocity anomalies become less pronounced as the lambda line is crossed at higher and higher pressures.

There have been three investigations of the attenuation of [100] longitudinal waves at one atmosphere[3–5]. The most detailed of these is by Garland and Yarnell[4] and indicates the presence of first-order instability and hysteresis very close to T_λ. The present work involves a study of the longitudinal acoustic attentuation as a function of pressure up to 3·5 kbar at various constant temperatures between 235–280°K. This will allow us to define the temperature and pressure dependence in both the ordered and disordered phases.

2. EXPERIMENTAL PROCEDURE

The ultrasonic equipment used in most of this work was essentially identical to that used by Garland and Yarnell[4]. Toward the end, runs at 270·2 and 281·8°K were made using new ultrasonic equipment manufactured by Matec. A Model 120 master synchronizer was used to trigger a Tektronix 546A oscilloscope and to alternately trigger (at one-half

---

*This work was supported in part by the Advanced Research Projects Agency and in part by the National Science Foundation, and in part by the Joint Services Electronics Program under Contract DA28-043-AMC-02536(E).

the oscilloscope repetition rate) a Model 6000 pulsed generator/receiver and a Model 666 pulse comparator. The pulse comparator operates at 60 MHz for use with the superheterodyne receiver, which eliminates the time-consuming tuning involved for variable frequency units. The sample echoes and the comparison pulse are displayed alternately on the screen, but persistence of vision causes the two traces to appear simultaneously. The comparison pulse is superimposed directly on the echo to be measured and its amplitude is adjusted by the use of a calibrated attenuator.

The pressure equipment and constant-temperature bath were the same as those described by Garland and Young[6], except that Univis J-43 oil was substituted for petroleum ether as the bath fluid above 265°K. Argon gas was used as the pressure fluid. The pressure could be held constant to within ±3 bar during a measurement, and the temperature was held constant to within ±0·05°K during an entire run.

The ammonium chloride single crystals, which were grown by Schumaker[7], had sample lengths L at 25°C of 1·1615 cm (I), 0·8286 cm (II) and 0·8465 cm (III). Parallel faces were flycut on crystal II with a high-speed milling machine. Natural faces were used for crystals I and III. The orientation of each specimen was checked by a back-reflection X-ray method, and the normal was found to be within 0·5 deg of the [100] axis in all cases. Chrome-gold plated X-cut quartz transducers were bonded to the samples with a phthallic anhydride-glycerin polymer[2], and measurements were made at 10, 20 and 30 MHz.

In making a run, the bath was brought to the desired temperature and the system was allowed to equilibrate for at least one hour. After the attenuation was measured at atmospheric pressure, the system was pressurized to about 3·5 kbar and allowed to equilibrate for another 15–20 min. Then a series of attenuation measurements was made as argon was vented from the cell. Well away from the transition line, a period of ten minutes was allowed for equilibration after each change in pressure. Close to the transition line, a period of twenty to thirty minutes was required. At the end of a pressure run, the one-atmosphere balance point of the manganin resistance bridge was remeasured and used to correct the readings for any drift from the original zero setting.

The echo pattern for all runs below 250°K deteriorated when the pressure had dropped to about 500 bar. Although about half the runs in the range 250·6–260·6°K also showed this deterioration, the runs at 265·6 and 270·2°K showed a good echo pattern at all pressures. Fortunately, the signal always reformed into a good echo pattern when the cell was repressurized, indicating difficulties with the bond rather than the sample. However, after prolonged use, crystals I and III developed small cleavage cracks (parallel to the direction of propagation and 1 to 2 mm deep) on the face bonded to the transducer. Reflections from these cracks distorted the echo display, and the crystals could no longer be used.

3. RESULTS AND DISCUSSION

Background attenuation

Separation of the anomalous attenuation associated with the order-disorder transition from the uninteresting but appreciable 'background' attenuation represent the principal difficulty in evaluating our data. The background attenuation is due to a combination of pressure-independent contributions (such as beam spread and scattering losses) and pressure-dependent losses. Both types of loss are appreciable in our case, but the dominant contribution arises from changes in the impedance match at the gas-sample interface. As the gas is compressed, its acoustic impedance increases and more ultrasonic energy is transmitted into the gas. This causes a considerable attenuation per echo at high pressures. In principle one could calculate the background attenuation, but in practice it is necessary to carry out an emprical determination. In doing this, we have assumed that the observed attenuation per echo, α_{total}, is a sum of background and intrinsic cooperative contributions. Once α_{back} is known, the desired attenuation coefficient α (in neper cm^{-1}) is obtained by simply dividing $(\alpha_{\text{total}} - \alpha_{\text{back}})$ by $8 \cdot 69\ (2L)$.

Total attenuation values obtained at 30 MHz as a function of pressure on a fused-silica test sample at 250 and 260°K showed very little change with temperature, which strongly suggests that the background attenuation is independent of temperature over a moderate range. All the 20 MHz runs were made on crystal I using transducers with an $\frac{1}{8}$ in. active spot, and these data at various temperatures were combined to construct a temperature-independent background as a function of pressure. Almost all the 30 MHz runs were made on crystal II, also using $\frac{1}{8}$ in. transducers, and the same analysis was made for these data. This analysis consisted of plotting α_{total} vs. $|T - T_\lambda|^{-1}$ at several constant pressures, where T_λ at each pressure is determined from the phase diagram of Renard and Garland[8]. This method of handling the data produces almost linear plots which can be easily extrapolated to zero (infinite ΔT) to yield the background attenuation. For Garland and Yarnell's 1-atm data[4], where there is little or no background attenuation, such plots are close to linear over a wide temperature range. It appears that a comparable behavior persists at high pressures even though the fraction of the total attenuation due to the background loss is increasing.

Another method of determining the background attenuation is to carry out isotherm runs which do not cross the lambda line in the range 0–3·5 kbar. This was done at 236·4°K on crystal I, and the results at pressures above 1 kbar (sufficiently far away from the lambda line) were in good agreement with those obtained with the first method. A series of runs were made at 10 and 30 MHz on crystal III using $\frac{1}{4}$ in. transducers. Data obtained at 240·5°K were used to establish a high-pressure ($p > 1 \cdot 5$ kbar) background curve for a 255·6°K run, and 281·8°K data provided a complete background curve for a 270·2°K run. It was observed that the pressure variation of the background attenuation was the same in the ordered and in the disordered phase.

Critical attenuation

One-atmosphere data has shown that the critical attenuation α is quadratic in frequency over the range 5–60 MHz except perhaps at temperatures very close to T_λ[3, 4]. Our present attenuation data at 10–30 MHz are proportional to ω^2 at all temperatures and pressures. Typical isotherms of ω^2/α vs. pressure are shown in Figs. 1 and 2. The arrow labelled p_λ on each plot indicates the critical pressure at that temperature as determined from shear velocity data[2]. Garland and Yarnell's ω^2/α values[4] are indicated by the crosses on the vertical axis, and the smooth curves were drawn so as to tie into these values. Smooth-curve ω^2/α values along all seven isotherms are listed in Table 1. These results are subject to both experimental errors in α_{total}, which are largely random in nature, and to systematic errors related to the choice of α_{back}. These two contributions to the

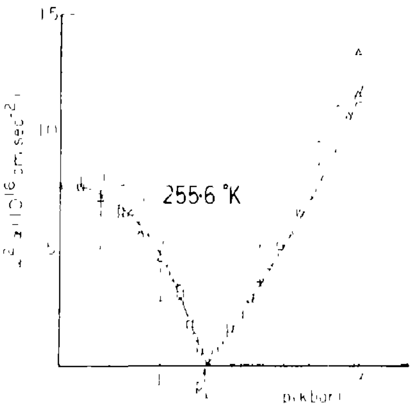

Fig. 1. Variation of ω^2/α with pressure at 255·6°K (see text). ○ 10 MHz, □ 20 MHz, △ 30 MHz.

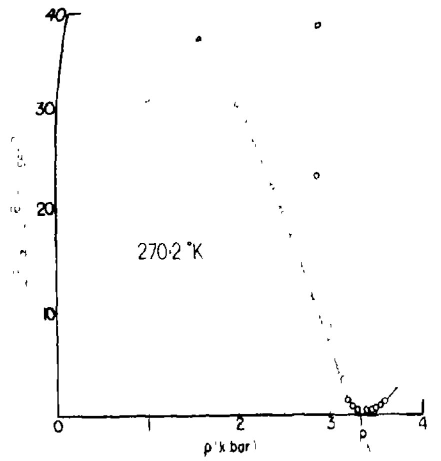

Fig. 2. Variation of ω^2/α with pressure at 270·2°K ○ 10 MHz, △ 30 MHz.

uncertainty are comparable near the transition but uncertainties due to α_{back} are dominant away from the transition region.

A somewhat non-exponential variation in the echo amplitudes is the limiting factor in the accuracy of our α_{total} values. However, the character of the echo pattern did not change during a pressure run, and ±5 per cent represents our estimate of the random error in measuring α_{total}. The effect of fluctuations or errors in the temperature and pressure varies considerably. Near the lambda line, where α is a sensitive function of p and T, this can cause ±4 per cent errors in α. In the essentially normal region away from the lambda line, this will cause only a 0·7 per cent uncertainty in α. An estimate of the systematic error in α due to the choice of α_{back} was obtained for the 255·6°K run by drawing an alternate background for each frequency. The vertical error bars shown in Fig. 1 illustrate the effect of this change on a few representative data points. Near the transition pressure, the α values change by about 10 per cent at 10 MHz and 5 per cent at 20 and 30 MHz. Far from the transition, the change

Table 1. *Smooth-curve values of ω^2/α, in units of* 10^{16} cm sec^{-2}, *as a function of pressure at various constant temperatures*

p (kbar)	241·0	246·5	250·6	255·6	260·6	265·6	270·2°K
0·001	0·80		4·95	7·70	10·40	13·60	16·7
0·2	1·55		4·55	7·60	10·90	14·50	19·5
0·4	2·45		3·80	7·30	11·00	15·00	22·4
0·6	3·55	1·35	2·55	6·75	10·85	15·25	25·2
0·8	4·75	2·25	0·95	5·90	10·50	15·35	27·9
1·0	6·00	3·25	0·75	4·70	9·85	15·15	30·5
1·2	7·35	4·30	1·75	2·90	9·00	14·70	32·3
1·4	8·80	5·45	2·85	0·80	7·75	14·00	33·0
1·6	10·30	6·65	4·25	0·85	6·00	12·85	32·9
1·8	11·80	7·90	6·05	2·10	3·70	11·20	32·0
2·0	13·35	9·15	8·15	3·40	1·00	9·20	30·1
2·2	14·90	10·45	10·45	4·75	0·80	6·90	26·4
2·4	16·50	11·75	12·80	6·15	2·50	4·45	21·9
2·6				7·70	4·15	1·90	17·0
2·7						0·60	
2·8				9·45	5·80		11·9
2·9						0·40	
3·0				11·45	7·45	1·15	6·60
3·2						2·75	1·50
3·3							0·35
3·4							0·40
3·5							0·80
3·6							1·35

is about 35 per cent at 10 MHz and 10 per cent at 20 and 30 MHz. It is felt that the original choices of background were definitely preferable, which is supported by the agreement among ω^2/α values at different frequencies. However, alternate background curves cannot be completely ruled out as limiting possibilities.

Figure 3 shows the NH_4Cl phase diagram with lines of constant ω^2/α added. In the low-temperature ordered phase these lines of constant attenuation lie nearly parallel to the lambda line. In the disordered phase, constant-attenuation lines are closely spaced at 3 kbar and spread apart considerably at lower pressures. This difference in behavior between the two phases is emphasized by the attenuation isobars shown in Fig. 4. These isobars were constructed from the smooth-curve values in Table 1. Although there was some scatter in the available points, no systematic curvature could be seen and the best straight lines were drawn (giving greater weight to those points close to the transition temperature). Lines corresponding to directly measured one-atmosphere data[4] have been added to this figure for comparison with our high pressure results. The isobars in the ordered phase are roughly parallel and have slopes approximately equal to the one-atmosphere value of $7{\cdot}2 \times 10^{15}$ cm sec^{-2} deg^{-1}. Isobars in the disordered phase have slopes which are a strong function of pressure ranging from $5{\cdot}1 \times 10^{15}$ cm sec^{-2} deg^{-1} at 1 atm to $16{\cdot}4 \times 10^{15}$ at 2000 bar. Figures 3 and 4 both indicate a corresponding-states behavior for the ordered phase but not for the disordered phase. However, the variation $\alpha \sim \omega^2|T - T_\lambda(p)|^{-1}$ seems to hold at all pressures up to 3 kbar in both phases.

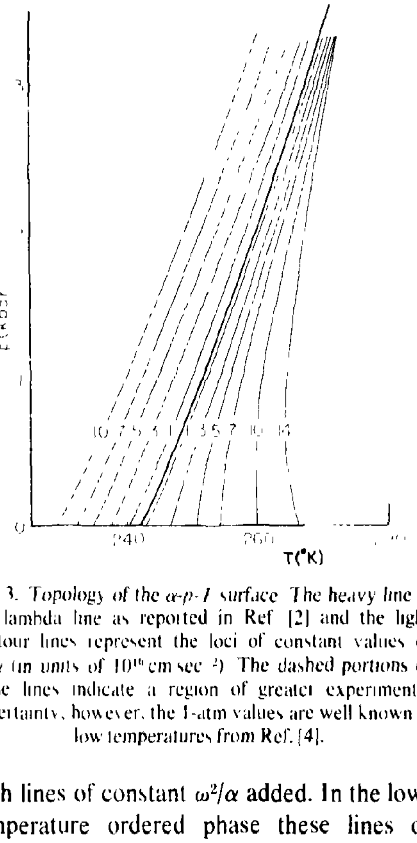

Fig. 3. Topology of the α-p-T surface. The heavy line is the lambda line as reported in Ref. [2] and the light contour lines represent the loci of constant values of ω^2/α (in units of 10^{16} cm sec^{-2}). The dashed portions of these lines indicate a region of greater experimental uncertainty, however, the 1-atm values are well known at low temperatures from Ref. [4].

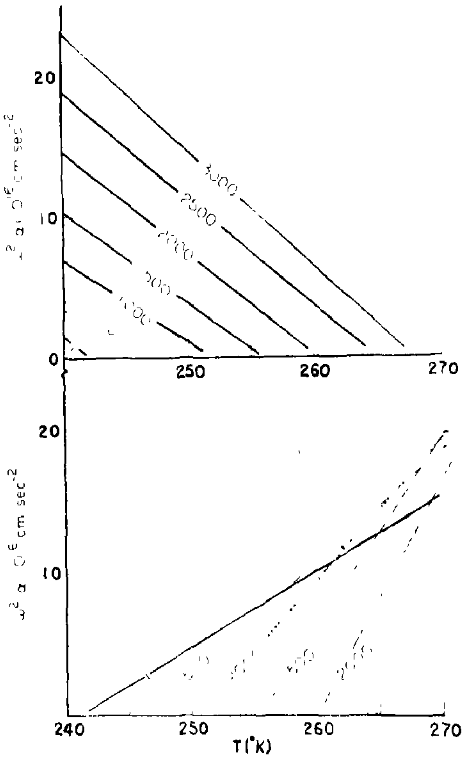

Fig. 4. Isobaric variation of ω^2/α with temperature. Pressure values indicated on each line are in bar.

A brief review of Landau theory for the critical relaxation of long-range ordering near an order-disorder transition has been given previously in connection with the 1-atm attenuation measurements on NH_4Cl [3, 4]. Recently, there has been a rapid development of fluctuation theories which predict that $\alpha \sim \omega^2|T-T_c|^{-\theta}$ but do not yet agree on the critical exponent θ[9]. No theoretical work has yet been done on the isothermal variation of α as a function of $|p-p_c|$.

In the future we hope to extend these measurements with special emphasis on the immediate vicinity of the lambda line. One can already notice a distinct difference in the sharpness of the attenuation peak as p_λ increases (see Figs. 1 and 2). It would be of interest to follow this behavior up to higher pressures.

REFERENCES

1. LEVY H. A. and PETERSON S. W., *Phys. Rev.* **86**, 766 (1952).
2. GARLAND C. W. and RENARD R., *J. chem. Phys.* **44**, 1130 (1966).
3. GARLAND C. W. and JONES J. S., *J. chem. Phys.* **42**, 4194 (1965).
4. GARLAND C. W. and YARNELL C. F., *J. chem. Phys.* **44**, 3678 (1966).
5. SHUSTIN O. A., YAKOVLEV I. A. and VELICHKINA T. S., *JETP Lett.* **5**, 3 (1967).
6. GARLAND C. W. and YOUNG R. A., *J. chem. Phys.* **49**, 5282 (1968).
7. SCHUMAKER N. E. and GARLAND C. W., *J. chem Phys.* To be published.
8. RENARD R. and GARLAND C. W., *J. chem. Phys.* **45**, 763 (1966).
9. GARLAND C. W., *Physical Acoustics*, Vol. 7. (Edited by W. P. Mason and R. N. Thurston), Academic Press, New York (1970).

J. Phys. Chem. Solids Pergamon Press 1970. Vol. 31, pp. 1765–1769. Printed in Great Britain.

THERMODYNAMIC PROPERTIES OF INTERSTITIAL SOLID SOLUTIONS BY RELAXATION METHODS

G. ALEFELD, J. VÖLKL and J. TRETKOWSKI*
Institut für Festkörper- und Neutronenphysik, Kernforschungsanlage Jülich, Germany

(*Received 5 September* 1969, *in revised form* 15 *October* 1969)

Abstract – By elastic relaxation methods the derivative $(\partial\mu/\partial\rho)_T$ of the chemical potential of solutes can be determined absolutely as a function of temperature and density ρ. Therefore useful parameters which characterize the solubility of gases in metals or which determine phase transitions of solutes can be found by elastic relaxation methods.

As an example experiments on hydrogen in niobium are discussed. On the basis of experimental parameters (trace of the elastic dipolemoment tensor, critical density, critical temperature) it will be argued that the attractive interaction of H in Nb, which is responsible for the phase transition, is of elastic nature.

1. INTRODUCTION

ELASTIC relaxation methods such as strain relaxation or internal friction which are based on orientational relaxation of dipoles have proved to be useful methods determining the rate of transition between equilibrium positions of interstitials, pairs of substitutionals and so on[1]. For many cases, especially for the interstitials like O, N or C in metals like V, Nb, Ta it has been possible to relate the experimental relaxation time to the macroscopic diffusion coefficient[2], although assumptions concerning the diffusion mechanism (e.g. octahedral–octahedral or tetrahedral–tetrahedral jumps) have to be made. From the relaxation strength the difference $(A-B)$ of the components of the dipolemoment tensor can be extracted[3].

The recently discovered diffusional relaxation process (Gorsky-Effect)[4] opens up new experimental possibilities to determine not only transport properties but equilibrium properties of solid solutions as well. The relaxation time of these processes can be converted directly into the diffusion coefficient without any assumption concerning the jump model[5]. From the relaxation strength equilibrium thermodynamic properties can be deduced.

2. THEORY

The relaxation strength Δ_E of the diffusional relaxation in a cubic system is given by[6, 7]:

$$\Delta_E = \Omega\frac{(A+2B)^2(s_{11}+2s_{12})^2}{9(\partial\mu/\partial\rho)_T s_{11}} \qquad (1)$$

with the orientation term Ω:

$$\Omega = \frac{s_{11}}{s_{11}-(2s_{11}-2s_{12}-s_{44})\Gamma} \qquad (2)$$

Γ is the usual orientation factor

$$\Gamma = \gamma_1^2\gamma_2^2+\gamma_2^2\gamma_3^2+\gamma_3^2\gamma_1^2 \qquad (3)$$

where the γ_i are the direction cosines of the angles between sample and crystal axes. s_{11}, s_{12} and s_{44} are the elastic coefficients and $A+2B$ is the trace of the elastic dipolemoment tensor. $A+2B$ is the same quantity which determines the change in lattice parameter due to the solid solution: $\Delta a/a = (A+2B)(s_{11}+2s_{12})\rho/3$; ρ = number of solutes per cm^3.

Finally $(\partial\mu/\partial\rho)_T$ is the derivative of the chemical potential μ of the solutes. Therefore the relaxation strength, equation (1), can be used to determine the dependence of $\partial\mu/\partial\rho$ on concentration and temperature. Since all quantities except $(\partial\mu/\partial\rho)_T$ in equation (1) are measurable directly, the value of the derivative of the chemical potential can even be determined absolutely by measurement of Δ_E. From the knowledge of the chemical potential predictions of such quantities as the solubility of gases in metals or phase transition of the solutes can be made. Therefore valuable parameters concerning these processes can be obtained by relaxation methods.

---

*Present address: Institut für Metallphysik, Universität Göttingen.

3. EXPERIMENTS

We have applied the diffusional relaxation to metal–hydrogen systems, especially to H in Nb. Due to the high mobility and high solubility of H in Nb just above room temperature this system can be studied conveniently over a large concentration range and in a practical temperature range. It has been pointed out recently[8] that hydrogen in metals can be considered as an example of a lattice gas[9]. There exists a phase transition (see Fig. 1), which corresponds to the gas–liquid transition. The critical temperature (the maximum in the miscibility gap) is approximately 180°C, the α-phase is the lattice gas, the α'-phase the lattice liquid. Due to the relation $(\partial\mu/\partial\rho)_T = 1(1)\rho^2 K_{\mathrm{iso}}$ (K_{iso} = isothermal compressibility) the relaxation strength is proportional to the lattice gas compressibility which approaches infinity at the critical point. The relaxation strength can more generally be called 'elastic susceptibility', its divergency at the critical point corresponds to the divergency of the magnetic susceptibility at the Curie point.

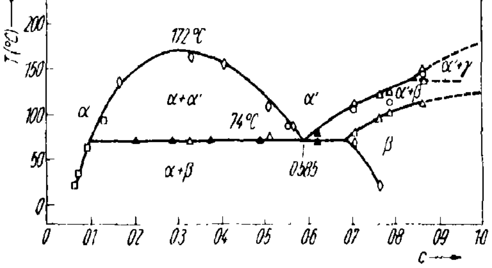

Fig. 1. Phase diagram for hydrogen in niobium[10] (c = concentration in atomic fraction.)

In contrast to H in the f.c.c.-lattice of Pd, interstitials in the b.c.c.-lattice of Nb have three sites with different symmetry. Assuming that the maximum concentration ρ_m is independent of the distribution over the three different sites and using mean field approximation, Alefeld and Buck[11] have derived the following expression for the chemical potential of H in Nb:

$$\mu = -ur + kT \ln \frac{r(1-\frac{2}{3}r)^2}{(1-r)^3} + f(T) \tag{4}$$

with $r = \rho/\rho_m$. The term ur represents an attractive interaction term similar to that in a van der Waals gas. From the conditions $\partial\mu/\partial\rho = 0$ and $\partial^2\mu/\partial\rho^2 = 0$ which define the critical point, the critical density ρ_c and critical temperature T_c have been determined by Alefeld and Buck[11] as:

$$\rho_c = 0{\cdot}393\,\rho_m \quad ; \quad kT_c = 0{\cdot}176\,u. \tag{5}$$

Using $\partial\mu/\partial\rho$ from equation (4) in equation (1) yields for the relaxation strength explicitly:

$$\Delta_E = \Omega r(1-r)(1-\tfrac{2}{3}r) \times \frac{\rho_m(A+2B)^2(s_{11}+2s_{12})^2}{9k(T-T_s)s_{11}} \tag{6}$$

with

$$kT_s = r(1-r)(1-\tfrac{2}{3}r)u. \tag{7}$$

For small concentrations ($r \ll 1$) equation (6) can be written as:

$$\Delta_E = \Omega \frac{2c(A+2B)^2(s_{11}+2s_{12})^2}{9kTs_{11}a^3} \tag{8}$$

ρ has been replaced by $2c/a^3$ (c = atomic concentration, a = lattice constant).

(a) By measuring the concentration dependence of the relaxation strength the trace of the dipolemoment tensor $(A+2B)$ was determined as 10·8 eV for Nb and 9·0 eV for V[7]. Both these values are consistent with lattice parameter changes reported in literature[10, 12].

(b) With decreasing temperature the relaxation strength increases as if it would approach infinity at the temperature T_s. $T_s(\rho)$ is defined by the condition $\partial\mu/\partial\rho = 0$, which is the definition of the socalled stability curve (spinodal)*. Therefore the temperature dependence of the relaxation strength allows to determine by extrapolation the position of the stability curve inside the coexistence curve. Assuming Curie–Weiss behaviour T_s is obtained by plotting $1/\Delta_E$ vs. T (see T_s in Fig. 2). Using equation (6) Schaumann[7] could show that for small concentrations the value of the temperature T_s is consistent with an interaction energy $u = 0{\cdot}21$ eV, which can be extracted from solubility measurements by Veleckis[13]. From similar measurements by Albrecht *et al.*[14] u can be determined as 0·16 eV yet with a relatively large error.

The onset of precipitation manifests itself as a well defined cusp in the relaxation strength (see T_p in Fig. 2). Therefore the shape and position of the phase boundary can be established as well.

(c) For temperatures $T > T_c$ the relaxation

---

*The physical significance of the stability curve is still a matter of controversy.

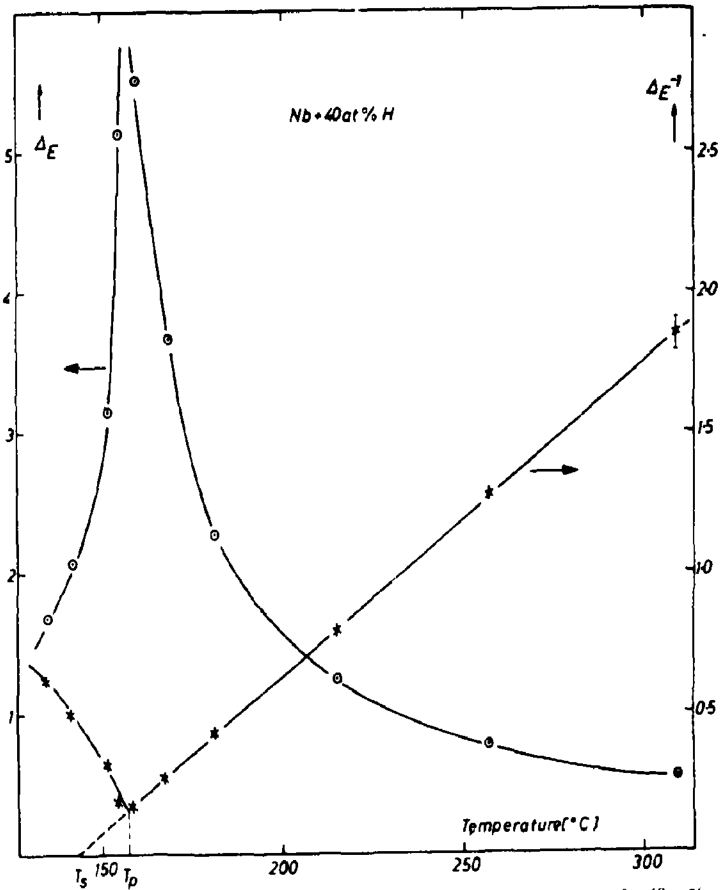

Fig. 2. Relaxation strength and reciprocal relaxation strength vs. temperature for 40 at% H in Nb.

strength, equation (6) or equation (1), passes through a maximum as a function of ρ. Assuming a weak dependence of the elastic constants s_{ij} and $(A+2B)$ on ρ, the maximum is defined by the condition $\partial^2\mu/\partial\rho^2 = 0$. This follows from equation (1). In mean field approximation this maximum is located at $\rho = \rho_c$, independent of temperature. For $T = T_c$ the maximum diverges into a singularity. In Fig. 3 the relaxation strength is plotted vs. concentration. Although for only 4 concentrations have measurements been performed, clearly a peak is resolved yielding C_c = (1)0·34 ± 0·02 at %.

From equation (5) the maximum concentration is derived as C_m = (1)0·87 ± 0·05 at %, which is in agreement with 0·89 at % as determined from solubility measurements[13]. The critical temperature was found as approximately T_c 450°K. Using equation (5) the interaction energy is determined as $u = 0{\cdot}21$ eV, again in agreement with Veleckis' solubility data[13] and with Schaumann's value[7] from the stability curve. Actually the agreement for u and C_m is much better than it could have been expected on the basis of the equation (4) with a linear interaction term only.

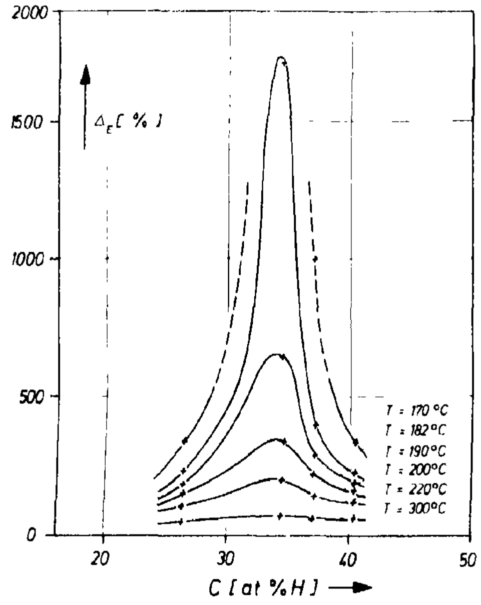

Fig. 3. Relaxation strength vs. concentration for different temperatures.

4. DISCUSSION

We have shown that several parameters which enter into the chemical potential of solutes can be determined by elastic relaxation methods. The derivative $\partial\mu/\partial\rho$ can be determined in temperature and concentration regions which are often not accessible to solubility measurements because of reluctance in surface reaction. Therefore the phase boundaries and especially the critical point can be found with more accuracy than it is possible by extrapolation from high temperatures. Also the knowledge of the components A, B of the dipolemoment tensor is of significance in understanding the phase transformations of the solutes. If the attractive interaction $u\rho/\rho_m$ in equation (4) is due purely to the elastic distortion, then for an isotropic solid u/ρ_m is in mean field approximation given by[15]:

$$\frac{u}{\rho_m} = \frac{2}{3} \cdot \frac{1-2\nu}{1-\nu} \cdot \frac{(A+2B)^2}{9\kappa} \tag{9}$$

(κ = bulk modulus, ν = Poisson ratio).
With $(A+2B) = 10{\cdot}8$ eV, $\kappa = 1{\cdot}72 \times 10^{12}$ dyn/cm^2 equation (9) yields $u = 0{\cdot}20$ eV for $\nu = \frac{1}{3}$ and $u = 0{,}27$ eV for $\nu = \frac{1}{4}$.

In spite of the uncertainty in regard to ν for the anisotropic Nb these values for u fall close to the experimental value. Therefore it may be concluded that elastic interaction is responsible for the attractive interaction which causes the gas-liquid transition at lower temperatures. It may be mentioned that the difference $A-B$, which determines the relaxation strength for orientation relaxation, plays an analogous role in further phase transitions at low temperatures and high concentrations.

Close to T_c, the meanfield approximation used to derive equation (4) is not applicable. Instead of the Curie–Weiß behaviour of equation (6) one expects a temperature dependence $\Delta_E \sim (T-T_c)^{-\gamma}$ for $\rho = \rho_c$. As a function of concentration Δ_E diverges as $\Delta_E \sim (\rho-\rho_c)^{-\delta+1}$ for $T = T_c$ ($\gamma \approx 1{\cdot}25$; $\delta \approx 5{\cdot}2$ for the Ising model). So far no deviation from the Curie–Weiss behaviour has been observed for temperatures $(T-T_c)/T_c \geqslant 0{\cdot}01$[16]. The validity of mean field approximation this close to the critical point indicates that the interaction must be fairly long range, which again is the case for elastic interaction[17].

In this paper we have discussed the application of the diffusional relaxation to H in metals. Other systems may be studied as well in temperature regions, in which the mobility is high enough to make relaxation times reasonable. By using samples with $\frac{1}{10}$ mm a factor 100 can easily be compensated in lower mobility compared to 1 mm samples, which we have used in our experiments on H.

REFERENCES

1. See e.g. WERT C.H., *Physical Acoustics*–III, Part A (Edited by W. P. Mason), Academic Press, New York (1966).
2. POWERS R. W. and DOYLE M., *J. appl. Phys.* **30**, 514 (1959).
3. See e.g. BERRY B. S. and NOWICK A. S., *Physical Acoustics*–III, Part A (Edited by W. P. Mason), Academic Press, New York (1966).
4. SCHAUMANN G., VÖLKL J. and ALEFELD G., *Phys. Rev. Lett.* **21**, 891 (1968).
5. VOLKL J., SCHAUMANN G. and ALEFELD G., submitted to this conference.
6. ALEFELD G., VOLKL J. and SCHAUMANN G., *Phys. Status Solidi* **37**, 337 (1970).
7. SCHAUMANN G., Thesis, Technische Hochschule Aachen (1969).
8. ALEFELD G., *Phys. Status Solidi* **32**, 67 (1969).
9. LEE T. D. and YANG C. N., *Phys. Rev.* **87**, 410 (1952).
10. WALTER R. J. and CHANDLER W. T., *Trans. AIME* **233**, 762 (1965).
11. ALEFELD G. and BUCK H., To be published.
12. MAELAND A. J., *J. phys. Chem.* **68**, 2197 (1964).
13. VELECKIS E., Thesis, Illinois Institute of Technology (1960). F. Veleckis has analysed his data for Nb, V and Ta by using a chemical potential which is valid only for systems with identical interstitial sites like H in Pd. Reevaluating his data yields $u = 0{\cdot}21$ eV.
14. ALBRECHT W. M., GOODE W. D. and MALLETT M. W., *J. Electrochem. Soc.* **106**, 981 (1959).
15. ALEFELD G., Unpublished.
16. TRETKOWSKI J., VOLKL J. and ALEFELD G., To be published.
17. SIEMS R., *Phys. Status Solidi* **30**, 645 (1968).

J. Phys. Chem. Solids Pergamon Press 1970. Vol. 31, pp. 1771–1783. Printed in Great Britain

DAMPING OF INTERSTITIAL ATOMS IN bcc METALS*

C. A. WERT
Department of Metallurgy and Mining Engineering, and Materials Research Laboratory,
University of Illinois at Urbana-Champaign, Urbana, Ill 61801, U.S.A.

(*Received* 5 *September* 1969, *in revised form* 25 *October* 1969)

Abstract—The internal friction of the bcc metals containing dissolved carbon, nitrogen, oxygen, and hydrogen is reviewed with special attention given to diffusion in these alloys. Three aspects of internal friction are considered, (a) the ideal Snoek effect, (b) the damping peaks associated with phase transformations and (c) the thermodynamics of small clusters of interstitials.

1. INTRODUCTION

THE USE of anelasticity in understanding point irregularities in crystal lattices—defects and point impurities—continues to make steady, if not spectacular, progress. This progress has come both from detailed studies of individual problems in specific materials and from more general investigations. A review of the entire scope of these problems is impractical, so attention is concentrated on three specific problems: (1) interstitially dissolved impurities in the bcc metals, (2) the acoustical energy loss associated with phase changes and (3) the thermodynamics of interstitial clustering, as it can be deduced from anelastic measurements.

2. THE IDEAL SNOEK EFFECT

Interstitial impurities in bcc metals produce nearly an ideal Snoek effect when they are in dilute enough solution. The damping peak is ideal in width and its height is a linear function of interstitial content. These facts have permitted a series of notable advances to be made in these alloys, first for carbon and nitrogen dissolved in iron and later for oxygen, nitrogen and carbon dissolved in V, Nb and Ta. Studies have been made both for diffusion in these alloys[1–6] and for precipitation in some of these alloys[7–11]. No insurmountable intrinsic difficulties were found to exist, although many detailed difficulties of specimen preparation had to be overcome.

One of the primary gains made in the diffusion studies has resulted from the combination of anelastic data with data obtained from long range diffusion studies. In general when sufficient care has been taken in both, good agreement between the two has been achieved; thus the diffusion range has been extended over some fifteen orders of magnitude in some instances. A summary of such investigations is presented in Table I(*a*) along with citations of some of the chief original or review papers[12–18]. One sees that reasonable agreement exists for the several cases in which both techniques can be used. A great many gaps exist, however, in bulk diffusion data.

Perhaps the most interesting case is that of carbon in iron, where a combination of anelastic and radio-tracer data shows marked curvature in the Arrhenius plot above 450°C [5, 13]. No doubt exists that this effect is real, but no proved explanation is known.

The VI B column of the periodic table has been extremely difficult for anelastic study because of metallurgical difficulties in specimen preparation. Chromium alloyed with nitrogen has gradually yielded to diligent investigation[19, 20] and the Snoek effect

---

*This research was supported in part by the U.S. Atomic Energy Commission, Contract AT(11-1)-1198.

Table 1(*a*). *Parameters characterizing diffusion in iron and the group* VB *elements*. D_0 *is in units* cm²/sec *and* ΔH *is in units* cal/mole. *For carbon diffusing in* Nb *and* Ta, *two measurements of bulk diffusion are reported separately*

Metal	Method	Carbon	Nitrogen	Oxygen
Iron	Anelastic	$D_0 = 0\cdot004$ $\Delta H = 19,160$	$D_0 = 0\cdot005$ $\Delta H = 18,350$	
	Bulk	$D_0 = 0\cdot1$ $\Delta H = 23,000$	$D_0 = 0\cdot066$ $\Delta H = 18,600$	
	Refs	[3], [5], [12], [13]	[4], [14], [15]	
Vanadium	Anelastic	$D_0 = 0\cdot0045$ $\Delta H = 27,290$	$D_0 = 0\cdot009$ $\Delta H = 34,060$	$D_0 = 0\cdot013$ $\Delta H = 29,010$
	Bulk	$D_0 = 0\cdot0049$ $\Delta H = 27,300$		
	Refs	[16], [16a]	[16]	[16]
Niobium	Anelastic	$D_0 = 0\cdot004$ $\Delta H = 33,020$	$D_0 = 0\cdot009$ ΔH 34,920	$D_0 = 0\cdot02$ $\Delta H = 26,910$
	Bulk	$D_0 = 0\cdot033$ $\Delta H = 37,900$ $D_0 = 0\cdot009$ $\Delta H = 35,000$		
	Refs	[16], [16a], [18]	[16]	[16]
Tantalum	Anelastic	$D_0 = 0\cdot006$ $\Delta H = 38,510$	$D_0 = 0\cdot006$ $\Delta H = 37,840$	$D_0 = 0\cdot0044$ $\Delta H = 25,450$
	Bulk	$D_0 = 0\cdot012$ $\Delta H = 40,300$ $D_0 = 0\cdot026$ $\Delta H = 43,000$		
	Refs	[16], [16a], [18]	[16]	[16]

for carbon in chromium has been reported[21]. Pertinent data for these and other systems are summarized in Table 1(*b*).

Molybdenum and tungsten have been extremely difficult, not because damping effects cannot be seen, but because interstitial peaks are difficult to interpret and identify. Schnitzel first reported such peaks after an arduous series of investigations, but gave only tentative correlations with specific interstitial impurities[22, 23]. Later papers have corroborated his results though perhaps with scantier data than he had[24, 25].

High temperature diffusion data are also scanty for these alloys, but measurements are gradually being made. Data for carbon diffusing in molybdenum and tungsten have been reported[24, 25, 27]. When these data are combined with the internal friction results quoted above, plots shown in Fig. 1 result. One sees that the combination yields somewhat lower values of ΔH than are derived from the high temperature data alone. Measurements for diffusion of nitrogen in molybdenum by effusion methods have been reported recently. The data of Evans and Eyre are reported in Table 1(*b*), although other measurements have also been made. (For an excellent summary see Table 1 of their paper[17].) A damping peak for nitrogen in molybdenum has been claimed, but the identification seems to be on too shaky grounds to warrant comparison[24]. A report of nitrogen diffusion in tungsten has been made[28]; the data are presented in Table 1(b). Both D_0 and the activation enthalpy seem very high. The reader can easily verify, though, that combination of these data with

Table 1(b). Parameters characterizing diffusion in the group VIB elements and in β-thorium. D_0 *is in units* cm²/sec *and* cm²/sec *and* ΔH *is in* cal/mole

Metal	Method	Carbon	Nitrogen	Oxygen
Chromium	Anelastic		$D_0 = 0{\cdot}016$ $\Delta H = 27{,}500$	
	Bulk			
	Combined	$D_0 = 0{\cdot}009$ $\Delta H = 26{,}500$		
	Refs	[21]	[19], [20]	
Molybdenum	Anelastic	(Damping peaks reported)		
	Bulk	$D_0 = 0{\cdot}02, 0{\cdot}03$ $\Delta H = 41{,}000$	$D_0 = 0{\cdot}003$ $\Delta H = 27{,}600$	
	Combined	$D_0 = 0{\cdot}003$ $\Delta H = 35{,}000$		
	Refs	[18], [22], [24], [27]	[17], [24]	[22], [24]
Tungsten	Anelastic	(Damping peaks reported)		
	Bulk	$D_0 = 0{\cdot}09$ $\Delta H = 53{,}500$	$D_0 = 5{\cdot}4$ $\Delta H = 62{,}000$	
	Combined	$D_0 = 0{\cdot}001$ $\Delta H = 40{,}000$		
	Refs	[18], [23], [25]	[25], [23], [25]	
β-Thorium	Bulk	$D_0 = 0{\cdot}02$ $\Delta H = 27{,}000$	$D_0 = 0{\cdot}032$ $\Delta H = 17{,}000$	$D_0 = 0{\cdot}0013$ $\Delta H = 11{,}000$
	Refs	[26]	[26]	[26]

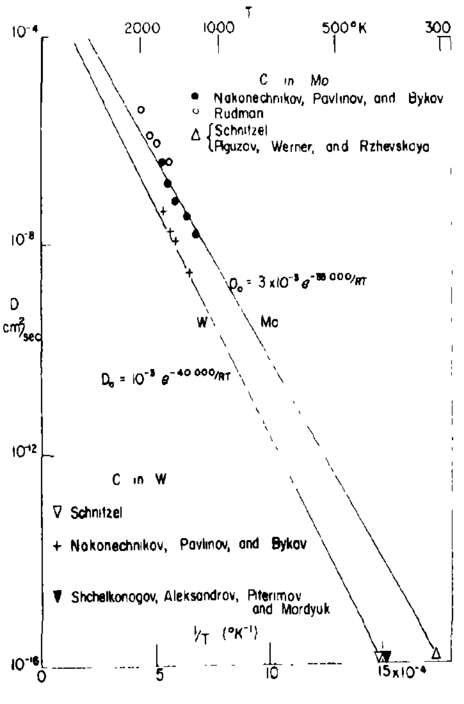

Fig. 1. Arrhenius plots for diffusion of C in Mo and W.

an extremely tentative damping peak yields values for both much lower, something like $D_0 \approx 5\times 10^{-2}$ and $\Delta H \approx 39{,}000$. These numbers are so tentative, however, that I hesitate to include them in the table.

The case for boron in iron is interesting. Snoek peaks are reported periodically [29–32] Most persistently, the peak is reported on top of (or near to) the Snoek peak for carbon in iron: This obviously leads to the surmise that carbon may inadvertently be added during boronizing, a position that is not easy to refute. The present status seems to this observer to be best drawn by the conclusions of Strocchi, Melandri, and Tamba[33], the Snoek peak for boron has not been seen and boron in bcc iron is most likely substitutional.

3. HYDROGEN IN THE bcc METALS

The diffusion of hydrogen in metals is of such intense current interest that it deserves a special section. It has been investigated quantitatively by several by several methods—by absorption and effusion, by nuclear magnetic resonance, by anelastic methods, and by low temperature aging of supersaturated solid solution. The importance of the study is two-fold; not only are the effects of hydrogen of immense importance in determining many of the mechanical properties, but the understanding of possible quantum effects in diffusion are of intense intellectual interest.

The diffusion of hydrogen in *iron* has been the subject of many investigations. Absorption and effusion studies have demonstrated the existence of two regimes in temperature—a high temperature region of low activation energy now thought to represent lattice diffusion of H-atoms and a lower temperature region of higher activation energy (and low values of D). This second region is apparently controlled by hydrogen trapping. The best of this work is that of Johnson and Hill, some representative values from their work are plotted in Fig. 2[34].

A more recent study involving charging of iron in electrolytic cell has been carried out by Choi[34]. His temperature range was necessarily limited, but he was able to extend the range of normal diffusion coefficients to lower temperatures. (See Fig. 2, where a few of his values are plotted.)

The first measurement of the Snoek peak of hydrogen in iron was made by Heller, using a torsional pendulum[36]. He found the peak near 30°K for a frequency of 1 Hz. A measurement at 80 kHz by Gibala put the Snoek peak at 48·5°K[37].

These four measurements are remarkably consistent. The straight line drawn in Fig. 2 shows no sign of curvature as would be expected if tunnelling were a factor at low temperature. The value of D_0 is 3×10^{-4}, that of ΔH is 1760 cal/mole (0·076 eV/atom).

The values of D which are deduced from the internal friction measurements are calculated according to the expression

$$D = \frac{a^2}{72\tau_r}. \quad (1)$$

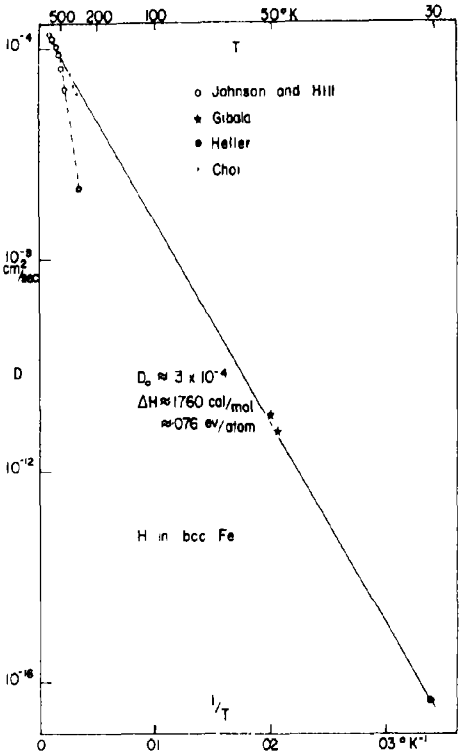

Fig. 2. Plot of diffusion coefficient of hydrogen in iron.

Here a is the cube edge of the bcc crystal and τ_r is the relaxation time. The number 72 is appropriate for tetrahedral site occupancy of hydrogen atoms with jumps being T–T jumps along ⟨110⟩ directions. Equation (1) is used throughout this paper for calculation of diffusion coefficients for hydrogen.

The diffusion of hydrogen in *niobium* has been the subject of numerous investigations. Unfortunately, considerable disagreement exists concerning the constants of diffusion. The first detailed study was an absorption-desorption series of measurements above 500°C yielding an activation energy around 9000 cal/mole[38]. An internal friction friction study in the range 90–105°K has been carried out by Cannelli and Verdini[39]. A few points in the same range have been added by Wert, Thompson and Buck (unreported data). Although these groups of measurements separately have quite different activation energies, the actual D values are relatively consistent; see the data and the line drawn in Fig. 3. The value of ΔH for this line is about 4150 cal/mole, the value of Cannelli and Verdini.

Several measurements have been reported yielding much lower activation energies. Two of these measurements of long range diffusion utilizing the Gorski effect yield an activation energy of only 2500 cal/mole[40, 41]. Although this value is much lower than that just cited, the actual D values are not much off the solid line drawn in Fig. 3, especially at the higher temperatures. These two measurements are in excellent agreement at temperatures above 250°K, but depart from each other below 250°K.

A determination of ΔH by the quench aging of supersaturated Hb-H alloys also yields a value near 2500 cal/mole[42]. Unfortunately, the method is incapable of giving explicit D values, so the data cannot be plotted in Fig. 3.

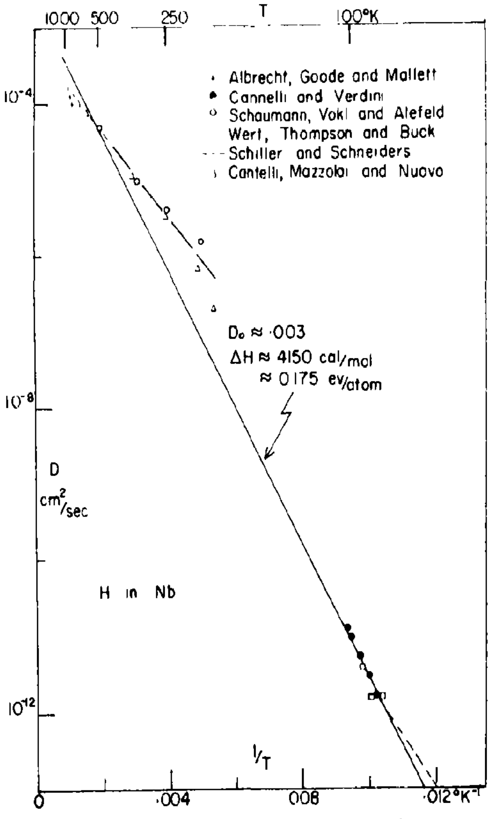

Fig. 3. Plot of diffusion coefficient of hydrogen in niobium.

Finally, a measurement of hydrogen diffusion using internal friction at frequencies lower than those of Cannelli and Verdini has been reported by Schiller and Schneiders [43]. They observed small changes in peak temperatures (and presumably then diffusion coefficients) as they varied the method of specimen preparation. Finally, they found a slight change in slope between their data and those of the earlier measurement (Fig. 3). Unfortunately, the break point comes right where the two pieces of data meet, with little overlap.

An overall assessment of this situation seems impossible at this time. Each of the measurements taken by itself seems to be well done. Yet the variation in reported activation energies of a factor of four is unreconcilable. Quite clearly, a simple comparison of slopes, as is usually made, is inadequate. At this time, it seems hard to discount the general correctness of the solid line close to the one drawn in Fig. 3. Were the data obtained using the Gorski effect consistent over the entire temperature range, the heavy dashed line in Fig. 3 would be a good possibility.

The nuclear magnetic resonance investigation of Zamir and Cotts bears an interesting relationship to the problem of hydrogen diffusion in niobium[44]. Although their work was mainly in two-phase regions where interpretation is difficult, one alloy is of extreme interest, the alloy $NbH_{0.7}$. If they knew their composition accurately and if the phase diagram is accurately known in that region of the phase diagram[45], this alloy cuts through the corner of the single-phase monohydride region at about 75°C. Consequently, the peculiar change in line narrowing which they observe (and could not fully explain) with increasing temperature between

60°–100°C can indeed be understood. It seems to have its origin in the passage through a two phase $\alpha+\beta$ region at low temperature, through a single phase β region, a two-phase $\alpha'+\beta$ region and finally into a single phase, α' (a solid solution of H in bcc Nb).

Values of proton correlation time, τ_c, (as given in Fig. 9 of their paper) can be converted to values of D, at least semiquantitatively, by the relation

$$D = r^2/12\tau_c. \qquad (2)$$

Here r is the interatomic distance and the factor of 12 is a constant given by Rowland [46]. These calculated values of D are plotted in Fig. 4. Whether the proportionality constant of twelve is precisely right for this case may perhaps be questioned, nevertheless the general correctness of the plot in Fig. 4 ought to be true.

Observe that ΔH for the α' region is about 3700 cal/mole, not much different from the solid line of Fig. 3 for diffusion in α. See also that the slope in the β-region gives a value of ΔH of about 9000 cal/mole, a value similar to the activation energy obtained for several kinetic processes involving changes in mechanical properties[47, 48]. Perhaps some of the reported property changes are due to phenomena in the hydride, not in the Nb–H solid solution.

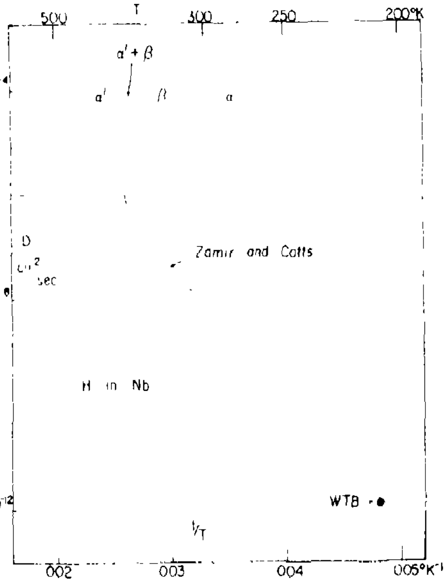

Fig. 4 Diffusion data calculated from NMR work of Zamir and Cotts.

Finally, a point labelled WTB is plotted in Fig. 4. This is the value of D calculated by single-point estimate for the 'precipitation peak' observed by Wert, Thompson and Buck. (See their paper in this issue.) This point was calculated assuming the applicability of equation (1) to this peak. An investigation is currently under way to see if that peak has an activation energy near 9000 cal/mole. If it does, the characteristics of that peak may provide valuable insight into the behaviour of hydrogen in the monohydride.

A short paragraph will suffice to discuss an excellent correlation which exists for diffusion of hydrogen in *tantalum*, Fig. 5. Massive absorption measurements at high temperature [49] and the internal friction work of Cannelli and Verdini[39] combine to give an overall

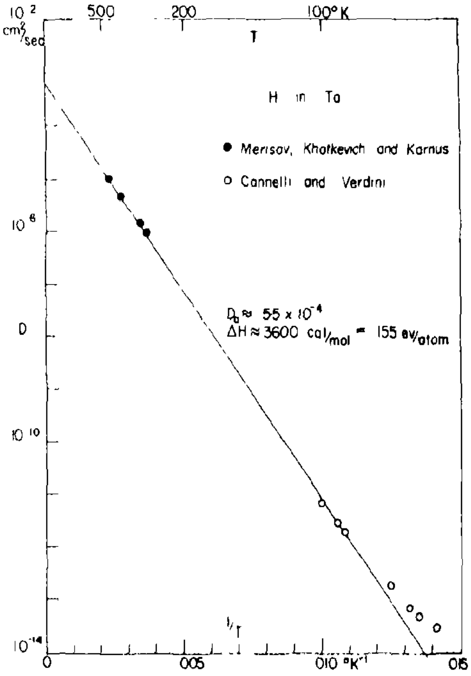

Fig 5. Plot diffusion coefficient of hydrogen in tantalum.

activation energy of 3600 cal/mole. If experience in other systems holds true here, this fit will be challenged as further data become available; for the present, however, it seems excellent.

Diffusion of hydrogen in *tungsten* has been measured quantitatively by Frauenfelder [50]. Using permeation methods, he found $D = 4{\cdot}1 \times 10^{-3} \exp(9000/RT)$. These values seem fairly consistent with data on other metals although ΔH may be too high compared to that for niobium and tantalum.

A few other data are available for several fcc metals. The results are listed in Table 2 along with those values just cited for the bcc metals Fe, Nb, Ta and W. Values of D_0 tend to be lower than those for C, N and O diffusing in the same metals. This is, in general, in accord with the proportionality between ΔH and ΔS[51], but quantitative correlation seems not possible at the present time.

A great deal has been written about the possibility of tunnelling-enhanced diffusion of light elements especially at low temperatures[36, 39, 41, 52, 53]. Tunnelling should manifest itself both in upward curvature of the Arrhenius plot at low temperatures and in differences in D with isotopic mass much larger than would be explained by mass differences in vibration frequency or correlation. Large differences in D are indeed observed between diffusion of hydrogen and deuterium in some instances, but no successful attempt has been made to use this variation in a quantitative way. Expected curvature of Arrhenius plots for diffusion of hydrogen has not been unambiguously proved in any instance. In particular, for the diffusion of hydrogen in iron, the activation energy is lower than any other so far measured, the ratio D_D/D_H seems to be at least a factor of 500[36], yet no curvature of the Arrhenius plot seems evident (Fig. 2). It would seem that any theory of tunnelling which attempts to explain effects seen in other systems should also explain why no enhancement is apparently seen in this one.

Table 2. *Values of* D_0 *and* ΔH *for Hydrogen diffusion in several metals. The values in parentheses for* Nb *are from the dashed line of Fig.* 4. D_0 *is in units* cm²/sec *and* ΔH *is in* cal/mole

Metal	D_0	ΔH
Iron	0·0004	1760
Niobium	0·003	4150
	(0·0005)	(2500)
Tantalum	0·00055	3600
Tungsten	0·0041	9000
Palladium	0·006	5990
Nickel	0·005	9560

4. NARROW DAMPING PEAKS

Most of the damping peaks associated with the Snoek effect are ideal; they fit the model of the standard linear solid and they can be interpreted in terms of thermally activated phenomena. In some instances, peaks are seen which are apparently not thermally activated: oftentimes these peaks are extremely narrow, only a few degrees wide.

A number of such peaks have been reported. The antiferromagnetic transformation in chromium displays such a peak[54]. The allotropic phase transformation $\alpha - \gamma$ iron has a pronounced peak[55–57]. A sharp peak exists in the $\alpha - \beta$ phase transformation in cobalt near 400°C. These peaks are all associated with phase transformations of some kind. Undoubtedly a great many more such damping peaks exist. At present, they are more of a curiosity than an aid in understanding the metals.

Another group of sharp peaks exist in some of the bcc metals. In Nb and Ta sharp peaks were found by deBatist between 200–250°K for frequencies near 1 Hz[58]. Sharp peaks were seen in Nb also near 200°K by Stanley and Szkopiak[59–61]. These peaks are around 5–10°K wide, as one can see from the figures in their papers. Three types of such narrow peaks are discussed in the paragraphs which follow, all three of which are found both in niobium and vanadium. (The original results quoted here are the joint work of Wert, Thompson and Buck – called here WTB).

The first type is that apparently associated with a eutectoid phase transformation. In niobium rods containing hydrogen, such damping peaks were seen on cooling through the temperature range 90–70°C. (See Fig. 8 of the paper WTB in this issue.) This is just region in which Walter and Chandler found the eutectoid phase transformation from α' to $\alpha+\beta$ to occur[45]. This peak was seen in spite of the fact that the overall hydrogen concentration was well within the α solid solution range at that temperature. Apparently some α' forms on cooling from above 155°C – perhaps in imperfect regions of the specimen. A similar peak is found at about 25°C in vanadium containing a small concentration of hydrogen; this observation would imply that such a eutectoid line must exist near room temperature in the vanadium–hydrogen system. (Thanks are due to Professor T. Scott for supplying the rod of vanadium.)

A second type of peak in these metals is the β-peak. In niobium it occurs near room temperature for frequencies near 15 kHz. If the peak (or cluster of peaks) near 200°K for frequencies near 1 Hz is also the β-peak, then the activation energy is close to 0·5 eV has been reported before[58–61]. From its position in temperature, one would also expect an energy of about 0·5–0·6 eV. However, the peak has a halfwidth only about half that required by such an activation energy.

A similar peak, thought also to be the β-peak, occurs in vanadium below room temperature at 18 kHz. It, too, is only about half the expected width for a peak occurring at that temperature.

These β-peaks have been seen in several well annealed samples of niobium and in an annealed rod of vanadium, all of which contained some hydrogen. We do not know the exact conditions under which they occur and we are unable to prescribe heat treatments necessary to ensure their presence or absence. Nevertheless we are not convinced that dislocations are necessary for their existence, and we tend to believe – as do Stanley and Szkopiak[61] – that they are caused by interstitial complexes (perhaps containing hydrogen). The narrowness may be caused by cooperative motion of the interstitials.

Finally, a third type of peak is the ultranarrow spike such as that seen near 235°K in niobium. One example of it is seen in Fig. 7 of WTB (this issue). Another is seen in Fig. 6 (this paper). This spike is less than 2°K wide at half maximum. It is also accompanied by a slight change either in sample length or in Young's modulus; from the little jog in the curve of frequency vs. temperature in Fig. 6, we cannot deduce which. The spike does not shift in temperature with change in frequency. A specimen heated slowly through this temperature range shows a slight thermal arrest at the temperature of the peak[62]. This peak shows hysteresis, on cooling it occurs near 205°K; see the data plotted in Fig. 7.

The phenomenon responsible for this effect may be a phase transformation similar to those which have been observed in certain hydrides of tantalum[63]. However, since it occurs in all specimens of our niobium, regardless of degree of attempted dehydrogenation, it may also be a martensitic type reaction in the α-solid solution.

Such sharp peaks as these are found in vanadium as well. An example is shown in Fig. 8 for a vanadium rod in two different conditions. Run 1 was made upon warming up from 20°K a specimen containing 80 ppm (wt.) of hydrogen. Run 2 was made upon such a warmup after the rod had been annealed in a vacuum of 10^{-6} torr for several hours at 600°C. These spikes are about 5° wide. Their existence may also indicate a transformation of some kind at about 125°K

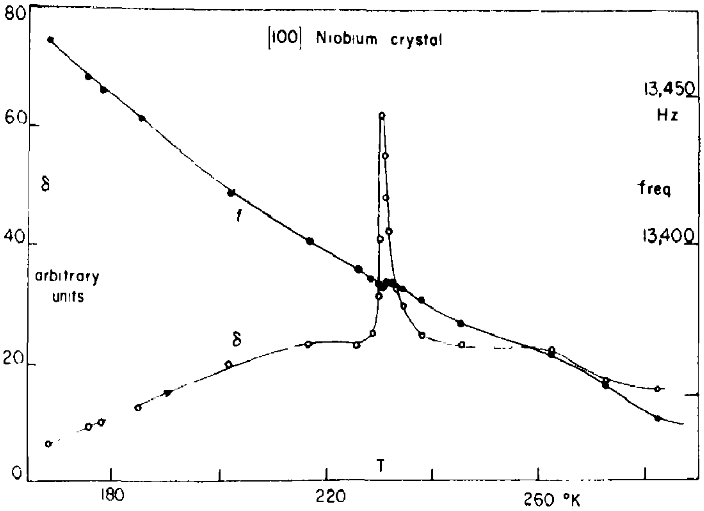

Fig. 6. Damping spike in niobium apparently associated with phase transformation.

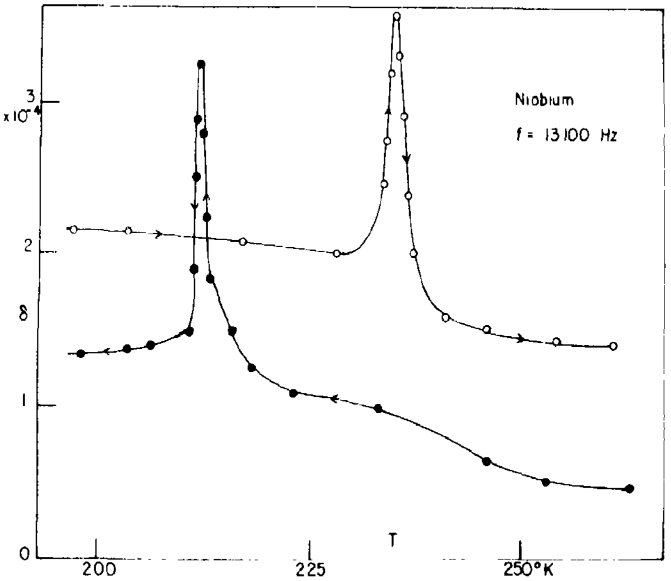

Fig. 7 Hysteresis of damping spike in niobium

in either the α-solid-solution or the hydride. Again one has to presume that some residual hydrogen may remain after the vacuum anneal.

Even though damping peaks associated with phase transformations have been known for at least 20 yr, no attempt has been made to deduce their relationship to the nature of the transformations. At present they are of most use in merely indicating the presence of transformations.

5. BROAD DAMPING PEAKS

Thermally activated damping peaks too

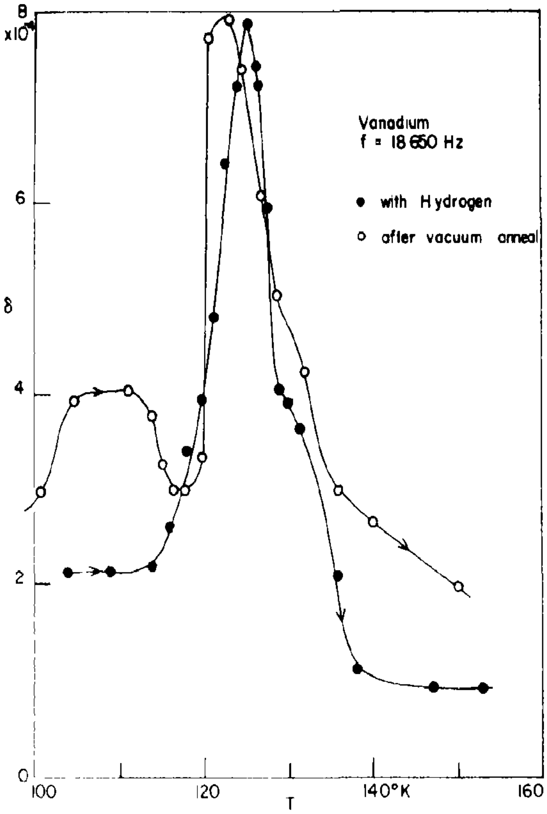

Fig. 8. Low temperature damping spikes in vanadium.

wide to be a single relaxation have been observed almost from the beginning of quantitative measurement of damping. Two chief techniques have been developed in analysis of such peaks; (1) assumption of a continuous distribution in both relaxation time and relaxation strength and description of the peaks in terms of appropriate analytical functions, (2) assumption of a limited set of discrete relaxations and determination of strengths and relaxation times of all components of the set. Discussion of decomposition of experimental curves in terms of one or the other of these models has been discussed adequately by Berry and Nowick [64] and Wert[65]. Those considerations will not be repeated here. Rather, a few comments will be made for the case of the discrete set and those comments mostly concerned with the thermodynamics of the entities which may be responsible for the relaxations.

These considerations have their origins in the paper of Dijkstra and Sladek which first reported such broadened peaks in alloys of iron and nitrogen with such other alloying elements as Mn, Cr and Mo[66]. They supposed that small clusters such as Mn–N, etc. were responsible for the relaxations additional to the normal iron–nitrogen Snoek peak. The simplest of these clusters is simply the substitutional-interstitial (S–i) pair, which is present in concentration given by

$$C_p = (Z_p/3) C_s C_i \exp(-\Delta S^0_{Si}/R) \times \exp(\Delta H^0_{Si}/RT). \qquad (3)$$

Here C_p, C_s and C_i are atom fractions of pairs, unpaired substitutional atoms and unpaired interstitials, respectively; Z_p is the multiplicity of the pairs; ΔS^0_{Si} and ΔH^0_{Si} are the entropy and enthalpy of binding, respectively. Equation (3) applies to dilute solution. Corresponding expressions may be written for *S–i–S* and *i–S–i* clusters and for higher order clusters as well.

This expression is not immediately applicable in all its details to a damping measurement since the specific damping capacity of a cluster of a given type must be known to permit its complete application. However, for determination of the most important thermodynamic quantity, the enthalpy of binding, this constant need not be known. In spite of this fact, no measurements of the enthalpy of binding have been reported. Several reasons exist for this fact, but with clever enough experimental technique they are not insurmountable.

The Zr–O pair in niobium forms one extreme case – that of a tightly bound cluster. The binding enthalpy is apparently so large that almost all oxygen added to the alloy is paired at normal temperature of measurement until the Zr is saturated; hence, no partitioning can be detected at low temperatures [67, 68]. In fact, the normal Snoek peak (which is proportional to C_i) does not appear at measuring temperatures near 200°C until the Zr atoms are almost all associated in an O–Zr–O complex. The binding enthalpy of the Zr–O pair must be several electron volts.

The other extreme, that of extremely weak binding is typified by the W–O complexes in niobium where no interaction peaks of any kind have been observed [69]. Neither has evidence been seen that complexes such as Ni–C, Cr–C and Mo–C exist in iron in appreciable numbers [70]. For complexes such as these, the binding enthalpy must be no greater than a few hundredths of an electron volt (or it may even be negative).

The possible candidates for successful measurement at present seem to be those for which the binding enthalpy is from 0·1 to perhaps 1 eV. Many of the ternary alloys Fe–Me–N would seem to fall into this category, although identification of the Mn–N complexes in iron is plagued by a third relaxation of unknown origin [66, 71]. Undoubtedly all of the refractory metal alloys will be found to exhibit many *S–i* clusters which may be metallurgically important. Mosher has proposed a tentative criterion by means of which one might predict the probable existence of such damping peaks [69].

The experimental problem is only that of making proper isothermal measurements at several temperatures so that equation (3) may be applied. This is an extremely difficult task for peaks widely different in relaxation time; perhaps the extrapolation method of Mosher will be found to be extremely useful [69].

The same general considerations apply to the self-clustering of interstitials. The initial notable paper of Powers and Doyle describing pairing of oxygen atoms in Ta [72] has been followed by several additional studies. The condition of equilibrium of clusters of various size can best be written in terms of the concentration of single interstitials, C_l.

$$C_i = (Z_i/Z_l^i)C_l^i \exp(-\Delta HS_i^0/R) \times \exp(DH_i^0/RT). \tag{4}$$

Here Z_i and Z_l are multiplicity of clusters of size i and l, respectively. The factors ΔS_i^0 and ΔH_i^0 are the entropy and enthalpy of binding of the cluster of size i. Again the range of enthalpy values for successful measurement by anelastic means seems to be from about 0·1–1·0 eV per cluster.

The basic problems here are the securing of data adequate for analysis into closely spaced component peaks and the interpretation of these components in terms of specific clusters. The several papers which have been published have been reviewed by Cost, Gibala and Wert [73].

Two additional considerations must be

cited here. First, several authors report that interstitials exhibit long range order in rather dilute solution in some of the refractory metals [74, 75]. Whether clusters of small size may form within these ordered domains is not known. Second, alternate means should be sought to measure the presence and number of the small clusters. This seems to be a formidable task.

Acknowledgements – The assembling of data for this review would have been impossible except for the cooperation of many authors who kindly supplied much information well in advance of its publication. Special thanks is due Professor R. Gibala for his long-continued assistance in the collection of data on diffusion of interstitials

REFERENCES

1. DIJKSTRA L. J., *Philips Res. Rep.* **2**, 357 (1947)
2. KÊRT.S., *Phys. Rev.* **71**, 533 (1947).
3. WERT C. A., *Phys. Rev.* **79**, 601 (1950)
4. WERT C. A. and ZENER C., *Phys. Rev.* **76**, 1169 (1949)
5. FORD A. F. and BESHERS D. N., *Acta metall* **14**, 1659 (1966)
6. POWERS R. W. and DOYLE M. V., *J. appl. Phys.* **30**, 514 (1959).
7. DIJKSTRA L. J., *Trans. AIME* **185**, 252 (1949)
8. WERT C. A., *Acta metall* **2**, 361 (1954)
9. ISON A., NUTTING J. and MENTER J., *J. Iron Steel Inst* **172**, 163 (1952)
10. THOMAS W. R. and LEAK G. M., *Phil. Mag.* **45**, 986 (1954)
11. DOLLINS C. and WERT C. A., *Acta metall* **17**, 711 (1969)
12. STANLEY J. K., *Trans. AIME* **185**, 752 (1949).
13. HOMAN C. G., *Acta metall* **12**, 1071 (1964)
14. WERT C. A., *J. appl. Phys.* **21**, 1196 (1950).
15. EAST J. D. and VERRIJP M. B., *J. Iron Steel Inst.* **176**, 24 (1964)
16. POWERS R. W. and DOYLE M. V., *J. appl. Phys.* **30**, 514 (1959)

16a. SON P., MIYAKA M., and SANO I., *Technology Rep. Osaka Univ* **18**, 828, 317 (1968)

18. NAKONECHNIKOV A. I., PAVLINOV L. V. and BYKOV V. N., *Physics Metals Metallogr* **22**, 2, 73 (1966).
19. KLEIN M. J., *J. appl. Phys.* **38**, 167 (1967).
20. de MORTON M. E., *J. appl. Phys.* **33**, 2768 (1962).
21. ZEMSKIY S. V. and SPASSKIY M. N., *Physics Metals Metallogr.* **21**, 1, 129 (1966).
22. SCHNITZEL R. H., *Trans. AIME* **230**, 609 (1964).
23. SCHNITZEL R. H., *Trans. AIME* **230**, 186 (1965).
24. PIGUZOV Y. V., WERNER W. D. and RZHEVSKAYA, I. Y., *Physics Metals Metallogr.* **24**, 3, 173 (1967).
25. SHCHELKONOGOV V. Y., ALEKSANDROV L. N., PITERIMOV V. A. and MORDYUK V. S., *Physics Metals Metallogr* **25**, 1, 68 (1968).
26. PETERSON D. T. and CARNAHAN T., *Trans. AIME* **245**, 213 (1969).
27. RUDMAN P. S., *Trans. AIME* **239**, 1949 (1967)
28. FRAUENFELDER R., *J. chem. Phys.* **48**, 3966 (1968).
29. HASIGUTI R. R. and KAMOSHITA H., *J. phys. Soc. Japan* **9**, 646 (1954).
30. THOMAS W. R. and LEAK G. M., *Nature, Lond.* **176**, 29 (1955).
31. PRIDANTSEV M. V., MESCHERINOVA O. N. and PIGUZOV Y. V., *Dokl. Akad. Nauk. SSSR* **111**, 98 (1956)
32. TAVADZE F. N., BAIRAMASHVILI I. A. and METREVELI V. S., *Soobsch Akad. Nauk. gruz. SSR* **40**, 401 (1965).
33. STROCCHI P. M., MELANDRI B. A and TAMBA A., *Nuovo Cim.* **51**, 1 (1967).
34. JOHNSON E. W. and HILL M. L., *Trans. AIME* **216**, 1105 (1960).
35. CHOI J. Y., *Trans. AIME* (Private Communication)
36. HELLER W. R., *Acta metall.* **9**, 600 (1961)
37. GIBALA R., *Trans. AIME* **239**, 1574 (1967).
38. ALBRECHT W. M., GOODE W. D. and MALLETT M. W., *J. electrochem. Soc.* **106**, 981 (1959)
39. CANNELLI G. and VERDINI L., *Ricerca scient.* **36**, (2), 98 (1966).
40. SCHAUMANN G., VÖKL J. and ALEFELD G., *Phys. Rev. Lett* **21**, 891 (1968).
41. CANTELLI R., MAZZOLAI F. M and NUOVO M., *Phys. Status. Solidi.* **34**, (1969).
42. SASAKI Y. and AMANO M., *Trans. Japan Inst Metals* **10**, 29 (1969).
43. SCHILLER P. and SCHNEIDERS A., *Int Conf Vacancies and Interstitials in Metals, Julich*, Vol. 2. 871 (1968).
44. ZAMIR D. and COTTS R. M., *Phys. Rev.* **134**, A666 (1964).
45. WALTER R. J. and CHANDLER W. T., *Trans AIME* **233**, 762 (1965)
46. ROWLAND T. J., *Progress in Metal Physics* (Edited by B. Chalmers), Vol 9, p 1. Pergamon Press, Oxford.
47. Wilcox B. A. and HUGGINS R. H., *J. less-common Metals* **2**, 292 (1960).
48. WILCOX B. A. and HUGGINS R. H., *Columbium Metallurgy* (Edited by D. A. Douglass and F. W. Kunz), p 257. Interscience, New York (1961).
49. MERISOV B., KHOTKEVICH V. and KARNUS A., *Physics Metals Metallogr.* **22**, 2, 163 (1966).
50. FRAUENFELDER R., *Westinghouse Int. Rep Scient. Paper* No. 68-1E1-HIVAC-P2 (1968); *J. Vacuum Science and Technology*, **6**, 388 (1969).
51. WERT C. and ZENER C., *Phys. Rev* **76**, 1169 (1949).
52. FLYNN C. P., *Phys. Rev.* **171**, 682 (1968).
53. BLAESSER G. and PERETTI J., *Int. Conf. Vacancies and Interstitials in Metals, Julich*, Vol. 2, p. 886 (1968).
54. EINE M. E., GREINER E. S. and ELLIS W. C., *Trans AIME* **191**, 56 (1951).
55. GARBER R. I., DATSKO O. I. and KHARITONOVA ZH. F., *Physics Metals Metallogr.* **25**, 1, 164 (1968).

56. KERR J. R., Thesis, Univ. of Illinois (Urbana) (1963).
57. GARBER R. I., DATSKO O. I., IVANOV I. G and KHARITONOVA ZH. F., *Physics Metals Metallogr* **25**, 3, 164 (1969).
58. deBATIST R., *Phys. Status Solidi*. **2**, 661 (1962).
59. STANLEY M. W. and SZKOPIAK Z. C., *J. Inst. Metals*. **94**, 80 (1966).
60. STANLEY M. W. and SZKOPIAK Z. C., *J. nucl. Mater*. **23**, 163 (1967).
61. STANLEY M. W. and SZKOPIAK Z. C., *J. mater Sci*. **2**, 559 (1966).
62. VISWANADHAM R. K., M. S. Thesis, Univ. of Illinois (Urbana) (1970).
63. WALLACE W. E., *J. chem. Phys* **35**, 2156 (1961).
64. BERRY B. S and NOWICK A. S., *Physical Acoustics* (Edited by W P. Mason), Vol. 3, Part A, Chap. 1 Academic Press, New York (1966).
65. WERT C., *Physical Acoustics* (Edited by W P. Mason), Vol. 3, Part A, Chap. 2. Academic Press, New York (1966)
66. DIJKSTRA L. J. and SLADEK R., *Trans. AIME* **197**, 69 (1953).
67. BUNN P. M., CUMMINGS D. G. and LEAVENWORTH H. W., JR., *J. appl. Phys*. **33**, 3009 (1962).
68. MINER R. E., Thesis, Case Western Reserve University (1968).
69. MOSHER D., Thesis, Univ. of Denver (1969).
70. WERT C. A., *Trans. AIME* **194**, 602 (1952)
71. ENRIETTO J. F., *Trans. AIME* **224**, 1119 (1962).
72. POWERS R. W and DOYLE M. V., *Trans. AIME* **215**, 655 (1959).
73. COST J. R., GIBALA R. and WERT C. A., *Energetics in Metallurgical Phenomena Series*, Vol. 5. Gordon and Breach, New York
74. VILLAGRANA R. E. and THOMAS G., *Phys. Status Solidi* **9**, 499 (1965).
75. JONES K. A., MOSS S. C. and ROSE R. M., *Acta Metall*. **17**, 365 (1969)

J. Phys. Chem. Solids Pergamon Press 1970. Vol. 31, pp. 1785–1791 Printed in Great Britain

INTERNAL FRICTION IN FERROELECTRICS DUE TO INTERACTION OF DOMAIN BOUNDARIES AND POINT DEFECTS

V. S. POSTNIKOV, V. S. PAVLOV and S. K. TURKOV

Voronezh Polytechnical Institute, Voronezh, Plelchenov Street 84, U.S.S.R.

(*Received 5 September 1969*)

Abstract—Torsion pendulum and resonance techniques were used for investigation of polycrystalline lead zirconate-titanate internal friction in the temperature range of 20–400°C. The compositions of samples were chosen close to the morphotropic phase boundary. Measurements of Q^{-1} were made on lead zirconate–titanate samples modified by the additions of niobium pentoxide (*B*-composition) and without any additions (*A*-composition). Two relaxation peaks were found on the $Q^{-1}(T)$ curves of the *A*-samples at 140 and 240°C; for *B*-samples these peaks were not observed. It is proposed that the peaks on the $Q^{-1}(T)$ curve are due to interaction of domain boundaries and charged point defects. The concentration of defects was changed by high-temperature annealing in different atmospheres. A calculation is presented of the value of internal friction caused by the diffusion of point defects to domain boundaries, where piezoelectric bound charges appear. The results of the calculations are in satisfactory agreement with the experimental data.

THE PROPERTIES of ferroelectrics largely depend on their domain structure geometry and the nature of interaction of domain boundaries and various imperfections of their crystal lattice. Along with other methods used for investigation into the structure of ferroelectrics and kinetics of various processes occuring in them due to external forces, the internal friction method is more and more widely used. Owing to some reasons of technological character polycrystalline ferroelectrics have high concentration of point defects. In view of this our work is concerned with internal friction of polycrystalline lead zirconate titanate solid solutions. Lead zirconate titanate has found wide application in different branches of technology due to good electromechanical properties.

Internal friction in the temperature range of 200–400°C was studied on lead zirconate titanate samples of the following stoichiometric composition:

A – $Pb_{0.95}Sr_{0.05}(Zr_{0.53}Ti_{0.47})O_3 + 3\%$ PbO

B – $Pb_{0.95}Sr_{0.05}(Zr_{0.53}Ti_{0.47})O_3 + 3\%$ PbO $+ 1\%$ Nb_2O_5.

The samples correspond to lead zirconate titanate solid solution which in its composition is close to the morphotropic phase boundary. At room temperature the samples have perovskite tetragonal structure with parameters $a = 4{\cdot}025$ Å, $c = 4{\cdot}112$ Å. The Curie temperatures of *A* and *B* compositions are 330 and 280°C, respectively. The synthesis of the samples was carried out according to industrial technology[1]. After cutting and polishing the samples were annealed for 8 hr at 750–800°C to remove stresses due to mechanical treatment.

The temperature dependence curve of internal friction which was studied in the papers[2, 3] had some relaxation peaks in the temperature range corresponding to ferroelectric phase (Fig. 1). For *B* composition samples the dependence of $Q^{-1}(T)$ (curve 2) has only one peak related to the phase transformation at the Curie temperature. In contrast to the *B* composition curve, the *A* composition curve measured at a frequency of about 1 c/s has relaxation peaks at temperatures about 140 and 240°C. Activation energies of the 140 and 240°C peaks calculated

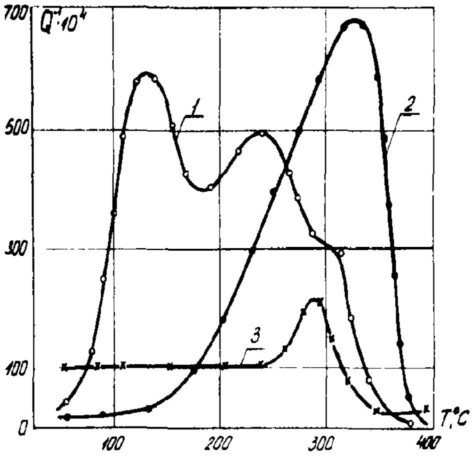

Fig 1 Internal friction temperature dependence measured at a frequency of about 1 c/s for *A* composition samples – curve 1, *B* composition samples – curve 2, and at a frequency of 180 c/s for an *A* composition sample – curve 3

by means of frequency shift are equal to 0·4 and 0·8 eV, respectively.

Curve 3 showing internal friction temperature dependence of *A* composition samples measured at a frequency of 180 c/s has no relaxation peaks. The 325°C peak is due to phase transformation from ferroelectric to paraelectric state. At this frequency the 140°C peak should occur at about 490°C. The absence of the peak in the above mentioned temperature range (curve 3) indicates that it is characteristic only of the ferroelectric phase. One can suppose that this peak is due to interaction of domain boundaries and point defects. It can be seen from the stoichiometric composition of the samples that these point defects may be oxygen and zirconium-titanium vacancies. This is supported by the absence of relaxation peaks on curve 2 for the *B* composition in which the number of vacancies is small due to the addition of Nb_2O_5. Two mechanisms related to point defects were proposed for the explanation of the peaks.

In the first case we consider energy losses due to vibration damping of 90° domain boundaries caused by their interaction with mobile point defects[2]. Then the process of relaxation proceeds in the following manner. Instantaneously applied stresses σ displaces the domain wall from the equilibrium position by the distance R, defined by the quasi-elastic forces κR and the forces of interaction f with point defects which remained in the original position. After a certain period of time sufficient for the diffusive disphacement of point defects to a new position of the wall, the latter forces become equal to zero. As a result, the wall shows additional displacement accompanied by additional strain, i.e. relaxation takes place.

The surface density of the wall and point defect interaction forces at small displacements R may be considered to be proportional to this displacement

$$f = \alpha R. \tag{1}$$

The calculation[2] showed that the relative modulus defect Δ for $\alpha \ll \kappa$ is given by

$$\Delta = 2\Omega^2\left(\frac{c}{a} - 1\right)^2 \Lambda \frac{\alpha}{s\kappa^2}, \tag{2}$$

where Ω is the orientation factor, Λ is the domain wall surface area per unit volume, s is the elastic shear compliance constant.

The coefficient α depends in magnitude on the nature of interaction of domain walls and point defects. We shall find this coefficient assuming that the interaction is of electrostatic nature.

Accidental deflection of a domain boundary from the position symmetrical with respect to spontaneous polarization vectors P_s of the neighbouring domains by the angle $\delta\psi/2$ gives rise to a bound charge at the boundary with the density.

$$\rho = \frac{1}{\sqrt{2}} P_s \delta\omega. \tag{3}$$

We shall also assume that the crystal contains point defects of opposite signs, some of them are mobile and the others—motionless. For calculation we shall adopt a simplified periodic scheme of domain boundary arrangement, the charges of the neighbouring domain boundaries being equal in magnitude and of opposite signs (Fig. 2). Then neglecting the dielectric constant ϵ anisotropy for the region $-L < x < L$ we can write the equation for the electrostatic potential

$$\frac{d^2\varphi}{dx^2} = -\frac{q(c-c_0)}{\epsilon\epsilon_0} - \frac{\rho}{\epsilon\epsilon_0}\left[\delta\left(x-\frac{L}{2}\right) - \delta\left(x+\frac{L}{2}\right)\right]. \tag{4}$$

Here q and c are the charge and the number of point defects per unit volume, respectively, c_0 is the equilibrium concentration in the absence of an electric field, $\epsilon_0 = 8{\cdot}85 \,.\, 10^{-12}$ f/m is the electrostatic constant, L is the distance between the neighbouring domain boundaries, ρ is the surface density of the wall charge, $\delta(x)$ is the Dirac delta function. The first term on the right-hand side of (4) is due to the point defect volume charge, the second—due to the charge of domain walls located at points $x = \pm L/2$ (domain boundaries are assumed to be infinitesimally thin). The equation (4) holds if domain boundaries are in the equilibrium positions.

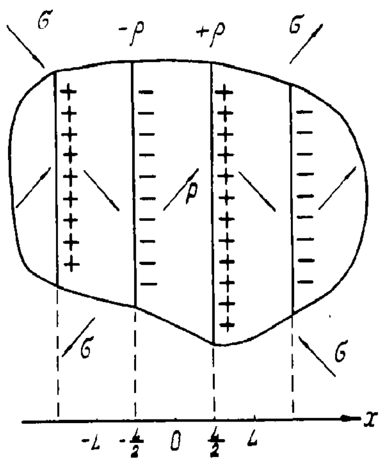

Fig. 2. A simplified diagram of 90° domain boundary arrangement in a crystal.

The first moment after the wall displacement the point defect concentration is given by

$$c = c_0 e^{-q\varphi/kT}. \tag{5}$$

If the interaction energy of a point defect and an electric field is far less than kT, i.e. when the condition

$$\left(\frac{q\varphi}{kT}\right)_{\max} \approx \frac{q\rho L}{kT\epsilon\epsilon_0} \ll 1 \tag{6}$$

is fulfilled, we have from equation (5)

$$c = c_0\left(1 - \frac{q\varphi}{kT}\right). \tag{7}$$

Substituting equation (3) into equation (6) and taking $P_s = 0{\cdot}25$ c/m², $q = 1{\cdot}6 \,.\, 10^{-19}$ c, $L \sim 10^{-7}$ m, $\epsilon \sim 1000$, $T = 400$°K, one can see that the condition (6) is fulfilled for $\delta\psi < 10^{-2}$.

From the equations (4) and (7) at periodic boundary conditions we obtain

$$c = c_0 - \frac{2qc_0\rho L}{\pi^2 kT\epsilon\epsilon_0} \sum_{n=1}^{\infty} \frac{(-1)^n \sin\frac{\pi(2n-1)x}{L}}{(2n-1)^2 + \frac{q^2 c_0 L^2}{\pi^2 kT\epsilon\epsilon_0}}. \tag{8}$$

The potential of the electrostatic field induced by point defects (the field induced by domain boundaries being subtracted) obeys the equation

$$\frac{d^2\varphi_c}{dx^2} = -\frac{q(c-c_0)}{\epsilon\epsilon_0}. \tag{9}$$

Substituting equation (8) into equation (9) we obtain

$$\varphi_c = -\frac{2q^2 c_0 \rho L^3}{\pi^4 kT\epsilon^2{\epsilon_0}^2} \sum_{n=1}^{\infty} \frac{(-1)^n \sin\frac{\pi(2n-1)x}{L}}{\left[(2n-1)^2 + \frac{q^2 c_0 L^2}{\pi^2 kT\epsilon\epsilon_0}\right]}. \tag{10}$$

If the domain wall is displaced from the equilibrium position by the distance $R \ll L$, the force acting on it due to point defects is given by the formula

$$f = -\rho \frac{d\varphi_e}{dx}\bigg|_{x=L/2+R} = \alpha R \tag{11}$$

where

$$\alpha = \frac{2q^2c_0\rho^2L}{\pi^2kT\epsilon^2\epsilon_0{}^2}\sum_{n=1}^{\infty}\frac{1}{(2n-1)^2+\dfrac{q^2c_0L^2}{\pi^2kT\epsilon\epsilon_0}}$$

$$= \frac{\pi\rho^2}{2\epsilon\epsilon_0L}\operatorname{th}\frac{q^2c_0L^2}{2\pi kT\epsilon\epsilon_0}. \tag{12}$$

If one relaxation time is assumed, it follows from equations 2, 3 and 12 that the internal friction peak height is

$$Q^{-1}_{\max} = \frac{\Delta}{2} = \frac{\pi\Omega^2\left(\dfrac{c}{a}-1\right)^2 AP_s{}^2(\delta\varphi)^2}{4s\kappa^2\epsilon\epsilon_0L}$$

$$\operatorname{th}\frac{q^2c_0L^2}{2\pi kT\epsilon\epsilon_0}. \tag{13}$$

Another mechanism of internal friction due to interaction of charged point defects and 90° domain boundaries was proposed in the paper [3]. Domain boundaries are assumed to be motionless. The process of relaxation proceeds as follows. Mechanical stresses induce piezoelectric charges at domain boundaries. As time passes these charges are compensated by charged point defects diffusing towards them. As a result, the electric field within the domain changes. This is accompanied by additional deformation of the crystal due to inverse piezoelectricity.

The derivation of internal friction for the domain structure represented in Fig. 2 gives the following expression

$$Q^{-1} = \frac{4q^2(d_{33}-d_{31})^2c_0D}{\pi^2\epsilon^2\epsilon_0{}^2kTs}\cdot\frac{\omega\tau^2}{1+\omega^2\tau^2} \tag{14}$$

where

$$\tau = \frac{1}{D}\left(\frac{\pi^2}{L^2}+\frac{q^2c_0}{\epsilon\epsilon_0kT}\right)^{-1}, \tag{15}$$

d_{33}, d_{31} are piezoelectric moduli, D is the point defect diffusion coefficient, ω is the vibration frequency.

At low concentrations of point defects when the condition

$$\frac{q^2c_0L^2}{\epsilon\epsilon_0kT\pi^2} \ll 1 \tag{16}$$

is fulfilled, the internal friction peak magnitude and the relaxation time are given by

$$Q^{-1}_{\max} = \frac{2(d_{33}-d_{31})^2c_0L^2q^2}{\pi^4\epsilon^2\epsilon_0{}^2kTs} \tag{17}$$

$$\tau = \frac{L^2}{\pi^2D}. \tag{18}$$

The fulfilment of the condition reciprocal to equation 16 gives

$$Q^{-1}_{\max} = \frac{2(d_{33}-d_{31})^2}{\pi^2\epsilon\epsilon_0s} \tag{19}$$

$$\tau = \frac{\epsilon\epsilon_0kT}{Dq^2c_0}. \tag{20}$$

The estimations of the internal friction peak at high concentration of point defects are in good agreement with the experiment [3].

In a general case in the presence of 180° and 90° domain boundaries the calculations become rather complicated due to inhomogeneity of the induced electric fields. However, if the distance between 90° domain boundaries is far greater than that of between 180° boundaries the contribution of the latter into internal friction is estimated using formulas (14–20) with the substitution of $\sqrt{2}d_{15}$ for $(d_{33}-d_{31})$.

Now compare the calculated values obtained for the above two models of energy dissipation. The difficulty in estimating the relaxation effect with the first model is connected with the fact that the quasi-elastic factor κ is unknown. However, one can estimate the minimum possible value of this factor in the following manner. Crystal strain due to domain boundary displacement $\Omega^2/\kappa((c/a)-1)^2\Lambda\sigma$ cannot exceed strain calculated by means of the known elastic constants $(s/2)\sigma$. Hence, we obtain

$$K > \frac{2\Omega^2\left(\frac{c}{a}-1\right)^2\Lambda}{s}. \tag{21}$$

Substituting (21) into (13) and comparing with (14) one can see that at $s = 2 \,.\, 10^{-11}$ m^2/N, $\Lambda \sim 1/L$, $(d_{33}-d_{31}) = 4 \,.\, 10^{10}$ c/N, $\delta\psi = 10^{-2}$, $P_s = 0{\cdot}25$ c/m², $\Omega \sim 10^{-1}$, internal friction associated with the vibrating 90° domain boundary damping is at least a factor of 10^3 lower than Q^{-1} due to piezoelectricity at domain boundaries.

Thus the second mechanism is likely to be dominant. It should be noted, however, that while estimating internal friction due to the first mechanism only electrostatic interaction of point defects with domain boundaries was taken into account. Consideration of other types of interaction can significantly increase the contribution of this energy loss mechanism.

In an attempt to verify the relaxation mechanism we studied the dependence of internal friction on the point defect concentration. The concentration was changed by thermal treatment in different atmospheres. Assuming that point defects responsible for relaxation are stoichiometric vacancies of oxygen and zirconium-titanium it is possible to suggest that isothermal annealing in the air at $T = 950$–$1000°$ must decrease vacancy concentration since such temperatures cause extensive evaporation of lead. Annealing in the air lasted for 1–8 hr. Isothermal annealing in a reducing atmosphere must lead to the build-up of oxygen vacancy concentration. The same effect may be expected from annealing in the atmosphere of saturated vapour of lead. We carried out annealing in a hydrogen atmosphere at 400–600°C for 0·5–6 hr. Annealing in saturated vapour of lead was made in an evacuated quartz ampule with lead. The time of annealing at about 1000°C was 1–8 hr. Building up of vacancy concentration may also be expected after annealing in a vacuum at elevated temperatures.

Annealing in a vacuum was accompanied by constant evacuation through a nitrogen trap which prevented the oil vapour of the diffusion pump hitting the surface of the samples. The temperature of annealing was 550–600°, the time 1–8 hr, a vacuum about 10^{-3} torr.

Internal friction measurement at ~ 1 c/s was made by the low frequency torsion pendulum technique[4]. The samples had the shape of prisms with the dimensions 3 × 3 × 90 mm. The sample relative strain amplitude was not more than 10^{-5}.

Internal friction at frequencies about 100 c/s was measured with flexural vibrations using the technique described in paper[4]. The samples were plates with the dimensions 3 × 35 × (0·2 + 0·3) mm. Since sample vibrations were excited electrostatically one of the plate sides was evaporated with aluminium.

Isothermal annealing in an air atmosphere causes the displacement of 140° peak to high temperature region and the increase of its value (Fig. 3). An opposite effect is observed

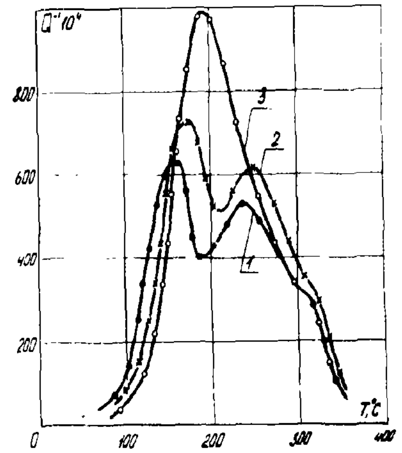

Fig. 3. Internal friction temperature dependence for *A* composition samples annealed in the air at *T* 1000°C for 1 hr – curve 1, 3 hr – curve 2, 8 hr – curve 3.

on the temperature dependence of internal friction of the samples annealed in a saturated lead vapour atmosphere. After the above mentioned thermal treatment the *B* composition internal friction did not change. Annealing in a hydrogen atmosphere was made on the original *B* composition and *A* composition samples subjected to preliminary isothermal annealing in the air at about 1000°C. As a result of this, the temperature dependence of the *B* composition internal friction (Fig. 4) shows a relaxation peak. Increasing the time of annealing in hydrogen raises the value of the peak and causes its displacement towards lower temperatures (curves 1–3). A similar peak appears for the *B* composition samples after their annealing in a vacuum at the temperature of 550°C (curve 4).

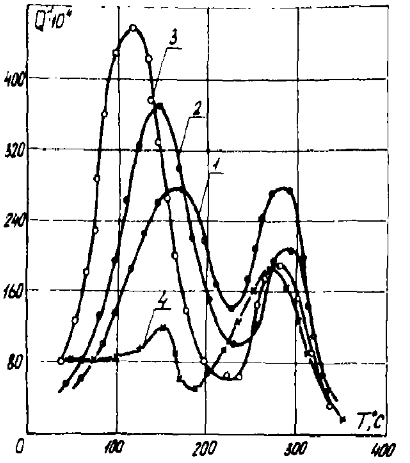

Fig. 4 Internal friction temperature dependence for *B* composition samples annealed in hydrogen at $T = 550°C$ for 1 hr – curve 1, 3 hr – curve 2, 5 hr – curve 3, and in a vacuum at $T = 550°C$ for 6 hr – curve 4.

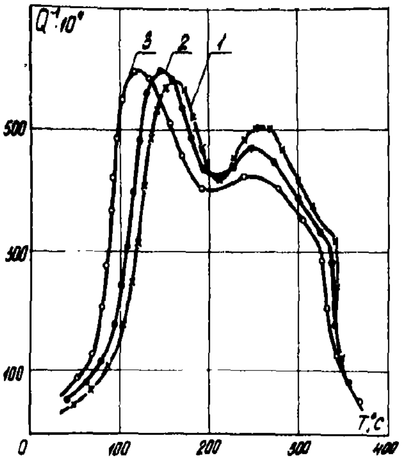

Fig. 5. Internal friction temperature dependence for *A* composition samples annealed in a hydrogen atmosphere for 1 hr – curve 2, 3 hr – curve 3, the original sample – curve 1.

Increasing the time of annealing in hydrogen at 550°C causes displacement of the 140° peak of the *A* composition samples towards lower temperatures (Fig. 5, curves 2, 3). Annealing in the air of the *B* composition samples subjected to preliminary thermal treatment in a hydrogen atmosphere causes decrease of the peak and its displacement to high temperature region. The peak disappears in the process of annealing for 8 hr. If the annealing is made in a vacuum for the same period of time the peak does not disappear.

At temperatures about 1000°C extensive evaporation of lead from the lead zirconate-titanate samples takes place. It decreases the number of stoichiometric vacancies and according to (15) this causes increase of the relaxation time and peak displacement towards higher temperatures.

Annealing in an atmosphere of lead saturated vapour gives the opposite effect, since it is accompanied by building up the stoichiometric vacancy concentration.

Long-term high-temperature annealing in the air may evidently give rise to lead vacancies, especially in *B* composition samples. However, corresponding relaxation peaks were not found . The reduction of samples in a hydrogen atmosphere at a temperature of 550°C builds up the concentration of point defects which may be oxygen vacancies and hydrogen ions. It is seen in Fig. 4 that the internal friction curves of the *B* composition reduced in hydrogen show a peak, the concentration dependence of which is in good agreement with the second model. The higher concentration of point defects (Fig. 5) may also account for the displacement of the 140° peak towards lower temperatures after the reduction in hydrogen. The lower concentration of point defects caused by the annealing of the reduced B composition samples in the samples in the air at $T = 550$–$600°C$ leads to the decrease of the peak height and to its displacement towards higher temperatures. Annealing in the air for 8 hr causes complete disappearance of this peak. It may be explained by the decrease of the vacancy number due to the absorption of oxygen or the isolation of hydrogen. The conservation of the peak in the reduced sample in the process of annealing in a vacuum for 8 hr (the temperature is 550°C) indicates that it is due to interaction of domains with oxygen vacancies. This is confirmed by the appearance of a small 150° peak on $Q^{-1}(T)$ for the B composition samples subjected to a 6 hr annealing in a vacuum (Fig. 4 curve 4).

The internal friction concentration dependence obtained experimentally is in qualitative agreement with the data calculated by means of the second model. According to (14–20) as the point defect concentration builds up the peak on the $Q^{-1}(T)$ curve becomes higher at first and then reaches saturation. In the latter case the peak is displaced towards lower temperatures. This dependence of the displacement of the peak on the point defect concentration is specific only for the given mechanism. Actually, the internal friction peak due to point defect diffusion to the vibrating domain boundaries must shift towards higher temperatures as the concentration builds up in the same manner as it takes place in the process of dislocation damping[5, 6].

REFERENCES

1 GLOSMAN I. A., *Piezoceramics, Energy* (1967).
2. POSTNIKOV V. S., PAPLOV V. S., GRIDNEV S. A., TURKOV S. K., DARINSKII B. M. and GLOZMAN I. A., *Izu Akad. Nauk.* **31**, 1845 (1967).
3. POSTNIKOV V. S., PAVLOV V. S., GRIDNEV S. A. and TURKOV S. K., *Soviet Phys. Solid State* **10**, 1267 (1968).
4 POSTNIKOV V. S., *Internal friction in metals, Metalurgy* (1969).
5 SHOEK G., *Acta Met.* **2**, 6, 617 (1963)
6. TURKOV S. K. and SHERMERGOR T. D., *Soviet Phys. Solid State* **6**, 12, 3503 (1964).

J. Phys. Chem. Solids Pergamon Press 1970. Vol. 31, pp. 1793–1798. Printed in Great Britain

INTERNAL FRICTION OF Nb–H ALLOYS

CHARLES WERT
Department of Metallurgy and Mining Engineering*†, and Materials Research Laboratory, University of Illinois at Urbana-Champaign Ill 61801 U S A

and

DONALD O. THOMPSON and OTTO BUCK
Science Center, North American Rockwell, Thousand Oaks, Calif 91360 U S A.

(*Received* 5 *September* 1969, *in revised form* 10 *October* 1969)

Abstract – A series of seven major peaks in the acoustical absorption spectrum of Nb–H alloys has been seen between 20–400°K. Some of these are attributed to effects that occur in the bcc solid solution, others to phenomena associated with the hydride

1. INTRODUCTION

ALLOYS of Nb with H form an extensive solid solution at temperatures above 500°K. Studies of equilibrium of solid Nb–H alloys with H_2 gas show Sievert's law to be obeyed in dilute alloys; hydrogen thus enters solution atomically dispersed[1]. The sites into which it goes are presumed to be the tetrahedrally co-ordinated sites of type (a/4, 0, 0). Six such sites exist for each lattice Nb atom; the possibility therefore exists that ordering of the hydrogen atoms among these sites may occur under certain conditions. Indeed such ordering has been observed in Ta–H alloys[2, 3].

At temperatures just above room temperature the phase diagram is controlled by the existence of a monohydride showing an extensive range of stoichiometry about the 1 : 1 ratio. An anomalous phase change around 75°C has been resolved by Walter and Chandler to be a eutectoid decomposition line[4]. The phase diagram they report is sketched in Fig. 1. The hydride NbH has an orthorhombic unit cell which departs only slightly from the parent bcc crystal from which it forms upon hydrogenation[5].

Many other features of the system are known and many effects of changes of mechanical properties of Nb after hydrogen addition have been observed. Those observations which bear on the present work will be presented at appropriate points.

The present investigation was undertaken to see if anelastic measurements could aid in the understanding of the Nb–H alloy system and of some of the property changes observed by other authors.

2. MATERIALS AND MEASUREMENTS

Three specimens of Nb metal were used. They are labelled as follows: Nb1, a [100] single crystal having a resistivity ratio of about 400 after growth. Microscopic examination showed it to contain a fine precipitate (which we believe to be either an oxide or a carbide); Nb2, a polycrystalline rod of electron-beam-melted stock; Nb3, a polycrystalline rod of commerical purity (containing 29 ppm hydrogen by weight). Since no effects of purity were seen and since all observations on all specimens can be fitted into a consistent scheme, no attempt was made to further characterize the purity of the three (rather, a continuation of the work is being made on several well characterized single crystals of various orientations). All specimens were about 0·25 in. in dia. and 5·0 in. in length.

---

*Visiting Scientist, North American Rockwell Corporation Science Center, Thousand Oaks, Calif., U.S.A.

†One of the authors (Charles Wert) acknowledges assistance from the U.S Atomic Energy Commission, Contract AT(11-1)-1198 in carrying out parts of this work.

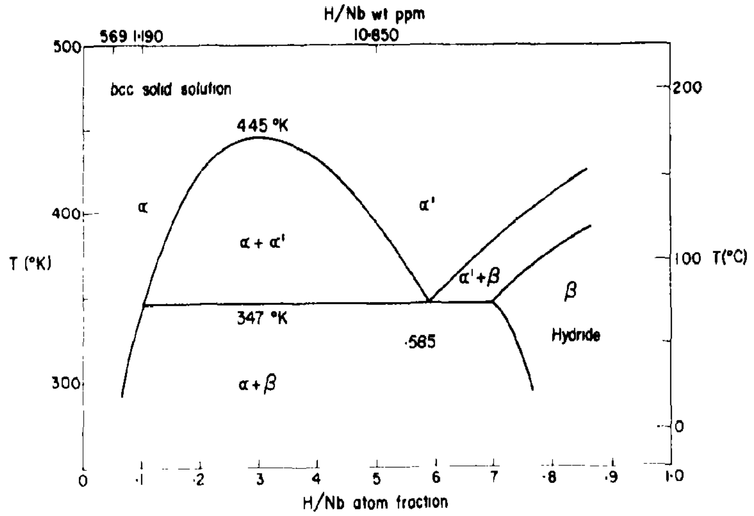

Fig. 1 The Nb–H phase diagram.

The internal friction measurements were made at about 13 kHz (or 39 kHz) between 20–450°K. The apparatus used was the self-regenerative oscillator described earlier[6] in which longitudinal vibrations are used. Automatic data acquisition permitted the recording of frequency, strain amplitude, internal friction and temperature as frequently as once every 20 sec. Since the rate of change of temperature could be made as slow as 0·2 deg/min in any temperature range, great detail of sharp relaxation peaks could be observed. The instrumental background damping was very low—of order $\delta \leq 4 \times 10^{-6}$—hence small variations in damping could be observed.

3. OVERALL DAMPING SPECTRUM

Seven major damping effects were observed in this study. They are sketched in Fig. 2.

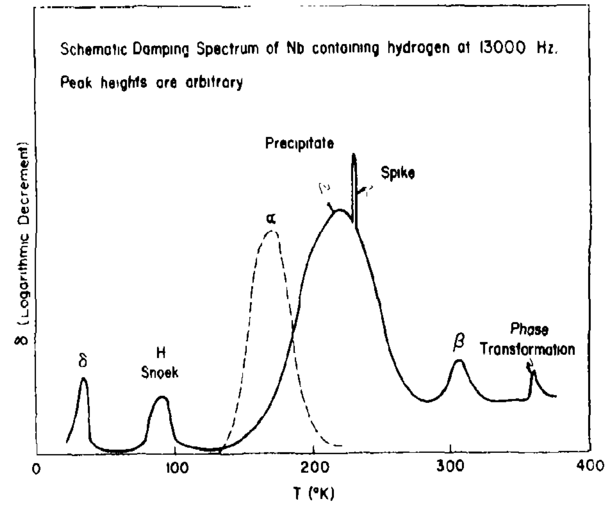

Fig. 2. Sketch of acoustical damping spectrum between 20–400°K.

From the lowest temperatures they are the following:

(1) A damping peak around 40°K. This is presumably the same peak observed in deformed Nb by Massolai and Nuovo and called by them the σ-peak[7]. They observed it at slightly lower temperatures, however (around 30°K).

(2) A peak at about 100°K first reported by Cannelli and Verdini and asserted by them to be the Snoek peak of H[8]. Discussion of this peak will be made at a later point.

(3) The α-peak at 170°K reported by Chambers and Schultz[9], by Bruner[10], by Bordoni, Nuovo and Verdini[11] and others.

(4) A striking peak at about 220–230°K which we call the precipitate peak. (It will be discussed later.)

(5) A very sharp spike at 230°K.

(6) A peak at 310°K which may be the β-peak of Bruner[10] and Chambers[9] and others. This is a highly symmetrical peak. It seems to wander about in temperature a little. Cold work is not required for its presence, and we believe it is associated with H in Nb. We have not yet been able to specify the heat treatment necessary to produce it, however.

(7) A sharp peak at about 360°K which is apparently associated with the eutectoid phase transformation.

Many more small peaks were observed below room temperature under certain conditions. They are not considered further in this paper. The existence of the many peaks in the dilute alloys we used (always less than 0·25 at% H) can only be accounted for by inhomogeneities inherent in the absorption or desorption of hydrogen during specimen preparation or treatment.

4. THE α-PEAK

We observed this peak in only one specimen, Nb3 – the commercially prepared rod – which we first measured without further heat treatment. It produced the α-peak but not a Snoek peak. We assume that it had been cold-worked during manufacture. This measurement of the α-peak fits well with earlier observations of the position of this peak, as shown in Fig. 3 [9–12].

After an anneal in vacuum for several hours at 900°C, the α-peak was gone but the Snoek peak, shown in Fig. 4, had appeared. Whether there is a causal relationship between the two events is not clear to us at this time. We assume that this vacuum anneal was sufficient to remove much of the hydrogen and destroy the structure which produced the α-peak. However, we assume that it was not sufficient to remove all the hydrogen.

5. THE PRECIPITATE PEAK

The new peak structure we identify as the precipitate peak is distinctly not the α-peak. It occurs at a considerably different temperature from the α-peak for the same measurement frequency with entirely different characteristics.

(a) It is a broad peak, being at least 100°K wide – much too wide for a single relaxation process, Fig. 5.

(b) The height of this peak is about a linear function of hydrogen concentration. (Compare the heights in Fig. 5. Although these data do not show strict linearity, further measurements over a much wider range of composition show good linearity.) It is also hysteretic – upon heating a specimen to high temperatures; i.e. 400°K or above, it disappears, to gradually reappear after low temperature aging. The kinetics of aging are presently under investigation. These results will be given in another publication.

(c) We have not measured its shift in temperature with frequency but from its position, we expect it to have an activation energy of about 9000 cal/mol. This value is remarkably close to the value obtained for absorption of hydrogen by Nb as measured by Albrecht, Goode and Mallett[13] and by Oakwood and Daniels[14] and for several measurements of activation energy for mechanical processes [15, 16].

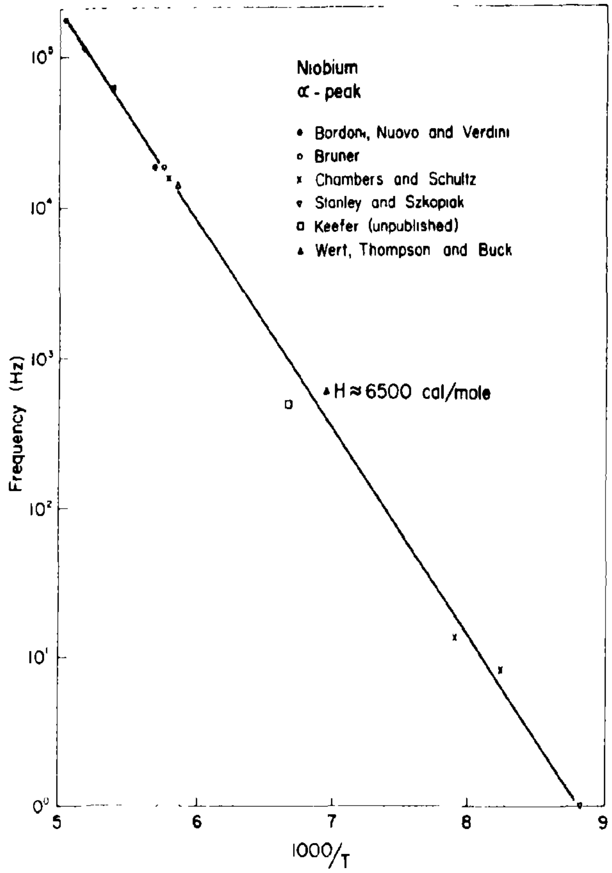

Fig. 3. The position of the α-peak in temperature for a number of measurements

We conclude that this may be a relaxation which occurs within the hydride since the magnitude of the peak is a linear function of the initial hydrogen concentration. It is perhaps caused by diffusion from site to site of H atoms in the hydride and the apparent activation energy of 9000 cal/mole may be that for diffusion of H in the hydride. Other explanations for the peak's origin have not as yet been excluded, however.

6. THE SNOEK PEAK

We have made at least a dozen measurements of the Snoek peak under various conditions of H doping. The damping is never larger than $\sigma = 2 \times 10^{-5}$. We assume that this level is due to the excess H concentration in equilibrium with the hydride, but do not yet know the specific damping factor. For frequencies near 13 kHz the Snoek Peak is near the temperature reported by Cannelli and Verdini; on the average, our peak temperature is a few degrees lower than theirs. We assume that their activation energy of 4150 cal/mole (0·18 eV) is about correct. Further corroboration of this value is available from the nuclear magnetic resonance data of Zamir and Cotts for line narrowing in Nb–H alloys[17]. They obtain, for their dilute alloys, an activation energy of about 3700 cal/mole (0·16 eV).

Measurement of long range diffusion of H in Nb around 500°K by relaxation methods yields values of activation energy distinctly lower than the numbers just cited—values around 2500 cal/mole (about 0·11 eV) have been reported[18–20]. Similarly, observations of quench aging of Nb-H alloys made by Sasaki and Amano at about 100°K yield an activation energy of about 0·11 eV[21].

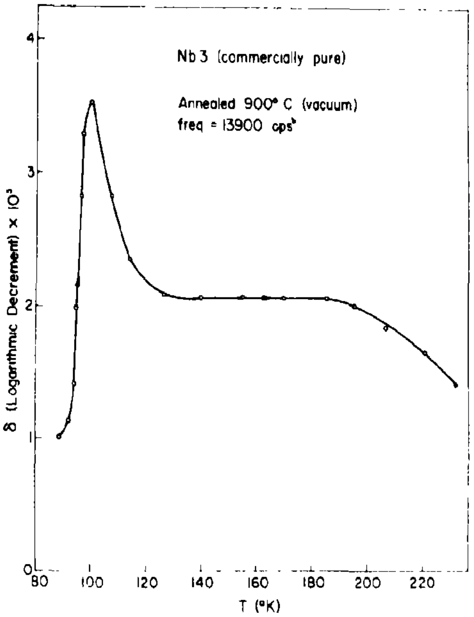

Fig. 4. The Snoek peak for specimen Nb3

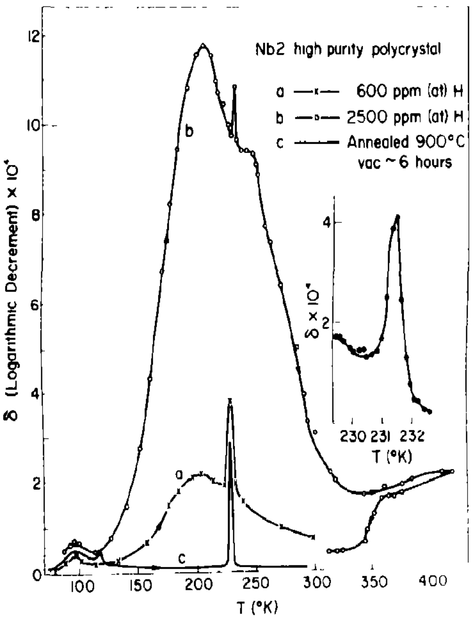

Fig. 5. The precipitate peak and the sharp spike at a frequency of 13,900 c/s. The inset shows the detail of the spike for a typical measurement.

Clearly a discrepancy exists between these groups of measurements well outside the probable error of each. The answer to this dilemma does not seem evident.

7. THE 230° SPIKE

This spike, seen for all three specimens, is a real effect and is not an instrumental artifact. It is seen for alloys of all compositions of H. See Fig. 5. Its breadth is about 1°K as shown in the inset of Fig. 5, and is hysteretic. It occurs at about 205° with decreasing temperature and about 230°K with increasing temperature. A measurement of the outgassed specimen at 39 kHz (the third harmonic) showed it at the identical temperature, although the Snoek peak caused by residual hydrogen had shifted appropriately. A measurement at 1 Hz in a torsional pendulum shows it at about 236°K.

We believe that this effect is caused by a transformation (perhaps martensitic) in the bcc solid solution (not in the hydride).

8. THE EUTECTOID PEAK

Damping peaks are known to be present near phase transformations. This system is no exception and an example of such a peak in this system is shown in Fig. 6. The peak is not precisely at the temperature of the eutectoid given by Walter and Chandler (74°C) being a few degrees higher. The NMR observations of Zamir and Cotts would also put the eutectoid temperature nearer to 90° than to 74°[17]. Nevertheless it seems evident that the eutectoid must lie between 70–90°C.

9. SUMMARY

Alloys of Nb with H have a rich acoustical absorption spectrum. Some of these absorption lines are apparently caused by effects in the hydride, others in the bcc solid

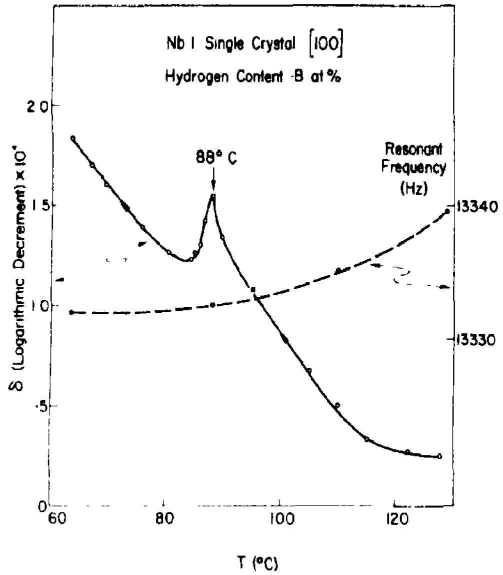

Fig. 6. The peak at the eutectoid temperature.

solution. A great deal of useful information can apparently be deduced from interpretation of these phenomena. Further experiments are currently in progress.

REFERENCES

1. SIEVERTS A. and HAGEN H., *Z. anorg. allg. Chem.* **185**, 225 (1930).
2. LEHMAN G. W. and GEHMAN W. G., *Progress in Solid State Chemistry* (Edited by H. Reiss), Vol. 2, Chap. 2, p. 414, Pergamon Press, Oxford (1965).
3. WALLACE W. E., *J. chem. Phys.* **35**, 2156 (1961).
4. WALTER R. J. and CHANDLER W. T., *Trans. AIME* **233**, 762 (1965).
5. WAINWRIGHT C., COOK A. J. and HOPKINS B. E., *J. less-common Metals* **6**, 362 (1964).
6. THOMPSON D. O. and GLASS F. M., *Rev. scient. Instrum.* **29**, 1034 (1958).
7. MAZZOLAI F. M. and NUOVO M., *Solid State Commun.* **7**, 103 (1969).
8. CANNELLI G. and VERDINI L., *Ricerca scient.* **36**, 98 (1966).
9. CHAMBERS R. H. and SCHULTZ J., *Acta metall.* **8**, 585 (1960).
10. BRUNER L. J., *Phys. Rev.* **118**, 399 (1960).
11. BORDONI P. B., NUOVO M. and VERDINI L., *Phys. Rev.* **123**, 1204 (1961).
12. STANLEY M. W. and SZKOPIAK Z. C., *J. mater. Sci.* **2**, 559 (1967).
13. ALBRECHT W. M., GOODE W. D. and MALLETT M. W., *J. electrochem. Soc.* **106**, 981 (1959).
14. OAKWOOD T. G. and DANIELS R. D., *Univ. Oklahoma Rep.* No. ORC-2570-10.
15. WILCOX B. A. and HUGGINS R. A., *J. less-common Metals* **2**, 292 (1960).
16. WILCOX B. A. and HUGGINS R. A., *Columbium Metallurgy* (Edited by D. Douglass and F. Kunz), p. 257, Interscience New York (1961).
17. ZAMIR D. and COTTS R. M., *Phys. Rev.* **134**, A666 (1964).
18. SCHAUMANN G., VÖLKL J. and ALEFELD G., *Phys. Rev. Lett.* **21**, 891 (1968).
19. SCHAUMANN G., VÖLKL J. and ALEFELD G., *Int. Conf. Vacancies and Interstitials in Metals*, Jülich, Vol. 2, p. 881 (1968).
20. CANTELLI R., MAZZOLAI F. M. and NUOVO M., *Phys. Status Solidi* **34**, 1 (1969).
21. SASAKI Y. and AMANO M., *Trans. Japan Inst. Metals* **10**, 29 (1969).

J. Phys. Chem. Solids Pergamon Press 1970. Vol. 31, pp. 1799–1804. Printed in Great Britain

SNOEK RELAXATION PEAKS IN SOLID SOLUTIONS OF NIOBIUM

M. S. AHMAD and Z. C. SZKOPIAK
Department of Metallurgy and Materials Technology, University of Surrey, Guildford, Surrey, England

(*Received 5 September 1969; in revised form 12 November 1969*)

Abstract – A detailed study has been carried out of the broadening effect of Snoek peaks due to oxygen and nitrogen in niobium. It is shown that the broadening is due to the presence of subsidiary Snoek peaks caused by the stress-induced migration of interstitial atoms associated in pairs and triplets. It is suggested that the stress-induced migration of interstitial atoms associated in pairs and triplets involves single atoms only, whilst the other atoms remain in their original positions. The present results indicate that clusters containing more than three atoms do not cause relaxation peaks.

1. INTRODUCTION

THE PROPERTIES of bcc transition metals vanadium, niobium and tantalum (Group VA metals) are strongly affected by intersitial impurities such as oxygen, nitrogen, carbon and hydrogen. Niobium can dissolve comparatively large quantities of oxygen[1, 2] and nitrogen[3] to form interstitial solid solutions. The Snoek peaks[4], caused by the stress-induced migration of oxygen and nitrogen atoms situated at the octahedral sites in the niobium lattice, are well documented[5, 6]. At low concentrations these peaks occur at 157 and 289°C respectively at a frequency of 1 Hz. At comparatively higher concentrations of the interstitials, the experimentally determined Snoek peaks are broader on the high temperature side, and are shifted to slightly higher temperatures[7]. This broadening effect can be attributed to additional relaxation peaks arising from the stress-induced migration of the interstitial atoms associated with other atoms in pairs, triplets or clusters of higher order[8].

Powers and Doyle[7] separated Snoek peaks due to oxygen and nitrogen in tantalum into two constituent peaks. The first peak was attributed to the relaxation of single, unassociated atoms, and the second peak to atoms associated in pairs. Keefer and Wert[9, 10] reported similar evidence for interstitial clustering in iron–nitrogen and iron–carbon alloys. They reported the presence of pairs and triplets of interstitial atoms in addition to unassociated atoms. More recently Gibala and Wert[8] reported detailed investigations of cluster formation in niobium containing 0·1–1·5 at% oxygen. They observed relaxation peaks due to pairs, triplets and quadruplets of oxygen atoms. Besides the association of like atoms, oxygen–nitrogen pairs have also been observed in niobium[11, 12]. It appears useful to study the nature of these clusters, as they are likely to have appreciable effect on the mechanical behaviour of these metals[13] particularly in the case of substitutional alloys [14].

In this paper an extensive internal friction study is reported on niobium–oxygen and niobium–nitrogen alloys containing various amounts of the interstitial impurities. The object of this investigation is the decomposition of experimentally measured internal friction spectra into constituent peaks and their interpretation in terms of elastic interactions of interstitial atoms.

2. MATERIAL AND EXPERIMENTAL PROCEDURE

2.1 *Material*

The material used in this investigation was Murex electron-beam-refined niobium wire 1·25 mm in dia. in the as drawn condition.

The chemical analysis, as supplied by the manufacturers, is given in Table 1. Although exceptional conditions exist for purification, doping and control of interstitials in niobium, it is nevertheless extremely difficult to prepare specimens containing only one type of interstitial. In view of this fact, specimens were first prepared with the lowest possible levels of oxygen and nitrogen, and then with varying amounts of one of the interstitials, while maintaining the other at the lowest possible level. The as-received wire was treated in the following way: (a) Cold swaged from 1·25 to 0·76 mm in dia. (b) Annealed by direct resistance heating at about 2300°C in a dynamic vacuum of 10^{-5}–10^{-6} torr to outgas and reduce the carbon content. (c) Oxygen or nitrogen charged (in the same furnace), in atmospheres of these gases at various pressures, at 1200 and 1500°C respectively. (d) Homogenised for 15–30 min at 1300°C and 1600°C respectively under dynamic vacuum of the order of 10^{-5}–10^{-6} torr.

Table 1. Analysis of electron-beam refined niobium

Element	ppm[*]
Oxygen (a)	870–1450
Oxygen (b)	2600–3200
Nitrogen (a)	260–400
Nitrogen (b)	800–930
Carbon	77
Hydrogen	400
Tantalum	410
Zirconium	trace
Iron	83
Titanium	194
Silicon	330

[*] In this paper ppm stands for atomic parts per million unless otherwise stated

2.2 *Experimental procedure*

Measurements were carried out in a *Ke* type torsion pendulum[15] with specimens in the form of a wire (0·76 mm dia. and 25 cm long) operating at a frequency of about 1 Hz. Measurements were taken on heating at a rate of about 1°C/min. Oxygen and nitrogen contents of test specimens were determined by the micro-vacuum-fusion technique.

2.3 *Analysis of the experimental data*

The experimental internal friction spectra required an accurate decomposition into constituent peaks. The major part of the present study, therefore, involved the separation of overlapping peaks, and the determination of the number of relaxation processes, with the help of a computer, using an Algol program based on the Gauss least squares algorithm. The program was based on the standard equation:-

$$\delta = \delta_{\max} \operatorname{sech}\left[\frac{Q}{R}\left(\frac{1}{T}-\frac{1}{T_p}\right)\right]. \qquad (1)$$

Where δ is the logarithmic decrement at a temperature T(°K), Q the activation energy of the relaxation process, $\delta_{\max}$ the height of the peak occurring at temperature Tp, and R the ideal gas constant.

The separation of each spectrum into constituent peaks was obtained by iterating for n individual processes each with three variables ($\delta_{\max}$, Q and Tp) until the best fit was attained.

3. RESULTS

3.1 *Niobium–oxygen*

For specimens containing up to about 300–400 ppm oxygen, the oxygen Snoek peaks consisted of only one relaxation peak [4]. However, for concentrations between about 400 and 2500 ppm the experimental spectra consisted of two constituent peaks. The new peak occurred at a higher temperature than the main oxygen Snoek peak. In the case of oxygen contents higher than 2500 ppm, the experimental spectra could only be separated into three constituent peaks. The third peak again occurred at a higher temperature than the second peak. An internal friction spectrum, decomposed into constituent peaks, of a specimen containing 8000 ppm oxygen is shown in Fig. 1. Besides the three constituent peaks (O, O-O and O-O-O), the internal friction spectrum contains the nitrogen Snoek peak (N) and another 5 small peak (O-N) which always occurred in specimens containing appreciable amounts of oxygen and nitrogen.

The variation of the heights (δ_{max}) of the three constituent peaks with oxygen concentration is shown in Fig. 2. From the log-log plot it is apparent that the heights of these peaks vary with the concentration of oxygen to power 1, 2 and 3 respectively.

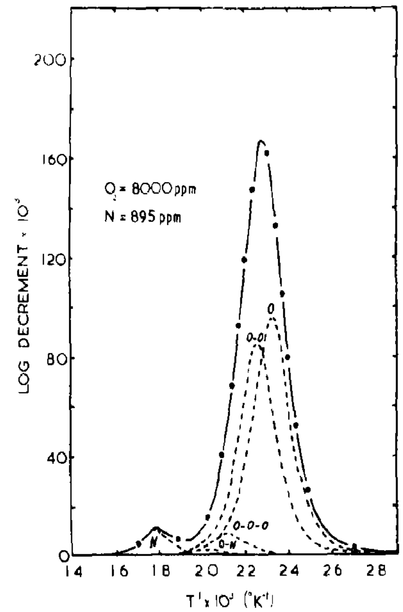

Fig 1. Oxygen and oxygen-oxygen interaction Snoek peaks in niobium.

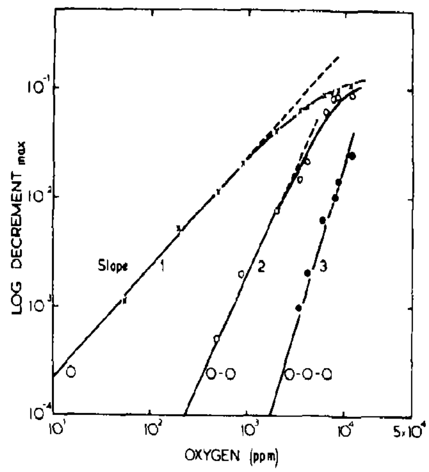

Fig 2. Variation of Snoek peak heights due to singles, pairs and triplets of oxygen atoms in niobium

3.2 *Niobium-nitrogen*

Analyses of the experimental internal friction peaks of niobium-nitrogen binary alloys revealed that the appearance of extra peaks, at temperatures higher than that of the main nitrogen Snoek peak, follows the same pattern observed in niobium-oxygen alloys. A typical complex spectrum of niobium containing 3820 ppm nitrogen, decomposed into the constituent peaks (O,O-N, N,N-N and N-N-N), is shown in Fig. 3. Peak heights (δ_{max}) of the constituent peaks (N, N-N and N-N-N) are plotted in Fig. 4 against nitrogen concentration on a log-log scale. From the figure it can be seen that, as in the case of oxygen, the heights of these peaks vary with concentration of nitrogen to power 1, 2 and 3 respectively.

3.3 *Activation energy of relaxation processes*

It is assumed that the relaxation processes causing the constituent Snoek peaks of the internal friction spectra studied obey the

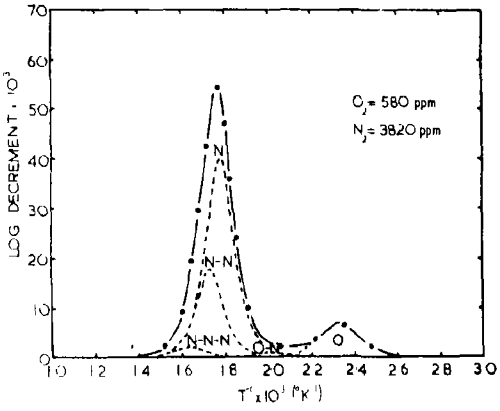

Fig 3. Nitrogen and nitrogen-nitrogen interaction Snoek peaks in niobium.

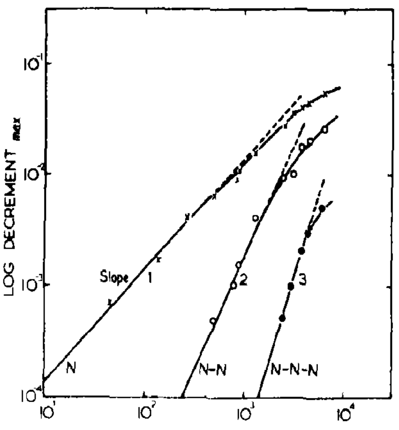

Fig. 4. Variation of Snoek peak heights due to singles, pairs and triplets of nitrogen atoms in niobium.

Arrhenius equation: $f=f_0 \exp(-Q/RT)$, where f is the applied frequency, f_0 the 'attempt frequency', Q the activation energy, R the gas constant and T the peak temperature in °K.

The activation energy for the process causing each constituent peak was determined by plotting the logarithm of applied frequency against the reciprocal of the corresponding peak temperature (Fig. 5). Attempt frequencies were then calculated in the usual manner. Relaxation rate parameters of the processes studied are summarized in Table 2 together with the average activation energies calculated by the computer for the best fit to the experimental data. The probable errors in Q and f_0 were ± 300 cal mol^{-1} and $\pm 1 \times 10^{13}$ Hz respectively. It can be seen from Table 2 that the experimental and the calculated activation energies are in good agreement, thus lending support to the method used for the decomposition of the complex peaks.

4. DISCUSSION

The appearance of extra peaks with increase in concentration of either oxygen or nitrogen (Figs. 1 and 3) indicates some form of association between the interstitial atoms. It is clear from Fig. 2 that the Law of Mass Action holds for an equilibrium between oxygen, singles, pairs and triplets of oxygen atoms in the niobium lattice. Slope 1 (Fig. 2) shows that up to about 1000 ppm, the height of the peak O (Fig. 1), which is due to stress induced migration of unassociated oxygen atoms[4], is proportional to oxygen content. Slope 2 (Fig. 2) indicates that for oxygen contents ranging from about 400 to 2500 ppm, the height of the peak O–O (Fig. 1) is a quadratic function of the oxygen concentration. Therefore, the relaxation process O–O causing the peak is due to stress induced migration of oxygen atoms associated in pairs. Similarly Slope 3 (Fig. 2) shows that the height of the

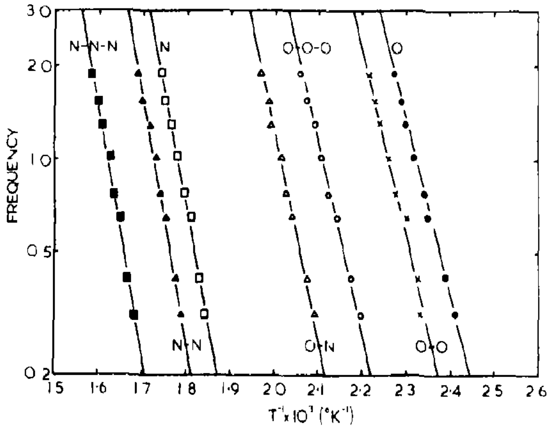

Fig. 5. Plot for the calculation of activation energies for Snoek peaks in niobium.

Table 2. Relaxation rate parameters of oxygen, nitrogen and their interaction Snoek peaks in niobium

Process	Peak temperature (at 1 Hz)		Activation energy ($Q \times 10^{-3}$ cal mol^{-1})		Attempt frequency
	$\left(\frac{1000}{T}(°K^{-1})\right)$	(°C)	Frequency shift	Computer calculated	($f_0 \times 10^{-13}$ Hz)
O	2·325	157	26·5	26·6	3·6
O-O	2·26	170	28·0	27·8	5·9
O-O-O	2·11	200	29·5	29·2	3·2
O-N	2·01	223	31·1	31·0	4·5
N	1·78	289	34·9	35·0	4·5
N-N	1·73	305	36·5	36·2	5·3
N-N-N	1·63	340	37·7	38·0	3·7

peak O-O-O (Fig. 1) is a cubic function of the oxygen concentration, and that the relaxation process is due to stress-induced migration of oxygen atoms associated as triplets. In an analogous manner, with reference to Fig. 4, we interpret that peaks N,N-N and N-N-N in Fig. 3 are due to stress- induced migration of unassociated nitrogen atoms, and atoms associated in pairs and triplets respectively.

A peak due to quadruplets of oxygen atoms, reported by Gibala and Wert[8], was not found in niobium-oxygen binary alloys up to a concentration of 12,000 ppm oxygen. Furthermore, a peak due to quadruplets of nitrogen atoms was also not observed in niobium-nitrogen alloys up to 6400 ppm nitrogen. The peak which Gibala and Wert[8] interpreted as being due to quadruplets of oxygen atoms, could be equally well interpreted as an oxygen-nitrogen interaction peak[11, 12]. This peak was always observed in the present study, but it will not be further discussed in this paper. Its detailed investigation will be published elsewhere.

Since a relaxation peak due to interstitial atoms associated in quadruplets was not observed in the present study, it may be assumed that atoms in clusters consisting of more than three atoms do not take part in relaxation. Probably, these small or medium sized clusters lead to nucleation and precipitation of new phases. This assumption is supported by the fact that the presence of precipitated nitrides was observed microscopically in alloys containing more than 5000 ppm nitrogen. Jones *et al.*[16] reported the existence of oxygen clusters of at least 250 Å in diameter in niobium containing 3300 ppm oxygen. At this concentration, it appears difficult to justify the presence of such large clusters in terms of the present study.

Attempt frequencies of the relaxation processes due to stress-induced migration of interstitial atoms from pairs and triplets are within experimental error, of the same magnitude ($4{\cdot}3 \times 10^{13}$) as those of stress-induced migration of unassociated atoms (Table 2). This indicates that the relaxation processes involve single atomic jumps to the preferred sites[4]. The migrating atom will move within the constraint provided by the presence of the other atoms in the cluster. For this reason the relaxation times of singles, pairs and triplets differ, and the corresponding relaxation peaks occur at different temperatures (Table 2).

The present work demonstrates the existence of attractive interactions between interstitial atoms. These interactions appear to be adequately described by the elastic models [17-19].

5. CONCLUSIONS

(1) It has been shown that the Snoek peaks due to oxygen or nitrogen in niobium consist of (a) a single peak for concentrations up to about 350 ppm of either oxygen or nitrogen,

(b) two peaks for concentrations between 350 and 2500 ppm. and (c) three peaks for concentration higher than 2500 ppm.

(2) The relaxation peaks are due to stress-induced migration of unassociated interstitial atoms, and like atoms associated in pairs and triplets respectively.

(3) In addition, there is always a peak due to the association of unlike atoms of oxygen and nitrogen when both interstitials are present in the specimen.

(4) It is believed that the migration of atoms associated in pairs and triplets involves only one atom migrating under the influence of the companion atoms which remain stationary in the cluster.

(5) The present results indicate that clusters containing more than three interstitial atoms do not cause relaxation.

Acknowledgements – One of the authors (M. S. A.) gratefully acknowledges the University of Surrey for the maintenance grant to carry out this work. Thanks are due to Professor M. B. Waldron, Head of the Department of Metallurgy and Materials Technology, University of Surrey, for his continued interest in and support of this work. The opportunity is also taken to express appreciation to Mr A. Ciesla for processing some of the results.

REFERENCES

1. ELLIOTT R., *Trans. Am. Soc. Metals* **52**, 990 (1960).
2. BRYANT R., *J. less-common Metals* **4**, 62 (1962).
3. COST J. and WERT C., *Acta metall.* **11**, 231 (1963).
4. SNOEK J. L., *Physica* **8**, 711 (1941).
5. POWERS R. W. and DOYLE M. V., *J. appl. Phys.* **30**, 514 (1959).
6. SCHULTZ H., *Mater. scient Engng* **3**, 189 (1968/69).
7. POWERS R. W. and DOYLE M. V., *Acta metall.* **4**, 233 (1956).
8. GIBALA R. and WERT C. A., *Acta metall* **14**, 1095 and 1105 (1966).
9. KEEFER D. and WERT C. A., *Acta metall.* **11**, 489 (1963).
10. KEEFER D. and WERT C. A., *J. phys. Soc. Japan* **18**, Suppl. III, 110 (1963).
11. VAN OOIJEN D. J. and VAN DER GOOT A. S., *Philips Res. Rep.* **10**, 505 (1964).
12. GIBALA R. and WERT C. A., *Trans. AIME* **236**, 924 (1966)
13. FRANK W., *Z. Naturf.* **22a**, 365 (1967); *Phys. Status Solidi* **19**, 239 (1967).
14. SZKOPIAK Z. C. and AHMAD M. S., *High Temperature Materials – Fundamentals and Developments, Proc. 6th Plansee Seminar* (Edited by F. Benesovsky), p. 345. Springer Berlin (1969).
15. KE T. S., *Phys. Rev.* **71**, 533 (1947).
16. JONES K. A., MOSS S. C. and ROSE R. M., *Acta metall.* **17**, 365 (1969)
17. FISHER J. C., *Acta metall.* **6**, 13 (1958).
18. YANG C. C., *Acta physiol. sin.* **22**, 282 and 294 (1966), *Chin. J. Phys.* **22**, 221 and 231 (1966).
19. JOHNSON R. A., *Acta metall.* **15**, 513 (1967)

J. Phys. Chem. Solids Pergamon Press 1970. Vol. 31, pp. 1805–1809. **Printed in Great Britain.**

DIFFUSIONAL RELAXATION OF H AND D IN V AND Nb

J. VÖLKL, G. SCHAUMANN and G. ALEFELD
Institut fur Festkorper- und Neutronenphysik, Kernforschungsanlage Julich, Germany

(*Received 5 September* 1969; *in revised form* 15 *October* 1969)

Abstract – The properties of the elastic diffusional relaxation processes of H and D in V and Nb are summarized. Results on the diffusion coefficients for both isotopes in these metals are also presented

1. INTRODUCTION

WE HAVE shown previously[1–2] that point defects like interstitial atoms give rise to a long-range diffusional relaxation process (Gorsky effect) if two conditions are fulfilled: The point defects must cause lattice distortion, which changes the volume of the host lattice and they must have relatively high mobility at accessible temperatures. Then if a gradient in dilatation is applied to the sample the point defects will follow this gradient. A gradient in defect concentration builds up in the sample with a time constant which is a simple function of the diffusion coefficient of the point defects and the sample diameter squared. Macroscopically a change in the concentration manifests itself as an anelastic strain. The high mobility is necessary because the defects must migrate over distances of half the sample diameter. Changes in sample thickness between $10\,\mu$ and 3 mm causes changes in the relaxation time of 5 orders of magnitude. Therefore by adjusting the sample diameter the diffusional relaxation process can be observed either dynamically or by static relaxation experiments. Furthermore relaxation times of 10^4 sec are still manageable in static experiments. Therefore by a proper choice of sample thickness roughly 9 orders of magnitude in relaxation time are available.

In this paper we give a brief survey of the experimental properties of the diffusional relaxation process for hydrogen and deuterium in several metals as determined by strain relaxation experiments. We will summarize results for dilute solutions, for which interaction between the solutes is negligible A more extensive description of experiments and results will be published elsewhere[3].

The systems H in V or Nb have several advantageous features and bear several interesting aspects· These metals have large solubility for hydrogen and deuterium. Therefore the concentration of these interstitials can be varied over a wide range. We have measurements on Nb between 0·2–40 at% H [1–6]. The maximum concentration is 89 at% but increasing brittleness probably will set a lower limit for elastic measurements. Furthermore from NMR measurements[7] it was expected, that e.g. H in Nb has a large diffusion coefficient although the absolute value was not known reliably. Diffusion coefficients in these systems are difficult to measure. The experimental technique of permeation commonly suffers from surface problems not easy to control. The possibility of measuring the isotope dependence of the diffusion constant was another reason for choosing these systems. The isotope dependence is of particular interest since deviations from the high temperature value $\sqrt{2}$ can be expected due to the low temperatures in our experiments (160–600°K) compared to the

Einstein temperature ($T \approx 1400$°K for H in Nb) for the localized mode of H in solution. The energy levels of H in solution have been determined by inelastic neutron scattering. The first level was found at 0·11 eV for H in Nb and 0·12 eV for H in V[8].

2. PROPERTIES OF THE DIFFUSIONAL RELAXATION PROCESS

(a) *Linearity and reversibility*

The anelastic strain increases linearly with stress and the relaxation time is independent of stress. Non-linear behavior of the diffusional relaxation can be expected close to the critical point of hydrogen.* Such a nonlinear elastic response would be analogous to the nonlinear susceptibility at the Curie point of a ferromagnet.

The anelastic strain is reversible at room temperature certainly within 95 per cent. This limit of observation is imposed by electronic drifts and by a small but observable dislocation background.

(b) *Time dependence of the strain relaxation*

The diffusional relaxation with which we are concerned obeys a simple exponential time law with one relaxation time. Examples of strain relaxation curves are published in Ref. [6]. For the corresponding internal friction peak one therefore expects the natural width, as has been confirmed recently[10]. This is quite unusual for elastic aftereffect and internal friction work, especially since the process is diffusion controlled. It has been shown by theory[11] which has been formulated analogously to Zener's theory for thermoelastic damping[12], that the relaxation process indeed consists of a spectrum with different relaxation times, but that the relaxation strength of the component with the largest relaxation time amounts to 98 per cent of the total relaxation strength. In contrast to the orientation relaxation process the diffusional relaxation obeys still a simple exponential law for high particle densities, for which interaction plays a role[6]. The reason for this difference is the averaging procedure resulting from the large number of jumps involved in the diffusional relaxation. According to theory [5, 12] the relation

$$13{\cdot}55 D\tau = d^2 \qquad (1)$$

between the diffusion coefficient D and the relaxation time τ should hold for a cylindrical specimen with the diameter d. Experiments have verified very well the predicted d^2-dependence of the relaxation time, thus confirming, that the diffusion process proceeds over the whole sample diameter and not between grains. This latter process can be exluded for the following reason as well: The samples had a bamboo structure with single crystals longer than sample diameter.

(c) *Relaxation strength*

For small concentrations theory[11] predicts a relaxation strength proportional to the density of H atoms, to the reciprocal temperature and to the trace of the dipolemoment tensor squared. The latter quantity determines as well the lattice parameter changes caused by hydrogen. Therefore from such measurements[13–15] the absolute value for the relaxation strength Δ_E can be predicted. The experiments show good agreement with the predicted density and temperature dependence and even consistency with the predicted absolute value. The latter has large error bars due to scatter in the lattice parameter measurements. Therefore we feel that from the results of our experiments

$$\Delta_E = (1{\cdot}7 \pm 0{\cdot}2)\cdot 10^{-2}/1\ \text{at\%H or D in Nb and V at 300°K}$$

the trace A + 2B of the dipolemoment tensor can be determined with more accuracy yielding the following result for H in Nb: A + 2B = (10·8 ± 0·6) eV and for H in V: A + 2B =

---

*The phase diagram for H in Nb has been discussed previously[9].

(9·0±0·6) eV. Theoretically one may expect a small difference for A + 2B for H and D, but this has not yet been resolved experimentally.

(d) *The diffusion coefficient*

The diffusion coefficient can be derived absolutely with the help of equation (1) from the experimentally well defined relaxation time. Figure 1 shows an Arrhenius plot for H and D in Nb, V. The concentrations were below 2 at%. The data published in Ref. [1] are included after a small correction for concentration dependence has been applied[5]. To avoid precipitation at low temperatures the measurements for H in Nb below 250°K were performed on a sample loaded with 0·2 at%H. Two points are included in Fig. 1 which have been measured by Gissler *et al.* [16] by quasielastic neutron scattering. The agreement is very good, especially if one takes into consideration that in both techniques no adjustable parameter is involved. For comparison in Fig. 2 the diffusion coefficient for H in Nb and H in V is plotted together with data for O and N in Nb[17] and for C in α-iron[18]. It should be pointed out that in a $1/T$-scale the range of our data for H in Nb is comparable with that for C in α-iron. Yet in our case all data points are measured with one technique, whereas for C in α-Fe at least six different methods had to be used [18]. This is not so much a consequence of the versatility of our technique but due to the extremely weak temperature dependence of the diffusion coefficient of H as compared to N or O. Whereas for H in Nb above 300°K an Arrhenius plot is still sensible (with U = 0·11 eV), for H in V a linear temperature de-

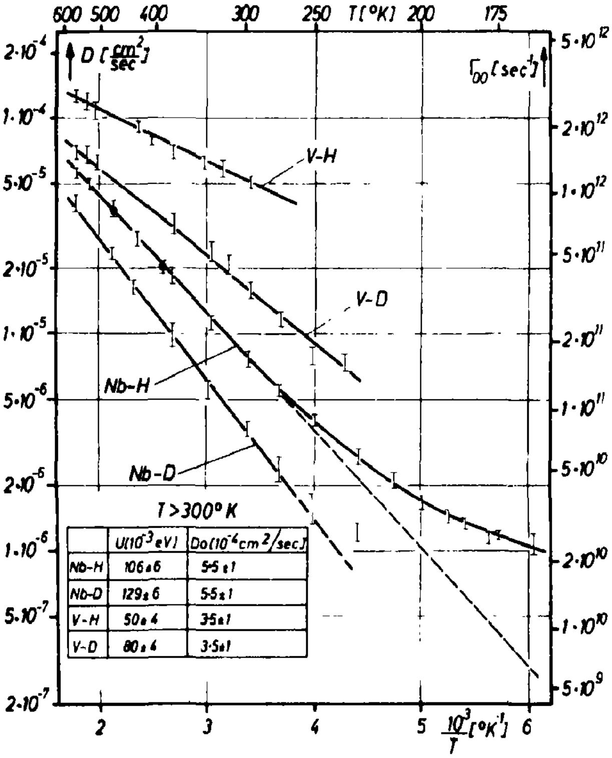

	U(10⁻³ eV)	Do(10⁻⁴ cm²/sec)
Nb-H	106±6	5·5±1
Nb-D	129±6	5·5±1
V-H	50±4	3·5±1
V-D	80±4	3·5±1

Fig. 1. Arrhenius plot of the diffusion coefficients of H and D in niobium and vanadium (Γ_{00} = mean jump rate, assuming octahedral-octahedral jumps [16]).

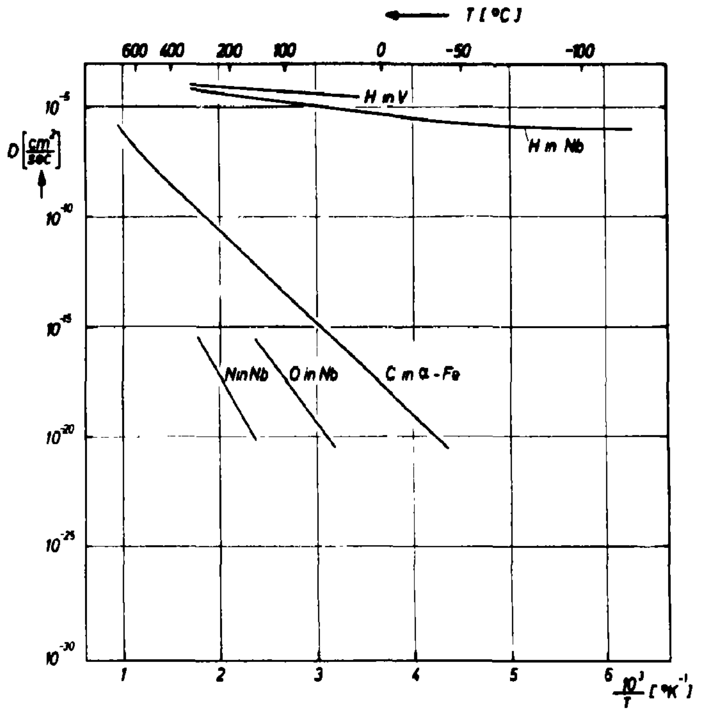

Fig. 2. Comparison of the diffusion coefficients of H in niobium and vanadium (present work) with those of N and O in niobium[17] and C in α-Iron[18].

pendence of D is compatible with the data as well. The table in Fig. 1 shows the slopes of the straight line segments and the values of D for $T \rightarrow \infty$ under the assumption of linear extrapolation. Below 300°K the temperature dependence of the diffusion coefficient D for H in Nb decreases strongly. Absolutely all diffusion coefficients in Fig. 1 are very large, e.g. at room temperature 15–20 orders of magnitude larger than for other interstitials. Assuming jumps between octahedral sites (for H in Nb this assumption has been confirmed recently[16]), the mean jump rate is plotted on the right hand side of Fig. 1. The jump rates at 300°C are comparable with the highest lattice frequencies of Nb[19]. Furthermore an abnormally large isotope dependence, which is even enhanced at low temperatures has been found for all systems. It is difficult to explain the data in Fig. 1 by classical rate theory. A more extensive discussion is given elsewhere[3]. It should be pointed out that recently Pfister[20] found similarly a transition from a nearly exponential to a linear temperature dependence combined with a large isotope effect for the rotational diffusion of the O_2 molecule in KCl below 4°K.

REFERENCES

1. SCHAUMANN G., VÖLKL J. and ALEFELD G., *Phys. Rev. Lett.* **21**, 891 (1968).
2. SCHAUMANN G., VÖLKL J. and ALEFELD G., (*2nd Int. Conf. Vacancies and Interstitials in Metals, Jülich*) Vol. 2, p. 881 (1968).
3. SCHAUMANN G., VÖLKL J. and ALEFELD G., to be published.
4. ALEFELD G., VÖLKL J. and TRETKOWSKI J., this Conference.
5. SCHAUMANN G., Thesis TH Aachen (1969).
6. ALEFELD G., SCHAUMANN G., TRETKOWSKI J. and VÖLKL J., *Phys. Rev. Lett.* **22**, 697 (1969).
7. ZAMIR D. and COTTS R. M., *Phys. Rev.* **134**, 666 (1964).

8. KLEY W., PERETTI J., RUBIN R. and VERDAN G., *Proc. Brookhaven Symp. Inelastic Scattering of Neutrons*, BNL 940 (1965).
9. ALEFELD G., *Phys. Status Solidi* **32**, 67 (1969).
10. CANTELLI R., MAZZOLAI F. M. and NUOVO M., this Conference.
11. ALEFELD G., VÖLKL J. and SCHAUMANN G., *Phys. Status Solidi* **37**, 339 (1970)
12. ZENER C., *Elasticity and Anelasticity of Metals* University of Chicago Press, Chicago Ill. (1948)
13. WALTER R. J. and CHANDLER W. T., Trans AIME **233**, 762 (1965).
14. ALBRECHT W. H., GOODE W. D. and MALLETT M. W., *J. electrochem. Soc.* **106**, 981 (1959).
15. MAELAND A. J., *J. phys. Chem.* **68**, 2197 (1964)
16. GISSLER W., ALEFELD G. and SPRINGER T., submitted for publication.
17. POWERS R. W. and DOYLE M. V., *J. appl. Phys.* **30**, 514 (1959)
18. LORD A. E. Jr. and BESHERS D. N., *Acta metall.* **14**, 1659 (1966)
19. WOODS A. D. B., *Proc. Symp. Inelastic Scattering of Neutrons, Bombay*, p. 87 IAEA, Vienna (1965)
20. PFISTER G., Thesis ETH Zurich (1969).

J. Phys. Chem. Solids Pergamon Press 1970. Vol. 31, pp. 1811–1817 Printed in Great Britain

INTERNAL FRICTION DUE TO LONG-RANGE DIFFUSION OF HYDROGEN AND DEUTERIUM IN VANADIUM

R. CANTELLI, F. M. MAZZOLAI and M. NUOVO
Consiglio Nazionale delle Ricerche, Istituto di Acustica 'O. M. Corbino', Rome, Italy

(*Received 5 September* 1969, *in revised form* 20 *October* 1969)

Abstract – The long-range diffusion (Gorsky effect) of hydrogen and deuterium in vanadium is invesitgated by internal friction measurements in the temperature range from 110 to 930°K; the vibration frequencies are included between 8 and 68 Hz. The diffusion coefficient of hydrogen and deuterium obeys an exponential law in a wide temperature range, the preexponential factors and the activation energies being, $D_{0H} = (4\cdot4 \pm 1\cdot5) \times 10^{-4}\ \text{cm}^2/\text{sec}$, $D_{0D} = (3\cdot1 \pm 0\cdot8) \times 10^{-4}\ \text{cm}^2/\text{sec}$, $W_H = (0\cdot059 \pm 0\cdot007)\ \text{eV}$, $W_D = (0\cdot073 \pm 0\cdot006)\ \text{eV}$.

1. INTRODUCTION

THE GORSKY effect due to long-range diffusion of hydrogen and deuterium in niobium has been recently investigated by measurements of elastic after-effect[1] and of internal friction[2]. The above investigations show that this anelastic effect is a suitable method for studying the diffusion in solid systems with high diffusivity.

The diffusion of hydrogen and deuterium in metals has been the object of several investigations[3–13]; however, the available experimental data are insufficient to obtain satisfactory knowledge of the diffusion behaviour of these elements.

In the present paper the Gorsky effect is investigated by internal friction measurements in the V–H and V–D systems and the diffusion coefficient of hydrogen and deuterium is evaluated over a wide temperature range.

2. EXPERIMENTAL

Measurements were made in zone refined 99·99 per cent pure vanadium supplied by Materials Research Corporation. The samples were two rectangular thin sheets prepared by cold rolling followed by chemical polishing. Their final dimensions were $5 \times 1\cdot2 \times 0\cdot0020\ \text{cm}^3$ (sample 1) and $5\cdot3 \times 1\cdot0 \times 0\cdot0016\ \text{cm}^3$ (sample 2). After machining, sheet 1 was recrystallized and hydrogen outgassed in vacuum ($\approx 2 \times 10^{-6}$ mm Hg) at 1270°K for about 13 hr, subsequently it was electrolytically loaded with hydrogen (0·05*A* for 2 min) and then homogeneized in vacuum at 490°K for 1 hr; the concentration of hydrogen introduced was 61·0 ppm by weight. Sheet 2 was recrystallized and hydrogen outgassed in vacuum ($\approx 2 \times 10^{-6}$ mm Hg) at 1220°K for about 43 hr, and subsequently it was loaded with deuterium by an alloying reaction with 99·95 per cent pure deuterium gas at 721°K and 2 mm Hg for 2 hr; the deuterium concentration was 880 ppm by weight.

The dissipation coefficient Q^{-1} was measured as a function of temperature (from $\approx$ 110 to $\approx$ 930°K) at different vibration frequencies, corresponding to flexural modes of the sample clamped at one end; the measurements were made in vacuum ($\approx 2 \times 10^{-6}$ mm Hg) both after the outgassing and after the hydrogen or deuterium loading treatments. The vibrations were excited and detected by the electrostatic technique described by Bordoni[14] and Nuovo[15].

3. RESULTS

The dissipation coefficient Q^{-1} of the outgassed specimen 1 is plotted as a function of

T^{-1} in Fig. 1, curve 1, the vibration frequency being 9·6Hz. The two pronounced peaks appearing at $2{\cdot}0 \times 10^{-3}\,{}^\circ K^{-1}$ and $1{\cdot}7 \times 10^{-3}\,{}^\circ K^{-1}$ are the Snoek peak due to oxygen and nitrogen, respectively. Curves 2 and 3 of the same figure are obtained during the same heating run and show the internal friction of the sample after the electrolytic hydrogen loading treatment at the vibration frequencies 9·6 and 64 Hz, respectively. The extra dissipation observed between $8{\cdot}0 \times 10^{-3}\,{}^\circ K^{-1}$–$3{\cdot}0 \times 10^{-3}\,{}^\circ K^{-1}$ in the hydrogen charged specimen, is due to the Gorsky effect.

The internal friction of sample 2 after the outgassing and the deuterium loading treatments is shown in Fig. 2, where the vibration frequencies are 8·0 Hz (curves 1 and 2) and 67·6 Hz (curve 3). The Gorsky effect, clearly evident in the deuterium loaded specimen, is about five times higher than that observed in hydrogen doped sample 1.

4. DISCUSSION

According to the theory of the diffusion relaxation process first formulated by Gorsky [16] and then further elaborated by Alefeld *et al.*[17, 18], the dissipation coefficient of a thin sheet having a constant thickness h is given by:

$$Q^{-1}(T) = \frac{\theta}{T - T_S} \times \sum_{n=1,3,5,} \frac{1}{n^4} \frac{2\omega\tau_n}{1 + \omega^2\tau_n^2}, \qquad (1)$$

where:

$$\tau_n = \frac{h^2}{n^2\pi^2 D} \qquad (2)$$

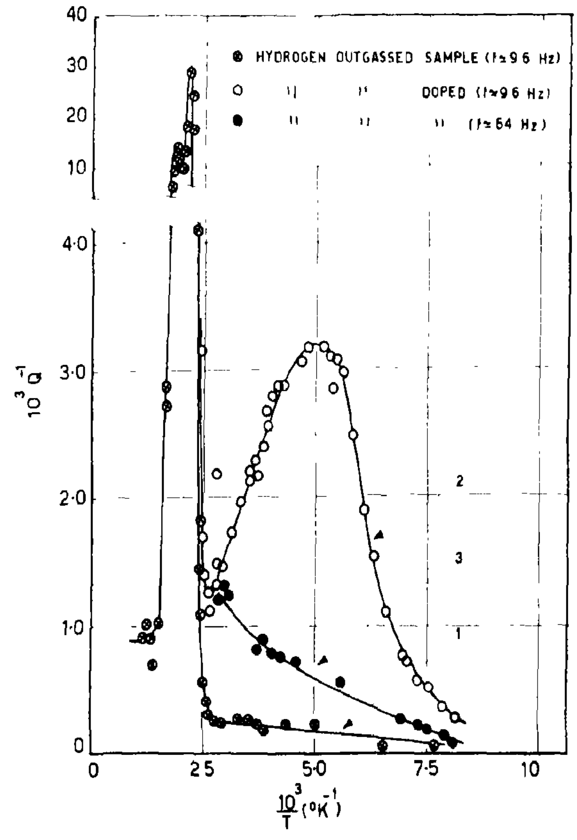

Fig. 1. Internal friction in pure and hydrogen doped vanadium.

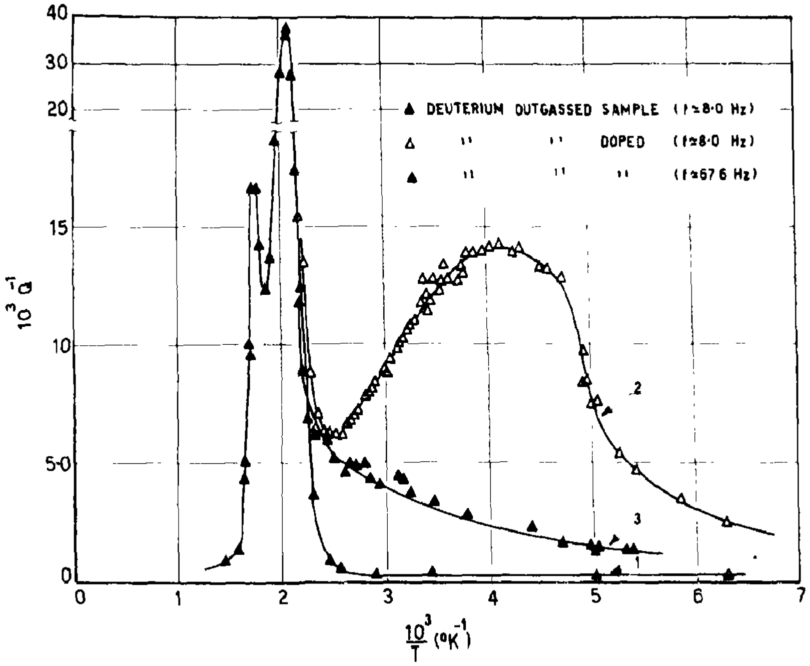

Fig. 2. Internal friction in pure and deuterium loaded vanadium

$$T_S = \frac{1}{k}\frac{c}{c_m}\left(1-\frac{c}{c_m}\right)\left(1-\frac{2}{3}\frac{c}{c_m}\right)U; \qquad (3)$$

θ is a constant, $D(T)$ the diffusion coefficient of the moving impurity, ω the angular frequency of the vibrating sample, k the Boltzmann constant, c the impurity concentration, c_m its maximum solubility and U the interaction energy between impurities. Within the limits of experimental accuracy, the contribution of higher order terms can be neglected, so that equation (1) can be approximated by the first term:

$$Q^{-1}(T) = \frac{\theta}{T-T_S}\frac{2\omega\tau_1}{1+\omega^2\tau_1^{\,2}}. \qquad (4)$$

In this approximation, θ represents the maximum value of the function $(T-T_S)Q^{-1}(T)$. This maximum value is reached at a temperature T_M given by the relation:

$$\omega\tau_1 = \omega\tau_0 \exp\left(\frac{W}{kT_M}\right) = 1. \qquad (5)$$

T_S has been estimated by means of equation (3) with $c_m = 48{\cdot}5$ at %[19] and $U = 0{\cdot}08$ eV, calculated by the expression given in[18]; the values obtained for T_S are 6 and 39°K for the V–H and V–D systems, respectively.

In Figs. 3 and 4, the quantity $(T-T_S)Q^{-1}$ has been plotted as a function of T^{-1} using the experimental data of Figs. 1 and 2, respectively. The resulting values of θ are 0·67°K for hydrogen and 3·05°K for deuterium.

Using relations (2) and (4) the diffusion coefficient $D(T)$ can be expressed in terms of measurable quantities according to the equation:

$$\ln\left(\frac{\pi^2}{\omega h^2}D\right) = -\operatorname{arcosh}\left(\frac{\theta}{(T-T_S)Q^{-1}(T)}\right). \qquad (6)$$

The diffusion coefficients of hydrogen and deuterium, evaluated using relation (6), are plotted in Fig. 5, where the data of Völkl *et al.*[20] are also shown. It can be seen that the lines which interpolate our high temperature points also pass through the points given by Völkl *et al.*, within the limits of experimental

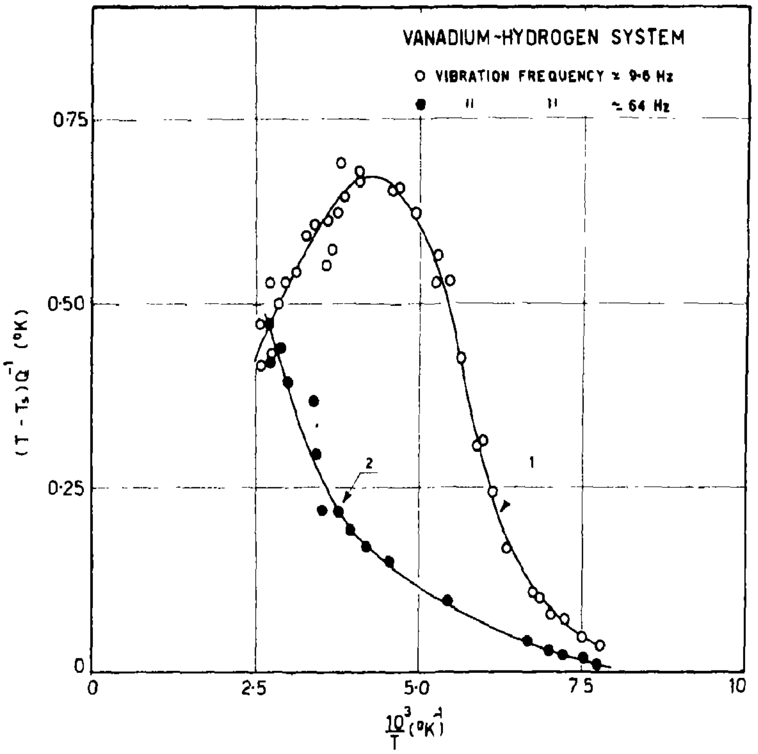

Fig. 3. Gorsky effect in hydrogen loaded vanadium sample 1.

error, indicating general agreement between the two kinds of experiment. Over a wide temperature range the diffusion coefficients obey the law of Arrhenius, whose parameters are:

$$W_H = (0{\cdot}059 \pm 0{\cdot}007)\ \text{eV},$$

$$W_D = (0{\cdot}073 \pm 0{\cdot}006)\ \text{eV},$$

$$D_{0H} = (4{\cdot}4 \pm 1{\cdot}5)\,10^{-4}\ \text{cm}^2/\text{sec},$$

$$D_{0D} = (3{\cdot}1 \pm 0{\cdot}8) \times 10^{-4}\ \text{cm}^2/\text{sec}.$$

As previously found for the diffusion coefficient of hydrogen in niobium[2], a deviation from the exponential law is observed at low temperatures. It is worth noting that the deviation of D_H in vanadium takes place near the $\alpha \rightarrow \beta$ transformation temperature, which is ≈ 200°K for a hydrogen content of 61 ppm by weight[21]. This deviation may be explained by the fact that relation (6) uses a constant value of θ, whereas it appears to decrease below the $\alpha \rightarrow \beta$ transformation temperature[22]. A similar conclusion may be drawn for the V–D and Nb–H systems, even if the details of the phase diagrams are incompletely known (Nb–H) or unknown (V–D) in this temperature range.

According to classical theory, D_H/D_D should be independent of temperature and equal to $(m_D/m_H)^{1/2} = \sqrt{2}$. This prediction appears to be only partially confirmed by the results shown in Fig. 5, which show that the ratio D_H/D_D tends to $\sqrt{2}$ as $T \rightarrow \infty$, but the ratio increases with decreasing temperature. Quantum effects, which have been extensively investigated in recent theoretical works[3–5, 10, 12, 13], may account for the above discrepancies. However, a comparison between theory and experiment cannot be easily accomplished because the theoretical formulae

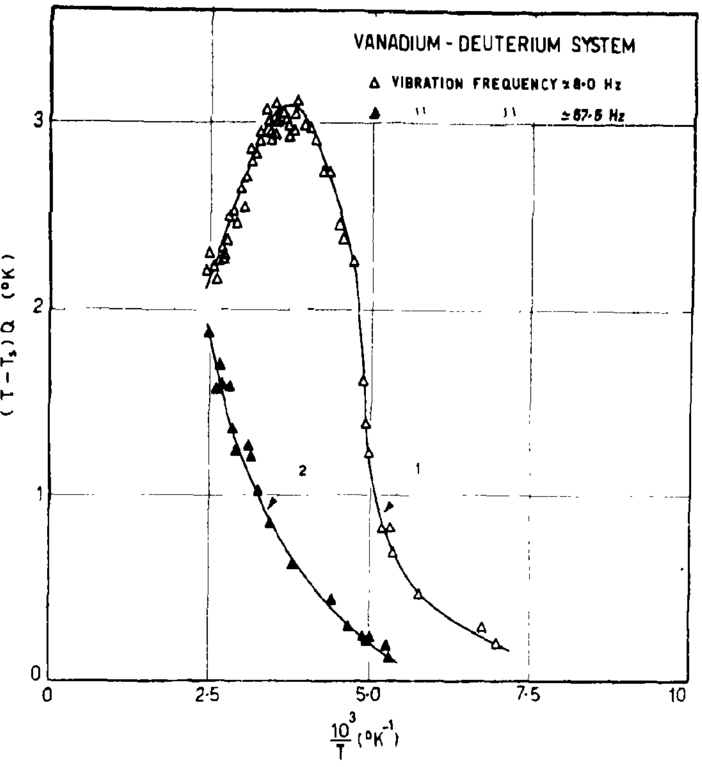

Fig. 4 Gorsky effect in deuterium loaded vanadium sample 2.

include parameters which are not well known.

It should be mentioned that the determination of the diffusion parameters by means of equation (6) involves the assumptions that there is a single relaxation process and that the background dissipation has a negligeable effect on the shape of the relaxation curve. The first hypothesis, suggested by the observation of a simple exponential time law of strain relaxation, has been proved to be valid in the case of niobium[2], where perfect agreement has been found between the hydrogen diffusion energy as measured by the shape of the relaxation curve, and that determined from the temperature dependence of the relaxation time. In order to have a further check of the validity of this assumption, a comparison has been made between the diffusion energy determined from Fig. 5 and that obtained from the Arrhenius plot of Fig. 6. In the case of the vanadium–hydrogen system the value of T_M^{-1} corresponding to the frequency of 9·6 Hz has been read from Fig. 3, while that corresponding to 64 Hz has been evaluated by extrapolating curve 2 of the same figure by means of equation (1), where the value $\theta = 0{\cdot}67$°K has been introduced. A third point at 21·5 Hz was obtained by shortening the free length of specimen 1. A similar procedure was used in the case of the V–D system for reading the values T_M^{-1}. Using the data shown in Fig. 6 it is possible to draw two straight lines which give the same activation energy as is derived from Fig. 5, within the limits of experimental error. This confirms the hypothesis of a single relaxation time.

In order to estimate the sensitivity of the results to the background dissipation the diffusion parameters have been recalculated by subtracting curve 1 from curves 2 and 3 of

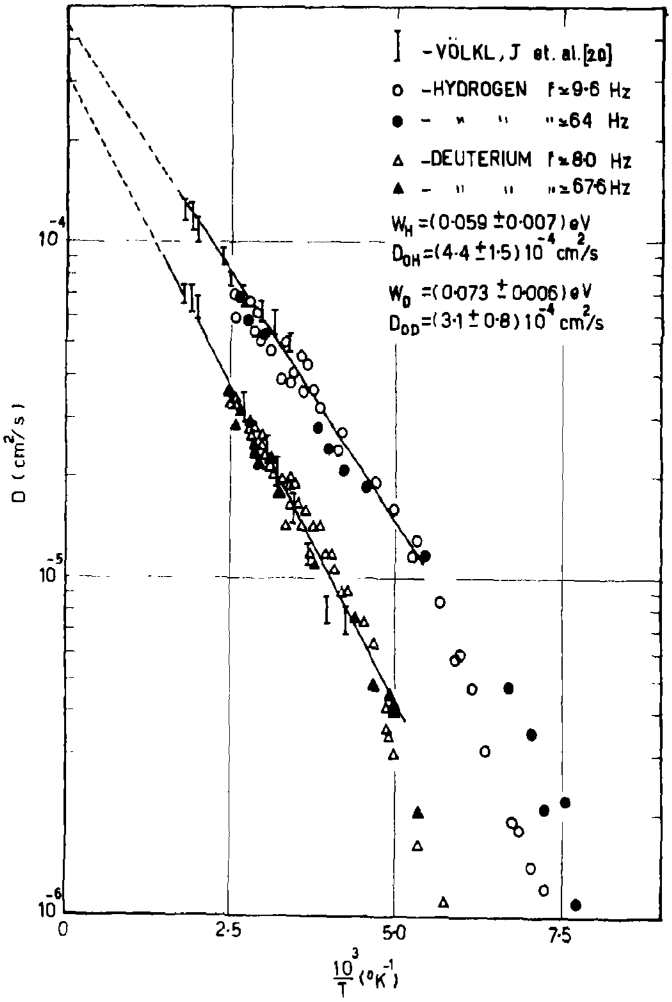

Fig. 5 Diffusion coefficients of hydrogen and deuterium in vanadium.

Figs. 1 and 2. The results obtained (W_H = (0·066 ± 0·006) eV, W_D = (0·075 ± 0·003) eV, D_{0H} = (6·6 ± 1·8) × 10^{-4} cm²/sec, D_{0D} = (3·6 ± 0·4) × 10^{-4} cm²/sec) are the same, within the experimental errors, as those evaluated without subtracting the background; however, with this background subtraction the agreement between measurements at 9·6 and 64 Hz is less satisfactory.

The above results and discussion indicate how successfully the Gorsky effect can be applied in studying the diffusion of hydrogen and deuterium in metals. Moreover our internal friction method allows diffusion measurements at concentrations as low as 61 ppm by weight. Lastly we remark that the measurement of the diffusion coefficients is accurate enough to show that the classical theory is unable to explain the observed isotopic effects.

Acknowledgements—The authors are indebted to Dr. Heinzel of Balzers A.G. for the hydrogen and deuterium determinations. The technical assistance of Mr. G. Libriani is acknowledged.

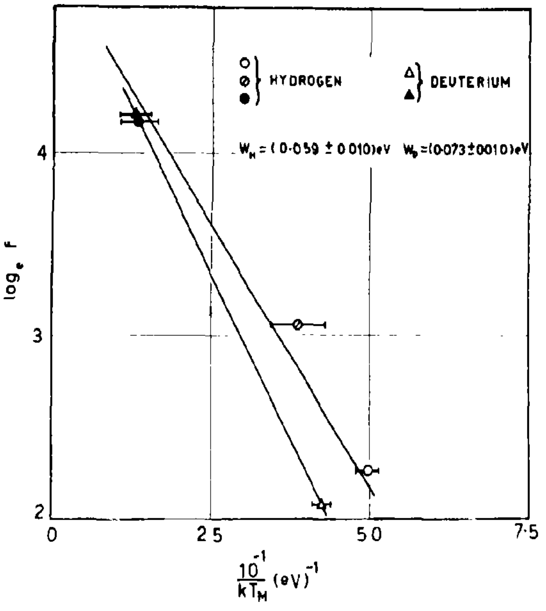

Fig. 6 Frequency dependence of the temperature T_M of Gorsky maximum.

REFERENCES

1. SCHAUMANN G., VÖLKL T. and ALEFELD G., *Phys. Rev. Lett.* **21**, 891 (1968)
2. CANTELLI R., MAZZOLAI F. M. and NUOVO M., *Phys. Status Solidi* **34**, 597 (1969)
3. LE CLAIRE A. D., *Phil. Mag.* **14**, 1271 (1966).
4. EBISUZAKY Y., KASS W. J. and O'KEEFFE M., *J. chem. Phys.* **46**, 1373 and 1378 (1967)
5. EBISUZAKY Y., KASS W. J. and O'KEEFFE M., *Phil. Mag.* **15**, 1071 (1967).
6. EICHENAUER W., LÖSER W. and WITTE H., *Z. Metallk.* **56**, 257 (1965).
7. KLEY W., PERETTI J., RUBIN R. and VERDAN G., *Brookhaven National Lab. Rep.* No. BNL-490, 1965.
8. CANNELLI G. and VERDINI L., *Ricerca scient.* **36**, 98 and 246 (1966).
9. BLAESSER G. and PERETTI J., *Int. Conf. on Vacancies and Interstitials in Metals, Jülich*, Vol. 2, 886 (1968)
10. ARONS R. R., *Int. Conf. on Vacancies and Interstitials in Metals, Jülich.* Vol. 2, p. 901 (1968).
11. SCHILLER P. and SCHNEIDERS A., *Int. Conf. on Vacancies and Interstitials in Metals, Jülich*, Vol. 2, p. 371 (1968).
12. PFEGEL B., *Phys. Status Solidi* **22**, 223 and k45 (1967).
13. PFEGEL B., *Phys. Status Solidi* **23**, 335 (1967)
14. BORDONI P. G., *Nuovo Cim.* **4**, 177 (1947)
15. NUOVO M., *Ricerca scient.* **31**, (II–A) 212 (1961)
16. GORSKY W. S., *Z. Phys.* **8**, 457 (1935)
17. ALEFELD G., VÖLKL J. and SCHAUMANN G., *Phys. Status Solidi* **37**, No. 1
18. ALEFELD G., VÖLKL J. and TRETKOWSKI J., Conference on Ultrasonic Attenuation in Crystalline Solids.
19. ELLIOTT R. P., *Constitution of Binary Alloys*, 1st Suppl. McGraw-Hill, New York (1965).
20. VÖLKL J., SCHAUMANN G. and ALEFELD G., This Conference
21. CANNELLI G. and MAZZOLAI F. M., This Conference
22. SCHAUMANN G., Thesis, Technische Hochschule Aachen (1969).

J. Phys. Chem. Solids Pergamon Press 1970. Vol. 31, pp 1819–1826. Printed in Great Britain

KINETICS OF ANELASTIC AND DIELECTRIC RELAXATION DUE TO REACTING POINT DEFECTS*

A. S. NOWICK
Henry Krumb School of Mines, Columbia University, New York, N.Y. 10027, U.S.A

(Received 5 September 1969)

Abstract – The theory of the kinetics of defect relaxations in crystals, developed previously for the case of a single defect species, is now extended to include defect reactions among several different species. In this way it becomes possible to obtain expressions for the various relaxation times in terms only of the symmetries of the crystal and of the interacting defects. It is shown that this generalization can be carried out using the same symmetry coordinates as were tabulated in an earlier paper. The example of a cubic crystal containing 3 species of interacting defects, which are tetragonal, trigonal and ⟨110⟩ orthorhombic, is considered in detail The results are applied to the specific problem of paired interstitial defects in the bcc lattice.

1. INTRODUCTION

In two previous papers[1, 2] (henceforth denoted by I and II, respectively) a general theory of dielectric and anelastic relaxation due to point defects in crystals was developed from the viewpoint that relaxation behavior can be characterized by the point symmetry of the defect as well as that of the crystal. Paper I confined itself to the calculation of the relaxation strength, i.e. the thermodynamics of the process, while II dealt with the relaxation times, i.e. the kinetics. Both papers, however, limited themselves to a single defect species which could occupy one of several crystallographically equivalent orientations. The complication of a defect 'reaction' between two or more non-equivalent species (e.g. an interstitial which can occupy more than one type of interstitial site, or a defect pair which can exist at both a nearest-neighbor and a next nearest-neighbor separation) was omitted in order to simplify the treatment. Nevertheless, the occurrence of defect reactions has been of importance in actual crystals studied and accordingly the theory of relaxation kinetics has been developed by various authors[3–5] for a number of specific cases. In these papers, as in I and II, group representation theory was used to greatly simplify the calculations; however, whereas the kinetic calculations in II were quite general in terms only of defect symmetry, references [3–5] considered only individual cases, and in fact confined themselves to paired defects.

The present paper is intended to show that the approach used in II can be extended to include defect reactions. In this way, it becomes possible to solve the problem for the reaction among defects of given symmetry only once, instead of having to start from first principles in each individual case. As before, a major step toward simplification of the problem of the calculation of relaxational normal modes is through the introduction of symmetry coordinates, which transform as the irreducible representation of the crystal point group. In fact, it is shown that the generalization to include defect reactions can be carried out with the very same symmetry coordinates of the individual defect species that are tabulated in II for many crystal structures. The results obtained are equally applicable to simple defects, e.g. interstitials, as well as to paired defects. Following the

---

*Work supported by the U.S. Atomic Energy Commission.

development of the general theory, a specific example will be given to illustrate the application of the theory.

2. GENERAL THEORY

We consider reactions among several (crystallographically inequivalent) defect species of the form $\alpha \rightleftarrows \beta \rightleftarrows \ldots \rightleftarrows \zeta \rightleftarrows \ldots$ i.e. confining ourselves to first-order reactions only. In addition, it is recognized that each defect species, ζ, may occupy a number n_ζ of crystallographically equivalent orientations, each of which may be numbered by an index $r(\zeta)$, e.g. following the numbering convention adopted in II. In general, jumps may take place from a defect $p(\alpha)$ to defect $r(\zeta)$ at a rate (i.e. with a probability per second) $\nu_{p(\alpha)r(\zeta)}$ in the absence of any applied electric or stress field (see Fig. 1). By analogy to II, we also define the rate $\nu_{p(\alpha)p(\alpha)}$ as the negative sum of all jump rates involving a departure from $p(\alpha)$, i.e. by

$$\nu_{p(\alpha)p(\alpha)} = -\sum\nolimits'_{q(\alpha)} \nu_{p(\alpha)q(\alpha)} - \sum\nolimits'_{\zeta} \sum\nolimits_{r(\zeta)} \nu_{p(\alpha)r(\zeta)} \qquad (1)$$

where $\Sigma'_{q(\alpha)}$ means a sum over all $q(\alpha)$ except $p(\alpha)$, while Σ'_ζ is over all species other than α. If we let $C_{p(\alpha)}$ be the concentration of defects of type $p(\alpha)$ expressed as a mole fraction of total number of molecules in the crystal, and write the kinetic equation for defect $p(\alpha)$, taking into account all jumps which increase and decrease $C_{p(\alpha)}$, we readily obtain with the aid of equation (1):

$$\dot{C}_{p(\alpha)} = \sum\nolimits_\zeta \sum\nolimits_{r(\zeta)} \nu_{r(\zeta)p(\alpha)} C_{r(\zeta)}. \qquad (2)$$

Similar equations may be written for each defect species and orientation (a total of n equations, where $n \equiv \Sigma_\zeta n_\zeta$ is the total number of defect orientations of all species). It is convenient to redefine the subscripts $r(\zeta)$ to a single index $u = 1, 2, \ldots n$ by numbering the defects in the following order: $1(\alpha)$, $2(\alpha), \ldots n_\alpha(\alpha)$, $1(\beta)$, $2(\beta), \ldots$ Equations (2) and (1) then become, respectively,

$$\dot{C}_u = \sum\nolimits_r C_r \nu_{ru} \qquad (3)$$

$$\nu_{uu} = -\sum\nolimits'_r \nu_{ur}. \qquad (4)$$

Equation (3) can also be written in matrix form as: $\dot{\mathbf{C}} = \mathbf{C}\boldsymbol{\nu}$ where $\mathbf{C}$ is a *row* vector made up of components C_r (i.e. in n-dimensional 'concentration space') while $\boldsymbol{\nu}$ is an $n \times n$ matrix. The frequency matrix $\boldsymbol{\nu}$ is not symmetric since $\nu_{p(\alpha)r(\zeta)} \neq \nu_{r(\zeta)p(\alpha)}$ due to the inequivalence of defects α and ζ, as shown in Fig. 1. In this sense the present case differs from that involving a single defect species (in II) where $\boldsymbol{\nu}$ was symmetric.

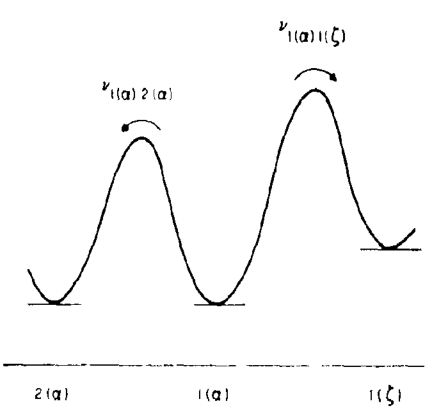

Fig. 1. Illustration of potential barriers and jump frequencies involved in moving a defect between two orientations of the same defect species, as well as between two different defect species.

To obtain the relaxational normal modes, we express the concentration vector in the form:

$$\mathbf{C} = \mathbf{A} \exp(-t/\tau) \qquad (5)$$

in terms of a relaxation time τ. The kinetic equations (3) then become the set of algebraic equations

$$\mathbf{A}(\boldsymbol{\nu} + \tau^{-1}\mathbf{E}) = 0 \qquad (6)$$

where $\mathbf{E}$ is the $n \times n$ unit matrix. The eigenvalues (relaxation rates τ^{-1}) are then the solutions of the determinental equation

$$|\boldsymbol{\nu} + \tau^{-1}\mathbf{E}| = 0 \qquad (7)$$

i.e. they are the negative roots of the matrix $\boldsymbol{\nu}$.

As in II, considerable simplification in the calculation of the eigenvalues is obtained by introducing the symmetry coordinates of concentration each of which transforms as an irreducible representation (abbreviated '*i.r.*') of the crystal point group. In the present case, this transformation in concentration space is given by

$$\mathbf{C}'\mathbf{W} = \mathbf{C}$$

where **W** is an $n \times n$ matrix in the block form

$$\mathbf{W} = \begin{pmatrix} \boxed{\mathbf{W}_\alpha} & & \\ & \boxed{\mathbf{W}_\beta} & \\ & & \ddots \end{pmatrix}.$$

Here $\mathbf{W}_\alpha$ is an $n_\alpha \times n_\alpha$ matrix, namely, that given in II (as **W**) which transforms the concentrations of species α into symmetry coordinates, and similarly for $\mathbf{W}_\beta$; further, all elements in the matrix outside the blocks are zeros. Since $\mathbf{W}_\alpha$, $\mathbf{W}_\beta$, etc. are unitary, the larger matrix **W** is also a unitary matrix in concentration space. The transformation converts equation (3) into

$$\dot{\mathbf{C}}' = -\mathbf{C}'\mathbf{\Omega} \tag{8}$$

in which

$$\mathbf{\Omega} = -\mathbf{W}\boldsymbol{\nu}\mathbf{W}\dagger. \tag{9}$$

(As usual the matrix **W**† represents the adjoint, or transposed complex conjugate, of **W**.) In view of the fact that $\boldsymbol{\nu}$ is negative semi-definite*, $\mathbf{\Omega}$ is positive semi-definite, i.e. it has non-negative eigenvalues. Equations (8) and (9), written in component form, become:

$$\dot{C}'^{(\gamma)}_{a\rho'} = -\sum_\rho C'^{(\gamma)}_{a\rho}\Omega_{\gamma,\rho\rho'} \tag{10}$$

$$\Omega_{\gamma,\rho\rho'} = -\sum_{u,r} W^{(\gamma)}_{a\rho,u}W^{(\gamma)*}_{a\rho',r}\nu_{ur}. \tag{11}$$

As in II, the components of the symmetrized frequency matrix, $\mathbf{\Omega}$, are identified by the i.r., γ, and by repeat indices ρ and ρ' taking into account the number of times that γ appears in the combined symmetry coordinates of all the defect species. The number of times that a given i.r. occurs, i.e. the range of the repeat index ρ, is simply obtained by adding the numbers of repeats for the various defect species taken separately, as given in the selection rule tables in I. Thus, for example, if i.r. γ appears once for species α and twice for species β, it will appear three times when the reaction $\alpha \rightleftharpoons \beta$ occurs. The components of Ω are independent of the degeneracy index **a** of the i.r., provided that the symmetry coordinates of different repeat indices are similarly oriented.† In addition to this independence of a, the fundamental theorems of representation theory (e.g., see papers I and II) assure that $\mathbf{\Omega}$ is diagonal with respect to components belonging to different γ and to different degeneracy indices a.

To find normal modes we may, similarly to equation (5), write $\mathbf{C}' = \mathbf{A}'\exp(-t/\tau)$ leading to the analog of equation (6):

$$\mathbf{A}'(\mathbf{\Omega} - \tau^{-1}\mathbf{E}) = \mathbf{0} \tag{12}$$

and the corresponding determinental equation. Due to the decoupling of terms for different γ and a, however, this determinental equation breaks up into separate equations, one for each i.r., of the form:

$$|\Omega_{\gamma,\rho\rho'} - \delta_{\rho\rho'}\tau^{-1}| = 0 \tag{13}$$

where $\delta_{\rho\rho'}$ is the Kronecker delta. This determinant is substantially reduced from that of equation (7), its dimensionality being simply the number of times that γ occurs. Most important, this reduction is carried out with the use of the same **W** matrices worked out and tabulated in II. In addition to the eigenvalues, τ^{-1}, obtained from (13), the corresponding eigenvectors (or normal coordinates) may be obtained for each i.r., in the usual way by substituting a given eigenvalue into the homogeneous equations (12).

---

*The proof that $\boldsymbol{\nu}$ is negative semi-definite follows along lines similar to that in II. First, $\boldsymbol{\nu}$ can be taken by a similarity transformation into a symmetric matrix via a transformation which multiplies each concentration $C_{r(\zeta)}$ by a constant $\sqrt{K_\zeta}$, where $K_\zeta = \nu_{s(\zeta)p(\alpha)}/\nu_{p(\alpha)r(\zeta)}$. It follows that $\boldsymbol{\nu}$ must have real roots. The fact that the roots are ≤ 0 follows form equation (4) and Gersgorin's theorem (paper II, Appendix A).

†This point was anticipated in II (see p. 15) so that all symmetry coordinates of a given degenerate i.r. given in that paper meet the requirement of similar orientation

In order to calculate the relaxation frequencies in practice, one requires more convenient expressions for $\Omega_{\gamma,\rho\rho'}$ than that given by equation (11). We therefore distinguish the case in which both repeat indices ρ and ρ' come from the same defect species and that where they come from different species. When they are from the same species, say α, it is advantageous to let ρ and ρ' become $\pi(\alpha)$ and $\pi'(\alpha)$, the repeat indices for that defect species (as denoted in II). It is then easy to show from equations (11), (1) and (4) that

$$\Omega_{\gamma,\pi(\alpha)\pi'(\alpha)} = \Omega_{\gamma,\pi\pi'}(\alpha \text{ only}) + \delta_{\pi\pi'} \sum\nolimits_{\zeta}' \sum\nolimits_{r(\zeta)} \nu_{p(\alpha)r(\zeta)} \tag{14}$$

where the first term on the right is that which was obtained for species α alone (as given in II). Equation (14) states that for $\pi \neq \pi'$ the term obtained is the same as if no reactions took place. For $\pi = \pi'$, we must add to the term for α alone the sum of all frequencies by which the defect in any particular orientation $p(\alpha)$ of species α may go into all possible orientations of all other defect species. It is thus possible to take full advantage of the methods already worked out (in Section 2 of II) for calculating $\Omega_{\gamma,\pi\pi'}$ for a single species. Further, if i.r. occurs only once for defect α, so that the index π is not needed, the term Ω_γ (α only) in (14) is simply the eigenvalue τ^{-1}, which is tabulated in II for most important crystal symmetries.

The other case to consider is that in which the repeat indices ρ and ρ' come from different defect species, say α and β, respectively. A simple but important situation is that in which i.r. γ occurs only once for one species, say β. Then if equation (9) is rewritten $\mathbf{\Omega W} = -\mathbf{W}\boldsymbol{\nu}$ and components are taken, we obtain

$$\Omega_{\gamma,\rho\rho'} = -\left(1/W^{(\gamma)}_{\alpha,q(\beta)}\right) \times \sum\nolimits_{p(\alpha)} W^{(\gamma)}_{a\pi(\alpha),p(\alpha)}\, \nu_{p(\alpha)q(\beta)}. \tag{15}$$

On the other hand, in the more general situation, we return to equation (11) and, by an argument analogous to that which yielded equation (2.19) of paper II, we obtain the relation

$$\begin{aligned}\Omega_{\gamma,\rho\rho'} &\equiv \Omega_{\gamma,\pi(\alpha)\pi'(\beta)}\\ &= (n_\alpha/b_\gamma) \sum\nolimits_a W^{(\gamma)}_{a\pi(\alpha),p(\alpha)}\\ &\quad\times \sum\nolimits_{q(\beta)} W^{(\gamma)*}_{a\pi'(\beta)q(\beta)}\, \nu_{p(\alpha)q(\beta)}\end{aligned} \tag{16}$$

where b_γ is the degeneracy of i.r. γ. Equation (16) applies also under conditions where (15) is valid, but the latter is somewhat easier to use where applicable.

The relaxations belonging to the totally symmetric i.r. (designated by $\gamma = A_1$) require special consideration. For a single defect species one always obtains $\tau^{-1}_{A_1} = 0$ (see II). This result stems from the fact that the total concentration of defects cannot be changed by means of reorientation jumps of the type being considered. On the other hand, in the presence of more than one reacting defect species, there is the possibility of relaxation via a net change in the concentration of one species at the expense of another. In the A_1 i.r. there is exactly one symmetry coordinate $C'^{(A_1)}_\rho$ for each species, in which all concentrations of that species are equal and the others are zero. Accordingly the repeat index ρ runs over the total number of species, say m. Writing equation (10) for the A_1 components only, and noting that in equilibrium all $\dot{C}'^{(A_1)}_\rho$ are zero while $C'^{(A_1)}_\rho \neq 0$, it follows that

$$|\Omega_{A_1,\rho\rho'}| = 0. \tag{17}$$

Accordingly, there exists a solution of equation (13) for which the eigenvalue $\tau^{-1} = 0$, namely that for which the eigenvector contains the equilibrium values of all the concentrations. This mode is often called the 'equilibrium mode.' The remaining $m-1$ modes belonging to the A_1 i.r. have non-zero relaxation rates. Thus, when 3 defect species are involved, the relaxation rates are obtained from the determinental equation (13), one solution being $\tau^{-1}=0$, and the other two given by:

$$\tau^{-1}=X\pm[X^2-Y]^{1/2} \tag{18}$$

where

$$X=(\Omega_{11}+\Omega_{22}+\Omega_{33})/2$$

$$\begin{aligned}Y=\Omega_{11}\Omega_{22}+\Omega_{22}\Omega_{33}+\Omega_{33}\Omega_{11}\\ -(\Omega_{12}\Omega_{21}+\Omega_{23}\Omega_{32}+\Omega_{31}\Omega_{13}).\end{aligned} \tag{19}$$

(For simplicity, the i.r. designation A_1 has been left out in all terms $\Omega_{1,\rho\rho'}$ of (19)).

It is easily shown that the A_1 modes involve only a net reaction and no reorientation among defects of the same species. The importance of such modes, (termed 'reaction modes') in relaxation studies will be the subject of a separate paper of this series which will deal particularly with the thermodynamics of the relaxation.

3. ILLUSTRATIVE EXAMPLE

In this section, we will illustrate the general theory by considering a particular example which includes, as special cases, most defect reactions of interest in cubic crystals[4]. This example is the reaction, in a cubic crystal, among the 3 defect species $\alpha\rightleftarrows\beta\rightleftarrows\eta$, in which α is tetragonal β is $\langle 110\rangle$ orthorhombic and η is trigonal. After working out this example in complete generality, we will consider a specific case, that of interstitial pairs in the bcc lattice. Mechanically active modes will only be considered, although the extension to include dielectric relaxation is straightforward and will be discussed briefly.

From the selection rules (see I), it is clear that in a cubic crystal, the tetragonal defect species gives rise to an E relaxation, the trigonal species to a T_2 (or F_2) relaxation and the $\langle 110\rangle$ orthorhombic to $E+T_2$.* Thus, the entire combination of 3 species yields two E and two T_2 relaxations. In addition, in view of the closing remarks of the previous section, two A_1 relaxations should also occur. Our object here is to calculate the relaxation rates of these six relaxations in terms of the various frequencies of the type $\nu_{r(\zeta)r'(\zeta')}$. As in II we use the numbering convention that $1(\alpha)$, $2(\alpha)$, and $3(\alpha)$ are the defects with tetragonal axis along [100], [010] and [001], respectively, that $1(\beta),\ldots 6(\beta)$ have a principal axis along [110], $[1\bar{1}0]$, [011], $[01\bar{1}]$, [101] and $[10\bar{1}]$, respectively, and finally, that $1(\eta),\ldots 4(\eta)$ have their trigonal axis along [111], $[\bar{1}11]$, $[1\bar{1}1]$ and $[11\bar{1}]$. We begin with the E relaxation, taking $\rho=1$ for the α and $\rho=2$ for the β species. (Since η is trigonal it does not contribute an E relaxation.)

For $\Omega_{E,11}$ we utilize equation (14) and note (from II) that $\Omega_{E,11}$ (α only) $=3\nu_{1(\alpha)2(\alpha)}$. Accordingly

$$\begin{aligned}\Omega_{E\,11}&=3\nu_{1(\alpha)2(\alpha)}+\sum_{q(\beta)=1}^{6}\nu_{1(\alpha)q(\beta)}\\&\quad+\sum_{r(\eta)=1}^{4}\nu_{1(\alpha)r(\eta)}\\&=3\nu_{1(\alpha)2(\alpha)}+4\nu_{1(\alpha)1(\beta)}\\&\quad+2\nu_{1(\alpha)3(\beta)}+4\nu_{1(\alpha)1(\eta)}\end{aligned} \tag{20}$$

where, in the last step we have expressed the result in terms only of the *independent* frequencies; relations such as $\nu_{1(\alpha)2(\beta)}=\nu_{1(\alpha)3(\beta)}$ are obtained from the above numbering convention together with the 'dot product' method for determining equivalent pairs of defects (see footnote to paper II, p. 18). In a similar way, we obtain:

$$\begin{aligned}\Omega_{E,22}&=6\nu_{1(\beta)3(\beta)}+2\nu_{1(\beta)1(\alpha)}+\nu_{3(\beta)1(\alpha)}\\&\quad+2\nu_{1(\beta)1(\eta)}+2\nu_{1(\beta)2(\eta)}.\end{aligned} \tag{21}$$

The calculation of Ω_{12} and Ω_{21} requires equation (15), since the two repeat indices are from different species and the i.r. E is non-repeating for each species. The results are:

---

*For the doubly degenerate E i.r., 'one relaxation' means 2 normal coordinates both having the same relaxation time; similarly for the triply degenerate T_2 i.r. (In I and II we have used the symbol F for triply degenerate i.r.'s. However, the symbol T is so much more widely used that we will adopt it henceforth.)

$$\Omega_{E,12} = \sqrt{2}(\nu_{1(\alpha)1(\beta)} - \nu_{1(\alpha)3(\beta)}) \quad (22)$$

$$\Omega_{E,21} = \sqrt{2}(\nu_{1(\beta)1(\alpha)} - \nu_{3(\beta)1(\alpha)}). \quad (23)$$

Finally, these $\Omega_{E,pp'}$ parameters may be inserted into equation (13) to obtain the two relaxation rates for the E modes

$$\tau^{-1} = \left(\frac{\Omega_{11}+\Omega_{22}}{2}\right) \pm \left[\left(\frac{\Omega_{11}-\Omega_{22}}{2}\right)^2 + \Omega_{12}\Omega_{21}\right]^{1/2} \quad (24)$$

where the i.r. subscript E has been dropped throughout.

Turning now to the T_2 mode, which appears once for each of the species η and β but not for α, we obtain in a completely analogous way:

$$\begin{aligned}\Omega_{T_2,11} = {} & 4\nu_{1(\eta)2(\eta)} + 3\nu_{1(\eta)1(\beta)} \\ & + 3\nu_{2(\eta)1(\beta)} + 3\nu_{1(\eta)1(\alpha)}\end{aligned} \quad (25)$$

$$\begin{aligned}\Omega_{T_2,22} = {} & 2\nu_{1(\beta)2(\beta)} + 4\nu_{1(\beta)3(\beta)} \\ & + 2\nu_{1(\beta)1(\alpha)} + \nu_{3(\beta)1(\alpha)} \\ = {} & 2\nu_{1(\beta)1(\eta)} + 2\nu_{1(\beta)2(\eta)}\end{aligned} \quad (26)$$

$$\Omega_{T_2,12} = -\sqrt{2}(\nu_{1(\eta)1(\beta)} - \nu_{2(\eta)1(\beta)}) \quad (27)$$

$$\Omega_{T_2,21} = -\sqrt{2}(\nu_{1(\beta)1(\eta)} - \nu_{1(\beta)2(\eta)}) \quad (28)$$

with two relaxation rates again given by equation (24).

Finally, for the A_1 modes, letting the repeat indices 1, 2 and 3 refer respectively to the defects α, β and η, we obtain:

$$\Omega_{A_1,11} = 4\nu_{1(\alpha)1(\beta)} + 2\nu_{1(\alpha)3(\beta)} + 4\nu_{1(\alpha)1(\eta)} \quad (29)$$

$$\begin{aligned}\Omega_{A_1,22} = {} & 2\nu_{1(\beta)1(\alpha)} + \nu_{3(\beta)1(\alpha)} \\ & + 2\nu_{1(\beta)1(\eta)} + 2\nu_{1(\beta)2(\eta)}\end{aligned} \quad (30)$$

$$\Omega_{A_1,33} = 3\nu_{1(\eta)1(\alpha)} + 3\nu_{1(\eta)1(\beta)} + 3\nu_{1(\eta)2(\beta)} \quad (31)$$

$$\Omega_{A_1,12} = -\sqrt{2}(2\nu_{1(\alpha)1(\beta)} + \nu_{1(\alpha)3(\beta)}) \quad (32)$$

$$\Omega_{A_1,21} = -\sqrt{2}(2\nu_{1(\beta)1(\alpha)} + \nu_{3(\beta)1(\alpha)}) \quad (33)$$

$$\Omega_{A_1,13} = -2\sqrt{3}\nu_{1(\alpha)1(\eta)} \quad (34)$$

$$\Omega_{A_1,31} = -2\sqrt{3}\nu_{1(\eta)1(\alpha)} \quad (35)$$

$$\Omega_{A_1,23} = -\sqrt{6}(\nu_{1(\beta)1(\eta)} + \nu_{1(\beta)2(\eta)}) \quad (36)$$

$$\Omega_{A_1,32} = -\sqrt{6}(\nu_{1(\eta)1(\beta)} + \nu_{2(\eta)1(\beta)}). \quad (37)$$

The corresponding relaxation rates are $\tau^{-1} = 0$ ('equilibrium mode') and the two rates given by equations (18)–(19).

Dielectric relaxation for this set of defect species is also easily treated; it is simply necessary to include the electrically active i.r.'s. To obtain dielectric relaxation, however, it is necessary that the defect have directionality, e.g. a defect consisting of an unlike pair. Two defects differing in orientation by 180° then produce the same elastic dipole but different electric dipoles. It is then easiest to treat the two types of i.r.'s separately. For the mechanically active i.r.'s one may number the defects without regard to directionality and so the above equations for the A_1, E and T_2 modes apply; for electrically active i.r.'s one must use a numbering system as described in Section 3 of II.

It should be noted that the example worked out in this section is applicable not only to the cases where all three defect species appear, but also where only two of them are involved. Thus, the case of a reaction involving only the tetragonal and ⟨110⟩ orthorhombic defects is covered by setting all frequencies containing η defects equal to zero. It is for this reason that we could state earlier that this one example covers essentially all specific cases dealt with in Chang's paper[4].

For a specific problem to illustrate the application of the theory, we choose that of the *i*-*i* (paired interstitial) defect in the bcc lattice. In this model, the pair is assumed to remain bound in one of three types of position: the nearest-neighbor (n.n.) configuration, α, which is tetragonal, the next-nearest neighbor (n.n.n.) configuration, β, which is ⟨110⟩ orthorhombic, and the third neighbor (t.n.n.) configuration, η, which is trigonal. This model, therefore, falls under the general example we have just discussed, and at the same time is of practical interest. Further, this problem has not been correctly worked out in the literature.*

The various configurations of the α, β and η defects are shown in Fig. 2. In this figure, one interstitial solute atom is placed at the center of the cube shown, while the other may occupy any one of the n.n., n.n.n., or t.n.n. sites, which are all numbered according to the convention quoted earlier. In Fig. 2, the centrally located interstitial atom sits in a tetragonal site (i.e. a Snoek 'octahedral' site) of the y-type, since the two nearest solvent atoms to it lie along the y axis. One can therefore draw two other crystallographically equivalent diagrams for which this central atom is located in x-type and z-type sites, or more conveniently, one can retain the figure as shown but permute the 3 axes, renumbering all the sites. Among the three diagrams so obtained, every possible type of defect jump can be obtained with motion of the outer interstitial, i.e. without a jump by the central interstitial atom. The fact that actually both members of the pair can jump is later taken into account by simply doubling all of the calculated frequencies. As in II, the complete solution of the kinetic problem requires that we obtain expressions for the relaxation rates in terms of all allowable atom jump rates, w'_j. In the present model, we shall first allow both nearest neighbor jumps (along $\langle 100\rangle$), and the next-nearest neighbor jumps (along $\langle 110\rangle$). Examination of Fig. 2, shows that there are four independent atom jump rates of the nearest neighbor type which may be defined as follows (giving, in each case the change in defect species produced by the particular jump):

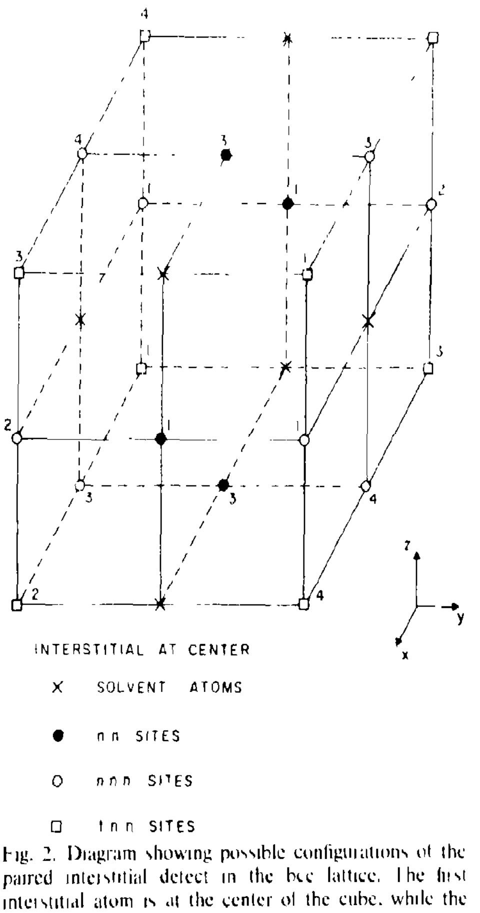

Fig. 2. Diagram showing possible configurations of the paired interstitial defect in the bcc lattice. The first interstitial atom is at the center of the cube, while the n.n., n.n.n. and t.n.n. positions of the second interstitial atom are shown, numbered according to the adopted convention.

$$w'_1(\alpha \to \beta),\ w'_2(\beta \to \alpha),$$
$$w'_3(\beta \to \eta),\ w'_4(\eta \to \beta).$$

Similarly, there are four distinct next-nearest-neighbor type jumps whose rates are:

$$w'_5(\alpha \to \alpha),\ w'_8(\beta \to \beta)$$
$$w'_6(\alpha \to \eta),\ w'_7(\eta \to \alpha).$$

These 8 jumps are the only independent ones in a model which allows the pair to separate no further than the t.n.n configuration, as we have presently assumed.

To complete this specific problem, then requires expressing the frequencies of the type $\nu_{p(\alpha),(\zeta)}$ in terms of the allowed atom jump rates $w'_1 - w'_8$. The use of the three diagrams (or a triply relabeled diagram) similar to Fig. 2, for this purpose may be illustrated by calculation of $\nu_{1(\alpha)1(\beta)}$. In Fig. 2, there is one path from a defect $1(\alpha)$ to $1(\beta)$, involving the jump of rate w'_1. On the other hand, in one of the other two diagrams the defect $1(\alpha)$ appears but has no available path to reach the defect numbered $1(\beta)$. Accordingly, the *average* rate at which a defect $1(\alpha)$ makes a transition into $1(\beta)$ is $w'_1/2$. Since both members of the pair can move, however, the desired frequency $\nu_{1(\alpha)1(\beta)}$ is w'_1. In a similar way, the following expressions obtained are the various independent frequencies $\nu_{r(\zeta)r'(\zeta')}$ in terms of the jump rates w'_j: $\nu_{1(\alpha)2(\alpha)} = 2w'_5$, $\nu_{1(\beta)1(\alpha)} = w'_2$, $\nu_{1(\alpha)1(\eta)} = 2w'_6$, $\nu_{1(\beta)3(\beta)} = w'_8$, $\nu_{1(\beta)1(\eta)} = 2w'_3$, $\nu_{1(\eta)1(\beta)} = 4w'_4/3$, $\nu_{1(\eta)1(\alpha)} = 4w'_7/3$, all the others being equal to zero. When these results are substituted into equations (20) through (37) the six relaxation rates are obtained.

---

*Chang[4] considers the problem but obtains a different relaxation rate for the E modes for different crystal orientations, and the same for T_2. Clearly, such a result is inconsistent with group representation theory

It is probably realistic to regard the next-nearest-neighbor jumps whose rates are w_5 to w_8 as far less probable than the nearest-neighbor jumps. We will therefore write the simpler expressions for the six relaxation times taking w_5 to w_8 equal to zero. These expressions are:

$$\tau_{I'}^{-1} = (2w'_1 + w'_2 + 2w'_3) \pm [(2w_1 - w'_2 - 2w'_3)^2 + 2w'_1 w'_2]^{1/2} \tag{38}$$

$$\tau_{I_2}^{-1} = (2w'_1 + w'_2 + 2w'_3) \pm [(2w'_4 - w'_2 - 2w'_3)^2 + (16/3)w'_3 w'_4]^{1/2} \tag{39}$$

$$\tau_{I_1}^{-1} = (2w'_1 + w'_2 + 2w'_3 + 2w'_4) \pm [(2w'_1 + w'_2 + 2w'_3 + 2w'_4)^2 - 16(w'_1 w'_3 + w'_1 w'_4 + w'_2 w'_4)]^{1/2}. \tag{40}$$

Insterstitial pairs in bcc lattices are known [6, 7] to give rise to complex relaxation spectra, consisting of a multiplicity of relaxation peaks. The present model, in spite of its restriction to pairs separated no further than t.n.n.'s, should be useful in the analysis of such relaxation spectra. In particular, the large number of relaxations with different τ-values which can arise even from as simplified a model as that considered here, tends to render doubtful the type of analysis often used, which assigns only one relaxation to interstitial pairs and all the others to higher order clusters.

4. CONCLUDING REMARKS

It has been possible to show that the kinetics of relaxation for a crystal containing a system of reacting defects can be worked out in general terms where the solution depends only on crystal and defect symmetry, just as had been done earlier (in II) for a single defect species. It is thus unnecessary to work out individually specific defects of interest, except for the last step, which is the conversion of the frequencies of the type $\nu_{1(\alpha)r(\zeta)}$ to atom jump rates w_j. The theory as presented here, however, is limited to first order reactions only and therefore does not take into account the important situation in which a paired defect may dissociate. This problem will be considered in a later paper in this series.

REFERENCES

1. NOWICK A. S. and HELLER W. R., *Adv. Phys.* **14**, 101 (1965).
2. NOWICK A. S., *Adv. Phys.* **16**, 1 (1967).
3. FRANKLIN A. D., *J. Res. natn. Bur. Stand.* **67A**, 291 (1963).
4. CHANG R., *J. Phys. Chem. Solids* **25**, 1081 (1964).
5. POVOLO F. and BISOGNI E. A., *Acta metall.* **14**, 711 (1966).
6. KEEFER D. and WERT C., *Acta metall.* **11**, 489 (1963).
7. GIBALA R. and WERT C., *Acta metall.* **14**, 1095, 1105 (1966).

J. Phys. Chem. Solids Pergamon Press 1970 Vol 31, pp 1827–1834 Printed in Great Britain.

ANELASTIC RELAXATION IN SILICON DOPED WITH LITHIUM AND BORON

B. S. BERRY
IBM Watson Research Center, Yorktown Heights, N.Y. 10598, U.S.A.

(*Received 5 September* 1969, *in revised form 25 October* 1969)

Abstract – Single crystals of Si doped interstitially with Li and substitutionally with B (up to $3{\cdot}7 \times 10^{19}$ atoms/cm^3) exhibit a well-defined internal friction peak at 150°C for a frequency of 1·2 kHz. The peak is governed by a single relaxation time, and has an activation energy Q of $0{\cdot}83 \pm 0{\cdot}015$ eV. The temperature and concentration dependence of the relaxation strength conform to a mass-action equation based on the reaction $Li^+ + B^- \rightleftarrows Li^+B^-$, and indicate that the relaxation is produced by the reorientation of bound Li^+B^- pairs rather than by unassociated Li^+ ions. The binding enthalpy Δh_b is found to be $0{\cdot}28 \pm 0{\cdot}025$ eV/pair. From measurements on ⟨100⟩ and ⟨111⟩ oriented samples, the symmetry of the Li^+B^- pair is found to be trigonal. The dipole shape factor $|\lambda_1 - \lambda_2|$ has the value 0·1. The defect symmetry indicates that the pair is composed of a Li^+ ion occupying a tetrahedral interstitial site in a nearest neighbor position to a substitutional B^- ion. All the available evidence is contrary to Weiser's suggestion that free Li^+ ions in Si enter the hexagonally coordinated interstitial sites which lie midway between the tetrahedral sites.

1. INTRODUCTION

THERE is general agreement that lithium dissolves interstitially in silicon and behaves electrically as a simple donor, ionizing to the singly-charged state Li^+. Diffusion studies performed by a variety of techniques are in good agreement on the activation energy ($Q_1 = 0{\cdot}65$ eV), and have shown the high diffusivities typical of an interstitial species [1–3]. Inspection of the diamond cubic structure of silicon shows that the largest interstitial sites are those represented by the small open circles in Fig. 1. These are known as the tetrahedral sites, since each one lies at the center of a regular tetrehedron defined by the four nearest neighbor silicon atoms. A second possible set of interstitial sites, of only slightly smaller size, is indicated in Fig. 1 by the small filled circles. These are located midway between adjacent tetrahedral sites. Each of the sites in this second group lies at the center of an array of six nearest neighbor silicon atoms delineating a symmetrically puckered hexagon. Hence these sites may be referred to for brevity as the 'hexagonal' sites.

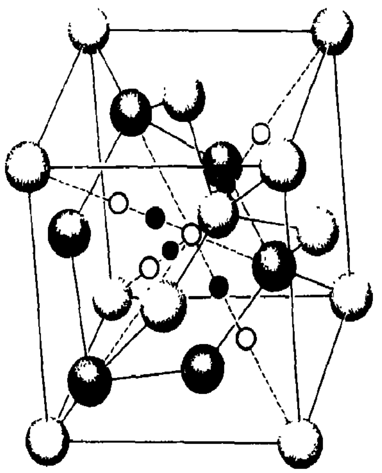

Fig. 1. The diamond cubic structure of silicon. The tetrahedral and hexagonal interstitial sites are indicated by the small open and filled circles, respectively. One of the tetrahedral sites is at the center of the cube; the others are located on the four cube diagonals half-way between the center and a corner of the cube. The hexagonal sites lie midway between adjacent tetrahedral sites.

Weiser[4] has performed theoretical calculations of the energy of an interstitial ion in these two types of site, and has concluded that Li^+ ions should enter the hexagonal, rather than the tetrahedral, sites. From an experimental viewpoint, anelastic relaxation measurements provide a method of investigating the question of tetrahedral vs. hexagonal site occupancy. The symmetry of the tetrahedral sites, like that of the host crystal, is cubic. Consequently, if Li^+ ions were to occupy these sites, it follows from the theory of point defect relaxations[5, 6] that the possibility of a relaxation under a shear stress is ruled out by symmetry considerations. On the other hand, the hexagonally coordinated sites possess trigonal symmetry. Occupancy of these sites leads to the prediction of a relaxation in the elastic compliance s_{44}. The experimental identification of the corresponding internal friction peak in Li-doped samples of pure Si would therefore provide clear-cut evidence in favor of Weiser's theory.[*] Unfortunately, a failure to detect this peak does not have an equally unique interpretation. (This was the situation encountered in practice.) Such a negative result could mean either that (a) the peak is absent because Li^+ occupies the tetrahedral site, or (b) Li^+ occupies the hexagonal sites but the sensitivity of the measurements (in terms of the peak-to-background ratio) was not high enough to resolve the peak. Since the peak height is proportional to the concentration of defects, the most serious problem affecting the sensitivity of the measurements was the low solubility of lithium in the temperature range of interest. At 100°C, for example, the work of Pell[8] and Fuller and Reiss[9] suggests a solubility of about 10^{-6} mole fraction.

To circumvent this problem, advantage was taken of the fact that pre-doping Si with the relatively soluble element boron (present substitutionally as B^- acceptor ions) both enhances the solubility of lithium and prevents its precipitation at lower temperatures. This behavior originates from the electron-hole equilibrium in the semiconductor, which favors an electrically compensated condition where the number of donors balances the number of acceptors[10, 11]. In using boron to enhance the solubility of lithium, it must be recognized that an added complication arises from the phenomenon of ion pairing[12, 13], which can be represented by the reaction

$$Li^+ + B^- \rightleftarrows Li^+B^-. \qquad (1)$$

Since the Li^+B^- pair constitutes an additional species of point defect that may produce relaxation, it is clearly of importance to obtain a positive identification of the defect responsible for a particular internal friction peak.

2. EXPERIMENTAL PROCEDURE

Float-zoned single crystal Si rods of approximately 4 mm dia. were purchased from the Dow-Corning Corporation. The high-purity samples contained ~ 10^{13} atoms/cm^3 of residual boron; the boron levels of the intentionally doped samples ranged from 3×10^{18} to $3{\cdot}7 \times 10^{19}$ atoms/cm^3 ($C_B = 6 \times 10^{-5}$–$7{\cdot}4 \times 10^{-4}$ mole fraction). Some samples were 3 in. long and of random crystallographic orientation. Others were specially supplied to a length of 6 in. and had either a ⟨100⟩ or ⟨111⟩ orientation to within 2° from the rod axis. The boron contents were obtained from the room temperature resistivities of the samples, using the calibration curve of Irvin[14].

The internal friction measurements were performed in the free-free modes of transverse vibration, using an electrostatic scheme of excitation and detection. The maximum frequency range (1–30 kHz) was obtained on the 6 in. crystals, where it was possible to perform measurements up to the 7th tone. Measurements of the logarithmic decrement in free decay were performed at pressures below 10^{-5} torr.

Preliminary attempts at Li doping by vacuum annealing samples painted with a dispersion of metallic lithium in oil[15] were not encouraging. In view of the desire to avoid surface cracks and restrict post-doping clean-up to no more than a light etch, it was decided to try doping by exposure to lithium vapor. This procedure worked very well. From a detailed analysis of the conductivity-temperature curves obtained before and after doping, it became clear that 80–90 per cent compensation could be easily achieved in all the boron doped specimens.

---

[*] It is of interest to contrast this situation with a parallel case concerning octahedral vs. tetrahedral site occupancy in some of the body centered cubic metals[6, 7]. In that case, an experimental distinction based on symmetry arguments alone is not possible, since the octahedral and tetrahedral sites are both of the same (tetragonal) symmetry.

Doping was carried out inside a long tantalum tube, enclosed in turn within a fused quartz tube evacuated by a LN_2-trapped diffusion pump. One end of the Ta tube was closed by a demountable Mo cap. Four wires, insulated by pure alumina tubing, were passed through this cap and attached to the specimen by tungsten spring clips, to provide for resistance measurements by the 4-lead method The end of the Ta tube containing the specimen was placed in the uniform temperature zone of a furnace; the other end of the tube projected from the furnace and remained cool. The metallic Li used as the doping source was placed in a boat attached to the inner end of a Ta plug, which could be pushed via a connecting rod to any desired depth inside the Ta tube. Due to the temperature gradient in this section of the tube, the positioning of the boat provided a convenient means of adjusting the Li vapor pressure. The system was first evacuated with the plug withdrawn, and the specimen heated to the diffusion temperature, usually chosen as 780°C to ensure complete homogenization across the diameter of the specimen in a convenient time. With the specimen at temperature, the plug was inserted to a depth producing a suitable boat temperature (commonly 500–600°C) Resistance measurements made during the diffusion anneal and subsequent cool-down clearly indicated the change towards electrical compensation.

3. RESULTS

The internal friction of Si samples containing Li or B separately was found to be a gently rising monotonic function of temperature, which increased by about a factor of two over the range 25–300°C. No evidence was obtained for peaks in any of these singly-doped samples, regardless of their orientation. (For measurements made at frequencies above 5 kHz, where the background loss* was less than 2×10^{-6}, the estimated minimum detectable peak height was 5×10^{-7}.) In contrast, a very well-resolved internal friction peak was observed in samples containing Li and B together. Data from $\langle 111 \rangle$ and $\langle 100 \rangle$ oriented samples, which serve to illustrate the strong anisotropy of this relaxation, are presented in Fig. 2. These data refer to samples of almost equal boron content. To assure that the difference in peak height reflected as closely as possible a difference in orientation only, these samples were Li-doped side by side in one operation. The ratio of the relaxation strengths $\Delta_{E\langle 111 \rangle}/\Delta_{E\langle 100 \rangle}$ is 17.6. It is also of interest to consider the relaxation of the compliance δE^{-1}, given by the relation $\delta E^{-1}/E^{-1} = \Delta$. Since the value of $E^{-1}_{\langle 111 \rangle}/E^{-1}_{\langle 100 \rangle}$ is 0·69[17], the ratio $\delta E^{-1}_{\langle 111 \rangle}/\delta E^{-1}_{\langle 100 \rangle}$ is found to be 12.

Measurements made on the $\langle 111 \rangle$ sample in a sequence of runs at different frequencies are shown in Fig. 3. These data are shown with the background removed and with the log. decrement-temperature product plotted vs. $1/T$. It should be noted that the first and last runs, performed at the same frequency, show a small (10 per cent) decrease in peak height due to Li outdiffusion. Since the thermal history of each run was about the same, this loss can be corrected for quite well by adding increments of $2\frac{1}{2}$, 5, $7\frac{1}{2}$ and 10 per cent to the peaks obtained in runs 2, 3, 4 and 5, respectively. Several important pieces of information are contained in Fig. 3. First, it is evident that the peak height-temperature product (which is proportional to the concentration of defects producing the relaxation) is a rather strongly decreasing function of temperature. Application of the mass-action relationship to equation (1) shows that the Li^+B^- pair must therefore be the defect responsible for the relaxation. Second, the variation of peak temperature with frequency can be used to obtain the activation energy Q and the pre-exponential factor τ_0 governing the relaxation time, τ. The plot shown in Fig. 4 yields the values $Q = 0{\cdot}83 \pm 0{\cdot}015$ eV and $\tau_0 = (2 \pm 0{\cdot}7) \times 10^{-14}$ sec. It should be

---

*Calculations indicate that a substantial part of this background damping originates within the specimen from the 'transverse thermal current' relaxation mechanism [16].

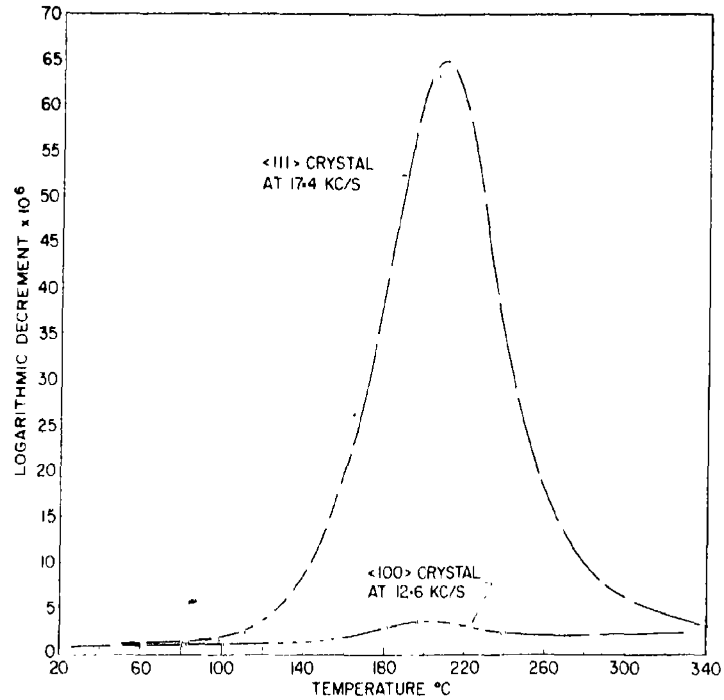

Fig. 2. Internal friction peaks in ⟨111⟩ and ⟨100⟩ oriented silicon rods containing $6{\cdot}6 \times 10^{18}$ atoms/cm^3 of boron and $5{\cdot}3 \times 10^{18}$ atoms/cm^3 of lithium

noted that this value of Q is significantly greater than the value 0·65 eV quoted earlier for the movement of unassociated Li^+ ions. From the value $Q = 0{\cdot}83$ eV, the internal friction peaks are found to have a width at half-maximum in excellent agreement with that calculated from the Debye equation [6], indicating the existence of only a single relaxation time. Finally, each peak shows an asymmetry of shape consistent with the decline observed directly in the peak height-temperature product. To point out this asymmetry, the broken curve in Fig. 3 represents the symmetrical Debye peak fitted to the temperature and half-width of the experimental peak for 1·20 kHz.

The data points in Fig. 5 show the variation of $\delta E^{-1}_{(111)}$ with boron concentration for samples with a compensation ratio close to 0·8. These results refer to a temperature of 209°C. For the purpose of the following analysis, the values of $\delta E^{-1}_{(111)}$ are expressed relative to the value in the most heavily doped sample. The mass action relation corresponding to equation (1) is

$$\frac{c_p}{(C_{Li}-c_p)(C_B-c_p)} = K(T) \qquad (2)$$

where C_{Li} and C_B denote the total mole fractions of lithium and boron, c_p is the mole fraction of pairs and $K(T)$ is the equilibrium constant. By choosing an arbitrary value of $K(T)$, it is thus possible to calculate values of c_p for selected values of C_B and $C_{Li}(= 0{\cdot}8\, C_B)$. When $K(T)$ is small (the weak binding limit) the curves of c_p vs. C_B are parabolic in shape, as indicated in the appropriately normalized form by the lower broken curve in Fig. 5. As $K(T)$ is made larger, the calculated curves progressively change shape, eventually becoming linear in the strong

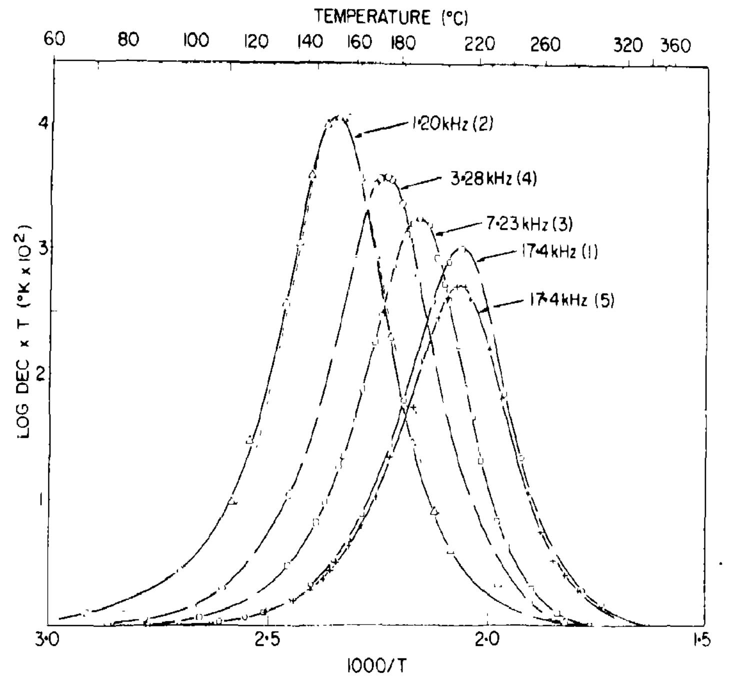

Fig. 3. Measurements on the (111) sample of Fig. 2 for a series of vibration frequencies. The numbers in parentheses denote the order in which the runs were performed.

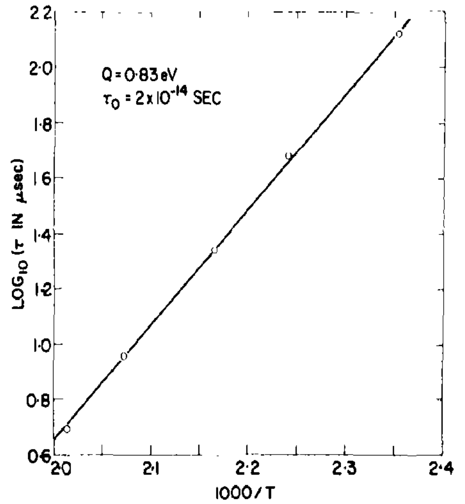

Fig. 4. Temperature dependence of the relaxation time τ for silicon samples co-doped with lithium and boron.

binding limit where every Li^+ is paired to a B^- ion. The major change in shape takes place for values of $K(T)$ in the range 500–50,000. As can be seen from the solid calculated curve in Fig. 5, an excellent fit to the data is obtained at $K(T) = 7200$. The uncertainty in this value of the equilibrium constant at 209°C is estimated to be ± 10 per cent.

To proceed further with the mass action analysis, $K(T)$ must be written in the explicit form

$$K(T) = A\exp(\Delta h_b/kT) \tag{3}$$

where

$$A = z\exp(-\Delta s_b/k). \tag{4}$$

Here, Δh_b and Δs_b are the enthalpy and entropy changes upon formation of a pair from its well-separated components. z is the number of distinguishable orientations that the pair can assume, and k and T are Boltzmann's constant and the absolute temperature.

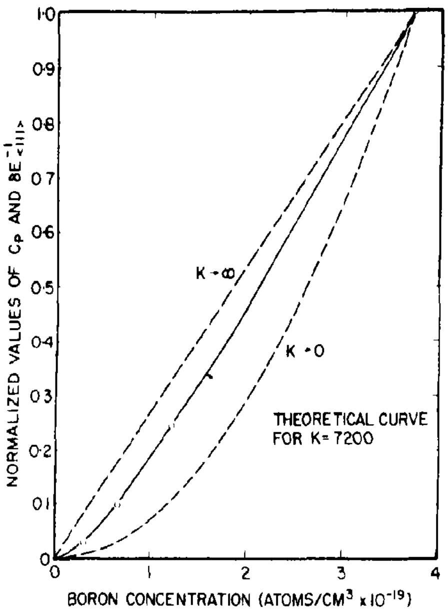

Fig. 5. The normalized variation of $\delta E^{-1}_{\langle 100\rangle}$ with boron concentration in samples with $C_{Li} = 0.8\,C_B$. The broken lines show the normalized c_p curves predicted by the mass action equation for $K \to 0$ and ∞. The best theoretical fit to the data points (solid curve) yields $K = 7200$ at 482°K

A unique determination of Δh_b and the entropy factor A is made possible by the requirement that these quantities must simultaneously satisfy the following two conditions: (a) $K(T) = 7200$ at $T = 482$°K, (b) the temperature dependence of c_p must match the observed peak height decrease with temperature shown in Fig. 3. It is thus found that the binding energy of the pair (Δh_b) is 0·275 ± 0·025 eV, and that $A = 9 \pm 4$. (Note that the high limit of Δh_b should be taken with the low value of A, and vice-versa.) Using these numbers it may be computed, for example, that the fraction of the total Li content present as pairs in the sample of Fig. 3 is 0·67, 0·45 and 0·28 at 120, 190 and 260°C, respectively.

4. DISCUSSION

The primary point evident from the results on co-doped samples is that only one peak is observed and this clearly originates from the reorientation of Li^+B^- pairs. Consideration will be given first to how this and other experimental observations compare with the behavior expected in the two alternative cases where Li^+ is assumed to enter the hexagonal or tetrahedral sites.

In the case of hexagonal site occupancy, the symmetry of the nearest neighbor (nn) Li^+B^- pair is low (monoclinic) and a relaxation of both the shear compliances s_{44} and $(s_{11}-s_{12})$ can be predicted[5]. It therefore seems doubtful that such a pair would produce a relaxation exhibiting the strong anisotropy evident in Fig. 2. Greater agreement could be obtained by postulating a next-nearest neighbor (nnn) pair, since this has trigonal symmetry for which the expressions for $\delta E^{-1}_{\langle 111\rangle}$ and $\delta E^{-1}_{\langle 100\rangle}$ are [6]:

$$\delta E^{-1}_{\langle 111\rangle} = \frac{4}{27}\frac{c_p v_0}{kT}(\lambda_1-\lambda_2)^2 \qquad (5)$$

and

$$\delta E^{-1}_{\langle 100\rangle} = 0. \qquad (6)$$

In equation (5) v_0 is the vol/atom in the host crystal and $(\lambda_1-\lambda_2)$ is the ellipticity or 'shape-factor' of the pair. The assumption of nnn pairs to the virtual exclusion of nn pairs appears however to be highly unrealistic, as the forces binding the pair are primarily coulombic in character. Added to these difficulties is the central point, noted in the Introduction, that unassociated Li^+ ions in hexagonal sites would be defects of trigonal symmetry. Accordingly, their presence should be revealed by a separate internal friction peak with characteristics conforming to Equation (5) and (6) after replacement of c_p by $(C_{Li}-c_p)$. From the previously quoted value $Q_{Li} = 0{\cdot}65$ eV, it can be reliably estimated that this peak would be located in the range 100–120°C for a vibration frequency of 10 kHz. No such peak has been observed. Furthermore, it is not possible to explain the absence of this peak on grounds of too low a concentration of defects, since the concentration of unassociated Li^+ at 120°C is typically only slightly smaller (by about a factor of 2) than the concentration of pairs producing the easily detected relaxation at higher temperatures. Taken together, therefore, the results show major incompatibilities with the assumption of hexagonal site occupancy.

Turning now to the assumption of tetrahedral occupancy, the absence of a peak from unassociated Li^+ ions is to be expected, because of the cubic symmetry of the tetrahedral site. Furthermore, the difficulties encountered above in explaining the anisotropy of the pair relaxation are also removed, since for tetrahedral occupancy the symmetry of the nn Li^+B^- pair is trigonal. Though the trend of the measurements shown in Fig. 2 is clearly in agreement with equations (5) and (6) for trigonal defects, the agreement is not perfect since equation (6) requires a strict null for the ⟨100⟩ orientation. (The magnitude of the ⟨100⟩ peak, though small, is still 10 times larger than could be accounted for by the allowable misorientation error of the sample.) As discussed below, the existence of the ⟨100⟩ peak is however readily explained by the presence of a small relaxation from the reorientation of nnn pairs. Hence, it appears certain that, contrary to Weiser's calculations, Li^+ occupies the tetrahedral interstitial sites in silicon. Other experimental work, utilizing spin resonance[18], optical excitation[19] and infrared[20] techniques, also leads to the same conclusion.

Since the mass action analysis of the previous section permits c_p to be calculated for given conditions, corresponding values of c_p and δE^{-1} may be inserted in equation (5) to find the shape factor of the pair. The result is $|\lambda_1-\lambda_2| = 0{\cdot}1$, which in terms of comparison with other defects corresponds to a moderately small value. It is convenient to note at this point that the nnn pair with tetrahedral occupancy is of tetragonal symmetry, and accordingly contributes to $\delta E^{-1}_{\langle 100\rangle}$ but not to $\delta E^{-1}_{\langle 111\rangle}$ [6]. Neglecting the possibility of an additional hydrostatic relaxation involving a reaction between nn and nnn pairs[5], the ratio of $\delta E^{-1}_{\langle 111\rangle}/\delta E^{-1}_{\langle 100\rangle}$ may then be written

$$\frac{3\delta E^{-1}_{\langle 111\rangle}}{2\delta E^{-1}_{\langle 100\rangle}} = \frac{c_p(\lambda_1-\lambda_2)^2}{c'_p(\lambda'_1-\lambda'_2)^2} \tag{7}$$

where the primed quantities refer to nnn pairs. While it is known from Fig. 2 that the experimental value of $3\delta E^{-1}_{\langle 111\rangle}/2\delta E^{-1}_{\langle 100\rangle}$ is 18 (at 210°C), it is unfortunately not possible to obtain $(\lambda'_1-\lambda'_2)$ from this equation without a knowledge of c'_p.

One parameter of a different kind that can be evaluated from the available data is the entropy of binding Δs_b. This follows from the fact that $z = 4$ for the nn Li^+B^- pair configuration identified above. Insertion of this value into equation (4) together with the value $A = 9 \pm 4$ gives the result $\Delta s_b/k = -0{\cdot}8 \pm 0{\cdot}5$.

At this point, attention will be turned to the kinetics of the relaxation and the magnitude of the activation energy Q. The reason that this quantity (0·83 eV) is significantly higher than the value 0·65 eV for free Li^+ is made evident by considering the paths available to a Li^+ ion in moving from one nn tetrahedral site to another around a B^- ion. From an inspection of the diamond structure, it can be seen that this reorientation cannot occur in one jump; any path requires the Li^+ ion to jump first *away* from the B^- ion to a less tightly bound site (either to one of three nnn sites or to one even more distant 3rd neighbor site). Since such jumps produce a partial dissociation of the pair, their activation energy can be expected to be higher than that for the movement of free Li^+ ions. Indeed, it is tempting to suggest that the difference (0·83–0·65) = 0·18 eV may represent a reasonable estimate of the difference in binding energies between the nearest and next-nearest neighbor sites*.

---

*Use of this assumption gives (c'_p/c_p) the value 0·02 at 210°C. From equation (7) it is then found that $(\lambda'_1-\lambda'_2) \simeq 2{\cdot}2(\lambda_1-\lambda_2)$. However, the uncertainties involved make this estimate of questionable value.

From Nowick's treatment[21] of the kinetics of point defect relaxations, the relaxation rate τ^{-1} for a trigonal defect in a cubic crystal is given by

$$\tau^{-1} = 4\nu_{12} \tag{8}$$

where ν_{12} is the rate at which reorientation takes place from one specified orientation to another (1 → 2). If w is the rate of the slow nn → nnn dissociation jump, the rate at which a Li^+ ion leaves an orientation No. 1 site is $3w$ (neglecting the single even slower jump to the 3rd neighbor site). The probability that the Li^+ ion returns to a B^- ion to produce a pair of orientation No. 2 is $\frac{1}{4}$, since there are 4 nn sites (each of which corresponds to a distinct orientation). With the assumption that the reorientation rate is dominated by the slow jump w, it follows that $\nu_{12} = 3w/4$ and thus, from equation (8)

$$\tau^{-1} = 3w. \tag{9}$$

The kinetics of Li^+ motion governing the relaxation are thus represented by $w = (\tau_0^{-1}/3) \exp(-Q/kT)$, or in numerical form by $w = 1{\cdot}7 \times 10^{13} \exp(-0{\cdot}83/kT)$.

Acknowledgements—Grateful acknowledgement is made to the U.S. Atomic Energy Commission for partial support in the early stages of this work, and to P. A. Roland and W. C. Pritchet for their assistance in the laboratory.

REFERENCES

1. FULLER C. S. and SEVERIENS J. C., *Phys. Rev.* **96**, 21 (1954).
2. PELL E. M., *Phys. Rev.* **119**, 1014, 1222 (1960).
3. PRATT B. and FRIEDMAN F., *J. appl. Phys.* **37**, 1893 (1966).
4. WEISER K., *Phys. Rev.* **126**, 1427 (1962).
5. NOWICK A. S. and HELLER W. R., *Adv. Phys.* **12**, 251 (1963); **14**, 101 (1965).
6. BERRY B. S. and NOWICK A. S., *Physical Acoustics* (Edited by W. P. Mason), Vol. 3A, p. 1. Academic Press, New York (1966).
7. BESHERS D. N., *J. appl. Phys.* **36**, 290 (1965).
8. PELL E. M., *J. Phys. Chem. Solids* **3**, 77 (1957).
9. FULLER C. S. and REISS H., *J. chem. Phys.* **27**, 318 (1957).
10. REISS H. and FULLER C. S., *J. Metals* **8**, 276 (1956).
11. FULLER C. S., *Semiconductors* (Edited by N. B. Hannay), Chap. 5, p. 192. Reinhold, New York (1959).
12. REISS H., FULLER C. S. and MORIN F. J., *Bell Syst. tech. J.* **35**, 535 (1956).
13. PELL E. M., *J. appl. Phys.* **31**, 1675 (1960), **32**, 1052 (1961).
14. IRVIN J. C., *Bell Syst. tech. J.* **41**, 387 (1962).
15. PELL E. M., *Solid State Physics in Electronics and Telecommunications* (Edited by M. Désirant and J. L. Michiels), Vol. 1, p. 261. Academic Press, New York (1960).
16. BERRY B. S., *J. appl. Phys.* **26**, 1221 (1955).
17. McSKIMIN H. J. and ANDREATCH, Jr. P., *J. appl. Phys.* **35**, 2161 (1964).
18. FEHER G., *Phys. Rev.* **114**, 1219 (1959).
19. AGGARWAL R. L., FISHER P., MOURZINE V., and RAMDAS A. K., *Phys. Rev.* **138**, A882 (1965).
20. BALKANSKI M. and NAZAREWICZ W., *J. Phys. Chem. Solids* **27**, 671 (1966).
21. NOWICK A. S., *Adv. Phys.* **16**, 1 (1967).

J. Phys. Chem. Solids Pergamon Press 1970. Vol. 31, pp. 1835-1841. Printed in Great Britain.

INTERNAL FRICTION MAXIMA DUE TO RELAXATION OF POINT DEFECTS IN NEUTRON IRRADIATED ALUMINIUM

K. EHRENSPERGER, V. FISCHER, J. KERSCHER and H. WENZL
Physik-Department, Technical University, Munich, Germany

(*Received* 5 *September* 1969)

Abstract – The internal friction and shear modulus of pure recrystallized polycrystalline aluminium wires has been studied as a function of temperature by measurement of the logarithmic decrement of the free vibrations (64 and 200 c/s) in shear strain ($\epsilon \approx 10^{-5}$) after irradiation with fast neutrons at 4·6°K. The elementary processes related to these internal friction maxima are discussed in terms of the corresponding elastic dipole tensors and the annealing model for irradiated aluminium.

1. INTRODUCTION

WE INTRODUCED interstitials and vacancies in aluminium at 4°K by irradiation with fast neutrons and studied the internal friction as a function of temperature and time (for a detailed discussion of the change of elastic modulus after irradiation in aluminium, copper and platinum see Ref. [1]).

The irradiation method has the advantage to allow homogeneous, nondestructive and reproducible production of defects in thick samples and complete removal of the defects by annealing treatments below the melting point.

2. EXPERIMENTAL RESULTS

The polycrystalline aluminium sample consisted of a spring. The logarithmic decrement δ of the free shear vibrations were measured in an amplitude range of 3 : 1 and with elastic strains ϵ in the range $10^{-6} < \epsilon < 10^{-5}$.

The spring could be excited in two different vibrational modes with different frequencies.

The free space inside the spring contained a thin aluminium wire for resistivity measurements.

The sample was irradiated in the core of the Munich research reactor FRM at 4·6°K[2]. Details of the experimental arrangement can be found in Ref. [1]. Maximum relative errors of frequency differences: $\pm 2 \times 10^{-4}$. Maximum relative errors of friction 5 per cent; maximum errors of electrical resistivity ±0·1 $n\Omega$cm, of temperature ±1°K ($T < 30$°K), ±0·5°K(30°K $< T <$ 100°K), ±0·2°K(100°K $< T <$ 300°K).

Table 1 presents a survey of the sample properties and the different irradiation experiments performed.

Five internal friction maxima were found in the temperature region 4–300°K (Fig. 1); the behaviour at higher temperatures is shown in Fig. 2.

In Figs. 3–5 and Table 2 details of the different internal friction peaks can be seen. Several observations indicate that the observed peaks are not connected with dislocation damping (see also Ref. [4]):

(a) The absence of the Bordoni peak shows that the dislocation density was very small. (b) The peak heights increased monotonously with dose. (c) The preexponential factor τ_0 is of the correct order of magnitude for the diffusion of single atoms (Table 2).

Although the annealing of some peaks [1–4] already starts at the peak-temperature, the details of the figures show that all can be considered as real internal friction maxima. The results are in agreement with measurements above 22°K after α-particle irradiation[4], although the necessity of using thin aluminium foils in this case prevented a more detailed and reliable analysis.

Table 1. *Irradiation dose and resistivity change* $\Delta\rho_{tot}$ *of aluminium. Polycrystalline samples, purity* 99·999 *per cent, air-annealed at* 350°K *for* 30 min *before each irradiation. Irradiations* 1–3 *and* 4–5 *were performed with the same sample, respectively*

No	Fast neutron dose $10^{18}\, n(E > 0{\cdot}1\ \mathrm{MeV})/\mathrm{cm}^2$	$\Delta\rho_{tot}/n\Omega\mathrm{cm}$
1	1·4	215·7 ± 0·1
2	5·3	585·2 ± 0·1
3	4·7	552·8 ± 0·1
4	0·4	57·5 ± 0·1
5	0·8	120·0 + 0·1

3. DISCUSSION

3.1 *Annealing model*

The activation enthalpy of annealing of the peaks 1 and 2 coincides with the activation enthalpy of resistivity annealing in stage I_A and I_D, respectively[7].

Therefore, peak 1 is attributed to the relaxation of close interstitial-vacancy pairs. Peak 2 may be due to the relaxation of a freely migrating interstitial (see Ref. [4] for a differ-

Table 2. *Characteristic data of the internal friction maxima. Explanation of symbols:* $\omega_1/2\pi$ = *frequency of fundamental vibrational mode;* $H_R{}^s$ = *activation enthalpy of relaxation, calculated from the shift of the peak-temperature with frequency.* $H_R{}^1$ *and* $H_R{}^2$ *were calculated from the half-width of the peaks for the two frequencies used. The activation enthalpy of annealing* H_A *was evaluated by the method of slope-change*[3, 5] *of the time dependence of the internal friction maxima.* n *indicates the number of jumps till annihilation at the beginning of the annealing, calculated from* H_A *and the measured time dependence of* Q^{-1}. *The value of* Δp *was calculated with the aid of equation* (1)

Max no		1	1*b*	2	3	4	5
Irradiation no ↓							
$\omega_1/2\pi$	1	63·8		63·9	63·9	63·8	63·8
	2		63·7		63·5		63·5
(sec^{-1})	3	63·0	63·0	63·2	63·0	63·0	63·0
$H_R{}^s$	1	35 + 9		97 ± 25	80 ... 220	135 ± 35	170 ... 470
	2				110 ± 20		
(MeV)	3	32 + 10	18 43				
$H_R{}^1$	1	19 ± 8		67 ± 20		96 ± 20	150 ± 30
	2		28 + 8		> 46		130 ... 230
(MeV)	3				> 48	> 50	90 ... 180
$H_R{}^2$	1	22 ± 8		75 + 25		150 ± 40	220 ± 60
	2						
(MeV)	3	18 ± 5					
$\log_{10}(\mathrm{sec}/\tau_0)$	5	14 ± 3		14 ± 2	13 ± 2	15 ± 2	16 ± 2
H_A (MeV)	5	63 ± 8		115 ± 15		195 ± 25	
$\log_{10} n$	5	1		4		1·8	
$(\Delta p)^2\,(\mathrm{eV})^2$	5	3 ... 5	0·3	10 ... 20	2 ... 3	100	0·5 ... 1

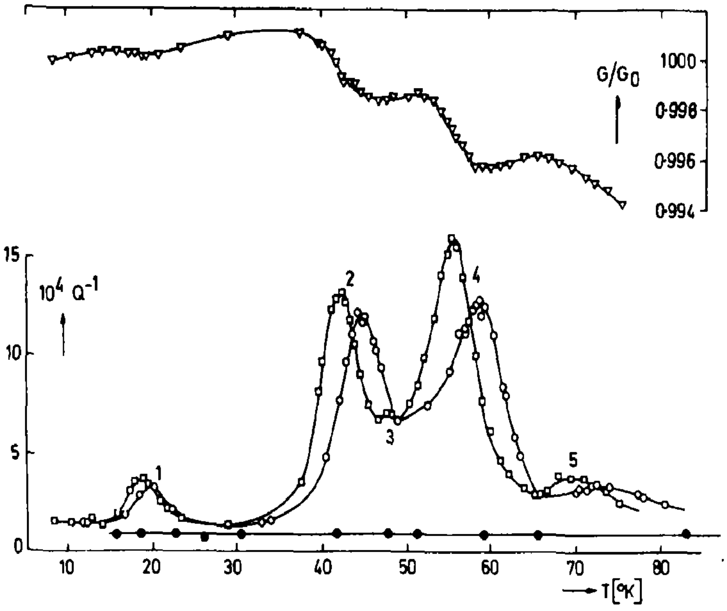

Fig. 1. Internal friction $Q^{-1} = \delta \cdot \pi$ and elastic shear modulus G normalized to the value G_0 at 8·4°K, during warming up (1°K/min). Measurement 4. Two different frequencies ν were used. 65 Hz (triangles circles) and 271 Hz (squares). The numbers indicate the position of identified peaks. Full circles: measurement after annealing at 350°K. No Bordoni peak can be observed due to the annealing treatments.

ent explanation). According to the resistivity measurements, the mean lifetime τ_L of the interstitial at 37°K (stage I_D) is $O(10^3\text{sec})$, with a number of jumps till annihilation $n = 1 \cdots 10$ and a certain jump frequency $f(n = f \cdot \tau_L)$.

At the temperature of peak 2 (42°K) the jump frequency is $f \leq \omega\, O(10^{+2}\,\text{sec}^{-1})$, whereas $\tau_L = O(10^3\text{ sec})$, too. Therefore, the number of jumps till annihilation must have increased by a factor of $10^3 \cdots 10^4$, if the same defect is assumed to participate in stage I_D and peak 2. This increase of n could be explained by the annealing of most of the reaction partners at the peak-temperature. The kinetics of the Q^{-1}-annealing follows a reaction order between 1 and 2[5, 11].

The peaks 3–5 can be attributed to the relaxation of smaller clusters of interstitials[4].

3.2 *Dumbbell interstitial*

The interstitials have probably the configuration of a ⟨100⟩-dumbbell, whose elastic stress field can be represented by a double force tensor with two independent components, p_1 and p_2[9–10].

In our case the largest splitting of energy levels of the elastic 'dipoles' under the applied strain $\epsilon = O(10^{-5})$, $|p_1 - p_2| \cdot \epsilon$ is always smaller than kT, since $|p_1 - p_2| = O(1\text{ eV})$. Therefore, the linear approximation of the relaxation process is valid, which leads to a relation between Q^{-1} and the microscopic parameters, namely[9, 11, 12]:

$$Q^{-1}_{\text{max}} = 3 \cdot 10^{-2} \frac{1}{G v_0} \frac{(\Delta p)^2}{k T_{\text{max}}} \cdot c, \qquad (1)$$

where G indicates the shear modulus, v_0 the atomic volume, $\Delta p = p_1 - p_2$, T_{max} the peak-temperature, and c the concentration of defects, given by the corresponding resistivity change $\Delta\rho$ and the resistivity per unit concentration of defects ρ_0 as $c = \Delta\rho/\rho_0$.

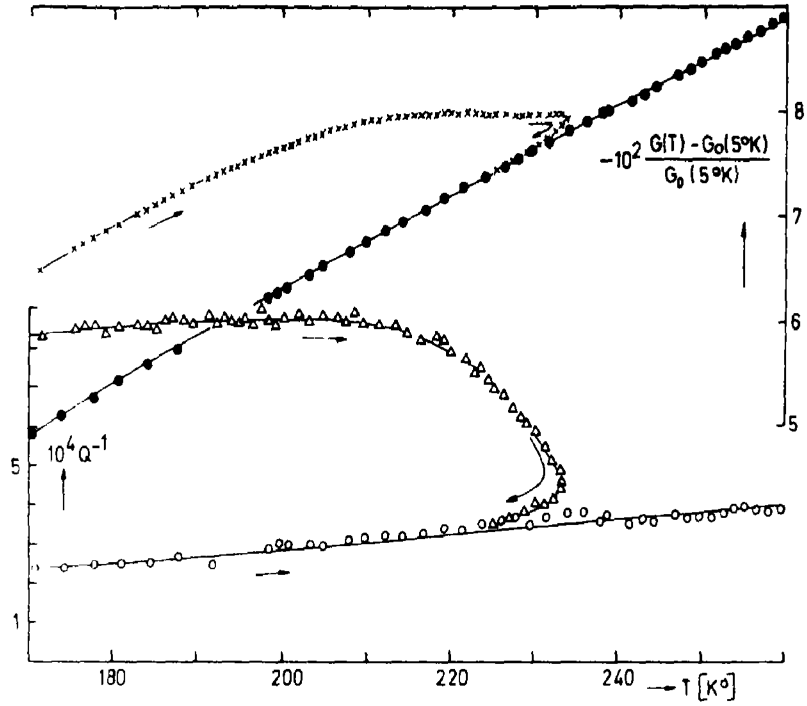

Fig. 2. Internal friction and elastic shear modulus, irradiation 2. Triangles and crosses measurement during warming up after irradiation (4°K/min), full circles and empty circles after annealing till 235°K (end of annealing stage III[3]). The increase of *G* superimposed on the normal decrease with rising temperature is discussed in Ref. [1]). Frequency $\nu = 62{\cdot}5$ Hz.

With the data of Table 2 and assuming interstitial-vacancy recombination as annealing mechanism ($\rho_0 = \rho_F = 400\,\mu\Omega$cm[6]), the result for peak 2 is: $|\Delta p| \approx 4$ eV.

Table 2 contains the corresponding values for the other peaks. The relative volume change due to the stress field is related to the trace of the dipol-tensor trp by the relation[12]:

$$\frac{\Delta V}{V} = \frac{C}{v_0} \cdot \frac{1}{3} \kappa \, trp$$

where κ is the compressibility. With $c = \Delta\rho/\rho_F$, $\Delta V/V = 3\Delta a/a$, and the experimental values of the relative lattice parameter change $\Delta a/a$ [6] this equation allows to estimate a lower limit for trp, by using the resistivity decrease measured during the annealing of the internal friction peak; trp = 38 eV. Then, the 'anisotropy' $3|\Delta p|/\text{trp}$ of the interstitial would be $\frac{1}{3}$.

In the conversion-two-interstitial model[8] the stable interstitial of dumbbell-type is expected to migrate in annealing stage III, with its maximum annealing rate at about 225°K[1]. If the activation enthalpy of relaxation of this interstitial is equal to the activation enthalpy of annealing in stage III (0·58 eV [3]), an internal friction maximum would be expected at about 230°K by using a vibration of $\omega = 300$ c/s and $\tau_0 = 10^{-15}$ sec.

In this temperature range no internal friction maximum could be detected (Fig. 2). The low temperature slope should have been visible already at 200°K. According to the experimental error of the Q^{-1}-measurements, and using equation (1), the largest possible value of $\Delta p| = 0{\cdot}4$ eV. Therefore, the 'aniso-

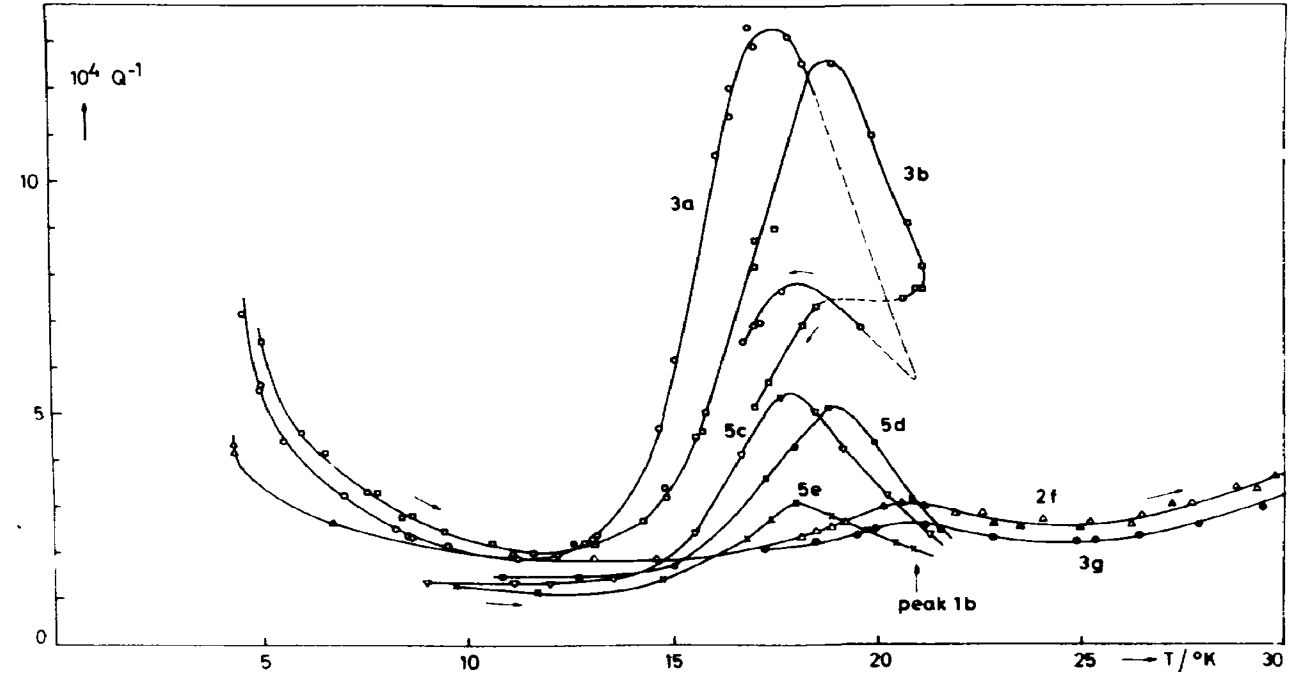

Fig 3 Internal friction peaks I and Ib, measured during heating or cooling (1°K/min). The numbers indicate different irradiations according to Table I Curves 3(a, b): 63.0, 258 Hz: measurement after irradiation at 4·6°K till 21°K and then cooling down with approx. the same velocity. Curves 5(c, d). 65.0; 271 Hz measurement after irradiation at 4·6°K till 22°K. Curve 5(e) 65.0 Hz, measurement after cooling 5(c) down again. Curve 2(*f*): 63,7 Hz; measurement after heating up till 68°K and cooling down again within a few seconds. Curve 3(g) 63.0 Hz; measurement after heating till 39°K. The high values of W^{-1} below 8°K are probably due to the presence of liquid helium droplets.

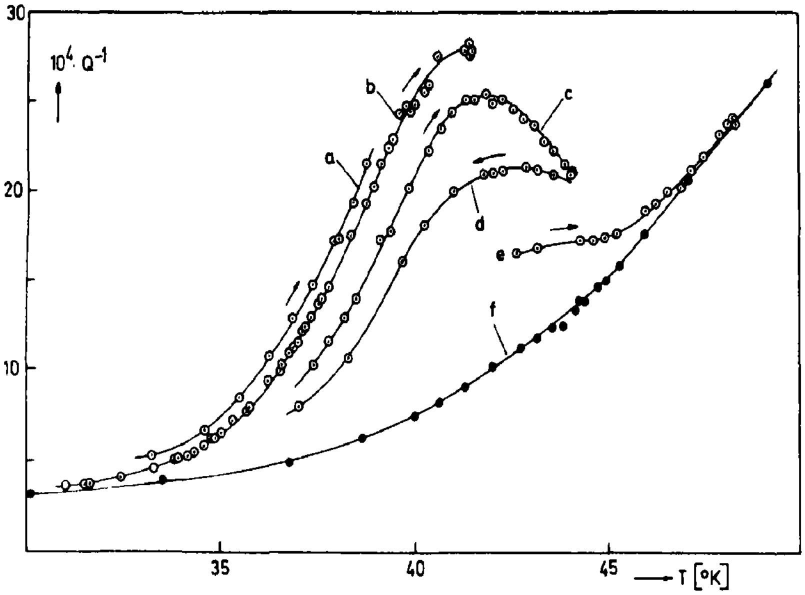

Fig. 4 Internal friction peak 2, irradiation No 3. Vibrational frequency $\nu = 63$ Hz The different curves were measured with 1°K/min after reaching a temperature of 28·6°K(a), 38·9°K(b), 41·5°K(c), 44·2°K(d), 43°K(e), (20 min at 43°K), 48·4°K(f) and cooling down again (except curve (d), which was measured during cooling)

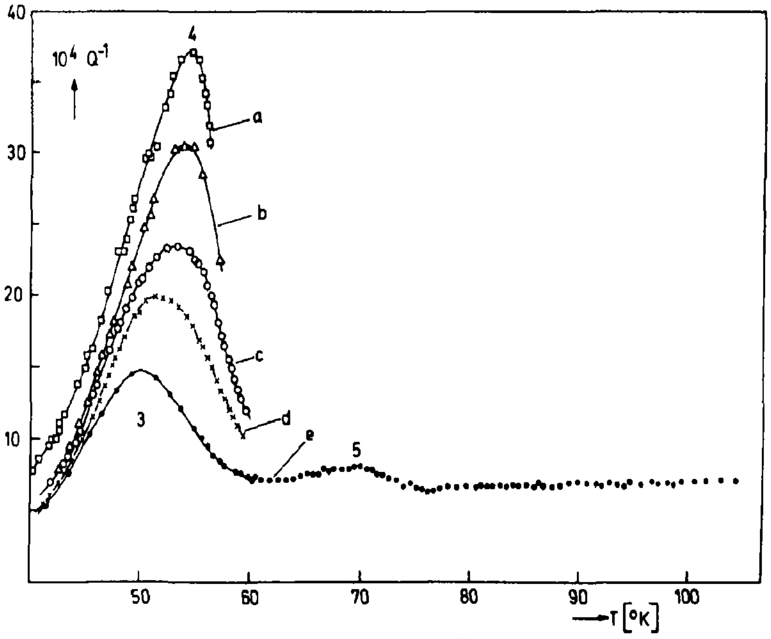

Fig. 5 Internal friction peaks 3, 4 and 5 Irradiation No. 3. Frequency $\nu =$ 63 Hz The different curves were measured during heating (1°K/min) after reaching a temperature of 48·4°K(a), 56·1°K(b), 57·3°K(c), 59·6°K(d), 60°K (70 min (e)) and cooling down again. Peak 3 is hidden under 4 and appears clearly after annealing at 60°K.

tropy' would be smaller than 1/30. Such a small value cannot be expected for a dumbbell configuration[10]. Since all peaks anneal at temperatures below stage III, the observed maxima cannot be due to the reorientation of the stage III-defect.

REFERENCES

1. EHRENSPERGER K., FISCHER V., KERSCHER F. and WENZL H., to be published.
2. MEIßNER H., SCHILLING W., WENZL H., *Europa. nucl* 2, 277 (1965); DOLL R., MEIßNER H., RIEHL N., SCHILLING W. and SCHMEIßNER F., *Z. angew. Phys.* 17, 321 (1964)
3. SCHILLING W., BURGER G., ISEBECK K. and WENZL H., Annealing stages of the electrical resistivity in fcc metals. *Vacancies and Interstitials in Metals* (Edited by J. Diehl, W. Schilling, D. Schumacher and A. Seeger). North-Holland, Amsterdam (1969).
4. RIGGAUER M., SCHILLING W., VÖLKL J. and WENZL H., *Phys. Status Solidi* 33, 843 (1969).
5. KERSCHER F., Thesis, Technische Hochschule Munchen (1968).
6. WENZL H., Physical properties of point defects in cubic crystals *Vacancies and Interstitials* (Edited by J. Diehl, W. Schilling, D. Schumacher and A. Seeger). North-Holland, Amsterdam (1969).
7. CORBETT J. W. *Electron Irradiation Damage in Semiconductors and Metals*. Academic Press, New York (1966)
8. SEEGER A., *Vacancies and Interstitials in Metals* (Edited by J. Diehl, W. Schilling, D. Schumacher and A. Seeger). North-Holland, Amsterdam (1969).
9. KRONMÜLLER H., *Vacancies and Interstitials in Metals* (Edited by J. Diehl, W. Schilling, D. Schumacher and A. Seeger). North-Holland, Amsterdam (1969)
10. SEEGER A., MANN E. and JAN R. V., *J. Phys. Chem. Solids* 23, 639 (1962)
11. FISCHER V., *Diplomarbeit*, Technische Hochschule Munchen (1969)
12. NOWICK A. S. and HELLER W. R., *Adv. Phys.* 14, 101 (1965).

J. Phys. Chem. Solids Pergamon Press 1970. Vol. 31, pp. 1843–1855. Printed in Great Britain

INTERNAL FRICTION IN LOW TEMPERATURE IRRADIATED bcc METALS

V. HIVERT, R. PICHON, H. BILGER, P. BICHON, J. VERDONE, D. DAUTREPPE and P. MOSER
Service de Physique du Solide et de Résonance Magnétique, Centre d'Etudes Nucleaires de Grenoble (38), France

(*Received* 5 *September* 1969, *in revised form* 7 *November* 1969)

Abstract—Internal friction peaks observed on irradiated iron and molybdenum are presented. An interpretation is proposed, which supposes a one-interstitial model.

1. INTRODUCTION

IN A RECENT review article[1] Schulze pointed out that body centred cubic metals may be divided into two groups. The first one, which includes Fe, Nb and Ta, is characterized by a small, apparently impurity dependent[2], stage III of the electrical resistivity recovery curve. The second group, which includes Mo and W, exhibits a large stage III which is less impurity dependent than for the first group.

In this article, we present internal friction results obtained on iron and molybdenum, metals belonging to the first and second groups respectively. Because the interstitial causes a local reduction in the symmetry of the lattice it should, by its reorientation, give rise to a mechanical relaxation phenomenon. The search for and the study of low frequency internal friction peaks is thus a method which should permit the identification of the free interstitials.

Several authors have suggested an interpretation of the difference in behaviour between the two groups of bcc metals. Some of them have proposed the following:

For the first group a one-interstitial model is suitable with the free interstitial annealing in substage I_E[3]. For the second group a two-interstitial model is needed, the first interstitial type being metastable and annealing in substage I_E and the second type being stable and annealing at stage III[4].

On the other hand, the results which we have obtained for two metals Fe and Mo, one of each group, are easily interpreted in terms of a single type of interstitial which anneals out at stage I. In the case of iron, we have furthermore been able to determine the mobility and symmetry of the interstitial.

2. SPECIMENS, IRRADIATIONS AND MEASURING TECHNIQUES

The polycrystalline iron was supplied by Light and Co. and purified by zone melting to yield a final total concentration of impurities of less than 0·003 wt. %. Single crystals were prepared by Dr. F. Terasaki at Irsid† starting from electrolytic iron heat treated in vacuum: the final total impurity concentration was less than 0·04 wt. %[5]. The specimens were in plate form with length 3 mm, width 1 mm and thickness 0·5 mm. We were able to cut single crystal samples with axes parallel to ⟨100⟩ and ⟨110⟩. The specimens were heat treated at 880°C for 6 hr in an atmosphere of pure hydrogen.

The molybdenum was supplied by N.R.C. The specimens, which were in the form of wires of 0·5 mm dia. and 66 mm length, were annealed at 2200°C in a chamber whose residual pressure did not rise above 10^{-9} torr.

---

†Institut de Recherche de la Siderurgie Saint-Germain en Laye (78) France

Neutron irradiations were carried out in the liquid neon or nitrogen irradiation facilities of the Melusine reactor at Grenoble. The molybdenum was irradiated at 28°K and the iron at 28 or 77°K. The samples were subsequently transferred to the internal friction pendulum and mounted without intervening warm-up. The transfer at 28°K is a particularly delicate operation as one must avoid the formation of solid air which introduces parasitic friction effects. It was effected in the present experiments under a neon atmosphere.

The electron irradiations were carried out in a 3 MeV Van der Graaf accelerator at a specimen temperature of 20°K. The specimens were then transferred at 28 or 77°K to the measuring pendulum. Certain molybdenum samples were studied *in situ*, by means of a pendulum which was housed in the irradiation cryostat. Measurements could then be started at 20°K after the evaporation of the liquid hydrogen.

All such internal friction studies were made at low frequency (0·25–1 Hz) on inverse pendulums. The tension in the samples was less than 4 g/mm². For the measurements on iron the sample was held in a magnetic field of 100 Oe which was sufficient to suppress internal friction effects due to motion of the Bloch walls.

3. EXPERIMENTAL RESULTS

(a) *Low temperature irradiation of polycrystalline iron*

(1) *Observation of internal friction peaks*. We have already demonstrated the existence of four peaks when iron is irradiated at 77°K [6]. Figure 1 shows the results obtained for an irradiation at 28°K, with specimen transfer and mounting effected at this temperature. The internal friction was monitored at a frequency of 0·5 Hz during a linear temperature increase of 160°/hr. No significant peaks appear between 28 and 110°K. Subsequently we observe the four peaks already mentioned: I_D^* at 110°K, I_E^* at 126°K, II^* at 151°K and III^* at 245°K.

The symbol used to label each peak indicates at which stage of the resistivity recovery it disappears. On this same figure we show the internal friction observed, still at 0·5 Hz, after a 3 MeV electron irradiation ($2{\cdot}7\times10^{18}$ electrons/cm²). For this case a single well defined peak is observed at 129°K.

Figure 2 presents the internal friction observed at 100 Hz after a neutron irradiation at 77°K. The peaks I_D^* and I_E^* do not appear because they are now displaced to higher temperatures where the annihilation of the defects with which they are associated is very rapid. This figure demonstrates the necessity of low frequency experiments in such point defect studies.

(2) *Annihilation of defects*. In the course of an isothermal treatment at 110°K, the peak I_D^* rapidly disappears, which implies that the corresponding defect undergoes only very few reorientations before annealing. Figure 3 shows the isochronal recovery of peak I_E^*. From this curve, we deduce that the kinetics of the annihilation of the associated defect is of order 2. This result is confirmed by the behaviour of the recovery process as a function of the irradiation dose. As the peak is diminishing with time at the temperature at which it is evident, the experimental peak height h_e is less than h_t which is the height that would be observed without any elimination of the associated defect. Also the temperature T_e, at which the apparent maximum occurs, is lower than that of the theoretical maximum T_t. The ratio h_t/h_e and the difference (T_t-T_e) both increase with increasing dose of irradiation.

For 10^{18} n.v.t., $h_t/h_e\simeq1{\cdot}6$ and $T_t-T_e\simeq$ 3°K whilst for 2×10^{18} n.v.t., $h_t/h_e\simeq2$ and $T_t-T_e\simeq$ 4°K.

The other characteristics of the defect responsible for the peak I_E are as follows:

Energy of reorientation $E_r=0{\cdot}25\pm0{\cdot}02$ eV.

Energy of migration $E_m=0{\cdot}25\pm0{\cdot}04$ eV.

Mean number of jumps effected by defect before annihilation = about 200 (for a dose of $1{\cdot}9\times10^{18}$ n.v.t.).

The peak observed at 129°K after electron

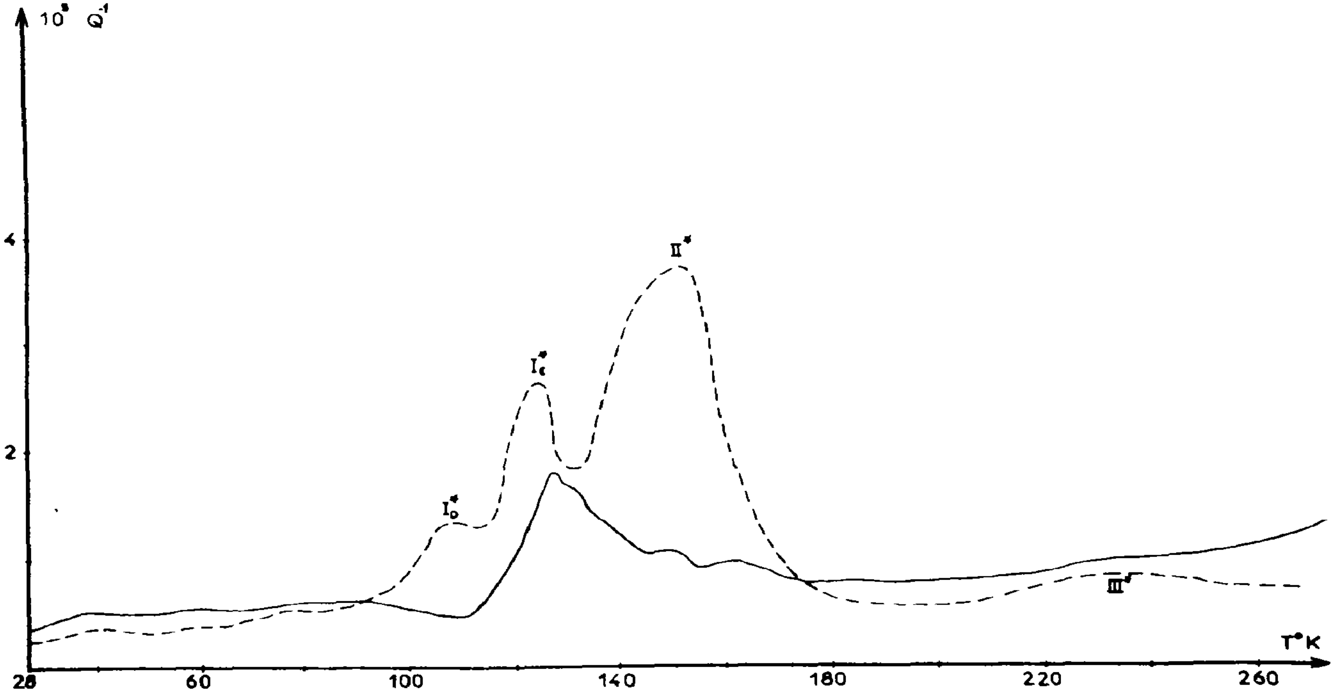

Fig. 1. Internal friction at low frequency (0·5 Hz) in pure polycrystalline iron during a linear increase of temperature at 160°/hr after neutron irradiation (---) at 28°K ($1{\cdot}9\ 10^{18}$ n v t, $E > 1$ MeV) and after 3 MeV electron irradiation (—) at 20°K ($2{\cdot}7 \times 10^{-18}$ electrons/cm^2), the study beginning at 28°K

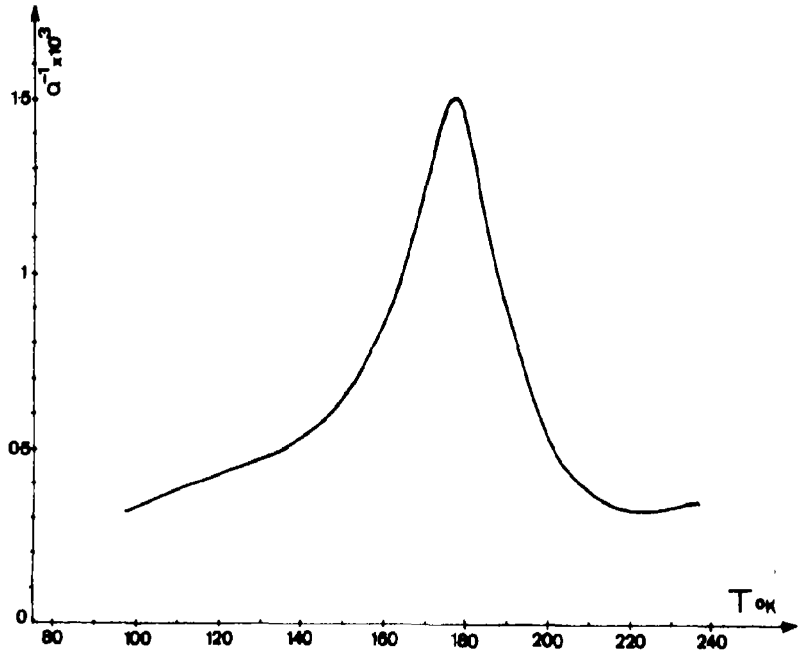

Fig. 2 Internal friction at frequency of 100 Hz, in pure polycrystalline iron after neutron irradiation at 77°K ($0{\cdot}9 \times 10^{18}$ n v t, $E > 1$ MeV).

irradiation (see Fig. 1) has exactly the same characteristics as the peak I_E^+ appearing at 126°K after neutron irradiation and which we have described immediately above. We therefore attribute these two peaks to the same defect. The different values for T_c may be explained (taking account of the different heights h_c) by the differing concentration of defects according as the irradiation is carried out with electrons or neutrons.

The elimination of peak II^+ is complex and extends over the temperature range 160–210°K when studied in the course of an isochronal anneal.

Peak III^+ which is centred at 245°K and was found to have a width very much greater than the theoretical value, does not appear to be related to a relaxation phenomenon because it is not accompanied by an associated reduction of the shear modulus. Furthermore, the isochronal annealing of the defect does not obey simple kinetics, its time dependence being approximately described by a $t^{-1/2}$ law.

(b) *Polycrystalline iron—low temperature irradiation and rolling*

Subsequent to irradiation the specimens were rolled at liquid nitrogen temperature. Figure 4 shows the dependence of the heights of the peak I_E^+, II^+ and III^+ on the degree of coldworking. The heights of peak I_E^+ and II^+ diminish with increasing coldwork probably because of the sweeping away of the point defects by the dislocations. On the other hand, peak III^+ grows quite clearly as a result of the treatment. The peak I_h^+ was found to be too small to be studied in this way.

A pure iron sample rolled at 77°K without prior irradiation yielded a peak rather analogous to peak III^+ but generally situated at some higher temperature whose exact value depended on the purity of the sample.

(c) *Irradiation of single crystals of pure iron*

Figure 5 shows the results of internal friction measurements after neutron irradiation of single crystals samples with axes parallel to

⟨100⟩ and ⟨110⟩. The corresponding results for electron irradiation are shown in Fig. 6.

Peak I_B^* (for neutron irradiation) is not evident in the specimen with axis parallel to ⟨100⟩.

Peak I_E^* appears for both types of irradiation and sample orientation.

The so-called peak II^+ (neutron irradiation) is in fact a combination of two peaks. One, appearing clearly for the sample whose axis is parallel to ⟨110⟩ is situated at 142°K and is labelled II_1^+ and the other, II_2^+, appearing for the sample whose axis is parallel to ⟨100⟩, is situated at 158°K.

After subtraction of the background contribution to the internal friction and separation of the overlapping peaks by the standard methods we obtain the experimental relaxation amplitude Δ_G, as listed in Table 1, for the two sample orientations. These results could then be used to determine the orientations of the defects responsible for the peaks, as we now show:

Table 1. Experimental values of $\Delta_G \times 10^3$

		Experimental results				
		I_B^*	I_E^*		II_1	II_2
		110°K neutron	126°K neutron	129°K electron	142°K neutron	158°K neutron
Crystal orientation	⟨100⟩	0+0·1	2·4±0·2	1·2±0·4	0±0·2	7±0·5
	⟨110⟩	2±0·2	1·2+0·1	1·2±0·4	4±0·4	2±0·2

Using the hypothesis that the relaxing point defect behaves as an elastic dipole[7, 8], we thus express the amplitude of relaxation as observed in torsional oscillation as:

$$\Delta_G = \frac{\delta s + 2(\delta s' - \delta s)\Gamma}{s + 2(s' - s)\Gamma} \qquad (1)$$

where $s = s_{11}$ and $s' = 2(s_{11} - s_{12})$; s_{11}: s_{12} and s_{44} are the elastic constants. Γ is defined by the relation:

$$\Gamma = \alpha_1{}^2\alpha_2{}^2 + \alpha_2{}^2\alpha_3{}^2 + \alpha_3{}^2\alpha_1{}^2$$

where the α_i's are the cosines of the angles between the specimen axis and the axes A_4 of the cubic lattice.

For iron[9]: $s = 0{\cdot}862 \times 10^{-12}\ \mathrm{cm^2/dyn}$

$$s' = 2{\cdot}078 \times 10^{-12}\ \mathrm{cm^2/dyn}.$$

Using the value of δs and $\delta s'$ given by Nowick and Heller[10] for the possible orientations of a point defect together with the corresponding values of s and s' for iron, we obtain the expression for Δ_G as presented in Table 2. We note that for a defect having its axis in the ⟨110⟩ direction Δ_G is independent of $\delta s'$ for the sample whose axis is parallel to ⟨100⟩ because in this case $\Gamma = 0$. For the sample with axis parallel to ⟨110⟩ $\Gamma = 1/4$, which gives:

$$\Delta_G = \frac{\delta s + \delta s'}{s' + s}$$

s and s' are positive, on account of thermodynamic considerations, similarly δs and $\delta s'$ are also positive. The minimum value of Δ_G for a known δs is obtained when $\delta s' = 0$, whence:

$$\Delta_G \geqslant \frac{\delta s}{s' + s}.$$

A comparison of Tables 1 and 2 leads to the following conclusions: (1) I_B^* is due to a defect of orientation ⟨100⟩ (2) I_E^* is probably due to

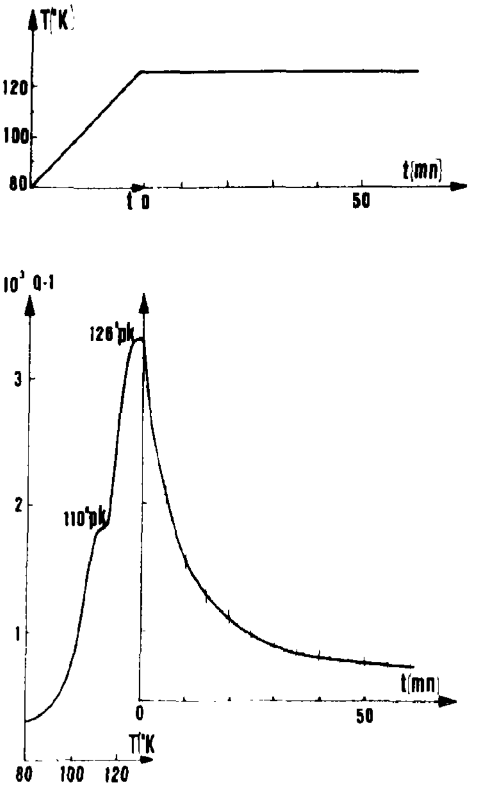

Fig. 3. Isothermal annealing of the 126°K peak. The critical curve for second order kinetics and experimental points

a defect of orientation ⟨110⟩† (for both neutron and electron irradiations). (3) II_1' is due to a defect of orientation ⟨100⟩ II_2^* may possibly be due to a defect of orientation ⟨111⟩.

(d) *Irradiation of polycrystalline iron doped with controlled concentrations of impurities*

If the impurity concentration is low (up to about 5 × 10^3 atomic ppm) peak I_F^* is observed and the characteristics of reorientation (reorientation energy and frequency factor) are unchanged. Nevertheless the characteristics of the recovery stage are strongly changed. The recovery process is very much more rapid and tends to kinetics of order 1[11, 12]. The mean number of jumps executed by a defect before its elimination decreases considerably (9 jumps for 5 × 10^3 ppm nickel). In the presence of nickel or silicon the disappearance of the peak I_F^* is accompanied by the emergence of another peak [11, 12].

Table 2. Theoretical values of $\Delta_G \times 10^{-12}$

Crystal orientation	Relaxing defect orientation ⟨100⟩ $\delta_s = 0$	⟨110⟩ $\delta_s \neq 0$ $\delta_{s'} \neq 0$	⟨111⟩ $\delta_{s'} = 0$
⟨100⟩ $\Gamma = 0$	0	$1{\cdot}16\,\delta_s$	$1{\cdot}16\,\delta_s$
⟨110⟩ $\Gamma = 1/4$	$0{\cdot}34\,\delta_s'$	$\geqslant 0{\cdot}34\,\delta_s$	$0{\cdot}34\,\delta_s$

(e) *Electron and neutron irradiations of molybdenum*

Figure 7 shows the resistivity recovery curve after electron irradiation. Stage I is seen to have a narrow substage at 41°K and a large stage III is evident. In Fig. 8 is shown the internal friction peak found after the two types of irradiation. This peak anneals out in the temperature range of the 41°K substage. No comparable peak appears in the vicinity of stage III (see Fig. 9). De Jong has found an elastic after effect in this vicinity[13] which he has attributed to a free migrating interstitial. However in this temperature range we sometimes found large peaks which were irreproducible both in position and annihilation behaviour and which were probably due to the superposition of several different effects such as: molybdenum structure, handling, irradiation conditions, etc.

4. DISCUSSION

As will have been seen from the introduction, we shall focus our attention on the search for

---

†Corresponding to the 126 and 129°K peaks, we found a magnetic after-effect zone. A complete study of this magnetic after-effect was carried out after neutron irradiation[3]. The results were not exactly identical (kinetics not exactly of a second order – symmetry nearer ⟨100⟩ than ⟨110⟩). Our explanation was that the magnetic after-effect cannot distinguish I_D^* and I_F^* defects

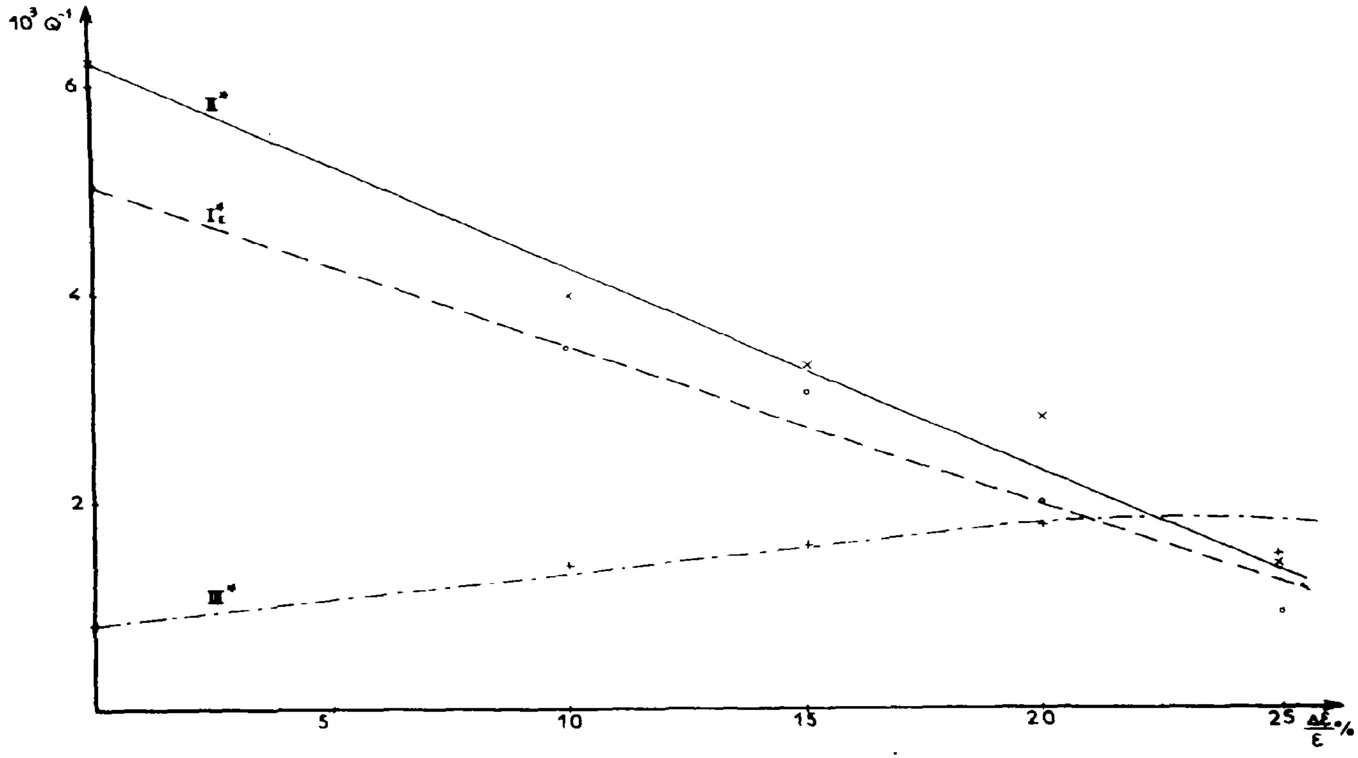

Fig. 4. The change of height of the internal friction peaks in low temperature neutron irradiated iron as a function at the degree of cold-working (after irradiation at 77°K the sample is maintained at this temperature and rolled in liquid nitrogen)

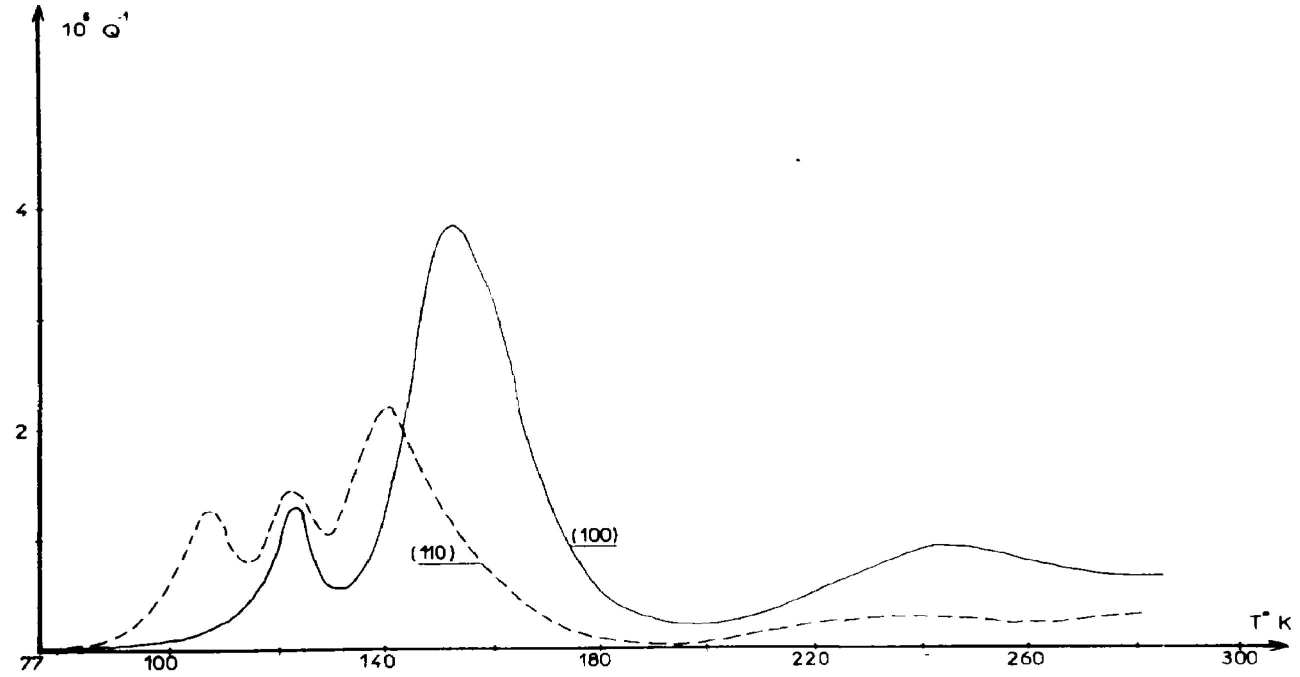

Fig. 5 Internal friction in monocrystalline iron (sample axis parallel to ⟨100⟩ and ⟨110⟩) after neutron irradiation at 77°K ($1 \cdot 9 \times 10^{18}$ n.v.t., $E > 1$ MeV).

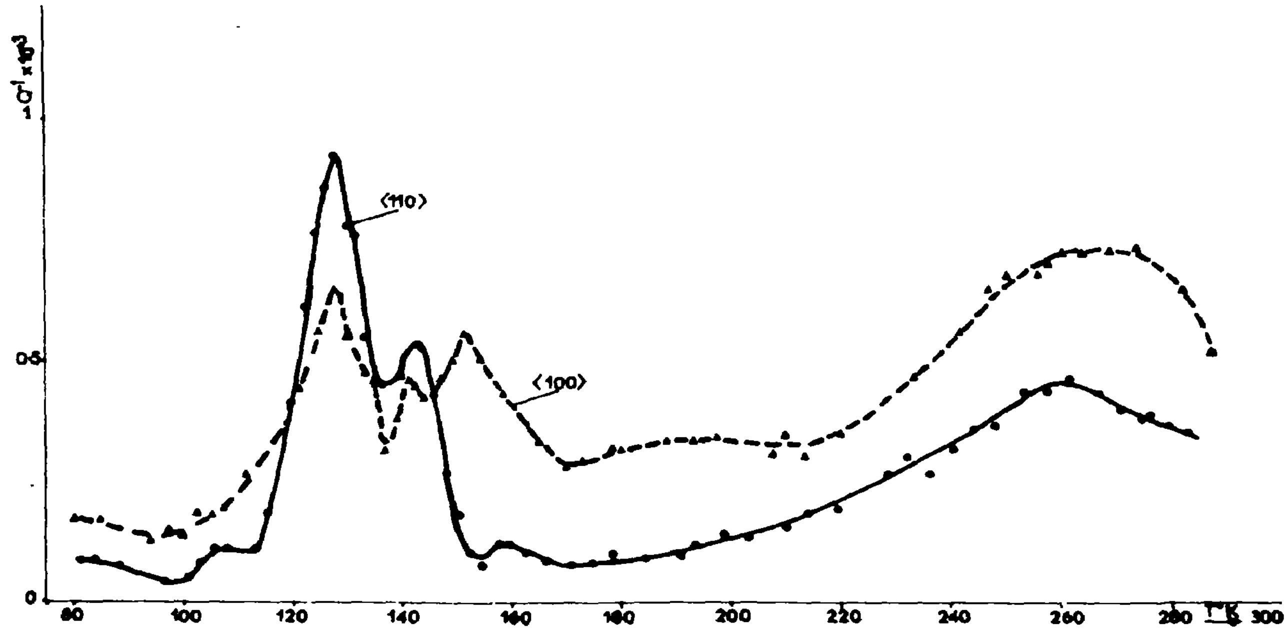

Fig. 6. Internal friction in monocrystalline iron (sample axis parallel ⟨100⟩ and ⟨110⟩) after 3 MeV electron irradiation at 20°K ($2{\cdot}7 \times 10^{16}$ electron/cm²), the study beginning at 77°K.

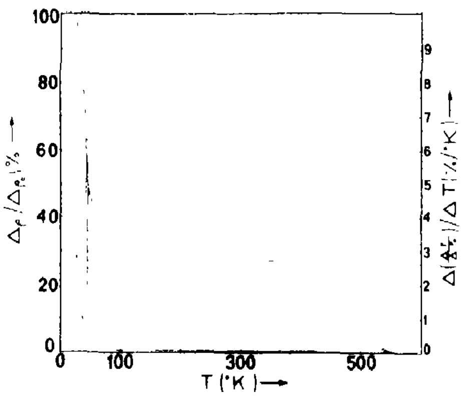

Fig. 7. Recovery of the resistivity after electron irradiation of pure molybdenum at 20°K. Isochronal annealing ($\Delta T = 1$°K $20°K < T < 80°K$, $\Delta T = 3$°K $80°K < T < 300°K$, $\Delta T = 5$°K $300°K < T < 550°K$, and $\Delta t = 10$ mn)

peaks which can be attributed to the free interstitial.

(a) *Model for iron*

The results of the experiments on coldworking after irradiation show that we can reject the hypothesis of a mechanism involving dislocations as an explanation of the behaviour of peaks I_L^* and II^*. Peak III^*, on the other hand, is directly related to the dislocations.

Peaks I_L^* and II^* are absent after electron irradiation. Peak I_L^* is the only one which can be attributed to the free interstitial. The following characteristics confirm this hyphotheis:

(1) The peak I_L^*, which is associated with a reduction of the shear modulus, is due to a simple relaxation phenomenon because its width is close to the theoretical value for such a phenomenon.

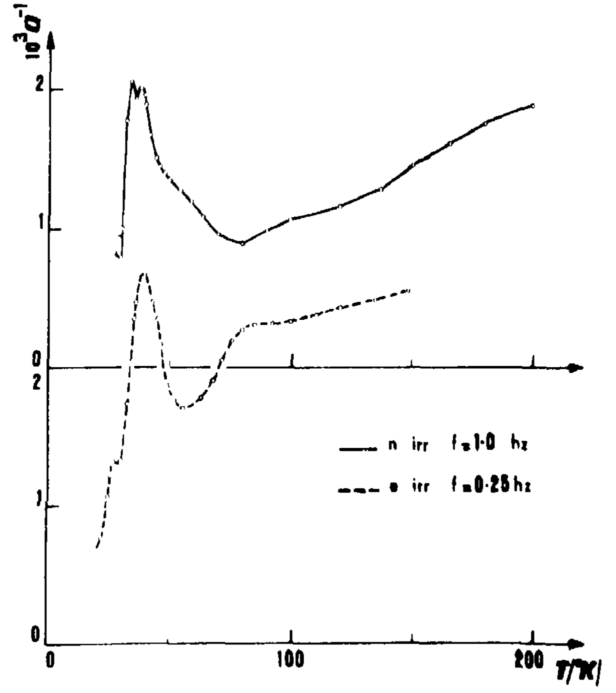

Fig. 8. Internal friction at the frequency of 0·25 Hz in polycrystalline molybdenum after 2 MeV electron irradiation (10^{18} electron/cm^2) at 20°K – and internal friction at the frequency of 1 Hz in molybdenum after neutron irradiation (5×10^{17} n.v.t. > 1 MeV) at 28°K.

(2) The second order kinetics of the annihilation of the corresponding defect, and the

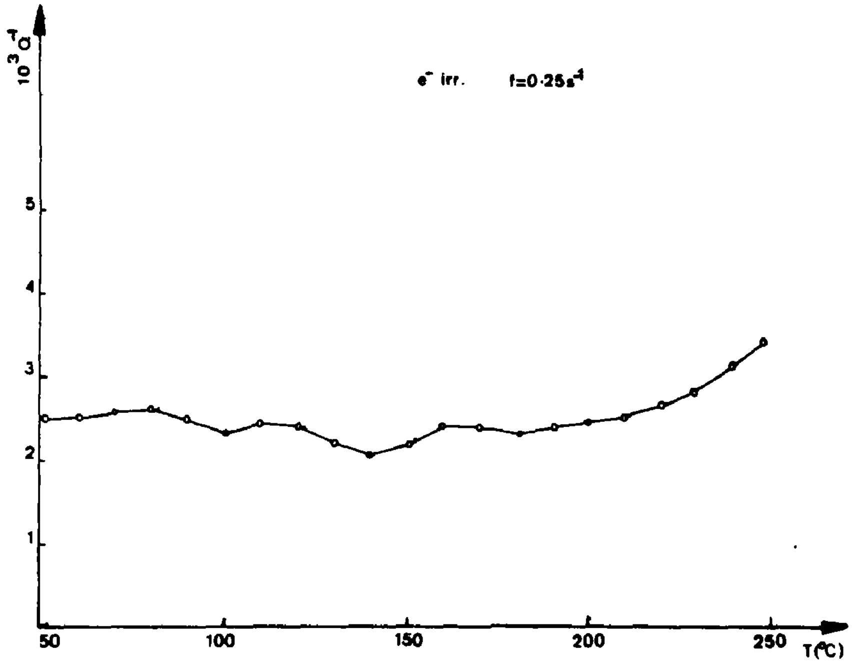

Fig. 9. Internal friction at the frequency of 0.5 Hz in molybdenum after room temperature irradiation ($E = 3$ MeV, 5×10^{18} electron/cm^2)

value of 200 found for the mean number of jumps prior to annihilation are both compatible with a random migration.

(3) The modification of the annihilation characteristics in the presence of impurities may be interpreted in terms of a free migration followed by trapping.

(4) The ⟨110⟩ symmetry of the defect responsible for I_E^* as well as the equality in the reorientation and migration energies are in agreement with the theoretical calculations of Johnson[14] for the self interstitial in iron. The experimental value of 0·025 ± 0·04 eV for these energies is lower than the calculated value of 0·32 eV but the difference is not surprising in view of the complexity of the parameters which must be introduced in a calculation of this type.

The broad peak III* is not accompanied by any measurable reduction in the shear modulus. It does not appear to be related to a relaxation process and so cannot be attributed to the reorientation of a second type of interstitial. This conclusion is confirmed by other characteristics of the peak, namely its modification after coldworking and the complex fashion in which it disappears. We thus explain this peak III* by a variation in the continuous background related to dislocations.

We shall not discuss peak I_D^* in the present article beyond the observation that we associate it with the orientation of close pairs which are characteristic of the neutron irradiation. Neither shall we discuss peaks II_1^* and II_2^* which are attributed to small agglomerates (di-interstitials and di-vacancies).

(b) *Anisotropy coefficient for the interstitial in iron*

To describe the interstitial in iron which is related to the peak I_E^* we now determine the parameters λ_1, λ_2 and λ_3 characterising the equivalent elastic dipole.

After Nowick and Heller[10], for a defect having its axis in the direction <110> we have the following relations:

$$\delta s = \frac{CV_0}{3kT}(\lambda_1 - \lambda_2)^2 \tag{2}$$

$$\delta s' = \frac{2CV_0}{3kT}\left(\frac{\lambda_1 + \lambda_2}{2} - \lambda_3\right)^2 \tag{3}$$

where δs and $\delta s'$ are the quantities employed in Section 3. C is the concentration of the defect responsible for the observed peak, V_0 is the atomic volume and T the temperature of the peak.

The interstitials giving rise to peak I_E^* are, according to our model of a single type, namely those which are annihilated at stage I_E or, after agglomeration, at later stages (annihilating at the same time as those agglomerates formed during the irradiation).

By analysis of the results obtained in diverse experiments (stored energy release[3], magnetic after effect[3], electrical resistivity[15]), we are able to estimate that a neutron dose of $1{\cdot}9 \times 10^{18}$ n.v.t. produces 1000 ppm Frenkel pairs and that 40 per cent of the interstitials in these pairs contribute to the peak I_E^*. We have seen that when the peak I_E^* is observed, about 50 per cent of the defects associated with it have already been annihilated. Thus the concentration C to be related to the experimental height of I_E^* is 200 ppm.

If we insert the data of Table 2 into equation (1), we obtain $\delta s = (2{\cdot}06 \pm 0{\cdot}20)\ 10^{-15}$ cm²/dyn and $\delta s' = (1{\cdot}46 \pm 0{\cdot}14)\ 10^{-15}$ cm²/dyn. V_0 is practically equal to 10^{-23} cm³, $k = 1{\cdot}38 \times 10^{-16}$ ergs/° and $T = 126$°K. To relations (2) and (3) we can add, as proposed by Di Carlo[16] the equation giving the relative increase in the volume produced by the introduction of the defect:

$$\frac{\Delta V}{V} = \lambda_1 + \lambda_2 + \lambda_3 \tag{4}$$

we take $\Delta V/V$ equal to 1·6 as calculated by Johnson for the interstitial in iron[14]. We thus obtain:

$$\lambda_1 = 0{\cdot}68 \pm 0{\cdot}07 \qquad \lambda_2 = 0{\cdot}47 \pm 0{\cdot}04 \qquad \lambda_3 = 0{\cdot}45 \pm 0{\cdot}04.$$

In the estimation of the errors we have only taken into account the uncertainties in Δ_G ⟨100⟩ and Δ_G ⟨110⟩ because the uncertainties in all other quantities are negligible.

(c) *Model for molybdenum*

For molybdenum the solution of the problem is at a somewhat less advanced stage than for iron. This is a consequence, in particular, of the absence of results on the isothermal annealing of the peak situated at 41°K. Nevertheless the presence of this peak after both neutron and electron irradiations, its width corresponding clearly to the theoretical value and its rapid annealing, seem to justify its identification as a peak having the same origin as the peak I_E^* in iron.

In the region of stage III no internal friction peak can be related to the large stage in the resistivity recovery. Furthermore the random effects mentioned above exhibit strong similarities with the peak III* observed after irradiation and coldworking or iron.

5. CONCLUSION

The results obtained for iron demonstrate the importance of the relaxation phenomenon related to the free interstitial migrating in the vicinity of stage I_E.

In the vicinity of stage III no peak could be associated with migration of a second type of interstitial. The internal friction effects observed in molybdenum in the vicinity of stages I and III are very similar to those observed in iron.

Consequently, although these two metals have different resistivity recoveries it appears that their behaviour can be interpreted in terms of a unique model requiring a single type of interstitial which migrates freely at stage I_E.

Acknowledgements—We wish to thank Dr. J. Philibert who kindly supplied us with the iron single crystals and G de Keating-Hart who as well as participating in the experiments, perfected the technique of sample transfer at 28°K We are also grateful to Dr. J. Belson for assistance in the translation of this paper.

REFERENCES

1. SCHULTZ H., *Mater. scient. Engng* **3**, 189 (1968/69).
2. LEVEQUE J. L., ANAGNOSTOPOULOS T., BILGER H. and MOSER P., *Phys. Status Solidi* **29**, K179 (1968).
3. MOSER P., *Mem. Sci. Rev. Metal.* **63**, 431 (1966)
4. STALS L. and NIHOUL J., *Physica* **42**, 165 (1969).
5. TERASAKI F., Thesis, Paris (1966).
6. DAUTREPPE D., HIVERT V., MOSER P. and SALVI A., *C. r. Acad. Sci.* **258**, 4539 (1964).
7. SERAPHINI D. P. and NOWICK A. S., *Acta metall* **9**, 85 (1961).
8. SEEGER E. and MANN E., *J. Phys. Chem. Solids* **23**, 639 (1962)
9. *American Institute of Physics Handbook*, 2nd Edn. pp. 3–89 (1963)
10. NOWICK A. S and HELLER W. R., *Adv. Phys.* **12**, 251 (1963).
11. VIGIER P., HIVERT V., MOSER P. et BONJOUR F., *C. r. Acad Sci.* **260**, 3359 (1965)
12. VIGIER P., MINIER C., MOSER P. et HIVERT V., *Phys Status Solidi* **17**, 1 (1966)
13. de JONG M. and WENSINK B. L., *Phys. Lett* **17**, 200 (1965).
14. JOHNSON R. A., *Phys. Rev* **134A**, 1329 (1964).
15. MINIER C. (Mme), Thesis Grenoble 1965 (CEN-G. Cédex 85- Grenoble, France (1965).
16. DI CARLO J. A., SNEAD C. L. Jr. and GOLAND A. N., *Phys. Rev.* **178**, 1059 (1969).

J. Phys. Chem. Solids Pergamon Press 1970. Vol. 31, pp. 1857–1861. Printed in Great Britain

ANOMALOUS ATTENUATION IN LITHIUM TANTALATE*

J. C. WORLEY, A. B. SMITH and M. KESTIGIAN
Sperry Rand Research Center, Sudbury, Mass. 01776, U.S.A.

(*Received 5 September* 1969; *in revised form* 1 *November* 1969)

Abstract – Longitudinal-wave attenuation measurements have been made in lithium tantalate single crystals grown from melts containing varying amounts of lithium and tantalum. These measurements covered a temperature range of 4–300°K and a frequency range of 1–10 GHz. A peak at about 30°K has been found in the temperature dependence of the attenuation. The shift of the position of this peak as the frequency is varied indicates that it is caused by an Arrhenius-type relaxation mechanism. Studies indicate that the height of the maximum is dependent on the Li/Ta ratio and independent of the amount of reduced tantalum or oxygen vacancies present in the sample.

It is of both scientific and practical interest to discover low-loss acoustic materials. Attenuation measurements in several promising new materials[1–8] have been reported in the last few years and among them is $LiTaO_3$[9]. We report here the presence of an anomalous peak in the temperature-dependent attenuation of this material.

Measurements were made on Czochralski-grown[10] *c*-axis crystals over a temperature range of 4–300°K and a frequency range of 1–10 GHz. The samples used in this study were cut from boules which had been poled [11] after growth in order to insure the presence of a single ferroelectric domain. The samples were rectangular parallelepipeds approximately 2·5 mm square by 10 mm long with the square faces polished flat to 1/10 wave and parallel to 5 sec of arc.

The arrangement used in this experiment was a typical pulse-echo setup, which is shown in Fig. 1. The ultrasonic waves were excited[12] at one of the 2·5 × 2·5 mm surfaces of this piezoelectric material and no separate transducer was needed. The attenuation measurements were made by observing the changes in relative echo heights, with a calibrated attenuator which was capable of measuring differences to an accuracy of ±0·02 dB. The sample was contained within a copper block, the temperature of which was measured by means of a carbon resistor at very low temperatures and by a gold-cobalt vs. copper thermocouple above 30°K. It was possible to maintain the temperature of the block to within ±0·01°K for any desired length of time by means of a heater within the block which was energized by a differential temperature controller connected to the thermocouple through a potentiometer.

The results of our measurements of longitudinal-wave attenuation on one $LiTaO_3$ sample are shown in Fig. 2. (In this and all subsequent figures, the attenuation has been normalized to zero at 4°K.) The results in Fig. 2 are in agreement with previous experiments[9] except that now in the low-temperature region the presence of a peak at approximately 30°K has been revealed. As is described below, the *height* of this peak is dependent on the ratio of Ta to Li in the melt from which the crystal is grown. In the sample of Fig. 2, the melt contained 5 per cent more Ta than the stoichiometric amount.

Barrett[13] has observed an attenuation peak in $KTaO_3$ which occurs in the same temperature range as the one reported here. He has explained the occurrence of the peak

---

*The work reported here was partially supported by the Air Force Materials Laboratory at Wright-Patterson Air Force Base under contract No. F33615-68-C-1099

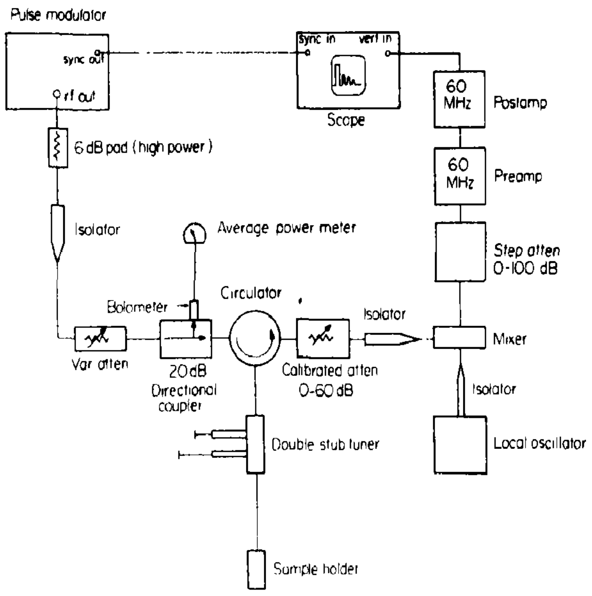

Fig. 1. Experimental set-up used for pulse-echo measurements.

in $KTaO_3$ in terms of interactions with thermally excited phonons in a transverse optical phonon mode. This is a 'soft' mode which has a very low frequency at long wavelength as can be independently verified by far-i.r. reflectivity measurements[14] and other techniques. It does not seem likely, however, that a similar effect is responsible for the peak we observe in $LiTaO_3$. The $KTaO_3$ data was taken in the paraelectric state as this material only approaches a ferroelectric state as $T \rightarrow 0$°K. On the other hand, $LiTaO_3$ with a Curie temperature of ~600°C[15] is a ferroelectric at all normal temperatures. (No comprehensive infrared or other studies of the phonon mode structure in $LiTaO_3$ are available. The only measurement we are aware of was made on a sample from the same batch which produced the 'pure' curve in Fig. 5. In an infrared transmission experiment the i.r. energy reaching the detector was seen to decline monotonically in going from 40 cm^{-1} to 10 cm^{-1} as might be expected from the normal frequency dependence of the dielectric constant.)

Peaks of the type shown in Fig. 2 have been successfully explained in a number of other materials[16–18] in terms of various relaxation processes. All these processes are assumed to have relaxation times τ_a which obey the so-called Arrhenius relation[19]

$$\tau_a = \tau_0 e^{\Delta E/kT}, \qquad (1)$$

where ΔE is the activation energy of the appropriate transition. Since the maximum energy will be absorbed from a sound wave of frequency ω when $\omega\tau_a = 1$, this type of absorption process leads to a peak superimposed on the usual attenuation vs. frequency curve.

The temperature at which the relaxation peak occurs, it should be noted, depends on ω. Hence ΔE and τ_0 can be determined by measuring the peak temperature T_p as a function of sound frequency. A plot of $1/T_P$ vs. $\ln \omega$ should be a straight line for this process as can be seen by taking the logarithm of equation (1). Figure 3 shows such a plot for the data given in Fig. 2. All the points fall very close to a straight line with the exception of the 8·5 GHz point, but at this frequency no peak

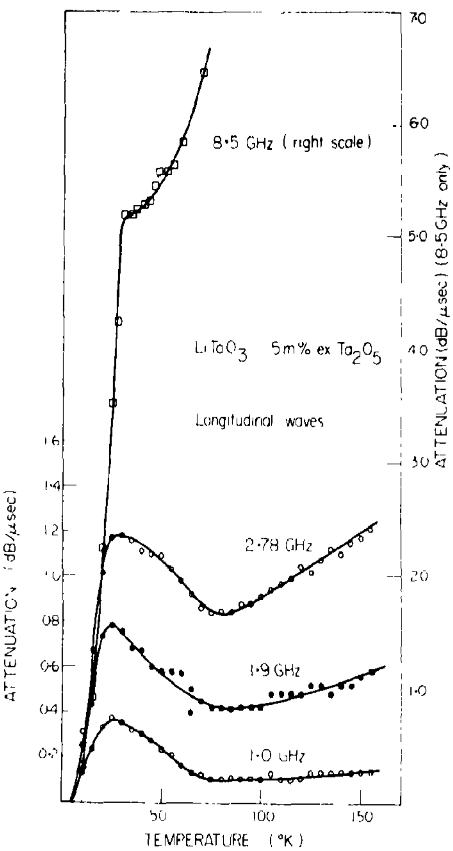

Fig. 2. Measured longitudinal-wave attenuation for various frequencies in a LiTaO$_3$ sample grown from a melt containing 5 mol% excess tantalum.

is apparent because of the high normal attenuation and the position of the peak must be estimated. From the figure, the characteristic time τ_0 is found to be $4{\cdot}27\times10^{-12}$ sec and the activation energy ΔE is $1{\cdot}02\times10^{-21}$ J.

Figure 4 shows a plot of attenuation vs. temperature for shear waves at 2·78 GHz in c-axis LiTaO$_3$. The existence of the anomalous attenuation under shear stress indicates[19] that the cause of the peak is such as to produce local strains which have a symmetry lower than that of the lattice.

Longitudinal-wave attenuation measurements were also made on a number of samples grown from melts of different compositions with the results shown in Fig. 5. It is seen that the height of the peak is dependent on the Ta/Li ratio. In an attempt to discover the specific cause of this dependence, several additional experiments were performed. X-ray powder patterns were taken of sections of the boules from which the samples with 5 m% excess tantalum and 5 m% excess lithium were cut. Within the accuracy of our measurements (±0·02 Å) there was no change in cell size. Also, no indication was seen of the existence of a different phase within the crystal. In order to determine whether the crystals which exhibited the peak were being affected by impurities, several samples were measured by means of emission spectrometry. The amounts of impurities were small (less than 2 ppm) and were the same within all samples.

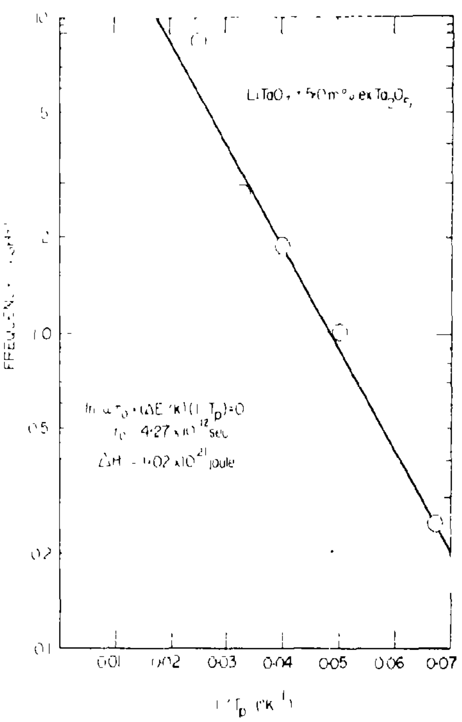

Fig. 3. Plot of frequency vs. $1/T_p$ for data given in Fig. 2.

It is evident from the pale yellow coloration of LiTaO$_3$ samples grown by the Czochralski technique that oxygen vacancies

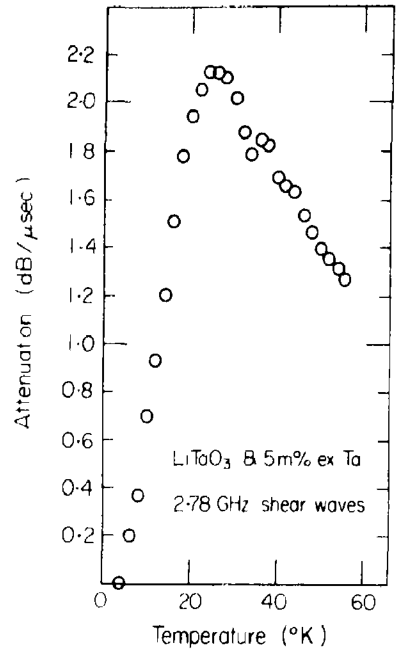

Fig. 4. Shear-wave attenuation as a function of temperature in $LiTaO_3$ grown from a melt containing 5 mol% excess tantalum

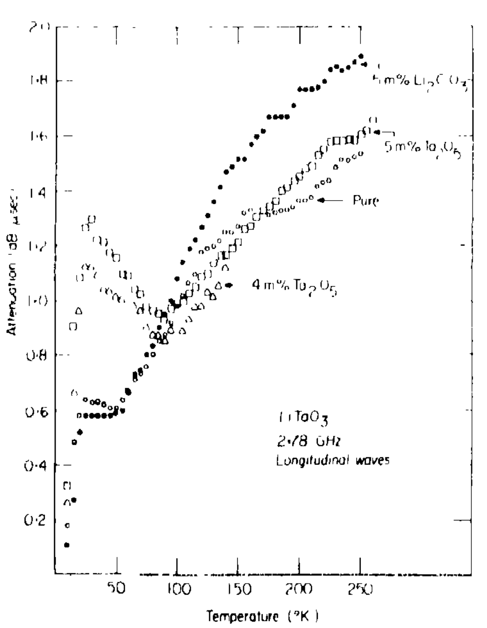

Fig. 5. Attenuation vs temperature at a constant frequency for crystals grown from different melt compositions

exist within these crystals. In order to discover whether or not these vacancies affect the attenuation, we measured two samples from the same boule, one of which had been annealed in oxygen at 1000°C and the other reduced in hydrogen at 1000°C until it was opaque. Figure 6 shows the results of this experiment. It can be seen that the attenuation peak is unaffected by the oxygen vacancies although the normal attenuation at higher temperatures does seem to be affected.

In conclusion, the anomalous attenuation in $LiTaO_3$ seems to be associated with the existence of a Ta/Li ratio which is greater than one. It appears that all $LiTaO_3$ samples grow with lithium vacancies because the high melting temperature of this compound (1600°C) causes the lithium to vaporize leaving a melt which is deficient in lithium. We feel that this is the reason that the anomalous attenuation is seen even in crystals grown from both stoichiometric melts and melts with excess lithium. (Precise analyses of the chemical composition of the grown crystals to settle this point have not been accomplished because of the difficulty in making accurate chemical determinations of

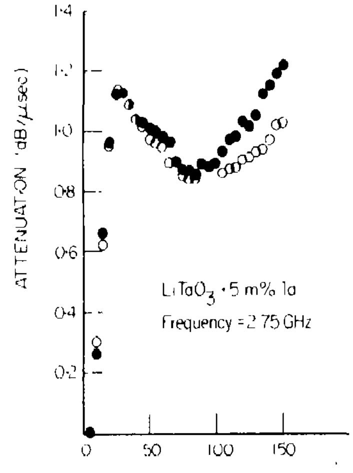

Fig. 6. Attenuation of two samples from the same boule, one of which (filled circles) had been reduced in hydrogen, the other (open circles) had been annealed in oxygen.

lithium content.) The anomalous attenuation is therefore possibly caused by either the motion of tantalum atoms in and around sites which they normally would not occupy in a stoichiometric crystal, or the motion of a combination of oxygen and tantalum atoms about an equilibrium position. There is also the possiblity that the attenuation could be associated with lithium vacancies, although Wert[20] has pointed out that attenuation due only to vacancies has never been observed.

Acknowledgement—The authors would like to thank P. Berger and H. H. Barrett for performing the infrared measurements referred to in the text and for several helpful discussions. We would also like to thank F. Bradlee and R. Brophy for technical assistance.

Note added in proof

Two recent papers which are related to this topic should be mentioned. Lines (*Phys. Rev.* **177**, 819 (1969)) discusses lattice modes in $LiTaO_3$ while Nassau and Lines (*J. appl. Phys.* **41**, 533 (1970)) discuss possible deviations from stoichiometry in this material.

REFERENCES

1. LEWIS M. F. and PATTERSON E., *J. appl. Phys.* **39**, 3420 (1968).
2. OLSON F. A., YAEGER J. R. and WILSON R. A., *5th Int. Congr. on Acoustics, Liége* (1965).
3. de KLERK J., *Phys. Rev.* **139**, A1635 (1965).
4. SHAW H. J., WINSLOW D. K., KARP A., WILSON R. A., *Appl. Phys. Lett.* **4**, 28 (1964).
5. MIDFORD L. A. and WANUGA S., *J. appl. Phys.* **36**, 3362 (1965).
6. HOLLAND M. G., PALADINO A. E., BIERIG R. W., *J. appl. Phys.* **38**, 4100 (1967).
7. GRACE M. I., KEDZIE R. W., KESTIGIAN M. and SMITH A. B., *Appl. Phys. Lett.* **9**, 155 (1966).
8. SMITH A. B., KESTIGIAN M., KEDZIE R. W. and GRACE M. I., *J. appl. Phys.* **38**, 4928 (1967).
9. SMITH A. B., KEDZIE R. W., McMAHON D. H. and KESTIGIAN M., *J. appl. Phys.* **40**, 2687 (1969).
10. BALLMAN A. A., *J. Am. Ceram. Soc.* **48**, 112 (1965); FEDULOV S. A., SHAPIRO Z. I. and LADYZHINSKII P. B., *Soviet Phys. Crystallogr.* **10**, 218 (1965).
11. LEVINSTEIN H. J., BALLMAN A. A. and CAPIO C. D., *J. appl. Phys.* **37**, 4585 (1966).
12. BOMMEL H. F. and DRANSFELD K., *Phys. Rev.* **117**, 1245 (1960).
13. BARRETT H. H., *Phys. Rev.* **178**, 743 (1969).
14. PERRY C. H. and McNELLY T. F., *Phys. Rev.* **154**, 456 (1967).
15. BALLMAN A. A., LEVINSTEIN H. J., CAPIO C. D., and BROWN H., *J. Am. Ceram. Soc.* **50**, 657 (1967).
16. MASON W. P., *Physical Acoustics* (Edited by W. P. Mason). Vol. 3B, p. 235. Academic Press, New York (1965). POMERANTZ M., *Proc. IEEE* **53**, 1438 (1965).
17. SPENCER E. G., DENTON R. T. and CHAMBERS R. P., *Phys. Rev.* **125**, 1950 (1962). EINSPRUCH N. G., *J. Phys. Chem. Solids* **23**, 1341 (1962). LEWIS M. F. and PATTERSON E., *J. appl. Phys.* **39**, 1932 (1968).
18. GIBBONS D. F., *J. appl. Phys.* **28**, 810 (1957). KAMIGAKI K., *J. phys. Soc. Japan* **16**, 1170 (1961).
19. BERRY B. S. and NOWICK A. S., *Physical Acoustics* (Edited by W. P. Mason), Vol. 3A, pp. 7–28. Academic Press, New York (1966).
20. WERT C., *Physical Acoustics* (Edited by W. P. Mason). Vol. 3A, p. 43. Academic Press, New York (1966).

J. Phys. Chem. Solids Pergamon Press 1970 Vol. 31, pp. 1863–1867 Printed in Great Britain

RERADIATION AND VISCOUS DISLOCATION DAMPING*

J. A. GARBER and A. V. GRANATO
Department of Physics, University of Illinois, Urbana, Ill. 61803, U S A.

(*Received* 5 *September* 1969, *in revised form* 3 *November* 1969)

Abstract—The vibrating string model has been useful in rationalizing dislocation damping measurements This model predicts that pinned dislocation line segments of the order of one micron in length will have resonances typically at about 10^9 Hz Comparisons of theory and experiment have shown that this resonance is normally overdamped by the viscous drag of the dislocation-phonon and dislocation-electron interaction so that the dislocation inertia cannot be measured. In the absence of these processes (low temperatures in insulators or superconductors), only dislocation reradiation of elastic waves should limit the resonance. This effect has been calculated using Eshelby's expression for the reradiation. It is found that the resonance is very sharp, and still persists even when a random distribution of pinning points is assumed.

ACCORDING to the vibrating string model of dislocation damping[1, 2], pinned dislocation line segments should show resonance effects at an appropriate frequency. Experiments have confirmed this result for the case where the resonance is overdamped by the viscous drag of the dislocation-phonon and dislocation-electron interaction[3]. For sufficiently low temperatures in insulators or superconductors, these mechanisms should be absent and only dislocation reradiation of elastic waves should limit the resonance. Calculations indicate that the resonance is very sharp[4] and still persists even when a random distribution of pinning points is assumed. In this case, the dislocation inertia could be experimentally determined. The derivation of these results, including both viscous and reradiation damping, follows.

The motion of a pinned-down dislocation segment in the vibrating string model is given by the following equation[1, 2]:

$$A\frac{\partial^2\xi}{\partial t^2}+B\frac{\partial\xi}{\partial t}-C\frac{\partial^2\xi}{\partial y^2}=b\sigma. \qquad (1)$$

where ξ is the displacement of the dislocation under the influence of an applied stress, A is the effective mass per unit length of dislocation line, the term in B is the viscous damping force per unit length, the term in C is the force per unit length due to the effective tension for a bowed-out dislocation, y is a coordinate along the dislocation line, and the term on the right is the force per unit length exerted on the dislocation by the external shearing stress. The boundary conditions are that ξ is zero at $y=0$ and $y=l$, where l is the length of a dislocation segment. B is proportional to the phonon or electron density. If there is negligible viscous drag, the resonant frequency $\omega_0=(\pi/l)(C/A)^{1/2}$ and is expected to lie in the range 100–1000 MHz for dislocation segment lengths of the order of 1–10 μ for typical materials. In the overdamped case, it is normally found at much lower frequencies (~ 10 MHz).

In order to take reradiation damping into account, an additional term can be added to the above equation. Eshelby[5] has shown that the radiation of elastic waves from an oscillating straight screw dislocation produces an effective reradiation damping force per unit length (F/l) which can be expressed in the form

$$\frac{F}{l}=-i\frac{\rho b^2\omega^2}{8}\xi, \qquad (2)$$

where ρ is the density of the medium, b is the Burger's vector, and the displacement ξ is

---

*Supported by the National Science Foundation.

expressed in complex notation as $\xi = \xi_0 e^{i\omega t}$. Eshelby has also shown that edge and screw dislocations radiate about the same amount. We will assume that the dislocation displacements are small enough so that the dislocations assumed to be straight with no stress applied remain approximately straight during their oscillations under stress. Thus equation (2) will be taken as an approximation to the radiation force for all displacements. An estimate of the stress induced curvatures will be given later in the discussion. Now equation (1), which does not take reradiation damping into account, may be written

$$-\omega^2 A\xi + i\omega B\xi - C\frac{\partial^2 \xi}{\partial y^2} = b\sigma \qquad (3)$$

due to the sinusoidal variation with time $e^{i\omega t}$ of the dislocation displacement. If we now introduce the reradiation damping given by equation (2), we have

$$-\omega^2 A\xi + i\omega\left(B + \frac{\rho b^2 \omega}{8}\right)\xi - C\frac{\partial^2 \xi}{\partial y^2} = b\sigma. \qquad (4)$$

From the above equation it is clear that we can apply all previously derived results for the viscous damping case to the case of viscous damping plus reradiation damping simply by substituting $(B + \rho b^2\omega/8)$ for B everywhere. Thus the attenuation α of the externally applied stress wave is given by [2, 3]

$$\alpha(\omega) = \frac{\omega}{2V}\frac{\Omega\Lambda\Delta_0\eta^2}{\pi}\sum_{n=0}^{\infty}\frac{1}{(2n+1)^2} \times \frac{\omega d}{[(\omega_n^2-\omega^2)^2+(\omega d)^2]}, \qquad (5)$$

and the velocity V of the stress wave is given by

$$V(\omega) = V_0\left[1 - \frac{\Omega\Lambda\Delta_0\eta^2}{2\pi}\sum_{n=0}^{\infty}\frac{1}{(2n+1)^2} \times \frac{(\omega_n^2-\omega^2)}{[(\omega_n^2-\omega^2)^2+(\omega d)^2]}\right], \qquad (6)$$

where Ω is an orientation factor taking into account the relations between the direction of propagation of the applied stress wave and the slip plane and slip direction in the crystal, Λ is the total length of movable dislocation line per unit volume, $\Delta_0 = (8Gb^2)/\pi^3 C$ where G is the shear modulus, $\eta^2 = \pi^2(C/A)$, $\omega_n = [(2n+1)\pi/l](C/A)^{1/2}$, $V_0 = (G/\rho)^{1/2}$, and $d = (B + \rho b^2\omega/8)/A$ if both viscous and reradiation damping are considered. Equations (5) and (6) were derived by applying Newton's law relating stress to strain, taking dislocation strain as well as elastic strain into account.

The decrement Δ (defined as the ratio of the energy lost per cycle to twice the maximum stored energy) is given by

$$\Delta = \alpha\lambda = \frac{2\pi V}{\omega}\alpha, \qquad (7)$$

where λ is the wave length of the applied stress wave. Then we have

$$\Delta = \Omega\Lambda\Delta_0\eta^2\sum_{n=0}^{\infty}\frac{1}{(2n+1)^2} \times \frac{\omega d}{[(\omega_n^2-\omega^2)^2+(\omega d)^2]}. \qquad (8)$$

The modulus change is equal to twice the velocity change $\Delta V/V_0$, where

$$\frac{\Delta V}{V_0} = \frac{V_0 - V}{V_0} = \frac{+\Omega\Lambda\Delta_0\eta^2}{2\pi}\sum_{n=0}^{\infty}\frac{1}{(2n+1)^2} \times \frac{(\omega_n^2-\omega^2)}{[(\omega_n^2-\omega^2)^2+(\omega d)^2]}. \qquad (9)$$

For small viscous damping (few phonons or electrons), equations (8) and (9) predict a sharp resonance near ω_0 limited by the elastic reradiation. In reality, this resonance peak would be expected to be broadened because not all dislocation segments are the same length [4]. The decrement and velocity change given by equations (8) and (9) are those due to the presence of Λ/l dislocation segments per unit volume, where all segments are of length l. If instead of a single length l, there is a distribution of lengths due to a random arrangement of pinning points along the dislocation line, then the distribution function $N(l)\mathrm{d}l$, or number of segments of length between l and $l+\mathrm{d}l$, is given by[1, 2]

$$N(l)\mathrm{d}l = (\Lambda/L^2)\exp(-l/L)\mathrm{d}l, \qquad (10)$$

where L is the average segment length. The decrement and velocity change are then given by

$$\tilde{\Delta} = \frac{1}{L^2}\int_0^\infty l\Delta \exp(l/L)\mathrm{d}l \qquad (11)$$

and

$$\frac{\widetilde{\Delta V}}{V_0} = \frac{1}{L^2}\int_0^\infty l\frac{\Delta V}{V_0}\exp(-l/L)\mathrm{d}l, \qquad (12)$$

where Δ and $\Delta V/V_0$ are as given in equations (8) and (9). Making the change of variable $x = \omega l/(2n+1)\eta$, and using the identity

$$\sum_{n=0}^{\infty} \exp[-(2n+1)a] = [2\sinh a]^{-1},$$

the summation in equations (11) and (12) using equations (8) and (9) can be evaluated to give the two-parameter integrals

$$\tilde{\Delta} = \frac{\Omega\Lambda\Delta_0 L^2}{2}\frac{s}{\nu^4} \times \int_0^\infty \frac{x^5\mathrm{d}x}{\sinh(x/\nu)[(1-x^2)^2+s^2x^4]} \qquad (13)$$

and

$$\frac{\widetilde{\Delta V}}{V_0} = \frac{\Omega\Lambda\Delta_0 L^2}{4\pi}\frac{1}{\nu^4} \times \int_0^\infty \frac{(1-x^2)x^3\mathrm{d}x}{\sinh(x/\nu)[(1-x^2)^2+s^2x^4]}, \qquad (14)$$

where s is a dimensionless damping factor given by $s = d/\omega$ and ν is a dimensionless frequency given by $\nu = \omega/\omega_0(L)$. Note that s can be expressed as

$$s = \frac{B}{A\omega} + \frac{1}{8}\frac{\rho b^2}{A} = \frac{\delta}{\nu} + \frac{1}{8}\frac{\rho b^2}{A}, \qquad (15)$$

where δ is a dimensionless viscous damping factor given by $\delta = B/A\omega_0(L)$. It has been theoretically determined[5] that A is of the order of ρb^2. If we assume that A equals ρb^2 exactly, then

$$s = \frac{\delta}{\nu} + \frac{1}{8}. \qquad (16)$$

The resulting normalized decrement and modulus change vs. dimensionless frequency (obtained by numerical integration of equations (13) and (14), using equation (16)) are shown in Figs. 1 and 2. For $\delta = 1000$, the resonance is overdamped by the viscous loss and the curves are those obtained previously [2]. The resonance is overdamped with the maximum occurring at a frequency much lower than that corresponding to the resonance frequency for the average segment length ($\nu = 1$ or $\log\nu = 0$). The velocity change, or dispersion, is small above the maximum, going through zero ($\log|\Delta V/V_0| \to -\infty$) as it changes sign. For $\delta = 10^{-3}$ the resonance is

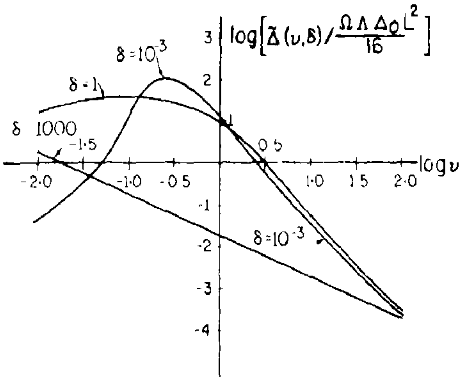

Fig. 1. Normalized decrement as a function of normalized frequency for different amounts of viscous damping. The frequency is normalized to the resonant frequency of the average segment $\nu = \omega/\omega_0(L)$. The resonance is overdamped for $\delta = 1000$ and radiation limited for $\delta = 10^{-3}$.

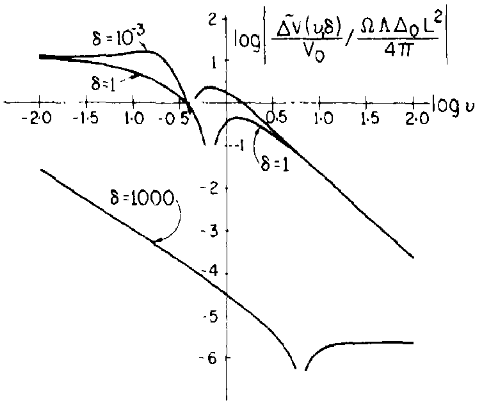

Fig. 2. Normalized velocity change as a function of frequency for different amounts of viscous damping. The breaks in the curves indicate logarithmic singularities where the velocity change changes sign

radiation limited. It still occurs at a frequency somewhat less than $\nu = 1$ as a consequence of the segment length distribution; the longer lengths are more effective.

It is difficult to make accurate measurements of the decrement and velocity as a function of frequency. However, the normalized frequency ν is proportional to ωL so that varying L (for example, by irradiation of the specimen) is equivalent to varying ω. Changes with L can be measured very accurately. The corresponding equations for fixed ω and varying L are given by

$$\tilde{\Delta}(\nu,\delta') = \left(\frac{\pi^2 C\Omega\Lambda\Delta_0}{2A\omega^2}\right)\frac{(\delta'+\frac{1}{8})}{\nu^2} \times \int_0^\infty \frac{x^5 \mathrm{d}x}{\sinh(x/\nu)[(1-x^2)^2+(\delta'+\frac{1}{8})^2x^4]} \tag{17}$$

and

$$\frac{\Delta\tilde{V}'(\nu,\delta')}{V_0} = \left(\frac{\pi C\Omega\Lambda\Delta_0}{4A\omega^2}\right)\frac{1}{\nu^2} \times \int_0^\infty \frac{(1-x^2)x^3 \mathrm{d}x}{\sinh(x/\nu)[(1-x^2)^2+(\delta'+\frac{1}{8})^2x^4]}, \tag{18}$$

where ν is now a dimensionless segment length given by $\nu = [\omega/\pi(A/C)^{1/2}]L$ and δ' is a dimensionless viscous damping factor given by $\delta' = \delta/\nu = B/A\omega$. Numerical evaluations of equations (17) and (18) are shown in Figs. 3 and 4. The curves are equivalent to Figs. 1 and 2 but have a somewhat different form because the normalizing factors of Figs. 1 and 2 also depend on L and because the parameters δ and δ' are different ($\delta' = \delta/\nu$). Figures 3 and 4 may be somewhat more useful for comparisons with experiment than Figs. 1 and 2.

At resonance ($\omega = \omega_0$) in the radiation limited case, the dislocation displacement is relatively large and predominantly out of phase with the applied stress. The largest

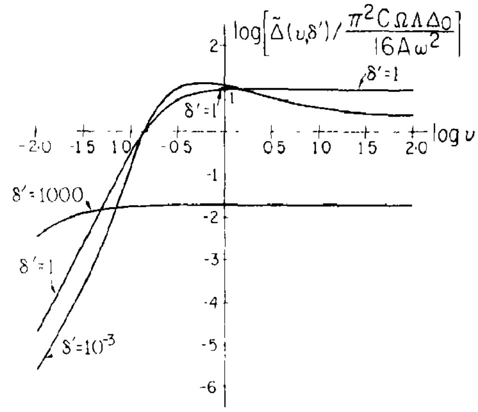

Fig. 3. Normalized decrement as a function of average segment length L for different amounts of viscous damping.

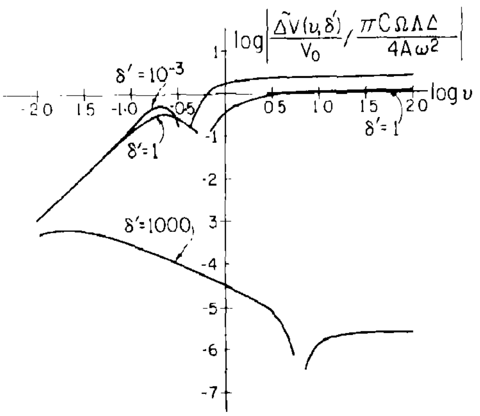

Fig. 4. Normalized velocity change as a function of average segment length L for different amounts of viscous damping.

displacement is, however, only 8·3 times that obtained at low frequencies[4] so that the maximum slope of the dislocation remains small and the dislocations remain nearly straight. Alternatively, the curvature (R) at low frequencies is given by equation (1) as $R \doteq (\xi_{yy})^{-1} = C/b\sigma$. Using the approximate relation $C \doteq Gb^2/2$ and $\sigma = G\epsilon$, one obtains $R \doteq b/2\epsilon$. With $b \doteq 2 \times 10^{-8}$ cm and the typical ultrasonic maximum strain amplitude of 10^{-7}, one obtains $R = 1$ mm. At resonance, the dislocation shape remains approximately sinusoidal with amplitude 8·3 times larger, so that the curvature remains greater than 10^{-2} cm.

The steady-state displacement is most conveniently expressed in terms of a relation given by Weertman[6] in the form

$$\xi = \left(\frac{b\sigma_0}{A\omega^2}\right)\left[F\left(\frac{y}{l}\right)\cos\omega t + G\left(\frac{y}{l}\right)\sin\omega t\right], \tag{19}$$

where y is the distance from the center of a segment of length $2l$. The in-phase component F and out-of-phase component G are shown in Fig. 5 for resonance ($\omega = \omega_0$). Again, $\delta = B/A\omega_0$. The F curves for $\delta = 0{\cdot}3$ and $\delta = 1$ are almost the same as the one for $\delta = 0$ on this scale.

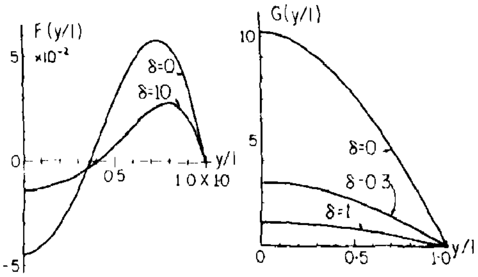

Fig 5 Dislocation displacement along a segment at resonance ($\omega = \omega_0$) for different amounts of viscous damping. F is proportional to the component of displacement in phase with the applied stress, while G is the out-of-phase component.

For $\delta = 0$ and $\nu = 0{\cdot}94$, F and G are both similar to the G curve with $\delta = 0$ of Fig. 5, but with half the maximum amplitude. For $\nu = 3$ and $\delta = 0$, G is nearly sinusoidal with two nodes and amplitude 3·5, while F has amplitude $-1{\cdot}33$.

REFERENCES

1. KOEHLER J S., *Imperfections in Nearly Perfect Crystals* (Edited by W. Shockley, J H Holloman, R. Maurer and F. Seitz) p. 197. Wiley, New York (1952).
2. GRANATO A. V. and LÜCKE K., *J. appl. Phys* **27**, 583 (1956).
3. GRANATO A V. and LÜCKE K., *Physical Acoustics* (Edited by W P. Mason), Vol. 4A. Academic Press, New York (1966).
4. GARBER J. A. and GRANATO A. V., *Bureau of Stand. Conf. Dislocation Theory*. April (1969) To be published.
5. ESHELBY J. D., *Proc. R Soc Lond.* **A266**, 222 (1962)
6. WEERTMAN J., *J. appl Phys.* **26**, 202 (1955)

J. Phys. Chem Solids Pergamon Press 1970. Vol. 31, pp. 1869–1875. Printed in Great Britain.

THE FREQUENCY DEPENDENCE OF SOUND RADIATION FROM MOBILE DISLOCATION WALLS[*]

R. O. SCHWENKER[†] and A. V. GRANATO
Department of Physics, University of Illinois, Urbana, Ill 61801, U S A.

(*Received* 5 *September* 1969, *in revised form* 7 *October* 1969)

Abstract – Macroscopic re-radiated plane waves from microscopic dislocation sources oscillating in a narrow slip band have been produced and detected in LiF and NaCl crystals in the 5–110 MHz frequency range The observed waves were shown to depend upon the dislocation motion through their dependence on the orientation of the exciting waves and their dependence on the number of pinning points on the dislocation lines during γ-irradiation of LiF and NaCl

The quantitative values of the re-radiated wave amplitudes were shown to be in good agreement with the values given by the model of the vibrating string for the dislocation displacements, both in the low frequency or frequency independent region and in the high frequency or ω^{-1} frequency region of the displacement. Since the measured re-radiated amplitudes were as large as is permitted by the vibrating string model, dislocation–dislocation interactions could not play an important role in limiting the dislocation motion for this configuration of dislocations

1. INTRODUCTION

THERE are two mechanisms by which a dislocation scatters elastic waves, strain-field scattering and re-radiation scattering. The interaction of an elastic wave with the dislocation elastic strain field produces a scattering of the elastic wave as a consequence of the non-linearity of the force-displacement law. The second scattering mechanism results from the emission of elastic waves from the dislocations which are driven into forced oscillations by the incident wave. This radiation of elastic waves is analogous to the radiation of electromagnetic waves by accelerated electric charges. The experiments reported here are a study of the re-radiation scattering mechanism for a simple system of dislocations in the megahertz frequency range of incident sound waves with relation to the available theory.

It must be noted that, while phonons interact with dislocations in essentially two different ways, by strain-field scattering and radiation scattering, there are also two different types of scattering according to the frequency of the waves which interact with the dislocations. The 'indirect' scattering is similar to the case of Browian motion of a particle in an external field, a dislocation moving through a phonon gas under the action of an externally applied stress is subject to a viscous drag and to fluctuations in displacement[1]. This is the strain-field scattering and radiation scattering of phonons or high frequency thermal waves These scattering mechanisms provide a damping force on the motion of the dislocations. Calculations[2–4] have been made of this viscous damping and a number of ultrasonic measurements of the damping constant at megahertz frequencies have been made for LiF[5–7] and NaCl[8]. The 'direct' scattering results from the interaction of megahertz frequency elastic waves with the dislocations, which can cause the dislocations to move in the crystal. This motion results in radiation of megahertz elastic waves as well as the scattering of phonons producing the viscous damping force.

---

[*] This work was supported by the National Science Foundation. It is based on a thesis by R O S., submitted to the University of Illinois in partial fulfillment of the requirements for the degree of Doctor of Philosophy in Physics.

[†] *Present address*: International Business Machines Corp. East Fishkill Laboratory, Hopewell Junction, N.Y. 12533, U.S.A

The 'direct' scattering losses can be studied by producing a thin slip band of dislocations in a single crystal[9]. The dislocations can be excited by a plane ultrasonic wave with its displacement in the slip direction of the dislocations. The dislocations then oscillate on their slip planes and each dislocation radiates a cylindrical wave with its displacement along the slip direction. Because all of the dislocations on one slip plane oscillate in phase with each other, this coherent motion produces a macroscopic plane wave from the microscopic dislocation sources.

Evidence that radiated signals come from moving dislocations and that these signals qualitatively fit orientation and pinning point predictions of the vibrating string model has been presented earlier[9–10]. In this study, the string model is developed for the dislocation wall geometry and a detailed quantitative study of measurements of attenuation, velocity and re-radiated amplitude as a function of pinning point density and frequency is given.

2. EXPERIMENTAL PROCEDURE

Harshaw lithium fluoride and sodium chloride single crystals having two sets of {110} faces and one set of {001} faces were used for this study. By using techniques which we have described elsewhere[10], thin, sharply defined bands of dislocations were formed in the crystals by applying a shear stress on a (110) slip plane and along the $[1\bar{1}0]$ slip direction. Etch pit studies of the LiF crystals showed that edge type dislocations were formed with densities up to $2 \times 10^7/\text{cm}^2$, while less than $10^6/\text{cm}^2$ screw type were observed.

The pulse-echo technique was used in making the ultrasonic measurements. AC-cut quartz transducers with resonant frequencies of either 5–10-MHz were bonded to the (110) faces. Matec ultrasonic comparators were used for most of the measurements. In addition to the usual pattern of large echoes from the opposite crystal face, the dislocation wall produces smaller echoes which are positioned between the main echoes. The wall echo amplitudes were measured relative to the main echo amplitudes by use of the comparator, which also was used to measure the main wave attenuation.

In order to determine the dependence of the wall echo amplitudes on the dislocation motion, the amplitudes were measured while the crystals were being γ-irradiated. Since γ-irradiation produces additional point defects which pin the dislocations, the dislocation wall echoes should decrease as a function of the irradiation dosage if the wall echoes are due to re-radiation. As shown in Fig. 1, this dependence was observed for incident shear waves with their polarization displacement in the $[1\bar{1}0]$ slip direction for the dislocations on the (110) slip planes. Shear waves polarized

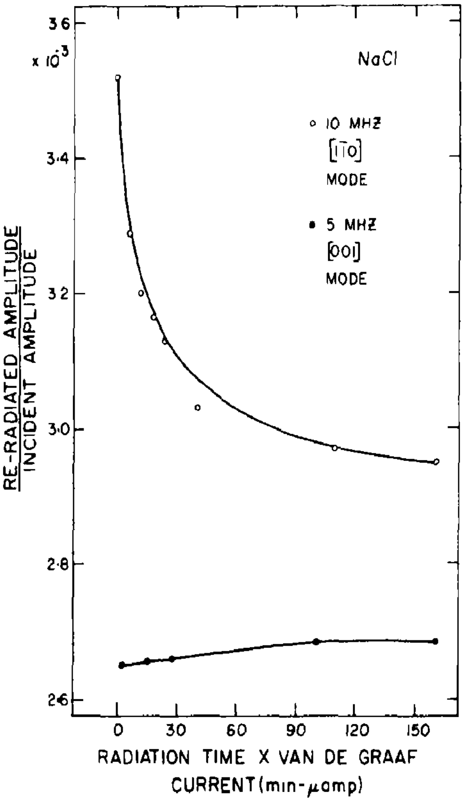

Fig. 1. Ratios of re-radiated wave amplitudes to their incident wave amplitudes for both dislocation sensitive and dislocation insensitive shear wave modes in a deformed NaCl crystal vs. the total γ-irradiation dosage.

in the [001] direction should not cause dislocation motion and the wall would not be expected to radiate. This is also seen in Fig. 1 where simultaneous measurements made of echoes of the two orientations are presented. While $\epsilon rr/\epsilon in$ ratios of only about 10^{-3} were observed with NaCl crystals, ratios for LiF crystals as large as four percent were observed.

For a thin slip band of dislocations, the radiated strain wave amplitude, ϵrr, has been shown[9] to be given by the equation

$$\left|\frac{\epsilon rr}{\epsilon in}\right| = \frac{W\omega}{v}\left[\left(\frac{\Delta G}{G}\right)^2 + \left(\frac{\Delta}{\pi}\right)^2\right]^{1/2} \qquad (1)$$

where ϵin is the incident wave amplitude, W is the width of the slip band, ω is the frequency of the incident wave, v is the velocity of the wave and $\Delta G/G$ and Δ are the relative modulus change and decrement respectively in the slip band.

From equation (1), it is seen that the relative modulus change should be measured in addition to the amplitudes of the wall echoes and the decrement, which is obtained from the attenuation of the main echoes. The modulus change, which results from that part of the dislocation displacement which is in phase with the incident wave while the decrement results from that part which is out of phase, is obtained from the change in velocity of the incident wave as it passes through the dislocation wall. A system for measuring the velocity change to one part in 10^6, developed by Jon Holder[11] of this laboratory was used for this. While operated at the same ten megahertz frequency as the comparator, the systems were completely separate except for the use of the same transducer which was mounted on the crystal.

Since our preliminary results[10] were consistent at low frequencies with the vibrating string model of Granato and Lücke[12], in which interactions between dislocations are neglected, this model was taken as the working model for the dislocation displacement. The experiments were then done in order to measure the frequency dependence of the re-radiated wave amplitude and to compare the results with the predictions from the string model of dislocations oscillating in phase but independently of each other. Although it was not possible to vary the exciting frequency while measuring the wall amplitudes, instead the average loop length of the dislocations was continuously decreased by γ-irradiation. As can be seen in Fig. 2, the average displacement of the dislocations, $[(\Delta G/G)^2 + (\Delta/\pi)^2]^{1/2}$, is given for the vibrating string model in terms of a normalized frequency, $\omega/(\pi^2 C/BL^2)$, where C is the effective dislocation tension, B is the viscous damping constant and L is the average loop length between pinning points. Thus the model can be checked by decreasing the loop length with γ-irradiation.

With a 10-MHz exciting wave, the normalized frequency was never large enough to check the expected ω^{-1} dependence of the dislocation displacement at high frequency when viscous damping should control the motion. In order to study this frequency range, measurements made on LiF crystals during their γ-irradiation were the attenuation of the main echoes at both 10 and 110 MHz, the velocity change of the 10 MHz wave, and wall echo amplitudes at both 10 and 110 MHz. Only one velocity measurement system was available so the higher frequency modulus change was calculated from the other variables by the use of Fig. 2. The ratio of $\Delta/(\Delta G/G)$ for 10 MHz could be used to determine $\Delta/(\Delta G/G)$ for 110 MHz from the r curve. Since Δ(110 MHz) was experimentally determined. $\Delta G/G$(110 MHz) could then be calculated. One transducer was used for all the measurements with separate Matec comparators used for each frequency.

Since narrow, high dislocation density walls were difficult to introduce into the crystals, a crystal with a good wall was often re-stressed at the original slip band in order to break the dislocations from the γ-irradiation pinning points.

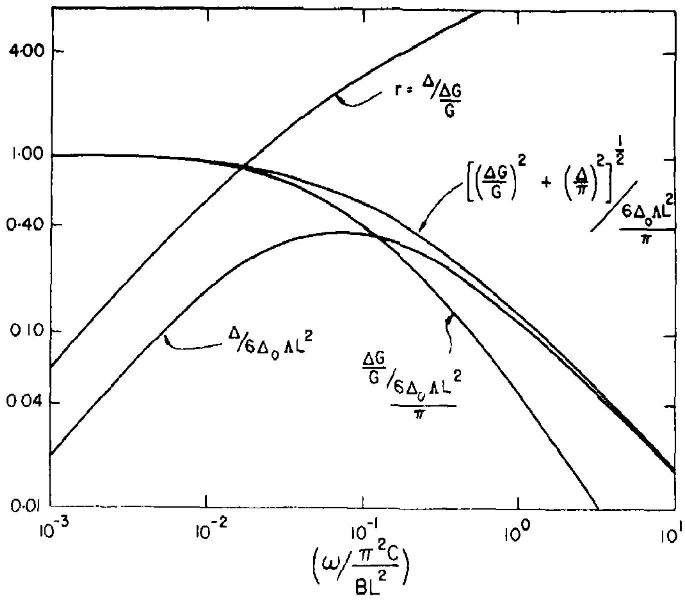

Fig. 2. The values predicted by the vibrating string model for the decrement, the modulus change, the ratio of the decrement to the modulus change, and the dislocation displacement for an exponential distribution of loop lengths vs the frequency of the exciting elastic wave.

3. RESULTS AND DISCUSSION

In order to compare the experimental results with the predictions of the vibrating string model for the dislocation motion, it is necessary to consider the effects of all of the frequency dependent factors which should be present in the re-radiated wave amplitude. We know from Fig. 2 that the average displacement of the dislocations in the wall should depend on the frequency of the exciting wave as shown schematically in the top part of Fig. 3 if the string model is used. At low frequencies, the displacement is nearly independent of frequency while at higher frequencies it goes according to ω^{-1}. According to Eshelby [3], the radiated strain wave amplitude, as is given in equation (1), is linearly dependent upon the exciting frequency times the average dislocation displacement in a single slip plane. The middle curve in Fig. 3 then gives the re-radiated wave amplitude from a very thin dislocation wall as a function of frequency. A third frequency dependent factor is present for walls with widths which are not small compared to a wavelength. Walls of these widths were produced experimentally and it was not possible to obtain very thin walls [10]. This third factor, $I(\omega)$, which is obtained by an integration of equation (1) over the width of the wall, is itself made up of two factors. One of these gives a ω^{-1} dependence which just cancels the linear frequency factor of equation (1), while the other gives a sinusoidal dependence on the frequency times the wall width. The lower curve in Fig. 3 gives a schematic representation of the product of all the frequency factors for the re-radiated wave amplitude from oscillating dislocations in a finite width slip band. For this finite width wall, equation (1) becomes

$$\left|\frac{\epsilon rr}{\epsilon in}\right| = \tfrac{1}{2}\left|1 - e^{i2\omega W/v} e^{-2\alpha W}\right| \left[\left(\frac{\Delta G}{G}\right)^2 + \left(\frac{\Delta}{\pi}\right)^2\right]^{1/2} \quad (2)$$

where α is the attenuation of the wave in the wall.

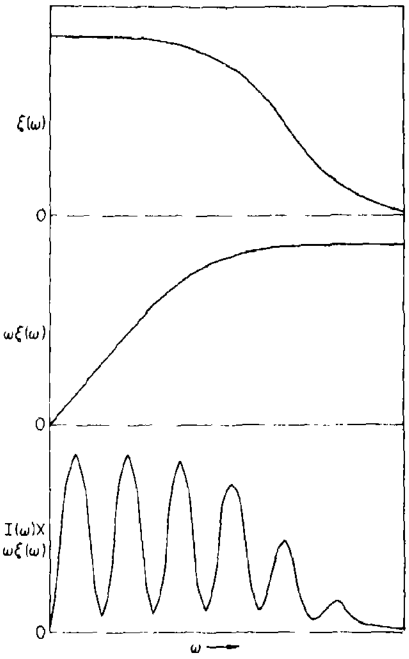

Fig. 3 A schematic representation of the average dislocation displacement, the radiated wave amplitude from a very thin wall, and the radiated wave amplitude from a finite width wall vs the frequency of the exciting wave.

Another interference effect also had to be considered since there were always echoes from other sources present in an echo pattern. These other echoes, which could have originated from strain-field scattering as well as several other possible sources[10], varied from specimen to specimen over a range of 10 per cent to nearly 100 per cent of the measured echo amplitude. The measured wall echo amplitude during a γ-irradiation must be the vector sum of the decreasing re-radiated wave and the constant wave.

$$\frac{\epsilon m}{\epsilon in} = \left|\frac{\epsilon c}{\epsilon in}\right| e^{i\varphi} + \left|\frac{\epsilon rr}{\epsilon in}\right| e^{i\theta} \qquad (3)$$

where ϵm is the measured amplitude, $|\epsilon c/\epsilon in|$ and φ are the magnitude ratio and phase of the constant echo, and $\theta = \tan^{-1}[(-\Delta/\pi)/(\Delta G/G)]$ is the phase of the re-radiated wave relative to the incident wave.

The L^4 and L^2 loop length dependence predicted by the string model for the decrement and re-radiated amplitude respectively at low frequencies has been reported previously[10]. The model also predicts that the relative modulus change and the ratio, $\Delta/(\Delta G/G)$, should go as L^2 and the ratio should have a magnitude of less than one in that low frequency range. This result is seen in Fig. 4 for 10 MHz. The model also predicts, as can be seen in Fig. 2, that the decrement at the higher frequency of a two frequency run should depend upon L less strongly than L^4 for long enough loop lengths, i.e. large enough r. This was observed as shown in the top of Fig. 5. As is shown in the figure, although initially having a larger value, the 10 MHz decrement decreased at a faster rate than the 110 MHz decrement. In the bottom part of Fig. 5, a function of the decrement which should be proportional to the number of pin-

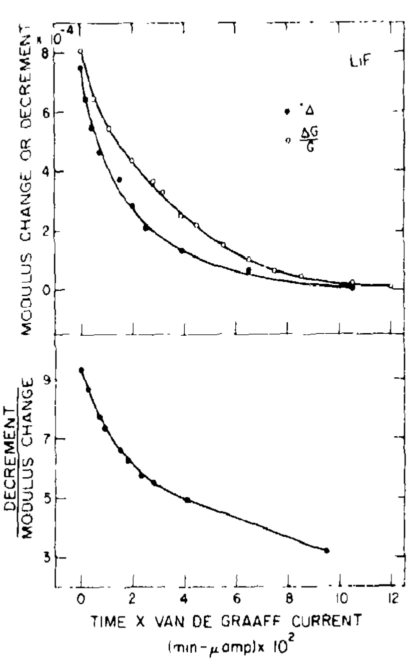

Fig. 4 The decrement, the modulus change, and their ratio for a 10 MHz incident wave in a LiF crystal vs the total γ-irradiation dosage

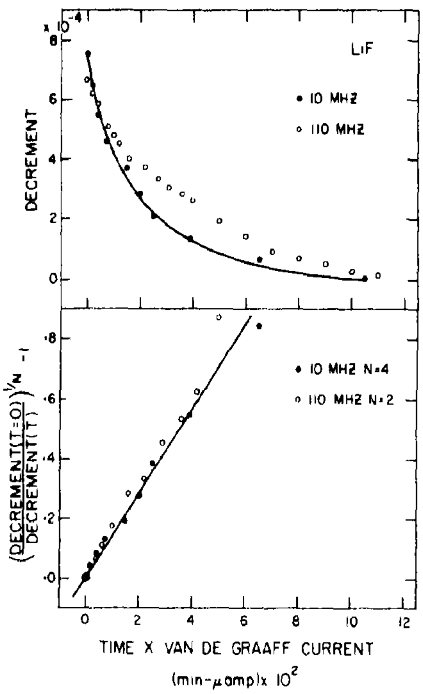

Fig. 5. The decrements for 10 and 110 MHz incident waves and functions of these decrements which should be proportional to the number of pinning points on the dislocation lines in a LiF crystal vs the total γ-irradiation dosage

ning points is plotted for both frequencies. For 10 MHz, $N = 4$ or $\Delta \propto L^4$ gives a linear relationship with the total γ-ray dosage while $\Delta \propto L^2$ gives the same relationship for 110 MHz. This is consistent with the string model since, for this case, the 110 MHz decrement should be near the top of the decrement curve as given in Fig. 2 and should depend approximately quadratically on the loop length in this range.

The measured wall echo amplitudes as a function of the irradiation dosage were used with the decrement and modulus change values given in Figs. 4 and 5 to obtain experimental values for the ratios $|\epsilon r r/\epsilon i n|$. A form of equation (3),

$$\left|\frac{\epsilon m}{\epsilon i n}\right|^2=\left|\frac{\epsilon c}{\epsilon i n}\right|+C^2\left[\left(\frac{\Delta G}{G}\right)^2+\left(\frac{\Delta}{\pi}\right)^2\right]$$

$$+2\left|\frac{\epsilon c}{\epsilon i n}\right| C\left[\cos\varphi\left(\frac{\Delta G}{G}\right)-\sin\varphi\left(\frac{\Delta}{\pi}\right)\right] \quad (4)$$

was used to fit the $|\epsilon m/\epsilon i n|$, $\Delta G/G$ and Δ data in order to determine C, $|\epsilon c/\epsilon i n|$ and φ. The experimental $|\epsilon r r/\epsilon i n|$ values, from equation (3) or equivalently from $C[(\Delta G/G)+(\Delta/\pi)^2]^{1/2}$, before the γ-irradiation, are then compared with the predicted range of values calculated by the use of equation (2)

$$\left|\frac{\epsilon r r}{\epsilon i n}\right|^{10\,\mathrm{MHz}}_{\mathrm{exp.}}=3{\cdot}8\times 10^{-2},$$

$$0{\cdot}5\times 10^{-2}\leqslant\left|\frac{\epsilon r r}{\epsilon i n}\right|^{10\,\mathrm{MHz}}_{\mathrm{model}}\leqslant 4{\cdot}4\times 10^{-2}$$

$$\left|\frac{\epsilon r r}{\epsilon i n}\right|^{110\,\mathrm{MHz}}_{\mathrm{exp.}}=5{\cdot}2\times 10^{-3},$$

$$3{\cdot}4\times 10^{-3}\leqslant\left|\frac{\epsilon r r}{\epsilon i n}\right|^{110\,\mathrm{MHz}}_{\mathrm{model}}\leqslant 10{\cdot}2\times 10^{-3}.$$

The agreement between these values is very good. Since the measurement systems were frequency tuned to give maximum amplitudes, comparison should be with the maximum values of the model. The numbers agree very well for 10 MHz and differ by only a factor of two for 110 MHz. If one of the frequency factors discussed earlier had been incorrect, completely different measured values would have resulted since the two frequencies are a factor of 11 different from each other.

4. CONCLUSION

It is concluded that the string model fits the data well in both the low frequency range where the dislocation displacement is nearly frequency independent and the higher frequency range where the displacement goes as ω^{-1}. If dislocation–dislocation interactions were important for these dislocation configurations, less dislocation displacement or smaller radiated amplitudes than the values calculated by the vibrating string model should have been measured. In addition, the measurements show that the direct scattered energy loss is not negligible, as is usually assumed, but, in the present case, the direct scattered amplitude is of the order of 4 per cent of the incident amplitude in LiF even at megahertz frequencies. This ratio could be even larger for thinner dislocation walls or lower temperatures where viscous damping is smaller.

Acknowledgements – We wish to thank Dr J. Holder, G. Wire, W. E. DeRossett, and E. R. Fuller for their assistance in making some of the measurements and J. Blanco for his assistance in specimen preparation

REFERENCES

1. GRANATO A. V., *Dislocation Dynamics* (Edited by A. R. Rosenfeld, G. T. Hahn, A. L. Bement, Jr and R. I. Jaffee), p. 138. McGraw-Hill, New York (1968)
2. LIEBFRIED G., *Z. Phys.* **127**, 344 (1950)
3. ESHELBY J. D., *Proc. R. Soc. Lond.* **A197**, 396 (1949).
4. MASON W. P., *J. acoust. Soc. Am.* **32**, 458 (1960).
5. FANTI F., HOLDER J. and GRANATO A. V., *J. acoust. Soc. Am.* **45**, 1356 (1969).
6. SUZUKI T., IKUSHIMA A. and AOKI M., *Acta. metall.* **12**, 1231 (1964).
7. MITCHELL O. M. M., *J. appl. Phys.* **36**, 2083 (1965)
8. MOOG R. A., Ph.D. Thesis, Cornell University (1965).
9. SCHWENKER R. O. and GRANATO A. V., *Bureau of Standards Int. Conf. on Dislocation Theory* (1969)
10. SCHWENKER R. O. and GRANATO A. V., *Phys. Rev. Lett.* **23**, 918 (1969).
11. HOLDER J., to be published.
12. GRANATO A. V. and LÜCKE K., *J. appl. Phys.* **27**, 583 (1956).

J Phys. Chem. Solids Pergamon Press 1970. Vol 31, pp. 1877–1881. Printed in Great Britain.

THE FREQUENCY DEPENDENCE OF DISLOCATION DAMPING IN NIOBIUM*

B. K. GANGULY, C. BAKER and H. K. BIRNBAUM
Department of Mining, Metallurgy and Petroleum Engineering and Materials Research Laboratory, University of Illinois at Urbana-Champaign, Urbana, Ill 61801, U S.A

(*Received 5 September* 1969)

Abstract – The frequency dependence of dislocation damping in niobium was measured in the megahertz frequency range at 293 and at 80°K. The results are interpreted in terms of an 'elastic string' dislocation mechanism and in terms of a dislocation motion mechanism based on the movement of kinks. Both models appear to be consistent with the experimental results. The 'elastic string' mechanism leads to a viscous damping constant of $1 \cdot 1 \times 10^{-4}$ dyn sec cm^{-2} at 293°K. The kink motion mechanism leads to a ratio of the kink density/kink damping constant of $0 \cdot 3 \times 10^{10}$ cm dyn^{-1} sec.$^{-1}$

1. INTRODUCTION

THE ANALOGY between dislocation motion under an oscillatory stress and the forced vibration of an elastic string in a viscous medium was originally proposed by Koehler[1] and extended by Granato and Lücke[2]. This model, in which the flexible dislocation line is characterized by a line tension, an effective mass, and a viscous drag coefficient, leads to a frequency dependent and stress amplitude independent damping at low stress amplitude. It has been shown to be in good agreement with measurements of the frequency dependence of the damping in the megahertz[3–5] and kilohertz[5] frequency range for f.c.c. crystals where the line tension approximation appears to be valid.

An alternative approach to the motion of dislocations is based on the formation and motion of kinks in a dislocation line which interacts strongly with a periodic potential field provided by the lattice. In this model the dislocations lie parallel to close packed crystallographic directions except at discrete points where a kink crosses from one energy minimum to the next. The motion of the dislocation line under a small oscillatory stress is then due to the motion of these kinks along the dislocation line. The kinks can be characterized by an effective mass and a viscous drag coefficient and their motion gives rise to an amplitude independent, frequency dependent damping at low stress amplitudes[6].

The behavior of dislocations in b.c.c. metals remains a matter of some controversy. The magnitude of the Peierls–Nabarro stress in these materials does not appear to be well established, and it is not clear whether the response of dislocations to low amplitude stresses can be described by a vibrating string approximation or by a kink motion model. It has been shown that dislocations contribute to the damping of b.c.c. metals and that they cause amplitude dependent damping[7]. The present work is part of a program in which damping measurements are being used to study dislocation behavior in a typical b.c.c. metal, niobium. In the present paper the results of a study of the frequency dependence of dislocation damping in the megahertz range are presented.

2. EXPERIMENTAL PROCEDURE

Crystals were grown from Wah Chang niobium containing several hundred ppm substitutional impurities (principally W, Mo and Ta) in a vacuum of 10^{-8} torr using electron beam heating. Specimens cut from these crystals had the ⟨110⟩ direction along their axis (to within 2°). The ends of the specimen were made flat and parallel to within 5×10^{-5} in. using a spark planing technique which minimized damage to the specimens.

---

*This research was supported in part by the United States Atomic Energy Commission, Contract AT(11-1)-1198.

The attenuation measurements were carried out using a double quartz crystal pulse-echo technique. Nonaq grease was used as a bond, although different bonding materials (Salol and Eastman 910) were used to establish that the bond was not affecting the measurement. Harmonics, of the fundamental frequencies of various X-cut quartz crystals were used in the frequency measurements to again establish the independence of the results from the bonding procedure and transducer crystals. *The damping was shown to be independent* of the driving voltage thus indicating that the measurements were made in the amplitude *independent range*.

Attempts to pin the dislocations by neutron irradiation at 290°K were not successful. Neutron doses of 10^{16} neutrons cm^{-2} (of energy greater than 1·5 MeV) had no effect on the damping in the frequency range 5–100 MHz. This is in contrast to the results for f.c.c. crystals where this dose would completely pin out the dislocation contribution to the damping. The dislocation contribution to the damping could, however, be pinned out using oxygen and nitrogen atoms as pins. The oxygen and nitrogen content of the specimens was controlled by annealing the specimens in controlled atmospheres[8, 9].

The dislocation densities were established by etch pitting[10] the (111) planes. It was established that repeated etching gave identical pit patterns. The dislocation densities were $3\text{-}4 \times 10^4$ cm^{-2}.

3. RESULTS AND DISCUSSION

The expression for the internal friction due to dislocation motion based on a flexible string model can be written:

$$\Delta = \Delta_0 \Omega \Lambda l^2 \omega\tau/(1+\omega^2\tau^2) \qquad (1)$$

where

$$\Delta_0 = 8Gb^2/\pi^3 C$$

$$\tau = Bl^2/\pi^2 C$$

and l is the average loop length, G is the shear modulus, ω is the frequency of the applied stress, Λ is the dislocation density, Ω is the orientation factor which depends on the distribution of the dislocations on the various slip systems, C is the line tension, b is the Burgers vector, and B is the damping force per unit length. In equation (1) it is assumed that $\omega \ll \omega_0$ $(\omega_0 = (\pi/1)\,(C/A)^{1/2}$; A is the effective mass per unit length) and that the loop length distribution is exponential. The maximum decrement is given by:

$$\Delta_m = 17{\cdot}6\,\Omega G b^2 \Lambda l^2/(\pi^3 C) \qquad (2)$$

and occurs at a frequency given by:

$$\omega_m = 0{\cdot}084\,\pi^2 C/(l^2 B). \qquad (3)$$

At frequencies $\omega \gg \omega_m$ the decrement is given by :

$$\Delta_h = 8\Lambda G b^2/(\pi B \omega). \qquad (4)$$

The amplitude independent decrement due to motion of kinks along a dislocation which lies in a Peierls–Nabarro energy minimum can be written in the form:

$$\Delta = \Delta_0 \Lambda n \omega\tau/(1+\omega^2\tau^2) \qquad (5)$$

where

$$\Delta_0 = 8Gb^2a^2/(\pi m \omega_0^2)$$

$$\tau = \pi d_0^3 B'/[Gb^2a^2\beta \sin^2(\pi d_0/2l)]$$

$$\omega_0 = 2[\sin(\pi d_0/2l)]ab[G\beta/(4\pi m d_0^3)]^{1/2}$$

and n is the number of kinks per unit length, a is the spacing of the Peierls–Nabarro minima, m is the effective mass of the kink, d_0 is the average kink spacing, B' is the kink damping coefficient and β is a constant of order one. The decrement has a maximum value of:

$$\Delta_m = 4Ga^2b^2\Lambda n/(\pi m\omega_0^2) \qquad (6)$$
$$= 16\Lambda l^2/(\pi^2\beta)$$

at a frequency:

$$\omega_m = Gb^2a^2\beta \sin^2(\pi d_0/2l)/(\pi d_0^3 B'). \quad (7)$$

At frequencies $\omega \gg \omega_m$ the decrement is given by:

$$\Delta_h = 8Ga^2b^2\Lambda n/(\pi\omega B'). \qquad (8)$$

As may be seen from the foregoing expressions, the dislocation decrement has the same functional forms in both models of dislocation motion. Measurements of the decrement at frequencies near ω_m lead to:

$$B = 14{\cdot}59\Omega Gb^2\Lambda/(\omega_m\Delta_m) \qquad (9)$$

in the elastic string model and to:

$$(B'/n) = 1{\cdot}4Ga^2b^2\Lambda/(\omega_m\Delta_m) \qquad (10)$$

in the kink motion model.

The as-grown crystals exhibited a ω^{-1} dependence for frequencies above 5 MHz as shown in Fig. 1. These results suggest that $\omega_m \ll 5$ MHz and are consistent with equations (4) and (8). As additional pinning points were added by alloying with oxygen and nitrogen, the maximum in the decrement was shifted to higher frequencies. Specimens which contained 1000 ppm (atomic) 0 and 1000 ppm (atomic) N exhibited a maximum decrement of $3{\cdot}7 \times 10^{-3}$ at 7 MHz at 290°K as shown in Fig. 2. The values of Δ_m and ω_m at 290°K for various concentrations of O and N solute atoms are summarized in Table 1 as are the values of B and (B'/n) which were calculated using equations (9) and (10). The experimental values of Δ_m can be used to calculate l using equation (2) or (6) and these values are also given in Table 1.

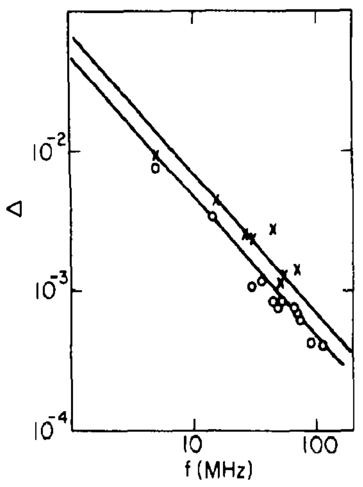

Fig. 1. Dislocation decrement vs. frequency at $\omega \gg \omega_m$ for two typical specimens containing 10 ppm (atomic) N Solid curve is the theoretical curve

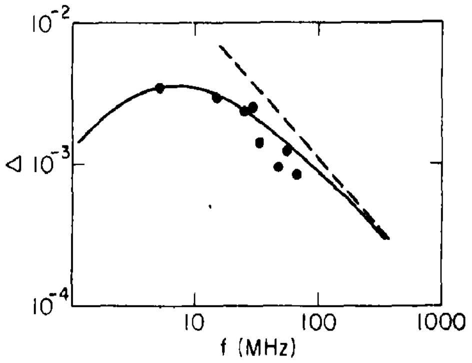

Fig. 2. Dislocation decrement vs. frequency for a specimen containing 1000 ppm (atomic) N and 1000 ppm (atomic) O Solid curve is the theoretical curve Dashed curve is the high frequency asymptote.

As shown by equations (4) and (8) the decrement at $\omega \gg \omega_m$ is independent of l and depends only on Λ/B (string model) or $\Lambda n/B'$ (kink model). Experimentally, the high frequency asymptote of the decrement was not a function of O or N concentration. The high frequency asymptote was also observed to be independent of temperature in the range 80–293°K as shown in Fig. 3. In this temperature range, therefore, B or B' is not a function

Table 1

Conc. O (atomic ppm)	Conc. N (atomic ppm)	Δ_{max}	ω_{max} (MHz)	B (dyn sec cm²)	n/B' (cm dyn sec)	l (cm)
20	400	$1{\cdot}2\times10^{-2}$	1·05	$1{\cdot}73\times10^{-4}$	$1{\cdot}4\times10^{19}$	4×10^{-4}
700	500	7×10^{-3}	3·5	$0{\cdot}89\times10^{-4}$	$2{\cdot}7\times10^{18}$	3×10^{-4}
1000	1000	$3{\cdot}7\times10^{-3}$	7	$0{\cdot}84\times10^{-4}$	$2{\cdot}9\times10^{18}$	2×10^{-4}

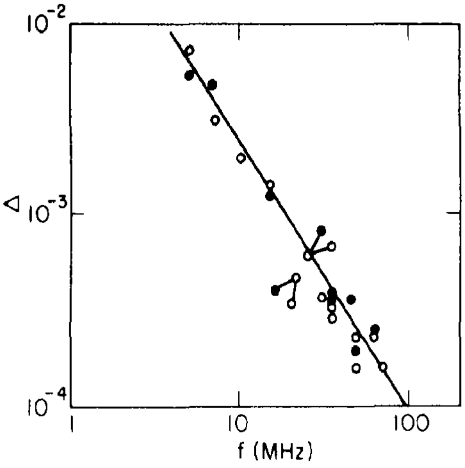

Fig. 3. Temperature dependence of dislocation decrement vs. frequency ● – 293°K ○ – 80°K

of temperature in contrast to the results obtained for f.c.c. crystals where B depends linearly on temperature[3]. The lack of temperature dependence of the damping constant is, however, in agreement with the results obtained on LiF crystals by Mitchell[11].

Various mechanisms have been proposed to account for the damping constants. If the dislocation is treated as an elastic string, it will experience a viscous damping force due to phonon scattering which has been calculated by Leibfried[12] to have the form:

$$B = 3kTz/10C_T a^2 \qquad (11)$$

where T is the temperature, k is Boltzman's constant, z is the number of atoms per unit cell, a is the lattice parameter, and C_T is the shear wave velocity. For niobium the value of B calculated from equation (11) is 10^{-4} dyn sec cm^{-2} at 300°K which is in good agreement with the observed value. The linear temperature dependence of equation (11) is not, however, in accord with the experimental results. A viscous drag mechanism based on the concept of phonon viscosity has been proposed by Mason[13] and leads to:

$$B \approx 0{\cdot}07E_0K/(C_V C_T) \qquad (12)$$

where E_0 is the thermal energy density, K is the lattice thermal conductivity, and C_V is the specific heat. While experimental values of K are not available for Nb, its value can be estimated from:[14]

$$K \approx DC_T^3 a/(\gamma^2 T) \qquad (13)$$

where D is the density and γ is Grüneisen's constant. At 293°K these relations lead to $B = 3{\cdot}9\times10^{-4}$ dyn sec cm^{-2} and at 77°K $B = 1{\cdot}5\times10^{-4}$ dyn sec cm^{-2}. The magnitude of these values is in good agreement with the experimental results, although the temperature dependence is greater than is observed.

Analysis of the data using the expressions for the kink mechanism requires an independent determination of either B' or n, since the damping results give n/B'. Dislocation stress-velocity measurements (using etch pitting techniques) in the high stress range could directly determine B' but have not been carried out for b.c.c. metals. However, B' can be estimated using Mason's phonon viscosity approach ($B' = BL$, where L is the link length) or the relations obtained by Lothe[15] for phonon scattering at kinks. These values and the resulting values of the kink density, n, are

Table 2

Kink length L	B' (viscosity) (dyn sec cm^{-1})	Kink energy W_k	B' (scattering) (dyn sec cm^{-1})	n (cm^{-1})
$2b$	$2\cdot2\times10^{-11}$			$6\cdot8\times10^{7}$
$7b$	$7\cdot7\times10^{11}$			$2\cdot4\times10^{8}$
$2b$		$10^{-2}Gb^{3}$	$3\cdot7\times10^{-12}$	$1\cdot1\times10^{7}$
$7b$		$10^{-2}Gb^{3}$	$1\cdot3\times10^{-11}$	4×10^{7}
$2b$		$10^{-1}Gb^{3}$	$3\cdot7\times10^{-13}$	$1\cdot1\times10^{6}$
$7b$		$10^{-1}Gb^{3}$	$1\cdot3\times10^{-12}$	4×10^{6}

given in Table 2. Use of the phonon viscosity value of B' results in very high kink densities; such that the kink approximation is no longer distinguishable from the elastic string approximation. The phonon scattering value for B' results in values of the kink density which are sufficiently low to allow the use of the kink damping mechanism.

4. CONCLUSIONS

The frequency dependence of the internal friction due to dislocations in niobium is described equally well by calculations based on a vibrating elastic string model or based on the motion of kinks. In the elastic string model the damping constant is $B = 1\cdot2\times10^{-4}$ dyn sec cm^{-2} and is in agreement with theoretical estimates based on phonon scattering or phonon viscosity. Experimentally, however, the temperature dependence of B in the range 80–293°K is observed to be much smaller than predicted by theory. In the kink model the ratio of the kink density to the kink damping constant n/B', is $0\cdot3\times10^{19}$ cm dyn^{-1} sec^{-1}. The theoretical estimates of B' based on phonon scattering lead to values of kink densities in the range of 1×10^{6} to 4×10^{7} cm^{-1}.

REFERENCES

1. KOEHLER J. S., *Imperfections in Nearly Perfect Crystals*, p. 197. Wiley, New York (1953).
2. GRANATO A. and LÜCKE K., *J appl Phys.* **27**, 583 (1956).
3. ALERS G. A and THOMSON D. O., *J. appl. phys.* **32**, 283 (1961).
4. GRANATO A. V. and STERN R M., *Acta metall.* **10**, 358 (1962).
5. HEIPLE C. R. and BIRNBAUM H. K., *J appl. Phys.* **38**, 3294 (1967).
6. SUZUKI T. and ELBAUM C., *J appl. Phys* **35**.
7. CHAMBERS R. H., *Physical Acoustics*, Vol 3A, p. 123. Academic Press, New York (1966).
8. COST J. and WERT C. A., *Acta metall.* **11**, 231 (1963).
9. FROMM E. and JEHN H, *Z. Metallk.* **58**, 61 (1967)
10. GUBERMAN H. D *Acta metall* **16**, 713 (1968).
11. MITCHELL O. M., *J. appl. Phys* **36**, 2083 (1965).
12. LEIBFRIED G., *Z. Phys.* **127**, 344 (1950).
13. MASON W. P., *J acoust. Soc. Am.* **32**, 458 (1960)
14. ZIMAN J M, *Principles of the Theory of Solids*. p 205 Cambridge Press, Cambridge (1965).
15. LOTHE J., *J. appl Phys* **33**, 2116 (1962).

J. Phys. Chem. Solids Pergamon Press 1970. Vol. 31. pp. 1883–1888. Printed in Great Britain.

FRICTIONAL FORCE COEFFICIENT OF A MOVING DISLOCATION IN URANIUM DIOXIDE WITH EXCESS OXYGEN

N. IGATA, K. DOMOTO* and R. R. HASIGUTI
Department of Metallurgy, University of Tokyo, Bunkyo-ku, Tokyo, Japan

(*Received* 5 *September* 1969; *in revised form* 13 *October* 1969)

Abstract—The frictional force coefficient *B* of moving dislocations in uranium dioxide with excess oxygen in the UO_2 to U_4O_9 range was measured at temperatures from −40 to +200°C by means of ultrasonic attenuation. The *B* values increase in the two temperature regions of relaxational internal friction peaks. These increases of *B* values are interpreted in terms of the redistribution of atoms, which brings forth the phase change, and the Snoek ordering of excess interstitial oxygen atoms, respectively, in the stress field of the moving dislocations.

1. INTRODUCTION

Two internal friction peaks are found at about 80°C and at about 105°C when measured at 5 Mc/sec in uranium dioxide with excess oxygen between $UO_{2\cdot 0}$ and $UO_{2\cdot 25}$. It was proposed in our preceding paper[1] that the first peak (80°C peak) is associated with the order-disorder type second order phase transition[2, 3] in U_4O_{9-y} and the second peak (105°C peak) is due to a Snoek type redistribution of interstitial oxygen atoms in UO_{2+x}. The purpose of the research reported here was to study the frictional force coefficient of dislocations in these peak temperature regions, because there relaxation phenomena would be expected to affect the frictional force behaviors of dislocations.

2. EXPERIMENTAL PROCEDURE

(a) *Specimens*

The same lots of sintered pellets of uranium dioxide between $UO_{2\cdot 00}$ and $UO_{2\cdot 25}$ as those used in the preceding research[1] were used. Their O/U ratios, grain sizes, densities and spectrographic analyses are shown in Table 1 of the preceding paper[1]. A fused single crystal of UO_2 with O/U = 2·001 was also used.

The size of specimens used is about 10·3 mm long by 12·50 mm in dia. and its faces are parallel within about 5 μ/cm. The sintered pellets were annealed at 1050°C for 40 hr in vacuum and cooled to room temperature at the rate of 20°C/hr.

(b) *Attenuation measurements*

The pulse echo method was used in the attenuation measurements with an 'Ultrasonic Comparator'. A quartz crystal was attached to the specimen with 'Nonac' silicone grease. The attenuation coefficient α(db/μsec), which was obtained from the exponential decay of the reflected echoes, was converted into the decrement Δ using the following equation:

$$\Delta = \alpha\lambda \frac{1}{8{\cdot}69\, V} \tag{1}$$

where V is the sound velocity, and λ is the wave length. The vibrational frequencies used were from 3 Mc/sec to 45 Mc/sec. The attenuation measurements were performed in a vacuum of about 10^{-4} mmHg.

The compressive stresses were applied to give plastic deformation to the specimen using a 10 ton universal testing machine to the level of 10 ~ 65 kg/mm². The attenuation was

---

*Power Reactor and Nuclear Fuel Development Corporation, Tokai-mura, Ibaraki-ken, Japan

Table 1. *Experimental results of* $UO_2 \sim U_4O_9$ *pellets and a fused* UO_2 *single crystal*

Specimens	O/U	Compression stress (kg/mm²)	Dislocation density (cm⁻²)	Temperature of measurement (°C)	Dislocation loop length (cm)	Frictional force coefficient (dynsec/cm²)
				−20	$0{\cdot}82\times10^{-4}$	$1{\cdot}2\times10^{-2}$
No. 1	2·002	65·0	$5{\cdot}6\times10^{7}$	+22	$0{\cdot}84\times10^{-4}$	$1{\cdot}0\times10^{-2}$
				+200	$0{\cdot}85\times10^{-4}$	$0{\cdot}78\times10^{-2}$
				−20	$0{\cdot}68\times10^{-4}$	$0{\cdot}76\times10^{-2}$
No. 2	2·15	47·4	$1{\cdot}9\times10^{8}$	+22	$0{\cdot}69\times10^{-4}$	$1{\cdot}1\times10^{-2}$
				+200	$0{\cdot}74\times10^{-4}$	$0{\cdot}82\times10^{-2}$
				−20	$0{\cdot}78\times10^{-4}$	$1{\cdot}3\times10^{-2}$
No 3	2·22	32·5	$1{\cdot}4\times10^{7}$	+22	$1{\cdot}7\times10^{-4}$	$0{\cdot}94\times10^{-2}$
				+200	$0{\cdot}79\times10^{-4}$	$1{\cdot}0\times10^{-2}$
No 4	1·18	40·7	$1{\cdot}4\times10^{8}$	−20	$0{\cdot}64\times10^{-4}$	$1{\cdot}5\times10^{-2}$
No 5	2·22	32·5	$8{\cdot}3\times10^{7}$	−20	$0{\cdot}99\times10^{-4}$	$4{\cdot}2\times10^{-2}$
No 6	2·23	30·0	$9{\cdot}0\times10^{7}$	−20	$1{\cdot}2\times10^{-4}$	$1{\cdot}6\times10^{-2}$
No. 7	2·016	40·6	$1{\cdot}5\times10^{7}$	+33	$1{\cdot}3\times10^{-4}$	$1{\cdot}4\times10^{-2}$
No. 8	2·016	28·5	$3{\cdot}9\times10^{7}$	+33	$0{\cdot}70\times10^{-4}$	$3{\cdot}1\times10^{-2}$
No 9	2·016	52·8	$7{\cdot}8\times10^{7}$	+33	$0{\cdot}83\times10^{-4}$	$2{\cdot}2\times10^{-2}$
No. 10	2·016	73·2	$6{\cdot}5\times10^{9}$	+33	$1{\cdot}0\times10^{-4}$	$1{\cdot}5\times10^{-2}$
No. 11*	2·001	10·0	$2{\cdot}2\times10^{6}$	+33	$3{\cdot}8\times10^{-4}$	$0{\cdot}96\times10^{-3}$
				+100	$4{\cdot}0\times10^{-4}$	$1{\cdot}0\times10^{-3}$

*No 11 used single crystal

measured before and after the compression. The internal friction due to dislocations is obtained by subtracting the attenuation value before compression from that after compression, because the attenuation includes many factors which are not concerned with the dislocation damping, and these factors must be eliminated. We shall consider only this differential damping in this paper.

The etch pit method was used to estimate the dislocation density after compression[5].

3. EXPERIMENTAL RESULTS

The differential damping of the specimens was obtained at different vibrational frequencies and at temperatures from −40 to +200°C. The differential damping as a function of vibrational frequencies show a maximum, of which two examples are shown in Figs. 1(a) and 1(b). That the differential decrement shows such a maximum as shown in Fig. 1 is evidence for the resonance damping of dislocations which were introduced by plastic deformation. The following Granato–Lücke relation can be used to describe the resonance damping of dislocations[4, 5]:

$$\Delta_l = \frac{8\Omega G b^2 \Lambda L^2}{\pi^3 C} \cdot \frac{\omega\tau_r}{1+\omega^2\tau_r^2}. \tag{2}$$

Here Ω is the orientation factor, G is the shear modulus, b is the magnitude of the Burgers vector and C is the line tension of the dislocation, Λ is the dislocation density, L is the dislocation loop length, ω is the applied angular frequency, and τ_r is the following quantity:

$$\frac{1}{\tau_r} = \frac{\pi^2 C}{BL^2} \tag{3}$$

where B is the frictional force coefficient of the dislocation. When $\omega\tau_r = 2\pi f \tau_r = 1$, the decrement shows the maximum. If the frequency f is much higher than the frequency f_m at which the decrement becomes maximum, the decrement is expressed by the following equation:

$$\Delta_\infty = \frac{4\Omega G b^2}{\pi^2} \cdot \frac{\Lambda}{B} \cdot \frac{1}{f} \quad \text{for} \quad f \gg f_m. \tag{4}$$

In Figs. 1(a) and 1(b) the solid curve, which

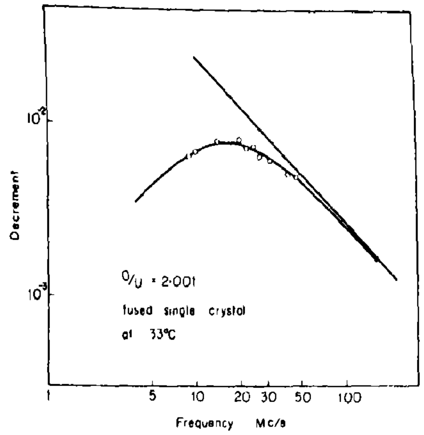

(a) Single crystal with O/U = 2·001.

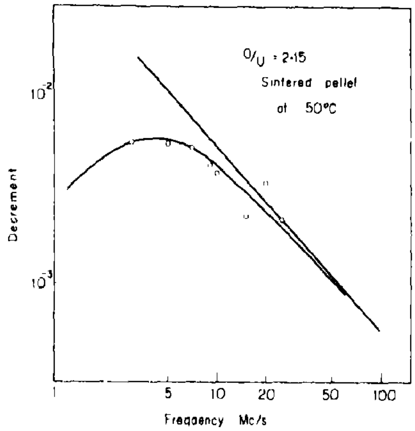

(b) Sintered pellet with O/U = 2·15.

Fig. 1. Differential decrements vs frequencies. The full curve shows the theoretical curve and the straight line shows the asymptote.

is the theoretical curve, is adjusted so as to fit the experimental data. Then the position of the asymptote is automatically determined. Thus from the asymptotic value of equation (4), the frictional force coefficient B is obtained, using the dislocation density Λ obtained by the etch pit method[5] and assuming $\Omega = 0{\cdot}05$[4]. The dislocation loop length is obtained from the decrement maximum value.

In Table 1, typical results of measurements of the dislocation density, the dislocation loop length and the frictional force coefficient are shown. In Fig. 2 the values of the frictional force coefficient B are plotted as a function of the temperature of measurements. The probable error of the B value is about ±10 per cent of the B value. The rises of B values are observed in the temperature regions of two internal friction peaks. The broken line shows the region where the B value cannot be obtained, because the attenuation at higher frequencies in that region is so large that reproducible measurements cannot be made. The B values are very large in our uranium oxides (Table 1 and Fig. 2). They cannot be the intrinsic B values, but they are the effective values for dislocations moving in the crystal with large lattice disturbances. In this paper we are only interested in the relative increase of B values in the internal friction peak regions.

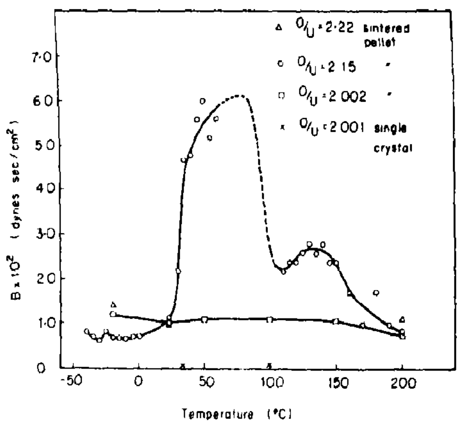

Fig. 2. Temperature dependence of the frictional force coefficients of the sintered pellets with various O/U ratios and a single crystal.

4. DISCUSSIONS

(a) *The first peak region*

The increase of the B values is observed in the first internal friction peak region, i.e. from about 30° to about 90°C.

As was reported in the preceding paper[1], the first internal friction peak is associated with the lambda type second order phase transition in U_4O_{9-y} crystal. Excess oxygen atoms enter into the UO_2 lattice interstitially resulting in $UO_{2+x} + U_4O_{9-y}$ crystals [6].

Above the transition temperature the interstitial oxygen atoms in U_4O_{9-y} are distributed randomly, while below the transition temperature they are redistributed to form an ordered U_4O_{9-y} phase. Thus below the transition temperature the specimen consists of an ordered U_4O_{9-y} phase and a disordered UO_{2+x} phase, the latter phase having no transition point in the temperature range concerned.

The internal friction due to a second order phase transition is expressed by the following equations[2, 3]:

$$Q^{-1} = M\frac{\omega\tau}{1+\omega^2\tau^2}, \tag{5}$$

$$\tau = \frac{A}{T_c - T}, \tag{6}$$

where M is the relaxation strength, τ is the relaxation time, T is the temperature, T_c is the transition temperature, and A is a constant. Equation (6) is often referred to as the Landau-Khalatnikov[2] relation.

Now let us consider the effect of phase transition on the frictional force of moving dislocations which were introduced by the plastic deformation. The stress field of a dislocation is considered to induce the redistribution of atoms, which brings forth the phase transition, in the vicinity of the dislocation core in the bulk matrix which has not yet undergone the phase transition as a whole. In other words a moving dislocation is considered to drag the phase change around the dislocation. This increases the B value below the transition temperature. This interpretation is supported by the fact that there is no increase of the B value in UO_2 without excess oxygen, which material shows no internal friction peak either (Fig. 2 of this paper and Fig. 4 in Ref. [1]).

The magnitude of B is proportional to the viscosity experienced by a moving dislocation. If the viscosity is due to the drag of the phase change, the viscosity or the B value is proportional to the relaxation time of the phase change τ. Equation (3) shows that B is proportional to the mechanical relaxation time of dislocation τ_r. Then we can conclude that τ_r is proportional to τ. If this proportionality relation holds, we obtain the relation

$$\tau_r = \frac{A'}{T_c - T}, \tag{7}$$

where A' is a constant which is different from A by the proportionality constant of τ/τ_r. The transition temperature T_c in equation (7) is the same as that in equation (6).

In Fig. 3 the values of $1/\tau_r$ corresponding to the B values in Fig. 2 are plotted against the temperature in the first peak region. As shown by a broken line in Fig. 3, the relation (7) holds reasonably well except a point at 30°C*, if the scattering of measured points, which is due to the difficulty in obtaining the B values in this temperature region, is considered. The temperature T_c is 84°C, which is the same as that obtained by the internal friction measurement[1].

The above shown Landau-Khalatnikov type relation in Fig. 3 supports the proposed mechanism of the drag of phase change for

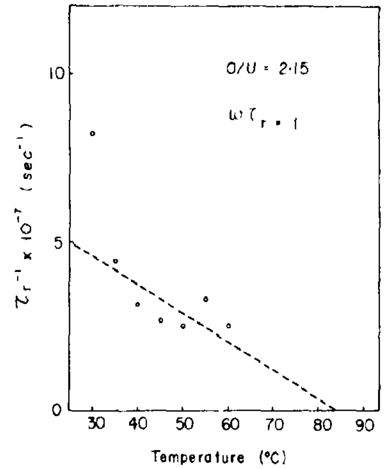

Fig. 3. The reciprocal relaxation time τ_r^{-1} vs. temperature in the first peak temperature region.

---

*The $1/\tau_r$ values deviate from the relation of equation (7) in the lower temperature region which is not shown in Fig. 3. This problem will not be discussed in this paper.

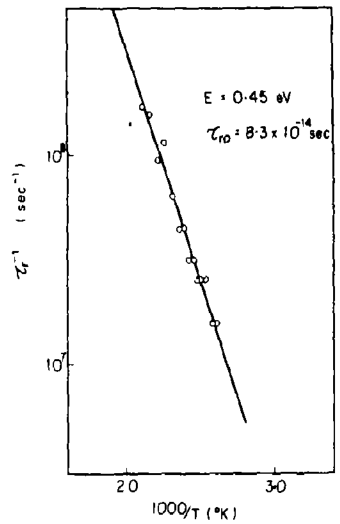

Fig. 4. The semilog plot of reciprocal relaxation time τ_r^{-1} vs. reciprocal temperature in the second peak temperature region.

the increased frictional force coefficient of a moving dislocation, because the Landau–Khalatnikov type relation shows that the second order phase change is involved in the process concerned.

(b) *The second peak region*

The increase of the B values is also observed in the second internal friction peak region, i.e. from about 100 to about 200°C.

The second internal friction peak was interpreted to be due to the Snoek type redistribution of excess interstitial oxygen atoms in the UO_{2+x} lattice[1].

Now it is considered that the increase in the B values is brought forth by the Snoek ordering of excess interstitial oxygen atoms in the stress field of the moving dislocations. The mechanical relaxation time of dislocations τ_r is proportional to the relaxation time of oxygen redistribution τ. This is proved in the same way as discussed in Section 4(a). The logarithm of $1/\tau_r$ is plotted against the reciprocal of temperature of the second peak region in Fig. 4, which gives the relation

$$\tau_r = \tau_{r0}\exp(E/kT) \qquad (8)$$

$$= 8{\cdot}3\times10^{-14}\exp(0{\cdot}45\,\mathrm{eV}/kT)\,\mathrm{sec}. \qquad (9)$$

The oxygen redistribution peak of internal friction[1] is expressed by the relation

$$\tau = \tau_0\exp(E/kT) \qquad (10)$$

$$= 1{\cdot}1\times10^{-14}\exp(0{\cdot}49\,\mathrm{eV}/kT)\,\mathrm{sec}. \qquad (11)$$

The activation energies in equations (9) and (11) are almost the same*. This, together with the fact that there is no increase of the B value in UO_2 without excess oxygen which shows no Snoek type peak either, supports the proposed mechanism of the Snoek ordering of excess interstitial oxygen atoms in the stress field of the moving dislocations which results in the increased frictional force coefficient of dislocations.

5. SUMMARY

(a) In uranium dioxide which consists of two phases, UO_{2+x} and U_4O_{9-y}, two relaxation peaks of internal friction were found. The first peak at about 80°C at 5 Mc/sec is due to an order–disorder transition of U_4O_{9-y} phase with interstitial oxygen atoms, and the second peak at about 105°C at 5 Mc/sec is due to a Snoek type redistribution of excess interstitial oxygen atoms in UO_{2+x}[1].

(b) The frictional force coefficients B of moving dislocations were found to increase from their background values of about 1×10^{-2} dynsec/cm^2 to their increased values of about 6×10^{-2} dynsec/cm^2 at the first peak temperature region and about $2{\cdot}5\times10^{-2}$ dynsec/cm^2 at the second peak temperature region. The increase of B at the first peak region is interpreted to be due to the redistribution of atoms, which brings forth the second order phase change, in the stress field of the moving dislocations in the U_4O_{9-y} phase, and the increase of B at the second peak region is considered to be due to the Snoek ordering of the excess interstitial oxygen atoms in the stress field of the moving dislocations in the UO_{2+x} phase.

---

*The ratio of the two pre-exponential factors in equations (9) and (11) comes from the proportionality constant of τ/τ_r.

Acknowledgement—The authors wish to thank Dr. T. Muto and Mr. J Komatsu of Power Reactor and Nuclear Fuel Development Corporation for their encouragement throughout this work

REFERENCES

1. DOMOTO K., IGATA N. and KOBAYASHI S., *J. nucl Mater.* **33**, 90 (1969).
2. LANDAU L. D. and KHALATNIKOV I. M., *Dokl. Akad. Nauk SSSR*, **96**, 469 (1954).
3. O'BRIEN E. J. and LITOVITZ T. A., *J. appl. Phys.* **35**, 180 (1964).
4. GRANATO A. and LÜCKE K., *J. appl. Phys.* **27**, 583, 789 (1956)
5. IGATA N., HASIGUTI R. R. and DOMOTO K., *The 1st Int. Conf. on Fracture*, Vol 2, p. 883, Sendai, Japan (1965).
6. WILLIS B. T. M., *J. Phys.* **25**, 431 (1964).

J. Phys. Chem. Solids Pergamon Press 1970. Vol. 31, pp. 1889-1899. Printed in Great Britain.

DISLOCATION RELAXATION IN SINGLE CRYSTALS OF bcc METALS

R. GIBALA, M. K. KORENKO*, M. F. AMATEAU† and T. E. MITCHELL
Division of Metallurgy and Materials Science, School of Engineering,
Case Western Reserve University, Cleveland, Ohio 44106, U.S.A

(*Received 5 September 1969, in revised form 8 October 1969*)

Abstract – The behavior of the α dislocation relaxation peak in bcc metals has been investigated for various orientations of high purity single crystals which were deformed in tension at temperatures in the range 77–450°K. The effects of substitutional alloying, interstitial impurities and strain aging were also examined These results coupled with results obtained by other investigators support a dislocation breakaway model as a likely mechanism of the α peak

1. INTRODUCTION

A DISLOCATION in motion in a vibrating crystal dissipates energy in processes which may be displayed as characteristic over-damped resonance or relaxation peaks in the internal friction spectrum of the crystal as a function of temperature or frequency[1]. One of the most familiar of such internal friction peaks is the Bordoni peak[2] in fcc metals which seems to have counterparts in many other crystal structures[3–6]. Although a great deal of experimental and theoretical work has been performed in order to disclose the mechanism of these peaks, considerable uncertainty still exists over their origin. In studies of fcc metals, a majority of investigators have concluded that the Bordoni peak has its origin in an intrinsic mechanism (i.e. a mechanism involving dislocation motion which is unaffected in a direct way by impurities and other defects). The mechanism which has perhaps received the greatest attention is the thermally activated formation of kink pairs in dislocation segments which lie along close-packed directions [7–11]. However, many other intrinsic mechanisms have been proposed and have not altogether been eliminated as possibilities. There is even doubt expressed by some investigators[12] concerning the suitability of intrinsic mechanisms as explanations for the Bordoni phenomenon. Rather, other defects, in particular point defects, in addition to dislocations may be involved in a direct way (i.e. an extrinsic mechanism may be occurring). In crystal structures other than fcc metals, the situation is even more unclear.

Chambers and co-workers[3] have made extensive studies of the dislocation relaxation spectra of deformed bcc metals. However, very little work has been performed on single crystals, and only cursory attempts have been made by other investigators[13–15]. Because of the great interest and controversy concerning the rate controlling deformation mechanism of bcc metals at low temperatures and the probable relationship between the internal friction spectrum and these mechanisms, we have studied dislocation relaxation peaks in single crystals of bcc metals which were deformed in ways for which the dislocation substructure could be well characterized.

Crystals of various crystallographic orientations were deformed in tension at various temperatures to allow easy comparison of the internal friction response with the extensive results obtained on dislocation substructures in bcc metals by transmission electron microscopy. The effects of substitutional alloying, interstitial impurities and strain aging were also examined. The present investigation was concerned primarily with one of the peaks, the α peak[16], observed in the internal friction spectrum of two bcc metals, niobium and molybdenum.

---

*Now at Massachusetts Institute of Technology, Cambridge, Mass. 02139, U.S.A.

†Now at Aerospace Corporation, El Segundo, Calif. 90245, U.S.A.

2. EXPERIMENTAL

All experiments have been performed on oriented single crystals prepared from $\frac{1}{4}$ in. dia. polycrystalline rods of ~99·95 per cent purity and appropriate seed crystals by electron-beam zone-melting under a vacuum $\leq 10^{-6}$ torr. Some crystals of niobium were further purified by solid state outgassing near the melting temperature in a vacuum of $\sim 10^{-8}$ torr. These treatments yielded niobium crystals containing ~20 ppm (outgassed) to ~150 ppm (zone-melted) of residual interstitials and molybdenum crystals containing ~7 ppm of interstitials.

The crystals were deformed in tension on a floor model Instron testing machine at a strain rate of $\sim 10^{-4}$ sec^{-1}, after which internal friction specimens of appropriate length (usually less than one-half the total length of the deformed crystal) were cut out or wafer machined. Various deformation temperatures in the range 77–450°K were obtained by the use of standard liquid baths.

In most experiments the internal friction was measured in the temperature range 4·2–400°K using a two component piezoelectric resonant bar technique for resonant frequencies near 100 kHz at strain amplitudes of $\sim 10^{-7}$. In a few experiments, designed largely to obtain activation energies, the above measurements were complemented by additional measurements at ~2 Hz obtained by use of a low temperature inverted torsion pendulum on wire specimens and at ~20 MHz by the pulse echo technique. The damping in all cases was strain amplitude independent.

More complete descriptions of the experimental procedures are available elsewhere [17, 18].

3. EXPERIMENTAL RESULTS

(a) *Effect of deformation*

In order to investigate the effect of the amount of deformation on the internal friction spectrum, single crystals of niobium were deformed in tension at 300°K for niobium and at 450°K for molybdenum. These temperatures are ideal for obtaining clearly defined three-stage hardening curves for 'easy glide' orientations[18, 19].

Figure 1 shows the internal friction spectrum for molybdenum crystals deformed to various stages of the stress-strain curve. It is seen that the damping is very small in stage 1. Deformation into the early part of stage 2 produces a step-like background with no peak but, as the deformation increases into stage 2 and stage 3, the α peak emerges and increases rapidly in height with increasing strain. Figure 1 also shows that the peak sharpens and moves to lower temperatures at higher deformations while the high temperature background damping decreases. The internal friction spectrum at 28 kHz of a deformed polycrystalline specimen of molybdenum due to Chambers and Schultz[16] is shown for comparison in Fig. 1: the peak height is much smaller and the peak temperature, even when corrected for frequency differences, is much lower than for the single crystals. We ascribe these differences to the higher purity of the crystals (see Section 3(c)).

We have observed somewhat different behavior in niobium crystals[15, 20]. Here a small α peak was evident even in stage 1 of the stress-strain curve and the peak again grew rapidly in stages 2 and 3. Very little high temperature background damping was observed in these zone-melted crystals. However, we have recently tested crystals which had been further purified by ultra-high vacuum outgassing: low deformations produced a step-like background and the α peak

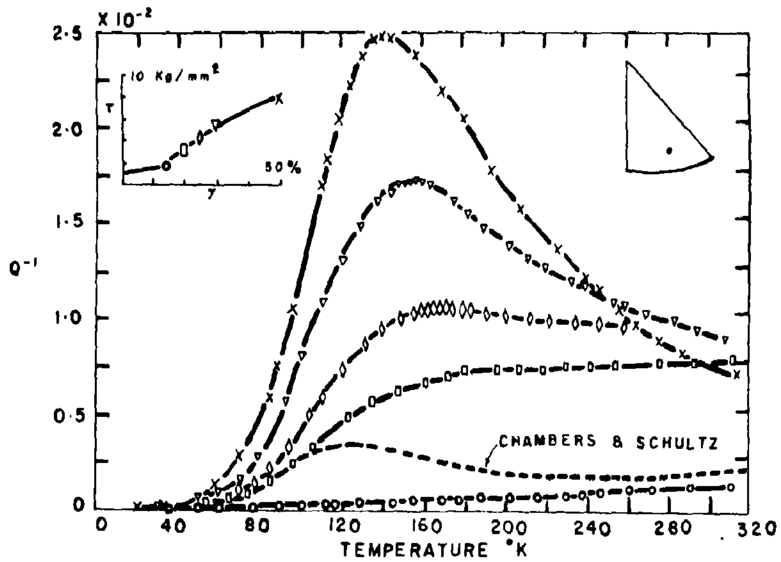

Fig. 1. Internal friction curves for molybdenum single crystals oriented near the center of the stereographic triangle and deformed in tension at 450°K to various points on the shear stress-shear strain $(\tau-\gamma)$ curve. Frequency $f = 100$ kHz. A curve for polycrystalline molybdenum prestrained 11·7 per cent at room temperature and tested at 28 kHz is shown for comparison (Chambers and Schultz[16]). The peak temperature is shifted to 131°K at 100 kHz.

emerged out of the background at higher deformation in a manner very similar to that described above for molybdenum. Apparently the high temperature background is very sensitive to loop-length effects. Thus, increasing the impurity content decreases the loop-length and decreases the background. Similarly at the highest deformations the background decreases (Fig. 1) because the loop-length in the dislocation substructure has decreased.

Orientations other than easy glide orientations have also been investigated[15, 20, 21]. For [101] crystals of molybdenum, parabolic hardening was observed (no stage 1). The step-like background internal friction was observed immediately after small deformations. For example, 2 per cent shear strain of a [101] crystal produced an internal friction spectrum similar to that obtained by 20 per cent shear strain of an easy glide crystal. The behavior with increasing deformation is much the same for the two orientations. A similar comparison of the orientation dependence can be made for niobium and, again, the major differences occur at low deformations according to whether stage I is present or absent[20].

The effects of orientation suggest that the stress level attained during deformation is more important in determining the internal friction spectrum than the strain level. In particular the level of work hardening may be significant; this is measured by the difference between the flow stress and yield stress, $(\tau-\tau_0)$. (In easy glide $(\tau-\tau_0)$ remains small, while in [101] crystals $(\tau-\tau_0)$ increases rapidly). Figure 2 shows a logarithmic plot of the α peak height, $Q^{-1}_{\max}$, against the work hardening stress, $(\tau-\tau_0)$. Results for both niobium and molybdenum are included using a variety of orientations, both easy glide and parabolic hardening types. There is a good deal of scatter in Fig. 2 but, even so, all the data fall around a single straight line of slope 2, indicating that $Q^{-1}_{\max} \propto (\tau-\tau_0)^2$. Since it has

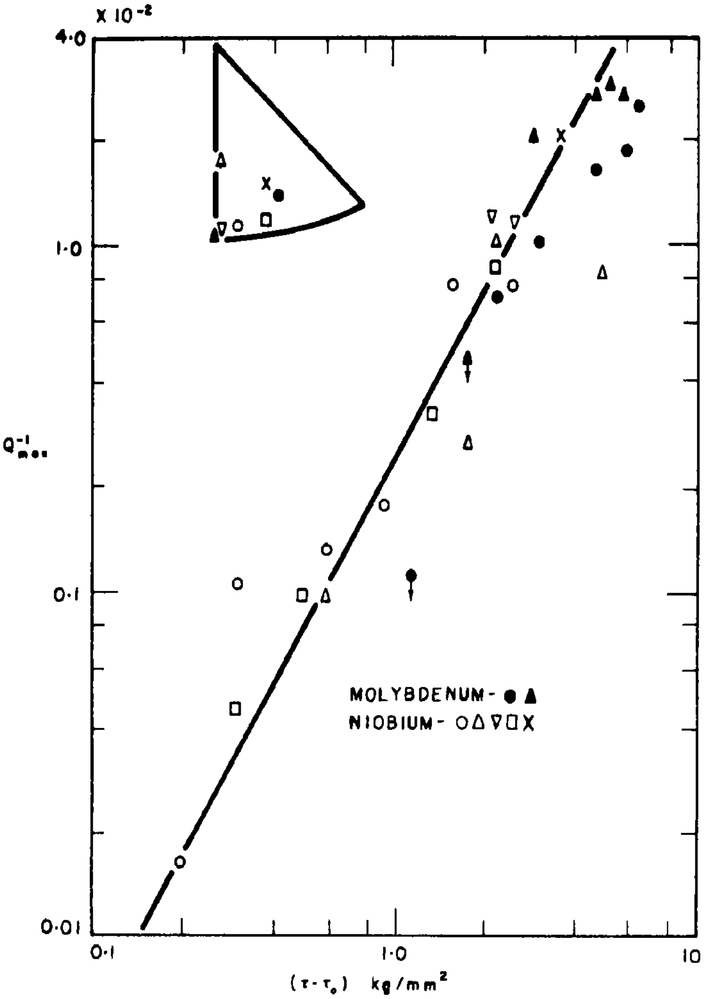

Fig. 2. Logarithmic plot of peak height, Q^{-1}_{max}, against work hardening stress, $\tau-\tau_0$, for niobium crystals deformed at 300°K and molybdenum crystals deformed at 450°K

been found by transmission electron microscopy[33–34] that the dislocation density, ρ, increases as the square of either τ or $(\tau-\tau_0)$, using the latter in the above equation gives that $Q^{-1}_{max} \propto \rho$. In other words, the peak height is directly proportional to the dislocation density. However, it is unlikely that the α peak height is controlled simply by the total dislocation line length for the following reasons. Figure 2 shows that the parabolic hardening crystals of molybdenum tend to have somewhat larger peaks than easy glide crystals. In addition, for molybdenum, Fig. 2 does not include any peak heights at low stresses because the α peak does not emerge from the background until high deformations. Finally, we note that Chambers[3] and Alefeld *et al.*[22] have shown that it is possible to induce the α peak or the Bordoni peak respectively in slightly strained specimens by subjecting them to large strain amplitudes or bias stresses. It is concluded, therefore, that the height of the α peak is controlled not only by the total line length of dislocations but probably by internal stresses as well.

(b) *Effects of deformation temperature*

Niobium and molybdenum crystals were deformed at different temperatures in order to investigate the effect of dislocation type and arrangement on the internal friction spectrum The dislocation arrangement induced by deformation depends strongly on temperature. At higher temperatures (where three-stage hardening is observed, i.e. ~300°K for Nb and ~450°K for Mo), dislocations are mostly near the edge orientation and occur in dipole and multipole patches in stage 1; with increasing stress in stages 2 and 3, the patches link up to form a cell structure with a high density of planar dislocations in the cell walls and a relatively low density inside the cells. After deformation at lower temperatures, the substructure consists predominantly of long, irregular screw dislocations with a high density of jogs; with increasing strain, the screw dislocation density increases but no cell structure develops[23-26].

The effect of deformation temperature on the internal friction spectrum is illustrated in Fig. 3, where selected curves for Nb and Mo crystals are shown[20-21]. The peak height which can be induced by deformation is found to decrease substantially with decreasing temperature; also, the background is lower. The behavior of Nb and Mo with respect to the peak temperature is quite different: for Nb the peak temperature decreases slightly with decreasing deformation temperature (by < 10°), while for Mo the peak temperature increases (by ~30-40°). If we regard the peak temperature as being controlled by a frequency factor which is inversely proportional to some loop length (the activation energy remaining approximately constant, as discussed in the next section), then we might expect the peak temperature to be lower after low temperature deformation because of the high density of jogs acting as pinning points. The observed low background internal friction would also be expected from this cause. However, if jog pinning were important, the same behavior of peak temperature should hold for molybdenum. This does not seem to be the case.

The lower peak heights in Fig. 3 for crystals containing a high density of screws infer that screw dislocations are not involved in the mechanism of the α peak. However, this is not a unique conclusion. Because the dislocation arrangement varies with deformation temperature, the internal stress state of the crystals varies. Thus the screw dislocation structure is rather uniform and consequently dislocations may have a lower internal stress acting on them than in the cell structure where local dislocation densities are very high. A lower internal stress could produce a lower peak height and also a higher peak temperature[9, 12] (agreeing with the behavior of molybdenum in this case).

(c) *Effects of alloying*

The effect of substitutional alloying has been investigated by the addition of Mo, Zr and V to Nb. The effect of interstitials has been studied for both Mo and Nb by comparing crystals of different purities and also by aging experiments.

Figure 4 shows selected internal friction curves for crystals of niobium and various substitutional niobium alloys deformed to shear strains ~40-50 per cent. All three substitutional elements are seen to reduce the peak height considerably: the peak height decreases by an order of magnitude by the addition of about one atomic per cent. Further additions of molybdenum, for example, eliminate the peak almost entirely, leaving a small stepped background with a maximum damping $\sim 3\times 10^{-4}$. In addition, the peak temperature is seen to be reduced by about 20°. Since there is a corresponding reduction in peak temperature at torsion pendulum

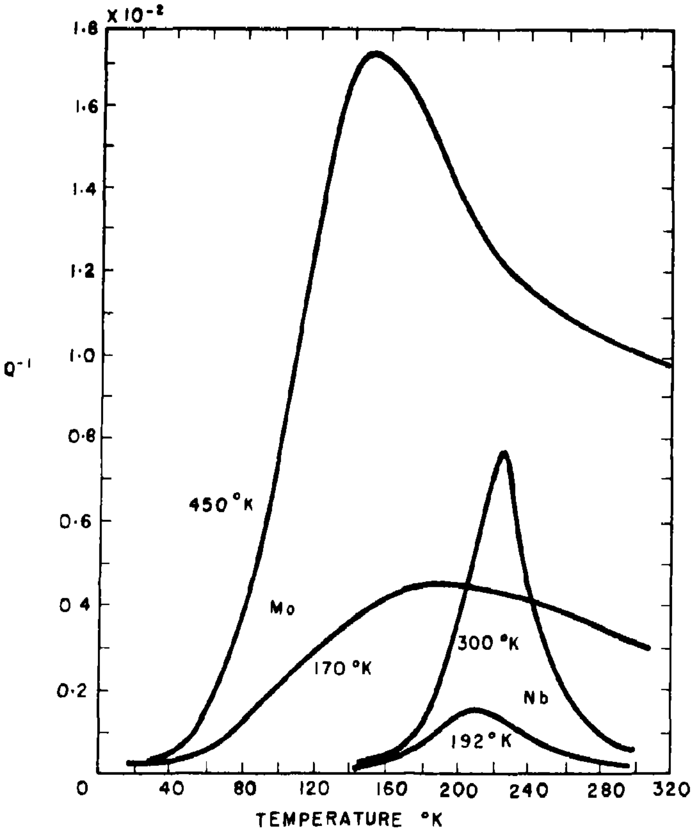

Fig. 3. Internal friction curves illustrating the effect of deformation temperature, T, on crystals pulled in tension as follows. Molybdenum $T = 450°K$, $\tau = 6·0 \text{ kg/mm}^2$, $\gamma = 0·28$; Molybdenum $T = 170°K$, $\tau = 34·0 \text{ kg/mm}^2$, $\gamma = 0·15$; Niobium $T = 300°K$, $\tau = 3·6 \text{ kg/mm}^2$, $\gamma = 0·44$; Niobium $T = 192°K$, $\tau = 8·0 \text{ kg/mm}^2$, $\gamma = 0·36$.

frequencies[20], this effect appears to be due mainly to a change in the frequency factor, f_0.

With regard to the effect of interstitials, for niobium crystals it has been found that reducing the interstitial impurity content from ~150 ppm to ~20 ppm has the effect of (a) increasing the α peak height by a factor of about four, (b) increasing the peak temperature by 20° and (c) increasing the background damping above the α peak. For molybdenum, the effect of interstitials may be discerned in Fig. 1 where the peak height and peak temperature for the relatively impure polycrystalline specimen of Chambers and Schultz[16] are much lower than for the single crystals. Thus interstitials and substitutional impurities produce qualitatively the same effect, namely a reduction in peak height and temperature, although quantitatively a concentration of interstitials about two orders of magnitude less than of substitutionals is required.

The effect of interstitial impurities is also illustrated in Fig. 5 which shows the influence of aging at 500 and 380°K on the internal friction of deformed crystals of molybdenum and niobium respectively. In both cases aging decreases both the peak height and background although the background appears to be more sensitive. The peak temperatures

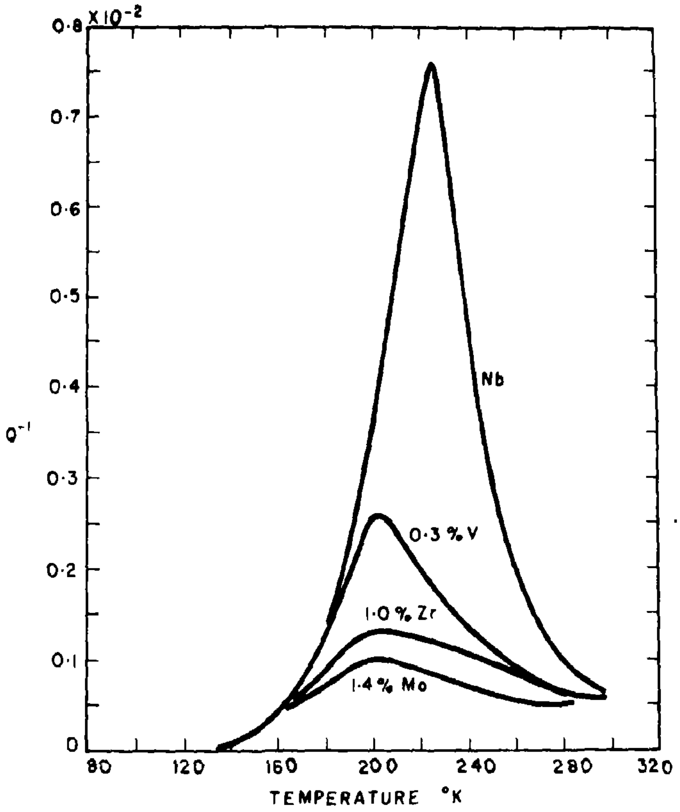

Fig. 4. Internal friction curves illustraing the effect of substitutional alloying in niobium. Crystals were deformed at room temperature as follows Nb. $\tau = 3{\cdot}6\ \text{kg/mm}^2$, $\gamma = 0{\cdot}44$; Nb–0·3% V, $\tau = 6{\cdot}1\ \text{kg/mm}^2$, $\gamma = 0{\cdot}42$, Nb–1·0% Zr, $\tau = 8{\cdot}8\ \text{kg/mm}^2$, $\gamma = 0{\cdot}55$, Nb–1·4% Mo, $\tau = 5{\cdot}7\ \text{kg/mm}^2$, $\gamma = 0{\cdot}48$

are also reduced in accordance with the impurity effects described above. The decreases in peak temperature and background can both be ascribed to reductions in loop length caused by segregation of interstitials to dislocations.

Figure 6 shows a collection of our data[20] combined with the data of others on the α peak in niobium, plotted as the logarithm of the measuring frequency against reciprocal peak temperature. Three parallel lines are drawn. One is for relatively impure polycrystalline material containing ~500 ppm impurities (this is not always specified). Another line is for zone-refined niobium (~150 ppm impurities) and a line is also drawn through our data for outgassed niobium (~20 ppm impurities). The implication of the parallel lines is that the activation energy is independent of impurity content but that the frequency factor, f_0, in the Arrhenius equation increases (roughly linearly) with impurity content. The data of Mazzolai and Nuovo[27] on tantalum given by the insert in Fig. 6 are in agreement with this implication. These data are for deformed specimens annealed at 373°K for various times; they show that the straight line plots of $\log f$ vs. $1/T$ are gradually displaced, such that f_0 increases with increasing annealing times (i.e. increasing impurity concentrations at the dislocations) and the activation energy remains approxi-

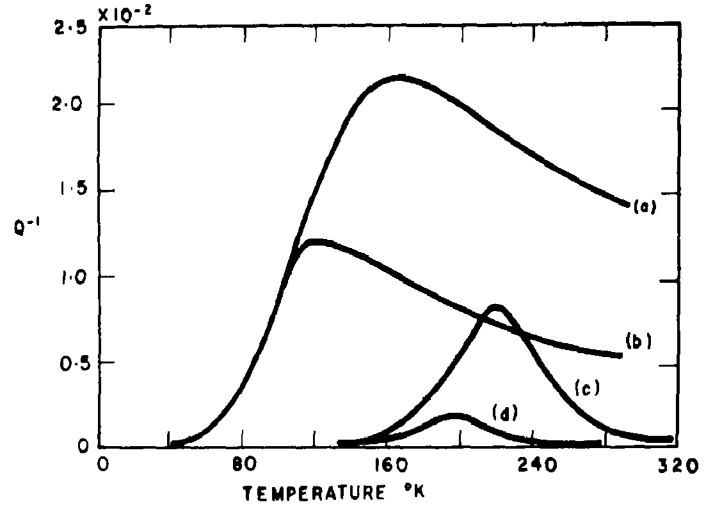

Fig. 5. Internal friction curves illustrating the effect of aging on deformed single crystals. (a) Molybdenum deformed at 450°K to $\tau = 4{\cdot}3\,\text{kg/mm}^2$, $\gamma = 0{\cdot}13$, (b) Aged 4 hr at 500°K, (c) Niobium deformed at 300°K to $\tau = 4{\cdot}2\,\text{kg/mm}^2$, $\gamma = 0{\cdot}57$; (d) Aged by heating to 380°K at ~1°K/min.

mately constant (within the limited frequency range investigated).

4. DISCUSSION

Most of the results of this investigation on the α peak can be interpreted in terms of the Seeger theory[7] of double kink formation if the theory is modified (1) to take into account the likely affect of internal stresses [9, 10] and (2) to recognize that the α peak probably involves dislocations in non-screw orientations[17, 18, 21]. However, there is one result to which we attach major significance in this paper and which the theory does not take into account in a simple way. This is the effect of purity, alloying, or strain aging on the relaxation rate parameter f_0 in the Arrhenius equation. Physically, one should expect for a relaxation process controlled by double kink generation that the larger the loop length between point defect pinning points, the more places along the dislocation line at which the kink pairs can be nucleated. Thus, increased purity should result in a larger f_0 and a lower peak temperature. Examination of Figs. 4–6 reveals that the inverse type of loop length dependence is observed experimentally.

The observed loop length dependence of f_0 is characteristic of mechanisms for which the entire loop length between pinning points is involved in the relaxation process, e.g. as in the Brailsford kink diffusion model[28]* or in various dislocation breakaway models [12, 29]. With such models, the longer the loop length, the fewer are the attempts at relaxation and the higher is the peak temperature.

Of course, it is possible to modify the double kink generation theory to account for the observed loop length dependence. One of the early theories of the Bordoni peak due to Mason[30] described the relaxation process in terms of a dislocation parallel to a close-packed direction which moves across the Peierls barrier essentially as a rigid rod between pinning points. Seeger and Schiller[8] interpret the relaxation time of the Bordoni peak as the sum of three time

---

*This theory is probably not applicable because of the finite dislocation modulus defect observed at temperatures below the α peak[3, 21].

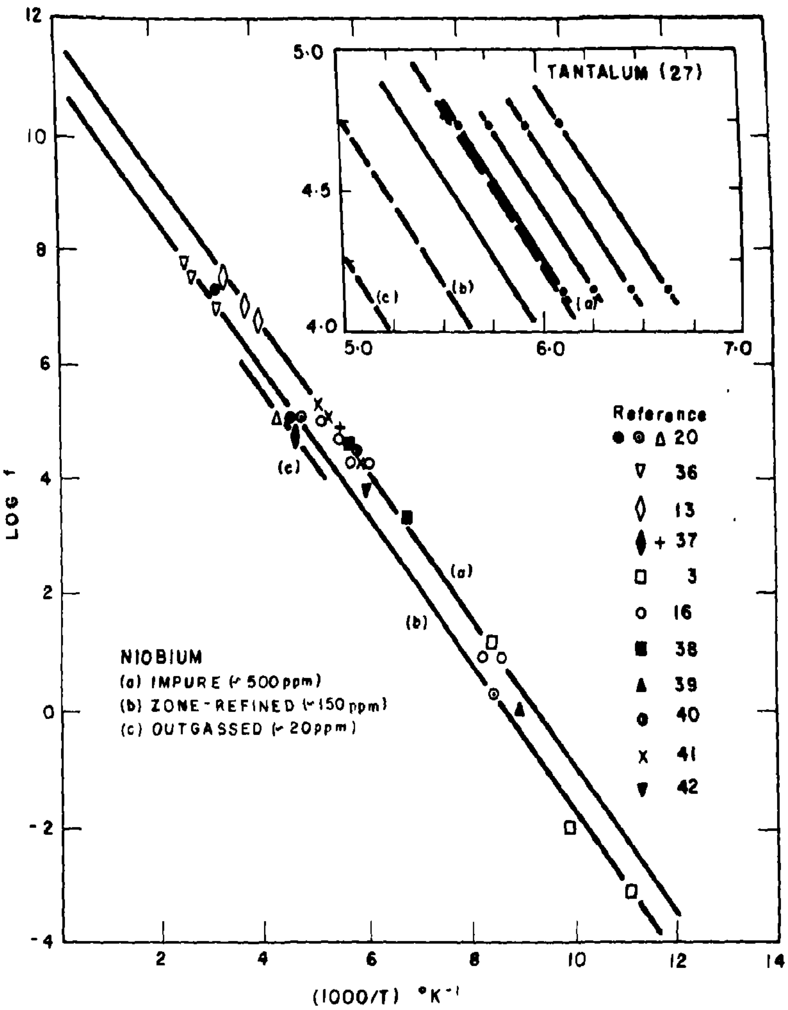

Fig. 6. Arrhenius plot of log measuring frequency against reciprocal peak temperature for niobium (center curves) and tantalum (insert). The parallel curves for tantalum were shifted to the right by progressive annealing at 373°K[27] (see text).

constants associated with kink formation, kink-kink and kink-phonon interactions, and kink-defect interactions. The latter two relaxation times are assumed to have slower temperature dependences than the former and contribute to the broadness of the peak, mainly on the high temperature side. However, the data of Fig. 6 do not indicate within experimental accuracy an effect of loop length on the activation energy ΔH of the α peak, such as would be expected from these models. Rather, the activation energy appears to be independent of loop length, quite like that expected for breakaway models for which $\Delta H \sim E_0$ or $E_0 - v\tau^*$, where E_0 is the dislocation-impurity interaction energy, v is the activation volume, and τ^* is the effective stress on the dislocation which is equal to the applied stress *plus* the internal stress[31].

Peguin and Birnbaum[12] have recently

suggested that the Bordoni peaks in fcc metals may result from thermally activated breakaway of a vibrating string dislocation from a dilute atmosphere of pinning points. This type of model *in general* accounts for the major features of the α peak observed in this paper, including the purity dependence, if internal stresses from deformation account for a major portion of the effective stress. However, in detail the model does not account for the low relaxation strength of crystals deformed at low temperatures unless the low peaks are due to insufficient internal stresses[9, 32]. In Section 3, our results on low temperature deformation inferred that, in addition to the possible deficiency of internal stress, the preponderance of non-contributing screw dislocations was probably responsible for the small size of the α peak. This suggests that the α peak is caused by breakaway of non-screw dislocations from pinning points.

Since the Peierls stress in bcc transition metals is probably finite, perhaps even large, it is reasonable from the above discussion to attribute the α peak more specifically to breakaway of moving kinked dislocations from impurity pinning points. Our visualization of such a process is similar to the trapped kink model of Hasiguti[33, 34] but with one exception: we regard the relaxation rate to be controlled by the rate at which kinks pile up at the pinning points (as in the Brailsford kink diffusion model) prior to breakaway. Thus qualitatively f_0 would be inversely proportional to the loop length as observed in Fig. 6.

Thus, our model for dislocation damping in the vicinity of the α peak is the following. At temperatures below the α peak, mixed dislocations move by kink diffusion behind pinning points which act as reflectors. The small loop lengths and the existence of internal stresses, which move the equilibrium positions of the kinks toward the pinning points, account for the low background damping in deformed bcc metals at low temperatures. The peak damping is directly associated with the breakaway process and at low amplitudes is displayed in a manner similar to peaks predicted by models of thermally activated breakaway of vibrating string dislocations from pinning points. At temperatures above the α peak, amplitude independent background damping with a new, larger effective loop length occurs, giving the stepped background seen in Figs. 1, 3, 4 and 5 and in much of the data of Chambers[3].

At high strain amplitudes, breakaway from additional pinning points occurs. In the entire internal friction spectrum, the extent to which dislocation damping is manifested as α peak damping or amplitude dependent hysteretic damping[35] will depend upon the relative roles played by stress and temperature in effecting breakaway. Increasing strain amplitude should shift the peak to lower temperatures in the manner seen in Fig. 1 for increasing *internal* stress and in amplitude dependent damping studies of Chambers[3]. Also, the release of dislocations by breakaway at α peak temperatures should permit strain amplitude dependent breakaway damping to be an easier process at temperatures above the peak. This is also confirmed by Chambers' studies.

The model presented infers that the classical Seeger double kink generation process either occurs as a relaxation peak at higher temperatures, perhaps in the range of Chambers' β or γ spectra[3], or is not displayed in the internal friction spectra of bcc metals. The strain aging phenomenon demonstrated in Fig. 5 prevented us from examining the appropriate temperature range to test these ideas.

With the exception of the effects of low temperature deformation (Fig. 3) and the *large* effect of impurities on the peak position (Fig. 6), all of the features displayed by the α peak are also displayed by the Bordoni peak in fcc single crystals[10]. Since both of these differences arise from properties apparently unique to the bcc crystals (e.g. a higher Peierls stress, much larger edge and screw dislocation-interstitial solute interaction energies), we suggest that the Bordoni peak involves the same mechanism as the α peak or a very similar one. If the Peierls stress of fcc metals is significantly smaller than that of bcc metals, the concept of kinked dislocations may not be as important as supposed here, and a vibrating string model of thermally activated breakaway may be a more appropriate description of the Bordoni peak. Bias stress experiments of the type described by Alefeld *et al.*[22] can be important in settling such questions.

REFERENCES

1. *Physical Acoustics* (Edited by W. P. Mason), Vol 3A, Academic Press, New York (1966).
2. NIBLETT D. H., *ibid.*, p. 77.
3. CHAMBERS R. H., *ibid.*, p. 123.
4. TSUI R. T. C. and SACK H. S., *Acta Met* **15**, 1715, 1723 (1967)
5. GIBBONS D. F. and CHIRBA V. G., *Acta Met.* **10**, 484 (1962).
6. CALZECCHI F., GONDI P. and MANTOVANI S., *Nuovo cim* **54B**, 165 (1968).
7. SEEGER A. K., *Phil. Mag.* **1**, 651 (1956).
8. SEEGER A. and SCHILLER P., *Acta Met* **10**, 348 also Chap. 8 in Ref. [1] p 361 (1962)
9. PARE V., *J. appl. Phys.* **32**, 332 (1961).
10. MECS B. M. and NOWICK A. S., *Phil. Mag.* **17**, 509 (1968)
11. ALEFELD G., *Lattice Defects and Their Interactions*, p. 409, Gordon and Breach, New York (1967).
12. PEGUIN P. and BIRNBAUM H. K., *J. appl. Phys.* **39**, 4428 (1968).
13. POLOTSKII I. G., PROKOPENKO G. I. and ZAPOROZHETS O. I., *Soviet Phys-solid St.* **8**, 2014 (1967).
14. POLOTSKII I. G. and PROKOPENKO G. I., *Soviet Phys Acoustics* **14**, 107 (1968).
15. AMATEAU M. F., GIBALA R. and MITCHELL T. E., *Scripta Met.* **2**, 123 (1968)
16. CHAMBERS R. H. and SCHULTZ J., *Acta Met.* **10**, 466 (1962).
17. AMATEAU M. F., Ph.D. Thesis, Case Western Reserve University (1968).
18. KORENKO M. K., M.S. Thesis, Case Western Reserve University (1968)
19. MITCHELL T. E., FOXALL R. A. and HIRSCH P. B., *Phil. Mag.* **8**, 1895 (1963).
20. AMATEAU M. F., MITCHELL T. E. and GIBALA R., *Phys. Status Solidi* **36**, 407 (1969).
21. KORENKO M. K., MITCHELL T. E. and GIBALA R., To be published (1970).
22. ALEFELD G., FILLOUX J. and HARPER H., *Dislocation Dynamics*, p. 191, McGraw-Hill, New York (1966).
23. TAYLOR G. and CHRISTIAN J. W., *Phil. Mag.* **15**, 893 (1967).
24. LOESCH H. W. Jr., and BROTZEN F. R., *J. less common Metals* **13**, 565 (1967)
25. FOXALL R. A., DUESBERY M. S., HIRSCH P. B., *can. J. Phys.* **45**, 607 (1967).
26. LAWLEY A., *Refractory Metals and Alloys IV: Research Development*, p 1419, Gordon and Breach, New York (1967)
27. MAZZOLAI F. M. and NUOVO M., *Ricerca Scient.* **36**, 1131 (1966)
28. BRAILSFORD A. D., *Phys. Rev.* **122**, 778 (1961)
29. KOIWA M. and HASIGUTI R. R., *Acta Met.* **13**, 1219 (1965)
30. MASON W. P., *Phys. Rev.* **98**, 1136 (1955); *J acoust. Soc. Am.* **27**, 643 (1955), *Bell System Tech. J.* **34**, 903 (1955).
31. SCHOECK G., *Phys. Status. Solidi* **8**, 499 (1965).
32. ALEFELD G., CHAMBERS R. H. and FIRLE T. E., *Phys. Rev* **A140**, 1771 (1965)
33. HASIGUTI R. R., *J. phys. Soc. Japan* **18**, Suppl. I. 114 (1963).
34. HASIGUTI R. R., *Phys. Status Solidi* **9**, 157 (1965).
35. GRANATO A. and LUCKE K., *J. appl Phys* **27**, 583, 789 (1956)
36. MITCHELL O. O. M., *J acoust. Soc Am.* **41**, 1058 (1967).
37. KRAMER E. J. and BAUER C. L., *Phys. Rev* 163, 407 (1967)
38. DEBATIST R., *Phys. Status Solidi* **2**, 661 (1962)
39. STANLEY M. W. and SZKOPIAK Z. C., *J. mat. Sci.* **2**, 559 (1967).
40. BRUNER L. J., *Phys Rev.* **118**, 399 (1960).
41. BORDONI P. G., NUOVO M. and VERDINI L., *Phys. Rev* **123**, 1204 (1961)
42. HANLON J. E. and WOLF J. D., *Trans AIME* **236**, 231 (1966)

J. Phys. Chem. Solids Pergamon Press 1970. Vol. 31, pp. 1901–1906. Printed in Great Britain

A CONTRIBUTION TO THE STUDY OF INTERNAL FRICTION PEAKS ASSOCIATED WITH DISLOCATIONS IN VARIOUS METALS, AND THEIR RELATIONS WITH COLD-WORK

J. de FOUQUET, P. BOCH, J. PETIT and G. RIEU

Ecole Nationale Supérieure de Mécanique et d'Aérotechnique, University of Poitiers, France

(*Received* 5 *September* 1969, *in revised form* 20 *October* 1969)

Abstract – Peaks of internal friction associated with dislocations were studied under the same experimental conditions between 77-700°K, in the frequency range 5–50 kHz, on various metals. Copper, Aluminum, Nickel, Zirconium, Molybdenum

Experimental results show a close relationship, characteristic of each metal, between the height of peaks and the amount of prestrain at room temperature. These relations and the influence of successive annealings after cold-work, or of the additional elements for Zirconium, confirm the consequence of internal stresses on these peaks, in accordance with the Seeger–Paré theory for Bordoni peaks, and with the Hasiguti first model for peaks observed at higher temperature

1. INTRODUCTION

THE INTERPRETATION of thermally activated internal friction peaks observed on metals at low temperature after plastic deformation necessitates a detailed study of the influence of cold-work amount, impurity concentration, and conditions of deformation (temperature, rate of deformation, ...) on peaks height and peaks temperature and the associated modulus defect[1, 2].

In the present investigation the influence of the amount of the room temperature prestrain on peaks observed between 77–700°K (Bordoni, Niblett and Wilks, and Hasiguti peaks) has been studied systematically, under the same experimental conditions on Copper, Aluminum, Nickel, Zirconium, and Molybdenum.

For this, all measurements were made on polycrystalline rods of about the same grain sizes, subjected to longitudinal vibrations in the frequency range 5–50 kHz, with excitation and detection by the capacitive method[3, 4, 5]. The vibration amplitude was sufficiently low to avoid hysteresis effects, and the background Q^{-1} of the apparatus was less than 5×10^{-6}. The diameter of the rods was 0·3–0·7 cm and their length 8–15 cm. The prestrains at room temperature were realized by successive tractions or compression on a 10 *T*. Instron machine, at a rate of 0·1 cm/min.

2. EXPERIMENTAL RESULTS

The principal results obtained on the different metals are following:

Copper. Data on 99·999 per cent pure Copper, with allowance made for background which decreases when the plastic prestrain increases, show a close relationship between the variations vs. prestrain of Bordoni peak P_0 and Hasiguti peak P_1 obtained at 77–225°K for a frequency of about 13 kHz.

These variations (Fig. 1) are characterized in particular by the existence of a maximum peak height for a 7 per cent prestrain. However, the thermal treatments before straining on hard-worked rods have a considerable influence on the height of peaks after a same deformation, and this influence is the same on the two peaks: the height is maximal for an initial annealing of 2 hr at 240°C leading to a near isotropic crystalline state, without texture, and with a mean grain size of about $70\,\mu$. On the contrary, the thermal treatments

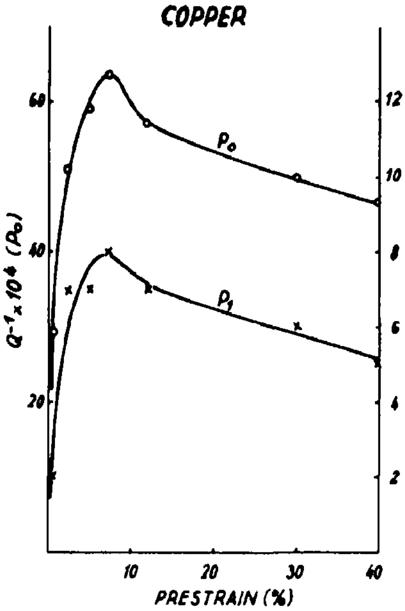

Fig. 1 Dependence of the height of P_0 and P_1 for polycrystalline Cu on amount of room temperature prestrain

after deformation affect P_0 and P_1 differently, and an annealing of 48 hr at 100°C eliminates P_1 while the disappearance of P_0 requires recrystallisation.

Aluminum. Unlike Copper, the height of peaks observed on 99·995 per cent pure Aluminum, P' at 143°K and P'' at 103°K for a frequency of about 17 kHz, increases uniformly with the prestrain (Fig. 2), at least to the 30 per cent cold-work obtained here. Also, the two peaks are very rapidly eliminated during annealing at temperatures below 100°C; but a difficulty is found in separating the spectrum only into two peaks P' and P'', from the variation of peaks during annealing. One better description seems to correspond with three peaks (P', P'', P'''); the activation energy for the third peak would be 0·1 eV and its temperature about 93°K. This decomposition gives a decrease of the temperature of each peak when the prestrain increases:

$\Delta T_{P'} = -11°$, $\Delta T_{P''} = -8°$, $\Delta T_{P'''} = -6°$ for an increasing prestrain from 0·33 per cent to 30 per cent.

Nickel. Figure 3 shows the evolution of damping obtained on 99·999 per cent pure Nickel for increasing cold-work. Very light prestrains at room temperature give rise to a broad peak P_{d} located at about 223°K for a

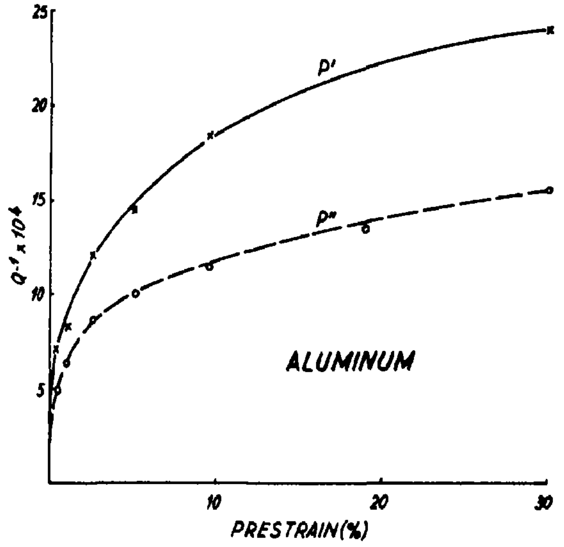

Fig. 2 Variation of the height of P' and P'' peaks for Aluminum vs. room temperature prestrain.

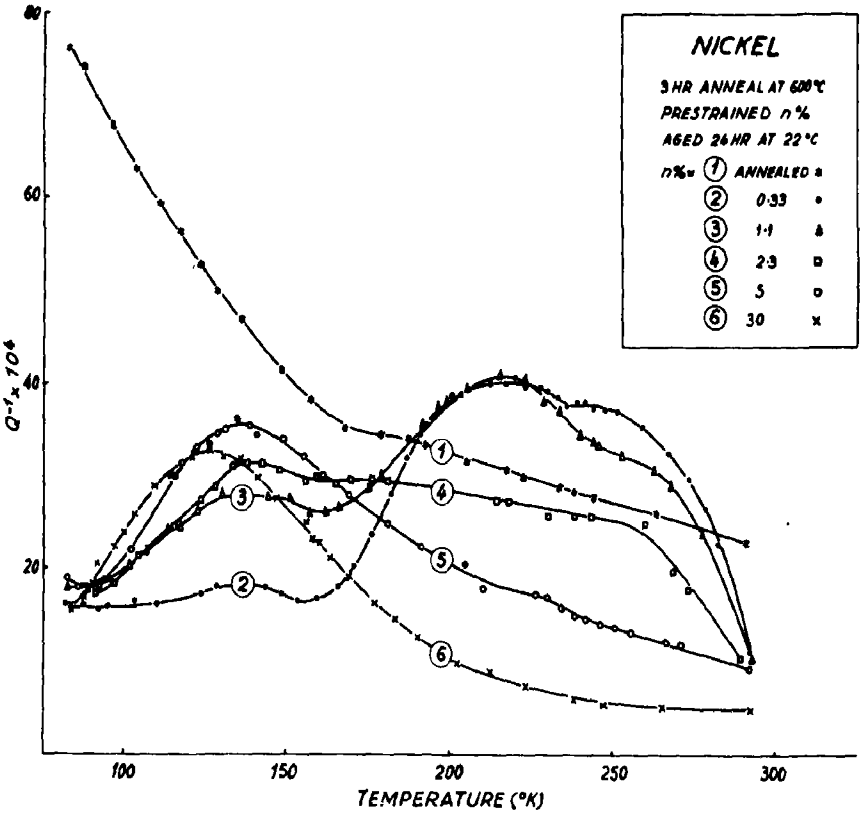

Fig. 3. Damping spectra of polycrystalline Ni after various amounts of plastic deformation at 22°C (measurement made at ~16 kHz)

frequency of 17 kHz; heavy cold-work gives another peak P_v situated at about 133°K. The height of peaks for a same amount of prestrain is dependent on pre-annealing and grain size, but the variation is lesser than on copper. The temperature of peaks decreases slightly when the grain size increases, but the shape of peak P_d is different and the peak seems to be made up by two peaks, one at about 208°K and another at 248°K.

This behaviour of Nickel has been already pointed out by Sommer and Beshers[6]; but we have not observed the same shift in temperature of P_x with cold-work and its reappearance during annealing after a heavy cold-work.

Zirconium. Unlike the preceding metals, the spectrum obtained on Zirconium and on its alloys (Zr-Cu 1·6% and 2·5%; Zr-Cu-Mo 2·5%) is remarkably simple, Fig. 4. The height of the peak situated at about 223°K for a frequency of about 13 kHz increases uniformly with cold-work, and the results are identical for pure Zirconium and for the alloys. But the height of peak which has an activation energy of 0·35 eV in every case is less for pure metal at the same amount of cold-work.

As for peak P_v of Nickel, successive annealings after prestrain lead to an increase of the peak for low temperatures annealings and to a gradual decrease above a certain temperature which is about 200°C for pure metal and alloys. So, the disappearance of the peak is obtained, as for Aluminum and

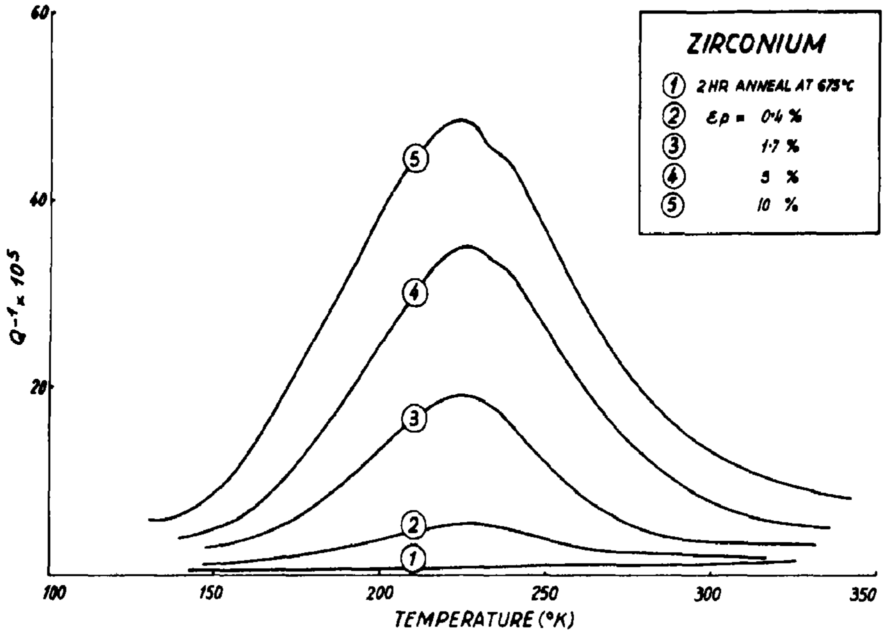

Fig. 4 Dependence of the height of peak for pure polycrystalline Zirconium on amount of room temperature prestrain (measurement made at 13 kHz)

unlike P_0 on copper, at rather lower temperature than the recrystallisation.

Molybdenum. Tests carried out recently on 99·995 per cent pure polycrystalline molybdenum, showing a clear yield point at room temperature, give three successive stages in the increase of peaks vs. the amount of prestrain; a small increase is observed for strains below the yield point, a rapid increase during Lüders band propagation, and another gradual increase during the strain-hardening process – Fig. 5. Four peaks at least are consistent with the spectrum obtained between 77°–700°K, and an annealing at 700°K leads in every case to the disappearance of peaks which reappear after a new deformation at 20°C. The peak at about 143°K ($P\alpha$) for a frequency of 19 kHz is lower than peaks $P\beta$ (at about 350, 430 and 650°K) for slight prestrains, and $P\alpha$ get higher than $P\beta$ from prestrain above 0·6 per cent. These results are in accordance with those obtained by Chambers and Schultz[1, 2] but the amounts of prestrain which give the same height for $P\alpha$ and $P\beta$ are very different. A better correspondence is observed between Q^{-1} and the stress σ than between Q^{-1} and the prestrain $\epsilon(\sigma)$.

3. CONCLUSION

The principal conclusions that can be drawn from these different results are:

(a) The close relationship between the evolution of peak P_0 and P_1 on copper in relation to prestrain and initial conditions of annealing.

(b) The monotonous increase of peaks P' and P'' in aluminum as opposed to P_0 and P_1 on copper and the difficulty in separating the spectrum into two peaks only.

(c) The peculiar behaviour of Nickel for which two peaks, P_x and P_y, are successively obtained for an increasing cold-work and the same influence of pre-annealing on the height of these two peaks.

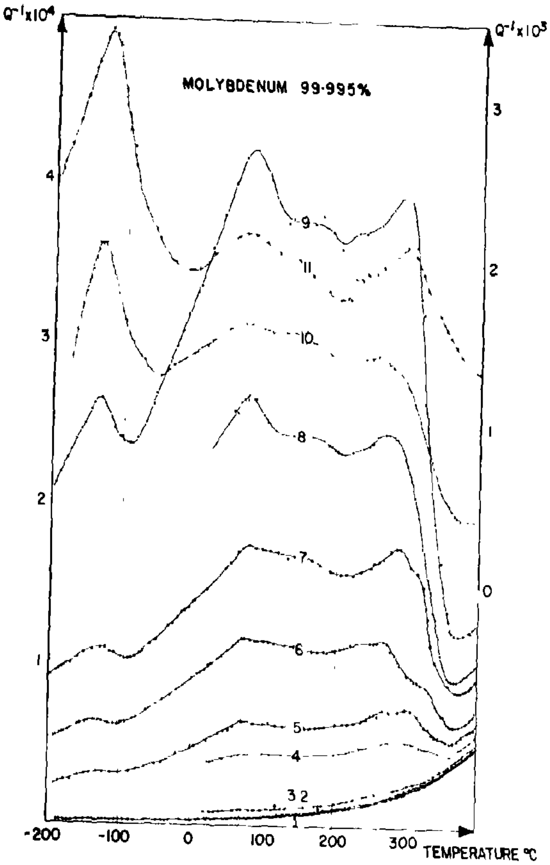

Fig. 5. Damping spectra of polycrystalline Mo after various amounts of prestrain at room temperature (measurements made at 19 kHz) Curve (1) As annealed 5 hr at 800°C – Curves (2)–(6): $\epsilon = 0$, $\sigma = 10$·25, 35, 40, 45 kg/mm² – Curves (7): $\epsilon = 0.01\%$, $\sigma = 50$ kg/mm² –(8): $\epsilon = 0.05\%$ $\sigma = 52.5$ kg/mm² –(9) $\epsilon = 0.1\%$, $\sigma = 55$ kg/mm² –(10) $\epsilon = 1\%$, $\sigma = 65$ kg/mm² –(11) $\epsilon = 5\%$; $\sigma = 90$ kg/mm².
Scales – left hand: Curves (1) to (9) $Q^{-1}\times 10^4$, – right hand: Curves (10) and (11), $Q^{-1}\times 10^3$

(d) The particularly simple shape of spectrum observed for Zirconium and its alloys, in contrast to the complex spectrum reported by Tsui and Sacks[1] for Magnesium, but the slip systems are different for these metals.

(e) The close relationship between the evolution of peaks for Molybdenum, and the different stages of the stress–strain curve of this metal at room temperature.

It is difficult from only these data, and the results obtained by different authors on the same metals, to give a sure interpretation of the variations of the height of peaks with the amount of prestrain. But the influence of pre-annealing and grain size on the height of peaks for the same deformation, the influence of additional elements on the height of peaks on Zirconium, and the close relationship between the variation of peaks and the temperature range 80–600°K and $\epsilon = 10^{-7}$ (c) one Elastometer Forster. Transverse mode of vibration: 2 kHz, temperature range 80–470°K.

The sample materials used here were: (a) polycrystalline aluminium 'Superaffinal' from Aluminium Suisse (99·999 per cent). After rolling or wire drawing the samples were annealed for one hour at 670°K under low vacuum. In the pendulum, before coldworking, the specimens are annealed *in situ* (2 hr at 470°K) to eliminate handling effects; (b) polycrystalline gold from Metaux Precieux, Neuchatel (99·999 per cent). After machining the samples are annealed under high vacuum for 4 hr at 1170°K. As before the samples are annealed *in situ* (4 hr at 670°K) to eliminate handling effects.

3. MODULUS EFFECTS

We will report here results obtained on both gold and aluminium. Figure 1 shows modulus defect $\Delta E/E$ of a gold and an aluminium sample, coldworked at liquid nitrogen temperature against the annealing temperature. The curve *A* for gold was obtained in flexure at 180 Hz, after it was coldworked at 3 per cent by traction at liquid nitrogen temperature. The curve *B* for aluminium was obtained after coldworking at 0·15 per cent.

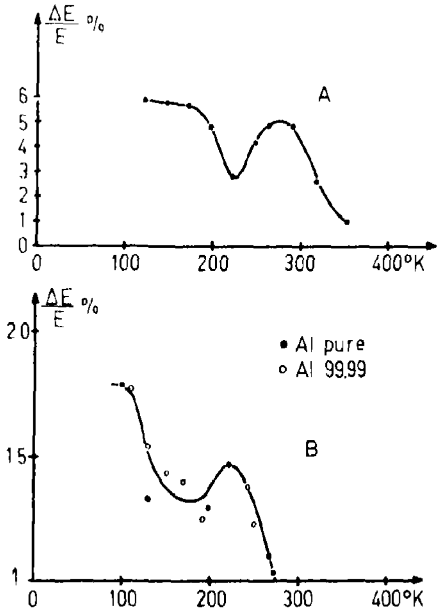

Fig. 1. $\Delta E/E$ measured at 100°K against annealing temperature, (a) gold; (b) aluminium.

If the theoretical explanation of dislocation pinning by point defects is accepted, we have to conclude that these modulus changes are produced by the arrival or the disappearance of point defects on dislocations. Following this, on the gold curve a pinning stage appears up to 220°K. Then a depinning stage is observed up to 270°K and is followed by a new pinning effect.

The same results are still observed in the aluminium case but with a temperature shift to lower temperatures (50°). We have verified that the height of Bordoni peak and background amplitude vary in the same way with annealing temperature, these two phenomena being due to the presence in metals of free dislocation lines.

4. HASIGUTI PEAKS

The results on internal friction measurements are shown on Figs. 2, 3 and 4. Figure 2 shows a result obtained on gold in an inverted torsion pendulum. The gold wire was coldworked *in situ* 3 per cent by torsion at liquid nitrogen temperature. Internal friction was measured during ten linear rises, from 90 up to 203°K. Successive rises were then carried out at 223, 243°K, etc.... according to the programme shown on Fig. 2.

On the first curve a peak is observed. Its maximum starts increasing (curve 2) and then decreases quickly (curves 3–11). It corresponds to Hasiguti peak P_2. Parallel to the annealing of P_2 a new peak P_3 appears, its maximum is near 210°K. At the same time as P_3 disappears a small peak P_1 appears at approximately 120°K.

A result obtained in flexure on an embedded foil is shown on Fig. 3. The foil is 100μm thick and is coldworked 3 per cent by traction at liquid nitrogen temperature. As for the

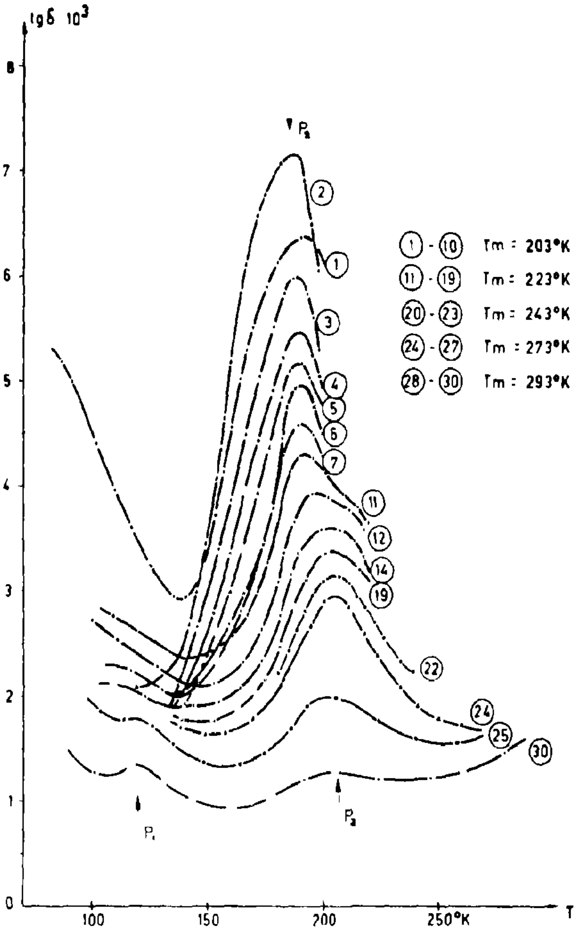

Fig. 2. Internal friction of gold against temperature Measurements have been made in a pendulum (0·5 Hz) after cold working 3 per cent in torsion

results of Fig. 2, internal friction is measured during a succession of linear annealings. The same peaks as before are observed but there is a shift of about 50° towards higher temperatures. The peak P_2 appears only the first rise; it disappears immediately and completely and two peaks P_1 and P_3 are observed on the following curves.

On Fig. 4, results obtained on aluminium wire in pendulum are presented. The wire is coldworked 0·5 per cent at liquid nitrogen temperature. These results are essentially similar to those obtained in gold. During the first run up to 133°K a first peak P_A is observed at 110°K. During the second run up to 223°K two new peaks are observed, the Bordoni peak at 95°K[4] and P_B at 155°K. The peak P_A seams already completely annealed. On the third and fourth curve only the Bordoni peak appears.

5. DISCUSSION

The preceeding results are sumed up on Fig. 5. Both modulus defect and internal friction peak height changes are reported different stages of the stress-strain curve (or of the strain-hardening process) of these different metals agree with the Seeger–Paré[7, 8] theory for the peaks at lower temperature, and for the others with Hasiguti's first model[9] which considered diffusion of kinks pinned by point defects or impurities.

REFERENCES

1. *Acta Met* **10**, 4 (1962). Conference on International Friction Due to Crystal Lattice Imperfections, Cornell University, July 1961.
2. *Physical Acoustics*, Vol. 3, Part A, "*The Effect of Imperfections*" (Edited by W. P. Mason). Academic Press, New York (1966).
3. BOCH P., MALLET J. M. et de FOUQUET J., *Mem. Sci. Rev. Met.* **6**, 507 (1967).
4. BOCH P. et de FOUQUET J., *Mem. Sci. Rev. Met.* **10**, 711 (1968)
5. BOCH P., These Dr Sc. Poitiers (1968).
6. SOMMER W. et BESHERS D. N., *J. appl. Phys* **37**, 4603 (1966).
7. SEEGER A., *Phil Mag.* **1**, 651 (1956).
8. PARÉ V K, *J. appl. Phys.* **32**, 332 (1961).
9. OKUDA S. et HASIGUTI R R., *Acta Met.* **2**, 257 (1963).

J. Phys. Chem. Solids Pergamon Press 1970. Vol. 31, pp. 1907–1912. Printed in Great Britain.

MODULUS EFFECTS AND HASIGUTI PEAKS ON TWO COLDWORKED fcc METALS: GOLD AND ALUMINIUM*

W. BENOIT, B. BAYS, P. A. GRANDCHAMP and B. VITTOZ
Laboratoire de Génie Atomique de l'Ecole Polytechnique Fédérale, Lausanne, Suisse

and

G. FANTOZZI, J. PEREZ and P. GOBIN
Département de Physique, Institut National des Sciences Appliquées, Lyon, France

(*Received* 30 *September* 1969)

Abstract–High purity polycrystalline gold and aluminium 99·999 per cent cold worked at liquid nitrogen temperature have been studied on several internal friction installations: torsion pendulums (0·04–2 Hz), embedded foils flexure (30–500 Hz) and bar flexure (2 kHz). Several internal friction peaks have been observed, already noticed by other authors (P_1, P_2, P_3, in gold, P_4 and P_B in aluminium).

Linear annealings make it possible to show the recovery stages of these peaks and to calculate the corresponding energies.

The modulus defect i.e. the pinning of the dislocation lines, is shown by the measurement of Young's modulus carried out at the same time as the internal friction measurement.

The results have been interpreted in terms of an interaction between dislocation lines and intrinsic point defects.

1. INTRODUCTION

THIS paper presents some results obtained on two fcc metals, gold and aluminium. The main goal is to observe interactions between dislocations and point defects. The most important part of the results have been obtained on specimens coldworked at liquid nitrogen temperature. During an increase in temperature different internal friction peaks and modulus effects are observed; only results obtained between liquid nitrogen temperature and room temperature will be presented.

It is well known that point defects on dislocation lines produce dislocation pinning. Modulus defect measurements are very sensitive to such dislocation pinning. As a matter of fact we have from both the bowing string model or from the kink model this expression[1]:

$$\frac{\Delta E}{E} = C\Lambda l^2 = \frac{f^2-f_0^2}{f_0^2}$$

where C = constant
Λ = dislocation density
l = mean loop length between two pinning points.

The arrival of point defects on dislocation lines reduces their mean loop length and the modulus defect decreases. Also the presence of point defects on dislocation lines seems to produce some relaxation peaks such as Hasiguti peaks[2] which appear between liquid nitrogen and room temperature in both gold and aluminium. Then modulus effects and Hasiguti peaks will be observed in view of studying dislocation pinning and depinning in the different stage of recovery.

2. EXPERIMENTAL PROCEDURE

The apparatus used in this work are of three kinds: (a) two inverted torsion pendulums[3, 4]: frequency range 0·04–2 Hz; temperature range: 80–600°K and $\epsilon = 5.10^{-6}$ (b) one embedded foil vibration installation[3]. Frequency range 30–500 Hz,

---

*This work was partially supported by the Swiss National Fund.

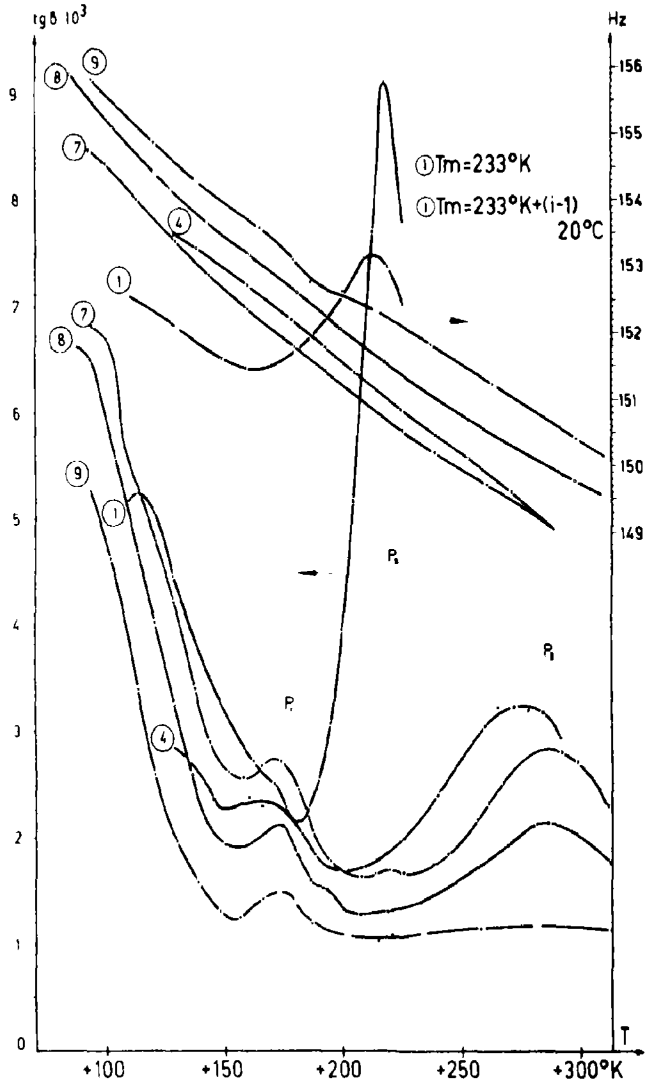

Fig. 3. Internal friction and frequency of a gold foil against temperature. Measurements have been made in a flexion installation after cold working 3 per cent in traction.

above for gold and below for aluminium. The annealing temperature is indicated in abscissa. The changes of $\Delta E/E$ show the pinning and depinning zone as it has been noted on Fig. 1. It can be observed that, on one hand, the P_2 and P_4 peaks appear and completely disappear in the first pinning zone, on the other hand, the P_3 and P_B peaks disappear in the depinning zone*. Thus, if we take into account the temperature shift a great similarity between gold and aluminium is observed. In conclusion there are very good

---

*In the case of gold there are actually two stages of annealing as reported on Fig. 5. But the first stage is the most important one[3].

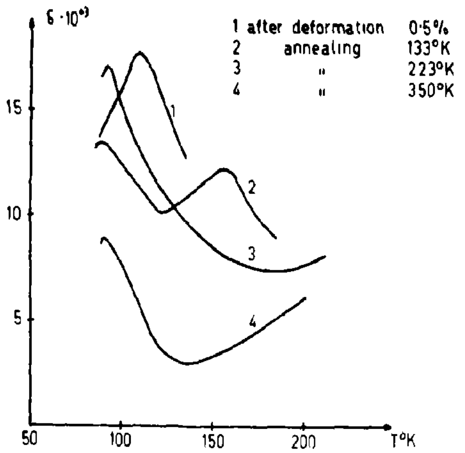

Fig. 4. Internal friction of aluminium against temperature. Measurements have been made in a torsion pendulum (1 Hz) after cold working 0·5 per cent in torsion.

reasons for thinking that P_A and P_B in the aluminium correspond to P_2 and P_3 in the gold, respectively.

It does not seem that these peaks are due to the elastic anistropy of any point defects for several reasons[3, 4]: (a) the limit frequency is too low (between 10^8 to 10^{12}); (b) the peaks are broader than those due to single reorientation processes; (c) the relaxation strength is high; (d) the relaxation strength increases with the ratio of cold working at low deformation but shows nearly a saturation at higher deformation (higher than 2 per cent in torsion); (e) annealing properties are difficult to explain with assumption of point defect reorientation.

The preceeding remarks lead us to think that both dislocations and point defects are responsible for the peaks. The exact mechanism is not yet known but several models such as those proposed by Hasiguti[5], Koïwa and Hasiguti[6] Peguin and Birnbaum[7] and Schlipf[8], can be accepted. The evolution of the modulus defect and of internal friction is now to be considered. The comparisons between the modulus defects and internal friction peaks cannot be considered unless one supposes that the defects which pin dislocations are the same as those which are responsible for the internal friction peaks.

First, the pinning effect can be associated with the increase of P_2 and P_A peaks; the temperature range corresponds to stage 2 observed by electric resistivity measurements in aluminium[9] and in gold[10]. The nature of defects responsible for this stage is not exactly known but generally authors attribute this stage to annihilation

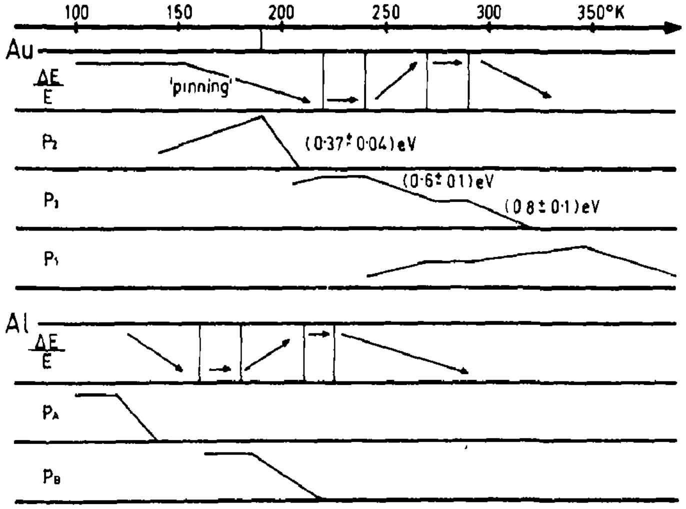

Fig. 5. Evolution of $\Delta E/E$ and peak height with annealing temperature. Upper part: gold, Lower part: aluminium

of interstitial type defects. Then, it can be thought that those defects migrate towards dislocation lines, pin them and are responsible for P_2 and P_A peaks.

However, the P_2 and P_A peaks disappear quite rapidly without depinning effect. At the same time, the P_3 and P_B peaks appear. Those observations can be interpreted by the migration of interstitials along dislocation lines leading to the formation of interstitial clusters which are more stable on dislocation lines and which interact more strongly with them. Then P_3 and P_B can be due to the interaction between such clusters and dislocation lines. The hypothesis of pipe diffusion is confirmed by Alefeld[11] who showed that mobile pinning point defects on or near dislocation lines tend to group together. The apparent activation energy of the annealing process of P_2 and P_A peaks is $(0{\cdot}37 \pm 0{\cdot}04)$eV and $(0{\cdot}25 \pm 0{\cdot}05)$eV respectively. Following the preceeding interpretation, these values would be the migration energy of interstitials along dislocation lines.

Secondly, the unpinning effect (gold 270–320°K, aluminium 170–220°K) can be associated with the disappearance of P_B (aluminium) and with the first stage of annealing of P_3 (gold). Thus, the clusters of interstitials which pin dislocation lines are eliminated; this annihilation can be due either to the migration of those defects towards sinks, or to the arrival of vacancy type defects on dislocation lines. The annealing of the P_3 peak in two stages and in a large temperature range, allow us to think that the latter assumption is more probable. In the case of gold, the activation energy found for these two stages are $(0{\cdot}6 \pm 0{\cdot}1)$eV and $(0{\cdot}8 \pm 0{\cdot}1)$eV; these values agree with the hypothesis of migration of di-vacancies and single vacancies respectively.

Finally, the last pinning stage can also be associated to the arrival of vacancy type defects in excess which can pin dislocation lines. In the case of gold, this pinning effect leads to the appearance of the P_1 peak which can be due to the interaction of dislocation lines with vacancies.

REFERENCES

1. FANTOZZI G., PEREZ J., PEGUIN P. and GOBIN P., *Mem. Sci. Revue. Metal.* **66**, 151 (1969).
2. OKUDA S. and HASIGUTI R. R. *Acta Met.* **11**, 257 (1963).
3. BENOIT W., Thesis, Lausanne (1968)
4. PEREZ J., GUENIN G. and GOBIN P., *Mem. Sci. Revue. Metal.* **65**, 185 (1968).
5. HASIGUTI R. R., *Phys. Status Solidi* **9**, 157 (1965).
6. KOÏWA M. and HASIGUTI R. R., *Acta Met.* **13**, 1219 (1965).
7. PEGUIN P. and BIRNBAUM H. K., *J. appl. Phys.* **39**, 4428 (1968).
8. SCHLIPF J., *Int. Conf. Providence* (1969).
9. FROIS C., *Acta Met.* **14**, 1325 (1966)
10. KOREVAAR B. M., *Acta Met* **6**, 572 (1968).
11. ALEFELD G., *Phil. Mag.* **11**, 809 (1965).

J. Phys. Chem. Solids Pergamon Press 1970. Vol. 31, pp. 1913–1919. Printed in Great Britain.

ANELASTIC RELAXATION EFFECTS IN COLD-WORKED AND HYDROGEN DOPED VANADIUM

G. CANNELLI and F. M. MAZZOLAI
Consiglio Nazionale delle Ricerche Istituto di Acustica 'O. M. Corbino', Rome, Italy

(*Received* 5 *September* 1969; *in revised form* 30 *October* 1969)

Abstract—The amplitude independent internal friction has been measured in a series of vanadium-hydrogen alloys in the temperature range from 4·2 to 450°K, the vibration frequencies being included between $2 \times 10^2 - 1 \times 10^5$ Hz. Experimental evidence has been obtained of an anelastic effect occuring near 20°K in cold-worked pure vanadium; its activation energy and its frequency factor are 0·012 eV and 5×10^7 Hz, respectively. The introduction of hydrogen in the prestrained material brings about a relaxation effect near 203°K, which is shown to be the hydrogen cold-work peak. A third relaxation effect, observed in prior annealed and then hydrogen doped vanadium, appears to be a suitable means for studying the phase diagram of V–H system.

1. INTRODUCTION

THE INTERNAL friction of bcc metals, chiefly of tantalum and niobium, has been extensively studied during last years[1–3]; it has been found that plastic deformation gives rise to several peaks in the damping versus temperature curve. It is generally agreed that these anelastic effects arise from lattice defects produced by cold-work; however, little is known so far about their structural causes.

Recently, an anelastic effect (δ peak) has been observed below the liquid nitrogen temperature in cold-worked tantalum and niobium and results have been presented which show that the so called α peak is a hydrogen cold-work peak (C W P)[4]. These observations modify to some extent previous interpretations of the anelastic behaviour of tantalum and niobium and suggest the opportunity of extending the experimental work to other bcc metals.

In this paper we present the results of an experimental investigation which has been undertaken to provide experimental evidence of the α and δ peaks in vanadium and to examine the effect of hydrogen impurities on the internal friction of this metal.

2. EXPERIMENTAL

The amplitude indipendent internal friction (Q^{-1}) has been measured during cooling runs in the temperature range from 4·2 to 450°K in 99·99 per cent pure vanadium, supplied by Materials Research Corporation. The flexural vibrations of the samples, whose thermal and mechanical history is described in Table 1, were excited and detected by a well known electrostatic technique [5, 6]; the frequencies covered the range from 2×10^2 to 1×10^5 Hz.

3. RESULTS

The damping of sample 1 after plastic deformation at room temperature (Table 1, treatment (a)) is plotted as a function of temperature in Fig. 1, curve 1, the vibration frequency is 39 kHz. Three peaks can be observed at about 18·5°K (δ peak), 250°K (β_1 peak) and 285°K (β_2 peak). As shown by curve 2 of Fig. 1, striking effects are produced on the elastic energy dissipation of prestrained sample 1 by a hydrogen contamination (Table 1; treatment (b)): it can be seen that while the δ peak is removed by the hydrogen impurities, a well developed peak (α peak) is introduced near 203°K. Curve 3 of the same

Table 1

Sample	Treatments undergone by the samples
1	(a) Machined and permanently strained 3·3% at room temperature. (b) Electrolytically loaded with hydrogen: At. concentration < 0·05%. (c) Hydrogen outgassed and recrystallized in vacuum (1×10^{-5} mm Hg) at 1170°K for about 50 hr (d) Electrolytically loaded with hydrogen: At. concentration < 0·05%.
2	(a) Hydrogen outgassed and recrystallized in vacuum (1×10^{-5} mm Hg) at 1170°K for about 25 hr. (b) Electrolytically loaded with hydrogen: At. concentration 0·27% (c) Electrolytically loaded with hydrogen: At. concentration 2·5%. (d) Electrolytically loaded with hydrogen At. concentration 4%. (e) Electrolytically loaded with hydrogen. At. concentration 6·5%.
3	(a) Hydrogen outgassed and recrystallized in vacuum (1×10^{-5} mm Hg) at 1170°K for about 25 hr (b) Electrolytically loaded with hydrogen: At concentration 0·5%. (c) Electrolytically loaded with hydrogen. At. concentration 1·2%.
4	(a) Permanently strained 5·5% at room temperature. (b) Machined to a rectangular shape by cold-rolling at room temperature

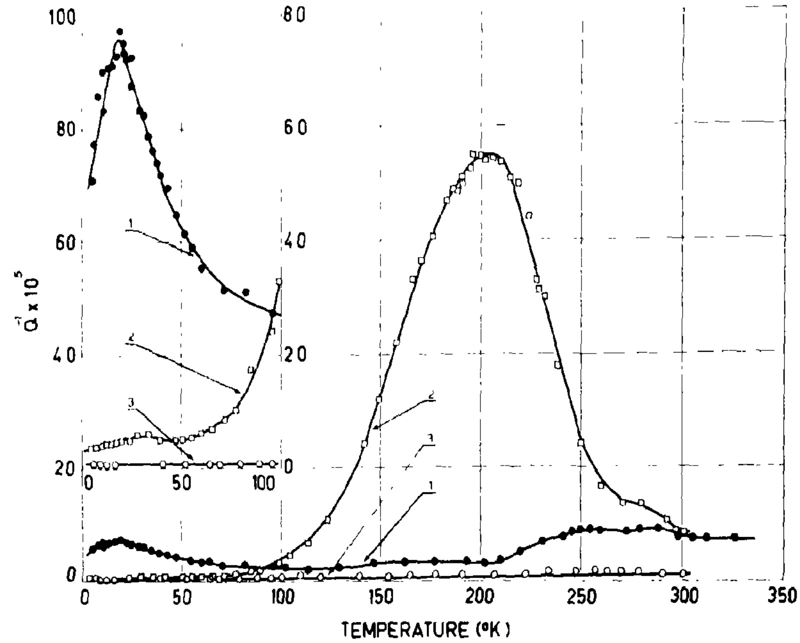

Fig. 1. Influence of the subsequent treatments of Table 1 on the internal friction of sample 1, curve 1 after cold working at room temperature; curve 2 after a subsequent loading treatment with hydrogen, curve 3 after an anneal at high temperature and a subsequent loading treatment with hydrogen.

figure, obtained after treatments (c) and (d) of sample 1, shows that a hydrogen content less than 0·05 per cent does not give rise to any observable relaxation effect in prior annealed material.

Figures 2 and 3 display the Arrhenius plots

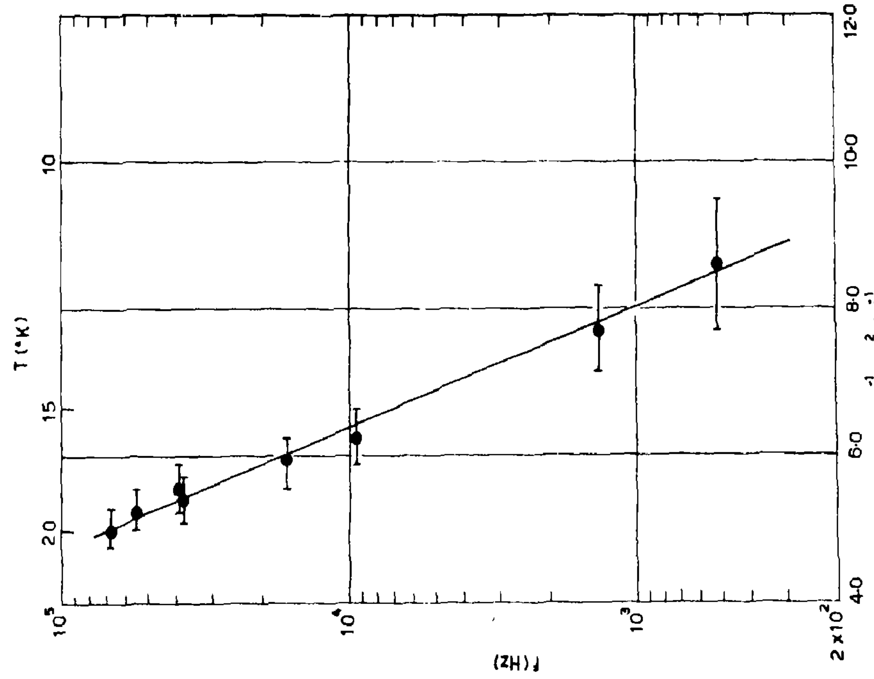

Fig. 2. Frequency dependence of the temperature of δ peak.

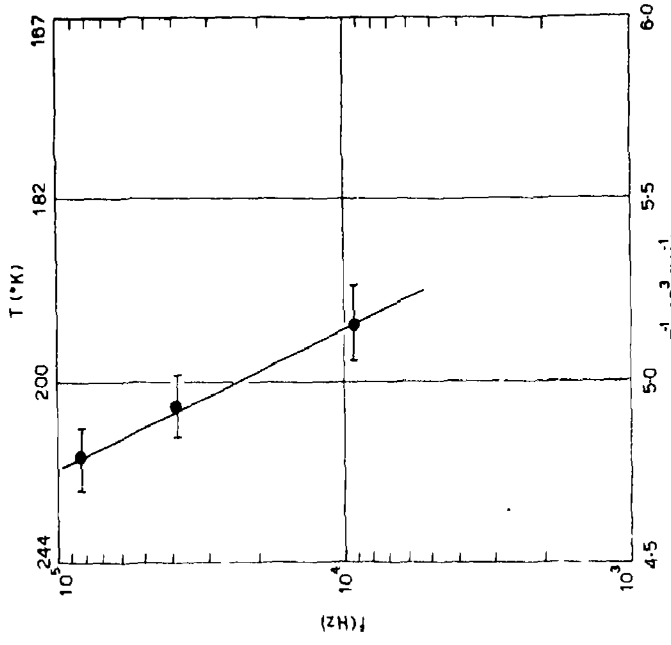

Fig. 3 Frequency dependence of the temperature of α peak.

of δ and α peaks, respectively; the high frequency measurements of Fig. 2 correspond to vibration modes of plates 1 and 4, those at low frequency to flexural modes of sheet 1, which was drawn from plate 4 by cold-rolling at room temperature (Table 1, treatment (b)). The measurements of Fig. 3 correspond to three vibration modes of sample 1 after hydrogen loading treatment (b) of Table 1. The relaxation parameters of δ and α peaks, evaluated from the above figures, are $W_\delta = (0{\cdot}012 \pm 0{\cdot}002)$ eV, $f_{0\delta} = 5 \times 10^7$ Hz; $W_\alpha = (0{\cdot}52 \pm 0{\cdot}10)$ eV, $f_{0\alpha} = 3 \times 10^{17}$ Hz.

In Fig. 4 a comparison is made between the experimental curve of δ peak corresponding to an activation energy of 0·012 eV and the Debye one; it can be seen that the theoretical curve is much narrower than the experimental one, showing the anelastic effect has a rather wide relaxation time spectrum.

The internal friction of samples 2 and 3 after the hydrogen doping treatments (d) and (c), respectively, is shown by Fig. 5. An asymmetric peak is observed, whose high temperature branch is even steeper than is expected for a single relaxation process. This abrupt rise in damping is more clearly shown by Fig. 6, where the high temperature part of some experimental curves is reported for several hydrogen contents.

4. DISCUSSION

The most important observations in the present investigation are: (1) cold-work gives rise to three peaks (δ, β_1 and β_2 peaks) in the internal friction versus temperature curve of pure vanadium; (2) hydrogen impurities, dissolved at low atomic concentration (< 0·05 per cent) in prior strained material, induce the α peak and remove the δ one, they do not produce any observable effect in prior annealed material; (3) a well evident asymmetric peak is induced by hydrogen impurities when their atomic concentration exceeds about 0·5 per cent.

Examination of the experimental data indicates that the occurrence of the α peak needs both plastic deformation and hydrogen impurities; this is the distinctive feature of the high temperature cold-work peaks, thus it can be inferred that the α peak is a C W P due to hydrogen. According to the atmosphere dragging model proposed by Schoeck to explain the C W P[7], the binding energy

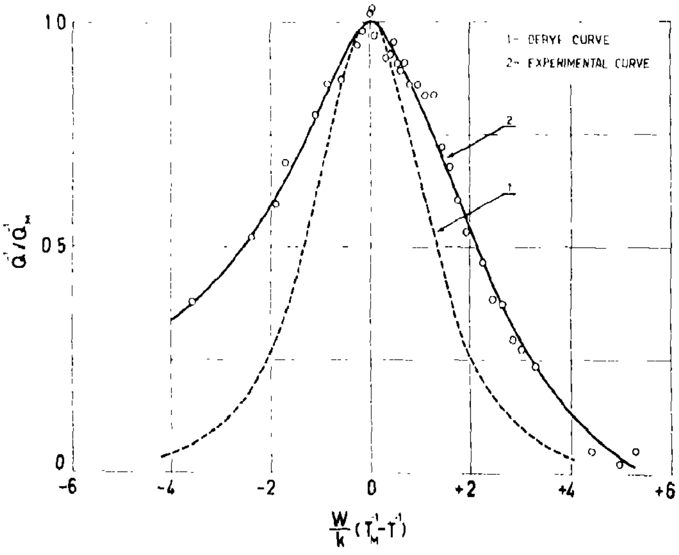

Fig. 4 Comparison between the experimental curve of δ peak corresponding to an activation energy of 0·012 eV and the Debye curve.

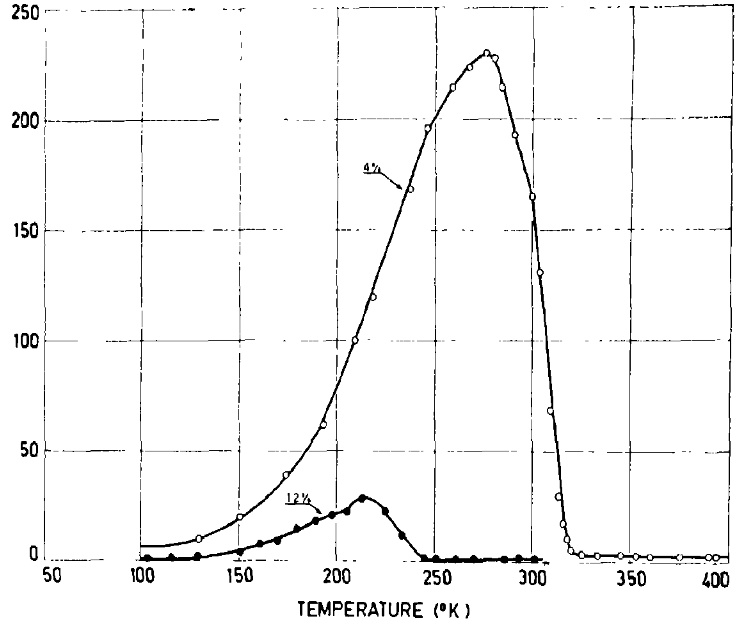

Fig. 5. Internal friction of prior annealed and then hydrogen charged samples 2(○) and 3(●) during cooling measurement runs The vibration frequencies are $2{\cdot}0 \times 10^4$ Hz (sample 2) and $1{\cdot}0 \times 10^4$ Hz (sample 3)

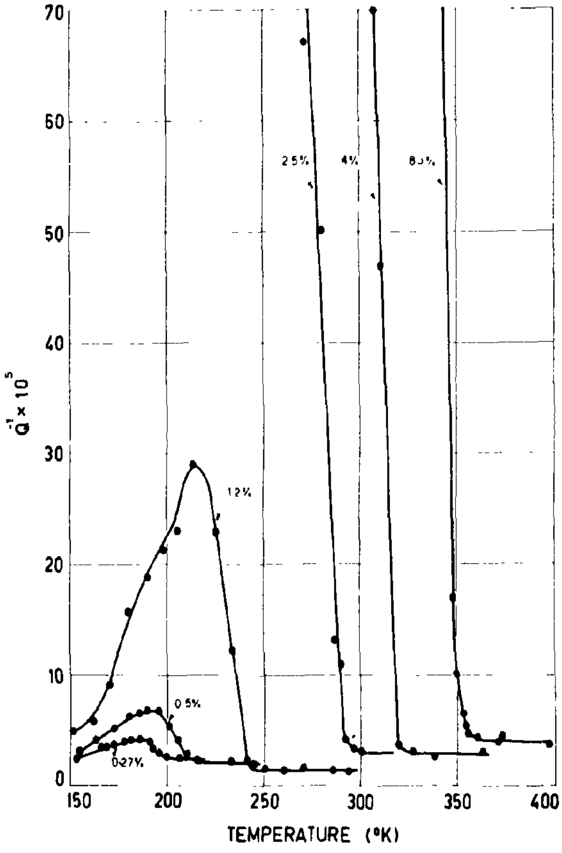

Fig 6. Internal friction of some V–H systems during the first cooling measurement run after hydrogenation.

W_b between a hydrogen impurity and a dislocation segment can be calculated as a difference between the activation energy W_α of the α peak and the diffusion energy W of hydrogen in vanadium. Assuming $W = 0{\cdot}059$ eV [8] and $W_\alpha = 0{\cdot}52$ eV, the value 0·46 eV is obtained for W_b, which is somewhat higher than those evaluated by means of the same procedure for the hydrogen-dislocation binding energy in Ta, Nb [4] and Fe [9].

The relatively low value of W_δ and $f_{0\delta}$ and the essential role played by cold-work in the occurrence of δ peak excludes that the motion of some impurity may be the source of this anelastic effect. Any explanation of δ peak, based on the stress-induced ordering of an isolated intrinsic point defect, meets also with difficulties; namely, due to the stability of δ peak at room temperature, the point defect should be endowed with an activation energy for diffusion exceedingly higher than that for reorientation; moreover, the low frequency factor and the wide spectrum of relaxation times could not be easily understood in terms of a stress-induced ordering mechanism. The influence of hydrogen on the relaxation strenght seems also to rule out the possibility that agglomerates of intrinsic point defects or impurity-defect complexes may originate this anelastic effect.

In the light of the above arguments the idea that δ peak may be due to the motion of dislocation segments seems the most convincing one. On the basis of this hypothesis, the disappearance of δ peak following a hydrogen doping treatment can be easily accounted for in terms of a dislocation pinning process, which is confirmed by the simoultaneous appearance of the hydrogen CWP (α peak). On the other hand a wide spectrum of relaxation times as well as a low value for the frequency factor have been proved to be usual features of the dislocation relaxation effects [10].

Since β_1 and β_2 peaks appear only after plastic deformation, it is definite that they are due to lattice defects produced by cold-working. Their position in the temperature

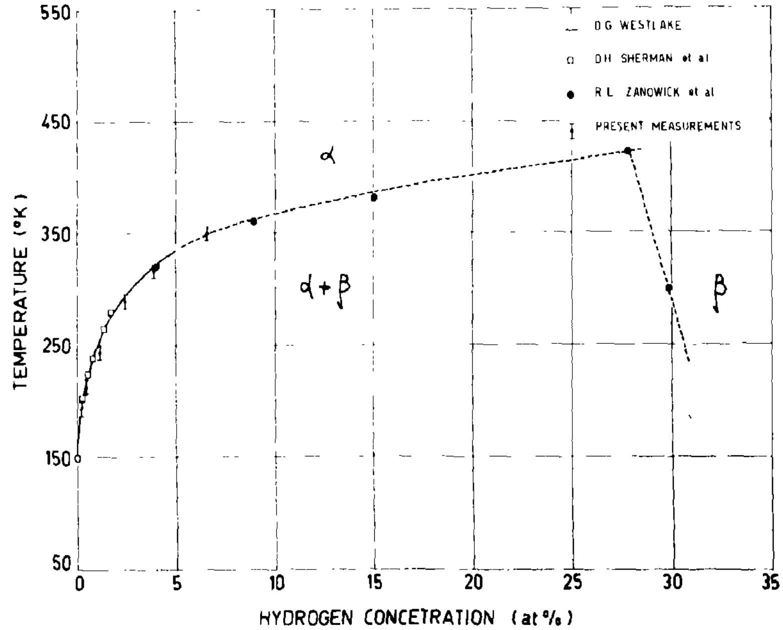

Fig. 7. Comparison between our data on the phase diagram of V–H system and those reported by other investigators.

scale suggests, for comparison with cold-worked fcc metals, that they may be related to some kind of association between dislocations and point defects.

The anelasticity of prior annealed and then hydrogen doped vanadium as measured during cooling runs (Figs. 5 and 6), does not differ significantly from that of heavily hydrogen loaded tantalum[11, 12] and can be thus interpreted in a similar way. According to the ideas put forward in a previous work[11], the observed anelasticity arises from the stress-induced ordering of interstitial hydrogen arranged in the body centered tetragonal lattice of the β phase of V–H system and the abrupt rise observed in the curves of Fig. 6 starts at the $\alpha \rightleftharpoons \beta$ transition temperature. On the basis of this interpretation the phase diagram of V–H system can be deduced from internal friction measurements; the results of the present work, together with those of other investigators[13–15] are reported in Fig. 7. Good agreement is found between different measurements, which supports the proposed explanation of the anelasticity of V–H system.

5. CONCLUSIONS

The results reported here show that the anelastic behaviour of vanadium at low temperatures is similar to that of tantalum and niobium and confirm that the δ peak is associated with a dislocation mechanism, which, perhaps, is the same as the one responsible for the Bordoni peak in cold-worked fcc metals. The essential role played by hydrogen in the occurrence of the α peak clearly shows that this is a cold-work type peak. The asymmetric anelastic effect brought about by hydrogen impurities in fully annealed vanadium is satisfactorily accounted for in terms of a stress-induced ordering mechanism taking place in the β phase of the V–H system.

Acknowledgements—We are grateful to Professor Nuovo for many useful discussions and we much appreciate the technical assistance of G. Libriani

REFERENCES

1. CHAMBERS R. H., *Physical Acoustics*, Vol. 3, Part A, p. 123. Academic Press, New York (1966).
2. BORDONI P. G., *Final Rep. of Contract* No. DA 91-591-EUC-2051.
3. KRAMER J. and BAUER C. L., *Phys. Rev.* **163**, 407 (1967)
4. MAZZOLAI F. M. and NUOVO M., *Solid State Commun.* 7 103 (1969).
5. BORDONI P. G., *Nuovo Cim.* **4**, 177 (1947).
6. NUOVO M., *Ricerce. scient.* **31**, 212 (1961).
7. SCHOECK G., *Acta Met.* **11**, 617 (1963)
8. CANTELLI R., MAZZOLAI F. M. and NUOVO M., This conference
9. GIBALA R., *Trans. AIME* **239**, 1574 (1967).
10. NIBLETT D. H., *Physical Acoustics*, Vol 3, Part A, p 78 Academic Press, New York (1966).
11. CANNELLI G. and MAZZOLAI F. M., *Nuovo Cim.* **64B**, 171 (1969)
12. BUTERA R. A. and KOFSTAD P. *J. appl. Phys.* **34**, 2172 (1963).
13. SHERMAN D. H., OWEN C. V. and SCOTT T. E., *Trans. AIME* **242**, 1775 (1968).
14. WESTLAKE D. G., *Trans. AIME* **239**, 1341 (1967).
15. ZANOWICK R. L. and WALLACE W. E., *J. chem. Phys.* **36**, 2059 (1962).

J. Phys. Chem. Solids Pergamon Press 1970 Vol. 31, pp. 1921–1923 Printed in Great Britain.

ANELASTICITY OF DISLOCATION DIPOLES

D. N. BESHERS
Henry Krumb School of Mines, Columbia University, New York, N.Y. 10027, U.S.A.

(*Received* 5 *September* 1969; *in revised form* 11 *November* 1969)

Abstract—Flipping of dislocation dipoles between two stable positions is shown to have too high an activation energy to be associated with Bordoni peaks.

GILMAN[1] has proposed that the thermally-activated flip-flopping of dislocation dipoles may lead to a detectable mechanical relaxation. The mechanism was originally proposed for the Bordoni peak, but a recent investigation of nickel[2, 3] revealed another peak (Peak Y) which was shown to be much more likely to be a dipole peak. A similar peak has been reported in aluminum[4]. The principal evidence against the dipole mechanism for the Bordoni peak is the stability of the Bordoni peak at high temperatures. The prospect that Peak Y is a dipole peak warrants further consideration of the model, which was somewhat heuristically developed.

The edge dislocation dipole (Fig. 1) consists of two parallel edge dislocations of opposite sign on parallel slip planes separated by a distance h. There are two positions of stable equilibrium in which the line of centers is at 45° and 135° to the slip plane. It is possible that the dipole can have segments of different orientation along its length, separated by regions of higher energy called orientation junctions where the dislocations cross over each other. An elasticity can be associated with either the creation or the propagation of these orientation junctions. If a dipole has no orientation junction, and a reversal is to take place somewhere along it, then two orientation junctions of opposite sense must be created, one at each end of the segment with reversed orientation. Gilman's calculations are based on thermal activation of this creation process. The propagation of the junctions along the dipole length may lead to a complete reversal, if the terminating segments are free to move appropriately[5, 6].

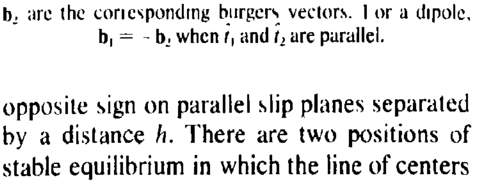

Fig. 1. Dipole with orientation junction as seen projected normal to the slip plane. $\hat{t}_1$ and $\hat{t}_2$ are unit vectors giving the (arbitrary) positive sense of direction of each line; $\mathbf{b}_1$ and $\mathbf{b}_2$ are the corresponding burgers vectors. For a dipole, $\mathbf{b}_1 = -\mathbf{b}_2$ when $\hat{t}_1$ and $\hat{t}_2$ are parallel.

Orientation junction theory has, as Gilman pointed out, a formal similarity to the theory of kink generation and motion[7] which leads us to three considerations which he omitted. First, in the dipole theory, the junctions of the dipoles (Fig. 1) play a role analogous to the glide kinks which are associated with the transition of a dislocation line from one Peierls valley to another. Seen in this light, the activation energy W_f for the dipole mechanism and the energy for the final state are expected to include terms involving the orientation junction energy W_j analogous to the kink formation energy W_k.

Second, because the Peierls energy is still present, we must remember that in forming the junction configuration, several glide kinks of the same sign are necessarily involved in each segment (Fig. 2) so that these kink energies must be included in the model. Indeed,

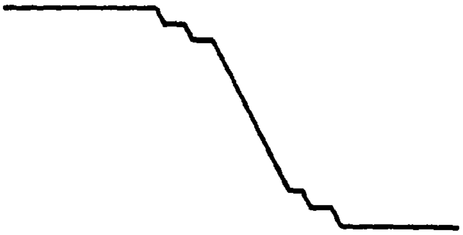

Fig. 2. The possible effects of the Peierls energy on one element of an orientation junction. There are several glide kinks at the bend, and the junction itself has fallen into a Peierls valley of another orientation

the first motion of the segments towards each other must be equivalent to doublekink formation. Unless the close proximity of the dipole elements drastically reduces the formation energy of a glide kink, it follows that the activation energy for dipole flipping is substantially higher than that for double-kink generation, W_{dk}.

Third, Paré's[8] general comments on the double-kink mechanism apply equally well to the dipole mechanism, or any other dislocation mechanism. Paré pointed out that the relaxation strength is very small unless the system is making transitions between states for which the total free energy of the system is the same within approximately kT, where k is Boltzmann's factor and T the absolute temperature. This equality of energies demands that only those dislocations subject to an internal stress $\sigma_i \gtrsim 2W_j/bh^2$ contribute appreciably to the relaxation process.

The problem, then, is to estimate W_j in the light of these general considerations. It suffices to proceed by elementary methods, approximating the junction by straight line segments making an angle φ with the longer lines. When the junction is very spread out, and the junction segments make only a small angle 2φ with each other, we may approximate the local interaction by using the well-known expressions for parallel dislocations of the given separation, and considering each segment to have a line tension $\frac{1}{2}Db\ln(h/r_0)$, where $D = \mu b/2\pi(1-\nu)$, μ is the shear modulus, ν Poisson's ratio and r_0 is the cutoff radius [9]. If the interaction between two parallel edges of a dipole, separated by y, is denoted by $W_d(y)$, then the interaction energy of a junction of length L is

$$\int_0^L W_d[y(x)]\,\mathrm{d}x = -2\int_h^0 W_d(y)\frac{\mathrm{d}y}{2\tan\varphi}$$

$$= Db\frac{h}{\tan\varphi}\left(\ln\frac{\sqrt{2}h}{r_0}+\frac{\pi}{2}-1\right)$$

and the increase in line energy is to a first approximation

$$Dbh\ln\left(\frac{h}{r_0}\right)\csc\varphi - Dbh\ln\left(\frac{h}{r_0}\right)\cot\varphi.$$

The total energy of the junction segment is

$$W_j = Dbh\ln\left(\frac{h}{r_0}\right)\csc\varphi$$

$$+ Dbh\cot\varphi\left[\ln\sqrt{2}+\frac{\pi}{2}-1\right].$$

Since both terms diverge as $\varphi \to 0$, it is clear that there is a strong tendency for the junction to shorten. The other extreme case, which can be treated by elementary methods, is to estimate the energy when $\varphi = \pi/2$, i.e. when the junction consists of a length of doubled screw perpendicular to the edge dipole. The elastic energy of the junction is then approximately $(1-\nu)Dbh\ln(h/r_0)$, which is smaller than the result obtained by extrapolation of the previous answer to $\varphi = \pi/2$. These elementary calculations imply that the junction is rather sharp with $W_j \approx Dbh\ln(h/r_0)$.

Next, consider a dipole with a reversed segment bounded by two orientation junctions of opposite sense. Assuming that the junctions are far enough apart that their recombination may be prevented by the action of internal stresses from other sources, then the reversed segment has become metastable with an energy $2W_j$ greater than the original dipole. The array is metastable since reversion to the dipole will require either that the junctions be freed or that a new reversal process, tending to return to the dipole, be started somewhere along the reversed segment, with a local increase of interaction energy. If the reversal segment is metastable then $W_f > 2W_j$. Kroupa and Brown[10] showed that jogs, and kinks, interact with energies that fall off as $1/r$, where r is the separation between them. Now the junctions approximate to doubled kinks, so their interaction energy should also fall off as $(1/r)$, with a force falling off as $1/r^2$, so there is some justification for our assumption above about their recombination.

Combining all the above considerations, we have the inequality

$$\tfrac{1}{2}W_f > W_j \gg W_{dk} \gtrsim 2W_k.$$

The emphatic inequality in the middle may be appreciated by considering the case of $h = 10b$, for which $W_j = 2\mu b^3$ or many electron volts. Bordoni peaks have activation energies of the order of several tenths of an electron volt. Further, W_j depends on h, while the Bordoni peaks have a fairly well-defined activation energy.

The dipoles seen in the electron microscope and discussed by Feltner[5] belong to Stages I and II of work hardening with $h > 100b$. They are eliminated as sources of anelasticity by the foregoing calculation and are also unsuitable for explaining phenomena associated with Stage III. Dipoles with $h \leqslant 10b$ will be invisible in the electron microscope[11] and their behavior will be quite different because of core-overlap effects.

It does not seem possible that the edge dipole mechanism can give rise to relaxations observed at small oscillatory stresses, such as the Bordoni peak. This conclusion is reinforced by Paré's point: the internal stress necessary for appreciable relaxation strength is $\mu \ln(h/r_0)/\pi(1-\nu)$ which turns out to be of the order of, or greater than, the yield strength for $h/b < 10^3$. Further, this condition is stronger when the junction energy, i.e. h, is lower. Large oscillatory stresses, as discussed by Feltner[5], are a different matter and the present considerations do not affect his discussion.

There is also the possibility than anelasticity is associated with the propagation of existing orientation junctions (see discussion to Ref. [1]). The high values calculated for W_j make it unlikely that a sufficient number of junctions exist in thermal equilibrium to be important, but if they exist, Fig. 2 shows that there may be Peierls stress resistance to the motion. If the Peierls stress is sensitive to the normal stress[12], it is possible that modified Peierls stresses in dipoles, or other special dislocation arrangements, may give rise to modified Bordoni peaks.

Acknowledgement—This work was supported in part by the Office of Naval Research

REFERENCES

1. GILMAN J. J. *J. phys Soc Japan* **18**, Suppl I 172 (1963)
2. SOMMER A. W. and BESHERS D. N. *J. appl Phys.* **37**, 4603 (1966)
3. VENKATESAN P. S. and BESHERS D. N., *J. appl Phys* **41**, 42 (1970).
4. LAX F. and FILSON D. H., *Phys. Rev.* **114**, 1273 (1959).
5. FELTNER C. E., *Phil. Mag.* **12**, 1229 (1965)
6. LI J. C. M. and SWANN P. R., *Phil. Mag.* **10**, 617 (1964)
7. SEEGER A. and SCHILLER P., *Physical Acoustics, Principles and Methods* (Edited by W. P. Mason), Vol. 3A, Academic Press, New York (1965)
8. PARÉ V. K., *J. appl. Phys.* **32**, 332 (1961).
9. KROUPA F., *J. Phys.* **27**, C154 (1966).
10. KROUPA F. and BROWN L. M., *Phil. Mag.* **6**, 1267 (1961).
11. HIRSCH P., HOWIE A., NICHOLSON R. B., PASHLEY D. W. and WHELAN M. J., *Electron Microscopy of Thin Crystals*. Butterworths, London (1965)
12. SANDERS W. I., *Phys. Rev.* **123**, 1540 (1962)

J. Phys. Chem. Solids Pergamon Press 1970. Vol. 31, pp. 1925–1933. Printed in Great Britain

INTERNAL FRICTION AND ULTRASONIC YIELD STRESS OF THE ALLOY 90 Ti 6 Al 4 V

WARREN P. MASON[*] **and JERZY WEHR**[†]

Department of Civil Engineering and Engineering Mechanics, Columbia University,
New York, N.Y. 10027, U.S.A

(*Received* 5 *September* 1969)

Abstract—The alloy 90 Ti 6 Al 4 V is used as a mechanical transformer to produce high strains in metal samples. The internal friction, modulus defect and limiting stable strain amplitudes have been studied over wide frequency and temperature ranges. The internal friction Q^{-1} of annealed samples has the low value of 5×10^{-5} which is independent of the frequency and decreases only slightly at high temperature. The result is consistent with a model in which the energy loss is produced by a non-linear motion across the Peierls kink barrier. The value found for the ratio of the internal friction to the modulus change is 0·03 which is intermediate between two theoretical calculations.

This material becomes unstable at strains from 3 to 5×10^{-4}. Evidence is presented which shows that this is a material with a Cottrell type pinning with pinning points on the average about 3 Burgers distances apart. Assuming that on the average one kink occurs between each pinning point, the modulus defect is consistent with about 10^{10} dislocations per cm^2. The frequency and temperature variations are consistent with this model.

1. INTRODUCTION

THE ALLOY 90 Ti 6 Al 4 V has been suggested for use in the supersonic plane. It also has been used as a mechanical transformer[1] for increasing the strain in a sample whose high amplitude and fatigue properties are to be studied. Hence it is important to determine its internal friction and modulus defect at both low amplitude and high amplitude vibration levels.

The internal friction at low amplitudes has been found to be independent of the frequency from 17 KHz to 10 MHz, and to be independent of the temperature (within about 30 per cent) from 4·2° up to 600°K. An impurity type peak is observed which peaks at 180°K for 10 MHz but after this effect is removed, the background internal friction is independent of the temperature. By annealing strained samples and straining annealed samples it is shown that this background internal friction is due to dislocations. The results obtained are in agreement with a 'low frequency' internal friction model[2] for which the damping results from the lattice vibrations generated when the kink crosses the kink Peierl's barrier. Theoretical studies[3, 4] have shown that this energy loss requires a dissipative stress τ_{dp} equal to from 0·01 to 0·1 of the kink stress σ_k, to replace this energy lost to the lattice vibrations. This ratio β can be measured by determining the ratio of the internal friction change ΔQ^{-1} to the modulus defect change determined when a strained sample is annealed. This value was found to be about 0·03 in agreement with the results in copper.

High amplitude measurements show that the internal friction is constant up to longitudinal strains of 4×10^{-4}. This is about half the static strain. The variation of the static stress with temperature indicates that the alloy is a material with Cottrell type pinning with pins on the average separated by about three times the Burger's distance b which is $2{\cdot}95\times10^{-8}$ cms for titanium. Assuming one kink on the average for each pinned loop, the internal friction and the modulus defect are consistent

---

[*] Supported by the Institute for the Study of Fatigue and Reliability.

[†] Supported by the Ford Foundation. Permanent address Polish Academy of Sciences, Warsaw, Poland.

with a dislocation density of about 10^{10} dislocation density of about 10^{10} dislocations per cm^2.

2. EXPERIMENTAL RESULTS FOR HIGH AMPLITUDE EFFECTS

The low frequency measurements (17 KHz) were performed using a transducer and transformer system described previously[1]. Since the system, the shape of the specimen and the method of calibration have been described previously, the reader is referred to this publication[1]. An evacuated container is used to eliminate the radiation resistance. The modulus change in the sample alone can be obtained by multiplying $2\Delta f/f$ by the ratio $(M_0+M_S)/M_0$ where M_0 is the effective mass of the transducer and transformer and M_S the mass of the sample; Δf is the change in frequency and f the frequency of the sample and system.

The internal friction and modulus change for a typical sample of the alloy are shown by Fig. 1. Instability sets in at maximum strain levels which may vary from 3×10^{-3} to 5×10^{-3}. The instability is accompanied by a sharp rise in the internal friction Q^{-1} and by the modulus defect $\Delta S/S$. *After this happens* the modulus defect has increased by about three per cent and the internal friction increases by nearly a factor of 10. Furthermore the critical longitudinal stress is reduced by over a factor of 10. It appears that this behavior is connected with the presence of long dislocation loops which are not repinned at room temperature. Specimens annealed in a vacuum at 750°C for 1 hr are sometimes returned to a normal condition but not always. The presence of long dislocation loops is confirmed by the non-linearity of the pick-up voltage as a function of the frequency, as shown by Fig. 2. Instead of a symmetrical response about a resonant frequency, the pick-up voltage builds up to a maximum as the frequency is reduced, after which it discontinuously drops to a low value. On the increasing cycle the response remains low for 34 cycles above the discontinuous decrease frequency after which it discontinuously increases to the value of the decreasing curve. This type of performance is

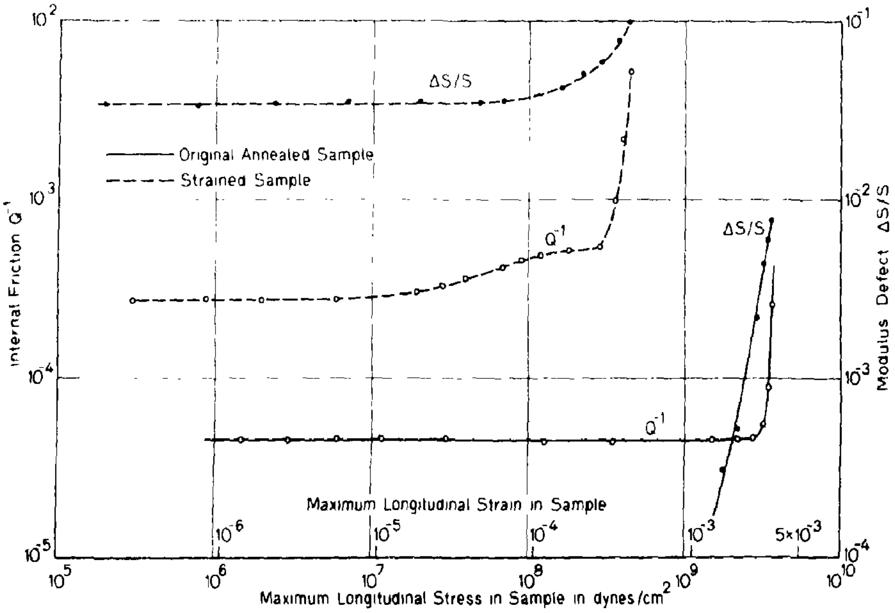

Fig. 1. Typical internal friction and modulus defect for an annealed sample of the alloy 90 Ti 6 Al 4 V. Dashed line shows the result obtained after the sample has become unstable.

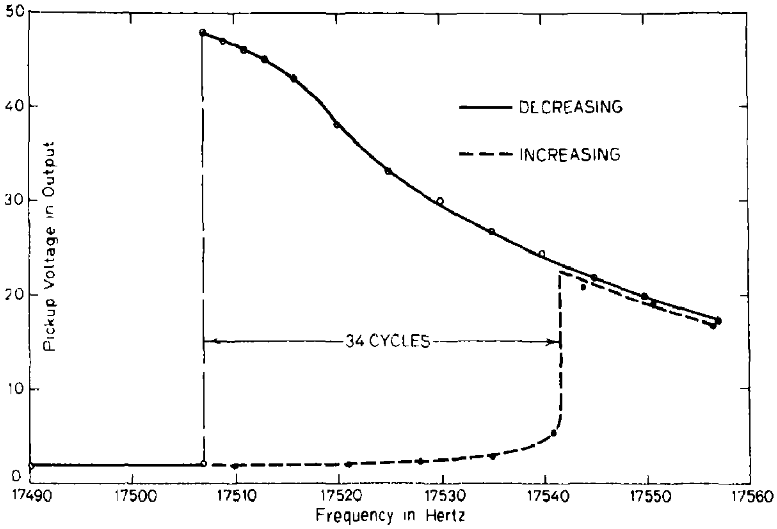

Fig. 2. Pick-up voltage plotted against the frequency for an unstable sample near its critical point. This result is indicative of a non-linear soft spring characteristic

characteristic of a non-linear spring which is softer at high amplitudes. This performance is in agreement with the existence of long dislocation loops which bow out and become less stiff as their displacement increases.

It appears that in the annealed state the dislocations are closely pinned in an atmosphere approximating a Cottrell type pinning [5]. This is shown by the yield stress curve for static stresses, Fig. 3, plotted as a function of the temperature. According to the Cottrell atmosphere concept the concentration along the dislocation is given by

$$c = c_0 e^{U/kT} \tag{1}$$

where c is the concentration along the dislocation, c_0 the density of the impurities in the body of the material, U the binding energy to the impurity, k Boltzmanns constant and T the absolute temperature. If we apply this concept to the data of Fig. 3, we find that U is about 0·5 eV and the average separation between pinning points is 10^{-7} cm or about 3 Burgers distances. From internal friction measurements it appears that on the average there is one kink between each pinning point.

Measurements were made of the ultrasonic yield stress as a function of the temperature. While the scatter is quite large, it appears that the ultrasonic yield stress is about half the static yield stress. Similar results are found for other metals [6]. This may be caused by the change in the positions of the pinning points with ultrasonic stress as suggested by Alefeld [7].

3. INTERNAL FRICTION MEASUREMENTS

Another important property of the alloy is its internal friction. This is connected with the motion of dislocations. This can be verified by annealing and straining experiments. When the sample is initially formed by the turning process its Q is lower and its frequency lower than found after being annealed for one hour at 760°C. Table 1 shows the resonance frequency and Q in the as formed condition and in the heat treated condition. The Q increases and the resonant frequency increases. If we take the average of the increase in Q^{-1}, i.e. ΔQ^{-1}, and the average increase in the modulus change $\Delta S/S$ the ratio is about 0·03 as shown by the last column. Similarly for a strain of

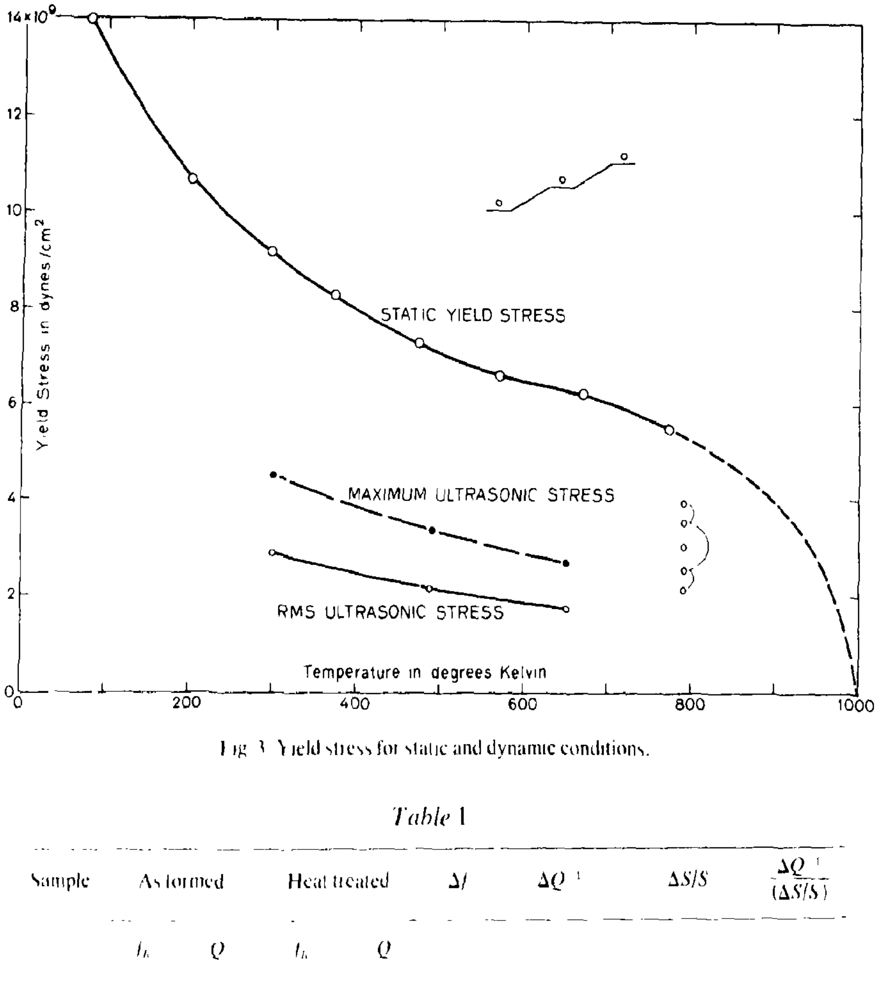

Fig. 3. Yield stress for static and dynamic conditions.

Table 1

Sample	As formed		Heat treated		Δf	ΔQ^{-1}	$\Delta S/S$	$\frac{\Delta Q^{-1}}{(\Delta S/S)}$
	f_R	Q	f_R	Q				
1	17326	1920	17418	6960	92	$8{\cdot}61 \times 10^{-4}$	$2{\cdot}48 \times 10^{-2}$	0·0346
2	17377	2480	17468	8750	87	$6{\cdot}56 \times 10^{-4}$	$2{\cdot}34 \times 10^{-2}$	0·0282
3	17335	2480	17415·5	9200	80·5	$6{\cdot}7 \times 10^{-4}$	$2{\cdot}17 \times 10^{-2}$	0·0308
4	17392	2900	17460	10900	68	$5{\cdot}55 \times 10^{-4}$	$1{\cdot}83 \times 10^{-2}$	0·0304

Average 0·0308

2 per cent, the internal friction increases to about 5×10^{-4} and the frequency drops by 160 cycles. Both of these experiments are indicative of a dislocation background.

Since the average pinning length is very small any dislocation dissipation due to a damping proportional to the dislocation velocity is negligible and all the damping must be due to the 'low frequency' component discussed in the next section. Since any other type of damping is negligible, this material provides an opportunity for evaluating the frequency and temperature variation of this 'low frequency' type of damping. Measurements were made on a number of unannealed samples with the result shown by Fig. 4. In order to cover a wide frequency range some shear wave measurements were made at 10 MHz. This raises the question of whether some of the attenuation was due to scattering losses from the polycrystalline grain structure of the material. This alloy has a fine grain structure with grains from 10^{-3} to 10^{-4} cm. Measurements were made over a frequency range and it was found that grain scattering effects did not produce an appreciable loss until a frequency of 30 MHz. Hence the values measured at 10 MHz are due to dislocations. Since the internal friction scatters over a range, it appears probable that the values are substantially independent of the frequency as shown by Fig. 4. Lower values still can be obtained by annealing the materials.

Measurements were then made to evaluate the internal friction as a function of the temperature. Since the pulsed 10 MHz system can be taken down to liquid helium temperature, measurements were made on two samples as shown by Fig. 5. Both samples showed an impurity type peak occurring at about 180°K. This did not appear to be due to dislocations since straining the sample changed the dislocation background but did not change the difference of the peak height from the background. If we analyze the peak as a single relaxation process, as shown by Fig. 6, it appears to be somewhat broader than a single relaxation and with an average relaxation energy of about 0·1 eV. If we subtract out the peak, the dislocation loss appears to be independent of the temperature.

Since it was not possible to go higher in temperature with this arrangement, measurements were made with the transducer transformer arrangement, using a furnace around the specimen with the combination mounted in an evacuated chamber. A number of different samples were taken up to 500°K with similar results. When a sample was taken up to 600°K an apparent increase seems to occur

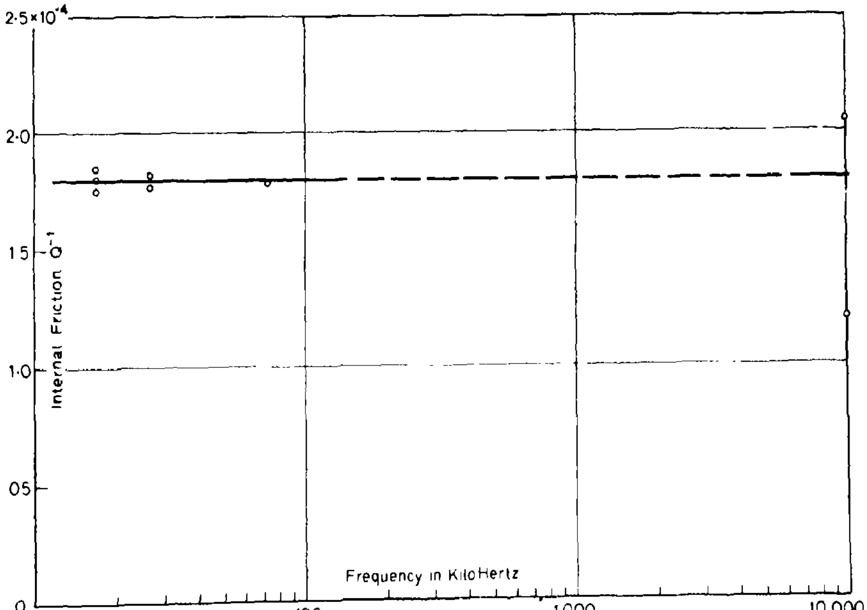

Fig. 4. Internal friction for unannealed samples as a function of the frequency Measurements up to 70 kHz were made with longitudinal vibrations. Measurements at 10 MHz were made by a pulsing method using shear waves.

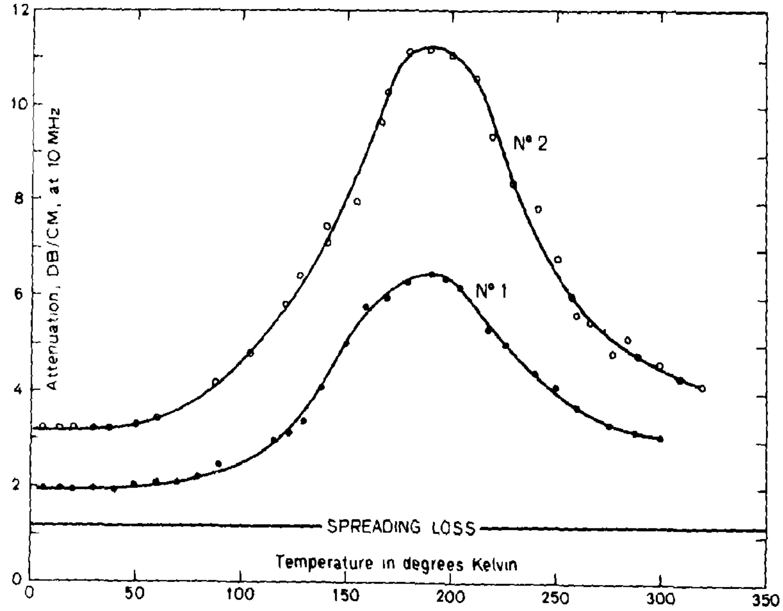

Fig. 5 Attenuation for shear waves at 10 MHz plotted against the temperature for two unannealed samples.

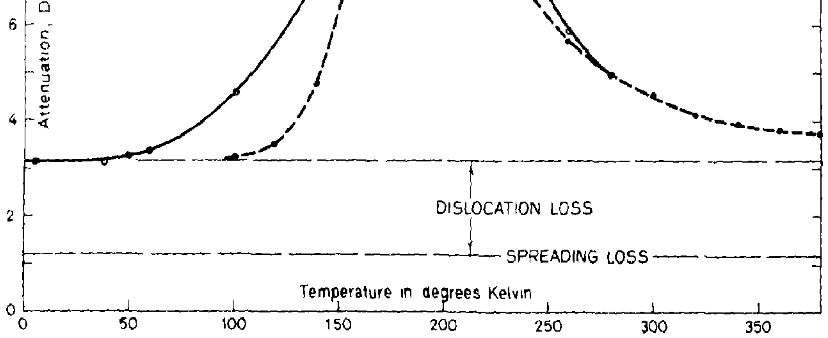

Fig. 6 Analysis of impurity peak in terms of a single activation energy. After subtracting this loss the dislocation component is independent of the temperature.

which may be connected with a partial unpinning. Hence up to 500°K there is a decrease in the internal friction of about 20 per cent. Figure 7 shows the measured variation of the internal friction with temperature for two well annealed samples.

4. THEORETICAL INTERPRETATION

The internal friction due to a drag coefficient proportional to the velocity has been worked out by Oen, Holmes, and Robinson. For a single loop length as would be consistent with the present case, the internal friction from this source will not be more than

$$Q^{-1} = 6 \times 10^{-9} \tag{2}$$

which is negligable compared to the measured value of $1 \cdot 5 \times 10^{-4}$. Hence another source of dissipation must be invoked which produces an internal friction independent of the frequency and nearly independent of the temperature.

Such a source of internal friction has been discussed previously[2] and has been applied to explaining the low frequency component for metals and for the earth's vibrations which also indicate a constant Q independent of the frequency. This source of dissipation is connected with the motion of dislocation kinks over Peierls-type kink barriers. This motion occurs non-linearly and results in the generation of lattice vibrations which abstract energy from the motion. For the present case with a single kink between pinning points the model is shown by Fig. 8. Here the kink occupies one minimum energy position and to move to the next energy minimum it has to cross the kink barrier of height W. According to calculations given by Seeger and Schiller[9], the energy W and the kink stress σ_k required to take the kink across the barrier are given by

$$W = \frac{\sigma_k b^3}{5}; \sigma_k = \frac{192}{\pi^2\sqrt{3}}\left(\frac{1-\nu}{1+\nu}\right)\frac{b}{w}\left(\frac{\sigma_p}{\mu}\right)^2\mu \tag{3}$$

where ν is the Poisson's ratio, w is the kink width, σ_p the Peierls stress and μ the shearing modulus. For reasonable values of $b/w \doteq 1$ and $(\sigma_p/\mu) \leqslant 10^{-2}$; it appears that σ_k will not be more than 10^8 d/cm^2 and $W \leqslant 5 \times 10^{-16}$ ergs $= 4 \cdot 1 \times 10^{-4}$ eV. This is a low enough energy so that it will not affect the internal friction down to 4°K.

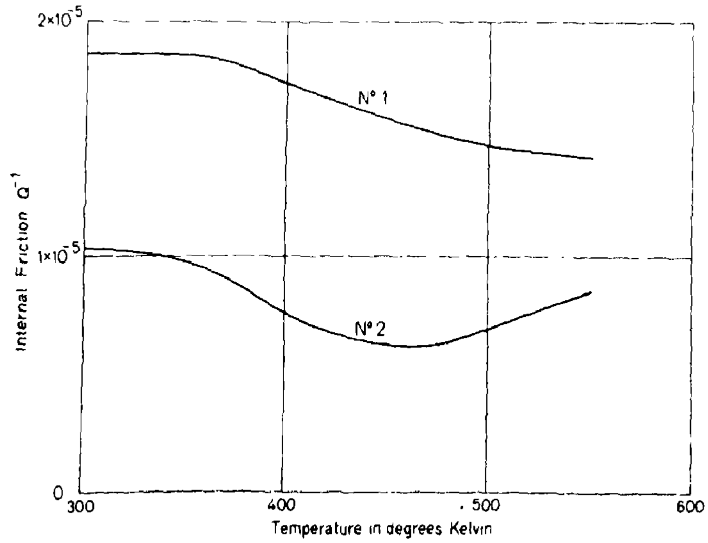

Fig. 7. Internal friction at 17·6 kHz as a function of the temperature

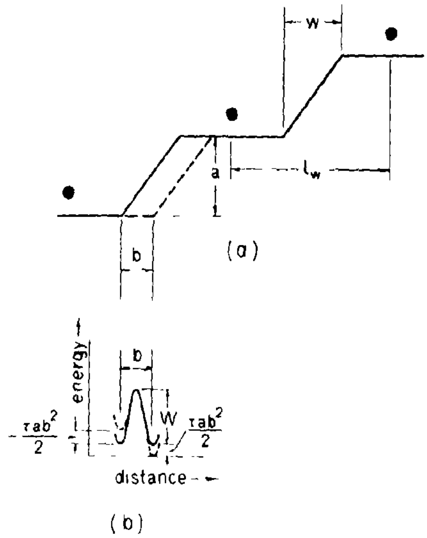

Fig. 8. Dislocation kinks and kink energy barriers. Dashed lines show the effect of an applied shearing stress τ.

For stresses less than the kink stress σ_k, it requires thermal energy to take the kink across the kink barrier. As shown by Fig. 8(b) the effect of a shearing stress τ is to lower one barrier by an amount $\tau ab^2/2$, where a is the height of the kink, and to raise the other barrier by the same amount. If this is the only stress applied, it is well known from reaction rate theory that the net rate of jumps per second is

$$(\alpha_{12} - \alpha_{21}) = \omega_0 e^{-W/kT}\left[e^{\tau ab^2/2kT} - e^{-\tau ab^2/2kT}\right]$$

$$\doteq \omega_0\left(\frac{\tau ab^2}{kT}\right)e^{-W/kT} \qquad (4)$$

since it can be shown that $\tau ab^2/2kT$ is much less than unity even for low temperatures. $\omega_0 = 2\pi$ times the frequency of the kink in the potential well. This is usually taken to be 10^{13} Hz.

When the kink has crossed the barrier it acquires an energy $\sigma_k ab^2/2$ from the negative slope of the potential barrier. If the kink had no interaction with adjacent kinks or pinning points and did not generate any lattice vibrations, this energy would be sufficient to carry it over the next barrier, etc. However Weiner [3] and Atkinson and Cabrera [4] have shown, using a Frenkel–Kontorowa model, that it takes a dynamic Peierls stress τ_{dp} of from 0·01 to 0·1 of the Peierls stress to keep the dislocation moving after it first crosses the barrier. This stress is necessary to replace the energy lost to mechanical lattice vibrations generated when the dislocation moves across the barrier. While the calculation is for a straight dislocation, it has generally been considered [9] that it applies to a kink also.

When the dislocation is pinned and interacts with adjacent kinks, the energy acquired from the negative slope of the barrier is stored in stretching the dislocation in a string model or in pushing the kinks closer together in the kink model. In either case the energy stored is

$$E = n\sigma_k ab^2/2 \qquad (5)$$

while the energy dissipated is

$$\Delta W = n\tau_{dp}ab^2/2 = n\beta\sigma_k ab^2/2 \qquad (6)$$

where β is the ratio of τ_{dp} to σ_k and n is the number of kink displacements. Hence for the dislocation system alone the internal friction Q^{-1}, which is by definition the ratio of the energy dissipated to the energy stored, is

$$Q^{-1} = \beta. \qquad (7)$$

For the complete system we have to consider the energy stored in the elastic part of the crystal and for this case

$$Q^{-1} = \beta\left(\frac{\Delta\mu}{\mu - \Delta\mu}\right) \doteq \frac{\beta\Delta\mu}{\mu} = \beta(\Delta S/S) \qquad (8)$$

where ΔS is the stiffness change for any mode such as the longitudinal mode used. From the measurements of Table 1, it is found that $\beta \doteq$ 0·03 which is intermediate to the two theoretical values. Since the number n of kink jumps is proportional to the applied stress and is equal to the total number n_0 when $\tau = \sigma_k$, then we have the relation

$$n = \tau n_0/\sigma_k. \qquad (9)$$

Some idea of the number of kinks moving can be obtained from the following calculation. The total shearing strain in the material is the sum of the elastic strain plus the plastic strain or

$$S = S^E + S^P = S^E + nsb = S^E + nab^2 \qquad (10)$$

where n is the number of kinks displaced and s their area equal to ab. But from Equation (9) this can be written

$$S = S^E + \frac{n_0\tau}{\sigma_k}ab^2. \qquad (11)$$

Dividing through by the shearing stress τ and collecting terms

$$\frac{\Delta\mu}{\mu} = \frac{\mu' - \mu}{\mu'} = \frac{n_0\mu' ab^2}{\sigma_k}. \qquad (12)$$

We found that σ_k may be in the order of 10^8 d/cm² and $\mu' = 4\times 10^{11}$ d/cm²; $b = 3\times 10^{-8}$ and a is in the same order. For the turned sample $\Delta S/S = 2\times 10^{-2}$. Hence we have

$$2\times 10^{-2} = n_0\times 4000\times 27\times 10^{-24}$$

or

$$n_0 \doteq 1{\cdot}85\times 10^{17}. \qquad (13)$$

If there is on the average of one kink between each pinning point and the separation between points is 10^{-7} cm then the number of dislocations for the strained sample is about $1{\cdot}5\times 10^{10}$. For the annealed sample this might drop to $1{\cdot}5\times 10^{9}$, which appears to be a reasonable value.

The frequency and temperature variations of the internal friction at low strain amplitudes are also in agreement with this model. Since the energy loss is proportional to the number of kink displacements and for a given strain the number of kink displacements is a constant, the energy loss is proportional to the frequency and the internal friction Q^{-1} is independent of the frequency. The energy loss is proportional to the height of the kink barrier and this should be constant up to higher temperatures when the height may drop somewhat. This is in agreement with the curves of Figs. 6 and 7.

REFERENCES

1 MASON W. P. *Plasticity* (Edited by C. J. McMahon), pp. 287–363. Interscience, New York (1968)

2 MASON W. P., *A Source of Dissipation That Produces An Internal Friction Independent of the Frequency* Tech. Report No. 61, Institute for the Study of Fatigue and Reliability, also published in *Int. Conf. Fundamentals of Dislocation Theory*, Natl. Bureau of Standards (1969)

3 WEINER J. H., *Phys. Rev.* **136**, A863–868 (1964).

4 ATKINSON W. and CABRERA N., *Phys. Rev.* **138**, A763–766 (1965).

5 COTTRELL A. H., *Dislocations and Plastic Flow In Crystals*, p. 139. Oxford University Press, Oxford (1953)

6 MASON W. P. and WOOD W. A., *J. appl. Phys.* **39**, 5581–5584 (1968)

7 ALEFELD G., *Phil. Mag.* **11**, 809–826 (1965)

8 OEN O. S., HOLMES D. K. and ROBINSON M. T., *U.S. At. Energy Comm. Rep.* No. ORNL-3017, 3

9 SEEGER A. and SCHILLER P., *Physical Acoustics* (Edited by W. P. Mason), Vol. 3A, Chap. 8. Academic Press, New York (1966)

J. Phys. Chem. Solids Pergamon Press 1970. Vol. 31, pp. 1935–1940. Printed in Great Britain.

INTERNAL FRICTION IN WHISKERS AND THIN FILMS

V. S. POSTNIKOV, S. A. AMMER, B. M. DARINSKY, I. V. ZOLOTUKHIN and A. T. KOSILOV

Voronezh Polytechnic Institute, Vorenezh, U.S.S.R

(*Received 5 September* 1969)

Abstract—Techniques have been developed (torsional oscillations, ν - cps; flexural oscillations, ν = kc/s) and measurements of the low-frequency internal friction of strained and annealed metal whiskers and thin films were made in the temperature range from 20 to 1000°C

A dissipation mechanism taking account of aftereffect is suggested and the value of internal friction calculated. The expression obtained for Q^{-1} is used for determining the length of the dislocation segments which tear away from the pinning points in the process of recovery. The theory suggested is in qualitative agreement with the experiment.

IT IS WELL known that whiskers and particularly thin films are widely applied in modern technology. This is primarily caused by the fact that the application of whiskers and film materials opens the way to designing different miniature devices and also by the fact that their properties can differ significantly from those of bulk materials. The latter opens new interesting possibilities for practice.

In addition to this, whiskers and thin films are unique objects for studying the most important problems of solid state physics including the problems of micromechanics of defects.

The purpose of the present study was to bring to light the peculiarities of low-frequency internal friction in metallic microobjects and to give their possible interpretation in the framework of existing solid state physical concepts.

We studied whiskers and thin films of copper. Whiskers were grown by the hydrogen reduction of the halide CuCl at about 570°C (according to the Brenner technique). The length of the whisker was up to 20 mm, the diameter up to 5–70 μ, the growth orientation –[111] or [100], or [110]. The length of the whiskers under study was 5–7 mm, the diameter 5–20 μ.

The technique used in our work allowed us to make a detailed study of internal friction, strain and aftereffect of whiskers within the temperature range from room temperature up to 1000°C All the experiments were made in 10^{-5} torr vacuum created by a standard vacuum evaporation installation. The measuring setup, mounted under a glass envelope of the vacuum installation, was a low-frequency torsion micropendulum (Fig. 1) consisting of a T-shaped suspension (1) and a micromirror (2). Iron filings were cemented at the ends of the suspension. The weight of the suspension was not more than 1–2 mg. The axial load on the sample did not exceed 100 g/mm² The maximum relative strain amplitude throughout the internal friction Q^{-1} measurement was not more than 10^{-5}. The measurement error at a low loss level ($Q^{-1} < 10^{-5}$) did not exceed 2–5 per cent, or 10–15 per cent at a high loss level The whisker was strained by rotation around the vertical axis of a thermocouple (radius 0·1 mm) to which joint the whisker was attached. The lower end of the whisker remained motionless since the suspension was fixed by a limiting fork (12). The limiting fork was placed on one axis of a galvanometer (13) and had a rigid connection with it. The torque applied to the galvanometer frame on the side of the twisted whisker was compensated by the flow of current through the frame, the amount of current being proportional to the moment M Knowing the moment one can calculate the maximum tangential stress $\tau_{\max}$ from the relation $M = (\pi r_0^3/2)\tau_{\max}$, where r_0 is the radius of the whisker, and hence the average stress τ_{mid}. It is easy to calculate the volume averaged mean strain, which is expressed in terms of the length L, the diameter $2r_0$ and the angle of twist θ_0

$$\left(\epsilon_{\text{mid}} = \frac{2\theta_0 r_0}{3L}\right).$$

In the process of heating, the recovery (untwisting) of the whisker was displayed on a strip chart recorder (17). For this purpose the light ray reflection of the micromirror was kept motionless and the untwisting of the

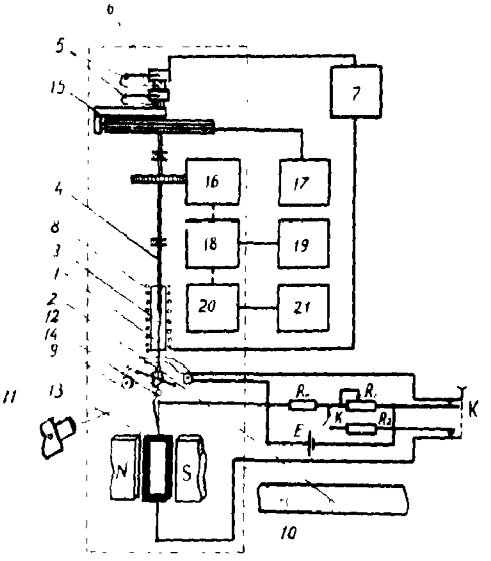

Fig. 1 Functional diagram of the installation for studying strain, recovery and internal friction of whiskers (1) 7-shaped suspension, (2) micromirror, (3) whisker, (4) thermocouple, (5) brushes, (6) rings, (7) potentiometer, (8) furnace, (9) electromagnets, (10) scale, (11) illuminator (12) limiting fork, (13) galvanometer frame, (14) micromirror (15) rheostat, (16) reductor, (17) potentiometer, (18) electric motor, (19) control circuit, (20) velocity pickup, (21) velocity meter

whisker was compensated by the rotation of the thermocouple and a rheostat (15) connected to it, the voltage from the battery being applied to the rheostat. The voltage u taken off from the sliding contacts of the rheostat was registered by the recorder ($u = f(\theta)$) Thus it was possible to record automatically the whisker twisting curves (strain) and untwisting curves (recovery)

The study of the whisker structure before and after strain and also after recovery was carried out metallographically and roentgenographically (Laue photographs were taken). The whisker strain was evidenced by the diffuseness of Laue spots and the recovery – by their restoration (by residual asterism).

The internal friction of thin metallic films was studied on an installation, the block diagram of which is given in Fig. 2. A metallic film (1) 1–2 μ thick is cemented to a thermocouple (2) and placed at a distance of about 1 mm from the fixed electrode of an ultra-short wave generator of frequency-modulated signals (3). The sample is excited electrostatically from an audio generator (4) through a thermocouple which must be isolated from the ground The resonant frequency of sample vibrations is equal to double the audio generator frequency. The ultra-short wave generator of frequency-modulated signals is a capacitive three-point circuit with an operating frequency of 120 Mc/s Frequency-modulated vibrations of the generator (3) are received by the antenna of a frequency modulation meter (5). From the

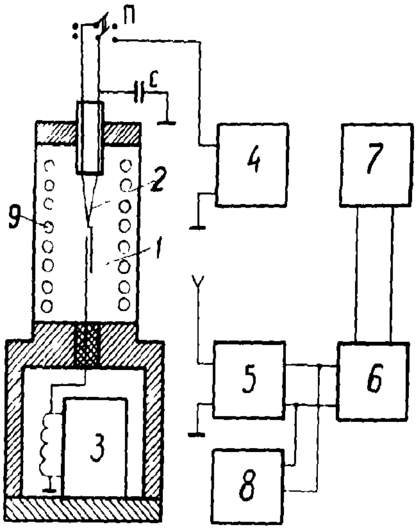

Fig. 2 Block diagram of the installation for measuring internal friction in thin films. (1) sample (film), (2) thermocouple, (3) high frequency generator, (4) audio generator, (5) frequency modulation meter; (6) differential discriminator, (7) pulse counter; (8) oscillograph, (9) heater

meter output, the modulating vibrations of the film are applied to a differential discriminator (6) which singles out attenuating vibrations between the two given amplitude levels and forms voltage pulses which are then applied to a counter (7) The pulse shape from the frequency modulation meter output is controlled by an electron oscillograph (8). The generator (3) enclosed into a case together with a pickup is placed into a vacuum chamber. The film is heated by an electric furnace (9) The internal friction measurement error does not exceed 1 per cent at room temperature and 3 per cent at high temperatures The natural frequency of film transverse vibrations was varied from 140 to 1000 c/s by the variation of the film length. The relative strain amplitude throughout the Q^{-1} measurement was $\sim 10^{-6}$. Copper films were obtained by condensation in $5 \cdot 10^{-6}$ torr vacuum. In order to get grains of different size the substrate temperature was varied from room temperature to 250°C. Mica was used as a substrate The film structure was observed in an electron microscope after decreasing the film thickness electrolytically.

The results of the study of $Q^{-1}(T)$ of whiskers deformed in tension (15 per cent) and of copper thin films deformed by transverse compression (15 per cent) are shown in Fig. 3. It can be seen that the 'temperature spectrum' of whiskers and that of thin films are identical, though the general level of internal friction of thin films is much higher.

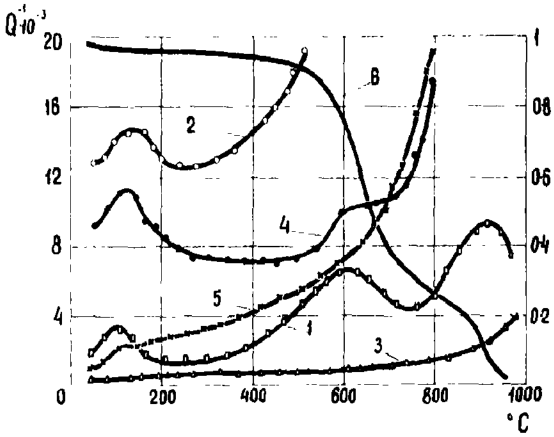

Fig. 3. Temperature dependence of internal friction (1–5) and of dislocation recovery (6) of whiskers and thin films of copper (1) whisker strained in tension by 15 per cent, (2) whisker strained by twisting ($\theta = 6\pi$); (3) whisker after annealing at 950°C and full recovery of its initial shape; (4) thin film after compression by 15 per cent, (5) thin film after annealing at 800°C; (6) recovery of the copper whisker shape

Figure 4 shows temperature dependence of polycrystalline film internal friction (curves 1, 2) compared with $Q^{-1}(T)$ of a single crystal film and of bulk copper samples. A bend on curve 1 in the region of 180°C is undoubtedly related to the polycrystalline nature of the film. If we subtract the background from curve 1 we shall obtain a rather high but very broad 'grainboundary' maximum. The peak is shifted to lower temperature region and its height is a factor of 1·5–2 less than that of the grain boundary maximum of $Q^{-1}(T)$ of bulk copper samples (99·992 per cent pure). The activation energy calculated by means of the peak shift as the vibration frequency of thin films is varied from 220 to 1000 c/s is equal to $1{\cdot}3\pm0{\cdot}1$ eV. The activation energy of the $Q^{-1}(T)$ grain boundary maximum in bulk copper samples is known to be within the limits of 1·4–1·55 eV, (see, for example, [1, 2]), and the self-diffusion activation energy at temperatures 550–850°C is 2·03 eV [3]. Thus it may be concluded from the study of thin polycrystalline films that the movement of defects along the intercrystalline boundary is responsible for grain boundary internal friction. Electron microscopy of copper films (curve 1) shows that they have small-grain structure (the size of the grain is of the order of 0·1 μ), considerable disorientation of grains, and contain many stacking faults and dislocations. Curve 2 corresponds to

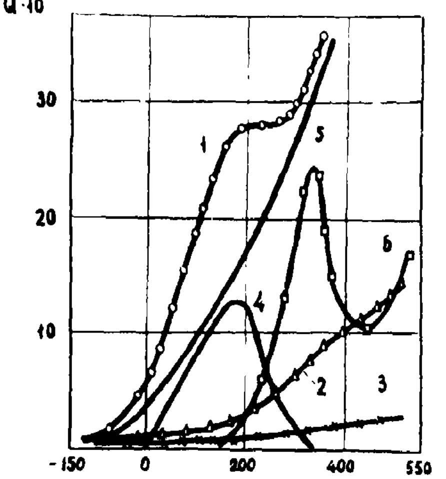

Fig 4 Temperature dependence of copper film internal friction (($\omega/2\pi$) 300 c/s). (1, 2) polycrystalline films; (3) single crystal film. (4) $Q^{-1}(T)$ peak, background (5) subtracted. (6) bulk copper samples (99·992 per cent). For curve (6), the abscissa should be read as °C Frequency ~ 1 c/s.

films containing larger crystals (4–5 μ) with preferential disorientation by angles not more than 12°.

As far as there is no generally accepted model of high-angle crystal boundaries there is no possibility to estimate theoretically the contribution to the total level of internal friction given by the mechanism of diffusion in the stress field of point defects at these boundaries.

The presented experimental material supports the conclusion that the high temperature internal friction background of single crystal films is far lower and of polycrystalline films somewhat higher than that of bulk copper samples.

A pronounced feature of a whisker is the recovery of the shape of the plastically strained crystal during its heating up to high temperatures. Bulk crystals do not exhibit such a feature. A typical recovery curve of a copper whisker is given in Fig. 3. The character of the recovery depends on the degree of prestrain determined by the angle of twist θ_0, the diameter and length of the sample, and also on the direction of the growth axis. An increase of θ_0 shifts the region of maximum recovery rate towards higher temperatures. Unlike other orientations, whiskers with the growth direction[100] even at small θ_0 do not recover their original shape at all or they do it only at high temperatures. The recovery of copper whiskers has three stages (see curve 6 in Fig. 3). It means that all the processes controlling the recovery of the shape are thermally activated and have different activation energies.

Figure 3 shows that curves 1,4 of prestrained whiskers and thin films have peaks corresponding to the three recovery stages.

The activation energy of the first recovery stage was about 0·9 eV. We can assume that the mechanism responsible for the first recovery stage and the first maximum of internal friction is displacement of jogs on screw dislocations emitting vacancies. It should be noted that an analogous mechanism was proposed by Seeger to explain the plastic deformation of copper in the same temperature range.

In order to explain the second peak and the second recovery stage we suggest that the principal process responsible for these phenomena is a thermally activated cutting through of intersections of screw dislocations moving in different systems of glide. The latter are formed in whiskers in the process of their twisting.

The process governing the third recovery stage and the formation of the $Q^{-1}(T)$ high temperature peak is, in our opinion, a non-conservative creep of edge dislocations. The polygonization of this stage confirms it.

From the above assumptions we can write the kinetic equation for the whisker recovery process at any of the mentioned stages

$$\dot{\epsilon} = -A(\epsilon)\exp\left(\frac{u}{kT}\right) \qquad (1)$$

where $\epsilon = (\theta/\theta_0)(r_0/L)$ is the whisker unelastic strain; $A(\epsilon)$ and u are the frequency factor and activation energy, respectively.

Superposition of external stresses

$$\tilde{\tau} = \tau_0 \exp(i\omega t)$$

throughout the internal friction measurement makes the activation energy a function of time as well

$$u(t) = u(\epsilon) - v\tilde{\tau} \qquad (2)$$

where v is an activation volume.

For sufficiently small τ_0, equation (1) may be written in the form

$$\dot{\epsilon} = -A\,(\epsilon_0)\,\mathrm{e}^{-\frac{u(\epsilon_0)}{kT}}\left(1+\frac{v\tilde{\tau}}{kT}\right). \qquad (3)$$

We shall have the solution of equation (3) as a sum

$$\epsilon = \epsilon_0 + \delta\epsilon.$$

Here ϵ_0 is the aftereffect strain in the absence of external cyclic stresses satisfying the equation

$$\dot{\epsilon}_0 = -A\exp\left(-\frac{u}{kT}\right). \qquad (4)$$

Time-dependent addition $\delta\epsilon$ results from the consideration of the influence of external stresses on the process of aftereffect. While obtaining $\delta\epsilon$ we shall take into account the fact that the period of the sample vibration $2\pi/\omega$ is far less than the characteristic time of the untwisting stage $t = \Delta T/\dot{T}$, where ΔT is the width of the stage, $\dot{T}$ is the rate of heating. This relationship holds at the rates of heating used in the experiment.

Substituting $\epsilon = \epsilon_0 + \delta\epsilon$ into equation (3) and taking into account the above mentioned considerations we obtain

$$\delta\epsilon = i\frac{\tau_0 v\dot{\epsilon}}{\omega kT}. \qquad (5)$$

In order to find Q^{-1} we shall divide the imaginary part of the strain $\delta\epsilon$ by the real part $\epsilon' = \tau_0/\mu$. As a result, we have

$$Q^{-1} = \frac{\mu v\dot{\epsilon}}{\omega \, . \, kT} \qquad (6)$$

where μ is the shear modulus. The latter equation shows that Q^{-1} is proportional to $\dot{\epsilon}$, which was supported by the experiment.

Having obtained experimentally the value of Q^{-1} and the aftereffect strain rate, one can calculate the value of the activation volume

$$v = \frac{Q^{-1}\omega kT}{\mu \, . \, \dot{\epsilon}}. \qquad (7)$$

For the initial part of the second recovery stage at 700°K $Q^{-1} = 16 \, . \, 10^{-3}$; $\dot{\epsilon} = 0{\cdot}5 \, . \, 10^{-7}$ sec^{-1}; $\omega = 25$ deg/sec. Substituting them into formula (7), we shall obtain the activation volume

$$v = dbl = 4 \, . \, 10^{-19}\ \text{cm}^3.$$

Knowing v, we can estimate the length l of the dislocation segments giving the principal contribution to Q^{-1}. We assume[4] that the energy barrier width is of the same order as that of the stacking fault d (for screw dislocations in copper $d = 5b$). Then $l \cong 10^3 b$.

Analysis of our Laue photographs shows the existence of separate fragments arising as a result of the shear along the slip planes. The shear may be due to generation on a whisker surface of screw dislocations with Burgers vectors normal to the sample axis and making small angles with it, and to their motion towards the crystal axis.

We assume that in crystal twisting screw dislocations move from the lateral surface a distance equal to the whisker radius r_0. Then the angle $\delta\theta$ of the turn of the lower whisker base when one dislocation passes through is given by

$$\delta\theta = \frac{b}{r_0}.$$

For the number of dislocations m ensuring the turn of the sample by the angle π, we have

$$m \cong \frac{\pi r_0}{b}.$$

Then the average length of the dislocation segments is

$$l = \sqrt{\frac{2}{\pi}Lb}.$$

Assuming the length of the sample to be 3 mm, we shall find $l \cong 2 \, . \, 10^3 b$, which coincides in the order of magnitude with the segment length estimated by means of the above formula (4). This coincidence may serve the basis for the statement that the mechanisms of the recovery of the shape and of internal friction at the second stage are associated with the cutting through of intersections of screw dislocations moving in different systems of glide.

The elementary mechanism of recovery and internal friction examined here may be made more complicated by the variety of types of intersections of both screw and edge dislocations, of the possible variants of their coming out to the surface, by dislocation reactions etc.

REFERENCES

1. GERTSRIKEN S D. and DEKHTER I. Y., *Diffusion in Metals and Alloys in the Solid Phase*, p. 159. Moscow (1960)
2. WILLIAMS T. M. and LEAK G M., *Acta Met.* **15**, 1111 (1967)
3. *Physical–Chemical Properties of Elements* (Edited by G V. Samsonov), p. 251. Moscow (1966).
4. SEEGER A, *Phil. mag.* **46**, 1194 (1955).

J. Phys. Chem. Solids Pergamon Press 1970. Vol. 31, pp. 1941–1945. Printed in Great Britain

DISLOCATION DAMPING IN COPPER SINGLE CRYSTALS OF CONTROLLED SUBSTRUCTURE*

H. AKITA[†] and N. F. FIORE

Department of Metallurgical Engineering and Materials Science, University of Notre Dame, Notre Dame, Indiana 46556, U.S.A.

(*Received 5 September* 1969, *in revised form* 20 *October* 1969)

Abstract – The dislocation substructure of ⟨111⟩ Cu single crystals has been controlled by varying crystal solidification rates between 1·57–109 cm/hr. Etch pitting and X-ray diffraction show that the random or inter-cell dislocation network is independent of growth rate and equal to $1 \times 10^6 \text{cm}^{-2}$ whereas the dislocation cell size and intra-cell misorientation increase with decreasing growth rates.

Resonance bar damping measurements at a fundamental frequency of 25 kHz and ultrasonic pulse echo measurements at 5–75 MHz show that the exact form of the damping vs. frequency or damping vs. amplitude behavior of the crystals is a function of cell size, and in general, damping increases with increasing cell size. They also suggest that damping from dislocations in cell boundaries may overshadow that from random dislocations.

1. INTRODUCTION

SINCE dislocation damping is so structure sensitive, the magnitude of the damping loss depends not only upon the number of mobile dislocations in a vibrating sample, but upon their spatial distribution as well. This fact is neglected in typical dislocation damping experiments, in which the damping is correlated with total dislocation density as determined by etch-pit count, or else the role of substructure is neglected altogether. Further, with few exceptions[1] the typical damping experiment is carried out with a single internal friction measurement technique and is thereby confined to a restricted range of frequency, amplitude, and other pertinent variables.

These two factors cause difficulty when attempts are made to describe the general characteristics of dislocation damping, because collections of data represent experiments made with a variety of techniques on specimens of unknown and, most probably, differing dislocation substructure. The experiments discussed in this paper have been conducted on ⟨111⟩ Cu single crystals whose substructure is systematically varied by control of crystal growth conditions and then specified by etch-pit and X-ray diffraction measurements. The damping of these crystals of known substructure is determined over a large range of frequency and amplitude with the resonance bar and pulse-echo measurements. It is hoped that the measurements in crystals of controlled substructure by two internal friction techniques will provide data which reflect general trends in the dislocation damping behavior of crystals.

2. EXPERIMENTAL

Crystal growth

The ⟨111⟩ Cu crystals are grown in AUC high purity graphite split molds from 99·999+ per cent pure Cu (American Smelting and Refining Company). They are in the form of right circular cylinders 1 cm in dia. by 15 cm in length.

The mold rests on a water-cooled pedestal enclosed in a mullite tube evacuated to 10^{-5} torr. The substructure is controlled by control of solidfication rate, i.e. by control of the rate at which a Kanthal-wound resistance furnace is raised parallel to the crystal axis.

---

*Submitted in partial fulfillment of the requirements for the degree of Doctor of Philosophy in the above department

Solidification rates vary from 1·57 cm/hr (hereafter called the slow rate) to 109 cm/hr (the fast rate).

Specimen preparation

The crystals are cut over size with a Servomet spark cutter, and are polished on an acid wheel[2] to remove dislocations introduced during cutting. The polishing solution (concentrated HCl saturated with $CuCl_2$) lies as a film between the independently rotated specimen and polishing wheel, and flat, smooth surfaces are obtained with no specimen contact. Previous work[3] has shown that 3 mm of material must be removed from each spark-cut surface to eliminate cutting damage. Final chemical polishing in a solution of 25 parts CH_3COOH, 20 parts HNO_3, 55 parts H_3PO_4 at 70–80°C produces the required flat, mirror-like surface required for etch pit studies.

Etch pit studies

Livingston's[4] etchant (1 part Br, 15 parts CH_3COOH, 25 parts HCl, 90 parts H_2O) is used to produce the triangular pits characteristic of dislocations emerging from {111} surfaces.

X-Ray studies

Etch pitting is unable to resolve individual dislocations in most cell walls, so the Guinier–Tennevin[5] focusing Laue method is employed for the purpose of obtaining cell wall densities. Foils 0·15 mm thick have been prepared by long and careful acid polishing of {111} slices of crystal. An X-ray beam generated by a Mo target and focused to a fine line is directed through the foil, and the splitting of the beam is used to provide a measure of the misorientation between cells in the foil, and therefore of the density of dislocations in the cell walls.

Transmission electron microscopy has also been employed in the substructure studies. It is unsatisfactory because the low dislocation densities and large cell sizes of the crystals make the probability of finding a useful field of view in the foils very small.

Damping measurements

The damping is measured at room temperature at both kilohertz and megahertz frequencies. In the kHz range the resonance bar Marx composite[6] oscillator technique is employed, with the specimen driven at 25 kHz in the longitudinal mode. This technique allows damping determination at 25 and 75 kHz at strain amplitudes ranging from 2×10^{-8} to 6×10^{-6}.

In the megahertz range, ultrasonic attenuation is measured by the pulse-echo technique with a commercial attenuation comparator similar to one described in the literature[7]. The same crystals are used for both resonance bar and pulse-echo studies, since the two {111} end surfaces of the rods are flat and parallel enough to allow direct bonding of X-cut or compressional wave transducers with Non-Aq stopcock grease. There are a number of extraneous energy losses[8] which make measurement of absolute values of attenuation difficult; however this study deals with relative values, and since transducer and specimen geometry are maintained from sample to sample, the general trends observed here are believed to be valid ones.

3. RESULTS

Substructure studies

Substructure and damping studies have been made on crystals grown within the entire range of rates, and all trends have been established from the accumulated data. For the purpose of discussion, only the results from slow-grown and fast-grown crystals will be treated in detail. Figure 1 shows the etch pitted {111} surfaces of slow- and fast-grown crystals. The average cell diameter for the fast-grown crystals is $1 \cdot 6 \times 10^{-2}$ cm and that of the slow-grown crystals is $5 \cdot 0 \times 10^{-2}$ cm, so it is evident that the slower the growth rate, the larger the cell size. This fact is consistent with previous studies[9, 10] of solidification substructure. Photomicrographs at higher magnification (Fig. 2 and 3) indicate that the

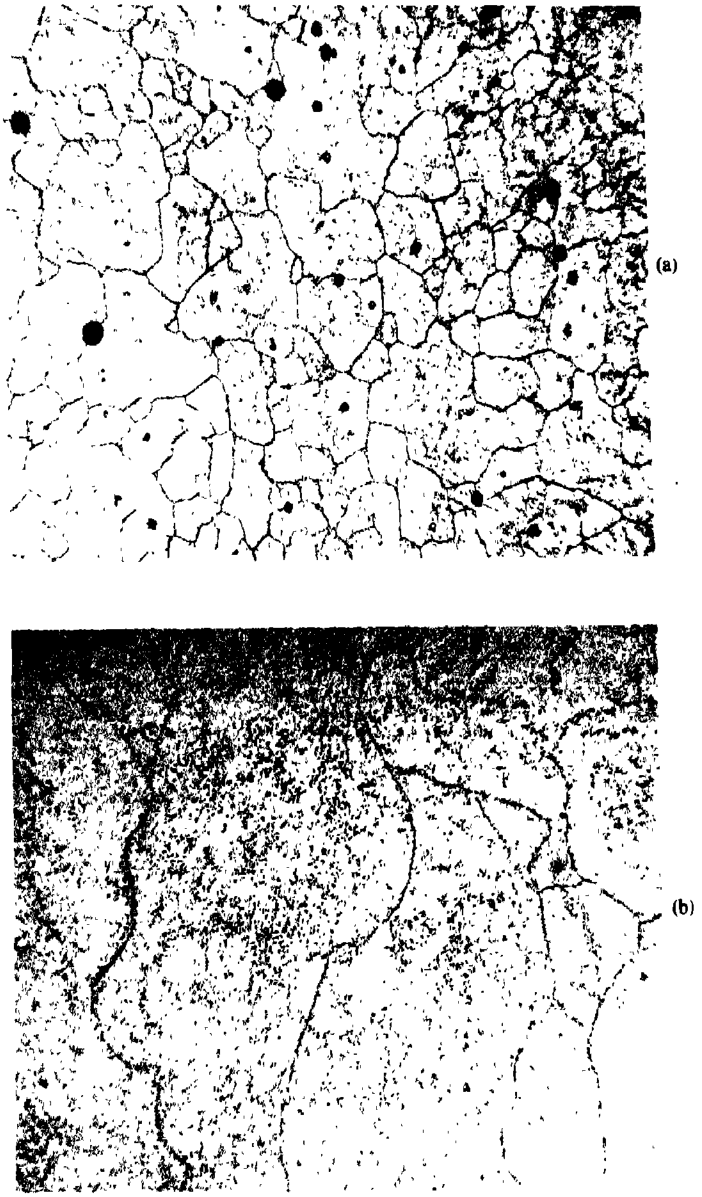

Fig. 1 The etch pitted (111) surfaces of slow- and fast-grown crystals (50×)
(a) Fast-grown; (b) Slow-grown.

Fig. 2. The etch pitted (111) surface of fast-grown crystal (400×)

Fig. 3 The etch pitted (111) surface of slow-grown crystal (400×).

density of the random or intra-cell dislocations (Λ^R) is independent of growth rate and equal to about 1×10^6 cm^{-2}. Etch pit counts on {111} faces inclined to the growth direction confirm these trends, although the cells tend to be elongated rather than equiaxed when viewed on faces not perpendicular to the growth direction.

The X-ray studies indicate that the average misorientation between adjacent cells in the slow-grown crystals ($\theta = 4 \times 10^{-3}$ rad.) is about twice that ($\theta = 2{\cdot}2 \times 10^{-3}$ rad.) between cells in fast-grown crystals. Assuming that the cell walls are simple tilt or twist boundaries, then the separation, h, between dislocations is equal to b, the magnitude of the Burgers vector, divided by θ, so that the slower the growth rate, the smaller the separation between cell wall dislocations.

Since the cells in the fast-grown crystals are about one third the size of those in the slow-grown crystals, the total length of boundary intersecting the ⟨111⟩ faces is larger for the fast-grown crystals. Thus, the absolute number of cell wall dislocations intersecting a cm^2 of ⟨111⟩ surface in the fast-grown crystals is about twice that intersecting the surface of the slow-grown crystals ($\Lambda^B(F) > \Lambda^B(S)$), in spite of the fact that the dislocations in the wall of the slow-grown crystals are more closely spaced than those in the fast-grown crystals ($h(F) < h(S)$). The results of the substructure measurements are summarized in Table 1.

Damping studies

Measurements as a function of strain amplitude at 25 kHz (Fig. 4) indicate that the damping, Δ, is considerably higher in the slow-grown crystals. Furthermore, the general form of the damping plots differs, with the fast-grown crystals tending to show a plateau at high strains. This figure points out the difficulty of making valid comparisons of various sets of damping data if the substructures of the crystals studied are not known to be identical. The figure also suggests that the damping difference is associated with cell size, since this is the only parameter which varies from crystal to crystal.

The total attenuation, α, in db/μsec is shown as a function of frequency in Fig. 5. These data are obtained with a 15 Mz transducer and have been duplicated with a 5 Mz transducer. The attenuation is higher in the slow-grown crystals than the fast-grown ones. Since Δ equals α divided by $8{\cdot}686f$, where f is the frequency of vibration, the ultrasonic data follow the trend of the kHz data, with damping increasing as cell size increases.

The crystal growth and damping measurements results are summarized as follows:

(1) Within the range of the growth rates employed, the random density (Λ^R) is independent of growth rate and equal to 1×10^6 cm^{-2}.

(2) As growth rate increases, average cell size decreases.

(3) As growth rate increases, the inter-cell misorientation and the average spacing

Table 1. Dislocation densities and cell sizes of slow- and fast-grown crystals

	Cell size ($L \times 10^{2}$ cm)	Random dislocation density ($\Lambda^R \times 10^{-6}$ cm^{-2})	Wall dislocations per cm^2 ($\Lambda^B \times 10^{-6}$ cm^{-2})	Maximum separation of dislocations in cell wall ($h \times 10^6$ cm)
Fast-Grown # 1	1·54	1·25	7·01	13·8
Fast-Grown # 2	1·67	1·13	10·3	13·2
Slow-Grown # 1	6·67	0·92	4·98	6·95
Slow-Grown # 2	4·17	1·24	4·42	8·82

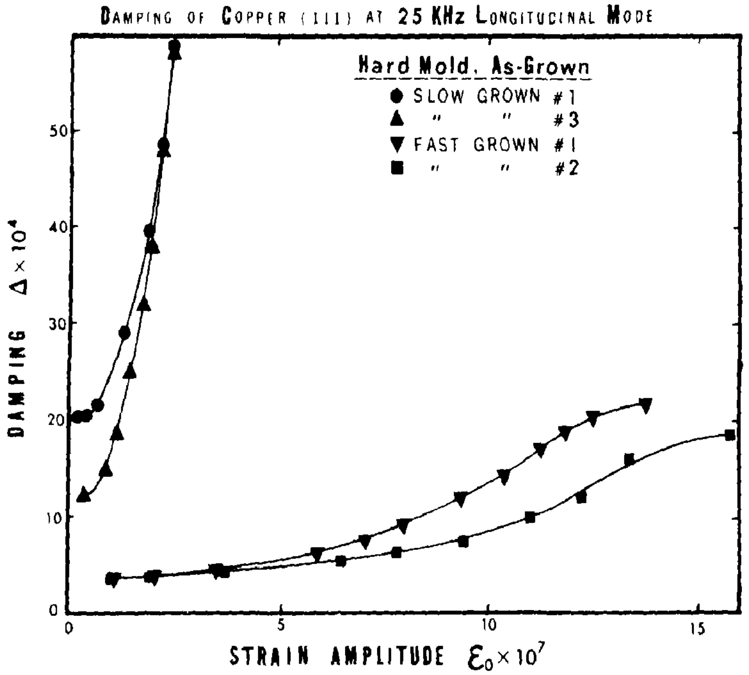

Fig. 4. Damping as a function of strain amplitude at 25 kHz.

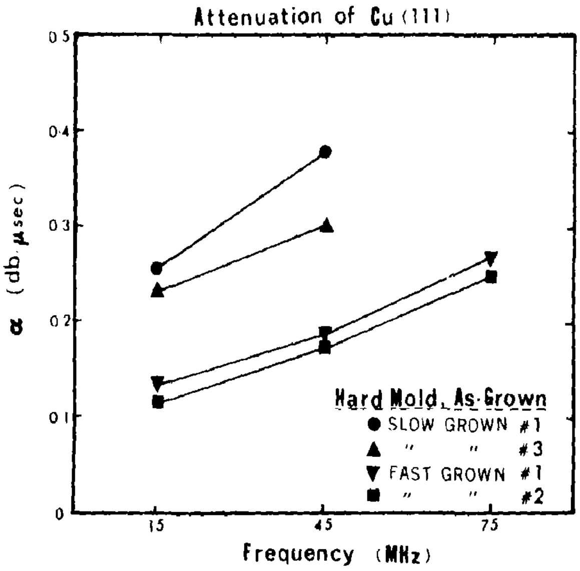

Fig. 5 Attenuation as a function of frequency in mHz

between wall dislocations decreases, but absolute number of (Λ^{II}) wall dislocations intersecting a cm^2 of {111} surface increases.

(4) Resonance bar measurements indicate that the damping of the slow-grown crystals is higher than the fast-grown crystals.

(5) Pulse-echo measurements indicate that the attenuation is higher in slow-grown than in fast-grown crystals.

(6) The damping behavior of the crystals seems to be associated with cell size.

The most successful theory of dislocation damping is due to Granato and Lücke[11, 12], who use Koehler's[13] model, and treat the dislocations as strings vibrating in a damping medium. They calculate that the total damping loss is composed of a dynamic contribution (Δ_I), which is a function of the frequency of vibration, and a hysteretic contribution (Δ_H), which depends upon vibrational strain amplitude.

The results obtained in this investigation indicate that this theory of damping, which is based on a random dislocation array, cannot account for the damping in crystals, which contain ordered dislocation arrangements. Since in the general case, as-grown, annealed, or deformed crystals contain large numbers of dislocations in ordered arrays, the model employed and the theory developed in Refs. [11–13] cannot be expected to account for the observed damping.

SUMMARY AND CONCLUSIONS

Substructure studies

(1) Within the range of growth rates studied, dislocation cell size can be decreased by increasing solidification rate.

(2) The slower the growth rate, the larger the misorientation between adjacent cells and the smaller the separation between cell wall dislocations.

(3) The intra-cell random dislocation network is independent of growth rate.

Damping studies

(1) Over large ranges of amplitude and frequency, dislocation damping is a strong function of cell size and cell wall make-up; this dependence may overshadow the damping contribution from network dislocations.

(2) Both resonance bar and pulse-echo measurements indicate that $\Delta_I(S)/\Delta_I(F) \cong 3$.

(3) Resonance bar measurements indicate that at a given ϵ_0, $\Delta_H(S) > \Delta_H(F)$, and that general shape of the Δ_H vs. ϵ_0 plot is a function of cell size.

Acknowledgements – The authors are indebted to the Metals and Ceramics Division of the Army Research Office, Durham for support of this work in the form of grant DA-ARO-D-31-124-G-936. They also express gratitude to Professor C. W. Allen for his helpful comments.

REFERENCES

1. HEIPLE C. R. and BIRNBAUM H. K., *J. appl. Phys.* **38**, 3294 (1967).
2. YOUNG JR. F. W. and WILSON J. R., *Rev. scient. Instrum.* **32**, 559 (1961).
3. McGUIRE M. F. and FIORE N. F., *Trans. AIME* **236**, 1753 (1966).
4. LIVINGSTON J. D., *J. appl. Phys.* **31**, 1071 (1960).
5. GUINIER A. and TENNEVIN J., *Acta crystallogr.* **2**, 133 (1949).
6. MARX J., *Rev. scient. Instrum.* **22**, 503 (1951).
7. CHICK B., ANDERSON G. and TRUELL R., *J. acoust. Soc. Am.* **32**, 186 (1960).
8. TRUELL R., ELBAUM C. and CHICK B. B., *Ultrasonic Methods in Solid State Physics*, Chap. 2. Academic Press, New York (1969).
9. GOSS A. J. and WEINTROUB S., *Proc. phys. Soc. Lond.* **B65**, 561 (1952).
10. RUTTER J. W. and CHALMERS B., *Can. J. Phys.* **31**, 15 (1953).
11. GRANATO A. and LÜCKE K., *J. appl. Phys.* **27**, 583 (1956).
12. GRANATO A. and LÜCKE K., *J. appl. Phys.* **27**, 789 (1956).
13. KOEHLER J. S., *Imperfections in Nearly Perfect Crystals*, p. 197. Wiley, New York (1952).

J. Phys. Chem. Solids Pergamon Press 1970. Vol. 31, pp. 1947–1953 Printed in Great Britain.

DISLOCATION STRUCTURE AND LOW FREQUENCY MECHANICAL HYSTERESIS IN COPPER SINGLE CRYSTALS*

J. DRALLA and J. C. BILELLO

Department of Materials Science, State University of New York at Stony Brook, Stony Brook,
N.Y. 11790, U.S.A.

(Received 5 September 1969, in revised form 8 October 1969)

Abstract—Copper single crystals of several orientations were grown and sectioned at various stages of prestrain such that both primary and forest dislocations could be directly observed using etch-pit techniques. Half-cycle hysteresis loops, at positive stress bias, representing damping frequencies in the range of $\approx 10^{-1}$ Hz were performed on these samples at room temperature. The results of the etch-pit and mechanical damping studies were correlated, and a model was formulated which describes the damping in terms of a dislocation-dislocation interaction model. The controlling pinning mechanism was associated with primary-forest dislocation combinations, and a discussion of the appropriate binding energy is made.

1. INTRODUCTION

AMPLITUDE-dependent internal friction in metals, at high frequencies, is generally thought to be hysteretic and associated with the interaction of the entire Frank network of dislocations with discrete impurity atoms in the lattice[1–4]. The dislocation unpins from the impurity atom by a combination of stress and thermal activation with typical binding energies of the order of 0·1 eV[5, 6]. Low frequency mechanical damping has been observed in the $\approx 10^{-1}$ Hz range and it was originally suggested that both types of damping were of similar origin[7]. However, recent evidence has cast considerable doubt on this earlier interpretation[8, 9] and instead has postulated that the latter range of damping is caused by primary dislocation-forest dislocation interactions with binding energies ~ 1 eV. If the forest pinning model governs, then a unique opportunity presents itself to make a direct correlation between a particular range of damping behavior and the pinning mechanism responsible for the hysteresis. The present experiments report the results of comparing the forest and primary dislocation structures observed from etch-pit analysis with the low frequency damping behavior of copper crystals of several orientations.

2. EXPERIMENTAL PROCEDURE

A modified Bridgman technique was used to grow copper crystals in vacuum from 99·999 per cent grade material purchased from ASARCO. The crystals were acid-sawed into samples which had 25 mm gage lengths and square cross-sectional areas of 22·5 mm². The tensile axes of the orientations studied are shown in Fig. 1 with: crystal *A* 19° from (100), *B* 14° from (110), and *C* 2° from (112); because of the proximity to these directions crystals *A*, *B*, *C* will be designated by these indices in the remainder of the text. These crystals were chosen at these orientations to represent the general range of slip character that can occur for fcc copper. All crystals were annealed in vacuum for 24 hr, in graphite trays, at 1070°C and then furnace cooled. Samples were chosen after this anneal so that for all orientations the initial grown-in

---

*This work was supported in part by the U.S. Atomic Energy Commission.

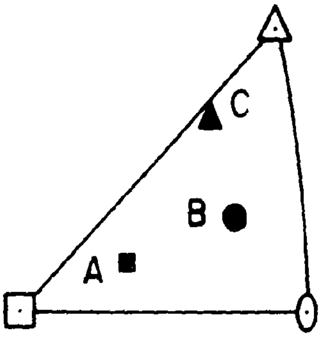

Fig. 1. Orientation of longitudinal axis for the three crystals.

density of dislocations was 2×10^{6} cm^{-2}, with an average sub-boundary spacing of $\sim \frac{1}{2}$ mm.

Tensile tests were performed on an Instron machine using a strain rate $1{\cdot}7 \times 10^{-1}$ sec.$^{-1}$ for prestraining and of 10^{-6} sec.$^{-1}$ for performing the low frequency damping experiments. A high strain resolution microstrain network capable of displacement sensitivities of 1×10^{-7} in. was employed in these experiments. A detailed description of the microstrain apparatus and calibration procedure for drift, linearity, and sensitivity appears elsewhere [8, 10].

A one micron crack-free chromium film was plated on all samples, because it was found convenient to extend the amplitude range of the decrement at any particular prestrain. The influence of the film and a discussion of any possible surface effect related to low frequency mechanical hysteresis have already been treated [8, 11].

It was important to be able to observe both the primary and forest-dislocation densities for each crystal in order to independently determine the number of primary dislocation loops and the number of possible forest pins available. In order to accomplish this, crystals were sectioned and polished along the appropriate (111) planes using a procedure similar to Young and Wilson (1961) [12], and then these surfaces were etched to reveal the dislocation structure using Livingston (1960) [13].

3. RESULTS AND DISCUSSION

General

In studying the influence of structure on low frequency mechanical damping behavior, the amplitude dependence of the decrement was taken at prestrains chosen so that the three orientations which were studied had a large range of overlap (e.g. samples at (110) orientation with prestrains $\approx 0{\cdot}025$ showed damping only over a 150 g/mm^2 to 300 g/mm^2). Also, it was necessary to keep the amount of prior deformation small enough so that the dislocation densities could be determined by etch-pit methods; yet large enough so that a significant range of amplitude dependence could be observed. Table 1, column 1 reports the results of the primary densities measured for the three crystals. The second aim was to keep the forest densities approximately constant (column 2, Table 1) and this was accomplished by experimentation using as a guideline the stress-forest density relationship of Basinski and Basinski [14]. Thus it was possible to vary the number of primary loops by about a factor of 2 while the number of available forest junctions stayed approximately constant. The amplitude dependence of the decrement is shown in Fig. 2 for the crystals reported in Table 1. Virtually no amplitude dependence is associated with (112) and even for the other two cases the dependence is rather small compared with that observed in the kHz range.

Figure 3 illustrates the orientation dependence of the decrement, Δ, over the amplitude range where the data in Fig. 2 coincides. The amplitude dependence is seen to be largest for the (110) crystal and becomes smaller as the stress axis moves from (100) through (112) directions. This effect is analogous to the prestrain dependence of the decrement at fixed orientation, which is shown in Fig. 4. In the strain-dependent case, the primary density for fcc copper increases through work-hardening Stage 1, but the forest density remains essentially

Table 1. *Measured etch-pit values*

Crystal	ρ_p Primary density (cm^{-2})	ρ_f Forest density (cm^{-2})	l_f (cm)	Prestress (g/mm^2)
(110)	$3{\cdot}5 \times 10^7$	$9{\cdot}6 \times 10^6$	$3{\cdot}2 \times 10^{-4}$	774
(100)	$6{\cdot}0 \times 10^7$	$1{\cdot}1 \times 10^7$	$3{\cdot}0 \times 10^{-4}$	550
(112)	$8{\cdot}0 \times 10^7$	$1{\cdot}3 \times 10^7$	$2{\cdot}8 \times 10^{-4}$	595

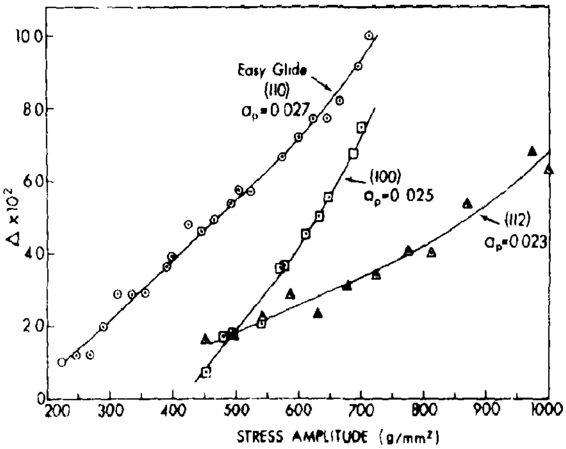

Fig. 2. Amplitude-dependence of the decrement, Δ, at the indicated prestrains a_p for each orientation. Stress, σ, is the axial component.

unchanged[14]. The conclusion, that is suggested by the results shown in Figs. 3 and 4, is that the amplitude dependence of the decrement for low frequency damping is independent of the mode in which a particular dislocation structure is produced, (i.e. either by producing relatively constant prestrains at various orientations or by varying the amount of prestrain for a fixed orientation).

4. DISLOCATION STRUCTURE

In the present experiments, both the primary and forest dislocation structures were measured directly using the method described in the experimental procedure section. A photo-micrograph of a typical forest plane section before and after prestrain is shown in Fig. 5. The section obtained before straining was produced from a section of the crystal immediately adjacent to the gage length at either end of the sample. About an order of magnitude rise in the forest density is apparent even though the sample was still in work-hardening stage 1. This is generally the case for coated crystals since secondary slip occurs before a well developed stage 2 hardening is observed in the macroscopic stress-strain curve. The observed increase in forest density agrees with the stress-forest density relationship of others [14]. The complete etch-pit data for all crystals appears in Table 1.

Previous work on low frequency mechanical hysteresis has not correlated directly measured damping behavior with structures. The dislocation structures have either been inferred from the dislocation measurements of others[8] or have been calculated from the assumed damping model[15]. In the next section a simplified damping model will be

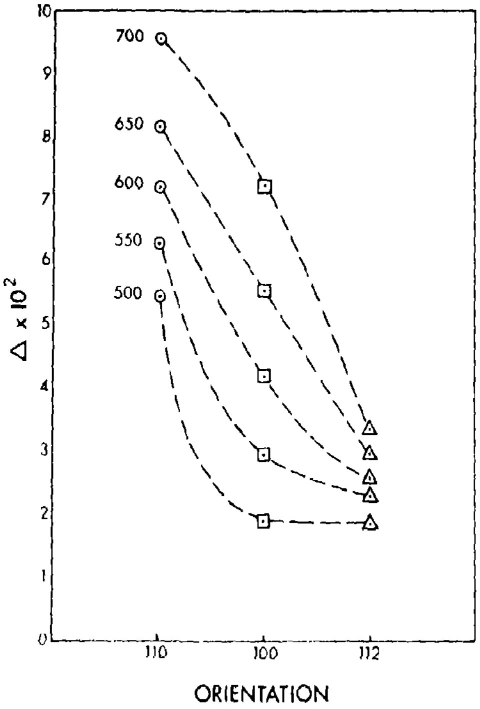

Fig. 3. Orientation dependence of the decrement for the three crystals with common forest dislocation densities i.e. nearly constant density and distribution of nodes. Stress amplitude indicated on each curve is in (g/mm²)

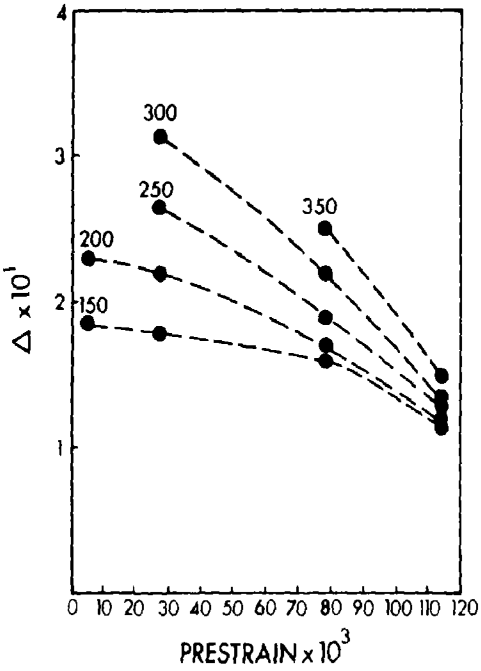

Fig. 4. Prestrain dependence of the decrement at constant orientation, for an easy glide crystal, longitudinal axis 8° from ⟨110⟩. Stress-amplitude indicated on each curve is in (g/mm²). (plot obtained from data in Ref. [8])

chosen and the magnitude of the damping level calculated from the measured etch-pit arrays.

Mechanism for energy loss

It has been shown earlier[8, 15] that the modulus defect can be quite large, of the order of 15–25 per cent for low frequency hysteresis experiments. This defect was found to be almost entirely caused by the large bowing strains associated with the excess primary loops produced by the plastic deformation[8]. Furthermore, at the large stress amplitudes which have been used here, i.e. up to ≈ ½ the flow stress, all loops have already broken away from impurity pins at stress levels equivalent to the preload level in the present experiments [8].

The strongest primary-forest dislocation interaction is assumed to be that between attractive triple point junctions[16]. Figure 6 shows a sequence which illustrates the motion of a primary loop pinned at four triple nodes (*T*). As the stress is increased, the loop breaks away from the weaker nodes; longer loops will generally break away first, if all nodes are of approximately the same binding energy. On reversing the stress, the loops collapse back and recombine. The general physical feature of the dislocation-strain vs. stress is analogous to that originally envisioned for impurity pinning in the Granato–Lücke model[4]. Yet for all the similarities, there are still some very important differences. These are: (1) binding energy of pinning agent is about an order of magnitude higher than for impurities, (2) there are no fixed node points since the nodes can move under the applied stress, and (3) bowing strain is very large, of the order of

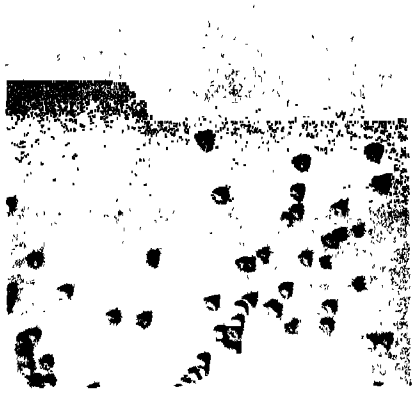

Fig 5(A).

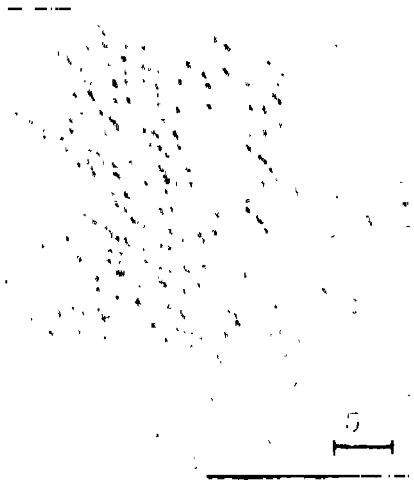

Fig. 5(B).

Fig. 5. Microphotographs of the forest dislocation structure for crystal A (100). Upper photo taken before straining and lower after a prestrain of ≈ 0·025. About an order of magnitude increase in dislocation density occurred. Magnifications indicated on photos.

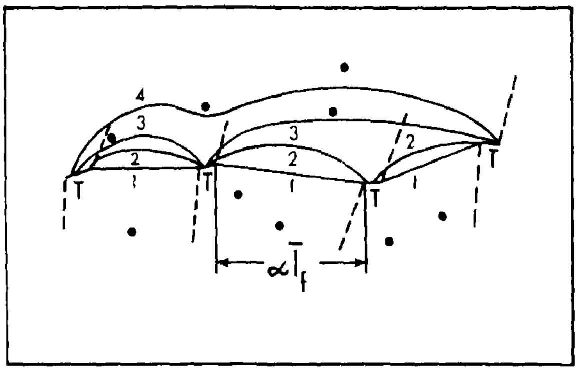

Fig. 6. Schematic illustrating mode in which mechanical hysteresis can arise from primary-forest dislocation interaction. Solid lines represent a primary dislocation which lies on the slip plane (plane of page). Dotted lines are the forest dislocations which thread through the slip plane. Where the primary and forest dislocations intersect a short segment of recombination occurs and a pair of triple nodes is formed, indicated by a *T*. Under stress primary bows out (1) junctions break down with increasing stress, (2), (3), (4). On relaxing the stress, primary dislocation moves back and the nodes (*T*) are reformed.

10^{-1}, and hence the assumption of small dislocation curvatures becomes untenable.

At low stress amplitudes, when the first loops break away, the dislocation array is similar to a collection of double loops. For this case, a quantitative comparison of the decrement level with dislocation structure can be made.

The decrement is given by $\Delta \approx 2\delta a/a$ where δa is the dislocation strain and a is the elastic shear strain[16]. For fcc copper, more than one slip system is operative, so that for the ith system:

$$a_i = \frac{N_i l_i^3 \tau_i}{6\mu}. \qquad (1)$$

Where, N_i are the number of loops, l_i the loop length, τ_i the resolved shear stress, all for the ith slip system. The appropriate shear modulus is μ.

The decrement is then given by $\Delta \approx 2\delta\mu/\mu \approx 2\delta a/a$ so that from equation (1):

$$\Delta \approx \sum_i \frac{(A_i N_i l_i^3)}{3} \qquad (2)$$

summed over all twelve slip systems. A_i is a distribution factor proportional to the stress operating on each slip system. If the number of dislocations on the primary is equal to that on another slip system, i.e. $\rho_p \approx \rho_f$ and the systems are equally stressed, then a significant proportion of the decrement would be due to dislocations lying on slip systems other than the primary. This could presumably be the case only at large strains in stage 2 for all crystal orientations studied in the present experiments. The (112) crystal would also be subject to this full summation at small strains; since both the primary and conjugate slip systems are nearly equally stressed, $\tau_c/\tau_p = 0{\cdot}93$, but at the prestrain used here $\rho_p \gg \rho_f$ so that only a few percent correction is introduced considering terms in the summation other than that due to the primary system. Thus for all crystals in the prestrain range considered

$$A_i \approx \begin{cases} 1, i = 1 \\ 0, 2 \leq i \leq 12 \end{cases}$$

Figure 6 illustrates the basis of applying equation (2) to the dislocation-dislocation interaction model. The distance between attractive junctions is a factor α times the forest spacing. For a random three dimensional network $\alpha = 3$, but for prestrained crystals, with forest multiplication, α is more nearly equal to 2 (16). The loop strength for the expanded double loop can then be seen to be $\approx 4\bar{l}_f$, where $\bar{l}_f$ is the modal forest spacing[†] taken from $\rho_f^{1/2} \approx \bar{l}_f$. The number of primary loops is likewise obtained from the measured values in Table 1, i.e. $2\rho_p \approx N_p$ (cm^{-1}). The decrement is thus from equation (2):

$$\Delta = \frac{N_p(4\bar{l}_f)^3}{3}. \tag{3}$$

The initial values of the decrement for the three crystals, calculated from equation (3) using the data in Table 1, are:

$$\Delta(110) = 0{\cdot}013,\ \Delta(100) = 0{\cdot}018,$$
$$\Delta(112) = 0{\cdot}018.$$

These are in good agreement with the initial decrements observed in Fig. 2 for the three crystals.

The amplitude-dependence, on the basis of this model, can arise from, (1) the activation of shorter loops with increasing applied stress, (2) breakdown of stronger junctions, (3) dislocations which have already broken-away becoming multi-loops i.e. a progressive breakdown of the primary dislocation – forest dislocation combinations. This view is consistent with etch-pit studies of the processes leading to yielding in copper crystals [17, 18].

Some final comments should be made concerning the binding energy associated with primary-forest dislocation combinations. The amplitude-dependent damping caused by impurity-dislocation interactions, which has been discussed by Granato–Lücke, leads to binding energies of the order of 0·1 eV [4]. The process considered here is formally the same, i.e. hysteretic, with the forest-primary attractive junctions forming the 'weak pins' and the incipient cell structure the strong nodes which limit catastrophic breakaway. The structures shown in Fig. 5 indicate that the forest is heterogeneous and that as a first approximation this idealized view is in reasonable qualitative agreement with the observed forest dislocation arrangements. This model can be checked for plausibility by calculating the binding energy which would be associated with the data reported in Table 1. From Teutonico, Granato, and Lücke [6] the binding energy U_0 required for mechanical breakaway is given by:

$$U_0 \approx \sigma_0 b^2 l \tag{4}$$

where σ_0 is the breakaway stress, taken here as the value of the minimum shear stress amplitude at which damping is observed. Thus, from Fig. 2 $\sigma_0 \sim 100$ g/mm^2; b is the burgers vector, $2{\cdot}5 \times 10^{-8}$ cm; and l is the spacing between pinning points, which is $\approx 3 \times 10^{-4}$ cm from Table 1. Using these results, one finds that $U_0 \approx 1$ eV which is in line with the values expected from the assumed forest-primary dislocation model.

The correlation between dislocation structure and low frequency mechanical hysteresis, given here, provides reasonable evidence that primary dislocation – forest dislocation interactions control the damping behavior in this low frequency, high amplitude range.

Acknowledgements—The authors wish to thank Mr. J. Pridans for his help in the etch-pit measurements and Mr. K. Tandon for building the acid-sectioning device.

REFERENCES

1. READ T. A., *Trans AIME* **143**, 30 (1941).
2. NOWICK A. S., *Phys. Rev.* **80**, 249 (1950).

[†] Because Δ is a very sensitive function of $\bar{l}_f$, careful statistics were taken for ρ_f. At least 2×10^4 etch-pits were counted for ρ_f on each crystal, with 90 per cent of the $\bar{l}_f$ values falling within ±20 per cent of the modal values for the prestrains used here.

3. WEERTMAN J. and SALKOVITZ E. I., *Acta Met.* **3**, 1 (1955)
4. GRANATO A. V. and LUCKE K., *J. appl. Phys* **27**, 583 789, (1956)
5. FRIEDEL J., *The Relation between the Structure and Mechanical Properties of Metals*, p. 409 (1963)
6. TEUTONICO L. J., GRANATO A. V. and LÜCKE K., *J. appl. Phys* **35**, 220 (1964).
7. ROBERTS J. M. and BROWN N., *Trans. AIME* **218**, 454 (1960).
8. BILELLO J. C. and METZGER J., *J. appl. Phys* **38**, 849 (1967).
9. ROBERTS J. M., *Proc. I.C.S.M.A., Suppl. Trans.*, J.I.M., Vol 9, p. 69 (1968)
10. BILELLO J. C., *Phil. Mag.* **19**, 583 (1969).
11. BILELLO J. C. and METZGER M., *Scripta Met* **2**, 581 (1968).
12. YOUNG F. W., Jr and WILSON T. R., *Rev. Scient. Instrum.* **32**, 559 (1961).
13. LIVINGSTON J. D., *J. appl. Phys* **31**, 1071 (1960).
14. BASINSKI Z. S. and BASINSKI S. J., *Phil. Mag* **9**, 51 (1964).
15. ROBERTS J. M. and BROWN N., *Acta Met.* **10**, 430 (1962)
16. FRIEDEL J., *Dislocations* pp. 222, 357. Addison-Wesley, Reading, Mass (1964)
17. YOUNG F. W., Jr., *J. appl. Phys.* **32**, 1815 (1961).
18. ARGON A. S., and BRYDGES W. T., *Phil. Mag.* **18**, 817 (1968).

J. Phys Chem Solids Pergamon Press 1970. Vol. 31, pp. 1955–1961. Printed in Great Britain.

DEFORMATION RATE EFFECTS ON THE ATTENUATION DURING LOADING, UNLOADING, AND RELOADING OF ALUMINUM CRYSTALS

WOLFGANG SACHSE and ROBERT E. GREEN, JR.
Department of Mechanics, The Johns Hopkins University, Baltimore, Md 21218, U.S.A.

(*Received 5 September 1969; in revised form 24 September 1969*)

Abstract – The influence of deformation rate on the ultrasonic attenuation of aluminum single crystals has been investigated over a strain rate range from 2×10^{-5} sec^{-1} to 20 sec^{-1}. In order to make this study a technique was developed which permits ultrasonic attenuation measurements to be made up to a rate of 1800 measurements/sec. The attenuation data exhibit marked strain rate effects in comparison with conventional stress–strain curves. In addition, attenuation data recorded during the rapid recovery period immediately subsequent to unloading show that the recovery behavior is dependent on the rate of removal of the externally applied load. Subsequent microplastic loading experiments are also affected by the initial deformation rate.

1. INTRODUCTION

DUE TO the extreme sensitivity of ultrasonic attenuation measurements for detecting dislocation motion and defect interactions in crystalline materials, various investigators have made ultrasonic attenuation measurements both during plastic deformation and in the subsequent recovery period following unloading of the test specimens[1–6]. The purpose of the present investigation was to make ultrasonic attenuation measurements with a time resolution of milliseconds and to compare the results obtained from these rapid measurements with the results of previous investigators who have been limited with regard to loading and unloading rates because each attenuation measurement required a time interval varying from seconds to minutes.

2. EXPERIMENTAL PROCEDURE

An Instron testing machine was used in the range 0·005–50 cm/min and a Sonntag Universal Impact Tester was modified to permit recording of load and deflection data from a specimen undergoing compressive deformation at a rate of 5000 cm/min. For the high speed tests, the load and deflection were measured using Tektronix *Q*-units. Cylindrical specimens were tested with one end cemented into a steel block to protect the quartz transducer. Square crystals were tested with the transducer held onto that lateral face for which the particle displacements of the ultrasonic wave had the largest shear component on the primary slip plane. A Fastax WF17 high speed camera and a Kodak Cine II camera were used to record the pulse echo patterns. The high speed camera was used in the streak mode and recorded simultaneously the echo pattern, either the load or deflection, and a timing light mark. The Kodak camera was used in time-lapse fashion with picture rates varying from 0·3 to 3 pictures/sec.

A Sperry Ultrasonic Attenuation Comparator and X-cut quartz transducers were used to generate and receive 10 MHz quasi-longitudinal waves. The maximum pulse repetition rate of 1800 pulses/sec was used. This repetition rate limited the testing speed of the experiments, since the other components of the system are capable of operation up to 8000 pulses/sec. The specimens used in this study were taken from 10-in. long mother crystals, of either $\frac{1}{2}$ in^2 or $\frac{1}{2}$ in. dia. round cross section, and were cut and polished to give an initial gauge length of 1½ in. The square crystals were polished on the lateral faces in a similar manner as the ends. All specimens used in a particular comparison study were from the same mother crystal and were of the same crystallographic orientation.

3. RESULTS AND DISCUSSION

Figure 1 shows the change of attenuation vs. strain curves as a function of specimen position along the 10-in. length of a mother crystal subjected to tensile elongation. Seven transducers, equally spaced along the length of the mother crystal, were connected through a switching circuit to the ultrasonic unit. The switching circuit was also connected to the time-lapse camera and was able to cycle all seven transducers in 3 sec. The results give the variation of attenuation during tensile deformation as a function of specimen location and show that the lowest crystal section exhibited the least change of attenuation with deformation.

Figure 2 shows the change of attenuation data and stress data plotted as a function of strain for six square cross section specimens. Bands indicate the variation of attenuation due to specimen location in the mother crystal. It is seen that the attenuation of the more rapidly deformed crystals increases more markedly with increasing strain than that of the slowly deformed ones. Note, for comparison, that the stress–strain curves exhibit essentially no strain rate influence.

The change of attenuation in cylindrical crystals as a function of time after deformation at 50 cm/min is shown in Fig. 3. All specimens were unloaded rapidly and show little, if any, recovery of attenuation for up to 0·1 min after load removal. Thereafter, the damping recovered according to an approximate $t^{-1/2}$ power law in agreement with the results of earlier work [7, 8].

Similarly, in square crystals deformed at 0·005 cm/min to 3·9 per cent strain and 5000 cm/min to 5·1 per cent strain and unloaded rapidly, it is seen from Fig. 4 that the recovery of damping does not begin until 0·01–

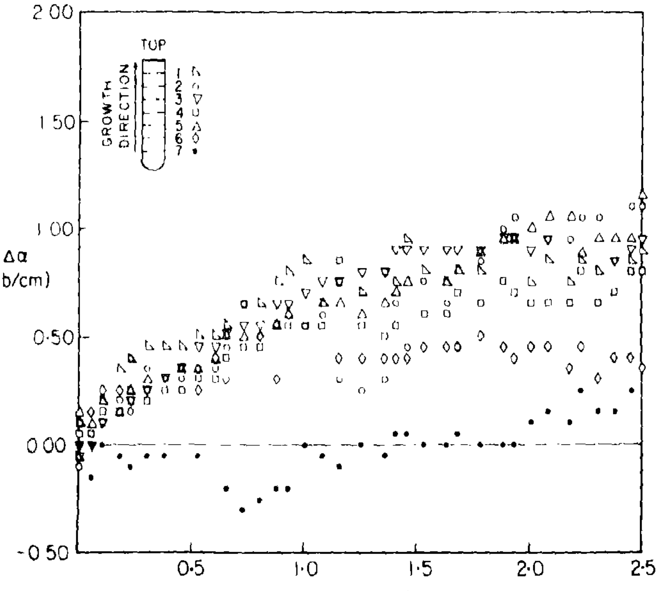

Fig. 1. Simultaneously measured attenuation changes at seven positions in a 10-in long square crystal undergoing tensile deformation at 0·05 cm/min. Tracings from computer plots of least square fit calculated attenuation data

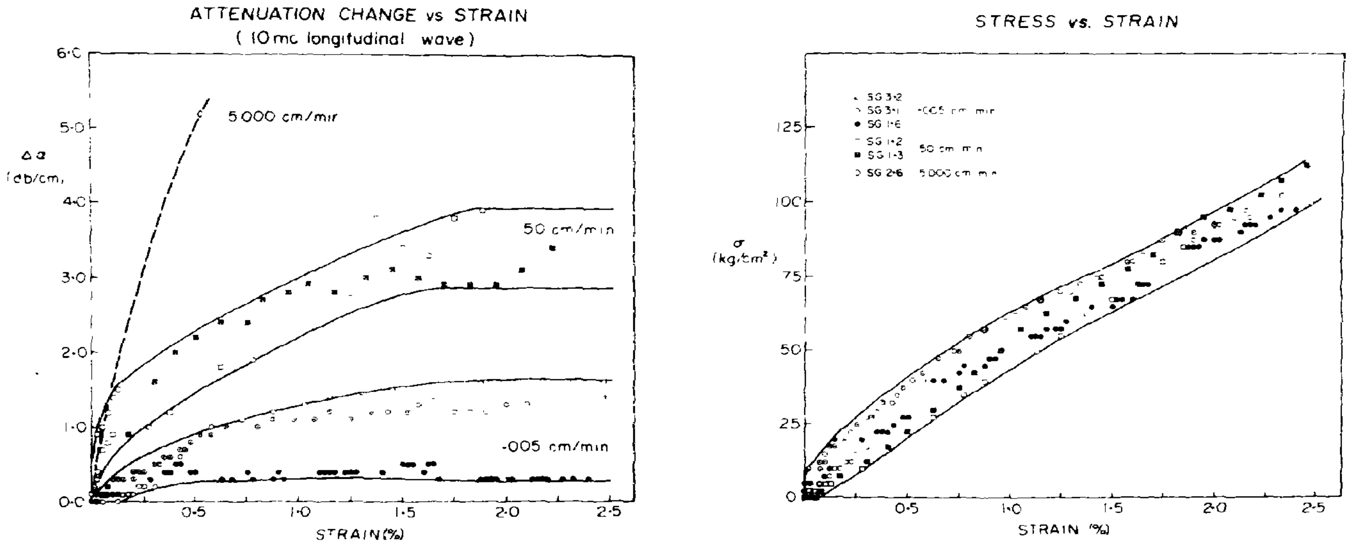

Fig. 2 Stress–strain change of attenuation–strain data for square cross section crystals deformed at deformation rates of 0 005, 50 and 5000 cm/min Tracings from computer plots of attenuation (using least square fit to pulse amplitude data) and stress as a function of strain

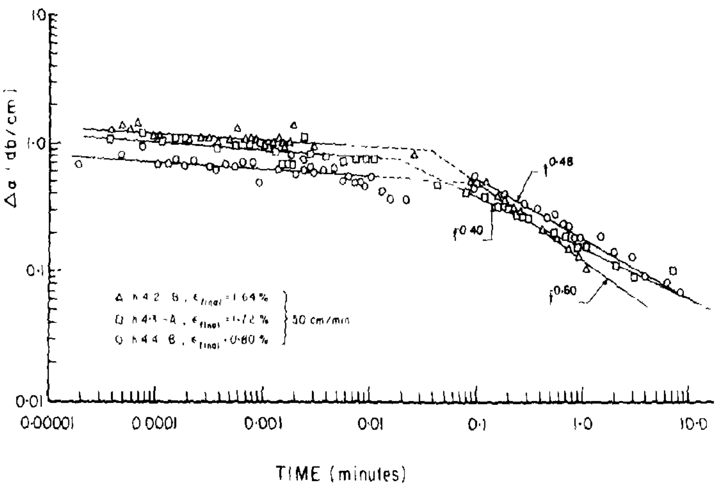

Fig. 3. The change of attenuation during recovery of cylindrical crystals which had been deformed at 50 cm/min to the indicated final strain levels.

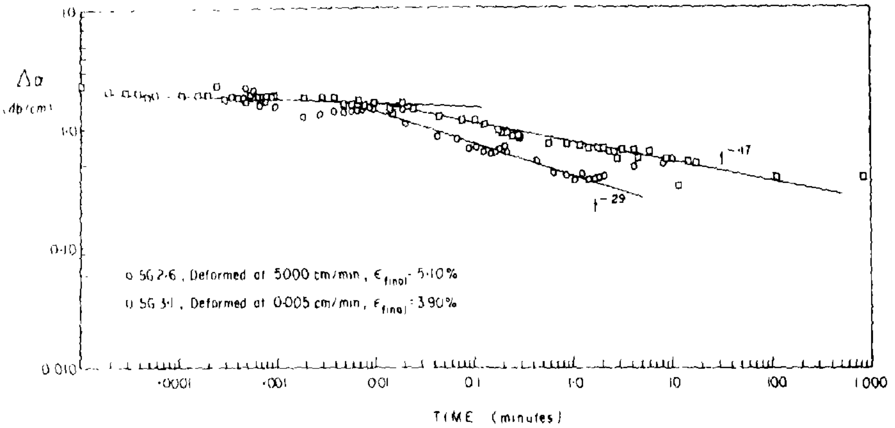

Fig. 4. The change of attenuation during recovery of square cross section crystals which had been deformed at 0·005 and 5000 cm/min to the indicated final strain levels.

0·1 min after loading has stopped. In this case, however, the recovery thereafter is much slower than that shown in Fig. 3—possibly due to the extent to which these specimens were deformed. This is in contrast to earlier conclusions with regard to the influence of degree of deformation on recovery [3].

The effect of rate of unloading could only be studied at a slow loading rate, since at rapid loading rates a slow unloading rate could not be achieved. A crosshead speed of 0·005 cm/min was chosen for the loading rate and for the slow unloading case the testing machine crosshead was merely reversed, so as to give an unloading rate of 0·005 cm/min, while for the fast unloading rate, breaking a piece of glass in series with the test specimen unloaded it in less than 40 μsec. The loading data of three crystals and the unloading data of two crystals are shown in Fig. 5. The result for the rapidly unloaded crystal has been discussed above. The slowly unloaded crystal at first exhibited the same behavior as the rapidly unloaded specimen but as soon as the crosshead began its reverse travel the attenuation increased initially and then recovered similarly to the rapidly unloaded specimen.

After an extended time following deformation, the attenuation of a crystal approaches its initial predeformation value. It has been found that upon subsequent reloading of the crystal to load levels far less than the maximum attained in the previous deformation, the attenuation exhibits a very reproducible change with loading and unloading[9]. Specimens have been repeatedly loaded and unloaded for 25 cycles and identical attenuation changes with loading in each cycle have been observed. The plastic strain associated with each cycle was less than 10^{-5}.

If a specimen is loaded and this load is maintained (except for the small decrease due to stress relaxation) for approximately 1 min, upon unloading and subsequent reloading the damping exhibits a distinct dip in the attenuation with loading curve at that load level which was previously maintained on the specimen for the short hold time[9]. Several dips can be seen if a specimen is loaded to a particular load level, maintained at that load for a short time, unloaded to a lower load level, maintained at this load level for a short time, and this procedure continued in steps until the specimen is completely unloaded. Upon subsequent reloading the attenuation curve will display distinct dips at those load levels which had been maintained on the specimen in the previous stepped unloading cycle. This is shown in Fig. 6 where the successively maintained loads were 60, 45, 30 and 15 kg on a specimen which had been previously loaded plastically to a load of 180 kg at a rate of 0·005 cm/min and unloaded at the same rate. The attenuation upon reloading shows distinct dips at all the load levels which had been maintained on the specimen during the previous cycle.

The specimen's prior history plays a part in the amplitude of the attenuation dip. In one test the specimen was plastically loaded at 0·005 cm/min and in another test the speci-

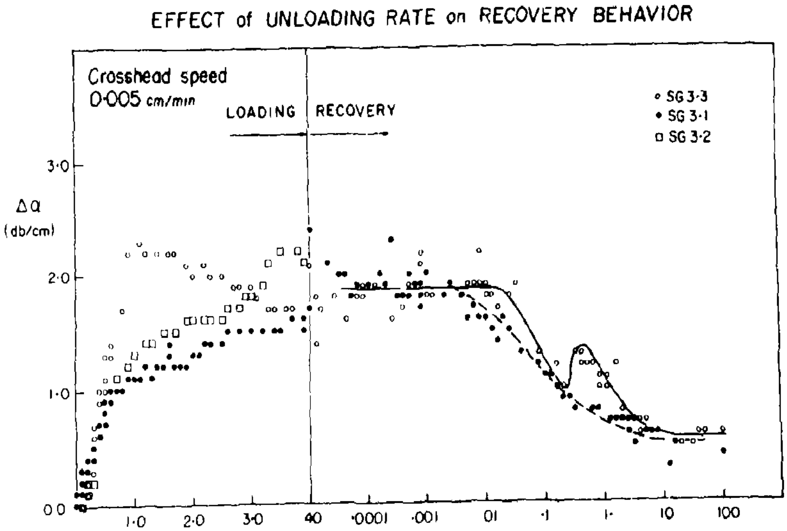

Fig. 5. The change of attenuation during loading at 0·005 cm/min and unloading at various rates. SG 3·1 was unloaded rapidly and SG 3·3 was unloaded at 0·005 cm/min.

men was plastically loaded at 50 cm/min. Both specimens were rapidly unloaded, then each crystal was carried through the same loading-hold-unloading-hold, etc. cycle as the crystal used with Fig. 6. The plots of Fig. 7 resulted upon reloading past each of the load levels 15, 30, 45 and 60 kg. In both cases one observes that the attenuation dip is either suppressed or eliminated. This result is associated with the rapidity of the previous plastic un-

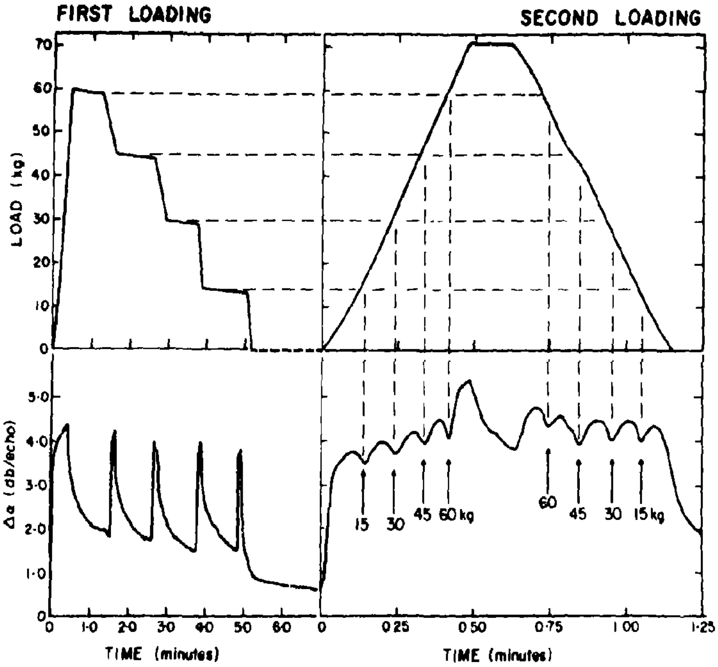

Fig. 6. Diagram depicting the reloading cycle used to observe the load memory attenuation dip

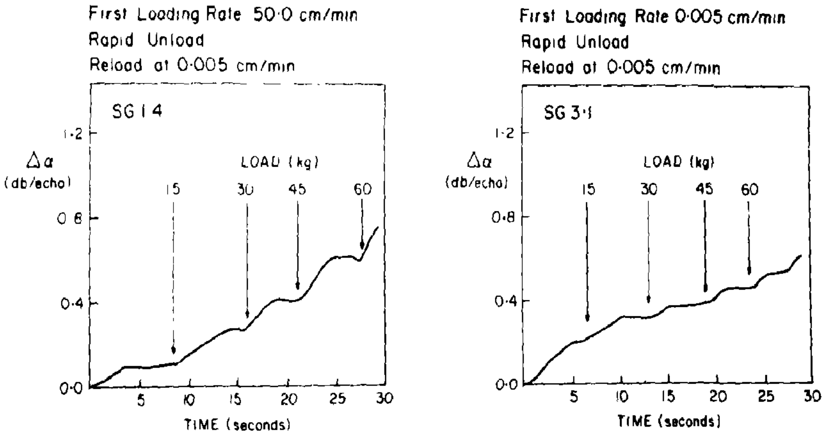

Fig. 7. Attenuation-time records which illustrate the influence of prior unloading rate on the magnitude of the load memory attenuation dip

loading, since the 0·005 cm/min deformed crystals are similarly affected as the 50 cm/min deformed crystals. The inability to load a specimen at a high deformation rate and then unload it slowly prevents a complete check of the hypothesis that only the unloading rate in the previous plastic deformation affects the observance of the attenuation dip in subsequent microplastic reloading. The dip amplitude decreases as a function of time after application of the microplastic load. In aluminum crystals the attenuation dip disappeared after 24 hr. Loading a specimen to a large plastic strain erased all memory of the dip instantaneously, but new dips could be observed by repeating the load-hold-unload cycle.

Acknowledgements—The authors wish to thank Professor Edmund G. Henneke, II, for critical review and Mrs Corinne Harness for typing the manuscript. They wish to thank Mrs. Faith Pacquet for preparing the illustrations. This research was supported, in part, by Aberdeen Proving Ground. One of the authors (W.S.) expresses his appreciation to the Society of the Sigma Xi for their grant-in-aid of research.

REFERENCES

1. ALERS G. A., *Phys. Rev.* **97**, 863 (1955)
2. HIKATA A., TRUELL R., GRANATO A., CHICK B. and LUCKE K., *J. appl. Phys.* **27**, 396 (1956)
3. GRANATO A., HIKATA A. and LUCKE K., *Acta metall.* **6**, 470 (1958)
4. HIKATA A., CHICK B., ELBAUM C. and TRUELL R., *Acta metall.* **10**, 423 (1962)
5. LENZ D., LUCKE K., OSTERMANN A. and SIBLEY W. A., *J. acoust. Soc. Am.* **45**, 1374 (1969)
6. SACHSE W. and GREEN R. E., *Trans. AIME* **242**, 2185 (1968)
7. HOLWECH I., *J. appl. Phys.* **31**, 928 (1960)
8. HULTGREN F. and LUCKE K., *Physical Acoustics* (Edited by W. P. Mason), Vol. 4, Part A, p. 260. Academic Press, New York (1966).
9. SACHSE W. and HSU, N. N., *Trans. AIME* (submitted for publication)

men w
specim
crystal
hold-u
used

NOTES FOR CONTRIBUTORS

I. GENERAL

1. Submission of a paper to *The Journal of Physics and Chemistry of Solids* will be taken to imply that it represents original research not previously published (except in the form of an abstract or preliminary report), that it is not being considered for publication elsewhere, and that if accepted it will not be published elsewhere in the same form, in any language, without the consent of the Editor-in-Chief. It should deal with original research work in the field of the physics and chemistry of solids.

2. Papers should be submitted to the appropriate regional editor (all English-language papers to be sent to the U.S. editor).

3. Short communications may be published as "Technical Notes" and will receive somewhat more rapid handling than full length articles. Short communications requiring the maximum speed of publication should be submitted to one of the editors of "Solid State Communications."

II. SCRIPT REQUIREMENTS

1. **Papers** submitted should be concise and written in a readily understandable style. Scripts should be typed and double spaced with good margins on one side of the paper only and submitted in duplicate to facilitate refereeing.

It will be appreciated if authors clearly indicate any special characters used. An abstract not exceeding 200 words, should be provided in the language of the paper. French and German papers should be submitted with English abstract and titles, but if this is not possible the abstract will be translated by the publishers. To conserve space, **authors are requested to mark less important parts of the paper,** such as details of experimental technique, methods, mathematical derivations, etc. **for printing in small type.** The technical description of methods should be given in detail only when such methods are new. Authors will receive proofs for correction when their papers are first set, and **alterations must be restricted to printer's errors.** Other than these, any substantial changes may be charged to the authors.

2. **Illustrations** should not be included in the typescript of the paper, and legends should be typed on a separate sheet. Line drawings which require redrawing should include all relevant details and clear instructions for the draughtsman. If figures are already well drawn it may be possible to reproduce them direct from the originals, or from good photo-prints if these can be provided. It is not possible to reproduce from prints with weak lines. Illustrations for reproduction should normally be about twice the final size required. The lettering should be sufficiently large and bold to permit this reduction. Photographs should only be included where they are essential.

3. **Tables and figures** should be so constructed as to be intelligible without reference to the text. Every table and column should be provided with an explanatory heading. Units of measure must always be clearly indicated. The same data should not be published in both tables and figures. The following standard symbols should be used on line drawings since they are easily available to the printers: ○, ●, +, ×, □, ■, △, ▲, ◇, ◆, ▽, ▼.

4. **References** are indicated in the text by numbers on the line in brackets, and the full reference should be given in a list at the end of the paper in the following form:

1. BARNES R. G., BORSA F. and PETERSON D., *J. appl. Phys.* **36**, 940 (1965).
2. KNIGHT W. D., In *Solid State Physics* (Edited by F. Seitz and D. Turnbull), Vol. 2, p. 93. Academic Press, New York (1957).

Abbreviations of journal titles should follow those given in *World List of Scientific Periodicals* (4th Edn.). It is particularly requested that authors' initials, and appropriate volume and page numbers, should be given in every case.

Footnotes, as distinct from literature references, should be indicated by the following symbols—*, †, ‡, §, commencing anew on each page; they should *not* be included in the numbered reference system.

5. Due to the international character of the journal no rigid rules concerning notation and spelling will be observed, but each paper should be consistent within itself as to symbols and units.

NOTES FOR CONTRIBUTORS

I. GENERAL

1. Submission of a paper to *The Journal of Physics and Chemistry of Solids* will be taken to imply that it represents original research not previously published (except in the form of an abstract or preliminary report), that it is not being considered for publication elsewhere, and that if accepted it will not be published elsewhere in the same form, in any language, without the consent of the Editor-in-Chief. It should deal with original research work in the field of the physics and chemistry of solids.

2. Papers should be submitted to the appropriate regional editor (all English-language papers to be sent to the U.S. editor).

3. Short communications may be published as "Technical Notes" and will receive somewhat more rapid handling than full length articles. Short communications requiring the maximum speed of publication should be submitted to one of the editors of "Solid State Communications."

II. SCRIPT REQUIREMENTS

1. **Papers** submitted should be concise and written in a readily understandable style. Scripts should be typed and double spaced with good margins on one side of the paper only and submitted in duplicate to facilitate refereeing.

It will be appreciated if authors clearly indicate any special characters used. An abstract not exceeding 200 words, should be provided in the language of the paper. French and German papers should be submitted with English abstract and titles, but if this is not possible the abstract will be translated by the publishers. To conserve space, **authors are requested to mark less important parts of the paper,** such as details of experimental technique, methods, mathematical derivations, etc. **for printing in small type.** The technical description of methods should be given in detail only when such methods are new. Authors will receive proofs for correction when their papers are first set, and **alterations must be restricted to printer's errors.** Other than these, any substantial changes may be charged to the authors.

2. **Illustrations** should not be included in the typescript of the paper, and legends should be typed on a separate sheet. Line drawings which require redrawing should include all relevant details and clear instructions for the draughtsman. If figures are already well drawn it may be possible to reproduce them direct from the originals, or from good photo-prints if these can be provided. It is not possible to reproduce from prints with weak lines. Illustrations for reproduction should normally be about twice the final size required. The lettering should be sufficiently large and bold to permit this reduction. Photographs should only be included where they are essential.

3. **Tables and figures** should be so constructed as to be intelligible without reference to the text. Every table and column should be provided with an explanatory heading. Units of measure must always be clearly indicated. The same data should not be published in both tables and figures. The following standard symbols should be used on line drawings since they are easily available to the printers: ○, ●, +, ×, □, ■, △, ▲, ◇, ◆, ▽, ▼.

4. **References** are indicated in the text by numbers on the line in brackets, and the full reference should be given in a list at the end of the paper in the following form:

1. BARNES R. G., BORSA F. and PETERSON D., *J. appl. Phys.* **36**, 940 (1965).
2. KNIGHT W. D., In *Solid State Physics* (Edited by F. Seitz and D. Turnbull), Vol. 2, p. 93. Academic Press, New York (1957).

Abbreviations of journal titles should follow those given in *World List of Scientific Periodicals* (4th Edn.). It is particularly requested that authors' initials, and appropriate volume and page numbers, should be given in every case.

Footnotes, as distinct from literature references, should be indicated by the following symbols—*, †, ‡, §, commencing anew on each page; they should *not* be included in the numbered reference system.

5. Due to the international character of the journal no rigid rules concerning notation and spelling will be observed, but each paper should be consistent within itself as to symbols and units.

THE JOURNAL OF PHYSICS AND CHEMISTRY OF SOLIDS

VOLUME 31, NUMBER 8 1970 AUGUST

CONTENTS

Foreword . . . 1655

E. Roland Dobbs: Electromagnetic generation of ultrasonic waves in metals . . . 1657

H. L. Grubin and T. Kjeldaas, Jr.: Application of translationally invariant wavefunctions in a magnetic field to frequency and wavelength dependent transport phenomena . . . 1669

J. Zucker and S. Zemon: Nonlinear attenuation of microsound in semiconducting CdS . . . 1673

J. L. Stevens and A. Houghton: Change in velocity of high frequency transverse sound at the superconducting transition temperature . . . 1677

Hilda A. Cerdeira, W. N. Cottingham and A. Houghton: Longitudinal ultrasonic attenuation in type II superconductors: clean limit . . . 1681

B. R. Tittmann: Ultrasonic attenuation in a type II superconducting alloy . . . 1687

J. N. Lange: Hypersonic attenuation in niobium in the mixed state. . . . 1693

J. J. Quinn: Direct generation of sound in metals and acoustic nuclear spin resonance . . . 1701

A. J. Budreau and P. H. Carr: Performance and applications of microwave photon–phonon double-quantum detection in MgO . . . 1709

B. A. Huberman, R. Ito, E. Burstein and Y. Sawada: The propagation and attenuation of acoustic waves in ferromagnetic metals . . . 1719

T. Ishiguro and N. Mikoshiba: Ultrasonic donor-spin resonance in germanium . . . 1729

T. J. Moran and B. Lüthi: Elastic and magnetoelastic effects in rare earth metals . . . 1735

B. Lüthi, T. J. Moran and R. J. Pollina: Sound propagation near magnetic phase transitions . 1741

C. W. Garland and D. D. Snyder: Ultrasonic attenuation near the lambda transition in NH_4Cl at high pressures . . . 1759

G. Alefeld, J. Völkl and J. Tretkowski: Thermodynamic properties of interstitial solid solutions by relaxation methods . . . 1765

C. A. Wert: Damping of interstitial atoms in bcc metals . . . 1771

V. S. Postnikov, V. S. Pavlov and S.K. Turkov: Internal friction in ferroelectrics due to interaction of domain boundaries and point defects . . . 1785

C. Wert, D. O. Thompson and O. Buck: Internal friction of Nb–H alloys . . . 1793

M. S. Ahmad and Z. C. Szkopiak: Snoek relaxation peaks in solid solutions of niobium . . 1799

J. Völkl, G. Schaumann and G. Alefeld: Diffusional relaxation of H and D in V and Nb . 1805

R. Cantelli, F. M. Mazzolai and M. Nuovo: Internal friction due to long-range diffusion of hydrogen and deuterium in vanadium . . . 1811

A. S. Nowick: Kinetics of anelastic and dielectric relaxation due to reacting point defects . 1819

B. S. Berry: Anelastic relaxation in silicon doped with lithium and boron . . . 1827

K. Ehrensperger, V. Fischer, J. Kerscher and H. Wenzl: Internal friction maxima due to relaxation of point defects in neutron irradiated aluminium . . . 1835

V. Hivert, R. Pichon, H. Bilger, P. Bichon, J. Verdone, D. Dautreppe and P. Moser: Internal friction in low temperature irradiated bcc metals . . . 1843

J. C. Worley, A. B. Smith and M. Kestigian: Anomalous attenuation in lithium tantalate . 1857

J. A. Garber and A. V. Granato: Reradiation and viscous dislocation damping . . . 1863

R. O. Schwenker and A. V. Granato: The frequency dependence of sound radiation from mobile dislocation walls . . . 1869

B. K. Ganguly, C. Baker and H. K. Birnbaum: The frequency dependence of dislocation damping in niobium . . . 1877

N. Igata, K. Domoto and R. R. Hasiguti: Frictional force coefficient of a moving dislocation in uranium dioxide with excess oxygen . . . 1883

R. Gibala, M. K. Korenko, M. F. Amateau and T. E. Mitchell: Dislocation relaxation in single crystals of bcc metals . . . 1889

J. de Fouquet, P. Boch, J. Petit and G. Rieu: A contribution to the study of internal friction peaks associated with dislocations in various metals, and their relations with cold-work. . 1901

W. Benoit, B. Bays, P. A. Grandchamp, B. Vittoz, G. Fantozzi, J. Perez and P. Gobin: Modulus effects and Hasiguti peaks on two coldworked fcc metals: gold and aluminium . . . 1907

G. Cannelli and F. M. Mazzolai: Anelastic relaxation effects in coldworked and hydrogen doped vanadium . . . 1913

D. N. Beshers: Anelasticity of dislocation dipoles . . . 1921

W. P. Mason and J. Wehr: Internal friction and ultrasonic yield stress of the alloy 90 Ti 6 Al 4 V 1925

V. S. Postnikov, S. A. Ammer, B. M. Darinsky, I. V. Zolotukhin and A. T. Kosilov: Internal friction in whiskers and thin films . . . 1935

H. Akita and N. F. Fiore: Dislocation damping in copper single crystals of controlled substructure 1941

J. Dralla and J. C. Bilello: Dislocation structure and low frequency mechanical hysteresis in copper single crystals . . . 1947

W. Sachse and R. E. Green, Jr.: Deformation rate effects on the attenuation during loading, unloading and reloading of aluminum crystals . . . 1955

PRINTED BY J. W. ARROWSMITH LTD., BRISTOL, ENGLAND